Understanding the Mechanism and Chemical Properties of High Valent Iron(IV) Oxo Intermediates in Enzymes Using Quantum Mechanical Methods

A thesis submitted to The Babasaheb Bhimrao Ambedkar University for the Award of the degree

of

Doctor in Science

in

Physics

By

Prof. (Dr.) Devesh Kumar, MNASc

Enrollment No.: 1086/18

Advisor

Prof. (Dr.) R. C. Sobti

Department of Physics

2020#

Understanding the Mechanism and Chemical Properties of High Valent Iron(IV) Oxo Intermediates in Enzymes Using Quantum Mechanical Methods

A thesis submitted to The Babasaheb Bhimrao Ambedkar University for the Award of the degree

of

Doctor in Science

in

Physics

By

Prof. (Dr.) Devesh Kumar, MNASc

Enrollment No.: 1086/18

Advisor

Prof. (Dr.) R. C. Sobti

Department of Physics

2020#

CANDIDATE'S DECLARATION

I, **Prof. (Dr.) Devesh Kumar**, declare that this thesis, entitled "**Understanding the Mechanism and Chemical Properties of High Valent Iron(IV) Oxo Intermediates in Enzymes Using Quantum Mechanical Methods**" submitted for the award of the degree of **D.Sc.** of this University, has not been submitted earlier for the award of any degree or diploma of this or any other University.

Date: 18/6/20

(Signature of the candidate)

Place: Lucknow

CERTIFICATE

This is to certify that this thesis entitled "**Understanding the Mechanism and Chemical Properties of High Valent Iron(IV) Oxo Intermediates in Enzymes Using Quantum Mechanical Methods**" has been submitted by **Prof. (Dr.) Devesh Kumar** for the award of the degree of **D.Sc.** of Babasaheb Bhimrao Ambedkar University, Lucknow.

.....
(Signature of the Advisor)

.....
(Signature of the Head of the Department & the Chairman of the DRC)

.....
(Name & Designation)

Acknowledgements

First of all I would like to thank the than Vice-Chancellor Prof (Dr.) R. C. Sobti (2018) without whose encouragement and support it was not possible for me to pursue for this degree.

I would also like to thank all the Faculty Members (Prof. (Dr.) B. C. Yadav, Dr. Ramesh Chandra, Dr. Anil K Yadav, Dr. Devendra Singh and Dr. K. B. Thapa) and office staff (Mr. Amit, Mr. Mukesh, Mr. Shtrudhan and Mr. Rahul) of the Deparment of Physics for their continous support.

All the former and present PhD students in my group (Dr Jitendra Kumar, Dr Suresh Kumar, Dr Pranav Upadhyaya, Dr. Deep Kumar, Dr. Devendra Singh, Dr. Dharmveer Singh, Dr. Ashish Kumar, Mr. Narinder Kumar, Miss Rolly Yadav, Miss Anamika Shukla, Miss Nidhi Awasti, Miss Shivani Choudhary), without their active participation in the projects discussed here this dissertation would not have been accomplished is acknowledged.

I also thank the National Service of Computational Chemistry Software (NSCCS), UK for very generous CPU support for our work. Funding from DST, New Delhi for Ramanujan Fellowship and DBT, New Delhi [BT/PR14510/BID/07/334/2010] is acknowledged for resources and person support is thanked.

Due to the interdisciplinary nature of the research, many of the projects described here are in collaboration with either experimentally based or computational research groups. I would like to thank all my collaborators over the years for their valuable contributions and stimulating discussions. In particular, I would like to thank the long-standing collaboration with Prof. (Dr.) C. V. Sastri, IIT, Guwahati.

I also need to give my special thanks to my close computational collaborator, Prof (Dr.) Sam P de Visser, Univrsity of Manchestor, UK who always is interested in working on joint projects with me. Our collaboration started during our joint postdoc in Jerusalem under supervision of Prof Sason Shaik

and continued after my move to initially the Max Planck Institute (with Late Prof Walter Thiel) and the Indian Institute of Chemical Technology in Hyderabad (with Prof G. Narahari Sastry).

Of course, I also thank for continous encouragement and support given by my family.

(Devesh Kumar)

Abstract:

In more than one third of enzymes metal ions play critical roles.These ions use to control an enzyme-catalyzed reaction by modify electron flow in enzyme or substrate. There are no general rules exist through which one may describe the behavior of given metal ion in an enzyme. These ions are usually positively charged and behave as electrophiles, always looking for the possibility of sharing electron pairs with other subgroups or atoms in order to form a bond or charge-charge interaction, hence, these ions behave like hydrogen ions. The ligands are usually negatively charged or neutral atom(s) or group(s) of atoms which can form bond with the metal ion in an electrostatic manner, generally by donating electron density to the metal ion. The number of ligand atoms bound to metal ion is the coordination number of a metal ion. It is viewed in terms of concentric spheres; the inner sphere containing those atoms is in contact with the metal ion while the second sphere containing those atoms is in contact with the inner sphere ligands. The sizes of metal ion as well as the sizes of the ligands decide the number of atoms in these spheres.

The theoretical model calculations, two decades before, had a minor role for explaining mechanisms of redox-active metalloenzymes. The available methods to describe transition metals were too slow for any meaningful applications and they were not accurate enough also. The computational models for the treatment of these enzymes were underdeveloped. But this situation changed now-a-days because of developments of methods as well as insights from applications. The developed density functional theory (DFT) methods with accuracy were not far from accuracy. The major improvements was the incorporation of density gradient terms for the exchange part and of fractions of exact exchange. The application of these methods showed that the accuracy was quite reasonable for transition-metal complexes. The experience of decades on small models with transition-metal complexes was the second important reason for the development in this area, it was surprisingly helpful for understanding many aspects of the mechanisms of large organometallic complexes, at least qualitatively, using small models. It is also observed that

the individual reaction steps as well as transition-state structures are quite insensitive to the size of the model in terms of explaining the mechanisms.

Originally two different approaches were developed to study mechanisms of redox-active metalloenzymes. The cluster model which is used to capture the important features of a mechanism in small quantum mechanical models is used. This model was used firstly in 1997, with DFT methods for understanding the mechanism of methane monooxygenase (MMO). The other approach in which the entire enzyme was treated with quantum mechanically described small core and the rest of enzyme was described with molecular mechanics, known as the quantum mechanics/molecular mechanics (QM/MM) model. The first application of QM/MM on the mechanism of galactose oxidase was made in 2000. Both approaches have been developed over the years from their original form. Now a day, with improvement in computer technology, QM cluster models can handle quite big model i.e. with more than 200 atoms, and even larger QM core can be used in the QM/MM approach.

Today, theoretical model calculations must be considered at least of equal importance for explaining/ determining mechanisms for metalloenzymes as compared with traditional spectroscopic techniques. Although the spectroscopic techniques have the advantage due to its application on the actual system, but their interpretations are often extremely difficult is the disadvantage. In theoretical modeling not only choices of the method but also the modeling of the real system has to be accurate. More than two decades of experience has made the understanding of the applicability and limitations of different models fully grown and it has reached at a mature stage.

Table of Contents:

1.	**Introduction.**	**Page 7**
2.	**Biological nonheme and heme based iron(IV)-oxo intermediates.**	**Page 9**
2.1	*Cytochrome P450s (P450s).*	**Page 9**
2.2	*Taurine/α-ketoglutarate dioxygenase (TauD).*	**Page 16**
2.3	*Cysteine Dioxygenase (CDO).*	**Page 17**
3.	**Methods and techniques.**	**Page 19**
3.1	*Density functional theory.*	**Page 19**
3.2	*Basis sets.*	**Page 23**
3.3	*Zero point energy (ZPE).*	**Page 26**
3.4	*Solvent effects.*	**Page 27**
3.5	*Quantum mechanics/molecular mechanics (QM/MM).*	**Page 28**
4.	**Results and Discussion.**	**Page 30**
4.1	*Cytochrome P450s (P450s).*	**Page 30**
4.1.1	*Compound I of P450.*	**Page 31**
4.1.2	*Chemical properties of Cpd I of peroxidases and catalases.*	**Page 32**
4.1.3	*Aliphatic hydroxylation by P450 Cpd I.*	**Page 33**
4.1.4	*Olefin epoxidation by P450 Cpd I.*	**Page 45**
4.1.5	*Sulphoxidation reaction by P450 Cpd I.*	**Page 50**
4.1.6	*Rearrangement patterns in aliphatic hydroxylation reactions by P450 Cpd I.*	**Page 50**
4.2	*Cysteine dioxygenase (CDO).*	**Page 53**
4.3	*Synthetic nonheme iron complexes.*	**Page 56**
4.3.1	*Electronic properties of iron(IV)-oxo complexes.*	**Page 56**
4.3.2	*Two-state reactivity patterns of mononuclear nonheme iron-oxo complexes.*	**Page 56**
4.3.3	*The* cis*-effect on the properties of the iron(IV)-oxo species.*	**Page 62**
5.	**Conclusions and Summary.**	**Page 64**
	References.	**Page 65**
	Appendix	**Page 76**

1. Introduction.

Oxygen activating metalloenzymes are highly versatile in nature and are involved in processes that include biodegradation, metabolism and biosynthesis. Many of the metalloenzymes in nature utilize iron in their active centre, which structurally contains either a heme or a nonheme ligand system. A large – and well studied – class of heme enzymes are the cytochromes P450, which are monoxygenases found, for instance, in the liver, where they catalyze the metabolism of drugs, detoxification processes as well as the biosynthesis of hormones.[1–8] These enzymes use a molecule of O_2 on a heme centre and with assistance of two electrons and two protons create a high-valent iron(IV)-oxo heme cation radical intermediate, $[Fe^{IV}(O)(heme^{+\bullet})]$ also known as Compound I (Cpd I), Eq 1. The monoxygenation reactions catalyzed by P450 enzymes cover a wide range of possible chemical reactions, but generally start from the active species, Cpd I.[8–13] A selection of the most often encountered mechanisms of oxygen atom transfer processes by Cpd I of P450 are given in Figure 1. The most common one of those is aliphatic hydroxylation leading to alcohol products. Other reactions include double bond activation that produces epoxides and challenging processes such as aromatic hydroxylation and heteroatom oxidation, such as sulphoxidation. In addition, the P450s occasionally give products originating from dehydrogenation and ring-closure processes, Figure 1.

$$[Fe^{III}(heme)] + O_2 + 2\ e^- + 2\ H^+ \rightarrow [Fe^{IV}(O)(heme^{+\bullet})] + H_2O \qquad (1)$$

Although the activity of Cpd I in oxygen atom transfer processes was predicted by biomimetic reaction mechanisms many years ago,[14] it was only characterized with spectroscopic methods very recently.[15] Due to the fact that P450 Cpd I was elusive for a long time, studies into its intrinsic electronic properties and reactivity patterns were performed using computational modelling, which characterized it as an extremely versatile oxidant.[4,8,16] Moreover, computational studies established the electronic properties, predicted spectroscopic parameters and reactivity patterns, and, as such guided and supported experiment. These studies gave insight into the nature of the

active species, the effect of ligands to the reaction centre and environmental influences on the oxidants and its activity towards substrates. In this dissertation, an overview will be given on the computational studies into heme and nonheme based iron(IV)-oxo species and synthetic analogues.

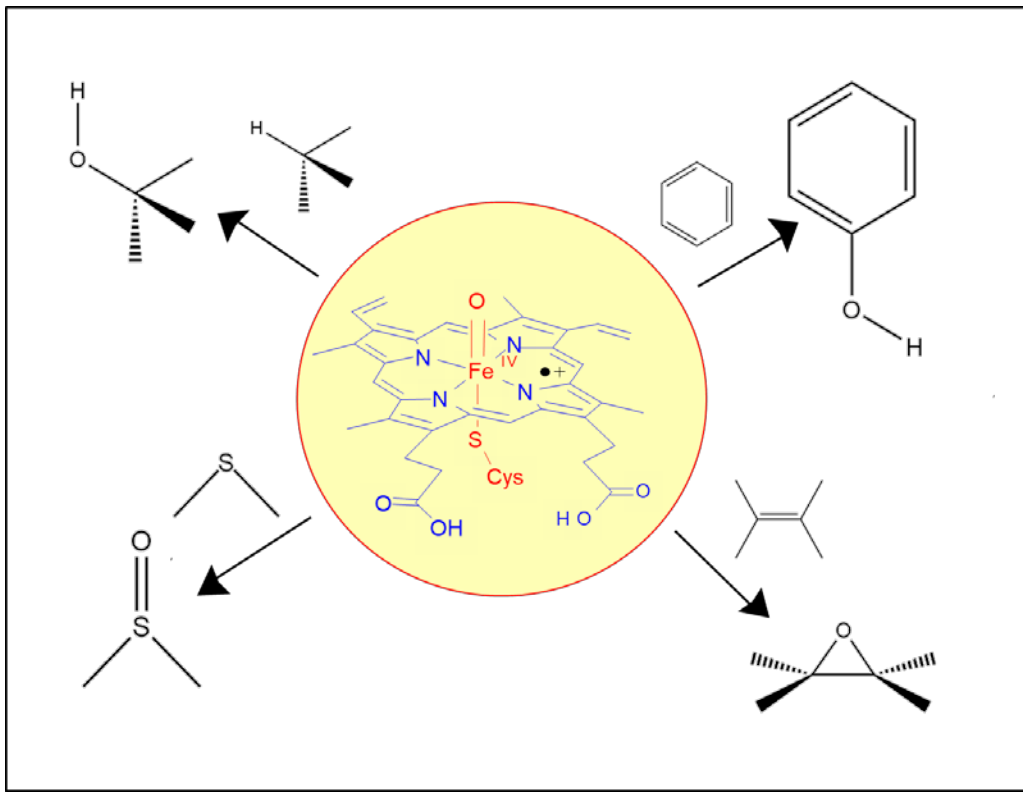

Figure 1: Reactivity patterns of Compound I of P450 enzymes with selected substrates.

Due to experimental difficulties in trapping and characterizing the active species of P450 enzymes, studies in the field moved to biomimetic model complexes and mononuclear nonheme iron enzymes instead. Over the past ten years the field of nonheme iron chemistry has blossomed, especially after the successful spectroscopic characterization of several iron(IV)-oxo complexes well before the first spectroscopic characterization of P450 Cpd I. Computational studies also investigated nonheme iron enzymes and synthetic analogues in detail and explained their reactivity patterns and predicted its chemical properties. Later we will give an overview of key advances in the field obtained from computational modelling. Before discussing the results of

our calculations, let me give a brief overview of heme and nonheme enzymes, their function and properties.

2. Biological nonheme and heme based iron(IV)-oxo intermediates.

Oxygen binding enzymes, generally, come in two varieties, namely with either a heme or a non-heme ligand system. Although in some enzymatic systems, such as methane monoxygenases,[17] a dimetal core is involved in the catalytic reaction mechanism, we will focus here on mononuclear iron systems only. Also oxygenases with other transition metals than iron in the catalytic site will not be covered. In the next sections we will give a brief overview on the mechanism and function of heme and non-heme iron containing mono- and dioxygenases. Subsequently, we will highlight how computational chemistry can assist in gaining understanding in catalytic transformations and the characterization of short-lived intermediates in reaction processes.

2.1 Cytochrome P450s (P450s).

Many heme enzymes utilize molecular oxygen on an iron centre, including monoxygenases, like the P450s,[1–10] but also the catalases and peroxidases.[18–20] The latter detoxify hydrogen peroxide to water, while the catalases convert it to molecular oxygen and water. The first heme enzyme where the complete catalytic cycle was resolved for using crystallographic methods was the one of cytochrome *c* peroxidase (C*c*P) and as a result it has become a template for heme studies in general.[21] However, spectroscopic studies on its Cpd I species as compared to that of other peroxidases and P450s showed that the active species of C*c*P is electronically quite different from the one obtained in other peroxidases, and, therefore, its active species cannot be considered as a model Cpd I species anymore.

The cytochromes P450 are probably, by far, the most extensively studied group of heme enzymes due to their relevance for human health and their potential in biotechnological applications. The name cytochrome P450 comes from the fact that the CO bound ferrous-heme gives a red-shifted strong Soret band through a high-energy π-π^* transition of the porphyrin ring at 450 nm,

due to the strong electron-donating character of the cysteinate axial ligand.[22–24] The P450s catalyze the transfer of one oxygen atom of molecular oxygen to substrates (SubH) concomitant with reduction of the other oxygen atom of O_2 to a water molecule.[1–8] The P450s are widespread in nature and have been found in virtually all forms of life, including bacteria, eukaryotes and fungi.[5,25,26] This is probably due to their versatility and their effectiveness of catalyzing oxidation reactions. They have been linked with the biosynthesis of antibiotics in prokaryotes as well as hormones in eukaryotes. In the human liver the P450s are involved with the metabolism and biodegradation of drugs and xenobiotics.[27] Since the P450s are highly versatile and able to hydroxylate substrates regio- as well as stereospecifically they are of big interest to the biotechnology industry. To gain insight into the fundamental building blocks of the P450s bioinorganic chemists have created biomimetic models of the P450 active site.[12,28–30] Subsequent computational studies have given further insight into the fundamental nature of the heme active site.[8,16,31–33]

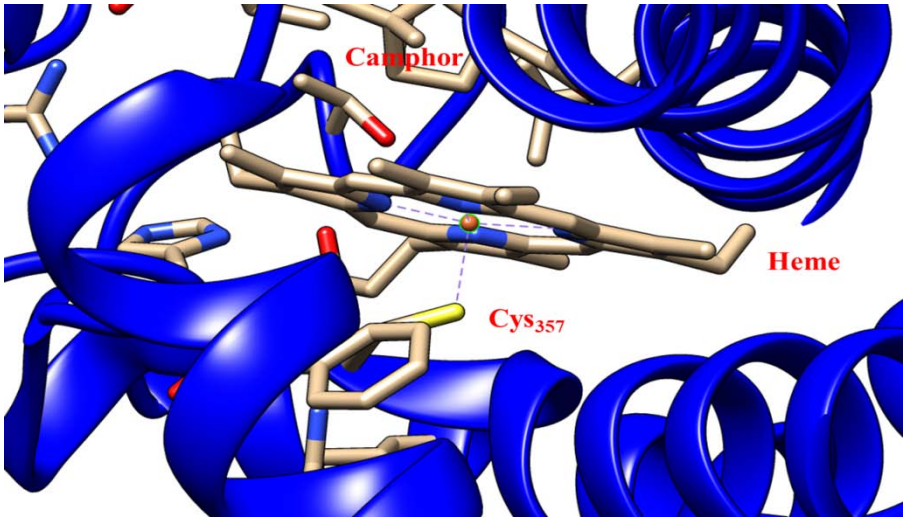

Figure 2: Extract of the crystal structure of substrate bound P450cam as taken from the 1DZ9 pdb file.

Poulos and co-workers were the first to determine an X-ray crystal structure of a P450 isozyme, namely the soluble bacterial $P450_{cam}$ isolated from the bacterium *Pseudomonas putida*,[34] which triggered a range of studies in the field and currently hundreds of P450 crystal structure coordinates are available

from the protein databank.[35] The P450 isozymes show considerable homology and all contain a central heme group, where the catalysis takes place. P450 enzymes contain a single polypeptide chain containing a heme *b* group (iron protoporphyrin IX) linked to a cysteine (Cys) amino acid via the axial ligand of the metal.[9] Figure 2 shows a snapshot of the active site of a typical P450 isozyme, namely $P450_{cam}$, as taken from the 1DZ9 protein databank (pdb) structure.[36] $P450_{cam}$ is a bacterial P450 that catalyses the regioselective hydroxylation of camphor at the C^5 position. It is one of the most extensively studied P450s and generally serves as a template for P450 chemistry.[37,38] The heme *b* group of $P450_{cam}$ is bound to the protein via a thiolate bond of Cys_{357} with the metal and is located deep inside the hydrophobic interior of the enzyme. This is important to accommodate hydrophobic substrates. Note that the axial cysteinate amino acid accepts hydrogen bonds from several neighbouring amino acids, including amide protons of three amino acids including Leu_{358} and Gly_{359}.[39] These hydrogen bonding interactions are believed to fine-tune the catalytic activity of the enzyme and affect the ionization potentials of several intermediates in the catalytic cycle.[40–45] Often the substrates of P450 isozymes bind in a very tight binding pocket where they are locked in position through electrostatic and hydrogen bonding interactions.[35]

The catalytic cycle of the P450s has been extensively studied but only recently the final evidence has been delivered for its mechanism. Thanks to efforts in the fields of enzymology, biomimetic chemistry and computational chemistry over the past four decades, a clear picture on the catalytic activity of P450 enzymes has emerged (Figure 3).[1–10,13,16] Computational modelling provided important insights into the molecular structures, spin states, and chemical and physical properties intermediates and reaction mechanisms.[4,8,16,31–33] Currently many excellent and detailed reviews are available on the catalytic cycle of P450 enzymes and the nature of the individual intermediates during the reaction process.[1–13,16]

The substrate-free resting state (**A**) is the starting (and end) point of the catalytic cycle and contains a six-coordinate low-spin iron(III) state with bound water molecule in the distal ligand position. This is the displaceable

ligand and upon substrate binding into the binding pocket the water molecule is removed as a result of a low-spin to high-spin state transition.[46]

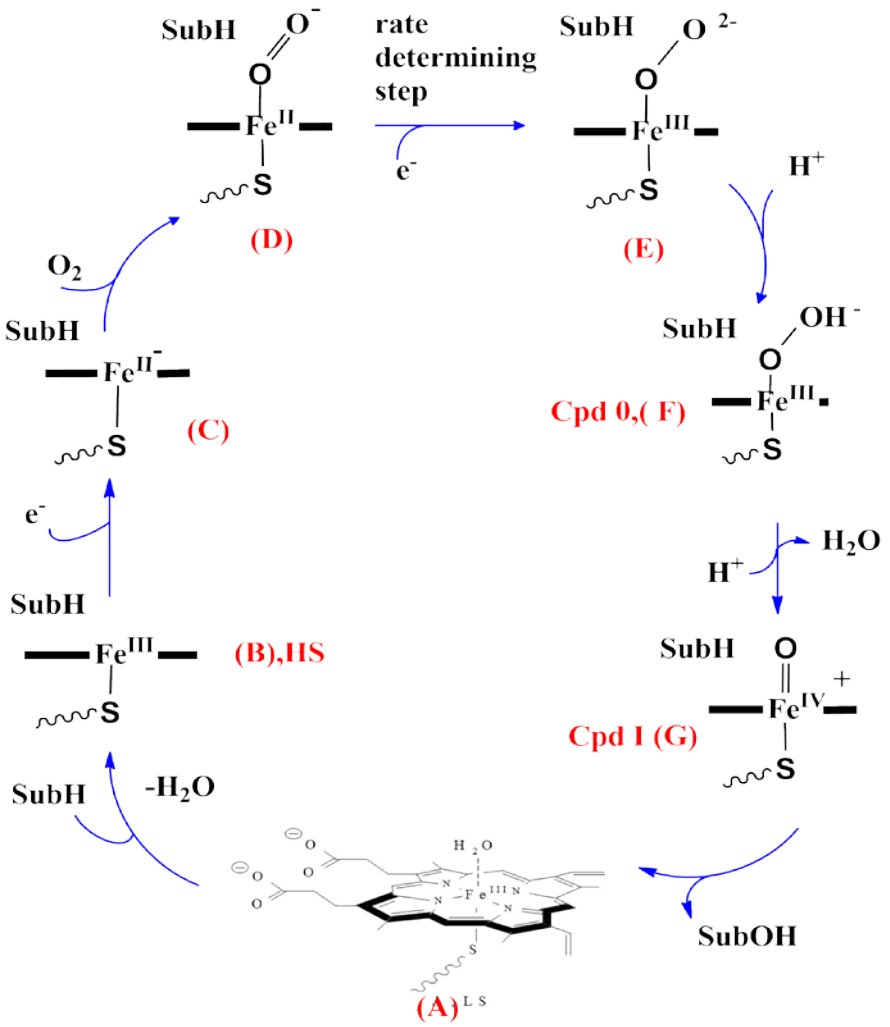

Figure 3: Catalytic cycle of P450 enzymes. SubH is the substrate.

Computational studies indeed confirmed a difference in spin-state ordering for **A** and **B** resulting in a favourable pentacoordinated complex in the high-spin state.[47–51] The spin-state change triggers an electron transfer process from the reductase domain to the heme and reduces the ferric complex **B** to a ferrous complex, **C**.[46] Subsequently, molecular oxygen binds to the ferrous heme to form a ferric-superoxo heme complex (Fe^{III}-O_2^{-}), **D**. The next step in the catalytic cycle is considered the rate-determining step and leads to a second electron transfer from the reductase domain to the heme,[52] to give the ferric-peroxo species (Fe^{III}-O_2^{2-}), **E**. This intermediate picks up a proton from a nearby carboxylic acid group and forms the ferric-hydroperoxo complex, **F**,

that is also known as Compound 0 (Cpd 0). Radiolytic cryoreduction of the ferric-superoxo of cytochrome $P450_{cam}$, **D**, with gradual temperature annealing produced the ferric-peroxo and ferric-hydroperoxo intermediates that were characterized by Electron Paramagnetic Resonance (EPR), Electron-Nuclear Double Resonance (ENDOR), and Ultraviolet-visible (UV-vis) spectroscopies.[36,53–55] A final proton transfer to the ferric-hydroperoxo species, **F**, results in heterolytic O–O bond cleavage to give the iron(IV)-oxo porphyrin π-cation radical intermediate or Cpd I (**G**) and a water molecule. Cpd I has recently been detected and characterized by UV-Visible, resonance Raman and Mössbauer spectroscopy and shown to react with substrates via hydrogen atom abstraction with a large kinetic isotope effect.[15] The spectroscopic properties of Compound I show similarities to the ones observed for the iron(IV)-oxo heme cation radical intermediates of chloroperoxidase (CPO) and horseradish peroxidase (HRP).[41,56] The final step in the catalytic cycle of P450 involves the transfer of the oxygen atom of **G** to the substrate (SubH) to give the alcohol products. This process returns the enzyme back to the resting state.

Due to the short lifetime of several intermediates in the catalytic cycle of P450, however, for a long time, alternative mechanisms have been proposed. One of these suggestions implicated activity of Cpd 0 in substrate epoxidation and sulphoxidation reactions.[57–59] Thus, site-directed mutagenesis studies on $P450_{cam}$ that supposedly blocked the second protonation step in the catalytic cycle and hence terminated the catalytic cycle at Cpd 0 still gave significant activity of the enzyme,[60] which was interpreted as the participation of Cpd 0 as a second electrophilic oxidant in substrate monoxygenation reactions, including olefin epoxidation and sulphoxidation. These mutants gave significant amounts of products originating from olefin epoxidation and sulphoxidation reactions but not from aliphatic hydroxylation reactions.[57–60] Further studies were done using so-called radical-clock substrates that distinguish between a radical and cationic reaction pathways,[61] and implicated ultrashort lifetimes indicative of two active oxidants in the reaction mechanism and hence assigned Cpd I and Cpd 0 as competitive oxidants.[60,62] Site-directed mutants were made where the proton-transfer processes in the catalytic cycle were affected through replacements of key amino acids in $P450_{cam}$ such as the

alcohol side-chain of Thr_{252} and the carboxylic acid group of Asp_{251}. The Thr252Ala mutation gave decreased activity of the enzyme with respect to wild-type and gave significant amounts of decoupling products whereby the ferric-hydroperoxo was converted into ferric-hydrogen peroxide instead and no substrate hydroxylation occured.[57] Interestingly, despite decreased activity of the Thr252Ala mutant with respect to aliphatic hydroxylation, by contrast, double bond epoxidation reactions apparently still proceeded. Based on these studies, a two-oxidant scenario was hypothesized[57] whereby Cpd I was assigned as the oxidant for aliphatic hydroxylation reactions, whereas Cpd 0 is responsible for double bond epoxidation.

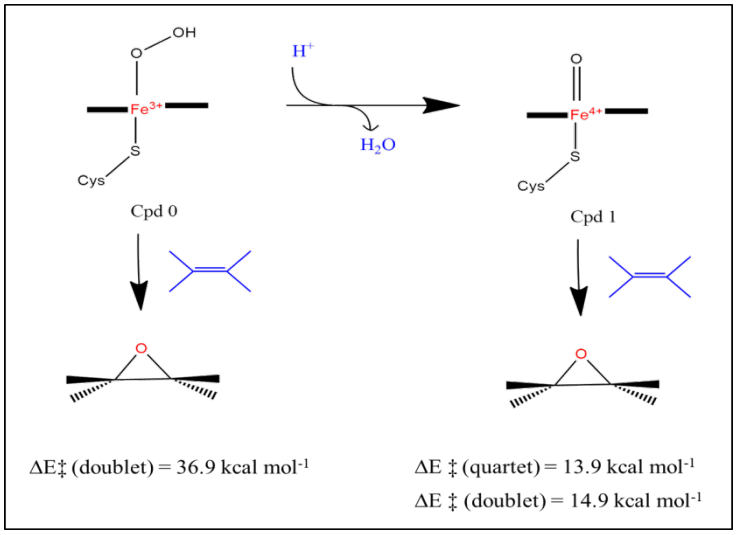

Figure 4: Computational studies of ethene epoxidation by Cpd 0 and Cpd I models of P450 with rate determining barriers in kcal mol–1.

Many computational and biomimetic studies have investigated the two-oxidant hypothesis, but all research showed the iron(III)-hydroperoxo species to be a sluggish oxidant.[63–66] The first evidence against Cpd 0 as an active oxidant came from computational modelling and addressed the relative performance of Cpd I and Cpd 0 in ethene epoxidation.[63] Figure 4 highlights the main results from these studies. Thus, Cpd I reacts with ethene in a stepwise mechanism via a radical intermediate, whereby the initial electrophilic addition is rate determining with a barrier of 13.9 kcal mol^{-1} on the quartet spin state surface and 14.9 kcal mol^{-1} on the doublet spin state surface. By contrast, the epoxidation reaction by Cpd 0 has a much higher reaction barrier of 36.9 kcal

mol^{-1}, and consequently, Cpd 0 is a sluggish oxidant and will not be able to compete with Cpd I.

Further detailed quantum mechanics/molecular mechanics (QM/MM) studies on dimethylsulphide sulphoxidation by Cpd I and Cpd 0 intermediates of P450 confirmed the conclusions of small model complexes and assigned Cpd I as the only viable oxidant in the catalytic cycle.[66] High barriers were found for the reaction mechanism starting from the iron(III)-hydroperoxo species, while much lower barriers for the same reaction by Cpd I were found. The computational studies were supported by biomimetic work on the substrate epoxidation and sulphoxidation reactions by three different nonheme iron(III)-hydroperoxo oxidants, namely $[(N4Py)Fe^{III}(OOH)]^{2+}$, $[(Bn\text{-}tpen)Fe^{III}(OOH)]^{2+}$ and $[(TPA)Fe^{III}(OOH)]^{2+}$ with N4Py = *N*,*N*-bis(2-pyridylmethyl)-*N*-bis(2-pyridyl)-methylamine, Bn-tpen = *N*-benzyl-*N*,*N*′,*N*′-tris(2-pyridylmethyl)ethane-1,2-diamine and TPA = tris(2-pyridylmethyl)amine. The work provided insight into electrophilic and nucleophilic reactivities of nonheme iron(III)-hydroperoxo intermediates.[67] The oxidants were found to be inactive towards thioanisole and cyclohexene, which implies that these intermediates cannot react via sulphoxidation and epoxidation mechanisms in support of the computational studies. The analogous iron(IV)-oxo complexes, by contrast, showed efficient catalysis of olefins and sulphides to their respective oxides and sulphoxides.[67] Similar conclusions were derived from the reaction of a mononuclear nonheme iron(III)-alkylperoxo complex, $[(TPA)Fe^{III}(t\text{-}BuOO)]^{2+}$ (*t*-BuOOH = *t*-butyl hydroperoxide), with substrates, where little reactivity was observed. This is further confirmation that iron(III)-alkylperoxo porphyrin intermediates are sluggish oxidants and that the iron(IV)-oxo intermediate is formed through O–O bond homolysis.[68,69]

Woggon, van Eldik, and their co-workers recently came with spectroscopic evidence for the formation of an iron(IV)-oxo porphyrin cation radical intermediate and its involvement in oxygen atom transfer processes to substrates.[70] Subsequently, they measured rate constants for the formation and decay of intermediates formed in the catalytic reaction of the iron porphyrin complex and *m*-CPBA (*m*-chloroperbenzoic acid) as well as oxygen atom transfer rate constants using low-temperature rapid-scan stopped-flow techniques. Nam and co-workers compared the reactivity of a high-valent

iron(IV)-oxo porphyrin cation radical with an iron(III)-alkylperoxo complex and found evidence that the former is an active oxidant in the catalytic oxygenation of organic substrates, while the latter is a sluggish oxidant.[71]

2.2 Taurine/α-ketoglutarate dioxygenase (TauD).

A large class of mononuclear nonheme iron containing enzymes that utilize molecular oxygen and react as dioxygenases are the α-ketoacid dependent dioxygenases of which α-ketoglutarate dependent dioxygenases (αKDD) are the most extensively studied of those.[8,28–30,72–78] By contrast to the catalytic cycle of the P450s that uses two external electrons and protons, the nonheme iron dioxygenases do neither utilize a cofactor nor a proton source, but instead use a co-substrate (α-ketoglutarate, αKG) to generate an iron(IV)-oxo active species. This intermediate is relatively long-lived and has been characterized by a range of spectroscopic methods, *vide supra*.[77,78] The αKDD are very versatile and catalyze many different reactions in biosystems, ranging from substrate hydroxylation, substrate halogenation and desaturation to ring-closure processes.[28,77–80] As such they catalyze a series of vital processes for human health with examples that include: DNA and RNA base repair in mammals,[81–83] cross-linking processes in collagen,[84] responses to hypoxia,[85] and the biosynthesis of the vancomycin, fosfomycin and carbapenem group of antibiotics in bacteria.[86–88] As both the nonheme iron dioxygenases and the P450 monoxygenases catalyze oxygen atom transfer reactions to substrates and specifically aliphatic hydroxylation reactions, the question remains why nature generated two sets of enzymes with essentially the same function. The detailed computational studies reported here will highlight the differences and comparisons between the heme and nonheme iron complexes in nature.

The nonheme iron dioxygenases, therefore, are highly versatile but show distinct structural differences between isoforms; however, most of them contain a characteristic iron-coordination site, where the metal is bound to the side chains of two histidine and one carboxylic acid (Asp/Glu) residue into a facial 2-His/1-Asp ligand system.[89,90] This motif has been identified in large numbers of nonheme iron dioxygenases, including clavaminic acid synthase,[91] AlkB repair enzymes,[92,93] and prolyl-4-hydroxylase.[94–106] The first nonheme iron enzyme of which the iron(IV)-oxo species was spectroscopically

characterized, and consequently the most extensively studied one, was taurine/α-ketoglutarate dioxygenase (TauD), and, hence, we will describe details of its spectroscopic characterization and reactivity in hydrogen atom abstraction reactions. To highlight the versatility of nonheme iron enzymes, we describe spectroscopic and reactivity studies on an alternative nonheme iron enzyme (cysteine dioxygenase, CDO) with a 3-His ligand system (Figure 5) that catalyzes the sulphoxidation reaction of a substrate. These two case studies highlight the effect of axial and equatorial ligands on the ground state properties of mononuclear nonheme iron(IV)-oxo intermediates and their reactivity patterns.

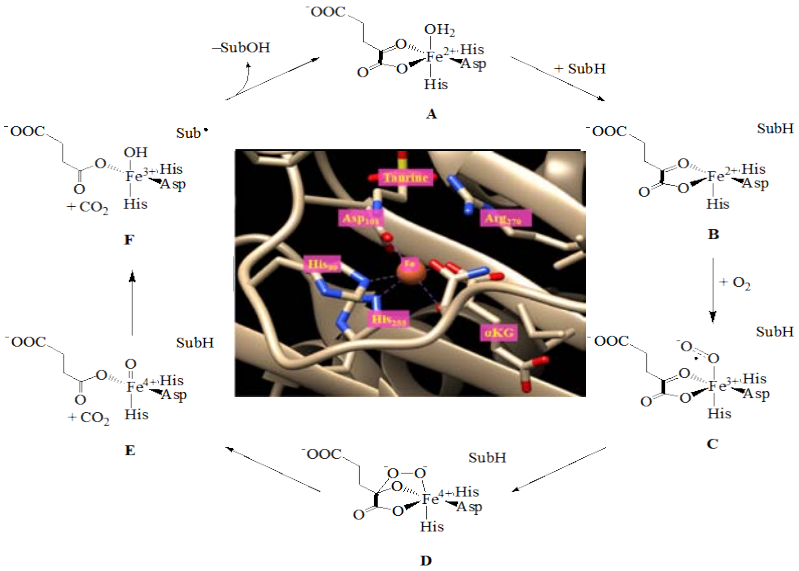

Figure 5: Catalytic cycle of TauD. The central structure is an extract of the 1OS7 pdb structure with key residues highlighted. SubH is substrate

2.3 Cysteine Dioxygenase (CDO).

Another nonheme iron enzyme that utilizes an iron(IV)-oxo species in its catalytic cycle is cysteine dioxygenase (CDO), which catalyzes the conversion of L-cysteine into L-cysteine sulphinic acid products. CDO is a vital enzyme for human health involved in the biodegradation and metabolism of toxic cysteine.[107,108] High concentrations of cysteine in the body are toxic and it precipitates into cystine stones.[109] Moreover, elevated levels of cysteine in the body have been correlated with neurological diseases such as Alzheimer's and

Parkinson's diseases.[110] The metabolism of cysteine is accomplished by a series of enzymes and the first one of these is CDO. Because of its importance in human physiology, the reaction has attracted a lot of scientific attention and is well studied.

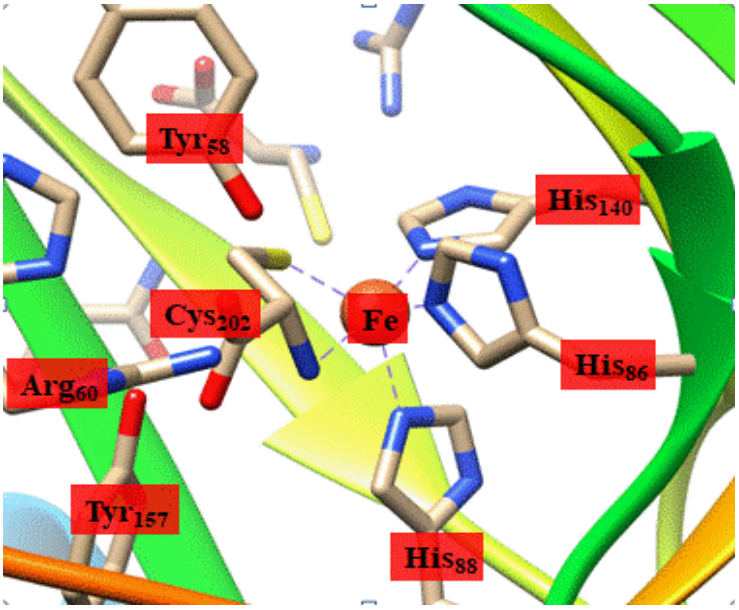

Figure 6: Active site structure of substrate bound CDO as taken from the 2IC1 pdb file with amino acids labelled as in the pdb file

By contrast to the chemical structure of TauD, the catalytic metal ion in CDO is bound into a 3-His ligand structure rather than the typical 2-His/1-Asp facial triad. Figure 6 gives an extract of the crystal structure of CDO enzymes as taken from the 2IC1 pdb file.[111] The metal is bound to the protein backbone via three histidine linkages of the side chains of His_{86}, His_{88} and His_{140}, whereas cysteine binds as a bidentate ligand to the metal with the thiolate group *trans* to His_{88} and the amino group *trans* to His_{140}. The carboxylic acid group of cysteine forms hydrogen bonding interactions with several residues in the binding pocket, including a salt bridge with Arg_{60}, as well as hydrogen bonding interactions with the imidazole side chain of His_{155} and the phenol groups of Tyr_{157} and Tyr_{58}. Because of this, the substrate binding pocket is tight and consequently CDO enzymes are highly substrate specific and will not even catalyze the reaction for structurally similar inhibitors.[112] The last ligand

position of iron is empty in the pdb file but it is the place where molecular oxygen will bind. EPR studies on NO bound CDO provided compelling evidence that substrate binds prior to molecular oxygen to the metal centre.[113] Moreover, experiments with $^{18}O_2$ showed that both oxygen atoms of O_2 are incorporated into cysteine sulphinic acid products.[114]

Another interesting and unusual feature of the enzyme active site is the Tyr_{157}–Cys_{93} crosslink. Currently, it is not clear what its function is, but it was shown to be correlated to substrate binding and catalytic turn-over.[115,116] It may, therefore, affect the active site geometry through structural changes, although recent Mössbauer spectroscopic studies revealed little effect on iron binding.[117] So far few experimental studies managed to stabilize and characterize catalytic cycle intermediates obtained after dioxygen binding, therefore, to gain insight into the dioxygenation reaction of CDO a string of high-level computational studies were performed.[118–120] The only two experimental reports on dioxygen bound intermediates refer to a crystal structure of an iron(III)-persulphenate and the spectroscopic characterization of an iron(III)-superoxo complex.[121,122] QM/MM calculations on the iron(III)-persulphenate structure,[120] however, found no evidence of its involvement of the catalytic mechanism of CDO, and its energy was found to be well higher than the iron(III)-superoxo structure. Therefore, it is more likely to be a by-product from a side reaction. The iron(III)-superoxo intermediate was synthesized from substrate bound CDO and mixed with superoxide generated from xanthine oxidase.[122] This created a transient species with UV-Vis features at 485 and 565 nm, which decayed very slowly. EPR spectroscopic studies on this transient species gave evidence of the septet spin iron(III)-superoxo intermediate with $S = {}^5/_2$ spin on the metal that is ferromagnetically coupled to an S = ½ superoxo radical.

3. Methods and techniques.

3.1 Density functional theory.

Our group uses well benchmarked and calibrated methods that are based on density functional theory (DFT) calculations as implemented in commercially available computational chemistry software packages, such as *Gaussian*, *Jaguar*, *Turbomole* or *Orca*.[123–126] Thus, these software packages describe the

electronic features of molecules with the Schrödinger equation,[127] Eq 2, that relates the wave function of electrical particles (Ψ) to the total energy of the system (E) by taking all perturbations that influence the wave function into account via the Hamilton operator (H). The Hamilton operator within the Born-Oppenheimer approximation includes the kinetic and potential energy of all the electrons and nuclei within a molecule and contains electron-electron, electron-nucleus and nucleus-nucleus interactions as described in Eq 3.[128–130] The distances between protons and electrons are given as r_{Ii}, while the distances between two electrons and two protons is described by either r_{ij} and R_{IJ}, respectively. The first term in Eq 3 represents the kinetic energy of the electrons, the second term is the electron-nuclei attractions and the third term gives the electron-electron repulsions. The final term in Eq 3 gives the nucleus-nucleus repulsions, which within the Born-Oppenheimer approximation is a constant value, because the electronic energy E is calculated for a rigid molecular geometry. In Eq 3, $\hbar$ is Planck's constant divided by 2π, m_{e} is the electron mass, e is the elementary charge and ε_0 represents the permittivity in vacuum. The Laplacian (∇) is defined in Eq 4 and represents the motion of an electron in three-dimensional space. The complexity of the Hamiltonian obviously is dependent on the number of electrons (N_{e}) and the number of protons (N_{p}) of the chemical system. Consequently, an increase of the chemical system with more atoms, i.e. with increased number of electrons and nuclei, gives enhanced complexity of the solution of the Schrödinger equation. As a result of this, the Schrödinger equation can only be solved exactly for the hydrogen atom and the $H_2^{+\bullet}$ molecule and for larger chemical systems approximations have to be used.

$$H\,\Psi = E\,\Psi \tag{2}$$

$$H = -\frac{\hbar^2}{2m_e}\sum_i^{N_e}\nabla_i^2 - \sum_i^{N_e}\sum_I^{N_p}\frac{Z_I e^2}{4\pi\varepsilon_0 r_{Ii}} + \frac{1}{2}\sum_{i,j}^{N_e}\frac{e^2}{4\pi\varepsilon_0 r_{ij}} + \frac{1}{2}\sum_{I,J}^{N_p}\frac{e^2}{4\pi\varepsilon_0 R_{IJ}} \tag{3}$$

$$\nabla_i^2 = \frac{\partial^2}{\partial x^2} + \frac{\partial^2}{\partial y^2} + \frac{\partial^2}{\partial z^2} \tag{4}$$

In Hartree-Fock theory (HF) the Schrödinger equation is solved numerically by multiplication of Eq 2 with the complex conjugate wave function followed by integration of the equation with respect to each individual spin orbital, Eq 5.

Solving Eq 5 gives the HF energy for a particular structure. In a subsequent step, the wave function coefficients are modified and the HF equations recalculated, which is an iterative process that is repeated until self-consistency is obtained, whereby the energy change from one step to the next stays below a certain cut-off value (the convergence energy). During a geometry optimization, this converged wave function is used as the starting point for a modified geometry based on the first derivatives of the energy to all individual distances and angles. The HF equations are again solved for the new structure until self-consistence and the process is repeated until a stationary structure, or minimum energy conformation, is found. This optimized geometry should be on a local minimum on the potential energy surface with first and second derivatives of the energy to the individual coordinates that are zero.

$$\int \Psi^* H \Psi d\tau = E \int \Psi^* \Psi d\tau \qquad (5)$$

Generally, HF gives reasonable geometries but its energies are not good enough for calculations on reaction mechanisms and barrier heights. For these processes, further improvements to the theory are necessary. One such method in wave function chemistry is the second order perturbation theory, such as Møller-Plesset theory or MP2, which gives much more accurate energies and chemical structures.[131] However, these methods are computationally demanding and even with current resources only accessible to chemical systems with less than 30 atoms.[132] To enable studies of larger chemical systems, including biosystems, the search for computationally cheap methods was started. Firstly, the advances in density functional theory (DFT) supplied an alternative to computationally expensive wave function methods such as MP2. Secondly, the development of quantum mechanics/molecular mechanics (QM/MM) opened up opportunities to study enzymatic systems with high accuracy.

In the 1960s Kohn and co-workers[133,134] showed that replacement of the wave function by a functional of the electron density, $\rho(\mathbf{r})$ with $\mathbf{r}$ the distance between two electrons, is more practical. Thus, in DFT the solution to the electronic energy (E_{el}) follows from the sum of the integrals given in Eq 6. Again, the first term represents the kinetic energy of the electrons, the second term the electron-nucleus attractions and the third integral gives the Coulombic

electron-electron repulsions. In addition, in DFT there is an exchange-correlation term E_{xc} for electron pair interactions with an exchange and a correlation component, E_{x} and E_{c}, respectively. The exchange energy, E_{x}, is dependent on ferromagnetic interactions of two electrons with the same spin (α or β) but in different orbitals. By contrast, the correlation energy, E_{c}, reflects the electron pairing energy of two electrons in the same molecular orbital. Unfortunately, no exact equations are known for the exchange and correlation energies so that they need to be approximated using empirical equations.

$$E_{el} = -\frac{1}{2}\sum_{i}\int \phi_i(\mathbf{r}_1)\nabla^2\phi_i(\mathbf{r}_1)d\mathbf{r}_1 + \sum_{A}\int \frac{Z_A}{|\mathbf{R}_A - \mathbf{r}_1|}\rho(\mathbf{r}_1)d\mathbf{r}_1 + \frac{1}{2}\int \frac{\rho(\mathbf{r}_1)\rho(\mathbf{r}_2)}{|\mathbf{r}_1 - \mathbf{r}_2|}d\mathbf{r}_1 d\mathbf{r}_2 + E_{xc} \tag{6}$$

Commonly used exchange and correlation energy equations are the Slater exchange, Eq 7,[135] and the correlation energy due to Vosco, Wilk and Nusair, Eq 8.[136] The Slater exchange uses the exchange scale factor (α_{ex}) that has a value of $^2/_3$ for an electron gas. The correlation energy is calculated per electron in a gas from the correlation functional $\varepsilon_c\left[\rho_1^\alpha, \rho_1^\beta\right]$ using spin densities ρ_1^α and ρ_1^β. The sole use of E_x^{Slater} and E_c^{VWN} gives the Local Density Approximation (LDA), which although it gives an improvement over Hartree-Fock (HF) wave function methods, it is not good enough to compete with, e.g., MP2 methods. As such, further corrections due to non-local interactions are needed. These are, for instance, implemented into the Lee, Yang and Parr (LYP) or Perdew and Wang (PW95) correlation methods.[137,138]

$$E_x^{Slater} = -\frac{9}{4\alpha_{ex}}\left(\frac{3}{4\pi}\right)^{\frac{1}{3}}\sum_{\gamma}\int\left[\rho_1^\gamma(\mathbf{r}_1)\right]^{\frac{4}{3}}d\mathbf{r}_1 \tag{7}$$

$$E_c^{VWN} = \int \rho_1(\mathbf{r}_1)\varepsilon_c\left[\rho_1^\alpha(\mathbf{r}_1), \rho_1^\beta(\mathbf{r}_1)\right]d\mathbf{r}_1 \tag{8}$$

It took until the 1990s until highly accurate density functional methods were developed that were able to accurately predict molecular properties. Thus, Becke developed a three parameter (*A*, *B*, *C*) hybrid density functional method that includes the exchange and correlation functionals of respectively Slater

and VWN in combination with the HF exchange and two correction factors: one for the correlation due to, e.g., LYP (ΔE_c^{LYP}) and the other for the exchange components (ΔE_x^{Becke}), Eq 9.[139] Becke then optimized the three parameters *A*, *B*, and *C* against experimentally determined electron affinities, ionization potentials and proton affinities for a test-set of molecules. As an example, we give the exchange correlation energy for the commonly used B3LYP hybrid density functional method in Eq 9. Obviously, since the hybrid density functional method contains fit-parameters that were calibrated against experiment, this method cannot be considered as an *ab initio* method. Hybrid density functional methods, however, combine high speed with reasonable accuracy, so that these methods are commonly used in computational chemistry problems for calculations on relatively large chemical systems with excess of 50 atoms. Becke's test-set predicted energies within 2 kcal mol^{-1} from experiment,[139] which is a reasonable accuracy to calculate chemical reactions. The Becke test-set, however, did not include transition metal containing complexes and recent calibration methods showed that for those types of chemical systems it is often better to use a modified hybrid density functional method like B3LYP* that uses less HF exchange, i.e. typically 10 or 15% rather than the standard 20%.[140] In addition, the energetics of these complexes often are overestimated due to lack of dispersion in the calculations. Grimme and co-workers developed a dispersion correction expression that gives improved energies, which we label as B3LYP-D.[141] Nevertheless, regardless on the DFT method chosen, the calculated result should be similar. Although often calculations show little sensitivity to the methodology, in transition metal complexes with close-lying spin states the ordering and spin-state energy splitting are occasionally dependent on the chosen method. It is of paramount importance, therefore, to calibrate DFT calculations on transition metal complexes to either experimental data or to do test calculations with alternative methods. In most projects described in this work that was done and examples of these benchmark results will be given later.

$$E_{xc}^{B3LYP} = AE_x^{Slater} + (1-A)E_x^{HF} + B\Delta E_x^{Becke} + E_c^{VWN} + C\Delta E_c^{LYP} \qquad (9)$$

3.2 Basis sets.

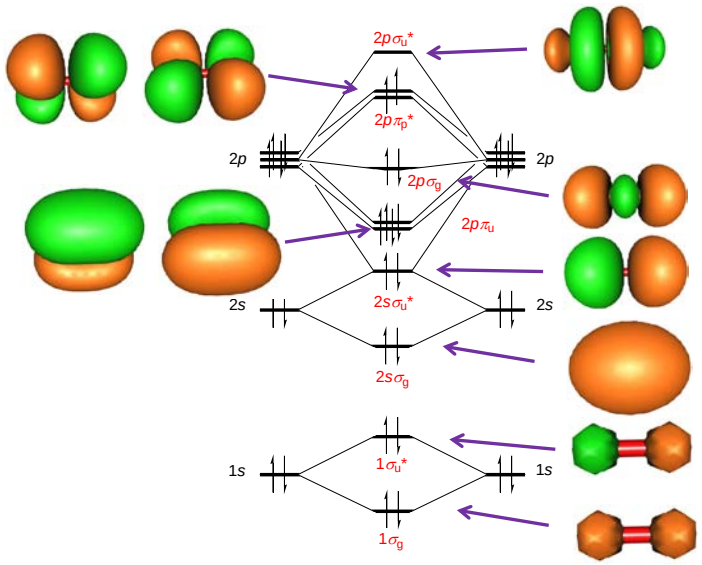

Figure 7: Molecular orbitals of O_2 in the triplet spin state as calculated with MP2/6-31G*.

In order to solve the Schrödinger equation one optimizes the wave function and using the perturbations from the Hamilton operator find the eigenvalues or energies associated with the equation. The wave function of molecules is not as straightforward as that of atoms, where distinct orbital levels can be identified, i.e. 1*s*, 2s, 2*p* etc. To overcome this problem, the molecular wave function, and consequently molecular orbitals, are usually described as a mathematical sum of atomic orbital components through the Linear Combination of Atomic Orbitals (LCAO) approach.[142] This approach takes all occupied and a selection of virtual atomic orbitals (χ) of all atoms in the molecule and creates a set of molecular orbitals (φ_i) through fractions (c_{ri}) of all atomic orbital components, Eq 10. The quality of these molecular orbitals obviously is dependent on the number of active orbitals taken into consideration and in particular the number of virtual orbitals included. Especially for wave function calculations large numbers of virtual orbitals are needed in the calculations as the energy tends to converge to the basis set limit. Since, the coefficients of hybrid density functional theory were benchmarked against experimental data using calculations using a double-ζ quality basis set,

this type of basis set is generally sufficient in DFT calculations for geometry optimizations.

$$\varphi_i = \sum_r c_{ri} \chi_r \qquad (10)$$

As an example of the mixing of atomic orbital components into molecular orbitals, we give in Figure 7 the orbital splitting for molecular oxygen. Thus, the left and right-hand-side levels represent the two individual oxygen atoms with $1s^2\ 2s^2\ 2p^4$ orbital occupation. The atomic orbitals on the two centres mix and form the set of molecular (O_2) orbitals depicted in the middle of Figure 7. The two 1*s* orbitals of the two oxygen atoms mix to form a bonding ($1\sigma_g$) and an anti-bonding ($1\sigma_u$*) pair of molecular orbitals, and the same happens between the atomic 2*s* pair of orbitals to generate the $2s\sigma_g$ and $2s\sigma_u$* set of molecular orbitals. In contrast to the 1σ orbitals the $2s\sigma$ molecular orbitals contain a certain degree of 2*p* character as well, and, therefore, have shapes that differ from the atomic orbitals. This is even more so for the valence orbitals ($2p\sigma$ and $2p\pi$), where several high lying (virtual) atomic orbitals are mixed in. Consequently, the calculated energy from the Schrödinger equation is dependent on the choice of basis set and the number of basis functions used. This is particularly important in wave function methods, such as MP2, where relatively large basis sets are required.

Due to the large number of electrons in transition metal elements there are special basis sets available that include an effective core potential (ECP).[143] Essentially, the core electrons, i.e. 1*s*, 2*s* and 2*p* electrons in Fe, are hardly affected by chemical bonding and, therefore, do not change much with respect to atomic orbitals. These orbitals in the ECP treatment are replaced by an electrical potential in the Hamiltonian. Often the ECP component contains relativistic corrections to the energy and improves the calculated energies. For iron, typical ECP containing basis sets are from the Los Alamos type, e.g. LACVP or LANL2DZ.[144] Generally, in our work we calculated energies using a triple ζ-type basis set (LACV3P+) that includes diffuse and polarization functions on the metal. Test calculations for a substrate hydroxylation potential energy profile by a Cpd I model using two different basis sets, namely BS1 (LACVP on iron and 6-31G on the rest of the atoms) and BS2 (LACV3P+ on

iron and 6-311+G* on the rest of the atoms), showed very little changes in optimized geometries and virtually identical relative energies along a reaction profile.[145] As such, usually geometries are optimized using a double-ζ basis set and the calculation is followed by a single point energy calculations with a triple-ζ basis set.

3.3 Zero point energy (ZPE).

Calculations of potential energy profiles and reaction mechanisms, as we have seen, start off from the Schrödinger equation with a choice of method and basis set. The eigenvalues obtained through this, however, are electronic energies, which are devoid of vibrational and entropical contributions.

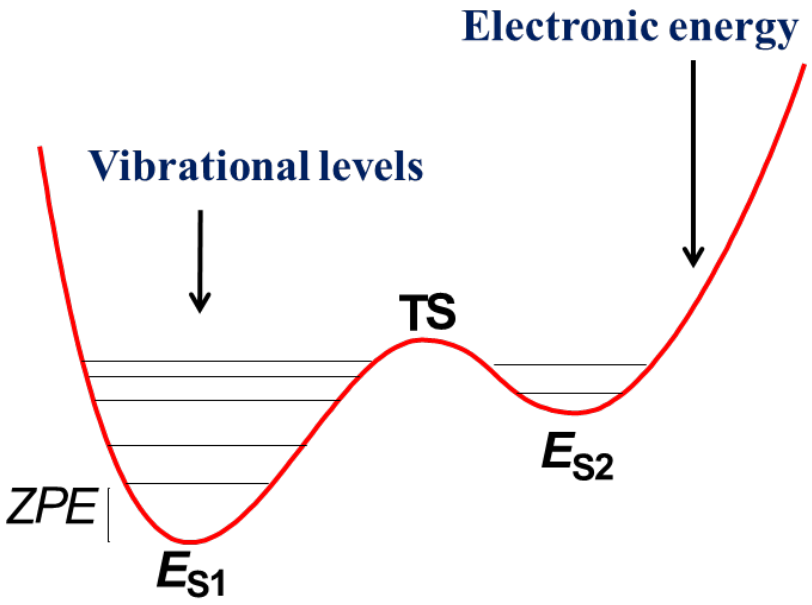

Figure 8: Potential energy profile from reactant state S1 to a product state S2 via a transition state TS. Highlighted are the electronic and ZPE contributions to the total energy.

In order to obtain these corrections to the electronic energy, a frequency calculation is performed that calculates the first and second derivatives of the energy with respect to the distances and angles between the atoms. From these derivatives the vibrational energy levels of a molecule are calculated. Thus, at 0 K temperature, the molecule resides in the lowest vibrational level above the

electronic energy of the local minimum as explained in Figure 8. This Figure gives the hypothetical potential energy profile of a molecule that can exist in two stable conformations, S1 and S2, for which local minima are calculated with energy E_{S1} and E_{S2}, respectively. The zero point energy (*ZPE*) is the lowest vibrational energy level above these electronic energies and hence E_{S1} + *ZPE* is the ground state energy for conformation S1. Calculations on a potential energy profile are given as ΔE + *ZPE* relative to a starting structure.

3.4 Solvent effects.

Calculated energies using computational chemistry methods refer to gas-phase data, whether they use ZPE corrections or not. In order to compare computational results to experiment, the solvent needs to be mimicked in into the calculations. This can be done by simply adding solvent molecules to the chemical model and reoptimizing the structures. However, calculations with large number of atoms require more resources and are not always practical, especially since solvent molecules can exist in several conformations.[146] Instead of addition of solvent molecules to the chemical structure, a more common approach is to add solvent corrections to the energetics using an implicit solvent model. This can either be done at single point level, whereby the energy is recalculated with a solvent model on the gas-phase optimized geometry, or by reoptimizing the structure using a solvent model.

Software packages, such as *Gaussian* and *Jaguar*, include solvent models like the Polarizable Continuum Model (PCM).[147] In PCM calculations the solvent is described as a perturbation of the molecule with a dielectric constant and the molecule is placed in a cavity that is surrounded by the dielectric continuum. The cavity is described as the area around the molecule that contains less than pre-defined amount of electron density of the molecule and is often based on van der Waals radii of atoms. The classical Poisson equations are then used to calculate the electronic potential arising from the molecule-solvent interactions using a defined dielectric constant.

3.5 Quantum mechanics/molecular mechanics (QM/MM).

Another approach to mimic perturbations of a surrounding into the energies of molecules is to use the quantum mechanics/molecular mechanics (QM/MM) approach. In QM/MM the chemical system, such as an enzyme, is divided into two or more regions (shells): the inner core that is calculated with accurate methods and the outer region, which contains the protein and solvent is calculated with computationally cheap methods, like molecular mechanics (MM).[148] The inner core is our region of interest and contains the basic features of the enzyme active site and the substrate, but is held in position by interactions with the rest of the protein. These chemical constraints fix the active site and substrate into a specific conformation that affect their interactions and reactivities. However, those chemical groups that do not contribute to the reaction mechanism and, therefore, are not essential for the quantum mechanical description of the system are not necessary in the QM region and are calculated with an MM force field.

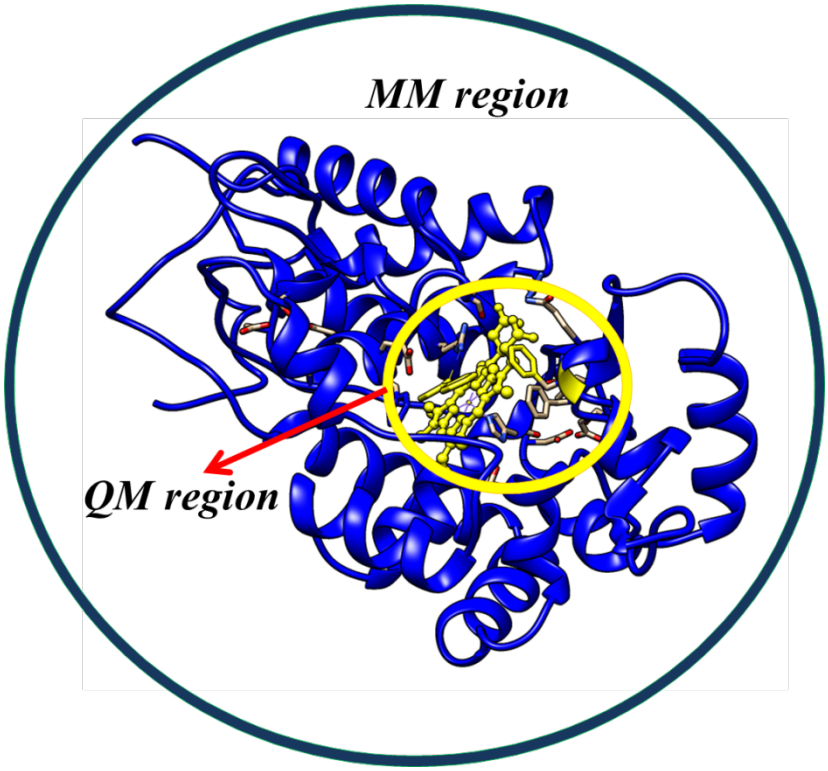

Figure 9: Description of an enzyme via QM/MM and the division of the system into a QM and an MM region.

The division of the system between QM and MM regions is not necessarily straightforward, since it may cut through bonds, and as such there are several methods to describe the interface between the QM and MM region. We use the link-atom approach whereby the region between the QM and MM areas is described with hydrogen link atoms using the charge shift model.[149]

The QM/MM methodology starts off from experimentally determined crystal structure coordinates, i.e. a protein data bank (pdb) file. Many pdb files of proteins are available from the protein databank on the internet.[35] Often these pdb files refer to a resting state structure of the enzyme rather than its catalytically active species. This, therefore, requires some modifications to the starting structure pdb and conversion of it into a later structure in the catalytic cycle. In addition, the pdb files tend not to contain hydrogen atoms, so that they need to be added as well as a solvent layer/box. Generally, this is done in the preliminary set up where the user carefully checks protonation states of residues, salt and disulphide bridges and ions. The pdbtopqr program was used to assign protonation states at pH = 7, whereas all individual histidine residues are manually checked for protonation state. Histidine groups in proteins can exist in one of three protonation states: deprotonated, singly protonated or doubly protonated. All His residues in the structure are manually and visually investigated for likely hydrogen bonding donor and acceptor groups and their protonation states assigned. Counterions are added to the surface to balance the overall charge of the system to neutral. After this initial set up the system is equilibrated and heated to room temperature in a stepwise protocol. First only hydrogen atoms are allowed to change position, but in a later stage also the backbone atoms are free to relax in the geometry optimization. The final molecular dynamics simulation creates a series of low energy snapshots that are used as starting points for the actual QM/MM calculations. There are several force fields available for these MD simulations, such as a universal force field (UFF),[150] Amber,[151] Charmm,[152] etc.

In our calculations we describe the QM region with a DFT method, such as B3LYP, in combination with one of the common basis sets mentioned above, e.g. LANL2DZ+ECP and 6-31G*. Since, the speed of the calculations is dependent on the number of atoms in the QM region, we test several sizes of QM region for consistency. Geometries refer to optimizations of all degrees of

freedom in the QM and MM regions unless otherwise noted. Frequencies are done on the geometry for the QM region only.

4. Results and Discussion.

Our studies use a combination of chemical techniques and are focused on gaining fundamental chemical insight into short-lived intermediates in enzymatic systems. In particular, the work describes the activity of enzymes vital for human health including the heme-based P450s and the nonheme iron dioxygenases. Both systems utilize molecular oxygen on an iron centre, but catalyze different reactions. Their reactivity patterns are still poorly understood, and hence these enzymes are under-used in commercial biotechnological applications. Moreover, due to the transient nature of several key intermediates in the reaction processes and the complications due to multiple possible spin state electromers it is difficult to study these chemical systems with experimental methods. Theoretical modelling assist here and guides experimental work in the field.

4.1 Cytochrome P450s (P450s).

Over the years our group has extensively studied the catalytic mechanism and chemical properties of P450 enzymes. Early studies focussed on establishing the catalytic mechanisms and rate determining steps of aliphatic hydroxylation,[153–155] olefin epoxidation,[154,156,157] sulphoxidation of dialkylsulphides,[65] and the aromatic hydroxylation of arenes by P450 Cpd I.[158] We will not discuss these studies in detail here, as they have been extensively reviewed,[8,13,16,32,33] but will describe more recent work where we have generalized the rate constants of the reaction processes using thermodynamic and valence bond (VB) models and the effect of ligands on the reaction mechanism. Those studies have predictive value and enable one to determine regioselectivities and activities of metal-oxo species. Before discussing the predictive studies, however, let me briefly summarize the key properties of the active species of P450, namely Cpd I.

4.1.1 Compound I of P450.

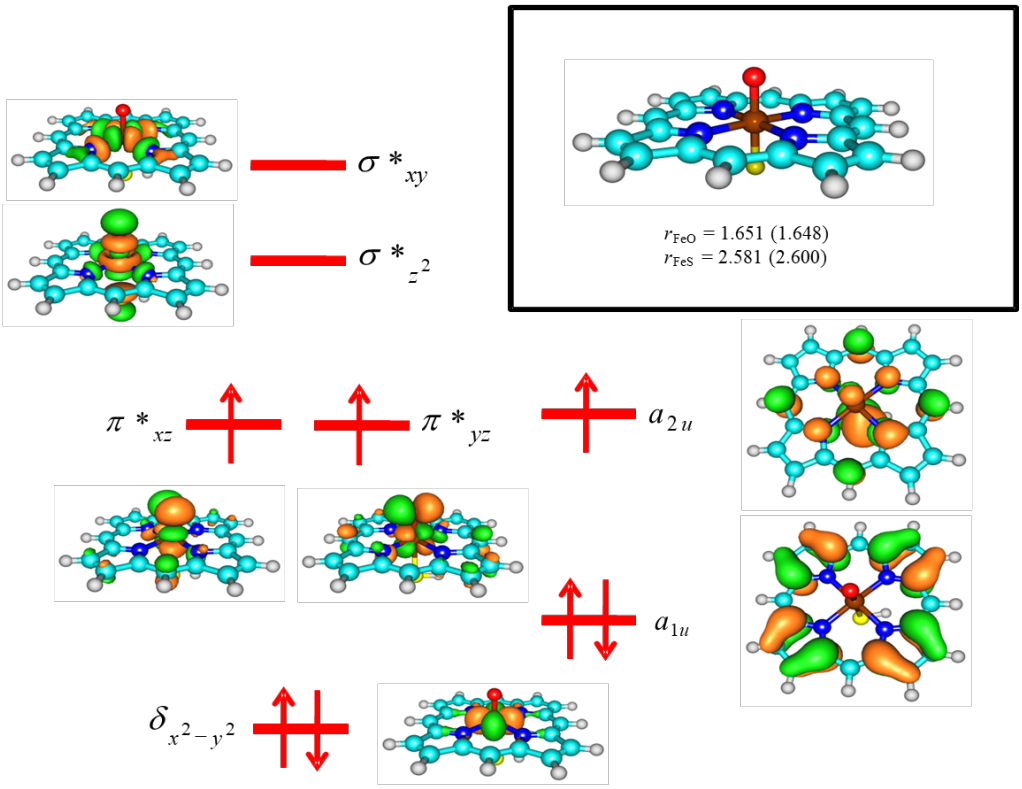

Figure 10: High-lying occupied and low-lying virtual orbitals of 4Cpd I. The inset gives the optimized geometry of 4,2Cpd I with bond lengths in angstroms.

As described above, the active species of the P450s is an iron(IV)-oxo heme cation radical species that is also known as Compound I (Cpd I). Cpd I has a characteristic electronic configuration with three unpaired electrons: two are in orthogonal π^*_{FeO} orbitals (labelled as π^*_{xz} and π^*_{yz}) while the third is in a heme-type π^* orbital with a_{2u} symmetry.[159,160] The latter orbital is known to mix with the axial ligand π-orbitals, and hence, its energy level is influenced by electron donating ligands.[161] In particular, a thiolate ligand of a cysteinate group gives strong mixing of the $3p_S$ orbital with the a_{2u} orbital that raises it in energy. This mixing was also shown to be dependent on environmental effects including donating hydrogen bonds toward thiolate.[161,162] The calculated geometry of Cpd I is shown in Figure 10 together with the key orbitals involved in the oxygen atom transfer reaction to substrates. Five of these orbitals originate from the metal 3*d* orbitals and the other two are π^*-type

porphyrin orbitals with a_{1u} and a_{2u} symmetry. Four electrons occupy the metal 3*d* set of orbitals: two reside into the nonbonding $\delta_x 2_{-y} 2$ orbital in the plane of the heme and two others are in a pair of almost degenerate π^*_{xz} and π^*_{yz} orbitals for the interactions of the $3d_{xz}/3d_{yz}$ iron orbitals with $2p_x/2p_y$ orbitals on oxygen. In a bare porphyrin ring ($PorH_2$) without the central metal ion, the a_{1u} and a_{2u} orbitals are degenerate,[163] but interactions of the a_{2u} with the axial thiolate ligand, raise it in energy. The overall electron configuration of Cpd I is $\delta_x 2_{-y} 2^2\ \pi^*_{xz}{}^1\ \pi^*_{yz}{}^1\ a_{1u}{}^2\ a_{2u}{}^1$ with a total of three unpaired electrons. Since, the interactions between the π^*_{xz}/π^*_{yz} and a_{2u} orbitals is small, the three unpaired electrons either couple to an overall doublet spin state ($\pi^*_{xz}{}^{\uparrow}\ \pi^*_{yz}{}^{\uparrow}\ a_{2u}{}^{\downarrow}$) or a quartet spin state ($\pi^*_{xz}{}^{\uparrow}\ \pi^*_{yz}{}^{\uparrow}\ a_{2u}{}^{\uparrow}$) that are very close in energy.[163] As a result Cpd I reacts with substrates via two-state-reactivity patterns on competing doublet and quartet spin state surfaces.[16,164] In the past we found examples, such as for substrate hydroxylation by *trans*-methylphenylcyclopropane, where the doublet spin mechanism is different from the one on the quartet spin state and consequently the two spin state surfaces give different reaction products.[165] Furthermore, two-state-reactivity was shown to affect and disturb kinetic isotope effects.

4.1.2 Chemical properties of Cpd I of peroxidases and catalases.

Most peroxidases in contrast to the P450s are heme enzymes that contain a histidine group in the axial position rather than a cysteinate residue, yet a tyrosinate group occupies that position in catalases. This, for a long time, was considered as the key chemical reason for the differences in biological function of these three classes of heme enzymes.[18,166,167] The biological function of peroxidases is to detoxify hydrogen peroxide to two water molecules, while catalases convert it to molecular oxygen and water. It has been proposed that a cysteinate axial ligand induces a “push”-effect of electron density toward the heme, whereas a histidine ligand withdraws electron density.[168,169] To understand the electron withdrawing/electron donating properties of the axial ligand and the effect this has on the catalysis of a substrate, we performed a series of DFT calculations on models of Cpd I of P450, horseradish peroxidase (HRP), cytochrome *c* peroxidase (C*c*P) and catalase (Cat).[163,170–172] Figure 11

displays optimized geometries of ^{4,2}Cpd I models of P450, HRP, C*c*P and Cat with relevant group spin densities (ρ) highlighted.

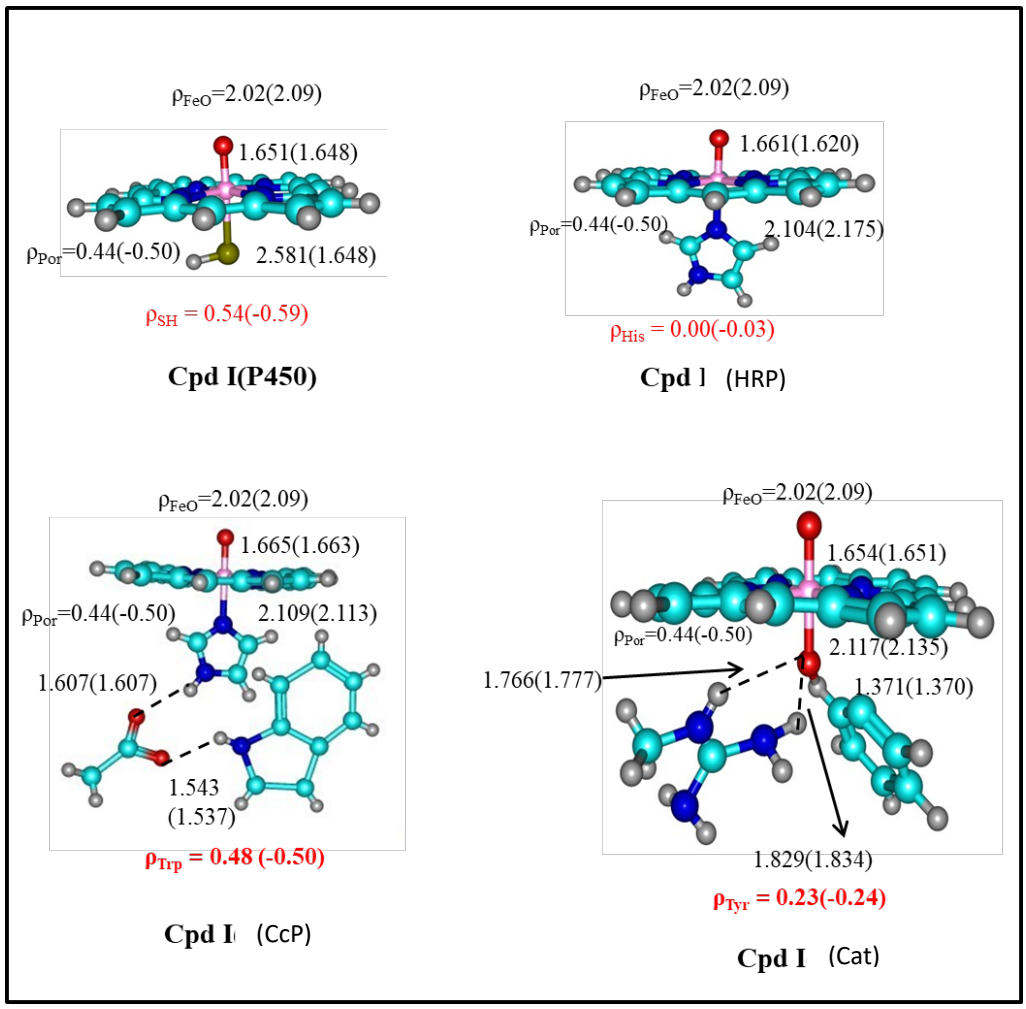

Figure 11: Optimized geometries of ^{4,2}Cpd I models of P450, HRP, CcP and Cat with bond lengths in angstroms and group spin densities (□) in atomic units. Data for the low-spin states are in parenthesis.

Geometrically, little variation is found in the iron(IV)-oxo distance in all Cpd I structures and generally the distance is about 1.66 Å in histidine ligated Cpd I, whereas it is slightly shorter in Cpd I systems with an anionic axial ligand. The group spin densities give a value of about 2 on the FeO group, which reflects single occupation of the π^*_{xz} and π^*_{yz} orbitals. In P450 Cpd I, the third electron is based in a mixed heme and axial ligand orbital as highlighted in Figure 12(*a*). Thus, the a_{2u} orbital mixes with a lone pair orbital (π_L, L = S) on the axial ligand along the O–Fe–S axis and splits into bonding and anti-bonding combination of orbitals ($a_{2u} + \pi_L$) and ($a_{2u} - \pi_L$). The former orbital is doubly occupied, whereas the anti-bonding orbital is destabilized in energy

and singly occupied. Since, this is the highest occupied molecular orbital (HOMO), the electron affinity of Cpd I(P450) is significantly reduced with respect to that of Cpd I(HRP), where this mixing does not occur.

The DFT model calculations on C*c*P Cpd I identify the electronic structure as a mixed state with partial unpaired spin density on the heme, in the a_{2u} orbital and partial single occupation of a tryptophan π-orbital, i.e. $\pi^*_{xz}{}^1\ \pi^*_{yz}{}^1\ a_{2u}{}^1\ \pi_{Trp}{}^2 \leftrightarrow \pi^*_{xz}{}^1\ \pi^*_{yz}{}^1\ a_{2u}{}^2\ \pi_{Trp}{}^1$.[170] In the gas-phase as well as in a solvent mimicked calculation, the energy differences between the two states are very small and hence a mixed state is found. To find out, whether environmental effects can change the ordering of these two states we added a point charge at a distance to our chemical system. Thus, a structurally close enzyme to C*c*P is ascorbate peroxidase (APX), which has a very similar heme active site that also contains a His-Asp-Trp triad, and the only difference in the structure appears to be a K^+ binding site at about 8 Å from the heme.[173] Experimental EPR studies on APX Cpd I, in contrast to those on Cpd I of C*c*P, identified the electronic state as a porphyrin radical rather than a Trp radical.

4.1.3 Aliphatic hydroxylation by P450 Cpd I.

Aliphatic hydroxylation is one of the most common chemical reactions catalyzed by the P450s as a means of detoxification of drugs and xenobiotics in the liver. As a result the P450s are well studied enzymes by the pharmacological industry.[174] Other P450 isozymes, such as the $P450_{BM3}$ isozymes, hydroxylate long-chain fatty acids stereospecifically and regioselectively.[175] Aliphatic C–H hydroxylation is a challenging reaction process, due to the fact that a strong C–H bond needs to be broken, Eq 11. Moreover, often the reaction takes place in a regioselective or stereospecific manner. As it is an important reaction in catalysis many studies have been performed to understand the catalytic mechanism, the origins of the regio- and stereoselectivity of the reaction, the nature of the by-products and predictions of chemical reactivity. However, as Cpd I is short-lived, experimental studies encounter difficulties. Computational modelling, therefore, can assist here and give insight into fast reaction processes of short-lived chemical intermediates.

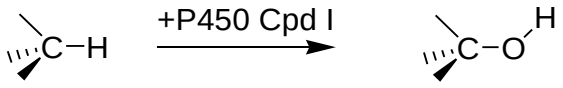

(11)

Technically, the aliphatic hydroxylation by Cpd I can start with a hydrogen atom abstraction, a proton abstraction or a hydride transfer from the substrate. We will start, however, with the most common reaction process that starts with a hydrogen atom abstraction, which essentially is the sum of a proton and electron transfer. In P450 chemistry the electron and proton transfer do not necessarily take place to the same site, so that different electromers can be formed after hydrogen atom abstraction from a substrate (SubH) to Cpd I, [Fe^{IV}=O(heme$^{+\bullet}$)], leading to either an iron(IV)-hydroxo heme or an iron(III)-hydroxo heme cation radical intermediate, Eqs 12 and 13. The reaction enthalpy for Eq 12 and 13 is $\Delta H_{HA,FeIV}$ and $\Delta H_{HA,FeIII}$, respectively.

$$[Fe^{IV}=O(heme^{+\bullet})] + SubH \rightarrow [Fe^{IV}(OH)(heme)] + Sub^{\bullet} + \Delta H_{HA,FeIV} \quad (12)$$

$$[Fe^{IV}=O(heme^{+\bullet})] + SubH \rightarrow [Fe^{III}(OH)(heme^{+\bullet})] + Sub^{\bullet} + \Delta H_{HA,FeIII} \quad (13)$$

Thus, the electron transfer from substrate to doublet or quartet Cpd I can lead to five low-lying radical intermediates (^{2,4}**I**), whereby the electron either fills the porphyrin hole (a_{2u} orbital) or fills the π^*_{xz} orbital with a second electron. Note that there are two isoelectronic doublet spin intermediates with the metal in the iron(III) oxidation state and electronic configuration $\pi^*_{xz}{}^2\ \pi^*_{yz}{}^{\uparrow}\ a_{2u}{}^{\downarrow}\ \phi_{Sub}{}^{\uparrow}$ (^{2}**I**$_{III}$) or $\pi^*_{xz}{}^2\ \pi^*_{yz}{}^{\uparrow}\ a_{2u}{}^{\uparrow}\ \phi_{Sub}{}^{\downarrow}$ (^{2}**I′**$_{III}$) with ϕ_{Sub} the orbital for the radical on Sub$^{\bullet}$. Table 1 gives an example of these five radical intermediates as calculated for hydrogen atom abstraction from propene by a Cpd I model.[176]

Table 1: Electronic configuration and relative energies of optimized geometries of radical intermediates (**I**) obtained after hydrogen atom abstraction from propene by P450 Cpd I.

Label	Electronic configuration	Orbital occupation	ΔE [a]
^{2}**I**$_{IV}$	[Fe^{IV}(OH)(heme)--Sub$^{\bullet}$]	$\pi^*_{xz}{}^{\uparrow}\ \pi^*_{yz}{}^{\uparrow}\ a_{2u}{}^2\ \phi_{Sub}{}^{\downarrow}$	0.0
^{4}**I**$_{IV}$	[Fe^{IV}(OH)(heme)--Sub$^{\bullet}$]	$\pi^*_{xz}{}^{\uparrow}\ \pi^*_{yz}{}^{\uparrow}\ a_{2u}{}^2\ \phi_{Sub}{}^{\uparrow}$	0.4

$^4\mathbf{I}_{III}$	[Fe^{III}(OH)(heme$^{+\bullet}$)--Sub$^{\bullet}$]	$\pi^*_{xz}{}^2\ \pi^*_{yz}{}^{\uparrow}\ a_{2u}{}^{\uparrow}\ \phi_{Sub}{}^{\uparrow}$	6.4
$^2\mathbf{I'}_{III}$	[Fe^{III}(OH)(heme$^{+\bullet}$)--Sub$^{\bullet}$]	$\pi^*_{xz}{}^2\ \pi^*_{yz}{}^{\uparrow}\ a_{2u}{}^{\uparrow}\ \phi_{Sub}{}^{\downarrow}$	6.4
$^2\mathbf{I}_{III}$	[Fe^{III}(OH)(heme$^{+\bullet}$)--Sub$^{\bullet}$]	$\pi^*_{xz}{}^2\ \pi^*_{yz}{}^{\uparrow}\ a_{2u}{}^{\downarrow}\ \phi_{Sub}{}^{\uparrow}$	9.9

[a] Energies in kcal mol^{-1} calculated at UB3LYP/BS2 and taken from Ref 176.

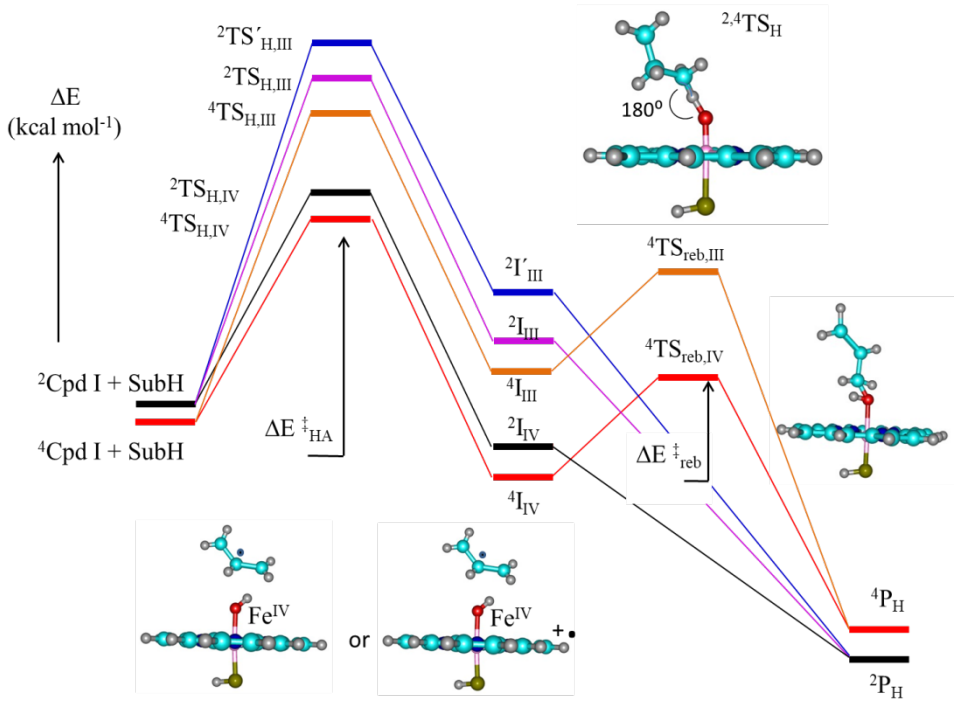

Figure 12: Typical two-state-reactivity potential energy profile for substrate hydroxylation by P450 Cpd I on competing doublet and quartet spin states and passing possible radical intermediate electromers.

Figure 12 displays a typical multistate-reactivity profile for aliphatic hydroxylation of a model substrate (propene) on competing doublet and quartet spin states.[176] The overall reaction mechanism starts from the degenerate doublet and quartet spin states of Cpd I and via an initial hydrogen atom abstraction followed by hydroxyl rebound to the radical restgroup gives 1-propenol products. Essentially, computation identified five low-lying reaction profiles via any of the $\mathbf{I}_{IV}$ or $\mathbf{I}_{III}$ intermediates. Obviously, these five radical intermediates connect to reactants via five different hydrogen atom abstraction barriers $\mathbf{TS}_H$. Radical rebound encounters significant barriers on the quartet spin state surface ($\mathbf{TS}_{reb}$), but is virtually barrierless on the low-spin surface. Nevertheless, the low-spin radical intermediates are local minima with real

frequencies only, but due to the small rebound barriers these states will have short lifetimes and collapse to the product complexes (^{2}**P**) spontaneously. By contrast, the quartet spin mechanisms have large barriers that will determine their lifetime during which the radical restgroup can undergo rearrangement leading to either by-products or stereochemical scrambling. These rearrangement patterns are not possible on the doublet spin state surface, hence the two spin state surfaces occasionally give differences in product distributions. The rebound barrier tend to be higher in energy for ^{4}**TS**$_{reb,III}$ than for ^{4}**TS**$_{reb,IV}$, since a double electron transfer takes place on the iron(III) surface. Thus, the quartet spin product (^{4}**P**) has orbital occupation $\pi^*_{xz}{}^{\uparrow}$ $\pi^*_{yz}{}^{\uparrow}$ $\sigma^*_z2^{\uparrow}$ $a_{2u}{}^2$, so that the process from ^{4}**I**$_{IV}$ will lead to electron transfer from substrate into the σ^*_z2 orbital, whereas the one starting from ^{4}**I**$_{III}$ gives an α-spin electron transfer from substrate to σ^*_z2 and a β-spin electron transfer from π^*_{xz} to a_{2u}. Because of this difference, the rebound barrier from ^{4}**I**$_{III}$ is larger than that for ^{4}**I**$_{IV}$, and consequently more rearrangement is expected on the quartet spin iron(III) surface.

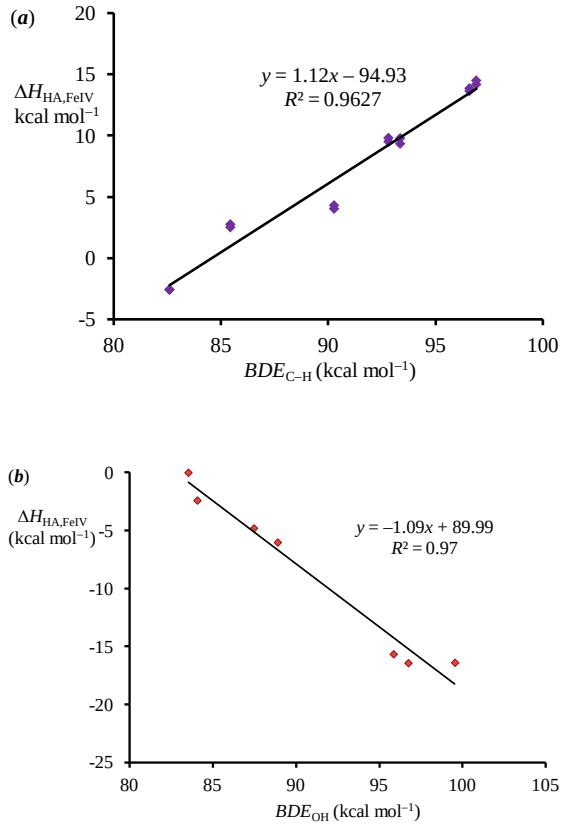

Figure 13: Hydrogen atom abstraction energy by Cpd I(P450) to form IIV intermediates as a function of (a) BDEC–H and (b) BDEO–H.

Let us in the following attempt to generalize and explain the energetics of the processes in Figure 12 and the corresponding reaction barriers. As shown in Eq 12 – 16 the reaction enthalpy for hydrogen atom abstraction is dependent on the strength of the C–H bond of the substrate that is broken or bond dissociation energy of the C–H bond ($BDE_{C–H}$) as well as on the strength of the O–H bond in the iron(IV)-hydroxo complex that is formed ($BDE_{O–H}$). The reaction enthalpy for the iron(IV)-process, therefore, can be written as the difference between $BDE_{C–H}$ and $BDE_{O–H}$.[177–179] This implies that the reaction energy from reactants to form $^4\mathbf{I}_{IV}$ should correlate with both $BDE_{C–H}$ and $BDE_{O–H}$. For the hydrogen atom abstraction from a range of substrates by a $^4[Fe^{IV}=O(Por^{+\bullet})SH]$ model of P450 Cpd I with Por = bare porphyrin ring without side chains, we plot the reaction enthalpy to form $^4\mathbf{I}_{IV}$ as a function of the calculated $BDE_{C–H}$ value of each substrate in Figure 13(*a*). As follows from Figure 13(*a*) the reaction enthalpy correlates linearly with $BDE_{C–H}$ and the correlation coefficient R^2 is close to unity. This implies that the standard deviation of the calculations is very small (within a few kcal mol^{-1}) and that indeed $\Delta H_{HA,FeIV}$ correlates with $BDE_{C–H}$ as predicted by Eq 16. The slope of the trend, however, deviates slightly from unity, probably because entropic effects were not taken into consideration in the calculations.

$$SubH \rightarrow Sub^{\bullet} + H^{\bullet} + BDE_{C–H} \quad (14)$$

$$[Fe^{IV}(OH)(heme)] \rightarrow [Fe^{IV}=O(heme^{+\bullet})] + H^{\bullet} + BDE_{O–H} \quad (15)$$

$$\Delta H_{HA,FeIV} = BDE_{C–H} - BDE_{O–H} \quad (16)$$

Subsequently, we calculated the hydrogen atom abstraction from propene by a range of iron(IV)-oxo species with either heme or nonheme ligand systems including a series of $[Fe^{IV}=O(Por^{+\bullet})X]$ intermediates with X = variable axial ligand.[180] A plot of the obtained $\Delta H_{HA,FeIV}$ enthalpies versus $BDE_{O–H}$ of these iron(IV)-oxo oxidants is given in Figure 14(*b*). As follows also the trend of $\Delta H_{HA,FeIV}$ against $BDE_{O–H}$ is linear with a correlation coefficient of $R^2 = 0.97$ and confirms the prediction made by Eq 14.

The Polanyi principle,[181] states that barrier heights of a chemical reaction are often proportional to the driving force of a reaction. Consequently for a

hydrogen atom abstraction from a substrate by Cpd I, the barrier height ($\mathbf{TS}_{H}$) should be proportional to ΔH_{HA} and also to either $BDE_{C–H}$ or $BDE_{O–H}$. In order to test this, two sets of calculations were performed. Firstly, for a model of P450 Cpd I the hydrogen atom abstraction of a range of substrates was calculated. Secondly, the aliphatic hydroxylation of propene was calculated for a set of iron(IV)-oxo species. These two sets of calculations aimed to correlate the barrier height of hydrogen atom abstraction against either $BDE_{C–H}$ or $BDE_{O–H}$.

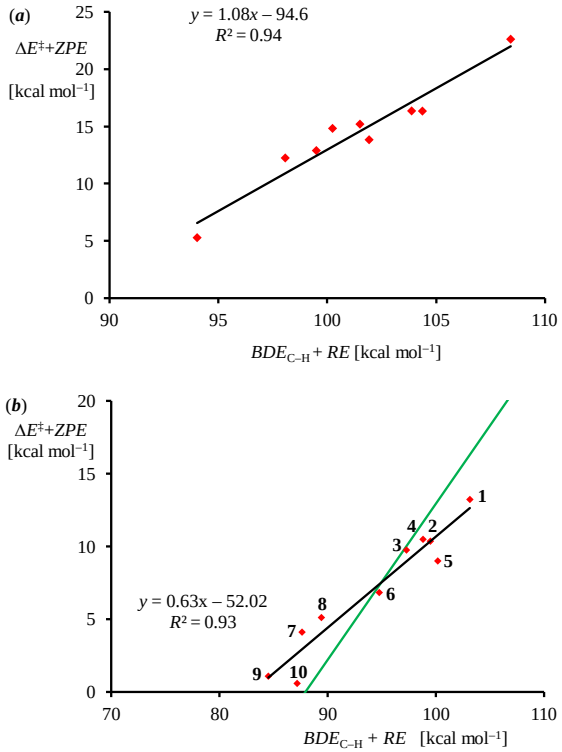

Figure 14: Trends of calculated hydrogen atom abstraction barrier height of an aliphatic group by an iron(IV)-oxo species versus the BDEC–H value of the substrate: (a) Using [Fe^{IV}=O(Por+•)SH] as an oxidant. (b) Using [Fe^{IV}=O(Cor+•)] as an oxidant. The green line in panel (b) gives the trend of panel (a).

In a first set of experiments we took one oxidant, [Fe^{IV}=O($Por^{+\bullet}$)SH] and calculated the hydrogen atom abstraction reaction of a set of substrates: methane, ethane, propane, propene, toluene, ethylbenzene, *trans*-methylphenylcyclopropane, *trans*-*i*-propylphenylcyclopropane, *N*,*N*-dimethylaniline and camphor. The hydrogen atom abstraction barrier was subsequently correlated to $BDE_{C–H}$ in Figure 14.[155,182] More recently, we also

calculated similar trends for [Fe^{IV}=O(corrole$^{+\bullet}$)],[183] displayed in Figure 15(*b*), and a model of the iron(IV)-oxo species of taurine/α-ketoglutarate dioxygenase (see section 4.4) and found similar trends. A corrole group resembles a porphyrin group but misses one of the *meso*-CH bridges and hence has overall charge –3 rather than –2. Because of this corroles are highly suitable ligand systems to stabilize transition metals in high oxidation states, such as Mn^{V} or Fe^{IV}. These figures give the $BDE_{C–H}$ energy corrected for the resonance energy of the substrate (*RE*), which reflects the distortions of the original substrate geometry in the transition state.[182] As can be seen from Figure 14 the hydrogen atom abstraction barrier correlates linearly with the strength of the C–H bond that is broken as predicted and found for experimentally observed trends by Bordwell, Mayer and their co-workers.[178,180]

As mentioned above substrate hydroxylation is a two step process with an initial hydrogen atom abstraction that is followed by OH rebound to Sub$^{\bullet}$ to form alcohol products. However, in some situations the latter step is replaced by a second hydrogen atom abstraction to give water and dehydrogenated substrate, such as an olefin or a ring-closure process. Technically, the dehydrogenation reaction competes with the hydroxylation reaction and the regioselectivity of these processes will be determined by the relative energies of the rebound *versus* dehydrogenation barriers.[184] Scheme 1 explains the competitive reaction mechanisms leading to alcohol and olefin products from aliphatic groups. Thus, both reactions start with a hydrogen atom abstraction from the substrate to form a radical intermediate. For simplicity we only show the iron(IV)-hydroxo intermediate in Scheme 1. Rebound of the OH group gives alcohol products with exothermicity $\Delta H_{reb,IV}$, but a second hydrogen atom abstraction from the substrate by the iron(IV)-hydroxo intermediate gives olefin and water products with reaction enthalpy $\Delta H_{dehydro}$.

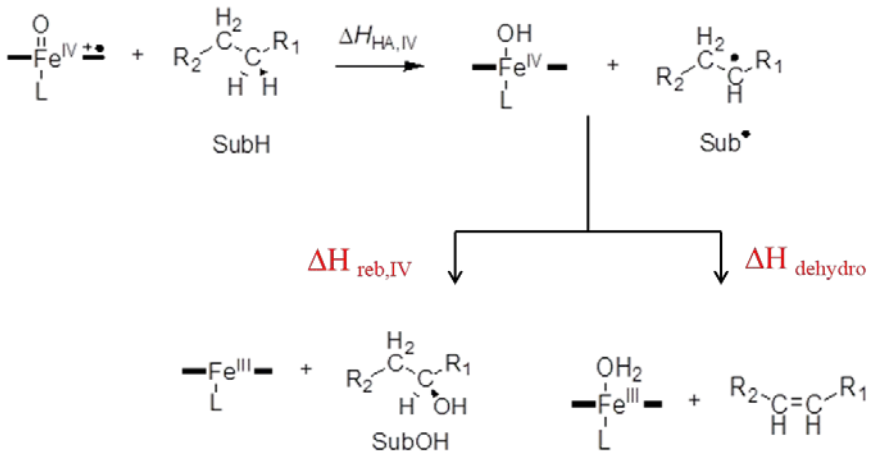

Scheme 1: Reaction mechanisms of Cpd I with alkanes leading to alcohol and olefin products.

Thermodynamically, the rebound barrier involves the breaking of the Fe^{IV}–OH bond in the radical intermediate and the formation of the Sub–OH bond. We calculated a value of 30.2 kcal mol^{-1} to break the Fe^{IV}–OH bond in the iron(IV)-hydroxo intermediate.[184] The bond dissociation energy of the C–O bond in the alcohol is defined as BDE_{COH} and we calculated this for a selection of substrates (Table 2). The bond is strong for aliphatic molecules such as ethane, *trans*-butane and cyclohexane, but is much weaker for olefins such as cyclohexene and cyclohexadiene. The dehydrogenation energy depends on the energy to break a C–H bond in Sub$^{\bullet}$ ($BDE_{C2–H}$) and the formation of an O–H bond to form water for which we calculated a value of 70.8 kcal mol^{-1} in $Fe^{III}(H_2O)$(heme). The values of $BDE_{C2–H}$ were calculated for a selection of substrates and are also given in Table 2.

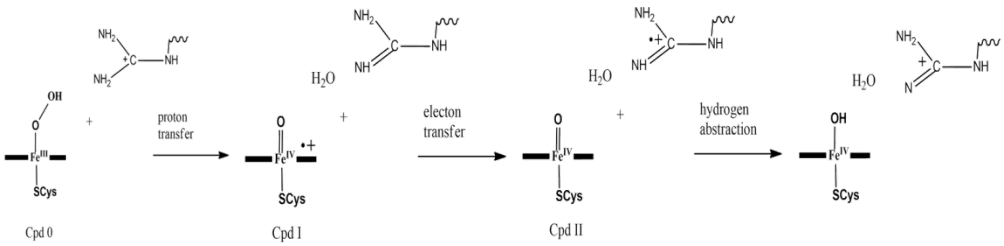

Scheme 2: Reaction mechanism of arginine hydroxylation by NOS enzymes as established by DFT.

Table 2: Calculated BDEs and reaction enthalpies for the reactions from Scheme 2.[a]

Substrate	BDE_{C-H}	$\Delta H_{HA,IV}$	BDE_{C2-H}	$\Delta H_{dehydro}$	BDE_{COH}	$\Delta H_{reb,IV}$
ethane	96.2	9.5	36.7	–34.0	85.8	–55.5
trans-butane	92.6	5.9	33.5	–37.3	85.4	–55.2
cyclohexane	93.0	6.4	33.6	–37.2	85.8	–55.6
cyclohexene	77.7	–9.0	47.5	–23.3	69.1	–38.9
cyclohexadiene	69.0	–17.6	21.8	–49.0	59.7	–29.5

[a] All values are in kcal mol^{-1} and taken from Ref 184.

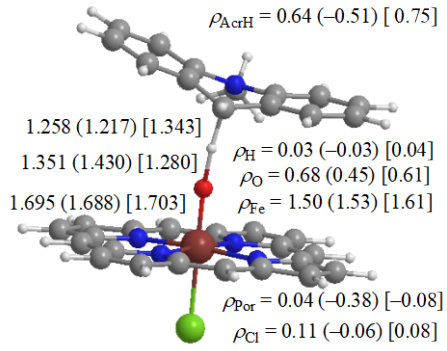

Figure 16: Optimized geometries of hydride transfer and hydrogen atom abstraction barriers from $AcrH_2$ by [Fe^{IV}=O(Por+•)Cl] with bond lengths in angstroms and group spin densities in atomic units.

Using these BDE values we then calculated reaction enthalpies for radical rebound and dehydrogenation from the iron(IV)-hydroxo complex and $Sub^{\bullet}$

and report these values in Table 2. As follows, for aliphatic substrates the rebound exothermicity is large mainly due to the formation of a strong C–O bond. With cyclohexene and cyclohexadiene the C–O bond formation is much lower. However, with cyclohexadiene the second hydrogen atom abstraction costs little energy, and, in addition, the formed product is benzene, which has considerable aromatic stabilization. By contrast, olefins formed from aliphatic groups do not have this resonance stabilization and hence have much lesser reaction exothermicities for dehydrogenation. As a consequence, cyclohexadiene will react with Cpd I by formation of benzene products through a dehydrogenation reaction, whereas linear alkanes give alcohol products instead. In principle, the reaction of Cpd I with an aliphatic group can lead to either hydrogen atom abstraction, proton transfer or hydride transfer. For the substrates discussed above only a hydrogen atom abstraction was observed, which was seen to be a separate electron and proton transfer to a different site, although the two events were found to be taking place during the same rate determining transition state. In the final paragraphs of this section we will give two examples of different reactivities. Firstly, we will give an example of a hydride transfer by Cpd I from a substrate with weak C–H bond strength, i.e., 10-methyl-9,10-dihydroacridine ($AcrH_2$). Secondly, we encountered a system, namely of the active site of nitric oxide synthase (NOS), where the reaction starts off with an initial electron transfer followed by a hydrogen atom abstraction.

The reaction of $[Fe^{IV}=O(Por^{+\bullet})Cl]$ with $AcrH_2$ was calculated with DFT methods and established a stepwise mechanism.[185] However, three barriers were located for the initial reaction step (Figure 16): $^{2,4}\mathbf{TS}_{H,HT}$ leading to a hydride transfer intermediate with orbital occupation $\delta_x 2_{-y} 2^2\ \pi^*_{xz}{}^2\ \pi^*_{yz}{}^1\ a_{2u}{}^2$ in the doublet spin state and $\delta_x 2_{-y} 2^2\ \pi^*_{xz}{}^1\ \pi^*_{yz}{}^1\ \sigma^*_z 2^1$ in the quartet spin state and configuration $[Fe^{III}(OH^-)(Por)Cl\text{---}AcrH^+]$. The third transition state ($^4\mathbf{TS}_{H,HA}$) is a hydrogen atom abstraction transition state similar to those discussed above that gives an iron(IV)-hydroxo radical intermediate. Thus, the hydride transfer transition states are substantially lower in energy than the hydrogen atom abstraction barrier. Furthermore, the cationic intermediates are also much lower in energy than the radical intermediates in this system.

However, although the overall reaction from reactants to intermediates implicates a hydride transfer step, actually, the charge and group spin densities in the $^{2,4}\mathbf{TS}_{H,HT}$ structures associate them as hydrogen atom abstraction barriers instead. In particular, the AcrH restgroup has considerable amount of unpaired spin density in all three transition states. Consequently, the hydride reaction step in the mechanism actually is a hydrogen atom transfer followed by a separate electron transfer. The hydrogen atom transfer then takes place in the transition states ($^{2,4}\mathbf{TS}_{H,HT}$), which are followed by an electron transfer en route from the transition state to the cationic intermediate. Replacement of the iron(IV) atom in Cpd I by manganese(V) gave similar reaction mechanisms of hydride versus hydrogen atom transfer reactions.[186]

Closely related to the P450 enzymes are the nitric oxide synthases (NOSs), which are involved in the biosynthesis of NO in the body. NO has diverse functions in the body, but due to its high reactivity it needs to be created close to the source where it is needed to avoid accidental damage. In the body NO functions as a neuronal messenger, and participates in blood pressure control and heart rate. NOS enzymes take one molecule of arginine and convert it to L-citrulline and NO through the use of two molecules of molecular oxygen on a heme centre. For a long time, it has been believed that the catalytic mechanism of the first step, i.e. the conversion of L-arginine into N^{ω}-L-hydroxy-arginine happens via a P450-type mechanism with an initial hydrogen atom abstraction followed by radical rebound. In order to understand its mechanism we did a series of DFT calculations on an active site model.[187,188] The calculations show that in the gas-phase protonated arginine substrate initially functions as a proton donor in the catalytic cycle, which can shuttle protons from the solvent to the iron(III)-superoxo and iron(III)-hydroperoxo (Cpd 0) intermediates. This eventually generates Cpd I and a neutral arginine residue. Test calculations for hydrogen atom abstraction or proton abstraction from protonated arginine by Cpd I revealed high energy barriers, and, therefore was ruled out as a possible mechanism. Neutral arginine transfers an electron to Cpd I rapidly in the gas phase to form Cpd II and ionized arginine. A hydrogen atom abstraction by Cpd II followed by OH rebound then gives N^{ω}-L-hydroxy arginine products.

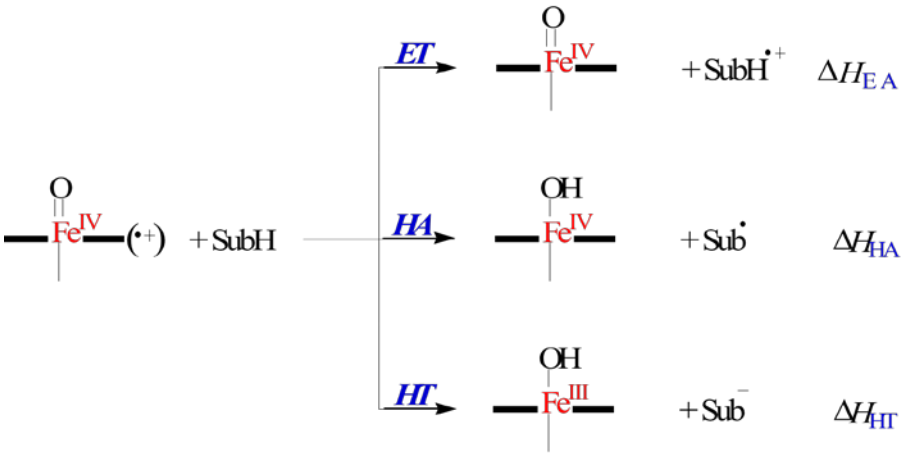

Figure 17: Possible reaction mechanisms between Cpd I and a substrate leading to electron transfer (ET), hydrogen atom abstraction (HA) and hydride transfer (HT).

In order to understand the reactivities of Cpd I with substrates and the possible mechanisms, i.e. electron transfer, hydrogen atom abstraction or hydride transfer, consider in Figure 17 the energetics for the individual processes. Thus, in a reaction where hydride transfer is preferential over hydrogen atom abstraction the reaction enthalpy ΔH_{HT} should be larger than ΔH_{HA}. Based on the strength of the C–H bond in the substrate and the electron affinity of Cpd I one can derive that the difference in enthalpy between hydrogen atom abstraction and hydride transfer is exactly equal to the electron affinity of a hydrogen atom minus the ionization potential of the hydrogen abstracted substrate (Sub):[185]

$$\Delta H_{HT} - \Delta H_{HA} > EA_H - IE_{Sub} \quad (18)$$

4.1.4 Olefin epoxidation by P450 Cpd I.

Olefin epoxidation is a common process catalyzed by P450 enzymes and, for instance, in the body takes place on unsaturated fatty acids in the liver,[189] whereas in cockroaches the epoxidation of methyl farnesoate by a P450 isozyme leads to the biosynthesis of a vital hormone.[190] A stepwise mechanism for substrate epoxidation by P450 Cpd I was established (Figure 18) with an initial C–O bond formation step to form a radical intermediate followed by a ring-closure barrier leading to epoxide products.[156] During the life-time of the radical intermediate stereochemical scrambling can occur leading, e.g., to *cis*-

epoxides from *trans*-olefins.[157] Furthermore, rearrangement patterns have been calculated leading to aldehyde and suicidal products via spin-state crossings from radical to cationic intermediates.[157,191,192] The features of the mechanism resemble that of aliphatic hydroxylation closely and were described as a stepwise process via a radical intermediate. As an example of a typical substrate epoxidation potential energy profile we present in Figure 19 the 1-butene epoxidation by ^{4,2}Cpd I of P450 as calculated with DFT.[145] In this study the geometries were optimized with a relatively large basis set, but despite this the energies were only a fraction different from those observed with UB3LYP/B1//UB3LYP/B2, hence the large basis set is not necessary for the geometry optimization itself. The potential energy profile resembles that of Figure 13 above and also can take place via either an iron(IV)(heme) or iron(III)(heme$^{+\bullet}$) radical intermediates, although we only give the low-lying iron(IV) structures here. Calculations on propene epoxidation by P450 Cpd I showed the mechanisms leading to iron(III) intermediates to be higher in energy by several kcal mol^{-1}, at least in the gas phase.[176] Ring closure of the epoxide ring leads to the product complexes and again the low-spin mechanism is virtually barrierless, whereas on the high-spin surface a small barrier (**TS**$_{rc}$) separates the radical intermediates from products. During the lifetime of the high-spin radical intermediate rearrangement patterns are possible leading to stereochemical scrambling. In addition, an internal electron transfer can take place to form two possible cationic intermediates; one that connects to suicidal intermediates and the other to aldehyde products.[157,191,192] The suicidal complexes originate from attack of the cationic site in Fe^{III}–OCH_2–CH^+–R onto a nitrogen atom of the porphyrin ring, which leads to a Fe–O–C–C–N five-membered ring. In enzymology these complexes have been detected and are called suicidal complexes as the formation of this highly stable complex destructs the activity of the heme.[193] We identified the cationic intermediate leading to these suicidal complexes as ^{4}**I**$_{III,cat,xy}$ with orbital occupation $\delta^2\ \pi^*_{xz}{}^1\ \pi^*_{yz}{}^1\ \sigma^*_{xy}{}^1\ a_{2u}{}^2\ \phi_R{}^0$.[157] An alternative cationic intermediate ^{4}**I**$_{III,cat,z2}$ with orbital occupation $\delta^2\ \pi^*_{xz}{}^1\ \pi^*_{yz}{}^1\ \sigma^*_z 2^1\ a_{2u}{}^2\ \phi_R{}^0$ was found to lead to a 1,2-hydrogen atom shift and the formation of aldehyde products.[191]

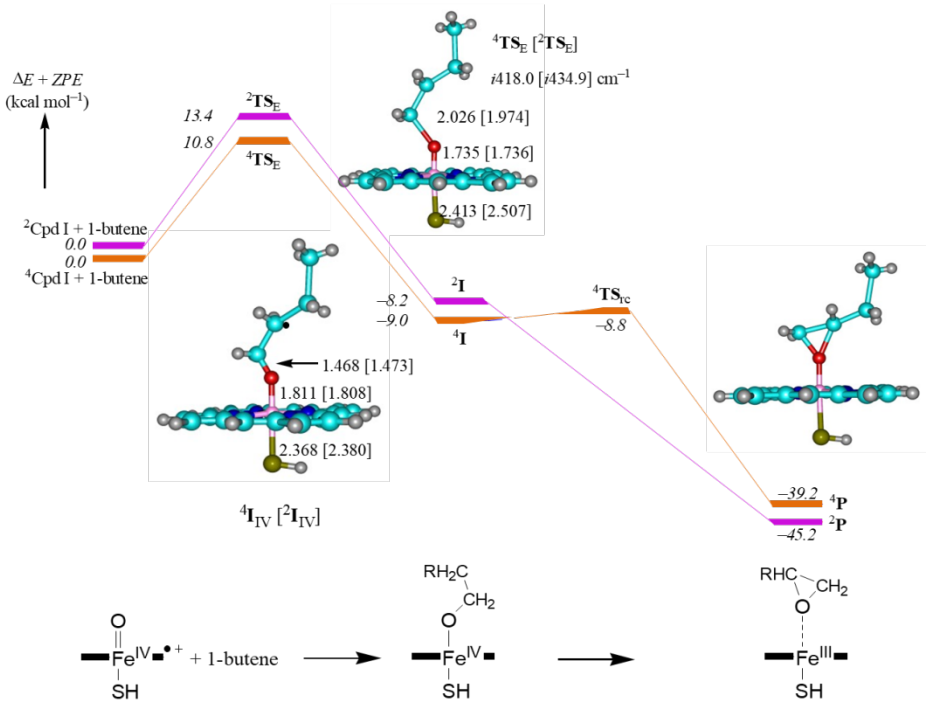

Figure 18: DFT calculated potential energy profile of 1-butene epoxidation by a Cpd I model. Bond lengths are in Ångstroms and relative energies in kcal mol–1. Data taken from Ref 145.

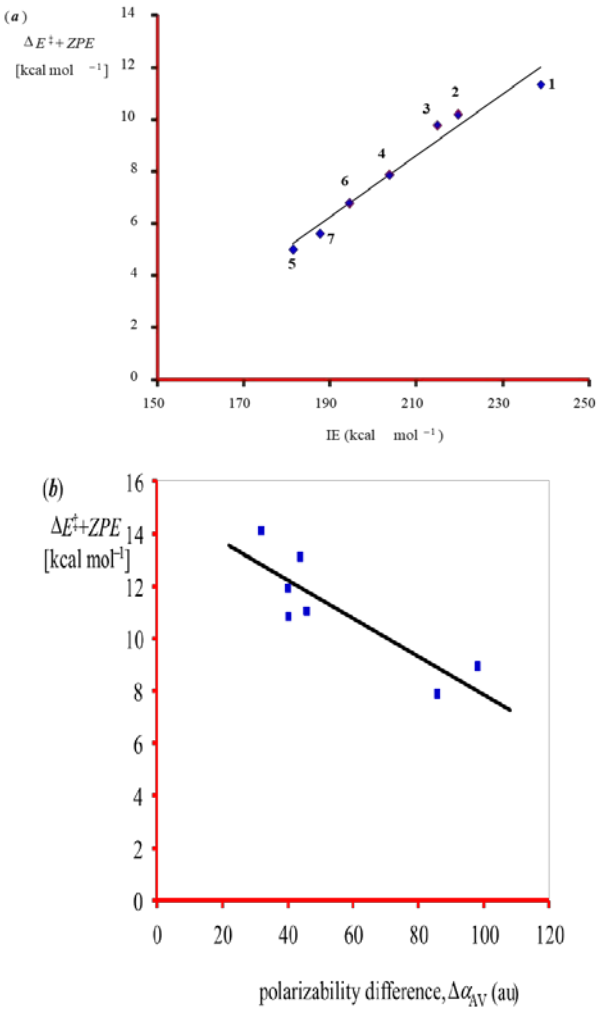

Figure 19: DFT calculated epoxidation barrier heights by Cpd I with a selection of substrates as a function of (a) the ionization potential of the substrate and (b) the polarizability change for the reaction. Data from Ref 145.

Subsequently, we investigated the intrinsic chemical properties of the oxidant and substrate that determine the barrier height or rate constant of olefin epoxidation. We first investigated olefin epoxidation by ^{4,2}Cpd I of P450 using a selection of substrates: ethene, propene, 1-butene, *trans*-2-butene, 1,3-cyclohexadiene, 1,4-cyclohexadiene and styrene. In a second set of calculations we took one substrate (propene) and varied the oxidant; this study included [Fe^{IV}=O($Por^{+\bullet}$)X] models with varying axial ligand X, as well as some nonheme iron(IV)-oxo complexes.[145] As the olefin epoxidation starts with the formation of a C–O bond and the transfer of an electron from the substrate into the a_{2u} molecular orbital, we attempted to correlate the barrier height ^{4,2}**TS**$_E$ with the ionization energy (IE) of the olefin. Figure 19 displays

the obtained correlation between epoxidation barrier height of olefins by ^{4}Cpd I(P450) as a function of IE. As follows a linear trend is observed that confirms that the rate constant is proportional to the ionization potential of the substrate. Recently, we showed that polarizability volume is a thermodynamic variable and is included in the van der Waals constants *a* and *b*.[194–196] To test if the barrier height of the reaction is proportional to the polarizability change from reactants to transition states, we extracted values of polarizability volume from the calculations and calculated the average value from the trace over α_{xx}, α_{yy} and α_{zz}. As follows from Figure 19(*b*) the polarizability volume correlates linearly with the barrier height, whereby the chemical system that undergoes the largest change in polarizability volume gives the lowest reaction barrier.

In a second set of calculations we investigated the properties of the oxidant in the epoxidation reaction process. We took one substrate (propene) and calculated its epoxidation by a set of iron(IV)-oxo complexes. Since, the epoxidation reaction is accomplished by the breaking of a π-bond in the substrate and the simultaneous formation of a C–O bond, we reasoned that the barrier height should correlate with the strength of the π-bond of the substrate that is broken and the strength of the C–O bond that is formed. The breaking of the π-bond, i.e. conversion of the double bond into a single bond, is essentially achieved upon ionizing the substrate as the π-orbital of the olefinic bond in most olefins is the HOMO. Indeed, the results in Figure 19 confirm a correlation between barrier height of substrate epoxidation with the ionization energy of the substrate. Subsequently, we mimicked the formation of the C–O bond between oxidant and substrate by the formation of an H–O bond. Thus, if the formation of a C–O bond is proportional to the formation of a H–O bond and the substrate encounters little stereochemical interactions with the oxidant then the $BDE_{O–H}$ value of the oxidant should correlate with the epoxidation barrier height for a range of oxidants. Our calculations indeed confirmed this for a range of iron(IV)-oxo complexes.[145]

4.1.5 Sulphoxidation reaction by P450 Cpd I.

Heteroatom oxidation, such as sulphoxidation and phosphorylation, are processes performed by P450 enzymes, for example in the biodegradation of neuroleptic drugs in the liver.[197] We studied the mechanism and detail and established a concerted, one-step, mechanism of heteroatom attack on the oxo group of Cpd I.[65,66,198–200] Experimental enzymology studies established a correlation between the rate constant of substrate sulphoxidation by P450 enzymes as a function of the substrate IE,[201] which was supported by a series of test calculations of sulphoxidation reactions catalyzed by Cpd I on a range of sulphides.[199] Since, both substrate epoxidation and sulphoxidation correlate with the IE of the substrate, these studies implicate that the regioselectivity of olefin epoxidation versus sulphide oxidation will be dependent on the nature of the substrate and can only be changed by external perturbations, such as in the substrate binding pocket that position the substrate for activation by Cpd I.

4.1.6 Rearrangement patterns in aliphatic hydroxylation reactions by P450 Cpd I.

Only recently P450 Cpd I was isolated and characterized as the active species in substrate hydroxylation reactions. Until that time studies were focused on establishing indirect evidence of its activity. A common method of this used, so-called, radical clock substrates.[58,61] From the kinetics of the reaction mechanism, it is believed that the lifetime of radical intermediates can be calculated. Thus, these P450 Cpd I reacts with the radical clock substrates via an initial hydrogen atom abstraction leading to a radical intermediate (Scheme 3) similarly to what was discussed in the previous section. During the lifetime of this intermediate, however, a rearranged may occur in the radical rest group Sub$^{\bullet}$. For instance, P450 Cpd I reacts with the radical clock substrate *trans*-methylphenylcyclopropane via aliphatic hydrogen atom abstraction from the methyl group. Rebound of the hydroxo group then gives the substrate with hydroxylated methyl group as unrearranged product (*U*) with rate constant $k_{reb,U}$. However, during the lifetime of the radical intermediate a ring-opening can take place with a rearrangement rate constant k_r, so that the subsequent

rebound with rate constant $k_{reb,R}$ leads to 4-hydroxo-4-phenyl-but-1-ene or rearranged products (*R*) instead. The product ratio [*U*/*R*] was used to experimentally determine the lifetime of the radical intermediate.[58] However, the obtained values were too short and a second-oxidant hypothesis was proposed to explain the observed trends, whereby Cpd 0 and Cpd I were considered as competing oxidants in the reaction mechanism.

To gain insight into the intricate details of the reaction mechanism, we performed a detailed DFT set of calculations on *trans*-methylphenylcyclo-propane hydroxylation by P450 Cpd I.[165,208,209] Figure 24 shows the calculated potential energy profile of the reaction leading to unrearranged and rearranged products. The initial mechanism is similar to that shown above in Figure 13 and starts with competing hydrogen atom abstraction barriers ($\mathbf{TS}_{H}$) on the doublet and quartet spin state surfaces leading to an iron(IV)-hydroxo intermediate with unrearranged radical rest group ($^{4,2}\mathbf{I}_{U}$). Radical rebound to form unrearranged products ($\mathbf{P}_{U}$) encounters a small barrier on the quartet spin state ($^{4}\mathbf{TS}_{reb,U}$) of 2.2 kcal mol^{-1} but is barrierless on the low-spin surface. The radical rest group in $^{4,2}\mathbf{I}_{U}$ can undergo a ring-opening to form the rearranged radical intermediate $^{4,2}\mathbf{I}_{R}$ via a barrier ($\mathbf{TS}_{rearr}$) of about 0.2 kcal mol^{-1} on the doublet as well as quartet spin state. The rearranged radical intermediate is considerably lower in energy than its unrearranged isomer and via subsequent radical rebound barriers ($\mathbf{TS}_{reb,R}$) it collapses to the rearranged product complexes ($^{4,2}\mathbf{P}_{R}$). As can be seen from Figure 24 the low-spin pathway has a lower radical rebound process then rearrangement barrier, so that the dominant pathway will lead to unrearranged products. By contrast, the high-spin unrearranged intermediate has lower rearrangement barrier than rebound barrier, hence the quartet spin profile will lead to dominant rearranged products instead. Therefore, the radical clock reaction mechanism gives an example of spin-state selective reactivity with different products on the doublet and quartet spin surfaces.

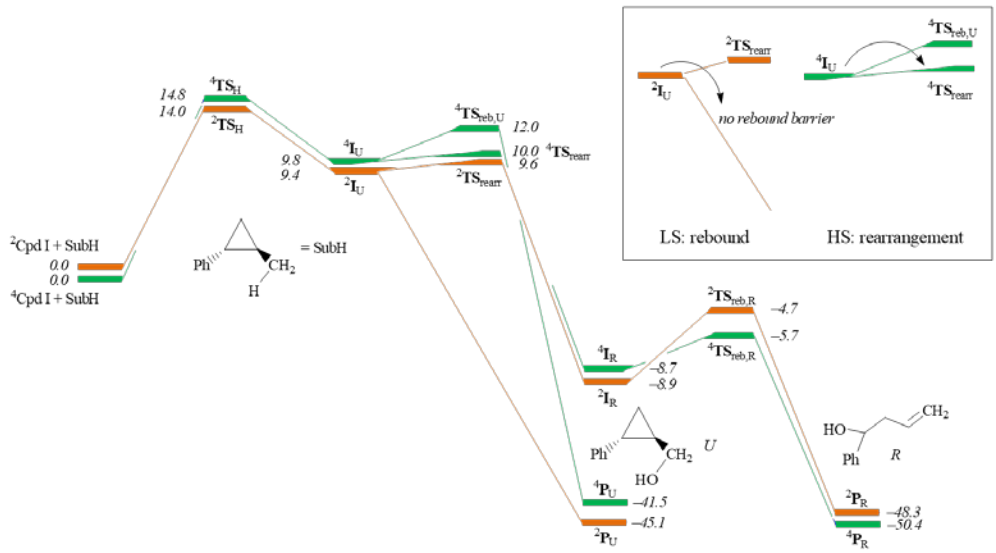

Figure 20: Potential energy profile for trans-methylphenylcyclopropane hydroxylation by P450 Cpd I leading to unrearranged (U) and rearranged (R) products. Energies are in kcal mol–1 and taken from Ref 208.

Experimental studies determined kinetic isotope effects (KIE) by replacement of the methyl hydrogen atoms by deuterium atoms and using the *U*/*R* product ratio a product isotope effect (PIE) was calculated.[58] In response to this we decided to calculate the KIEs for unrearranged and rearranged pathways and find the origin of the PIE values. Based on the mechanism in Figure 20 it can be envisaged that the KIE value for the unrearranged pathway originated from the low-spin surface and the KIE value for the rearranged mechanism from the high-spin surface, Eq 19.

$$\mathrm{PIE}(U/R) = \mathrm{KIE}(U)/\mathrm{KIE}(R) = \mathrm{KIE(LS)/KIE(HS)} \qquad (19)$$

DFT calculations established KIE values using the semiclassical Eyring equation (Eq 20) using 298 K free energies of activation ($\Delta G^{\ddagger}$) of the reaction using hydrogen and deuterium-substituted substrates. In Eq 20 the temperature is given by T and R is the gas constant.

$$\mathrm{KIE}_{\mathrm{Eyring}} = \exp[(\Delta G^{\ddagger}_{\mathrm{D}} - \Delta G^{\ddagger}_{\mathrm{H}})/RT] \qquad (20)$$

Further tunnelling-corrected KIEs due to Wigner (KIE_{Wigner}) and Bell (KIE_{Bell}) use models as described in Eq 21 – 23. In these equations, k_B is the Boltzmann constant, h is Planck's constant and ν is the imaginary frequency in the transition state.

$$KIE_{tunneling} = KIE_{Eyring} \times Q_{t,H}/Q_{t,D} \quad (21)$$

$$Q_{t,Wigner} = 1 + u_t^2/24 \text{ with } u_t = h\nu/k_B T \quad (22)$$

$$Q_{t,Bell} = \frac{u_t}{2\sin\left(\frac{1}{2}u_t\right)} - \sum_{n=1}^{\infty}(-1)^n \frac{\exp\left(\left(u_t - 2n\pi\right)\frac{\Delta E}{u_t}\right)}{\left(u_t - 2n\pi\right)/u_t} \quad (23)$$

DFT calculations for hydrogen atom abstraction by P450 Cpd I of *trans*-methylphenylcyclopropane versus *trans*-d_1-methylphenylcyclopropane gave values of PIE_{Eyring} = 1.03, PIE_{Wigner} = 1.07 and PIE_{Bell} = 1.20 in very good agreement with the experimentally reported PIE value of 1.14.[165,208] These calculations, therefore, ruled out a second oxidant in the reaction mechanism and explained the reactivity via Cpd I using multistate reactivity. To further ascertain that Cpd 0 cannot compete with Cpd I, the reaction mechanism of olefin epoxidation and dimethylsulphide oxidation by Cpd 0 and Cpd I was calculated.[63,65,66] Substantially higher barriers were obtained for the reactions starting with Cpd 0 than Cpd I, which implies that Cpd 0 is a sluggish oxidant that cannot compete with Cpd I.

4.2 Cysteine dioxygenase (CDO).

Cysteine dioxygenase, in contrast to TauD, has an active site with iron bound to a facial 3-His ligand system rather than the more common 2-His/1-Asp features of most nonheme iron dioxygenases. Computational studies were initially focussed on small model complexes,[118,119] but more recent work used QM/MM on the complete enzyme.[120] Due to the tight substrate binding pocket of CDO and the large number of stabilizing hydrogen bonds, a QM region was chosen that includes all characteristic features of the active site, namely most groups in the first and second coordination sphere of the metal: FeO_2, substrate

cysteine and the amino acid side chains of His_{86}, His_{88}, His_{140}, Arg_{60}, His_{155}, Tyr_{157} and Cys_{93}. The calculations revealed a mechanism as given in Figure 21(*a*) that starts from an iron(III)-superoxo complex (**A**), which has close lying singlet, triplet, quintet and septet spin states. The reaction proceeds with attack on the sulphur of cysteinate to for a bicyclic ring structure (**B**) on close-lying singlet, triplet and quintet spin state surfaces. Attempts to calculate this mechanism on the septet spin state surface failed and did not lead to products,[118] therefore, the experimentally trapped septet spin state iron(III)-superoxo intermediate may not be the catalytically relevant species, although the calculations showed it to be close in energy to the quintet spin state. During this process the O–O bond is significantly weakened from 1.338 to 1.513 Å, and in a subsequent step breaks to form an iron(IV)-oxo species with a bound cysteine sulfoxide (**C**). Figure 21(*b*) gives the results of the QM/MM calculations starting from the iron(IV)-oxo intermediate with extracts of the optimized geometries. Thus, in structure **C** the transfer of the second oxygen atom to the substrate is blocked by the sulfoxide group, so that an initial isomerisation step occurs, whereby the SO group rotates, the Fe–S bond breaks and the sulfoxide binds the metal instead to form isomer **C′**. In analogy to biomimetic nonheme iron(IV)-oxo species,[228,229] the ground state of both complexes **C** and **C′** is a triplet spin state. However, the triplet-quintet energy gap is strongly dependent on the ligands bound to the metal and whether cysteine-sulfoxide binds to metal with the sulphur or oxygen atom. The isomerisation step has barriers of 11.3 and 13.2 kcal mol^{-1} on the quintet and triplet spin state surfaces, therefore, a certain degree of spin equilibration is expected at this stage of the reaction with two-state reactivity patterns. After the isomerisation the second oxygen atom transfer takes place on a dominant quintet spin state surface to give cysteine sulphinic acid products (**D**).

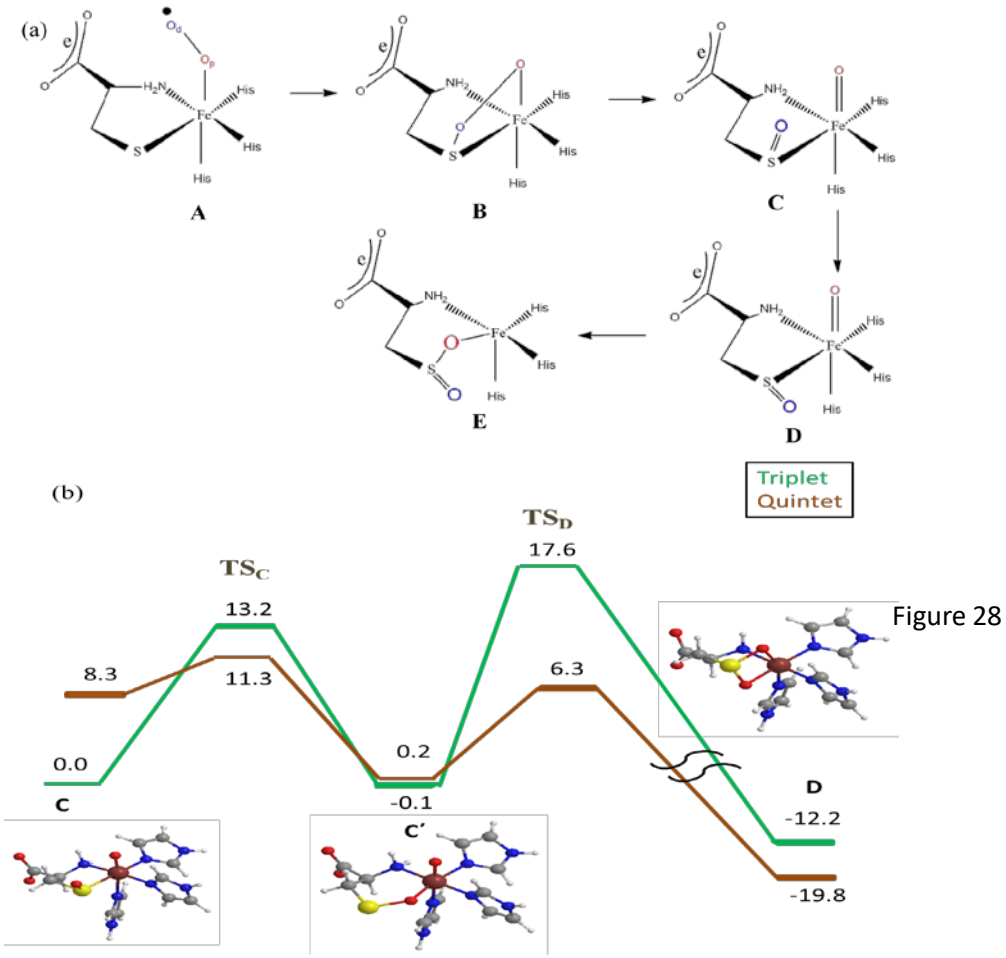

Figure 28

Figure 21: (a) Catalytic mechanism of CDO enzymes. (b) QM/MM calculated oxygenation of cysteine sulfinic acid by a nonheme iron(IV)-oxo intermediates. Energies are in kcal mol–1 and contain ZPE corrections.

Due to the structural differences between TauD and CDO, also calculations on active site mutants were performed where one of the three histidine ligands of the iron in CDO was replaced by a carboxylic acid group to create a 2-His/1-Asp bound motif, i.e. H86D, H88D and H140D mutants.[119] Thus, the mutants have higher dioxygenation barriers, which implies that the 3-His ligand motif in CDO is essential for optimal dioxygenation of the substrate. In particular, a weakening of the Fe–S bond is found for the situation where a carboxylic acid group located *trans* to this bond. On the other hand, a carboxylic acid group *trans* to the superoxo group increases the oxygen atom transfer barriers as a result of a pull-effect of electrons.

4.3 Synthetic nonheme iron complexes.

As discussed in the introduction, mononuclear nonheme iron(IV)-oxo complexes are potent catalysts of oxygenation reactions but the catalytic properties seem to be dependent on the ligands bound to the metal centre. Specifically, two types of interactions have been identified, namely from the axial ligand (i.e. the ligand *trans* to the oxo group) and the equatorial ligands (those perpendicular to the oxo group; the *cis*-ligands). To explain the differences in electronic properties of those types of systems and the factors that determine their reactivity patterns, a series of DFT studies have been performed to elucidate the electronic properties of the oxidants and their reactivity towards substrates. We will start this section with an in-depth overview of the factors that distinguish the individual iron(IV)-oxo catalysts as elucidated from quantum chemical modelling.

4.3.1 Electronic properties of iron(IV)-oxo complexes.

As described above, all experimentally characterized enzymatic mononuclear iron(IV)-oxo species have a quintet spin (S = 2) ground state, whereas most biomimetic complexes tend to have a triplet spin (S = 1) ground state. To understand these differences, we plot in Figure 29 the high-lying occupied and low-lying virtual orbitals of two mononuclear nonheme iron(IV)-oxo complexes, namely the active species of TauD and $[Fe^{IV}(O)(N4Py)]^{2+}$, N4Py = *N*,*N*-bis(2-pyridylmethyl)-*N*-bis(2-pyridyl)-methylamine.[205,215] Other non-heme mononuclear iron(IV)-oxo complexes give a similar set of occupied and virtual orbitals although small variations, e.g. due to differences in the axial ligand may occur. In particular, the axial ligand is known to entice a push-effect and thereby influence the orbitals along the molecular *z*-axis, i.e. along the Fe–O bond.[168,169] All orbitals originate from the metal type 3*d* atomic orbitals that split into a series of three t_{2g} and two e_g set of π^* and σ^* orbitals, where we allocate the *z*-axis along the Fe–O bond. A pair of orthogonal $3d_{xz}$ and $3d_{yz}$ atomic orbitals mix with $2p_x$ and $2p_y$ atomic orbitals on the oxo group to give a set of bonding and anti-bonding combinations, designated π_{xz},

π_{yz}, π^*_{xz}, and π^*_{yz}. The π^*_{xy} orbital is located in the equatorial ligand plane and its corresponding orbital in heme enzymes ($\delta_x 2_{-y}2$) is nonbonding.[163] The same situation appears for $[Fe^{IV}(O)(N4Py)]^{2+}$ where the four equatorial ligands are identical. As a consequence, this orbital in $[Fe^{IV}(O)(N4Py)]^{2+}$ is significantly lowered in energy with respect to the other π^* orbitals, i.e. π^*_{xz} and π^*_{yz}, and hence the triplet spin state is the ground state.[226–228] High in energy and virtual are two σ-type anti-bonding combinations of the metal with the nitrogen atoms (in $\sigma^*_x 2_{-y}2$) and along the O–Fe axis (in $\sigma^*_z 2$). The latter orbital also interacts with orbitals on the axial ligand and in particular this effect is strong with a sulfur atom in that position.[163] Indeed, in iron(IV)-oxo complexes the ligand environment has been shown to influence the energy level of, in particular, the $\sigma^*_z 2$ orbital.[145]

The set of orbitals displayed in Figure 22 is occupied with ten electrons but in the enzymatic system this gives a quintet spin ground state, whereas it is a triplet spin ground state in $[Fe^{IV}(O)(N4Py)]^{2+}$. These two states are close in energy for both systems, whereby the triplet/quintet spin state ordering is found to be dependent on the nature of the other ligand(s) bound to iron. In particular, with an increase of the electron-withdrawing power of the axial ligand the π^*_{xy}–$\sigma^*_x 2_{-y}2$ energy gap decreases considerably and so does the quintet-triplet energy gap.[145] A consequence of close lying spin states is the phenomenon designated two-state reactivity (TSR) that originally was described to explain the reactivity patterns of iron(IV)-oxo heme systems, but has been extended to nonheme systems as well.[226–228] The next section explains this phenomenon in detail and how it affects reactivity patterns, product distributions and kinetic isotope effects.

Geometries of several mononuclear nonheme iron(IV)-oxo complexes were optimized with DFT methods in the triplet and quintet spin states.[205–207,226] Generally, the Fe–O bond in nonheme iron(IV)-oxo complexes is short (in the range of 1.65 Å) typical for a double bond. The four equatorial Fe–N distances are of similar size and the average value of these bonds ($r_{FeN,av}$) is shorter for the triplet spin state structures than for the quintet spin state systems, as a result of differences in orbital occupation. The axial Fe–N bond ($r_{FeN,ax}$) is

quite different in length to the equatorial Fe–N bonds again as a result of the orbital occupation in the structure.

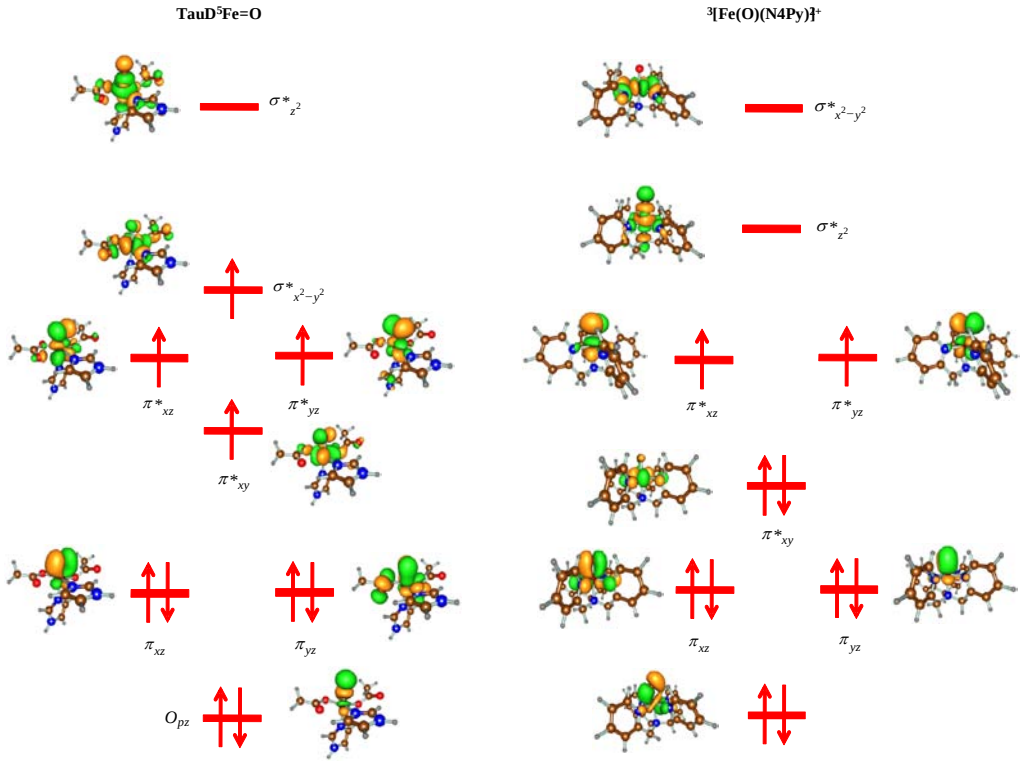

Figure 22: High-lying occupied and virtual orbitals and orbital occupation of the ground states of the iron(IV)-oxo species of TauD (left-hand-side) and [FeIV(O)(N4Py)]2+ (right-hand-side).

4.3.2 Two-state reactivity patterns of mononuclear nonheme iron-oxo complexes.

Enzymatic iron(IV)-oxo complexes have a quintet spin ground state, whereas biomimetic complexes have a lower lying triplet spin state. The oxygen transfer reaction with substrates, therefore, can take place on competing spin-state surfaces with different rate constants, KIEs and barrier heights on each of these spin state surfaces. This phenomenon has been termed two-state reactivity (TSR) and was originally designed to explain the reactivity patterns of the iron(IV)-oxo active species of the heme enzyme cytochrome P450

(P450).[8,16,164] In analogy to this, in nonheme iron(IV)-oxo complexes there are also close lying spin state surfaces, usually triplet and quintet spin. However, the two spin states in nonheme iron chemistry are not degenerate and the spin state energy is dependent on the interactions of the metal with its ligands. Figure 23 displays a schematic drawing of a TSR potential energy profile for a nonheme iron(IV)-oxo complex in a reaction with substrate AlkH. The reaction starts from the two close-lying reactant (**R**) spin states with triplet and quintet spin respectively that are identified with a superscript. These two spin states are generally close in energy in nonheme iron(IV)-oxo complexes, whereby in biomimetic model complexes the triplet spin is usually the ground state, although there are a few examples, where the quintet spin state is the ground state. The hydroxylation mechanism proceeds with an initial hydrogen atom abstraction via barriers $^{3,5}\mathbf{TS}_{HA}$ to form an iron(III)-hydroxo complex and a nearby Alk radical: the intermediate complex **I**. In a subsequent radical rebound step via barrier $^{3,5}\mathbf{TS}_{reb}$ the hydroxylated product (**P**) is formed. All hydroxylation studies of mononuclear nonheme iron(IV)-oxo complexes reported so far follow essentially this reaction mechanism.[205,207,226–228]

Although the triplet spin state is the ground state in all biomimetic iron(IV)-oxo complexes, in fact the hydrogen abstraction barriers on this spin state surface tend to be relatively high and in most cases much higher in energy than the corresponding quintet spin state hydrogen abstraction barriers. As a consequence, it is expected that along the reaction mechanism a spin state crossing from the triplet to quintet spin state takes place. The higher reactivity of the high-spin state has been explained with differences in substrate approach to the iron(IV)-oxo group.[226] In the triplet spin state mechanism the hydrogen abstraction step is accomplished by a simultaneous electron transfer from the substrate into the π^*_{xz} orbital and as a consequence the substrate attacks the Fe–O group sideways to get maximum orbital overlap with this orbital. By contrast, in the quintet spin state the electron transfer is into the $\sigma^*_{z}2$ orbital, which is along the Fe–O bond and the substrate, is aligned with this bond. In this particular orientation there is little electrostatic repulsion of the approaching substrate with the iron ligands, whereas in the triplet spin there is considerable repulsion that destabilizes this transition state. As a consequence

of these differences in electron transfer processes in the hydrogen abstraction step of the mechanism, the approach of the substrate onto the iron(IV)-oxo group also is different in the triplet and quintet spin states. The in-sets of Figure 30 show the geometries of the hydrogen abstraction transition states in the triplet and quintet spin states (^{3,5}**TS**$_{HA}$). In both transition states the O–H–C angle is around 180°, but due to differences in electron transfer the Fe–O–C angle is 180° in the quintet spin state while it is around 120° (dependent on the nature of the ligands bound to iron) in the triplet spin state.[226] Because of repulsive interactions of the approaching substrate with the ligands bound to iron, the triplet spin state barriers generally are higher in energy than those in the quintet spin state. Consequently, similarly to the heme models also biomimetic nonheme iron-oxo complexes give rise to two-state reactivity patterns on close lying triplet and quintet spin state surfaces. The difference, however, is that the orbital occupation of the triplet and quintet spin state is quite different, so that the nature of the other ligands determines the triplet-quintet energy splitting. In the next few sections we will give some examples of results of theoretical studies of oxygen atom transfer reaction by nonheme models and how TSR patterns affect the product distributions and KIEs. After the initial hydrogen abstraction step an iron(III)-hydroxo complex is formed with a radical rest group, and hydroxylated products (**P**) are formed via a radical rebound transition state (**TS**$_{reb}$). In most examples studied so far, the rebound barrier is significantly lower in energy than the hydrogen abstraction barrier that is the rate-determining step in the reaction mechanism.

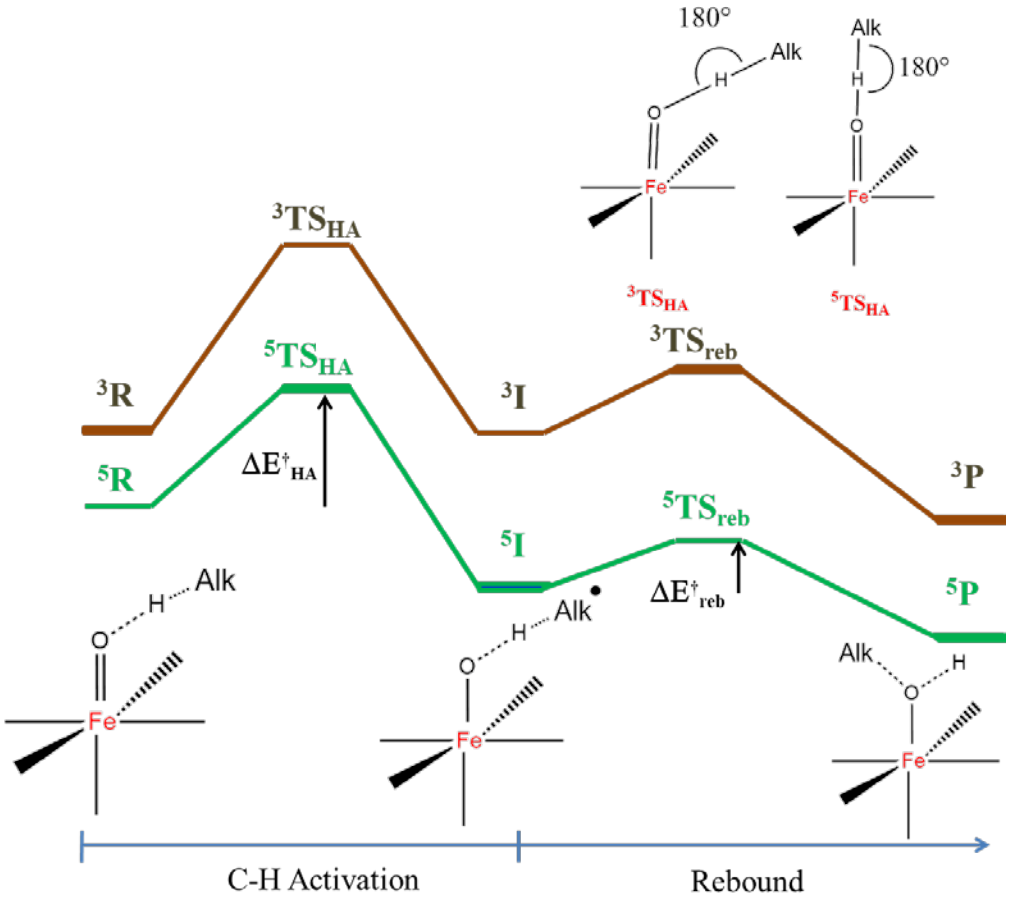

Figure 23: Reactivity differences of biomimetic iron(IV)-oxo species with triplet spin ground state as compared to enzymatic iron(IV)-oxo species with a quintet spin ground state.

A comparative DFT study on substrate hydroxylation by a TauD model vis-à-vis a heme model mimicking the active site of cytochrome P450 revealed that mononuclear nonheme iron(IV)-oxo oxidants are more efficient and powerful oxidants as compared to heme-type iron(IV)-oxo oxidants.[215,223] This was ascribed to the formation of a much stronger O–H bond in nonheme systems, which as a consequence also lowers the reaction barriers. More recent studies on the reactions of mononuclear iron(IV)-oxo oxidants with a 2-His/1-Asp ligand motif with a range of different substrates, with C–H bond strengths from 82.4 kcal mol^{-1} for ethylbenzene to 101.6 kcal mol^{-1} for methane, showed that the barrier of substrate hydroxylation is linearly related to the strength of the C–H bond that is broken in the process.[224]

4.3.3 The cis*-effect on the properties of the iron(IV)-oxo species.*

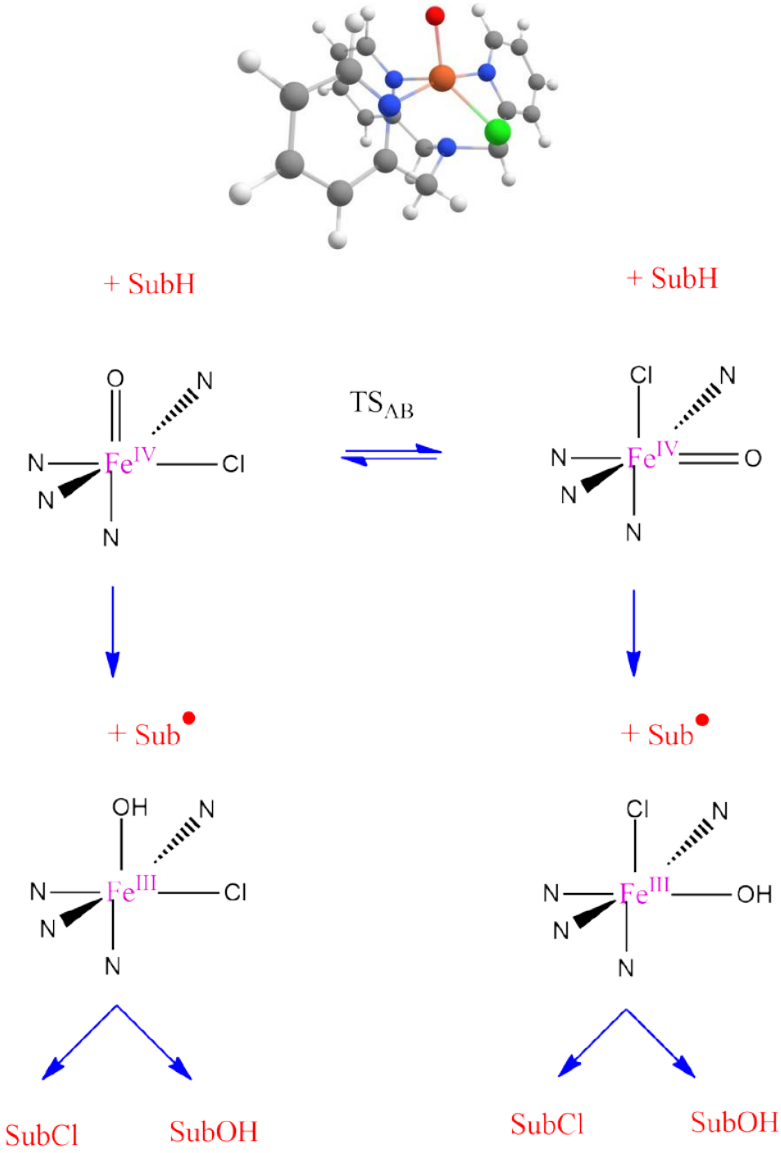

Scheme 2: Calculated reaction mechanisms of halogenation versus hydroxylation of a substrate with an iron(IV)-oxo(halide) system.

As shown in the previous section ligands *trans* to the oxo group (axial ligands) determine key properties of the iron(IV)-oxo centre and influence reactivity patterns. To establish whether or not ligands perpendicular to the iron(IV)-oxo bond influence the spectroscopic and catalytic properties of the system, a series of density functional theory studies on the nature of the *cis*-effect and *cis*-influence of ligands on iron(IV)-oxo nonheme complexes have been performed

using $[Fe^{IV}(O)(TPA)L]^+$ with L = F^-, Cl^-, and Br^-.[231] This particular ligand system with a hydroxyl group in the *cis*-position (L = OH^-) has been shown to react with olefins to give *cis*-dihydroxylation and epoxide products.[232–234] DFT calculations showed that the barrier leading to *cis*-dihydroxylation is 1 kcal mol^{-1} lower in energy than the one leading to epoxide products, hence both products are expected for the reactions as indeed observed by experiment.[235] Combined experimental and DFT studies using a mononuclear iron(IV)-oxo in a pentadentate bispidine ligand showed that it reacts with olefins to form competitive *cis*-dihydroxylation and epoxide products.[236,237]

The calculations of a series of $[Fe^{IV}(O)(TPA)X]^+$ complexes with X = F^-, Cl^- or Br^- showed that the interaction between the metal and a first-row element leads to an electronic *cis*-effect due to favourable orbital overlap, which is missing between the metal and second/third row elements.[231] As a consequence, the HOMO/LUMO energy gap is widened for the metal-second row element interaction with respect to the system with L = F^-. Despite the larger HOMO/LUMO gap no large differences in electron affinities of the complexes is observed. Similarly to other mononuclear nonheme iron-oxo complexes also $[Fe^{IV}(O)(TPA)X]^+$ with X = F^-, Cl^-, and Br^- have close lying triplet and quintet spin states, but only the quintet spin state is reactive with substrates. Therefore, the efficiency of the oxidant will be determined with the triplet-quintet spin state crossing of the reaction.

An interesting feature of iron(IV)-oxo complexes with a labile *cis*-ligand is the fact that under certain conditions this ligand is transferred to substrates. Thus, the α-ketoglutarate dependent halogenases have a catalytic cycle that closely resembles that of TauD reported in Figure 5 and all steps until the iron(IV)-oxo species are the same. However, in the halogenases, the *cis*-bound halide atom (usually Cl^-) is transferred to the radical to form halogenated products rather than rebound of the hydroxyl group to form alcohols. In biomimetic complexes substrate halogenation has been reported for $[Fe^{IV}(O)(Cl)(TPA)]^+$. Technically this system has two stable isomers, Scheme 4, with either the oxo or halide *trans* to the amide nitrogen atom of TPA. We calculated the isomerisation between the two forms as well as the hydrogen atom abstraction leading to radical intermediates and the halide and hydroxyl rebound to form halogenated

and hydroxylated products.[239] We show that the two isomers give different regioselectivities, where one isomer gives halogenated products, whereas the other gives dominant hydroxylation. As such we predict that it is essential for efficient substrate halogenation that an initial isomerisation takes place whereby the halide group is moved to a position *trans* to the amide nitrogen of TPA as it weakens its bond and makes the halide transfer to substrate more likely.

The all above discussion with elebortaded explainations and VB model explanations can be found in Ref. 261. There are nice discussions and detail experimental and theoretical presentation can be found in Ref. 262-271.

5. Conclusions and Summary

As highlighted in this dissertation, computational chemistry methods are highly accurate and these days are applicable to 'real life' systems including enzymatic intermediates and synthetic catalysts. As these oxidants tend to react very fast with substrates, computational methods can assist experimental studies in the field and gain valuable understanding on the chemical properties of the oxidant that drive the reaction mechanism and the nature of the active oxidant. Thus our studies established mechanisms for oxygen atom transfer reactions, including aliphatic and aromatic hydroxylation, olefin epoxidation, dehydrogenation of olefins and heteroatom oxidation (sulphoxidation/phosphorylation), of transition metal containing complexes. The research characterized the active oxidant in the reaction processes and the rate determining step in the mechanism. Moreover, in several cases we have devised models that rationalize reaction processes and barrier heights and that can be used to predict rate constants of processes. The work established the difference in reactivity of heme and nonheme iron(IV)-oxo intermediates and assigned the nonheme ones as the more reactive. The calculations rationalized the rate constants and reaction mechanisms and identified the origin of the rate constants, the electron/proton transfer processes involved and the regioselectivity preferences. These studies have set the scene for collaborative computational modelling in close relationship with experimental biomimetic and enzymatic work.

References:

1 M. Sono, M. P. Roach, E. D. Coulter and J. H. Dawson, *Chem. Rev*., 1996, **96**, 2841.

2 J. T. Groves, *Proc. Natl. Acad. Sci. USA*, 2003, **100**, 3569.

3 P. R. Ortiz de Montellano, Ed. *Cytochrome P450: Structure, Mechanism and Biochemistry*. 3rd ed.; Kluwer Academic/Plenum Publishers, New York, 2004.

4 B. Meunier, S. P. de Visser and S. Shaik, *Chem. Rev*., 2004, **104**, 3947.

5 A. W. Munro, H. M. Girvan and K. J. McLean, *Nat. Prod. Rep*., 2007, **24**, 585.

6 K. M. Kadish, K. M. Smith and R, Guilard, Eds. *Handbook of Porphyrin Science*. World Scientific Publishing Co., New Jersey, 2010.

7 P. R. Ortiz de Montellano, *Chem. Rev*., 2010, **104**, 932.

8 S. P. de Visser and D. Kumar, Eds. *Iron-containing enzymes: Versatile catalysts of hydroxylation reaction in nature*. RSC Publishing, Cambridge (UK), 2011.

9 I. G. Denisov, T. M. Makris, S. G. Sligar and I. Schlichting, *Chem. Rev*., 2005, **105**, 2253.

10 Y. Watanabe, H. Nakajima and T. Ueno, *Acc. Chem. Res*., 2007, **40**, 554.

11 J. T. Groves, *Models and Mechanisms of Cytochrome P450 Action*. In *Cytochrome P450: Structure, Mechanism and Biochemistry*. P. R. Ortiz de Montellano, Ed., 3rd Ed., Kluwer Academic/Plenum Publishers: New York, 2005, Chapter 1, pp 1–44.

12 W. Nam, *Acc. Chem. Res*., 2007, **40**, 522.

13 S. P. de Visser and W. Nam, *High-valent iron-oxo porphyrins in oxygenation reactions*. In *Handbook of Porphyrin Science*, K. M. Kadish, K. M. Smith and R. Guilard, Eds., World Scientific Publishing Co., New Jersey, 2010, Chapter 44, pp. 85–140.

14 J. T. Groves and G. A. McClusky, *J. Am. Chem. Soc*., 1976, **98**, 859.

15 J. Rittle and M. T. Green, *Science*, 2010, **330**, 933.

16 S. Shaik, D. Kumar, S. P. de Visser, A. Altun and W. Thiel, *Chem. Rev*., 2005, **105**, 2279.

17 P. E. M. Siegbahn, R. H. Crabtree and P. Nordlund, *J. Biol. Inorg. Chem*., 1998, **3**, 314.

18 P. R. Ortiz de Montellano, *Annu. Rev. Pharmacol. Toxicol.*, 1992, **32**, 89.

19 G. I. Berglund, G. H. Carlsson, A. T. Smith, H. Szöke, A. Henriksen and J. Hajdu, *Nature*, 2002, **417**, 463.

20 E. L. Raven, *Nat. Prod. Rep*., 2003, **20**, 367.

21 M. Sivaraja, D. B. Goodin, M. Smith and B. M. Hoffman, *Science*, 1989, **245**, 738.

22 M. Klingenberg, *Arch. Biochem. Biophys*., 1958, **75**, 376.

23 T. Omura and R. Sato, *J. Biol. Chem*., 1962, **237**, 1375.

24 T. Omura and R. Sato, *J. Biol. Chem*., 1964, **239**, 2370.

25 F. P. Guengerich, *Chem. Res. Toxicol.*, 2001, **14**, 611.

26 P. R. Ortiz de Montellano and J. J. De Voss, *Nat. Prod. Rep*., 2002, **19**, 477.

27 O. Pylypenko and I. Schlichting, *Annu. Rev. Biochem*., 2004, **73**, 991.

28 M. Costas, M. P. Mehn, M. P. Jensen and L. Que Jr, *Chem. Rev*., 2004, **104**, 939.

29 S. V. Kryatov, E. V. Rybak-Akimova and S. Schindler, *Chem. Rev*., 2005, **105**, 2175.

30 P. C. A. Bruijnincx, G. van Koten, R. J. M. Klein Gebbink, *Chem. Soc. Rev*., 2008, **37**, 2716

31 G. H. Loew and D. L. Harris, *Chem. Rev*., 2000, **100**, 407.

32 S. Shaik, S. Cohen, Y. Wang, H. Chen, D. Kumar and W. Thiel, *Chem. Rev*., 2010, **110**, 949.

33 S. P. de Visser, *Adv. Inorg. Chem.*, 2012, **64**, 1.

34 T. L. Poulos, B. C. Finzel, I. C. Gunsalus, G. C. Wagner and J. Kraut, *J. Biol. Chem*., 1985, **260**, 16122.

35 H. M. Berman, J. Westbrook, Z. Feng, G. Gilliland, T. N. Bhat, H. Weissig, I. N. Shindyalov and P. E. Bourne, *Nucleic Acids Res*., 2000, **28**, 235.

36 I. Schlichting, J. Berendzen, K. Chu, A. M. Stock, S. A. Maves, D. E. Benson, R. M. Sweet, D. Ringe, G. A. Petsko and S. G. Sligar, *Science*, 2000, **287**, 1615.

37 T. L. Poulos, B. C. Finzel and A. J. Howard, *Biochemistry*, 1986, **25**, 5314.

38 T. L. Poulos, B. C. Finzel and A. J. Howard, *J. Mol. Biol*., 1987, **195**, 687.

39 R. Raag and T. L. Poulos, *Biochemistry*, 1989, **28**, 7586.

40 J. H. Dawson, *Science*, 1988, **240**, 433.

41 M. T. Green, J. H. Dawson and H. B. Gray, *Science*, 2004, **304**, 1653.

42 M. T. Green, *Curr. Opin. Chem. Biol*., 2009, **13**, 84.

43 F. Ogliaro, S. P. de Visser and S. Shaik, *J. Inorg. Biochem*., 2002, **91**, 554.

44 K. L. Stone, R. K. Behan and M. T. Green, *Proc. Natl. Acad. Sci. USA*, 2005, **102**, 16563.

45 A. Dey, Y. Jiang, P. R. Ortiz de Montellano, P. O. Hodgson, B. Hedman and E. I. Solomon, *J. Am. Chem. Soc*., 2009, **131**, 7869.

46 S. G. Sligar, *Biochemistry*, 1976, **15**, 5399.

47 P. Rydberg, E. Sigfridsson and U. Ryde, *J. Biol. Inorg. Chem*., 2004, **9**, 203.

48 M. Swart, A. R. Groenhof, A. W. Ehlers and K. Lammertsma, *Chem. Phys. Lett*., 2005, **403**, 35.

49 A. Altun and W. Thiel, *J. Phys. Chem. B*, 2005, **109**, 1268.

50 A. R. Groenhof, M. Swart, A. W. Ehlers and K. Lammertsma, *J. Phys. Chem. A*, 2005, **109**, 3411.

51 P. R. Balding, C. S. Porro, K. J. McLean, M. J. Sutcliffe, J.-D. Maréchal, A. W. Munro and S. P. de Visser, *J. Phys. Chem. A*, 2008, **112**, 12911.

52 C. B. Brewer and J. A. Peterson, *J. Biol. Chem*., 1988, **263**, 791.

53 R. Davydov, T. M. Makris, V. Kofman, D. E. Werst, S. G. Sligar and B. M. Hoffman, *J. Am. Chem. Soc*., 2001, **123**, 1403.

54 I. G. Denisov, T. M. Makris and S. G. Sligar, *J. Biol. Chem*., 2001, **276**, 11648.

55 I. G. Denisov, S.-C. Hung, K. E. Weiss, M. A. McLean, Y. Shiro, S.-Y. Park, P. M. Champion and S. G. Sligar, *J. Inorg. Biochem*., 2001, **87**, 215.

56 J. E. Roberts, B. M. Hoffman, R. Rutter and L. P. Hager, *J. Am. Chem. Soc*., 1981, **103**, 7654.

57 A. D. N. Vaz, D. F. McGinnity and M. J. Coon, *Proc. Natl. Acad. Sci. USA*, 1998, **95**, 3555.

58 M. Newcomb, R. Shen, S.-Y. Choi, P. H. Toy, P. F. Hollenberg, A. D. N. Vaz and M. J. Coon, *J. Am. Chem. Soc*., 2000, **122**, 2677.

59 M. J. Cryle and J. J. De Voss, *Angew. Chem. Int. Ed*., 2006, **45**, 8221.

60 A. D. N. Vaz, S. J. Pernecky, G. M. Raner and M. J. Coon, *Proc. Natl. Acad. Sci. USA*, 1996, **93**, 4644.

61 P. R. Ortiz de Montellano and R. A. Stearns, *J. Am. Chem. Soc*., 1987, **109**, 3415.

62 M. Newcomb and P. H. Toy, *Acc. Chem. Res*., 2000, **33**, 449.

63 F. Ogliaro, S. P. de Visser, S. Cohen, P. K. Sharma and S. Shaik, *J. Am. Chem. Soc*., 2002, **124**, 2806.

64 T. Kamachi, Y. Shiota, T. Ohta and K. Yoshizawa, *Bull. Chem. Soc. Jpn*., 2003, **76**, 721.

65 P. K. Sharma, S. P. de Visser and S. Shaik, *J. Am. Chem. Soc*., 2003, **125**, 8698.

66 C. S. Porro, M. J. Sutcliffe and S. P. de Visser, *J. Phys. Chem. A*, 2009, **113**, 11635.

67 M. J. Park, J. Lee, Y. Suh, J. Kim and W. Nam, *J. Am. Chem. Soc*., 2006, **128**, 2630.

68 J. Kaizer, M. Costas and L. Que Jr., *Angew. Chem. Int. Ed*., 2003, **42**, 3671.

69 M. S. Seo, T. Kamachi, T. Kouno, K. Murata, M. J. Park, K. Yoshizawa and W. Nam, *Angew. Chem. Int. Ed*., 2007, **46**, 2291.

70 N. Hessenauer-Ilicheva, A. Franke, D. Meyer, W.-D. Woggon and R. van Eldik, *J. Am. Chem. Soc*., 2007, **129**, 12473.

71 A.-R. Han, Y. J. Jeong, Y. Kang, J. Y. Lee, M. S. Seo and W. Nam, *Chem. Commun*., 2008, 1076.

72 S. J. Lange and L. Que Jr, *Curr. Opin. Chem. Biol*., 1998, **2**, 159.

73 E. I. Solomon, T. C. Brunold, M. I. Davis, J. N. Kemsley, S.-K. Lee, N. Lehnert, F. Neese, A. J. Skulan, Y.-S. Yang and J. Zhou, *Chem. Rev*., 2000, **100**, 235.

74 T. D. H. Bugg, *Curr. Opin. Chem. Biol*., 2001, **5**, 550.

75 M. J. Ryle and R. P. Hausinger, *Curr. Opin. Chem. Biol*., 2002, **6**, 193.

76 M. M. Abu-Omar, A. Loaiza and N. Hontzeas, *Chem. Rev*., 2005, **105**, 2227.

77 J. M. Bollinger Jr and C. Krebs, *Curr. Opin. Chem. Biol*., 2007, **11**, 151.

78 C. Krebs, D. G. Fujimori, C. T. Walsh and J. M. Bollinger Jr, *Acc. Chem. Res*., 2007, **40**, 484.

79 C. J. Schofield and Z. Zhang, *Curr. Opin. Chem. Biol*., 1999, **9**, 722.

80 T. D. H. Bugg, *Tetrahedron*, 2003, **59**, 7075.

81 J. M. Simmons, T. A. Müller and R. P. Hausinger, *Dalton Trans*., 2008, 5132.

82 Y. Mishina, E. M. Duguid and C. He, *Chem. Rev*., 2006, **106**, 215.

83 P. J. O'Brien, *Chem. Rev*., 2006, **106**, 720.

84 C. Loenarz and C. J. Schofield, *Nat. Chem. Biol*., 2008, **4**, 152.

85 R. Chowdhury, A. Hardy and C. J. Schofield, *Chem. Soc. Rev*., 2008, **37**, 1308.

86 O. W. Choroba, D. H. Williams and J. B. Spencer, *J. Am. Chem. Soc*., 2000, **122**, 5389.

87 L. J. Higgins, F. Yan, P. Liu, H.-W. Liu and C. L. Drennan, *Nature*, 2005, **437**, 838.

88 M. C. Bodner, R. M. Phelan, M. F. Freeman, R. Li and C. A. Townsend, *J. Am. Chem. Soc*., 2010, **132**, 12.

89 E. L. Hegg and L. Que Jr., *Eur. J. Biochem*., 1997, **250**, 625.

90 E. G. Kovaleva and J. D. Lipscomb, *Nat. Chem. Biol*., 2008, **4**, 186.

91 Z. Zhang, J. Ren, D. K. Stammers, J. E. Baldwin, K. Harlos and C. J. Schofield, *Nat. Struct. Biol*., 2000, **7**, 127.

92 S. C. Trewick, T. F. Henshaw, R. P. Hausinger, T. Lindahl and B. Sedgwick, *Nature*, 2002, **419**, 174.

93 J. M. Simmons, T. A. Müller and R. P. Hausinger, *Dalton Trans*., 2008, 5132.

94 H. M. Hanauske-Abel and V. Günzler, *J. Theor. Biol*., 1982, **94**, 421.

95 K. I. Kivirikko, R. Myllyla and T. Pihlajaniemi, *FASEB J*., 1989, **3**, 1609.

96 A. D. Winter and A. P. Page, *Mol. Cell Biol*., 2000, 4084.

97 J. R. O'Brien, D. J. Schuller, V. S. Yang, B. D. Dillard and W. N. Lanzilotta, *Biochemistry*, 2003, **42**, 5547.

98 A. Bassan, T. Borowski and P. E. M. Siegbahn, *Dalton Trans*., 2004, 3153.

99 J. M. Bollinger Jr, J. C. Price, L. M. Hoffart, E. W. Barr, C. Krebs, *Eur. J. Inorg. Chem*., 2005, 4245.

100 S. P. de Visser, *Coord. Chem. Rev*., 2009, **253**, 754.

101 T. Borowski, A. Bassan and P. E. M. Siegbahn, *Chem. Eur. J*., 2004, **10**, 1031.

102 M. J. Ryle, R. Padmakumar and R. P. Hausinger, *Biochemistry*, 1999, **38**, 15278.

103 J. C. Price, E. W. Barr, B. Tirupati, J. M. Bollinger Jr and C. Krebs, *Biochemistry*, 2003, **42**, 7497.

104 D. A. Proshlyakov, T. F. Henshaw, G. R. Monterosso, M. J. Ryle and R. P. Hausinger, *J. Am. Chem. Soc*., 2004, **126**, 1022.

105 P. J. Riggs-Gelasco, J. C. Price, R. B. Guyer, J. H. Brehm, E. W. Barr, J. M. Bollinger Jr and C. Krebs, *J. Am. Chem. Soc*., 2004, **126**, 8108.

106 J. C. Price, E. W. Barr, T. E. Glass, C. Krebs, J. M. Bollinger Jr., *J. Am. Chem. Soc*., 2003, **125**, 13008.

107 M. H. Stipanuk, *Annu. Rev. Nutr*., 2004, **24**, 539.

108 C. A. Joseph and M. J. Maroney, *Chem. Commun*., 2007, 3338.

109 C. L. Weinstein, R. H. Haschemeyer and O. W. Griffin, *J. Biol. Chem*., 1988, **263**, 16568.

110 M. T. Heafield, S. Fearn, G. B. Steventon, R. H. Waring, A. C. Williams and S. G. Sturman, *Neurosci. Lett*., 1990, **110**, 216.

111 S. Ye, X. Wu, L. Wei, D. Tang, P. Sun, M. Bartlam and Z. Rao, *J. Biol. Chem*., 2007, **282**, 3391.

112 S. C. Chai, J. R. Bruyere and M. J. Maroney, *J. Biol. Chem*., 2006, **281**, 15774.

113 B. S. Pierce, J. D. Gardner, L. J. Bailey, T. C. Brunold and B. G. Fox, *Biochemistry*, 2007, **46**, 8569.

114 J. B. Lombardini, T. P. Singer and P. D. Boyer, *J. Biol. Chem*., 1969, **244**, 1172.

115 J. E. Dominy Jr, J. Hwang, S. Guo, L. L. Hirschberger, S. Zhang and M. H. Stipanuk, *J. Biol. Chem*., 2008, **283**, 12188.

116 T. Kleffmann, S. A. K. Jongkees, G. Fairweather, S. M. Wilbanks and G. N. L. Jameson, *J. Biol. Inorg. Chem*., 2009, **14**, 913.

117 E. P. Tchesnokov, S. M. Wilbanks and G. N. L. Jameson, *Biochemistry*, 2012, **51**, 257.

118 S. Aluri and S. P. de Visser, *J. Am. Chem. Soc*., 2007, **129**, 14846.

119 S. P. de Visser and G. D. Straganz, *J. Phys. Chem. A*, 2009, **113**, 1835.

120 D. Kumar, W. Thiel and S. P. de Visser, *J. Am. Chem. Soc*., 2011, **133**, 3869.

121 C. R. Simmons, K. Krishnamoorthy, S. L. Granett, D. J. Schuller, J. E. Dominy Jr, T. P. Begley, M. H. Stipanuk and P. A. Karplus, *Biochemistry*, 2008, **47**, 11390.

122 J. A. Crawford, W. Li and B. S. Pierce, *Biochemistry*, 2011, **51**, 10241.

123 M. J. Frisch *et al*. *Gaussian*-09, Revision A.02, Wallingford, CT, 2009.

124 *Jaguar* 7.6, Schrödinger LLC, New York NY, 2007.

125 R. Ahlrichs, M. Bär, M. Häser, H. Horn and C. Kölmel, *Chem. Phys. Lett*., 1989, **162**, 165.

126 F. Neese, *ORCA – an ab initio, DFT and semiempirical SCF-MO package*, Bonn, Germany, Version 2.7-00, 2009.

127 E. Schrödinger, *Phys. Rev.*, 1926, **28**, 1049.

128 P. W. Atkins and R. S. Friedman, *Molecular Quantum Mechanics*, 3rd Ed., Oxford University Press, 1997.

129 F. Jensen, *Introduction to Computational Chemistry*, 2nd Ed., John Wiley & Sons, Ltd., Chichester, 2007.

130 S. P. de Visser. *Introduction to quantum behaviour – a primer*. In *Quantum Tunnelling in Enzyme-Catalysed Reactions*, R. K. Alleman and N. S. Scrutton, Eds.; RSC Publishing, Cambridge, 2009, Chapter 2, p 18.

131 C. Møller and M. S. Plesset, *Phys. Rev*., 1934, **46**, 0618.

132 S. P. de Visser, *J. Biocatal. Biotransf*., 2012, **1**, 1.

133 P. Hohenberg and W. Kohn, *Phys. Rev. B*, 1964, **136**, 864.

134 W. Kohn and L. J. Sham, *Phys. Rev. A*, 1965, **140**, 1133.

135 J. C. Slater, *The self-consistent field for molecular and solids*. In *Quantum Theory of Molecular and Solids*, McGraw-Hill, New York, 1974, Vol. 4.

136 S. H. Vosko, L. Wilk and M. Nusair, *Can. J. Phys*., 1980, **58**, 1200.

137 C. Lee, W. Yang and R. G. Parr, *Phys. Rev. B*, 1988, **37**, 785.

138 J. P. Perdew and Y. Wang, *Phys. Rev. B*, 1992, **45**, 13244.

139 A. D. Becke, *J. Chem. Phys*., 1993, **98**, 5648.

140 M. Reiher, O. Salomon and B. A. Hess, *Theor. Chem. Acc*., 2001, **107**, 48.

141 T. Schwabe and S. Grimme, *Phys. Chem. Chem. Phys*., 2007, **9**, 3397.

142 E. Hückel, *Z. Physik*, 1931, **70**, 204.

143 H. Hellmann, *J. Chem. Phys*., 1935, **3**, 61.

144 P. J. Hay and W. R. Wadt, *J. Chem. Phys.*, 1985, **82**, 270.

145 D. Kumar, B. Karamzadeh, G. N. Sastry and S. P. de Visser, *J. Am. Chem. Soc*., 2010, **132**, 7656.

146 J. H. Jensen, *Molecular Modeling Basics*. CRC Press, Boca Raton, 2010.

147 J. Tomasi, B. Mennucci and R. Cammi, *Chem. Rev*., 2005, **105**, 2999.

148 H. M. Senn and W. Thiel, *Top. Curr. Chem*., 2007, **268**, 173.

149 D. Bakowies and W. Thiel, *J. Phys. Chem*., 1996, **100**, 10580.

150 A. K. Rappé, C. J. Casewit, K. S. Colwell, W. A. Goddard III and W. M. Skiff, *J. Am. Chem. Soc*., 1992, **114**, 10024.

151 W. D. Cornell, P. Cieplak, C. I. Bayly, I. R. Gould, K. M. Merz Jr., D. M. Ferguson, D. C. Spellmeyer, T. Fox, J. W. Caldwell and P. A. Kollman, *J. Am. Chem. Soc*., 1995, **117**, 5179.

152 A. D. MacKerell Jr, *et al*, *J. Phys. Chem. B*, 1998, **102**, 3586.

153 F. Ogliaro, N. Harris, S. Cohen, M. Filatov, S. P. de Visser and S. Shaik, *J. Am. Chem. Soc*., 2000, **122**, 8977.

154 S. P. de Visser, F. Ogliaro, P. K. Sharma and S. Shaik, *Angew. Chem. Int. Ed*., 2002, **41**, 1947.

155 S. P. de Visser, D. Kumar, S. Cohen, R. Shacham and S. Shaik, *J. Am. Chem. Soc*., 2004, **126**, 8362.

156 S. P. de Visser, F. Ogliaro, N. Harris and S. Shaik, *J. Am. Chem. Soc*., 2001, **123**, 3037.

157 S. P. de Visser, F. Ogliaro and S. Shaik, *Angew. Chem. Int. Ed*., 2001, **40**, 2871.

158 S. P. de Visser and S. Shaik, *J. Am. Chem. Soc*., 2003, **125**, 7413.

159 M. T. Green, *J. Am. Chem. Soc*., 1999, **121**, 7939.

160 F. Ogliaro, S. P. de Visser, S. Cohen, J. Kaneti and S. Shaik, *ChemBioChem*., 2001, **2**, 848.

161 F. Ogliaro, S. Cohen, S. P. de Visser and S. Shaik, *J. Am. Chem. Soc*., 2000, **122**, 12892.

162 J. C. Schöneboom, H. Lin, N. Reuter, W. Thiel, S. Cohen, F. Ogliaro and S. Shaik, *J. Am. Chem. Soc*., 2002, **124**, 8142.

163 S. P. de Visser, S. Shaik, P. K. Sharma, D. Kumar and W. Thiel, *J. Am. Chem. Soc*., 2003, **125**, 15779.

164 S. Shaik, S. P. de Visser, F. Ogliaro, H. Schwarz and D. Schröder, *Curr. Opin. Chem. Biol*., 2002, **6**, 556.

165 D. Kumar, S. P. de Visser and S. Shaik, *J. Am. Chem. Soc*., 2003, **125**, 13024.

166 P. Nicholls, I. Fita and P. C. Loewen, *Adv. Inorg. Chem*., 2000, **51**, 51.

167 N. G. Veitch and A. T. Smith, *Adv. Inorg. Chem.*, 2000, **51**, 107.

168 J. H. Dawson, R. H. Holm, J. R. Trudell, G. Barth, R. E. Linder, E. Bunnenberg, C. Djerassi and S. C. Tang, *J. Am. Chem. Soc*., 1976, **98**, 3707.

169 T. L. Poulos, *J. Biol. Inorg. Chem*., 1996, **1**, 356.

170 S. P. de Visser, *J. Phys. Chem. A*, 2005, **109**, 11050.

171 S. P. de Visser, *Inorg. Chem*., 2006, **45**, 9551.

172 R. Wang and S. P. de Visser, *J. Inorg. Biochem*., 2007, **101**, 1464.

173 C. A. Bonagura, B. Bhaskar, H. Shimizu, H. Li, M. Sundaramoorthy, D. E. McRee, D. B. Goodin and T. L. Poulos, *Biochemistry*, 2003, **42**, 5600.

174 E. O'Reilly, V. Köhler, S. L. Flitch and N. J. Turner, *Chem. Commun*., 2010, **47**, 2490.

175 H. M. Girvan, C. W. Levy, P. Williams, K. Fisher, M. R. Cheesman, S. E. Rigby, D. Leys and A. W. Munro, *Biochem. J*., 2010, **427**, 455.

176 S. P. de Visser, F. Ogliaro, P. K. Sharma and S. Shaik, *J. Am. Chem. Soc*., 2002, **124**, 11809.

177 L. E. Friedrich, *J. Org. Chem*., 1983, **48**, 3851.

178 F. G. Bordwell and J.-P. Cheng, *J. Am. Chem. Soc*., 1991, **113**, 1736.

179 J. M. Mayer, *Acc. Chem. Res*., 1998, **31**, 441.

180 S. P. de Visser, *J. Am. Chem. Soc*., 2010, **132**, 1087.

181 M. G. Evans and M. Polanyi, *J. Chem. Soc., Faraday Trans*., 1936, **32**, 1340.

182 S. Shaik, D. Kumar and S. P. de Visser, *J. Am. Chem. Soc*., 2008, **130**, 10128.

183 R. Latifi, J. S. Valentine, W. Nam and S. P. de Visser, *Chem. Commun*., 2012, **48**, 3491.

184 D. Kumar, L. Tahsini, S. P. de Visser, H. Y. Kang, S. J. Kim and W. Nam, *J. Phys. Chem. A*, 2009, **113**, 11713.

185 L. Tahsini, M. Bagherzadeh, W. Nam and S. P. de Visser, *Inorg. Chem*., 2009, **48**, 6661.

186 R. Latifi, L. Tahsini, B. Karamzadeh, N. Safari, W. Nam and S. P. de Visser, *Arch. Biochem. Biophys*., 2011, **507**, 4.

187 S. P. de Visser and L. S. Tan, *J. Am. Chem. Soc*., 2008, **130**, 12961.

188 S. P. de Visser, *Biochem. Soc. Trans*., 2009, **37**, 373.

189 B. E. Daikh, J. M. Lasker, J. L. Raucy and D. R. Koop, *J. Pharmacol. Exp. Therap*., 1994, **271**, 1427.

190 C. Helvig, J. F. Koener, G. C. Unnithan and R. Feyereisen, *Proc. Natl. Acad. Sci. USA*, 2004, **101**, 4024.

191 S. P. de Visser, D. Kumar and S. Shaik, *J. Inorg. Biochem*., 2004, **98**, 1183.

192 D. Kumar, S. P. de Visser and S. Shaik, *Chem. Eur. J*., 2005, **11**, 2825.

193 K. L. Kunze, B. L. K. Mangold, C. Wheeler, H. S. Beilan and P. R. Ortiz de Montellano, *J. Biol. Chem*., 1983, **258**, 4202.

194 S. P. de Visser, *Phys. Chem. Chem. Phys*., 1999, **1**, 749.

195 S. P. de Visser, *J. Phys. Chem. B*, 2011, **115**, 4709.

196 S. P. de Visser, *Chem. Phys. Lett*., 2011, **515**, 170.

197 J. Wójcikowski, P. Maurel and W. A. Daniel, *Drug Metabol. Disp*., 2006, **34**, 471.

198 D. Kumar, S. P. de Visser, P. K. Sharma, H. Hirao and S. Shaik. *Biochemistry*, 2005, **44**, 8148.

199 D. Kumar, G. N. Sastry and S. P. de Visser, *Chem. Eur. J*., 2011, **17**, 6196.

200 K. A. Prokop, H. M. Neu, S. P. de Visser and D. P. Goldberg, *J. Am. Chem. Soc*., 2011, **133**, 15874.

201 Y. Watanabe, T. Iyanagi and S. Oae, *Tetrahedron Lett*., 1982, **23**, 533.

202 S. P. de Visser, *Chem. Eur. J*., 2006, **12**, 8168.

203 C. Hazan, D. Kumar, S. P. de Visser and S. Shaik, *Eur. J. Inorg. Chem*., 2007, 2966.

204 D. Kumar, G. N. Sastry and S. P. de Visser, *J. Phys. Chem. B*, 2012, **116**, 718.

205 S. P. de Visser, K. Oh, A.-R. Han and W. Nam, *Inorg. Chem*., 2007, **46**, 4632.

206 S. P. de Visser, L. Tahsini and W. Nam, *Chem. Eur. J*., 2009, **15**, 5577.

207 S. P. de Visser, R. Latifi, L. Tahsini and W. Nam, *Chem. Asian J*., 2011, **6**, 493.

208 D. Kumar, S. P. de Visser, P. K. Sharma, S. Cohen and S. Shaik, *J. Am. Chem. Soc*., 2004, **126**, 1907.

209 D. Kumar, S. P. de Visser and S. Shaik, *J. Am. Chem. Soc*., 2004, **126**, 5072.

210 S. P. de Visser, *Chem. Commun*., 2007, 171.

211 I. A. Topol, A. V. Nemukhin, K. Salnikow, R. E. Cachau, Y. G. Abashkin, K. S. Kasprzak and S. K. Burt, *J. Phys. Chem. A*, 2006, **110**, 4223.

212 A. R. Diebold, C. D. Brown-Marshall, M. L. Neidig, J. M. Brownlee, G. R. Moran and E. I. Solomon, *J. Am. Chem. Soc*., 2011, **133**, 18148.

213 L. M. Mirica, K. P. McCusker, J. W. Munos, H.-w. Liu and J. P. Klinman, *J. Am. Chem. Soc*., 2008, **130**, 8122.

214 E. Godfrey, C. S. Porro and S. P. de Visser, *J. Phys. Chem. A*, 2008, **112**, 2464.

215 S. P. de Visser, *J. Am. Chem. Soc*., 2006, **128**, 9813.

216 S. Sinnecker, N. Svensen, E. W. Barr, S. Ye, J. M. Bollinger Jr, F. Neese and C. Krebs, *J. Am. Chem. Soc*., 2007, **129**, 6168.

217 A. V. Nemukhin, I. A. Topol, R. E. Cachau and S. K. Burt, *Theor. Chem. Acc*., 2006, **115**, 348.

218 S. Ye and F. Neese, *Proc. Natl. Acad. Sci. USA*, 2011, **108**, 1228.

219 B. Karamzadeh, D. Kumar, G. N. Sastry and S. P. de Visser, *J. Phys. Chem. A*, 2010, **114**, 13234.

220 P. K. Grzyska, E. H. Appelman, R. P. Hausinger and D. A. Proshlyakov, *Proc. Natl. Acad. Sci. USA*, 2010, **107**, 3982.

221 Z. Gross, *J. Biol. Inorg. Chem*., 1996, **1**, 368.

222 M. T. Green, *J. Am. Chem. Soc*., 2006, **128**, 1902.

223 S. P. de Visser, *Angew. Chem. Int. Ed*., 2006, **45**, 1790.

224 R. Latifi, M. Bagherzadeh and S. P. de Visser, *Chem. Eur. J*., 2009, **15**, 6651.

225 C. Geng, S. Ye and F. Neese, *Angew. Chem. Int. Ed*., 2010, **49**, 5717.

226 S. P. de Visser, *J. Am. Chem. Soc*., 2006, **128**, 15809.

227 D. Kumar, H. Hirao, L. Que Jr. and S. Shaik, *J. Am. Chem. Soc*., 2005, **127**, 8026.

228 H. Hirao, D. Kumar, L. Que Jr. and S. Shaik, *J. Am. Chem. Soc*., 2006, **128**, 8590.

229 K. A. Prokop, S. P. de Visser and D. P. Goldberg, *Angew. Chem. Int. Ed*., 2010, **49**, 5091.

230 P. Leeladee, R. A. Baglia, K. A. Prokop, R. Latifi, S. P. de Visser and D. P. Goldberg, *J. Am. Chem. Soc*., 2012, **134**, 10397.

231 S. P. de Visser and W. Nam, *J. Phys. Chem. A*, 2008, **112**, 12887.

232 K. Chen and L. Que Jr, *J. Am. Chem. Soc*., 2001, **123**, 6327.

233 A. Company, Y. Feng, M. Güell, X. Ribas, J. M. Luis, L. Que Jr. and M. Costas, *Chem. Eur. J*., 2009, **15**,3359.

234 I. Prat, J. S. Mathieson, M. Güell, X. Ribas, J. M. Luis, L. Cronin and M. Costas, *Nature Chem*., 2011, **3**, 788.

235 A. Bassan, M. R. A. Blomberg, P. E. M. Siegbahn and L. Que Jr, *Angew. Chem. Int. Ed*., 2005, **44**, 2939.

236 J. Bautz, P. Comba, C. Lopez de Laorden, M. Menzel and G. Rajaraman, *Angew. Chem. Int. Ed*., 2007, **46**, 8067.

237 P. Comba and G. Rajaraman, *Inorg. Chem*., 2008, **47**, 78.

238 S. P. de Visser and R. Latifi, *J. Phys. Chem. B*, 2009, **113**, 12.

239 M. G. Quesne and S. P. de Visser, *J. Biol. Inorg. Chem*., 2012, **17**, 841.

240 S. J. Lange, H. Miyake and L. Que Jr, *J. Am. Chem. Soc*., 1999, **121**, 6330.

241 M. P. Jensen, S. J. Lange, M. P. Mehn, E. L. Que and L. Que Jr, *J. Am. Chem. Soc*., 2003, **125**, 2113.

242 N. Y. Oh, M. S. Seo, M. H. Lim, M. B. Consugar, M. J. Park, J.-U. Rohde, J. Han, K. M. Kim, J. Kim, L. Que Jr and W. Nam, *Chem. Commun*., 2005, 5644.

243 M. R. Bukowski, K. D. Koehntop, A. Stubna, E. L. Bominaar, J. A. Halfen, E. Münck, W. Nam and L. Que Jr, *Science*, 2005, **310**, 1000.

244 Y. M. Badlei, M. Siegler and D. P. Goldberg, *J. Am.Chem. Soc*., 2011, **133**, 1274.

245 M. Sallmann, I. Siewert, L. Fohlmeister, C. Limberg and C. Knispel, *Angew. Chem., Int. Ed*., 2012, **51**, 2234.

246 D. Kumar, G. N. Sastry, D. P. Goldberg and S. P. de Visser, *J. Phys. Chem. A*, 2012, **116**, 582.

247 L. E. Gonzalez-Ovalle, M. G. Quesne, D. Kumar, D. P. Goldberg and S. P. de Visser, *Org. Biomol. Chem*., 2012, **10**, 5401.

248 S. P. de Visser, J. S. Valentine and W. Nam, *Angew. Chem. Int. Ed*., 2010, **49**, 2099.

249 A. K. Vardhaman, C. V. Sastri, D. Kumar and S. P. de Visser, *Chem. Commun*., 2011, **47**, 11044.

250 J. Annaraj, J. Cho, Y.-M. Lee, S. Y. Kim, R. Latifi, S. P. de Visser and W. Nam, *Angew. Chem. Int. Ed*., 2009, **48**, 4150.

251 R. Latifi, L. Tahsini, D. Kumar, G. N. Sastry, W. Nam and S. P. de Visser, *Chem. Commun*., 2011, **47**, 10674.

252 R. Latifi, L. Tahsini, W. Nam and S. P. de Visser, *Phys. Chem. Chem. Phys*., 2012, **14**, 2518.

253 R. Latifi, M. Bagherzadeh, B. F. Milne, M. Jaspars and S. P. de Visser, *J. Inorg. Biochem*., 2008, **102**, 2171.

254 S. J. Kim, R. Latifi, H. Y. Kang, W. Nam and S. P. de Visser, *Chem. Commun*., 2009, 1562.

255 S. P. de Visser, *J. Phys. Chem. B*, 2006, **110**, 20759.

256 S. P. de Visser, *J. Phys. Chem. B*, 2007, **111**, 12299.

257 S. P. de Visser, *The axial ligand effect on substrate monoxygenation by the oxo-iron active species of heme enzymes. How does cytochrome c peroxidase compare to cytochrome P450?* In *Inorganic Biochemistry: Research Progress*, J. G. Hughes and A. J. Robinson, Eds.; Nova Science Publishers, Inc., New York, 2008, Chapter 7, pp. 197–224.

258 S. P. de Visser, *J. Biol. Inorg. Chem*., 2006, **11**, 168.

259 S. P. de Visser, Y.-M. Lee and W. Nam, *Eur. J. Inorg. Chem*., 2008, 1027.

260 S. P. de Visser, *Chem. Eur. J*., 2008, **14**, 4533.

261 S. P. De Visser, **D.Sc. Thesis**, University of Mancestor, 2012

262 S. Kumar, A. S. Faponle, P. Barman, A. K. Vardhaman, C. V. Sastri, Devesh Kumar, and S. P. de Visser, *J. Am. Chem. Soc.*, 2014, **136**, 17102.

263 B. Karamzadeh, D. Singh, W. Nam, Devesh Kumar and S. P. de Visser, *Phys. Chem. Chem. Phys*., 2014, **16**, 22611.

264 M. A. Sainna, S. Kumar, Devesh Kumar, S. Fornarini, M. E. Crestoni, and S. P. de Visser, *Chem.Sci.*, 2015, **6**, 1516.

265 M. A. Sainna, Devendra Singh, Devesh Kumar, and S. P. de Visser, *Organometallics* 2015, **34**, 1651.

266 Li Ji, A. S. Faponle, M. G. Quesne, M. A. Sainna, J. Zhang, A. Franke, Devesh Kumar, R. van Eldik, W. Liu, and S. P. de Visser, *Chem. Eur. J*. 2015, **21**, 9083.

267 Madleen Sallmann, Suresh Kumar, Petko Chernev, Joscha Nehrkorn, Alexander Schnegg, Devesh Kumar, Holger Dau, Christian Limberg, and Sam P. de Visser, *Chem. Eur. J*. 2015, **21**, 7470.

268 P. Barman, P. Upadhyay, A. S. Faponle, J. Kumar, S. S. Nag, Devesh Kumar, C. V. Sastri, and S. P. de Visser, *Angew. Chem. Int. Ed*., 2016, **55**, 11091.

269 F. G. C. Reinhard, P. Barman, G. Mukherjee, J. Kumar, D. Kumar, Devesh Kumar, Chivukula V. Sastri, and Sam P. de Visser, *J. Am. Chem. Soc.*, 2017, **139**, 18328.

270 G Mukherjee, A Alili, P Barman, Devesh Kumar, C V Sastri, and S P de Visser, *Chem.–A Euro. J.*, 2019, **25**, 5086.

271 P Barman, F C Reinhard, U K Bagha, Devesh Kumar, C V Sastri, and S P de Visser *Angew. Chem. Int. Ed.* 2019, **58**, 10639.

Appendix

Paper #1:

P Barman, F C Reinhard, U K Bagha, **Devesh Kumar**, C V Sastri, S P de Visser

Hydrogen by Deuterium Substitution in an Aldehyde Tunes the Regioselectivity by a Nonheme Manganese (III)-Peroxo Complex.

***Angew. Chem. Int. Ed.* 2019**, *58*, 10639 –10643

Paper #2:

G Mukherjee, A Alili, P Barman, **Devesh Kumar**, C V Sastri, S P de Visser

Interplay Between Steric and Electronic Effects: A Joint Spectroscopy and Computational Study of Nonheme Iron (IV)-Oxo Complexes.

***Chem.–A Euro. J.* 2019**, *25*, 5086-5098.

Paper #3:

F S T Khan, S Banerjee, **Devesh Kumar**, S P Rath

Diheme Cytochrome c: Structure–Function Correlation and Effect of Heme−Heme Interactions.

Inorg. Chem. **2018**, *57*, 11498-11510.

Paper #4:

G. Mukherjee, C WZ Lee, S. Sekhar Nag, A. Alili, F. G Cantú Reinhard, **Devesh Kumar**, C V Sastri, S P de Visser

Dramatic rate-enhancement of oxygen atom transfer by an iron (iv)-oxo species by equatorial ligand field perturbations.

Dalton Trans. **2018**, *42*, 14945-14957.

Paper #5:

F. G. C. Reinhard, P. Barman, G. Mukherjee, J. Kumar, D. Kumar, **Devesh Kumar**, Chivukula V. Sastri, and Sam P. de Visser

Keto−Enol Tautomerization Triggers an Electrophilic Aldehyde Deformylation Reaction by a Nonheme Manganese(III)-Peroxo Complex.

J. Am. Chem. Soc. **2017**, *139*, 18328−18338.

Paper #6:

F. G. C. Reinhard, M. A. Sainna, P. Upadhyay, G. A. Balan, **Devesh Kumar**, S. Fornarini, M. E. Crestoni, Sam P. de Visser

A Systematic Account on Aromatic Hydroxylation by a Cytochrome P450 Model Compound I: A Low-Pressure Mass Spectrometry and Computational Study.

Chem. Eur. J. **2016**, *22*, 18608 – 18619.

Paper #7:

P. Barman, P. Upadhyay, A. S. Faponle, J. Kumar, S. S. Nag, **Devesh Kumar**, C. V. Sastri, S. P. de Visser

Deformylation Reaction by a Nonheme Manganese(III)–PeroxoComplex via Initial Hydrogen-Atom Abstraction.

Angew. Chem. Int. Ed. **2016**, *55*, 11091 –11095.

Paper #8:

M. G. Quesne, D. Senthilnathan, D. Singh, **Devesh Kumar**, P. Maldivi, A. B. Sorokin, Sam P. de Visser

Origin of the Enhanced Reactivity of μ-Nitrido-Bridged Diiron(IV)-Oxo Porphyrinoid Complexes over Cytochrome P450 Compound I.

ACS Catal. **2016**, *6*, 2230−2243.

Paper #9:

Madleen Sallmann, Suresh Kumar, Petko Chernev, Joscha Nehrkorn, Alexander Schnegg, **Devesh Kumar**, Holger Dau, Christian Limberg, Sam P. de Visser

Structure and Mechanism Leading to Formation of the Cysteine Sulfinate Product Complex of a Biomimetic Cysteine Dioxygenase Model.

Chem. Eur. J. **2015**, *21*, 7470 – 7479.

Paper #10:

Li Ji, A. S. Faponle, M. G. Quesne, M. A. Sainna, J. Zhang, A. Franke, **Devesh Kumar**, R. van Eldik, W. Liu, S. P. de Visser

Drug Metabolism by Cytochrome P450 Enzymes: What Distinguishes the Pathways Leading to Substrate Hydroxylation Over Desaturation?

Chem. Eur. J. **2015**, *21*, 9083 – 9092.

Paper #11:

M. A. Sainna, Devendra Singh, **Devesh Kumar**, S. P. de Visser

A Trimetal Carbene with Reactivity Reminiscent of Fischer−Tropsch Catalysis.

Organometallics **2015**, *34*, 1651-1660.

Paper #12:

M. A. Sainna, S. Kumar, **Devesh Kumar**, S. Fornarini, M. E. Crestoni, S. P. de Visser

A comprehensive test set of epoxidation rate constants for iron(IV)--oxo porphyrin complexes.

Chem.Sci. **2015**, *6*, 1516–1529.

Paper #13:

S. Kumar, A. S. Faponle, P. Barman, A. K. Vardhaman, C. V. Sastri, Devesh Kumar, S. P. de Visser

Long-Range Electron Transfer Triggers Mechanistic Differences between Iron(IV)-Oxo and Iron(IV)-Imido Oxidants.

J. Am. Chem. Soc. **2014**, *136*, 17102-17115.

Paper #14:

B. Karamzadeh, D. Singh, W. Nam, **Devesh Kumar,** S. P. de Visser

Properties and reactivities of nonheme iron(IV)–oxo versus iron(V)–oxo: long-range electron transfer versus hydrogen atom abstraction.

Phys. Chem. Chem. Phys. **2014**, *16*, 22611-22622.

Paper #15:

. D. Saha, Ravi Verma, **Devesh Kumar**, S. Pathak, S. Bhunya, A. Sarkar

A “Hemilabile” Palladium−Carbon Bond: Characterization and Its Implication in Catalysis.

Organometallics **2014**, *33*, 3243−3246.

Paper #16:

L. R. Widger, Y. Jiang, A. C. McQuilken, T. Yang, M. A. Siegler, H. Matsumura, P. Moënne-Loccoz, **Devesh Kumar**, S. P. de Visser, D. P. Goldberg

Thioether-ligated iron (II) and iron (III)-hydroperoxo/alkylperoxo complexes with an H-bond donor in the second coordination sphere.

Dalton Transactions **2014**, *43*, 7522-7532.

Paper #17:

M. G. Quesne, R. Latifi, L. E. Gonzalez-Ovalle, **Devesh Kumar**, and S. P. de Visser

Quantum Mechanics/Molecular Mechanics Study on the Oxygen Binding and Substrate Hydroxylation Step in AlkB Repair Enzymes.

Chem. Eur. J. **2014**, *20*, 435 – 446.

Paper #18:

Anil Kumar Vardhaman, Prasenjit Barman, Suresh Kumar, C. V. Sastri, **Devesh Kumar**, Sam P. de Visser

Mechanistic insight into halide oxidation by non-heme iron complexes. Haloperoxidase versus halogenase activity.

***Chem.Commun.* 2013**, 49, 10926-10928.

Paper #19:

A. K. Vardhaman, P. Barman, S. Kumar, C. V. Sastri, **Devesh Kumar**, Sam P. de Visser

. Comparison of the Reactivity of Nonheme Iron(IV)–Oxo versus Iron(IV)–Imido Complexes: Which is the Better Oxidant?

Angew. Chem. Int. Ed. **2013***, 52,*12288-12292.

Paper #20:

L. R. Widger, Y. Jiang, M. Siegler, **Devesh Kumar**, R. Latifi, S. P. de Visser, G. N. L. Jameson, D. P. Goldberg

Synthesis and Ligand Non-Innocence of Thiolate-Ligated (N4S) Iron(II) and Nickel(II) Bis(imino)pyridine Complexes.

InorgChem* 2013, 52,* 10467–10480.

Paper #21:

S. M. Pratter, C. Konstantinovics, C. L. M. DiGiuro, E. Leitner, **Devesh Kumar**, S. P. de Visser, G. Grogan, and G. D. Straganz

. Inversion of Enantioselectivity of a Mononuclear Non-Heme Iron(II)-dependent Hydroxylase by Tuning the Interplay of Metal-Center Geometry and Protein Structure.

Angew. Chem. Int. Ed. 2013*, 52,*9677-9681,

Paper #22:

Devesh Kumar, R. Latifi, S. Kumar, E. V. Rybak-Akimova, M. A. Sainna, Sam P. de Visser

Rationalization of the Barrier Height for p-Z-styrene Epoxidation by Iron(IV)-Oxo Porphyrin Cation Radicals with Variable Axial Ligands.

***Inorg. Chem.* 2013**, *52*, 7968–7979.

Paper #23:

P. Leeladee, G. Jameson, M. Siegler, **Devesh Kumar**, Sam de Visser, David P. Goldberg

Generation of a High-Valent Iron Imido Corrolazine Complex and NR Group Transfer Reactivity.

Inorg. Chem. **2013**, *52*, 4668-4682.

Paper #24:

L. E. Gonzalez-Ovalle, M. G. Quesne, **Devesh Kumar**, D. P. Goldberg, Sam P. de Visser

Axial and equatorial ligand effects on biomimetic cysteine dioxygenase model complexes.

Org. Biomolec. Chem. **2012**, *10*, 5401-5409.

Paper #25:

Devesh Kumar, G. Narahari Sastry, Sam P. de Visser

Axial Ligand Effect On The Rate Constant of Aromatic Hydroxylation By Iron(IV)- Oxo Complexes Mimicking Cytochrome P450 Enzymes.

J. Phys. Chem. B **2012**, *116*, 718-730.

Paper #26:

Devesh Kumar, G. Narahari Sastry, David P. Goldberg, Sam P. de Visser

Mechanism of S-Oxygenation by a Cysteine Dioxygenase Model Complex.

J. Phys. Chem. A **2012**, *116*, 582-591.

Paper #27:

A. K. Vardhaman, C. V. Sastri, **Devesh Kumar**, Sam P. de Visser

Nonheme Ferric Hydroperoxo Intermediates Are Efficient Oxidants of Bromide Oxidation.

ChemComm 2011, *47*, 11044 - 11046.

Paper #28:

R. Latifi, L. Tahsini, **Devesh Kumar**, G. Narahari Sastry, W. Nam, Sam P. de Visser

Oxidative properties of a nonheme Ni(II)(O_2) complex: Reactivity patterns for C–H activation, aromatic hydroxylation and heteroatom oxidation.

ChemComm 2011, *47*, 10674-10676.

Paper #29:

Devesh Kumar

Drug metabolism by Cytochrome P450: A tale of multistate reactivity.

In:

"*Iron-Containing Enzymes: Versatile Catalysts of Hydroxylation Reactions in Nature", Eds. S. P. Visser, D. Kumar, The Royal Society of Chemistry, U.K., (2011) Ch. 9 pp 281-329.*

Paper #30:

Sam P. de Visser and Devesh Kumar (Eds.)

Iron-containing enzymes: Versatile catalysts of hydroxylation reactions in nature;

Royal Society of Chemistry Publishing, Cambridge (UK),

2011.

Paper #31:

Devesh Kumar, Walter Thiel, S. P. de Visser

Theoretical study on the mechanism of the oxygen activation process in cysteine dioxygenase enzymes.

***J. Am. Chem. Soc.* 2011**, *133*, 3869-3882.

Paper #32:

Devesh Kumar, G. N. Sastry, S. P. de Visser

Effect of the Axial Ligand on Substrate Sulfoxidation Mediated by Iron (IV)–Oxo Porphyrin Cation Radical Oxidants.

Chem. Eur. J. **2011**, *17*, 6196-6205.

Paper #33:

Devesh Kumar, A. Altun, S. Shaik, W. Thiel

Water as biocatalyst in cytochrome P450.

Faraday Discussions* 2011, 148*, 373-383.

Paper #34:

B. Karamzadeh, **Devesh Kumar**, G. N. Sastry, S. P. de Visser

Steric Factors Override Thermodynamic Driving Force in Regioselectivity of Proline Hydroxylation by Prolyl-4-hydroxylase Enzymes.

J. Phys. Chem. A **2010**, *114*; 13234-13243.

Paper #35:

Devesh Kumar, B. Karamzadeh, G. Narahari Sastry, S. P. de Visser

What Factors Influence the Rate Constant of Substrate Epoxidation by Compound I of Cytochrome P450 and Analogous Iron(IV)-Oxo Oxidants.

***J. Am. Chem. Soc.* 2010**,*132*, 7656–7667.

Paper #36:

M. Altarsha, T. Benighaus, **Devesh Kumar**, W. Thiel

Coupling and uncoupling mechanisms in the methoxythreonine mutant of cytochrome P450cam: a quantum mechanical/ molecular mechanical study.

Biol. Inorg. Chem. **2010**, *15*, 361-372.

Paper #37:

S. Shaik, S. Cohen, Y. Wang, H. Chen, **D. Kumar** & W. Thiel

. P450 Enzymes: Their Structure, Reactivity and Selectivity, Modeled by QM/MM Calculations.

***Chem. Rev*. 2010**, *110*, 949-1017.

Paper #38:

Devesh Kumar, L. Tahsini, S. P. de Visser, H. Y. Kang, S. J. Kim, W. Nam

Effect of Porphyrin Ligands on the Regioselective Dehydrogenation versus Epoxidation of Olefins by Oxoiron(IV) Mimics of Cytochrome P450.

***J. Phys. Chem. A* 2009**, *113*, 11713-11722.

Paper #39:

C. S. Porro, **Devesh Kumar**, S. P. de Visser

Electronic properties of pentacoordinated heme complexes in cytochrome P450 enzymes: Search for an Fe(I) Oxidation State

Phys. Chem. Chem. Phys. **2009**, *11*, 10219-10226.

Paper #40:

M. Altarsha, W. Dongqi, T. Benighaus, **Devesh Kumar**, W. Thiel

QM/MM Study of the Second Proton Transfer in the Catalytic Cycle of the D251N Mutant of Cytochrome P450cam.

J. Phys. Chem. B **2009**, *113*, 9577-9588.

Paper #41:

M. Altarsha, T. Benighaus, **Devesh Kumar**, W. Thiel

How is the Reactivity of Cytochrome P450cam Affected by Thr252X Mutation? A QM/MM Study for X = Serine, Valine, Alanine, Glycine.

J. Am. Chem. Soc. **2009**, *131*, 4755-4763.

Paper #42:

A. Altun, **Devesh Kumar**, F. Neese, W. Thiel

Multi-reference Ab Initio QM/MM Study on Intermediates in the Catalytic Cycle of Cytochrome P450cam.

J. Phys. Chem. A **2008**, *112*, 12904-12910.

Paper #43:

S. Shaik, **Devesh Kumar**, S. P. de Visser

A Valence Bond Modeling of Trends in Hydrogen Abstraction Barriers and Transition States of Hydrogen Reactions Catalyzed by Cytochrome P450 Enzymes.

***J. Am. Chem. Soc.* 2008**, *130*, 10128-10140.

Paper #44:

Y. Wang, **Devesh Kumar**, C. Yang, K. Han, S. Shaik

Theoretical Study of N-Demethylation of Substituted N,N-Dimethylanilines by Cytochrome P450: The Mechanistic Significance of Kinetic Isotope Effect Profiles.

J. Phys. Chem. B **2007**, *111*, 7700-7710.

Paper #45:

C. Hazan, **Devesh Kumar**, S. P. de Visser, S. Shaik

A Density Functional Study of the Factors that Influence the regioselectivity of Toluene Hydroxylation by Cytochrome P450 enzyme?

Eur. J. Inorg. Chem. **2007**, 2966-2974.

Paper #46:

S. Shaik, H. Hirao, **Devesh Kumar**

Reactivity patterns of cytochrome P450 enzymes: Multifunctionality of the active species and the two states – two oxidants conundrum.

Natural Product Reports **2007**, *24*, 533-552..

Paper #47:

S. Shaik, H. Hirao, **Devesh Kumar**

Reactivity of High-Valent Iron Oxo Species in Enzymes and Synthetic Reagents: A Tale of Many States.

***Acc. Chem. Res.* 2007**, *40*, 532-542.

Paper #48:

C. A. Grapperhaus, P. M. Kozlowski, **Devesh Kumar**, H. N. Frye, K. B. Venna, S. Poturovic

Singlet Diradical Character of an Oxidized Ruthenium Trithiolate: Electronic Structure and Reactivity.

Angew. Chem. Int. Ed. **2007**, *46*, 4085-4088..

Paper #49:

K.-B. Cho, Y. Moreau, **DeveshKumar**, D. Rock, J. P. Jones, S. Shaik

Formation of the Active Species of Cytochrome P450 Using Iodosylbenzene: A Case for Spin Selective Reactivity.

Chem. Eur. J. **2007,** *13*, 4103 - 4115.

Paper #50:

H. Hirao, **Devesh Kumar**, S. Shaik

On the Identity and Reactivity Patterns of the "Second Oxidant" of the T252A Mutant of Cytochrome P450cam in the Oxidation of 5-Methylenenylcamphor.

***J. Ing. Biochem.* 2006**, *100*, 2054-2068.

Paper #51:

Devesh Kumar, H. Hirao, S. Shaik, P. M. Kozlowski

Proton-shuffle mechanism of O-O activation for formation of a high-valent oxo-iron species of Bleomycin.

***J. Am. Chem. Soc.* 2006,** *128*, 16148-16158.

Paper #52:

H. Hirao, **Devesh Kumar**, Lawrence Que Jr. & S. Shaik

Two-State Reactivity in Alkane Hydroxylation by Non-Heme Iron-Oxo Complexes.

***J. Am. Chem. Soc.* 2006**, *128*, 8590-8606.

Paper #53:

S. Cohen, **Devesh Kumar**, S. Shaik

In silico design of a mutant of cytochrome P450 containing selenocysteine.

***J. Am. Chem. Soc.* 2006,** *128*, 2649-2653.

Paper #54:

E. Derat, **Devesh Kumar**, H. Hirao, S. Shaik

Gauging the Relative Oxidative Powers of Compound I, Ferric-Hydroperoxide and the Ferric-Hydrogen Peroxide Species of Cytochrome P450 Towards C-H Hydroxylation of a Radical Probe Substrate.

***J. Am. Chem. Soc.* 2006**, *128*, 473-484.

Paper #55:

C. Li, W. Wu, **Devesh Kumar**, S. Shaik

Kinetic Isotope Effect is A Sensitive Probe of Spin State Reactivity in C-H Hydroxylation of N,N-Dimethyl Aniline by Cytochrome P450.

***J. Am. Chem. Soc.* 2006**, *128*, 394-395.

Paper #56:

Devesh Kumar, H. Hirao, S. P. de Visser, J. Zheng , D. Wang, W. Thiel, S. Shaik

New Feature in the Catalytic Cycle of Cytochrome P450 during the formation of Compound I from Compound 0.

J. Phys. Chem. B **2005,** *109*, 19946-19951.

Paper #57:

H.Hirao, **Devesh Kumar**, W. Thiel, S. Shaik

Two States and Two More in the Mechanisms of Hydroxylation and Epoxidation by Cytochrome P450.

***J. Am. Chem. Soc.* 2005,** *127*, 13007-13018.

Paper #58:

S. Shaik, **Devesh Kumar**, S. P. de Visser, A. Ahmet, W. Thiel

A Theoretical Perspective on Structure and Mechanisms of Cytochrome P450 Enzymes.

***Chem. Rev*. 2005**, *105*, 2279-2328.

Paper #59:

Devesh Kumar, S. P. de Visser, P. K. Sharma, H. Hirao, S. Shaik

Sulfoxidation Mechanisms Catalyzed by Cytochrome P450 and Horseradish Peroxidase Models: Spin-Selection Induced by the Ligand.

Biochemistry **2005,** *44*, 8148-8158.

Paper #60:

Devesh Kumar, S. P. de Visser, S. Shaik

Theory Favors A Stepwise Mechanism of Porphyrin Degradation By a Ferric Hydroperoxide Model of Active Speices of Heme Oxygenase.

***J. Am. Chem. Soc.* 2005**, *127*, 8204-8213.

Paper #61:

Devesh Kumar, H. Hirao, Lawrence Que Jr., S. Shaik

Theoretical Investigation of C-H Hydroxylation by $(N_4Py)Fe^{IV}=O^{2+}$: An Oxidant More Powerful than P450?

J. Am. Chem. Soc. **2005,** *127*, 8026 -8027.

Paper #63:

Devesh Kumar, S. P. de Visser, S. Shaik

Multi-state Reactivity in Styrene Epoxidation by Compound I of Cytochrome P450: Mechanisms of Products and Side Product Formations.

***Chem. Eur. J.* 2005,** *11*, 2825–2835.

Paper #64:

S. Shaik, S. P. de Visser, **Devesh Kumar**

One oxidant, many pathways: A theoretical perspective of monoxygenation mechanisms by cytochrome P450 enzymes.

J. Biol. Inorg. Chem. **2004,** *9*, 661-668.

Paper #65:

S. Shaik, S. P. de Visser, **Devesh Kumar**

External Electric Field Will Control the Selectivity of Enzymatic-Like Bond Activations.

***J. Am. Chem. Soc.* 2004,** *126*, 11746-11749.

Paper #66:

S. P. de Visser, **Devesh Kumar**, S. Cohen, R. Shacham, S. Shaik

A Predictive Pattern of Computed Barriers for C-H Hydroxylation by Compound I of Cytochrome P450.

***J. Am. Chem. Soc.* 2004,** *126*, 8362-8363.

Paper #67:

S. Shaik, S. Cohen, S. P.de Visser, P. K. Sharma, **Devesh Kumar**, S. Kozuch, F. Ogliaro, D. Danovich

The "Rebound Controversy": An Overview and Theoretical Modeling of the Rebound Step in C-H Hydroxylation by Cytochrome P450.

***Eur. J. Inorg. Chem*. 2004**, 207-226.

Paper #68:

S. P. de Visser, **Devesh Kumar**, S. Shaik

How Do Aldehyde Side Products Occur During Alkene Epoxidation by Cytochrome P450? Theory Reveals a State-Specific Multi-State Scenario Where the High-Spin Component Leads to All Side Products.

***J. Inorg. Biochem*. 2004,** *98*, 1183-1193.

Paper #69:

Devesh Kumar, S. P. de Visser, S. Shaik

Oxygen Economy of Cytochrome P450: What is the Origin of the Mixed Functionality as a Dehydrogenating-Oxidase Enzyme Compared with its Normal Function?

***J. Am. Chem. Soc.* 2004,** *126*, 5072-5073.

Paper #70:

P. K. Sharma, R. Kerkokiants, S. P. de Visser, **Devesh Kumar**, S. Shaik

Porphyrin Traps its Terminator! Concerted and Stepwise Porphyrin Degradation Mechanisms Induced by Heme-Oxygenase and Cytochrome P450.

***Angew. Chem. Int. Ed.* 2004**, *43*, 1129-1132.

Paper #71:

Devesh Kumar, S. P. de Visser, P. K. Sharma, S. Cohen, S. Shaik

Radical Clock Substrates, their C–H Hydroxylation Mechanism by Cytochrome P450 and Other Reactivity Patterns:; What Does Theory Reveal About the Clocks'- Behavior?

***J. Am. Chem. Soc.* 2004**, *126*, 1907-1920.

Paper #72:

S. P. de Visser, S. Shaik, P. K. Sharma, **Devesh Kumar**, W. Thiel

Active Species of Horseradish Peroxidase (HRP) and Cytochrome P450: Two Electronic Chameleons.

J. Am. Chem. Soc. **2003,** *125*, 15779-15788.

Paper #73:

Devesh Kumar, S. P. de Visser, S. Shaik

How Does Product Isotopes Effect Prove the Operation of a Two-State 'Rebound' Mechanism in C-H Hydroxylation by Cytochrome P450?

***J. Am. Chem. Soc.* 2003,** *125*, 13024 - 13025.

JACS
JOURNAL OF THE AMERICAN CHEMICAL SOCIETY
Article
Cite This: J. Am. Chem. Soc. 2017, 139, 18328–18338
pubs.acs.org/JACS

Keto–Enol Tautomerization Triggers an Electrophilic Aldehyde Deformylation Reaction by a Nonheme Manganese(III)-Peroxo Complex

Fabián G. Cantú Reinhard,[†] Prasenjit Barman,[‡] Gourab Mukherjee,[‡] Jitendra Kumar,[§] Deep Kumar,[§] Devesh Kumar,[§] Chivukula V. Sastri,*[,‡] and Sam P. de Visser*[,†]

[†]The Manchester Institute of Biotechnology and School of Chemical Engineering and Analytical Science, The University of Manchester, 131 Princess Street, Manchester M1 7DN, United Kingdom

[‡]Department of Chemistry, Indian Institute of Technology Guwahati 781039, Assam, India

[§]Department of Applied Physics, School for Physical Sciences, Babasaheb Bhimrao Ambedkar University, Lucknow 226025, UP, India

Supporting Information

ABSTRACT: Oxygen atom transfer by high-valent enzymatic intermediates remains an enigma in chemical catalysis. In particular, manganese is an important first-row metal involved in key biochemical processes, including the biosynthesis of molecular oxygen (through the photosystem II complex) and biodegradation of toxic superoxide to hydrogen peroxide by superoxide dismutase. Biomimetic models of these biological systems have been developed to gain understanding on the structure and properties of short-lived intermediates but also with the aim to create environmentally benign oxidants. In this work, we report a combined spectroscopy, kinetics and computational study on aldehyde deformylation by two side-on manganese(III)-peroxo complexes with bispidine ligands. Both manganese(III)-peroxo complexes are characterized by UV–vis and mass spectrometry techniques, and their reactivity patterns with aldehydes was investigated. We find a novel mechanism for the reaction that is initiated by a hydrogen atom abstraction reaction, which enables a keto–enol tautomerization in the substrate. This is an essential step in the mechanism that makes an electrophilic attack on the olefin bond possible as the attack on the aldehyde carbonyl is too high in energy. Kinetics studies determine a large kinetic isotope effect for the replacement of the transferring hydrogen atom by deuterium, while replacing the transferring hydrogen atom by a methyl group makes the substrate inactive and hence confirm the hypothesized mechanism. Our new mechanism is confirmed with density functional theory modeling on the full mechanism and rationalized through valence bond and thermochemical cycles. Our unprecedented new mechanism may have relevance to biological and biomimetic chemistry processes in general and gives insight into the reactivity patterns of metal-peroxo and metal-hydroperoxo intermediates in general.

INTRODUCTION

Metalloenzymes are powerful oxidants in nature that catalyze important reactions for Biosystems.[1] Most of these metalloenzymes utilize iron as their central cofactor, due to its high natural abundance. Another transition metal in relatively large abundance in the Earth Crust is manganese and, as such, nature has found key uses of it in various biological transformations.[2] Thus, manganese complexes are strong oxidizers, and consequently, the active site of superoxide dismutase (SOD) contains a central Mn atom.[3] SOD is involved in the biodegradation of superoxide radicals and converts them on a manganese center to hydrogen peroxide. Often SOD enzymes are anchored to a catalase enzyme that react and detoxify hydrogen peroxide. Another biological system with manganese coordination is the Photosystem II (PSII) active cluster, which contains four manganese atoms held together with bridging oxygen atoms and a dangling Ca^{2+} ion in a cubane-type Mn_4O_5Ca cluster.[4] This cluster binds water molecules and reacts them to one molecule of molecular oxygen with the release of four protons.

In biomimetic chemistry, synthetic manganese containing models of SOD and PSII have been created and studied for their chemical properties and reactivity.[5] In several of these studies a manganese-peroxo was investigated and the spectroscopic features of the complexes was established with UV–vis, resonance Raman, infrared absorption and electron paramagnetic resonance (EPR) spectroscopy.[6,7] Furthermore, the reactivity of manganese-peroxo with respect to substrates was investigated and efficient conversion to aldehyde products via deformylation was obtained.[8] However, the exact details of the mechanism remain a mystery. Therefore, manganese(III)-peroxo shows interesting reactivity patterns with substrates that are still poorly understood.

Received: September 23, 2017
Published: November 17, 2017

ACS Publications © 2017 American Chemical Society

DOI: 10.1021/jacs.7b10033
J. Am. Chem. Soc. 2017, 139, 18328–18338

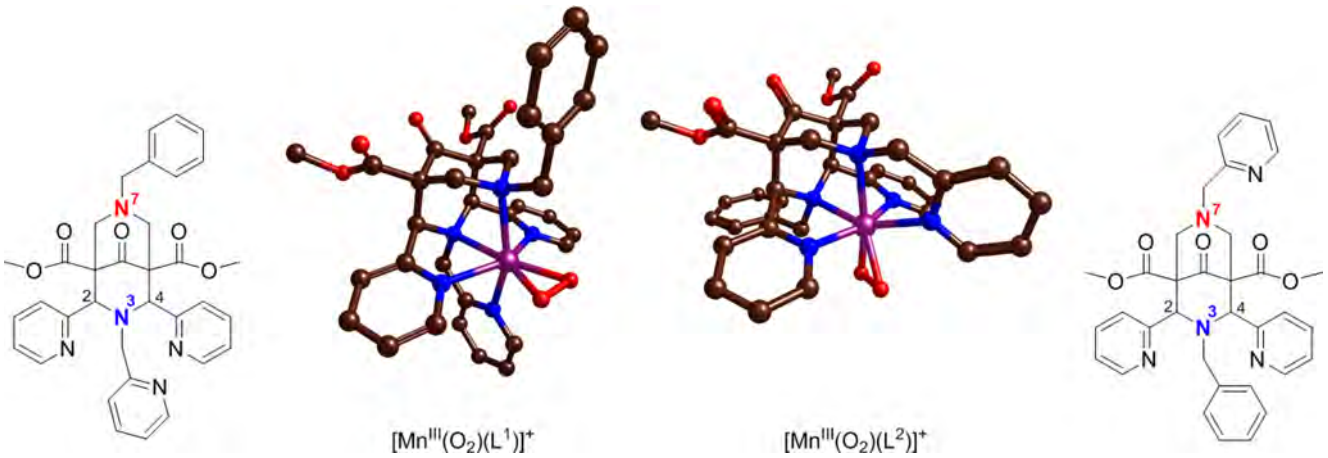

Figure 1. Manganese(III)-peroxo complexes investigated in this work.

Recently, our groups have shown that bispidine ligated manganese(III)-peroxo reacts with aldehydes through a rate-determining hydrogen atom abstraction reaction as evidenced from a large kinetic isotope effect (KIE) for the replacement of the α-hydrogen atom by deuterium.[9] Radical trapping experiments and density functional theory calculations further confirmed the rate-determining hydrogen atom abstraction and rationalized that this is originating from a more feasible electron transfer from peroxo to Mn as compared to substrate carbonyl. The question, therefore, is how the ligand system of the metal influences the bifurcation pathways between hydrogen atom abstraction (i.e., the electrophilic pathway) versus a nucleophilic pathway.

To test the ligand effect on the bifurcation pathways, we followed our previous work up with a detailed study on two functionally isomeric pentadentate manganese(III)-peroxo complexes, resulting in different orientations of two pyridine groups with respect to N^3 nitrogen of the bispidine backbone. In particular, we synthesized manganese(III)-peroxo complexes with bispidine ligand systems (see Figure 1), namely $[Mn^{III}(O_2)(L^1)]^+$ (**1**) and $[Mn^{III}(O_2)(L^2)]^+$ (**2**) with L^1 = dimethyl-2,4-di(2-pyridyl)3-(pyridin-2-ylmethyl)-7-benzyl-3,7-diaza-bicyclo[3.3.1] nonan-9-one-1,5-dicarboxylate) and L^2 = dimethyl 2,4-di(2-pyridyl)-3-benzyl-7-(pyridin-2-ylmethyl)-3,7-diazabicyclo[3.3.1] nonan-9-one-1,5-dicarboxylate). Thus, ligand L^1 has three pyridine groups pointing upward (i.e., along the molecular *z*-axis with the ortho-C−H groups in hydrogen bonding distance to the sixth ligand), whereas in ligand L^2 only one of those points upward and the other two are aligned with the *xy*-plane. Our combined experimental and computational study gives evidence of a novel reaction mechanism starting with a rate-determining hydrogen atom abstraction reaction and followed by a reshuttle of the hydrogen atom through a keto−enol tautomerization to set up a low-energy nucleophilic attack of peroxo on an olefin bond of the substrate. Alternative reaction mechanisms were tested and ruled out. Our observations are confirmed with computational modeling that rationalize the reaction mechanism with valence bond and thermochemical cycles.

METHODS

Experimental Procedures. Our procedures are similar to previous studies of our groups and will be summarized briefly here.[10] All reagents were obtained from Aldrich Chemical Co. and obtained at the best available purity and used without further purification unless otherwise indicated. Solvents were dried according to published procedures and distilled under argon prior to use.[11] The piperidone backbone of the ligands L^1 and L^2 were prepared according to a literature protocol[12] and used to generate the $[Mn^{II}(L^1)](ClO_4)_2$ and $[Mn^{II}(L^2)](ClO_4)_2$ complexes. Subsequently, the manganese(III)-peroxo complexes were prepared by reacting their corresponding Mn^{II} systems with 10 equiv of H_2O_2 and 2.5 equiv of triethylamine (TEA) in acetonitrile (2 mL) at 15 °C.

2-Methyl-2-phenylpropionaldehyde (2-Me-PPA) was synthesized in our laboratory according to a literature procedure,[13] while α-[D_1]-2-phenylpropionaldehyde (α-[D_1]-PPA, ∼90%, D enriched) was purchased from RVL Scientific & Engineering Pvt. Ltd. (Lucknow, India) and the purity of the compound was confirmed by NMR. All NMR spectra were recorded in $CDCl_3$.

Syntheses and Characterization. Bispidine ligands (0.17 mmol) were dissolved in acetonitrile and mixed with $Mn^{II}(ClO_4)_2{\cdot}2CH_3CN$ salt (0.22 mmol in CH_3CN) under inert conditions. The pale yellow solution was refluxed overnight and filtered through a 0.2 μm syringe filter and layered with diethylether to obtain a white crystal suitable for X-ray diffraction. The cif file of the complexes is deposited at the Cambridge Crystallographic Data Centre (CCDC) with the following deposition numbers: CCDC 1022749 and 1022750. Caution! Metal perchlorate salts are potentially explosive and should be handled with excessive care.

Instrumentation. NMR (^{1}H and ^{13}C) spectra were recorded with a Bruker 600/150 MHz spectrometer. UV−vis spectra and kinetic measurements were performed with a Hewlett-Packard 8453 spectrophotometer equipped with either a constant temperature circulating water bath or a liquid nitrogen cryostat (Unisoku) with a temperature controller. High-resolution electrospray ionization mass spectra (ESI-MS) of $[Mn^{III}(O_2)(L^1)]^+$ and $[Mn^{III}(O_2)(L^2)]^+$ were recorded on a Waters (Micromass MS Technologies) Q-TOF Premier mass spectrometer by infusing precooled samples directly into the source at 15 μL min^{-1} using a syringe pump. The spray voltage was set at 2 kV and the capillary temperature at 80 °C.

Reactivity Studies. The chemical reactions were monitored in a 10 mm path length cuvette by measuring the UV−vis spectral changes of the reaction solutions as a function of time. The rate constants were determined by fitting the changes in absorbance of the intermediates as a function of time under study. The rate constants were averaged from three individual experiments and resulted in a standard deviation of less than 10% of the given values.

Product Analysis. Product analysis was performed on a WATERS ACQUITY UPLC equipped with a variable wavelength UV-200 detector. Products were separated on a Waters Symmetry C18 reverse phase column (4.6 × 250 mm) and detection was made at 215 and 254 nm. Product yields were determined by comparison with standard curves of known authentic samples. All experiments were done at least in triplicate.

DOI: 10.1021/jacs.7b10033
J. Am. Chem. Soc. 2017, 139, 18328−18338

Computational Procedures. Density functional theory (DFT) calculations were performed on the catalytic reaction mechanism of deformylation of 2-phenylpropionaldehyde (2-PPA) by $[Mn^{III}(O_2)(L^1)]^+$ and $[Mn^{III}(O_2)(L^2)]^+$ following previously tested and benchmarked procedures.[14] We took initial structures from our previous study[9] but reoptimized all geometries in Gaussian-09 with a full solvent model as mimicked by a polarized continuum model (PCM) with a dielectric constant of 37.5 mimicking acetonitrile.[15,16] These geometry optimizations utilized the unrestricted B3LYP hybrid density functional method in combination with an LACVP basis set with core potential on Mn and 6-31G* on the rest of the atoms (basis set BS1).[17,18] The nature of the stationary points was confirmed through a frequency calculation also under solution conditions calculated with the PCM model. All local minima had real frequencies only, while the transition states were characterized by a single imaginary mode for the correct transition. To improve the energetics, single-point calculations using an LACV3P+ basis set with core potential on Mn and 6-311+G* on the rest of the atoms was performed: basis set BS2. Previously, we showed that little changes in structure and energetics are obtained for UB3LYP/BS1 versus UB3LYP/BS2 geometry optimizations.[19] Furthermore, the spin state ordering and relative energies of related manganese complexes were tested using a range of alternative DFT and ab initio methods.[20] On the basis of the fact that manganese(III)-peroxo has a high-spin ground state, we selected B3LYP as computational method and the results reproduce the experimental trends well.

Kinetic isotope effects (KIE) were evaluated computationally by reevaluating the free energy and vibrational frequencies of the structures, whereby one or more hydrogen atom is replaced by deuterium.[21] The Eyring kinetic isotope effect (KIE_{Eyring}) is determined from the change in free energy of activation ($\Delta G^{\ddagger}$) between the system with hydrogen and deuterium atoms, eq 1, with R representing the gas constant and T the temperature (298 K).

$$KIE_{Eyring} = \exp\{(\Delta G^{\ddagger}_{D} - \Delta G^{\ddagger}_{H})/RT\} \quad (1)$$

In addition, we estimated the Wigner kinetic isotope effect (KIE_{Wigner}), which corrects KIE_{Eyring} with tunneling corrections Q_t for the hydrogen and deuterium reactions through eqs 2 and 3. These equations contain Planck's constant (h), Boltzmann's constant (k_B), and the imaginary frequency in the transition state (ν).

$$KIE_{Wigner} = KIE_{Eyring} \times Q_{t,H}/Q_{t,D} \quad (2)$$

$$Q_t = 1 + (h\nu/k_BT)^2/24 \quad (3)$$

RESULTS

In this work, we describe the synthesis, characterization and reactivity patterns of two novel side-on manganese(III)-peroxo complexes with a pentadentate bispidine N5 ligand {i.e., $[Mn^{III}(O_2)(L^1)]^+$ (**1**) and $[Mn^{III}(O_2)(L^2)]^+$ (**2**)}, Figure 1. These two ligand systems have their equatorial pyridine groups either axial or equatorial to the manganese(III)-peroxo group and, hence, interact differently with an approaching substrate. The weak intermolecular interactions separating the two complexes may incur in functional differences due to the way substrate can approach to the catalytic center and/or the stability of the reactant complex. Therefore, these models may give insight into the properties and functions of enzymatic catalysts where substrate approach is often tightly controlled.[22]

Upon addition of 10 equiv of H_2O_2 to $[Mn^{II}(L^2)(ClO_4)_2]^{2+}$ in the presence of 2.5 equiv of TEA, a brown intermediate is formed with distinctive absorption features, Figure S2. The ESI mass spectra of **1** and **2** exhibit prominent peaks with m/z 678 and an isotope pattern that identify them as $[Mn^{III}(O_2)(L^1)]^+$ and $[Mn^{III}(O_2)(L^2)]^+$. When $H_2{}^{16}O_2$ was replaced by $H_2{}^{18}O_2$ in the reaction mixture, the mass of the parent ion increased with four units indicative of a dioxygen-bound complex. We attempted to resolve the resonance Raman spectrum of **1** and **2**, but due to degradation of the manganese complexes caused by scattering, all our efforts failed.

Subsequently, we investigated the deformylation behavior of compounds **1** and **2** in a reaction with 2-phenylpropionaldehyde (2-PPA). This was done by monitoring the change in UV–vis absorption spectra as a function of time after the addition of substrate. In particular, the aldehyde deformylation reaction and the mechanism of substrate activation by side-on manganese(III)-peroxo was investigated from the reactivity of $[Mn^{III}(O_2)(L^1)]^+$ and $[Mn^{III}(O_2)(L^2)]^+$ with 2-PPA under the same experimental reaction conditions (Figure 2). Addition of 2-PPA to **2** in acetonitrile at 15 °C led to immediate decay of the intermediate and the formation of acetophenone product as

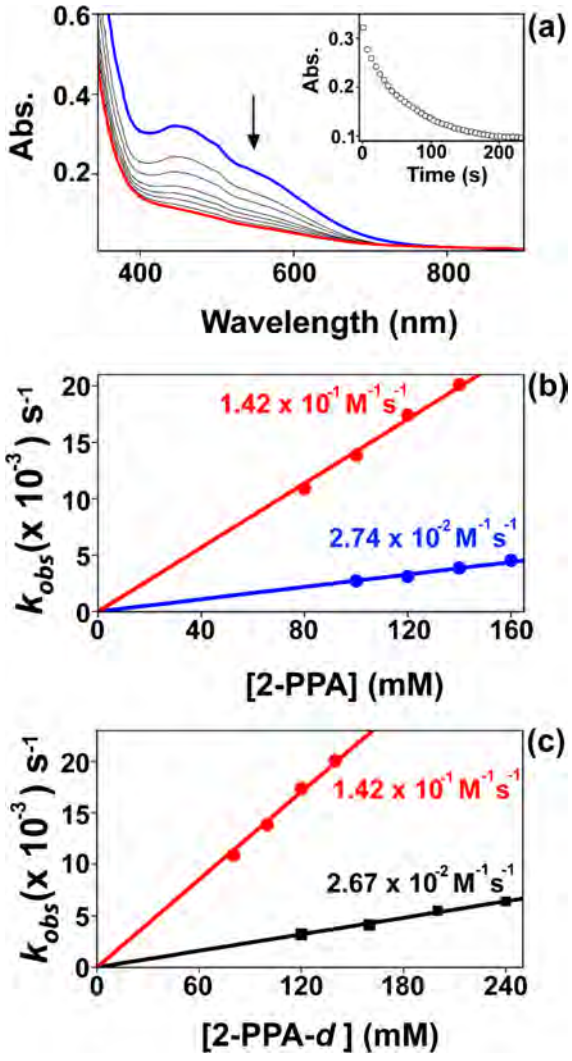

Figure 2. Kinetics of the reaction of **2** with 2-PPA. (a) UV–vis spectral changes of **2** (2 mM) upon addition of 2-PPA (120 mM) in the presence of TEA (5 mM) and hydrogen peroxide (20 mM) in CH_3CN at 15 °C. The inset shows the time course of the absorbance at 450 nm. (b) Plot of k_{obs} against the concentration of 2-PPA and the derived second-order rate constant for the reaction of 2 mM **1** and **2** with 2-PPA at various concentrations in CH_3CN at 15 °C [data for **2** (red •) and **1** (blue •) are given]. (c) Plot of k_{obs} against the concentration of α-[D_1]-PPA (~90%, D enriched, ■) with **2** in CH_3CN at 15 °C.

DOI: 10.1021/jacs.7b10033
J. Am. Chem. Soc. 2017, 139, 18328–18338

identified by NMR. The pseudo first-order rate constant for the decay of **2** increased linearly with increasing concentration of 2-PPA and enabled us to measure the second-order rate constant: $k_2 = 1.42 \times 10^{-1}$ M^{-1} s^{-1}. For comparison, the second-order rate constant for the reaction of $[Mn^{III}(O_2)(L^1)]^+$ with 2-PPA was 2.74×10^{-2} M^{-1} s^{-1}.[9] Therefore, it appears that $[Mn^{III}(O_2)(L^2)]^+$ reacts with 2-PPA about five times faster than the isomeric oxidant with ligand L^1. These results were in fact in opposite trend to those obtained in the reactivity of the corresponding manganese(IV)-oxo complexes $[Mn^{IV}(O)(L^1)]^{2+}$ and $[Mn^{IV}(O)(L^2)]^{2+}$.[12d] A possible reason for the change in rate constant ordering is the shape of the ligand system, whereby the L^1 ligand (see Figure 1) has protons pointing upward toward the peroxo group, whereas in the L^2 ligand the pyridine moieties are in the *xy*-plane and will not interact with the approaching substrate.

To understand the details of the rate-determining step for the reaction of $[Mn^{III}(O_2)(L^1)]^+$ and $[Mn^{III}(O_2)(L^2)]^+$ with 2-PPA, we decided to investigate the kinetic isotope effect (KIE) for replacing the α-hydrogen atom with deuterium (Figure 2c). Thus, upon addition of α-$[D_1]$-PPA (~90%, D-enriched) to **2** in acetonitrile at 15 °C, the absorption of the intermediates shows decay from which we determined a second-order rate constant of $k_2 = 2.67 \times 10^{-2}$ M^{-1} s^{-1}. Hence, the reaction between **2** and 2-PPA proceeds with a KIE = 5.3, and it can be concluded that the reaction has a rate-determining hydrogen atom abstraction step. A comparable KIE value of 5.4 was determined for the reactivity difference of **1** with 2-PPA/α-$[D_1]$-PPA.[9] Consequently, both $[Mn^{III}(O_2)(L^1)]^+$ and $[Mn^{III}(O_2)(L^2)]^+$ react with 2-PPA through a rate-determining hydrogen atom abstraction and a KIE that deviates from unity and most likely their reaction mechanisms will be similar.

To further ascertain that hydrogen atom abstraction from the α-position is key to the reaction mechanism, we used a mechanistic probe, namely 2-methyl-2-phenyl propionaldehyde (2-Me-PPA), Scheme 1. Lack of reactivity with this probe

Scheme 1. Reaction of $[Mn^{III}(O_2)(L^2)]^+$ with Substrates

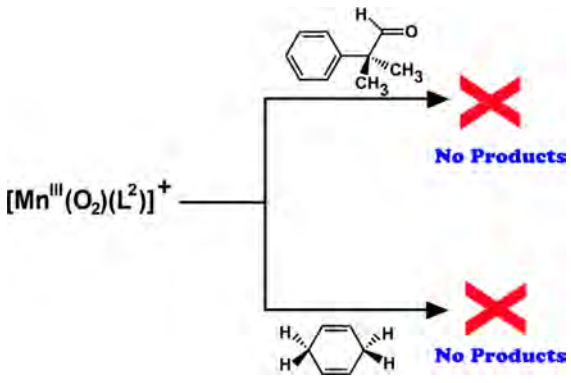

would confirm that the rate-determining step is indeed α-hydrogen atom abstraction and no nucleophilic pathway is possible. When we add 2-Me-PPA to **2** at 15 °C, however, no reaction products are observed and only natural decay profiles back to $[Mn^{II}(L^2)]^{2+}$ are seen due to the short lifetime of the parent complex in solution ($t_{1/2}$ ~ 45 min). After analyzing the reaction solution with ESI-MS, we do not find any evidence of deformylated products. Consequently, the reactivity study with 2-Me-PPA as a mechanistic probe confirms that the reaction of **2** with 2-PPA does not proceed through a rate-determining nucleophilic attack on the carbonyl group but is initiated by activation of the α-hydrogen atom instead.

To test whether the manganese(III)-peroxo can react efficiently through hydrogen atom abstraction, we decided to test alternative substrates with weak C–H bonds. Addition of 1,4-cyclohexadiene to either **1** or **2** did not lead to decay of the spectroscopic features of the manganese(III)-peroxo structures, Scheme 1, hence $[Mn^{III}(O_2)(L^1)]^+$ and $[Mn^{III}(O_2)(L^2)]^+$ are unable to react via desaturation pathways. This is surprising as the deformylation reaction described above appears to have a rate-determining hydrogen atom abstraction step from 2-PPA to $[Mn^{III}(O_2)(L^2)]^+$. Moreover, the mechanistic probes ruled out the more commonly seen nucleophilic attack on the carbonyl group. Computational modeling, vide infra, established the reasons behind the lack of reactivity toward cyclohexadiene as resulting from an energetically high second hydrogen atom abstraction.

Finally, a radical trapping experiment with bromotrichloromethane was performed to establish that the reaction mechanism of manganese(III)-peroxo with aldehydes proceeds through a radical intermediate species.[9,23] Addition of 2-PPA to intermediate **2** in the presence of excess $CBrCl_3$ or CBr_4 in acetonitrile at 15 °C leads to the formation of α-brominated product of the 2-PPA exclusively, Scheme 2, which was

Scheme 2. Reaction of $[Mn^{III}(O_2)(L^2)]^+$ with Radical Trapping Substrates

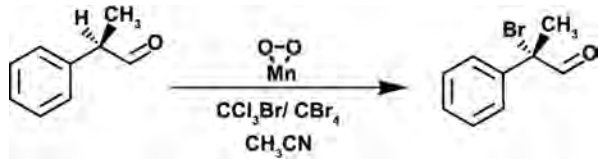

confirmed by NMR analysis (see Figure S4). Consequently, our radical trapping experiment confirms a radical mechanism that most likely starts with hydrogen atom abstraction from the α-position of 2-PPA.

In conclusion, experimental kinetics studies find that aldehyde deformylation starts with a rate-determining hydrogen atom abstraction from the α-position of 2-PPA leading to a radical intermediate. On the other hand, no reactivity is observed between $[Mn^{III}(O_2)(L^2)]^+$ and substrates with weak C–H bonds such as cyclohexadiene. To understand the reaction mechanisms and explain the reactivity patterns of side-on manganese(III)-peroxo with substrates, a computational study was performed.

Computational Modeling. To explain the experimentally obtained results on the reactivity of side-on manganese(III)-peroxo with aldehydes, we embarked on a density functional theory study on the possible reaction mechanisms leading to aldehyde deformylation by these complexes. Although we tested many possible mechanisms and spin states (vide infra), our lowest-energy pathway leading to the first oxygen atom transfer is on a quintet spin state, Figure 3. The reaction starts with a hydrogen atom abstraction via transition state TS_{HAT1} and forms a manganese(II)-hydroperoxo with a radical intermediate I_1.

In the quintet spin state, the barrier is 19.2 kcal mol^{-1} and the reaction is endothermic by 7.0 kcal mol^{-1}. Rather than radical rebound, however, as is common in typical hydrogen atom abstraction reactions,[24] actually the hydrogen atom is bounced back to substrate to give the enol form of the substrate

DOI: 10.1021/jacs.7b10033
J. Am. Chem. Soc. 2017, 139, 18328–18338

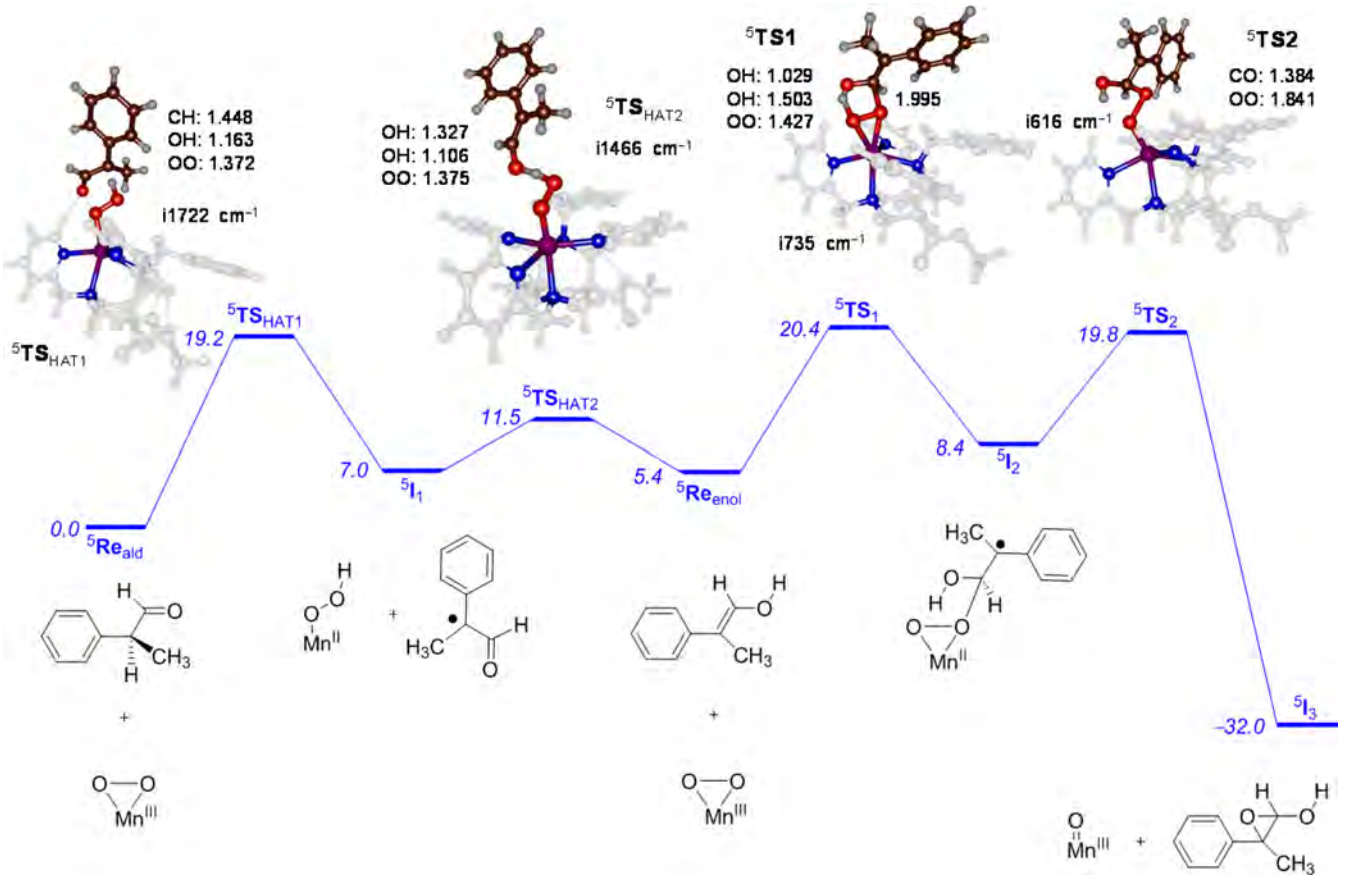

Figure 3. Potential energy profile (UB3LYP/BS2//UB3LYP/BS1+ZPE) for oxygen atom transfer from $[Mn^{III}(O_2)(L^2)]^+$ to 2-PPA with energies in kcal mol^{-1}. Transition state structures give distances in angstroms and the imaginary frequency in cm^{-1}.

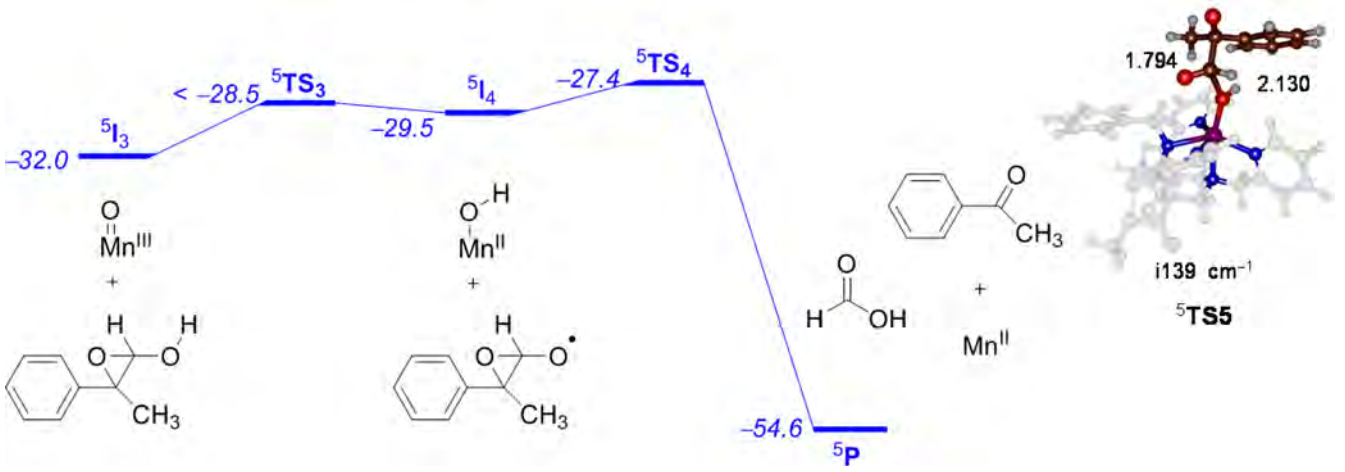

Figure 4. Potential energy profile (UB3LYP/BS2//UB3LYP/BS1+ZPE) for oxygen atom transfer from $^5\mathbf{I}_3$ leading to products with energies in kcal mol^{-1}. Transition state structure gives distances in angstroms and the imaginary frequency in cm^{-1}.

and manganese(III)-peroxo via a subsequent barrier $\mathbf{TS}_{HAT2}$ of 4.5 kcal mol^{-1}. The enol form of the reactant ($^5\mathbf{Re}_{enol}$) is slightly lesser stable than the keto form (by 5.4 kcal mol^{-1}). Once the reactant is in the enol-form, the manganese(III)-peroxo part of the reactant complex attacks the substrate olefin bond via a nucleophilic transition state ^{5}**TS1** of 20.4 kcal mol^{-1} to form the radical intermediate $^5\mathbf{I}_2$. Energetically, $^5\mathbf{I}_2$ is close in energy to $^5\mathbf{I}_1$ and $^5\mathbf{Re}_{enol}$ and will react via an O−O cleavage barrier (^{5}**TS2**) to form a manganese(III)-oxo complex and an epoxide ($^5\mathbf{I}_3$) in a highly exothermic process. As such, the computational studies implicate that probably the first steps in the reaction mechanism will be reversible, but the step from $^5\mathbf{I}_2$ to $^5\mathbf{I}_3$ will be irreversible. We also tested the triplet spin pathway but found it at least 20 kcal mol^{-1} higher in energy along the full profile (see the Supporting Information).

Geometrically, $^5\mathbf{TS}_{HAT1}$ and $^5\mathbf{TS}_{HAT2}$ have features typical of hydrogen atom abstraction barriers seen before for the reaction of heme and nonheme iron(IV)-oxo with aliphatic substrates.[25] Both barriers have a large imaginary frequency, which implies that substitution of the transferring hydrogen atom by

DOI: 10.1021/jacs.7b10033
J. Am. Chem. Soc. 2017, 139, 18328−18338

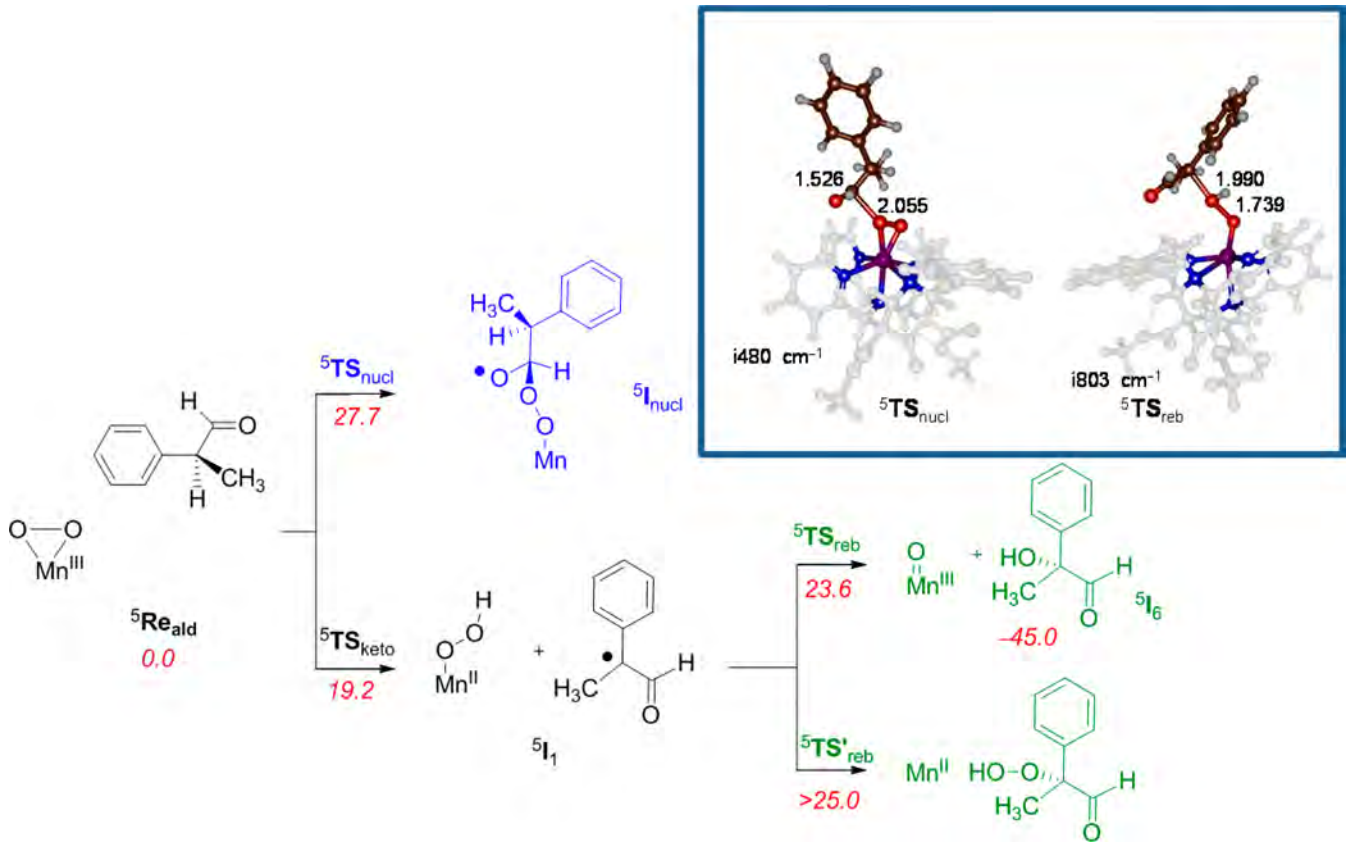

Figure 5. Alternative nucleophilic transition states along the pathway of aldehyde deformylation by side-on manganese(III)-peroxo as calculated at the UB3LYP/BS2//UB3LYP/BS1+ZPE level of theory. Energies are in kcal mol^{-1}. Transition state structures give distances in angstroms and the imaginary frequency in cm^{-1}.

deuterium should give a major change in the value of the free energy of activation and, hence, a large kinetic isotope effect,[26] as indeed observed experimentally and reported above in Figure 2. Moreover, the transition states are late with long C−H and short O−H distances for ^{5}**TS**$_{HAT1}$ (1.448 and 1.163 Å, respectively), while the transferring hydrogen atom in ^{5}**TS**$_{HAT2}$ is closer to the donor hydroperoxo group (1.106 Å) than the accepting alcohol oxygen atom (1.327 Å).

In the enol-form, a nucleophilic attack takes the place of the manganese(III)-peroxo group on the double bond through a C−O bond formation via ^{5}**TS1**. This transition state has a relatively large imaginary frequency of i735 cm^{-1} due to the simultaneous C−O bond formation and proton transfer from enol to peroxo. Thus, the peroxo bond weakens to 1.427 Å, and a C−O interaction of 1.995 Å is formed.

After the transition state, the system relaxes to a local minimum that has a single bond for the C−O interaction and a radical on the neighboring carbon atom. In addition, the dioxygen moiety moves from a side-on to an end-on conformation. The dioxygen bond cleaves in ^{5}**TS2** at an energetic cost of 19.8 kcal mol^{-1}. In this step, simultaneous to the O−O bond breaking, an epoxide ring is formed to give a low-energy manganese(III)-oxo species. The imaginary mode in the transition state indeed reflects the O−O bond cleavage on the one hand with the epoxide ring-closure on the other hand.

The next stage in the mechanism from epoxide to final deformylation products is given in Figure 4. Thus, the manganese(III)-oxo group abstracts a hydrogen atom in ^{5}**I**$_3$ from the alcohol position of substrate, which breaks the epoxide ring to form a complex between manganese(II)-hydroxo and a radical (^{5}**I**$_4$). This step has an almost barrierless reaction pathway via ^{5}**TS3**, and hence the ^{5}**TS3** structure could not be properly characterized. An estimate from the geometry scan predicts it to be less than 1 kcal mol^{-1} in energy above the value of ^{5}**I**$_4$. The subsequent OH rebound leads to simultaneous epoxide ring-opening, C−C bond cleavage and the formation of formic acid and methylphenylketone products via transition state ^{5}**TS4**. The imaginary frequency of i139 cm^{-1} indeed reflects the C−C bond breaking and the dissociation of methylphenylketone from the complex. At the same time the OH rebound to the HCO leaving group results in formic acid as the second product. The overall reaction mechanism has two highly exothermic reaction steps, namely the formation of the manganese(III)-oxo species (^{5}**I**$_3$) and the final reaction step leading to methylphenylketone and formic acid products. These two steps will be irreversible, although other reactions steps may be reversible.

In summary, the lowest-energy pathway for aldehyde deformylation by side-on manganese(III)-peroxide of 2-PPA is α-hydrogen atom abstraction followed by reshuttle and tautomerization to form the enol form and nucleophilic attack on the olefin bond. Oxygen atom transfer then gives epoxide that through a low-barrier hydrogen atom transfer gives formic acid and methylphenylketone products.

Alternative Mechanisms. Several alternative pathways for aldehyde deformylation by side-on manganese(III)-peroxo complexes were considered, as shown in Figure 5. First, a direct nucleophilic attack on the carbonyl group of 2-PPA was considered by side-on manganese(III)-peroxo. The nucleo-

DOI: 10.1021/jacs.7b10033
J. Am. Chem. Soc. 2017, 139, 18328−18338

philic pathway proceeds via a transition state ^{5}**TS**$_{nucl}$ to form the nucleophilic addition intermediate ^{5}**I**$_{nucl}$ (Figure 5). Similarly to the results reported previously,[9] this is a high-energy pathway with a barrier of $\Delta E^{\ddagger}$ + ZPE = 27.7 kcal mol^{-1}. The transition state has an imaginary frequency of i480 cm^{-1}, which reflects the C−O bond formation between peroxo and carbonyl moieties and simultaneously the peroxo moves from side-on to end-on. Clearly, the direct nucleophilic addition from side-on peroxo is well higher in energy than the hydrogen atom abstraction reported above in Figure 4 by at least 8.5 kcal mol^{-1} and hence will not be competitive.

We also investigated mechanisms starting from the manganese(III)-hydroperoxo intermediate ^{5}**I**$_1$ and, in particular, looked at OH rebound to form manganese(III)-oxo and 2-hydroxo-2-phenyl-propionaldehyde (^{5}**I**$_6$). Although, ^{5}**I**$_6$ is considerably more stable than the epoxide intermediate ^{5}**I**$_3$ reported above. Actually, its formation barrier is considerably higher in energy. Therefore, despite the fact that ^{5}**I**$_6$ is a more stable intermediate than ^{5}**I**$_3$, the preferred reaction intermediate leading to aldehyde deformylation will pass ^{5}**I**$_3$. The OH rebound transition state (^{5}**TS**$_{reb}$) has typical features seen before for OH transfer from iron(III)-hydroperoxo complexes,[27] with simultaneous O−O cleavage and C−O bond formation in a concerted reaction step. The OH group is located midway between donor and acceptor groups through long interactions of 1.990 and 1.739 Å.

Additionally, various other pathways were tested (see Supporting Information), including rebound of the OH group to the aldehyde carbon atom. However, this OH rebound pathway formed a biradical species that is very high in energy (>50 kcal mol^{-1}). Also, OOH transfer from the manganese(II)-hydroperoxo intermediate (^{5}**I**$_1$) to the radical gave a barrier (^{5}**TS'**$_{reb}$) of well over 25 kcal mol^{-1} in energy. Unfortunately, no subsequent pathways leading to aldehyde deformylation products could be identified, and therefore, the mechanism was ruled out. Finally, a mechanism was considered for nucleophilic attack of manganese(III)-peroxo on the secondary carbon atom of the enol form of 2-PPA. The intermediate formed through this pathway is high in energy (>40 kcal mol^{-1} with respect to ^{5}**Re**$_{ald}$), and consequently, the pathway is ruled out as a viable reaction mechanism.

In conclusion, the lowest-energy reaction mechanism for aldehyde deformylation by manganese(III)-peroxo complexes we have identified starts with hydrogen atom abstraction from the α-position followed by a reshuttle, whereby the aldehyde is converted into an enol that can efficiently react via nucleophilic addition with the side-on manganese(III)-peroxo.

DISCUSSION

To understand the unusual mechanism found for aldehyde deformylation by manganese(III)-peroxo complexes, we analyzed the structure and electronic configuration of all species in detail and set up valence bond and thermo-chemical cycles to explain the mechanism and rationalize the observed reactivities.

Thermochemical Modeling. Let us first try to predict the hydrogen atom abstraction barriers for the keto and enol form of 2-PPA by side-on manganese(III)-peroxo complexes. The driving force for the hydrogen atom abstraction can be written as the difference in energy between the C−H/O−H bond that is broken and the O−H bond formed to give the manganese-(II)-hydroperoxo, which in general terms using substrate SubH is given in eq 4.

$$[Mn^{III}(O_2)(L^2)]^+ + SubH \rightarrow [Mn^{II}OOH(L^2)]^+ + Sub^{\bullet} \quad (4)$$

The overall reaction (eq 4) has an energy corresponding to the driving force ΔE_{rp} and can be written as the difference between two bond dissociation free energies (BDFEs) of the bonds that are formed and broken as defined in eqs 5−7. Thus, the BDFE values for the substrate C−H bond of the aldehyde from 2-PPA and the O−H bond of the enol form of 2-PPA are defined as through eq 5 as BDFE$_{CH}$(2-PPA) and BDFE$_{OH}$(2-PPA). Values were calculated from a full geometry optimization of 2-PPA and 2-PPA with the transferring hydrogen atom removed (Sub$^{\bullet}$) and the free energy difference obtained from eq 5. Subsequently, we calculated the BDFE$_{OH}$ value of the manganese(II)-hydroperoxo species from its free energy difference with the manganese(III)-peroxo and a hydrogen atom (eq 6) as defined as BDFE$_{OH}$(Ox).

$$SubH \rightarrow Sub^{\bullet} + H^{\bullet} + BDFE_{AH}(SubH) \quad (5)$$

$$[Mn^{II}OOH(L^2)]^+ \rightarrow [Mn^{III}(O_2)(L^2)]^+ + H^{\bullet} + BDFE_{OH}(Ox) \quad (6)$$

$$\Delta G_{rp} = BDFE_{AH}(SubH) - BDFE_{OH}(Ox) \quad (7)$$

Therefore, the free energy driving force for the hydrogen atom abstraction from substrate (ΔG_{rp}), be it in the keto or enol form, by $[Mn^{III}(O_2)(L^2)]^+$ can be written in terms of BDFE of donor and acceptor groups, eq 7. We calculate BDFE values of 66.1 and 55.9 kcal mol^{-1} for hydrogen atom abstraction from the keto and enol forms of 2-PPA, respectively. In agreement with the potential energy landscape in Figure 4 above, these BDFE$_{CH}$ values implicate that it is easier to abstract a hydrogen atom from the enol form of substrate than from the α-position of the aldehyde.

Furthermore, BDFE$_{OH}$ values of 56.6 and 61.1 kcal mol^{-1} were obtained for $[Mn^{II}OOH(L^1)]^+$ and $[Mn^{II}OOH(L^2)]^+$, respectively. Consequently, the driving forces for hydrogen atom abstraction of $[Mn^{III}(O_2)(L^2)]^+$ from 2-PPA in its keto form is ΔG = 5.0 kcal mol^{-1}, which is in excellent agreement with the reaction free energy from ^{5}**Re**$_{ald}$ to ^{5}**I**$_1$ of 6.2 kcal mol^{-1} (Table S3). Similarly, the driving force from hydrogen atom abstraction of the enol form of 2-PPA by $[Mn^{III}(O_2)(L^2)]^+$ of ΔG = −5.2 kcal mol^{-1} matches the free-energy difference between ^{5}**Re**$_{enol}$ and ^{5}**I**$_1$ reasonably well.

To compare the BDFE$_{CH}$ of 2-PPA with typical substrates used in hydrogen atom transfer reactions, we calculated the BDFE$_{CH}$ of 1,4-cyclohexadiene. Interestingly, the BDFE$_{CH}$ of 1,4-cyclohexadiene is 61.9 kcal mol^{-1}, which is midway in between the values for breaking the C−H bond of the keto-form of 2-PPA and the O−H bond of the enol form. Therefore, theory would expect the first aliphatic hydrogen atom abstraction of 1,4-cyclohexadiene by side-on manganese(III)-peroxo to proceed with similar rate constants as 2-PPA. However, no benzene products are obtained, which probably means that the subsequent reaction step between manganese-(II)-hydroperoxo and the C_6H_7 radical does not lead to products, and a further hydrogen atom abstraction is hampered. As side-on manganese(III)-peroxo can abstract a hydrogen atom from 2-PPA, this implies that the cyclohexadiene reaction is prevented due to an energetically unfavorable second hydrogen atom abstraction performed by the manganese(II)-hydroperoxo species. Thus, side-on manganese(III)-peroxo will

DOI: 10.1021/jacs.7b10033
J. Am. Chem. Soc. 2017, 139, 18328−18338

not react with aliphatic C−H bonds through substrate hydroxylation.

To test this hypothesis, we calculated the hydrogen atom abstraction energy by $[Mn^{II}OOH(L^2)]^+$ at either the distal or proximal oxygen atom, Scheme 3. In particular, we calculated

Scheme 3. Reactivity Channels of $[Mn^{II}(OOH)(L^2)]^+$ through Hydrogen Atom Abstraction (top) or O−O Bond Cleavage (Bottom)

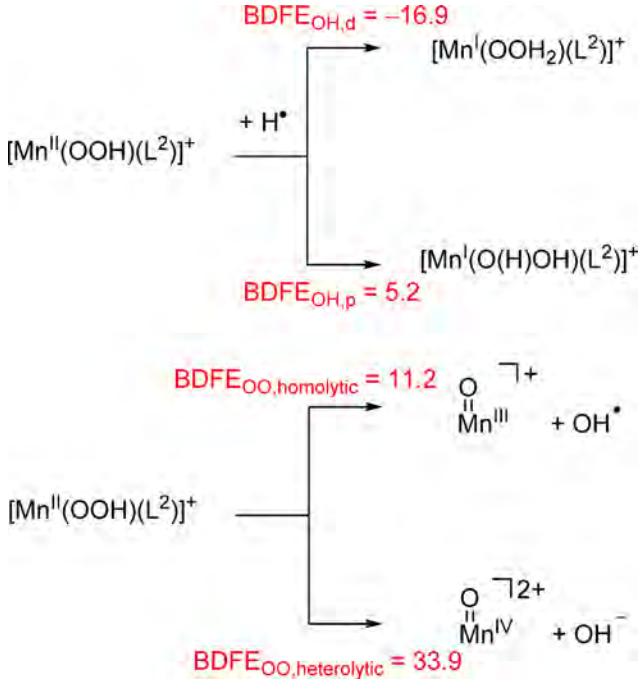

the diabatic hydrogen atom abstraction energy by the manganese(II)-hydroperoxo species as a full geometry optimization of either $[Mn^I(OOH_2)(L^2)]^+$ or $[Mn^I(O(H)OH)(L^2)]^+$, which led to dissociation of both complexes. Proximal donation of a hydrogen atom has a driving force of only 5.2 kcal mol^{-1}, whereas distal donation gives an endothermic BDFE value. Consequently, despite the fact that manganese(III)-peroxo is able to abstract hydrogen atoms from weak aliphatic C−H bonds, the resulting manganese(II)-hydroperoxo is inactive and thermodynamically unable to react further to give either alcohols or a dehydrogenation of the substrate.

To find out, whether the manganese(II)-hydroperoxo has other catalytic abilities, we calculated its homolytic and heterolytic O−O bond cleavage free energies, see bottom part of Scheme 3. Similar to that seen for nonheme iron(III)-hydroperoxo complexes,[28] also here the heterolytic cleavage is high in free energy (>30 kcal mol^{-1}) and can be ruled out. Homolytic cleavage is endothermic by 11.2 kcal mol^{-1} and, therefore, although a slow process, may be feasible. As such, the only probable reaction pathway for manganese(II)-hydroperoxo is homolytic cleavage of the O−O bond but will only be possible if the bond that is subsequently formed is strong enough to balance the energetic cost of the O−O bond breaking mechanism.

Valence Bond Rationalization of the Mechanism. Figure 6 gives the electronic delineation of the properties a rate-determining reaction barrier should possess and how this links to the properties of reactants and products.[9,21,29] Thus, as

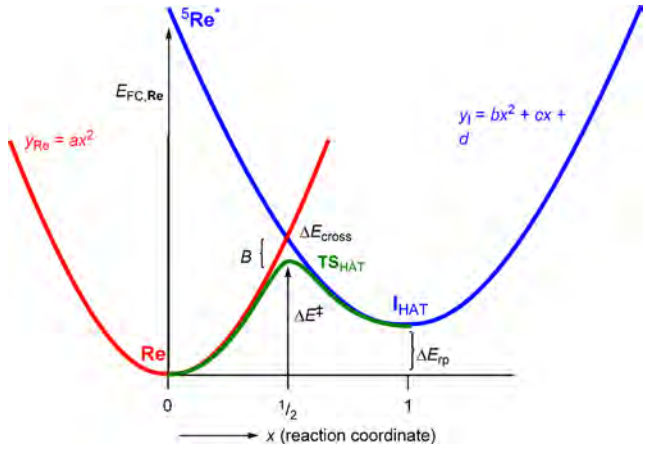

Figure 6. Definition of a reaction barrier and its connection to the vertical excitation energy in the reactants ($E_{FC,R}$) and the driving force for the reaction (ΔE_{rp}).

an example, we consider the hydrogen atom abstraction reaction from a reactant complex (*Re*) via a transition state ($\mathbf{TS}_{HAT}$) leading to a radical intermediate ($\mathbf{I}_{HAT}$). We now envisage the local minima to reside in a parabolic function (y, representing the potential energy) along the reaction coordinate axis (x) for the hydrogen atom abstraction with the reactants in the origin ($x = 0$) and the radical intermediate at the value $x = 1$. Mathematically, the potential energy functions for the reactant and intermediate states can then be described as shown in eqs 8 and 9 with a, b, c, and d some constants that determine the shape and curvature of the two parabolic functions.

$$y_{Re} = ax^2 \tag{8}$$

$$y_I = bx^2 + cx + d \tag{9}$$

It has been shown through valence bond modeling that the transition state connecting two local minima is located nearby the curve crossing of the valence bond (VB) curves of the reactant and product wave functions.[30] If we assume the crossing happens in $x = {}^1/_2$ then we can derive a function for the crossing point of the two curves as a function of two variables, namely the difference in energy between the two functions in $x = 0$ [i.e., the Franck−Condon energy in the reactants ($E_{FC,Re}$)] and the driving force for the hydrogen atom abstraction reaction (ΔE_{rp}), eq 10.

$$\Delta E_{cross} = 1/4E_{FC,Re} + 3/4\Delta E_{rp} \tag{10}$$

Further, it has been shown that the curve crossing energy is a fraction B (the resonance energy) above the actual transition state,[30] so that the height of the reaction barrier can be estimated from the Franck−Condon energy between the two states in the reactants, the driving force and the resonance energy. Previously, we used this procedure successfully to predict trends in aromatic hydroxylation reactions by iron(IV)-oxo porphyrin cation radical models and benchmarked the results against experimental rate constants.[31] In addition, we predicted regioselectivity ratios of aliphatic hydroxylation versus decarboxylation reactions in cytochrome P450 peroxygenase enzymes using VB models.[32]

Subsequently, we attempted to estimate the Franck−Condon energies ($E_{FC,Re}$) from electronic changes along the reaction mechanism for hydrogen atom abstraction (HAT) and

DOI: 10.1021/jacs.7b10033
J. Am. Chem. Soc. 2017, 139, 18328−18338

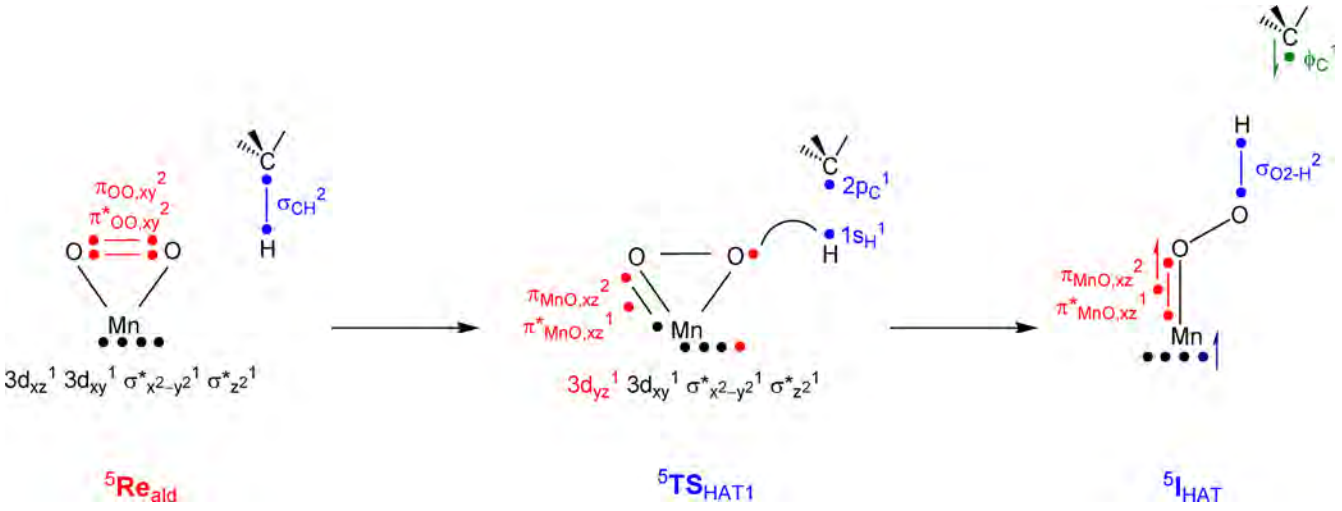

Figure 7. Electronic changes during the hydrogen atom abstraction from substrate by quintet spin side-on manganese(III)-peroxo. Dots represent electrons and lines between dots represent a bond orbital.

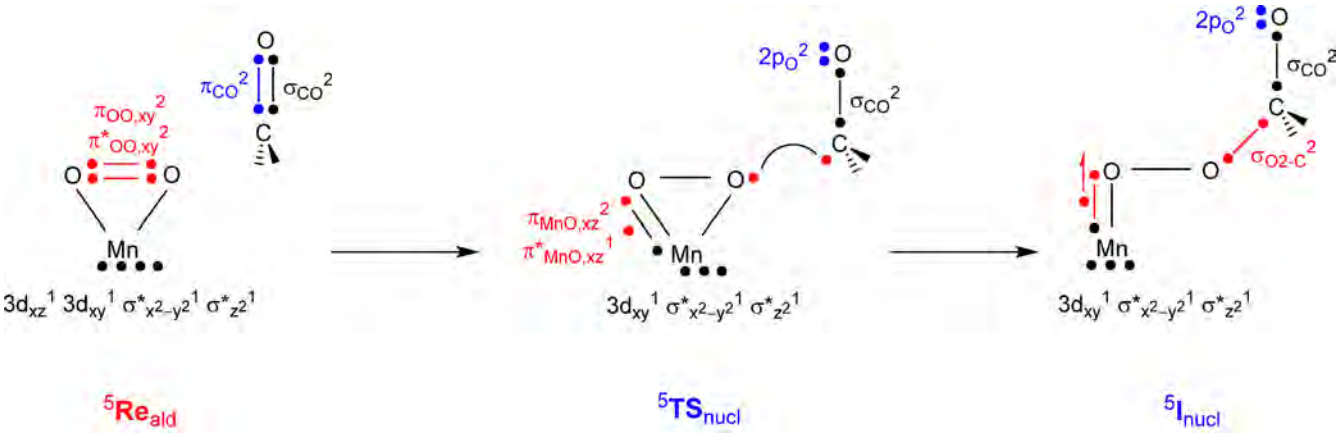

Figure 8. Electronic changes during the nucleophilic addition from substrate by quintet spin side-on manganese(III)-peroxo. Dots represent electrons and lines between dots a bond orbital.

nucleophilic addition (NA). Figure 7 displays the electronic changes during the hydrogen atom abstraction step between $^5[Mn^{III}(O_2)(L^2)]^+$ and substrate. Obviously, the hydrogen atom abstraction implies the breaking of a substrate C−H (or O−H in the case of the enol structure) bond orbital of the substrate (σ_{CH}) that splits into two atomic orbitals ($2p_C$ and $1s_H$ each with one electron). Therefore, the value of $E_{FC,Re}$ will contain the energy to break the σ_{CH} bond, $E_{\sigma(C-H)}$.

In addition, the peroxo double bond ($\pi_{OO,xy}/\pi^*_{OO,xy}$) breaks with energy $E_{\pi/\pi^*OO,xy}$, and the four electrons are redistributed over the manganese-peroxo system: two of those will pair up with the $3d_{xz}$ on manganese to form a three-electron MnO bond ($\pi_{MnO,xz}^2\ \pi^*_{MnO,xz}^1$), the third electron stays as a 2p on oxygen and will pair up with $1s_H$ to form the O−H orbital (σ_{O2-H}), while the fourth electron is promoted into the virtual $3d_{yz}$ orbital on manganese ($E_{exc,Mn}$). Consequently, the Franck−Condon energy should correlate with the breaking of the $\pi_{MnO,xz}$ orbitals, the formation of the O−H orbital, the breaking of the C−H orbital, and the electron transfer from peroxo to manganese, eq 11.

$$E_{FC,Re,HAT} = E_{\sigma(C-H)} + E_{\pi/\pi^*OO,xy} + E_{exc,Mn} \quad (11)$$

The $E_{\sigma(C-H)}$ was determined from the adiabatic values using eq 5 above as 82.6 kcal mol^{-1}. The $E_{\pi/\pi^*OO,xy}$ energy was determined from the orbital energy difference of the α-type $\pi_{OO,xy}$ and $\pi^*_{OO,xy}$ orbitals in the quintet spin reactant complex (78.2 kcal mol^{-1}), whereas $E_{exc,Mn}$ was taken as the energy difference between the $\pi^*_{OO,xy}$ and π^*_{yz} orbitals with β spin. These values gave us a prediction of $E_{FC,Re,HAT}$, whereas the energy difference of the BDE_{CH} of the substrate and the BDE_{OH} of $^6[MnOOH(L^2)]^+$ gave ΔE_{rp} = 8.0 kcal mol^{-1}. On the basis of eqs 10 and 11, we estimated the hydrogen atom abstraction barrier from the keto position as $\Delta E^{\ddagger}_{VB,HAT}$ = 18.5 kcal mol^{-1}. For comparison, using transition state theory, the experimental second-order rate constant of k_2 = 0.142 M^{-1} s^{-1} corresponds to a free energy of activation of $\Delta G^{\ddagger}_{2,exp}$ = 18.9 kcal mol^{-1} at 15 °C. Therefore, our DFT model predicts the hydrogen atom abstraction barrier perfectly and explains the contributions from orbital/bond breaking and forming processes.

Finally, we analyze the VB electronic configuration changes for the nucleophilic reaction of manganese(III)-peroxo with aldehyde in Figure 8. Similarly to the hydrogen atom abstraction step, the $\pi_{OO,xy}/\pi^*_{OO,xy}$ orbital couple is rehybridized and converted back into atomic orbitals, whereby again two of those electrons will form a new three-electron bond along the Mn−O axis ($\pi_{MnO,xz}^2\ \pi^*_{MnO,xz}^1$). The remaining two electrons originating from the $\pi_{OO,xy}/\pi^*_{OO,xy}$ orbitals are donated into the new σ-bond for the C−O interaction. This

DOI: 10.1021/jacs.7b10033
J. Am. Chem. Soc. 2017, 139, 18328−18338

results in the breaking of the π-bond of the carbonyl (in the keto-form) or olefin (in the enol-form) bond of the substrate.

To estimate the VB barrier for the nucleophilic attack, we again took the energy to break the $\pi_{OO,xy}/\pi^*_{OO,xy}$ orbitals ($E_{\pi/\pi^*oo,xy}$) as well as the energy to break the double bond ($E_{\pi,Sub}$), eq 12. The energy $E_{\pi,Sub}$ for the keto and enol forms of the substrate was determined from the singlet−triplet energy gap in the isolated forms as 83.1 and 77.5 kcal mol^{-1}, respectively. That way, we predict a nucleophilic barrier height of 24.8 kcal mol^{-1} for direct attack of aldehyde on side-on manganese(III)-peroxo. This value is in good quantitative agreement with the DFT barrier reported above and explains the electrostatic interactions relevant for the barrier height. It also shows that it will be easier for the enol form to react through nucleophilic addition then the keto form as the singlet−triplet energy gap in the double bond is much higher.

$$E_{FC,Re,NA} = E_{\pi,Sub} + E_{\pi/\pi^*OO,xy} \quad (12)$$

CONCLUSIONS

In this work, a combined experimental and computational study is reported on aldehyde deformylation by side-on manganese(III)-peroxo complexes. We identify a novel reaction mechanism that starts with a hydrogen atom abstraction and reshuttle to give a keto−enol tautomerization in the substrate as the rate-determining step. Subsequently, a nucleophilic attack on the olefin bond in the enol form leads to a low-energy mechanism to products. Alternative pathways were tested and ruled out. A detailed thermochemical and valence bond analysis of the structures of intermediates and reactants explains the need of the keto−enol tautomerization. Thus, in the enol form the olefin π-bond is easy to break, whereas breaking the carbonyl π-bond is more energetically demanding. As the reaction starts with a hydrogen atom abstraction from aldehyde, we also considered the manganese(III)-peroxo species as a general oxidant for substrate hydroxylation and desaturation reactions. Unfortunately, high reaction barriers for radical rebound are encountered and substrate hydroxylation and desaturation are unfeasible pathways at room temperature.

ASSOCIATED CONTENT

Supporting Information

The Supporting Information is available free of charge on the ACS Publications website at DOI: 10.1021/jacs.7b10033.

Mass, UV-vis, and NMR spectra; tables with energies, group spin densities, charges, and optimized geometries; Cartesian coordinates of all structures reported; and optimized structures (PDF)

AUTHOR INFORMATION

Corresponding Authors

*sam.devisser@manchester.ac.uk
*sastricv@iitg.ernet.in

ORCID

Prasenjit Barman: 0000-0002-4409-2782
Gourab Mukherjee: 0000-0002-7150-5570
Chivukula V. Sastri: 0000-0003-0477-7741
Sam P. de Visser: 0000-0002-2620-8788

Author Contributions

The manuscript was written through contributions of all authors. All authors have given approval to the final version of the manuscript.

Notes

The authors declare no competing financial interest.

ACKNOWLEDGMENTS

F.G.C.R. thanks the Conacyt (Mexico) for a studentship. D.K. and S.P.d.V. thank the University of Manchester for a Targeting GCRF Applications in Industrial Biotechnology: Enhancing International Collaborations award. Research support was provided by the Department of Science and Technology (SERB), India (EMR/2014/000279), to C.V.S. D.K. and J.K. acknowledge financial support from DBT, New Delhi (BT/PR14510/BID/07/334/2010).

REFERENCES

(1) See, for example: (a) Solomon, E. I.; Brunold, T. C.; Davis, M. I.; Kemsley, J. N.; Lee, S.-K.; Lehnert, N.; Neese, F.; Skulan, A. J.; Yang, Y.-S.; Zhou, J. *Chem. Rev.* **2000**, *100*, 235−349. (b) Bugg, T. D. H. *Curr. Opin. Chem. Biol.* **2001**, *5*, 550−555. (c) Ryle, M. J.; Hausinger, R. P. *Curr. Opin. Chem. Biol.* **2002**, *6*, 193−201. (d) Costas, M.; Mehn, M. P.; Jensen, M. P.; Que, L., Jr *Chem. Rev.* **2004**, *104*, 939−986. (e) Abu-Omar, M. M.; Loaiza, A.; Hontzeas, N. *Chem. Rev.* **2005**, *105*, 2227−2252. (f) Krebs, C.; Galonić Fujimori, D.; Walsh, C. T.; Bollinger, J. M., Jr *Acc. Chem. Res.* **2007**, *40*, 484−492. (g) Bruijnincx, P. C. A.; van Koten, G.; Klein Gebbink, R. J. M. *Chem. Soc. Rev.* **2008**, *37*, 2716−2744. (h) Solomon, E. I.; Light, K. M.; Liu, L. V.; Srnec, M.; Wong, S. D. *Acc. Chem. Res.* **2013**, *46*, 2725−2739. (i) McDonald, A. R.; Que, L., Jr *Coord. Chem. Rev.* **2013**, *257*, 414−428.

(2) (a) Zhu, W.; Richards, N. G. J. *Essays Biochem.* **2017**, *61*, 259−270. (b) Aguirre, J. D.; Culotta, V. C. *J. Biol. Chem.* **2012**, *287*, 13541−13548.

(3) (a) Jackson, T. A.; Brunold, T. C. *Acc. Chem. Res.* **2004**, *37*, 461−470. (b) Streit, B. R.; Blanc, B.; Lukat-Rodgers, G. S.; Rodgers, K.; Dubois, J. L. *J. Am. Chem. Soc.* **2010**, *132*, 5711−5724. (c) Hofbauer, S.; Gruber, C.; Pirker, K. F.; Sündermann, A.; Schaffner, I.; Jakopitsch, C.; Oostenbrink, C.; Furtmüller, P. G.; Obinger, C. *Biochemistry* **2014**, *53*, 3145−3157. (d) Grove, L. E.; Xie, J.; Yikilmaz, E.; Miller, A.-F.; Brunold, T. C. *Inorg. Chem.* **2008**, *47*, 3978−3992. (e) Kenkel, I.; Franke, A.; Dürr, M.; Zahl, A.; Dücker-Benfer, C.; Langer, J.; Filipović, M. R.; Yu, M.; Puchta, R.; Fiedler, S. R.; Shores, M. P.; Goldsmith, C. R.; Ivanović-Burmazović, I. *J. Am. Chem. Soc.* **2017**, *139*, 1472−1484. (f) Miller, A.-F. *FEBS Lett.* **2012**, *586*, 585−595. (g) Lee, A. Q.; Streit, B. R.; Zdilla, M. J.; Abu-Omar, M. M.; DuBois, J. L. *Proc. Natl. Acad. Sci. U. S. A.* **2008**, *105*, 15654−15659.

(4) (a) Vinyard, D. J.; Ananyev, G. M.; Dismukes, G. C. *Annu. Rev. Biochem.* **2013**, *82*, 577−606. (b) Renger, G.; Renger, T. *Photosynth. Res.* **2008**, *98*, 53−80. (c) Barber, J. *Q. Rev. Biophys.* **2003**, *36*, 71−89. (d) Siegbahn, P. E. M. *Chem. - Eur. J.* **2008**, *14*, 8290−8302.

(5) (a) Kryatov, S. V.; Rybak-Akimova, E. V.; Schindler, S. *Chem. Rev.* **2005**, *105*, 2175−2226. (b) Nam, W. *Acc. Chem. Res.* **2007**, *40*, 522−531. (c) Sahu, S.; Goldberg, D. P. *J. Am. Chem. Soc.* **2016**, *138*, 11410−11428. (d) Saisaha, P.; de Boer, J. W.; Browne, W. R. *Chem. Soc. Rev.* **2013**, *42*, 2059−2074.

(6) (a) Roelfes, G.; Vrajmasu, V.; Chen, K.; Ho, R. Y. N.; Rohde, J.-U.; Zondervan, C.; la Crois, R. M.; Schudde, E. P.; Lutz, M.; Spek, A. L.; Hage, R.; Feringa, B. L.; Münck, E.; Que, L., Jr *Inorg. Chem.* **2003**, *42*, 2639−2653. (b) Annaraj, J.; Suh, Y.; Seo, M. S.; Kim, S. O.; Nam, W. *Chem. Commun.* **2005**, 4529−4531. (c) Thibon, A.; Bartoli, J.-F.; Bourcier, S.; Banse, F. *Dalton Trans.* **2009**, 9587−9584. (d) Mukherjee, A.; Cranswick, M. A.; Chakrabarti, M.; Paine, T. K.; Fujisawa, K.; Münck, E.; Que, L., Jr *Inorg. Chem.* **2010**, *49*, 3618−3628. (e) Cho, J.; Jeon, S.; Wilson, S. A.; Liu, L. V.; Kang, E. A.; Braymer, J. J.; Lim, M. H.; Hedman, B.; Hodgson, K. O.; Valentine, J. S.; Solomon, E. I.; Nam, W. *Nature* **2011**, *478*, 502−505.

DOI: 10.1021/jacs.7b10033
J. Am. Chem. Soc. 2017, 139, 18328−18338

(7) (a) Annaraj, J.; Cho, J.; Lee, Y.-M.; Kim, S. Y.; Latifi, R.; de Visser, S. P.; Nam, W. *Angew. Chem., Int. Ed.* **2009**, *48*, 4150−4153. (b) Leto, D. F.; Chattopadhyay, S.; Day, V. W.; Jackson, T. A. *Dalton Trans.* **2013**, *42*, 13014−13025. (c) Zlatar, M.; Gruden, M.; Vassilyeva, O. Y.; Buvaylo, E. A.; Ponomarev, A. N.; Zvyagin, S. A.; Wosnitza, J.; Krzystek, J.; Garcia-Fernandez, P.; Duboc, C. *Inorg. Chem.* **2016**, *55*, 1192−1201. (d) Lee, C.-M.; Chuo, C.-H.; Chen, C.-H.; Hu, C.-C.; Chiang, M.-H.; Tseng, Y.-J.; Hu, C.-H.; Lee, G.-H. *Angew. Chem., Int. Ed.* **2012**, *51*, 5427−5430. (e) Gennari, M.; Brazzolotto, D.; Pécaut, J.; Cherrier, M. V.; Pollock, C. J.; DeBeer, S.; Retegan, M.; Pantazis, D. A.; Neese, F.; Duboc, C. *J. Am. Chem. Soc.* **2015**, *137*, 8644−8653. (f) Brazzolotto, D.; Cantú Reinhard, F. G.; Smith-Jones, J.; Retegan, M.; Amidani, L.; Faponle, A. S.; Ray, K.; Philouze, C.; de Visser, S. P.; Gennari, M.; Duboc, C. *Angew. Chem., Int. Ed.* **2017**, *56*, 8211−8215.

(8) (a) Coggins, M. K.; Kovacs, J. A. *J. Am. Chem. Soc.* **2011**, *133*, 12470−12473. (b) Coggins, M. K.; Martin-Diaconescu, V.; DeBeer, S.; Kovacs, J. A. *J. Am. Chem. Soc.* **2013**, *135*, 4260−4272. (c) Colmer, H. E.; Howcroft, A. W.; Jackson, T. A. *Inorg. Chem.* **2016**, *55*, 2055−2069. (d) Cho, J.; Sarangi, R.; Nam, W. *Acc. Chem. Res.* **2012**, *45*, 1321−1330. (e) Zhang, Q.; Bell-Taylor, A.; Bronston, F. M.; Gorden, J. D.; Goldsmith, C. R. *Inorg. Chem.* **2017**, *56*, 773−782.

(9) Barman, P.; Upadhyay, P.; Faponle, A. S.; Kumar, J.; Nag, S. S.; Kumar, D.; Sastri, C. V.; de Visser, S. P. *Angew. Chem., Int. Ed.* **2016**, *55*, 11091−11095.

(10) (a) Vardhaman, A. K.; Barman, P.; Kumar, S.; Sastri, C. V.; Kumar, D.; de Visser, S. P. *Angew. Chem., Int. Ed.* **2013**, *52*, 12288−12292. (b) Kumar, S.; Faponle, A. S.; Barman, P.; Vardhaman, A. K.; Sastri, C. V.; Kumar, D.; de Visser, S. P. *J. Am. Chem. Soc.* **2014**, *136*, 17102−17115. (c) Barman, P.; Faponle, A. S.; Vardhaman, A. K.; Angelone, D.; Löhr, A.-M.; Browne, W. R.; Comba, P.; Sastri, C. V.; de Visser, S. P. *Inorg. Chem.* **2016**, *55*, 10170−10181.

(11) Armarego, W. L. F. In *Purification of Laboratory Chemicals*, Perrin, D. D., Ed.; Pergamon Press: Oxford, 1997.

(12) (a) Börzel, H.; Comba, P.; Hagen, K. S.; Lampeka, Y. D.; Lienke, A.; Linti, G.; Merz, M.; Pritzkow, H.; Tsymbal, L. V. *Inorg. Chim. Acta* **2002**, *337*, 407−419. (b) Comba, P.; Kuwata, S.; Linti, G.; Pritzkow, H.; Tarnai, M.; Wadepohl, H. *Chem. Commun.* **2006**, 2074−2076. (c) Comba, P.; Kanellakopulos, B.; Katsichtis, C.; Lienke, A.; Pritzkow, H.; Rominger, F. *J. Chem. Soc., Dalton Trans.* **1998**, 3997−4001. (d) Barman, P.; Vardhaman, A. K.; Martin, B.; Wörner, S. J.; Sastri, C. V.; Comba, P. *Angew. Chem., Int. Ed.* **2015**, *54*, 2095−2099.

(13) Goto, Y.; Wada, S.; Morishima, I.; Watanabe, Y. *J. Inorg. Biochem.* **1998**, *69*, 241−247.

(14) (a) de Visser, S. P.; Quesne, M. G.; Martin, B.; Comba, P.; Ryde, U. *Chem. Commun.* **2014**, *50*, 262−282. (b) Sainna, M. A.; Kumar, S.; Kumar, D.; Fornarini, S.; Crestoni, M. E.; de Visser, S. P. *Chem. Sci.* **2015**, *6*, 1516−1529.

(15) Frisch, M. J.; Trucks, G. W.; Schlegel, H. B.; Scuseria, G. E.; Robb, M. A.; Cheeseman, J. R.; Scalmani, G.; Barone, V.; Mennucci, B.; Petersson, G. A.; Nakatsuji, H.; Caricato, M.; Li, X.; Hratchian, H. P.; Izmaylov, A. F.; Bloino, J.; Zheng, G.; Sonnenberg, J. L.; Hada, M.; Ehara, M.; Toyota, K.; Fu-kuda, R.; Hasegawa, J.; Ishida, M.; Nakajima, T.; Honda, Y.; Kitao, O.; Nakai, H.; Vreven, T.; Montgomery, J. A., Jr.; Peralta, J. E.; Ogliaro, F.; Bearpark, M.; Heyd, J. J.; Brothers, E.; Kudin, K. N.; Staroverov, V. N.; Keith, T.; Kobayashi, R.; Normand, J.; Raghavachari, K.; Rendell, A.; Burant, J. C.; Iyengar, S. S.; Tomasi, J.; Cossi, M.; Re-ga, N.; Millam, J. M.; Klene, M.; Knox, J. E.; Cross, J. B.; Bakken, V.; Adamo, C.; Jaramillo, J.; Gomperts, R.; Stratmann, R. E.; Yazyev, O.; Austin, A. J.; Cammi, R.; Pomelli, C.; Ochterski, J. W.; Martin, R. L.; Morokuma, K.; Zakrzewski, V. G.; Voth, G. A.; Salvador, P.; Dannen-berg, J. J.; Dapprich, S.; Daniels, A. D.; Farkas, O.; Foresman, J. B.; Ortiz, J. V.; Cioslowski, J.; Fox, D. J. *Gaussian 09*, revision C.01; Gaussian, Inc.: Wallingford, CT, 2010.

(16) Tomasi, J.; Mennucci, B.; Cammi, R. *Chem. Rev.* **2005**, *105*, 2999−3093.

(17) (a) Becke, A. D. *J. Chem. Phys.* **1993**, *98*, 5648−5652. (b) Lee, C.; Yang, W.; Parr, R. G. *Phys. Rev. B: Condens. Matter Mater. Phys.* **1988**, *37*, 785−789.

(18) (a) Hay, P. J.; Wadt, W. R. *J. Chem. Phys.* **1985**, *82*, 270−283. (b) Hehre, W. J.; Ditchfield, R.; Pople, J. A. *J. Chem. Phys.* **1972**, *56*, 2257−2262.

(19) (a) de Visser, S. P. *J. Am. Chem. Soc.* **2010**, *132*, 1087−1097. (b) Quesne, M. G.; Senthilnathan, D.; Singh, D.; Kumar, D.; Maldivi, P.; Sorokin, A. B.; de Visser, S. P. *ACS Catal.* **2016**, *6*, 2230−2243.

(20) (a) Cantú Reinhard, F. G.; Faponle, A. S.; de Visser, S. P. *J. Phys. Chem. A* **2016**, *120*, 9805−9814. (b) Yang, T.; Quesne, M. G.; Neu, H. M.; Cantú Reinhard, F. G.; Goldberg, D. P.; de Visser, S. P. *J. Am. Chem. Soc.* **2016**, *138*, 12375−12386.

(21) (a) de Visser, S. P. *Chem. - Eur. J.* **2006**, *12*, 8168−8177. (b) Li, X.-X.; Postils, V.; Sun, W.; Faponle, A. S.; Solà, M.; Wang, Y.; Nam, W.; de Visser, S. P. *Chem. - Eur. J.* **2017**, *23*, 6406−6418.

(22) (a) Quesne, M. G.; Latifi, R.; Gonzalez-Ovalle, L. E.; Kumar, D.; de Visser, S. P. *Chem. - Eur. J.* **2014**, *20*, 435−446. (b) Timmins, A.; Saint-André, M.; de Visser, S. P. *J. Am. Chem. Soc.* **2017**, *139*, 9855−9866.

(23) (a) Groves, J. T.; Nemo, T. E. *J. Am. Chem. Soc.* **1983**, *105*, 6243−6248. (b) Rana, S.; Dey, A.; Maiti, D. *Chem. Commun.* **2015**, *51*, 14469−14472.

(24) (a) Yoshizawa, K.; Kamachi, T.; Shiota, Y. *J. Am. Chem. Soc.* **2001**, *123*, 9806−9816. (b) Shaik, S.; Kumar, D.; de Visser, S. P.; Altun, A.; Thiel, W. *Chem. Rev.* **2005**, *105*, 2279−2328. (c) Shaik, S.; Kumar, D.; de Visser, S. P. *J. Am. Chem. Soc.* **2008**, *130*, 10128−10140. (d) Li, D.; Wang, Y.; Han, K. *Coord. Chem. Rev.* **2012**, *256*, 1137−1150.

(25) (a) de Visser, S. P.; Kumar, D.; Cohen, S.; Shacham, R.; Shaik, S. *J. Am. Chem. Soc.* **2004**, *126*, 8362−8363. (b) Kumar, D.; Hirao, H.; Que, L., Jr.; Shaik, S. *J. Am. Chem. Soc.* **2005**, *127*, 8026−8027. (c) Geng, C. Y.; Ye, S. F.; Neese, F. *Angew. Chem., Int. Ed.* **2010**, *49*, 5717−5720. (d) Srnec, M.; Solomon, E. I. *J. Am. Chem. Soc.* **2017**, *139*, 2396−2407.

(26) Latifi, R.; Bagherzadeh, M.; de Visser, S. P. *Chem. - Eur. J.* **2009**, *15*, 6651−6662.

(27) Faponle, A. S.; Quesne, M. G.; Sastri, C. V.; Banse, F.; de Visser, S. P. *Chem. - Eur. J.* **2015**, *21*, 1221−1236.

(28) Faponle, A. S.; Banse, F.; de Visser, S. P. *JBIC, J. Biol. Inorg. Chem.* **2016**, *21*, 453−462.

(29) (a) Hernández-Ortega, A.; Quesne, M. G.; Bui, S.; Heyes, D. J.; Steiner, R. A.; Scrutton, N. S.; de Visser, S. P. *J. Am. Chem. Soc.* **2015**, *137*, 7474−7487. (b) Cantú Reinhard, F. G.; de Visser, S. P. *Chem. - Eur. J.* **2017**, *23*, 2935−2944.

(30) Shaik, S. *Phys. Chem. Chem. Phys.* **2010**, *12*, 8706−8720.

(31) Cantú Reinhard, F. G.; Sainna, M. A.; Upadhyay, P.; Balan, G. A.; Kumar, D.; Fornarini, S.; Crestoni, M. E.; de Visser, S. P. *Chem. - Eur. J.* **2016**, *22*, 18608−18619.

(32) Faponle, A. S.; Quesne, M. G.; de Visser, S. P. *Chem. - Eur. J.* **2016**, *22*, 5478−5483.

DOI: 10.1021/jacs.7b10033
J. Am. Chem. Soc. 2017, 139, 18328−18338

Dalton Transactions

PAPER

Cite this: *Dalton Trans.*, 2018, **47**, 14945

Dramatic rate-enhancement of oxygen atom transfer by an iron(IV)-oxo species by equatorial ligand field perturbations†

Gourab Mukherjee, [a] Calvin W. Z. Lee,[b] Sayanta Sekhar Nag, [a] Aligulu Alili,[b] Fabián G. Cantú Reinhard, [b] Devesh Kumar, [c] Chivukula V. Sastri *[a] and Sam P. de Visser *[b]

Received 25th May 2018,
Accepted 20th September 2018

DOI: 10.1039/c8dt02142b

rsc.li/dalton

Nonheme iron dioxygenases are efficient enzymes with relevance for human health that regio- and stereospecifically transfer an oxygen atom to substrates. How they perform this task with such selectivity remains unknown, but may have to do with substrate binding, positioning and oxidant approach. To understand substrate approach on a catalytic reaction centre, we investigated the structure and reactivity of a biomimetic oxidant with ligand features that affect the interactions between oxidant and substrate. Thus, we report here the synthesis and characterization of an iron(IV)-oxo complex with pentadentate nonheme ligand, where structurally induced perturbations in the equatorial ligand field affect the spectroscopy and reactivity of the complex. We tested the activity of the complex with respect to oxygen atom transfer to and hydrogen atom abstraction from substrates. This oxidant shows improved reaction rates toward heteroatom oxidation with respect to the nonsubstituted ligand complex by ~10^4 fold. The origin of the enhanced reactivity is explained with a series of density functional theory studies that show an enhanced electron affinity of the oxidant through equatorial ligand perturbations.

Introduction

Iron-containing metalloenzymes are well-known oxidants that carry out metabolically vital oxidative transformations in the human body.[1] High valent iron(IV)-oxo complexes have often been identified as the key reacting species in such oxidative transformations,[2] and indeed have been characterized for several nonheme iron dioxygenases.[3] Most nonheme iron dioxygenases display a typical facial iron coordination *via* two histidine and one carboxylate based residue; usually from Asp or Glu. Many details on the catalytic reaction mechanisms of heme and nonheme metalloenzymes remain unknown. Moreover, many nonheme iron dioxygenases react with substrates in a stereoselective or regiospecific manner. For instance, prolyl-4-hydroxylase activates a proline residue in a peptide chain to give solely the *R*-4-hydroxyproline product as part of its natural biosynthesis pathway.[4] Recent QM/MM studies showed that even though 5-hydroxyproline would be a thermodynamically more stable product, the enzyme manages to avoid this product through substrate binding and orientation.[5] In particular, substrate is held in a tight binding pocket and can only approach the active site through a narrow funnel lined up by a Trp and Tyr residue. Moreover, key hydrogen bonding interactions hold the substrate in a tight conformation and site-selective mutations of one of the residues in the substrate binding pocket leads to either loss of specificity or complete loss of activity. Other enzymes with tight substrate binding pockets that catalyse a regioselective reaction include the camphor hydroxylating heme enzyme cytochrome $P450_{cam}$,[6] and the nonheme iron dioxygenase AlkB, which is involved in DNA base repair mechanisms through the demethylation of methylated DNA bases.[7] Clearly, the substrate binding position and orientation in enzymes is important and can determine and affect the product distributions.

To understand the mechanistic aspects of metalloenzymes biomimetic models have been developed that contain the coordination features of the metal but lack the protein environment.[8] Artificial/synthetic mimics of these biological systems provide necessary information about their catalytic

[a]*Department of Chemistry, Indian Institute of Technology Guwahati, Assam 781039, India. E-mail: sastricv@iitg.ernet.in; Fax: +91-361-258-2349*
[b]*The Manchester Institute of Biotechnology and the School of Chemical Engineering and Analytical Science, The University of Manchester, 131 Princess Street, Manchester M1 7DN, UK. E-mail: sam.devisser@manchester.ac.uk*
[c]*Department of Applied Physics, School for Physical Sciences, Babasaheb Bhimrao Ambedkar University, Lucknow 226025, India. E-mail: dkclcre@yahoo.com*

†Electronic supplementary information (ESI) available: Experimental and computational raw data, including Cartesian coordinates of optimized structures, absolute and relative energies and group spin densities and charges. See DOI: 10.1039/c8dt02142b

This journal is © The Royal Society of Chemistry 2018

cycle and their mode of operation. There are several reports in the literature regarding the tuning of the primary coordination sphere of these high valent intermediates and the various factors that affect their reactivity, such as ligand topology, axial ligation, spin-state of the metal atom, *etc*.[9] As changes in the primary coordination sphere can be quite dramatic, research has also focused on the influence of secondary coordination sphere modifications, where changes are more subtle.[10] Non-covalent interactions in the vicinity of the active site, such as charge induction or stereochemical perturbations influence reaction mechanisms and can change bifurcation pathways.[11]

A biomimetic iron(IV)-oxo species that has received quite a lot of attention over the years is the $[Fe^{IV}(O)(N4Py)]^{2+}$ complex with N4Py = *N*,*N*-bis(2-pyridylmethyl)-*N*-bis(2-pyridyl) methylamine: structure **2b** in Fig. 1. The complex was originally synthesized by Feringa and Que and their co-workers[12] and was one of the first biomimetic iron(IV)-oxo species that was characterized by electron paramagnetic resonance, resonance Raman, Mössbauer, UV-vis absorption and nuclear magnetic resonance (NMR) spectroscopic methods as well as by X-ray crystallography.[13] In addition, many reactivity studies with substrates have been reported, which showed it efficiently reacts through oxygen atom transfer.[14] Very recently Que and co-workers showed that substitution of the three pyridine rings of the tetradentate TPA, tris-(2-pyridylmethyl)amine, ligand by quinoline moieties enabled the synthesis of a high-spin (S = 2) iron(IV)-oxo species.[15] However, replacement of the pyridine rings by *N*-methylbenzimidazole moieties, instead generated an S = 1 iron(IV)-oxo ground state.[16] Nevertheless, in both of these systems enhanced reactivity towards substrates was observed. Interestingly, such ligand modifications are much less explored in pentadentate iron(IV)-oxo intermediates. Nordlander and co-workers have shown that a systematic replacement of the pyridine groups with *N*-methylbenzimidazole in the N4Py ligand framework leads to enhanced reaction rates.[17]

In particular, the introduction of *ortho*-substituents to a pyridine ring is a well-established design strategy to significantly affect the iron(IV)-oxo core by weakening the Fe–N_{eq} bonds. To gain insight into the influence of the equatorial ligand perturbations in biomimetic complexes, we engineered the N4Py ligand system to 2PyN2Q (1,1-di(pyridin-2-yl)-*N*,*N*-bis(quinolin-2-ylmethyl)methanamine). The introduction of bulky quinoline moieties is expected to influence the electronic orbitals and spectroscopic features of the iron(IV)-oxo oxidant and hence its reactivity with substrates. Specifically, we compare the spectroscopy and reactivity of the two nonheme iron(IV)-oxo complexes **1b** and **2b** (Fig. 1), namely $[Fe^{IV}(O)(2PyN2Q)]^{2+}$ and $[Fe^{IV}(O)(N4Py)]^{2+}$. In these complexes the equatorial ligand perturbations on the oxo group are different, whereby in **1b** the oxo group experiences two weak C–H···O hydrogen bonding interactions that are absent in complex **2b**. We predicted that the changes in ligand coordination may give different spectroscopic and reactivity patterns. Indeed, the results described in this work show a dramatic rate-enhancement with the new ligand system, which is explained through a combination of experimental and computational studies.

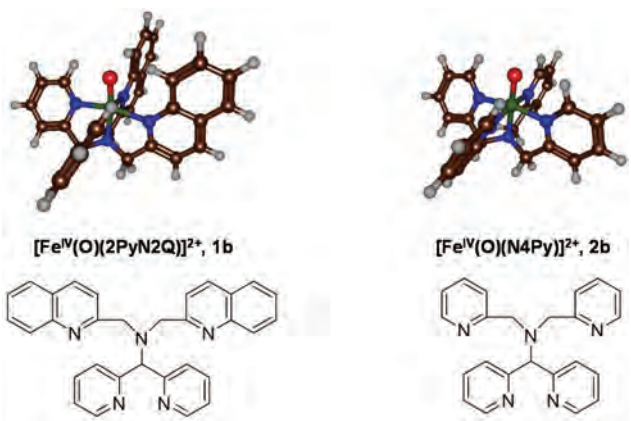

Fig. 1 Oxidants investigated in this study.

Results and discussion

In this work we report a combined experimental and computational study on the reactivity of a modified N4Py ligand system (2PyN2Q) that when bound to an iron(IV)-oxo influences substrate approach and therefore leads to significant enhancement of oxidative properties. Various experiments are performed to understand the mechanism of the reaction and are supported by computational studies.

Experiment

Our initial work started from a pentadentate nonheme iron complex $[Fe^{II}(2PyN2Q)(OTf)_2]$, **1a**, supported by the 2PyN2Q ligand bearing quinoline moieties.[18] Dropwise addition of an acetonitrile solution containing $Fe^{II}(OTf)_2{\cdot}2CH_3CN$ to the ligand resulted in the formation of a dark yellow compound (**1a**) in 95% yield that could be characterized with UV-vis spectroscopy, electrospray ionization-mass spectrometry (ESI-MS) and NMR spectroscopy, see Fig. S2 and S3 (ESI†). Treatment of **1a** with 1.5 equivalents of $PhI(OAc)_2$ in CH_3CN under ambient conditions generated the corresponding iron(IV)-oxo complex $[Fe^{IV}(O)(2PyN2Q)]^{2+}$, **1b** ($\lambda_{max}$ = 770 nm, ε = 340 L M^{-1} cm^{-1}, $t_{1/2}$ = 50 min at RT), Fig. 2a. These values are similar to those reported recently by Rasheed *et al.*[19] The intermediate **1b** was also prepared by the addition of PhIO (in CF_3CH_2OH) and 1-^{t}butylsulfonyl-2-iodosylbenzene with a half-life of 3 and 50 min respectively. The UV-vis absorption spectrum of **2b** when generated under the same experimental conditions gave an absorption band at λ_{max} = 695 nm with a half-life of over 60 hours typical of $[Fe^{IV}(O)(N4Py)]^{2+}$. Thus, substitution of the pyridine rings in N4Py with quinoline groups to form 2PyN2Q resulted in a bathochromic shift of the d–d transition band by 75 nm and a significant loss of the thermal stability of the complex. These lifetimes indicate that the ligand architecture at the equatorial site influences its stability and reactivity.

This journal is © The Royal Society of Chemistry 2018

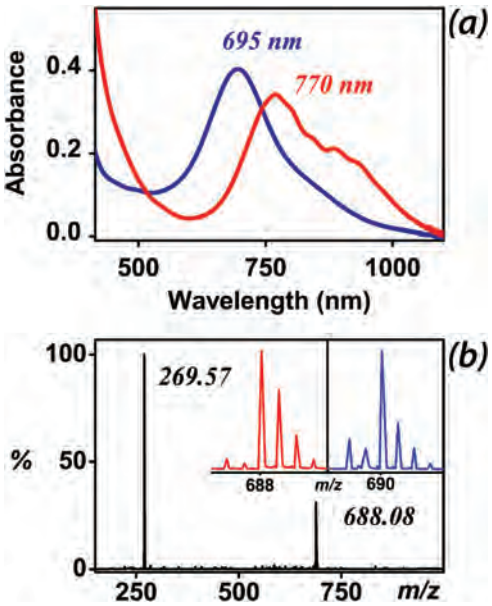

Fig. 2 (a) UV-vis spectra of **1b** (red) and **2b** (blue) in CH_3CN at 298 K; (b) electrospray ionization mass spectra of **1b** in CH_3CN at 298 K. Inset shows expanded isotopic distribution pattern of $[Fe^{IV}(O^{16})(2PyN2Q)(OTf)]^+$ (red) and $[Fe^{IV}(O^{18})(2PyN2Q)(OTf)]^+$ (blue).

The ESI-MS gives a major peak at *m*/*z* 269.57 corresponding to $[Fe^{IV}(O)(2PyN2Q)]^{2+}$ and a minor peak at *m*/*z* 688.08 representing the $[Fe^{IV}(O)(2PyN2Q)(OTf)]^+$ ion (Fig. 2b). The isotopic patterns for the two species confirm the assignments of the two ions. The formation of $[Fe^{IV}(O)(2PyN2Q)]^{2+}$ was further established by an isotopic labelling experiment using $H_2{}^{18}O$, which leads to oxygen atom exchange with the oxo group. The experiment with $H_2{}^{18}O$ moves the peak in the ESI mass spectrum for $[Fe^{IV}(O)(2PyN2Q)(OTf)]^+$ from *m*/*z* 688.08 to *m*/*z* 690.08, while the peak representing the $[Fe^{IV}(O)(2PyN2Q)]^{2+}$ ion shifts by one unit. Hence the isotopic labelling experiment shows that one oxygen atom is incorporated into the metal complex in the form of an iron(IV)-oxo species. We further employed ^{1}H-NMR spectrometry to see the differences between the two iron(IV)-oxo complexes (see Fig. S3, ESI†). The ^{1}H-NMR spectra for complex **2b** as reported by Klinker *et al*. reveals the presence of mirror symmetry.[13b] However, for complex **1b**, as expected, a more complicated spectrum with a larger number of signals is obtained compared to **2b**, due to the presence of quinoline groups instead of pyridine rings. The observed range of paramagnetic shift in the ^{1}H-NMR spectrum of **1b** decreased with respect to its Fe(II) precursor and gave a typical $S = 1$ shift.[10a,13b,20]

To gain more insight into the electronic structure of **1b**, we performed a variable temperature NMR experiment over a temperature range from 233–298 K. With a lowering of the temperature, no upfield shift of peaks was observed in the Curie plot, thereby confirming an $S = 1$ ferryl species as the ground state, see Fig. S4 and S5 (ESI†). This observation was further supported by a recent report of Rasheed *et al*. using Mössbauer spectroscopy.[19] The Fourier transform infrared spectral data of **1b** showed a Fe=O stretch vibration at 834 cm^{-1} which was at a lower frequency in comparison with **2b**.[19] Nevertheless, the lifetime of **1b** is sufficiently long to enable us do a detailed kinetics and spectroscopy study at room temperature alongside those for the analogous complex **2b**, *i.e.* $[Fe^{IV}(O)(N4Py)]^{2+}$.

In order to find out whether the change in spectroscopic properties of the oxidant (**1b** *versus* **2b**) has an effect on the oxidation properties, we did a thorough kinetics study using a range of different substrates. Thus, we employed thioanisole and benzyl alcohol as model substrates for heteroatom oxidation and alcohol oxidation reactions, respectively.

Addition of thioanisole to **1b** at 233 K led to the decay of the iron(IV)-oxo characteristic band at 770 nm in the UV-vis spectrum concomitant with the appearance of its iron(II) precursor (λ_{max} = 475 nm) with an isosbestic point at 605 nm, thereby generating methyl phenyl sulfoxide as the major product (Fig. 3a). We measured the change in absorbance

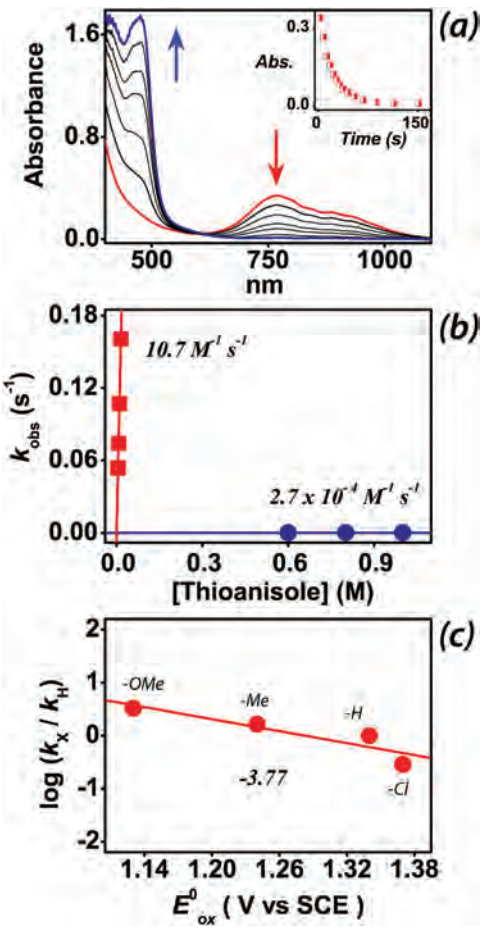

Fig. 3 (a) UV-vis spectral changes of **1b** upon addition of 7 equiv. thioanisole in CH_3CN at 233 K. Inset shows the decay profile of the 770 nm band; (b) second order rate constant determined for the reaction of **1b** (1 mM) (■) and **2b** (1 mM) (●) with thioanisole at 233 K; (c) plot of log(k_X/k_H) against one-electron oxidation potentials (E^0_{ox}) of *p*-X-thioanisols in their reaction with **1b** (●) at 233 K in CH_3CN, where k_X and k_H are the pseudo first-order rate constants of *p*-X-thioanisole and thioanisole, respectively.

from the UV-vis spectra at 770 nm and plotted it as a function of time, which enabled us to determine the pseudo first-order rate constant (k_{obs}) for the reaction. Subsequently, these observed rate constants were converted into second-order rate constants by plotting k_{obs} as a function of substrate concentration. The second-order rate constant (k_2) for the reaction of thioanisole with **1b** was evaluated to be 10.7(4) M^{-1} s^{-1} at 233 K (Fig. 3b). Previous work on the reaction of thioanisole with **2b** under the same reaction conditions,[16] provided a second-order rate constant of 2.7 × 10^{-4} M^{-1} s^{-1}. Consequently, under the same experimental conditions, the reactivity of **1b** with thioanisole is faster than that of **2b** by a factor of almost 4 × 10^4 fold. This rate increment is much higher than those observed for an analogous ligand system with *N*-methylbenzimidazole substituents by at least 30 times.[17] The enhanced reaction rate probably originates from the introduction of the *ortho*-substituent on the pyridine ring and consequent weakening of the Fe–N_{eq} bonds relative to that in **2b**. To gain insight into the mechanistic details of the reaction, we studied the reaction of **1b** with various *para*-X-substituted thioanisole substrates (X = OCH_3, CH_3, H, Cl) and measured their reaction rates (Table 1 and Fig. S6, ESI†).[21] A plot of the logarithm of the rate constant ratio (k_X/k_H) as a function of the one-electron oxidation potentials (E^0_{ox}) of various *para*-X-substituted thioanisole substrates gives a linear correlation with a slope of ρ = −3.77 (Fig. 3c). The negative ρ value and slope implicates that the reaction proceeds *via* atom transfer through an electrophilic reaction mechanism.[21b]

To compare the reactivity difference of **1b** over **2b** in C–H activation reactions, we subsequently monitored the hydrogen atom abstraction ability of both complexes toward benzyl alcohols. Upon addition of different concentrations of benzyl alcohol to **1b** in acetonitrile, the 770 nm band decayed in a pseudo first-order manner as a function of time. Product analysis reveal the formation of benzaldehyde in almost stoichiometric yields (>80% with respect to intermediate formed). The second-order rate constant (k_2) for the reaction of **1b** with benzyl alcohol is found to be 51.04(1) × 10^{-2} M^{-1} s^{-1} at 298 K (Fig. 4a), whereas previous work for **2b** found a value of 8.27 × 10^{-2} M^{-1} s^{-1} under the same reaction conditions.[22]

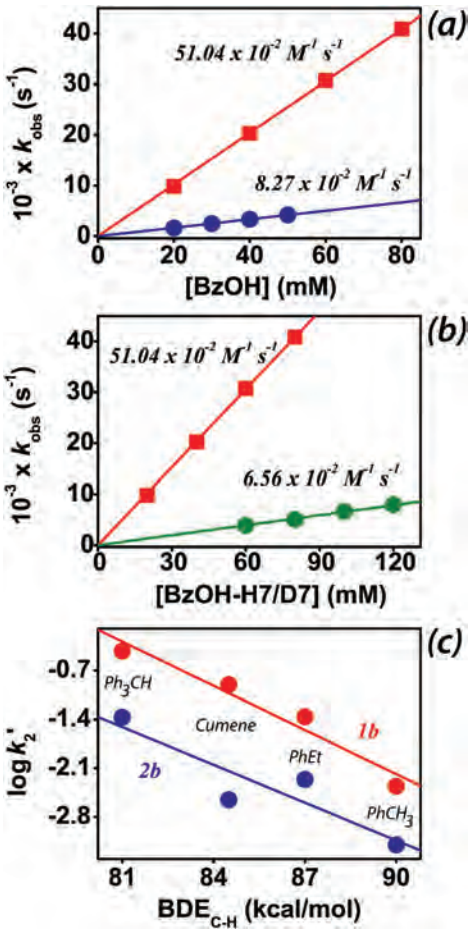

Fig. 4 Second-order rate constant determined for the reaction of (a) 1 mM **1b** (■) and 1 mM **2b** (●) with benzyl alcohol in CH_3CN at 298 K; (b) 1 mM **1b** with benzyl alcohol (■) and benzyl alcohol-d_7 (●) in CH_3CN at 298 K; (c) correlation between C–H bond dissociation energies of different hydrocarbons and log k'_2 for their reactions with **1b** (●) and **2b** (●) at 298 K; k'_2 is the second-order rate constant divided by the number of equivalent C–H bonds on the substrate that would react with the iron(IV)-oxo.

Table 1 Pseudo first-order rate constants (k_{obs}) determined for the reaction of **1b** (1 mM solution in CH_3CN) with 5 equivalents of *para*-X-substituted thioanisole at −40 °C in CH_3CN[a]

X[b]	σ_P[c]	σ_P^+[c]	E^0_{ox}[d]	k_{obs}[e]	k_X/k_H[f]	log(k_X/k_H)
$-OCH_3$	−0.27	−0.78	1.13	0.177(4)	3.29	0.52
$-CH_3$	−0.17	−0.31	1.24	0.088(2)	1.64	0.22
–H	0.00	0.00	1.34	0.054(2)	1.00	0.00
–Cl	0.23	0.11	1.37	0.015(3)	0.28	−0.55.

[a] All the reactions were followed by monitoring the UV-vis spectral changes of the reaction solution. [b] *para*-Substituents in *para*-X-thioanisole. [c] Data taken from ref. 21*a*. [d] Data taken from ref. 21*b*. [e] In s^{-1}. [f] Relative rate constant obtained by dividing the k_{obs} of *p*-X-thioanisole by k_{obs} of *p*-H-thioanisole.

As such, $[Fe^{IV}(O)(2PyN2Q)]^{2+}$ reacts with benzyl alcohol with rates that are more than six times faster than $[Fe^{IV}(O)(N4Py)]^{2+}$. Therefore, the equatorial ligand environment has significant effect on the reaction rates of alcohol oxidation reactions. Its rate-enhancement, however, is not as strong as in oxygen atom transfer (compare Fig. 3b and 4a), but clearly both reaction processes are favoured with **1b** as an oxidant.

To ascertain that hydrogen atom abstraction is indeed the rate-determining step in the reaction mechanism, we repeated the experiment with benzyl alcohol-d_7 or $C_6D_5CD_2OH$ as the substrate. A comparison of the rate constants depicted in Fig. 4b (and Table S1, ESI†) clearly shows that substitution of the active hydrogen atom by deuterium reduces the reaction rate by a factor of about 8. Hence, we determine a kinetic isotope effect (KIE) value of 8 for the reaction of **1b** with benzyl alcohol at 298 K. This KIE value is indicative of a rate-determining hydrogen atom abstraction step in the reaction

This journal is © The Royal Society of Chemistry 2018

mechanism. Our mechanism, therefore, is in excellent agreement with that derived for **2b** with benzyl alcohol although an even larger KIE value is obtained upon replacement of hydrogen by deuterium.[22,23]

We then studied the hydrogen atom abstraction ability of **1b** and **2b** with a selection of substrates with known C–H bond strengths. Previously, it was shown that reactions proceeding with a rate-determining hydrogen atom abstraction have the natural logarithm of the rate constant linearly related to the C–H bond dissociation energy (BDE_{C-H}).[24] We investigated the hydrogen atom abstraction reactions of **1b** with substrates including triphenylmethane, cumene, ethylbenzene and toluene (Fig. 4c and Table 2). These substrates span a range of C–H bond dissociation energies (BDE_{C-H}) typical for hydrogen atom abstraction reaction rates.[13a,25] As can be seen from Fig. 4c, a linear correlation between the natural logarithm of the rate constant *versus* BDE_{C-H} is found for the reactions of **1b**/**2b** with substrates. The linearity of the Bell–Evans–Polanyi plot ($\log k'_2$ *versus* BDE_{C-H}) provides evidence of a rate-determining hydrogen atom abstraction. Product analysis of the dead reaction mixture after the decay of the characteristic band in UV-vis spectrum indicated the production of the corresponding alcohols (and aldehydes) in variable yields (*e.g.* Ph_3C–OH, 88%; $PhC(OH)(CH_3)_2$, 60%; $PhCH(OH)CH_3$, 32% and PhCHO, 55%). It is not surprising to see that the rate enhancement for sulfoxidation is different from hydrogen atom abstraction as sulfoxidation generally is a concerted two-electron reaction mechanism, whereas substrate hydroxylation is stepwise reaction *via* a radical intermediate.[26] Clearly, the change of the ligand and the introduction of equatorial ligand perturbations do not affect the reaction mechanism of **1b**/**2b** with substrates. However, the change in ligand does affect the absolute reactivities.

Further evidence of the mechanism was obtained through studies of *para*-X-substituted benzyl alcohols in a reaction with $[Fe^{IV}(O)(2PyN2Q)]^{2+}$, **1b**. In particular, we monitored the influence of electron-withdrawing or electron-donating *para*-X-substituents on the reaction rate of **1b** with benzyl alcohols at 298 K. When we plot the $\log(k_X/k_H)$ values as a function of the Hammett parameters, σ_p, a linear trend is found with a slope of $\rho = -0.27$, Fig. S7 and Table S2 (ESI†). This small Hammett ρ value implicates little electronic effects as a result of the addition of *para*-substituents to the benzyl alcohol. Mechanistically, therefore, **1b** shows a reactivity pattern close to that previously reported on **2b**, where a ρ value of −0.10 was found under similar reaction conditions.[22]

Finally, a reactivity study of **1b** with cyclobutanol was performed, which is often used as a mechanistic probe.[22,23] In particular, formation of cyclobutanone as a product indicates a single step two-electron process, whereas two sequential one-electron steps involve ring opening of the substrate and the subsequent formation of 4-hydroxybutyraldehyde. We find that **1b** reacts with cyclobutanol to give cyclobutanone as the major product, thereby, confirming that alcohol oxidation by complex **1b** proceeds by a direct two-electron transfer pathway.

Table 2 C–H Bond dissociation energies and second-order rate constant values for the reaction of **1b** (1 mM) and **2b** (1 mM) with various substrates in CH_3CN at 25 °C

Substrate[a]	BDE_{C-H}[b] (kcal mol^{-1})	Complex	k_2[c]	k'_2[c,d]	$\log k'_2$
Ph_3CH (1)	81	**1b**	0.376(4)	0.376	−0.42
		2b	0.043(2)	0.043	−1.37
$PhCH(CH_3)_2$ (1)	84.5	**1b**	0.125(3)	0.125	−0.90
		2b	0.003(3)	0.003	−2.55
$PhCH_2CH_3$ (2)	87	**1b**	0.082(2)	0.041	−1.38
		2b	0.011(1)	0.005	−2.26
$PhCH_3$ (3)	90	**1b**	0.015(4)	0.005	−2.29
		2b	0.0006(2)	0.0002	−3.68

[a] The number in parenthesis indicates the number of equivalent H-atoms on the substrate that would react with the iron(IV)-oxo species. [b] From ref. 13. [c] In M^{-1} s^{-1}. [d] The k'_2 values are obtained by dividing k_2 values by the number of equivalent hydrogen atoms in the substrate that would react with the iron(IV)-oxo species.

Theory

In order to understand the rate-enhancement of **1b** over **2b** in oxygen atom transfer reactions, we initiated a density functional theory (DFT) study using methods and procedures calibrated against experimental rate constants for $[Fe^{IV}(O)(N4Py)]^{2+}$ reactivities previously.[22,27] Our previous studies reproduced experimental free energies of activation to within 3 kcal mol^{-1} using the methods and procedures used here.[28] Particularly, test calculations using about 50 different computational methods and basis sets showed that B3LYP/BS2//B3LYP/BS1 with solvent corrections was one of the best performing procedures.[27b] Further tests using this procedure found good structures and potential energy landscapes that were generally within 0.5 kcal mol^{-1} of those obtained with B3LYP/BS2.[29] This was indeed confirmed here for the toluene reaction mechanism (see ESI†). Furthermore, in case of bifurcation pathways leading to multiple products, the methods predicted the correct product distributions for the reactivities of nonheme iron(IV)-oxo complexes and consequently correct transition state ordering.[30]

We started with a detailed analysis of the electronic and structural configuration of **1b** or $[Fe^{IV}(O)(2PyN2Q)]^{2+}$ in the triplet and quintet spin states, see Fig. 5. At the ΔE + ZPE level of theory with solvent corrections included, the triplet spin state is the ground state by 2.8 kcal mol^{-1}. This energy difference is considerably smaller to that found for ^{3,5}**2b** or $^{3,5}[Fe^{IV}(O)(N4Py)]^{2+}$, where a value of 7.5 kcal mol^{-1} was found using the same methods.[22,31] Interestingly, the structural differences between ^{3}**1b** and ^{3}**2b** are relatively minor with similar Fe–O distances (1.658 *vs.* 1.660 Å). The only changes appear to be a drop in the Fe–O stretch vibration (859 *vs.* 846 cm^{-1}) and a more tilted O–Fe–N_{axial} angle (from 179.5° to 171.3°) for ^{3}**2b** *versus* ^{3}**1b**, respectively.

The geometric differences between ^{3}**1b** and ^{3}**2b** can affect the high-lying occupied and low-lying virtual orbitals and hence influence physical variables such as electron affinity (EA), ionization energy (IE) and proton affinity. To highlight

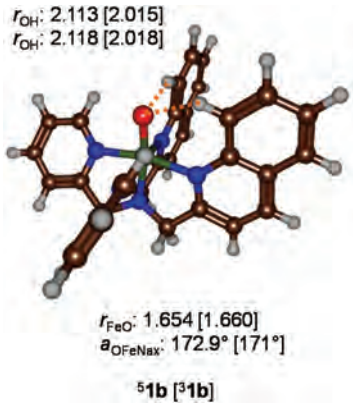

Fig. 5 UB3LYP/BS1 optimized geometries of ^{3,5}**1b** as obtained in Gaussian. Bond lengths are in angstroms and angles in degrees.

the differences in high-lying occupied molecular orbitals we display orbital diagrams of ^{3}**1b** and ^{3}**2b** in Fig. 6. This Figure displays the metal-type molecular orbitals of ^{3}**1b** and ^{3}**2b** and particularly focus on orbitals that include an iron 3d contribution that interacts with neighbouring atoms. The lowest in energy are the bonding pair of orbitals (π_{xz}/π_{yz}) for the interaction of the metal $3d_{xz}/3d_{yz}$ with the $2p_x/2p_y$ on oxygen. A little bit higher in energy is the π^*_{xy} molecular orbital, which is perpendicular to the Fe–O axis inside the plane of the four pyridine nitrogen atoms. In heme-type iron complexes this π^*_{xy} orbital is nonbonding and generally labelled as δ,[32] but here interactions are seen with the aromatic groups of the 2PyN2Q ligand. These antibonding interactions will raise the π^*_{xy} in energy and may result in a stabilization of the quintet spin state as seen from the relative energies. A bit higher in energy than the π^*_{xy} orbital are the almost degenerate π^*_{xz} and π^*_{yz} molecular orbitals for the antibonding interaction of the metal $3d_{xz}/3d_{yz}$ atomic orbitals with the $2p_x/2p_y$ atomic orbitals of the oxo group. Also these two orbitals interact with orbitals on the aromatic 2PyN2Q ligand system and particularly with the hydrogen atoms that hydrogen bond with the oxo group. Higher in energy and virtual in the triplet spin state are two σ* orbitals, namely the $\sigma^*_{z^2}$ orbital for the antibonding Fe–O interaction and the $\sigma^*_{x^2-y^2}$ orbital for the interaction of iron with four nitrogen atoms. The latter is the only molecular orbital where few or little extra interactions between the metal and ligand are observed.

The molecular ground state in the triplet spin state is $\pi^*_{xy}{}^2$ $\pi^*_{xz}{}^1$ $\pi^*_{yz}{}^1$, whereas the quintet spin state has configuration $\pi^*_{xy}{}^1$ $\pi^*_{xz}{}^1$ $\pi^*_{yz}{}^1$ $\sigma^*_{x^2-y^2}{}^1$.

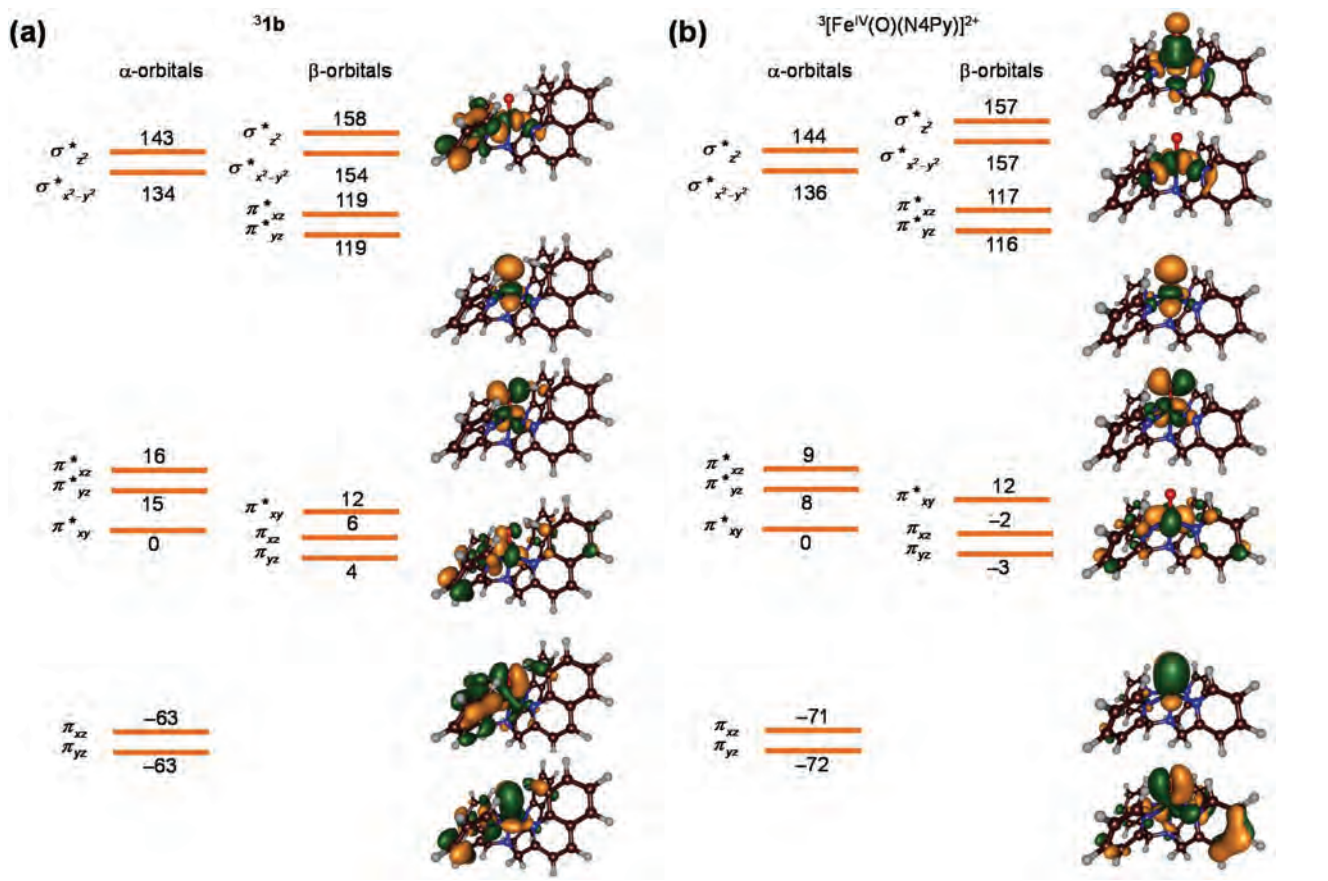

Fig. 6 Orbital energy levels of ^{3}**1b** (part a) and ^{3}**2b** (part b) as obtained at the UB3LYP/BS1 level of theory in Gaussian. Orbital energies are given in kcal mol^{-1} relative to the α-orbital for π^*_{xy}.

This journal is © The Royal Society of Chemistry 2018

Orbital energies (Fig. 6) are calculated relative to the π^*_{xy} orbital from the α-set of orbitals. As can be seen most relative energies are similar between the two structures and those for the π_{xz}/π_{yz} and π^*_{xz}/π^*_{yz} set of orbitals. These orbitals are all raised in energy in ^{3}**1b** as compared to ^{3}**2b**, which should lead to a lowering of the triplet–quintet energy gap as indeed found here. More dramatic changes are seen in the orbital shapes as depicted in Fig. 6 alongside the orbital diagram. In particular, the π-orbitals of the pyridine ligands interact with the metal strongly in ^{3}**1b** and even the π^*_{xy} and $\sigma^*_{x^2-y^2}$ orbitals are seen to be affected by this. Clearly, the equatorial ligand perturbation has a major effect on the molecular orbital shapes and energies that deviate dramatically from those typically found for pentadentate nonheme iron(IV)-oxo complexes without these effects.[33] Nevertheless, the molecular orbitals show clear metal–ligand interactions that affect the relative ordering and energies of the orbitals of the complex. As a result the triplet–quintet spin state gap is narrowed from 7.5 kcal mol^{-1} for [Fe(O)(N4Py)]$^{2+}$ to 2.8 kcal mol^{-1} for [Fe(O)(2PyN2Q)]$^{2+}$. This result is in line with Nordlander *et al.*[18b] who also observed enhanced reactivities for hydrogen atom abstraction processes through equatorial ligand perturbations. In recent work, a nonheme iron(IV)-oxo complex with a tetra cyclic-NHC ligand was investigated, which showed considerable widening of the triplet and quintet spin state gap resulting in unexpected triplet spin reactivity patterns.[34] A reduced energy gap between triplet and quintet spin states is expected to enhance the reactivity dramatically.

Thus, in the triplet spin state a hydrogen atom abstraction results in filling of the π^*_{xz} orbital with a second electron, whereas in the quintet spin state the virtual $\sigma^*_{z^2}$ orbital is occupied. In most nonheme iron(III)-hydroxo complexes the intermediate with $\pi^*_{xy}{}^1\ \pi^*_{xz}{}^1\ \pi^*_{yz}{}^1\ \sigma^*_{x^2-y^2}{}^1\ \sigma^*_{z^2}{}^1$ is the lowest in energy and hence the quintet pathway has the largest driving force.[35] As such, nonheme iron(IV)-oxo complexes react through two-state reactivity (TSR),[36] whereby in model complexes the reaction starts from a triplet spin state and cross over to the lower-lying quintet spin state during the reaction.

In our particular system, the ^{3,5}**1b** complex has a small triplet–quintet energy gap due to equatorial ligand perturbations that affect the structure and molecular orbitals along the Fe–O axis. Particularly, the change in O–Fe–N_{axial} angle will affect the $\sigma_{z^2}/\sigma^*_{z^2}$ orbital interactions of the oxo with iron atoms and specifically their energy levels and energy splitting. Since, the reduction of the iron(IV)-oxo complexes leads to filling of the $\sigma^*_{z^2}$ orbital with one electron this bending also should lower the energy of the complex to pick up an electron, *i.e.* its electron affinity (EA). As such, we calculated the electron affinities of **1b** as compared to **2b**. Indeed, we find a considerably lower electron affinity for **1b** than for **2b** as predicted: EA_{1b} = 123 kcal mol^{-1} and EA_{2b} = 134 kcal mol^{-1}. Therefore, the change in electron affinity should affect the reactivity differences with substrates as well in agreement with the experimental data reported above.

To further test the reactivity changes of **1b** *versus* **2b** with substrates for either hydrogen atom abstraction or oxygen atom transfer, we calculated the reaction mechanisms of **1b**/**2b** with several model substrates, namely 1,3-cyclohexadiene (CHD), toluene (Tol) and dimethylsulfide (DMS). These substrates were used in various previous studies with [Fe^{IV}(O)(N4Py)]$^{2+}$ and enable a direct comparison between the two oxidants, while toluene is one of the substrates reported above in our experimental study.[22,27]

Let us first start with a discussion on the hydrogen atom abstraction from toluene and 1,3-cyclohexadiene by **1b** and **2b**. In particular, we investigated the dehydrogenation of 1,3-cyclohexadiene to benzene by ^{3,5}**1b** and ^{3,5}**2b**, and the results are given in Fig. 7. The reaction is stepwise with an initial hydrogen atom abstraction *via* transition state $\mathbf{TS}_{HA}$ leading to a radical intermediate $\mathbf{I}_{HA}$. In the next step, a second hydrogen atom abstraction occurs *via* transition state $\mathbf{TS}_{desat}$ to form benzene products ($\mathbf{P}_{HA}$). On the triplet spin state with oxidant **1b** as well as with both spin states for oxidant **2b** all these transition states and local minima could be characterized. However, starting from ^{5}**1b**, the reaction has an almost barrierless hydrogen atom abstraction transition state (that could not be characterized and was estimated from the geometry scan) and collapses to form products directly. This was established with detailed geometry scans that fixed one degree of freedom and optimized all others. As such the reaction will be facile on the quintet spin state and lead to products very rapidly.

As can be seen from Fig. 7, during the hydrogen atom abstraction a spin-state crossing occurs from the triplet to the quintet spin state to give the quintet spin products. With ^{3,5}**1b** this spin-state crossing is early and probably happens before the hydrogen atom abstraction transition state, so that $^5\mathbf{TS}_{HA,1b}$ will be rate-determining. On the triplet spin state the barrier is well higher in energy and located at 11.4 kcal mol^{-1} above ^{3}**Re**. These barriers are considerably lower than those found for ^{3}**2b** (^{5}**2b**) where values of 11.6 (21.1) kcal mol^{-1} were found. Previous calculations for this reaction found similar trends.[22] Therefore, the changes in molecular orbitals and the second-coordination sphere effects of the ligand present an ideal approach in the quintet spin state as well as significant triplet–quintet spin state separation. The combination of these effects raises the quintet barriers well above those for the triplet. Consequently, ^{3,5}**1b** will be a much better oxidant and is expected to react with substrates through hydrogen atom abstraction with significantly lower barriers than those reported for ^{3,5}**2b**. The experimental work reported above indeed confirms these calculations. Fig. 7 gives barriers as calculated at ΔE + ZPE and ΔG level of theory. Similarly as seen before, thermal and entropy corrections to the enthalpy contribute to a shift of about 10 kcal mol^{-1} and hence, on average ΔG values are 10 kcal mol^{-1} higher than ΔE + ZPE values.[37]

Optimized geometries of the hydrogen atom abstraction transition states are given in Fig. 7. The triplet spin structures are very similar with C–H and H–O distances of 1.239/1.421 Å for $^3\mathbf{TS}_{HA,2b}$ *versus* 1.260/1.381 Å for $^3\mathbf{TS}_{HA,1b}$. These structures match previously calculated hydrogen atom abstraction barriers well. Furthermore, the equatorial ligand perturbations of structure **1b** do not affect the geometry of the hydrogen atom

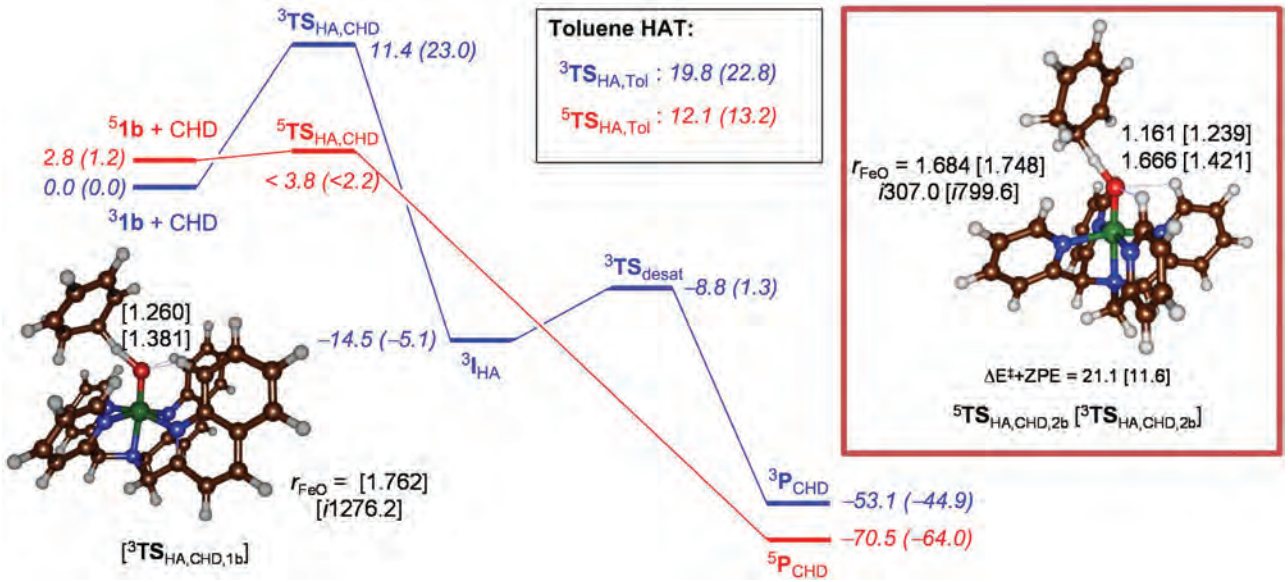

Fig. 7 Potential energy profile, ΔE + ZPE + E_{solv} and ΔG + E_{solv} (in parenthesis) with values in kcal mol^{-1} for CHD dehydrogenation and toluene hydrogen atom abstraction by ^{3,5}**1b** as calculated at UB3LYP/BS2//UB3LYP/BS1 level of theory. Also shown are optimized geometries of ^{3,5}TS$_{HA,CHD,1b}$ with bond lengths in angstroms, angles in degrees and the imaginary frequency in wave numbers. The value for ^{5}TS$_{HA,CHD}$ was estimated from the geometry scan.

abstraction barriers dramatically. Group spin densities of ^{3}**TS**$_{HA,1b}$ give a spin of 1.52 on the FeO unit and 0.51 on CHD, which implicates the transfer of a down-spin electron from substrate to π^*_{xz}. Indeed, the radical intermediate (^{3}**I**$_{HA,1b}$) has configuration $\pi^*_{xy}{}^2$ $\pi^*_{xz}{}^2$ $\pi^*_{yz}{}^1$ $\phi_{Sub}{}^1$. This type of mechanism has been labelled a $^3\pi$-pathway and usually proceeds *via* a transition state with a strongly bent angle of about 120° for the Fe–O–H interaction.[34,35] Our optimized geometry of ^{3}**TS**$_{HA,1b}$ is 127.2° in line with what is expected. Similar structure and electronic configuration was found for ^{3}**TS**$_{HA,2b}$.[22]

In the quintet spin state, by contrast, the hydrogen atom abstraction results in a transfer of an α-electron from substrate into the $\sigma^*_{z^2}$ orbital, which usually gives a radical intermediate with configuration $\pi^*_{xy}{}^1$ $\pi^*_{xz}{}^1$ $\pi^*_{yz}{}^1$ $\sigma^*_{z^2}{}^1$ $\sigma^*_{x^2-y^2}{}^1$ $\phi_{Sub}{}^1$, whereby all the unpaired electrons on the metal are up-spin and the substrate radical is down-spin. This mechanism is called the $^5\sigma$-pathway and generally gives a highly stable intermediate that is well below that of the triplet spin state. In the case of **1b** the radical intermediate is a shoulder on the potential energy profile and no stable, local minimum could be located. All attempts to optimize the structure of ^{5}**I**$_{HA,1b}$ converged to the product complex instead.

Also given in Fig. 7 are the hydrogen atom abstraction barriers from toluene by **1b**. In general, the barriers are considerably higher than those seen for 1,3-cyclohexadiene as a significantly stronger C–H bond is broken in the process. Indeed triplet and quintet spin free energies of activation of 22.8 and 13.2 kcal mol^{-1}, respectively for hydrogen atom abstraction from toluene are found. These values are in reasonable agreement with the rate constants reported in Table 2 above. Moreover, in comparison with the toluene hydrogen atom abstraction barriers by [Fe^{IV}(O)(N4Py)]$^{2+}$ reported previously,[31a] it implies a substantial rate-enhancement can be expected. This is in excellent agreement with the experimental rate-enhancement reported above.

To further understand the reactivity differences of **1b** and **2b** with substrates, we investigated oxygen atom transfer (OAT) to dimethylsulfide as a typical substrate for sulfoxidation reactions. Fig. 8 shows the potential energy landscape of OAT by ^{3,5}**1b** from DMS. As can be seen, the reaction proceeds by forming a reactant complex (^{3,5}**Re**) of oxidant and substrate in a highly exothermic reaction step of −16.0 kcal mol^{-1}, which retains the spin-state ordering between triplet and quintet. No charge transfer is encountered in this step and the electronic configuration stays the same as isolated reactants. Upon approach of the substrate on the oxo group an OAT transition state (**TS**$_{SO}$) is encountered prior to the formation of the sulfoxide product complexes (**P**$_{DMS}$). The quintet spin state barrier is very small (1.7 kcal mol^{-1} above ^{5}**Re**), whereas the triplet spin barrier is considerably higher in energy. Therefore, the reaction will proceed through a spin-state crossing from triplet to quintet during the OAT reaction. Moreover, these calculations imply much faster oxygen atom transfer than the bare N4Py complex, whereas the reactivity differences between **1b** and **2b** are much less for hydrogen atom abstraction in line with the experimental observations.

Previously,[22] we calculated a quintet spin barrier for OAT from [Fe^{IV}(O)(N4Py)]$^{2+}$ to DMS of 20.6 kcal mol^{-1} above a reactant complex. As such, the computational modelling agrees with a rate-enhancement upon replacing the oxidant of **2b** with **1b** as shown in Fig. 2b. Consequently, **1b** is a more efficient oxidant than **2b** because of a lower-lying quintet spin

This journal is © The Royal Society of Chemistry 2018

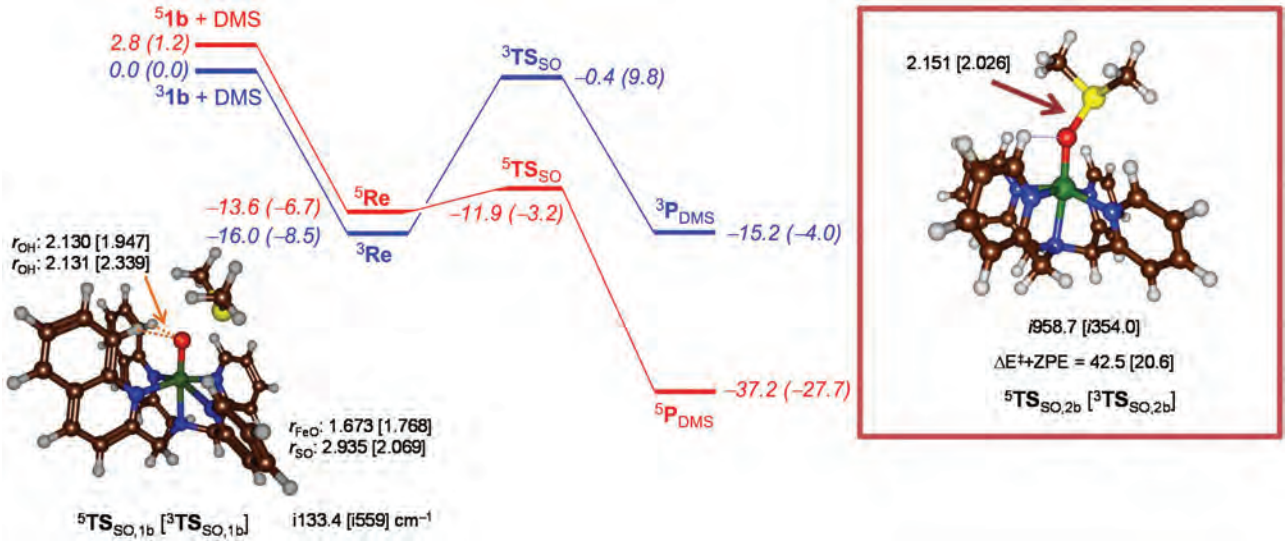

Fig. 8 Potential energy profile (ΔE + ZPE + E_{solv}) with values in kcal mol^{-1} for DMS sulfoxidation by ^{3,5}**1b** as calculated at UB3LYP/BS2//UB3LYP/BS1 level of theory. Also shown are optimized geometries of ^{3,5}**TS**$_{SO,1b}$ with bond lengths in angstroms, angles in degrees and the imaginary frequency in wave numbers. The inset gives the ^{3,5}**TS**$_{SO,2b}$ optimized geometries from ref. 21.

state that enables a fast spin-state crossing from triplet to quintet.

Optimized geometries of the oxygen atom transfer transition states using ^{3,5}**1b** and ^{3,5}**2b** as oxidants are shown in Fig. 8. These transition states show typical features of sulfoxidation transition states seen before with elongated Fe–O and O–S bonds.[38] In the ^{3}**TS**$_{SO,1b}$ structure the Fe–O and O–S distances are 1.768 and 2.069 Å and hence the transition state is late on the potential energy surface. By contrast, the quintet spin state transition state is much earlier with a very long O–S distance of 2.935 Å and still a relatively short Fe–O distance of 1.673 Å. The quintet spin state structure has a small imaginary frequency of i133 cm^{-1}, while a much larger value was obtained with model **2b**. Therefore, considerable differences of the potential energy profile are seen through the modification of the N4Py ligand system with aromatic rings that clearly affect substrate approach and activation.

In summary, the DFT calculations show that ^{3,5}**1b** is much more reactive with substrates than ^{3,5}**2b**. This is the result from changes in the σ_{z^2} and $\sigma^*_{z^2}$ molecular orbitals, which are perturbed by equatorial interactions particularly of C–H groups to the oxo. As a consequence, the electron affinity of **1b** is significantly lower than that of **2b** and hence it is more reactive.

Experimental

Materials and methods

All Chemicals were obtained from Aldrich Chemical Co., and were of the best available purity and used without further purification unless otherwise stated. Solvents were dried according to published procedures[39] and distilled under argon prior to use. $H_2{}^{18}O$ (99.9% pure and enrichment 97.1 atom%) was purchased from Berry and Associates (Icon Isotopes). Benzyl alcohol-d_7 was purchased from Cambridge Isotope Laboratories, Inc. Iodosylbenzene and 1-^{t}butylsulfonyl-2-iodosylbenzene were prepared using previously reported literature methods.[40] The ligand (2PyN2Q) was synthesized using previously reported procedures.[18a] Iron(II) complex, [Fe^{II}(2PyN2Q)](CF$_3$SO$_3$)$_2$, (**1a**) was synthesized inside a glove-box by an equimolar reaction of 2PyN2Q and Fe^{II}(CF$_3$SO$_3$)$_2$·2CH$_3$CN in CH$_3$CN. The reaction mixture was stirred overnight, filtered with the help of syringe filters. Excess diethyl ether was slowly added to the resulting filtrate and the bilayer solution was left undisturbed inside the glovebox at −40 °C. The ethereal solution was decanted off after a few days and the yellowish residue was washed several times with diethyl ether and dried under vacuum to get the desired complex **1a** in excellent yield (95%). The [Fe^{IV}(O)(2PyN2Q)]$^{2+}$ (**1b**) was synthesized *in situ* in CH$_3$CN by adding 1.5 equivalents of PhI(OAc)$_2$ in CH$_3$CN at ambient temperature and was further used for all the kinetic studies. The [Fe^{II}(N4Py)](CF$_3$SO$_3$)$_2$ complex (**2a**) and corresponding [Fe^{IV}(O)(N4Py)]$^{2+}$ intermediate (**2b**) were synthesized by previously reported procedures.[12,13]

Instrumentation

Bruker Avance III HD 600 and 400 MHz NMR spectrometers were used for recording NMR spectra using TMS as an internal standard. Variable temperature-NMR spectra were recorded on a Jeol Advanced Solution State 400 MHz spectrometer (JNM ECZ400S). UV-vis spectra were recorded on a Hewlett Packard 8453 spectrophotometer equipped with either constant temperature circulating water bath or a liquid nitrogen cryostat (Unisoku) with a temperature controller. The purified complexes and intermediates were characterized by mass spectrometry on an Agilent-Q-TOF 6520 instrument in positive ESI

mode equipped with a Mass hunter workstation. The samples were infused directly into the source. The spray voltage was set at 3 kV and the drying gas flow and temperature were maintained as 5.0 L min^{-1} and 200 °C respectively. The products were analysed by ^{1}H and ^{13}C-NMR recorded with Bruker Avance III HD 600 and 400 MHz spectrometers and LCMS with Waters ACQUITY UPLC equipped with a variable wavelength UV-200 detector. Product yields were determined by comparison with standard curves of authentic samples.

Reactivity studies

All reactions were run in a 10 mm path length UV-vis cuvette by monitoring UV-vis spectral changes of reaction solutions. The kinetics studies were performed under pseudo first-order conditions with excess substrate in acetonitrile. The reactions were monitored by following the decrease of the absorbance of the characteristic peaks as a function of time. The rate constants were determined by fitting the changes in absorbance of the intermediates under study. Reactions were run at least in triplicate and the data reported represents the average of those.

Computational modelling

Computational studies used density functional theory as implemented in the Gaussian program package.[41] Due to the overall charge of +2 in our chemical system full geometry optimizations were performed with a solvent model, *i.e.* the polarized continuum model mimicking acetonitrile. We did initial optimizations and frequency calculations using the hybrid density functional method UB3LYP and the LACVP basis set on iron and 6-31G on the rest of the atoms (BS1).[42,43] Subsequent single points utilized a triple-ζ LACV3P + basis set on iron and 6-311 + G* on the rest of the atoms (BS2). All structures were calculated on the lowest lying triplet and quintet spin state surfaces and all structures were characterized by a frequency calculation at the same level of theory as the optimization as either a local minimum (without imaginary frequencies) or a transition state structure (with one imaginary frequency for the correct mode). Reactivities were investigated with dimethylsulfide (DMS), cyclohexadiene (CHD) and toluene (Tol) as model substrates for sulfoxidation and HAT reactions.

Conclusions

In conclusion, we have synthesized a room temperature stable iron(IV)-oxo intermediate (**1b**) that acts as an efficient oxidant of substrates. Instead of contributing to the steric fencing around the iron(IV)-oxo core and prohibiting molecular approach, the introduction of two bulky quinoline groups in the N4Py ligand framework has notably enhanced the HAT and OAT reactivity of the iron(IV)-oxo complex. We did a comparative study of thioanisole oxidation and hydrogen atom abstraction reactions with various substrates. We show that **1b** reacts with substrates with increased rate constants with respect to those obtained with oxidant **2b** which is attributed to subtle changes in the ligand skeleton that position the oxo group and lower the virtual $\sigma^*_{z^2}$ orbital in energy. These engineered structures show that small perturbations on the equatorial ligand may have major influences in substrate positioning and reactivity in line with what is found for enzymatic reaction mechanisms. The work highlights how tweaking the ligand architecture of a catalyst can affect its performance, which will help in designing novel synthetic scaffolds for enzymatic mimics.

Conflicts of interest

There are no conflicts to declare.

Acknowledgements

CVS acknowledges financial support by the Department of Science and Technology (SERB), India (EMR/2014/000279). CSIR-IICB is duly acknowledged for providing access to VT-NMR equipment. SdV and CVS thank the British Council for a UK-India Education Research Initiative (UKIERI) award (DST/INT/UK/P-151/2017). FC thanks the Conacyt Mexico for a studentship. DK acknowledges financial support from the DBT, New Delhi (BT/PR14510/BID/07/334/2010).

Notes and references

1 (*a*) E. I. Solomon, T. C. Brunold, M. I. Davis, J. N. Kemsley, S. K. Lee, N. Lehnert, F. Neese, A. J. Skulan, Y. S. Yang and J. Zhou, *Chem. Rev.*, 2000, **100**, 235; (*b*) M. Costas, M. P. Mehn, M. P. Jensen and L. Que Jr., *Chem. Rev.*, 2004, **104**, 939; (*c*) M. M. Abu-Omar, A. Loaiza and N. Hontzeas, *Chem. Rev.*, 2005, **105**, 2227; (*d*) P. C. A. Bruijnincx, G. van Koten and R. J. M. Klein Gebbink, *Chem. Soc. Rev.*, 2008, **37**, 2716; (*e*) A. R. McDonald and L. Que Jr., *Coord. Chem. Rev.*, 2013, **257**, 414; (*f*) W. Nam, Y.-M. Lee and S. Fukuzumi, *Acc. Chem. Res.*, 2014, **47**, 1146.

2 (*a*) M. Sono, M. P. Roach, E. D. Coulter and J. H. Dawson, *Chem. Rev.*, 1996, **96**, 2841; (*b*) J. T. Groves, *Proc. Natl. Acad. Sci. U. S. A.*, 2003, **100**, 3569; (*c*) B. Meunier, S. P. de Visser and S. Shaik, *Chem. Rev.*, 2004, **104**, 3947; (*d*) I. G. Denisov, T. M. Makris, S. G. Sligar and I. Schlichting, *Chem. Rev.*, 2005, **105**, 2253; (*e*) S. V. Kryatov, E. V. Rybak-Akimova and S. Schindler, *Chem. Rev.*, 2005, **105**, 2175; (*f*) R. van Eldik, *Coord. Chem. Rev.*, 2007, **251**, 1649; (*g*) P. R. Ortiz de Montellano, *Chem. Rev.*, 2010, **110**, 932; (*h*) *Iron-containing enzymes: Versatile catalysts of hydroxylation reactions in nature*, ed. S. P. de Visser and D. Kumar, RSC Publishing, Cambridge, 2011.

3 (*a*) D. A. Proshlyakov, T. F. Henshaw, G. R. Monterosso, M. J. Ryle and R. P. Hausinger, *J. Am. Chem. Soc.*, 2004, **126**, 1022; (*b*) J. M. Bollinger Jr., J. C. Price, L. M. Hoffart, E. W. Barr and C. Krebs, *Eur. J. Inorg. Chem.*, 2005, 4245.

 This journal is © The Royal Society of Chemistry 2018

4 (*a*) K. Gorres and R. T. Raines, *Crit. Rev. Biochem. Mol. Biol.*, 2010, **45**, 106; (*b*) M. A. McDonough, V. Li, E. Flashman, R. Chowdhury, C. Mohr, B. M. Lienard, J. Zondlo, N. J. Oldham, I. J. Clifton, J. Lewis, L. A. McNeill, R. J. Kurzeja, K. S. Hewitson, E. Yang, S. Jordan, R. S. Syed and C. J. Schofield, *Proc. Natl. Acad. Sci. U. S. A.*, 2006, **103**, 9814.

5 (*a*) A. Timmins, M. Saint-André and S. P. de Visser, *J. Am. Chem. Soc.*, 2017, **139**, 9855; (*b*) A. Timmins and S. P. de Visser, *Front. Chem.*, 2017, **5**, 94, DOI: 10.3389/fchem.2017.00094.

6 See, e.g.: R. Davydov, T. M. Makris, V. Kofman, D. E. Werst, S. G. Sligar and B. M. Hoffman, *J. Am. Chem. Soc.*, 2001, **123**, 1403.

7 (*a*) P. J. O'Brien, *Chem. Rev.*, 2006, **106**, 720; (*b*) C. Yi, C. G. Yang and C. He, *Acc. Chem. Res.*, 2009, **42**, 519.

8 (*a*) M. Atanasov, P. Comba, S. Hausberg and B. Martin, *Coord. Chem. Rev.*, 2009, **253**, 2306; (*b*) M. Costas, *Coord. Chem. Rev.*, 2011, **255**, 2912; (*c*) C. V. Sastri, J. Lee, K. Oh, Y. J. Lee, J. Lee, T. A. Jackson, K. Ray, H. Hirao, W. Shin, J. A. Halfen, J. Kim, L. Que Jr., S. Shaik and W. Nam, *Proc. Natl. Acad. Sci. U. S. A.*, 2007, **104**, 19181; (*d*) C. Buron, K. Sénéchal-David, R. Ricoux, J.-P. Le Caër, V. Guérineau, P. Méjanelle, R. Guillot, C. Herrero, J.-P. Mahy and F. Banse, *Chem. – Eur. J.*, 2015, **21**, 12188; (*e*) X. Engelmann, I. Monte-Pérez and K. Ray, *Angew. Chem., Int. Ed.*, 2016, **55**, 7632.

9 See, e.g.: (*a*) I. Prat, L. Gómez, M. Canta, X. Ribas and M. Costas, *Chem. – Eur. J.*, 2013, **19**, 1908; (*b*) M. G. Quesne, D. Senthilnathan, D. Singh, D. Kumar, P. Maldivi, A. B. Sorokin and S. P. de Visser, *ACS Catal.*, 2016, **6**, 2230; (*c*) P. Barman, A. S. Faponle, A. K. Vardhaman, D. Angelone, A.-M. Löhr, W. R. Browne, P. Comba, C. V. Sastri and S. P. de Visser, *Inorg. Chem.*, 2016, **55**, 10170; (*d*) S. P. de Visser, L. Tahsini and W. Nam, *Chem. – Eur. J.*, 2009, **15**, 5577; (*e*) J. Annaraj, J. Cho, Y.-M. Lee, S. Y. Kim, R. Latifi, S. P. de Visser and W. Nam, *Angew. Chem., Int. Ed.*, 2009, **48**, 4150; (*f*) A. Takahashi, D. Yamaki, K. Ikemura, T. Kurahashi, T. Ogura, M. Hada and H. Fujii, *Inorg. Chem.*, 2012, **51**, 7296; (*g*) T. A. Jackson, J.-U. Rohde, M. S. Seo, C. V. Sastri, R. DeHont, A. Stubna, T. Ohta, T. Kitagawa, E. Münck, W. Nam and L. Que Jr., *J. Am. Chem. Soc.*, 2008, **130**, 12394.

10 (*a*) S. Sahu, L. R. Widger, M. G. Quesne, S. P. de Visser, H. Matsumura, P. Moënne-Loccoz, M. A. Siegler and D. P. Goldberg, *J. Am. Chem. Soc.*, 2013, **135**, 10590; (*b*) D. C. Lacy, R. Gupta, K. L. Stone, J. Greaves, J. W. Ziller, M. P. Hendrich and A. S. Borovik, *J. Am. Chem. Soc.*, 2010, **132**, 12188; (*c*) Ü. İşci, A. S. Faponle, P. Afanasiev, F. Albrieux, V. Briois, V. Ahsen, F. Dumoulin, A. B. Sorokin and S. P. de Visser, *Chem. Sci.*, 2015, **6**, 5063; (*d*) J.-G. Liu, T. Ohta, S. Yamaguchi, T. Ogura, S. Sakamoto, Y. Maeda and Y. Naruta, *Angew. Chem., Int. Ed.*, 2009, **48**, 9262; (*e*) T. Taguchi, R. Gupta, B. Lassalle-Kaiser, D. W. Boyce, V. K. Yachandra, W. B. Tolman, J. Yano, M. P. Hendrich and A. S. Borovik, *J. Am. Chem. Soc.*, 2012, **134**, 1996; (*f*) Z. Gordon, M. J. Drummond, E. M. Matson, J. A. Bogart, E. J. Schelter, R. L. Lord and A. R. Fout, *Inorg. Chem.*, 2017, **56**, 4852; (*g*) M. Sørensen Vad, A. Lennartson, A. Nielsen, J. Harmer, J. E. McGrady, C. Frandsen, S. Mørup and C. J. McKenzie, *Chem. Commun.*, 2012, **48**, 10880; (*h*) F. Wang, W. Sun, C. Xia and Y. Wang, *J. Biol. Inorg. Chem.*, 2017, **22**, 987; (*i*) F. Burg, M. Gicquel, S. Breitenlechner, A. Pöthig and T. Bach, *Angew. Chem., Int. Ed.*, 2018, **57**, 2953.

11 See, e.g.: (*a*) C. E. MacBeth, R. Gupta, K. R. Mitchell-Koch, V. G. Young Jr., G. H. Lushington, W. H. Thompson, M. P. Hendrich and A. S. Borovik, *J. Am. Chem. Soc.*, 2004, **126**, 2556; (*b*) T. Ishizuka, S. Ohzu, H. Kotani, Y. Shiota, K. Yoshizawa and T. Kojima, *Chem. Sci.*, 2014, **5**, 1429; (*c*) M. Mitra, J. Lloret-Fillol, M. Haukka, M. Costas and E. Nordlander, *Chem. Commun.*, 2014, **50**, 1408.

12 M. Lubben, A. Meetsma, E. C. Wilkinson, B. Feringa and L. Que Jr., *Angew. Chem., Int. Ed. Engl.*, 1995, **34**, 1512.

13 (*a*) J. Kaizer, E. J. Klinker, N. Y. Oh, J.-U. Rohde, W. J. Song, A. Stubna, J. Kim, E. Münck, W. Nam and L. Que Jr., *J. Am. Chem. Soc.*, 2004, **126**, 472; (*b*) E. J. Klinker, J. Kaizer, W. W. Brennessel, N. L. Woodrum, C. J. Cramer and L. Que Jr., *Angew. Chem., Int. Ed.*, 2005, **44**, 3690.

14 See, e.g.: (*a*) D. Lakk-Bogáth, R. Csonka, G. Speier, M. Réglier, A. J. Simaan, J.-V. Naubron, M. Giorgi, K. Lázár and J. Kaizer, *Inorg. Chem.*, 2016, **55**, 10090; (*b*) S. K. Padamati, A. Draksharapu, D. Unjaroen and W. R. Browne, *Inorg. Chem.*, 2016, **55**, 4211; (*c*) S. Kim, K.-B. Cho, Y.-M. Lee, J. Chen, S. Fukuzumi and W. Nam, *J. Am. Chem. Soc.*, 2016, **138**, 10654; (*d*) D. Wang, K. Ray, M. J. Collins, E. R. Farquhar, J. R. Frisch, L. Gómez, T. A. Jackson, M. Kerscher, A. Waleska, P. Comba, M. Costas and L. Que Jr., *Chem. Sci.*, 2013, **4**, 282; (*e*) A. Draksharapu, D. Angelone, M. G. Quesne, S. K. Padamati, L. Gómez, R. Hage, M. Costas, W. R. Browne and S. P. de Visser, *Angew. Chem., Int. Ed.*, 2015, **54**, 4357; (*f*) A. K. Vardhaman, P. Barman, S. Kumar, C. V. Sastri, D. Kumar and S. P. de Visser, *Chem. Commun.*, 2013, **49**, 10926; (*g*) C. V. Sastri, K. Oh, Y. J. Lee, M. S. Seo, W. Shin and W. Nam, *Angew. Chem., Int. Ed.*, 2006, **45**, 3992; (*h*) S. P. de Visser, Y.-M. Lee and W. Nam, *Eur. J. Inorg. Chem.*, 2008, 1027; (*i*) J. Park, Y. Morimoto, Y.-M. Lee, W. Nam and S. Fukuzumi, *J. Am. Chem. Soc.*, 2011, **133**, 5236; (*j*) K. Benzing, P. Comba, B. Martin, B. Pokrandt and F. Keppler, *Chem. – Eur. J.*, 2017, **23**, 10465; (*k*) R. Turcas, D. Lakk-Bogáth, G. Speier and J. Kaizer, *Dalton Trans.*, 2018, **47**, 3248.

15 A. N. Biswas, M. Puri, K. K. Meier, W. N. Oloo, G. T. Rohde, E. L. Bominaar, E. Münck and L. Que Jr., *J. Am. Chem. Soc.*, 2015, **137**, 2428.

16 M. S. Seo, N. H. Kim, K. B. Cho, J. E. So, S. K. Park, M. Clémancey, R. G. Serres, J. M. Latour, S. Shaik and W. Nam, *Chem. Sci.*, 2011, **2**, 1039.

17 M. Mitra, H. Nimir, S. Demeshko, S. S. Bhat, S. O. Malinkin, M. Haukka, J. Lloret-Fillol, G. C. Lisensky,

F. Meyer, A. A. Shteinman, W. R. Browne, D. A. Hrovat, M. G. Richmond, M. Costas and E. Nordlander, *Inorg. Chem.*, 2015, **54**, 7152.

18 (*a*) W. K. C. Lo, C. J. McAdam, A. G. Blackman, J. D. Crowley and D. A. McMorran, *Inorg. Chim. Acta*, 2015, **426**, 183; (*b*) A. A. Massie, M. C. Denler, L. T. Cardoso, A. N. Walker, M. K. Hossain, V. W. Day, E. Nordlander and T. A. Jackson, *Angew. Chem., Int. Ed.*, 2017, **56**, 4178; (*c*) A. A. Massie, A. Sinha, J. D. Parham, E. Nordlander and T. A. Jackson, *Inorg. Chem.*, 2018, **57**, 8253.

19 W. Rasheed, A. Draksharapu, S. Banerjee, V. G. Young Jr., R. Fan, Y. Guo, M. Ozerov, J. Nehrkorn, J. Krzystek, J. Telser and L. Que Jr., *Angew. Chem., Int. Ed.*, 2018, **57**, 9387.

20 (*a*) K. Ray, J. England, A. T. Fiedler, M. Martinho, E. Münck and L. Que Jr., *Angew. Chem., Int. Ed.*, 2008, **47**, 8068; (*b*) A. Company, G. Sabenya, M. González-Béjar, L. Gómez, M. Clémancey, G. Blondin, A. J. Jasniewski, M. Puri, W. S. Browne, J. M. Latour, L. Que Jr., M. Costas, J. Pérez-Prieto and J. Lloret-Fillol, *J. Am. Chem. Soc.*, 2014, **136**, 4624; (*c*) S. Sahu, M. G. Quesne, C. G. Davies, M. Dürr, I. Ivanović-Burmazović, M. A. Siegler, G. N. L. Jameson, S. P. de Visser and D. P. Goldberg, *J. Am. Chem. Soc.*, 2014, **136**, 13542; (*d*) L. R. Widger, C. G. Davies, T. Yang, M. A. Siegler, O. Troeppner, G. N. L. Jameson, I. Ivanović-Burmazović and D. P. Goldberg, *J. Am. Chem. Soc.*, 2014, **136**, 2699; (*e*) S. Sahu, B. Zhang, C. J. Pollock, M. Dürr, C. G. Davies, A. M. Confer, I. Ivanović-Burmazović, M. A. Siegler, G. N. L. Jameson, C. Krebs and D. P. Goldberg, *J. Am. Chem. Soc.*, 2016, **138**, 12791.

21 (*a*) H. C. Brown and Y. Okamoto, *J. Am. Chem. Soc.*, 1958, **80**, 4979; (*b*) Y. Goto, T. Matsui, S. I. Ozaki, Y. Watanabe and S. Fukuzumi, *J. Am. Chem. Soc.*, 1999, **121**, 9497.

22 S. Kumar, A. S. Faponle, P. Barman, A. K. Vardhaman, C. V. Sastri, D. Kumar and S. P. de Visser, *J. Am. Chem. Soc.*, 2014, **136**, 17102.

23 N. Y. Oh, Y. Suh, M. J. Park, M. S. Seo, J. Kim and W. Nam, *Angew. Chem., Int. Ed.*, 2005, **44**, 4235.

24 (*a*) L. E. Friedrich, *J. Org. Chem.*, 1983, **48**, 3851; (*b*) F. G. Bordwell and J.-P. Cheng, *J. Am. Chem. Soc.*, 1991, **113**, 1736; (*c*) J. M. Mayer, *Acc. Chem. Res.*, 1998, **31**, 441; (*d*) J. M. Mayer, *Annu. Rev. Phys. Chem.*, 2004, **55**, 363.

25 (*a*) J. Yoon, S. A. Wilson, Y. K. Jang, M. S. Seo, K. Nehru, B. Hedman, K. O. Hodgson, E. Bill, E. I. Solomon and W. Nam, *Angew. Chem., Int. Ed.*, 2009, **48**, 1257; (*b*) D. E. Lansky and D. P. Goldberg, *Inorg. Chem.*, 2006, **45**, 5119; (*c*) A. J. McGown, W. D. Kerber, H. Fujii and D. P. Goldberg, *J. Am. Chem. Soc.*, 2009, **131**, 8040; (*d*) S. R. Bell and J. T. Groves, *J. Am. Chem. Soc.*, 2009, **131**, 9640; (*e*) Y. Kang, H. Chen, Y. J. Jeong, W. Lai, E. H. Bae, S. Shaik and W. Nam, *Chem. – Eur. J.*, 2009, **15**, 10039; (*f*) J. J. Warren, T. A. Tronic and J. M. Mayer, *Chem. Rev.*, 2010, **110**, 6961; (*g*) K. A. Prokop, S. P. de Visser and D. P. Goldberg, *Angew. Chem., Int. Ed.*, 2010, **49**, 5091; (*h*) J. M. Mayer, E. A. Mader, J. P. Roth, J. R. Bryant, T. Matsuo, A. Dehestani, B. C. Bales, E. J. Watson, T. Osako, K. Valliant-Saunders, W. H. Lam, D. A. Hrovat, W. T. Borden and E. R. Davidson, *J. Mol. Catal. A: Chem.*, 2006, **251**, 24; (*i*) C. Arunkumar, Y. M. Lee, J. Y. Lee, S. Fukuzumi and W. Nam, *Chem. – Eur. J.*, 2009, **15**, 11482; (*j*) A. K. Vardhaman, P. Barman, S. Kumar, C. V. Sastri, D. Kumar and S. P. de Visser, *Angew. Chem., Int. Ed.*, 2013, **52**, 12288.

26 See, e.g.: T. Yang, M. G. Quesne, H. M. Neu, F. G. Cantú Reinhard, D. P. Goldberg and S. P. de Visser, *J. Am. Chem. Soc.*, 2016, **138**, 12375.

27 (*a*) A. K. Vardhaman, C. V. Sastri, D. Kumar and S. P. de Visser, *Chem. Commun.*, 2011, **47**, 11044; (*b*) F. G. Cantú Reinhard, A. S. Faponle and S. P. de Visser, *J. Phys. Chem. A*, 2016, **120**, 9805.

28 (*a*) M. A. Sainna, S. Kumar, D. Kumar, S. Fornarini, M. E. Crestoni and S. P. de Visser, *Chem. Sci.*, 2015, **6**, 1516; (*b*) F. G. Cantú Reinhard, M. A. Sainna, P. Upadhyay, G. A. Balan, D. Kumar, S. Fornarini, M. E. Crestoni and S. P. de Visser, *Chem. – Eur. J.*, 2016, **22**, 18608.

29 (*a*) S. P. de Visser, *J. Am. Chem. Soc.*, 2010, **132**, 1087; (*b*) M. A. Kaczmarek, A. Malhotra, G. A. Balan, A. Timmins and S. P. de Visser, *Chem. – Eur. J.*, 2018, **24**, 5293; (*c*) A. Timmins, M. G. Quesne, T. Borowski and S. P. de Visser, *ACS Catal.*, 2018, **8**, 8685.

30 (*a*) L. Ji, A. S. Faponle, M. G. Quesne, M. A. Sainna, J. Zhang, A. Franke, D. Kumar, R. van Eldik, W. Liu and S. P. de Visser, *Chem. – Eur. J.*, 2015, **21**, 9083; (*b*) B. Karamzadeh, D. Kumar, G. N. Sastry and S. P. de Visser, *J. Phys. Chem. A*, 2010, **114**, 13234.

31 (*a*) D. Kumar, H. Hirao, L. Que Jr. and S. Shaik, *J. Am. Chem. Soc.*, 2005, **127**, 8026; (*b*) T. Z. H. Gani and H. J. Kulik, *ACS Catal.*, 2018, **8**, 975.

32 (*a*) S. P. de Visser, S. Shaik, P. K. Sharma, D. Kumar and W. Thiel, *J. Am. Chem. Soc.*, 2003, **125**, 15779; (*b*) X.-X. Li, V. Postils, W. Sun, A. S. Faponle, M. Solà, Y. Wang, W. Nam and S. P. de Visser, *Chem. – Eur. J.*, 2017, **23**, 6406.

33 (*a*) L. Bernasconi and E.-J. Baerends, *J. Am. Chem. Soc.*, 2013, **135**, 8857; (*b*) Y. Liu, X. Guan, E. L.-M. Wong, P. Liu, J.-S. Huang and C.-M. Che, *J. Am. Chem. Soc.*, 2013, **135**, 7194; (*c*) A. Dey, *J. Am. Chem. Soc.*, 2010, **132**, 13892; (*d*) H. Hirao, F. Li, L. Que Jr. and K. Morokuma, *Inorg. Chem.*, 2011, **50**, 6637; (*e*) D. Usharani, D. C. Lacy, A. S. Borovik and S. Shaik, *J. Am. Chem. Soc.*, 2013, **135**, 17090; (*f*) S. P. de Visser, *J. Am. Chem. Soc.*, 2006, **128**, 9813.

34 (*a*) F. G. Cantú Reinhard and S. P. de Visser, *Chem. – Eur. J.*, 2017, **23**, 2935; (*b*) R. Latifi, M. A. Sainna, E. V. Rybak-Akimova and S. P. de Visser, *Chem. – Eur. J.*, 2013, **19**, 4058; (*c*) M. G. Quesne, R. Latifi, L. E. Gonzalez-Ovalle, D. Kumar and S. P. de Visser, *Chem. – Eur. J.*, 2014, **20**, 435.

35 (*a*) L. Bernasconi and E. J. Baerends, *Eur. J. Inorg. Chem.*, 2008, 1672; (*b*) S. P. de Visser, *J. Am. Chem. Soc.*, 2006, **128**, 15809; (*c*) S. Ye and F. Neese, *Proc. Natl. Acad. Sci. U. S. A.*, 2011, **108**, 1228; (*d*) H. Tang, J. Guan, H. Liu and X. Huang, *Dalton Trans.*, 2013, **42**, 10260; (*e*) A. Ansari, A. Kaushik and G. Rajaraman, *J. Am. Chem. Soc.*, 2013, **135**, 4235.

 This journal is © The Royal Society of Chemistry 2018

36 (*a*) S. Shaik, H. Chen and D. Janardanan, *Nat. Chem.*, 2011, **3**, 19; (*b*) C. T. Saouma and J. M. Mayer, *Chem. Sci.*, 2014, **5**, 21.
37 (*a*) D. Kumar, B. Karamzadeh, G. N. Sastry and S. P. de Visser, *J. Am. Chem. Soc.*, 2010, **132**, 7656; (*b*) D. Kumar, R. Latifi, S. Kumar, E. V. Rybak-Akimova, M. A. Sainna and S. P. de Visser, *Inorg. Chem.*, 2013, **52**, 7968.
38 (*a*) D. Kumar, G. N. Sastry and S. P. de Visser, *Chem. – Eur. J.*, 2011, **17**, 6196; (*b*) A. S. Faponle, F. P. Seebeck and S. P. de Visser, *J. Am. Chem. Soc.*, 2017, **139**, 9259.
39 *Purification of Laboratory Chemicals*, ed. W. L. F. Armarego and D. D. Perrin, Pergamon Press, Oxford, 1997.
40 (*a*) *Organic Syntheses*, ed. H. Saltzman and J. G. Sharefkin, Wiley, New York, 1973, collect. vol. V, p. 658; (*b*) D. Macikenas, E. Skrzypczak-Jankun and J. D. Protasiewicz, *J. Am. Chem. Soc.*, 1999, **121**, 7164.
41 M. J. Frisch, G. W. Trucks, H. B. Schlegel, G. E. Scuseria, M. A. Robb, J. R. Cheeseman, G. Scalmani, V. Barone, B. Mennucci, G. A. Petersson, H. Nakatsuji, M. Caricato, X. Li, H. P. Hratchian, A. F. Izmaylov, J. Bloino, G. Zheng, J. L. Sonnenberg, M. Hada, M. Ehara, K. Toyota, R. Fukuda, J. Hasegawa, M. Ishida, T. Nakajima, Y. Honda, O. Kitao, H. Nakai, T. Vreven, J. A. Montgomery Jr., J. E. Peralta, F. Ogliaro, M. Bearpark, J. J. Heyd, E. Brothers, K. N. Kudin, V. N. Staroverov, T. Keith, R. Kobayashi, J. Normand, K. Raghavachari, A. Rendell, J. C. Burant, S. S. Iyengar, J. Tomasi, M. Cossi, N. Rega, J. M. Millam, M. Klene, J. E. Knox, J. B. Cross, V. Bakken, C. Adamo, J. Jaramillo, R. Gomperts, R. E. Stratmann, O. Yazyev, A. J. Austin, R. Cammi, C. Pomelli, J. W. Ochterski, R. L. Martin, K. Morokuma, V. G. Zakrzewski, G. A. Voth, P. Salvador, J. J. Dannenberg, S. Dapprich, A. D. Daniels, O. Farkas, J. B. Foresman, J. V. Ortiz, J. Cioslowski and D. J. Fox, *Gaussian 09, Revision C.01*, Gaussian, Inc., Wallingford, CT, 2010.
42 (*a*) A. D. Becke, *J. Chem. Phys.*, 1993, **98**, 5648; (*b*) C. Lee, W. Yang and R. G. Parr, *Phys. Rev. B: Condens. Matter Mater. Phys.*, 1988, **37**, 785.
43 (*a*) P. J. Hay and W. R. Wadt, *J. Chem. Phys.*, 1985, **82**, 270; (*b*) W. J. Hehre, R. Ditchfield and J. A. Pople, *J. Chem. Phys.*, 1972, **56**, 2257.

This journal is © The Royal Society of Chemistry 2018

Inorganic Chemistry
Article
Cite This: Inorg. Chem. 2018, 57, 11498−11510
pubs.acs.org/IC

Diheme Cytochrome *c*: Structure−Function Correlation and Effect of Heme−Heme Interactions

Firoz Shah Tuglak Khan,[†] Sayantani Banerjee,[†] Devesh Kumar,*[,‡] and Sankar Prasad Rath*[,†]

[†]Department of Chemistry, Indian Institute of Technology Kanpur, Kanpur-208016, India

[‡]Department of Physics, School for Physical and Decision Sciences, Babasaheb Bhimrao Ambedkar University, Lucknow-226025, India

Supporting Information

ABSTRACT: We explore here the structure−function relationship of the diheme cytochrome *c* using synthetic diheme analogs which serve as a convenient tool to investigate various aspects of Nature's sophisticated design *in vitro*. A large series of diiron ethane-bridged porphyrin dimers, both in the oxidized and the reduced states, are synthesized and their structural, chemical, and electrochemical properties have been scrutinized. Interestingly, the iron-to-iron nonbonding separation observed in such dihemes ranges from 9.49 to 10.06 Å which is very similar to the separation of 9.4 and 9.9 Å observed in the crystal structures of diheme cytochromes *c* isolated from *Geobacter sulfurreducens* and *Haemophilus influenza*, respectively. The Fe^{III}/Fe^{II} redox couple in the diheme complex is shifted toward more positive than their monomeric analog. Present study unmasks the electronic structure and properties of diheme centers and also highlights the significance of their structural arrangement and axial ligand orientation, and heme-to-heme separation. The Atoms in Molecules (AIM) analysis suggests long-range attractive dispersion forces between the heme units for the observed structure and properties in dihemes.

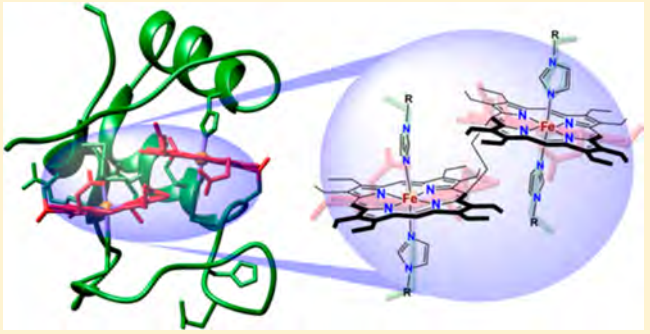

INTRODUCTION

Multiheme cytochromes represent an extensive class of hemoproteins with consequential role in enzymatic catalysis and electron transport in biology.[1−4] The majority of them belong to the family of cytochromes *c* in which the heme units are covalently connected to the polypeptide chain via formation of two thioether bonds between two cysteine residues and the vinyl side-chains of the porphyrin ring.[1−5] A low amino acid residue to heme ratio and bis-histidine coordination, with few exceptions, characterizes them. Understanding the structural arrangement of multiheme units is crucial to gain more insights into the highly optimized properties of these multiheme cytochromes *c*. However, their spectroscopic investigation is often complicated due to the presence of large number of heme centers along with substantial intermacrocyclic coupling in between.[1−4]

However, several closely packed diheme blocks have been found in the structural arrangements of multiheme proteins.[5] Interestingly, the array of such diheme motifs generates large and almost super imposable superheme motifs.[1−3] Diheme cytochrome *c* (DHC2), found in the bacteria *Geobacter sulfurreducens*, is the simplest member of the multiheme family which has two spectroscopically inequivalent heme units having different redox properties.[6a] Stereoviews of the two diheme cytochromes are shown in Figure 1 in which diheme centers are also highlighted. Iron-to-iron nonbonding separation of 9.4 Å has been observed in DHC2 which, however, results in an efficient coupling between the heme centers. An interplanar angle of 36° has been observed between two axially coordinated histidine ligands in heme unit I, whereas two axial ligands are nearly coplanar in heme unit II. Moreover, the porphyrin macrocycle of heme group I is almost planar whereas it is highly distorted in heme group II. Such differences in the porphyrin ring deformations as well as axial ligand orientations between the heme units in DHC2[6a] have been proposed to be caused by interheme interactions. Heme arrangement similar to DHC2 has also been observed in the small subunit (NapB) of the periplasmic nitrate reductase occurring in *Haemophilus influenza*.[6b] In NapB, the two heme groups are oriented almost parallel to each other with dihedral angles of 11° and 21° between the two axially ligated imidazoles in the two heme groups. Iron-to-iron separation of 9.9 Å has been observed here which is also similar to the split-Soret diheme cytochrome *c* found in *Desulfovibrio desulfuricans* ATCC 27774.[6c]

The above state of affairs has prompted us to investigate the structure−function correlation for diheme cytochrome *c* and the effect of the interheme interactions therein. The separation mediated sharp decrease in intramolecular interactions makes

Received: May 18, 2018
Published: August 27, 2018

Downloaded via BABASAHEB BHIMRAO AMBEDKAR UNIV on January 9, 2020 at 07:32:38 (UTC).
See https://pubs.acs.org/sharingguidelines for options on how to legitimately share published articles.

© 2018 American Chemical Society

DOI: 10.1021/acs.inorgchem.8b01368
Inorg. Chem. 2018, 57, 11498−11510

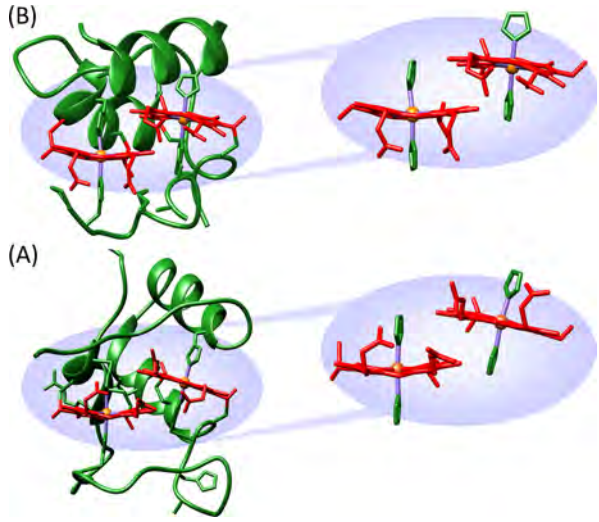

Figure 1. Relative stereoviews of (A) diheme cytochrome *c* isolated from *G. sulfurreducens* (PDB code 2CZS)[6a] and (B) split-Soret cytochrome *c* isolated from *D. desulfuricans* (PDB code 1H21).[6c]

close proximity of the heme units susceptible to significant modification of their intrinsic properties.[3d,4b] However, the study of structure–function activity relationships of such diheme cytochromes *c* are complicated by the presence of large polypeptide chains. Synthetic metalloporphyrins, therefore, serve as convenient systems for testing mechanistic hypotheses of enzymatic processes as they are unhindered by the absence of any associated biological superstructure. Active site analogs of such diheme cytochromes provide a tool to investigate various aspects of Nature's sophisticated design *in vitro* which cannot be obtained through the native enzyme.

We have been engaged in exploiting the significance and outcome of the heme–heme interactions using metalloporphyrin dimers.[7−12] In the present work, we explore the structure–function relationship of the diheme cytochrome *c* using a series of synthetic diheme analogs. For that, covalently linked porphyrin dimer with highly flexible ethane bridge has been employed as a diheme analog in which two-heme units orient in an *anti*-conformation. A large series of such analogs, both in the oxidized as well as in the reduced states, are synthesized and their structural, chemical, and electrochemical properties have been scrutinized. Interestingly, the iron-to-iron nonbonding separation observed in such dihemes ranges from 9.49 to 10.06 Å (*vide infra*) which is very similar to the iron-to-iron separation of 9.4 and 9.9 Å observed in the crystal structures of diheme cytochromes *c* isolated from *G. sulfurreducens* and *H. influenza*, respectively.[6] Such similar iron-to-iron separation as well as relative structural arrangement of diheme units make the diiron ethane-bridged porphyrin dimer an excellent synthetic analog for exploring several aspects of Nature's sophisticated design.

RESULTS AND DISCUSSION

μ-Oxo-*syn*-1,2-bis[5-(2,3,7,8,12,13,17,18 octaethylporphyrinato)iron(III)]ethane, **1**, was synthesized using a procedure reported earlier.[10a] UV–vis spectroscopic data of **1** shows a Soret band at 399 nm and a Q-band at 579 nm in dichloromethane in which two porphyrin macrocycles are in face- to-face orientation. Upon addition of excess acid (HX) such as HCl, $HClO_4$ and 2,4,6-trinitrophenol (HTNP), **1**, converts immediately into **1**·X_2 in quantitative yields (Scheme 1).[8]

Scheme 1. Synthetic Outline

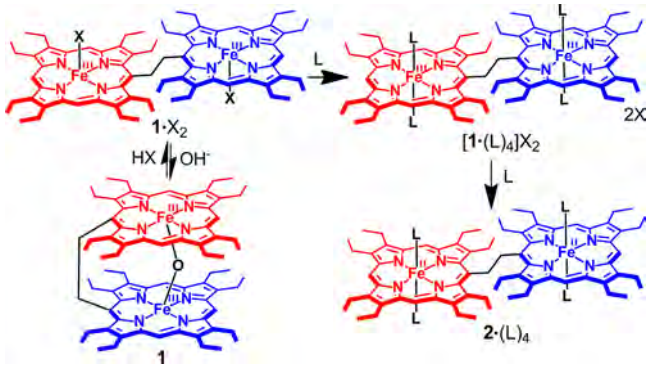

However, addition of axial ligand L into the dichloromethane solution of **1**·X_2 (X: ClO_4, Cl and TNP) results in the formation of the six-coordinate complex [**1**·$(L)_4$]$(X)_2$ which has been isolated and structurally characterized. The axial ligands (L) that are used in the present investigation are imidazole (Im), 1-methylimidazole (1-MeIm), 2-methylimidazole (2-MeIm), 4-methylimidazole (4-MeIm), pyridine (Py), 3-cyanopyridine (3-CNPy), and 4-cyanopyridine (4-CNPy). Moreover, upon standing with excess L, the complex [**1**·$(L)_4$]$(ClO_4)_2$ spontaneously autoreduces[13] into air-stable **2**·$(L)_4$ in quantitative yield. During such a process, large changes in the UV–visible spectra are observed. For example, gradual addition of imidazole to **1**·$(ClO_4)_2$ produces a large spectral change in which peaks at 390 and 515 nm corresponding to **1**·$(ClO_4)_2$ transformed into peaks at 418 and 549 nm due to the formation of [**1**·$(Im)_4$]$(ClO_4)_2$; Figure 2 demonstrates such spectral changes in the UV–visible region. Similar changes are also obtained with other imidazoles/pyridines as axial ligands. Figure 2 (trace B) compares the absorption spectra between [**1**·$(4\text{-MeIm})_4$]$(ClO_4)_2$ and **2**·$(4\text{-MeIm})_4$ in dichloromethane. Scheme 1 shows the synthetic outline and list of the complexes reported here along with their abbreviations used.

The UV–vis spectra of the diheme complexes reported here are similar to the native diheme cytochrome *c* (DHC2) in their oxidized and reduced states. For example, the Soret and Q-bands of [**1**·$(4\text{-MeIm})_4$]$(ClO_4)_2$ are observed at 408 and 539 nm while in the reduced complex **2**·$(4\text{-MeIm})_4$, the bands are, respectively, at 419 and 551 nm. It is, however, interesting to note here that the oxidized form of the diheme cytochrome *c*, DHC2, from *G. sulfurreducens* shows absorption maxima at 408 and 530 nm whereas the reduced form exhibits the same maxima at 419 nm (Soret) and 523, 552 nm.[6a] As one can see, electronic spectra of the synthetic diheme complexes are nearly identical with the DHC2 both in the oxidized and reduced forms.

Crystallographic Characterizations. Dark red crystals of [**1**·$(1\text{-MeIm})_4$]$(ClO_4)_2$ were grown by slow diffusion of *n*-hexane into the benzene solutions of **1**·$(ClO_4)_2$ containing 1-methylimidazole in 1:5 molar ratio at room temperature in air. The complex crystallizes in the triclinic crystal system with the $P\bar{1}$ space group. Two perspective views of the molecule are shown in Figure 3. Similarly, the crystals of [**1**·$(2\text{-MeIm})_4$]Cl_2, [**1**·$(4\text{-CNPy})_4$]$(ClO_4)_2$ and [**1**·$(Py)_4$]$(TNP)_2$ were grown. In all the complexes, the iron centers are in a six-coordinate

DOI: 10.1021/acs.inorgchem.8b01368
Inorg. Chem. 2018, 57, 11498−11510

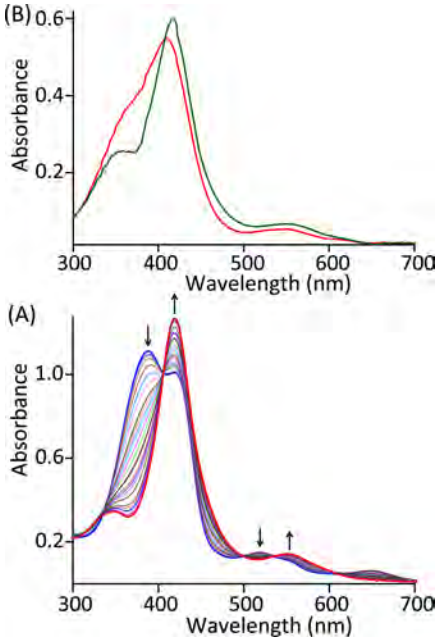

Figure 2. (A) Time resolved UV−vis spectral changes upon gradual addition of imidazole up to 6 equiv to a solution of $\mathbf{1}\cdot(ClO_4)_2$ in dichloromethane at 295 K. Arrows indicate an increase or decrease of band intensity. (B) UV−vis spectra (in dichloromethane at 295 K) comparing $[\mathbf{1}\cdot(4\text{-MeIm})_4](ClO_4)_2$ (red line) and $\mathbf{2}\cdot(4\text{-MeIm})_4$ (green line).

octahedral geometry. The complex $[\mathbf{1}\cdot(2\text{-MeIm})_4]Cl_2$ crystallizes in the monoclinic crystal system with the $P2_1/n$ space group while $[\mathbf{1}\cdot(4\text{-CNPy})_4](ClO_4)_2$ crystallizes in triclinic and $[\mathbf{1}\cdot(Py)_4](TNP)_2$ in monoclinic crystal system having space groups of $P\bar{1}$ and $P2_1/c$, respectively. Perspective views and molecular packing diagrams of the complexes are given in Figures S1−S7 and the out-of-plane displacement plots comparing the ring deformations are given in Figure S8. The selected bond distances and angles are given in Table S1 while the crystal data and data collection parameters are given in Table S2. As observed from Table S1, Fe−N_{por} distances are in the narrow range of 1.948 to 1.974 Å while Fe−N_{ax} distances are within 1.961−2.101 Å. These values are in the range of six-coordinate low-spin iron(III) porphyrins reported earlier.[13−18] The X-ray structures of $[\mathbf{1}\cdot(1\text{-MeIm})_4](ClO_4)_2$, $[\mathbf{1}\cdot(2\text{-MeIm})_4]Cl_2$, $[\mathbf{1}\cdot(Py)_4](TNP)_2$, and $[\mathbf{1}\cdot(4\text{-CNPy})_4](ClO_4)_2$ demonstrate nearly perpendicular axial ligand orientations in the distorted macrocyclic environments.

Dark brown crystals of $\mathbf{2}\cdot(L)_4$ were grown at room temperature in air by slow diffusion of acetonitrile into the chloroform solution of $\mathbf{1}\cdot(ClO_4)_2$ containing large excess of pyridine, 3-cyanopyridine and 4-cyanopyridine yielding $\mathbf{2}\cdot(Py)_4$, $\mathbf{2}\cdot(3\text{-CNPy})_4$, and $\mathbf{2}\cdot(4\text{-CNPy})_4$, respectively. All the complexes crystallize in triclinic crystal system having the $P\bar{1}$ space group. A perspective view of $\mathbf{2}\cdot(Py)_4$ is shown in Figure 4 (trace B) while the perspective views and molecular packing diagrams of $\mathbf{2}\cdot(3\text{-CNPy})_4$ and $\mathbf{2}\cdot(4\text{-CNPy})_4$ are shown in Figures S9−S13. Here also, the axial ligands are in perpendicular orientations. Interestingly, iron-to-iron nonbonding distances along with other structural and geometrical parameters of these synthetic dihemes are very similar to the naturally occurring DHC2 as summarized in Table 1. The selected bond distances and angles are listed in Table S1 while the crystal data and data collection parameters are listed in Table S3. As observed from Table 1, Fe−N_{por} distances are in the narrow range of 1.988 to 1.991 Å while Fe−N_{ax} distances are within 1.972 to 2.003 Å. These values are in the range of low spin iron(II) porphyrins observed in the literature.[13−18]

As can be seen in Table 1, iron(III) complexes are more distorted compared to their iron(II) analogs and the out-of-plane displacements of the porphyrin core atoms of $\mathbf{2}\cdot(L)_4$ and $[\mathbf{1}\cdot(L)_4]X_2$ are compared in Figures 5 and S14. One reason for such a decrease in the ring deformation on going from iron(III) to iron(II) is the difference in the ionic radii of iron. It is interesting to compare the porphyrin ring deformations in $[\mathbf{1}\cdot(Py)_4](TNP)_2$, $\mathbf{2}\cdot(Py)_4$, and their monomeric iron(II) analog $Fe(OEP)(Py)_2$ (Tables S4 and S5), which, however, produces a nearly planar porphyrin ring. It has been observed that the macrocycles in the porphyrin dimers are much more distorted as compared to their monomeric analog. In a nonplanar porphyrinic environment, the axial ligand orienta-

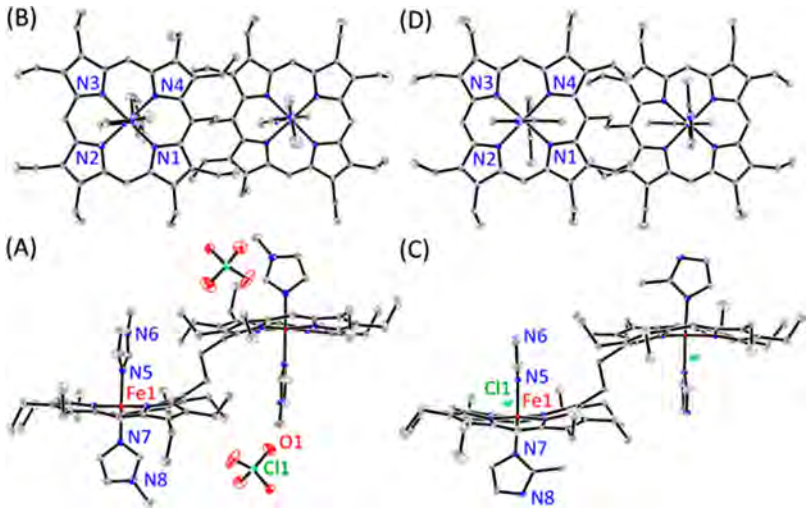

Figure 3. (A) Perspective views of $[\mathbf{1}\cdot(1\text{-MeIm})_4](ClO_4)_2$ (A, side view and B, top view without counteranions) and $[\mathbf{1}\cdot(2\text{-MeIm})_4]Cl_2$ (C, side view and D, top view without counteranions) showing 50% thermal contours for all the non-hydrogen atoms at 100 K (hydrogen atoms have been omitted for clarity).

DOI: 10.1021/acs.inorgchem.8b01368
Inorg. Chem. 2018, 57, 11498−11510

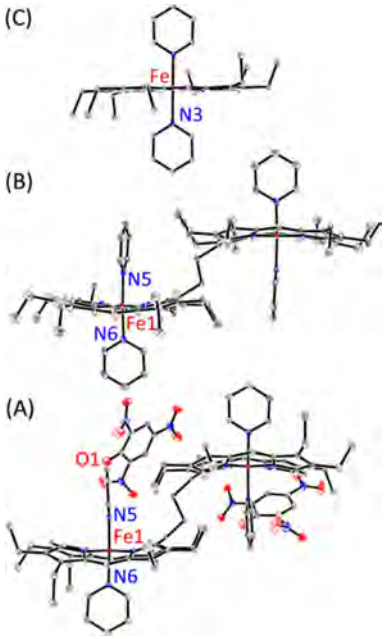

Figure 4. Perspective views of (A) $[\mathbf{1}\cdot(Py)_4](TNP)_2$, (B) $\mathbf{2}\cdot(Py)_4$, and (C) $Fe(OEP)(Py)_2$ showing 50% thermal contours for all the non-hydrogen atoms at 100 K (hydrogen atoms have been omitted for clarity).

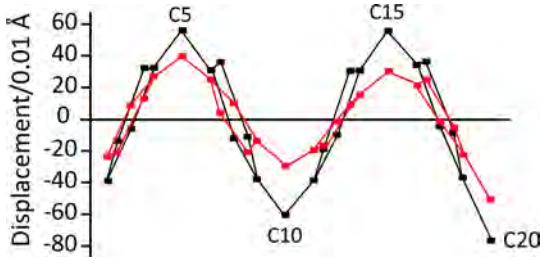

Figure 5. Out-of-plane displacement (in units of 0.01 Å) of the porphyrin core atoms of $[\mathbf{1}\cdot(Py)_4](TNP)_2$ (black line) and $\mathbf{2}\cdot(Py)_4$ (red line) from the least-squares plane of the $C_{20}N_4$ porphyrinato core. The horizontal axis represents the bond connectivity between atoms.

tions have been demonstrated to switch between perpendicular and parallel upon changing the oxidation state of iron,[13] however, no such change is observed in the diheme complexes reported here. Moreover, in case of $Fe(OEP)(Py)_2$ the axial ligands are found to be in parallel orientation, whereas in its diheme analog $\mathbf{2}\cdot(Py)_4$, it was found to be perpendicular. The heme–heme interaction in diheme has increased the porphyrin ring deformations, and subsequently, the perpendicular alignment of axial ligands are stabilized in both diiron(III) and diiron(II) porphyrin dimers reported here.

Table 1. Selected Structural and Geometrical Parameters of $[\mathbf{1}\cdot(L)_4](X)_2$, $\mathbf{2}\cdot(L)_4$, and $Fe(OEP)(Py)_2$ along with the Native Diheme Cytochrome *c*

Complex		$Fe-N_{por}$ (Å)[a]	$Fe-N_{ax}$ (Å)	Φ (deg)[b]	θ (deg)[c]	Δ_{24} (Å)[d]	Fe···Fe (Å)	ref
$[\mathbf{1}\cdot(1\text{-MeIm})_4](ClO_4)_2$		1.974(2)	1.961(2)	37.7	85.2	0.25	9.89	this work
			1.982(2)					
$[\mathbf{1}\cdot(2\text{-MeIm})_4]Cl_2$		1.973(2)	1.991(4)	43.5	87.6	0.26	9.91	this work
			1.999(4)					
$[\mathbf{1}\cdot(Py)_4](TNP)_2$		1.956(2)	1.986(2)	42.2	87.6	0.31	9.49	this work
			2.101(2)					
$[\mathbf{1}\cdot(4\text{-CNPy})_4](ClO_4)_2$	core-I	1.959(4)	1.991(3)	42.7	87.2	0.28	9.67	this work
			1.996(3)					
	core-II	1.948(4)	1.998(3)	39.7	81.9	0.36		
			2.003(4)					
$\mathbf{2}\cdot(4\text{-CNPy})_4$		1.991(3)	1.972(3)	42.7	88.2	0.17	9.86	this work
			2.003(3)					
$\mathbf{2}\cdot(3\text{-CNPy})_4$		1.9888(18)	1.9840(19)	38.1	81.8	0.20	10.06	this work
			1.9977(18)					
$\mathbf{2}\cdot(Py)_4$		1.988(3)	1.990(3)	44.1	87.4	0.19	9.94	this work
			2.003(3)					
$Fe(OEP)(Py)_2$		2.001(2)	2.048(2)	32.1	0.0	0.02		this work
DHC2	core-I	2.044	1.935	44.1	36	0.07	9.38	6a
(isolated from *G. sulfurreducens*)			1.979					
	core-II	2.033	2.007	30.0	2	0.21		
			2.032					
DHC2	core-I	1.982	2.007	42.6	21	0.13	9.90	6b
(isolated from *H. influenza*)			2.051					
	core-II	1.996	2.003	44.4	14	0.14		
			2.073					
DHC2	core-I	1.942	1.970	33.7	74	0.22	9.17	6c
(isolated from *D. desulfuricans*)			2.037					
	core-II	1.976	2.000	38.6	23	0.15		
			2.019					

[a]Average value. [b]Dihedral angle between the plane of the closest $N_{por}-Fe-N_{ax}$ and the axial ligand plane. [c]Dihedral angle between two axial ligands. [d]Average displacement of atoms from the least-squares plane of the $C_{20}N_4$ porphyrinato core.

DOI: 10.1021/acs.inorgchem.8b01368
Inorg. Chem. 2018, 57, 11498–11510

Mössbauer Spectroscopy. Mössbauer parameters are one of the most important tools to determine the spin states of iron(III) porphyrins.[17,18] The spectra of the polycrystalline samples of $[\mathbf{1}\cdot(L)_4](X)_2$ (X = ClO_4 and Cl) were recorded in zero magnetic field at 295 K and are shown in Figure 6. All the

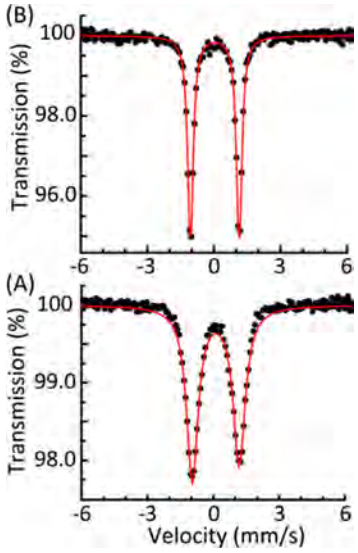

Figure 6. Zero-field Mössbauer spectra of the polycrystalline samples of (A) $[\mathbf{1}\cdot(1\text{-MeIm})_4](ClO_4)_2$ and (B) $[\mathbf{1}\cdot(Im)_4](ClO_4)_2$ at 295 K.

complexes show only one quadrupole doublet: for $[\mathbf{1}\cdot(Im)_4](ClO_4)_2$, δ (ΔE_Q) = 0.19 (2.12) mm s^{-1}; $[\mathbf{1}\cdot(1\text{-MeIm})_4](ClO_4)_2$, δ (ΔE_Q) = 0.18 (2.19) mm s^{-1}; $[\mathbf{1}\cdot(2\text{-MeIm})_4]Cl_2$, δ (ΔE_Q) = 0.16 (1.55) mm s^{-1}. Similarly, one quadrupole doublet was observed for $[\mathbf{1}\cdot(Py)_4](TNP)_2$ having δ (ΔE_Q) = 0.15 (2.29) mm s^{-1}. These values are characteristic of the iron(III) low-spin complex.[17,18] Therefore, Mössbauer parameters are in line with the results obtained from the X-ray structures of the complexes (*vide supra*).

EPR Spectroscopy. X-band EPR spectra were measured for $[\mathbf{1}\cdot(L)_4](ClO_4)_2$ at 77 K which show rhombic type spectral features both in solid and solution phases. The spectra for the representative complexes in dichloromethane are shown in Figure 7. Upon simulations, g values that are obtained are as follows: g_3 = 2.70, g_2 = 2.27, and g_1 = 1.75 for $[\mathbf{1}\cdot(Im)_4](ClO_4)_2$; g_3 = 2.67, g_2 = 2.26, and g_1 = 1.75 for $[\mathbf{1}\cdot(4\text{-MeIm})_4](ClO_4)_2$; g_3 = 2.86, g_2 = 2.25, and g_1 = 1.53 for $[\mathbf{1}\cdot(1\text{-MeIm})_4](ClO_4)_2$. The spectra are of typical rhombic type that are usually observed for low-spin ($S = {}^1/_2$) iron(III) porphyrins with two axially ligated imidazoles. It is interesting to note here that the X-band EPR of DHC2 also exhibits similar rhombic type spectra.[6a] However, with 4-fold symmetric porphyrins, the appearance of a rhombic spectrum for a low-spin iron(III) porphyrin usually indicates the two axial ligands lying in a common plane.[13−16] The low-spin iron(III) porphyrins with perpendicularly oriented planar axial ligand usually display "large g_{max}" EPR spectra that mark the near degeneracy of the d_{xz} and d_{yz} orbitals.[13−16] However, in the diheme complexes reported here, the intrinsic asymmetry in the porphyrin dimer lowers the symmetry leading to rhombic type EPR spectra, even though the planar axial ligands are in perpendicular orientations. Similar rhombic-type EPR data were also observed for the meso-hydroxy heme in which two axial imidazoles are in perpendicular orientation.[16a]

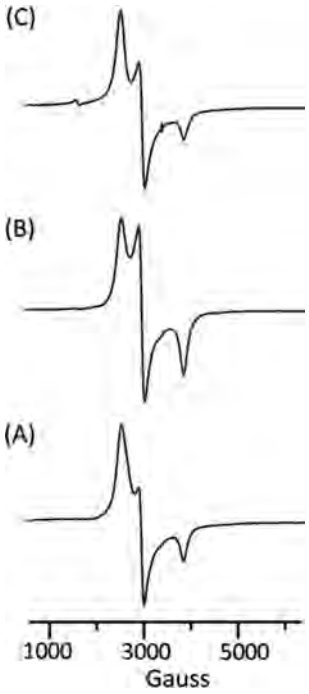

Figure 7. X-band EPR spectra of (A) $[\mathbf{1}\cdot(Im)_4](ClO_4)_2$, (B) $[\mathbf{1}\cdot(4\text{-MeIm})_4](ClO_4)_2$ and (C) $[\mathbf{1}\cdot(1\text{-MeIm})_4](ClO_4)_2$ in dichloromethane at 77 K.

^{1}H NMR Spectroscopy. The solution structure and properties of the complexes can be analyzed through their ^{1}H NMR spectra. The ^{1}H NMR spectrum for $[\mathbf{1}\cdot(Py)_4](TNP)_2$ has been recorded in pyridine-d_5. Eight methylene signals are observed at a region between 6.1 and 11.3 ppm while the bridging protons are further downfield shifted to 18.3 ppm. The *meso* protons are upfield shifted and observed at 0.8 and −5.9 ppm in a 2:1 intensity ratio (Figure 8). Similar peak

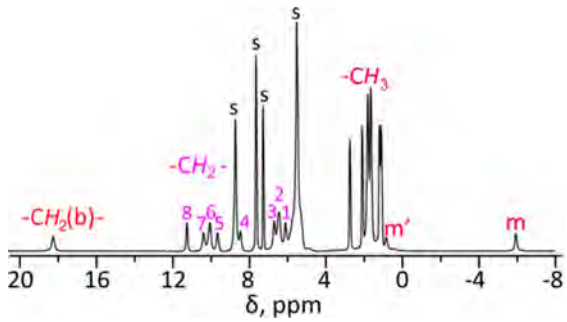

Figure 8. ^{1}H NMR spectrum (in pyridine-d_5 at 295 K) of $[\mathbf{1}\cdot(Py)_4](TNP)_2$. Peaks marked as "s" correspond to signals from solvent.

patterns have also been observed in the ^{1}H NMR spectra of $[\mathbf{1}\cdot(Im)_4](ClO_4)_2$, recorded in $CDCl_3$, where eight methylene signals at 2.9(2), 4.6, 5.3, 6.0, 6.2, 6.4, and 6.9 ppm, bridging CH_2 protons at 15.9, and two *meso* signals at −1.9 and −8.5 ppm in intensity ratio 2:1 are observed. Mulliken spin density calculation of $[\mathbf{1}\cdot(Py)_4]^{2+}$ (Figure S15) shows positive spin densities at the *meso* carbons while negative spins at the bridging carbons, thus, ascertaining the upfield and downfield shifting of corresponding proton signals as observed in their ^{1}H NMR spectrum. The observed ^{1}H NMR spectral pattern is of a typical hexacoordinated iron(III) low-spin complex.[14,16−19]

DOI: 10.1021/acs.inorgchem.8b01368
Inorg. Chem. 2018, 57, 11498−11510

The ^{1}H NMR spectra of $[\mathbf{1}\cdot(L)_4](X)_2$ (X = ClO_4 and Cl), where L are substituted imidazoles, have also been recorded and it was observed that the proton signals from imidazoles are shifted to both downfield and upfield regions which indicate π-spin delocalization from iron(III) center to axially coordinated imidazole. In order to assign the proton peaks of the coordinated imidazole species, several substituted imidazoles have been used here. The ^{1}H NMR spectra of the complexes are compared in Figure 9. The H_a proton of coordinated

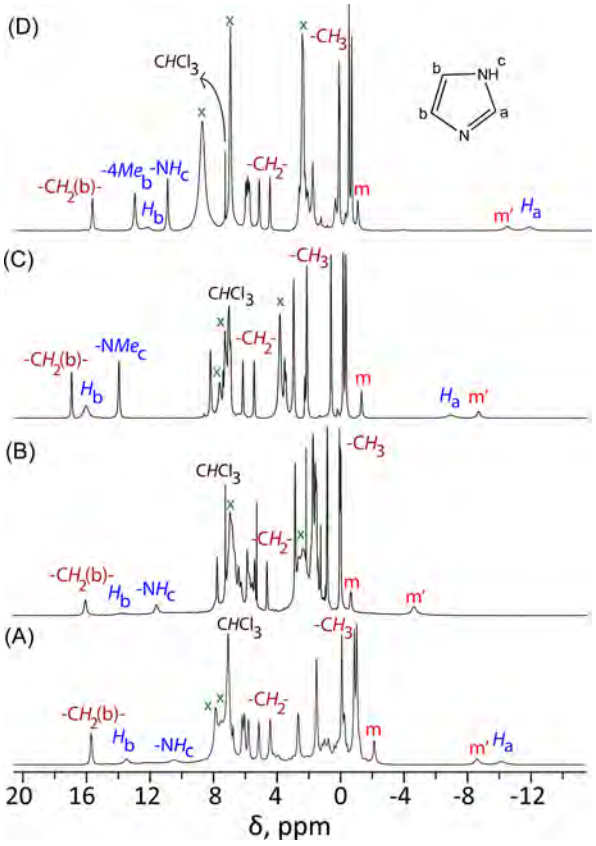

Figure 9. ^{1}H NMR spectra (in $CDCl_3$ at 295 K) of (A) $[\mathbf{1}\cdot(Im)_4](ClO_4)_2$, (B) $[\mathbf{1}\cdot(2\text{-MeIm})_4]Cl_2$, (C) $[\mathbf{1}\cdot(1\text{-MeIm})_4](ClO_4)_2$, and (D) $[\mathbf{1}\cdot(4\text{-MeIm})_4](ClO_4)_2$. Peaks marked as "x" belong to proton signals from free ligands.

imidazole in $[\mathbf{1}\cdot(Im)_4](ClO_4)_2$ shifts to the upfield regions at −9.9 whereas the H_b and H_c protons shift downfield to 13.7 and 10.7 ppm, respectively. Mulliken spin density calculation on $[\mathbf{1}\cdot(2\text{-MeIm})_4]Cl_2$ (Figure S16) displays considerable spin delocalization to the axially coordinated imidazole also. The spin densities observed is negative at C_b position while positive at C_a position. Therefore, the C_b protons should be downfield shifted while C_a proton is to be upfield shifted which is indeed observed in the ^{1}H NMR spectra of the complex.

Electrochemistry. Cyclic voltammetric experiments were done at 295 K under nitrogen in dichloromethane using 0.1 M tetra(*n*-butyl)ammonium hexafluorophosphate (TBAH) as the supporting electrolyte. The first oxidation couples for $[\mathbf{1}\cdot(Im)_4](ClO_4)_2$, $[\mathbf{1}\cdot(4\text{-MeIm})_4](ClO_4)_2$, $[\mathbf{1}\cdot(1\text{-MeIm})_4](ClO_4)_2$, and $[\mathbf{1}\cdot(2\text{-MeIm})_4]Cl_2$ are observed at 0.60, 0.61, 0.62, and 0.64 V vs Ag/AgCl, respectively, which correspond to porphyrin-centered oxidation and two representative cyclic voltammograms are shown in Figure 10. Similarly, the electrochemical measurements for the monomeric analogs

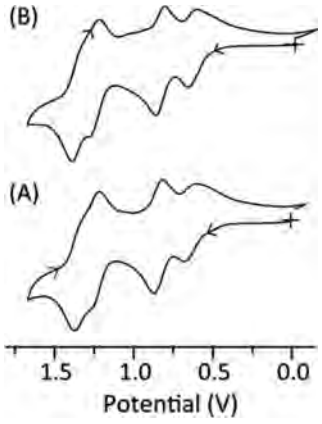

Figure 10. Portion of cyclic voltammograms of (A) $[\mathbf{1}\cdot(4\text{-MeIm})_4](ClO_4)_2$, and (B) $[\mathbf{1}\cdot(2\text{-MeIm})_4]Cl_2$ in CH_2Cl_2 (scan rate 100 mV/s) with 0.1 M tetra(*n*-butyl)ammonium hexafluorophosphate as supporting electrolyte. The reference electrode was Ag/AgCl.

were also carried out under identical conditions and the first oxidation couples for $[Fe(OEP)(Im)_2]ClO_4$, $[Fe(OEP)(4\text{-MeIm})_2]ClO_4$, $[Fe(OEP)(1\text{-MeIm})_2]ClO_4$, and $[Fe(OEP)(2\text{-MeIm})_2]Cl$ are observed at 0.83, 0.84, 0.85, and 0.86 V, respectively. Thus, the first oxidation potential of the diheme species occurs at a potential much lower than its monomeric analog.

The reduction of diheme complex $[\mathbf{1}\cdot(L)_4](X)_2$ has also been performed and the $E_{1/2}$ of Fe^{III}/Fe^{II} redox couple are observed at −0.27, −0.36, −0.37, and −0.42 V vs. Ag/AgCl for L= Im, 4-MeIm, 1-MeIm, and 2-MeIm, respectively, and three representative cyclic voltammograms are shown in Figure 11.

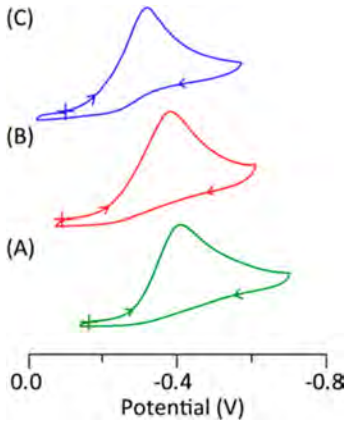

Figure 11. Portion of cyclic voltammograms of (A) $[\mathbf{1}\cdot(2\text{-MeIm})_4]Cl_2$, (B) $[\mathbf{1}\cdot(4\text{-MeIm})_4](ClO_4)_2$, and (C) $[\mathbf{1}\cdot(Im)_4](ClO_4)_2$ in CH_2Cl_2 (scan rate 100 mV/s) with 0.1 M tetra(*n*-butyl)ammonium hexafluorophosphate as supporting electrolyte. The reference electrode was Ag/AgCl.

Coulometric reduction of $[\mathbf{1}\cdot(L)_4](ClO_4)_2$ in dichloromethane at a constant potential has also been done and the progress of the reaction was monitored continuously by UV−vis spectroscopy as shown in Figure S17 for $[\mathbf{1}\cdot(4\text{-MeIm})_4](ClO_4)_2$, as a representative case. A gradual decrease of the Soret band characteristics of iron(III) porphyrin and the appearance of a new Soret band corresponding to iron(II) confirms the corresponding potential as that of the iron(III)/iron(II) redox couple. The cyclic voltammogram for the monomeric analog has also been recorded: the $E_{1/2}$ of Fe^{III}/Fe^{II} redox

DOI: 10.1021/acs.inorgchem.8b01368
Inorg. Chem. 2018, 57, 11498−11510

couple for $[Fe(OEP)(Im)_2]ClO_4$, $[Fe(OEP)(4\text{-}MeIm)_2]ClO_4$, $[Fe(OEP)(1\text{-}MeIm)_2]ClO_4$, and $[Fe(OEP)(2\text{-}MeIm)_2]Cl$ are observed at −0.41, −0.42, −0.43, and −0.45 V, respectively. This observation demonstrates that not only the oxidation but also the reduction become easier in the diheme complexes as compared to their monoheme analogs. The plots of first oxidation potential and Fe^{III}/Fe^{II} redox couple of diheme complexes vs p*K*a of the axial ligands (i.e., Im, 4-MeIm, 1-MeIm, and 2-MeIm) are shown in Figure 12 in which both

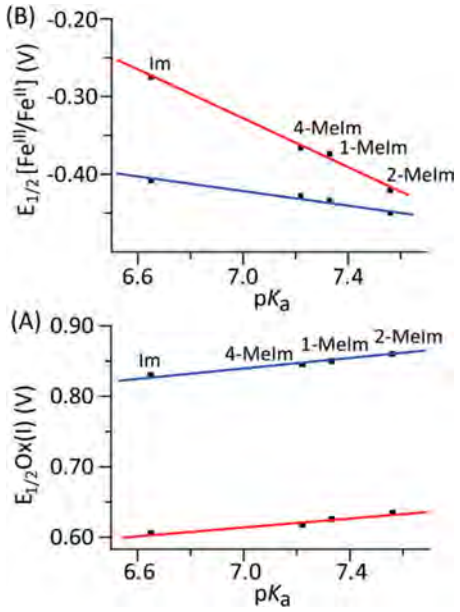

Figure 12. Plots of pK_a[20] of axial ligands vs (A) first oxidation, and (B) Fe^{III}/Fe^{II} reduction potential (in V) of $[\mathbf{1}\cdot(L)_4](X)_2$ and $[Fe(OEP)(L)_2]X$ (X = ClO_4,Cl). Red and blue lines correspond to diiron(III) porphyrin dimer and its corresponding monomeric analog, respectively.

diheme and monoheme complexes show a linear relationship. To gain more insights into such electronic effect in the diheme species, a series of theoretical calculations are performed (*vide infra*).

Molecular Modeling. Density functional calculations have been carried out for several six-coordinate low-spin diiron(III) and diiron(II) porphyrin dimers in which the atom coordinates are taken directly from their single crystal X-ray structures. The geometries of $[\mathbf{1}\cdot(L)_4]^{2+}$, $\mathbf{2}\cdot(L)_4$, $[Fe^{III}(OEP)(L)_2]^+$ and $Fe^{II}(OEP)(L)_2$ (where L= Im, 2-MeIm, 1-MeIm and Py) are optimized and the calculations virtually reproduce the geometrical parameters observed in their X-ray structures (Figures 13 and S18−S22). Computational studies were done employing the Gaussian 09, revision B.01 package[21] with unrestricted hybrid B3LYP[22] exchange-correlation functionals and the basis set combination, termed as BS1, used is LANL2DZ (for Fe) and 6-31G** (for C, H, N, Cl and O). Upon going from diiron(III) to diiron(II), some structural changes are observed in the optimized structures as obtained in the experiment also (*vide infra*). The Fe−N_{por} bond distance elongates from 1.982 to 2.023 Å (for L = Py, as a representative case) which results in porphyrin core expansion. The intramolecular iron-to-iron distance increases on going from diiron(III) to diiron(II) which was also observed experimentally. Moreover, the optimized structures reproduce the perpendicular axial ligand orientation as observed in the

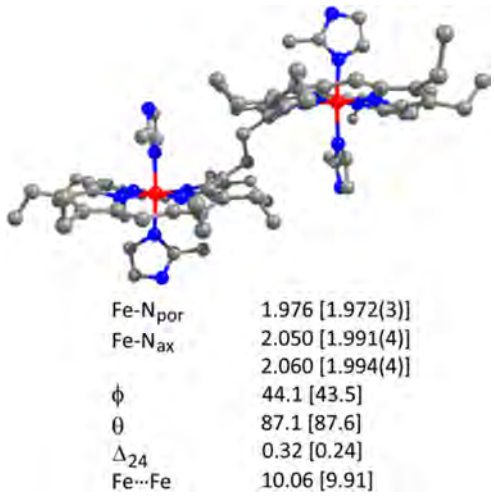

Figure 13. uB3LYP/BS1 optimized geometry of $[\mathbf{1}\cdot(2\text{-}MeIm)_4]^{2+}$ with bond lengths in Å and angles in degrees. Parentheses contain the experimental value obtained from the X-ray structure of $[\mathbf{1}\cdot(2\text{-}MeIm)_4]Cl_2$ (hydrogen atoms have been omitted for clarity).

experiment. For example, the optimized geometry of $[\mathbf{1}\cdot(1\text{-}MeIm)_4](ClO_4)_2$ displays angles of 94.3° and 85.4° between the two axial ligands in cores I and II, respectively, which are, however, close to the values observed in the X-ray structure of the complex.

To gain more insights into the stabilization of such perpendicular orientation, 1D potential energy surface (PES) scan on $[\mathbf{1}\cdot(1\text{-}MeIm)_4](ClO_4)_2$ has also been performed. One of the axial ligand from each of the cores was rotated in steps of 10° keeping other two axial ligands intact in their positions. The relative energy of the complex was then plotted against the dihedral angle as shown in Figure 14 (trace A). The lowest energy was observed when the dihedral angle between the axial ligands is ∼90° which is also close to the angle observed in the X-ray structure of the complex. Similar calculations are also

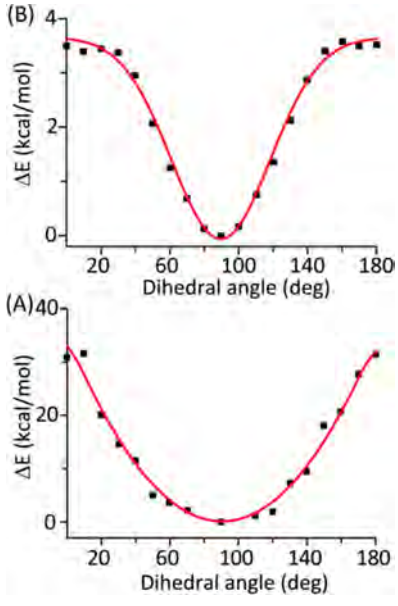

Figure 14. Plots showing the relative energy (Δ*E*) upon changing dihedral angles between the two 1-methylimidazole axial ligands for (A) $[\mathbf{1}\cdot(1\text{-}MeIm)_4](ClO_4)_2$ and (B) $\mathbf{2}\cdot(1\text{-}MeIm)_4$.

DOI: 10.1021/acs.inorgchem.8b01368
Inorg. Chem. 2018, 57, 11498−11510

done on the uB3LYP/BS1 optimized geometry of its iron(II) analog **2**·(1-MeIm)$_4$; the relative energy plot with respect to dihedral angle also shows the stabilization of geometry having perpendicular axial ligand orientations only (Figure 14, trace B). The calculation on the optimized geometry of [**1**·(Py)$_4$]$^{2+}$ (without counteranions) also displays the perpendicular axial ligand orientation being stabilized by 36.9 kcal/mol over the parallel one. To understand more about the stability of the perpendicular orientation of the axial ligands, several single-point calculations are done on the optimized geometries of [**1**·(Im)$_4$]$^{2+}$ and **2**·(Im)$_4$ after removing ethyl substituents and the ethane bridge keeping everything else intact in the complexes. While perpendicular orientations in [**1**·(Im)$_4$]$^{2+}$ and **2**·(Im)$_4$ are stabilized over parallel by 13.5 and 3.8 kcal/mol, respectively, the energy differences, however, have reduced to 8.1 and 1.4 kcal/mol, respectively, after removal of ethyl substituents as well as the ethane bridge (Table S6).

Interestingly, no change in the axial ligand orientation has been observed on going from diiron(III) to diiron(II) state; i.e., both the complexes were stabilized with a perpendicular orientation of the axial ligands. In contrast, axial ligand orientation has been found to vary between parallel and perpendicular just upon changing iron oxidation states from +3 to +2 in saddle-distorted iron porphyrins.[13] This further justify the judicious choice of diheme over monohemes where the reorganization energy, on going from Fe(III) to Fe(II), has been minimized in diheme as there is negligible structural change with identical axial ligand orientation. To gain more insights into this reduction of reorganization energy, two monoheme complexes were optimized, in Fe(III) as well as Fe(II) state, having *meso*-methyl OEP core with imidazole and 2-methylimidazole axial ligands. Such a porphyrin core was chosen as it structurally resembled one-half of its porphyrin dimer. Fe(III) to Fe(II) reductions in diheme complexes having imidazole and 2-methylimidazole as axial ligands are found to be stabilized by 7.8 and 6.6 kcal/mol, respectively, over their monomeric analogs. This justifies the reduction in structural reorganization energy in dihemes over monohemes. The selected structural and geometrical parameters for the optimized geometries of [**1**·(L)$_4$]$^{2+}$ and **2**·(L)$_4$ (L= Py, Im, 1-MeIm, and 2-MeIm) are compared in Table S7 and are also shown in Figures S18−S22.

It has been experimentally found that the Fe(III) to Fe(II) reduction is much easier in dihemes as compared to their monoheme analogs (*vide supra*) which has also been reproduced by theoretical calculations. The redox potentials of [**1**·(Im)$_4$]$^{2+}$ and [**1**·(2-MeIm)$_4$]$^{2+}$ were calculated using a method reported earlier.[23] The calculated Fe^{III}/Fe^{II} redox potential was −0.06 V in diheme complex [**1**·(2-MeIm)$_4$]$^{2+}$ whereas it was −0.19 V in the monoheme [Fe(OEP)(2-MeIm)$_2$]$^+$. Similarly, the redox potential for [**1**·(Im)$_4$]$^{2+}$ was 0.04 V which was −0.11 V in [Fe(OEP)(Im)$_2$]$^+$ (Table S8). This is also in line with the decrease of reorganization energy in diheme as compared to the monoheme analog which results in an easier reduction of diheme as compared to the monoheme.

To gain more insights into the effect of heme−heme interactions in diheme, a series of DFT calculations were performed on [**1**·(Im)$_4$]$^{2+}$ by varying iron-to-iron separation from 9.5 to 11.0 Å in the increments of 0.1 Å in each step (Tables S9 and S10) and subsequently optimizing the geometry. This variation alters the interheme interaction between the heme units in the porphyrin dimer. The most stable geometry was observed when the iron-to-iron separation was 10.05 Å which is in close agreement with the experiment. Upon varying the interheme separation, by increasing or decreasing the Fe···Fe distance, the molecule was more and more destabilized as evident from the relative energy curve (Figure 15). Eventually, at a distance beyond 11.0 Å, the curve

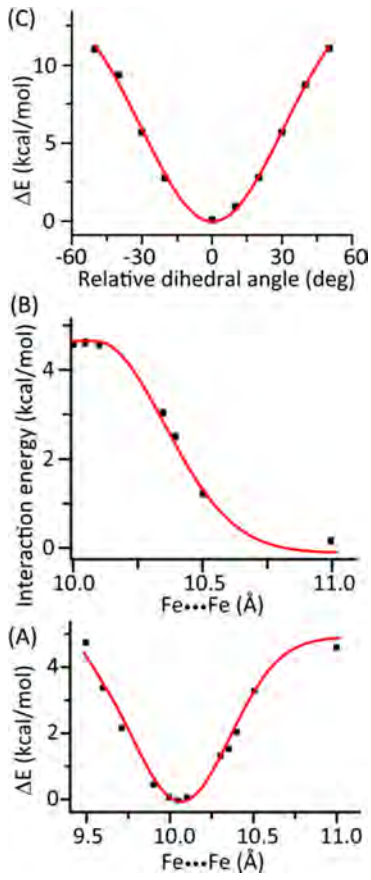

Figure 15. Plots of (A) relative energy (ΔE) of optimized geometries with Fe···Fe separation, (B) distance dependence of the pairwise interactions between the heme centers and (C) relative energy (ΔE) upon changing dihedral angle between two heme centers of [**1**·(Im)$_4$]$^{2+}$.

becomes almost parallel with respect to the *X*-axis, which indicates a negligible change in energy. This signifies that the diheme complex behaves as two separate monohemes at that distance. This gain in stabilization energy facilitates faster reduction of the iron(III) centers as compared to its monoheme counterpart which also closely agrees with the experiment. The redox potential for Fe^{III}/Fe^{II} redox couple of [**1**·(Im)$_4$]$^{2+}$ at a Fe···Fe separation of 11.0 Å has also been calculated to be −0.22 V. However, when two hemes are brought closer, the redox potential for Fe^{III}/Fe^{II} couple gradually decreases which has been found to be only 0.04 V at a iron-to-iron separation of 10.05 Å.

Not only the iron-to-iron separations in dihemes but the spatial arrangement might also be responsible in modulating the redox property of the diheme. To explore such effect on the heme-to-heme relative orientation, a sequence of calculations were done on [**1**·(Im)$_4$]$^{2+}$ varying the relative dihedral angle (θ') between two heme units from 0° (found as most stable orientation), in steps of 10° in either directions until the dihedral angle of 50° and the molecules are

DOI: 10.1021/acs.inorgchem.8b01368
Inorg. Chem. 2018, 57, 11498−11510

subsequently optimized with fixed θ' (Tables S11 and S12). A plot of relative energy of the optimized geometries vs θ' has been shown in Figure 15 (trace C). The redox potentials of Fe^{III}/Fe^{II} couples for $[\mathbf{1}\cdot(Im)_4]^{2+}$ were calculated to be −0.12 and 0.04 V, respectively, for 50° and 0° dihedral angles (θ'). This suggests that not only the iron-to-iron separation but also the relative heme orientations are also responsible for the change in their Fe^{III}/Fe^{II} redox couple. Such structurally mediated heme−heme interactions thus serve as an efficient tool to modulate the redox potentials in dihemes.

To understand the interaction between the two-heme units, AIM (atoms in molecules) analysis was executed. The software DAMQT 2.1.0[24] was utilized for the topographical analysis of uB3LYP/BS1 optimized geometry of $[\mathbf{1}\cdot(Im)_4]^{2+}$ and subsequent mapping shows several critical points between the two heme units (Figure 16, trace A). Analysis of such points

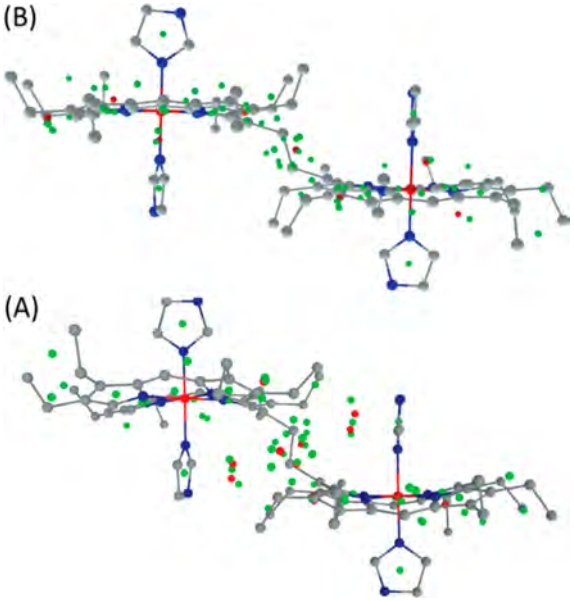

Figure 16. DAMQT 2.1.0 picture of $[\mathbf{1}\cdot(Im)_4]^{2+}$ highlighting critical points [(3,+3) CP in red and (3,+1) CP in green] between two heme units at fixed Fe···Fe separation of (A) 10.05 Å (as in most stable optimized geometry) and (B) 11.00 Å. Hydrogen atoms have been omitted for clarity.

suggest long-range attractive dispersion forces between the heme units which contribute to the through space heme-to-heme interaction in diheme. Moreover, AIM analysis of uB3LYP/BS1 optimized geometry of $[\mathbf{1}\cdot(Im)_4]^{2+}$ at fixed Fe··· Fe separation of 11.0 Å was also done (Figure 16, trace B) which displays insignificant numbers of critical points between the two heme centers since they are substantially far from each other. Thus, such long-range dispersion forces between two heme centers in diheme are responsible for functional superiority of dihemes over monoheme analogs.

CONCLUSION

A large series of six-coordinated diiron(III) and diiron(II) ethane-bridged porphyrin dimers, as synthetic analogs of diheme cytochromes *c*, have been isolated and structurally characterized. Gradual addition of axial ligand L (L = imidazoles and pyridines) into pentacoordinated $\mathbf{1}\cdot X_2$ (X = ClO_4,Cl and TNP) produces hexacoordinated diiron(III) porphyrin dimer $[\mathbf{1}\cdot(L)_4](X)_2$ which, in presence of excess of L, quantitatively auto reduces into air-stable diiron(II) porphyrin dimer $\mathbf{2}\cdot(L)_4$. Such autoreduction produces large changes in the UV−vis spectra of the dihemes. Also, the spectral changes are similar as observed in the native diheme cytochromes *c* (DHC2) in their oxidized and reduced states.

The X-ray structures of seven such dihemes along with a monoheme analog have been determined successfully which demonstrate low-spin state of iron. Structurally these diheme analogs closely resemble with the naturally occurring DHC2. The solid-state structures are also intact in solution which is further supported by ^1H NMR and EPR studies. X-band EPR spectra measured for $[\mathbf{1}\cdot(L)_4](ClO_4)_2$ show rhombic type spectral features both in solid and solution phases, similar to that of the DHC2 isolated from *G. sulfurreducens*. Electrochemical data reveal good linear relationships for the first oxidation as well as Fe^{III}/Fe^{II} redox couples with the pK_a of axial ligand L. The Fe^{III}/Fe^{II} redox couple in the diheme complex is shifted toward more positive than their monomeric analog which demonstrates easier reduction of diheme as compared to their monomeric analog.

In order to substantiate the effect of interheme interaction in dihemes, a series of computational studies were performed. DFT studies reproduce the positive shifts of the Fe^{III}/Fe^{II} redox couple on moving from monohemes to dihemes. It has also been observed that the redox potential could easily be tuned by changing the relative orientation of the two heme units in dihemes and also through the variation of iron-to-iron non bonding distance which eventually affects the interheme interactions. This could be well correlated with the variable redox properties shown by several DHC2 in nature. The atoms in molecules (AIM) analysis suggests long-range attractive dispersion forces between the heme units. The present investigation explores the effect of interheme interactions in diiron(III) and diiron(II) porphyrin dimers. The large variation in the structure and properties of dihemes, as compared to the analogous monohemes, accounts for the role played by interheme interactions in diheme.

EXPERIMENTAL SECTION

Materials. *μ*-Oxo-*syn*-1,2-bis[5-(2,3,7,8,12,13,17,18-octaethylporphyrinato)iron(III)]ethane (**1**), 1,2-bis[(chloro){5-(2,3,7,8,12,13,17,18-octaethylporphyrinato)}iron(III)]ethane ($\mathbf{1}\cdot Cl_2$), 1,2-bis[(perchlorato){5-(2,3,7,8,12,13,17,18-octaethylporphyrinato)}iron(III)]ethane ($\mathbf{1}\cdot(ClO_4)_2$), and 1,2-bis-[(2,4,6-trinitrophenolato){5-(2,3,7,8,12,13,17,18-octaethylporphyrinato)}iron(III)]ethane ($\mathbf{1}\cdot(TNP)_2$) have been synthesized following the reported procedures.[8c,d,10a] Reagents and solvents were purchased from commercial sources and purified by standard procedures before use.

Preparation of [1·(1-MeIm)$_4$](ClO$_4$)$_2$. Complex $[\mathbf{1}\cdot(L)_4](ClO_4)_2$, where X = Cl, ClO_4, and TNP, was prepared using a general procedure; details are given for $[\mathbf{1}\cdot(1\text{-MeIm})_4](ClO_4)_2$ as a representative case.

$\mathbf{1}\cdot ClO_4$ (60 mg, 0.043 mmol) was dissolved in 20 mL of distilled dichloromethane, and 1-methylimidazole (70 mg, 0.260 mmol) was added to it and stirred for nearly 5 min to form a deep red solution. The solution was then quickly filtered to remove any solid residue and was evaporated to dryness. The solid thus obtained was then dissolved in a minimum volume of benzene and carefully layered with *n*-hexane. After 5−6 days in air at room temperature, a dark crystalline solid was formed that was then collected by filtration, was washed well with mother liquor, and dried under vacuum. Yield: 58 mg (78%). UV−vis (dichloromethane) [λ_{max}, nm (ε, M^{-1} cm^{-1})]: 415 nm (1.7×10^5), 545 (7.2×10^3). ^1H NMR ($CDCl_3$, 295 K): *meso-H*, −1.3, −8.6; CH_3, −0.3, −0.2, 0.6, 2.1; CH_2, 2.2, 3.5, 5.4, 6.1, 6.9, 7.2(2), 8.1; CH_2(b),

DOI: 10.1021/acs.inorgchem.8b01368
Inorg. Chem. 2018, 57, 11498−11510

16.8; $-H_a$, −7.0; $-H_b$, 15.9; $-NMe_c$, 13.5 ppm. EPR data: in dichloromethane (77 K), g_1 = 1.53, g_2 = 2.25, g_3 = 2.86. Mössbauer: (α-Fe, 295 K): δ = 0.18 mm s^{-1}, ΔE_Q = 2.19 mm s^{-1}.

*Preparation of [**1**·(Im)$_4$](ClO$_4$)$_2$.* Yield: 52 mg (72%). UV−vis (dichloromethane) [λ_{max}, nm (ε, M^{-1} cm^{-1})]: 418 (1.6×10^5), 549 (9.9×10^3). ^{1}H NMR ($CDCl_3$, 295 K): *meso-H*, −1.9, −8.5; CH_3, −0.9, −0.7, −0.1, 1.7; CH_2, 2.9(2), 4.6, 5.3, 6.0, 6.2, 6.4 and 6.9; CH(b), 15.9; $-H_a$, −9.9; $-H_b$, 13.7; $-H_c$, 10.7 ppm. EPR data: in dichloromethane (77 K), g_1 = 1.75, g_2 = 2.27, g_3 = 2.70. Mössbauer: (α-Fe, 295 K): δ = 0.19 mm s^{-1}, ΔE_Q = 2.12 mm s^{-1}.

*Preparation of [**1**·(4-MeIm)$_4$](ClO$_4$)$_2$.* Yield: 51 mg (70%). UV−vis (dichloromethane) [λ_{max}, nm (ε, M^{-1} cm^{-1})]: 408 (1.6×10^5), 539 (1.1×10^4). ^{1}H NMR ($CDCl_3$, 295 K): *meso-H*, −1.1, −10.6; CH_3, −0.7, −0.6, 0.1, 1.7; CH_2, 2.1, 2.2, 2.6, 4.4, 5.1, 5.7, 5.8, 5.9; CH_2(b), 15.6; $-H_a$, −11.9; $-H_b$, 12.2; $-H_c$, 10.9; $-4Me_b$, 12.9 ppm. EPR data: in dichloromethane (77 K), g_1 = 1.75, g_2 = 2.26, g_3 = 2.67.

*Preparation of [**1**·(2-MeIm)$_4$]Cl$_2$.* Yield: 44 mg (65%). UV−vis (dichloromethane) [λ_{max}, nm (ε, M^{-1} cm^{-1})]: 411 (1.5×10^5), 556 (8.6×10^3). ^{1}H NMR ($CDCl_3$, 295 K): *meso-H*, −0.7, −4.6; CH_3, 0.0, 0.2, 0.8, 1.7; CH_2, 4.6, 5.4, 5.9, 6.4, 6.6, 6.8, 6.9, 7.8; CH_2(b), 16.1; $-H_b$, 13.8; $-H_c$, 11.6 ppm. Mössbauer: (α-Fe, 295 K): δ = 0.16 mm s^{-1}, ΔE_Q = 1.55 mm s^{-1}.

*Preparation of [**1**·(Py)$_4$](TNP)$_2$.* Yield: 53 mg (80%); UV−vis (dichloromethane) [λ_{max}, nm (ε, M^{-1} cm^{-1})]: 398 nm (1.7×10^5), 519 (1.4×10^4), 552 (1.3×10^4). ^{1}H NMR ($CDCl_3$, 295 K): *meso-H*, 0.8, −5.9; CH_3, 1.2, 1.7, 2.1, 2.8; CH_2, 6.1, 6.5, 6.7, 8.5, 9.7, 10.1, 10.4, 11.3; CH_2(b), 18.3 ppm. Mössbauer: (α-Fe, 295 K): δ = 0.15 mm s^{-1}, ΔE_Q = 2.29 mm s^{-1}.

*Preparation of [**1**·(4-CNPy)$_4$](ClO$_4$)$_2$.* Yield: 36 mg (65%); UV−vis (dichloromethane) [λ_{max}, nm (ε, M^{-1} cm^{-1})]: 393 nm (1.6×10^5), 517 (1.4×10^4), 552 (1.1×10^4).

*Preparation of **2**·(Py)$_4$.* Complex **2**·(L)$_4$ was prepared using a general procedure; details are given for **2**·(Py)$_4$ as a representative case.

1·ClO_4 (50 mg, 0.036 mmol) was dissolved in 20 mL of distilled chloroform, pyridine (22 mg, 0.288 mmol) was added to it, and the mixture was stirred for nearly 10 min to form a deep red solution. The solution was then quickly filtered and was concentrated under reduced pressure. The solution was, then, carefully layered with acetonitrile. After 7−8 days in air at room temperature, dark crystalline solids were obtained which were collected by filtration, well washed with mother liquor, and dried under vacuum. Yield: 29 mg (54%); UV−vis (dichloromethane) [λ_{max}, nm (ε, M^{-1} cm^{-1})]: 413 nm (2.0×10^5), 523 (1.4×10^4), 565 (1.3×10^4).

*Preparation of **2**·(3-CNPy)$_4$.* Yield: 30 mg (51%); UV−vis (dichloromethane) [λ_{max}, nm (ε, M^{-1} cm^{-1})]: 396 nm (1.9×10^5), 521 (1.4×10^4), 556 (1.2×10^4).

*Preparation of **2**·(4-CNPy)$_4$.* Yield: 32 mg (55%); UV−vis (dichloromethane) [λ_{max}, nm (ε, M^{-1} cm^{-1})]: 395 nm (1.8×10^5), 519 (1.5×10^4), 548 (1.3×10^4).

Instrumentation. UV−vis spectra were recorded on a PerkinElmer UV/vis spectrometer. Electron paramagnetic resonance (EPR) spectra were obtained on a Bruker EMX EPR spectrometer. ^{1}H NMR spectra were recorded on a JEOL 500 MHz instrument. The spectra for paramagnetic molecules were recorded over a 100-kHz bandwidth with 64 K data points and a 5 ms 90° pulse. For a typical spectrum between 2000 and 3000 transients were accumulated with a 50-s delay time. The residual ^{1}H resonances of the solvents were used as a secondary reference. ^{57}Fe Mössbauer spectra were recorded using a Wissel 1200 spectrometer and a proportional counter. ^{57}Co(Rh) in a constant acceleration mode was used as the radioactive source. Isomer shifts (δ) are given related to α-iron foil at room temperature. Cyclic voltammetric studies were performed on a BAS Epsilon electrochemical workstation in dichloromethane with 0.1 M tetra(*n*-butyl)ammonium hexafluorophosphate (TBAH) as supporting electrolyte and the reference electrode was Ag/AgCl and the auxiliary electrode was a Pt wire. The concentration of the compounds was in the order of 10^{-3} M. The ferrocene/ferrocenium couple occurs at $E_{1/2}$ = +0.45 (65) V versus Ag/AgCl under the same experimental conditions.

X-ray Structure Solution and Refinement. Single-crystal X-ray data were collected at 100 K on a Bruker SMART APEX CCD diffractometer equipped with CRYO Industries low-temperature apparatus and intensity data were collected using graphite-monochromated Mo Kα radiation (λ= 0.71073 Å). The data integration and reduction were processed with SAINT software.[25] An absorption correction was applied.[26] The structure was solved by the direct method using SHELXS-97 and was refined on F^2 by full-matrix least-squares technique using the SHELXL-2014 program package.[27] Non-hydrogen atoms were refined anisotropically. The hydrogen atoms were included in calculated positions. In the refinement, hydrogens were treated as riding atoms using SHELXL default parameters. CCDC 1824035−1824041 and 1837539 contain the supplementary crystallographic data for this paper. These data are provided free of charge by the Cambridge Crystallographic Data Centre.

Computational Details. All DFT optimizations have been carried out by employing a B3LYP hybrid functional using the Gaussian 09, revision B.01, package software package.[21] The method used was Becke's three parameter hybrid exchange functional, the nonlocal correlation provided by the Lee, Yang, and Parr expression, and Vosko, Wilk, and Nuair 1980 correlation functional (III) for local correction.[22] The basis set was LANL2DZ for iron atom and 6-31G** for carbon, nitrogen, oxygen, chlorine and hydrogen atoms, combination labeled as BS1. The coordinates are taken directly from the single crystal X-ray data and subsequently unconstrained geometry optimization of the molecules are done keeping the spin-state (low-spin) constant both for iron(III) and iron(II) porphyrin dimers. For 1D potential energy surface (PES) scan and for molecular orbital calculation, the coordinates are taken from the optimized geometry. Each one of the axial ligand from both the heme units was rotated in simultaneous steps of 10° keeping the corresponding other two axial ligands intact in their position. Solvent corrections were included in all the calculations using chloroform as solvent. Frequency calculations were also carried out on all optimized structures to ensure that there are zero or very few imaginary frequencies. Energies were taken from the Gaussian frequencies, and contain zero-point corrections at 298.15 K and 1 atm. The optimized geometry diagrams were made employing the Chemcraft software.[28]

Unless otherwise specified, the counteranions were removed for the full geometry optimization of [**1**·(L)$_4$]$^{2+}$ (where L is substituted imidazoles and pyridines) giving an overall +2 charge to the molecule with a overall spin multiplicity of triplet. For geometry optimization of **2**·(L)$_4$, the charge and spin multiplicity given was 0 and 1, respectively. To estimate the reduction potential for Fe^{III}/Fe^{II} associated with $2Fe^{3+} + 2e^- \rightarrow 2Fe^{2+}$ occurring during diiron(III) porphyrin dimer reduction, the diiron(III) as well as corresponding diiron(II) i.e. $2e^-$ reduced complex were geometrically optimized. The free energy change (ΔA^0) associated with the $2e^-$ reduction was calculated using the following equation: $E^0 = -\Delta A^0/nF$, with F is the Faraday constant, and n is the number of electrons involved in the redox process Fe^{III}/Fe^{II} which is 2 for dihemes and 1 for monohemes. The calculations provide absolute E^0 values, which were subsequently reported as relative to SHE, by subtracting the IUPAC recommended 4.420 V value for the hydrogen semireaction.[29] Similarly, the redox potentials for Fe^{III}/Fe^{II} for monoheme complexes were calculated by geometry optimization of iron(III) and its $1e^-$ reduced iron(II) porphyrin complex.

For a better understanding of such heme−heme interaction linked reduction potential, a series of DFT calculations were done which involved variable iron−iron separation. The geometries of several conformers of [**1**·(Im)$_4$]$^{2+}$ were optimized with the iron to iron non bonding distance varying from 9.5 to11.0 Å in small steps. At 11.0 Å, both the diiron(III) as well as its diiron(II) analog, i.e., **2**·(Im)$_4$ was optimized and the potential for Fe^{III}/Fe^{II} redox couple was calculated in a similar fashion described above. Similarly, the relative orientations of both the porphyrins rings were changed by varying the dihedral angle (θ°) between the heme units in [**1**·(Im)$_4$]$^{2+}$ from 0° (most stabilized geometry obtained through optimization) to 50° in either

DOI: 10.1021/acs.inorgchem.8b01368
Inorg. Chem. 2018, 57, 11498−11510

directions. At 50°, the potential for Fe^{III}/Fe^{II} redox couple for $[\mathbf{1}\cdot(Im)_4]^{2+}$ was similarly calculated.

■ ASSOCIATED CONTENT

Supporting Information

The Supporting Information is available free of charge on the ACS Publications website at DOI: 10.1021/acs.inorgchem.8b01368.

X-ray structures, packing diagrams, and out-of-plane displacement plots of $[\mathbf{1}\cdot(1\text{-MeIm})_4](ClO_4)_2$, $[\mathbf{1}\cdot(2\text{-MeIm})_4]Cl_2$, $[\mathbf{1}\cdot(4\text{-CNPy})_4](ClO_4)_2$, and $[\mathbf{1}\cdot(Py)_4](TNP)_2$ (Figures S1−S8); X-ray structures, packing diagrams, and out-of-plane displacement plots of $\mathbf{2}\cdot(Py)_4$, $\mathbf{2}\cdot(3\text{-CNPy})_4$ and $\mathbf{2}\cdot(4\text{-CNPy})_4$ (Figures S9−S14); Mulliken spin density plots for $[\mathbf{1}\cdot(Py)_4]^{2+}$ and $[\mathbf{1}\cdot(2\text{-MeIm})_4]Cl_2$ (Figures S15 and S16); UV−visible spectral change upon two-electron reduction of $[\mathbf{1}\cdot(4\text{-MeIm})_4](ClO_4)_2$ (Figure S17); uB3LYP/BS1 optimized structures of $[\mathbf{1}\cdot(2\text{-MeIm})_4]Cl_2$, $\mathbf{2}\cdot(2\text{-MeIm})_4$, $[\mathbf{1}\cdot(Py)_4]^{2+}$, and $\mathbf{2}\cdot(Py)_4$ (Figure S18−S22), Cartesians of all optimized geometries; selected bond distances (Å) and bond angles (deg) for the complexes along with crystal data and data collection parameters (Tables S1−S5); relative energies of axial ligand orientations (Table S6); and selected structural and geometrical parameters of optimized species with relative energies (Tables S7−S12) (DOCX)

Accession Codes

CCDC 1824035−1824041 and 1837539 contain the supplementary crystallographic data for this paper. These data can be obtained free of charge via www.ccdc.cam.ac.uk/data_request/cif, or by emailing data_request@ccdc.cam.ac.uk, or by contacting The Cambridge Crystallographic Data Centre, 12 Union Road, Cambridge CB2 1EZ, UK; fax: +44 1223 336033.

■ AUTHOR INFORMATION

Corresponding Authors

*(S.P.R.) E-mail: sprath@iitk.ac.in. Telephone: (+91)-512-259-7251. Fax: (+91)-512-259-7436.

*(D.K.) E-mail: dkclcre@yahoo.com.

ORCID

Sankar Prasad Rath: 0000-0002-4129-5074

Notes

The authors declare no competing financial interest.

■ ACKNOWLEDGMENTS

The authors thank Science and Engineering Research Board (SERB), New Delhi, and Council of Scientific and Industrial Research (CSIR) New Delhi for financial support. F.S.T.K. thanks University Grants Commission (UGC), India, and S.B. thanks Innovation in Science Pursuit for Inspired Research (INSPIRE) of Department of Science and Technology, New Delhi for their fellowships.

■ DEDICATION

Dedicated to Professor Akhil R. Chakravarty on the occassion of his 65th birthday.

■ REFERENCES

(1) (a) Liu, J.; Chakraborty, S.; Hosseinzadeh, P.; Yu, Y.; Tian, S.; Petrik, I.; Bhagi, A.; Lu, Y. Metalloproteins containing cytochrome, iron−sulfur, or copper redox centers. *Chem. Rev.* **2014**, *114*, 4366−4469. (b) Paquete, C. M.; Louro, R. O. Unveiling the details of electron transfer in multicenter redox proteins. *Acc. Chem. Res.* **2014**, *47*, 56−65. (c) Bewley, K. D.; Ellis, K. E.; Firer-Sherwood, M. A.; Elliott, S. J. Multi-heme proteins: Nature's electronic multi-purpose tool. *Biochim. Biophys. Acta, Bioenerg.* **2013**, *1827*, 938−948. (d) Mayfield, J. A.; Dehner, C. A.; DuBois, J. L. Recent advances in bacterial heme protein biochemistry. *Curr. Opin. Chem. Biol.* **2011**, *15*, 260−266. (e) Sharma, S.; Cavallaro, G.; Rosato, A. A systematic investigation of multiheme *c*-type cytochromes in prokaryotes. *JBIC, J. Biol. Inorg. Chem.* **2010**, *15*, 559−571. (f) Akutsu, H.; Takayama, Y. Functional roles of the heme architecture and its environment in tetraheme cytochrome *c*. *Acc. Chem. Res.* **2007**, *40*, 171−178. (g) Shi, L.; Squier, T. C.; Zachara, J. M.; Fredrickson, J. K. Respiration of metal (hydr)oxides by *Shewanella* and *Geobacter*: A key role for multihaem *c*-type cytochromes. *Mol. Microbiol.* **2007**, *65*, 12−20. (h) Stevens, J. M.; Daltrop, O.; Allen, J. W. A.; Ferguson, S. J. *C*-type cytochrome formation: chemical and biological enigmas. *Acc. Chem. Res.* **2004**, *37*, 999−1007.

(2) Pereira, I. A.; Xavier, A. V. in *Encyclopedia of Inorganic Chemistry*; King, R. B., Ed.; John Wiley & Sons: New York, 2005, vol *5*, pp 3360−3376.

(3) (a) Watanabe, H. C.; Yamashita, Y.; Ishikita, H. Electron transfer pathways in a multiheme cytochrome MtrF. *Proc. Natl. Acad. Sci. U. S. A.* **2017**, *114*, 2916−2921. (b) Santos, T. C.; Silva, M. A.; Morgado, L.; Dantas, J. M.; Salgueiro, C. A. Diving into the redox properties of *Geobacter sulfurreducens* cytochromes: a model for extracellular electron transfer. *Dalton Trans* **2015**, *44*, 9335−9344. (c) Zhang, Y.; Liu, C.; Balaeff, A.; Skourtis, S. S.; Beratan, D. N. Biological charge transfer via flickering resonance. *Proc. Natl. Acad. Sci. U. S. A.* **2014**, *111*, 10049−10054. (d) Burggraf, F.; Koslowski, T. Charge transfer through a cytochrome multiheme chain: Theory and simulation. *Biochim. Biophys. Acta, Bioenerg.* **2014**, *1837*, 186−192. (e) Soares, C. M.; Baptista, A. M. Simulation of multihaem cytochromes. *FEBS Lett.* **2012**, *586*, 510−518.

(4) (a) Breuer, M.; Rosso, K. M.; Blumberger, J. Electron flow in multiheme bacterial cytochromes is a balancing act between heme electronic interaction and redox potentials. *Proc. Natl. Acad. Sci. U. S. A.* **2014**, *111*, 611−616. (b) Fonseca, B. M.; Paquete, C. M.; Salgueiro, C. A.; Louro, R. O. The role of intramolecular interactions in the functional control of multiheme cytochromes *c*. *FEBS Lett.* **2012**, *586*, 504−509. (c) Paquete, C. M.; Louro, R. O. Molecular details of multielectron transfer: the case of multiheme cytochromes from metal respiring organisms. *Dalton Trans* **2010**, *39*, 4259−4266. (d) Zatsman, A. I.; Zhang, H.; Gunderson, W. A.; Cramer, W. A.; Hendrich, M. P. Heme-heme interactions in the cytochrome b_6f complex: EPR spectroscopy and correlation with structure. *J. Am. Chem. Soc.* **2006**, *128*, 14246−14247. (e) Mowat, C. G.; Chapman, S. K. Multi-heme cytochromes—new structures, new chemistry. *Dalton Trans* **2005**, *34*, 3381−3389.

(5) (a) Pokkuluri, P. R.; Londer, Y. Y.; Duke, N. E. C.; Long, W. C.; Schiffer, M. Family of cytochrome c_7-type proteins from *Geobacter sulfurreducens*: Structure of one cytochrome c_7 at 1.45 Å Resolution. *Biochemistry* **2004**, *43*, 849−859. (b) Leys, D.; Meyer, T. E.; Tsapin, A. S.; Nealson, K. H.; Cusanovich, M. A.; Van Beeumen, J. J. Crystal structures at atomic resolution reveal the novel concept of "electron-harvesting" as a role for the small tetraheme cytochrome *c*. *J. Biol. Chem.* **2002**, *277*, 35703−35711. (c) Matias, P. M.; Coelho, A. V.; Valente, F. M. A.; Plácido, D.; LeGall, J.; Xavier, A. V.; Pereira, I. A. C.; Carrondo, M. A. Sulfate respiration in *Desulfovibrio vulgaris* Hildenborough. *J. Biol. Chem.* **2002**, *277*, 47907−47916. (d) Einsle, O.; Stach, P.; Messerschmidt, A.; Simon, J.; Kröger, A.; Huber, R.; Kroneck, P. M. H. Cytochrome *c* nitrite reductase from *Wolinella succinogenes*. *J. Biol. Chem.* **2000**, *275*, 39608−39616. (e) Matias, P. M.; Coelho, R.; Pereira, I.; Coelho, A. V.; Thompson, A. W.; Sieker, L. C.; Gall, J. L.; Carrondo, M. A. The primary and three-dimensional structures of a nine-haem cytochrome *c* from *Desulfovibrio desulfuricans* ATCC 27774 reveal a new member of the Hmc family. *Structure* **1999**, *7*, 119−130.

DOI: 10.1021/acs.inorgchem.8b01368
Inorg. Chem. 2018, 57, 11498−11510

(6) (a) Heitmann, D.; Einsle, O. Structural and biochemical characterization of DHC2, a novel diheme cytochrome *c* from *Geobacter sulfurreducens*. *Biochemistry* **2005**, *44*, 12411−12419. (b) Brige, A.; Leys, D.; Meyer, T. E.; Cusanovich, M. A.; Van Beeumen, J. J. The 1.25 Å resolution structure of the diheme NapB subunit of soluble nitrate reductase reveals a novel cytochrome *c* fold with a stacked heme arrangement. *Biochemistry* **2002**, *41*, 4827−4836. (c) Abreu, I. A.; Lourenço, A. I.; Xavier, A. V.; LeGall, J.; Coelho, A. V.; Matias, P. M.; Pinto, D. M.; Arménia Carrondo, M.; Teixeira, M.; Saraiva, L. M. A novel iron centre in the split-Soret cytochrome *c* from *Desulfovibrio desulfuricans* ATCC 27774. *JBIC, J. Biol. Inorg. Chem.* **2003**, *8*, 360−370. (d) De March, M.; Di Rocco, G.; Hickey, N.; Geremia, S. High-resolution crystal structure of the recombinant diheme cytochrome *c* from *Shewanella baltica* (OS155). *J. Biomol. Struct. Dyn.* **2015**, *33*, 395−403.

(7) (a) Lai, D.; Khan, F. S. T.; Rath, S. P. Multiheme proteins: Effect of heme-heme interactions. *Dalton Trans* **2018**, DOI: 10.1039/C8DT00518D. (b) Sil, D.; Rath, S. P. An ethane-bridged porphyrin dimer as model of di-heme proteins: inorganic and bioinorganic perspectives and consequences of heme-heme interactions. *Dalton Trans* **2015**, *44*, 16195−16211. (c) Singh, A. K.; Khan, F. S. T.; Rath, S. P. Silver(III)···Silver(III) interactions that stabilize the *syn* form in a porphyrin dimer upon oxidation. *Angew. Chem., Int. Ed.* **2017**, *56*, 8849−8854. (d) Dey, S.; Rath, S. P. *Syn-anti* conformational switching in an ethane-bridged Co(II)bisporphyrin induced by external stimuli: effects of inter-macrocyclic interactions, axial ligation and chemical and electrochemical oxidations. *Dalton Trans* **2014**, *43*, 2301−2314. (e) Brahma, S.; Asif Ikbal, S.; Rath, S. P. *Syn-anti* conformational switching: Synthesis and X-ray structures of *tweezer* and *anti* form in a zinc porphyrin dimer induced by axial ligands. *Inorg. Chim. Acta* **2011**, *372*, 62−70.

(8) (a) Khan, F. S. T.; Pandey, A. K.; Rath, S. P. Modulation of iron spin in ethane-bridged diiron(III) porphyrin dimer: Anion dependent spin state switching. *J. Chem. Sci.* **2018**, DOI: 10.1007/s12039-018-1488-2. (b) Sil, D.; Khan, F. S. T.; Rath, S. P. Axial thiophenolate coordination on diiron(III)bisporphyrin: influence of heme-heme interactions on structure, function and electrochemical properties of the individual heme center. *Inorg. Chem.* **2014**, *53*, 11925−11936. (c) Bhowmik, S.; Dey, S.; Sahoo, D.; Rath, S. P. Unusual stabilization of an intermediate spin of iron upon axial phenoxide coordination on a diiron(III)bisporphyrin: Effect of heme-heme interactions. *Chem. - Eur. J.* **2013**, *19*, 13732−13744. (d) Bhowmik, S.; Ghosh, S. K.; Rath, S. P. Control of spins by ring deformation in a diiron(III)-bisporphyrin: reversal of ClO_4^- and $CF_3SO_3^-$ ligand field strength on the magnetochemical series. *Chem. Commun.* **2011**, *47*, 4790−4792. (e) Bhowmik, S.; Sil, D.; Patra, R.; Rath, S. P. Axial phenoxide coordination on di-iron(III)bisporphyrin: Insights from experimental and DFT studies. *J. Chem. Sci.* **2011**, *123*, 827−837.

(9) (a) Pandit, Y. A.; Sanfui, S.; Rath, S. P. Intermacrocyclic interaction triggers facile one-pot synthesis of a chlorin-porphyrin heterodimer. *Chem. - Eur. J.* **2017**, *23*, 13415−13422. (b) Guchhait, T.; Sarkar, S.; Pandit, Y. A.; Rath, S. P. Probing bis-Fe^{IV} MauG: Isolation of highly reactive radical intermediates. *Chem. - Eur. J.* **2017**, *23*, 10270−10275. (c) Dey, S.; Sil, D.; Rath, S. P. A highly oxidized cobalt porphyrin dimer: Spin coupling and stabilization of the four-electron oxidation product. *Angew. Chem., Int. Ed.* **2016**, *55*, 996−1000. (d) Sil, D.; Dey, S.; Kumar, A.; Bhowmik, S.; Rath, S. P. Oxidation triggers extensive conjugation and unusual stabilization of two di-heme dication diradical intermediates: Role of bridging group for electronic communication. *Chem. Sci.* **2016**, *7*, 1212−1223. (e) Dey, S.; Sil, D.; Pandit, Y. A.; Rath, S. P. Effect of Two Interacting Rings in Metalloporphyrin Dimers upon Stepwise Oxidations. *Inorg. Chem.* **2016**, *55*, 3229−3238. (f) Pandit, Y. A.; Shah, S. J.; Rath, S. P. Unusual Stabilization of Dication Diradical Intermediate of. *Z. Anorg. Allg. Chem.* **2018**, *644*, 856−863.

(10) (a) Ghosh, S. K.; Patra, R.; Rath, S. P. Synthesis and characterization of *anti*-bisFe(III) porphyrins, *syn*-bisFe(III)-*μ*-oxo porphyrin and *syn*-bisFe(III)-*μ*-oxo porphyrin cation radical. *Inorg. Chem.* **2010**, *49*, 3449−3460. (b) Ghosh, S. K.; Patra, R.; Rath, S. P. Remarkably bent, ethane-linked, diiron(III) *μ*-oxobisporphyrin: Synthesis, structure, conformational switching, and photocatalytic oxidation. *Inorg. Chem.* **2008**, *47*, 10196−10198. (c) Ghosh, S. K.; Patra, R.; Rath, S. P. Synthesis, Structure and photocatalytic activity of a remarkably bent, cofacial ethene-linked diiron(III) *μ*-oxobisporphyrin. *Inorg. Chim. Acta* **2010**, *363*, 2791−2799.

(11) (a) Guchhait, T.; Sasmal, S.; Khan, F. S. T.; Rath, S. P. Oxo- and hydroxo-bridged diiron(III) porphyrin dimers: inorganic and bioinorganic perspectives and effects of intermacrocyclic interactions. *Coord. Chem. Rev.* **2017**, *337*, 112−144. (b) Khan, F. S. T.; Guchhait, T.; Sasmal, S.; Rath, S. P. Hydroxo-bridged diiron(III) and dimanganese(III) bisporphyrins: modulation of metal spins by counter anions. *Dalton Trans* **2017**, *46*, 1012−1037.

(12) (a) Khan, F. S. T.; Pandey, A. K.; Rath, S. P. Remarkable anion dependent spin state switching in diiron(III)-*μ*-hydroxo bisporphyrins: What role do counter ions play? *Chem. - Eur. J.* **2016**, *22*, 16124−16137. (b) Sil, D.; Khan, F. S. T.; Rath, S. P. Effect of inter-porphyrin distance on spin-state in diiron(III) *μ*-hydroxo bisporphyrins. *Chem. - Eur. J.* **2016**, *22*, 14585−14597. (c) Sil, D.; Kumar, A.; Rath, S. P. Diiron(III)-*μ*-fluoro bisporphyrins: Effect of bridging ligand on the metal spin state. *Chem. - Eur. J.* **2016**, *22*, 11214−11223. (d) Sil, D.; Bhowmik, S.; Khan, F. S. T.; Rath, S. P. Experimental and theoretical investigation of a series of novel dimanganese(III) *μ*-hydroxo bisporphyrins: magneto−structural correlation and effect of metal spin on porphyrin core deformation. *Inorg. Chem.* **2016**, *55*, 3239−3251. (e) Sainna, M. A.; Sil, D.; Sahoo, D.; Martin, B.; Rath, S. P.; Comba, P.; de Visser, S. P. Spin state ordering in hydroxo bridged diiron(III)bisporphyrin complexes. *Inorg. Chem.* **2015**, *54*, 1919−1930. (f) Ghosh, S. K.; Bhowmik, S.; Sil, D.; Rath, S. P. Effect of heme-heme interactions and modulation of metal spins by counter anions in a series of diiron(III)-*μ*-hydroxo bisporphyrins: Unusual stabilization of two different spins in a single molecular framework. *Chem. - Eur. J.* **2013**, *19*, 17846−17859. (g) Bhowmik, S.; Ghosh, S. K.; Layek, S.; Verma, H. C.; Rath, S. P. Protonation of an oxo-Bridged diiron unit makes two iron centers different: A new class of Diiron(III)-*μ*-hydroxo bisporphyrin and control of spins by counter anions. *Chem. - Eur. J.* **2012**, *18*, 13025−13037. (h) Ghosh, S. K.; Rath, S. P. A remarkably bent diiron(III)-*μ*-hydroxo bisporphyrin: Unusual stabilization of two spin states of iron in a single molecular framework. *J. Am. Chem. Soc.* **2010**, *132*, 17983−17985.

(13) (a) Patra, R.; Sahoo, D.; Dey, S.; Sil, D.; Rath, S. P. Switching orientation of two axial imidazole ligands between parallel and perpendicular in low-spin Fe(III) and Fe(II) nonplanar porphyrinates. *Inorg. Chem.* **2012**, *51*, 11294−11305. (b) Patra, R.; Bhowmik, S.; Ghosh, S. K.; Rath, S. P. Effects of axial pyridine coordination in a saddle-distorted porphyrin macrocycle: stabilization of hexa-coordinated high-spin Fe(III) and air-stable low-spin iron(II) porphyrinates. *Dalton Trans* **2010**, *39*, 5795−5806. (c) Patra, R.; Chaudhary, A.; Ghosh, S. K.; Rath, S. P. Axial ligand orientations in a distorted porphyrin macrocycle: Synthesis, structure and properties of low-spin bis (imidazole) Fe(III) and Fe(II) porphyrinates. *Inorg. Chem.* **2010**, *49*, 2057−2067.

(14) (a) Walker, F. A. Models of the bis-histidine-ligated electron-transferring cytochromes. Comparative geometric and electronic structure of low-spin ferro- and ferrihemes. *Chem. Rev.* **2004**, *104*, 589−615. (b) Teschner, T.; Yatsunyk, L.; Schünemann, V.; Paulsen, H.; Winkler, H.; Hu, C.; Scheidt, W. R.; Walker, F. A.; Trautwein, A. X. Models of the membrane-bound cytochromes: Mössbauer spectra of crystalline low-spin ferriheme complexes having axial ligand plane dihedral angles ranging from 0° to 90°. *J. Am. Chem. Soc.* **2006**, *128*, 1379−1389. (c) Yatsunyk, L. A.; Dawson, A.; Carducci, M. D.; Nichol, G. S.; Walker, F. A. Models of the cytochromes: Crystal structures and EPR spectral characterization of low-spin bis-imidazole complexes of (OETPP)Fe^{III} having intermediate ligand plane dihedral angles. *Inorg. Chem.* **2006**, *45*, 5417−5428. (d) Yatsunyk, L. A.; Carducci, M. D.; Walker, F. A. Low-Spin ferriheme models of the cytochromes: Correlation of molecular structure with EPR spectral type. *J. Am. Chem. Soc.* **2003**, *125*, 15986−16005.

DOI: 10.1021/acs.inorgchem.8b01368
Inorg. Chem. 2018, 57, 11498−11510

(15) (a) Li, J.; Nair, S. M.; Noll, B. C.; Schulz, C. E.; Scheidt, W. R. Relative axial ligand orientation in bis(imidazole)iron(ii) porphyrinates: Are "Picket Fence" derivatives different? *Inorg. Chem.* **2008**, *47*, 3841−3850. (b) Hu, C.; Noll, B. C.; Schulz, C. E.; Scheidt, W. R. Ligand Orientation Control in Low-Spin Six-Coordinate (Porphinato)iron(II) Species. *Inorg. Chem.* **2005**, *44*, 4346−4358.
(16) (a) Rath, S. P.; Olmstead, M. M.; Balch, A. L. Electron distribution in iron octaethyloxophlorin complexes. Importance of the Fe(III) oxophlorin trianion form in the bis-pyridine and bis-imidazole complexes. *Inorg. Chem.* **2006**, *45*, 6083−6093. (b) Rath, S. P.; Olmstead, M. M.; Balch, A. L. The effects of axial ligands on electron distribution and spin states in iron complexes of octaethyloxophlorin, intermediates in heme degradation. *J. Am. Chem. Soc.* **2004**, *126*, 6379−6386.
(17) (a) Sahoo, D.; Quesne, M. G.; de Visser, S. P.; Rath, S. P. Hydrogen bonding interactions trigger a spin-flip in iron(III)-porphyrin complexes. *Angew. Chem., Int. Ed.* **2015**, *54*, 4796−4800. (b) Sahoo, D.; Rath, S. P. Controlled generation of highly saddled (porphyrinato) iron(III) iodide, tri-iodide and one-electron oxidized complex. *Chem. Commun.* **2015**, *51*, 16790−16790. (c) Sahoo, D.; Guchhait, T.; Rath, S. P. Spin modulation in highly distorted Fe(III) porphyrinates using axial coordination and their π-cation radicals. *Eur. J. Inorg. Chem.* **2016**, *2016*, 3441−3453. (d) Patra, R.; Rath, S. P. Cyanide binding to iron in a highly distorted porphyrin macrocycle: Synthesis and structure of low-spin Fe(II) dicyano porphyrin. *Inorg. Chem. Commun.* **2009**, *12*, 515−519. (e) Patra, R.; Chaudhary, A.; Ghosh, S. K.; Rath, S. P. Modulation of metal displacement in a saddle distorted macrocycle: Synthesis, structure and properties of high spin Fe(III) porphyrins and implications for the hemoproteins. *Inorg. Chem.* **2008**, *47*, 8324−8335.
(18) (a) Weiss, R.; Gold, A.; Terner, J. Cytochromes *c*': Biological models for the S = $^3/_2$,$^5/_2$ spin-state admixture? *Chem. Rev.* **2006**, *106*, 2550−2579. (b) Sakow, D.; Baabe, D.; Böker, B.; Burghaus, O.; Funk, M.; Kleeberg, C.; Menzel, D.; Pietzonka, C.; Bröring, M. Iron 10-Thiacorroles: Bioinspired Iron(III) complexes with an intermediate spin (S = 3/2) ground state. *Chem. - Eur. J.* **2014**, *20*, 2913−2924.
(19) (a) Ikezaki, A.; Ohgo, Y.; Nakamura, M. NMR studies on the electronic structure of one-electron oxidized complexes of iron(III) porphyrinates. *Coord. Chem. Rev.* **2009**, *253*, 2056−2069. (b) Kouno, S.; Ikezaki, A.; Ikeue, T.; Nakamura, M. Spin−spin interactions in iron(III) porphyrin radical cations with ruffled and saddled structure. *J. Inorg. Biochem.* **2011**, *105*, 718−721.
(20) Safo, M. K.; Gupta, G. P.; Watson, C. T.; Simonis, U.; Walker, F. A.; Scheidt, W. R. Models of the Cytochromes *b*. Low-Spin Bis-Ligated (Porphinato)iron(III) Complexes with "Unusual" Molecular Structures and NMR, EPR, and Mössbauer Spectra. *J. Am. Chem. Soc.* **1992**, *114*, 7066−7075.
(21) Frisch, M. J.; Trucks, G. W.; Schlegel, H. B.; Scuseria, G. E.; Robb, M. A.; Cheeseman, J. R.; Scalmani, G.; Barone, V.; Mennucci, B.; Petersson, G. A.; Nakatsuji, H.; Caricato, M.; Li, X.; Hratchian, H. P.; Izmaylov, A. F.; Bloino, J.; Zheng, G.; Sonnenberg, J. L.; Hada, M.; Ehara, M.; Toyota, K.; Fukuda, R.; Hasegawa, J.; Ishida, M.; Nakajima, T.; Honda, Y.; Kitao, O.; Nakai, H.; Vreven, T.; Montgomery, J. A., Jr., Peralta, J. E.; Ogliaro, F.; Bearpark, M.; Heyd, J. J.; Brothers, E.; Kudin, K. N.; Staroverov, V. N.; Kobayashi, R.; Normand, J.; Raghavachari, K.; Rendell, A.; Burant, J. C.; Iyengar, S. S.; Tomasi, J.; Cossi, M.; Rega, N.; Millam, J. M.; Klene, M.; Knox, J. E.; Cross, J. B.; Bakken, V.; Adamo, C.; Jaramillo, J.; Gomperts, R.; Stratmann, R. E.; Yazyev, O.; Austin, A. J.; Cammi, R.; Pomelli, C.; Ochterski, J. W.; Martin, R. L.; Morokuma, K.; Zakrzewski, V. G.; Voth, G. A.; Salvador, P.; Dannenberg, J. J.; Dapprich, S.; Daniels, A. D.; Farkas, Ö.; Foresman, J. B.; Ortiz, J. V.; Cioslowski, J.; Fox, D. J. *Gaussian 09*, revision B.01; Gaussian, Inc.: Wallingford CT, 2010.
(22) (a) Becke, A. D. Density-functional thermochemistry. III. The role of exact exchange. *J. Chem. Phys.* **1993**, *98*, 5648−5652. (b) Lee, C.; Yang, W.; Parr, R. G. Development of the Colle-Salvetti correlation-energy formula into a functional of the electron density. *Phys. Rev. B: Condens. Matter Mater. Phys.* **1988**, *37*, 785−789. (c) Stephens, P. J.; Devlin, F. J.; Chabalowski, C. F.; Frisch, M. *Ab Initio* calculation of vibrational absorption and circular dichroism spectra using density functional force fields. *J. Phys. Chem.* **1994**, *98*, 11623−11627.
(23) Daidone, I.; Paltrinieri, L.; Amadei, A.; Battistuzzi, G.; Sola, M.; Borsari, M.; Bortolotti, C. A. Unambiguous assignment of reduction potentials in diheme cytochromes. *J. Phys. Chem. B* **2014**, *118*, 7554−7560.
(24) (a) López, R.; Rico, J. F.; Ramírez, G.; Ema, I.; Zorrilla, D.; Kumar, A.; Yeole, S. D.; Gadre, S. R. Topology of molecular electron density and electrostatic potential with DAMQT. *Comput. Phys. Commun.* **2017**, *214*, 207−215. (b) Kumar, A.; Yeole, S. D.; Gadre, S. R.; López, R.; Rico, J. F.; Ramírez, G.; Ema, I.; Zorrilla, D. DAMQT 2.1.0: A new version of the damqt package enabled with the topographical analysis of electron density and electrostatic potential in molecules. *J. Comput. Chem.* **2015**, *36*, 2350−2359.
(25) *SAINT+, 6.02 ed.*, Bruker AXS, Madison, WI, 1999.
(26) Sheldrick, G. M. *SADABS 2.0*; University of Göttingen: Göttingen, Germany, 2000.
(27) Sheldrick, G. M. *SHELXL-2014*; Program for Crystal Structure Refinement; University of Göttingen: Göttingen, Germany, 2014.
(28) http://www.chemcraftprog.com.
(29) (a) Fawcett, W. R. The ionic work function and its role in estimating absolute electrode potentials. *Langmuir* **2008**, *24*, 9868−9875. (b) Isse, A.; Gennaro, A. Absolute potential of the standard hydrogen electrode and the problem of interconversion of potentials in different solvents. *J. Phys. Chem. B* **2010**, *114*, 7894−7899.

DOI: 10.1021/acs.inorgchem.8b01368
Inorg. Chem. 2018, 57, 11498−11510

ChemPubSoc Europe

DOI: 10.1002/chem.201806430

CHEMISTRY A European Journal Full Paper

Coordination Chemistry | *Hot Paper* |

Interplay Between Steric and Electronic Effects: A Joint Spectroscopy and Computational Study of Nonheme Iron(IV)-Oxo Complexes

Gourab Mukherjee,[a] Aligulu Alili,[b] Prasenjit Barman,[a] Devesh Kumar,[c] Chivukula V. Sastri,*[a] and Sam P. de Visser*[b]

Abstract: Iron is an essential element in nonheme enzymes that plays a crucial role in many vital oxidative transformations and metabolic reactions in the human body. Many of those reactions are regio- and stereospecific and it is believed that the selectivity is guided by second-coordination sphere effects in the protein. Here, results are shown of a few engineered biomimetic ligand frameworks based on the N4Py (*N*,*N*-bis(2-pyridylmethyl)-*N*-bis(2-pyridyl)methylamine) scaffold and the second-coordination sphere effects are studied. For the first time, selective substitutions in the ligand framework have been shown to tune the catalytic properties of the iron(IV)-oxo complexes by regulating the steric and electronic factors. In particular, a better positioning of the oxidant and substrate in the rate-determining transition state lowers the reaction barriers. Therefore, an optimum balance between steric and electronic factors mediates the ideal positioning of oxidant and substrate in the rate-determining transition state that affects the reactivity of high-valent reaction intermediates.

Introduction

Metalloenzymes play vital functions for human health and are involved in the biosynthesis of essential compounds in the body as well as the biodegradation of xenobiotics and damaging products.[1,2] Due to the large natural abundance of iron, metalloenzymes with either mononuclear or binuclear iron are relatively common in biology. Studies on the details of enzymatic reaction mechanisms are challenging due to the short lifetime of catalytic cycle intermediates and hence, it is not always clear what the active species is that performs the transformations or what features of the active site affect the rate-determining reaction step. To understand the functional properties of these metal-containing active sites, biomimetic models have been developed that comprise the metal with a similar coordination environment but dissolved in an organic solvent.[3] Biomimetic models give insight into the effect of the ligands on the chemical properties and reactivity of the oxidant as well as the first and second coordination sphere on the reaction mechanism and rate constants.

Often biomimetic models contain mononuclear iron embedded in a ligand scaffold and pentadentate ligands have proven to be very popular because they generally give few isomeric structures. One particular N5-based pentadentate ligand that has been extensively studied is *N*,*N*-bis(2-pyridylmethyl)-*N*-bis(2-pyridyl)methylamine (N4Py, Figure 1).[4] In the iron(IV)-oxo form, the $[Fe^{IV}(O)(N4Py)]^{2+}$ complex (**1b**) bears four equatorially bound nitrogen donor atoms (N_{eq}) perpendicular to the iron(IV)-oxo axis and an axial amine nitrogen atom (N_{ax}) *trans* to the oxo group. Structurally, this ligand framework offers a perfect bowl-like cavity for the iron(IV)-oxo for reactions with substrates. In terms of bond-atom distances, all the equatorial Fe–N_{eq} distances appear to be equivalent and give the iron an octahedral symmetry. Over the years, the Fe^{IV}-oxo complex (**1b**) has been thoroughly characterized and extensively studied, which makes it an ideal candidate to engineer with substituents and ligands and study the interplay between the steric and electronic effects on its properties and reactivity.

There have been quite a few reports on the derivatization of pyridine rings that are bound to the iron(IV)-oxo core in **1b**,[5,6] particularly at the pyridine 6-position, which is closest to the oxo group. However, most studies on modified N4Py structures have focused on the two pyridine rings that are tethered to the axial nitrogen atom (N_{ax} atom) through methylene carbon atoms. Therefore, we were wondering what the effect would

[a] *G. Mukherjee, Dr. P. Barman, Dr. C. V. Sastri*
Department of Chemistry, Indian Institute of Technology Guwahati
Guwahati 781039, Assam (India)
E-mail: sastricv@iitg.ac.in

[b] *A. Alili, Dr. S. P. de Visser*
The Manchester Institute of Biotechnology and School of Chemical Engineering and Analytical Science, The University of Manchester
131 Princess Street, Manchester M1 7DN (UK)
E-mail: sam.devisser@manchester.ac.uk

[c] *Dr. D. Kumar*
Department of Applied Physics, Babasaheb Bhimrao Ambedkar University
School for Physical Sciences, Vidya Vihar, Rae Bareilly Road
Lucknow 226025, UP (India)

Supporting information and the ORCID identification number(s) for the author(s) of this article can be found under: https://doi.org/10.1002/chem.201806430.

© 2019 Wiley-VCH Verlag GmbH & Co. KGaA, Weinheim

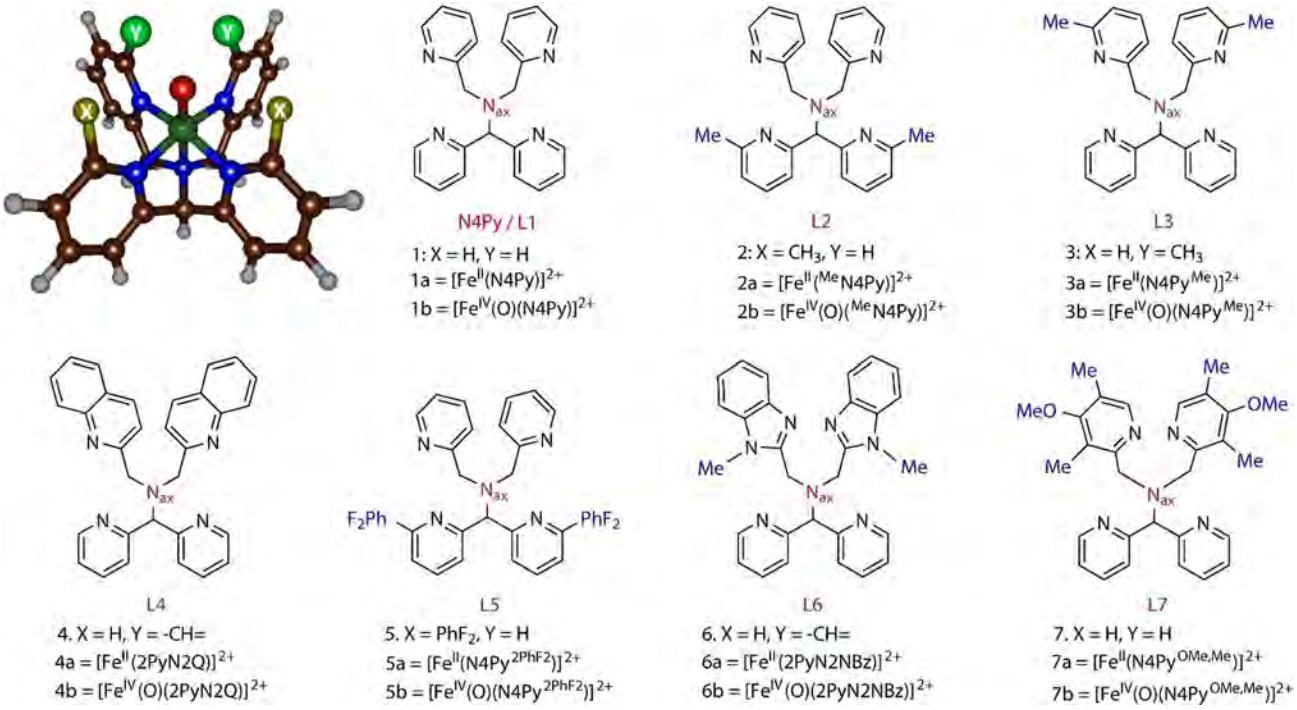

Figure 1. Structures of oxidants discussed in this work.

be of *ortho*-substitution of the two pyridine rings that bind through a methine carbon to the axial N-atom. Our study reveals the inequivalence of the four bound pyridine rings, which otherwise appear similar in terms of equatorial ligand field perturbation, when the pyridine C6 positions are substituted and this results in dramatic changes in reactivity.

It has been shown that substitution of the sixth position of a pyridine ring leads to the weakening of the equatorial field resulting in elongation of the Fe–N_{eq} bonds due to enhanced electrophilicity of the iron(IV)-oxo species.[6] Thus, using the tetradentate TPA ligand system [TPA = tris-(2-pyridylmethyl)-amine], Que and co-workers showed that introduction of at least one methyl group in the ligand framework (in the form of 6-MeTPA, 6-Me_2TPA and 6-Me_3TPA) led to changes in the electronic ground state of the ferrous and ferric species from low to high spin.[7]

Introduction of bulkier quinoline groups instead of pyridine led to the formation of a highly reactive high-spin ferryl-oxo intermediate with spectroscopic features analogous to the active species of the enzyme taurine/α-ketoglutarate dioxygenase (TauD).[8] Furthermore, drastic improvement in catalytic reactivity has been successfully achieved by replacement of pyridine groups in TPA by bulkier heterocycles such as *N*-methylbenzimidazole.[9] There are also reports of other ($S = 2$) iron(IV)-oxo intermediates, in which the metal center is positioned in a sterically encumbered cavity with forceful occupation of a trigonal bipyramidal geometry.[10]

On account of steric bulk and better σ-donor ability, these engineered ligand frameworks can offer enhanced perturbations in the equatorial ligand field that can make the iron(IV)-oxo core more susceptible to approaching substrates. Steric and electronic effects are two vital tuning probes that manifests the reactivity profiles for these systems and a delicate borderline exists between the two factors.[11] It is understood that along with the stretched Fe–N_{eq} bonds, the distortion in the ferryl axis, specifically the N_{ax}-Fe-O bond angle, plays a pivotal role in their stabilities, spectroscopic properties and various oxidative reactivities.[6] These examples from the literature implicate that substitution of the sixth position of a metal-bound pyridine ring leads to better hydrogen-atom abstraction (HAA) and oxygen-atom transfer (OAT) reactivity. However, what most of these metal complexes have in common is that the manipulations have been done in the sixth position of two specific methylene bound pyridine rings in N4Py, whereas any sort of engineering on the other two methine-carbon-bound pyridine rings in the primary coordination sphere has rarely been reported. Hence, an effort has been made by our groups to dig deeper into this issue. Both experimental and theoretical studies reveal the intrinsic parity between the two sets of pyridine rings, contributing to the overall reactivity profiles of the two catalysts. Considering the frameworks shown in Figure 1, the ligands are named 2(6-MePy)N_{ax}2Py or ^{Me}N4Py and 2PyN_{ax}2(6-MePy) or N4Py^{Me} in short and their iron(II) complexes are designated **2a** and **3a**, respectively.

The distinct spectroscopic properties and stability of the two complexes $[Fe^{IV}(O)(^{Me}N4Py)]^{2+}$ (**2b**) and $[Fe^{IV}(O)(N4Py^{Me})]^{2+}$ (**3b**) allowed us to pursue a detailed kinetic analysis and probe the very definitive factors that govern the reactivity and stability of these high valent metal-oxo species. Our studies concern the fine line between steric and electronic factors that orchestrate the reaction rates and selectivity, and also reveal the intricate details of second coordination sphere effects related to substrate approach to a metal-oxo species.

© 2019 Wiley-VCH Verlag GmbH & Co. KGaA, Weinheim

Results

Experimental characterization

Ligands ^{Me}N4Py and N4Py^{Me} were synthesized starting from di(6-methyl-pyridin-2-yl)methanone or di(pyridine-2-yl)methanone and, in a reaction with hydroxylamine, converted into an oxime, and subsequently over Zn, were reduced further to their amine form. Upon addition of either 2-(chloromethyl)-pyridine or 2-(chloromethyl)-6-methyl-pyridine in NaOH, we reacted the amines to form the ^{Me}N4Py and N4Py^{Me} structures, respectively, in good yield (detailed synthetic procedures are discussed in the Supporting Information, Schemes S1 and S2). Subsequently, the ^{Me}N4Py and N4Py^{Me} ligands were reacted with $[Fe^{II}(CH_3CN)_2{\cdot}2ClO_4]$ in acetonitrile to form the metal complexes $[Fe^{II}(^{Me}N4Py)](ClO_4)_2$ (**2a**) and $[Fe^{II}(N4Py^{Me})](ClO_4)_2$ (**3a**), which were characterized with UV/Vis absorption spectroscopy, electrospray ionization-mass spectrometry (ESI-MS), and crystallographic methods.[12] Single crystals of **2a** were obtained by vapor diffusion of diethyl ether into an acetonitrile solution of $[Fe^{II}(^{Me}N4Py)(CH_3CN)]^{2+}{\cdot}2BF_4$.

The crystal structure (Figure 2a and Table 1) shows clear penta-coordination of the metal to the ^{Me}N4Py ligand in a structural orientation analogous to the reported complexes $[Fe^{II}(N4Py)]^{2+}$ and $[Fe^{II}(N4Py^{Me})(CH_3CN)]^{2+}{\cdot}2ClO_4$.[13] The Fe–N bond distances for **2a**, as shown in Table 1, are typical for low spin Fe^{II} complexes reported previously.[5,6,11,13] In comparison to the crystal structure of Feringa and co-workers,[13b] (Figure 2b, Table 1) the two metal complexes **2a** and **3a** indicate minor differences. In particular, the sixth coordination position, *trans* to the N_{ax}, is occupied by the solvent CH_3CN in both complexes, but there is a substantial bending in the N_{ax}-Fe-solvent axis for **3a** (167.5°), as compared to **2a** (179.3°). This is the largest bend observed among the fellow structures (Table 1) and is close to that in **4a** reported by Rana et al., in which a triflate counter-anion occupies the apical position instead of a solvent molecule.[6c] The huge tilt accounts for an induced steric effect imparted by the methyl groups in the structure of **3a**. Another interesting observation is that in **2a**, the

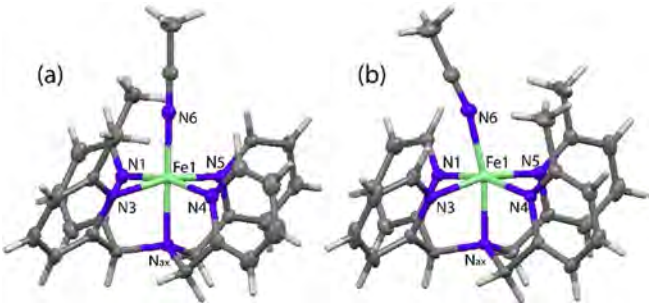

Figure 2. ORTEP diagram (with 30% ellipsoid probability) of complex (a) $Fe^{II}(^{Me}N4Py)(CH_3CN)](BF_4)_2$ and (b) $Fe^{II}(N4Py^{Me})(CH_3CN)](ClO_4)_2$.[13b] Color-coding: Hydrogen (off-white), carbon (gray), iron (green), nitrogen (violet). Counter-ions have been omitted for clarity.

N_{ax}-Fe-solvent axis is close to 180° in agreement with **1a** (177.3°). Thus, in the absence of any substituent the bond angle deviates from 180° to an acute value (177.3° in **1a**), and substituents in the methylene bound pyridine rings (167.5° in **3a**, 168.3° in **4a**, 175.7° in **6a** and 176.9° in **7a**) as well as methine bound pyridine rings (as in **5a**) display the same tilt. By contrast, in **2a**, the steric effect acts from the opposite direction thereby making the axis almost as straight as 180°. The $\measuredangle N_{eq}$-Fe-N_{ax} and $\measuredangle N_{eq}$-Fe-N_6 angles (compiled in Table 1) give a measure of the position of Fe in the equatorial plane inside the ligand framework and signifies the depth to which the metal center is located inside the cavity. Again, complex **4a** and **3a** both have the lowest $\measuredangle N_{eq}$-Fe-N_{ax} and highest $\measuredangle N_{eq}$-Fe-N_6 values compared to the rest, indicative of the strain inside the cavity (although there are intrinsic differences in ligation ability for the sixth donor, which is N for **3a** and O for **4a**).

Furthermore, the average Fe–N bond distance is higher in **3a** (2.016 Å) than that in **1a** (1.960 Å), **2a** (1.991 Å), **5a** (1.988 Å), **6a** (1.965 Å) and **7a** (1.96 Å). This is suggestive of a weakened equatorial ligand field in complex **3a**. Considering the cavity provided by the N5 donor center in all the ligand systems, the sixth coordination site is occupied by the solvent molecule that is susceptible to be replaced by the oxygen

Table 1. Selected bond lengths [Å] and bond angles [°] for Fe^{II} complexes **1a**–**7a**.

Complex:	**1a**[a]		**2a**[b]		**3a**[c]		**4a**[d]		**5a**[e]		**6a**[f]		**7a**[g]	
Bond	Bond length	Avg	Bond length	Avg	Bond length	Avg	Bond length	Avg	Bond length	Avg	Bond length	Avg	Bond length	Avg
Fe1–N1	1.976 (3)		2.049 (5)		2.004 (4)		2.199 (6)		2.057 (1)		1.964 (3)		1.963 (8)	
Fe1–N3	1.967 (3)	1.971[h]	2.043 (6)	2.012[h]	1.981 (4)	2.036[h]	2.233 (8)	2.220[h]	2.031 (1)	2.008[h]	1.983 (3)	1.977[h]	1.971 (8)	1.971[h]
Fe1–N4	1.975 (3)		1.974 (5)		2.083 (4)		2.223 (6)		1.979 (1)		1.983 (3)		1.965 (7)	
Fe1–N5	1.968 (3)		1.981 (5)		2.078 (3)		2.226 (6)		1.966 (1)		1.979 (2)		1.984 (8)	
Fe1–N_{ax}	1.961 (3)	1.938[i]	1.968 (5)	1.949[i]	1.990 (2)	1.974[i]	2.192 (6)	2.118[i]	1.967 (1)	1.949[i]	1.983 (3)	1.942[i]	1.959 (7)	1.938[i]
Fe1–N6	1.915 (3)		1.930 (5)		1.959 (3)		2.045 (6)		1.931 (1)		1.901 (3)		1.918 (7)	
Avg Fe–N	1.960		1.991		2.016		2.186		1.988		1.965		1.960	
Angles							Bond angles							
N_{eq}-Fe-N_{ax}[j]	84.0		83.3		82.7		77.2		83.5		83.6		84.0	
N_{eq}-Fe-N6[j]	96.0		96.6		97.1		102.6		96.6		96.4		96.0	
N_{ax}-Fe-N6	177.3		179.3		167.5		168.3		175.5		175.7		176.9	

[a] Ref. [13a]. [b] This work. [c] Ref. [13b]. [d] Ref. [6c]. [e] Ref. [5d]. [f] Ref. [5f]. [g] Ref. [5g]. [h] Average of all the equatorial bonds. [i] Average of all the axial bonds. [j] Average *cis*-bond angle of equatorial Fe1–N bonds with N_{ax} and N6. Avg = average.

© 2019 Wiley-VCH Verlag GmbH & Co. KGaA, Weinheim

atom during the formation of the oxo species. Indeed, the fragility of the Fe-solvent bond is indicated by the Fe1–N6 bond length, which is also longer in **3a** (1.959(3) Å) compared to **1a** (1.915(3) Å), **2a** (1.930(5) Å), **5a** (1.931(1) Å), **6a** (1.901(3) Å) and **7a** (1.918(7) Å). The Fe–O_{OTf} bond length in **4a** (2.045(6) Å) is even longer than the Fe–N6 bond in **3a**. The higher bond length values in **4a** are most probably due to the high-spin nature of the complex, as a result of anion binding (triflate) to the sixth coordination site instead of CH_3CN, which generally results in low spin complexes. Thus, notwithstanding the intrinsic differences between the Fe–N and Fe–O bonds, the quinoline groups impart strong influence on the vertical N_{ax}-Fe-O axis, which is obvious from the huge OAT rates.[6b] Clearly, the positioning of the methyl groups is responsible for similar steric effects in **3a** that can be anticipated for the corresponding oxo complex (**3b**) as well.

Unlike in the solid state, structural tuning of the ligand skeleton of such Fe^{II} complexes often leads to spin equilibrium in the solution phase. The absorption spectra of all Fe^{II} complexes **1a**, **2a** and **3a**, show two MLCT bands with notable differences in their epsilon values ($^{1a}\varepsilon = 8120$, 6600 L M^{-1} cm^{-1}, $^{2a}\varepsilon =$ 5360, 4920 L M^{-1} cm^{-1} and $^{3a}\varepsilon = 880$, 400 L M^{-1} cm^{-1}; see Figure S6a, Supporting Information). The very low value is speculative of substantial spin crossover in **3a** and **2a**, which is absent in **1a**. Steric hindrance of the methyl groups increases the bond lengths in the solid state; however, in the solution state, the spin equilibrium is mostly shifted towards the high-spin form that also rationalizes the low ε values of the new complexes. As the temperature is lowered to 233 K, the population of the low-spin state increases effectively in **3a** and **2a** thereby increasing their absorbance values (see Figure S6, Supporting Information). The ^{1}H-NMR spectra of **2a** and **3a** further support these findings and expectedly, paramagnetic shifting of the peaks were observed in both cases (see Figure S7, Supporting Information). However, the extent of peak-shifting and broadening is more so in the case of **3a** than in **2a**, thereby confirming larger contribution of the high-spin form in **3a** in equilibrium with the low-spin species. Similar paramagnetic shifting of proton resonances for ferrous complexes was also observed for **4a** and **6a**.[5f,6]

Complexes **2b** and **3b** were generated in situ by treating the iron(II) precursor complexes with 1.5 equivalents of $PhI(OAc)_2$ in an acetonitrile solution at room temperature. These ferryl-oxo complexes were characterized by UV/Vis, ESI-MS and ^{1}H-NMR spectroscopy. Upon addition of oxidant to the Fe^{II} species, the Fe^{IV}=O chromophores were formed almost instantaneously for both **2b** and **3b**, as observed from the UV/Vis spectrum. Subtle differences in the absorption spectrum were seen for the iron(IV)-oxo complexes **1b**, **2b** and **3b** (Figure 3). Cumulative bathochromic and hypochromic shifts range from 695 nm ($\varepsilon = 400$ L M^{-1} cm^{-1}) for **1b** to 750 nm ($\varepsilon =$ 340 L M^{-1} cm^{-1}) for **2b** to 775 nm ($\varepsilon = 200$ L M^{-1} cm^{-1}) for **3b**. These changes in the d–d transition bands are indicative of the sequential increment of the equatorial ligand field perturbation along the series and weakening of the same. Furthermore, this also leads to distortions in the bell-shaped absorption curve of **2b** and **3b** due to the appearance of shoulder humps in the NIR region as compared to that of **1b**. The stability of these complexes also follows the same trend with half-lives of 3600, 130 and 30 minutes, respectively.

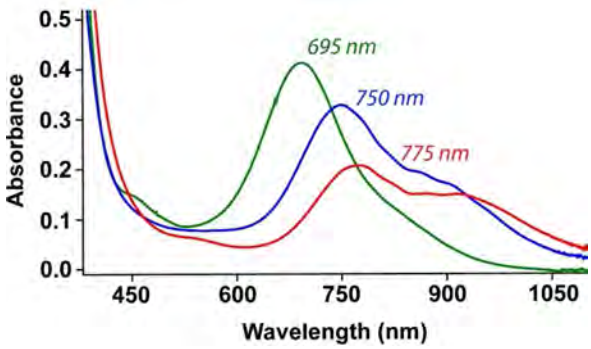

Figure 3. UV/Vis absorption spectrum of **1b** (green), **2b** (blue) and **3b** (red) in CH_3CN at 298 K.

The relatively less stable nature of the new oxo complexes (as evident from their half-lives) made it difficult to record their ESI-MS spectra at room temperature. Therefore, the ESI-MS spectra for **2b** and **3b** were recorded at lower temperatures by infusing cold samples directly into the source. Both complexes gave a major peak at *m/z* 233.6 corresponding to $[Fe^{IV}(O)(L)]^{2+}$ (Figure S8, Supporting Information). To further confirm the existence of iron(IV)-oxo, we did an isotope-labelling experiment. The iron-oxo complexes are known to exchange oxygen from water.[14] Thus upon addition of $H_2{}^{18}O$ to the new iron-oxo complexes, a positive peak shift of one unit for the *M*/2 ion-cluster was observed in the mass spectrum after an incubation spell of 10–15 minutes thereby confirming the existence of iron(IV)-oxo complexes (see insets in Figures S8).

We also carried out ^{1}H-NMR spectroscopy experiments to discriminate between the two new iron(IV)-oxo species, **2b** and **3b**, (Figure 4) and compare the spectra with the existing

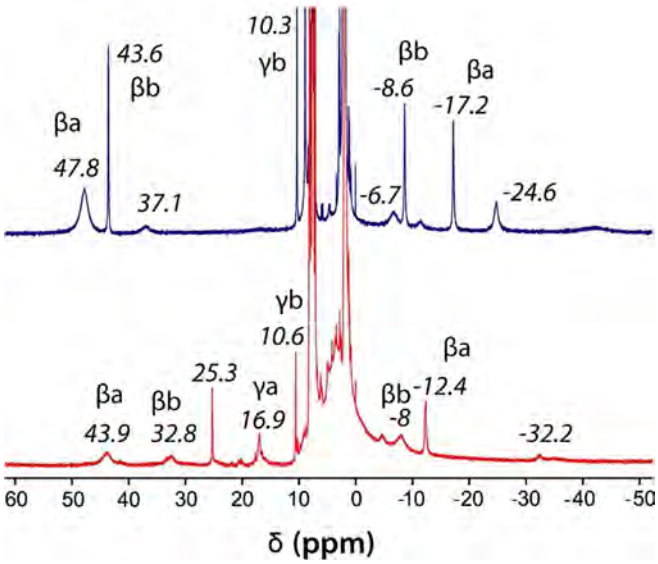

Figure 4. ^{1}H-NMR spectra of **2b** (top) and **3b** (bottom) in CD_3CN at 298 K.

© 2019 Wiley-VCH Verlag GmbH & Co. KGaA, Weinheim

^{1}H-NMR spectrum of complex **1b**.[15a] Clearly, there are shifting of peaks resulting from the typical $S=1$ ferryl species that unequivocally exists in the octahedral environment.[15] The low spin Fe^{IV} center in **2b** exhibits more relaxation properties compared to **3b**, thereby producing sharper signals although both the complexes give rise to paramagnetically shifted proton resonances. As compared to the ^{1}H-NMR spectra of **4b**, the same for **2b** and **3b** appears less complex due to the absence of the quinoline ring protons.[6b,c] The ^{1}H-NMR spectra for **2b** and **3b** were recorded over a spectral width of 200 ppm at 298 K temperature (Figure 4). Both complexes show a unique shift pattern for the pyridine protons of low spin Fe^{IV} centers, with one β-proton shifted upfield (−17.2, −8.6 ppm for **2b** and −12.4, −8 ppm for **3b**) and one β-proton shifted downfield (43.6, 47.8 ppm for **2b** and 32.8, 43.9 ppm for **3b**), as observed previously for analogous complexes.[5b–e,15] However, in case of Fe^{III}-pyridine complexes, both the β-protons shift downfield with comparable paramagnetic shift.[7] The difference in extent of paramagnetic shifting and peak integrations in the NMR spectra of **2b** and **3b** justify the unequal interaction of the two different sets of pyridine rings with the Fe d-orbitals that have an uneven load of unpaired spin density.

Reaction kinetics

The reactivity of these complexes was investigated for the oxygen-atom transfer (OAT) and hydrogen-atom abstraction (HAA) reactions from substrates. Thioanisole was employed initially for OAT reactivity, whereas HAA properties were tested using a range of substrates having varied C–H bond dissociation energies and active hydrogen availability. Addition of substrates to a solution containing **2b** or **3b** in acetonitrile led to the first-order decay of the characteristic d–d transition band in the respective UV/Vis spectrum. The second-order rate constants (k_2) were determined by plotting the pseudo-first-order rate constants (k_{obs}) as a function of the proportional increment of substrate concentration. In the case of OAT, the sulfur atom of the organic substrate acts as the active recipient of the oxygen atom and eventually forms the oxidized product in the form of sulfoxides or sulfones.[16–18] $[Fe^{IV}(O)(N4Py)]^{2+}$ (**1b**) reacts with thioanisole with a k_2 of 50×10^{-3} M^{-1} s^{-1} at 273 K.[17]

Under identical conditions, complex **2b** shows enhanced reaction rates (see Figure 5b). However, upon addition of 10 equivalents of thioanisole to 1 mM solution of **3b**, the 775 nm band vanished in less than 20 seconds at even lower temperatures (233 K). As such, complex **3b** reacts with thioanisole at even faster rates than the recently reported $[Fe^{IV}(O)(2PyN2Q)]^{2+}$ complex (**4b**) under identical conditions: for 5 equivalents THA at 233 K, the k_{obs} values for **3b** and **4b** are $8.9(4)\times10^{-2}$ s^{-1} and $5.4(2)\times10^{-2}$ s^{-1}, respectively.[6b] Therefore, to procure a comparative analysis for S-oxidation under identical conditions, we employed dibenzothiophene (DBT) as the model substrate for OAT reactions for all three oxidants. DBT has two benzene rings fused to a thiophene, in conjugation with the heteroatom, and delocalizes the electron density through a number of canonical structures thereby making the reaction slower compared to thioanisole.[18] Thus, it is a more suitable substrate for a comparative study of all three complexes than thioanisole. Complex **3b** transfers an oxygen atom to DBT about a thousand times faster ($k_2=4.1$ M^{-1} s^{-1}) than **1b** ($k_2=3.2\times10^{-3}$ M^{-1} s^{-1}),[18] whereas **2b** ($k_2=9.5\times10^{-3}$ M^{-1} s^{-1}) could only triple the rate of **1b** (see Figure 5c) at 298 K. These rates agree with the fact that complex **3b**, compared to **2b**, has an underlying weaker equatorial Fe–N bonding and more ferryl-oxo distortions thereby making the catalyst more susceptible towards heteroatom oxidation reactions. Hence, introduction of methyl groups at the two methylene bound pyridine rings exerts a prolific effect on the iron-oxo core compared to the one containing methyl groups on the pyridine rings connected by the methine carbon in the case of OAT reactions.

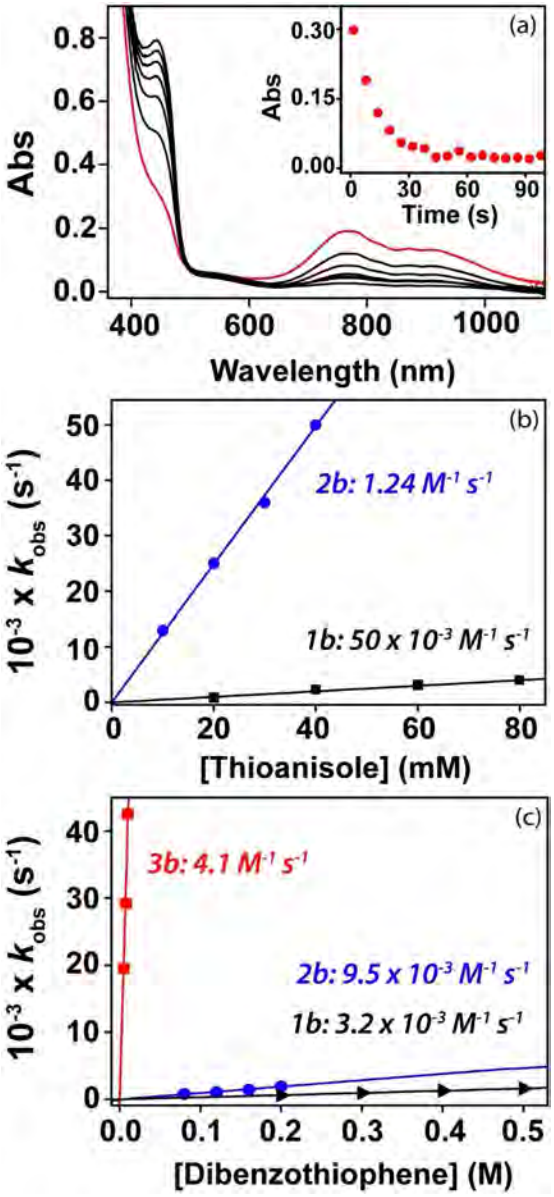

Figure 5. (a) Decay profile for the reaction of **3b** with THA (5 equivalents) at 233 K. Inset shows the time trace for the decay of the 775 nm band. Second-order rate constants determined for the reaction of **1b** (1 mM, ▶), **2b** (1 mM, ●) and **3b** (1 mM, ■) with (b) thioanisole at 273 K; (c) DBT kinetics plot obtained at 298 K.

© 2019 Wiley-VCH Verlag GmbH & Co. KGaA, Weinheim

To verify the sustainability of this reactivity trend for HAA, we evaluated the C–H activation abilities of the complexes under study. The conversion of ethylbenzene to 1-phenylethanol was tested with **1b**, **2b** and **3b**. Reaction rates with **3b** ($k_2 = 155.3 \times 10^{-3}$ M^{-1} s^{-1}) was around twenty times faster than **1b** ($k_2 = 8 \times 10^{-3}$ M^{-1} s^{-1}), whereas **2b** ($k_2 = 9.7 \times 10^{-3}$ M^{-1} s^{-1}) almost mirrors **1b** in terms of C–H activation rates at 298 K (see Figure 6a). To ensure that HAA is the rate-determining step, we repeated the experiment with ethylbenzene-[D_{10}] (see Figure S12, Table S8, Supporting Information).[4b] The isotopomers react differently due to vibrational differences in the C–H and C–D bond frequencies, and kinetic isotope effect (KIE) values of 14 and 13 were obtained for **2b** and **3b**, respectively. Hence, C–H bond cleavage is the rate-determining step in the HAA reactions.

A more pragmatic approach was taken to study the effect of the methyl groups towards substrate approach and reactivity using the conventionally available substrates with varying C–H bond dissociation energies (BDE).[4b,17a] As can be seen in the Bell–Evans–Polanyi plot, the log k_2' values for five different complexes (**1b**, **2b**, **3b**, **4b** and **6b**) are portrayed against the C–H BDE of the sacrificial C–H bond(s) ranging from 77–90 kcal mol^{-1} (see Table S9, Supporting Information). As is evident from Figure 6b, **1b** and **2b** display comparable reaction rates for all the substrates. The only exceptions being 9,10-dihydroanthracene (DHA), fluorene and triphenylmethane, in which **2b** happens to react very sluggishly compared to **1b**. Clearly the steric effect imparted by the methyl groups in **2b** during the approach of these three bulky substrates can be perceived. Other complexes, such as **3b**, **4b** and **6b**, have substantially higher reaction rates than **1b**/**2b** for all the substrates irrespective of the C–H bond strength, one specific case, again, being the reactivity of **3b** with triphenylmethane, in which a significant drop in reaction rate is observed. All the points in the plot shown here have been recorded under similar reaction conditions. Therefore, the sudden drop in reactivity for **2b** and **3b** with triphenylmethane can only be attributed to the steric factor between the oxo complex and the approaching substrate. The only active hydrogen atom in Ph_3CH is deeply embedded inside its "propeller shaped" structure, abstraction of which by **2b** and/or **3b** is highly hindered by the steric fencing provided by the methyl groups in both the complexes. This observation is unique and novel and portrays the steric effect of Fe^{IV}-oxo complexes with bulky substrates like Ph_3CH (also 9,10-DHA and fluorene), whereas all other complexes (like **1b**, **4b** and **6b**) follow the thermodynamic trend of bond strength versus reactivity and the corresponding points for BDE 81 kcal mol^{-1} falls close to the best fitted line. For substrates other than Ph_3CH, the active hydrogen(s) is/are easily accessible to all the complexes depending on the geometry and approach pathway.

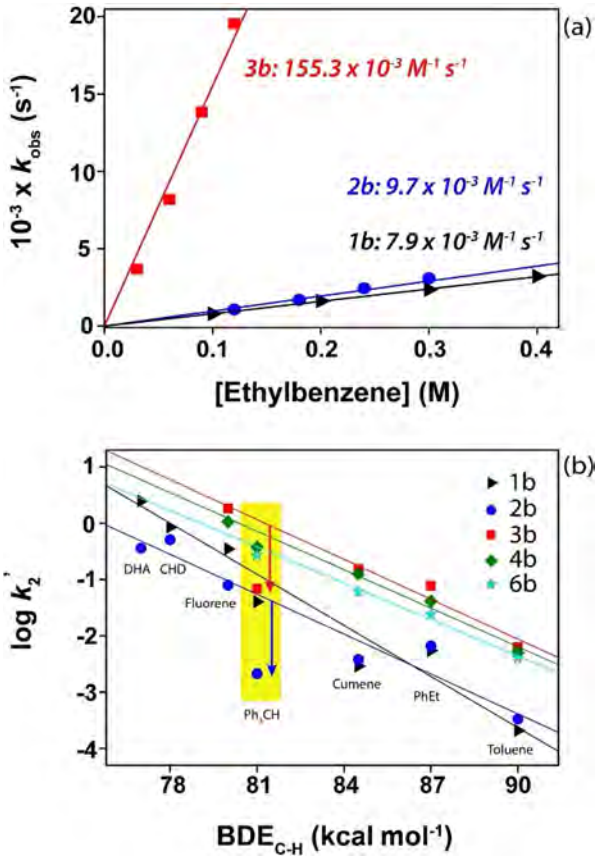

Figure 6. (a) Second-order rate constants determined for the reaction of **1b** (1 mM, ▶), **2b** (1 mM, ●) and **3b** (1 mM, ■) with ethylbenzene at 298 K; (b) Bell–Evans–Polanyi plot for their reaction of **1b** (▶), **2b** (●) **3b** (■), **4b** (◆) and **6b** (★) with different substrates at 298 K in CH_3CN; k_2' is k_2 divided by the number of equivalent C–H bonds on the substrate that would react with the iron(IV)-oxo species. Best fit lines exclude points for Ph_3CH to show the deviation.

Complexes **4b** and **6b** have almost similar reactivity profile to **3b** but do not show reluctance towards Ph_3CH; as such, the influence of the added substituents in the pyridine-6 position is primarily electronic, thereby enhancing their reactivity compared to **1b**.[5f,6] The longer Fe–N bond length in Fe^{IV}-oxo, in general, gives rise to a more reactive complex. The average Fe–N bond lengths in **4b** and **6b** are 2.053 Å and 1.999 Å, respectively, whereas the same for **1b** is 1.972 Å.[6a] Again in complex **2b** and **3b**, the introduction of the methyl groups in the *ortho*-position of the pyridine rings leads to a flagpole-like interaction with the oxo moiety, and the sp^3-hybridization of the methyl carbon thus adds up to the flexibility in terms of C–C bond rotation and bending. In **4b** and **6b**, however, the added bulk is tethered to the *ortho*- and *meta*-positions of the pyridine ring and that to the immediate vicinity of the binding N is an sp^2-carbon, thereby restricting its free movement and rotation (see Figure 1).

Overall, in **2b** and **3b**, the steric factor precedes the electronic factor to determine the fate and rate of a reaction, and triphenylmethane (in spite of having a lower BDE_{C-H}) is an ideal substrate to make such an inference.

Computational studies

To understand the anomaly in reactivity of **1b** versus **2b** and **3b**, a theoretical investigation was conducted. Before going into the details of the various reaction mechanisms we will dis-

© 2019 Wiley-VCH Verlag GmbH & Co. KGaA, Weinheim

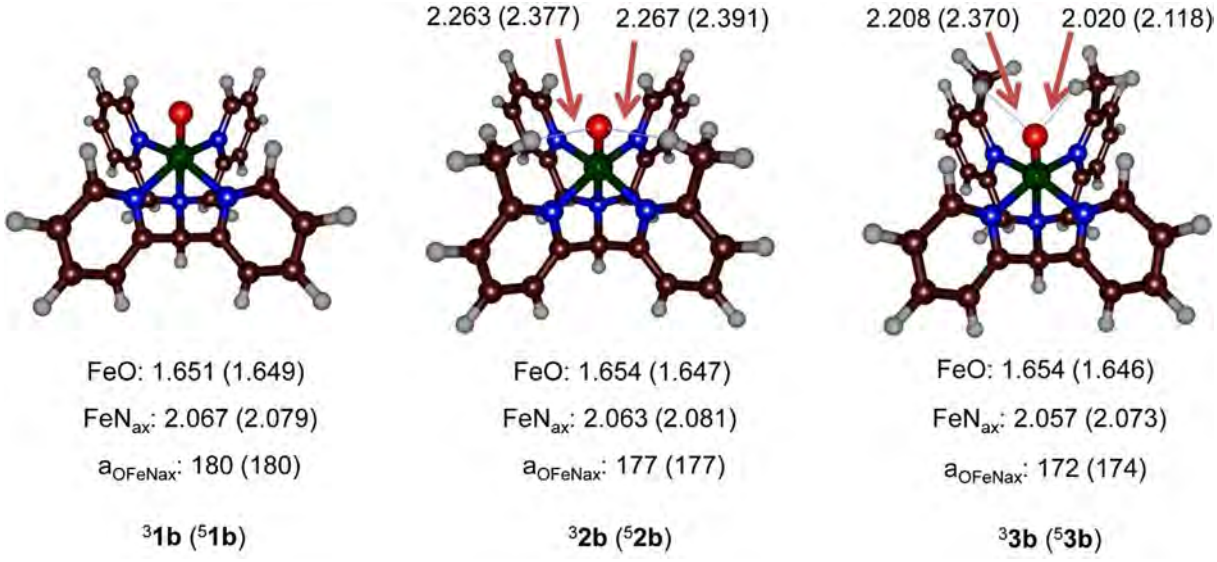

Figure 7. Optimized UB3LYP/BS1 geometries of ^{3,5}**1b**, ^{3,5}**2b** and ^{3,5}**3b** with bond lengths in angstroms and the O-Fe-N$_{ax}$ angle in degrees with N$_{ax}$ the axial amine nitrogen atom.

cuss the electronic and structural differences of the oxidants first.

Figure 7 displays optimized geometries of complexes **1b**, **2b** and **3b** in the lowest triplet and quintet spin states. In all cases, the triplet spin state is the ground state and well-separated from the nearest quintet spin state. In particular, triplet-quintet energy gaps of 4.0 and 2.3 kcal mol^{-1} are found for **2b** and **3b**, respectively. For structure **3b**, we also calculated the lowest lying singlet and septet spin states, which we find 28.9 and 20.6 kcal mol^{-1} higher in energy, respectively. As such, these spin state surfaces were not explored further. Our spin-state energies and spin-state orderings match previously calculated DFT studies on [Fe^{IV}(O)(N4Py)]$^{2+}$ (**1b**) excellently, in which triplet-quintet energy gaps of well over 4 kcal mol^{-1} were calculated.[17] Moreover, experimental EPR and Mössbauer studies identified **1b** as a triplet spin iron(IV)-oxo species.[4] Therefore, methyl substituents have a small effect on the spin-state energies of **1b**, **2b** and **3b** but do not change the spin-state ordering.

The Fe—O distances are short and typical for a double bond between the iron and oxo group. Although the Fe—O distances in ^{3}**2b** and ^{3}**3b** are the same (1.654 Å), the Fe—O stretch vibration changes from 856 cm^{-1} for the former to 848 cm^{-1} for ^{3}**3b**. These distances match previously reported bond lengths and vibrations of calculated geometries as well as experimental crystal structure distances of iron(IV)-oxo complexes well.[19,20] No dramatic changes in iron(IV)-oxo distances are seen upon addition of methyl substituents to the pyridine scaffold. Similarly, the distances of the iron atom to the axial amine nitrogen atom (N$_{ax}$) do not vary a lot between the individual complexes. The only structural change that is seen comes from a modestly bent O-Fe-N$_{ax}$ angle in ^{3,5}**3b** to 172° (triplet) and 174° (quintet), respectively, that was envisaged from the crystal structures for the ferrous complexes. This bending may affect the orbital shapes and energies. Note also the weak interactions of the methyl protons to the oxo group at a distance of 2.0–2.4 Å in the ^{3,5}**2b** and ^{3,5}**3b** structures. The electronic configuration of the iron(IV)-oxo complexes is determined by the interaction of the metal 3d orbitals with first-coordination sphere ligands and particularly the oxo group. With the molecular *z*-axis associated along the Fe—O bond, this gives a pair of bonding and antibonding orbitals for the π and π^* interaction of 3d(Fe) with 2p(O) with a total for six electrons: $\pi_{xz}^2\ \pi_{yz}^2\ \pi^*_{xz}{}^1\ \pi^*_{yz}{}^1$. A final π-type orbital is located in the *xy*-plane and is non-bonding (π^*_{xy}). Two σ-type orbitals associated with the bonding and antibonding interactions along the Fe-O axis (σ_{z^2} and $\sigma^*_{z^2}$) and in the *xy*-plane with pyridine nitrogen atoms ($\sigma_{x^2-y^2}$ and $\sigma^*_{x^2-y^2}$). Figure 8 gives orbital depictions of ^{3}**2b** as calculated in Gaussian for the α- and β-set of molecular orbitals. The σ_{z^2} and $\sigma_{x^2-y^2}$ orbitals are low in energy and not shown. In general, all triplet spin states have orbital occupation $\sigma_{z^2}^2\ \sigma_{x^2-y^2}^2\ \pi_{xz}^2\ \pi_{yz}^2\ \pi^*_{xy}{}^2\ \pi^*_{xz}{}^1\ \pi^*_{yz}{}^1$, whereas the quintet spin state had $\sigma_{z^2}^2\ \sigma_{x^2-y^2}^2\ \pi_{xz}^2\ \pi_{yz}^2\ \pi^*_{xy}{}^1\ \pi^*_{xz}{}^1\ \pi^*_{yz}{}^1\ \sigma^*_{x^2-y^2}{}^1$ configuration. Therefore, a triplet-to-quintet transition results from the promotion of one electron from π^*_{xy} into $\sigma^*_{x^2-y^2}$.

A comparison of the orbital shapes of ^{3}**2b** (Figure 8) and ^{3}**3b** (Figure S14, Supporting Information) shows very little differences in orbital shapes. Relative orbital energies as taken from the UB3LYP/BS2 and UB3LYP/BS1 calculations are given in Figure 8. Little variation between the data is seen and most numbers are within a few kcal mol^{-1}. Moreover, when the orbital energies are compared relative to the β-spin π^*_{xy} molecular orbital, we only see minor shifts in energy levels between the two structures. Consequently, the addition of methyl substituents to the N4Py scaffold nearby the oxo group in the iron(IV)-oxo species has little effect on the electronic configuration of the oxidant and the orbital energies and shapes. Thus, any change in reactivity must therefore come from differences in substrate approach through electrostatic interactions. Further evidence for the small changes in orbital energies comes from

© 2019 Wiley-VCH Verlag GmbH & Co. KGaA, Weinheim

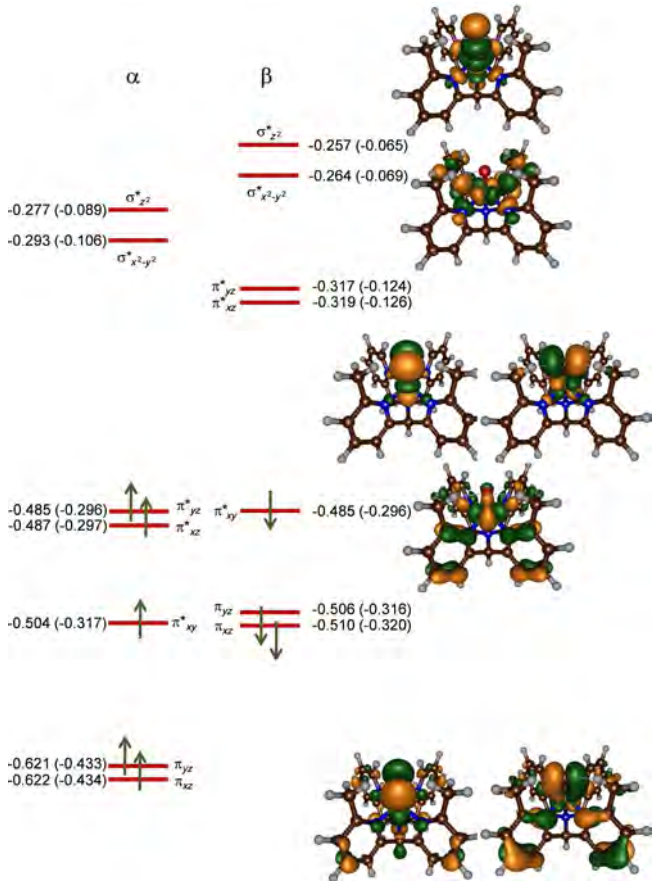

Figure 8. Orbital shapes and energies of ^{3}**2b** as calculated at UB3LYP/BS1 and UB3LYP/BS2 (in parenthesis) in Gaussian. Orbital energies are given in kcal mol^{-1}.

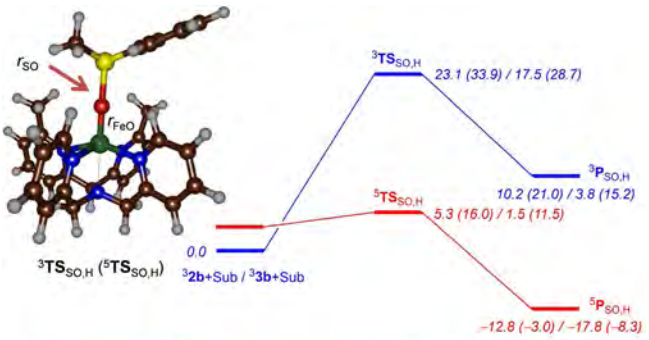

Z	r_{FeO}		r_{SO}		Imag freq	
	triplet	quintet	triplet	quintet	triplet	quintet
H-2b	1.764	1.773	2.072	2.196	i473	i116
H-3b	1.768	1.777	2.078	2.230	i500	i76

Figure 9. Calculated sulfoxidation reaction mechanism for the reaction of ^{3,5}**2b**/^{3,5}**3b** with *p*-H-thioanisole (Sub) obtained at UB3LYP/BS1//UB3LYP/BS2. Energies (free energies) are in kcal mol^{-1} and contain solvent and zero-point corrections. Quintet spin data in parenthesis.

the calculated (adiabatic) electron affinities of the various complexes, in which we find values of 119.3, 119.2 and 120.7 kcal mol^{-1} for ^{3}**1b**, ^{3}**2b** and ^{3}**3b**, respectively. Therefore, any change in rate constant should result from second-coordination sphere effects through interactions of the approaching substrate with the oxidant.

Subsequently, we investigated the OAT from ^{3,5}**2b** and ^{3,5}**3b** to *para*-Z-substituted thioanisole with Z = OCH_3, CH_3, H, Cl and NO_2. As before, the reactions were concerted with a single OAT to form sulfoxide products (^{3,5}**P**$_{SO,Z}$) with a transition state ^{3,5}**TS**$_{SO,Z}$. Figure 9 shows the general energy landscape for the reactions starting from ^{3,5}**2b** and ^{3,5}**3b** with *para*-H-thioanisole as an example. Although the triplet spin state is the ground state upon reaching the S–O bond formation transition state, a spin state crossing from the triplet to the quintet spin state occurs and hence ^{5}**TS**$_{SO}$ is well below ^{3}**TS**$_{SO}$. As a matter of fact, ^{5}**TS**$_{SO}$ is only a fraction higher in energy than the quintet spin reactants, which implies the reaction must be really fast on the quintet spin state surface. Energetically, for structure **2b**, the quintet spin state sulfoxidation barrier is $\Delta E^{\neq}$ + ZPE = 5.3 kcal mol^{-1}, whereas it is much lower for **3b**, in which we find a value of only 1.5 kcal mol^{-1}. Despite the large drop in barrier height between ^{5}**TS**$_{SO,H}$ for **2b** versus **3b**, they are geometrically alike (Figure S17, Supporting Information). The drop in barrier height, therefore, must originate from second-coordination sphere effects rather than first-coordination sphere effects or changes in the oxidant structure. In particular, a change in the N_{ax}-Fe-O angle is seen for all transition states. As discussed above in Figure 7, the ^{3,5}**2b** structures have an almost linear N_{ax}-Fe-O angle of about 177°, whereas in ^{3,5}**3b** the angle is slightly tilted to 172°–174°. In the sulfoxidation transition states displayed in Figure 9, all structures have an N_{ax}-Fe-O angle in the range 168–172.5°. Therefore, the change in angle is stronger for complexes ^{3,5}**2b** than for ^{3,5}**3b**, in which the metal stays in virtually the same position as in reactants. As a result of smaller changes in geometry the sulfoxidation barriers are considerably lower. The overall sulfoxidation reaction is exothermic by 12.8 (for **2b**) and 17.8 (for **3b**) kcal mol^{-1} to form products.

Optimized geometries of the triplet and quintet spin transition states for the reaction of ^{3,5}**3b** with *para*-Z-thioanisole are given in Figure 10. In the transition state, the Fe–O distance is elongated from 1.654 Å in ^{3}**3b** and 1.647 Å in ^{5}**3b** to values ranging from 1.765–1.784 Å in ^{3}**TS**$_{SO,Z}$ and from 1.775–1.792 Å in the ^{5}**TS**$_{SO,Z}$ structures. A plot of the triplet spin Fe–O bond lengths against the σ_p Hammett parameter gives a linear correlation and as such, the structure changes smoothly upon replacement of the *para*-Z group of thioanisole (Supporting Information Figure S15). Similar correlations of the S–O and Fe–N_{ax} distances with σ_P also give a linear correlation. Therefore, the transition state geometries change smoothly depending on the *para*-Z substituent that causes electron-donating or -withdrawing properties on the sulfide group.

The imaginary frequency in the triplet spin state is relatively large, namely ranging from *i*491 cm^{-1} for *para*-OCH_3-thioanisole to *i*519 cm^{-1} for *para*-NO_2-thioanisole. Interestingly, in the quintet spin state the imaginary frequencies are much lower, that is, *i*72–*i*158 cm^{-1}. Also, the imaginary frequency in the transition state follows the Hammett correlation with σ_P which means that the *para*-Z substituent affects the shape of the po-

© 2019 Wiley-VCH Verlag GmbH & Co. KGaA, Weinheim

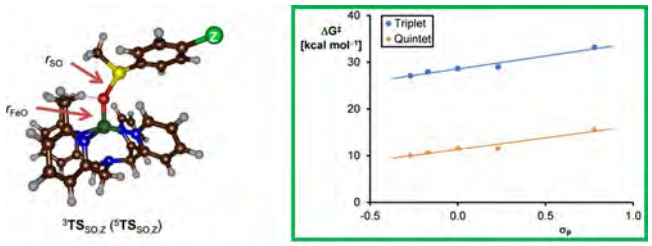

Z	r_{FeO}	r_{SO}	Imag freq
OCH_3	1.765 (1.786)	2.090 (2.218)	i491 (i146)
CH_3	1.765 (1.775)	2.084 (2.241)	i495 (i72)
H	1.768 (1.777)	2.078 (2.230)	i500 (i76)
Cl	1.774 (1.786)	2.070 (2.197)	i507 (i130)
NO_2	1.784 (1.792)	2.052 (2.166)	i519 (i158)

Figure 10. Transition state geometries for the reaction of ^{3,5}**3b** with *para*-Z-thioanisole (Z = OCH_3, CH_3, H, Cl and NO_2) as calculated at UB3LYP/BS1 in Gaussian. Data represent the Fe–O and S–O bond lengths in angstroms and the imaginary frequency of the transition state in cm^{-1}. Quintet spin data is given in parenthesis.

tential energy surface and broadens it when more electron-withdrawing substituents are added to the *para*-position of the aromatic ring of the substrate. A similar observation was found for *para*-Z-styrene epoxidation by iron(IV)-oxo porphyrins, in which a linear correlation between σ_p and the imaginary frequency was also found.[21] These correlations are found irrespective of the spin-state surface.

Finally, we investigated HAA from ethylbenzene (EB) by ^{3,5}**2b** and ^{3,5}**3b** and the results are given in Figure 11. As shown, the approach of substrate onto the iron(IV)-oxo changes upon substitution of the sixth position with methyl groups; in ^{3,5}**2b**, the substrate comes from the left, whereas it enters from the right in ^{3,5}**3b**. The methyl groups form weak C–H···O hydrogen-bonding interactions that stabilize the oxo group and hold it in a specific orientation. Nevertheless, the C–H and O–H distances do not vary dramatically between the structures in the triplet spin state with values of 1.322 (1.303) Å for the C–H interaction and 1.289 (1.316) Å for the O–H distance in ^{3}**TS**$_{HA,2b}$ (^{3}**TS**$_{HA,3b}$), respectively. All triplet spin state transition state structures have a large imaginary frequency for the C-H-O stretch vibration. Values of those magnitudes typically correspond to a significant amount of tunneling and a large KIE as also reported experimentally (see above).[22] Despite similar bond lengths, the triplet spin HAA barrier for **3b** is 2.0 kcal mol^{-1} lower in energy than that for **2b**, which matches the experimental rate changes well. Lower in energy, however, are the quintet spin hydrogen atom abstraction barriers, which are 7.9 and 4.0 kcal mol^{-1} for system **2b** and **3b**. Therefore, in line with the OAT to sulfides, the HAA transition states are also lower for **3b** as compared with **2b**. These rate changes obtained computationally match the experimentally determined trends from Figures 5 and 6 excellently and show that **3b** is a much better oxidant than **2b** for oxidation reactions.

Discussion

To understand the reactivity differences of **1b**, **2b** and **3b**, we analyzed the thermochemical and electronic properties of the reactant complexes and set up a valence-bond model to describe their oxidative differences. The electronic changes for the HAA from the substrate by the iron(IV)-oxo complexes ^{5}**1b**, ^{5}**2b** and ^{5}**3b** in the quintet spin state is depicted in Scheme 1. As described in Figure 8, all complexes have an orbital occupation with $\pi_{xz}^2\ \pi_{yz}^2\ \pi^*_{xy}{}^1\ \pi^*_{xz}{}^1\ \pi^*_{yz}{}^1\ \sigma^*_{x^2-y^2}{}^1$ configuration as identified in Scheme 1 with dots for each electron, while a line separating two dots represents a doubly occupied orbital. Thus, the π_{xz}/π^*_{xz} and π_{yz}/π^*_{yz} pairs of orbitals form two three-electron bonds along the Fe-O axis. In addition, there are two unpaired electrons with dominant contribution on iron in the *xy*-plane, namely π_{xy} and $\sigma^*_{x^2-y^2}$. Finally, the substrate has a doubly occupied σ_{CH} orbital for the C–H bond that is activated in the process.

Upon HAA, the σ_{CH} bond splits back up into atomic orbitals and the leaving H-atom pairs its electron up with a 2p electron on oxygen. The latter originates from the three-electron π_{xz}/π^*_{xz} pair of orbitals (highlighted in red in Scheme 1) that revert

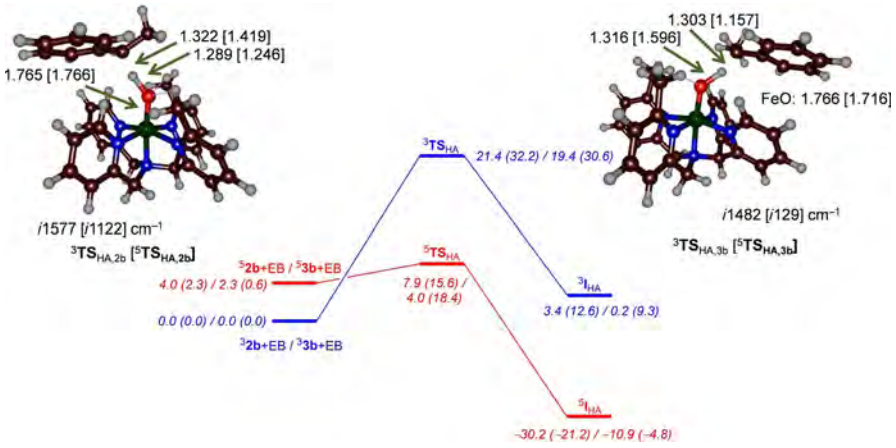

Figure 11. HAA energies for the reaction of ^{3,5}**2b** and ^{3,5}**3b** with ethylbenzene as calculated at UB3LYP/BS1//UB3LYP/BS2 in Gaussian. Energies (in kcal mol^{-1}) represent $\Delta E + ZPE + E_{solv}$ values with free energies (at 298 K) in parenthesis. Transition-state geometries give bond lengths in angstroms and the imaginary frequency in cm^{-1}.

© 2019 Wiley-VCH Verlag GmbH & Co. KGaA, Weinheim

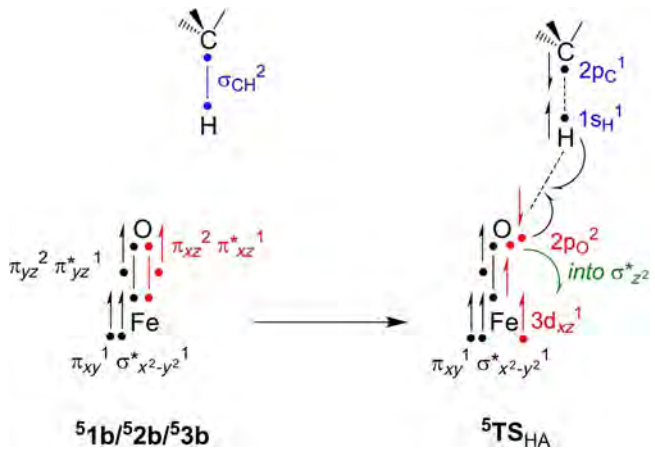

Scheme 1. Valence bond orbital diagram for the electronic changes during hydrogen atom abstraction.

to atomic orbitals. The other two electrons lead to the non-bonding $3d_{xz}$ with one electron and the $\sigma^*_{z^2}$ orbital with one electron. We previously showed that based on these electron-transfer mechanisms, the HAA barrier is correlated with the energies to break the π_{xz}/π^*_{xz} bond, break the σ_{CH} bond and form the σ_{OH} orbital for the interaction of $2p_O$ with $1s_H$.[23] Following from Scheme 1, the oxidation state of iron is reduced from iron(IV) to iron(III) during HAA. Therefore, we decided to do a thermochemical analysis on the physical–chemical properties of complexes **1b**, **2b** and **3b** and, particularly, focus on the electron-and proton-abstraction ability. Thus, the electron affinity (EA) for the one-electron reduction of the triplet spin iron(IV)-oxo complexes were calculated from the adiabatic energy differences (at $\Delta E + ZPE + E_{solv}$) with the iron(III)-oxo complex, see Figure 12. Interestingly, the electron affinity of the three complexes is virtually the same and ranges from 119.2 kcal mol^{-1} for **2b** to 120.7 kcal mol^{-1} for **3b**. Consequently, the changes in reactivity pattern do not originate from differences in the reduction potential of the three complexes.

Subsequently, we calculated the energy for the iron(IV)-oxo species to abstract a hydrogen atom as the energy difference between the iron(III)-hydroxo complex and the sum of the iron(IV)-oxo and a hydrogen atom, which is termed the O–H bond dissociation energy (BDE_{OH}). Similar to the EA values, the

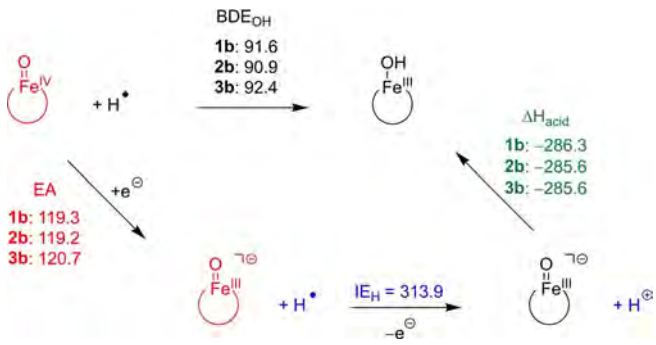

Figure 12. Thermochemical analysis of the differences of structure **1b**, **2b** and **3b** in EA, gas-phase acidity (ΔH_{acid}) and O–H bond strength (BDE_{OH}) with values in kcal mol^{-1}.

BDE_{OH} values of **1b**, **2b** and **3b** are very close in energy and range from 90.9 kcal mol^{-1} for **2b** to 92.4 kcal mol^{-1} for **3b**. Previously, the BDE_{OH} of the oxidant was correlated with the rate constant for HAA and, as such, would imply similar HAA barriers from substrates.[24] To complement the reaction cycle in Figure 12, we also calculated the acidity of the iron(III)-hydroxo complex (ΔH_{acid}). Obviously, given that there are little changes between the complexes for the EA and BDE_{OH} values, no dramatic changes for the acidity were seen. Therefore, the three complexes **1b**, **2b** and **3b** have similar physical-chemical properties and as a result should also show comparable reactivity patterns with substrates. The fact that this is not the case means external perturbations must be at play and influence the reactivity of these oxidants with substrates. Most likely the reaction rates are affected due to differences in the approach of the substrate to the oxidant, which must show structural and electronic differences. To understand the reactivity differences, we did a detailed analysis of the structural and electronic differences of the rate-determining transition states.

To identify the structural differences between the rate-determining transition states better, we give an overlay of ^{5}**TS**$_{SO,2b}$ and ^{5}**TS**$_{SO,3b}$, on the one hand, and ^{5}**TS**$_{EB,2b}$ and ^{5}**TS**$_{EB,3b}$ on the other hand in Figure 13. As can be seen from Figure 13, the substrate is located in roughly the same position with respect to the oxidant. However, the metal center has shifted slightly within the ligand scaffold. Thus, in ^{5}**TS**$_{SO,3b}$ and ^{5}**TS**$_{EB,3b}$ the metal is located nearby the center of the four pyridine nitrogen atoms that give Fe–N distances within a range of 0.038 and 0.021 Å, respectively. By contrast, for the structures originating from **2b** the Fe–N distances are much wider apart (0.089 and 0.090 Å), so that the metal is not located in the center of the ligand scaffold. The deviation of the metal from the axis will affect the orbital shapes and particularly influence the energy level of the $\sigma^*_{z^2}$ orbital that accepts one electron during the rate-determining step. Interestingly, although the metal is displaced from the center, the group spin densities for ^{5}**TS**$_{SO,2b}$ and ^{5}**TS**$_{SO,3b}$ are virtually the same. Specifically, the complexes give a spin of 3.82/3.84 on iron, 0.27/0.28 on oxygen and −0.43/−0.47 on the substrate.

These spin densities indeed confirm the electron transfer, as proposed in Scheme 1, that leaves a down-spin electron on the substrate antiferromagnetically coupled to five unpaired metal-based electrons. Overall, the sulfoxidation barrier heights hardly vary in electronic configuration despite the large energetic differences. Overall, the calculations show that methyl substituents on the sixth position, as in **3b**, have an effect on the position of the metal in the ligand framework such that the metal is pulled back into the center of the four pyridine rings during the rate-determining transition state. This has a dramatic effect on lowering the barrier height and consequently the reaction rate due to more favorable overlap between the donating (π^*_{xz}) and accepting ($\sigma^*_{z^2}$) orbital of the electron, although the reactant complexes do not appear to be systematically different. As such, the methyl substituents masquerade the oxidant and effectively position the substrate and oxidant for ideal HAA or OAT reactions.

© 2019 Wiley-VCH Verlag GmbH & Co. KGaA, Weinheim

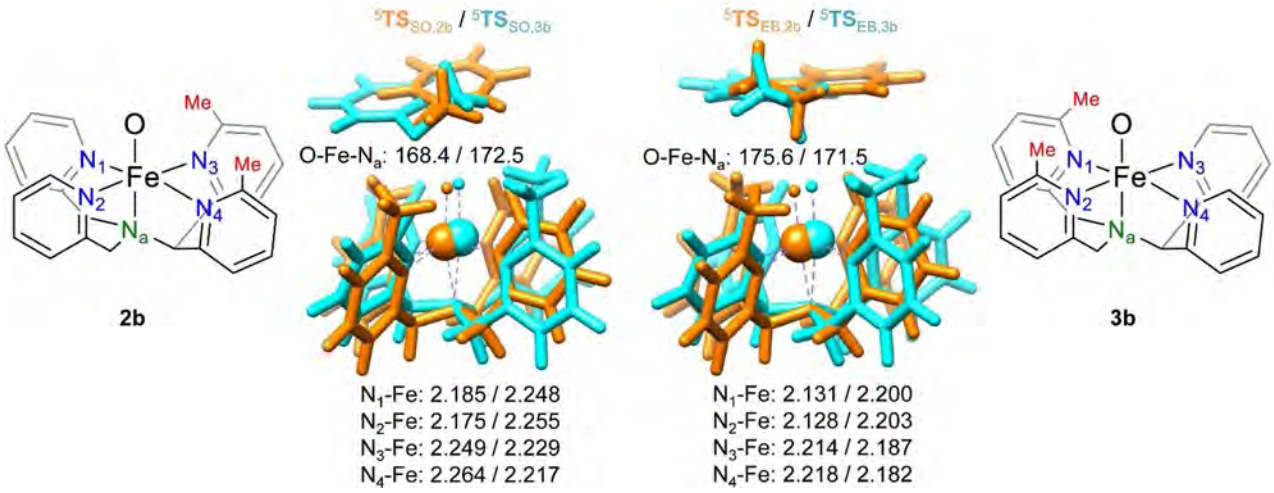

Figure 13. Overlay of optimized geometries of the quintet spin transition states for sulfoxidation and HAA by ^{5}**2b** and ^{5}**3b**. Bond lengths are given in angstroms and the O-Fe–N_{ax} angle is in degrees.

Conclusion

The reactivity of nonheme ferryl-oxo systems are very difficult to generalize and rational optimization of the ligand scaffolds are very tricky because these systems are extremely sensitive to backbone modifications. However, with the benchmarking of existing and new iron(IV)-oxo complexes in oxidation reactions, we have provided an experimental overview of the various reactivity trends. The theoretical study allows us to understand the fine interplay between electronic and steric effects generated by substituents that can be utilized as guidelines for a more rational synthetic approach to develop more efficient and selective systems. Overall, this research highlights the intricate details of subtle modifications to the primary- and secondary-coordination sphere of mononuclear nonheme iron(IV)-oxo model systems in an octahedral environment that brings forth the competitiveness of electronic and steric factors that influence their reactivity. With the synthesis and characterization of two new pentadentate ligand frameworks that are isomeric in mass and geometry, we have evidenced that the corresponding iron(IV)-oxo complexes possess differences in reactivity profiles towards HAA and OAT reactions. In fact, this study is unique in that regioselective substitution by methyl moieties in the same ligand skeleton provoke substantially different reactivity of the oxo species. In addition, the methyl groups shield the bulkier substrates like 9,10-DHA, fluorene and mainly triphenylmethane to make the catalysts reluctant towards these substrates, a phenomenon not observed before. Computational modelling rules out the electronic features of the complexes under study and establishes that a steric factor is the driving force behind this eccentric reactivity. Indeed, the methyl groups employed at the specified positions act as shafts to position the substrate and oxidant in a definite orientation in space. These substituents direct the corridors of substrate approach to the active site thereby tuning the efficiency of HAA or OAT reactions similar to what enzymatic catalysts do in proteins that channel the substrate and position the oxidant in an ideal conformation.

Experimental Section

Materials and methods: All chemicals were obtained from Sigma Aldrich Chemical Co., were of the best available purity and used without further purification unless otherwise stated. Solvents were dried according to published procedures[25] and distilled under argon prior to use. $H_2{}^{18}O$ (99.9% pure and enrichment 97.1 atom%) was purchased from Berry and Associates (Icon Isotopes). Substrates were passed through silica before reactivity study. Ethyl chloroformate, 95%, was purchased from Avra synthesis Pvt. Ltd. and purified prior to use. Metal complexes, including $[Fe^{II}(N4Py)](ClO_4)_2$ (**1a**), $[Fe^{II}(^{Me}N4Py)](ClO_4)_2$ (**2a**) and $[Fe^{II}(N4Py^{Me})](ClO_4)_2$ (**3a**) were synthesized inside a Jacomex glovebox filled with argon using procedures as described in the Supporting Information. Subsequently, the iron(IV)-oxo complexes, that is, $[Fe^{IV}(O)(N4Py)]^{2+}$ (**1b**), $[Fe^{IV}(O)(^{Me}N4Py)]^{2+}$ (**2b**) and $[Fe^{IV}(O)(N4Py^{Me})]^{2+}$ (**3b**) were prepared from their corresponding iron(II) complexes with 1.5 equivalents of $PhI(OAc)_2$ in CH_3CN at ambient temperature and pressure.

Characterization: UV/Vis spectra were recorded on a Hewlett Packard 8453 spectrophotometer equipped with either constant temperature circulating water bath or a liquid nitrogen cryostat (Unisoku) with a temperature controller. High-resolution electrospray ionization-mass spectra (ESI-MS) were recorded on a Waters (Micromass MS Technologies) Q-TOF Premier mass spectrometer by infusing samples directly into the source at 15 μL min^{-1} using a syringe pump. The spray voltage was set at 2 kV and the capillary temperature at 80 °C unless otherwise mentioned. NMR spectra were recorded on a Bruker Avance III HD 600 MHz spectrometer and a Jeol Advanced Solution State 400 MHz spectrometer (JNM-ECZ400S) using TMS as internal standard under ambient conditions. Product analysis of the reaction mixtures were done by ESI-MS, NMR (^{1}H and ^{13}C) with a Varian 400/100 MHz spectrometer and LCMS with WATERS ACQUITY UPLC equipped with a variable wavelength UV-200 detector. The crystal structure was recorded on an Agilent Single Crystal X-Ray Diffractometer (XRD) equipped with Mo X-ray source (Mova), CCD detector (Eos), Oxford cryo system and crystal AlisPRO and Autochem software.

Kinetics experiments: Upon addition of substrate to in situ generated iron(IV)-oxo species, the decay of the absorption band against time was monitored in the UV/Vis spectrum. Substrate concentrations were maintained in excess to obtain pseudo-first-order reac-

© 2019 Wiley-VCH Verlag GmbH & Co. KGaA, Weinheim

tion conditions. Kinetic profiles were obtained at four different substrate concentrations, which were plotted against the k_{obs} values to obtain a linear correlation and enabled us to determine second-order rate constants (k_2) for each reaction. The slopes pass through the origin to ensure minimum standard deviation and zero intercept on either axes. All UV/Vis spectra were measured in a 10 mm quartz cell.

Computations: Density functional theory calculations were performed for the reaction mechanisms of **1b**, **2b** and **3b** with ethylbenzene and *para*-Z-thioanisole with Z = OCH_3, CH_3, H, Cl and NO_2. Extensive benchmarking and testing of computational methods and procedures on this particular system was reported in previous work on the reactivity of $[Fe^{IV}(O)(N4Py)]^{2+}$ with *para*-Z-substituted thioanisole as well as dimethylsulfide.[26] These studies showed that the methods used here are in excellent agreement with experimentally determined free energies and enthalpies of activation. In particular, experimental rate constants were converted into free energy of activation values using transition state theory. Those values were within 4 kcal mol^{-1} from those calculated with DFT methods as used in this work. Full geometry optimizations (without constraints) were done with either UB3LYP/BS1 or UB3LYP/BS2 level of theory in Gaussian 09.[27–29] BS1 stands for LACVP with core potential on iron and 6-31G on the rest of the atoms, while BS2 represents a triple-ζ basis set (LACV3P+ on iron and 6–311+G* on the rest of the atoms). The calculations included a conductor polarized continuum model (CPCM) with a dielectric constant mimicking acetonitrile. In general, calculations obtained with UB3LYP/BS2 and UB3LYP/BS1//UB3LYP/BS2 gave virtually the same structures and energies. Transition states were characterized with a frequency calculation that gave a single imaginary frequency for the correct mode. In addition, for a selection of structures, intrinsic reaction coordinate (IRC) scans were performed. These IRCs connected the transition states to the reactants in one direction and to products in the reverse direction.

Crystallographic data: CCDC 1876766 (**2a**) and 232796 (**3a**) contains the supplementary crystallographic data for this paper. These data are provided free of charge by The Cambridge Crystallographic Data Centre.

Acknowledgements

Research support was provided by the Department of Science and Technology (SERB), India (EMR/2014/000279) to C.V.S.. S.d.V. and C.V.S. thank the British Council for a UK-India Education and Research Initiative grant (DST/INT/UK/P-151/2017). D.K. acknowledges financial support from the Department of Biotechnology, New Delhi (BT/PR14510/BID/07/334/2010). We also thank Central Instrumentation Facility (CIF) IIT Guwahati for providing instrumental facilities.

Conflict of interest

The authors declare no conflict of interest.

Keywords: biomimetic models · density functional calculations · iron-oxo · kinetics · steric effect

[1] a) M. Costas, M. P. Mehn, M. P. Jensen, L. Que, Jr., *Chem. Rev.* **2004**, *104*, 939–986; b) M. M. Abu-Omar, A. Loaiza, N. Hontzeas, *Chem. Rev.* **2005**, *105*, 2227–2252; c) C. Krebs, D. G. Fujimori, C. T. Walsh, J. M. Bollinger, Jr., *Acc. Chem. Res.* **2007**, *40*, 484–492; d) P. C. A. Bruijnincx, G. van Koten, R. J. M. Klein Gebbink, *Chem. Soc. Rev.* **2008**, *37*, 2716–2744; e) E. I. Solomon, K. M. Light, L. V. Liu, M. Srnec, S. D. Wong, *Acc. Chem. Res.* **2013**, *46*, 2725–2739; f) K. Ray, F. F. Pfaff, B. Wang, W. Nam, *J. Am. Chem. Soc.* **2014**, *136*, 13942–13958; g) X. Engelmann, I. Monte-Pérez, K. Ray, *Angew. Chem. Int. Ed.* **2016**, *55*, 7632–7649; *Angew. Chem.* **2016**, *128*, 7760–7778.

[2] a) B. Meunier, S. P. de Visser, S. Shaik, *Chem. Rev.* **2004**, *104*, 3947–3980; b) I. G. Denisov, T. M. Makris, S. G. Sligar, I. Schlichting, *Chem. Rev.* **2005**, *105*, 2253–2278; c) P. R. Ortiz de Montellano, *Chem. Rev.* **2010**, *110*, 932–948; d) D. Li, Y. Wang, K. Han, *Coord. Chem. Rev.* **2012**, *256*, 1137–1150; e) M. R. A. Blomberg, T. Borowski, F. Himo, R.-Z. Liao, P. E. M. Siegbahn, *Chem. Rev.* **2014**, *114*, 3601–3658; f) *Iron-containing enzymes: Versatile catalysts of hydroxylation reaction in nature* (Eds.: S. P. de Visser, D. Kumar), RSC, Cambridge, **2011**.

[3] a) E. I. Solomon, T. C. Brunold, M. I. Davis, J. N. Kemsley, S. K. Lee, N. Lehnert, F. Neese, A. J. Skulan, Y. S. Yang, J. Zhou, *Chem. Rev.* **2000**, *100*, 235–349; b) J. U. Rohde, J. H. In, M. H. Lim, W. W. Brennessel, M. R. Bukowski, A. Stubna, E. Münck, W. Nam, L. Que Jr, *Science* **2003**, *299*, 1037–1039; c) C. V. Sastri, J. Lee, K. Oh, Y. J. Lee, T. A. Jackson, K. Ray, H. Hirao, W. Shin, J. A. Halfen, J. Kim, L. Que Jr, S. Shaik, W. Nam, *Proc. Natl. Acad. Sci. USA* **2007**, *104*, 19181–19186; d) P. Comba, S. Wunderlich, *Chem. Eur. J.* **2010**, *16*, 7293–7299; e) S. V. Kryatov, E. V. Rybak-Akimova, S. Schindler, *Chem. Rev.* **2005**, *105*, 2175–2226.

[4] a) M. Lubben, A. Meetsma, E. C. Wilkinson, B. Feringa, L. Que, Jr., *Angew. Chem. Int. Ed.* **1995**, *34*, 1512–1515; *Angew. Chem.* **1995**, *107*, 1610–1612; b) J. Kaizer, E. J. Klinker, N. Y. Oh, J.-U. Rohde, W. J. Song, A. Stubna, J. Kim, E. Münck, W. Nam, L. Que, Jr., *J. Am. Chem. Soc.* **2004**, *126*, 472–473; c) E. J. Klinker, T. A. Jackson, M. P. Jensen, A. Stubna, G. Juhász, E. L. Bominaar, E. Münck, L. Que, Jr., *Angew. Chem. Int. Ed.* **2006**, *45*, 7394–7397; *Angew. Chem.* **2006**, *118*, 7554–7557; d) D. Wang, K. Ray, M. J. Collins, E. R. Farquhar, J. R. Frisch, L. Gómez, T. A. Jackson, M. Kerscher, A. Waleska, P. Comba, M. Costas, L. Que, Jr., *Chem. Sci.* **2013**, *4*, 282–292.

[5] a) A. C. McQuilken, Y. Jiang, M. A. Siegler, D. P. Goldberg, *J. Am. Chem. Soc.* **2012**, *134*, 8758–8761; b) S. Sahu, L. R. Widger, M. G. Quesne, S. P. de Visser, H. Matsumura, P. Moënne-Loccoz, M. A. Siegler, D. P. Goldberg, L. R. Widger, C. G. Davies, T. Yang, M. A. Siegler, O. Troeppner, G. N. L. Jameson, I. Ivanović-Burmazović, D. P. Goldberg, *J. Am. Chem. Soc.* **2013**, *135*, 10590–10593; c) L. R. Widger, C. G. Davies, T. Yang, M. A. Siegler, O. Troeppner, G. N. L. Jameson, I. Ivanović-Burmazović, D. P. Goldberg, *J. Am. Chem. Soc.* **2014**, *136*, 2699–2702; d) S. Sahu, M. G. Quesne, C. G. Davies, M. Dürr, I. Ivanović-Burmazović, M. A. Siegler, G. N. L. Jameson, S. P. de Visser, D. P. Goldberg, *J. Am. Chem. Soc.* **2014**, *136*, 13542–13545; e) S. Sahu, B. Zhang, C. J. Pollock, M. Dürr, C. G. Davies, A. M. Confer, I. Ivanović-Burmazović, M. A. Siegler, G. N. L. Jameson, C. Krebs, D. P. Goldberg, *J. Am. Chem. Soc.* **2016**, *138*, 12791–12802; f) M. Mitra, H. Nimir, S. Demeshko, S. S. Bhat, S. O. Malinkin, M. Haukka, J. Lloret-Fillol, G. C. Lisensky, F. Meyer, A. A. Shteinman, W. R. Browne, D. A. Hrovat, M. G. Richmond, M. Costas, E. Nordlander, *Inorg. Chem.* **2015**, *54*, 7152–7164; g) S. Rana, A. Dey, D. Maiti, *Chem. Commun.* **2015**, *51*, 14469–14472.

[6] a) W. Rasheed, A. Draksharapu, S. Banerjee, V. G. Young Jr, R. Fan, Y. Guo, M. Ozerov, J. Nehrkorn, J. Krzystek, J. Telser, L. Que Jr, *Angew. Chem. Int. Ed.* **2018**, *57*, 9387–9391; *Angew. Chem.* **2018**, *130*, 9531–9535; b) G. Mukherjee, C. W. Z. Lee, S. S. Nag, A. Alili, F. G. Cantú Reinhard, D. Kumar, C. V. Sastri, S. P. de Visser, *Dalton Trans.* **2018**, *47*, 14945–14957; c) S. Rana, J. P. Biswas, A. Sen, M. Clémancey, G. Blondin, J.-M. Latour, G. Rajaraman, D. Maiti, *Chem. Sci.* **2018**, *9*, 7843–7858.

[7] Y. Zang, J. Kim, Y. Dong, E. C. Wilkinson, E. H. Appelman, L. Que, Jr., *J. Am. Chem. Soc.* **1997**, *119*, 4197–4205.

[8] A. N. Biswas, M. Puri, K. K. Meier, W. N. Oloo, G. T. Rohde, E. L. Bominaar, E. Münck, L. Que, Jr., *J. Am. Chem. Soc.* **2015**, *137*, 2428–2431.

[9] M. S. Seo, N. H. Kim, K.-B. Cho, J. E. So, S. K. Park, M. Clémancey, R. G. Serres, J.-M. Latour, S. Shaik, W. Nam, *Chem. Sci.* **2011**, *2*, 1039–1045.

[10] a) C. E. Macbeth, A. P. Golombek, V. G. Young Jr, C. Yang, K. Kuczera, M. P. Hendrich, A. S. Borovik, *Science* **2000**, *289*, 938–941; b) J. England, M. Martinho, E. R. Farquhar, J. R. Frisch, E. L. Bominaar, E. Münck, L. Que Jr, *Angew. Chem. Int. Ed.* **2009**, *48*, 3622–3626; *Angew. Chem.* **2009**, *121*, 3676–3680; c) J. P. Bigi, W. H. Harman, B. Lassalle-Kaiser, D. M.

© 2019 Wiley-VCH Verlag GmbH & Co. KGaA, Weinheim

Robles, T. A. Stich, J. Yano, R. D. Britt, C. J. Chang, *J. Am. Chem. Soc.* **2012**, *134*, 1536 – 1542.

[11] a) A. K. Patra, M. M. Olmstead, P. K. Mascharak, *Inorg. Chem.* **2002**, *41*, 5403 – 5409; b) S. Kundu, J. V. K. Thompson, A. D. Ryabov, T. J. Collins, *J. Am. Chem. Soc.* **2011**, *133*, 18546 – 18549; c) S. A. Wilson, J. Chen, S. Hong, Y.-M. Lee, M. Clémancey, R. Garcia-Serres, T. Nomura, T. Ogura, J.-M. Latour, B. Hedman, K. O. Hodgson, W. Nam, E. I. Solomon, *J. Am. Chem. Soc.* **2012**, *134*, 11791 – 11806; d) I. Prat, A. Company, T. Corona, T. Parella, X. Ribas, M. Costas, *Inorg. Chem.* **2013**, *52*, 9229 – 9244; e) E. Wong, J. Jeck, M. Grau, A. J. P. White, G. J. P. Britovsek, *Catal. Sci. Technol.* **2013**, *3*, 1116 – 1122; f) M. Mitra, J. Lloret-Fillol, M. Haukka, M. Costas, E. Nordlander, *Chem. Commun.* **2014**, *50*, 1408 – 1410; g) X. Sun, C. Geng, R. Huo, U. Ryde, Y. Bu, J. Li, *J. Phys. Chem. B* **2014**, *118*, 1493 – 1500; h) R. Turcas, D. Lakk-Bogath, G. Speier, J. Kaizer, *Dalton Trans.* **2018**, *47*, 3248 – 3252.

[12] Crystals of complex **2a** were obtained as $[Fe(^{Me}N4Py)(CH_3CN)](BF_4)_2{\cdot}2H_2O$ while that for complex **3a** was reported as $[Fe(N4Py^{Me})(CH_3CN)](ClO_4)_2{\cdot}H_2O$.

[13] a) G. Roelfes, M. Lubben, K. Chen, R. Y. N. Ho, A. Meetsma, S. Genseberger, R. M. Hermant, R. Hage, S. K. Mandal, V. G. Young, Jr., Y. Zang, H. Kooijman, A. L. Spek, L. Que Jr., B. L. Feringa, *Inorg. Chem.* **1999**, *38*, 1929 – 1936; b) A. L. Spek, M. F. J. Schoondergang, B. L. Feringa, CCDC 232796, *CSD Communication* **2004**.

[14] M. S. Seo, J.-H. In, S. O. Kim, N. Y. Oh, J. Hong, J. Kim, L. Que, Jr., W. Nam, *Angew. Chem. Int. Ed.* **2004**, *43*, 2417 – 2420; *Angew. Chem.* **2004**, *116*, 2471 – 2474.

[15] a) E. J. Klinker, J. Kaizer, W. W. Brennessel, N. L. Woodrum, C. J. Cramer, L. Que, Jr., *Angew. Chem. Int. Ed.* **2005**, *44*, 3690 – 3694; *Angew. Chem.* **2005**, *117*, 3756 – 3760; b) K. Ray, J. England, A. T. Fiedler, M. Martinho, E. Münck, L. Que, Jr., *Angew. Chem. Int. Ed.* **2008**, *47*, 8068 – 8071; *Angew. Chem.* **2008**, *120*, 8188 – 8191; c) A. Company, G. Sabenya, M. González-Béjar, L. Gómez, M. Clémancey, G. Blondin, A. J. Jasniewski, M. Puri, W. S. Browne, J. M. Latour, L. Que, Jr., M. Costas, J. PérezPrieto, J. Lloret-Fillol, *J. Am. Chem. Soc.* **2014**, *136*, 4624 – 4633.

[16] a) M. H. Lim, J.-U. Rohde, A. Stubna, M. R. Bukowski, M. Costas, R. Y. N. Ho, E. Münck, W. Nam, L. Que, Jr., *Proc. Natl. Acad. Sci. U. S. A.* **2003**, *100*, 3665 – 3670; b) M. S. Seo, H. G. Jang, J. Kim, W. Nam, *Bull. Korean Chem. Soc.* **2005**, *26*, 971 – 974; c) M. You, M. S. Seo, K. M. Kim, W. Nam, J. Kim, *Bull. Korean Chem. Soc.* **2006**, *27*, 1140 – 1144; d) W. Nam, *Acc. Chem. Res.* **2007**, *40*, 522 – 531; e) S. Paria, S. Chatterjee, T. K. Paine, *Inorg. Chem.* **2014**, *53*, 2810 – 2821; f) D. Sheet, T. K. Paine, *Chem. Sci.* **2016**, *7*, 5322 – 5331.

[17] a) A. K. Vardhaman, P. Barman, S. Kumar, C. V. Sastri, D. Kumar, S. P. de Visser, *Angew. Chem. Int. Ed.* **2013**, *52*, 12288 – 12292; *Angew. Chem.* **2013**, *125*, 12514 – 12518; b) S. Kumar, A. S. Faponle, P. Barman, A. K. Vardhaman, C. V. Sastri, D. Kumar, S. P. de Visser, *J. Am. Chem. Soc.* **2014**, *136*, 17102 – 17115.

[18] A. K. Vardhaman, S. Sikdar, C. V. Sastri, *Ind. J. Chem.* **2011**, *50A*, 427 – 431.

[19] a) D. Kumar, H. Hirao, L. Que, Jr., S. Shaik, *J. Am. Chem. Soc.* **2005**, *127*, 8026 – 8027; b) S. P. de Visser, *J. Am. Chem. Soc.* **2006**, *128*, 9813 – 9824; c) L. Bernasconi, E.-J. Baerends, *Eur. J. Inorg. Chem.* **2008**, 1672 – 1681; d) S. D. Wong, C. B. Bell III, L. V. Liu, Y. Kwak, J. England, E. E. Alp, J. Zhao, L. Que, Jr., E. I. Solomon, *Angew. Chem. Int. Ed.* **2011**, *50*, 3215 – 3218; *Angew. Chem.* **2011**, *123*, 3273 – 3276; e) S. F. Ye, F. Neese, *Proc. Natl. Acad. Sci. USA* **2011**, *108*, 1228 – 1233; f) R. Latifi, M. A. Sainna, E. V. Rybak-Akimova, S. P. de Visser, *Chem. Eur. J.* **2013**, *19*, 4058 – 4068; g) T. Z. H. Gani, H. J. Kulik, *ACS Catal.* **2018**, *8*, 975 – 986.

[20] a) M. Martinho, F. Banse, J.-F. Bartoli, T. A. Mattioli, P. Battioni, O. Horner, S. Bourcier, J.-J. Girerd, *Inorg. Chem.* **2005**, *44*, 9592 – 9596; b) A. S. Borovik, *Acc. Chem. Res.* **2005**, *38*, 54 – 61; c) S. P. de Visser, J.-U. Rohde, J.-M. Lee, J. Cho, W. Nam, *Coord. Chem. Rev.* **2013**, *257*, 381 – 393; d) N. Y. Lee, D. Mandal, S. H. Bae, M. S. Seo, Y.-M. Lee, S. Shaik, K.-B. Cho, W. Nam, *Chem. Sci.* **2017**, *8*, 5460 – 5467.

[21] D. Kumar, R. Latifi, S. Kumar, E. V. Rybak-Akimova, M. A. Sainna, S. P. de Visser, *Inorg. Chem.* **2013**, *52*, 7968 – 7979.

[22] a) S. P. de Visser, *Chem. Eur. J.* **2006**, *12*, 8168 – 8177; b) L. Ji, A. S. Faponle, M. G. Quesne, M. A. Sainna, J. Zhang, A. Franke, D. Kumar, R. van Eldik, W. Liu, S. P. de Visser, *Chem. Eur. J.* **2015**, *21*, 9083 – 9092; c) M. G. Quesne, D. Senthilnathan, D. Singh, D. Kumar, P. Maldivi, A. B. Sorokin, S. P. de Visser, *ACS Catal.* **2016**, *6*, 2230 – 2224.

[23] a) S. P. de Visser, *J. Am. Chem. Soc.* **2010**, *132*, 1087 – 1097; b) X.-X. Li, V. Postils, W. Sun, A. S. Faponle, M. Solà, Y. Wang, W. Nam, S. P. de Visser, *Chem. Eur. J.* **2017**, *23*, 6406 – 6418; c) A. Timmins, M. G. Quesne, T. Borowski, S. P. de Visser, *ACS Catal.* **2018**, *8*, 8685 – 8698.

[24] a) L. E. Friedrich, *J. Org. Chem.* **1983**, *48*, 3851 – 3852; b) J. M. Mayer, *Acc. Chem. Res.* **1998**, *31*, 441 – 450; c) S. P. de Visser, D. Kumar, S. Cohen, R. Shacham, S. Shaik, *J. Am. Chem. Soc.* **2004**, *126*, 8362 – 8363.

[25] *Purification of Laboratory Chemicals* (Ed.: D. D. Perrin), Pergamon Press, Oxford, **1997**.

[26] a) T. Yang, M. G. Quesne, H. M. Neu, F. G. Cantú Reinhard, D. P. Goldberg, S. P. de Visser, *J. Am. Chem. Soc.* **2016**, *138*, 12375 – 12386; b) F. G. Cantú Reinhard, A. S. Faponle, S. P. de Visser, *J. Phys. Chem. A* **2016**, *120*, 9805 – 9814.

[27] a) C. Lee, W. Yang, R. G. Parr, *Phys. Rev. B* **1988**, *37*, 785 – 789; b) A. D. Becke, *J. Chem. Phys.* **1993**, *98*, 5648 – 5652.

[28] P. J. Hay, W. R. Wadt, *J. Chem. Phys.* **1985**, *82*, 270 – 283.

[29] Gaussian 09, Revision D.01, M. J. Frisch, G. W. Trucks, H. B. Schlegel, G. E. Scuseria, M. A. Robb, J. R. Cheeseman, G. Scalmani, V. Barone, B. Mennucci, G. A. Petersson, H. Nakatsuji, M. Caricato, X. Li, H. P. Hratchian, A. F. Izmaylov, J. Bloino, G. Zheng, J. L. Sonnenberg, M. Hada, M. Ehara, K. Toyota, R. Fukuda, J. Hasegawa, M. Ishida, T. Nakajima, Y. Honda, O. Kitao, H. Nakai, T. Vreven, J. A. Montgomery, Jr., J. E. Peralta, F. Ogliaro, M. Bearpark, J. J. Heyd, E. Brothers, K. N. Kudin, V. N. Staroverov, R. Kobayashi, J. Normand, K. Raghavachari, A. Rendell, J. C. Burant, S. S. Iyengar, J. Tomasi, M. Cossi, N. Rega, J. M. Millam, M. Klene, J. E. Knox, J. B. Cross, V. Bakken, C. Adamo, J. Jaramillo, R. Gomperts, R. E. Stratmann, O. Yazyev, A. J. Austin, R. Cammi, C. Pomelli, J. W. Ochterski, R. L. Martin, K. Morokuma, V. G. Zakrzewski, G. A. Voth, P. Salvador, J. J. Dannenberg, S. Dapprich, A. D. Daniels, Ö. Farkas, J. B. Foresman, J. V. Ortiz, J. Cioslowski, D. J. Fox, Gaussian, Inc., C. T. Wallingford, **2009**.

Manuscript received: December 29, 2018
Accepted manuscript online: February 5, 2019
Version of record online: March 12, 2019

© 2019 Wiley-VCH Verlag GmbH & Co. KGaA, Weinheim

Bioinorganic Chemistry

International Edition: DOI: 10.1002/anie.201905416
German Edition: DOI: 10.1002/ange.201905416

Hydrogen by Deuterium Substitution in an Aldehyde Tunes the Regioselectivity by a Nonheme Manganese(III)–Peroxo Complex

Prasenjit Barman, Fabián G. Cantú Reinhard, Umesh Kumar Bagha, Devesh Kumar, Chivukula V. Sastri, and Sam P. de Visser**

Abstract: *Mononuclear nonheme Mn^{III}-peroxo complexes are important intermediates in biology, and take part in oxygen activation by photosystem II. Herein, we present work on two isomeric biomimetic side-on Mn^{III}-peroxo intermediates with bispidine ligand system and reactivity patterns with aldehydes. The complexes are characterized with UV/Vis and mass spectrometric techniques and reaction rates with cyclohexane carboxaldehyde (CCA) are measured. The reaction gives an unusual regioselectivity switch from aliphatic to aldehyde hydrogen atom abstraction upon deuteration of the substrate, leading to the corresponding carboxylic acid product for the latter, while the former gives a deformylation reaction. Mechanistic details are established from kinetic isotope effect studies and density functional theory calculations. Thus, replacement of C–H by C–D raises the hydrogen atom abstraction barriers and enables a regioselectivity switch to a competitive pathway that is slightly higher in energy.*

In general, dioxygen in nature is mostly inert and will not react with substrates directly. To activate oxygen to its more reactive form, enzymes bind dioxygen on a transition metal center and through the use of either protons/electrons or a co-substrate convert it into a high-valent metal–oxo, metal–peroxo, metal–hydroperoxo, or metal–superoxo species.[1] These intermediates are responsible for the biological transformations of substrates in enzymes.[2] As the active oxygen species in enzymes are short-lived and highly reactive they are difficult to study experimentally. Manganese ions are present in the active site structure of numerous enzymes that utilize molecular oxygen, and are involved in harmful superoxide detoxification, decomposition of hydrogen peroxide, and water splitting.[3] Most of these enzymes include either a manganese–oxo, manganese–superoxo or manganese–peroxo structure as active intermediate in their catalytic cycle; however, these structures are short-lived and few have been characterized experimentally. As a consequence, biomimetic models have been created of manganese(III)–peroxo complexes that have ligand features of the enzymatic structures but lack the protein surrounding.[4]

A number of biomimetic manganese(III)–peroxo complexes have been synthesized and characterized with spectroscopic methods.[5] Furthermore, for some of those the reactivity against substrates has been tested.[6] In general, side-on manganese(III)–peroxo reacts via nucleophilic pathways, for instance, through deformylation of aldehydes.[7] Several of these metal–peroxo complexes have shown unusual reactivity patterns, whereby, for instance, aldehydes are converted into alkanes in the presence of a switchable H-atom donor.[8] Recent work of our groups implicated aldehyde deformylation of 2-phenylpropionaldehyde (2-PPA) to start with an initial and rate-determining hydrogen-atom abstraction, followed by keto-enol tautomerization and a deformylation reaction, and confirmed the electrophilic nature of these oxidants.[9] Clearly, side-on manganese(III)-peroxo complexes show a versatile reactivity pattern with a variety of substrates that is poorly understood, which encouraged us to look deeper into their reactivity with substrates.

In this work, we report the synthesis and characterization of two side-on manganese(III)–peroxo complexes (Figure 1) with a pentadentate N5 bispidine ligand backbone, namely $[Mn^{III}(O_2)(L^1)]^+$ (**1**) and $[Mn^{III}(O_2)(L^2)]^+$ (**2**) with L^1 = dimethyl-2,4-di(2-pyridyl)3-(pyridin-2-ylmethyl)-7-benzyl-3,7-diaza-bicyclo[3.3.1] nonan-9-one-1,5-dicarboxylate and L^2 = dimethyl 2,4-di(2-pyridyl)-3-benzyl-7-(pyridin-2-ylmethyl)-3,7-diazabicyclo[3.3.1] nonan-9-one-1,5-dicarboxylate.[9–11] Treatment of a colorless solution of the manganese(II) precursor with 10 equivalents of H_2O_2 and triethylamine

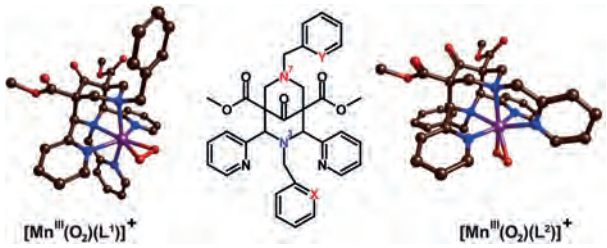

Figure 1. Oxidants investigated in this work. DFT-optimized structures of $[Mn^{III}(O_2)(L^1)]$ (left, X = N, Y = OH), and $[Mn^{III}(O_2)(L^2)]$ (right, X = CH, Y = N).

[*] Dr. P. Barman, U. K. Bagha, Dr. C. V. Sastri
Department of Chemistry, Indian Institute of Technology Guwahati, Guwahati (Assam), 781039 (India)
E-mail: sastricv@iitg.ernet.in
Dr. F. G. Cantú Reinhard, Dr. S. P. de Visser
Manchester Institute of Biotechnology and
School of Chemical Engineering and Analytical Science,
The University of Manchester
131 Princess Street, Manchester M1 7DN (UK)
E-mail: sam.devisser@manchester.ac.uk
Dr. D. Kumar
Department of Physics, School of Physical and Decision Sciences,
Babasaheb Bhimrao Ambedkar University
Lucknow, 226025 (India)
Supporting information and the ORCID identification number(s) for the author(s) of this article can be found under: https://doi.org/10.1002/anie.201905416.

 © 2019 Wiley-VCH Verlag GmbH & Co. KGaA, Weinheim

(TEA; 2.5 equivalents) in CH_3CN at 15 °C results in the formation of a blue and brown intermediate for **1** and **2**, respectively.[10] The identity of complexes **1** and **2** was confirmed by ultraviolet-visible absorption spectroscopy (UV/Vis) and electrospray ionization-mass spectrometry (ESI-MS) studies.[9,10] Few metal–peroxo oxidants have been reported that react via hydrogen-atom abstraction reactions, therefore, we decided to extend our work to other substrates to evaluate the factors responsible for such unique reaction pathways. As such we investigated the reactivity of complexes **1** and **2** with cyclohexane carboxaldehyde (CCA) as it is a classical substrate used in several reactivity studies by manganese(III)–peroxo complexes and generally gives cyclohexanone as product.[7d,12]

Upon addition of 40 equivalents of CCA to **1** in CH_3CN at 15 °C, the intermediate decayed immediately and led to cyclohexanone as product (Figure 2). The pseudo-first-order rate constant of the decay of **1** increased linearly with increasing CCA concentration, thus enabling us to determine the second-order rate constant of the reaction: $k_2 = 0.064\,M^{-1}s^{-1}$ (Figure 2b). In contrast, the second-order rate constant for the oxidation of CCA by **2** gave a rate constant k_2 of $0.291\,M^{-1}s^{-1}$. The rate changes between **1** and **2** are similar to those reported previously for the oxidation of 2-PPA.[9]

As previous work reported a rate-determining hydrogen-atom abstraction reaction, we decided to synthesize α-[D_1]-CCA and repeat the kinetics experiments with **1** and **2** (Figure 2c). Surprisingly, upon addition of 40 equivalents of α-[D_1]-CCA to **1** at 15 °C, an enhanced reaction rate compared to CCA was observed. The second-order rate constant for the reactivity of α-[D_1]-CCA with **1** was 50 times faster when compared with parent CCA and implicated an effective kinetic isotope effect (KIE) of 0.02. The product analysis by NMR spectroscopy revealed that the product for the reaction of α-[D_1]-CCA with **1** was cyclohexane carboxylic acid (Scheme 1), rather than the expected cyclohexanone.

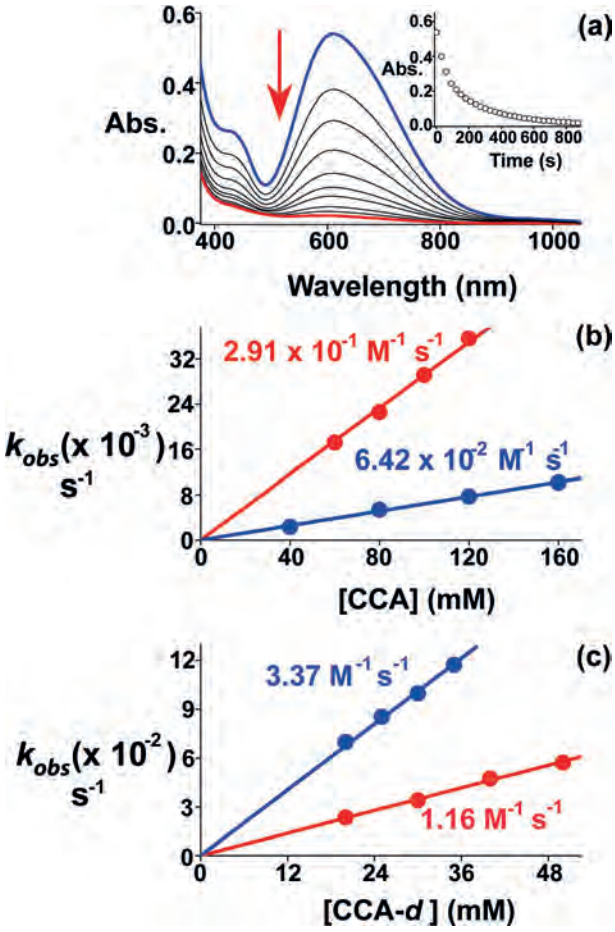

Figure 2. Kinetic studies for the reaction of **1** and **2** with CCA: a) UV/Vis spectral changes of **1** (2 mM) upon addition of CCA (120 mM) in the presence of TEA (5 mM) and hydrogen peroxide (20 mM) in CH_3CN at 15 °C. Inset shows the time course of the absorbance at 605 nm. b) Plot of k_{obs} against the concentration of CCA: second-order rate constant for the reaction of 2 mM **1** (blue) and **2** (red) with various substrate concentrations in CH_3CN at 15 °C. c) Plot of k_{obs} against the concentration of α-[D_1]-CCA (approximately 90%, D enriched) with 2 mM **1** (blue) and **2** (red) in CH_3CN at 15 °C.

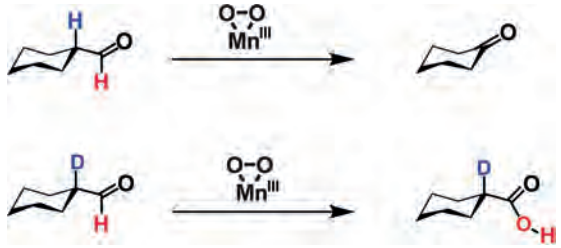

Scheme 1. Products obtained for the reaction of 1 and 2 with substrates.

This clearly indicates a regioselectivity switch for hydrogen-atom abstraction from the α-position of substrate to the aldehyde hydrogen atom. The observed second-order rate constants for the reaction of α-[D_1]-CCA with **1** and **2** were $3.37\,M^{-1}s^{-1}$ and $1.16\,M^{-1}s^{-1}$, respectively. These observed trends are in contrast to those obtained for the reaction of **1** and **2** with 2-PPA. As far as we know, our observation of the oxidation of α-[D_1]-CCA to its corresponding acid is the first experimental evidence of a Mn^{III}–peroxo intermediate that reacts via an electrophilic oxidation reaction. The observed oxidation rates of **1** and **2** follow a similar trend as shown previously for $[Mn^{IV}(O)(L^1)]^{2+}$ versus $[Mn^{IV}(O)(L^2)]^{2+}$.[10] This unique regioselectivity switch observed here may be the result of two competing pathways that are close in energy and deuteration reverses the ordering of the transition states and hence the product distributions, as seen, for instance, in the hydroxylation of ethylbenzene versus ethylbenzene-[D_{10}] with iron(IV)–oxo complexes.[13]

To substantiate our hypothesis further, we synthesized 1,2-di-deuterio-cyclohexane carboxaldehyde (approximately 90%, D enriched, 1,2-[D_2]-CCA). Upon addition of 40 equivalents of 1,2-[D_2]-CCA to **1** in CH_3CN at 15 °C, the corresponding intermediate readily decayed, enabling us to follow the reaction spectroscopically. A second-order rate constant of $4.8 \times 10^{-2}\,M^{-1}s^{-1}$ with an effective KIE of 70 was determined.

To gain insight into the regioselectivity switch and the nature of the oxidant and reactivity patterns, we decided to

 © 2019 Wiley-VCH Verlag GmbH & Co. KGaA, Weinheim

These are not the final page numbers!

complement our work with a density functional theory (DFT) study. Although several DFT methods were tested (see the Supporting Information for details), we will focus on the B3LYP and B3LYP-D3 results in the main text only. In general, all methods predict the same trends and give analogous optimized structures. We then calculated a reactant complex (**Re**) of CCA with **1**. The geometry and electronic configuration of the manganese–peroxo complex changed little upon complexation with CCA. Thereafter, two hydrogen-atom abstraction pathways were investigated, namely via transition state ^{5}**TS**$_{HA,ald}$ for hydrogen-atom abstraction from the aldehyde C–H bond, and via transition state ^{5}**TS**$_{HA,\alpha}$ for hydrogen-atom abstraction from the C$^\alpha$–H bond of CCA.

In both cases an end-on manganese–hydroperoxo with a substrate radical is formed (**I**$_{HA,ald}$ and **I**$_{HA,\alpha}$) after hydrogen-atom abstraction. The two hydrogen-atom abstraction transition states are shown in Figure 3 and give the typical features seen before.[9] Thus, ^{5}**TS**$_{HA,Ald}$ is late with a long C–H distance of 1.425 {1.406} Å and a short O–H distance of 1.147 {1.173} Å and with the hydroperoxo group in end-on configuration as calculated at the B3LYP/BS1 {B3LYP-D3/BS2} level of theory. As such there is little effect of changing the basis set on the optimized geometries of the transition state structures. Although the optimized geometries have end-on features, an intrinsic reaction coordinate scan (Supporting Information, Figure S23) shows the structure to connect to the side-on Mn^{III}–peroxo reactant, but upon approach of substrate to oxidant it reorients from side-on to end-on Mn^{III}–peroxo without an isomerization barrier. The aliphatic hydrogen-atom abstraction barrier (^{5}**TS**$_{HA,\alpha}$) also is late with similar C–H and O–H distances with respect to ^{5}**TS**$_{HA,ald}$ with distances of 1.422 {1.447} and 1.161 {1.155} Å as calculated at the B3LYP/BS1 {B3LYP-D3/BS2} level of theory, respectively. In general, late hydrogen-atom abstraction transition states correspond to energetically high barriers,[14] which indeed is seen for this process and matches the experimental reaction rates well.

Free energies of activation for the two reaction pathways were calculated from the Gaussian frequencies using thermal, solvent, and entropic corrections to the enthalpy. As gas-phase calculated entropies tend to be overestimated with respect to experiment,[15] we applied two entropic correction models. Firstly, we used the Wertz correction (model 1) that scales the molecular entropy of each compound ($\Delta G_{Wertz}^{\ddagger}$). Secondly, the lowest entropy contributions for low vibrational frequencies ($< 50\ cm^{-1}$) were ignored from the free energies in model 2 ($\Delta G_{vibr}^{\ddagger}$). These two different free energies of activation for hydrogen-atom abstraction from the α- and aldehyde C–H positions are given in the Table in Figure 3. As can be seen from Figure 3, the two barriers (^{5}**TS**$_{HA,ald}$ and ^{5}**TS**$_{HA,\alpha}$) are within 1 kcal mol^{-1} of each other and dependent on the model and calculation procedure (see the Supporting Information for a detailed comparison of different methods and basis sets) either ^{5}**TS**$_{HA,\alpha}$ or ^{5}**TS**$_{HA,ald}$ is lower in energy. Within transition state theory, the experimental rate constant of $6.4 \times 10^{-2}\ M^{-1}s^{-1}$ would correspond to a free energy of activation of 18.4 kcal mol^{-1}. Therefore, our computed barriers with vibrational corrections included are in excellent agreement with the experimental values and also predict the correct regioselectivity.

With vibrational corrections applied, the lowest free energy of activation is via ^{5}**TS**$_{HA,\alpha}$ with a $\Delta G^{\ddagger}_{\alpha,vibr}$ of 18.1 kcal mol^{-1}, while the aldehyde hydrogen atom abstraction is $\Delta G^{\ddagger}_{ald,vibr} = 18.6$ kcal mol^{-1}. As such, the calculations reproduce the experimental product distributions and predict regioselective hydrogen-atom abstraction of the C$^\alpha$–H bond. Although the Wertz-corrected free energies point to a reversed regioselectivity, actually upon deuteration of the

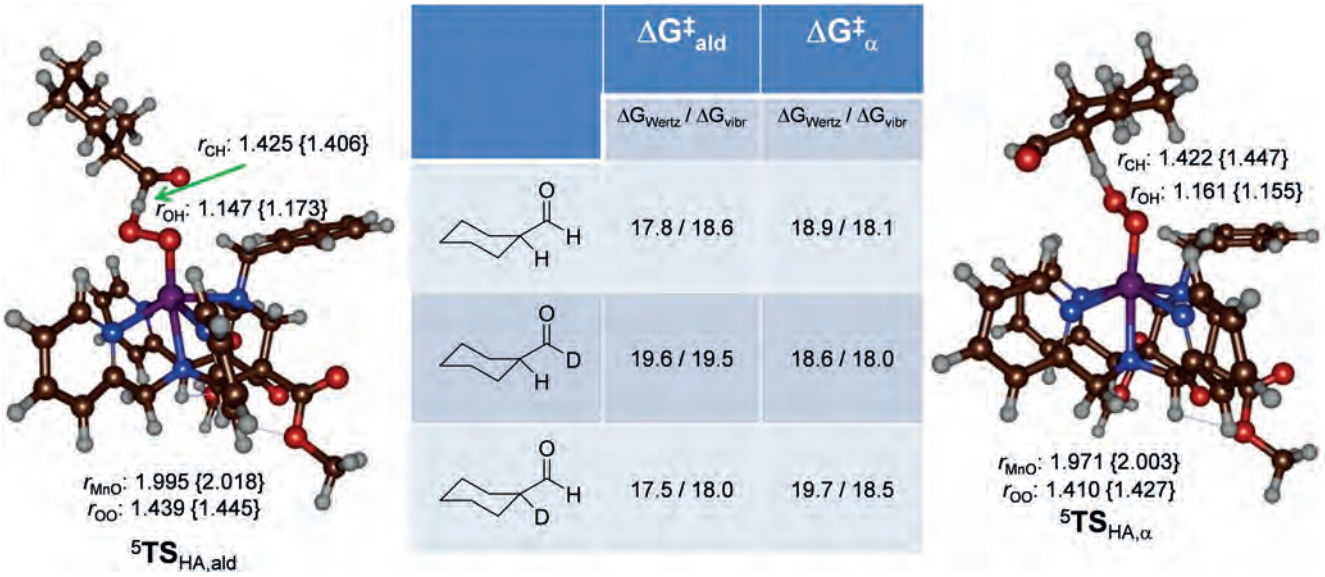

Figure 3. Hydrogen-atom abstraction transition states optimized at UB3LYP/BS1 {UB3LYP-D3/BS2} from aldehyde group (left) and C$^\alpha$–H bond (right) with bond lengths in angstroms. The table gives corrected (Wertz/vibrational) free energies of activation calculated at UB3LYP/BS2//UB3LYP/BS1 level of theory for the two pathways for hydrogen-atom subtraction by **1** from CCA, 1-[D$_1$]-CCA and, 2-[D$_1$]-CCA with values in kcal mol^{-1}.

© 2019 Wiley-VCH Verlag GmbH & Co. KGaA, Weinheim

C^{α}–H group both models predict a rise of $^{5}\mathbf{TS}_{HA,\alpha}$ by about 1 kcal mol^{-1}, while the $^{5}\mathbf{TS}_{HA,ald}$ barrier drops slightly. Therefore, singly deuterating the C^{α}–H group results in a regioselectivity switch from C^{α}–H hydrogen-atom abstraction to aldehyde hydrogen-atom abstraction. On the other hand, deuteration of the aldehyde position of substrate raises the $^{5}\mathbf{TS}_{HA,ald}$ barriers, but keeps the $^{5}\mathbf{TS}_{HA,\alpha}$ barriers more or less the same. The computational trends, therefore, agree with experimental observation and implicate a regioselectivity switch upon deuteration of the α-position of CCA substrate. As reasoned before,[15] a hydrogen-atom transfer (HAT) reaction has a large zero-point energy due to the loss of one C–H vibration in the complex. In general, HAT barriers increase in energy by a few kcal mol^{-1} upon deuteration of the transferring hydrogen atom.[16] Thus, with two competing barriers very close in energy, substrate deuteration raises the lowest barrier in energy and leads to a regioselectivity switch.

As shown before, hydrogen-atom abstraction reactions often have barriers that correlate with the strength of the C–H bond that is broken in the process.[14,17] Therefore, we calculated the C–H bond dissociation energy (BDE) of the C^{α}–H and $C_{aldehyde}$–H bonds from the energy of the substrate with respect to an isolated hydrogen atom and the substrate radical, and find values of ΔG of 72.1 and 79.5 kcal mol^{-1}, respectively. Based on these values, the reaction should give dominant hydrogen-atom abstraction from the C^{α}–H bond, as seen for the natural substrate. The reason the $^{5}\mathbf{TS}_{HA,\alpha}$ and $^{5}\mathbf{TS}_{HA,ald}$ barriers are within 1 kcal mol^{-1} is probably due to electrostatic repulsions between the L^{1} ligand protons and those from the approaching substrate that are stronger in $^{5}\mathbf{TS}_{HA,\alpha}$ than in $^{5}\mathbf{TS}_{HA,ald}$, where the cyclohexane ring is further away from the ligand structure.

In summary, a couple of Mn^{III}–peroxo complexes bearing pentadentate bispidine backbone were synthesized and characterized with various spectroscopic techniques and studied with DFT. We demonstrate here for the first time that the Mn^{III}–peroxo complex can perform electrophilic oxidation of substrates through the hydrogen-atom abstraction from the C–H bond of an aldehyde to give the corresponding acid as the product.

Acknowledgements

Research support was provided by the Department of Science and Technology (SERB), India (EMR/2014/000279) to C.V.S. S.dV. and C.V.S. thank the British Council for a UK-India Research Initiative grant (DST/INT/UK/P-151/2017). F.C. thanks the Conacyt Mexico for a studentship. D.K. acknowledges financial support from the Department of Biotechnology, New Delhi (BT/PR14510/BID/07/334/2010).

Conflict of interest

The authors declare no conflict of interest.

Keywords: biomimetic models · density functional theory · hydrogen atom abstraction · kinetic isotope effects · oxidation

[1] a) *Cytochrome P450: Structure, Mechanism, and Biochemistry*, 3rd ed. (Ed.: P. R. Ortiz de Montellano), Kluwer Academic/Plenum Publishers, New York, **2005**; b) *Biomimetic Oxidations Catalyzed by Transition Metal Complexes* (Ed.: B. Meunier), Imperial College Press, London, **2000**.

[2] a) M. Costas, M. P. Mehn, M. P. Jensen, L. Que, Jr., *Chem. Rev.* **2004**, *104*, 939–986; b) C. Krebs, D. G. Fujimori, C. T. Walsh, J. M. Bollinger, Jr., *Acc. Chem. Res.* **2007**, *40*, 484–492; c) E. I. Solomon, K. M. Light, L. V. Liu, M. Srnec, S. D. Wong, *Acc. Chem. Res.* **2013**, *46*, 2725–2739.

[3] a) A. F. Miller, *Acc. Chem. Res.* **2008**, *41*, 501–510; b) R. Eisenberg, H. B. Gray, *Inorg. Chem.* **2008**, *47*, 1697–1699; c) A. J. Wu, J. E. Penner-Hahn, V. L. Pecoraro, *Chem. Rev.* **2004**, *104*, 903–938.

[4] a) S. V. Kryatov, E. V. Rybak-Akimova, S. Schindler, *Chem. Rev.* **2005**, *105*, 2175–2226; b) M. M. Abu-Omar, A. Loaiza, N. Hontzeas, *Chem. Rev.* **2005**, *105*, 2227–2252; c) W. Nam, *Acc. Chem. Res.* **2007**, *40*, 522–531; d) P. C. A. Bruijnincx, G. van Koten, R. J. M. Klein Gebbink, *Chem. Soc. Rev.* **2008**, *37*, 2716–2744; e) M. Atanasov, P. Comba, S. Hausberg, B. Martin, *Coord. Chem. Rev.* **2009**, *253*, 2306–2314; f) M. Costas, *Coord. Chem. Rev.* **2011**, *255*, 2912–2932; g) A. R. McDonald, L. Que, Jr., *Coord. Chem. Rev.* **2013**, *257*, 414–428; h) P. Saisaha, J. W. de Boer, W. R. Browne, *Chem. Soc. Rev.* **2013**, *42*, 2059–2074.

[5] a) G. Roelfes, V. Vrajmasu, K. Chen, R. Y. N. Ho, J.-U. Rohde, C. Zondervan, R. M. la Crois, E. P. Schudde, M. Lutz, A. L. Spek, R. Hage, B. L. Feringa, E. Münck, L. Que, Jr., *Inorg. Chem.* **2003**, *42*, 2639–2653; b) J. Annaraj, Y. Suh, M. S. Seo, S. O. Kim, W. Nam, *Chem. Commun.* **2005**, 4529–4531; c) A. Thibon, J.-F. Bartoli, S. Bourcier, F. Banse, *Dalton Trans.* **2009**, 9587–9594; d) A. Mukherjee, M. A. Cranswick, M. Chakrabarti, T. K. Paine, K. Fujisawa, E. Münck, L. Que, Jr., *Inorg. Chem.* **2010**, *49*, 3618–3628; e) J. Cho, S. Jeon, S. A. Wilson, L. V. Liu, E. A. Kang, J. J. Braymer, M. H. Lim, B. Hedman, K. O. Hodgson, J. S. Valentine, E. I. Solomon, W. Nam, *Nature* **2011**, *478*, 502–505; f) D. F. Leto, S. Chattopadhyaay, V. W. Day, T. A. Jackson, *Dalton Trans.* **2013**, *42*, 13014–13025; g) D. Brazzolotto, F. G. Cantú Reinhard, J. Smith-Jones, M. Retegan, L. Amidani, A. S. Faponle, K. Ray, C. Philouze, S. P. de Visser, M. Gennari, C. Duboc, *Angew. Chem. Int. Ed.* **2017**, *56*, 8211–8215; *Angew. Chem.* **2017**, *129*, 8323–8327.

[6] a) M. K. Coggins, J. A. Kovacs, *J. Am. Chem. Soc.* **2011**, *133*, 12470–12473; b) J. Cho, R. Sarangi, W. Nam, *Acc. Chem. Res.* **2012**, *45*, 1321–1330; c) M. K. Coggins, V. Martin-Diaconescu, S. DeBeer, J. A. Kovacs, *J. Am. Chem. Soc.* **2013**, *135*, 4260–4272; d) H. E. Colmer, A. W. Howcroft, T. A. Jackson, *Inorg. Chem.* **2016**, *55*, 2055–2069; e) Q. Zhang, A. Bell-Taylor, F. M. Bronston, J. D. Gorden, C. R. Goldsmith, *Inorg. Chem.* **2017**, *56*, 773–782.

[7] a) R. B. VanAtta, C. E. Strouse, L. K. Hanson, J. S. Valentine, *J. Am. Chem. Soc.* **1987**, *109*, 1425–1434; b) N. Kitajima, H. Komatsuzaki, S. Hikichi, M. Osawa, Y. Moro-Oka, *J. Am. Chem. Soc.* **1994**, *116*, 11596–11597; c) M. S. Seo, J. Y. Kim, J. Annaraj, Y. Kim, Y.-M. Lee, S.-J. Kim, J. Kim, W. Nam, *Angew. Chem. Int. Ed.* **2007**, *46*, 377–380; *Angew. Chem.* **2007**, *119*, 381–384; d) R. A. Geiger, S. Chattopadhyay, V. W. Day, T. A. Jackson, *Dalton Trans.* **2011**, *40*, 1707–1715.

[8] A. Shokri, L. Que, Jr., *J. Am. Chem. Soc.* **2015**, *137*, 7686–7691.

[9] a) P. Barman, P. Upadhyay, A. S. Faponle, J. Kumar, S. S. Nag, D. Kumar, C. V. Sastri, S. P. de Visser, *Angew. Chem. Int. Ed.* **2016**,

 © 2019 Wiley-VCH Verlag GmbH & Co. KGaA, Weinheim

These are not the final page numbers!

55, 11091 – 11095; *Angew. Chem.* **2016**, *128*, 11257 – 11261; b) F. G. Cantú Reinhard, P. Barman, G. Mukherjee, J. Kumar, D. Kumar, D. Kumar, C. V. Sastri, S. P. de Visser, *J. Am. Chem. Soc.* **2017**, *139*, 18328 – 18338.

[10] P. Barman, A. K. Vardhaman, B. Martin, S. J. Wörner, C. V. Sastri, P. Comba, *Angew. Chem. Int. Ed.* **2015**, *54*, 2095 – 2099; *Angew. Chem.* **2015**, *127*, 2123 – 2127.

[11] L^1 = dimethyl-2,4-di(2-pyridyl)3-(pyridin-2-ylmethyl)-7-benzyl-3,7-diaza-bicyclo[3.3.1] nonan-9-one-1,5-dicarboxylate and L^2 = dimethyl 2,4-di(2-pyridyl)-3-benzyl-7-(pyridin-2-ylmethyl)-3,7-diazabicyclo[3.3.1] nonan-9-one-1,5-dicarboxylate.

[12] R. L. Shook, W. A. Gunderson, J. Greaves, J. W. Ziller, M. P. Hendrich, A. S. Borovik, *J. Am. Chem. Soc.* **2008**, *130*, 8888 – 8889.

[13] a) W. J. Song, Y. O. Ryu, R. Song, W. Nam, *J. Biol. Inorg. Chem.* **2005**, *10*, 294 – 304; b) S. P. de Visser, *Chem. Eur. J.* **2006**, *12*, 8168 – 8177.

[14] S. Shaik, D. Kumar, S. P. de Visser, *J. Am. Chem. Soc.* **2008**, *130*, 10128 – 10140.

[15] S. P. de Visser, F. Ogliaro, P. K. Sharma, S. Shaik, *Angew. Chem. Int. Ed.* **2002**, *41*, 1947 – 1951; *Angew. Chem.* **2002**, *114*, 2027 – 2031.

[16] X.-X. Li, V. Postils, W. Sun, A. S. Faponle, M. Solà, Y. Wang, W. Nam, S. P. de Visser, *Chem. Eur. J.* **2017**, *23*, 6406 – 6418.

[17] F. G. Cantú Reinhard, A. S. Faponle, S. P. de Visser, *J. Phys. Chem. A* **2016**, *120*, 9805 – 9814.

Manuscript received: May 1, 2019
Accepted manuscript online: May 20, 2019
Version of record online: ■■ ■■, ■■■■

 © 2019 Wiley-VCH Verlag GmbH & Co. KGaA, Weinheim

Communications

Bioinorganic Chemistry

P. Barman, F. G. Cantú Reinhard, U. K. Bagha, D. Kumar, C. V. Sastri,* S. P. de Visser* _____ ■■■■–■■■■

Hydrogen by Deuterium Substitution in an Aldehyde Tunes the Regioselectivity by a Nonheme Manganese(III)–Peroxo Complex

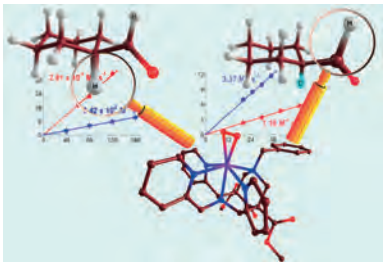

Regioselective hydrogen-atom abstraction: A combined experimental and computational study gives evidence of electrophilic reactivity of a side-on manganese(III)–peroxo complex. Furthermore, isotopic substitution of the substrate changes the regioselectivity of the reaction and the product distributions.

© 2019 Wiley-VCH Verlag GmbH & Co. KGaA, Weinheim

These are not the final page numbers!

ChemPubSoc Europe

DOI: 10.1002/chem.201604361

CHEMISTRY A European Journal Full Paper

Reaction Mechanisms

A Systematic Account on Aromatic Hydroxylation by a Cytochrome P450 Model Compound I: A Low-Pressure Mass Spectrometry and Computational Study

Fabián G. Cantú Reinhard[+],[a] Mala A. Sainna[+],[a] Pranav Upadhyay,[b] G. Alex Balan,[a] Devesh Kumar,[b] Simonetta Fornarini,*[c] Maria Elisa Crestoni,*[c] and Sam P. de Visser*[a]

Abstract: Cytochrome P450 enzymes are heme-containing mono-oxygenases that mainly react through oxygen-atom transfer. Specific features of substrate and oxidant that determine the reaction rate constant for oxygen atom transfer are still poorly understood and therefore, we did a systematic gas-phase study on reactions by iron(IV)-oxo porphyrin cation radical structures with arenes. We present herein the first results obtained by using Fourier transform-ion cyclotron resonance mass spectrometry and provide rate constants and product distributions for the assayed reactions. Product distributions and kinetic isotope effect studies implicate a rate-determining aromatic hydroxylation reaction that correlates with the ionization energy of the substrate and no evidence of aliphatic hydroxylation products is observed. To further understand the details of the reaction mechanism, a computational study on a model complex was performed. These studies confirm the experimental hypothesis of dominant aromatic over aliphatic hydroxylation and show that the lack of an axial ligand affects the aliphatic pathways. Moreover, a two-parabola valence bond model is used to rationalize the rate constant and identify key properties of the oxidant and substrate that drive the reaction. In particular, the work shows that aromatic hydroxylation rates correlate with the ionization energy of the substrate as well as with the electron affinity of the oxidant.

Introduction

Aromatic hydroxylation is a challenging catalytic reaction because a very strong C–H bond of a substrate needs to be broken in the process. Several enzymes in nature have developed procedures to enable an aromatic hydroxylation or even a dioxygenation.[1] Among those are the nonheme iron dioxygenases that regio- and stereospecifically dihydroxylate an aromatic substrate into a catechol.[2] Highly relevant for environmental purposes are, for instance, the naphthalene dioxygenases that have functions in biotechnology that include the cleaning up of oil-spills and removal of aromatic compounds from soil.[3] Also, in the human body applications of heme and nonheme iron dioxygenases are found, for instance, for the biodegradation of aromatic amino acids starting with a mono- or dihydroxylation reaction.[4] Further arene-activating enzymes in the body include the thiolate-ligated heme mono-oxygenases called cytochromes P450 (P450) that have been shown to hydroxylate arenes to phenols as a means to metabolize drugs as well as xenobiotic molecules in the liver.[5]

The full details of the mechanism of the latter processes are still shrouded in many mysteries and so far, no experimental reaction rates have been obtained. Progress in understanding the P450-type reaction mechanisms has been made in the fields of computational chemistry and low-pressure mass spectrometry.[6,7] In particular, recently, Fourier transform-ion cyclotron resonance mass spectrometry (FT-ICR MS) has been used by us to trap and characterize a pentacoordinated model complex of the active species of P450 enzymes (Compound I, CpdI).[8] We have utilized this experience and measured low-pressure thermal rate constants of aromatic hydroxylation by this CpdI model for the first time and present these results here.

P450 CpdI is a high-valent iron(IV)-oxo heme cation radical, which is bound to the enzyme through a thiolate bridge of a conserved cysteinate residue. It has been spectroscopically

[a] F. G. Cantú Reinhard,[+] Dr. M. A. Sainna,[+] G. A. Balan, Dr. S. P. de Visser
Manchester Institute of Biotechnology and School of Chemical Engineering and Analytical Science
The University of Manchester, 131 Princess Street
Manchester M1 7DN (UK)
E-mail: sam.devisser@manchester.ac.uk

[b] P. Upadhyay, Dr. D. Kumar
Department of Applied Physics, School for Physical Sciences
Babasaheb Bhimrao Ambedkar University, Vidya Vihar
Rae Bareilly Road, Lucknow (UP) 226025, (India)

[c] Prof. Dr. S. Fornarini, Prof. Dr. M. E. Crestoni
Dipartimento di Chimica e Tecnologie del Farmaco
Università di Roma "La Sapienza", P.le A. Moro 5
00185, Roma, (Italy)
E-mail: simonetta.fornarini@uniroma1.it
mariaelisa.crestoni@uniroma1.it

[+] Both authors contributed equally to this work.

Supporting information and the ORCID identification number(s) for the author(s) of this article can be found under http://dx.doi.org/10.1002/chem.201604361.

© 2016 Wiley-VCH Verlag GmbH & Co. KGaA, Weinheim

trapped and characterized at low temperature for one specific isozyme, but experimental rate constants could be determined for only very few substrates due to its short lifetime.[9] As such, much is to be gained from understanding the reactivity patterns of CpdI with substrates and particularly on the regioselectivity and bifurcation patterns leading to a variety of products. On the other hand, CpdI and its reactivity patterns with substrates have been extensively studied with computational methods and detailed mechanisms of aromatic and aliphatic hydroxylation as well as sulfoxidation were established.[10]

Figure 1 shows the active site description of P450 CYP120 A1 with the heme and its link to Cys_{391} highlighted. These crystal structure coordinates contain retinoic acid as a substrate in the vicinity of the heme on its distal site.[11] CpdI was shown to be a versatile oxidant and to react efficiently with a variety of different substrates. In our previous work we reported a combined mass spectrometric and computational study on a biomimetic model of CpdI, in which the protoporphyrin IX was replaced by 5,10,15,20-tetrakis(pentafluorophenyl) porphyrin (TPFPP), Figure 1 b.[12] The ensuing $[Fe^{IV}(O)(TPFPP^{+\bullet})]^+$ cation was trapped in the cell of an FT-ICR mass spectrometer and its reactivity studied with a selection of olefins.

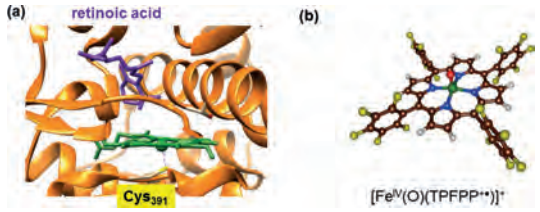

Figure 1. Enzymatic and biomimetic models of cytochrome P450 CpdI. (a) Active site structure as taken of substrate bound-resting state P450 from the 2VE3 pdb file. (b) Biomimetic model investigated here.

These studies established rate constants for olefin epoxidation, showing them to correlate with the ionization energy (IE) of the substrate that is activated. Subsequently, DFT calculations confirmed the observed trend and using a valence bond (VB) scheme highlighted the major components of the oxidant and substrate that contribute to the free energy of activation. To gain further insight into the reactivity patterns of CpdI model complexes using a combined FT-ICR MS and DFT approach, we decided to follow up our studies with work on aromatic hydroxylation. We propose a nucleophilic addition pathway as the rate determining reaction step, whereby the rate is determined by the ionization potential of the substrate and the π/π^* energy splitting of the CpdI models as well as electron reorganization energies within the complex. Furthermore, it is found that the removal of the axial cysteinate ligand as in the FT-ICR MS model used here raises the energies of the aliphatic hydroxylation pathways dramatically and prevents these product channels. The studies, therefore, give evidence of the axial ligand to be crucial in determining the activity and potential of the reactive oxidant of P450 enzymes.

Results

Experiment

In previous work, we established working procedures for the trapping of high-valent transition-metal-oxo intermediates in an FT-ICR MS.[7,12] These studies identified structures with *m/z* 1044 in the mass spectrum representing $[Fe^{IV}(O)(TPFPP^{+\bullet})]^+$ ions in good abundance and with long enough lifetime to enable ion-molecule reactions in the gas-phase. These procedures enabled us to do a systematic study into olefin epoxidation by these ions,[12] which established reactivity trends and a model that accounts for the observed reactivity. We decided to follow the study up with a systematic account on arene hydroxylation processes. In particular, a series of 16 aromatic substrates were investigated and their second-order rate constants (k_{exp}) determined in a reaction with $[Fe^{IV}(O)(TPFPP^{+\bullet})]^+$. Note that due to bifurcation processes, multiple reaction channels and products are possible, leading to aromatic and aliphatic hydroxylation products. Using the Average Dipole Orientation (ADO) theory (see Methods), the experimental rate constants were converted into reaction efficiencies (Φ) that represent the fraction of reactive collisions.

Table 1 summarizes the experimentally determined reaction rates for all substrates as well as their individual product distributions. Also included are ionization energies (IE) taken from the NIST database.[13] Thus, the reaction of $[Fe^{IV}(O)(TPFPP^{+\bullet})]^+$ with arenes typically gives two reaction channels, namely oxygen atom transfer (OAT) and an addition process (Add), see Scheme 1. The OAT reaction leads to the formation of $[Fe^{III}(TPFPP)]^+$ ions with *m/z* 1028 and consequently release of oxygenated substrate. In addition, in several cases an adduct

Table 1. FT-ICR MS reactivity of $[Fe^{IV}(O)(TPFPP^{+\bullet})]^+$ with arenes: Second-order rate constants, reaction efficiencies and product distributions for OAT and Add.

Substrate	IE[a]	k_{exp}[b,c]	k_{ADO}[b]	Φ_{OAT}	Φ_{Add}	[%] OAT	[%] Add
benzaldehyde	9.50	0.15	11.4	–	1.3	0	100
α-[D_1]-benzaldehyde	9.50	0.14	11.4	–	1.2	0	100
benzene	9.20	0.012	8.8	0.14	–	100	–
toluene	8.80	0.36	9.2	3.1	0.78	80	20
ethylbenzene	8.77	0.58	9.5	4.3	1.8	70	30
[D_5]-ethylbenzene	8.77	0.56	9.5	4.2	1.7	72	28
[D_{10}]-ethylbenzene	8.77	0.57	9.5	4.4	1.6	73	27
i-propylbenzene	8.73	1.2	10.0	7.8	4.2	65	35
tert-butylbenzene	8.68	1.0	10.0	9.5	0.5	95	5
o-xylene	8.56	1.4	9.5	9.5	5.2	65	35
[D_4]-*o*-xylene	8.56	1.4	9.5	9.1	5.6	62	38
[D_6]-*o*-xylene	8.56	1.3	9.5	8.9	4.8	65	35
m-xylene	8.55	1.6	9.5	15.8	1.2	93	7
p-xylene	8.44	1.3	8.9	9.4	5.1	65	35
mesitylene	8.40	1.9	9.0	12.6	8.4	60	40
naphthalene	8.14	0.93	9.1	7.6	2.4	76	24

[a] from NIST database, in eV. [b] second-order rate constants (k_{exp}) in units of 10^{-10} cm^3 $molecule^{-1}$ s^{-1}, at the temperature of the FT-ICR cell (300 K). [c] The estimated error is ±30%; the internal consistency of the data is within ±10%.

© 2016 Wiley-VCH Verlag GmbH & Co. KGaA, Weinheim

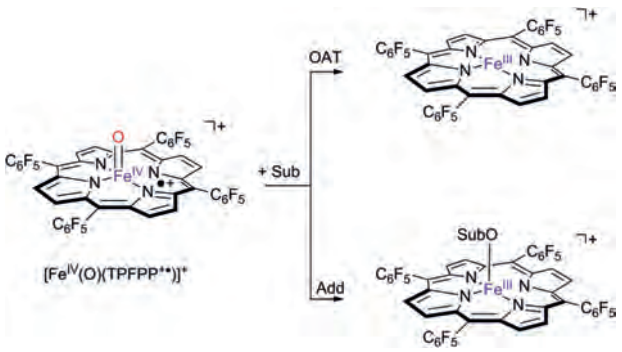

Scheme 1. Reaction products observed from the reaction of $[Fe^{IV}(O)(TPFPP^{+\bullet})]^+$ with arenes (Sub).

complex is observed with mass corresponding to $[Fe^{III}(TPFPP)(SubO)]^+$, whereby Sub represents the substrate.

Figure S1 in the Supporting Information shows an example of a mass spectrum recorded along the kinetic run for the reaction of $[Fe^{IV}(O)(TPFPP^{+\bullet})]^+$ with toluene at 3.8×10^{-8} mbar and displays signals at 120 s reaction time for the reactant $[Fe^{IV}(O)(TPFPP^{+\bullet})]^+$ centered at *m/z* 1044, product ions $[Fe^{III}(TPFPP)]^+$ at *m/z* 1028, and $[Fe^{III}(TPFPP)(SubO)]^+$ at *m/z* 1136.

The actual formation of an oxidation product remaining in the coordination sphere of $[Fe^{III}(TPFPP)]^+$ assigned to the $[Fe^{III}(TPFPP)(SubO)]^+$ ion at *m/z* 1136 has been verified by isolating the complex and submitting it to low-energy collision induced dissociation. As shown in Figure S2 (Supporting Information), the ion at *m/z* 1136 undergoes fragmentation, releasing $[Fe^{III}(TPFPP)]^+$ by loss of SubO, namely the oxidation product of toluene. Additional evidence for the formation of a SubO ligand is inferred from a reaction that is observed at longer reaction times whereby the $[Fe^{III}(TPFPP)(SubO)]^+$ ion undergoes a ligand substitution process by a Sub molecule, the neutral present in the FT-ICR cell, to give $[Fe^{III}(TPFPP)(Sub)]^+$. This process is clearly observed for the reaction of benzaldehyde. In this case, one finds that the efficiency for the $[Fe^{III}(TPFPP)(SubO)]^+ + Sub \rightarrow [Fe^{III}(TPFPP)(Sub)]^+ +$ SubO reaction is less than 1.3% (this value represents the efficiency for the $[Fe^{IV}(O)(TPFPP^{+\bullet})]^+ + Sub \rightarrow [Fe^{III}(TPFPP)(SubO)]^+$ reaction, with Sub equal to benzaldehyde).

On this basis, an indirect probe for the structure of $[Fe^{III}(TPFPP)(SubO)]^+$ ions has been sought by forming distinct model complexes and studying their gas phase reactivity towards benzaldehyde. In methanol solution $[Fe^{III}(TPFPP)]^+$ reacts with both (*m*/*p*)-hydroxy-benzaldehyde and benzoic acid to give an addition complex which is delivered by electrospray ionization (ESI) into the gas phase, led into the ICR cell and tested for bimolecular reactivity with benzaldehyde. The complex with benzoic acid is found to be substantially more reactive in the ligand transfer process than both complexes with (*m*/*p*)-hydroxy-benzaldehyde (reaction efficiencies are equal to 14% and around 0.60%, respectively, Equations 1–3). This result is indicative that the gas phase oxidation of benzaldehyde by $[Fe^{IV}(O)(TPFPP^{+\bullet})]^+$ is directed at the aromatic ring rather than at the formyl group. The same experiment could not be extended to other substrates, given the scant ligand transfer reactivity typically displayed by arenes, but this outcome in the favorable case of benzaldehyde suggests that $[Fe^{IV}(O)(TPFPP^{+\bullet})]^+$ prefers attack at the aromatic ring rather than at a side chain substituent.

$$[Fe^{III}(TPFPP)(C_6H_5COOH)]^+ + C_6H_5CHO \rightarrow [Fe^{III}(TPFPP)(C_6H_5CHO)]^+ + C_6H_5COOH \quad (1)$$
$$\Phi = 14\,\%$$

$$[Fe^{III}(TPFPP)(p\text{-}OH\text{-}C_6H_4CHO)]^+ + C_6H_5CHO \rightarrow [Fe^{III}(TPFPP)(C_6H_5CHO)]^+ + p\text{-}OH\text{-}C_6H_4CHO \quad (2)$$
$$\Phi = 0.64\,\%$$

$$[Fe^{III}(TPFPP)(m\text{-}OH\text{-}C_6H_4CHO)]^+ + C_6H_5CHO \rightarrow [Fe^{III}(TPFPP)(C_6H_5CHO)]^+ + m\text{-}OH\text{-}C_6H_4CHO \quad (3)$$
$$\Phi = 0.56\,\%$$

As follows from Table 1, the rate constant ranges from 0.012×10^{-10} $cm^3\,molecule^{-1}\,s^{-1}$ for the reaction of $[Fe^{IV}(O)(TPFPP^{+\bullet})]^+$ with benzene increasing to a value of 1.9×10^{-10} $cm^3\,molecule^{-1}\,s^{-1}$ for the reaction with mesitylene. As such, a spread of two orders of magnitude in rate constant is found for the series of substrates investigated here. In all cases (except for benzaldehyde) the dominant product complex obtained is the $[Fe^{III}(TPFPP)]^+$ ion representing the OAT channel. However, addition products are obtained in significant amounts with percentages of up to 40% (with mesitylene), whereas for benzaldehyde this is the sole reaction channel. Figure 2 displays the reactant and product abundancies as

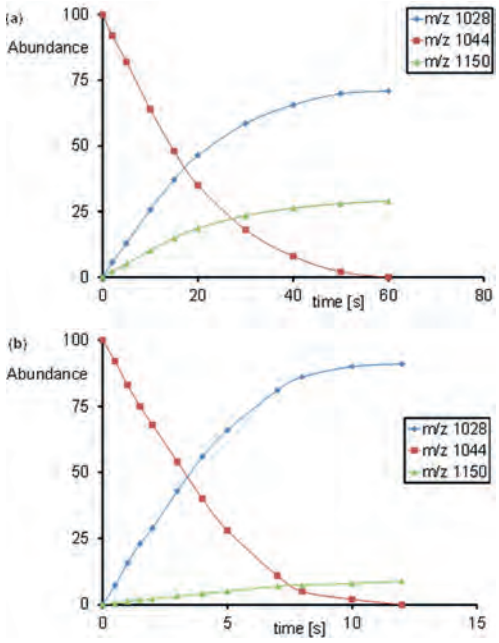

Figure 2. Ion distributions as a function of time for the reaction of $[Fe^{IV}(O)(TPFPP^{+\bullet})]^+$ with (a) ethylbenzene and (b) *m*-xylene.

© 2016 Wiley-VCH Verlag GmbH & Co. KGaA, Weinheim

a function of time for the reaction of $[Fe^{IV}(O)(TPFPP^{+\bullet})]^+$ with ethylbenzene and *m*-xylene. The reactant ion abundance decays according to pseudo first-order kinetics as expected for a bimolecular reaction in the gas-phase. Thus, the ion abundance at *m/z* 1044 decays slowly as a function of time as the $[Fe^{IV}(O)(TPFPP^{+\bullet})]^+$ reacts away and the decay patterns were used to establish the experimental second-order rate constants k_{exp}. In the case of ethylbenzene as a substrate (Figure 2a) two products are formed with *m/z* 1028 and *m/z* 1150 representing the OAT and Add channels. The shape of the curves shown in Figure 2 is used to determine the efficiencies Φ_{OAT} and Φ_{Add} described in Table 1. As follows the ratio of the abundancies of the OAT and Add channels are constant as a function of time for ethylbenzene as well as *m*-xylene with ratios of *m/z* 1028: *m/z* 1150 ion abundancies of 2.5 and 13, respectively. This implies that these products originate from the same source and most probably, product release from the iron(III) complex and, most probably, is a slow process.

To find out whether the reactivities and, in particular, the product distributions relate to aromatic or aliphatic hydroxylation pathways, we repeated some of the reactions with deuterated substrates. Thus, we tested ethylbenzene with all aliphatic hydrogen atoms replaced by deuterium ($[D_5]$-ethylbenzene) and fully deuterated ethylbenzene ($[D_{10}]$-ethylbenzene). As can be seen from Table 1, the substrate deuteration has a small but nonsignificant effect on the reaction efficiencies and product distributions. Therefore, it can be concluded that the reaction between $[Fe(O)(TPFPP^{+\bullet})]^+$ and ethylbenzene does not proceed with a rate-determining hydrogen atom abstraction. The indication is rather that these reactions with deuterated substrates strongly implicate an aromatic hydroxylation of substrates. The product ratios also suggest that an ethylphenol product (as obtained from ethylbenzene) is more strongly bound to the iron(III) complex than the dimethylphenol product obtained from *m*-xylene.

To further confirm the reactions as aromatic hydroxylation, we investigated *o*-xylene with all aromatic hydrogen atoms replaced by deuterium ($[D_4]$-*o*-xylene) and all aliphatic hydrogen atoms replaced by deuterium ($[D_6]$-*o*-xylene). Table 1 gives the product distributions and reaction efficiencies for *o*-xylene, $[D_4]$-*o*-xylene and $[D_6]$-*o*-xylene. Within our experimental error margin all reaction efficiencies, rate constants and product distributions are the same, which gives evidence that in the reaction of $[Fe(O)(TPFPP^{+\bullet})]^+$ with *o*-xylene no rate determining hydrogen atom abstraction takes place.

Theory

To support the experiments and gain insight into the details of the reaction mechanism, we followed the work up with an extensive DFT study to establish reactivity trends. Our initial work was aimed at the aromatic hydroxylation mechanism of arenes by [4,2]$[Fe^{IV}(O)(TPFPP^{+\bullet})]^+$, although we utilized a model without porphyrin substituents here, that is, porphyrin (Por). The investigated arenes in this work were mesitylene (**1**), toluene (**2**), ethylbenzene (**3**), fluorobenzene (**4**), chlorobenzene (**5**), naphthalene (**6**), *iso*-propylbenzene (**7**) and *tert*-butylbenzene (**8**). Test calculations with the full TPFPP model were also performed but found to give only minor differences in structure and reactivity with respect to the smaller porphyrin complex without side groups (see Supporting Information). Figure 3 shows the aromatic hydroxylation reaction of the *para*-position of toluene (PhMe; henceforth indicated with the subscript 2 beside the label of the structure) by the doublet and quartet spin states of $[Fe^{IV}(O)(Por^{+\bullet})]^+$ as calculated with DFT as an example. Thus, the reaction starts with an electrophilic attack of the oxo group on the *para*-carbon atom of the substrate that

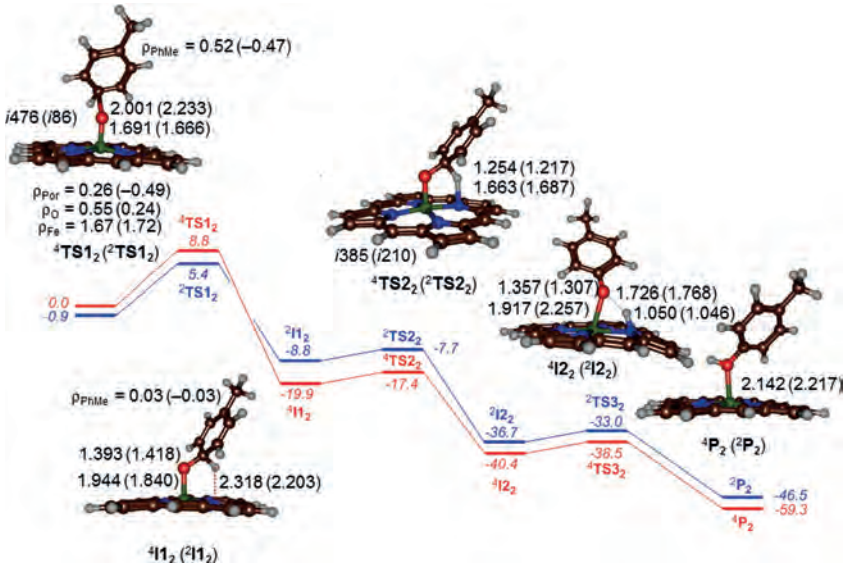

Figure 3. Potential energy profile (in kcal mol^{-1}) of aromatic hydroxylation of toluene (PhMe) by $[Fe^{IV}(O)(Por^{+\bullet})]^+$ as calculated with DFT at UB3LYP/BS2//UB3LYP/BS1 level of theory. All data include ZPE corrections and are calculated relative to isolated reactants. Bond lengths are given in angstroms and group spin densities (ρ) in atomic units.

© 2016 Wiley-VCH Verlag GmbH & Co. KGaA, Weinheim

via a transition state **TS1** leads to the intermediate **I1**. As shown previously by calculations on P450 model complexes, the *ipso*-proton is abstracted by the porphyrin group via transition state **TS2** to form the protonated porphyrin structure **I2**. Finally, the proton is relayed to the phenolate group via transition state **TS3** to form phenol products (**P**).[14]

An analysis of the group spin densities and charges establishes the intermediates **I1** as cationic on the substrate moiety ($\rho_{PhMe} = 0.03/-0.03$ in ^{4}**I1**$_2$/^{2}**I1**$_2$), which implies that two electrons have transferred from substrate to oxidant. We made several attempts to find radical intermediates through the swapping of molecular orbitals, but in all of these cases the wave functions converged back to the cationic intermediates instead. Recent experimental studies of Asaka and Fujii found experimental evidence of fast electron transfer during the C–O bond formation step and hence support the formation of a cationic intermediate.[15]

After the cationic intermediates (**I1**) the substrate loses its *ipso*-proton to the porphyrin ring via a small reaction barrier of 2.5 kcal mol^{-1} on the quartet spin state and 1.1 kcal mol^{-1} on the doublet spin surface. This proton-transfer intermediate (**I2**) then relays the proton back to the phenolate oxygen atom to form phenol products via another transition state **TS3** lying close in energy to **I2**.

The rate determining step in the reaction mechanism, however, is the electrophilic addition step via **TS1**, which elongates the Fe–O bond to 1.691/1.666 Å in ^{4,2}**TS1**$_2$ and has the substrate in an almost upright position. An analysis of the group spin densities (ρ) establishes it as a radical-type transition state with spin densities of 2.22 (1.96), 0.26 (−0.49) and 0.52 (−0.47) on the FeO, Por and PhMe groups, respectively, in ^{4}**TS1**$_2$ (^{2}**TS1**$_2$). As the reactant state has an electronic configuration $\pi^*_{xz}{}^1\ \pi^*_{yz}{}^1\ a_{1u}{}^1$ with spin density of about 2 on the FeO group and 1 on the porphyrin ring, this implies that radical character on the porphyrin manifold is lost in the transition state. In particular, an electron transfer from substrate into the a_{1u} orbital has occurred to create a transition state with configuration approximating $\pi^*_{xz}{}^1\pi^*_{yz}{}^1 a_{1u}{}^2\ \phi_{PhMe}{}^1$.

After the transition state the system relaxes to the cationic intermediate **I1**, which involves a second electron transfer from the substrate to the metal to generate an intermediate with orbital occupation $\pi^*_{xz}{}^1\pi^*_{yz}{}^1\sigma^*_{z2}{}^1 a_{1u}{}^2\ \phi_{PhMe}{}^0$. Geometrically, this second electron transfer and the single occupation of the σ^*_{z2} orbital results in considerable lengthening of the Fe–O bond from 1.691 Å in ^{4}**TS1**$_2$ to 1.944 Å in ^{4}**I1**$_2$. At the same time the C–O distance shortens from 2.001 Å in the transition state to 1.393 Å in the intermediate.

In the subsequent step we located transition states for proton transfer from the *ipso*-position to one of the nitrogen atoms of the porphyrin ligand in the doublet and quartet spin states. These proton transfer barriers have relatively small imaginary frequencies, i385 cm^{-1} (^{4}**TS2**$_2$) and i210 cm^{-1} (^{2}**TS2**$_2$), as compared to typical hydrogen atom abstraction transition states where values of well over i1000 cm^{-1} were found.[16] From the **I2** intermediates another proton transfer leads to the phenol product complexes with high exothermicity. A small barrier **TS3** is obtained in both spin states.

Overall, the aromatic hydroxylation reaction is stepwise with a rate determining electrophilic addition step with a barrier of $\Delta E^{\neq} + ZPE = 8.8$ (5.4) kcal mol^{-1} on the quartet (doublet) spin states. These values compare well with previous studies of aliphatic and aromatic hydroxylation by iron(IV)-oxo porphyrin cation radical complexes.[12,16–18]

Thereafter, we completed the investigation of ^{4,2}[Fe^{IV}(O)(Por$^{+\bullet}$)]$^+$ and its aromatic hydroxylation of a range of arenes and initially calculated the full landscape for chlorobenzene hydroxylation by ^{4,2}[Fe^{IV}(O)(Por$^{+\bullet}$)]$^+$, see Supporting Information for details. The landscape gives the same pattern as that seen for toluene in Figure 3 with a rate-determining electrophilic addition barrier **TS1**$_5$ leading to a cationic intermediate **I1**$_5$. Similarly to the toluene data reported above, ^{2}**TS1**$_5$ is below ^{4}**TS1**$_5$ as seen before in aromatic hydroxylation by P450 CpdI models.[14]

In addition, we calculated ^{4,2}**TS1** and ^{4,2}**I1** for the following substrates: mesitylene, ethylbenzene, fluorobenzene, naphthalene, *iso*-propylbenzene and *tert*-butylbenzene, whereby we give the label as a subscript after the structure name. In general, the same structural trends are observed in the quartet and doublet spin states and the mechanism is the same.

As can be seen strong geometric differences are found upon changing the *para*-substituent of the arene, whereby the ^{4}**TS1** structure for fluorobenzene gives Fe–O and O–C distances of 1.703 and 1.942 Å, while with ethylbenzene these distances change to 1.689 and 2.005 Å, respectively. Similar differences are seen for the other complexes as well as in the value of the imaginary frequency in the transition state. Nevertheless, all **TS1** structures shown in Figure 4 represent the same electronic transition of electron transfer from arene to a_{1u} and the accumulation of radical character on the arene group. Moreover, the transition state structures are geometrically alike with the substrate in virtually the same orientation in all cases. The occurrence of an electron transfer equilibrium preceding aromatic hydroxylation by a compound I model within a solvent cage has been highlighted.[15] The electrophilic addition transition states shown in Figure 4 differ strongly in the barrier height and values of $\Delta E^{\neq} + ZPE$ range from 1.8 kcal mol^{-1} for ^{2}**TS**$_6$ (naphthalene) to 12.4 kcal mol^{-1} for ^{4}**TS1**$_4$ (fluorobenzene). Nevertheless, all of them are radical type transition states with group spin densities similar to those reported for ^{4,2}**TS1**$_2$ above in Figure 3.

To ascertain that the lowest energy pathway indeed is aromatic hydroxylation rather than aliphatic hydroxylation, we also calculated the aliphatic hydroxylation mechanisms of toluene and ethylbenzene by ^{4}[Fe^{IV}(O)(Por$^{+\bullet}$)]$^+$, see Figure 5. These reactions are also stepwise with an initial hydrogen atom abstraction via transition state ^{4}**TS**$_H$ that leads to a radical intermediate ^{4}**I**$_H$. In both aliphatic hydrogen atom abstraction transition states significant radical character ($\rho = -0.52$ for both) is obtained. In a subsequent radical rebound barrier the OH group is transferred to substrate to form alcohol product complexes ^{4}**P**$_H$. The hydrogen atom abstraction is rate determining and has a relatively central transition state with elongated C–H distances of 1.202 Å for both toluene and ethylbenzene. In both structures the Fe–O bond has elongated to well over 1.7 Å.

© 2016 Wiley-VCH Verlag GmbH & Co. KGaA, Weinheim

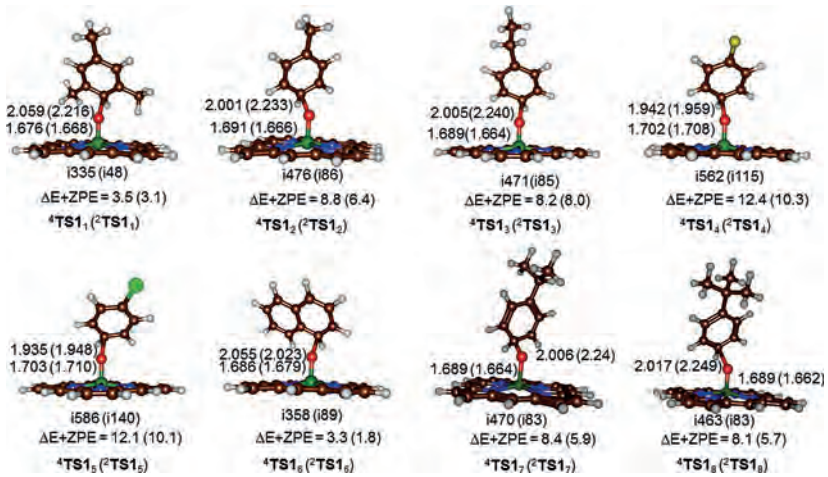

Figure 4. Optimized electrophilic addition transition states for the reaction of $^{4,2}[Fe^{IV}(O)(Por^{+\bullet})]^{+}$ with arenes. Barrier heights (in kcal mol^{-1}) given are relative to isolated reactants and calculated at UB3LYP/BS2//UB3LYP/BS1 level of theory. Bond lengths are in angstroms and imaginary frequencies in wave numbers.

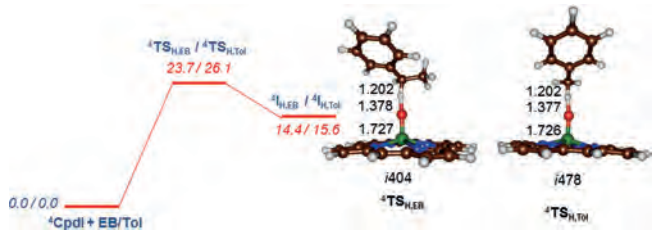

Figure 5. Aliphatic hydroxylation potential energy landscape as calculated at UB3LYP/BS2//UB3LYP/BS1 level of theory. Energies are in kcal mol^{-1} and include ZPE correction, while geometries give bond distances in angstroms and the imaginary frequency in wave numbers.

Energetically, the hydrogen atom abstraction barriers are higher than the arene activation barriers **TS1** shown in Figure 4 by well over 15 kcal mol^{-1}. Therefore, the dominant pathway is expected to be aromatic hydroxylation of arenes by $[Fe^{IV}(O)(Por^{+\bullet})]^{+}$ and little or no aliphatic hydroxylation products should be observed. The $[Fe^{IV}(O)(Por^{+\bullet})]^{+}$ system, as a consequence, reacts sluggishly with aliphatic groups, in contrast to iron(IV)-oxo porphyrins with an anionic axial ligand. Previously, we and others showed that the barrier heights of aliphatic hydroxylation reactions correlate with the bond dissociation energy (BDE_{OH}) for the formation of the iron(IV)-hydroxo species from the iron(IV)-oxo species and a hydrogen atom.[19] This implies that the BDE_{OH} of the $[Fe^{IV}(O)(Por^{+\bullet})]^{+}$ system will be considerably smaller than that of P450 CpdI and unable to react via hydrogen atom abstraction. Indeed, we calculate a BDE_{OH} for the reaction of $^{3}[Fe^{III}(OH)(Por^{+\bullet})]^{+}$ into CpdI and a hydrogen atom of $\Delta E + ZPE = 66.3$ kcal mol^{-1}, whereas for a P450 CpdI model a value of 88.9 kcal mol^{-1} was obtained.[20] In aliphatic hydroxylation the energy of the hydrogen atom abstraction step is equal to the difference in BDE_{CH} of the substrate and the BDE_{OH} of the oxidant. The BDE_{CH} of ethylbenzene is 82.5 kcal mol^{-1}.[14b] In the case of $[Fe^{IV}(O)(Por^{+\bullet})]^{+}$, therefore, hydrogen atom abstraction from ethylbenzene will be endothermic by 16.2 kcal mol^{-1}, whereas the P450 CpdI model should give an exothermic hydrogen atom abstraction by −6.4 kcal mol^{-1}. Indeed, the radical intermediate $^{4}\mathbf{I}_{H}$ for ethylbenzene as a substrate is 14.4 kcal mol^{-1} higher in energy than reactants and therefore matches the difference in energy between BDE_{OH} and BDE_{CH} of oxidant and substrate. The endothermicity for the hydrogen atom abstraction reactions of substrates by $[Fe^{IV}(O)(Por^{+\bullet})]^{+}$ is too high and, therefore; this process will not be able to compete with lower energy reaction channels, such as substrate epoxidation and aromatic hydroxylation.

Thus, the efficiency and reaction rate constant of aliphatic hydroxylation was shown to be linearly correlated with BDE_{OH},[19b] hence the system without axial ligand, that is $[Fe^{IV}(O)(Por^{+\bullet})]^{+}$, has reduced catalytic efficiency for aliphatic hydroxylation. Clearly, the axial cysteinate ligand in P450 enzymes affects the reactivity properties of the oxo group and thereby makes it a better oxidant. Electrophilic reactions, such as aromatic hydroxylation and epoxidation, however, tend to connect with the ionization energy of the substrate and the electron affinity of the oxidant,[21] which is appropriate for $[Fe^{IV}(O)(Por^{+\bullet})]^{+}$ to perform these reactions.

Discussion

In this work a comprehensive overview of arene activation by $[Fe^{IV}(O)(Por^{+\bullet})]^{+}$ and $[Fe^{IV}(O)(TPFPP^{+\bullet})]^{+}$ is given as mimics of P450 CpdI reactivity with substrates. As some of the substrates have aliphatic substituents to the arene, our initial work focused on establishing the nature of the reaction products. Unfortunately, aliphatic and aromatic hydroxylation of arenes gives products with equal mass and as such cannot be distinguished by mass spectrometry. Moreover, the fragmentation patterns of the products did not give direct evidence of what pathway was followed either. Hence, FT-ICR MS cannot distinguish the two products directly. We, therefore, repeated the experiments with deuterium-labelled compounds, which gave only minor changes to the rate constants and implicated that

© 2016 Wiley-VCH Verlag GmbH & Co. KGaA, Weinheim

the rate determining step does not include a hydrogen atom abstraction.

To gain further insight into the details of the reaction mechanism and the bifurcation processes, computational modelling was performed. In particular, DFT studies on the relative barriers for aliphatic versus aromatic hydroxylation reactions were performed (Figures 4 and 5) and confirmed the latter to be well lower in energy. As such, in the gas-phase the $[Fe^{IV}(O)(TPFPP^{+\bullet})]^+$ complex will preferentially react via aromatic hydroxylation over aliphatic hydroxylation with substrates. Nam et al.[22] studied the aliphatic versus aromatic hydroxylation of ethylbenzene by $[Fe^{IV}(O)(TPFPP^{+\bullet})(X)]$ with $X = Cl^-$/$CF_3SO_3^-$ in dichloromethane. Aliphatic hydroxylation products were obtained with $[Fe^{IV}(O)(TPFPP^{+\bullet})(Cl)]$ as an oxidant, whereas aromatic hydroxylation products were detected in a reaction with $[Fe^{IV}(O)(TPFPP^{+\bullet})(CF_3SO_3)]$. Subsequent computational modelling showed that the axial ligand affects the electron affinity and O–H bond strength (bond dissociation energy, BDE_{OH}) and hence affected the relative barriers of aliphatic versus aromatic hydroxylation.[14b,23] To gain further insight into the intricate details of the bifurcation processes, below, a molecular orbital and valence bond interpretation of the mechanisms is shown. First, however, a discussion of the experimental reaction trends is presented.

To find trends and a rationale in the obtained rate constants and particularly find evidence on the properties of the catalyst/oxidant that determines the reaction process, we decided to search for physicochemical properties of substrate and oxidant in correlation with the rate constant. These analyses should give insight into the fundamental properties of P450 CpdI and how it is able to activate arenes. To this end, we decided to plot the natural logarithm of the rate constant against physical chemical properties of the substrate and oxidant, including the ionization energy of the substrate. Thus, previously it was shown that reactions starting with a rate-determining hydrogen atom abstraction generally correlate with the strength of the C–H bond that is broken, that is, the bond dissociation energy (BDE_{CH}).[24,25] However, aromatic hydroxylation pathways by metal-oxo complexes were shown to connect to the ionization energy (IE) of the substrate.[25]

Figure 6 displays plots of the natural logarithm of the experimentally determined rate constant versus the ionization energy of the substrate (part a) and the BDE_{CH} value of the aliphatic group of the substrate (part b). As can be seen from Figure 6, the ionization energy of the substrate follows a linear correlation with the ln k_{exp} value with an R^2 value of 0.88. Interestingly, the rate constants for benzene and naphthalene activation by $[Fe^{IV}(O)(TPFPP^{+\bullet})]^+$ do not fit the trend. This may be due to the fact that these substrates approach the oxidant differently and give extra interactions with the oxidant. Aromatic hydroxylation, similarly to double bond epoxidation, therefore, gives rate constants that are proportional to the IE of the substrate involved.[25] This means that any oxidant reacting with a substrate containing an arene and a double bond as a separate group will give preferential aromatic hydroxylation rather than double bond epoxidation.

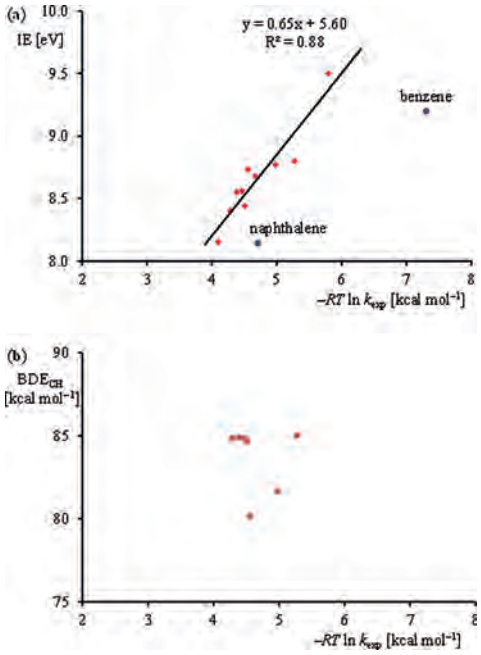

Figure 6. Correlation of the natural logarithm of the rate constant with (a) ionization energy from the substrate. (b) BDE_{CH} value of the aliphatic group of the substrate. Ionization energies taken from the NIST Database.[13] BDE_{CH} values calculated with DFT at B3LYP/BS2//UB3LYP/BS1 including ZPE corrections.

For the set of substrates with aliphatic substituents also a plot of ln k_{exp} versus BDE_{CH} was attempted (Figure 6b), however, no clear linear correlation is found. Based on this evidence the aliphatic hydroxylation pathway can be ruled out as a viable mechanism for arene activation by $[Fe^{IV}(O)(TPFPP^{+\bullet})]^+$ and, based on the reactivity trends as well as the kinetic isotope effect (KIE) values, the dominant pathway is aromatic hydroxylation.

Figure 7 gives the corresponding plot for the correlation between the ionization energy and the computationally determined aromatic hydroxylation free energy of activation calculated for the various ^{4,2}**TS1** structures for the substrates in Figure 4. In agreement with the experimental result, a linear correlation between barrier height and ionization energy is found with an $R^2 = 0.91$ (quartet) and 0.93 (doublet). As such, both experimental reaction rates and computational barrier heights implicate a linear correlation between the natural logarithm of the rate constant and ionization energy. As both experiment and theory give the same correlation, of course, the experimental rates also correlate linearly with the computational barrier heights. Moreover, using the found trends, this enables us to predict reaction rates of alternative substrates. For instance, the rate constants for aromatic hydroxylation of chlorobenzene and fluorobenzene could not be measured. However, the trend from Figure 6a and Figure 7a enable us to predict their values as 4.8 and 5.0×10^{-11} $cm^3\,molecule^{-1}\,s^{-1}$, respectively. Similarly, we predict barrier heights at B3LYP level of theory from the experimental trend in Figure 6a of $\Delta G^{\neq} = 19.5$, 19.9 and 24.4 kcal mol^{-1} for *iso*-propylbenzene, *tert*-butylbenzene and benzaldehyde, respectively, whereas values of $\Delta G^{\neq} =$

© 2016 Wiley-VCH Verlag GmbH & Co. KGaA, Weinheim

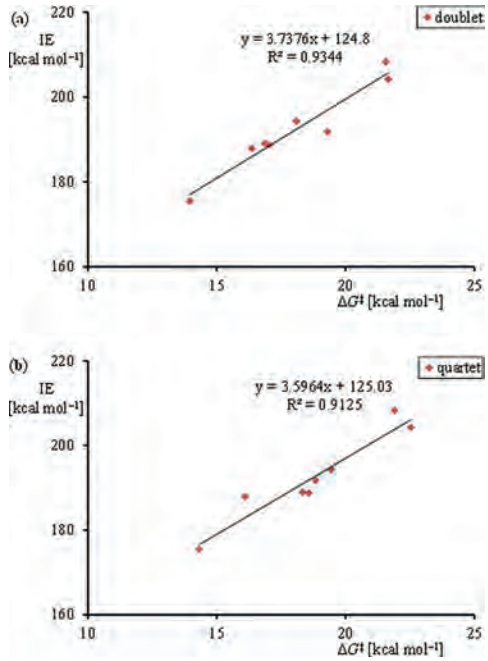

Figure 7. Correlation of the computationally determined free energy of activation of aromatic hydroxylation (**TS1**) with calculated ionization energy of the substrate.

18.8, 19.2 and 19.3 kcal mol^{-1} are expected for *m*-, *o*-, and *p*-xylene. As such the two plots from Figure 6 and Figure 7 enable one to predict experimental rates from computational trends or computational barriers from experimental trends. To verify the accuracy of this procedure we predicted the DFT barriers for toluene, ethylbenzene and mesitylene from the trend in Figure 6a and find values of $\Delta G^{\ddagger}=22.3$, 21.2 and 16.4 kcal mol^{-1}, respectively, which are within a mean error of 2.8 kcal mol^{-1} of the DFT calculated results (Supporting Information).

Electronically, the fact that the trends correlate with ionization energy implicate that the electron transfer from substrate to oxidant will determine the reaction rate. The trends in reactivity also imply that none of the products observed in the mass spectra can correlate with aliphatic hydroxylation products. Therefore, the product ions with *m/z* 1028 and *m/z* 1150 (Figure 2) originate from the aromatic hydroxylation of substrates. Clearly, product release from the iron(III) complex is a slow process and a mixture of metal-ligated and free phenol products are obtained.

Evidently, the rate constant and reactivity patterns of the iron(IV)-oxo porphyrin complex with arenes is dependent on key properties of the oxidant and substrate. In order to improve catalyst design and find novel oxidants for this reaction process, we delineated the transition-state barrier into fundamental properties of oxidant and substrate. This analysis identifies the origin of the reaction mechanism and explains how the oxidant can be further improved for better catalysis.

To understand the obtained trends and correlations we used a parabolic approximation of previously described VB models to explain the reaction barrier.[26] Figure 8 displays the basic

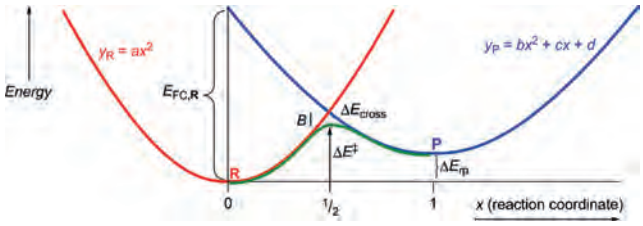

Figure 8. Two-parabola curve crossing model for the prediction of barrier heights.

features of the two-parabola crossing model, where we assume the reactant complex (**R**) to reside in a local minimum that can be described by a parabola with function $y_R=ax^2$ with y_R being the energy function of the reactant complex, x the reaction coordinate and a is a constant that describes the curvature of the reaction coordinate function. The reactant complex is defined as the starting point of the reaction with coordinates $x_R=0$ and $y_R=0$. For the product complex we describe the potential energy surface with another parabola that is shifted from the reactant parabola and hence has function $y_P=bx^2+cx+d$ with b, c, and d being some constants that describe the curvature and extremes of the parabola. We now assume that the product local minimum is located at a reaction coordinate with value $x=1$ and the transition state at the half-way point ($x={}^1/_2$). That means the two curves for y_R and y_P will cross at $x_{cross}={}^1/_2$ and create a crossing point, at energy $y_P({}^1/_2)=\Delta E_{cross}$, which will ultimately lead to an avoided crossing and a transition state for the reaction. One can see from Figure 8 that $y_P(0)=d=E_{FC,R}$, whereby $E_{FC,R}$ represents the Franck–Condon energy at the reactant geometry. Furthermore, $y_P(1)$ is equal to the driving force for the reaction (ΔE_{rp}). Using the information for the first derivative of y_P at the point $x=1$, that is, $y_P'(1)=0$, we can now derive Equation 4 for $y_P({}^1/_2)$ as a function of the driving force for the reaction and the Franck–Condon energy at the reactants geometry.

$$y_P({}^1/_2)=\Delta E_{cross}=\frac{1}{4}E_{FC,R}+\frac{3}{4}\Delta E_{rp} \quad (4)$$

The actual transition state, however, with energy $\Delta E^{\ddagger}$ will be below the crossing point by an amount B that represents the resonance energy, Equation 5.

$$\Delta E^{\ddagger}=\Delta E_{cross}-B \quad (5)$$

Using Equations 4 and 5 we can predict the barrier height for the reaction in terms of the driving force for the reaction (ΔE_{rp}), the change in electronic configuration between the reactant and product state in the geometry of the reactants ($E_{FC,R}$) and the resonance energy B. Values for the driving force are taken as the difference in energy ($\Delta E+ZPE$) between reactant complex (**R**) of ^{4}CpdI and substrate with the radical intermediate ^{4}**I1**.

Figure 9 shows the curve crossing diagram with key valence bond (VB) structures of critical points along the reaction mechanism. The difference in VB structure between the reactant and product structures in the geometry of the reactants will

© 2016 Wiley-VCH Verlag GmbH & Co. KGaA, Weinheim

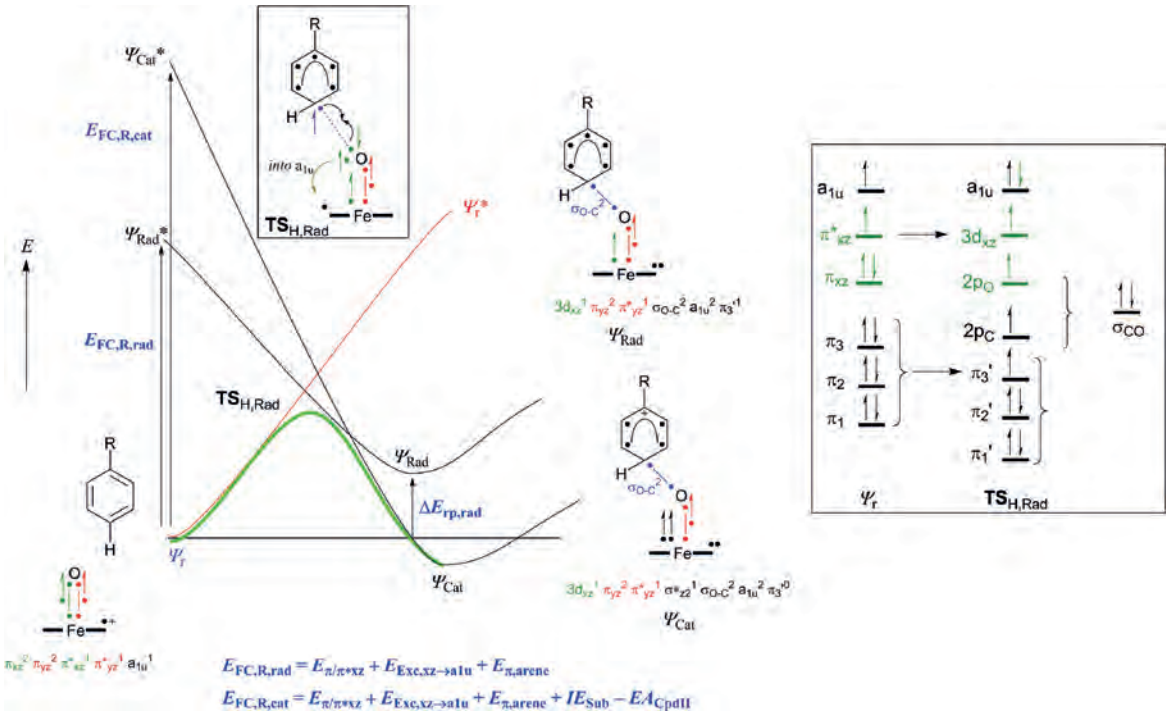

Figure 9. Valence bond curve crossing diagram and orbital/bonding changes along the electrophilic addition pathway of arene activation by $[Fe^{IV}(O)(Por^{+\bullet})]^+$. Valence bond structures give electrons as dots. Orbital occupation and hybridization changes are indicated with the orbital diagram.

determine the value of $E_{FC,R}$. These diagrams have been used previously to rationalize barrier heights of chemical reactions and explain what features of substrate and oxidant affect the value of the barrier height.[21,27]

The diagram starts on the bottom-left with the reactant configuration of $[Fe^{IV}(O)(Por^{+\bullet})]^+$ and arene. Thus, in the ground state the system has three unpaired electrons distributed over the π^*_{xz}, π^*_{yz} and a_{1u} molecular orbitals. The π_{xz}/π^*_{xz} and π_{yz}/π^*_{yz} molecular orbitals represent the bonding and antibonding combinations of 3d orbitals on Fe with 2p orbitals on oxygen.

The a_{1u} orbital is a nonbonding π-orbital on the porphyrin ring and is close in energy to the a_{2u} orbital. In previous work on $[Fe^{IV}(O)(Por^{+\bullet})]^+$ we found several close-lying electronic states with either doublet or quartet spin and single occupation of a_{1u} or a_{2u}.[12] The three green dots along the Fe–O bond in Figure 9 represent the π_{xz}/π^*_{xz} electrons, while the ones in red are the π_{yz}/π^*_{yz} electrons. Both sets of π/π^* orbitals form a three-electron bond along the Fe–O group. Upon formation of the intermediate complex either a radical or cationic structure is formed. In both cases the C–O bond is formed from one of the electrons of the π-cloud of the substrate plus an electron from the π_{xz}/π^*_{xz} system. This means that electrophilic addition will result in the breaking of the π-system of the substrate and the set of six electrons in the substrate π-system (π_1, π_2 and π_3 orbitals), will be split into a $2p_C$ atomic orbital for one carbon and a conjugated π-system over the remaining five carbon atoms with orbitals π_1', π_2' and π_3'. Breaking the π-cloud of the substrate, will cost the system an energy $E_{\pi,arene}$. Of course, the breaking of the π-cloud will also be correlated to the excitation energy in the π-system as well as the ionization energy for removal of an electron from one of the π-orbitals.

As such, the barrier height and the driving force for the reaction are likely to correlate with the ionization energy of the substrate as indeed shown in Figure 6a and Figure 7 . By contrast, the cationic pathway will more likely be connected to the second ionization energy of the substrate as apart from the breaking of the π-orbitals of the substrate and also an electron will have to transfer to the oxidant.

In the calculations presented in Figures 3 and 4 the intermediates are of a cationic nature with an electronic configuration of $3d_{xz}{}^1 \pi_{yz}{}^2 \pi^*_{yz}{}^1 \sigma^*_{z2}{}^1 a_{1u}{}^2 \pi'_3{}^0$ with spin density of less than 0.1 on the aromatic ring and a value of about 3 on the FeO unit. Interestingly, the transition states give significant radical character on the aromatic ring, typically 0.50–0.70, so that these transition states should be considered as radical-type transition states connecting the reactants with the radical intermediates. For the estimation of the barrier heights from the VB structures, therefore, we will use the driving force to reach the radical intermediates, $\Delta E_{rp,rad}$. On the oxidant side of the reaction, a number of electron transfer and orbital reorganizations happen, which enable us to predict the value for $E_{FC,R,rad}$. Firstly, the π_{xz}/π^*_{xz} set of orbitals (highlighted in green in the VB structures for the reactant and the transition state) split back into atomic orbitals ($3d_{xz}$ and $2p_O$), which will cost the system E_{π/π^*xz} in energy. One of the electrons of $2p_O$ pairs up with the single electron in $2p_C$ and forms the new C–O bonding orbital σ_{CO}. The value of E_{π/π^*xz} is determined from the relative energies of the two orbitals in the reactant complex and is 85.2 kcal mol^{-1}. The remaining two electrons stay on the metal-

© 2016 Wiley-VCH Verlag GmbH & Co. KGaA, Weinheim

porphyrin side of the system and one of those electrons is promoted into the a_{1u} orbital to fill it with a second electron with excitation energy $E_{Exc,xz\rightarrow a1u}$. From the relative energies of the π_{xz} and a_{1u} orbitals in the reactant complex a value of 51.5 kcal mol^{-1} is obtained. Finally, the Franck–Condon energy between the reactant and the radical state is dependent on the breaking of the π-system of the arene, $E_{\pi,arene}$. The overall Franck–Condon energy for the transition from the reactant to the radical state is given in Equation 6.

$$E_{FC,\mathbf{R},rad} = E_{\pi/\pi*xz} + E_{Exc,xz\rightarrow a1u} + E_{\pi,arene} \quad (6)$$

Using Equations 4–6 we have estimated VB predicted barrier heights of $\Delta E + ZPE = 12.5$, 12.1, 5.1 and 6.2 kcal mol^{-1} for the reaction of $[Fe^{IV}(O)(Por^{+\bullet})]^{+}$ with chlorobenzene, fluorobenzene, toluene and ethylbenzene, respectively. These values are in good quantitative agreement with those obtained from full DFT optimizations and shown in Figure 3 and 4 above. As such, the two-parabola curve crossing diagram gives a good quantitative representation of the reaction mechanism and the kinetics obtained. Moreover, the model gives hints on the key electronic properties of oxidant and substrate that determine the rate determining reaction step.

Equation 6 shows that the barrier height for aromatic hydroxylation should be proportional to the excitation energy of the π-cloud of the substrate arene, which, of course, is proportional to the ionization energy. Indeed that is what we observe above in Figure 6 and Figure 7. The fact that the rate constants for benzene and naphthalene do not fit the trend displayed in Figure 6 could be explained as those systems following a cationic pathway rather than a more radical pathway and hence should correlate with $E_{FC,\mathbf{R},cat}$ rather than $E_{FC,\mathbf{R},rad}$.

In the case of electrophilic addition, however, there is also a pathway leading to a cationic intermediate with wave function Ψ_{Cat}. This electronic configuration can be formed from the radical intermediate through an electron transfer from the substrate π-system into the σ^*_{z2} orbital of the metal. As such, we expect there to be a direct transition state leading to the radical intermediate as well as one to form the cationic intermediate, although the latter is higher in energy. These transition states will be proportional to the Franck–Condon energy from the reactant state to the excited state representing the product electronic configuration. Figure 8 gives descriptions for the Franck–Condon energies reaching the radical state ($E_{FC,\mathbf{R},rad}$) and the one leading to the cationic state ($E_{FC,\mathbf{R},cat}$). Based on the electronic differences between ground and excited state configurations, we established the individual contributions determining these excitation energies. As it happens, the excitation energy leading to the cationic state contains all features of the one leading to the radical state plus two additional terms, namely the ionization energy of the substrate (IE_{Sub}) and the electron affinity of the metal in the radical intermediate, which is the reduced form of the iron(IV)-oxo species, namely EA_{CpdII}. Therefore, in the transition state the cationic process is higher in energy and only after the barrier a crossover from radical to cationic pathway will be observed leading to the cationic intermediate and fast conversion to phenol products. The DFT and VB models, therefore, implicate a rate determining electrophilic addition step with a radical-type transition state. However, upon C–O bond formation en route to the intermediate a state crossing occurs to the lower lying cationic intermediate.

In summary, the VB diagram highlights the factors of the substrate and oxidant that affect the barrier height and predicts that the rate constant is proportional to the ionization energy of the substrate regarded that the oxidant stays the same.

Conclusion

A combined FT-ICR MS and DFT study is performed on the reactivity of arenes with a model of P450 CpdI without axial ligand. It is shown that removal of the axial ligand gives a dominant aromatic hydroxylation pathway and no evidence of aliphatic hydroxylation is found. In general, the natural logarithm of the rate constant of aromatic hydroxylation links linearly with the ionization energy of the substrate. The explanation of this finding is supported within the framework of a Valence Bond model.

Experimental Section

Materials

All chemicals and solvents used for this work were research grade and purchased from commercial sources. Iodosylbenzene was used as a terminal oxidant for the synthesis of the iron(IV)-oxo complex and was generated according to a literature procedure,[29] and subsequently stored at −20 °C prior to usage.

Instrumental

A Bruker BioApex FT-ICR mass spectrometer was used for all experiments described here, which includes a cylindrical infinity cell, a 4.7 T superconducting magnet and an Apollo I electrospray ionization (ESI) source. Analyte solutions of reactants were infused into the mass spectrometer through a fused-silica capillary with internal diameter of 50 μm at a continuous flow rate of 120 μL h^{-1} by a syringe pump. Ions were desolvated by applying an N_2 counter current drying gas heated at 380 K and then accumulated for 0.8 seconds in a radiofrequency-only hexapole ion guide. Thereafter, the ions were pulsed into the ICR cell that is held at room temperature (300 K). The ions of interest, $[Fe^{IV}(O)(TPFPP^{+\bullet})]^{+}$ at *m/z* 1044, were mass selected by ion ejection procedures and ion-molecule reactions were studied by inserting neutral collision gases and monitoring the abundance of product ions as a function of time. Neutral reagents were admitted into the FT-ICR cell at stationary pressures (in the range from 1.0–15×10^{-8} mbar) by a needle valve. The pressure in the FT-ICR cell was measured with a cold-cathode sensor (IKR Pfeiffer Balzers S.p.A., Milan, Italy) and calibrated against the rate constant of proton transfer from methane cation radical to methane, Eq 7, which is known to have a rate constant $k = 1.1\times 10^{-9}$ cm^3 s^{-1}.[29]

$$CH_4^{+\bullet} + CH_4 \rightarrow CH_5^{+} + CH_3^{\bullet} \quad (7)$$

In the mass spectra, corrections for ^{13}C isotopic contributions were applied in order to reveal possible species deriving from a hydro-

© 2016 Wiley-VCH Verlag GmbH & Co. KGaA, Weinheim

gen atom transfer channel, namely $[Fe^{IV}(OH)(TPFPP)]^+$ ions at *m/z* 1045, presenting a formally protonated ferryl unit.

Ion abundances were monitored as a function of time and pseudo first-order rate constants were obtained from the slope of the semi-logarithmic plots. These values, determined at least in triplicate, were then converted into second-order rate constants (k_{exp}) by dividing the parent ion abundances by the substrate concentration at 300 K. Reaction efficiencies (Φ) were calculated from the ratio of the second-order rate constant and the collision rate constant (k_{ADO}), Equation 8. Values for k_{ADO} were calculated using the parametrized trajectory theory.[30]

$$\Phi = k_{exp}/k_{ADO} \times 100\,\% \quad (8)$$

Product ion branching ratios and reaction efficiencies were found to be independent of the pressure in the ICR cell. The error in the estimated second-order rate constants (k_{exp}) is to within 10% with an absolute error of $\pm 30\%$, caused largely by the uncertainty affecting the pressure of the neutral.[31]

Sample preparation

The $[Fe^{IV}(O)(TPFPP^{+\bullet})]^+$ ion was synthesized in a methanol/dichloromethane (1:1) mixture by adding iodosylbenzene (0.5 mM) to the corresponding iron(III)chloride complex, 10 μM of $[Fe^{III}(TPFPP)Cl]$, and cooled to −40 °C. The iron(IV)-oxo complex remained stable at this temperature for at least 1 hour. The ESI FT-ICR mass analysis of the reaction mixture gave a prominent peak centered at *m/z* 1044 with isotopic pattern conforming to an iron(IV)-oxo complex, $[Fe^{IV}(O)(TPFPP^{+\bullet})]^+$, together with the reduced form $[Fe^{III}(TPFPP)]^+$ at *m/z* 1028. Nonetheless, the ion population at *m/z* 1044 comprises a fraction of isomeric species, likely corresponding to an isobaric ion oxidized on the porphyrin ring, and unable to attain any oxidation process. This fraction was titrated by its complete trapping by NO yielding the $[Fe^{III}(TPFPP{-}O)(NO)]^+$ adduct, in analogy with the reduced form, $[Fe^{III}(TPFPP)]^+$. The presence of this unreactive form was taken into account in treating the kinetic data.

Computation

To support the experimental observations and determine further trends and features of the reaction mechanism, we did a detailed DFT study on aromatic hydroxylation by $[Fe^{IV}(O)(Por^{+\bullet})]^+$, where Por represents an unsubstituted porphyrin ligand. We also tested the full $[Fe^{IV}(O)(TPFPP^{+\bullet})]^+$ system but found very little differences in geometry, electronic description and reactivity with respect to the $[Fe^{IV}(O)(Por^{+\bullet})]^+$ system (Supporting Information Figure S4), hence the latter was used here. All calculations were performed in Gaussian-09,[32] and implemented DFT methods. Test calculations with a range of density functional methods show little sensitivity of the amount of exchange and correlation to optimized geometries and the potential energy landscape gives the same pattern (Supporting Information Tables S1–S20), therefore, we will show results obtained with the B3LYP[33] density functional method only as that will enable a direct comparison with our previous work.[12]

Initial geometry optimizations and constraint geometry scans were performed at the UB3LYP/BS1 level of theory: BS1 is LACVP on iron (with core potential) and 6–31G on the rest of the atoms.[34] The maxima of the geometry scans were then used as starting points for the transition state searches, which established first-order saddle points with a single imaginary frequency for the correct mode. Improved energies were obtained through single point calculations at the UB3LYP/BS2 level of theory: BS2 is LACV3P+ on iron (with core potential) and 6–311+G* on the rest of the atoms. Free energies are reported at a temperature of 298 K and 1atm pressure and include zero-point, thermal and entropic corrections under standard conditions. Although the experiments were performed in the gas-phase, we also tested the effect of solvent on the obtained rate constants from single point calculations using the polarized continuum model in Gaussian with a dielectric constant mimicking acetonitrile. All structures represent full geometry optimizations without constraints and were characterized with a frequency calculation as either a local minimum (real frequencies only) or a first-order saddle point.

Acknowledgements

M.A.S. and F.G.C.R. thank the Petroleum Technology Development Fund and the Conacyt Mexico for a studentship. SdV acknowledges CPU time support from the National Service of Computational Chemistry Software (NSCCS). The EU-COST Network Explicit Control Over Spin-states in Technology and Biochemistry (ECOSTBio, CM1305) is acknowledged for support. M.E.C. and S.F. are grateful to the Università di Roma "La Sapienza" for funding of the FT-ICR MS work.

Keywords: arenes · density functional theory · fourier transform-ion cyclotron resonance · mass spectrometry · oxygen atom transfer

[1] a) M. Costas, M. P. Mehn, M. P. Jensen, L. Que Jr, *Chem. Rev.* **2004**, *104*, 939–986; b) M. M. Abu-Omar, A. Loaiza, N. Hontzeas, *Chem. Rev.* **2005**, *105*, 2227–2252; c) W. Nam, *Acc. Chem. Res.* **2007**, *40*, 522–531; d) P. Comba, M. Kerscher, *Coord. Chem. Rev.* **2009**, *253*, 564–574; e) *Iron-containing enzymes: Versatile catalysts of hydroxylation reaction in nature* (Eds.: S. P. de Visser, D. Kumar), RSC Publishing, Cambridge (UK), **2011**.

[2] a) E. I. Solomon, T. C. Brunold, M. I. Davis, J. N. Kemsley, S. K. Lee, N. Lehnert, F. Neese, A. J. Skulan, Y. S. Yang, J. Zhou, *Chem. Rev.* **2000**, *100*, 235–349; b) S. V. Kryatov, E. V. Rybak-Akimova, S. Schindler, *Chem. Rev.* **2005**, *105*, 2175–2226; c) P. C. A. Bruijnincx, G. van Koten, R. J. M. Klein Gebbink, *Chem. Soc. Rev.* **2008**, *37*, 2716–2744; d) M. Costas, *Coord. Chem. Rev.* **2011**, *255*, 2912–2932; e) A. R. McDonald, L. Que Jr, *Coord. Chem. Rev.* **2013**, *257*, 414–428; f) W. Nam, Y.-M. Lee, S. Fukuzumi, *Acc. Chem. Res.* **2014**, *47*, 1146–1154.

[3] A. Karlsson, J. V. Parales, R. E. Parales, D. T. Gibson, H. Eklund, S. Ramaswamy, *Science* **2003**, *299*, 1039–1042.

[4] a) T. D. H. Bugg, *Tetrahedron* **2003**, *59*, 7075–7101; b) E. G. Kovaleva, J. D. Lipscomb, *Science* **2007**, *316*, 453–457; c) S. Fetzner, R. A. Steiner, *Appl. Microbiol. Biotechnol.* **2010**, *86*, 791–804.

[5] a) M. Sono, M. P. Roach, E. D. Coulter, J. H. Dawson, *Chem. Rev.* **1996**, *96*, 2841–2888; b) J. T. Groves, *Proc. Natl. Acad. Sci. USA* **2003**, *100*, 3569–3574; c) B. Meunier, S. P. de Visser, S. Shaik, *Chem. Rev.* **2004**, *104*, 3947–3980; d) *Cytochrome P450: Structure, Mechanism and Biochemistry* (Ed.: P. R. Ortiz de Montellano) 3rd Ed., Kluwer Academic/Plenum Publishers, New York, **2005**; e) A. W. Munro, H. M. Girvan, K. J. McLean, *Nat. Prod. Rep.* **2007**, *24*, 585–609; f) G. Grogan, *Curr. Opin. Chem. Biol.* **2011**, *15*, 241–248; g) *Handbook of Porphyrin Science* (Eds.: K. M. Kadish, K. M. Smith, R. Guilard), World Scientific Publishing Co., New Jersey, **2010**; h) T. L. Poulos, *Chem. Rev.* **2014**, *114*, 3919–3962.

[6] a) S. Shaik, D. Kumar, S. P. de Visser, A. Altun, W. Thiel, *Chem. Rev.* **2005**, *105*, 2279–2328; b) M. R. A. Blomberg, T. Borowski, F. Himo, R.-Z. Liao, P. E. M. Siegbahn, *Chem. Rev.* **2014**, *114*, 3601–3658.

[7] a) F. Lanucara, M. E. Crestoni, *Chem. Eur. J.* **2011**, *17*, 12092–12100; b) M. E. Crestoni, S. Fornarini, F. Lanucara, J. J. Warren, J. M. Mayer, *J. Am. Chem. Soc.* **2010**, *132*, 4336–4343; c) B. Chiavarino, R. Cipollini, M. E. Crestoni, S. Fornarini, F. Lanucara, A. Lapi, *J. Am. Chem. Soc.* **2008**,

© 2016 Wiley-VCH Verlag GmbH & Co. KGaA, Weinheim

130, 3208 – 3217; d) M. E. Crestoni, S. Fornarini, F. Lanucara, *Chem. Eur. J.* **2009**, *15*, 7863 – 7866; e) M. E. Crestoni, S. Fornarini, *Inorg. Chem.* **2005**, *44*, 5379 – 5387.
[8] M. E. Crestoni, S. Fornarini, *Inorg. Chem.* **2007**, *46*, 9018 – 9020.
[9] J. Rittle, M. T. Green, *Science* **2010**, *330*, 933 – 937.
[10] a) M. T. Green, *J. Am. Chem. Soc.* **1999**, *121*, 7939 – 7940; b) F. Ogliaro, N. Harris, S. Cohen, M. Filatov, S. P. de Visser, S. Shaik, *J. Am. Chem. Soc.* **2000**, *122*, 8977 – 8989; c) D. Li, Y. Wang, K. Han, *Coord. Chem. Rev.* **2012**, *256*, 1137 – 1150; d) S. P. de Visser, *Adv. Inorg. Chem.* **2012**, *64*, 1 – 31.
[11] K. Kühnel, N. Ke, M. J. Cryle, S. G. Sligar, M. A. Schuler, I. Schlichting, *Biochemistry* **2008**, *47*, 6552 – 6559.
[12] M. A. Sainna, S. Kumar, D. Kumar, S. Fornarini, M. E. Crestoni, S. P. de Visser, *Chem. Sci.* **2015**, *6*, 1516 – 1529.
[13] NIST Chemistry WebBook, *NIST Standard Reference Database*, Number 69 (Eds.: P. J. Linstrom, W. G. Mallard) National Institute of Standards and Technology, Gaithersburg MD, 20899, http://webbook.nist.gov.
[14] a) S. P. de Visser, S. Shaik, *J. Am. Chem. Soc.* **2003**, *125*, 7413 – 7424; b) S. P. de Visser, R. Latifi, L. Tahsini, W. Nam, *Chem. Asian J.* **2011**, *6*, 493 – 504.
[15] M. Asaka, H. Fujii, *J. Am. Chem. Soc.* **2016**, *138*, 8048 – 8051.
[16] S. Kumar, A. S. Faponle, P. Barman, A. K. Vardhaman, C. V. Sastri, D. Kumar, S. P. de Visser, *J. Am. Chem. Soc.* **2014**, *136*, 17102 – 17115.
[17] L. Ji, A. S. Faponle, M. G. Quesne, M. A. Sainna, J. Zhang, A. Franke, D. Kumar, R. van Eldik, W. Liu, S. P. de Visser, *Chem. Eur. J.* **2015**, *21*, 9083 – 9092.
[18] S. M. Pratter, C. Konstantinovics, C. L. M. DiGiuro, E. Leitner, D. Kumar, S. P. de Visser, G. Grogan, G. D. Straganz, *Angew. Chem. Int. Ed.* **2013**, *52*, 9677 – 9681; *Angew. Chem.* **2013**, *125*, 9859 – 9863.
[19] a) J. M. Mayer, *Acc. Chem. Res.* **1998**, *31*, 441 – 450; b) S. P. de Visser, *J. Am. Chem. Soc.* **2010**, *132*, 1087 – 1097.
[20] S. P. de Visser, L.-S. Tan, *J. Am. Chem. Soc.* **2008**, *130*, 12961 – 12974.
[21] D. Kumar, B. Karamzadeh, G. N. Sastry, S. P. de Visser, *J. Am. Chem. Soc.* **2010**, *132*, 7656 – 7667.
[22] W. J. Song, Y. O. Ryu, R. Song, W. Nam, *J. Biol. Inorg. Chem.* **2005**, *10*, 294 – 304.
[23] S. P. de Visser, *Chem. Eur. J.* **2006**, *12*, 8168 – 8177.
[24] a) J. M. Mayer, *Annu. Rev. Phys. Chem.* **2004**, *55*, 363 – 390; b) J. Kaizer, E. J. Klinker, N. Y. Oh, J.-U. Rohde, W. J. Song, A. Stubna, J. Kim, E. Münck, W. Nam, L. Que Jr., *J. Am. Chem. Soc.* **2004**, *126*, 472 – 473; c) J. Yoon, S. A. Wilson, Y. K. Jang, M. S. Seo, K. Nehru, B. Hedman, K. O. Hodgson, E. Bill, E. I. Solomon, W. Nam, *Angew. Chem. Int. Ed.* **2009**, *48*, 1257 – 1260; *Angew. Chem.* **2009**, *121*, 1283 – 1286; d) D. P. Goldberg, *Acc. Chem. Res.* **2007**, *40*, 626 – 634; e) Y. Kang, H. Chen, Y. J. Jeong, W. Lai, E. H. Bae, S. Shaik, W. Nam, *Chem. Eur. J.* **2009**, *15*, 10039 – 10046.
[25] a) S. Shaik, P. Milko, P. Schyman, D. Usharani, H. Chen, *J. Chem. Theory Comput.* **2011**, *7*, 327 – 339; b) D. Kumar, G. N. Sastry, S. P. de Visser, *J. Phys. Chem. B* **2012**, *116*, 718 – 730.
[26] a) S. S. Shaik, *J. Am. Chem. Soc.* **1981**, *103*, 3692 – 3701; b) S. Shaik, *Phys. Chem. Chem. Phys.* **2010**, *12*, 8706 – 8720.
[27] a) S. Shaik, D. Kumar, S. P. de Visser, *J. Am. Chem. Soc.* **2008**, *130*, 10128 – 10140; b) D. Kumar, R. Latifi, S. Kumar, E. V. Rybak-Akimova, M. A. Sainna, S. P. de Visser, *Inorg. Chem.* **2013**, *52*, 7968 – 7979.
[28] H. Saltzman, J. G. Sharefkin, *Organic Syntheses*, Wiley, Hoboken, **1973**, Collect. Vol. 5, p 658.
[29] a) M. Meot-Ner in *Gas Phase Ion Chemistry*, (Ed.: M. T. Bowers), Academic Press, New York, **1979**, Vol. 1; b) J. E. Bartmess, R. M. Georgiadis, *Vacuum* **1983**, *33*, 149 – 154.
[30] T. Su, W. J. Chesnavich, *J. Chem. Phys.* **1982**, *76*, 5183 – 5185.
[31] F. Angelelli, B. Chiavarino, M. E. Crestoni, S. Fomarini, *J. Am. Soc. Mass Spectrom.* **2005**, *16*, 589 – 598.
[32] M. J. Frisch, *Gaussian* 09, revision D.01; M. J. Frisch, G. W. Trucks, H. B. Schlegel, G. E. Scuseria, M. A. Robb, J. R. Cheeseman, G. Scalmani, V. Barone, B. Mennucci, G. A. Petersson, H. Nakatsuji, M. Caricato, X. Li, H. P. Hratchian, A. F. Izmaylov, J. Bloino, G. Zheng, J. L. Sonnenberg, M. Hada, M. Ehara, K. Toyota, R. Fukuda, J. Hasegawa, M. Ishida, T. Nakajima, Y. Honda, O. Kitao, H. Nakai, T. Vreven, J. A. Montgomery, Jr., J. E. Peralta, F. Ogliaro, M. Bearpark, J. J. Heyd, E. Brothers, K. N. Kudin, V. N. Staroverov, T. Keith, R. Kobayashi, J. Normand, K. Raghavachari, A. Rendell, J. C. Burant, S. S. Iyengar, J. Tomasi, M. Cossi, N. Rega, J. M. Millam, M. Klene, J. E. Knox, J. B. Cross, V. Bakken, C. Adamo, J. Jaramillo, R. Gomperts, R. E. Stratmann, O. Yazyev, A. J. Austin, R. Cammi, C. Pomelli, J. W. Ochterski, R. L. Martin, K. Morokuma, V. G. Zakrzewski, G. A. Voth, P. Salvador, J. J. Dannenberg, S. Dapprich, A. D. Daniels, O. Farkas, J. B. Foresman, J. V. Ortiz, J. Cioslowski, D. J. Fox, Gaussian, Inc., Wallingford, CT, 2004.
[33] a) A. D. Becke, *J. Chem. Phys.* **1993**, *98*, 5648 – 5652; b) C. Lee, W. Yang, R. G. Parr, *Phys. Rev. B* **1988**, *37*, 785 – 789.
[34] a) P. J. Hay, W. R. Wadt, *J. Chem. Phys.* **1985**, *82*, 270 – 283; b) W. J. Hehre, R. Ditchfield, J. A. Pople, *J. Chem. Phys.* **1972**, *56*, 2257 – 2261.

Received: September 14, 2016
Published online on November 15, 2016

© 2016 Wiley-VCH Verlag GmbH & Co. KGaA, Weinheim

Biomimetic Models Very Important Paper

International Edition: DOI: 10.1002/anie.201604412
German Edition: DOI: 10.1002/ange.201604412

Deformylation Reaction by a Nonheme Manganese(III)–Peroxo Complex via Initial Hydrogen-Atom Abstraction

Prasenjit Barman, Pranav Upadhyay, Abayomi S. Faponle, Jitendra Kumar, Sayanta Sekhar Nag, Devesh Kumar, Chivukula V. Sastri,* and Sam P. de Visser**

Abstract: *Metal–peroxo intermediates are key species in the catalytic cycles of nonheme metalloenzymes, but their chemical properties and reactivity patterns are still poorly understood. The synthesis and characterization of a manganese(III)–peroxo complex with a pentadentate bispidine ligand system and its reactivity with aldehydes was studied. Manganese(III)–peroxo can react through hydrogen-atom abstraction reactions instead of the commonly proposed nucleophilic addition reaction. Evidence of the mechanism comes from experiments which identify a primary kinetic isotope effect of 5.4 for the deformylation reaction. Computational modeling supports the established mechanism and identifies the origin of the reactivity preference of hydrogen-atom abstraction over nucleophilic addition.*

The chemistry of metal–dioxygen intermediates has attracted interest in the field of biological as well as bioinorganic chemistry communities for many decades. These complexes are key intermediates in the catalytic cycles of metalloenzymes that activate and utilize molecular oxygen for vital biological processes in the human body, including the metabolism of drugs and the biosynthesis of hormones.[1] Although many metalloenzymes use iron as the central cofactor, several actually use manganese instead. Biologically active manganese ions are included, for instance, in the oxygen-evolving complex of photosystem II,[2] but also in superoxide dismutase that catalyzes the detoxification of superoxide and hydrogen peroxide to water.[3] The manganese–peroxo intermediate has been postulated as an important intermediate in these catalytic cycles; however, as it is short-lived, there currently is no experimental evidence available. Therefore, synthetic biomimetic models have been developed that have a ligand architecture suitable for studies in solution but have a coordination sphere that resembles enzyme analogues and consequently may give insight into the chemical and spectroscopic properties of enzymatic intermediates and their reactivity patterns.[4]

In the past few years, several biomimetic metal–peroxo adducts of iron and manganese have been prepared and characterized with UV/Vis, electronic absorption, electron paramagnetic resonance (EPR), and X-ray absorption spectroscopy techniques.[5,6] Furthermore, reactivity patterns with model substrates were studied, which showed that these metal–peroxo species mainly react through nucleophilic addition reactions.[7,8] Recently, a nonheme manganese(III)–peroxo complex with cyclam-type ligand was spectroscopically characterized with electronic absorption, EPR, and X-ray absorption techniques. Moreover, the complex was shown to react with manganese(II) chloride to form manganese(IV)–oxo and manganese(III)–hydroxo complexes.[9]

Synthetic metal–peroxo complexes are known to react with aldehydes efficiently in a proposed nucleophilic reaction mechanism. However, an alternative mechanism, not considered previously, concerns a rate determining hydrogen-atom abstraction from the α-position prior to oxygen-atom transfer. Recent work on metal–bispidine ligand systems showed that these complexes react efficiently with substrates through hydrogen-atom abstraction, owing to their rigid ligand framework, and reaction rates could be monitored effectively over a broad temperature and concentration range.[10] Therefore, we decided to investigate the relative reactivity of the $[Mn^{III}(L^1)(O_2)]^+$ complex (Scheme 1) with aldehydes and study the possible nucleophilic addition versus hydrogen-atom abstraction mechanisms. In particular, we report the synthesis and characterization of a novel side-on manganese(III)–peroxo complex with a pentadentate bispidine N5 ligand, $[Mn^{III}(L^1)(O_2)]^+$ (**1**),[11] Scheme 1, and study its reactivity patterns with 2-phenylpropionaldehyde (2-PPA) and its α-deuterated form.

The starting manganese(II) complex, $[Mn^{II}(L^1)(ClO_4)_2]^{2+}$ (**2**), was synthesized by reacting $Mn^{II}(ClO_4)_2{\cdot}2CH_3CN$ with the pentadentate bispidine ligand (L^1) in CH_3CN under an argon atmosphere, in analogy to previously reported procedures.[12] Addition of 10 equivalents of H_2O_2 to a colorless solution containing $[Mn^{II}(L^1)(ClO_4)_2]^{2+}$ (**2**; 2 mM) and triethylamine (TEA; 2.5 equivalents) in an acetonitrile solution at 15 °C afforded a blue intermediate (**1**) with an absorption band at 605 nm ($\varepsilon = 270\ L\,mol^{-1}\,cm^{-1}$; with a half-life of about 60 minutes (Figure 1a; see the Supporting Information for experimental details). The blue intermediate is characterized with various spectroscopic techniques including UV/Vis, high-

[*] P. Barman, S. S. Nag, Dr. C. V. Sastri
Department of Chemistry, Indian Institute of Technology Guwahati
Assam, 781039 (India)
E-mail: sastricv@iitg.ernet.in
P. Upadhyay, J. Kumar, Dr. D. Kumar
Department of Applied Physics, School of Physical Sciences
Babasaheb Bhimrao Ambedkar University
Lucknow, 226025 (India)
E-mail: dkclcre@yahoo.com
A. S. Faponle, Dr. S. P. de Visser
Manchester Institute of Biotechnology and School of Chemical Engineering and Analytical Science, The University of Manchester
131 Princess Street, Manchester M1 7DN (UK)
E-mail: sam.devisser@manchester.ac.uk
Supporting information and the ORCID identification number(s) for the author(s) of this article can be found under http://dx.doi.org/10.1002/anie.201604412.

 © 2016 Wiley-VCH Verlag GmbH & Co. KGaA, Weinheim

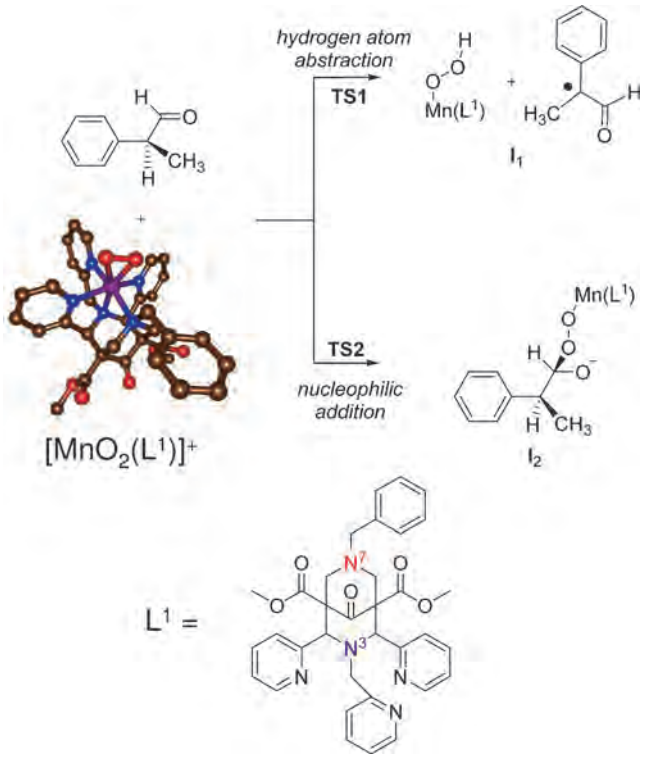

Scheme 1. Reactant complex $[Mn^{III}(L^1)(O_2)]^+$ and the possible reactivity patterns with 2-PPA substrate.

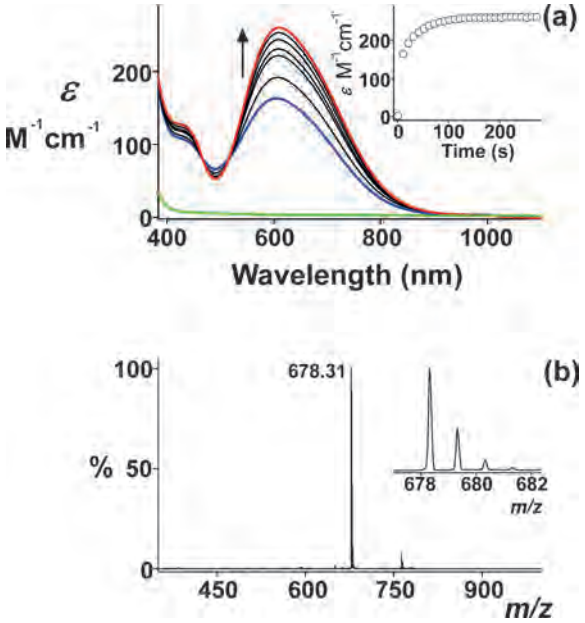

Figure 1. a) UV/Vis spectra of formation of **1** (2 mM) upon addition of $[Mn(L^1)]^{2+}$ (**2**; green line) in the presence of TEA (5 mM) and H_2O_2 (20 mM) in CH_3CN at 15 °C. Inset: the time trace for the formation the **1**. b) ESI-MS spectrum of **1**. Inset: the observed isotope distribution patterns for $[Mn(L^1)(O_2)]^+$.

resolution electrospray ionization-mass spectrometry (ESI-MS), and DFT. The ESI mass spectra of **1** exhibit a prominent ion peak with *m*/*z* 678.31, its isotopic distribution pattern

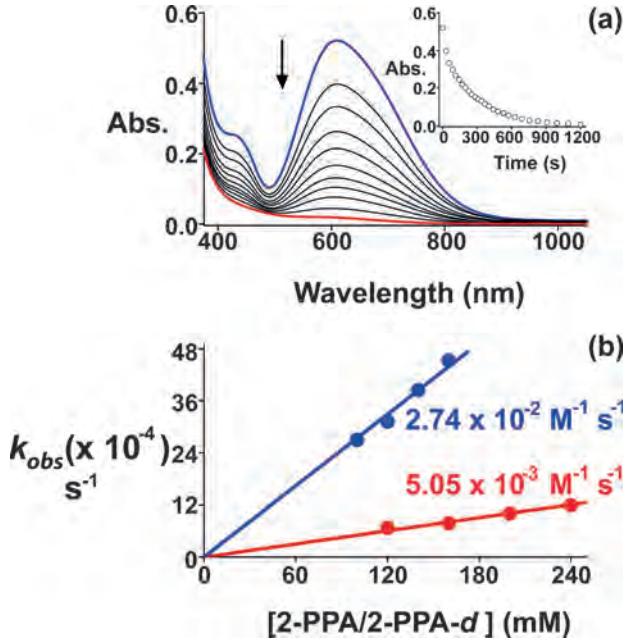

Figure 2. Kinetics of the reaction of **1** with 2-PPA: a) UV/Vis spectral changes of **1** (2 mM) upon addition of 2-PPA (160 mM) in the presence of TEA (5 mM) and hydrogen peroxide (20 mM) in CH_3CN at 15 °C. Inset: time course of the absorbance at 605 nm. b) Plot of k_{obs} against the concentration of 2-PPA and α-[D_1]-PPA (ca. 90%, D-enriched) and the derived second-order rate constant for the reaction of 2 mM **1** with substrate at various concentrations in CH_3CN at 15 °C for 2-PPA (●, blue) and α-[D_1]-PPA (●, red).

corresponds to $[Mn^{III}(L^1)(O_2)]^+$ (Figure 1b). These spectra are similar to those found by Jackson et al. on an analogous manganese(III)–peroxo complex.[9]

The nucleophilic and electrophilic character of **1** was then investigated in a reaction with 2-PPA as a substrate. Previous work showed that manganese(III)–peroxo complexes react with aldehydes to give the corresponding deformylated products by attacking the carbonyl group in a nucleophilic reaction.[6c,d] Upon addition of 2-PPA to **1** in CH_3CN at 15 °C, the intermediate decayed immediately and led to acetophenone as product (Figure 2a). The pseudo first-order rate constant of the decay of **1** increased linearly with increasing 2-PPA concentration, thus giving a second-order rate constant of 2.74×10^{-2} L mol^{-1} s^{-1}.

To establish whether the mechanism proceeds through a nucleophilic attack on the carbonyl group we used 2-methyl-2-phenylpropionaldehyde (2-Me-2-PPA) as a mechanistic probe. Upon addition of 2-Me-2-PPA to **1** at 15 °C, the intermediate decays at the rate of its natural decay. However, when the reaction solutions were analyzed with ESI-MS no deformylated products were observed. These results demonstrate that the manganese(III)–peroxo does not react with 2-PPA through a nucleophilic attack on the carbonyl group. As such, the work contradicts previous studies on the reactivity of nonheme and heme metal–peroxo complexes with aldehydes, that all reported a nucleophilic mechanism.[5b,6a,13]

To find out whether an alternative pathway was possible starting with an initial hydrogen-atom abstraction, we decided to investigate the reaction with α-[D_1]-PPA. Thus, upon

 © 2016 Wiley-VCH Verlag GmbH & Co. KGaA, Weinheim

addition of α-[D_1]-PPA (ca. 90%, D-enriched) to **1** in CH_3CN at 15 °C we determined a second-order rate constant of 5.05×10^{-3} L mol^{-1} s^{-1} (Figure 2b). Therefore, our kinetics studies establish the manganese(III)–peroxo complex to react with 2-PPA via a rate determining hydrogen-atom abstraction reaction from the α-position with a kinetic isotope effect (KIE) of 5.4.

To find further evidence of this novel reaction mechanism, we performed a radical trapping experiment with bromotrichloromethane using procedures reported previously.[14] Addition of 2-PPA to intermediate **1** in the presence of excess CCl_3Br (or CBr_4) in CH_3CN at 15 °C, leads to the formation of α-brominated product of the 2-PPA exclusively, which was confirmed by NMR analysis (Supporting Information). Consequently, our kinetics and reactivity studies clearly reveal a novel reaction mechanism between manganese(III)–peroxo complexes with aldehydes starting from an α-hydrogen-atom abstraction step.

To gain further insight into the rate determining step for the reaction of manganese(III)–peroxo with aldehydes, we decided to follow the experimental work up with a set of density functional theory calculations using previously reported procedures.[15] Two pathways were investigated, namely 1) hydrogen-atom abstraction by **1** from the α-position of 2-PPA; and 2) nucleophilic attack of the peroxo group on the carbonyl moiety of 2-PPA. The optimized geometries of the hydrogen-atom abstraction (^{5}**TS**$_{HA}$) and nucleophilic transition state (^{5}**TS**$_{NA}$) are given in the Supporting Information, Figures S15 and S18. Herein, we will focus on the analysis of the results and the understanding as to why the hydrogen-atom abstraction pathway is favorable. The hydrogen-atom abstraction barrier is relatively central with close values of the C–H and H–O distances and as expected happens with a large imaginary frequency for the C–H–O stretch typical for hydrogen-atom abstraction reactions.[16] In agreement with experimental observation the lowest barrier is ^{5}**TS**$_{HA}$ ($\Delta E + ZPE^{\ddagger} = 23.9$ kcal mol^{-1}). By contrast, the nucleophilic transition state (^{5}**TS**$_{NA}$) is well higher in energy ($\Delta E + ZPE^{\ddagger} = 28.7$ kcal mol^{-1}).

To understand the mechanistic preference of hydrogen-atom abstraction over nucleophilic addition, we devised a novel two-parabola curve crossing diagram to explain the reaction mechanism, which shows analogy to the valence bond curve crossing diagrams of Shaik.[17] Figure 3 shows details of the two-parabola curve crossing model. Thus, we consider the reaction along the reaction coordinate (x) that starts in the reactants (at $x = 0$) that is connected to another local minimum at $x = 1$ via a reaction barrier. We assume that the potential energy curve (y) can be described with a parabola with function $y_R = ax^2$ for the reactant complex and $y_P = bx^2 + cx + d$ for the products. If we assume that the transition state for the reaction happens at a reaction coordinate $x = {}^1/_2$ then these two curves will cross at $x = {}^1/_2$ and using the values for $y_P(0)$, $y_P({}^1/_2)$, $y_P(1)$, and $y_P'(1)$, we can derive an equation for the curve crossing energy (ΔE_{cross}) as a function of the Franck-Condon energy in the reactants

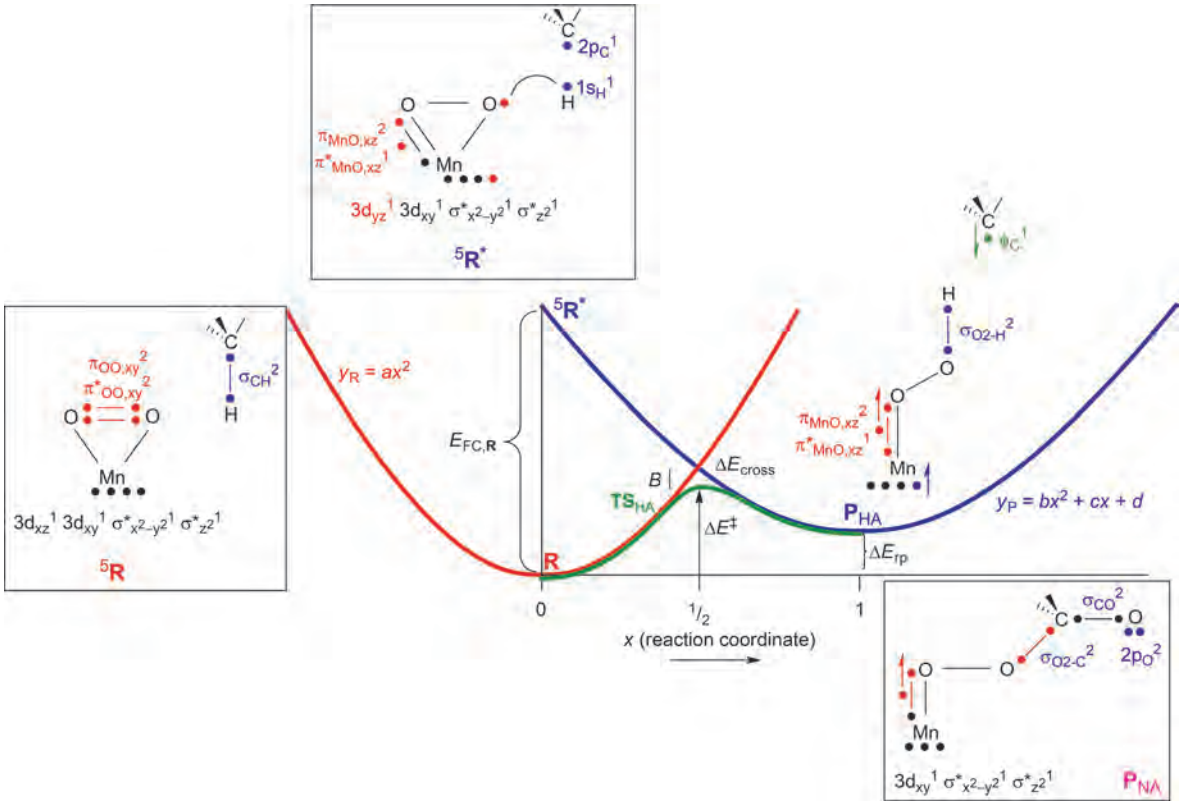

Figure 3. Two-parabola curve-crossing rationalization of the hydrogen-atom abstraction pathway in the reaction of **1** with 2-PPA. Bond orbital changes along the pathways highlighted. Dots represent electrons, and a line between two dots is a bond occupied by two electrons. Straight arrows indicate spin orbitals. Also shown is the VB representation of the alternative nucleophilic intermediate **P**$_{NA}$.

 © 2016 Wiley-VCH Verlag GmbH & Co. KGaA, Weinheim

($E_{FC,\mathbf{R}}$) and the driving force for the reaction (ΔE_{rp}), Equation (1), as defined in Figure 3.

$$\Delta E_{cross} = {}^1\!/_4 E_{FC,R} + {}^3\!/_4 \Delta E_{rp} \quad (1)$$

As shown previously using valence-bond curve-crossing diagrams,[17] the actual transition state is below the curve crossing energy by an amount B (the resonance energy), so that we can predict the value of the transition state based on estimates for $E_{FC,\mathbf{R}}$, ΔE_{rp}, and B with Equation (2).

$$\Delta E^{\neq}_{VB,HAT} = \Delta E_{cross} - B \quad (2)$$

We then analyzed the bond breaking and orbital changes between reactants, transition states and intermediates for the rate determining reaction step to predict the Franck–Condon energy between $^5\mathbf{R}$ and $^5\mathbf{R}$* and give details in Figure 3 in a valence bond format. These VB schemes were used previously to predict reactivities and rationalize reactivity trends.[18,19] Thus, the hydrogen-atom abstraction is accomplished through the breaking of the σ_{CH} bond of the substrate leading to atomic $2p_C$ and $1s_H$ orbitals, which energetically is equal to the bond dissociation energy of the C–H bond (BDE_{CH}). On the oxidant side of the reaction the $\pi_{OO,xy}{}^2$ $\pi^*_{OO,xy}{}^2$ pair of orbitals revert back to atomic orbitals and will cost an energy $E_{O=O}$. This will generate two doubly occupied 2p atomic orbitals, one on each oxygen atom. One of those 2p electrons on the terminal oxygen atom will form a bond with the incoming hydrogen atom, while the other electron is transferred to the $3d_{yz}$ orbital on Mn. Finally, the other 2p orbital on oxygen atom O1 will form a three-electron bond with the $3d_{xz}$ orbital on manganese and form the $\pi_{MnO,xz}$ and $\pi^*_{MnO,xz}$ pair of orbitals. The Franck–Condon energy, therefore, can be described as the sum of BDE_{CH}, $E_{O=O}$, and E_{ET}. We calculate a BDE_{CH} value for the α-position of 2-PPA of 80.3 kcal mol^{-1}, while the energy difference between the $\pi_{OO,xy}$ and $\pi^*_{OO,xy}$ was found to be 129.1 kcal mol^{-1} in the side-on manganese(III)–peroxo complex. Finally, the excitation energy from $\pi^*_{OO,xy}$ to $3d_{yz}$ was estimated to be 96.6 kcal mol^{-1}. The resonance energy, as before,[17] was taken as one half of the weakest bonds that are either broken or formed, which in this case is the sum of the O–H and Mn–O bond. As such, we estimate a hydrogen-atom abstraction barrier of 24.5 kcal mol^{-1}, which is in excellent agreement with the DFT barrier reported above.

Subsequently, we investigated the bond breaking and electron rearrangements for the nucleophilic addition reaction of which we show the VB representation of the product configuration in Figure 3. The reaction is initiated with the breaking of the carbonyl π-bond ($E_{PPA,\pi}$) as well as the splitting of the $\pi_{OO,xy}{}^2$ $\pi^*_{OO,xy}{}^2$ pair of orbitals on the peroxo group into atomic orbitals, that is, $E_{O=O}$. Similarly to the hydrogen-atom abstraction process the $2p_{O1}$ pair of electrons form a three-electron bond with the $3d_{xz}$(Mn) electron. Finally, a C–O bond is formed between peroxo and carbonyl. However, in contrast to the hydrogen-atom abstraction process no electron transfer from peroxo to manganese takes place. Instead, two electrons from the peroxo are donated into the C–O bond and the two electrons from the C=O π-bond move to the carbonyl oxygen atom. The resonance energy for the nucleophilic pathway is one-half of the sum of the C–O and Mn–O bonds that are formed, while a value of $E_{PPA,\pi=}$184.7 kcal mol^{-1} was estimated. Based on first principles, we estimate the nucleophilic barrier to be $\Delta E^{\neq}_{VB,NA} = 44.9$ kcal mol^{-1}.

The VB modeling, therefore, predicts that the side-on manganese–peroxo will react with 2-PPA through preferential α-hydrogen-atom abstraction rather than via nucleophilic addition. This is possible thanks to its small redox potential that enables efficient electron transfer from peroxo to manganese, which is a lower energy pathway than transferring an electron from peroxo to substrate carbonyl. Furthermore, the C–H bond strength of the substrate is only 80.3 kcal mol^{-1} and despite the fact that the side-on peroxo will give a weaker O–H bond, actually a strong Mn–O three-electron bond is formed, which gives the reaction to large driving force. By contrast, the nucleophilic pathway gains a rather weak C–O bond probably due to stereochemical repulsions of the ligand substituents interfering with the bond formation, so that this process overall will cost more energy. Therefore, the side-on manganese–peroxo with bispidine ligand system will preferentially react via hydrogen-atom abstraction rather than nucleophilic addition with aldehydes through its availability of low-energy metal 3d orbitals that can pick up an electron from the peroxo group. Further research will need to be done on synthetic and enzymatic manganese and iron–peroxo complexes, such as the aldehyde deformylating dioxygenases,[20] to find out whether this is a general mechanism.

Acknowledgements

Research support was provided by the Department of Science and Technology (SERB), India (EMR/2014/000279) to C.V.S. The National Service of Computational Chemistry Software (NSCCS) is acknowledged for CPU time to S.d.V. A.S.F. thanks the Tertiary Education Trust Fund Nigeria for a studentship. D.K. is the Ramanujan Fellow of the Department of Science and Technology, New Delhi (India).

Keywords: biomimetic models · density functional theory · enzyme models · hydrogen-atom abstraction · reaction mechanisms

How to cite: *Angew. Chem. Int. Ed.* **2016**, *55*, 11091–11095
Angew. Chem. **2016**, *128*, 11257–11261

[1] a) *Biomimetic Oxidations Catalyzed by Transition Metal Complexes* (Ed.: B. Meunier), Imperial College Press, London, **2000**; b) *Cytochrome P450: Structure, Mechanism, and Biochemistry*, 3rd ed. (Ed.: P. R. Ortiz de Montellano), Kluwer Academic/Plenum Publishers, New York, **2005**.

[2] a) D. J. Vinyard, G. M. Ananyev, G. C. Dismukes, *Annu. Rev. Biochem.* **2013**, *82*, 577–606; b) G. Renger, T. Renger, *Photosynth. Res.* **2008**, *98*, 53–80; c) J. Barber, *Q. Rev. Biophys.* **2003**, *36*, 71–89; d) P. E. M. Siegbahn, *Chem. Eur. J.* **2008**, *14*, 8290–8302.

[3] a) T. A. Jackson, T. C. Brunold, *Acc. Chem. Res.* **2004**, *37*, 461–470; b) B. R. Streit, B. Blanc, G. S. Lukat-Rodgers, K. R. Lukat-Rodgers, J. L. Dubois, *J. Am. Chem. Soc.* **2010**, *132*, 5711–5724;

 © 2016 Wiley-VCH Verlag GmbH & Co. KGaA, Weinheim

c) S. Hofbauer, C. Gruber, K. F. Pirker, A. Sündermann, I. Schaffner, C. Jakopitsch, C. Oostenbrink, P. G. Furtmüller, C. Obinger, *Biochemistry* **2014**, *53*, 3145 – 3157.
[4] a) M. Costas, M. P. Mehn, M. P. Jensen, L. Que, Jr., *Chem. Rev.* **2004**, *104*, 939 – 986; b) P. C. A. Bruijnincx, G. van Koten, R. J. M. Klein Gebbink, *Chem. Soc. Rev.* **2008**, *37*, 2716 – 2744; c) M. M. Abu-Omar, A. Loaiza, N. Hontzeas, *Chem. Rev.* **2005**, *105*, 2227 – 2252; d) S. V. Kryatov, E. V. Rybak-Akimova, S. Schindler, *Chem. Rev.* **2005**, *105*, 2175 – 2226.
[5] a) G. Roelfes, V. Vrajmasu, K. Chen, R. Y. N. Ho, J.-U. Rohde, C. Zondervan, R. M. la Crois, E. P. Schudde, M. Lutz, A. L. Spek, R. Hage, B. L. Feringa, E. Münck, L. Que, Jr., *Inorg. Chem.* **2003**, *42*, 2639 – 2653; b) J. Annaraj, Y. Suh, M. S. Seo, S. O. Kim, W. Nam, *Chem. Commun.* **2005**, 4529 – 4531; c) A. Thibon, J.-F. Bartoli, S. Bourcier, F. Banse, *Dalton Trans.* **2009**, 9587 – 9594; d) A. Mukherjee, M. A. Cranswick, M. Chakrabarti, T. K. Paine, K. Fujisawa, E. Münck, L. Que, Jr., *Inorg. Chem.* **2010**, *49*, 3618 – 3628; e) J. Cho, S. Jeon, S. A. Wilson, L. V. Liu, E. A. Kang, J. J. Braymer, M. H. Lim, B. Hedman, K. O. Hodgson, J. S. Valentine, E. I. Solomon, W. Nam, *Nature* **2011**, *478*, 502 – 505.
[6] a) J. Annaraj, J. Cho, Y.-M. Lee, S. Y. Kim, R. Latifi, S. P. de Visser, W. Nam, *Angew. Chem. Int. Ed.* **2009**, *48*, 4150 – 4153; *Angew. Chem.* **2009**, *121*, 4214 – 4217; b) D. F. Leto, S. Chattopadhyaay, V. W. Day, T. A. Jackson, *Dalton Trans.* **2013**, *42*, 13014 – 13025; c) M. Zlatar, M. Gruden, O. Y. Vassilyeva, E. A. Buvaylo, A. N. Ponomarev, S. A. Zvyagin, J. Wosnitza, J. Krzystek, P. Garcia-Fernandez, C. Duboc, *Inorg. Chem.* **2016**, *55*, 1192 – 1201; d) C.-M. Lee, C.-H. Chuo, C.-H. Chen, C.-C. Hu, M.-H. Chiang, Y.-J. Tseng, C.-H. Hu, G.-H. Lee, *Angew. Chem. Int. Ed.* **2012**, *51*, 5427 – 5430; *Angew. Chem.* **2012**, *124*, 5523 – 5526.
[7] W. Nam, *Acc. Chem. Res.* **2007**, *40*, 522 – 531.
[8] a) M. K. Coggins, J. A. Kovacs, *J. Am. Chem. Soc.* **2011**, *133*, 12470 – 12473; b) M. K. Coggins, V. Martin-Diaconescu, S. DeBeer, J. A. Kovacs, *J. Am. Chem. Soc.* **2013**, *135*, 4260 – 4272.
[9] H. E. Colmer, A. W. Howcroft, T. A. Jackson, *Inorg. Chem.* **2016**, *55*, 2055 – 2069.
[10] a) P. Comba, M. Kerscher, W. Schiek, *Prog. Inorg. Chem.* **2007**, *55*, 613 – 704; b) P. Comba, S. Fukuzumi, H. Kotani, S. Wunderlich, *Angew. Chem. Int. Ed.* **2010**, *49*, 2622 – 2625; *Angew. Chem.* **2010**, *122*, 2679 – 2682.
[11] L^1 = dimethyl-2,4-di(2-pyridyl)3-(pyridin-2-ylmethyl)-7-benzyl-3,7-diaza-bicyclo[3.3.1] nonan-9-one-1,5-dicarboxylate.
[12] P. Barman, A. K. Vardhaman, B. Martin, S. J. Wörner, C. V. Sastri, P. Comba, *Angew. Chem. Int. Ed.* **2015**, *54*, 2095 – 2099; *Angew. Chem.* **2015**, *127*, 2123 – 2127.
[13] a) M. S. Seo, J. Y. Kim, J. Annaraj, Y. Kim, Y.-M. Lee, S.-J. Kim, J. Kim, W. Nam, *Angew. Chem. Int. Ed.* **2007**, *46*, 377 – 380; *Angew. Chem.* **2007**, *119*, 381 – 384; b) R. A. Geiger, S. Chattopadhyay, V. W. Day, T. A. Jackson, *Dalton Trans.* **2011**, *40*, 1707 – 1715; c) Y. Goto, S. Wada, I. Morishima, Y. Watanabe, *J. Inorg. Biochem.* **1998**, *69*, 241 – 247; d) J. Cho, R. Sarangi, J. Annaraj, S. Y. Kim, M. Kubo, T. Ogura, E. I. Solomon, W. Nam, *Nat. Chem.* **2009**, *1*, 568 – 572; e) R. L. Shook, W. A. Gunderson, J. Greaves, J. W. Ziller, M. P. Hendrich, A. S. Borovik, *J. Am. Chem. Soc.* **2008**, *130*, 8888 – 8889; f) J. Cho, R. Sarangi, H. Y. Kang, J. Y. Lee, M. Kubo, T. Ogura, E. I. Solomon, W. Nam, *J. Am. Chem. Soc.* **2010**, *132*, 16977 – 16986; g) R. V. Ottenbacher, D. G. Samsonenko, E. P. Talsi, K. P. Bryliakov, *ACS Catal.* **2016**, *6*, 979 – 988; h) J. A. Kovacs, *Acc. Chem. Res.* **2015**, *48*, 2744 – 2753; i) C.-M. Lee, C.-H. Chuo, C.-H. Chen, C.-C. Hu, M.-H. Chiang, Y.-J. Tseng, C.-H. Hu, G.-H. Lee, *Angew. Chem. Int. Ed.* **2012**, *51*, 5427 – 5430; *Angew. Chem.* **2012**, *124*, 5523 – 5526.
[14] a) J. T. Groves, T. E. Nemo, *J. Am. Chem. Soc.* **1983**, *105*, 6243 – 6248; b) S. Rana, A. Dey, D. Maiti, *Chem. Commun.* **2015**, *51*, 14469 – 14472.
[15] a) A. K. Vardhaman, P. Barman, S. Kumar, C. V. Sastri, D. Kumar, S. P. de Visser, *Angew. Chem. Int. Ed.* **2013**, *52*, 12288 – 12292; *Angew. Chem.* **2013**, *125*, 12514 – 12518; b) S. P. de Visser, M. G. Quesne, B. Martin, P. Comba, U. Ryde, *Chem. Commun.* **2014**, *50*, 262 – 282; c) S. Kumar, A. S. Faponle, P. Barman, A. K. Vardhaman, C. V. Sastri, D. Kumar, S. P. de Visser, *J. Am. Chem. Soc.* **2014**, *136*, 17102 – 17115.
[16] L. Ji, A. S. Faponle, M. G. Quesne, M. A. Sainna, J. Zhang, A. Franke, D. Kumar, R. van Eldik, W. Liu, S. P. de Visser, *Chem. Eur. J.* **2015**, *21*, 9083 – 9092.
[17] a) S. S. Shaik, *J. Am. Chem. Soc.* **1981**, *103*, 3692 – 3701; b) S. Shaik, *Phys. Chem. Chem. Phys.* **2010**, *12*, 8706 – 8720.
[18] a) D. Kumar, B. Karamzadeh, G. N. Sastry, S. P. de Visser, *J. Am. Chem. Soc.* **2010**, *132*, 7656 – 7667; b) D. Kumar, R. Latifi, S. Kumar, E. V. Rybak-Akimova, M. A. Sainna, S. P. de Visser, *Inorg. Chem.* **2013**, *52*, 7968 – 7979.
[19] A. S. Faponle, M. G. Quesne, S. P. de Visser, *Chem. Eur. J.* **2016**, *22*, 5478 – 5483.
[20] L. J. Rajakovich, H. Nørgard, D. M. Warui, W.-C. Chang, N. Li, S. J. Booker, C. Krebs, J. M. Bollinger, Jr., M.-E. Pandelia, *J. Am. Chem. Soc.* **2015**, *137*, 11695 – 11709.

Received: May 6, 2016
Revised: June 3, 2016
Published online: July 8, 2016

 © 2016 Wiley-VCH Verlag GmbH & Co. KGaA, Weinheim

This is an open access article published under a Creative Commons Attribution (CC-BY) License, which permits unrestricted use, distribution and reproduction in any medium, provided the author and source are cited.

ACS Catalysis

Research Article

pubs.acs.org/acscatalysis

Origin of the Enhanced Reactivity of μ-Nitrido-Bridged Diiron(IV)-Oxo Porphyrinoid Complexes over Cytochrome P450 Compound I

Matthew G. Quesne,[†] Dhurairajan Senthilnathan,[‡,$] Devendra Singh,[&] Devesh Kumar,[&] Pascale Maldivi,[*,‡,◇] Alexander B. Sorokin,[*,⊥] and Sam P. de Visser[*,†]

[†]Manchester Institute of Biotechnology and School of Chemical Engineering and Analytical Science, The University of Manchester, 131 Princess Street, Manchester M1 7DN, United Kingdom

[‡]Univ. Grenoble Alpes, INAC-SCIB, Reconnaissance Ionique et Chimie de Coordination, F-38000 Grenoble, France

[◇]CEA, INAC-SCIB, F-38000 Grenoble, France

[$]Center for Computational Chemistry, CRD, PRIST University, Vallam, Thanjavur, Tamilnadu 613403, India

[&]Department of Applied Physics, Babasaheb Bhimrao Ambedkar University, School for Physical Sciences, Vidya Vihar, Rae Bareilly Road, Lucknow, Uttar Pradesh 226025, India

[⊥]Institut de Recherches sur la Catalyse et l'Environnement de Lyon (IRCELYON), UMR 5256, CNRS-Université Lyon 1, 2, av. A. Einstein, 69626 Villeurbanne, France

Supporting Information

ABSTRACT: μ-Nitrido-bridged diiron porphyrins and phthalocyanines are known to be efficient oxidants that are able to oxidize some of the strongest C−H bonds in nature, such as the one in methane. The origin of their catalytic efficiency is poorly understood, and in order to gain insight into the structural and electronic features of this chemical system, we performed a detailed and systematic study into their chemical properties and reactivities using density functional theory. Our work shows that μ-nitrido-bridged diiron porphyrins and phthalocyanines are highly active catalytic oxidants, which react with methane with very low reaction barriers and a rate-determining hydrogen-atom-abstraction step. Furthermore, the μ-nitrido-bridged diiron porphyrin and phthalocyanine complexes react with a free energy of activation that is more than 10 kcal mol^{-1} lower in energy than that found for cytochrome P450 Compound I, which is known to be one of the most efficient C−H hydroxylating agents in Nature. We have analyzed the electronic configuration of reactants and transition states in detail and have identified the key properties of the oxidants that lead to this rate enhancement. In particular, the potency of the oxidant is related to the orbital mixing patterns along the Fe−O axis, whereby the axial iron(IV)-nitrido group donates sufficient electron density to affect the pK_a of the oxo group as well as the strength of the O−H bond formed in the iron(IV)-hydroxo complex. The studies confirm that μ-nitrido diiron-oxo complexes should react via oxygen atom transfer readily even with strong C−H bonds as in methane. The results are analyzed with orbital diagrams, valence bond, and thermochemical cycles and explain the intricate details of the mechanism and the properties of the oxidant.

KEYWORDS: *biomimetic models, hydrogen abstraction, hydroxylation, iron, ligand effects*

INTRODUCTION

Cytochrome P450 enzymes are versatile enzymes in human physiology that mainly react with compounds through oxygen atom transfer, including the hydroxylation of C−H bonds. P450s activate their substrates with the aim to initiate their metabolism and detoxification but, on the other hand, also assist in biosynthetic pathways of e.g., hormones.[1] Thus, the biodegradation of long chain fatty acids and xenobiotics is catalyzed by P450 liver isozymes through a mechanism that is considered to proceed via an iron(IV)-oxo heme cation radical intermediate called Compound I (CpdI). To understand the fundamental features of the oxidant in the P450-enzyme-catalyzed reaction mechanism, synthetic models have been prepared that model the enzyme active site composition and coordination.[2] These so-called biomimetic model complexes enable one to study the reactivity patterns and the intrinsic chemical properties of iron porphyrins and gain understanding into the intricate structural and electronic features of the active site. Biomimetic work indeed confirmed a high-valent iron(IV)-oxo porphyrin cation radical to be the active oxidant in chemical transformations of substrates and ruled out many alternative suggestions.[3]

Recent biochemical studies isolated and characterized Compound I in a P450 isozyme and established the electronic

Received: November 30, 2015
Revised: January 11, 2016
Published: February 19, 2016

 © 2016 American Chemical Society

DOI: 10.1021/acscatal.5b02720
ACS Catal. 2016, 6, 2230−2243

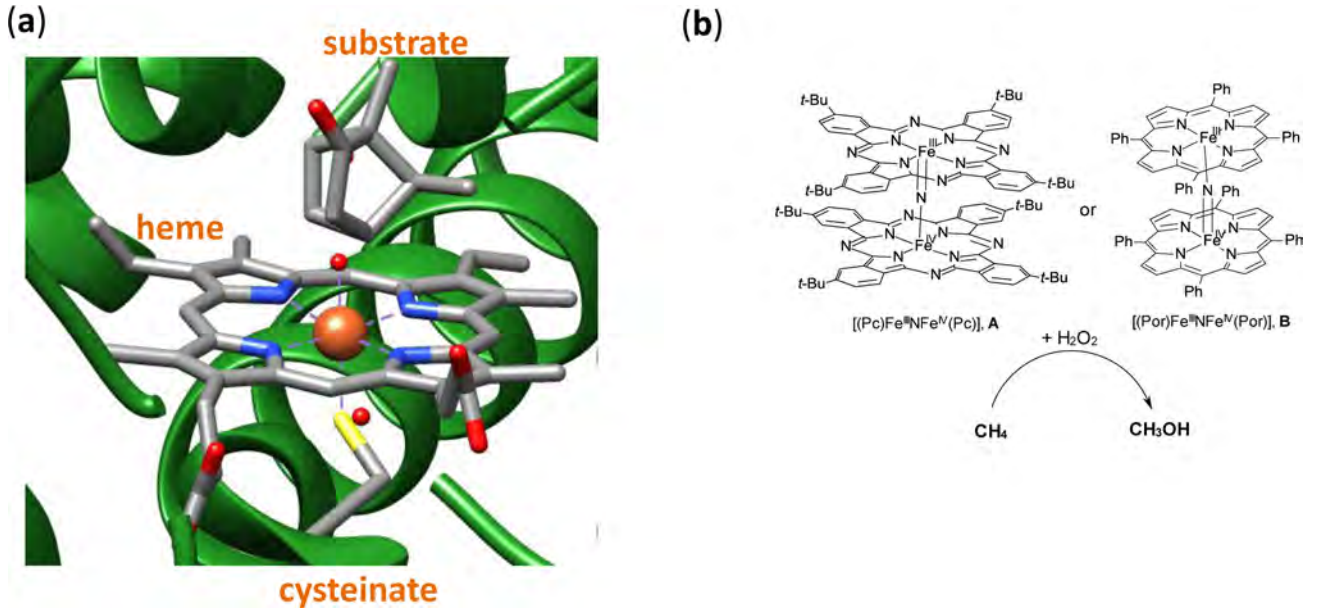

Figure 1. Comparative structural features of the active site of $P450_{cam}$ (a) and μ-nitrido-bridged diiron-oxo porphyrin and phthalocyanine complexes (b).

configuration with spectroscopic methods.[4] Although the P450s are known to be efficient and powerful oxidants in nature, native enzymes do not catalyze the conversion of methane to methanol, which requires the breaking of a very strong C−H bond with a bond dissociation energy (BDE) of 104.9 kcal mol^{-1}. However, using iodosylbenzene as an oxidant, it was shown that CYP153A6 is able to oxidize methane at room temperature, although very low turnover numbers of 0.02−0.05 were obtained.[5] On the other hand, guest/host activation of $P450_{BM3}$ with perfluorocarboxylic acids as decoy molecules enabled the oxidation of all short alkanes tested except for methane.[6,7]

Structurally, the P450s all contain an active heme group (Figure 1a) linked to the protein through a cysteinate bridge. To mimic the active site features of P450 CpdI, over the years, work on synthetic iron porphyrins has been performed with the aim of improving the oxidative power of the active species through modifications of the porphyrin scaffold. In particular, research was done to find a metal porphyrin system able to hydroxylate methane, but so far, only a few of these studies have been successful. Thus, several μ-nitrido-bridged diiron-oxo phthalocyanines and porphyrin (**A** and **B**, Figure 1b) complexes prepared using H_2O_2 or *m*-chloroperbenzoic acid (m-CPBA) are able to oxidize methane to methanol efficiently.[8,9] Experimental and computational studies on these exciting catalysts also show that these μ-nitrido-bridged systems are stable and maintain their dimerization throughout the reactions that they catalyze, unlike many of the μ-oxo dimers.[8]

It appears, therefore, that these diiron complexes are more potent oxidants than the active species of P450 enzymes, an example of which is shown using the active site structure from $P450_{cam}$ as taken from the protein databank[10] for structural comparison in Figure 1. The question is, then, what makes **A**/**B** a stronger oxidant than the enzyme, and what is the effect of the bridging μ-nitrido group on the chemical properties of the oxidant and the catalysis?

The origin of the reactivity differences between μ-nitrido-bridged diiron complexes and P450 CpdI may derive from a range of chemical and structural differences. First, some P450 isozymes have a tight substrate binding pocket and selectively activate substrates,[11] and the pocket may not be setup to hydroxylate methane efficiently, resulting in an uncoupling reaction. However, the use of decoy molecules, such as inert perfluorocarboxylic acids, makes it possible to accommodate methane into the cavity, but this did not lead to the oxidation of methane.[7] On the other hand, there are clear structural differences between **A**/**B** and P450 CpdI and particularly related to the axial ligand (i.e., cysteinate versus nitrido-iron(IV)-phthalocyanine).

It is known that the axial ligand of iron-porphyrins has a major effect on catalysis as well as on the spectroscopic properties (e.g., Fe−O vibrations) of the oxidant.[12] These biomimetic studies on axial ligand effects in iron(IV)-oxo complexes are in analogy to those derived from biochemical work on enzymes including heme-peroxidases and heme-monoxygenases. Thus, peroxidases generally have a histidine axial ligand coordinating the heme, whereas heme-monooxygenases such as the P450s have a cysteinate axial ligand. The axial ligand incurs a push- or a pull effect of electron density and thereby gives fundamental differences between the two heme enzyme classes.[13] This difference in function of P450 monoxygenases, heme peroxidases, and catalases has been assigned to the axial ligand bound to the heme.[14] In addition, biomimetic work has shown equatorial ligand may also have an effect on reactivity patterns but usually to a lesser extent than the axial ligand.[15]

Clearly, the reactivity and electronic properties of iron porphyrin/heme complexes is sensitive to the axial ligand bound and, in particular, experimental evidence appears to suggest that an axial μ-nitrido iron(IV) makes the oxidant so powerful that it can even hydroxylate methane. Therefore, we decided to investigate the electronic properties and reactivity patterns of μ-nitrido-bridged diiron-oxo complexes and find out the key factors that influence their catalytic activity with strong C−H bonds. The work shows that the axial μ-nitrido iron(IV) group has π and π^* orbitals that mix with the iron(IV)-oxo π/π^* orbitals and thereby make the oxidant more reactive.

DOI: 10.1021/acscatal.5b02720
ACS Catal. 2016, 6, 2230−2243

Scheme 1. Models of μ-Nitrido-Bridged Diiron Porphyrazine (1) and Porphyrin (2) as well as P450 CpdI (3) Investigated in This Work

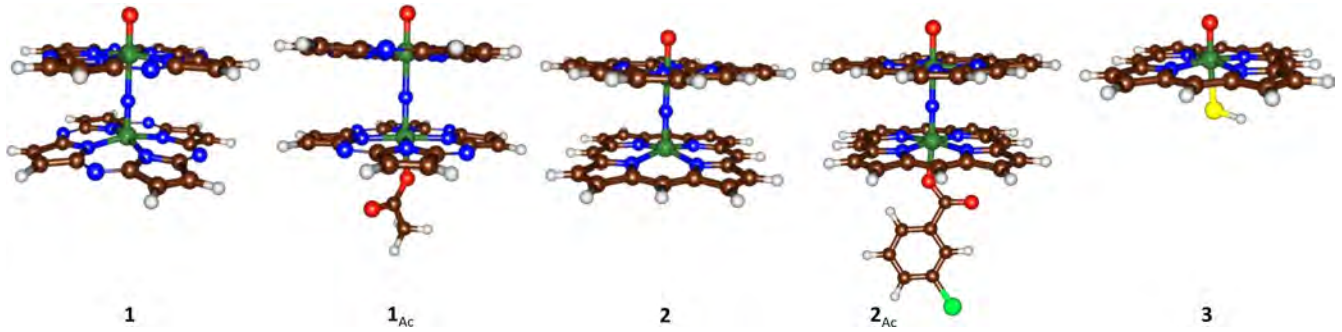

METHODS

Models. To understand the chemical properties of **A**/**B**, we created a number of models with different equatorial and axial ligands included, see Scheme 1. First, we created a "small" μ-nitrido-bridged diiron-oxo chemical structure of 68 atoms, whereby the phthalocyanine units were abbreviated to porphyrazine macrocycles (**1**). However, experimental Mössbauer studies indicated the possible presence of an anionic axial ligand in μ-nitrido-bridged high-valent diiron porphyrin oxo species,[9] when a concentrated solution of the complex and m-CPBA was used at very low temperatures. Although the presence of the axial ligand could not be ascertained under catalytic conditions in the experiments, we decided to include a model with an axial acid anion ligand and investigated its possible influence on the oxidizing properties of the oxo species in model $\mathbf{1}_{Ac}$. As a comparison, we also investigated the properties of μ-nitrido-bridged diiron-oxo porphyrin without an anionic axial ligand attached to Fe_2 (structure **2**) and with 3-chlorobenzoate ligated (structure $\mathbf{2}_{Ac}$) to reflect the use of m-CPBA experimentally. Structures **1** and **2** are overall charge neutral, whereas $\mathbf{1}_{Ac}$ and $\mathbf{2}_{Ac}$ have a total charge of −1.

A complete model with tetraphenylporphyrin (TPP) ligands ($\mathbf{2}_{TPP}$) was also studied, but the addition of substituents to the *meso*-position of the porphyrin had little effect on the optimized geometries and electronic configuration of the reactant complexes, see Supporting Information for details.

All structures and reactivities were compared with model complexes of P450 CpdI, which was modeled, as before,[16] as an iron(IV)-oxo-porphyrin cation radical ($\mathbf{3}_{SH}$, [Fe^{IV}(O) ($Por^{+\bullet}$)-SH]) but also with an elaborate cysteinate axial ligand description ($\mathbf{3}_{Cys}$, [Fe^{IV}(O) ($Por^{+\bullet}$)Cys]). In previous work, we extensively tested various enzyme models and compared those to results obtained from QM/MM studies and experiment.[17] Indeed, in recent work, model clusters were compared to QM/MM results with increasing QM size.[17b] The energy differences upon the barrier heights fluctuated within a range of a few kcal mol^{-1} and did not affect the shape of the landscape or the overall conclusions. The models discussed here were shown to reproduce QM/MM obtained results well and gave similar electronic configuration as well as reactivity patterns with barrier heights reproduced within 1.1 kcal mol^{-1}.[17a] For example, the charge and spin distributions of CpdI and the spin-state ordering and relative energies follow similar trends. In addition, studies on product isotope effects through bifurcation pathways gave excellent agreement with experimentally determined values.[18] The small model complexes used here enable one to understand the fundamental chemical differences between the active site of P450 and the synthetic μ-nitrido-bridged diiron-oxo complexes described here by elimination of the protein interactions. The P450 models were overall charge neutral and were calculated in the lowest-lying doublet and quartet spin states. Our study produced a comprehensive set of data of which the highlights are presented here, and all the details can be found in the Supporting Information.

Computational Procedures. The studies presented in this work used density functional theory methods as implemented in the Gaussian-09, Jaguar 7.8, and ORCA program packages.[19] The potential energy surfaces of the reaction of methane with **1**, $\mathbf{1}_{Ac}$, $\mathbf{2}_{TPP}$, and **3** on all low-lying spin states were initially explored at the UB3LYP level of theory[20] in Gaussian-09 in combination with a double-ζ quality LACVP basis set on iron with core potential and 6-31G on the rest of the atoms: basis set BS1.[21] Subsequently, full geometry optimizations of local minima and transition states were calculated at UB3LYP[20] and UBP86[22] level of theory and followed by an analytical frequency, see Supporting Information for details. Transition states were characterized with a single imaginary frequency for the correct mode, while local minima had real frequencies only. Subsequently, single-point calculations were done using a triple-ζ type LACV3P+ basis set on iron with core potential and 6-311+G* on the rest of the atoms: basis set BS2. Test calculations, whereby the geometries were optimized with UB3LYP/BS2 gave a potential energy profile of substrate hydroxylation that was within a few tenths of a kcal mol^{-1} from those obtained with UB3LYP/BS2//UB3LYP/BS1;[23] therefore, the rest of the systems were geometry optimized with UB3LYP/BS1.

As the experimental work used acetonitrile as a solvent, we performed solvent calculations using the polarized continuum model (PCM) with a dielectric constant of ε = 37.5 and a probe radius of 2.183 Å as implemented in Jaguar using a triple-ζ or better basis set on all atoms. Test calculations, whereby the geometry was optimized with a solvent model included, were performed (see Supporting Information Figure S19). However, this did not lead to changes in the electronic structure of the local minima and gave very similar optimized geometries.

Detailed geometry scans along one degree of freedom were performed between reactants and intermediates as well as between intermediates and products. These constrained geometry optimizations had one degree of freedom fixed, while all other coordinates were optimized. Geometry scans confirmed the reaction mechanisms and electron-transfer processes. Due to the size of the chemical systems investigated here, we only were able to run Intrinsic Reaction Coordinate (IRC) scans for a selection of systems. Those studies confirmed

DOI: 10.1021/acscatal.5b02720
ACS Catal. 2016, 6, 2230−2243

the mechanism and did not give results that were dramatically different from the geometry scans. The methods and procedures used in this work were extensively tested and benchmarked. For instance, in previous work, we reproduced experimental free energies of activation within 3 kcal mol^{-1},[24] but also experimental rate enhancements,[25] as well as kinetic isotope effects.[26]

The calculations of the reaction mechanism of methane with **2** and $\mathbf{2}_{Ac}$ were explored at the UB3LYP/BS1 level of theory in Jaguar with basis set BS1, and with Orca using a basis set that contains LANL2DZ on iron and 6-31G on the rest of the atoms. As for the porphyrazine species, stationary points were characterized with a frequency calculation with minima and transition states having all real or one imaginary frequency, respectively. In the latter case, the imaginary mode was displayed using the Orca Pltvib utility[19c] and GOpenMol[19d] to check its nature. Solvent effects were incorporated through the Conductor-like Screening Model (Cosmo) as implemented in Orca using a dielectric constant of 37 mimicking acetonitrile. Optimizations for both minima and transition states were done in solvent at the UB3LYP/BS1 level of theory, but the resulting structures, spin densities, and energy differences were very similar to the gas-phase results. Single points at the UB3LYP/BS2 level of theory were also performed on stationary points. Natural bond order analysis calculations were performed in Gaussian-09.

Structure **1** and $\mathbf{1}_{Ac}$ were investigated in Gaussian-09 on all low lying spin states: doublet, quartet, sextet and octet. As before,[27] we tested a range of ferromagnetically and antiferromagnetically coupled spin-state occupations of the reactant complexes. In particular, we attempted to create a P450 CpdI-type electronic configuration with a metal radical coupled to a ligand radical. However, all our attempts to generate an electronic state with ligand radical failed, and converted back to a state with only radical character on the OFe_1NFe_2 atoms. The same efforts were also done for **2** and $\mathbf{2}_{Ac}$ in Orca and Jaguar with the same effects: namely, no radical character on the macrocycle was obtained. Although several spin states were investigated, the doublet spin state was found to be the ground state and well separated from the nearest quartet, sextet, and octet spin states. Therefore, the other models were calculated in the doublet spin state only.

To test the reproducibility of the work, we did a range of single-point calculations on the UB3LYP/BS1 optimized geometries in Gaussian using a number of (unrestricted) density functional methods with basis set BS2, namely B3LYP,[20] BP86,[22] B3LYP* (B3LYP with 15% HF),[28] dispersion-corrected B3LYP (B3LYP-D3),[29] M06-L,[30] and PBE0.[31] In general, the same spin-state ordering is obtained regardless of the density functional method, and all chemical trends are reproduced. For clarity, we will focus in the main text on the B3LYP results, but all other results can be found in the Supporting Information.

Multireference perturbation theory of the N-electron valence type (NEVPT2) was applied to test the electronic configuration of the reactant and radical intermediate complexes. These calculations were done in Orca using procedures described previously.[32]

Kinetic Isotope Effects. We estimated the kinetic isotope effect (KIE) for the hydrogen-atom-abstraction reactions by replacing one or more of the hydrogen atoms of the substrate by deuterium atoms. Thus, the ratio of the rate constants of the substrate and the deuterated substrate (k_H/k_D) is a measure of the KIE, whereby we estimated the primary KIE for replacing the transferring hydrogen atom by deuterium as well as the secondary KIE, where the other hydrogen atoms of the substrate were replaced.[33] Semiclassical KIEs (eq 1) were estimated from the Eyring equation using the free energies of activation ($\Delta G^{\ddagger}_H$) of the deuterium substituted and reference systems.

$$KIE_E = k_H/k_D = \exp\{(\Delta G^{\ddagger}_D - \Delta G^{\ddagger}_H)/RT\} \quad (1)$$

In this equation, R is the gas constant, and T the temperature (298.15 K). Further corrections due to tunneling were obtained from the Wigner model (KIE_W, eq 2) by multiplying KIE_E with the tunneling ratio (Q_{tH}/Q_{tD}, eq 3) as follows:

$$KIE_W = KIE_E \times Q_{tH}/Q_{tD} \quad (2)$$

$$Q_t = 1 + (h\nu/k_BT)^2/24 \quad (3)$$

Here, k_B is Boltzmann's constant, h is Planck's constant, and ν is the magnitude of the imaginary frequency in the transition state. Kinetic isotope effects were calculated using the data from the Gaussian frequency calculations for the hydrogen-atom-abstraction process from methane by **1**, $\mathbf{1}_{Ac}$ and **3**.

Thermochemistry. The O−H and C−H bond dissociation energies (BDE_{OH} and BDE_{CH}) were determined from the relative energy (ΔE + ZPE + E_{solv}) for the following two equations:

$$Fe^{IV} = O(L) + H^{\bullet} \rightarrow Fe^{III}OH(L) + BDE_{OH} \quad (4)$$

$$A^{\bullet} + H^{\bullet} \rightarrow A - H + BDE_{CH} \quad (5)$$

Electron affinities (EA) and ionization energies (IE) reported here are adiabatic values calculated with UB3LYP/BS2 with ZPE and solvent included.

RESULTS

In this work, we focus on the chemical properties of the μ-nitrido bound diiron complexes and their reactivity with methane and, in particular, aim to elucidate why **A**/**B** react faster by hydrogen atom abstraction than P450 CpdI. We used extensively benchmarked and calibrated methods, which on analogous chemical systems are known to give the correct spin-state ordering and kinetics.[34] Subsequently, the electronic properties and the origin of the reactivity differences of **1**/**2** versus **3** were elucidated through thermochemical cycles, valence bond schemes and electronic properties of the various species involved.

Substrate Hydroxylation Mechanism. Let us start with evaluating the reactivity differences of methane hydroxylation by **1**, $\mathbf{1}_{Ac}$, **2**, $\mathbf{2}_{Ac}$, and **3** as obtained with B3LYP. We investigated the methane hydroxylation by **1**, $\mathbf{1}_{Ac}$, **2**, and $\mathbf{2}_{Ac}$ and compare the obtained result with those calculated previously for $[Fe^{IV}(O)(Por^{+\bullet})SH]$ or **3**.[35] We initially created a long-range complex (**Re**) of structures **1**, $\mathbf{1}_{Ac}$, **2**, and $\mathbf{2}_{Ac}$ with methane and optimized the geometries in the doublet, quartet, sextet, and octet spin states. However, the doublet spin state was the ground state in isolated reactants as well as the reactant complexes and remained the lowest-lying spin state along the full reaction mechanism. The results of the alternative spin states are given in the Supporting Information Figures S2−S4 and S6−S8, Tables S5 and S9−S16.

The reaction is stepwise with an initial hydrogen atom abstraction via transition state $\mathbf{TS}_{HA}$ to form the radical

DOI: 10.1021/acscatal.5b02720
ACS Catal. 2016, 6, 2230−2243

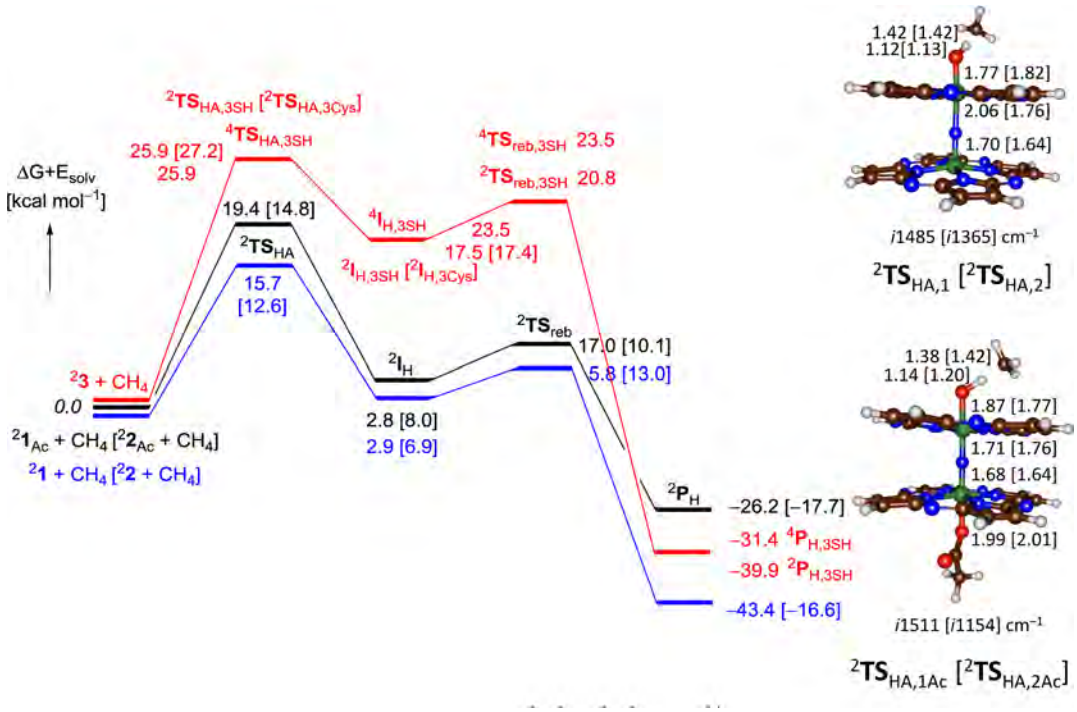

Figure 2. DFT calculated methane hydroxylation pathway by $^{2}\mathbf{1}$, $^{2}\mathbf{1}_{Ac}$, $^{2}\mathbf{2}$, $^{2}\mathbf{2}_{Ac}$, and $^{2,4}\mathbf{3}$. Data for $\mathbf{1}/\mathbf{1}_{Ac}$ and **3** were calculated in Gaussian at the UB3LYP/BS2//UB3LYP/BS1 level of theory, whereas the values for $\mathbf{2}/\mathbf{2}_{Ac}$ are obtained in Orca at UB3LYP/BS2//UB3LYP/BS1. Free energies are in kcal mol^{-1} and include ZPE, entropic, thermal, and solvent corrections. Also shown are optimized geometries of the rate-determining transition states with bond lengths in Å and the imaginary frequency of the **TS** in wave numbers. Data for model $\mathbf{1}/\mathbf{2}$ are given in blue, $\mathbf{1}_{Ac}/\mathbf{2}_{Ac}$ in black and values for complex **3** are shown in red.

intermediate $\mathbf{I}_{H}$, which is a complex of iron(IV)-hydroxo with $CH_3^{\bullet}$. In the next step, the OH rebounds to the $CH_3^{\bullet}$ group via transition state $\mathbf{TS}_{reb}$ to form the methanol-bound product complex $\mathbf{P}_{H}$. In all cases, $\mathbf{TS}_{HA}$ is the rate-determining reaction step, and $\mathbf{TS}_{reb}$ is smaller. This is in agreement with previous aliphatic hydroxylation mechanisms for iron(IV)-oxo complexes.[36]

Figure 2 shows the free energy landscape for methane hydroxylation by $^{2}\mathbf{1}$, $^{2}\mathbf{1}_{Ac}$, $^{2}\mathbf{2}$, $^{2}\mathbf{2}_{Ac}$, and $^{2,4}\mathbf{3}$. For comparison, in previous work, a free energy of activation of 25.9 kcal mol^{-1} in solvent using the same computational methods was obtained for the reaction of $[Fe^{IV}(O)(Por^{+\bullet})SH] + CH_4$.[35b] However, the free energy of activation of hydrogen atom abstraction from methane by **1**, in contrast, only has a value of $\Delta G^{\ddagger}$ = 15.7 kcal mol^{-1}, which raises to 19.4 kcal mol^{-1} when acetate binds as an axial ligand. The ratio of the rate constants for methane hydroxylation by **3** versus **1** would imply a rate enhancement of about 10^7 for this reaction. As such, it appears that μ-nitrido-bridged diiron-oxo complexes are highly effective oxidants of substrate hydroxylation reactions and should be able to hydroxylate methane at ambient temperatures and pressures. Indeed, experimental work of Sorokin and co-workers confirmed methanol products from the reaction of μ-nitrido-bridged diiron phthalocyanine with methane.[8b,c] To further ascertain that this rate enhancement is not due to the choice of the density functional method, we repeated the calculations of all rate-determining steps with alternative density functional methods (see Supporting Information Tables S9, S10, and S60−S63 for details). However, in all cases, the free energy of activation for the reaction of methane with $\mathbf{1}/\mathbf{1}_{Ac}$ was considerably lower than that with a P450 CpdI model.

In order to test whether the rate enhancement from **3** to $\mathbf{1}/\mathbf{1}_{Ac}$ is due to the phthalocyanine ligand or the μ-nitrido-bridged diiron arrangement, we decided to also investigate the reactivity of the analogous porphyrin complexes $\mathbf{2}/\mathbf{2}_{Ac}$. As follows from the data shown in Figure 2, the same trend is obtained for the couple $^{2}\mathbf{2}/^{2}\mathbf{2}_{Ac}$, where the hydrogen-atom-abstraction barrier is raised by 2.2 kcal mol^{-1} for the latter. Consequently, all μ-nitrido-bridged diiron-oxo complexes (**1**, $\mathbf{1}_{Ac}$, **2**, $\mathbf{2}_{Ac}$) give low free energies of activation for methane hydroxylation, which implies that they should catalyze the reaction at room temperature, which is in agreement with experimental data.[8b]

Geometrically, all transition states are product-like with considerably longer C−H than O−H distances. Previous studies on aliphatic hydrogen abstraction reactions by iron(IV)-oxo complexes showed that methane hydroxylation generally proceeds with a barrier characterized by a short O−H distance, a much longer C−H distance, and a geometry resembling the radical intermediate.[35,36] The two Fe_1−N and Fe_2−N distances for the bridging nitrido group in $\mathbf{TS}_{HA,1}$ and $\mathbf{TS}_{HA,1Ac}$ are considerably different due to the electron-donating properties of the acetate ligand that pull Fe_2 into the plane of the phthalocyanine/porphyrin ring.

All hydrogen-atom-abstraction transition states are characterized with a single large imaginary frequency of well over i1100 cm^{-1} that reflects a mode for the asymmetrical stretch vibration along the O−H−C bond and hence corresponds to a hydrogen atom transfer. These values are typical of hydrogen-atom-abstraction barriers by metal-oxo oxidants and implicate a narrow barrier with potentially significant amount of tunneling.[37] The nature of the barrier and its connection to reactants and radical intermediates was further established by initially running constraint geometry scans (with one degree of freedom

DOI: 10.1021/acscatal.5b02720
ACS Catal. 2016, 6, 2230−2243

fixed) as well as IRCs, see Supporting Information for details, which confirmed the mechanism shown in Figure 2.

Interestingly, we find a considerably larger dipole moment for $\mathbf{TS}_{HA,1}$ of 4.7 D versus that for $\mathbf{TS}_{HA,3}$ [0.8 D], and additionally, it points in the opposite direction. Similar dipole moments are found for the reactant complexes. Obviously, an enlarged dipole moment will lead to stabilization of the complex in solution and interactions with polar solvent molecules, which may affect the relative reactivities through their environment. To find further electronic factors that contribute to the transition state energy, we calculated the change in polarizability volume ($\delta\alpha$) for the geometric change from reactants to $\mathbf{TS}_{HA}$, eq 6.[38] The value $\delta\alpha$ was calculated from the difference in polarizability volume between the transition state structure and those of the isolated reactants.

$$\delta\alpha_i = \alpha_{TS} - \alpha_i - \alpha_{CH4},\ \mathbf{i} = \mathbf{1}, \mathbf{1}_{Ac} \quad (6)$$

Previously, we showed that the polarizability change correlates linearly with enthalpy change for chemical reactions as well as for transition state formation.[23,39] This polarizability change is then plotted as a function of barrier height for a range of hydrogen-atom-abstraction reactions by [Fe^{IV}(O) ($Por^{+\bullet}$)-SH] in the doublet and quartet spin states (Figure 3). As can be

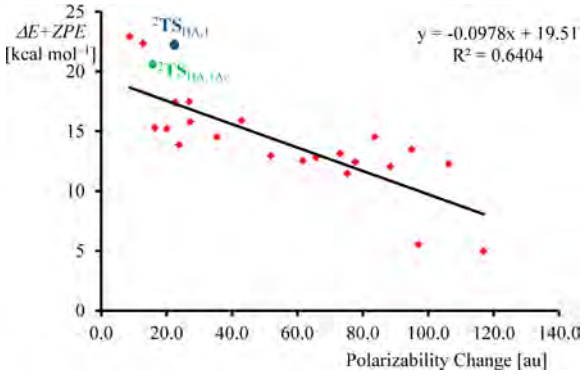

Figure 3. Plot of the change in polarizability volume ($\delta\alpha$) as a function of barrier height (ΔE + ZPE) for the reaction of [Fe^{IV}(O) ($Por^{+\bullet}$)SH] with aliphatic substrates.

seen, the correlation is reasonably linear, which implies that all transition states are characterized as electronically similar and are connected through the same electron-transfer processes. The calculated values for $^2\mathbf{TS}_{HA,1}$ and $^2\mathbf{TS}_{HA,1Ac}$ fit the trend and support the obtained correlation.

As the rate-determining step in the reaction mechanism is a hydrogen atom abstraction, we investigated the kinetic isotope effects (KIE) by replacing one or more hydrogen atoms of the CH_4 reactant with deuterium atoms. Thus, we replaced the transferring hydrogen atom of methane by deuterium to get the primary KIE but also the three other hydrogen atoms (secondary KIE); lastly, we replaced all hydrogen atoms of CH_4 by deuterium atoms and the obtained results for reactions with **1**, $\mathbf{1}_{Ac}$, and **3** are given in Table 1. We calculated KIE values using the semiclassical Eyring model but also the Wigner model with tunneling corrections included. The KIE values are dependent on the magnitude of the imaginary frequency in the transition state and the free energy of activation, see Methods section for details. Although a considerably larger imaginary frequency in the transition state for $^2\mathbf{TS}_{HA,1}$ (i1485 cm^{-1}) is found as compared to $^{2,4}\mathbf{TS}_{HA,3}$ (values of i946 and i791 cm^{-1} for doublet and quartet spin states, respectively), actually, the

Table 1. Calculated Kinetic Isotope Effects Using the Eyring (Wigner) Models for Replacing Hydrogen Atoms in Methane by Deuterium Atoms[a]

oxidant	O−D−CH_3	O−H−CD_3	O−D−CD_3
1	7.0 (9.9)	2.2 (2.3)	16.3 (23.4)
$\mathbf{1}_{Ac}$	7.1 (10.1)	1.4 (1.4)	10.3 (14.9)
3	5.7 (9.2)	1.4 (2.3)	8.6 (13.7)

[a]Data from Gaussian frequency calculation at 298 K for doublet spin states.

Wigner KIE effects are not dramatically different for the two complexes. Nevertheless, replacement of the transferring hydrogen atom by deuterium leads to major differences in KIE values. We calculated KIE values of 7.0 (9.9) using the Eyring (Wigner) models for **1** for replacement of the transferring hydrogen atom by deuterium. Note that a significant secondary KIE value of about 1.4−2.3 for replacing the nontransferrable hydrogen atoms by deuterium atoms is obtained for all systems. The results in Table 1 show that **1** should give a considerably larger KIE value than $\mathbf{1}_{Ac}$ and **3** for hydrogen atom abstraction from unactivated, sp^3 hybridized, carbon centers.

DISCUSSION

As shown in the previous section and in agreement with experimental observation, μ-nitrido-bridged diiron-oxo complexes are efficient oxidants of aliphatic hydroxylation reactions and can even hydroxylate methane at room temperature. To understand the origin of these reactivity differences with P450 CpdI, which does not hydroxylate methane at room temperature, we did a detailed analysis of the physicochemical properties of the reactants and an evaluation of the obtained transition states, which will be covered in detail in the following.

Electronic Configuration of the Reactants. To gain insight into the nature of the reactivity differences observed above, let us start our analysis with an evaluation of the electronic configuration of the isolated reactants (i.e., without methane) and compare $\mathbf{1}/\mathbf{1}_{Ac}/\mathbf{2}/\mathbf{2}_{Ac}$ on the one hand with **3** on the other hand.

Figure 4 displays the orbital energy levels of P450 CpdI, that is, [Fe^{IV}(O) ($Por^{+\bullet}$)Cys], and how the mixing with an axial iron(IV)-nitrido group of [Fe^{IV}(N) (Por)] gives the new orbital energy levels for the μ-nitrido diiron-oxo complexes **1** and **2**. Thus, P450 CpdI is a triradical system with two unpaired electrons in π^*_{FeO} orbitals and a third one in a heme orbital with a_{2u} symmetry (Figure 4: left-hand-side). These three orbitals are either ferromagnetically coupled into a quartet spin state or antiferromagnetically coupled into a doublet spin state and usually DFT calculations find the two states within 1 kcal mol^{-1}.[17,40]

The π_{FeO}/π^*_{FeO} orbitals reflect the interaction of the $3d_{xz}/3d_{yz}$ atomic orbitals on iron with the $2p_x/2p_y$ orbitals on oxygen, whereas the a_{2u} orbital is a nonbonding heme orbital. Addition of an axial ligand to CpdI leads to mixing of orbitals on the ligand with both the a_{2u} and π^*_{FeO} orbitals. In particular, a cysteinate axial ligand results in mixing of the $3p_z$ orbital of the sulfur atom with the a_{2u} orbital on the porphyrin and the antibonding combination ($3p_z-a_{2u}$) is raised in energy with respect to the original a_{2u} orbital.[41] This change in orbital energy lowers the electron affinity of CpdI and it has been

DOI: 10.1021/acscatal.5b02720
ACS Catal. 2016, 6, 2230−2243

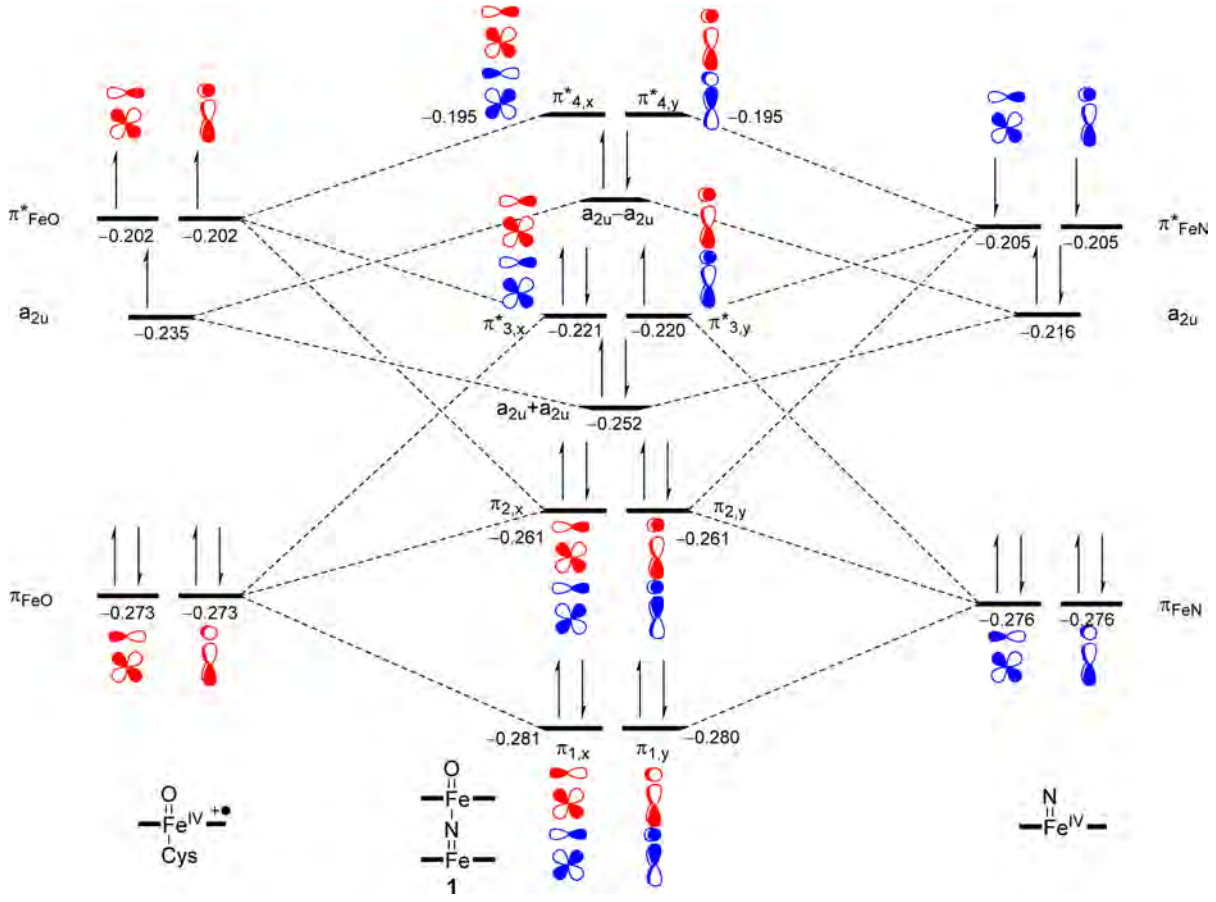

Figure 4. Orbital energy splitting of μ-nitrido-bridged diiron(IV)-oxo phthalocyanine and porphyrin species and how the orbital mixing originates from iron(IV)-oxo porphyrin cation radical (left-hand-side) and iron(IV)-nitrido (right-hand-side). Orbital energies are given for ^{2}**2** in au.

proposed that this could make it a better oxidant than an iron(IV)-oxo porphyrin without axial ligand.[26,41]

On the right-hand-side of Figure 4, we give the orbital occupation of the iron(IV)-nitrido group, which is essentially the one-electron reduced form of CpdI with orbital occupation $\pi_{FeN,xz}^{2}\ \pi_{FeN,yz}^{2}\ a_{2u}^{2}\ \pi^*_{FeN,xz}^{1}\ \pi^*_{FeN,yz}^{1}$. The iron(IV)-nitrido group has the same orbital shapes as the iron(IV)-oxo species with a pair of π_{FeN}/π^*_{FeN} orbitals and a close-lying a_{2u} orbital.

Upon formation of a μ-nitrido-bridged diiron-oxo complex, the orbitals along the molecular z-axis (i.e., along the O−Fe_1−N−Fe_2 axis) will mix and form a new set of orbitals, as shown in the middle panel of Figure 4. Thus, addition of an axial iron(IV)-nitrido group to an iron(IV)-oxo porphyrin cation radical changes the orbital interactions and energies along the z-axis dramatically. Due to alignment of the O, Fe_1, N, and Fe_2 atoms along the molecular z-axis in **1**, their atomic orbitals interact and form new molecular orbitals that span the complete molecular z-axis. The orbital interactions of the two iron $3d_{xz}/3d_{yz}$ atomic orbitals with the $2p_x/2p_y$ orbitals on the oxo and bridging nitrido groups leads to a set of bonding and antibonding combinations; namely four sets of molecular orbitals along the x and y-axis labeled as $\pi_{1,x}/\pi_{1,y}$, $\pi_{2,x}/\pi_{2,y}$, $\pi^*_{3,x}/\pi^*_{3,y}$, and $\pi^*_{4,x}/\pi^*_{4,y}$. In addition, the porphyrin π-orbitals, such as the a_{1u} and a_{2u} orbitals, mix and form bonding and antibonding sets of orbitals due to π-stacking interactions as well as the mixing with the $\sigma_{z2}/\sigma^*_{z2}$ orbitals on Fe_1 and Fe_2.

The orbital diagram in Figure 4 shows that complexes **1**/**2** should have a dominant doublet spin state with a singly occupied $\pi^*_{3,y}$ orbital and a closed-shell ligand system. This contrast of the orbital occupation and energy levels of P450 CpdI, where the high-lying π^*_{FeO} orbitals are close in energy to the a_{2u} orbital, so that a combination of ferromagnetically and antiferromagnetically coupled spin states are possible. In structures **1**/$\mathbf{1}_{Ac}$/**2**/$\mathbf{2}_{Ac}$, the separation between the a_{2u} and π^*_3 orbitals is large, and no low-lying states were found with radical character spread over metal and ligands. In particular, antiferromagnetic (or ferromagnetic) coupling of spin states where unpaired electrons on the metal(s) is coupled to an unpaired electron on the porphyrazine group was attempted but did not converge to stable, low-energy conformations. Furthermore, the spin-state ordering, relative energies, and group spin densities of the calculated doublet, quartet, sextet, and octet spin states of **1** and $\mathbf{1}_{Ac}$ all show little radical character on the porphyrazine ligand (see Supporting Information, Tables S11 and S15).

Experimental Mössbauer spectra implicated a doublet spin ground state, which is reproduced excellently by our calculations. We attempted to create an electronic state with porphyrazine or porphyrin radical by swapping molecular orbitals or imposing local spin polarizations. Therefore, an extensive series of additional calculations were done to locate the alternative $^2A_{2u}$ state with occupation (core) $\pi^*_{3,x}{}^2\ \pi^*_{3,y}{}^2\ \pi^*_{4,x}{}^0\ (a_{2u}-a_{2u})^1$. However, in all cases during the SCF convergence the system reverted back to the $^2\Pi$ state described in Figure 4. Test calculations with a range of unrestricted density functional theory methods, i.e. B3LYP, B3LYP-D3, BP86, M06, PBE0 and B3LYP*, either after a full geometry optimization or a single-point calculation at the UB3LYP/BS1

DOI: 10.1021/acscatal.5b02720
ACS Catal. 2016, 6, 2230−2243

geometry consistently gave the same spin state ordering and predicted the $^2\Pi$ state as the ground state, Supporting Information Table S17. Group spin densities obtained with these methods show small differences as seen in Table 2. In all cases the spin density on the equatorial ligand, i.e. porphyrazine or porphyrin, is negligible and all radical character is dominantly located on the OFeNFe group. The spin density contributions in Table 2 characterize all structures as a $^2\Pi$ state with a single unpaired electron in the $\pi^*_{3,y}$ orbital.

Table 2. Group Spin Densities of Reactant Configurations of 1, 1_{Ac}, 2, and 2_{Ac} As Calculated with Various Computational Methods[a]

oxidant	method	ρ_{OFeNFe}	ρ_{Por}/ρ_{Pz}
1	UB3LYP	1.16	−0.10
	UBP86	1.01	0.00
	UB3LYP*	1.11	−0.01
	UB3LYP-D3	0.85	0.02
	M06-L	1.12	−0.12
$\mathbf{1}_{Ac}$	UB3LYP	1.18	−0.04
	UBP86	1.02	−0.01
	UB3LYP*	1.20	−0.04
	UB3LYP-D3	1.20	−0.04
	NEVPT2	1.00	0.00
2	UB3LYP	1.16	−0.05
	UBP86	1.01	0.00
	UB3LYP*	1.11	−0.01
	UB3LYP-D3	0.86	0.01
$\mathbf{2}_{Ac}$	UB3LYP	1.18	−0.02
	UBP86	1.02	0.00
	UB3LYP*	1.20	−0.02
	UB3LYP-D3	1.21	−0.02

[a]Data obtained for $\mathbf{1}/\mathbf{1}_{Ac}$ are from a Gaussian single-point calculation with basis set BS2 on a UB3LYP/BS1 optimized geometry, whereas data for $\mathbf{2}/\mathbf{2}_{Ac}$ were calculated in Orca.

The optimized geometries appear reasonably consistent between the various density functional theory methods (Supporting Information, Table S17). Thus, without an axial ligand bound, the Fe_1−O and Fe_2−N bond lengths are short (most values are between 1.62 and 1.66 Å) and implicate a double bond for both the Fe_1═O and Fe_2═N groups. Interestingly, upon addition of an acetate ligand to **1**, the nitrido group moves more to the center of the Fe_1−Fe_2 atoms at distances of 1.81 and 1.88 Å. Although to a much lesser extent, the same is true for structure **2**, where binding of an chlorobenzoate axial ligand leads to Fe_2−N bond elongation. Optimized geometries of **1** and **2** are virtually the same for each density functional method and implicate little changes upon replacing the porphyrin ligand with porphyrazine. This is in line with previous studies on *meso*-substituted metal-oxo porphyrinoid systems that showed little changes upon ligand substitution.[12d,32,42] The BP86 optimized geometries of the *μ*-nitrido diiron oxo species supported by phthalocyanine ligands provided the following distances: Fe_1−O = 1.73 Å, Fe_1−N = 1.77 Å, and Fe_2−N = 1.61 Å.[42b] These values are very close to those obtained for **1** and **2** with the same BP86 functional.

To test the effect of the environment on the spin state ordering and the nature of the electronic state of $^2\mathbf{1}_{Ac}$, we performed a full UB3LYP/BS2 optimization in solvent, for structure $^2\mathbf{1}_{Ac}$; however, there was very little structural or spin density change during the optimization as compared to the structure minimized in the gas-phase with basis set BS1 (Supporting Information Figure S19).

In a final attempt to unequivocally establish the molecular ground state of complexes **1** and $\mathbf{1}_{Ac}$, we performed a NEVPT2 single-point calculation on these chemical systems. In support of the DFT studies, a molecular ground state with $^2\Pi$ configuration with no radical character on the porphyrin/porphyrazine ligands observed. Therefore, the most likely ground state of complexes **1**, $\mathbf{1}_{Ac}$, **2**, and $\mathbf{2}_{Ac}$ is the $^2\Pi$ state in the gas-phase. However, the presence of explicit solvent molecules, electric, and/or magnetic fields as well as the inclusion of entropy and interactions of the oxidant with ions and solvent may change the ordering of the electronic states.[43] Thus, DFT calculations of P450 CpdI models showed that hydrogen bonding interactions toward the thiolate ligand, or an electric field effect changed the electronic description of CpdI and moved radical character from the axial ligand to the porphyrin manifold.[43b] Furthermore, CpdI models of both of cytochrome *c* peroxidase and ascorbate peroxidase, showed that the addition of a point charge at 12 Å distance from the iron center changed the electronic configuration from a heme cation radical to a tryptophan radical.[44] As such, environmental

Scheme 2. Electron-Transfer Pathways for the Hydrogen Atom Abstraction from Methane by CpdI (top) and *μ*-Nitrido-Bridged Diiron-Oxo Species (bottom)

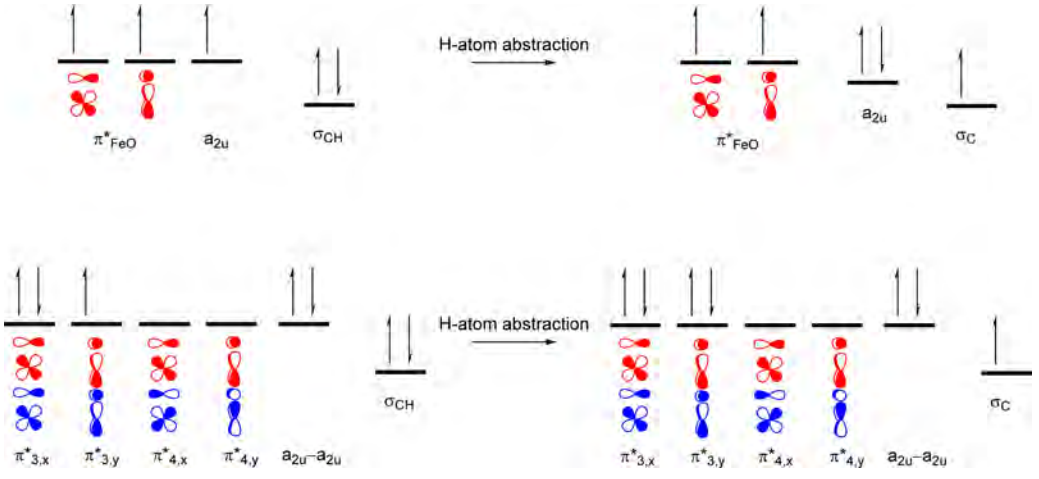

DOI: 10.1021/acscatal.5b02720
ACS Catal. 2016, 6, 2230−2243

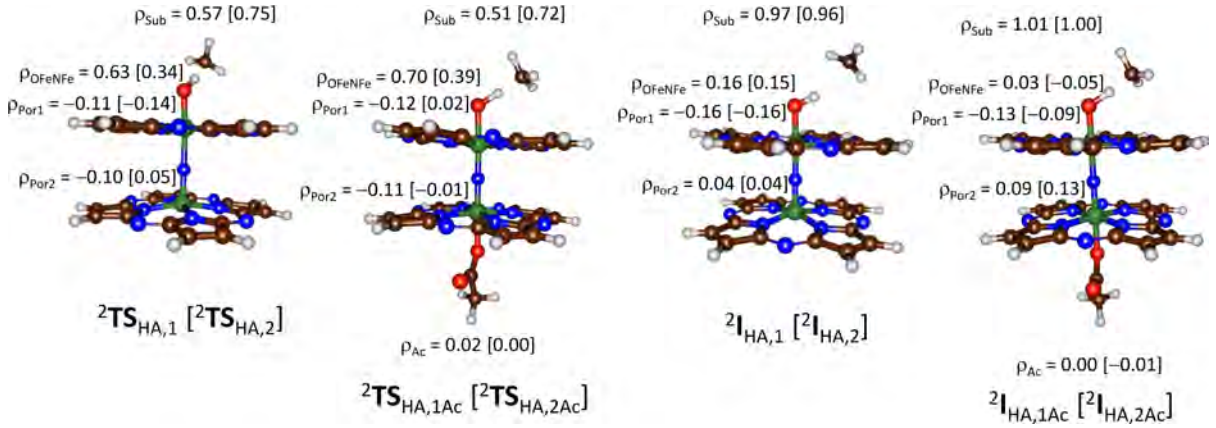

Figure 5. Group spin densities of hydrogen-atom-abstraction barriers and radical intermediates as taken from the B3LYP/BS2 results.

perturbations can have a major effect on spin-state ordering and relative energies. However, single-point calculations using the conductor-like polarized continuum model (CPCM) on species **1**, $\mathbf{1}_{Ac}$, **2**, and $\mathbf{2}_{Ac}$ did not change the electronic ground states.

Our DFT studies on **1** are in good agreement with calculations reported in the literature.[45] All these reports predict a doublet spin ground state, in agreement with experiment, with most unpaired spin density located on the O−Fe_1−N−Fe_2 group. Interestingly, Anasari et al.[45b] report an electronic ground state of ^{2}**1** with spin densities of 3.78 and −2.92 on Fe_1 and Fe_2, respectively, which implicates a state with four unpaired electrons on Fe_1 antiferromagnetically coupled to three unpaired electrons on Fe_2. This state is different from the state proposed on the basis of experimental Mössbauer and EPR spectra[9,46] and also to the considerably larger chemical model studied here.

Electron Transfer during the Mechanism. The hydrogen-atom-abstraction reaction from a substrate leads to formation of a hydroxo bond and the transfer of an electron from the oxo group into the metal−ligand system. Scheme 2 summarizes the main electron-transfer pathways that were observed in the hydrogen-atom-abstraction step from methane by **3** (top) and **1**/$\mathbf{1}_{Ac}$ (bottom). Thus, the breaking of the C−H bond leads to the splitting of the σ_{CH} orbital into an atomic hydrogen orbital ($1s_H$) and a substrate radical orbital (σ_C). The $1s_H$ orbital then mixes with a 2p orbital on oxygen to form the σ_{OH} bond with two electrons. This process results in the one electron transferred from the oxo group into a metal or ligand type orbital and in P450 it moves into the a_{2u} orbital.

In the μ-nitrido-bridged diiron-oxo species the electron transfer is different from P450 CpdI due to a closed-shell a_{2u} orbital in the reactant state. As a result the electron moves into the $\pi^*_{3,y}$ orbital to fill it with a second electron. Indeed, the group spin densities of the hydrogen-atom-abstraction transition states (Figure 5) give a considerable reduction of the spin on the OFe_1NFe_2 group, which drops to almost zero in the radical intermediates. At the same time, a spin density of about +1 on the substrate rest-group is obtained.

We tested several possibilities for alternative radical intermediates and electron-transfer pathways with ferromagnetically and antiferromagnetically coupled states, but all those attempts gave higher energy structures. Therefore, the lowest-lying electron transfer appeared to lead to a radical intermediate with configuration $\pi^*_{3,x}{}^2\ \pi^*_{3,y}{}^2\ \sigma_C{}^{\uparrow}$. A subsequent NEVPT2 single-point calculation gave spin density contributions corresponding to the same electronic state and confirms it to be the lowest-lying radical intermediate and hydrogen-atom-abstraction barrier. Attempts to swap molecular orbitals were done to generate the electronic state with occupation $\pi^*_{3,x}{}^2\ \pi^*_{3,y}{}^{\uparrow}\ \pi^*_{4,x}{}^{\uparrow}\ \sigma_C{}^{\downarrow}$; however, during the SCF convergence, they fell back to the state shown in Scheme 2, and hence, it is an excited state. Similarly, attempts to swap orbitals and generate a state with the (a_{2u}−a_{2u}) orbital singly occupied failed and led to the radical intermediate described above.

Group spin densities of the hydrogen abstraction transition states and radical intermediates are given in Figure 5. As can be seen, significant radical character on the CH_3 group is accumulating already in the transition state, which grows to a value of around 1 for the radical intermediates. The growth in spin density on the CH_3 group happens simultaneously with the loss of total spin density on the OFe_1NFe_2 group. The radical character on both porphyrin or porphyrazine groups remains small and never grows beyond a value of 0.2. Therefore, the calculations, in contrast to those on P450 CpdI, give no porphyrin radical in the oxidant and also not along the calculated reaction mechanism.

Physicochemical Properties of Reactant Complexes. The above studies show that structures **1** and **2** have well-separated electronic states, which are fundamentally different from the electronic ground state ($^{2,4}A_{2u}$ state) found in P450 Cpd I with three unpaired electrons and $\pi^*_{FeO,x}{}^1\ \pi^*_{FeO,y}{}^1\ a_{2u}{}^1$ occupation. Therefore, the difference in molecular valence orbitals between **1** or **2**, on the one hand, with **3**, on the other hand, will affect the relative energies of the molecular orbitals, such as the HOMO−LUMO energy gap, and as a consequence also the ionization potential, the electron affinity and pK_a values of the oxidant. This means that the spectroscopic and catalytic properties of the oxidants will be dramatically different as well as the H atom abstraction reaction, which involves a combined proton and electron transfer.[47] These factors influence the reactivity patterns with substrates and in this particular case enhance the reactivity. In addition, the potential energy landscapes shown in Figure 2 above shows that the binding of an axial ligand raises the hydrogen-atom-abstraction barriers by several kcal mol^{-1} and hence make it a weaker oxidant.

To understand how the intricate details of individual components can cause a change in the electron affinity of **1** and $\mathbf{1}_{Ac}$ as compared to P450 CpdI, we dissected the electron affinities into several factors, namely the electric field effect due to the axial ligand (E_{field}), a quantum mechanical effect from orbital overlap between the oxidant and the axial ligand (E_{QM}) and a π-stacking effect of the two porphyrazine groups (E_{π_π}),

DOI: 10.1021/acscatal.5b02720
ACS Catal. 2016, 6, 2230−2243

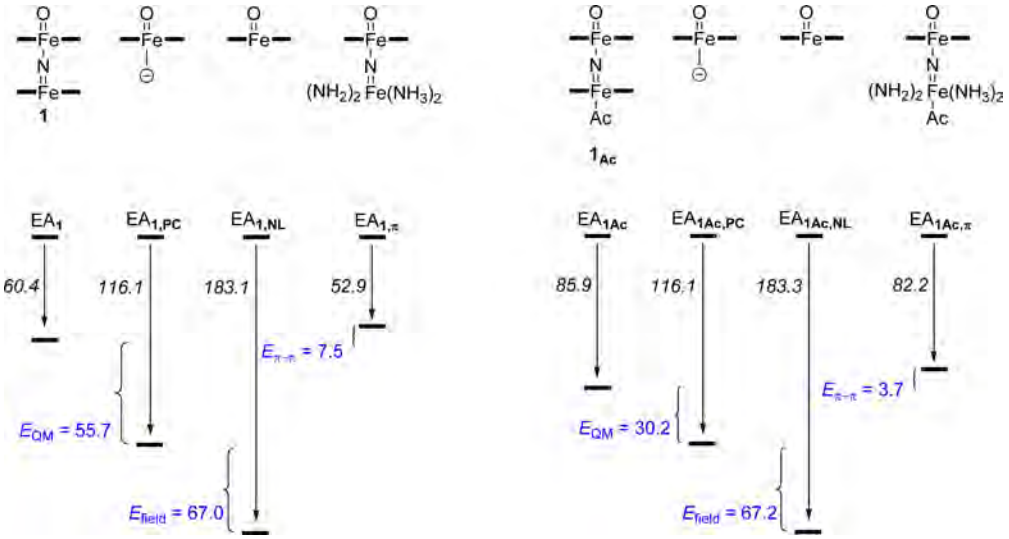

Figure 6. Axial ligand effects contributing to the electron affinity of **1** (left) and $\mathbf{1}_{Ac}$ (right). All values represent ΔE + ZPE + E_{solv} energies (in kcal mol^{-1}) and contain solvent corrections.

see Figure 6. Thus, we took the optimized structures of **1** and $\mathbf{1}_{Ac}$ and in one set of calculations removed the axial nitrido-iron(IV)porphyrazine group (no ligand, NL) and did a single-point electron affinity calculation to give EA_{NL}.

Subsequently, we did another set of single-point electron affinity calculations on these systems without axial ligand, where a point charge (PC) was placed in the position of the nitrido group (EA_{PC}). The difference in energy between EA and EA_{PC}, represents the quantum mechanical effect (E_{QM}) of the axial ligand group due to mixing of axial ligand orbitals with the iron(IV)-oxo group, eq 7. On the other hand, the difference in energy between EA_{PC} and EA_{NL} gives the electric field effect of the interaction of the charges of the axial ligand with the iron(IV)-oxo group, eq 8.

$$E_{QM} = EA - EA_{PC} \quad (7)$$

$$E_{field} = EA_{PC} - EA_{NL} \quad (8)$$

In a final set of calculations we attempted to estimate the π-stacking contribution for the two porphyrazine ligands. To this end, we replaced the porphyrazine group of the iron(IV)-nitrido group by $(NH_3)_2(NH_2^-)_2$, which keeps the same charge and coordination number but lacks the second porphyrazine unit, and calculated the electron affinity of [O═Fe(Pz)−N═$Fe(NH_3)_2(NH_2^-)_2$] with and without Ac axial ligand. We call this electron affinity, the π-stacking electron affinity, EA_π, as it lacks the π-stacking interactions. The resulting data on EA, EA_{PC}, EA_{NL}, and EA_π as well as the values of E_{QM} and E_{field} are depicted in Figure 6 for comparison. On the basis of the orbital energy levels above, we predict an increased EA upon axial ligand binding, which indeed is confirmed with the calculations in Figure 2. This contrasts the behavior of P450 CpdI that sees a decrease in electron affinity upon addition of an axial ligand (cysteinate) or replacing it with a neutral molecule or solvent molecule.[23] The reason for this disparity comes from the orbital interactions that raise the antibonding a_{2u}-axial ligand interaction in P450 CpdI, whereas the π^*_3 orbitals are stabilized (and π^*_4 orbitals destabilized) in $\mathbf{1}_{Ac}$ with respect to **1** due to the additional acetate ligand.

The latter also is highlighted from our dissection of the electron affinity contributions, where **1** has a much larger quantum mechanical contribution of the axial ligand than $\mathbf{1}_{Ac}$ (E_{QM} is 55.7 kcal mol^{-1} for **1** and 30.2 kcal mol^{-1} for $\mathbf{1}_{Ac}$). As such, binding of an acetate group has a major influence on the electron distribution within the oxidant and changes the orbital interactions so drastically that the electron affinity is raised by about 25 kcal mol^{-1}, which will affect its oxidation potential with substrates. Needless to say, the electric field effect due to the iron(IV)-nitrido porphyrazine group is virtually the same for $\mathbf{1}/\mathbf{1}_{Ac}$ at a value of 67.0/67.2 kcal mol^{-1}. By contrast, the π-stacking energy (E_{π_π}) is small, and only in the order of 3.7−7.5 kcal mol^{-1}, and hence will not be the dominant factor. However, the electron affinity of both complexes **1** and $\mathbf{1}_{Ac}$ are larger with a porphyrazine group attached to the iron(IV)-nitrido unit (compare $EA_{1,\pi}$ vs EA_1), which confirms an important interaction between the axial ligand and the porphyrazine moiety exists.

The values of E_{field} and E_{QM} calculated previously for the axial ligand effect of [Fe^{IV}(O) ($Por^{+\bullet}$)SH] were 54.0 and 38.8 kcal mol^{-1}, respectively.[48] The field effect calculated here is somewhat larger as the point charge was placed in the position of the bridging nitrogen atom at 2.06 Å, whereas in P450 CpdI, it was in the position of the sulfur atom at 2.49 Å.[48] Obviously, a shorter distance will lead to a larger Coulomb interaction and a larger field effect. In addition to an increased field effect, a comparison of **1** and [Fe^{IV}(O) ($Por^{+\bullet}$)SH] also gives an increased quantum chemical effect by 16.9 kcal mol^{-1} due to better orbital interactions along the O−Fe_1−N−Fe_2 system. However, most of this benefit is lost when acetate binds to Fe_2. Nevertheless, **1** has a considerably lower electron affinity than P450 CpdI (EA_{CpdI} = 92.9 kcal mol^{-1}), which is partially due to a larger electric field effect and partially as a result of a quantum mechanical effect. Based on the much smaller electron affinity of **1** versus **3**, one would expect the former to be a much weaker oxidant in hydrogen-atom-abstraction reactions. Nevertheless, as will be shown later in this work, system **1** has also a decreased pK_a value, which makes it more basic and leads to a larger driving force for hydrogen atom abstraction as shown previously.[25]

Thermochemical Properties Affecting Reactivities. In order to assign the origin of reactivity differences one has to take the thermochemical properties of the oxidant and substrate

DOI: 10.1021/acscatal.5b02720
ACS Catal. 2016, 6, 2230−2243

into consideration. Experimental studies on hydrogen-atom-abstraction reactivities showed that the rate constant generally correlates with the strength of the C−H bond of the substrate that is broken (BDE_{CH}) as well as with the strength of the O−H bond that is formed (BDE_{OH}).[49] The BDE_{OH} and BDE_{CH} values are defined for the reactions described in eq 4 and 5 above. However, the BDE_{OH} value can be split into an electron transfer (electron affinity, EA of the oxidant), a proton affinity of the reduced oxidant (ΔG_{acid}) and the ionization energy (IE_H) of a hydrogen atom as described in eqs 9−11.

$$AH \rightarrow A^- + H^+ + \Delta G_{acid} \quad (9)$$

$$A \rightarrow A^- + EA_A \quad (10)$$

$$H \rightarrow H^+ + IE_H \quad (11)$$

Combination of reactions 9−11 adds up to reaction 4 and will give a BDE_{OH} description as given in eq 12.

$$-BDE_{OH} = \Delta G_{acid} - EA_{FeO} - IE_H \quad (12)$$

The ionization energy of a hydrogen atom is taken here from the NIST database.[50] Subsequently, we calculated the EA, ΔG_{acid}, and BDE_{OH} values of **1**, $\mathbf{1}_{Ac}$, and **3** and give the results graphically in Figure 7 but also tabulate the results in Table 3.

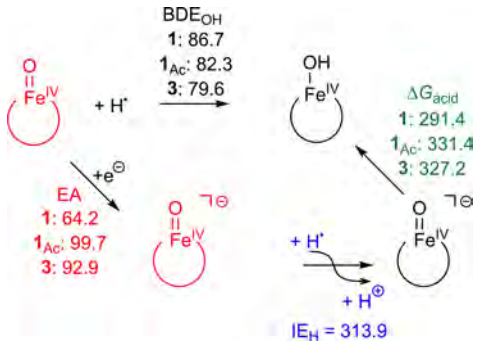

Figure 7. Calculated thermochemical variables for **1** and $\mathbf{1}_{Ac}$. Data represents $\Delta G + E_{solv}$ values with free energies that include solvent, thermal, and entropic corrections (in kcal mol^{-1}).

Table 3. Calculated Thermochemical Variables for 1, $\mathbf{1}_{Ac}$, and 3[a]

oxidant	BDE_{OH}	ΔG_{acid}	EA
1	86.7	291.4	64.2
$\mathbf{1}_{Ac}$	82.3	331.4	99.7
$\mathbf{3}_{SH}$	79.6	327.2	92.9

[a]Free energies with solvent corrections given in kcal mol^{-1}.

Extensive experimental studies implicated that the dominant component to the BDE_{OH} trends relates to the acidity of the oxo group (i.e., ΔG_{acid}).[51] With a solvent model included, we calculated a value of $BDE_{OH}(\mathbf{1}) = 86.7$ kcal mol^{-1}, which is only slightly higher in energy than the value we calculated before for $\mathbf{1}_{Ac}$, $BDE_{OH}(\mathbf{1}_{Ac}) = 82.3$ kcal mol^{-1} and the one for $\mathbf{3}_{SH}$, $BDE_{OH}(\mathbf{3}_{SH}) = 79.6$ kcal mol^{-1}.[43a] This change is likely due to the push-effect of electron density from the axial ligand to the metal-oxo group, which affects the orbital energies and consequently the electron affinity as well as the acidity of the iron(IV)-hydroxo group. However, **1** has an electron affinity that is about 35 kcal mol^{-1} lower in energy than that for $\mathbf{1}_{Ac}$, and as a consequence, **1** has a 40 kcal mol^{-1} lower ΔG_{acid} value. It is this acidity change that will make **1** a much better oxidant than either $\mathbf{1}_{Ac}$ or $\mathbf{3}_{SH}$ for substrate hydroxylation reactions.

Therefore, **1** is found to be a more powerful oxidant of hydrogen-atom-abstraction reactions than **3** due to an increased basicity of the iron(IV)-hydroxo complex that is formed, which is mainly due to orbital reorganization that affects the electron affinity of the oxidant. Figure 7 breaks down this basicity change into BDE_{OH} and EA components for species **1**, $\mathbf{1}_{Ac}$, and **3**.

In summary, the μ-nitrido diiron(IV)-oxo complexes have dramatically altered electronic configurations with respect to P450 CpdI, which is mainly due to charge and orbital delocalization along the O−Fe_1−N−Fe_2 axis. Because of this, the electron affinity of **1** is much lower than that of P450 CpdI; however, its interaction with ligands bound to the iron(IV)-nitrido group is also less. These orbital interactions lower the ability to abstract hydrogen atoms efficiently and make **1** a considerably better oxidant of hydrogen-atom-abstraction reactions than P450 CpdI. In addition, these electronic effects also influence the pK_a value of the corresponding iron(IV)-hydroxo group. As such, both thermochemical and electronic analysis point to the reasons for the reactivity differences of μ-nitrido-bridged diiron oxo complexes with respect to P450 CpdI.

Valence Bond Rationalization of the Reaction Mechanism. Finally, we have tried to understand the reaction mechanism obtained and rationalize why structures **1** and **2** are better oxidants than P450 CpdI in methane hydroxylation processes by setting up a valence bond (VB) curve crossing diagram, see Figure 8. These diagrams were used previously to rationalize hydrogen-atom-abstraction barriers and double bond epoxidation barriers by iron(IV)-oxo complexes and explained the obtained rate constant trends, but also identified the origin of the stepwise processes.[23,36,37,39] The figure starts on the bottom left with the reactant states, and in the case of **1** and **2**, the system has orbital occupation (core) $\pi^*_{3,x}{}^2\ \pi^*_{3,y}{}^1\ (a_{2u}-a_{2u})^2$ in a doublet spin ground state, which essentially implicates an iron(V)-oxo that is connected to an iron(IV)-nitrido group. This system has electrons in the $\pi_{1,x}$, $\pi_{2,x}$, and $\pi^*_{3,x}$ orbitals as identified by the dots next to the O, Fe_1, N, and Fe_2 atoms. The dots on the right-hand-side of the labels refer to the six electrons in $\pi_{1,x}{}^2\ \pi_{2,x}{}^2\ \pi^*_{3,x}{}^2$, and those on the left-hand-side of the labels represent the five electrons in $\pi_{1,y}{}^2\ \pi_{2,y}{}^2\ \pi^*_{3,y}{}^1$. In the VB structures, the equatorial ligand is given as a bold horizontal bar and both doubly occupied a_{2u} orbitals on each of the porphyrazine groups are identified with two dots next to these bars. Lastly, the C−H bond is occupied with two electrons and is given as a bar connected with two dots.

In the transition state for hydrogen atom abstraction, the C−H bond splits back into atomic orbitals, whereby the up-spin electron is retained by the CH_3 radical, while the down-spin electron leaves as a $1s_H$ orbital with hydrogen. In addition, in the transition state the $\pi_{1,x}/\pi_{2,x}/\pi^*_{3,x}/\pi^*_{4,x}$ set of orbitals is rehybridized and separated into a $2p_y$ orbital on oxygen with two electrons and three new orbitals for the interaction between Fe_1, N, and Fe_2 ($\pi'_{1,x}/\pi'_{2,x}/\pi^{*\prime}_{3,x}$). One of the electrons of the $2p_x$ orbital forms a bond (σ_{OH}) with the incoming $1s_H$ orbital of hydrogen, whereas the other electron is transferred into the $\pi'_{1,x}/\pi'_{2,x}/\pi^{*\prime}_{3,x}$ that ends up with five electrons. In the subsequent step in the reaction mechanism, namely, the OH rebound step (not shown in Figure 8), the set of $\pi_{1,y}/\pi_{2,y}/\pi^*_{3,y}/\pi^*_{4,y}$ orbitals is split into a $2p_y$ and a set of new π'_y orbitals. The radical on the substrate then forms a bond

DOI: 10.1021/acscatal.5b02720
ACS Catal. 2016, 6, 2230−2243

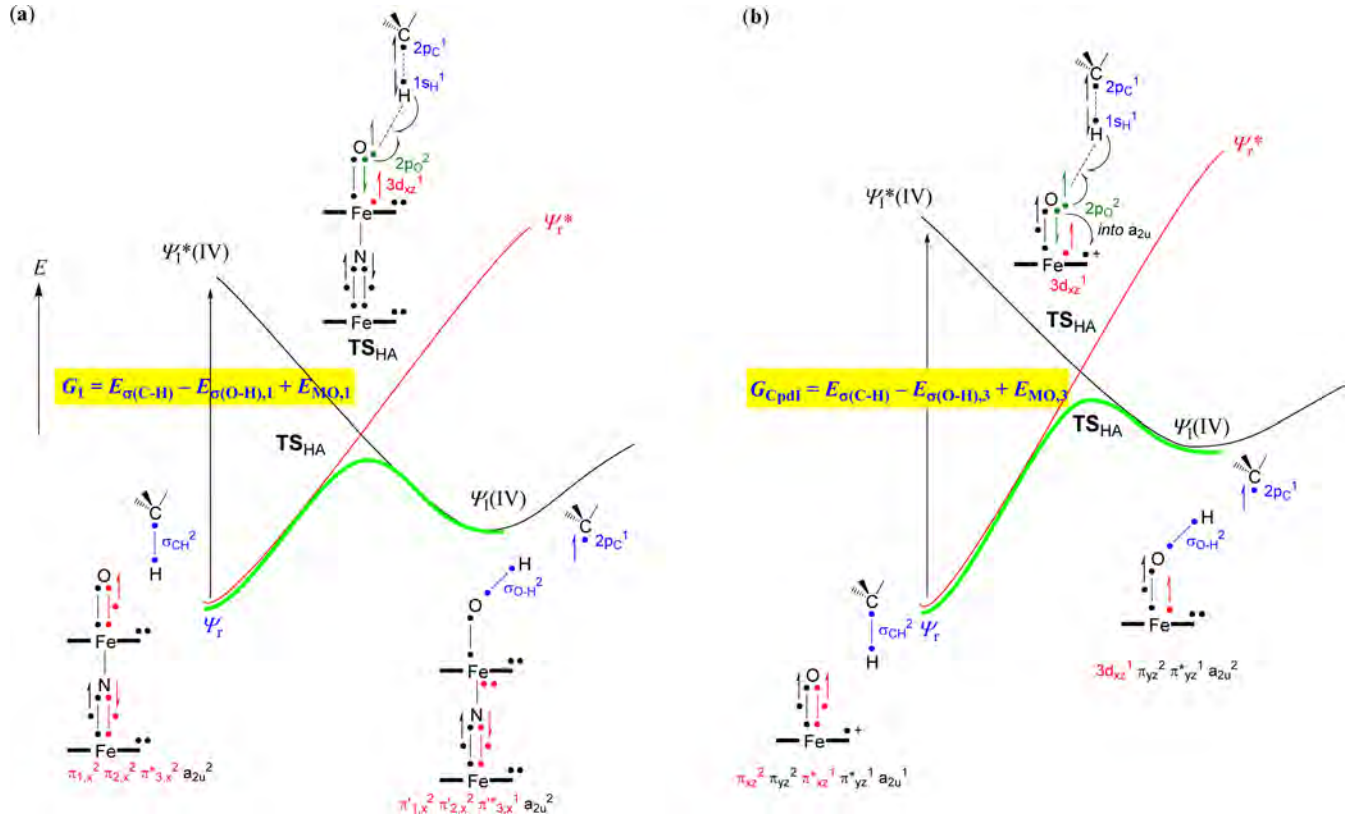

Figure 8. Valence bond curve crossing diagram for the methane hydroxylation by **1** (panel a) and P450 Cpd I (panel b). Dots represent valence electrons and lines (curved or straight) implicate chemical bonds.

with the electron in $2p_y$ to form the methanol product complex. These electron-transfer pathways and orbital occupations agree with the spin densities reported above.

The reactant configuration can be described quantum mechanically with a reactant wave function (Ψ_r) and the radical intermediate with the intermediate wave function Ψ_I. In valence bond theory, the reactant wave function represents an excited state in the intermediate geometry (i.e., Ψ_r*), whereas the intermediate configuration links to an excited state in the reactant geometry (i.e., Ψ_I*).

It has been shown that the barrier height from reactants to products is proportional to the excitation energy (or promotion gap G) from Ψ_r to Ψ_I*.[52] A comparison of the VB structures of the Ψ_r and Ψ_I* (i.e., TS) configurations gives insight into the chemical and physical components that determine the transition state for the reaction and enable us to estimate the promotion gap of **1** or **2**. Thus, the barrier is determined by the energy of the σ_{CH} bond of the substrate that is broken into atomic orbitals (i.e., $E_{\sigma(C-H)}$). In addition, it is based on the energy of the σ_{OH} bond that is formed (i.e., $E_{\sigma(O-H)}$). As discussed above, the barrier height is also dependent on molecular orbital changes (E_{MO}) in the oxidant and particularly on the electron-transfer energies and rehybridization of some of the orbitals due to bond formation and breaking. For instance, the E_{MO} value contains the energy to split the $\pi_{1,x}/\pi_{2,x}/\pi^*_{3,x}/\pi^*_{4,x}$ set of orbitals into a $2p_x$ on oxygen and a $\pi'_{1,x}/\pi'_{2,x}/\pi^{*\prime}_{3,x}$ set of orbitals along the Fe_1-N-Fe_2 axis. The overall value of the promotion gap of **1** or **2** is given in eq 13.

$$G_{\mathbf{1}} = E_{\sigma(C-H)} - E_{\sigma(O-H),\mathbf{1}} + E_{MO,\mathbf{1}} \quad (13)$$

On the right-hand-side of Figure 8, we show the analogous VB curve crossing diagram for methane hydroxylation by P450 CpdI. Thus, the dots along the Fe−O bond represent the three electrons in the π_{xz}/π^*_{xz} (in red) and the three electrons in the π_{yz}/π^*_{yz} (in black) orbitals. Similarly, as discussed above for **1** and $\mathbf{1}_{Ac}$, the $\pi_{xz}^2\,\pi^*_{xz}{}^1$ orbitals split into atomic orbitals with two electrons in $2p_x(O)$ and one in the metal $3d_{xz}$. One of the electrons of $2p_x(O)$ forms the σ_{OH} bond with the incoming $1s_H$ hydrogen atom, whereas the other atom of $2p_x(O)$ is promoted to the nearest available electronic orbital, namely, the a_{2u} orbital. The promotion gap for this reaction ($G_{\mathbf{CpdI}}$) is described in eq 14. Obviously, since we use the same substrate (methane) as in the reaction with **1**, the value $E_{\sigma(C-H)}$ will be the same for **1** and **3**.

$$G_{\mathbf{CpdI}} = E_{\sigma(C-H)} - E_{\sigma(O-H),\mathbf{3}} + E_{MO,\mathbf{3}} \quad (14)$$

In principle, the $E_{\sigma(O-H)}$ represents the strength of the O−H bond that is formed and will be proportional to the BDE_{OH} value. As shown above in Table 3, the BDE_{OH} value for **1** is about 4.4 kcal mol^{-1} larger than that for $\mathbf{1}_{Ac}$ and 7.1 kcal mol^{-1} larger than that found for **3**. Therefore, we expect a smaller promotion gap for **1** than for $\mathbf{1}_{Ac}$ and **3**, which should result in a lower hydrogen-atom-abstraction barrier for **1** than for **3**. Indeed, the potential energy profiles (Figure 2) show a $\mathbf{TS}_{HA}$ ordering of $\mathbf{TS}_{HA,1} < \mathbf{TS}_{HA,1Ac} < \mathbf{TS}_{HA,3}$ in agreement with the promotion gap differences. Thus, part of the differences in BDE_{OH} values relate to differences in the acidity of the iron-hydroxo complex. However, part of this benefit is canceled out by changes in the electron affinity of the oxidants, Table 3.

The major difference between complex **1** and **3** is related to the rehybridization energy or E_{MO}, which is determined by the

DOI: 10.1021/acscatal.5b02720
ACS Catal. 2016, 6, 2230−2243

difference in electron affinity of **1** versus **3**. Thus, in **3**, the π_{xz}/π^*_{xz} couple is rehybridized into atomic orbitals $2p_x(O)$ and $3d_{xz}(Fe)$ of which the $2p_x(O)$ mixes with the $1s_H$ orbital to form the new σ_{CH} orbital. By contrast, in **1** the set of four coupled orbitals $(\pi_{1,x}/\pi_{2,x}/\pi^*_{3,x}/\pi^*_{4,x})$ is reduced to a set of three coupled orbitals and the atomic $2p_x(O)$ orbital, which amounts to a much lesser orbital reorganization and consequently a much smaller E_{MO} value. Therefore, **1** will have a smaller E_{MO} value than **3** and hence also a smaller excitation energy as well as higher reactivity in H atom abstraction reactions. Because of the larger quantum chemical changes upon reduction of **3** versus the reduction of **1** and the increased stability of the product, it is evident that **3** will be a lesser good oxidant of hydrogen-atom-abstraction reactions. Indeed, that is what is observed by the relative methane hydrogen-atom-abstraction reactions when **1** and **3** are compared.

CONCLUSION

The calculations presented in this work highlight how small external perturbations, such as those of an axially coordinated nitrido iron porphyrin ligand can lead to dramatic changes in molecular orbital interactions of the metal(IV)-oxo group with aligned ligand-orbitals as well as the dipole moment of the oxidant. In particular, an μ-nitrido-bridged diiron-oxo complex, with either porphyrin or phthalocyanine, has an increased basicity of the oxo group that is highly susceptible to hydrogen atom abstraction. This explains the enhanced reactivity observed for **A**/**B** over P450 Compound I. Moreover, these insights will assist in the design of efficient and powerful oxidants of hydrogen-atom-abstraction reactions. A detailed thermochemical, valence bond, and orbital analysis has given insight into the intricate details of μ-nitrido-bridged diiron(IV) complexes and gives hints on how this complex can be further modified to improve its catalytic properties.

ASSOCIATED CONTENT

Supporting Information

The Supporting Information is available free of charge on the ACS Publications website at DOI: 10.1021/acscatal.5b02720.

Computational details, including tables with absolute and relative energies, group spin densities and charges, as well as figures with geometry scans, IRCs, and Cartesian coordinates of optimized geometries (PDF)

AUTHOR INFORMATION

Corresponding Authors

*E-mail: sam.devisser@manchester.ac.uk.
*E-mail: alexander.sorokin@ircelyon.univ-lyon1.fr.
*E-mail: pascale.maldivi@cea.fr.

Notes

The authors declare no competing financial interest.

ACKNOWLEDGMENTS

The National Service of Computational Chemistry Software (NSCCS) is thanked for CPU time provided. M.G.Q. thanks the BBSRC for a studentship. D.K. holds the Ramanujan Fellowship (SR/S2/RJN-11/2008) from the Department of Science and Technology (DST), New Delhi (India). A.B.S. is indebted to ANR (France) for financial support (grant ANR-08-BLANC-0183-01). P.M. is grateful to the French National Agency for Research (ANR) "Programme Labex" (ARCANE project no. ANR-11-LABX-003) for partial funding. D.S. wishes to thank Prof Sason Shaik for fruitful discussions and support in this study. S.d.-V. and P.M. also thank Prof Jean-Marc Latour for useful discussions on the structure and spectroscopy of the reactant complex. The COST action CM1305 ECostBio is acknowledged for support. This work was partially performed using HPC resources from GENCI- CINES (Grant 2015-089173).

REFERENCES

(1) (a) Sono, M.; Roach, M. P.; Coulter, E. D.; Dawson, J. H. *Chem. Rev.* **1996**, *96*, 2841−2888. (b) Groves, J. T. *Proc. Natl. Acad. Sci. U. S. A.* **2003**, *100*, 3569−3574. (c) Ortiz de Montellano, P. R., Ed., *Cytochrome P450: Structure, Mechanism and Biochemistry*, 3rd ed.; Kluwer Academic/Plenum Publishers: New York, 2005. (d) Munro, A. W.; Girvan, H. M.; McLean, K. J. *Nat. Prod. Rep.* **2007**, *24*, 585−609. (e) Kadish, K. M., Smith, K. M., Guilard, R., Eds.; *Handbook of Porphyrin Science*; World Scientific Publishing Co.: Singapore, 2010. (f) de Visser, S. P., Kumar, D., Eds.; *Iron-containing enzymes: Versatile catalysts of hydroxylation reaction in nature*; RSC Publishing: Cambridge, U.K., 2011. (g) Grogan, G. *Curr. Opin. Chem. Biol.* **2011**, *15*, 241−248. (h) Poulos, T. L. *Chem. Rev.* **2014**, *114*, 3919−3962. (i) Blomberg, M. R. A.; Borowski, T.; Himo, F.; Liao, R.-Z.; Siegbahn, P. E. M. *Chem. Rev.* **2014**, *114*, 3601−3658.

(2) (a) Costas, M. *Coord. Chem. Rev.* **2011**, *255*, 2912−2932. (b) Bruijnincx, P. C. A.; van Koten, G.; Klein Gebbink, R. J. M. *Chem. Soc. Rev.* **2008**, *37*, 2716−2744. (c) Kryatov, S. V.; Rybak-Akimova, E. V.; Schindler, S. *Chem. Rev.* **2005**, *105*, 2175−2226. (d) McDonald, A. R.; Que, L., Jr *Coord. Chem. Rev.* **2013**, *257*, 414−428. (e) Nam, W.; Lee, Y.-M.; Fukuzumi, S. *Acc. Chem. Res.* **2014**, *47*, 1146−1154.

(3) (a) Groves, J. T. Models and Mechanisms of Cytochrome P450 Action. In *Cytochrome P450: Structure, Mechanism and Biochemistry*, 3rd ed.; Ortiz de Montellano, P. R., Ed.; Kluwer Academic/Plenum Publishers: New York, 2005; Chapter 1, pp 1−44. (b) Nam, W. *Acc. Chem. Res.* **2007**, *40*, 522−531. (c) Denisov, I. G.; Makris, T. M.; Sligar, S. G.; Schlichting, I. *Chem. Rev.* **2005**, *105*, 2253−2277.

(4) Rittle, J.; Green, M. T. *Science* **2010**, *330*, 933−937.

(5) Chen, M. M.; Coelho, P. S.; Arnold, F. H. *Adv. Synth. Catal.* **2012**, *354*, 964−968.

(6) Zilly, F. E.; Acevedo, J. P.; Augustyniak, W.; Deege, A.; Häusig, U. W.; Reetz, M. T. *Angew. Chem., Int. Ed.* **2011**, *50*, 2720−2724; Corrigendum: *Angew. Chem., Int. Ed.* **2013**, *52*, 13503.

(7) (a) Kawakami, N.; Shoji, O.; Watanabe, Y. *Angew. Chem., Int. Ed.* **2011**, *50*, 5315−5318. (b) Kawakami, N.; Shoji, O.; Watanabe, Y. *Chem. Sci.* **2013**, *4*, 2344−2348.

(8) (a) Sorokin, A. B.; Mangematin, S.; Pergrale, C. *J. Mol. Catal. A: Chem.* **2002**, *182-183*, 267−281. (b) Sorokin, A. B.; Kudrik, E. V.; Bouchu, D. *Chem. Commun.* **2008**, 2562−2564. (c) Sorokin, A. B.; Kudrik, E. V.; Alvarez, L. X.; Afanasiev, P.; Millet, J. M. M.; Bouchu, D. *Catal. Today* **2010**, *157*, 149−154. (d) Sorokin, A. B. *Chem. Rev.* **2013**, *113*, 8152−8191. (e) Afanasiev, P.; Kudrik, E. V.; Millet, J-M. M.; Bouchu, D.; Sorokin, A. B. *Dalton Trans.* **2011**, *40*, 701−740. (f) Colomban, C.; Kudrik, E. V.; Afanasiev, P.; Sorokin, A. B. *J. Am. Chem. Soc.* **2014**, *136*, 11321−11330.

(9) Kudrik, E. V.; Afanasiev, P.; Alvarez, L. X.; Dubourdeaux, P.; Clémancey, M.; Latour, J.-M.; Blondin, G.; Bouchu, D.; Albrieux, F.; Nefedov, S. E.; Sorokin, A. B. *Nat. Chem.* **2012**, *4*, 1024−1029.

(10) Berman, H. M.; Westbrook, J.; Feng, Z.; Gilliland, G.; Bhat, T. N.; Weissig, H.; Shindyalov, I. N.; Bourne, P. E. *Nucleic Acids Res.* **2000**, *28*, 235−242.

(11) (a) Butler, C. F.; Peet, C.; Mason, A. E.; Voice, M. W.; Leys, D.; Munro, A. W. *J. Biol. Chem.* **2013**, *288*, 25387−25399. (b) Batabyal, D.; Poulos, T. L. *Biochemistry* **2013**, *52*, 8898−8906. (c) Müller, C. S.; Knehans, T.; Davydov, D. R.; Bounds, P. L.; von Mandach, U.; Halpert, J. R.; Caflisch, A.; Koppenol, W. H. *Biochemistry* **2015**, *54*, 711−721. (d) Xu, K.; Wang, Y.; Hirao, H. *ACS Catal.* **2015**, *5*, 4175−4179.

DOI: 10.1021/acscatal.5b02720
ACS Catal. 2016, 6, 2230−2243

(12) (a) Gross, Z.; Nimri, S. *Inorg. Chem.* **1994**, *33*, 1731−1732. (b) Czarnecki, K.; Nimri, S.; Gross, Z.; Proniewicz, L. M.; Kincaid, J. R. *J. Am. Chem. Soc.* **1996**, *118*, 2929−2935. (c) Song, W. J.; Ryu, Y. O.; Song, R.; Nam, W. *JBIC, J. Biol. Inorg. Chem.* **2005**, *10*, 294−304. (d) Takahashi, A.; Yamaki, D.; Ikemura, K.; Kurahashi, T.; Ogura, T.; Hada, M.; Fujii, H. *Inorg. Chem.* **2012**, *51*, 7296−7305.
(13) For examples, see the following: (a) Alfonso-Prieto, M.; Biarnés, X.; Vidossich, P.; Rovira, C. *J. Am. Chem. Soc.* **2009**, *131*, 11751−11761. (b) Colin, J.; Wiseman, B.; Switala, J.; Loewen, P. C.; Ivancich, A. *J. Am. Chem. Soc.* **2009**, *131*, 8557−8563. (c) Raven, E. L. *Nat. Prod. Rep.* **2003**, *20*, 367−381. (d) Veitch, N. C. *Phytochemistry* **2004**, *65*, 249−259.
(14) (a) Dawson, J. H.; Holm, R. H.; Trudell, J. R.; Barth, G.; Linder, R. E.; Bunnenberg, E.; Djerassi, C.; Tang, S. C. *J. Am. Chem. Soc.* **1976**, *98*, 3707−3709. (b) Poulos, T. L. *JBIC, J. Biol. Inorg. Chem.* **1996**, *1*, 356−359.
(15) (a) Zhou, Y.; Shan, X.; Mas-Ballesté, R.; Bukowski, M. R.; Stubna, A.; Chakrabarti, M.; Slominski, L.; Halfen, J. A.; Münck, E.; Que, L., Jr *Angew. Chem., Int. Ed.* **2008**, *47*, 1896−1899. (b) de Visser, S. P.; Nam, W. *J. Phys. Chem. A* **2008**, *112*, 12887−12895. (c) Takahashi, A.; Kurahashi, T.; Fujii, H. *Inorg. Chem.* **2011**, *50*, 6922−6928.
(16) Shaik, S.; Kumar, D.; de Visser, S. P.; Altun, A.; Thiel, W. *Chem. Rev.* **2005**, *105*, 2279−2328.
(17) (a) Porro, C. S.; Sutcliffe, M. J.; de Visser, S. P. *J. Phys. Chem. A* **2009**, *113*, 11635−11642. (b) Hernández-Ortega, A.; Quesne, M. G.; Bui, S.; Heyes, D. J.; Steiner, R. A.; Scrutton, N. S.; de Visser, S. P. *J. Am. Chem. Soc.* **2015**, *137*, 7474−7487. (c) Quesne, M. G.; Borowski, T.; de Visser, S. P. *Chem. - Eur. J.* **2016**, *22*, 2562−2581.
(18) (a) de Visser, S. P.; Quesne, M. G.; Martin, B.; Comba, P.; Ryde, U. *Chem. Commun.* **2014**, *50*, 262−282. (b) Kumar, D.; de Visser, S. P.; Sharma, P. K.; Cohen, S.; Shaik, S. *J. Am. Chem. Soc.* **2004**, *126*, 1907−1920. (c) Kumar, D.; de Visser, S. P.; Shaik, S. *J. Am. Chem. Soc.* **2004**, *126*, 5072−5073.
(19) (a) Frisch, M. J. et al. *Gaussian 09*, revision D.01; Gaussian, Inc.: Wallingford, CT, 2009. (b) *Jaguar*, version 8.4; Schrodinger, Inc.: New York, NY, 2013. (c) Neese, F. *ORCA − an ab initio, DFT and semiempirical SCF-MO package*, version 2.9; University of Bonn: Bonn, Germany, 2009. (d) Visualizing Molecules with gOpenMol. http://www.chem.utah.edu/directory/anderson/research-group/gopen/ (accessed January 2016).
(20) (a) Becke, A. D. *J. Chem. Phys.* **1993**, *98*, 5648−5652. (b) Lee, C.; Yang, W.; Parr, R. G. *Phys. Rev. B: Condens. Matter Mater. Phys.* **1988**, *37*, 785−789.
(21) (a) Hay, P. J.; Wadt, W. R. *J. Chem. Phys.* **1985**, *82*, 299−310. (b) Hehre, W. J.; Ditchfield, K.; Pople, J. A. *J. Chem. Phys.* **1972**, *56*, 2257−2261.
(22) (a) Becke, A. D. *Phys. Rev. A: At., Mol., Opt. Phys.* **1988**, *38*, 3098−3100. (b) Perdew, J. P. *Phys. Rev. B: Condens. Matter Mater. Phys.* **1986**, *33*, 8822−8824.
(23) de Visser, S. P. *J. Am. Chem. Soc.* **2010**, *132*, 1087−1097.
(24) (a) Vardhaman, A. K.; Sastri, C. V.; Kumar, D.; de Visser, S. P. *Chem. Commun.* **2011**, *47*, 11044−11046. (b) Vardhaman, A. K.; Barman, P.; Kumar, S.; Sastri, C. V.; Kumar, D.; de Visser, S. P. *Angew. Chem., Int. Ed.* **2013**, *52*, 12288−12292. (c) Vardhaman, A. K.; Barman, P.; Kumar, S.; Sastri, C. V.; Kumar, D.; de Visser, S. P. *Chem. Commun.* **2013**, *49*, 10926−10928.
(25) Prokop, K. A.; de Visser, S. P.; Goldberg, D. P. *Angew. Chem., Int. Ed.* **2010**, *49*, 5091−5095.
(26) de Visser, S. P. *Chem. - Eur. J.* **2006**, *12*, 8168−8177.
(27) (a) Sainna, M. A.; Kumar, S.; Kumar, D.; Fornarini, S.; Crestoni, M. E.; de Visser, S. P. *Chem. Sci.* **2015**, *6*, 1516−1529. (b) Sainna, M. A.; Sil, D.; Sahoo, D.; Martin, B.; Rath, S. P.; Comba, P.; de Visser, S. P. *Inorg. Chem.* **2015**, *54*, 1919−1930.
(28) Reiher, M.; Salomon, O.; Hess, B. A. *Theor. Chem. Acc.* **2001**, *107*, 48−55.
(29) Grimme, S.; Antony, J.; Ehrlich, S.; Krieg, H. *J. Chem. Phys.* **2010**, *132*, 154104−154104.
(30) Zhao, Y.; Truhlar, D. G. *J. Chem. Phys.* **2006**, *125*, 194101−194101.
(31) Adamo, C.; Barone, V. *J. Chem. Phys.* **1999**, *110*, 6158−6169.
(32) Neu, H. M.; Quesne, M. G.; Yang, T.; Prokop-Prigge, K. A.; Lancaster, K. M.; Donohoe, J.; DeBeer, S.; de Visser, S. P.; Goldberg, D. P. *Chem. - Eur. J.* **2014**, *20*, 14584−14588.
(33) Heyes, D. J.; Sakuma, M.; de Visser, S. P.; Scrutton, N. S. *J. Biol. Chem.* **2009**, *284*, 3762−3767.
(34) For examples, see the following: Neu, H. M.; Yang, T.; Baglia, R. A.; Yosca, T. H.; Green, M. T.; Quesne, M. G.; de Visser, S. P.; Goldberg, D. P. *J. Am. Chem. Soc.* **2014**, *136*, 13845−13852.
(35) (a) Yoshizawa, K.; Kamachi, T.; Shiota, Y. *J. Am. Chem. Soc.* **2001**, *123*, 9806−9816. (b) de Visser, S. P.; Kumar, D.; Cohen, S.; Shacham, R.; Shaik, S. *J. Am. Chem. Soc.* **2004**, *126*, 8362−8363.
(36) Shaik, S.; Kumar, D.; de Visser, S. P. *J. Am. Chem. Soc.* **2008**, *130*, 10128−10140.
(37) For examples, see the following: Kumar, S.; Faponle, A. S.; Barman, P.; Vardhaman, A. K.; Sastri, C. V.; Kumar, D.; de Visser, S. P. *J. Am. Chem. Soc.* **2014**, *136*, 17102−17115.
(38) de Visser, S. P. *Phys. Chem. Chem. Phys.* **1999**, *1*, 749−754.
(39) (a) Kumar, D.; Karamzadeh, B.; Sastry, G. N.; de Visser, S. P. *J. Am. Chem. Soc.* **2010**, *132*, 7656−7667. (b) Kumar, D.; Sastry, G. N.; de Visser, S. P. *Chem. - Eur. J.* **2011**, *17*, 6196−6205.
(40) de Visser, S. P.; Shaik, S.; Sharma, P. K.; Kumar, D.; Thiel, W. *J. Am. Chem. Soc.* **2003**, *125*, 15779−15788.
(41) Ogliaro, F.; de Visser, S. P.; Cohen, S.; Kaneti, J.; Shaik, S. *ChemBioChem* **2001**, *2*, 848−851.
(42) (a) Kumar, D.; Tahsini, L.; de Visser, S. P.; Kang, H. Y.; Kim, S. J.; Nam, W. *J. Phys. Chem. A* **2009**, *113*, 11713−11722. (b) Colomban, C.; Kudrik, E. V.; Briois, V.; Shwarbrick, J. C.; Sorokin, A. B.; Afanasiev, P. *Inorg. Chem.* **2014**, *53*, 11517−11530.
(43) (a) de Visser, S. P.; Tan, L. S. *J. Am. Chem. Soc.* **2008**, *130*, 12961−12974. (b) Shaik, S.; de Visser, S. P.; Kumar, D. *J. Am. Chem. Soc.* **2004**, *126*, 11746−11749.
(44) de Visser, S. P. *J. Phys. Chem. A* **2005**, *109*, 11050−11057.
(45) (a) Silaghi-Dumitrescu, R.; Makarov, S. V.; Uta, M.-M.; Dereven'kov, I. A.; Stuzhin, P. A. *New J. Chem.* **2011**, *35*, 1140−1145. (b) Ansari, M.; Vyas, N.; Ansari, A.; Rajaraman, G. *Dalton Trans.* **2015**, *44*, 15232−15243. (c) İşci, Ü.; Faponle, A. S.; Afanasiev, P.; Albrieux, F.; Briois, V.; Ahsen, V.; Dumoulin, F.; Sorokin, A. B.; de Visser, S. P. *Chem. Sci.* **2015**, *6*, 5063−5075.
(46) Bocian, D. F.; Findsen, E. W.; Hofmann, J. A., Jr; Schick, G. A.; English, D. R.; Hendrickson, D. N.; Suslick, K. S. *Inorg. Chem.* **1984**, *23*, 800−807.
(47) For examples, see the following: (a) Latifi, R.; Bagherzadeh, M.; de Visser, S. P. *Chem. - Eur. J.* **2009**, *15*, 6651−6662. (b) Faponle, A. S.; Quesne, M. G.; Sastri, C. V.; Banse, F.; de Visser, S. P. *Chem. - Eur. J.* **2015**, *21*, 1221−1236.
(48) Ogliaro, F.; de Visser, S. P.; Shaik, S. *J. Inorg. Biochem.* **2002**, *91*, 554−567.
(49) (a) Friedrich, L. E. *J. Org. Chem.* **1983**, *48*, 3851−3852. (b) Bordwell, F. G.; Cheng, J.-P. *J. Am. Chem. Soc.* **1991**, *113*, 1736−1743. (c) Mayer, J. M. *Acc. Chem. Res.* **1998**, *31*, 441−450.
(50) *NIST Chemistry WebBook*, NIST Standard Reference Database, Number 69; Linstrom, P. J., Mallard, W. G., Eds.; National Institute of Standards and Technology: Gaithersburg, MD, 2016. http://webbook.nist.gov.
(51) (a) Green, M. T.; Dawson, J. H.; Gray, H. B. *Science* **2004**, *304*, 1653−1656. (b) Parsell, T. H.; Yang, M.-Y.; Borovik, A. S. *J. Am. Chem. Soc.* **2009**, *131*, 2762−2763.
(52) Shaik, S. S. *J. Am. Chem. Soc.* **1981**, *103*, 3692−3701.

DOI: 10.1021/acscatal.5b02720
ACS Catal. 2016, 6, 2230−2243

Chemical Physics 456 (2015) 41–46

Contents lists available at ScienceDirect

Chemical Physics

journal homepage: www.elsevier.com/locate/chemphys

Polarizability study of nematic liquid crystal 4-cyano-4′-pentylbiphenyl (5CB) and its nitrogen derivatives

Pranav Upadhyay, Manoj Kumar Rastogi, Devesh Kumar *

Department of Applied Physics, Babasaheb Bhimrao Ambedkar University, Lucknow 226025, U.P., India

ARTICLE INFO

Article history:
Received 22 January 2015
In final form 25 March 2015
Available online 16 April 2015

Keywords:
Liquid crystal
Polarizability
Density functional theory
5CB

ABSTRACT

The effect of electric field on the molecular polarizability and HOMO–LUMO gap for 4-cyano-4′-pentylbiphenyl (**1**) and its nitrogen derivatives 2-cyano-5-(4-pentylphenyl)pyridine (**2**), 2-(4-cyanophenyl)-5-pentylpyrimidine (**3**) and 5-cyano-2-(4-pentylphenyl)pyrimidine (**4**) has been studied using density functional theory (DFT). The effect on polarizability and HOMO–LUMO gap due to presence of substituent in the molecules is also investigated by comparing results obtained from two different DFT approaches B3LYP and M062X. It was observed that variation of polarizability with change in electric field for all molecules show a common feature that is stabilization of polarizability between two values of electric field (or for a range of electric field). 4-cyano-4′-pentylbiphenyl (**1**) polarizes more in comparison to all other derivatives and has widest stability region among all.

© 2015 Published by Elsevier B.V.

1. Introduction

Now-a-days liquid crystals (LC) are widely used for commercial applications such as electro-optical flat panel display devices for consumer audio-visual and office equipment. Among the all type of liquid crystals, nematic phase is characterized by long range orientational order, i.e. the long axis of the molecule tend to align along a preferred direction and its orientational order can also be altered by an applied magnetic or electric field [1–3].

Williams et al. [4] studied the effect of dc field on nematic liquid crystal by confining it between two electrodes and observed a convective instability beyond a threshold voltage (∼5 V) resulting in breakdown of the nematic phase and formation of regular patterns or domains. These domains become visible in polarized light with direction of polarization parallel to the direction of initial molecular alignment [5]. It was also observed that the electro-convection and flexo-electric pattern was formed upon application of superimposed dc and ac electric fields [6].

The effect of electric field on liquid crystals can be studied by analyzing an important parameter known as polarizability, which is a crucial property responsible for dispersion as well as induction forces in molecules and materials. Depending on the polarizability of a material, an applied electric field causes its polarization so that material can be used for a desired purpose. In liquid crystals, the molecular polarizability and its anisotropy are important inherent molecular properties because the intermolecular interaction energies depend on them [7].

To measure polarizability and other physical properties, different theoretical models and approaches have been proposed over past few decades; Vuks [8], Neugebauer [9], Lippincott δ-function model [10] and their modifications are the methods to name a few.

As dielectric anisotropy ($\Delta\varepsilon = \varepsilon_{||} - \varepsilon_{\perp}$, $\varepsilon_{||}$ and $\varepsilon_{\perp}$ are the permittivity parallel and perpendicular to the director respectively) dominates the reorientation of liquid crystal molecules under an external electric field, so it becomes critical for most of the electro-optic applications [11]. Maier–Meier theory [12] either with some alterations or hybridizing it with other methods [13–15] had been used by many researchers for determining dielectric anisotropy. Semi-empirical molecular orbit (MO) methods to calculate the dielectric anisotropy was first used by Bremer and Tarumi [16] in which they were successful in finding reasonable correlation between $\Delta\varepsilon$ and dipole moment with some scatter. *ab initio* method (B3LYPD/6-31G(d)) was compared with semi-empirical method (MOPAC/AM1) by Demus and Inukai [17,18] with different conformers and they found latter was more near to experiments. Aver'yanov studied the influence of the orientational order of molecules in a nematic liquid crystal on the average dielectric permittivity and anisotropy of the molecular polarizability in the framework of the molecular statistical approach with a perturbation of the electronic structure of molecules due to the change in the conformation of their aromatic core and intermolecular interactions [19].

* Corresponding author.
E-mail address: dkclcre@yahoo.co.in (D. Kumar).

http://dx.doi.org/10.1016/j.chemphys.2015.03.011
0301-0104/© 2015 Published by Elsevier B.V.

Presently liquid crystals are experiencing a revolutionary phase of research in which aspects other than display properties are brought forward by studying the applicability of liquid crystalline states of matter in the field of organic electronics [20,21], nanoparticle organization [22,23]. Photonics [24], polymers [25,26], complexes [27], biology [28,29], pharmacology [30] and food science [31] as well [32]. Electro-optical properties of liquid crystals after being doped with different kind of dopants have been analyzed [23,33]. Materials like graphene oxide [34,35], active matter [36] possessing liquid crystalline phase have been demonstrated.

In this paper we present a comparative study of polarizability of 4-cyano-4′-pentylbiphenyl (**1**) (commonly known as 5CB) and its nitrogen derivatives 2-cyano-5-(4-pentylphenyl)pyridine (**2**), 2-(4-cyanophenyl)-5-pentylpyrimidine (**3**) and 5-cyano-2-(4-pentylphenyl)pyrimidine (**4**), which are nematic liquid crystal. 5CB is about 20 Å long and exhibit liquid crystal phases near room temperature. The molecular structure along with transition temperatures and dielectric constants of these molecules is summarized in Table I. They have positive dielectric anisotropy ($\Delta\varepsilon$) and are useful for parallel or twist alignment.

2. Geometry optimization and methodology

Geometry optimization and total-energy calculations were carried out by using density-functional theory which is proven good for characterization/correlation/explanation of properties of various types of molecules [41–43]. The structures were created using GaussView 5.0. The molecular structures were fully optimized without any constrain and frequency were calculated with B3LYP [44,45] hybrid functional for Gaussian type orbitals (GTOs) and 6-31G** [46] basis set using Gaussian 09 [47]. Inter-ring distance and inter-ring twist after optimization is given in Table 2. Effect of electric field along the long axis (*x*-axis) on polarizability (α) was calculated using B3LYP and M062X [48] methods with 6-31G** basis set using Gaussian 09. These methods are already proven in the area of intramolecular interactions, conformational studies [49], enzymatic reaction mechanism [50–53], investigations on molecular structure, spectroscopy [54], and studies of clusters [55].

M06-2X belongs to M06-class functional which relies on spin densities, spin density gradients, spin kinetic energy densities, and for nonlocal hybrid functionals, Hartree–Fock exchange. M06-2X, is hybrid meta functional, has excellent performance for main group chemistry. It is quite accurate in predicting valence and Rydberg electronic excitation energies, including dispersion corrections and provide excellent results for aromatic–aromatic stacking interactions [48].

Table 2
Inter-ring distance and inter-ring twist of compounds.

Compound	Inter-ring distance (Å)	Inter-ring twist (°)
1	1.48276	143.581
2	1.47949	143.227
3	1.48557	180.262
4	1.47469	180.084

Table 3
Showing the conversion factor for atomic unit to SI unit.

Physical parameter	Atomic unit (a.u.)	SI unit
Electric field	1	5.142206×10^{11} Vm^{-1}
Polarizability	1	1.648777×10^{-41} C^2 m^2 J^{-1}
Energy	1 hartree	4.3597×10^{-18} J

Calculation of effect of field as implemented in Gaussian 09 is well explained by Jensen [56]. Molecular geometry was not allowed to change during calculation of polarizability. The field was varied from 0.000 a.u. to 0.050 a.u. with an increment of 0.002 a.u. Polarizability was calculated from the trace of polarizability tensor. Table 3 presents conversion different parameters from atomic unit to SI unit.

3. Results

Fig. 1 presents the optimized geometry of the molecules **1**, **2**, **3**, and **4**.

3.1. 4-cyano-4′-pentylbiphenyl

Fig. 2 presents the variation of polarizability and HOMO–LUMO band gap with the electric field for molecule **1**. The polarizability varies exponentially with respect to electric field till it reaches a point (0.018 a.u. for B3LYP and 0.022 a.u. for M062X) where it gets stabilized and remains constant till 0.042 a.u. for both B3LYP and M062X. HOMO–LUMO gap also varies with electric field as shown in Fig. 2. It gets stabilized after continuous decrement at the same field value for which polarizability gets stabilized.

3.2. 2-cyano-5-(4-pentylphenyl)pyridine

Replacement of carbon at *ortho* position with nitrogen in second benzene ring from the chain side has pushed the stability range by 0.006 a.u. Starting points of stability region is 0.022 a.u. for B3LYP and 0.024 a.u. for M062X and stability region ends at 0.038 a.u. for

Table 1
List of molecules studied with their transition temperature and values for dielectric anisotropy (measured at $0.98 \times T_{N-I}$, where T_{N-I} is nematic clearing point) (Ref. [37]).

Compound	Molecular structure	Transition temperature (crystal) (°C)	Transition temperature (nematic) (°C)[a]	Dielectric anisotropy ($\Delta\varepsilon$)	References
1		22.5	35	+8.5	[38]
2	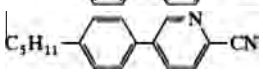	73	[31]	+9.4	[39]
3	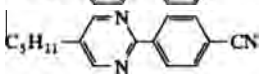	71	(52)	+21	[40]
4	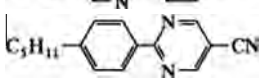	96	109[b]	+3.4	[41]

[a] The parenthesis represent a monotropic transition temperature and square bracket represent an extrapolated "virtual" transition temperature.
[b] Smectic A phase at 93.5 °C.

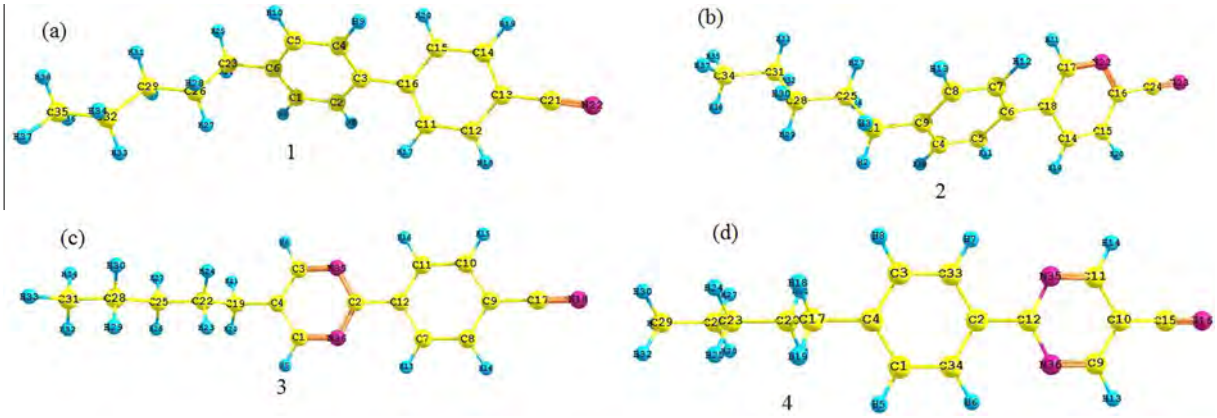

Fig. 1. The optimized geometry for the molecules (a) 4-cyano-4′-pentylbiphenyl (b) 2-cyano-5-(4-pentylphenyl)pyridine, (c) 2-(4-cyanophenyl)-5-pentylpyrimidine, (d)5-cyano-2-(4-pentylphenyl)pyrimidines. Atoms labelled are used for finding inter-ring twist.

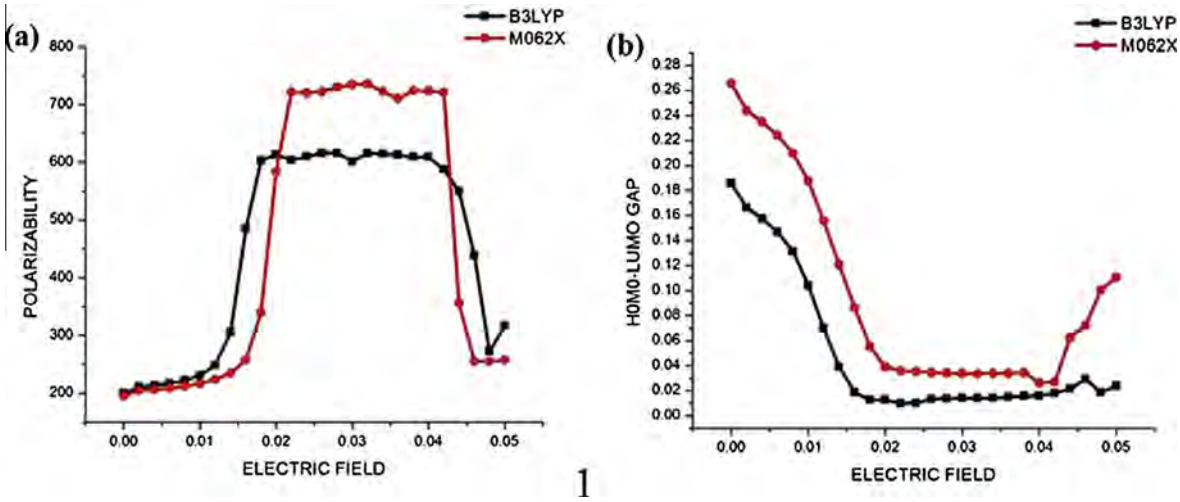

Fig. 2. (a) Variation of polarizability with electric field and (b) variation of HOMO–LUMO gap for molecule 1.

B3LYP and 0.040 a.u. for M062X. HOMO–LUMO gap variation gets modified accordingly with electric field as shown in Fig. 3.

3.3. 2-(4-cyanophenyl)-5-pentylpyrimidine

From Fig. 4, it can be observed that on replacing both *ortho* carbons with nitrogen in the first ring from chain side, the stability range achieves nearly the same value as that of molecule **1** for both B3LYP and M062X. The starting point for B3LYP is 0.02 a.u. and 0.024 a.u. for M062X, while dropping value is 0.04 a.u. For B3LYP and 0.044 a.u. for M062X. Stability of HOMO–LUMO gap is also between the same ranges of field values.

3.4. 5-cyano-2-(4-pentylphenyl) pyrimidine

Replacement of both *meta* carbons in the second ring with nitrogen gives us a stability range similar to molecule **2**.Stability starts at 0.022 a.u. for B3LYP and 0.024 a.u. for M062X which ends at 0.038 a.u. for B3LYP and 0.042 for M062X (Fig. 5). Plot for HOMO–LUMO gap follows accordingly.

3.5. Effect of high field on charge distribution

There is fall of polarizability on field above 0.42 a.u. in most cases. Tables 4 and 5 shows the Mullikan charge distribution for all compounds at 0.46 a.u. electric field. At this field even few hydrogen atoms also bears negative charge.

4. Discussion and conclusions

Polarizability versus electric field plot for all molecules shows a common feature of stabilized polarizability between two values of electric field (or for a range of electric field values). 5CB (**1**) polarizes more in comparison to all other derivatives and has widest stability region among all.

For 5CB, stability region always remains above the level of 600 a.u. but for its nitrogen derivatives, stability region is below 600 a.u. Similarly for M062X, 5CB has more polarizability than its nitrogen derivatives (**2**, **3**, **4**).

Initially both M062X and B3LYP start with similar values of polarizability. M062X gives higher value in comparison to B3LYP. Fall for M062X is sharper while for B3LYP it is quite smooth. For all the molecules, HOMO–LUMO gap is flat in the stability region of the respective molecule.

To conclude, we found that the polarizability as well as HOMO–LUMO gap remains stable within a particular range of electric field and around a certain level. The possible reason is that the increase in magnitude of field results in conjugation effect whereby electrons prefer to delocalize instead of being localized. The mobile electrons which are available as a result of this conjugation (delocalization) are responsible for an increased polarizability.

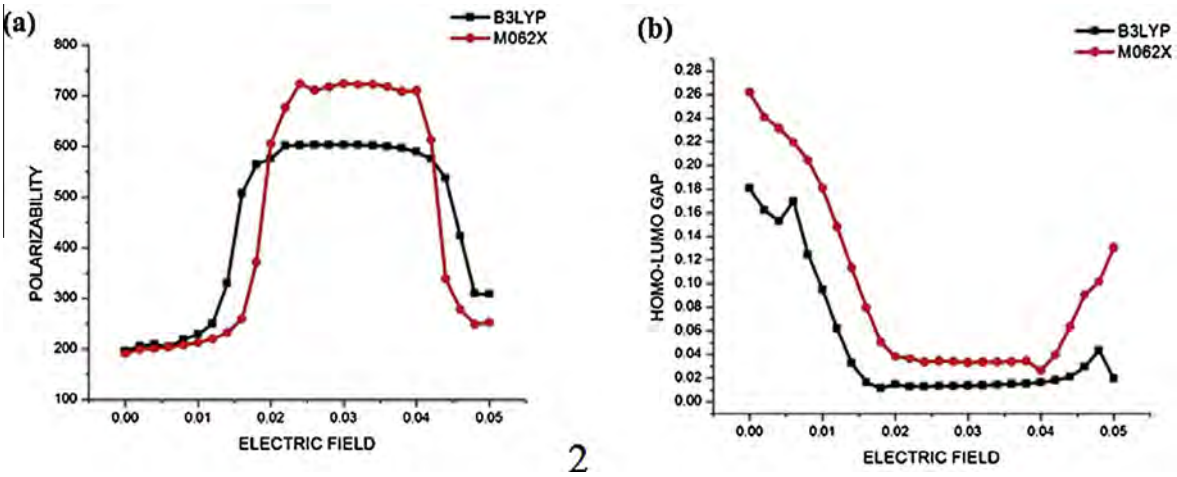

Fig. 3. (a) Variation of polarizability with electric field and (b) variation of HOMO–LUMO gap for molecule 2.

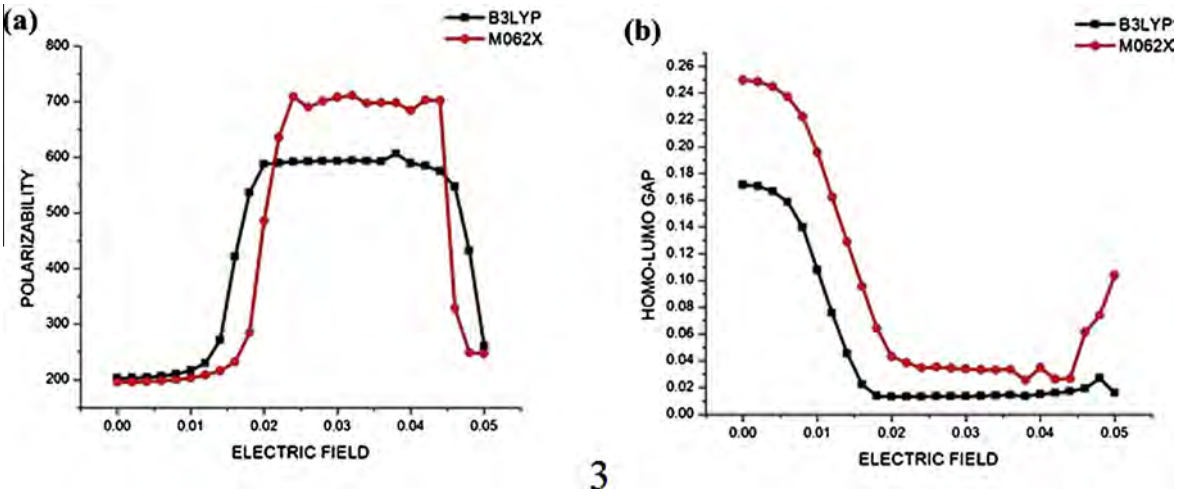

Fig. 4. (a) Variation of polarizability with electric field and (b) variation of HOMO–LUMO gap for molecule 3.

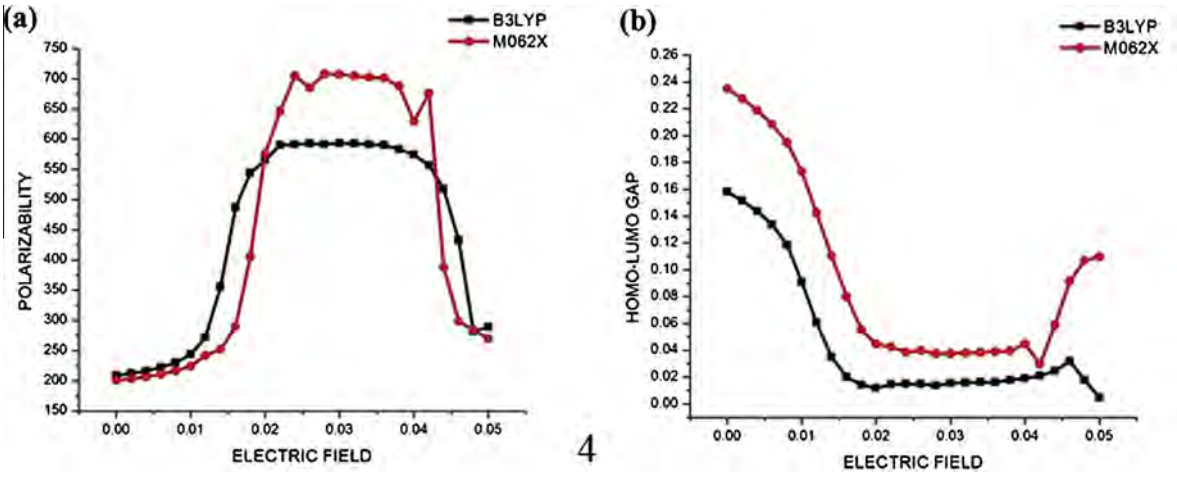

Fig. 5. (a) Variation of polarizability with electric field and (b) variation of HOMO–LUMO gap for molecule 4.

Table 4
Below is the charge on the atoms (along with number showing their label as per Fig. 1) of molecule **1** and molecule **2** at an electric field 0.46 a.u. At this field even few hydrogen atoms also bears negative charge.

Molecule 1				Molecule 2			
B3LYP		M062X		B3LYP		M062X	
Atom	Charge	Atom	Charge	Atom	Charge	Atom	Charge
1 C	−0.106952	1 C	−0.133739	1 C	−0.272783	1 C	−0.305298
2 C	−0.130472	2 C	−0.151885	2 H	0.194829	2 H	0.215619
3 C	0.071506	3 C	0.041636	3 H	0.188529	3 H	0.209565
4 C	−0.129848	4 C	−0.151047	4 C	−0.108535	4 C	−0.131893
5 C	−0.108796	5 C	−0.135126	5 C	−0.130910	5 C	−0.151430
6 C	0.111276	6 C	0.072510	6 C	0.069187	6 C	0.042380
7 H	0.162151	7 H	0.190161	7 C	−0.128521	7 C	−0.149455
8 H	−0.002686	8 H	0.021733	8 C	−0.107823	8 C	−0.131457
9 H	0.003350	9 H	0.027779	9 C	0.110871	9 C	0.068179
10 H	0.160909	10 H	0.189030	10 H	0.166995	10 H	0.198928
11 C	−0.106311	11 C	−0.123124	11 H	0.010615	11 H	0.038237
12 C	−0.173103	12 C	−0.193774	12 H	−0.008761	12 H	0.018861
13 C	0.080857	13 C	0.044794	13 H	0.154694	13 H	0.186753
14 C	−0.156672	14 C	−0.177652	14 C	−0.080025	14 C	−0.097778
15 C	−0.101844	15 C	−0.119514	15 C	−0.134952	15 C	−0.159389
16 C	−0.015856	16 C	−0.045458	16 C	0.140832	16 C	0.126896
17 H	0.085379	17 H	0.118690	17 C	−0.011578	17 C	−0.010253
18 H	−0.167330	18 H	−0.136005	18 C	−0.033042	18 C	−0.064789
19 H	−0.244051	19 H	−0.212995	19 H	0.034833	19 H	0.069156
20 H	0.035047	20 H	0.068118	20 H	−0.253879	20 H	−0.218983
21 C	−0.477575	21 C	−0.480141	21 H	0.086766	21 H	0.117889
22 N	−0.867158	22 N	−0.876627	22 N	−0.578246	22 N	−0.601324
23 C	−0.273206	23 C	−0.306147	23 N	−0.867764	23 N N	−0.877294
24 H	0.195485	24 H	0.207441	24 C	−0.411950	24 C	−0.410744
25 H	0.193595	25 H	0.207229	25 C	−0.209482	25 C	−0.244894
26 C	−0.209470	26 C	−0.249957	26 H	0.143177	26 H	0.157444
27 H	0.139028	27 H	0.143048	27 H	0.137423	27 H	0.150286
28 H	0.137051	28 H	0.144271	28 C	−0.243577	28 C	−0.294578
29 C	−0.243058	29 C	−0.314832	29 H	0.303379	29 H	0.322739
30 H	0.297745	30 H	0.333861	30 H	0.292126	30 H	0.311233
31 H	0.302180	31 H	0.335331	31 C	−0.316701	31 C	−0.383574
32 C	−0.317298	32 C	−0.424723	32 H	0.333522	32 H	0.367202
33 H	0.358611	33 H	0.426065	33 H	0.358460	33 H	0.399700
34 H	0.327459	34 H	0.427253	34 C	−0.224698	34 C	−0.265855
35 C	−0.225756	35 C	−0.298803	35 H	0.482233	35 H	0.513851
36 H	0.432923	36 H	0.535205	36 H	0.486310	36 H	0.525778
37 H	0.478920	37 H	0.460534	37 H	0.428442	37 H	0.458291
38 H	0.483968	38 H	0.536863				

Table 5
Below is the charge on the atoms (along with number showing their label as per Fig. 1) of molecule **3** and molecule **4** at an electric field 0.46 a.u. At this field even few hydrogen atoms also bears negative charge.

Molecule 3				Molecule 4			
B3LYP		M062X		B3LYP		M062X	
Atom	Charge	Atom	Charge	Atom	Charge	Atom	Charge
1 C	0.052251	1 C	0.047005	1 C	−0.110861	1 C	−0.136575
2 C	0.281837	2 C	0.309511	2 C	0.106206	2 C	0.059961
3 C	0.050341	3 C	0.045206	3 C	−0.110666	3 C	−0.136314
4 C	0.070346	4 C	0.021892	4 C	0.113301	4 C	0.070232
5 H	0.164444	5 H	0.192650	5 H	0.156254	5 H	0.187345
6 H	0.147118	6 H	0.175596	6 H	0.021837	6 H	0.052943
7 C	−0.107216	7 C	−0.122112	7 H	0.026949	7 H	0.057955
8 C	−0.166211	8 C	−0.188420	8 H	0.161162	8 H	0.191650
9 C	0.072714	9 C	0.031567	9 C	−0.021188	9 C	−0.025511
10 C	−0.161262	10 C	−0.183348	10 C	0.045060	10 C	0.011418
11 C	−0.105618	11 C	−0.120957	11 C	−0.020985	11 C	−0.025098
12 C	0.013114	12 C	−0.045675	12 C	0.167624	12 C	0.179625
13 H	0.083775	13 H	0.118593	13 H	−0.170911	13 H	−0.139818
14 H	−0.164968	14 H	−0.139052	14 H	−0.163626	14 H	−0.132425
15 H	−0.189966	15 H	−0.164631	15 C	−0.479875	15 C	−0.473988
16 H	0.066921	16 H	0.101590	16 N	−0.842733	16 N	−0.852825
17 C	−0.407839	17 C	−0.414523	17 C	−0.272401	17 C	−0.305030
18 N	−0.819774	18 N	−0.838138	18 H	0.194590	18 H	0.213245
19 C	−0.266471	19 C	−0.294839	19 H	0.189653	19 H	0.211739

(*continued on next page*)

Table 5 (*continued*)

Molecule 3				Molecule 4			
B3LYP		M062X		B3LYP		M062X	
Atom	Charge	Atom	Charge	Atom	Charge	Atom	Charge
20 H	0.160755	20 H	0.180367	20 C	−0.209472	20 C	−0.244972
21 H	0.146005	21 H	0.168852	21 H	0.143992	21 H	0.155411
22 C	−0.206873	22 C	−0.245119	22 H	0.136339	22 H	0.152619
23 H	0.172722	23 H	0.190895	23 C	−0.242904	23 C	−0.293905
24 H	0.156828	24 H	0.177794	24 H	0.297779	24 H	0.321026
25 C	−0.245983	25 C	−0.298120	25 H	0.296551	25 H	0.313544
26 H	0.262488	26 H	0.290181	26 C	−0.315986	26 C	−0.382781
27 H	0.251999	27 H	0.275287	27 H	0.361464	27 H	0.362879
28 C	−0.303373	28 C	−0.369811	28 H	0.324875	28 H	0.399101
29 H	0.390503	29 H	0.398197	29 C	−0.227147	29 C	−0.267586
30 H	0.347346	30 H	0.427873	30 H	0.433362	30 H	0.522136
31 C	−0.233901	31 C	−0.269783	31 H	0.480015	31 H	0.512308
32 H	0.412778	32 H	0.510140	32 H	0.479391	32 H	0.459210
33 H	0.506401	33 H	0.541933	33 C	−0.130594	33 C	−0.151148
34 H	0.455606	34 H	0.436625	34 C	−0.130287	34 C	−0.150612
35 N	−0.447741	35 N	−0.477812	35 N	−0.342514	35 N	−0.356970
36 N	−0.439096	36 N	−0.469415	36 N	−0.344255	36 N	−0.358793

As the field is increased gradually, the polarizability attains nearly constant value due to availability of large number of mobile electrons. Further, availability of mobile electrons due to conjugation results in decrease of HOMO–LUMO separation.

When the applied electric field is increased further, it results in drop of polarizability due to excessive and random distribution of electrons (negative charge). As we can see from the Tables 4 and 5 that even hydrogen of benzene ring (near to CN group) and carbon of CN group bears some negative charge.

Replacement of carbon with nitrogen has not only reduced the stability range but has also pushed it further. Presence of more electronegative nitrogen makes derivatives less polarizable by countering the effect of cyano group hence higher field is required to reach the stability region.

Conflict of interest

No conflict of interest.

Acknowledgments

Authors are thankful to Mr. Ankur Trivedi for scientific discussions and suggestions. DK is DST-Ramanujan Fellow (SR/S2/RJN-11/2008).

References

[1] P.G. de Gennes, J. Prost, The Physics of Liquid Crystals, second ed., Oxford University Press, Oxford, 1993.
[2] S. Chandrasekhar, Liquid Crystals, second ed., Cambridge University Press, Cambridge, 1992.
[3] M.J. Stephen, J.P. Straley, Rev. Mod. Phys. 46 (1974) 617.
[4] R. Williams, J. Chem. Phys. 39 (1963) 384.
[5] D.T. Teaney, A. Migliori, J. Appl. Phys. 41 (1970) 998.
[6] K. Alexei, Phys. Rev. E 89 (2014) 052507.
[7] P.R. Alapati, D. Bhuyan, D. Madhavilatha, P. Pardhasaradhi, V.G.K.M. Pisipati, P.V. Datta Prasad, K.N. Singh, World J. Condens. Matter Phys. 1 (2011) 167.
[8] M.F. Vuks, Opt. Spectrosc. 20 (1966) 361.
[9] H.E.J. Neugebauer, Can. J. Phys. 18 (1950) 292.
[10] E.R. Lippincott, J.M. Stutman, J. Phys. Chem. 68 (1964) 2926.
[11] Z. Ran, H. Jun, P. Zeng-Hui, X. Li, Chin. Phys. Soc. 18 (2009) 7.
[12] W. Maier, G.Z. Meier, Naturforschung 16 (1961) 262.
[13] G. Saitoh, M. Satoh, E. Hasegawa, Mol. Cryst. Liq. Cryst. 301 (1997) 13.
[14] M. Klasen, M. Bremer, A. Gäotz, S. Manabe, S. Naemura, K. Tarumi, Jpn. J. Appl. Phys. 37 (1998) 945.
[15] A. Fujita, M. Ushioda, H. Takeuchi, T. Inukai, D. Demus, Mol. Cryst. Liq. Cryst. 331 (1999) 305.
[16] M. Bremer, K. Tarumi, Adv. Mater. 5 (1993) 842.
[17] D. Demus, T. Inukai, Liq. Cryst. 26 (1999) 1257.
[18] D. Demus, T. Inukai, Mol. Liq. Cryst. 400 (2003) 39.
[19] E.M. Aver'yanov, Phys. Solid State 56 (2014) 1058.
[20] M. O'Neill, S. Kelly, Adv. Mater. 23 (2011) 566.
[21] J. Harden, M. Chambers, R. Verduzco, P. Luchette, J.T. Gleeson, S. Sprunt, A. Jakli, Appl. Phys. Lett. 96 (2010) 102907.
[22] H. Chen, W. Lee, Opt. Rev. 12 (2005) 223.
[23] P. van der Schoot, V. Popa-Nita, S. Kralj, J. Phys. Chem. B 112 (2008) 4512.
[24] R. Won, Nat. Photon 5 (2011) 133.
[25] J. Clapper, S. Iverson, C. Guymon, Biomacromolecules 8 (2007) 2104.
[26] C. Mock-knoblauch, O.S. Enger, U.D. Schalkowsky, SID Dig. (2006) 1673.
[27] A.P. Kovshika, E.S. Krainyukova, S.A. Kovshika, A.A. Knyazevb, Yu.G. Galyametdinovb, E.I. Ryumtsev, Opt. Spectrosc. 116 (2014) 56.
[28] S. Sivakumar, K.L. Wark, J.K. Gupta, N.L. Abbott, F. Caruso, Adv. Funct. Mater. 19 (2009) 2260.
[29] C. Jang, L. Cheng, C. Olsen, N. Abbott, Nano Lett. 6 (2006) 1053.
[30] C. Muller-goymann, Eur. J. Pharm. Biopharm. 58 (2004) 343.
[31] L. Sagalowicz, M. Leser, H. Watzke, M. Michel, Trends Food Sci. Technol. 17 (2006) 204.
[32] J.P.F. Lagerwall, G. Scalia, Curr. Appl. Phys. 12 (2012) 1387.
[33] M. Urbanski, J. Mirzaei, T. Hegmann, H.S. Kitzerow, ChemPhysChem 15 (2014) 1395.
[34] J.E. Kim, T.H. Han, S.H. Lee, J.Y. Kim, Chi Won Ahn, Je Moon Yun, Sang Ouk Kim, Angew. Chem. Int. Ed. 50 (2011) 3043.
[35] J.Y. Kim, S.O. Kim, Nat. Mater. 32 (2014) 325.
[36] S. Zhoua, A. Sokolovb, O.D. Lavrentovicha, I.S. Aranson, PNAS 111 (2014) 1265.
[37] S.M. Kelly, M. O'Neill, Liquid Crystals, Display and Laser Materials, vol. 7, Academic Press, U.K., 2000. Chapter 1.
[38] G.W. Gray, K.J. Harrison, J.A. Nash, Electron. Lett. 9 (1973) 130.
[39] L.A. Karamysheva, E.I. Kovshev, A.I. Pavluchenko, K.V. Roitman, V.V. Titov, S.I. Torgova, M.F. Grebyonkin, Mol. Cryst. Liq. Cryst. 67 (1981) 241.
[40] A. Boller, M. Cereghetti, M. Schadt, H. Scherrer, Mol. Cryst. Liq. Cryst. 42 (1977) 1225.
[41] S. Kumar, A.S. Faponle, P. Barman, A.K. Vardhaman, C.V. Sastri, D. Kumar, S.P. de Visser, J. Am. Chem. Soc. 136 (2014) 17102.
[42] A.K. Vardhaman, P. Barman, S. Kumar, C.V. Sastri, D. Kumar, S.P. de Visser, Angew. Chem. Int. Ed. 52 (2013) 12288.
[43] D. Umadevi, S. Panigrahi, G.N. Sastry, Acc. Chem. Res. 47 (2014) 2574.
[44] A.D. Becke, J. Chem. Phys. 1993 (98) (1993) 5648.
[45] C. Lee, W. Yang, R.G. Parr, Phys. Rev. B 37 (1988) 785.
[46] P.J. Hay, W.R. Wadt, J. Chem. Phys. 82 (1985) 270.
[47] M.J. Frisch, G.W. Trucks, H.B. Schlegel, G.E. Scuseria, M.A. Robb, J.R. Cheeseman, G. Scalmani, V. Barone, B. Mennucci, G.A. Petersson, H. Nakatsuji, M. Caricato, X. Li, H.P. Hratchian, A.F. Izmaylov, J. Bloino, G. Zheng, J.L. Sonnenberg, M. Hada, M. Ehara, K. Toyota, R. Fukuda, J. Hasegawa, M. Ishida, T. Nakajima, Y. Honda, O. Kitao, H. Nakai, T. Vreven, J.A. Montgomery Jr., J.E. Peralta, F. Ogliaro, M. Bearpark, J.J. Heyd, E. Brothers, K.N. Kudin, V.N. Staroverov, T. Keith, R. Kobayashi, J. Normand, K. Raghavachari, A. Rendell, J.C. Burant, S.S. Iyengar, J. Tomasi, M. Cossi, N. Rega, J.M. Millam, M. Klene, J.E. Knox, J.B. Cross, V. Bakken, C. Adamo, J. Jaramillo, R. Gomperts, R.E. Stratmann, O. Yazyev, A.J. Austin, R. Cammi, C. Pomelli, J.W. Ochterski, R.L. Martin, K. Morokuma, V.G. Zakrzewski, G.A. Voth, P. Salvador, J.J. Dannenberg, S. Dapprich, A.D. Daniels, O. Farkas, J.B. Foresman, J.V. Ortiz, J. Cioslowski, D.J. Fox, Gaussian-09, Revision B.01, Gaussian Inc., Wallingford CT, 2010.
[48] Y. Zhao, D.G. Truhlar, Theor. Chem. Acc. 120 (2008) 215.
[49] U. Yadava, M. Singh, M. Roychaudhury, Comput. Theor. Chem. 977 (2011) 134.
[50] S. Shaik, S.P. de Visser, D. Kumar, J. Am. Chem. Soc. 126 (2004) 11746.
[51] S.P. de Visser, J. Phys. Chem. A 109 (2005) 11050.
[52] S.P. de Visser, Inorg. Chem. 45 (2006) 9551.
[53] Rong-Zheng Liao, Jian-Guo Yu, F. Himo, J. Phys. Chem. B 114 (2010) 2533.
[54] U. Yadava, D.K. Gupta, M. Roychoudhury, J. Mol. Liq. 156 (2010) 187.
[55] A. Sorkin, D.G. Truhlar, E.A. Amin, J. Chem. Theory Comput. 5 (2009) 1254.
[56] F. Jensen, Introduction to Computational Chemistry, second ed., John Wiley & Sons Ltd, UK, 2006. Chapter 10, p. 315.

ChemPubSoc Europe

DOI: 10.1002/chem.201500329

CHEMISTRY A European Journal Full Paper

Reaction Mechanisms |*Hot Paper*|

Drug Metabolism by Cytochrome P450 Enzymes: What Distinguishes the Pathways Leading to Substrate Hydroxylation Over Desaturation?

Li Ji,[a] Abayomi S. Faponle,[b] Matthew G. Quesne,[b] Mala A. Sainna,[b] Jing Zhang,[a] Alicja Franke,[c] Devesh Kumar,[e] Rudi van Eldik,[c, d] Weiping Liu,*[a] and Sam P. de Visser*[b]

Abstract: Cytochrome P450 enzymes are highly versatile biological catalysts in our body that react with a broad range of substrates. Key functions in the liver include the metabolism of drugs and xenobiotics. One particular metabolic pathway that is poorly understood relates to the P450 activation of aliphatic groups leading to either hydroxylation or desaturation pathways. A DFT and QM/MM study has been carried out on the factors that determine the regioselectivity of aliphatic hydroxylation over desaturation of compounds by P450 isozymes. The calculations establish multistate reactivity patterns, whereby the product distributions differ on each of the spin-state surfaces; hence spin-selective product formation was found. The electronic and thermochemical factors that determine the bifurcation pathways were analysed and a model that predicts the regioselectivity of aliphatic hydroxylation over desaturation pathways was established from valence bond and molecular orbital theories. Thus, the difference in energy of the O–H versus the O–C bond formed and the π-conjugation energy determines the degree of desaturation products. In addition, environmental effects of the substrate binding pocket that affect the regioselectivities were identified. These studies imply that bioengineering P450 isozymes for desaturation reactions will have to include modifications in the substrate binding pocket to restrict the hydroxylation rebound reaction.

Introduction

The cytochrome P450s (P450s) are key drug metabolizing enzymes in the human body,[1] and are widely distributed in living organisms, such as eukaryotic animals, but also in plants, fungi and bacteria. As of January 2015, more than 20000 different sequences had been identified, making the P450s one of the major biological enzyme classes.[2] In the human body, P450s are predominantly found in the liver, where they catalyse the biodegradation of xenobiotics but are also involved in the biosynthesis of hormones.[3] As such the P450s have multiple functions in the body, which also shows their versatility in substrate activation. For instance, the $P450_{BM3}$ subclass hydroxylates long-chain fatty acids,[4] and has a substrate binding pocket that accommodates long and thin substrates. By contrast, $P450_{cam}$ is a bacterial isozyme that regioselectively hydroxylates camphor at the carbon-5 position and has a fit-for-purpose substrate binding pocket.[5] A key drug metabolizing P450 isozyme is $P450_{2D6}$, which has a more open substrate binding pocket and can activate a large range of different substrate shapes and sizes. As P450 isozymes are highly efficient in substrate activation, they have gained interest from the biotechnology industry for the regioselective and/or stereospecific activation of substrates.[6] Despite decades of extensive scientific research into P450 chemistry, there are still major gaps in our understanding of its reactivity and activity, in particular related to the metabolism of drug molecules and xenobiotics, which is important for drug development and the pharmaceutical industry.

The name cytochrome P450 derives from the fact that the CO bound heme complex has an absorption band at 450 nm.[7] Their heme active site is linked to the protein via a thiolate linkage of a cysteinate residue covalently bound to the iron

[a] *Dr. L. Ji, J. Zhang, Prof. Dr. W. Liu*
College of Environmental and Resource Sciences
Zhejiang University, Yuhangtang Road 866, Hangzhou 310058 (China)
E-mail: wliu@zju.edu.cn

[b] *A. S. Faponle, Dr. M. G. Quesne, M. A. Sainna, Dr. S. P. de Visser*
Manchester Institute of Biotechnology and School of
Chemical Engineering and Analytical Science
The University of Manchester, 131 Princess Street
Manchester M1 7DN (UK)
E-mail: sam.devisser@manchester.ac.uk

[c] *Dr. A. Franke, Prof. Dr. R. van Eldik*
Inorganic Chemistry, Department of Chemistry and Pharmacy
University of Erlangen-Nuremberg
Egerlandstrasse 1, 91058 Erlangen (Germany)

[d] *Prof. Dr. R. van Eldik*
Faculty of Chemistry, Jagiellonian University
Ingardena 3, 30-060 Krakow (Poland)

[e] *Dr. D. Kumar*
Department of Applied Physics, School for Physical Sciences
Babasaheb Bhimrao Ambedkar University, Vidya Vihar
Rai Bareilly Road, Lucknow 226 025 (India)

Supporting information for this article is available on the WWW under http://dx.doi.org/10.1002/chem.201500329.

© 2015 Wiley-VCH Verlag GmbH & Co. KGaA, Weinheim

centre,[8] while the substrate binding pocket varies in shape and size for the different P450 isozymes. As an example we show in Figure 1 the active site of $P450_{2C19}$ with substrate warfarin bound as taken from the 4GQS protein databank (PDB) file.[9] The heme is linked to the protein through an iron–thiolate linkage with Cys435 and *trans* to this ligand the substrate (warfarin) binds.

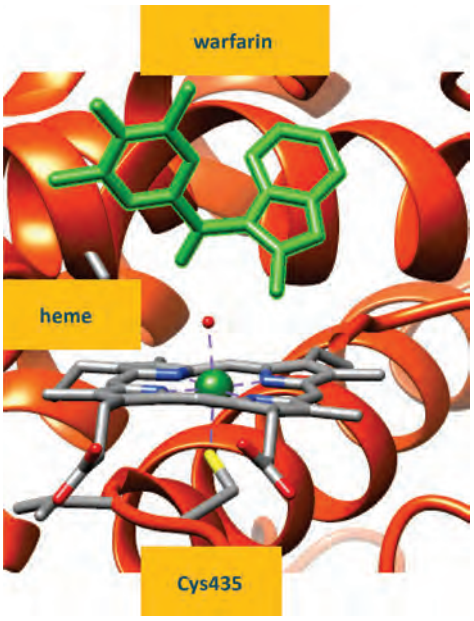

Figure 1. Extract of the active site of $P450_{2C19}$ as taken from the 4GQS PDB file.

The active species of P450 enzymes is an iron(IV)–oxo heme cation radical species called Compound I (Cpd I).[10] Due to its transient nature, Cpd I is short-lived and difficult to study with experimental means and as a consequence many details of its catalytic mechanism with substrates are unknown. The most common reaction mechanism performed by the P450s is aliphatic hydroxylation of substrates,[11] which was experimentally revealed as a stepwise process leading to alcohol product complexes.[12] Computational modelling confirmed the general mechanism and showed that the oxidation actually contains two close-lying spin states that lead to two-state reactivity patterns, each with an individual rate constant of the reaction.[13] Moreover, the two-state reactivity pattern also predicted that the lifetime of the radical intermediate could lead to a bifurcation of the potential energy profile, thereby generating, for instance, rearrangement patterns on one spin-state surface but not on the other.[14]

A key reaction mechanism in P450 chemistry with great relevance to drug metabolism is the desaturation of aliphatic groups to form olefins. As shown in Scheme 1 desaturation is a reaction mechanism that shows similarities to aliphatic hydroxylation, whereby both processes start with an initial hydrogen atom abstraction. However, thereafter the reaction bifurcates into two possible product channels: one giving OH rebound to form alcohol products (aliphatic hydroxylation) and the other leading to a second hydrogen atom abstraction to give an olefin and water (desaturation). Although the basic mechanism of substrate desaturation has been studied previously,[15] the origin and consequences of the bifurcation pathways in P450 catalysis are currently unknown and no predictive model exists that gives product distributions as a function of substrate chemical properties.

Several drug molecules have been shown to produce desaturation metabolites by P450 enzymes. Namely, valproic acid, an antiepileptic drug, is converted by P450 enzymes to form both alcohol and olefin products.[16] Another example is ethylcarbamate,[17] that in a reaction with $P450_{2E1}$ enzymes leads to a small amount of vinyl carbamate as a precursor to its epoxide.[18] The latter is considered the ultimate carcinogen[19] and its biosynthesis requires an essential desaturation step. Over the years a range of substrates of P450 isozymes have been identified that are desaturated to form olefins, including lauric acid,[20] but also a step in the biosynthesis of ergosterol includes a desaturation.[21]

Clearly, the mechanistic pathways surrounding drug metabolism by the P450s produce a large versatility of product patterns and currently it is not clear why certain substrates lead to desaturation, whereas others solely give hydroxylation products. To gain insight into the origin of the regioselectivity of desaturation versus hydroxylation processes by P450 enzymes, we decided to carry out a comprehensive computational study that includes density functional theory (DFT) modelling, quantum mechanics/molecular mechanics (QM/MM) and valence

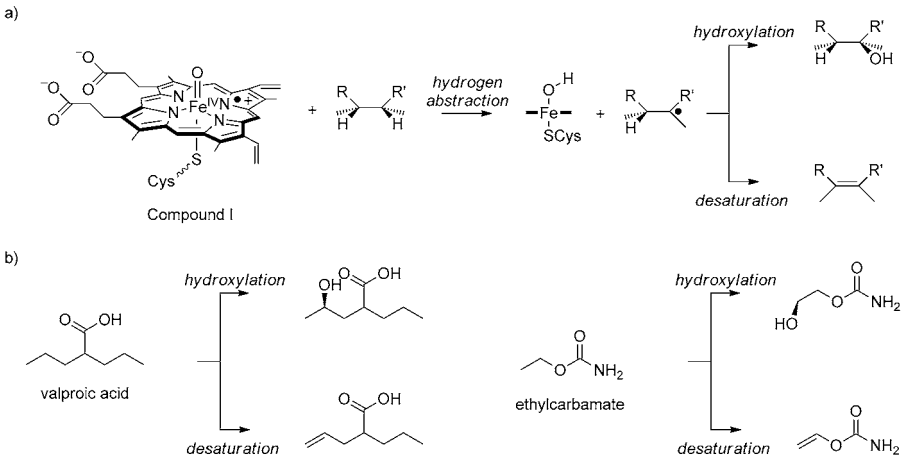

Scheme 1. a) Competitive hydroxylation and desaturation metabolism pathways of drug molecules by P450 Cpd I. b) Reaction products observed for valproic acid and ethylcarbamate.

© 2015 Wiley-VCH Verlag GmbH & Co. KGaA, Weinheim

bond (VB) theory. The overall study gives an electronic structure description on the metabolism of a variety of drug molecules and enables us to provide a predictive pattern that anticipates desaturation versus hydroxylation product distributions. Our studies explain the experimentally observed bifurcation reactions and may be used to develop computer-aided toxic risk assessment of potential carcinogens resulting from desaturation reactions catalysed by P450 isozymes.

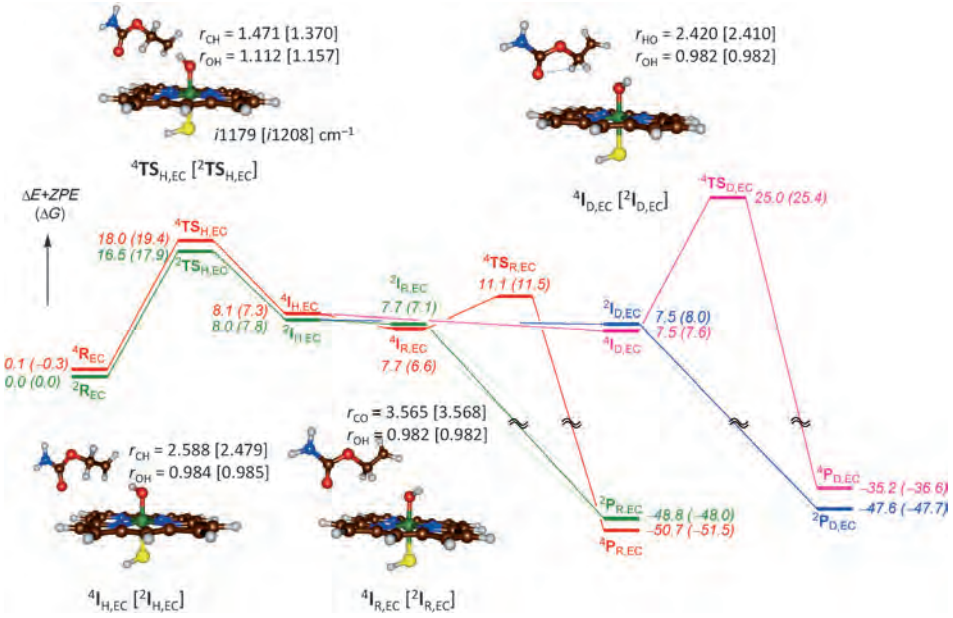

Figure 2. Potential energy profile of ethylcarbamate activation by ^{4,2}Cpd I of P450 as calculated with DFT. Energies are given in kcal mol^{-1} and are calculated at UB3LYP/BSII//UB3LYP/BSI level of theory with *ZPE* and solvent corrections included. Values in parenthesis are free energies in solvent. Optimized geometries give bond lengths in Å and the imaginary frequency in the transition states in wave numbers.

Results and Discussion

DFT model reactions

Before going into detail of the mechanism of drug metabolism by P450 enzymes, let us first go through a typical reaction mechanism of substrate activation leading to desaturation and hydroxylation products by taking ethylcarbamate (EC) as an example. Scheme 2 displays the calculated reaction mechanisms of EC activation by Cpd I of P450 and the bifurcation mechanism leading to desaturation and hydroxylation products.

We calculated the reaction between Cpd I and ethylcarbamate, as shown in Figure 2, starting from a reactant complex (^{4,2}**R**$_{EC}$), which exists in close-lying doublet and quartet spin states, both with electronic configuration $\delta_{x^2-y^2}{}^2\pi^*_{xz}{}^1\pi^*_{yz}{}^1a_{2u}{}^1$. Attack of the oxo group of Cpd I on the substrate leads to a hydrogen atom abstraction via a transition state ^{4,2}**TS**$_{H,EC}$ to form a radical intermediate (^{4,2}**I**$_{H,EC}$) with electronic configuration $\delta_{x^2-y^2}{}^2\pi^*_{xz}{}^1\pi^*_{yz}{}^1a_{2u}{}^2\ \phi_{Rad}{}^1$. During the lifetime of the radical intermediate it can isomerize to structures ^{4,2}**I**$_{D,EC}$, whereby the C–H group of the substrate forms a hydrogen-bonding interaction with the oxygen atom of the OH group as a precursor to the second hydrogen atom abstraction step via transition state ^{4,2}**TS**$_{D,EC}$ to form desaturated products ^{4,2}**P**$_{D,EC}$. The alternative mechanism from ^{4,2}**I**$_{H,EC}$ gives an isomerization to form the pro-hydroxylation radical intermediate ^{4,2}**I**$_{R,EC}$, where the radical is aligned to the oxygen atom for rebound via transition state ^{4,2}**TS**$_{R,EC}$ to give the alcohol product complexes ^{4,2}**P**$_{R,EC}$. Our calculations were focused on establishing whether isomerization barriers exist from **I**$_H$ to **I**$_D$ and **I**$_R$, and what the factors are that determine the height of these barriers and consequently the regioselectivity of the reaction.

As shown in Figure 2, the hydrogen atom abstraction step is endergonic by $\Delta G^{\neq} = 19.4$ (17.9) kcal mol^{-1} in the quartet (doublet) spin states, respectively. Addition of dispersion corrections to the calculated relative energies lowers ^{4,2}**TS**$_{H,EC}$ in energy by about 4 kcal mol^{-1}, which is in accord with analogous previous findings for transition metal complexes.[22] The hydrogen atom abstraction transition states are characterized by an almost linear O–H–C configuration and a large imaginary frequency (HS: *i*1179 cm^{-1}; LS: *i*1208 cm^{-1}), and consequently a considerable kinetic isotope effect (KIE) for the reaction may be expected.[23]

We then investigated the OH rebound to form alcohol products and the second hydrogen atom abstraction to give desaturation products. We propose this to happen (Scheme 2) by an initial isomerization of the radical intermediate from ^{4,2}**I**$_{H,EC}$ to ^{4,2}**I**$_{R,EC}$, which sets up the molecular orientation for the OH rebound leading to the 2-hydroxyethyl-carbamate product. Similarly to previous studies,[24]

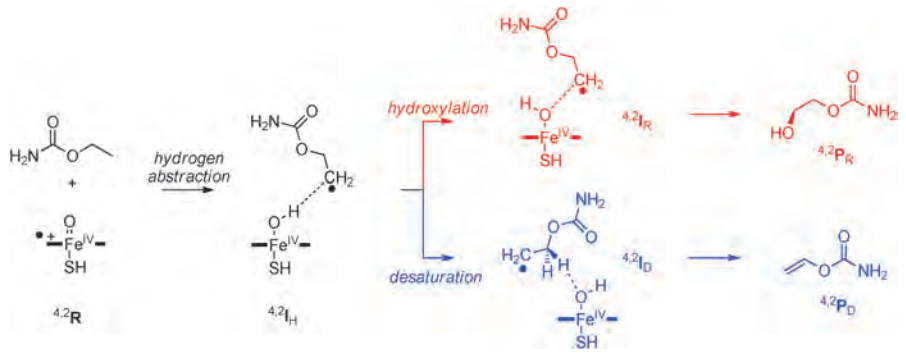

Scheme 2. Reaction mechanism of ethylcarbamate activation by Cpd I of P450.

© 2015 Wiley-VCH Verlag GmbH & Co. KGaA, Weinheim

a small but significant rebound barrier ($\Delta G = 4.9$ kcal mol^{-1}) is found on the quartet spin surface, while the doublet spin pathway is barrier free. Dispersion corrections lower the rebound barriers by about 1 kcal mol^{-1}, which is a significant smaller change than that found for the hydrogen atom abstraction step. The radical rebound pathway from $^{4,2}\mathbf{I}_{H,EC}$ is exergonic by $\Delta G = 58.8$ (55.8) kcal mol^{-1} on the quartet (doublet) spin state surfaces as expected for the formation of a stable alcohol product complex.

The alternative isomerization pathway from $^{4,2}\mathbf{I}_{H,EC}$, leads to a substrate rotation to form $^{4,2}\mathbf{I}_{D,EC}$, whereby the oxygen atom of the OH group is aligned with a hydrogen atom of the substrate to enable a second hydrogen atom abstraction. Note that the difference in orientation between $^{4,2}\mathbf{I}_{R,EC}$ and $^{4,2}\mathbf{I}_{D,EC}$ is similar to those reported for a synthetic manganese–hydroxo porphyrin complex.[25] The DFT calculations give negligible isomerization barriers between structures $\mathbf{I}_H$, $\mathbf{I}_R$ and $\mathbf{I}_D$, however, as shown below the effect of the protein changes this dramatically.

The doublet spin radical intermediate $^{2}\mathbf{I}_{D,EC}$ collapses to the desaturation product complex virtually barrier-free, whereas the quartet spin complex $^{4}\mathbf{I}_{D,EC}$ encounters a large activation barrier ($^{4}\mathbf{TS}_{D,EC}$) of $\Delta G^{\ddagger} = 17.8$ kcal mol^{-1} instead. Similarly to the above-mentioned rebound process, the activation barrier only decreases by 1.5 kcal mol^{-1} after dispersion corrections are added. The large $^{4}\mathbf{TS}_{D,EC}$ barrier implicates that desaturation is an unlikely process on the quartet spin-state surface. Moreover, the difference in kinetics between the quartet and doublet spin desaturation routes suggests that the doublet spin state surface is the only viable pathway responsible for vinyl carbamate formation. Consequently, the regioselectivity of desaturation versus hydroxylation is a spin-selective reaction process, whereby the high-spin pathway gives solely hydroxylation products whereas a mixture of products may be expected on the low-spin surface instead.

Experimental reports on ethylcarbamate activation by $P450_{2E1}$ isozymes reveal only a small but significant proportion of biotransformation leading to desaturation reactions.[18] The DFT calculations presented in Figure 2, therefore, are in line with these experimental product distributions of hydroxylation versus desaturation, which predict a mixture of products. Moreover, when we look at the driving force for desaturation versus hydroxylation, both pathways on the low-spin surface have similar exergonicity, that is, $\Delta G = -48.0$ versus -47.7 kcal mol^{-1}. As such, P450s should exhibit mixed hydroxylase/desaturase activity toward EC as indeed observed experimentally.

To find a general trend in desaturation versus hydroxylation regioselectivity preferences, we did a further set of calculations using alternative substrates that should give the chemical extremes of the two processes. In Figure 3 we display studies on desaturation versus hydroxylation mechanisms using valproic acid (VA), ethane (ET) and 9,10-dihydroanthracene (DHA) as substrates. Thus, experimentally, DHA in a reaction with P450 enzymes is known to lead to anthracene as major product, whereas ethane leads solely to alcohol products instead. For all chemical systems the full potential energy profile like the one shown in Figure 2 is calculated on both spin-state surfaces, and mechanisms are analogous to those reported above; for details see the Supporting Information. Thus, for valproic acid as a substrate the DFT calculations predict mixed desaturase/hydroxylase activity on a low-spin surface (Figure S1 in the Supporting Information). Key optimized geometries of the hydrogen atom abstraction transition states are given in Figure 3. In general, all substrates reveal the same catalytic mechanism as calculated above and previously reported in the literature[13,26] with a rate determining hydrogen-atom abstraction leading to a radical intermediate. Differences, however, are found for the relative energies for radical rebound versus desaturation.

On the quartet spin-state surface a small but significant radical rebound barrier exists (0.8–4.9 kcal mol^{-1}), whereas all low-spin rebound pathways are essentially barrier-free. Details of the rebound and desaturation barriers for all substrates are given in Table 1. By contrast to the radical rebound process, the desaturation barriers ($\mathbf{TS}_D$) show considerably more variation in relative energies. Similarly to the ethylcarbamate mechanism from Figure 2, a substantial desaturation barrier of 4.2–35.6 kcal mol^{-1} is required for valproic acid, ethane and DHA desaturation on the quartet spin state. Note as well that there is a significant desaturation barrier on the low-spin pathway for ethane, which is further evidence that desaturation is an unlikely process for a substrate like ethane.

The barrier heights displayed in Table 1 implicate competitive hydroxylation and desaturation on the doublet spin-state surface for all substrates except ethane. On the high-spin surface, on the other hand, there appears to be a clear preference for radical rebound. This is similar to previous studies on the

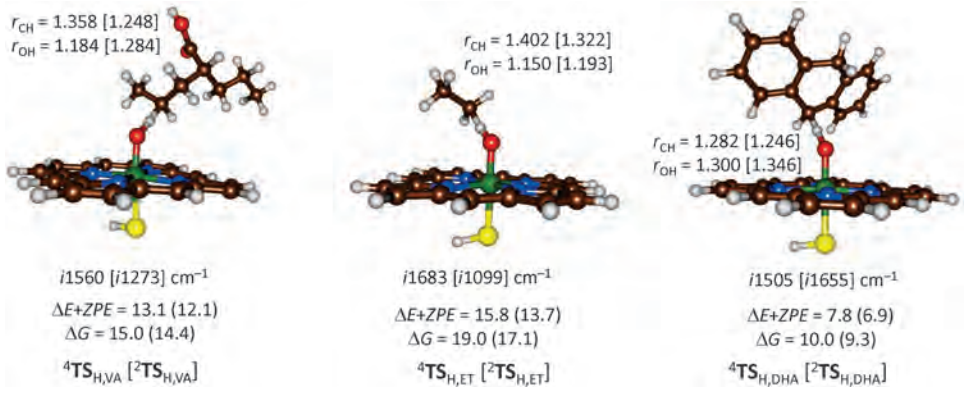

Figure 3. Optimized geometries of hydrogen-atom abstraction transition states of VA, ET and DHA by ^{4,2}CpdI of P450 as calculated with DFT. Bond lengths are in Å, the imaginary frequency is in wave numbers and (free) energies are given in kcal mol^{-1} and are calculated at UB3LYP/BSII//UB3LYP/BSI level of theory with *ZPE* and solvent corrections included.

© 2015 Wiley-VCH Verlag GmbH & Co. KGaA, Weinheim

Table 1. Free energies of activation of hydrogen-atom abstraction, rebound and desaturation barriers and the overall free energies for the hydroxylation and desaturation reactions.[a]

Substrate	TS_H[b]	TS_R[c]	TS_D[d]	P_R/P_D[b]
LS				
ethylcarbamate	17.9	0.0	0.0	−48.0/−47.7
valproic acid	14.4	0.0	0.0	−51.5/−49.1
ethane	17.1	0.0	14.7	−49.1/−43.0
DHA	9.3	0.0	0.0	−47.1/−61.5
HS				
ethylcarbamate	19.4	4.9	17.8	−51.5/−36.6
valproic acid	15.0	1.3	23.0	−56.0/−49.7
ethane	19.0	1.7	35.6	−51.9/−32.3
DHA	10.0	0.8	4.2	−50.8/−64.7

[a] ΔG values at 298 K in kcal mol^{-1}. [b] ΔG relative to **R**. [c] ΔG relative to $\mathbf{I}_H$. [d] ΔG relative to $\mathbf{I}_D$.

regioselectivity of substrate epoxidation versus suicidal complex formation in olefin activation by P450 isozymes that was predicted to only lead to by-products on the high-spin surface.[14] It should be noted, however, that the driving force for hydroxylation as compared to desaturation is larger for EC, VA and ethane as substrates, whereas it is favourable for desaturation for DHA. Thermodynamically, therefore, DHA should preferentially undergo the desaturation pathway, in accord with experimental studies on iron(IV)–oxo porphyrins that observed anthracene as the major product.[27] It seems the precursor leading to the aromatic species on the desaturation pathway gives the highest desaturase activity, because of its increased resonance stabilization of the benzene product.[28] By contrast, VA gives a thermodynamically dominant hydroxylase activity in analogy to EC. This is in agreement with experiment, where the ratio of desaturated to hydroxylated metabolites produced during P450-mediated VA activation is 1:37 for $P450_{2B1}$, and 1:2 for $P450_{4B1}$.[16c] Regardless of the external factors, we conclude that the P450-catalyzed desaturation reaction can occur, but is competitive with hydroxylation reactions on the low-spin state. However, as seen in the P450-mediated VA case, the proportion of desaturated metabolites also depends on the P450 isoforms and hence the substrate binding pocket must incur a significant effect on the regioselectivity of the reaction.

To further assess the calculated results, we estimated kinetic isotope effects for the replacement of the transferring hydrogen atom by deuterium using the semi-classical Eyring equation as well as the tunnelling-corrected Wigner isotope effect.[29] We re-evaluated the free energy and imaginary frequency for the hydrogen-atom abstraction step for $[D_2]$VA-4,4 and based on a comparison with the fully hydrogenated system establish a KIE = 6.4 (8.4) using the Eyring model and a KIE = 7.2 (12.1) at the doublet (quartet) spin states with tunnelling corrections included. These values compare well with the experimentally determined KIE value of 5.58 for the same substrate.[16b]

QM/MM studies of desaturation

As follows from the DFT model calculations in the previous section, both the radical rebound and second hydrogen-atom abstraction processes are barrierless on the doublet spin-state surface, whereas a substantial barrier on the quartet spin state surface is found. This implies that the mechanistic switch from substrate hydroxylation to desaturation by P450-catalyzed drug metabolism reactions is not kinetically controlled by the properties of the oxidant and/or substrate, but must be affected—at least in part—by external influences, such as the substrate binding into the substrate binding pocket. Therefore, we followed up our study by a set of QM/MM calculations on a system that is known to desaturate its natural substrate. These calculations take the size and shape of the substrate binding pocket into consideration and should give a realistic picture of the regioselectivity switch from hydroxylation to desaturation.

The $OleT_{JE}$ P450 isozyme binds long-chain fatty acids, such as eicosanoic acid (EA), and converts them to olefins, CO_2 and water on an iron(IV)–oxo heme cation radical system. We calculated the potential energy landscape as obtained by QM/MM for the hydrogen-atom abstraction by Cpd I from the C^{β}–H group of eicosanoic acid. The pathways leading to desaturation and hydroxylation starting from the radical intermediate ($^4\mathbf{I}_{H\beta,EA}$) are given in Figure 4. The hydrogen-atom abstraction barrier is low and of the same order of magnitude as those reported above for the DFT models as well as to previous hydrogen-atom abstraction barriers from the literature.[13,24,26]

The hydrogen-atom abstraction leads, as above, to an iron(IV)–hydroxo intermediate and substrate radical ($^{4,2}\mathbf{I}_{H\beta,EA}$) with electronic configuration $\delta^2\pi^*_{xz}{}^1\pi^*_{yz}{}^1\ \phi_{Sub}{}^1$. These structures have the O–H–C atoms aligned with an angle close to linearity. Subsequently, we investigated the pathways leading to desaturation and hydroxylation. We initially ran stepwise geometry

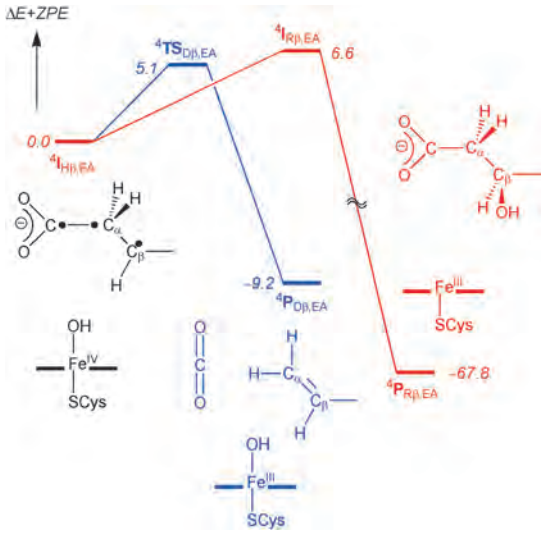

Figure 4. Potential energy profile of eicosanoic acid activation by ^{4}Cpd I of P450 as calculated with QM/MM. Energies are given in kcal mol^{-1} and are calculated at UB3LYP/BSIV//UB3LYP/BSIII level of theory with *ZPE* corrections included relative to $^4\mathbf{I}_{H\beta,EA}$.

© 2015 Wiley-VCH Verlag GmbH & Co. KGaA, Weinheim

scans, whereby one degree of freedom (the reaction coordinate) was fixed and all other parameters were minimized. However, all local minima and maxima of the scans were subjected to geometry optimizations and characterized with a frequency. The geometry of $\mathbf{TS}_{H\beta,EA}$ (see the Supporting Information) is analogous to the hydrogen atom abstraction barriers of ethylcarbamate, valproic acid and ethane, where long C–H and short H–O distances are found to be 1.33 and 1.18 Å, respectively. At the same time, the Fe–O bond elongates from about 1.602 Å in $\mathbf{R}_{EA}$ to 1.730 Å in $\mathbf{TS}_{H\beta,EA}$, which is indicative of electron rearrangement within the Fe–O bond (see below).

The energy landscape starting from $^4\mathbf{I}_{H\beta,EA}$ is shown in Figure 4. We located a small barrier ($^4\mathbf{TS}_{D\beta,EA}$) of $\Delta E + ZPE = 5.1$ kcal mol^{-1} for desaturation and the formation of a terminal olefin and CO_2 as reaction products ($^4\mathbf{P}_{D\beta,EA}$) with a modest exothermicity of -9.2 kcal mol^{-1}. Optimized geometries of local minima are shown in Figure 5. The desaturation transition state results in elongation of the OOC–$C_\alpha H_2 C_\beta$ bond to 1.874 Å with an imaginary frequency for the C–C_α stretch vibration of *i*541.3 cm^{-1}. This results in heterolytic splitting of the C–C bond and the formation of a double bond between C_α and C_β by pairing of the radical on C_β with the electron from the C–C_α bond. At the same time an electron is transferred from the carboxylate group to the iron(IV)–hydroxo group to form an iron(III)–hydroxo complex and enables the carboxylate group to leave as CO_2 and desaturate the fatty acid to a terminal olefin. In the iron(III)–hydroxo complex the metal has $\delta^2\pi^*_{xz}{}^1\pi^*_{yz}{}^1\sigma^*_{z^2}{}^1$ orbital occupation, whereby the latter orbital is antibonding along the S–Fe–O axis and hence elongates the Fe–S and Fe–O distances, as seen in Figure 5.

The alternative pathway starting with a rotation of the OH group around the Fe–O axis is, in contrast to the DFT calculations reported above, endothermic by 6.6 kcal mol^{-1}. Analysis of the chemical structure of $^4\mathbf{I}_{R\beta,EA}$ shows stereochemical clashes of the OH proton with a proline (Pro246) residue that blocks the rotation process.

In addition, a network of water molecules and polar groups force the iron(IV)–hydroxo group in $^4\mathbf{I}_{H\beta,EA}$ in a tight conformation. Several water molecules (three are shown in Figure 5) bridge the iron(IV)–hydroxo to the salt bridge of Arg245 with the carboxylate group of the substrate, but also links the water network to the propionate side chains of the heme. By contrast, the substrate binding pocket of $P450_{cam}$ is very tight and has few water molecules present.[8] Clearly, the subtle network of hydrogen bonding interactions affects the regioselectivity of the reaction and destabilizes the OH rebound pathway. A geometry scan for the C^α–COO dissociation in the substrate and subsequent transition-state characterization leads to release of CO_2 and the formation of olefin as shown in Figure 4. This pathway has a lower barrier than the alternative OH rotation and therefore, the desaturation degree of freedom will be C–C cleavage here rather than OH rotation. The regioselectivity of hydroxylation versus desaturation, therefore, in $OleT_{JE}$ is guided by the hydrogen-bonding network in the substrate binding pocket that destabilizes the rebound pathways that are barrierless in the gas-phase and in model complexes. This is the first example of a P450 isozyme that has accommodated its substrate binding pocket with polar residues to enable a substrate desaturation reaction.

Valence bond rationalization of rebound and desaturation mechanisms

To understand the origin of the regioselectivity of desaturation over hydroxylation, we set up valence bond (VB) curve-crossing diagrams that rationalize the kinetics of the reactions. These curve-crossing diagrams were used previously to rationalize oxygen-atom transfer reactions to heme and nonheme metal–oxo and metal–nitrido complexes.[30] Figure 6 shows the VB curve-crossing diagrams for the radical rebound and desaturation pathways leading to the competitive hydroxylation and desaturation products. These curve-crossing diagrams

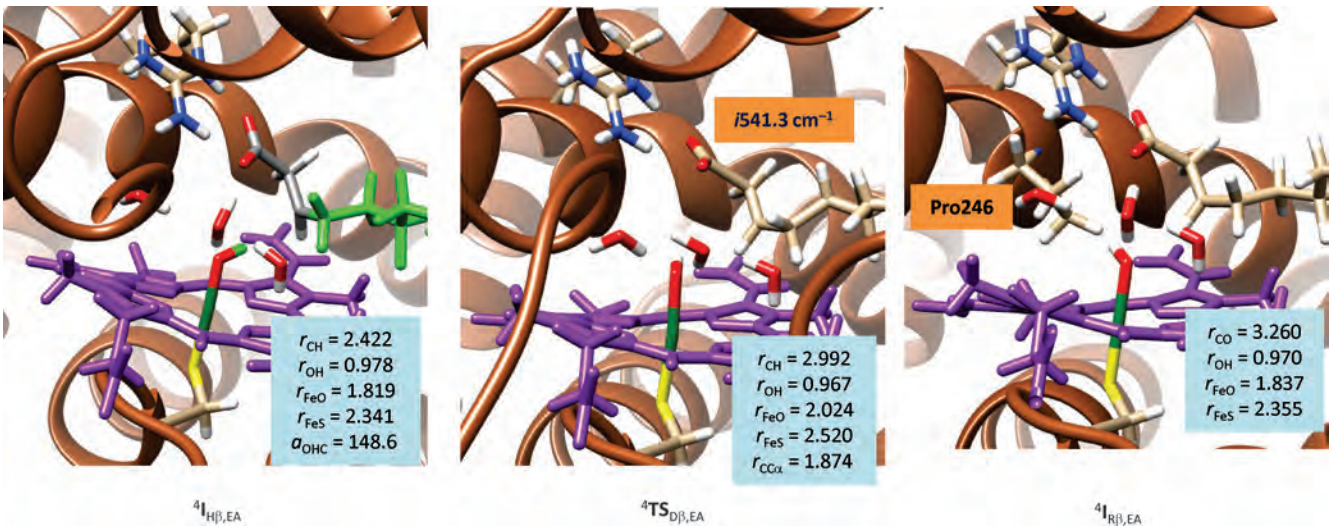

Figure 5. QM/MM optimized geometries (B3LYP/Charmm) of local minima along the reaction profile from Figure 4. Bond lengths (*r*) are in Å, angles (*a*) in degrees and the imaginary frequency in the transition state in wave numbers.

© 2015 Wiley-VCH Verlag GmbH & Co. KGaA, Weinheim

start on the left-hand side with the radical intermediates, that is, $^{4,2}\mathbf{I}_H$, which are described as an iron(IV)–hydroxo (porphyrin) complex with a nearby radical. The wave function Ψ_I represents structure $^{4,2}\mathbf{I}_H$ and corresponds to an electronic configuration $\delta_{x^2-y^2}{}^2\pi^*_{xz}{}^1\pi^*_{yz}{}^1\ \phi_{Rad}{}^1$ with two unpaired electrons along the Fe–O bond and a third on the substrate in the ϕ_{Rad} orbital. On the bottom right-hand side of each Figure the product complexes are drawn, which are either alcohol products or olefin products. The product complexes $^{4,2}\mathbf{P}_R$ and $^{4,2}\mathbf{P}_D$ have wave function Ψ_P and Ψ_D, respectively, whereby the doublet spin states have configuration $\delta_{x^2-y^2}{}^2\pi^*_{xz}{}^2\pi^*_{yz}{}^1$ and the quartet spin states $\delta_{x^2-y^2}{}^2\pi^*_{xz}{}^1\pi^*_{yz}{}^1\sigma^*_{z^2}{}^1$. In a curve-crossing diagram, as displayed in Figure 6, the reactant wave function (Ψ_I) connects with an excited-state wave function (Ψ_P* in part a and Ψ_D* in part b) in the product geometry. At the same time, the ground state product wave function connects to an excited state in the reactant geometry ($\Psi_{I,reb}$* in part a and $\Psi_{I,D}$* in part b). These two curves cross and lead to an avoided crossing and hence a transition state for the reaction pathway from intermediate to products.

Mathematically, the height of the barrier ($\Delta E^{\neq}$) can be determined from a VB curve-crossing diagram by estimating the excitation energy (or promotion gap G) in the reactant geometry from Ψ_I to Ψ_I*. Thus, as has been shown previously,[31] the barrier height is equal to the curve-crossing energy (ΔE_X) minus the resonance energy (B). Since, ΔE_X is proportional to a fraction (f) of the promotion gap, the barrier height can be estimated from Equation (1):

$$\Delta E^{\neq} = \Delta E_X - B = fG - B \qquad (1)$$

A careful look at the VB structures in the reactant geometry for the hydroxylation pathway shows that upon excitation the two electrons on the carbon of the substrate and the donor oxygen atom in $\Psi_{I,reb}$* have formed a bond and at the same time an electron has transferred from the OH group to iron. The rebound excitation energy G_{reb}, therefore, depends on the strength of the CO bond formed, that is, the bond-dissociation energy of the CO bond (BDE_{CO}), but also on the excitation energy ($E_{ex,FeOH}$) within the iron–hydroxo complex from $2p_z$(OH) into the iron 3d-block [Eq. (2)].

This excitation energy will fill the π^*_{xz} orbital with a second electron in the doublet spin state and the $\sigma^*_{z^2}$ orbital in the quartet spin state.

$$G_{reb} = BDE_{CO} + E_{ex,FeOH} \qquad (2)$$

The desaturation pathway, by contrast, shows somewhat different electron-transfer mechanisms as compared to the hydroxylation pathway (Figure 6b). Thus, in the excited state $\Psi_{I,D}$* the secondary hydrogen atom forms a chemical bond with the hydroxo moiety, whereas this bond is missing but it forms a bond with the carbon atom of the substrate instead. Therefore, the excitation energy is proportional to the difference in strength of the O–H bond that is formed (BDE_{OH}) and the C–H bond that is broken (BDE_{CH}). In addition, the two radicals on the adjacent carbon atoms in $\Psi_{I,D}$* have formed a π-bond with energy E_π. Obviously, π-conjugation will have a major effect on the excitation energy and lower it dramatically in value. Similarly to the radical rebound also in the desaturation pathway there is an internal electron transfer from the hydroxo group to the metal ($E_{ex,FeOH}$) [Eq. (3)]:

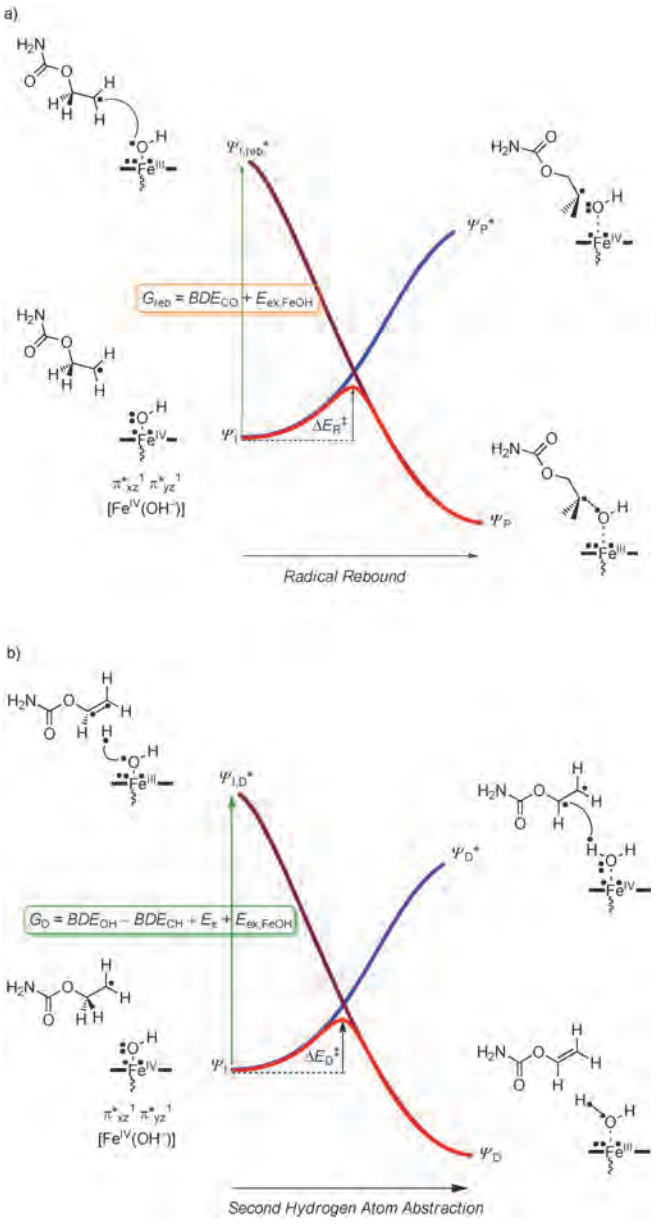

Figure 6. Valence bond curve-crossing diagrams for product formation from radical intermediates. a) Radical rebound leading to hydroxylation products. b) Hydrogen-atom transfer to give desaturation products.

In order to stabilize a desaturation pathway over a hydroxylation pathway the barrier for the latter should be higher in energy than that for the desaturation mechanism, that is, $\Delta E_{reb}{}^{\neq} > \Delta E_D{}^{\neq}$. Considering Equation (1) above, the difference in barrier height of radical rebound versus desaturation then depends on the promotion gap values, G, of the two processes

© 2015 Wiley-VCH Verlag GmbH & Co. KGaA, Weinheim

and the resonance energies, *B*. Generally, *f* is found to have a constant value of 0.30.[32] Therefore, if both pathways incur similar resonance energy values, *B*, the change in product distributions will only depend on the relative values of G_{reb} versus G_D [Eq. (4)]:

$$G_{reb} - G_D = BDE_{CO} - BDE_{OH} + BDE_{CH} - E_\pi \quad (4)$$

The BDE_{OH} value was calculated from the iron(III)–water complex and iron(IV)–hydroxo intermediate to be 70.8 kcal mol^{-1} for the iron–porphyrin model used here.[28] The corresponding C–H bond strength of the substrate that is broken ranges from 36.7 kcal mol^{-1} for $C_2H_5^\bullet$ to 21.8 kcal mol^{-1} for cyclo-$C_6H_7^\bullet$. By contrast, the C–O bond strength of the alcohol product that is formed ranges from BDE_{CO} = 85.8 kcal mol^{-1} for ethane to 59.7 kcal mol^{-1} for cyclohexadiene. Furthermore, DFT calculations predicted a π-conjugation energy of about 36 kcal mol^{-1} for a benzene molecule.[33] Based on this, we calculate a difference $G_{reb} - G_D = +16$ kcal mol^{-1} for a molecule like ethane, whereas a value of −25 kcal mol^{-1} is found for cyclohexadiene. This implies that a regioselective hydroxylation of ethane may be expected, whereas the desaturation will be favourable for cyclohexadiene. These values, therefore, implicate strong effects of the nature of the substrate on the regioselectivity of hydroxylation over desaturation, which is determined by a much stronger C–O bond formed in ethanol (by 26 kcal mol^{-1}) than the corresponding alcohol of cyclohexadiene and in addition has a stronger C–H bond for the second hydrogen atom that is abstracted in the desaturation process (by another 15 kcal mol^{-1}).

As the difference $G_{reb} - G_D$ for ethane is calculated to be +16 kcal mol^{-1} in favour of substrate hydroxylation, this implies that perturbations through binding of the substrate in the enzyme binding pocket will have to overcome 16 kcal mol^{-1} in order to change the regioselectivity of hydroxylation over desaturation for this particular substrate. As seen in Figures 4 and 5, a substrate with an aliphatic chain like eicosanoic acid can be desaturated by P450 enzymes due to a tight substrate binding pocket that through hydrogen-bonding networks prevent the OH rotation and, thereby, blocks the OH-rebound process efficiently.

Subsequently, we calculated the difference $G_{reb} - G_D$ for the drug molecules EC and VA as well as for DHA and find values of 10, 13 and −4 kcal mol^{-1}, respectively. This implies that the DHA reaction will naturally be driven towards desaturation and the formation of anthracene products. However, in the case of EC and VA the balance in the isolated system is in favour of hydroxylation rather than desaturation. The P450 isozymes involved in detoxification of EC and VA, therefore, have a specific substrate binding pocket that will change the balance in favour of desaturation rather than hydroxylation due to environmental perturbations affecting the rebound process. Consequently, subtle perturbations in the substrate binding pocket can have a major effect on the regioselectivity of substrate activation by P450 isozymes and are necessary to change the preference from hydroxylation to desaturation. This may be an important point to consider in bioengineering P450s for commercial purposes.

Conclusion

We present here a detailed set of computational results on the potential regioselectivity of aliphatic hydroxylation versus desaturation. We identify key steps in the mechanisms that both are initiated by a hydrogen atom abstraction step followed by OH isomerization to form either the pro-hydroxylation radical intermediate or the pro-desaturation radical intermediate. A VB and molecular orbital analysis (Supporting Information) identifies the electron-transfer processes for both reaction steps and highlights the substrate-specific factors and orbitals that drive the regioselectivity to hydroxylation or desaturation. Further evidence from QM/MM calculations shows that the regioselectivity can be modified through external perturbations that block one of the isomerization pathways.

Experimental Section

Our work uses two main computational approaches, namely DFT calculations on model complexes and QM/MM on a full P450 isozyme.

DFT model calculations

As in previous studies of our groups,[34] Cpd I of P450 was modelled as a six-coordinated iron(IV)–oxo porphyrin (Por) cation radical complex, [Fe^{IV}(O)($Por^{+\cdot}$)(SH)]. For simplicity, the heme is replaced by protoporphyrin IX, whereby all side chains are abbreviated with hydrogen atoms and the axial cysteinate ligand is changed to thiolate. All geometries were optimized using the unrestricted hybrid B3LYP density functional[35] in combination with an LACVP basis set on iron and 6–31G on the rest of the atoms;[36] basis set BSI. A subsequent analytical frequency calculation was run to confirm that all ground states had no imaginary frequencies, and all transition states had a single one for the correct mode. The computed vibrational frequencies were then used further for quantifying the zero-point energy (*ZPE*), and enabled us to calculate thermal and entropic corrections to the free energy at 298.15 K and 101.325 kPa. More accurate energies were determined by single-point calculations with the SDD basis set on iron coupled to 6–311++G** on the rest of the atoms; basis set BSII. To test the effect of the basis set on the optimized geometries, we calculated a full potential energy profile of 1-butene epoxidation by Cpd I using different basis sets. However, a single point calculation with a triple-ζ quality basis set on all atoms performed on a geometry that was optimized with either a double-ζ or a triple-ζ quality basis set did only give minor differences in the relative energies to within 0.1 kcal mol^{-1} of each other,[37] hence the former procedure was used in this work.

Bulk protein environment was simulated with the polarized continuum-solvation model with a dielectric constant of $\varepsilon = 5.62$. Dispersion interactions were added to the energy at the UB3LYP-D3 level of theory with zero damping.[38] All calculations were carried out using the Gaussian 09 program package.[39]

As density functional theory occasionally struggles with the correct description of spin-state ordering of transition metal complexes,[40] we tested the effect of the density functional method on the spin-state ordering and relative energies of the rebound versus desatu-

© 2015 Wiley-VCH Verlag GmbH & Co. KGaA, Weinheim

ration reactions. We did full geometry optimizations at the UBLYP/BSI,[35b,41] UB3PW91/BSI[35a,42] and TPSS/BSI[43] levels of theory. However, no change in spin state ordering was observed and only minor differences in the relative energies of the barrier heights were obtained (see the Supporting Information). Therefore, the same qualitative picture is obtained with alternative DFT methods and we will focus on the B3LYP results only.

QM/MM calculations

To support the DFT calculations and gain insight into whether the model would be applicable to realistic systems, we did a further set of calculations using an actual P450 isozyme that is known to desaturate its natural substrate. $OleT_{JE}$ was recently identified as a P450 isozyme that converts long-chain fatty acids into terminal olefins.[44] We investigated the pathways of β-hydroxylation and desaturation of eicosanoic acid by the P450 isozyme $OleT_{JE}$ using QM/MM methods. The starting coordinates for the calculations were taken from crystal structure data.[45] We followed the set-up procedures of the QM/MM system as reported and benchmarked before, which we will briefly summarize here.[46]

Starting from the crystal structure coordinates, hydrogen atoms and oxo group were added to the structure using the PDB2PQR program package[47] and the active site was manually modified from a resting state iron(III)–water(heme) complex into an iron(IV)–oxo heme cation radical (Cpd I) structure. We did a careful and visual analysis of all acidic and basic amino acid side chains for their protonation states, whereby we chose all glutamic and aspartic acid residues to be deprotonated at the carboxylic acid group and all arginine and lysine residues protonated. All histidine groups were visually inspected for proton-donor and -acceptor possibilities. The histidine residues His120 and His210 were doubly protonated, whereas the other six (His85, His92, His222, His259, His325 and His363) were singly protonated. The overall structure was neutralized with counter-ions (Mg^{2+} and Cl^{-}). Solvent water (with a sphere of radius of 35 Å) was added to this structure, and equilibrated, followed by a molecular dynamics minimization and heating procedure to 298 K of the full structure using the CHARMM force field.[48] The thus obtained QM/MM model had a total number of 32992 atoms including 8739 TIP3P water molecules.

In these QM/MM calculations the inner core including all residues and water molecules within a radius of 8 Å from the heme iron were fully geometry optimized, whereas all other atoms were fixed in the MD simulated coordinates. The iron(IV)–hydroxo species was geometry optimized in the doublet and quartet spin states and a frequency calculation on the QM region established these structures as stationary points.

QM/MM calculations employed the Turbomole program package[49] for the calculations of the QM region and Charmm as implemented in DL-Poly[50] for the MM region all linked through the ChemShell interface.[51] For consistency with the DFT studies reported above, we selected the UB3LYP[35] density functional for the QM region in combination with the Turbomole built-in basis set SVP, BSIII.[49] The QM region contained the iron(IV)–oxo group, the heme (without side chains), thiolate for the axial cysteinate group and the butanoate group of the substrate. To improve the energetics, single-point calculations were performed with a Wachters all electron basis set on iron and 6–311+G** on the rest of the atoms; basis set BSIV.[52] These methods and basis sets are of similar quality to those used for the model complexes and have been shown to give comparable results for analogous systems.[46] Electronic embedding procedures were implemented,[53] thereby taking into consideration to electronic interactions of electrons in the QM region with charges in the MM region.

The QM region selected in the QM/MM calculations contains the heme (without side chains) and its ligands and part of the substrate. As the substrate has a terminal carboxylate group that is linked through a salt bridge with an arginine residue, we kept the methylguanidinium component of Arg245 in the QM region and terminated the substrate at the sixth carbon atom. All side chains of the heme were in the MM region and the axial cysteinate residue was abbreviated by methylmercaptane. Subsequently, we investigated hydrogen atom abstraction from the C^{β} position of the substrate and the pathways leading to desaturation and hydroxylation.

Acknowledgements

L.J. and W.L. gratefully thank support from the National Natural Science Foundation of China (Grant No. 21307107 and 21320102007). A.F. and R.v.E. gratefully acknowledge financial support from the Deutsche Forschungsgemeinschaft and the National Science Centre of Poland (grant no. 2012/05/B/ST5/00389). The China National Supercomputing Centre in Shenzhen (Shenzhen Cloud Computing Centre, Contract No. S13037 and S14011) and the National Service of Computational Chemistry Software UK are acknowledged for providing computational resource and CPU time to L.J. and S.d.V. A.S.F., M.G.Q. and M.A.S. thank the Tertiary Education Trust Fund, the BBSRC and the Petroleum Technology Development Fund, respectively, for studentships. D.K. is the Ramanujan Fellow of the DST, New Delhi (India).

Keywords: compound I · density functional calculations · enzyme catalysis · reaction mechanisms · oxygen atom transfer

[1] a) M. Sono, M. P. Roach, E. D. Coulter, J. H. Dawson, *Chem. Rev.* **1996**, *96*, 2841–2888; b) J. T. Groves, *Proc. Natl. Acad. Sci. USA* **2003**, *100*, 3569–3574; c) *Cytochrome P450: Structure, Mechanism and Biochemistry* (Ed.: P. R. Ortiz de Montellano), 3rd ed., Kluwer, New York, **2004**; d) I. G. Denisov, T. M. Makris, S. G. Sligar, I. Schlichting, *Chem. Rev.* **2005**, *105*, 2253–2277; e) B. Meunier, S. P. de Visser, S. Shaik, *Chem. Rev.* **2004**, *104*, 3947–3980; f) *Handbook of Porphyrin Science* (Eds.: K. M. Kadish, K. M. Smith, R. Guilard) World Scientific, New Jersey, **2010**; g) P. R. Ortiz de Montellano, *Chem. Rev.* **2010**, *110*, 932–948.

[2] D. R. Nelson, *Human Genomics* **2009**, *4*, 59–65.

[3] a) F. P. Guengerich, *Chem. Res. Toxicol.* **2001**, *14*, 611–650; b) G. H. Posner, P. M. O'Neill, *Acc. Chem. Res.* **2004**, *37*, 397–404; c) A. W. Munro, H. M. Girvan, K. J. McLean, *Nat. Prod. Rep.* **2007**, *24*, 585–609.

[4] a) M. H. Gelb, D. C. Heimbrook, P. Mälkönen, S. G. Sligar, *Biochemistry* **1982**, *21*, 370–377; b) W. M. Atkins, S. G. Sligar, *J. Am. Chem. Soc.* **1987**, *109*, 3754–3760.

[5] a) R. T. Ruettinger, L. P. Wen, A. J. Fulco, *J. Biol. Chem.* **1989**, *264*, 10987–10995; b) D. R. Davydov, G. H. Bon Hoa, J. A. Peterson, *Biochemistry* **1999**, *38*, 751–761.

[6] a) E. O'Reilly, V. Koehler, S. Flitsch, N. Turner, *Chem. Commun.* **2011**, *47*, 2490–2501; b) G. Grogan, *Curr. Opin. Chem. Biol.* **2011**, *15*, 241–248.

[7] T. Omura, R. Sato, *J. Biol. Chem.* **1962**, *237*, 1375–1376.

[8] a) T. L. Poulos, B. C. Finzel, I. C. Gunsalus, G. C. Wagner, J. Kraut, *J. Biol. Chem.* **1985**, *260*, 6122–6130; b) I. Schlichting, J. Berendzen, K. Chu, A. M. Stock, S. A. Maves, D. E. Benson, R. M. Sweet, D. Ringe, G. A. Petsko, S. G. Sligar, *Science* **2000**, *287*, 1615–1622; c) K. Auclair, P. Moënne-Loccoz, P. R. Ortiz de Montellano, *J. Am. Chem. Soc.* **2001**, *123*, 4877–4885.

© 2015 Wiley-VCH Verlag GmbH & Co. KGaA, Weinheim

[9] R. L. Reynald, S. Sansen, C. D. Stout, E. F. Johnson, *J. Biol. Chem.* **2012**, *287*, 44581 – 44591.
[10] J. Rittle, M. T. Green, *Science* **2010**, *330*, 933 – 937.
[11] a) J. T. Groves, *Models and Mechanisms of Cytochrome P450 Action, in Cytochrome P450: Structure, Mechanism and Biochemistry* (Ed.: P. R. Ortiz de Montellano), 3rd ed., Kluwer, New York, **2005**, Chapter 1, pp. 1 – 44; b) Y. Watanabe, H. Nakajima, T. Ueno, *Acc. Chem. Res.* **2007**, *40*, 554 – 562.
[12] J. T. Groves, G. A. McClusky, *J. Am. Chem. Soc.* **1976**, *98*, 859 – 861.
[13] a) T. Kamachi, K. Yoshizawa, *J. Am. Chem. Soc.* **2003**, *125*, 4652 – 4661; b) S. Shaik, D. Kumar, S. P. de Visser, A. Altun, W. Thiel, *Chem. Rev.* **2005**, *105*, 2279 – 2328.
[14] a) S. P. de Visser, F. Ogliaro, S. Shaik, *Angew. Chem. Int. Ed.* **2001**, *40*, 2871 – 2874; *Angew. Chem.* **2001**, *113*, 2955 – 2958; b) D. Kumar, S. P. de Visser, P. K. Sharma, S. Cohen, S. Shaik, *J. Am. Chem. Soc.* **2004**, *126*, 1907 – 1920.
[15] a) D. Kumar, S. P. de Visser, S. Shaik, *J. Am. Chem. Soc.* **2004**, *126*, 5072 – 5073; b) W. Lai, H. Chen, S. Cohen, S. Shaik, *J. Phys. Chem. Lett.* **2011**, *2*, 2229 – 2235.
[16] a) A. E. Rettie, A. W. Rettenmeier, W. N. Howald, T. A. Baillie, *Science* **1987**, *235*, 890 – 893; b) A. E. Rettie, M. Boberg, A. W. Rettenmeier, T. A. Baillie, *J. Biol. Chem.* **1988**, *263*, 13733 – 13738; c) A. E. Rettie, P. R. Sheffels, K. R. Korzekwa, F. J. Gonzalez, R. M. Philpot, T. A. Baillie, *Biochemistry* **1995**, *34*, 7889 – 7895; d) A. J. M. Sadeque, M. B. Fisher, K. R. Korzekwa, F. J. Gonzalez, A. E. Rettie, *J. Pharmacol. Exp. Ther.* **1997**, *283*, 698 – 703; e) X. Wen, J. S. Wang, K. T. Kivistö, P. J. Neuvonen, J. T. Backman, *Br. J. Clin. Pharmacol.* **2001**, *52*, 547 – 553; f) A. Gunes, E. Bilir, H. Zengil, M. O. Babaoglu, A. Bozkurt, U. Yasar, *Pharmacol. Toxicol.* **2007**, *100*, 383 – 386.
[17] a) J. M. Loch, J. Potter, K. A. Bachmann, *Pharmacol.* **1995**, *50*, 146 – 153; b) P. G. Forkert, R. P. Lee, *Toxicol. Appl. Pharmacol.* **1997**, *146*, 245 – 254; c) R. P. Lee, A. Parkinson, P.-G. Forkert, *Drug Metabol. Disp.* **1998**, *26*, 60 – 65; d) F. P. Guengerich, *Chem. Res. Toxicol.* **2008**, *21*, 70 – 83.
[18] F. P. Guengerich, D. H. Kim, *Chem. Res. Toxicol.* **1991**, *4*, 413 – 421.
[19] M. T. Leithauser, A. Liem, B. C. Stewart, E. C. Miller, J. A. Miller, *Carcinogenesis* **1990**, *11*, 463 – 473.
[20] X. Guan, M. B. Fisher, D. H. Lang, Y. M. Zheng, D. R. Koop, A. E. Rettie, *Chem. Biol. Interact.* **1998**, *110*, 103 – 121.
[21] S. L. Kelly, D. C. Lamb, D. E. Kelly, *FEBS Lett.* **1997**, *412*, 233 – 235.
[22] a) R. Lonsdale, J. N. Harvey, A. J. Mulholland, *J. Phys. Chem. Lett.* **2010**, *1*, 3232 – 3237; b) A. K. Vardhaman, P. Barman, S. Kumar, C. V. Sastri, D. Kumar, S. P. de Visser, *Angew. Chem. Int. Ed.* **2013**, *52*, 12288 – 12292; *Angew. Chem.* **2013**, *125*, 12514 – 12518.
[23] S. P. de Visser, *Chem. Eur. J.* **2006**, *12*, 8168 – 8177.
[24] S. Shaik, D. Kumar, S. P. de Visser, *J. Am. Chem. Soc.* **2008**, *130*, 10128 – 10140.
[25] J. F. Hull, D. Balcells, E. L. O. Sauer, C. Raynaud, G. W. Brudvig, R. H. Crabtree, O. Eisenstein, *J. Am. Chem. Soc.* **2010**, *132*, 7605 – 7616.
[26] See, for example: a) F. Ogliaro, N. Harris, S. Cohen, M. Filatov, S. P. de Visser, S. Shaik, *J. Am. Chem. Soc.* **2000**, *122*, 8977 – 8989; b) S. P. de Visser, D. Kumar, S. Cohen, R. Shacham, S. Shaik, *J. Am. Chem. Soc.* **2004**, *126*, 8362 – 8363; c) R. Latifi, M. Bagherzadeh, S. P. de Visser, *Chem. Eur. J.* **2009**, *15*, 6651 – 6662; d) L. Ji, G. Schüürmann, *Angew. Chem. Int. Ed.* **2013**, *52*, 744 – 748; *Angew. Chem.* **2013**, *125*, 772 – 776.
[27] a) Y. J. Jeong, Y. Kang, A. R. Han, Y. M. Lee, H. Kotani, S. Fukuzumi, W. Nam, *Angew. Chem. Int. Ed.* **2008**, *47*, 7321 – 7324; *Angew. Chem.* **2008**, *120*, 7431 – 7434; b) L. Ji, A. Franke, M. Brindell, M. Oszajca, A. Zahl, R. van Eldik, *Chem. Eur. J.* **2014**, *20*, 14437 – 14450.
[28] D. Kumar, L. Tahsini, S. P. de Visser, H. Y. Kang, S. J. Kim, W. Nam, *J. Phys. Chem. A* **2009**, *113*, 11713 – 11722.
[29] D. J. Heyes, M. Sakuma, S. P. de Visser, N. S. Scrutton, *J. Biol. Chem.* **2009**, *284*, 3762 – 3767.
[30] a) S. Kumar, A. S. Faponle, P. Barman, A. K. Vardhaman, C. V. Sastri, D. Kumar, S. P. de Visser, *J. Am. Chem. Soc.* **2014**, *136*, 17102 – 17115; b) M. A. Sainna, S. Kumar, D. Kumar, S. Fornarini, M. E. Crestoni, S. P. de Visser, *Chem. Sci.* **2015**, *6*, 1516 – 1529.
[31] S. Shaik, P. C. Hiberty, *A Chemist's Guide to Valence Bond Theory*, Wiley-Interscience, New York, **2007**.
[32] D. Usharani, W. Lai, C. Li, H. Chen, D. Danovich, S. Shaik, *Chem. Soc. Rev.* **2014**, *43*, 4968 – 4988.
[33] I. Fernández, G. Frenking, *Chem. Commun.* **2006**, 5030 – 5032.
[34] a) S. P. de Visser, L. S. Tan, *J. Am. Chem. Soc.* **2008**, *130*, 12961 – 12974; b) L. Ji, J. Zhang, W. Liu, S. P. de Visser, *Chem. Asian J.* **2014**, *9*, 1175 – 1182.
[35] a) A. D. Becke, *J. Chem. Phys.* **1993**, *98*, 5648 – 5652; b) C. Lee, W. Yang, R. G. Parr, *Phys. Rev. B* **1988**, *37*, 785 – 789.
[36] a) P. J. Hay, W. R. Wadt, *J. Chem. Phys.* **1985**, *82*, 299 – 310; b) W. J. Hehre, K. Ditchfield, J. A. Pople, *J. Chem. Phys.* **1972**, *56*, 2257 – 2261.
[37] a) D. Kumar, B. Karamzadeh, G. N. Sastry, S. P. de Visser, *J. Am. Chem. Soc.* **2010**, *132*, 7656 – 7667; b) A. S. Faponle, M. G. Quesne, C. V. Sastri, F. Banse, S. P. de Visser, *Chem. Eur. J.* **2015**, *21*, 1221 – 1236.
[38] S. Grimme, *J. Comput. Chem.* **2006**, *27*, 1787 – 1799.
[39] Gaussian 09, Revision D.01, M. J. Frisch, G. W. Trucks, H. B. Schlegel, G. E. Scuseria, M. A. Robb, J. R. Cheeseman, G. Scalmani, V. Barone, B. Mennucci, G. A. Petersson, H. Nakatsuji, M. Caricato, X. Li, H. P. Hratchian, A. F. Izmaylov, J. Bloino, G. Zheng, J. L. Sonnenberg, M. Hada, M. Ehara, K. Toyota, R. Fukuda, J. Hasegawa, M. Ishida, T. Nakajima, Y. Honda, O. Kitao, H. Nakai, T. Vreven, J. A. Montgomery, Jr., J. E. Peralta, F. Ogliaro, M. Bearpark, J. J. Heyd, E. Brothers, K. N. Kudin, V. N. Staroverov, T. Keith, R. Kobayashi, J. Normand, K. Raghavachari, A. Rendell, J. C. Burant, S. S. Iyengar, J. Tomasi, M. Cossi, N. Rega, J. M. Millam, M. Klene, J. E. Knox, J. B. Cross, V. Bakken, C. Adamo, J. Jaramillo, R. Gomperts, R. E. Stratmann, O. Yazyev, A. J. Austin, R. Cammi, C. Pomelli, J. W. Ochterski, R. L. Martin, K. Morokuma, V. G. Zakrzewski, G. A. Voth, P. Salvador, J. J. Dannenberg, S. Dapprich, A. D. Daniels, O. Farkas, J. B. Foresman, J. V. Ortiz, J. Cioslowski, D. J. Fox, Gaussian, Inc., Wallingford CT, **2013**.
[40] S. P. de Visser, M. G. Quesne, B. Martin, P. Comba, U. Ryde, *Chem. Commun.* **2014**, *50*, 262 – 282.
[41] A. D. Becke, *Phys. Rev. A* **1988**, *38*, 3098 – 3100.
[42] J. P. Perdew, Y. Wang, *Phys. Rev. B* **1992**, *45*, 13244 – 13249.
[43] J. Tao, J. P. Perdew, V. N. Staroverov, G. E. Scuseria, *Phys. Rev. Lett.* **2003**, *91*, 146401.
[44] M. A. Rude, T. S. Baron, S. Brubaker, M. Alibhai, S. B. Del Cardayre, A. Schirmer, *Appl. Environ. Microbiol.* **2011**, *77*, 1718 – 1727.
[45] J. Belcher, K. J. McLean, S. Matthews, L. S. Woodward, K. Fisher, S. E. J. Rigby, D. R. Nelson, D. Potts, M. T. Baynham, D. A. Parker, D. Leys, A. W. Munro, *J. Biol. Chem.* **2014**, *289*, 6535 – 6550.
[46] a) D. Kumar, W. Thiel, S. P. de Visser, *J. Am. Chem. Soc.* **2011**, *133*, 3869 – 3882; b) M. G. Quesne, R. Latifi, L. E. Gonzalez-Ovalle, D. Kumar, S. P. de Visser, *Chem. Eur. J.* **2014**, *20*, 435 – 446.
[47] T. J. Dolinsky, P. Czodrowski, H. Li, J. E. Nielsen, J. H. Jensen, G. Klebe, N. A. Baker, *Nucl. Acids Res.* **2007**, *35*, W522 – W531.
[48] B. R. Brooks, R. E. Bruccoleri, B. D. Olafson, D. J. States, S. Swaminathan, M. Karplus, *J. Comput. Chem.* **1983**, *4*, 187 – 217.
[49] R. Ahlrichs, M. Bär, M. Häser, H. Horn, C. Kölmel, *Chem. Phys. Lett.* **1989**, *162*, 165 – 169.
[50] W. Smith, T. R. Forester, *J. Mol. Graphics* **1996**, *14*, 136 – 141.
[51] P. Sherwood, *J. Mol. Struct.* **2003**, *632*, 1 – 28.
[52] A. J. H. Wachters, *J. Chem. Phys.* **1970**, *52*, 1033 – 1036.
[53] D. Bakowies, W. Thiel, *J. Phys. Chem.* **1996**, *100*, 10580 – 10594.

Received: January 26, 2015
Published online on April 29, 2015

© 2015 Wiley-VCH Verlag GmbH & Co. KGaA, Weinheim

ORGANOMETALLICS

Article

pubs.acs.org/Organometallics

A Trimetal Carbene with Reactivity Reminiscent of Fischer–Tropsch Catalysis

Mala A. Sainna,[†,§] Devendra Singh,[‡,§] Devesh Kumar,*[,‡] and Sam P. de Visser*[,†]

[†]Manchester Institute of Biotechnology and School of Chemical Engineering and Analytical Science, The University of Manchester, 131 Princess Street, Manchester M1 7DN, United Kingdom

[‡]Department of Applied Physics, School for Physical Sciences, Babasaheb Bhimrao Ambedkar University, Vidya Vihar, Rae Bareilly Road, Lucknow (U. P.) 226 025, India

Supporting Information

ABSTRACT: Metal-carbenes are common reaction intermediates in chemical catalysis; however, very few catalysts are known with a trimetal-carbene active center. In this work, we describe a computational study into the chemical and catalytic properties of a unique trimetal carbene containing a Ru_2Pt-carbene core, $[(CpRu)_2(\mu_2\text{-}CH_2)(\mu_3\text{-}NCH_3)Pt(P(CH_3)_3)_2]$, with and without bound CO. The chemical structure and individual orbital interactions are identified from a natural bond orbital analysis, and the reaction pathways for consecutive intramolecular CH_3 and H transfer (or vice versa) are investigated. The studies show that CO binding has dramatic effects on the reaction mechanism and weakens the Ru–H bond strength. The reaction processes are rationalized by valence bond models and thermochemical bond strength studies. The work leads to suggestions on how to improve this chemical system for enhanced alkane synthesis.

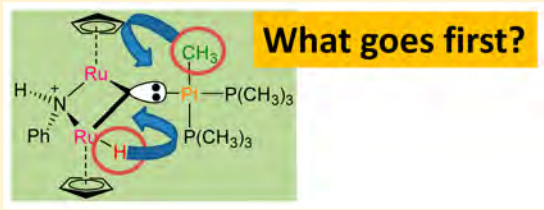

INTRODUCTION

In industrial Fischer–Tropsch catalysis, alkanes are being synthesized from H_2 and CO gas on a metal surface, which is a process that was developed and exploited in Germany in the 1920s and 1930s as an alternative to fossil fuels.[1] With dwindling supplies of fossil fuels, urgent alternative sources are needed; however, the Fischer–Tropsch process is energetically demanding and usually requires high pressures and/or temperatures as well as expensive heterogeneous catalysts.[2] Research on improving Fischer–Tropsch catalysis is hampered due to the lack of knowledge of details of the reaction mechanism and the properties played by the metal surface. In addition, few homogeneous catalysts are known that perform a Fischer–Tropsch-type reaction.[3]

Recently, the Matsuzaka group[4] reported the synthesis and spectroscopic characterization of $[(Cp^*Ru)_2(\mu_2\text{-}CH_2)(\mu_3\text{-}NPh)Pt(P(CH_3)_3)_2]$, which was treated with CH_3OTf in diethyl ether and, after heating in toluene, produced a unique structure (labeled as **3** in ref 4) with a trigonal sp^2 hybridized carbon atom linked to three transition-metal atoms. It was reported that structure **3** reacted via a Fischer–Tropsch-type reaction via H and CH_3 migration from the RuH and $PtCH_3$ ligands to form μ_2-$CHCH_3$ products (Scheme 1). Therefore, structure **3** catalyzes the C–C and C–H bond formation reactions for the synthesis of alkanes alike to the Fischer–Tropsch process, which are thermodynamically difficult processes. As such, structure **3** is one of the few homogeneous Fischer–Tropsch catalysts available currently. However, little is known of the reaction process and the overall potential of this type of chemical system. In order to explore its possibilities further, it is important to fully understand the origin of the reaction mechanism and the chemical properties that drive the process. Currently, there is limited knowledge on the chemical system displayed in Scheme 1, and experimental studies failed to identify intermediates along the reaction mechanism. Hence, it is unclear how and why this chemical system operates and how it can be further improved. Moreover, there are very few examples in the literature of analogous processes, and this chemical system may pose a novel synthetic route for the generation of alkanes on a carbene center.

Scheme 1. Chemical Reaction Investigated in This Work

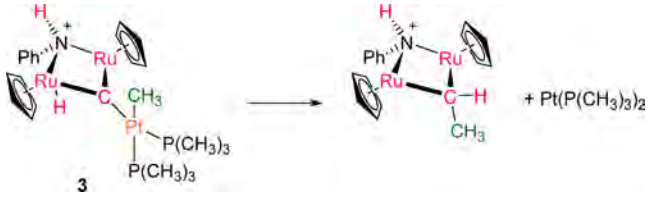

The aim of the studies in this work, therefore, is focused on establishing the reaction mechanism of alkyl chain growth on the carbene center and the chemical properties of the reaction center shown in Scheme 1. First, the chemical properties of the trimetal carbene center are poorly understood, and theory may give insight into whether it would be a suitable catalytic center. Second, it is unclear whether there is an initial H transfer, followed by a CH_3 transfer or the reverse. Moreover, it may very well be that both mechanisms are kinetically and thermodynamically possible. Third, as shown in iron-porphyrin

Received: February 7, 2015
Published: April 30, 2015

ACS Publications © 2015 American Chemical Society

DOI: 10.1021/acs.organomet.5b00305
Organometallics 2015, 34, 1651–1660

Scheme 2. Definition of the Chemical Model, and Nomenclature of Structures along the Reaction Mechanism

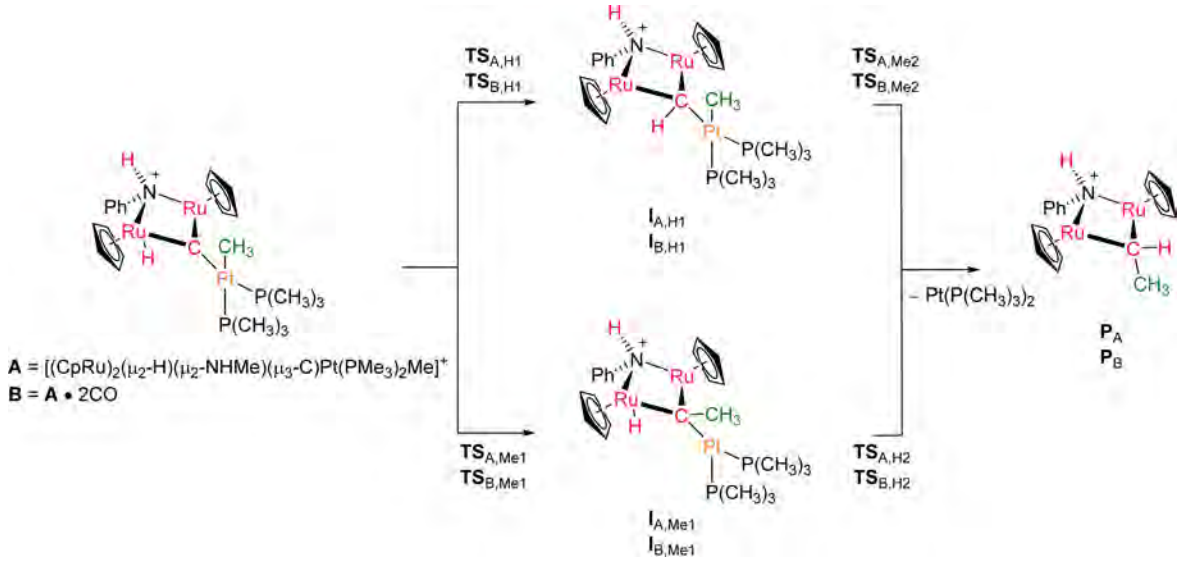

chemistry, for many examples, the reaction can take place via proton transfer, hydrogen atom transfer, or hydride transfer.[5] Furthermore, hydrogen atom and hydride transfer processes may happen via proton-coupled electron transfer (PCET), whereby the electrons move to a different donor site than the protons involved in the reaction. Theory is the ideal tool to distinguish between these mechanistic pathways and to establish the electronic features that drive this important mechanism. In addition to the reactivity questions and the synthesis of alkyl groups on this carbon center, there are also questions related to the chemical structure of the central carbon atom in **3** itself. Thus, an sp^2 hybridized carbon atom would make **3** a carbocation with a planar conformation, which is unlikely given the fact that the carbon atom is surrounded by positively charged metal ions. On the other hand, if the carbon atom is negatively charged, i.e., a carbanion, it would have a pyramidal structure because of its sp^3 hybridization, which is in disagreement with the experimental crystal structure coordinates. Clearly, the structural and reactivity features of this complex are poorly understood, and theory may provide insight into its electronic and structural features.

The Ru_2PtC core of structure **3** is an unusual structure in chemical catalysis but shows some resemblance to Grubbs catalyst,[6] where the metal is covalently linked to a carbon atom through either a single, a double, or a triple bond. However, as far as we know, there are no reported catalysts in the literature, where the carbon atom is ligated to two Ru atoms and a Pt atom. There are several examples in the literature of carbido centered structures, where the carbon atom is bound to three or more metal atoms,[7] but very few of these show catalytic activity. It, therefore, remains unclear why structure **3** is reactive for the formation of alkyl groups from individual methyl, hydrogen, and carbon groups. In order to gain insight into the peculiar structure and reactivity of **3**, we decided to do a computational study and establish the electronic and thermochemical features. As we will show here, our studies give fundamental insight into the nature of the metal−carbon bond and characterizes structure **3** as a trimetal carbene that can react via sequential methyl and hydrogen atom transfer to form μ_2-$CHCH_3$. These results may have direct relevance to heterogeneous catalysis on metal surfaces.

METHODS

The calculations reported in this work were performed using density functional theory (DFT) methods as used previously on transition-metal complexes by our groups,[8] and are implemented in the Jaguar 7.7[9] and Gaussian 09[10] program packages. Initial geometries were optimized (without constraints) in Jaguar using the hybrid density functional theory method B3LYP[11] coupled with an LACVP basis set (including a core potential) on ruthenium and platinum and 6-31G on the rest of the atoms: basis set BS1.[12] A subsequent analytical frequency in Gaussian confirmed the structures as local minima with real frequencies only or first-order saddle points with one imaginary frequency for the correct mode. Energies were then improved by running a single point calculation in Jaguar using a triple-ζ quality LACV3P+ basis set on iron and 6-311+G* on the rest of the atoms: basis set BS2. We also tested the effect of dispersion on the reaction energies by doing a UB3LYP-D3 single point calculation in Jaguar using the model of Grimme and co-workers.[13] For a selection of chemical systems, i.e., reactants and transition states, we did geometry optimizations at UB3LYP/BS2 and UB3LYP-D3/BS2, but found very little changes with respect to those obtained at UB3LYP/BS1. Since transition-metal complexes often react via multistate reactivity,[14] we calculated the complete potential energy profile on the lowest-lying singlet, triplet, and quintet spin states; however, in all cases, the singlet spin state was the ground state and well separated from the other spin states. Energies reported in this work contain B3LYP/BS2 energies and include zero-point and solvent corrections (calculated with B3LYP/BS2 using the polarized continuum model with a dielectric constant mimicking toluene).

As occasionally DFT calculations on spin state ordering and relative energies of transition-metal complexes show fluctuations depending on the choice of the density functional method,[15] we decided to do a series of test calculations with alternative DFT methods, namely, B3LYP-D3,[13] BP86,[16] M06,[17] OPBE, and PBE0; see the Supporting Information.[18] Similar to previously reported calculations on analogous systems,[19] these studies confirmed the trends and did not change the conclusions.

The methods described here were benchmarked previously on transition-metal-containing systems and compared with experimentally determined data, which gave free energies of activation within 4 kcal mol^{-1} from experiment,[20] but also gave reasonable agreement for spectroscopic data, where they reproduced resonance Raman, EXAFS, and Mössbauer data excellently.[21] To locate transition-state structures, we ran extensive geometry scans between the various local minima and used the maximum of those scans as a starting point for the actual transition state searches. Moreover, these scans confirmed that

DOI: 10.1021/acs.organomet.5b00305
Organometallics 2015, 34, 1651−1660

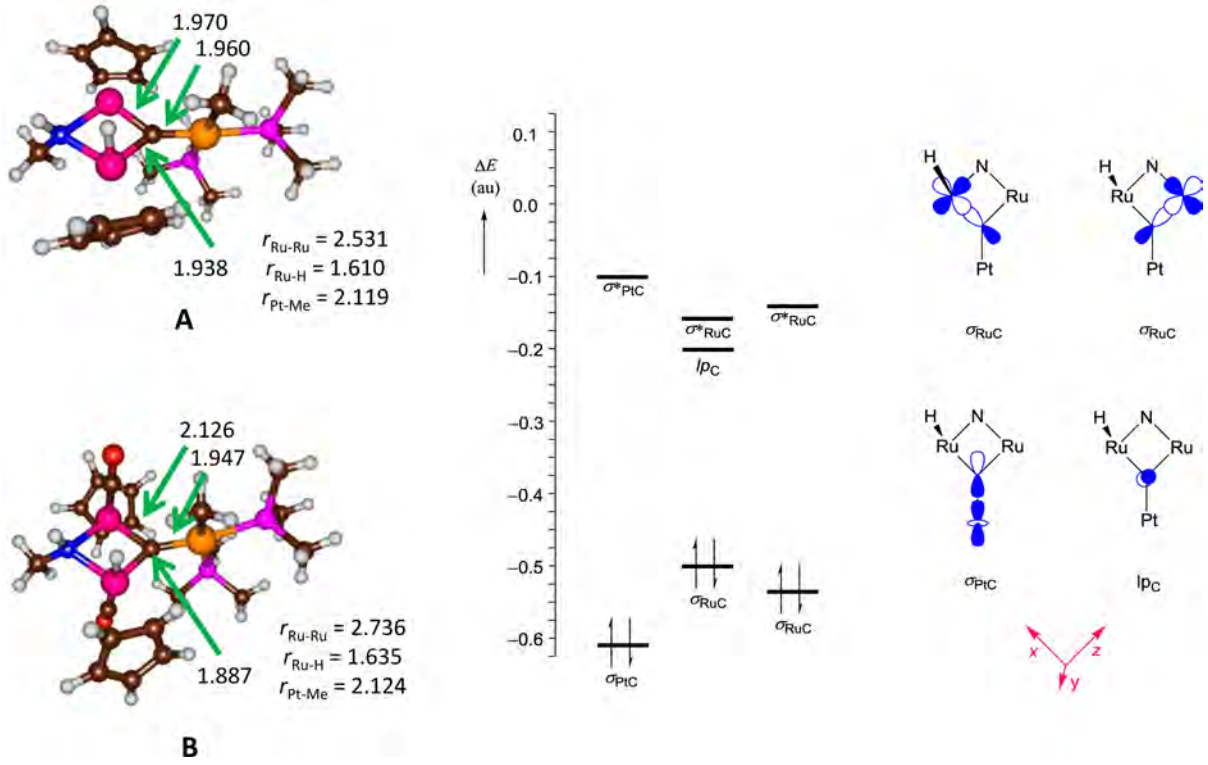

Figure 1. Optimized geometry of **A** and **B** as calculated with B3LYP with bond lengths given in angstroms. The right-hand side displays relative energies of the natural orbitals of **A** and gives drawings of the metal-carbon interactions.

reactants and products indeed connect via the reported transition state.

Our chemical model (Scheme 2) is based on the crystal structure coordinates of $[(Cp^*Ru)_2(\mu_2\text{-}H)(\mu_2\text{-}NHPh)(\mu_3\text{-}C)PtCH_3(P(CH_3)_3)_2]^+$,[4] whereby we replaced the Cp* groups with Cp and phenyl by methyl: Structure **A**. The stereochemical effects of the methyl groups of the $P(CH_3)_3$ groups on the reaction mechanism were investigated by replacement of the $P(CH_3)_3$ groups with PH_3. The latter structures are identified as **A′**, $\mathbf{I}_{A,Me}'$, and $\mathbf{I}_{A,H}'$. As the chemical system is saturated in carbon monoxide, we also created a model with two CO molecules bound (one on each Ru center): Structure **B**. We investigated the pathways starting from structures **A** and **B** for hydrogen atom abstraction to form $\mathbf{I}_{A,H1}/\mathbf{I}_{B,H1}$ intermediates via transition state $\mathbf{TS}_{A,H1}/\mathbf{TS}_{B,H1}$ as well as the alternative pathway for initial methyl transfer via transition states $\mathbf{TS}_{A,Me1}/\mathbf{TS}_{B,Me1}$ to form intermediates $\mathbf{I}_{A,Me1}/\mathbf{I}_{B,Me1}$. Subsequently, the methyl group is transferred to $\mathbf{I}_{A,H1}/\mathbf{I}_{B,H1}$ via transition state $\mathbf{TS}_{A,Me2}/\mathbf{TS}_{B,Me2}$ to form products. Alternatively, in the reactant, a methyl group is relayed to form $\mathbf{I}_{A,Me1}/\mathbf{I}_{B,Me1}$, followed by a hydrogen atom migration via transition state $\mathbf{TS}_{A,H2}/\mathbf{TS}_{B,H2}$ to form products (Scheme 2).

Charges reported in this work were obtained from a natural bond occupation (NBO) calculation as implemented in the Gaussian program package at the B3LYP/BS2 level of theory.[22]

In order to fully understand the thermodynamics and kinetics of the mechanism of the overall chemical reaction, we calculated the bond dissociation free energies (BDFEs) of key Ru/C−H and Pt/C−CH_3 bonds in complexes **A**, **B**, $\mathbf{I}_{A,Me1}$, $\mathbf{I}_{B,Me1}$, $\mathbf{I}_{A,H1}$, $\mathbf{I}_{B,H1}$, $\mathbf{P}_{A,H}$, and $\mathbf{P}_{B,H}$. The release of either $H^\bullet$, H^+, $CH_3^\bullet$, or CH_3^+ from these four complexes as described by eqs 1−4, whereby each individual structure was calculated through a full geometry optimization to give the adiabatic bond dissociation free energies. In addition, we calculated the methylenium transfer Gibbs free energy (MTFE) and the proton transfer Gibbs free energy (PTFE). The latter was calculated through the use of the H_2O/H_3O^+ couple to balance the equation. As there were large structural changes upon H/CH_3 bond breaking on the various complexes, we also calculated the diabatic bond dissociation free energies, or vertical bond dissociation free energies, whereby we took the optimized geometries of **A**, **B**, $\mathbf{I}_{A,Me1}$, $\mathbf{I}_{B,Me1}$, $\mathbf{I}_{A,H1}$, $\mathbf{I}_{B,H1}$, $\mathbf{P}_{A,H}$, and $\mathbf{P}_{B,H}$ and ran single point calculations with either $H^\bullet$, H^+, $CH_3^\bullet$, or CH_3^+ removed.

$$\mathbf{A}^+ \rightarrow [\mathbf{A} - H]^+ + H^\bullet + BDFE_H \quad (1)$$

$$\mathbf{A}^+ \rightarrow [\mathbf{A} - CH_3]^+ + CH_3^\bullet + BDFE_{Me} \quad (2)$$

$$\mathbf{A}^+ + H_2O \rightarrow [\mathbf{A}{-}H]^0 + H_3O^+ + PTFE \quad (3)$$

$$\mathbf{A}^+ \rightarrow [\mathbf{A} - CH_3]^0 + CH_3^+ + MTFE \quad (4)$$

RESULTS AND DISCUSSION

Before we discuss our calculated reaction mechanisms, let us briefly summarize the main results on our reactant structures, **A** and **B**, and establish their chemical properties. The optimized geometries of **A** and **B** are shown in Figure 1. The obtained bond distances of **A** are to within 0.011 Å of the crystal structure coordinates reported in ref 4, and as such, the DFT calculations give reasonable chemical structures. The Pt−C bond of 1.960/1.947 Å in **A**/**B** represents a single bond and is in good agreement with several reported Pt−C containing crystal structures from the literature.[23] The two Ru−C bonds are very close in bond length in **A**, and the fact that one of the two atoms is protonated, therefore, appears to have little effect on its interaction with carbon. However, addition of two CO molecules strongly affects the Ru−C bond lengths, and one of those is elongated to 2.126 Å in **B**. Ru−C bond lengths found here are typical for a single bond and compare to analogous structures reported before.[24] Therefore, addition of two CO molecules to structure **A** does not appear to have drastically changed the molecular geometry and keeps its original features.

The experimental studies of ref 4 implicate the hydride to bind as a bridging ligand to both Ru atoms, whereas Figure 1 gives a terminal-hydride atom that is linked to a single Ru atom.

DOI: 10.1021/acs.organomet.5b00305
Organometallics 2015, 34, 1651−1660

We created starting structures for a geometry optimization using both a bridging hydride atom as well as a terminal hydride atom. However, both of these calculations (whether CO was used as ligands or not) converged to the structure with a terminal hydride atom. This implies that a structure with a bridging hydride atom will be a higher energy state and possibly inaccessible.

As transition-metal complexes containing iron or ruthenium generally contain close-lying spin states and often react via multistate reactivity patterns,[14] structure **A** was optimized in the singlet, triplet, and quintet spin states. The closed-shell singlet spin state is the ground state and is well separated from the triplet and quintet spin states by ΔG_{gas} = 17.1 and 44.8 kcal mol^{-1}, respectively. These values change by less than 1 kcal mol^{-1} when solvent corrections are included. Clearly, structure **A** is a closed-shell species that will react via single-state reactivity in contrast to metal(IV)-oxo and metal(IV)-nitrido complexes from the literature.[25]

In order to shed light on the bonding pattern of the central carbon atom, we did a natural bond orbital (NBO) analysis of structure **A**. Thus, the NBO analysis reveals three bonding type orbitals for the central carbon atom, namely, three single bonds for the interaction with the two Ru atoms and the Pt atom. The σ_{PtC} orbital represents the σ-bonding orbital between Pt and C and is built up from the interaction of the $5d_{z^2}$ orbital on Pt with the $2p_z$ orbital on C. In addition, there are two single bonds between the carbido atom and the two Ru atoms, which result from the mixing of the 2s, $2p_x$, and $2p_z$ atomic orbitals on C with the $4d_{z^2}$ orbital on Ru or the $4d_{x^2-z^2}$ on Ru(H). As such, the central carbon atom is sp^2 hybridized. However, the fourth valence orbital on carbon is a virtual $2p_y$ atomic orbital. The NBO analysis, therefore, assigns the central carbon atom as a carbene with three sp^2 hybridized orbitals that are occupied with two electrons in an orbital donating to Pt (σ_{PtC}), and two bonding orbitals where both C and Ru donate one electron each into the bond (σ_{RuC}, σ_{RuC}). This hybridization scheme gives the central carbon atom its planar structure (Scheme 3).

Scheme 3. Hybridization Scheme of A and B

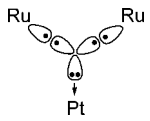

As such, the chemical structure of Ru_2CPt represents a Fischer-carbene, where the lone pair of the carbon atom interacts with an empty Pt orbital and the π-type Pt orbitals give backbonding into the empty $2p_y$ orbital of the carbene.[26] The NBO charges displayed in Figure 1 reveal a charge-neutral carbon atom (Q_C = 0.04) that is surrounded by slightly negatively charged metal atoms. Consequently, there is very little charge built up in this chemical system.

Subsequently, we calculated the potential energy profile for μ_2-$CHCH_3$ formation starting from **A** and **B**. We tested two mechanisms as shown in Figure 2: (i) initial hydrogen transfer from RuH to the carbene, followed by methyl abstraction, and (ii) initial methyl transfer from $PtCH_3$, followed by hydrogen/proton transfer. Figure 2 starts from the center with **A**/**B** and follows the two possible reaction mechanisms: The initial H transfer (mechanism to the right) and the initial CH_3 transfer (mechanism to the left). The two mechanisms are described as follows: In the first case, the metal-carbene group abstracts a hydrogen atom from the RuH group via a transition state $\mathbf{TS}_{H1}$ to form the H-transfer intermediate $\mathbf{I}_{H1}$. A subsequent CH_3 transfer from the $PtCH_3$ group via a barrier $\mathbf{TS}_{Me2}$ gives the μ_2-$CHCH_3$ bound product **P**. We also tested the alternative pathway starting with an initial CH_3 abstraction by the metal-carbene group via transition state $\mathbf{TS}_{Me1}$ leading to the methyl transfer intermediate $\mathbf{I}_{Me1}$. This intermediate then reacts further by H abstraction from RuH via a transition state $\mathbf{TS}_{H2}$ to form product **P**.

We attempted to also locate the alternative synchronous transfer of both hydrogen and methyl group at the same time to the carbene atom; however, all calculations converged to one of the lower-lying transition states (or local minima) described in this work. Previously, we calculated the concerted epoxidation reaction of an olefin by an iron(IV)-oxo heme cation radical system and found it to be a second-order saddle point that is well higher in energy than the stepwise transition states.[27]

Dramatic differences in relative energies and optimized structures are found for the pathways starting from **A** or **B**; however, in both cases, the H-atom transfer reaction has the lowest Gibbs free energy of activation of $\Delta G^{\ddagger}$ = 19.6 (3.1) kcal mol^{-1} for **A** (**B**). Nevertheless, in both cases, it is not the rate-determining step as the subsequent CH_3 transfer to form products gives an additional barrier with a maximum of 23.1 (24.2) kcal mol^{-1}. Therefore, the reaction that is initiated with H-atom transfer from **A** has an unfeasible Gibbs free energy of activation of 42.7 kcal mol^{-1} for $\mathbf{TS}_{A,Me2}$ with respect to **A** and will not be able to proceed through that pathway. On the other hand, this barrier for structure **B** is much lower in energy, but still would imply a relatively slow reaction process. This is in agreement with experimental observation that found evidence of a structure with analogy to $\mathbf{I}_H$, but the methyl group bound to one of the Ru atoms, which would imply a fast hydrogen abstraction, followed by a much slower methyl transfer. The origin of the enhanced stabilization of CO bound intermediate $\mathbf{I}_{B,H1}$ with respect to $\mathbf{I}_{A,H1}$ comes from the structural differences. Thus, without CO bound, the carbene carbon atom pyramidalizes much more and the dihedral angle $d_{CRuRuPt}$ = 43.3° in $\mathbf{I}_{A,H1}$, whereas it is 25.7° in $\mathbf{I}_{B,H1}$. The large pyramidalization causes contraction of the chemical system and more stereochemical repulsions of the $P(CH_3)_3$ groups with the RuCp groups that destabilize the structure.

The alternative pathway with an initial CH_3 transfer, on the other hand, has a calculated Gibbs free energy of activation of $\Delta G^{\ddagger}$ = 21.5 (25.4) kcal mol^{-1} for **A** (**B**) and, therefore, is disfavored over the initial H-atom transfer process. However, this reaction leads to a very stable intermediate $\mathbf{I}_{A,Me1}$ with an exergonicity of almost 10 kcal mol^{-1}, whereas the reaction is endothermic for the formation of $\mathbf{I}_{B,Me1}$. Its subsequent H-atom transfer leading to products only has a Gibbs free energy of activation of 18.3 (6.2) kcal mol^{-1} from intermediates for **A** (**B**). Therefore, product formation is a viable, but kinetically slow, pathway through this channel for both structures **A** and **B**, whereby it is the dominant mechanism for **A** and competitive with initial hydrogen atom abstraction for **B**. Binding of CO molecules to the reaction center, therefore, changes the regioselectivity of the chemical reaction in favor of initial hydrogen atom abstraction. In previous work on the regioselectivity of substrate epoxidation versus hydroxylation by iron(IV)-oxo complexes, we showed that changes to the ligand system of the iron or even replacing hydrogen atoms of the substrate by deuterium atoms can reverse a regioselectivity, and as such, the Ru_2Pt-carbene complex is another example of a

DOI: 10.1021/acs.organomet.5b00305
Organometallics 2015, 34, 1651−1660

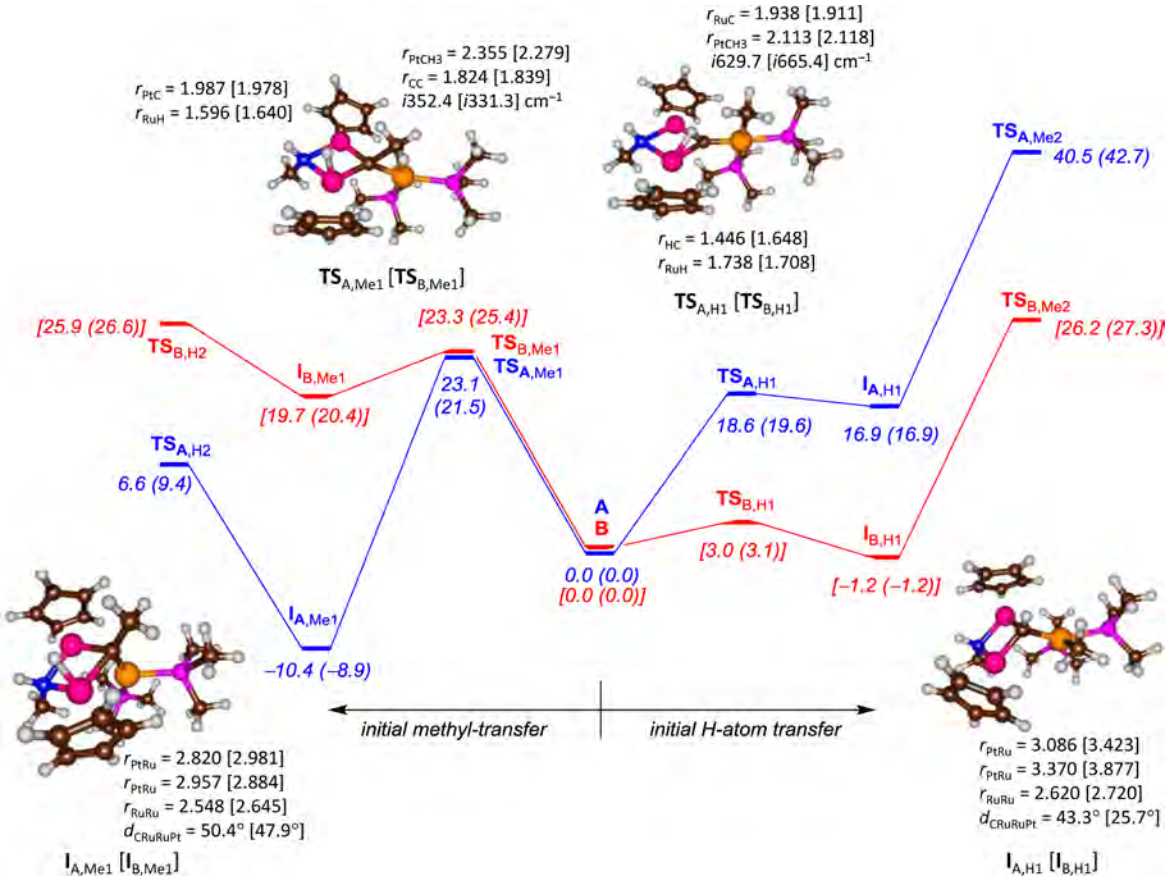

Figure 2. Gibbs free energy profile of alkyl chain growth on **A** and **B** via either (i) CH_3 transfer, followed by H transfer (mechanism from the center to the left), or (ii) H transfer, followed by CH_3 transfer (mechanism from the center to the right). Energies (ΔE + ZPE) and free energies (ΔG, in parentheses) obtained with B3LYP/BS2 with values in kcal mol^{-1}. All data include solvent corrections to the energy. Optimized geometries report bond lengths in angstroms, angles in degrees, and the imaginary frequency of the transition states in wavenumbers.

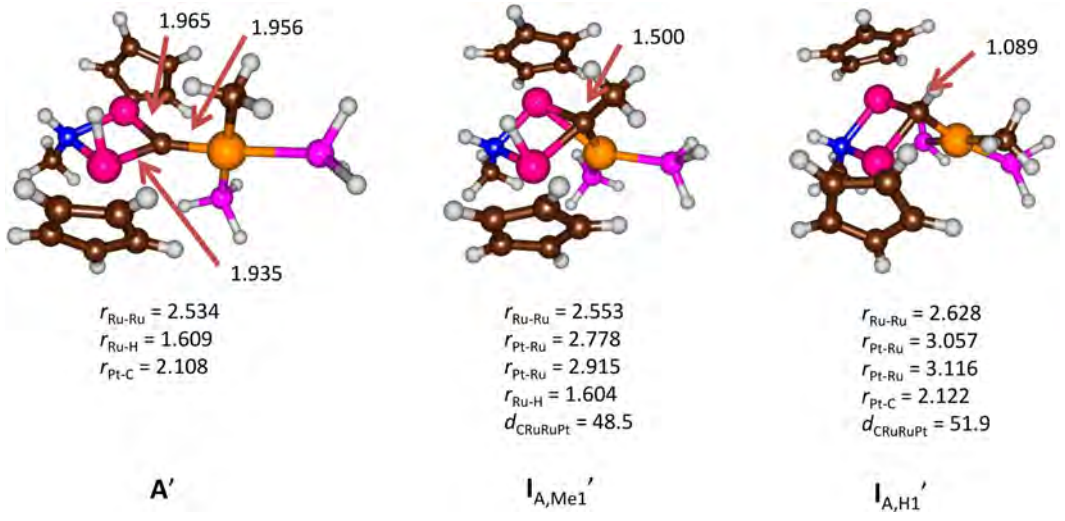

Figure 3. Optimized geometries of **A**′, $I_{A,Me1}$′, and $I_{A,H1}$′ with bond lengths in angstroms.

chemical catalyst that changes its reactivity upon ligand modifications.[28]

The origin of the differences in stability of $I_{A,Me1}$ versus $I_{B,Me1}$ stems from differences in location of the transferring hydrogen atom. Thus, in $I_{A,Me1}$, the hydrogen atom is located close to one Ru atom with Ru1−H and Ru2−H distances of 1.604 and 2.521 Å, whereas they change to 1.736 and 1.943 Å, respectively, in $I_{B,Me1}$. The structure with the bridging proton is considerably destabilized with respect to singly protonated Ru atom.

In summary, DFT establishes a possible alkyl synthesis mechanism for **A** as a stepwise mechanism with an initial CH_3 transfer, followed by H-atom transfer, whereas structure **B** proceeds with competitive mechanisms via either initial CH_3-

DOI: 10.1021/acs.organomet.5b00305
Organometallics 2015, 34, 1651−1660

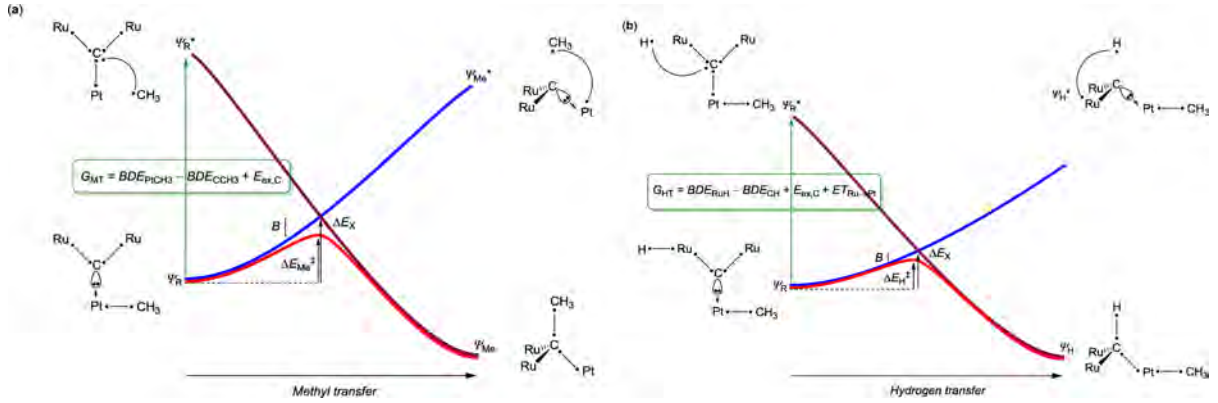

Figure 4. Valence bond curve crossing diagrams for methyl transfer (part a) and hydrogen atom transfer (part b) from reactants (**A** or **B**). Valence electrons are identified with a dot.

or H-transfer processes. An analysis of the group spin densities and charges (Supporting Information) along the complete reaction mechanism shows that all local minima and transition states are closed-shell singlet species with no radical built up during the reaction. Accordingly, the reaction starts with either proton transfer or CH_3^+ transfer.

So, why is the reaction displayed in Figure 2 stepwise with consecutive CH_3- or H-transfer processes, and what is the function of the Ru_2Pt scaffold? These questions will be answered in the following discussion. Structurally, there are major changes happening at the Ru_2Pt-carbene center during the reaction mechanism. Although **A** and **B** have an sp^2 hybridized carbon atom that lies in the plane of the Ru_2Pt atoms, upon H/CH_3 transfer, the planarity is distorted and the carbon atom relaxes to a pyramidal conformation due to sp^3 hybridization. The pyramidalization is considerably more pronounced for the CH_3-transfer process than in the H-atom transfer pathway as dihedral angles C−Ru−Ru−Pt of 50.4° for $\mathbf{I}_{A,Me1}$ and 43.3° for $\mathbf{I}_{A,H1}$ are found. At the same time, the Pt−Ru distances in $\mathbf{I}_{A,Me1}$ shorten by as much as 0.8 Å with respect to **A** to well below 3 Å, while, in $\mathbf{I}_{A,H1}$, they stay considerably longer: r_{PtRu} = 3.086 and 3.370 Å. These large structural changes for the CH_3-transfer pathway will have an effect on the reaction energetics and kinetics as well as on the relative stability of $\mathbf{I}_{A,Me1}$ versus $\mathbf{I}_{A,H1}$. Thus, the Pt atom in $\mathbf{I}_{A,Me1}$ only has three ligands due to CH_3 transfer to the carbon atom, which means limited stereochemical interactions between the two $P(CH_3)_3$ groups and the rest of the molecule so that the Pt atom can approach the two Ru atoms closely. In $\mathbf{I}_{A,H1}$, the Pt atom remains tetracoordinated and the stereochemical interactions between all ligands and the rest of the molecule prevent a close approach to the Ru_2C center. As a consequence of the stereochemical repulsions, $\mathbf{I}_{A,H1}$ is considerably destabilized over $\mathbf{I}_{A,Me1}$ and the reaction pathway with initial H-atom transfer is energetically disfavored.

To further establish these stereochemical interactions in $\mathbf{I}_{A,H1}$ versus $\mathbf{I}_{A,Me1}$, we did a subsequent set of calculations on these structures, but with the $P(CH_3)_3$ groups replaced by PH_3: structures $\mathbf{I}_{A,H1}'$ and $\mathbf{I}_{A,Me1}'$ (Figure 3). The optimized geometry of **A′** (Figure 3) is very close to that reported above for **A** in Figure 1, and only minor changes in bond lengths are obtained. Clearly, the $P(CH_3)_3$ groups have little effect on the structure of the Ru_2PtC core of our chemical system. A similar situation occurs for $\mathbf{I}_{A,Me1}'$, which has large structural similarities with $\mathbf{I}_{A,Me}$ reported in Figure 2. Major changes, however, are seen when $\mathbf{I}_{A,H1}$ is compared to $\mathbf{I}_{A,H1}'$. Thus, one of the Ru−Pt distances decreases from 3.370 to 3.116 Å, and as a consequence, the pyramidality of the carbon center changes from $d_{CRuRuPt}$ = 43.3° in $\mathbf{I}_{A,H1}$ to a value of 51.9° in $\mathbf{I}_{A,H1}'$. This has a major effect on the stability of $\mathbf{I}_{A,H1}'$, and it is stabilized by 6.0 kcal mol^{-1} with respect to **A′**; however, the $\mathbf{I}_{A,Me1}'$ remains the most stable conformation. This implies that the $P(CH_3)_3$ groups incur a destabilizing effect on the reaction mechanism, but will not reverse the preference of initial CH_3 transfer over H-atom transfer.

To gain insight into the electronic changes during the reaction mechanism, a NBO analysis was also performed on the intermediate and product complexes. The NBO calculation reveals a configuration on the central carbon atom of $2s^{1.08}2p^{2.92}$ for $\mathbf{I}_{A,Me1}$ and $2s^{1.18}2p^{3.10}$ for $\mathbf{I}_{A,H1}$. Both intermediate complexes, therefore, have an electronic configuration close to sp^3 hybridization, and as a consequence, their geometries have changed from planar to pyramidal, in agreement with the optimized structures.

In order to fully understand the thermodynamics and kinetics of the mechanism displayed in Figure 2, and, in particular, gain insight into the electron transfer mechanisms during the reaction processes, we set up valence bond (VB) curve crossing diagrams (Figure 4) for the methyl transfer and hydrogen atom transfer steps. We applied these VB curve crossing diagrams previously to rationalize the reaction mechanisms of substrate activation (hydroxylation, epoxidation, desaturation, and sulfoxidation) by Compound I of cytochrome P450 enzymes as well as the nonheme iron(IV)-oxo species of dioxygenases.[29] These studies rationalized reaction mechanisms and, for instance, explained why a reaction was stepwise via a radical intermediate rather than synchronous (concerted). Furthermore, in the case of P450 Compound I, several possible electron transfer pathways in substrate hydroxylation by Compound I were identified via either an iron(IV)-hydroxo intermediate or an iron(III)-hydroxo heme cation radical, and different activation barriers (and consequently rate constants) were identified that passed these individual intermediates.[30] VB diagrams explained the differences in electron transfer pathways and rationalized the ordering of the various electronic and spin states. Finally, the VB diagrams were used to find patterns in activation energies/rate constants and create predictive models. As such, these VB curve crossing diagrams may also find their use in organometallic chemistry, and therefore, we applied it to the chemical system described here.

The VB curve crossing diagrams start at the bottom-left with the reactant electronic configuration and wave function (Ψ_R) of

DOI: 10.1021/acs.organomet.5b00305
Organometallics 2015, 34, 1651−1660

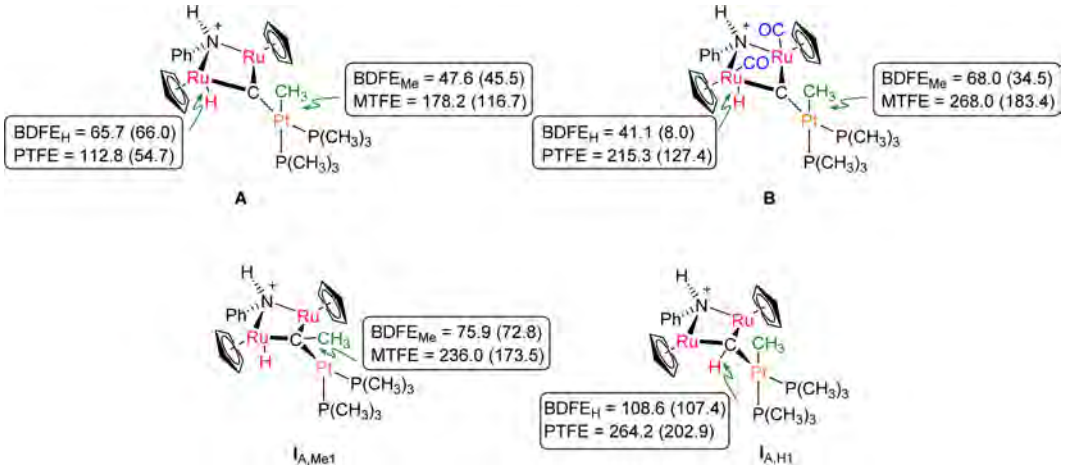

Figure 5. Bond dissociation free energies (BDFEs in kcal mol^{-1}) of key bonds in structures **A**, **B**, $\mathbf{I}_{A,Me1}$, and $\mathbf{I}_{A,H1}$. Reactions calculated according to eqs 1−4. Values in parentheses are solvent-corrected free energies, whereas those out of parentheses are gas-phase data. PTFE and MTFE are the proton and methyl transfer Gibbs free energies, respectively.

A/**B**, which is a carbene where two sp^2 electrons form bonding orbitals with electrons on the two ruthenium atoms and the other two electrons represent a lone pair orbital that donates a bond to Pt. Each of the dots in Figure 4 represents one of these valence electrons. In part (a) in Figure 4, the reaction follows the methyl transfer from Pt to carbene and the structure on the right-hand side gives the electronic configuration of $\mathbf{I}_{Me}$ with wave function Ψ_{Me}. In $\mathbf{I}_{Me}$, the central carbon atom is sp^3 hybridized and forms a single bond with Ru, Ru, Pt, and CH_3. In VB theory, the wave functions of the reactant and product complexes cross, i.e., Ψ_R and Ψ_{Me} in Figure 4a, and lead to an avoided crossing and a transition state for the reaction from reactants to intermediates.[31] Thus, the curve crossing energy (ΔE_X) is above the actual transition state ($\Delta E_{Me}^{\ddagger}$) by a factor *B*, which is called the resonance energy. It has been shown that the barrier height can be described by the difference in energy by a fraction (f) of the promotion gap (G) and the resonance energy *B*: $\Delta E_{Me}^{\ddagger} = fG_{MT} - B$. The promotion gap signifies the excitation energy from the ground state wave function to the product wave function in the geometry of the reactants; i.e., G_{MT} is the energy difference between Ψ_R and Ψ_R* in the reactant geometry. The VB diagrams also give chemical structures of the reactant and product wave functions of the ground and excited state species with valence electrons identified with a dot.

A close inspection of the VB diagrams in Figure 4 shows that the promotion gap for methyl transfer (G_{MT}) represents the breaking of the Pt−CH_3 bond and the formation of a new C−CH_3 bond. In addition, the VB structures of Ψ_R and Ψ_R* show that the carbene carbon is rehybridized from sp^2 to sp^3 hybridization and one electron of the lone pair orbital pointing toward Pt is promoted into the new sp^3 orbital. At the same time, the electron from the broken Pt−CH_3 bond moves into the carbene−Pt bond. Thus, the promotion gap also contains a component for the excitation energy of the carbene from sp^2 to sp^3 hybridization ($E_{ex,C}$), which essentially requires a promotion of an electron from the σ_{PtC} orbital to the virtual 2p$_y$ molecular orbital on carbon. Energetically, G_{MT} can be described in terms of the bond dissociation energies (BDEs) of the respective bonds that are broken and formed in the reaction process (eq 5), whereby BDE_{PtCH_3} represents the Gibbs free energy to break the Pt−CH_3 bond in **A**/**B** and BDE_{CCH_3} is the Gibbs free energy to form the C−CH_3 bond in $\mathbf{I}_{A,Me1}$/$\mathbf{I}_{B,Me1}$.

$$G_{MT} \propto BDE_{PtCH_3} - BDE_{CCH_3} + E_{ex,C} \quad (5)$$

The situation is dramatically different for hydrogen atom transfer from **A**/**B**, as shown in Figure 4b. Thus, the barrier height for hydrogen atom transfer ($\Delta E_H^{\ddagger}$) is proportional to the promotion gap for hydrogen atom transfer (G_{HT}), which correlates with the strength of the Ru−H bond that is broken (BDE_{RuH}), the strength of the C−H bond that is formed (BDE_{CH}), and again the excitation energy for the carbene to change from sp^2 to sp^3 hybridization. In addition to these three terms, the promotion gap G_{HT} also contains a component for the electron transfer energy from Ru to Pt ($ET_{Ru\rightarrow Pt}$). The hydrogen atom transfer process, therefore, incurs extra electron reorganization energy in the Ru_2Pt-carbene scaffold, which is not necessary for the methyl transfer step. The overall preference of hydrogen atom transfer versus methyl transfer will depend on the relative strengths of the bonds that are broken and formed in the process and the electron reorganization energy. To find out whether there are major differences between the BDE values in eq 5 and those in eq 6, we decided to calculate their values with DFT.

$$G_{HT} \propto BDE_{RuH} - BDE_{CH} + E_{ex,C} + ET_{Ru\rightarrow Pt} \quad (6)$$

As the VB drawings in Figure 4 only give qualitative analysis of electron transfer processes and no actual quantitative values, we decided to calculate BDEs and bond dissociation free energies (BDFEs) of key Ru/C−H and Pt/C−CH_3 bonds in complexes **A**, **B**, $\mathbf{I}_{A,Me1}$, and $\mathbf{I}_{A,H1}$ by calculating the release of a H$^{\bullet}$, H$^+$, $CH_3^{\bullet}$, and CH_3^+ from these four complexes according to eqs 1−4 above. Figure 5 displays the diabatic driving forces for H/CH_3 release from complexes **A**, **B**, $\mathbf{I}_{A,H1}$, and $\mathbf{I}_{A,Me1}$. We initially calculated the adiabatic BDFE calculations, whereby we did a full geometry optimization of all individual chemical structures in eqs 1−4 and then took the difference in Gibbs free energy for each of these reactions. However, due to considerable rehybridization of the central carbon atom and, as a consequence, large geometrical changes in some of the structures, the adiabatic BDFE values gave unrealistic results. For instance, the adiabatic bond dissociation energy for the breaking of the Ru−H bond in **A** appears negative, which

DOI: 10.1021/acs.organomet.5b00305
Organometallics 2015, 34, 1651−1660

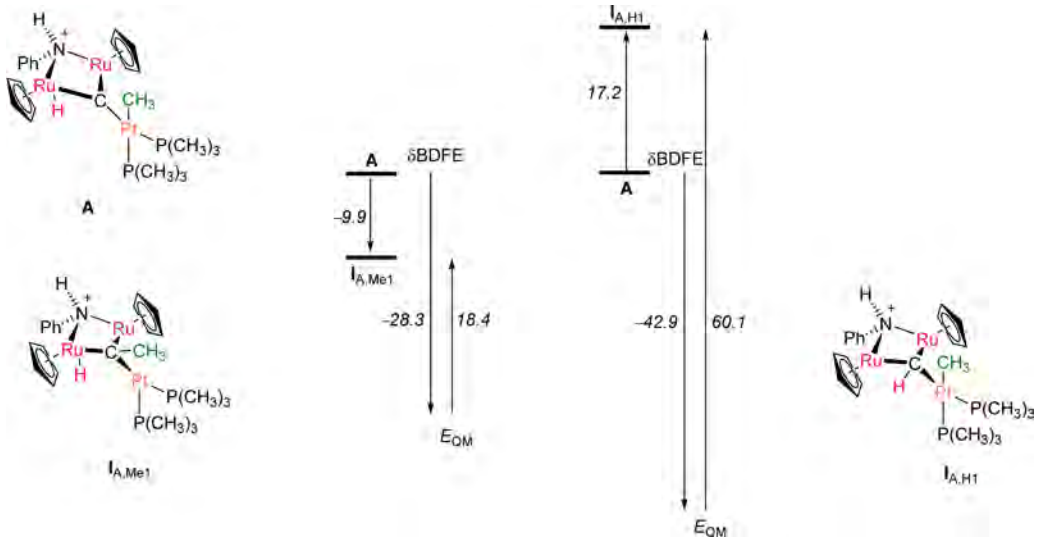

Figure 6. Energy decomposition of the methyl and hydrogen atom transfer reaction from **A**. Gibbs free energies given are in kcal mol^{-1}.

would imply spontaneous dissociation, in disagreement with the experimental crystal structure. However, this did not happen during the geometry optimization, and consequently, there is a significant barrier for this process. Another reason the adiabatic energies give unrealistic results is the dramatic structural changes upon removal of one ligand, i.e., H or CH_3, which changes systems from hexacoordination to pentacoordination, i.e., from an octahedral to a trigonal bipyramical structure, which leads to major changes in electronic structure.[32] Conversely, when we calculate the diabatic Gibbs free energy change by taking the H and [**A**−H] products in the geometry of **A**, then the BDFE is positive. The same is found for the dissociation of a methyl group from **A**. By contrast to structure **A**, the adiabatic and diabatic bond energies in structures $\mathbf{I}_{A,Me1}$ and $\mathbf{I}_{A,H1}$ are very similar and vary by less than 6 kcal mol^{-1}. In the following, however, we will focus on the diabatic bond dissociation free energies.

As can be seen, the strength of the C−H bond in **A** is considerably different from that obtained for **B**. Thus, the $BDFE_H$ for **A** is 45.5 kcal mol^{-1} in solvent, whereas a value of 34.5 kcal mol^{-1} is found for **B**, and as a consequence, the hydrogen atom transfer should be much easier with the CO bound complex then with complex **A**. Indeed, the potential energy landscape in Figure 2 shows that formation of $\mathbf{I}_{B,H1}$ is exergonic by −1.2 kcal mol^{-1}, whereas it is endergonic for $\mathbf{I}_{A,H1}$. Thus, CO binding affects the chemical structure of the Ru centers and weakens the Ru−H bond and makes it more susceptible for hydrogen atom transfer. Despite the fact that the subsequent methyl transfer still has a barrier of about 28 kcal mol^{-1} (virtually unchanged with respect to **A**), it is now sufficiently low to cross at ambient temperatures and pressures. On the other hand, the platinum−methyl bond is much stronger in the CO bound structures and results in a considerable raise in the $\mathbf{I}_{B,Me1}$ energy.

Thermodynamically, the driving force to form $\mathbf{I}_{A,Me1}/\mathbf{I}_{A,H1}$ from **A** represents the breaking of a weak Pt−CH_3 or Ru−H bond and the formation of a much stronger C−CH_3/C−H bond. Hence, the reaction should be strongly exergonic, which is seen for the reaction via $\mathbf{I}_{A,Me1}$ in Figure 2, but not for the one via $\mathbf{I}_{A,H1}$. Thus, the hydrogen atom transfer from Ru in **A** to the carbene to form $\mathbf{I}_{A,H1}$ results in the breaking of the Ru−H bond of $BDFE_H$ = 65.7 kcal mol^{-1} in the gas phase and the formation of a C−H bond with a diabatic value of 108.6 kcal mol^{-1}, and if the driving force was solely dependent on the change in bond strength, the reaction would have been exergonic by 42.9 kcal mol^{-1}. As shown in Figure 2, however, this reaction is endergonic by 17.2 kcal mol^{-1}, which implies that the stereochemical and electronic effects, i.e., the sp^2 to sp^3 rehybridization ($E_{ex,C}$) and the Ru → PT electron transfer ($ET_{Ru\rightarrow Pt}$), account for a destabilization of $\mathbf{I}_{A,H1}$ by about 60 kcal mol^{-1} in Gibbs free energy. This is explained schematically in Figure 6, where we deconvolute the processes from **A** to $\mathbf{I}_{A,Me1}$ and from **A** to $\mathbf{I}_{A,H1}$ into factors for bond breaking and formation (δBDFE) and quantum mechanical effects (E_{QM}). Thus, the methyl transfer reaction from **3** results in the breaking of the Pt−CH_3 bond, which requires a $BDFE_{Me,diabatic}$ = 47.6 kcal mol^{-1}, and, at the same time, the formation of the C−CH_3 bond ($BDFE_{Me,diabatic}$ = 75.9 kcal mol^{-1}). Therefore, the change in bond dissociation Gibbs free energy for the methyl transfer is −28.3 kcal mol^{-1}. The reaction mechanism in Figure 2 found the methyl transfer process to be exergonic by 9.9 kcal mol^{-1}, which implies that the quantum mechanical effect of the process accounts for 18.4 kcal mol^{-1}. The quantum mechanical effect includes the rehybridization energy of the carbene group and the geometric and stereochemical factors associated with the methyl transfer. By comparison, the hydrogen atom transfer shows a much larger change in bond dissociation energy due to the strong C−H bond that is formed ($\delta BDFE_{H,diabatic}$ = −42.9 kcal mol^{-1}). However, this reaction incurs a large quantum mechanical effect of 60.1 kcal mol^{-1} and thereby makes the overall process highly endergonic. The quantum mechanical effect includes the rehybridization of the carbon atom, which will probably be of the same order of magnitude as that found for the methyl transfer process, i.e., about 18 kcal mol^{-1}. In addition, there are the above-mentioned stereochemical repulsions of the methyl groups of the $P(CH_3)_3$ moieties that raise $\mathbf{I}_{A,H1}$ by about 6 kcal mol^{-1}. Finally, the electronic effects (E_{QM}) for the hydrogen atom transfer reaction include the electron transfer energy from Ru to Pt, as described in the VB diagram in Figure 4.

In addition to removal of H/CH_3 from our reactant complexes and intermediates, the breaking of the bond into two ions was also investigated and is described as the proton transfer Gibbs free energy (PTFE) and methyl transfer Gibbs

DOI: 10.1021/acs.organomet.5b00305
Organometallics 2015, 34, 1651−1660

free energy (MTFE). As follows from the data in Figure 5, it requires considerably more energy to break the Ru−H and Pt−CH_3 bonds than a homogeneous splitting into $Ru^{\bullet}$ + $H^{\bullet}$ and $Pt^{\bullet}$ + $CH_3^{\bullet}$. The thermodynamic analysis confirms the results described above in Figure 2, where either an $H^{\bullet}$ or $CH_3^{\bullet}$ is transferred rather than H^+ and CH_3^+.

So what about the next step for the formation of μ_2-$CHCH_3$ products? The reaction from $\mathbf{I}_{A,Me1}$ to products results in the breaking of the Ru−H bond and the formation of a new C−H bond. By contrast, the pathway from $\mathbf{I}_{A,H1}$ leads to the breaking of the Pt−CH_3 bond and the transfer of the methyl group to carbon. However, this process breaks the C−Pt bond and the $Pt(P(CH_3)_3)_2$ group is left behind with two unpaired electrons. Thus, an electron on Pt is promoted into a virtual orbital and the reaction proceeds via a high energy pathway. Indeed, the DFT calculated potential energy profile in Figure 2 gives a high barrier for $\mathbf{TS}_{A,Me2}$, in agreement with this.

In summary, DFT calculations presented here show a novel pathway for the synthesis of linear alkanes on a trimetal-carbene center. The chemical system discussed here, however, is inefficient as the lowest-lying initial barrier is for hydrogen atom transfer, which leads to a dead-end reaction intermediate. By contrast, the initial methyl transfer can be followed by hydrogen atom transfer to lead to products. The question is how this catalyst may be improved for alkane synthesis. The thermodynamic and VB schemes above give some clear indication to this. As shown in eqs 5 and 6, above, the barrier heights $\mathbf{TS}_{H1}$ and $\mathbf{TS}_{Me1}$ are dependent on the Ru−H and Pt−CH_3 bonds that are broken and the C−H and C−CH_3 bonds being formed. Consequently, a chemical system with a weaker metal−CH_3 bond should react predominantly via initial methyl transfer and may be more efficient. The work described here may have relevance to biological and heterogeneous catalysis for the synthesis of alkanes. In particular, in heterogeneous catalysis, linear alkanes are generated on a metal surface using often CO and H_2 as reactants. It may very well be that the trimetal-carbene structure discussed here is a common type intermediate in heterogeneous catalysis, but further research will have to be performed to establish this.

CONCLUSIONS

In summary, our calculations establish the key features of a synthetic homogeneous catalyst for alkyl chain growth. A combination of DFT, NBO, VB, and thermochemical studies has been performed and establish the intrinsic chemical properties of **A** or **B**. First, we characterize reactants as having a Ru_2Pt-carbene core where the lone pair is donated to Pt via a bonding/backbonding configuration. Second, we find a low energy mechanism of alkyl formation through consecutive $CH_3^{\bullet}$ and $H^{\bullet}$ transfer to the carbene with low Gibbs free energy of activation and exergonic driving force. We show that the reverse process is thermochemically hampered and would lead to an excited triplet configuration.

Overall, our work identifies a novel reaction for the synthesis of alkanes that starts from a trimetal carbene. This unique structure is shown to be capable of intramolecular methyl and hydrogen atom transfer to the carbene to form μ_2-$CHCH_3$ products as precursor to alkanes.

ASSOCIATED CONTENT

Supporting Information

Supporting Information with Cartesian coordinates as well as tables with group spin densities, charges, and absolute and relative energies is provided. The Supporting Information is available free of charge on the ACS Publications website at DOI: 10.1021/acs.organomet.5b00305.

AUTHOR INFORMATION

Corresponding Authors

*E-mail: Sam.devisser@manchester.ac.uk (S.P.d.V.).
*E-mail: dkclcre@yahoo.com (D.K.).

Author Contributions

§These authors contributed equally.

Notes

The authors declare no competing financial interests.

ACKNOWLEDGMENTS

The National Service of Computational Chemistry Software is thanked for CPU time provided. D.K. holds the Ramanujan Fellowship (SR/S2/RJN-11/2008) from the Department of Science and Technology (DST), New Delhi (India). M.A.S. thanks the Petroleum Technology Development Fund in Nigeria for a studentship.

REFERENCES

(1) (a) Rofer-de Poorter, C. K. *Chem. Rev.* **1981**, *81*, 447−474. (b) Schulz, H. *Appl. Catal., A* **1999**, *186*, 3−12. (c) Khodakov, A. Y.; Chu, W.; Fongarland, P. *Chem. Rev.* **2007**, *107*, 1692−1744. (d) Maitlis, P. M.; Zanotti, V. *Chem. Commun.* **2009**, 1619−1634.

(2) See, e.g.: (a) Tsakoumis, N. E.; Rønning, M.; Borg, Ø.; Rytter, E.; Holmen, A. *Catal. Today* **2010**, *154*, 162−182. (b) Shetty, S.; van Santen, R. A. *Catal. Today* **2011**, *171*, 168−173. (c) Inderwildi, O. R.; Jenkins, S. J. *Chem. Soc. Rev.* **2008**, *37*, 2274−2309.

(3) (a) Perkins, P.; Vollhardt, K. P. C. *J. Am. Chem. Soc.* **1979**, *101*, 3985−3987. (b) Inderwildi, O. R.; King, D. A.; Jenkins, S. J. *Phys. Chem. Chem. Phys.* **2009**, *11*, 11110−11112.

(4) Takemoto, S.; Morita, H.; Karitani, K.; Fujiwara, H.; Matsuzaka, H. *J. Am. Chem. Soc.* **2009**, *131*, 18026−18027.

(5) (a) Mayer, J. M. *Acc. Chem. Res.* **1998**, *31*, 441−450. (b) Weinberg, D. R.; Gagliardi, C. J.; Hull, J. F.; Murphy, C. F.; Kent, C. A.; Westlake, B. C.; Paul, A.; Ess, D. H.; McCafferty, D. G.; Meyer, T. J. *Chem. Rev.* **2012**, *112*, 4016−4093.

(6) See, e.g.: (a) Love, J. A.; Sanford, M. S.; Day, M. W.; Grubbs, R. H. *J. Am. Chem. Soc.* **2003**, *125*, 10103−10109. (b) Alcaide, B.; Almendros, P.; Luna, A. *Chem. Rev.* **2009**, *109*, 3817−3858. (c) Bernal, M. J.; Torres, O.; Martín, M.; Sola, E. *J. Am. Chem. Soc.* **2013**, *135*, 19008−19015.

(7) (a) Miller, R. L.; Wolczanski, P. T.; Rheingold, A. L. *J. Am. Chem. Soc.* **1993**, *115*, 10422−10423. (b) Su, C.-J.; Su, P.-C.; Chi, Y.; Peng, S.-M.; Lee, G.-H. *J. Am. Chem. Soc.* **1996**, *118*, 3289−3290. (c) Peters, J. C.; Odom, A. L.; Cummins, C. C. *Chem. Commun.* **1997**, 1995−1996. (d) Caselli, A.; Solari, E.; Scopelliti, R.; Floriani, C. *J. Am. Chem. Soc.* **2000**, *122*, 538−539. (e) Buchowicz, W.; Herbaczyńska, B.; Jerzykiewicz, L. B.; Lis, T.; Pasynkiewicz, S.; Pietrzykowski, A. *Inorg. Chem.* **2012**, *51*, 8292−8297. (f) Harding, D. J.; Kerpal, C.; Meijer, G.; Fielicke, A. *J. Phys. Chem. Lett.* **2013**, *4*, 892−896. (g) Borren, E. S.; Hill, A. F.; Shang, R.; Sharma, M.; Willis, A. C. *J. Am. Chem. Soc.* **2013**, *135*, 4942−4945. (h) Li, X.; Wang, L.-S.; Boldyrev, A. I.; Simons, J. *J. Am. Chem. Soc.* **1999**, *121*, 6033−6038.

(8) (a) de Visser, S. P.; Tan, L. S. *J. Am. Chem. Soc.* **2008**, *130*, 12961−12974. (b) Latifi, R.; Bagherzadeh, M.; de Visser, S. P. *Chem.—Eur. J.* **2009**, *15*, 6651−6662.

(9) *Jaguar 7.7*, version 7.9; Schrodinger, LLC: New York, NY, 2011.

(10) Frisch, M. J.; Trucks, G. W.; Schlegel, H. B.; Scuseria, G. E.; Robb, M. A.; Cheeseman, J. R.; Scalmani, G.; Barone, V.; Mennucci, B.; Petersson, G. A.; Nakatsuji, H.; Caricato, M.; Li, X.; Hratchian, H. P.; Izmaylov, A. F.; Bloino, J.; Zheng, G.; Sonnenberg, J. L.; Hada, M.; Ehara, M.; Toyota, K.; Fukuda, R.; Hasegawa, J.; Ishida, M.; Nakajima, T.; Honda, Y.; Kitao, O.; Nakai, H.; Vreven, T.; Montgomery, J. A., Jr.;

DOI: 10.1021/acs.organomet.5b00305
Organometallics 2015, 34, 1651−1660

Peralta, J. E.; Ogliaro, F.; Bearpark, M.; Heyd, J. J.; Brothers, E.; Kudin, K. N.; Staroverov, V. N.; Kobayashi, R.; Normand, J.; Raghavachari, K.; Rendell, A.; Burant, J. C.; Iyengar, S. S.; Tomasi, J.; Cossi, M.; Rega, N.; Millam, J. M.; Klene, M.; Knox, J. E.; Cross, J. B.; Bakken, V.; Adamo, C.; Jaramillo, J.; Gomperts, R.; Stratmann, R. E.; Yazyev, O.; Austin, A. J.; Cammi, R.; Pomelli, C.; Ochterski, J. W.; Martin, R. L.; Morokuma, K.; Zakrzewski, V. G.; Voth, G. A.; Salvador, P.; Dannenberg, J. J.; Dapprich, S.; Daniels, A. D.; Farkas, Ö.; Foresman, J. B.; Ortiz, J. V.; Cioslowski, J.; Fox, D. J. *Gaussian 09*, Revision A.1; Gaussian, Inc.: Wallingford, CT, 2009.

(11) (a) Becke, A. D. *J. Chem. Phys.* **1993**, *98*, 5648−5652. (b) Lee, C.; Yang, W.; Parr, R. G. *Phys. Rev. B* **1988**, *37*, 785−789.

(12) Hay, P. J.; Wadt, W. R. *J. Chem. Phys.* **1985**, *82*, 299−310.

(13) Grimme, S.; Antony, J.; Ehrlich, S.; Krieg, H. *J. Chem. Phys.* **2010**, *132*, 154104.

(14) (a) Shaik, S.; de Visser, S. P.; Ogliaro, F.; Schwarz, H.; Schröder, D. *Curr. Opin. Chem. Biol.* **2002**, *6*, 556−567. (b) de Visser, S. P. *Angew. Chem., Int. Ed.* **2006**, *45*, 1790−1793.

(15) (a) de Visser, S. P.; Quesne, M. G.; Martin, B.; Comba, P.; Ryde, U. *Chem. Commun.* **2014**, *50*, 262−282. (b) Quesne, M. G.; Latifi, R.; Gonzalez-Ovalle, L. E.; Kumar, D.; de Visser, S. P. *Chem.—Eur. J.* **2014**, *20*, 435−446.

(16) (a) Becke, A. D. *Phys. Rev. A* **1988**, *38*, 3098−3100. (b) Perdew, J. P. *Phys. Rev. B* **1986**, *33*, 8822−8824.

(17) Zhao, Y.; Truhlar, D. G. *Theor. Chem. Acc.* **2008**, *120*, 215−241.

(18) (a) Adamo, C.; Barone, V. *J. Chem. Phys.* **1999**, *110*, 6158−6169. (b) Perdew, J. P.; Burke, K.; Ernzerhof, M. *Phys. Rev. Lett.* **1996**, *77*, 3865−3868.

(19) (a) Sainna, M. A.; Kumar, S.; Kumar, D.; Fornarini, S.; Crestoni, M. E.; de Visser, S. P. *Chem. Sci.* **2015**, *6*, 1516−1529. (b) Sainna, M. A.; Sil, D.; Sahoo, D.; Martin, B.; Rath, S. P.; Comba, P.; de Visser, S. P. *Inorg. Chem.* **2015**, *54*, 1919−1930.

(20) (a) Vardhaman, A. K.; Sastri, C. V.; Kumar, D.; de Visser, S. P. *Chem. Commun.* **2011**, *47*, 11044−11046. (b) Kumar, S.; Faponle, A. S.; Barman, P.; Vardhaman, A. K.; Sastri, C. V.; Kumar, D.; de Visser, S. P. *J. Am. Chem. Soc.* **2014**, *136*, 17102−17115.

(21) (a) Karamzadeh, B.; Kumar, D.; Sastry, G. N.; de Visser, S. P. *J. Phys. Chem. A* **2010**, *114*, 13234−13243. (b) Kumar, D.; Latifi, R.; Kumar, S.; Rybak-Akimova, E. V.; Sainna, M. A.; de Visser, S. P. *Inorg. Chem.* **2013**, *52*, 7968−7979. (c) Draksharapu, A.; Angelone, D.; Quesne, M. G.; Padamati, S. K.; Gómez, L.; Hage, R.; Costas, M.; Browne, W. R.; de Visser, S. P. *Angew. Chem., Int. Ed.* **2015**, *54*, 4357−4361. (d) Sallmann, M.; Kumar, S.; Chernev, P.; Nehrkorn, J.; Schnegg, A.; Kumar, D.; Dau, H.; Limberg, C.; de Visser, S. P. *Chem.—Eur. J.* **2015**, DOI: 10.1002/chem.201500644.

(22) Weinhold, F.; Carpenter, J. E. The Natural Bond Orbital Lewis Structure Concept for Molecules, Radicals, and Radical Ions. In *The Structure of Small Molecules and Ions*; Naaman, R., Vager, Z., Eds.; Plenum Press: New York, 1988; pp 227−236.

(23) (a) de Quadras, L.; Bauer, E. B.; Stahl, J.; Zhuravlev, F.; Hampel, F.; Gladysz, J. A. *New. J. Chem.* **2007**, *31*, 1594−1604. (b) Che, C.-M.; Huang, J.-S. *Coord. Chem. Rev.* **2002**, *231*, 151−164. (c) Das, R. K.; Saha, B.; Rahaman, S. M. W.; Bera, J. K. *Chem.—Eur. J.* **2010**, *16*, 14459−14468. (d) Algarra, A. G.; Grushin, V. V.; MacGregor, S. A. *Organometallics* **2012**, *31*, 1467−1476.

(24) (a) Mutter, S. T.; Platts, J. A. *J. Phys. Chem. A* **2011**, *115*, 11293−11302. (b) Conner, D.; Jayaprakash, K. N.; Wells, M. B.; Manzer, S.; Gunnoe, T. B.; Boyle, P. D. *Inorg. Chem.* **2003**, *42*, 4759−4772. (c) Patra, S. K.; Sadhukhan, N.; Bera, J. K. *Inorg. Chem.* **2006**, *45*, 4007−4015. (d) Patra, S. K.; Bera, J. K. *Organometallics* **2006**, *25*, 6054−6060. (e) MacGregor, S. A.; McKay, D.; Panetier, J. A.; Whittlesey, M. K. *Dalton Trans.* **2013**, *42*, 7386−7395. (f) Sharma, P. K.; de Visser, S. P.; Ogliaro, F.; Shaik, S. *J. Am. Chem. Soc.* **2003**, *125*, 2291−2300.

(25) (a) Latifi, R.; Sainna, M. A.; Rybak-Akimova, E. V.; de Visser, S. P. *Chem.—Eur. J.* **2013**, *19*, 4058−4068. (b) Vardhaman, A. K.; Barman, P.; Kumar, S.; Sastri, C. V.; Kumar, D.; de Visser, S. P. *Angew. Chem., Int. Ed.* **2013**, *52*, 12288−12292.

(26) See, e.g.: (a) Diver, S. T. *Coord. Chem. Rev.* **2007**, *251*, 671−701. (b) Barluenga, J.; Fernández-Rodríguez, M. A.; Aguilar, E. *J. Organomet. Chem.* **2005**, *690*, 539−587. (c) Bernasconi, C. F. *Chem. Soc. Rev.* **1997**, *26*, 299−307.

(27) (a) de Visser, S. P.; Ogliaro, F.; Shaik, S. *Angew. Chem., Int. Ed.* **2001**, *40*, 2871−2874. (b) de Visser, S. P.; Ogliaro, F.; Shaik, S. *Chem. Commun.* **2001**, 2322−2323.

(28) (a) de Visser, S. P. *Chem.—Eur. J.* **2006**, *12*, 8168−8177. (b) de Visser, S. P.; Tahsini, L.; Nam, W. *Chem.—Eur. J.* **2009**, *15*, 5577−5587.

(29) Previous work that used VB diagrams to explain reaction mechanisms: (a) Shaik, S.; Kumar, D.; de Visser, S. P. *J. Am. Chem. Soc.* **2008**, *130*, 10128−10140. (b) de Visser, S. P. *J. Am. Chem. Soc.* **2010**, *132*, 1087−1097. (c) Kumar, D.; Karamzadeh, B.; Sastry, G. N.; de Visser, S. P. *J. Am. Chem. Soc.* **2010**, *132*, 7656−7667. (d) Ji, L.; Faponle, A. S.; Quesne, M. G.; Sainna, M. A.; Zhang, J.; Franke, A.; Kumar, D.; van Eldik, R.; Liu, W.; de Visser, S. P. *Chem. Eur. J.* **2015**, DOI: 10.1002/chem.201500329.

(30) de Visser, S. P.; Ogliaro, F.; Sharma, P. K.; Shaik, S. *J. Am. Chem. Soc.* **2002**, *124*, 11809−11826.

(31) Shaik, S.; Hiberty, P. C. *A Chemist's Guide to Valence Bond Theory*; Wiley-Interscience: New York, NY, 2007.

(32) Quesne, M. G.; de Visser, S. P. *J. Biol. Inorg. Chem.* **2012**, *17*, 841−852.

DOI: 10.1021/acs.organomet.5b00305
Organometallics 2015, 34, 1651−1660

ChemPubSoc Europe

DOI: 10.1002/chem.201500644

CHEMISTRY A European Journal Full Paper

Enzyme Models

Structure and Mechanism Leading to Formation of the Cysteine Sulfinate Product Complex of a Biomimetic Cysteine Dioxygenase Model

Madleen Sallmann,[a] Suresh Kumar,[b] Petko Chernev,[c] Joscha Nehrkorn,[d] Alexander Schnegg,[d] Devesh Kumar,*[b] Holger Dau,*[c] Christian Limberg,*[a] and Sam P. de Visser*[e]

Abstract: Cysteine dioxygenase is a unique nonheme iron enzyme that is involved in the metabolism of cysteine in the body. It contains an iron active site with an unusual 3-His ligation to the protein, which contrasts with the structural features of common nonheme iron dioxygenases. Recently, some of us reported a truly biomimetic model for this enzyme, namely a trispyrazolylborato iron(II) cysteinato complex, which not only has a structure very similar to the enzyme–substrate complex but also represents a functional model: Treatment of the model with dioxygen leads to cysteine dioxygenation, as shown by isolating the cysteine part of the product in the course of the work-up. However, little is known on the conversion mechanism and, so far, not even the structure of the actual product complex had been characterised, which is also unknown in case of the enzyme. In a multidisciplinary approach including density functional theory calculations and X-ray absorption spectroscopy, we have now determined the structure of the actual sulfinato complex for the first time. The Cys-SO_2^- functional group was found to be bound in an η^2-*O*,*O*-coordination mode, which, based on the excellent resemblance between model and enzyme, also provides the first support for a corresponding binding mode within the enzymatic product complex. Indeed, this is again confirmed by theory, which had predicted a η^2-*O*,*O*-binding mode for synthetic as well as the natural enzyme.

Introduction

Mononuclear nonheme iron dioxygenases (MNHID) are found in all forms of life and catalyse vital reactions in biosystems.[1] These nonheme iron dioxygenases are highly versatile in nature and are involved in biodegradation pathways, for example, in the metabolism of cysteine in the body, as well as biosynthesis functions, for example, antibiotics synthesis in microbes, and in DNA and RNA repair mechanisms.[2] They utilise molecular oxygen on a nonheme iron centre and transfer both oxygen atoms to either one or two substrate molecules. Thus, in the α-ketoglutarate dioxygenases, which is a common and well-studied nonheme iron dioxygenase, an α-ketoglutarate co-substrate binds to the iron centre, which is converted into succinate, CO_2 and a high-valent iron(IV)-oxo species.[3] The latter has been characterised spectroscopically for a number of α-ketoglutarate dioxygenases and halogenases and was shown to react with aliphatic groups with a large kinetic isotope effect through C–H abstraction.[4] A common theme within the α-ketoglutarate dependent dioxygenases, and also in other MNHID, is the active site structural features, whereby the metal is linked to the protein through a conserved 2-His/1-Asp (or Glu) ligand system in a facial orientation.[5] However, there are a handful of representatives of the MNHID enzyme family that show a different organisation. The cysteine dioxygenase (CDO) belongs to those because it features an iron centre bound by

[a] *M. Sallmann,[+] Prof. Dr. C. Limberg*
Humboldt-Universität zu Berlin, Institut für Chemie
Brook-Taylor-Strasse 2, 12489 Berlin (Germany)
Fax: (+49) 30-2093-6966
E-mail: christian.limberg@chemie.hu-berlin.de

[b] *S. Kumar,[+] Dr. D. Kumar*
Department of Applied Physics
Babasaheb Bhimrao Ambedkar University
School for Physical Sciences, Vidya Vihar
Rae Bareilly Road, Lucknow, UP (India)
E-mail: dkclcre@yahoo.com

[c] *Dr. P. Chernev, Prof. Dr. H. Dau*
Freie Universität Berlin, FB Physik
Arnimallee 14, 14195 Berlin (Germany)
E-mail: holger.dau@fu-berlin.de

[d] *Dr. J. Nehrkorn, Dr. A. Schnegg*
Helmholtz-Zentrum Berlin für Materialien und Energie GmbH
Institut für Silizium-Photovoltaik, Kekuléstrasse 5
12489 Berlin (Germany)

[e] *Dr. S. P. de Visser*
Manchester Institute of Biotechnology
and School of Chemical Engineering and Analytical Science
The University of Manchester
131 Princess Street, Manchester M1 7DN (UK)
E-mail: sam.devisser@manchester.ac.uk

[+] *These authors contributed equally to this work.*

Supporting information for this article is available on the WWW under http://dx.doi.org/10.1002/chem.201500644.

© 2015 Wiley-VCH Verlag GmbH & Co. KGaA, Weinheim

three histidine ligands.[6] The origin and demand for this structural arrangement is still poorly understood[7] and has led to much speculation on the function of the 3-His ligand binding, triggering interest from a range of disciplines including biomimetic chemistry.

CDO catalyses the metabolism of cysteine with molecular oxygen to yield cysteine sulfinic acid (Scheme 1), which is

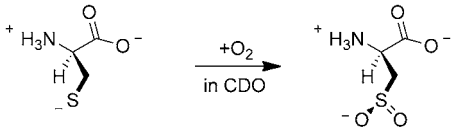

Scheme 1. Catalytic reaction mechanism of cysteine oxygenation by CDO enzymes.

needed for the assembly of central metabolites in the human organism.[8] A CDO structure has been known since 2006,[6] and a substrate-bound structure was also characterised: the substrate cysteine coordinates to the 3-His Fe^{II} centre through the sulfur atom and the nitrogen atom, so that a pentagonal coordination sphere results for the iron(II) ion and one coordination site remains open for the potential coordination and activation of O_2. However, little information is available on the events that take place after dioxygen binding. The exact mechanism of cysteine oxidation is thus still controversial and several possible intermediates and reaction pathways have been suggested.[9] One particular problem in CDO enzymes comes from the fact that most dioxygen-bound structures are short-lived and, for instance, no product complex has ever been characterised.

Whereas the functions of many oxygenating iron enzymes have been successfully imitated within the last decades by using molecular model compounds, such as biomimetic complexes,[1,10] only in the past three years have major advances with respect to the modelling of CDO been made.[11] Some of us have recently reported the successful coordination and dioxygenation of a protected cysteinato ligand at a $(His)_3Fe^{II}$ analogue with three facially arranged *N*-heterocyclic donor functions coordinating to iron(II) and thus about a truly biomimetic model system for CDO had been developed.[11d] For the simulation of the His_3 coordination sphere at the iron centre of CDO, the well-known trispyrazolylborato (Tp) ligand system was chosen, with phenyl residues at the 3-positions of the pyrazole units to create a protective reaction pocket imitating the one in the actual enzyme. L-Cysteine ethyl ester was employed as the substrate ligand, which coordinated to the TpFe unit in a fashion very similar to that found for the CDO-cysteinate complex (Scheme 2). O_2 treatment led to dioxygenation, as evidenced by the results of electrospray ionisation/mass spectrometry (ESI/MS). Unfortunately, due to the instability of the actual product, so far, all attempts to grow single crystals that might have allowed a characterisation through X-ray diffraction, failed. However, aqueous work-up (Scheme 2) provided the cysteine sulfinic acid derivative, suggesting a constitution $[Tp^{Me,Ph}Fe(O_2S\text{-}CH_2\text{-}CH(NH_2)CO_2Et)]$, **1**, for the initially formed product complex.

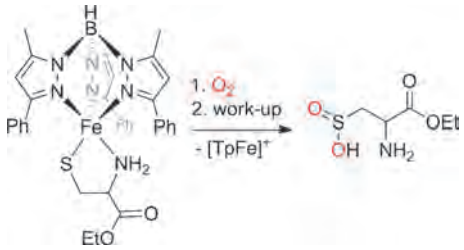

Scheme 2. Reactivity of $[Tp^{Me,Ph}Fe(CysOEt)]$ towards O_2.

With this knowledge, the structure of the dioxygenated compound **1** is of high interest, especially bearing in mind that no experimental data is available for the product complex of the natural enzyme. It can be safely assumed that the cysteine sulfinate will bind as a chelating ligand, but there are several possibilities: The SO_2 unit can bind through one oxygen atom, through two oxygen atoms or—as recently found in an experimental model study—through the sulfur atom.[11f] Given that no experimental data has been reported on the product complex of the enzyme, a quantum mechanics/molecular mechanics (QM/MM) study was performed, which provided insight into the enzymatic reaction mechanism leading to the cysteine sulfinic product complex, of which we highlight the active site structure in Figure 1.[9g] These calculations led to the conclu-

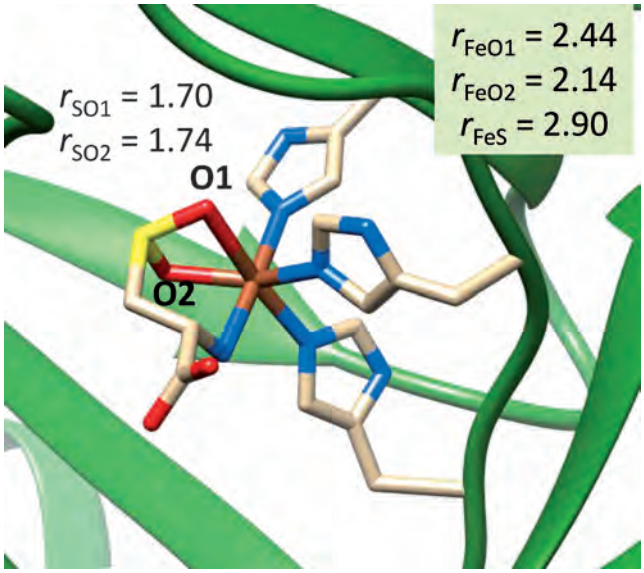

Figure 1. QM/MM optimised structure of the quintet spin product complex as taken from Reference [9g]. Bond lengths are given in angstroms.

sion that the coordination proceeds through a η^2-*O*,*O*-binding mode. However, until today there has been no experimental support for this finding, and hence we hoped to gain such evidence through the investigation of the biomimetic model system **1**, which is sufficiently stable to allow investigations in solutions.

Herein, we present the results of a combined theoretical and experimental study on the product structure of our realistic

© 2015 Wiley-VCH Verlag GmbH & Co. KGaA, Weinheim

model of the CDO and propose a catalytic mechanism for the formation of this complex starting from the reactants. This multidisciplinary approach leads to the conclusion that the biomimetic model truly reflects the enzymatic system with a closely related catalytic cycle and a product complex that binds through η^2-*O*,*O*-coordination.

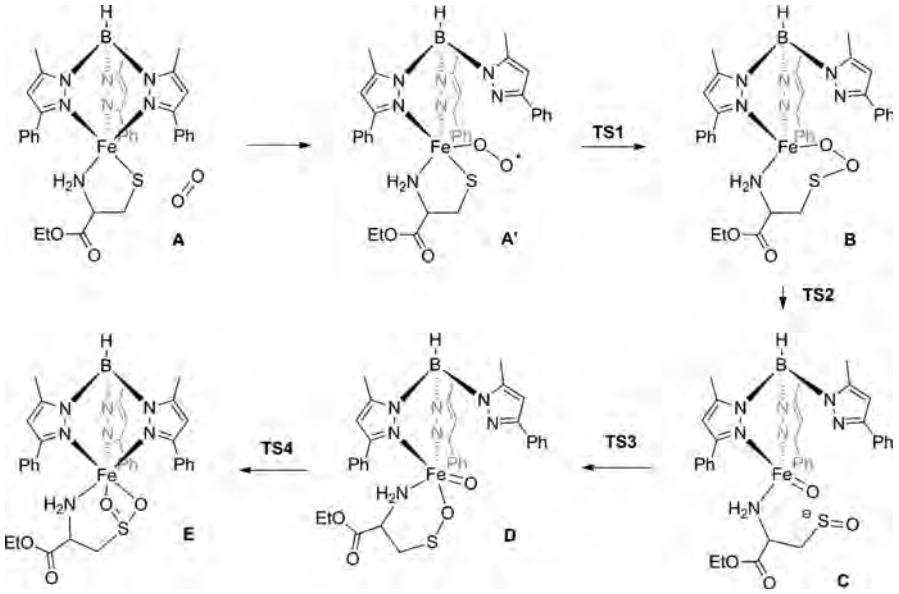

Scheme 3. Mechanism and nomenclature of cysteine dioxygenation by a biomimetic model complex.

Results and Discussion

At the outset of this work, we initiated a computational study on the mechanism of substrate dioxygenation within the biomimetic CDO complex leading to the product complex. The optimised geometries were then compared with the results of experimental spectroscopic analysis. Before we discuss the latter, we will highlight the major computational results on the conversion of our biomimetic CDO complex and underline the key differences and similarities with respect to the enzymatic system.

Computational studies on the oxygen activation process of [Tp^{Me,Ph}Fe(CysOEt)] with O_2

We calculated the complete dioxygenation reaction starting from an iron(II) complex, [Tp^{Me,Ph}Fe(CysOEt)], with a nearby dioxygen molecule, as described in detail in Scheme 3. We set out from a long-range complex of [Tp^{Me,Ph}Fe(CysOEt)] and O_2, designated **A**. Subsequently, we allowed the oxygen to approach the iron centre to form iron(III)-superoxo complex **A′**. The terminal oxygen atom attacks the sulfur atom to form ring-structure **B**, via transition-state **TS1**, followed by O–O breaking via transition-state **TS2** to give an iron(IV)-oxo complex and sulfoxide **C**. A subsequent barrier via **TS3** leads to binding of the sulfoxide to the iron centre, structure **D**, followed by transfer of the second oxygen atom via transition-state **TS4** to give cysteine sulfinate complex **E**.

This mechanism shows analogy to that calculated for CDO enzymes and biomimetic models published previously,[9c,g,12] although we will highlight some critical differences below. The postulated mechanism proceeds stepwise via multiple local minima for the sequential oxygen atom transfer, on several close-lying potential energy surfaces. Although, we calculated the full mechanism on the singlet, triplet, quintet and septet spin state surfaces, actually the ground state of all local minima in Scheme 3 is either triplet or quintet spin. Full details of all calculations on the alternative (singlet and septet) spin states are given in the Supporting Information; we focus herein on the triplet and quintet spin state structures only.

Let us start with a detailed analysis of the reactant structures **A** and **A′** as depicted schematically in Figure 2. Thus, without oxygen bound to the iron centre (as in **A**) the metal is pentacoordinated with the Tp^{Me,Ph} ligand bound as a tripodal tridentate ligand and cysteinate as a bidentate ligand that binds through the amine and thiolate groups to the metal. The ground state of **A** is a triplet spin state with the septet, open-shell singlet and quintet spin states higher in energy by $\Delta G_d =$ 9.2, 11.0 and 11.8 kcal mol^{-1}, respectively, whereby the free energy was calculated with UB3LYP-D/BS2 energies and corrected with zero-point, thermal and entropic corrections at UB3LYP/BS1 in the gas-phase. The optimised geometry and the resulting bond parameters are in reasonable agreement with those determined by a single-crystal X-ray analysis for [Tp^{Me,Ph}Fe(CysOEt)]. Whereas the Fe–S bond revealed by XRD (Fe–S 2.3122(8) Å) is somewhat shorter than that in the calculated structure, all Fe–N bonds are somewhat longer (experiment: Fe–N_{Cys} 2.290(3) Å, Fe–N_{Pz} 2.106(2), 2.112(2), 2.275(2) Å;

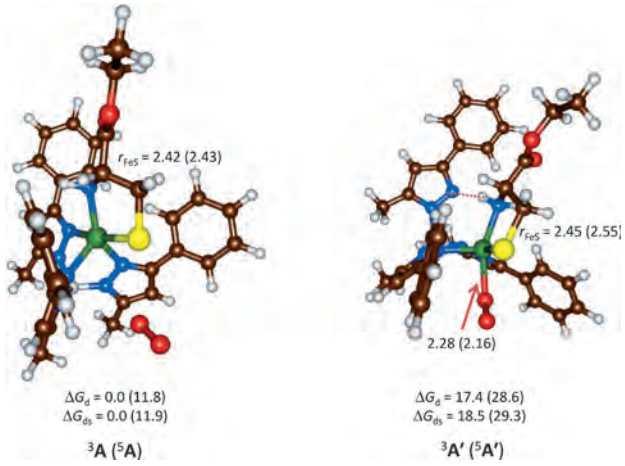

Figure 2. DFT optimised geometries of ^{3,5}**A** and ^{3,5}**A′** with Fe–O and Fe–S bond lengths in angstroms and free energies in the gas phase (ΔG_d) and in solvent (ΔG_{ds}) in kcal mol^{-1}.

© 2015 Wiley-VCH Verlag GmbH & Co. KGaA, Weinheim

calculations: Fe–N_{Cys} 2.182 [2.179] Å; Fe–N_{Pz} 2.082 [2.085], 2.092 [2.089], 2.216 [2.212] Å). The three pyrazole groups form a facial triad in close analogy to the 3-His ligand system in CDO enzymes. In addition, substrate cysteinate in the enzyme also binds as a bidentate ligand; therefore, structure **A** faithfully mimics the active sites of CDO enzymes. To test the effect of the basis set on the structure, we also performed a B3LYP/BS2 geometry optimisation (see the Supporting Information, Figure S10), however, only small changes in bond lengths were found.

The bulky phenyl substituents of the $Tp^{Me,Ph}$ ligand, however, prevent binding of a sixth ligand to the metal centre. Thus, approach of molecular oxygen to the iron centre with formation of the iron(III)-superoxo complex **A′** is accompanied by the release of one of the pyrazole groups from the iron centre in a barrierless process. While the pyrazole group loses a covalent linkage with the iron, it forms a new hydrogen bond with the amine group of the cysteinate residue. Thus, dioxygen binding to our biomimetic CDO model contrasts with the dioxygen binding process in CDO enzymes, in which all original metal–ligand and metal–substrate interactions remain intact. Another difference of the iron(III)-superoxo complex **A′** with respect to the analogous system calculated for CDO enzymes relates to the orientation of the substrate with respect to the superoxo group: In CDO, both amine and thiolate groups are *cis* with respect to the superoxo group, whereas in structure **A′**, the thiolate is in the *cis* position and the amine is *trans* to the superoxo group.

The loss of one of the iron-pyrazole interactions has little effect on the spin-state ordering, and the triplet spin state remains the ground state, although an open-shell singlet spin state approaches it to within 2 kcal mol^{-1}. However, on the singlet spin state surface, the rest of the mechanism is at least 15 kcal mol^{-1} higher in energy. The large structural changes upon dioxygen binding to the iron centre means that this O_2-binding step of the mechanism is strongly endergonic.

The spin-state ordering for structures **A** and **A′** contrast with the one found in calculations on CDO enzymes, for which an open-shell singlet spin state was found as the ground state.[9c,g] However, test calculations using the BP86, PBE0 and B3LYP-D3 methods gave the same spin state ordering for **A** and **A′** as the one found for B3LYP with a triple-ζ quality basis set. Calculations on $[Fe^{III}(LN_3S)O_2]$, for which LN_3S was a bis(imino)pyridine ligand with a pendant thiolate arm, gave an open-shell singlet ground state, too, although both the triplet and the quintet spin states were located within 5.5 kcal mol^{-1}.[12a] The origin of the triplet spin ground state for the iron(III)-superoxo complex probably stems from the fact that complexes **A** and **A′** are pentacoordinated iron(III) complexes, whereas the CDO enzymatic and reported model systems have the metal in an environment of six ligands. Given that iron(III)-superoxo complexes are known to have a large variety of close-lying electronic and spin states, it is reasonable that subtle changes in the coordination environment and electrostatic interactions will lead to changes in the spin state energy.[13] In a similar vein, we recently showed that iron(IV)-oxo complexes in a pentacoordinated environment stabilise structures in a high-spin state, whereas hexacoordination favours the intermediate (triplet) spin state instead.[14]

After dioxygen binding and the formation of the iron(III)-superoxo structure **A′**, the reaction continues with attack of the terminal oxygen atom of the superoxo group on the sulfide group of cysteinate. The formation of the S–O bond leads to ring-structure **B** via a rate-determining transition state **TS1** of $\Delta G_d = 12.3$ and $\Delta G_{ds} = 11.3$ kcal mol^{-1} with respect to **A′**, whereby the latter represents the free energies with solvent corrections included (Figure 3). This is similar to the mechanism of CDO and other nonheme iron dioxygenases for which the iron(III)-superoxo group attacks with the terminal oxygen atom to form a bicyclic ring-structure.[9c,g,15] The barriers are of the same order of magnitude as those obtained for the enzymatic system. Similar to the mechanism calculated for CDO enzymes and model complexes, here also the reaction from ^{3}**A′** to ^{3}**B** is endothermic, whereas it is exothermic on the quintet spin state surface.[9c,g,15] It is expected that a spin-state-crossing from the triplet to the quintet spin state will occur either en route from ^{3}**TS1** to **B** or during the lifetime of ^{3}**B**.

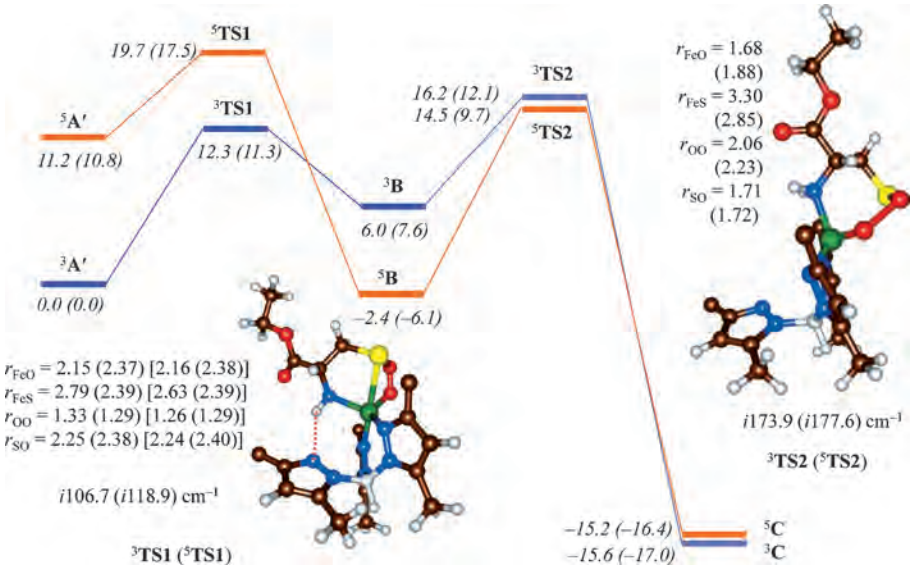

Figure 3. Potential energy landscape for the mechanism of the first oxygen atom transfer from O_2 to cysteinate with free energies in the gas phase and in solvent (in parenthesis) in kcal mol^{-1}. Optimised geometries of ^{3,5}**TS1** and ^{3,5}**TS2** with bond lengths in angstroms; the imaginary frequency in wave numbers are also shown. UB3LYP/BS2 optimised geometries are given in square brackets. Phenyl substituents have been removed for clarity.

© 2015 Wiley-VCH Verlag GmbH & Co. KGaA, Weinheim

Formation of the cyclic ring structure **B** leads to weakening of the O–O bond and it formally changes from a bond order of 1.5 in the iron(III)-superoxo complex (1.26 Å in ^{3}**A**′ and 1.28 Å in ^{5}**A**′) to a single bond in **B** (1.38 Å in ^{3}**B** and 1.46 Å in ^{5}**B**). The dioxygen bond subsequently breaks in **TS2** and an iron(IV)-oxo complex with dangling cysteine sulfoxide is formed (**C**) in a highly exothermic and possibly irreversible process. The exothermicity is as expected and is consistent with the results of previous computational studies of oxygen activation by nonheme iron dioxygenases.[9c,g,15] However, in all these previous studies it was found that the formation of iron(IV)-oxo and sulfoxide units keeps the sulfur atom bound to the iron centre, whereas in the complex studied here the Fe–S bond is broken and the sulfoxide is dangling away from the metal centre. Nevertheless, this moiety is still bound to the iron through the amine group, and sulfoxide products cannot be released at this stage. Instead, the sulfoxide rebinds to the iron centre to form structure **D** later in the mechanism.

The spin-state ordering of the iron(IV)-oxo complex **C** gives the triplet spin in close energy to the quintet spin state and their ordering depends on whether relative enthalpies or free energies, or gas-phase versus solvent models are chosen. Previous computational studies of iron(IV)-oxo complexes also showed close-lying triplet and quintet spin states, whereby the spin-state ordering and relative energies were found to be sensitive to the ligand binding, environmental effects and to the computational methods used.[14,16]

Optimised geometries of the triplet and quintet spin states of **B**, **C** and **D** are given in Figure 4. The cyclic structure **B** has

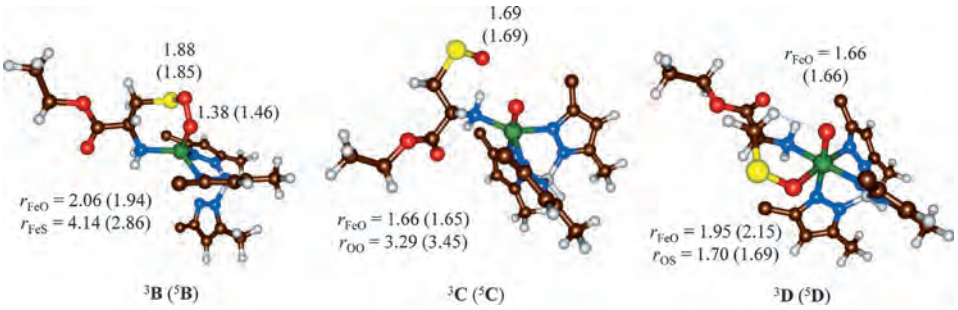

Figure 4. Optimised geometries of ^{3,5}**B**, ^{3,5}**C** and ^{3,5}**D** with bond lengths in angstroms. Phenyl substituents have been removed for clarity.

a sulfur atom that is not bound to the metal and is located at a distance of 2.86 Å in ^{5}**B** and well over 4 Å in ^{3}**B**. In ^{3}**B**, the $Tp^{Me,Ph}$ binds again as a tridentate ligand, thus keeping the metal pentacoordinated. In ^{5}**B**, one arm of the $Tp^{Me,Ph}$ ligand remains unbound, so that the metal is coordinated by only four donor ligands, probably because low-coordination favours high-spin states. In fact the stabilisation reached in this way is considerable, so that the quintet state drops below the triplet spin state, whereas the two spin states are isoenergetic in **C**. The first oxygen atom transfer to form cysteine sulfoxide **C** brings the $Tp^{Me,Ph}$ ligand back in its original position as a tridentate ligand also in the case of ^{5}**B**; **C** contains the sulfoxide group as a free dangling group in hydrogen-bonding interaction with the amine group of cysteinate. Rebound of the sulfoxide group to the iron centre via **TS3** has a negligible barrier on all spin state surfaces and gives structure **D**, which is a hexacoordinated iron complex. This chemical structure resembles the optimised geometries calculated for the iron(IV)-oxo-sulfoxide intermediates in CDO enzymes and model complexes closely.[9c,g,15,17] Energetically, there is no dramatic stabilisation upon sulfoxide binding to the iron centre and we find ^{3}**D** to be more stable than ^{3}**C** by $\Delta G_d = 2.3$ kcal mol^{-1} and $\Delta G_{ds} = 1.3$ kcal mol^{-1}. Similarly, we calculate ^{5}**D** to be more stable than ^{5}**C** by $\Delta G_d = 6.5$ kcal mol^{-1} and $\Delta G_{ds} = 6.6$ kcal mol^{-1}.

The oxygen atom transfer within the iron(IV)-oxo-sulfoxide complex **D** to give the product complex **E**, with both oxygen atoms bound to the iron, was then investigated. A small barrier ^{3}**TS4** was characterised on the triplet spin state, whereas the quintet spin pathway had a negligible barrier. The optimised geometries of ^{3}**TS3** and ^{3}**TS4** are given in Figure 5. At the ΔG_d (ΔG_{ds}) levels of theory, we find ^{3}**TS3** to be 3.4 (3.5) kcal mol^{-1} above ^{3}**C**, and ^{3}**TS4** was located at less than 0.5 kcal mol^{-1} above ^{3}**D**. Therefore, the conversion of ^{3}**C** into ^{3}**D** and conversion from ^{3}**D** into ^{3}**E** are fast processes, and complexes **C** and **D** are expected to have a short lifetime. These small barriers also have an effect on the imaginary frequencies in the transition states, which also tend to be small. These barriers are also small on the quintet spin state and we were unable to fully characterise these transition states. Therefore, the second oxygen atom transfer is a facile and fast process. This part of the mechanism shows good resemblance to the enzymatic reaction mechanism in which an exothermic second oxygen atom transfer with small individual barriers was calculated, too.

We also investigated an alternative mechanism, whereby molecular oxygen attacks the sulfur atom of the substrate directly, that is, without binding to iron and the formation of an iron(III)-superoxo structure first. A mechanism of this type was suggested for a cofactor-independent dioxygenase, in which molecular

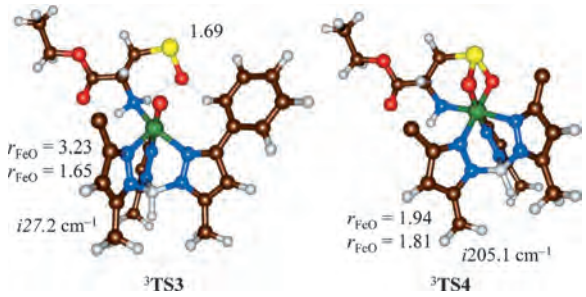

Figure 5. Optimised geometries of ^{3}**TS3** and ^{3}**TS4** with bond lengths in angstroms and the imaginary frequency in wave numbers. Phenyl substituents have been removed for clarity.

© 2015 Wiley-VCH Verlag GmbH & Co. KGaA, Weinheim

oxygen attacks the (1*H*)-3-hydroxy-4-oxoquinaldine substrate directly without involvement of a metal centre.[18] All geometry scans for closing the distance between the O_2 moiety and the sulfur atom, however, led to binding of O_2 to the iron centre upon close approach. Clearly, direct attack of O_2 on sulfur is a high-energy pathway that cannot compete with the formation of an iron(III)-superoxo structure. Previous calculations on CDO model complexes as well as synthetic model complexes for intradiol catechol dioxygenases established similar conclusions that O_2 needs to bind the iron first.[12b,19]

Structure and electronic properties of the product complex

The product complex obtained by following the mechanism as described in Scheme 3 leads to chemical structures with η^2-*O*,*O*-coordination, but, in principle, binding of the cysteine sulfinic acid in alternative orientations could be conceivable. Therefore, we undertook a detailed study into all possible cysteine sulfinic acid binding orientations. These calculations were then used to interpret the results of experimental spectroscopic measurements, which will be discussed in the next section.

Firstly, the triplet and quintet geometries that followed the final step in the mechanism described in the previous section were optimised. This led to the structures ^{3}**E** and ^{5}**E** shown on the left of Figure 6. The optimised geometries give relatively short Fe–O distances of 1.92 (2.05) Å for ^{3}**E** (^{5}**E**), which is somewhat shorter than the distances found for the enzymatic product complex with QM/MM, for which a value of 2.30 Å was obtained. A similar shortening of the Fe–S distance was found from 2.90 Å in the QM/MM structure to 2.80 Å for ^{5}**E**. Note that a geometry optimisation at the BP86 and PBE0 density functional level of theory (see the Supporting Information) gives structures that are similar to those located with B3LYP, as can be seen from the central panel in Figure 6. Furthermore, a geometry optimisation at UB3LYP/BS2 rather than UB3LYP/BS1 (see the Supporting Information) also did not lead to dramatic changes in the optimised geometry: *r*(Fe–O, average) = 2.15 Å and *r*(Fe–S) = 2.75 Å. Therefore, the geometric differences observed between the structures in Figure 1 and Figure 6 are the result of electronic differences between the enzymatic and biomimetic product complexes. Furthermore, they may also highlight the effect of the protein as a ligand. At the ΔG_d level of theory, triplet and quintet spin states are almost degenerate, with the quintet spin state slightly more stable by 0.4 kcal mol^{-1}. Solvent corrections to the structures, however, reverse the order and make the triplet slightly more stable by 2.6 kcal mol^{-1}. A subsequent solvent optimisation gives the same spin state ordering with the triplet lower in energy than the quintet by 1.6 kcal mol^{-1}, and, hence, gives a qualitatively similar result.

In addition, we investigated alternative cysteine sulfinate binding modes and attempted to optimise the geometries of product complexes with coordination through just one oxygen atom to the metal centre. All these attempts, however, converged to structure ^{3,5}**E**, as displayed in Figure 6, with the cysteine sulfinate bound to iron as a tridentate ligand in a facial *N*,*O*,*O*-coordination mode.

We tested one more possible product complex orientation with the iron bound to one oxygen atom and the sulfur atom by taking the ^{5}**E** optimised structure with the SO_2 group rotated by 180°. Although the optimisation yielded structures with one C–O and one Fe–O bond (**E′**, Figure 6, right), close inspection of the optimised geometries revealed that it is not a product complex as such. Thus, the oxygen atom that forms the Fe–O bond has attacked the *ortho*-carbon position of one of the phenyl substituents in an aromatic-type electrophilic addition step. In particular, the *ortho*-carbon atom in ^{3,5}**E′** is in sp^3 hybridisation and forms four bonding interactions. The resulting structure has the iron in oxidation state +II, with four unpaired electrons, and no radical character is found on the Tp ligand or cysteine sulfinate unit. Consequently, a product complex with η^2-*S*,*O*-coordination mode is not a likely intermediate due to stereochemical constraints of the three phenyl groups of the $Tp^{Me,Ph}$ ligand. To test whether ^{3,5}**E′** are dead-end products or not, we investigated the S–O bond breakage leading to a sulfoxide and oxidised phenyl ring of the $Tp^{Me,Ph}$ unit. We calculated the electrophilic attack on the *ortho*-carbon atom and located transition states (^{3,5}**TS5**) and electrophilic oxidation products (^{3,5}**F**). The barriers were found to be considerable, however, with values of ΔG_d (ΔG_{ds}) = 20.8 (28.9) kcal mol^{-1} above ^{5}**E′** on the quintet spin state surface, although the reaction is exergonic by 12.5 (8.0) kcal mol^{-1} leading to ^{5}**F**, which is

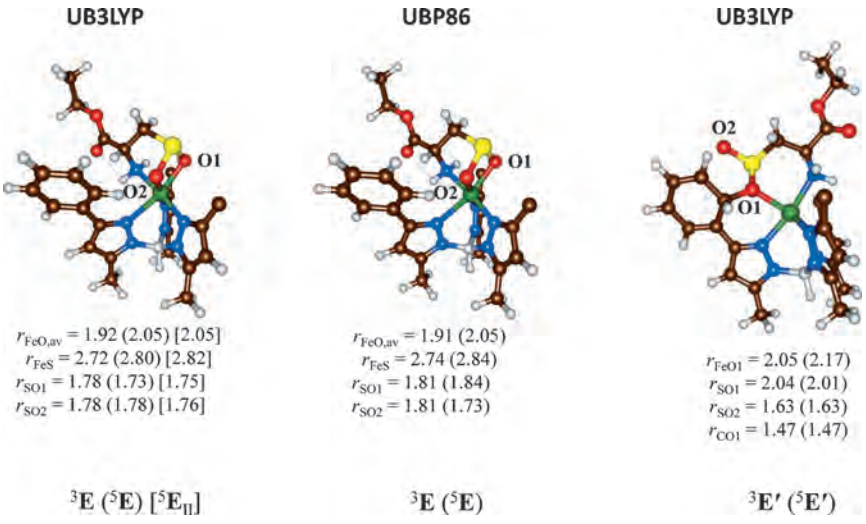

Figure 6. Optimised geometries of ^{3,5}**E** and ^{3,5}**E′** as obtained with either B3LYP or BP86 with bond lengths given in angstroms. Phenyl substituents have been removed for clarity.

© 2015 Wiley-VCH Verlag GmbH & Co. KGaA, Weinheim

a cysteine sulfoxide ligated to an iron(II) centre with the $Tp^{Me,Ph}$ ligand hydroxylated at the phenyl group. Therefore, electrophilic attack of the cysteine sulfinic acid group on one of the aromatic rings of the ligand is a high-energy pathway that is unlikely to occur in the real system. It should also be noted that formation of ^{3,5}**E**′ itself from either ^{3,5}**D** or ^{3,5}**E** is energetically costly because it will lead to the destruction of aromaticity in one of the Ph ligands.

In summary, the computational studies on model **1**, similar to the calculations on the CDO product complex, predict a η^2-*O*,*O*-binding mode for cysteine sulfinate product complex, which underlined the model character of **1** and encouraged us to continue with attempts to confirm the structure experimentally.

Comparison of the theoretical results with experimental findings

Given that the product complex **1** eluded crystallisation (see above), we performed solution X-ray absorption spectroscopy (XAS) at the KMC1 beamline of the BESSY synchrotron in Berlin (see the Supporting Information for details). The spectrum in the X-ray absorption near-edge structure (XANES) region of the starting material in comparison with the oxygenated product is shown in Figure 7. The pre-edge feature (insets in Figure 7) is lower in the product complex than in the precursor

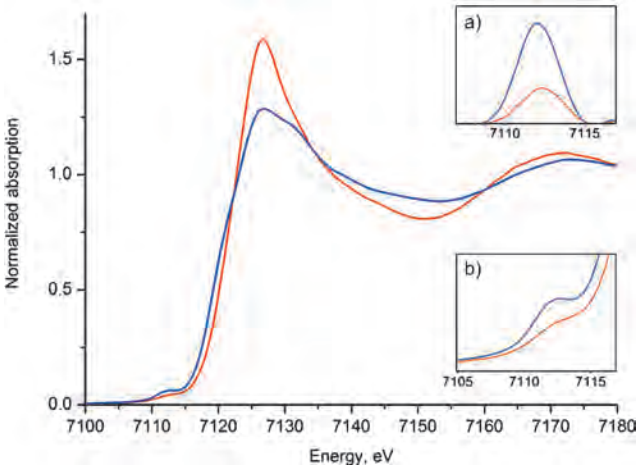

Figure 7. Normalised Fe *K*-edge XANES of [$Tp^{Me,Ph}$Fe(CysOEt)] (dark blue) and **1** (red). The insets shows magnified pre-edge features a) extracted by background subtraction and b) expanded (without background subtraction).

[$Tp^{Me,Ph}$Fe(CysOEt)]; furthermore, the principal edge maximum (white line) is much sharper and higher. Both these observations suggest that oxygenation results in an increase of the coordination number from five, in the precursor, to six, in **1**. The observed spectral changes are prototypical for transformation to an octahedrally coordinated compound, as discussed elsewhere, in the framework of molecular orbital and scattering theory.[20,21] After oxygenation, the white-line height of **1** reaches an especially high value (more than 1.5) typically observed only for octahedral $Fe(N/O)_6$ coordination in the absence of any sulfur ligation.[22] This already argues in favour of an η^2-*O*,*O*-binding mode of the sulfinate unit, and the extended X-ray absorption fine-structure (EXAFS) data were also consistent with this conclusion.

The position of the edge jump is indicative of the oxidation state of the absorbing atom. The edge position of complex **1** shifted up only slightly (by ca. 0.6 eV) compared with [$Tp^{Me,Ph}$Fe(CysOEt)]. This shift can also be partly attributed to the change from five- to six-coordinated iron. We conclude therefore that complex **1**, as the precursor [$Tp^{Me,Ph}$Fe(CysOEt)], contained mostly iron(II) species.

The EXAFS spectrum of the precursor and that of the product of O_2 treatment are compared in Figure 8. Comparison of

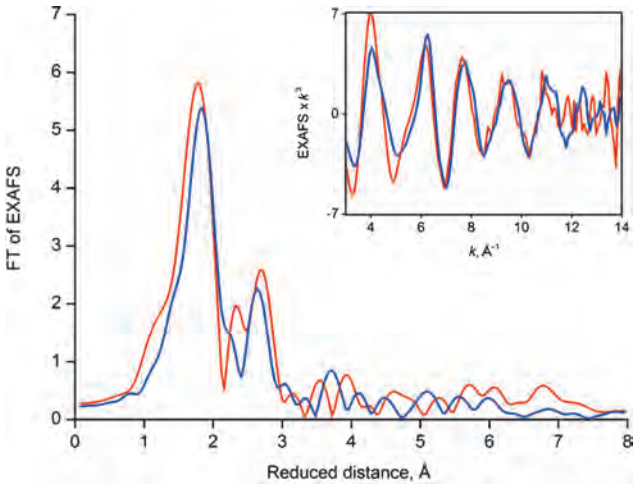

Figure 8. Overlay of the Fourier transforms of the EXAFS data for [$Tp^{Me,Ph}$Fe(CysOEt)] (blue) and **1** (red). The inset shows *k*-space data for [$Tp^{Me,Ph}$Fe(CysOEt)] (blue) and **1** (red). The distances between ligands of the first, second and third coordination sphere were determined by EXAFS simulations and typically exceed the indicated "reduced distance" by 0.4 Å.

the bond distances obtained for [$Tp^{Me,Ph}$Fe(CysOEt)], **A**, with those determined by X-ray diffraction shows relatively small differences (one Fe–N shell with coordination number four at 2.13 Å from EXAFS vs. four Fe–N distances between 2.11 and 2.29 Å from XRD; Fe–S at 2.30 Å from EXAFS vs. Fe–S at 2.31 Å from XRD, see the Supporting Information, Figure S1 and Table S1). In the product of O_2 treatment, the most notable feature is a new peak at a reduced distance of 2.32 Å. Indeed, setting out from the DFT-optimised geometry, a very good fit of the EXAFS data could be reached, which indicated two scattering O atoms at 2.08 Å and an S atom at 2.70 Å (Figure 9 and Table 1). These distances are in reasonable agreement with those calculated and reported for **E** in Figure 6 above, with EXAFS favouring the quintet, although the Fe–O/N distances determined by DFT calculations are somewhat shorter than suggested by EXAFS. Note however that a geometry optimisation at UB3LYP/BS2 rather than UB3LYP/BS1 gives minor differences with respect to the structure displayed in Figure 6, but with Fe–O distances of 2.12 and 2.18 Å in the quintet spin state that are instead slightly longer than those determined by EXAFS. Generally, the B3LYP method gives reasonable energies

© 2015 Wiley-VCH Verlag GmbH & Co. KGaA, Weinheim

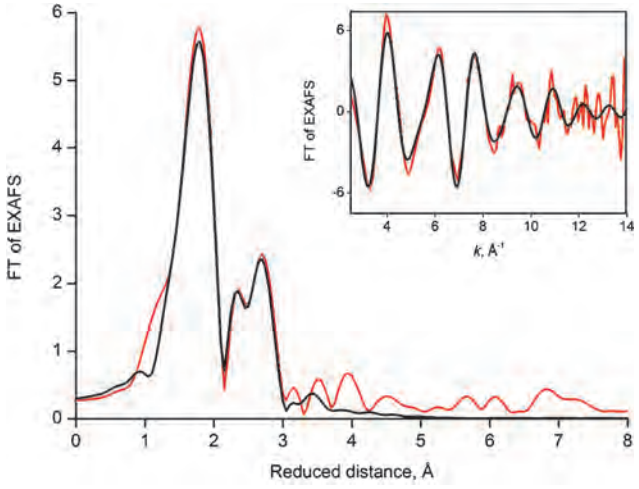

Figure 9. Fourier-transformed Fe *K*-edge EXAFS spectra of **1** (experiment: red; simulation: black). Goodness-of-fit parameters: $\chi^2 = 75$, $R_f = 9.1$.

Table 1. Parameters obtained by simulation of the k^3-weighted EXAFS spectrum of **1** shown in Figure 9. The errors represent the 68% confidence interval of the respective fit parameter (*N*, coordination number; *R*, absorber-backscatter distance; σ, Debye–Waller parameter). The coordination numbers were not fitted but were fixed to the values suggested by the structure.

Shell	*N*	*R* [Å]	σ [Å]
Fe–O	2	2.08 ± 0.01	0.06 ± 0.01
Fe–N	4	2.22 ± 0.01	0.06 ± 0.01
Fe–S	1	2.70 ± 0.02	0.09 ± 0.01
Fe–N	3	3.06 ± 0.01	0.05 ± 0.01

for calculations of reaction mechanisms, but tends to be weak at reproducing experimental geometries.[23] Therefore, we re-optimised ^{3,5}**E** by using the BP86 density functional method. We calculate an average Fe–O distance of 1.91 (2.05) Å in the triplet (quintet) spin states and an Fe–S separation of 2.74 (2.84) Å. These optimised geometries are not dramatically different from those observed at the B3LYP level of theory. Clearly, for this particular case, the agreement between experimental and computational Fe–S distances is very good, which is not always the case for distances between second-row elements, for which the differences can be quite large.[24] In conclusion, the experimental data on the structure of product complex **1** match nicely the findings made on **E** in the theoretical analysis. Other aspects of the calculated structures and reaction barriers also rationalise the experimental findings:

i) A $S = 2$ ground state was predicted for **A** and, indeed, investigations on the magnetic properties of the precursor complex [Tp^{Me,Ph}Fe(S-CH$_2$-CH(NH$_2$)(CO$_2$Et)] confirmed that: The magnetic moment for the precursor complex in solution at room temperature ($\mu_{eff} = 5.05\ \mu_B$), as determined by using the Evans method, is in accordance with the spin only (s.o.) value for four unpaired electrons with a total spin quantum number of $S = 2$ ($\mu_{s.o.} = 4.90\ \mu_B$). The isolated solid exhibits a magnetic moment of $\mu_{eff} = 4.96\ \mu_B$. We also tried to monitor the course of the reaction with O_2 by EPR. However, because this is an even-spin system, such studies are far from routine. Measurements in the parallel mode were performed but they were further complicated by the fact that the system is highly sensitive towards both O_2 and water, and at the same time had to be investigated at rather low concentrations. Hence, no reproducible results were obtained.

ii) The calculated mechanism shows why all of our attempts to detect the iron(III) superoxo species failed: Its formation is endergonic and the barrier back to **A** is virtually nonexistent.

iii) The comparatively high barrier for the rate-determining step, the further reaction to **B**, explains why the model reaction is comparatively slow and takes hours to reach completion.

Conclusion

Taken together, the theoretical results of the CDO product complex as well as the combined computational and experimental results on a closely related biomimetic model complex strongly suggest that the cysteine sulfinate also binds in a η^2-*O*,*O*-binding mode in the product complex of the CDO. Moreover, calculations were performed with the aim of further clarifying mechanistic details, and the results have helped rationalise the experimental observations. Finally, the results have revealed how to proceed to achieve an even closer resemblance between enzyme and model: The steric demand of residues at the Tp ligand (or at least one of the residues) has to be decreased to an extent that avoids intermediate dissociation of one of the pyrazole donors. At the same time, as before, it has to be sufficiently large to allow for the isolation of [TpFe(S-CH$_2$-CH(NH$_2$)CO$_2$Et)] and prohibit Fe^{III}-O-Fe^{III} formation in the oxygenation process; that is, a subtle balance has to be found. Corresponding investigations are underway.

Experimental Section

Preparation of a sample of 1 for XAS

All manipulations were carried out in a glove box, or by using Schlenk techniques under a dry argon atmosphere. [Tp^{Me,Ph}Fe(CysOEt)] was prepared and crystallised as described earlier.[11d] The preparation of complex **1** proceeded by the direct reaction of a solution of [Tp^{Me,Ph}Fe(CysOEt)] in dichloromethane with dioxygen. Below we give information on how this sample was treated for XAS studies.

XAS measurements and simulations

X-ray absorption spectroscopy at the K-edge of iron was performed at the KMC-1 beamline at the BESSY-II synchrotron (Helmholtz-Zentrum Berlin, Germany) at 20 K in a liquid-helium cryostat as described elsewhere.[25] Spectra were recorded in fluorescence mode using a 13-element Ge detector (Canberra). The extracted spectrum was weighted by k^3 and simulated in *k*-space; an E_0 value of 7112 eV was used for conversion of the energy scale to a *k*-scale. All EXAFS simulations were performed by using in-house software (SimX) after calculation of the phase functions with the FEFF program[26,27] (version 8.4, self-consistent field option activated). Atomic coordinates of the FEFF input files were generated for

© 2015 Wiley-VCH Verlag GmbH & Co. KGaA, Weinheim

several reasonable structural models; the EXAFS phase functions did not depend strongly on the details of the used model. An amplitude reduction factor S_0^2 of 0.94 was used. The data range used in the simulation was 15–750 eV (2–14 $Å^{-1}$). The EXAFS simulation was optimised by a minimisation of the error sum obtained by summation of the squared deviations between measured and simulated values (least-squares fit). The fit was performed by using the Levenberg–Marquardt method with numerical derivatives. The error ranges of the fit parameters were estimated from the covariance matrix of the fit, and indicate the 68% confidence intervals of the corresponding fit parameters. The fit error was calculated as in ref.[28]

Simulation of the EXAFS spectrum of [$Tp^{Me,Ph}$Fe(CysOEt)]

A simulation using only three shells (shown in Table S1) readily reproduces the experimental spectrum (Figure S1) and is in agreement with the known structure of [$Tp^{Me,Ph}$Fe(CysOEt)].

Computational studies

All calculations reported here were performed by using DFT as implemented in the Jaguar 7.7[29] and Gaussian 09[30] program packages. Initial geometries were optimised in Jaguar at the UB3LYP level of theory[31] coupled with an LACVP basis set on iron and 6–31G on the rest of the atoms: basis set BS1.[32] A subsequent analytic frequency in Gaussian confirmed the structures as local minima with real frequencies only or first order saddle points with one imaginary frequency for the correct mode. Energies were then improved by running a single-point calculation in Jaguar using a triple-ζ quality LACV3P+ basis set on iron and 6–311+G* on the rest of the atoms: basis set BS2. We also tested the effect of dispersion on the reaction energies by performing a UB3LYP-D3 single-point calculation in Jaguar by using the model of Grimme and coworkers.[33] The complete potential energy profile was calculated on the singlet, triplet, quintet and septet spin states. Previously, we used these methods for analogous systems and they reproduced free energies of activation within 4 kcal mol^{-1},[34] but also gave reasonable agreement for spectroscopic data.[35] We also showed previously that energies obtained at UB3LYP/BS2//UB3LYP/BS1 were within 0.1 kcal mol^{-1} of those obtained after a geometry optimisation at UB3LYP/BS2 level of theory.[36]

The product complex was investigated as a structure with the two oxygen atoms bound to the metal (structure **E**), as well as with the sulfur bound to the metal (structure **E′**). Although the latter structure was started without Fe–O bonding interactions, during the optimisation the sulfinic acid group rotated onto structure **E′** with one Fe–S and one Fe–O bond. To test the effect of solvent, we reoptimised ^{3,5}**E** in a solvent model (^{3,5}$\mathbf{E}_{solvopt}$) but this had only minor effects on the final structure. We used the polarised continuum model as implemented in Jaguar with a dielectric constant of 37.5 and a probe radius of 2.183 Å.

To test the effect of the density functional method and the basis set on the optimised geometries and spin-state ordering of the product complexes, we performed a further set of test calculations. First, we reoptimised ^{3,5}**A**, ^{3,5}**TS1** and ^{3,5}**E** at the UB3LYP/BS2 level of theory. In addition, we calculated ^{3,5}**E** by using the pure density functional method BP86.[37] These test calculations gave only minor changes in the structural features of the complexes and did not affect the conclusions.

Acknowledgements

We are grateful to the Humboldt-Universität zu Berlin and to UniCat (Unifying Concepts in Catalysis, Cluster of Excellence, Berlin) for financial support. We thank the Helmholtz-Zentrum Berlin for the allocation of synchrotron radiation beamtime. The National Service of Computational Chemistry Software (NSCCS) is acknowledged for cpu time to S.d.V. D.K. acknowledges the Department of Science and Technology (New Delhi) for a Ramanujan Fellowship. The EU-COST Network (CM1305) on spin state reactivity is acknowledged for support.

Keywords: density functional calculations · enzyme catalysis · enzyme models · oxygenation · reaction mechanisms

[1] a) E. I. Solomon, T. C. Brunold, M. I. Davis, J. N. Kemsley, S.-K. Lee, N. Lehnert, F. Neese, A. J. Skulan, Y.-S. Yang, J. Zhou, *Chem. Rev.* **2000**, *100*, 235–349; b) T. D. H. Bugg, *Curr. Opin. Chem. Biol.* **2001**, *5*, 550–555; c) M. J. Ryle, R. P. Hausinger, *Curr. Opin. Chem. Biol.* **2002**, *6*, 193–201; d) M. Costas, M. P. Mehn, M. P. Jensen, L. Que Jr, *Chem. Rev.* **2004**, *104*, 939–986; e) M. M. Abu-Omar, A. Loaiza, N. Hontzeas, *Chem. Rev.* **2005**, *105*, 2227–2252; f) P. C. A. Bruijnincx, G. van Koten, R. J. M. Klein Gebbink, *Chem. Soc. Rev.* **2008**, *37*, 2716–2744; g) S. V. Kryatov, E. V. Rybak-Akimova, S. Schindler, *Chem. Rev.* **2005**, *105*, 2175–2226.

[2] a) R. Chowdhury, A. Hardy, C. J. Schofield, *Chem. Soc. Rev.* **2008**, *37*, 1308–1319; b) J. M. Simmons, T. A. Müller, R. P. Hausinger, *Dalton Trans.* **2008**, 5132–5142; c) C. Loenarz, C. J. Schofield, *Nat. Chem. Biol.* **2008**, *4*, 152–156.

[3] a) A. Bassan, T. Borowski, P. E. M. Siegbahn, *Dalton Trans.* **2004**, 3153–3162; b) C. Krebs, D. Galonić Fujimori, C. T. Walsh, J. M. Bollinger Jr., *Acc. Chem. Res.* **2007**, *40*, 484–492; c) *Iron-Containing Enzymes: Versatile Catalysts of Hydroxylation Reaction in Nature* (Eds.: S. P. de Visser, D. Kumar), RSC Publishing, Cambridge, **2011**.

[4] a) D. A. Proshlyakov, T. F. Henshaw, G. R. Monterosso, M. J. Ryle, R. P. Hausinger, *J. Am. Chem. Soc.* **2004**, *126*, 1022–1023; b) P. J. Riggs-Gelasco, J. C. Price, R. B. Guyer, J. H. Brehm, E. W. Barr, J. M. Bollinger Jr, C. Krebs, *J. Am. Chem. Soc.* **2004**, *126*, 8108–8109.

[5] a) L. Que Jr, *Nat. Struct. Biol.* **2000**, *7*, 182–184; b) E. G. Kovaleva, J. D. Lipscomb, *Nat. Chem. Biol.* **2008**, *4*, 186–193.

[6] a) C. R. Simmons, Q. Liu, Q. Q. Huang, Q. Hao, T. P. Begley, P. A. Karplus, M. H. Stipanuk, *J. Biol. Chem.* **2006**, *281*, 18723–18733; b) S. Ye, X. Wu, L. Wei, D. Tang, P. Sun, M. Bartlam, Z. Rao, *J. Biol. Chem.* **2007**, *282*, 3391–3402.

[7] D. Buongiorno, G. D. Straganz, *Coord. Chem. Rev.* **2013**, *257*, 541–563.

[8] a) M. H. Stipanuk, *Annu. Rev. Nutr.* **2004**, *24*, 539–577; b) G. D. Straganz, B. Nidetzky, *ChemBioChem* **2006**, *7*, 1536–1548; c) C. A. Joseph, M. J. Maroney, *Chem. Commun.* **2007**, 3338–3349.

[9] a) J. G. McCoy, L. J. Bailey, E. Bitto, C. A. Bingman, D. J. Aceti, B. G. Fox, G. N. Phillips Jr., *Proc. Natl. Acad. Sci. USA* **2006**, *103*, 3084–3089; b) B. S. Pierce, J. D. Gardner, L. J. Bailey, T. C. Brunold, B. G. Fox, *Biochemistry* **2007**, *46*, 8569–8578; c) S. Aluri, S. P. de Visser, *J. Am. Chem. Soc.* **2007**, *129*, 14846–14847; d) C. R. Simmons, K. Krishnamoorthy, S. L. Granett, D. J. Schuller, J. E. Dominy Jr., T. P. Begley, M. H. Stipanuk, P. A. Karplus, *Biochemistry* **2008**, *47*, 11390–11392; e) T. Kleffmann, S. A. K. Jongkees, G. Fairweather, S. M. Wilbanks, G. N. L. Jameson, *J. Biol. Inorg. Chem.* **2009**, *14*, 913–921; f) J. D. Gardner, B. S. Pierce, B. G. Fox, T. C. Brunold, *Biochemistry* **2010**, *49*, 6033–6041; g) D. Kumar, W. Thiel, S. P. de Visser, *J. Am. Chem. Soc.* **2011**, *133*, 3869–3882; h) E. P. Tchesnokov, S. M. Wilbanks, G. N. L. Jameson, *Biochemistry* **2012**, *51*, 257–264; i) R. J. Souness, T. Kleffmann, E. P. Tchesnokov, S. M. Wilbanks, G. B. Jameson, G. N. L. Jameson, *Biochemistry* **2013**, *52*, 7606–7617.

[10] a) W. Nam, *Acc. Chem. Res.* **2007**, *40*, 522–531; b) I. Siewert, C. Limberg, *Chem. Eur. J.* **2009**, *15*, 10316–10328; c) S. Friedle, E. Reisner, S. J. Lippard, *Chem. Soc. Rev.* **2010**, *39*, 2768–2779.

[11] a) Y. Jiang, L. R. Widger, G. D. Kasper, M. A. Siegler, D. P. Goldberg, *J. Am. Chem. Soc.* **2010**, *132*, 12214–12215; b) A. R. McDonald, M. R. Bukowski,

 © 2015 Wiley-VCH Verlag GmbH & Co. KGaA, Weinheim

E. R. Farquhar, T. A. Jackson, K. D. Koehntop, M. S. Seo, R. F. De Hont, A. Stubna, J. A. Halfen, E. Münck, W. Nam, L. Que, Jr., *J. Am. Chem. Soc.* **2010**, *132*, 17118 – 17129; c) Y. M. Badiei, M. A. Siegler, D. P. Goldberg, *J. Am. Chem. Soc.* **2011**, *133*, 1274 – 1277; d) M. Sallmann, I. Siewert, L. Fohlmeister, C. Limberg, C. Knispel, *Angew. Chem. Int. Ed.* **2012**, *51*, 2234 – 2237; *Angew. Chem.* **2012**, *124*, 2277 – 2280; e) A. C. McQuilken, D. P. Goldberg, *Dalton Trans.* **2012**, *41*, 10883 – 10899; f) A. C. McQuilken, Y. Jiang, M. A. Siegler, D. P. Goldberg, *J. Am. Chem. Soc.* **2012**, *134*, 8758 – 8761; g) A. C. McQuilken, Y. Ha, K. D. Sutherlin, M. A. Siegler, K. O. Hodgson, B. Hedman, E. I. Solomon, G. N. L. Jameson, D. P. Goldberg, *J. Am. Chem. Soc.* **2013**, *135*, 14024 – 14027.

[12] a) D. Kumar, G. N. Sastry, D. P. Goldberg, S. P. de Visser, *J. Phys. Chem. A* **2012**, *116*, 582 – 591; b) L. E. Gonzalez-Ovalle, M. G. Quesne, D. Kumar, D. P. Goldberg, S. P. de Visser, *Org. Biomol. Chem.* **2012**, *10*, 5401 – 5409.

[13] S. P. de Visser, *Chem. Commun.* **2007**, 171 – 173.

[14] R. Latifi, M. A. Sainna, E. V. Rybak-Akimova, S. P. de Visser, *Chem. Eur. J.* **2013**, *19*, 4058 – 4068.

[15] a) T. Borowski, A. Bassan, P. E. M. Siegbahn, *Chem. Eur. J.* **2004**, *10*, 1031 – 1041; b) V. Georgiev, T. Borowski, P. E. M. Siegbahn, *J. Biol. Inorg. Chem.* **2006**, *11*, 571 – 585.

[16] a) D. Kumar, H. Hirao, L. Que Jr, S. Shaik, *J. Am. Chem. Soc.* **2005**, *127*, 8026 – 8027; b) H. Hirao, L. Que Jr, W. Nam, S. Shaik, *Chem. Eur. J.* **2008**, *14*, 1740 – 1756; c) S. Ye, F. Neese, *Proc. Natl. Acad. Sci. USA* **2011**, *108*, 1228 – 1233; d) S. P. de Visser, J.-U. Rohde, Y.-M. Lee, J. Cho, W. Nam, *Coord. Chem. Rev.* **2013**, *257*, 381 – 393.

[17] a) D. Kumar, G. N. Sastry, S. P. de Visser, *Chem. Eur. J.* **2011**, *17*, 6196 – 6205; b) A. K. Vardhaman, P. Barman, S. Kumar, C. V. Sastri, D. Kumar, S. P. de Visser, *Angew. Chem. Int. Ed.* **2013**, *52*, 12288 – 12292; *Angew. Chem.* **2013**, *125*, 12514 – 12518.

[18] A. Hernandez-Ortega, M. G. Quesne, S. Bui, D. P. H. M. Heuts, R. A. Steiner, D. J. Heyes, S. P. de Visser, N. S. Scrutton, *J. Biol. Chem.* **2014**, *289*, 8620 – 8632.

[19] R. Jastrzebski, M. G. Quesne, B. M. Weckhuysen, S. P. de Visser, P. C. A. Bruijnincx, *Chem. Eur. J.* **2014**, *20*, 15686 – 15691.

[20] H. Dau, P. Liebisch, M. Haumann, *Anal. Bioanal. Chem.* **2003**, *376*, 562 – 583.

[21] H. Dau, P. Liebisch, M. Haumann, *Phys. Scr.* **2005**, *T115*, 844 – 846.

[22] M. Haumann, A. Porthun, T. Buhrke, P. Liebisch, W. Meyer-Klaucke, B. Friedrich, H. Dau, *Biochemistry* **2003**, *42*, 13786 – 13786.

[23] M. G. Quesne, R. Latifi, L. E. Gonzalez-Ovalle, D. Kumar, S. P. de Visser, *Chem. Eur. J.* **2014**, *20*, 435 – 446.

[24] a) S. P. de Visser, S. Shaik, P. K. Sharma, D. Kumar, W. Thiel, *J. Am. Chem. Soc.* **2003**, *125*, 15779 – 15788; b) D. Kumar, R. Latifi, S. Kumar, E. V. Rybak-Akimova, M. A. Sainna, S. P. de Visser, *Inorg. Chem.* **2013**, *52*, 7968 – 7979.

[25] M. Barra, M. Haumann, P. Loja, R. Krivanek, A. Grundmeier, H. Dau, *Biochemistry* **2006**, *45*, 14523 – 14532.

[26] J. J. Rehr, R. C. Albers, *Rev. Mod. Phys.* **2000**, *72*, 621 – 654.

[27] A. L. Ankudinov, B. Ravel, J. J. Rehr, S. D. Conradson, *Phys. Rev. B* **1998**, *58*, 7565 – 7576.

[28] M. Risch, K. Klingan, J. Heidkamp, D. Ehrenberg, P. Chernev, I. Zaharieva, H. Dau, *Chem. Commun.* **2011**, *47*, 11912 – 11914.

[29] Jaguar 7.7, version 7.9, Schrodinger, LLC, New York, NY, **2011**.

[30] Gaussian 09, Revision B.01, M. J. Frisch, G. W. Trucks, H. B. Schlegel, G. E. Scuseria, M. A. Robb, J. R. Cheeseman, G. Scalmani, V. Barone, B. Mennucci, G. A. Petersson, H. Nakatsuji, M. Caricato, X. Li, H. P. Hratchian, A. F. Izmaylov, J. Bloino, G. Zheng, J. L. Sonnenberg, M. Hada, M. Ehara, K. Toyota, R. Fukuda, J. Hasegawa, M. Ishida, T. Nakajima, Y. Honda, O. Kitao, H. Nakai, T. Vreven, J. A. Montgomery, Jr., J. E. Peralta, F. Ogliaro, M. Bearpark, J. J. Heyd, E. Brothers, K. N. Kudin, V. N. Staroverov, T. Keith, R. Kobayashi, J. Normand, K. Raghavachari, A. Rendell, J. C. Burant, S. S. Iyengar, J. Tomasi, M. Cossi, N. Rega, J. M. Millam, M. Klene, J. E. Knox, J. B. Cross, V. Bakken, C. Adamo, J. Jaramillo, R. Gomperts, R. E. Stratmann, O. Yazyev, A. J. Austin, R. Cammi, C. Pomelli, J. W. Ochterski, R. L. Martin, K. Morokuma, V. G. Zakrzewski, G. A. Voth, P. Salvador, J. J. Dannenberg, S. Dapprich, A. D. Daniels, O. Farkas, J. B. Foresman, J. V. Ortiz, J. Cioslowski, and D. J. Fox, Gaussian, Inc., Wallingford CT, **2010**.

[31] a) A. D. Becke, *J. Chem. Phys.* **1993**, *98*, 5648 – 5652; b) C. Lee, W. Yang, R. G. Parr, *Phys. Rev. B* **1988**, *37*, 785 – 789.

[32] P. J. Hay, W. R. Wadt, *J. Chem. Phys.* **1985**, *82*, 299 – 310.

[33] S. Grimme, J. Antony, S. Ehrlich, H. Krieg, *J. Chem. Phys.* **2010**, *132*, 154104.

[34] a) D. Kumar, S. P. de Visser, S. Shaik, *Chem. Eur. J.* **2005**, *11*, 2825 – 2835; b) K. A. Prokop, S. P. de Visser, D. P. Goldberg, *Angew. Chem. Int. Ed.* **2010**, *49*, 5091 – 5095; *Angew. Chem.* **2010**, *122*, 5217 – 5221; c) A. K. Vardhaman, C. V. Sastri, D. Kumar, S. P. de Visser, *Chem. Commun.* **2011**, *47*, 11044 – 11046.

[35] a) B. Karamzadeh, D. Kumar, G. N. Sastry, S. P. de Visser, *J. Phys. Chem. A* **2010**, *114*, 13234 – 13243; b) P. Leeladee, G. N. L. Jameson, M. A. Siegler, D. Kumar, S. P. de Visser, D. P. Goldberg, *Inorg. Chem.* **2013**, *52*, 4668 – 4682.

[36] a) S. P. de Visser, *J. Am. Chem. Soc.* **2010**, *132*, 1087 – 1097; b) S. P. de Visser, M. G. Quesne, B. Martin, P. Comba, U. Ryde, *Chem. Commun.* **2014**, *50*, 262 – 282.

[37] a) A. D. Becke, *Phys. Rev. A* **1988**, *38*, 3098 – 3100; b) J. P. Perdew, *Phys. Rev. B* **1986**, *33*, 8822 – 8824.

Received: February 15, 2015
Published online on March 30, 2015

© 2015 Wiley-VCH Verlag GmbH & Co. KGaA, Weinheim

Computational and Theoretical Chemistry 1061 (2015) 1–5

Contents lists available at ScienceDirect

Computational and Theoretical Chemistry

journal homepage: www.elsevier.com/locate/comptc

On copper–copper bond in hydrated cupric acetate

Nirmal K. Shee [a], Ravi Verma [b], Devesh Kumar [b], Dipankar Datta [a,*]

[a] Department of Inorganic Chemistry, Indian Association for the Cultivation of Science, Calcutta 700 032, India
[b] Department of Applied Physics, Babasaheb Bhimrao Ambedkar University, Vidya Vihar, Lucknow 226 025, India

ARTICLE INFO

Article history:
Received 6 February 2015
Received in revised form 3 March 2015
Accepted 3 March 2015
Available online 20 March 2015

Keywords:
Copper(II)acetate
DFT
Broken symmetry
Copper–copper bond
Wiberg's bond index

ABSTRACT

Broken symmetry (BS) calculations within the framework of density functional theory are performed on hydrated copper(II)acetate and its anhydrous variety using LACVP*(Cu)/6-31G*(rest) and LACVP*(Cu)/6-311G++**(rest) basis sets. The experimentally known Cu—Cu distance of 2.617 Å in hydrated copper(II)acetate is reproduced well as 2.619 Å. Using the second basis set, the singlet–triplet separations in both the compounds come out as 497 cm^{-1}. The Cu—Cu distance in anhydrous copper(II)acetate is calculated as 2.480 Å. Bader's AIM calculations show presence of a bond critical point (BCP) of the type (3, −1) between the two copper atoms in both the compounds indicating the existence of a chemical bond between the metal atoms. The sign of the Laplacian associated with the electron density at the BCP is found to be negative indicating a covalent bond between the two copper centers. For the Cu—Cu bond in both the compounds, Wiberg's bond index comes out as ~0.3 suggesting a reasonably strong metal–metal bond in cupric acetate. Calculations of the energies of the BS and the triplet states around the Cu—Cu distance of 2.6 Å (to be specific, in the range of 2.4–2.9 Å) reveal that the observed magnetic behavior of hydrated cupric acetate is the resultant of two opposing pathways for the interaction between the two unpaired metal electrons – (1) through the ligand framework and (2) through a direct Cu—Cu bond. The Cu—Cu bond results in an antiferromagnetic exchange while the acetato framework provides a means of ferromagnetic interactions.

© 2015 Elsevier B.V. All rights reserved.

1. Introduction

Copper(II)acetate monohydrate (abbreviated as $Cu(OAc)_2H_2O$) plays a lead role in magnetochemistry and related studies. Understanding the magnetic properties of this compound is very crucial, which is still not fully clear. Lifschitz and Rosenbohm [1] first observed in 1915 that the molar magnetic susceptibility of $Cu(OAc)_2H_2O$ at room temperature is much lower than expected. This has been corroborated by several subsequent studies [2]. First variable temperature (83–304 K) magnetic susceptibility measurements on a single crystal of $Cu(OAc)_2H_2O$ have been reported by Guha [3] in 1951. In the following year, Bleany and Bowers [4] have explained the experimental data of Guha by assuming direct magnetic exchange coupling between a pair of copper(II) atoms with the exchange coupling constant J of $-315\ cm^{-1}$. Later on many such measure-ments [5] have been made lowering the temperature much below 83 K. J value obtained by Elmali [5] in 2000 in the temperature range 4.2–300 K, is $-292.2\ cm^{-1}$ by using Bleany–Bowers equation [6]. The X-ray crystal structure of $Cu(OAc)_2H_2O$ was first determined by Niekerk and Schoening [7] in 1953 to show that it is an acetato bridged dimer with a Cu—Cu distance of 2.64 Å, a bit longer than the interatomic distance of 2.556 Å in metallic copper at 293 K. This substantiated the idea of Bleany and Bowers. It is interesting to note that a search of CCDC shows that the X-ray crystal structure of $Cu_2(OAc)_4{\cdot}2H_2O$ has been determined at least thirteen times after Niekerk and Schoening, the latest one [8] being in 2012 where the Cu—Cu distance is found to be 2.6107(4) Å. From neutron-diffraction [9], Cu—Cu separation comes out as 2.614(2) Å. The number of times the variable temperature magnetic susceptibility and the crystal structure of $Cu_2(OAc)_4{\cdot}2H_2O$ have been repeated only shows the importance of this very compound in the magnetic studies of inorganic complexes.

Variable temperature magnetic susceptibility studies show that in $Cu_2(OAc)_4{\cdot}2H_2O$, singlet is the ground state, i.e. the unpaired electrons on the two copper(II) centers are antiferromagnetically coupled. MO studies of Malrieu and co-workers [10] in 1982 indicate that the observed magnetic behavior of $Cu(OAc)_2H_2O$ is a resultant of direct exchange (ferromagnetic), super-exchange (antiferromagnetic), double-spin polarization (overall antiferromagnetic) and some higher order effects (antiferromagnetic). Earlier in 1975 Hoffman and co-workers [11] have ruled

* Corresponding author. Tel.: +91 33 2473 5374; fax: +91 33 2473 2805.
E-mail address: icdd@iacs.res.in (D. Datta).

http://dx.doi.org/10.1016/j.comptc.2015.03.003
2210-271X/© 2015 Elsevier B.V. All rights reserved.

out the possibility of copper–copper bond in $Cu_2(OAc)_4{\cdot}2H_2O$ saying that the Cu—Cu distance is too long for a direct overlap between the d_x^2–y^2 orbitals on the metal (from EPR studies it is known that the unpaired electron of each copper atom remains in the respective d_x^2–y^2 orbital). Herein we re-examine this aspect by Bader's theory [12–14] of Atoms-in-Molecule (AIM). For comparison, we have done the same calculations for anhydrous copper(II) acetate, $Cu_2(OAc)_4$ also.

2. Computational

All calculations were done by using the hybrid density functional BP86 in Jaguar 7.9 program package [15]. Analytical frequency calculations were done using Gaussian 09 [16]. One set of basis (**1**) used is LACVP*(Cu)/6-31G*(rest) [17,18]. Single point calculations were done using basis set **2** comprising LACVP*(Cu)/6-311G++**(rest) on the geometry optimized by basis set **1**, to generate the wave function necessary for AIM calculations, as implemented in AIM 2000 program package [19]. Deviations from these protocols have been specified on appropriate occasions.

3. Results and discussion

To apply Bader's theory, one has to know the ground state wave function. Theoretically for two interacting spins S_1 and S_2, J is calculated from the energies of the low spin (LS) and high spin (HS) state. As mentioned above, singlet i.e. the LS state is the ground state in $Cu_2(OAc)_4{\cdot}2H_2O$ and $Cu_2(OAc)_4$ [2]. While the HS state can be readily described by single determinant wave function, LS state requires extensive treatment of electron–electron correlation. The LS state can be easily approximated by "broken symmetry" (BS) state in BS-DFT approach of Ginsberg, Noodleman and Yamaguchi [20–23]. Alvarez and co-workers [24,25] have shown that for $S_1 \geqslant S_2$,

$$J = \frac{E_{BS} - E_{HS}}{2S_1S_2 + S_2} \quad (1)$$

For $S_1 = S_2 = 1/2$ as in $Cu_2(OAc)_4{\cdot}2H_2O$ and $Cu_2(OAc)_4$, Eq. (1) becomes

$$J = E_{BS} - E_{HS} \quad (2)$$

One way to test whether the wave function for the BS state truly represent the singlet states in $Cu_2(OAc)_4{\cdot}2H_2O$ and $Cu_2(OAc)_4$ is to calculate the expectation value of total spin squared $\langle S_{BS}^2 \rangle$. It should be close to unity for a system where two unpaired electrons interact [26,27]. Our values for $Cu_2(OAc)_4{\cdot}2H_2O$ is 0.95 and for $Cu_2(OAc)_4$ 0.93 when basis set **1** is used. For basis set **2**, $\langle S_{BS}^2 \rangle$ for $Cu_2(OAc)_4{\cdot}2H_2O$ is 0.90 and for $Cu_2(OAc)_4$ 0.89. Thus in our calculations the singlet state has been simulated by the BS states quite satisfactorily.

From our calculations, the triplet state for $Cu_2(OAc)_4{\cdot}2H_2O$ is found to be higher than the singlet one by 528 and 497 cm^{-1} for basis set **1** and basis set **2** respectively. These are much higher than the experimental values. On the other hand, the experimental Cu—Cu distance in $Cu_2(OAc)_4{\cdot}2H_2O$ is very well reproduced in our calculations (Table 1). In the case of $Cu_2(OAc)_4$, the triplet state is higher than the singlet state by 574 and 497 cm^{-1} for the basis set **1** and basis set **2** respectively. Figgis and Martin [2] have experimentally determined the J for anhydrous copper(II)acetate as 286 cm^{-1}.

Figs. 1 and 2 present Bader's bond critical points (BCP) of (3, −1) type and Tables 1 and 2 summarize calculated bond distances as well as the electron density ρ at the BCP and its associated Laplacian, $\nabla^2\rho$, of some representative bonds in $Cu_2(OAc)_4{\cdot}2H_2O$ and $Cu_2(OAc)_4$ respectively. In Bader's theory, existence of a BCP between two atoms ensures chemical bonding between them. From the figures, it is clear that BCP is centrally located on the Cu—Cu bonds. The magnitude of the corresponding ρ and the sign of $\nabla^2\rho$ suggest a weak covalent bond [28] between the two Cu atoms. The topological analysis of the experimental charge density maps of $Cu_2(OAc)_4{\cdot}2H_2O$ at 100 K, performed by Bertolotti et al. in 2012, shows the expected bond critical points with the corresponding bond paths, including Cu—Cu bond [8]. The magnitudes of experimental ρ and $\nabla^2\rho$ for the Cu—Cu bond are somewhat higher than those obtained here (Table 1). Further, the sign of $\nabla^2\rho$ obtained experimentally is positive [8], while that obtained by us theoretically is negative. An interesting consequence of our BS calculations is presented in Fig. 3 where the orbitals of the two Cu(II) are different despite the D_{4h} symmetry of $Cu_2(OAc)_4{\cdot}2H_2O$. This indicates a breakdown of the simple molecular orbital picture, which is just a limiting case of BS calculations.

Existence of a bond between two copper atoms in $Cu_2(OAc)_4{\cdot}2H_2O$ and $Cu_2(OAc)_4$ is further supported by Wiberg's

Table 1
Lengths r, the electron density ρ at bond critical point and its associated Laplacian $\nabla^2\rho$ for some bonds in $Cu_2(CH_3COO)_4{\cdot}2H_2O$ as obtained from BP86/LACVP*(Cu)/6-311G++**(rest)//BP86/LACVP*(Cu)/6-31G*(rest) calculations on the BS state and comparison with the experimental data.[a]

Bond	r (Å)		ρ (e Å^{-3})		$\nabla^2\rho$ (e Å^{-5})		WBI
	calc	exp	calc	exp	calc	exp	
Cu_1—Cu_2	2.619	2.617	0.202	0.182(1)	−0.24	1.68(1)	0.31
Cu_1—Ow_1	2.378	2.157	0.202	0.378(6)	−0.96	6.07(1)	0.16
Cu_2—Ow_2	2.366	2.157	0.202	0.378(6)	−0.96	6.07(1)	0.16
Cu_1—O_1	2.013	1.947	0.472	0.521(1)	−2.65	9.22(1)	0.29
Cu_1—O_2	1.980	1.954	0.472	0.512(4)	−3.13	9.06(1)	0.31
Cu_2—O_3	2.050	1.954	0.472	0.512(4)	−2.65	9.06(1)	0.29
Cu_2—O_4	2.019	1.947	0.472	0.521(1)	−3.13	9.22(1)	0.31
Cu_1—O_5	2.027	1.996	0.405	0.558(1)	−2.65	9.86(1)	0.28
Cu_1—O_6	1.981	1.987	0.472	0.595(1)	−3.13	10.47(1)	0.30
Cu_2—O_7	2.050	1.987	0.405	0.595(1)	−2.41	10.47(1)	0.27
Cu_2—O_8	2.005	1.996	0.472	0.558(1)	−2.89	9.86(1)	0.28

[a] For atom labeling scheme, see Fig. 1. The experimental (exp) bond lengths are quoted from Ref. 5 and those for ρ and $\nabla^2\rho$ at 100 K are from Ref. 8.

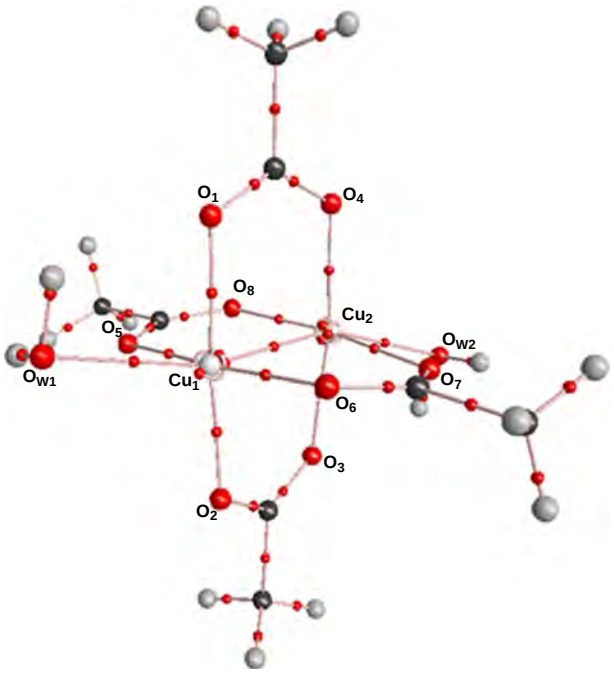

Fig. 1. Calculated bond critical points of $Cu_2(CH_3COO)_4{\cdot}2H_2O$.

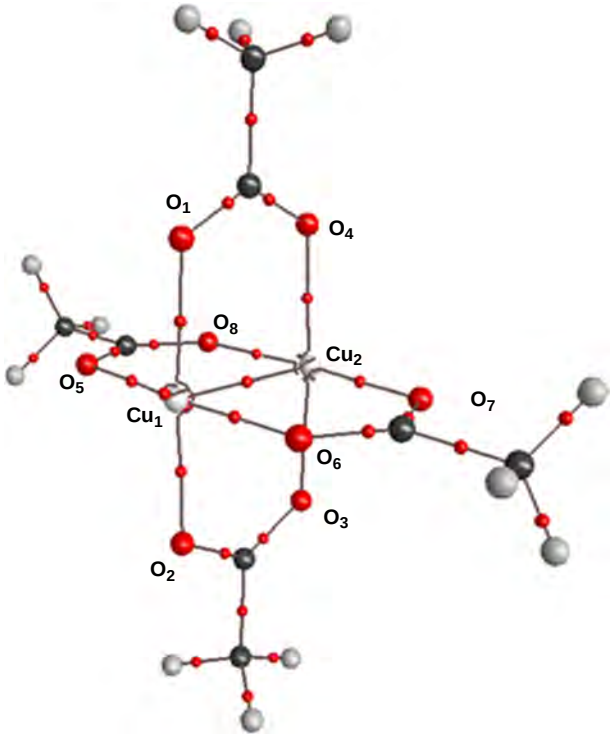

Fig. 2. Calculated bond critical points of $Cu_2(CH_3COO)_4$.

bond index (WBI) which is "the sum of the squares of the bond orders between any one atomic orbital and all other orbitals in a molecule" [29]. WBI of the Cu—Cu bond in $Cu_2(OAc)_4{\cdot}2H_2O$ is 0.31. It is one of the highest among all the bonds listed in Table 1. For anhydrous copper(II)acetate also, similar conclusion is drawn (Table 2). In the anhydrous variety, Cu—Cu distance comes out as somewhat smaller than that in the hydrated one with WBI remaining the same.

An interesting scenario emerges when we try to estimate the energies of the BS state and the triplet states for $Cu_2(OAc)_4{\cdot}2H_2O$ around the Cu—Cu distance of 2.6 Å – specifically in the range of 2.4–2.9 Å (Table 3, Fig. 4). For this purpose and to generate the wave functions in these cases necessary for AIM analyses, a single point calculation was done with B3LYP/6-31++G** after geometry optimization of $Cu_2(OAc)_4{\cdot}2H_2O$ with B3LYP/6-31G at a given Cu—Cu distance for each multiplicity. At Cu—Cu distances below 2.85 Å, the BS state is lower than the triplet state (*J* value negative). At 2.85 Å, the value of *J* is 0. Beyond that, the *J* value becomes positive indicating surfacing of ferromagnetic interaction. There are actually two opposing pathways in $Cu_2(OAc)_4{\cdot}2H_2O$ for the intramolecular magnetic interaction – (i) copper–copper bond and (ii) the acetato bridge. The van der Waals radius of copper, according to Bondi [30], is 1.4 Å. Consequently, beyond 2.8 Å, there should not be any Cu—Cu bond. An indirect support for this argument is provided by the alkoxo bridged dinuclear 3-amino-propanolato Cu(II) complexes of Farrugia et al. [31] where no bond path is found between the two copper(II) nuclei which are at a distance of 2.96 Å. The WBI values at the different Cu—Cu bond distances given in Table 3 show that as the distance between the two copper(II) centers approaches 2.9 Å, the Cu—Cu bond weakens very much. Our calculations reveal that the geometric parameters of the ligand framework remain more or less unperturbed (Table 4) in the explored vicinity of Cu—Cu distance of 2.6 Å. Thus the point is when Cu—Cu distance >2.85, the anti-ferromagnetic exchange interaction in $Cu_2(OAc)_4{\cdot}2H_2O$ through the Cu—Cu bond is much diminished or lost. But there remains the exchange interactions through the acetato bridge which is evidently ferromagnetic. Factorisation of magnetic exchange in a dinulear compound through different bridges has been attempted earlier [32].

Table 2
Lengths *r*, the electron density ρ at the bond critical point and its associated Laplacian $\nabla^2\rho$ of some bonds in $Cu_2(CH_3COO)_4$ as obtained from BP86/LACVP*(Cu)/6-311G++**(rest)//BP86/LACVP*(Cu)/6-31G*(rest) calculations on the BS state.[a]

Bond	*r* (Å)	ρ (e Å^{-3})	$\nabla^2\rho$ (e Å^{-5})	WBI
Cu_1—Cu_2	2.480	0.20	−0.48	0.30
Cu_1—O_1	1.987	0.47	−2.89	0.28
Cu_1—O_2	1.986	0.47	−2.89	0.28
Cu_2—O_3	1.994	0.47	−2.89	0.28
Cu_2—O_4	1.993	0.47	−2.89	0.28
Cu_1—O_5	1.987	0.47	−2.89	0.28
Cu_1—O_6	1.990	0.47	−2.89	0.28
Cu_2—O_7	1.995	0.47	−2.89	0.28
Cu_2—O_8	1.997	0.47	−2.89	0.28

[a] For atom labeling scheme, see Fig. 2.

Table 3
Variation of B3LYP BS-DFT energies of the BS (i.e. singlet; S) and the triplet (T) states and electron density ρ at the bond critical point and its associated Laplacian $\nabla^2\rho$ as obtained from B3LYP/6-31++G**//B3LYP/6-31G calculations on $Cu_2(CH_3COO)_4{\cdot}2H_2O$ with Cu—Cu distance.

Cu—Cu distance (Å)	Spin multiplicity	Energy (a.u.)	ρ (e Å^{-3})	$\nabla^2\rho$ (e Å^{-5})	WBI
2.4	S	−4348.311476	0.34	−0.48	0.13
	T	−4348.310571	0.34	−0.48	0.13
2.5	S	−4348.314778	0.27	−0.48	0.11
	T	−4348.313812	0.27	−0.48	0.11
2.6	S	−4348.315976	0.20	−0.48	0.09
	T	−4348.314948	0.20	−0.48	0.02
2.7	S	−4348.315458	0.13	−0.48	0.08
	T	−4348.314362	0.13	−0.48	0.02
2.8	S	−4348.313102	0.13	−0.24	0.06
	T	−4348.311926	0.13	−0.24	0.01
2.9	S	−4348.309734	0.13	−0.24	0.05
	T	−4348.310720	0.13	−0.24	0.01

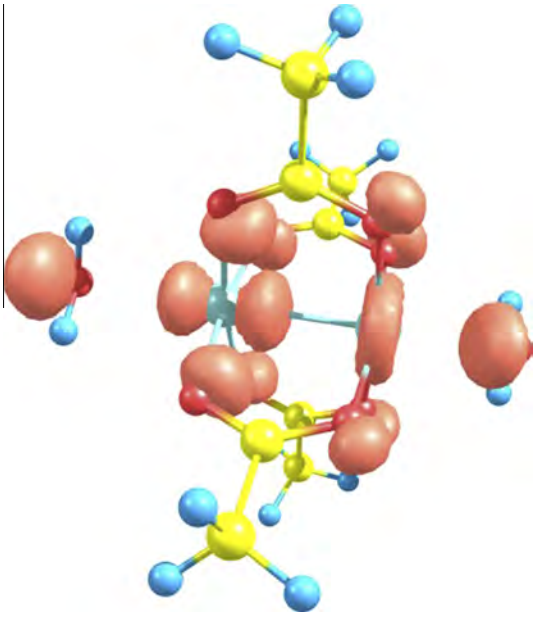

Fig. 3. An orbital picture of the interaction between the oxygen atoms of the water molecules with Cu(II) in $Cu_2(CH_3COO)_4{\cdot}2H_2O$ complex emerging out of our BS-DFT calculations.

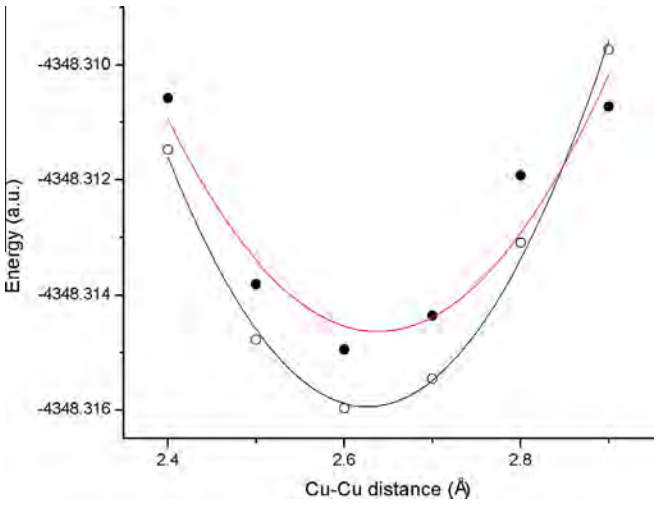

Fig. 4. Variation of the energies of the BS (black line, open circles) and the triplet (red line, filled circles) states in $Cu_2(CH_3COO)_4{\cdot}2H_2O$ with Cu—Cu distance. For data, see Table 3. Curves drawn are least squares fitted. Correlation coefficient *r*: black, 0.995; red, 0.914. (For interpretation of the references to color in this figure legend, the reader is referred to the web version of this article.)

Table 4
Variation of some structural parameters of $Cu_2(CH_3COO)_4{\cdot}2H_2O$ in the BS (i.e. singlet; S) and the triplet (T) states with Cu—Cu distance as obtained from B3LYP/6-31G optimization.[a]

Cu—Cu (Å)	Spin multiplicity	⟨C=O⟩ (Å)	⟨Cu—O⟩ (Å)	⟨Cu—O—C⟩ (°)	⟨O—C—O⟩ (°)
2.4	S	1.29	1.98	119.7	122.8
	T	1.29	1.98	119.7	122.7
2.5	S	1.29	1.98	120.8	123.2
	T	1.29	1.98	120.8	123.2
2.6	S	1.29	1.98	121.9	123.7
	T	1.29	1.98	121.9	123.6
2.7	S	1.29	1.98	123.0	124.1
	T	1.29	1.98	123.0	124.0
2.8	S	1.29	1.99	124.4	124.5
	T	1.29	1.99	124.5	124.4
2.9	S	1.29	1.99	126.2	124.8
	T	1.29	1.96	119.3	123.8

[a] Experimental data [5]: ⟨C=O⟩, 1.26 Å; ⟨Cu—O⟩, 1.97 Å; ⟨Cu—O—C⟩, 122.8°; ⟨O—C—O⟩, 125.2°.

4. Concluding remarks

Here we have shown that the interaction between the two spins on the two copper atoms in cupric acetate is actually a resultant of two pathways of counteracting nature. One path is through the ligand framework and another through the direct Cu—Cu bond. The Cu—Cu bond induces an antiferromagnetic exchange while the acetato framework provides a pathway for ferromagnetic interactions. Incidentally, presence of a Cu—Cu bond in cupric acetate was first proposed by Figgis and Martin in 1956 [2]. They envisaged a δ bonding between the two $d_{x^2-y^2}$ orbitals of the two copper atoms. Actually a $\delta \rightarrow \delta^*$ transition is observed in complexes of second-row and third row transition metals having metal–metal quadruple bonds [33]. Gray and co-workers have estimated this transition to be around 100 nm in $Cu_2(OAc)_4{\cdot}2H_2O$ [33], which they consider as "the archetypal weakly metal–metal-interacting dimer". It is mentioned that there is no correlation between the $\delta \rightarrow \delta^*$ transition energy and metal–metal bond strength.

Here we have relied on AIM. Alternative bonding pictures can be obtained from more rigorous methods like Domain Average Fermi Hole approach and delocalization indices [34]. Of these, Bertolotti et al. [8] have attempted to calculate the delocalization index for the Cu—Cu bond to conclude that there is a rather small amount of electron delocalization in the internuclear metallic region in $Cu_2(OAc)_4{\cdot}2H_2O$. It is cautioned that delocalization indices cannot be related to bond order.

Acknowledgement

Thanks are due to a reviewer for various help.

References

[1] J. Lifschitz, E. Rosenbohm, Magneto-chemistry of Internally Complex Compounds, Z. Electrochem. 21 (1915) 499–501.
[2] B.N. Figgis, R.L. Martin, Magnetic studies with copper(II) salts. Part I. Anomalous pasramagnetism and δ-bonding in anhydrous and hydrated copper(II) acetates, J. Chem. Soc. (1956) 3837–3846.
[3] B.C. Guha, Magnetic properties of some paramagnetic crystals at low temperature, Proc. Roy. Soc. Ser. A (London) 206 (1951) 353–373.
[4] B. Bleaney, K.D. Bowers, Anomalous paramagnetism of copper acetate, Proc. Roy. Soc. Ser. A (London) 214 (1952) 451–465.
[5] A. Elmali, The magnetic super-exchange coupling in copper(II) acetate monohy-drate and a redetermination of the crystal structure, Turk. J. Phys. 24 (2000) 667–672.
[6] G. Mostafa, G.K. Patra, J.M. Jana, D. Datta, A ferromagnetically coupled acetato bridged copper(II) dimer, Ind. J. Chem. 39A (2000) 1174–1176.
[7] J.N. van Niekerk, F.R.L. Schoening, A new type of copper complex as found in the crystal structure of cupric acetate, $Cu_2(CH_3COO)_4{\cdot}2H_2O$, Acta Cryst. 6 (1953) 227–232.
[8] F. Bertolotti, A. Forni, G. Gervasio, D. Marabello, E. Diana, Experimental and theoretical charge density of hydrated cupric acetate, Polyhedron 42 (2012) 118–127.
[9] G.M. Brown, R. Chidambaram, Dinuclear copper(II) acetate monohydrate: a redetermination of the structure by neutron-diffraction analysis, Acta Cryst. B29 (1973) 2393–2403.
[10] P. de Loth, P. Cassoux, J.P. Daudey, J.P. Malrieu, Ab initio direct calculation of the singlet-triplet separation in cupric acetate hydrate dimer, J. Am. Chem. Soc. 103 (1981) 4007–4016.
[11] P.J. Hay, J.C. Thibeault, R. Hoffmann, Orbital interactions in metal dimer complexes, J. Am. Chem. Soc. 97 (1975) 4884–4899.
[12] R.F.W. Bader, A quantum theory of molecular structure and its applications, Chem. Rev. 91 (1991) 893–928.
[13] S. Hati, D. Datta, Electronegativity and Bader's bond critical point, J. Comput. Chem. 13 (1992) 912–918.
[14] A.K. Samanta, D. Datta, A DFT and AIM study of the interactions of pyridine and pyrazine with alkali hydrides. Identification of dihydrogen bonds involving aromatic C–H hydrogen, Ind. J. Chem. 49A (2010) 176–179.
[15] Jaguar, version 7.9, Schrodinger, LLC, New York, NY, 2011.
[16] Gaussian-09, Revision C.01, M.J. Frisch, G.W. Trucks, H.B. Schlegel, G.E. Scuseria, M.A. Robb, J.R. Cheeseman, G. Scalmani, V. Barone, B. Mennucci, G.A. Petersson, H. Nakatsuji, M. Caricato, X. Li, H.P. Hratchian, A.F. Izmaylov, J. Bloino, G. Zheng, J.L. Sonnenberg, M. Hada, M. Ehara, K. Toyota, R. Fukuda, J. Hasegawa, M. Ishida, T. Nakajima, Y. Honda, O. Kitao, H. Nakai, T. Vreven, J.A. Montgomery, Jr., J.E. Peralta, F. Ogliaro, M. Bearpark, J.J. Heyd, E. Brothers, K.N. Kudin, V.N. Staroverov, T. Keith, R. Kobayashi, J. Normand, K. Raghavachari, A. Rendell, J.C. Burant, S.S. Iyengar, J. Tomasi, M. Cossi, N. Rega, J.M. Millam, M. Klene, J.E. Knox, J.B. Cross, V. Bakken, C. Adamo, J. Jaramillo, R. Gomperts, R.E. Stratmann, O. Yazyev, A.J. Austin, R. Cammi, C. Pomelli, J.W. Ochterski, R.L. Martin, K. Morokuma, V.G. Zakrzewski, G.A. Voth, P. Salvador, J.J. Dannenberg, S. Dapprich, A.D. Daniels, O. Farkas, J.B. Foresman, J.V. Ortiz, J. Cioslowski, D.J. Fox, Gaussian Inc., Wallingford CT, 2010.
[17] P.J. Hay, W.R. Wadt, Ab initio effective core potentials for molecular calculations. Potentials for the transition metal atoms Sc to Hg, J. Chem. Phys. 82 (1985) 270–283.
[18] W.J. Hehre, R. Ditchfield, J.A. Pople, Self-consistent molecular orbital methods. XII. Further extensions of Gaussian-type basis sets for use in molecular orbital studies of organic molecules, J. Chem. Phys. 56 (1972) 2257–2261.
[19] F. Biegler-König, J. Schönbohm, D. Bayles, AIM2000 – A program to analyze and visualize atoms in molecules, J. Comp. Chem. 22 (2001) 545–559.
[20] A.P. Ginsberg, Magnetic exchange in transition metal complexes. 12. Calculation of cluster exchange coupling constants with the X. alpha.-scattered wave method, J. Am. Chem. Soc. 102 (1980) 111–117.
[21] L. Noodleman, Valence bond description of antiferromagnetic coupling in transition metal dimers, J. Chem. Phys. 74 (1981) 5737–5743.
[22] K. Yamaguchi, Y. Takahara, T. Fueno, K.N. Houk, Extended Hartree-Fock (EHF) theory of chemical reactions, Theor. Chim. Acta 73 (1988) 337–364.
[23] F. Neese, Prediction of molecular properties and molecular spectroscopy with density functional theory: from fundamental theory to exchange-coupling, Coord. Chem. Rev. 253 (2009) 526–563.
[24] E. Ruiz, J. Cano, S. Alvarez, P. Alemany, Broken symmetry approach to calculation of exchange coupling constants for homobinuclear and heterobinuclear transition metal complexes, J. Comput. Chem. 20 (1999) 1391–1400.

[25] E. Ruiz, S. Alvarez, J. Cano, V. Polo, About the calculation of exchange coupling constants using density-functional theory: the role of the self-interaction error, J. Chem. Phys. 123 (2005) 164110.
[26] K. Yamaguchi, Y. Takahara, T. Fueno, in: J.V.H. Smith, H.F. Schaefer III, K. Morokuma (Eds.), Ab-initio molecular orbital studies of structure and reactivity of transition metal-oxo compounds, Appl. Quantum Chem., D. Reidel, Dordrecht, 1986, pp. 155–184.
[27] A. Bencini, Some considerations on the proper use of computational tools in transition metal chemistry, Inorg. Chim. Acta 361 (2008) 3820–3831.
[28] L. Zhang, F. Ying, W. Wu, P.C. Hiberty, S. Shaik, Topology of electron charge density for chemical bonds from valence bond theory: a probe of bonding types, Chem. Eur. J. 15 (2009) 2979–2989.
[29] K.B. Wiberg, Application of the Pople-Santry-Segal CNDO method to the cyclopropylcarbinyl and cyclobutyl cation and to bicyclobutane, Tetrahedron 24 (1968) 1083–1096.
[30] A. Bondi, Van der Waals volumes and radii, J. Phys. Chem. 68 (1964) 441–451.
[31] L.J. Farrugia, D.S. Middlemiss, R. Sillanpää, P. Seppälä, A combined experimental and theoretical charge density study of the chemical bonding and magnetism in 3-amino-propanolato Cu(II) complexes containing weakly coordinated anions, J. Phys. Chem. A 112 (2008) 9050–9067.
[32] S. Sarkar, A. Datta, A. Mondal, D. Chopra, J. Ribas, K.K. Rajak, S.M. Sairam, S.K. Pati, Competing magnetic interactions in a dinuclear Ni(II) complex: antiferromagnetic O–H···O moiety and ferromagnetic N_3^- ligand, J. Phys. Chem. B 110 (2006) 12–15.
[33] V.M. Miskowski, M.D. Hopkins, J.R. Winkler, H.B. Gray, Multiple metal–metal bonds, in: E.I. Solomon, A.B.P. Lever (Eds.), Inorganic Electronic Structure and Spectroscopy, vol. II, John Wiley & Sons, Inc., New York, 1999, (chapter 6).
[34] R. Ponec, C. Gatti, Do the structural changes defined by the electron density topology necessarily affect the picture of the bonding?, Inorg Chem. 48 (2009) 11024–11031.

Author's personal copy

J Mol Model (2015) 21:96
DOI 10.1007/s00894-015-2631-3

ORIGINAL PAPER

Pyrazolo[3,4-*d*]pyrimidines as novel inhibitors of O-acetyl-L-serine sulfhydrylase of *Entamoeba histolytica*: an in silico study

Umesh Yadava · Bindesh Kumar Shukla · Mihir Roychoudhury · Devesh Kumar

Received: 20 June 2014 / Accepted: 22 February 2015
© Springer-Verlag Berlin Heidelberg 2015

Abstract Amoebiasis, a worldwide explosive epidemic, caused by the gastrointestinal anaerobic protozoan parasite *Entamoeba histolytica*, infects the large intestine and, in advance stages, liver, kidney, brain and lung. Metronidazole (MNZ)—the first line medicament against amoebiasis—is potentially carcinogenic to humans and shows significant side-effects. Pyrazolo[3,4-*d*]pyrimidine compounds have been reported to demonstrate antiamoebic activity. In silico molecular docking simulations on nine pyrazolo[3,4-*d*]pyrimidine molecules without linkers (molecules **1–9**) and nine pyrazolo[3,4-*d*]pyrimidine molecules with a trimethylene linker (molecules **10–18**) along with the reference drug metronidazole (MNZ) were conducted using the modules of the programs Glide-SP, Glide-XP and Autodock with O-acetyl-L-serine sulfhydrylase (OASS) enzyme—a promising target for inhibiting the growth of *Entamoeba histolytica*. Docking simulations using Glide-SP demonstrate good agreement with reported biological activities of molecules **1**–**9** and indicate that molecules **2** and **4** may act as potential high affinity inhibitors. Trimethylene linker molecules show improved binding affinities among which molecules **15** and **16** supersede. MD simulations on the best docked poses of molecules **2, 4, 15, 16** and **MNZ** were carried out for 20 ns using DESMOND. It was observed that the docking complexes of molecules **4, 15** and **MNZ** remain stable in aqueous conditions and do not undergo noticeable fluctuations during the course of the dynamics. Relative binding free energy calculations of the ligands with the enzyme were executed on the best docked poses using the molecular mechanics generalized Born surface area (MM-GBSA) approach, which show good agreement with the reported biological activities.

Keywords *Entamoeba histolytica* · Glide docking · Schrodinger · ADME · Molecular dynamics

Introduction

Amoebiasis, the most aggressive disease of the human intestine, is caused by the anaerobic protozoan parasite *Entamoeba histolytica*, and is the third most common cause of death from parasitic infections, surpassing Schistosomiasis and malaria [1, 2]. It is more common in the young but may affect people of any age. It has a very high incidence in tropical countries like India, Mexico, Central and South America etc. and spreads commonly through contaminated water, feces and from food served with contaminated hands. The *E. histolytica* parasite penetrates the human gastrointestinal tract and burrows deep into the intestinal walls, which can cause abscesses and ulcers and may infect the bowel. Without treatment, it can travel to the other parts of the body, such as the liver, through the veins of the intestines. Other body parts that are reached by this protozoa may also become infected and adorned with abscesses and ulcers. The formation of pus in the liver (liver abscess), lungs (lung abscess), and brain (brain abscess), is a sign of advanced stage of amoebiasis, which may be highly fatal to a person. When the cyst of *E. histolytica* enters the small intestine, active amoebic parasites (trophozoites) are released, which can invade the epithelial cells of the large intestines, causing flask-shaped ulcers. Cysteine is an

Electronic supplementary material The online version of this article (doi:10.1007/s00894-015-2631-3) contains supplementary material, which is available to authorized users.

U. Yadava (✉) · B. K. Shukla · M. Roychoudhury
Department of Physics, D.D.U. Gorakhpur University, Gorakhpur 273009, India
e-mail: u_yadava@yahoo.com

D. Kumar
Department of Applied Physics, Babasaheb Bhimrao Ambedkar University, Vidya Vihar, Rae Bareilly Road, Lucknow 226025, India

Published online: 25 March 2015

Author's personal copy

important amino acid for the attachment and growth of trophozites of *E. histolytica* [3]. In this organism, the condensation of O-acetylserine with sulfide is the major route of cysteine biosynthesis, which involves two key enzymes: O-acetyl-L-serine sulfhydrylase (OASS) and serine acetyl transferase (SAT). These enzymes can act as promising targets for inhibiting the growth of *E. histolytica* [4, 5]. Metronidazole (MNZ)—the first line medicament against amoebiasis—produces significant side effects and is potentially carcinogenic to human cells on account of its genotoxicity [6]. Moreover, resistance of *E. histolytica* to MNZ and relapses of intestinal and hepatic amoebiasis have also been reported [7]. Because of multidrug resistance and the significant side effects of an assortment of available antiamoebic drugs, the development of novel effective antiamoebic drugs that produce fewer or no side effects is required.

Development of inhibitors of OASS using in silico docking methods and their in vitro testing have been reported in the literature [8]. Pyrazolo[3,4-d]pyrimidines constitute a class of naturally occurring fused uracils that exhibit diverse biological activities. These compounds are reported as potential anti-inflammatory agents [9], anti-coagulation inhibitors [10], xanthine oxidase inhibitors [11], antiproliferative and proapoptotic agents in several tumor types [12]. They are also known as SRC kinase inhibitors [13] and are useful in the treatment of human cancers sustaining oncogenic activation of RET [14]. Due to the structural similarity of pyrazolo[3,4-d]pyrimidine cores with almost all the antiamoebic drugs, e.g., metronidazole, tinidazole, and ornidazole (Fig. 1), pyrazolo[3,4-d]pyrimidine analogues were synthesized and found to be endowed with antiamoebic activity [15–18]. The in vitro antiamoebic activity of compounds **1**–**9** (Fig. 2a) against HM1:IMSS strain of *E. histolytica*, indicates that these compounds may have better inhibitor activity in comparison to the reference drug metronidazole [18]. Further, these compounds are also found to have low cytotoxicity against the human breast cancer cell line MCF-7. These preliminary results illustrate that pyrazolo[3,4-d]pyrimidine analogues could help in designing better molecules with improved antiamoebic activity. Pyrazolo[3,4-d]pyrimidine molecules having trimethylene linkers; the flexible models to facilitate aromatic π–π interactions also possess useful pharmaceutical properties [10, 19]. It is fascinating to consider these trimethylene linker molecules to investigate their potential as anti-amoebic agents in addition to molecules without this linker. The in silico molecular docking studies of nine pyrazolo[3,4-d]pyrimidine molecules with no linker (molecules **1**–**9**) and nine molecules with a trimethylene linker (molecules **10**–**18**) along with the reference molecule metronidazole (MNZ) (Fig. 2a, b) were carried out with the O-acetyl-L-serine sulfhydrylase (OASS) enzyme—the prime target for inhibiting the growth of *E. histolytica*. In order to study the stability and dynamic changes of predicted binding conformations, molecular dynamics (MD) simulations were performed on the best docking complexes. Molecular mechanics-generalized Born/surface area (MM-GB/SA) analysis was carried out to estimate the relative binding free energies of the ligands with OASS. To ensure success at clinical trial level, we carried out ADME (absorption, distribution, metabolism and excretion) predictions on ligand molecules.

Methods

GLIDE docking

The three-dimensional crystal structure of O-acetyl-L-serine sulfhydrylase enzyme complexed with cysteine and pyridoxal-5′-phosphate (PLP) ligands (PDB ID: 3BM5) determined by X-ray crystallography was retrieved from the Protein Data Bank (http://www.rcsb.org). This crystal structure was inspected carefully and processed in order to overcome a variety of potential problems, e.g., missing atoms, bond orders, added waters, chain breaks, alternate binding locations, etc. Preparations of protein and ligands were carried out and an electron affinity grid was subsequently generated. Docking of ligands with the receptor has been carried out using GLIDE5.2 module with standard precision (SP) and extra precision (XP) protocols both, as implemented in the SCHRÖDINGER Suite [20]. During docking, the receptor was kept rigid while ligands were treated as flexible, which enables generation of multiple poses of the receptor–ligand complexes. Each pose includes unique structural conformation of the ligand that

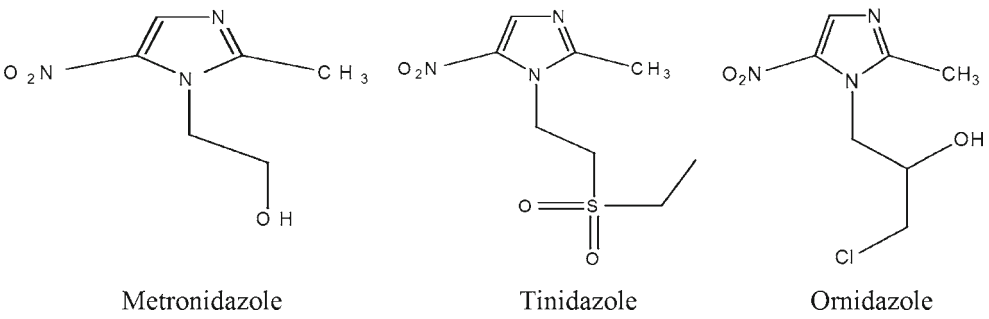

Fig. 1 Chemical structure of antiamoebic drugs bearing a nitrogen-containing heterocyclic ring

Author's personal copy

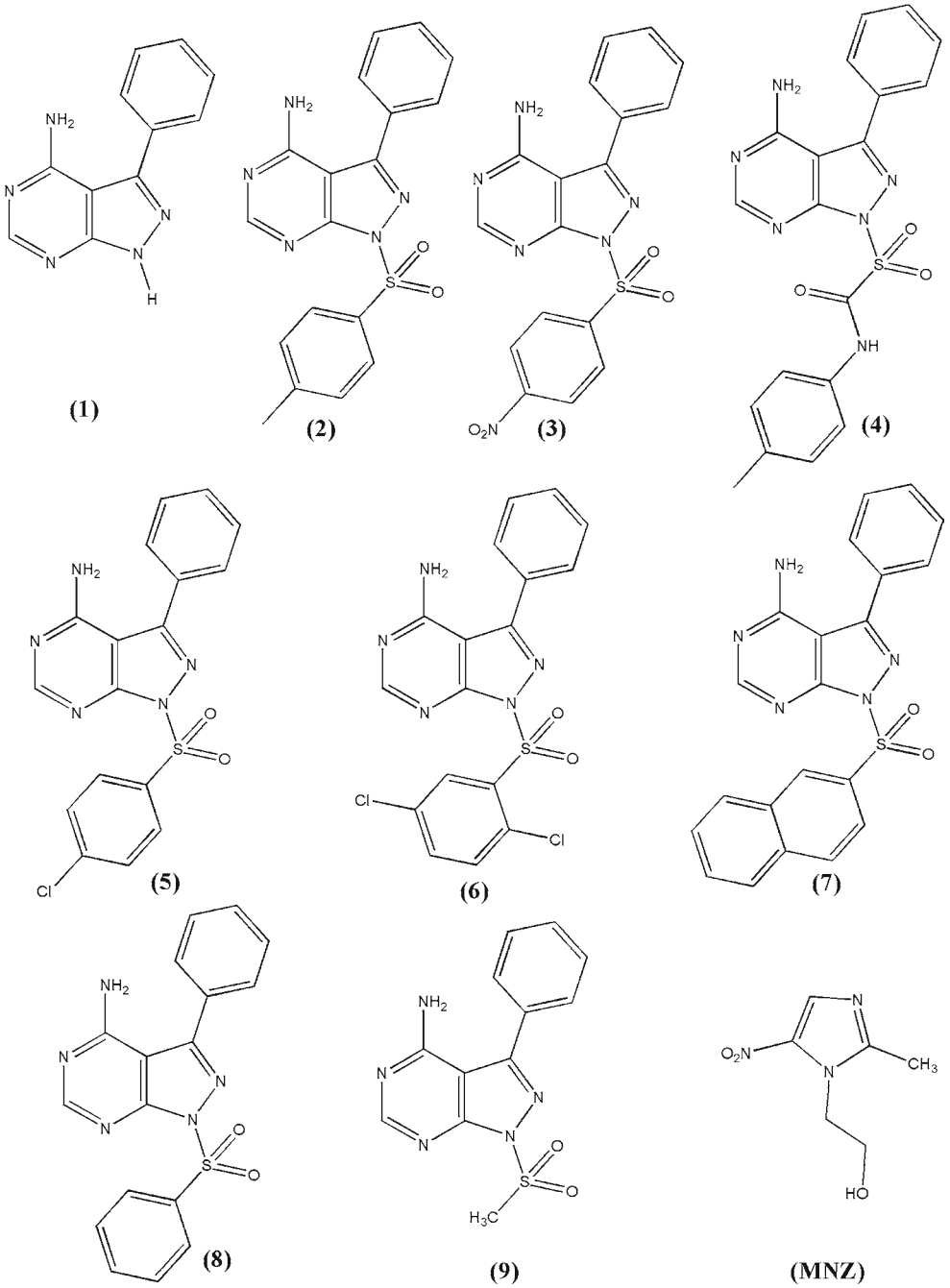

Fig. 2 **a** Chemical structures of pyrazolo[3,4-d]pyrimidines with no linker: **1** 3-phenyl-1H-pyrazolo[3,4-d]pyrimidin-4-amine, **2** 3-phenyl-1-tosyl-1H-pyrazolo[3,4-d]pyrimidin-4-amine, **3** 1-[(4-nitrophenyl)sulfonyl]-3-phenyl-1H-pyrazolo[3,4-d]pyrimidine-4-amine, **4** N-{4-[(4-amino-3-phenyl-1H-pyrazolo[3,4-d]pyrimidin-1-yl)sulfonyl]phenyl}acetamide, **5** 1-[(4-Chlorophenyl)sulfonyl]-3-phenyl-1H-pyrazolo[3,4-d]pyrimidine-4-amine, **6** 1-[(2,5-Dichlorophenyl)sulfonyl]-3-phenyl-1Hpyrazolo[3,4-d]pyrimidine-4-amine, **7** 1-(2-Naphthylsulfonyl)-3-phenyl-1H-pyrazolo[3,4-d]pyrimidin-4-amine, **8** 3-Phenyl-1-(phenylsulfonyl)-1H-pyrazolo[3,4-d]pyrimidine-4-amine, **9** 3-Phenyl-1-(methylsulfonyl)-1H-pyrazolo[3,4-d]pyrimidine-4-amine and Metronidazole (MNZ). **b** Chemical structures of pyrazolo[3,4-d]pyrimidines with trimethylene linkers: **10** 1,3-bis(4,6-diethylthio-1H-pyrazolo[3,4-d]pyrimidin-1-yl)propane; **11** 1,3-bis(4-ethoxy-6-methyl-sulfanyl-1H-pyrazolo[3,4-d]pyrimidin-1-yl)propane; **12** 1,10-(1,3-propanediyl)bis(5-methyl-6-methylthio-4,5-dihydro-1H-pyrazolo[3,4-d]pyrimidin-4-one); **13** 1,10-(1,3-propanediyl)bis(5-ethyl-6-methylthio-4,5-dihydro-1H-pyrazolo[3,4-d]pyrimidin-4-one); **14** 1,10-(1,3-propanediyl)bis(5-benzyl-6-methylsulfanyl-4,5-dihydro-1H-pyrazolo[3,4-d]pyrimidin-4-one); **15** 1-(4,6-dimethylsulfanyl-1H-pyrazolo[3,4-d]pyrimidin-1-yl)-3-(5-methyl-6-methylsulfanyl-4-oxo-1,5-dihydropyrazolo[3, 4-d]pyrimidin-1-yl)propane; **16** 4,6-bis(methylsulfanyl)-1-phthalimidopropyl-1H-pyrazolo[3,4-d]-pyrimidine; **17** 6-methylsulfanyl-1-phthalimidopropyl-4(pyrrolidin-1-yl)-1H-pyrazolo[3,4-d]pyrimidine; **18** and 6-methylsulfanyl-1-(3-phenylpropyl)-4,5-dihydro-1H-pyrazolo[3,4-d]pyrimidin-4-one

Author's personal copy

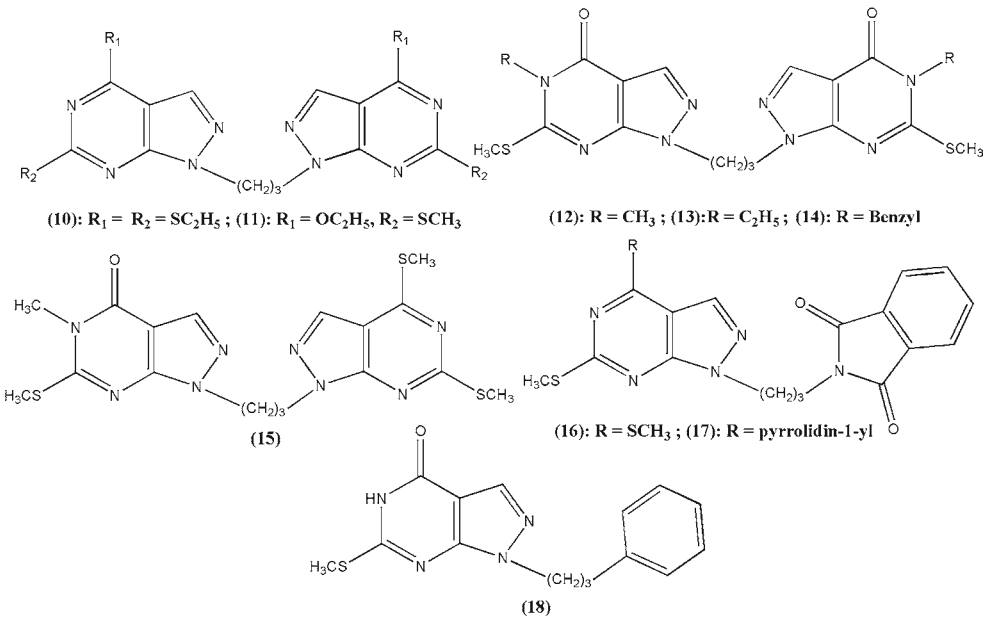

Fig. 2 (continued)

fit in the binding site of the receptor. Docking complexes were ranked by Glide scores (G-score). G-Score is an empirical scoring function that uses the combination of various parameters like hydrogen bonds, hydrophobic contacts, van der Waals, coulombic, polar interactions in the binding site, a metal binding term, penalties for buried polar groups and freezing rotatable bonds, etc. [21].

Ligand preparation

Geometries of all the ligands (molecules **1**–**18** and MNZ) were optimized using density functional theory (DFT) B3LYP method in conjunction with the 6-31G** basis set as implemented in GAUSSIAN03 [22]. Optimized coordinates of the ligands were prepared using the LIGPREP module, bond orders were modified according to their data and different conformers were generated using CONFGEN. Each generated conformer was subjected to a full minimization in the gas phase with the OPLS-2005 (optimized potential for liquid simulations) force field [23] to eliminate the bond length and bond angles biased from the crystal structure. LIGPREP produced the structures with various ionization states, tautomers, stereo-chemistries, and ring conformations.

Protein preparation

The three dimensional (3D) structure of OASS complexed with PLP was prepared using protein preparation wizard, where hydrogens were added automatically and subsequent refinement of the structure was carried out. Water molecules in the crystallographic complex are not critical to the functioning of the protein–ligand interaction, hence all the crystallographic waters were deleted and the bond orders were re-assigned. Further, the whole system was minimized to a root mean square deviation (RMSD) of 0.30 Å. Missing residues were added through the PRIME application of the SCHRODINGER Suite [24].

Receptor grid generation

The affinity and electrostatic potential grid for each type of atoms in ligands at different grid points, at the active site of the receptor were calculated. The position of PLP was taken as the center of the active site of the protein for all ligands. During the grid generation, no van der Waals radius sampling was done and the partial charge cutoff was taken as 0.25.

Ligand docking

SP and XP modes of Glide were used for flexible molecular docking of the prepared ligands within the active site of the receptor. For the minimization of ligands, the distance-dependent dielectric constant with a value of 2.0 and a conjugate gradient algorithm with 1,000 steps were used. All of the inhibitors were passed through a scaling factor of 0.80 and partial charge cutoff of 0.15 Å. After docking, post-docking minimization was performed to improve the geometry of the poses, which specifies a full force-field minimization of those poses that are considered for final scoring. After minimization, the results were used for binding energy calculations and docking scores.

Author's personal copy

Autodock docking

Docking simulations were also performed through Autodock4.2 [25], which hits upon favorable docking in a protein-binding site. Autodock tools were used to prepare the protein and the ligands. During preparation of the macromolecule, polar hydrogens were added in the crystal structure of OASS and Kollman United atom charges and atomic solvation parameters were then allocated. Autogrid4 was employed for the calculation of electron affinity and electrostatic potential grid. The grid center was taken as the location of the co-crystallized ligand PLP. The grid map was generated with 70×70×70 points with a grid spacing of 0.625 Å using distance-dependent dielectric constants. Molecular docking was performed using the GA–LS method, with the parameters defined in our earlier paper [10]. After docking, all the generated structures were assigned to clusters based on a tolerance of 1.0 Å all-atom RMSD from the lowest-energy structure. Hydrogen bonding and hydrophobic interactions between docked potent agents and the macromolecule were analyzed using ADT [25].

MD simulation

The coordinates of the best docking poses were subjected to MD simulation using DESMOND software [26, 27]. Each complex was neutralized using 3-sodium counter-ions. The complexes and the counter ions were "immersed" in a Monte-Carlo-equilibrated, periodic TIP3P water bath, such that the whole system was surrounded by a periodic box of transferable intermolecular potential (TIP3P) waters, which extended approximately 10 Å in each direction. The system thus constructed, had one protein molecule (solute), 3-sodium ions and water molecules in the box. The Verlet-leap-frog algorithm [28] was used in numerical integration with a 1.0 fs time step length for minimization and 2.0 fs for dynamics [29]. Hydrogen-atom bonds were constrained to "ideal" lengths using SHAKE. A cut-off of 9.0 Å was applied to the Lennard-Jones interactions, and constant pressure was maintained with isotropic-molecule-based scaling. Water molecules and counter-ions were first energy minimized by steps of steepest descent until gradient threshold 25 kcal mol^{-1} $Å^{-2}$ and then by conjugate-gradient energy minimization with a satisfactory convergence of rms gradient of 0.1 kcal mol^{-1} $Å^{-2}$. The entire system was subjected to 10, 000 steps of steepest-descent minimization followed by conjugate-gradient minimization. The velocities were assigned at 100 K to all the atoms according to Boltzmann's distribution. The temperature of the system was raised from 100 to 298 K over 2.0 ps by scaling velocities according to Berendsen algorithm followed by a constant-pressure-dynamics run over 25 ps. After initial equilibration, MD production run was performed over 20.0 ns.

Binding free energy calculation

The Prime/MM-GB/SA approach [24] was used to calculate the relative binding free energies of the ligands to the receptor. The best docked poses were minimized and energies of the complexes were computed using the OPLS-AA(2005) force field and GB/SA continuum solvent model as implemented in PRIME. The binding free energies were calculated as the sum of three terms: (1) ΔE, the difference of the minimized energies of the complex and ligand plus receptor ($\Delta E = E_{complex} - E_{ligand} - E_{protein}$); (2) ΔG_{solv}, the difference of solvation free energies of complex and ligand plus receptor ($\Delta G_{solv} = G_{solv(complex)} - G_{solv(ligand)} - G_{solv(protein)}$); and (3) ΔG_{SA}, the difference of surface area energies of the complex and ligand plus receptor ($\Delta G_{SA} = G_{SA(complex)} - G_{SA(ligand)} - G_{SA(protein)}$) [30].

ADME prediction

In order to ensure success at the clinical testing level [31, 32], ADME parameters and other pharmaceutically important properties of the ligands were also predicted using QikProp3.5 module [33]. The program was processed in normal mode and predicted 44 properties for all the molecules, consisting of principal descriptors and physiochemical properties with a detailed analysis of the logP (octanol/water), QP %, and logHERG etc. It also evaluates the acceptability of the analogues based on Lipinski's rule of 5, which is essential for rational drug design [34]. The rule describes the molecular properties important for a drug's pharmacokinetics in the human body, including its ADME. However, the rule does not predict whether a compound is pharmacologically active [35].

Results and discussion

Analysis of the crystal structure of O-acetyl-L-serine sulfhydrylase (OASS)—the prime target for the inhibition of *E. histolytica*—revealed that the polypeptide folds into two subunits comprising α and β domains. Each domain consists of a relatively small mobile N-terminal domain (residues 57–164) and a large rigid C-terminal domain (residues 1–56 and 165–336) [36]. The cofactor PLP is linked covalently to Lys-58, which is conserved in all OASS structures and is positioned in between these two domains. Other highly conserved residues, such as Gly236, Ser280 and Pro307, interact with the aromatic ring of PLP. These observations prompt us to view the position of PLP as the center of the active site.

GLIDE docking

Ligand docking of different pyrazolo[3,4-d]pyrimidines with OASS revealed a large variation in their binding energies.

Author's personal copy

Initially, five poses of each ligand were selected from the docking results, out of which the poses with better glide scores, better hydrogen bonding and better non-covalent interactions with lower glide energy values were chosen as the best poses for each molecule. Although the predicted free energy of binding is a useful descriptor of ligand–receptor complementarities, the choice of the 'best' docking model was ultimately dictated by various parameters of the ADME study. These best docked complexes were considered for further analysis and the results were compared.

Standard precision docking

Docking calculations of pyrazolo[3,4-d]pyrimidine molecules without linkers (molecules **1**–**9** and MNZ) through Glide-SP revealed that molecules **2** and **4** have better glide scores (−6.305 and −6.104 kcal mol^{-1}, respectively) than the reference drug MNZ, which has a socre of −5.934 (Table S1a). These results are consistent with the experimental results predicted on the basis of IC50 values [17], which proves the validity of the method used. The electron withdrawing group ($-NO_2$) in compound **3** causes it to have a lower glide score than **2**, **4** and MNZ. Molecules **7**, **1** and **6**, which contain planar aromatic moieties, exhibit the next best glide scores, while others have poorer scores. SP docking further demonstrates that almost all the molecules exhibit better glide energies than MNZ. Molecule **4** is the best, while molecule **7** exhibits the next best binding energy value. The electrostatic energy contribution of molecule **4** is most appreciable, followed by MNZ and molecule **2** (Table S1a). Other molecules have lower electrostatic contributions. The value of cross-correlation function of glide scores with IC50 values was found to be relatively good (R^2=0.631).

The hydrogen bonding interactions in the best poses of the docking of these ligands (without linkers) show that most of the molecules have same type of interactions as the reference molecule MNZ (Table S1b). Evidence for hydrogen bonding interactions with residue Lys58 is displayed by molecules **2**, **4**, **5**, **7** and MNZ, which is important from the molecular recognition point of view. Molecule **8** shows π-cation interaction with Lys58. Since PLP is linked covalently to residue Lys58 in all the structures of OASS, interactions with Lys58 play an important role in amoebiasis inhibition. Molecules **2**, **3**, **4**, **6**, **8** and **9** display hydrogen bonding interactions with residue Thr85. Hydrophobic interactions are exhibited by ligands with conserved residues of both the N– and C-terminal domains of the active site like Tyr313, Ile237, Pro307, Ala190, Val191, Val197, Val61, Val57, Met136, Phe160, Met112 and Ala239. Polar interactions with residues Asn88, Gln159, Gln235, Hie232, Ser113, Ser280, Ser308, Ser86, Ser56, Thr111, Thr193, Thr196, Thr85 and Thr89 were also observed. On the basis of Glide scores, Glide energies and non-covalent interactions as obtained through Glide SP docking and corresponding IC50 values, it can be concluded that compounds **2**, **3** and **4** might be better inhibitors than MNZ against amoebic histolytica disease.

Inspired by the successes with pyrazolo[3,4-d]pyrimidines without linker, SP docking studies with the target OASS were also performed using pyrazolo[3,4-d]pyrimidine molecules containing trimethylene linkers (molecules **10**–**18**). These molecules—well known flexible models for aromatic π–π interactions—have either two pyrazolo[3,4-d]pyrimidine moieties (molecules **10**–**15**) or one pyrazolo[3,4-d]pyrimidine moiety and another aromatic moiety connected through a trimethylene linker (molecules **16**–**18**). Interestingly, some of these molecules (**12**, **15**, **16** and **18**) show better glide scores than molecule **2**, which received the top glide score among the molecules without a linker. Molecule **16** showed the best glide score at −7.800 kcal mol^{-1}. It was observed that, when one of the thiomethyl substituents at the 4th position was replaced by a non-aromatic moiety pyrrolidin-1-yl (**17**), the glide score was reduced significantly to −5.266 kcal mol^{-1}, probably because of steric hindrance. Compound **15**, which belongs to the dissymmetric class of molecules containing two pyrazolo[3,4-d]pyrimidine moieties and a methyl substituent at the 5th position of one moiety, established the second best glide score of −7.404 kcal mol^{-1}. The symmetrical class of molecule **12**, containing a methyl group at the 5th position of both pyrazolo[3,4-d]pyrimidine moities, exhibited the third best glide score of −7.172 kcal mol^{-1}. However, replacing the methyl group with an ethyl group (**13**) or a benzyl group (**14**) reduces the glide scores. Molecules **10**, **11** and **18** have lower modulus of glide scores but higher than the originally crystallized molecule MNZ. Glide energies of all the ligands with the trimethylene linker were higher than those of both molecules without linker and MNZ.

Hydrogen bonding interactions in the best docking poses, revealed by ligands **2**, **4**, **12**, **15**, **16** and MNZ, as obtained through Glide-SP docking with target OASS are shown in Fig. 3. Both molecules **12** and **16** demonstrate four hydrogen bonding interactions whereas molecule **18** shows three. It can be observed from Fig. 3 and Table S1b, that molecules **10**, **11**, **12**, **14**, **16** and **18** demonstrate hydrogen bonding interactions with the residue Lys58—vital for the inhibition of OASS. Other residues that take part in hydrogen bonding interactions with different ligands are Arg116, Tyr313, Ser280, Thr85, Asn88, Gln159, Ser86, Gly236 and Thr193. Hydrophobic and polar interactions are also exhibited by ligands with different residues. Non covalent π–π interactions and cation–π interactions are exhibited by molecules **17** and **18** with residues His232 and Lys58, respectively.

Extra precision docking

In the XP module of GLIDE, protein–ligand structural motifs leading to enhanced binding affinity were included in addition

Author's personal copy

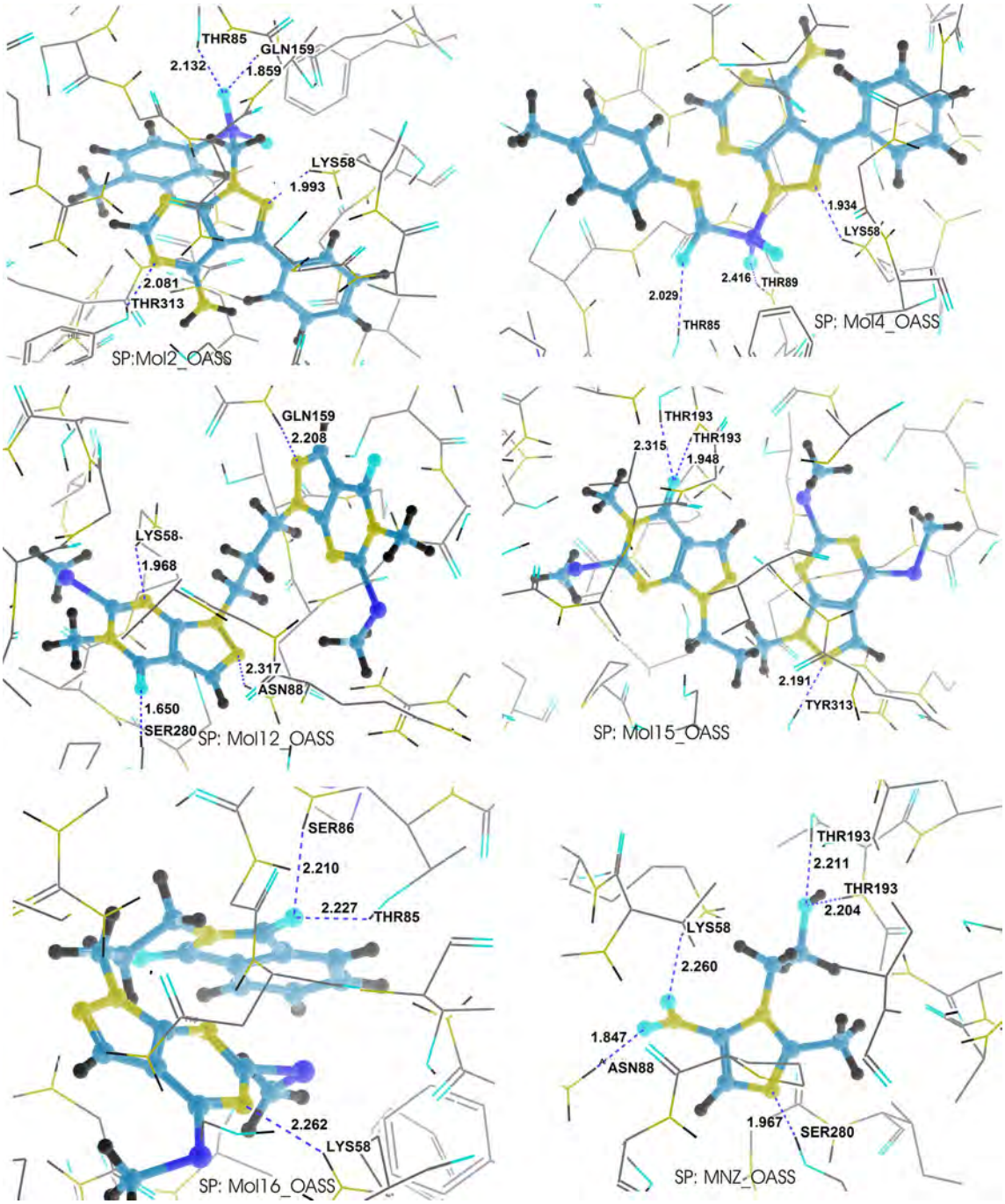

Fig. 3 Hydrogen bonding interactions in the best docking poses of molecules **2**, **4**, **12**, **15**, **16** and MNZ as obtained through Glide-SP docking

to unique water desolation energy terms. The Glide docking results of the XP protocol are summarized in Tables S2a, S2b and Fig. 4. It was observed that the Glide scores and docking energies differ from those of the SP mode. Glide scores of XP docking were reduced in comparison to SP docking. XP docking of the ligands without linker revealed that molecule **4** has the best glide score of −5.190 kcal mol^{-1}. Molecules **7** and **2** have the next best glide scores of −4.573 and −4.290 kcal mol^{-1}, respectively. It was further observed that all the ligands except molecule **3** exhibit better glide scores than MNZ. Comparison of glide energies divulge that molecule **4** has the minimum value of glide energy −51.232 kcal mol^{-1}. Molecules **2**, **6** and **8** received the next best values of glide energies. Binding energies of molecules **1**–**8** were better than MNZ, while molecule **9** had the lowest magnitude of binding energy. The relative strength of compounds **2** and **4** were reversed compared to SP docking. Overall, the performance of Glide SP is better than Glide XP and extended funnel does not advance the results, as reported by other authors [37]. The cross-correlation between XP_Glide

Author's personal copy

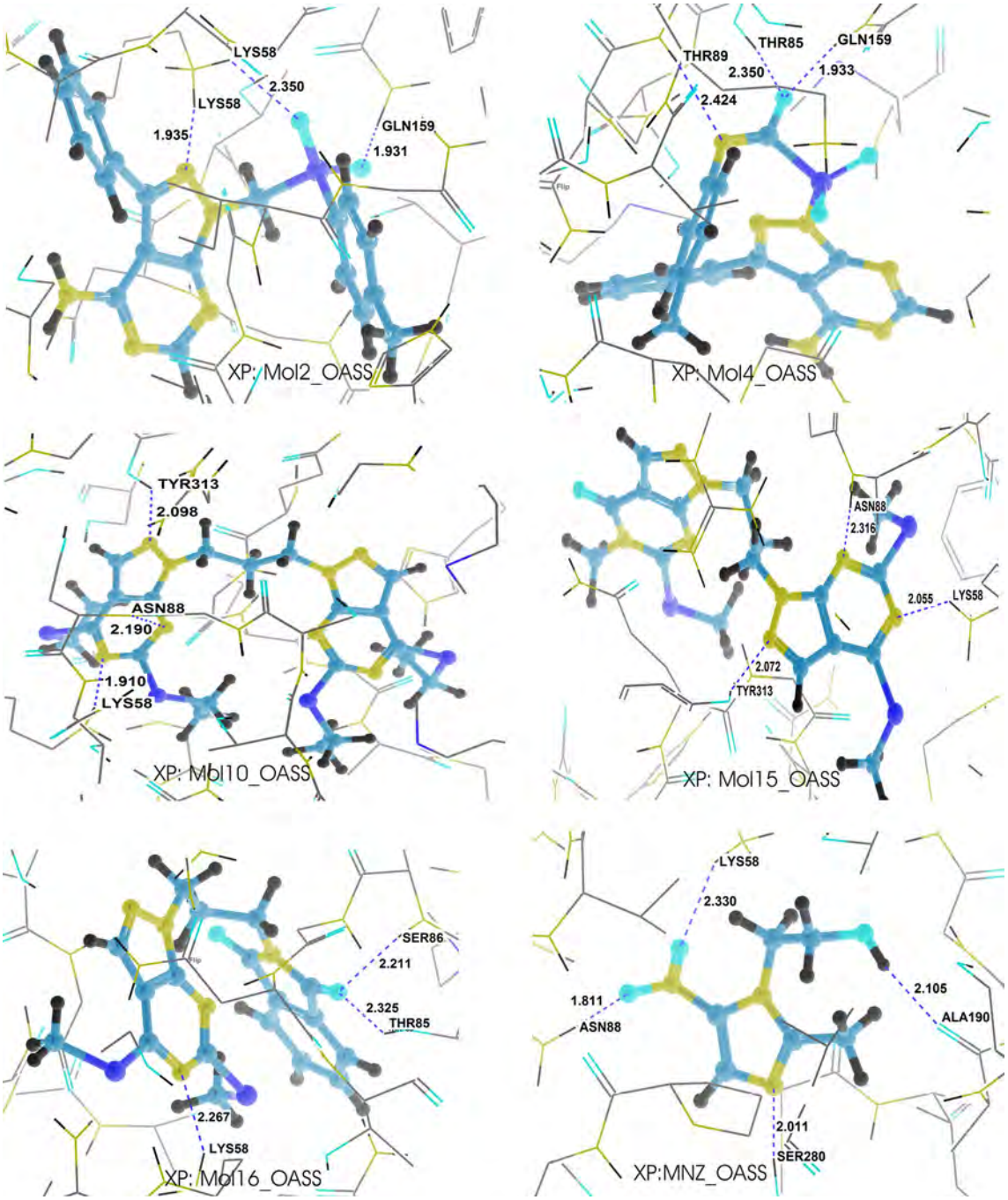

Fig. 4 Hydrogen bonding interactions in the best docking poses of molecules **2**, **4**, **10**, **15**, **16** and MNZ as obtained through Glide-XP docking

score and IC50 values was found to be relatively poor (R^2= 0.180).

The hydrogen bonding interactions as obtained through XP docking of pyrazolo[3,4-d]pyrimidine ligands containing no linkers with the target OASS were almost same as the reference molecule MNZ (Fig. 4 and Table S2b). Hydrogen bonding interactions with residue Lys58 were exhibited by molecules **1**, **2**, **5**, **8**, **9** and MNZ. Most of the ligands also exhibited interactions with residue Thr85. Non-covalent π–π stacking interactions with residue Phe160 were shown by molecule **6**, while molecule **8** revealed cation–π interactions with Lys58. Ligands **2** and **7** interact with different residues of the active site of the target each through five hydrogen bonding interactions, whereas each of the molecules **4**, **9** and MNZ exhibits four hydrogen bonding interactions. The residues Tyr313, Ile237, Pro307, Ala190, Val57, Met136, Phe160, Phe241, Ala239, Met112, Val191 in the active site of the protein form a hydrophobic packet. Polar interactions also exist between ligands and these residues. The residues that interact through polar interactions are Ser86, Ser308, Gln235, Ser280, Asn88,

Author's personal copy

Thr89, Gln159, Thr85, Gln159, Ser113, Thr193, Thr196, Ser56, His232 and Ser56.

XP docking of pyrazolo[3,4-d]pyrimidine molecules having trimethylene linker (molecules **10**–**18**) with target OASS shows that all these molecules in their best docked poses, except molecule **18**, have better glide scores than MNZ. In this respect, molecules **16** and **14** can be placed at the first and second place globally, i.e., they have the highest scores among all the ligands. Molecule **16** has a less aromatic phthallimide moiety whereas molecule **14** has a less aromatic pyrazolo[3,4-d]pyrimidine moiety and bulky benzyl substituent. Through SP docking, molecule **14** had a poorer glide score due to steric hindrance but showed better glide scores after inclusion of a hydrophobic enclosure. However, the glide score of molecule **15** was reduced in XP docking, and showed a better glide score through SP docking. The glide score of molecule **17**, obtained through replacement of the methylsulfanyl substituent at the 4th position of molecule **16** by a pyrollidin-1-yl moiety, was greatly reduced in the case of XP docking. Molecules **10**, **11**, **12** and **15** have comparatively better glide scores. However, molecules **13** and **18** had poorer scores than that of molecule **2**. Glide energies for molecules **10**, **11**, **13**, **14** and **15** were more negative than the highest negative value of glide energy of the ligands without linker. The glide energy value of molecule **16** was nearly the same as that of molecule **4**.

The hydrogen bonding and other non-covalent interactions of ligands with the residues of the active site, as obtained through XP docking, are presented in Table S2b. The hydrogen bonding interactions in the best docked poses of molecules **2**, **4**, **10**, **15**, **16** and MNZ are shown in Fig. 4. It can be seen that molecule **18** shows a cation–π interaction with Lys58 and molecule **17** exhibits an aromatic π–π interaction with residue His232. Hydrogen bonding interactions with backbone amino acids exist with residues Thr193, Gly236 and Ser86 bonded with molecules **15**, **16** and **17**, respectively. Side chain hydrogen bonding interactions in the conserved active site were displayed by all the molecules. Molecules **16** and **12** have four hydrogen bonds in each case, while molecule **18** have three hydrogen bonds. Hydrophobic and electrostatic interactions were similar to the case of molecules without linkers.

Autodock docking

The various energies and inhibitory coefficients (KI) as obtained through Autodock docking of the ligands with OASS (Table S3a) indicate the important role played by electronic interactions in ligand docking. The docking of molecules with no linker showed that molecule **2** has the best docking energy(−8.13 kcal mol^{-1}) and inhibition coefficient as obtained through Glide-SP and experimental observations. Molecules **7** and **4** have the next best energies, and show better results with Glide XP. Also, molecule **4** was found to have second best preference on the basis of experimental as well as Glide-SP calculations. Among the top five molecules, four (**2**, **4**, **7** and **6**) show agreement with Glide-SP results. Calculations further depict that the minimum inhibitory concentrations have the lowest docking energy. Intermolecular interaction energies also display parallel preferences. Docking simulations through Autodock on molecules with the trimethylene linker with OASS demonstrate that molecule **15** has the best docking energy followed by molecules **12** and **16**. Consequently, molecules **12**, **15** and **16** are common among the top three molecules as obtained through Glide SP. Also, as discussed, molecule **16** shows the best docking score through Glide-XP.

The noncovalent hydrogen bonding interactions in the best docking complexes are depicted in Table S3b and Figure S1. Intermolecular N–H···O and O–H···O type hydrogen bonding interactions, flanked by the ligands and residues of the active site, assist in stabilizing the complexes. Residues that are involved in N–H···O type hydrogen bonding interactions with ligands are Ser315, Glu311, Ala98, Glu34, Lys121, Arg312, Glu115, Arg10, Ser8, Arg116, Ser315, Asp317, Ser7, Thr111, Gly233, Gln235, Leu314, Ser113 etc. Also, in the best docking complexes, molecule **9** and MNZ exhibit O–H···O type hydrogen bonding interactions involving Tyr14 and Ser315 residues, respectively. Molecules **17** and **18** do not show any significant hydrogen bonding interactions.

ADME prediction

The ADME properties inspected using QIKPROP3.5 (Table S4) indicate that the molecules without linker (molecules **1**–**9**) do not exhibit any violation of Lipinski's rule of '5' while MNZ shows one violation. It has also been reported that molecules **10** and **14** have two violations and molecule **11** has one [13]. Molecules violating more than one or two of these rules may have problems with bioavailability. Molecules **1**–**9**, MNZ and molecule **10** of the linker-containing molecules have an octanol-water partition coefficient (LogP) greater than that of the range of 95 % of drugs while molecules **11**–**18** have LogP values within the range. Higher logP values are associated with poor absorption. ADME calculations and docking results suggest that pyrazolo[3,4-d]pyrimidine molecules may be good inhibitors of OASS, and molecules with trimethylene linker may have improved activity over molecules without linker.

Molecular dynamics simulation

On the basis of docking and ADME predictions, better docked complexes of the two molecules without linker (molecules **2** and **4**) and better docked complexes of the two molecules with trimethylene linkers (molecules **15** and **16**) along with the best

Author's personal copy

docked complex of MNZ, were subjected to MD simulation for 20.0 ns to ensure the stability of the ligands in the enzyme active site. In many cases, even the best docked structure flies away from the enzyme active site within a few picoseconds of MD simulations; consequently, a long MD run was carried out. The MD simulation was performed in water and neutralized with Na^+ counter ions to come close to the real situation. The average RMSDs of heavy atoms during MD simulation of each complex are plotted in Fig. 5. Small fluctuations and constant heavy atom RMSD is a good indication of system stability. The results indicate that the complexes OASS_Mol4, OASS_Mol15 and OASS_MNZ show small fluctuations in the beginning but transit quickly to nearly constant average RMSDs, with reasonably small oscillations centered around them. However, RMS deviations increase with simulation time in the case of OASS_Mol2 and OASS_Mol16 complexes, indicating that these complexes are not able to sustain stability in aqueous medium. The range of oscillation of each dynamic structure around the MD average is about ±0.30 Å. The OASS_Mol2 complex shows fluctuations at 3.6 ns with an RMSD of 5.6 Å; afterwards, it turned out to be centered around 2.5 Å at 5.0 ns. The RMSD of the complex OASS_Mol2 increased smoothly after 5.0 ns and approached a value of 5.6 Å at the end of 20.0 ns dynamics. The smoothed average RMSD of 3.6 Å was exhibited by OASS_Mol4 complex for dynamics over 3.0 ns. Although complex OASS_Mol15 showed smaller fluctuations in the beginning, with RMSDs 2.2 Å and 2.8 Å for 1.0 ns to 4.8 ns and 4.8 ns to 5.2 ns dynamics, respectively, a constant RMSD of 2.5 Å was seen for the rest of the dynamics. During the course of MD, increasing average RMSD behavior was displayed by OASS_Mol16 complex as it increased from 2.5 Å at 1.0 ns to 5.5 Å at 19.0 ns. After initially exhibiting small fluctuations, the heavy atom average RMSD of the complex with MNZ attained a constant value of 4.4 Å over 5.0 ns dynamics.

The average RMS fluctuations of individual residue positions from their mean positions indicate that residue Lys58 has very small fluctuations in almost all structures, indicating the possibility of non-covalent interactions. The RMS fluctuations of residues His79, Tyr168, Phe177 and Trp221 were smaller. It was also observed that the main contribution to the total energy in all cases comes from the electrostatic energy (receptor, complex and ligand), while the difference in van der Waals energy was more negative with respect to electrostatic energy. Strong van der Waals interactions also imply a reasonable geometry for binding with the receptor. High contributions of polar groups indicate that enzyme inhibition is supported mostly by hydrophilic interactions. The negative binding energy is a sign of the strong binding of the ligand with its receptor (Fig. S2). Small fluctuations in total energy specify that hydrogen bonding and other non-covalent interactions alternate among the residues of the active site, as no constraint was applied to the hydrogen bonding. It is noteworthy that the fluctuations in the total energy of the complexes falls within 10 kcal mol^{-1} for molecules **2**, **15**, **16** and MNZ and 50 kcal mol^{-1} for molecule **4**.

Protein–ligand interactions throughout the simulation exhibited four types of interaction: hydrogen bonds, hydrophobic, ionic and water bridges. Cation–π, aromatic π–π and other non-specific interactions fall into the category of

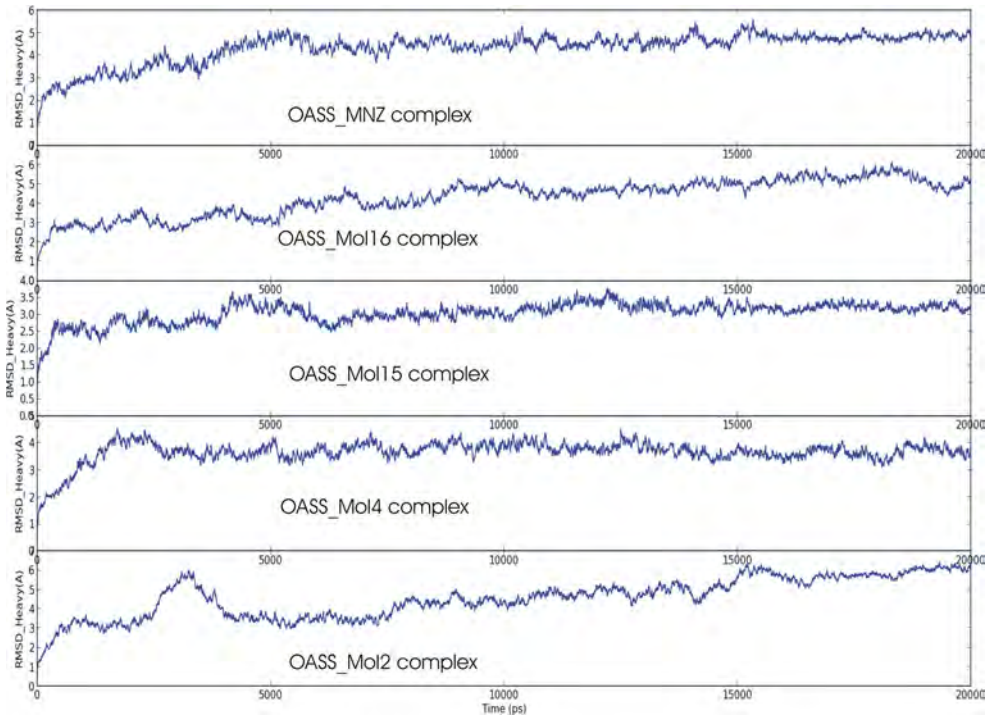

Fig. 5 **a**–**e** Average root mean square deviation (RMSD) of heavy atoms of the complexes during molecular dynamics (MD) simulation. **a** OASS_Mol2 complex, **b** OASS_Mol4 complex, **c** OASS_Mol15 complex, **d** OASS_Mol16 complex, **e** OASS_MNZ complex

Author's personal copy

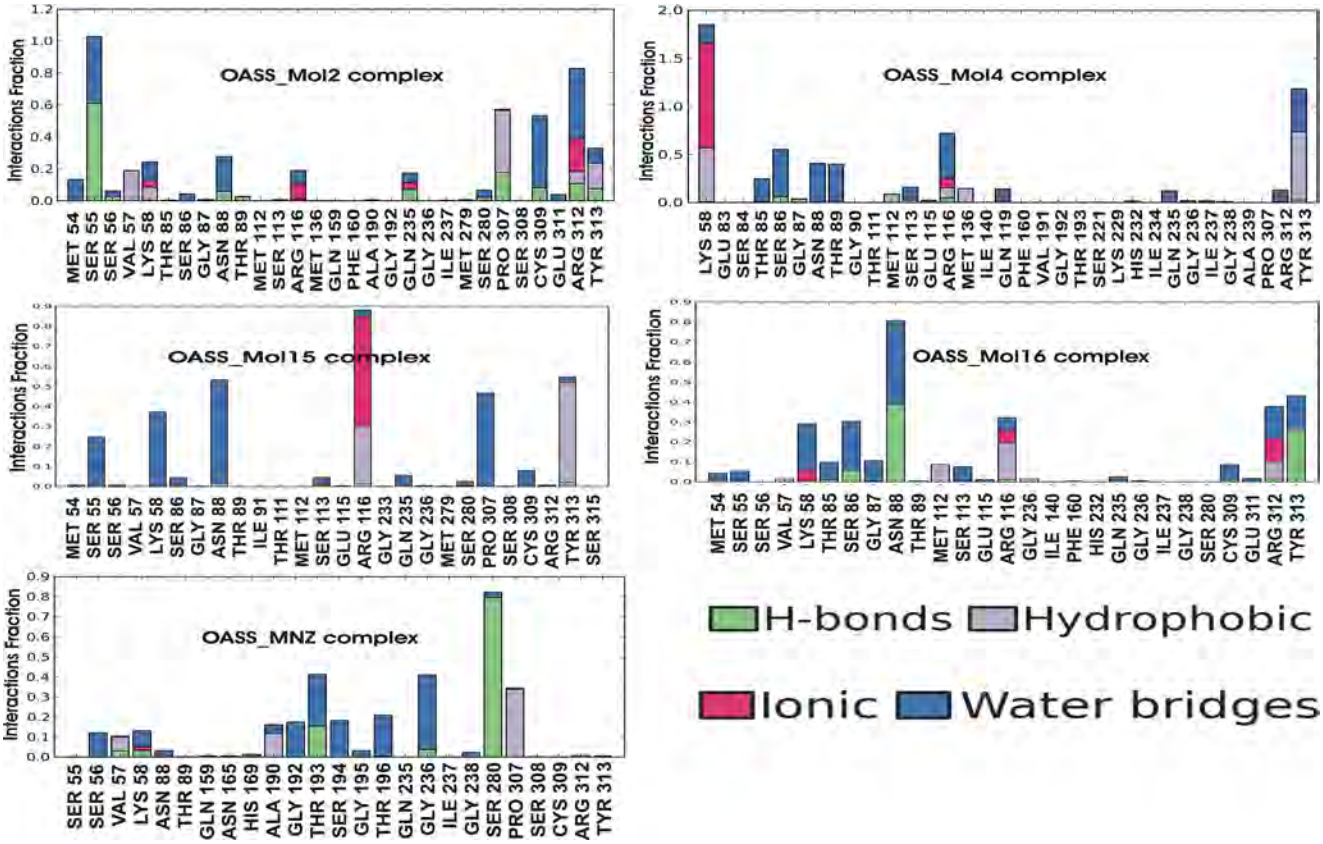

Fig. 6 Normalized stacked bar chart representation of interactions and contacts over the course of the MD trajectory. Values > 1.0 are possible as some residues make multiple contacts of the same subtype with ligands

hydrophobic interactions. These interactions were monitored throughout the MD (Fig. 6). It was observed, in the MD simulation of OASS_Mol2 complex, that H-bonding, hydrophobic, ionic and water bridge interactions of Arg312 with the ligand, were maintained at about 12 %, 8 %, 20 % and 40 %, respectively, of the simulation time, while hydrogen bonding and water bridge interactions of Ser55 were maintained about 60 and 40 %, respectively, of the simulation time. The interactions fraction diagram of the OASS_Mol4 complex revealed multiple ionic, hydrophobic and water bridge interactions of Lys58 with the ligand during 100 %, 55 % and 30 % of the simulation time. Ionic interactions were the major

Table 1 IC50 and relative binding free binding energy differences along with Glide SP, Glide XP and Autodock scores. *MM/GBSA* Molecular mechanics generalized Born surface area, *SP* standard precision, *XP* extra precision

Molecule	IC50 (μg/ml)	Relative Binding free energy difference (MM/GBSA) (kcal mol^{-1})	Best glide score (SP) (kcal mol^{-1})	Best Glide score (XP) (kcal mol^{-1})	Autodock score (kcal mol^{-1})
1	4.73	16.73	−5.722	−4.546	−5.85
2	0.57	−0.44	−6.305	−4.257	−8.13
3	2.52	2.87	−5.399	−3.590	−6.80
4	0.68	−4.84	−6.104	−5.190	−7.84
5	3.23	2.95	−5.399	−4.139	−6.98
6	2.37	1.75	−5.720	−3.620	−7.11
7	3.11	−1.51	−5.885	−4.573	−7.92
8	4.24	8.58	−5.363	−3.762	−7.67
9	5.15	8.97	−5.211	−3.868	−6.82
MNZ	1.80	0.00	−5.934	−3.824	−4.81
15	NA	−5.93	−7.404	−5.456	−7.16
16	NA	−22.66	−7.800	−7.811	−6.28

Author's personal copy

interactions in the OASS_Mol4 complex and were strong enough to be maintained throughout the dynamics. Strong electrostatic and hydrophobic interactions of the ligands with Arg116 remained prominent during the dynamics of the OASS_Mol15 complex for 52 % and 30 % of the simulation time, respectively. Other residues that maintained interactions over 50 % simulation time in OASS_Mol15 were Asn88 and Tyr313. On the other hand, Lys58 showed interactions during 40 % of the simulation time. Although molecule16_OASS and MNZ_OASS complexes made a major contribution to hydrogen bonding interactions, other interactions, also present within the binding site, were interchangeable in nature. A timeline representation of the interactions between residues of the active site and ligands revealed that the number of specific contacts varies between 1 and 9 in each complex over the course of the trajectory (Fig. S3). The alteration in the number of hydrogen bonds clearly demonstrates the flexibility of binding site residues. Lys58 forms more than four contacts in OASS_Mol4 and more than two contacts in the OASS_Mol16 complex. More than three contacts are exhibited by residues Arg116 and Ser280 in OASS_Mol15 and OASS_MNZ complexes, respectively, throughout the dynamics. In the OASS_Mol16 complex, Lys58 and Asn88 have more than three interactions up to 4.0 ns. Later interactions evolved with Arg312, Arg116 and Tyr313 with two or more interactions.

MM/GBSA binding free energy analysis

The MM/GBSA approach was undertaken in order to correlate relative binding free energies ($\Delta\Delta G_{binding}$) of the MD-optimized complexes with the corresponding IC50 values of compounds with the intention of predicting the relative activity of compounds with unknown activities. The MM/GBSA estimation of relative free energies on the representative structures was carried out with a partially flexible protein structure within 12 Å of the center of the ligand in the binding site. Table 1 depicts the relative binding free energies and glide scores, with corresponding IC50 values of the molecules. These calculations were performed on ten molecules (molecule **1** to **9** and MNZ) of known IC50 values to compare the results, and two molecules **15** and **16** to predict the relative binding affinity. The value of cross correlation coefficient R^2 (=0.702) between relative binding free energies and IC50 values was found to be excellent. Results also indicate that molecules **15** and **16** exhibit better relative binding free energies compared to other molecules, which is in good agreement with Glide scores.

Conclusions

Molecular docking studies of 18 pyrazolo[3,4d]pyrimidine analogues and MNZ were carried out with OASS enzyme, using Glide-SP, Glide-XP and Autodock docking protocols. Docking simulation and reported IC50 values of the ligands without linker indicate that molecules **2** and **4** may be better inhibitors than molecules **1**, **3**, **5**, **6**, **7**, **8** and **9**. The trimethylene linker pyrazolo[3,4-d]pyrimidine molecules had improved glide scores and binding energies over the molecules without linker. Docking simulation and ADME limitation demonstrate that linker-containing molecules **15** and **16** have better binding capabilities with the target than any other molecule under study. SP docking further indicates that the methyl substituents have enhanced glide scores, while bulky substitutions of the benzyl group reduces the score. It has also been observed that inclusion of a non-aromatic pyrollidin-1-yl moiety reduces the glide score significantly. On the basis of docking simulation, ADME calculation and reported IC50 values; molecules **2** and **4** without linkers, and trimethylene linker molecules **15** and **16** were screened as potential high affinity inhibitors. MD simulation of the best docked complexes of these molecules (molecules **2**, **4**, **15**, **16**, MNZ) demonstrated that the docking complexes of molecules **4**, **15** and MNZ remained stable during the course of dynamics. Timeline simulation interaction studies demonstrated several interactions (polar, hydrophobic and water bridges) of binding site residues with ligands that were maintained throughout the course of the trajectory. MM/GBSA estimation of relative binding free energies showed good agreement with experimental observations. These studies indicate that pyrazolo[3,4-d]pyrimidine analogues can act as lead molecules for the development of high affinity inhibitors of OASS enzyme—a promising target for inhibiting the growth of *E. histolytica* disease.

Acknowledgments U. Y. is thankful to DST, New Delhi, India for financial support through SERC Fast Track Young Scientist scheme(SR/FT/CS-78/2010) and UGC, New Delhi, India for the award of a Raman Fellowship for postdoctoral studies in the United States [F.No. 5-1/2013(IC)].

References

1. Lejeune M, Rybicka JM, Chadee K (2009) Recent discoveries in the pathogenesis and immense response towards *Entamoeba histolytica*. Future Microbiol 4:105–118
2. Salles JM, Moraes LA, Salles MC (2003) Hepatic amebiasis. Braz J Infect Dis 7:96–100
3. Takeuchi T, Weinbach EC, Gottlieb M, Diamond LS (1979) Mechanism of L-serine oxidation in *Entamoeba histolytica*. Comp Biochem Physiol B 62:281–285
4. Kumar S, Raj I, Nagpal I, Subbarao N, Gourinath S (2011) Structural and biochemical studies of serine acetyltransferase reveal why the parasite *Entamoeba histolytica* cannot form a cysteine synthase complex. J Biol Chem 286:12533–12541
5. Chinthalapudi K, Kumar M, Kumar S, Jain S, Alam N (2008) Crystal structure of native O-acetyl-serine sulfhydrylase from *Entamoeba histolytica* and its complex with cysteine: structural evidence for

Author's personal copy

cysteine binding and lack of interactions with serine acetyl transferase. Proteins 72:1222–1232
6. Bendesky A, Menendez D, Ostosky-Wegman P (2002) Is metonidazole carcinogenic? Mutat Res 511:134–144
7. Becker S, Hoffman P, Houpt ER (2011) Efficiency of antiamoebic drugs in a mouse model. Am J Trop Med Hyg 84:581–586
8. Nagpal I, Raj I, Subbarao N, Gourinath S (2012) Virtual screening, identification and in vitro testing of novel inhibitors of O-acetyl-L-serine sulfhydrylase of *Entamoeba histolytica*. PLoS ONE 7(2): e30305. doi:10.1371/journal.pone.0030305
9. Bekhit AA, Abdel-Azeim T (2004) Design, synthesis and biological evaluation of some pyrazole derivatives as anti-inflammatory-antimicrobial agents. Bioorg Med Chem 12:1935–1945
10. Yadava U, Singh M, Roychoudhury M (2013) Pyrazolo[3,4-d]pyrimidines as inhibitor of anti-coagulation and inflammation activities of phospholipase A2: insight from molecular docking studies. J Biol Phys 39:419–438
11. Elion GB, Callahan SW, Nathan H, Bieber S, Rundles RW, Hilching GH (1963) Pontetiation by inhibition of drug degradation:6-substituted purines and xanthine oxidase. Biochem Pharmacol 12:85–93
12. Schenone S, Brullo C, Musumeci F, Botta M (2010) Novel dual Src/Abl inhibitors for hematologic and solid malignancies. Expert Opin Investig Drugs 19:931–945
13. Indovina P, Giorgi F, Rizzo V, Khadang B, Schenone S, Marzo D, Forte IM, Tomei V, Mattioli E, Urso VD, Grilli B, Botta M, Giordano A, Pentimalli F (2012) New pyrazolo[3,4-d]pyrimidiine SRC inhibitors induce apoptosis in mesothelioma cell lines through p 27 nuclear nuclear stabilization. Oncogenes 31:929–938
14. Carlomagno F, Vitagliano D, Guida T, Basolo F, Castellone MD, Melillo RM, Fusco A, Santro M (2003) Efficient inhibition of RET/papillary thyroid carcinoma oncogenic kinases by 4-amino-5-(4-chloro-phenyl)-7-(t-Butyl)Pyrazolo[3,4-d]Pyrimidine (PP2). J Clin Endocrinol Metab 88:1897–1902
15. Hayat F, Salahudin A, Ummar S, Azam A (2010) Synthesis charasterization, antiamoebic activity and cytotoxicity of novel series of pyrazoline derivatives bearing quinoline tail. Eur J Med Chem 45: 4669–4675
16. Budakoti A, Abid M, Azam A (2007) Synthesis, characterization and in vitro antiamoebic activity of new Pd(II) complexes with 1-N-substituted thiocarbonyl1-3,5-dimethyl-2-pyrazoline derivatives. Eur J Med Chem 42:544–551
17. Parveen H, Hayat F, Mukhtar S, Salahudin A, Khan A, Islam F, Azam A (2011) Synthesis, characterization and biological evaluation of novel 2,4, 6 trisubstituted bis-pyrimidine derivatives. Eur J Med Chem 46:4669–4675
18. Siddiqui SM, Salahudin A, Azam A (2013) Pyrazolo[3,4-d]pyrimidine analogues: synthesis, characterization and their in-vitro antiamoebic activity. Med Chem Res 22:775–781
19. Yadava U, Singh M, Roychoudhury M (2011) Gas-phase conformational and intramolecular π-π interaction studies on some pyrazolo[3,4-d]pyrimidine derivatives. Comput Theo Chem 977:134–139
20. (2012) Glide: version 5.2 Schrödinger. LLC, New York
21. Friesner RA, Banks JL, Murphy RB, Halgren TA, Kliclic JJ, Mainz DT, Repasky MP, Knoll EH, Shelley M, Perry JK, Shaw DE, Francis P, Shenkin PS (2004) Glide: a new approach for rapid accurate docking and scoring, method and assessment of docking accuracy. J Med Chem 47:1739–1749
22. Frisch MJ, Trucks GW, Schlegel HB, Scuseria GE, Robb MA, Cheeseman JR, Montgomery JA, Vreven JT, Kudin KN, Burant JC, Millam JM, Iyengar SS, Tomasi J, Barone V, Mennucci B, Cossi M, Scalmani G, Rega N, Petersson GA, Nakatsuji H, Hada M, Ehara M, Toyota K, Fukuda R, Hasegawa J, Ishida M, Nakajima T, Honda Y, Kitao O, Nakai H, Klene M, Li X, Knox JE, Hratchian HP, Cross JB, Adamo C, Jaramillo J, Gomperts R, Stratmann RE, Yazyev O, Austin AJ, Cammi R, Pomelli C, Ochterski JW, Ayala PY, Morokuma K, Voth GA, Salvador P, Dannenberg JJ, Zakrzewski VG, Dapprich S, Daniels AD, Strain MC, Farkas O, Malick DK, Rabuck AD, Raghavachari K, Foresman JB, Ortiz JV, Cui Q, Baboul AG, Clifford S, Cioslowski J, Stefanov BB, Liu G, Liashenko A, Piskorz P, Komaromi I, Martin RL, Fox DJ, Keith T, Al-Laham MA, Peng CY, Nanayakkara A, Challacombe M, Gill PMW, Johnson B, Chen W, Wong MW, Gonzalez C, Pople JA (2003) GAUSSIAN 03, revision B.04. Gaussian, Inc, Pittsburgh
23. Jorgenson WL, Maxwell DS, Tirado-Rives J (1996) Development and testing of the OPLS all atom force field on conformational energetic and properties of organic liquids. J Am Chem Soc 118:11225–11236
24. (2012) Prime, version 3.1. Schrödinger, LLC, New York
25. Morris GM, Huey R, Lindstrom W, Sanner MF, Belew RK, Goodsell DS, Olson AJ (2009) Autodock 4 and Autodock Tools 4: automated docking with selective receptor flexibility. J Comput Chem 30:2785–2791
26. (2012) DESMOND molecular dynamics system, version 3.1. Shaw, New York
27. Bowers KJ, Chow E, Xu H, Dror RO, Eastwood MP, Gregersen BA, Klepeis JL, Kolossvary I, Moraes MA, Sacerdoti FD, Salmon JK, Shan Y and Shaw DE (2006) Scalable algorithms for molecular dynamics simulations on commodity clusters. Proc ACM/IEEE Conf Supercomp (SC06), Tampa, FL
28. Verlet L (1967) Computer "Experiments" on classical fluids I. Thermodynamical properties of Lennard–Jones molecules. Phys Rev 159:98–103
29. Swegat W, Schlitter JR, Kruger P, Wollmer A (2003) MD simulation of protein-ligand interaction: formation and dissociation of an insulin-phenol complex. Biophys J 84:1493–1506
30. Tripathi SK, Muttineni R, Singh SK (2013) Extra precision docking, free energy calculation and molecular dynamics simulation studies of CDK2 inhibitors. J Theor Biol 334:87–100
31. Kennedy T (1997) Managing the discovery/development interface. Drug Discov Today 2:436–444
32. DiMassi JA (1995) Success rates for new drugs entering clinical testing in the Unites States. Clin Pharmacol Ther 58:1–14
33. (2012) QikProp: version 3.5. Schrödinger, LLC, New York
34. Lipinski CA (2000) Drug-like properties and the causes of poor solubility and poor permeability. J Pharmacol Toxicol Methods 44:235–249
35. Lipinski CA, Lombardo F, Dominy BW, Feeney PJ (1997) Experimental and computational approaches to estimate solubility and permeability in drug discovery and development settings. Adv Drug Deliv Rev 23:3–25
36. Krishna C, Jain R, Kashav T, Wadhwa D, Alam N (2007) Crystallization and preliminary crystallographic analysis of cysteine synthase from *Entamoeba histolytica*. Acta Crystallogr F63:512–515
37. Kawatkar S, Wang H, Czerminski R, Joseph-McCarthy D (2009) Virtual fragment screening: an exploration of various docking and scoring protocols for fragments using glide. J Comput Aided Mol Des 23:527–539

Chemical Science

EDGE ARTICLE

View Article Online
View Journal | View Issue

CrossMark click for updates

Cite this: *Chem. Sci.*, 2015, **6**, 1516

Open Access Article. Published on 08 December 2014. Downloaded on 22/01/2015 17:11:53.
This article is licensed under a Creative Commons Attribution 3.0 Unported Licence.

A comprehensive test set of epoxidation rate constants for iron(IV)–oxo porphyrin cation radical complexes†

Mala A. Sainna,[a] Suresh Kumar,[b] Devesh Kumar,*[b] Simonetta Fornarini,*[c] Maria Elisa Crestoni*[c] and Sam P. de Visser*[a]

Cytochrome P450 enzymes are heme based monoxygenases that catalyse a range of oxygen atom transfer reactions with various substrates, including aliphatic and aromatic hydroxylation as well as epoxidation reactions. The active species is short-lived and difficult to trap and characterize experimentally, moreover, it reacts in a regioselective manner with substrates leading to aliphatic hydroxylation and epoxidation products, but the origin of this regioselectivity is poorly understood. We have synthesized a model complex and studied it with low-pressure Fourier transform-ion cyclotron resonance (FT-ICR) mass spectrometry (MS). A novel approach was devised using the reaction of $[Fe^{III}(TPFPP)]^+$ (TPFPP = *meso*-tetrakis(pentafluorophenyl) porphinato dianion) with iodosylbenzene as a terminal oxidant which leads to the production of ions corresponding to $[Fe^{IV}(O)(TPFPP^{+\bullet})]^+$. This species was isolated in the gas-phase and studied in its reactivity with a variety of olefins. Product patterns and rate constants under Ideal Gas conditions were determined by FT-ICR MS. All substrates react with $[Fe^{IV}(O)(TPFPP^{+\bullet})]^+$ by a more or less efficient oxygen atom transfer process. In addition, substrates with low ionization energies react by a charge-transfer channel, which enabled us to determine the electron affinity of $[Fe^{IV}(O)(TPFPP^{+\bullet})]^+$ for the first time. Interestingly, no hydrogen atom abstraction pathways are observed for the reaction of $[Fe^{IV}(O)(TPFPP^{+\bullet})]^+$ with prototypical olefins such as propene, cyclohexene and cyclohexadiene and also no kinetic isotope effect in the reaction rate is found, which suggests that the competition between epoxidation and hydroxylation – in the gas-phase – is in favour of substrate epoxidation. This notion further implies that P450 enzymes will need to adapt their substrate binding pocket, in order to enable favourable aliphatic hydroxylation over double bond epoxidation pathways. The MS studies yield a large test-set of experimental reaction rates of iron(IV)–oxo porphyrin cation radical complexes, so far unprecedented in the gas-phase, providing a benchmark for calibration studies using computational techniques. Preliminary computational results presented here confirm the observed trends excellently and rationalize the reactivities within the framework of thermochemical considerations and valence bond schemes.

Received 4th September 2014
Accepted 8th December 2014

DOI: 10.1039/c4sc02717e

www.rsc.org/chemicalscience

Introduction

The cytochromes P450 are part of the body's natural defence mechanism in the liver and perform vital functions for human health that include the biodegradation of xenobiotic and drug molecules.[1] Due to this broad chemical function the P450s can bind and activate a large range of substrates with varying shapes and sizes. Generally, the P450s act as monoxygenases, whereby they bind and utilize molecular oxygen *via* a heme centre and transfer one of the oxygen atoms of O_2 to a substrate, while the second oxygen atom leaves the process as a water molecule. The P450s react with substrates activating aliphatic and aromatic hydroxylation, epoxidation and sulfoxidation reactions, but have also been reported to catalyse desaturation and *N*-dealkylation reactions.[2] There are many different P450 isozymes and until early 2014 thousands of different structures had been characterized.[3] All P450s share common features which include a catalytically active heme group with a central iron atom that is linked to the protein by the thiolate sulphur atom of a cysteinate side chain.[4]

[a]*Manchester Institute of Biotechnology and School of Chemical Engineering and Analytical Science, The University of Manchester, 131 Princess Street, Manchester M1 7DN, UK. E-mail: sam.devisser@manchester.ac.uk*

[b]*Department of Applied Physics, School for Physical Sciences, Babasaheb Bhimrao Ambedkar University, Vidya Vihar, Rai Bareilly Road, Lucknow 226 025, India. E-mail: dkclcre@yahoo.com*

[c]*Dipartimento di Chimica e Tecnologie del Farmaco, Università di Roma "La Sapienza", P.le A. Moro 5, 00185, Roma, Italy. E-mail: mariaelisa.crestoni@uniroma1.it; simonetta.fornarini@uniroma1.it*

† Electronic supplementary information (ESI) available: Details of the computational results, including Tables with group spin densities, charges, absolute and relative energies as well as structures and Cartesian coordinates is provided. See DOI: 10.1039/c4sc02717e

This journal is © The Royal Society of Chemistry 2015

Open Access Article. Published on 08 December 2014. Downloaded on 22/01/2015 17:11:53.
This article is licensed under a Creative Commons Attribution 3.0 Unported Licence.

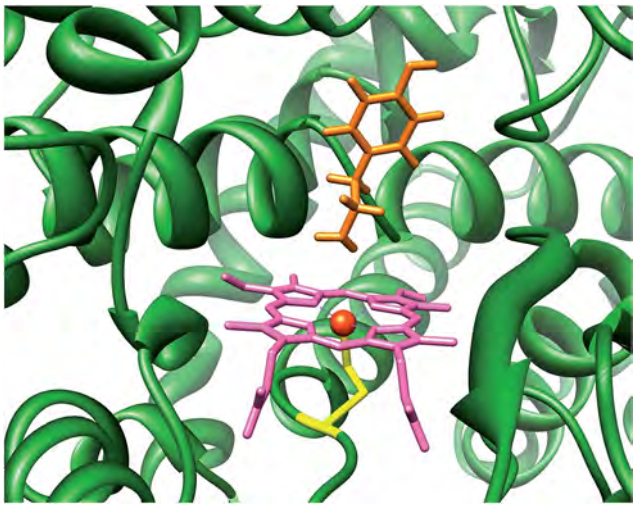

Fig. 1 Active site of P450 as taken from the 2WM4 pdb file. Substrate tyramine is highlighted in orange.

Fig. 1 displays the structure of a typical P450 active site, namely the one belonging to the CYP124 isozyme as taken from the 2WM4 protein databank (pdb) file.[5] As shown in Fig. 1 the substrate (tyramine) is located in a cleft nearby the heme, the substrate binding pocket, which is in a tight orientation with stabilizing hydrogen bonding interactions by several residues. The vacant sixth coordination site of iron is the position where molecular oxygen will bind during the catalytic cycle. The process includes two reduction and two protonation steps to synthesize the active species of P450 called Compound I (Cpd I).[6] Cpd I is highly reactive and therefore difficult to study experimentally, however, a few reports on its spectroscopic properties have appeared in the literature.[7]

Due to the short lifetime of Cpd I, studying catalytic mechanisms and reaction rates of P450 catalysed reactions is challenging;[8] therefore, many studies have focused on biomimetic iron–porphyrin complexes instead.[9] These studies gave detailed insight into the effect of axial and equatorial ligands,[10] but also on the local environment such as the substrate binding pocket. A particularly useful method to establish the properties and reactivity patterns of short-lived complexes, such as catalytic intermediates, is Fourier transform – ion cyclotron resonance (FT-ICR) mass spectrometry (MS).[11] In FT-ICR MS, the charged species of interest (either positive or negative ion) is trapped in a collision cell for a specific time during which reactions with neutral gases can occur and be studied at the prevailing low pressure of the instrument. FT-ICR MS allows one to measure the ion distributions and fragmentation patterns at varying trapping time, thereby yielding insight into reactivities, and enabling one to calculate rate constants and thermochemical properties. In recent work, Crestoni, Fornarini and co-workers have succeeded in trapping and characterizing the Cpd I analogues of iron and manganese porphyrin complexes and studied their reactivity with a selection of substrates.[12] Thus, the $[Mn^{V}(O)(TPFPP)]^{+}$ complex (TPFPP = *meso*-tetrakis (pentafluorophenyl)porphinato dianion) was found to react with model substrates through oxygen atom transfer (OAT), electron transfer (ET), hydride transfer and ligand addition. However, no direct hydrogen atom transfer (HAT) with any tested substrate took place.

In order to find out what drives the OAT reaction of Cpd I with olefins, we decided to investigate the properties and reactivities of $[Fe^{IV}(O)(Por^{+\bullet})]^{+}$ (Por = porphine dianion) and $[Fe^{IV}(O)(TPFPP^{+\bullet})]^{+}$ with FT-ICR MS and with density functional theory (DFT) methods. These studies represent the first comprehensive – experimental and computational – study on olefin epoxidation by iron(IV)–oxo porphyrin cation radical models and allow correlations to be established between the OAT rate constant and the ionization energy (IE) of the olefin. These correlations are further supported and rationalized by computational modelling.

Methods

Materials

All chemicals used in the experiments, including (5,10,15,20-tetrakis(pentafluorophenyl)porphinato)iron(III) chloride, $[Fe^{III}(TPFPP)]Cl$, were research grade products purchased from commercial sources and used as received. All the solvents were analytical grade. Ethylene, propylene, and *E*-2-butene were high purity gases from Matheson Gas Products Inc. Iodosylbenzene (C_6H_5IO) was prepared according to a published procedure and stored at −20 °C.[13]

Instrumental

All experiments were run on a Bruker BioApex Fourier transform-ion cyclotron resonance (FT-ICR) mass spectrometer equipped with an Apollo I electrospray ionization source, a 4.7 T superconducting magnet, and a cylindrical infinity cell. Analyte solutions were continuously infused through a 50 μm internal diameter fused-silica capillary at a flow rate of 120 μL h^{-1} by a syringe pump and ions were accumulated in a radiofrequency-only hexapole ion guide for 0.8 s. The ion population, desolvated by a heated (380 K) N_2 counter current drying gas, was pulsed into the ICR cell at room temperature (300 K), where the ion of interest was isolated by ion ejection procedures and allowed to react with the selected neutral reagent (L) admitted by a needle valve at stationary pressures in the range of 1.0–15 × 10^{-8} mbar. The pressure was measured with a cold-cathode sensor (IKR Pfeiffer Balzers S.p.A., Milan, Italy) calibrated by using the rate constant, $k_{methane} = 1.1 \times 10^{-9}$ cm^3 s^{-1}, for the reference reaction $CH_4^{+\bullet} + CH_4 \rightarrow CH_5^{+} + CH_3^{\bullet}$ and corrected for different response factors.[14]

Pseudo-first order rate constants were obtained from the slope of the semi-logarithmic decrease of the parent ion abundance as a function of time and divided by the substrate concentration to determine the second-order rate constants (k_{exp}) at 300 K. The reaction efficiencies (Φ) are percentages of the second-order rate constant with respect to the collision rate constant (k_{ADO}), *i.e.* $\Phi = k_{exp}/k_{ADO}$, calculated by the parametrized trajectory theory.[15] These values and product ion branching ratios were found to be independent of the pressure

Open Access Article. Published on 08 December 2014. Downloaded on 22/01/2015 17:11:53.
This article is licensed under a Creative Commons Attribution 3.0 Unported Licence.

of the neutral and of the additional presence of an inert bath gas, *i.e.* argon. The reproducibility of the k_{exp} values was within 10%, while the error of the absolute rate constants is estimated to be ±30%.

Sample preparation

The $[Fe^{IV}(O)(TPFPP^{+\bullet})]^+$ ion of interest was prepared by adding iodosylbenzene (0.5 mM) to $[Fe^{III}(TPFPP)]Cl$ (10 μM) in a CH_3OH/CH_2Cl_2 (1 : 1) solvent mixture cooled at −40 °C. The so-formed $[Fe^{IV}(O)(TPFPP^{+\bullet})]^+$ ion persisted at this temperature for about 1 h. The high-resolution electrospray ionization FT-ICR mass analysis shows the presence of ions $[Fe^{IV}(O)(TPFPP^{+\bullet})]^+$ as a prominent cluster centered at *m*/*z* 1044, along with the resting form $[Fe^{III}(TPFPP)]^+$, characterized by the same isotopic pattern, and centered at *m*/*z* 1028.

As already pointed out,[16] the synthetic method yields a portion of an isomeric species, likely oxidized on the porphyrin ligand and ineffective in any OAT reaction to reductants. This OAT-unreactive fraction of the overall ion population at *m*/*z* 1044 has been identified as a four-coordinate iron(III) complex incorporating an O-atom on the porphyrin ligand, henceforth denoted as $[Fe^{III}(TPFPP\text{-}O)]^+$.[16] Its relative amount has been evaluated exploiting the characteristic reaction with NO, displaying different paths from the two isomeric species. In fact, while $[Fe^{III}(TPFPP\text{-}O)]^+$ yields a ligand addition product, $[Fe^{III}(TPFPP\text{-}O)(NO)]^+$, the genuine iron(IV)–oxo complex $[Fe^{IV}(O)(TPFPP^{+\bullet})]^+$ undergoes an OAT process by releasing $[Fe^{III}(TPFPP)]^+$.

Computation

All calculations discussed here utilize density functional theory (DFT) methods as implemented in the Jaguar and Gaussian-09 program packages.[17] Two different models were investigated: (i) $[Fe^{IV}(O)(Por^{+\bullet})]^+$ (**A**) that includes a porphyrin (Por) ring with all side-chains abbreviated to hydrogen atoms, and (ii) $[Fe^{IV}(O)(TPFPP^{+\bullet})]^+$ (**B**), Scheme 1. Similar to previous work of ours in the field,[18] we use the unrestricted hybrid density functional method UB3LYP[19] as it was shown to reproduce the kinetics of metal(iv)–oxo oxidants well.[20] Initial exploratory calculations employed a modest LANL2DZ basis set on iron and 6-31G on the rest of the atoms (basis set BS1)[21] for geometry optimizations, analytical frequencies and geometry scans. These studies explored the potential energy surfaces involving reactants, intermediates and products on different spin states in detail and generated starting structures for the transition state optimizations. All local minima reported here had real frequencies only and the transition states were characterized by a single imaginary frequency for the correct mode. To improve the energetics of these structures we did single point calculations in the gas-phase with a triple-ζ quality basis set on iron (LACV3P+) and 6-311+G* on the rest of the atoms, basis set BS2. Subsequently, all geometries (local minima and transition states) were reoptimized at the UB3LYP/BS2 and UB3LYP-D3/BS2 levels of theory[19,22] and characterized by an analytical frequency analysis. Barrier heights reported in this work were calculated relative to isolated reactants, although using reactant complexes instead only minor changes are observed (ESI†).

The effect of solvent on the rate constants was tested through single point calculations using the self-consistent reactant field model as implemented in Gaussian with a dielectric constant representing chloroform ($\varepsilon = 4.7113$).

Ionization energies and bond dissociation energy (BDE_{OH}) values were calculated as before[23] and represent adiabatic values for reaction 1 and 2, respectively and report UB3LYP/BS2//UB3LYP/BS1 energies including ZPE and dispersion corrections.

$$A \rightarrow A^{+\bullet} + e^- + IE_A \quad (1)$$

$$[Fe^{IV}(OH)(Por)]^+ \rightarrow [Fe^{IV}(O)(Por^{+\bullet})]^+ + H^\bullet + BDE_{OH} \quad (2)$$

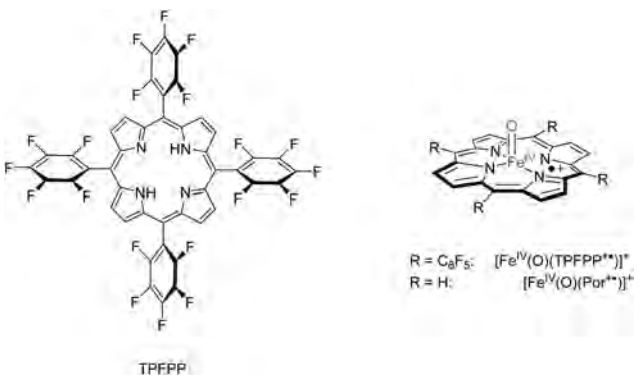

Scheme 1 Models investigated in this work.

Results

Gas phase reactivity with FT-ICR MS

Formation and characterization of naked $[Fe^{IV}(O)(TPFPP^{+\bullet})]^+$ ions. In an early survey, the preparation of a high-valent iron(IV)–oxo porphyrin cation radical was achieved by controlled oxidation of $[Fe^{III}(TPFPP)]Cl$ with H_2O_2 in a methanol solution. This solution was then sampled by electrospray ionization FT-ICR MS.[12a] However, under the selected experimental conditions, in addition to the heterolytic cleavage of the peroxide bond also a homolytic pathway is observed that yields a high-valent iron(IV)–hydroxo porphyrin complex $[Fe^{IV}(OH)(TPFPP)]^+$. Because the latter complex differs by one mass unit only from the species of interest, this presence complicates the ion distribution and the assignment of the oxidant in the reaction mixture. Therefore, we aimed to synthesize $[Fe^{IV}(O)(TPFPP^{+\bullet})]^+$ through an alternative, neater mechanism. A methanol/dichloromethane solution of $[Fe^{III}(TPFPP)]Cl$ was treated with iodosylbenzene (PhIO) as oxygen atom donor. The reaction mixture, assayed by electrospray ionization and high resolution mass measurements by FT-ICR mass spectrometry, displays an ion cluster centered at *m*/*z* 1044.0116, which corresponds to the acquisition of just one oxygen atom by the reactant species $[Fe^{III}(TPFPP)]^+$.

 This journal is © The Royal Society of Chemistry 2015

Open Access Article. Published on 08 December 2014. Downloaded on 22/01/2015 17:11:53.
This article is licensed under a Creative Commons Attribution 3.0 Unported Licence.

The thus generated, naked five-coordinate species proves to be resistant with respect to any unimolecular dissociation process ($k_{diss} \leq 0.001$ s^{-1}). However, when the ion-molecule reactivity of the ion cluster at *m*/*z* 1044 is examined through the addition of NO into the FT-ICR cell, two reaction products are observed: (i) a major fraction of ions reacts by OAT and forms $[Fe^{III}(TPFPP)]^+$ and NO_2 as the likely neutral product, (ii) a significant percentage of the starting ions undergo a ligand addition reaction to give a product with *m*/*z* 1074.

The product formed in the latter pathway has been sampled by collision induced dissociation (CID), and displays the loss of NO as unique fragmentation channel thus suggesting that NO has become part of the complex as intact ligand at a formerly vacant axial position. Note here that ligand addition is typical for the reactivity of tetracoordinate $[Fe^{III}(TPFPP)]^+$ ions.[12a] This finding provides circumstantial evidence for an ion population of the same elemental composition as $[Fe^{IV}(O)(TPFPP^{+\bullet})]^+$, that may correspond to an isomeric structure oxidized on the porphyrin ligand, designated as $[Fe^{III}(TPFPP\text{-}O)]^+$.

The chemical titration reaction with NO is a way to resolve the isomeric distribution of electrosprayed ions at *m*/*z* 1044 and allowed us to establish the relative amount of $[Fe^{IV}(O)(TPFPP^{+\bullet})]^+$ in each experiment, which is consistently found to be equal to or larger than 60% of the total ion population at *m*/*z* 1044.

Reactivity of naked $[Fe^{IV}(O)(TPFPP^{+\bullet})]^+$ ions with olefins. Our initial studies focused on experimentally determining the reactivity of $[Fe^{IV}(O)(TPFPP^{+\bullet})]^+$ with the selected olefins depicted in Scheme 2, and the results are summarized in Table 1. These olefins vary in molecular size and structure and their reported ionization energies span from 8.1 to 10.51 eV.[24] The $[Fe^{IV}(O)(TPFPP^{+\bullet})]^+$ ion was prepared from the reaction of iodosylbenzene with $[Fe^{III}(TPFPP)]Cl$ in methanol/dichloromethane solution and transferred by electrospray ionization into the mass spectrometer as described above. Subsequently, the $[Fe^{IV}(O)(TPFPP^{+\bullet})]^+$ ion was mass selected and trapped in the FT-ICR cell. The chosen olefin (Sub) was present at constant pressure in the cell and mass spectra were recorded at regular time intervals after isolation of the parent ion. Over time, all $[Fe^{IV}(O)(TPFPP^{+\bullet})]^+$ was found to react and new peaks corresponding to product ions appeared in the spectrum. Three different reaction paths were observed and monitored, namely oxygen atom transfer (OAT), hydride transfer (HT) and charge transfer (CT), as illustrated in Scheme 3.

These three pathways lead to different product ions in the recorded spectra: (i) $[Fe^{III}(TPFPP)]^+$ ions are the products of the OAT channel; (ii) ions at *m*/*z* corresponding to $[Sub\text{-}H]^+$ are obtained from the HT processes; (iii) ions corresponding to $Sub^{+\bullet}$ arise from a CT reaction. Interestingly, no evidence of hydrogen atom abstraction (HAT) is observed with any of the selected olefins listed in Table 1. In the case of two substrates, cyclohexene and 1,4-cyclohexadiene, molecular addition (Add) to the complex is also observed, leading to an ion with *m*/*z* value formally corresponding to $[Fe(O)(TPFPP)(Sub)]^+$. It is possible that these addition complexes are products from a hydrogen atom abstraction reaction but currently this cannot be established from the product ions. However, experiments with fully deuterated cyclohexene (cyclohexene-d_{10}) *versus* that of cyclohexene-h_{10} gave a rate constant ratio k_H/k_D very close to 1. Reactions starting with an initial hydrogen atom abstraction reaction normally encounter a large kinetic isotope effect (KIE = k_H/k_D) of well greater than 1, hence these KIE experiments implicate that no rate determining hydrogen atom abstraction takes place here.

Because the selected ions at *m*/*z* 1044 comprise isomeric species as described in the previous paragraph, it is important to mention that in all experiments with the selected substrates (olefins and unsaturated hydrocarbons) an unreactive fraction

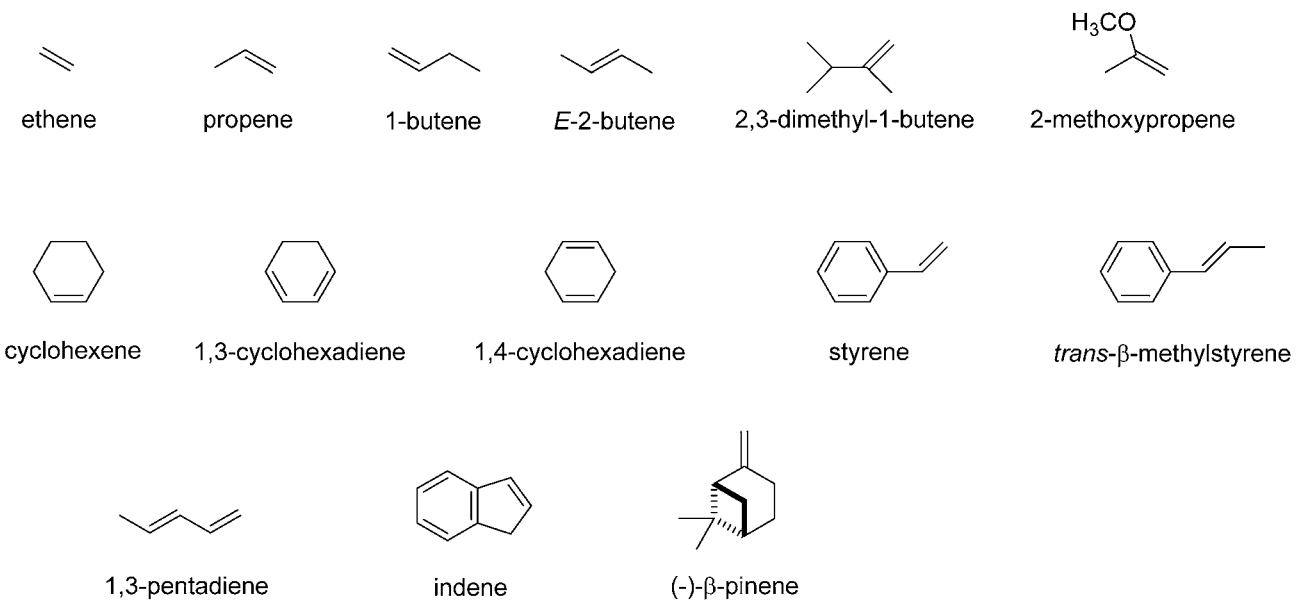

Scheme 2 Substrates investigated in this work.

Open Access Article. Published on 08 December 2014. Downloaded on 22/01/2015 17:11:53.
This article is licensed under a Creative Commons Attribution 3.0 Unported Licence.

Table 1 Kinetic data and product distributions obtained for the gas phase reaction of $[Fe^{IV}(O)(TPFPP^{+\bullet})]^+$ with selected olefins as determined by FT-ICR MS

Substrate	IE[a]	k_{exp}[b]	k_{ADO}[c]	Φ[d]	HT	CT	OAT	Add
Ethene	10.51	8.5×10^{-5}	8.5	1×10^{-3}	—	—	100	—
Propene	9.73	7.6×10^{-3}	9.45	0.080	—	—	100	—
1-Butene	9.55	0.029	9.6	0.30	—	—	100	—
E-2-Butene	9.10	0.080	10.8	0.74	—	—	100	—
2,3-Dimethyl-1-butene	9.07	0.145	9.5	1.5	—	—	100	—
Cyclohexene[e]	8.95	0.194–0.291	9.7	2–3	—	—	75	25
1,4-Cyclohexadiene	8.82	0.511	9.29	5.5	—	—	90	10
2-Methoxy-1-propene	8.64	0.819	10.5	7.8	—	—	100	—
1,3-Pentadiene	8.60	0.826	9.6	8.6	—	—	100	—
Styrene	8.46	1.40	9.26	15	—	—	100	—
1,3-Cyclohexadiene	8.25	1.58	9.29	17	—	—	100	—
trans-β-Methylstyrene	8.1–8.2	2.97	11.9	25	4	—	96	—
Indene	8.14	3.18	8.6	37	2	12	86	—
β-Pinene[f]	N/A	4.32–4.7	9.4	46–50	—	—	100	—

[a] Ionization energies (IE, eV) are from ref. 24. N/A stands for not available. [b] Second-order rate constants (k_{exp}) in units of 10^{-10} cm^3 molecule^{-1} s^{-1} are measured at a temperature of 300 K in the FT-ICR cell. The estimated error in k_{exp} is ±30%, although the internal consistency of the data is within ±10%. [c] Collision rate constants (k_{ADO}) evaluated with the parameterized trajectory theory. [d] Reaction efficiency (%), $\Phi = k_{exp}/k_{ADO} \times 100$. [e] The reaction with cyclohexene-d_{10} gave a rate constant within experimental error of that for cyclohexene-h_{10}. [f] The IE for α-pinene is 8.07 eV.

is observed in a corresponding relative amount as the species yielding the NO addition product in the probe reaction with nitric oxide. This species has been assigned the features of a porphyrin-oxidized complex and its contribution to the experiments has been thoroughly subtracted, an operation allowed by the distinctly different (un)reactivity of the two isomeric

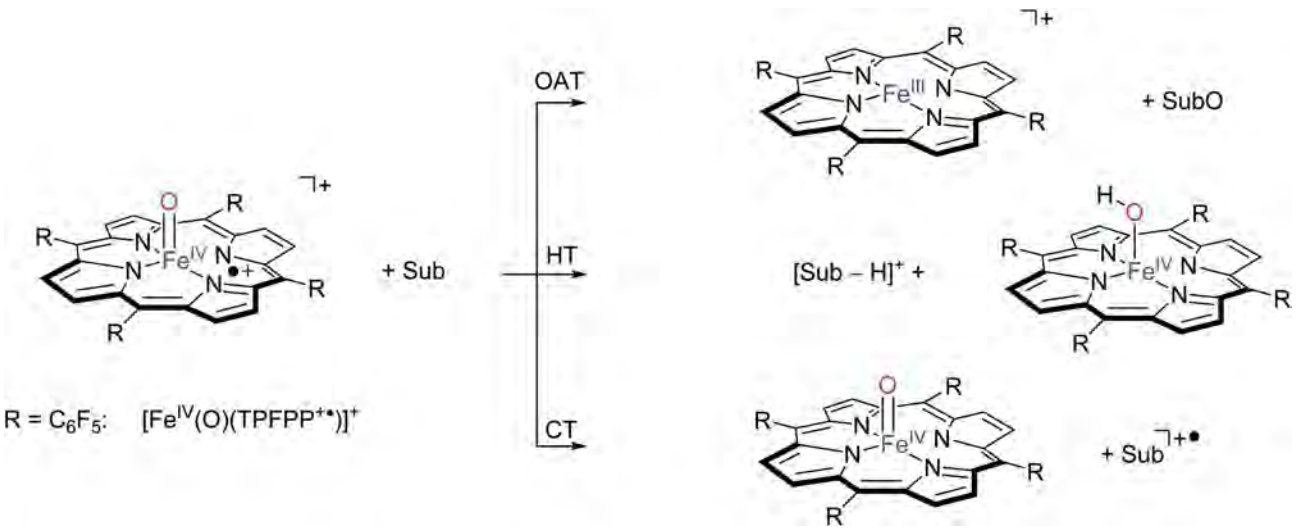

Scheme 3 Pathways observed for the reaction of $[Fe^{IV}(O)(TPFPP^{+\bullet})]^+$ ions (R = C_6F_5) with selected substrates (Sub) as studied with FT-ICR MS.

 This journal is © The Royal Society of Chemistry 2015

Open Access Article. Published on 08 December 2014. Downloaded on 22/01/2015 17:11:53.
This article is licensed under a Creative Commons Attribution 3.0 Unported Licence.

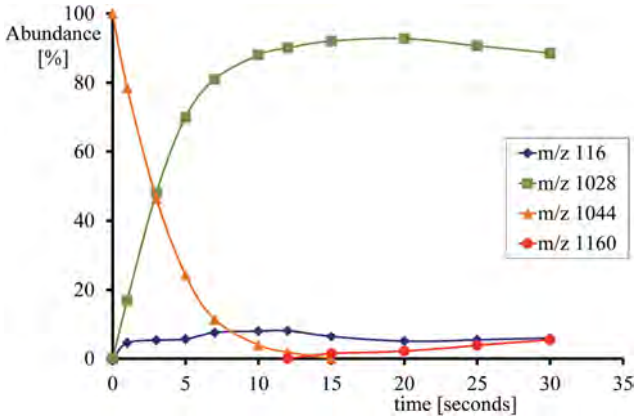

Fig. 2 Time dependence of relative ion abundancies for the reaction of $[Fe^{IV}(O)(TPFPP^{+\bullet})]^+$ (*m*/*z* 1044) with indene. Product ions are $[Fe^{III}(TPFPP)]^+$ (*m*/*z* 1028), $[Fe(TPFPP)(C_9H_8)O]^+$ (*m*/*z* 1160) and $C_9H_8^{+\bullet}$ (*m*/*z* 116). Experiments were performed in the presence of indene at 5.2×10^{-8} mbar in the FT-ICR cell.

complexes $[Fe^{IV}(O)(TPFPP^{+\bullet})]^+$ and $[Fe^{III}(TPFPP\text{-}O)]^+$. Henceforth, the implication of this species will not be further discussed.

Fig. 2 gives an example of the time dependence of the relative ion abundance of reactant and product ions as a function of time for the reaction of $[Fe^{IV}(O)(TPFPP^{+\bullet})]^+$ with indene. In general, the ion abundance of $[Fe^{IV}(O)(TPFPP^{+\bullet})]^+$ follows an exponential decay as a function of time, as illustrated by its reaction with indene in Fig. 2. The pseudo-first order decay of the reactant ion abundance as a function of time was then converted into a bimolecular rate constant, k_{exp}, which was normalized by the respective collision rate constant (k_{ADO}) to give the relative efficiency ($\Phi = k_{exp}/k_{ADO} \times 100$).[15] The gas phase reactivity of $[Fe^{IV}(O)(TPFPP^{+\bullet})]^+$ spans a wide range of reaction efficiencies, with values varying from 0.001% to 0.08% for terminal olefins, like ethene and propene, up to *ca.* 50% for electron-rich monoterpenes.

With most substrates a clean OAT conversion from reactants to products is observed without production of by-products and the time dependence shows a pattern like that displayed in Fig. 2. In the case of cyclohexene, about 25% addition occurs with the formation of an ion formally corresponding to $[Fe(TPFPP)(c\text{-}C_6H_{10})O]^+$. The formation of a long-lived complex with this substrate suggests that, within the metal coordination sphere, the olefin is activated to form an O-containing species endowed with appreciable affinity for the metal. Ligand binding to iron porphyrin complexes has been found to correlate with the gas phase basicity of the ligand.[25] It may thus be inferred that the olefin has turned into a more basic species, either an epoxide by O-addition across the double bond or an alcohol by allylic C–H bond activation. The nature of the adduct complex has been further probed and confirmed by low-energy CID, and reveals the formation of the reduced species $[Fe^{III}(TPFPP)]^+$ through the release of SubO. The so-formed complex from the reaction of $[Fe^{IV}(O)(TPFPP^{+\bullet})]^+$ with the olefin substrate may then be depicted as $[Fe^{III}(TPFPP)(SubO)]^+$. Similar product complexes have been observed previously from other substrates through oxygen atom-acceptor properties such as sulphides, amines, and phosphorus containing complexes.[12a,16]

In addition, substrates with low ionization potential are found to react *via* hydride transfer (*trans*-β-methylstyrene, and indene) and/or charge transfer reactions (indene) as side-reactions. We examined whether a charge-transfer (CT) reaction occurs between $[Fe^{IV}(O)(TPFPP^{+\bullet})]^+$ and sampled substrates. As in FT-ICR MS only exothermic reactions are able to occur due to the low number of collisions in the gas, the data in Table 1 show that the charge-transfer reaction is exothermic with indene as a substrate (eqn (3)), but endothermic with other substrates. Thus, the enthalpy change for the charge-transfer between $[Fe^{IV}(O)(TPFPP^{+\bullet})]^+$ and indene should be equal to the difference between the ionization energy of the substrate and the electron affinity (EA) of $[Fe^{IV}(O)(TPFPP^{+\bullet})]^+$. Since, no charge-transfer reaction occurs with substrates with an ionization energy above 8.2 eV (Table 1), this implies that the EA of gaseous $[Fe^{IV}(O)(TPFPP^{+\bullet})]^+$ ions must be lower than 8.2 eV. Previous FT-ICR MS studies predicted a lower limit of 7.5 eV for the EA of $[Fe^{IV}(O)(TPFPP^{+\bullet})]^+$,[16] which is in good general agreement with the data in Table 1. DFT calculations on $[Fe^{IV}(O)(Por^{+\bullet})X]$ with different axial ligands X have yielded electron affinities of 3.06 eV for $X = SH^-$, whereas values of 6.41 and 6.12 eV are found for systems with an imidazole or tyrosinate axial ligand, respectively.[26] Clearly, removal of the axial ligand is expected to raise the EA of the iron(IV)–oxo porphyrin cation radical substantially with respect to axially ligated systems due to the loss of interaction between the a_{2u} molecular orbital with axial ligand orbitals, *vide infra*.

$$[Fe^{IV}(O)(TPFPP^{+\bullet})]^+ + \text{indene} \rightarrow [Fe^{IV}(O)(TPFPP)] + \text{indene}^{+\bullet} \quad (3)$$

$$\Delta H_{Eq3} = IE_{indene} - EA_{[Fe^{IV}(O)(TPFPP^{+})]} < 0 \text{ kcal mol}^{-1} \quad (4)$$

Interestingly, although cytochrome P450 isozymes react with typical olefins, such as propene, cyclohexene and *Z*- and *E*-butene, to give a mixture of epoxide and enol products, actually the precise product distributions depend on the specific P450 isozyme.[27] Clearly, the substrate binding pocket and substrate orientation within the enzyme play a key role in determining the regioselectivity of the enzymatic reaction. In fact, enzymes manage to control the regioselectivity of substrate activation probably by binding the substrate under a specific orientation, which raises the epoxidation barriers and/or lowers the hydrogen atom abstraction barriers. Unfortunately, the FT-ICR MS results are unable to unequivocally distinguish hydroxylation products from epoxidation products as both have the same mass and are released as neutral molecules. As such, the experiments do not provide direct evidence supporting olefin epoxidation over a C–H activation channel in the reactions of $[Fe^{IV}(O)(TPFPP^{+\bullet})]^+$ with the selected olefins. However, we are able to show indirect evidence, *vide infra*. Computational studies on the regioselectivity of propene epoxidation *versus* hydroxylation by $[Fe^{IV}(O)(Por^{+\bullet})(SH)]$ gave lower epoxidation barriers in the gas-phase reaction,[28] but solvent and

Open Access Article. Published on 08 December 2014. Downloaded on 22/01/2015 17:11:53.
This article is licensed under a Creative Commons Attribution 3.0 Unported Licence.

environmental effects reversed the ordering. The computational studies from ref. 28, therefore, confirm the experimental trends in Table 1. This finding underlines the benchmark role played by a mechanistic study in the gas phase.

Theoretically derived reaction paths, energetics and structures. The experimental studies reported above present a comprehensive test set of model reactions of iron(IV)–oxo porphyrin cation radical complexes with olefins for the first time and enable extensive benchmarking and calibration of computational methods and procedures against gas-phase (Ideal Gas conditions) rate constants. We decided to take the opportunity and calibrate previously used methods and procedures for DFT studies on these chemical systems and compare to the results of the FT-ICR rates from Table 1. In addition, the computational studies were performed to further understand the substrate activation patterns by $[Fe^{IV}(O)(TPFPP^{+\bullet})]^{+}$ with olefins, and rationalize the obtained trends. Before we discuss details of the reaction mechanism and possible reactivity trends, let us start with a detailed analysis of the reactant species, namely $[Fe^{IV}(O)(Por^{+\bullet})]^{+}$, ^{4,2}**A**, and $[Fe^{IV}(O)(TPFPP^{+\bullet})]^{+}$, ^{4,2}**B**.

Fig. 3 displays the high-lying occupied and low-lying virtual orbitals of ^{4,2}**A**; the orbitals for ^{4,2}**B** look very similar. These orbitals are dominated by the interactions of the metal 3d orbitals with its ligands and several π-type porphyrin orbitals. Lowest in energy are a pair of σ-type orbitals (σ_{z2} and σ_{xy}): σ_{z2} represents the σ-interactions of the $3d_{z2}$ orbital on iron with the $2p_z$ orbital on oxygen, whereas the σ_{xy} gives the interactions of the $3d_{xy}$ orbital on iron with $2p_{x,y}$ orbitals on the four nitrogen atoms of the porphyrin ligand. The antibonding combinations of these two orbitals (σ^*_{z2} and σ^*_{xy}) are high in energy and virtual. Also doubly occupied is the δ_{x2-y2} orbital, which is a lone-pair orbital located in the plane of the porphyrin ring. Finally, the interaction of the metal $3d_{xz}/3d_{yz}$ with the $2p_x/2p_y$ on the oxygen atom leads to a pair of π_{xz}/π_{yz} and a pair of π^*_{xz}/π^*_{yz} set of orbitals. The σ_{z2}, σ_{xy}, π_{xz} and π_{yz} bonding orbitals are doubly occupied and low-lying in all calculations reported here. In addition to the metal-type orbitals there are also two porphyrin-type π-orbitals that in D_{4h} symmetry have the labels a_{1u} and a_{2u}. With a thiolate as axial ligand the a_{2u} orbital strongly mixes with a $3p_z$ orbital on sulphur and hence is destabilized in energy,[29] which strongly affects the electron affinity of the oxidant and consequently is responsible for its push-effect.[30]

The set of orbitals displayed in Fig. 3 is occupied with 15 electrons and as several of these orbitals are close in energy there are a number of possibilities to distribute the electrons

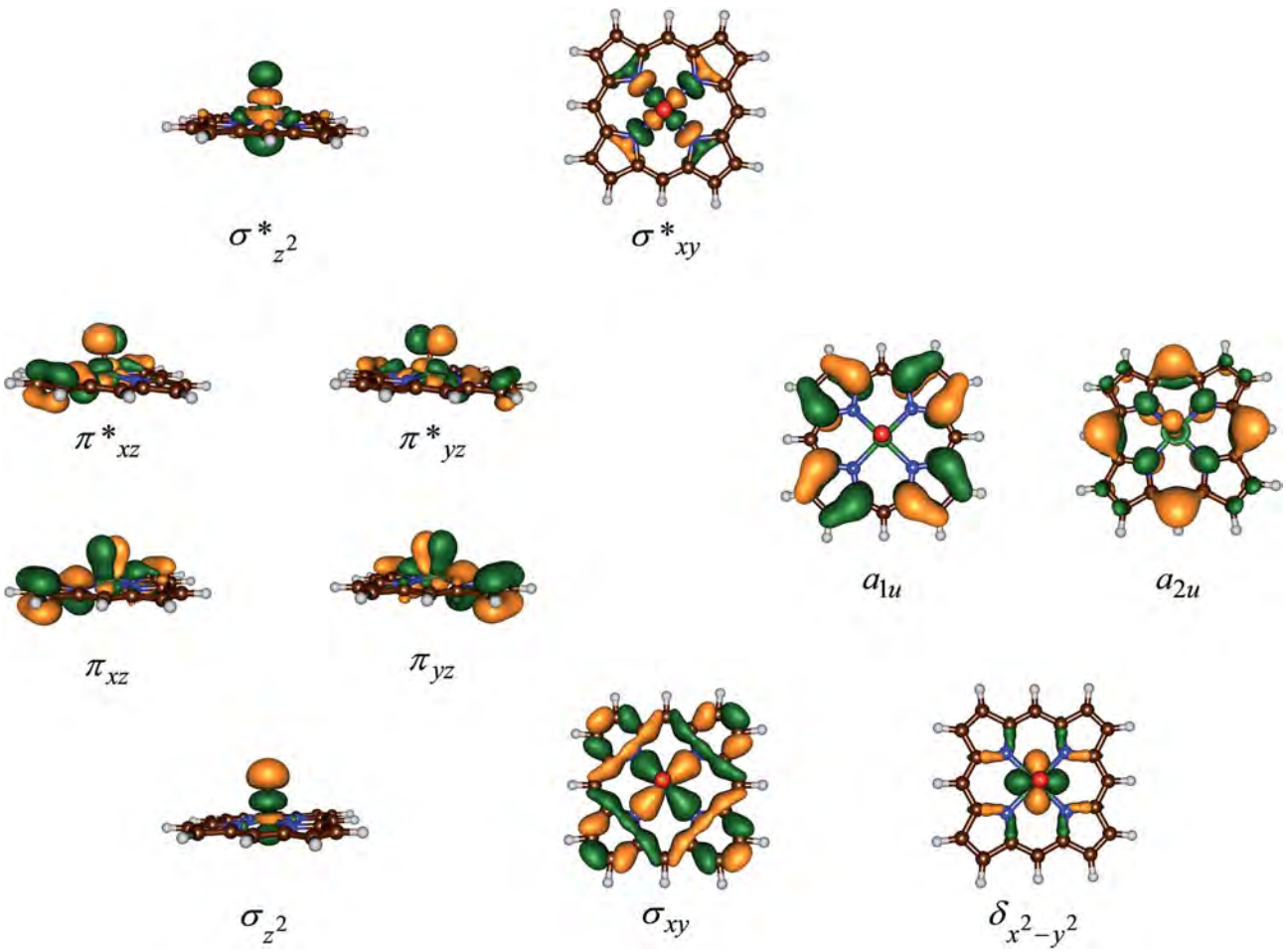

Fig. 3 Molecular valence orbitals of ^{4}A.

This journal is © The Royal Society of Chemistry 2015

Open Access Article. Published on 08 December 2014. Downloaded on 22/01/2015 17:11:53.
This article is licensed under a Creative Commons Attribution 3.0 Unported Licence.

over the orbitals. In addition, states can also be found in various spin states ranging from doublet to quartet and sextet, where we identify the spin state with a superscript in front of the electronic state label. Thus, the electronic state labelled as $^4A_{2u}$ has an overall quartet spin state and singly occupied a_{2u} molecular orbital with overall electronic configuration: $\sigma_{z2}^2\ \sigma_{xy}^2\ \pi_{xz}^2\ \pi_{yz}^2\ \delta_{x2-y2}^2\ \pi_{xz}^{*1}\ \pi_{yz}^{*1}\ a_{1u}^2\ a_{2u}^1$ or in short [core] $\delta_{x2-y2}^2\ \pi_{xz}^{*1}\ \pi_{yz}^{*1}\ a_{1u}^2\ a_{2u}^1$. Similarly, we calculated the doublet spin state ($^2A_{2u}$ state), where the unpaired electron in the a_{2u} orbital is antiferromagnetically coupled to the unpaired electrons in the two π* orbitals: $^2A_{2u}$ = [core] $\delta_{x2-y2}^2\ \pi_{xz}^{*\uparrow}\ \pi_{yz}^{*\uparrow}\ a_{1u}^2\ a_{2u}^{\downarrow}$.

Previous studies with either imidazole, acetonitrile or thiolate as axial ligand,[29,31] showed the $^{4,2}A_{2u}$ states to be close in energy and well below alternative states. However, this was due to considerable mixing of the a_{2u} orbital with the axial ligand orbitals, which obviously is not possible in our chemical system that lacks an axial ligand. However, in an isolated porphyrin macrocycle, the a_{1u} and a_{2u} orbitals are degenerate;[32] therefore, we decided to investigate a range of possible electronic states for the pentacoordinated iron(IV)–oxo porphyrin cation radical system, $[Fe^{IV}(O)(Por^{+\bullet})]^+$. Firstly, we tested the stability of the $^{4,2}A_{2u}$ states and the alternative $^{4,2}A_{1u}$ states with [core] $\delta_{x2-y2}^2\ \pi_{xz}^{*1}\ \pi_{yz}^{*1}\ a_{1u}^1\ a_{2u}^2$ orbital occupation. In addition, we attempted to generate models with the iron in oxidation state iron(V), *i.e.* $^2\Pi_{xz}$ state with occupation [core] $\delta_{x2-y2}^2\ \pi_{xz}^{*1}\ a_{1u}^2\ a_{2u}^2$, or the iron in oxidation state iron(III), *i.e.* the ^4A state with orbital occupation [core] $\delta_{x2-y2}^2\ \pi_{xz}^{*2}\ \pi_{yz}^{*1}\ a_{1u}^1\ a_{2u}^1$ and the $^6\Sigma_{xy,III}$ state with [core] $\delta_{x2-y2}^2\ \pi_{xz}^{*1}\ \pi_{yz}^{*1}\ \sigma_{xy}^{*1}\ a_{1u}^1\ a_{2u}^1$ occupation. However, all our attempts to calculate iron(III) or iron(V) states failed and converged back to lower lying solutions with four electrons on the metal in a formal iron(IV) oxidation state, hence the $^2\Pi_{xz}$, ^4A and $^6\Sigma_{xy,III}$ states are high in energy and inaccessible to our chemical system.

Table 2 summarizes relative energies of optimized geometries of the various electronic spin states as calculated with different DFT methods for ^{2,4,6}**A**. As follows from Table 2 all calculations of **A** give a $^2A_{1u}$ ground state that is nearly degenerate with the corresponding quartet spin state. In general, calculations done at UB3LYP/BS2 and UB3LYP-D3/BS2 give almost identical spin state orderings and relative energies, which shows that dispersion is not a critical component for these chemical structures. Nevertheless, the $^{4,2}A_{2u}$ and $^{4,2}A_{1u}$ states are close in energy and all four states could have a finite lifetime.

Optimized geometries of the $^{4,2}A_{2u}$ and $^{4,2}A_{1u}$ states are given in Fig. 4. Geometrically, no dramatic changes in bond lengths are obtained between the three optimization techniques. A small basis set gives slightly longer Fe–O distances than those found with a triple-ζ basis set. The effect of dispersion is negligible on the optimized geometries: UB3LYP/BS2 and UB3LYP-D3/BS2 give virtually the same chemical structures. Addition of *meso*-substituents to the porphyrin ring such as pentafluorophenyl groups is not expected to dramatically change key bond lengths in the optimized geometries and relative energies of individual spin states.[33] Thus, recent work of the Goldberg group showed that *meso*-substituted manganese–oxo porphyrinoid complexes retained the spin state ordering and converged to a closed-shell singlet manganese(V)–oxo state in all cases.[33a]

The calculations on the low-lying $^{4,2}A_{2u}$ and $^{4,2}A_{1u}$ states reported in Table 2 and Fig. 4 show that geometrically there are very little differences between these states, but the spin state ordering and relative energies are sensitive to the method and basis set. Recent complete active site (CASSCF) and restricted active site (RASSCF) calculations of Pierloot and co-workers[34] calculated the $^{4,2}A_{2u}$ and $^{4,2}A_{1u}$ states of **A** within 1 kcal mol^{-1} of each other with a small preference for the A_{1u} states. However, they also located two low-lying iron(V) states, which we were unable to characterize and for which no experimental evidence exist. Unfortunately, our chemical systems (in particular structure **B**) are too large to attempt calculations using the CASSCF and RASSCF methods; therefore, we decided to continue with UB3LYP instead.

Subsequently, we investigated the substrate epoxidation by $[Fe^{IV}(O)(Por^{+\bullet})]^+$, *i.e.* ^{4}**A**. We find the lowest lying barriers to proceed from the $^4A_{2u}$ state and will focus on those in the following. Previous studies on the epoxidation of olefins by $[Fe^{IV}(O)(Por^{+\bullet})(L)]$ with L = $NCCH_3$ or Cl^- showed that the same trends in reactivity are observed when the Por ligand is replaced by TPFPP,[35] hence the smaller model was used in this study. We investigated substrate epoxidation with a range of olefins:

Table 2 Relative energies of several low-lying electronic states of $[Fe(O)(Por^{+\bullet})]^+$ (**A**)[a]

		A[b]	**A**[c]	**A**[d]
State	Configuration	Δ*E* + ZPE	Δ*E* + ZPE	Δ*E* + ZPE
$^2A_{1u}$	$\delta^2\ \pi_{xz}^{*\uparrow}\ \pi_{yz}^{*\uparrow}\ a_{1u}^{\downarrow}$	0.00	0.00	0.00
$^4A_{1u}$	$\delta^2\ \pi_{xz}^{*\uparrow}\ \pi_{yz}^{*\uparrow}\ a_{1u}^{\uparrow}$	0.71	0.19	0.21
$^2A_{2u}$	$\delta^2\ \pi_{xz}^{*\uparrow}\ \pi_{yz}^{*\uparrow}\ a_{2u}^{\downarrow}$	1.65	3.75	3.80
$^4A_{2u}$	$\delta^2\ \pi_{xz}^{*\uparrow}\ \pi_{yz}^{*\uparrow}\ a_{2u}^{\uparrow}$	1.25	3.42	3.47
$^6A_{2u}$	$\delta^{\uparrow}\ \pi_{xz}^{*\uparrow}\ \pi_{yz}^{*\uparrow}\ \sigma_{xy}^{*\uparrow}\ a_{2u}^{\uparrow}$	9.25	18.68	19.38
$^4\Delta_{xy}$	$\delta^{\uparrow}\ \pi_{xz}^{*\uparrow}\ \pi_{yz}^{*\uparrow}\ \sigma_{xy}^{*\uparrow}\ a_{1u}^{\downarrow}$	9.69	ND	ND
$^4\Delta_{zz}$	$\delta^{\uparrow}\ \pi_{xz}^{*\uparrow}\ \pi_{yz}^{*\uparrow}\ \sigma_{z2}^{*\uparrow}\ a_{2u}^{\downarrow}$	19.53	ND	ND

[a] Relative energies in kcal mol^{-1} with respect to the $^2A_{1u}$ state, ND stands for not determined. [b] Energies obtained at UB3LYP/BS2//UB3LYP/BS1 level of theory. [c] Energies and geometries calculated at UB3LYP/BS2 level of theory. [d] Energies and geometries calculated at UB3LYP-D3/BS2 level of theory.

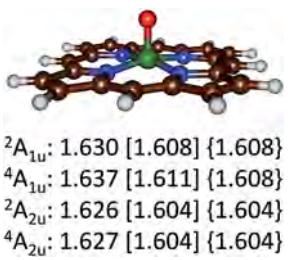

Fig. 4 Optimized geometries of the $^{4,2}A_{2u}$ and $^{4,2}A_{1u}$ states of ^{4,2}**A** as calculated with UB3LYP/BS1 [UB3LYP/BS2] {UB3LYP-D3/BS2} with Fe–O bond lengths in angstroms.

Open Access Article. Published on 08 December 2014. Downloaded on 22/01/2015 17:11:53.
This article is licensed under a Creative Commons Attribution 3.0 Unported Licence.

ethene (**1**), propene (**2**), 1-butene (**3**), *E*-2-butene (**4**), cyclohexene (**5**), 1,3-cyclohexadiene (**6**), styrene (**7**), *trans*-β-methylstyrene (**8**), *Z*-2-butene (**9**) and 2-pinene (**10**). For all substrates we calculated the full potential energy profile from reactants to epoxide products, see ESI,† but for space restrictions we will focus on the rate determining C–O bond formation transition states ($\mathbf{TS}_{CO}$) only. All reactions are concerted with a single C–O activation barrier leading to epoxide product complexes $\mathbf{P}_E$. This is unusual as previous calculations on substrate epoxidation by Cpd I models gave a stepwise mechanism *via* a radical intermediate that *via* a ring-closure barrier was separated from epoxide product complexes.[36] The orientation of the substrate and the strong displacement of the metal from the porphyrin plane are the likely reason for the fact that radical intermediates are saddlepoints here. Thus, the ring-closure barrier on the quartet spin state surface involves an electron transfer from substrate into σ^*_{z2}. The latter orbital in iron–porphyrin complexes with axial ligand, *e.g.* thiolate, contains a strong contribution from axial ligand orbitals ($3p_z$) and therefore is high in energy. Since our particular system lacks an axial ligand, the σ^*_{z2} orbital is considerably lower in energy and as a consequence the lifetime of the radical intermediate is reduced and the reaction to form products is now concerted.

Fig. 5 gives the optimized geometries of the C–O activation transition states ($\mathbf{TS}_{CO}$) for all substrates. Generally, the transition states occur early with a long C–O distance and relatively short Fe–O distance that has not dramatically changed from what it was in the iron(IV)–oxo porphyrin cation radical state. As expected the metal is considerably displaced from the plane through the four nitrogen atoms of the porphyrin ring by as much as 0.268–0.299 Å. These transition states bear resemblance to substrate epoxidation barriers calculated previously for P450 Cpd I reactions with olefins.[36] Electronically, all transition states are accomplished by single electron transfer from the substrate into the a_{2u} orbital and the formation of an $[Fe^{IV}(OSub)(TPFPP)]^+$ transition state with orbital occupation [core] $\delta_{x2-y2}^2\ \pi^{*1}_{xz}\ \pi^{*1}_{yz}\ a_{1u}^2\ a_{2u}^2\ \phi_{Sub}^1$ with ϕ_{Sub} a radical on the substrate group.

Discussion

The present work gives a detailed and extensive overview on the reactivity of iron(IV)–oxo porphyrin cation radical systems with a test-set of olefins. We determined rate constants and measured product ion distributions in the gas phase using FT-ICR MS. This comprehensive set of transition metal containing reactivities is unique and will enable computation to benchmark and calibrate its methods effectively. This is particularly important for transition metal complexes, such as iron(IV)-oxo species, where the reproducibility of the computational (DFT) methods sometimes varies strongly depending on the density functional method used, the basis set, environmental perturbations, dispersion effects *etc.*[37] In this work, we supplemented the experimental studies with a series of preliminary DFT calculations for two reasons: (i) to validate and calibrate computational methods against experiment; (ii) to establish the physicochemical properties that influence the rate constant of the chemical reaction.

Let us first start with a comparison of the experimental and computational reaction rates. As FT-ICR MS experiments are being performed at very low pressures, these experimental conditions are close to Ideal Gas conditions with very few

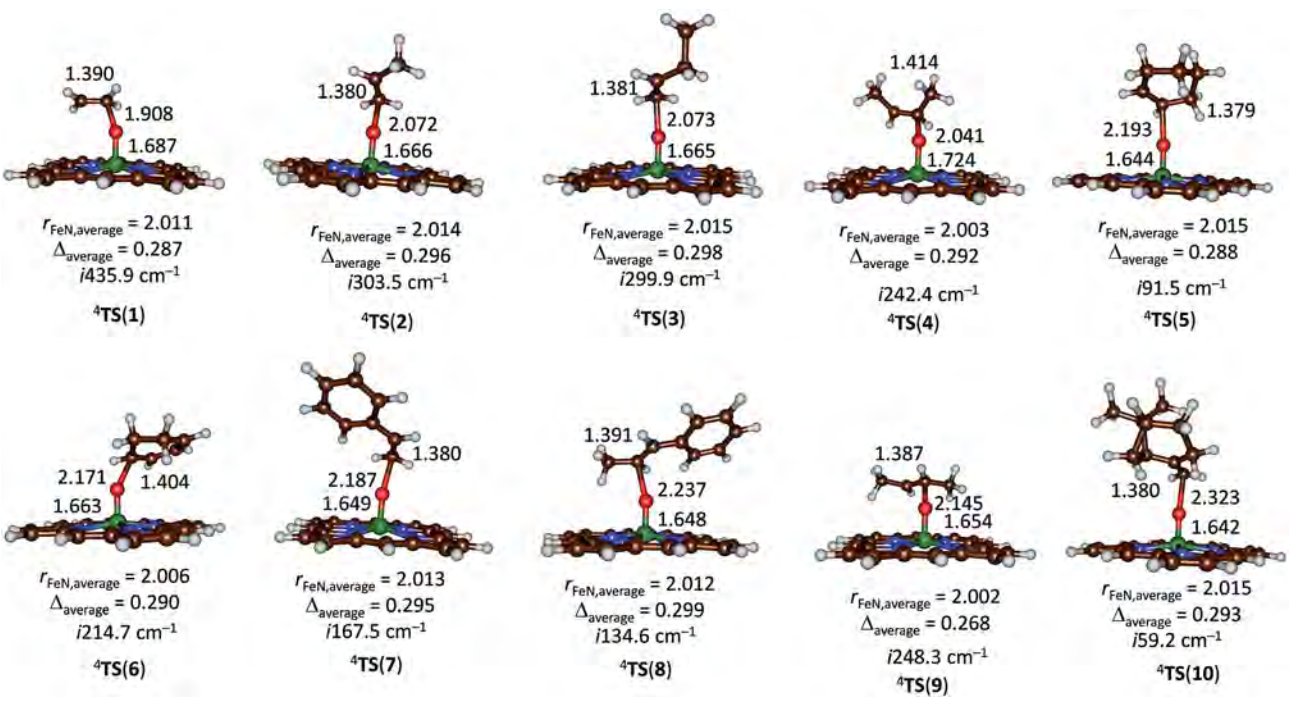

Fig. 5 UB3LYP/BS1 optimized geometries of epoxidation transition states with bond lengths in angstroms.

 This journal is © The Royal Society of Chemistry 2015

Open Access Article. Published on 08 December 2014. Downloaded on 22/01/2015 17:11:53.
This article is licensed under a Creative Commons Attribution 3.0 Unported Licence.

molecular collisions per second. In the kinetic study of ion-molecule reactions in the gas phase one needs to consider that thermal equilibration of the reacting system with the environment is in general not granted. On the contrary, when small species react at low pressures, the absence of thermalizing collisions leads to non-equilibrium energy distributions. In the absence of solvation, the double-well potential model first proposed by Brauman in 1977 to account for the kinetic behaviour of displacement reactions by anionic nucleophiles predicts that the energy of the intermediate and transition state must lie below the energy of the combined reactants.[38] Because at low pressure the intermediates cannot be stabilized by unreactive collisions, determining the transition state energy is less straightforward than in solution. However, the kinetics results presently reported deal with a relatively large reactant ion that effectively establishes thermal equilibrium with the environment through coupling with the background radiation field allowed by the several low frequency infrared modes of the iron(IV)–oxo macrocyclic ligand complex. This condition is responsible, for example, for the consistency between the kinetics of NO ligand addition to iron(II/III) porphyrin complexes and the equilibrium data independently established through equilibrium measurements.[25] Because of these considerations, the notion can be adopted that the presently investigated systems are in prevailing thermal equilibrium with the environment and reaction kinetics can be interpreted within the framework of transition state theory. Consequently, reaction rates represent bimolecular reactions and as such they should compare to computationally determined reaction rates well.

The experimental rate constants (Table 1) were converted into free energy units *via* $-RT \ln k_{exp}$, with R the gas constant and T the temperature, using transition state theory and plotted against the calculated enthalpy of activation for the same substrates, see Fig. 6. Although only a limited computational study is reported here, when we calculate the deviation between experiment and theory for each data point, we find an average difference between experiment and theory of 1.5 kcal mol^{-1} with a standard deviation of 3.4 kcal mol^{-1}. As such, the DFT methods used here reproduce the trends obtained from experimental enthalpies of activation well and the linearity and reproducibility of the calculations is well within the typical error reported for DFT calculations using this method of about 5 kcal mol^{-1}.[39] There is, however, a large systematic error as well as a relatively large standard deviation that require further studies. Note that the experimental data in Fig. 6 refers to free energies of activation, whereas the computational results are enthalpy changes instead. The systematic error between experiment and theory contains entropic corrections to the energy.

Subsequently, we investigated the origin of the rate constant, and in particular, the physical and chemical properties of the substrate and oxidant that determine the reaction mechanism and the enthalpy of activation of an epoxidation reaction. Previous studies on heteroatom oxidation and double bond epoxidation by P450 enzymes implicated a correlation between the natural logarithm of the rate constant with the ionization energy of the substrate.[12d,e,28,40] To find out whether the data in Table 1 follow these trends as well, we plot $RT \ln k_{exp}$ *versus* experimentally known ionization energies,[24] in Fig. 7. The set of data shown in Table 1 and Fig. 7 gives a linear correlation between the natural logarithm of the rate constant and the ionization energy of the substrate with an $R^2 = 0.96$. Fig. 7b displays the correlation between the DFT calculated enthalpy of

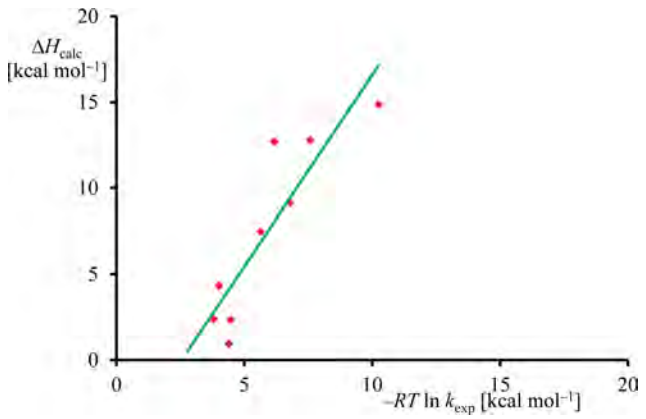

Fig. 6 Correlation between experimental and computational barrier heights.

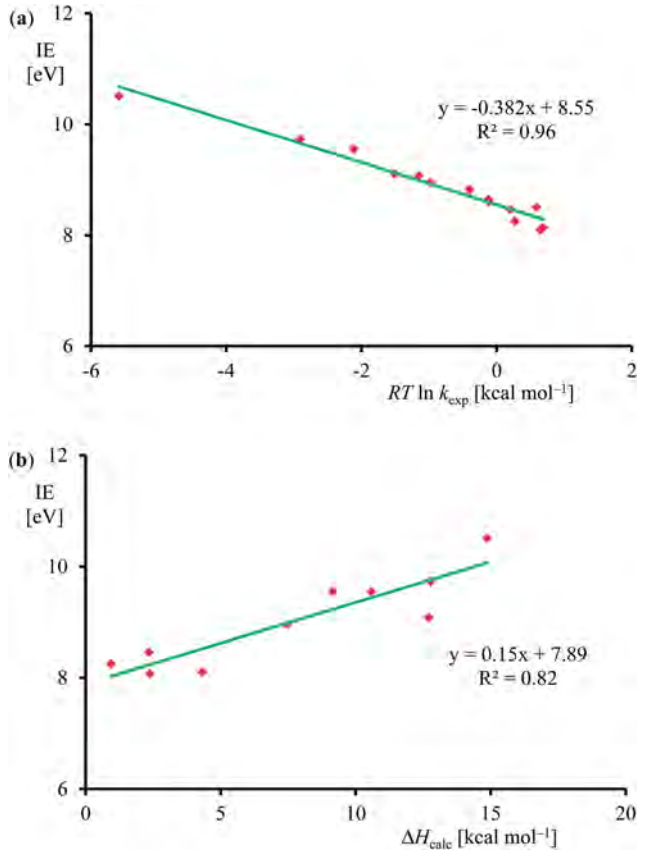

Fig. 7 (a) Correlation between experimentally determined $RT \ln k_{exp}$ (for raw data, see Table 1) *versus* known ionization energies (IE). (b) Correlation between calculated epoxidation activation enthalpy (in kcal mol^{-1}) and experimental ionization energy for the substrates in Fig. 5.

Open Access Article. Published on 08 December 2014. Downloaded on 22/01/2015 17:11:53.
This article is licensed under a Creative Commons Attribution 3.0 Unported Licence.

activation of the reaction of $[Fe^{IV}(O)(Por^{+\bullet})]^+$ with olefins. In agreement with the experimental trends given in part (a) of Fig. 7 also the computational trends link the natural logarithm of the rate constant to the ionization energy of the substrate. Clearly, the key physicochemical property that drives the reaction mechanism and affects the rate constant of substrate epoxidation by iron(IV)–oxo porphyrin cation radical complexes is the ionization energy of the substrate.

In order to explain the experimental and computational trends in the reaction mechanisms, we devised a valence bond (VB) curve crossing diagram, which is schematically depicted in Fig. 8. This diagram starts bottom left with the reactant configuration of $[Fe^{IV}(O)(TPFPP^{+\bullet})]^+$ in electronic configuration $\pi_{xz}^2\,\pi_{yz}^2\,\delta_{x2-y2}^2\,\pi_{xz}^{*1}\,\pi_{yz}^{*1}\,a_{2u}^1$. The π and π* electrons along the FeO bond are identified with dots in the VB diagram and due to occupation of $\pi_{xz}^2\,\pi_{xz}^{*1}$ there are three dots on the left-hand-side of the Fe–O bond. In addition, there are three electrons in the π_{yz} and π_{yz}^* orbitals, which are identified with the other three dots on the right-hand-side of the Fe–O bond. Furthermore, the oxidant has a radical on the porphyrin ring for single occupation of the a_{2u} molecular orbital. The substrate double bond is also highlighted with four electrons spread out over the interaction. Upon approach of the substrate on the iron(IV)–oxo species a radical intermediate is formed that has a single bond between the oxygen and carbon atoms and a doubly occupied a_{2u} orbital.

In VB theory the electronic configuration in the reactant complex (Ψ_R) connects to an excited state in the product geometry (Ψ_P^*) as shown with the blue line in Fig. 8. At the same time the product electronic configuration (Ψ_P) connects to an excited state in the reactant geometry (Ψ_R^*), black line in Fig. 8. These two VB curves cross and lead to an avoided crossing and a transition state for the C–O bond formation with barrier $\Delta E^{\ddagger}$. The barrier height is linearly proportional to the curve crossing energy, which in its own right is a fraction of the excitation energy (G_H) from the reactant wave function to the product wave function in the geometry of the reactants, *i.e.* for $\Psi_R \rightarrow \Psi_R^*$. The difference in VB structures for Ψ_R and Ψ_R^* thereby should give a reflection of the key electron transfer/migrations upon product formation. Moreover, based on the excitation energy, the factors that determine the barrier height can be predicted.

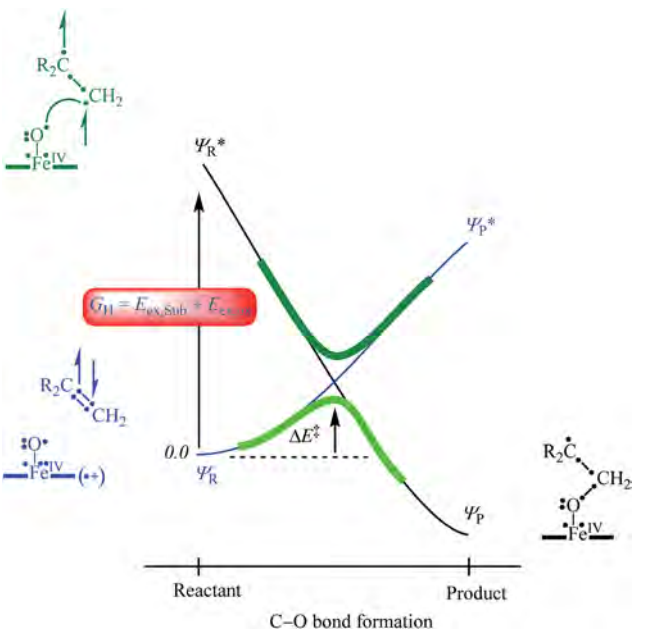

Fig. 8 VB curve crossing diagram for the C–O bond formation step in olefin epoxidation ($R_2C{=}CH_2$) by $[Fe^{IV}(O)(TPFPP^{+\bullet})]^+$. Valence electrons are identified with a dot and lines (curved and straight) in the VB structures represent bonds.

An analysis of the differences between the reactant and product wave functions in the reactant geometry reveals the following information: First of all, a comparison of the VB structures of Ψ_R and Ψ_R^* shows that the electrons in the π-bond of the olefin are singlet paired in the ground state and triplet coupled in the excited state, hence the excitation energy G_H includes the π–π* electron excitation in the substrate, $E_{ex,Sub}$. Generally, the first ionization potential of an olefin corresponds to the removal of an electron from a π-orbital, and, hence, is proportional to the π–π* excitation energy. Indeed, our experimentally and computationally determined barrier heights correlate linearly with the ionization energy of the olefin, and therefore support the VB model.

One of the electrons originating from the π-bond of the olefin forms a bond with the π_{xz}^* electron along the FeO bond, to create the C–O bonding pair of electrons. This means that the π_{xz}/π_{xz}^* pair of orbitals during the reaction splits back into individual atomic orbitals namely $3d_{xz}$(Fe) and $2p_x$(O). The $2p_x$(O) electron pairs with the electron from the substrate, while one of the electrons of the $3d_{xz}$(Fe) orbital is transferred into the a_{2u} orbital through internal excitation/rehybridization of the oxidant, $E_{ex,ox}$. The promotion gap, G_H, therefore, will be proportional to the π–π* excitation in the substrate and the $3d_{xz}$ to a_{2u} electron transfer in the oxidant: $G_H = E_{ex,Sub} + E_{ex,ox}$. Obviously, since the ionization energy represents the energy to remove an electron from a π-type orbital of an olefin, this will imply a linear correlation between the first excited state and the ionization energy of the substrate.[28] The VB diagram, therefore, confirms a linear correlation between the ionization energy of the substrate and the C–O bond formation enthalpy of activation as shown above.

Although, the oxygen atom transfer reaction between $[Fe^{IV}(O)(TPFPP^{+\bullet})]^+$ and an olefin could lead to either epoxide or hydroxylated products, unfortunately the FT-ICR MS experiments cannot distinguish the two. Thus, several substrates in Scheme 2 and Table 1 contain aliphatic groups that in a reaction with an iron(IV)–oxo group can be converted into an alcohol. A correlation between the rate constant of oxygen atom transfer and the ionization energy, Fig. 7a, of the olefin provides indirect experimental evidence that all reactions lead to epoxidation products. In fact, hydrogen atom abstraction reactions should not correlate with the ionization potential of the substrate, but were shown to be proportional to the strength of the C–H bond of the substrate that is formed.[12e,40] To test that the rate constants do not correlate with the bond dissociation energy (BDE_{CH}) of the C–H bond of the substrate that is broken, we plot

 This journal is © The Royal Society of Chemistry 2015

Open Access Article. Published on 08 December 2014. Downloaded on 22/01/2015 17:11:53.
This article is licensed under a Creative Commons Attribution 3.0 Unported Licence.

in Fig. 9 calculated BDE_{CH} and barrier heights of selected olefins, namely propene, *Z*-2-butene, *E*-2-butene, cyclohexene and 1,3-cyclohexadiene. As can be seen from Fig. 9, no correlation between BDE_{CH} and barrier height exists, and, therefore, hydrogen atom abstraction is not the rate determining step in the reaction mechanism. Further evidence that hydrogen atom abstraction reactions can be ruled out here comes from kinetic isotope effect (KIE) studies. We measured the rate constant of oxygen atom transfer with cyclohexene and cyclohexene-d_{10} and determined a KIE $= k_H/k_D \sim 1$ (Table 1). Consequently, the oxygen atom transfer is unlikely to proceed with an initial hydrogen atom abstraction and double bond epoxidation will be the dominant pathway.

The experimental trends, therefore, provide the first indirect experimental evidence that in the gas-phase the regioselectivity of double bond epoxidation *versus* aliphatic hydroxylation will be in favour of the epoxidation pathway. This implies that in enzymatic systems, such as the cytochromes P450, the shape and size of the substrate binding pocket will influence the regioselectivity of hydroxylation over epoxidation and can change the natural preference away from epoxidation.

Finally, the calculations presented in this work obviously refer to gas-phase results and hence correlate well with gas-phase mass spectrometric data. In order to further establish that the work can be extrapolated to solution phase, we did a series of single point calculations using the polarized continuum model with a dielectric constant of $\varepsilon = 4.7$ to mimic a solution. The obtained correlation between solvent corrected free energies of activation of epoxidation reactions by $[Fe^{IV}(O)(Por^{+\bullet})]^+$ is plotted against the solvent corrected ionization energy of all substrates in Fig. S1, ESI.† Even in solvent, the linear trend in the correlation between free energy of activation and ionization energy is retained, therefore, we expect to be able to extrapolate our results to the solution phase as well.

Conclusions

In this work we report a comprehensive combined mass spectrometric and computational study on substrate epoxidation by iron(IV)–oxo porphyrin cation radical complexes in the gas phase. We present a novel method to synthesize $[Fe^{IV}(O)(TPFPP^{+\bullet})]^+$ in the gas phase at low pressure. Furthermore, we report a large set of experimentally derived rate constants and product distributions. All olefins undergo oxygen atom transfer, whereas compounds with low ionization energy also give a certain degree of hydride transfer and charge transfer reactions. Our experimentally determined reaction rates correlate linearly with the ionization potential of the substrate and show that the electron transfer from substrate to oxidant is rate determining. A thorough computational survey has confirmed the suggested mechanism and provides a rationale for the observed trend in the rate constants. Moreover, the work highlights a regioselective epoxidation over hydroxylation in the gas phase.

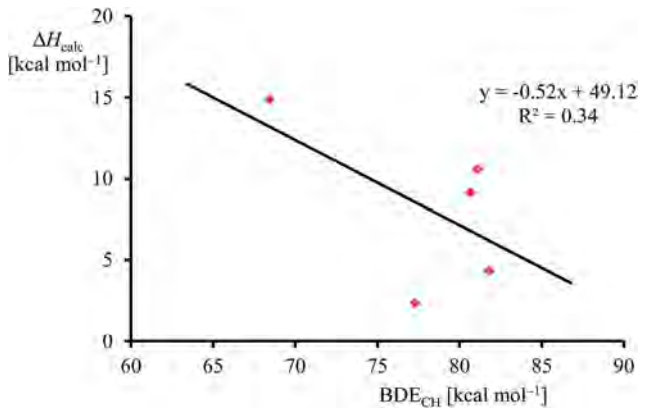

Fig. 9 Correlation between calculated epoxidation activation enthalpy (in kcal mol^{-1}) and BDE_{CH} for the substrates.

Acknowledgements

MAS thanks the Petroleum Technology Development Fund for a studentship. The National Service of Computational Chemistry Software (NSCCS) is thanked for providing valuable cpu time to SdV. DK acknowledges the Department of Science and Technology (New Delhi) for a Ramanujan Fellowship. MEC and SF thank the Università degli Studi di Roma La Sapienza for support.

Notes and references

1 (*a*) M. Sono, M. P. Roach, E. D. Coulter and J. H. Dawson, *Chem. Rev.*, 1996, **96**, 2841; (*b*) J. T. Groves, *Proc. Natl. Acad. Sci. U. S. A.*, 2003, **100**, 3569; (*c*) *Cytochrome P450: Structure, Mechanism and Biochemistry*, ed. P. R. Ortiz de Montellano, Kluwer Academic/Plenum Publishers, New York, 3rd edn, 2004; (*d*) I. G. Denisov, T. M. Makris, S. G. Sligar and I. Schlichting, *Chem. Rev.*, 2005, **105**, 2253; (*e*) *Handbook of Porphyrin Science*, ed. K. M. Kadish, K. M. Smith and R. Guilard, World Scientific, New Jersey, 2010; (*f*) P. R. Ortiz de Montellano, *Chem. Rev.*, 2010, **110**, 932; (*g*) E. O'Reilly, V. Koehler, S. Flitsch and N. Turner, *Chem. Commun.*, 2011, **47**, 2490; (*h*) G. Grogan, *Curr. Opin. Chem. Biol.*, 2011, **15**, 241.

2 (*a*) J. T. Groves, Models and Mechanisms of Cytochrome P450 Action, in *Cytochrome P450: Structure, Mechanism and Biochemistry*, ed. P. R. Ortiz de Montellano, Kluwer Academic/Plenum Publishers, New York, 3rd edn, 2005, ch. 1, pp. 1–44; (*b*) Y. Watanabe, H. Nakajima and T. Ueno, *Acc. Chem. Res.*, 2007, **40**, 554.

3 D. R. Nelson, *Methods Mol. Biol.*, 2006, **320**, 1.

4 (*a*) T. L. Poulos, B. C. Finzel, I. C. Gunsalus, G. C. Wagner and J. Kraut, *J. Biol. Chem.*, 1985, **260**, 6122; (*b*) T. L. Poulos, B. C. Finzel and A. J. Howard, *Biochemistry*, 1986, **25**, 5314.

5 J. B. Johnston, P. M. Kells, L. M. Podust and P. R. Ortiz de Montellano, *Proc. Natl. Acad. Sci. U. S. A.*, 2009, **106**, 20687.

6 (*a*) B. Meunier, S. P. de Visser and S. Shaik, *Chem. Rev.*, 2004, **104**, 3947; (*b*) *Iron-containing enzymes: Versatile catalysts of hydroxylation reaction in nature*, ed. S. P. de Visser and D. Kumar, RSC Publishing, Cambridge, UK, 2011.

7 J. Rittle and M. T. Green, *Science*, 2010, **330**, 9337.

Open Access Article. Published on 08 December 2014. Downloaded on 22/01/2015 17:11:53.
This article is licensed under a Creative Commons Attribution 3.0 Unported Licence.

8 (*a*) K. Auclair, Z. Hu, D. M. Little, P. R. Ortiz de Montellano and J. T. Groves, *J. Am. Chem. Soc.*, 2002, **124**, 6020; (*b*) P. Lafite, F. André, D. C. Zeldin, P. M. Dansette and D. Mansuy, *Biochemistry*, 2007, **46**, 10237; (*c*) T. S. Dowers, D. A. Rock, D. A. Rock and J. P. Jones, *J. Am. Chem. Soc.*, 2004, **126**, 8868; (*d*) H. L. R. Cooper and J. T. Groves, *Arch. Biochem. Biophys.*, 2011, **507**, 111; (*e*) K. M. Roberts and J. P. Jones, *Chem.–Eur. J.*, 2010, **16**, 8096.

9 See, *e.g.*, (*a*) J. T. Groves and R. S. Myers, *J. Am. Chem. Soc.*, 1983, **105**, 5791; (*b*) J. T. Groves and Y. Watanabe, *J. Am. Chem. Soc.*, 1986, **108**, 507; (*c*) D. Ostović and T. C. Bruice, *J. Am. Chem. Soc.*, 1989, **111**, 6511; (*d*) J. T. Groves, Z. Gross and M. K. Stern, *Inorg. Chem.*, 1994, **33**, 5065; (*e*) N. Stephenson and A. T. Bell, *Inorg. Chem.*, 2006, **45**, 2758; (*f*) N. Hessenauer-Ilicheva, A. Franke, D. Meyer, W.-D. Woggon and R. van Eldik, *J. Am. Chem. Soc.*, 2007, **129**, 12473; (*g*) R. Mas-Balleste and L. Que Jr, *J. Am. Chem. Soc.*, 2007, **129**, 15964; (*h*) P. Comba and G. Rajaraman, *Inorg. Chem.*, 2008, **47**, 78; (*i*) P. C. A. Bruijnincx, I. L. C. Buurmans, S. Gosiewska, M. A. H. Moelands, M. Lutz, A. L. Spek, G. van Koten and R. J. M. Klein Gebbink, *Chem.–Eur. J.*, 2008, **14**, 1228; (*j*) J. F. Hull, E. L. O. Sauer, C. D. Incarvito, J. W. Faller, G. W. Brudvig and R. H. Crabtree, *Inorg. Chem.*, 2009, **48**, 488; (*k*) A. McGown, W. D. Kerber, H. Fujii and D. P. Goldberg, *J. Am. Chem. Soc.*, 2009, **131**, 8040; (*l*) A. Company, Y. Feng, M. Güell, X. Ribas, J. M. Luis, L. Que Jr and M. Costas, *Chem.–Eur. J.*, 2009, **15**, 3359; (*m*) A. Franke, M. Wolak and R. van Eldik, *Chem.–Eur. J.*, 2009, **15**, 10182; (*n*) N. Hessenauer-Ilicheva, A. Franke, M. Wolak, T. Higuchi and R. van Eldik, *Chem.–Eur. J.*, 2009, **15**, 12447.

10 (*a*) Z. Gross and S. Nimri, *Inorg. Chem.*, 1994, **33**, 1731; (*b*) Z. Gross, *J. Biol. Inorg. Chem.*, 1996, **1**, 368; (*c*) K. Czarnecki, S. Nimri, Z. Gross, L. M. Proniewicz and J. R. Kincaid, *J. Am. Chem. Soc.*, 1996, **118**, 2929.

11 (*a*) A. G. Marshall, C. L. Hendrickson and G. S. Jackson, *Mass Spectrom. Rev.*, 1998, **17**, 1; (*b*) J. Roithová and D. Schröder, *Chem. Rev.*, 2010, **110**, 1170; (*c*) N. M. M. Nibbering, *Mass Spectrom. Rev.*, 2006, **25**, 962.

12 (*a*) M. E. Crestoni and S. Fornarini, *Inorg. Chem.*, 2005, **44**, 5379; (*b*) M. E. Crestoni and S. Fornarini, *Inorg. Chem.*, 2007, **46**, 9018; (*c*) M. E. Crestoni, S. Fornarini, F. Lanucara, J. J. Warren and J. M. Mayer, *J. Am. Chem. Soc.*, 2010, **132**, 4336; (*d*) M. E. Crestoni, S. Fornarini and F. Lanucara, *Chem.–Eur. J.*, 2009, **15**, 7863; (*e*) F. Lanucara and M. E. Crestoni, *Chem.–Eur. J.*, 2011, **17**, 12092.

13 H. Saltzman and J. G. Sharefkin, *Organic Syntheses*, Wiley, New York, 1973, vol. 5, p. 658, Collect.

14 (*a*) M. Meot-Ner, in *Gas Phase Ion Chemistry*, ed. M. T. Bowers, Academic Press, New York, 1979, vol. 1; (*b*) J. E. Bartmess and R. M. Georgiadis, *Vacuum*, 1983, **33**, 149.

15 T. Su and W. J. Chesnavich, *J. Chem. Phys.*, 1982, **76**, 5183.

16 B. Chiavarino, R. Cipollini, M. E. Crestoni, S. Fornarini, F. Lanucara and A. Lapi, *J. Am. Chem. Soc.*, 2008, **130**, 3208.

17 (*a*) Schrodinger, *Jaguar, version 7.9*, LLC, New York, NY, 2011; (*b*) M. J. Frisch, *Gaussian 09, revision D.01*, Gaussian, Inc., Wallingford, CT, 2004.

18 (*a*) R. Latifi, M. A. Sainna, E. V. Rybak-Akimova and S. P. de Visser, *Chem.–Eur. J.*, 2013, **19**, 4058; (*b*) M. G. Quesne, R. Latifi, L. E. Gonzalez-Ovalle, D. Kumar and S. P. de Visser, *Chem.–Eur. J.*, 2014, **20**, 435.

19 (*a*) A. D. Becke, *J. Chem. Phys.*, 1993, **98**, 5648; (*b*) C. Lee, W. Yang and R. G. Parr, *Phys. Rev. B: Condens. Matter Mater. Phys.*, 1988, **37**, 785.

20 (*a*) A. K. Vardhaman, C. V. Sastri, D. Kumar and S. P. de Visser, *Chem. Commun.*, 2011, **47**, 11044; (*b*) A. K. Vardhaman, P. Barman, S. Kumar, C. V. Sastri, D. Kumar and S. P. de Visser, *Angew. Chem., Int. Ed.*, 2013, **52**, 12288; (*c*) S. Kumar, A. S. Faponle, P. Barman, A. K. Vardhaman, C. V. Sastri, D. Kumar and S. P. de Visser, *J. Am. Chem. Soc.*, 2014, **136**, 17102.

21 P. J. Hay and W. R. Wadt, *J. Chem. Phys.*, 1985, **82**, 270.

22 S. Grimme, J. Antony, S. Ehrlich and H. Krieg, *J. Chem. Phys.*, 2010, **132**, 154104.

23 S. P. de Visser, *J. Am. Chem. Soc.*, 2010, **132**, 1087.

24 S. G. Lias, J. E. Bartmess, J. F. Liebman, J. L. Holmes, R. D. Levin and W. G. Mallard, in *Ion Energetics Data in NIST Chemistry WebBook*, ed. P. J. Linstrom and W. G. Mallard, National Institute of Standards and Technology, Gaithersburg, MD, 20899, http://webbook.nist.gov, NIST Standard Reference Database Number 69, retrieved in September 2014.

25 F. Angelelli, B. Chiavarino, M. E. Crestoni and S. Fornarini, *J. Am. Soc. Mass Spectrom.*, 2005, **16**, 589.

26 S. P. de Visser, *Inorg. Chem.*, 2006, **45**, 9551.

27 (*a*) R. E. White, J. T. Groves and G. A. McClusky, *Acta Biol. Med. Ger.*, 1979, **38**, 475; (*b*) R. T. Ruettinger and A. J. Fulco, *J. Biol. Chem.*, 1981, **256**, 5728; (*c*) J. T. Groves and D. V. Subramanian, *J. Am. Chem. Soc.*, 1984, **106**, 2177; (*d*) J. T. Groves, G. E. Avaria-Neisser, K. M. Fish, M. Imachi and R. L. Kuczkowski, *J. Am. Chem. Soc.*, 1986, **108**, 3837; (*e*) J. F. Bartoli, O. Brigaud, P. Battioni and D. Mansuy, *J. Chem. Soc., Chem. Commun.*, 1991, 440; (*f*) T. Ohno, N. Suzuki, T. Dokoh, Y. Urano, K. Kikuchi, M. Hirobe, T. Higuchi and T. Nagano, *J. Inorg. Biochem.*, 2000, **82**, 123; (*g*) S. Yoshioka, S. Takahashi, K. Ishimori and I. Morishima, *J. Inorg. Biochem.*, 2000, **81**, 141.

28 S. P. de Visser, F. Ogliaro, P. K. Sharma and S. Shaik, *J. Am. Chem. Soc.*, 2002, **124**, 11809.

29 (*a*) M. T. Green, *J. Am. Chem. Soc.*, 1999, **121**, 7939; (*b*) F. Ogliaro, S. P. de Visser, S. Cohen, J. Kaneti and S. Shaik, *ChemBioChem*, 2001, **11**, 848.

30 J. H. Dawson, R. H. Holm, J. R. Trudell, G. Barth, R. E. Linder, E. Bunnenberg, C. Djerassi and S. C. Tang, *J. Am. Chem. Soc.*, 1976, **98**, 3707.

31 (*a*) S. P. de Visser, S. Shaik, P. K. Sharma, D. Kumar and W. Thiel, *J. Am. Chem. Soc.*, 2003, **125**, 15779; (*b*) T. Kamachi and K. Yoshizawa, *J. Am. Chem. Soc.*, 2003, **125**, 4652; (*c*) C. M. Bathelt, J. Zurek, A. J. Mulholland and J. N. Harvey, *J. Am. Chem. Soc.*, 2005, **127**, 12900; (*d*) S. P. de Visser, *J. Phys. Chem. A*, 2005, **109**, 11050; (*e*) S. P. de Visser, L. Tahsini and W. Nam, *Chem.–Eur. J.*, 2009, **15**, 5577; (*f*) R. Lonsdale, J. Oláh, A. J. Mulholland and J. N. Harvey, *J. Am. Chem. Soc.*, 2011, **133**, 15464; (*g*)

 This journal is © The Royal Society of Chemistry 2015

Open Access Article. Published on 08 December 2014. Downloaded on 22/01/2015 17:11:53.
This article is licensed under a Creative Commons Attribution 3.0 Unported Licence.

H. Isobe, S. Yamanaka, M. Okumura, K. Yamaguchi and J. Shimada, *J. Phys. Chem. B*, 2011, **115**, 10730.

32 A. Ghosh, *Acc. Chem. Res.*, 1998, **31**, 189.

33 (*a*) H. M. Neu, M. G. Quesne, T. Yang, K. A. Prokop-Prigge, K. M. Lancaster, J. Donohoe, S. DeBeer, S. P. de Visser and D. P. Goldberg, *Chem.–Eur. J.*, 2014, **20**, 14584; (*b*) F. Lanucara, B. Chiavarino, M. E. Crestoni, D. Scuderi, R. K. Sinha, P. Maitre and S. Fornarini, *Inorg. Chem.*, 2011, **50**, 4445.

34 M. Radoń, E. Broclawic and K. Pierloot, *J. Chem. Theory Comput.*, 2011, **7**, 898.

35 (*a*) D. Kumar, L. Tahsini, S. P. de Visser, H. Y. Kang, S. J. Kim and W. Nam, *J. Phys. Chem. A*, 2009, **113**, 11713; (*b*) D. Kumar, R. Latifi, S. Kumar, E. V. Rybak-Akimova, M. A. Sainna and S. P. de Visser, *Inorg. Chem.*, 2013, **52**, 7968.

36 (*a*) S. P. de Visser, F. Ogliaro, N. Harris and S. Shaik, *J. Am. Chem. Soc.*, 2001, **123**, 3037; (*b*) S. P. de Visser, F. Ogliaro and S. Shaik, *Angew. Chem., Int. Ed.*, 2001, **40**, 2871; (*c*) S. P. de Visser, F. Ogliaro, P. K. Sharma and S. Shaik, *Angew. Chem., Int. Ed.*, 2002, **41**, 1947; (*d*) D. Kumar, B. Karamzadeh, G. N. Sastry and S. P. de Visser, *J. Am. Chem. Soc.*, 2010, **132**, 7656; (*e*) D. Kumar, S. P. de Visser and S. Shaik, *Chem.–Eur. J.*, 2005, **11**, 2825.

37 See, *e.g.*, (*a*) A. Ghosh and P. R. Taylor, *Curr. Opin. Chem. Biol.*, 2003, **7**, 113; (*b*) M. Swart, A. R. Groenhof, A. W. Ehlers and K. Lammertsma, *J. Phys. Chem. A*, 2004, **108**, 5479; (*c*) S. P. de Visser, M. G. Quesne, B. Martin, P. Comba and U. Ryde, *Chem. Commun.*, 2014, **50**, 262.

38 M. L. Chabinyc, S. L. Craig, C. K. Regan and J. I. Brauman, *Science*, 1998, **279**, 1882.

39 (*a*) Y. Zhao and D. G. Truhlar, *Acc. Chem. Res.*, 2008, **41**, 157; (*b*) T. Schwabe and S. Grimme, *Acc. Chem. Res.*, 2008, **41**, 569; (*c*) T. Weymuth, E. P. A. Couzijn, P. Chen and M. Reiher, *J. Chem. Theory Comput.*, 2014, **10**, 3092.

40 Y. Watanabe, T. Iyanagi and S. Oae, *Tetrahedron Lett.*, 1980, **21**, 3685.

JACS
JOURNAL OF THE AMERICAN CHEMICAL SOCIETY
Article
pubs.acs.org/JACS

Long-Range Electron Transfer Triggers Mechanistic Differences between Iron(IV)-Oxo and Iron(IV)-Imido Oxidants

Suresh Kumar,[†] Abayomi S. Faponle,[‡] Prasenjit Barman,[⊥] Anil Kumar Vardhaman,[⊥] Chivukula V. Sastri,*[,⊥] Devesh Kumar,*[,†] and Sam P. de Visser*[,‡]

[†]Department of Applied Physics, School for Physical Sciences, Babasaheb Bhimrao Ambedkar University, Vidya Vihar, Rae Bareilly Road, Lucknow, 226025 Uttar Pradesh, India

[⊥]Department of Chemistry, Indian Institute of Technology Guwahati, Assam 781039, India

[‡]Manchester Institute of Biotechnology and School of Chemical Engineering and Analytical Science, The University of Manchester, 131 Princess Street, Manchester M1 7DN, United Kingdom

Supporting Information

ABSTRACT: Nature often utilizes molecular oxygen for oxidation reactions through monoxygenases and dioxygenases. In many of these systems, a high-valent iron(IV)-oxo active species is found. In recent years, evidence has accumulated of possible iron(IV)-imido and iron(V)-nitrido intermediates in enzymatic catalysis, although little is known about their activity. In this work, we report a detailed combined kinetics and computational study on the difference in reactivity and chemical properties of nonheme iron(IV)-oxo compared with iron(IV)-tosylimido. We show here that iron(IV)-tosylimido complex is much more reactive with sulfides than the corresponding iron(IV)-oxo complex; however, the reverse trend is obtained for hydrogen atom abstraction reactions. The latter proceed with a relatively small kinetic isotope effect of k_H/k_D = 7 for the iron(IV)-tosylimido complex. Moreover, a Hammett analysis of hydrogen atom abstraction from para-X-benzyl alcohol reveals a slope of close to zero for the iron(IV)-oxo, whereas a strong negative slope is found for the iron(IV)-tosylimido complex. These studies implicate dramatic changes in the reaction mechanisms and suggest a considerable charge transfer in the transition states. Density functional theory calculations were performed to support the experiments and confirm an initial long-range electron transfer for the iron(IV)-tosylimido complex with substrates, due to a substantially larger electron affinity compared with the iron(IV)-oxo species. As a consequence, it also reacts more efficiently in electrophilic addition reactions such as those with sulfides. By contrast, the long-range electron transfer for the iron(IV)-tosylimido complex results in a rate constant that is dependent on the $\pi^*_{xz} \rightarrow \sigma^*_{z^2}$ excitation energy, which raises the hydrogen atom abstraction barrier above that found for the iron(IV)-oxo. On the other hand, sulfimidation has much earlier electron transfer steps with respect to sulfoxidation. All data has been analyzed and rationalized with valence bond models and thermochemical cycles. Our studies highlight the catalytic potential of iron(IV)-tosylimido complexes in chemistry and biology.

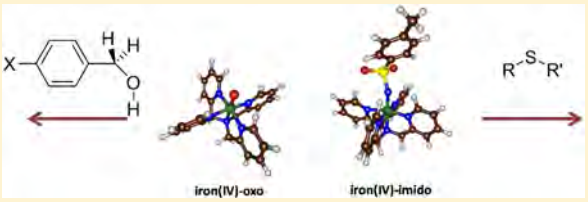

INTRODUCTION

Monoxygenases and dioxygenases are common enzymes in biology that utilize molecular oxygen usually on a transition metal center that can be bound into either a heme or nonheme environment.[1,2] A well-studied class of monoxygenases are the cytochromes P450 (P450s) that are found in all forms of life and catalyze the regioselective and stereospecific hydroxylation and epoxidation of substrates. These reactions have important functions in biology that include the biosynthesis of hormones in the liver, as well as the detoxification of metabolites and xenobiotics, such as drug molecules, in the body.[3] As such there is interest in understanding their function and mechanism from a pharmaceutical as well as biotechnological viewpoint. The P450s form a high-valent iron(IV)-oxo heme cation radical species in the catalytic cycle that is called compound I (Cpd I),[4] which is a highly reactive oxidant that reacts with substrates through aliphatic and aromatic hydroxylation, N-dealkylation, and sulfoxidation reactions.[5]

Despite the fact that much research has been devoted to P450 catalysis and synthetic model complexes there are still major gaps in our understanding of its catalytic mechanism and function. For instance, why does nature use molecular oxygen in the catalytic cycle of P450 enzymes and not, for instance, nitrogen, which is more abundant in the atmosphere? Technically, an iron(IV)-imido (Fe^{IV}═NR, R = alkyl) or iron(V)-nitrido (Fe^{V}≡N) complex should be a stable intermediate in P450 catalyzed reactions. Moreover, an iron(IV)-imido or iron(V)-nitrido could be reactive in NR group reactivity to substrates analogous to Cpd I. Indeed, over the years several examples in P450 catalysis, for example, in

Received: August 16, 2014
Published: November 12, 2014

ACS Publications © 2014 American Chemical Society

dx.doi.org/10.1021/ja508403w | J. Am. Chem. Soc. 2014, 136, 17102−17115

aziridation and imidation reactions, have been reported that include an iron(IV)-nitrido intermediate.[6] For example, the reaction of iron(III)-porphyrin complexes with *N*-tosyliminophenyliodinane (PhINTs) in the presence of olefins led to efficient aziridination of the substrate. More recent work on the amination of substrates by engineered $P450_{BM3}$ enzymes gave several examples of efficient nitrogen group transfer reactions.[7]

Despite being relatively rare in enzymology, actually in inorganic chemistry there are many examples of high-valent metal-imido and metal-nitrido complexes, where they have been shown to be reactive in various processes.[8] Bioinspired P450 analogues have been developed to understand the chemical and physical properties of the active species of P450 enzymes.[9] In a number of these synthetic complexes an iron-nitrido or iron-imido complex could be formed, spectroscopically characterized, and studied for reactivity with selected substrates.[10] In addition, studies have been reported on high-valent ruthenium-nitrido porphyrin complexes, which were shown to efficiently activate sp^3 hybridized C−H bonds of substrates.[11]

In more recent work, attention has shifted to nonheme iron and ruthenium based nitrido and imido complexes. These structures range from pentacoordinated to heptacoordinated iron complexes and have been spectroscopically characterized.[12] The studies showed that aliphatic substrates with a C−H bond strength analogous to that of cyclohexane could be activated efficiently. In addition to mononuclear iron and ruthenium complexes, evidence of diiron(III,IV)-tosylimido complexes has also been reported.[13] Thus, Latour and coworkers[13] observed hydrogen atom abstraction and nitrene transfer reactions by the diiron(III,IV)-tosylimido complex efficiently, whereby the sulfimidation of *para*-substituted thioanisoles was found to correlate linearly with the Hammett constant in an electrophilic pathway.

The iron(IV)-tosylimido (NTs) complex, tosylimido = NTs, with pentadentate N4Py ligand (N4Py = *N*,*N*-bis(2-pyridylmethyl)-*N*-bis(2-pyridyl) methylamine) was synthesized by Klinker et al.[14] and spectroscopically characterized with UV−vis, NMR, EPR, EXAFS, and Mössbauer spectroscopies. Because the analogous iron(IV)-oxo species is also known, we used the opportunity to study the reactivity of $[Fe^{IV}(O)(N4Py)]^{2+}$ (**1**) versus $[Fe^{IV}(NTs)(N4Py)]^{2+}$ (**2**), Figure 1, against selected substrates.[15] It is found that the iron(IV)-oxo oxidant is more effective in hydrogen atom abstraction reactions, but the iron(IV)-tosylimido species, surprisingly, is seen to be much more reactive with sulfides. The intricate details of the catalysts that are responsible for these reactivity differences between **1** and **2** could not be established in detail in our previous study; therefore, we decided to follow up our original study with a broader substrate range, as well as a comprehensive computational study on the reactivity of **1** and **2** with either sulfides (dimethylsulfide, DMS) or hydrogen abstraction donors. We show here, for the first time, that iron(IV)-oxo and iron(IV)-tosylimido have different valence orbital shapes, which lead to differences in electron affinity values that trigger reactivity changes.

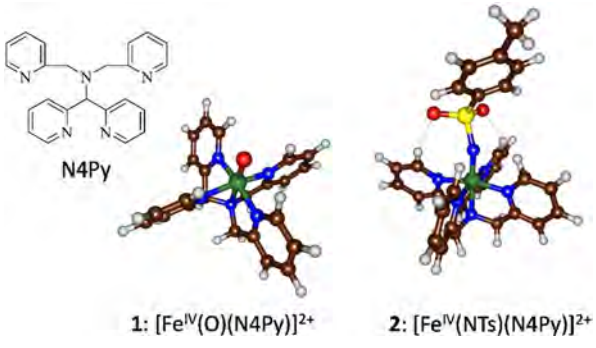

Figure 1. Iron(IV)-oxo and iron(IV)-tosylimido complexes studied in this work.

METHODS

Materials. All chemicals were obtained at the best available purity from Aldrich Chemical Co. and used as specified. Solvents were dried according to published procedures and distilled under argon prior to use.[16] Iodosylbenzene (PhIO) and *N*-tosyliminophenyliodinane (PhINTs) were prepared following literature procedures.[17] Iron(II) complex $[Fe^{II}(N4Py)](CF_3SO_3)_2$ was prepared in a glovebox as reported before.[18] Iron(IV) complexes, $[Fe^{IV}(O)(N4Py)]^{2+}$ and $[Fe^{IV}(NTs)(N4Py)]^{2+}$, were synthesized at ambient temperatures in acetonitrile by reacting the corresponding iron(II) complex with PhIO and PhINTs, respectively.[14,19] The oxidants (**1** and **2**) were characterized with UV−vis spectrophotometry and electrospray ionization mass spectrometry (ESI-MS) methods that confirmed their purity, see Figures S1 and S2 (Supporting Information).[15,19b] Benzyl alcohol-d_7 ($C_6D_5CD_2OH$) was purchased from C/D/N Isotopes Inc. (Pointe-Claire, Quebec, Canada).

Instrumentation. UV−vis spectra and kinetic measurements were recorded on a Hewlett-Packard 8453 spectrophotometer equipped with either a constant temperature circulating water bath or a liquid nitrogen cryostat (Unisoku) with a temperature controller. High resolution ESI-MS spectra of $[Fe^{IV}(O)(N4Py)]^{2+}$ and $[Fe^{IV}(NTs)(N4Py)]^{2+}$ were recorded on a Waters (Micromass MS Technologies) Q-TOF Premier mass spectrometer by infusing precooled (233 K) samples directly into the source at 15 μL min^{-1} using a syringe pump. The spray voltage was set at 2 kV, and the capillary temperature was set at 80 °C. Product analysis was done using NMR (^1H and ^{13}C), whereby the spectra were recorded with a Varian 400/100 MHz spectrometer and LCMS with WATERS ACQUITY UPLC equipped with a variable wavelength UV-200 detector.

Reactivity Studies. All reactions were run in a 10 mm path length UV cuvette by monitoring the UV−vis spectral changes of reaction solutions. Rate constants were determined by fitting the changes in absorbance of the intermediates under study. Their values were measured in triplicate and averaged, which gave a standard deviation of less than 10% of the given values.

Computation. The studies presented in this work use density functional theory (DFT) methods as implemented in the *Jaguar* 7.9 and *Gaussian*-09 program packages.[20] Calculations were performed on $[Fe^{IV}(O)(N4Py)]^{2+}$ (**1**) and $[Fe^{IV}(NTs)(N4Py)]^{2+}$ (**2**) as shown in Figure 1, and their reactivity patterns with 1,3-cyclohexadiene (CHD), benzyl alcohol (BA), and dimethylsulfide (DMS) as model substrates for hydrogen atom abstraction and sulfoxidation processes were investigated. Although calculations have been reported on the reaction mechanism of $[Fe^{IV}(NTs)(N4Py)]^{2+}$ with CHD and DMS,[15] those studies were based on gas-phase geometry optimizations and the effect of solvent was only treated at the single point level. However, because our chemical systems are multiply charged ions, we repeated all studies, whereby full geometry optimizations were performed using a solvent model (polarized continuum model) included that mimics an acetonitrile solution.[21]

Because the spin state ordering of transition metal complexes occasionally varies with the density functional method in the calculations,[22] we tested geometry optimizations with a range of DFT functionals, but all methods converged to very similar spin state orderings and relative energies. Initial studies utilized the unrestricted hybrid density functional method UB3LYP[23] in combination with a double-ζ quality LACVP basis set on iron and 6-31G on the rest of the atoms, basis set BS1.[24] With UB3LYP/BS1, the full potential energy

dx.doi.org/10.1021/ja508403w | J. Am. Chem. Soc. 2014, 136, 17102−17115

landscape from reactants to products on all possible low-lying spin and electronic states was investigated, and local minima and transition states were characterized. Furthermore, intrinsic reaction coordinate scans established the connectivity of the reactants with products via transition states. An analytical frequency calculation at this level of theory confirmed the structures as local minima (with real frequencies only) or first-order saddle points with a single imaginary frequency for the correct mode.

Subsequently all local minima and transition states were reoptimized with a triple-ζ quality basis set that contains an LACV3P+ basis set on iron coupled to 6-311+G* on the rest of the atoms, BS2. To test the reliability of the density functional method, we ran a series of single point calculations at the UB3LYP optimized structures using B3LYP-D3,[25] BP86,[26] PBE0,[27] and M06.[28] These studies did not change the spin state ordering (see Supporting Information) and confirmed the reactivity patterns and the conclusions drawn here.

Kinetic isotope effects (KIEs) were calculated using two models, namely, the semiclassical Eyring model (KIE_E) and the Wigner model (KIE_W), which includes tunneling corrections.[29] KIEs for the hydrogen atom abstraction step of substrates were evaluated from the frequency calculations, whereby the analytical frequencies of the reactants and transition states were recalculated with one or more of the hydrogen atoms of the substrate replaced by deuterium atoms. This led to a change in free energy of activation ($\Delta G^{\ddagger}$) for the original substrate versus that of the deuterium substituted one. The rate constant ratio (k_H/k_D) is then equal to the Eyring KIE, KIE_E, at a specific temperature T (298 K) via eq 1. Further corrections for tunneling are included in the Wigner KIE, KIE_W, which multiplies the KIE_E with the tunneling correction Q_{tH}/Q_{tD}, eqs 2 and 3. In eqs 1−3, R is the gas constant, h is Planck's constant, k_B is the Boltzmann constant, and ν is the imaginary frequency in the transition state.

$$KIE_E = k_H/k_D = \exp[(\Delta G_D^{\ddagger} - \Delta G_H^{\ddagger})/(RT)] \quad (1)$$

$$KIE_W = KIE_E Q_{tH}/Q_{tD} \quad (2)$$

$$Q_t = 1 + \frac{1}{24}\left(\frac{h\nu}{k_B T}\right)^2 \quad (3)$$

The free energy of activation for electron transfer ($\Delta G_{ET}^{\ddagger}$) was calculated using previously described methods,[30] from the driving force for the electron transfer reaction (ΔG_{ET}) and the solvent reorganization energy, λ_0, via eqs 4 and 5. These equations use Avogadro's number (N_A), the elementary charge (e), and the permittivity of vacuum (ε_0). The static and optical dielectric constants (ε_s and ε_{op}) were taken from the Gaussian calculation and had values of 35.688 (acetonitrile) and 1.807, respectively. The hard sphere radii (in Å) of the donor and acceptor molecules of the electron are labeled with r_1 and r_2.

$$\Delta G_{ET}^{\ddagger} = \frac{\lambda_0}{4}\left(1 + \frac{\Delta G_{ET}}{\lambda_0}\right)^2 \quad (4)$$

$$\lambda_0 = \frac{N_A e^2}{4\pi\varepsilon_0}\left(\frac{1}{\varepsilon_{op}} - \frac{1}{\varepsilon_s}\right)\left(\frac{1}{2r_1} + \frac{1}{2r_2} - \frac{1}{r_1 + r_2}\right) \quad (5)$$

RESULTS AND DISCUSSION

Experiment. The reactivity of high valent iron(IV)−oxo complexes has been extensively studied over the past few decades,[2,9,31] but, by contrast, only very few studies have been reported on its closely related iron(V)−nitrido ($Fe^V{\equiv}N$) or the iron(IV)−imido ($Fe^{IV}{=}NR$) species. The origin and chemical details of the reaction mechanism of iron(IV)-oxo compared with iron(IV)-imido with substrates are poorly understood; therefore, we decided to do a comparative kinetics study on the two complexes. Two of the most common reaction mechanisms found for enzymatic iron(IV)-oxo intermediates include hydrogen atom abstraction (HAT) and heteroatom oxidation; therefore, we studied the reactivity of **1** and **2** with *para*-X-benzyl alcohol and fluorene as models for HAT and *para*-X-thioanisole as models for heteroatom oxidation.

Complexes **1** and **2** were generated in an acetonitrile solution *in situ*, and subsequently substrate was added. Upon addition of substrate to a solution of **1** and **2**, the intermediates decayed by pseudo-first-order kinetics and the d−d transitions were monitored in the UV−vis spectrum (Figure 2a). The first-order rate constants were then plotted as a function of substrate concentration to obtain the second-order rate constants (k_2) of which we show the example for *para*-H-benzyl alcohol in Figure 2b. Table 1 summarizes the thus obtained second-order rate constants for all substrates discussed here.

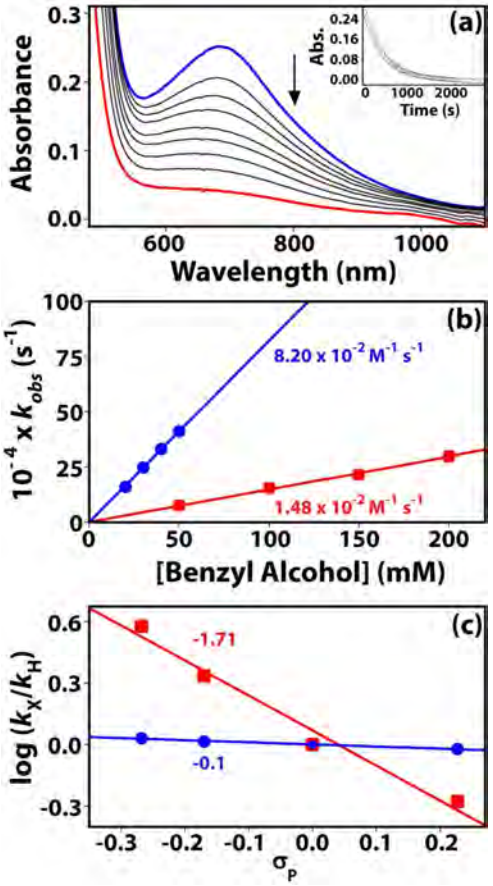

Figure 2. (a) UV−vis spectral changes of **2** (1 mM, blue line) upon the addition of *para*-H-benzyl alcohol (150 equiv diluted in 50 μL of CH_3CN) at 298 K. Inset shows decay profile of 660 nm band. (b) Second-order rate constants determined in the reactions of 1 mM of **1** (●) and **2** (■) in CH_3CN solution against various concentrations of benzyl alcohol at 298 K. (c) Plot of $\log(k_X/k_H)$ against σ_p values of *para*-X-benzyl alcohol in reaction with **1** (●) and **2** (■) at 298 K. The k_X and k_H are the second order rate constants of *para*-X-benzyl alcohol at 298 K.

The second-order rate constant, k_2, obtained for benzyl alcohol at 25 °C was determined to be 1.48×10^{-2} M^{-1} s^{-1} for $[Fe^{IV}(NTs)(N4Py)]^{2+}$, whereas a value of 8.20×10^{-2} M^{-1} s^{-1} was found for $[Fe^{IV}(O)(N4Py)]^{2+}$. Therefore, the $[Fe^{IV}(O)(N4Py)]^{2+}$ complex reacts with benzyl alcohol with rate

dx.doi.org/10.1021/ja508403w | J. Am. Chem. Soc. 2014, 136, 17102−17115

Table 1. Second-Order Rate Constants for the Reaction of 1 and 2 with Selected Substrates

	1			2		
substrate	k_2 (M^{-1} s^{-1})	KIE	Hammett (ρ)	k_2 (M^{-1} s^{-1})	KIE	Hammett (ρ)
thioanisole[a,b]	5.00×10^{-2}		−0.87	2.60×10^{-1}		−3.35
fluorene[b,c]	6.97×10^{-1}	30		1.16×10^{-1}	7	
para-X-benzyl alcohol[c]						
X = OCH_3	8.8×10^{-2}			5.6×10^{-2}		
X = CH_3	8.5×10^{-2}			3.2×10^{-2}		
X = H	8.20×10^{-2}	48[d]	−0.10	1.48×10^{-2}	7	−1.71
X = Cl	7.8×10^{-2}			7.8×10^{-3}		

[a]At 273 K. [b]From ref 15. [c]At 298 K. [d]From ref 32.

constants that are almost six times larger than those found for the $[Fe^{IV}(NTs)(N4Py)]^{2+}$ complex. Similar rate enhancements were found for fluorene, for example, by **1** and **2**.[15] As such the rate enhancement is not dependent on the HAT donor in these cases and most likely proceeds via the same mechanism for both oxidants.

To gain more insight into the details of the hydrogen atom abstraction mechanism, we repeated the experiments with benzyl alcohol-d_7 ($C_6D_5CD_2OH$) and give the comparative second-order rate plots in Figure S6, Supporting Information. These studies established a kinetic isotope effect (KIE) of 7.0, which is relatively low for typical hydrogen atom abstraction reactions but can still be considered as a rate determining HAT step in the reaction mechanism. In the case of HAT of fluorene by **1** and **2**, also a KIE = 7 for the iron(IV)-tosylimido complex was established, whereas a value of 30 was obtained for the iron(IV)-oxo species. Clearly, there are fundamental differences in reactivity between iron(IV)-oxo and iron(IV)-tosylimido that lead to this dramatic lowering of the kinetic isotope effects. Our studies, reported here, are in line with those reported on hydrogen atom abstraction from benzyl alcohol by $[Fe^{IV}(O)(N4Py)]^{2+}$, which also found a large KIE of 48 at 0 °C.[32]

To further understand the intrinsic details of the reaction mechanism of benzyl alcohol with **1** and **2**, we decided to study *para*-substituted benzyl alcohols and create a Hammett plot, see Figure 2c. Reaction of $[Fe^{IV}(O)(N4Py)]^{2+}$ with *para*-substituted benzyl alcohol indicates that the reaction rates are not greatly dependent on the *para*-substituent and whether it is electron-withdrawing or electron-donating gives similar reaction rates. When we plot the reaction rate as a function of σ_p of the substituent, a small Hammett ρ value, approximately −0.1, is found in agreement with the literature.[32] This clearly indicates that there is no substituent effect in the reaction of $[Fe^{IV}(O)(N4Py)]^{2+}$ with benzyl alcohol.

By contrast to the reaction of **1** with benzyl alcohol, the same reaction with **2** gives a dramatic change in substituent effect with a Hammett ρ value of approximately −1.71. This large Hammett value indicates that during the hydrogen atom abstraction from the substrate, there is a considerable amount of positive charge built-up in the transition state. Most likely it originates from additional stabilization of positive charge on the substrate in the transition state by electron-donating groups in the *para*-position of benzyl alcohol and thereby enhances the overall rate of oxidation. The large Hammett value and low KIE indicates that there is a large amount of charge transfer in the rate-determining step.[33]

To unequivocally establish that the rate-determining step is indeed one-electron transfer, we did a subsequent set of experiments with cyclobutanol as mechanistic probe. It has been shown previously that the oxidation of cyclobutanol proceeds through either an initial one-electron or two-electron transfer process, which leads to different products.[32,34] Thus, the one-electron transfer reaction is followed by ring-opening of the substrate to give 4-hydroxybutyraldehyde products, whereas the reaction initiated by a two-electron transfer results in the formation of cyclobutanone products. In the oxidation of cyclobutanol by **2**, we observe 4-hydroxybutyraldehyde as the major products; hence the reaction of **2** with aliphatic substrates proceeds via a dominant radical pathway. By contrast, cyclobutanol reacts with **1** to yield cyclobutanone products after a specific C−H bond cleavage.[32] This observation is in agreement with our earlier observation for the oxidation reaction of fluorene by **1** and **2**, where the latter gives 9,9′-bifluorene as the major product, while with the former fluorenone was obtained.[15]

In addition to the HAT mechanism of **1** versus **2** with selected substrates, we also investigated the sulfoxidation or sulfimidation reaction with *para*-X-thioanisole substrates, X = OCH_3, CH_3, H, and Cl.[15] A plot of the logarithm of the rate constant ratio k_X/k_H gave a linear correlation with the σ_p Hammett parameter with a slope of −0.87 for **1** and −3.35 for **2**, which implicated differences in reaction mechanism. This was assigned as a possible group transfer for the reaction of sulfides with $[Fe^{IV}(O)(N4Py)]^{2+}$ and electron transfer for the reaction with $[Fe^{IV}(NTs)(N4Py)]^{2+}$.

Computation. To gain further insight into the chemical differences between **1** and **2** in hydrogen atom abstraction and heteroatom transfer reactions, we decided to do a detailed density functional theory (DFT) study. To this end, we calculated the catalytic reaction mechanism of hydrogen atom abstraction from 1,3-cyclohexadiene (CHD) and benzyl alcohol (BA) by these oxidants as well as the reaction of **1** and **2** with dimethylsulfide (DMS). Full details of the calculations and the benchmarking of the computational methods are given in the Supporting Information, while we focus on the major trends in the paper here.

Before we discuss the substrate activation by **1** and **2**, let us first do an in-depth analysis of the reactant complexes with and without substrate. Figure 3 displays optimized geometries of $[Fe^{IV}(O)(N4Py)]^{2+}$ (**1**) and $[Fe^{IV}(NTs)(N4Py)]^{2+}$ (**2**) in the lowest lying singlet, triplet, and quintet spin states as obtained after a geometry optimization in a polarized continuum model. In both systems, the triplet spin state is the ground state by more than 4 kcal mol^{-1} over the nearest singlet and quintet spin states.

Optimized geometries of ^{1,3,5}**1** are similar to structures reported previously for gas-phase optimized structures and also to analogous iron(IV)-oxo intermediates from the literature.[35,36] Dramatic geometric differences are found between **1** and **2**. In particular, the Fe−O distance is short, about 1.65−

dx.doi.org/10.1021/ja508403w | J. Am. Chem. Soc. 2014, 136, 17102−17115

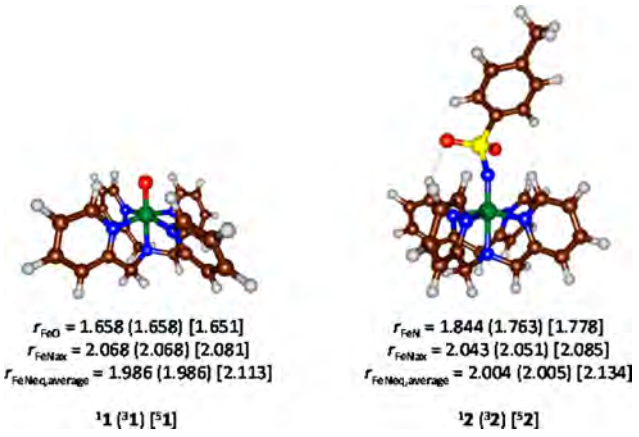

Figure 3. UB3LYP optimized geometries in a dielectric constant mimicking acetonitrile of **1** and **2** with bond lengths in angstroms. The distance between the iron and amide nitrogen atom is labelled as r_{FeNax}, whereas $r_{FeNeq,average}$ represents the average distance of the four iron-pyridine interactions.

1.66 Å in all spin states, typical for a double bond. By contrast, much longer Fe−N bonds are found for structure **2** that range from 1.763 Å for ^{3}**2** to 1.844 Å for ^{1}**2**. Similar bond lengths were obtained from a gas-phase geometry optimization.[15] Despite these differences, structures **1** and **2** have the same electronic configuration with orbital occupation of $\pi^*_{xy}{}^2\pi^*_{xz}{}^1\pi^*_{yz}{}^1$ in the triplet spin state. However, the interactions of the NTs group with the metal differs from that of an oxo group with the metal, and as a result changes in orbital energy levels, orbital ordering, and orbital stability is found.

Figure 4 displays the orbital energy levels of the π^*_{xy}, π^*_{xz}, π^*_{yz}, $\sigma^*_{z^2}$ and $\sigma^*_{x^2-y^2}$ molecular orbitals of ^{3}**1** and ^{3}**2**. The π^*_{xy} orbital is the lowest in energy typical for hexacoordinated iron complexes and its lobes are placed between the nitrogen atoms of the N4Py ligand. However, because the pyridine ligands are orthogonal to the four Fe−N axes, the equatorial nitrogen atoms can still form bonding and antibonding overlap interactions of $2p_x/2p_y$ orbitals with the $3d_{xy}$ orbital on the metal, and hence the π^*_{xy} orbital is higher in energy than in corresponding porphyrin complexes.

The $3d_{xz}$ and $3d_{yz}$ atomic orbitals on Fe interact with a pair of $2p_x/2p_y$ atomic orbitals on the oxo group and form a degenerate pair of π_{xz}/π^*_{xz} and π_{yz}/π^*_{yz} molecular orbitals in **1**. In $[Fe^{IV}(NTs)(N4Py)]^{2+}$, by contrast, the donating nitrogen atom also binds the tosyl group, and as a consequence, the π^*_{xz} and π^*_{yz} are not degenerate anymore. As seen in Figure 4, the $3d_{xz}$ orbital on Fe interacts with the σ_{SN} bonding orbital along the S−N bond to form the π_{xz}/π^*_{xz} set of orbitals, whereas the

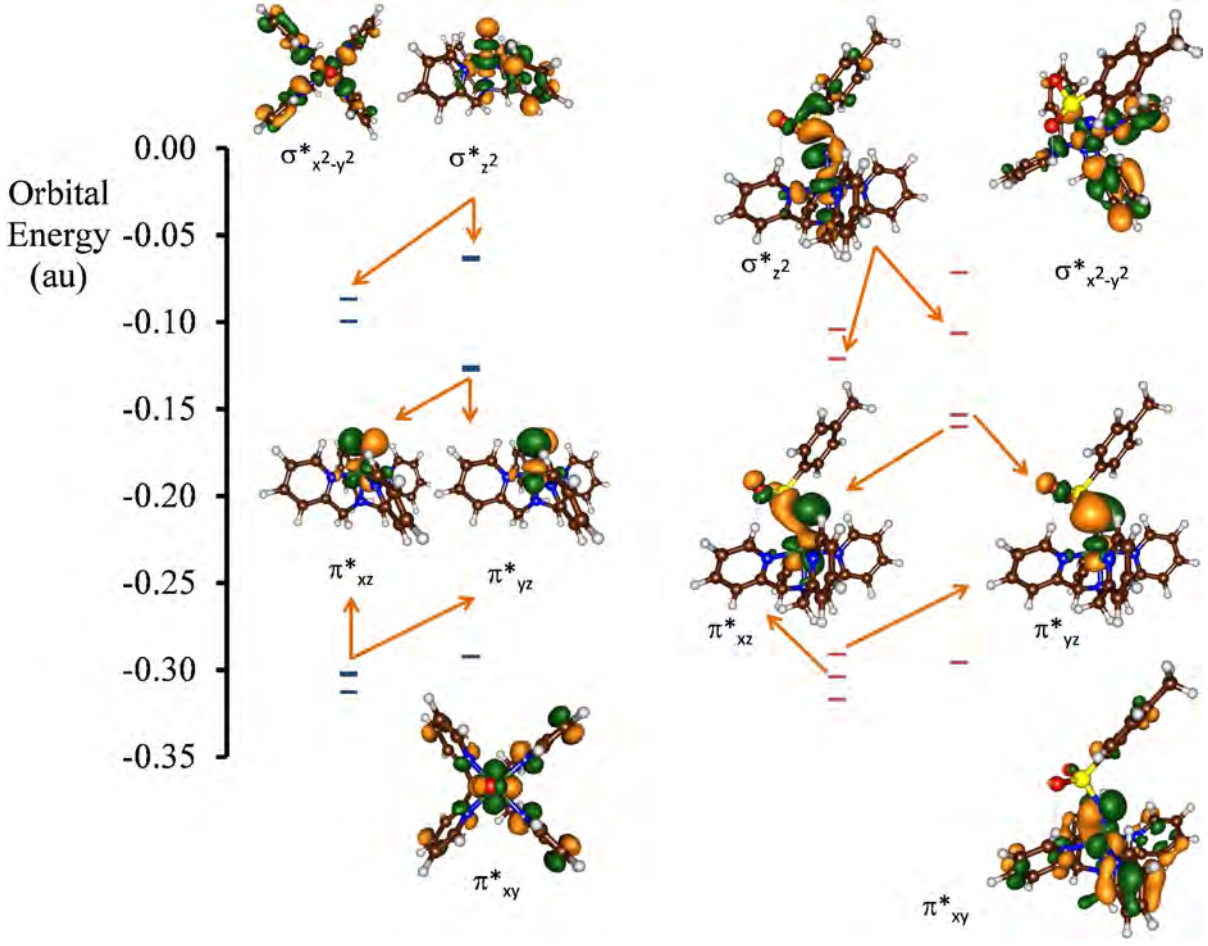

Figure 4. Orbital diagram of $[Fe^{IV}(O)(N4Py)]^{2+}$ (**1**) on the left-hand-side and $[Fe^{IV}(NTs)(N4Py)]^{2+}$ (**2**) on the right-hand-side. The energy levels of the α- and β-set of molecular valence orbitals are given (with energies in au) of both complexes. Also shown are orbital drawings of the relevant molecular orbitals.

dx.doi.org/10.1021/ja508403w | J. Am. Chem. Soc. 2014, 136, 17102−17115

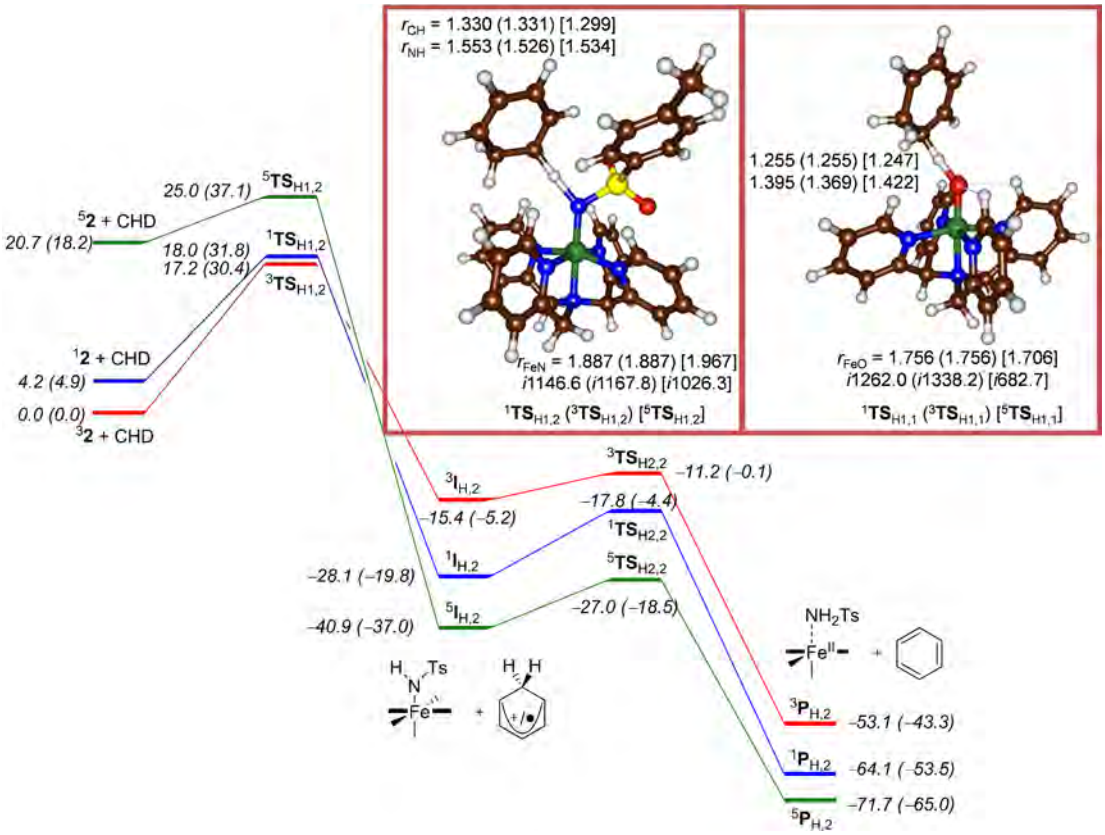

Figure 5. Potential energy landscape of dehydrogenation of CHD by $[Fe^{IV}(NTs)(N4Py)]^{2+}$ with energies relative to isolated reactants in kcal mol^{-1}. Out of parentheses are given ΔE + ZPE values in solvent, whereas free energies with solvent and entropic and thermal corrections are given in parentheses. Also shown are optimized geometries of $\mathbf{TS}_{H1,1}$ and $\mathbf{TS}_{H1,2}$ with bond lengths in angstroms and the imaginary frequency in wave numbers.

$3d_{yz}$ orbital pairs up with a lone pair ($2p_y$) on the nitrogen atom to form π_{yz}/π^*_{yz}.

Two virtual orbitals, $\sigma^*_{z^2}$ and $\sigma^*_{x^2-y^2}$, complement the set of valence orbitals in Figure 4. The $\sigma^*_{x^2-y^2}$ orbital is in the plane of the N4Py ligand and is similar in shape and orbital energy in **1** and **2**. The major orbital differences between **1** and **2** are found along the Fe−O/Fe−N axis. Thus, the $\sigma^*_{z^2}$ molecular orbital for the antibonding interactions of the $3d_{z^2}$ atomic orbital on Fe with the $2p_z$ orbital on O/N is affected strongly.

In **1**, the $\sigma^*_{z^2}$ orbital in $[Fe^{IV}(O)(N4Py)]^{2+}$ is the result of the interaction of the $3d_{z^2}$ orbital on iron with the $2p_z$ atomic orbital on oxygen. By contrast, the $\sigma^*_{z^2}$ orbital in $[Fe^{IV}(NTs)(N4Py)]^{2+}$ is built up from the $3d_{z^2}$ orbital on iron with the $2p_y$ orbital on nitrogen but also includes the $3p_z$ orbital on sulfur. These differences in molecular orbital interactions of the $\sigma^*_{z^2}$ orbital in **1** and **2** affect the energy level dramatically and change the ordering of $\sigma^*_{x^2-y^2}$ over $\sigma^*_{z^2}$, whereby the latter is lower in energy in **2**. The changes in orbital energies affect the HOMO−LUMO gaps, which are reduced in **2** with respect to **1** and thereby increase the electrophilicity of **2** as well. As such, based on the orbital diagrams, differences in chemical reactivity are expected between **1** and **2**.

Hydrogen Atom Abstraction Mechanisms. We then calculated the dehydrogenation of CHD by **1** and **2** with DFT methods, as well as the hydrogen atom abstraction of benzyl alcohol (Supporting Information). As an example of a typical potential energy profile of C−H activation by iron(IV)-tosylimido complexes, we display the dehydrogenation of CHD by ^{1,3,5}**2** in Figure 5. The reaction is stepwise with an initial hydrogen atom abstraction via a transition state $\mathbf{TS}_{H1}$ to form a radical intermediate $\mathbf{I}_H$. A second hydrogen atom abstraction then via transition state $\mathbf{TS}_{H2}$ gives dehydrogenated products, that is, benzene and water/H_2NTs. The labels in superscript refer to the spin multiplicity and the subscript label to the reactant, that is, either **1** or **2**. Thus, $^3\mathbf{TS}_{H1,1}$ is the initial hydrogen atom abstraction transition state from CHD by **1** on the triplet spin state surface.

Note that in the case of the iron(IV)-tosylimido system, actually the reaction starts with an electron transfer from substrate to oxidant prior to the hydrogen atom abstraction. Therefore, we first estimated the electron transfer barrier for reaction 6 using the Marcus equation described with eq 4 above. We estimate the electron transfer free energy of activation ($\Delta G^{\ddagger}_{ET}$) to be 3.4 kcal mol^{-1}, and hence it is well lower than the hydrogen atom abstraction barrier. Note that long-range electron transfer of high-valent iron(IV)-oxo complexes has been calculated before in the reaction of $[Fe(O)(BQEN)(NCCH_3)]^{3+}$, BQEN = *N*,*N*′-dimethyl-*N*,*N*′-bis(8-quinolyl)ethane-1,2-diamine, in a reaction with ethylbenzene as well as in a reaction of Cpd I of P450 with an arginine substrate.[37]

$$^3\mathbf{2} + \text{CHD} \rightarrow [Fe^{III}(NTs)(N4Py)]^+ + \text{CHD}^{\bullet+} + \Delta G_{ET} \quad (6)$$

The initial hydrogen atom abstraction barrier, $\mathbf{TS}_{H1}$, is rate determining in all cases and leads to very stable intermediates $\mathbf{I}_H$ with large exothermicity. The lowest lying barrier, $\mathbf{TS}_{H1,2}$, is on the triplet spin state surface with an energy of $\Delta E^{\ddagger}$ + ZPE =

dx.doi.org/10.1021/ja508403w | J. Am. Chem. Soc. 2014, 136, 17102−17115

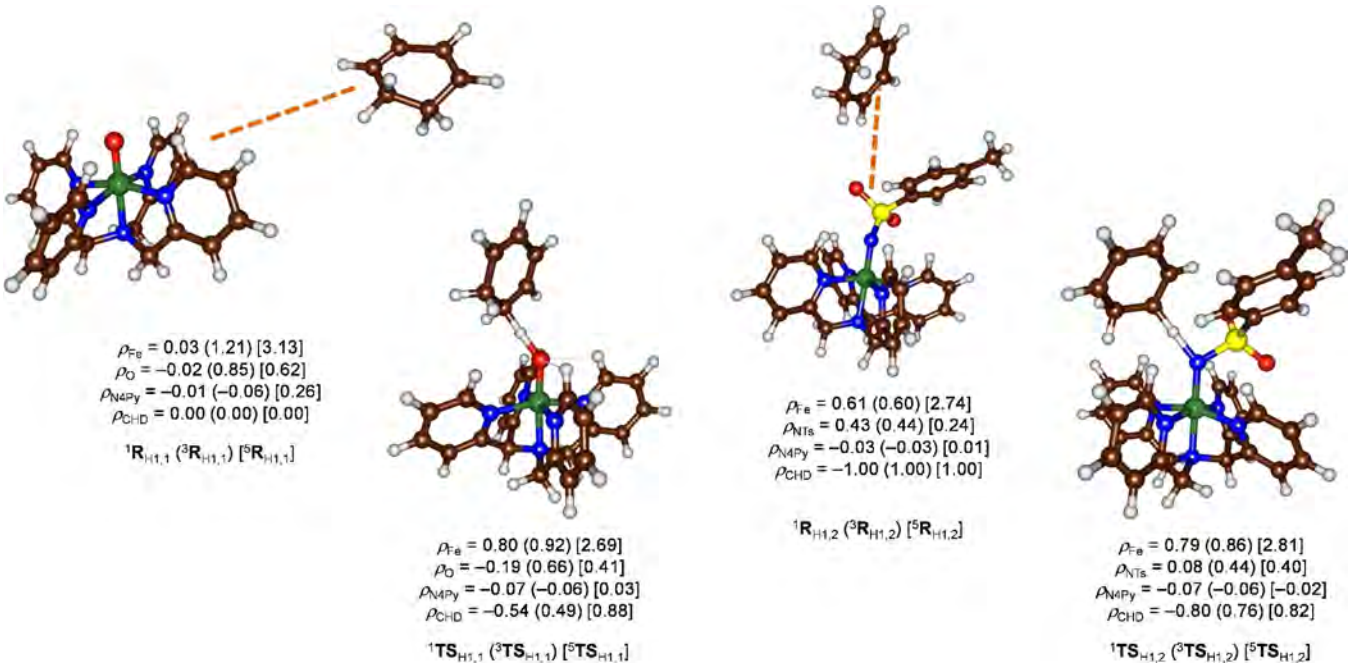

Figure 6. Group spin densities of $\mathbf{R}_{H1,1}$, $\mathbf{TS}_{H1,1}$, $\mathbf{R}_{H1,2}$, and $\mathbf{TS}_{H1,2}$ as obtained at UB3LYP/BS2 in a dielectric constant of 35.688.

17.2 kcal mol^{-1}. By contrast, the reaction of ^{3}**1** with CHD has a hydrogen atom abstraction barrier of 15.7 kcal mol^{-1} at the same level of theory (Supporting Information, Table S31). A change in enthalpy of 1.5 kcal mol^{-1} between the reaction of CHD with **1** and of CHD with **2** leads to a rate enhancement of about 11, which compares well with the one reported experimentally of 6 for *para*-H benzyl alcohol (Table 1), as well as with our previously reported reaction rates for CHD and fluorene.[15]

Although the absolute error of DFT calculated barrier heights is typically several kcal mol^{-1},[38] actually extensive reactivity trends showed that the error is mostly systematic. Thus, for a series of oxygen atom transfer reactions from Cpd I of P450 to substrates, a linear correlation was found with the strength of the C−H bond broken (in the case of HAT) or the ionization potential of the olefin (for epoxidation reactions) with a standard deviation of less than 2 kcal mol^{-1}.[39] Furthermore, DFT calculations on the reaction of ^{4,2}Cpd I with *trans*-2-phenylmethylcyclopropane gave a mixture of rearrangement and nonrearrangement pathways, which enabled the calculation of product isotope effect.[40] The calculated product isotope effect of 1.11 was very close to the experimental value of 1.14; hence DFT can calculate small regioselectivity differences of a few kcal mol^{-1} with good accuracy.

Past the transition state, $\mathbf{TS}_{H1,2}$, a spin crossing to a higher spin state occurs to form $\mathbf{I}_{H,2}$ in the quintet spin state. In the transition state, however, the triplet is well below the quintet spin. With iron(IV)-oxo as an oxidant, the second hydrogen atom abstraction has negligible barriers, but for [Fe^{IV}(NTs)(N4Py)]$^{2+}$, significant barriers, for example, ΔE + ZPE = 13.9 kcal mol^{-1} for $^{5}\mathbf{TS}_{H2,2}$, are found. This will imply that the radical intermediates have a finite lifetime during which rearrangement processes may occur leading to side reactions and byproducts.[41]

Geometrically, $\mathbf{TS}_{H1,1}$ is different from $\mathbf{TS}_{H1,2}$, although the value of the imaginary frequency is of the same order of magnitude. In particular, the N−H bond in $\mathbf{TS}_{H1,2}$ is rather long with values well over 1.5 Å, whereas the O−H distance in $\mathbf{TS}_{H1,1}$ is between 1.369 and 1.422 Å for the three spin states. Optimized geometries of intermediates and products are in line with previous studies on dehydrogenation processes by iron(IV)-oxo and iron(IV)-tosylimido complexes.[42,43]

To understand the differences between $\mathbf{TS}_{H1,1}$ and $\mathbf{TS}_{H1,2}$, we plot in Figure 6 the group spin densities of these transition states as well as the reactant complexes. At first glance, the two sets of spin densities for the transition states look very similar: In the triplet spin state there is about 1.5 spin density on the FeO/FeNTs group and considerable radical character on the substrate. However, a careful look at the reactant complexes $\mathbf{R}_{H1,1}$ and $\mathbf{R}_{H1,2}$ shows that the iron(IV)-tosylimido complex has undergone an electron transfer upon approach of the substrate, and $^{1,3,5}\mathbf{R}_{H1,2}$ all show a spin density of approximately 1 at the CHD unit. This may affect the spin densities and charge distributions in the transition states as well.

The group spin densities of the iron(IV)-oxo species in ^{1,3,5}**1** and $^{1,3,5}\mathbf{R}_{H1,1}$ are very similar, and little spin density has accumulated on the substrate moiety in $\mathbf{R}_{H1,1}$. Therefore, approach of the substrate on the iron(IV)-oxo species has little effect on the charge distributions, and in $\mathbf{R}_{H1,1}$ the oxidant is still an iron(IV)-oxo species. A comparison of the group spin densities of ^{1,3,5}**2** and $^{1,3,5}\mathbf{R}_{H1,2}$, on the other hand, shows that an electron transfer has occurred at relatively large distance and in $\mathbf{R}_{H1,2}$ the metal is reduced and the substrate is a cation radical, that is, [Fe^{III}(NTs)(N4Py)]$^{+}$···CHD$^{+\bullet}$ rather than [Fe^{IV}(NTs)(N4Py)]$^{2+}$···CHD. Hence the actual oxidant that performs the hydrogen atom abstraction is the iron(III)-tosylimido species rather than an iron(IV)-tosylimido species. Because experimental rate constants were measured after addition of substrate, this implies that we cannot use the reactant complex $\mathbf{R}_{H1,2}$ as a comparison with experiment but have to use isolated reactants instead. Clearly, the electron affinity of [Fe^{IV}(NTs)(N4Py)]$^{2+}$ is large, and the electron transfer happens prior to the substrate activation step. In recent work, we showed that binding of Zn^{2+} to a manganese-porphyrinoid system resulted in valence tautomerism and changes in electronic configuration

dx.doi.org/10.1021/ja508403w | J. Am. Chem. Soc. 2014, 136, 17102−17115

Scheme 1. Reaction Mechanisms Established for Iron(IV)-oxo and Iron(IV)-tosylimido Complexes

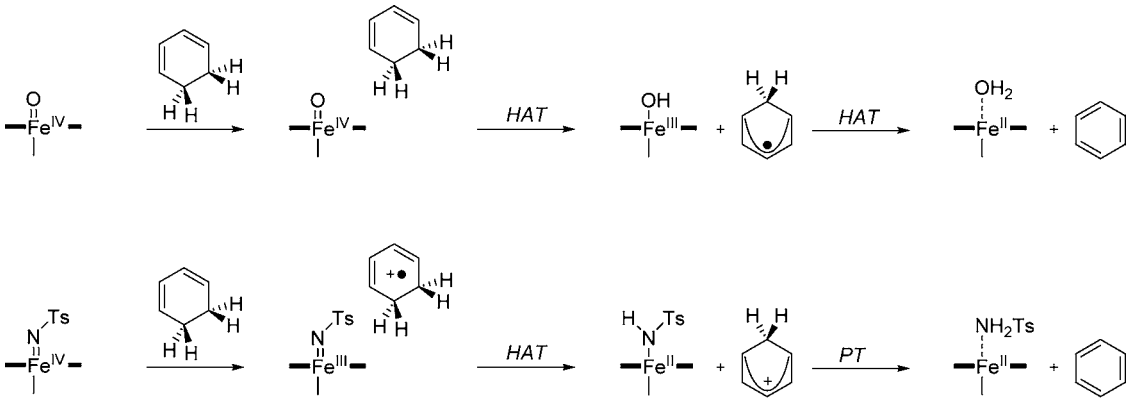

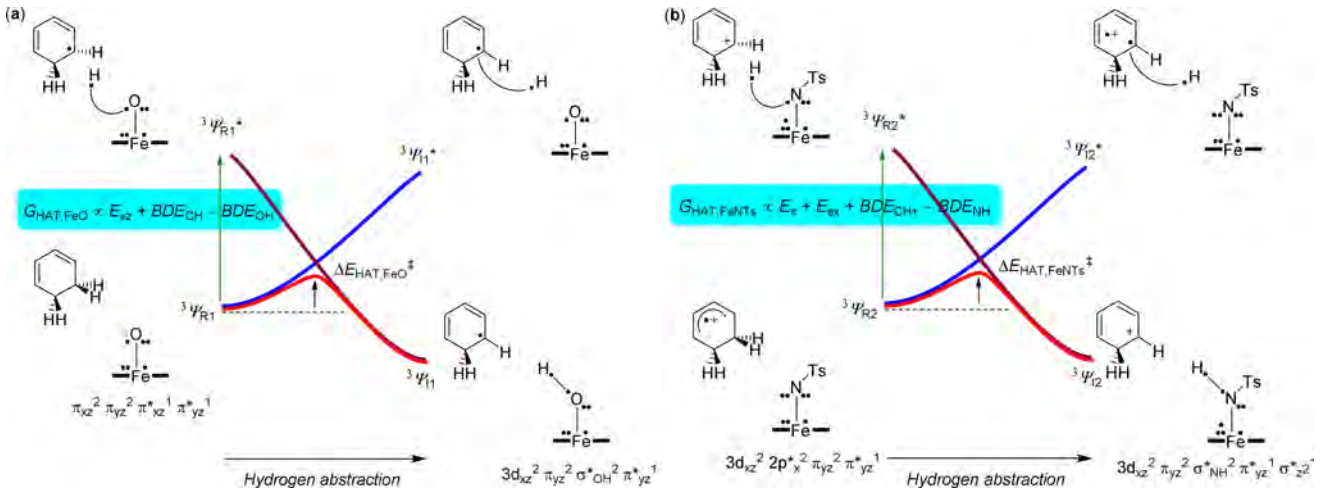

Figure 7. Valence bond curve crossing diagrams for hydrogen atom abstraction from substrate by $[Fe^{IV}(O)(N4Py)]^{2+}$ (a) and $[Fe^{III}(NTs)(N4Py)]^{+}$ (b). Valence electrons are identified with a dot, and lines (straight or bent) in chemical structures refer to bonds.

and consequently catalysis.[44] The $[Fe^{IV}(NTs)(N4Py)]^{2+}$ system, therefore, is another example of a catalyst where its activity is strongly dependent on environmental variables.

Note that the spin densities on the quintet spin state surface for $\mathbf{R}_{H1,2}$ and $\mathbf{TS}_{H1,2}$ implicate the ferromagnetic coupling of three electrons on iron with one on the substrate rest group. Previous studies on nonheme iron(IV)-oxo reactivity[35,36] found quintet spin states with five unpaired electrons on the iron(IV)-oxo antiferromagnetically coupled to a radical on the substrate rest group as the most stable radical intermediate. In these systems, the hydrogen atom typically attacks from the top and aligns itself with the Fe−O axis. In iron(IV)-tosylimido, this site is blocked by the tosylimido group, and the substrate attacks along an angle, thus stabilizing the π-pathway. We made attempts to swap molecular orbitals and create alternative quintet spin states with five unpaired electrons on the metal antiferromagnetically coupled to a substrate radical for transition states and intermediate complexes. However, all these calculations failed and led to high energy structures only.

The group spin densities and, in particular, the differences between $\mathbf{R}_{H1,1}$ and $\mathbf{TS}_{H1,1}$ and between $\mathbf{R}_{H,2}$ and $\mathbf{TS}_{H1,2}$ show that in both cases between the reactant complex and the **TS** a hydrogen atom abstraction takes place. The differences between the two processes are that in the iron(IV)-tosylimido already one electron had transferred upon formation of a long-range complex **R**, thereby generating a triplet ground state with $\pi^{*}_{xy}{}^{2}\pi^{*}_{xz}{}^{2}\pi^{*}_{xz}{}^{1}\pi_{CHD}{}^{1}$ configuration representing a state corresponding to $[Fe^{III}(NTs)(N4Py)]^{+}\cdots CHD^{+\bullet}$. Therefore, the subsequent hydrogen atom abstraction includes a second electron to be transferred and the formation of a $[Fe^{II}(NHTs)(N4Py)]$ intermediate. This complex then abstracts a proton to form the product complex. The $^{3}\mathbf{TS}_{H1,2}$ structure, therefore, has an electronic configuration closely resembling the product complexes, where the aromaticity in the benzene group is starting to form and an electron transfer from substrate into $\sigma^{*}_{z^2}$ takes place.

The singlet spin state reactant complex has the same electronic configuration as $^{3}\mathbf{R}_{H1,2}$, and its transition state is very close in energy to $^{3}\mathbf{TS}_{H1,2}$ and leads through an electron transfer to the closed-shell singlet intermediate $^{1}\mathbf{I}_{H,2}$ with configuration $\pi^{*}_{xy}{}^{2}\pi^{*}_{xz}{}^{2}\pi^{*}_{yz}{}^{2}$. The most stable intermediate, however, is $^{5}\mathbf{I}_{H,2}$ with configuration $\pi^{*}_{xy}{}^{2}\pi^{*}_{xz}{}^{1}\pi^{*}_{yz}{}^{1}\sigma^{*}_{z^2}{}^{1}\sigma^{*}_{x^2-y^2}{}^{1}$. Scheme 1 summarizes the mechanisms that we obtained for dehydrogenation of olefins, such as CHD, by **1** and **2**. The $\sigma^{*}_{z^2}$ orbital in $^{3}\mathbf{TS}_{H1,2}$ mixes strongly with a π-orbital on the aromatic substrate and hence is strongly affected in shape and energy level by the *para*-substituent on the ring. We can anticipate a large Hammett effect upon changing the *para*-H substituent by a more electron donating or withdrawing group.

The reaction mechanisms shown in Scheme 1 also explain the Hammett plot for benzyl alcohol in Figure 2c. Thus, the iron(IV)-oxo complex reacts with little charge accumulation on

dx.doi.org/10.1021/ja508403w | J. Am. Chem. Soc. 2014, 136, 17102−17115

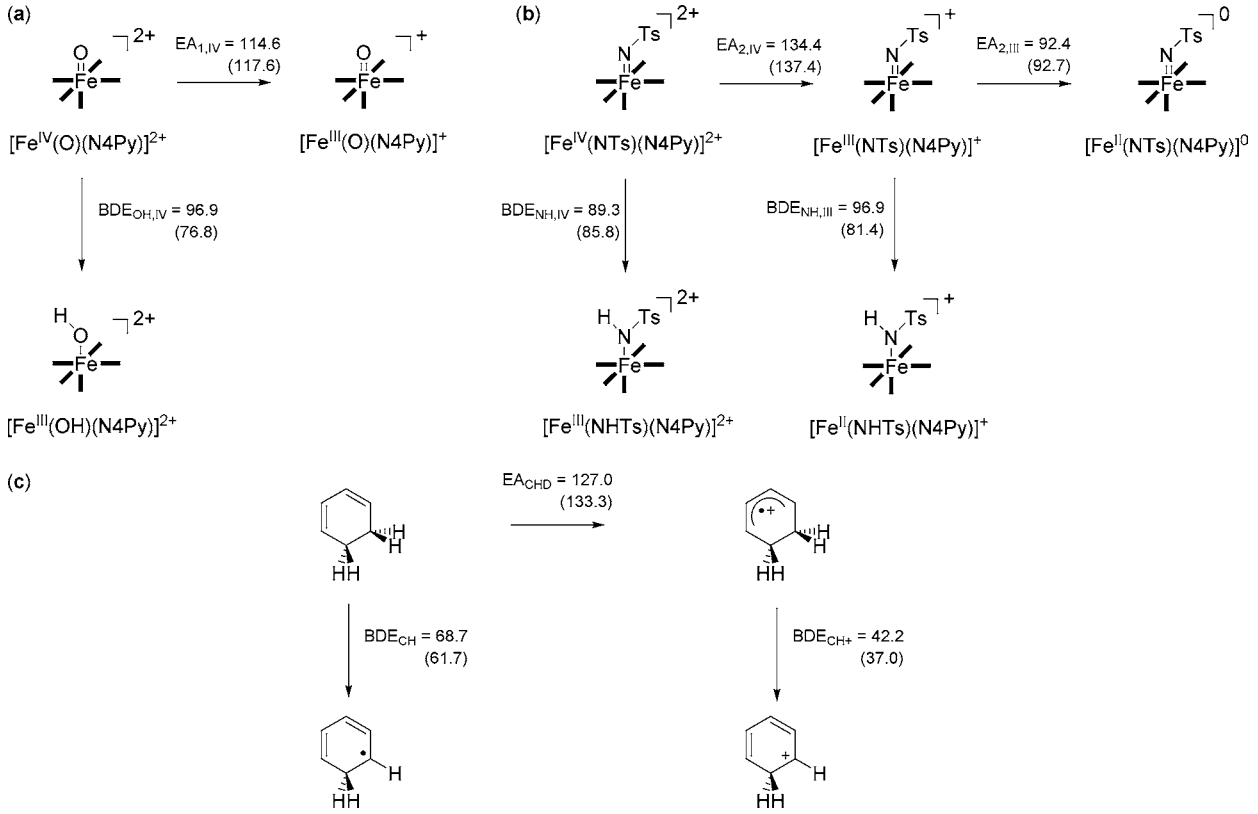

Figure 8. Thermochemical cycles for electron and hydrogen atom transfer from $[Fe^{IV}(O)(N4Py)]^{2+}$ (a), $[Fe^{IV}(NTs)(N4Py)]^{2+}$ (b), and cyclohexadiene (c). All data obtained after a UB3LYP/BS2//UB3LYP/BS1 calculation in a dielectric constant. Data out of parentheses are ΔE + ZPE values in solvent, whereas free energies are in parentheses.

the substrate and hence has an almost zero Hammett ρ value. By contrast, the iron(IV)-tosylimido complex starts the reaction with an electron transfer and the formation of a substrate cation radical. This large charge accumulation on the substrate has a strong effect on the Hammett parameter and as a result a value of $\rho = -1.71$ is obtained.

To further understand the intricate details of HAT reaction mechanisms by $[Fe^{IV}(O)(N4Py)]^{2+}$ versus $[Fe^{IV}(NTs)(N4Py)]^{2+}$, we did a valence bond (VB) and thermochemical analysis on the basic chemical properties of oxidants and substrates. Figure 7 displays the curve crossing diagrams of hydrogen atom abstraction by the reactant complexes $\mathbf{R}_{H1,1}$ and $\mathbf{R}_{H1,2}$. As discussed above, approach of CHD on an iron(IV)-oxo species gives $\mathbf{R}_{H1,1}$ or $[Fe^{IV}(O)(N4Py)]^{2+}\cdots$CHD. However, when CHD approaches the $[Fe^{IV}(NTs)(N4Py)]^{2+}$ complex instead, an electron transfer takes place to form $\mathbf{R}_{H1,2}$ or $[Fe^{III}(NTs)(N4Py)]^{+}\cdots CHD^{+\bullet}$. Figure 7 reflects these starting conditions and discusses the hydrogen atom abstraction mechanism from the reactant complexes.

The valence bond (VB) curve crossing diagrams start at the bottom left with the reactant complexes, that is, $\mathbf{R}_{H1,1}$ or $\mathbf{R}_{H1,2}$, which have a reactant wave function Ψ_{R1} and Ψ_{R2}, respectively. We then consider the hydrogen atom abstraction leading to intermediates $\mathbf{I}_{H1}/\mathbf{I}_{H2}$, which are described on the bottom right-hand-side of the figure with product wave function Ψ_{I1}/Ψ_{I2}. The crossing of the reactant and product wave functions leads to an avoided crossing and a hydrogen atom abstraction barrier with energy $\Delta E^{\ddagger}_{HAT}$. Previously, it has been shown that $\Delta E^{\ddagger}_{HAT}$ is proportional to a fraction of the excitation energy (G) for the excitation from Ψ_R to Ψ_R* in the reactant geometry.[45] In order to understand the factors that determine the actual value of G in the reaction of $[Fe^{IV}(O)(N4Py)]^{2+}$ and $[Fe^{IV}(NTs)(N4Py)]^{2+}$ with CHD, we display the VB structures of the ground and excited states corresponding to the Ψ_R and Ψ_R* wave functions. Note that upon approach of the substrate to $[Fe^{IV}(NTs)(N4Py)]^{2+}$ an electron transfer has taken place; therefore, we use $[Fe^{III}(NTs)(N4Py)]^{+}\cdots CHD^{+\bullet}$ as a reactant configuration instead.

The iron(IV)-oxo complex has electronic configuration $\pi_{xz}{}^2\pi_{yz}{}^2\pi^*_{xy}{}^2\pi^*_{xz}{}^1\pi^*_{yz}{}^1$ in a ground state triplet. The π_{xz}/π^*_{xz} and π_{yz}/π^*_{yz} pair of orbitals are located along the Fe−O bond, and the electrons in these orbitals are identified with dots, while the π^*_{xy} electrons have been omitted from Figure 7 for clarity. Hydrogen atom abstraction splits the π_{xz}/π^*_{xz} pair of orbitals back into atomic orbitals with two electrons in $3d_{xz}$ and a single electron in $2p_x$. The latter electron pairs up with the electron of the incoming hydrogen atom to form a σ_{OH} bond.

A comparison between the VB structures representing Ψ_{R1} and Ψ_{R1}* should give information on the components that affect the excitation energy and consequently the hydrogen atom abstraction barrier. The difference between the two VB structures highlights the breaking of the C−H bond of the substrate, the formation of the O−H bond, and the dehybridization of the π_{xz}/π^*_{xz} pair of orbitals. The excitation energy, $G_{HAT,FeO}$, therefore, includes the energy to break the C−H bond of the substrate, that is, BDE_{CH}, the energy to form an O−H bond, that is, BDE_{OH}, and finally the energy to split the π_{xz}/π^*_{xz} pair of molecular orbitals into atomic orbitals, E_{xz}, eq 7.

$$G_{HAT,FeO} = E_{xz} + BDE_{CH} - BDE_{OH} \quad (7)$$

dx.doi.org/10.1021/ja508403w | J. Am. Chem. Soc. 2014, 136, 17102−17115

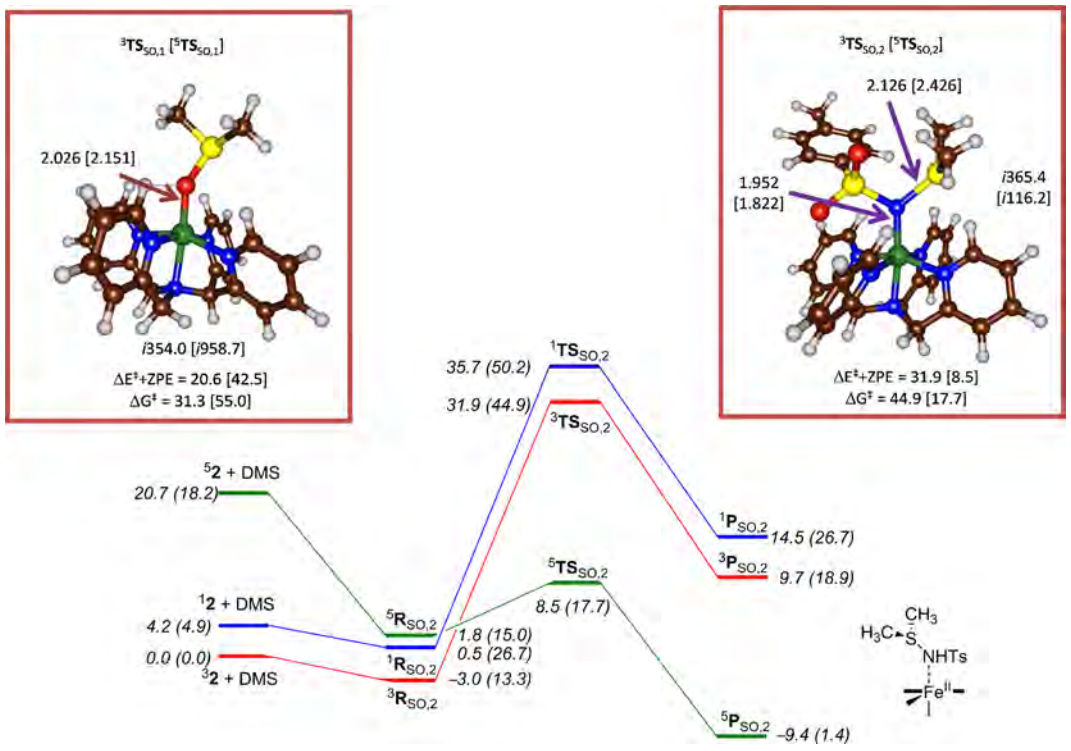

Figure 9. Potential energy landscape of dehydrogenation of CHD by $[Fe^{IV}(NTs)(N4Py)]^{2+}$ with energies relative to isolated reactants in kcal mol^{-1}. Out of parentheses are given ΔE + ZPE values in solvent, whereas free energies with solvent and entropic and thermal corrections are given in parentheses. Also shown are optimized geometries of $\mathbf{TS}_{SO,1}$ and $\mathbf{TS}_{SO,2}$ with bond lengths in angstroms and the imaginary frequency in wave numbers.

The situation is radically different for the reaction of $[Fe^{IV}(NTs)(N4Py)]^{2+}$ with CHD, where prior to the formation of the reactant complex an electron transfer has taken place. Figure 7b, therefore, starts bottom left with the $[Fe^{III}(NTs)(N4Py)]^{+}$ in close approach with CHD cation radical. The reactant wave function for this system is $3d_{xz}{}^{2}2p_{x}{}^{2}\pi_{yz}{}^{2}\pi^{*}_{xy}{}^{2}\pi^{*}_{yz}{}^{1}$. In the hydrogen atom abstraction, the C−H bond of the substrate ($CHD^{+\bullet}$) is broken, which will cost BDE_{CH+}. Note that with the iron(IV)-oxo species a hydrogen atom abstraction is from CHD, whereas with the iron(III)-tosylimido group it is from $CHD^{+\bullet}$. The values of BDE_{CH} and BDE_{CH+} are different, *vide infra*.

The hydrogen atom attacks the $2p_x$ orbital and forms a new σ_{NH} bond; however, since there are three electrons in the interaction, one of those is promoted into the $\sigma^{*}_{z^2}$ orbital, and therefore the bond formation energy is equal to the energy to form the N−H bond, that is, BDE_{NH}, plus the excitation energy from $2p_x$ to $\sigma^{*}_{z^2}$, E_{ex}. In addition, the radical left behind on the carbon atom, which originally bound the hydrogen atom conjugates with the remaining electrons of the $CHD^{+\bullet}$ π-system with energy E_{π}, eq 8.

$$G_{HAT,FeNTs} = E_{\pi} + E_{ex} + BDE_{CH+} - BDE_{NH} \quad (8)$$

To get a feeling for the magnitude of $G_{HAT,FeO}$ versus $G_{HAT,FeNTs}$, we calculated the various bond dissociation energies (BDEs) and ionization energies (IEs) as summarized in the thermochemical cycles in Figure 8. We calculate values ΔE + ZPE of 68.7 kcal mol^{-1} for BDE_{CH} and 96.9 kcal mol^{-1} for BDE_{OH}. The value of E_{xz} in eq 7 is estimated from the energy gap between the π_{xz} and π^{*}_{xz} α-orbitals in $^{3}[Fe^{IV}(O)(N4Py)]^{2+}$ for which we find 76.7 kcal mol^{-1}. Therefore, $G_{HAT,FeO}$ is estimated to have a value of 48.5 kcal mol^{-1}. Generally, the barrier height is about one-third of the height of the excitation energy G,[46] which in our case would lead to a VB predicted barrier height of $\Delta E^{\ddagger}_{HAT,FeO}$ = 16.2 kcal mol^{-1} for the reaction between **1** and CHD. The VB predicted barrier matches the DFT calculated one of 15.7 kcal mol^{-1} (Supporting Information, Table S31) perfectly.

Using a similar approach, we estimate the excitation energy $G_{HAT,FeNTs}$: the bond energy of the C−H bond in $CHD^{+\bullet}$ is BDE_{CH+} = 42.2 kcal mol^{-1}, whereas the N−H bond formation energy between $[Fe^{III}(NTs)(N4Py)]^{+}$ and a hydrogen atom is BDE_{NH} = 96.9 kcal mol^{-1} (Figure 8).

The $2p_x \rightarrow \sigma^{*}_{z^2}$ excitation energy is taken from the difference in energy of these orbitals in $[Fe^{III}(NTs)(N4Py)]^{+}$ and estimated to be 72.9 kcal mol^{-1}. The π-conjugation energy of olefins was previously reported to be about 32 kcal mol^{-1}.[47] As such, a value of $G_{HAT,FeNTs}$ = 50.2 kcal mol^{-1} is predicted from VB theory. A fraction of one-third of this value would give a $\Delta E^{\ddagger}_{HAT,FeNTs}$ = 16.7 kcal mol^{-1} again in good agreement with the DFT calculations reported in Figure 5. Furthermore, the VB estimated barriers reproduce the experimentally observed and DFT calculated ordering.

In conclusion, the VB curve crossing diagrams predict the iron(IV)-oxo species to be more reactive with CHD than the corresponding iron(III)-tosylimido system, because of a large contribution to the excitation energy for $2p_x$ to $\sigma^{*}_{z^2}$ promotion. Even though the driving force of the reaction for $[Fe^{III}(NTs)(N4Py)]^{+}$ with $CHD^{+\bullet}$ is larger than the one for $[Fe^{IV}(O)(N4Py)]^{2+}$ with CHD as also follows from the differences in BDE values.

The data in Figure 8 also shows that the electron affinity of **2** is considerably larger than that of **1** by about 20 kcal mol^{-1}. As

dx.doi.org/10.1021/ja508403w | J. Am. Chem. Soc. 2014, 136, 17102−17115

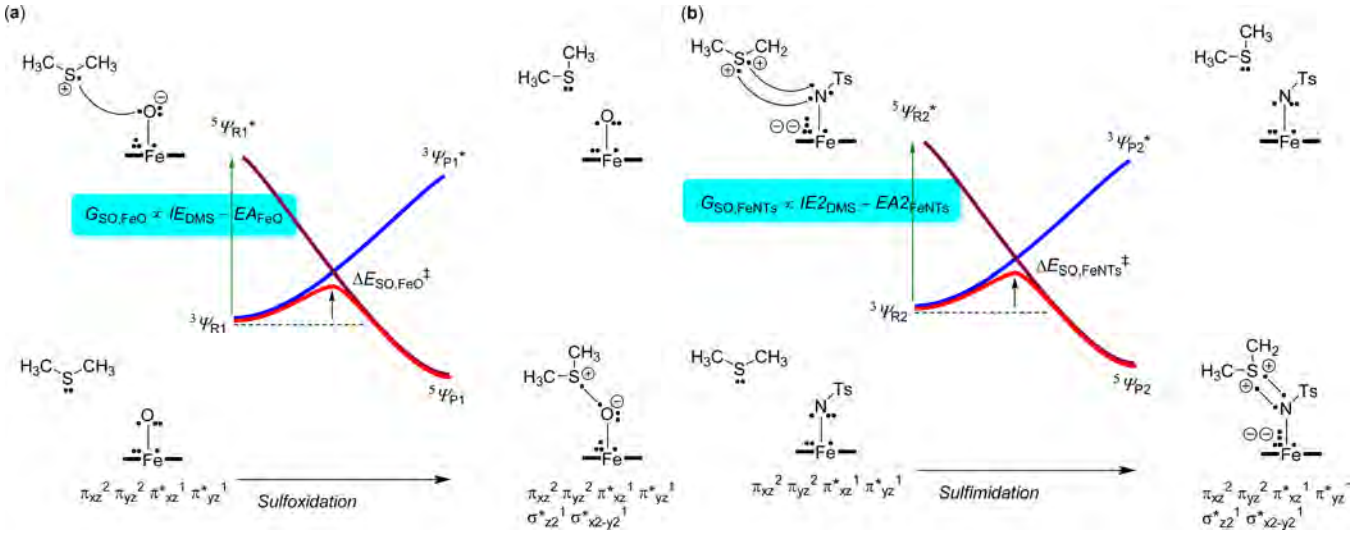

Figure 10. Valence bond curve crossing diagrams for sulfoxidation/sulfimidation from substrate by $[Fe^{IV}(O)(N4Py)]^{2+}$ (a) and $[Fe^{III}(NTs)(N4Py)]^{+}$ (b). Valence electrons are identified with a dot, and lines (straight or bent) in chemical structures refer to bonds.

a result of this, the electron transfer reaction of **1** with CHD is endergonic, whereas it is exergonic with **2**, eqs 9 and 10.

$$\mathbf{1} + \mathrm{CHD} \rightarrow [Fe^{III}(O)(N4Py)]^{+} + \mathrm{CHD}^{+\bullet} \qquad \Delta G = 15.8\ \mathrm{kcal\ mol^{-1}} \tag{9}$$

$$\mathbf{2} + \mathrm{CHD} \rightarrow [Fe^{III}(NTs)(N4Py)]^{+} + \mathrm{CHD}^{+\bullet} \qquad \Delta G = -4.1\ \mathrm{kcal\ mol^{-1}} \tag{10}$$

Indeed, a geometry optimization of the reactant complexes $\mathbf{R}_{H1,1}$ and $\mathbf{R}_{H1,2}$ shows that the iron(IV)-tosylimido group is reduced to an iron(III) species, whereas no electron transfer has occurred for the iron(IV)-oxo intermediate. As a consequence, the hydrogen atom abstraction in $\mathbf{TS}_{H1,1}$ is from CHD, whereas it is from $\mathrm{CHD}^{+\bullet}$ in $\mathbf{TS}_{H1,2}$. The C−H bond strength in $\mathrm{CHD}^{+\bullet}$ is considerably weaker than that in CHD by ΔG = 24.7 kcal $\mathrm{mol^{-1}}$, which should lower the barrier as well.

In order to find out whether the thermodynamics and kinetics of eq 10 is affected by the tosyl group bound to the iron(IV)-imido, we decided to calculate the same reaction for $[Fe^{IV}(NCH_3)(N4Py)]^{2+}$ and $[Fe^{IV}(NC_6H_5)(N4Py)]^{2+}$ as possible oxidants. We find free energy values (ΔG with solvent corrections) for eq 10 of 25.1 kcal $\mathrm{mol^{-1}}$ for $[Fe^{IV}(NCH_3)(N4Py)]^{2+}$ and 20.1 kcal $\mathrm{mol^{-1}}$ for $[Fe^{IV}(NC_6H_5)(N4Py)]^{2+}$. Consequently, the tosylimido group is strongly electron-withdrawing and enables a long-range electron transfer, while this is not possible with the alternative $[Fe^{IV}(NCH_3)(N4Py)]^{2+}$ and $[Fe^{IV}(NC_6H_5)(N4Py)]^{2+}$ complexes.

A HAT reaction of a substrate with **1** or **2** will lead to radical intermediates **I** with a reaction (free) energy equal to the difference in BDE_{CH} and BDE_{NH}/BDE_{OH}. Moreover, often the natural logarithm of the rate constant for HAT also is proportional to either BDE_{CH} or BDE_{OH} as seen in several examples of metal-oxo complexes.[48] Technically, however, the BDE_{OH} value essentially represents an electron and a proton transfer, which do not necessarily transfer to the same place. The BDE_{OH} is described in eq 11 into individual components for the electron affinity (EA), the acidity of the hydroxo group (ΔG_{acid}), and the ionization energy of an isolated hydrogen atom (IE_H).[49]

$$BDE_{OH} = -EA - \Delta G_{acid} - IE_H \tag{11}$$

The ionization energy of a hydrogen atom is 13.598 eV,[50] and together with our reported values of BDE_{OH}/BDE_{NH} and EA from Figure 8, we calculate a ΔG_{acid} = 211.8 kcal $\mathrm{mol^{-1}}$ for $[Fe^{IV}(O)(N4Py)]^{2+}$, whereas values of 262.1 and 343.5 kcal $\mathrm{mol^{-1}}$ are found for $[Fe^{IV}(NTs)(N4Py)]^{2+}$ and $[Fe^{III}(NTs)(N4Py)]^{2+}$. Thus, based on the acidity values, one would expect the iron(IV)-tosylimido and iron(III)-tosylimido complexes to be much better oxidants of HAT reactions. Indeed, the DFT calculated reaction energy for the HAT reaction is well larger for **2** than it is for **1** in agreement with the relative acidity values. The fact that the barrier heights do not follow this trend is due to stereochemical interactions of the approaching substrate with the bulky tosylimido group. The iron(IV)-oxo group, on the other hand, experiences very little stereochemical interactions with the approaching substrate.

Sulfoxidation Mechanisms. Subsequently, we investigated the sulfoxidation and sulfimidation of dimethylsulfide (DMS) by **1** and **2**, respectively, and the calculated potential energy profile for $[Fe^{IV}(NTs)(N4Py)]^{2+}$ is given in Figure 9, as well as the rate determining transition states for all systems calculated. The collision of DMS with oxidant leads to the formation of a reactant complex $\mathbf{R}_{SO}$, and heteroatom oxidation proceeds via barrier $\mathbf{TS}_{SO}$ to form the product complexes $\mathbf{P}_{SO}$. In both sets of calculations, the substrate approaches the oxidant from the side and reacts in a concerted pathway by insertion of the sulfide into the O/N system. Optimized geometries of the transition states give an FeN−SMe_2 distance that is only slightly longer than the FeO−SMe_2 distance, and in both cases it is longer in the quintet than in the triplet spin state.

The imaginary frequencies found for the $\mathbf{TS}_{SO}$ barriers are significantly lower than the ones reported above for the hydrogen atom abstraction barriers because heavier atoms are involved in the motion. The geometries and imaginary frequencies are in good agreement with previous substrate sulfoxidation transition states from the literature.[51]

In both chemical systems, the product complexes are most stable in the quintet spin state, whereas reactants (**1** and **2**) have a triplet spin ground state. This indicates that a spin crossover from triplet to quintet will need to take place on the potential energy surface during the course of the reaction. In

dx.doi.org/10.1021/ja508403w | J. Am. Chem. Soc. 2014, 136, 17102−17115

the sulfimidation reaction, the quintet spin transition state is well below the triplet in energy ($\Delta G^{\ddagger}$ = 17.7 kcal mol^{-1} for ^{5}**TS**$_{SO,2}$ and $\Delta G^{\ddagger}$ = 44.9 kcal mol^{-1} for ^{3}**TS**$_{SO,2}$), and consequently the spin state crossing happens well before the sulfimidation barrier.

The opposite is found for the reaction starting with the iron(IV)-oxo species, where ^{3}**TS**$_{SO,1}$ is lower in energy than ^{5}**TS**$_{SO,1}$. Furthermore, the absolute value of the barrier height for sulfoxidation is well higher than the sulfimidation reaction. Therefore, DFT predicts dimethylsulfide to react faster with [Fe^{IV}(NTs)(N4Py)]$^{2+}$ than with [Fe^{IV}(O)(N4Py)]$^{2+}$ in agreement with experimental observation (compare with Table 1).

Note that in the corresponding reactant complexes (**R**$_{SO,1}$ and **R**$_{SO,2}$) no charge transfer has occurred from substrate to oxidant in contrast to the results described in Figure 6 for **R**$_{H,2}$. This implies that the reactivities of **1** as well as the sulfimination by **2** start from an iron(IV) species, whereas the reaction of hydrogen atom abstraction by **2** is performed by its reduced species, that is, [Fe^{III}(NTs)(N4Py)]$^{+}$, and ionized CHD. Because of this difference the reactivity pattern has changed.

To further understand the heteroatom oxidation mechanism by **1** and **2** and to find the origin of the reactivity differences, we developed the corresponding VB curve crossing diagrams (Figure 10). These diagrams are similar to those reported above for the HAT processes but now connect the reactant wave function ($^{3}\Psi_{R}$) with the product wave function ($^{5}\Psi_{P}$) directly in a concerted reaction step. The sulfoxidation by iron(IV)-oxo complexes follows a VB diagram as reported before,[45c,52] whereby essentially a single electron transfer in the transition state for S−O bond formation occurs.

One of the electrons from one of the lone-pairs of the DMS substrate is transferred to the iron (into the $\sigma^{*}_{z^2}$ orbital), and a new S−O bond is formed between the singly occupied orbital on S with the singly occupied 2p$_x$ orbital on oxygen. The corresponding promotion gap for the sulfoxidation of DMS by **1** will, therefore, be proportional to the ionization potential of DMS (IE$_{DMS}$) as well as the electron affinity of **1** (EA$_{FeO}$). Indeed previous studies on trends in substrate sulfoxidation by iron(IV)-oxo complexes showed a linear correlation between the barrier height (**TS**$_{SO}$) and the IE of the substrate.[51c]

In the case of the reaction of DMS with **2**, the orbital occupation and group spin densities in the transition state implicate a double electron transfer and the formation of an electronic state that resembles the product complex. Thus, the double electron transfer with **2** occurs early on the potential energy surface and both electrons are transferred in the **TS**, while with **1** only one electron has moved yet in **TS**$_{SO}$. Because of this, the barrier height according to the VB curve crossing diagram will be dependent on the second ionization potential of DMS (IE2$_{DMS}$) for the removal of two electrons (from both lone pairs on sulfur) from DMS. At the same time, the oxidant accepts two electrons (into $\sigma^{*}_{x^2-y^2}$ and $\sigma^{*}_{z^2}$), and hence the double electron affinity (EA2$_{FeNTs}$) will determine the barrier height. The free energy (ΔG_{solv}) for conversion of [Fe^{IV}(NTs)(N4Py)]$^{2+}$ into [Fe^{III}(NTs)(N4Py)]$^{+}$ is 137.4 kcal mol^{-1} and the subsequent electron abstraction another 92.7 kcal mol^{-1} (Figure 8).

By contrast, the first electron affinity for [Fe^{IV}(O)(N4Py)]$^{2+}$ is 117.6 kcal mol^{-1}, and the addition of a second electron is 74.8 kcal mol^{-1}. Consequently, the two electron abstraction by **2** is 37.7 kcal mol^{-1} more favorable than that by **1**, which makes the two-electron transfer process for the heteroatom oxidation thermochemically favorable for the [Fe^{IV}(NTs)(N4Py)]$^{2+}$ complex, and as a result **TS**$_{SO,1}$ is higher in energy than **TS**$_{SO,2}$. Therefore, the iron(IV)-tosylimido complex will react with higher rate constants with sulfides than the corresponding iron(IV)-oxo complex.

The DFT and VB analyses, therefore, highlight the differences in chemical properties of [Fe^{IV}(NTs)(N4Py)]$^{2+}$ versus [Fe^{IV}(O)(N4Py)]$^{2+}$ that enable differences in reactivity patterns.

CONCLUSIONS

A combined kinetics and computational study is presented on the relative oxidative power of iron(IV)-oxo and iron(IV)-tosylimido. The experimental studies show that the iron(IV)-tosylimido reacts faster in heteroatom oxidation reactions, such as sulfimidation, compared with the iron(IV)-oxo species. However, the opposite trend is found for HAT reactions from, for example, *para*-X-benzyl alcohol and fluorene. Subsequent DFT calculations confirmed the experimentally observed trends and gave smaller barriers for HAT by iron(IV)-oxo complexes relative to iron(IV)-imido, whereas the reverse trend is found for heteroatom transfer. The origin of the rate reversal was investigated through a thermochemical analysis of the bond breaking and electron transfer processes. It was found that the electron affinity of [Fe^{IV}(NTs)(N4Py)]$^{2+}$ is so high that it accepts electrons from HAT substrates at a large distance, which was due to differences in orbital interactions compared with the iron(IV)-oxo species. As a result of that, the actual HAT is performed by its reduced species, that is, [Fe^{III}(NTs)(N4Py)]$^{+}$, which is catalytically much less potent than an iron(IV)-oxo species. On the other hand, heteroatom transfer reactions do not start with a long-range electron transfer but proceed via a rate determining group transfer, whereby two-electrons are transferred to the iron(IV)-imido, whereas only one electron is transferred yet at the same point along the potential energy profile in the reaction with the iron(IV)-oxo complex. A thermochemical and valence bond analysis has identified the key components that drive the reaction mechanism and cause a reactivity preference switch from preferred heteroatom transfer for iron(IV)-tosylimido to hydrogen atom transfer for iron(IV)-oxo.

ASSOCIATED CONTENT

Supporting Information

Detailed description of methods and techniques as well as full data of the calculations, including optimized geometries and Cartesian coordinates, as well as tables with group spin densities, group charges, absolute (free) energies, and relative (free) energies. This material is available free of charge via the Internet at http://pubs.acs.org.

AUTHOR INFORMATION

Corresponding Authors

sam.devisser@manchester.ac.uk
dkclcre@yahoo.com
sastricv@iitg.ernet.in

Notes

The authors declare no competing financial interest.

ACKNOWLEDGMENTS

The National Service of Computational Chemistry Software (NSCCS) is thanked for providing generous CPU time. Research support was provided by the Department of Science

and Technology, India (SR/S1/IC-02/2009), and Council for Scientific & Industrial Research (01(2527)/11/EMR-II) to C.V.S. D.K. acknowledges Department of Science and Technology (New Delhi) for a Ramanujan Fellowship. A.S.F. thanks the Tertiary Education Trust Fund for a studentship.

REFERENCES

(1) (a) Sono, M.; Roach, M. P.; Coulter, E. D.; Dawson, J. H. *Chem. Rev.* **1996**, *96*, 2841−2888. (b) Groves, J. T. *Proc. Natl. Acad. Sci. U.S.A.* **2003**, *100*, 3569−3574. (c) Ortiz de Montellano, P. R., Ed. *Cytochrome P450: Structure, Mechanism and Biochemistry*, 3rd ed.; Kluwer Academic/Plenum Publishers: New York, 2004. (d) Denisov, I. G.; Makris, T. M.; Sligar, S. G.; Schlichting, I. *Chem. Rev.* **2005**, *105*, 2253−2277. (e) Kadish, K. M., Smith, K. M., Guilard, R., Eds. *Handbook of Porphyrin Science*; World Scientific: Hackensack, NJ, 2010. (f) Ortiz de Montellano, P. R. *Chem. Rev.* **2010**, *110*, 932−948. (g) O'Reilly, E.; Koehler, V.; Flitsch, S.; Turner, N. *Chem. Commun.* **2011**, *47*, 2490−2501. (h) Grogan, G. *Curr. Opin. Chem. Biol.* **2011**, *15*, 241−248.

(2) (a) Solomon, E. I.; Brunold, T. C.; Davis, M. I.; Kemsley, J. N.; Lee, S.-K.; Lehnert, N.; Neese, F.; Skulan, A. J.; Yang, Y.-S.; Zhou, J. *Chem. Rev.* **2000**, *100*, 235−349. (b) Bugg, T. D. H. *Curr. Opin. Chem. Biol.* **2001**, *5*, 550−555. (c) Costas, M.; Mehn, M. P.; Jensen, M. P.; Que, L., Jr. *Chem. Rev.* **2004**, *104*, 939−986. (d) Bruijnincx, P. C. A.; van Koten, G.; Klein Gebbink, R. J. M. *Chem. Soc. Rev.* **2008**, *37*, 2716−2744. (e) Bugg, T. D. H.; Ramaswamy, S. *Curr. Opin. Chem. Biol.* **2008**, *12*, 134−140. (f) Abu-Omar, M. M.; Loaiza, A.; Hontzeas, N. *Chem. Rev.* **2005**, *105*, 2227−2252. (g) Kryatov, S. V.; Rybak-Akimova, E. V.; Schindler, S. *Chem. Rev.* **2005**, *105*, 2175−2226. (h) Kovaleva, E. G.; Lipscomb, J. D. *Nat. Chem. Biol.* **2008**, *4*, 186−193. (i) He, P.; Moran, G. R. *Curr. Opin. Chem. Biol.* **2009**, *13*, 443−450.

(3) (a) Guengerich, F. P. *Chem. Res. Toxicol.* **2001**, *14*, 611−650. (b) Munro, A. W.; Girvan, H. M.; McLean, K. J. *Nat. Prod. Rep.* **2007**, *24*, 585−609.

(4) (a) Rittle, J.; Green, M. T. *Science* **2010**, *330*, 933−937. (b) de Visser, S. P.; Kumar, D., Eds., *Iron-Containing Enzymes: Versatile Catalysts of Hydroxylation Reactions in Nature*. RSC Publishing: Cambridge, U.K., 2011.

(5) (a) Groves, J. T. *J. Inorg. Biochem.* **2006**, *100*, 434−447. (b) Meunier, B.; de Visser, S. P.; Shaik, S. *Chem. Rev.* **2004**, *104*, 3947−3980.

(6) (a) White, R. E.; McCarthy, M. B. *J. Am. Chem. Soc.* **1984**, *106*, 4922−4926. (b) Svastits, E. W.; Dawson, J. H.; Breslow, R.; Gellman, S. H. *J. Am. Chem. Soc.* **1985**, *107*, 6427−6428. (c) Mahy, J.-P.; Bedi, G.; Battioni, P.; Mansuy, D. *J. Chem. Soc., Perkin Trans. II* **1988**, 1517−1524.

(7) (a) McIntosh, J. A.; Coelho, P. S.; Farwell, C. C.; Wang, Z. J.; Lewis, J. C.; Brown, T. R.; Arnold, F. H. *Angew. Chem., Int. Ed.* **2013**, *52*, 9309−9312. (b) Singh, R.; Bordeaux, M.; Fasan, R. *ACS Catal.* **2014**, *4*, 546−552.

(8) (a) Eikey, R. A.; Abu-Omar, M. M. *Coord. Chem. Rev.* **2003**, *243*, 83−124. (b) Berry, J. F. *Comments Inorg. Chem.* **2009**, *30*, 28−66. (c) Saouma, C. T.; Peters, J. C. *Coord. Chem. Rev.* **2011**, *255*, 920−937.

(9) (a) Bukowski, M. R.; Koehntop, K. D.; Stubna, A.; Bominaar, E. L.; Halfen, J. A.; Münck, E.; Nam, W.; Que, L., Jr. *Science* **2005**, *310*, 1000−1002. (b) Rohde, J.-U.; In, J.-H.; Lim, M. H.; Brennessel, W. W.; Bukowski, M. R.; Stubna, A.; Münck, E.; Nam, W.; Que, L., Jr. *Science* **2003**, *299*, 1037−1039. (c) Martinho, M.; Banse, F.; Bartoli, J.-F.; Mattioli, T. A.; Battioni, P.; Horner, O.; Bourcier, S.; Girerd, J.-J. *Inorg. Chem.* **2005**, *44*, 9592−9596. (d) Sastri, C. V.; Seo, M. S.; Park, M. J.; Kim, K. M.; Nam, W. *Chem. Commun.* **2005**, 1405−1407.

(10) (a) Che, C.-M.; Lo, V. K.-Y.; Zhou, C.-Y.; Huang, J.-S. *Chem. Soc. Rev.* **2011**, *40*, 1950−1975. (b) Lu, H.; Zhang, X. P. *Chem. Soc. Rev.* **2011**, *40*, 1899−1909. (c) Long, Z.; Liang, D. *Chin. Sci. Bull.* **2012**, *57*, 2352−2360. (d) Zdilla, M. J.; Dexheimer, J. L.; Abu-Omar, M. M. *J. Am. Chem. Soc.* **2007**, *129*, 11505−11511.

(11) See, for example, Zardi, P.; Caselli, A.; Macchi, P.; Ferretti, F.; Gallo, E. *Organometallics* **2014**, *33*, 2210−2218.

(12) (a) Scepaniak, J. J.; Bontchev, R. P.; Johnson, D. L.; Smith, J. M. *Angew. Chem., Int. Ed.* **2011**, *50*, 6630−6633. (b) Hohenberger, J.; Ray, K.; Meyer, K. *Nat. Commun.* **2012**, *3*, 1−13. (c) Torres-Alacan, J.; Das, U.; Filippou, A. C.; Vöhringer, P. *Angew. Chem., Int. Ed.* **2013**, *52*, 12833−12837. (d) Liu, Y.; Guan, X.; Wong, E. L.-M.; Liu, P.; Huang, J.-S.; Che, C.-M. *J. Am. Chem. Soc.* **2013**, *135*, 7194−7204. (e) Man, W.-L.; Xie, J.; Pan, Y.; Lam, W. W. Y.; Kwong, H.-K.; Ip, K.-W.; Yiu, S.-M.; Lau, K.-C.; Lau, T.-C. *J. Am. Chem. Soc.* **2013**, *135*, 5533−5536. (f) Man, W.-L.; Lam, W. W. Y.; Kwong, H.-K.; Yiu, S.-M.; Lau, T.-C. *Angew. Chem., Int. Ed.* **2012**, *51*, 9101−9104.

(13) Gouré, E.; Avenier, F.; Dubourdeaux, P.; Sénèque, O.; Albrieux, F.; Lebrun, C.; Clémancey, M.; Maldivi, P.; Latour, J.-M. *Angew. Chem., Int. Ed.* **2014**, *53*, 1580−1584.

(14) Klinker, E. J.; Jackson, T. A.; Jensen, M. P.; Stubna, A.; Juhász, G.; Bominaar, E. L.; Münck, E.; Que, L., Jr. *Angew. Chem., Int. Ed.* **2006**, *45*, 7394−7397.

(15) Vardhaman, A. K.; Barman, P.; Kumar, S.; Sastri, C. V.; Kumar, D.; de Visser, S. P. *Angew. Chem., Int. Ed.* **2013**, *52*, 12288−12292.

(16) Perrin, D. D., Ed., *Purification of Laboratory Chemicals*; Pergamon Press: Oxford, U.K., 1997.

(17) (a) Sharefkin, J. G., Ed. *Organic Syntheses*; Wiley: New York, 1973; Vol. *5*, p 658. (b) Taylor, S.; Gullick, J.; McMorn, P.; Bethell, D.; Bulman Page, P. C.; Hancock, F. E.; King, F.; Hutchings, G. J. *J. Chem. Soc., Perkin Trans. II* **2001**, 1714−1723.

(18) (a) Lubben, M.; Meetsma, A.; Wilkinson, E. C.; Feringa, B.; Que, L., Jr. *Angew. Chem., Int. Ed.* **1995**, *34*, 1512−1515. (b) Vardhaman, A. K.; Barman, P.; Kumar, S.; Sastri, C. V.; Kumar, D.; de Visser, S. P. *Chem. Commun.* **2013**, *49*, 10926−10928.

(19) (a) Kaizer, J.; Klinker, E. J.; Oh, N. Y.; Rohde, J.-U.; Song, W. J.; Stubna, A.; Kim, J.; Münck, E.; Nam, W.; Que, L., Jr. *J. Am. Chem. Soc.* **2004**, *126*, 472−473. (b) Vardhaman, A. K.; Sastri, C. V.; Kumar, D.; de Visser, S. P. *Chem. Commun.* **2011**, *47*, 11044−11046.

(20) (a) *Jaguar*, version 7.9, Schrodinger, LLC: New York, NY, 2011. (b) Frisch, M. J. et al. *Gaussian 09*, revision C.01; Gaussian, Inc.: Wallingford, CT, 2010.

(21) Cossi, M.; Barone, V.; Cammi, R.; Tomasi, J. *Chem. Phys. Lett.* **1996**, *255*, 327−335.

(22) See, for example, (a) Latifi, R.; Sainna, M. A.; Rybak-Akimova, E. V.; de Visser, S. P. *Chem.—Eur. J.* **2013**, *19*, 4058−4068. (b) Quesne, M. G.; Latifi, R.; Gonzalez-Ovalle, L. E.; Kumar, D.; de Visser, S. P. *Chem.—Eur. J.* **2014**, *20*, 435−446. (c) de Visser, S. P.; Quesne, M. G.; Martin, B.; Comba, P.; Ryde, U. *Chem. Commun.* **2014**, *50*, 262−282.

(23) (a) Becke, A. D. *J. Chem. Phys.* **1993**, *98*, 5648−5652. (b) Lee, C.; Yang, W.; Parr, R. G. *Phys. Rev. B* **1988**, *37*, 785−789.

(24) Hay, P. J.; Wadt, W. R. *J. Chem. Phys.* **1985**, *82*, 270−283.

(25) Grimme, S. *J. Chem. Phys.* **2006**, *124*, No. 034108.

(26) (a) Becke, A. D. *Phys. Rev. A* **1988**, *38*, 3098−3100. (b) Perdew, J. P. *Phys. Rev. B* **1986**, *33*, 8822−8824.

(27) Adamo, C.; Barone, V. *J. Chem. Phys.* **1999**, *110*, 6158−6169.

(28) Zhao, Y.; Truhlar, D. G. *Theor. Chem. Acc.* **2008**, *120*, 215−241.

(29) (a) de Visser, S. P. *Chem.—Eur. J.* **2006**, *12*, 8168−8177. (b) Heyes, D. J.; Sakuma, M.; de Visser, S. P.; Scrutton, N. S. *J. Biol. Chem.* **2009**, *284*, 3762−3767.

(30) Ji, L.; Zhang, J.; Liu, W.; de Visser, S. P. *Chem.—Asian J.* **2014**, *9*, 1175−1182.

(31) Nam, W.; Lee, Y.-M.; Fukuzumi, S. *Acc. Chem. Res.* **2014**, *47*, 1146−1154.

(32) Oh, N. Y.; Suh, Y.; Park, M. J.; Seo, M. S.; Kim, J.; Nam, W. *Angew. Chem., Int. Ed.* **2005**, *44*, 4235−4239.

(33) Cheng, W.-C.; Yu, W.-Y.; Li, C.-K.; Che, C.-M. *J. Org. Chem.* **1995**, *60*, 6840−6846.

(34) See, for example, (a) Meyer, K.; Roček, J. *J. Am. Chem. Soc.* **1972**, *94*, 1209−1214. (b) Pestovsky, O.; Bakac, A. *J. Am. Chem. Soc.* **2004**, *126*, 13757−13764. (c) Hanson, S. K.; Baker, R. T.; Gordon, J. C.; Scott, B. L.; Silks, L. A.; Thorn, D. L. *J. Am. Chem. Soc.* **2010**, *132*, 17804−17816.

(35) (a) Kumar, D.; Hirao, H.; Que, L., Jr.; Shaik, S. *J. Am. Chem. Soc.* **2005**, *127*, 8026−8027. (b) Hirao, H.; Kumar, D.; Que, L., Jr; Shaik, S. *J. Am. Chem. Soc.* **2006**, *128*, 8590−8606.
(36) (a) de Visser, S. P. *J. Am. Chem. Soc.* **2006**, *128*, 15809−15818. (b) de Visser, S. P. *Angew. Chem., Int. Ed.* **2006**, *45*, 1790−1793. (c) Ye, S.; Neese, F. *Proc. Natl. Acad. Sci. U.S.A.* **2011**, *108*, 1228−1233.
(37) (a) Karamzadeh, B.; Singh, D.; Nam, W.; Kumar, D.; de Visser, S. P. *Phys. Chem. Chem. Phys.* **2014**, *16*, 22611−22622. (b) de Visser, S. P.; Tan, L. S. *J. Am. Chem. Soc.* **2008**, *130*, 12961−12974.
(38) (a) Zhao, Y.; Truhlar, D. G. *Acc. Chem. Res.* **2008**, *41*, 157−167. (b) Schwabe, T.; Grimme, S. *Acc. Chem. Res.* **2008**, *41*, 569−579. (c) Weymuth, T.; Couzijn, E. P. A.; Chen, P.; Reiher, M. *J. Chem. Theory Comput.* **2014**, *10*, 3092−3103.
(39) (a) de Visser, S. P. *J. Am. Chem. Soc.* **2010**, *132*, 1087−1097. (b) Kumar, D.; Karamzadeh, B.; Sastry, G. N.; de Visser, S. P. *J. Am. Chem. Soc.* **2010**, *132*, 7656−7667. (c) Kumar, D.; Latifi, R.; Kumar, S.; Rybak-Akimova, E. V.; Sainna, M. A.; de Visser, S. P. *Inorg. Chem.* **2013**, *52*, 7968−7979.
(40) Kumar, D.; de Visser, S. P.; Sharma, P. K.; Cohen, S.; Shaik, S. *J. Am. Chem. Soc.* **2004**, *126*, 1907−1920.
(41) de Visser, S. P.; Ogliaro, F.; Shaik, S. *Angew. Chem., Int. Ed.* **2001**, *40*, 2871−2874.
(42) Kumar, D.; Tahsini, L.; de Visser, S. P.; Kang, H. Y.; Kim, S. J.; Nam, W. *J. Phys. Chem. A* **2009**, *113*, 11713−11722.
(43) (a) Conradie, J.; Ghosh, A. *Inorg. Chem.* **2010**, *49*, 243−248. (b) Jaccob, M.; Rajaraman, G. *Dalton Trans.* **2012**, *41*, 10430−10439.
(44) Leeladee, P.; Baglia, R. A.; Prokop, K. A.; Latifi, R.; de Visser, S. P.; Goldberg, D. P. *J. Am. Chem. Soc.* **2012**, *134*, 10397−10400.
(45) (a) Shaik, S.; Kumar, D.; de Visser, S. P. *J. Am. Chem. Soc.* **2008**, *130*, 10128−10140. (b) Shaik, S. *Phys. Chem. Chem. Phys.* **2010**, *12*, 8706−8720. (c) Shaik, S.; Lai, W.; Chen, H.; Wang, Y. *Acc. Chem. Res.* **2010**, *43*, 1154−1165.
(46) Shaik, S. S. *J. Am. Chem. Soc.* **1981**, *103*, 3692−3701.
(47) Fernández, I.; Frenking, G. *Chem. Commun.* **2006**, 5030−5032.
(48) See, for example, (a) Bordwell, F. G.; Cheng, J.-P.; Ji, G.-Z.; Satish, A. V.; Zhang, X. *J. Am. Chem. Soc.* **1991**, *113*, 9790−9795. (b) Mayer, J. M. *Acc. Chem. Res.* **1998**, *31*, 441−450. (c) Goldberg, D. P. *Acc. Chem. Res.* **2007**, *40*, 626−634. (d) Kang, Y.; Chen, H.; Jeong, Y. J.; Lai, W.; Bae, E. H.; Shaik, S.; Nam, W. *Chem.—Eur. J.* **2009**, *15*, 10039−10046.
(49) Green, M. T.; Dawson, J. H.; Gray, H. B. *Science* **2004**, *304*, 1653−1656.
(50) Lias, S. G. Ionization energy evaluation. In *NIST Chemistry Webbook*; Linstrom, P. J., Mallard, W. G., Eds.; NIST Standard Reference Database Number 69; National Institute of Standards andTechnology: Gaithersburg, MD, 2009; 20899 (http://webbook.nist.gov).
(51) (a) Sharma, P. K.; de Visser, S. P.; Shaik, S. *J. Am. Chem. Soc.* **2003**, *125*, 8698−8699. (b) Prokop, K. A.; Neu, H. M.; de Visser, S. P.; Goldberg, D. P. *J. Am. Chem. Soc.* **2011**, *133*, 15874−15877. (c) Kumar, D.; Sastry, G. N.; de Visser, S. P. *Chem.—Eur. J.* **2011**, *17*, 6196−6205.
(52) Shaik, S.; Wang, Y.; Chen, H.; Song, J.; Meir, R. *Faraday Discuss.* **2010**, *145*, 49−70.

PCCP

PAPER

Cite this: *Phys. Chem. Chem. Phys.*, 2014, **16**, 22611

Properties and reactivities of nonheme iron(IV)–oxo *versus* iron(V)–oxo: long-range electron transfer *versus* hydrogen atom abstraction†

Baharan Karamzadeh,[a] Devendra Singh,[b] Wonwoo Nam,*[c] Devesh Kumar*[b] and Sam P. de Visser*[a]

Received 11th July 2014,
Accepted 8th September 2014

DOI: 10.1039/c4cp03053b

www.rsc.org/pccp

Recent work of Nam and co-workers [J. Yoon, S. A. Wilson, Y. K. Jang, M. S. Seo, K. Nehru, B. Hedman, K. O. Hodgson, E. Bill, E. I. Solomon and W. Nam, *Angew. Chem., Int. Ed.*, 2009, **48**, 1257] on a biomimetic iron complex implicated a mixture of iron(IV)–oxo and iron(V)–oxo intermediates but the latter could not be spectroscopically characterized, hence its involvement was postulated. To gain insight into the relative activity of these iron(IV)–oxo *versus* iron(V)–oxo intermediates, we have performed an extensive density functional theory (DFT) study on the chemical properties of the chemical system of Nam *et al.*, namely $[Fe(O)(BQEN)(NCCH_3)]^{2+/3+}$ with BQEN = *N*,*N*′-dimethyl-*N*,*N*′-bis(8-quinolyl)ethane-1,2-diamine and their reactivity in hydrogen atom abstraction from ethylbenzene. We show that the perceived iron(V)–oxo species actually is an iron(IV)–oxo ligand cation radical, similar to cytochrome P450 compound I. Moreover, this intermediate has an extremely large electron affinity and therefore can abstract electrons from substrates readily. In our particular system, this means that prior to the hydrogen atom abstraction, an electron is abstracted to form an iron(IV)–oxo species, which subsequently abstracts a hydrogen atom from the substrate. Thus, our calculations show for the first time how some nonheme iron complexes react by long-range electron transfer and others directly *via* hydrogen atom abstraction. We have rationalized our results with detailed thermochemical cycles that explain the observed reactivity patterns.

Introduction

Nonheme iron dioxygenases are important enzymes for human health with essential functions that include DNA base repair mechanisms and oxidative cleavage of carotenoids.[1] In several organisms, natural product biosynthesis is catalysed by nonheme iron dioxygenases, and, therefore, they have important functions in biology as well as in biotechnology. In order to understand enzymatic reaction processes, synthetic model complexes have been developed and designed.[2] These biomimetic model complexes of nonheme iron oxidants are well studied and many biomimetic high-valent catalytic intermediates have been characterized in recent years.[3] For instance, to tackle the controversy in Rieske dioxygenases regarding the active oxidant in the reaction process, several biomimetic model complexes with iron(V)–oxo(hydroxo) as reactive features have been studied and their reactivity patterns established.[4]

All biomimetic Rieske dioxygenase models contain a hydroxo group in a *cis*-position of the iron(IV/V)–oxo group. Only few examples exist of biomimetic iron(V)–oxo intermediates without this *cis*-hydroxo ligand and spectroscopic studies gave indirect evidence of its existance.[5] Thus, McKenzie and co-workers reported the structural characterization of an iron(V)–oxo species with a monoionic multidentate ligand and found it to react with thioanisole efficiently.[6] Kim and co-workers used a tetradentate ligand system and formed the corresponding iron(V)–oxo species by heterolytic cleavage of an iron–acylperoxo intermediate.[7] They determined kinetic isotope effects (KIE, k_H/k_D), $H_2{}^{18}O$ exchange reactions and measured product distributions. Using a tetraamido macrocyclic ligand, Collins and co-workers studied the sulfoxidation of substrates by an iron(V)–oxo species and compared the rates with analogous iron(IV)–oxo species.[8] Finally, Nam and co-workers studied the reaction of $[Fe^{II}(BQEN)]^{2+}$, BQEN = *N*,*N*′-dimethyl-*N*,*N*′-bis(8-quinolyl) ethane-1,2-diamine, with CH_3CO_3H and found evidence of competing reaction mechanisms originating from

[a] *Manchester Institute of Biotechnology and School of Chemical Engineering and Analytical Science, the University of Manchester, 131 Princess Street, Manchester M1 7DN, UK. E-mail: sam.devisser@manchester.ac.uk; Fax: +44 (0)1613065201; Tel: +44 (0)1613064882*

[b] *Department of Applied Physics, School for Physical Sciences, Babasaheb Bhimrao Ambedkar University, Vidya Vihar, Rai Bareilly Road, Lucknow 226 025, India. E-mail: dkclcre@yahoo.com*

[c] *Department of Chemistry and Nano Science, Ewha Womans University, Seoul 120-750, Korea. E-mail: wwnam@ewha.ac.kr*

† Electronic supplementary information (ESI) available: Tables with absolute and relative energies as well as group spin densities and charges. See DOI: 10.1039/c4cp03053b

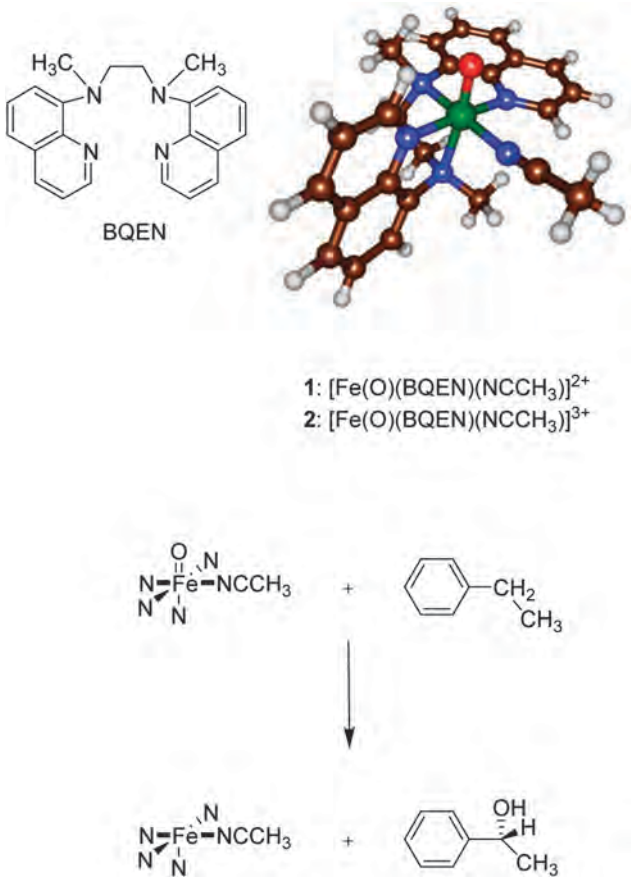

Scheme 1 Iron–oxo oxidants and ligand system studied in this work.

two oxidants in the reaction mixture that were tentatively assigned as $[Fe^{IV}(O)(BQEN)]^{2+}$ and $[Fe^{V}(O)(BQEN)]^{3+}$.[9] Their studies failed to unequivocally assign the active oxidant in the reaction mechanism, and therefore could not determine the relative reactivity of iron(IV)–oxo *versus* iron(V)–oxo. In order to resolve this dichotomy and gain general insight into the relative reactivity of iron(IV)–oxo *versus* iron(V)–oxo with nonheme ligand systems a computational study was conducted using the $[Fe^{IV}(O)(BQEN)(NCCH_3)]^{2+}$ (**1**) and $[Fe^{V}(O)(BQEN)(NCCH_3)]^{3+}$ (**2**) systems, Scheme 1.

Currently, very little is known regarding the catalytic activity of iron(V)–oxo intermediates and to the best of our knowledge, no direct comparison in reactivity between iron(IV)–oxo and iron(V)–oxo has been reported. We present here a DFT study to gain insight into the potential use of iron(V)–oxo intermediates as catalytic oxidants with ethylbenzene as the selected substrate. We present the first comparative study on the aliphatic hydroxylation by iron(IV)–oxo *versus* iron(V)–oxo using the BQEN ligand system shown in Scheme 1 and follow the mechanism of ethylbenzene activation leading to benzyl alcohol product complexes.

Methods

All studies reported here utilize density functional theory (DFT) methods as implemented in the Jaguar and Gaussian program packages.[10] We initially did exploratory gas-phase optimizations on $[Fe(O)(BQEN)(NCCH_3)]^{3+/2+}$ in Jaguar at the UB3LYP level of theory[11] and explored the catalytic mechanism of ethylbenzene hydroxylation. However, as most of our chemical systems are multiply charged ions we decided to do a subsequent set of calculations, where the complete project was done using a polarized continuum solvent model included during the geometry optimizations. These studies gave considerable differences from the gas-phase results and therefore we will focus on the solvent optimized calculations mainly. Details of the gas-phase calculations can be found in the ESI.† Thus, all geometry optimizations and frequencies were performed with a solvent model included with a dielectric constant mimicking acetonitrile. All local minima are characterized with a frequency calculation and have real frequencies only, whereas the transition states have one imaginary frequency for the correct mode. As transition metal containing complexes give close-lying electronic and spin states,[12] we calculated the $[Fe(O)(BQEN)(NCCH_3)]^{3+}$ complexes in the lowest lying doublet, quartet and sextet spin states and the $[Fe(O)(BQEN)(NCCH_3)]^{2+}$ complexes in the singlet, triplet and quintet spin states.

We tested the reproducibility and reliability of the density functional method by applying a range of unrestricted DFT methods, including B3LYP,[11] B3LYP-D3,[13] B3LYP*,[14] and OPBE.[15] There is a certain degree of fluctuation observed in the relative energies, spin state ordering and geometric details as commonly observed in nonheme iron complexes.[16] However, the results confirmed the assignment of the electron configuration of all complexes and reproduce experimental trends.

All optimizations and frequencies use a triple-ζ quality basis set (BS2) with LACV3P+ on iron and 6-311+G* on the rest of the atoms.[17] Previously, we used these methods extensively for the description of nonheme iron complexes and reproduced experimental free energies of activation within several kcal mol^{-1}.[18] To test the effect of the overall charge on the calculations we also performed a set of test calculations on charge neutral complexes, whereby the reactants and rate determining transition states were modified by counter-ions at a fixed distance of 15 Å from the axial nitrogen atom and with an angle of 120 degrees with respect to iron and the axial nitrogen atom. Point charges, Cl^- counter-ions and OH^- counter-ions were applied, but all results reproduced the solvent optimized results and did not give changes to the charge and spin distributions.

Kinetic isotope effects (KIEs) were calculated for the hydrogen atom abstraction reaction of ethylbenzene by **1** for the replacement of one or more hydrogen atoms of the substrate by deuterium atoms. We initially used the semi-classical Eyring equation (eqn (1)) to calculate KIE_E from the difference in free energies of activation ($\Delta G^{\ddagger}$) of the substrate and its deuterium substituted form following previously reported methods.[19] Eqn (1) uses the gas constant (R) and the actual temperature (273.15 K).

$$KIE_E = k_H/k_D = \exp\left\{\left(\Delta G^{\ddagger}_D - \Delta G^{\ddagger}_H\right)\Big/RT\right\} \qquad (1)$$

Further corrections due to tunnelling were applied using the Wigner model[20] that corrects KIE_E with the tunnelling ratio (Q_{tH}/Q_{tD}) as described in eqn (2) and (3).

 This journal is © the Owner Societies 2014

$$KIE_W = KIE_E \times Q_{tH}/Q_{tD} \quad (2)$$

$$Q_t = 1 + \frac{1}{24}\left(\frac{h\nu}{k_B T}\right)^2 \quad (3)$$

In eqn (3), k_B represents the Boltzmann's constant, h is Planck's constant and ν is the imaginary frequency in the transition state.

Results

Isolated reactants 1 and 2

Our study uses density functional theory (DFT) methods and is focused on the chemical systems of ref. 9 as described in Scheme 1, where we included an acetonitrile solvent molecule in the sixth ligand position of the metal: $[Fe(O)(BQEN)(NCCH_3)]^{2+}$ (**1**) and $[Fe(O)(BQEN)(NCCH_3)]^{3+}$ (**2**). These structures have the metal in formal oxidation state iron(IV) and iron(V), respectively. Before we will look into the reactivity patterns of structures **1** and **2** with substrates, we will describe the electronic properties of the optimized geometries of **1** and **2**, Fig. 1.

The lowest lying singlet, triplet and quintet spin states of **1** were calculated, but the singlet state was found to be high in energy. Similarly, **2** was investigated in the doublet and quartet spin states only. Fig. 1 displays the molecular valence orbitals of **1** and **2**, which are determined by the mixing of the metal 3d orbitals with its ligands. Thus, there are three π* molecular orbitals (π^*_{xy}, π^*_{yz}, π^*_{xz}) representing the anti-bonding interactions of the 3d iron orbitals with 2p orbitals on the oxo group. High in energy are two σ* orbitals for the anti-bonding interactions of the metal with the ligands in the *xy*-plane ($\sigma^*_{x^2-y^2}$) and with ligands along the *z*-axis ($\sigma^*_{z^2}$), whereby the *z*-axis is defined as parallel to the Fe–O bond. In the iron(IV)–oxo complex, *i.e.* ^{3,5}**1**, the set of orbitals shown in Fig. 1 is occupied by four electrons, which gives two low-lying solutions with either triplet or quintet spin: **1** has a triplet spin ground state with electronic configuration $\pi^*_{xy}{}^2\ \pi^*_{xz}{}^1\ \pi^*_{yz}{}^1$ (^{3}**1**) that is somewhat lower in energy than the quintet spin state with configuration $\pi^*_{xy}{}^1\ \pi^*_{xz}{}^1\ \pi^*_{yz}{}^1\ \sigma^*_{x^2-y^2}{}^1$ (^{5}**1**), *vide infra*. In both spin states **1** has the metal in formal oxidation state iron(IV). The spin state ordering matches previous studies on hexacoordinated non-heme iron biomimetic model complexes and also supports the experimentally reported absorption band at λ_{max} = 740 nm characteristic for triplet iron(IV)–oxo species and assigned by Nam *et al.* on $[Fe(O)(BQEN)(NCCH_3)]^{2+}$.[3,9,21]

Upon oxidation of ^{3,5}**1**, however, several possibilities arise for the electronic configuration of **2**. Firstly, ^{3}**1** can lose an electron from π^*_{yz} to give a doublet spin configuration with $\pi^*_{xy}{}^2\ \pi^*_{xz}{}^1$ orbital occupation or lose an electron from the

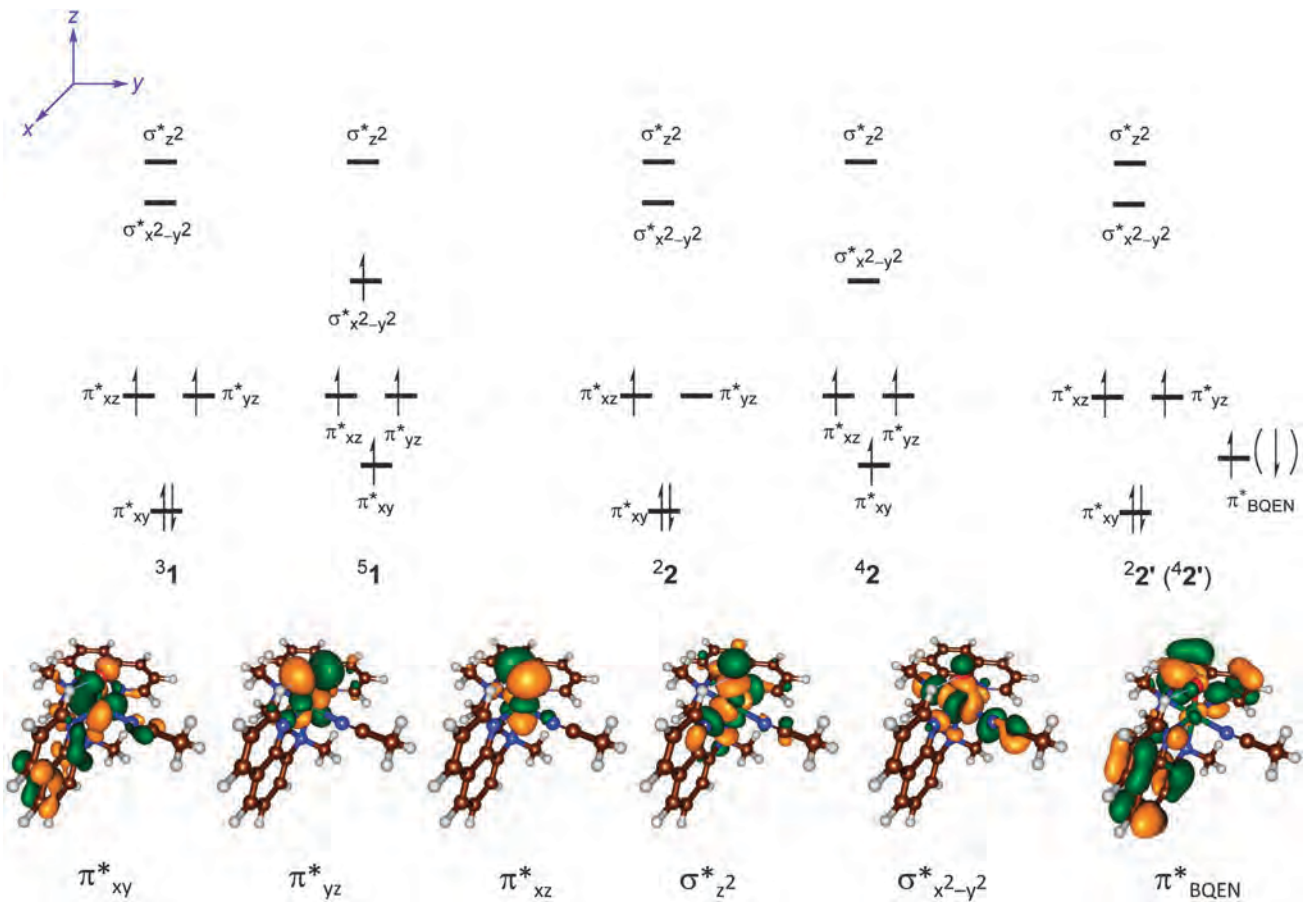

Fig. 1 High-lying occupied and low-lying virtual orbitals of **1** and **2**. The top panel shows the different electronic configurations of **1** and **2** considered and the bottom shows the orbital shapes of the valence orbitals.

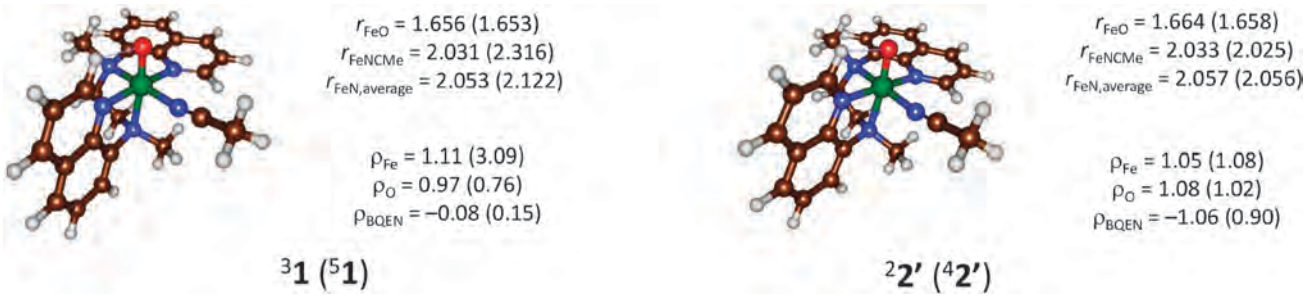

Fig. 2 Gas-phase optimized geometries (UB3LYP/BS1) of ^{3,5}**1** and ^{2,4}**2** with bond lengths in angstroms and group spin densities (ρ) in atomic units.

doubly occupied π^*_{xy} orbital to give a quartet spin complex with $\pi^*_{xy}{}^1\ \pi^*_{xz}{}^1\ \pi^*_{yz}{}^1$ configuration. These two states have the metal in formal oxidation state iron(v) and are labelled as ^{2,4}**2** in Fig. 1. In addition, the oxidation of ^{3}**1** can expel an electron from a ligand π-type orbital, such as π^*_{BQEN}, and lead to an electronic configuration $\pi^*_{xy}{}^2\ \pi^*_{xz}{}^1\ \pi^*_{yz}{}^1\ \pi^*_{BQEN}{}^1$, whereby the radical on the ligand can be either ferromagnetically or anti-ferromagnetically coupled to the metal-based unpaired electrons in an overall quartet or doublet spin state (^{4,2}**2**′). The latter, therefore, can be seen as an iron(IV)–oxo ligand cation radical species with configuration $[Fe^{IV}(O)(BQEN^{+\bullet})(NCCH_3)]^{3+}$ and is reminiscent of compound I of cytochrome P450 enzymes, which was characterized as an iron(IV)–oxo heme cation radical species, *i.e.* $[Fe^{IV}(O)(heme^{+\bullet})Cys]$.[22]

Details of the optimized geometries of ^{3,5}**1** and ^{2,4}**2**′ in the gas phase are reported in Fig. 2. In the gas-phase the triplet spin state is the ground state by ΔE + ZPE (ΔG) = 2.0 (0.2) kcal mol^{-1}. Optimized geometries are in line with previously reported structures on non-heme iron(IV)–oxo complexes with a short Fe–O bond of 1.66 Å, which implicates a double bond.[21,23] Group spin densities and charges confirm the orbital assignment of ^{3,5}**1** as described in Fig. 2 with electronic configuration of $\pi^*_{xy}{}^2\ \pi^*_{xz}{}^1\ \pi^*_{yz}{}^1$ for ^{3}**1** and $\pi^*_{xy}{}^1\ \pi^*_{xz}{}^1\ \pi^*_{yz}{}^1\ \sigma^*_{x^2-y^2}{}^1$ for ^{5}**1**.

Nam and co-workers[9] using absorption and infrared spectroscopy and extended X-ray absorption fine structure (EXAFS) studied the $[Fe(O)(BQEN)(NCCH_3)]^{2+}$ complex experimentally. They identified an iron–oxo bond of 1.67 Å and an average Fe–N distance of 1.97 Å. Our calculated Fe–O distances for ^{3,5}**1** in Fig. 2 match the experimental values excellently. The experimentally reported Fe–N distances are in good agreement with the triplet spin structures, but not with the quintet spin state structures due to single occupation of the $\sigma^*_{x^2-y^2}$ orbital that elongates the distances between the metal and its ligands. Therefore, the computational studies support the characterization of a triplet spin ground state of **1**.

Geometry optimizations of ^{2,4}**2**′, however, gives a low-lying solution with two singly occupied π* orbitals coupled to a radical on the BQEN unit with spin densities of ρ_{BQEN} = −1.06 (0.90) in the doublet and quartet spin states. The optimized geometries, therefore, correspond to an electronic state $[Fe^{IV}(O)(BQEN^{+\bullet})(NCCH_3)]^{3+}$, *i.e.* ^{2,4}**2**′ in Fig. 1, rather than the anticipated iron(v)–oxo species. Although we attempted to swap molecular orbitals to generate the iron(v) solution (^{2,4}**2**) these calculations converged back to ^{2,4}**2**′, which therefore is the molecular ground state.

As the complex has a large overall charge of +3, we decided to reoptimize these structures using the polarized continuum model mimicking an acetonitrile solution. However, the new model did not affect the spin state ordering and electronic configuration of the ground state and the same electronic state was found. It appears, therefore, that ^{2,4}**2**′ is the electronic ground state that can be described as $[Fe^{IV}(O)(BQEN^{+\bullet})(NCCH_3)]^{3+}$ with an iron(IV)–oxo group coupled to a ligand radical. As both doublet and quartet spin states represent the same orbital occupation, namely $\pi^*_{xy}{}^2\ \pi^*_{xz}{}^1\ \pi^*_{yz}{}^1\ \pi^*_{BQEN}{}^1$, we calculate them within 2 kcal mol^{-1}. This result is similar to the spin state energies of ferromagnetically *versus* antiferromagnetically coupled doublet and quartet spin states of compound I of P450, where these spin states were also found to be within a couple of kcal mol^{-1} from each other. Moreover, the energy gap was found to be sensitive to the local environment, including hydrogen bonding interactions to the oxidant as well as solvent effects.[24] Furthermore, these two spin states result in two-state-reactivity patterns with substrates on competing spin-state surfaces.[25] Analogously to P450 compound I, the iron(v)–oxo species is an excited state of the molecular ground state with configuration $[Fe^{IV}(O)(BQEN^{+\bullet})(NCCH_3)]^{3+}$. Geometrically ^{2,4}**2**′ has metal–ligand bond lengths close to those found for ^{3}**1**, which is also an iron(IV)–oxo species.

Reactant complexes

Subsequently, ethylbenzene (EB) was added to the model complexes to create a long-range reactant complex (**RC**) as this was one of the substrates used in the experimental study and we investigated the benzyl hydroxylation processes. The electronic features of ^{3,5}**RC**$_1$ or $^{3,5}[Fe(O)(BQEN)(NCCH_3)\cdots EB]^{2+}$ and ^{2,4}**RC**$_2$ or $^{2,4}[Fe(O)(BQEN)(NCCH_3)\cdots EB]^{3+}$ will be discussed prior to the investigation of the catalytic mechanism. Considering that computational modelling occasionally is sensitive to the choice of the density functional used as well as on environmental variables,[26] some thorough testing of the structures, spin-state energetics and electronic configurations of ^{3,5}**RC**$_1$ and ^{2,4}**RC**$_2$ using a selection of density functional methods and procedures was carried out. Thus, we performed geometry optimizations of all complexes in the gas-phase at UB3LYP/BS1, but also did a full geometry optimization in a dielectric constant mimicking acetonitrile at UB3LYP/BS2 and finally a full geometry optimization in a dielectric constant at the UB3LYP-D3/BS2. In addition, single point calculations on the UB3LYP/BS2 optimized geometries using B3LYP with 15% HF exchange (B3LYP*), UB3LYP-D3 and OPBE were

 This journal is © the Owner Societies 2014

Table 1 Spin state energies and optimized geometries of reactant complexes as calculated using various DFT methods

				ΔE + ZPE						
				UB3LYP	UB3LYP	UB3LYP-D3	UB3LYP-D3	UB3LYP	UB3LYP*	OPBE
Structure	r_{FeO} [a,b]	r_{FeO} [b,c]	r_{FeO} [b,e]	Gas[a,d]	Solv[c,d]	Solv[c,d]	Solv[d,e]	PC[c,f]	Solv[c,d]	Solv[c,d]
^{3}**RC**$_1$	1.656	1.633	1.657	0.0	0.0	0.0	0.0	0.0	0.0	0.0
^{5}**RC**$_1$	1.653	1.627	1.653	10.3	2.5	7.4	8.2	8.7	6.0	2.4
^{2}**RC**$_2$	1.664	1.638	1.656	0.0	0.0	0.0	0.0	0.0	0.0	0.0
^{4}**RC**$_2$	1.664	1.631	1.653	0.6	−3.6	10.0	8.4	10.0	6.9	3.8

[a] UB3LYP/BS1 geometry optimization in the gas-phase. [b] Values in Å. [c] UB3LYP/BS2 geometry optimization in solvent. [d] ΔE + ZPE value with energies at the BS2 level of theory in kcal mol^{-1}. [e] UB3LYP-D3/BS2 geometry optimization in solvent. [f] Structure with added point charges that neutralize the system at 15 Å.

performed. Finally, single point calculations in the gas-phase with additional counter-ions or point charges included in the model at a distance of 15 Å that neutralize the chemical systems were carried out.

Table 1 presents the optimized Fe–O distance and spin-state energies as obtained using these different DFT models and methods. As can be seen all methods, models and optimization techniques give the same spin state ordering, but a certain degree of variation in the relative energies is observed typical for DFT calculated iron complexes.[26] In all cases ^{3}**RC**$_1$ and ^{5}**RC**$_1$ are characterized as $[Fe^{IV}(O)(BQEN)(NCCH_3)\cdots EB]^{2+}$ with orbital occupation $\pi^*_{xy}{}^2\,\pi^*_{xz}{}^1\,\pi^*_{yz}{}^1$ and $\pi^*_{xy}{}^1\,\pi^*_{xz}{}^1\,\pi^*_{yz}{}^1\,\sigma^*_{x^2-y^2}{}^1$, respectively, in agreement with what was found for structure ^{3,5}**1** above. Regardless of the method and whether the optimization is done in the gas-phase or in solvent, a triplet spin ground state that is well separated from the quintet spin state by 2.4–10.3 kcal mol^{-1} is found. Although this appears to be a large variation in spin state energies, actually for transition metal complexes, and, in particular iron(IV)–oxo complexes a strong variation of the ordering and relative energies is normal in DFT upon changing the density functional method or environmental effects.[27] Nevertheless, all methods give a triplet spin ground state in support of experimental studies.[17]

The situation is dramatically changed when ^{2,4}**RC**$_2$ is investigated with these methods and models. Whereas ^{2,4}**2′** was found as the electronic ground state with configuration $[Fe^{IV}(O)(BQEN^{+\bullet})(NCCH_3)]^{3+}$ with two unpaired π* electrons coupled to a radical on the ligand, by contrast, in ^{2,4}**RC**$_2$ we find yet another electronic configuration with two unpaired π* electrons that are coupled to an ethylbenzene radical, *i.e.* orbital occupation $\pi^*_{xy}{}^2\,\pi^*_{xz}{}^1\,\pi^*_{yz}{}^1\,\pi^*_{BQEN}{}^2\,\pi_{EB}{}^1$, where the latter orbital is a singly occupied π-orbital on ethylbenzene. Therefore, addition of an ethylbenzene molecule to ^{2,4}**2′** results in an intermolecular electron transfer from the substrate into the π^*_{BQEN} orbital of the oxidant and the creation of a complex $[Fe^{IV}(O)(BQEN)(NCCH_3)]^{2+}\cdots EB^{+\bullet}$. This happens regardless of the method and whether gas-phase or solvent models are used. It implies that $[Fe^{IV}(O)(BQEN^{+\bullet})(NCCH_3)]^{3+}$ is a strong oxidant and can abstract electrons from substrates readily. Most probably this is caused by its extremely large electron affinity, *vide infra*.

Note that outer-sphere electron transfer upon approach of a substrate onto a metal–oxo species has been calculated before on metal–porphyrins,[28,29] including a potential intermediate of nitric oxide synthase, where the arginine substrate was found to donate an electron to an iron(IV)–oxo heme cation radical species quickly. Furthermore, approach of a Zn^{2+} ion onto a high-valent manganese(V)–oxo corrolazine also led to the formation of a manganese(IV)–oxo corrolazine cation radical through valence tautomerization.[29] Finally, studies on the comparative electronic features of the iron(IV)–oxo heme species of cytochrome *c* peroxidase (C*c*P) *versus* ascorbate peroxidase implicated differences in electronic configuration as a result of a bound cation at a distance of 15 Å from the heme. DFT modelling on compound **I** of C*c*P tested the effect of a point charge with magnitude $Q = -1/+1$ on the electronic configuration.[30] It was found that a charge of $Q = +1$ gave an electronic state $[Fe^{IV}(O)(heme^{+\bullet})\cdots Trp_{191}]$, whereas a value of $Q = -1$ resulted in an alternative state corresponding to $[Fe^{IV}(O)(heme)\cdots Trp_{191}{}^{+\bullet}]$. These studies have shown that seemingly small external (but long-range) perturbations can have a major impact on the electronic configuration of the oxidant and consequently on its ability to react with substrates. However, for nonheme metal–oxo species this would be the first example of outer-sphere electron transfer upon substrate approach and is likely caused by the large electron affinity of the ligand. In the following we will describe whether the change in electronic configuration is beneficial or disadvantageous to the catalysis.

Ethylbenzene hydroxylation by 1 and 2

Subsequently, the benzyl hydroxylation of ethylbenzene by ^{3,5}**RC**$_1$ and ^{2,4}**RC**$_2$ was calculated. Fig. 3 displays the calculated reaction mechanism with optimized geometries of the rate determining transition states of the reaction starting from ^{3,5}**RC**$_1$. We calculate a stepwise mechanism with an initial hydrogen atom abstraction from the benzyl position of ethylbenzene *via* a transition state (**TS**$_{HA}$) to form a radical intermediate (**I**) followed by hydroxyl rebound *via* a transition state (**TS**$_{reb}$) to form alcohol products (**P**). In all cases the hydrogen atom abstraction is rate determining and the rebound barriers are small or negligible, so that we will focus on the **TS**$_{HA}$ pathway only here. Full details of the rest of the mechanism are given in the ESI.† In the gas phase very little energy difference between hydrogen atom abstraction from the *pro-S versus pro-R* site of the benzyl position of ethylbenzene by iron(IV)–oxo complexes was found. Recent computational studies on *S*-mandalate synthase showed that the shape and size of the substrate binding pocket determines

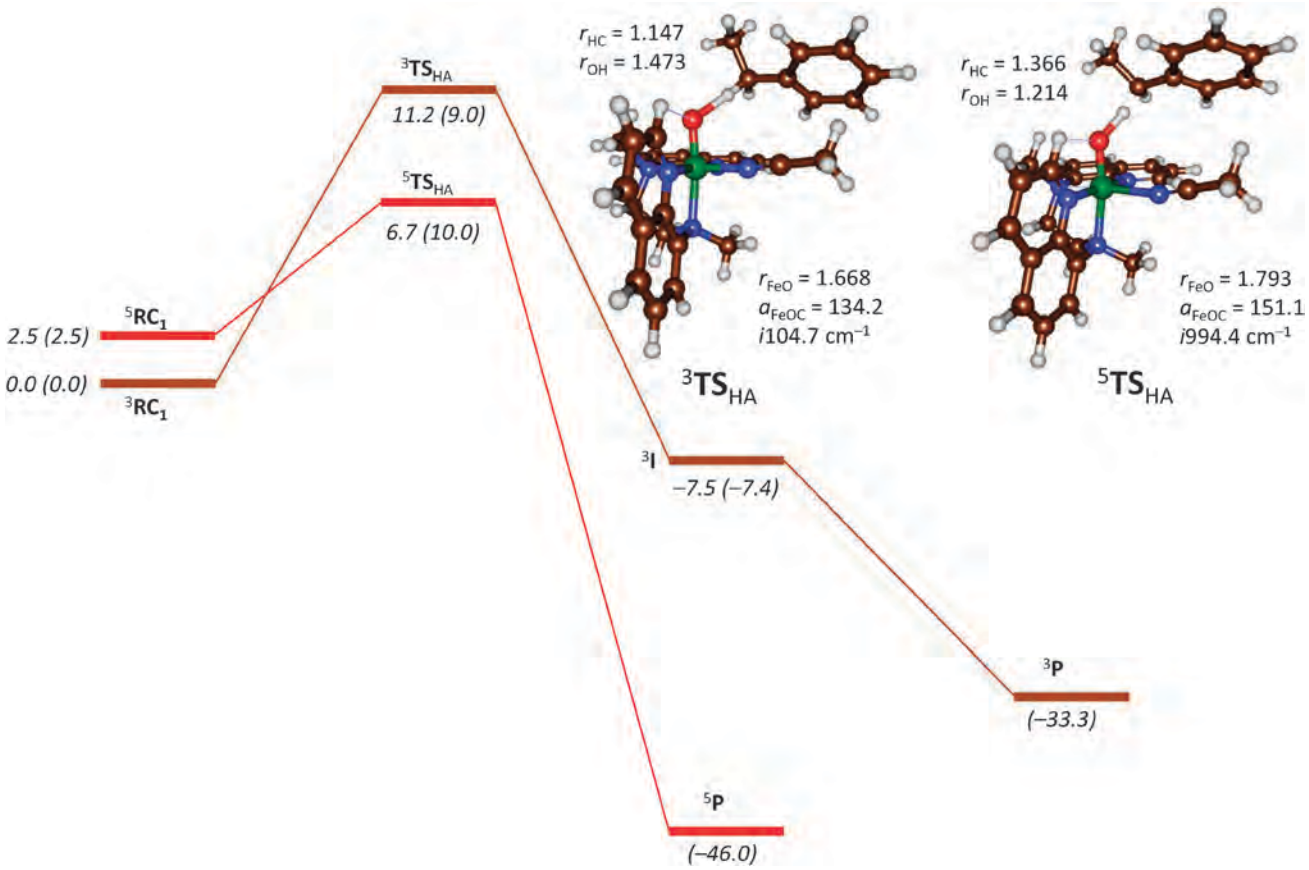

Fig. 3 DFT calculated potential energy profile for the hydrogen atom abstraction from EB by ^{3,5}**1** with energies given in kcal mol^{-1}. Also shown are optimized UB3LYP/BS2(solvent) geometries of ^{3,5}**TS**$_{HA}$ with bond lengths in angstroms, angles in degrees and the imaginary frequency in wave numbers. Relative energies represent ΔE + ZPE + E_{solv} values obtained after a full geometry optimization in solvent at the UB3LYP/BS2 (out of parenthesis) or at UB3LYP/BS2//UB3LYP/BS1 level of theory on a gas-phase optimized geometry.

whether the *pro-R* or *pro-S* hydrogen atom can be abstracted.[31] Indeed, site-selective mutations confirmed the computationally proposed hypothesis.

Geometrically, the ^{3,5}**TS**$_{HA}$ structures are quite distinct due to differences in electron transfer processes that happen in these transition states. In the triplet spin state the hydrogen atom transfer is accompanied with electron transfer from the substrate into the π^*_{xz} orbital and hence the substrate attacks under an angle (a_{FeOC} = 134.2°) to get ideal orbital overlap between donor and acceptor orbitals.[32] In the quintet spin state the hydrogen atom abstraction is accompanied with electron transfer from the substrate into the vacant $\sigma^*_{z^2}$ orbital and hence the substrate attacks from the top with considerably larger FeOC angles than found in the triplet spin state (a_{FeOC} = 151.1°), which gives an iron(III)–hydroxo complex with a fully exchange coupled metal 3d system with five singly occupied orbitals that is antiferromagnetically coupled to a benzyl radical: ^{5}**I** has electronic configuration $\pi^*_{xy}{}^1\,\pi^*_{xz}{}^1\,\pi^*_{yz}{}^1\,\sigma^*_{x^2-y^2}{}^1\,\sigma^*_{z^2}{}^1\,\pi_{EB}{}^1$. This exchange stabilization makes ^{5}**I** considerably lower in energy than the corresponding triplet spin complex. As a consequence, ^{5}**TS**$_{HA}$ is stabilized over ^{3}**TS**$_{HA}$, although dispersion corrections make them almost degenerate. Nevertheless, the barrier heights on both spin state surfaces are small and implicate an efficient hydrogen atom abstraction process in agreement with experiment.[9] When the enthalpy values from Fig. 3 are converted to a free energy of activation, a value of ΔG_{solv} = 10.8 kcal mol^{-1} on the triplet spin state surface is found, which is in reasonable agreement with the experimentally reported free energy of activation of Nam *et al.*[9]

The experimental studies on ethylbenzene hydroxylation by **RC**$_1$ were found to proceed with a kinetic isotope effect (KIE) of 10 for the replacement of hydrogen atoms by deuterium in the substrate. To estimate the isotope effects for replacement of the transferrable hydrogen atom by deuterium in the reaction passing ^{3}**TS**$_{HA}$ we used the Eyring and Wigner models (see Methods section) to estimate the KIE. Values of KIE$_E$ and KIE$_W$ of 4.9 and 5.4 were obtained, whereas these values increased up to 5.1 and 5.7, respectively, when the fully deuterated substrate was used. Our calculated isotope effect, therefore, predicts the same trends as experiment.

We then calculated a reaction complex of **2** with ethylbenzene (^{2,4}**RC**$_2$) in the gas phase as well as with solvent models included during the geometry optimizations. As mentioned above, the optimized geometry and group spin densities of ^{2}**RC**$_2$ characterize the reactant complex as ^{3}[Fe^{IV}(O)(BQEN)(NCCH$_3$)]$^{2+}\cdots{}^{2}$EB$^{+\bullet}$. The hydrogen atom abstraction from EB$^{+\bullet}$ by the iron(IV)–oxo complex then leads to electron transfer from the substrate into the π^*_{xz} orbital of the oxidant and spin density changes that are

 This journal is © the Owner Societies 2014

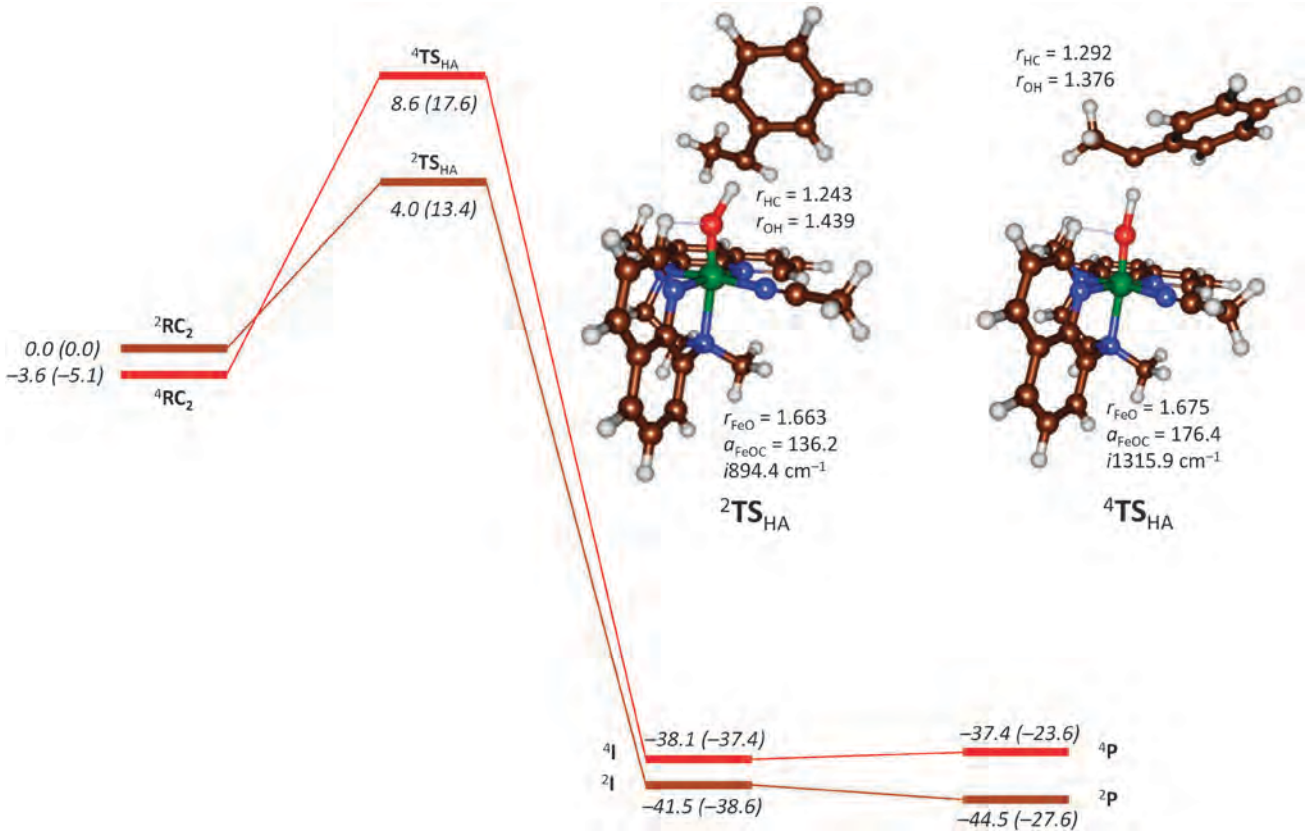

Fig. 4 DFT calculated potential energy profile for the hydrogen atom abstraction from EB by ^{2,4}**2** with energies given in kcal mol^{-1}. Also shown are optimized UB3LYP/BS2(solvent) geometries of ^{2,4}**TS**$_{HA}$ with bond lengths in angstroms, angles in degrees and the imaginary frequency in wave numbers. Relative energies represent ΔE + ZPE + E_{solv} values obtained after a full geometry optimization in solvent at the UB3LYP/BS2 (out of parenthesis) or at UB3LYP/BS2//UB3LYP/BS1 level of theory on a gas-phase optimized geometry.

very similar to those observed for ^{3}**TS**$_{HA}$. Technically, the differences in the hydrogen atom abstraction barrier between ^{3}**RC**$_1$ and ^{2}**RC**$_2$ should be very small as both are an iron(IV)–oxo oxidant. However, the outer-sphere electron transfer from the substrate to the oxidant has oxidized the approaching substrate, and hence the differences in barrier heights observed in Fig. 3 and 4 relate to hydrogen atom abstraction of the C–H bonds of EB and EB$^{+\bullet}$, respectively. Previously, it was shown that the hydrogen atom abstraction barrier correlates with the strength of the C–H bond of the substrate that is broken in the process.[33] Indeed, experimentally determined rate constants of hydrogen atom abstraction reactions by nonheme iron oxidants were shown to correspond to the bond dissociation energy (BDE$_{CH}$) for the breaking of the C–H bond of the substrate.[34] We, therefore, decided to calculate the BDE$_{CH}$ values of EB and EB$^{+\bullet}$ into $C_6H_5CHCH_3^{\bullet/+}$ and a hydrogen atom and find values of ΔE + ZPE = 82.3 and 41.2 kcal mol^{-1} in the gas phase, respectively. Thus, the oxidized ethylbenzene substrate has considerably weaker benzyl C–H bond strength as compared to the neutral system, and, therefore, the barrier heights for hydrogen atom abstraction obtained for **2′** are significantly lower than those for **1** in agreement with the differences in BDE$_{CH}$. Although, the higher reactivity of **2′** *versus* **1** is perceived as due to differences in the oxidation state of the two oxidants, it actually represents the same oxidant but a difference in the ionization state of the substrate with weakened BDE$_{CH}$. Also the reaction of **2′** with ethylbenzene incurs a significant KIE value, where we find a KIE$_E$ = 5.6 and a KIE$_W$ = 7.2. These values, therefore, are similar to those found for **1** above.

We also calculated the alternative quartet spin state of **2′** and the hydrogen atom abstraction *via* ^{4}**TS**$_{HA}$. Thus, ^{4}**RC**$_2$ has orbital occupation $\pi^*_{xy}{}^2\ \pi^*_{xz}{}^{\uparrow}\ \pi^*_{yz}{}^{\uparrow}\ \pi_{EB}{}^{\uparrow}$ and refers to ^{3}[Fe^{IV}(O)(BQEN)(NCCH$_3$)]$^{2+}\cdots{}^2$EB$^{+\bullet}$, but in contrast to ^{2}**RC**$_2$ the spin on EB is ferromagnetically coupled to the unpaired electrons on the metal. Energetically, ^{2}**RC**$_2$ and ^{4}**RC**$_2$ are close in energy. However, during the hydrogen atom abstraction in ^{2}**TS**$_{HA}$ the unpaired electron from EB$^{+\bullet}$ is transferred with down-spin to give a $\pi^*_{xy}{}^2\ \pi^*_{xz}{}^2\ \pi^*_{yz}{}^1$ configuration, but in ^{4}**TS**$_{HA}$ the unpaired electron has up-spin so a $\pi^*_{xy}{}^2\ \pi^*_{xz}{}^1\ \pi^*_{yz}{}^1\ \sigma^*_{z^2}{}^1$ configuration is formed. As this involves a higher lying orbital than in the corresponding doublet spin pathway, the barrier height for ^{4}**TS**$_{HA}$ is higher in energy than that for ^{2}**TS**$_{HA}$.

Discussion

Our DFT calculations on ^{3,5}**1** and ^{2,4}**2′** reported above show that both systems are in the iron(IV) oxidation state and the oxidation

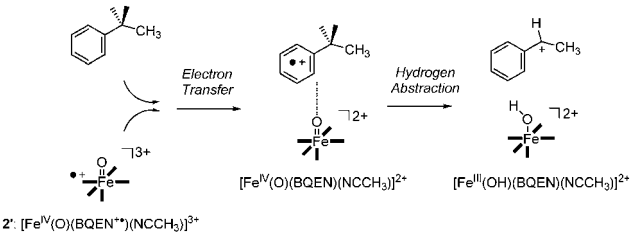

Scheme 2 Calculated reaction mechanism for **2** with oxidation states of critical intermediates identified.

of **2′** does not oxidize the metal to iron(VI) but rather keeps it at the lower oxidation state of iron(IV) due to electron release from the BQEN macrocycle rather than the metal. Therefore, although **2′** is perceived as an iron(V)–oxo species, it actually is an iron(IV)–oxo with BQEN cation radical. Moreover, the DFT calculations reported in this work show that approach of a substrate, *e.g.* ethylbenzene, onto ^{4,2}**2′**, leads to a long-range electron transfer upon formation of the reactant complex ^{4,2}**RC**$_2$: ^{3}[Fe^{IV}(O)(BQEN)(NCCH$_3$)]$^{2+}\cdots{}^2$EB$^{+\bullet}$, Scheme 2. The subsequent hydrogen atom abstraction then gives an iron(III)–hydroxo complex and a $C_6H_5CH^+CH_3$ cation.

In previous studies, we showed that the driving force of a hydrogen atom abstraction correlates linearly with the free energy of activation.[24d,27c,33] Therefore, to understand the thermodynamics and kinetics of the reaction mechanisms reported in Fig. 2 and 3 above, we did a detailed analysis of the individual thermodynamic reaction steps for electron and hydrogen atom transfer processes, which are summarized in Fig. 5. Panel (a) in Fig. 5 starts on the top left with ^{2}**2′** and the reaction to the right reflects a one-electron abstraction to form ^{3}**1** and the subsequent one-electron abstraction to form [Fe^{III}(O)(BQEN)(NCCH$_3$)]$^+$. The vertical arrows reflect the hydrogen atom abstraction processes from both ^{2}**2′** and ^{3}**1**. Thermodynamically, the energy for these reactions is associated with the bond dissociation energy of the O–H bond in the metal–hydroxo complex to revert back into the iron–oxo and an isolated H-atom, as defined as BDE$_{OH}$. The calculated BDE$_{OH}$ values for ^{2}**2′** and ^{3}**1** are virtually the same in the gas phase, which is not surprising as both complexes are iron(IV)–oxo intermediates. Therefore, geometrically very little differences in the hydrogen atom abstraction reactions will be obtained. The energy gap between the two BDE$_{OH}$ values widens to 10.2 kcal mol^{-1} in favour of ^{2}**2′** when solvent, thermal and entropical corrections to the energy are included.

In the case of BDE$_{OH}$, solvent corrections stabilize the value of **2′** over **1** by 7.3 kcal mol^{-1}, whereas thermal and entropic

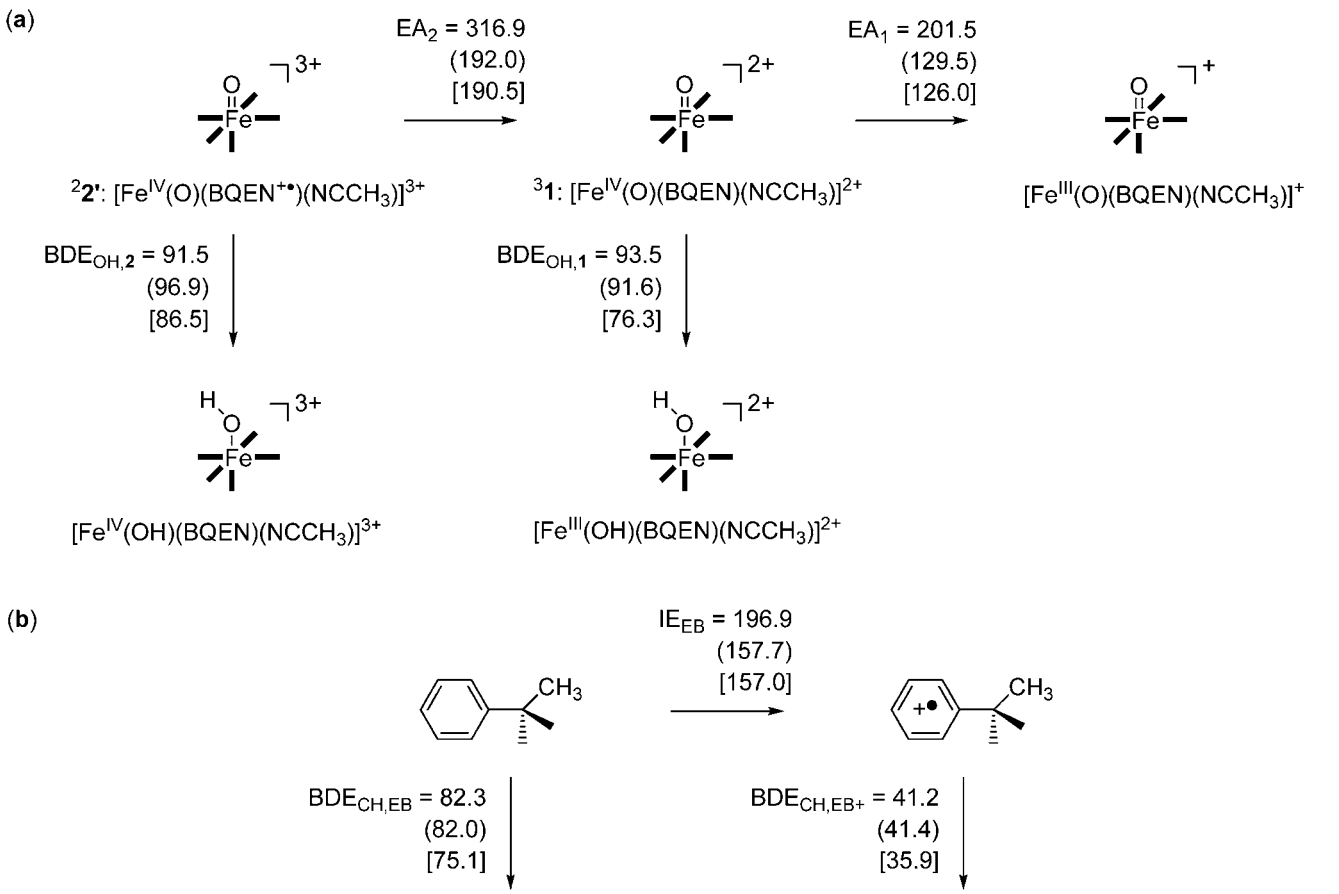

Fig. 5 (a) Thermodynamic reaction pathways for electron and hydrogen atom abstraction by **1** and **2**. (b) Thermodynamic reaction pathways for electron and hydrogen atom abstraction by EB. All data obtained from a geometry optimization at UB3LYP/BS2. Data (in kcal mol^{-1}) reported are ΔE + ZPE in the gas-phase (ΔE + ZPE in solvent) [ΔG in solvent].

 This journal is © the Owner Societies 2014

corrections add a further 4.9 kcal mol^{-1}. These BDE_{OH} values, therefore, would predict higher reactivity of $^2\mathbf{2}'$ over $^3\mathbf{1}$ in solvent for hydrogen atom abstraction reactions.

The major differences between **1** and **2′**, however, are related to their electron affinities or reduction potentials. Thus, $^2\mathbf{2}'$ has a large electron affinity (EA_2) of 316.9 kcal mol^{-1} in the gas-phase and ΔG_{solv} = 190.5 kcal mol^{-1}. It is worth noting that for all calculations we find almost equal values for ΔE + ZPE + E_{solv} and ΔG_{solv}, therefore, entropic and thermal corrections to the solvent corrected enthalpies have a negligible effect on the individual reactions studied. The electron affinity of $^2\mathbf{2}'$ is considerably larger than that found for $^3\mathbf{1}$, where values of EA_1 = 201.5 kcal mol^{-1} in the gas-phase and ΔG_{solv} = 126.0 kcal mol^{-1} are found. Consequently, $^2\mathbf{2}'$ has a ΔG_{solv} = 63.5 kcal mol^{-1} larger electron affinity than $^3\mathbf{1}$ and will be more susceptible to react by electron abstraction from substrates.

For completeness we also include in Fig. 6 the thermodynamics for the ethylbenzene substrate for removal of an electron and the C–H bond strengths of the benzyl group of ethylbenzene and the ethylbenzene cation radical. As already mentioned above the ethylbenzene cation radical has a considerably weakened C–H bond strength of ΔG_{solv} = 35.9 kcal mol^{-1} as compared to EB. Consequently, hydrogen atom abstraction from $EB^{+\bullet}$ will have a low barrier.

To find out whether a reaction of $^2\mathbf{2}'$ and $^3\mathbf{1}$ with EB would lead to a large thermodynamic driving force for electron transfer, the free energy in solvent for the reactions given in eqn (4) and (5) was calculated. Thus, the electron transfer from EB to $^2\mathbf{2}'$ is calculated to be exergonic by 33.5 kcal mol^{-1}, whereas the one originating from $^3\mathbf{1}$ is endergonic by 31.0 kcal mol^{-1} instead. These two reactions implicate that in a collision between $^2\mathbf{2}'$ and EB the driving force will trigger an electron abstraction from EB, whereas that will not be the case in a collision between $^3\mathbf{1}$ and EB. The large EA_2 value will, therefore, lead to a large driving force for electron transfer from suitable substrates including ethylbenzene to **2′**. Moreover, the thermodynamic reaction pathways given in Fig. 5 give further evidence of a likely electron transfer between EB and $^2\mathbf{2}'$.

$$^2\mathbf{2}' + EB \rightarrow {}^3\mathbf{1} + EB^{+\bullet} \quad [\Delta G_{solv} = -33.5 \text{ kcal mol}^{-1}] \quad (4)$$

$$^3\mathbf{1} + EB \rightarrow {}^4[Fe^{III}(O)(BQEN)(NCCH_3)]^+ + EB^{+\bullet} \quad [\Delta G_{solv} = +31.0 \text{ kcal mol}^{-1}] \quad (5)$$

Despite the fact that the BDE_{OH} values of **1** and **2′** are virtually the same, actually at the free energy level with solvent included they are separated by about 10 kcal mol^{-1}. However, much more dramatic differences in the electron affinity of both complexes are found. Thus, the bond dissociation energy to break the A–H bond (BDE_{AH}) – or hydrogen atom abstraction ability of compound A – can be split into an individual electron and proton transfer *via* eqn (6), whereby ΔG_{acid} represents the acidity of the weak acid AH, EA_A is the electron affinity of A, and IE_H the ionization energy of a H-atom. The experimentally reported value of IE_H is 13.598 eV.[35]

$$A\text{–}H \rightarrow A + H + BDE_{AH} \quad (6a)$$

$$BDE_{AH} = \Delta G_{acid,AH} - EA_A - IE_H \quad (6b)$$

Using the data from Fig. 5 and the known IE_H value we calculate a ΔG_{acid} of 590.5 kcal mol^{-1} for $[Fe^{IV}(OH)(BQEN)(NCCH_3)]^{3+}$, whereas proton transfer to **1** gives the complex $[Fe^{III}(OH)(BQEN)(NCCH_3)]^{2+}$ with ΔG_{acid} = 515.9 kcal mol^{-1}. The large difference between EA_2 and EA_1, therefore, has a direct impact on the acidity of the iron(III)–hydroxo group and makes it considerably more acidic. The origin of the difference in electron affinity of **1** and **2′** is due to difference in electron transfer processes. Upon reduction of $^2\mathbf{2}'$ an electron is transferred into the low-lying π^*_{BQEN} orbital to form a triplet spin $\pi^*_{xy}{}^2\,\pi^*_{xz}{}^1\,\pi^*_{yz}{}^1\,\pi^*_{BQEN}{}^2$ configuration.

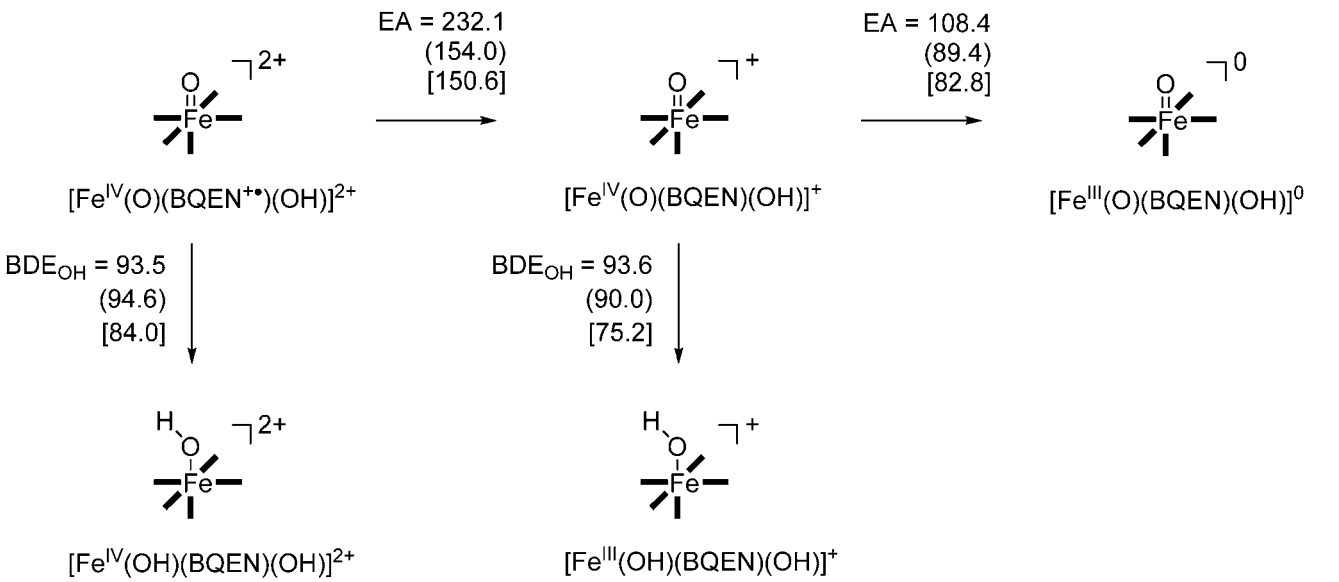

Fig. 6 Thermodynamic reaction pathways for electron and hydrogen atom abstraction by $[Fe(O)(BQEN)(OH)]^{2+}$ and $[Fe(O)(BQEN)(OH)]^{+}$. All data obtained from a geometry optimization at UB3LYP/BS2. Data (in kcal mol^{-1}) reported are ΔE + ZPE in the gas-phase (ΔE + ZPE in solvent) [ΔG in solvent].

On the other hand, reduction of ^{3}**1** leads to filling of the virtual $\sigma^*_{z^2}$ orbital with a single electron. As the $\sigma^*_{z^2}$ orbital is significantly higher in energy than the π^*_{BQEN} orbital this means the reduction of **1** will incur a much smaller electron affinity than adding an electron to π^*_{BQEN}, which is indeed what is found in Fig. 5.

To find out whether the *cis*-ligand of the metal–oxo group affects the EA and ΔG_{acid} values, we did a further set of calculations on the electron and hydrogen atom transfer reactions for complexes $[Fe^{IV}(O)(BQEN^{+\bullet})(OH)]^{2+}$ and $[Fe^{IV}(O)(BQEN)(OH)]^{+}$, *i.e.* complexes **2′** and **1** that have the acetonitrile ligand replaced by OH^-. We should note here that replacement of the acetonitrile equatorial ligand by hydroxide does not change the spin state ordering and electronic configuration and these complexes are characterized like **2′** and **1** above. Fig. 6 displays the thermodynamic reaction pathways for $[Fe^{IV}(O)(BQEN^{+\bullet})(OH)]^{2+}$ and $[Fe^{IV}(O)(BQEN)(OH)]^{+}$. Firstly, a very little effect of replacing the acetonitrile with hydroxide is found on the BDE_{OH} values of the complexes. For $[Fe^{IV}(OH)(BQEN)(OH)]^{2+}$ we find a BDE_{OH} value of ΔG_{solv} = 84.0 kcal mol^{-1}, whereas its one-electron reduced counterpart has a ΔG_{solv} = 75.2 kcal mol^{-1}. These values are within 2.5 kcal mol^{-1} from those obtained with an acetonitrile molecule in the *cis*-position. The situation, however, changes dramatically for the electron affinities and acidity values of the complexes when the acetonitrile ligand is replaced by hydroxide. Thus, $[Fe^{IV}(O)(BQEN^{+\bullet})(OH)]^{2+}$ has an electron affinity of ΔG_{solv} = 150.6 kcal mol^{-1}, whereas the much lower value of 82.8 kcal mol^{-1} is found for $[Fe^{IV}(O)(BQEN)(OH)]^{+}$. These lowered electron affinities with respect to complexes **2′** and **1** also mean reduced acidity of the protonated complexes, for which we find values of 548.2 and 471.6 kcal mol^{-1}, respectively.

In addition, a reaction of $[Fe^{IV}(O)(BQEN^{+\bullet})(OH)]^{2+}$ with ethylbenzene is calculated to give an endergonic electron transfer of 6.4 kcal mol^{-1} using the data given in Fig. 5 and 6. Therefore, replacing the acetonitrile equatorial ligand in complex **2′** with an anion such as a hydroxide will affect the stability and reactivity of the complex and will prevent a long-range electron transfer with substrates like ethylbenzene. The electron transfer from ethylbenzene to $[Fe^{IV}(O)(BQEN)(OH)]^{+}$ is calculated to be even more endergonic (ΔG_{solv} = 74.2 kcal mol^{-1}) and consequently is not likely to happen.

In summary, we establish reasons for the large thermodynamic driving force for electron transfer from ethylbenzene to **2′** as originating from a high electron affinity of the oxidant of ΔG_{solv} = 190.5 kcal mol^{-1}. This implies that the electron transfer to the approaching substrate could be spontaneous for substrates with an ionization potential below 190.5 kcal mol^{-1} or 8.26 eV. Although, we calculate an ionization energy of 8.54 eV in the gas phase actually in solution the value drops to ΔG_{solv} = 6.81 eV. Therefore, in solution the ionization potential of ethylbenzene is sufficiently low to incur a long-range electron transfer to the oxidant and create $^3[Fe^{IV}(O)(BQEN)(NCCH_3)]^{2+}\cdots{}^2EB^{+\bullet}$.

Finally, the thermodynamics values of Fig. 6 and 7 also enable us to predict the hydrogen atom transfer driving force in complexes $\mathbf{RC}_2$ and $\mathbf{RC}_1$. As described above, $\mathbf{RC}_2$ undergoes a long-range electron transfer and converts to $[Fe^{IV}(O)(BQEN)(NCCH_3)]^{2+}$ and $EB^{+\bullet}$. This complex reacts *via* hydrogen atom transfer *via*

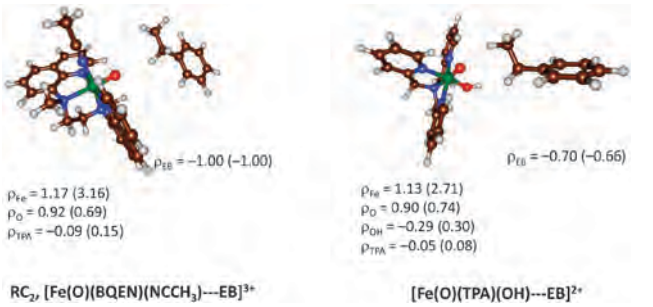

Fig. 7 Group spin densities of $^{4,2}\mathbf{RC}_2$ and $[Fe(O)(TPA)(OH)\cdots EB]^{2+}$ as calculated with UB3LYP/BS2 in solvent. High-spin data in parenthesis.

eqn (7) with a free energy change of −40.4 kcal mol^{-1}. The DFT calculations for this process, see ESI,† implicated a free energy change of ΔG_{solv} = −42.4 kcal mol^{-1} for the formation of the radical intermediate ^{2}**I**, and therefore its calculated value is in good agreement with the value estimated from our thermodynamic cycles.

$$[Fe^{IV}(O)(BQEN)(NCCH_3)]^{2+} + EB^{+\bullet} \rightarrow [Fe^{III}(OH)(BQEN)(NCCH_3)]^{2+} + C_6H_5CH^+CH_3\ [\Delta G_{solv} = -40.4\ \text{kcal mol}^{-1}] \quad (7)$$

By contrast, if we do the same for complex $\mathbf{RC}_1$ and take the difference in free energy between the BDE_{CH} and BDE_{OH} values of oxidant and substrate, we find an almost thermoneutral hydrogen atom abstraction reaction, eqn (8). Indeed, the DFT calculations above predict a radical intermediate with an exergonicity of 6.9 kcal mol^{-1} with respect to the reactant complex in good agreement with the thermodynamically estimated value.

$$[Fe^{IV}(O)(BQEN)(NCCH_3)]^{2+} + EB \rightarrow [Fe^{III}(OH)(BQEN)(NCCH_3)]^{2+} + C_6H_5CH^{\bullet}CH_3\quad [\Delta G_{solv} = -1.2\ \text{kcal mol}^{-1}] \quad (8)$$

To test whether the electron transfer observed here in our reactant complexes is a general feature that could be found in alternative iron(v)–oxo complexes as well, we also decided to investigate the well-studied $[Fe(O)(TPA)(OH)]^{2+}$, TPA = tris-(2-pyridylmethyl)amine, system of Costas and co-workers.[10b] Previously, $[Fe(O)(TPA)(X)]^{2+}$ with X = halide or OH^- has been used in studies of the *cis*-effect on substrate activation by metal–oxo species, but also as a model for non-heme iron halogenases. Technically the $[Fe(O)(TPA)(OH)]^{2+}$ is an iron(v)–oxo complex as indeed confirmed by DFT calculations.[36] The question, of course, arises whether the oxidation state of the complex stays in the iron(v) state upon approach of an ethylbenzene molecule. Thus, we optimized the reactant complex $[Fe(O)(TPA)(OH)\cdots EB]^{2+}$ in the doublet and quartet spin states at UB3LYP-D3/BS2 level of theory and show the structures and group spin densities of the complexes alongside those of $^{4,2}\mathbf{RC}_2$ in Fig. 7.

The results in Fig. 7 show that upon approach of an ethylbenzene molecule to an iron(v)–oxo center, a long-range electron transfer takes place from substrate to oxidant. Therefore, the group spin densities of $^{2,4}\mathbf{RC}_2$ and $[Fe(O)(TPA)(OH)\cdots EB]^{2+}$ both refer to an iron(iv)–oxo complex with a nearby $EB^{+\bullet}$ ion. Both complexes have a doublet spin state with $\pi^*_{xy}{}^2\ \pi^*_{xz}{}^1\ \pi^*_{yz}{}^1\ \pi_{EB}{}^1$ configuration,

 This journal is © the Owner Societies 2014

i.e. a triplet spin iron(IV)–oxo complex with a nearby doublet cation radical ethylbenzene. By contrast the quartet spin state configurations of these complexes have orbital occupation $\pi^{*}_{xy}{}^{2}$ $\pi^{*}_{xz}{}^{1}$ $\pi^{*}_{yz}{}^{1}$ $\sigma^{*}_{z^2}{}^{1}$ $\pi_{EB}{}^{1}$ configuration with the ethylbenzene radical anti-ferromagnetically coupled to three unpaired electrons on the iron(IV)–oxo complex. Note that without ethylbenzene the $[Fe(O)(TPA)(OH)]^{2+}$ complex converges to an iron(V)–oxo species and no ligand radical is found. The TPA ligand, therefore, has much lower lying molecular orbitals than a BQEN ligand system and as a result the π_{BQEN} orbitals become competitive with the $\pi^{*}_{xz}/\pi^{*}_{yz}$ orbitals on the FeO group. As a result of this $[Fe(O)(BQEN)(NCCH_3)]^{3+}$ has an electronic configuration representing an iron(IV)–oxo coupled to a ligand radical, whereas $[Fe(O)(TPA)(OH)]^{2+}$ is an iron(V)–oxo species.

Conclusions

In summary, we present here the first comparative study on the reactivity patterns of nonheme iron(IV)–oxo *versus* iron(V)–oxo intermediates. Upon approach of the substrate to the iron(IV)–oxo ligand cation radical it abstracts an electron from the substrate readily, and thereby creates an iron(IV)–oxo ligand cation radical species. The perceived reactivity of the iron(V)–oxo species, therefore, is due to the activity of the iron(IV)–oxo ligand cation radical instead. We also show that oxidation of ethylbenzene weakens the C–H bond strength of the substrate and thereby lowers the hydrogen atom abstraction barriers and leads to higher reactivity. This is an example of how outer-sphere (long-range) electron transfer can change the C–H bond strength of the substrate so that a more efficient H-transfer becomes possible. The outer-sphere electron transfer may be a common feature in transition metal catalysis, but further research will be needed to find more examples of this type of reactivity patterns.

Acknowledgements

SdV thanks the Royal Society for an International Exchanges with Korea grant. The National Service of Computational Chemistry Software (NSCCS) is acknowledged for cpu time. DK acknowledges Department of Science and Technology (New Delhi) for a Ramanujan Fellowship. The research at EWU was supported by NRF of Korea through CRI (NRF-2012R1A3A2048842) and GRL (NRF-2010-00353).

Notes and references

1 (*a*) E. I. Solomon, T. C. Brunold, M. I. Davis, J. N. Kemsley, S.-K. Lee, N. Lehnert, F. Neese, A. J. Skulan, Y.-S. Yang and J. Zhou, *Chem. Rev.*, 2000, **100**, 235; (*b*) T. D. H. Bugg and S. Ramaswamy, *Curr. Opin. Chem. Biol.*, 2008, **12**, 134; (*c*) M. J. Ryle and R. P. Hausinger, *Curr. Opin. Chem. Biol.*, 2002, **6**, 193; (*d*) Y. Mishina, E. M. Duguid and C. He, *Chem. Rev.*, 2006, **106**, 215; (*e*) *Iron-containing enzymes: Versatile catalysts of hydroxylation reactions in nature*, ed. S. P. de Visser and D. Kumar, RSC Publishing, Cambridge (UK), 2011; (*f*) P. He and G. R. Moran, *Curr. Opin. Chem. Biol.*, 2009, **13**, 443; (*g*) D. Buongiorno and G. D. Straganz, *Coord. Chem. Rev.*, 2013, **257**, 541.

2 (*a*) M. Costas, M. P. Mehn, M. P. Jensen and L. Que Jr, *Chem. Rev.*, 2004, **104**, 939; (*b*) S. V. Kryatov, E. V. Rybak-Akimova and S. Schindler, *Chem. Rev.*, 2005, **105**, 2175; (*c*) M. M. Abu-Omar, A. Loaiza and N. Hontzeas, *Chem. Rev.*, 2005, **105**, 2227; (*d*) R. van Eldik, *Coord. Chem. Rev.*, 2007, **251**, 1649; (*e*) P. C. A. Bruijnincx, G. van Koten and R. J. M. Klein Gebbink, *Chem. Soc. Rev.*, 2008, **37**, 2716; (*f*) S. P. de Visser, J.-U. Rohde, Y.-M. Lee, J. Cho and W. Nam, *Coord. Chem. Rev.*, 2013, **257**, 381; (*g*) W. Nam, Y.-M. Lee and S. Fukuzumi, *Acc. Chem. Res.*, 2014, **47**, 1146.

3 See, *e.g.*, (*a*) M. R. Bukowski, K. D. Koehntop, A. Stubna, E. L. Bominaar, J. A. Halfen, E. Münck, W. Nam and L. Que Jr, *Science*, 2005, **310**, 1000; (*b*) J.-U. Rohde, J.-H. In, M. H. Lim, W. W. Brennessel, M. R. Bukowski, A. Stubna, E. Münck, W. Nam and L. Que Jr, *Science*, 2003, **299**, 1037; (*c*) M. Martinho, F. Banse, J.-F. Bartoli, T. A. Mattioli, P. Battioni, P. Horner, S. Bourcier and J.-J. Girerd, *Inorg. Chem.*, 2005, **44**, 9592; (*d*) C. V. Sastri, M. S. Seo, M. J. Park, K. M. Kim and W. Nam, *Chem. Commun.*, 2005, 1405; (*e*) F. T. De Oliveira, A. Chanda, D. Banerjee, X. Shan, S. Mondal, L. Que Jr, E. L. Bominaar, E. Münck and T. J. Collins, *Science*, 2007, **315**, 835; (*f*) T. A. Jackson, J.-U. Rohde, M. S. Seo, C. V. Sastri, R. DeHont, A. Stubna, T. Ohta, T. Kitagawa, E. Münck, W. Nam and L. Que Jr, *J. Am. Chem. Soc.*, 2008, **130**, 12394.

4 (*a*) K. Chen, M. Costas, J. Kim, A. K. Tipton and L. Que Jr, *J. Am. Chem. Soc.*, 2002, **124**, 3026; (*b*) A. Company, L. Gómez, M. Güell, X. Ribas, J. M. Luis, L. Que Jr and M. Costas, *J. Am. Chem. Soc.*, 2007, **129**, 15766; (*c*) R. Mas-Ballesté, M. Fujita and L. Que Jr, *Dalton Trans.*, 2008, 1828; (*d*) P. Comba, M. Maurer and P. Vadivelu, *Inorg. Chem.*, 2009, **48**, 10348; (*e*) A. Company, Y. Feng, M. Güell, X. Ribas, J. M. Luis, L. Que Jr and M. Costas, *Chem. – Eur. J.*, 2009, **15**, 3359; (*f*) I. Prat, J. S. Mathieson, M. Güell, X. Ribas, J. M. Luis, L. Cronin and M. Costas, *Nat. Chem.*, 2011, **3**, 788.

5 (*a*) K. Chen and L. Que Jr, *J. Am. Chem. Soc.*, 2001, **123**, 6327; (*b*) A. D. Ryabov, *Adv. Inorg. Chem.*, 2013, **65**, 117.

6 (*a*) A. Nielsen, F. B. Larsen, A. D. Bond and C. J. McKenzie, *Angew. Chem., Int. Ed.*, 2006, **45**, 1602; (*b*) A. Lennartson and C. J. McKenzie, *Angew. Chem., Int. Ed.*, 2012, **51**, 6767.

7 S. H. Lee, J. H. Han, H. Kwak, S. J. Lee, E. Y. Lee, H. J. Kim, J. H. Lee, C. Bae, S. N. Lee, Y. Kim and C. Kim, *Chem. – Eur. J.*, 2007, **13**, 9393.

8 S. Kundu, J. Van Kirk Thompson, A. D. Ryabov and T. J. Collins, *J. Am. Chem. Soc.*, 2011, **133**, 18546.

9 J. Yoon, S. A. Wilson, Y. K. Jang, M. S. Seo, K. Nehru, B. Hedman, K. O. Hodgson, E. Bill, E. I. Solomon and W. Nam, *Angew. Chem., Int. Ed.*, 2009, **48**, 1257.

10 (*a*) *Jaguar, version 7.9*, Schrodinger, LLC, New York, NY, 2011; (*b*) *Gaussian-09, Revision C.01*, Gaussian Inc., Wallingford CT, 2010.

11 (*a*) A. D. Becke, *J. Chem. Phys.*, 1993, **98**, 5648; (*b*) C. Lee, W. Yang and R. G. Parr, *Phys. Rev. B: Condens. Matter Mater. Phys.*, 1988, **37**, 785.

12 (*a*) S. P. de Visser, *Angew. Chem., Int. Ed.*, 2006, **45**, 1790; (*b*) D. Kumar, W. Thiel and S. P. de Visser, *J. Am. Chem. Soc.*, 2011, **133**, 3869.
13 S. Grimme, *J. Chem. Phys.*, 2006, **124**, 034108.
14 M. Reiher, O. Salomon and B. A. Hess, *Theor. Chem. Acc.*, 2001, **107**, 48.
15 (*a*) N. C. Handy and A. J. Cohen, *Mol. Phys.*, 2001, **99**, 403; (*b*) J. P. Perdew, K. Burke and M. Ernzerhof, *Phys. Rev. Lett.*, 1996, **77**, 3865.
16 S. P. de Visser, M. G. Quesne, B. Martin, P. Comba and U. Ryde, *Chem. Commun.*, 2014, **50**, 262.
17 (*a*) P. J. Hay and W. R. Wadt, *J. Chem. Phys.*, 1985, **82**, 270; (*b*) W. J. Hehre, R. Ditchfield and J. A. Pople, *J. Chem. Phys.*, 1972, **56**, 2257.
18 (*a*) A. K. Vardhaman, C. V. Sastri, D. Kumar and S. P. de Visser, *Chem. Commun.*, 2011, **47**, 11044; (*b*) A. K. Vardhaman, P. Barman, S. Kumar, C. V. Sastri, D. Kumar and S. P. de Visser, *Angew. Chem., Int. Ed.*, 2013, **52**, 12288; (*c*) A. K. Vardhaman, P. Barman, S. Kumar, C. V. Sastri, D. Kumar and S. P. de Visser, *Chem. Commun.*, 2013, **49**, 10926.
19 (*a*) S. P. de Visser, *Chem. – Eur. J.*, 2006, **12**, 8168; (*b*) D. J. Heyes, M. Sakuma, S. P. de Visser and N. S. Scrutton, *J. Biol. Chem.*, 2009, **284**, 3762.
20 D. Kumar, S. P. de Visser, P. K. Sharma, S. Cohen and S. Shaik, *J. Am. Chem. Soc.*, 2004, **126**, 1907.
21 (*a*) D. Kumar, H. Hirao, L. Que Jr and S. Shaik, *J. Am. Chem. Soc.*, 2005, **127**, 8026; (*b*) S. P. de Visser, *J. Am. Chem. Soc.*, 2006, **128**, 15809; (*c*) S. Ye and F. Neese, *Proc. Natl. Acad. Sci. U. S. A.*, 2011, **108**, 1228.
22 (*a*) M. T. Green, *J. Am. Chem. Soc.*, 1999, **121**, 7939; (*b*) J. Rittle and M. T. Green, *Science*, 2010, **330**, 933; (*c*) K. Yoshizawa, Y. Shiota and T. Yamabe, *J. Am. Chem. Soc.*, 1999, **121**, 147.
23 (*a*) S. P. de Visser, *J. Am. Chem. Soc.*, 2006, **128**, 9813; (*b*) L. Bernasconi and E.-J. Baerends, *Eur. J. Inorg. Chem.*, 2008, 1672; (*c*) C. Y. Geng, S. Ye and F. Neese, *Angew. Chem., Int. Ed.*, 2010, **49**, 5717; (*d*) S. Shaik, H. Chen and D. Janardanan, *Nat. Chem.*, 2011, **3**, 19; (*e*) P. Comba, M. Maurer and P. Vadivelu, *Inorg. Chem.*, 2009, **48**, 10389.
24 (*a*) J. C. Schöneboom, H. Lin, N. Reuter, W. Thiel, S. Cohen, F. Ogliaro and S. Shaik, *J. Am. Chem. Soc.*, 2002, **124**, 8142; (*b*) S. P. de Visser, S. Shaik, P. K. Sharma, D. Kumar and W. Thiel, *J. Am. Chem. Soc.*, 2003, **125**, 15779; (*c*) S. P. de Visser, L. Tahsini and W. Nam, *Chem. – Eur. J.*, 2009, **15**, 5577; (*d*) D. Kumar, G. N. Sastry and S. P. de Visser, *Chem. – Eur. J.*, 2011, **17**, 6196.
25 S. Shaik, H. Hirao and D. Kumar, *Nat. Prod. Rep.*, 2007, **24**, 533.
26 M. G. Quesne, R. Latifi, L. E. Gonzalez-Ovalle, D. Kumar and S. P. de Visser, *Chem. – Eur. J.*, 2014, **20**, 435.
27 See, *e.g.*, (*a*) M. Güell, J. M. Luis, M. Solà and M. Swart, *J. Phys. Chem. A*, 2008, **112**, 6384; (*b*) R. Latifi, M. A. Sainna, E. V. Rybak-Akimova and S. P. de Visser, *Chem. – Eur. J.*, 2013, **19**, 4058; (*c*) D. Kumar, R. Latifi, S. Kumar, E. V. Rybak-Akimova, M. A. Sainna and S. P. de Visser, *Inorg. Chem.*, 2013, **52**, 7968.
28 S. P. de Visser and L. S. Tan, *J. Am. Chem. Soc.*, 2008, **130**, 12961.
29 P. Leeladee, R. A. Baglia, K. A. Prokop, R. Latifi, S. P. de Visser and D. P. Goldberg, *J. Am. Chem. Soc.*, 2012, **134**, 10397.
30 S. P. de Visser, *J. Phys. Chem. A*, 2005, **109**, 11050.
31 S. M. Pratter, C. Konstantinovics, C. L. M. DiGiuro, E. Leitner, D. Kumar, S. P. de Visser, G. Grogan and G. D. Straganz, *Angew. Chem., Int. Ed.*, 2013, **52**, 9677.
32 S. Sahu, L. R. Widger, M. G. Quesne, S. P. de Visser, H. Matsumura, P. Moënne-Loccoz, M. A. Siegler and D. P. Goldberg, *J. Am. Chem. Soc.*, 2013, **135**, 10590.
33 R. Latifi, M. Bagherzadeh and S. P. de Visser, *Chem. – Eur. J.*, 2009, **15**, 6651.
34 X. Wu, M. S. Seo, K. M. Davis, Y.-M. Lee, J. Chen, K.-B. Cho, Y. N. Pushkar and W. Nam, *J. Am. Chem. Soc.*, 2011, **133**, 20088.
35 S. G. Lias, in *Ionization Energy Evaluation in NIST Chemistry WebBook*, NIST Standard Reference Database Number 69: ed. P. J. Linstrom and W. G. Mallard, National Institute of Standards and Technology, Gaithersburg MD, 2005, p. 20899, http://webbook.nist.gov.
36 (*a*) Y. Ma and P. B. Balbuena, *J. Phys. Chem. B*, 2007, **111**, 2711; (*b*) P. Comba, G. Rajaraman and H. Rohwer, *Inorg. Chem.*, 2007, **46**, 3826; (*c*) A. Bassan, M. R. A. Blomberg, P. E. M. Siegbahn and L. Que Jr, *J. Am. Chem. Soc.*, 2002, **124**, 11056; (*d*) S. P. de Visser and W. Nam, *J. Phys. Chem. A*, 2008, **112**, 12887.

 This journal is © the Owner Societies 2014

ORGANOMETALLICS

Communication

pubs.acs.org/Organometallics

A "Hemilabile" Palladium–Carbon Bond: Characterization and Its Implication in Catalysis

Debajyoti Saha,[†] Ravi Verma,[‡] Devesh Kumar,[‡] Shubhrodeep Pathak,[§] Sourav Bhunya,[§] and Amitabha Sarkar*[,†]

[†]Department of Organic Chemistry, Indian Association for the Cultivation of Science, Raja S. C. Mullik Road, Kolkata 700032, India

[‡]Department of Applied Physics, School for Physical Sciences, Babasaheb Bhimrao Ambedkar University, Ramabai Ambedkar Raili Sthal Road, Lucknow 226 025, India

[§]Raman Centre for Atomic, Molecular and Optical Sciences, Indian Association for the Cultivation of Science, Raja S. C. Mullik Road, Kolkata 700032, India

Supporting Information

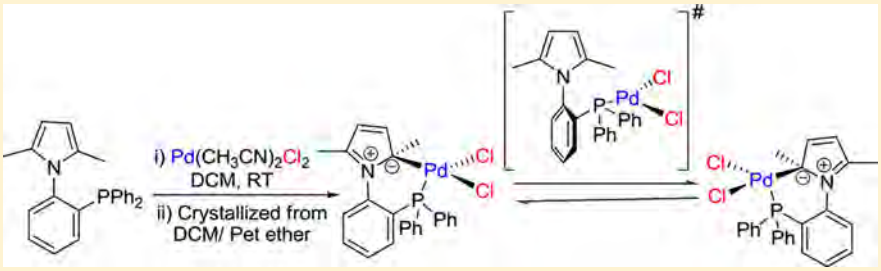

ABSTRACT: An unusual palladium–carbon bond was identified in the crystal structure of a Pd(II) complex (**VI**) derived from 1-(2-diphenylphosphinophenyl)-2,5-dimethyl-1*H*-pyrrole (**L4**). Theoretical calculations indicate that the Pd–C bond is covalent in nature. The complex exhibits fluxional behavior in solution at ambient temperature—the Pd binds alternately to C2 and C5 of pyrrole, generating equivalent, enantiomeric structures. Theory predicts that the transition state of this interconversion probably occurs through an unsaturated 14e complex, where the ligand binds the metal in a monodentate fashion. Comparison with related structures reported earlier has been made, and the possible implication of such unusual bonding in the context of catalysis of coupling reactions is discussed.

Palladium is known to have rather unusual bonding interactions with an ipso carbon of an aromatic ring in complexes with ligands featuring a β-aryl ring[1] or a biaryl motif,[2,3] as revealed in their crystal structures. Such structures are known for both Pd(0) and Pd(II) complexes, a selection of which, viz. **I**–**V**, are presented in Figure 1. A few of these have been scrutinized by theoretical calculations, and a covalent bond is inferred from the existence of a typical bond critical point between the metal and the carbon atoms.[4]

If we replace the ipso carbon with nitrogen as in 1-(2-diphenylphosphino)phenyl-2,5-dimethylpyrrole (**L4**), the biphenyl motif is technically retained and its similarity to the reported ligands **L1**–**L3** is evident (Figure 2).

We report herein the synthesis and structural characterization of a palladium(II) complex derived from ligand **L4**. The unusual η^1 bonding of palladium with the C2 of pyrrole in this molecule is indeed unique. The covalent nature of the bond is substantiated by theoretical calculations. We further established that the structure of the complex in solution is fluxional—the palladium can form a bond with either of the two equivalent carbons (C2 and C5) of pyrrole with equal facility—and metallotropy is fast on the NMR time scale at room temperature. Theory suggests that the interconversion most likely occurs via a monoligated 14e intermediate.

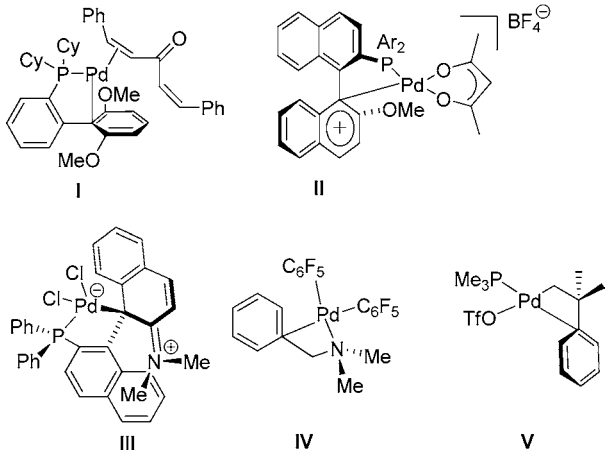

Figure 1. Palladium complexes with Pd–C_{arene} interactions.

Received: May 21, 2014
Published: July 2, 2014

 © 2014 American Chemical Society dx.doi.org/10.1021/om5005435 | *Organometallics* 2014, 33, 3243–3246

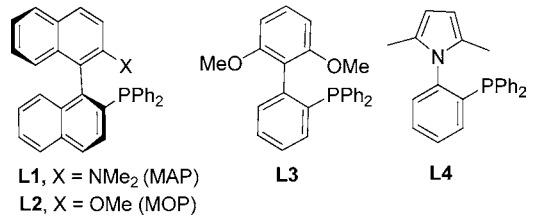

Figure 2. Structures of ligands.

Treatment of equimolar amounts of the ligand **L4** (for details of synthesis and characterization, see the Supporting Information) with $(CH_3CN)_2PdCl_2$ in dichloromethane (Figure 3a) afforded the red complex **VI**, a suitable crystal of which was grown from dichloromethane and light petroleum for crystal structure determination.

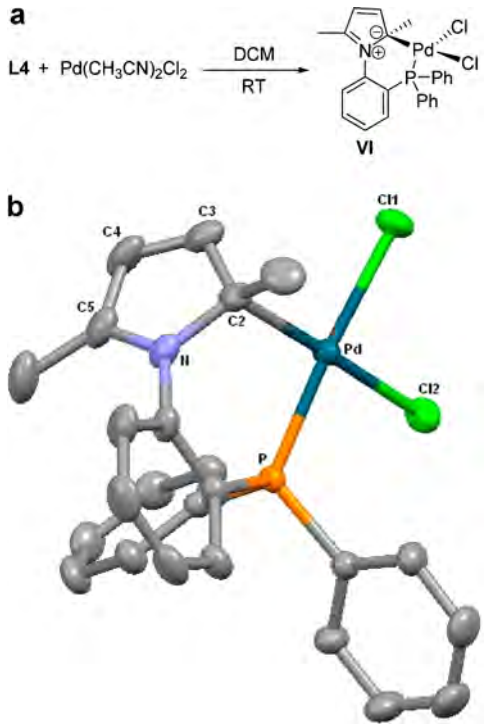

Figure 3. (a) Synthesis of complex **VI**. (b) ORTEP diagram for the molecular complex **VI** with ellipsoids at the 30% probability level. Selected bond lengths (Å): Pd–C2, 2.169(4); C2–C3, 1.434(6); C3–C4, 1.353(7); C4–C5, 1.386(6); C5–N, 1.344(5); N–C2, 1.437(5); Pd–P, 2.2373(9); Pd–Cl1, 2.3626(10); Pd–Cl2, 2.3125(10).

The ORTEP diagram (Figure 3b) reveals a near-planar ligand arrangement at the palladium center, where the metal is coordinated to the phosphorus and two chlorine atoms as anticipated. In addition, an unusual bond is formed between the C2 of pyrrole and palladium. There is no bonding interaction between the metal center and the nitrogen atom that substitutes for the ipso carbon in the heterocycle. Not only is the bonding site different in this unusual structure but also compound **VI** has by far one of the shortest metal–carbon bonds (2.169(4) Å) in such a complex.[5]

In some structures of palladium η^1-arene complexes, the planarity of the arene ring with sp^2-hybridized carbon atoms is said to be conserved despite the bonding interaction.[2] In the case of other complexes, however, pyramidality of the coordinated ipso carbon (as distinct from planarity of an aromatic system) has been mentioned.[3] Where the bonding interaction is strong, the Pd–C bond length is short (<2.22 Å) and deviation from planarity is significant. For structures with Pd–C bonds larger than 2.33 Å, the deviation from planarity is minimal. Complex **VI** presents another such unequivocal example where the C2 of pyrrole connected to Pd is clearly tetrahedral. The bond between N and C5 and the bond between C4 and C3 of pyrrole are shorter (1.344(5) and 1.353(7) Å) with pronounced double-bond character, while the bonds between C3 and C2 as well as between C2 and N are longer (1.434(6) and 1.437(5) Å) with greater single-bond character. These parameters prompted the formulation of the zwitterionic structure **VI** depicted in Figure 3a. The lone pair of nonbonded electrons of nitrogen is allowed to delocalize all the way to C2, where increased electron density would allow σ donation to palladium, which now attains the stable 16e configuration.[6]

The computed optimized geometry is shown in Figure 4a (see the Supporting Information for computational details).

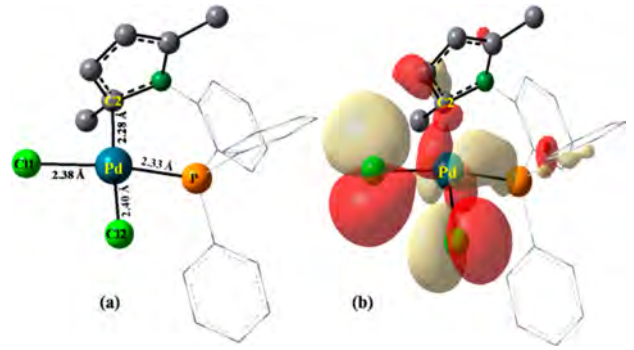

Figure 4. (a) Optimized geometry showing bond lengths and (b) highest occupied molecular orbitals showing overlap between Pd and C2.

The associated frontier molecular orbital picture clearly shows the presence of a significant bonding overlap between palladium and carbon of the pyrrole ring, as depicted in Figure 4b. The trend of bond length shrinkage or elongation observed in the crystal structure is reflected in the calculated bond lengths. Planarity around the palladium atom is also reproduced by the calculations. In many respects, therefore, the energy-minimized structure is similar to the crystal structure, as seen from a comparison of structural parameters (Table 1).

Table 1. Bond Lengths (r), Electron Density (ρ), and the Associated Laplacian ($\nabla^2\rho$) of Representative Bonds

	r (Å)	ρ	$\nabla^2\rho$	WBI[a]	NAO-BO[b]
Pd–P	2.33	0.09	−0.03	0.1486	0.5437
Pd–Cl1	2.38	0.07	−0.04	0.1603	0.4791
Pd–Cl2	2.40	0.07	−0.04	0.1522	0.4864
Pd–C2	2.28	0.07	−0.31	0.0745	0.3253

[a]Wiberg bond index. [b]Natural atomic orbital bond order.

Figure 5 indicates the presence of bond critical points (BCP) of the (3,−1) type. From Figure 5, it is clear that the BCP is centrally situated in the Pd–C2 bond and parameters ρ and $\nabla^2\rho$ (Table 1) suggest a covalent nature of the bond.[7]

The Mulliken population analysis places a net negative charge on the carbon bound to palladium and a net positive

dx.doi.org/10.1021/om5005435 | Organometallics 2014, 33, 3243–3246

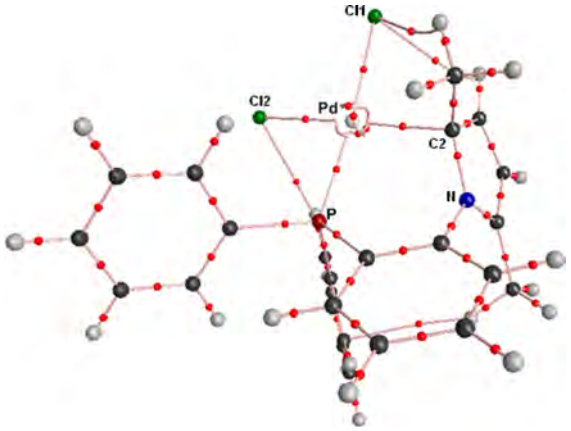

Figure 5. Calculated bond critical point of (3,−1) type.

charge on the nitrogen,[8] which is in agreement with our proposed zwitterionic structure **VI**.

The structure of complex **VI** implies that the symmetry of the pyrrole ring is destroyed; thus, the two methyl groups on pyrrole should have different chemical shift values in the proton NMR spectrum. However, the ^{1}H NMR spectrum of the complex recorded at ambient temperature exhibits one six-proton singlet at 1.46 ppm. Indeed, lowering the temperature led to decoalescence of the six-proton singlet. At −73 °C, two three-proton singlets are clearly seen to emerge at 1.71 and 1.04 ppm (Figure 6), which is to be expected from the nature of the

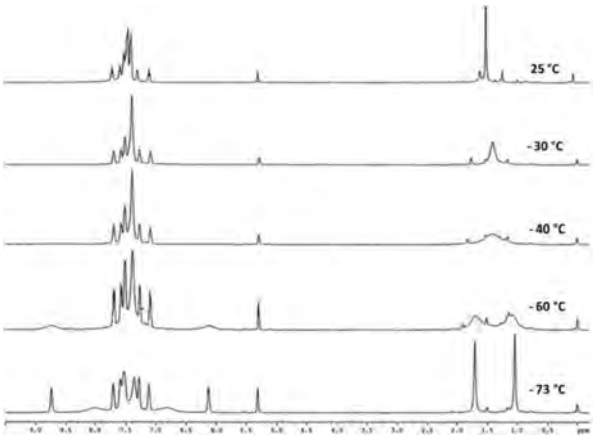

Figure 6. Low-temperature ^{1}H NMR spectra of complex **VI**.

two methyl groups depicted in the crystal structure. Similarly, two distinct and unsymmetrical pyrrole proton signals (H's at C3 and C4) also emerged at 8.74 and 6.13 ppm. A gradual shift of the ^{31}P signal of the phosphine coordinated to the metal was also observed (see the Supporting Information). Thus, the low-temperature NMR spectrum is consistent with the molecular structure of complex **VI**.

It is worthwhile to speculate on the mechanism of the fluxional process. The C−Pd bond is a relatively weak bond. It can be easily disrupted, allowing for a bond rotation along the arene−pyrrole axis leading to a similar bond formation on the other side of the pyrrole: the two structures are enantiomeric (Figure 7). The postulated metallotropy might involve an η^3-2-azaallyl group coordinated to palladium(II) as the transition state between two equal-energy ground-state conformations of η^1 complexes. Formation of an open-chain, coordinatively

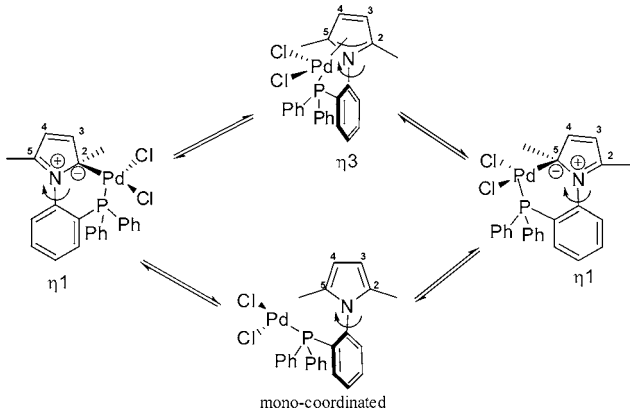

Figure 7. Possible modes of interconversion between two enantiomeric structures of **VI**.

unsaturated $-PPh_2PdCl_2$ intermediate that allows for rotation around the C−N bond is the other possibility.

A frontier molecular orbital analysis shows that the transition state goes through neither the η^3-2-azaallyl complex nor any Pd−N intermediate (see the Supporting Information for computational details). In the transition state there is no bonding overlap between the metal and the pyrrole ring (Figure 8), which suggests that the fluxional process involves

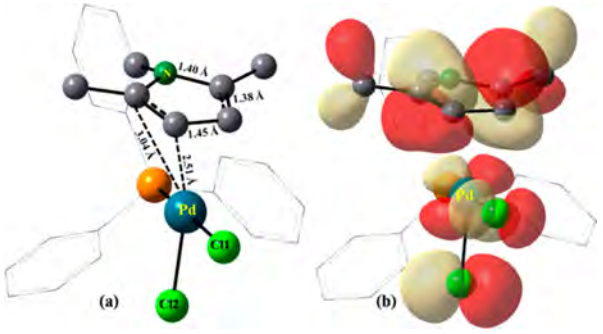

Figure 8. (a) Transition state geometry showing bond lengths and (b) highest occupied molecular orbitals of antibonding type.

Pd−C bond dissociation only. The free energy barrier for the fluxional process is calculated to be 11.5 kcal mol^{-1}. It is in good agreement with the value of 10.42 kcal mol^{-1} estimated[9] from DNMR data.

However curious the metal−pyrrole bond is, it appears to have a significant effect on the catalytic efficiency of the complex in coupling reactions of chloroarenes,[10] which are generally difficult substrates for such reactions. It is also a fact that several such complexes cited in the references do display significant catalytic activity.[11] It can perhaps be attributed to an unconventional, "hemilabile" participation on the part of the presumed monodentate phosphine that stabilizes reactive intermediates in the catalytic cycle.

Hemilabile ligands are potentially chelating ligands with one (or more) donor that has a strong affinity for the metal center and another which is "substitutionally labile".[12b] At the precatalyst stage or catalyst "resting" stage, the ligand acts as a bidentate ligand and stabilizes the metal species by a "chelating" effect. For hetero donor ligands of P, X type, where X = O, N, etc., the metal remains bound to phosphorus throughout the reaction; the weaker donor, O or N, dissociates

dx.doi.org/10.1021/om5005435 | *Organometallics* 2014, 33, 3243−3246

in the presence of the substrate molecules to trigger the catalytic cycle. It has also been stated that "hemilability of a chelate can be observed via fluxional processes that involve the dissociation and recoordination of weakly bonding moieties via intramolecular ligand exchange processes",[12a] which is exactly what we observed. It is possible that oxidative addition of ArCl takes place when the palladium is monocoordinated, as suggested earlier by Buchwald.[4a]

We cannot overlook the fact that several complexes that catalyze coupling reaction with ArCl feature a *triarylphosphine* as donor,[13] not an *aryldialkylphosphine*. Whether and how a weak Pd−C interaction can impart adequate electron richness of palladium to facilitate oxidative addition across a less reactive Ar−Cl bond remains an open question.

To sum up, we have isolated and structurally characterized an unusual palladium(II) complex which reveals an uncommon η^1 coordination of a pyrrole ring to metal that is characterized as a covalent bond by theoretical calculations. The bond is weak, however, as evidenced by a rapid interconversion between two enantiomeric structures at ambient temperature. However, such an interaction strengthens the possibility of "hemilabile" participation of the ligand to stabilize Pd(II) intermediates and facilitate coupling reaction of chloroarenes, notably with triarylphosphines. This merits a closer scrutiny, a theme that is currently being pursued in this laboratory.

■ ASSOCIATED CONTENT

Supporting Information

Text, figures, and a CIF file giving experimental details, characterization data, including ^{1}H, ^{13}C and ^{31}P NMR spectra for the compounds prepared in this paper, and crystallographic data for **VI**. This material is available free of charge via the Internet at http://pubs.acs.org.

■ AUTHOR INFORMATION

Corresponding Author

*E-mail for A.S.: ocas@iacs.res.in.

Notes

The authors declare no competing financial interest.

■ ACKNOWLEDGMENTS

We thank thr DST of India for financial support. D.K. is a Ramanujan Fellow of the Department of Science and Technology (DST), New Delhi, India. D.S. is grateful to the CSIR of India for a Senior Research Fellowship. Crystallographic studies were performed at the facility of the Department of Inorganic Chemistry, IACS. The authors thank Mr. Ranjan Dutta for his valuable assistance. We thank the reviewers for valuable suggestions and references. S.P. and S.B. thank their mentor, Dr. Ankan Paul for his support and encouragement.

■ REFERENCES

(1) (a) Falvello, L. R.; Fornies, J.; Navarro, R.; Sicilia, V.; Tomas, M. *Angew. Chem., Int. Ed.* **1990**, *29*, 891. (b) Falvello, L. R.; Fornies, J.; Navarro, R.; Sicilia, V.; Tomas, M. *J. Chem. Soc., Dalton Trans.* **1994**, 3143. (c) Cámpora, J.; López, J. A.; Palma, P.; Valerga, P.; Spillner, E.; Carmona, E. *Angew. Chem., Int. Ed.* **1999**, *38*, 147.

(2) (a) Murahashi, T.; Otani, T.; Okuno, T.; Kurosawa, H. *Angew. Chem., Int. Ed.* **2000**, *39*, 537. (b) Reid, S. M.; Boyle, R. C.; Mague, J. T.; Fink, M. J. *J. Am. Chem. Soc.* **2003**, *125*, 7816. (c) Wang, Y.; Li, X.; Sun, J.; Ding, K. *Organometallics* **2003**, *22*, 1856. (d) Walker, S. D.; Barder, T. E.; Martinelli, J. R.; Buchwald, S. L. *Angew. Chem., Int. Ed.* **2004**, *43*, 1871. (e) Chaouche, N.; Fornies, J.; Fortuno, C.; Kribii, A.; Martín, A. *J. Organomet. Chem.* **2007**, *692*, 1168.

(3) (a) Kočovsky, P.; Vyskočil, Š.; Cisařová, I.; Sejbal, J.; Tislerova, I.; Smrcina, M.; Lloyd-Jones, G. C.; Stephen, S. C.; Butts, C. P.; Murray, M.; Langer, V. *J. Am. Chem. Soc.* **1999**, *121*, 7714. (b) Dotta, P.; Kumar, P. G. A.; Pregosin, P. S. *Organometallics* **2003**, *22*, 5345.

(4) (a) Barder, T. E.; Walker, S. D.; Martinelli, J. R.; Buchwald, S. L. *J. Am. Chem. Soc.* **2005**, *127*, 4685. (b) Yamashita, M.; Takamiya, I.; Jin, K.; Nozaki, K. *J. Organomet. Chem.* **2006**, *691*, 3189. (c) Barder, T. E. *J. Am. Chem. Soc.* **2006**, *128*, 898.

(5) For comparable C_{ipso}−Pd bond distances, see 2.336(4) Å in ref 2a, 2.676(5) Å in ref 2b, 2.338(11) Å in ref 2c, 2.374(3) Å in ref 2d, 2.391(5) Å in ref 2e, 2.187 Å in ref 3a, and 2.226(8) and 2.129(2) Å in ref 3b.

(6) Kočovsky and Lloyd-Jones reported[3a] a structure that has a tetrahedral arene carbon bound to the Pd(II) center (see structure **III** in Figure 1). The lone pair of electrons on the nitrogen of the Me_2N− group is shown to delocalize (like an enamine) to increase electron density of the ipso carbon that coordinates with the palladium ion. The nitrogen now carries a positive charge; the palladium is shown as a "palladate" species in conformity with its +2 oxidation state. Similar polarizations have also been described by others.[3b]

(7) Zhang, L.; Ying, F.; Wu, W.; Hiberty, P. C.; Shaik, S. *Chem. Eur. J.* **2009**, *15*, 2979.

(8) Mulliken charges on different atoms of **VI**: Pd, 0.504499; P, 1.504727; N, 0.581628; C2, −0.346059.

(9) Eliel, E. L.; Wilen, S. H. In *Stereochemistry of Organic Compounds*; Wiley: New York, 1994; p 502.

(10) Selected reviews: (a) Littke, A. F.; Fu, G. C. *Angew. Chem., Int. Ed.* **2002**, *41*, 4176. (b) Zapf, A.; Beller, M. *Chem. Commun.* **2005**, 431. (c) Martin, R.; Buchwald, S. L. *Acc. Chem. Res.* **2008**, *41*, 1461. (d) Kambe, N.; Iwasaki, T.; Terao, J. *Chem. Soc. Rev.* **2011**, *40*, 4937. (e) Wong, S. M.; So, C. M.; Kwong, F. Y. *Synlett* **2012**, *23*, 1132. (f) Bruno, N. C.; Tudge, M. T.; Buchwald, S. L. *Chem. Sci.* **2013**, *4*, 916.

(11) (a) See refs 3a and 4a. See also: Iwasawa, T.; Komano, T.; Tajima, A.; Tokunaga, M.; Obora, Y.; Fujihara, T.; Tsuji, Y. *Organometallics* **2006**, *25*, 4665. (b) Preliminary experiments show that complex **VI** (2 mol %) catalyzes Suzuki−Miyaura coupling of 4-chloroanisole and 4-chlorotoluene with phenylboronic acid with 76% and 82% isolated yields of coupled products, respectively, in toluene at 100 °C for 6 h: Saha, D.; Sarkar, A. Unpublished results.

(12) (a) Slone, C. S.; Weinberger, D. A.; Mirkin, C. A. *Prog. Inorg. Chem.* **1999**, *48*, 233−350. (b) Braunstein, P.; Naud, F. *Angew. Chem., Int. Ed.* **2001**, *40*, 680.

(13) (a) Liu, S.-Y.; Choi, M. J.; Fu, G. C. *Chem. Commun.* **2001**, 2408. (b) Pramick, M. R.; Rosemeier, S. M.; Beranek, M. T.; Nickse, S. B.; Stone, J. J.; Stockland, R. A., Jr.; Baldwin, S. M.; Kastner, M. E. *Organometallics* **2003**, *22*, 523. (c) Kwong, F. Y.; Chan, K. S.; Yeung, C. H.; Chan, A. S. C. *Chem. Commun.* **2004**, 2336. (d) Mukherjee, A.; Sarkar, A. *Tetrahedron Lett.* **2004**, *45*, 9525. (e) So, C. M.; Chow, W. K.; Choy, P. Y.; Lau, C. P.; Kwong, F. Y. *Chem. Eur. J.* **2010**, *16*, 7996. (f) Chow, W. K.; Yuen, O. Y.; So, C. M.; Wong, W. T.; Kwong, F. Y. *J. Org. Chem.* **2012**, *77*, 3543. (g) See also ref 11a..

Published on 27 March 2014. Downloaded by INDIAN INSTITUTE OF TECHNOLOGY GUWAHATI on 30/09/2014 14:45:32.

Dalton Transactions

PAPER

View Article Online
View Journal | View Issue

Cite this: *Dalton Trans.*, 2014, **43**, 7522

Thioether-ligated iron(II) and iron(III)-hydroperoxo/alkylperoxo complexes with an H-bond donor in the second coordination sphere†

Leland R. Widger,[a] Yunbo Jiang,[a] Alison C. McQuilken,[a] Tzuhsiung Yang,[a] Maxime A. Siegler,[a] Hirotoshi Matsumura,[b] Pierre Moënne-Loccoz,*[b] Devesh Kumar,[c,d] Sam P. de Visser*[c] and David P. Goldberg*[a]

Received 25th January 2014,
Accepted 26th March 2014

DOI: 10.1039/c4dt00281d

www.rsc.org/dalton

The non-heme iron complexes, $[Fe^{II}(N3PySR)(CH_3CN)](BF_4)_2$ (**1**) and $[Fe^{II}(N3Py^{amide}SR)](BF_4)_2$ (**2**), afford rare examples of metastable Fe(III)-OOH and Fe(III)-OO*t*Bu complexes containing equatorial thioether ligands and a single H-bond donor in the second coordination sphere. These peroxo complexes were characterized by a range of spectroscopic methods and density functional theory studies. The influence of a thioether ligand and of one H-bond donor on the stability and spectroscopic properties of these complexes was investigated.

Introduction

Iron-(hydro)peroxo and (alkyl)peroxo species are postulated to be critical intermediates in a number of biologically relevant processes, from the utilization of dioxygen for substrate oxidation, to the processing and detoxification of reactive oxygen-derived species (ROS).[1–5] Some specific examples of non-heme Fe centers involved in this chemistry include isopenicillin N-synthase (IPNS),[6] superoxide reductase (SOR),[7] aromatic amino acid hydroxylase (AAH),[8] Bleomycin,[9] and cysteine dioxygenase (CDO) (Fig. 1).[10] In one case, the alkylperoxo intermediate of an extradiol ring-cleaving dioxygenase, homoprotocatechuate 2,3-dioxygenase (2,3-HPCD), was structurally characterized by X-ray crystallography.[2] The physical and spectroscopic properties of these species have been studied in a number of inorganic model complexes,[11–25] but most of these models utilize only polyamino/polypyridyl ligands. In contrast, some of the enzymes shown in Fig. 1 also include a sulfur donor in the first coordination sphere, but the incorporation of sulfur or other heteroatoms in model complexes is rare.[23,25–41] In addition, little work has been done to determine the effect of secondary sphere interactions, such as hydrogen-bonding networks, on the structures and spectroscopic properties of iron-peroxo complexes,[42,43] despite their roles in many of the corresponding enzyme intermediates. Recently our lab has focused on determining the first and second coordination sphere effects on non-heme iron model complexes, including the incorporation of S donors in the first coordination sphere, and oxidizable substrates or H-bond donors in the second coordination sphere.[44–47]

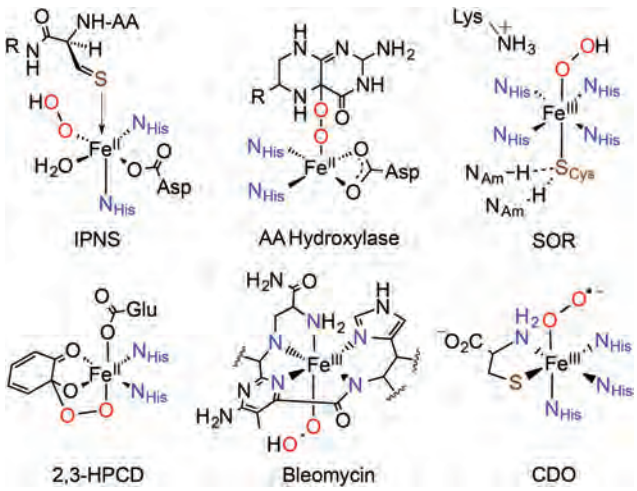

Fig. 1 Selected examples of iron-dioxygen complexes in biology.

The thiolate-ligated complex $[Fe^{II}(N3PyS)(CH_3CN)]BF_4$ was among the first examples of a biomimetic iron(II) complex to

[a]*Department of Chemistry, The Johns Hopkins University, 3400 North Charles Street, Baltimore, Maryland 21218, USA. E-mail: dpg@jhu.edu; Fax: +1-410-516-8420; Tel: +1-410-516-6658*
[b]*Oregon Health & Science University, Institute of Environmental Health, Mail code: HRC3, 3181 SW Sam Jackson Park Road, Portland, OR 97239, USA. E-mail: moennelo@ohsu.edu; Fax: +1-503-346-3427; Tel: +1-503-346-3429*
[c]*Manchester Institute of Biotechnology and School of Chemical Engineering and Analytical Science, The University of Manchester, 131 Princess Street, Manchester, M1 7DN, UK. E-mail: sam.devisser@manchester.ac.uk*
[d]*Department of Applied Physics, School of Physical Sciences, Babasaheb, Bhimrao Ambedkar University, Vidya Vihar, Rae Bareilly Road, Lucknow 226-025, India. E-mail: dkclcre@yahoo.com*

†Electronic supplementary information (ESI) available: Computational details. CCDC 976172–976174. For ESI and crystallographic data in CIF or other electronic format see DOI: 10.1039/c4dt00281d

This journal is © The Royal Society of Chemistry 2014

Published on 27 March 2014. Downloaded by INDIAN INSTITUTE OF TECHNOLOGY GUWAHATI on 30/09/2014 14:45:32.

undergo S-oxygenation with O_2 to yield a doubly-oxygenated sulfinate product.[44] This complex was also useful for studying the fundamental electronic structure and photolability of complexes while employing NO$^{\bullet}$ as a surrogate for O_2.[45] We have examined secondary coordination sphere effects by utilizing the aryl appended complexes, $[Fe^{II}(N4Py^{2Ph})(CH_3CN)](BF_4)_2$ and $[Fe^{II}(N4Py^{amide,2Ph})(CH_3CN)](BF_4)_2$. Without a stabilizing H-bond donor positioned near the open site on iron, the alkylperoxo complex $[Fe^{III}(N4Py^{2Ph})(OOtBu)]^{2+}$ likely undergoes rapid O–O bond cleavage to give a putative $Fe^{IV}(O)$ intermediate. The $Fe^{IV}(O)$ would then be situated for attack of the appended aryl group, giving the arene-hydroxylated product. However, in the presence of an amide H-bond donor, $[Fe^{III}(N4Py^{amide,2Ph})(OOtBu)]^{2+}$ is stabilized and only the alkylperoxoiron(III) complex is observed.[46] We also determined the influence of first and second coordination sphere modifications in a system in which an equatorial thioether donor was included in the first coordination sphere and an amide H-bond donor was included in the second coordination sphere. The $[Fe^{II}(N3Py^{amide}SR)](BF_4)_2$ starting material was shown to react with O-atom donors to give $[Fe^{IV}(O)(N3Py^{amide}SR)]^{2+}$ in CH_3CN at −40 °C. This complex is a rare example of a metastable $Fe^{IV}(O)$ complex with a pendant thioether donor, and it does not undergo *intramolecular* oxygen-atom transfer (OAT) to the thioether group. However, this complex does exhibit rapid *intermolecular* OAT to *exogenous* thioether substrates (PhSMe), and it was proposed that amide H-bond donation to the terminal oxo ligand was causing the significant rate accelerations seen for intermolecular OAT.[47]

Herein we report the synthesis and characterization of Fe(III)-OOH and -OO*t*Bu complexes derived from two biomimetic starting compounds, $[Fe^{II}(N3PySR)(CH_3CN)](BF_4)_2$ (**1**) and $[Fe^{II}(N3Py^{amide}SR)](BF_4)_2$ (**2**), shown in Scheme 1. These complexes were synthesized by metallation with $Fe(BF_4)_2$ of their respective purified ligand precursors. Both **1** and **2** possess a thioether ligand in the first coordination sphere, while complex **2** incorporates a single amide N–H group within H-bonding distance of the preferred binding site for anionic ligands. We demonstrate the generation of meta-stable Fe^{III}-OO(H/R) complexes in the presence of the thioether donor ligands starting from **1** and **2**. The influence of a first coordination sphere thioether donor and a second coordination sphere H-bond donor on the stability and spectroscopic properties of the (hydro/alkyl)peroxo iron(III) complexes is assessed.

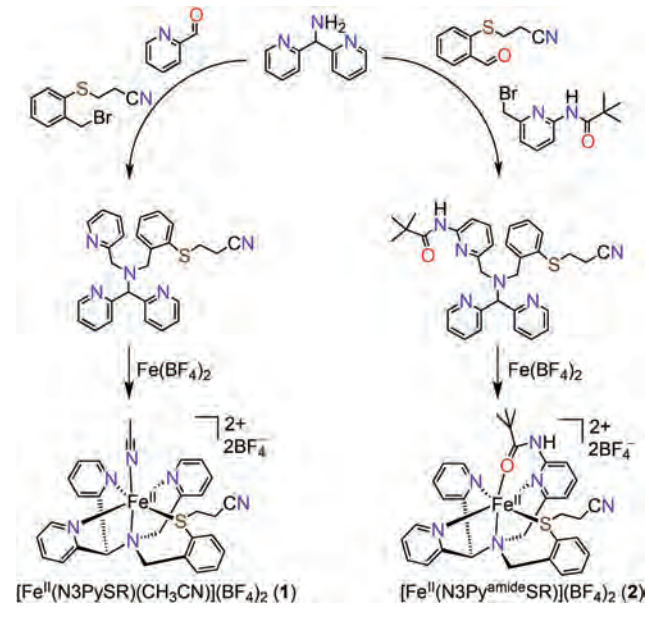

Scheme 1 Convergent syntheses of **1** and **2**.

Results and discussion

Synthesis and characterization

Compound **1** is prepared by metallation of the ligand N3PySR with $Fe(BF_4)_2$ in MeCN, followed by vapor diffusion of Et_2O into the resulting solution to give dark red blocks of **1** in 68% yield (Scheme 1). The structure of the cation of **1** is shown in Fig. 2 and structural data are summarized in Table 1. The ferrous ion is bound in a pseudo-octahedral geometry by three pyridyl and an aryl thioether donor in the equatorial plane, with a tertiary nitrogen donor and solvent nitrile molecule occupying the axial positions. The Fe–N bond distances (1.9260(14)–1.9969(13) Å, Table 2) are consistent with a low spin (ls) iron(II) center. The spin state was also confirmed by observation of a diamagnetic ^{1}H-NMR spectrum in $CDCl_3$.

Metallation of the ligand N3Py^{amide}SR with $Fe(BF_4)_2$, followed by vapor diffusion of Et_2O into the resulting dark orange solution yielded dark red crystals of **2** in 88% yield. The structure of the cation of **2** (Fig. 3) was reported previously and is repeated here for comparison with the other complexes.[47] As in **1**, the ferrous ion is low-spin and bound in a pseudo-octahedral geometry with three pyridyl and one aryl thioether donor in the equatorial plane, with the tertiary nitrogen donor occupying the axial position. In **2** however, the amide ligand has displaced the

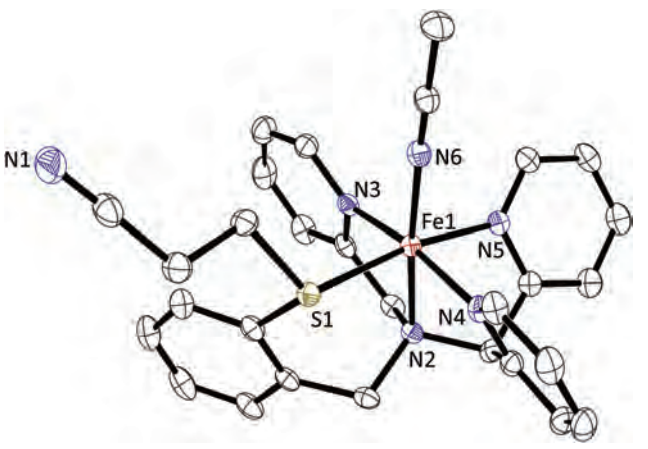

Fig. 2 Displacement ellipsoid plot of the cation of **1** shown at the 50% probability level. H-atoms are removed for clarity.

Published on 27 March 2014. Downloaded by INDIAN INSTITUTE OF TECHNOLOGY GUWAHATI on 30/09/2014 14:45:32.

Table 1 Summary of the crystallographic data for **1**, **3**·CH_3CN and **8**

Complex	**1**	**3**·CH_3CN	**8**
Formula	$C_{29}H_{28}B_2F_8FeN_6S$	$C_{34}H_{37}BF_{4.67}FeN_8OS$	$C_{44}H_{42}B_2F_8FeN_6OS$
Formula weight	722.10	761.13	932.37
T (K)	110	110	110
Color, morphology	Dark red, irregular shape	Yellow, lath	Yellow, block
Class	Triclinic	Orthorhombic	Triclinic
Space group	$P\bar{1}$	$Pbcn$	$P\bar{1}$
a (Å)	10.6689(2)	35.1087(4)	10.4419(3)
b (Å)	12.0355(2)	10.08753(9)	14.5834(3)
c (Å)	13.0403(3)	19.9277(2)	17.2950(4)
α (°)	80.5885(18)	90	90.6304(19)
β (°)	88.0024(18)	90	105.768(2)
γ (°)	68.543(2)	90	106.791(2)
V (Å^3)	1536.85(5)	7057.59(12)	2415.01(10)
ρ (g cm^{-3})	1.560	1.433	1.282
μ (mm^{-1})	0.640	4.546	0.425
$(\sin\theta/\lambda)_{max}$ (Å^{-1})	0.65	0.62	0.62
No. reflections collected	35 673	44 026	29 736
No. unique reflections	7051	6942	9709
R_{int}	0.0247	0.0273	0.0305
No. variable parameters	425	511	648
R_1 [$I > 2\sigma(I)$]	0.0325	0.0322	0.0401
wR_2 [$I > 2\sigma(I)$]	0.0877	0.0791	0.1117
R_1 [all data]	0.0373	0.0366	0.0475
R_2 [all data]	0.0905	0.0821	0.1155
Goodness-of-fit (GOF) on F^2	1.061	1.026	1.102
Largest difference in hold and peak (e A^{-3})	−0.50, 0.63	−0.33, 0.63	−0.46, 0.58

Table 2 Selected bond distances (Å) and angles (°) for **1**

Bond lengths		Bond angles	
Fe1 N6	1.9260(14)	N6 Fe1 N4	94.41(6)
Fe1 N4	1.9569(13)	N6 Fe1 N3	97.35(6)
Fe1 N3	1.9619(13)	N4 Fe1 N3	168.23(6)
Fe1 N5	1.9790(13)	N6 Fe1 N5	94.24(5)
Fe1 N2	1.9969(13)	N4 Fe1 N5	86.41(5)
Fe1 S1	2.2848(4)	N3 Fe1 N5	92.09(5)
		N6 Fe1 N2	175.10(5)
		N4 Fe1 N2	83.35(5)
		N3 Fe1 N2	84.88(5)
		N5 Fe1 N2	81.29(5)
		N6 Fe1 S1	93.13(4)
		N4 Fe1 S1	87.26(4)
		N3 Fe1 S1	92.70(4)
		N5 Fe1 S1	170.63(4)
		N2 Fe1 S1	91.12(4)

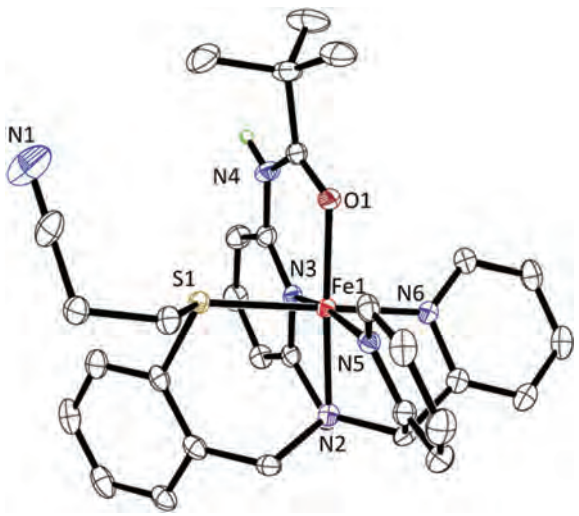

Fig. 3 Displacement ellipsoid plot for the cation of **2** shown at the 50% probability level. H-atoms, except the amide N–H, are removed for clarity. The existence of the H atom attached to N4 was confirmed by difference Fourier map.

bound solvent molecule and is coordinated through the amide oxygen.

When the propionitrile protecting group of the ligand for **1** is removed prior to metal binding, the corresponding Fe^{II}-thiolate complex is accessed, which has been shown to undergo sulfur oxidation in the presence of O_2.[44] However, in compounds **1** and **2** the thioether donor appears to make these complexes stable toward O_2, with no visible decomposition over several days stored under aerobic conditions.

Prior to attempting to make iron-peroxo complexes from **1** and **2**, we wanted to test the substitution chemistry of **2** toward anionic donors to show that the amide group could be displaced and reoriented into a favorable hydrogen-bonding position. We also wanted to confirm whether hydrogen bonding would be favored with the anionic ligands found in the axial position. Stirring of **2** with 1.0 equiv. NaN_3 in MeCN, followed by vapor diffusion of Et_2O into the solution produced a small amount of yellow crystals that were manually separated from the bulk precipitate for X-ray structure determination. This structure revealed the new compound, $[Fe^{II}(N3Py^{amide}SR)(F/N_3)]BF_4$ (**3**), which shows that the amide C=O donor has been displaced, and there is a mixture of F^- (67%) and N_3^- (33%) anions that are occupying the desired axial position.

 This journal is © The Royal Society of Chemistry 2014

Published on 27 March 2014. Downloaded by INDIAN INSTITUTE OF TECHNOLOGY GUWAHATI on 30/09/2014 14:45:32.

Table 3 Selected bond lengths (Å) and angles (°) for **3**

Bond lengths		Bond angles	
Fe1 F1	1.850(4)	F1 Fe1 N2	98.05(14)
Fe1 N7	2.063(14)	N7 Fe1 N2	105.6(5)
Fe1 N2	2.1703(16)	F1 Fe1 N1	108.09(14)
Fe1 N1	2.1892(14)	N7 Fe1 N1	102.8(4)
Fe1 N3	2.2012(14)	N2 Fe1 N1	82.68(6)
Fe1 N5	2.2448(13)	F1 Fe1 N3	173.68(12)
Fe1 S1	2.6007(5)	N7 Fe1 N3	176.6(4)
		N2 Fe1 N3	77.62(6)
		N1 Fe1 N3	76.14(5)
		F1 Fe1 N5	98.62(14)
		N7 Fe1 N5	103.3(4)
		N2 Fe1 N5	95.76(5)
		N1 Fe1 N5	153.22(5)
		N3 Fe1 N5	77.41(5)
		F1 Fe1 S1	94.88(14)
		N7 Fe1 S1	87.7(5)
		N2 Fe1 S1	166.53(5)
		N1 Fe1 S1	96.89(4)
		N3 Fe1 S1	89.18(4)
		N5 Fe1 S1	78.52(4)

The Fe–S bond is rather long (2.6007(5) Å), but the sulfur is oriented correctly for a weak bonding interaction with the Fe center (Table 3). The Fe^{II}–N(py) distances (2.1703(16)–2.2448(13) Å) for **3** are indicative of a high-spin (hs) ferrous center, and the difference in Fe–F and Fe–N_3 distances allows for reliable determination of the N_3^- ligand despite its low occupancy. The N_3^--containing component of **3** is shown in Fig. 4, as it more closely resembles the structure of an anionic peroxo ligand than does the F^- component. The source of fluoride for the F^--containing component of **3** can be assigned to BF_4^-. This structure shows that the axial amide carbonyl is labile, and can be displaced by anionic donors. The structure of **3** also shows that the pendant amide is positioned such that H-bonding interactions to anionic ligands are favored (N6···N7 = 2.914(16) Å, N6···F1 = 2.784(5) Å, N6–H–N7 = 174(2)°, N6–H–F1 = 170(2)°; amide N–H is located in the difference map). This complex provides good evidence that Fe-OO(H/R) complexes will likely exhibit the same H-bonding interaction.

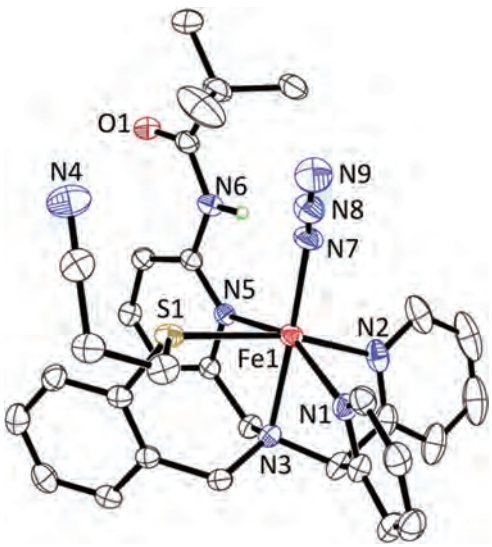

Fig. 4 Displacement ellipsoid plot of the N_3^--containing disordered component of the cation of **3** shown at the 50% probability level. H-atoms, except the amide N–H, are removed for clarity. The existence of the H atom attached to N6 was confirmed by difference Fourier map.

Fe^{III}-OOH complexes

Complex **1** reacts with excess H_2O_2 at 25 °C (Fig. 5) to generate a new transient red species, **4** ($t_{1/2} \approx 1$ min). Monitoring the reaction by UV-vis shows isosbestic conversion of the peaks corresponding to **1** (λ_{max} = 360, 430 nm) into a new spectrum for **4** (λ_{max} = 542 nm, ε = 1000 M^{-1} cm^{-1}). The peak at 542 nm is characteristic of a hydroperoxo-to-iron(III) LMCT band. Attempts to trap this species by generation at −40 °C were unsuccessful, leading only to decomposition, with no observable UV-vis peaks corresponding to **4**. Samples of **4** for analysis by EPR and resonance Raman were therefore prepared at 25 °C and flash-frozen immediately after mixing. From EPR and RR (*vide infra*) complex **4** is assigned as the Fe^{III}-OOH complex $[Fe^{III}(OOH)(N3PySR)]^{2+}$.

Complex **2** reacts with excess H_2O_2 at −40 °C (Fig. 6), and changes in color from orange to deep purple over the course of 30 min. The new purple species (**5**) persists for at least several hours at −40 °C, but immediately decays upon warming to 25 °C. Monitoring by low-temperature UV-vis spectroscopy shows isosbestic conversion from **2** (λ_{max} = 350, 450 nm) to a new peak (λ_{max} = 567 nm, ε = 900 M^{-1} cm^{-1}) that is characteristic of a hydroperoxo-to-iron(III) LMCT band. The EPR and RR spectra (*vide infra*), confirmed that the new species (**5**) is the Fe^{III}-OOH complex, $[Fe^{III}(OOH)(N3Py^{amide}SR)]^{2+}$.

The X-band EPR spectra of **4** and **5** are shown in Fig. 5 and 6, respectively. Both complexes show axial spectra corresponding to ls iron(III) centers with signals at g = 2.17, 2.11,

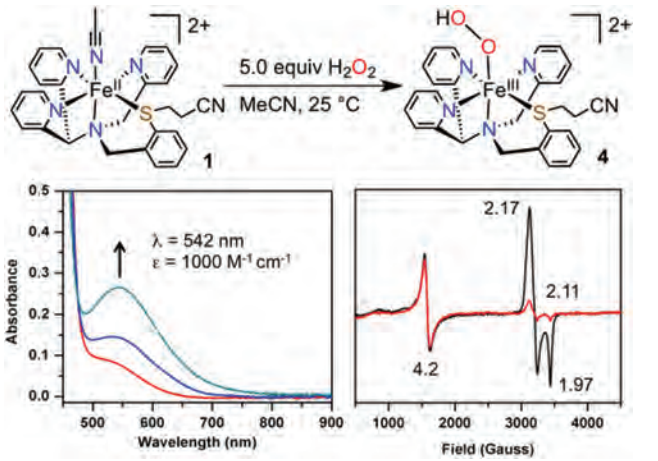

Fig. 5 Formation of $[Fe^{III}(OOH)(N3PySR)]^{2+}$ (**4**) (top). Changes in the electronic absorption spectrum for the reaction of **1** + H_2O_2 in CH_3CN (25 °C), red = **1**, blue = 30 s, green = 60 s (bottom left). X-band EPR spectra of the reaction mixture of **1** + H_2O_2, flash frozen after mixing at 25 °C for 1 min (black line) and 3 min (red line) (bottom right). EPR parameters: T = 15 K, frequency = 9.46 GHz, power = 2.01 mW.

Published on 27 March 2014. Downloaded by INDIAN INSTITUTE OF TECHNOLOGY GUWAHATI on 30/09/2014 14:45:32.

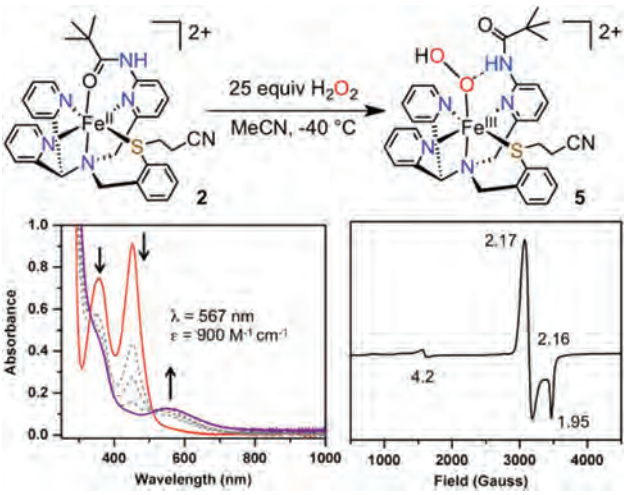

Fig. 6 Formation of $[Fe^{III}(OOH)(N3Py^{amide}SR)]^{2+}$ (**5**) (top). Changes in the electronic absorption spectrum for the reaction of **2** + H_2O_2 in CH_3CN, over 30 min at −40 °C (bottom left). X-band EPR spectrum of the reaction mixture of **2** + H_2O_2, flash frozen after mixing at −40 °C for 30 min. EPR parameters: T = 77 K, frequency = 9.46 GHz, power = 2.01 mW.

1.97, for **4** and g = 2.17, 2.16, 1.95, for **5**. These values are similar to other Fe^{III}-OOH complexes reported in the literature.[18] The mononuclear complex $[Fe^{III}(N4Py)(OOH)]^{2+}$ in methanol has a signal at g = 2.17, 2.12 and 1.97,[13] while the TPA analogue $[Fe^{III}(TPA)(OOH)]^{2+}$ affords a spectrum with g = 2.19, 2.15 and 1.96 in acetone/acetonitrile.[48] EPR spectra of reaction mixtures of **4**, taken at different timepoints (1–5 min) clearly show the rapid decomposition of the ls-Fe^{III} signal at room temperature. Samples frozen after 1 min show a relatively strong ls-Fe^{III} signal along with an additional signal at g = 4.2. After 3 minutes, the ls-Fe^{III} signal appears to be mostly decayed, and after 5 min no ls-Fe^{III} signal is observed. The peak at g = 4.2 does not increase with the decay of the Fe^{III}-OOH feature, indicating it is not a decomposition product and is likely a byproduct of Fe^{III}-OOH formation. The peak at g = 4.2 is much more prominent in **4** relative to that seen in the spectrum of **5**, which was prepared at −40 °C and frozen after 30 min, allowing for full formation of **5** with much less possibility for decay.

The identity of the Fe^{III}-OOH complex **4** was confirmed by RR spectroscopy. Frozen CD_3CN solutions were analyzed at 110 K with a 568 nm laser excitation to avoid overlap of RR bands with non-resonant vibrations from CH_3CN. The RR spectra of **4** show a cluster of bands in the ν(Fe–O) region with prominent bands at 615, 629, 647 and 664 cm^{-1}, and two bands at 787 and 809 cm^{-1} in the ν(O–O) region (Fig. 7A). Labeled samples prepared with $H_2{}^{18}O_2$ exhibit greatly simplified spectra with unique ν(Fe–O) and ν(O–O) modes at 590 and 763 cm^{-1}, respectively. RR spectra of samples prepared with D_2O_2 in the presence of excess D_2O also show a single set of ν(Fe–O) and ν(O–O) bands at 607 cm^{-1} and 809 cm^{-1}. These data clearly indicate that the complexity of the RR spectra of unlabeled complex **4** results from vibrational coupling of the

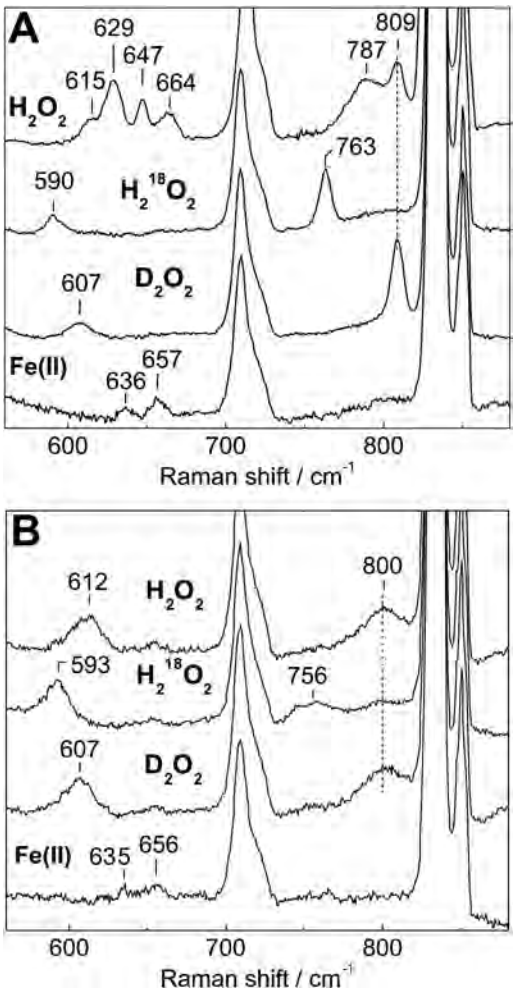

Fig. 7 Resonance Raman spectra of complexes **1** and **4** (A), and **2** and **5** (B) in CD_3CN.

Fe–O–O–H unit with internal vibrations of the (N3PyS) ligand. Using Hooke's law to calculate the $\nu(^{16}O–^{16}O)$ frequency based on an isolated diatomic oscillator with a $\nu(^{18}O–^{18}O)$ at 763 cm^{-1} leads to an 809 cm^{-1} value that matches the ν(O–O) mode seen in D_2O and the sharper component of the doublet observed with unlabeled complex **4**. Accordingly, the 809 cm^{-1} band is assigned to the ν(O–O) mode of **4**. Using the same approach to interpret the RR bands observed in the ν(Fe–O) region is less successful,[49] presumably because of admixture between Fe–O stretch and Fe–O–O bend vibrations, as seen previously with other Fe(III)-hydroperoxo complexes.[13,50]

The pendant amide complex $[Fe^{III}(N3Py^{amide}SR)(OOH)]^{2+}$ (**5**) was also studied by RR spectroscopy under the same conditions (Fig. 7b). In contrast with **4**, the RR spectra of **5** shows no evidence of vibrational coupling and assigning the ν(Fe–O) and ν(O–O) bands is straightforward. The unlabeled complex shows a single ν(O–O) mode at 800 cm^{-1} that downshifts to 756 cm^{-1} with samples prepared with $H_2{}^{18}O_2$ and that is unchanged in samples prepared with D_2O_2 in the presence of excess D_2O. A single band at 612 cm^{-1} in the ν(Fe–O) region shifts to 593 cm^{-1} with $H_2{}^{18}O_2$ and to 607 cm^{-1} with D_2O_2.

 This journal is © The Royal Society of Chemistry 2014

Published on 27 March 2014. Downloaded by INDIAN INSTITUTE OF TECHNOLOGY GUWAHATI on 30/09/2014 14:45:32.

Table 4 Comparison of RR data for ls non-heme Fe^{III}-OOH complexes

Complex	ν(Fe–O), [ν(O–O)]	$\Delta^{18}O_2$	ΔD_2O
$[Fe^{III}(N3PySR)(OOH)]^{2+}$	615, [809]	−25, [−46]	−8, [0]
$[Fe^{III}(N3Py^{amide}SR)(OOH)]^{2+}$	612, [800]	−19, [−44]	−5, [0]
$[Fe^{III}(N4Py)(OOH)]^{2+}$ [a]	632, [790]	−16, [−44]	−5, [0]
$[Fe^{III}(TPA)(OOH)]^{2+}$ [b]	624, [803]	−19, [44]	−3, [0]

[a] Ref. 13. [b] Ref. 51.

Comparing ν(Fe–O) and ν(O–O) frequencies for **4** and **5** with previously characterized Fe(III)-OOH complexes (Table 4), confirms their identity and suggests that the amide H-bond donor group exerts limited influence on the Fe–O–O unit.

Comparison of the RR data for complexes **4** and **5** with $[Fe^{III}(N4Py)(OOH)]^{2+}$ reveals a 19 ± 2 cm^{-1} downshift in ν(Fe–O), and a 10 to 19 cm^{-1} (for **5** and **4**, respectively) upshift of the $\Delta\nu$(O–O) upon incorporation of the thioether donor. This effect of the equatorial thioether donor on ν(O–O) differs from a previous study, where the replacement of an axial triflate (OTf^-) ligand with aryl-thiolate donors (ArS^-) in hs $[Fe^{III}(Me_4[15]aneN_4)(SAr)(OOR)]^+$ complexes was shown to have little influence on ν(O–O) ($\Delta\nu$(O–O) = 1 cm^{-1}).[23] In contrast, the effect of the equatorial thioether donor on ν(Fe–O) in **4** and **5** is similar to the effect previously seen for the aryl-thiolate complexes, in which inclusion of sulfur induced a lowering of this band.[23]

Fe^{III}-OO*t*Bu complexes

Complex **1** reacts with 10 equiv. of *t*BuOOH (Fig. 8) at −40 °C in MeCN to give a new deep blue species (**6**) that persists at low temperature for 15–20 min before slowly decaying. Monitoring the reaction by UV-vis spectroscopy shows the isosbestic conversion of the peaks corresponding to **1**, into a new spectrum (λ_{max} = 600 nm, ε = 1670 M^{-1} cm^{-1}) that is characteristic of an alkylperoxo-to-iron(III) LMCT band and is in good agreement with similar compounds reported in the literature.[14,29] The UV-vis spectra reveal that **1** reacts with *t*BuOOH to form **6** within 10 min, but is only stable for a short period and begins to decay after 15 min. The new species (**6**) is assigned as the alkylperoxo complex $[Fe^{III}(OOtBu)(N3PySR)]^{2+}$.

Complex **2** also reacts with *t*BuOOH at −40 °C to give a deep blue solution, similar to that seen for **1**. This new complex (**7**, Fig. 9) is formed *via* isosbestic conversion from **2**, to a new spectrum characteristic for Fe^{III}-OOR complexes (λ_{max} = 620 nm, ε = 2000 M^{-1} cm^{-1}) within 15 min. As seen for **6**, complex **7** is not stable at −40 °C, and slowly decays to a broad, featureless spectrum over 1 h. This species (**7**) is assigned as the ferric-alkylperoxo complex, $[Fe^{III}(OOtBu)(N3Py^{amide}SR)]^{2+}$.

It has been shown that a lowering in energy of peroxo-to-iron(III) charge transfer bands can be correlated with an increasing number of pyridine ligands bound to the iron center, as the π-accepting ability of py ligands lowers the energy of LMCT bands.[18,52] It is therefore interesting to compare the energy of the LMCT band for compounds **6** and **7**

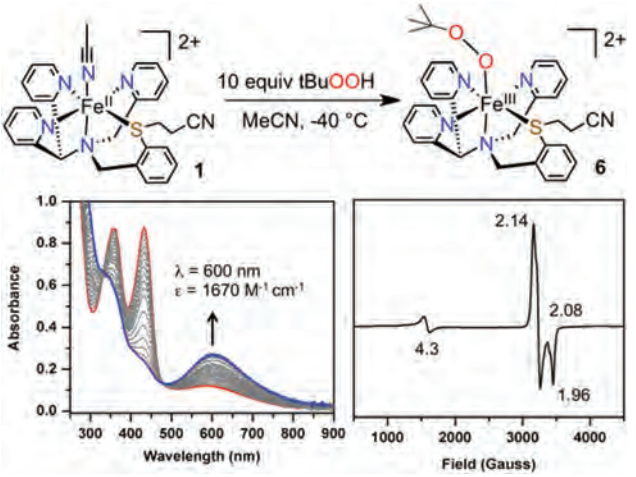

Fig. 8 Formation of $[Fe^{III}(OOtBu)(N3PySR)]^{2+}$ (**6**) (top). Changes in the electronic absorption spectrum for the reaction of **1** + *t*BuOOH in CH_3CN, over 10 min at −40 °C (bottom left). X-band EPR spectrum of the reaction mixture of **1** + *t*BuOOH, flash frozen after mixing at −40 °C for 15 min. EPR parameters: T = 15 K, frequency = 9.46 GHz, power = 2.01 mW.

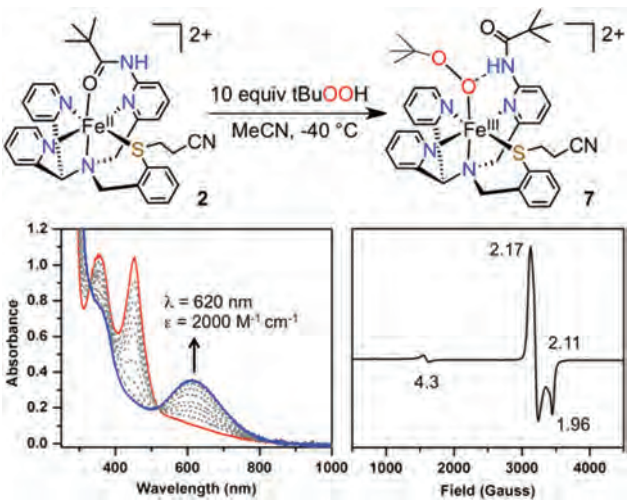

Fig. 9 Formation of $[Fe^{III}(OOtBu)(N3Py^{amide}SR)]^{2+}$ (**7**) (top). Changes in the electronic absorption spectrum for the reaction of **2** + *t*BuOOH in CH_3CN, over 10 min at −40 °C (bottom left). X-band EPR spectrum of the reaction mixture of **2** + *t*BuOOH, flash frozen after mixing at −40 °C for 15 min. EPR parameters: T = 77 K, frequency = 9.46 GHz, power = 2.01 mW.

to the parent $[Fe^{III}(N4Py)(OOtBu)]^{2+}$ compound (λ_{max} = 560 nm, ε = 2400 M^{-1} cm^{-1}).[15] Relative to N4Py, the thioether-ligated complexes exhibit bands that are shifted to lower energy by 40 nm for **6**, and 60 nm for **7**. These shifts indicate that replacement of a pyridine with a thioether donor causes a significant lowering of the energy of the LMCT band. This change is consistent with stabilization of the metal acceptor orbital caused by the weaker ligand field presented by the thioether donor. In addition, the LMCT bands for both the (hydro) and (alkyl) peroxo-iron(III) complexes are further lowered in energy by the

Published on 27 March 2014. Downloaded by INDIAN INSTITUTE OF TECHNOLOGY GUWAHATI on 30/09/2014 14:45:32.

addition of the H-bond donor, as evidenced by the ~20 nm red-shift in the absorption band for both **5** and **7**, relative to the non H-bonded **4** and **6**.

The X-band EPR spectra for **6** and **7** (Fig. 8 and 9) show that the alkylperoxo species are also low-spin iron(III) with *g* values of 2.14, 2.08, 1.96 (**6**), and 2.17, 2.11, 1.96 (**7**), that are in good agreement with similar compounds previously reported in the literature.[14,28,29] As seen with the hydroperoxo complexes, spectra of **6** and **7** do show a small peak at $g = 4.3$, consistent with a small amount of high-spin decomposition product.

Resonance Raman spectra of **6** and **7** were collected on frozen samples in CD_3CN at 110 K with a 647 nm laser excitation (Fig. 10). The spectrum of **6** shows two resonance-enhanced vibrations at 700 and 796 cm^{-1} that are in the expected range for ν(Fe–O) and ν(O–O), respectively. The RR spectrum of **7** shows similar vibrations at 691 and 796 cm^{-1}.

These ν(O–O) frequencies below 800 cm^{-1} are consistent with the ls configuration of **6** and **7** and both ν(O–O) and ν(Fe–O) closely match reported results for $[Fe^{III}(TPA)(OH_n)(OOtBu)]^{n+}$ (see Table 5). The presence of the intramolecular H-bond donor in **7** has no effect on the ν(O–O), but it results in a −9 cm^{-1} downshift of the ν(Fe–O) relative to **6**. RR spectra of complex **7** after H/D exchange of the amide N–H group showed that deuteration of the amide group has no effect on the ν(Fe–O) and ν(O–O) signals, which suggests that the H-bonding interaction might be weak. The 7 cm^{-1} downshift of the ν(Fe–O) in **7**, relative to $[Fe^{III}(TPA)(OOtBu)]^{2+}$, could be due to changes in Fe–O–O–R angle and level of admixture between Fe–O stretch and Fe–O–O bend rather than changes in Fe–O bond strength.

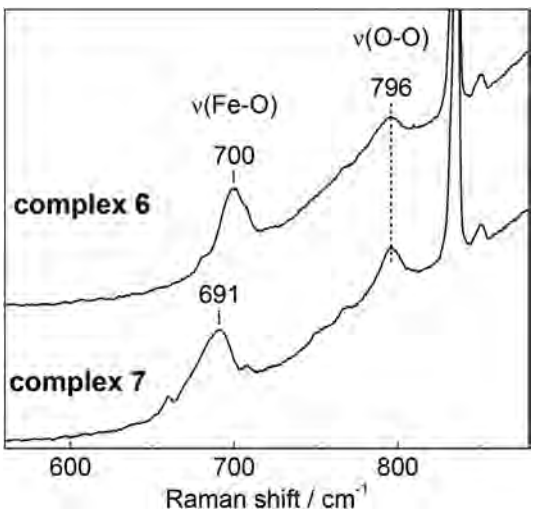

Fig. 10 Resonance Raman spectra of **6** and **7** in CD_3CN.

Table 5 Comparison of RR data for ls non-heme Fe^{III}-OO*t*Bu complexes

Complex	ν(Fe–O)	ν(O–O)	Reference
$[Fe^{III}(N3PySR)(OOtBu)]^{2+}$	700	796	This work
$[Fe^{III}(N3Py^{amide}SR)(OOtBu)]^{2+}$	691	796	This work
$[Fe^{III}(TPA)(OOtBu)]^{2+}$	696	796	22
$[Fe^{III}([15]aneN_4)(SPh)(OOtBu)]^{+}$	612	803	23

Density functional theory

Density functional computations at the UB3LYP-D level of theory were utilized to model complexes **4**–**7** (see ESI† for details). Our initial work explored the spin state ordering of complex **5**, for which we calculated the lowest lying doublet (^{2}**5**), quartet (^{4}**5**), and sextet (^{6}**5**) spin states. The doublet spin state was found to be the ground state by 1.5 and 8.5 kcal mol^{-1} over the sextet and quartet spin states, respectively. This spin state ordering reproduces the experimental EPR characterization of **5**, which indicates an $S = 1/2$ spin state. Optimized geometries of ^{2}**5** and ^{2}**7** are shown in Fig. 11 and are consistent with the proposed structures for complexes **5** and **7**, where the iron(III) center is bound in a pseudo-octahedral geometry by the equatorial pyridine and thioether donors, and the tertiary amine and (hydro/alkyl)peroxide ligands occupy the axial positions. The structures also show that the pendant amide H-bond donor has reoriented in both cases, and reveals an NH···O hydrogen bond, with calculated N···O distances of 2.774 Å (**5**) and 2.815 Å (**7**) and angles of 158.1° (**5**) and 153.3° (**7**).

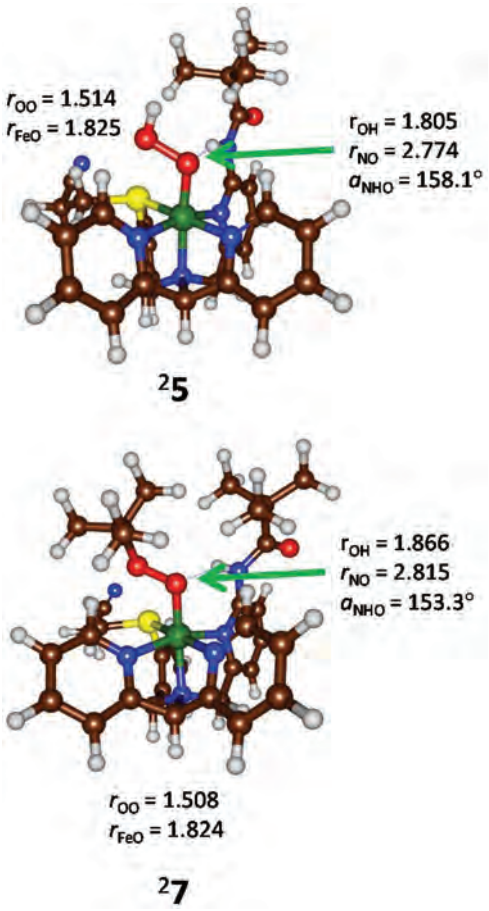

Fig. 11 DFT optimized structures of ^{2}**5** (top) and ^{2}**7** (bottom), calculated at the UB3LYP-D level of theory with bond lengths given in angstroms.

 This journal is © The Royal Society of Chemistry 2014

Published on 27 March 2014. Downloaded by INDIAN INSTITUTE OF TECHNOLOGY GUWAHATI on 30/09/2014 14:45:32.

Steric influences in the secondary coordination sphere

In further efforts to stabilize the Fe^{III}-OO(H/R) species, we synthesized the new ligand shown in Scheme 2. The resulting complex, $[Fe^{II}(N3Py^{amide,2Ph}SR)](BF_4)_2$ (**8**), incorporates two phenyl substituents in the second coordination sphere, providing additional steric protection around the putative peroxide binding site (Fig. 12). The synthesis of the $N3Py^{amide,2Ph}SR$ ligand is shown in Scheme 2. The key synthetic step, incorporation of the phenyl substituents onto the pyridine rings, was accomplished in high yield using Suzuki–Miyaura cross coupling reaction.[46] Metallation of the free ligand with $Fe(BF_4)_2$ was accomplished by stirring in MeCN, and single crystals of **8** were grown from vapor diffusion of Et_2O into the solution. The light yellow crystals reveal Fe–N bond distances (2.1842–2.2267 Å, Table 6) consistent with a high-spin (hs) iron(II) center. As in **2**, the iron(II) ion is bound in a pseudo-octahedral geometry with the 3 pyridine donors and aryl thioether occupying the equatorial positions, while the tertiary amine and the amide carbonyl are bound in the axial positions. The incorporated phenyl substituents are projected orthogonal to the pseudo-equatorial plane, and are oriented to provide significant steric protection around the axial binding site. In contrast to low-spin **1** and **2**, as well as some other hs Fe^{II} complexes,[28,46] **8** does not react with H_2O_2 or *t*BuOOH to afford the corresponding ferric-peroxo complexes, and appears to only undergo outer-sphere oxidation upon addition of a large excess of oxidant (150 equiv.). The lack of reactivity may be due to significant steric encumbrance around the metal center with incorporation of the new phenyl substituents. However, we should point out that the related diphenyl-substituted hs Fe^{II} complex, $[Fe^{II}(N4Py^{amide,2Ph})(CH_3CN)]^{2+}$, does react with *t*BuOOH to give an $Fe^{III}(OOtBu)$ complex at low temperature,[46] and therefore some additional factors may also be involved in inhibiting the reactivity of **8**.

Table 6 Selected bond distances (Å) and angles (°) for **8**

Bond lengths		Bond angles	
Fe1 O1	2.0085(13)	O1 Fe1 N4	83.37(6)
Fe1 N4	2.1842(16)	O1 Fe1 N3	159.27(6)
Fe1 N3	2.1954(15)	N4 Fe1 N3	76.66(6)
Fe1 N1	2.1959(15)	O1 Fe1 N1	111.24(6)
Fe1 N2	2.2267(16)	N4 Fe1 N1	98.60(6)
Fe1 S1	2.6097(5)	N3 Fe1 N1	77.62(6)
		O1 Fe1 N2	120.85(6)
		N4 Fe1 N2	154.51(6)
		N3 Fe1 N2	78.35(6)
		N1 Fe1 N2	80.75(6)
		O1 Fe1 S1	83.97(4)
		N4 Fe1 S1	84.45(4)
		N3 Fe1 S1	88.61(4)
		N1 Fe1 S1	164.70(4)
		N2 Fe1 S1	90.05(4)

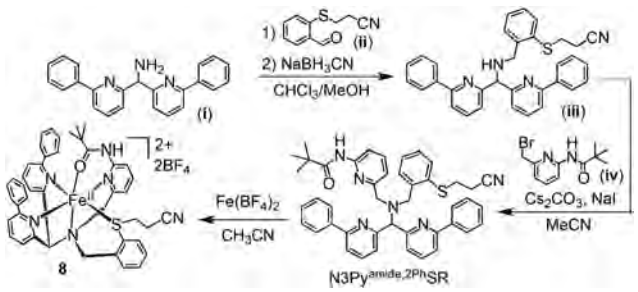

Scheme 2 Synthesis of the ligand precursor ($N3Py^{amide,2Ph}SR$) to **8**.

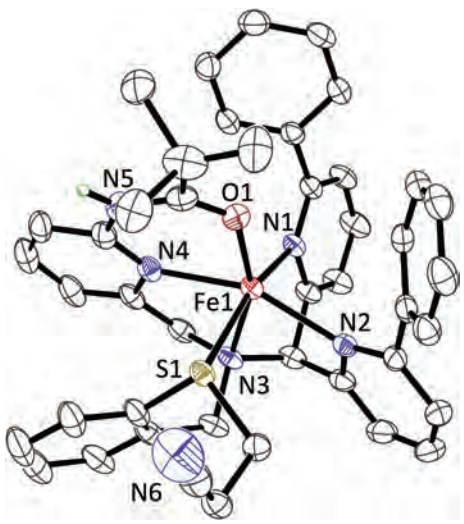

Fig. 12 Displacement ellipsoid plot of the cation of **8** shown at the 50% probability level. H-atoms, except the amide N–H, are removed for clarity.

Conclusions

We have synthesized a series of new biomimetic iron(II) model complexes that incorporate a pendant thioether ligand in the equatorial plane. Complexes **1** and **2** react to generate rare examples of Fe^{III}-hydroperoxo and -alkylperoxo complexes with a pendant thioether donor (**4**–**7**). These peroxo species were characterized by UV-vis, EPR and resonance Raman spectroscopy, and DFT calculations supported the proposed structures and spin states. All four peroxo complexes are low-spin species with rhombic EPR resonances centered around $g = 2$, and ν(O–O) at 800 ± 10 cm^{-1}. The hydroperoxo (**4** and **5**) and alkylperoxo (**6** and **7**) complexes show ν(Fe–O) at 618 ± 5 cm^{-1} and ν(Fe–O) at 695 ± 5 cm^{-1}, respectively, which are also in the expected range for ls peroxo species. While the addition of an equatorial thioether donor has minimal effects on the alkylperoxo Fe–O–O vibrations, substantial ν(Fe–O) and ν(O–O) upshifts are seen in the hydroperoxo complexes. The UV-vis data show a significant decrease in the energy of the alkylperoxo-to-iron(III) charge transfer bands, indicating that incorporation of a thioether donor in the first coordination sphere likely stabilizes the key metal acceptor orbital for the LMCT bands in **6** and **7**. Modification of the second coordination

Published on 27 March 2014. Downloaded by INDIAN INSTITUTE OF TECHNOLOGY GUWAHATI on 30/09/2014 14:45:32.

sphere by addition of a single H-bond donor was also shown to affect the properties of these non-heme Fe complexes. Structural characterization of the azide/fluoride-ligated complex **3** showed that the axial amide ligand was indeed labile toward displacement by anionic donors, and that formation of a single hydrogen bond between the amide N–H and anionic ligands in the open site is favored. The inclusion of an amide H-bond donor in the second coordination sphere also appears to shift the peroxo-to-iron LMCT band to lower energy by ~20 nm in both the hydro- and alkylperoxo cases. In contrast, the RR spectra of the peroxo complexes are minimally affected by the addition of the amide H-bond donor. The largest change corresponds to a 9 cm^{-1} downshift of the ν(Fe–O) in the Fe^{III}-OO*t*Bu complex **7**. It appears that the addition of the phenyl substituents in **8** inhibits formation of the Fe^{III}-OO(H/R) complexes, and further work is needed to tease out the factors that contribute to this second coordination sphere effect. The results presented here suggest that both first and second coordination sphere effects can be employed by non-heme iron complexes and proteins to subtly tune the reactivity and properties of Fe^{II} and Fe^{III}-OO(H/R) species.

Experimental section

General considerations

All reagents were purchased from commercial vendors and used without further purification unless noted otherwise. The N3PySR ligand[44] and **2**[47] were synthesized as previously reported. All reactions were carried out under an atmosphere of N_2 inside a glovebox or under Ar by standard Schlenk and vacuum line techniques. UV-visible spectra were recorded on a Varian Cary 50 spectrophotometer. Electron paramagnetic resonance (EPR) spectra were obtained on a Bruker EMX EPR spectrometer controlled with a Bruker ER 041 XG microwave bridge at 15 or 77 K. The EPR spectrometer was equipped with a continuous-flow liquid He or N_2 cryostat and an ITC503 temperature controller made by Oxford Instruments, Inc. NMR was performed on a Bruker Avance 400 MHz FT-NMR spectrometer at 25 °C. Elemental analysis was performed by Atlantic Microlab Inc., Norcross, GA. LDI-ToF mass spectra were obtained using a Bruker Autoflex III Maldi ToF/ToF instrument (Billerica, MA). Samples were dissolved in CH_2Cl_2 and deposited on the target plate in the absence of any added matrix. Samples were irradiated with a 355 nm UV laser and mass-analyzed by ToF mass spectrometry in the reflectron mode. Resonance Raman spectra were recorded at 110 K using a backscattering geometry with a McPherson 2061/207 spectrograph and a liquid-N_2-cooled CCD camera. The 568 and 647 nm excitations were obtained from a Kr and Ar ion laser, respectively (Innova 300, Coherent). Longpass filters (Razor-Edge, Semrock) were used to attenuate the Raleigh scattering. The samples were kept at 110 K inside a liquid-N_2 coldfinger and spun continuously to prevent photodamage. Frequencies were calibrated relative to an aspirin standard and are accurate to ±1 cm^{-1}. Density functional theory calculations were performed using previously calibrated and benchmarked methods[53] and are explained in detail in the ESI.†

Synthesis of reported compounds

$[Fe^{II}(N3PySR)(CH_3CN)](BF_4)_2$ (1). The free ligand N3PySR (399 mg, 0.89 mmol) was dissolved in CH_3CN (10 mL). A slurry of $Fe(BF_4)_2{\cdot}6H_2O$ (298 mg, 0.88 mmol) in CH_3CN (10 mL) was added dropwise to the ligand, affording a red suspension. The mixture was allowed to stir for 2 h, and filtered through celite. Diffusion of diethyl ether into a CH_3CN solution afforded dark red blocks after two days. Yield: 409 mg (68%). ^1H NMR ($CDCl_3$): δ 9.48 (2H), 9.34 (1H), 8.23 (1H), 8.14 (1H), 7.99 (2H), 7.76 (1H), 7.70 (1H), 7.56 (1H), 7.44 (3H), 7.21 (2H), 6.81 (1H), 6.71 (1H), 4.40 (1H), 4.26 (1H), 3.88 (1H), 3.66 (1H), 3.10 (1H), 2.73 (1H), 2.60 (1H). *Anal. Calc.* for $C_{29}H_{28}B_2F_8N_6SFe$: C, 48.24; H, 3.91; N, 11.64. Found: C, 48.22; H, 3.93; N, 11.70.

$[Fe^{II}(N3Py^{amide}SR)(F/N_3)](BF_4){\cdot}CH_3CN$ (F^- = 67%, N_3^- = 33%) (3·CH_3CN). A stock solution of NaN_3 (5.8 mg in 0.5 mL MeOH) was prepared, and 50 μL of this solution was added to complex **2** (6.5 mg, 9 μmol) dissolved in 0.5 mL MeCN. Vapor diffusion of Et_2O into the mixture resulted in a small amount of yellow crystals (**3**) suitable for X-ray structure determination, which were separated manually from the bulk material. UV-vis (CH_3CN): λ_{max} = 355, 430 nm, ε = 1620, 1680 M^{-1} cm^{-1}.

$[Fe^{III}(N3PySR)(OOH)]^{2+}$ (4). A solution of **1** (0.8 mM) was prepared in MeCN before H_2O_2 (30%, 5.0 equiv.) was added at 25 °C. The yellow solution immediately turned red, then brown. Monitoring by UV-vis (Fig. 5) showed the decay of peaks corresponding to **1** (λ_{max} = 350, 450 nm), with isosbestic conversion to a new spectrum (λ_{max} = 542 nm) that corresponds to **4**. Complex **4** was formed within 60 s and immediately began to decay to a brown species with no prominent UV-vis features. UV-vis: λ_{max} = 542 nm, ε = 1000 M^{-1} cm^{-1}; EPR: g = [2.17, 2.11, 1.97]; RR: ν(Fe–O) = 615, 629, 647 and 664 cm^{-1}, ν(O–O) = 809 cm^{-1}.

$[Fe^{III}(N3Py^{amide}SR)(OOH)]^{2+}$ (5). An amount of **2** (1.25 mg, 1.7 μmol) was dissolved in 4.0 mL of MeCN and cooled to −40 °C. A solution of H_2O_2 (0.88 M, 25 equiv., 0.05 mL) in MeCN was added and the color immediately began to change from orange to purple. Monitoring by UV-vis (Fig. 6) revealed full formation of **5** (λ_{max} = 567 nm) within 30 min. UV-vis: λ_{max} = 567 nm, ε = 900 M^{-1} cm^{-1}; EPR: g = [2.17, 2.16, 1.95]; RR: ν(Fe–O) = 612 cm^{-1}, ν(O–O) = 800 cm^{-1}.

$[Fe^{III}(N3PySR)(OO\mathit{t}Bu)]^{2+}$ (6). A solution of **1** (0.8 mM) was prepared in MeCN and cooled to −40 °C. A solution of *t*BuOOH (5.5 M, 10.0 equiv.) diluted in MeCN was added, and the yellow solution immediately turned green, then blue. Monitoring by UV-vis (Fig. 8) showed the peaks corresponding to **1** decay with isosbestic conversion to a new spectrum (λ_{max} = 600 nm) that corresponds to **6**. UV-vis: λ_{max} = 600 nm, ε = 1670 M^{-1} cm^{-1}; EPR: g = [2.14, 2.08, 1.96]; RR: ν(Fe–O) = 700 cm^{-1}, ν(O–O) = 796 cm^{-1}.

$[Fe^{III}(N3Py^{amide}SR)(OO\mathit{t}Bu)]^{2+}$ (7). A solution of **2** (1.1 mM) in MeCN was prepared and cooled to −40 °C. A solution of *t*BuOOH (5.5 M, 10 equiv.) in MeCN was then added and allowed to stir for 20 min. The orange solution of **2** turns

 This journal is © The Royal Society of Chemistry 2014

Published on 27 March 2014. Downloaded by INDIAN INSTITUTE OF TECHNOLOGY GUWAHATI on 30/09/2014 14:45:32.

green and finally deep blue, as monitoring by UV-vis (Fig. 9) shows the decay of the peaks corresponding to **2** with the isosbestic growth of a new peak (λ_{max} = 620 nm) corresponding to **7**. UV-vis: λ_{max} = 620 nm, ε = 2000 M^{-1} cm^{-1}; EPR: g = [2.17, 2.11, 1.96]; RR: ν(Fe–O) = 691 cm^{-1}, ν(O–O) = 796 cm^{-1}.

Secondary amine (iii). Primary amine (**i**)[46] (825 mg, 2.5 mmol) and aldehyde (**ii**)[47] (468 mg, 2.5 mmol) were dissolved in a 1 : 1 mixture of $CHCl_3$–MeOH (see Scheme 2). Molecular sieves (4 Å) were added and the mixture was stirred under Ar for 48 h. Excess $NaBH_3CN$ (315 mg, 5.0 mmol) was added and allowed to mix for 2 h before being quenched with 1 M HCl. The crude reaction mixture was concentrated, dissolved in $CHCl_3$, washed with H_2O, dried and re-concentrated, before being purified on neutral alumina (EtOAc–hexanes) to give 680 mg (53%) of secondary amine **iii** as a pale yellow solid. ^{1}H-NMR ($CDCl_3$): δ 8.09–8.07 (m, 4H), 7.72 (t, 2H), 7.63 (d, 2H), 7.54–7.49 (m, 6H), 7.46–7.42 (m, 6H), 5.30 (s, 1H), 4.06 (s, 2H), 3.06 (t, 2H), 2.47 (t, 2H).

N3Py^{amide,2Ph}SR. Secondary amine (**iii**) (200 mg, 0.4 mmol) and Cs_2CO_3 (196 mg, 0.6 mmol) were combined in 100 mL MeCN, followed by alkyl bromide (**iv**)[46] (109 mg, 0.4 mmol) and NaI (90 mg, 0.6 mmol) (see Scheme 2). After stirring for 72 h, the crude mixture was filtered through celite and concentrated. The crude solid was dissolved in $CHCl_3$, washed with H_2O, dried, and purified by column chromatography on neutral alumina (EtOAc–hexanes) to give 272 mg (97%) of the final ligand as a pale yellow solid. ^{1}H-NMR ($CDCl_3$): δ 8.07–8.03 (m, 5H), 7.92–9.90 (m, 2H), 7.73 (t, J = 8.1 Hz, 2H), 7.67 (dd, J = 8.8, 1.0 Hz, 2H), 7.60 (t, J = 7.8 Hz, 2H), 7.50–7.39 (m, 9H), 7.33 (dd, J = 7.6, 1.5 Hz, 1H), 7.25 (dd, J = 7.6, 1.3 Hz, 1H), 7.19 (td, 7.5, 1.8 Hz, 1H), 5.53 (s, 1H), 4.29 (s, 2H), 4.06 (s, 2H), 2.94 (t, J = 7.1 Hz, 2H), 2.37 (t, J = 7.1 Hz, 2H), 1.31 (s, 9H); ^{13}C NMR ($CDCl_3$): δ 177.2, 160.1, 159.1, 156.5, 150.8, 141.8, 139.8, 138.7, 137.1, 133.0, 131.4, 130.4, 129.1, 128.9, 127.9, 127.8, 127.3, 123.0, 119.1, 118.8, 118.3, 111.8, 72.0, 57.5, 54.6, 51.9, 40.0, 30.1, 27.8, 18.2, 8.6. FAB-MS (+): m/z = 703.32127 $[M + H]^+$ (calcd for $C_{44}H_{43}N_6OS$, 703.32191).

[Fe^{II}(N3Py^{amide,2Ph}SR)](BF$_4$)$_2$ (8). The free ligand N3Py^{amide,2Ph}SR (461 mg, 0.66 mmol) was dissolved in 5 mL MeCN before $Fe(BF_4)_2{\cdot}6H_2O$ (221 mg, 0.66 mmol) was added. After stirring for 2 h, the yellow solution was filtered through celite and vapor diffusion of Et_2O gave **8** as yellow crystals suitable for X-ray structure determination (510 mg, 83% yield). ^{1}H-NMR (CD_3CN): δ 80.67, 65.78, 64.29, 63.25, 53.03, 47.52, 32.37, 24.80, 20.33, 19.42, 13.40, 11.65, 9.19, 8.22, 7.38, 6.22, 4.08, 3.50, 2.33, 1.17, 0.45, −0.45, −2.33, −14.63, −32.73. LDI-MS: m/z = 757.6 $[M - H]^+$. UV-vis (CH_3CN): λ_{max} = 405 nm, ε = 2650 M^{-1} cm^{-1}. *Anal. Calc.* for [**8**] ($C_{44}H_{42}B_2F_8FeN_6OS$): predicted: C, 56.68, H, 4.54; N, 9.01; Found: C, 56.53; H 4.72; N, 9.44.

Acknowledgements

The NIH (D.P.G., GM62309 and GM101153, P.M.L. GM074785) is gratefully acknowledged for financial support. The National Service of Computational Chemistry Software (NSCCS) is thanked for providing cpu time to SdV. H.M. acknowledges support from the JSPS.

Notes and references

1 E. G. Kovaleva, M. B. Neibergall, S. Chakrabarty and J. D. Lipscomb, *Acc. Chem. Res.*, 2007, **40**, 475–483.
2 E. G. Kovaleva and J. D. Lipscomb, *Science*, 2007, **316**, 453–457.
3 E. I. Solomon, A. Decker and N. Lehnert, *Proc. Natl. Acad. Sci. U. S. A.*, 2003, **100**, 3589–3594.
4 M. Costas, M. P. Mehn, M. P. Jensen and L. Que, Jr., *Chem. Rev.*, 2004, **104**, 939–986.
5 E. I. Solomon, S. D. Wong, L. V. Liu, A. Decker and M. S. Chow, *Curr. Opin. Chem. Biol.*, 2009, **13**, 99–113.
6 P. L. Roach, I. J. Clifton, C. M. H. Hensgens, N. Shibata, C. J. Schofield, J. Hajdu and J. E. Baldwin, *Nature*, 1997, **387**, 827–830.
7 T. Santos-Silva, J. Trincão, A. L. Carvalho, C. Bonifácio, F. Auchère, P. Raleiras, I. Moura, J. J. G. Moura and M. J. Romão, *J. Biol. Inorg. Chem.*, 2006, **11**, 548–558.
8 P. C. A. Bruijnincx, G. van Koten and R. J. M. Klein Gebbink, *Chem. Soc. Rev.*, 2008, **37**, 2716–2744.
9 L. Que, Jr., *J. Biol. Inorg. Chem.*, 2004, **9**, 684–690.
10 S. Ye, X. Wu, L. Wei, D. M. Tang, P. Sun, M. Bartlam and Z. H. Rao, *J. Biol. Chem.*, 2007, **282**, 3391–3402.
11 M. J. Vasbinder and A. Bakac, *Inorg. Chem.*, 2007, **46**, 2921–2928.
12 G. Roelfes, M. Lubben, K. Chen, R. Y. N. Ho, A. Meetsma, S. Genseberger, R. M. Hermant, R. Hage, S. K. Mandal, V. G. Young, Y. Zang, H. Kooijman, A. L. Spek, L. Que, Jr. and B. L. Feringa, *Inorg. Chem.*, 1999, **38**, 1929–1936.
13 G. Roelfes, V. Vrajmasu, K. Chen, R. Y. N. Ho, J.-U. Rohde, C. Zondervan, R. M. la Crois, E. P. Schudde, M. Lutz, A. L. Spek, R. Hage, B. L. Feringa, E. Münck and L. Que, Jr., *Inorg. Chem.*, 2003, **42**, 2639–2653.
14 J. Kim, E. Larka, E. C. Wilkinson and L. Que, Jr., *Angew. Chem., Int. Ed.*, 1995, **34**, 2048–2051.
15 J.-U. Rohde, S. Torelli, X. P. Shan, M. H. Lim, E. J. Klinker, J. Kaizer, K. Chen, W. Nam and L. Que, Jr., *J. Am. Chem. Soc.*, 2004, **126**, 16750–16761.
16 A. Dey and E. I. Solomon, *Inorg. Chim. Acta*, 2010, **363**, 2762–2767.
17 A. J. Simaan, S. Döpner, F. Banse, S. Bourcier, G. Bouchoux, A. Boussac, P. Hildebrandt and J.-J. Girerd, *Eur. J. Inorg. Chem.*, 2000, 1627–1633.
18 M. Martinho, F. Banse, J. Sainton, C. Philouze, R. Guillot, G. Blain, P. Dorlet, S. Lecomte and J.-J. Girerd, *Inorg. Chem.*, 2007, **46**, 1709–1717.
19 A. E. Anastasi, A. Lienke, P. Comba, H. Rohwer and J. E. McGrady, *Eur. J. Inorg. Chem.*, 2007, 65–73.
20 M. R. Bukowski, P. Comba, C. Limberg, M. Merz, L. Que, Jr. and T. Wistuba, *Angew. Chem., Int. Ed.*, 2004, **43**, 1283–1287.

Published on 27 March 2014. Downloaded by INDIAN INSTITUTE OF TECHNOLOGY GUWAHATI on 30/09/2014 14:45:32.

21 N. Lehnert, R. Y. N. Ho, L. Que, Jr. and E. I. Solomon, *J. Am. Chem. Soc.*, 2001, **123**, 12802–12816.
22 N. Lehnert, R. Y. N. Ho, L. Que, Jr. and E. I. Solomon, *J. Am. Chem. Soc.*, 2001, **123**, 8271–8290.
23 F. Namuswe, T. Hayashi, Y. B. Jiang, G. D. Kasper, A. A. N. Sarjeant, P. Moënne-Loccoz and D. P. Goldberg, *J. Am. Chem. Soc.*, 2010, **132**, 157–167.
24 Y. B. Jiang, J. Telser and D. P. Goldberg, *Chem. Commun.*, 2009, 6828–6830.
25 J. Stasser, F. Namuswe, G. D. Kasper, Y. B. Jiang, C. M. Krest, M. T. Green, J. Penner-Hahn and D. P. Goldberg, *Inorg. Chem.*, 2010, **49**, 9178–9190.
26 J. Shearer, R. C. Scarrow and J. A. Kovacs, *J. Am. Chem. Soc.*, 2002, **124**, 11709–11717.
27 T. Kitagawa, A. Dey, P. Lugo-Mas, J. B. Benedict, W. Kaminsky, E. I. Solomon and J. A. Kovacs, *J. Am. Chem. Soc.*, 2006, **128**, 14448–14449.
28 D. Krishnamurthy, G. D. Kasper, F. Namuswe, W. D. Kerber, A. A. N. Sarjeant, P. Moënne-Loccoz and D. P. Goldberg, *J. Am. Chem. Soc.*, 2006, **128**, 14222–14223.
29 F. Namuswe, G. D. Kasper, A. A. N. Sarjeant, T. Hayashi, C. M. Krest, M. T. Green, P. Moënne-Loccoz and D. P. Goldberg, *J. Am. Chem. Soc.*, 2008, **130**, 14189–14200.
30 K. N. Green, S. M. Brothers, R. M. Jenkins, C. E. Carson, C. A. Grapperhaus and M. Y. Darensbourg, *Inorg. Chem.*, 2007, **46**, 7536–7544.
31 C. A. Grapperhaus and M. Y. Darensbourg, *Acc. Chem. Res.*, 1998, **31**, 451–459.
32 M. Sallmann, I. Siewert, L. Fohlmeister, C. Limberg and C. Knispel, *Angew. Chem., Int. Ed.*, 2012, **51**, 2234–2237.
33 C. S. Mullins, C. A. Grapperhaus, B. C. Frye, L. H. Wood, A. J. Hay, R. M. Buchanan and M. S. Mashuta, *Inorg. Chem.*, 2009, **48**, 9974–9976.
34 P. Lugo-Mas, W. Taylor, D. Schweitzer, R. M. Theisen, L. Xu, J. Shearer, R. D. Swartz, M. C. Gleaves, A. DiPasquale, W. Kaminsky and J. A. Kovacs, *Inorg. Chem.*, 2008, **47**, 11228–11236.
35 A. C. McQuilken and D. P. Goldberg, *Dalton Trans.*, 2012, **41**, 10883–10899.
36 G. Musie, C. H. Lai, J. H. Reibenspies, L. W. Sumner and M. Y. Darensbourg, *Inorg. Chem.*, 1998, **37**, 4086–4093.
37 E. Nam, P. E. Alokolaro, R. D. Swartz, M. C. Gleaves, J. Pikul and J. A. Kovacs, *Inorg. Chem.*, 2011, **50**, 1592–1602.
38 J. C. Noveron, M. M. Olmstead and P. K. Mascharak, *J. Am. Chem. Soc.*, 2001, **123**, 3247–3259.
39 M. G. O'Toole, M. Kreso, P. M. Kozlowski, M. S. Mashuta and C. A. Grapperhaus, *J. Biol. Inorg. Chem.*, 2008, **13**, 1219–1230.
40 M. J. Rose, N. M. Betterley, A. G. Oliver and P. K. Mascharak, *Inorg. Chem.*, 2010, **49**, 1854–1864.
41 L. A. Tyler, J. C. Noveron, M. M. Olmstead and P. K. Mascharak, *Inorg. Chem.*, 1999, **38**, 616–617.
42 D. C. Lacy, J. Mukherjee, R. L. Lucas, V. W. Day and A. S. Borovik, *Polyhedron*, 2013, **52**, 261–267.
43 R. L. Shook and A. S. Borovik, *Inorg. Chem.*, 2010, **49**, 3646–3660.
44 A. C. McQuilken, Y. B. Jiang, M. A. Siegler and D. P. Goldberg, *J. Am. Chem. Soc.*, 2012, **134**, 8758–8761.
45 A. C. McQuilken, Y. Ha, K. D. Sutherlin, M. A. Siegler, K. O. Hodgson, B. Hedman, E. I. Solomon, G. N. L. Jameson and D. P. Goldberg, *J. Am. Chem. Soc.*, 2013, **135**, 14024–14027.
46 S. Sahu, L. R. Widger, M. G. Quesne, S. P. de Visser, H. Matsumura, P. Moënne-Loccoz, M. A. Siegler and D. P. Goldberg, *J. Am. Chem. Soc.*, 2013, **135**, 10590–10593.
47 L. R. Widger, C. G. Davies, T. Yang, M. A. Siegler, O. Troeppner, G. N. L. Jameson, I. Ivanović-Burmazović and D. P. Goldberg, *J. Am. Chem. Soc.*, 2014, **136**, 2699–2702.
48 C. Kim, K. Chen, J. H. Kim and L. Que, Jr., *J. Am. Chem. Soc.*, 1997, **119**, 5964–5965.
49 Calculations based on an isolated diatomic oscillator with a ν(Fe–^{18}O) at 590 cm^{-1} predict a ν(Fe–^{16}O) at 617 cm^{-1} which does not match any of the most prominent bands seen in the ν(Fe–O) region of the RR spectra of unlabeled complex **4** nor the 607 cm^{-1} frequency observed in D_2O.
50 N. Lehnert, F. Neese, R. Y. N. Ho, L. Que, Jr. and E. I. Solomon, *J. Am. Chem. Soc.*, 2002, **124**, 10810–10822.
51 A. M. I. Payeras, R. Y. N. Ho, M. Fujita and L. Que, Jr., *Chem. – Eur. J.*, 2004, **10**, 4944–4953.
52 J.-J. Girerd, F. Banse and A. J. Simaan, *Struct. Bonding*, 2000, **97**, 145–177.
53 R. Latifi, M. A. Sainna, E. V. Rybak-Akimova and S. P. de Visser, *Chem. – Eur. J.*, 2013, **19**, 4058–4068.

 This journal is © The Royal Society of Chemistry 2014

ChemPubSoc Europe

DOI: 10.1002/chem.201303282

CHEMISTRY A European Journal Full Paper

DNA Damage

Quantum Mechanics/Molecular Mechanics Study on the Oxygen Binding and Substrate Hydroxylation Step in AlkB Repair Enzymes

Matthew G. Quesne,[a] Reza Latifi,[a, b] Luis E. Gonzalez-Ovalle,[a] Devesh Kumar,[c] and Sam P. de Visser*[a]

Abstract: AlkB repair enzymes are important nonheme iron enzymes that catalyse the demethylation of alkylated DNA bases in humans, which is a vital reaction in the body that heals externally damaged DNA bases. Its mechanism is currently controversial and in order to resolve the catalytic mechanism of these enzymes, a quantum mechanics/molecular mechanics (QM/MM) study was performed on the demethylation of the N^1-methyladenine fragment by AlkB repair enzymes. Firstly, the initial modelling identified the oxygen binding site of the enzyme. Secondly, the oxygen activation mechanism was investigated and a novel pathway was found, whereby the catalytically active iron(IV)–oxo intermediate in the catalytic cycle undergoes an initial isomerisation assisted by an Arg residue in the substrate binding pocket, which then brings the oxo group in close contact with the methyl group of the alkylated DNA base. This enables a subsequent rate-determining hydrogen-atom abstraction on competitive σ- and π-pathways on a quintet spin-state surface. These findings give evidence of different locations of the oxygen and substrate binding channels in the enzyme and the origin of the separation of the oxygen-bound intermediates in the catalytic cycle from substrate. Our studies are compared with small model complexes and the effect of protein and environment on the kinetics and mechanism is explained.

Introduction

Nonheme iron dioxygenases catalyse a range of important reactions in Nature including the biosynthesis of antibiotics in microbes and the metabolism of, for instance, cysteine in mammals.[1,2] In addition, nonheme iron dioxygenases have been linked to oxygen sensing and collagen cross-linking processes in the body, and as such they have vital functions for the biosystem,[3] but unfortunately there are many unanswered questions related to their activity and the catalytic transformation of substrates and detailed computational studies can shed light on this and predict a mechanism. The nonheme iron dioxygenases generally contain an iron active centre that is bound to the protein via a facial triad of amino acids that includes two histidine and one aspartate or glutamate residue in a 2-His/1-Asp feature.[4] They utilise a co-substrate (α-ketoglutarate, αKG) on an iron centre to convert molecular oxygen into a high-valent iron(IV)–oxo species, which has been proposed to be the active species of these enzymes.[5] For several nonheme iron dioxygenases, this active species has been characterised by spectroscopic methods, including resonance Raman and Mössbauer spectroscopies, and it was found that the iron(IV)–oxo intermediate reacts by hydrogen-atom abstraction from the substrate with a large kinetic isotope effect.[6] These experimental studies, however, mostly focused on the bacterial enzyme taurine/α-ketoglutarate dioxygenase.

A special class of enzymes within the nonheme iron dioxygenase family are the AlkB repair enzymes that repair methylated DNA (and RNA) bases that have been damaged by intra- or extracellular chemicals.[7] This has a dramatic effect on normal cellular function as, for instance, N^3-methylation of an adenine residue of a DNA strain blocks DNA replication through the prevention of formation of Watson–Crick base-pairs.[8] In addition, chemicals such as methylmethane sulfonate and methyl halides have been shown to generate N^1-methyladenine and N^3-methylcytosine. AlkB repair enzymes are the body's natural defence mechanism and react with damaged DNA and RNA chains by demethylation of these alkylated bases in a reaction that uses one molecule of αKG and molecular oxygen.[9] Biochemical studies were performed on the characterisation of the enzyme,[10] the protein structure,[11]

[a] M. G. Quesne, Dr. R. Latifi, L. E. Gonzalez-Ovalle, Dr. S. P. de Visser
Manchester Institute of Biotechnology and School of Chemical Engineering and Analytical Science
The University of Manchester, 131 Princess Street
Manchester M1 7DN (UK)
E-mail: sam.devisser@manchester.ac.uk

[b] Dr. R. Latifi
Department of Chemistry, Tufts University
Medford MA, 02155 (USA)

[c] Dr. D. Kumar
Department of Applied Physics, School of Physical Sciences
Babasaheb, Bhimrao Ambedkar University, Vidya Vihar
Rae Bareilly Road, Lucknow 226-025 (India)

Supporting information for this article is available on the WWW under http://dx.doi.org/10.1002/chem.201303282.

© 2013 The Authors. Published by Wiley-VCH Verlag GmbH & Co. KGaA. This is an open access article under the terms of the Creative Commons Attribution License, which permits use, distribution and reproduction in any medium, provided the original work is properly cited.

and the substrate selectivity and binding of inhibitors.[12] Moreover, crystal structure coordinates were measured for the reactant as well as the substrate and hydroxylated product bound complexes.[13] These studies highlight a tight bonding pocket for substrate and a catalytic mechanism that leads to hydroxylation of the methylated DNA base.

It has been hypothesised that the catalytic mechanism of AlkB repair enzymes is analogous to the nonheme iron dioxygenases and proceeds by aliphatic hydroxylation of the methyl group followed by release of formaldehyde.[7] Isotopic labelling and product distributions indeed confirmed that iron(II), αKG and molecular oxygen are needed in the process and that formaldehyde and CO_2 are formed.[7a,b] Crystallographic data provided further evidence that AlkB repair enzymes belong to the αKG-dependent dioxygenases and highlighted a nonheme iron active site, where the metal is bound to a 2-His/1-Asp ligand system (Figure 1).[14] However, a close inspection of the crystal structure coordinates reveals that the sixth binding site of the metal, that is, the O_2 binding site, is located perpendicular to the substrate orientation rather than in its vicinity. As such, an oxygen atom transfer within this conformation may be difficult and might proceed over a relatively large distance.

Furthermore, previous computational studies of the Gauld group on the catalytic cycle of the AlkB repair enzyme using active-site models found a rate-determining hydrogen-atom abstraction barrier of 20.9 kcal mol^{-1} for methylated adenine.[15] This is a relatively high barrier for a nonheme iron(IV)–oxo complex, since, for a series of hydrogen-atom abstraction reactions by analogous models much lower barriers were obtained for alternative substrates. As such, the value of 20.9 kcal mol^{-1} in the gas phase would compare to that found for a substrate like propane,[16] which as far as we know is not hydroxylated by nonheme iron enzymes. Consequently, a barrier with a magnitude over 20 kcal mol^{-1} may be a very slow process that is not efficient enough to happen in Nature. However, there may be effects of the protein and the local environment that were not taken into consideration in the models of Gauld et al. that have affected the barrier heights. The studies, therefore, warrant a further set of calculations and in particular one using quantum mechanics/molecular mechanics (QM/MM) that takes the full scale of the protein and solvent into effect.

Here we report this QM/MM study and focus on the catalytic mechanism of oxygen activation by AlkB enzymes and the hydroxylation of methylated DNA bases (Scheme 1). We investigate two possible oxygen binding positions on the iron(II) reactant complex with the superoxo either *trans* to His_{131} (structure **A**) or *trans* to His_{187} (structure **B**). In the following step in the catalytic cycle the superoxo group is expected to attack the α-keto-position of αKG to give an iron(IV)–oxo species, CO_2 and succinate.[17] Technically two isomeric iron(IV)–oxo struc-

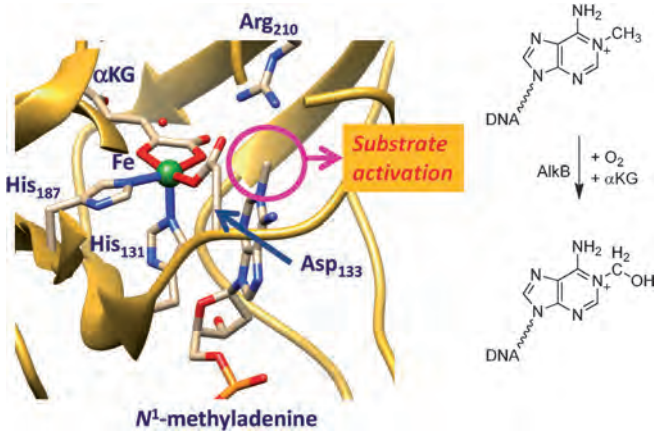

Figure 1. Extract of the active site of AlkB repair enzyme as taken from the 3I2O PDB file and the reaction catalysed by the enzyme. The proposed oxygen binding site *trans* to His_{131} is filled with a water molecule.

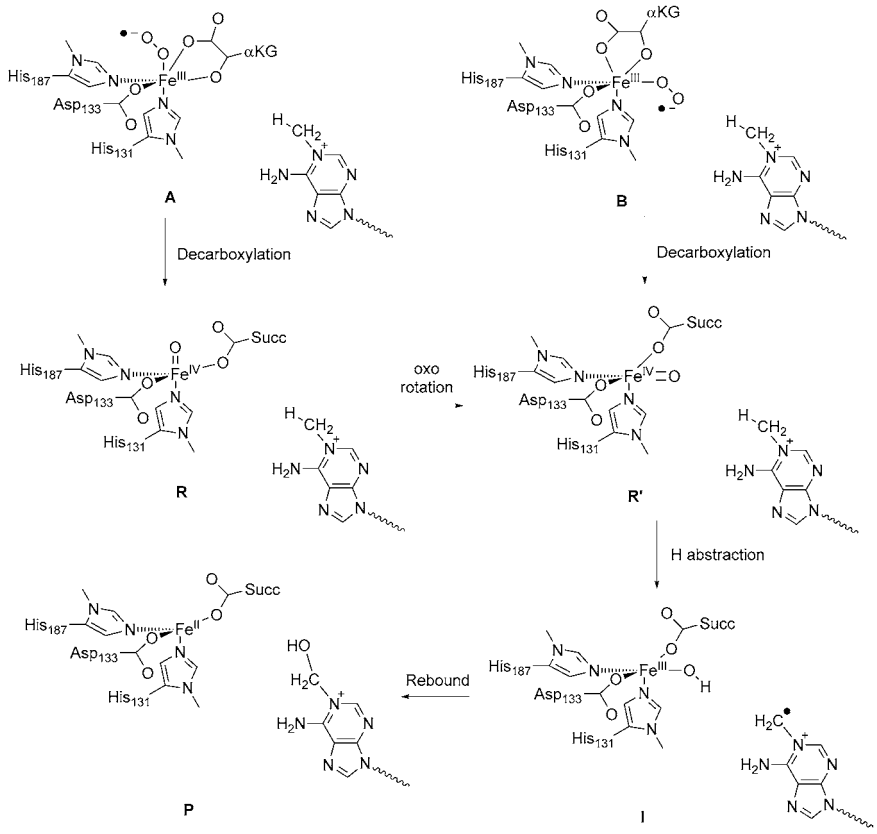

Scheme 1. Mechanism of substrate hydroxylation by an iron(IV)–oxo in AlkB repair enzymes.

 © 2014 The Authors. Published by Wiley-VCH Verlag GmbH & Co. KGaA, Weinheim

tures are possible (**R** and **R′**), which may interconvert into each other. In this work we identify **A** as the oxygen-binding position and propose a novel mechanism whereby the iron(IV)–oxo undergoes an isomerisation from **R** to **R′** prior to hydrogen-atom abstraction. We also highlight the electronic changes during the reaction and the effect the isomerisation has on the electron-transfer pathways and the barrier heights for the reaction.

Results and Discussion

Oxygen binding site on the metal

A recent QM/MM study investigated the hydrogen-atom abstraction step of N^1-methyladenine (CH_3Ade) by AlkB repair enzymes.[18] They used a molecular geometry, whereby the oxo group was aligned with the substrate, that is, *trans* to His_{187}, and an almost linear Fe-O-HCH_2-Ade angle, analogous to structure **R′** in Scheme 1. However, the iron(IV)–oxo species is formed in a catalytic cycle from an iron(III)–superoxo complex in a reaction with αKG (Scheme 1), and in the crystal structure displayed in Figure 1 there seems to be a dioxygen binding site *trans* to His_{131}. We decided, therefore, to first investigate the oxygen binding site of the enzyme, and thereby assign either **R** or **R′** as the reactant of the catalytic hydroxylation.

We started the work with locating the oxygen binding site of AlkB, whereby we attempted to model dioxygen into the protein structure at various metal binding sites, that is, create structures **A** and **B** (Figure 2). Firstly, molecular oxygen was inserted into the sixth binding site *trans* to His_{131} by replacing the water ligand. The binding pocket has sufficient space to accommodate molecular oxygen and no stereochemical clashes are noted that would prevent it from binding in this position. The binding pocket is lined up with apolar and aromatic residues, such as the side chains of Ile_{143}, Phe_{154} and Trp_{178}. Solvation of the protein still finds sufficient space in the binding pocket *trans* to His_{131} for two water molecules; this binding pocket, therefore, is large enough to accommodate molecular oxygen. Figure 2 gives the equilibrated MM structure of **A**.

Thereafter, we inserted molecular oxygen into the metal position *trans* to His_{187} with the distal oxygen atom on the line through the iron and the hydrogen atom from N^1-methyladenine that is abstracted by AlkB in order to generate structure **B**. However, this structure has considerable stereochemical constraints and we failed to optimise its geometry and converge it to a local minimum. In particular, the proximal oxygen atom of the iron(III)–superoxo with the oxygen *trans* to His_{187} gives close contacts (<1.7 Å) to the carboxylate group of Asp_{133} and the methyl group of N^1-methyladenine. Furthermore, the distal oxygen atom of the iron(III)–superoxo has close contact with the carboxylate group of αKG (1.75 Å), therefore, stereochemically it is not a stable structure. Consequently, these MM models show that molecular oxygen does not fit into the binding pocket in a position *trans* to His_{187} as it is too tight with too many closely packed residues. As structure **B** is not a stable entity it cannot be a catalytic cycle intermediate and as a result molecular oxygen can only bind in the position *trans* to His_{131}, that is, **A**. Our studies, therefore, have identified the molecular oxygen binding site as *trans* to His_{131} that in a reaction with αKG will give the iron(IV)–oxo species in the **R** conformation. This also implies that a subsequent isomerisation will be needed to form the rotated iron(IV)–oxo species (**R′**) with the oxo group *trans* to His_{187}, which is expected to precede the hydrogen-atom abstraction reaction.

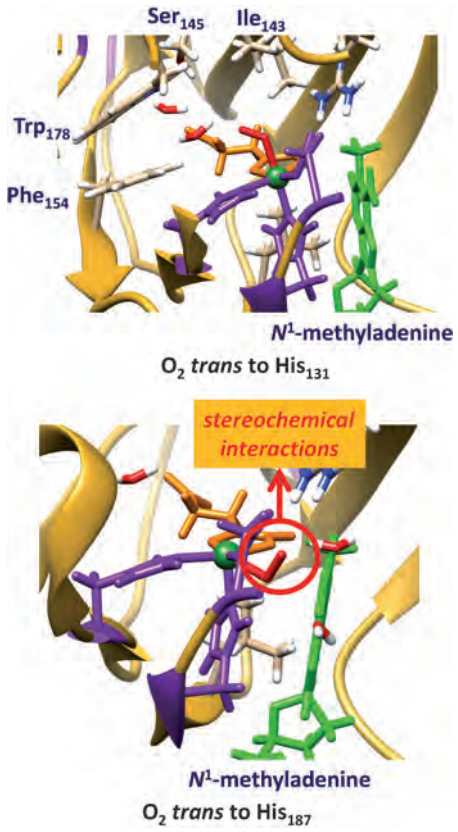

Figure 2. Isomeric structures for dioxygen binding to the iron(II) centre of AlkB enzymes with either the O_2 *trans* to His_{131} (top) or *trans* to His_{187} (bottom). The former structure is MM minimised, whereas the latter failed to converge due to stereochemical clashes. The 2-His/1-Asp structure is in purple, substrate in green and αKG in orange.

The reported QM/MM results in ref. [18] did not consider this isomerisation and as a result may not reflect the correct mechanism of the chemical reaction as they may have used a wrong starting structure of the chemical process. To gain further insight into the mechanism of substrate hydroxylation by DNA base repair enzymes, we decided to carry out a QM/MM study. We started the work from the iron(IV)–oxo species as displayed in Figure 1 and we followed the mechanism as described in Scheme 1 until hydroxylated products. The work started from the iron(IV)–oxo species with the oxo group *trans* to His_{131} (**R**), which is expected to isomerise to a position with the oxo group *trans* to His_{187} in **R′**. In the latter conformation the oxo group is in hydrogen bonding distance to the methyl group of N^1-methyladenine and takes up a hydrogen atom to form a radical intermediate (**I**) before hydroxyl rebound to form alcohol product complexes (**P**).

 © 2014 The Authors. Published by Wiley-VCH Verlag GmbH & Co. KGaA, Weinheim

QM/MM set up and validation

The work described in here uses the quantum mechanics/molecular mechanics (QM/MM) procedure, whereby the inner core of the enzyme is described by density functional theory methods and the rest of the protein and solvent with a molecular mechanics force field as explained in detail in the Experimental Section. Generally, the methodology follows previous QM/MM calculations of our group that were carefully benchmarked and calibrated.[19] The calculations start from the 3I2O PDB file,[14] which is a substrate bound iron(III)–water complexed with αKG as described in Figure 1. The water ligand was replaced by an oxo group and αKG by succinate to obtain our reactant structure (**R′**): an iron(IV)–oxo group in a 2-His/1-Asp ligand environment and succinate bound as a bidentate ligand. Subsequently, hydrogen atoms were added and the protonation state of residues checked as described below. Thereafter, the structure was subjected to an iterative solvation procedure to give a chemical model with a total amount of 10011 atoms.

After the set-up was completed we ran a molecular dynamics (MD) simulation for 800 ps at 298 K and 1 bar using the Charmm force field,[20] whereby the protein and solvent were allowed to relax. Figure 3 displays the total energy and the root mean square deviation (RMSD) of the protein structure of the MD trajectory of our reactant structure. As follows from Figure 3 after 20–30 ps of simulation the total energy reaches a plateau and the energy stabilises. At the same time the fluctuations in the protein structure and geometry stabilise and the RMSD values converges to a value of close to 1. These MD simulations match those found for the analogous nonheme iron enzymes proline hydroxylase that revealed conformational stability and rigidity after substrate binding.[21]

We selected three snapshots from the MD simulations as starting points for the QM/MM calculations after 300, 400 and 500 ps; designated Sn_{300}, Sn_{400} and Sn_{500}, respectively. An overlay of the three structures of these snapshots (Supporting Information, Figure S1) shows little differences in the protein orientation and the enzyme active site. The only differences obtained between these snapshots originate at distances far away from the reaction centre and generally are on the surface of the protein. We do not expect these motions and structural differences to be dramatic, but decided to carry out some test calculations for all three snapshots to determine the reproducibility and stability of the calculations. In all studies, we selected a large QM region containing the iron(IV)–oxo group, methylimidazole groups for His_{131} and His_{187}, acetate for succinate and Asp_{133}, methylguanidinium for Arg_{210}, and the N^1-methyladenine part of the substrate (Figure 4).

Subsequently, we optimised the geometry of the iron(IV)–oxo species using Sn_{300}, Sn_{400} and Sn_{500} in the lowest lying singlet, triplet, quintet and septet spin states. In all cases, the geometry optimisation converged to a structure corresponding to **R′**, in which the oxo-group bridges between the methyl group of methylated adenine and the iron atom. The quintet spin state is the ground state in each snapshot and the spin state ordering follows quintet–triplet–septet and singlet throughout, which implies that the quintet spin state will be

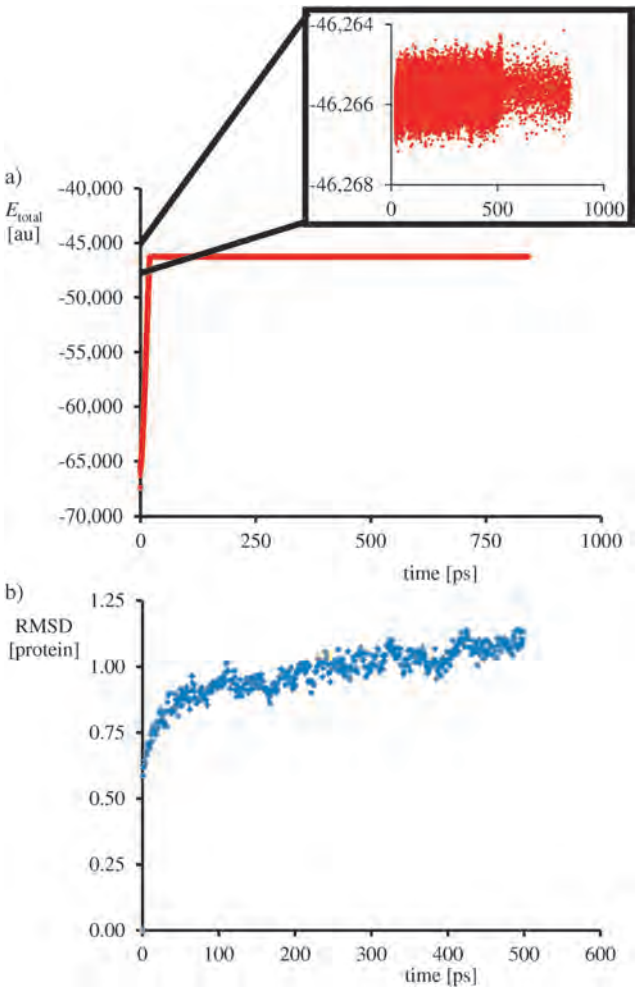

Figure 3. Molecular dynamics scan at 298 K of the protein. a) Plot of the total MM energy as a function of time. b) RMSD value of the protein structure as a function of time.

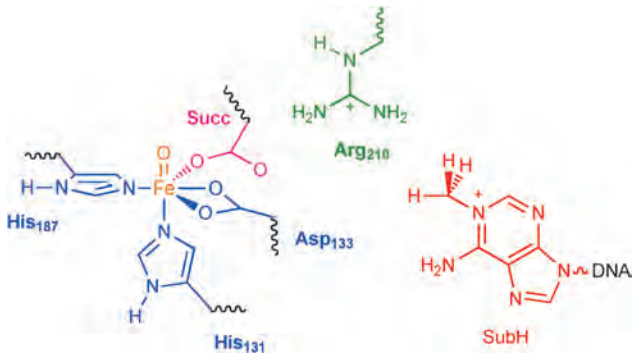

Figure 4. QM region selected for the QM/MM calculations. Waved lines represent QM/MM linkages that were described with the link atom method. Succ stands for succinate and SubH for substrate.

the reactive state. Previous studies of nonheme iron reactivities showed higher barriers on the triplet spin state than on the quintet spin state,[22] therefore, it is not expected that the triplet spin state will play a key role in this part of the catalytic cycle. Our calculations are in agreement with the experimental EPR characterisation of nonheme iron(IV)–oxo complexes in en-

 © 2014 The Authors. Published by Wiley-VCH Verlag GmbH & Co. KGaA, Weinheim

zymes that were found to be in a high-spin state.[23] Previous calculations on the iron(IV)–oxo species of DNA base repair enzymes[15,18] and analogous nonheme iron dioxygenases[24] also identified it as a high-spin ground state. This contrasts biomimetic nonheme iron(IV)–oxo complexes that generally are described with a triplet spin ground state.[25] Recent computations, however, showed that pentacoordinated iron(IV)–oxo complexes stabilise the quintet spin state, whereas hexacoordinated iron(IV)–oxo usually has a triplet spin ground state.[26]

All three snapshots give the same spin-state ordering and a well-separated quintet spin ground state from other states, therefore, we have focused in the following on the quintet spin mechanism of oxygen atom transfer only. Optimised geometries of ^{5}**R**′ as calculated in Sn_{300}, Sn_{400} and Sn_{500} are given in Figure 5. The iron(IV)–oxo bond is short, that is, 1.660–1.671 Å,

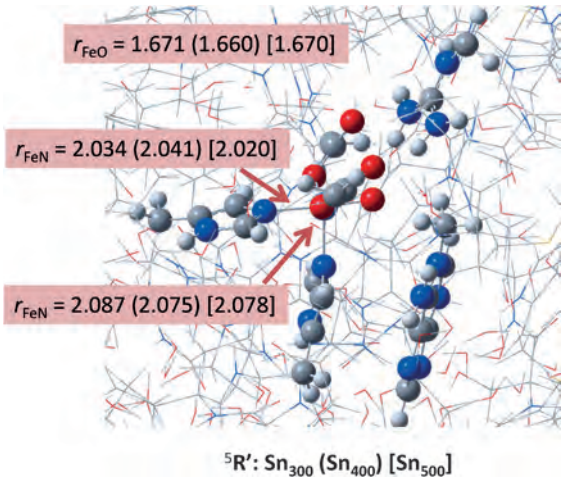

Figure 5. Optimised geometries of ^{5}**R**′ as obtained for Sn_{300}, Sn_{400} and Sn_{500} with bond lengths in Ångstroms.

which is indicative of a double bond and in agreement with previous calculations on related complexes.[24,27] The structures show little deviations between the three snapshots, and consequently the QM region is highly rigid and constraint. Furthermore, the optimised geometries of the three snapshots implicates that the reproducibility of the results is high and that little movement in the central components of the protein and in particular the catalytic centre has occurred during the MD simulation. Further test calculations using different density functional methods were carried out, namely B3LYP, B3LYP*, BP86 and M06.[28–31] In all cases a spin state ordering quintet < triplet < singlet was found with the quintet spin state as the ground state (see the Supporting Information). As the DFT methodology does not appear to give dramatic differences in spin-state ordering and relative energies, we decided to continue with UB3LYP only.

Iron(IV)–oxo group isomerisation

In the next set of calculations, we investigated ^{5}**R** as well as its barrier (^{5}**TS**$_I$) for the isomerisation into ^{5}**R**′. A comparison of the structure and electronic properties of ^{5}**R** and ^{5}**R**′ reveals some interesting features that may affect the reactivity of these complexes. Let us start with a description of the electronic changes upon rotation from ^{5}**R** to ^{5}**R**′. Thus, the rotation of the oxo group from a position *trans* to His_{131} in ^{5}**R** to a position *trans* to His_{187} in ^{5}**R**′ changes the shapes of the molecular orbitals. Figure 6 displays the valence orbitals of ^{5}**R** and ^{5}**R**′, in which we used the nomenclature of Shaik, Solomon and co-workers for nonheme iron oxidants.[22] The labelling uses a molecular *z* axis as taken along the Fe–O bond in ^{5}**R**. In the lowest quintet spin state of ^{5}**R** the metal 3d block of orbitals interact with ligands and split into a set of three π^* (π^*_{xz}, π^*_{yz}, π^*_{xy}) orbitals and a pair of two σ^* ($\sigma^*_{z^2}$, $\sigma^*_{x^2-y^2}$) orbitals. The π^* orbitals represent the antibonding combinations of the 3d atomic orbital on Fe with a $2p_{x/y}$ orbital on oxygen, whereas the $\sigma^*_{z^2}$ orbital reflects the antibonding combination of $3d_{z^2}$ on Fe with $2p_z$ on O. Finally, the $3d_{x^2-y^2}$ orbital on the metal forms antibonding combinations with ligands in the *xy* plane of symmetry. In pentacoordinated iron(IV)–oxo complexes the π^*_{xy} and $\sigma^*_{x^2-y^2}$ orbitals are close in energy and hence a high-spin situation is favourable.[32] Indeed, ^{5}**R**, as found for analogous complexes,[15,18,19,24] has orbital occupation $\pi^*_{xy}{}^1\pi^*_{xz}{}^1\pi^*_{yz}{}^1\sigma^*_{x^2-y^2}{}^1\sigma^*_{z^2}{}^0$. By contrast, the nearest triplet spin state is calculated to have $\pi^*_{xy}{}^2\pi^*_{xz}{}^1\pi^*_{yz}{}^1$ configuration.

Upon rotation of the oxo group, whereby ^{5}**R**′ is formed the molecular orbital interactions have altered. Thus, the Fe–O bond is now located along the molecular *y* axis and hence the labels of some of the orbitals have changed. In particular, the π^*_{xy} orbital in ^{5}**R**′ has a shape that matches the π^*_{xz} orbital in ^{5}**R** and the π^*_{xz} orbital in ^{5}**R**′ looks like the π^*_{xy} orbital in ^{5}**R**′. However, since both are singly occupied in ^{5}**R** and ^{5}**R**′, that will not affect the relative energies of these isomers dramatically. The major differences between ^{5}**R** and ^{5}**R**′ relate to the two σ^* orbitals, that is, the HOMO and LUMO orbitals, which, therefore, also affect the reactivities. In ^{5}**R** the $\sigma^*_{x^2-y^2}$ is singly occupied and the $\sigma^*_{z^2}$ orbital is virtual, whereas the ordering is reversed for ^{5}**R**′ and the $\sigma^*_{z^2}$ orbital is singly occupied instead. In this orientation the $\sigma^*_{z^2}$ orbital in ^{5}**R**′ has lesser antibonding interactions than the HOMO, that is, $\sigma^*_{x^2-y^2}$ in ^{5}**R** and consequently ^{5}**R**′ is more stable than ^{5}**R**. We calculated an isomerisation energy difference of $\Delta E + ZPE = -6.0$ kcal mol^{-1} for Sn_{500} at the UB3LYP level of theory. Changing the method to UB3LYP* gives negligible changes to the energy difference between ^{5}**R** and ^{5}**R**′ and a value of -7.0 kcal mol^{-1} is obtained.

Despite the fact that the orbital interactions have changed between ^{5}**R** and ^{5}**R**′, there are actually very little changes in the group spin densities and charges of these complexes (see the Supporting Information). The spin density on the metal is slightly increased from 2.96 in ^{5}**R** to 3.01 in ^{5}**R**′ and at the same time the oxygen atom loses spin density from 0.75 in ^{5}**R** to 0.69 in ^{5}**R**′. Generally, the more radical character obtained at the oxygen atom, the more reactive a metal–oxo group is, and it may be anticipated that this small change of spin polarisation from oxo to iron will make ^{5}**R**′ a slightly lesser oxidant than ^{5}**R**. Our group spin densities and electronic state assignment matches those reported in previous DFT and QM/MM studies on analogous systems.[15–20]

 © 2014 The Authors. Published by Wiley-VCH Verlag GmbH & Co. KGaA, Weinheim

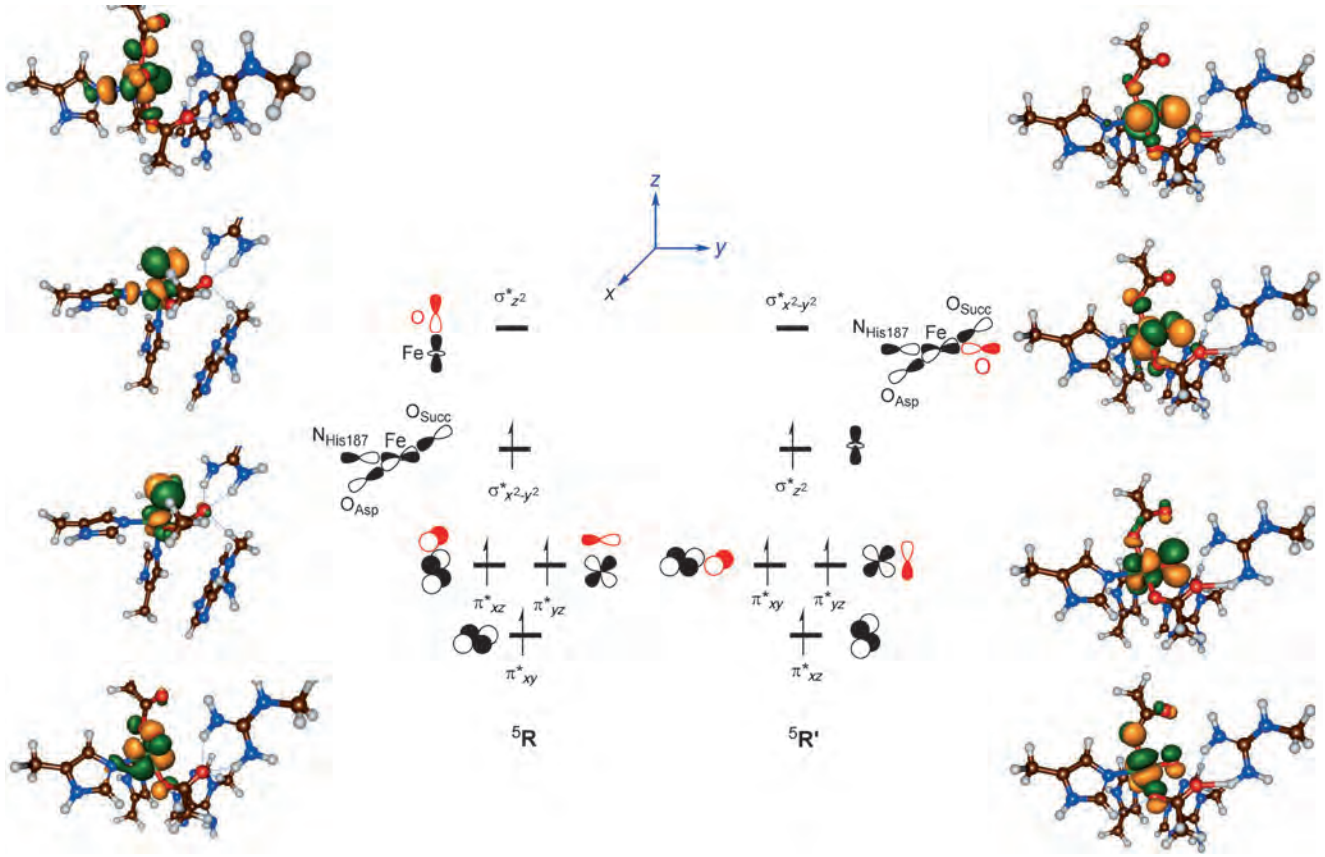

Figure 6. Orbital occupation of ^{5}**R** and ^{5}**R**′. Also given are the natural orbitals for ^{5}**R** and ^{5}**R**′.

In addition to differences in orbital interactions of the HOMO orbital in ^{5}**R** versus ^{5}**R**′ there are similar changes noted for the LUMO orbital. In ^{5}**R** the LUMO orbital is the antibonding interaction along the Fe–O bond, which shows little involvement of other ligands. By contrast, the $\sigma^*_{x^2-y^2}$ orbital displays interactions with four groups in the *xy* plane, namely the oxo, Asp_{133}, His_{187} and succinate groups, and, therefore, it will be considerably higher in energy than the LUMO in ^{5}**R**. Consequently, ^{5}**R**′ will have a much larger electron affinity than ^{5}**R** and it will cost ^{5}**R** more energy to abstract electrons from substrates. As hydrogen-atom abstraction is accompanied by a one-electron transfer from substrate to oxidant; this implies that ^{5}**R**′ will react with higher barriers than ^{5}**R**. There must, therefore, be a fundamental reason for the enzyme to initiate the reaction with an isomerisation from ^{5}**R** to ^{5}**R**′. A possible reason is that the enzyme has to separate the dioxygen and substrate binding processes to avoid side reactions and by-products. Thus, after dioxygen binding to the iron centre an iron(III)–superoxo complex is formed that reacts with αKG to form an iron(IV)–oxo and succinate.[24] In several nonheme iron enzymes, however, the iron(III)–superoxo complex is known to abstract hydrogen atoms from substrates directly. For instance, in the enzyme isopenicillin N synthase, the tripeptide δ-(L-α-amino adipoyl)-L-cysteinyl-D-valine, by four sequential hydrogen-atom abstraction reactions, is converted into isopenicillin N through two ring-closure processes.[33] The first step of this reaction proceeds via an iron(III)–superoxo intermediate. It may very well be that in AlkB repair enzymes the iron(III)–superoxo has to be separated from substrate to prevent multiple hydroxylation reactions to occur on the methylated group, which would prevent the subsequent demethylation reaction into formaldehyde.

To test the relative reactivity of an iron(III)–superoxo versus an iron(IV)–oxo complex with N^1-methyladenine, we set up a DFT model complex based on the QM region displayed in Figure 4 and calculated the hydrogen-atom abstraction of both complexes. We found a hydrogen-atom abstraction barrier of $\Delta E + \mathrm{ZPE} = 32.8\ \mathrm{kcal\,mol^{-1}}$ for the iron(III)–superoxo, whereas a value of $\Delta E + \mathrm{ZPE} = 23.4\ \mathrm{kcal\,mol^{-1}}$ for the iron(IV)–oxo was calculated. The latter matches the hydrogen-atom abstraction barrier reported by Gauld et al. well although slightly different methods were used.[15] Thus, the energy difference between the two hydrogen-atom abstraction barriers implicate faster reactivity of the iron(IV)–oxo than the iron(III)–superoxo complex. However, it is conceivable that the iron(III)–superoxo reacts with aliphatic groups by abstraction of hydrogen atoms although it probably will be slow.

Nevertheless, any reactivity of the iron(III)–superoxo species would lead to the disruption of the catalytic cycle and the failure to hydroxylate N^1-methyladenine to form N^1-hydroxymethyl adenine. It is, thus, very well possible that the enzyme has separated the oxygen binding and substrate binding positions in the active site of AlkB to prevent reactivity by the iron(III)–superoxo species. The substrate is shielded from the iron(III)–

 © 2014 The Authors. Published by Wiley-VCH Verlag GmbH & Co. KGaA, Weinheim

superoxo group by an arginine residue (Arg_{210}) in the binding pocket. The superoxo group is too bulky to slide underneath Arg_{210} and attack the substrate, but once the iron(III)–superoxo has reacted with αKG and formed an iron(IV)–oxo species an oxidant is formed that can migrate to a position *trans* to His_{187} and attack the substrate. This way the enzyme retains the regioselectivity of substrate hydroxylation and prevents the occurrence of by-products. Most probably the enzyme pays a small thermodynamic price for this isomerisation process, which now happens with elevated hydrogen-atom abstraction barriers.

Next we calculated the isomerisation barrier (^{5}**TS**$_I$) from ^{5}**R** to ^{5}**R**′ in Sn_{500} and the optimised geometry is given in Figure 7. Energetically, ^{5}**TS**$_I$ is higher in energy than ^{5}**R** by $\Delta E + ZPE = 9.0$ kcal mol^{-1}. QM/MM studies of the Borowski group[34] on the nonheme iron halogenase SyrB2 were also predicted to start

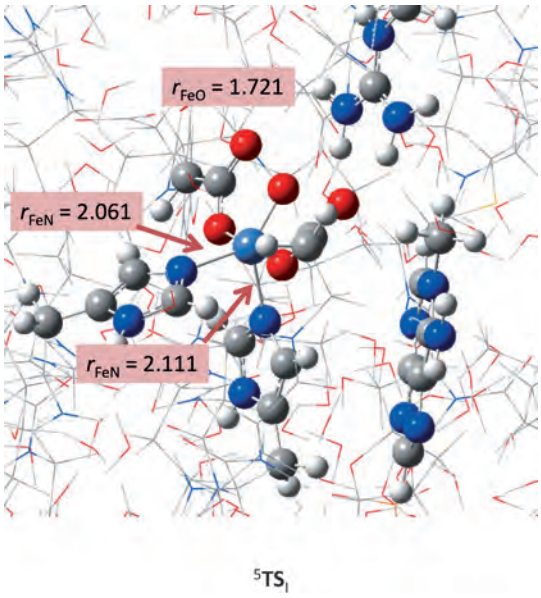

Figure 7. QM/MM optimised geometry of ^{5}**TS**$_I$ using snapshot Sn_{500} with bond lengths in Ångstroms.

with an isomerisation, whereby the positions of the oxo and halide ligands to the metal centre were interchanged. They calculated an isomerisation barrier of 13.4 kcal mol^{-1} for that process, which is not dramatically different from the value we found here. Our isomerisation is slightly lower in energy because in AlkB only the oxo group migrates whereas in SyrB2 both the oxo and halide groups interchange, which will raise the barrier heights.

The optimised geometry of ^{5}**TS**$_I$ shows some differences with respect to ^{5}**R** and ^{5}**R**′. Obviously the $NHis_{131}$-Fe-O angle changes along the rotation from 173.3° in ^{5}**R** to 135.7° in ^{5}**TS**$_I$ and to 97.2° in ^{5}**R**′. In addition in ^{5}**TS**$_I$ there is minor elongation of the two Fe–N distances with His_{131} and His_{187}, but more dramatically is the lengthening of the Fe–O bond to 1.721 Å. This is because of a tight interaction of the oxo group with one of the protons of Arg_{210}, which is shortened from 2.414 Å in ^{5}**R** to 1.888 Å in ^{5}**TS**$_I$ and then elongates again toward ^{5}**R**′ to a value of 2.470 Å. The Arg_{210} residue, therefore, acts as a switch and assists with the rotation of the oxo group from *trans* to His_{131} to a position *trans* of His_{187}.

Substrate hydroxylation by the iron(IV)–oxo complex

We subsequently continued with calculations of the rest of the potential energy profile for the hydrogen-atom abstraction and followed by radical rebound to form alcohol product complexes (**P**). The hydrogen-atom abstraction passes a transition state ($\mathbf{TS}_H$) to form a radical intermediate (**I**) that is separated from products by a rebound transition state ($\mathbf{TS}_{reb}$). We calculated the hydrogen-atom abstraction with QM/MM using snapshot Sn_{300}, Sn_{400} and Sn_{500}, whereas the rebound was only investigated for Sn_{500}. Despite the fact that we calculated the full potential energy profile of N^1-methyladenine hydroxylation on the singlet, triplet, quintet and septet spin state surfaces with QM/MM, actually only the quintet spin state is accessible for this part of the catalytic cycle and the other spin states are much higher in energy (see the Supporting Information). This is in agreement with previous studies of nonheme iron(IV)–oxo complexes in which single-state reactivity on a dominant quintet spin state surface was found.[24a] Hence, we will focus on the quintet spin state results only and the other spin state structures and energetics are given in the Supporting Information for completeness.

Figure 8 displays the complete potential energy profile from **R** to **P** as calculated with QM/MM in Sn_{500}. As mentioned above, the isomerisation barrier is about 9.0 kcal mol^{-1} and leads to the energetically more stable structure **R**′. Geometrically, the isomerisation step is assisted by Arg_{210} that hydrogen bonds with the oxo and succinate groups. Arg_{210} keeps the oxo group in a specific orientation and guides its rotation toward the substrate. To highlight the motion of the Arg residue upon rotation from **R** to **R**′ we have drawn a yellow box around its atoms. The isomerisation then brings the oxo group in close proximity to the substrate to enable a regioselective hydrogen-atom abstraction and prevent reactivity of its precursor the iron(III)–superoxo species. The tight substrate binding pocket and the Arg-assisted isomerisation mechanism enable regioselective hydroxylation of the methylated DNA base without activation of any of the other C–H bonds in the substrate.

We located two distinct pathways for hydrogen-atom abstraction by ^{5}**R**′. Hydrogen-atom abstraction from N^1-methyladenine by ^{5}**R**′ can either lead to electron transfer into the virtual $\sigma^*_{x^2-y^2}$ orbital, the so-called $^5\sigma$-pathway, or to double occupation of the π^*_{xz} orbital through the so-called $^5\pi$-pathway.[35] Usually, in nonheme iron(IV)–oxo complexes the $^5\sigma$-pathway is considerably lower in energy than the $^5\pi$-pathway, and, hence is the dominating quintet spin electron transfer mechanism.[22,24,26] Generally, in the $^5\sigma$-pathway the substrate attacks from the top and incurs little stereochemical interactions with the metal ligands, whereas in the $^5\pi$-pathway the substrate approaches under an Fe-O-H angle of about 120° that is stereochemically disfavoured.[36] Due to the rotation of the iron(IV)–oxo group and a change of orbital shapes (Figure 6), the $^5\sigma$-pathway is not the dominating pathway anymore. We located

 © 2014 The Authors. Published by Wiley-VCH Verlag GmbH & Co. KGaA, Weinheim

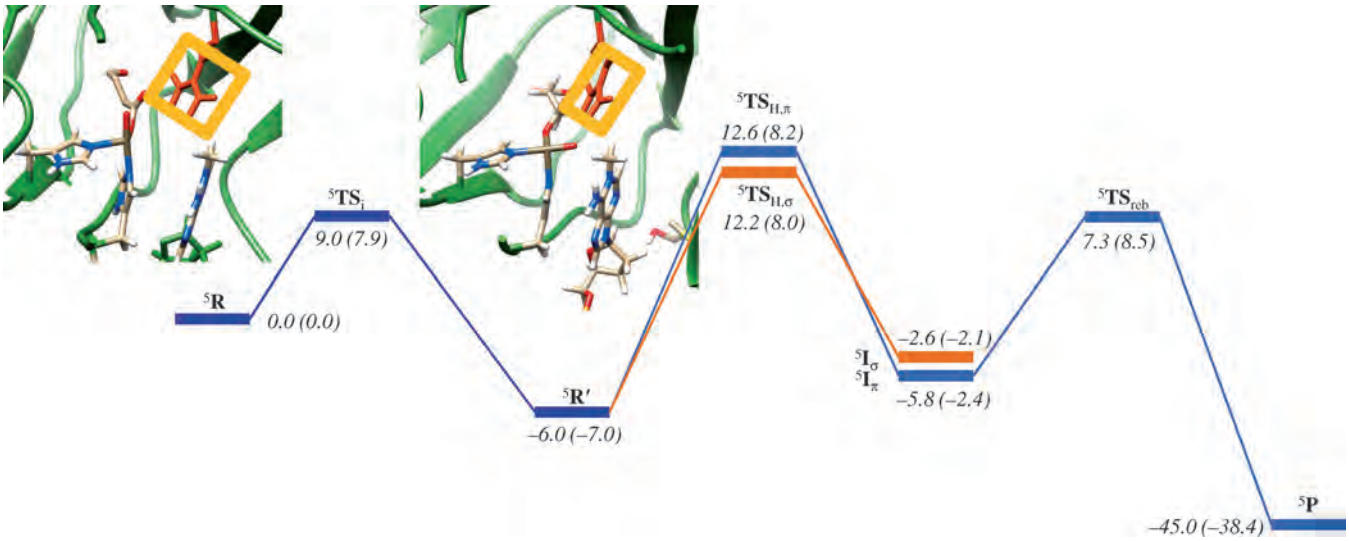

Figure 8. Potential energy landscape for the hydroxylation of N^1-methyladenine as calculated with QM/MM. Energies are obtained at UB3LYP/B2//UB3LYP/B1-Amber, whereas in parenthesis are given UB3LYP*/B2//UB3LYP/B1-Amber results. All energies contain zero-point corrections and are given in kcal mol^{-1}.

transition states for both pathways, designated ^{5}**TS**$_{H,\sigma}$ and ^{5}**TS**$_{H,\pi}$, as well as the two isomeric radical intermediates, ^{5}**I**$_\sigma$ and ^{5}**I**$_\pi$.

Based on the orbital diagram for ^{5}**R** and the unfavourable angle between the $\sigma^*_{z^2}$ and the substrate location, one might have expected high barriers for ^{5}**TS**$_{H,\sigma}$ but actually due to the change of the ordering of $\sigma^*_{z^2}$ and $\sigma^*_{x^2-y^2}$ upon rotation of the iron(IV)–oxo group from ^{5}**R** to ^{5}**R**′ the σ-pathway is still a viable reaction pathway. Moreover, the $^5\pi$-pathway is stabilised and becomes competitive with the $^5\sigma$-pathway. Nevertheless, the rate-determining step in the reaction mechanism in Figure 8 is the hydrogen-atom abstraction via barrier ^{5}**TS**$_H$, and both located transition states ^{5}**TS**$_{H,\sigma}$ and ^{5}**TS**$_{H,\pi}$ originate from the same reactant structure ^{5}**R**′. Thus, during the hydrogen-atom abstraction an electron is transferred into the $\sigma^*_{x^2-y^2}$ orbital in ^{5}**TS**$_{H,\sigma}$ to form an exchange coupled radical intermediate (^{5}**I**$_\sigma$) with $\pi^*_{xz}{}^{\uparrow}\pi^*_{yz}{}^{\uparrow}\pi^*_{xy}{}^{\uparrow}\sigma^*_{z^2}{}^{\uparrow}\sigma^*_{x^2-y^2}{}^{\uparrow}\phi_{Sub}{}^{\downarrow}$ configuration. By contrast in ^{5}**TS**$_{H,\pi}$ a low-lying π^* orbital is doubly occupied to give a radical intermediate (^{5}**I**$_\pi$) with configuration $\pi^*_{xz}{}^2\pi^*_{yz}{}^{\uparrow}\pi^*_{xy}{}^{\uparrow}\sigma^*_{z^2}{}^{\uparrow}\sigma^*_{x^2-y^2}{}^0\phi_{Sub}{}^{\uparrow}$. As the isomerisation has led to an inversion of the ordering of $\sigma^*_{z^2}$ and $\sigma^*_{x^2-y^2}$ the σ-pathway now involves electron transfer into the $\sigma^*_{x^2-y^2}$ orbital and an alignment of the substrate along the molecular *y* axis. Indeed, an Fe-O-C angle of 141.4° is found for ^{5}**TS**$_{H,\sigma}$, whereas ^{5}**TS**$_{H,\pi}$ gives a much smaller angle of 131.4°.

Because of the fact that the angle in ^{5}**TS**$_{H,\sigma}$ deviates significantly from the ideal angle of a linear Fe-O-C conformation due to constraints on the enzyme substrate and co-factor binding pocket, the σ-pathway is destabilised. By contrast, the π-pathway requires angles of typically 120° and indeed here we find an Fe-O-C angle of 131.4°. Because of the unfavourable angle in the σ-pathway, it is destabilised in energy and the π-pathway becomes competitive. This is fundamentally different from hydrogen-atom abstraction along the molecular *z* axis as is normally the case for nonheme iron enzymes that appear to mostly react through the σ-pathway. Note as well that the LUMO orbital in ^{5}**R**, that is, the $\sigma^*_{z^2}$ orbital is lower in energy than the LUMO orbital in ^{5}**R**′, that is, the $\sigma^*_{x^2-y^2}$ which has considerably more antibonding interactions between the metal and its ligands, and, therefore, it requires more energy to fill it.

Energetically in Sn_{500}, ^{5}**TS**$_{H,\sigma}$ and ^{5}**TS**$_{H,\pi}$ are of comparable energies: 18.2 versus 18.6 kcal mol^{-1} at UB3LYP level of theory, and 15.0 versus 15.2 kcal mol^{-1} at UB3LYP* level of theory with respect to ^{5}**R**′. We also calculated ^{5}**R**′ and ^{5}**TS**$_{H,\pi}$ in Sn_{300} and Sn_{400}, but similar group spin densities and charges are found and a minor stabilisation of the barrier heights is observed: 13.0 kcal mol^{-1} for Sn_{300} and 15.1 kcal mol^{-1} for Sn_{400}. As such there is a small effect of the protein on the barrier heights of the hydrogen-atom abstraction, although, geometrically they look very similar to the structure displayed in Figure 8 for Sn_{500} (see the Supporting Information). Our values are also close, but slightly lower in energy than those reported by Cisneros and co-workers.[18] Furthermore, DFT studies using an active-site complex found a rate-determining hydrogen-atom abstraction barrier of 20.9 kcal mol^{-1}.[15] It appears, therefore, that the protein has a minor but stabilising effect on the transition state of the reaction. These high energetic barriers are caused through the isomerisation of the iron(IV)–oxo species, which raises the electron affinities and the corresponding hydrogen-atom abstraction barriers.

Figure 9 gives QM/MM optimised geometries for hydrogen-atom abstraction transition states and intermediates on the competing σ- and π-pathways. In both cases the hydrogen-atom abstraction is late on the potential energy surface with short O–H distances of 1.141 and 1.160 Å for ^{5}**TS**$_{H,\sigma}$ and ^{5}**TS**$_{H,\pi}$, whereas their corresponding H–C distances are considerably longer: 1.367 and 1.500 Å, respectively. As previously shown,[37] late transition states generally correspond with high energetic barriers. Due to single occupation of the $\sigma^*_{x^2-y^2}$ orbital in ^{5}**TS**$_{H,\sigma}$ the Fe–O and Fe–$NHis_{187}$ distances are somewhat longer than those in ^{5}**TS**$_{H,\pi}$, in which this orbital is virtual. The Arg_{210} residue

 © 2014 The Authors. Published by Wiley-VCH Verlag GmbH & Co. KGaA, Weinheim

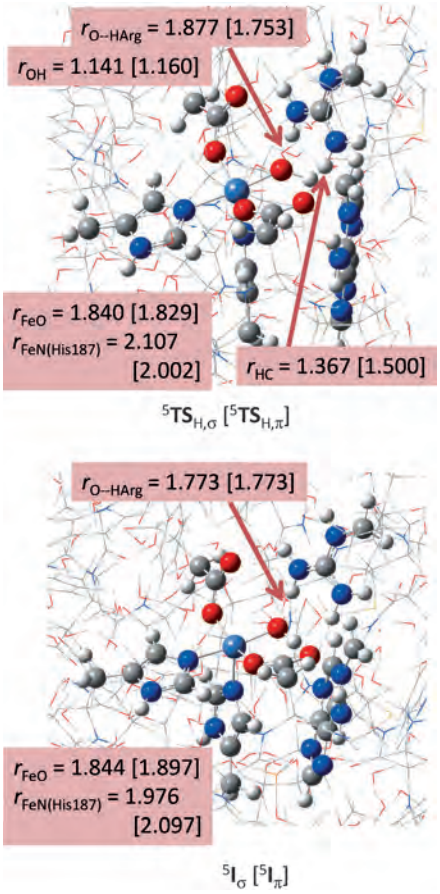

Figure 9. Optimised geometries of $^5TS_{H,\sigma}$, $^5TS_{H,\pi}$, $^5I_\sigma$ and $^5I_\pi$ as obtained from QM/MM calculations with bond lengths in Ångstroms.

forms hydrogen bonding interactions with the carboxylate groups of succinate and Asp_{133} as well as with the oxo group at a distance 1.877 (1.753) Å for $^5TS_{H,\sigma}$ ($^5TS_{H,\pi}$).

After the hydrogen-atom abstraction the system relaxes to a radical intermediate ($^5I_\sigma$ or $^5I_\pi$), whereby the former has orbital occupation $\pi^{*\uparrow}_{xz}\pi^{*\uparrow}_{yz}\pi^{*\uparrow}_{xy}\sigma^{*\uparrow}_{z^2}\sigma^{*\uparrow}_{x^2-y^2}\phi^{\downarrow}_{Sub}$ whereas it is $\pi^{*2}_{xz}\pi^{*\uparrow}_{yz}\pi^{*\uparrow}_{xy}\sigma^{*\uparrow}_{z^2}\sigma^{*0}_{x^2-y^2}\phi^{\uparrow}_{Sub}$ for the latter. The hydroxyl group in $^5I_\sigma$ and $^5I_\pi$ is locked in hydrogen-bonding interactions with the carboxylate group of Asp_{133} at a short distance of 1.701 (1.781) Å for $^5I_\sigma$ ($^5I_\pi$). As such it is not surprising that hydroxyl rebound to the substrate radical gives a significant barrier: on the π-pathway we located a $^5TS_{reb}$ barrier of 13.1 kcal mol^{-1} above $^5I_\pi$, although this is lower in energy than the hydrogen-atom abstraction barrier of 18.6 kcal mol^{-1} for the π-pathway. This substantial rebound barrier was previously shown to lead to rearrangement patterns and the formation of by-products due to the relatively long lifetime of the radical intermediate.[38] Despite the large rebound barriers, therefore, the hydrogen-atom abstraction step is still the rate-determining step in the reaction mechanism. The large rebound barrier obtained in this work contrasts the result of DFT model calculations,[15] in which a rebound barrier of just 0.6 kcal mol^{-1} was found. Clearly, the strong hydrogen-bonding interactions of the OH group to the carboxylate groups of succinate and Asp_{133} and the methylguanidinium group of Arg_{210} stabilise the radical intermediates and raise the barrier for OH transfer to the radical. This highlights the importance of inclusion of part of the protein and particularly the hydrogen bonding network in the model.

To find out whether the hydrogen abstraction barrier is dependent on the substrate, we also calculated it for N^1-methylguanine, N^1-methyladenine, N^3-methylcytosine and N^3-methylthymine using DFT model complexes and compared the results with the QM/MM studies described above (Figure 10). Our calculated hydrogen-abstraction barrier for N^1-methylade-

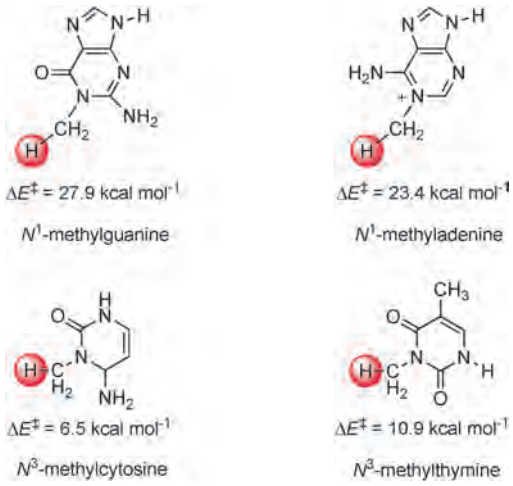

Figure 10. DFT calculated hydrogen-atom abstraction barriers from methylated DNA bases as calculated with DFT model complexes. All energies are in kcal mol^{-1} and contain ZPE and solvent corrections.

nine of 23.4 kcal mol^{-1} is close in energy to the one reported by Gauld and co-workers.[15] We located hydrogen-atom abstraction barrier heights from the *N*-methyl positions of N^3-methylcytosine, N^1-methylguanine and N^3-methylthymine of $\Delta E + ZPE = 6.5$, 27.9 and 10.9 kcal mol^{-1}, respectively. To find out whether this trend correlates with the strength of the C–H bond that is broken for these substrates, we calculated the bond dissociation energy (BDE_{CH}) for these bonds using procedures used before.[39] The BDE_{CH} value of substrates (SubH) was calculated from the energy difference of the isolated substrate with the sum of an isolated hydrogen atom and the substrate minus one hydrogen atom. As follows the BDE_{CH} values for these four substrates fall within a narrow window of about 5 kcal mol^{-1}, and should have resulted in very similar barrier heights for all substrates. Inspection of the optimised geometries (see the Supporting Information) shows that in the DFT model complexes the substrates have reoriented in several cases and formed multiple hydrogen-bonding interactions with the carboxylic acid groups of succinate and Asp_{133} as well as the oxo-group. As shown before,[26] hydrogen-bonding interactions reduce catalytic efficiency and raise hydrogen-abstraction barriers and therefore these model complexes are not a good representative of the catalysis in the actual enzyme. Thermodynamically, the AlkB repair enzyme should, therefore, also be able to hydroxylate, and, consequently, repair N^3-methylcytosine and N^3-methylthymine.

 © 2014 The Authors. Published by Wiley-VCH Verlag GmbH & Co. KGaA, Weinheim

Conclusion

In this work we report a series of QM/MM and DFT studies on the catalytic mechanism of substrate activation by AlkB repair enzymes. We analysed PDB structures and attempted to insert a dioxygen molecule in several positions and found only one feasible binding position to iron *trans* to His_{131}. The iron(III)–superoxo species is separated from the substrate by a considerable distance and its approach is blocked by an Arg residue. This Arg_{210} residue acts as a latch and only allows the isomerisation of iron(IV)–oxo and prevents the iron(III)–superoxo from reacting with substrate. It is proposed that the iron(III)–superoxo reacts with αKG to form iron(IV)–oxo, succinate and CO_2. The iron(IV)–oxo initially has the oxo *trans* to His_{131} and isomerises to a position *trans* to His_{187}. The isomeric iron(IV)–oxo species was found to react via hydrogen-atom abstraction on competing $^5\sigma$- and $^5\pi$-pathways to form a radical intermediate followed by rebound to give alcohol products. The hydrogen-atom abstraction is the rate-determining step in the reaction mechanism.

The studies presented in this work give important insight into the substrate and oxygen binding channels in the enzyme. We show that it is essential to separate the substrate and oxygen binding channels as otherwise the iron(III)–superoxo will react with substrate and prevent the repair reaction of the DNA. We also show that the isomerisation reorganises the high-lying occupied and low-lying virtual orbitals and, thereby, affects the electron transfer abilities of the oxidant. The isomeric iron(IV)–oxo reacts with substantially larger barriers as a result, which is a price the enzyme pays for separating the substrate and dioxygen binding channels.

Experimental Section

For the set-up of the QM/MM system we used well-tested and benchmarked methods as reported before.[19] Starting from the 3I2O PDB file,[14] hydrogen atoms were added to the structure using the PDB2PQR program package[40] and the active site was manually modified from the iron(II)—water αKG complex into an iron(IV)–oxo succinate (Succ) active site. Apart from the two histidine groups that are bound to the metal, all other histidine side chains were doubly protonated. Furthermore, we made sure that all arginine and lysine side chains were protonated and all glutamic acid and aspartic acid side chains were deprotonated. This resulted in a structure with overall neutral charge. Solvent (with sphere of radius of 35 Å) was added to this structure, and equilibrated, followed by a molecular dynamics minimisation and heating procedure to 298 K of the full structure using the CHARMM force field.[20] The total model has 10011 atoms and includes 2269 TIP3P water molecules. We selected several snapshots from this MD simulation as starting points for the QM/MM calculations at different time intervals. The iron(IV)–oxo reactant was geometry optimised in all low-lying and accessible spin states, that is, singlet, triplet, quintet and septet, and the spin state ordering and relative energies of these snapshots at 300, 400 and 500 ps (Sn_{300}, Sn_{400}, Sn_{500}) gave consistent and reproducible results. Subsequently, we investigated the full potential energy profile with Sn_{500} as well as the hydrogen-atom abstraction step by Sn_{300} and Sn_{400}. We chose to start the work from the iron(III)–superoxo complex and studied the mechanism until formation of alcohol product complexes as this procedure means the number of atoms in the model stays constant during the reaction.

QM/MM calculations employed the ONIOM program package as implemented in Gaussian 09.[41] The QM region was described by density functional theory and the unrestricted B3LYP functional,[28] while we used the Amber force field for the MM region.[42] The QM region contained the iron(IV)–oxo group, methylimidazole groups for His_{131} and His_{187}, acetate for succinate and Asp_{133}, methylguanidinium for Arg_{210}, and the N^1-methyladenine part of the substrate. All structures described here are the result of a full QM/MM geometry optimisation of all degrees of freedom. Stationary points were characterised by running an analytical frequency calculation on the QM region only at the same level of theory. Geometry optimisation and frequency were carried out with a double-ζ quality LACVP basis set on iron that contains a core potential and 6-31G on the rest of the atoms (basis set B1).[43] Single-point energy calculations with a Wachters all-electron basis set on iron and 6-31+G* on the rest of the atoms (basis set B2) was carried out on the optimised geometries at QM/MM to improve the energetics.[44] All energies reported in this work were obtained with basis set B2 and include ZPE corrections. Previous studies of our group on nonheme iron(IV)–oxo complexes showed these methods to be sufficiently accurate to match experimentally determined free energies of activation.[44] We used electronic embedding procedures whenever possible. To ascertain that the obtained results are reproducible we also calculated single-point energies using the UB3LYP* density functional in which the amount of HF exchange was reduced to 15%,[29] as well as single points using either the BP86 or M06 methods.[30,31]

To gain further insight into the reaction kinetics and energetics we supplemented our studies with DFT model calculations in which we took a model containing iron(IV)–oxo with two imidazole and two acetate groups as the active species of the enzyme in analogy to previous model calculations.[16,24a] We then treated this oxidant with methylated DNA bases: N^1-methyladenine, N^1-methylguanine, N^3-methylcytosine and N^3-methylthymine. The geometries were optimised with UB3LYP/B1 and characterised with a frequency calculation. Single-point calculations were carried out with UB3LYP/B2 and solvent corrections were included.

We also calculated a DFT model complex based on the above-mentioned QM region for an iron(III)–superoxo complex and calculated the hydrogen-atom abstraction from N^1-methyladenine at UB3LYP/B1. Geometries and frequencies were carried out in Gaussian using this level of theory and energies were corrected with single points at UB3LYP/B2 and solvent corrections.

Acknowledgements

The National Service of Computational Chemistry Software (NSCCS) is thanked for generous CPU time. M.G.Q. thanks the BBSRC for a studentship. D.K. is DST–Ramanujan Fellow (SR/S2/RJN-11/2008) and also acknowledges financial support from the Department of Biotechnology, New Delhi (BT/PR14510/BID/07/334/2010). Dr. Kakali Sen and Prof. Walter Thiel (Max Planck Institute in Mülheim an der Ruhr) are thanked for fruitful discussions and assistance with the QM/MM set-up.

Keywords: density functional calculations · DNA base repair · DNA damage · hydroxylation · nonheme iron enzymes

 © 2014 The Authors. Published by Wiley-VCH Verlag GmbH & Co. KGaA, Weinheim

[1] a) E. I. Solomon, T. C. Brunold, M. I. Davis, J. N. Kemsley, S.-K. Lee, N. Lehnert, F. Neese, A. J. Skulan, Y.-S. Yang, J. Zhou, *Chem. Rev.* **2000**, *100*, 235 – 349; b) T. D. H. Bugg, *Curr. Opin. Chem. Biol.* **2001**, *5*, 550 – 555; c) M. J. Ryle, R. P. Hausinger, *Curr. Opin. Chem. Biol.* **2002**, *6*, 193 – 201; d) M. Costas, M. P. Mehn, M. P. Jensen, L. Que Jr, *Chem. Rev.* **2004**, *104*, 939 – 986; e) M. M. Abu-Omar, A. Loaiza, N. Hontzeas, *Chem. Rev.* **2005**, *105*, 2227 – 2252; f) P. C. A. Bruijnincx, G. van Koten, R. J. M. Klein Gebbink, *Chem. Soc. Rev.* **2008**, *37*, 2716 – 2744; g) S. V. Kryatov, E. V. Rybak-Akimova, S. Schindler, *Chem. Rev.* **2005**, *105*, 2175 – 2226.

[2] a) M. H. Stipanuk, *Annu. Rev. Nutr.* **2004**, *24*, 539 – 577; b) G. D. Straganz, B. Nidetzky, *ChemBioChem* **2006**, *7*, 1536 – 1548; c) C. A. Joseph, M. J. Maroney, *Chem. Commun.* **2007**, 3338 – 3349.

[3] a) R. Chowdhury, A. Hardy, C. J. Schofield, *Chem. Soc. Rev.* **2008**, *37*, 1308 – 1319; b) J. M. Simmons, T. A. Müller, R. P. Hausinger, *Dalton Trans.* **2008**, 5132 – 5142; c) C. Loenarz, C. J. Schofield, *Nat. Chem. Biol.* **2008**, *4*, 152 – 156.

[4] a) L. Que Jr, *Nat. Struct. Biol.* **2000**, *7*, 182 – 184; b) E. G. Kovaleva, J. D. Lipscomb, *Nat. Chem. Biol.* **2008**, *4*, 186 – 193.

[5] a) W. Nam, *Acc. Chem. Res.* **2007**, *40*, 522 – 531; b) *Iron-Containing Enzymes: Versatile Catalysts of Hydroxylation Reaction in Nature* (Eds.: S. P. de Visser, D. Kumar), RSC, Cambridge, **2011**; c) A. R. McDonald, L. Que, Jr., *Coord. Chem. Rev.* **2012**, *257*, 414 – 428.

[6] a) D. A. Proshlyakov, T. F. Henshaw, G. R. Monterosso, M. J. Ryle, R. P. Hausinger, *J. Am. Chem. Soc.* **2004**, *126*, 1022 – 1023; b) P. J. Riggs-Gelasco, J. C. Price, R. B. Guyer, J. H. Brehm, E. W. Barr, J. M. Bollinger Jr, C. Krebs, *J. Am. Chem. Soc.* **2004**, *126*, 8108 – 8109.

[7] a) S. C. Trewick, T. F. Henshaw, R. P. Hausinger, T. Lindahl, B. Sedgwick, *Nature* **2002**, *419*, 174 – 178; b) P. Ø. Falnes, R. F. Johansen, E. Seeberg, *Nature* **2002**, *419*, 178 – 182; c) P. J. O'Brien, *Chem. Rev.* **2006**, *106*, 720 – 752; d) C. Yi, C. G. Yang, C. He, *Acc. Chem. Res.* **2009**, *42*, 519 – 529.

[8] a) Y. Mishina, E. M. Duguid, C. He, *Chem. Rev.* **2006**, *106*, 215 – 232; b) Y. Mishina, C. He, *J. Inorg. Biochem.* **2006**, *100*, 670 – 678; c) K. I. Ladwein, M. Jung, *Angew. Chem.* **2011**, *123*, 12347 – 12349; *Angew. Chem. Int. Ed.* **2011**, *50*, 12143 – 12145.

[9] a) B. Yu, J. F. Hunt, *Proc. Natl. Acad. Sci. USA* **2009**, *106*, 14315 – 14320; b) Y. Fu, Q. Dai, W. Zhang, J. Ren, T. Pan, C. He, *Angew. Chem.* **2010**, *122*, 9069 – 9072; *Angew. Chem. Int. Ed.* **2010**, *49*, 8885 – 8888; c) N. C. Giri, H. Sun, H. Chen, M. Costa, M. J. Maroney, *Biochemistry* **2011**, *50*, 5067 – 5076; d) D. Li, J. C. Delaney, C. M. Page, X. Yang, A. S. Chen, C. Wong, C. L. Drennan, J. M. Essigmann, *J. Am. Chem. Soc.* **2012**, *134*, 8896 – 8901.

[10] a) M. A. Kurowski, A. S. Bhagwat, G. Papaj, J. M. Bujnicki, *BMC Genomics* **2003**, *4*, 48 – 53; b) Y. Mishina, L. X. Shen, C. He, *J. Am. Chem. Soc.* **2004**, *126*, 16930 – 16936.

[11] B. Bleijlevens, T. Shivarattan, K. S. van den Boom, A. de Haan, G. van der Zwan, P. J. Simpson, S. J. Matthews, *Biochemistry* **2012**, *51*, 3334 – 3341.

[12] a) R. W. D. Welford, I. Schlemminger, L. A. McNeill, K. S. Hewitson, C. J. Schofield, *J. Biol. Chem.* **2003**, *278*, 10157 – 10161; b) S. C. Peck, H. A. Cooke, R. M. Cicchillo, P. Malova, F. Hammerschmidt, S. K. Nair, W. A. van der Donk, *Biochemistry* **2011**, *50*, 6598 – 6605; c) A. M. Maciejewska, J. Poznański, Z. Kaczmarska, B. Krowisz, J. Nieminuszczy, A. Polkowska-Nowakowska, E. Grzesiuk, J. T. Kuśmierek, *J. Biol. Chem.* **2013**, *288*, 432 – 441.

[13] C. Yi, G. Jia, G. Hou, Q. Dai, G. Zheng, X. Jian, C.-G. Yang, Q. Cui, C. He, *Nature* **2010**, *468*, 330 – 335.

[14] B. Yu, W. C. Edstrom, J. Benach, Y. Hamuro, P. C. Weber, B. R. Gibney, J. F. Hunt, *Nature* **2006**, *439*, 879 – 884.

[15] H. Liu, J. Llano, J. W. Gauld, *J. Phys. Chem. B* **2009**, *113*, 4887 – 4898.

[16] a) R. Latifi, M. Bagherzadeh, S. P. de Visser, *Chem. Eur. J.* **2009**, *15*, 6651 – 6662; b) S. P. de Visser, *J. Am. Chem. Soc.* **2010**, *132*, 1087 – 1097.

[17] a) A. Bassan, T. Borowski, P. E. M. Siegbahn, *Dalton Trans.* **2004**, 3153 – 3162; b) S. P. de Visser, *Chem. Commun.* **2007**, 171 – 173.

[18] D. Fang, R. L. Lord, G. A. Cisneros, *J. Phys. Chem. B* **2013**, *117*, 6410 – 6420.

[19] a) E. Godfrey, C. S. Porro, S. P. de Visser, *J. Phys. Chem. A* **2008**, *112*, 2464 – 2468; b) D. Kumar, W. Thiel, S. P. de Visser, *J. Am. Chem. Soc.* **2011**, *133*, 3869 – 3882.

[20] B. R. Brooks, R. E. Bruccoleri, B. D. Olafson, D. J. States, S. Swaminathan, M. Karplus, *J. Comput. Chem.* **1983**, *4*, 187 – 217.

[21] C. R. Wick, H. Lanig, C. M. Jäger, N. Burzlaff, T. Clark, *Eur. J. Inorg. Chem.* **2012**, 4973 – 4985.

[22] a) D. Kumar, H. Hirao, L. Que Jr, S. Shaik, *J. Am. Chem. Soc.* **2005**, *127*, 8026 – 8027; b) A. Decker, J.-U. Rohde, E. J. Klinker, S. D. Wong, L. Que Jr, E. I. Solomon, *J. Am. Chem. Soc.* **2007**, *129*, 15983 – 15996.

[23] a) J. C. Price, E. W. Barr, B. Tirupati, J. M. Bollinger, Jr., C. Krebs, *Biochemistry* **2003**, *42*, 7497 – 7508; b) D. Galonić Fujimori, E. W. Barr, M. L. Matthews, G. M. Koch, J. R. Yonce, C. T. Walsh, J. M. Bollinger Jr., C. Krebs, P. J. Riggs-Gelasco, *J. Am. Chem. Soc.* **2007**, *129*, 13408 – 13409; c) P. K. Grzyska, E. H. Appelman, R. P. Hausinger, D. A. Proshlyakov, *Proc. Natl. Acad. Sci. USA* **2010**, *107*, 3982 – 3987.

[24] a) S. P. de Visser, *J. Am. Chem. Soc.* **2006**, *128*, 9813 – 9824; b) T. Borowski, A. Bassan, P. E. M. Siegbahn, *Chem. Eur. J.* **2004**, *10*, 1031 – 1041; c) S. P. de Visser, *Angew. Chem.* **2006**, *118*, 1822 – 1825; *Angew. Chem. Int. Ed.* **2006**, *45*, 1790 – 1793; d) S. Ye, F. Neese, *Proc. Natl. Acad. Sci. USA* **2011**, *108*, 1228 – 1233; e) S. Aluri, S. P. de Visser, *J. Am. Chem. Soc.* **2007**, *129*, 14846 – 14847.

[25] a) S. Shaik, H. Chen, D. Janardanan, *Nat. Chem.* **2011**, *3*, 19 – 27; b) S. P. de Visser, J.-U. Rohde, Y.-M. Lee, J. Cho, W. Nam, *Coord. Chem. Rev.* **2013**, *257*, 381 – 393.

[26] R. Latifi, M. A. Sainna, E. V. Rybak-Akimova, S. P. de Visser, *Chem. Eur. J.* **2013**, *19*, 4058 – 4068.

[27] a) I. A. Topol, A. V. Nemukhin, K. Salnikow, R. E. Cachau, Y. G. Abashkin, K. S. Kasprzak, S. K. Burt, *J. Phys. Chem. A* **2006**, *110*, 4223 – 4228; b) C. Geng, S. Ye, F. Neese, *Angew. Chem.* **2010**, *122*, 5853 – 5856; *Angew. Chem. Int. Ed.* **2010**, *49*, 5717 – 5720.

[28] a) A. D. Becke, *J. Chem. Phys.* **1993**, *98*, 5648 – 5652; b) C. Lee, W. Yang, R. G. Parr, *Phys. Rev. B* **1988**, *37*, 785 – 789.

[29] M. Reiher, O. Salomon, B. A. Hess, *Theor. Chem. Acc.* **2001**, *107*, 48 – 55.

[30] J. P. Perdew, *Phys. Rev. B* **1986**, *33*, 8822 – 8824.

[31] Y. Zhao, D. G. Truhlar, *J. Chem. Phys.* **2006**, *125*, 1 – 18.

[32] H. Hirao, L. Que Jr, W. Nam, S. Shaik, *Chem. Eur. J.* **2008**, *14*, 1740 – 1756.

[33] a) J. E. Baldwin, M. Bradley, *Chem. Rev.* **1990**, *90*, 1079 – 1088; b) M. Lundberg, P. E. M. Siegbahn, K. Morokuma, *Biochemistry* **2008**, *47*, 1031 – 1042.

[34] T. Borowski, H. Noack, M. Radoń, K. Zych, P. E. M. Siegbahn, *J. Am. Chem. Soc.* **2010**, *132*, 12887 – 12898.

[35] a) L. Bernasconi, E.-J. Baerends, *Eur. J. Inorg. Chem.* **2008**, 1672 – 1681; b) S. D. Wong, C. B. Bell III, L. V. Liu, Y. Kwak, J. England, E. E. Alp, J. Zhao, L. Que Jr, E. I. Solomon, *Angew. Chem.* **2011**, *123*, 3273 – 3276; *Angew. Chem. Int. Ed.* **2011**, *50*, 3215 – 3218; c) S. Sahu, L. R. Widger, M. G. Quesne, S. P. de Visser, H. Matsumura, P. Moënne-Loccoz, M. A. Siegler, D. P. Goldberg, *J. Am. Chem. Soc.* **2013**, *135*, 10590 – 10593.

[36] S. P. de Visser, *J. Am. Chem. Soc.* **2006**, *128*, 15809 – 15818.

[37] a) S. P. de Visser, D. Kumar, S. Cohen, R. Shacham, S. Shaik, *J. Am. Chem. Soc.* **2004**, *126*, 8362 – 8363; b) S. Shaik, D. Kumar, S. P. de Visser, *J. Am. Chem. Soc.* **2008**, *130*, 10128 – 10140; c) D. Kumar, B. Karamzadeh, G. N. Sastry, S. P. de Visser, *J. Am. Chem. Soc.* **2010**, *132*, 7656 – 7667.

[38] a) S. P. de Visser, F. Ogliaro, S. Shaik, *Angew. Chem.* **2001**, *113*, 2955 – 2958; *Angew. Chem. Int. Ed.* **2001**, *40*, 2871 – 287; b) D. Kumar, S. P. de Visser, S. Shaik, *J. Am. Chem. Soc.* **2004**, *126*, 5072 – 5073; c) D. Kumar, S. P. de Visser, S. Shaik, *Chem. Eur. J.* **2005**, *11*, 2825 – 2835; d) S. M. Prather, C. Konstantinovics, C. L. M. DiGiuro, E. Leitner, D. Kumar, S. P. de Visser, G. Grogan, G. D. Straganz, *Angew. Chem.* **2013**, *125*, 9859 – 9863; *Angew. Chem. Int. Ed.* **2013**, *52*, 9677 – 9681.

[39] a) K. A. Prokop, S. P. de Visser, D. P. Goldberg, *Angew. Chem.* **2010**, *122*, 5217 – 5221; *Angew. Chem. Int. Ed.* **2010**, *49*, 5091 – 5095; b) K. A. Prokop, H. M. Neu, S. P. de Visser, D. P. Goldberg, *J. Am. Chem. Soc.* **2011**, *133*, 15874 – 15877; c) P. Leeladee, R. A. Baglia, K. A. Prokop, R. Latifi, S. P. de Visser, D. P. Goldberg, *J. Am. Chem. Soc.* **2012**, *134*, 10397 – 10400.

[40] T. J. Dolinsky, P. Czodrowski, H. Li, J. E. Nielsen, J. H. Jensen, G. Klebe, N. A. Baker, *Nucleic Acids Res.* **2007**, *35*, 522.

[41] Gaussian 09, Revision C.01, M. J. Frisch, G. W. Trucks, H. B. Schlegel, G. E. Scuseria, M. A. Robb, J. R. Cheeseman, G. Scalmani, V. Barone, B. Mennucci, G. A. Petersson, H. Nakatsuji, M. Caricato, X. Li, H. P. Hratchian, A. F. Izmaylov, J. Bloino, G. Zheng, J. L. Sonnenberg, M. Hada, M. Ehara, K. Toyota, R. Fukuda, J. Hasegawa, M. Ishida, T. Nakajima, Y. Honda, O. Kitao, H. Nakai, T. Vreven, J. A. Montgomery, Jr., J. E. Peralta, F. Ogliaro, M. Bearpark, J. J. Heyd, E. Brothers, K. N. Kudin, V. N. Staroverov, T. Keith, R. Kobayashi, J. Normand, K. Raghavachari, A. Rendell, J. C. Burant, S. S. Iyengar, J. Tomasi, M. Cossi, N. Rega, J. M. Millam, M. Klene, J. E. Knox,

 © 2014 The Authors. Published by Wiley-VCH Verlag GmbH & Co. KGaA, Weinheim

J. B. Cross, V. Bakken, C. Adamo, J. Jaramillo, R. Gomperts, R. E. Stratmann, O. Yazyev, A. J. Austin, R. Cammi, C. Pomelli, J. W. Ochterski, R. L. Martin, K. Morokuma, V. G. Zakrzewski, G. A. Voth, P. Salvador, J. J. Dannenberg, S. Dapprich, A. D. Daniels, O. Farkas, J. B. Foresman, J. V. Ortiz, J. Cioslowski, D. J. Fox, Gaussian, Inc., Wallingford CT, **2010**.

[42] W. D. Cornell, P. Cieplak, C. I. Bayly, I. R. Gould, K. M. Merz, Jr., D. M. Ferguson, D. C. Spellmeyer, T. Fox, J. W. Caldwell, P. A. Kollman, *J. Am. Chem. Soc.* **1995**, *117*, 5179 – 5197.

[43] P. J. Hay, W. R. Wadt, *J. Chem. Phys.* **1985**, *82*, 299 – 310.

[44] A. J. H. Wachters, *J. Chem. Phys.* **1970**, *52*, 1033 – 1036.

[45] a) A. K. Vardhaman, C. V. Sastri, D. Kumar, S. P. de Visser, *Chem. Commun.* **2011**, *47*, 11044 – 11046; b) A. K. Vardhaman, P. Barman, S. Kumar, C. V. Sastri, D. Kumar, S. P. de Visser, *Angew. Chem.* **2013**, *125*, 12514 – 12518; *Angew. Chem. Int. Ed.* **2013**, 52, 12288 – 12292.

Received: August 21, 2013
Published online on December 11, 2013

 © 2014 The Authors. Published by Wiley-VCH Verlag GmbH & Co. KGaA, Weinheim

ChemComm

RSC Publishing

COMMUNICATION

Mechanistic insight into halide oxidation by non-heme iron complexes. Haloperoxidase *versus* halogenase activity†

Cite this: *Chem. Commun.*, 2013, **49**, 10926

Received 5th September 2013, Accepted 8th October 2013

DOI: 10.1039/c3cc46792a

www.rsc.org/chemcomm

Anil Kumar Vardhaman,[a] Prasenjit Barman,[a] Suresh Kumar,[b] Chivukula V. Sastri,*[a] Devesh Kumar*[b] and Sam P. de Visser*[c]

This work presents the first detailed study on mechanistic aspects of halide oxidation by non-heme iron complexes. We show that while iron(III)–hydroperoxo complexes oxidise halides *via* oxygen atom transfer, the corresponding iron(IV)–oxo complex reacts *via* electron transfer.

A large variety of natural product biosynthesis reactions involve the halogenation of aromatic and aliphatic carbon centres.[1] Halogenating enzymes are divided into H_2O_2 required haloperoxidases (heme systems) and oxygen dependent halogenases (non-heme systems).[2,3] Over the years many heme containing haloperoxidases have been discovered that utilize chloride, bromide and iodide ions and in a reaction with hydrogen peroxide lead to hypohalide products.[4] The α-ketoglutarate dependent halogenases, by contrast, form a high-valent non-heme iron(IV)–oxo (halide) intermediate that abstracts a hydrogen atom from an aliphatic group and rebound the halide ligand to form a halogenated substrate in a stepwise radical process.[5] While haloperoxidases catalyse electrophilic halogenation (X^+) reactions, the non-heme iron halogenases, on the other hand, usually react *via* a radical process ($X^\bullet$).

Despite the fact that the enzymatic mechanism is well explored, surprisingly, few studies have been reported on analogous biomimetic models. As such, we report the first detailed mechanistic study on the reaction of halides with biomimetic iron(IV)–oxo complexes. The catalytic halogenation of organic substrates by these models was reported for a number of complexes that are likely to form a high-valent metal–oxo intermediate.[6] In addition, the reactivity of non-heme iron(III)–hydroperoxo intermediates as effective electrophilic oxidants in substrate halogenation has been reported, and it was found that under certain conditions they are catalytically more active than iron(IV)–oxo intermediates.[7] Further studies on the relative activity of non-heme iron(IV)–oxo *versus* iron(III)–hydroperoxo in aromatic hydroxylation and sulfoxidation of substrates have been reported.[8] To gain insight into the mechanistic pathways by non-heme iron(III)–hydroperoxo intermediates in electrophilic reactions, we decided to explore the direct reactivity of halides (X^- = F^-, Cl^-, Br^- and I^-) with $[Fe^{III}(OOH)(N4Py)]^{2+}$ (**1a**) and $[Fe^{III}(OOH)(Bn\text{-}tpen)]^{2+}$ (**2a**) and compare the kinetics with those of the corresponding iron(IV)–oxo complexes, *i.e.* $[Fe^{IV}(O)(N4Py)]^{2+}$ (**1b**) and $[Fe^{IV}(O)(Bn\text{-}tpen)]^{2+}$ (**2b**) (Fig. S1, ESI†).[9]

The iron(III)–hydroperoxo complexes, **1a** and **2a**, were generated *in situ* in a methanol solution at 253 K by addition of 10 equiv. of H_2O_2 following a reported procedure.[10] Subsequently, tetrabutyl ammonium halides (TBA–X; X = Cl^-, Br^-, I^-) were added to **1a** at the same temperature, which led to decay of the characteristic 548 nm peak in the UV-vis spectra. The second order rate constants extracted from these experiments (Fig. 1 and Table 1) showed a difference of as large as a factor of 6, and the reactivity decreased in the order $I^- > Br^- > Cl^-$. Surprisingly, the observed trend does not correlate with the electron affinities of these halides. Moreover, when TBA–F was added to **1a** no oxidation reaction of F^- was observed, which may be due to the fact that H_2O_2 lacks the thermodynamic potential to oxidize fluoride ions.[11]

In order to compare the reactivities of iron(III)–hydroperoxo with iron(IV)–oxo in halide oxidation, we generated **1b** and **2b** in CH_3CN using a procedure reported previously.[12] Addition of halides to **1b** under the same conditions as those for **1a** enabled us to evaluate the second order rate constants: **1b** reacted with halides (Cl^-, Br^-) with much lower rate constants than **1a**; *however, a reversal of the trend was observed in the presence of* I^-. In fact, for iodide oxidation, **1b** was found to react about six times faster than **1a**. This reversal in trend may be attributed to the steric factor influenced by the bulky I^- group upon approach of **1a**. Additionally, the reactivity of **1b** was found to be sensitive to the one electron oxidation potential of halides thus demonstrating that the reactivity of non-heme iron(IV)–oxo

[a] *Department of Chemistry, Indian Institute of Technology Guwahati, Assam 781039, India. E-mail: sastricv@iitg.ernet.in; Fax: +91-361-258-2349*

[b] *Department of Applied Physics, School for Physical Sciences, Babasaheb Bhimrao Ambedkar University, Vidya Vihar, Rai Bareilly Road, Lucknow 226 025, India. E-mail: dkclcre@yahoo.com*

[c] *Manchester Institute of Biotechnology and School of Chemical Engineering and Analytical Science, The University of Manchester, 131 Princess Street, Manchester M1 7DN, UK. E-mail: sam.devisser@manchester.ac.uk*

† Electronic supplementary information (ESI) available: Experimental and computational methods, and experimental and computational raw data in the form of tables and figures. See DOI: 10.1039/c3cc46792a

This journal is © The Royal Society of Chemistry 2013

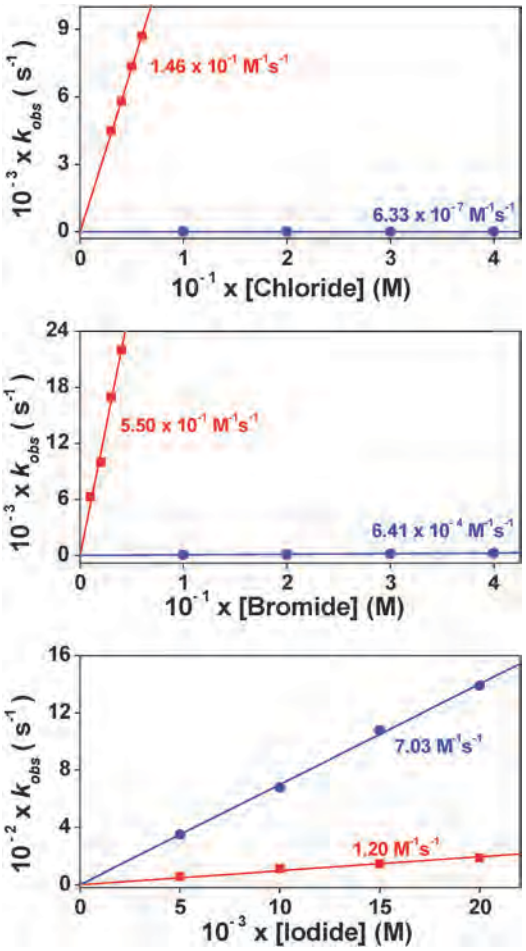

Fig. 1 Comparison of the second order rate constants for halide oxidation by **1a** (■) and **1b** (●) in the presence of (a) TBA-Cl, (b) TBA-Br and (c) TBA-I at 253 K.

Table 1 Second order rate constants for the oxidation of halides

	k_2 (M^{-1} s^{-1}) (253 K)			
X^-	**1a**	**1b**	**2a**	**2b**
Cl^-	1.46×10^{-1}	6.33×10^{-7}	4.00×10^{-2}	6.00×10^{-5}
Br^-	5.50×10^{-1}	6.41×10^{-4}	2.70×10^{-1}	1.00×10^{-2}
I^-	1.20	7.03	8.01×10^{-1}	19.01

complexes can be significantly affected by the identity of substrates. The difference in the reactivity between **1a** and **1b** was in the order of $\sim 10^3$ in the oxidation reaction of Br^- and increased to $\sim 10^5$ for Cl^-. A similar trend was observed when the halide oxidation reactions of **2a** and **2b** were compared.

To quantify the difference in the oxidation pathways for iron(III)–hydroperoxo and iron(IV)–oxo intermediates, we then made a plot of the second order rate constants log(k_2) against the one electron oxidation potential (E^0_{ox}) of these halides. A linear correlation was observed with a slope of –0.88 and –6.62 for **1a** and **1b** respectively (Fig. 2). Similar slopes were obtained for **2a** (–1.23) and **2b** (–5.16) (ESI†). Such large negative values of slopes from a plot of log(k_2) *versus* one electron oxidation potential implicates a rate determining electron transfer step in the reaction from halides to oxidants, *i.e.* **1b** and **2b**, rather than a group transfer.[13] The ease of a plausible electron transfer from I^- to

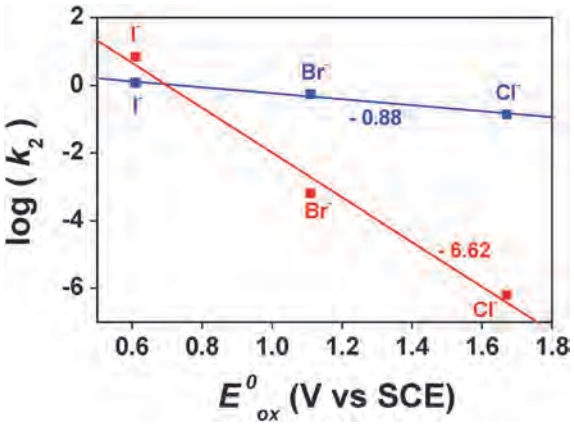

Fig. 2 Plot of log(k_2) against the one-electron oxidation potentials (E^0_{ox}) of halides of **1a** (■, blue) and **1b** (■, red) at 253 K.

iron(IV)–oxo can now account for the higher oxidation rates observed. The difference in the reaction mechanism for the oxidation of halides by iron(IV)–oxo as compared to iron(III)–hydroperoxo complexes can be attributed to the interactions of the negatively charged substrates with the electrophilic iron centre.

Further evidence of the mechanistic insights was obtained from the catalytic oxidation of anisole by **1a** and **1b** in the presence of TBA-Cl (see ESI† for details). These two chlorinating species yield different products with anisole. The oxidation of chloride involves either a one-electron oxidation ($Cl^- \rightarrow Cl^{\bullet} + e^-$) to form a chloride radical or an overall two electron oxidation ($Cl^- \rightarrow Cl^+ + 2e^-$) to give the chloronium ion. Chlorination by **1a** gave only monochlorinated products (*para* and *ortho* isomers). In stark contrast, the chlorination of anisole by **1b** gave a mixture of mono- and di-substituted chlorinated products, Scheme 1. The isomer distribution and product ratios indicate that the chlorinating agent in the presence of **1a** is Cl^+. The formation of di-substituted anisole and phenoxymethyl chloride is characteristic of free radical chlorination of anisole in the presence of **1b**.[14]

To gain further insight into the difference in reactivity of **1a** *versus* **1b** in a reaction with halides we performed a set of DFT studies on their reactivity with Br^-, as explained in detail in the ESI.†[15] Bromide oxidation by either **1a** or **1b** proceeds in a

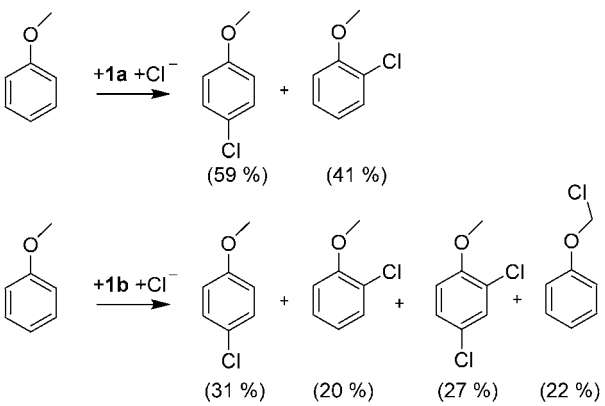

Scheme 1 Products obtained from the reaction of anisole with **1a** and **1b** in the presence of TBA-Cl at 298 K. The values in parentheses represent relative yields in mole%.

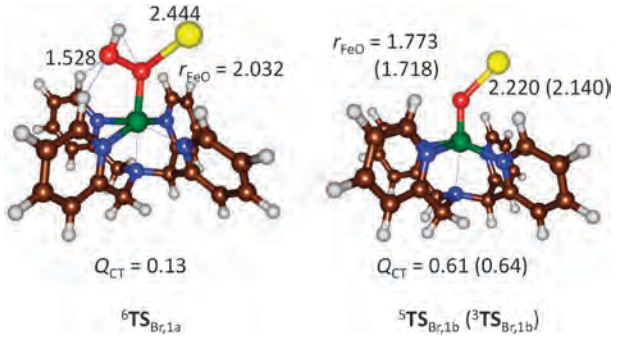

Fig. 3 Optimized geometries of bromide oxidation transition states by **1a** and **1b** with bond lengths (in Å) and spin densities and charges (in au).

concerted manner *via* a single transition state ($\mathbf{TS}_{Br}$) to form a product complex of hypobromide bound to iron(II)(N4Py). Fig. 3 displays the rate determining transition states for the reactions of **1a**/**1b** with Br^-. Geometrically, the reaction of **1a** with Br^- gives early transition states with longer O–Br distances as compared to the reaction of **1b** with Br^-. The large differences between the transition states, however, relate to the spin densities and charges. Thus, the iron(IV)–oxo complex reacts *via* an initial one-electron transfer to the substrate to produce a transition state with a large degree of radical character on the approaching halide: ρ_{Br} = −0.49 (−0.51) for $^5\mathbf{TS}_{Br}$ ($^3\mathbf{TS}_{Br}$), similar to what was observed before for electrophilic reaction mechanisms by non-heme iron(IV)–oxo complexes.[16] In addition, we calculated a large amount of charge transfer (Q_{CT}) from the oxidant to the substrate as obtained from the difference in charge of the halide in the reactant complex with respect to $\mathbf{TS}_{Br}$. This way, we obtained values of Q_{CT} to be 0.61 (0.64) for $^5\mathbf{TS}_{Br}$ ($^3\mathbf{TS}_{Br}$), respectively. On the other hand, the bromide oxidation transition state of **1a**, *i.e.* $^6\mathbf{TS}_{Br,1a}$, shows little changes in group spin densities with respect to the reactant complex and only a small degree of charge transfer (Q_{CT} = 0.13),[7] hence the iron(III)–hydroperoxo species reacts *via* group transfer rather than one-electron transfer.

These computational studies show that the electron transfer processes in electrophilic reaction mechanisms are dependent on the nature of the oxidant, whereby iron(IV)–oxo abstracts electrons early, whereas the electron transfer by iron(III)–hydroperoxo will happen after the transition state, on the way to product formation. The electron affinity difference of **1a** *versus* **1b** will, therefore, determine the electrophilic reaction rates with halides. We calculated electron affinities for **1a** and **1b** of ΔE + ZPE + E_{solv} = 102.6 and 108.7 kcal mol^{-1}, respectively. Thus, the larger electron affinity of the iron(IV)–oxo as compared to the iron(III)–hydroperoxo species will enable a much quicker and efficient electron transfer by the iron(IV)–oxo complexes. Indeed, the transition states show much earlier electron transfer from the iron(IV)–oxo as compared to the iron(III)–hydroperoxo species. These computational results are also in perfect agreement with the plot in Fig. 2 that shows a correlation of the reaction rate with the electron oxidation potential.

In summary, we reported a comparative study of the reactivity of non-heme iron(III)–hydroperoxo *versus* iron(IV)–oxo in halide oxidation reactions. We identified dramatic differences in the electron transfer processes for the two reactions, whereby iron(IV)–oxo reacts *via* a one-electron transfer and iron(III)–hydroperoxo by group transfer.

The authors acknowledge support from the Department of Science and Technology, India, for the Ramanujan Fellowship (SR/S2/RJN-11/2008) to DK and grants to CVS: SR/S1/IC-02/2009 and support from the Council for Scientific & Industrial Research (01(2527)/11/EMR-II). CPU time was provided by the National Service of Computational Chemistry Software (NSCCS) to SdV.

Notes and references

1 (*a*) G. W. Gribble, *J. Chem. Educ.*, 2004, **81**, 1441; (*b*) A. Butler and M. Sandy, *Nature*, 2009, **460**, 848.
2 (*a*) F. H. Vaillancourt, E. Yeh, D. A. Vosburg, S. Garneau-Tsodikova and C. T. Walsh, *Chem. Rev.*, 2006, **106**, 3364; (*b*) K. H. Van Peé, C. Dong, S. Flecks, J. Naismith, E. P. Patallo and T. Wage, *Adv. Appl. Microbiol.*, 2006, **59**, 127; (*c*) J. L. Anderson and S. K. Chapman, *Mol. Biosyst.*, 2006, **2**, 350; (*d*) D. G. Fujimori and C. T. Walsh, *Curr. Opin. Chem. Biol.*, 2007, **11**, 553.
3 L. P. Hager, D. R. Morris, F. S. Brown and H. Eberwein, *J. Biol. Chem.*, 1966, **241**, 1769.
4 (*a*) J. A. Manthey and L. P. Hager, *Biochemistry*, 1989, **28**, 3052; (*b*) J. A. Manthey and L. P. Hager, *J. Biol. Chem.*, 1985, **260**, 9654; (*c*) M. P. Roach, Y. P. Chen, S. A. Woodin, D. E. Lincoln, C. R. Lovell and J. H. Dawson, *Biochemistry*, 1997, **36**, 2197.
5 (*a*) C. Krebs, D. Galonić Fujimori, C. T. Walsh and J. M. Bollinger Jr, *Acc. Chem. Res.*, 2007, **40**, 484; (*b*) *Iron-containing enzymes: Versatile catalysts of hydroxylation reactions in nature*, ed. S. P. de Visser and D. Kumar, Royal Society of Chemistry Publishing, Cambridge, UK, 2011.
6 (*a*) T. Kojima, R. A. Leising, S. Yan and L. Que Jr., *J. Am. Chem. Soc.*, 1993, **115**, 11328; (*b*) A. Bakac, C. Shi and O. Pestovsky, *Inorg. Chem.*, 2004, **43**, 5416; (*c*) J. Y. Kravitz and V. L. Pecoraro, *Pure Appl. Chem.*, 2005, **77**, 1595; (*d*) P. Comba and S. Wunderlich, *Chem.–Eur. J.*, 2010, **16**, 7293; (*e*) W. Liu and J. T. Groves, *J. Am. Chem. Soc.*, 2010, **132**, 12847; (*f*) W. Liu, X. Huang, M.-J. Cheng, R. J. Nielsen, W. A. Goddard III and J. T. Groves, *Science*, 2012, **337**, 1322; (*g*) P. Galloni, M. Mancini, B. Floris and V. Conte, *Dalton Trans.*, 2013, **42**, 11963.
7 A. K. Vardhaman, C. V. Sastri, D. Kumar and S. P. de Visser, *Chem. Commun.*, 2011, **47**, 11044.
8 (*a*) A. Thibon, V. Jollet, C. Ribal, K. Sénéchal-David, L. Billon, A. B. Sorokin and F. Banse, *Chem.–Eur. J.*, 2012, **18**, 2715; (*b*) J. Cho, S. Jeon, S. A. Wilson, L. V. Liu, E. A. Kang, J. J. Braymer, M. H. Lim, B. Hedman, K. O. Hodgson, J. S. Valentine, E. I. Solomon and W. Nam, *Nature*, 2011, **478**, 502.
9 Abbreviations used: N4Py, *N*,*N*-bis(2-pyridylmethyl)-*N*-bis(2-pyridyl)-methylamine; Bn-tpen, *N*-benzyl-*N*,*N*′,*N*′-tris(2-pyridylmethyl)ethane-1,2-diamine.
10 (*a*) A. Hazell, C. J. McKenzie, L. P. Nielsen, S. Schindler and M. Weitzer, *J. Chem. Soc., Dalton Trans.*, 2002, 310; (*b*) K. D. Koehntop, J.-U. Rohde, M. Costas and L. Que Jr, *Dalton Trans.*, 2004, 3191.
11 (*a*) O. Nashiru, D. L. Zechel, D. Stoll, T. Mohammadzadeh, R. A. J. Warren and S. G. Withers, *Angew. Chem., Int. Ed.*, 2001, **40**, 417; (*b*) D. L. Zechel, S. P. Reid, O. Nashiru, C. Mayer, D. Stoll, D. L. Jakeman, R. A. J. Warren and S. G. Withers, *J. Am. Chem. Soc.*, 2001, **123**, 4350.
12 J. Kaizer, E. J. Klinker, N. Y. Oh, J.-U. Rohde, W. J. Song, A. Stubna, J. Kim, E. Münck, W. Nam and L. Que Jr., *J. Am. Chem. Soc.*, 2004, **126**, 472.
13 Y. Goto, T. Matsui, S.-I. Ozaki, Y. Watanabe and S. Fukuzumi, *J. Am. Chem. Soc.*, 1999, **121**, 9497.
14 F. S. Brown and L. P. Hager, *J. Am. Chem. Soc.*, 1967, **89**, 719.
15 (*a*) D. Kumar, W. Thiel and S. P. de Visser, *J. Am. Chem. Soc.*, 2011, **133**, 3869; (*b*) R. Latifi, M. A. Sainna, E. V. Rybak-Akimova and S. P. de Visser, *Chem.–Eur. J.*, 2013, **19**, 4058.
16 (*a*) D. Kumar, B. Karamzadeh, G. N. Sastry and S. P. de Visser, *J. Am. Chem. Soc.*, 2010, **132**, 7656; (*b*) D. Kumar, G. N. Sastry and S. P. de Visser, *Chem.–Eur. J.*, 2011, **17**, 6196.

 This journal is © The Royal Society of Chemistry 2013

Iron(IV)–Imido Complexes

DOI: 10.1002/anie.201305370

Comparison of the Reactivity of Nonheme Iron(IV)–Oxo versus Iron(IV)–Imido Complexes: Which is the Better Oxidant?**

Anil Kumar Vardhaman, Prasenjit Barman, Suresh Kumar, Chivukula V. Sastri, Devesh Kumar,* and Sam P. de Visser**

High-valent heme and nonheme iron(IV)–oxo complexes play key roles in biology as catalytic intermediates in enzymes, where they catalyze vital biotransformations for human health, including detoxification processes in the liver and also the biosynthesis of hormones.[1,2] Mono- and dioxygenases bind and utilize molecular oxygen on an iron center and form a catalytically active iron(IV)–oxo species that transfers the oxygen atom to substrate. Technically, using a nitrogen donor one should be able to synthesize the analogous iron(IV)–imido and/or iron(V)–nitrido complexes. Although these complexes are rare in nature, evidence exists of substrate aziridination by cytochrome P450 enzymes that presumably takes place by a high-valent iron(IV)–nitrido or –imido complex.[3] Several iron–porphyrin models with nitrene or imido ligands have been synthesized and their reactivity patterns implicated efficient aziridination of olefins.[4,5]

By contrast to iron(IV)–oxo complexes, which have been extensively studied over the years, only few studies have been reported on its closely related iron(V)–nitrido species ($Fe^{V}\equiv N$) or the iron(IV)–imido (Fe^{IV}=NR) species. In principle, these high-valent metal–nitrido/imido complexes should have strong oxidative power and capable to catalyze isolobal amination reactions. During the past decade, the chemistry of metal-catalyzed aziridination of alkenes and aminidation of aliphatic C–H bonds using iminoiodane reagents have been studied by several groups.[6,7] In recent years, the putative metal–nitrogen multiple-bonded species have been isolated and spectroscopically characterized, which led to significant progress on the understanding of its fundamental chemical properties.[6,8] However, details on its potential as nitrogen atom transfer agent are lacking and little knowledge exists in its relative reactivity with respect to the well-known iron(IV)–oxo species.[8h]

In nonheme iron chemistry, the aromatic amination of ligands by an iron–nitrido complex was reported by several groups,[6e,9] and recently, the spectroscopic characterization of the iron(IV)–tosylimido (tosylimido^{2-} = NTs) complex with pentadentate N4Py ligand (N4Py = *N*,*N*-bis(2-pyridylmethyl)-*N*-bis(2-pyridyl)methylamine), $[Fe^{IV}(NTs)(N4Py)]^{2+}$, was described (Figure 1).[10] As this species was shown to have a relatively long lifetime, it makes it highly suitable for reactivity studies, especially since the iron(IV)–oxo analogue can be studied in tandem. We therefore took the opportunity to pursue a comparative reactivity study of $[Fe^{IV}(NTs)(N4Py)]^{2+}$ (**1**) and $[Fe^{IV}(O)(N4Py)]^{2+}$ (**2**) with substrates.

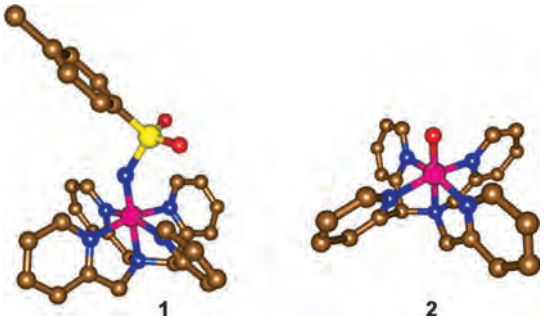

Figure 1. Structures of $[Fe^{IV}(NTs)(N4Py)]^{2+}$ (**1**) and $[Fe^{IV}(O)(N4Py)]^{2+}$ (**2**) derived from computational and crystallographic results. Hydrogen atoms are omitted for clarity. Fe magenta, C brown, O red, N blue, S yellow.

Complexes **1** and **2** were generated in an acetonitrile solution in situ using either PhINTs as tosylimido donor or PhIO as oxygen atom donor using procedures reported before.[10,11] The identity of complex **1** was confirmed on the basis of visible features with an intense LMCT band at 445 nm ($\varepsilon = 2700\ L\,mol^{-1}\,cm^{-1}$) and a low energy 660 nm band ($\varepsilon = 250\ L\,mol^{-1}\,cm^{-1}$) that arises from ligand field transitions characteristic for $S = 1$ iron(IV) complexes (Supporting Information, Figure S2). The electron spray ionization mass spectrum (Supporting Information, Figure S3) gave a major

[*] A. K. Vardhaman, P. Barman, Dr. C. V. Sastri
Department of Chemistry
Indian Institute of Technology Guwahati
Assam, 781039 (India)
E-mail: sastricv@iitg.ernet.in
S. Kumar, Dr. D. Kumar
Department of Applied Physics
Babasaheb Bhimrao Ambedkar University
School for Physical Sciences
Vidya Vihar, Rae Bareilly Road, Lucknow (UP), 226025 (India)
E-mail: dkclcre@yahoo.com
Dr. S. P. de Visser
Manchester Institute of Biotechnology and School of Chemical Engineering and Analytical Science, The University of Manchester
131 Princess Street, Manchester M1 7DN (United Kingdom)
E-mail: sam.devisser@manchester.ac.uk

[**] Research support was provided by the Department of Science and Technology, India (SR/S1/IC-02/2009) and Council for Scientific & Industrial Research (01(2527)/11/EMR-II) to C.V.S. The National Service of Computational Chemistry Software (NSCCS) is acknowledged for CPU time. D.K. acknowledges Department of Science and Technology (New Delhi) for a Ramanujan Fellowship.

Supporting information for this article is available on the WWW under http://dx.doi.org/10.1002/anie.201305370.

 © 2013 Wiley-VCH Verlag GmbH & Co. KGaA, Weinheim

peak at $m/z = 741.0751$ corresponding to {[Fe^{IV}(NTs)N4Py](OTf)}$^+$ with an isotope pattern that matches the theoretically expected distribution. Thioanisole was added to the solution of **1** at 273 K, which led to the decay of the characteristic peak at 660 nm in the UV/Vis spectrum concomitant with the appearance of its iron(II) precursor ($\lambda_{max} = 450$ nm) with an isosbestic point at 516 nm (Supporting Information, Figure S4). Aminidation of thioanisole to *N*-*p*-tosylmethylphenyl sulfilimine was obtained in about 85% yield,[12] and a second-order rate constant for this reaction was evaluated of 0.260 $L\,mol^{-1}\,s^{-1}$ (Supporting Information, Table S5). In contrast, the second-order rate constant for **2** determined under the same reaction conditions was found to be only 0.050 $L\,mol^{-1}\,s^{-1}$ (Figure 2a; Supporting Information, Table S6). It appears, therefore, that the [Fe^{IV}(NTs)(N4Py)]$^{2+}$ complex reacts with thioanisole with rate constants that are about five times higher than those found for the [Fe^{IV}(O)(N4Py)]$^{2+}$ complex.

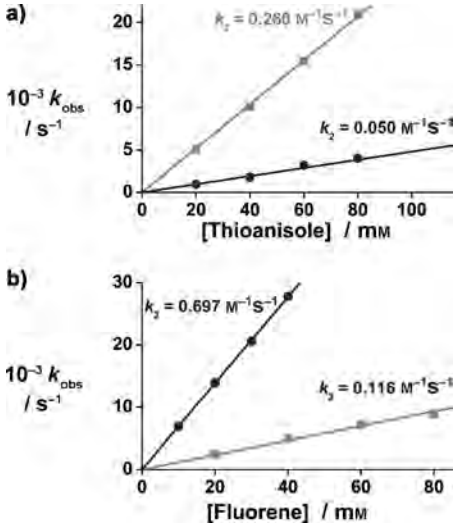

Figure 2. Second-order rate constants determined in the reactions of 1 mM [Fe^{IV}(NTs)(N4Py)]$^{2+}$ **1** (■) and [Fe^{IV}(O)(N4Py)]$^{2+}$ **2** (●) in CH_3CN solution against various concentrations of a) thioanisole at 273 K and b) fluorene at 298 K.

The pseudo first-order rate constants were then determined for the reaction of **1** and **2** with various *p*-substituted thioanisoles (Supporting Information, Table S7). From a direct comparison of the k_{obs} values for the reactions of **1** and **2** with different *para*-substituted thioanisoles, it is evident that the reactivity of **1** is more sensitive than that of **2** to substitution at the *para* position of the substrate. In fact, the difference in reactivity between **1** and **2** increased when electron-donating groups at the *para* position were employed; for instance, in the reaction with *p*-methoxythioanisole the difference in reactivity was found to be more than 50 times. We then created Hammett plots, for a quantitative examination of the substituent effect on the reaction rates. For **2**, a linear correlation with σ was found with a $\rho = -0.90$. In contrast, when a similar plot was made for **1**, non-linearity was observed with $\rho = -3.36$ (Supporting Information, Figure S8), which is likely as a result of additional stabilization of positive charge in the transition state by electron-donating groups in the *para* position of thioanisole and thus enhanced the overall rate of oxidation, as also will be discussed in the computational section. To accommodate the additional stabilization of the positive charge in the transition state, new Hammett plots were now made using σ^+ values leading to ρ values of -1.92 and -0.52, respectively, for **1** and **2** (Supporting Information, Figure S9). This difference is slopes quantitatively reflect that **1** is more sensitive to electronic effects of the *para* substituents than **2**. Further, the plot of $\log(k_X/k_H)$ values against the E^0_{ox} of sulfides gave a linear correlation with a slope of -7.1 and -1.92 for **1** and **2**, respectively (Supporting Information, Figure S10). Such a large negative slope obtained from these plots implicates a rate determining electron transfer from sulfides to **1** rather than a group transfer.[13]

Considering the high reactivity of **1** over **2** in the oxidation of thioanisole, we then evaluated the hydrogen atom transfer (HAT) capability of **1**. It has been shown that the rate constant of HAT reactions often correlates with the strength of the C–H bond that is broken, that is, BDE_{C-H} or bond dissociation energy,[14] we therefore studied the rates of HAT between **1** and substrates with a range of BDE_{C-H} values: xanthene, 9,10-dihydroanthracene (DHA), 1,4-cyclohexadiene (CHD), fluorene, and triphenylmethane. Indeed a plot of the logarithm of the rate constant of HAT by **1** versus the BDE_{C-H} value of the substrate gives a linear correlation, Figure 3, (Supporting Information, Table S11, Figure S12). However, when excess triphenylmethane ($BDE_{C-H} = 81$ kcal mol^{-1}) was added to a solution of **1** at 298 K, no change in 660 nm absorption band was observed, despite observable reactivity with fluorene, which has a comparable BDE_{C-H}.[11] Most probably the difference in reactivity between these two substrates with closely related BDE_{C-H} values is due to stereochemical clashes of **1** with the approaching substrate. This is particularly important for substrates with bulky groups adjacent to the hydrogen abstraction center, such as triphenylmethane.

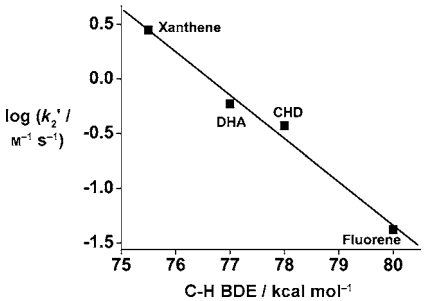

Figure 3. Correlation of the second-order rate constants (determined at 288 K) for HAT by **1** with BDE_{C-H} of substrates.

Subsequently, we compared the relative activity in HAT processes of **1** and **2** using fluorene as the substrate (Supporting Information, Table S13). The reaction of **1** and **2** follows pseudo first-order kinetics, and second-order rate constants were determined for each system (Figure 2b;

 © 2013 Wiley-VCH Verlag GmbH & Co. KGaA, Weinheim

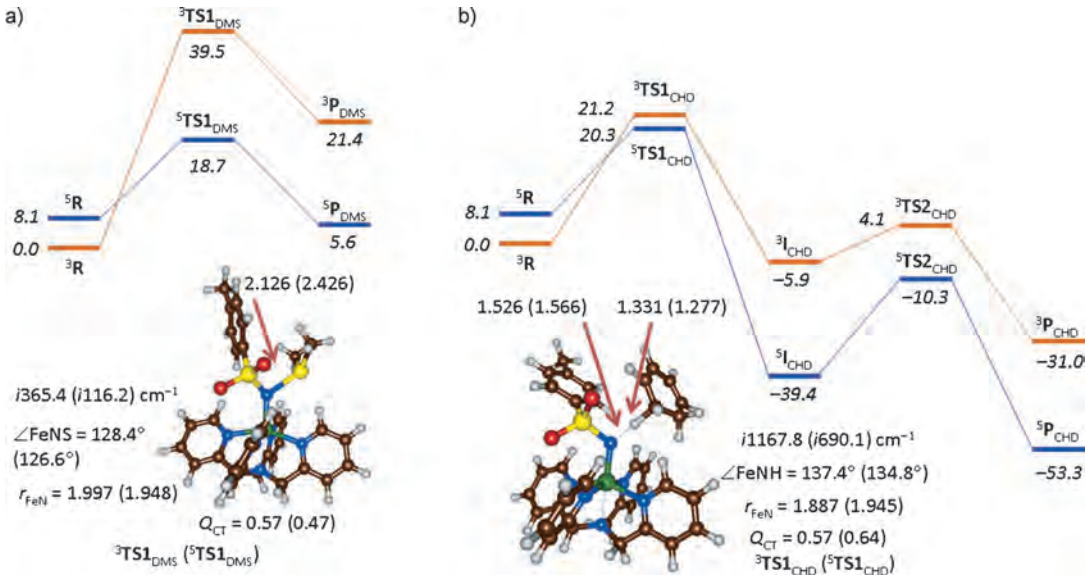

Figure 4. DFT calculated potential-energy landscapes for DMS sulfoxidation and hydrogen atom abstraction from CHD by $[Fe^{IV}(NTs)(N4Py)]^{2+}$. Energies are ΔG^{+} in kcal mol^{-1} relative to a reactant complex with solvent and dispersion energy corrections included. Also given are optimized geometries of the transition states with bond lengths [Å], the degree of charge transfer (Q_{CT}), and the imaginary frequency in the **TS** [cm^{-1}].

Supporting Information, Table S6). At 298 K, complex **1** decayed with a second order rate constant of 0.116 L mol^{-1} s^{-1} to form 9*H*,9′*H*-[9,9′]bifluorenyl (9,9′-bifluorene) products in about 32% yield. These results indicate that **1** effectively acts as a one-electron oxidizing agent in HAT reactions, whereby the 32% yield of 9,9′-bifluorene reflects the conversion of about 64% of iron(IV)–imido complex in two one-electron oxidation steps of fluorene. By comparison, complex **2** decays with a $k_2 =$ 0.697 L mol^{-1} s^{-1} to form fluorenone as the dominant product.[15] The observed slower rate (ca. 6 times) of **1** relative to **2** for C–H bond activation is opposite to that observed for thioanisole oxidation (see above). This observation indicates that iron(IV)–tosylimido complex is a less-effective oxidant than iron(IV)–oxo for hydrogen atom abstraction reactions. Indeed, recent computational studies on nonheme iron(IV)–oxo versus iron(IV)–nitrido complexes gave higher hydrogen atom abstraction barriers from methane for the latter system, in agreement with our results herein.[16]

Further evidence of a rate-determining HAT reaction comes from kinetic isotope effect (KIE) studies of **2** with fluorene (KIE = 30). Such large KIE values exceed the semi-classical limit and suggest strong tunneling behavior in the reaction mechanism. On the other hand, the reaction of deuterated fluorene with **1** gave a KIE of only 7, although it is still regarded as a HAT mechanism (Supporting Information, Figures S14, S15).

To gain insight into the details of the reaction mechanisms of substrate activation by iron(IV)–tosylimido complexes, we decided to do an additional density functional theory study and compare the work with the experimental work reported above and earlier computational studies on the reactivity of **2** with substrates.[17] We calculated the reaction mechanisms of **1** with dimethylsulfide (DMS) and CHD as model substrates for sulfoxidation and HAT reactions. Dehydrogenation of CHD is a stepwise process with two sequential hydrogen-atom abstraction barriers $\mathbf{TS1}_{CHD}$ and $\mathbf{TS2}_{CHD}$ by a radical intermediate $\mathbf{I}_{CHD}$ leading to benzene products $\mathbf{P}_{CHD}$. Figure 4 displays the calculated free energy landscapes and the rate-determining transition states (**TS1**) for the two reactions on the lowest lying triplet and quintet spin-state surfaces. Similar to previous studies, we find a concerted one-step,mechanism via a transition state $\mathbf{TS1}_{DMS}$ for substrate sulfoxidation by both **2** and **1**, leading to products $\mathbf{P}_{DMS}$.[18] Despite the fact that substrate sulfoxidation by either **1** or **2** appears to be concerted through a single rate-determining transition state, actually there are some critical differences between the two sulfoxidation processes that lead to changes in the Hammett plots for **1** versus **2**. In case of **1**, the analysis of the orbital occupation and group spin densities and charges of $^{3,5}\mathbf{TS1}_{DMS}$ shows that in the sulfoxidation transition states a large amount of charge transfer has taken place from substrate to oxidant; $Q_{CT} = 0.57$ (0.47) for $^3\mathbf{TS1}_{DMS}$ ($^5\mathbf{TS1}_{DMS}$), respectively. Furthermore, the orbital occupations and group spin densities (Supporting Information, Tables S18, S31) implicate a product-like electronic configuration. In contrast, the electron-transfer processes from substrate to iron(IV)–oxo happen at a much later timescale and give group spin densities much more in line with the reactant structure.[18] To find the origin of these differences in reactivity we calculated the electron affinities of **1** and **2**, which gave values of $\Delta E + \mathrm{ZPE} + E_{solv} =$ 120.5 and 94.6 kcal mol^{-1}, respectively. Therefore, **1** is more electrophilic than **2**.

The substrate sulfoxidation mechanism by $[Fe^{IV}(NTs)(N4Py)]^{2+}$ shows analogy to aromatic hydroxylation by **2**, where also a large energy difference between $^3\mathbf{TS1}$ and $^5\mathbf{TS1}$ was calculated.[17b] However, there are critical differences and one relates to the orientation of the substrate. Thus, on the quintet spin-state surface the substrate usually attacks from the top and aligns itself along the Fe–O/N bond owing to

© 2013 Wiley-VCH Verlag GmbH & Co. KGaA, Weinheim

electron transfer into the $\sigma^*_{z^2}$ orbital.[17,19] In $[Fe^{IV}(NTs)(N4Py)]^{2+}$ this alignment is not possible because of stereochemical constraints of the NTs group with the approaching substrate and thus a more sideways approach is essential. As a consequence, the quintet spin barriers have increased in energy and in the case of HAT from CHD ^{5}**TS1**$_{CHD}$ is competitive with ^{3}**TS1**$_{CHD}$. These studies support the experimental observation mentioned above that **2** will be better in catalyzing HAT reaction mechanisms owing to lesser stereochemical interactions between substrate and oxidant as compared to **1**. Furthermore, the stereochemical interactions between oxidant and the approaching substrate destabilize the transition states and increase the HAT process for **1**. This effect is larger for HAT processes by **1** than by **2** as the (almost) linearity of the Fe-O-H angle in the quintet spin state will ensure large distances between the rest of the substrate and the oxidant. Approach under an angle of 120° as in **1**, however, brings the substrate closer to the equatorial ligand of the oxidant and hence stereochemical repulsions are larger and barriers are raised. As a consequence, the HAT barriers for **1** are above those for **2** in support of the experimental rate constants in Figure 2.

The dehydrogenation reaction has low barriers **TS1**$_{CHD}$ on the triplet and quintet spin states, leading to a radical intermediate. However, the subsequent dehydrogenation of hydrogen atom abstraction via **TS2** encounters significantly larger barriers of well over $\Delta G + E_{solv} > 25$ kcal mol^{-1}, and consequently will be difficult. Instead theory predicts that the radical will dissipate from the reaction center rather than donating a second hydrogen atom to the oxidant. A subsequent collision of two of these radicals will then form a dimer at much lower energetic costs than dehydrogenation products, which is indeed what was observed experimentally. The fact that these dimers are not formed in the reaction of **1** with triphenylmethane may be due to stereochemical restrictions in dimer formation. The large **TS2** barrier obtained for the reaction of **1** with CHD contrasts that found for the reaction of **2** with CHD, where typically barriers of less than 5 kcal mol^{-1} are obtained.[20] This change in **TS2** barrier leads to fundamental differences in substrate activation and consequently product distributions.

So what is the origin of the differences in reactivity of **1** over **2** and why is sulfoxidation preferred for **1**, whereas hydrogen atom abstraction is favored by **2**? Hydrogen atom abstraction is accompanied by the breaking of the C–H bond of the substrate and the formation of an O/N–H bond with the oxidant. It has been shown that hydrogen atom abstraction barriers tend to correlate with the BDE_{C-H} bond of the substrate as well as the BDE_{O-H} bond of the oxidant.[14,21] We calculated values of $BDE_{N-H} = 94.4$ kcal mol^{-1} and $BDE_{O-H} = 96.7$ kcal mol^{-1} for **1** and **2**, respectively, which implies that **2** and **1** should be similarly good oxidants of HAT reactions. Instead, differences in HAT catalysis are most likely originated by stereochemical repulsions of the approaching substrate with the oxidant. Thus, as shown in Figure 4, during HAT the substrate attacks the NTs group under an angle Fe-N-H of 137.4° (134.8°) for ^{3}**TS**$_{CHD}$ (^{5}**TS**$_{CHD}$), respectively, whereas in $[Fe^{IV}(O)(N4Py)]^{2+}$ the approach will be along the Fe–O axis in the quintet spin state.[22] Consequently, the attack of substrate on **1** will be more stereochemically constraint than in **2** and thus generally higher barriers for HAT reactions.

In summary, we present herein the first comparative study on the reactivity patterns of nonheme iron(IV)–oxo versus iron(IV)–imido. We show that owing to the larger electron affinity of the oxidant iron(IV)–imido is a better oxidant of sulfoxidation reactions than iron(IV)–oxo. By contrast, these trends are reversed for stepwise one-electron transfer reactions, such as hydrogen atom abstraction reactions where stereochemical interactions upon substrate approach determine the relative rate constants.

Experimental Section

Detailed procedures and methods of the experiments and computations, which follow those of our previous studies in the field,[23] are given in detail in the Supporting Information.

Received: June 21, 2013
Revised: August 12, 2013
Published online: September 25, 2013

Keywords: C–H activation · enzyme models · imido ligands · iron · sulfoxidation

[1] a) M. Sono, M. P. Roach, E. D. Coulter, J. H. Dawson, *Chem. Rev.* **1996**, *96*, 2841 – 2888; b) J. T. Groves, *Proc. Natl. Acad. Sci. USA* **2003**, *100*, 3569 – 3574; c) *Cytochrome P450: Structure, Mechanism and Biochemistry*, 3rd ed. (Ed.: P. R. Ortiz de Montellano), Kluwer Academic/Plenum Publishers, New York, **2004**; d) *Handbook of Porphyrin Science* (Eds.: K. M. Kadish, K. M. Smith, R. Guilard), World Scientific Publishing Co., New Jersey, **2010**; e) *Iron-containing enzymes: Versatile catalysts of hydroxylation reactions in nature* (Eds.: S. P. de Visser, D. Kumar), RSC Publishing, Cambridge, **2011**.

[2] a) M. Costas, M. P. Mehn, M. P. Jensen, L. Que, Jr., *Chem. Rev.* **2004**, *104*, 939 – 986; b) S. V. Kryatov, E. V. Rybak-Akimova, S. Schindler, *Chem. Rev.* **2005**, *105*, 2175 – 2226; c) M. M. Abu-Omar, A. Loaiza, N. Hontzeas, *Chem. Rev.* **2005**, *105*, 2227 – 2252; d) R. van Eldik, *Coord. Chem. Rev.* **2007**, *251*, 1649 – 1662; e) P. C. A. Bruijnincx, G. van Koten, R. J. M. Klein Gebbink, *Chem. Soc. Rev.* **2008**, *37*, 2716 – 2744; f) A. R. McDonald, L. Que, Jr., *Coord. Chem. Rev.* **2013**, *257*, 414 – 428.

[3] a) R. E. White, M. B. McCarthy, *J. Am. Chem. Soc.* **1984**, *106*, 4922 – 4926; b) E. W. Svastits, J. H. Dawson, R. Breslow, S. H. Gellman, *J. Am. Chem. Soc.* **1985**, *107*, 6427 – 6428; c) J. Hohenberger, K. Ray, K. Meyer, *Nat. Commun.* **2012**, *3*, 1 – 13.

[4] a) D. Mansuy, P. Battioni, J.-P. Mahy, *J. Am. Chem. Soc.* **1982**, *104*, 4487 – 4489; b) J.-P. Mahy, P. Battioni, D. Mansuy, J. Fisher, R. Weiss, J. Mispelter, I. Morgenstern-Badarau, P. Gans, *J. Am. Chem. Soc.* **1984**, *106*, 1699 – 1706; c) J.-P. Mahy, P. Nattioni, D. Mansuy, *J. Am. Chem. Soc.* **1986**, *108*, 1079 – 1080.

[5] a) C.-M. Che, C.-Y. Zhou, E. L.-M. Wong, *Top. Organomet. Chem.* **2011**, *33*, 111 – 138; b) T. W.-S. Chow, G.-Q. Chen, Y. Liu, C.-Y. Zhou, C.-M. Che, *Pure Appl. Chem.* **2012**, *84*, 1685 – 1704.

[6] a) J. F. Berry, E. Bill, E. Bothe, S. DeBeer George, B. Mienert, F. Neese, K. Wieghardt, *Science* **2006**, *312*, 1937 – 1941; b) P. Comba, C. Lang, C. Lopez de Laorden, A. Muruganatham, G. Rajaraman, H. Wadepohl, M. Zajaczkowski, *Chem. Eur. J.* **2008**, *14*, 5313 – 5328; c) K. L. Klotz, L. M. Slominski, M. E. Riemer, J. A. Phillips, J. A. Halfen, *Inorg. Chem.* **2009**, *48*, 801 – 803; d) J. J. Scepaniak, J. A. Young, R. P. Bontchev, J. M. Smith,

 © 2013 Wiley-VCH Verlag GmbH & Co. KGaA, Weinheim

Angew. Chem. **2009**, *121*, 3204 – 3206; *Angew. Chem. Int. Ed.* **2009**, *48*, 3158 – 3160; e) P. Leeladee, G. N. L. Jameson, M. A. Siegler, D. Kumar, S. P. de Visser, D. P. Goldberg, *Inorg. Chem.* **2013**, *52*, 4668 – 4682.

[7] a) M. J. Zdilla, M. M. Abu-Omar, *J. Am. Chem. Soc.* **2006**, *128*, 16971 – 16979; b) S. Kundu, E. Miceli, E. Farquhar, F. F. Pfaff, U. Kuhlmann, P. Hildebrandt, B. Braun, C. Greco, K. Ray, *J. Am. Chem. Soc.* **2012**, *134*, 14710 – 14713; c) J. W. W. Chang, P. W. H. Chan, *Angew. Chem.* **2008**, *120*, 1154 – 1156; *Angew. Chem. Int. Ed.* **2008**, *47*, 1138 – 1140.

[8] a) T. Petrenko, S. DeBeer George, N. Aliaga-Alcalde, E. Bill, B. Mienert, Y. Xiao, Y. S. Guo, W. Sturhahn, S. P. Cramer, K. Wieghardt, F. Neese, *J. Am. Chem. Soc.* **2007**, *129*, 11053 – 11060; b) R. E. Cowley, N. A. Eckert, S. Vaddadi, T. M. Figg, T. R. Cundari, P. L. Holland, *J. Am. Chem. Soc.* **2011**, *133*, 9796 – 9811; c) M. P. Mehn, J. C. Peters, *J. Inorg. Biochem.* **2006**, *100*, 634 – 643; d) C. M. Thomas, N. P. Mankad, J. C. Peters, *J. Am. Chem. Soc.* **2006**, *128*, 4956 – 4957; e) I. Nieto, F. Ding, R. P. Bontchev, H. Wang, J. M. Smith, *J. Am. Chem. Soc.* **2008**, *130*, 2716 – 2717; f) E. R. King, E. T. Hennessy, T. A. Betley, *J. Am. Chem. Soc.* **2011**, *133*, 4917 – 4923; g) Y. Liu, X. Guan, E. L. M. Wong, P. Liu, J. S. Huang, C.-M. Che, *J. Am. Chem. Soc.* **2013**, *135*, 7194 – 7204; h) E. T. Hennessy, T. A. Betley, *Science* **2013**, *340*, 591 – 595.

[9] a) M. P. Jensen, M. P. Mehn, L. Que, Jr., *Angew. Chem.* **2003**, *115*, 4493 – 4496; *Angew. Chem. Int. Ed.* **2003**, *42*, 4357 – 4360; b) H. S. Soo, M. T. Sougrati, F. Grandjean, G. J. Long, C. J. Chang, *Inorg. Chim. Acta* **2011**, *369*, 82 – 91.

[10] E. J. Klinker, T. A. Jackson, M. P. Jensen, A. Stubna, G. Juhász, E. L. Bominaar, E. Münck, L. Que, Jr., *Angew. Chem.* **2006**, *118*, 7554 – 7557; *Angew. Chem. Int. Ed.* **2006**, *45*, 7394 – 7397.

[11] J. Kaizer, E. J. Klinker, N. Y. Oh, J.-U. Rohde, W. J. Song, A. Stubna, J. Kim, E. Münck, W. Nam, L. Que, Jr., *J. Am. Chem. Soc.* **2004**, *126*, 472 – 473.

[12] Small amounts (< 15 %) of methylphenylsulfoxide products were detected that are likely to be due to hydrolysis of sulfilimine.

[13] a) Y. Goto, T. Matsui, S.-I. Ozaki, Y. Watanabe, S. Fukuzumi, *J. Am. Chem. Soc.* **1999**, *121*, 9497 – 9502; b) J. Park, Y. Morimoto, Y.-M. Lee, W. Nam, S. Fukuzumi, *J. Am. Chem. Soc.* **2011**, *133*, 5236 – 5239.

[14] a) L. E. Friedrich, *J. Org. Chem.* **1983**, *48*, 3851 – 3852; b) F. G. Bordwell, J.-P. Cheng, *J. Am. Chem. Soc.* **1991**, *113*, 1736 – 1743; c) C. V. Sastri, J. Lee, K. Oh, Y. J. Lee, J. Lee, T. A. Jackson, K, Ray, H. Hirao, W. Shin, J. A. Halfen, J. Kim, L. Que, Jr., S. Shaik, W. Nam, *Proc. Natl. Acad. Sci. USA* **2007**, *104*, 19181 – 19186; d) J. J. Warren, T. A. Tronic, J. M. Mayer, *Chem. Rev.* **2010**, *110*, 6961 – 7001; e) K. A. Prokop, S. P. de Visser, D. P. Goldberg, *Angew. Chem.* **2010**, *122*, 5217 – 5221; *Angew. Chem. Int. Ed.* **2010**, *49*, 5091 – 5095.

[15] J. R. Bryant, J. M. Mayer, *J. Am. Chem. Soc.* **2003**, *125*, 10351 – 10361.

[16] H. Tang, J. Guan, H. Liu, X. Huang, *Inorg. Chem.* **2013**, *52*, 2684 – 2696.

[17] a) H. Hirao, D. Kumar, L. Que, Jr., S. Shaik, *J. Am. Chem. Soc.* **2006**, *128*, 8590 – 8606; b) S. P. de Visser, K. Oh, A.-R. Han, W. Nam, *Inorg. Chem.* **2007**, *46*, 4632 – 4641; c) S. P. de Visser, *J. Am. Chem. Soc.* **2010**, *132*, 1087 – 1097.

[18] a) S. Aluri, S. P. de Visser, *J. Am. Chem. Soc.* **2007**, *129*, 14846 – 14847; b) D. Kumar, S. P. de Visser, P. K. Sharma, H. Hirao, S. Shaik, *Biochemistry* **2005**, *44*, 8148 – 8158; c) D. Kumar, G. N. Sastry, S. P. de Visser, *Chem. Eur. J.* **2011**, *17*, 6196 – 6205.

[19] a) S. P. de Visser, *J. Am. Chem. Soc.* **2006**, *128*, 15809 – 15818; b) C. Y. Geng, S. F. Ye, F. Neese, *Angew. Chem.* **2010**, *122*, 5853 – 5856; *Angew. Chem. Int. Ed.* **2010**, *49*, 5717 – 5720; c) S. Sahu, L. R. Widger, M. G. Quesne, S. P. de Visser, H. Matsumura, P. Moënne-Loccoz, M. A. Siegler, D. P. Goldberg, *J. Am. Chem. Soc.* **2013**, *135*, 10590 – 10593.

[20] a) R. Latifi, M. A. Sainna, E. V. Rybak-Akimova, S. P. de Visser, *Chem. Eur. J.* **2013**, *19*, 4058 – 4068; b) S. M. Pratter, C. Konstantinovics, C. L. M. DiGiuro, E. Leitner, D. Kumar, S. P. de Visser, G. Grogan, G. D. Straganz, *Angew. Chem.* **2013**, *125*, 9859 – 9863; *Angew. Chem. Int. Ed.* **2013**, *52*, 9677 – 9681.

[21] a) J. M. Mayer, *Acc. Chem. Res.* **1998**, *31*, 441 – 450; b) J. Yoon, S. A. Wilson, Y. K. Jang, M. S. Seo, K. Nehru, B. Hedman, K. O. Hodgson, E. Bill, E. I. Solomon, W. Nam, *Angew. Chem.* **2009**, *121*, 1283 – 1286; *Angew. Chem. Int. Ed.* **2009**, *48*, 1257 – 1260; c) D. E. Lansky, D. P. Goldberg, *Inorg. Chem.* **2006**, *45*, 5119 – 5125.

[22] a) S. P. de Visser, *J. Am. Chem. Soc.* **2006**, *128*, 9813 – 9824; b) D. Kumar, W. Thiel, S. P. de Visser, *J. Am. Chem. Soc.* **2011**, *133*, 3869 – 3882.

[23] A. K. Vardhaman, C. V. Sastri, D. Kumar, S. P. de Visser, *Chem. Commun.* **2011**, *47*, 11044 – 11046.

 © 2013 Wiley-VCH Verlag GmbH & Co. KGaA, Weinheim

Inorganic Chemistry

Article

pubs.acs.org/IC

Synthesis and Ligand Non-Innocence of Thiolate-Ligated (N_4S) Iron(II) and Nickel(II) Bis(imino)pyridine Complexes

Leland R. Widger,[†] Yunbo Jiang,[†] Maxime A. Siegler,[†] Devesh Kumar,[⊥] Reza Latifi,[§] Sam P. de Visser,*[,§] Guy N. L. Jameson,*[,‡] and David P. Goldberg*[,†]

[†]Department of Chemistry, The Johns Hopkins University, 3400 North Charles Street, Baltimore, Maryland 21218, United States

[‡]Department of Chemistry, and MacDiarmid Institute for Advanced Materials and Nanotechnology, University of Otago, PO Box 56, Dunedin 9054, New Zealand

[§]Manchester Institute of Biotechnology and School of Chemical Engineering and Analytical Science, The University of Manchester, 131 Princess Street, Manchester M1 7DN, United Kingdom

[⊥]Department of Applied Physics, School for Physical Sciences, Babasaheb Bhimrao Ambedkar University, Vidya Vihar, Rae Bareilly Road, Lucknow (U. P.) 226 025, India

Supporting Information

ABSTRACT: The known iron(II) complex [$Fe^{II}(LN_3S)$-(OTf)] (**1**) was used as starting material to prepare the new biomimetic (N_4S(thiolate)) iron(II) complexes [$Fe^{II}(LN_3S)$-(py)](OTf) (**2**) and [$Fe^{II}(LN_3S)$(DMAP)](OTf) (**3**), where LN_3S is a tetradentate bis(imino)pyridine (BIP) derivative with a covalently tethered phenylthiolate donor. These complexes were characterized by X-ray crystallography, ultraviolet−visible (UV-vis) spectroscopic analysis, ^{1}H nuclear magnetic resonance (NMR), and Mössbauer spectroscopy, as well as electrochemistry. A nickel(II) analogue, [$Ni^{II}(LN_3S)$](BF_4) (**5**), was also synthesized and characterized by structural and spectroscopic methods. Cyclic voltammetric studies showed **1**−**3** and **5** undergo a single reduction process with $E_{1/2}$ between −0.9 V to −1.2 V versus Fc^+/Fc. Treatment of **3** with 0.5% Na/Hg amalgam gave the monoreduced complex [$Fe(LN_3S)$(DMAP)]^0 (**4**), which was characterized by X-ray crystallography, UV-vis spectroscopic analysis, electron paramagnetic resonance (EPR) spectroscopy (g = [2.155, 2.057, 2.038]), and Mössbauer (δ = 0.33 mm s^{-1}; ΔE_Q = 2.04 mm s^{-1}) spectroscopy. Computational methods (DFT) were employed to model complexes **3**−**5**. The combined experimental and computational studies show that **1**−**3** are 5-coordinate, high-spin (S = 2) Fe^{II} complexes, whereas **4** is best described as a 5-coordinate, intermediate-spin (S = 1) Fe^{II} complex antiferromagnetically coupled to a ligand radical. This unique electronic configuration leads to an overall doublet spin (S_{total} = 1/2) ground state. Complexes **2** and **3** are shown to react with O_2 to give S-oxygenated products, as previously reported for **1**. In contrast, the monoreduced **4** appears to react with O_2 to give a mixture of sulfur oxygenates and iron oxygenates. The nickel(II) complex **5** does not react with O_2, and even when the monoreduced nickel complex is produced, it appears to undergo only outer-sphere oxidation with O_2.

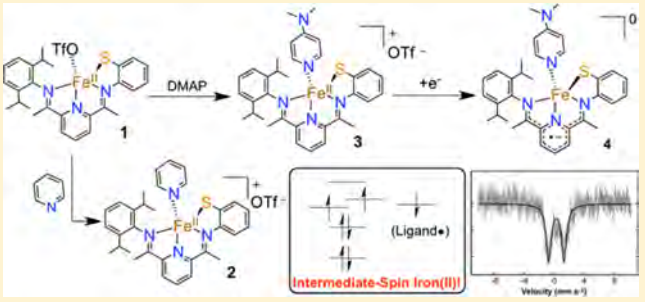

INTRODUCTION

Thiolate-ligated non-heme iron sites play key roles in biology, exhibiting diverse structural features as well as contributing to a wide range of reactivity.[1−7] The mononuclear, thiolate-ligated non-heme iron enzymes superoxide reductase,[8−12] nitrile hydratase,[13−15] and cysteine dioxygenase (CDO)[16−23] utilize single iron sites coordinated in mixed N/S ligand environments. Work by some of us has focused on the preparation of synthetic analogues of these sites, including some of the first structural and functional models of CDO.[1,24−33] A bis(imino)-pyridine (BIP) ligand scaffold was employed, leading to the synthesis of $Fe^{II}(LN_3S)$ complexes that mimicked certain structural and functional features of CDO.[24,25] The key thiolate donor was incorporated into these complexes by either covalent attachment to the BIP backbone, or by addition of an exogenous phenylthiolate (PhS^-) ligand to the iron(II) center, yielding $Fe^{II}(N_3S)$ complexes in both cases. These complexes were among the first mononuclear thiolato-iron(II) complexes to selectively react with O_2 to give S-oxygenated products, reproducing the gross reactivity of the enzymatic system. However, the Cys-bound iron(II) form of CDO contains an iron center held in an (N_4S) donor set, comprised of three His ligands and one Cys substrate chelated through both the amino and side-chain S groups. Thus, we are currently interested in the design and synthesis of $Fe^{II}(N_4S)$ complexes in which a fourth neutral N donor is included in the first coordination

Received: May 29, 2013
Published: August 30, 2013

 © 2013 American Chemical Society dx.doi.org/10.1021/ic4013558 | Inorg. Chem. 2013, 52, 10467−10480

sphere to more closely match the active site of CDO prior to S-oxygenation.

Herein, we describe the synthesis, spectroscopic characterization and O_2 reactivity of a new series of $Fe^{II}(N_4S)$ complexes (Figure 1) that contain a covalently linked, BIP-derived ligand

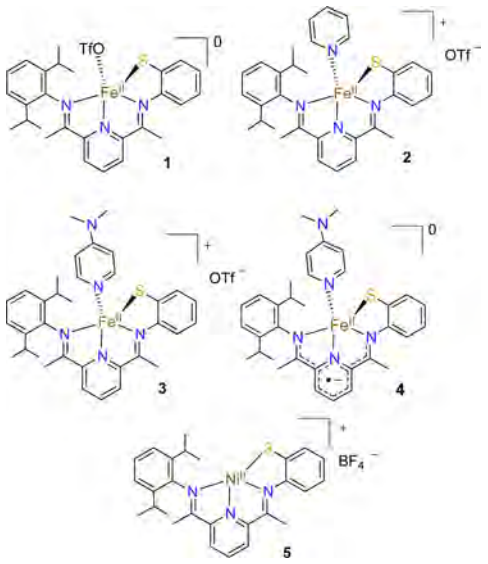

Figure 1. Complexes described in the present study.

providing an N_3S(thiolate) donor set (LN_3S^-), and a fourth N donor derived from exogenous pyridine derivatives. The general synthetic strategy was to incorporate a fourth N donor without the need for covalent modification of the BIP backbone. This strategy proved productive, and the new iron(II) complexes $[Fe^{II}(LN_3S)(py)](OTf)$ (**2**) and $[Fe^{II}(LN_3S)(DMAP)](OTf)$ (**3**) were synthesized and characterized by X-ray crystallography, NMR, electrochemistry, Mössbauer spectroscopy and density functional theory (DFT) calculations. A nickel(II) analogue, $[Ni^{II}(LN_3S)](BF_4)$ (**5**), was also prepared for comparative spectroscopic and reactivity studies.

The BIP platform is also well-known to behave as a non-innocent ligand, allowing for the storage of multiple reducing equivalents on the ligand backbone. The BIP framework has been shown to accept up to three electrons, which are stabilized by delocalization over the conjugated ligand scaffold.[34−45] However, the reduced analogues of these BIP complexes are generally restricted to derivatives in which only minor changes to the aryl substitution patterns on the imino positions have been made, with no major modification of the chelating abilities of the BIP framework. There is significant interest in the development of non-innocent, polydentate ligands for their use as redox-active partners in combination with metal ions to assist with various chemical transformations such as the reduction of small-molecules (e.g., CO_2, N_2) and other redox reactions. With the thiolate-modified LN_3S system in hand, we thus wanted to determine if it could also function as a non-innocent ligand, perhaps stabilizing one or more reducing equivalents across the ligand backbone. A question to be addressed concerns the influence of the additional, covalently linked phenylthiolate arm on the stability, spin delocalization, and spectroscopic and redox properties of possible (multi)reduced ligand−metal complexes. It is also of interest to determine if multiple reducing equivalents stored on both the ligand and the metal can be employed together for the activation of O_2, and how this combination will affect subsequent sulfur- or metal-based oxygenation steps.

The new complexes $[Fe^{II}(LN_3S)(py)]OTf$ (**2**), $[Fe^{II}(LN_3S)(DMAP)]OTf$ (**3**) and $[Ni^{II}(LN_3S)]BF_4$ (**5**) were shown to accept a single electron to give the respective monoreduced products. In one case, successful crystallization of the monoreduced species was achieved, and the structure of $[Fe(LN_3S)(DMAP)]^0$ (**4**) was obtained by X-ray crystallography. A detailed experimental and computational (DFT) investigation into the electronic and structural properties of **4**, as well as the other monoreduced analogues, was conducted, revealing several insights regarding the interplay between the structures and the electronic configurations of these complexes. The influence of the strong field thiolate donor, the extent of non-innocence in the BIP ligand, and the oxidation and spin state of the metal center are addressed. A major finding from these studies is that complex **4**, based on experimental and computational results, is a monoreduced bis(imino)pyridine complex with an intermediate-spin iron(II) center coupled with a stable ligand-based radical.

The O_2 reactivity of these complexes was also examined, and for the starting iron(II) complexes **2** and **3**, selective S-oxygenation to give sulfonato (RSO_3^-) products was observed, as seen previously for $[Fe^{II}(LN_3S)(OTf)]$ (**1**).[24] In contrast, the monoreduced complex **4** reacts with O_2, leading to a mixture of products that suggest both iron oxygenation and sulfur oxygenation readily occur for this monoreduced species. However, both the Ni^{II} complex **5**, and its monoreduced analog, do not exhibit any sulfur-based or metal-based oxygenation in the presence of O_2, even after prolonged reaction times. This lack of reactivity is in contrast to the iron analogues, as well as some nickel-thiolate complexes that do react with O_2 to give sulfur-oxygenated sulfinato and sulfonato products, although these reactions can be sluggish.[46−54]

EXPERIMENTAL SECTION

General Procedures. All reagents were purchased from commercial vendors and used without further purification, unless noted otherwise. All reactions were carried out under an atmosphere of N_2 inside a glovebox or under an argon atmosphere by standard Schlenk and vacuum line techniques. Ultraviolet−visible (UV-vis) spectra were recorded on an Agilent 8453 photodiode array spectrophotometer. Electron paramagnetic resonance (EPR) spectra were obtained on a Bruker EMX EPR spectrometer that was controlled using a Bruker ER 041 X G microwave bridge at 15 K. The EPR spectrometer was equipped with a continuous-flow liquid helium cryostat and an ITC503 temperature controller made by Oxford Instruments, Inc. Nuclear magnetic resonance (NMR) was performed on a Bruker Avance 400 MHz FT-NMR spectrometer at 25 °C. Elemental analysis was performed by Atlantic Microlab, Inc. (Norcross, GA). LDI-ToF mass spectra were obtained using a Bruker Autoflex III Maldi ToF/ToF instrument (Billerica, MA). Samples were dissolved in CH_2Cl_2 and deposited on the target plate in the absence of any added matrix. Samples were irradiated with a 355-nm UV laser and mass-analyzed by ToF mass spectrometry in reflectron mode. $Fe^{II}(LN_3S)(OTf)$ (**1**) was prepared according to a literature procedure.[24] ^{57}Fe Mössbauer spectra were recorded on a Mössbauer spectrometer from SEE Co. (Science Engineering & Education Co., Edina, MN) equipped with a closed-cycle refrigerator system from Janis Research Co. and Sumitomo Heavy Industries, Ltd. (SHI)). Approximately 10 mg of sample was placed in a custom sample holder made from Teflon and specifically designed for solid samples. Data were collected in constant acceleration mode in transmission geometry with an applied field of 47 mT parallel to the γ-rays. The zero velocity of the Mössbauer spectra refers to the centroid of the room

dx.doi.org/10.1021/ic4013558 | Inorg. Chem. 2013, 52, 10467−10480

temperature spectrum of a 25 μm metallic iron foil. Analysis of the spectra was conducted using the WMOSS program (SEE Co., formerly WEB Research Co., Edina, MN).

Computational Methods. Density functional theory calculations were performed on complexes **3**–**5**, using methods and procedures that we have tested and calibrated previously.[55,56] The complexes were calculated in several possible spin states. The spin state ordering of transition-metal complexes can be dependent on the density functional theory (DFT) functional chosen, and thus we tested several different methods for our calculations. In an initial set of calculations, the unrestricted hybrid density functional method B3LYP was used in combination with an LACVP basis set on the metal and 6-31G on the rest of the atoms (referenced as basis set B1) for geometry optimizations and frequencies.[57−59] Optimized structures were employed as the starting point for single-point calculations using (a) the LACV3P+ basis set on the metal and 6-311+G* on the rest of the atoms; (b) the M06/B1 method;[60] and (c) B3LYP/B1 with the polarized continuum model with a dielectric constant of ε = 5.7. In a second set of calculations, we used the unrestricted BP86 density functional method[61,62] in combination with an LACV3P+ basis set on the metal and 6-311+G* on the rest of the atoms (referenced as basis set B2). Full geometry optimizations were run with the Jaguar 7.6 program, followed by a frequency calculation using these methods.[63] Single-point calculations with dispersion-corrected DFT were performed as proposed by Schwabe and Grimme;[64] however, this had a negligible effect on the spin state ordering and relative energies.

Synthesis of [Fe^{II}(LN$_3$S)(py)]OTf (2). Crystalline [Fe^{II}(LN$_3$S)(OTf)] (**1**) (100 mg, 0.16 mmol) was dissolved in CH_2Cl_2 and pyridine (15 μL, 0.19 mmol) was added. After stirring for 2 h, the solution was filtered through Celite. Slow vapor diffusion of diethyl ether or layering with pentane gave the desired product as dark brown plates suitable for X-ray diffraction (XRD) analysis in 97% yield (110 mg). ^{1}H NMR (CD_2Cl_2): δ 107.0, 95.4, 91.6, 45.2, 13.1, 11.6, 3.1, 1.3, −4.1, −10.3, −16.2, −30.4. LDI-MS (+): m/z 484.2 ([**2**−py−OTf]$^+$). Anal. Calc. for Fe^{II}(LN$_3$S)(py)(OTf)·CH_2Cl_2 ($C_{34}H_{37}Cl_2F_3FeN_4O_3S_2$): C, 51.20; H, 4.68; N, 7.02. Found: C, 51.21; H, 4.88; N, 7.67.

Synthesis of [Fe^{II}(LN$_3$S)(DMAP)]OTf (3). Crystalline [Fe^{II}(LN$_3$S)(OTf)] (**1**) (110 mg, 0.17 mmol) was dissolved in CH_2Cl_2 and DMAP (25 mg, 0.21 mmol) was added. After stirring for 2 h, the solution was filtered through Celite. Slow vapor diffusion of diethyl ether or layering with pentane gave **3** as black plates suitable for XRD analysis in 95% yield (125 mg). ^{1}H NMR (CD_2Cl_2): δ 128.0, 102.4, 92.8, 37.6, 19.4, 10.4, 8.4, 3.1, 1.4, −4.9, −7.7, −10.4, −13.7, −22.8. LDI-MS (+): m/z 484.2 ([**3**−DMAP−OTf]). Anal. Calc. for Fe^{II}(LN$_3$S)(DMAP)(OTf) ($C_{35}H_{40}F_3FeN_5O_3S_2$): C, 55.63; H, 5.34; N, 9.27. Found: C, 55.37; H, 5.29; N, 9.07.

Synthesis of [Fe^{II}(LN$_3$S)(DMAP)]·2Et$_2$O (4·2Et$_2$O). Crystalline [Fe^{II}(LN$_3$S)(DMAP)](OTf) (**3**) (125 mg, 0.17 mmol) was combined with 1.5 equiv of 0.5% Na/Hg amalgam (6.0 mg Na^0, 1.15 g Hg) and suspended in 5 mL of Et_2O. Upon stirring, the insoluble starting material (**3**) slowly dissolves into solution as it reacts, giving a dark green/brown solution. After stirring for 2 h, the reaction mixture was filtered through Celite, layered with pentane, and placed in the freezer for several days, giving **4·2Et$_2$O** as dark brown crystals suitable for XRD in 37% yield (38 mg). UV-vis (THF) (nm): 566, 625, 785 (ε = 890 M^{-1} cm^{-1}). ^{1}H NMR (THF-d_8): δ 95.7, 33.8, 24.7, 5.8. EPR: g = 2.155, 2.057, 2.038. Mössbauer: $\Gamma_{L=R}$ = 0.8 mm s^{-1}, δ = 0.33 mm s^{-1}, ΔE_Q = 2.04 mm s^{-1}. Anal. Calc. for [**4** + Et_2O + 0.25 NaOTf] ($C_{38.25}H_{50}F_{0.75}FeN_5Na_{0.25}O_{1.75}S_{1.25}$): C, 63.48; H, 6.96; N, 9.68. Found: C, 62.85; H, 6.74; N, 9.73. Crystalline samples of **4·2Et$_2$O** coprecipitate with a small amount of white solid impurity that could not be separated from **4·2Et$_2$O**. The impurity was identified as NaOTf by ^{19}F NMR (see Figure S2). Inclusion of 0.25 equiv of NaOTf was necessary to obtain a good fit for elemental analysis.

Synthesis of [Ni^{II}(LN$_3$S)]BF$_4$ (5). An amount of 2-(O=CMe)-6-(2,6-(^{i}Pr$_2$−C_6H_3N=CMe)-C_5H_3N (50 mg, 0.155 mmol) and Ni^{II}(BF$_4$)$_2$·6H_2O (55 mg, 0.163 mmol) was suspended in EtOH (5 mL) and heated at 80 °C for 30 min. The solids slowly dissolved to give a deep green solution, and then a solution of 2-aminothiophenol (17 μL, 0.155 mmol) and triethylamine (22 μL, 0.155 mmol) in EtOH (1 mL) was added to the reaction mixture. The reaction was allowed to stir at 80 °C for 24 h before being cooled to room temperature and concentrated. The resulting solid residue was brought into a glovebox where it was redissolved in a minimum amount of CH_2Cl_2 and filtered through Celite. Slow vapor diffusion of diethyl ether into the filtrate yielded 96 mg (94% yield) of **5** as dark red crystals suitable for X-ray analysis, together with colorless crystals of $Et_3NH·BF_4$. Samples for elemental analysis were prepared by manual separation of crystals of **5** from the colorless $Et_3NH·BF_4$ crystals. ^{1}H NMR (CD_2Cl_2): δ 8.30 (br, 1H), 7.89 (br, 2H), 7.35 (t, 1H), 7.22 (d, 2H), 7.09 (d, 1H), 6.92 (t, 1H), 6.82−6.72 (m, 2H), 3.18 (br), 2.69 (s, 3H), 2.14 (s, 3H), 1.50 (d, 6H), 1.33 (br), (1.17 (d, 6H). LDI-MS (+): m/z 488.3 [**5**-BF$_4$]$^+$. Anal. Calc. for [Ni^{II}(LN$_3$S)](BF$_4$)·CH_2Cl_2 ($C_{28}H_{32}BCl_2F_4N_3NiS$): Predicted: C, 51.03; H, 4.89; N, 6.38. Found: C, 51.28; H 4.76; N, 6.66.

O_2 Reactivity. Reactions of **2**, **3**, and **5** with excess O_2 were conducted as previously reported for **1** in CH_2Cl_2.[24] The one-electron-reduced complexes were reacted with O_2 by freshly preparing solutions of **4** or reduced **5** via Na/Hg amalgam in Et_2O, followed by filtration through Celite, as described for the synthesis of **4**. Reaction mixtures following O_2 addition were then analyzed directly by LDI-MS.

RESULTS AND DISCUSSION

Synthesis of Iron(II) and Nickel(II) Complexes. The synthesis of the unsymmetrical, thiolate-ligated complex [Fe^{II}(LN$_3$S)(OTf)] (**1**) was accomplished by reacting the imino-ketone precursor[65] 2-(O=CMe)-6-(2,6-(^{i}Pr$_2$−C_6H_3N=CMe)-C_5H_3N with the commercially available 2-aminothiophenol and Fe(OTf)$_2$ in a metal-assisted template reaction as previously described.[24] We sought to determine if this complex could be used as a precursor to generate Fe^{II} complexes with biologically relevant [N_4S] donor sets via substitution at the OTf$^-$ position. Displacement of the OTf$^-$ ligand in **1** was an attractive route when compared to the more challenging strategy involving multistep organic synthesis to produce covalently linked N_4S-donating ligands.[26,66−68] The addition of 1 equiv of either pyridine or *N*,*N*′-dimethylaminopyridine (DMAP) to dark red-purple **1** in CH_2Cl_2 at room temperature does not result in any color change. However, vapor diffusion of diethyl ether into the reaction mixture after stirring for 2 h afforded single crystals as dark brown plates of the pyridine-ligated [Fe^{II}(LN$_3$S)(py)](OTf) (**2**), and black plates in the case of the DMAP-ligated [Fe^{II}(LN$_3$S)(DMAP)](OTf) (**3**). These crystals yielded the X-ray structures of **2** and **3** (Figures 2 and 3, vide infra), confirming that the OTf$^-$ anion was displaced by the pyridine derivatives. For large-scale preparations of **2** and **3**, layering of pentane was used in place of vapor diffusion of Et_2O to give both **2** and **3** in high yield.

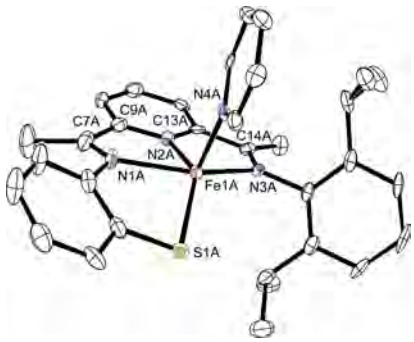

Figure 2. Displacement ellipsoid plot for the cation of complex **2** (50% probablility level). The H atoms are removed for clarity.

dx.doi.org/10.1021/ic4013558 | Inorg. Chem. 2013, 52, 10467−10480

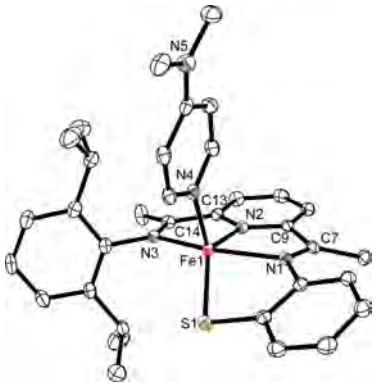

Figure 3. Displacement ellipsoid plot for the cation of complex **3** (50% probablility level). The H atoms are removed for clarity.

The synthesis of the Ni^{II} analogue of **1** was also targeted for comparison of spectroscopic features and its reactivity toward O_2. The use of $Ni^{II}(BF_4)_2$ in place of $Fe^{II}(OTf)_2$ in Scheme 1 results in a dark green solution. Vapor diffusion of Et_2O afforded dark red crystals, together with clusters of large colorless needles. The red crystals were separated by hand and analyzed by X-ray crystallography, revealing the Ni^{II} complex $[Ni^{II}(LN_3S)](BF_4)$ (**5**). The colorless crystals were presumed to be $Et_3NH^+BF_4^-$, the expected byproduct of the template reaction. Peaks corresponding to $Et_3NH^+BF_4^-$ were confirmed in the ^1H NMR of **5**. The coprecipitation of $Et_3NH^+BF_4^-$ could not be avoided even upon successive recrystallizations; therefore, it was necessary to isolate complex **5** by manual separation of crystalline material for elemental analysis and further reactivity studies.

X-ray Structures of the Iron(II) and Nickel(II) Complexes. The X-ray structures for the iron(II) complexes $[Fe^{II}(LN_3S)(py)](OTf)$ (**2**) and $[Fe^{II}(LN_3S)(DMAP)](OTf)$ (**3**) are shown in Figures 2 and 3. Selected bond distances and angles are given in Tables 1 and 2. The structures reveal that the triflate ligand has been displaced in each case by the heterocyclic N donor to afford the 5-coordinate $Fe^{II}(N_4S$-(thiolate)) products. There is a clear preference for forming the 5-coordinate complexes over the 6-coordinate species, in which the OTf^- would be retained in the first coordination sphere. The Fe−N distances of 2.073(5)−2.196(5) Å for **2** and 2.0667(14)−2.2179(15) Å for **3** are indicative of high-spin (S = 2) Fe^{II} complexes. The pyridine-derived Fe−N bonds are shorter than the imine N−Fe distances in both **2** and **3**, whereas the Fe−S bonds are nearly identical. There is minimal effect of substitution of the *para* position of the pyridine derivatives on the bond lengths in **2** and **3**. An analysis of the bond angles for **2** and **3** and their τ values (τ = 0.15 for **2**, and τ = 0.18 for **3**; where τ = 0 for square pyramidal and τ = 1 for trigonal bipyramidal)[69] show that, in both cases, the Fe^{II} ions are held in a distorted square pyramidal geometry, with the pyridine derivatives occupying the axial position. The molecular structure of **1** has been reported,[24] and selected bond distances are reproduced in Table 1. The Fe−N distances are very similar to those found in **2** and **3**, whereas the Fe−S distance appears slightly shorter. Complex **1** exhibits a more idealized square pyramidal geometry than **2** or **3**, with τ = 0.12, and a comparison of the τ values for **1**−**3** reveals that the geometry becomes more distorted from square pyramidal with increasing axial ligand donor strength ($\tau_{(OTf)}$ = 0.12 < $\tau_{(py)}$ = 0.15 < $\tau_{(DMAP)}$ = 0.18). In all three complexes **1**−**3**, the pyridine diimine backbone remains planar, while the ferrous ion sits 0.276 Å above the N_3 plane for **1**, but less out of plane for **2** (0.116 Å) and **3** (0.200 Å). In addition, the thiolate donor never sits in the ideal equatorial position, but rather lies well below the N_3 plane. For **1** and **2**, the N_{plane}−S distances are 0.824 and 1.18 Å, respectively, while for **3**, it is significantly more distorted with $d(N_{plane}-S)$ = 1.8 Å. The C_{imine}−N and $C_{imine}-C_{ipso}$ bond distances for the ligand are similar for complexes **1**−**3** (Table 1), and are consistent with a neutral-ligand bis(imino)pyridine backbone (LN_3S^-).[34,43]

The X-ray structure for the Ni^{II} complex $[Ni^{II}(LN_3S)](BF_4)$ (**5**) is shown in Figure 4. Selected bond distances and angles for **5** are given in Table 3. The molecular structure of **5** shows a square planar geometry for the Ni^{II} ion. The observed Ni−N distances are 1.8151(14)−1.9159(15) Å, and are somewhat shorter (∼0.1−0.4 Å) than other BIP-derived nickel(II) complexes.[45,70−73] The Ni−S distance of 2.1386(5) Å is significantly shorter than the Fe^{II}−S distances seen for **1**−**3**, as are the Ni−N distances. The bond angles about the Ni^{II} center deviate slightly from the idealized square-planar geometry (82.44°−102.37°), likely due to the constraints imposed by the three 5-membered chelate rings. The Ni^{II} ion and S atom sit directly in the plane of the bis(imino)pyridine ligand as seen by Ni−N_3(plane) and S−N_3(plane) distances of 0.030 Å and 0.082 Å, respectively. This structure contrasts those found for **1**−**3**, where both the metal ion and sulfur donor lie significantly

Scheme 1. Synthesis of Iron(II) Complexes (1−3), and Nickel(II) Complex (5)

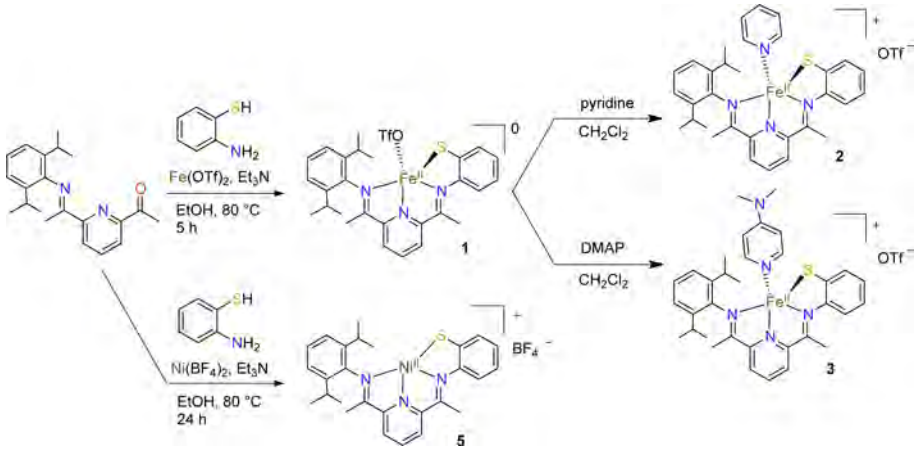

dx.doi.org/10.1021/ic4013558 | *Inorg. Chem.* 2013, 52, 10467−10480

Table 1. Selected Bond Distances for $[Fe(LN_3S)]^{n+}$ Complexes[a]

	Bond Distances (Å)			
	$[Fe^{II}(LN_3S)(OTf)]$[a]	$[Fe^{II}(LN_3S)(py)]OTf$	$[Fe^{II}(LN_3S)(DMAP)]OTf$	$[Fe^{II}(LN_3S)(DMAP)]^0$
Fe1−N1	2.188(2)	2.173(5)	2.1859(15)	1.9255(15)
Fe1−N2	2.072(2)	2.090(5)	2.0960(14)	1.8278(15)
Fe1−N3	2.184(2)	2.196(5)	2.2179(15)	1.9179(16)
Fe1−N4	N/A	2.073(5)	2.0667(14)	2.0508(16)
Fe1−S1	2.2942(8)	2.3246(18)	2.3295(5)	2.2179(5)
Fe−O1	2.0870(18)	N/A	N/A	N/A
N1−C7 (imine)	1.293(3)	1.298(8)	1.292(2)	1.347(2)
C7(imine)− C9(ipso)	1.480(4)	1.485(9)	1.486(2)	1.432(3)
C9(ipso)−N2(pyr)	1.343(3)	1.342(8)	1.341(2)	1.376(2)
N3−C14(imine)	1.284(3)	1.275(7)	1.290(2)	1.341(2)
C14(imine)−C13(ipso)	1.483(4)	1.494(8)	1.487(3)	1.426(3)
C13(ipso)−N2(pyr)	1.334(3)	1.334(8)	1.343(2)	1.381(2)

[a]Data taken from ref 24.

Table 2. Selected Bond Angles for $[Fe(LN_3S)]^{n+}$ Complexes

	Bond Angles (deg)		
	$[Fe^{II}(LN_3S)(py)]OTf$	$[Fe^{II}(LN_3S)(DMAP)]OTf$	$[Fe^{II}(LN_3S)(DMAP)]^0$
N4−Fe1−N2	109.79(19)	112.91(6)	99.92(6)
N4−Fe1−N1	95.3(2)	99.69(6)	95.84(6)
N2−Fe1−N1	74.0(2)	73.08(5)	81.26(7)
N4−Fe1−N3	99.29(19)	99.82(6)	99.88(6)
N2−Fe1−N3	73.4(2)	73.94(6)	80.65(7)
N1−Fe1−N3	147.24(19)	146.17(5)	157.78(7)
N4−Fe1−S1	106.05(15)	107.20(4)	105.25(5)
N2−Fe1−S1	138.08(14)	135.18(4)	153.58(5)
N1−Fe1−S1	81.79(15)	81.40(4)	88.27(5)
N3−Fe1−S1	121.28(13)	118.28(4)	102.49(5)

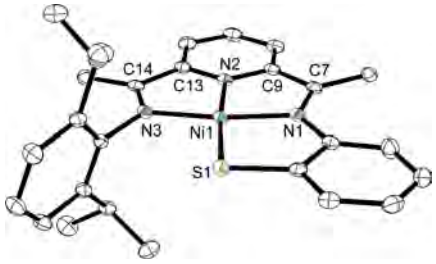

Figure 4. Displacement ellipsoid plot for the cation of complex **5** (50% probablility level). The H atoms are removed for clarity.

Table 3. Selected Bond Distances and Angles for Complex 5

Bond Distances (Å)	
Ni1−N1	1.8981(15)
Ni1−N2	1.8151(14)
Ni1−N3	1.9159(15)
Ni1−S1	2.1386(5)
N1−C7 (imine)	1.312(2)
C7(imine)−C9(ipso)	1.480(2)
C9(ipso)−N2(pyr)	1.341(2)
N3−C14(imine)	1.299(2)
C14(imine)−C13(ipso)	1.480(2)
C13(ipso)−N2(pyr)	1.338(2)
Bond Angles (deg)	
N2−Ni1−N1	83.56(6)
N2−Ni1−N3	82.44(6)
N1−Ni1−N3	165.91(6)
N2−Ni1−S1	175.17(5)
N1−Ni1−S1	91.64(5)
N3−Ni1−S1	102.37(5)

out of the bis(imino)pyridine plane for these 5-coordinate complexes.

NMR Spectroscopy. The paramagnetic ^{1}H NMR spectra for complexes **1**−**3** in CD_2Cl_2 are shown in Figure 5. Each complex exhibits sharp, paramagnetically shifted peaks over a broad range (from 130 ppm to −30 ppm), indicative of high-spin (S = 2) Fe^{II} complexes. Detailed ^{1}H NMR assignments have been made for bis(imino)pyridine iron(II) complexes that carry the same aryl imino substituents.[34,65,74,75] These data can be used as a guide for interpreting the spectra for **1**−**3**, although the unsymmetrical structures of **1**−**3** make their ^{1}H NMR patterns difficult to definitively assign. For all three complexes, the downfield region (130−80 ppm) contains three sharp peaks, with the exception of **3**, in which the most downfield resonance at 130 ppm is significantly broadened. In comparison to symmetrical (BIP)FeX_2 complexes, two of the three resonances in this region can be assigned to the *meta* and *para* pyridyl backbone protons, with the most intense resonance (82.8, 95.4, and 92.8 ppm for **1**−**3**, respectively) likely arising from the *meta* protons that are apparently not split in the local symmetry. We tentatively assign the third resonance to a proton on the phenylthiolate ring. No peaks appear in the spectrum for **1** between 80 ppm and 20 ppm, whereas complex **2** shows a broad peak at 45.2 ppm and complex **3** exhibits a sharp peak at 37.6 ppm and a broad feature at 43.5 ppm. The latter peaks for **2** and **3** can be assigned to the axial pyridine ligands, which are absent in **1**. This assignment was confirmed by the generation in situ of **2** with the addition of 1 equiv of pyridine-d_5 to **1**. As seen in Figure 5, the spectrum for deuterated **2**-d_5 is a good match for **2**, except for the disappearance of the resonance at 45.2 ppm. The broadness of the py peak and the absence of distinct signals for the *ortho*, *meta*, and *para* protons suggest that the py ligand in **2** is labile on the NMR time scale. In contrast, two peaks are observed for **3** in the region of the axial DMAP donor, and one is relatively sharp, suggesting that DMAP is significantly less labile than py; this observation is consistent with it being a more strongly donating py derivative. Further upfield, the diisopropyl methyl groups can easily be assigned to the intense singlets between 1.20 ppm and 1.36 ppm for **1**−**3**, and the peaks found from −14 ppm to −16 ppm are assigned to the *para* C−H on the

dx.doi.org/10.1021/ic4013558 | Inorg. Chem. 2013, 52, 10467−10480

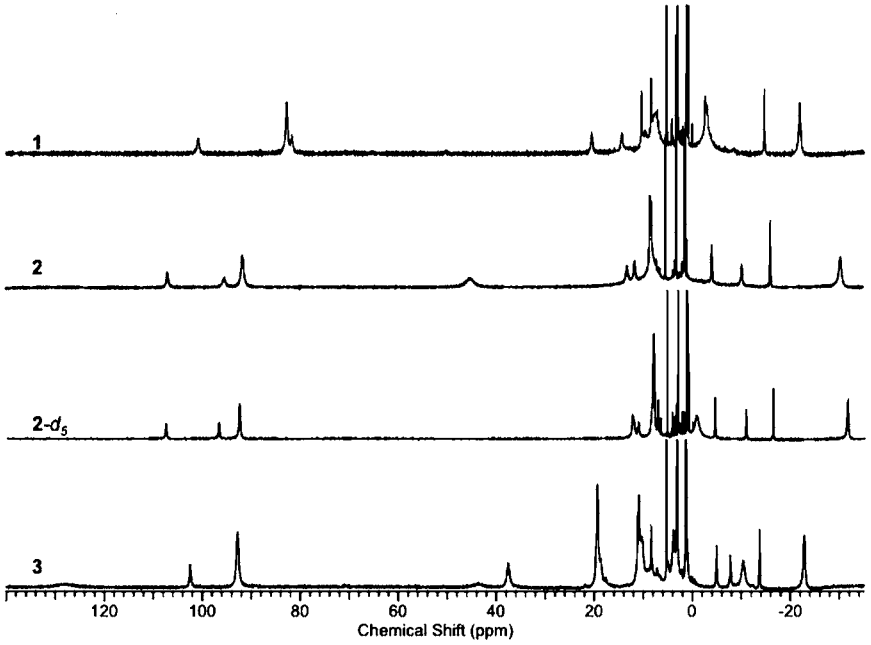

Figure 5. ^{1}H NMR spectra of complexes **1**−**3** in CD_2Cl_2 at 25 °C.

iPr$_2$Ph substituent based on earlier work.[34,65,74,75] The upfield resonances at −21.9, −30.3, and −22.8 ppm for **1**, **2**, and **3**, respectively, likely arise from the isopropyl methine protons.

The ^{1}H NMR spectrum of the diamagnetic Ni(II) complex **5** is shown in Figure 6. The peaks for the pyridyl protons are seen

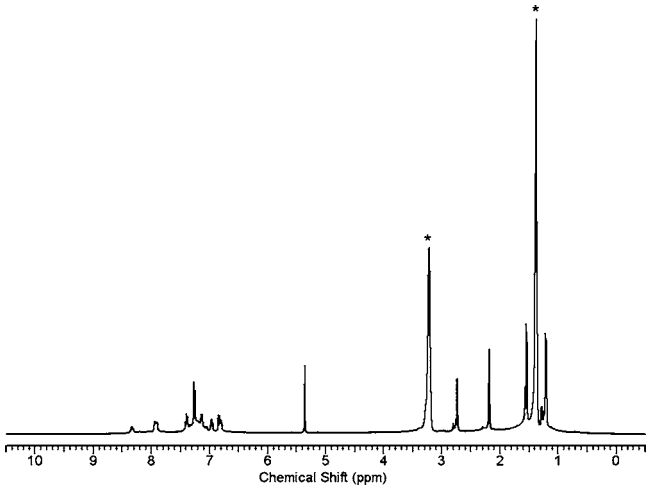

Figure 6. ^{1}H NMR spectrum of **5** in CD_2Cl_2 at 25 °C. The $Et_3NH^+BF_4^-$ impurity signal is denoted by an asterisk (*).

at δ 8.30 and 7.88, and the diisopropylphenyl peaks are assigned to δ 7.35 (t, 1H) and 7.22 (d, 2H). Other peaks in the aromatic region include δ 7.09 (d, 1H), 6.92 (t, 1H), and overlapping peaks at 6.79 (d, 1H) and 6.75 (t, 1H), which can be attributed to the phenylthiolate ring. The peaks found at 3.18 and 1.33 ppm come from a small amount of $Et_3NH^+BF_4^-$ impurity (vide supra), and the peak at 3.18 ppm likely masks the isopropyl methine C−H peaks for **5**. The ketimine CH_3 resonances are located at δ 2.70 (s, 3H) and 2.14 (s, 3H). There are two distinct isopropyl CH_3 peaks found at δ 1.50 (d, 6H) and 1.17 (d, 6H), indicating restricted rotation of the diisopropylphenyl substituent about the N_{imino}−C_{ipso} bond.

Electrochemistry. Cyclic voltammetry of the iron(II) and nickel(II) complexes was measured to gain insights regarding the influence of the exogenous py derivatives and covalently tethered phenylthiolato donor on the redox properties of these complexes. The cyclic voltammograms for compounds **1**, **2**, **3**, and **5** are shown in Figure 7. The triflate complex **1** and the

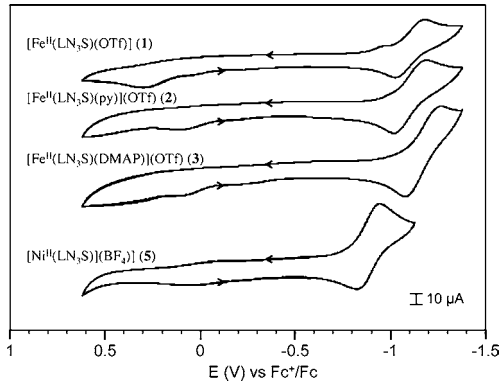

Figure 7. Cyclic voltammograms of compounds **1**−**3** and **5** in MeCN. $E_{1/2}$: **1** = −1.1 V, **2** = −1.1 V, **3** = −1.2 V, and **5** = −0.9 V; ΔE_p: **1** = 120 mV, **2** = 130 mV, **3** = 130 mV, and **5** = 66 mV. Working electrode, glassy carbon; counter electrode, platinum; and reference electrode, Ag/Ag^+. Electrolyte: $LiClO_4$, 100 mM. Scan rate = 100 mV/s.

pyridine complex **2** exhibit quasireversible waves at $E_{1/2}$ = −1.1 V, while the DMAP complex **3** reveals a more negative $E_{1/2}$ value (−1.2 V). No other obvious redox processes for these complexes are present within the solvent window for CH_3CN. The fact that the $E_{1/2}$ values for **1** and **2** are the same suggests that the axial pyridine donor in **2** does not exhibit any influence on the redox potential, but is also consistent with the pyridine ligand dissociating to some extent in solution, as indicated by the NMR data. Substitution of py for DMAP does have a clear impact, shifting the redox potential by ∼100 mV more negative in **3**, compared to **2**. This result is consistent with DMAP being a more strongly donating ligand than unsubstituted pyridine.

dx.doi.org/10.1021/ic4013558 | Inorg. Chem. 2013, 52, 10467−10480

Scheme 2. Reduction of Thiolate-Ligated M^{II} Bis(imino)pyridine Complexes

The nickel(II) complex is the easiest to reduce in the series, with $E_{1/2}$ = −0.9 V.

Non-innocent BIP ligands have been shown previously to undergo up to three sequential reductions in which the electrons are delocalized over the BIP backbone.[34−45] The negative $E_{1/2}$ values for **1**−**3** are consistent with ligand-based reduction, and covalent attachment of the phenylthiolate group exerts a strong influence on the redox properties, in comparison to other BIP complexes.[25] The non-thiolate-ligated BIP complexes typically show two reversible reduction waves, whereas **1**−**3** exhibit only one reduction process, suggesting that the next reduction for **1**−**3**, if it exists, lies outside the solvent window. Similarly, the nickel(II) analogue **5** exhibits only one redox process at −0.9 V, which is within the range of ligand-based reductions for the iron complexes, but is more positive by ≥200 mV. These data show that the BIP-derived ligand of the Ni^{II} complex **5** is significantly easier to reduce than **1**−**3**.

One-Electron Reduction of the Iron(II) and Nickel(II) Complexes. A summary of the possible redox transformations for the phenylthiolate-appended $[M(LN_3S)(L)]^+$ complexes are shown in Scheme 2. The CV data for **1**−**3** and **5** each show well-separated, quasi-reversible reduction waves, indicating that one-electron-reduced complexes should be synthetically accessible. The lack of a second reduction process suggests that the one-electron-reduced complexes can be isolated without the complication of forming two-electron-reduced species, in contrast to other BIP complexes.[39] Several methods have been employed to reduce M^{n+}(BIP) complexes, including treatment with aluminum/lithium alkyl reagents, $NaBEt_3H$, KC_8, and Na/Hg amalgam.[35,70,76,77] The latter method was a convenient choice for the controlled reduction of the thiolate-ligated complexes described here.

Reduction of the DMAP complex **3** was accomplished by stirring a suspension of **3** in Et_2O over a slight excess of 0.5% Na/Hg amalgam, affording the one-electron-reduced $[Fe(LN_3S)(DMAP)]^0$ (**4**), as shown in Scheme 3. The progress

Scheme 3. Synthesis of the Monoreduced Complex $[Fe(LN_3S)(DMAP)]^0$ (4)

of the reaction is easily followed by the colorless ethereal suspension of **3** converting to a deep green, homogeneous solution. The UV-vis spectrum following the Na/Hg reduction is shown in Figure 8, where the solvent is THF instead of Et_2O to maintain the solubility of **3**. Distinct features appear at 566, 625, and 785 nm that are indicative of **4**. It should be noted that solutions of **4** in either THF or Et_2O are extremely air-sensitive,

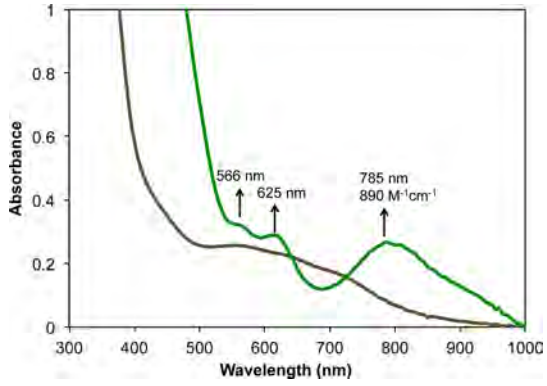

Figure 8. UV-vis spectral change for the conversion of **3** (brown trace) to **4** (green trace) with 0.5% Na/Hg amalgam in tetrahydrofuran (THF).

and will decompose upon prolonged standing, even at −35 °C in a drybox freezer, as seen by spontaneous conversion of dark green solutions of **4** to a brown precipitate. Crystals for XRD can be grown from layering of pentane into Et_2O at −35 °C, but the crystals must be obtained within 48 h or decomposition occurs and no crystalline product will form. Crystalline **4** is also difficult to isolate outside of the mother liquor without further decomposition. Attempts to scale up the reaction failed to give crystalline product: instead, it led to more-rapid decomposition.

Many reduced Fe(BIP) complexes have been reported, most involving doubly reduced species relative to the M^{II} complexes analogous to **1**−**3**. However, a few examples of monoreduced and triply reduced Fe(BIP) complexes have been described.[37−39] The monoreduced Fe(BIP) complexes were prepared by either reduction of iron(II) starting materials (e.g., $[(^{iPr}BIP)Fe^{II}Cl_2] + e^- \rightarrow [(^{iPr}BIP)FeCl]^0$), or oxidation of doubly reduced (formally Fe^0) Fe(BIP) complexes (e.g., $[(^{iPr}BIP)Fe(N_2)]^0 \rightarrow [(^{iPr}BIP)Fe(OEt_2)]^+ + e^-$) and, in both cases, yield 4-coordinate iron complexes.[37−39] The 5-coordinate complexes $[(^{iPr}BIP)Fe(Br)(THF)]$ and $[(^{iPr}BIP)Fe(CO)_2]^+$, were prepared via one-electron oxidation of their respective doubly reduced precursors, while $[(^{Et}BIP)Fe(Cl)(Et_2O)]$ was prepared by reduction of the starting material.[37,40,78] However, the doubly reduced species generally are more easily obtained than the monoreduced analogs, and careful stoichiometric control must be used to synthesize monoreduced complexes. In contrast, the putative doubly reduced analog of **3** is not accessible as seen by electrochemistry, and thus reduction of **3** leads to the selective isolation of a rare 5-coordinate, monoreduced complex.

Attempted reductions of the iron(II) complexes **1** and **2** suspended in Et_2O led to deep green solutions similar to those seen for **4**, but the products were highly soluble, even in mixtures with pentane, and crystals could not be isolated. The nickel(II) complex **5**, which is insoluble in Et_2O, reacts similarly with Na/Hg amalgam to give a homogeneous bright green solution which presumably contains the monoreduced nickel analogue. This product was also highly soluble and could not be

dx.doi.org/10.1021/ic4013558 | Inorg. Chem. 2013, 52, 10467−10480

crystallized, but provides a useful comparison to iron-containing **4**; therefore, it was prepared in situ from **5** and characterized by EPR spectroscopy (vide infra).

X-ray Structure of Monoreduced [Fe(LN$_3$S)(DMAP)]^0 (4). The crystal structure of **4** (Figure 9) shows an overall

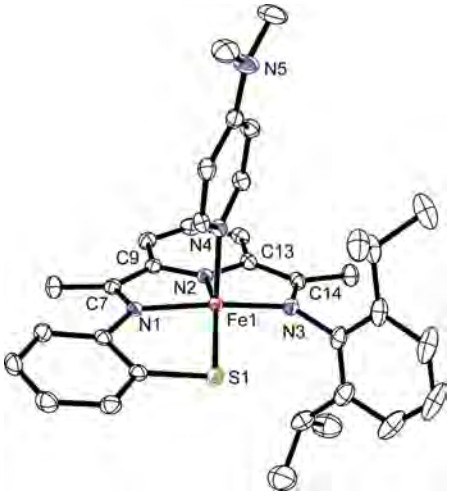

Figure 9. Displacement ellipsoid plot for **4** (50% probablility level). The H atoms are removed for the sake of clarity.

neutral iron complex with no additional counterions. Therefore, charge balance indicates that this complex is the one-electron-reduced analogue of the cation of **3**. The DMAP is retained in the axial position and, together with the LN$_3$S ligand, gives a 5-coordinate Fe center. Selected bond distances and angles are given in Tables 1 and 2. The Fe and S atoms in **4** have moved toward the equatorial plane of the bis(imino)pyridine backbone (Fe−N$_3$(plane) = 0.254 Å and S−N$_3$(plane) = 0.411 Å), compared to **3**. This flattening of the geometry around the Fe center is characterized by a change in τ value from τ = 0.18 for **3** to τ = 0.08 for **4**. There is a significant shortening of the Fe−N and Fe−S bonds for LN$_3$S, with the Fe−S bond decreasing by 0.1 Å and the Fe−N bonds decreasing by 0.3 Å. These changes are opposite to what would be expected for a metal-centered reduction to give a formal high-spin iron(I) complex, and they are more consistent with ligand-based reduction.

It has been shown that the C−C and C−N bond distances in BIP complexes are indicative of ligand reduction, and an analysis of ligand backbone distances is essential when assigning the locus of reduction in these complexes.[37−43] To gain insight into the electronic structure of **4**, it is useful to compare metrical parameters with other structurally characterized 5-coordinate monoreduced complexes reported in the literature. The complexes [Fe(^{iPr}BIP)(Br)(THF)][78] and [Fe(^{Et}BIP)(Cl)][40] exhibit similar C$_{imine}$−N$_{imine}$, C$_{imine}$−C$_{ipso}$, and C$_{ipso}$−C$_{pyridyl}$ bond distances in the BIP backbone that are consistent with one-electron ligand reduction. In contrast, [Fe(^{iPr}BIP)(CO)$_2$](BAr$^F_4$),[37] another monoreduced complex, has bond distances closer to a non-reduced BIP ligand and has been assigned as an iron(I) complex. The critical metrical parameters for **4** are highlighted in the structural fragments shown in Figure 10, in which **4** can be compared with its non-reduced precursor **3**. The C−N$_{imine}$ and C−N$_{pyridyl}$ bonds are elongated, while the C$_{imine}$−C$_{ipso}$ bonds are shortened in **4**, compared to **3**. These changes in the ligand backbone clearly point to the complex undergoing ligand-based reduction upon conversion of

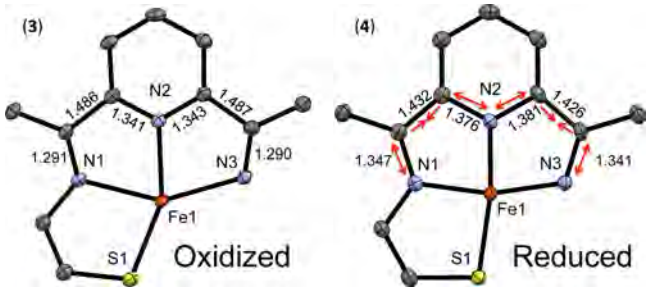

Figure 10. Comparison of selected ligand bond lengths for **3** (left) and **4** (right).

3 to **4**. A careful comparison of the bond distances in **4** to those reported in the literature suggests that the ligand in **4** is similar to a two-electron reduced BIP ligand. However, **4** would need to be formulated as an Fe^{III} complex with a doubly reduced (LN$_3$S)$^{3-}$ ligand, which is unlikely, given that iron(III) complexes are often not stable in the presence of monoanionic thiolate donors. Further evidence from Mössbauer spectroscopy and DFT calculations point to **4** as being an iron(II) complex with a one-electron-reduced ligand (vide infra). The phenylthiolate-appended LN$_3$S ligand appears capable of behaving as a non-innocent ligand by accommodating a reducing equivalent delocalized over the BIP backbone.

EPR Spectroscopy. Further information regarding the electronic structure of the monoreduced **4** was obtained by EPR spectroscopy. Crystalline **4** was dissolved in Et$_2$O and EPR data were recorded at 15 K. A nearly axial EPR spectrum was observed, and a good simulation was obtained for an S = 1/2 system with g values of 2.155, 2.057, and 2.038 (Figure 11).

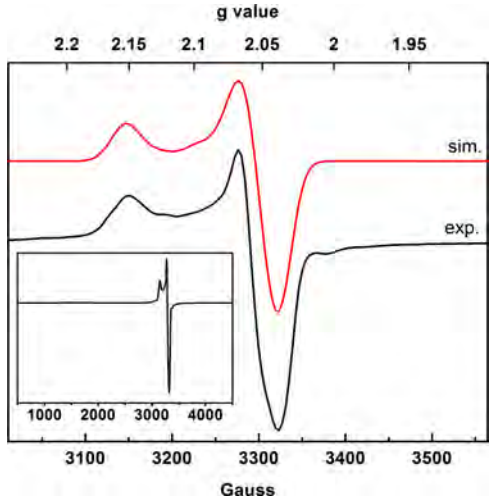

Figure 11. X-band EPR spectrum of **4** (2.4 mM) in Et$_2$O at 16 K (black line). Inset: full-range experimental spectrum. Parameters: frequency, 9.479 GHz; microwave power, 2 mW; modulation amplitude, 10 G; modulation frequency, 100 kHz. Parameters for simulation (red line): S = 1/2; g = [2.155, 2.057, 2.038]; Lorentzian linewidths, W = 33, 32, and 30 G.

The S = 1/2 ground state could arise from a low-spin (ls) iron(I) center resulting from metal-based reduction, a ls-iron(II) (S = 0) center with a ligand-based radical, or an intermediate-spin (is) iron(II) (S = 1) center antiferromagnetically coupled to a ligand-based radical. An additional possibility is a high-spin (hs) iron(II) (S = 2) antiferromagnetically

dx.doi.org/10.1021/ic4013558 | Inorg. Chem. 2013, 52, 10467−10480

coupled to a ligand-based radical, but this configuration would give rise to a total spin ground state of $S = 3/2$, which should exhibit g values spread over a much wider range than that observed in Figure 11.[38] To make a definitive assignment, it is useful to draw comparisons with other monoreduced BIP-Fe complexes. For the monoreduced complex $[(^{iPr}BIP)Fe(CO)_2](BAr^F{}_4)$, a rhombic EPR spectrum with $g = 2.111, 2.043, 1.994$ is observed and attributed to a low-spin Fe^I configuration with an $S = 1/2$ ground state.[37] In contrast, the monoreduced $[(^{iPr}BIP)Fe(OEt_2)](BAr^F{}_4)$ exhibits an EPR spectrum assigned to an $S = 3/2$ species derived from a high-spin Fe^{II} ion antiferromagnetically coupled to the BIP radical anion.[38] The spectrum in Figure 11 does not match the spectra for either of the former complexes. These results suggest that the LN_3S complex **4**, which contains a covalently tethered phenylthiolate group, exhibits a new electronic configuration, consisting of either ls-Fe^{II} and a ligand-based radical or an is-Fe^{II} center antiferromagnetically coupled to a ligand-based radical, not previously observed in other monoreduced complexes.

The in situ reduction of the nickel complex **5** helps clarify the EPR properties and electronic ground states of the LN_3S complexes described in this work. The monoreduced analogue of **5**, $[Ni(LN_3S)]^0$, was generated in situ and its EPR spectrum is shown in Figure 12. A sharp singlet at $g = 2.00$ ($\Delta pp = 20$ G)

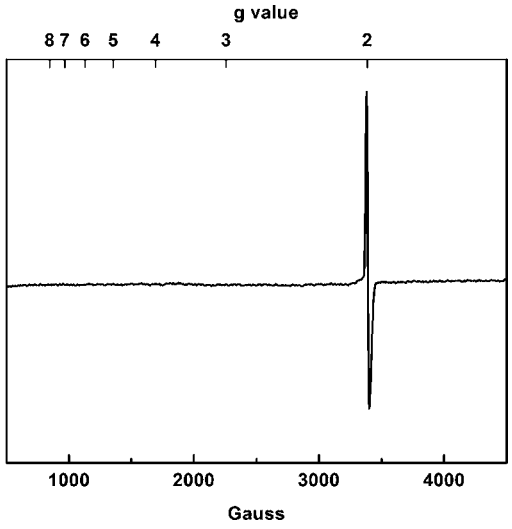

Figure 12. X-band EPR spectrum of **5** (3.0 mM) + Na/Hg (0.5%) amalgam in THF at 16 K. Parameters: frequency, 9.479 GHz; microwave power, 2 mW; modulation amplitude, 10 G; modulation frequency, 100 kHz.

is observed and can be assigned to a purely ligand-based radical.[70] Such a spectrum would be expected for **4** if this complex contained an ls-Fe^{II} ion and a single, unpaired e^- delocalized over the LN_3S ligand. Taken together, these data suggest that **4** may be best described as an intermediate-spin iron(II) ion antiferromagnetically coupled with a ligand radical, giving rise to the axial EPR spectrum in Figure 11.

Mössbauer Spectroscopy. Mössbauer spectra of microcrystalline samples of complexes **3** and **4** with natural abundance ^{57}Fe were collected at 5.3 K and with a weak applied field (47 mT) and are given in Figure 13. Mössbauer parameters for these complexes, together with complexes from the literature, are given in Tables 4 and 5. Both **3** and **4** produced spectra that consisted of broad quadrupole doublets. The broad spectra may be attributed to the fact that the

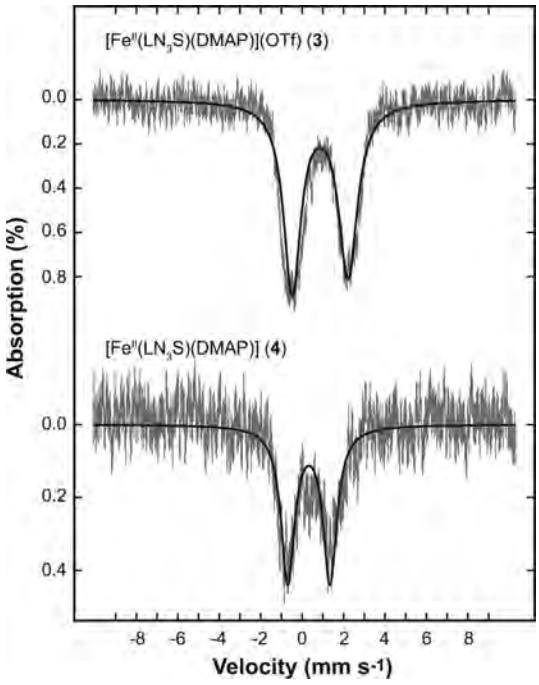

Figure 13. Mössbauer spectra at 5.3 K in a weak applied field (47 mT) of **3** (starting material) and **4** (monoreduced). Both spectra consist of broad quadrupole doublets ($\Gamma_{L=R} = 0.8$ mm s^{-1}). Complex **3** has parameters that can be assigned to a high-spin iron(II) species: ($\delta = 0.87$ mm s^{-1}; $\Delta E_Q = 2.70$ mm s^{-1}), while **4** is consistent with an intermediate-spin iron(II) species coupled to a S = 1/2 radical: ($\delta = 0.33$ mm s^{-1}; $\Delta E_Q = 2.04$ mm s^{-1}).

samples for **3** and **4** were mixtures of both crystalline and amorphous solids. The spectrum of **3** can be fitted to a quadrupole doublet with parameters that are highly distinctive[79] for a high-spin iron(II) ion ($\delta = 0.87$ mm s^{-1}; $\Delta E_Q = 2.70$ mm s^{-1}). However, the isomer shift is on the low end of the expected range, and this lowering is likely caused by both covalency of the thiolate iron bond and the five-coodinate nature of the complex. We previously reported an analogous ^{iPr}BIP complex, $[Fe^{II}(^{iPr}BIP)(SPh)Cl]$, which contains an exogenous thiolate donor in place of the tethered PhS^- group in **1**–**3** and Cl^- as the fifth ligand, and its Mössbauer spectrum was collected and is displayed in Figure S7 in the Supporting Information.[25] Complex **3** and $[Fe^{II}(^{iPr}BIP)(SPh)Cl]$ exhibit similar isomer shifts and quadrupole splittings, suggesting that substitution of the neutral DMAP ligand with the anionic Cl^- ligand has little effect on the Mössbauer spectra and, hence, electronic structure. These complexes can also be compared favorably with data for the thiolate-ligated non-heme iron enzymes CDO[20] and SOR.[81]

We next examined the one-electron-reduced complex **4** by Mössbauer spectroscopy. Analysis of crystalline **4** affords a Mössbauer spectrum distinct from **3**, with a significant decrease in both isomer shift and quadrupole splitting ($\delta = 0.33$ mm s^{-1}; $\Delta E_Q = 2.04$ mm s^{-1}). Comparison with the monoreduced and doubly reduced complexes in Table 5 shows that **4** exhibits Mössbauer parameters with values between those of monoreduced $[(BIP)Fe(CO)_2]^+$, which contains two strong-field CO donors and an ls-Fe^I center, and monoreduced $[(BIP)Fe(OEt_2)]^+$, which has a single, weak-field Et_2O donor and an hs-Fe^{II} ion. Surprisingly, the isomer shift and quadrupole splitting values for **4** are, in fact, closest to those seen for the *doubly*

dx.doi.org/10.1021/ic4013558 | Inorg. Chem. 2013, 52, 10467−10480

Table 4. ^{57}Fe Mössbauer Parameters for Selected High-Spin Iron(II) Complexes

	δ (mm s^{-1})	ΔE_Q (mm s^{-1})	ground state, S	source
[Fe^{II}(LN$_3$S)(DMAP)](OTf) (**3**)	0.87	2.70	2	this work
[(^{iPr}BIP)FeCl$_2$]	0.89	2.40	2	ref 39
[(^{iPr}BIP)FeCl$_2$]	0.92	2.40	2	this work
[(^{iPr}BIP)Fe(SPh)Cl]	0.78	2.62	2	this work
[(^{Mes}BIP)FeCl$_2$]	0.90	1.12	2	ref 80

Table 5. ^{57}Fe Mössbauer Parameters for Monoreduced and Doubly Reduced BIP-Iron Complexes

	δ (mm s^{-1})	ΔE_Q (mm s^{-1})	S_{total}	S_{Fe}	S_{ligand}	source
Monoreduced Complexes						
[Fe^{II}(LN$_3$S)(DMAP)] (**4**)	0.33	2.04	1/2	1	1/2	this work
[(^{iPr}BIP)Fe(CO)$_2$](BAr$^F_4$)	0.17	0.62	1/2	1/2	0	ref 37
[(^{iPr}BIP)Fe(OEt$_2$)](BAr$^F_4$)	1.13	2.51	3/2	2	1/2	ref 38
[(^{iPr}BIP)FeCl]	0.77	0.73	3/2	2	1/2	ref 39
Doubly Reduced Complexes						
[(^{iPr}BIP)Fe(DMAP)]	0.31	1.94	0	1	1	ref 39
[(^{iPr}BAP)Fe(DMAP)]^a	0.30	2.04	0	1	1	ref 82
[(^{iPr}BIP)Fe(CO)$_2$]	0.03	1.17	1	0	1	refs 39, 82

^{a}BAP = bis(aldimino)pyridine.

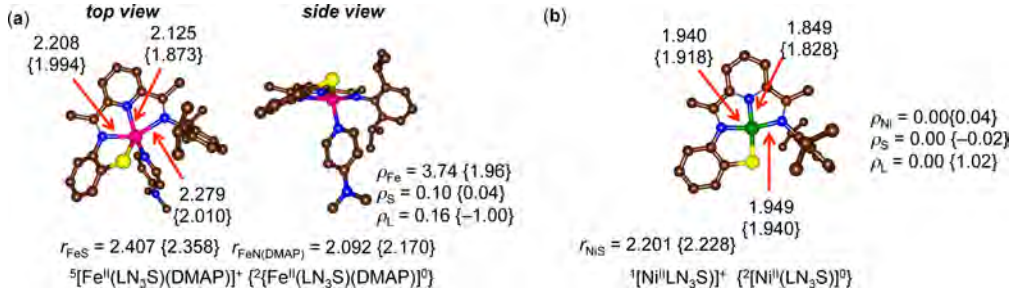

Figure 14. Optimized UB3LYP/B1 geometries of ^{5}[Fe^{II}(LN$_3$S)(DMAP)]$^+$ and ^{1}[Ni^{II}(LN$_3$S)]$^+$, and their reduced complexes (bond lengths given in angstroms). Also given are group spin densities.

reduced complexes, which have been assigned as intermediate-spin (is) iron(II) species with diradical ligands. The Mössbauer data for **4** thus point to an is-Fe^{II} center as the best assignment for this complex, and this conclusion is in good agreement with both the structural and EPR data. The strong-field thiolate ligand in **4**, coupled with the relatively weak-field DMAP donor, gives rise to this unique electronic configuration.

Computational Studies. The iron(II) and nickel(II) complexes, and their monoreduced analogues, were studied by DFT calculations to gain further insight into their structures and electronic configurations. The optimized geometries of [(LN$_3$S)Fe^{II}(DMAP)]$^+$ (**3**) and [Ni^{II}(LN$_3$S)]$^+$ (**5**) were calculated with the B3LYP functional on all low-lying spin states and are given in Figure 14. A quintet spin ground state (S = 2, hs-Fe^{II}) was found for **3**. At ΔE+ZPE level of theory, the quintet state (^{5}**3**) for the iron(II) complex is more stable than either the triplet state (S = 1, is-Fe^{II}, (^{3}**3**)) or the singlet state (^{1}**3**), by 13.8 and 17.0 kcal mol^{-1}, respectively. Inclusion of dispersion corrections further increases the energy gaps to 21.6 and 32.7 kcal mol^{-1}, respectively. These results indicate that the singlet and triplet spin states should be inaccessible at room temperature, and match nicely with the experimental observations (structural parameters, ^{1}H NMR) that show **3** has an hs-Fe^{II} ground state. The Fe−N bond lengths in the DFT-optimized structure of ^{5}**3** are within the range of 2.092−2.279 Å, and they are in good agreement with the X-ray structure (Fe−N for **3**: 2.073(5)−2.196(5)). The Fe−S distance of 2.407 Å for ^{5}**3** in Figure 14 is slightly elongated, compared to the X-ray structure (Fe−S = 2.3246(18) Å). Note that when geometry optimizations for **3** were run with a pure density functional such as BP86 instead of B3LYP, a different spin state ordering was found, in which a degenerate singlet/triplet ground state was obtained and the quintet spin state was calculated to be much higher in energy (see the Supporting Information). Consequently, pure density functional methods such as BP86 give results that are inconsistent with the experimental findings, and therefore we did not proceed further with these types of methods.

For the nickel(II) complex **5**, a closed-shell singlet spin state (S = 0) was found to be the ground state. We also calculated the triplet and quintet spin states for **5**, but we found these states to be higher in energy than ^{1}**5**, by 4.2 and 33.3 kcal mol^{-1}, respectively. No changes in spin state ordering were found for this complex when alternative density functional methods were employed. The optimized geometry for the ground state singlet is approximately square planar, consistent with the X-ray structure. The Ni−N distances for ^{1}**5** are in excellent agreement with those derived from the crystal structure (Table 3), although the Ni−S distance is slightly elongated (2.201 Å via the DFT method, 2.1386(5) Å according to the experimental data), similar to the trend seen for the Fe−S distance in ^{5}**3** versus the X-ray structure. The DFT calculations at the B3LYP level of theory often slightly overestimate metal−sulfur bond lengths.[83] The other main

dx.doi.org/10.1021/ic4013558 | Inorg. Chem. 2013, 52, 10467−10480

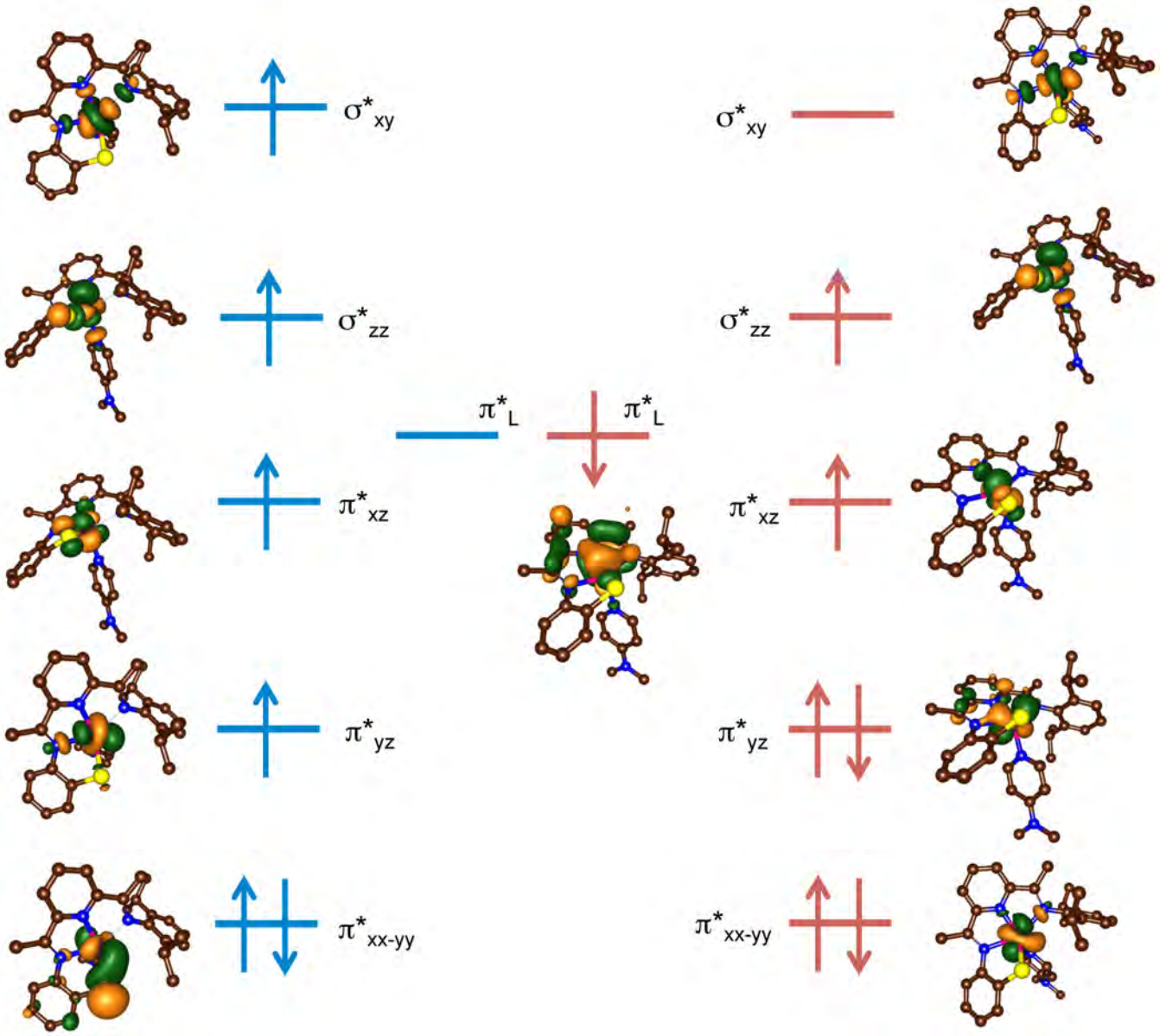

Figure 15. Orbital diagrams of $^{5}[Fe^{II}(LN_3S)(DMAP)]^{+}$ (left) and $^{2}[Fe^{II}(LN_3S)(DMAP)]^{0}$ (right).

structural features—and, importantly, the spin ground states—are well-reproduced by the calculations.

The monoreduced complex **4** was also studied at the B3LYP level of theory, taking into consideration the possible doublet (S = 1/2) and quartet (S = 3/2) spin states for this complex. Calculations were initiated by using the coordinates from the X-ray structure of **4** as a starting point, and the results led to an overall doublet spin ground state (S = 1/2) for the monoreduced complex. The doublet spin state is found to be stabilized by 6.3 kcal mol^{-1} over the quartet spin state, and solvent corrections raise this energy gap to 6.5 kcal mol^{-1}; however, dispersion corrections reduce it to 0.6 kcal mol^{-1}. The computationally derived S = 1/2 ground state thus matches that derived from the EPR spectrum observed in Figure 9 for complex **4**. The bond distances for the doublet spin ground state of **4** are shown in Figure 14, and both the Fe−N and Fe−S distances are significantly shortened compared to the starting complex **3**. The Fe−N bond lengths for the in-plane LN_3S ligand are in good agreement with the structural parameters for **4** (Table 1), but the Fe−S distance is somewhat longer, following the trend seen for **3** and **5**. In addition the Fe−N distance for the axial DMAP ligand is also slightly elongated (DFT, 2.170 Å; expt, 2.0508(16) Å).

The molecular orbital diagram for the doublet spin ground state of **4** is given in Figure 15, together with the MO diagram for the quintet spin ground state of starting complex **3**. For complex **4**, the computational results are consistent with an is-Fe^{II} (S_{Fe} = 1) center antiferromagnetically coupled with a ligand-based radical to give an overall doublet spin (S_{total} = 1/2) ground state. As seen in Figure 15, two α spin electrons reside in metal-based orbitals, while a predominantly ligand-based orbital (π^*_L) contains one β spin electron. The two unpaired electrons on the metal are reflected by a calculated spin density of ρ_{Fe} = 1.96, whereas the unpaired electron on the ligand leads to ρ_{LN3S} = −1.00 (Figure 14). In contrast, the MO diagram for **3** reveals four half-filled (α-spin) metal-based orbitals resulting in ρ_{Fe} = 3.74, as expected for a hs-Fe^{II} center. The calculations show that one-electron reduction of **3** occurs by the filling of a

dx.doi.org/10.1021/ic4013558 | Inorg. Chem. 2013, 52, 10467−10480

low-lying virtual ligand (π^*_L) orbital in preference to filling of an empty metal-based orbital, confirming the non-innocent nature of the LN_3S ligand. The spin state change that occurs at the Fe center upon reduction of **3** (hs-Fe^{II}) to **4** (is-Fe^{II}) appears to be a consequence of the destabilization of the σ^*_{xy} orbital. This destabilization is likely brought on by an increase in ligand field strength for the one-electron-reduced LN_3S ligand and a consequent shortening of the Fe−N and Fe−S bonds. Destabilization of σ^*_{xy} leads to depopulation of this orbital and occupation of the lower-lying π^*_{yz} orbital, resulting in an overall is-Fe^{II} center. Finally, the ligand-based β electron in **4** is mainly located on the bis(imino)pyridine backbone, which leads to the significant bond length perturbations shown in Figure 16, where the backbones for ^{5}**3** and ^{2}**4** are compared.

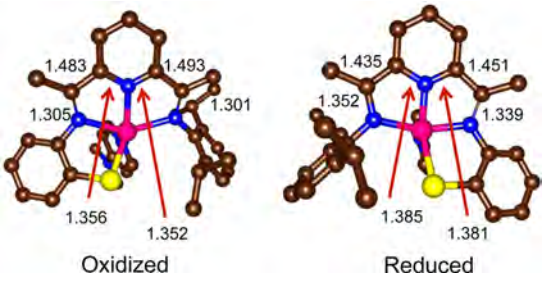

Figure 16. Optimized UB3LYP/B1 geometries of $^5[Fe^{II}(LN_3S)(DMAP)]^+$ and $^2[Fe^{II}(LN_3S)(DMAP)]^0$, highlighting BIP ligand backbone (bond lengths given in angstroms).

The trends in the perturbations provide a satisfying match to what is seen experimentally in Figure 10 and help to further validate the DFT results. The close agreement of the calculated ligand backbone bond distances (Figure 16) with the X-ray structure of **4** provides additional evidence for the assignment of **4** as a one-electron reduced ligand radical coupled to an is-Fe^{II} ion (ρ_{Fe} = 1.96, ρ_L = −1.00; see Figure 14a).

The monoreduced product of ^{1}**5** was also investigated by DFT, giving the optimized geometry for the doublet spin ground state of $^2[Ni^{II}(LN_3S)]^0$ shown in Figure 14. In this case, there are only very minor perturbations on the metal−ligand bond lengths, compared to the non-reduced starting material. Analysis of the spin density shows that the extra electron clearly lies on the LN_3S ligand and not the closed-shell nickel center, with an α electron occupying a π^*_L orbital (Figure S8 in the Supporting Information). The DFT calculations for the monoreduced nickel complex provide further confirmation that LN_3S functions easily as a non-innocent ligand, and the ligand-based radical predicted by DFT is in full agreement with the sharp organic radical seen in the EPR spectrum for monoreduced **5**.

O_2 Reactivity. We previously found that **1** reacts with excess O_2[24] in CH_2Cl_2 to give an S-oxygenated sulfonate complex, providing the first example of an Fe^{II}-thiolate complex that reacts with O_2 to give selective sulfur oxygenation. This reaction mimicked some of the general features of the reaction seen for CDO, but was lacking in the fact that the donor set at the metal center was N_3S(thiolate), not N_4S(thiolate), and the sulfur-oxygenated product was a triply oxygenated RSO_3^- complex, as opposed to the doubly oxygenated RSO_2^- product generated by the enzymatic system. In a subsequent report, we prepared an improved N_4S(thiolate) iron(II) model complex based on the tripodal N4Py ligand, $[Fe^{II}(N3PyS)(solvent)]^+$, and we found that it reacts with O_2 to give a biomimetic, doubly oxygenated sulfinato-iron(II) complex.[26] We thus sought to test the new N_4S(thiolate) iron(II) complexes **2** and **3** to determine their reactivity toward O_2.

Reactions of complexes **2** and **3** with excess O_2 in CH_2Cl_2 were analyzed directly by LDI-MS. The mass spectral data (Figures S3 and S4 in the Supporting Information) show dominant ions that correspond to the triply oxygenated sulfonato-iron(II) complex, $[Fe(LN_3SO_3)]^+$ (m/z = 532). This oxygenation pattern is the same as that seen for **1**.[24] Conversion of **1** to an N_4S(thiolate) coordination environment by addition of py or DMAP does not alter the O_2 reactivity such that sulfur oxygenation results in a doubly oxygenated sulfinato product, as seen for our other N_4S(thiolate) system.[25]

Some nickel(II) thiolate complexes can undergo sulfur oxygenation, most likely through a mechanism involving direct attack of O_2 on the coordinated sulfur atom, while other Ni^{II}-thiolates are inert toward O_2, and orbital compositions have been analyzed to explain these differences in O_2 reactivity.[46−54] We did not observe any reaction between complex **5** and excess O_2 in CH_2Cl_2, even after prolonged stirring for several days. Solutions of the monoreduced nickel(II) complex $[Ni(LN_3S)]^0$ generated from Na/Hg amalgam in THF were next tested for their reactivity toward O_2. In this case, a rapid reaction with O_2 was indeed observed by an immediate color change from bright to dark green, but LDI-MS analysis of the reaction mixture revealed only a peak (m/z = 488.3) for the starting material **5**, suggesting only outer-sphere oxidation had occurred. In contrast, a related Ni^{II}(BIP) complex undergoes outer-sphere reduction to give a one-electron-reduced product that then reacts with O_2 via an inner-sphere mechanism to afford ligand-oxidized products.[70]

The monoreduced compound **4** also exhibits rapid reactivity with O_2. Exposure of solutions of **4** in Et_2O to air, or bubbling O_2, leads to an immediate color change from dark green to brown with concurrent formation of a brown precipitate. Analysis by LDI-MS reveals a mixture that can be assigned to iron oxygenates and sulfur oxygenates, with multiple major peaks assigned to $[SOFe^{III}-O-Fe^{III}SO]^{2+}$ (m/z = 508.3), $[SO_2Fe^{III}-O-Fe^{III}SO_2]^{2+}$ (m/z = 524.4), and $[SO_3Fe^{III}-O-Fe^{III}-SO_3]^{2+}$ (m/z = 540.4). While complexes **1**−**3** exhibit S-centered oxidation, the monoreduced complex **4** appears to show significant oxidation at the Fe center. This represents a significant change in the observed reactivity of these complexes, as a result of the change in electronic structure.

■ CONCLUSIONS

The triflate-ligated ferrous complex $[Fe^{II}(LN_3S)(OTf)]$ (**1**) serves as a useful precursor for the facile synthesis of the biomimetic N_4S(thiolate) complexes $[Fe^{II}(LN_3S)(DMAP)]$-OTf (**2**) and $[Fe^{II}(LN_3S)(DMAP)]OTf$ (**3**). Template assembly with nickel(II) tetrafluoroborate leads to the Ni^{II} analogue $[Ni^{II}(LN_3S)]BF_4$ (**5**). Structural and spectroscopic methods show that the iron complexes are 5-coordinated, high-spin (S = 2) iron(II) species, while the nickel complex is a 4-coordinate square-planar nickel(II) species. Electrochemical measurements revealed that these complexes uniformly exhibit only one reversible reduction wave between −0.9 V and −1.2 V, vs Fc^+/Fc, within the CH_3CN solvent window. Bulk chemical reduction of **3** by Na/Hg amalgam gives the extremely air-sensitive, monoreduced complex $[Fe(LN_3S)(DMAP)]^0$ (**4**), which was isolated and crystallographically characterized. No evidence for a two-electron reduced product was observed, which was consistent with the electrochemical analysis. This

dx.doi.org/10.1021/ic4013558 | Inorg. Chem. 2013, 52, 10467−10480

behavior contrasts other bis(imino)pyridine complexes, which typically can house up to two or three reducing equivalents beginning at the $M^{2+}(BIP^0)$ redox level, and have been shown to form two-electron reduced products from Na/Hg reduction. It can be concluded that the anionic thiolate arm appended to the new LN_3S system likely causes multiple reductions to be thermodynamically unfavorable. The X-ray structure of **4** shows it is a 5-coordinated complex, with one DMAP ligand remaining coordinated in the axial position following reduction. The electronic structure of the monoreduced complex **4** was firmly established through a combination of structural analysis, EPR and Mössbauer spectroscopies as well as computational (DFT) methods. The ground state of **4** is clearly a doublet state that arises from an intermediate-spin ($S = 1$) iron(II) center antiferromagnetically coupled to a ligand-based radical. The spin state of the Fe center is reflected in the unusual Mössbauer parameters for this monoreduced BIP complex, with $\delta = 0.33$ mm s^{-1} and $\Delta E_Q = 2.04$ mm s^{-1}. These parameters differ significantly from other monoreduced Fe(BIP) complexes that exhibit either hs-Fe^{II} ($S = 2$) or ls-Fe^{II} ($S = 0$) configurations, and they, in fact, are consistent with the doubly reduced Fe(BIP) species, which have been previously assigned as is-Fe^{II} complexes carrying diradical ligands. The computational studies show that the doublet spin ground state is comprised of two α electrons occupying metal-based orbitals of d_{z2} and d_{xz} parentage and one β electron residing on a ligand-based π^* orbital with most of the spin density localized on the bis(imino)pyridine backbone and not on the phenylthiolate arm. The DFT results are nicely validated by their agreement with the findings from Mössbauer and EPR spectroscopies, as well as by their reproduction of the experimentally observed, yet subtle bond length distortions that occur in the BIP backbone upon one-electron reduction. This study shows that the tetradentate LN_3S ligand can serve as a non-innocent ligand in the same fashion as the parent BIP system; however, in this case, it only accepts one electron delocalized over the ligand backbone. Taken together, our experimental and computational data strongly suggest that monoreduction of the starting iron(II) complex provides the first example of an intermediate-spin iron(II) complex antiferromagnetically coupled with a ligand-based radical.

The O_2 reactivity of the new Fe^{II} complexes **2** and **3** seems to mirror that of **1**, to give sulfonato-iron complexes. Interestingly, the thiolate-ligated Ni^{II} complex **5** is completely unreactive toward O_2, as opposed to some thiolate-ligated Ni^{II} complexes that can become oxygenated at the sulfur positions. The monoreduced iron complex **4** is extremely air-sensitive and rapidly reacts with O_2, but instead of leading only to sulfur oxygenation, yields a mixture of products involving both Fe-centered and S-centered oxygenates. Now that the ability to store reducing equivalents on thiolate-appended BIP ligands has been established, future work may involve designing systems where reducing equivalents on both the non-innocent ligand and the metal can be harnessed in a more-controlled fashion for O_2 activation.

■ ASSOCIATED CONTENT

Supporting Information

Crystallographic details for $[Fe^{II}(LN_3S)(py)](OTf)$, $[Fe^{II}(LN_3S)(DMAP)](OTf)$, $[Fe(LN_3S)(DMAP)]^0$, and $[Ni^{II}(LN_3S)](BF_4)$ in CIF format. ^1H and ^{19}F NMR spectra of **4**, and LDI-MS data for O_2 reactions. Computational details, including energies and Cartesian coordinates for DFT calculated structures. This material is available free of charge via the Internet at http://pubs.acs.org.

■ AUTHOR INFORMATION

Corresponding Author

*E-mail: dpg@jhu.edu.

Notes

The authors declare no competing financial interest.

■ ACKNOWLEDGMENTS

The National Institute of Health (NIH) is gratefully acknowledged for financial support to D.P.G. (No. GM62309). The National Service of Computational Chemistry Software (NSCCS) is thanked for generous CPU time to S.P.d.V. D.K. is a DST-Ramanujan Fellow (SR/S2/RJN-11/2008). G.N.L.J. thanks the Marsden Fund and The International Mobility Fund administered by the Royal Society of New Zealand.

■ REFERENCES

(1) McQuilken, A. C.; Goldberg, D. P. *Dalton Trans.* **2012**, *41*, 10883.
(2) Fox, B. G. *Iron Cofactors: Non-heme Handbook of Proteins*; John Wiley & Sons, Ltd.: Chichester, U.K., 2007; pp 611−618.
(3) Kovacs, J. A.; Brines, L. M. *Acc. Chem. Res.* **2007**, *40*, 501.
(4) Mascharak, P. K. *Coord. Chem. Rev.* **2002**, *225*, 201.
(5) Solomon, E. I.; Decker, A.; Lehnert, N. *Proc. Natl. Acad. Sci. U.S.A.* **2003**, *100*, 3589.
(6) Ryle, M. J.; Hausinger, R. P. *Curr. Opin. Chem. Biol.* **2002**, *6*, 193.
(7) Bruijnincx, P. C. A.; van Koten, G.; Klein Gebbink, R. J. *Chem. Soc. Rev.* **2008**, *37*, 2716.
(8) Nivière, V.; Bonnot, F.; Bourgeois, D. *Handb. Metalloproteins* **2011**, 246.
(9) Yeh, A. P.; Hu, Y. L.; Jenney, F. E.; Adams, M. W. W.; Rees, D. C. *Biochemistry* **2000**, *39*, 2499.
(10) Matias, P. M.; Morais, J.; Coelho, A. V.; Meijers, R.; Gonzalez, A.; Thompson, A. W.; Sieker, L.; LeGall, J.; Carrondo, M. A. *J. Biol. Inorg. Chem.* **1997**, *2*, 507.
(11) Santos-Silva, T.; Trincão, J.; Carvalho, A. L.; Bonifâcio, C.; Auchère, F.; Raleiras, P.; Moura, I.; Moura, J. J. G.; Romão, M. J. *J. Biol. Inorg. Chem.* **2006**, *11*, 548.
(12) Adam, V.; Royant, A.; Niviere, V.; Molina-Heredia, F. P.; Bourgeois, D. *Structure* **2004**, *12*, 1729.
(13) Kobayashi, M.; Nagasawa, T.; Yamada, H. *Trends Biotechnol.* **1992**, *10*, 402.
(14) Endo, I.; Nojiri, M.; Tsujimura, M.; Nakasako, M.; Nagashima, S.; Yohda, M.; Odaka, M. *J. Inorg. Biochem.* **2001**, *83*, 247.
(15) Kobayashi, M.; Shimizu, S. *Nat. Biotechnol.* **1998**, *16*, 733.
(16) de Visser, S. P., Kumar, D., Eds. *Iron-Containing Enzymes: Versatile Catalysts of Hydroxylation Reactions in Nature*; Royal Society of Chemistry: Cambridge, U.K., 2011.
(17) Joseph, C. A.; Maroney, M. J. *Chem. Commun.* **2007**, 3338.
(18) Straganz, G. D.; Nidetzky, B. *ChemBioChem* **2006**, *7*, 1536.
(19) Siakkou, E.; Rutledge, M. T.; Wilbanks, S. M.; Jameson, G. N. L. *Biochim. Biophys. Acta, Proteins Proteomics* **2011**, *1814*, 2003.
(20) Tchesnokov, E. P.; Wilbanks, S. M.; Jameson, G. N. L. *Biochemistry* **2012**, *51*, 257.
(21) McCoy, J. G.; Bailey, L. J.; Bitto, E.; Bingman, C. A.; Aceti, D. J.; Fox, B. G.; Phillips, G. N. *Proc. Natl. Acad. Sci. U.S.A.* **2006**, *103*, 3084.
(22) Simmons, C. R.; Liu, Q.; Huang, Q. Q.; Hao, Q.; Begley, T. P.; Karplus, P. A.; Stipanuk, M. H. *J. Biol. Chem.* **2006**, *281*, 18723.
(23) Ye, S.; Wu, X.; Wei, L.; Tang, D. M.; Sun, P.; Bartlam, M.; Rao, Z. H. *J. Biol. Chem.* **2007**, *282*, 3391.
(24) Jiang, Y. B.; Widger, L. R.; Kasper, G. D.; Siegler, M. A.; Goldberg, D. P. *J. Am. Chem. Soc.* **2010**, *132*, 12214.
(25) Badiei, Y. M.; Siegler, M. A.; Goldberg, D. P. *J. Am. Chem. Soc.* **2011**, *133*, 1274.

(26) McQuilken, A. C.; Jiang, Y. B.; Siegler, M. A.; Goldberg, D. P. *J. Am. Chem. Soc.* **2012**, *134*, 8758.
(27) Kovacs, J. A. *Science* **2003**, *299*, 1024.
(28) Kovacs, J. A. *Chem. Rev.* **2004**, *104*, 825.
(29) Artaud, I.; Chatel, S.; Chauvin, A. S.; Bonnet, D.; Kopf, M. A.; Leduc, P. *Coord. Chem. Rev.* **1999**, *192*, 577.
(30) Cho, J.; Woo, J.; Nam, W. *J. Am. Chem. Soc.* **2012**, *134*, 11112.
(31) Sallmann, M.; Siewert, I.; Fohlmeister, L.; Limberg, C.; Knispel, C. *Angew. Chem., Int. Ed.* **2012**, *51*, 2234.
(32) Gonzalez-Ovalle, L. E.; Quesne, M. G.; Kumar, D.; Goldberg, D. P.; de Visser, S. P. *Org. Biomol. Chem.* **2012**, *10*, 5401.
(33) Kumar, D.; Sastry, G. N.; Goldberg, D. P.; de Visser, S. P. *J. Phys. Chem. A* **2012**, *116*, 582.
(34) Britovsek, G. J. P.; Bruce, M.; Gibson, V. C.; Kimberley, B. S.; Maddox, P. J.; Mastroianni, S.; McTavish, S. J.; Redshaw, C.; Solan, G. A.; Stromberg, S.; White, A. J. P.; Williams, D. J. *J. Am. Chem. Soc.* **1999**, *121*, 8728.
(35) Scott, J.; Gambarotta, S.; Korobkov, I.; Budzelaar, P. H. M. *Organometallics* **2005**, *24*, 6298.
(36) Scott, J.; Gambarotta, S.; Korobkov, I.; Knijnenburg, Q.; de Bruin, B.; Budzelaar, P. H. M. *J. Am. Chem. Soc.* **2005**, *127*, 17204.
(37) Tondreau, A. M.; Milsmann, C.; Lobkovsky, E.; Chirik, P. J. *Inorg. Chem.* **2011**, *50*, 9888.
(38) Tondreau, A. M.; Stieber, S. C. E.; Milsmann, C.; Lobkovsky, E.; Weyhermuller, T.; Semproni, S. P.; Chirik, P. J. *Inorg. Chem.* **2013**, *52*, 635.
(39) Bart, S. C.; Chlopek, K.; Bill, E.; Bouwkamp, M. W.; Lobkovsky, E.; Neese, F.; Wieghardt, K.; Chirik, P. J. *J. Am. Chem. Soc.* **2006**, *128*, 13901.
(40) Bouwkamp, M. W.; Bart, S. C.; Hawrelak, E. J.; Trovitch, R. J.; Lobkovsky, E.; Chirik, P. J. *Chem. Commun.* **2005**, 3406.
(41) Bart, S. C.; Lobkovsky, E.; Bill, E.; Wieghardt, K.; Chirik, P. J. *Inorg. Chem.* **2007**, *46*, 7055.
(42) Stieber, S. C. E.; Milsmann, C.; Hoyt, J. M.; Turner, Z. R.; Finkelstein, K. D.; Wieghardt, K.; DeBeer, S.; Chirik, P. J. *Inorg. Chem.* **2012**, *51*, 3770.
(43) Darmon, J. M.; Turner, Z. R.; Lobkovsky, E.; Chirik, P. J. *Organometallics* **2012**, *31*, 2275.
(44) Enright, D.; Gambarotta, S.; Yap, G. P. A.; Budzelaar, P. H. M. *Angew. Chem., Int. Ed.* **2002**, *41*, 3873.
(45) de Bruin, B.; Bill, E.; Bothe, E.; Weyhermuller, T.; Wieghardt, K. *Inorg. Chem.* **2000**, *39*, 2936.
(46) Farmer, P. J.; Solouki, T.; Mills, D. K.; Soma, T.; Russell, D. H.; Reibenspies, J. H.; Darensbourg, M. Y. *J. Am. Chem. Soc.* **1992**, *114*, 4601.
(47) Farmer, P. J.; Solouki, T.; Soma, T.; Russell, D. H.; Darensbourg, M. Y. *Inorg. Chem.* **1993**, *32*, 4171.
(48) Darensbourg, M. Y.; Tuntulani, T.; Reibenspies, J. H. *Inorg. Chem.* **1995**, *34*, 6287.
(49) Buonomo, R. M.; Font, I.; Maguire, M. J.; Reibenspies, J. H.; Tuntulani, T.; Darensbourg, M. Y. *J. Am. Chem. Soc.* **1995**, *117*, 5427.
(50) Grapperhaus, C. A.; Darensbourg, M. Y.; Sumner, L. W.; Russell, D. H. *J. Am. Chem. Soc.* **1996**, *118*, 1791.
(51) Grapperhaus, C. A.; Darensbourg, M. Y. *Acc. Chem. Res.* **1998**, *31*, 451.
(52) Mullins, C. S.; Grapperhaus, C. A.; Frye, B. C.; Wood, L. H.; Hay, A. J.; Buchanan, R. M.; Mashuta, M. S. *Inorg. Chem.* **2009**, *48*, 9974.
(53) Herdt, D. R.; Grapperhaus, C. A. *Dalton Trans.* **2012**, *41*, 364.
(54) Mullins, C. S.; Grapperhaus, C. A.; Kozlowski, P. M. *J. Biol. Inorg. Chem.* **2006**, *11*, 617.
(55) Kumar, D.; Karamzadeh, B.; Sastry, G. N.; de Visser, S. P. *J. Am. Chem. Soc.* **2010**, *132*, 7656.
(56) Vardhaman, A. K.; Sastri, C. V.; Kumar, D.; de Visser, S. P. *Chem. Commun.* **2011**, *47*, 11044.
(57) Becke, A. D. *J. Chem. Phys.* **1993**, *98*, 1372.
(58) Lee, C. T.; Yang, W. T.; Parr, R. G. *Phys. Rev. B* **1988**, *37*, 785.
(59) Hay, P. J.; Wadt, W. R. *J. Chem. Phys.* **1985**, *82*, 299.
(60) Grimme, S.; Antony, J.; Ehrlich, S.; Krieg, H. *J. Chem. Phys.* **2010**, *132*, 154104.
(61) Becke, A. D. *Phys. Rev. A* **1988**, *38*, 3098.
(62) Perdew, J. P. *Phys. Rev. B* **1986**, *33*, 8822.
(63) *Jaguar, version 7.9*; Schrödinger, LLC: New York, 2011.
(64) Schwabe, T.; Grimme, S. *Phys. Chem. Chem. Phys.* **2007**, *9*, 3397.
(65) Bianchini, C.; Mantovani, G.; Meli, A.; Migliacci, F.; Zanobini, F.; Laschi, F.; Sommazzi, A. *Eur. J. Inorg. Chem.* **2003**, 1620.
(66) Fiedler, A. T.; Halfen, H. L.; Halfen, J. A.; Brunold, T. C. *J. Am. Chem. Soc.* **2005**, *127*, 1675.
(67) Theisen, R. M.; Shearer, J.; Kaminsky, W.; Kovacs, J. A. *Inorg. Chem.* **2004**, *43*, 7682.
(68) Shearer, J.; Nehring, J.; Lovell, S.; Kaminsky, W.; Kovacs, J. A. *Inorg. Chem.* **2001**, *40*, 5483.
(69) Addison, A. W.; Rao, T. N.; Reedijk, J.; Vanrijn, J.; Verschoor, G. C. *J. Chem. Soc., Dalton Trans.* **1984**, 1349.
(70) Manuel, T. D.; Rohde, J. U. *J. Am. Chem. Soc.* **2009**, *131*, 15582.
(71) Fan, R. Q.; Fan, R. J.; Lv, Z. W.; Yang, Y. L.; An, F.; Gu, D. M. *J. Coord. Chem.* **2007**, *60*, 919.
(72) Dunn, T. J.; Ramogida, C. F.; Simmonds, C.; Paterson, A.; Wong, E. W. Y.; Chiang, L.; Shimazaki, Y.; Storr, T. *Inorg. Chem.* **2011**, *50*, 6746.
(73) Chen, Y. J.; Hao, P.; Zuo, W. W.; Gao, K.; Sun, W. H. *J. Organomet. Chem.* **2008**, *693*, 1829.
(74) Bryliakov, K. P.; Talsi, E. P.; Semikolenova, N. V.; Zakharov, V. A. *Organometallics* **2009**, *28*, 3225.
(75) Britovsek, G. J. P.; Gibson, V. C.; Spitzmesser, S. K.; Tellmann, K. P.; White, A. J. P.; Williams, D. J. *J. Chem. Soc., Dalton Trans.* **2002**, 1159.
(76) Bart, S. C.; Lobkovsky, E.; Chirik, P. J. *J. Am. Chem. Soc.* **2004**, *126*, 13794.
(77) Nakajima, Y.; Nakao, Y.; Sakaki, S.; Tamada, Y.; Ono, T.; Ozawa, F. *J. Am. Chem. Soc.* **2010**, *132*, 9934.
(78) Trovitch, R. J.; Lobkovsky, E.; Chirik, P. J. *J. Am. Chem. Soc.* **2008**, *130*, 11631.
(79) Gütlich, P.; Bill, E.; Trautwein, A. X. *Mössbauer Spectroscopy and Transition Metal Chemistry: Fundamentals and Applications*; Springer–Verlag: Berlin, Heidelberg, 2011.
(80) Britovsek, G. J. P.; Clentsmith, G. K. B.; Gibson, V. C.; Goodgame, D. M. L.; McTavish, S. J.; Pankhurst, Q. A. *Catal. Commun.* **2002**, *3*, 207.
(81) Moura, I.; Tavares, P.; Moura, J. J. G.; Ravi, N.; Huynh, B. H.; Liu, M. Y.; Legall, J. *J. Biol. Chem.* **1990**, *265*, 21596.
(82) Russell, S. K.; Milsmann, C.; Lobkovsky, E.; Weyhermuller, T.; Chirik, P. J. *Inorg. Chem.* **2011**, *50*, 3159.
(83) Kumar, D.; Thiel, W.; de Visser, S. P. *J. Am. Chem. Soc.* **2011**, *133*, 3869.

Biocatalysis

DOI: 10.1002/anie.201304633

Inversion of Enantioselectivity of a Mononuclear Non-Heme Iron(II)-dependent Hydroxylase by Tuning the Interplay of Metal-Center Geometry and Protein Structure**

*Sarah M. Pratter, Cornelia Konstantinovics, Cristiana M. L. Di Giuro, Erich Leitner, Devesh Kumar, Sam P. de Visser, Gideon Grogan, and Grit D. Straganz**

Natural stereoselective oxidations by molecular oxygen have long fascinated chemists and these chemically challenging, "green" reactions have great potential for industrial processes.[1] However, the natural enzymes have a finite synthetic repertoire. A major goal is therefore to control their stereoselectivity and to produce a desired stereo-center within a certain target molecule. There have been some major successes recently in the design of stereo-controlled reactions by cytochrome P450 enzymes (P450s),[2] which have great potential as a source for site-specific oxygenation reactions.[3] By contrast, O_2 and mononuclear non-heme (MNH) Fe^{II} dependent hydroxylases have not been the focus of enzyme design studies. This is surprising because the catalytic potential of MNH Fe^{II} dependent hydroxylases complements that of P450s, with their ability to oxidize aliphatic carbon atoms in a regio- and stereoselective manner.[4] One example is the (*S*)-selective *p*-hydroxymandelate synthase (HMS) from *Amycalotopsis orientalis* (*Ao*HMS), which has homologues in other organisms including *Streptomyces coelicolor* (*Sc*HMS).[5,6] Recently, it was found that the high enantioselectivity of *Sc*HMS, which naturally converts the substrate *p*-hydroxyphenylpyruvate, can be compromised by substituents on the aromatic ring of phenylpyruvate (PP).[7] However, no structural features have been identified that cause the generally observed (*S*)-enantioselectivity of HMS enzymes. Herein, we have used modeling, molecular dynamics (MD), and density functional theory (DFT) calculations to redesign the (*S*)-selective *Sc*HMS to give a biocatalyst of inverted enantioselectivity, yielding (*R*)-mandelate as the product.

The reaction mechanism of HMS enzymes follows that of α-ketoacid dependent MNH Fe^{II} enzymes: *p*-hydroxyphenylpyruvate binding primes the iron center for activation of O_2, which in turn decarboxylates the substrate. The resulting high-valent Fe^{IV}=O species abstracts a benzylic hydrogen atom. In a rebound reaction, the formed Fe^{III}–OH species transfers a hydroxyl radical to the benzylic position resulting in the *p*-hydroxymandelate product, which leaves the active site (Figure 1).[6,8] The crystal structure of the (*S*)-selective *Ao*HMS has been determined and shows the native reaction product coordinated to the metal center.[9]

Upon close inspection of in silico docked complexes of *Sc*HMS with mandelate (MA) analogues of the (*S*)-configuration, as well as in the *Ao*HMS crystal structure,[9] it was found that the ligands were oriented in a slightly distorted trigonal bipyramidal geometry at the metal center. The α-hydroxy group of MA and the metal-coordinating glutamate were in the axial positions and two nitrogen atoms from the coordinating histidines, together with the carboxylate oxygen of the ligand, formed the trigonal basis of the pyramid. In contrast, the analogous (*R*)-MA–enzyme complex showed more pronounced deviations from the ideal symmetry (Supporting Information, Figure S1).[7] DFT calculations of the reactive Fe^{IV}=O and Fe^{III}–OH species in the catalytic cycle of α-ketoacid dependent enzymes showed that a trigonal bipyramidal geometry was one of two probable organizations

[*] S. M. Pratter, C. Konstantinovics, Dr. C. M. L. Di Giuro, Dr. G. D. Straganz
Institute of Biotechnology and Biochemical Engineering
Graz University of Technology
Petersgasse 12, 8010 Graz (Austria)
E-mail: grit.straganz@tugraz.at
Prof. Dr. E. Leitner
Institute of Analytical Chemistry and Food Chemistry
Graz University of Technology
Stremayrgasse 9, 8010 Graz (Austria)
Dr. D. Kumar
Department of Applied Physics, School for Physical Sciences,
Babasaheb Bhimrao Ambedkar University
Vidya Vihar, Rae Bareilly Road, Lucknow 226-025 (India)
Dr. S. P. de Visser
Manchester Institute of Biotechnology and School of Chemical Engineering and Analytical Science
The University of Manchester
131 Princess Street, Manchester M1 7DN (UK)
Dr. G. Grogan
York Structural Biology Laboratory, Department of Chemistry,
University of York
Heslington, York, YO10 5DD (UK)

[**] The financial support by the Austrian Science Fund (FWF) grant W901-B05 DK Molecular Enzymology and FWF research grant P18828 is gratefully acknowledged. G.D.S. thanks the VVRC at the Graz University of Technology for computational resources and Kim Carstens for technical assistance. S.d.V. thanks the National Service of Computational Chemistry Software for CPU time. D.K. holds a Ramanujan Fellowship from the Department of Science and Technology (DST), New Delhi (India) and acknowledges its financial support (Research Grants SR/S2/RJN-11/2008 and SR/S1/PC-58/2009).

Supporting information for this article is available on the WWW under http://dx.doi.org/10.1002/anie.201304633.

© 2013 Wiley-VCH Verlag GmbH & Co. KGaA, Weinheim

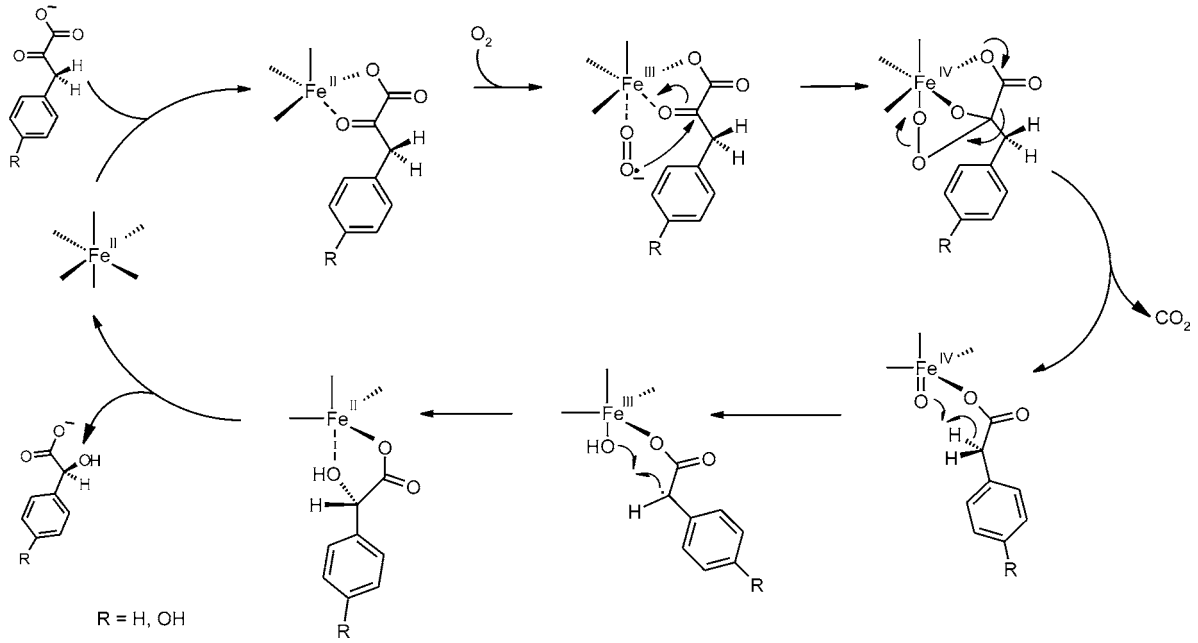

Figure 1. Generally accepted reaction mechanism of HMS enzymes.[8]

of these high-valent iron centers.[10] This posed the question of what impact the ligand field symmetry may have on enantioselectivity during catalysis. In models of (*R*)-MA and (*S*)-MA bound *Sc*HMS, in which the trigonal bipyramidal geometry was constrained, the (*R*)-MA ligand did not occupy the hydrophobic pocket that accommodates the aromatic substituent of (*S*)-MA. In contrast, the aromatic ring pointed toward the presumed substrate entrance channel and thereby collided with residue Tyr359 (Figure S1). *pro*-(*S*) and *pro*-(*R*) transition states of H-abstraction and rebound hydroxylation gave analogous principle spatial orientations when docked into the trigonal bipyramidal metal center of *Sc*HMS. Consequently, we investigated how the destabilization of the aromatic ring in the hydrophobic pocket and its stabilization in the alternative orientation influenced enantioselective catalysis. The steric clash with residue Tyr359 upon (*R*)-MA binding in our model could be removed by substituting it with alanine. To obstruct the hydrophobic pocket of *Sc*HMS, potentially effective point mutations were identified using in silico site-saturation mutagenesis with the following set of criteria: the variation 1) results in a low-energy apo-enzyme structure to prevent energetically driven reorganization of the active site; 2) has low-energy amino acid conformers that all interfere with the hydrophobic binding pocket; and 3) does not interact with the first coordination sphere of the metal ion and thus with its electronic or geometric structure. Using the algorithm described in the Supporting Information (Figure S2), six target single-point substitutions (Ser221Met, Val223Phe, Val223Met, Val223Trp, Ile236Phe and Tyr359Ala) were identified and introduced into the *Sc*HMS scaffold in vitro.

Spectra of PP conversion products by the wild-type (WT) and the resulting enzyme variants were subsequently analyzed using GC-MS and HPLC-MS (Table S1): all but one variation had a significant impact on the enantioselectivity of the WT enzyme, which gave an enantiomeric ratio (e.r.) of 0.4% (*R*)-MA:99.6% (*S*)-MA (Figure 2a). The most pronounced effect was an appoximately 1900-fold increase in (*R*)-selectivity with the mutation Ser221Met, which was predicted to obstruct the hydrophobic pocket, and resulted in the formation of 88.5% (*R*)-MA versus 11.5% (*S*)-MA. This efficacy was followed by the mutant Val223Phe, which gave an e.r. of 65.1% (*R*)-MA:34.9% (*S*)-MA. The opening of space for (*R*)-MA binding by the Tyr359Ala mutation resulted in only an approximately 47-fold increase of (*R*)-enantioselectivity compared to WT. Notably, Ser221, Val223, and Tyr359 are strongly conserved throughout all annotated putative *p*-hydroxyphenylpyruvate dioxygenases and HMSs. Combinations of the most successful substitutions further enhanced enantioselectivity: the best variant, triple mutant Ser221Met_Val223Phe_Tyr359Ala increased the e.r. to 97.4% in favor of (*R*)-selective hydroxylation, which corresponds to an approximately 9300-fold enhancement compared to WT. The latter translates to a difference in transition state energy $\Delta\Delta G^{\ddagger}$ of 22.6 kJ mol^{-1}. No reaction side products that are indicative of C2–C3 cleavage or uncoupled decarboxylation[11] were formed in detectable amounts and product recovery for MA was greater than 95% for all variants, except for variants Ile236Phe and Val223Trp, which showed substantial losses of approximately 60% and 20% that were not accounted for. This may indicate the formation of alternative oxygenation products in these variants that escaped our analysis. Notably, ring oxidation products have been reported from mutational studies of the active site of HMS.[12]

All *Sc*HMS variants had enzymatic activities towards PP that were roughly in the same range of the WT enzyme (Figure 2b, Table S1). The point mutations Val223Phe and Ser221Met increased catalytic efficiencies by an order of

 © 2013 Wiley-VCH Verlag GmbH & Co. KGaA, Weinheim

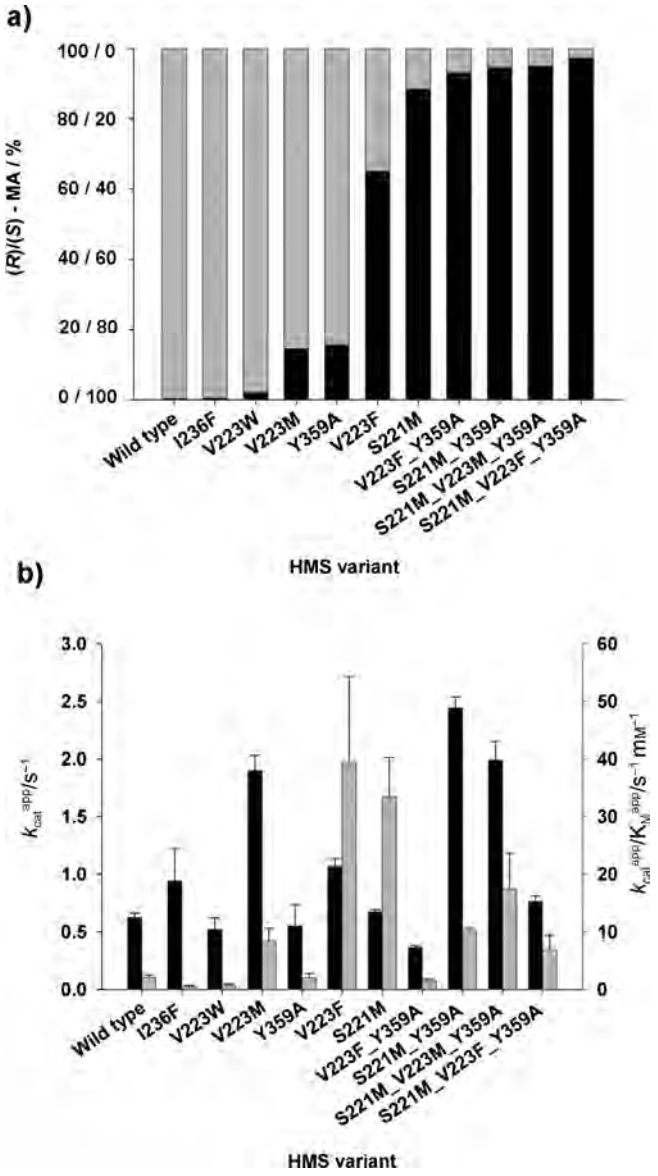

Figure 2. Enantioselectivities and activities of *Sc*HMS WT and variants. (a) The percentage of (*R*)-MA (black) and (*S*)-MA (gray) products and (b) steady-state kinetic constants k_{cat}^{app} (black) and k_{cat}^{app}/K_M^{app} (gray) are shown.

magnitude with k_{cat}^{app}/K_M^{app} values of 40 mM^{-1}s^{-1} and 34 mM^{-1}s^{-1} respectively, while the open active-site variant Tyr359Ala did not significantly alter WT efficiency ($k_{cat}^{app}/K_M^{app} = 2.1$ mM^{-1}s^{-1}). For the enzyme with the highest (*R*)-enantioselectivity, the triple mutant Ser221Met_Val223Phe_Tyr359Ala, the apparent turnover number was raised by 22% ($k_{cat}^{app} = 0.76$ s^{-1}) and the k_{cat}^{app}/K_M^{app} of 6.9 mM^{-1}s^{-1} was approximately three times higher compared to the WT enzyme.

The structure of the newly designed (*R*)-MA synthase, *Sc*HMS variant Ser221Met_Val223Phe_Tyr359Ala, in complex with (*R*)-MA and cobalt, which is a redox inactive Fe^{II} mimic,[9] was solved and refined to a resolution of 1.95 Å with an R_{cryst} value of 17.5% and an R_{free} value of 21.5% (Table S2). The aromatic substituent of the product filled the free space, which was created by the Tyr359Ala mutation, while Met221 and Phe223 occupied space in the hydrophobic binding pocket of the enzyme. Both protein molecules of the asymmetric unit showed (*R*)-MA ligation to the metal ions in a trigonal bipyramidal geometry and thus mirrored the product coordinated active site in the native structure of *Ao*HMS[11] (Figure 3a).

Computational MD studies of reaction intermediates in the scaffolds of WT *Sc*HMS and its Ser221Met_Val223Phe_Tyr359Ala variant shed light on the impact of particular catalytic steps for the overall enantioselectivity of the reaction. In each case, intermediates and transition states from phenylacetate (PA) ligated Fe^{IV}=O centers up to the final products were analyzed, whereby the ideal initial *pro*-(*S*) and *pro*-(*R*) geometries, which had been geometrically optimized by DFT calculations (Figure S3–S5), were the starting points of all simulations. The complexes generally showed two distinct localizations of the phenyl rings on the intermediates that were prototypical for either the *pro*-(*S*) or the *pro*-(*R*) pathway (Figure 3b and Figure S6–S13). Inspection of the ligand geometries and energies in the *Sc*HMS WT protein suggested that product chirality was determined by the final hydroxylation step. The pro-(*S*) mechanism, to which the ligand is predisposed by preceding catalytic steps,[7,10d] resulted in a PA radical that displayed considerable out-of-plane flexibility. It oscillated between a *pro*-(*S*) (43%) and a *pro*-(*R*) (57%) conformation, thus apparently making both hydroxylation pathways equally feasible (Figure S10 and Table S4). The *pro*-(*S*) rebound transition state was then kinetically favored compared to the (*R*)-selective pathway. By contrast, during MD simulations of the newly designed (*R*)-MA synthase the first, high-valent Fe^{IV}=O complex of both *pro*-(*R*) and *pro*-(*S*) starting geometries adopted the *pro*-(*R*) conformation. The subsequent PA radicals were entrapped in their respective *pro*-(*S*) (99%) and *pro*-(*R*) positions (97%) (Figure S10), while the *pro*-(*S*) pathway was kinetically favored during hydroxylation. This suggests that the primary Fe^{IV}=O complex geometry co-determines enantioselectivity in the variant and apparently compensates for the kinetically favored (*S*)-trajectory during hydroxylation (Table S4). Overall, our computational method rationalized the experimentally observed enantioselectivities of the two enantio-complementary enzymes.

In summary, we demonstrated for the first time how the interplay of metal-center geometry and protein structure control enantioselective hydroxylation in a metalloenzyme. The consideration of this principle has allowed for the design of a highly (*R*)-selective MA synthase from an enantio-complementary HMS through the in vitro construction of a total of only ten enzyme variants. The resulting approximately 9300-fold enantioselectivity switch, the most pronounced change ever reported for an oxygenation, is accompanied by a threefold improvement of enzyme efficiency. The designed hydroxylase, which has no natural precedent, may open up a new route for efficient, sustainable (*R*)-MA biosynthesis from readily available renewable feedstocks. This work and its underlying principles may, furthermore, be

 © 2013 Wiley-VCH Verlag GmbH & Co. KGaA, Weinheim

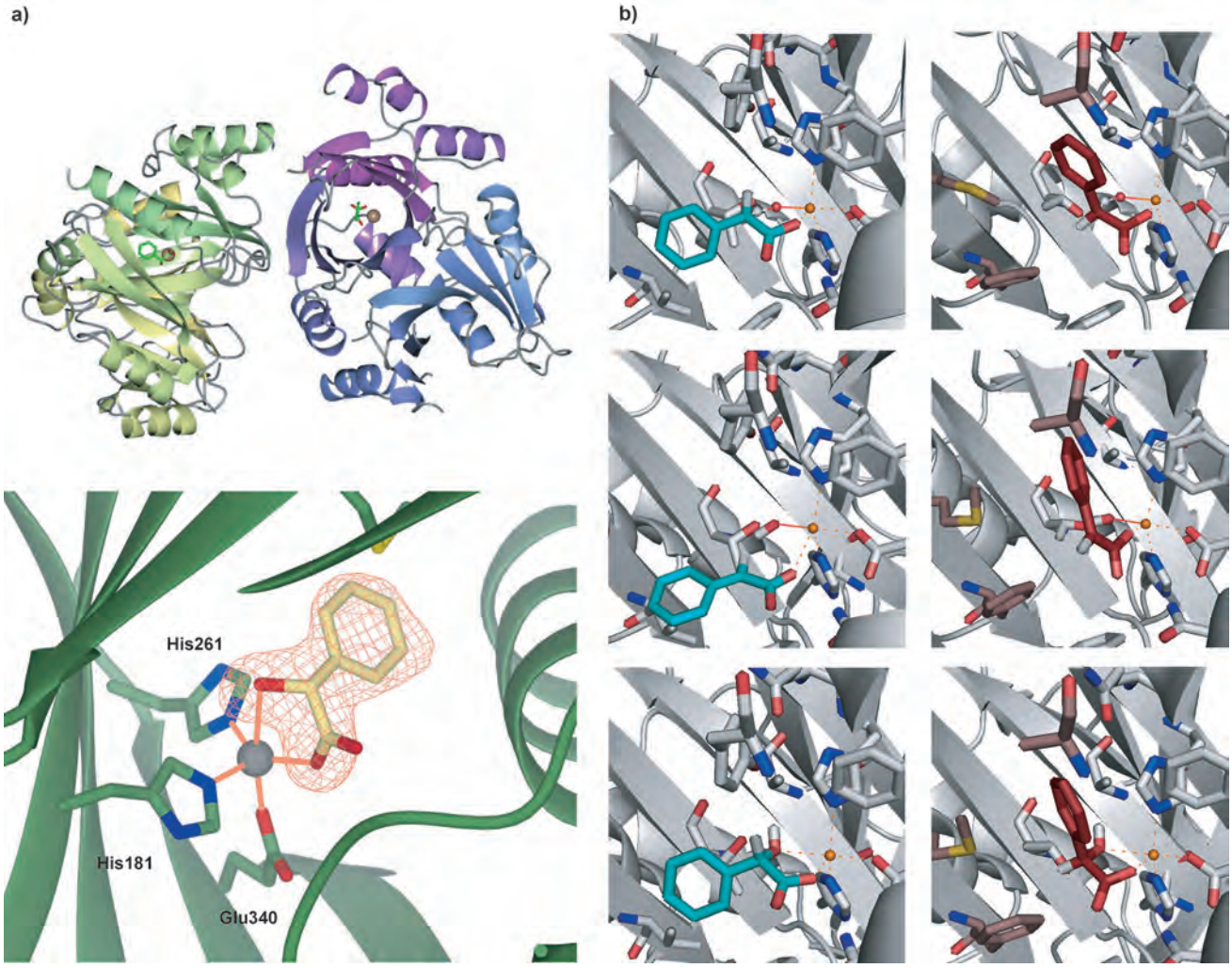

Figure 3. Interplay of protein structure and ligand orientation in the *Sc*HMS WT and the Ser221Met_Val223Phe_Tyr359Ala variant. a) Crystal structure of the (*R*)-selective *Sc*HMS triple variant. Top: overall structure of the observed dimer in complex with cobalt (brown) and the reaction product (*R*)-MA (green). Bottom: close-up of the active site. The coordinating oxygen atoms of (*R*)-MA (yellow) and the side chains of His261, His181, and Glu340 form a trigonal bipyramidal geometry around the cobalt atom (gray). The electron density of the ligand (coral) corresponds to the omit map (F_o-F_c map) contoured at a level of 3 σ obtained after the final rounds of refinement in the absence of the ligand. b) A structural representation of the catalytic steps that lead to chiral hydroxylation in WT *Sc*HMS (left) and in the (*R*)-selective triple mutant (right). The average structures of 10 ns MD simulations are shown, except in the lower right panel, which depicts the crystal structure of the mutant solved in this study. (Note that MD simulations gave similar active site geometries). The transition state of H-abstraction from PA by the Fe^{IV}=O center (upper row) results in an iron-bound hydroxy group and a substrate radical (middle row). The subsequent rebound step yields the chiral products (lower row). Residues within 5 Å of the metal (orange) are displayed—Ile335, Leu358, and Ile236 are omitted for clarity. Ligands of the (*S*)- and (*R*)-selective pathways are in teal and dark red, respectively. Mutations in the triple variant are shown in brown.

a first step in making enzymatic MNH Fe^{II} centers accessible as a resource for tailor-made biosynthetic oxygenations.

Received: May 29, 2013
Revised: July 1, 2013
Published online: July 23, 2013

Keywords: asymmetric catalysis · hydroxylation · metalloenzymes · non-heme iron · protein design

[1] K. Sanderson, *Nature* **2011**, *469*, 18–20.
[2] a) S. Kille, F. E. Zilly, J. P. Acevedo, M. T. Reetz, *Nat. Chem.* **2011**, *3*, 738–743; b) R. Agudo, G. D. Roiban, M. T. Reetz, *ChemBioChem* **2012**, *13*, 1465–1473; c) W. L. Tang, Z. Li, H. Zhao, *Chem. Commun.* **2010**, *46*, 5461–5463; d) S. Q. Pham, G. Pompidor, J. Liu, X. D. Li, Z. Li, *Chem. Commun.* **2012**, *48*, 4618–4620.
[3] V. B. Urlacher, M. Girhard, *Trends Biotechnol.* **2012**, *30*, 26–36.
[4] E. G. Kovaleva, J. D. Lipscomb, *Nat. Chem. Biol.* **2008**, *4*, 186–193.
[5] B. K. Hubbard, M. G. Thomas, C. T. Walsh, *Chem. Biol.* **2000**, *7*, 931–942.
[6] O. W. Choroba, D. H. Williams, J. B. Spencer, *J. Am. Chem. Soc.* **2000**, *122*, 5389–5390.
[7] C. M. L. Di Giuro, C. Konstantinovics, U. Rinner, C. Nowikow, E. Leitner, G. D. Straganz, *PLoS One* **2013**, DOI: 10.1371/journal.pone.0068932.
[8] D. D. Shah, J. A. Conrad, B. Heinz, J. M. Brownlee, G. R. Moran, *Biochemistry* **2011**, *50*, 7694–7704.

© 2013 Wiley-VCH Verlag GmbH & Co. KGaA, Weinheim

[9] J. Brownlee, P. He, G. R. Moran, D. H. Harrison, *Biochemistry* **2008**, *47*, 2002 – 2013.
[10] M. L. Neidig, A. Decker, O. W. Choroba, F. Huang, M. Kavana, G. R. Moran, J. B. Spencer, E. I. Solomon, *Proc. Natl. Acad. Sci. USA* **2006**, *103*, 12966 – 12973; b) S. P. de Visser, *Angew. Chem.*, **2006**, *118*, 1822 – 1825; *Angew. Chem. Int. Ed.*, **2006**, 45, 1790 – 1793; c) S. Sinnecker, N. Svensen, E. W. Barr, S. Ye, J. M. Bollinger, Jr., F. Neese, C. Krebs, *J. Am. Chem. Soc.* **2007**, 129, 6168 – 6179; d) A. Wojcik, E. Broclawik, P. E. Siegbahn, T. Borowski, *Biochemistry* **2012**, 51, 9570-9580.
[11] T. K. Paine, H. Zheng, L. Que Jr. , *Inorg. Chem.* **2005**, *44*, 474 – 476.
[12] a) M. Gunsior, J. Ravel, G. L. Challis, C. A. Townsend, *Biochemistry* **2004**, *43*, 663 – 674; b) J. M. Brownlee, B. Heinz, J. Bates, G. R. Moran, *Biochemistry* **2010**, *49*, 7218 – 7226.

 © 2013 Wiley-VCH Verlag GmbH & Co. KGaA, Weinheim

Inorganic Chemistry

Article

pubs.acs.org/IC

Rationalization of the Barrier Height for *p*-Z-styrene Epoxidation by Iron(IV)-Oxo Porphyrin Cation Radicals with Variable Axial Ligands

Devesh Kumar,*[,†] Reza Latifi,*[,‡,§] Suresh Kumar,[†] Elena V. Rybak-Akimova,[§] Mala A. Sainna,[‡] and Sam P. de Visser*[,‡]

[†]Department of Applied Physics, School of Physical Sciences, Babasaheb Bhimrao Ambedkar University, Vidya Vihar, Rae Bareilly Road, Lucknow 226-025, India

[‡]Manchester Institute of Biotechnology and School of Chemical Engineering and Analytical Science, University of Manchester, 131 Princess Street, Manchester M1 7DN, U.K.

[§]Department of Chemistry, Tufts University, Medford, Massachusetts 02155, United States

Supporting Information

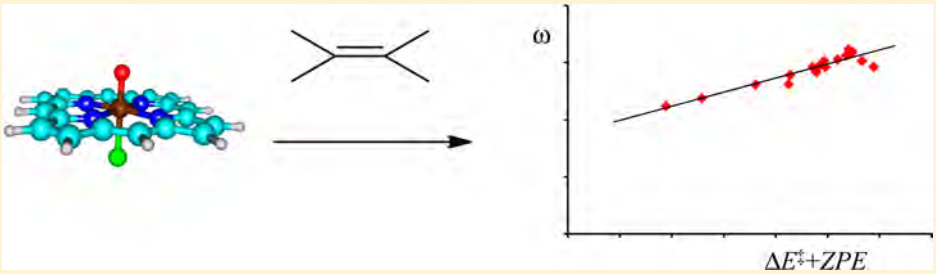

ABSTRACT: A versatile class of heme monoxygenases involved in many vital functions for human health are the cytochromes P450, which react via a high-valent iron(IV) oxo heme cation radical species called Compound I. One of the key reactions catalyzed by these enzymes is C=C epoxidation of substrates. We report here a systematic study into the intrinsic chemical properties of substrate and oxidant that affect reactivity patterns. To this end, we investigated the effect of styrene and para-substituted styrene epoxidation by Compound I models with either an anionic (chloride) or neutral (acetonitrile) axial ligand. We show, for the first time, that the activation enthalpy of the reaction is determined by the ionization potential of the substrate, the electron affinity of the oxidant, and the strength of the newly formed C−O bond (approximated by the bond dissociation energy, BDE_{OH}). We have set up a new valence bond model that enables us to generalize substrate epoxidation reactions by iron(IV)-oxo porphyrin cation-radical oxidants and make predictions of rate constants and reactivities. We show here that electron-withdrawing substituents lead to early transition states, whereas electron-donating groups on the olefin substrate give late transition states. This affects the barrier heights in such a way that electron-withdrawing substituents correlate the barrier height with BDE_{OH}, while the electron affinity of the oxidant is proportional to the barrier height for substrates with electron-donating substituents.

INTRODUCTION

An important class of enzymes in human physiology are the cytochromes P450, which are a large set of heme enzymes involved in the biodegradation and metabolism of toxic compounds in the liver.[1] These enzymes utilize molecular oxygen on a heme center in a catalytic cycle that uses two electrons and two protons to generate an iron(IV) oxo heme cation-radical active species called Compound I (CpdI).[2] This species is the active oxidant of the P450 enzymes and reacts with substrates via, for instance, aliphatic and aromatic hydroxylation, double-bond epoxidation, N-dealkylation, and sulfoxidation.[3] Because of its versatility in substrate activation, the group of enzymes has attracted interest from the biotechnological and pharmaceutical industries, although the intricate details of its catalytic mechanism and reactivity with substrates are still poorly understood. The epoxidation of olefins is a common reaction in P450 enzymes for a variety of important bioprocesses in the body including the activation of unsaturated fatty acids.[4] As a result, substrate epoxidation by P450 isozymes is well studied for a wide range of (non)natural substrates.[5] For instance, the reactions were shown to be highly enantioselective, whereby the *cis*-*β*-methylstyrene substrate gave an 89:11 epoxide product ratio of the 1*S*,2*R* form over the 1*R*,2*S* form.[6]

Because CpdI is a very versatile oxidant, many studies investigated synthetic analogues and models in substrate oxidation.[7] A number of these biomimetic studies focused on double-bond epoxidation mechanisms, and one of the most common substrates in these studies is styrene. Thus, a series of styrene epoxidation studies with a CpdI mimic and various axial ligands gave rate constants that were proportional to its

Received: February 27, 2013
Published: July 3, 2013

 © 2013 American Chemical Society dx.doi.org/10.1021/ic4005104 | *Inorg. Chem.* 2013, 52, 7968−7979

electron-donating ability.[8] Green and co-workers[9] characterized the axial-ligand effect as arising from changes in the pK_a values of the oxo group, which was confirmed with density functional theory (DFT) calculations on model complexes.[10]

Experimental studies reported rate constants for styrene epoxidation by synthetic iron(IV) oxo complexes: $[Fe^{IV}(O)(TPFPP^{\bullet+})X]^{0/+}$ with TPFPP = *meso*-tetrakis(pentafluorophenyl)porphyrinato and X = Cl^- or $NCCH_3$.[11] In an intriguing set of experiments, it was shown that the reaction of $[Fe^{IV}(O)(TPFPP^{\bullet+})NCCH_3]^+$ with ethylbenzene gave aromatic hydroxylation products, whereas the one using $[Fe^{IV}(O)(TPFPP^{\bullet+})Cl]$ as an oxidant led to benzylic hydroxylation instead; hence, the axial ligand in iron(IV)-oxo porphyrins seems to affect the product distributions in the reaction processes and the regioselectivity of aromatic over aliphatic hydroxylation.[11] The two oxidants with chloride versus acetonitrile as the axial ligand also gave differences in styrene epoxidation using para-substituted styrene derivatives. The work identified a correlation between the rate constant of styrene epoxidation with the ρ^+ Hammett factor, but the slopes were different for the CpdI models with anionic versus neutral axial ligands. The fundamental nature of this axial-ligand effect and how it affects the reaction mechanisms, rate constants and product distributions of iron(IV)-oxo porphyrins is unknown and, therefore, warrants a computational study. Thus, to gain insight into the effect of axial ligands on the reactivity of iron(IV)-oxo porphyrins with olefins, we have done a DFT study of the activation barriers using a selection of para-substituted styrenes as substrates and CpdI models with meso-substituted porphyrin.

Fujii and co-workers did a systematic investigation into the redox potentials of $[Fe^{IV}(O)(TMP^{+\bullet})X]^{n+}$ with TMP = 5,10,15,20-tetramesitylporphyrinate and X an axial ligand that is either anionic or neutral.[12] They found a positive $E_{1/2}$ shift upon binding of an anionic axial ligand that was virtually constant for a range of ligands. By contrast, binding of neutral ligands, such as imidazole, gave redox potentials in line with those found for peroxidases corresponding to a negative $E_{1/2}$ shift. They then replaced the TMP group with a meso-substituted porphyrin ligand with electron-withdrawing groups, which led to an increase of the $E_{1/2}$ values. Currently, it is not clear what factors determine the redox potentials of iron porphyrins and whether there is a relationship with catalysis. Therefore, to gain insight into the effect of meso substitution on the intrinsic chemical properties of the oxidant and the subsequent catalysis of substrates, we decided to include this study in the present work.

The model we chose for our studies presented here is given in Figure 1 and is based on the system used in ref 11. The basic features of the oxidant are an iron(IV) oxo group embedded in a protoporphyrin IX (Por) without side chains and with either chloride or acetonitrile as the axial ligand: $[Fe^{IV}(O)(Por^{\bullet+})X]^{0/+}$ with X = Cl^- or $NCCH_3$. In addition, we also investigated a more elaborate model that uses pentafluorophenyl substituents on the meso position of the porphyrin ring, i.e., TPFPP. Substrate epoxidation was studied using a range of *p*-Z-substituted styrenes with Z = H, F, Cl, CH_3, *t*-Bu, CN, NO_2, OCH_3, NH_2, and $N(CH_3)_2$. We show that para substitution affects the ionization potential of the substrate and its electron-donating ability, which leads to changes in the activation barrier of oxygen atom transfer. Although we reported a detailed analysis of substrate epoxidation by iron(IV)-oxo porphyrins before,[10] the systematic study described here goes beyond that of the previous work and highlights the differences in reactivity of substrates with electron-donating versus electron-withdrawing substituents. Moreover, a new model is presented that correlates with the obtained reactivity trends.

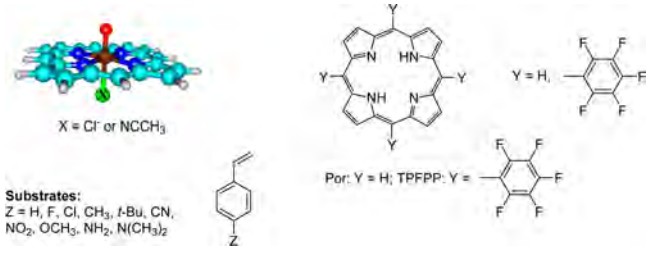

Figure 1. Oxidants and substrates used in this work.

METHODS

The study presented here uses DFT methods, as implemented in the *Jaguar*, *Gaussian03*, and *Gaussian09* program packages.[13] All geometries are the result of a full geometry optimization, whereby all degrees of freedom are minimized. A subsequent analytical frequency calculation characterized the structures as local minima (with real frequencies only) or first-order saddle points with one imaginary frequency for the correct mode. The hybrid B3LYP method[14] was employed throughout in combination with the Los Alamos-type LACVP basis set on iron and 6-31G on the rest of the atoms (BS1) for the geometry optimizations and frequencies.[15] Energies were then improved by single-point calculations with a triple-ζ-type basis set on iron (LACV3P+) and 6-311+G* on the rest of the atoms (BS2). Benchmark studies against experimental data reproduced free energies of activation using these methods to within 3 kcal mol^{-1}.[16] Previously, we calculated a full potential energy profile for substrate hydroxylation by an iron(IV)-oxo porphyrin cation-radical system at UB3LYP/BS2 and obtained relative energies within a few tenths of a kilocalorie per mole for local minima and first-order saddle points along a reaction mechanism compared to those obtained at UB3LYP/BS2//UB3LYP/BS1; hence, the latter method was used here.[17] Single-point calculations in a dielectric constant with ε = 37.5 mimicking acetonitrile with a probe radius of 2.1 Å were performed in *Jaguar* using basis set BS2. Free energies reported here were calculated at 298 K temperature and 1 bar pressure and are based on the UB3LYP/BS2//UB3LYP/BS1 energies and corrected with zero-point energy (ZPE), thermal and entropic corrections from the frequency file, and solvent corrections from the single-point solvent calculation. Further corrections to the energy were made by performing single-point calculations with dispersion-corrected B3LYP, B3LYP-D, as implemented in *Jaguar*.[18] For selected structures, we also did geometry optimizations and frequencies using UB3LYP-D/BS1 in *Jaguar*, although little changes in the optimized geometries were obtained.

We used two synthetic iron porphyrin models that are distinguished by the choice of the axial ligand, which was either chloride or acetonitrile. Note that $[Fe^{IV}(O)(Por^{\bullet+})Cl]^0$ is overall charge neutral, while $[Fe^{IV}(O)(Por^{\bullet+})NCCH_3]^+$ is positively charged. In our initial calculations, we used a bare porphyrin ring, whereby all side chains were replaced by hydrogen atoms. In a second set of calculations, we studied a TPFPP ligand system. We studied styrene epoxidation using a selection of para-substituted styrene substrates, as described in Figure 1.

To ascertain that the results are not influenced by the DFT method chosen here, we ran a selection of single-point calculations using dispersion-corrected DFT[18] and B3LYP with 15% HF exchange (designated as B3LYP*).[19] As before,[20] these test calculations reproduced the trends obtained with the B3LYP method, so that the results give a systematic error, which does not affect our discussion and analysis because we are dealing with trends only here. Nevertheless, for comparison, we give here the results obtained for ΔE + ZPE

dx.doi.org/10.1021/ic4005104 | *Inorg. Chem.* 2013, 52, 7968−7979

(UB3LYP), $\Delta G + E_{solv}$ (UB3LYP), and $\Delta G + E_{solv} + E_{disp}$ (UB3LYP-D).

RESULTS

We started the work with a detailed study into the electronic properties of iron(IV) oxo complexes, the effects of axial versus equatorial ligands, and finally the reactivity patterns with a selection of para-substituted styrenes. Our models include $[Fe^{IV}(O)(Por^{\bullet+})X]^{0/+}$, designated as $\mathbf{1}_X$, and $[Fe^{IV}(O)(TPFPP^{\bullet+})X]^{0/+}$, designated as $\mathbf{2}_X$, with X = Cl^- and $NCCH_3$ (Figure 1). Similar to previous studies on CpdI of P450 and biomimetic iron(IV)-oxo porphyrin complexes,[21] all complexes have the same electronic ground state with four electrons in metal 3d-type orbitals and a radical on the porphyrin macrocycle. High-lying occupied molecular orbitals include the $\delta_{x^2-y^2}$ orbital, which is nonbonding, doubly occupied, and located in the plane of the porphyrin. Slightly higher in energy are two π^*_{FeO} orbitals (π^*_{xz}, π^*_{yz}) for the antibonding interaction of the metal $3d_{xz/yz}$ with $2p_{x/y}$ atomic orbitals on oxygen. Higher-lying and virtual are the $\sigma^*_{z^2}$ and σ^*_{xy} orbitals for the antibonding interactions along the Fe−O axis and between the Fe−N groups in the plane of the porphyrin ring. In addition, there is a radical on a porphyrin-type orbital that in D_{4h} symmetry has the label a_{2u}. The orbital occupation gives close-lying doublet and quartet spin states with configuration $\delta_{x^2-y^2}{}^2\pi^*_{xz}{}^1\pi^*_{yz}{}^1a_{2u}{}^1$, whereby the two π^* electrons are either ferromagnetically or antiferromagnetically coupled to the a_{2u} electron in the quartet and doublet spin states. As a consequence, the two spin states are close in energy and the oxidant reacts via two-state-reactivity patterns on close-lying doublet and quartet spin state surfaces.[22]

Figure 2 gives optimized geometries of $^{4,2}\mathbf{1}_X$ and $^{4,2}\mathbf{2}_X$ with X = Cl^-/$NCCH_3$, as calculated with DFT. Optimized geometries of $^{4,2}\mathbf{1}_X$ (X = Cl^-/$NCCH_3$) are almost identical with those reported before.[23] The Fe−O distances are short and typical for an iron(IV) oxo species and shorten somewhat with an axially ligated acetonitrile molecule compared to chloride. This is due to mixing of the a_{2u} and π^* orbitals in $^{4,2}\mathbf{1}_{Cl}$ with 3p atomic orbitals on the chloride ligand,[23] which brings the metal more inside the plane through the porphyrin ring. This type of mixing has been identified before as the key reason for the intrinsic electronic differences of CpdI in monoxygenases and peroxidases.[24] We did additional geometry optimizations of $^2\mathbf{1}_X$ (X = Cl^-/$NCCH_3$) at the UB3LYP-D/BS1 level of theory, which reproduced the UB3LYP/BS1 structures within 0.010 Å.

As can be seen, meso substitution of the porphyrin ring with pentafluorophenyl groups has little effect on the optimized geometries, and the Fe−O, Fe−Cl, and Fe−N_{ax} distances for structures **1** and **2** are almost the same. Note also that very little saddling is found for the $[Fe^{IV}(O)(TPFPP^{\bullet+})X]$ structures. Not surprisingly, because the same molecular orbitals are singly occupied in the doublet and quartet spin-state structures, their geometries are virtually identical for each CpdI set of data. To establish whether the *meso*-pentafluorophenyl groups give electronic changes to the iron(IV) oxo species, we also show in Figure 2 the group spin densities (ρ), but only minor differences are observed between the data for structures **1** and **2**.

Subsequently, we calculated styrene epoxidation using a range of para-substituted styrene derivatives. Before we discuss the results on the substituted styrenes, let us focus on the general overall mechanism first. All epoxidation reactions described in this work proceed with the same stepwise

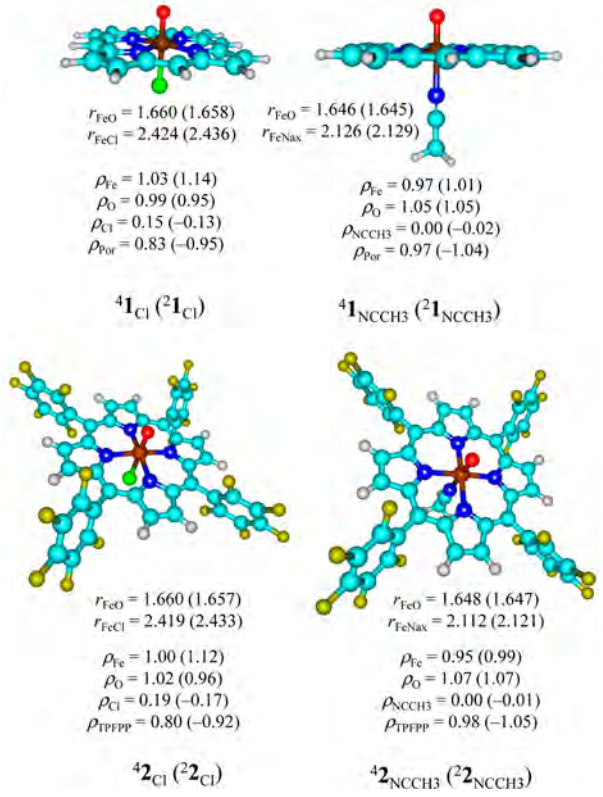

Figure 2. UB3LYP/BS1-optimized geometries of $^{4,2}\mathbf{1}_X$ and $^{4,2}\mathbf{2}_X$ in the gas phase with bond lengths in angstroms. Group spin densities are obtained at UB3LYP/BS2//UB3LYP/BS1 and are reported in atomic units.

mechanism that starts with the formation of a reactant complex between CpdI and substrate, **R**. As an example, we give the reaction profile for $[Fe^{IV}(O)(Por^{\bullet+})Cl]$ with *p*-H-styrene in Figure 3 on the lowest doublet and quartet spin states. The spin multiplicity is given as a superscript, and in the subscript, we give the axial ligand (X) and the *p*-Z substituent of styrene. The mechanism resembles that found in earlier studies of substrate epoxidation of olefins by metal(IV) oxo oxidants[23,25,26] and starts with an initial electrophilic addition of the oxo group to the double olefinic bond of styrene via a transition state $\mathbf{TS}_{X,Z}$ to form a radical intermediate ($\mathbf{I}_{X,Z}$), whereby the subscript X refers to the axial ligand, i.e., X = Cl^- or AN (acetonitrile), and the subscript Z to the para substituent of styrene. In a final reaction step, a ring-closure transition state ($\mathbf{TS}_{rc,Z}$) leads to epoxide product complexes ($\mathbf{P}_{X,Z}$). Optimized geometries obtained at UB3LYP-D/BS1 show little difference from those obtained at UB3LYP/BS1 (Figure 3).

Although the ring-closure barrier was calculated for a selection of chemical systems, in all cases its barrier was much smaller than the C−O bond-formation barrier via $\mathbf{TS}_{X,Z}$; therefore, we will focus here on the rate-determining barrier only. In particular, in the quartet spin state, ring-closure barriers were located and found to be small, whereas in the doublet spin state, the ring closure was virtually barrierless. The origin of this difference is due to differences in electron-transfer processes in the ring-closure step, whereby on the doublet spin-state surface, the π^*_{xz} orbital is filled with an extra electron, while on the quartet spin state, a higher-lying and virtual $\sigma^*_{z^2}$ orbital is filled with one electron.[26a] Energies obtained for the reaction of $[Fe^{IV}(O)(Por^{\bullet+})Cl]$ with *p*-H-styrene are very similar to those

dx.doi.org/10.1021/ic4005104 | Inorg. Chem. 2013, 52, 7968−7979

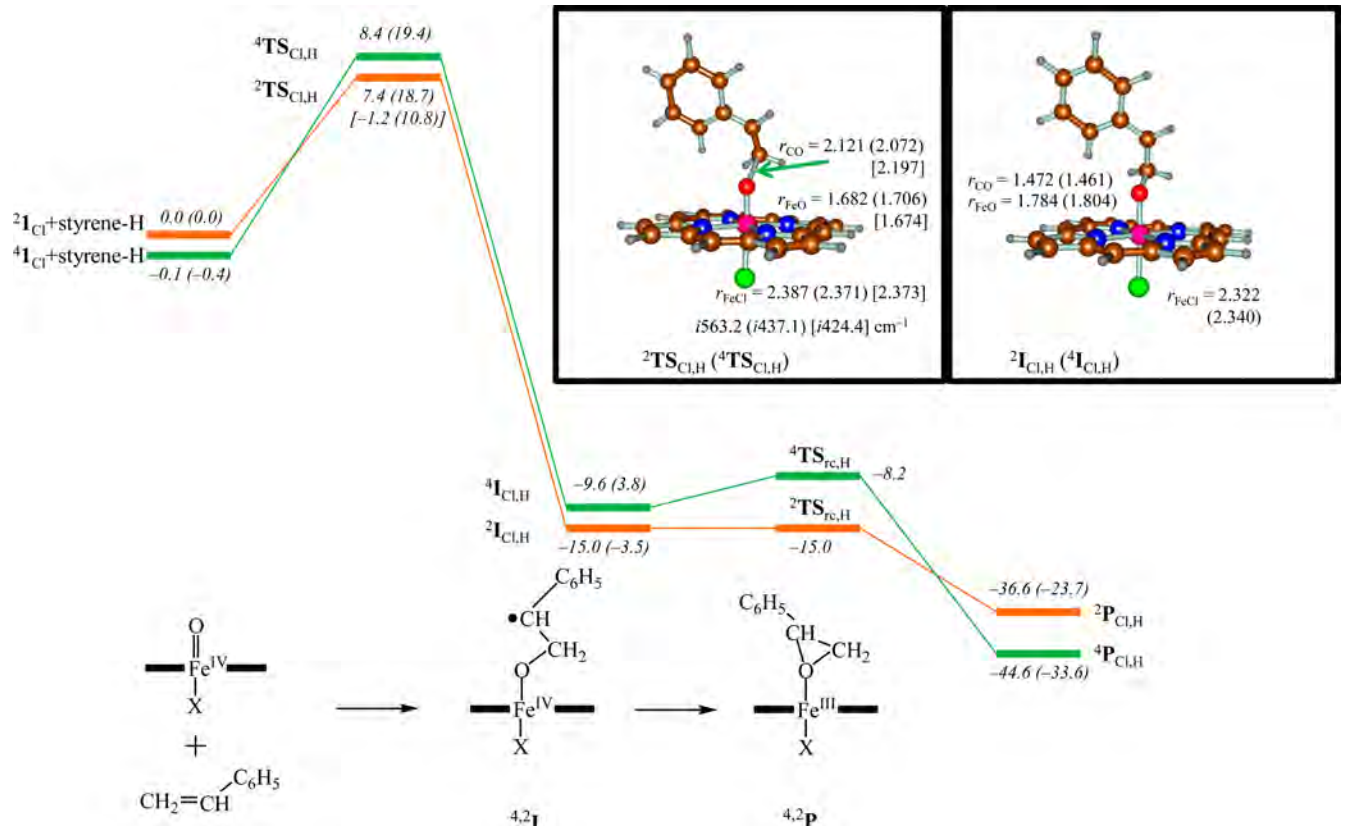

Figure 3. Potential energy profile of styrene epoxidation by $^{4,2}\mathbf{1}_{Cl}$ as calculated with UB3LYP/BS2//UB3LYP/BS1. All energies are in kilocalories per mole relative to isolated reactants in the doublet spin state and include ZPE corrections. Also shown are optimized geometries of critical points with bond lengths in angstroms and the imaginary frequencies in the transition state in wavenumbers. Free energies are given in parentheses and include UB3LYP/BS2 energies corrected with thermal and entropic corrections at 298 K. Data in square brackets were obtained from a UB3LYP-D/BS2//UB3LYP-D/BS1 calculation.

reported before using $[Fe^{IV}(O)(Por^{\bullet+})SH]$ as an oxidant.[23,26b] That is not surprising because the pK_a and electron affinity (EA) of $[Fe^{IV}(O)(Por^{\bullet+})X]$, X = Cl^-/SH^-, are virtually the same. Geometries are typical for epoxidation structures from previous calculations for P450-catalyzed reaction mechanisms.[25,26] In the transition state, the Fe−O bond elongates slightly with respect to reactants and further extends in the intermediate to 1.784 Å. At the same time, considerable shortening of the C−O distance occurs to a formally single bond in $^{4,2}\mathbf{I}_{Cl,H}$ of 1.472 Å.

Subsequently, we investigated the reaction mechanisms of $[Fe^{IV}(O)(Por^{\bullet+})X]^{0/+}$, X = Cl^- or $NCCH_3$, with para-substituted styrene, and the optimized geometries of the transition states are given in Figure 4. Interestingly, structural differences are found between the two axially ligated oxidants, whereby the Cl^--bound $\mathbf{TS}_{X,Z}$ structures are with styrene in an upright position, whereas the acetonitrile-bound ones are more sideways-bound. Test calculations using an upright starting structure and an acetonitrile axial ligand, however, converged back to the sideways-bound structure instead, which implies that the upright structures are higher in energy for the axially ligated acetonitrile transition states. The differences in the substrate orientation affect the bond distances of the respective transition states. For instance, the bond-forming C−O distances vary from 2.017 to 2.241 Å for the transition states with X = Cl^-, whereas for X = $NCCH_3$, distances between 2.083 and 2.439 Å are found. This implies that the barriers for the acetonitrile-ligated structures are somewhat earlier than the ones for the chloride-bound systems. Although variations in the Fe−O and Fe−X distances are considerably smaller than those for the C−O distance, variations between the oxidant with chloride and acetonitrile ligands are also found.

The epoxidation barriers ($\mathbf{TS}_{Cl,Z}$) range from 3.92 kcal mol^{-1} for *p*-N$(CH_3)_2$-styrene to 7.40 kcal mol^{-1} for *p*-H-styrene, i.e., vary by 3.48 kcal mol^{-1} upon para substitution. With acetonitrile as the axial ligand, the lowest barrier is 10.56 kcal mol^{-1} below isolated reactants for *p*-N$(CH_3)_2$-styrene, although it should be noted that the reactant complex is more stable than isolated reactants by 14.75 kcal mol^{-1}. Thus, the epoxidation barrier height varies by 20 kcal mol^{-1} between *p*-N$(CH_3)_2$-styrene and *p*-NO_2-styrene for $\mathbf{TS}_{AN,Z}$; hence, the substituent located at a distance of over 4 Å from the reaction center causes a rate constant change by a factor of ca. 10^{15} (estimated using transition state theory for an enthalpy-derived free energy change of 20 kcal mol^{-1}; the entropy of activation was not included in this estimate). The ordering of the barrier heights is virtually the same for the two oxidants studied, namely, Z = N$(CH_3)_2$ < NH_2 < OCH_3 < CH_3/*t*-Bu < F/Cl < CN < H. A plot of the barriers $^2\mathbf{TS}_{Cl,Z}$ versus those calculated for $^2\mathbf{TS}_{AN,Z}$ with the same methods gives a linear correlation; see Figure S27 in the Supporting Information (SI). Furthermore, calculations using a solvent model included give free energies of activation that follow the same trends as values found in the gas phase (Figure S28 in the SI). Inclusion of dispersion corrections on the solvent-corrected free energies of activation gives a further systematic change of the energetics, as shown in

dx.doi.org/10.1021/ic4005104 | Inorg. Chem. 2013, 52, 7968−7979

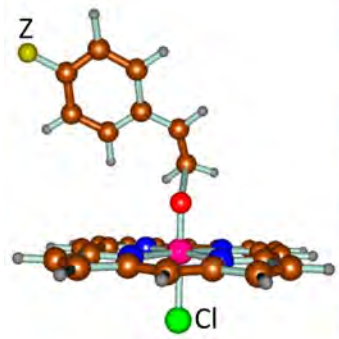

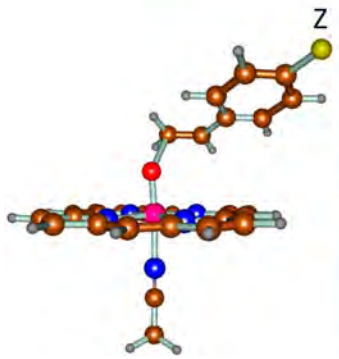

Z	H	F	Cl	CH_3	*t*-Bu	CN	NO_2	OCH_3	NH_2	$N(CH_3)_2$
X = Cl^-										
r_{C-O}	2.121	2.107	2.090	2.142	2.143	2.053	2.017	2.163	2.232	2.241
r_{O-Fe}	1.682	1.684	1.685	1.680	1.680	1.689	1.692	1.679	1.674	1.674
r_{Fe-Cl}	2.387	2.386	2.385	2.390	2.389	2.383	2.382	2.392	2.399	2.401
imag	*i*563.2	*i*600.4	*i*641.0	*i*500.3	*i*500.1	*i*693.3	*i*697.8	*i*421.5	*i*269.4	*i*245.7
ΔE+ZPE	7.40	7.01	7.06	6.79	6.85	7.30	7.28	5.97	4.80	3.92
$\Delta G+E_{solv}+E_{disp}$	13.8	11.2	11.9	9.4	11.3	12.7	11.8	10.1	6.5	−0.3
X = $NCCH_3$										
r_{C-O}	2.187	2.178	2.160	2.244	2.272	2.117	2.083	2.305	2.430	2.439
r_{O-Fe}	1.668	1.673	1.677	1.659	1.653	1.692	1.703	1.653	1.648	1.646
$r_{Fe-NCCH3}$	2.103	2.099	2.096	2.115	2.128	2.088	2.084	2.130	2.150	2.163
imag	*i*209.8	*i*220.3	*i*234.3	*i*181.1	*i*238.2	*i*274.4	*i*310.5	*i*147.8	*i*75.3	*i*66.0
ΔE+ZPE	3.55	4.15	4.66	1.39	1.25	8.30	9.44	-1.94	-7.11	-10.56
$\Delta G+E_{solv}+E_{disp}$	6.3	8.7	10.7	5.7	7.7	24.8	27.0		4.9	−1.0

Figure 4. Optimized geometries of rate-determining transition states $^2\mathbf{TS}_{X,Z}$ for the reaction of *p*-Z-styrene with $^2\mathbf{1}_X$ (X = Cl^-/$NCCH_3$). Geometries optimized at UB3LYP/BS1 with bond lengths given in angstroms and the imaginary frequencies in wavenumbers. Also given are barrier heights (ΔE + ZPE) for $^2\mathbf{TS}_{X,Z}$ with energies calculated at UB3LYP/BS2//UB3LYP/BS1+ZPE relative to isolated reactants in kilocalories per mole and free energies of activation in a solvent ($\Delta G + E_{solv} + E_{disp}$) relative to $^2\mathbf{RC}_{X,Z}$.

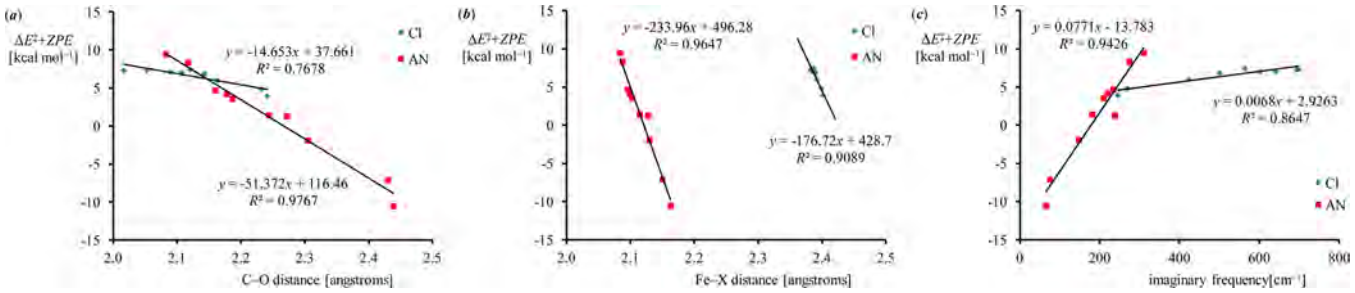

Figure 5. Analysis of the structural features of the transition states $\mathbf{TS}_{X,Z}$ calculated at UB3LYP/BS1 as a function of the height of the epoxidation barrier with respect to the (a) C−O distance, (b) Fe−X distance, and (c) imaginary frequency in the transition state. Data are given for X = Cl^- axial ligand (blue diamonds) and X = acetonitrile (red squares).

Figures S29 and S30 in the SI. This highlights the fact that for the assignment of reactivity trends it does not matter whether ΔE + ZPE, ΔG, $\Delta G + E_{solv}$, or $\Delta G + E_{solv} + E_{disp}$ energies are used. Because the enthalpies in a reaction mechanism are determined by the electronic changes of the reactants and we aim to establish the intrinsic chemical properties that determine the reactivity patterns, we will focus in the following on establishing trends through the ΔE + ZPE sets of data.

To understand the changes in the transition-state geometry between the para-substituted styrene substrates, we plot in Figure 5 a selection of bond distances versus the barrier height ($\Delta E^{\ddagger}$ + ZPE) for the two CpdI models with either a chloride or an acetonitrile axial ligand. Figure 5a shows the distance of the C−O bond that is formed in the process versus the barrier height. An almost perfect linear correlation (R^2 = 0.98) is obtained for the acetonitrile-ligated transition states, and a satisfactory linear correlation is found for the chloride-ligated system. Thus, a drop in the C−O bond length of 0.224 Å is found between the weakest epoxidating substrate (*p*-NO_2-styrene) and the strongest one [*p*-$N(CH_3)_2$-styrene] using a chloride axial ligand, whereas the difference between these substrates is 0.256 Å for an axially ligated acetonitrile molecule. This implies that the para substituent of styrene has a single possibly electrostatic effect on the C−O bond-formation step and, consequently, the barrier height of the reaction. To further ascertain that the optimized geometries and barrier heights are reproducible, we reoptimized a selection of **TS** structures with UB3LYP-D/BS1. Thus, $^2\mathbf{TS}_{AN,CN}$ and $^2\mathbf{TS}_{Cl,CN}$ give Fe−O distances of 1.683 and 1.680 Å and C−O distances of 2.131 and 2.107 Å, respectively. These values are close to those given in Figure 4 calculated at the UB3LYP/BS1 level of theory.

dx.doi.org/10.1021/ic4005104 | *Inorg. Chem.* 2013, 52, 7968−7979

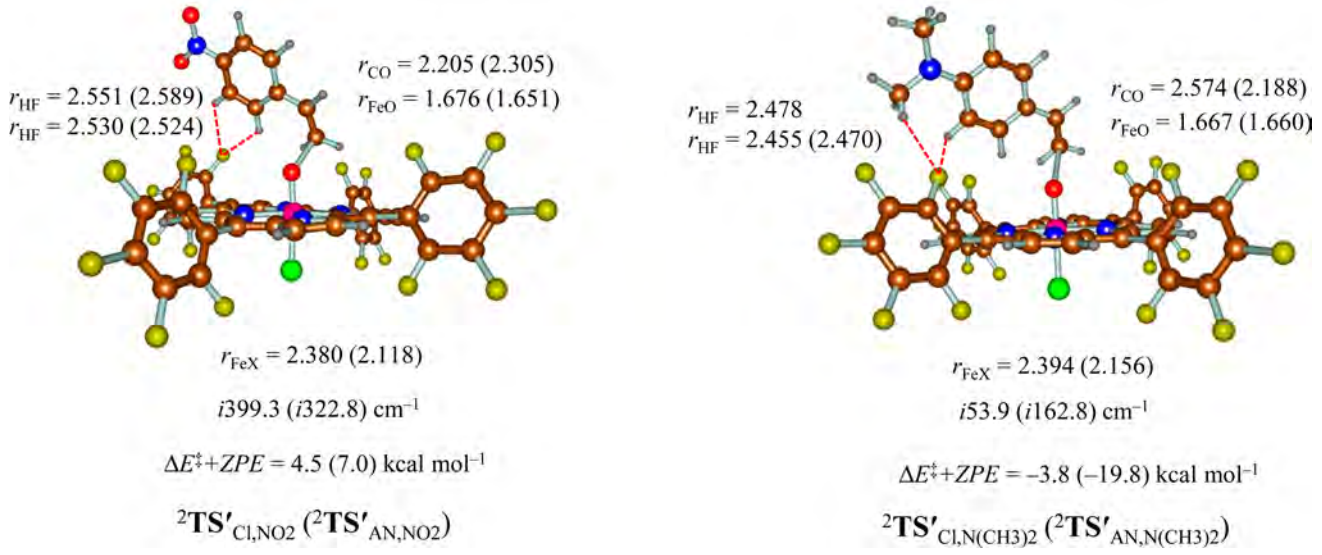

Figure 6. Optimized geometries of epoxidation transition states ^{2}**TS′**$_{X,Z}$ for the reaction of **2**$_{X}$ (X = Cl^{-}/NCCH$_3$) with *p*-Z-styrene. Bond lengths are in angstroms and the values of the imaginary frequencies in wavenumbers.

We also investigated the correlations of the epoxidation barrier height with the Fe−O and Fe−X distances in the transition states, and indeed these correlations are linear as well. With a chloride axial ligand, modest Fe−O and Fe−Cl changes are seen throughout the series of −0.018 and +0.019 Å, respectively, between the outer ranges for *p*-NO_2-styrene and *p*-$N(CH_3)_2$-styrene. Much larger differences are found for the weakly bound acetonitrile system, where the Fe−$NCCH_3$ distance is elongated from 2.084 to 2.163 Å (+0.079 Å shift) between *p*-NO_2-styrene and *p*-$N(CH_3)_2$-styrene. Thus, the para substituent of styrene affects bond distances well over 5 Å from the catalytic center and weakens the metal-to-axial ligand distances of the Fe−Cl and Fe−$NCCH_3$ bonds dramatically.

Interestingly, even the value of the imaginary frequency gives a linear correlation with the barrier height, i.e., are that the para substituent of styrene affects the height as well as the width of the potential energy curve around the transition state. Because both the height and width of the barrier change linearly for our series of substrates, this means that the area under the curve could stay the same for these substrates. However, changes to the width of the potential energy curve may have important effects on, for instance, the kinetic isotope effects (KIEs) for a reaction.[27] Thus, a small imaginary frequency correlates with a broad and wide potential energy surface, whereas a large imaginary frequency implies a narrow and high peak. Tunnelling through a narrow and high peak should be easier than through a broad peak; therefore, KIEs associated with this reaction may be affected as well. It is interesting to note that the imaginary frequencies are substantially larger for [Fe^{IV}(O)(Por$^{\bullet+}$)Cl] than for [Fe^{IV}(O)(Por$^{\bullet+}$)$NCCH_3$]$^{+}$; hence, the barriers for the latter oxidant will be much broader in shape. If this trend also applies to the hydrogen-atom-abstraction reaction, then this would imply that the calculations predict [Fe^{IV}(O)(Por$^{\bullet+}$)Cl] to react with considerably larger KIEs for the replacement of hydrogen by deuterium atoms than [Fe^{IV}(O)(Por$^{\bullet+}$)$NCCH_3$]$^{+}$ with substrates. Indeed, Nam and co-workers reported differences in the KIE values for the two oxidants in aliphatic hydrogen-atom-abstraction reactions.[11]

In a final set of calculations, we investigated the effect of meso substitution of the porphyrin ring on the electronic properties of CpdI and the epoxidation of para-substituted styrenes. We selected the TPFPP ligand system with pentafluorophenyl groups on the meso position of the porphyrin and calculated styrene epoxidation using the TPFPP oxidant: [Fe^{IV}(O)(TPFPP$^{\bullet+}$)X]$^{0/+}$ with X = Cl^{-} and $NCCH_3$ or **2**$_{X}$. We studied styrene epoxidation for *p*-$N(CH_3)_2$-styrene and *p*-NO_2-styrene and compared the mechanism and energy profiles with those observed above for **1**$_{X}$. Figure 6 displays optimized geometries of the epoxidation transition states **TS′**$_{X,Z}$ for the reaction of styrene with **2**$_{X,Z}$ with Z = NO_2 or $N(CH_3)_2$, as calculated with DFT methods.

Geometrically, there are striking differences between **TS**$_{X,Z}$, on the one hand, and **TS′**$_{X,Z}$, on the other hand. Thus, the epoxidation barriers with the TPFPP ligand system are characterized with long C−O and short Fe−O distances, which implies much earlier transition states along the potential energy surface. Furthermore, both acetonitrile- and chloride-ligated **TS′**$_{X,Z}$ structures are in the upright configuration, with a structure similar to the **TS**$_{Cl,Z}$ geometries reported in Figure 4. Probably, the stereochemical interactions with meso substituents prevent a substrate orientation analogous to **TS**$_{AN,Z}$ with a sideways attack on the oxo group. In addition, the structures are stabilized with hydrogen-bonding interactions of substrate C−H groups with the fluoride atoms from the TPFPP ligand and specifically those located in the ortho position of the meso substituent. As a consequence, both the reactant complexes and the transition states for epoxidation are considerably stabilized with respect to isolated reactants. Each transition state structure in Figure 6 is stabilized by at least two or three C−H---F hydrogen-bonding interactions with distances between 2.4 and 2.6 Å. F−H hydrogen-bonding interactions can be dramatic; for instance, trifluoromethanol as a solvent has been shown to lead to a considerable lowering of the epoxidation and halogenation barriers heights because of hydrogen-bonding and charge-transfer interactions.[28]

Recent computational studies of dehydrogenation of cyclohexadiene by [Fe^{IV}(O)(TPCPP$^{\bullet+}$)Cl] with TPCPP = *meso*-tetrakis(pentachlorophenyl)porphyrin also showed substrate stabilization due to weak hydrogen-bonding interactions of chloride atoms of the TPCPP ligand with C−H groups of the

dx.doi.org/10.1021/ic4005104 | *Inorg. Chem.* 2013, 52, 7968−7979

approaching substrate.[29] These interactions were shown to be particularly strong for epoxidation barrier heights because of a closer approach to the oxidant compared to hydrogen-atom-abstraction reactions and lowered epoxidation barriers significantly.[30] In line with this, it is not surprising that we find a considerable lowering of the epoxidation barriers from 7.3 to 4.5 kcal mol^{-1} for X = Cl/Z = NO_2, from 9.4 to 7.0 kcal mol^{-1} for X = AN/Z = NO_2, from 3.9 to −3.8 kcal mol^{-1} for X = Cl/Z = $N(CH_3)_2$, and from −10.6 to −19.8 kcal mol^{-1} for X = AN/Z = $N(CH_3)_2$ upon replacement of the equatorial ligand from Por to TPFPP. The big changes in geometry for $\mathbf{TS}_{X,Z}$ compared to $\mathbf{TS}'_{X,Z}$ also affect the shape of the potential energy surface and the values of the imaginary frequencies. Both $\mathbf{TS}'_{Cl,NO_2}$ and $\mathbf{TS}'_{Cl,N(CH_3)_2}$ structures have lower imaginary frequencies than $\mathbf{TS}_{Cl,NO_2}$ and $\mathbf{TS}_{Cl,N(CH_3)_2}$, whereas this is not the case for the axially ligated acetonitrile structures.

Thus, we report here the effect of meso substitution on the electronic and reactivity properties of iron(IV) oxo porphyrin cation-radical models. We find little changes in the electronic configuration of the various CpdI reactants. However, fluorine substituents on the meso position of TPFPP entice favorable electrostatic interactions with the approaching substrate and stabilize the epoxidation transition states. In the following, we will try to rationalize these observations.

DISCUSSION

In this work, we report a systematic set of epoxidations of substituted styrenes using four different oxidants, namely, $\mathbf{1}_{Cl}$, $\mathbf{1}_{NCCH_3}$, $\mathbf{2}_{Cl}$, and $\mathbf{2}_{NCCH_3}$. During the substrate epoxidation process, two electrons are transferred from the substrate to the oxidant, which is reduced from $[Fe^{IV}(O)(Por^{\bullet+})X]$ to $[Fe^{III}(Por)X]$. As a consequence, the EA of the oxidant and the ionization energy (IE) of the substrate should reflect the electron-transfer processes that take place. Indeed, several experimental studies found a correlation between the IE of substrates and the rate constant of substrate epoxidation and sulfoxidation.[7s,31] So far, no experimental studies have been reported on the activation parameters of substrate epoxidation by synthetic biomimetic iron(IV)-oxo porphyrin cation-radical models, but the rate constants are expected to correlate with the activation enthalpies. In earlier work, we reported a systematic study of olefin epoxidation by iron(IV) oxo complexes and set up a model that predicts barrier heights from known ionization potentials. Although that correlation still applies, we generalize it further in this work using the data described here.

To understand the individual contributions of the oxidant and substrate to the reaction process, i.e., transition states, we will investigate those separately. Let us start with a discussion of the differences and a comparison between $\mathbf{1}_{Cl}/\mathbf{2}_{Cl}$ and $\mathbf{1}_{NCCH_3}/\mathbf{2}_{NCCH_3}$ in styrene epoxidation reactions and their corresponding EAs. Thus, as shown in Figure 2, the reactant complexes give little differences in the geometric and electronic features upon a change in the equatorial ligand from Por to TPFPP.

We calculated EA values of 79.4 kcal mol^{-1} for $\mathbf{1}_{Cl}$, 101.4 kcal mol^{-1} for $\mathbf{2}_{Cl}$, 148.7 kcal mol^{-1} for $\mathbf{1}_{NCCH_3}$, and 163.8 kcal mol^{-1} for $\mathbf{2}_{NCCH_3}$ in the gas phase. Note here that, despite the fact that the valence orbital occupations and orbital shapes seem little influenced by the nature of the meso substituents of the porphyrin ring, actually the EA values increase by as much as 15.1−22.0 kcal mol^{-1}. This observation is in excellent agreement with the electrochemical studies of Fujii and coworkers, who found similar trends.[12]

Because the electrophilic reaction mechanism results in electron transfer from substrate to oxidant orbitals, these differences in the EAs of the four oxidants also affect the subsequent reaction mechanisms and reactivities with substrates. The transition state structures for these reactions, however, show dramatic differences in group spin densities, as displayed in Figure 7. Thus, generally the reaction proceeds

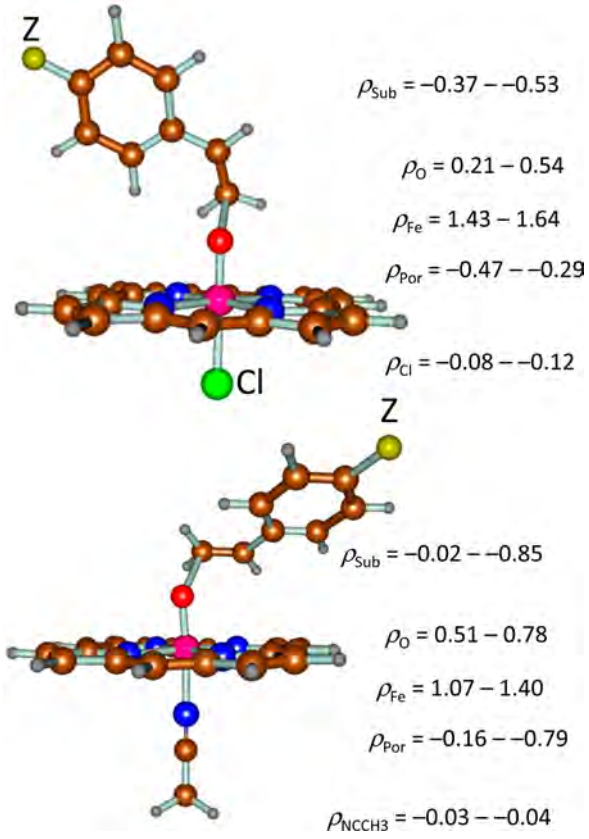

Figure 7. UB3LYP/BS2//UB3LYP/BS1-calculated group spin density ranges for *p*-Z-styrene epoxidation by $\mathbf{1}_{Cl}$ (top) and $\mathbf{1}_{AN}$ (bottom).

with electron transfer from the substrate to the half-filled a_{2u} porphyrin orbital, whereby a decrease in the spin density of the porphyrin group is found. The electronic configuration of the $\mathbf{TS}_{Cl,Z}$ structures is very much product-like with ρ_{Por} in the range from −0.29 to −0.47, whereas the $\mathbf{TS}_{AN,Z}$ values are reactant-like with considerably more spin density on the porphyrin ring.

Similarly, polarization of the FeO spin density from almost equal oxygen and iron spin densities in the reactants to a dominant iron radical in $\mathbf{TS}_{Cl,Z}$ occurs, whereby ρ_{Fe} ranges from 1.43 to 1.64 and ρ_O ranges from 0.21 to 0.54. By contrast, ρ_{Fe} varies from 1.07 to 1.40 and ρ_O ranges from 0.51 to 0.78 in the set of $\mathbf{TS}_{AN,Z}$ structures. The axial ligand, therefore, has an electronic effect on the charge and spin distributions in the rate-determining transition states, and, in particular, an anionic axial ligand, such as chloride, polarizes the FeO biradical toward the metal. Consequently, the anionic ligand will incur a "push" effect on the metal oxo group and formally change it from an $Fe^{V}O^{\bullet-}$ configuration in the reactant state to $Fe^{IV}O^{2-}$ in the transition state. By contrast, an iron(IV) oxo oxidant with a neutral axial ligand retains much larger radical character on the

dx.doi.org/10.1021/ic4005104 | Inorg. Chem. 2013, 52, 7968−7979

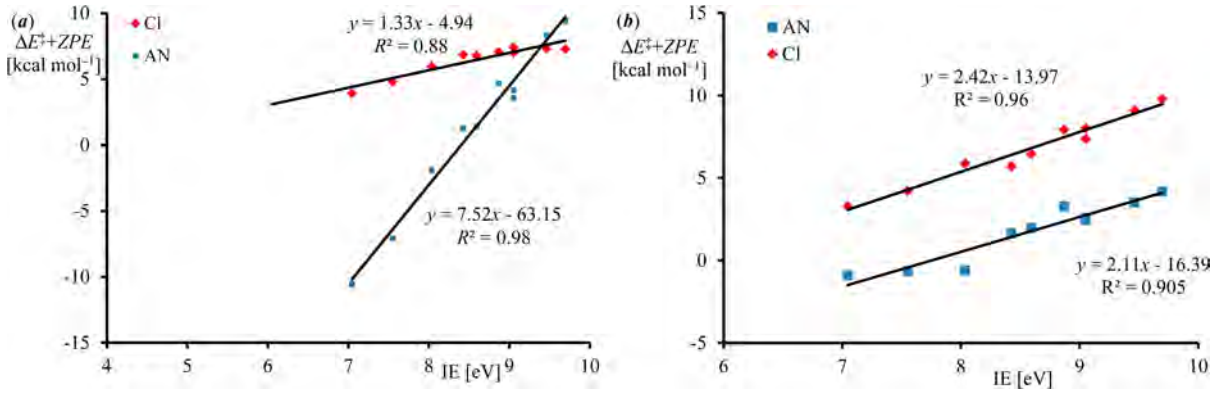

Figure 8. Styrene epoxidation barrier heights ($\Delta E^{\ddagger}$ + ZPE) of $^{2}\mathbf{TS}_{X,Z}$ plotted against the IE of the corresponding substrate. (a) Energies relative to isolated reactants. (b) Energies relative to a reactant complex (**RC**).

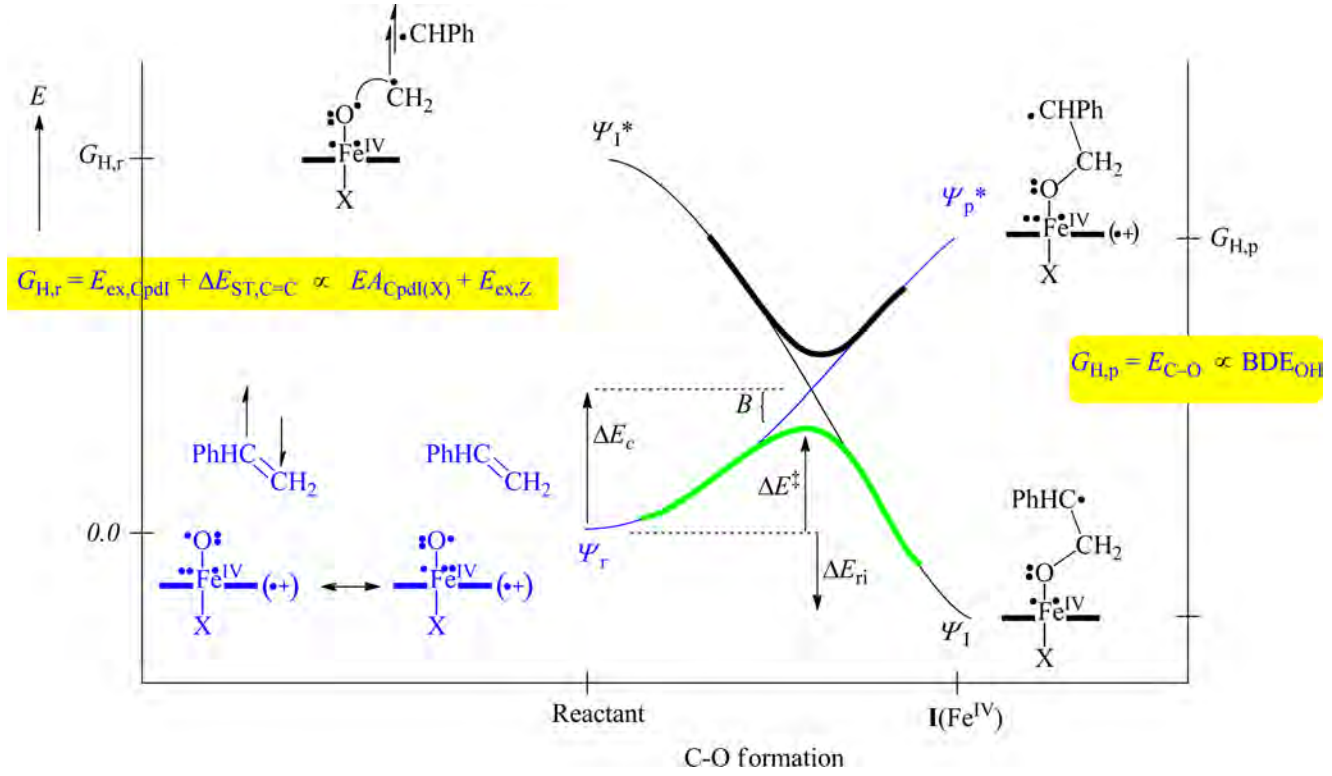

Figure 9. VB curve crossing diagram for *p*-Z-styrene epoxidation by iron(IV)-oxo porphyrin cation-radical oxidants. Lewis structures give relevant valence π orbitals with a dot.

oxygen atom in the electrophilic transition states and keeps the metal oxo group in a formal $Fe^{V}O^{\bullet-}$ configuration. This is important because it reduces the barrier heights of the electrophilic reaction mechanisms.

Let us in the following look into the barrier heights of styrene epoxidation and elucidate the enthalpic contributions to the relative values of the associated rate constants. Experimental studies on substrate sulfoxidation by P450 enzymes indicated a correlation between the rate constants and IEs of the selected substrates.[31] More recent mass spectrometric and computational studies showed that this correlation also applies to substrate epoxidation reactions.[7s,10] To test this relationship for the set of data studied here, we plot in Figure 8 the calculated barrier heights $^{2}\mathbf{TS}_{Cl,Z}$ and $^{2}\mathbf{TS}_{AN,Z}$ as a function of the IEs of the *p*-Z-styrene substrates. We calculated the trends using two sets of relative energies: In the first, we take the isolated reactants as a reference point, whereas in the second set, a reactant complex (**RC**) is used. DFT-calculated ionization potentials at the same level of theory as the transition states for the epoxidation reactions were used for consistency. Our calculated IE values are close to those reported in the literature;[32] however, because not all IE values are experimentally known, we will use the calculated data in our analysis here. As can be seen, both series of *p*-Z-styrene epoxidation reactions give barriers that correlate linearly with the ionization potential, whether energies relative to isolated reactants or a reactant complex are used. Interestingly, the two correlations that use energies relative to isolated reactants have different slopes and intercepts, and indeed the two curves cross at an IE of about 9.40 eV. Therefore, $[Fe^{IV}(O)(Por^{\bullet+})NCCH_3]^{+}$ in the gas phase is a better oxidant than $[Fe^{IV}(O)(Por^{\bullet+})Cl]$ in epoxidation reactions with substrates with IE below 9.40 eV,

dx.doi.org/10.1021/ic4005104 | Inorg. Chem. 2013, 52, 7968−7979

whereas it is reversed for substrates with higher ionization potentials, i.e., for *p*-CN-styrene and *p*-NO_2-styrene. This observation is in excellent agreement with the experimental studies of Nam et al.,[11] who also found improved reactivity of $[Fe^{IV}(O)(Por^{\bullet+})NCCH_3]^+$ over $[Fe^{IV}(O)(Por^{\bullet+})Cl]$ for the epoxidation of para-substituted styrenes with a large ρ^+_p Hammett value of the substituent. The study that uses a reactant complex as the reference point, by contrast does not find this change in reactivity but instead produces almost parallel trends (Figure 8b). It may very well be, therefore, that the reactant complexes are unrealistic models and do not compare well with the experiment. Thus, in a reactant complex, the structures of the oxidant and substrate are solvated by solvent molecules and the interactions between all particles. In our reactant complex, no solvent molecules were included, and as a consequence, full freedom of optimization was possible, which may have resulted in an experimentally unrealistic structure.

To further understand the reactivity trends and the effect of the substrate and oxidant on the obtained barrier heights and, by extension, the rate constants, we set up a valence bond (VB) curve crossing diagram for styrene epoxidation by iron(IV)-oxo porphyrin cation-radical systems (Figure 9). The VB curve crossing diagram displayed here is analogous to that presented before for hydrogen-atom-abstraction reactions by iron(IV) oxo oxidants[33] but is further generalized to accommodate substrate epoxidation reactions.

This diagram starts on the bottom-left with the reactant configurations, i.e., styrene and $[Fe^{IV}(O)(Por^{\bullet+})X]$. The latter appears in two VB configurations, where we highlight the valence π-orbital electrons with dots. Thus, the electronic ground state of $[Fe^{IV}(O)(Por^{\bullet+})X]$ is $\delta_{x^2-y^2}{}^2\pi_{xz}{}^2\pi_{yz}{}^2\pi^*_{xz}{}^1\pi^*_{yz}{}^1a_{2u}{}^1$ in both the quartet and doublet spin states, and its wave function is labeled as Ψ_r in Figure 9. The $\delta_{x^2-y^2}$ orbital is a nonbonding orbital in the plane of the porphyrin ring. The perpendicular set of orbitals, π_{xz}/π^*_{xz} and π_{yz}/π^*_{yz}, are the bonding and antibonding combinations of the metal $3d_{xz}/3d_{yz}$ with the oxygen $2p_x/2p_y$ atomic orbitals and contain three electrons in each pair.

In the C−O bond-formation step in the epoxidation mechanism, one electron is transferred from the substrate to the oxidant and it fills the a_{2u} orbital with a second electron to give the radical intermediate wave function Ψ_I. In VB theory,[33] the reactant (Ψ_r) and product (Ψ_I) wave functions cross each other and connect to excited states in the product and reactant conformations, respectively. Thus, Ψ_I* is an excited reactant state with an electronic configuration that represents a C−O bond pair, a radical on the styrene group, and a closed-shell a_{2u} orbital. The two VB curves give an avoided crossing and a barrier height for C−O bond formation, $\Delta E^{\ddagger}$. On the basis of a series of hydrogen-atom-abstraction reactions,[33,34] it was shown that $\Delta E^{\ddagger}$ is proportional to the curve crossing energy (ΔE_c) minus the resonance energy B via $\Delta E^{\ddagger} = \Delta E_c - B$. However, the curve crossing energy is proportional to the promotion gap ($G_{H,r}$) or excitation energy from the reactant to product configuration in the geometry of the reactants so that the barrier height can be written as

$$\Delta E^{\ddagger} = fG_{H,r} - B \quad (1)$$

In a recent study, we showed that the relationship in eq 1 is also valid for substrate epoxidation and sulfoxidation reactions and that the promotion gap $G_{H,r}$ reflects the excitation energy or ionization potential of the substrate.[10,35]

A comparison of the VB structures for the Ψ_r and Ψ_I* configurations shows that there is an electron transfer from the iron(IV) oxo group to the porphyrin a_{2u} orbital, reflecting an electron excitation in CpdI ($E_{ex,CpdI}$), which can be approximated with the EA of the oxidant. In addition, it can be seen that the electrons in the C=C bond are singlet-paired in the reactant ground state but triplet-coupled in the excited state in the reactant geometry, which implies a singlet−triplet energy gap in the C=C bond, ΔE_{ST}. Thus, a singlet−triplet energy gap in the C=C bond reflects the excitation energy of an electron in the π bond of the C=C moiety, namely, $E_{ex,Z}$, which, in turn, can be approximated with the IE of the substrate. Consequently, $G_{H,r}$ is proportional to $EA_{CpdI(X)} + E_{ex,Z}$ and so should the barrier height of the epoxidation reaction. Of course, electron excitation from the π orbital of the substrate, which is the highest occupied molecular orbital, is also proportional to the IE of the substrate. Indeed, the plot in Figure 8 confirms a relationship between the barrier height and ionization potential, as predicted by the VB diagram in Figure 9.

For the reverse reaction, that is, from radical intermediates to reactants, the epoxidation barrier height ($\Delta E^{\ddagger}_{rev}$) is equal to $\Delta E^{\ddagger}$ plus the exothermicity to form radical intermediates (ΔE_{ri}). In VB, the reverse barrier is proportional to the promotion gap in the radical intermediates, i.e., Ψ_I to Ψ_p* or $G_{H,p}$. The VB structures on the radical intermediate side of Figure 9 show that the excitation energy $G_{H,p}$ corresponds to the formation energy of the C−O bond plus the electron transfer from the substrate into the a_{2u} orbital. The VB structures in Figure 9 indicate that the electrons in the C−O bond are singlet-coupled in Ψ_I but triplet-coupled in Ψ_p*, which implies that a singlet−triplet excitation in the C−O bond has occurred. The singlet−triplet excitation in the C−O bond refers to the bond breaking of the C−O bond. In earlier work, we showed that the C−O bond-formation energy is proportional to a H−O bond-formation energy, so that it can be mimicked with BDE_{OH}, defined as the reaction enthalpy for eq 2.[10]

To test whether the VB curve crossing diagram can predict the barrier heights from empirical values, we calculated the gas-phase EAs of all four oxidants from Figure 1 and the π−π* excitation energies and IEs of all *p*-Z-styrene substrates, and the results are given in Table 1. We calculated the EA of the

Table 1. Substrate Chemical Properties and Charge-Transfer (Q_{CT}) Values in the Transition States

Z	IE_Z[a]	$E_{ex,Z}$[a]	$Q_{CT,Cl}$[b]	$Q_{CT,AN}$[c]
H	9.05	3.82	0.10	0.25
F	9.05	3.81	0.07	0.24
Cl	8.87	3.70	0.08	0.16
CH_3	8.59	3.75	0.12	0.32
t-Bu	8.43	3.76	0.12	0.42
CN	9.46	3.46	0.01	0.10
NO_2	9.70	2.88	−0.03	−0.01
OCH_3	8.03	3.73	0.16	0.42
NH_2	7.55	3.61	0.22	0.55
$N(CH_3)_2$	7.05	3.57	0.27	0.63

[a]In electronvolts. [b]Charge transfer in $^2TS_{Cl,Z}$. [c]Charge transfer in $^2TS_{AN,Z}$.

dx.doi.org/10.1021/ic4005104 | Inorg. Chem. 2013, 52, 7968−7979

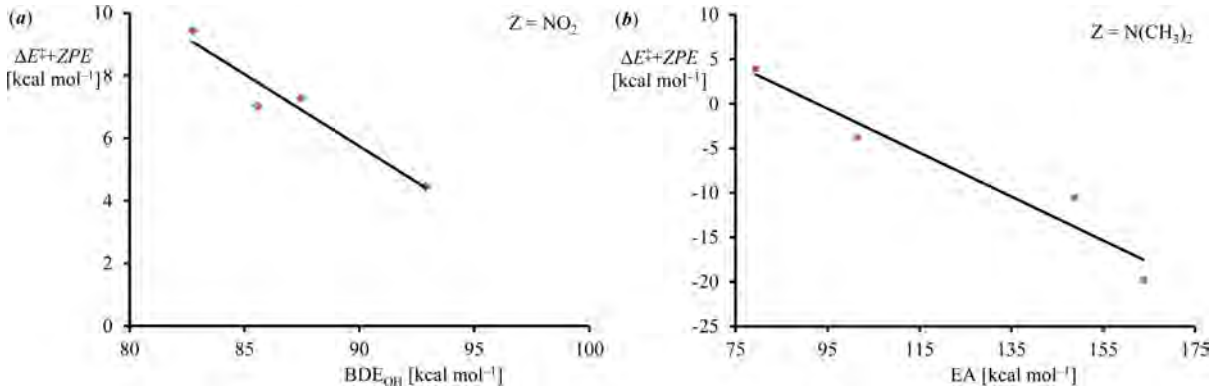

Figure 10. Correlations of (a) the epoxidation barrier height of *p*-NO_2-styrene with BDE_{OH} and (b) the epoxidation barrier height of *p*-$N(CH_3)_2$-styrene with $EA_{CpdI(X)}$.

oxidant, the $\pi-\pi^*$ excitation energy in the *p*-Z-styrene substrates, and the promotion gap via eq 2. Subsequently, we used these values to estimate $\Delta E^{\ddagger}_{VB}$ for all substrates. Although these VB-calculated barrier heights are, on average, within −0.05 kcal mol^{-1} of the DFT-calculated ones, actually the standard deviation is quite large (about 2 kcal mol^{-1}). This implies that the model has shortcomings, which we address with a slightly modified model as described below.

$$G_{H,r} = 2(EA_{CpdI(X)} + E_{ex,Z}) \quad (2)$$

$$[Fe^{IV}(O)(Por^{\bullet+})X] + H^{\bullet} \rightarrow [Fe^{IV}(OH)(Por)X] \quad (3)$$

Thus, the forward reaction barrier is dependent on the intrinsic chemical properties of the substrate, i.e., the IE, whereas the reverse reaction barrier depends on the variables of the oxidant, i.e., the BDE_{OH} value. We calculated gas-phase values of BDE_{OH} = 87.5 kcal mol^{-1} for $[Fe^{IV}(O)(Por^{\bullet+})Cl]$ and BDE_{OH} = 82.8 kcal mol^{-1} for $[Fe^{IV}(O)(Por^{\bullet+})NCCH_3]^+$, respectively.[23] This energy difference narrows to almost equal values in a dielectric constant of ε = 5.7: BDE_{OH} = 82.3 and 81.3 kcal mol^{-1} for $[Fe^{IV}(O)(Por^{\bullet+})X]$, X = Cl^- or $NCCH_3$, respectively.

The VB diagram of Figure 9 shows that the transition state described from reactants to intermediates, i.e., forward, is proportional to $EA_{CpdI(X)} + E_{ex,Z}$, whereas the transition state in the reverse reaction, i.e., backward, is proportional to the BDE_{OH} value of the oxidant. Thus, the location of the barrier on the potential energy surface will determine whether the barrier correlates with $EA_{CpdI(X)} + E_{ex,Z}$ or BDE_{OH}. So, for a substrate epoxidation reaction where the transition state has a very reactant-like electronic configuration, i.e., an early transition state, very little electron transfer from the substrate to the oxidant has taken place and consequently the reactant wave function dominates in the transition state. As a result, an early transition state should be proportional to BDE_{OH}. On the other hand, a late transition state has an electronic configuration closely resembling the radical intermediate state because of a significant amount of electron transfer that has taken place already. Therefore, late transition states, based on the VB diagram in Figure 8, should correlate with the EA of the oxidant. Indeed, the group spin density of the epoxidation transition state with *p*-NO_2-styrene as a substrate shows only a small amount of electron transfer from the substrate to the oxidant, and consequently the charge transfer from the substrate to the oxidant (Q_{CT}) is almost zero. This implies that the epoxidation barriers for *p*-NO_2-styrene will be early on the potential energy surface, and little electron transfer has taken place. As reasoned above, these barrier heights should, therefore, correlate with BDE_{OH} and not with $EA_{CpdI(X)} + E_{ex,Z}$. To test this, we display in Figure 10 the correlation of *p*-NO_2-styrene epoxidation with BDE_{OH} for $\mathbf{1}_X/\mathbf{2}_X$ (X = Cl^- and $NCCH_3$). As can be seen for this set of four data points, a linear correlation is found between the epoxidation barrier of *p*-NO_2-styrene and the corresponding BDE_{OH} value of the oxidant.

The group spin densities of $^2\mathbf{TS}_{X,N(CH_3)_2}$, in contrast to those found for $^2\mathbf{TS}_{X,NO_2}$, show considerably larger amounts of spin density on the substrate part of the structure. At the same time, the spin density on the porphyrin ring has dropped because of electron transfer from the substrate to the oxidant. Thus, the $^2\mathbf{TS}_{X,N(CH3)2}$ structures are electronically late and resemble product-type conformations. Because of that, in $^2\mathbf{TS}_{X,N(CH_3)_2}$, electron transfer has taken place already (or at least most of it) and, consequently, the barrier height will be driven by the differences in the EAs of the individual oxidants. To test this, we plot in Figure 10b the correlation between the epoxidation barrier height of *p*-$N(CH_3)_2$-styrene epoxidation by $\mathbf{1}_X/\mathbf{2}_X$ oxidants as a function of the EA of the oxidant. We find a linear correlation between the EA and barrier height, as predicted by the VB diagram in Figure 8.

As follows from the correlations depicted in Figure 10, the amount of electron transfer from the substrate to the oxidant determines whether a transition state correlates either with the sum of $EA_{CpdI(X)} + E_{ex,Z}$ or with BDE_{OH} instead. Thus, we extracted the degree of charge transfer from the substrate to the oxidant (Q_{CT}) from the UB3LYP/B2//UB3LYP/B1 calculations and summarize these values for the $^2\mathbf{TS}_{X,Z}$ transition states in Table 1. We now define the variable ω, which describes the position of the transition state on the potential energy profile through eq 4, and link ω to the degree of charge transfer (Q_{CT}), BDE_{OH}, and $EA_{CpdI(X)} + E_{ex,Z}$.

$$\omega = Q_{CT}BDE_{OH} + (1 - Q_{CT})(EA_{CpdI(X)} + E_{ex,Z}) \quad (4)$$

Essentially, ω is proportional to BDE_{OH} when the charge transfer is maximal, i.e.. an early transition state, but it is proportional to $EA_{CpdI(X)} + E_{ex,Z}$ for a late transition state with a small value of Q_{CT}. We calculated ω for all transition states $^2\mathbf{TS}_{X,Z}$, X = Cl^-/$NCCH_3$ and *p*-Z-styrene as substrates, and a plot of all data is given in Figure 11. Thus, the full set of transition states, irrespective of the axial ligand of the oxidant, fits a linear correlation. Consequently, we described the trend in epoxidation barriers for early as well as late transition states

dx.doi.org/10.1021/ic4005104 | Inorg. Chem. 2013, 52, 7968−7979

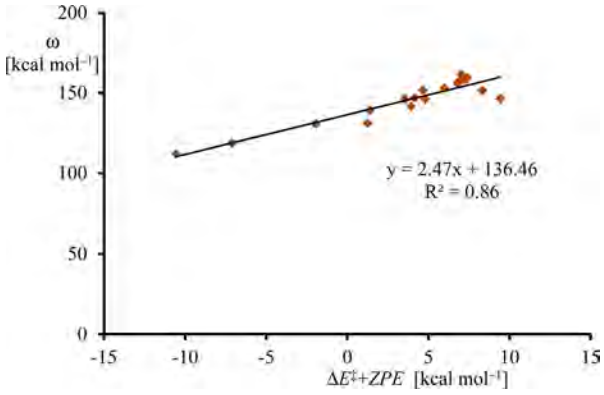

Figure 11. Correlation between the epoxidation barrier height of all data for $\mathbf{1}_X$ (X = Cl^-, $NCCH_3$) with parameter ω.

as a function of the intrinsic chemical properties of the oxidant and substrate and the amount of charge transfer in the TS during the reaction process.

In summary, we show here that the barrier height of an epoxidation reaction by a metal oxo oxidant is dependent on the electron-donating/withdrawing character of the substituents of the substrate. Thus, substrates with high electron-donating power such as *p*-$N(CH_3)_2$-styrene result in low barrier heights and rapid electron transfer from the substrate to the oxidant well before the epoxidation barrier height has been overcome. On the other hand, electron-withdrawing groups such as *p*-NO_2-styrene result in much later electron transfer from the substrate to the oxidant, and now the height of the barrier is determined by the strength of the C−O bond that is formed.

CONCLUSIONS

In this work, we report a systematic computational study into substrate epoxidation by four iron(IV)-oxo porphyrin cation-radical models. We investigated the effect of the axial ligand, chloride versus acetonitrile, as well as the equatorial ligand, Por versus TPFPP. It is shown that the substituents on the porphyrin ring can guide substrate binding through electrostatic interactions with halide atoms, which lowers the barrier heights. A neutral axial ligand leads to displacement of the metal from the plane through the porphyrin ring and results in different orbital interactions between the metal and porphyrin ring compared to systems with an anionic ligand. This has profound effects on the EA of the oxidant and the subsequent reactivity patterns. Finally, we investigated *p*-Z-styrene epoxidation by four iron(IV)-oxo porphyrin cation-radical models and highlight the differences in reactivity for olefins with electron-withdrawing versus electron-donating substituents. In particular, it is shown that electron-donating substituents give early transition states and lower reaction barriers than substrates with electron-withdrawing substituents.

ASSOCIATED CONTENT

Supporting Information

Tables with group spin densities, charges, and relative energies of all complexes described in this work as well as Cartesian coordinates of all optimized geometries. This material is available free of charge via the Internet at http://pubs.acs.org.

AUTHOR INFORMATION

Corresponding Author

*E-mail: sam.devisser@manchester.ac.uk (S.P.d.V.), dkclcre@yahoo.com (D.K.), rezalatifi@gmail.com (R.L.).

Notes

The authors declare no competing financial interest.

ACKNOWLEDGMENTS

The research was supported by the CPU time provided by the National Service of Computational Chemistry Software. D.K. is Ramanujan Fellow of the Department of Science and Technology, New Delhi, India (Research Grants SR/S2/RJN-11/2008), and also acknowledges financial support from the OSDD unit of the Council of Scientific & Industrial Research, New Delhi, India (Grant OSDD/HCP0001/12FYP/2012-13/Fin/2455). M.A.S. thanks the Petroleum Technology Development Fund of the Nigerian Government for a scholarship. E.V.R.-A. thanks the U.S. Department of Energy, Office of Basic Energy Science (Grant DE-FG02-06ER15799).

REFERENCES

(1) (a) Sono, M.; Roach, M. P.; Coulter, E. D.; Dawson, J. H. *Chem. Rev.* **1996**, *96*, 2841−2888. (b) Groves, J. T. *Proc. Natl. Acad. Sci. U.S.A.* **2003**, *100*, 3569−3574. (c) Ortiz de Montellano, P. R., Ed. *Cytochrome P450: Structure, Mechanism and Biochemistry*, 3rd ed.; Kluwer Academic/Plenum Publishers: New York, 2004. (d) Kadish, K. M., Smith, K. M., Guilard, R., Eds. *Handbook of Porphyrin Science*; World Scientific Publishing Co.: New York, 2010. (e) Ortiz de Montellano, P. R. *Chem. Rev.* **2010**, *110*, 932−948. (f) de Visser, S. P., Kumar, D., Eds. *Iron-containing enzymes: Versatile catalysts of hydroxylation reactions in nature*; RSC Publishing: Cambridge, U.K., 2011.

(2) (a) Denisov, I. G.; Makris, T. M.; Sligar, S. G.; Schlichting, I. *Chem. Rev.* **2005**, *105*, 2253−2277. (b) Rittle, J.; Green, M. T. *Science* **2010**, *330*, 933−937.

(3) (a) Groves, J. T.; Shalyaev, K.; Lee, J. In *The Porphyrin Handbook*; Kadish, K. M., Smith, K. M., Guilard, R., Eds.; Academic Press: New York; 2000; Vol. *4*, Chapter 27, pp 17−40. (b) Nam, W. *Acc. Chem. Res.* **2007**, *40*, 522−531.

(4) (a) Ruettinger, R. T.; Fulco, A. J. *J. Biol. Chem.* **1981**, *256*, 5728−5734. (b) Guengerich, F. P. *Arch. Biochem. Biophys.* **2003**, *409*, 59−71. (c) McLean, K. J.; Munro, A. W. *Drug Metabol. Rev.* **2008**, *40*, 427−446.

(5) (a) Groves, J. T.; Avaria-Neisser, G. E.; Fish, K. M.; Imachi, M.; Kuczkowski, R. L. *J. Am. Chem. Soc.* **1986**, *108*, 3837−3838. (b) Alcalde, M.; Farinas, E. T.; Arnold, F. H. *J. Biomol. Screen.* **2004**, *9*, 141−146. (c) Dansette, P. M.; Bertho, G.; Mansuy, D. *Biochem. Biophys. Res. Commun.* **2005**, *338*, 450−455. (d) Yuan, X.; Wang, Q.; Horner, J. H.; Sheng, X.; Newcomb, M. *Biochemistry* **2009**, *48*, 9140−9146. (e) Shinkyo, R.; Xu, L.; Tallman, K. A.; Cheng, Q.; Porter, N. A.; Guengerich, T. P. *J. Biol. Chem.* **2011**, *286*, 33021−33028.

(6) Ortiz de Montellano, P. R.; Fruetel, J. A.; Collins, J. R.; Campere, D. L.; Loew, G. H. *J. Am. Chem. Soc.* **1991**, *113*, 3195−3196.

(7) For example, see: (a) Groves, J. T.; Myers, R. S. *J. Am. Chem. Soc.* **1983**, *105*, 5791−5796. (b) Groves, J. T.; Watanabe, Y. *J. Am. Chem. Soc.* **1986**, *108*, 507−508. (c) Collman, J. P.; Kodadek, T.; Brauman, J. I. *J. Am. Chem. Soc.* **1986**, *108*, 2588−2594. (d) Ostović, D.; Bruice, T. C. *J. Am. Chem. Soc.* **1989**, *111*, 6511−6517. (e) Collman, J. P.; Brauman, J. I.; Hampton, P. D.; Tanaka, H.; Bohle, D. S.; Hembre, R. T. *J. Am. Chem. Soc.* **1990**, *112*, 7980−7984. (f) Groves, J. T.; Gross, Z.; Stern, M. K. *Inorg. Chem.* **1994**, *33*, 5065−5072. (g) Stephenson, N. A.; Bell, A. T. *Inorg. Chem.* **2006**, *45*, 2758−2766. (h) Collman, J. P.; Zeng, L.; Wang, H. J. H.; Lei, A.; Brauman, J. I. *Eur. J. Org. Chem.* **2006**, 2707−2714. (i) Hessenauer-Ilicheva, N.; Franke, A.; Meyer, D.; Woggon, W.-D.; van Eldik, R. *J. Am. Chem. Soc.* **2007**, *129*, 12473−12479. (j) Mas-Balleste, R.; Que, L., Jr. *J. Am. Chem. Soc.* **2007**, *129*,

15964−15972. (k) Comba, P.; Rajaraman, G. *Inorg. Chem.* **2008**, *47*, 78−93. (l) Bruijnincx, P. C. A.; Buurmans, I. L. C.; Gosiewska, S.; Moelands, M. A. H.; Lutz, M.; Spek, A. L.; van Koten, G.; Klein Gebbink, R. J. M. *Chem.—Eur. J.* **2008**, *14*, 1228−1237. (m) Hull, J. F.; Sauer, E. L. O.; Incarvito, C. D.; Faller, J. W.; Brudvig, G. W.; Crabtree, R. H. *Inorg. Chem.* **2009**, *48*, 488−495. (n) McGown, A. J.; Kerber, W. D.; Fujii, H.; Goldberg, D. P. *J. Am. Chem. Soc.* **2009**, *131*, 8040−8048. (o) Company, A.; Feng, Y.; Güell, M.; Ribas, X.; Luis, J. M.; Que, L., Jr.; Costas, M. *Chem.—Eur. J.* **2009**, *15*, 3359−3362. (p) Franke, A.; Wolak, M.; van Eldik, R. *Chem.—Eur. J.* **2009**, *15*, 10182−10198. (q) Hessenauer-Ilicheva, N.; Franke, A.; Wolak, M.; Higuchi, T.; van Eldik, R. *Chem.—Eur. J.* **2009**, *15*, 12447−12459. (r) Leeladee, P.; Goldberg, D. P. *Inorg. Chem.* **2010**, *49*, 3083−3085. (s) Lanucara, F.; Crestoni, M. E. *Chem.—Eur. J.* **2011**, *17*, 12092−12100.

(8) (a) Gross, Z.; Nimri, S. *Inorg. Chem.* **1994**, *33*, 1731−1732. (b) Gross, Z. *J. Biol. Inorg. Chem.* **1996**, *1*, 368−371. (c) Czarnecki, K.; Nimri, S.; Gross, Z.; Proniewicz, L. M.; Kincaid, J. R. *J. Am. Chem. Soc.* **1996**, *118*, 2929−2935.

(9) Green, M. T.; Dawson, J. H.; Gray, H. B. *Science* **2004**, *304*, 1653−1656.

(10) Kumar, D.; Karamzadeh, B.; Sastry, G. N.; de Visser, S. P. *J. Am. Chem. Soc.* **2010**, *132*, 7656−7667.

(11) Song, W. J.; Ryu, Y. O.; Song, R.; Nam, W. *J. Biol. Inorg. Chem.* **2005**, *10*, 294−304.

(12) (a) Takahashi, A.; Kurahashi, T.; Fujii, H. *Inorg. Chem.* **2011**, *50*, 6922−6928. (b) Cong, Z.; Kurahashi, T.; Fujii, H. *Angew. Chem., Int. Ed.* **2011**, *50*, 9935−9939.

(13) (a) *Jaguar*, version 7.9; Schrödinger, LLC: New York, 2011. (b) Frisch, M. J.; et al. *Gaussian03*, revision C.01; Gaussian, Inc.: Wallingford, CT, 2004. (c) Frisch, M. J.; et al. *Gaussian09*, revision A.1; Gaussian, Inc.: Wallingford, CT, 2009.

(14) (a) Becke, A. D. *J. Chem. Phys.* **1993**, *98*, 5648−5652. (b) Lee, C.; Yang, W.; Parr, R. G. *Phys. Rev. B* **1988**, *37*, 785−789.

(15) (a) Hay, P. J.; Wadt, W. R. *J. Chem. Phys.* **1985**, *82*, 270−283. (b) Hehre, W. J.; Ditchfield, R.; Pople, J. A. *J. Chem. Phys.* **1972**, *56*, 2257−2261.

(16) (a) de Visser, S. P.; Oh, K.; Han, A.-R.; Nam, W. *Inorg. Chem.* **2007**, *46*, 4632−4641. (b) Vardhaman, A. K.; Sastri, C. V.; Kumar, D.; de Visser, S. P. *Chem. Commun.* **2011**, *47*, 11044−11046.

(17) de Visser, S. P. *J. Am. Chem. Soc.* **2010**, *132*, 1087−1097.

(18) Schwabe, T.; Grimme, S. *Phys. Chem. Chem. Phys.* **2007**, *9*, 3397−3406.

(19) Reiher, M.; Salomon, O.; Hess, B. A. *Theor. Chem. Acc.* **2001**, *107*, 48−55.

(20) Kumar, D.; Thiel, W.; de Visser, S. P. *J. Am. Chem. Soc.* **2011**, *133*, 3869−3882.

(21) (a) Green, M. T. *J. Am. Chem. Soc.* **1999**, *121*, 7939−7940. (b) Ogliaro, F.; de Visser, S. P.; Cohen, S.; Kaneti, J.; Shaik, S. *ChemBioChem* **2001**, *11*, 848−851. (c) Kamachi, T.; Yoshizawa, K. *J. Am. Chem. Soc.* **2003**, *125*, 4652−4661. (d) Bathelt, C. M.; Zurek, J.; Mulholland, A. J.; Harvey, J. N. *J. Am. Chem. Soc.* **2005**, *127*, 12900−12908. (e) Lonsdale, R.; Oláh, J.; Mulholland, A. J.; Harvey, J. N. *J. Am. Chem. Soc.* **2011**, *133*, 15464−15474. (f) Isobe, H.; Yamanaka, S.; Okumura, M.; Yamaguchi, K.; Shimada, J. *J. Phys. Chem. B* **2011**, *115*, 10730−10738.

(22) Shaik, S.; Kumar, D.; de Visser, S. P.; Altun, A.; Thiel, W. *Chem. Rev.* **2005**, *105*, 2279−2328.

(23) de Visser, S. P.; Tahsini, L.; Nam, W. *Chem.—Eur. J.* **2009**, *15*, 5577−5587.

(24) de Visser, S. P.; Shaik, S.; Sharma, P. K.; Kumar, D.; Thiel, W. *J. Am. Chem. Soc.* **2003**, *125*, 15779−15788.

(25) (a) Linde, C.; Åkermark, B.; Norrby, P.-O.; Svensson, M. *J. Am. Chem. Soc.* **1999**, *121*, 5083−5084. (b) Kamachi, T.; Shiota, Y.; Ohta, T.; Yoshizawa, K. *Bull. Chem. Soc. Jpn.* **2003**, *76*, 721−732. (c) Quiñinero, D.; Musaev, D. G.; Morokuma, K. *Inorg. Chem.* **2003**, *42*, 8449−8455. (d) Sharma, P. K.; de Visser, S. P.; Ogliaro, F.; Shaik, S. *J. Am. Chem. Soc.* **2003**, *125*, 2291−2300. (e) Hirao, H.; Kumar, D.; Thiel, W.; Shaik, S. *J. Am. Chem. Soc.* **2005**, *127*, 13007−13018. (f) Kumar, D.; Derat, E.; Khenkin, A. M.; Neumann, R.; Shaik, S. *J. Am. Chem. Soc.* **2005**, *127*, 17712−17718. (g) Bassan, A.; Blomberg, M. R. A.; Siegbahn, P. E. M.; Que, L., Jr. *Angew. Chem., Int. Ed.* **2005**, *44*, 2939−2941.

(26) (a) de Visser, S. P.; Ogliaro, F.; Harris, N.; Shaik, S. *J. Am. Chem. Soc.* **2001**, *123*, 3037−3047. (b) de Visser, S. P.; Ogliaro, F.; Shaik, S. *Angew. Chem., Int. Ed.* **2001**, *40*, 2871−2874. (c) de Visser, S. P.; Ogliaro, F.; Sharma, P. K.; Shaik, S. *Angew. Chem., Int. Ed.* **2002**, *41*, 1947−1951. (d) de Visser, S. P.; Ogliaro, F.; Sharma, P. K.; Shaik, S. *J. Am. Chem. Soc.* **2002**, *124*, 11809−11826. (e) Kumar, D.; de Visser, S. P.; Shaik, S. *Chem.—Eur. J.* **2005**, *11*, 2825−2835.

(27) (a) Kumar, D.; de Visser, S. P.; Shaik, S. *J. Am. Chem. Soc.* **2003**, *125*, 13024−13025. (b) Kumar, D.; de Visser, S. P.; Sharma, P. K.; Cohen, S.; Shaik, S. *J. Am. Chem. Soc.* **2004**, *126*, 1907−1920. (c) Kumar, D.; de Visser, S. P.; Shaik, S. *J. Am. Chem. Soc.* **2004**, *126*, 5072−5073. (d) de Visser, S. P. *Chem.—Eur. J.* **2006**, *12*, 8168−8177.

(28) (a) Ben-Daniel, R.; de Visser, S. P.; Shaik, S.; Neumann, R. *J. Am. Chem. Soc.* **2003**, *125*, 12116−12117. (b) de Visser, S. P.; Kaneti, J.; Neumann, R.; Shaik, S. *J. Org. Chem.* **2003**, *68*, 2903−2912.

(29) Kumar, D.; Tahsini, L.; de Visser, S. P.; Kang, H. Y.; Kim, S. J.; Nam, W. *J. Phys. Chem. A* **2009**, *113*, 11713−11722.

(30) de Visser, S. P. *J. Am. Chem. Soc.* **2006**, *128*, 15809−15818.

(31) (a) Watanabe, Y.; Iyanagi, T.; Oae, S. *Tetrahedron Lett.* **1980**, *21*, 3685−3688. (b) Watanabe, Y.; Numata, T.; Iyanagi, T.; Oae, S. *Bull. Chem. Soc. Jpn.* **1981**, *54*, 1163−1170. (c) Watanabe, Y.; Iyanagi, T.; Oae, S. *Tetrahedron Lett.* **1982**, *23*, 533−536.

(32) Lide, D. R. *CRC Handbook of Chemistry and Physics*, 76th ed.; CRC Press: Boca Raton, FL, 1996.

(33) Shaik, S. S. *J. Am. Chem. Soc.* **1981**, *103*, 3692−3701.

(34) (a) Shaik, S.; Kumar, D.; de Visser, S. P. *J. Am. Chem. Soc.* **2008**, *130*, 10128−10140. (b) Latifi, R.; Bagherzadeh, L.; de Visser, S. P. *Chem.—Eur. J.* **2009**, *15*, 6651−6662.

(35) Kumar, D.; Sastry, G. N.; de Visser, S. P. *Chem.—Eur. J.* **2011**, *17*, 6196−6205.

Inorganic Chemistry

Article

pubs.acs.org/IC

Generation of a High-Valent Iron Imido Corrolazine Complex and NR Group Transfer Reactivity

Pannee Leeladee,[†] Guy N. L. Jameson,*[,‡] Maxime A. Siegler,[†] Devesh Kumar,[⊥] Sam P. de Visser,*[,∥] and David P. Goldberg*[,†]

[†]Department of Chemistry, The Johns Hopkins University, 3400 North Charles Street, Baltimore, Maryland 21218, United States

[‡]Department of Chemistry and MacDiarmid Institute for Advanced Materials and Nanotechnology, University of Otago, P.O. Box 56, Dunedin 9054, New Zealand

[⊥]Department of Applied Physics, Babasaheb Bhimrao Ambedkar University, Vidya Vihar, Rai Bareilly Road, Lucknow 226 025, India

[∥]Manchester Institute of Biotechnology and School of Chemical Engineering and Analytical Science, The University of Manchester, 131 Princess Street, Manchester M1 7DN, United Kingdom

Supporting Information

ABSTRACT: The generation of a new high-valent iron terminal imido complex prepared with a corrolazine macrocycle is reported. The reaction of $[Fe^{III}(TBP_8Cz)]$ (TBP_8Cz = octakis(4-*tert*-butylphenyl)corrolazinato) with the commercially available chloramine-T (Na^+TsNCl^-) leads to oxidative N-tosyl transfer to afford $[Fe^{IV}(TBP_8Cz^{+\bullet})(NTs)]$ in dichloromethane/acetonitrile at room temperature. This complex was characterized by UV−vis, Mössbauer (δ = −0.05 mm s^{-1}, ΔE_Q = 2.94 mm s^{-1}), and EPR (X-band (15 K), g = 2.10, 2.00) spectroscopies, and together with reactivity patterns and DFT calculations has been established as an iron(IV) species antiferromagnetically coupled with a Cz-π-cation-radical (S_{total} = $^1/_2$ ground state). Reactivity studies with triphenylphosphine as substrate show that $[Fe^{IV}(TBP_8Cz^{+\bullet})(NTs)]$ is an efficient NTs transfer agent, affording the phospharane product $Ph_3P{=}NTs$ under both stoichiometric and catalytic conditions. Kinetic analysis of this reaction supports a bimolecular NTs transfer mechanism with rate constant of 70(15) M^{-1} s^{-1}. These data indicate that $[Fe^{IV}(TBP_8Cz^{+\bullet})(NTs)]$ reacts about 100 times faster than analogous Mn terminal arylimido corrole analogues. It was found that two products crystallize from the same reaction mixture of $Fe^{III}(TBP_8Cz)$ + chloramine-T + PPh_3, $[Fe^{IV}(TBP_8Cz)(NPPh_3)]$ and $[Fe^{III}(TBP_8Cz)(OPPh_3)]$, which were definitively characterized by X-ray crystallography. The sequential production of $Ph_3P{=}NTs$, $Ph_3P{=}NH$, and $Ph_3P{=}O$ was observed by ^{31}P NMR spectroscopy and led to a proposed mechanism that accounts for all of the observed products. The latter Fe^{III} complex was then rationally synthesized and structurally characterized from $Fe^{III}(TBP_8Cz)$ and $OPPh_3$, providing an important benchmark compound for spectroscopic studies. A combination of Mössbauer and EPR spectroscopies led to the characterization of both intermediate spin (S = $^3/_2$) and low spin (S = $^1/_2$) Fe^{III} corrolazines, as well as a formally Fe^{IV} corrolazine which may also be described by its valence tautomer $Fe^{III}(Cz^{+\bullet})$.

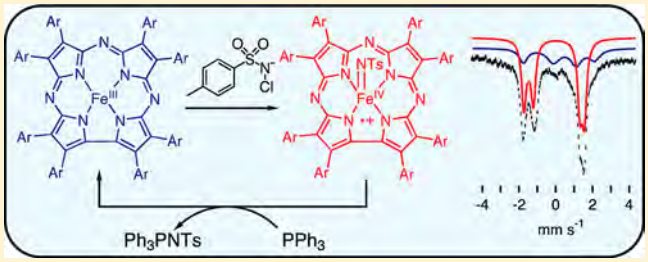

INTRODUCTION

Iron−nitrogen multiply bonded complexes have been implicated in biological systems and industrial processes. For instance, in the Haber−Bosch process, iron-bound surface nitrides have been postulated as the reactive intermediates responsible for ammonia production.[1,2] The iron-containing metalloenzyme nitrogenase likely relies upon one or more multiply bonded Fe−N intermediates during the dinitrogen reduction process.[3−5] An Fe=NR porphyrin species was suggested as the reactive intermediate for reactions involving NR insertion into C−H bonds by the heme enzyme Cytochrome P450-LM 3,4.[6] In analogy to this chemistry, much effort has gone into accessing transient Fe−N(R) multiply bonded species as potent catalysts for C−H activation and functionalization.[7−11] There is great interest in preparing metal-nitrido and metal-imido complexes, including iron-based systems, for similar potential applications in atom or group transfer processes.[12−17]

The synthesis of mid- to late-transition metal-imido complexes has been quite challenging. The stability of these compounds depends on their geometry, the oxidation state of the metal, and the nature of the ancillary ligands. In particular, 5- or 6-coordinate Fe-imido complexes are usually considered highly unstable, making it difficult to generate and/or characterize such species. It can be seen from qualitative d-orbital splitting diagrams that these high coordination number iron complexes would normally have filled, or partially filled,

Received: February 2, 2013
Published: March 25, 2013

 © 2013 American Chemical Society dx.doi.org/10.1021/ic400280x | Inorg. Chem. 2013, 52, 4668−4682

Chart 1. Representative Examples of Multiply-Bonded, Terminal-Imido/Nitrene Fe and Mn Complexes (Ad = adamantyl; Ts = tosyl; Mes = mesityl)

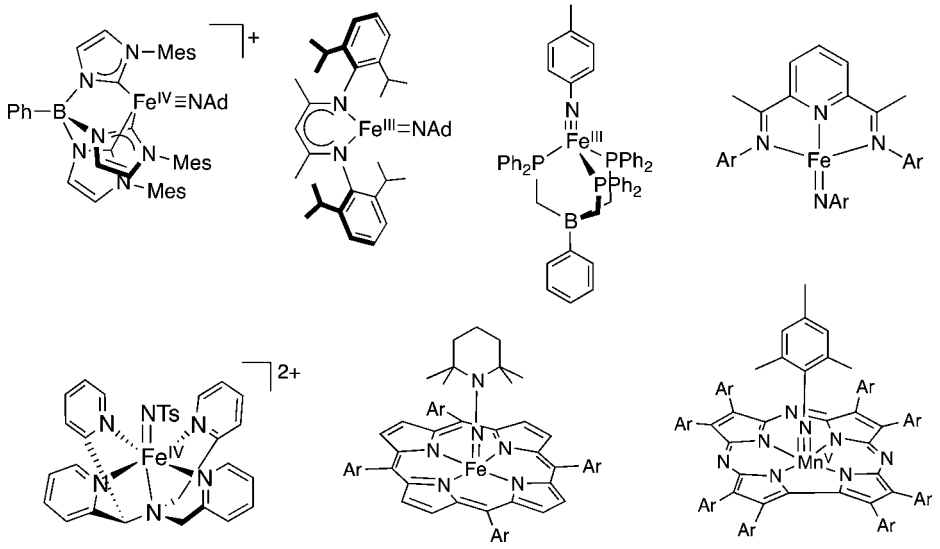

dπ-pπ antibonding orbitals with respect to the Fe−N interaction. The Fe ion needs to be in an unusually high oxidation state, e.g., Fe(6+), to avoid this destabilizing influence,[18] and iron compounds in relatively low oxidation states, e.g. Fe(2+), Fe(3+), are destabilized due to the population of the antibonding dπ(Fe)−pπ(N) orbitals.[9,10,17,19] To our knowledge, there is only one example of an Fe(NR) complex with a coordination number ≥5 that has been crystallographically characterized, and this complex is an iron porphyrin derivative.[20] Interestingly, this complex was formulated as a high-spin Fe^{II}-nitrene compound, as indicated by Mössbauer spectroscopy. In addition, a 6-coordinate, nonheme Fe^{IV}-imido complex supported by a tetrapyridylamine ligand was described, but this complex could not be characterized by X-ray crystallography (Chart 1).[21]

An alternative, elegant strategy to prepare stable Fe terminal imido complexes is to construct them from compounds with low coordination number (Chart 1). Peters and co-workers have shown that triply bonded Fe^{II}-, Fe^{III}-, and Fe^{IV}-imido complexes can be stabilized in pseudotetrahedral coordination environments by sterically encumbered tris(phosphino)borane, tris(phosphino)borate, and bis(phosphine)pyrazolyl ligands.[22−26] Similarly, Smith and co-workers introduced strong field, bulky tris(carbene)borate ligands to stabilize Fe^{III}- and Fe^{IV}-imido complexes with 3-fold symmetry.[27] Iron-imide complexes with redox-active bis(imino)pyridine (BIP) ligands have been constructed from distorted square planar geometries,[28,29] although the assignment of the iron oxidation states in these compounds is not straightforward.[28] Highly unsaturated, three-coordinate iron(III) terminal imido complexes have also been prepared with either bulky bidentate, β-diketiminate ligands,[30,31] or bidentate, dipyrromethene-based systems.[8] In all of these cases it seems that the steric encumbrance of the surrounding ligands is essential to engender the low-coordinate environments that stabilize iron-imido species.

Our group has focused on the stabilization and characterization of high-valent manganese and iron complexes with multiply bonded terminal ligands encapsulated in the heme-like corrolazine (Cz) platform. The strongly donating and oxidatively resistant Cz macrocycle has allowed for the isolation and X-ray crystallographic characterization of a high-valent Mn^{V}-imido complex, [Mn^{V}(TBP$_8$Cz)(NMes)] (Mes = 2,4,6-trimethylphenyl; TBP$_8$Cz = octakis(4-*tert*-butylphenyl)-corrolazinato) (Chart 1).[32] The related corrole (Cor) complex, [Mn^{V}(tpfc)(NMes)] (tpfc = *meso*-tris(pentafluorophenyl)-corrole), was also isolated and fully characterized, including an X-ray structure determination.[33] Isoelectronic Mn^{V} terminal oxo complexes have also been generated with Cz and Cor supporting ligands, and the first example of this class, Mn^{V}(O)(TBP$_8$Cz), was isolable and stable as a solid at room temperature.[34−38] In these cases the paradigm does not involve enforcing low-coordinate environments at the metal center; rather the Cz and Cor ligands are designed to provide strong, in-plane σ donation that helps stabilize metal ions in high-valent states, depopulating the key, dπ−pπ antibonding orbitals involved in terminal imido/oxo ligation.

The synthesis of these rare, manganese-imido/oxo complexes suggested to us that the Cz scaffold might support the preparation of analogous high-valent, iron-imido complexes. Indeed, we had already described the generation, low-temperature stabilization, and C−H activation chemistry of a high-valent, iron-oxo corrolazine π-cation-radical (Fe^{IV}(O)-(TBP$_8$Cz$^{+\bullet}$)), equivalent to the compound-I intermediate in heme enzymes.[39,40] It has been shown that Fe^{III} corroles can catalyze aziridinations using PhINTs as the nitrogen source, and a high-valent Fe-imido species was postulated as the reactive intermediate.[41] In the same study, an Fe^{IV} corrole was also found to be a potent catalyst for aziridinations when PhINTs was replaced with chloramine-T (Na^{+}TsNCl^{-}) as the nitrogen source. However, no direct spectroscopic evidence for the existence of high-valent Fe-imido corroles in this study, or any other, has thus far been obtained.

Herein, we report the generation of a high-valent iron-imido corrolazine, (TBP$_8$Cz$^{+\bullet}$)Fe^{IV}(NTs), and its characterization through a combination of UV−vis, EPR, and Mössbauer spectroscopies. Density functional theory (DFT) calculations were performed to support and analyze the electronic structure assignment, and simulate the Mössbauer parameters for the high-valent iron-imido complex. This complex is a rare example of a metastable Fe-imido porphyrinoid compound, and the first example of such a species housed in a corrole-type macrocycle.

dx.doi.org/10.1021/ic400280x | *Inorg. Chem.* 2013, 52, 4668−4682

It is shown that this compound is capable of NR group transfer to PPh_3 to give the $TsN{=}PPh_3$ product with concomitant two-electron reduction of the iron-imido complex. Kinetic studies show that the reactivity of the Fe=NTs complex is dramatically enhanced over Mn=NAr corroles. However, $(TBP_8Cz^{+\bullet})Fe^{IV}(NTs)$ is, in general, significantly more stable (and less reactive) than expected for a multiply bonded, iron-imido species. Crystal structures were determined for the PPh_3-derived products $[Fe^{IV}(TBP_8Cz)(NPPh_3)]$ and $[Fe^{III}(TBP_8Cz)(OPPh_3)]$, and these structures have aided in our understanding of the mechanism of NR transfer and subsequent product transformations. Combined EPR and Mössbauer studies on the series of iron complexes described here provide insights into the oxidation state assignments and ligand noninnocence for such compounds.

EXPERIMENTAL DETAILS

All reactions were performed using dry solvents and standard Schlenk or drybox techniques at room temperature unless otherwise noted. The complex $[Fe^{III}(TBP_8Cz)]$ (**1**)[42] and metal-free corrolazine TBP_8CzH_3[43] were synthesized as reported previously. The $^{57}FeCl_2$ was prepared according to a published procedure.[44] Dichloromethane and acetonitrile were purified via a Pure-Solv solvent purification system from Innovative Technologies, Inc. Deuterated solvents for NMR samples were purchased from Cambridge Isotope Laboratories, Inc. Chloramine-T trihydrate ($Na^+TsNCl^-{\cdot}3H_2O$) was purchased from Sigma-Aldrich and used as received. Triphenylphosphine (PPh_3) was received from Sigma-Aldrich and recrystallized from diethyl ether. Triphenylphosphine oxide (Ph_3PO) was purchased from Sigma-Aldrich and recrystallized from ethanol. Authentic samples of (*N*-tosylimino)triphenylphosphorane (Ph_3PNTs) and Ph_3PNH were synthesized according to published methods.[45,46]

Instrumentation. UV−vis spectroscopy was performed on a Varian Cary 50 Bio spectrophotometer. Kinetic experiments were run on a Hewlett-Packard 8542 diode-array spectrophotometer equipped with HPChemstation software. Electron paramagnetic resonance (EPR) spectra were obtained on a Bruker EMX EPR spectrometer controlled with a Bruker ER 041 X G microwave bridge at 15 K, and equipped with a continuous-flow liquid helium cryostat (ESR900) coupled to a TC503 temperature controller made by Oxford Instruments, Inc. ^1H NMR and ^{31}P NMR spectra were recorded on a Bruker Avance 400 MHz FT-NMR spectrometer. Chemical shifts were referenced to the residual solvent peaks for ^1H NMR and to the H_3PO_4 peak for ^{31}P NMR. Electrospray ionization mass spectra (ESI-MS) were collected on a Thermo Finnigan LCQ Duo ion-trap mass spectrometer fitted with an electrospray ionization source in positive ion mode. Samples were infused into the instrument at a rate of 25 μL/min using a syringe pump via a silica capillary line. The spray voltage was set at 5 kV, and the capillary temperature was held at 250 °C. ^{57}Fe Mössbauer spectra were recorded on a Mössbauer spectrometer from SEE Co. (Science Engineering & Education Co., MN) equipped with a closed cycle refrigerator system from Janis Research Co. and SHI (Sumitomo Heavy Industries Ltd.). Data were collected in constant acceleration mode in transmission geometry. The zero velocity of the Mössbauer spectra refers to the centroid of the room temperature spectrum of a 25 μm metallic iron foil. Analysis of the spectra was conducted using the WMOSS program (SEE Co, formerly WEB Research Co. Edina, MN). Magnetic spectra were fitted using the spin Hamiltonian:

$$H = D\left[\hat{S}_z^2 - \frac{1}{3}S(S+1)\right] + E(\hat{S}_x^2 - \hat{S}_y^2) + \beta\hat{S}\cdot g\cdot\hat{B} \qquad (1)$$

Computational Calculations and Spectroscopic Parameter Determination. All calculations were done using previously described methods[47] with density functional theory at the unrestricted hybrid density functional level UB3LYP[48,49] as implemented in the *Jaguar 7.9* and *Gaussian-03* program packages.[50,51] All geometries described here were the result of a full optimization without geometric constraints, and the local minima were ascertained with an analytical frequency calculation that established real frequencies only. These optimizations and frequencies were done with an LACVP basis set on Fe that includes a core potential and a 6-31G basis set on the rest of the atoms: basis set B1.[52] This basis set was shown to give adequate structures for the investigation of a potential energy profile of a chemical reaction by an iron(IV)-oxo species.[53] To improve the energetics we did single point calculations using a triple-ζ quality LACV3P+ basis set on Fe (with core potential) and 6-311+G* on the rest of the atoms: basis set B2. Energies reported in here are taken from the UB3LYP/B2 results and are corrected for zero-point energies at UB3LYP/B1. Free energies use UB3LYP/B2 energies and UB3LYP/B1 zero-point energies, thermal and entropic corrections. We also did single point calculations in Jaguar using the Polarized Continuum Model using a dielectric constant of $\varepsilon = 5.708$ and probe radius of 2.722 Å.

Spectroscopic parameters (Mössbauer and EPR parameters) were obtained from single point calculations on the optimized geometries using the ORCA program package.[54] These calculations used the B3LYP method in combination with the CP(PPP) basis set on Fe coupled to a TZVP basis set on the rest of the atoms.[55] The electric field gradients V_i ($i = x, y,$ or z) were used to calculate the quadrupole splitting (ΔE_Q) using eqs 2 and 3 with e the elementary charge of a proton/electron, Q the nuclear quadrupole moment, $Q(^{57}Fe) = 0.16$ barn, and η the asymmetry parameter of the nuclear quadrupole tensor.[56]

$$\Delta E_Q = \frac{1}{2}eQ\cdot V_z\cdot\sqrt{1+\frac{1}{3}\eta^2} \qquad (2)$$

$$\eta = (V_x - V_y)/V_z \qquad (3)$$

The isomer shift δ was calculated from the spin density at the iron nucleus $\rho_0(Fe)$ using previously determined fit-parameters in ORCA.[57] The magnetic hyperfine parameters, A_i ($i = x, y,$ or z), were obtained using the scalar relativistic zero-order regular approximation (ZORA) at the B3LYP level of theory. These methods were shown to reproduce well experimentally determined Mössbauer and EPR parameters of transition metal complexes.

Generation of $[Fe^{IV}(TBP_8Cz^{+\bullet})(NTs)]$ (2) in Situ. To a solution of $[Fe^{III}(TBP_8Cz)]$ (16 μM) in CH_2Cl_2 was added $Na^+TsNCl^-{\cdot}3H_2O$ (1 equiv dissolved in CH_3CN). A color change of the solution from green to brown was noted. The reaction was monitored by UV−vis spectroscopy, revealing isosbestic conversion from the spectrum for **1** to that of the new brown species $[Fe^{IV}(TBP_8Cz^{+\bullet})(NTs)]$ (**2**) (λ_{max} = 395, $\varepsilon = 4.3\times10^4\ M^{-1}\ cm^{-1}$). The spectrum for **2** is stable for at least 2 h at room temperature. An EPR sample was prepared as follows: to a solution of $[Fe^{III}(TBP_8Cz)]$ (2.0 mM) in toluene (300 μL) was added chloramine-T (1 equiv dissolved in CH_3CN) to give a final concentration of 1.5 mM of the iron complex. A color change from green to brown was observed. The reaction mixture was then transferred to a Wilmad quartz EPR tube (3 mm i.d.), and the sample was frozen and stored at 77 K.

Precipitation of Solid $[Fe^{IV}(TBP_8Cz^{+\bullet})(NTs)]$ (2). To an amount of $[Fe^{III}(TBP_8Cz)]$ (20.6 mg, 14.6 μmol) in CH_2Cl_2 (1.00 mL) was added $Na^+TsNCl^-{\cdot}3H_2O$ (6.2 mg, 22 μmol, 1.5 equiv) dissolved in CH_3CN (0.40 mL). The reaction mixture was stirred for 30 min, and the color change from green to brown was observed. An amount of CH_3CN was added until a solid precipitate had formed in the reaction mixture. The resulting solid was filtered, isolated on filter paper, and washed with CH_3CN to afford a dark brown-green solid (8.0 mg).

Kinetics of NR Group Transfer to Triphenyl Phosphine. In a custom-made 100-mL round-bottom flask adapted with a 1-cm path-length side arm UV−vis cell was prepared a solution of $[Fe^{IV}(TBP_8Cz^{+\bullet})(NTs)]$ (**2**) by addition of $Na^+TsNCl^-{\cdot}3H_2O$ (100 μL of an 0.8 mM stock solution in CH_3CN, 1 equiv) to a solution of **1** (16 μM) dissolved in CH_2Cl_2 (5 mL). The cell was placed in the spectrophotometer, and a 400 nm long-pass filter was placed between the spectrophotometer light source and the sample solution in order to

dx.doi.org/10.1021/ic400280x | Inorg. Chem. 2013, 52, 4668−4682

avoid any potential photodegradation of iron corrolazine. After complete conversion of **1** to **2** was noted by UV−vis, excess PPh_3 (30−75 equiv dissolved in CH_2Cl_2) was added to start the reaction, and an immediate color change from brown to green was noted, indicating the recovery of the starting material **1**. The time-course of the reaction was monitored by UV−vis and showed a smooth conversion of **2** to **1** over a 100−200 s period depending on the concentration of PPh_3. The pseudo-first-order rate constants, k_{obs}'s, for this reaction were obtained by nonlinear least-squares fitting of the plots of absorbance (Abs) at 440 nm versus time (t) to the following equation:

$$Abs_t = Abs_f - (Abs_f - Abs_0)e^{-k_{obs}t} \quad (4)$$

Here, Abs_f = final absorbance and Abs_0 = initial absorbance. The reaction was repeated over a range of substrate concentrations, and a plot of k_{obs} versus substrate concentration was found to be linear. The second-order rate constant (k) was obtained from the slope of the best-fit line to this plot.

Monitoring of NR Group Transfer by ^{31}P NMR Spectroscopy. To a solution of **1** (12−15 mM) in CD_2Cl_2 was added $Na^+TsNCl^-{\cdot}3H_2O$ (1−3 equiv dissolved in CD_3CN). A color change from green to brown was noted, consistent with formation of **2**. An aliquot of the reaction mixture was checked by UV−vis spectroscopy to ensure the complete formation of **2**. Excess PPh_3 (5−10 equiv dissolved in CD_2Cl_2) was added, causing an immediate color change from brown to green. An aliquot of the reaction mixture was removed and analyzed by UV−vis spectroscopy, revealing the return of **1**. The solution was then transferred to an NMR tube, and the reaction was monitored by ^{31}P NMR over 14 d.

Synthesis of [Fe(TBP$_8$Cz)(NPPh$_3$)] (3). A reaction of **2** with PPh_3 substrate was performed as described above for ^{31}P NMR experiments, and then the reaction mixture was allowed to stand in an NMR tube under ambient conditions. Good quality single crystals appeared after 2 weeks. A crystal was selected for X-ray structure determination and revealed the structure for [Fe(TBP$_8$Cz)(NPPh$_3$)] (**3**). ESI-MS, EPR, and Mössbauer data indicated that the bulk material of these crystals was contaminated with a small amount of [Fe(TBP$_8$Cz)(OPPh$_3$)], and a separate X-ray structure determination of a second crystal confirmed the presence of this complex, whose structure was solved as [Fe(TBP$_8$Cz)(OPPh$_3$)] (**4a**).

Synthesis of [Fe(TBP$_8$Cz)(OPPh$_3$)] (4b). To a solution of **1** (9.8 mg, 6.9 μmol) in CH_2Cl_2 (400 μL) was added Ph_3PO (5 equiv in 100 μL of CH_2Cl_2). An amount of CH_3CN (100 μL) was added, and good quality single crystals (black blocks) (8 mg, 68%) were obtained by slow evaporation of this mixture for one week. UV−vis (CH_2Cl_2): λ_{max} = 439, 607, 732 nm. ESI-MS (m/z): isotopic cluster centered at 1689.7 (M^+). ^{1}H NMR (CD_2Cl_2): δ (ppm) 13.05 (br), 11.26 (br), 9.95 (br), 7.47 (br), 2.00, 1.82, 1.66, 1.57, 1.26, 0.88. ^{31}P NMR (CD_2Cl_2): δ (ppm) 27.4. Anal. Calcd for $C_{114}H_{119}FeN_7OP$: C, 81.02: H, 7.10; N, 5.80. Found: C, 81.18; H, 7.03; N, 5.78.

X-ray Crystallography. All reflection intensities were measured at 110(2) K using a KM4/Xcalibur (detector: Sapphire3) with enhanced graphite-monochromated Mo Kα radiation (λ = 0.710 73 Å) under the program CrysAlisPro (Version 1.171.33.55 or 1.171.35.11, Agilent Technologies, 2010/2011). The temperature of the data collection was controlled using the system Cryojet (manufactured by Oxford Instruments). The program CrysAlisPro (Version 1.171.33.55 or 1.171.35.11, Agilent Technologies, 2010/2011) was used to refine the cell dimensions and data reduction. The structure was solved with the program SHELXS-97 and was refined on F^2 with SHELXL-97. Analytical numeric absorption corrections based on a multifaceted crystal model were applied using CrysAlisPro (Version 1.171.33.55 or 1.171.35.11, Agilent Technologies, 2010/2011). The H-atoms were placed at calculated positions using the instructions AFIX 23, AFIX 43, or AFIX 137 with isotropic displacement parameters having values 1.2 or 1.5 times U_{eq} of the attached C atoms.

The asymmetric unit of **3**, **4a**, and **4b** contains one Fe complex, and some lattice dichloromethane and acetonitrile solvent molecules. All structures are partly disordered. The t-butyl group C73→C76 of one aryl group is disordered over two orientations, and the occupancy factor for the major component refines to 0.876(5) for **3**, 0.870(5) for **4a**, and 0.895(4) for **4b**. In the structure of **3**, disorder was modeled for the four crystallographically independent dichloromethane molecules, and the occupancy factors for the major components are 0.831(4), 0.880(2), 0.695(5), and 0.529(8). In the structures of **4a** and **4b**, free variables for the major occupancy factors of one disordered CH_2Cl_2 and one ordered CH_3CN solvent molecules were used in the final refinement. Their refined values are 0.753(4), 0.131(3), and 0.902(8) for **4a**, and 0.792(4), 0.113(3), and 0.923(8) for **4b**. Other solvent molecules were found in the crystal lattice but were significantly more disordered, and therefore, their contributions were taken out by using the program SQUEEZE (Spek, 2003) for the final refinement.

Data for **3** follow: fw = 2068.75, black block, 0.34 × 0.31 × 0.26 mm^3, monoclinic, $P2_1/c$ (No. 14), a = 17.2124(2) Å, b = 33.4786(5) Å, c = 19.9855(2) Å, β = 102.6307(12)°, V = 11237.9(2) Å^3, Z = 4, D_x = 1.223 g cm^{-3}, μ = 0.390 mm^{-1}, abs corr range 0.894−0.923. There were 65 453 reflections measured up to a resolution of $(\sin\theta/\lambda)_{max}$ = 0.59 Å^{-1}. There were 19 786 unique reflections (R_{int} = 0.0377), of which 13 559 were observed [$I > 2\sigma(I)$]. There were 1354 parameters refined using 180 restraints. R1/wR2 [$I > 2\sigma(I)$]: 0.0666/0.1901. R1/wR2 [all reflns]: 0.0961/0.2026. S = 1.069. Residual electron density found between −0.93 and 0.78 e Å^{-3}.

Data for **4a** follow (asterisk indicates exclusion of the contribution of the unresolved residual electron density): *fw = 1802.09, *black block, 0.62 × 0.51 × 0.30 mm^3, monoclinic, $P2_1/c$ (No. 14), a = 17.2614(8) Å, b = 33.4143(11) Å, c = 19.9714(8) Å, β = 102.610(4)°, V = 11241.2(8) Å^3, Z = 4, D_x = 1.065 g cm^{-3}, *μ = 0.239 mm^{-1}, *abs corr range 0.899−0.941. *There were 59 539 reflections measured up to a resolution of $(\sin\theta/\lambda)_{max}$ = 0.59 Å^{-1}. There were 19 795 unique reflections (R_{int} = 0.0449), of which 15 006 were observed [$I > 2\sigma(I)$]. There were 1221 parameters refined using 63 restraints. R1/wR2 [$I > 2\sigma(I)$]: 0.0605/0.1733. R1/wR2 [all reflns]: 0.0759/0.1822. S = 1.069. Residual electron density found between −0.47 and 0.66 e Å^{-3}.

Data for **4b** follow: *fw = 1804.71, *black block, 0.35 × 0.24 × 0.20 mm^3, monoclinic, $P2_1/c$ (No. 14), a = 17.2502(2) Å, b = 33.4217(5) Å, c = 19.9821(2) Å, β = 102.7119(12)°, V = 11237.9(2) Å^3, Z = 4, D_x = 1.067 g cm^{-3}, *μ = 0.240 mm^{-1}, *abs corr range 0.900−0.937. There were *64 199 reflections measured up to a resolution of $(\sin\theta/\lambda)_{max}$ = 0.59 Å^{-1}. There were 19 786 unique reflections (R_{int} = 0.0375), of which 14 933 were observed [$I > 2\sigma(I)$]. There were 1221 parameters refined using 63 restraints. R1/wR2 [$I > 2\sigma(I)$]: 0.0611/0.1662. R1/wR2 [all reflns]: 0.0791/0.1750. S = 1.073. Residual electron density found between −0.40 and 0.66 e Å^{-3}.

Synthesis of [^{57}Fe^{III}(TBP$_8$Cz)]. The metal-free corrolazine TBP_8CzH_3 (62 mg, 0.046 mmol) was combined with $^{57}FeCl_2$ (29 mg, 0.23 mmol) in dimethylformamide (10 mL) and heated at reflux for 2 h. After removing the solvent *in vacuo*, the crude product was purified by flash column chromatography (CH_2Cl_2/MeOH 99:1 v/v; silica gel) to obtain [^{57}Fe^{III}(TBP$_8$Cz)] as a dark-green solid (51 mg, 79%). UV−vis (CH_2Cl_2): λ_{max} = 441, 610, 746 nm.

Samples for Mössbauer Studies. The ^{57}Fe-labeled complexes [^{57}Fe^{III}(TBP$_8$Cz)] and [^{57}Fe^{III}(TBP$_8$Cz)(NPPh$_3$)] were used for Mössbauer measurements. An isotopically labeled sample of **3** ([^{57}Fe^{III}(TBP$_8$Cz)(NPPh$_3$)]) was synthesized from [^{57}Fe^{III}(TBP$_8$Cz)] starting material. In the case of [Fe^{III}(TBP$_8$Cz)(OPPh$_3$)] (**4b**), Mössbauer data were collected on samples that were not enriched in ^{57}Fe. Samples were either measured as solid-state samples (~10 mg) or as frozen solutions (~400 μL) in toluene or pyridine in custom-made Teflon sample holders.

RESULTS AND DISCUSSION

Synthesis and Characterization of a High-Valent Iron Imido Corrolazine Complex. A variety of discrete metal-imido complexes have been synthesized by the reaction of the appropriate metal precursors and alkyl- or aryl-azides.[9,32,33,58−61] This strategy was used to synthesize the Mn^V-imido complex [Mn^V(TBP$_8$Cz)NMes], in which the Mn^{III}

dx.doi.org/10.1021/ic400280x | Inorg. Chem. 2013, 52, 4668−4682

precursor [$Mn^{III}(TBP_8Cz)$] was reacted with mesityl azide (2,4,6-$(CH_3)_3C_6H_2N_3$) at elevated temperature.[32] Corrole analogues [Mn(tpfc)NAr] (Ar = 2,4,6-$(CH_3)_3C_6H_2$, 2,4,6-$Cl_3C_6H_2$) have been similarly prepared.[33] Our initial efforts to gain access to a high-valent Fe-imido corrolazine followed the same methodology. Attempts were made to react the previously synthesized Fe^{III} complex [$Fe^{III}(TBP_8Cz)$] with both alkyl- and aryl-azides. For example, [$Fe^{III}(TBP_8Cz)$] was stirred with 50 equiv of mesityl azide in toluene for 24 h, but even at elevated temperature (90 °C) no evidence of reaction in the form of a color change, UV−vis spectroscopic conversion, or TLC change was noted. The azides AdN_3 (Ad = adamantyl), PhN_3, and Me_3SiN_3 were examined under similar conditions, but none led to any noticeable reaction with the Fe^{III} corrolazine. We speculated that the coordination of the azide reagents, or the triplet nitrene that potentially forms upon thermal activation of the azides,[61] was not occurring because even small changes in the UV−vis spectrum of [$Fe^{III}(TBP_8Cz)$] were not observed. The failure of the azide reagents to react with [$Fe^{III}(TBP_8Cz)$] prompted us to examine alternative NR group transfer reagents.

The inexpensive, commercially available reagent chloramine-T ($Na^+TsNCl^-\cdot 3H_2O$) was shown to be a good NTs-transfer agent in catalytic aziridinations involving Fe corrole [$(Fe^{IV}(tpfc)$],[41] and both chloramine-T and bromamine-T have been used as a nitrene source in metal-catalyzed C−H insertions.[41,62−65] Addition of a stock solution of chloramine-T in CH_3CN to [$Fe^{III}(TBP_8Cz)$] dissolved in CH_2Cl_2 at room temperature led to the conversion of green [$Fe^{III}(TBP_8Cz)$] (λ_{max} = 440, 611, 747 nm) to a new, brown species with λ_{max} = 395 nm (Figure 1). Isosbestic points are observed at 392, 490,

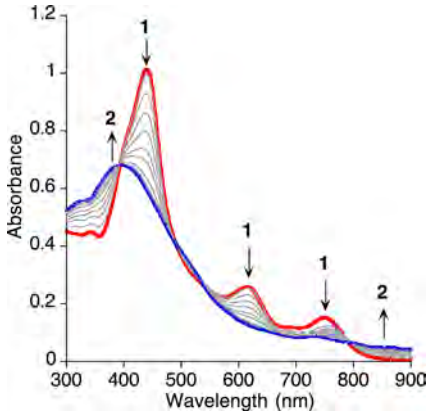

Figure 1. UV−vis spectral change upon addition of chloramine-T trihydrate (0−1.0 equiv) to [$Fe^{III}(TBP_8Cz)$] at 23 °C in CH_2Cl_2/CH_3CN.

538, and 792 nm. The new species with λ_{max} = 395 nm appears surprisingly stable for more than 2 h at room temperature as monitored by UV−vis. The changes in the UV−vis following addition of chloramine-T are similar to those observed for the reaction of [$Fe^{III}(TBP_8Cz)$] and pentafluoroiodosylbenzene to give the high-valent iron-oxo complex [$Fe^{IV}(TBP_8Cz^{+\bullet})(O)$], although in this case the iron-oxo product is thermally unstable and had to be observed at low temperature (−78 °C) (Figure 2). The UV−vis data are consistent with the formation of the expected product, [$Fe^{IV}(TBP_8Cz^{+\bullet})(NTs)$] (**2**), in which the tosylimido group replaces the terminal oxo ligand of [$Fe^{IV}(TBP_8Cz^{+\bullet})(O)$] and the Fe^{III} complex is oxidized by

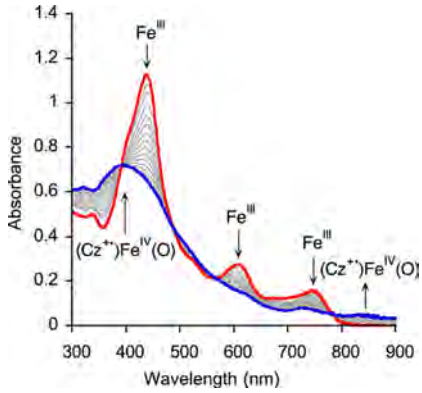

Figure 2. UV−vis spectral change upon addition of pentafluoroiodosylbenzene (PFIB) to [$Fe^{III}(TBP_8Cz)$] at −78 °C in CH_2Cl_2/CH_3OH.

two electrons, as shown in Scheme 1. The stoichiometry of the reaction was determined by titration of chloramine-T followed by monitoring by UV−vis spectroscopy, as shown in Figures 1 and S1. Addition of chloramine-T in 0.1 equiv increments results in isosbestic conversion of the Fe^{III} complex up to a total of 1 equiv, at which point a loss of isosbestic behavior is observed together with a decrease at 395 nm corresponding to the oxidized product. This spectral titration confirms that chloramine-T and [$Fe^{III}(TBP_8Cz)$] (**1**) react in a ratio of 1:1 to form [$Fe^{IV}(TBP_8Cz^{+\bullet})(NTs)$] (**2**). The imido complex **2** is thus remarkably stable in solution at room temperature, and this stability is likely a consequence of the previously established ability of the corrolazine platform to stabilize high-valent, multiply bonded terminal oxo and terminal imido complexes.

Several attempts were made to grow single crystals of the product from chloramine-T for X-ray structure determination, but thus far these efforts have remained unsuccessful. However, the complex can be isolated as a solid by solvent precipitation. Relatively concentrated solutions of [$Fe^{IV}(TBP_8Cz^{+\bullet})(NTs)$] (10 mM) can be generated in CH_2Cl_2 from [$Fe^{III}(TBP_8Cz)$] and chloramine-T, and the resulting Fe═NTs product is then precipitated from the reaction mixture by the addition of excess CH_3CN. Formation of a brown-green solid and a brown solution results, and the solid is then isolated by filtration. This solid exhibited similar UV−vis and other spectroscopic properties as seen for a sample of [$Fe^{IV}(TBP_8Cz^{+\bullet})(NTs)$] freshly generated in CH_2Cl_2, indicating that the precipitated material contains the [$Fe^{IV}(TBP_8Cz^{+\bullet})(NTs)$] complex prepared in situ. However, Mössbauer spectroscopic measurements show that this solid cannot be isolated in pure form, and contains up to ∼25% of the starting Fe^{III} complex (vide infra). Autoreduction of the iron-imido complex likely occurs upon precipitation, which is similar to what we have observed previously in attempts to isolate high-valent Mn-oxo corrolazines in the solid state.

NR Group Transfer. The brown complex **2**, generated from the reaction of chloramine-T and [$Fe^{III}(TBP_8Cz)$], was next examined for its ability to transfer the NTs group to phosphine substrates. The analogous reaction with corrole derivatives (e.g. [$Mn^V(tpfc)(NAr)$]) and phosphine substrates occurs smoothly, and has yielded kinetic and mechanistic information regarding NR group transfer.[66] Reaction of [$Fe^{IV}(TBP_8Cz^{+\bullet})(NTs)$] (freshly prepared in situ) with excess triphenylphosphine (Scheme 2) led to the isosbestic return of the spectrum for [$Fe^{III}(TBP_8Cz)$] as shown in Figure 3. Production of the two-

dx.doi.org/10.1021/ic400280x | Inorg. Chem. 2013, 52, 4668−4682

Scheme 1. Reaction of $Fe^{III}(TBP_8Cz)$ with Chloramine-T

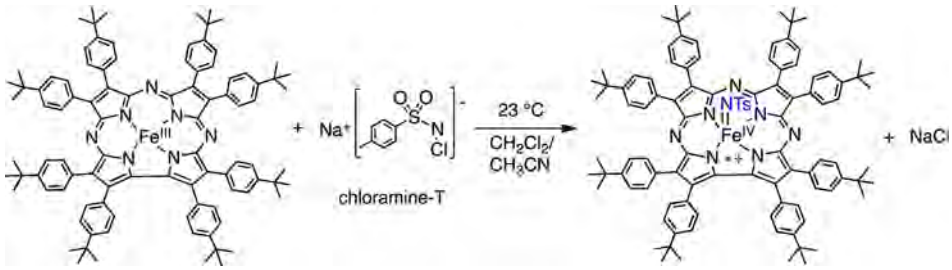

Scheme 2. Reaction of $[Fe^{IV}(TBP_8Cz^{+\bullet})(NTs)]$ with PPh_3

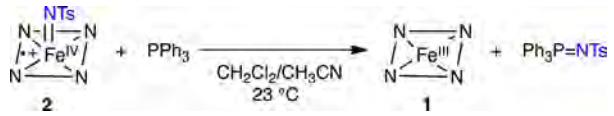

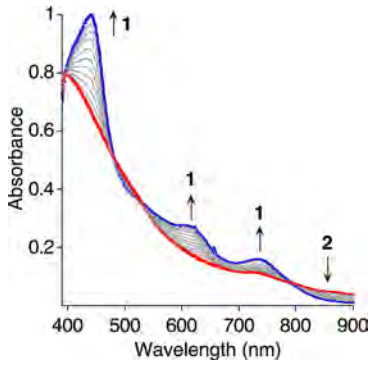

Figure 3. Time-resolved UV−vis spectra of $[Fe^{IV}(TBP_8Cz^{+\bullet})(NTs)]$ + PPh_3 (30 equiv) at 23 °C in CH_2Cl_2/CH_3CN (100:1 v:v).

electron-reduced Fe^{III} product is consistent with the formulation of $[Fe^{IV}(TBP_8Cz^{+\bullet})(NTs)]$, which is two oxidizing equivalents above that of the Fe^{III} starting material. Analysis of the reaction mixture by ^{31}P NMR following addition of PPh_3 reveals a single peak at 14.8 ppm (Figure S11). This peak matches that seen for the expected phosphorane product, $Ph_3P{=}NTs$, providing confirmation of NTs transfer to the phosphine substrate. No signal for unreacted PPh_3 was observed by ^{31}P NMR at the end of the NTs transfer reaction. This observation is consistent with the lack of a ^{31}P signal for independent solutions of $[Fe^{III}(TBP_8Cz)]$ + excess PPh_3, which is likely due to paramagnetic effects from the Fe^{III} complex on PPh_3. The PPh_3 also may coordinate to one or both axial positions at the Fe^{III} center, enhancing the paramagnetic influence.

The generation of $[Fe^{IV}(TBP_8Cz^{+\bullet})(NTs)]$ and subsequent reaction with PPh_3 was monitored by ^1H NMR spectroscopy (Figure S13). The initial spectrum for the Fe^{III} complex **1** reveals paramagnetically shifted peaks between −10 and +15 ppm. Addition of a slight excess of chloramine-T causes the clear disappearance of the paramagnetic signals for **1**, revealing a featureless paramagnetic spectrum for the iron-imido complex **2**. Subsequent addition of excess PPh_3 to the reaction mixture causes an immediate return of the peaks from −10 to 15 ppm associated with the starting complex **1**. These data are nicely consistent with the proposed mechanism of formation of the iron-imido complex and subsequent NTs transfer to PPh_3, which also causes the concomitant return of the Fe^{III} starting material.

Preliminary investigation of the reaction of the imido complex **2** with styrene was also performed to determine its potential reactivity toward aziridination of alkene substrates. As seen in Figure S14, a titration experiment with styrene leads to the reduction of **2** back to the starting Fe^{III} complex **1**, but a very large excess of substrate (48 000 equiv) is needed for this reaction to go to completion over a 25 min period. These data suggest that **2** is a very sluggish NR transfer agent for alkene substrates, and this finding is consistent with the general, inherent stability of **2** in solution at room temperature compared to other high-valent Fe-imido complexes. Given the low reactivity of **2** toward styrene, further studies regarding aziridination of styrene or other substrates were not pursued at this time.

Turnover. The UV−vis and NMR data suggested that the reactions involving the generation of the Fe=NTs complex and the subsequent NR transfer to PPh_3 were relatively fast, and therefore we attempted to determine if catalytic turnover could be achieved. The NR transfer reaction was run under catalytic conditions with a small excess of oxidant (3 equiv) and PPh_3 substrate (10 equiv). The initial formation of **2** from **1** + chloramine-T was first confirmed by UV−vis spectroscopy, and then the substrate was added immediately to initiate the NR transfer reaction. As seen in Figure 4, monitoring of this

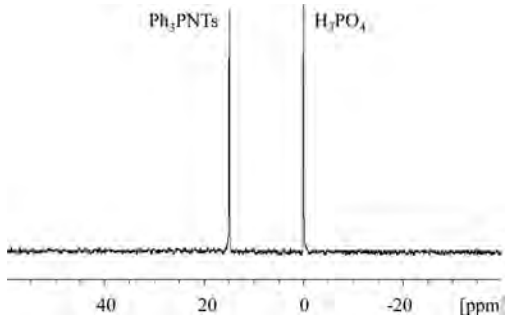

Figure 4. ^{31}P NMR spectrum showing the production of $Ph_3P{=}NTs$ from the reaction of $[Fe^{III}(TBP_8Cz)]$ + chloramine-T trihydrate (3 equiv) + PPh_3 (10 equiv) after 15 min in CD_2Cl_2/CD_3CN at 23 °C.

reaction by ^{31}P NMR showed the rapid production of $Ph_3P{=}NTs$ with no other phosphorane products. The catalytic cycle is summarized in Scheme 3. A background reaction does occur in the absence of **1** under these conditions; however, a significant amount of triphenylphosphine oxide is also produced in this case (Figure S12). The $OPPh_3$ is presumably obtained from oxidation of PPh_3 by hypochlorite anion (OCl^-), which is known to readily form from chloramine-T and exogenous H_2O. There is no $OPPh_3$ observed by ^{31}P NMR in Figure 4, indicating that the catalytic NR transfer must be highly efficient, preventing any background reaction from occurring. We can

dx.doi.org/10.1021/ic400280x | Inorg. Chem. 2013, 52, 4668−4682

Scheme 3. Catalytic Turnover

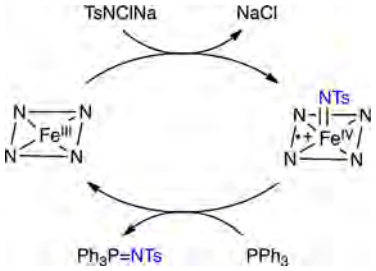

conclude that **1** is capable of catalytic turnover in the NR transfer to phosphines, and that the high-valent iron imido complex **2** is the likely active oxidant in the catalytic cycle.

Kinetics of NR Group Transfer. The kinetics of the reaction between $[Fe^{IV}(TBP_8Cz^{+\bullet})(NTs)]$ and PPh_3 were examined at 23 °C to gain further insight into the reaction mechanism for NR group transfer. The Fe═NTs complex was generated in situ, and excess PPh_3 (30−75 equiv) was added to yield pseudo-first-order conditions. An example of time-resolved UV−vis spectra used for kinetic measurements is shown in Figure 3. Monitoring this transformation at 440 nm over time gives the plot in Figure 5, which was satisfactorily fit

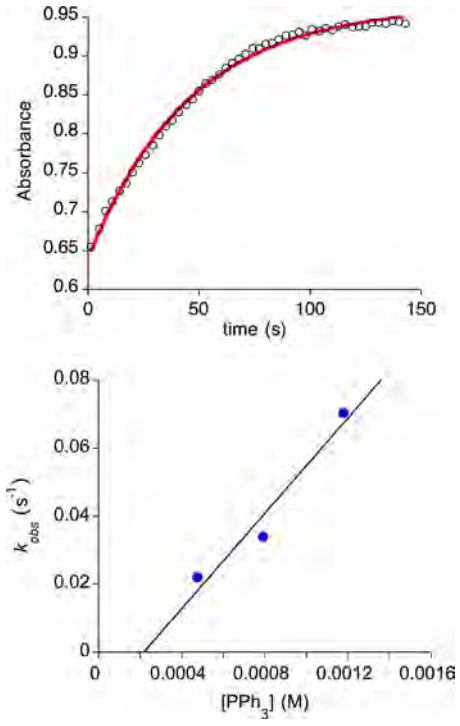

Figure 5. Representative change in absorbance at 440 nm vs time for **2** + PPh_3 corresponding to the return of $Fe^{III}(TBP_8Cz)$ (open circles), and best fit line (red) (top). Plot of the pseudo-first-order rate constants (k_{obs}) vs $[PPh_3]$ (bottom). A second-order rate constant of 70(15) M^{-1} s^{-1} was obtained from the best fit line (black).

with a first-order kinetics model and yielded a k_{obs} = 0.022 s^{-1}. The concentration of PPh_3 was varied and led to a linear correlation of k_{obs} versus $[PPh_3]$ as shown in Figure 5, consistent with an overall second-order rate law of rate = $k_2[Fe^{IV}(TBP_8Cz^{+\bullet})(NTs)][PPh_3]$. The slope of this plot gave a derived second-order rate constant of 70(15) M^{-1} s^{-1}. In comparison, the Mn^V-imido corrole $[Mn^V(tpfc)(NMes)]$ underwent NR group transfer to PPh_3 with a rate constant of 0.71(5) M^{-1} s^{-1}.[66] Thus, the Fe═NTs corrolazine exhibits a 100-fold rate enhancement over an Mn^V imido corrole analogue. These findings are in line with the enhanced reactivity of high-valent iron-oxo versus manganese-oxo corrolazines.[40] In addition, the electron-withdrawing nature of a tosyl group, as compared to a 2,4,6-trichlorophenyl substituent, can be expected to enhance the electrophilicity of **2** and make it more reactive for NR group transfer to nucleophiles such as PPh_3.

Structural Characterization of an NR Group Transfer Product. Efforts were made to obtain single crystals for structural characterization of the phosphine product following reaction of $[Fe^{IV}(TBP_8Cz^{+\bullet})(NTs)]$ with PPh_3. An NMR sample of this reaction mixture in CD_2Cl_2/CD_3CN was allowed to stand for two weeks, affording black crystalline blocks suitable for X-ray diffraction. The structure revealed an iron corrolazine complex with a phospharaniminato ligand coordinated in the axial position, corresponding to $[Fe^{IV}(TBP_8Cz)(NPPh_3)]$ (**3**). A displacement ellipsoid plot for complex **3** is shown in Figure 6, and selected bond distances and angles are

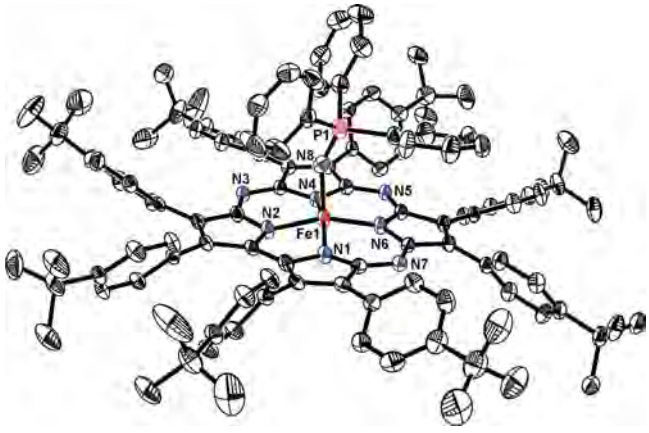

Figure 6. Displacement ellipsoid plot (50% probability level) of $[Fe(TBP_8Cz)(NPPh_3)]$ (**3**). H atoms and disorder are omitted for clarity.

given in Table 1. The tosyl substituent is absent, presumably having been hydrolytically cleaved from the initial Ph_3P═NTs product during crystallization. The remaining anionic Ph_3P═N^- axial ligand indicates that the iron is formally in the +4 oxidation state. We attempted to model the donor atom attached to Fe as an oxygen atom given the possibility of forming $OPPh_3$ in the reaction mixture. However, substitution of O for N in the axial position invariably leads to an unusually large thermal ellipsoid (Figure S3). In addition, substitution of O for N does not alter bond distances significantly, and the resulting P—O bond length would be unusually short (Table 2). These results rule out the presence of an $OPPh_3$ axial donor in **3**. The structural parameters for **3** are also not reasonable for a protonated Ph_3P═NH ligand, and no evidence for a hydrogen atom could be found in the final difference Fourier maps.

To our knowledge there are only two other crystallographically characterized mononuclear Fe—N═PPh_3 complexes reported to date, and relevant structural data for these complexes are given in Table 2. These iron complexes are four-coordinate iron(II) species derived from sterically encumbered tris(carbene)borate ancillary ligands. The Fe−N distance for

dx.doi.org/10.1021/ic400280x | Inorg. Chem. 2013, 52, 4668−4682

Table 1. Selected Bond Distances (Å) and Angles (deg) for 3, 4a, and 4b

	3	4a	4b
Fe(1)−N(1)	1.840(3)	1.843(2)	1.840(2)
Fe(1)−N(2)	1.844(3)	1.849(2)	1.848(2)
Fe(1)−N(4)	1.862(3)	1.867(2)	1.864(2)
Fe(1)−N(6)	1.866(3)	1.866(2)	1.865(2)
Fe(1)−$(N_{pyrrole})_{plane}$	0.292	0.291	0.291
Fe(1)−$(23\text{-atom})_{core}$	0.271	0.262	0.259
C_β−C_β (av)	1.393	1.388	1.390
C_α−C_β (av)	1.446	1.448	1.447
C_α−C_α (C4−C5)	1.425(5)	1.436(4)	1.430(4)
C_α−$N_{pyrrole}$(av)	1.373	1.367	1.369
C_α−N_{meso} (av)	1.338	1.338	1.339
Fe1−X (X = N8 or O1)	1.963(3)	2.002(2)	2.001(2)
P(1)−X	1.427(3)	1.494(2)	1.500(2)
N(1)−Fe(1)−N(2)	80.9(1)	81.12(9)	81.1(1)
N(2)−Fe(1)−N(4)	90.2(1)	90.45(9)	90.3(1)
N(4)−Fe(1)−N(6)	92.9(1)	92.62(9)	92.6(1)
N(6)−Fe(1)−N(1)	90.4(1)	90.17(9)	90.3(1)
N(1)−Fe(1)−X	97.9(1)	98.60(9)	98.50(9)
N(2)−Fe(1)−X	95.9(1)	96.13(8)	95.95(9)
N(4)−Fe(1)−X	100.1(1)	99.30(8)	99.47(9)
N(6)−Fe(1)−X	101.9(1)	101.72(8)	101.85(9)
Fe(1)−X−P(1)	154.5(2)	154.5(1)	154.4(1)

$[Fe^{IV}(TBP_8Cz)(NPPh_3)]$ of 1.963(3) Å is considerably longer than the Fe−N distances seen for the tris(carbene)borate complexes (Fe−N = 1.807(2)−1.894(2) Å). The shorter Fe−N bonds in the latter complexes may be assigned to the $NPPh_3$ ligand functioning as both a σ- and π-donor to the metal. In these approximate C_3-symmetric complexes, the d_{xz}/d_{yz} orbitals can serve as π-acceptors, whereas in the tetragonal Cz complex the orbitals of similar parentage are π^* in character with respect to the Fe−N bond and are partly filled, leading to the elongated Fe−N distance. In contrast, the N−P distance for **3** is significantly shorter than the N−P distances found in the other Fe—N═PPh_3 complexes in Table 2. The origin of this discrepancy is not known at this time, although the N−P distance for **3** is clearly shorter than that expected for either M−$OPPh_3$ or M−(H)$NPPh_3$ complexes, as seen in Table 2.

Efforts to characterize a bulk crystalline sample of $[Fe^{IV}(TBP_8Cz)(NPPh_3)]$ by ESIMS(+) revealed an isotopic cluster centered at m/z 1689.7, whose main peak was +2 above that expected for $[Fe(TBP_8Cz)(NPPh_3)]^{+\bullet}$, but a close match for $[Fe(TBP_8Cz)(OPPh_3)]^{+\bullet}$ (theoretical m/z 1689.8, see Supporting Information). However, the isotope pattern did not fit well for the $OPPh_3$ complex, and suggested that a possible mixture of Fe−$NPPh_3$ and Fe−$OPPh_3$ products crystallized in the same bulk material. This result prompted the analysis of a new batch of crystals from the PPh_3 reaction by X-ray diffraction. A unit cell check on an independently prepared crystal from the PPh_3 reaction mixture revealed a similar cell to that obtained for **3**. However, we speculated that an Fe^{III}−$OPPh_3$ complex might have nearly identical unit cell dimensions to those of **3**, and thus, another full set of data was collected. The structure solution for this second crystal revealed an $OPPh_3$ rather than $NPPh_3$ axial ligand. The crystal structure of this complex, $[Fe^{III}(TBP_8Cz)(OPPh_3)]$ (**4a**), is provided in the Supporting Information, and relevant bond distances and angles are given in Table 1. In this case, the presence of an O atom was confirmed, but the refinement of an N atom in the axial position was attempted. As expected, an N atom in this position led to a significantly smaller thermal ellipsoid, and three residual electron density peaks as large as 0.69 e^- $Å^{-3}$ were found at 0.43−0.48 Å from the N atom, which strongly suggests that not enough electron density has been assigned to this atomic site. The metrical parameters for the second crystal structure from the reaction of $[Fe(TBP_8Cz^{+\bullet})(NTs)]$ + PPh_3 are fully consistent with an Fe^{III}−$OPPh_3$ complex. These findings indicate that a mixture of Fe-$NPPh_3$ and Fe-$OPPh_3$ products ultimately form in the PPh_3 reaction and both crystallize under the same conditions.

Synthesis of $[Fe^{III}(TBP_8Cz)(OPPh_3)]$. The $Fe^{III}(OPPh_3)$ complex was independently prepared for comparison purposes. Addition of excess $OPPh_3$ to a solution of $[Fe^{III}(TBP_8Cz)]$ led to the crystalline complex $[Fe^{III}(TBP_8Cz)(OPPh_3)]$ (**4b**) in good yield (Scheme 4). A displacement ellipsoid plot is shown in Figure 7, and selected bond distances and angles are given in Table 1. The metrical parameters match well with those found for **4a**. The UV−vis and ESIMS spectra for **4b** are shown in Figure 8. The mass spectral data show a dominant cluster centered at m/z 1689.7, and its position and isotope pattern match nicely for $[Fe(TBP_8Cz)(OPPh_3)]^+$. This result can be contrasted with Figure S4, in which a different isotope pattern was obtained for the mixture of **3** + **4a** from the chloramine-T reaction. The UV−vis spectrum is similar to that of the Fe^{III} starting material, but a blue-shift of ∼15 nm is seen for the 732 nm band, resulting from coordination of $OPPh_3$ to Fe^{III}. Elemental analysis confirmed the high purity of **4b** as a bulk crystalline solid, and this material provided a key benchmark for further studies, including ^{31}P NMR and Mössbauer spectroscopies, while also confirming our assignment of the **3** + **4a** mixture from the PPh_3 oxidation reaction.

Scheme 4. Synthesis of $Fe^{III}(TBP_8Cz)(OPPh_3)$

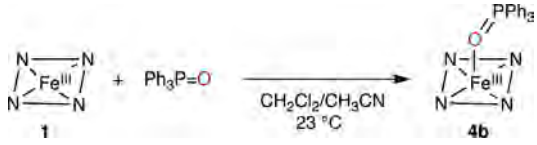

Monitoring Production of Hydrolyzed Products by ^{31}P NMR Spectroscopy. The reaction of $[Fe^{IV}(TBP_8Cz^{+\bullet})$-

Table 2. Comparison of Selected Bond Distances (Å) for Metal-$XPPh_3$ Compounds (X = N, O)

	M−X	P−X	ref
$[Fe^{IV}(TBP_8Cz)(NPPh_3)]$ (**3**)	1.963(3)	1.427(3)	this study
$[Fe^{III}(TBP_8Cz)(OPPh_3)]$ (**4b**)	2.001(2)	1.500(2)	this study
M-(H)$NPPh_3$ (M = Os, Cu, Zr, Ta)	1.931−2.367	1.511−1.843	67, 81−84
Fe^{III}−$OPPh_3$	1.912−2.056	1.483−1.507	85−89
$PhB(^tBuIm)_3Fe^{II}$−$NPPh_3$	1.894(2)	1.527(2)	59
$PhB(MesIm)_3Fe^{II}$−$NPPh_3$	1.807(2)−1.855(2)	1.524(2)−1.549(2)	90

dx.doi.org/10.1021/ic400280x | Inorg. Chem. 2013, 52, 4668−4682

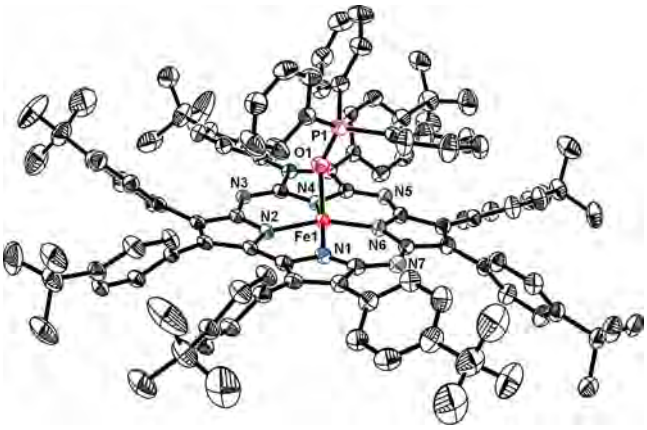

Figure 7. Displacement ellipsoid plot (50% probability level) of $[Fe^{III}(TBP_8Cz)(OPPh_3)]$ (**4b**). H atoms and disorder are omitted for clarity.

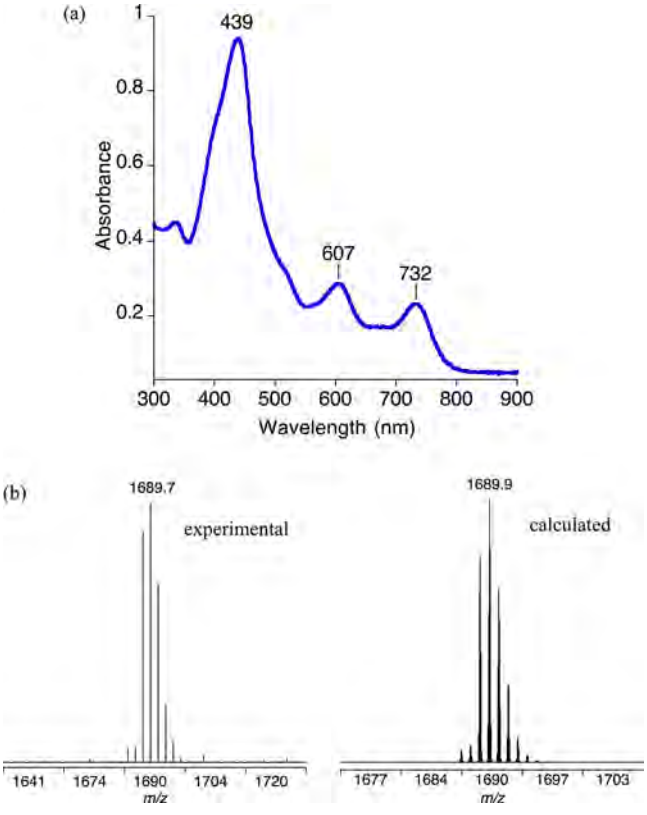

Figure 8. (a) UV–vis and (b) ESIMS spectra for $[Fe^{III}(TBP_8Cz)(OPPh_3)]$ (**4b**) as a crystalline solid dissolved in CH_2Cl_2.

(NTs)] (**2**) + PPh_3 was monitored by ^{31}P NMR spectroscopy over an extended time-course to gain insight into the mechanism of NR transfer and formation of the final phosphine-derived products $[Fe^{IV}(TBP_8Cz)(NPPh_3)]$ (**3**) and $[Fe^{III}(TBP_8Cz)(OPPh_3)]$ (**4**). Examination of the reaction mixture after day 1 shows only the Ph_3PNTs product, as expected (Figure 9). Following this initial spectrum, there is a slow build-up of the detosylated Ph_3PNH compound at 21.8 ppm (verified by comparison with an authentic sample). By day 7, a broad peak appears at 27.9 ppm, which then grows in intensity after a further week of reaction (day 14). An independent sample of pure $[Fe^{III}(TBP_8Cz)(OPPh_3)]$ (**4b**) exhibited the same broad peak in the ^{31}P NMR spectrum

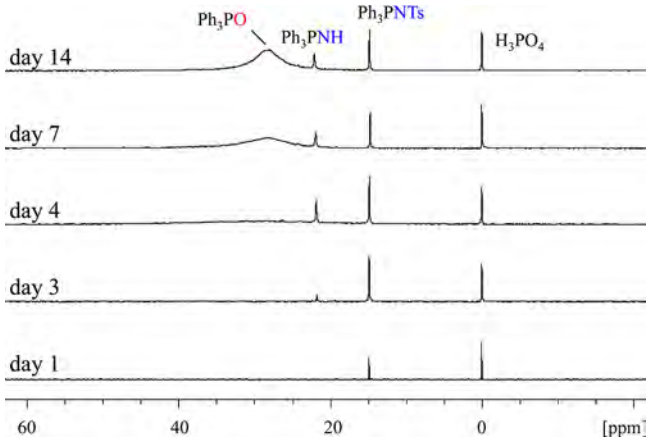

Figure 9. ^{31}P NMR spectra of the reaction of $[Fe^{III}(TBP_8Cz)]$ + chloramine-T trihydrate (3 equiv) + PPh_3 (10 equiv) in CD_2Cl_2/CD_3CN over 2 weeks.

(Figure S7). Thus, the ^{31}P NMR time-course shows the production of all three phosphorus products, Ph_3PNTs, $Ph_3PN(H)$, and Ph_3PO, over a two-week period.

Mechanism. A proposed mechanism for NR group transfer and generation of the different phosphine products is shown in Scheme 5. Initial formation of the Fe=NTs complex is followed by nucleophilic attack of PPh_3 to give Ph_3PNTs and an iron(III) corrolazine. The Ph_3PNTs may be activated by Fe^{III} toward hydrolytic cleavage of the tosyl group, resulting in production of Ph_3PNH. Coordination of this phosphinimine product can then lead to the formation of $Fe^{IV}(NPPh_3)$, following oxidation of an Fe^{III} precursor. Although the identity of the oxidant is not known, oxidation of Fe^{III} to Fe^{IV} is likely facilitated by a strong axial donor such as Ph_3PN^-. The generation of Ph_3PO occurs upon hydrolysis of Ph_3PNH, which is known to readily hydrolyze to Ph_3PO and NH_4OH in the presence of residual water.[67] The presence of Ph_3PO can then give rise to the final $Fe^{III}(OPPh_3)$ complex. This mechanism accounts for both the NMR time-course experiments and the observation of the different products from X-ray crystallography.

EPR and Mössbauer Spectroscopies. To obtain information about the oxidation states and spin states of the Fe corrolazine complexes described here, EPR and Mössbauer spectra were collected. Previous work on iron corrole complexes[68−71] has shown that it is often difficult to determine their electron configurations due to the noninnocent nature of the corrolate ligand. Similar complications arise with the related iron corrolazines presented in this study. Further complexity is to be expected when Mössbauer spectra of frozen solutions are collected because corrolazines, like other porphyrinoid compounds, are prone to aggregation, which can lead to intermolecular spin–spin relaxation.[72−74] For these reasons the Mössbauer and EPR data have to be treated as a whole. To support the Mössbauer and EPR assignments we ran a set of DFT calculations in tandem with the experiments.

A solid state, crystalline sample of **4b** formed from the reaction of $[Fe^{III}(TBP_8Cz)]$ with Ph_3PO provides a well-defined reference compound for spectroscopic measurements because the structure has been determined with high precision by single-crystal X-ray diffraction, and the oxidation state of the iron center can be definitively assigned as +3. A sample of **4** exhibits a Mössbauer spectrum at 5.3 K with a single, sharp

dx.doi.org/10.1021/ic400280x | Inorg. Chem. 2013, 52, 4668−4682

Scheme 5. Proposed Mechanism

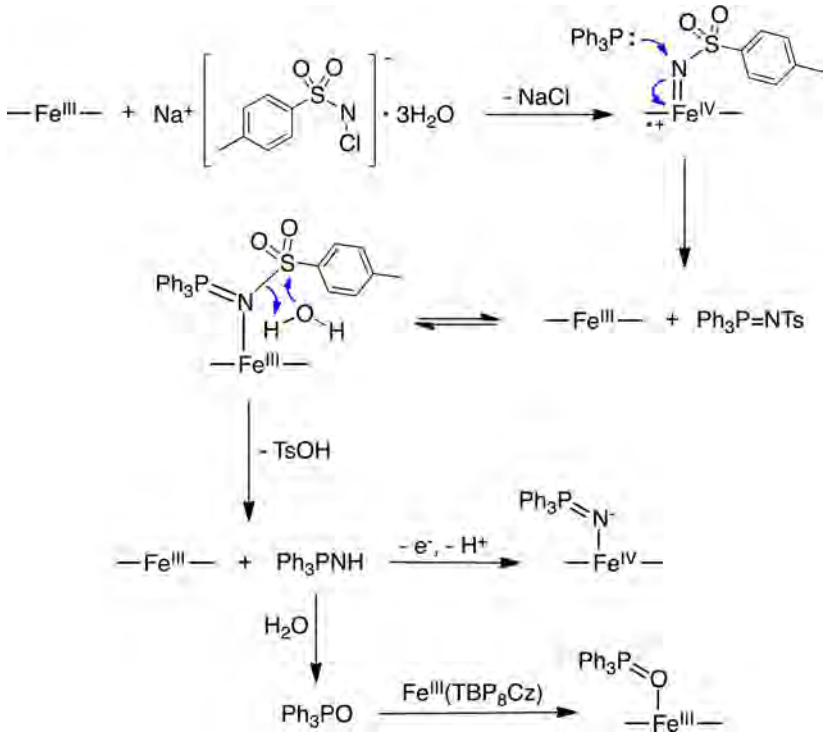

quadrupole doublet (δ = 0.13 mm s^{-1}; ΔE_Q = 4.40 mm s^{-1}, Figure 10). The isomer shift is consistent with an intermediate spin (S = $^3/_2$) Fe^{III} ion as seen by comparison with other intermediate spin iron(III) complexes (see Table 5 in ref 56), and the large quadrupole splitting is in part due to the square pyramidal geometry (see bond angles above). Indeed, the square pyramidal geometry of the iron center revealed by the crystal structure of [Fe^{III}(TBP$_8$Cz)(OPPh$_3$)] (Figure 7) and the presence of the strong-field equatorial corrolazine ligand should greatly destabilize the $d_{x^2-y^2}$ orbital relative to the other d orbitals and therefore stabilize the S = $^3/_2$ state relative to the high spin S = $^5/_2$ state. The intermediate spin state of this compound is further confirmed by EPR spectroscopy. The X-band EPR spectrum of a crystalline sample of **4** dissolved in toluene and measured at 15 K (Figure 11) shows an axial signal with $g_\perp$ = 4.43, $g_\parallel$ = 1.99, which is typical for an S = $^3/_2$ ion.

In comparison, the Mössbauer spectrum of solid [Fe^{III}(TBP$_8$Cz)], which lacks an OPPh$_3$ axial ligand, was measured at 293 K and consists of two quadrupole doublets (δ = 0.06 mm s^{-1}, ΔE_Q = 4.00 mm s^{-1} and δ = 0.30 mm s^{-1}, ΔE_Q = 1.00 mm s^{-1}, Figure 10) in a ratio of approximately 3:1.

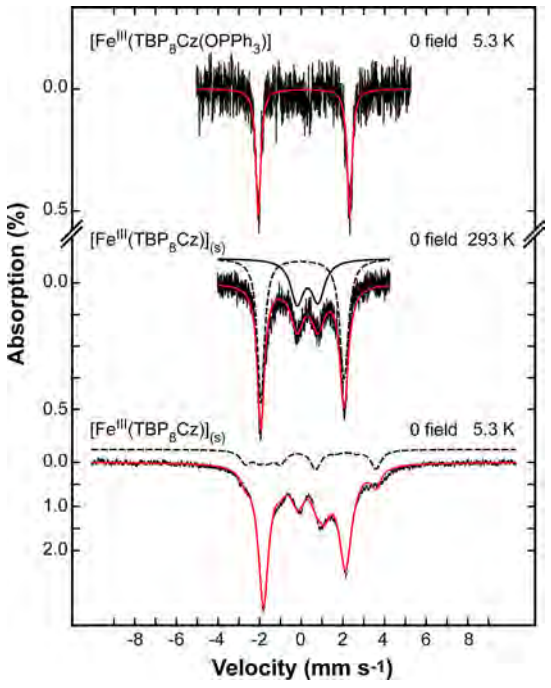

Figure 10. Mössbauer spectra of a crystalline sample of [Fe^{III}(TBP$_8$Cz)(O═PPh$_3$)] (**4b**) measured at 5.3 K and a solid sample of [Fe^{III}(TBP$_8$Cz)] (**1**) measured at 293 K (solid black line = high spin Fe^{III}; dashed black line = intermediate spin Fe^{III}) and 5.3 K with no applied magnetic field (dashed line = slow relaxing intermediate spin Fe^{III}). The red lines show the best fit to the data.

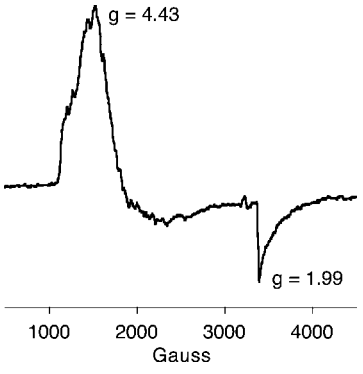

Figure 11. X-band EPR spectrum at 15 K of crystalline [Fe^{III}(TBP$_8$Cz)(OPPh$_3$)] (**4b**) dissolved in toluene. Experimental conditions: frequency = 9.49 GHz, microwave power = 0.201 mW, modulation amplitude 10.0 G, modulation frequency = 100 kHz.

dx.doi.org/10.1021/ic400280x | Inorg. Chem. 2013, 52, 4668−4682

These parameters and intensities are similar to those recently reported for [$Fe^{III}(TBP_8Cz)$] by Nakamura and co-workers,[75] who measured temperature-dependent Mössbauer spectra down to 77 K. In this study the quadrupole splitting was seen to be temperature-independent, but the isomer shift increased with a decrease in temperature, as one would expect, as a result of the second-order Doppler shift.[76] As seen in Figure 10, the spectrum at 5.3 K for **1** consists of two quadrupole doublets with a slight increase in the isomer shifts (δ = 0.15 mm s^{-1} and δ = 0.47 mm s^{-1}) as compared to the data at 293 K. These isomer shifts can be assigned to a mixture of intermediate spin Fe^{III} and high spin Fe^{III} ($S = {}^5/_2$) ions. Additionally, there is a broad component (~20%, dashed line Figure 10) caused by slow relaxation of the intermediate spin iron(III) centers relative to the Mössbauer time scale of ~10^7 s^{-1}, resulting in splitting of the nuclear magnetic spin states and giving rise to the broad spectrum observed. The parameters used to simulate this magnetic spectrum were those used to fit the frozen solution spectrum of [$Fe^{III}(TBP_8Cz)$] described below.

Dissolution of the [$Fe^{III}(TBP_8Cz)$] complex in toluene provides Mössbauer spectra that help to clarify the spectral assignments. A frozen toluene solution of the Fe^{III} complex produces a single quadrupole doublet at 100 K (δ = 0.11 mm s^{-1}, ΔE_Q = 3.96 mm s^{-1}, Figure 12), consistent with the

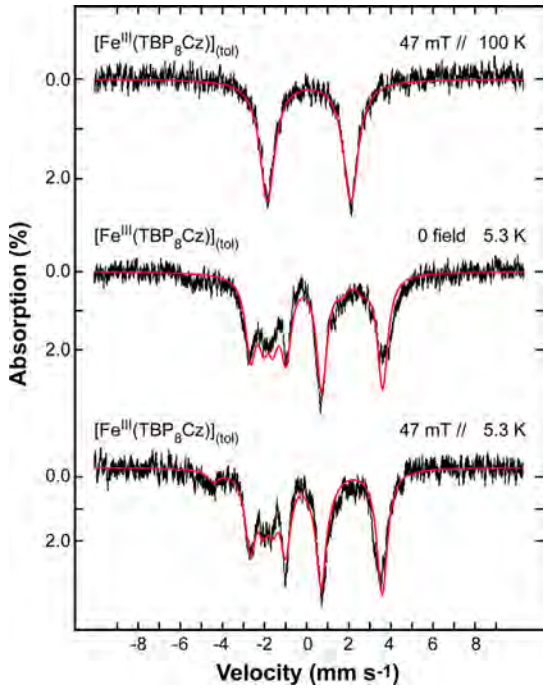

Figure 12. Mössbauer spectra of [$Fe^{III}(TBP_8Cz)$] dissolved in toluene and measured at 100 K with an applied magnetic field of 47 mT parallel to the γ-rays, 5.3 K with no magnetic field and 5.3 K with an applied magnetic field of 47 mT parallel to the γ-rays. The red line through the data shows the best fit using the parameters given in the text.

presence of a pure intermediate spin species. If the sample is then suitably diluted and carefully frozen,[72] the spectra collected at the lower temperature of 5.3 K are clearly in the slow relaxation regime (Figure 12), and can be fitted to a single $S = {}^3/_2$ species. This result is in good agreement with EPR spectra of the same complex in a frozen solution of toluene, which revealed an intermediate spin iron(III) spectrum at 15 K.[42] Careful comparison of the Mössbauer spectra in the presence and absence of a small magnetic field (47 mT) allows this species to be fitted with the values δ = 0.15 mm s^{-1}; ΔE_Q = +3.98 mm s^{-1}; $D = -4$ cm^{-1}; $E/D = 0$; $A_x = A_y = 19$ T, $A_z = 6$ T, which are comparable with intermediate spin Fe^{III} tetraamido complexes.[77] We can conclude that dissolution in toluene provides a uniform environment for complex **1** and leads to the observation of a single iron(III) intermediate spin ground state, in contrast to the solid state, in which stacking or other aggregation effects appear to give rise to a mixture of the two different spin states $S = {}^3/_2$ and $S = {}^5/_2$ for **1**.

The third possible spin state for an Fe^{III} species is a low-spin ($S = {}^1/_2$) configuration, and this state can be accessed for iron(III) corrolazine by addition of excess pyridine. Previous work has shown that addition of pyridine to [$Fe^{III}(TBP_8Cz)$] gives the axially ligated complex [$Fe^{III}(TBP_8Cz)(py)_2$], which reveals an intense rhombic EPR spectrum (g 2.39, 2.20, 1.90) that is characteristic of a low spin Fe^{III} porphyrinoid compound.[42] The Mössbauer spectrum of this species at 100 K consists of a symmetrical quadrupole doublet (δ = 0.01 mm s^{-1}, ΔE_Q = 3.99 mm s^{-1}, Figure 13). The isomer shift is consistent with low spin Fe^{III}, and indeed the value is lower than that of the intermediate spin species discussed above. At 5.3 K, the spectrum consists of both slow (dashed line, Figure 13) and fast relaxing low spin Fe^{III} signals (δ = 0.03 mm s^{-1}, ΔE_Q = 4.03 mm s^{-1}), as seen for the intermediate spin complex (Figure 10). These parameters are similar to, but slightly larger than, those recently described[75] for the analogous bis(cyano) complex [$Fe^{III}(TBP_8Cz)(CN)_2]^{2-}$ ($\delta = -0.09$ mm s^{-1}, ΔE_Q = 2.74 mm s^{-1} at 77 K).

The Mössbauer spectrum of bulk, crystalline **3** consists of a quadrupole doublet at 293 K (δ = 0.13 mm s^{-1}, ΔE_Q = 4.25 mm s^{-1}, Figure 13). However, a bulk sample of this material consists of both [$Fe^{IV}(TBP_8Cz)(NPPh_3)$] and [$Fe^{III}(TBP_8Cz)$-$(OPPh_3)$] as shown by independent X-ray analysis. An EPR spectrum of a bulk sample of **3** at 15 K revealed only a weak signal with broad features at g 5.39, 2.02 (Figure S10), consistent with the presence of [$Fe^{III}(TBP_8Cz)(OPPh_3)$] as a minor impurity. The Mössbauer spectrum of **3** at 5.3 K can be fitted to an Fe^{IV} (S = 1) species (δ = 0.13 mm s^{-1}; ΔE_Q = 4.25 mm s^{-1}; $D = +5$ cm^{-1}; $E/D = 0$; $A_x = A_y = 8$ T, $A_z = 10$ T; Figure 13) together with [$Fe^{III}(TBP_8Cz)(OPPh_3)$] as a minor component (~10%, fitted with the parameters found for the pure $Fe^{III}(OPPh_3)$ complex). Thus, Mössbauer and EPR spectroscopy are in agreement with the assignment of the bulk crystalline material for **3**. Interestingly, the isomer shift for the Fe^{IV} complex (δ = 0.13 mm s^{-1}) is comparable to the isomer shift found for the intermediate spin Fe^{III} corrolazines, which suggests that the Fe^{IV}–$NPPh_3$ complex may be better described as an intermediate spin Fe^{III} center coupled to a corrolazine π-cation radical. This dichotomy for iron(IV) corroles has been discussed at length by Walker and co-workers,[70] but these two options cannot be distinguished for the current complex from the available data. We note that the quadrupole splitting parameters are distinct for the Fe^{IV} complex **3** (4.25 mm s^{-1}) and the intermediate spin-Fe^{III} complex **4** (4.40 mm s^{-1}), although not by as much as might be expected. Future experimental/computational work may shed light on this issue.

Finally, Mössbauer spectroscopy was also employed to analyze a ^{57}Fe-labeled sample of [$Fe^{IV}(TBP_8Cz^{+\bullet})(NTs)$], which was isolated as a precipitated solid from the reaction

dx.doi.org/10.1021/ic400280x | Inorg. Chem. 2013, 52, 4668–4682

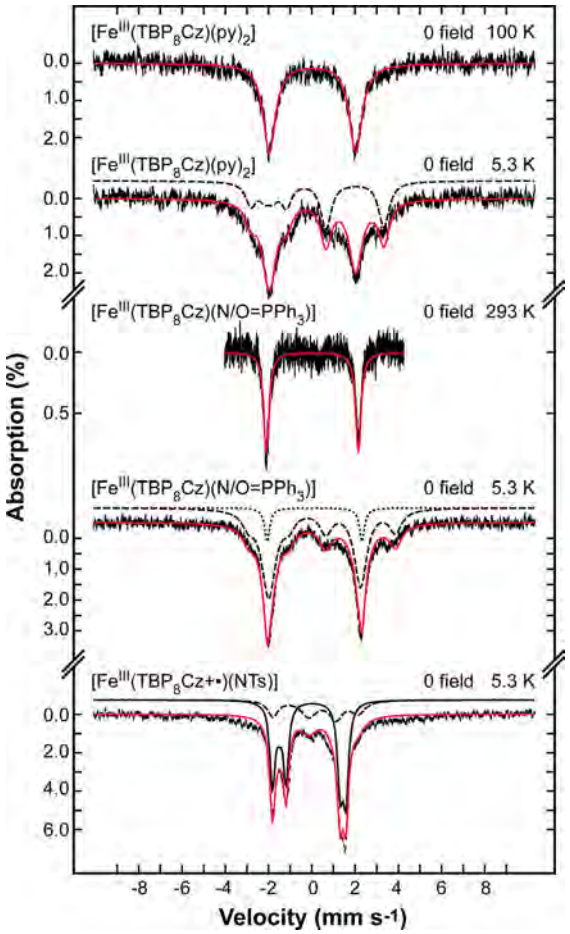

Figure 13. Mössbauer spectra of $[Fe^{III}(TBP_8Cz)]$ dissolved in pyridine at 100 and 5.3 K with no applied field (dashed line = slow relaxing low spin Fe^{III}). Mössbauer spectra of a solid sample of $[Fe^{III}(TBP_8Cz)(N/OPPh_3)]$ measured at 293 and 5.3 K (dotted line = $[Fe^{III}(TBP_8Cz)(OPPh_3)]$; dashed line = $[Fe^{IV}(TBP_8Cz)(NPPh_3)]$). Frozen solution spectrum of $[Fe^{IV}(TBP_8Cz^{+\bullet})(NTs)]$ measured at 5.3 K (dashed line = ~25% $[Fe^{III}(TBP_8Cz)]$). The red line through the data shows the best fit using the parameters given in the text.

mixture of $[Fe^{III}(TBP_8Cz)]$ and chloramine-T. The spectrum measured at 5.3 K in toluene (Figure 13) can be fitted to two species: ~25% of unreacted $[Fe^{III}(TBP_8Cz)]$ (dashed line, parameters given above), and an Fe^{IV} (S = 1) ion antiferromagnetically coupled to a Cz-π-cation-radical (δ = −0.05 mm s^{-1}; ΔE_Q = 2.94 mm s^{-1}; $A_x = A_y$ = 26 T, A_z = 3.5 T; J ~ 30 cm^{-1}). The sign of the quadrupole splitting cannot be unambiguously defined, but if positive, a rotation of the electric field gradient (EFG) relative to the principle axes is required. In fact there is no reason why the principal axes should be collinear and the EFG tensor can be rotated by a set of Euler angles α, β, and γ (0, 105, 0). The low isomer shift and smaller quadrupole splitting of this species as compared to those found for the Fe^{III} complexes strongly suggest that this complex contains an iron(IV) center as proposed.[68] In addition, EPR spectroscopy of this complex at 15 K gives a sharp axial signal with $g_\perp$ = 2.10, $g_\parallel$ = 2.00, consistent with an overall $S = {}^1/_2$ ground state as expected for an Fe^{IV}−Cz-π-cation-radical and in good agreement with the Mössbauer analysis.

Altogether, the Mössbauer data show consistent findings across all species as summarized in Table 3. The intermediate spin $S = {}^3/_2$ Fe^{III} species all have isomer shifts of ~+0.13 mm s^{-1}. The isomer shift for $[Fe^{IV}(TBP_8Cz)(NPPh_3)]$ also falls in this range, and this complex may be best described as an Fe^{III} coupled to a π-radical-cation. Conversion to a low spin Fe^{III} center by addition of pyridine to form $[Fe^{III}(TBP_8Cz)(py)_2]$ lowers the isomer shift to +0.03 mm s^{-1}. Further oxidation to form $[Fe^{IV}(TBP_8Cz^{+\bullet})(NTs)]$ leads to an isomer shift of −0.05 mm s^{-1}, consistent with a high-valent iron(IV) ion.

Computational Studies. To further confirm the spectroscopic data and gain structural insight into the iron-imido complex we have calculated the Mössbauer and EPR parameters of $[Fe^{IV}(H_8Cz^{+\bullet})(NTs)]$ in both the doublet and quartet spin states using DFT. To reduce calculation time a model where the eight peripheral ^{t}Bu-phenyl groups from the corrolazine ring were replaced by hydrogen atoms was implemented, H_8Cz. Initial geometric optimization led to a structure with reasonable bond lengths (Figure 15). The Fe−N

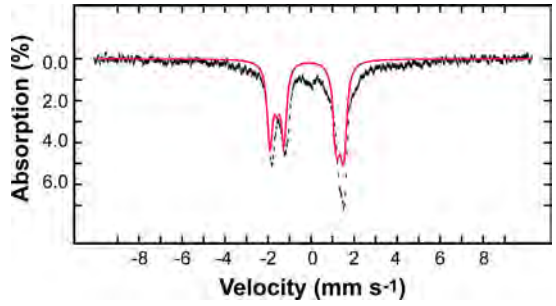

Figure 14. Mössbauer spectra of $[Fe^{IV}(TBP_8Cz^{+\bullet})(NTs)]$ measured at 5.3 K. Overlaid is a simulation (red line) using the parameters determined by DFT with the EFG and A rotated by the following Euler angles (19, 100, 51) and (70, 92, 3).

Table 3. Mössbauer Parameters for Iron Corrolazine Complexes

		spin state	δ (mm s^{-1})	ΔE_Q (mm s^{-1})	Γ (mm s^{-1})	D (cm^{-1})	E/D	$A_x/g_n\mu_n$ [a] (T)	$A_y/g_n\mu_n$ [a] (T)	$A_z/g_n\mu_n$ [a] (T)
$[Fe^{III}(TBP_8Cz)]$		$^3/_2$	0.15	+3.98	0.6	−4	0	19	19	6
$[Fe^{III}(TBP_8Cz)(py)_2]$		$^1/_2$	0.03	4.03	0.7					
$[Fe^{III}(TBP_8Cz)(OPPh_3)]$		$^3/_2$	0.13	4.40	0.3					
$[Fe^{IV}(TBP_8Cz)(NPPh_3)]$		1 [b]	0.13	4.25	0.7	+5	0	8	8	10
$[Fe^{IV}(TBP_8Cz^{\bullet+})(NTs)]$	expt	$^1/_2$ [c]	−0.05	2.95	0.3			26	26	3.5
	calcd	$^1/_2$ [d]	−0.12	+2.92				−4.8	24.0	30.9

[a] The sign of the hyperfine coupling constants cannot be determined. [b] The spin state is not fully determined and can be considered an intermediate spin Fe^{III} coupled to a radical cation, as the isomer shift suggests. [c] The S = 1 Fe^{IV} is antiferromagnetically coupled to a $S = {}^1/_2$ radical cation with an exchange coupling constant of ~30 cm^{-1}. The electric field gradient (EFG) is rotated using the following Euler angles (0, 105, 0). [d] η = 0.38. To fit experiment, both the EFG and A tensors have to be rotated by the following Euler angles (19, 100, 51) and (70, 92, 3), respectively, because the principal axes used are different.

dx.doi.org/10.1021/ic400280x | Inorg. Chem. 2013, 52, 4668−4682

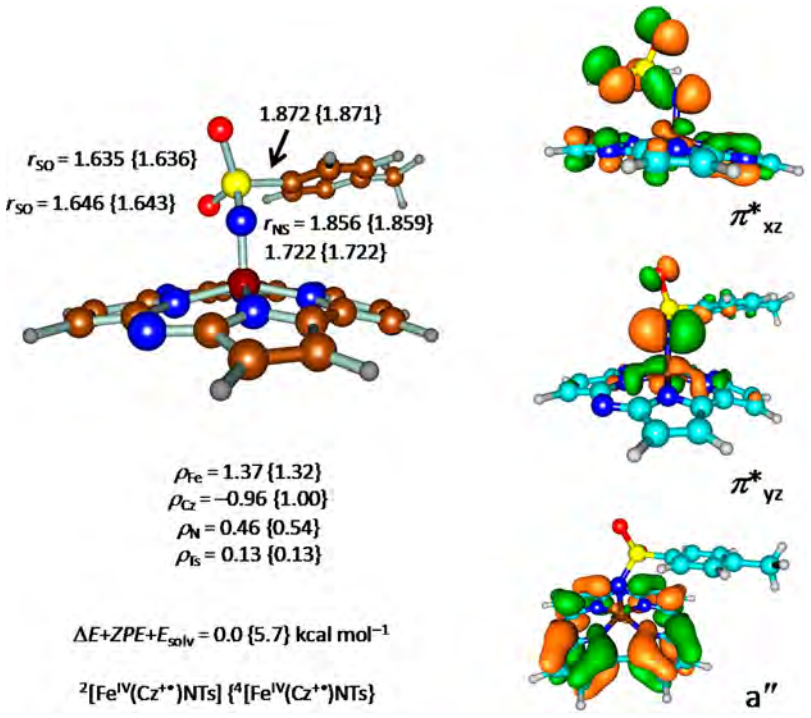

Figure 15. DFT calculated structures of ^{2,4}[Fe^{IV}(H$_8$Cz$^{+\bullet}$)(NTs)] with bond lengths in angstroms and group spin densities (ρ) in atomic units. Also given are the spin state energy differences in kcal mol^{-1} as calculated at UB3LYP/B2//UB3LYP/B1 including solvent and zero-point corrections. Orbital drawings of the singly occupied molecular orbitals are given on the right.

bond length of 1.722 Å is comparable to other iron-imido complexes both experimental and calculated.[8,78] The doublet spin state is the ground state and is found to lie 5.7 kcal mol^{-1} below the quartet spin state, consistent with the spectroscopic results given above. The spin densities were then calculated and molecular orbitals analyzed, which revealed two unpaired electrons in the $\pi^*_{xz/yz}$ orbitals antiferromagnetically coupled to a single electron in the a″-type Cz orbital. The orbital shapes and the electronic configuration show resemblance to that calculated for [Mn^V(H$_8$Cz$^{+\bullet}$)(O)], which also gave single occupation of the a″ orbital.[38] Due to mixing of the atomic $3d_{xz}/3d_{yz}$ orbitals on Fe with $2p_x/2p_y$ orbitals on nitrogen, the π^*_{xz} and π^*_{yz} orbitals are mixed iron/nitrogen antibonding orbitals, and consequently, considerable spin density is observed on the nitrogen and tosylate group. This mixing is similar to that observed on the oxo group in heme and nonheme iron(IV)-oxo species.[79,80]

Finally, the Mössbauer and EPR parameters were then calculated and are given in Table 3. The parameters compare favorably with the experimentally determined ones and provide further strong evidence that our understanding of the electronic state is correct. The calculated g values (2.00, 2.03, 2.07) are rhombic rather than axial, but the Mössbauer isomer shift and quadrupole splitting reproduce the experimental data within the error of the calculations. A simulation of the Mössbauer spectrum with these parameters is given in Figure 14 and shows graphically how close the match is. To obtain a reasonable fit both the electric field gradient (EFG) and hyperfine (A) tensors had to be rotated relative to each other. The following Euler angles were used: (19, 100, 51) for the EFG and (70, 92, 3) for A.

CONCLUSIONS

The reaction of [Fe^{III}(TBP$_8$Cz)] with the NR transfer agent chloramine-T results in the formation of the high-valent iron(IV) terminal imido complex [Fe^{IV}(TBP$_8$Cz$^{+\bullet}$)(NTs)] (**2**). Previously iron terminal imido complexes have been stabilized through a combination of steric encumbrance and the enforcement of relatively low-coordinate geometries about the iron center. The stability of **2** is likely a consequence of the oxidatively resistant, trianionic corrolazine supporting ligand favoring high-valent iron(IV) together with the strong σ and π donation of the terminal tosylimido donor. The stability of **2** is significant because high-valent, multiply bonded terminal imido complexes of the mid- to late-transition metals are normally considered to be highly reactive, but the data presented here indicates that **2** is much more stable (and consequently less reactive) than is expected for an iron-imido complex. Thus, catalytic mechanisms that rely on proposed intermediates of this type, especially in porphyrinoid chemistry, may need to be carefully scrutinized when identifying the actual oxidizing species.

Mössbauer and EPR spectroscopies show that [Fe^{IV}(TBP$_8$Cz$^{+\bullet}$)(NTs)] contains a high-valent Fe^{IV} ion with an extra oxidizing equivalent stored on the Cz ring as a π-cation-radical, analogous to the previously described compound-I-like terminal oxo complex [Fe^{IV}(TBP$_8$Cz$^{+\bullet}$)(O)].[39] This view has been further corroborated by DFT calculations. The spin state of both the imido and oxo complexes is proposed to be a doublet with iron(IV) antiferromagnetically coupled to the Cz π-cation-radical. It was demonstrated that **2** is capable of NR group transfer to triphenylphosphine to give Ph$_3$PNTs, leading to the two-electron reduction of **2** to give the Fe^{III} complex **1**. Catalytic NR transfer to PPh$_3$ by **1** was also successful, suggesting that further design of suitable metallocorrolazines (or corroles) may yield potent NR transfer

dx.doi.org/10.1021/ic400280x | Inorg. Chem. 2013, 52, 4668−4682

catalysts. The kinetic data For NR transfer from **2** to PPh_3 was in agreement with the proposed bimolecular mechanism, and a comparison of rate constants shows that **2** exhibits a dramatic rate enhancement (~100-fold) for NR transfer as compared to $Mn^V(NAr)$ corrole analogues. Structural analyses of complexes formed following initial NR transfer reveal that both $[Fe^{IV}(TBP_8Cz)(NPPh_3)]$ and $[Fe^{III}(TBP_8Cz)(OPPh_3)]$ crystallize from the same reaction mixture. A mechanism was described that can account for the NR transfer reactivity of **2** as well as the subsequent formation of the former complexes.

■ ASSOCIATED CONTENT

Ⓢ Supporting Information

Spectroscopic and crystallographic data (CIF), and details of the DFT calculations, including relative and absolute energies, group spin densities, charges, and Cartesian coordinates of all structures. This material is available free of charge via the Internet at http://pubs.acs.org.

■ AUTHOR INFORMATION

Corresponding Author

*E-mail: dpg@jhu.edu (D.P.G.); gjameson@chemistry.otago.ac.nz (G.N.L.J.); sam.devisser@manchester.ac.uk (S.P.d.V.).

Notes

The authors declare no competing financial interest.

■ ACKNOWLEDGMENTS

This work was supported by the NSF (CHE0909587 and CHE1213836 to D.P.G.). P.L. is grateful for the Queen Sirikit Scholarship (Thailand). We thank Dr. Yosra M. Badiei for the synthesis of $^{57}FeCl_2$ and Dr. Victoria J. A. Jameson for help with Mössbauer sample preparation. The computational work was supported by CPU time provided by the National Service of Computational Chemistry Software (NSCCS). D.K. holds a Ramanujan Fellowship from the Department of Science and Technology (DST), New Delhi (India), and acknowledges its financial support (Research Grants SR/S2/RJN-11/2008 and SR/S1/PC-58/2009).

■ REFERENCES

(1) Ertl, G. *Angew. Chem., Int. Ed.* **1990**, *29*, 1219−1227.
(2) Smil, V. *Enriching the Earth: Fritz Haber, Carl Bosch, and the Transformation of World Food Production*; MIT Press: Cambridge, 2004.
(3) Hoffman, B. M.; Dean, D. R.; Seefeldt, L. C. *Acc. Chem. Res.* **2009**, *42*, 609−619.
(4) Seefeldt, L. C.; Hoffman, B. M.; Dean, D. R. *Annu. Rev. Biochem.* **2009**, *78*, 701−722.
(5) Pickett, C. J. *J. Biol. Inorg. Chem.* **1996**, *1*, 601−606.
(6) Svastits, E. W.; Dawson, J. H.; Breslow, R.; Gellman, S. H. *J. Am. Chem. Soc.* **1985**, *107*, 6427−6428.
(7) King, E. R.; Betley, T. A. *Inorg. Chem.* **2009**, *48*, 2361−2363.
(8) King, E. R.; Hennessy, E. T.; Betley, T. A. *J. Am. Chem. Soc.* **2011**, *133*, 4917−4923.
(9) Berry, J. F. *Comments Inorg. Chem.* **2009**, *30*, 28−66.
(10) Mehn, M. P.; Peters, J. C. *J. Inorg. Biochem.* **2006**, *100*, 634−643.
(11) Saouma, C. T.; Peters, J. C. *Coord. Chem. Rev.* **2011**, *255*, 920−937.
(12) Zalatan, D. N.; Du Bois, J. *Top. Curr. Chem.* **2010**, *292*, 347−378.
(13) Müller, P.; Fruit, C. *Chem. Rev.* **2003**, *103*, 2905−2919.
(14) Chow, T. W. S.; Chen, G. Q.; Liu, Y. G.; Zhou, C. Y.; Che, C. M. *Pure Appl. Chem.* **2012**, *84*, 1685−1704.
(15) Eikey, R. A.; Abu-Omar, M. M. *Coord. Chem. Rev.* **2003**, *243*, 83−124.
(16) Abu-Omar, M. M. *Dalton Trans.* **2011**, *40*, 3435−3444.
(17) Smith, J. M.; Subedi, D. *Dalton Trans.* **2012**, *41*, 1423−1429.
(18) To our knowledge, there are only two reported Fe compounds with +6 oxidation state: Berry, J. F.; Bill, E.; Bothe, E.; DeBeer George, S.; Mienert, B.; Neese, F.; Wieghardt, K. *Science* **2006**, *312*, 1937−1941.
(19) Hohenberger, J.; Ray, K.; Meyer, K. *Nat. Commun.* **2012**, *3*, 720.
(20) Mahy, J. P.; Battioni, P.; Mansuy, D.; Fisher, J.; Weiss, R.; Mispelter, J.; Morgensternbadarau, I.; Gans, P. *J. Am. Chem. Soc.* **1984**, *106*, 1699−1706.
(21) Klinker, E. J.; Jackson, T. A.; Jensen, M. P.; Stubna, A.; Juhasz, G.; Bominaar, E. L.; Münck, E.; Que, L., Jr. *Angew. Chem., Int. Ed.* **2006**, *45*, 7394−7397.
(22) Brown, S. D.; Betley, T. A.; Peters, J. C. *J. Am. Chem. Soc.* **2003**, *125*, 322−323.
(23) Moret, M. E.; Peters, J. C. *Angew. Chem., Int. Ed.* **2011**, *50*, 2063−2067.
(24) Betley, T. A.; Peters, J. C. *J. Am. Chem. Soc.* **2003**, *125*, 10782−10783.
(25) Brown, S. D.; Peters, J. C. *J. Am. Chem. Soc.* **2005**, *127*, 1913−1923.
(26) Thomas, C. M.; Mankad, N. P.; Peters, J. C. *J. Am. Chem. Soc.* **2006**, *128*, 4956−4957.
(27) Nieto, I.; Ding, F.; Bontchev, R. P.; Wang, H. B.; Smith, J. M. *J. Am. Chem. Soc.* **2008**, *130*, 2716−2717.
(28) Bowman, A. C.; Milsmann, C.; Bill, E.; Turner, Z. R.; Lobkovsky, E.; DeBeer, S.; Wieghardt, K.; Chirik, P. J. *J. Am. Chem. Soc.* **2011**, *133*, 17353−17369.
(29) Bart, S. C.; Lobkovsky, E.; Bill, E.; Chirik, P. J. *J. Am. Chem. Soc.* **2006**, *128*, 5302−5303.
(30) Cowley, R. E.; Eckert, N. A.; Vaddadi, S.; Figg, T. M.; Cundari, T. R.; Holland, P. L. *J. Am. Chem. Soc.* **2011**, *133*, 9796−9811.
(31) Cowley, R. E.; Holland, P. L. *Inorg. Chem.* **2012**, *51*, 8352−8361.
(32) Lansky, D. E.; Kosack, J. R.; Sarjeant, A. A. N.; Goldberg, D. P. *Inorg. Chem.* **2006**, *45*, 8477−8479.
(33) Eikey, R. A.; Khan, S. I.; Abu-Omar, M. M. *Angew. Chem., Int. Ed.* **2002**, *41*, 3592−3595.
(34) Mandimutsira, B. S.; Ramdhanie, B.; Todd, R. C.; Wang, H. L.; Zareba, A. A.; Czernuszewicz, R. S.; Goldberg, D. P. *J. Am. Chem. Soc.* **2002**, *124*, 15170−15171.
(35) Lansky, D. E.; Mandimutsira, B.; Ramdhanie, B.; Clausén, M.; Penner-Hahn, J.; Zvyagin, S. A.; Telser, J.; Krzystek, J.; Zhan, R. Q.; Ou, Z. P.; Kadish, K. M.; Zakharov, L.; Rheingold, A. L.; Goldberg, D. P. *Inorg. Chem.* **2005**, *44*, 4485−4498.
(36) Prokop, K. A.; Goldberg, D. P. *J. Am. Chem. Soc.* **2012**, *134*, 8014−8017.
(37) Prokop, K. A.; de Visser, S. P.; Goldberg, D. P. *Angew. Chem., Int. Ed.* **2010**, *49*, 5091−5095.
(38) Prokop, K. A.; Neu, H. M.; de Visser, S. P.; Goldberg, D. P. *J. Am. Chem. Soc.* **2011**, *133*, 15874−15877.
(39) McGown, A. J.; Kerber, W. D.; Fujii, H.; Goldberg, D. P. *J. Am. Chem. Soc.* **2009**, *131*, 8040−8048.
(40) Cho, K.; Leeladee, P.; McGown, A. J.; DeBeer, S.; Goldberg, D. P. *J. Am. Chem. Soc.* **2012**, *134*, 7392−7399.
(41) Simkhovich, L.; Gross, Z. *Tetrahedron Lett.* **2001**, *42*, 8089−8092.
(42) Kerber, W. D.; Ramdhanie, B.; Goldberg, D. P. *Angew. Chem., Int. Ed.* **2007**, *46*, 3718−3721.
(43) Ramdhanie, B.; Stern, C. L.; Goldberg, D. P. *J. Am. Chem. Soc.* **2001**, *123*, 9447−9448.
(44) Aresta, M.; Nobile, C. F.; Petruzzelli, D. *Inorg. Chem.* **1977**, *16*, 1817−1818.
(45) Bittner, S.; Assaf, Y.; Krief, P.; Pomerantz, M.; Ziemnicka, B. T.; Smith, C. G. *J. Org. Chem.* **1985**, *50*, 1712−1718.
(46) Davidson, M. G.; Goeta, A. E.; Howard, J. A. K.; Lehmann, C. W.; McIntyre, G. M.; Price, R. D. *J. Organomet. Chem.* **1998**, *550*, 449−452.

(47) Kumar, D.; Karamzadeh, B.; Sastry, G. N.; de Visser, S. P. *J. Am. Chem. Soc.* **2010**, *132*, 7656−7667.
(48) Becke, A. D. *J. Chem. Phys.* **1993**, *98*, 5648−5652.
(49) Lee, C. T.; Yang, W. T.; Parr, R. G. *Phys. Rev. B* **1988**, *37*, 785−789.
(50) *Jaguar, version 7.9*; Schrodinger, LLC: New York, 2011.
(51) Frisch, M. J.; et al. *Gaussian 03, revision C.02*; Gaussian, Inc.: Wallingford, CT, 2004. See Supporting Information.
(52) Hay, P. J.; Wadt, W. R. *J. Chem. Phys.* **1985**, *82*, 270−283.
(53) de Visser, S. P. *J. Am. Chem. Soc.* **2010**, *132*, 1087−1097.
(54) Neese, F. *ORCA—An Ab Initio, DFT and Semiempirical SCF-MO Package, Version 2.9*; Bonn, Germany, 2009.
(55) Neese, F. *Inorg. Chim. Acta* **2002**, *337*, 181−192.
(56) Sinnecker, S.; Svensen, N.; Barr, E. W.; Ye, S.; Bollinger, J. M., Jr.; Neese, F.; Krebs, C. *J. Am. Chem. Soc.* **2007**, *129*, 6168−6179.
(57) Karamzadeh, B.; Kumar, D.; Sastry, G. N.; de Visser, S. P. *J. Phys. Chem. A* **2010**, *114*, 13234−13243.
(58) Betley, T. A.; Peters, J. C. *J. Am. Chem. Soc.* **2004**, *126*, 6252−6254.
(59) Scepaniak, J. J.; Fulton, M. D.; Bontchev, R. P.; Duesler, E. N.; Kirk, M. L.; Smith, J. M. *J. Am. Chem. Soc.* **2008**, *130*, 10515−15017.
(60) Mankad, N. P.; Muller, P.; Peters, J. C. *J. Am. Chem. Soc.* **2010**, *132*, 4083−4085.
(61) Abu-Omar, M. M.; Shields, C. E.; Edwards, N. Y.; Eikey, R. A. *Angew. Chem., Int. Ed.* **2005**, *44*, 6203−6207.
(62) Fructos, M. R.; Trofimenko, S.; Diaz-Requejo, M. M.; Perez, P. J. *J. Am. Chem. Soc.* **2006**, *128*, 11784−11791.
(63) Fantauzzi, S.; Caselli, A.; Gallo, E. *Dalton Trans.* **2009**, 5434−5443.
(64) Vyas, R.; Gao, G. Y.; Harden, J. D.; Zhang, X. P. *Org. Lett.* **2004**, *6*, 1907−1910.
(65) Harden, J. D.; Ruppel, J. V.; Gao, G. Y.; Zhang, X. P. *Chem. Commun.* **2007**, 4644−4646.
(66) Edwards, N. Y.; Eikey, R. A.; Loring, M. I.; Abu-Omar, M. M. *Inorg. Chem.* **2005**, *44*, 3700−3708.
(67) Bennett, B. K.; Saganic, E.; Lovell, S.; Kaminsky, W.; Samuel, A.; Mayer, J. M. *Inorg. Chem.* **2003**, *42*, 4127−4131.
(68) Cai, S.; Walker, F. A.; Licoccia, S. *Inorg. Chem.* **2000**, *39*, 3466−3474.
(69) Walker, F. A.; Licoccia, S.; Paolesse, R. *J. Inorg. Biochem.* **2006**, *100*, 810−837.
(70) Zakharieva, O.; Schünemann, V.; Gerdan, M.; Licoccia, S.; Cai, S.; Walker, F. A.; Trautwein, A. X. *J. Am. Chem. Soc.* **2002**, *124*, 6636−6648.
(71) Schwalbe, M.; Dogutan, D. K.; Stoian, S. A.; Teets, T. S.; Nocera, D. G. *Inorg. Chem.* **2011**, *50*, 1368−1377.
(72) Amusa, A.; Debrunner, P.; Frauenfe, H.; Münck, E.; DePasqua, G. *J. Phys. C* **1974**, *7*, 1881−1891.
(73) Teschner, T.; Yatsunyk, L.; Schunemann, V.; Paulsen, H.; Winkler, H.; Hu, C. J.; Scheidt, W. R.; Walker, F. A.; Trautwein, A. X. *J. Am. Chem. Soc.* **2006**, *128*, 1379−1389.
(74) Simonneaux, G.; Schunemann, V.; Morice, C.; Carel, L.; Toupet, L.; Winkler, H.; Trautwein, A. X.; Walker, F. A. *J. Am. Chem. Soc.* **2000**, *122*, 4366−4377.
(75) Kurahashi, S.; Ikeue, T.; Sugimori, T.; Takahashi, M.; Mikuriya, M.; Handa, M.; Ikezaki, A.; Nakamura, M. *J. Porphyrins Phthalocyanines* **2012**, *16*, 518−529.
(76) Gütlich, P.; Bill, E.; Trautwein, A. X. *Mössbauer Spectroscopy and Transition Metal Chemistry: Fundamentals and Applications*; Springer-Verlag: Berlin, 2011.
(77) Kostka, K. L.; Fox, B. G.; Hendrich, M. P.; Collins, T. J.; Rickard, C. E. F.; Wright, L. J.; Münck, E. *J. Am. Chem. Soc.* **1993**, *115*, 6746−6757.
(78) Jaccob, M.; Rajaraman, G. *Dalton Trans.* **2012**, *41*, 10430−10439.
(79) de Visser, S. P. *J. Am. Chem. Soc.* **2006**, *128*, 15809−15818.
(80) *Iron-Containing Enzymes: Versatile Catalysts of Hydroxylation Reactions in Nature*; de Visser, S. P., Kumar, D., Eds.; Royal Society of Chemistry Publishing: Cambridge, U.K., 2011.
(81) Stephens, J. C.; Khan, M. A.; Houser, R. P. *Inorg. Chem.* **2001**, *40*, 5064−5065.
(82) Chen, G.; Man, W. L.; Yiu, S. M.; Wong, T. W.; Szeto, L.; Wong, W. T.; Lau, T. C. *Dalton Trans.* **2011**, *40*, 1938−1944.
(83) Gröb, T.; Geiseler, G.; Harms, K.; Greiner, A.; Dehnicke, K. *Z. Anorg. Allg. Chem.* **2002**, *628*, 217−221.
(84) Schrumpf, F.; Roesky, H. W.; Noltemeyer, M. *Z. Naturforsch., B* **1990**, *45*, 1600−1602.
(85) Tomi, F.; Wah, H. L. K.; Postel, M. *New J. Chem.* **1988**, *12*, 289−292.
(86) Ding, Z. R.; Bhattacharya, S.; Mccusker, J. K.; Hagen, P. M.; Hendrickson, D. N.; Pierpont, C. G. *Inorg. Chem.* **1992**, *31*, 870−877.
(87) Chekhlov, A. N. *Russ. J. Inorg. Chem.* **2005**, *50*, 1207−1211.
(88) Atkinson, F. L.; Blackwell, H. E.; Brown, N. C.; Connelly, N. G.; Crossley, J. G.; Orpen, A. G.; Rieger, A. L.; Rieger, P. H. *J. Chem. Soc., Dalton. Trans.* **1996**, 3491−3502.
(89) Olejnik, Z.; Lis, T.; Ondrejkovicova, I. *Acta Crystallogr., Sect. C* **1995**, *51*, 2246−2249.
(90) Scepaniak, J. J.; Harris, T. D.; Vogel, C. S.; Sutter, J.; Meyer, K.; Smith, J. M. *J. Am. Chem. Soc.* **2011**, *133*, 3824−3827.

View Online / Journal Homepage / Table of Contents for this issue
Dynamic Article Links

Organic & Biomolecular Chemistry

Cite this: *Org. Biomol. Chem.*, 2012, **10**, 5401

www.rsc.org/obc

PAPER

Axial and equatorial ligand effects on biomimetic cysteine dioxygenase model complexes†

Luis E. Gonzalez-Ovalle,[a] Matthew G. Quesne,[a] Devesh Kumar,*[b] David P. Goldberg*[c] and Sam P. de Visser*[a]

Received 24th February 2012, Accepted 30th May 2012
DOI: 10.1039/c2ob25406a

Published on 31 May 2012 on http://pubs.rsc.org | doi:10.1039/C2OB25406A
Downloaded by The University of Manchester Library on 28 June 2012

Density functional theory (DFT) calculations are presented on biomimetic model complexes of cysteine dioxygenase and focus on the effect of axial and equatorial ligand placement. Recent studies by one of us [Y. M. Badiei, M. A. Siegler and D. P. Goldberg, *J. Am. Chem. Soc*. 2011, **133**, 1274] gave evidence of a nonheme iron biomimetic model of cysteine dioxygenase using an *i*-propyl-bis(imino)pyridine, equatorial tridentate ligand. Addition of thiophenol, an anion – either chloride or triflate – and molecular oxygen, led to several possible stereoisomers of this cysteine dioxygenase biomimetic complex. Moreover, large differences in reactivity using chloride as compared to triflate as the binding anion were observed. Here we present a series of DFT calculations on the origin of these reactivity differences and show that it is caused by the preference of coordination site of anion *versus* thiophenol binding to the chemical system. Thus, stereochemical interactions of triflate and the bulky iso-propyl substituents of the ligand prevent binding of thiophenol in the *trans* position using triflate. By contrast, smaller anions, such as chloride, can bind in either *cis* or *trans* ligand positions and give isomers with similar stability. Our calculations help to explain the observance of thiophenol dioxygenation by this biomimetic system and gives details of the reactivity differences of ligated chloride *versus* triflate.

Introduction

Nonheme iron enzymes are versatile oxidants that catalyze a range of vital processes for human health, and are involved in repair mechanisms, biosynthesis as well as biodegradation of compounds. Generally, they use molecular oxygen on an iron center and transfer either one or both oxygen atoms of molecular oxygen to a substrate, whereby a monoxygenation, dioxygenation or dehydrogenation type of reaction occurs. Nature has developed a large arsenal of these nonheme iron enzymes with various differences in ligand orientation and binding as well as functional properties.[1] Studies on nonheme iron containing enzymes and synthetic analogues (biomimetic compounds) are important for the understanding of biochemical reaction mechanisms but also for industrial (biotechnological) applications.

[a]*Manchester Interdisciplinary Biocenter and School of Chemical Engineering and Analytical Science, The University of Manchester, 131 Princess Street, Manchester M1 7DN, UK. E-mail: sam.devisser@manchester.ac.uk; Fax: +44 (0)161306 5201*
[b]*Department of Applied Physics, School of Physical Sciences, Babasaheb, Bhimrao Ambedkar University, Vidya Vihar, Rae Bareilly Road, Lucknow 226-025, India. E-mail: dkclcre@yahoo.com*
[c]*Department of Chemistry, The Johns Hopkins University, 3400 N. Charles Street, Baltimore, Maryland 21218, USA. E-mail:dpg@jhu.edu*

†Electronic supplementary information (ESI) available. See DOI: 10.1039/c2ob25406a

An extensively studied class of nonheme iron enzymes is the α-ketoglutarate dependent dioxygenases, which anchor the metal *via* a facial 2-His-1-Asp ligand orientation to the protein.[2] These enzymes catalyze the biosynthesis of several antibiotics in bacteria; including vancomycin, fosfomycin and carbapenem.[3] In addition, these enzymes have been implicated with DNA and RNA repair mechanisms.[4] A structurally similar enzyme to the α-ketoglutarate dependent dioxygenases is the human enzyme cysteine dioxygenase (CDO), which is involved in the detoxification and metabolism of cysteine in the body.[5] It catalyzes the first step in the biodegradation of cysteine and converts the substrate to cysteine sulfinic acid. This is a unique reaction and of interest to the biotechnology industry for the catalytic dioxygenation of sulphides.

CDO contains an unusual ligand system where the metal is bound to three histidine ligands of the protein *via* a 3-His facial ligand orientation, but compared to the α-ketoglutarate dependent dioxygenases lacks the carboxylate ligand and the 2-His/1-Asp motif. Current evidence suggests the substrate cysteinate binds the metal in a bidentate fashion through the thiolate and amine groups and is locked in hydrogen bonding interactions *via* several nearby polar amino acids. Fig. 1 displays the active site of substrate bound CDO as taken from the 2IC1 protein databank (pdb) structure.[6] Similar to the nonheme iron dioxygenases, the protein binds the metal in a facial orientation and the ligand position *trans* to His_{86} is vacant and is reserved for molecular oxygen. In recent years a number of spectroscopic and kinetic

Published on 31 May 2012 on http://pubs.rsc.org | doi:10.1039/C2OB25406A
Downloaded by The University of Manchester Library on 28 June 2012

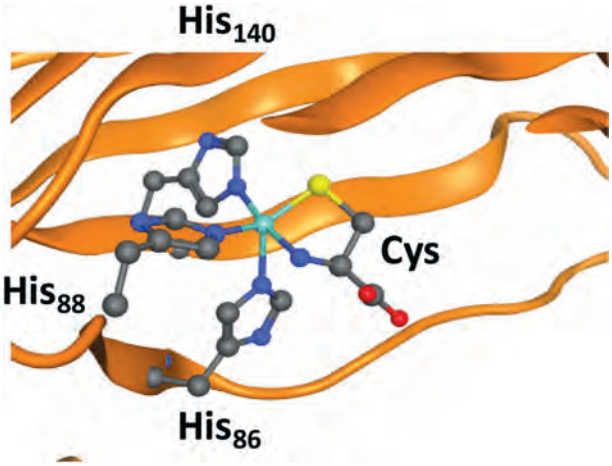

Fig. 1 Extract of the active site of CDO as taken from the 2IC1 pdb file.[6] Amino acids are labelled as in the pdb.

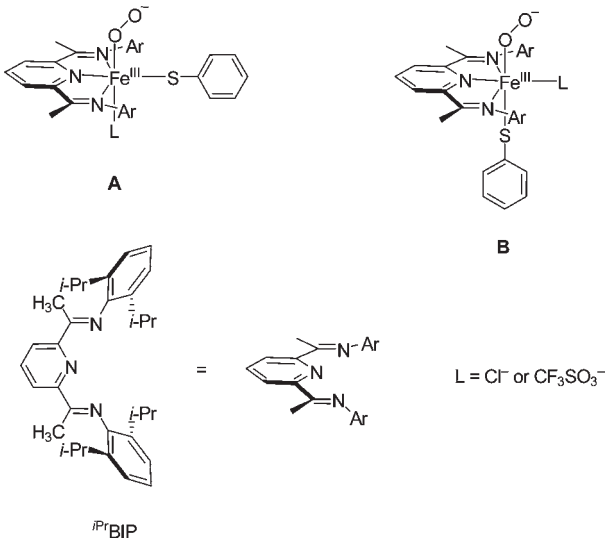

Scheme 1 Models investigated in this study.

studies have provided important insight on the catalytic mechanism of CDO, but there is little knowledge of oxygen bound intermediates.[7] A series of computational studies in our groups have given insight into the CDO ligand system and its mechanism of substrate activation.[8] These studies showed that replacing the 3-His ligand system of CDO by a 2-His-1-Asp ligand system disrupts the dioxygenation process of cysteine and, in particular, leads to weakening of the Fe–S bond. It appears, therefore, that the 3-His ligand system is essential for optimal dioxygenation of cysteine.

In biomimetic chemistry, active site analogues are created with the aim to understand the basic features of enzyme active site structures and reactivity.[1c,d,9] Recently, a few biomimetic models of CDO enzymes were published and spectroscopically characterized.[10–12] One of these contains an Fe(II)(^{iPr}BIP) complex (^{iPr}BIP = iso-propyl-bis(imino)pyridine), Scheme 1.[11] Studies focused on the relative orientation of thiophenol and dioxygen on the metal center. Thus, the ^{iPr}BIP ligand occupies three ligand positions of the metal in the same plane. Dioxygen will occupy the ligand position *cis* with respect to the three nitrogen atoms of the ^{iPr}BIP ligand. The remaining two ligand positions are occupied by thiophenolate (SPh^-) and an anion, which is either Cl^- or $CF_3SO_3^-$. Consequently, these complexes have two possible stereoisomers (Scheme 1) for the Fe(III)-superoxo complex, *i.e.* [$Fe^{III}O_2$(^{iPr}BIP)(SPh)(L)] with L = Cl^- or $CF_3SO_3^-$ (OTf^-), which are designated with **A** and **B** in Scheme 1, respectively. It also should be noted that in contrast to the facial triad of histidine ligands in CDO enzymes, the ^{iPr}BIP ligand coordinates in one plane thereby leaving the axial ligand position vacant for either substrate or an anion. The previous experimental studies revealed dramatic differences in reactivity that were induced by changing the ligand L from Cl^- to $CF_3SO_3^-$, whereby the chloride ligated complex gave disulfide products, whereas the triflate ligated system reacted with O_2 to give an *S*-oxygenated sulfonato product.[11] These differences were assigned to axial *versus* equatorial ligand effects on the iron complex, however, direct evidence for this mechanistic hypothesis was lacking. To gain insight into this matter we performed a density functional theory (DFT) study, and the results are present here.

The effect of axial and equatorial ligands on heme and nonheme iron oxidants is well documented. Thus, heme monoxygenases such as the cytochromes P450 contain an iron-heme active center where the heme is linked to the protein *via* an axial cysteinate ligand.[13] By contrast, heme peroxidases have an axially ligated histidine group, which has been proposed to be a key reason for their differences in catalytic function.[14] These studies proposed the cysteinate to act with a "push"-effect and the push/pull-effect of the axial ligand is thought to contribute to the reactivity differences of P450s *vis-à-vis* peroxidases. Indeed, a series of density functional theory (DFT) calculations confirmed that peroxidase models reacted with much higher barriers in aliphatic hydroxylation and epoxidation reactions using the same substrate.[15] Moreover, the differences between an axially ligated cysteinate *versus* histidine were explained as originating from the charge of the axial ligand and the molecular orbital interactions between metal and ligand.[16]

In biomimetic models, the effect of the axial ligand on spectroscopic properties (*trans*-influence) as well as on reactivity patterns (*trans*-effect) was demonstrated by Gross and co-workers[17] using studies of styrene epoxidation by a range of iron(IV)-oxo porphyrin cation radical systems. Subsequent studies of Nam *et al*[18] showed differences in oxidative properties of iron(IV)-oxo oxidants with chloride *trans* to the oxo group as compared to those with acetonitrile, leading to reactivity differences of those oxidants with *cis versus trans* olefins, the regioselectivity of aliphatic over aromatic hydroxylation, as well as epoxidation *versus* hydroxylation processes. Further studies also revealed axial ligand effects on the reactivity and spectroscopic parameters of a selection of nonheme iron complexes,[19] including a series of thiolate-ligated nonheme iron model complexes by one of us.[20] Recent, combined experimental and computational studies in our groups on the reactivity of manganese(V)-oxo embedded in a corrolazine ligand system identified a pronounced axial ligand effect on the rate constant of hydrogen atom abstraction from C–H substrates (*e.g.* dihydroanthracene) as a function of the axial ligand.[21] By contrast, very little is known of the ligand effect of iron(III)-superoxo complexes,

 This journal is © The Royal Society of Chemistry 2012

Published on 31 May 2012 on http://pubs.rsc.org | doi:10.1039/C2OB25406A
Downloaded by The University of Manchester Library on 28 June 2012

which we will address in this work. The computational study presented here provides insight into the equatorial and axial ligand effect of the CDO biomimetic model displayed in Scheme 1.

Methods

The studies presented in this work use density functional theory methods as implemented in the *Gaussian*-03 program package.[22] Following previous experience in the field,[23] we initially used the unrestricted hybrid density functional method UB3LYP[24] in combination with a double-ζ quality LANL2DZ basis set on iron that includes a core potential and 6-31G on the rest of the atoms,[25] basis set BS1. We performed a full geometry optimization (without constraints) followed by an analytical frequency calculation. All structures were confirmed as local minima and had no imaginary frequencies. Subsequent geometry optimization and frequency calculations were done with a triple-ζ quality basis set: BS2 represents a triple-ζ LACV3P+ basis set on iron and 6-311+G* on the rest of the atoms and BS3 is 6-311+G* on all atoms. It should be noted that very little differences in energy and optimized geometries are obtained between UB3LYP/BS2//UB3LYP/BS1 calculations as compared to those found for UB3LYP/BS2 optimizations, therefore, we will focus on only the latter results.[26] All calculations were done for the lowest lying singlet, triplet, quintet and septet spin states. To test the effect of the environment on the ordering and relative energies of the various spin states, we did single point calculations using the polarized continuum model (PCM) with a dielectric constant of $\varepsilon = 35.7$ mimicking an acetonitrile solution at UB3LYP/BS2.

To confirm the obtained spin state ordering and relative energies we did a further set of calculations using dispersion corrected density functional theory (B3LYP-D).[27] We reoptimized $^{3,5,7}\mathbf{A}_L$ and $^{3,5,7}\mathbf{B}_L$ (L = Cl^-/OTf^-) at B3LYP-D/BS1 level of theory followed by a single point calculation at B3LYP-D/BS2 level of theory. The methods used in this work are well tested and benchmarked. For example, they have reproduced experimental free energies of activation of oxygen atom transfer processes within about 3 kcal mol^{-1}.[28]

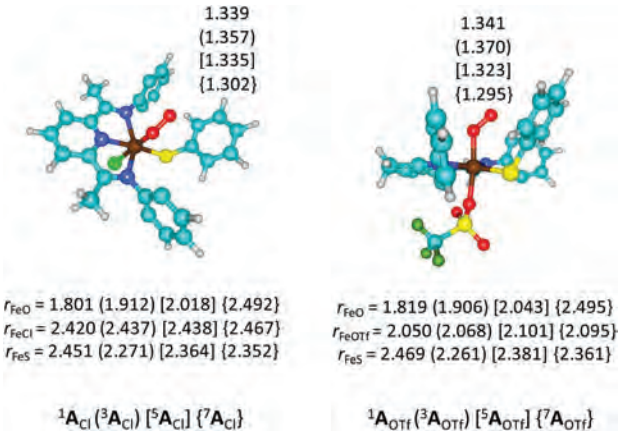

Fig. 2 Optimized geometries of $^{1,3,5,7}\mathbf{A}_{Cl}$ (left-hand-side) and $^{1,3,5,7}\mathbf{A}_{OTf}$ (right-hand-side) with bond lengths in angstroms. Isopropyl groups have been hidden.

Table 1 Spin state ordering and relative energies of $^{1,3,5,7}\mathbf{A}_L$ and $^{1,3,5,7}\mathbf{B}_L$ (L = Cl^-/OTf^-) as obtained using different methods and techniques[a]

	B3LYP/BS1	B3LYP/BS2	B3LYP + E_{solv}/BS2	B3LYP-D/BS1	B3LYP-D/BS2
$^1\mathbf{A}_{Cl}$	26.05	25.55	32.00		
$^3\mathbf{A}_{Cl}$	12.56	11.73	16.13	27.16	39.19
$^5\mathbf{A}_{Cl}$	0.00	0.00	0.00	0.00	0.00
$^7\mathbf{A}_{Cl}$	−0.27	−8.11	−2.66	−0.11	0.21
$^1\mathbf{A}_{OTf}$	26.16	31.84	32.36		
$^3\mathbf{A}_{OTf}$	5.94	11.47	11.31	18.50	31.27
$^5\mathbf{A}_{OTf}$	0.00	0.00	0.00	0.00	0.00
$^7\mathbf{A}_{OTf}$	−0.55	−1.91	−2.41	0.65	1.46
$^1\mathbf{B}_{Cl}$	29.73	28.18	32.72		
$^3\mathbf{B}_{Cl}$	10.72	9.42	15.49	24.58	35.71
$^5\mathbf{B}_{Cl}$	2.62	1.16	7.46	20.96	12.15
$^7\mathbf{B}_{Cl}$	−7.56	−18.40	−11.75	−7.55	−9.21
$^1\mathbf{B}_{OTf}$	37.05	41.67	37.51		
$^3\mathbf{B}_{OTf}$	19.70	31.24	26.60	61.03	75.68
$^5\mathbf{B}_{OTf}$	15.03	23.73	20.15	43.55	39.19
$^7\mathbf{B}_{OTf}$	5.09	9.16	5.03	27.42	33.90

[a] All data are in kcal mol^{-1} and include zero-point corrections. E_{solv} stands for solvent corrected energy.

Results and discussion

We started our investigation with a series of calculations on $^{1,3,5,7}\mathbf{A}_L$ (L = Cl^- and OTf^-) and the optimized geometries are given in Fig. 2, whereas the relative energies of the individual spin states are given in Table 1. The method has very little effect on the spin state ordering, which is virtually constant for all models described in this work. Generally, the septet and triplet spin states are destabilized with dispersion corrections included. Nevertheless, the results appear to give close lying quintet and septet spin iron(III)-superoxo intermediates.

We, generally, find minor structural differences between geometries optimized at UB3LYP/BS1 (Fig. 2) and UB3LYP-D/BS1 (Fig. S3, ESI†) level of theory for most key intermediates. In both cases the quintet and septet spin states are degenerate, whereby the septet state is the lowest by a few kcal mol^{-1} at B3LYP but dispersion corrections make the quintet slightly lower in energy. The triplet (singlet) spin states are well higher in energy by 19.8 (33.7) kcal mol^{-1} for $\mathbf{A}_{Cl}$ and 13.4 (33.8) kcal mol^{-1} for $\mathbf{A}_{OTf}$, and we conclude that these two spin states are unlikely to play a role of importance in the reaction mechanism. With dispersion corrections included, these spin states are further raised in energy. Recent spectroscopic studies on a synthetically generated iron(III)-superoxo CDO intermediate found evidence of a septet spin ground state.[29] Although these enzymatic CDO studies contradict other nonheme iron(III)-superoxo work,[30] where quintet spin ground states are found, the work does support the calculations presented here. Consequently, the availability of a low-lying septet spin state may be inherent to the ligand system of CDO enzymes and their biomimetic model complexes. However, these results do not require that the reactivity take place on the septet spin state surface, as will be seen later.

Optimized geometries are in line with previous computational studies on Fe(III)-superoxo complexes that typically find O–O

Published on 31 May 2012 on http://pubs.rsc.org | doi:10.1039/C2OB25406A
Downloaded by The University of Manchester Library on 28 June 2012

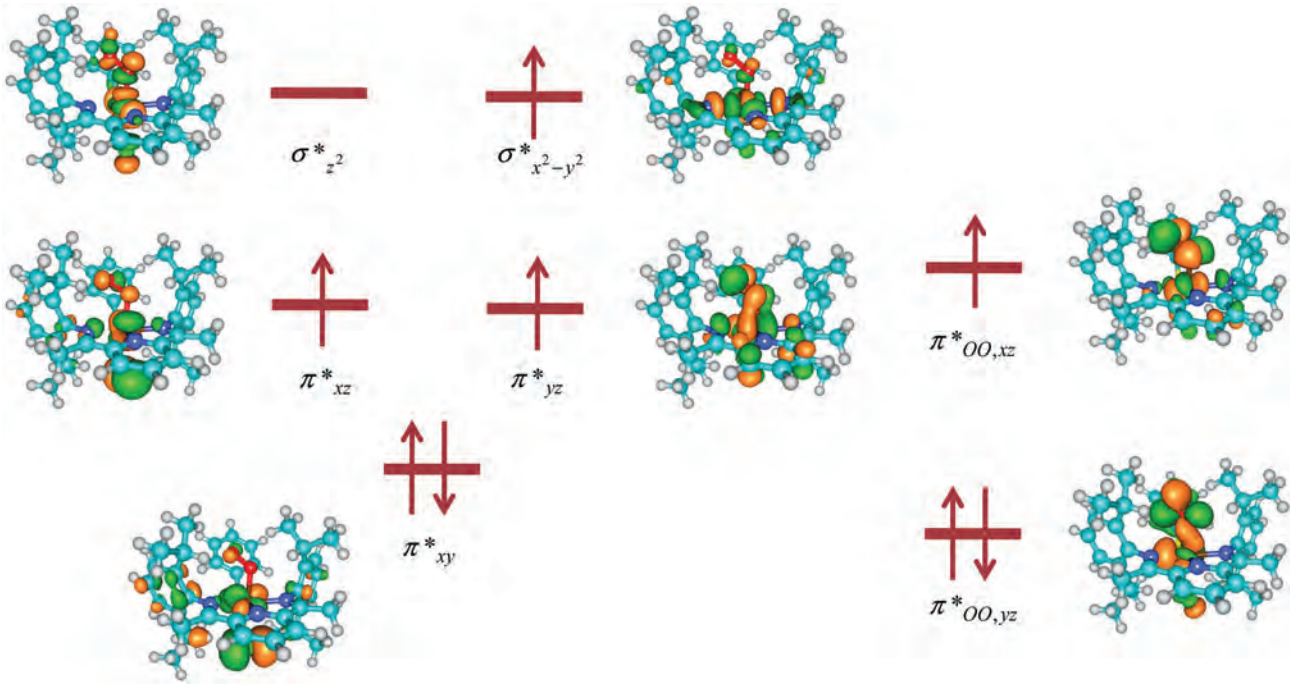

Fig. 3 High-lying occupied and low-lying virtual orbitals of $^{5}\mathbf{A}_{Cl}$.

distances in the range of 1.295–1.370 Å.[31] The Fe–Cl distance is in a narrow range from 2.420–2.467 Å, which is in good agreement with previous studies of iron(IV)-oxo porphyrin cation radical systems that also had an axially ligated Cl^- anion.[32] There is some fluctuation in the Fe–S bond length between the four different spin states, however, this follows from the molecular orbital occupations, *vide infra*.

To understand these spin state energetics and the differences between models $\mathbf{A}_{Cl}$ and $\mathbf{A}_{OTf}$, consider in Fig. 3 the high-lying occupied and virtual orbitals for both systems as taken from the quintet spin calculations. The metal-type orbitals originate from a linear combination of the 3d atomic orbitals on iron with ligand based orbitals. The lowest lying orbital is the π^*_{xy} orbital that is in the plane of the ^{iPr}BIP ligand. A bit higher in energy are the π^*_{xz} and π^*_{yz} orbitals; the former is in the plane of the Fe–O–O group and interacts with a π-orbital on the axial ligand, while the π^*_{yz} orbital interacts with both the axial ligand and the proximal oxygen atom. Higher in energy are two σ* orbitals: one for the antibonding interaction of the axial ligand and the proximal oxygen atom with the iron ($\sigma^*_{z^2}$) and the second for the antibonding interactions of the metal with the BIP and phenylthiolate ligands ($\sigma^*_{x^2-y^2}$). Two antibonding orbitals along the superoxo bond are also depicted in Fig. 3 ($\pi^*_{OO,yz}$ and $\pi^*_{OO,xz}$), which are occupied with three electrons. The metal-based orbitals are occupied with five electrons, and the system is characterized as an Fe(III)-superoxo complex with a quintet spin state.

The quintet spin state has orbital occupation $\pi^*_{xy}{}^2\ \pi^*_{xz}{}^1\ \pi^*_{yz}{}^1\ \sigma^*_{x^2-y^2}{}^1\ \pi^*_{OO,yz}{}^2\ \pi^*_{OO,xz}{}^1$ and includes the ferromagnetic coupling of the $\pi^*_{OO,xz}$ electron with three metal based unpaired electrons. The lowest lying triplet spin state, by contrast, has $\pi^*_{xy}{}^2\ \pi^*_{yz}{}^2\ \pi^*_{xz}{}^1\ \pi^*_{OO,yz}{}^2\ \pi^*_{OO,xz}{}^1$ and is distinguished from the quintet spin state by the transfer of one electron from $\sigma^*_{x^2-y^2}$ to π^*_{yz}. This conversion is equivalent to a change from intermediate-spin Fe^{III} to a low-spin Fe^{III} ion. Both of these states, therefore, can be characterized as Fe(III)-superoxo complexes. The septet and singlet spin states, by contrast, are Fe(II)-dioxygen complexes with orbital occupation $\pi^*_{xy}{}^2\ \pi^*_{xz}{}^1\ \pi^*_{yz}{}^1\ \sigma^*_{x^2-y^2}{}^1\ \sigma^*_{z^2}{}^1\ \pi^*_{OO,yz}{}^1\ \pi^*_{OO,xz}{}^1$ and $\pi^*_{xy}{}^2\ \pi^*_{xz}{}^2\ \pi^*_{yz}{}^2\ \pi^*_{OO,yz}{}^2$, respectively. We made several attempts to swap orbitals for the singlet spin state and calculate a low-spin Fe(III)-superoxo complex but all our calculations converged back to the Fe(II)-dioxygen situation instead. It appears therefore that there is no lower lying low-spin state for these complexes. The orbital occupation is in line with previous experimental and computational studies of six-coordinate iron(III)-superoxo complexes.[30,33,34]

The pentacoordinated iron(II)-^{iPr}BIP(X) reactant complex with $X = Cl^-$ or OTf^- was characterized as a quintet spin state,[11] therefore, dioxygen binding may continue on the quintet spin state surface rather than generating a septet spin iron(II)-dioxygen state. In light of the large geometric differences between the quintet and septet structures, this would imply small spin–orbit coupling between the two states and little equilibration between the two spin states. Our optimized geometries are also in support of the orbital occupations, and, for instance, in the quintet spin state due to single occupation of a $\sigma^*_{x^2-y^2}$ orbital with antibonding character along the Fe–SPh axis, the Fe–S distances are elongated with respect to the triplet spin state, where this orbital is virtual. The same trend is also observed for $^{1,3,5,7}\mathbf{A}_{OTf}$. On the other hand, occupation of the $\sigma^*_{z^2}$ orbital in the quintet spin state would have elongated the Fe–O and Fe-axial ligand distances considerably, as observed before.[35] The geometries, therefore, support the assignment of a singly occupied $\sigma^*_{x^2-y^2}$ orbital and virtual $\sigma^*_{z^2}$ orbital in the quintet spin states.

The group spin densities (Fig. 4) give further evidence for the assignment of the orbital occupations discussed above. In the triplet spin state the unpaired spin density on the superoxo group is 0.92 for both $^{3}\mathbf{A}_{Cl}$ and $^{3}\mathbf{A}_{OTf}$, which is coupled to an unpaired electron on the metal; the spin density on iron is 0.91 in $^{3}\mathbf{A}_{Cl}$

 This journal is © The Royal Society of Chemistry 2012

Published on 31 May 2012 on http://pubs.rsc.org | doi:10.1039/C2OB25406A
Downloaded by The University of Manchester Library on 28 June 2012

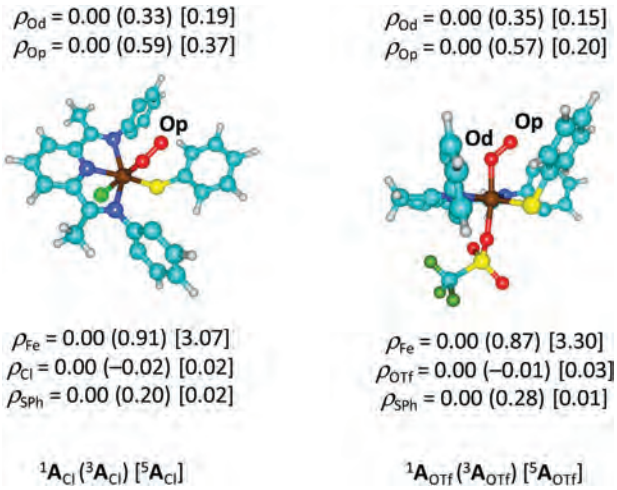

Fig. 4 Group spin densities calculated at UB3LYP/B2//UB3LYP/B1 for $^{1,3,5,7}\mathbf{A}_{Cl}$ (left-hand-side) and $^{1,3,5,7}\mathbf{A}_{OTf}$ (right-hand-side). H-atoms and isopropyl group have been hidden.

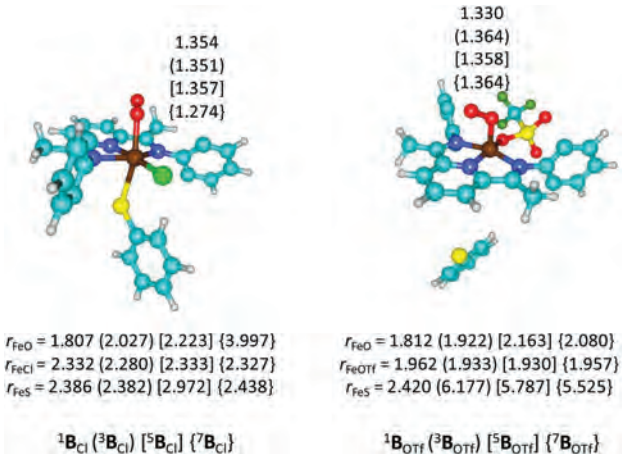

Fig. 5 Optimized geometries of $^{1,3,5,7}\mathbf{B}_{Cl}$ (left-hand-side) and $^{1,3,5,7}\mathbf{B}_{OTf}$ (right-hand-side) with bond lengths in angstroms. Isopropyl groups have been hidden.

and 0.87 in $^{3}\mathbf{A}_{OTf}$. These spin densities confirm the single occupation of the π^*_{xz} and $\pi^*_{OO,xz}$ orbitals in these triplet spin states. In the quintet spin states, by contrast, the metal unpaired spin density is increased to 3.07 and 3.30 for $^{5}\mathbf{A}_{Cl}$ and $^{5}\mathbf{A}_{OTf}$, respectively. The metal is involved in all four singly occupied molecular orbitals, although the contribution is small in $\pi^*_{OO,xz}$ (Fig. 3). In the quintet spin states there is also significant spin density on the BIP ligand system (0.30 in $^{5}\mathbf{A}_{Cl}$ and 0.33 in $^{5}\mathbf{A}_{OTf}$), which further supports the assignment of a singly occupied $\sigma^*_{x^2-y^2}$ orbital.

Subsequently, we investigated the isomers $^{1,3,5,7}\mathbf{B}_{Cl}$ and $^{1,3,5,7}\mathbf{B}_{OTf}$, which have the axial and equatorial ligands swapped as compared to structure $\mathbf{A}_L$ (L = Cl^- or OTf^-), Scheme 1, *i.e.* the thiophenolate is put in the axial position of the iron(III)-superoxo and the anionic ligand (Cl^- or OTf^-) is in the equatorial position. Optimized geometries of the lowest lying singlet, triplet, quintet and septet spin state structures are depicted in Fig. 5. Similarly to the results described above on $^{1,3,5,7}\mathbf{A}_{Cl}$, also for $\mathbf{B}_{Cl}$ the septet spin state is the ground state followed by the quintet and triplet spin states, whereas the closed-shell singlet spin state is well higher in energy. Relative energies of the four spin states are: $^{7}\mathbf{B}_{Cl}$ (0.0 kcal mol^{-1}), $^{5}\mathbf{B}_{Cl}$ (19.6 kcal mol^{-1}) $^{3}\mathbf{B}_{Cl}$ (27.8 kcal mol^{-1}) and $^{1}\mathbf{B}_{Cl}$ (46.6 kcal mol^{-1}). It appears, therefore, that the septet spin state is considerably stabilized over the other three spin states, although the relative energies between $^{1,3,5}\mathbf{A}$ and $^{1,3,5}\mathbf{B}$ are not dramatically different.

Geometrically, there are similarities as well as differences between the structures $^{1,3,5,7}\mathbf{A}_{Cl}$, on the one hand, and $^{1,3,5,7}\mathbf{B}_{Cl}$, on the other hand. First of all in $^{7}\mathbf{B}_{Cl}$ the oxygen group is not bound to the metal center, whereas in $^{7}\mathbf{B}_{OTf}$ one ligand (SPh) has split off the metal center. Recent studies of ours[36] showed that it is essential for sulphur oxygenation that dioxygen binds to the metal center prior to the reaction. Consequently, the septet structures are unlikely to be involved in the reaction mechanism for *S*-oxygenation. Despite the fact that the dioxygen bond length is virtually the same in all complexes, actually the metal–ligand distances show big differences. Thus, the metal–oxygen bond is significantly elongated from 1.912 Å in $^{3}\mathbf{A}_{Cl}$ to 2.027 Å in $^{3}\mathbf{B}_{Cl}$ and from 2.018 Å in $^{5}\mathbf{A}_{Cl}$ to 2.223 Å in $^{5}\mathbf{B}_{Cl}$. At the same time elongation of the Fe–S bond occurs from 2.271 Å in $^{3}\mathbf{A}_{Cl}$ to 2.382 Å in $^{3}\mathbf{B}_{Cl}$ and from 2.364 Å in $^{5}\mathbf{A}_{Cl}$ to 2.972 Å in $^{5}\mathbf{B}_{Cl}$. The latter structure has a very weak thiophenolate bound and with a bond length of that magnitude cannot be considered as a covalent bond.

In the triflate bound isomers ($^{3,5,7}\mathbf{B}_{OTf}$) this situation is even worse and the thiophenolate has dissociated completely from the metal and is optimized with a distance of around 6 Å. Hence, $^{3,5,7}\mathbf{B}_{OTf}$ are pentacoordinate complexes. The reason for this is the considerable steric strain from the di-iso-propylphenyl groups that are attached to the BIP ligand. The group spin densities of these complexes characterize these structures as Fe(II)-superoxo with a nearby thiophenol radical, *i.e.* an electron transfer from thiophenol to the metal has taken place. This electron transfer fills the π^*_{xz} orbital with a second electron in both the triplet and quintet spin states. A single point calculation in a dielectric constant does not change the spin and charge distributions dramatically and keeps the system in a Fe(II)-superoxo-^{iPr}BIP-(OTf) with a nearby $SPh^{\cdot}$ radical. Therefore, upon approach of molecular oxygen to the [Fe^{III}(SPh)(*cis*-OTf)-(^{iPr}BIP)]^0 complex, during its binding to the vacant ligand position, the thiophenolate splits off as a $SPh^{\cdot}$ radical, Scheme 2. Collision of two thiophenyl radicals then will form PhS–SPh. Clearly, the binding affinity of molecular oxygen and the electron affinity of the complexes change from ligated triflate to chloride in the *cis*-position and as a consequence the complexes give differences in reactivity patterns.

An oxygen atom transfer reaction from complexes **A** or **B** to give sulfoxides or double oxygen atom transfer leads to sulfinic acid products. Both processes starting from iron(III)-superoxo will be initiated by breaking the dioxygen bond. In previous work, we showed that the hydrogen atom abstraction reaction by iron(IV)-oxo porphyrin cation radical oxidants is proportional to the strength of the C–H bond that is broken as well as with the O–H bond that is formed, *i.e.* the bond dissociation energy of the O–H bond or BDE_{OH}.[23b,26,37] On the other hand, in sulfoxidation reactions by metal–oxo oxidants it was shown that the O–S bond formation step is linearly proportional to the O–H bond

Published on 31 May 2012 on http://pubs.rsc.org | doi:10.1039/C2OB25406A
Downloaded by The University of Manchester Library on 28 June 2012

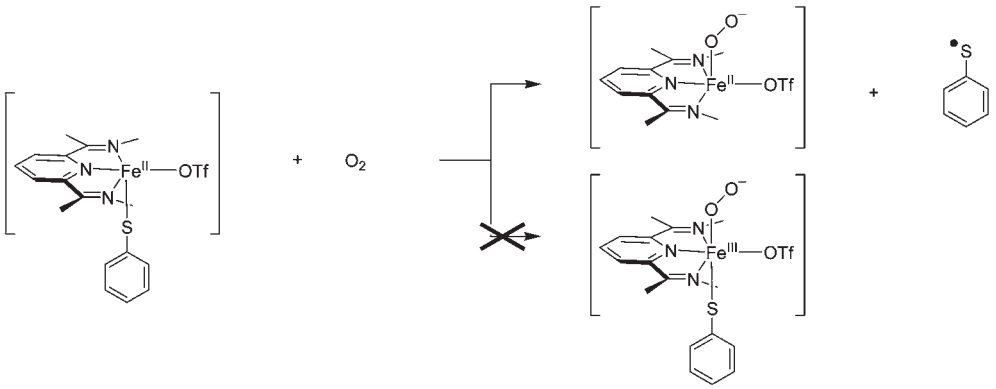

Scheme 2 Reaction of iron(II)-thiophenolate with dioxygen.

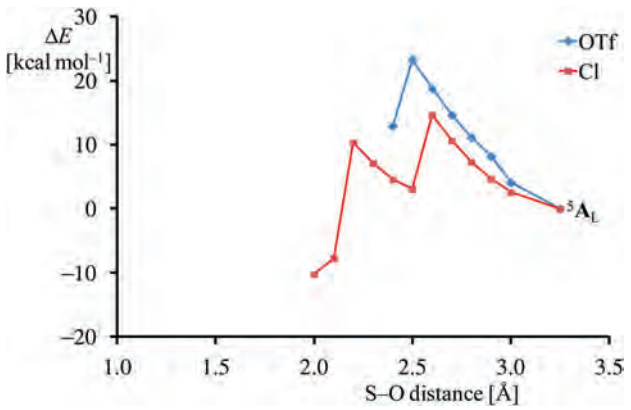

Fig. 6 Geometry scans for the attack of superoxo on the SPh^- group in $^5\mathbf{A}_L$ (L = Cl^- or OTf^-). Each point in the figure represents a full geometry optimization (UB3LYP/B1) with fixed S–O distance in Gaussian. Energies are relative to $^5\mathbf{A}_L$ (L = Cl^- or OTf^-).

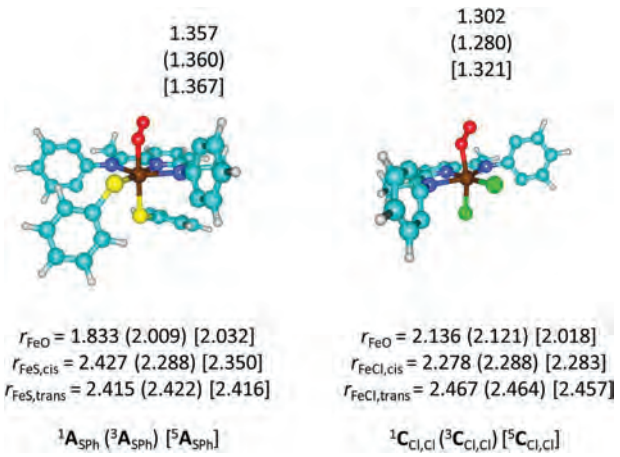

Fig. 7 Optimized geometries of $^{1,3,5}\mathbf{A}_{SPh}$ (left-hand-side) and $^{1,3,5}\mathbf{C}_{Cl,Cl}$ (right-hand-side) with bond lengths in angstroms. Isopropyl groups have been hidden.

formation energy, and hence correlates with BDE_{OH} as well.[37d,38] In a similar vein we predict complex $^5\mathbf{A}_{Cl}$ to be more efficient in oxygen atom transfer reactions to substrates since the superoxo bond is weaker, hence it should be easier to break in the process. To test this we ran a geometry scan for the attack of the terminal oxygen atom of the superoxo group on the sulfur atom of SPh^- for $^5\mathbf{A}_{Cl}$ and $^5\mathbf{A}_{OTf}$ and the results are given in Fig. 6. As follows, both reactions efficiently lead to a bicyclic ring structure, whereby an S–O bond is formed and the O–O bond is still intact, although weakened. This mechanism was also found for CDO enzymes using DFT and QM/MM methods.[8] Indeed, as predicted from the optimized geometries of $^5\mathbf{A}_{Cl}$ and $^5\mathbf{A}_{OTf}$, the barrier height for oxygen attack on sulfur is smaller for $^5\mathbf{A}_{Cl}$ than for $^5\mathbf{A}_{OTf}$.

How do our computations match the experiments reported on these particular systems? First of all, the crystal structure of Fe(II)-^{iPr}BIP with either chloride or triflate bound gave a structure of the **B**-type with chloride bound, but of **A**-type with triflate bound. These structures, of course, are pentacoordinated and no molecular oxygen is attached to the metal center. Nevertheless, we will compare the results obtained in this work with the pentacoordinate crystal structures from ref. 11. The relative energy between structures $^5\mathbf{A}_{Cl}$ and $^5\mathbf{B}_{Cl}$ is calculated to be 1.2 kcal mol^{-1} in favour of structure **A**. Therefore both isomers could exist in equilibrium in solution. On the other hand, for the triflate structure $^5\mathbf{A}_{OTf}$ is well lower in energy than $^5\mathbf{B}_{OTf}$ by 23 kcal mol^{-1} due to the dissociation of the thiophenol from the metal center in **B**. It appears therefore that the cavity within the ^{iPr}BIP ligand is too small to fit the triflate ligand. On the other hand, small anions, such as chloride, fit into the cavity easily. As a consequence, the triflate bound structure resides in an orientation with the thiophenolate in the *cis*-position (equatorial), *i.e.* in a position adjacent to the superoxo group. Because of this positioning, the sulphur atom will be accessible for attack by dioxygen and efficient dioxygenation may occur. This result is indeed what Goldberg and co-workers observed with this complex. By contrast, the thiophenolate ligand is in the *trans*-position (axial) in the chloride bound structure, and it is located too far away from molecular oxygen to enable reactivity. However, these stable complexes may have a finite lifetime and during the course of that lifetime collisions of two $^5\mathbf{A}_{Cl}$ structures may occur that lead to disulfide product complexes.

To further ascertain the effect of *cis*-triflate on binding of thiophenolate in the *trans*-position, we calculated two additional structures, namely one with thiophenolate in both *cis* and *trans* positions ($\mathbf{A}_{SPh}$) and one with chloride in both *cis* and *trans* positions ($\mathbf{C}_{Cl,Cl}$), Fig. 7. Both structures, in analogy with $\mathbf{A}_{Cl}$, $\mathbf{A}_{OTf}$,

 This journal is © The Royal Society of Chemistry 2012

Published on 31 May 2012 on http://pubs.rsc.org | doi:10.1039/C2OB25406A
Downloaded by The University of Manchester Library on 28 June 2012

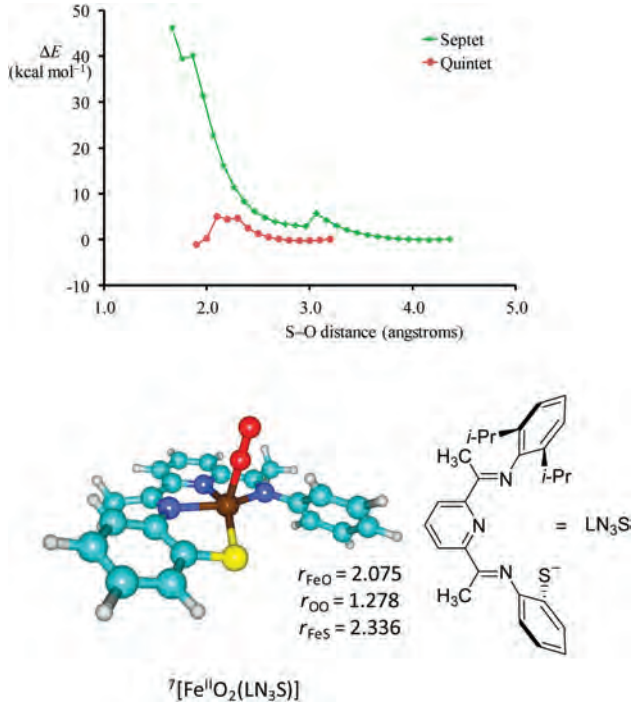

Fig. 8 Septet and quintet S–O bond formation scan and optimized geometry of $[FeO_2(LN_3S)]$ with distances in angstroms.

$\mathbf{B}_{Cl}$ and $\mathbf{B}_{OTf}$ discussed above have the quintet spin state well below the triplet and singlet spin states by more than 10 kcal mol^{-1}. Optimized geometries are in line with the structures displayed in Fig. 2 above with iron-*cis*-ligand distances of 2.350 and 2.283 Å for $^5\mathbf{A}_{SPh}$ and $^5\mathbf{C}_{Cl,Cl}$, respectively. The metal-*trans*-ligand distances are somewhat longer than the metal-*cis*-ligand ones, namely 2.416 and 2.457 Å for $^5\mathbf{A}_{SPh}$ and $^5\mathbf{C}_{Cl,Cl}$, respectively, which is a result of orbital occupation. Nevertheless, thiophenolate binds in the axial ligand position, but only when either chloride or thiophenolate is in the *cis*-position. Bulky triflate ligands, therefore, in the *cis*-position prevent binding of thiophenolate in the axial position and a dissociative system is found for $\mathbf{B}_{OTf}$.

In summary, the key feature that determines dioxygenation of thiophenol by these nonheme iron complexes appears to be the availability of a *cis*-binding site on the metal adjacent to the dioxygen binding position. Stereochemical interactions of ligands as in the case of structure **B** prevent binding of thiophenolate in an appropriate position and consequently cannot bind it. However, these complexes can donate electrons rather than binding substrate that will then lead to formation of PhS–SPh products.

How does the work compare to other computational studies of CDO model complexes? Recent computational studies[36] on a related CDO mimic with a bis(imino)pyridyl ligand and pendant thiolate group (LN_3S) revealed a sulphur dioxygenation mechanism similar to CDO enzymes on competing singlet, triplet and quintet spin state surfaces. In these studies the possible septet spin state was not considered. However, in light of recent experimental studies on CDO enzymes that seem to implicate a septet spin iron(III)-superoxo species,[29] as well as the studies presented in this work, we decided to revisit our study and calculate the septet spin $[Fe^{II}O_2(LN_3S)]$ and its oxygen activation reaction.

As follows from Fig. 8 the iron(III)-superoxo structure in the septet spin state is slightly lower in energy to that found for the quintet spin state; in the gas-phase ΔE + ZPE is 1.8 kcal mol^{-1} whereas in solvent it is 0.9 kcal mol^{-1}. This implies that technically, the structure can exist in close lying septet and quintet spin state structures. To find out whether the septet spin state is reactive, we investigated the S–O bond formation step in the dioxygenation process of the LN_3S ligand. In the quintet spin state a low barrier of 5.0 kcal mol^{-1} was found. A geometry scan starting from the septet spin state (top panel in Fig. 8), however, shows a continuous climbing energy curve that does not reach a local minimum for an intermediate in the dioxygenation process. The maximum point of the scan is well higher in energy than reactants, *i.e.* by more than 40 kcal mol^{-1}. Clearly, the septet spin state, even if it exists, is an unreactive state that will not be able to participate in the reaction mechanism. Consequently, a spin crossing from septet back to quintet will be required for the dioxygenation process to proceed.

Conclusions

Density functional theory calculations are presented on biomimetic model complexes of cysteine dioxygenase. Our studies show that it is vital to have a thiolate substrate bound in the *cis*-position of the dioxygen moiety. Preventing substrate binding through stereochemical interactions of other ligands prevents substrate dioxygenation. However, the iron(III)-superoxo complex is a good electron acceptor and easily abstracts electrons from thiophenols so that they can react further to form PhS–SPh *via* a bimolecular reaction.

Acknowledgements

The authors thank the National Service for Computational Chemistry Software (NSCCS) for cpu time and MGQ thanks the BBSRC for a studentship. The University of Manchester is acknowledged for a travel grant. DK holds a Ramanujan Fellowship from the Department of Science and Technology (DST), New Delhi (India), and acknowledges its financial support (Research Grants SR/S2/RJN-11/2008 and SR/S1/PC-58/2009). The NIH (GM62309 to D.P.G.) is gratefully acknowledged for partial support of this work.

Notes and references

1 (*a*) E. I. Solomon, T. C. Brunold, M. I. Davis, J. N. Kemsley, S.-K. Lee, N. Lehnert, F. Neese, A. J. Skulan, Y.-S. Yang and J. Zhou, *Chem. Rev.*, 2000, **100**, 235; (*b*) T. D. H. Bugg, *Curr. Opin. Chem. Biol.*, 2001, **5**, 550; (*c*) M. Costas, M. P. Mehn, M. P. Jensen and L. Que Jr., *Chem. Rev.*, 2004, **104**, 939; (*d*) P. C. A. Bruijnincx, G. van Koten and R. J. M. Klein Gebbink, *Chem. Soc. Rev.*, 2008, **37**, 2716; (*e*) *Iron-Containing Enzymes: Versatile Catalysts of Hydroxylation Reactions in Nature*, ed. S. P. de Visser and D. Kumar, RSC Publishing, Cambridge (UK), 2011.

2 (*a*) C. Krebs, D. G. Fujimori, C. T. Walsh and J. M. Bollinger Jr, *Acc. Chem. Res.*, 2007, **40**, 484; (*b*) C. J. Schofield and Z. Zhang, *Curr. Opin. Chem. Biol.*, 1999, **9**, 722; (*c*) T. D. H. Bugg, *Tetrahedron*, 2003, **59**, 7075.

View Online

Published on 31 May 2012 on http://pubs.rsc.org | doi:10.1039/C2OB25406A
Downloaded by The University of Manchester Library on 28 June 2012

3 (*a*) O. W. Choroba, D. H. Williams and J. B. Spencer, *J. Am. Chem. Soc.*, 2000, **122**, 5389; (*b*) L. J. Higgins, F. Yan, P. Liu, H.-W. Liu and C. L. Drennan, *Nature*, 2005, **437**, 838; (*c*) M. J. Bodner, R. M. Phelan, M. F. Freeman, R. Li and C. A. Townsend, *J. Am. Chem. Soc.*, 2010, **132**, 12.

4 (*a*) S. C. Trewick, T. F. Henshaw, R. P. Hausinger, T. Lindahl and B. Sedgwick, *Nature*, 2002, **419**, 174; (*b*) P. Ø. Falnes, R. F. Johansen and E. Seeberg, *Nature*, 2002, **419**, 178; (*c*) Y. Mishina, E. M. Duguid and C. He, *Chem. Rev.*, 2006, **106**, 215.

5 (*a*) M. H. Stipanuk, *Annu. Rev. Nutr.*, 2004, **24**, 539; (*b*) G. D. Straganz and B. Nidetzky, *ChemBioChem*, 2006, **7**, 1536; (*c*) C. A. Joseph and M. J. Maroney, *Chem. Commun.*, 2007, 3338.

6 S. Ye, X. Wu, L. Wei, D. Tang, P. Sun, M. Bartlam and Z. Rao, *J. Biol. Chem.*, 2007, **282**, 3391.

7 (*a*) J. G. McCoy, L. J. Bailey, E. Bitto, C. A. Bingman, D. J. Aceti, B. G. Fox and G. N. Phillips Jr, *Proc. Natl. Acad. Sci. U. S. A.*, 2006, **103**, 3084; (*b*) S. C. Chai, J. R. Bruyere and M. J. Maroney, *J. Biol. Chem.*, 2006, **281**, 15774; (*c*) C. R. Simmons, Q. Liu, Q. Huang, Q. Hao, T. P. Begley, P. A. Karplus and M. H. Stipanuk, *J. Biol. Chem.*, 2006, **281**, 18723; (*d*) J. E. Dominy Jr, C. R. Simmons, P. A. Karplus, A. M. Gehring and M. H. Stipanuk, *J. Bacteriol.*, 2006, **188**, 5561; (*e*) B. D. Pierce, J. D. Gardner, L. J. Bailey, T. C. Brunold and B. G. Fox, *Biochemistry*, 2007, **46**, 8569; (*f*) J. E. Dominy Jr, J. Hwang, S. Guo, L. L. Hirschberger, S. Zhang and M. H. Stipanuk, *J. Biol. Chem.*, 2008, **283**, 12188; (*g*) T. Kleffmann, S. A. K. Jongkees, G. Fairweather, S. M. Wilbanks and G. N. L. Jameson, *J. Biol. Inorg. Chem.*, 2009, **14**, 913; (*h*) J. D. Gardner, B. S. Pierce, B. G. Fox and T. C. Brunold, *Biochemistry*, 2010, **49**, 6033; (*i*) E. P. Tchesnokov, S. M. Wilbanks and G. N. L. Jameson, *Biochemistry*, 2012, **51**, 257.

8 (*a*) S. Aluri and S. P. de Visser, *J. Am. Chem. Soc.*, 2007, **129**, 14846; (*b*) S. P. de Visser and G. D. Straganz, *J. Phys. Chem. A*, 2009, **113**, 1835; (*c*) D. Kumar, W. Thiel and S. P. de Visser, *J. Am. Chem. Soc.*, 2011, **133**, 3869.

9 (*a*) S. V. Kryatov, E. V. Rybak-Akimova and S. Schindler, *Chem. Rev.*, 2005, **105**, 2175; (*b*) M. M. Abu-Omar, A. Loaiza and N. Hontzeas, *Chem. Rev.*, 2005, **105**, 2227; (*c*) W. Nam, *Acc. Chem. Res.*, 2007, **40**, 522.

10 (*a*) Y. Jiang, L. R. Widger, G. D. Kasper, M. A. Siegler and D. P. Goldberg, *J. Am. Chem. Soc.*, 2010, **132**, 12214; (*b*) A. C. McQuilken, Y. Jiang, M. A. Siegler and D. P. Goldberg, *J. Am. Chem. Soc.*, 2012, **134**, 8758–8761.

11 Y. M. Badiei, M. A. Siegler and D. P. Goldberg, *J. Am. Chem. Soc.*, 2011, **133**, 1274.

12 M. Sallmann, I. Siewert, L. Fohlmeister, C. Limberg and C. Knispel, *Angew. Chem., Int. Ed.*, 2012, **51**, 2234.

13 (*a*) J. H. Dawson, R. H. Holm, J. R. Trudell, G. Barth, R. E. Linder, E. Bunnenberg, C. Djerassi and S. C. Tang, *J. Am. Chem. Soc.*, 1976, **98**, 3707; (*b*) T. L. Poulos, *J. Biol. Inorg. Chem.*, 1996, **1**, 356.

14 (*a*) M. T. Green, J. H. Dawson and H. B. Gray, *Science*, 2004, **304**, 1653; (*b*) W.-D. Woggon, *Acc. Chem. Res.*, 2005, **38**, 127.

15 D. Kumar, S. P. de Visser, P. K. Sharma, E. Derat and S. Shaik, *J. Biol. Inorg. Chem.*, 2005, **10**, 181.

16 F. Ogliaro, S. P. de Visser and S. Shaik, *J. Inorg. Biochem.*, 2002, **91**, 554.

17 (*a*) Z. Gross and S. Nimri, *Inorg. Chem.*, 1994, **33**, 1731; (*b*) Z. Gross, *J. Biol. Inorg. Chem.*, 1996, **1**, 368; (*c*) K. Czarnecki, S. Nimri, Z. Gross, L. M. Proniewicz and J. R. Kincaid, *J. Am. Chem. Soc.*, 1996, **118**, 2929.

18 (*a*) W. Nam, Y. O. Ryu and S. J. Song, *J. Biol. Inorg. Chem.*, 2004, **9**, 654; (*b*) W. J. Song, Y. O. Ryu, R. Song and W. Nam, *J. Biol. Inorg. Chem.*, 2005, **10**, 294.

19 (*a*) C. V. Sastri, J. Lee, K. Oh, Y. J. Lee, J. Lee, T. A. Jackson, K. Ray, H. Hirao, W. Shin, J. A. Halfen, J. Kim, L. Que Jr, S. Shaik and W. Nam, *Proc. Natl. Acad. Sci. U. S. A.*, 2007, **104**, 19181; (*b*) A. E. Anastasi, P. Comba, J. McGrady, A. Lienke and H. Rohwer, *Inorg. Chem.*, 2007, **46**, 6420; (*c*) M. P. Jensen, A. Mairata i Payeras, A. T. Fiedler, M. Costas, J. Kaizer, A. Stubna, E. Münck and L. Que Jr, *Inorg. Chem.*, 2007, **46**, 2398; (*d*) T. A. Jackson, J.-U. Rohde, M. S. Seo, C. V. Sastri, R. DeHont, A. Stubna, T. Ohta, T. Kitagawa, E. Münck, W. Nam and L. Que Jr, *J. Am. Chem. Soc.*, 2008, **130**, 12394; (*e*) Y. Zhou, X. Shan, R. Mas-Ballesté, M. R. Bukowski, A. Stubna, M. Chakrabarti, L. Slominski, J. A. Halfen, E. Münck and L. Que Jr, *Angew. Chem., Int. Ed.*, 2008, **47**, 1896; (*f*) H. Hirao, L. Que Jr, W. Nam and S. Shaik, *Chem.–Eur. J.*, 2008, **14**, 1740; (*g*) S. Fukuzumi, H. Kotani, T. Suenobu, S. Hong, J.-M. Lee and W. Nam, *Chem.–Eur. J.*, 2010, **16**, 354; (*h*) K.-B. Cho, Y. Moreau, D. Kumar, D. A. Rock, J. P. Jones and S. Shaik, *Chem.–Eur. J.*, 2007, **13**, 4103.

20 (*a*) F. Namuswe, G. D. Kasper, A. A. N. Sarjeant, T. Hayashi, C. M. Krest, M. T. Green, P. Moënne-Loccoz and D. P. Goldberg, *J. Am. Chem. Soc.*, 2008, **130**, 14189; (*b*) J. Stasser, F. Namuswe, G. D. Kasper, Y. Jiang, C. M. Krest, M. T. Green, J. Penner-Hahn and D. P. Goldberg, *Inorg. Chem.*, 2010, **49**, 9178; (*c*) F. Namuswe, T. Hayashi, Y. Jiang, G. D. Kasper, A. A. N. Sarjeant, P. Moënne-Loccoz and D. P. Goldberg, *J. Am. Chem. Soc.*, 2010, **132**, 157.

21 (*a*) K. A. Prokop, S. P. de Visser and D. P. Goldberg, *Angew. Chem., Int. Ed.*, 2010, **49**, 5091; (*b*) K. A. Prokop, H. M. Neu, S. P. de Visser and D. P. Goldberg, *J. Am. Chem. Soc.*, 2011, **133**, 15874.

22 M. J. Frisch, G. W. Trucks, H. B. Schlegel, G. E. Scuseria, M. A. Robb, J. R. Cheeseman, J. A. Montgomery Jr, T. Vreven, K. N. Kudin, J. C. Burant, J. M. Millam, S. S. Iyengar, J. Tomasi, V. Barone, B. Mennucci, M. Cossi, G. Scalmani, N. Rega, G. A. Petersson, H. Nakatsuji, M. Hada, M. Ehara, K. Toyota, R. Fukuda, J. Hasegawa, M. Ishida, T. Nakajima, Y. Honda, O. Kitao, N. Nakai, M. Klene, X. Li, J. E. Knox, H. P. Hratchian, J. B. Cross, C. Adamo, J. Jaramillo, R. Gomperts, R. E. Stratmann, O. Yazyev, A. J. Austin, R. Cammi, C. Pomelli, J. W. Ochterski, P. Y. Ayala, K. Morokuma, G. A. Voth, P. Salvador, J. J. Dannenberg, V. G. Zakrzewski, S. Dapprich, A. D. Daniels, M. C. Strain, O. Farkas, D. K. Malick, A. D. Rabuck, K. Raghavachari, J. B. Foresman, J. V. Ortiz, Q. Cui, A. G. Baboul, S. Clifford, J. Cioslowski, B. B. Stefanov, G. Liu, A. Liashenko, P. Piskorz, I. Komaromi, R. L. Martin, D. J. Fox, T. Keith, M. A. Al-Laham, C. Y. Peng, A. Nanayakkara, M. Challacombe, P. M. W. Gill, B. Johnson, W. Chen, M. W. Wong, C. Gonzalez and J. A. Pople, *GAUSSIAN 03 (Revision C.02)*, Gaussian, Inc., Wallingford, CT, 2004.

23 (*a*) S. P. de Visser, *Chem.–Eur. J.*, 2006, **12**, 8168; (*b*) S. P. de Visser, *Angew. Chem., Int. Ed.*, 2006, **45**, 1790; (*c*) S. P. de Visser, *J. Am. Chem. Soc.*, 2006, **128**, 9813; (*d*) D. Kumar, B. Karamzadeh, G. N. Sastry and S. P. de Visser, *J. Am. Chem. Soc.*, 2010, **132**, 7656.

24 (*a*) A. D. Becke, *J. Chem. Phys.*, 1993, **98**, 5648; (*b*) C. Lee, W. Yang and R. G. Parr, *Phys. Rev. B*, 1988, **37**, 785.

25 P. J. Hay and W. R. Wadt, *J. Chem. Phys.*, 1985, **82**, 270.

26 S. P. de Visser, *J. Am. Chem. Soc.*, 2010, **132**, 1087.

27 T. Schwabe and S. Grimme, *Phys. Chem. Chem. Phys.*, 2007, **9**, 3397.

28 (*a*) D. Kumar, S. P. de Visser and S. Shaik, *Chem.–Eur. J.*, 2005, **11**, 2825; (*b*) S. P. de Visser, K. Oh, A.-R. Han and W. Nam, *Inorg. Chem.*, 2007, **46**, 4632; (*c*) A. K. Vardhaman, C. V. Sastri, D. Kumar and S. P. de Visser, *Chem. Commun.*, 2011, **47**, 11044.

29 J. A. Crawford, W. Li and B. S. Pierce, *Biochemistry*, 2011, **50**, 10241.

30 M. M. Mbughuni, M. Chakrabarti, J. A. Hayden, E. L. Bominaar, M. P. Hendrich, E. Münck and J. D. Lipscomb, *Proc. Natl. Acad. Sci. U. S. A.*, 2010, **107**, 16788.

31 (*a*) P. Rydberg, E. Sigfridsson and U. Ryde, *J. Biol. Inorg. Chem.*, 2004, **9**, 203; (*b*) K. P. Jensen, B. O. Roos and U. Ryde, *J. Inorg. Biochem.*, 2005, **99**, 45; (*c*) H. Nakashima, J.-Y. Hasegawa and H. Nakatsuji, *J. Comput. Chem.*, 2006, **27**, 1363; (*d*) J. Annaraj, J. Cho, Y.-M. Lee, S. Y. Kim, R. Latifi, S. P. de Visser and W. Nam, *Angew. Chem., Int. Ed.*, 2009, **48**, 4150; (*e*) S. P. de Visser, *Coord. Chem. Rev.*, 2009, **253**, 754; (*f*) W. Lai and S. Shaik, *J. Am. Chem. Soc.*, 2011, **133**, 5444; (*g*) R. Latifi, T. Tahsini, D. Kumar, G. N. Sastry, W. Nam and S. P. de Visser, *Chem. Commun.*, 2011, **47**, 10674; (*h*) K.-B. Cho, H. Chen, D. Janardanan, S. P. de Visser, S. Shaik and W. Nam, *Chem. Commun.*, 2012, **48**, 2189.

32 (*a*) S. P. de Visser, *J. Biol. Inorg. Chem.*, 2006, **11**, 168; (*b*) S. P. de Visser, L. Tahsini and W. Nam, *Chem.–Eur. J.*, 2009, **15**, 5577.

33 (*a*) J. P. Emerson, E. R. Farquhar and L. Que Jr, *Angew. Chem., Int. Ed.*, 2007, **46**, 8553; (*b*) W. A. van der Donk, K. Crebs and J. M. Bollinger Jr, *Curr. Opin. Struct. Biol.*, 2010, **20**, 1; (*c*) Y.-M. Lee, S. Hong, Y. Morimoto, W. Shin, S. Fukuzumi and W. Nam, *J. Am. Chem. Soc.*, 2010, **132**, 10668; (*d*) A. Mukherjee, M. A. Cranswick, M. Chakrabarti, T. K. Paine, K. Fujisawa, E. Münck and L. Que Jr, *Inorg. Chem.*, 2010, **49**, 3618.

34 (*a*) A. Bassan, T. Borowski and P. E. M. Siegbahn, *Dalton Trans.*, 2004, 3153; (*b*) S. Shaik, D. Kumar, S. P. de Visser, A. Altun and W. Thiel, *Chem. Rev.*, 2005, **105**, 2279; (*c*) V. Georgiev, T. Borowski, M. R. A. Blomberg and P. E. M. Siegbahn, *J. Biol. Inorg. Chem.*, 2008, **13**, 929; (*d*) L. T. Haahr, K. P. Jensen, J. Boesen and H. E. M. Christensen, *J. Inorg. Biochem.*, 2010, **104**, 136.

35 (*a*) S. P. de Visser, *J. Am. Chem. Soc.*, 2006, **128**, 15809; (*b*) L. Bernasconi and E. J. Baerends, *Eur. J. Inorg. Chem.*, 2008, 1672.

 This journal is © The Royal Society of Chemistry 2012

View Online

36 D. Kumar, G. N. Sastry, D. P. Goldberg and S. P. de Visser, *J. Phys. Chem. A*, 2012, **116**, 582.
37 (*a*) S. P. de Visser, D. Kumar, S. Cohen, R. Shacham and S. Shaik, *J. Am. Chem. Soc.*, 2004, **126**, 8362; (*b*) S. Shaik, D. Kumar and S. P. de Visser, *J. Am. Chem. Soc.*, 2008, **130**, 10128; (*c*) R. Latifi, M. Bagherzadeh and S. P. de Visser, *Chem.–Eur. J.*, 2009, **15**, 6651; (*d*) D. Kumar, G. N. Sastry and S. P. de Visser, *Chem.–Eur. J.*, 2011, **17**, 6196; (*e*) D. Kumar, G. N. Sastry and S. P. de Visser, *J. Phys. Chem. B*, 2012, **116**, 718; (*f*) R. Latifi, J. S. Valentine, W. Nam and S. P. de Visser, *Chem. Commun.*, 2012, **48**, 3491.
38 D. Kumar, S. P. de Visser, P. K. Sharma, H. Hirao and S. Shaik, *Biochemistry*, 2005, **44**, 8148.

Downloaded by The University of Manchester Library on 28 June 2012
Published on 31 May 2012 on http://pubs.rsc.org | doi:10.1039/C2OB25406A

Journal of Molecular Catalysis A: Chemical 356 (2012) 152–157

Contents lists available at SciVerse ScienceDirect

Journal of Molecular Catalysis A: Chemical

journal homepage: www.elsevier.com/locate/molcata

An antimony(V) substituted Keggin heteropolyacid, $H_4PSbMo_{11}O_{40}$: Why is its catalytic activity in oxidation reactions so different from that of $H_4PVMo_{11}O_{40}$?

Hila Goldberg[a], Devesh Kumar[b,1], G. Narahari Sastry[b], Gregory Leitus[c], Ronny Neumann[a,*]

[a] Department of Organic Chemistry, Weizmann Institute of Science, Rehovot 76100, Israel
[b] Molecular Modeling Group, Indian Institute of Chemical Technology, Hyderabad 500 607, India
[c] Chemical Research Support Unit, Weizmann Institute of Science, Rehovot 76100, Israel

ARTICLE INFO

Article history:
Received 16 August 2011
Received in revised form
19 December 2011
Accepted 21 December 2011
Available online 18 January 2012

Keywords:
Polyoxometalate
Antimony
Molybdenum
Oxidation
DFT

ABSTRACT

An antimony(V) containing α-Keggin type *acidic* polyoxometalate, $H_4PSbMo_{11}O_{40}$, was prepared by reacting $NaMoO_4$, H_3PO_4 and Sb_2O_3 in the presence of aqua regia to appraise its reactivity compared to the well known vanadate analog, $H_4PVMo_{11}O_{40}$. Characterization was by X-ray diffraction, MALDI-TOF MS, IR, UV–vis and ^{31}P NMR spectroscopy. Catalytic redox reactions, such as oxidative dehydrogenation using O_2 and N_2O as terminal oxidants were studied and showed very different reactivity of $H_4PSbMo_{11}O_{40}$ versus $H_4PVMo_{11}O_{40}$. It was found by DFT calculations that in contrast to analogous $H_4PVMo_{11}O_{40}$ where vanadium centered catalysis is observed, in $H_4PSbMo_{11}O_{40}$ catalysis is molybdenum and not antimony centered.

© 2012 Elsevier B.V. All rights reserved.

1. Introduction

Polyoxometalates exhibit a variety of structures and properties that make them useful in catalysis, material science and medicine [1]. They can be viewed as polyanions of discrete structure composed of mixtures of metal oxides containing both main group and transition metal elements. Our interest in polyoxometalates has been as liquid phase homogeneous catalysts, but heterogeneous, gas phase oxidation catalysis is also an important area of research [2]. The catalytic activity and reaction selectivity in polyoxometalate catalyzed reactions is dependent on many parameters most notably the elemental composition. Equally important are the overall structure, acidity and/or counter cation, and charge and within the polyoxometalate structure. Specifically, *acidic* phosphovanadomolybdates, $H_{3+x}PV_xMo_{12-x}O_{40}$ where $x = 1$, 2, but especially $x = 2$ show interesting redox activity that can be translated to oxidation and oxygenation of organic substrates by electron transfer and electron transfer–oxygen transfer mechanisms as reported extensively by us [3,4]. Importantly the reduced catalyst can be conveniently reoxidized with dioxygen under mild conditions even though they are stable also at significantly higher temperatures [3,4].

Antimony oxides are well-known components of heterogeneous oxidation catalysts, such as $VSbO_4$ for propane ammonoxidation, alkylaromatic ammonoxidation and in allylic oxidations [24]. It is also known that antimony in the secondary structure of polyoxometalates as counter cations have a stabilizing effect on polyoxometalates at high temperatures (>400 °C) [25]. There are quite a significant number of polyoxomolybdates and polyoxotungstates reported in the literature containing Sb(III) atoms, where the lone pair on Sb occupies a coordination position and the compounds are non-acidic, that is they are not heteropolyacids [26–44]. Most of these studies are based on structural aspects with only sparse use in catalysis. Our search of the literature has revealed only five Sb(V) containing compounds [45–49]. In this context it should be emphasized that we have reported on the tetrabutyl ammonium salt of $[PSb(V)Mo_{11}O_{40}]^{4-}$ via oxidation of an antimony(III) compound with ozone but an antimony(V) containing Keggin *heteropolyacid* has not been disclosed. The distinction is important for only the acids are reactive in electron transfer (ET) and electron transfer–oxygen transfer (ET–OT) reactions [3–23].

In this research we were interested in probing the question on how the replacement of vanadium(V) in $H_{3+x}PV_xMo_{12-x}O_{40}$ by antimony(V) to yield the similar $H_{3+x}PSb_xMo_{12-x}O_{40}$ compounds would effect the catalytic activity in electron transfer and electron transfer–oxygen transfer type reactions? [3] Differences were

* Corresponding author. Tel.: +972 8 934 3354; fax: +972 8 934 4142.
E-mail address: Ronny.Neumann@weizmann.ac.il (R. Neumann).
[1] Present address: Department of Applied Physics, School for Physical Sciences, Babasaheb Bhimrao Ambedkar University, Vidya Vihar, Rae Bareilly Road, Lucknow (U.P.) 226 025, India.

1381-1169/$ – see front matter © 2012 Elsevier B.V. All rights reserved.
doi:10.1016/j.molcata.2011.12.033

Table 1
Crystallographic Data for $H_4PSbMo_{11}O_{40}{\cdot}14H_2O$.

Empirical formula	$PSb_1Mo_{11}O_{40}+14O$
Molecular weight	2072.06
Crystal system	Triclinic
Space group	$P\bar{1}$
a, Å	13.602(3)
b, Å	13.944(2)
c, Å	13.946(3)
α,°	60.72(3)
β,°	68.44(3)
γ,°	70.50(2)
Volume, Å^3; Z	2106.7(10); 2
Density$_{calc}$, mg cm^{-1}	3.267
μ, mm^{-1}	3.962
Reflections	33,799
Unique reflections	11,289
R_{int}	0.0224
R_1; wR_2 ($I>2\sigma(I)$)[a]	0.0307; 0.0697
R_1; wR_2 (all data)[a]	0.0377; 0.0730

[a] $R_1=\sum||F_o|-|F_c||/\sum|F_o|$; $wR_2=\{\sum[w(F_o^2-F_c^2)^2]/\sum w(F_o^2)^2\}^{1/2}$.

expected for a number of reasons: (1) The common oxidation states of vanadium in polyoxometalates are 4+ and 5+, whereas for antimony typically 3+ and 5+ oxidation states have been observed. This could conceivably lead to a one-step two-electron oxidation of substrates with $H_{3+x}PSb_xMo_{12-x}O_{40}$ versus two consecutive one-electron oxidations commonly observed for $H_{3+x}PV_xMo_{12x}O_{40}$. (2) The significantly higher electronegativity of antimony versus vanadium should render the neighboring oxygen atoms more electropositive and in this way could conceivably improve the oxygen donation reactivity of $H_{3+x}PSb_xMo_{12-x}O_{40}$.

2. Results and discussion

The synthesis of $H_{3+x}PSb_xMo_{12-x}O_{40}$ for $x=1$ and 2 was carried out in the typical manner for such polyoxometalates [50] which involves the reaction of the required stoichiometric amounts of phosphate, antimonate and molybdate under acidic conditions. The major difference vis-a-vis the analogous $H_{3+x}PV_xMo_{12-x}O_{40}$ synthesis was to prepare the antimony(V) precursor in situ by oxidation of Sb_2O_3 with aqua regia. Extraction with ether and recrystallization of $H_4PSbMo_{11}O_{40}$ was successful while the synthesis of $H_5PSb_2Mo_{10}O_{40}$ was not due to insufficient stability of the product obtained. Subsequent research was on $H_4PSbMo_{11}O_{40}$ only. It should be noted that a different procedure used in the past using Sb_2O_5 as antimony(V) precursor failed [35].

$H_4PSbMo_{11}O_{40}$ crystallized in the triclinic space group *P-1* with two slightly different α-Keggin moieties per asymmetric unit. For details of the structural analysis, see Table 1, Section 4, and the cif file in the Supporting Information. Generally, in most mono-substituted α-Keggin structures the substituted metal atom positions are fully disordered due to the cubic crystal structure [51]. Here, the lower triclinic symmetry has allowed us to determine that when the compound crystallizes it showed a Sb content of 1.02 Sb atoms (also observed in elemental analysis) per PMo(Sb)O cluster. The refinement when the sum of the Sb occupancies was fixed to be equal 1 gives an *R* factor of 0.0307 whereas when it was assumed that no Sb was incorporated the *R* factor was significantly higher, 0.052, Fig. 1. The Mo—O and Sb—O bonds lengths are typical for phosphomolybdates and not statistically different from each other that is, the Sb—O bonds lengths are within one standard deviation of those of the respective Mo—O bond lengths. It should be noted that 14 water molecules were located for each polyoxometalate unit. This amount of water was confirmed also by thermogravimetric analysis which showed a loss of 11.5% water at up to circa 100 °C.

The X-ray diffraction characterization of $H_4PSbMo_{11}O_{40}$ was complemented by further spectroscopic and electrochemical

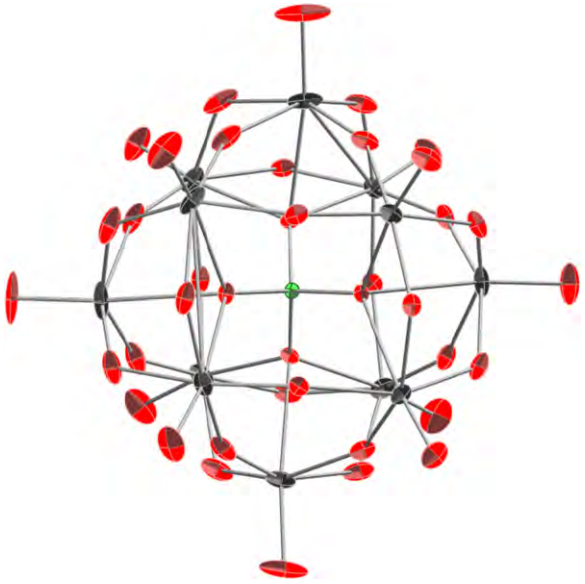

Fig. 1. ORTEP representation (50% probability) of $H_4PSbMo_{11}O_{40}{\cdot}14H_2O$. Water molecules and protons not shown; P – green, Mo/Sb – black, O – red. (For interpretation of the references to color in this figure legend, the reader is referred to the web version of this article.)

characterization. The IR spectrum of $H_4PSbMo_{11}O_{40}$ has four peaks at 1064, 960, 869, and 781 cm^{-1} due to four different types of oxygen atoms (internal, edge shared, corner shared and terminal) and is typical for non-distorted α-Keggin structures of general T_d symmetry and essentially the same as the spectrum of $H_3PMo_{12}O_{40}$. A MALDI-TOF-MS of $H_4PSbMo_{11}O_{40}$ deposited from an acetonitrile solution showed a cluster of peaks at $m/z=1894.0540$ (90%) and 1771.0132 (100%) attributable to a protonated $H_4PSbMo_{11}O_{40}{\cdot}CH_3CN$ species and a lacunary species, respectively. No peak associable to the analogous $H_3PMo_{12}O_{40}$ compound was observed. The IR spectrum does not indicate the presence of a lacunary species in the sample itself that would lead to a split peak for the P—O vibration at 1064 cm^{-1} indicating that the lacunary species is formed as a metastable species upon ionization within the mass spectrometer. The ^{31}P NMR of $H_4PSbMo_{11}O_{40}$ has a single peak at $\delta=-2.298$ ppm, close to that of $H_3PMo_{12}O_{40}$ which has a peak at $\delta=-2.313$. The peaks, however, are *distinct* as shown by measuring the spectrum of a mixture of the two compounds. The cyclic voltammogram (1 mM $H_4PSbMo_{11}O_{40}$, 1 M $TBABF_4$ in CH_3CN) shows two reductions at 0.48 and 0.63 mV versus NHE.

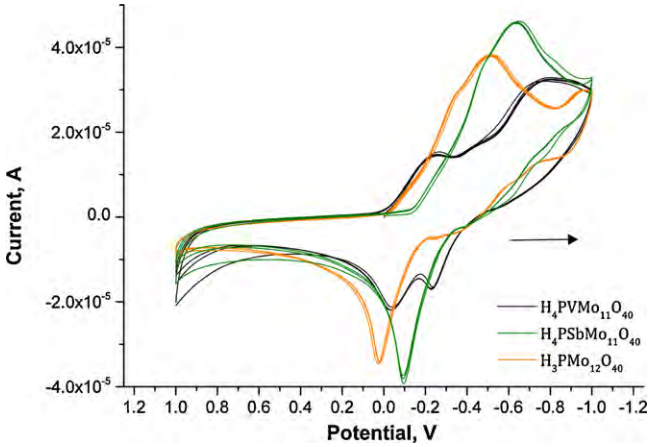

Fig. 2. Cyclic voltammograms of $H_4PSbMo_{11}O_{40}$ and $H_3PMo_{12}O_{40}$ (1 mM polyoxometalate, 1 M $(n\text{-}C_4H_9)_4NBF_4$ in CH_3CN, scan rate – 100 mV/s).

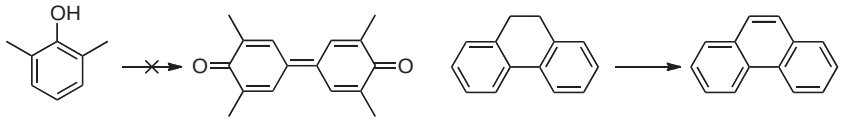

Scheme 1. Aerobic oxidation of 2,6-dimethyl phenol and dihydrophenanthrene catalyzed by $H_4PSbMo_{11}O_{40}$.

This is in contrast to the cyclic voltammogram of the $H_3PMo_{12}O_{40}$ "parent" polyoxometalate, which under identical conditions, also showed two reductions, however, at different and lower potentials, 0.33 and 0.48 mV versus NHE, Fig. 2. $H_4PSbMo_{11}O_{40}$ has a higher oxidation potential compared to $H_3PMo_{12}O_{40}$. $H_4PVMo_{11}O_{40}$ has oxidation potentials intermediate that of $H_4PSbMo_{11}O_{40}$ and $H_3PMo_{12}O_{40}$.

As mentioned in the introduction, we have shown that $H_{3+x}PV_xMo_{12-x}O_{40}$ is active in electron transfer (ET) and electron transfer–oxygen transfer (ET–OT) reactions. The reactions all begin by electron transfer from the organic substrate to the polyoxometalate to yield vanadium(IV) species. In ET only reactions there is no oxygen transfer from the catalyst to the activated substrate and the eventual product is a dehydrogenated compound. Examples include arenes from dihydroarenes [3,6], or diphenoquinones from phenols [5]. In ET–OT reactions, initial electron transfer is followed by oxygen transfer from the polyoxometalate to the activated substrate to yield oxygenated products. Examples include ketones and quinones from arenes and alkylarenes, respectively [9,10], the carbon—carbon bond cleavage in the oxidation of primary alcohols [19], and the oxygenation of sulfides [22]. We wished to gauge the reactivity of $H_4PSbMo_{11}O_{40}$ in both ET and ET–OT reactions.

In the presence of $H_4PVMo_{11}O_{40}$, 2,6-dimethyl phenol gives the corresponding diphenoquinone in quantitative yields through a four-electron oxidative dimerization reaction. In this reaction the corresponding $H_4PSbMo_{11}O_{40}$ showed no catalytic activity, Scheme 1. On the other hand, $H_4PSbMo_{11}O_{40}$ was reactive in electron transfer initiated oxidative dehydrogenations of dihydroarenes to arenes. For example, in Table 2, one can see the relative conversions using various catalysts and two oxidants for the oxidative dehydrogenation of dihydrophenanthrene to phenanthrene. In the aerobic oxidation, $H_4PSbMo_{11}O_{40}$ and $H_4PVMo_{11}O_{40}$ showed the same conversion after 15 h, while $H_3PMo_{12}O_{40}$ was significantly less reactive. The use of nitrous oxide as oxidant was also effective although the yields were significantly lower. It should be noted that in the absence of catalyst with both oxidants only trace amounts, ~1%, of dihydrophenanthrene were oxidized via a disproportionation pathway, that is reduced tetrahydro- and octahydrophenanthrene were also formed.

In order to differentiate more clearly between the catalytic activities of the various catalysts, the initial rates of the aerobic oxidative dehydrogenation of limonene to *para*-cymene were measured. This was done by observing the reduction of the polyoxometalate catalyst by UV–vis spectroscopy, through formation of the known reduced blue species at 700 nm. The relative reactivity was $H_4PVMo_{11}O_{40}$ (~20) > $H_4PSbMo_{11}O_{40}$ (~10) ≫ $H_3PMo_{12}O_{40}$ (1). Clearly, the antimony and vanadium substituted phosphomolybdates have similar activity for the aforementioned aromatization reactions that are in any case higher than that of the non-substituted compound. However, the scope of reactivity of $H_4PSbMo_{11}O_{40}$ was lower.

Table 2
Oxidative dehydrogenation of dihydrophenanthrene to phenanthrene.

Catalyst	Conversion, mol% O_2	Conversion, mol% N_2O
$H_4PSbMo_{11}O_{40}$	>99	26
$H_4PVMo_{11}O_{40}$	>99	24
$H_3PMo_{12}O_{40}$	31	25

Reaction conditions: dihydrophenanthrene (5 mmol), catalyst (0.5 mmol), acetic acid (1 mL), 1 bar O_2 or N_2O, 15 h, 110 °C. Conversions were measured by GC and no products besides phenanthrene were observed.

In contrast to $H_4PVMo_{11}O_{40}$ in ET–OT reactions no catalytic activity of $H_4PSbMo_{11}O_{40}$ was found for the oxygenation of active arenes and alkyl arenes such as anthracene and xanthene. Also no oxygenation of thioanisole with $H_4PSbMo_{11}O_{40}$ was observed. On the other hand for the oxidative carbon—carbon cleavage reaction of 1-butanol where phosphovanadomolybdates yielded *selective* 1:1 formation of butylformate and butylpropionate, the use of $H_4PSbMo_{11}O_{40}$ led to a mixture of products. Thus, oxidation of 1-butanol (1 mmol), $H_4PSbMo_{11}O_{40}$ (0.01 mmol), sulfolane (1 mL), 1 bar O_2 100 °C, 15 h, gave a low conversion of 1-butanol and a mixture of products, including the cleavage products, butylformate and butylpropionate, the autooxidation product, butanal, and the acid catalyzed etherification product, di-*n*-butylether, Scheme 2. The same reaction with $H_3PMo_{12}O_{40}$ gave *no* oxidation products and only di-*n*-butylether (17% yield). Clearly, $H_4PSbMo_{11}O_{40}$ was a significantly inferior catalyst for ET–OT reactions as compared to the analogous vanadium substituted compounds but did show some activity as opposed to $H_3PMo_{12}O_{40}$ which is totally inactive for such reactions. A post reaction measurement of the ^{31}P NMR spectrum of the reaction mixture showed no compounds except the original $H_4PSbMo_{11}O_{40}$ indicating that the catalyst was stable under reaction conditions.

In order to gain further insight into the potential of $H_4PSbMo_{11}O_{40}$ as an ET and ET–OT catalyst, calculations were carried out on $[PSbMo_{11}O_{40}]^{4-}$ to determine its energies and spin states using the same methodology previously used for the analogous $[PV_xMo_{12-x}O_{40}]^{(3+x)-}$ polyoxometalates [52]. Fig. 3 shows the numbering scheme used for the designation of the atoms in the calculations.

DFT calculations have been performed on all possible spin states and the stationary points have been characterized as minima on the potential energy surface. The two basis sets yielded essentially identical results and therefore the results are independent of basis set employed. However, the gas phase results were unable to provide any meaningful correlations with the observations. A cursory look at Tables 3–5 indicates the importance of calculations in solvent phase for corroboration with the observations. The two solvents employed, water and acetonitrile (ACN) yielded similar values. The following observations can be made from the systematic computational study: (1) For the fully oxidized compound $[PSbMo_{11}O_{40}]^{4-}$, the ground state is unambiguously characterized as a singlet. (2) All the compounds are expected to be low spin and only the one-electron reduced $[PSbMo_{11}O_{40}]^{5-}$ is expected to be paramagnetic with a doublet ground state; the oxidized and two-electron compounds are expected to be diamagnetic. (3) The one-electron reduced compound, $[PSbMo_{11}O_{40}]^{5-}$, is more

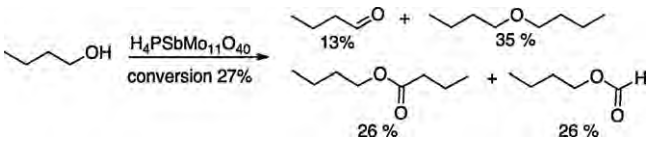

Scheme 2. Aerobic oxidation of 1-butanol catalyzed by $H_4PSbMo_{11}O_{40}$.

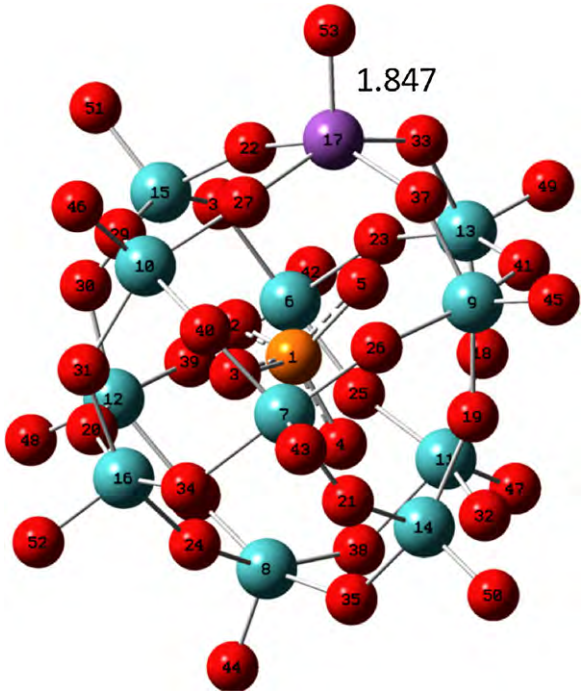

Fig. 3. The numbering scheme for the $[PSbMo_{11}O_{40}]^{q-}$ (q = 4, 5, 6) anion. Mo – blue, O – red, P – orange, Sb – purple. (For interpretation of the references to color in this figure legend, the reader is referred to the web version of this article.)

Table 3
B3LYP/B1 (top) and B3LYP/B2D//B1 (bottom) relative energies in kcal/mol for $^{1,3,5}[PSbMo_{11}O_{40}]^{4-}$.

	DE[a]			D(E+ZPC)[a]		
	Gas	Water	ACN	Gas	Water	ACN
M1	0.00	0.00	0.00	0.00	0.00	0.00
	0.00	0.00	0.00	0.00	0.00	0.00
M3	27.21	26.85	27.00	26.09	25.73	25.88
	36.14	35.78	35.93	35.02	34.66	34.81
M5	69.04	69.73	69.8	66.74	67.43	67.58
	88.51	89.20	89.35	86.21	86.90	87.05

[a] Values are with respect to $^{1}[PSbMo_{11}O_{40}]^{4-}$; M1 – singlet, M3 – triple, M5 – quintet, ACN – acetonitrile.

stable than the oxidized $[PSbMo_{11}O_{40}]^{4-}$ as may be expected for an oxidizing compound and the two-electron reduced compound, $[PSbMo_{11}O_{40}]^{6-}$, is yet more stable. The results support the electrochemical measurements and the positive oxidation potential of these compounds.

The B3LYP/B1 spin densities and charges (see ESI for the tables) for $^{1}[PSbMo_{11}O_{40}]^{4-}$, $^{2}[PSbMo_{11}O_{40}]^{5-}$, and $^{1}[PSbMo_{11}O_{40}]^{6-}$, shows that the charge on antimony remains unchanged over all three of the lowest energy states indicating that reduction *does not take place at the antimony atom.* Indeed, for the one-electron reduced $^{2}[PSbMo_{11}O_{40}]^{5-}$, the negative charge and spin density are mostly concentrated on the distal (to antimony) molybdenum atom, Mo14. Further, for the two-electron reduced $^{1}[PSbMo_{11}O_{40}]^{6-}$, the negative charge tends to be more delocalized over all molybdenum atoms with preference for Mo11 and Mo14. The calculations point out that although $H_4PSbMo_{11}O_{40}$ is isostructural to $H_4PVMo_{11}O_{40}$ and have similar ground state energies (−427.1 and −443.6 kcal/mol) the electronic ground states of the reduced compounds are very different. $H_4PVMo_{11}O_{40}$ shows vanadium-centered redox properties, whereas $H_4PSbMo_{11}O_{40}$ shows molybdenum-based redox chemistry. This indicates that $H_4PSbMo_{11}O_{40}$ is more similar to $H_3PMo_{12}O_{40}$, albeit with a higher oxidation potential, than to $H_4PVMo_{11}O_{40}$. The catalytic oxidation chemistry supports this conclusion.

Table 4
B3LYP/B1 (top) and B3LYP/B2D//B1 (bottom) relative energies in kcal/mol for $^{2,4,6}[PSbMo_{11}O_{40}]^{5-}$.

	DE[a]			D(E+ZPC)[a]		
	Gas	Water	ACN	Gas	Water	ACN
M2	128.83	−115.80	−111.41	127.66	−116.97	−112.58
	143.73	−100.90	−96.51	142.57	−102.06	−97.67
M4	172.17	−71.74	−67.46	169.57	−74.34	−70.06
	197.50	−46.41	−42.13	194.90	−49.01	−44.73
M6	211.01	−31.92	−27.54	207.53	−35.40	−31.02
	246.64	3.71	8.09	243.16	0.23	4.61

[a] Values are with respect to $^{1}[PSbMo_{11}O_{40}]^{4-}$; M2 – doublet, M4 – quartet, M6 – hextet.

Table 5
B3LYP/B1 (top) and B3LYP/B2D//B1 (bottom) relative energies in kcal/mol for $^{1,3,5}[PSbMo_{11}O_{40}]^{6-}$.

	DE[a]			D(E+ZPC)[a]		
	Gas	Water	ACN	Gas	Water	ACN
M1	327.08	−219.22	−208.70	324.85	−221.45	−210.93
	355.99	−190.31	−179.79	353.75	−192.55	−182.03
M3	324.18	−221.66	−211.11	321.45	−224.39	−213.84
	353.59	−192.25	−181.70	350.86	−194.98	−184.43
M5	364.84	−179.19	−168.67	360.83	−183.20	−172.68
	404.00	−140.03	−129.51	399.99	−144.04	−133.52

[a] Values are with respect to $^{1}[PSbMo_{11}O_{40}]^{4-}$; M1 – singlet, M3 – triple, M5 – quintet.

3. Conclusions

Phosphovanadomolybdates, $H_{3+x}PV_xMo_{12-x}O_{40}$ especially where x = 1 and 2, have unique and well-defined catalytic activity in electron transfer and electron transfer–oxygen transfer reactions. In an attempt to find yet more active catalysts, a new antimony(V) containing α-Keggin type acidic polyoxometalate, $H_4PSbMo_{11}O_{40}$, was prepared and characterized based on the assumption that compared to the well-known $H_4PVMo_{11}O_{40}$, $H_4PSbMo_{11}O_{40}$ would engender two-electron reactions at the antimony center and oxygen transfer would be facilitated by the lower electronegativity of Sb. Cyclic voltammetry showed that $H_4PSbMo_{11}O_{40}$ compound has a higher oxidation potential compared to the parent $H_3PMo_{12}O_{40}$, but catalytic activity was inferior to $H_4PVMo_{11}O_{40}$. In some cases no reactivity was observed, ET phenol oxidative dimerization and ET–OT sulfide, arene and alkylarene oxygenation. In other cases, dihydroarene aromatization and primary alcohol oxidation was observed, but the activity was lower than that of $H_4PVMo_{11}O_{40}$. DFT calculations show that $[PSbMo_{11}O_{40}]^{4-}$ is low spin as are the one and two-electron reduced compounds. The reduction of $[PSbMo_{11}O_{40}]^{4-}$ does not take place at the antimony atom as originally hypothesized. The first electron reduction occurs at a molybdenum center distal to the antimony atom while the two-electron reduction yields negative charge density quite delocalized over all molybdenum atoms.

4. Experimental

4.1. Synthesis of $H_4PSbMo_{11}O_{40}\cdot 14H_2O$

$H_4PSbMo_{11}O_{40}\cdot 14H_2O$ was synthesized by dissolving antimony(III) oxide (1.45 g, 5 mmol) in aqua regia (60 mL) on a hot plate at 70 °C to oxidize it to an antimony(V) species. This solution was

added to a solution of sodium phosphate (709.8 mg, 5 mmol) in 10 mL water. A drop of H_2SO_4 was added and the solution was stirred for 10 min at 70 °C then let cool to room temperature. Sodium molybdate dihydrate (12.1 g, 50 mmol) dissolved in 20 mL water was added. The color gradually changed from pale orange to clear yellow. The solution was further acidified by adding 8 mL HNO_3 dropwise and the solution was let to stir at room temperature for 15 h. The desired $H_4PSbMo_{11}O_{40}$ was extracted with diethyl ether to yield an etherate phase; the ether was then removed by evaporation. The crude mixture was dissolved in water and let to crystallize to give yellowish crystals with a green tint. Yield – 2.6 g (27%). Elemental Analysis $H_4PSbMo_{11}O_{40}{\cdot}14H_2O$ experimental (calculated) P: 1.11 (1.47), Sb: 5.53 (5.79), Mo: 49.78 (50.15) H_2O: 12.07 (11.87).

4.2. X-ray diffraction analyses

Crystal data for $H_4PSbMo_{11}O_{40}$ was measured at 100(2) K on a Bruker Kappa Apex2 CCD diffractometer [λ(Mo Kα) = 0.71073 Å] with a graphite monochromator. The data were processed with Apex2 software, respectively. The structures were solved by direct methods using the program SHELXS-97 and refined using SHELXL-97. All non-hydrogen atoms were refined anisotropically, using weighted full-matrix least squares on F^2 crystal data collection and refinement parameters are given in Table 1.

4.3. Other characterizations of $H_4PSbMo_{11}O_{40}$

The ^{31}P NMR spectra were measured in acetonitrile on a Bruker Avance DPX 300 spectrometer with H_3PO_4 as external standard. The IR spectra were measured on a Nicolet 6700 FTIR; samples were prepared as ~5 wt% KBr based pellets. Cyclic voltammetry was measured on CH Instruments, 680 Amp Booster model using glassy carbon working electrode and a platinum reference electrode. The UV/vis spectra were recorded on Agilent 89090A spectrophotometer using 0.3 mM solution in acetonitrile.

4.4. Catalytic oxidation reactions

Typically, oxidation reactions were carried out in 13 mL glass pressure tubes by loading the tube with appropriate amounts of the polyoxometalate, substrate and solvent. $H_4PSbMo_{11}O_{40}$ was treated with ozone prior to each reaction to ensure that all the catalyst is in its oxidized form. The tube was purged three times with the desired gas before loading it to 1 bar. The reaction tube was placed in a thermostated oil bath and the mixture stirred magnetically. Oxidation reaction products were characterized quantitatively and qualitatively using GC and GC/MS, respectively. The compounds were separated using a 30 m, 0.32 mm i.d. 5% phenyl methylsilicone column with a 0.25 mm coating using He as eluent.

4.5. DFT calculations

All calculations were performed with Gaussian 03 using the unrestricted UB3LYP density functional theoretic (DFT) method. Geometry optimization was performed with a Los Alamos-type LACVP basis set on Mo, Sb (with a small core ECP) and 6-31G on the rest of the atoms, henceforth, B1. Single point calculations were done using PCM model on B3LYP/B1 optimized geometries in two different solvents (water and acetonitrile) and single point B3LYP/Def2-TZVP calculations were also done on B3LYP/B1 optimized geometries i.e. B3LYP/B2D//B1.

Acknowledgement

This research was supported by the Israel Science Foundation grant # 1073/10 and the Helen and Martin Kimmel Center for Molecular Design. R. N. is the Rebecca and Israel Sieff Professor of Chemistry and D. K. is Ramanujan Fellow of the Department of Science and Technology (New Delhi, India).

Appendix A. Supplementary data

Supplementary data associated with this article can be found, in the online version, at doi:10.1016/j.molcata.2011.12.033.

References

[1] M.T. Pope, Heteropoly and Isopoly Oxometalates, Springer, Berlin, 1983.
[2] Catalysts for Fine Chemical Synthesis, Volume 2, Catalysis by Polyoxometalates, Kozhevnikov, I.V. Wiley, Weinheim, Germany, 2002.
[3] R. Neumann, M. Lissel, J. Org. Chem. 54 (1989) 4607–4610.
[4] R. Neumann, M. Levin, J. Org. Chem. 56 (1991) 5707–5710.
[5] M. Lissel, H. Jansen van de Wal, R. Neumann, Tetrahedron Lett. 33 (1992) 1795–1798.
[6] R. Neumann, M. Levin, J. Am. Chem. Soc. 114 (1992) 7278–7286.
[7] R. Neumann, I. Dror, Appl. Catal. A: Gen. 172 (1998) 67–72.
[8] A.M. Khenkin, I. Vigdergauz, R. Neumann, Chem. Eur. J. 6 (2000) 875–882.
[9] A.M. Khenkin, R. Neumann, Angew. Chem. Int. Ed. 39 (2000) 4088–4090.
[10] A.M. Khenkin, L. Weiner, Y. Wang, R. Neumann, J. Am. Chem. Soc. 123 (2001) 8531–8542.
[11] R. Ben-Daniel, R. Neumann, Angew. Chem. Int. Ed. 42 (2003) 92–95.
[12] R. Ben-Daniel, P. Alsters, R. Neumann, J. Org. Chem. 66 (2001) 8650–8653.
[13] O.V. Branytska, R. Neumann, J. Org. Chem. 68 (2003) 9510–9512.
[14] A.M. Khenkin, R. Neumann, J. Am. Chem. Soc. 126 (2004) 6356–6362.
[15] A.M. Khenkin, L. Weiner, R. Neumann, J. Am. Chem. Soc. 127 (2005) 9988–9989.
[16] O.V. Branytska, R. Neumann, Synlett (2005) 2525–2527.
[17] G. Maayan, B. Ganchegui, W. Leitner, R. Neumann, Chem. Commun. (2006) 2230–2232.
[18] R. Neumann, A.M. Khenkin, Chem. Commun. (2006) 2529–2538.
[19] A.M. Khenkin, R. Neumann, J. Am. Chem. Soc. 130 (2008) 14474–14476.
[20] H. Goldberg, I. Kaminker, D. Goldfarb, R. Neumann, Inorg. Chem. 48 (2009) 7947–7952.
[21] I. Kaminker, H. Goldberg, R. Neumann, D. Goldfarb, Chem. Eur. J. 16 (2010) 10014–10020.
[22] A.M. Khenkin, G. Leitus, R. Ronny Neumann, J. Am. Chem. Soc. 132 (2010) 11446–11448.
[23] A.M. Khenkin, R. Neumann, ChemSusChem 4 (2011) 346–348.
[24] F. Cavani, A. Tanguy, F. Trifirò, M. Koutrev, J. Catal. 174 (1998) 231–241.
[25] Y.-K. Lu, J.-N. Xu, X.-B. Cui, J. Jin, S.-Y. Shi, J.-Q. Xu, Inorg. Chem. Commun. 13 (2010) 46–49.
[26] L.H. Bi, E.B. Wang, R.D. Huang, C.W. Hu, J. Mol. Struct. 553 (2000) 167–174.
[27] M. Bösing, I. Loose, H. Pohlmann, B. Krebs, Chem. Eur. J. 3 (1997) 1232–1237.
[28] J. Fischer, L. Richard, R. Weiss, J. Am. Chem. Soc. 98 (1976) 3050–3052.
[29] I. Loose, E. Droste, M. Bösing, H. Pohlmann, M.H. Dickman, C. Rosu, M.T. Pope, B. Krebs, Inorg. Chem. 38 (1999) 2688–2694.
[30] U. Kortz, N.K. Al-Kassem, M.G. Savelieff, N.A.A. Kadi, M. Sadakane, Inorg. Chem. 40 (2001) 4742–4749.
[31] U. Kortz, M.G. Savelieff, B.S. Bassil, B. Keita, L. Nadjo, Inorg. Chem. 41 (2002) 783–789.
[32] L.J. Zhang, X.L. Zhao, J.Q. Xu, T.G. Wang, J. Chem. Soc., Dalton Trans. (2002) 3275–3276.
[33] X.X. Hu, J.Q. Xu, X.B. Cui, J.F. Song, T.G. Wang, Inorg. Chem. Commun. 7 (2003) 264–271.
[34] S.-Y. Shi, Y.-H. Sun, Y. Chen, J.-N. Xu, X.-B. Cui, Y. Wang, G.-W. Wang, G.-D. Yang, J.-Q. Xu, Dalton Trans. 39 (2010) 1389–1394.
[35] A.M. Khenkin, L.J.W. Shimon, R. Neumann, Eur. J. Inorg. Chem. 3 (2001) 789–794.
[36] U. Kortz, M.G. Savelieff, B.S. Bassil, M.H. Dickman, Angew. Chem. Int. Ed. 40 (2001) 3384–3386.
[37] U. Kortz, M.G. Savelieff, F.Y.A. Ghali, L.M. Khalil, S.A. Maalouf, D.I. Sinno, Angew. Chem. Int. Ed. 41 (2002) 4070–4073.
[38] Y.K. Lu, J.N. Xu, X.B. Cui, J. Jin, S.Y. Shi, J.Q. Xu, Inorg. Chem. Commun. 13 (2010) 46–49.
[39] R. Kiebach, C. Näther, W. Bensch, R. Kiebach, Solid State Sci. 8 (2006) 964–970.
[40] J.P. Wang, P.T. Ma, J.W. Zhao, J.Y. Niu, Inorg. Chem. Commun. 10 (2007) 523–526.
[41] J.P. Wang, P.T. Ma, J. Li, J.Y. Niu, Chem. Lett. 35 (2006) 994–995.
[42] W. Zhang, S.X. Liu, P. Sun, C.D. Zhang, F.J. Ma, D. Feng, J. Mol. Struct. 969 (2010) 76–80.
[43] W. Zhang, S.X. Liu, D. Feng, C.D. Zhang, P. Sun, F.J. Ma, J. Mol. Struct. 936 (2010) 194–198.
[44] S. Yao, Z.M. Zhang, Y.G. Li, E.B. Wang, Inorg. Chem. Commun. 12 (2009) 937–940.
[45] Y.-Y. Zhang, S.-X. Liu, C.-J. Yu, Q. Tang, D.D. Liang, C.D. Zhang, F.J. Ma, S.-J. Li, S.-W. Zhang, R.-K. Tan, Rui-Kang, Inorg. Chem. Commun. 13 (2010) 1418–1420.

[46] A. Ogawa, H. Yamato, U. Lee, H. Ichida, A. Kobayashi, Y. Sasaki, Acta Crystallogr. C44 (1988) 1879–1881.
[47] D. Drewes, G. Vollmer, B. Krebs, Z. Anorg. Allg. Chem. 630 (2004) 2573–2575.
[48] G.L. Xue, X.M. Liu, H.S. Xu, H.M. Hu, F. Fu, J.W. Wang, Inorg. Chem. 47 (2008) 2011–2016.
[49] Y.Z. Zhen, Q. Shen, L.L. Li, G.L. Xue, H.M. Hu, F. Fu, J.W. Wang, Inorg. Chem. Commun. 11 (2008) 886–888.
[50] G.A. Tsigdinos, C.J. Hallada, Inorg. Chem. 7 (1968) 437–441.
[51] H.T. Evans Jr., Perspect. Struct. Chem. 4 (1971) 1–59.
[52] H. Hirao, D. Kumar, H. Chen, R. Neumann, S. Shaik, J. Phys. Chem. C 111 (2007) 7711–7719.

THE JOURNAL OF PHYSICAL CHEMISTRY B

ARTICLE

pubs.acs.org/JPCB

Axial Ligand Effect On The Rate Constant of Aromatic Hydroxylation By Iron(IV)—Oxo Complexes Mimicking Cytochrome P450 Enzymes

Devesh Kumar,*[†,‡] G. Narahari Sastry,[‡] and Sam P. de Visser[§]

[†]Department of Applied Physics, School for Physical Sciences, Babasaheb Bhimrao Ambedkar University, Vidya Vihar, Rae Bareilly Road, Lucknow 226 025, India

[‡]Molecular Modelling Group, Indian Institute of Chemical Technology, Hyderabad 500-607, India

[§]Manchester Interdisciplinary Biocenter and School of Chemical Engineering and Analytical Science, University of Manchester, 131 Princess Street, Manchester M1 7DN, United Kingdom

Supporting Information

ABSTRACT:

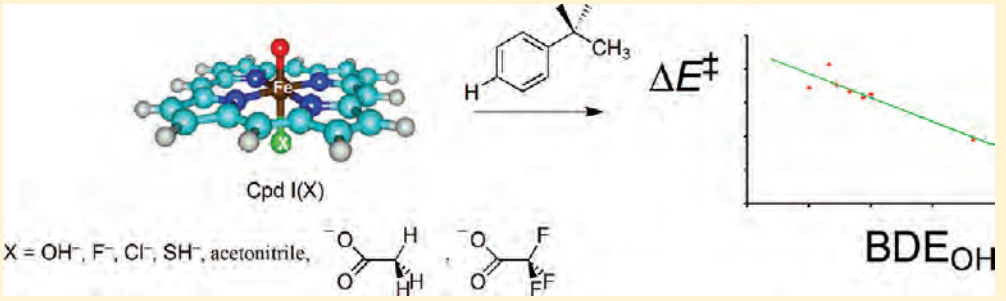

The cytochromes P450 are important iron-heme based monoxygenases that catalyze a range of different oxygen atom transfer reactions in nature. One of the key bioprocesses catalyzed by these enzymes is the aromatic hydroxylation of unactivated arenes. To gain insight into axial ligand effects and, in particular, how it affects aromatic hydroxylation processes by P450 model complexes, we studied the effects of the axial ligand on spectroscopic parameters (trans-influence) as well as on aromatic hydroxylation kinetics (trans-effect) using a range of $[Fe^{IV}(O)(Por^{+\bullet})X]$ oxidants with X = SH^-, Cl^-, F^-, OH^-, acetonitrile, $GlyGlyCys^-$, CH_3COO^-, and CF_3COO^-. These systems give red-shifted Fe—O vibrations that are dependent on the strength of the axial ligand. Despite structural changes, however, the electron affinities of these oxidants are very close in energy, but sharp differences in pK_a values are found. The aromatic hydroxylation of the para-position of ethylbenzene was tested with these oxidants, and they all show two-state-reactivity patterns although the initial low-spin C—O bond formation barrier is rate determining. We show, for the first time, that the rate determining barrier for aromatic hydroxylation is proportional to the strength of the O—H bond in the corresponding iron(IV)—hydroxo complex, i.e., BDE_{OH}, hence this thermochemical property of the oxidant drives the reaction and represents the axial ligand effect. We have rationalized our observed barrier heights for these axially ligated systems using thermochemical cycles and a valence bond curve crossing diagram to explain the origins of the rate constants.

The cytochromes P450 (P450) are important enzymes found in most biosystems ranging from eukaryotes to prokaryotes. In humans they are mainly found in the liver, where they catalyze detoxification processes including the metabolism of drugs.[1] In addition, the P450s are known to be involved in biosynthetic pathways producing, for instance, hormones. Generally, the P450s react as monoxygenases that transfer one oxygen atom originating from molecular oxygen to a substrate, which is either hydroxylated (aliphatic or aromatic), epoxidized, or sulfoxidized.[2] Because of this large versatility in substrate activation, they are very important enzymes in biology but also biotechnological and pharmaceutical applications are being investigated.[3] Moreover, understanding their mechanism and function is important, but despite intense efforts in the field there still remain many questions to be answered.

Aromatic hydroxylation by P450 enzymes has always intrigued scientists, since a very strong C—H bond of an aromatic ring has to be broken. Despite this, the P450s seem to catalyze this reaction with relative ease. In biosystems, many important and vital processes include an aromatic hydroxylation step, and as such it contributes in biosynthesis and biodegradation of compounds. Thus, the metabolism of the hormone estrogen leads to the carcinogen 16-α-hydroxy-estrogen through an aromatic hydroxylation process and is catalyzed by liver P450 enzymes, whereby the P450 converts the hormone into a compound that can trigger breast cancer.[4] On the other hand, the aromatic hydroxylation of isoliquiritigenin by plant P450 enzymes gives a

Received: November 25, 2011
Published: December 01, 2011

ACS Publications © 2011 American Chemical Society

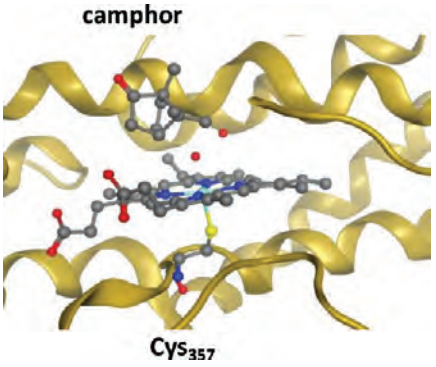

Figure 1. Active site structure of $P450_{cam}$ as taken from the 1DZ9 pdb file.[16d] Amino acids are labeled according to the pdb file.

product that has antitumor, antioxidant, and phytoestrogenic activity.[5] Aromatic hydroxylation reactions by the cytochromes P450 are also vital from a drug metabolism perspective. Examples of aromatic hydroxylation reactions of drug molecules by the P450s includes the para-hydroxylation of amphetamine and tamoxifen[6] as well as other substrates, such as, the β-blocker alprenolol[7] and the neurotoxin 1-methyl-4-phenyl-1,2,3,6-tetrahydropyridine that is a chemical inducer of Parkinson's disease.[8] The P450 isozyme CYP1B1 is particularly effective in catalyzing aromatic hydroxylation reactions and has been shown to hydroxylate, for instance, resveratrol, a cancer preventative agent found in red wine, and convert it into the anticancer agent piceatannol.[9] Finally, site-specific P450 mutants have been created that react regiospecifically by aromatic ring hydroxylation of substrates with the aim to create biotechnologically relevant P450s.[10]

Generally, the P450s utilize molecular oxygen on a heme center and convert it into an iron(IV)−oxo heme cation radical species $[Fe^{IV}(O)(heme^{+\bullet})]$ through a catalytic cycle that uses two electrons and two protons.[2,11] This iron(IV)−oxo heme cation radical species, which is also called Compound I (Cpd I), is the catalytic active species of P450 enzymes.[2,12] Until recently, this species was elusive and support for the assignment of Cpd I as active oxidant only came from indirect evidence, biomimetic and computational studies.[13,14] This was until Rittle and Green characterized Cpd I using Mössbauer, electron paramagnetic resonance, and UV−vis spectroscopic methods and found unambiguous proof for its activity in substrate hydroxylation.[15]

The active site of P450 enzymes includes an iron atom that is embedded into a heme (protoporphyrin IX) subunit, which is linked to the protein via a covalent linkage with a side chain of a cysteinate residue via a thiolate bridge (Figure 1).[16] Other oxygen activating enzymes, such as peroxidases and catalases, by contrast, bind the heme to the protein via either a bridging histidine or tyrosinate ligand.[17] This difference in iron-ligand binding between the P450s on the one hand with peroxidases and catalases on the other hand, has been proposed to be the reason for their differences in catalytic function, whereby cysteinate creates a "push-effect" and donates electrons to the heme center, while a histidine axial ligand withdraws electrons.[18] Indeed, a series of elegant biomimetic experiments of Gross et al.[19] and Nam et al.[20] have identified an axial ligand effect on substrate oxidation by iron(IV)−oxo oxidants with variable axial ligands. These studies used biomimetic iron-porphyrin oxidants where the ligand position trans to the oxo group was occupied by either an anion, e.g., F^-, Cl^-, acetate, perchlorate, etc., or a neutral solvent molecule, e.g., acetonitrile. Thus, rate constants for styrene epoxidation and hydrogen abstraction reactions were measured and shown to vary with the nature of the axial ligand. Moreover, Nam et al.[20b] investigated the reactivities of $[Fe^{IV}(O)(TPFPP^{+\bullet})X]$ with TPFPP = *meso*-tetrakis(pentafluoro-phenyl)porphyrinato and X = $NCCH_3$ or Cl^-. The reaction of $[Fe^{IV}(O)(TPFPP^{+\bullet})NCCH_3]^+$ with ethylbenzene gave aromatic hydroxylation products, whereas the one using $[Fe^{IV}(O)(TPFPP^{+\bullet})Cl]$ as an oxidant led to benzyl hydroxylation instead.

Understanding the catalytic mechanism of P450 enzymes is, therefore, important but sadly many fundamental details of the processes that take place are still unknown. In recent years, the technical details of hydrogen atom abstraction processes have been revealed through detailed valence bond (VB) curve crossing mechanisms.[21] More recent studies have also addressed the fundamental nature of double bond epoxidation,[22] dialkylsulfide sulfoxidation mechanisms,[23] as well as aromatic hydroxylation[24] by P450 enzymes. All these studies have in common that they investigate the reactivity of Cpd I of P450 with a systematic set of substrates. This indeed gives insight into the effects of the substrate on reactivity patterns. However, to gain insight into the effect of the oxidant on the reaction mechanisms, and in particular the choice of the axial ligand, we have performed a further set of calculations where we vary Cpd I but keep the substrate constant. The work described herein will generalize aromatic hydroxylation reactions by metal−oxo oxidants. Although aromatic hydroxylation reactions by P450 enzymes have been extensively studied by several groups,[25−28] the effect of the axial ligand remains elusive. Indeed, experimental studies identified a strong axial ligand effect upon aromatic hydroxylation reactions of arenes.[20b] Our previous studies on aliphatic hydroxylation by a range of Cpd I models established the role of the oxidant in reaction kinetics.[29] To gain insight into the axial ligand effect of aromatic hydroxylation and the implications on P450 catalysis, we have performed a density functional theory study. We show here that indeed the barrier heights and, consequently, the rate constants are affected by the choice of the axial ligand. In particular, we show here, for the first time, that using thermochemical properties of the oxidant and substrate the barrier height of the reaction and consequently the rate constant can be predicted for aromatic hydroxylation reactions.

METHODS

The calculations described in this work use methods that have been thoroughly tested and benchmarked against experimental data.[30] The geometries were fully optimized with the *Jaguar* 7.7 and *Gaussian* 03 program packages, and a subsequent frequency calculation (at the same level of theory) confirmed the structures as local minima with real frequencies only or first order saddle points with a single imaginary frequency for the correct mode.[31] In order to compare the studies with related previous work, we chose the B3LYP hybrid density functional method for all calculations,[32] in combination with a Los Alamos type LACVP basis set on iron that includes a core potential coupled to 6-31G on the rest of the atoms (basis set B1).[33] Single point calculations were done using the triple-ζ quality LACV3P+ basis set on iron in combination with 6-311+G* on the rest of the atoms (basis set B2) on the UB3LYP/B1 geometries on all structures described here. Test calculations that compared a potential energy landscape of a chemical reaction calculated with UB3LYP/B2 and UB3LYP/B2//UB3LYP/B1 showed only small changes in energy and geometry;[22]

dx.doi.org/10.1021/jp2113522 |*J. Phys. Chem. B* 2012, 116, 718–730

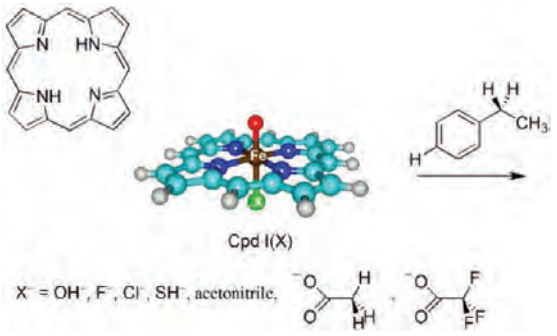

Figure 2. Oxidants and substrate used in this work.

therefore, the latter method was used here. Frequencies reported here were scaled with the recommended value of 0.9614.[34] All energies discussed in this work were obtained with UB3LYP/B2 and corrected with zero-point energy from the frequency calculations. To test the effect of the environment, we did single point calculations with the polarized continuum model with a dielectric constant of $\varepsilon = 5.7$ and probe radius of 2.7 Å mimicking a chlorobenzene solution and in-line with values found for enzymatic systems. These methods have been thoroughly tested, benchmarked, and shown, for instance, to reproduce experimental free energies of activation for these types of reactions within 3 kcal mol^{-1} and give vibrational frequencies that are on average about 10−15 cm^{-1} from experiments.[35,36]

To ascertain that the methods are not influenced by the density functional method chosen here, we ran a selection of single point calculations using OPBE[37] and B3LYP with 15% HF exchange (designated B3LYP*).[38] These test calculations reproduced the B3LYP barrier heights within 2 kcal mol^{-1} and gave similar trends, see the Supporting Information.

Cpd I was modeled as an iron(IV)−oxo embedded in protoporphyrin IX, whereby all side chains were abbreviated by hydrogen atoms. Previous work showed that replacing the heme side chains with hydrogen atoms gives little changes in the high-lying occupied and low-lying virtual orbitals of the chemical system, although some steric effects on substrate approach may occur.[39] We initially tested the description of the ligand system to mimic Cpd I of P450 by using an iron(IV)−oxo porphyrin cation radical model [Fe^{IV}(O)(Por$^{+\bullet}$)X] with two types of axial ligands (X$^-$): The first one uses thiolate and the second one a short peptide containing GlyGlyCys$^-$ that binds the metal via a thiolate bridge. The sets of geometry optimizations give similar geometries and group spin densities and charges. Moreover, it is shown that both the electron affinity of the oxidants and the BDE$_{OH}$ remain virtually the same for both ligand systems; therefore, we continued the reactivity profile with X = SH$^-$ as the P450 Cpd I. In a subsequent set of calculations we replaced the axial ligand (X$^-$) in [Fe^{IV}(O)(Por$^{+\bullet}$)X] with X = F$^-$, Cl$^-$, OH$^-$, acetonitrile, CF_3COO^-, and CH_3COO^-. Because of two-state-reactivity patterns,[40] we calculated all reactions on the doublet and quartet spin state surfaces. Full details of all results are given in the Supporting Information document, while we focus on the main trends only.

RESULTS

Here, the axial ligand effect on aromatic hydroxylation by iron(IV)−oxo porphyrin cation radical oxidants, which in the case of heme enzymes are known under the name Compound I

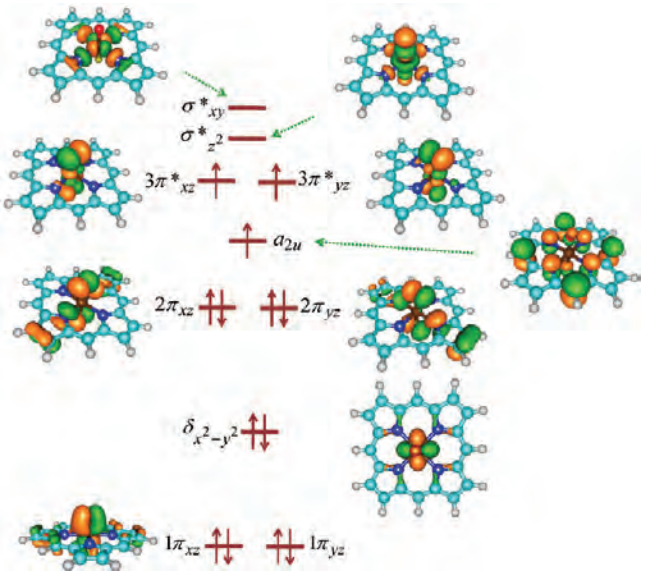

Figure 3. High-lying occupied and low-lying virtual orbitals of ^{4}Cpd I(F).

(Cpd I), is investigated. We varied the axial ligand (X) bound to the metal trans to the oxo group and with X = OH$^-$, F$^-$, Cl$^-$, SH$^-$, acetonitrile, acetate (CH_3COO^-), and trifluoroacetate (CF_3COO^-); Figure 2. This is a broad selection of ligand types with varying ligand effects and includes neutral (acetonitrile) as well as anionic axial ligands. As a model of aromatic hydroxylation reactions in general, we studied the aromatic hydroxylation on the para-position of ethylbenzene with DFT methods. To identify the type of Cpd I, we give the axial ligand in parentheses after Cpd I or in subscript after the label, while in superscript we give the overall spin multiplicity of the structure. For example, ^{2}Cpd I(F) is an iron(IV)−oxo porphyrin cation radical model of Cpd I with an axial fluoride ligand and in overall doublet spin state.

Before we will discuss the reactivity patterns of these iron(IV)−oxo porphyrin cation radical models, let us first highlight the electronic, geometric, and spectroscopic differences and comparisons between the various Cpd I complexes. Figure 3 gives the high-lying occupied and low-lying virtual orbitals of ^{4}Cpd I(F), where we focus on those orbitals that involve the metal 3d contributions plus a high lying π^*-type heme orbital. This labeling assumes that the z-axis is along the Fe−O bond and the x- and y-axes in between two Fe−N bonds of the porphyrin. As such, the metal $3d_{xz}$ and $3d_{yz}$ atomic orbitals interact with $2p_x/2p_y$ atomic orbitals on the oxo group as well as with those on the axial ligand. These orbitals form pairs of bonding ($1\pi_{xz}$ and $1\pi_{yz}$), nonbonding ($2\pi_{xz}$ and $2\pi_{yz}$), and antibonding ($3\pi_{xz}^*$ and $3\pi_{yz}^*$) set of molecular orbitals. The bonding and nonbonding pairs of orbitals are all doubly occupied in Cpd I, but both π^* orbitals are singly occupied. These two unpaired electrons are either ferromagnetically or antiferromagnetically coupled to an unpaired electron in a mixed porphyrin-axial ligand type orbital designated a_{2u} to give an overall quartet or doublet spin state, respectively. The a_{2u} orbital mixes somewhat with the $2p_z$ orbital on the axial ligand.[41] The remaining three 3d-type orbitals on the metal are the nonbonding $\delta_{x^2-y^2}$ orbital that is in the plane of the porphyrin and two sets of σ/σ^* pair of orbitals. The σ_{z^2} and σ_{xy} orbitals (not shown in Figure 3) are low-lying and doubly occupied, while the σ^* orbitals ($\sigma_{z^2}^*$ and σ_{xy}^*) are virtual.

dx.doi.org/10.1021/jp2113522 |J. Phys. Chem. B 2012, 116, 718–730

Table 1. Optimized Fe−O Bond Lengths (r_{FeO} in Å) of Cpd I(X) Structures in the Low-Spin (LS) and High-Spin (HS) Spin States[a]

Cpd I(L)	OH^-	F^-	Cl^-	SH^-	CH_3COO^-	CF_3COO^-	GlyGlyCys$^-$
LS Data							
r_{FeO}[b]	1.664	1.681	1.659	1.648	1.665	1.662	
ν_{FeO}[c]	783.2	786.1	821.3	837.2	793.8	802.5	
ν_{FeX}[c]	406.4	510.0	219.2	152.0	867.9	650.1	
HS Data							
r_{FeO}[b]	1.691	1.683	1.661	1.652	1.667	1.662	1.641
ν_{FeO}[c]	696.6	772.0	811.9	821.2	782.3	799.6	850.7
ν_{FeX}[c]	407.2	513.7	224.2	161.9	868.6	650.2	259.6
EA(Cpd I)[d]	113.5	111.8	112.1	109.2	112.9	111.3	
BDE_{OH}[d]	96.5	88.2	82.3	87.6	86.3	85.7	88.1

[a] Also given are vibrational frequencies (ν_{FeO} and ν_{FeX}) for the Fe−O and Fe−X stretch vibration (in wavenumbers). [b] Values in Å. [c] Values in cm^{-1}. [d] Energies are in kcal mol^{-1} relative to [2]Cpd I(X) and include ZPE and solvent corrections.

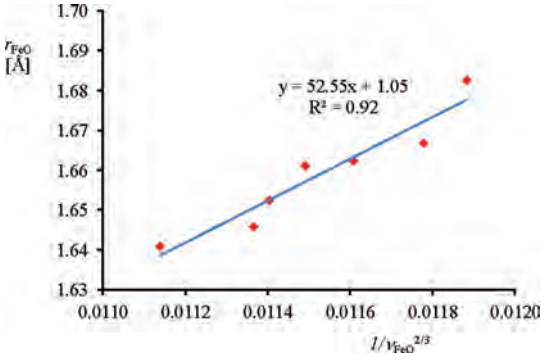

Figure 4. Badger plot for the Fe−O bond length versus $1/\nu_{FeO}^{2/3}$ with ν_{FeO} the stretch vibration for the Fe−O bond for the series of Cpd I species of Figure 2 plus Cpd I($NCCH_3$). Data for high-spin Cpd I(X) structures were used.

The σ_{z^2}* orbital reflects the antibonding σ-interaction of the metal with the distal and axial ligands, whereas the σ_{xy}* orbital is orthogonal to the σ_{z^2}* orbital and interacts in the plane of the porphyrin with σ-orbitals on the four pyrrole nitrogen atoms. The σ_{xy}* orbital is high in energy and remains virtual during the complete reaction mechanism. The $\delta_{x^2-y^2}$ orbital is also located in this plane but due to the symmetry of the porphyrin ring cannot form bonding and antibonding pairs and hence is a nonbonding orbital.

Gross and co-workers showed that the axial ligand displays a trans-influence due to changes in the spectroscopic parameters of complexes with different axial ligands as well as a trans-effect on the reactivity patterns.[19] Therefore, we first did an in-depth analysis of the structures and spectroscopic parameters of the Cpd I models shown in Figure 2 together with an elaborate P450 Cpd I model, where the axial ligand is described by a small chain of amino acids containing GlyGlyCys$^-$: Cpd I(GlyGlyCys). Thus, this model includes the amide−sulfur hydrogen bonding interactions on the axial ligand site that are known to be important in regulating the electronic properties of Cpd I, i.e. through a push effect of the thiolate ligand, and consequently the reactivity patterns.[42] In all cases we find the quartet and doublet spin state structures within 1 kcal mol^{-1}, but the quartet spin state is slightly lower in energy. This is in agreement with EPR studies on oxo−iron porphyrin cation radical models of Gross, which implicated these structures as high-spin states.[19b] Optimized Fe−O bond lengths are given in Table 1 as well as vibrational stretch frequencies for the Fe−O and Fe−X modes.

The Fe−O distances range from 1.641 Å for [4]Cpd I(GlyGlyCys) to 1.691 Å for [4]Cpd I(OH), which implies that a difference of 0.05 Å has occurred due to the change in axial ligand bound trans to the iron(IV)−oxo bond. Although this is a minor change from a mechanistic point of view, it causes a significant effect on the spectroscopic parameters for these Cpd I species. In particular, a difference in Fe−O bond strength should influence the Fe−O vibrational frequency. Indeed, our calculated Fe−O vibrational frequencies in the quartet spin state range from 696.6 cm^{-1} for [4]Cpd I(OH) to 850.7 cm^{-1} for [4]Cpd I(GlyGlyCys), whereby a long Fe−O distance corresponds to the lowest Fe−O stretch vibration and a short Fe−O distances with high vibrational modes. Thus, the experimentally determined value of ν_{FeO} for $[Fe^{IV}(O)(TMP^{+\bullet})X]$, X = F^-/Cl^- and TMP = tetramesitylporphyrin,[19b] is 801 cm^{-1}. Our calculated value of [4]Cpd I(Cl) is within 10 cm^{-1} of this; however, the calculations predict a strong deviation in Fe−O stretch vibration between Cpd I(F) and Cpd I(Cl) that was not found experimentally. This may be due to the fact that our calculated model lacks meso-substituents and/or was optimized in the gas-phase.

Badger[43] proposed a correlation between the Fe−O bond strength (r_{FeO}) and the strength of the stretch vibration (ν_{FeO}) for this bond (eq 1), via two constants c_{ij} and d_{ij}. Green showed that this equation successfully predicts the Fe−O bond strength in peroxidases and P450 Cpd I species.[44] To find out whether the equation also applies to our series of axially ligated Cpd I mimics, we determined the Fe−O stretch vibrations and plotted those against the Fe−O bond length in Figure 4. As can be seen from Figure 4, the trend is linear and indeed Badger's rule applies to axially ligated iron(IV)−oxo porphyrin cation radical systems. Note here that the trend includes neutral (acetonitrile) as well as anionic axial ligands.

$$r_{FeO} = \frac{c_{ij}}{(\nu_{FeO})^{2/3}} + d_{ij} \quad (1)$$

To understand the changes in vibrational frequencies upon changing the axial ligand, we did an in-depth analysis of the

dx.doi.org/10.1021/jp2113522 |J. Phys. Chem. B 2012, 116, 718–730

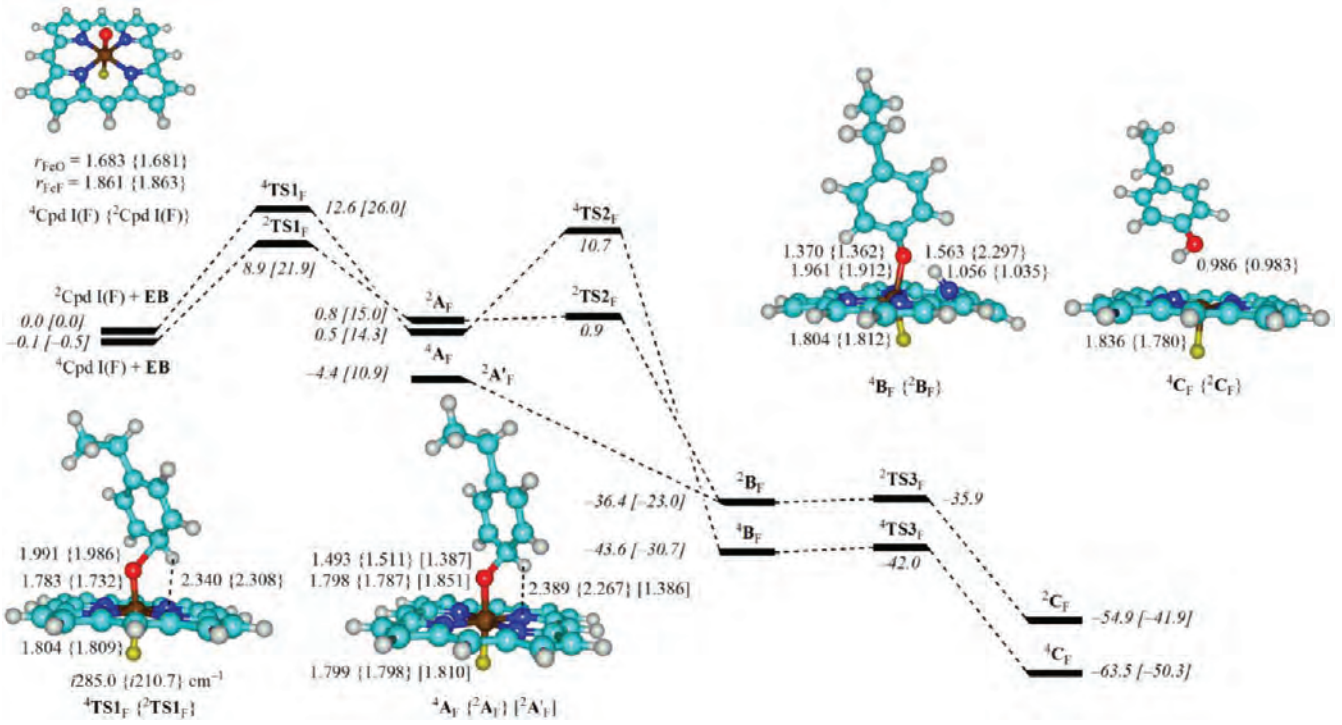

Figure 5. Potential energy surface of aromatic hydroxylation of ethylbenzene by Cpd I(F) as calculated with DFT methods. All energies are in kilocalories mole^{-1} relative to isolated reactants in the quartet spin state. Also shown are optimized geometries of critical points with bond lengths in angstroms and the imaginary frequency in the transition states in wave numbers. The energies are calculated at the UB3LYP/BS2//UB3LYP/BS1 level of theory and contain zero point corrections, while values in square brackets are free energies.

different Cpd I species with the aim to elucidate the quantum chemical origins of these differences. Thus, we calculated the electron affinity (EA) and hydrogen atom abstraction ability (bond dissociation energy, BDE_{OH}) of each Cpd I structure. BDE_{OH} is defined as the negative of the enthalpy change for reaction 2 and can be written in terms of a separate electron and proton abstraction, eq 3.

$$[Fe^{IV}(O)(Por^{+\bullet})X] + H^{\bullet} \rightarrow [Fe^{IV}(OH)(Por)X] \quad (2)$$

$$BDE_{OH} = EA + 2.303RT\, pK_a + 54.9 \text{ kcal mol}^{-1} \quad (3)$$

The EA values in Table 1 give a spread of only 4.3 kcal mol^{-1} for the various Cpd I species; therefore, the axial ligand hardly affects the reduction potential of Cpd I. Electron abstraction by these Cpd I models, in all cases, fills the porphyrin-type a_{2u} orbital with a second electron. This orbital is a pure porphyrin based orbital for Cpd I(F), Cpd I(CH_3COO), and Cpd I (CF_3COO) but contains significant mixing with a $2p_z$ orbital on the axial ligand in Cpd I(OH) and Cpd I(SH). The latter two structures, in the gas-phase, give spin densities of −0.71 and −0.50 on the porphyrin ring and −0.36 and −0.60 on the axial ligand, respectively. Because of this, the latter two structures have the highest and lowest EA values. The amount of mixing between the a_{2u} and $3p_z$ (thiolate) orbitals was shown to be dependent on hydrogen bonding donor groups, and a QM/MM approach reduced the amount of radical character on the thiolate of Cpd I dramatically.[45] Calculations on small model complexes showed a large effect on the electronic properties of Cpd I(SH) due to hydrogen bonding interactions but very little influence on hydrogen abstraction reactions.[46] In agreement with that, the data in Table 1 shows a negligible effect of hydrogen bonding on BDE_{OH} so that the hydrogen abstraction ability of Cpd I(SH) and Cpd I(GlyGlyCys) is expected to be the same.

The BDE_{OH} values vary from 81.3 kcal mol^{-1} for Cpd I-($NCCH_3$) to 96.5 kcal mol^{-1} for Cpd I(OH) and, hence, cover a range of more than 15 kcal mol^{-1}. Thermodynamically, BDE_{OH} can be described as the sum of an electron and a proton transfer and is split into an EA and pK_a term as shown in eq 3, with R the gas constant and T the temperature.[47] The constant of 54.9 kcal mol^{-1} in eq 3 represents the ionization potential of a hydrogen atom and solvent corrections to the equation. As follows from the data in Table 1, the EA values are virtually independent of the axial ligand and fairly constant. The change in BDE_{OH} along the axial ligand series, therefore, correlates with a change in the pK_a value of the oxidant. This is in agreement with experimental studies of Green and Goldberg that came to the same conclusion.[16c,48]

Table 1 also gives the values of the Fe−X stretch vibrations as taken from the Gaussian frequency calculations. Thus, very strong differences in Fe−axial ligand frequencies are found that range from 152.0 cm^{-1} for the Fe−S stretch vibration in ^{2}Cpd I(SH) to 868.6 cm^{-1} for the Fe−$OOCCH_3$ stretch vibration in ^{4}Cpd I(CH_3COO). In contrast to the iron(IV)−oxo frequencies, therefore, the Fe−X vibrations do not seem to be proportional to the strength of the Fe−X bond. At first glance a higher vibrational frequency for Fe−$OOCH_3$ than Fe═O may look odd, but experimental $^{16}O_2/^{18}O_2$ studies on the iron(IV)−oxo-(carboxylato) species of taurine/α-ketoglutarate dioxygenase (TauD) found similar vibrational frequencies as those reported here.[49] The difference spectrum showed isotope sensitive peaks at 821 and 859 cm^{-1}, whereby the lower one was identified as the Fe═O vibration, while the latter was shown to be an Fe−carboxylate vibration.

dx.doi.org/10.1021/jp2113522 |J. Phys. Chem. B 2012, 116, 718–730

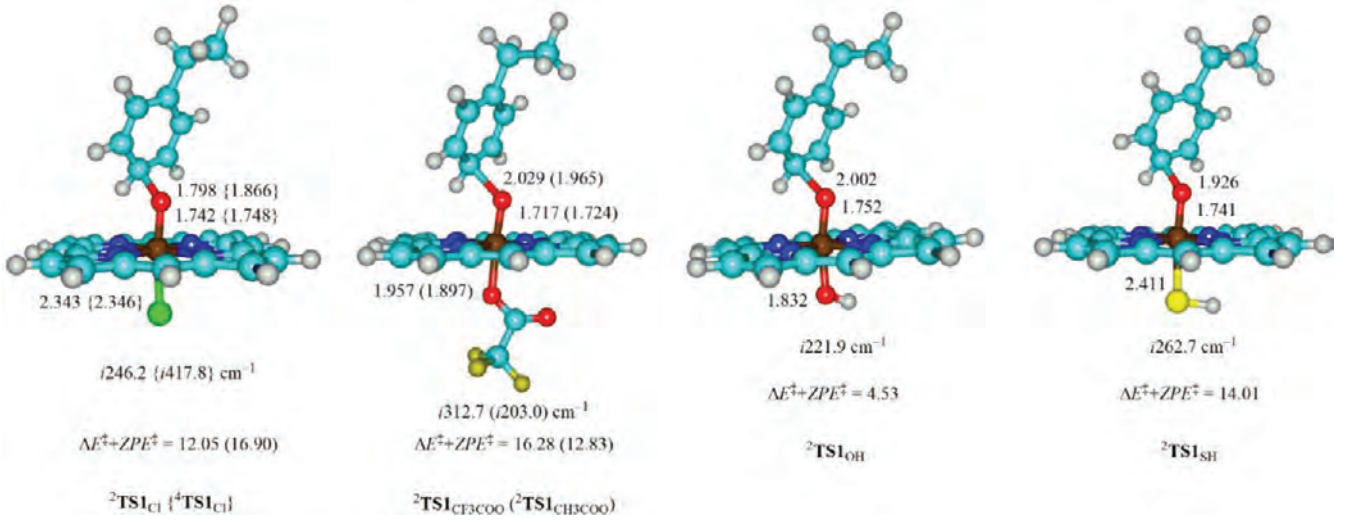

Figure 6. Optimized geometries of rate determining transition states **TS1** from the reaction of ethylbenzene with Cpd I(X), X = Cl^-, CF_3COO^-, CH_3COO^-, OH^-, and SH^-. Geometries optimized at UB3LYP/B1 with bond lengths given in angstroms and the imaginary frequency in the transition state in wavenumbers.

Our axial carboxylate system gives vibrational frequencies for the Fe−OOCCH$_3$ that are very close to these values.

Subsequently, we investigated the aromatic hydroxylation of ethylbenzene (EB) by the selection of Cpd I models with varying axial ligands. As an example, we give in Figure 5 the aromatic hydroxylation mechanism of ethylbenzene by Cpd I(F). All other oxidants give similar potential energy profiles and the only difference arises from the relative energies. The aromatic hydroxylation mechanism found here is similar to those reported before for P450 model complexes, although different substrates were used.[26,27] The reaction starts with an electrophilic attack of the oxo group on the carbon atom in the para-position from ethylbenzene to give a Meisenheimer complex (**A**) via an electrophilic transition state **TS1**. In this complex, the aromaticity of the benzene ring is distorted and as a consequence its basicity is very large. Structure **A** either has a radical on the aromatic ring or a cation on the aromatic ring (in **A′**). The ipso-proton is shuttled to one of the nitrogen atoms of the porphyrin ring via a barrier **TS2** to form the proton transfer intermediate **B**. During this process, the aromaticity is put back into the aromatic ring and **B**, therefore, can be regarded as a phenolate bound to an iron(III) ion inside a protonated porphyrin. Because of the protonation of one of its pyrrole groups, the porphyrin ring in structure **B** is not planar but significantly distorted, where the protonated pyrrole ring is tilted out of the plane through the other nitrogen atoms. In a final step, the proton is relayed to the phenolate to give para-hydroxoethylbenzene products (**C**) via a transition state **TS3**. This brings the porphyrin ring back to planarity and removes the temporary tilt that is characteristic for structure **B**. Note that an early report of Siegbahn and co-workers on a nonheme metal−oxo oxidant found a direct hydrogen atom migration rather than the proton-shuttle mechanism found for iron−porphyrin systems.[50] Detailed DFT studies that compared the two mechanisms, however, found the proton-shuttle mechanism to be significantly lower in energy;[26a] hence, we focus on that mechanism here only.

As follows from Figure 5, the first step in this mechanism is the rate determining step with a barrier of 8.9 kcal mol^{-1} on the low-spin surface and 12.6 kcal mol^{-1} on the high-spin surface. This difference in barrier between the low- and high-spin surfaces was explained by the differences in electron transfer that take place in an electrophilic attack.[26] After passing the barrier (^{4,2}**TS1**) the system relaxes to the radical intermediates (^{4,2}**A**), which have an electronic configuration that resembles the transition state structures closely. The overall reaction energy (driving force) for the formation of radical intermediates is almost thermoneutral. There is, however, a slightly more stable intermediate, namely, the cationic intermediate (**A′**), although, it is a first-order saddle point with an imaginary frequency of *i*630.5 cm^{-1} for the proton transfer from the ipso-position to the nearest nitrogen atom of the porphyrin ring. By contrast, the radical intermediates (^{4,2}**A**) are genuine local minima, although the subsequent proton transfer mechanism via **TS2** is virtually barrierless on the low-spin surface while it encounters a somewhat larger barrier in the high-spin surface. Previous computational studies[26,27] also calculated the cationic intermediate (**A′**) below the radical intermediates ^{4,2}**A** by several kilocalories mole^{-1}. However, the relative energies between the radical and cationic intermediates and the degree of charge-transfer in the transition state were found to be dependent on the substrate.[24] Moreover, in previous work the rate determining barriers had strong cationic character, whereas here **TS1** is a radical, later we will give an in-depth discussion on these differences.

The reaction leading to complexes **C** is highly exothermic due to the fact that the aromaticity is put back into the arene ring and the proton transfer gives a phenolate anion bound to an iron(III) center. The protonated heme structure (**C**) has a twisted pyrrole ring and can relay its proton back to the phenolate to form phenol products. QM/MM studies[27c] showed that there is sufficient space in the heme binding pocket to accommodate for these structural changes. Nevertheless, the barriers leading to products are very small (<2 kcal mol^{-1}), so the last step will proceed very fast. In the past, we showed that structure **C** in the benzene hydroxylation mechanism of P450 is also an intermediate en route to cyclohexadienone products through proton relay to the ortho-carbon atom.[26a] However, the barrier leading to cyclohexadienone products was found to be significantly higher in energy than the one giving phenol products; therefore, we will not focus on this alternative mechanism here.

dx.doi.org/10.1021/jp2113522 |*J. Phys. Chem. B* 2012, 116, 718–730

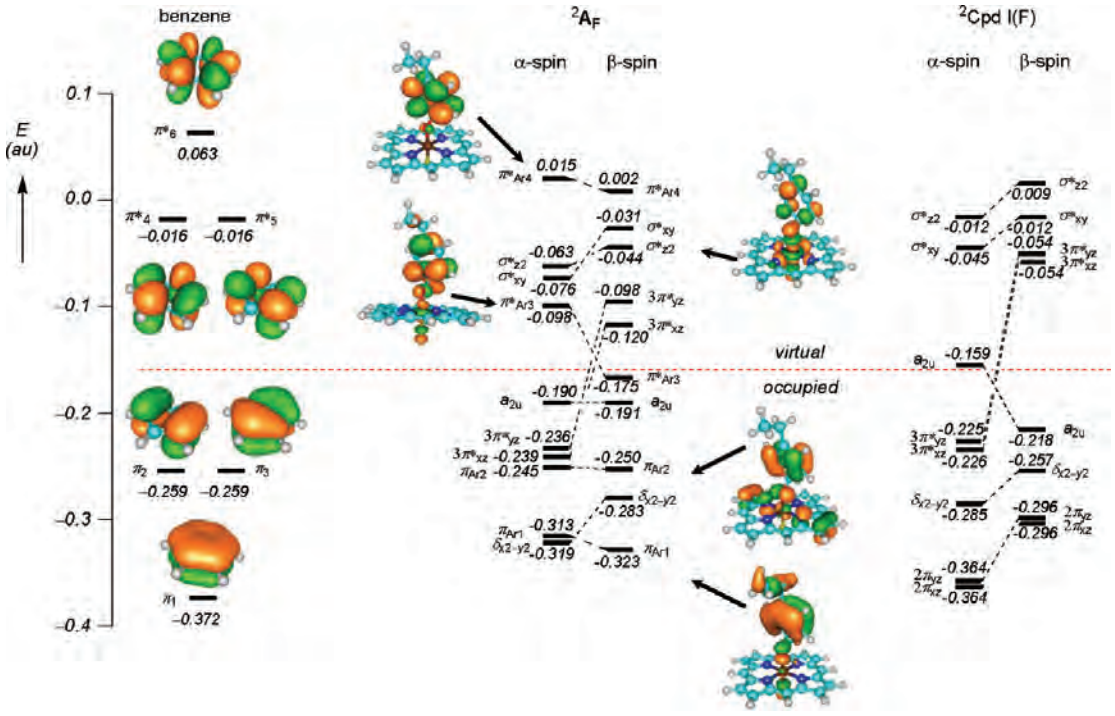

Figure 7. Orbital diagram of benzene (left-hand-side), $^2\mathbf{A}_F$ (middle), and ^{2}Cpd I(F) (right-hand-side). Orbital energies taken from UB3LYP/B2//UB3LYP/B1 calculations.

A series of density functional theory studies on iron(IV)−oxo porphyrins identified a large axial ligand effect on the kinetics of substrate activation by substrates, whereby neutral ligands such as imidazole (mimicking peroxidases) gave substantial differences in reactivity patterns over anionic ligands like thiolate or phenolate (mimicking catalase).[51] To this end, we investigated the axial ligand effect on aromatic hydroxylation reactions and optimized the geometries of all rate determining transition states which are given in Figure 6. The geometries are typical for an electrophilic attack of an iron(IV)−oxo on an aromatic ring and all optimized geometries give structures that are very similar. Despite this, there are remarkable differences in C−O activation barrier height (**TS1**) of ethylbenzene by Cpd I models that on the low-spin surface range from 4.5 kcal mol^{-1} for Cpd I(OH) to 16.3 kcal mol^{-1} for Cpd I(CF_3COO). The difference in barrier height between these two processes should correlate with a considerable rate enhancement for the aromatic hydroxylation reaction (k_{OH}/k_{CF3COO}) of several orders of magnitude. Similar trends are observed for the driving force of the reaction, i.e., the energy between reactants and ^{2}**A** (Supporting Information). Therefore, the axial ligand effect manifests itself by changing the driving force and kinetics of the aromatic hydroxylation reaction.

Attempts to find a correlation between either the Fe−O distance and/or the C−O distance with the barrier height gave no linear correlation (Supporting Information). The imaginary frequencies in the transition states range from *i*203.0 cm^{-1} for ^{2}**TS1**$_{CF3COO}$ to *i*312.7 cm^{-1} for ^{2}**TS1**$_{CH3COO}$ and compare well to values found before for aromatic hydroxylation reactions.[26−28] Note that all transition states are characterized via a side-on approach of the substrate on the iron(IV)−oxo group, where the ipso-hydrogen atom forms a hydrogen bonding interaction with one of the nitrogen atoms of the porphyrin ring. In the case of Cpd I(SH), we also calculated a face-on transition state, where the aromatic ring of the substrate is parallel to the porphyrin ring (Supporting Information Figure S20). In analogy to previous work,[27c] however, the face-on approach has a barrier that is a several kilocalories mole^{-1} higher in energy than the side-on TS, i.e., 17.1 versus 14.0 kcal mol^{-1}.

DISCUSSION

So what is the origin of the axial ligand effect and what are the intrinsic properties of the reactant and/or substrate that determine the barrier heights/rate constants for aromatic hydroxylation? In the following sections, we will try to give an in-depth understanding of the fundamental properties that lead to the dramatic differences in aromatic hydroxylation rate constant by these Cpd I mimics with varying axial ligands.

To understand the electron transfer process that takes place for the conversion from ^{2}Cpd I to ^{2}**A** via the transition state ^{2}**TS1**, consider in Figure 7 the orbital energy levels of the two reactants (outer left- and right-hand-side of Figure 7) and those for $^2\mathbf{A}_F$ for the system with fluoride axial ligand, where we use benzene as the aromatic substrate for simplicity. All other chemical systems discussed here follow the same principles. Thus, a substrate with an aromatic ring, such as benzene, will have a set of six π/π^*-orbitals of which the lowest three are doubly occupied (π_1, π_2 and π_3); the latter two are degenerate. Higher in energy are the virtual π^* orbitals on the aromatic ring (π_4^*, π_5^*, and π_6^*). As discussed above, ^{2}Cpd I(F) has orbital occupation (core) $1\pi_{xz}^2$ $1\pi_{yz}^2$ $2\pi_{xz}^2$ $2\pi_{yz}^2$ $\delta_{x^2-y^2}^2$ $3\pi_{xz}^{*1}$ $3\pi_{yz}^{*1}$ a_{2u}^1, whereby the unpaired electrons in the π^* orbitals are antiferromagnetically coupled to the a_{2u} electron.

Electrophilic attack of the iron(IV)−oxo group on one of the carbon atoms of the aromatic ring leads to a C−O bond formation and distortion of the aromatic ring from planarity. Consequently,

dx.doi.org/10.1021/jp2113522 |*J. Phys. Chem. B* 2012, 116, 718–730

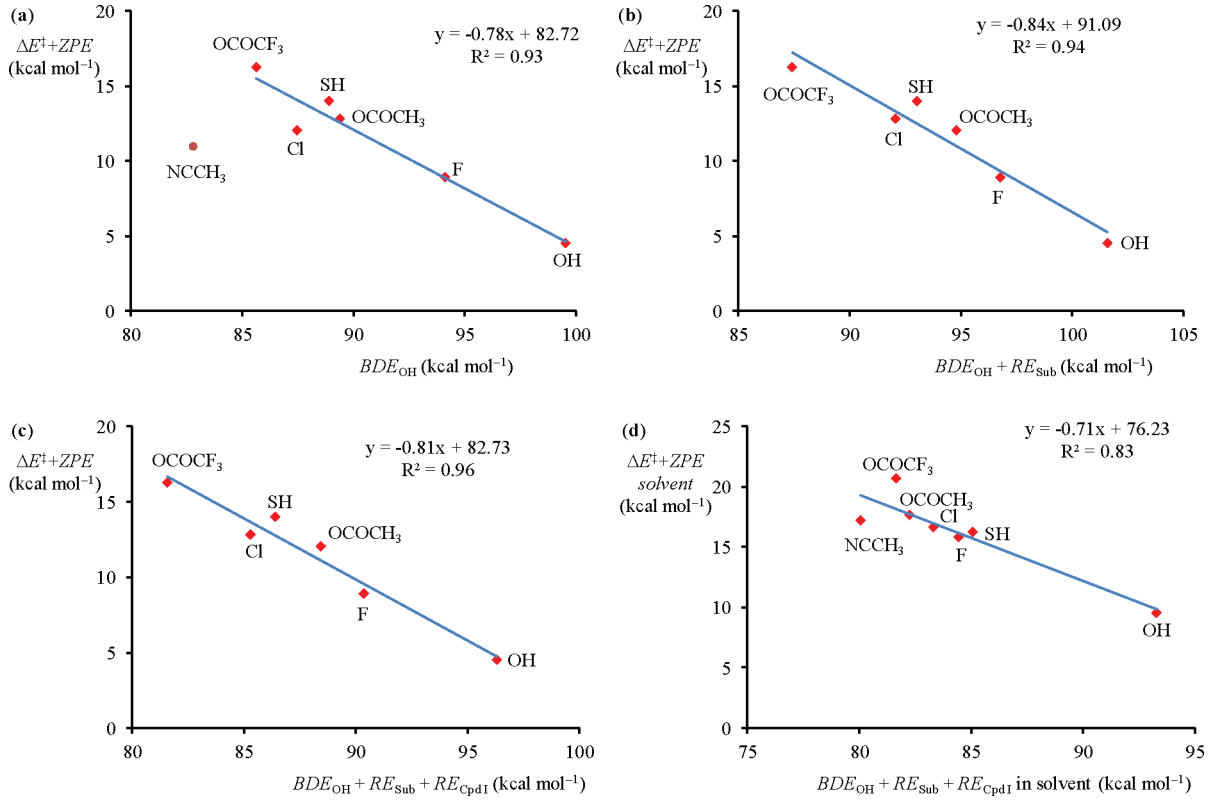

Figure 8. Correlation between aromatic hydroxylation barrier height and BDE_{OH} value. Data for low-spin structures only.

the aromatic ring of the substrate in ^{2}**A** has a conjugated π-system spread out over only five of its carbon atoms. This has a major effect on the orbital energy levels as can be seen from the middle panel in Figure 7. The lowest aromatic ring orbital (π_{Ar1}) is raised from −0.372 au in isolated benzene to −0.313 (α) and −0.323 (β) au in $^2\mathbf{A}_F$ due to decreased π-conjugation. Not all substrate π-type orbitals change as much in energy as π_{Ar1}. For instance, the π_2 orbital in benzene does not have orbital occupation on the carbon atom that binds oxygen in ^{2}**A**, hence the corresponding π_{Ar2} orbital energy level is close to that of π_2 in isolated benzene. The π_3 orbital of benzene is significantly raised in energy after oxygen binds to the ipso-carbon atom and splits into a virtual π_{Ar3}* α-orbital and an occupied β-orbital. Its reactant electron is transferred into the vacant a_{2u} orbital to create a radical intermediate with configuration $\pi_{Ar1}{}^2\ \pi_{Ar2}{}^2\ \delta_{x^2-y^2}{}^2\ 3\pi_{xz}{}^{*1}\ 3\pi_{yz}{}^{*1}\ a_{2u}{}^2\ \pi_{Ar3}{}^{*1}$. Note as well the mixing of π_{Ar3}* with the σ_{z^2}* orbital along the axial ligand−Fe−O axis. Obviously, the larger the contribution of the axial ligand effect into the σ_{z^2}* orbital is, the stronger the effect on the energy level of this mixed $\pi^*_{Ar3}-\sigma_{z^2}{}^*$ orbital will be the case. This will affect the electron transfer possibility during the C−O bond formation step. Electron transfer from the β-occupied π^*_{Ar3} orbital in $^2\mathbf{A}_F$ to the vacant $3\pi_{xz}$* converts $^2\mathbf{A}_F$ into the lowering lying $^2\mathbf{A}'_F$. Thus, the orbital occupation shows favorable side-on approach that results in stabilization due to mixing of the π_{Ar3}* and σ_{z^2}* molecular orbitals. This is in agreement to the lowering of the barrier height as compared to a face-on transition state (Supporting Information). Further stabilization of the side-on structure is as a result of a hydrogen bonding interaction between the ipso-proton and one of the nitrogen atoms of the porphyrin ring.

Let us in the following focus on the thermodynamics of the electrophilic reaction mechanism and try to find a correlation that will enable us to make predictions of rate constants of aromatic hydroxylation processes. Thus, in an aliphatic hydroxylation reaction between Cpd I(X) and a substrate (SubH), the reaction enthalpy of a hydrogen atom abstraction (ΔH_{HA}) can be described by the differences in bond dissociation energy (BDE) of the aliphatic C−H bond that is broken (BDE_{CH}) and the strength of the O−H bond that is formed (BDE_{OH}), eqs 4−6.[47] Many experimental and computational studies confirmed a correlation between rate constant and BDE_{CH} for a series of hydrogen atom abstraction reactions.[52,53]

$$\mathrm{CpdI(X)} + \mathrm{SubH} \rightarrow [\mathrm{Fe^{IV}(OH)(Por)X}] + \mathrm{Sub^{\bullet}} \quad (4)$$

$$\Delta H_{HA}(\mathrm{eq2}) = \mathrm{BDE_{CH}} - \mathrm{BDE_{OH}} \quad (5)$$

$$\mathrm{SubH} \rightarrow \mathrm{Sub^{\bullet}} + \mathrm{H^{\bullet}} + \mathrm{BDE_{CH}} \quad (6)$$

In an aromatic hydroxylation reaction, by contrast, a C−O rather than a H−O bond is formed. However, recent studies on trends in substrate epoxidation reactions by a range of Cpd I oxidants showed that the formation of the C−O bond in this mechanism can be approximated by the formation of a H−O bond. Therefore, a plot of the epoxidation barrier height against BDE_{OH} for the reaction of propene with Cpd I(X) gave a linear correlation.[22] In a similar vein, a correlation between sulfoxidation barrier height and BDE_{OH} was found to be linear, so that BDE_{OH} appears to be a good representation of a C−O as well as an S−O bond formation step.[54] To find out whether the same applies to aromatic hydroxylation, we plot in Figure 8 the aromatic hydroxylation barriers versus BDE_{OH} for the reaction of ethylbenzene with Cpd I(X), X = F^-, Cl^-, SH^-, OH^-, acetonitrile, CH_3COO^-, and CF_3COO^-.

dx.doi.org/10.1021/jp2113522 |J. Phys. Chem. B 2012, 116, 718–730

If we exclude acetonitrile from the correlation and focus on the Cpd I oxidants with anionic ligands only, then the correlation is good and an R^2 value of 0.93 is found. Following previous studies in the field,[21] we also calculated the reorganization energy (RE) of both the substrate (RE_{Sub}) and the oxidant ($RE_{Cpd\ I}$) in the transition states. The values of RE_{Sub} were calculated from the energies obtained from the substrate geometry in the transition state minus that for the fully relaxed structure. Similarly, the $RE_{Cpd\ I}$ values were calculated from the difference in energy between the structure of Cpd I in the transition state geometry minus that for the fully relaxed geometry. Correcting the BDE_{OH} values for RE_{Sub} gives a small improvement of the correlation with barrier height (Figure 8b). Further corrections with $RE_{Cpd\ I}$ gives an even better R^2 value of 0.96 for the relationship with barrier height (Figure 8c). Consequently, the barrier heights of aromatic hydroxylation by iron(IV)−oxo porphyrin cation radical systems are proportional to BDE_{OH}. This implies that barrier heights of substrates can be predicted using known values of BDE_{OH} of the oxidants used.

The series of oxidants discussed so far all have in common that the axial ligands used are anionic. To find out whether Cpd I species with a neutral ligand will also fit the trend, we did a further set of calculations using Cpd I($NCCH_3$) as an oxidant and overall charge 1+. As follows from Figure 8a, the barrier height of ^{2}**TS1**$_{NCCH3}$ does not fit the trend through the Cpd I series with anionic ligands. Corrections for RE_{Sub} and $RE_{Cpd\ I}$ have no effect and keep the deviation for the acetonitrile reaction. It appears that the gas-phase results are only applicable to oxidants with the same total charge. We then tested whether single point calculations in a dielectric constant would solve the problems and calculated BDE_{OH} values and barrier heights in a dielectric constant for the complete series of oxidants. As can be seen from Figure 8d, the solvent corrected BDE_{OH} values correlate excellently with solvent corrected aromatic hydroxylation barrier heights for all reaction mechanisms that include overall neutral and cationic oxidants. Therefore, a comparison of Cpd I species with neutral versus anionic axial ligand systems will require solvent corrections to all energies, i.e. BDEs as well as barrier heights. Moreover, these studies show that the differences in reaction kinetics of neutral versus cationic oxidants is not due to the electronic properties of the oxidant but is purely a solvent effect, where the cationic species are stabilized strongly.

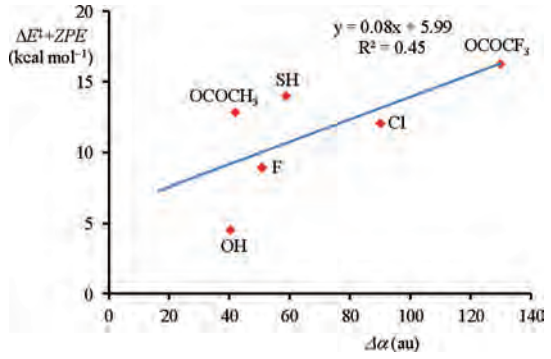

Figure 9. Correlation between aromatic hydroxylation barrier height and reaction polarizability for the low-spin reactions by Cpd I(X), X = OH^-, F^-, Cl^-, SH^-, acetate, and CF_3COO^-.

Recent studies of ours showed that reaction energies and barrier heights often correlate with a polarizability change for a reaction.[55] To find out whether that is also the case for the aromatic hydroxylation trends here, we calculated the polarizability trace from the Gaussian frequency calculations and converted this to a reaction polarizability ($\Delta\alpha_r$) using eq 7. Thus, the polarizability trace in the barrier height is calculated from the individual polarizabilities of the transition state structure, Cpd I, and the substrate. In eq 7, these variables are given as α_{TS}, $\alpha_{Cpd\ I}$, and α_{SubH}, respectively.

$$\Delta\alpha_r = \alpha_{TS} - \alpha_{Cpd\ I} - \alpha_{SubH} \quad (7)$$

Figure 9 displays the correlation between reaction polarizability ($\Delta\alpha_r$) and barrier height for the aromatic hydroxylation barriers on low-spin states. The correlation is not perfect, but a trend is seen that gives a low polarizability change for systems

Scheme 1. Thermodynamic Cycle Describing the Electron Transfer and Bond Formation Steps in the Electrophilic Addition Step in an Aromatic Hydroxylation Reaction by Cpd I(SH)

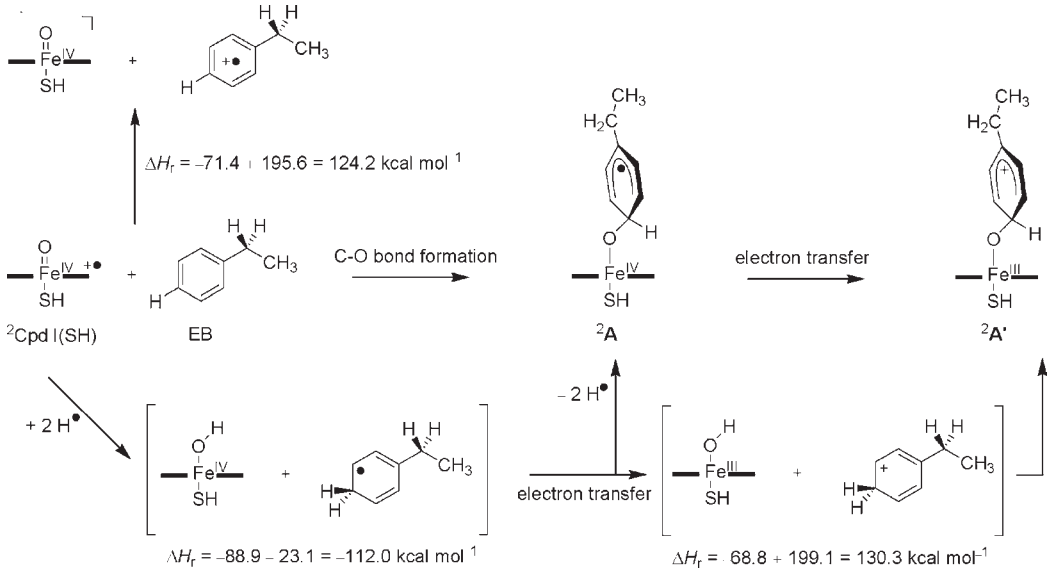

dx.doi.org/10.1021/jp2113522 |J. Phys. Chem. B 2012, 116, 718–730

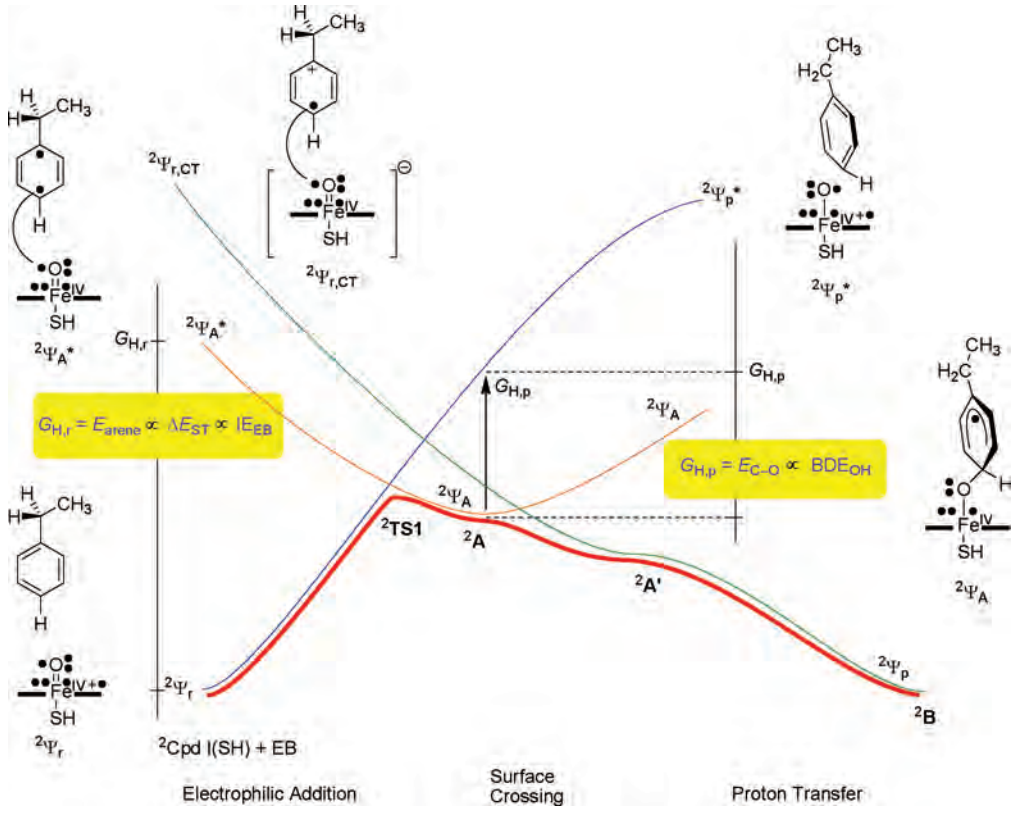

Figure 10. Valence bond curve crossing diagram for aromatic hydroxylation by ^{2}Cpd I(SH) via radical and cationic intermediates (^{2}**A**, ^{2}**A**′) leading to the proton transfer intermediate ^{2}**B**. The valence 2π and $3\pi^*$ orbitals are indicated with dots next to the Fe−O bond.

with low reaction barriers and a significantly larger barrier for systems that undergo a large change in polarizability.

Thus, the various thermodynamic correlations in Figures 8 and 9 show that the barrier height and consequently the rate constant of the aromatic hydroxylation reaction catalyzed by iron(IV)−oxo porphyrin cation radical oxidants is proportional to BDE_{OH} as well as to polarizability volume changes. So what is the origin of the correlation between barrier height and BDE_{OH} and why does the reaction pass a radical type **TS1** barrier? Previous studies[26−28] implicated mechanisms proceeding via a cationic intermediate, and hence our work seems to give a different reaction mechanism than that generally known.

In order to gain insight into the electron transfer processes in the initial stages of the reaction mechanism, we set up a thermodynamic cycle (Scheme 1) that explains the origins of electron and hydrogen atom transfer processes between ethylbenzene and Cpd I(SH). The scheme starts on the left with Cpd I(SH) and ethylbenzene (EB) as starting points and the reaction horizontal and to the right reflects the aromatic hydroxylation mechanism found above in Figure 5. An initial electrophilic addition step leads to the formation of a C−O bond and the transfer of one electron from the substrate into the half-filled a_{2u} orbital to give the radical complex ^{2}**A**. This complex converts into the cationic intermediate ^{2}**A**′ via a second electron transfer from substrate to oxidant. We calculated all individual electron, proton, and hydrogen atom transfers involved in the overall reaction mechanism. Thus, an electron transfer in isolated reactions gives the one-electron reduced form of Cpd I and ionized ethylbenzene with an endothermicity of 124.2 kcal mol^{-1} due to an endothermic ionization potential of ethylbenzene of 195.6 kcal mol^{-1} and an exothermic electron affinity of Cpd I of 71.4 kcal mol^{-1}. Solvent effects reduce the total electron transfer energy to 45.1 kcal mol^{-1} and additional thermal and entropic corrections give an electron transfer free energy of 45.3 kcal mol^{-1}. This large endothermicity for electron transfer, therefore, makes it unlikely that the reaction will be initiated by a single electron transfer.

To mimic the C−O bond formation step, we calculated the energy to add a hydrogen atom to both Cpd I(SH) and ethylbenzene to form ^{3}[Fe^{IV}(OH)(Por)(SH)] and ^{3}[EB + H]. This reaction will distort the geometries of Cpd I and EB into geometries that apart from the C−O bond resemble those of intermediate complex **A** with the same electronic configuration and orbital occupation. The hydrogen abstraction enthalpy of Cpd I, of course, is equal to $-BDE_{OH}$ by definition (eq 2). Both hydrogen atom abstraction processes are exothermic, namely, by 88.9 and 23.1 kcal mol^{-1}, respectively; hence, C−O bond formation should be the recommended process.

In a subsequent set of calculations, we calculate the electron affinity of ^{3}[Fe^{IV}(OH)(Por)(SH)] and the ionization potential of ^{2}[EB + H], which creates the two components that describe the cationic intermediate, namely, ^{4}[Fe^{III}(OH)(Por)(SH)]$^-$ and ^{1}[EB + H]$^+$. The reaction enthalpy is endothermic by a significant amount (+130.3 kcal mol^{-1}) mainly due to the large ionization potential of ^{2}[EB + H]. Corrections due to solvent, thermal, and entropic contributions reduce the overall reaction enthalpy to 49.0 kcal mol^{-1}. On the basis of this thermochemical analysis, we predict the aromatic hydroxylation to proceed with an initial electrophilic addition step leading to a radical intermediate. The second electron transfer will take place later in the mechanism in the direction of the proton-transfer intermediate **B**.

dx.doi.org/10.1021/jp2113522 |*J. Phys. Chem. B* 2012, 116, 718–730

Technically, there are two mechanisms from ^{2}**A** to ^{2}**B**: (1) directly via **TS2** and (2) through initial electron transfer from ^{2}**A** to ^{2}**A′** followed by relaxation toward ^{2}**B**. The barrier (^{2}**TS2**) leading to the proton transfer intermediate (^{2}**B**) from ^{2}**A** is relatively small (<1 kcal mol^{-1}) hence the electron transfer from ^{2}**A** to ^{2}**A′** may not be needed and ^{2}**A** will collapse to ^{2}**B** quickly and efficiently. Nevertheless, conversion of ^{2}**A** to ^{2}**A′** will also lead to ^{2}**B** products, hence whether or not conversion from a radical to cationic intermediate in **A** happens or not, it will not affect the overall rate constants and product distributions.

Recent studies of Shaik and co-workers[24] on the aromatic oxidation by Cpd I(SH) explained the observed trends with a valence bond (VB) curve crossing diagram. These studies, however, used only one oxidant and a series of substrates. In this work we generalized the reactivity trends further by varying also the oxidant while keeping the same substrate. That way we can expand the VB diagram of Shaik et al. into the more general form as shown in Figure 10. This valence bond curve crossing diagram has analogies to those reported before for hydrogen atom transfer and double bond epoxidation reactions and most recently also shown for aromatic hydroxylation by Cpd I(SH).[21−25,54,56]

Figure 10 starts on the bottom left-hand-side with the reactant complexes ^{2}Cpd I(SH) and ethylbenzene (EB), where Cpd I has the common $2\pi_{xz}^2\ 2\pi_{yz}^2\ 3\pi_{xz}^{*1}\ 3\pi_{yz}^{*1}\ a_{2u}^1$ configuration with reactant wave function $^2\Psi_r$. The figure is virtually independent of the axial ligand bound to Cpd I, although the relative energies may vary. In a VB curve crossing diagram, the reactant wave function connects to an excited state in the product geometry $^2\Psi_p$*. Thus, $^2\Psi_p$* has the electronic configuration of the reactants but the geometry of the products, whereas $^2\Psi_r$ has both reactant configuration and geometry. In our mechanism, however, the wave functions of reactant and products are crossed by several extra wave functions that represent the various intermediates along the reaction mechanism. The first of these is the radical intermediate (^{2}**A**) that is described by the electronic configuration $2\pi_{xz}^2\ 2\pi_{yz}^2\ 3\pi_{xz}^{*1}\ 3\pi_{yz}^{*1}\ a_{2u}^2\ \pi_{Ar3}^{*1}$ and wave function $^2\Psi_A$, which connects to the excited state $^2\Psi_A$* in the reactants geometry. The crossing of these two VB curves leads to an avoided crossing and a transition state for the electrophilic reaction mechanism (^{2}**TS1**).

In VB theory, one can describe the barrier heights from physical properties of the reactants and/or products. Thus, it was shown that the barrier height ($\Delta E^{\ddagger}$) that results from the crossing of two VB curves can be described (eq 8) as the difference of the curve crossing energy (ΔE_c) and the resonance energy B, so that the actual barrier is a factor B below the crossing point. It was further shown that the curve crossing energy is a fraction (f) of the excitation energy from the reactant to the product wave function in the reactant geometry, $G_{H,r}$.

$$\Delta E^{\ddagger} = \Delta E_c - B = fG_{H,r} - B \qquad (8)$$

In the case of aromatic hydroxylation leading to ^{2}**A** intermediates, the barrier height, therefore, is proportional to the excitation from $^2\Psi_r \rightarrow {}^2\Psi_A$*. The electron distributions of the VB structures on the left-hand-side of Figure 10 give the electronic differences between $^2\Psi_r$ and $^2\Psi_A$*, which determine $G_{H,r}$. For the electrophilic addition barrier leading to the radical intermediate, it follows that the height of **TS1**, therefore, is proportional to the excitation energy in the aromatic ring of the substrate (E_{arene}). The latter is proportional to the singlet−triplet energy (ΔE_{ST}) in that bond and, hence, the ionization energy of the substrate (IE_{EB}). Indeed DFT calculated barrier heights of aromatic hydroxylation by Cpd I(SH) were found to correlate linearly with the ionization potential of the substrate.[24]

In this work we varied the oxidant and used a single substrate. Because of this difference, the VB modeling of the axial ligand effect calculations discussed here will represent the reverse reaction process and hence we should consider the barrier height starting in ^{2}**A** in the direction of reactants. Equation 8 for the reverse reaction implies that the barrier height will be proportional to the excitation energy ($G_{H,p}$) for the excitation from the radical wave function ($^2\Psi_A$) to the reactant wave function in the geometry of the radical intermediate. As follows from the VB structure on the right-hand-side of Figure 10, the excitation $G_{H,p}$ involves a singlet−triplet excitation in the C−O bond plus an electron transfer from substrate into a_{2u}. The C−O bond formation can be modeled via the use of BDE_{OH};[29] hence, the VB curve crossing diagram confirms the correlation between the electrophilic addition steps in aromatic hydroxylation with BDE_{OH}, as indeed observed before for a range of Cpd I species with varying axial ligands.

Finally, the VB curve crossing diagram also gives the charge-transfer VB curve that ultimately leads to the proton-transfer intermediate ^{2}**B** and in reverse direction passes the cationic intermediate (^{2}**A′**) and ends up as a high-lying excited state in the reactants with wave function $^2\Psi_{r,CT}$. In the reactants geometry, this state reflects the electron transfer state or the long-range complex between reduced Cpd I and ionized ethylbenzene, [Fe^{IV}(O)(Por)(SH)- - -$EB^{+\bullet}$]. The wave function $^2\Psi_{r,CT}$ crosses $^2\Psi_A$ and converts the radical intermediate via the cationic intermediate into the proton transfer intermediate **B**. The Fe−O and O−C bond lengths of ^{2}**A** are in between those found for ^{2}**TS1** and ^{2}**A′** (see Figure 5 above); therefore, it seems most likely that the surface crossing from $^2\Psi_A$ to $^2\Psi_{r,CT}$ takes place after ^{2}**A** en route to the proton transfer intermediate. This is further supported by the charge and spin distributions of the various ^{2}**TS1** and ^{2}**A** structures, which are very similar (Supporting Information). Subsequently, ^{2}**A** can either convert into ^{2}**B** via the negligible barrier ^{2}**TS2** directly or via a surface crossing to the saddle point ^{2}**A′**, which also relaxes to ^{2}**B**. Energetically there is very little difference between these two options and none affect the rate constant of the reaction. The exact position of the surface crossing will depend on the nature of the oxidant and the substrate. Thus, in the case of benzene hydroxylation by Cpd I(SH), we showed that the surface crossing appears early in the reaction mechanism, where the charge-transfer transition state was below the radical transition state.[26a] However, with ethylbenzene as a substrate, the surface crossing appears to take place later in the reaction mechanism. Earlier DFT studies on aromatic hydroxylation of ethylbenzene by heme and nonheme iron(IV)−oxo complexes also found C−O activation barriers with a large radical contribution on the substrate.[26c,e,f]

The correlation between barrier heights of electrophilic addition, such as aromatic hydroxylation, with BDE_{OH} will have consequences on regioselectivity reactions. Thus, recent work of ours[22,29,54] showed that the barrier heights for hydrogen atom abstraction, double bond epoxidation, and sulfoxidation reactions by Cpd I(X) models all are proportional to BDE_{OH}. This implies that the barrier heights, and consequently rate constants, of hydrogen atom abstraction, double bond epoxidation, sulfoxidation, and aromatic hydroxylation all correlate with BDE_{OH} and as a result their regioselectivities should not be dependent on

the oxidant but only on the substrate. These correlations further imply that the regioselectivity of a chemical reaction as catalyzed by enzymatic metal−oxo systems can only be varied through changes in the substrate binding pocket and not through chemical modifications of the oxidant itself.

CONCLUSIONS

We have performed a systematic density functional theory study into the trans-influence of spectroscopic properties of Cpd I(X) species and the trans-effect on the kinetics and mechanism of aromatic hydroxylation reactions. Our studies show that the trans-influence is due to changes in the acidity of the oxidant due to the axial ligand. Surprisingly, the electronic effects appear to be lesser affected by the axial ligand and little changes in, for instance, the electron affinity of the oxidant is found. Furthermore, we investigated the aromatic hydroxylation of a model substrate (ethylbenzene) by these Cpd I(X) species. We show that the reaction barriers, and hence rate constants of the rate determining electrophilic addition step, are proportional to BDE_{OH}. These results enable one to predict barrier heights of aromatic hydroxylation reactions empirically. The reactivity patterns are rationalized with thermochemical cycles and a valence bond curve crossing diagram, which explain the mechanism observed and also give evidence to the reason behind the correlation of barrier height with BDE_{OH}. Thus, the reaction proceeds via a radical intermediate, which can interconvert into a cationic intermediate. The latter is a saddle point en route to the proton-transfer intermediate that is the precursor to the phenol product complex. We also show, for the first time, that trends through series of anionic and neutral axial ligands are linear when solvent corrected energies and BDEs are used, which enabled us to generalize reactivity patterns further. Consequently, the reactivity differences between neutral and cationic oxidants are solvent dependent and do not originate from electronic differences.

ASSOCIATED CONTENT

Supporting Information. Detailed supporting information including group spin densities, charges, and absolute and relative energies of all structures described in this work as well as Cartesian coordinates of all optimized geometries, and references 31b and 31c. This material is available free of charge via the Internet at http://pubs.acs.org.

AUTHOR INFORMATION

Corresponding Author

*E-mail: sam.devisser@manchester.ac.uk (S.P.d.V.); dkclcre@yahoo.com (D.K.).

ACKNOWLEDGMENT

The authors thank the National Service for Computational Chemistry Software (NSCCS) for CPU time. D.K. holds a Ramanujan Fellowship from the Department of Science and Technology (DST), New Delhi (India), and acknowledges its financial support (Research Grants SR/S2/RJN-11/2008 and SR/S1/PC-58/2009).

REFERENCES

(1) (a) Guengerich, F. P. *Chem. Res. Toxicol.* **2001**, *14*, 611–650. (b) Munro, A. W.; Girvan, H. M.; McLean, K. J. *Nat. Prod. Rep.* **2007**, *24*, 585–609.

(2) (a) Sono, M.; Roach, M. P.; Coulter, E. D.; Dawson, J. H. *Chem. Rev.* **1996**, *96*, 2841–2888. (b) Groves, J. T. *Proc. Natl. Acad. Sci. U.S.A.* **2003**, *100*, 3569–3574. (c) Ortiz de Montellano, P. R., Ed.; *Cytochrome P450: Structure, Mechanism and Biochemistry*, 3rd ed.; Kluwer Academic/Plenum Publishers: New York, 2004. (d) Kadish, K. M., Smith, K. M., Guilard, R., Eds.*Handbook of Porphyrin Science*; World Scientific Publishing Co.: Singapore, 2010. (e) Ortiz de Montellano, P. R. *Chem. Rev.* **2010**, *110*, 932–948. (f) de Visser, S. P., Kumar, D., Eds. *Iron-Containing Enzymes: Versatile Catalysts of Hydroxylation Reaction in Nature*; RSC Publishing: Cambridge, U.K., 2011.

(3) O'Reilly, E.; Köhler, V.; Flitch, S. L.; Turner, N. J. *Chem. Commun.* **2010**, *47*, 2490–2501.

(4) (a) Sarabia, S. F.; Zhu, B. T.; Kurosawa, T.; Tohma, M.; Liehr, J. G. *Chem. Res. Toxicol.* **1997**, *10*, 767–771. (b) Huang, Z.; Guengerich, F. P.; Kaminsky, L. S. *Carcinogenesis* **1998**, *19*, 867–872. (c) Lee, A. J.; Cai, M. X.; Thomas, P. E.; Conney, A. H.; Zhu, B. T. *Endocrinology* **2003**, *144*, 3382–3398.

(5) Guo, J.; Liu, D.; Nikolic, D.; Pezzuto, J. M.; Van Breemen, R. B. *Drug Metab. Dispos.* **2008**, *36*, 461–468.

(6) (a) Jonsson, J. *Acta Pharmacol. Toxicol.* **1977**, *40*, 517–528. (b) Carvalho, F.; Soares, M. E.; Fernandes, E.; Remião, F.; Carvalho, M.; Duarte, J. A.; Pires-das-Neves, R.; De Lourdes Pereira, M.; De Lourdes Bastos, M. *J. Health Sci.* **2007**, *53*, 371–377. (c) Hu, Y.; Dehal, S. S.; Hynd, G.; Jones, G. B.; Kupfer, D. *Xenobiotica* **2003**, *33*, 141–151.

(7) Narimatsu, S.; Tachibana, M.; Masubuchi, Y.; Imaoka, S.; Funae, Y.; Suzuki, T. *Biol. Pharm. Bull.* **1995**, *18*, 1060–1065.

(8) Herraiz, T.; Guillén, H.; Arán, V. J.; Idle, J. R.; Gonzalez, F. J. *Toxicol. Appl. Pharmacol.* **2006**, *216*, 387–398.

(9) Potter, G. A.; Patterson, L. H.; Wanogho, E.; Perry, P. J.; Butler, P. C.; Ijaz, T.; Ruparelia, K. C.; Lamb, J. H.; Farmer, P. B.; Stanley, L. A.; Burke, M. D. *Br. J. Cancer* **2002**, *86*, 774–778.

(10) Pfister, T. D.; Ohki, T.; Ueno, T.; Hara, I.; Adachi, S.; Makino, Y.; Ueyama, N.; Lu, Y.; Watanabe, Y. *J. Biol. Chem.* **2005**, *280*, 12858–12866.

(11) (a) Denisov, I. G.; Makris, T. M.; Sligar, S. G.; Schlichting, I. *Chem. Rev.* **2005**, *105*, 2253–2277. (b) Watanabe, Y.; Nakajima, H.; Ueno, T. *Acc. Chem. Res.* **2007**, *40*, 554–562. (c) Nam, W. *Acc. Chem. Res.* **2007**, *40*, 522–531.

(12) (a) Groves, J. T.; Shalyaev, K.; Lee, J. In *The Porphyrin Handbook*; Kadish, K. M., Smith, K. M., Guilard, R., Eds.; Academic Press: New York, 2000; Vol. 4, Chapter 27, pp 17−40. (b) Shaik, S.; Hirao, H.; Kumar, D. *Acc. Chem. Res.* **2007**, *40*, 532–542.

(13) (a) Egawa, T.; Shimada, H.; Ishimura, Y. *Biochem. Biophys. Res. Commun.* **1994**, *201*, 1464–1469. (b) Kellner, D. G.; Hung, S. C.; Weiss, K. E.; Sligar, S. G. *J. Biol. Chem.* **2002**, *277*, 9641–9644. (c) Hessenauer-Ilicheva, N.; Franke, A.; Meyer, D.; Woggon, W.-D.; van Eldik, R. *J. Am. Chem. Soc.* **2007**, *129*, 12473–12479. (d) Chiavarino, B.; Cipollini, R.; Crestoni, M. E.; Fornarini, S.; Lanucara, F.; Lapi, A. *J. Am. Chem. Soc.* **2008**, *130*, 3208–3217.

(14) (a) Green, M. T. *J. Am. Chem. Soc.* **1999**, *121*, 7939–7940. (b) Ogliaro, F.; de Visser, S. P.; Cohen, S.; Kaneti, J.; Shaik, S. *ChemBioChem.* **2001**, *11*, 848–851.

(15) Rittle, J.; Green, M. T. *Science* **2010**, *330*, 933–937.

(16) (a) Poulos, T. L.; Finzel, B. C.; Howard, A. J. *J. Mol. Biol.* **1987**, *195*, 687–700. (b) Raag, R.; Poulos, T. L. *Biochemistry* **1989**, *28*, 7586–7592. (c) Green, M. T.; Dawson, J. H.; Gray, H. B. *Science* **2004**, *304*, 1653–1656. (d) Schlichting, I.; Berendzen, J.; Chu, K.; Stock, A. M.; Maves, S. A.; Benson, D. E.; Sweet, R. M.; Ringe, D.; Petsko, G. A.; Sligar, S. G. *Science* **2000**, *287*, 1615–1622.

(17) (a) Dunford, H. B. *Heme Peroxidases*; Wiley-VCH: New York, 1999. (b) Poulos, T. L. Peroxidases and Cytochrome P450. In *The Porphyrin Handbook*; Kadish, K. M., Smith, K. M., Guilard, R., Eds.; Academic Press: San Diego, CA, 2000; Vol. 4, Chapter 32, pp 189−218. (c) Veitch, N. C.; Smith, A. T. *Adv. Inorg. Chem.* **2000**, *51*, 107–162.

(d) Gajhede, M. *The Handbook of Metalloproteins*; Messerschmidt, A., Huber, R., Poulos, T. L., Wieghardt, K., Eds.; Wiley: New York, 2001; Vol. 1, pp 195−210.

(18) Dawson, J. H.; Holm, R. H.; Trudell, J. R.; Barth, G.; Linder, R. E.; Bunnenberg, E.; Djerassi, C.; Tang, S. C. *J. Am. Chem. Soc.* **1976**, *98*, 3707–3709.

(19) (a) Gross, Z.; Nimri, S. *Inorg. Chem.* **1994**, *33*, 1731–1732. (b) Gross, Z. *J. Biol. Inorg. Chem.* **1996**, *1*, 368–371. (c) Czarnecki, K.; Nimri, S.; Gross, Z.; Proniewicz, L. M.; Kincaid, J. R. *J. Am. Chem. Soc.* **1996**, *118*, 2929–2935.

(20) (a) Sastri, C. V.; Park, M. J.; Ohta, T.; Jackson, T. A.; Stubna, A.; Seo, M. S.; Lee, J.; Kim, J.; Kitagawa, T.; Münck, E.; et al. *J. Am. Chem. Soc.* **2005**, *127*, 12494–12495. (b) Song, W. J.; Ryu, Y. O.; Song, R.; Nam, W. *J. Biol. Inorg. Chem.* **2005**, *10*, 294–304. (c) Sastri, C. V.; Lee, J.; Oh, K.; Lee, Y. J.; Lee, J.; Jackson, T. A.; Ray, K.; Hirao, H.; Shin, W.; Halfen, J. A.; Nam, W.; et al. *Proc. Natl. Acad. Sci. U.S.A.* **2007**, *104*, 19181–19186. (d) Hirao, H.; Que, L., Jr.; Nam, W.; Shaik, S. *Chem.—Eur. J.* **2008**, *14*, 1740–1756. (e) Jackson, T. A.; Rohde, J.-U.; Seo, M. S.; Sastri, C. V.; DeHont, R.; Stubna, A.; Ohta, T.; Kitagawa, T.; Münck, E.; Nam, W.; Que, L., Jr. *J. Am. Chem. Soc.* **2008**, *130*, 12394–12407. (f) Fukuzumi, S.; Kotani, H.; Suenobu, T.; Hong, S.; Lee, Y.-M.; Nam, W. *Chem.—Eur. J.* **2009**, *15*, 354–361. (g) Kang, Y.; Chen, H.; Jeong, Y. J.; Lai, W.; Bae, E. H.; Shaik, S.; Nam, W. *Chem.—Eur. J.* **2009**, *15*, 10039–10046.

(21) (a) Shaik, S.; Kumar, D.; de Visser, S. P. *J. Am. Chem. Soc.* **2008**, *130*, 10128–10140. (b) Shaik, S.; Lai, W.; Chen, H.; Wang, Y. *Acc. Chem. Res.* **2010**, *43*, 1154–1165.

(22) Kumar, D.; Karamzadeh, B.; Sastry, G. N.; de Visser, S. P. *J. Am. Chem. Soc.* **2010**, *132*, 7656–7667.

(23) Shaik, S.; Wang, Y.; Chen, H.; Song, J.; Meir, R. *Faraday Discuss.* **2010**, *145*, 49–70.

(24) Shaik, S.; Milko, P.; Schyman, P.; Usharani, D.; Chen, H. *J. Chem. Theory Comput.* **2011**, *7*, 327–339.

(25) (a) Jones, J. P.; Mysinger, M.; Korzekwa, K. R. *Drug Metab. Dispos.* **2002**, *30*, 7–12. (b) Dowers, T. S.; Rock, D. A.; Rock, D. A.; Perkins, B. N. S.; Jones, J. P. *Drug Metab. Dispos.* **2004**, *32*, 328–332. (c) Dowers, T. S.; Jones, J. P. *Drug Metab. Dispos.* **2006**, *34*, 1288–1290.

(26) (a) de Visser, S. P.; Shaik, S. *J. Am. Chem. Soc.* **2003**, *125*, 7413–7424. (b) Kumar, D.; de Visser, S. P.; Shaik, S. *Chem.—Eur. J.* **2005**, *11*, 2825–2835. (c) de Visser, S. P. *Chem.—Eur. J.* **2006**, *12*, 8168–8177. (d) Hazan, C.; Kumar, D.; de Visser, S. P.; Shaik, S. *Eur. J. Inorg. Chem.* **2007**, 2966–2974. (e) de Visser, S. P.; Tahsini, L.; Nam, W. *Chem.—Eur. J.* **2009**, *15*, 5577–5587. (f) de Visser, S. P.; Latifi, R.; Tahsini, L.; Nam, W. *Chem. Asian J.* **2011**, *6*, 493–504.

(27) (a) Bathelt, C. M.; Ridder, L.; Mulholland, A. J.; Harvey, J. N. *J. Am. Chem. Soc.* **2003**, *125*, 15004–15005. (b) Bathelt, C. M.; Ridder, L.; Mulholland, A. J.; Harvey, J. N. *Org. Biomol. Chem.* **2004**, *2*, 2998–3005. (c) Bathelt, C. M.; Mulholland, A. J.; Harvey, J. N. *J. Phys. Chem. A* **2008**, *112*, 13149–13156.

(28) Rydberg, P.; Ryde, U.; Olsen, L. *J. Phys. Chem. A* **2008**, *112*, 13058–13065.

(29) de Visser, S. P. *J. Am. Chem. Soc.* **2010**, *132*, 1087–1097.

(30) (a) Li, C.; Wu, W.; Kumar, D.; Shaik, S. *J. Am. Chem. Soc.* **2006**, *128*, 394–395. (b) Kumar, D.; Thiel, W.; de Visser, S. P. *J. Am. Chem. Soc.* **2011**, *133*, 3869–3882.

(31) (a) *Jaguar*, version 7.7; Schrodinger, LLC: New York, 2010. (b) Frisch, M. J. et al. *Gaussian 03*, revision C.01; Gaussian, Inc.: Wallingford, CT, 2004. (c) Frisch, M. J. et al. *Gaussian 09*; Gaussian, Inc.: Wallingford, CT, 2009.

(32) (a) Becke, A. D. *J. Chem. Phys.* **1993**, *98*, 5648–5652. (b) Lee, C.; Yang, W.; Parr, R. G. *Phys. Rev. B* **1988**, *37*, 785–789.

(33) (a) Hay, P. J.; Wadt, W. R. *J. Chem. Phys.* **1985**, *82*, 270–283. (b) Hehre, W. J.; Ditchfield, R.; Pople, J. A. *J. Chem. Phys.* **1972**, *56*, 2257–2261.

(34) Scott, A. P.; Radom, L. *J. Phys. Chem.* **1996**, *100*, 16502–16513.

(35) (a) Derat, E.; Kumar, D.; Hirao, H.; Shaik, S. *J. Am. Chem. Soc.* **2006**, *128*, 473–484. (b) de Visser, S. P.; Oh, K.; Han, A.-R.; Nam, W. *Inorg. Chem.* **2007**, *46*, 4632–4641.

(36) (a) Heyes, D. J.; Sakuma, M.; de Visser, S. P.; Scrutton, N. S. *J. Biol. Chem.* **2009**, *284*, 3762–3767. (b) Porro, C. S.; Kumar, D.; de Visser, S. P. *Phys. Chem. Chem. Phys.* **2009**, *11*, 10219–10226. (c) Karamzadeh, B.; Kumar, D.; Sastry, G. N.; de Visser, S. P. *J. Phys. Chem. A* **2010**, *114*, 13234–13243.

(37) (a) Handy, N. C.; Cohen, A. J. *Mol. Phys.* **2001**, *99*, 403–412. (b) Hoe, W.-M.; Cohen, A.; Handy, N. C. *Chem. Phys. Lett.* **2001**, *341*, 319–328. (c) Perdew, J. P.; Burke, K.; Ernzerhof, M. *Phys. Rev. Lett.* **1996**, *77*, 3865–3868.

(38) Reiher, M.; Salomon, O.; Hess, B. A. *Theor. Chem. Acc.* **2001**, *107*, 48–55.

(39) Kumar, D.; Tahsini, L.; de Visser, S. P.; Kang, H. Y.; Kim, S. J.; Nam, W. *J. Phys. Chem. A* **2009**, *113*, 11713–11722.

(40) Shaik, S.; Kumar, D.; de Visser, S. P.; Altun, A.; Thiel, W. *Chem. Rev.* **2005**, *105*, 2279–2328.

(41) de Visser, S. P.; Shaik, S.; Sharma, P. K.; Kumar, D.; Thiel, W. *J. Am. Chem. Soc.* **2003**, *125*, 15779–15788.

(42) (a) Poulos, T. L. *J. Biol. Inorg. Chem.* **1996**, *1*, 356–359. (b) Sigman, J. A.; Pond, A. E.; Dawson, J. H.; Lu, Y. *Biochemistry* **1999**, *38*, 11122–11129. (c) Suzuki, N.; Higuchi, T.; Urano, Y.; Kikuchi, K.; Uekusa, H.; Ohashi, Y.; Uchida, T.; Kitagawa, T.; Nagano, T. *J. Am. Chem. Soc.* **1999**, *121*, 11571–11572.

(43) Badger, R. M. *J. Chem. Phys.* **1935**, *3*, 710–714.

(44) Green, M. T. *J. Am. Chem. Soc.* **2006**, *128*, 1902–1906.

(45) (a) Schöneboom, J. C.; Lin, H.; Reuter, N.; Thiel, W.; Cohen, S.; Ogliaro, F.; Shaik, S. *J. Am. Chem. Soc.* **2002**, *124*, 8142–8151. (b) Bathelt, C. M.; Zurek, J.; Mulholland, A. J.; Harvey, J. N. *J. Am. Chem. Soc.* **2005**, *127*, 12900–12908.

(46) Siegbahn, P. E. M.; Borowski, T. *Acc. Chem. Res.* **2006**, *39*, 729–736.

(47) (a) Friedrich, L. E. *J. Org. Chem.* **1983**, *48*, 3851–3852. (b) Bordwell, F. G.; Cheng, J.-P. *J. Am. Chem. Soc.* **1991**, *113*, 1736–1743. (c) Bordwell, F. G.; Cheng, J.-P.; Ji, G.-Z.; Satish, A. V.; Zhang, X. *J. Am. Chem. Soc.* **1991**, *113*, 9790–9795.

(48) (a) Prokop, K. A.; de Visser, S. P.; Goldberg, D. P. *Angew. Chem., Int. Ed.* **2010**, *49*, 5091–5095. (b) Prokop, K. A.; Neu, H. M.; de Visser, S. P.; Goldberg, D. P. *J. Am. Chem. Soc.* **2011**, *133*, 15874–15877.

(49) Proshlyakov, D. A.; Henshaw, T. F.; Monterosso, G. R.; Ryle, M. J.; Hausinger, R. P. *J. Am. Chem. Soc.* **2004**, *126*, 1022–1023.

(50) Bassan, A.; Blomberg, M. R. A.; Siegbahn, P. E. M. *Chem.—Eur. J.* **2003**, *9*, 4055–4067.

(51) (a) Rydberg, P.; Sigfridsson, E.; Ryde, U. *J. Biol. Inorg. Chem.* **2004**, *9*, 203–223. (b) Kumar, D.; de Visser, S. P.; Sharma, P. K.; Derat, E.; Shaik, S. *J. Biol. Inorg. Chem.* **2005**, *10*, 181–189. (c) de Visser, S. P. *J. Biol. Inorg. Chem.* **2006**, *11*, 168–178. (d) de Visser, S. P. *J. Phys. Chem. B* **2006**, *110*, 20759–20761. (e) Wang, R.; de Visser, S. P. *J. Inorg. Biochem.* **2007**, *101*, 1464–1472.

(52) (a) Mayer, J. M. *Acc. Chem. Res.* **1998**, *31*, 441–450. (b) Mayer, J. M. *Annu. Rev. Phys. Chem.* **2004**, *55*, 363–390. (c) Mader, E. A.; Manner, V. W.; Markle, T. F.; Wu, A.; Franz, J. A.; Mayer, J. M. *J. Am. Chem. Soc.* **2009**, *131*, 4335–4345. (d) Kaizer, J.; Klinker, E. J.; Oh, N. Y.; Rohde, J.-U.; Song, W. J.; Stubna, A.; Kim, J.; Münck, E.; Nam, W.; Que, L., Jr. *J. Am. Chem. Soc.* **2004**, *126*, 472–473. (e) Yoon, J.; Wilson, S. A.; Jang, Y. K.; Seo, M. S.; Nehru, K.; Hedman, B.; Hodgson, K. O.; Bill, E.; Solomon, E. I.; Nam, W. *Angew. Chem., Int. Ed.* **2009**, *48*, 1257–1260. (f) Lansky, D. E.; Goldberg, D. P. *Inorg. Chem.* **2006**, *45*, 5119–5125. (g) Bell, S. R.; Groves, J. T. *J. Am. Chem. Soc.* **2009**, *131*, 9640–9641.

(53) (a) de Visser, S. P.; Kumar, D.; Cohen, S.; Shacham, R.; Shaik, S. *J. Am. Chem. Soc.* **2004**, *126*, 8362–8363. (b) Latifi, R.; Bagherzadeh, M.; de Visser, S. P. *Chem.—Eur. J.* **2009**, *15*, 6651–6662.

(54) Kumar, D.; Sastry, G. N.; de Visser, S. P. *Chem.—Eur. J.* **2011**, *17*, 6196–6205.

(55) (a) de Visser, S. P. *Phys. Chem. Chem. Phys.* **1999**, *1*, 749–753. (b) de Visser, S. P. *J. Phys. Chem. B* **2011**, *115*, 4709–4717. (c) de Visser, S. P. *Chem. Phys. Lett.* **2011**, *515*, 170–172.

(56) Shaik, S. *Phys. Chem. Chem. Phys.* **2010**, *12*, 8706–8720.

THE JOURNAL OF PHYSICAL CHEMISTRY A

ARTICLE

pubs.acs.org/JPCA

Mechanism of S-Oxygenation by a Cysteine Dioxygenase Model Complex

Devesh Kumar,[*,†,‡] G. Narahari Sastry,[†] David P. Goldberg,[*,§] and Sam P. de Visser[*,⊥]

[†]Molecular Modelling Group, Indian Institute of Chemical Technology, Hyderabad 500-607, India

[‡]Department of Applied Physics, School for Physical Sciences, Babasaheb Bhimrao Ambedkar University, Vidya Vihar, Rai Bareilly Road, Lucknow 226 025, India

[§]Department of Chemistry, Johns Hopkins University, 3400 North Charles Street, Baltimore, Maryland 21218, United States

[⊥]Manchester Interdisciplinary Biocenter and School of Chemical Engineering and Analytical Science, University of Manchester, 131 Princess Street, Manchester M1 7DN, United Kingdom

Supporting Information

ABSTRACT:

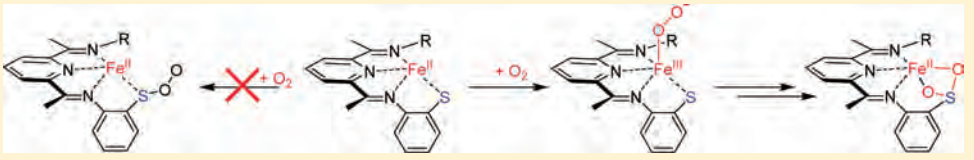

In this work, we present the first computational study on a biomimetic cysteine dioxygenase model complex, $[Fe^{II}(LN_3S)]^+$, in which LN_3S is a tetradentate ligand with a bis(imino)pyridyl scaffold and a pendant arylthiolate group. The reaction mechanism of sulfur dioxygenation with O_2 was examined by density functional theory (DFT) methods and compared with results obtained for cysteine dioxygenase. The reaction proceeds via multistate reactivity patterns on competing singlet, triplet, and quintet spin state surfaces. The reaction mechanism is analogous to that found for cysteine dioxygenase enzymes (Kumar, D.; Thiel, W.; de Visser, S. P. *J. Am. Chem. Soc.* **2011**, *133*, 3869−3882); hence, the computations indicate that this complex can closely mimic the enzymatic process. The catalytic mechanism starts from an iron(III)−superoxo complex and the attack of the terminal oxygen atom of the superoxo group on the sulfur atom of the ligand. Subsequently, the dioxygen bond breaks to form an iron(IV)−oxo complex with a bound sulfenato group. After reorganization, the second oxygen atom is transferred to the substrate to give a sulfinic acid product. An alternative mechanism involving the direct attack of dioxygen on the sulfur, without involving any iron−oxygen intermediates, was also examined. Importantly, a significant energetic preference for dioxygen coordinating to the iron center prior to attack at sulfur was discovered and serves to elucidate the function of the metal ion in the reaction process. The computational results are in good agreement with experimental observations, and the differences and similarities of the biomimetic complex and the enzymatic cysteine dioxygenase center are highlighted.

INTRODUCTION

Biosystems often utilize molecular oxygen on a transition metal center for the biotransformation of substrates. Two characteristic types of transition metal containing oxygenases have been identified—namely, the heme and nonheme oxygenases—that either transfer one oxygen atom of molecular oxygen to the substrate (monoxygenases) or both oxygen atoms (dioxygenases).[1,2] The heme enzymes include the—well studied—cytochrome P450 enzymes that are monoxygenases and mainly found in the liver, where they catalyze the metabolism of drugs and the biosynthesis of hormones.[1] By contrast, the nonheme iron dioxygenases take part in biocatalysis via oxygen-sensing mechanisms, reactions to hypoxia, and DNA and RNA base repair.[2,3] Essentially, both classes of oxygenases utilize molecular oxygen on a transition metal center and catalyze an oxygen atom transfer reaction to a substrate via a substrate hydroxylation (aromatic as well as aliphatic), epoxidation, or heteroatom oxidation.

A large group of nonheme iron dioxygenases uses α-ketoglutarate as a cosubstrate in the catalytic cycle and, therefore, are called the α-ketoglutarate dependent dioxygenases (αKDDs).[4] Structurally, the αKDDs have a characteristic active site where the metal is bound to the protein via a 2-His-1-Asp facial motif.[5] Figure 1a shows the active site of substrate-bound taurine/α-ketoglutarate dioxygenase (TauD) as taken from the 1OS7 protein databank file (pdb).[6] Substrate taurine is not bound to the iron center directly, but in its close vicinity, and held in position through a series of hydrogen bonding interactions; for instance, with Arg_{270} and His_{70}.

There are a small number of nonheme iron dioxygenases, however, that do not possess the 2-His-1-Asp facial ligand motif, but still catalyze a dioxygenation reaction.[7] One of these enzymes is cysteine dioxygenase (CDO), which is involved in the first step of the catalytic metabolism of cysteine in the body.[8] This is a vital process in our biosystem, since a decline in CDO activity has

Received: August 25, 2011
Revised: November 9, 2011
Published: November 18, 2011

ACS Publications © 2011 American Chemical Society

been associated with neurological disorders and can give rise to diseases such as Alzheimer's and Parkinson's.[9] Despite the important function of CDO in human health, there is surprisingly little known about the mechanism of action of this enzyme. A few single-crystal X-ray diffraction studies have provided important structural information on CDO, and a small number of spectroscopic measurements on the enzyme have been reported, but thus far, there has been no experimental observation of any mechanistic intermediates for the cysteine oxidation carried out by CDO enzymes.[10]

In contrast to other nonheme iron dioxygenases, such as TauD, the metal in CDO enzymes is locked in position through bonds with three histidine groups in a facial orientation (see Figure 1b), as taken from the 2IC1 pdb file.[11] Substrate cysteinate binds as a bidentate ligand to the iron center with the sulfide group trans to His_{88} and the amide group trans to His_{140}. The substrate is held in a tight binding pocket and forms a salt bridge between its carboxylic acid group and the side chain of Arg_{60}, but also forms hydrogen bonding interactions with Tyr_{157} and His_{155}. Note also the unusual covalent linkage between Tyr_{157} and Cys_{93}. The sixth ligand site (trans to His_{86}) is vacant in the pdb file and reserved for molecular oxygen.

To understand the catalytic mechanism of CDO enzymes and the effect of the 3-His ligand system on the reactivity patterns, a series of computational studies were performed.[12] In these calculations, it was found that the 3-His ligand system is essential for the dioxygenation process in CDO enzymes, since replacing one of the His ligands by Asp led to weakening of the Fe−S bond and less efficient dioxygenation as compared with wild-type enzyme. In this regard, the influence of a 3-His coordination environment versus the canonical 2-His-1-carboxylate motif is of broad interest.[13] Furthermore, the computational studies gave insight into the mechanism of dioxygen activation by CDO enzymes and the rate-determining step in the reaction mechanism.

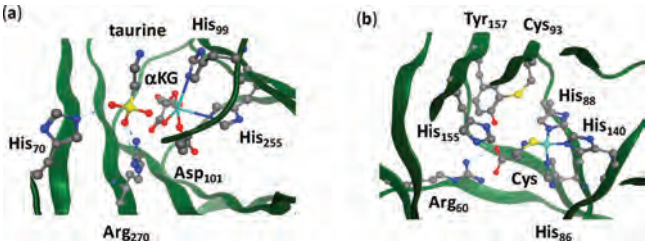

Figure 1. The active sites of TauD (panel a) and CDO (panel b) as taken from the 1OS7 and 2IC1 pdb files. Amino acids are labeled as in the pdb files.

Scheme 1 summarizes the computationally derived mechanism of dioxygen activation by CDO enzymes. It was shown that the reaction starts from an end-on Fe(III)−superoxo complex (**A**), where the distal oxygen atom (O_d) is hydrogen-bonded to the amide group of the cysteinate moiety. This distal oxygen atom subsequently attacks the sulfur atom of cysteinate to form a bicyclic ring structure (**B**) via a rate-determining S−O bond formation step. In structure **B**, the dioxygen bond is significantly weakened with considerable bond lengthening upon moving from **A** to **B** and breaks via a small barrier to form an Fe(IV)−oxo bound to cysteine sulfenate (**C**). In structure **C**, the sulfur atom is inaccessible to the second oxygen atom; hence, an internal rotation takes place to move the sulfenate into the trans position in structure **D**. Finally, the second oxygen atom is transferred to the substrate to form the cysteine sulfinic acid product (**E**). Computational modeling at the density functional theory (DFT) and quantum mechanics/molecular mechanics (QM/MM) levels of theory showed the reaction to proceed via multistate reactivity on close lying singlet, triplet, and quintet spin states. As such, CDO enzymes follow mechanisms that resemble heme and nonheme dioxygenases, which also show two-state-reactivity and multistate reactivity patterns.[14]

Another method to investigate the influence of structure and coordination environment on the mechanism of metalloenzymes is through the synthesis and study of synthetic analogs of their active sites.[15] Some of the best studied of these synthetic models are the iron porphyrins. High-valent iron-oxo porphyrins are postulated as the key intermediates in many heme enzymes, and many synthetic analogs of these intermediates have been generated through the addition of hydrogen peroxide or peracids to a reduced iron porphyrin precursor.[16] Examination of synthetic high-valent iron−oxo porphyrins has provided many important insights regarding structure and function. For example, the binding of variable axial ligands to iron(IV)−oxo porphyrin complexes helped establish a trans effect on reactivity patterns as well as a trans influence on spectroscopic parameters.[17] Reactivity patterns of systems with different axial ligands (neutral versus anionic) showed changes in the regioselectivity of aromatic versus aliphatic hydroxylation, reactivity patterns of cis versus trans olefins, and kinetic isotope effects for hydrogen atom abstraction reactions.[18] A trans influence of thiolate donors on nonheme Fe^{III}−OOR model complexes has also been described, providing evidence for a weakening of the Fe−O bond upon increasing thiolate electron donation.[19] These findings suggested a role for the unusual trans-ligated Cys

Scheme 1. Dioxygen Activation Mechanism of CDO Enzymes as Established by Computational Studies[12]

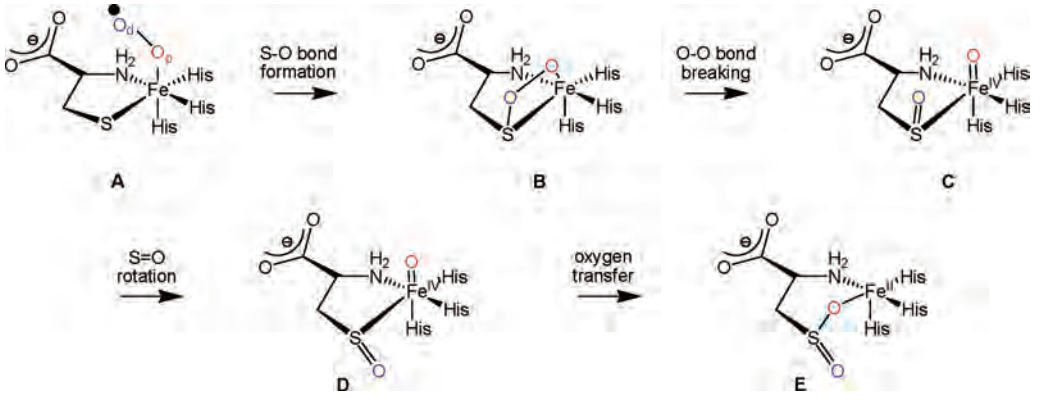

dx.doi.org/10.1021/jp208230g |J. Phys. Chem. A 2012, 116, 582–591

Scheme 2. Biomimetic Model of CDO

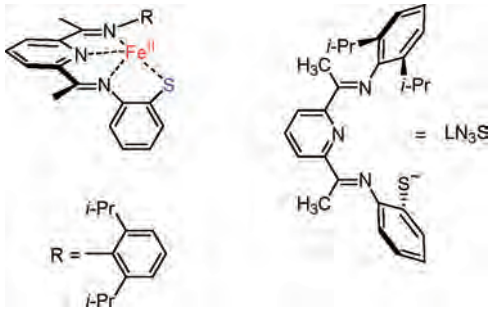

donor in the nonheme iron enzyme superoxide reductase.[20] These previous studies highlight the role that model complexes play in defining the fundamental influences of biomimetic ligands on the properties of biologically relevant metal centers.

Some of the first functional synthetic models of the active site of CDO have been reported by one of us, including the iron(II) model complex displayed in Scheme 2.[21] The CDO biomimetic model contains a bis(imino)pyridine ligand with a pendant thiolate group (LN_3S), which binds iron as a tetradentate ligand through the three nitrogen atoms and the thiolate group. Reaction of this complex with excess dioxygen affords a product in which the thiolate donor has been oxygenated to give a terminal $-SO_3^-$ (sulfonato) group. Studies involving the use of ^{18}O isotopically labeled dioxygen revealed that all three oxygen atoms of the sulfonato product originate from O_2, as opposed to H_2O, and mixed $^{18}O_2/^{16}O_2$ experiments indicated that two oxygens in the $-SO_3^-$ group derive from one molecule of O_2. A reasonable mechanistic hypothesis for S-oxygenation in the model complex involves dioxygenation of the sulfur atom, similar to the enzyme, followed by a second monoxygenation event. However, what the mechanism of dioxygen activation is, and whether it is analogous to CDO enzymes, remain open questions that are ripe for computational analysis.

The selective S-oxygenation of sulfur-bound metal complexes with O_2 as oxidant is a relatively rare process, although several biomimetic Ni(II) complexes were found to perform this process efficiently.[22] There are also a few examples of Ru(II) and Fe(III) thiolates reacting with O_2 to give S-oxygenated products.[23,24] Although not much mechanistic information is available for the former complexes, it is possible that these complexes proceed through a mechanism similar to that postulated for the Ni(II) thiolates, in which the coordinated S atom functions as a nucleophile for direct attack on O_2. In this scenario, S-oxygenation does not involve O_2 activation at the metal in a redox process. Alternatively, a related possible mechanism for S-oxygenation could be similar to the mechanism proposed for extradiol dioxygenases, in which the nonheme iron center serves to activate the bound substrate toward a coordinated O_2 molecule, but there are no formal redox state changes at Fe to activate O_2.[25] Thus, one or more of these mechanisms are possible for both CDO and the synthetic analog in Scheme 2. The question of whether an Fe(III)−superoxo species is formed prior to S-oxygenation is a question of fundamental importance to both CDO and related model complexes.

To establish a reaction mechanism of dioxygen transfer to the iron(II) model complex in Scheme 2 as well as the S-oxygenation process of the LN_3S ligand, we decided to do a series of density functional theory calculations and specifically focus on the difference between a reaction starting from an iron(III)−superoxo complex and one in which molecular oxygen directly reacts with the thiolate ligand. We then compare the obtained results with those recently published on CDO enzymes, nonheme iron dioxygenases, and biomimetic model complexes.

METHODS

Following previous experience in the field,[26] we use density functional theory studies on the biomimetic model of CDO as displayed in Scheme 2. The calculations were performed with the Jaguar and Gaussian program packages.[27] The unrestricted hybrid density functional method B3LYP was selected,[28] since previous studies of ours showed that this method gives rate constants within 2−3 kcal mol^{-1} from experiment.[29] Moreover, QM/MM studies using a series of density functional methods describing the QM region showed that B3LYP gives results close in energy to other methods tested.[12c] Furthermore, the use of methods and techniques similar to those in ref 12 enables us to make a direct comparison between the performance of the biomimetic model studied here and the enzymatic system.

Initial geometry optimizations were performed with a Los Alamos-type LACVP basis set on iron that contains a core potential, whereas the rest of the atoms are described with 6-31G, basis set BS1.[30] Subsequent single-point calculations utilize the LACV3P+ basis set on iron that includes a core potential and 6-311+G* on the rest of the atoms; basis set BS2. Previous studies of ours showed that this combination of methods gives reliable geometries and energetics that are within a few tenths of a kilocalories per mole of those obtained after a full geometry optimization at UB3LYP/BS2.[31] Relative energies reported here were obtained with basis set BS2 and corrected for zero-point energy from the Gaussian frequency calculations. Free energies contain UB3LYP/BS1 zero-point, thermal, and entropy calculated corrections at 298 K and use UB3LYP/BS2 energies.

All structures were subjected to a full geometry optimization without constraints and followed by an analytical frequency calculation at the same level of theory. To establish a reaction mechanism between the various local minima, first we performed extensive geometry scans whereby one degree of freedom (the reaction coordinate) was frozen and all other degrees of freedom were fully optimized. These geometry scans established pathways between the various local minima, and the maxima of these scans were used as starting points for the transition state geometry searches. The effect of the environment was tested through single-point calculations in a dielectric constant of $\varepsilon = 5.7$, mimicking a chlorobenzene solution using the Poisson−Boltzmann solvation model as implemented in Jaguar 7.7.

RESULTS AND DISCUSSION

Iron(III)−Superoxo Species in Biomimetic and Enzymatic CDO Complexes. Following previous experience in the field,[12] we started the dioxygenation studies from an iron(III)−superoxo complex shown in Figure 2. This complex was generated from the crystal structure coordinates of $[Fe^{II}(LN_3S)(OTf)]$ reported in ref 21a, whereby the *iso*-propyl groups were replaced by hydrogen atoms to help facilitate the computations. Mass spectrometric analysis of the product distributions identified $[Fe^{II}(LN_3SO_2)]^+$ products, although it reacted over time to the triply oxygenated product, probably in reaction with a second molecule of O_2. The CDO enzymes contain an active site where there is a neutral

dx.doi.org/10.1021/jp208230g |*J. Phys. Chem. A* 2012, 116, 582–591

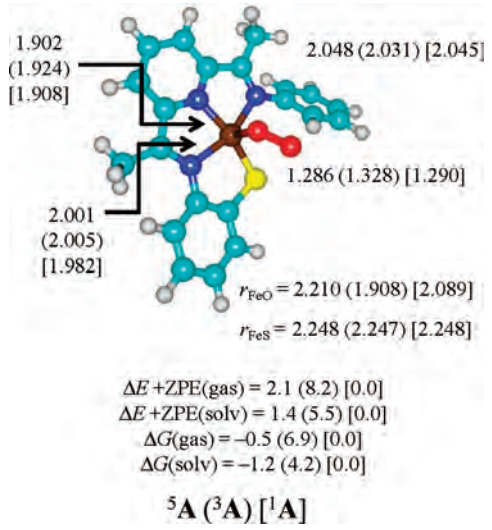

Figure 2. Optimized UB3LYP/BS1 geometries of ^{1,3,5}**A** with bond lengths in angstroms. Also given are relative energies in the gas phase and relative free energies with values in kilocalories per mole.

histidine group trans to the dioxygen binding site on the metal, and therefore, we decided to remove the triflate anion and replace it with molecular oxygen. Computational studies of the axial ligand effect of hydrogen atom abstraction versus aromatic hydroxylation by iron(IV)−oxo complexes with axial acetonitrile versus chloride showed dramatic differences due to the charge of the axial ligand, that is, neutral versus anionic axial ligands.[32] With triflate removed, our computational model shows close similarity to the active site of CDO enzymes. These coordinates were optimized and resulted in a structure that showed little deviation from the crystal structure.

Optimized geometries of the Fe(III)−superoxo complexes (^{1,3,5}**A**) in the lowest lying singlet, triplet and quintet spin states are shown in Figure 2. The structures are characteristic of an iron(III)−superoxo complex in which the superoxo group is bound in an end-on fashion. The bond lengths obtained are similar to those calculated for iron(III)−superoxo complexes in heme and nonheme environments.[14a,33] Crystallographic data on enzymatic, end-on, ferric−superoxo complexes gave Fe−O and O−O distances of ∼2.06 and 1.22 Å, respectively, which are values close to those given in Figure 2.[34] Relative energies give close-lying singlet, triplet, and quintet spin state structures, in which the spin state ordering varies with the method chosen. Gas-phase relative energies give the singlet spin state below the quintet by ∼2.1 kcal mol^{-1}, but free energy and solvent corrections reverse this and make the quintet spin state the ground state by 1.2 kcal mol^{-1}. No experimental data are available on the iron(III)−superoxo complex; however, the Fe(II) complex without O_2 is in a quintet spin state,[21a] which makes it likely that the Fe(III)−superoxo complex should be in a high-spin state, too. Nevertheless, it is clear that the iron(III)−superoxo species exists in close-lying spin states and, therefore, will react via multistate reactivity patterns.

The spin-state ordering and relative energies for ^{1,3,5}**A** found here is considerably different from that reported before for the CDO enzyme active site derived from either DFT methods or QM/MM. To understand these differences, let us analyze the orbital differences in more detail: Figure 3 shows the high-lying occupied and low-lying virtual orbitals for ^{5}**A** as an example of the orbital shapes. The other spin states have similar molecular orbitals, but the only difference is their occupation. The molecular orbitals displayed in Figure 3 originate from the metal 3d orbitals and the interactions they undergo with the 2p orbitals on the superoxo group and the nitrogen and sulfur atoms of the LN_3S ligand and consist of six π^* type and three σ^* type orbitals, which we label as $\pi_1^*-\pi_6^*$ and $\sigma_1^*-\sigma_3^*$. The lowest-lying molecular orbital with metal 3d contribution is the doubly occupied π_1^* (π_{xy}^*) orbital that consists of the $3d_{xy}$ orbital on Fe in interaction with a 3p orbital on sulfur. Another doubly occupied orbital is the σ_{z2} + $\pi_{OO,yz}^*$ mixed orbital that has the bonding combination of the out-of-plane $3d_{z2}$ orbital with the antibonding π_{OO}^* orbital along the yz axis: σ_1^*. The antibonding combination of this orbital, labeled as σ_2^*, is singly occupied and has a dominant $3d_{z2}$ component on the metal. The metal $3d_{xz}$ and $3d_{yz}$ atomic orbitals form bonding and antibonding combinations with the $\pi_{OO,xz}^*$ and $\pi_{OO,yz}^*$ orbitals on the superoxo group, respectively. Along the yz axis, there is one pair of $\pi_{yz}^* \pm \pi_{OO,yz}^*$; the positive combination (π_3^*) is singly occupied, and the negative one (π_5^*) is a virtual orbital. By contrast, along the xz axis, there are three possible combinations: namely, bonding (π_2^*), nonbonding (π_4^*), and antibonding (π_6^*). The bonding combination ($\pi_{xz}^* + \pi_{OO,xz}^*$) and the nonbonding $\pi_{OO,xz}^*$ orbitals are singly occupied in the quintet spin state, and the antibonding $\pi_{xz}^*-\pi_{OO,xz}^*$ is virtual. Finally, high-lying and virtual is the σ_{x2-y2}^* orbital for the antibonding interactions of the metal with the four ligand atoms in the xy plane (σ_3^*). These sets of orbitals have an occupation of $\pi_1^{*2}\sigma_1^{*2}\sigma_2^{*1}\pi_2^{*1}\pi_3^{*1}\pi_4^{*1}$ for ^{5}**A**, whereas ^{3}**A** has an occupation of $\pi_1^{*2}\sigma_1^{*2}\pi_2^{*2}\pi_3^{*1}\pi_4^{*1}$, and ^{1}**A** has an occupation of $\pi_1^{*2}\sigma_1^{*2}\sigma_2^{*\uparrow}\pi_2^{*\downarrow}\pi_3^{*\uparrow}\pi_4^{*\downarrow}$. Double occupation of π_2^* in the triplet spin state leads to enhanced bonding between the metal and oxygen atom and considerable shortening of the Fe−O bond with respect to the singlet and quintet spin state structures.

As follows from the orbital diagrams in Figure 3, the $3d_{xz}$ and $3d_{yz}$ atomic orbitals on Fe mix with orbitals on the π system on the LN_3S ligand and the π^*_{OO} orbitals to create a series of mixed orbitals, for example, $\pi_2^*-\pi_6^*$. As a consequence of this, the orbital energy levels in our biomimetic CDO model are very different from those found for the enzymatic system. Note, for instance, that in CDO enzymes, the ligands in the xy-plane are histidine amino acids, but their aromatic rings are not aligned with the xy plane; instead, they are perpendicular to it. Consequently, the iron(III)−superoxo species in CDO enzymes has a singlet spin ground state that is well separated from the quintet spin state by more than 10 kcal mol^{-1},[12c] whereas in the biomimetic system, the singlet and quintet spin states are close in energy. This will also affect the subsequent oxygen atom transfer processes, as will be shown later.

Reaction Mechanism of S-Oxygenation. Next, we investigated the dioxygenation of the thiolate group of the LN_3S ligand according to the mechanism found for CDO enzymes (Scheme 1), and the results are shown in Figure 4. The reaction starts from the iron(III)−superoxo complexes (^{1,3,5}**A**) with the attack of the distal oxygen atom on the sulfur atom to form a bicyclic ring structure (^{1,3,5}**B**) via an S−O bond formation barrier (^{1,3,5}**TS1**). In the bicyclic structure, the dioxygen bond is weakened and breaks via a barrier, ^{1,3,5}**TS2**, to form a sulfenate bound to an iron(IV)−oxo moiety (^{1,3,5}**C**). Thereafter, the sulfenate group undergoes an internal rotation to form the isomeric structure ^{1,3,5}**D** via a barrier, ^{1,3,5}**TS3**. In a final step, the second oxygen atom is transferred via a transition state, ^{1,3,5}**TS4**, to give the sulfinic acid product complex (^{1,3,5}**E**).

Although the singlet spin state is low in energy for the iron(III)−superoxo complex, it actually has little effect on the reaction

dx.doi.org/10.1021/jp208230g |J. Phys. Chem. A 2012, 116, 582–591

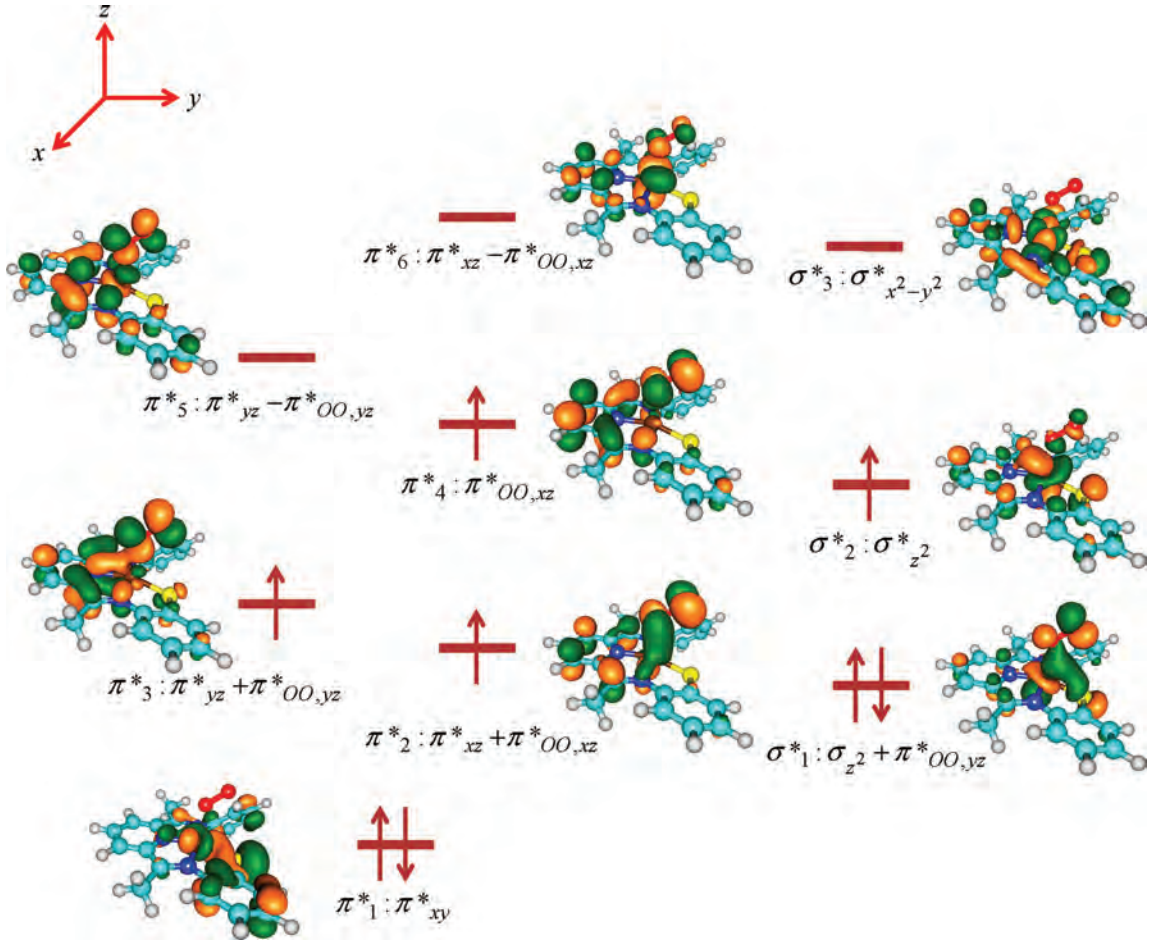

Figure 3. High-lying occupied and low-lying virtual orbitals of ^{5}**A** as calculated with DFT methods. Orbital diagrams are taken from the β set of molecular orbitals.

mechanism due to the fact that ^{1}**TS1** and ^{1}**TS2** barriers are very high in energy, that is, well over 25 kcal mol^{-1}. As a matter of fact, the complete singlet spin potential energy surface beyond ^{1}**TS1** is at least 10 kcal mol^{-1} above the lowest-lying spin state surface, which means that the singlet spin state will contribute very little to the overall reaction mechanism.

At the free energy level, the quintet spin iron(III)−superoxo complex is the ground state. Similar to gas-phase DFT studies on CDO enzymes,[12a] the S−O bond formation barrier (**TS1**) is also the lowest on the quintet spin state surface. As follows from Figure 4 at the free energy level, the mechanism starting from the iron(III)−superoxo complex until the iron(IV)−sulfenate complex will take place on a dominant quintet spin state surface only. The nearest other spin state is at least 7 kcal mol^{-1} higher in energy in the mechanism leading up to the iron(IV)−sulfenate complex (**C**), but the triplet and quintet spin states converge in this point, and ^{3,5}**C** are energetically close, with a small preference for the triplet spin state. As shown before, biomimetic nonheme iron(IV)−oxo complexes have a triplet spin ground state,[35] which contrasts with the situation for enzymatic nonheme iron(IV)−oxo complexes that have been characterized as high-spin states.[36] Computational studies explained this difference through differences in orbital interactions of the π^*_{xy} and σ^*_{x2-y2} molecular orbitals that change their relative energy and thereby affect the triplet−quintet energy splitting and ordering.[37]

The rotational barrier from ^{3,5}**C** to reach ^{3,5}**D** (i.e. ^{3,5}**TS3**) is relatively small; therefore, the system will interconvert to **D** rapidly. The final oxygen atom transfer via barrier **TS4** is large on the quintet spin state but much smaller on the triplet spin state surface, although it is not the highest barrier. The rate-determining step in the CDO biomimetic reaction mechanism is the process passing **TS2**, which has a free energy of activation of 22 kcal mol^{-1} relative to reactant complexes on the quintet spin state surface. This contrasts the mechanisms found for CDO enzymes in which the step passing **TS1** was found to be rate-determining.[12]

Optimized geometries of the local minima along the reaction mechanism are displayed in Figure 5, and the optimized transition state structures are given in Figure 6. Optimized geometries are in line with previous DFT and QM/MM studies on the catalytic mechanism of dioxygen transfer from the iron center in the enzyme to cysteinate substrate. As discussed above, the reaction starts from an iron(III)−superoxo structure that is in close-lying singlet and quintet spin states, with the latter slightly lower in energy. Attack of the terminal oxygen atom of the superoxo group on the thiolate sulfur creates an O−S bond and forms the ring structure **B**. In these structures, the superoxo O−O bond is weakened, elongating from 1.286 to 1.328 Å in ^{1,3,5}**A** to a distance near 1.5 Å in ^{1,3,5}**B**, which is consistent with a formal single bond. At the same time, the Fe−S bond is weakened from 2.248 Å in ^{1,3,5}**A** to 2.359 Å in ^{1}**B** and 2.613 Å in ^{5}**B**. In the quintet spin state,

dx.doi.org/10.1021/jp208230g |*J. Phys. Chem. A* 2012, 116, 582–591

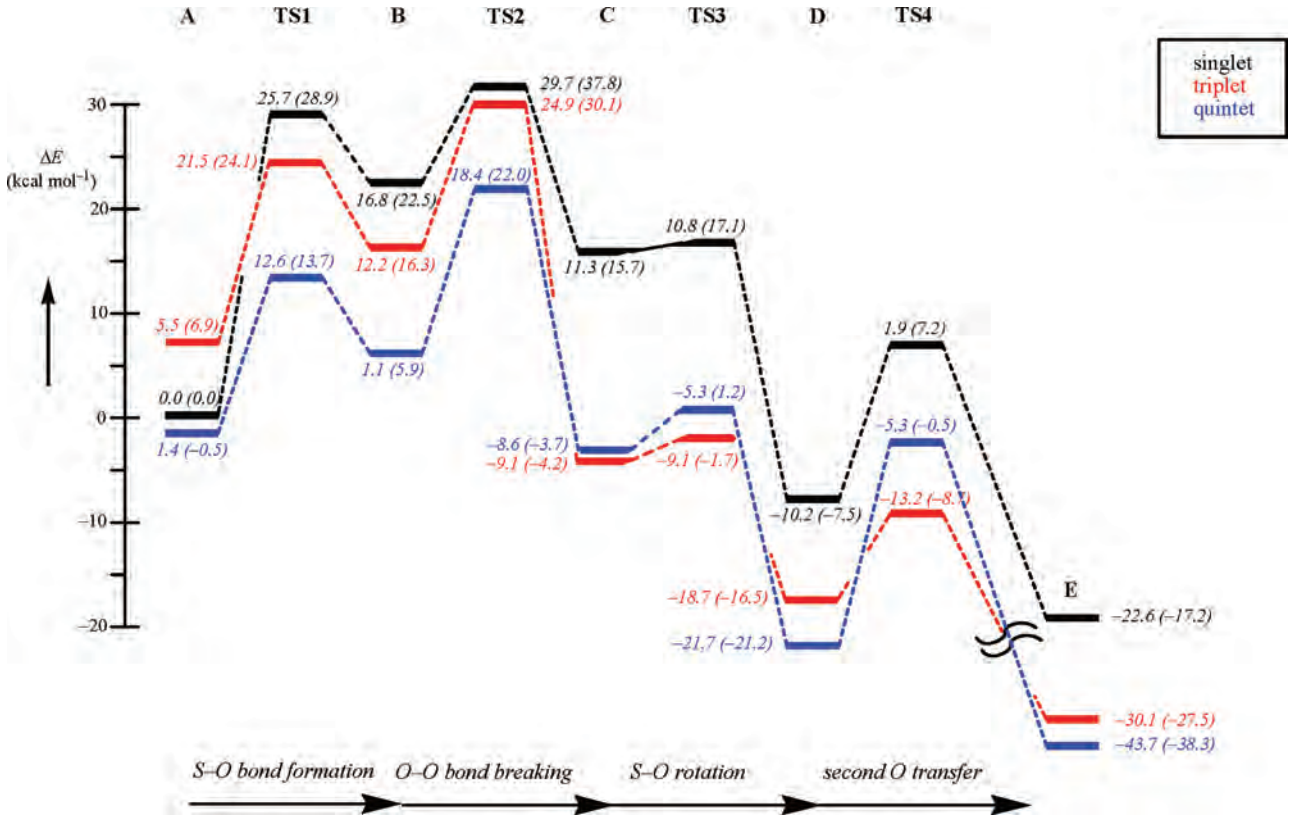

Figure 4. Potential energy profile of oxygen transfer to the thiolate group of the LN_3S ligand starting from the $[Fe^{III}(LN_3S)O_2]^+$ complex. All energies are in kilocalories per mole relative to ^{1}**A**. Out of parentheses are ΔE + ZPE + E_{solv} values, and in parentheses are free energies. The latter include entropic and thermal corrections at 298 K.

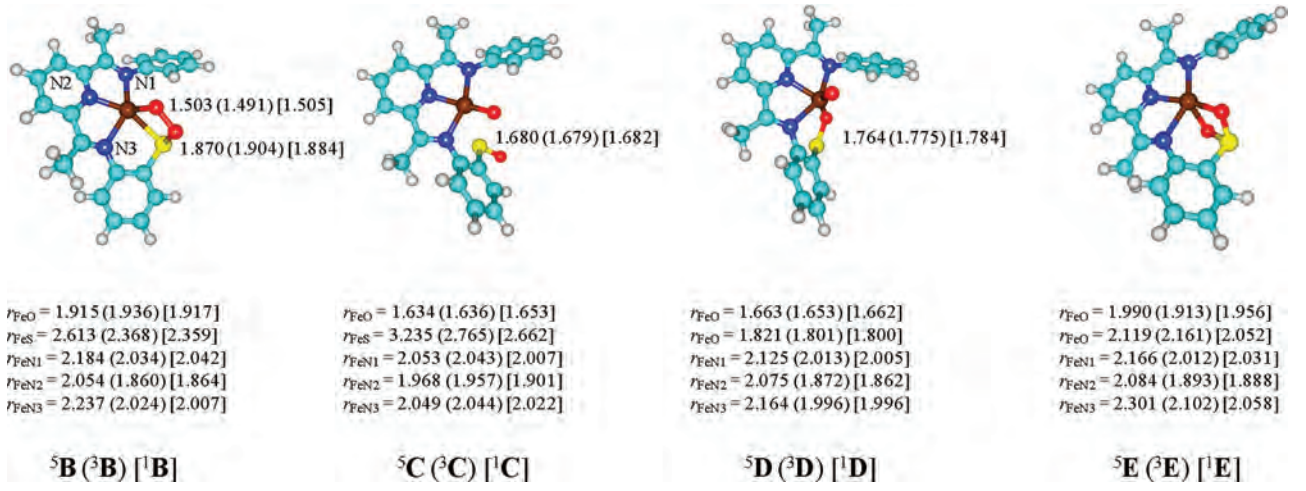

Figure 5. Optimized UB3LYP/BS1 geometries of the critical points from Figure 3 with bond lengths in angstroms. Optimized geometries of ^{5,3,1}**A** are given above in Figure 2.

there is also a certain degree of bond lengthening among the metal and the three bound nitrogen atoms. Because of the weakening of the superoxide O−O bond, it costs relatively little extra energy to break it and form the iron(IV)−oxo with a sulfenate ligand, structure **C**. In this structure, the iron−sulfur bond is weakened further, and in particular, in the quintet spin state, it has dissociated (Fe−S distance of 3.235 Å in ^{5}**C**). Subsequently, the oxygen atom of the sulfenate binds to the metal to form structures **D** followed by the final oxygen atom transfer to form products, **E**.

The transition state structures are analogous to those found for CDO enzymes.[12] The O−O bond lengthens in **TS1** to a value ranging from 1.421 to 1.432 Å. The imaginary frequency in the transition state represents the S−O stretch vibration and is characteristic for an S−O bond formation step. In **TS2**, the O−O bond is further elongated, and the imaginary frequency shows an

dx.doi.org/10.1021/jp208230g |*J. Phys. Chem. A* 2012, 116, 582–591

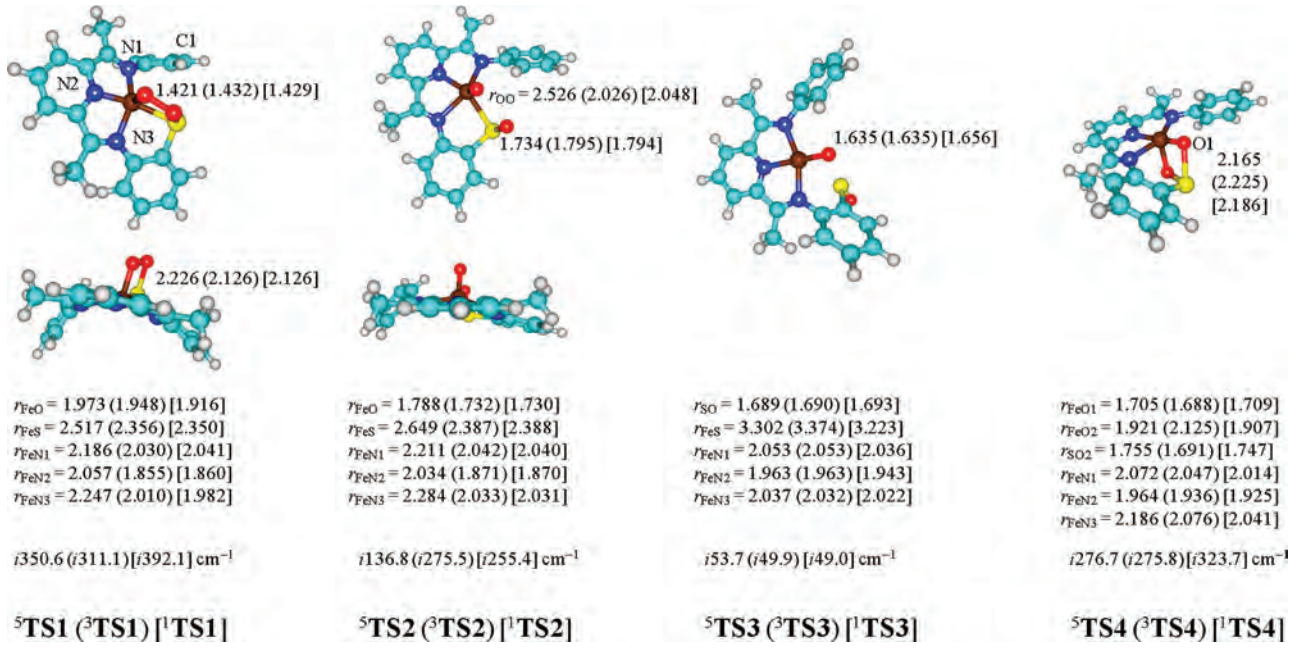

Figure 6. Optimized UB3LYP/BS1 geometries of the transition states from Figure 4. Bond lengths are in angstroms, and the imaginary frequency in the transition state, in wave numbers.

O−O stretch vibration that represents the O−O dissociation step in the reaction mechanism. Note also that some saddling in the LN_3S ligand structure has taken place in **TS1**, although the saddling is lost in **TS2** and onward. If we define a dihedral angle through the three nitrogen atoms of the LN_3S ring and the para carbon atom of the R group (C1−N1−N3−N2) in Figure 6, we find a saddling of −165.7° in ^{3}**TS1**, −169.9° in ^{1}**TS1**, and −175.3° in ^{5}**TS1**, which implicates deviations from planarity of 14.3, 10.1, and 4.7°, respectively. Consequently, the orbital occupation in the triplet spin state with shortened Fe−O distances causes structural distortion and saddling.

Thus, the calculations predict that the iron center of the model complex functions to coordinate and activate O_2 toward O−O bond cleavage and oxygen transfer to the thiolate group. They also show that O-atom transfer to the thiolate S atom is relatively facile, providing a smooth mechanism for S-oxygenation. The computed mechanism predicts a dioxygenase type mechanism wherein two oxygen atoms in the final product are derived from one molecule of O_2, which is nicely consistent with experimental evidence from $^{18}O_2$ isotope-labeling mass spectrometry studies. It may further be anticipated that the third oxygen atom transfer to form the $-SO_3$ complex will proceed after binding a second molecule of molecular oxygen and a subsequent monoxygenation step of the sulfinic acid intermediate.

Comparison between CDO Enzyme and the Biomimetic Model. No experimental data on wild-type CDO or biomimetic model complexes exists after dioxygen binding so that a comparison of the obtained results with experiment is not possible; therefore, we will compare the work with previous computations in the field. At a first glance, the obtained results of the synthetic model seem to give considerable differences as compared with DFT and QM/MM studies on the CDO enzyme, which we will compare in detail in the following. Table 1 gives relative energies of the dioxygen transfer process in $[Fe^{III}(LN_3S)O_2]^+$ as described in this work as compared with two published sets of calculations on CDO enzymes: the first uses a DFT model complex of 81 atoms from ref 12a, whereas the second is the result of the full QM/MM calculation reported in ref 12c. The calculations on $[Fe^{III}(LN_3S)O_2]^+$ and the CDO model complex use the same methods and techniques and energetics, including ZPE and solvent corrections. As can be seen from Table 1, the obtained potential energy landscape for these two chemical systems is very similar, with some minor deviations we will discuss below. On the basis of the energetic profile, therefore, it appears that the $[Fe^{III}(LN_3S)O_2]^+$ is a good model of CDO enzymes. At this level of theory, the singlet spin state is the ground state of the iron-superoxo complex, but as discussed above, at the free energy level, the quintet spin state becomes the ground state. This lowering of the quintet spin state surface in the Fe(III)−superoxo reactant has further consequences for the overall kinetics of the reaction. Thus, in the enzymatic system using DFT model complexes, a rate-determining ^{5}**TS1** barrier was found, and all subsequent barriers were found to be smaller than their precursors: ^{5}**TS1** > ^{5}**TS2** > ^{5}**TS3** > ^{5}**TS4**. Lowering of the energy of ^{5}**A** in the synthetic model leads to a lowering of the energy in ^{5}**TS1**. Accordingly, the biomimetic CDO model complex has a rate-determining step via ^{5}**TS2**, whereas the enzymatic DFT model has a rate-determining ^{5}**TS1** step. These differences in barriers should lead to different kinetic behavior for these two systems. The rest of the mechanism is very much alike for the biomimetic and CDO model complexes, apart from a relatively high ^{5}**TS4** barrier in the biomimetic model system.

On the singlet spin potential energy surface, the deviation between the biomimetic and enzymatic model complexes is <5.7 kcal mol^{-1} for all structures. This is also the case for the triplet spin state surface until ^{3}**TS3**; beyond this point, significant deviations occur between the enzymatic and biomimetic model complexes, and the biomimetic ^{3}**D** and ^{3}**TS4** structures are stabilized considerably. It should be noted, however, that the actual barrier from ^{3}**D** to ^{3}**TS4** is similar in energy to that found in the enzymatic calculations. Hence, this affects only the driving force for ^{3}**D** to ^{3}**E**, not the kinetics.

The differences between the QM/MM studies on CDO enzymes and the biomimetic model system are more pronounced and require further elaboration. As mentioned above, the quintet spin state of the iron(III)−superoxo structure is significantly higher in energy in the QM/MM studies than in either DFT model complexes. This is not only due to destabilization of the quintet but also a result of stabilization of the singlet spin state surface. The latter further leads to a low ^{1}**TS1** barrier that is competitive with the quintet spin barrier. Accordingly, in the QM/MM calculations, multistate reactivity patterns on competing singlet, triplet, and quintet spin state surfaces are found, in which the reaction starts in ^{1}**A** and proceeds via ^{1}**TS1** to ^{1}**B** or via a spin-state crossing to ^{3}**B**. Depending on the lifetime of this intermediate, a further electron transfer process can lead to a second spin-state crossing to the quintet spin state. However, the **TS2** barriers are low, and the most stable **C** structure is in the triplet spin state. The ^{5}**TS3** and ^{5}**TS4** barriers are considerably lower in energy than ^{3}**TS3** and ^{3}**TS4**, so it is likely that the spin-state crossing to the quintet spin state will take place in or around **TS3**/**TS4** in the reaction mechanism to give quintet spin state products. This multistate reactivity mechanism has a rate-determining ^{1}**TS1** barrier and will contain two spin state crossings: one from singlet to triplet and another from triplet to quintet.

Table 1. Relative Energies (in kilocalories per mole) of Dioxygen Transfer from Iron(III)−Superoxo to Sulfur-Based Substrate in (a) the Biomimetic CDO Model, (b) the CDO Enzyme Model As Calculated Using DFT Model Complex, and (c) the CDO Enzyme Model As Calculated with QM/MM

	$[Fe^{III}(LN_3S)O_2]^+$	CDO enzyme model	
	DFT [a]	DFT [a,b]	QM/MM [c,d]
^{1}**A**	0.00	0.00	0.00
^{3}**A**	5.51	2.01	5.80
^{5}**A**	1.39	8.36	13.84
^{1}**TS1**	25.70	23.69	13.68
^{3}**TS1**	21.53	25.39	24.19
^{5}**TS1**	12.61	17.72	14.44
^{1}**B**	16.77	12.31	12.12
^{3}**B**	12.20	10.26	10.88
^{5}**B**	1.12	−0.42	2.87
^{1}**TS2**	29.75	29.08	14.93
^{3}**TS2**	24.88	21.67	10.32
^{5}**TS2**	18.41	5.92	5.75
^{1}**C**	11.27	9.33	−5.88
^{3}**C**	−9.14	−9.85	−18.94
^{5}**C**	−8.62	−8.54	−10.62
^{1}**TS3**	10.79	5.13	7.76
^{3}**TS3**	−9.11	−4.66	−5.73
^{5}**TS3**	−5.28	−5.29	−7.61
^{1}**D**	−10.23	−5.48	−9.87
^{3}**D**	−18.67	−1.15	−19.02
^{5}**D**	−21.66	−14.59	−18.73
^{1}**TS4**	1.93	1.70	−2.03
^{3}**TS4**	−13.20	4.90	−1.31
^{5}**TS4**	−5.32	−13.10	−12.58
^{1}**E**	−22.57	−26.10	−25.48
^{3}**E**	−30.13	−32.88	−31.13
^{5}**E**	−43.71	−40.72	−38.66

[a] ΔE + ZPE values with solvent corrections included. [b] From ref 12b. [c] ΔE + ZPE result. [d] From ref 12c.

Despite the differences in relative energies of **A** and **TS1** in the biomimetic model complex as compared with the QM/MM calculations on the enzyme, in the ring structures **B**, all energies converge to very similar values. The dioxygen bond-breaking step has small barriers on each spin state surface in the QM/MM calculations, but much larger barriers are found in the biomimetic model system, where this step is even rate-determining. Presumably, the hydrogen bonding and polar interactions in the substrate binding pocket of the enzyme facilitate smooth dioxygen bond breakage and the formation of the sulfenate intermediate. These interactions are absent in the biomimetic model, and hence, the dioxygen bond breaking barriers are higher.

Direct Oxygen Atom Transfer to Sulfur without Metal Assistance. One of the key remaining questions in CDO catalysis relates to the involvement of the transition metal in the conversion of cysteine into cysteine sulfinic acid products. Thus, does the metal just hold the substrate into position, while being electronically inactive, or does it play an active role by donating electrons into the process? To address this question, we did a subsequent experiment in which molecular oxygen is not bound to the transition metal at the start of the reaction but approaches the thiolate-bound $[Fe^{II}(LN_3S)]^+$ from a large (>6 Å) distance. The obtained geometry scan is given in Figure 7 for the singlet, triplet, and quintet spin states. In these studies, we investigate the direct attack of molecular oxygen on the thiolate group without binding the metal first. To this end, the dioxygen starts at a large distance

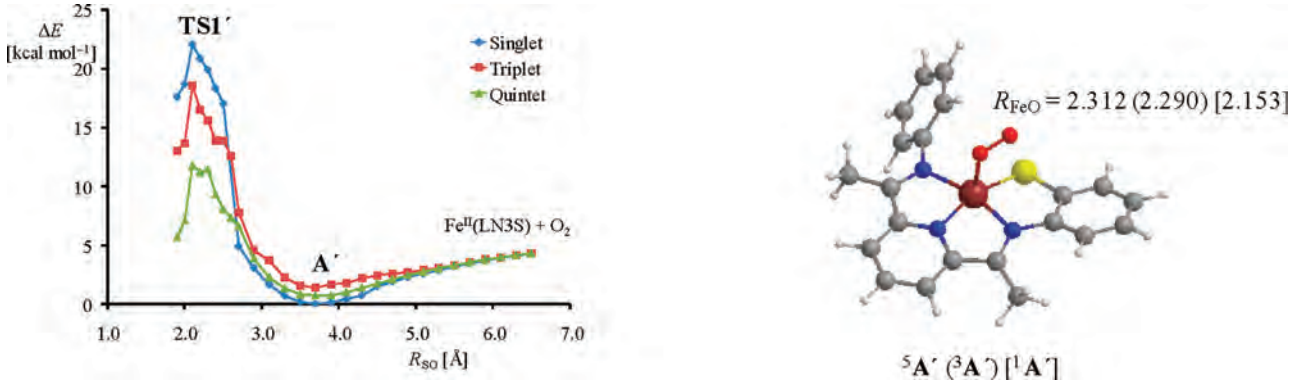

Figure 7. Geometry scans for the approach of the dioxygen on the sulfur atom starting at a S−O distance of over 6 Å. Also shown is the geometry of the minimum point of the scan for the singlet, triplet, and quintet spin states with the Fe−O distance (R_{FeO}) given in angstroms.

dx.doi.org/10.1021/jp208230g |J. Phys. Chem. A 2012, 116, 582–591

from the metal and sulfur centers, and in stepwise (full geometry) optimizations, we move the dioxygen moiety closer to the sulfur atom by fixing the S−O distance while optimizing all other degrees of freedom.

During the geometry scan, however, prior to the formation of an actual O−S bond, the dioxygen molecule approaches the metal center and binds in the usual Fe(III)−superoxo form, thereby stabilizing our chemical system with a couple of kilocalories per mole. This happens on all three spin state surfaces. As a consequence, the minimum points in the scans shown in Figure 7, labeled as ^{1,3,5}**A**′, geometrically resemble the Fe(III)−superoxo optimized geometries discussed above in Figure 5. Consequently, approach of molecular oxygen onto the sulfur atom bound to a metal center will first lead to a stable metal−superoxo complex. These results predict that direct attack of the thiolate group by molecular oxygen should be high in energy.

From the local minima in Figure 7, we continued the geometry scans for the S−O bond formation. The reaction proceeds in a way similar to that shown in Figure 4, with similar barrier heights and rate constants. Shortening of the S−O bond farther indeed gives transition state structures similar to those reported above that started from ^{1,3,5}**A** and lead to analogous ring-structure complexes. Therefore, direct attack of dioxygen on the thiolate group is unlikely to take place, and binding of molecular oxygen will give a stable iron(III)−superoxo complex that is able to transfer both oxygen atoms to a sulfur-containing substrate located in the cis position.

In summary, it is essential for the reaction that molecular oxygen binds the metal center first, since it leads to stable open-shell spin states, as shown by the orbital diagram in Figure 2. Furthermore, it enables a stepwise oxygen atom transfer mechanism as described in Scheme 1, in which the first step is focused on O−O bond weakening and breaking. The results on the model complex suggest that the iron center in CDO has dual functions in the S-oxygenation mechanism. First, it holds the substrate into a tight but specific orientation. Second, it binds molecular oxygen, whereby the electrons are redistributed in metal−superoxo type orbitals that enable efficient oxygen atom transfer mechanisms.

CONCLUSIONS

Density functional theory calculations have been performed on the mechanism of LN_3S dioxygenation on an iron center. This reaction mimics that found for CDO enzymes and gives fundamental insight into the metal ligand system on reactivity. We investigated two reaction mechanisms: one involves binding of dioxygen to iron, and the other involves a direct attack of dioxygen on the sulfur atom. The calculations show that the binding of O_2 to Fe is energetically favorable, and during the geometry scan for dioxygen approach to the sulfur atom, the O_2 molecule binds the iron atom immediately. These calculations indicate that the formation of the iron(III)−superoxo complex is thermodynamically driven and will lead to the reaction mechanism analogous to the one calculated for CDO enzymes. A detailed structural, thermodynamic, and kinetic comparison of the CDO mimic and the enzyme gives close similarities between the biomimetic model system and wild-type enzyme and supports the assignment of iron(II)-(LN_3S) as a CDO mimic.

ASSOCIATED CONTENT

Supporting Information. Group spin densities, charges, and absolute and relative energies of all structures described in this work as Cartesian coordinates of optimized geometries. This material is available free of charge via the Internet at http://pubs.acs.org.

AUTHOR INFORMATION

Corresponding Author

*E-mail: (S.P.d.V.) sam.devisser@manchester.ac.uk, (D.K.) dkclcre@yahoo.com, (D.P.G.) dpg@jhu.edu.

ACKNOWLEDGMENT

The authors thank the National Service for Computational Chemistry Software (NSCCS) for CPU time. D.K. holds a Ramanujan Fellowship from the Department of Science and Technology (DST), New Delhi (India), and acknowledges its financial support (Research Grants SR/S2/RJN-11/2008 and SR/S1/PC-58/2009). The NIH (GM62309 to D.P.G.) is gratefully acknowledged for support, in part, of this work. S.d.V. thanks the University of Manchester for a travel grant.

REFERENCES

(1) (a) Sono, M.; Roach, M. P.; Coulter, E. D.; Dawson, J. H. *Chem. Rev.* **1996**, *96*, 2841–2888. (b) Kadish, K. M.; Smith, K. M.; Guilard, R., Eds. *The Porphyrin Handbook*; Academic Press: San Diego, CA, 2000; Vol. 4. (c) Guengerich, F. P. *Chem. Res. Toxicol.* **2001**, *14*, 611–650. (d) Groves, J. T. *Proc. Natl. Acad. Sci. U.S.A.* **2003**, *100*, 3569–3574. (e) Ortiz de Montellano, P. R., Ed. *Cytochrome P450: Structure, Mechanism and Biochemistry*, 3rd ed.; Kluwer Academic /Plenum Publishers: New York, 2004. (f) Munro, A. W.; Girvan, H. M.; McLean, K. J. *Nat. Prod. Rep.* **2007**, *24*, 585–609. (g) Shaik, S.; Hirao, H.; Kumar, D. *Nat. Prod. Rep.* **2007**, *24*, 533–552. (h) Meunier, B.; de Visser, S. P.; Shaik, S. *Chem. Rev.* **2004**, *104*, 3947–3980.

(2) (a) Solomon, E. I.; Brunold, T. C.; Davis, M. I.; Kemsley, J. N.; Lee, S.-K.; Lehnert, N.; Neese, F.; Skulan, A. J.; Yang, Y.-S.; Zhou, J. *Chem. Rev.* **2000**, *100*, 235–349. (b) Bugg., T. D. H. *Curr. Opin. Chem. Biol.* **2001**, *5*, 550–555. (c) Costas, M.; Mehn, M. P.; Jensen, M. P.; Que, L., Jr. *Chem. Rev.* **2004**, *104*, 939–986. (d) Bruijnincx, P. C. A.; van Koten, G.; Klein Gebbink, R. J. M. *Chem. Soc. Rev.* **2008**, *37*, 2716–2744. (e) Bugg, T. D. H.; Ramaswamy, S. *Curr. Opin. Chem. Biol.* **2008**, *12*, 134–140. (f) de Visser, S. P.; Kumar, D., Eds. *Iron-Containing Enzymes: Versatile Catalysts of Hydroxylation Reactions in Nature*; RSC Publishing: Cambridge (UK), 2011.

(3) (a) Trewick, S. C.; Henshaw, T. F.; Hausinger, R. P.; Lindahl, T.; Sedgwick, B. *Nature* **2002**, *419*, 174–178. (b) Falnes, P. Ø.; Johansen, R. F.; Seeberg, E. *Nature* **2002**, *419*, 178–182. (c) Mishina, Y.; Duguid, E. M.; He, C. *Chem. Rev.* **2006**, *106*, 215–232.

(4) (a) Krebs, C.; Fujimori, D. G.; Walsh, C. T.; Bollinger, J. M. *Acc. Chem. Res.* **2007**, *40*, 484–492. (b) Schofield, C. J.; Zhang, Z. *Curr. Opin. Chem. Biol.* **1999**, *9*, 722–731. (c) Bugg, T. D. H. *Tetrahedron* **2003**, *59*, 7075–7101.

(5) Que, L., Jr. *Nat. Struct. Biol.* **2000**, *7*, 182–184.

(6) O'Brien, J. R.; Schuller, D. J.; Yang, V. S.; Dillard, B. D.; Lanzilotta, W. N. *Biochemistry* **2003**, *42*, 5547–5554.

(7) Straganz, G. D.; Nidetzky, B. *ChemBioChem* **2006**, *7*, 1536–1548.

(8) (a) Stipanuk, M. H. *Annu. Rev. Nutr.* **2004**, *24*, 539–577. (b) Joseph, C. A.; Maroney, M. J. *Chem. Commun.* **2007**, *Issue 32*, 3338–3349. (c) Stipanuk, M. H.; Ueki, I.; Dominy, J. E., Jr.; Simmons, C. R.; Hirschberger, L. L. *Amino Acids* **2009**, *37*, 55–63.

(9) (a) Perry, T. L.; Norman, M. G.; Yong, V. W.; Whiting, S.; Crichton, J. U.; Hansen, S.; Kish, S. *J. Ann. Neurol.* **1985**, *18*, 482–489. (b) Heafield, M. T.; Fearn, S.; Steventon, G. B.; Waring, R. H.; Williams, A. C.; Sturman, S. G. *Neurosci. Lett.* **1990**, *110*, 216–220.

(10) (a) McCoy, J. G.; Bailey, L. J.; Bitto, E.; Bingman, C. A.; Aceti, D. J.; Fox, B. G.; Phillips, G. N., Jr. *Proc. Natl. Acad. Sci. U.S.A.* **2006**, *103*, 3084–3089. (b) Simmons, C. R.; Liu, Q.; Huang, Q.; Hao, Q.; Begley, T. P.; Karplus, P. A.; Stipanuk, M. H. *J. Biol. Chem.* **2006**, *281*, 18723–18733. (c) Dominy, J. E., Jr.; Simmons, C. R.; Karplus, P. A.;

Gehring, A. M.; Stipanuk, M. H. *J. Bacteriol.* **2006**, *188*, 5561–5569. (d) Pierce, B. D.; Gardner, J. D.; Bailey, L. J.; Brunold, T. C.; Fox, B. G. *Biochemistry* **2007**, *46*, 8569–8578. (e) Dominy, J. E., Jr.; Hwang, J.; Guo, S.; Hirschberger, L. L.; Zhang, S.; Stipanuk, M. H. *J. Biol. Chem.* **2008**, *283*, 12188–12201. (f) Kleffmann, T.; Jongkees, S. A. K.; Fairweather, G.; Wilbanks, S. M.; Jameson, G. N. L. *J. Biol. Inorg. Chem.* **2009**, *14*, 913–921. (g) Gardner, J. D.; Pierce, B. S.; Fox, B. G.; Brunold, T. C. *Biochemistry* **2010**, *49*, 6033–6041.

(11) Ye, S.; Wu, X.; Wei, L.; Tang, D.; Sun, P.; Bartlam, M.; Rao, Z. *J. Biol. Chem.* **2007**, *282*, 3391–3402.

(12) (a) Aluri, S.; de Visser, S. P. *J. Am. Chem. Soc.* **2007**, *129*, 14846–14847. (b) de Visser, S. P.; Straganz, G. D. *J. Phys. Chem. A* **2009**, *113*, 1835–1846. (c) Kumar, D.; Thiel, W.; de Visser, S. P. *J. Am. Chem. Soc.* **2011**, *133*, 3869–3882. (d) de Visser, S. P. *Coord. Chem. Rev.* **2009**, *253*, 754–768.

(13) Diebold, A. R.; Neidig, M. L.; Moran, G. R.; Straganz, G. D.; Solomon, E. I. *Biochemistry* **2010**, *49*, 6945–6952.

(14) (a) Shaik, S.; Kumar, D.; de Visser, S. P.; Altun, A.; Thiel, W. *Chem. Rev.* **2005**, *105*, 2279–2328. (b) Hirao, H.; Kumar, D.; Que, L., Jr.; Shaik, S. *J. Am. Chem. Soc.* **2006**, *128*, 8590–8606.

(15) (a) Kryatov, S. V.; Rybak-Akimova, E. V.; Schindler, S. *Chem. Rev.* **2005**, *105*, 2175–2226. (b) Abu-Omar, M. M.; Loaiza, A.; Hontzeas, N. *Chem. Rev.* **2005**, *105*, 2227–2252. (c) Nam, W. *Acc. Chem. Res.* **2007**, *40*, 522–531.

(16) (a) Groves, J. T. In *Cytochrome P450: Structure, Mechanism and Biochemistry*; 3rd ed.; Ortiz de Montellano, P. R., Ed.; Kluwer Academic/Plenum Publishers: New York, 2005, Chapter 1, pp 1−44. (b) de Visser, S. P.; Nam, W. In *Handbook of Porphyrin Science*; Kadish, K. M., Smith, K. M., Guilard, R., Eds.; World Scientific Publishing Co.: Singapore, 2010; Chapter 44; pp 85−140.

(17) (a) Gross, Z.; Nimri, S. *Inorg. Chem.* **1994**, *33*, 1731–1732. (b) Gross, Z. *J. Biol. Inorg. Chem.* **1996**, *1*, 368–371. (c) Czarnecki, K.; Nimri, S.; Gross, Z.; Proniewicz, L. M.; Kincaid, J. R. *J. Am. Chem. Soc.* **1996**, *118*, 2929–2935.

(18) (a) Sastri, C. V.; Park, M. J.; Ohta, T.; Jackson, T. A.; Stubna, A.; Seo, M. S.; Lee, J.; Kim, J.; Kitagawa, T.; Münck, E.; Que, L., Jr.; Nam, W. *J. Am. Chem. Soc.* **2005**, *127*, 12494–12495. (b) Song, W. J.; Ryu, Y. O.; Song, R.; Nam, W. *J. Biol. Inorg. Chem.* **2005**, *10*, 294–304. (c) Sastri, C. V.; Lee, J.; Oh, K.; Lee, Y. J.; Lee, J.; Jackson, T. A.; Ray, K.; Hirao, H.; Shin, W.; Halfen, J. A.; Kim, J.; Que, L., Jr.; Shaik, S.; Nam, W. *Proc. Natl. Acad. Sci. U.S.A.* **2007**, *104*, 19181–19186. (d) Prokop, K. A.; de Visser, S. P.; Goldberg, D. P. *Angew. Chem., Int. Ed.* **2010**, *49*, 5091–5095. (e) Prokop, K. A.; Neu, H. M.; de Visser, S. P.; Goldberg, D. P. *J. Am. Chem. Soc.* **2011**, *133*, 15874–15877.

(19) (a) Namuswe, F.; Hayashi, T.; Jiang, Y.; Kasper, G. D.; Sarjeant, A. A. N.; Moënne-Loccoz, P.; Goldberg, D. P. *J. Am. Chem. Soc.* **2010**, *132*, 157–167. (b) Namuswe, F.; Kasper, G. D.; Sarjeant, A. A. N.; Hayashi, T.; Krest, C. M.; Green, M. T.; Moënne-Loccoz, P.; Goldberg, D. P. *J. Am. Chem. Soc.* **2008**, *130*, 14189–14200. (c) Krishnamurthy, D.; Kasper, G. D.; Namuswe, F.; Kerber, W. D.; Sarjeant, A. A. N.; Moënne-Loccoz, P.; Goldberg, D. P. *J. Am. Chem. Soc.* **2006**, *128*, 14222–14223.

(20) (a) Kurtz, D. M., Jr. *J. Inorg. Biochem.* **2006**, *100*, 679–693. (b) Dey, A.; Jenney, F. E.; Adams, M. W. W.; Johnson, M. K.; Hodgson, K. O.; Hedman, B.; Solomon, E. I. *J. Am. Chem. Soc.* **2007**, *129*, 12418–12431. (c) Brines, L. M.; Kovacs, J. A. *Eur. J. Inorg. Chem.* **2007**, 29–38.

(21) (a) Jiang, Y.; Widger, L. R.; Kasper, G. D.; Siegler, M. A.; Goldberg, D. P. *J. Am. Chem. Soc.* **2010**, *132*, 12214–12215. (b) Badlei, Y. M.; Siegler, M. A.; Goldberg, D. P. *J. Am. Chem. Soc.* **2011**, *133*, 1274–1277.

(22) (a) Farmer, P. J.; Solouki, T.; Mills, D. K.; Soma, T.; Russell, D. H.; Reibenspies, J. H.; Darensbourg, M. Y. *J. Am. Chem. Soc.* **1992**, *114*, 4601–4605. (b) Grapperhaus, C. A.; Darensbourg, M. Y. *Acc. Chem. Res.* **1998**, *31*, 451–459. (c) Maroney, M. J.; Choudhury, S. B.; Bryngelson, P. A.; Mirza, S. A.; Sherrod, M. J. *Inorg. Chem.* **1996**, *35*, 1073–1076. (d) Mirza, S. A.; Pressler, M. A.; Kumar, M.; Day, R. O.; Maroney, M. J. *Inorg. Chem.* **1993**, *32*, 977–987.

(23) (a) Masitas, C. A.; Mashuta, M. S.; Grapperhaus, C. A. *Inorg. Chem.* **2010**, *49*, 5344–5346. (b) Masitas, C. A.; Kumar, M.; Mashuta, M. S.; Kozlowski, P. M.; Grapperhaus, C. A. *Inorg. Chem.* **2010**, *49*, 10875–10881.

(24) (a) Heinrich, L.; Li, Y.; Vaissermann, J.; Chottard, G.; Chottard, J. C. *Angew. Chem., Int. Ed.* **1999**, *38*, 3526–3528. (b) Noveron, J. C.; Olmstead, M. M.; Mascharak, P. K. *J. Am. Chem. Soc.* **2001**, *123*, 3247–3259. (c) Galardon, E.; Giorgi, M.; Artaud, I. *Chem. Commun.* **2004**, 286–287. (d) O'Toole, M. G.; Kreso, M.; Kozlowski, P. M.; Mashuta, M. S.; Grapperhaus, C. *J. Biol. Inorg. Chem.* **2008**, *13*, 1219–1230.

(25) Lipscomb, J. D. *Curr. Opin. Struct. Biol.* **2008**, *18*, 644–649.

(26) (a) Li, C.; Wu, W.; Kumar, D.; Shaik, S. *J. Am. Chem. Soc.* **2006**, *128*, 394–395. (b) Latifi, R.; Bagherzadeh, M.; de Visser, S. P. *Chem.—Eur. J.* **2009**, *15*, 6651–6662. (c) Kumar, D.; Sastry, G. N.; de Visser, S. P. *Chem.—Eur. J.* **2011**, *17*, 6196–6205.

(27) (a) *Jaguar 7.6*, Schrödinger, LLC.: New York, NY, 2007. (b) Frisch, M. J.; Trunks, G. W.; Schlegel, H. B.; Scuseria, G. E.; Robb, M. A.; Cheeseman, J. R.; Montgomery, Jr., J. A.; Vreven, T.; Kudin, K. N.; Burant, J. C.; Millam, J. M.; Iyengar, S. S.; Tomasi, J.; Barone, V.; Mennucci, B.; Cossi, M.; Scalmani, G.; Rega, N.; Petersson, G. A.; Nakatsuji, H.; Hada, M.; Ehara, M.; Toyota, K.; Fukuda, R.; Hasegawa, J.; Ishida, M.; Nakajima, T.; Honda, Y.; Kitao, O.; Nakai, H.; Klene, M.; Li, X.; Knox, J. E.; Hratchian, H. P.; Cross, J. B.; Bakken, V.; Adamo, C.; Jaramillo, J.; Gomperts, R.; Stratmann, R. E.; Yazyev, O.; Austin, A. J.; Cammi, R.; Pomelli, C.; Ochterski, J. W.; Ayala, P. Y.; Morokuma, K.; Voth, G. A.; Salvador, P.; Dannenberg, J. J.; Zakrzewski, V. G.; Dapprich, S.; Daniels, A. D.; Strain, M. C.; Farkas, O.; Malick, D. K.; Rabuck, A. D.; Raghavachari, K.; Foresman, J. B.; Ortiz, J. V.; Cui, Q.; Baboul, A. G.; Clifford, S.; Cioslowski, J.; Stefanov, B. B.; Liu, G.; Liashenko, A.; Piskorz, P.; Komaromi, I.; Martin, R. L.; Fox, D. J.; Keith, T.; Al-Laham, M. A.; Peng, C. Y.; Nanayakkara, A.; Challacombe, M.; Gill, P. M. W.; Johnson, B.; Chen, W.; Wong, M. W.; Gonzalez, C.; Pople, J. A. *Gaussian 03, revision C.02*; Gaussian, Inc.: Wallingford, CT, 2004.

(28) (a) Becke, A. D. *J. Chem. Phys.* **1993**, *98*, 5648–5652. (b) Lee, C.; Yang, W.; Parr, R. G. *Phys. Rev. B* **1988**, *37*, 785–789.

(29) (a) Kumar, D.; de Visser, S. P.; Shaik, S. *Chem.—Eur. J.* **2005**, *11*, 2825–2835. (b) de Visser, S. P.; Oh, K.; Han, A.-R.; Nam, W. *Inorg. Chem.* **2007**, *46*, 4632–4641. (c) Vardhaman, A. K.; Sastri, C. V.; Kumar, D.; de Visser, S. P. *Chem. Commun.* **2011**, *47*, 11044–11046.

(30) Hay, P. J.; Wadt, W. R. *J. Chem. Phys.* **1985**, *82*, 270–283.

(31) (a) de Visser, S. P. *J. Am. Chem. Soc.* **2010**, *132*, 1087–1097. (b) Kumar, D.; Karamzadeh, B.; Sastry, G. N.; de Visser, S. P. *J. Am. Chem. Soc.* **2010**, *132*, 7656–7667.

(32) (a) de Visser, S. P. *Chem.—Eur. J.* **2006**, *12*, 8168–8177. (b) de Visser, S. P.; Tahsini, L.; Nam, W. *Chem.—Eur. J.* **2009**, *15*, 5577–5587. (c) de Visser, S. P.; Latifi, R.; Tahsini, L.; Nam, W. *Chem.—Asian J.* **2011**, *6*, 493–504.

(33) (a) Bassan, A.; Borowski, T.; Schofield, C. J.; Siegbahn, P. E. M. *Chem.—Eur. J.* **2006**, *12*, 8835–8846. (b) Lai, W.; Shaik, S. *J. Am. Chem. Soc.* **2011**, *133*, 5444–5452. (c) Latifi, R.; Tahsini, L.; Kumar, D.; Sastry, G. N.; Nam, W.; de Visser, S. P. *Chem. Commun.* **2011**, *47*, 10674–10676.

(34) Emerson, J. P.; Farquhar, E. R.; Que, L., Jr *Angew. Chem., Int. Ed.* **2007**, *46*, 8553–8556.

(35) (a) Rohde, J.-U.; In, J.-H.; Lim, M. H.; Brennessel, W. W.; Bukowski, M. R.; Stubna, A.; Münck; Nam, W.; Que, L., Jr. *Science* **2003**, *299*, 1037–1039. (b) Martinho, M.; Banse, F.; Bartoli, J.-F.; Mattioli, T. A.; Battioni, P.; Horner, O.; Bourcier, S.; Girerd, J.-J. *Inorg. Chem.* **2005**, *44*, 9592–9596. (c) Sastri, C. V.; Seo, M. S.; Park, M. J.; Kim, K. M.; Nam, W. *Chem. Commun.* **2005**, 11, 1405−1407. (d) De Oliveira, F. T.; Chanda, A.; Banerjee, D.; Shan, X.; Mondal, S.; Que, L., Jr; Bominaar, E. L.; Münck, E.; Collins, T. J. *Science* **2007**, *315*, 835–838. (e) Jackson, T. A.; Rohde, J.-U.; Seo, M. S.; Sastri, C. V.; DeHont, R.; Stubna, A.; Ohta, T.; Kitagawa, T.; Münck, E.; Nam, W.; Que, L., Jr. *J. Am. Chem. Soc.* **2008**, *130*, 12394–12407.

(36) Riggs-Gelasco, P. J.; Price, J. C.; Guyer, R. B.; Brehm, J. H.; Barr, E. W.; Bollinger, J. M., Jr.; Krebs, C. *J. Am. Chem. Soc.* **2004**, *126*, 8108–8109.

(37) (a) Kumar, D.; Hirao, H.; Que, L., Jr.; Shaik, S. *J. Am. Chem. Soc.* **2005**, *127*, 8026–8027. (b) de Visser, S. P. *J. Am. Chem. Soc.* **2006**, *128*, 15809–15818. (c) Hirao, H.; Que, L., Jr.; Nam, W.; Shaik, S. *Chem.—Eur. J.* **2008**, *14*, 1740–1756. (d) Ye, S.; Neese, F. *Proc. Natl. Acad. Sci. U.S.A.* **2011**, *108*, 1228–1233.

ChemComm

View Online
Dynamic Article Links

Cite this: *Chem. Commun.*, 2011, **47**, 11044–11046

www.rsc.org/chemcomm

COMMUNICATION

Nonheme ferric hydroperoxo intermediates are efficient oxidants of bromide oxidation†

Anil Kumar Vardhaman,[a] Chivukula V. Sastri,*[a] Devesh Kumar*[b] and Sam P. de Visser*[c]

Received 24th June 2011, Accepted 24th August 2011
DOI: 10.1039/c1cc13775a

This work presents the first combined experimental and computational study that gives evidence of the electrophilic reactivity of a nonheme iron(III)-hydroperoxo species. We show that in contrast to their heme counterparts the nonheme iron(III)-hydroperoxo complexes are catalytically much more active and even more so than nonheme iron(IV)-oxo species.

Oxygen atom transfer reactions are vital processes in biosystems and take part in biodegradation, biosynthesis and bioconversion reactions in the body. Many of the enzymes utilize molecular oxygen on an iron center and, for instance, contain the class of cytochrome P450 enzymes (P450s), which is a versatile group of enzymes involved in drug metabolism, hormone biosynthesis and detoxification processes.[1] The active species of the P450s is an iron(IV)-oxo heme cation radical (Compound I, Cpd I) and its precursor in the catalytic cycle is the iron(III)-hydroperoxo species (Compound 0, Cpd0). CpdI and Cpd0 have both been characterized with spectroscopic methods and are relatively short-lived.[2] Reactivity studies together with supporting computational modeling provided evidence, however, that only CpdI is an active oxidant of oxygen atom transfer reactions, while Cpd 0 is a sluggish oxidant.[3]

The nonheme iron chemistry of biomimetic systems and enzymes led to the characterization of a number of high-valent iron(IV)-oxo intermediates in electrophilic and nucleophilic oxygenation reactions.[4] However, the reactivity patterns of the corresponding nonheme Fe(III)-hydroperoxo intermediates are not well understood. To gain insight into the reactivity patterns of nonheme Fe(III)-hydroperoxo intermediates in electrophilic reaction mechanisms, we decided to investigate the bromide oxidation by $[Fe^{III}OOH(N4Py)]^{2+}$ (**1a**) and $[Fe^{III}OOH(Bn\text{-}tpen)]^{2+}$ (**2a**),[5] Scheme 1, using combined experimental and computational techniques. These nonheme complexes contain pentadentate ligands and their corresponding iron(IV)-oxo complexes have been shown to give efficient electrophilic reactivity patterns with substrates including hydrogen atom abstraction mechanisms.[6] Nam and co-workers studied **1a** and **2a** and found them to be inactive with thioanisole and cyclohexene.[7]

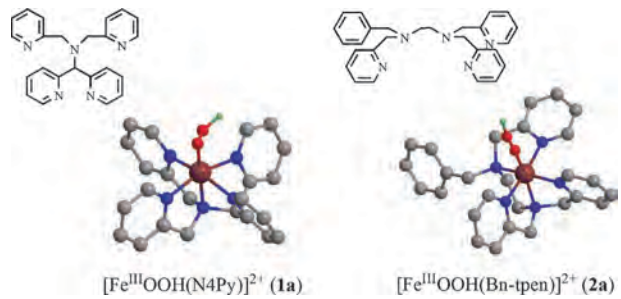

Scheme 1 Oxidants used in this study.

The ferric hydroperoxo complexes, **1a** and **2a**, were generated in a methanol solution *in situ* by adding excess H_2O_2 following a previously reported procedure.[8] Subsequently, tetrabutyl ammonium bromide (TBABr) was added to the solution of **1a** at 253 K, which led to the rapid decay of the characteristic 548 nm peak in the UV-Vis spectra and the efficient formation of $[Fe^{III}(OH)(N4Py)]^{2+}$, see Fig. 1a. We evaluated the second order rate constant for this reaction to be 5.5×10^{-1} M^{-1} s^{-1}. This is a very fast reaction and is several orders of magnitude faster than, for instance, the same reaction catalyzed by the corresponding Fe(IV)-oxo complexes (**1b**) for which we determined a second order rate constant of 6.4×10^{-4} M^{-1} s^{-1} using the same experimental conditions (Fig. 1b). *This implies that the Fe(III)-hydroperoxo complex reacts with bromide with rate constants that are about three orders of magnitude higher than those found for the ferryl-oxo complex*. To highlight the difference in reactivity between **1a** and **1b** with bromide we plot the rate constants of bromide oxidation at different concentrations in Fig. 1c. To find out whether the same rate enhancement is observed with other nonheme iron ligand systems, we investigated the same reactions for the iron(III)-hydroperoxo and iron(IV)-oxo species with the Bn-tpen ligand system: structures **2a** and **2b**, respectively. Indeed, a similar

[a] *Department of Chemistry, Indian Institute of Technology Guwahati, Assam 781039, India. E-mail: sastricv@iitg.ernet.in; Fax: +91-361-258-2349*
[b] *Department of Applied Physics, School for Physical Sciences, Babasaheb Bhimrao Ambedkar University, Vidya Vihar, Rae Bareilly Road, Lucknow 226 025, India. E-mail: dkclcre@yahoo.com*
[c] *The Manchester Interdisciplinary Biocentre and the School of Chemical Engineering and Analytical Science, The University of Manchester, 131 Princess Street, Manchester M1 7DN, UK. E-mail: sam.devisser@manchester.ac.uk*

† Electronic supplementary information (ESI) available: Detailed experimental and computational methods, tables with group spin densities, charges and absolute and relative energies of calculated structures. Also given are figures with optimized geometries, geometry scans and experimental data on **2a** and **2b**. See DOI: 10.1039/c1cc13775a

This journal is © The Royal Society of Chemistry 2011

View Online

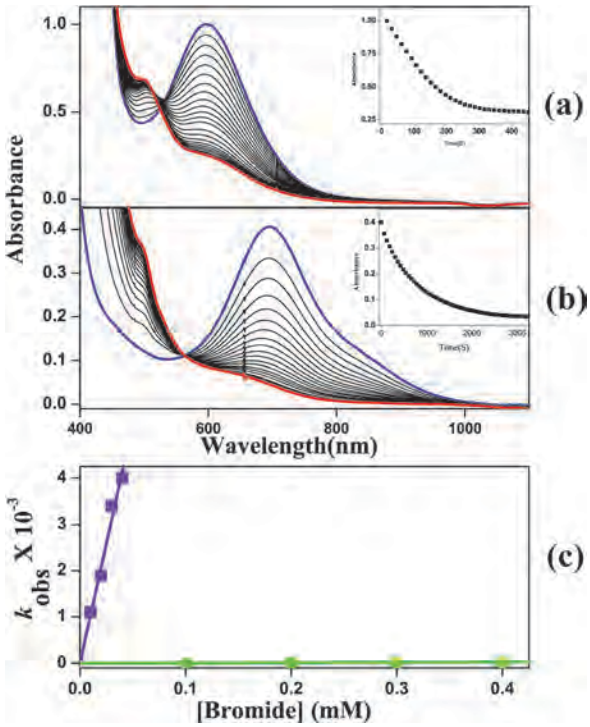

Fig. 1 UV-vis spectral changes of (a) **1a** (1 mM) upon addition of 10 equiv. of TBABr at 253 K. Scan interval was 10 s. The inset shows the time course of **1a** monitored at 548 nm. (b) **1b** (1 mM) upon addition of 10 equiv. of TBABr at 298 K. Scan interval was 10 s. The inset displays the time course of **1b** monitored at 695 nm. (c) Comparison of the second order rate constants of bromide oxidation by **1a**, 5.5×10^{-1} M^{-1} s^{-1} (■), and **1b**, 6.4×10^{-4} M^{-1} s^{-1} (●) with TBABr at 253 K.

enhanced bromide oxidation rate was observed for **2a** (2.7×10^{-1} M^{-1} s^{-1}) as compared to **2b** (1.0×10^{-2} M^{-1} s^{-1}) at 253 K, ESI†, Fig. S10. It should be noted here that the order of reactivity for the ferryl complexes was **2b** > **1b**, which is consistent with previous reactivity studies of these oxidants.[6] By contrast, the reverse ordering was observed for the Fe(III)-hydroperoxo complexes, *i.e.* **1a** > **2a**.

To understand the apparent disparity between the reactivity of **1a**/**2a** on the one hand *versus* that of **1b**/**2b** on the other hand, as compared to what is known for heme-enzymes and biomimetic analogues, we monitored the product distributions of all processes. Thus, bromide oxidation of phenol red by a high-valent Fe(III)-hydroperoxo species leads to the production of bromophenol blue, or the tetrabrominated product of phenol red.[9] However, in the presence of HOBr, Br_2 or Br_3^-, phenol red is easily tetra-brominated to form bromophenol blue. The addition of H_2O_2 to our solution containing $[Fe^{II}(N4Py)]^{2+}$ (or $[Fe^{II}(Bn\text{-}tpen)]^{2+}$) and phenol-red in the presence of excess TBABr resulted in a red-shift in the UV-Vis spectra from 441 nm (orange-red) to 590 nm (blue), indicative of the conversion from phenol red to bromophenol blue (Fig. 2). Similar results were obtained under inert conditions. The yield of bromophenol blue was ~80% based on the molar absorption coefficient of bromophenol blue and showed a time-dependent absorbance change, arising from the formation of bromophenol blue (inset, Fig. 2; ESI†, Fig. S11). As can be seen from Fig. 2, the bromophenol blue was initially produced slowly (long lag phase) due

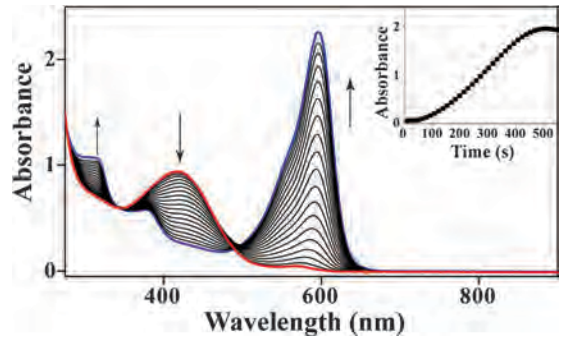

Fig. 2 Catalytic conversion of phenol red (62.5 μM) to bromophenol blue in the presence of $[Fe^{II}(N4Py)]^{2+}$ (0.1 mM) and TBABr (80 mM) upon addition of H_2O_2 (10 mM). The inset shows the time course of formation of bromophenol blue monitored at 590 nm.

to the absence of BrO^-, but after the concentration of BrO^- increases, so does the amount of bromophenol blue. However, when a steady-state concentration of BrO^- is reached, the formation rate of bromophenol blue is equal to the rate of bromide oxidation by **1a**. The duration of the initial lag decreased with the increasing concentration of the catalyst. The systematic variation of the catalyst concentration and the measurements of the initial rate of bromophenol blue formation are found to be of first-order, which is in agreement with the results given above. The uncatalyzed bromide oxidation by H_2O_2 in the absence of a catalyst was reported to be in the order of 10^{-7} M^{-1} s^{-1}.[10]

Due to the fact that **1a**/**2a** cannot be generated in an acetonitrile solution, whereas **1b**/**2b** cannot be studied in a methanol solution as a result of alcohol oxidation, the above mentioned experiments of **1a** *vs.* **1b** and **2a** *vs.* **2b** refer to studies in a different solvent. To confirm that **1a**/**2a** are better oxidants than **1b**/**2b** of bromination reactions we decided to run a series of density functional theory studies. Essentially, we do full geometry optimizations with the polarized continuum model with a dielectric constant of $\varepsilon = 35.7$ (acetonitrile) or 32.6 (methanol) using previously described procedures.[11] Fig. 3 displays the free energy landscape for bromination with **1a** and **2a** as oxidants. Thus, the reaction is concerted *via* the bromination transition state $\mathbf{TS_{Br}}$ and leads to an Fe^{III}-hydroxo complex with nearby OBr^- (**P**). The reactants have a sextet spin ground state, while the doublet and quartet spin states are 7.2/6.7 and 32.8/7.8 kcal mol^{-1} higher in energy.

The bromination reactions by ^{6}**1a** and ^{6}**2a** have free energies of activation of 21.8 and 27.1 kcal mol^{-1}, respectively. Using transition state theory the rate constant for **1a** reported in Fig. 1 corresponds to $\Delta G^{\ddagger} = 18.5$ kcal mol^{-1}, therefore, we find good agreement between experiment and computation with similar $\Delta G^{\ddagger}$ differences as before.[12] We also calculated the bond dissociation energy of the O–O bond in **1a**/**2a** to give the corresponding iron(IV)-oxo complexes and found enthalpies that are 32/13 kcal mol^{-1} above those of $^6\mathbf{TS_{1a}}$/$^6\mathbf{TS_{2a}}$. Therefore, the observed products are due to reactivity of **1a**/**2a** and not from interconversion of **1a**/**2a** into **1b**/**2b** first. As can be seen from Fig. 3, the optimized geometries of $\mathbf{TS_{Br,1a}}$ and $\mathbf{TS_{Br,2a}}$ are very similar and consequently cannot be the origin of the difference in reaction barrier between the two processes.

View Online

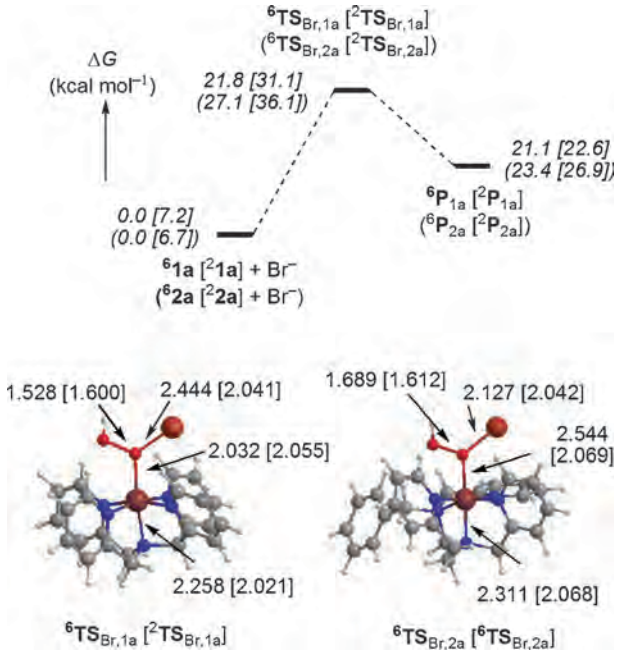

Fig. 3 DFT calculated mechanism of bromination by **1a** and **2a**. Free energies are reported in kcal mol^{-1} with energies and solvent corrections taken from the UB3LYP/B2//UB3LYP/B1 calculations and include zero point, thermal, and entropic corrections at UB3LYP/B1. Also given are optimized geometries of the **TS**s with bond lengths in angstroms.

The DFT calculations, therefore, do support the experimental observations of higher reactivity of **1a** over **2a** in bromination reactions.

The origin of the high reactivity of nonheme iron(III)-hydroperoxo can be traced to the orbital occupation. Thus, nonheme iron(IV)-oxo species are stabilized in high-spin states with an elevated π^*_{xy} orbital as compared to heme iron(IV)-oxo species.[6b,13] The same is true for iron(III)-hydroperoxo that is low-spin in heme systems but high-spin in nonheme systems. These high-spin species are more reactive and can abstract hydrogen atoms/electrons more easily than their low-spin counterparts. To assess the oxidative potential of the iron(III)-hydroperoxo species, we calculate the reaction energy (BDE_{OH}) for reaction (1) using isolated molecules.

$$[Fe^{III}OOH(N4Py)]^{2+} + H^{\bullet} \rightarrow [Fe^{IV}{=}O(N4Py)]^{2+} + H_2O \quad (1)$$

Thus, the calculated reaction energy starting from **1a** is 91.1 kcal mol^{-1}, while that from **2a** is found to be 85.6 kcal mol^{-1}. By contrast, the H-abstraction energy calculated for Cpd0 of P450 is only 81.2 kcal mol^{-1} due to two doubly occupied 3d-type orbitals.[14] As shown previously, differences in BDE_{OH} values are proportional to H-abstraction rate constants and a larger BDE_{OH} value should correspond to faster reactions.[15] Indeed the relative BDE_{OH} values for **1a** and **2a** follow the trend in barrier heights and rate constants discussed here. These BDE_{OH} values are close to those calculated for CpdI of P450 (88.9 kcal mol^{-1}),[14] hence, in particular, **1a** should be an efficient oxidant of electrophilic reaction mechanisms.

We provide the first experimental and computational evidence that nonheme iron(III)-hydroperoxo species are efficient oxidants of electrophilic oxidation reactions. This makes nonheme iron(III)-hydroperoxo complexes fundamentally different from heme iron(III)-hydroperoxo species.

Research support was provided to CVS by Department of Science and Technology, India (SR/S1/IC-02/2009), and Board of Research in Nuclear Sciences, India (2010/37C/3/BRNS). CPU time was provided by the National Service of Computational Chemistry Software (NSCCS). DK acknowledges Department of Science and Technology (New Delhi) for the Ramanujan Fellowship.

Notes and references

1 (*a*) M. Sono, M. P. Roach, E. D. Coulter and J. H. Dawson, *Chem. Rev.*, 1996, **96**, 2841; (*b*) J. T. Groves, *Proc. Natl. Acad. Sci. U. S. A.*, 2003, **100**, 3569; (*c*) *Cytochrome P450: Structure, Mechanism and Biochemistry*, ed. P. R. Ortiz de Montellano, 3rd edn, Kluwer Academic/Plenum Publ., New York, 2005.

2 (*a*) R. Davydov, T. M. Makris, V. Kofman, D. E. Werst, S. G. Sligar and B. M. Hoffman, *J. Am. Chem. Soc.*, 2001, **123**, 1403; (*b*) P. J. Mak, I. G. Denisov, D. Victoria, T. M. Makris, T. Deng, S. G. Sligar and J. R. Kincaid, *J. Am. Chem. Soc.*, 2007, **129**, 6382; (*c*) J.-G. Liu, T. Ohta, S. Yamaguchi, T. Ogura, S. Sakamoto, Y. Maeda and Y. Naruta, *Angew. Chem., Int. Ed.*, 2009, **48**, 9262; (*d*) J. Rittle and M. T. Green, *Science*, 2010, **330**, 933.

3 (*a*) F. Ogliaro, S. P. de Visser, S. Cohen, P. K. Sharma and S. Shaik, *J. Am. Chem. Soc.*, 2002, **124**, 2806; (*b*) S. Shaik, H. Hirao and D. Kumar, *Nat. Prod. Rep.*, 2007, **24**, 533; (*c*) S. P. de Visser, J. S. Valentine and W. Nam, *Angew. Chem., Int. Ed.*, 2010, **49**, 2099.

4 (*a*) M. Costas, M. P. Mehn, M. P. Jensen and L. Que Jr, *Chem. Rev.*, 2004, **104**, 939; (*b*) M. M. Abu-Omar, A. Loaiza and N. Hontzeas, *Chem. Rev.*, 2005, **105**, 2227; (*c*) P. C. A. Bruijnincx, G. van Koten and R. J. M. Klein Gebbink, *Chem. Soc. Rev.*, 2008, **37**, 2716; (*d*) L. Que Jr, *Acc. Chem. Res.*, 2007, **40**, 493; (*e*) W. Nam, *Acc. Chem. Res.*, 2007, **40**, 522.

5 Abbreviations used: N4Py, *N*,*N*-bis(2-pyridylmethyl)-*N*-bis(2-pyridyl)-methylamine; Bn-tpen, *N*-benzyl-*N*,*N*′,*N*′-tris(2-pyridylmethyl)ethane-1,2-diamine.

6 (*a*) J. Kaizer, E. J. Klinker, N. Y. Oh, J.-U. Rohde, W. J. Song, A. Stubna, J. Kim, E. Münck, W. Nam and L. Que Jr, *J. Am. Chem. Soc.*, 2004, **126**, 472; (*b*) D. Kumar, H. Hirao, L. Que Jr and S. Shaik, *J. Am. Chem. Soc.*, 2005, **127**, 8026; (*c*) C. V. Sastri, K. Oh, Y. J. Lee, M. S. Seo, W. Shin and W. Nam, *Angew. Chem., Int. Ed.*, 2006, **45**, 3992.

7 M. J. Park, J. Lee, Y. Suh, J. Kim and W. Nam, *J. Am. Chem. Soc.*, 2006, **128**, 2630.

8 (*a*) A. Hazell, C. J. McKenzie, L. P. Nielsen, S. Schindler and M. Weitzer, *J. Chem. Soc., Dalton Trans.*, 2002, 310; (*b*) K. D. Koehntop, J.-U. Rohde, M. Costas and L. Que Jr, *Dalton Trans.*, 2004, 3191.

9 Phenol red is commonly used as a standard assay for haloperoxidase activity, see *e.g.* J. V. Walker, M. Morey, H. Carlssom, A. Davidson, G. D. Stucky and A. Butler, *J. Am. Chem. Soc.*, 1997, **119**, 6921.

10 M. S. Reynolds, S. J. Morandi, J. W. Raebiger, S. P. Melican and E. Smith, *Inorg. Chem.*, 1994, **33**, 4977.

11 (*a*) D. Kumar, B. Karamzadeh, G. N. Sastry and S. P. de Visser, *J. Am. Chem. Soc.*, 2010, **132**, 7656; (*b*) D. Kumar, G. N. Sastry and S. P. de Visser, *Chem.–Eur. J.*, 2011, **17**, 6196.

12 D. Kumar, S. P. de Visser and S. Shaik, *Chem.–Eur. J.*, 2005, **11**, 2825.

13 S. P. de Visser, *J. Am. Chem. Soc.*, 2006, **128**, 15809.

14 (*a*) S. P. de Visser, *Chem.–Eur. J.*, 2006, **12**, 8168; (*b*) S. P. de Visser and L. S. Tan, *J. Am. Chem. Soc.*, 2008, **130**, 12961.

15 (*a*) J. M. Mayer, *Acc. Chem. Res.*, 1998, **31**, 441; (*b*) K. A. Prokop, S. P. de Visser and D. P. Goldberg, *Angew. Chem., Int. Ed.*, 2010, **49**, 6111; (*c*) S. P. de Visser, *J. Am. Chem. Soc.*, 2010, **132**, 1087.

 This journal is © The Royal Society of Chemistry 2011

ChemComm

Dynamic Article Links

Cite this: *Chem. Commun.*, 2011, **47**, 10674–10676

www.rsc.org/chemcomm

COMMUNICATION

Oxidative properties of a nonheme Ni(II)(O_2) complex: Reactivity patterns for C–H activation, aromatic hydroxylation and heteroatom oxidation†

Reza Latifi,[ab] Laleh Tahsini,[ab] Devesh Kumar,*[cd] G. Narahari Sastry,[c] Wonwoo Nam*[b] and Sam P. de Visser*[a]

Received 4th July 2011, Accepted 17th August 2011
DOI: 10.1039/c1cc13993b

Density functional theory calculations on the reactivity of a Ni(II)-superoxo complex in C–H bond activation, aromatic hydroxylation and heteroatom oxidation reactions have been explored; the Ni(II)-superoxo complex is able to react with substrates with weak C–H bonds and PPh_3.

Nature utilizes molecular oxygen for many important biotransformations, including biocatalysis, biodegradation and biosynthesis. Despite the abundance of nickel on earth, there are only a few enzymes in nature that utilize a nickel active center for aerobic oxidations.[1] In coordination chemistry, many nickel-superoxide complexes have been structurally characterized with spectroscopic techniques,[2] and of several of those reactivity studies have been performed.[2b,h] Metal-superoxo species have attracted much attention recently, since the intermediates have been proposed as active oxidants in C–H bond activation reactions by metalloenzymes and their biomimetic counterparts.[3,4] Therefore, to assess the oxidative power of metal-superoxo species, we have performed a density functional theory (DFT) study.

A well studied chemical system is a Ni(II)-superoxo complex embedded in a TMC ligand (TMC = 1,4,8,11-tetramethyl-1,4,8,11-tetraazacyclotetradecane), which has been characterized using resonance Raman, EXAFS and EPR spectroscopy.[2b] Moreover, reactivity studies showed efficient electrophilic oxygen atom transfer to PPh_3 and H-abstraction from xanthene, but no reactivity with olefins and sulfides.[2b,5] To gain insight into the oxidative properties of Ni(II)-superoxo complexes, we have done a DFT study on the various possible oxygenation reactions using Ni(II)-superoxo complexes bearing two possible TMC conformers, namely with either a *trans* or a *cis* conformer. The latter isomer was used in the studies of reference 5 and will enable us to make a detailed comparison. Preliminary experimental data using the *trans*-TMC Ni(II)-superoxo complex show that it reacts with xanthenes and cyclohexadiene efficiently.[6] Thus, to establish the potency of Ni(II)-superoxo species in oxygenation reactions, including aromatic and aliphatic hydroxylation and heteroatom oxidation, we have performed a set of DFT calculations using the reactions displayed in Scheme 1. H-abstraction is investigated for xanthene, cyclohexadiene and the benzyl position of ethylbenzene and aromatic hydroxylation at the *para*-position of ethylbenzene by $[Ni^{II}O_2(trans\text{-TMC})]^+$, $\mathbf{R_1}$, while H-abstraction from xanthene by $[Ni^{II}O_2(cis\text{-TMC})]^+$, $\mathbf{R_2}$, was also investigated. Heteroatom oxidation is studied for the oxidation of PPh_3 and $S(CH_3)_2$ by $\mathbf{R_1}$.

The reactant species, $\mathbf{R_1}$ as well as $\mathbf{R_2}$, has close lying doublet and quartet spin states as the ground state. Dependent on the density functional chosen for the calculations (see ESI for details) the energetic differences are small. Moreover, the choice

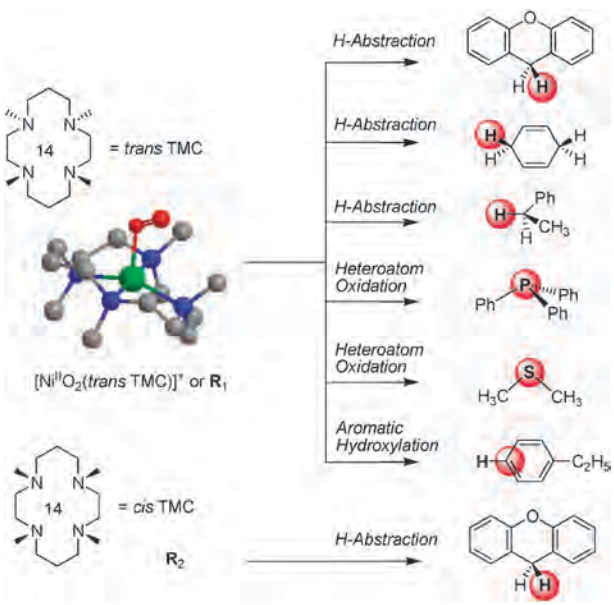

Scheme 1 Oxidants, $\mathbf{R_1}$ and $\mathbf{R_2}$, and the reactions studied in this work.

[a] *Manchester Interdisciplinary Biocenter and School of Chemical Engineering and Analytical Science, University of Manchester, 131 Princess Street, Manchester M1 7DN, UK. E-mail: sam.devisser@manchester.ac.uk; Fax: +44 161 306 5201*
[b] *Department of Chemistry and Nano Science, Department of Bioinspired Science, Centre for Biomimetic Systems, Ewha Womans University, Seoul 120-750, Korea. E-mail: wwnam@ewha.ac.kr; Fax: +82 3277 4441*
[c] *Molecular Modelling Group, Indian Institute of Chemical Technology, Hyderabad 500-607, India. E-mail: dkclcre@yahoo.com*
[d] *Department of Applied Physics, School for Physical Sciences, Babasaheb Bhimrao Ambedkar University, Vidya Vihar, Rae Bareilly Road, Lucknow (U. P.) 226 025, India.*
† Electronic supplementary information (ESI) available: Detailed methods, tables with electronic properties and optimized geometries. See DOI: 10.1039/c1cc13993b

This journal is © The Royal Society of Chemistry 2011

of the density functional does not seem to affect the relative barrier heights calculated and does not change the conclusions. Optimized geometries of $^{4,2}\mathbf{R}_1$ are given in Fig. 1(a), whereas those for $^{4,2}\mathbf{R}_2$ are given in Fig. S1 (ESI†). The Ni–O distances are rather long, and are considerably longer than those typically found for other superoxo complexes, such as Fe^{II}-superoxo, where bond lengths around 1.94 Å were found.[7] The reason for the enhanced bond lengths follows from the molecular orbital occupation. Thus, the Ni(II)-superoxo complexes are characterized by an $\pi^*_{xy}{}^2\ \pi^*_{xz}{}^2\ \pi^*_{yz}{}^2\ \sigma^*_{z2}{}^1\ \sigma^*_{x2-y2}{}^1\ \pi^*_{OO,yz}{}^2\ \pi^*_{OO,xz}{}^1$ orbital occupation. The σ^*_{x2-y2} orbital represents the antibonding interaction of the $3d_{x2-y2}$ atomic orbital on Ni with 2p orbitals on the nitrogen atoms of the TMC ligand, while the σ^*_{z2} orbital is antibonding along the Ni–O bond. Both of these orbitals are singly occupied in the lowest spin states and the electrons are either ferromagnetically or antiferromagnetically coupled to the unpaired electron in the $\pi^*_{OO,xz}$ orbital for the quartet and doublet spin states. Fig. 1(b) gives orbital drawings of these singly occupied molecular orbitals. As follows from Fig. 1(b), the σ^*_{z2} orbital symbolizes the antibonding interaction along the Ni–O axis and gives significant mixing with the π_{OO} and π^*_{OO} orbitals on the superoxide moiety. Our optimized geometries and charge distributions are in good agreement with earlier DFT studies on this complex.[2b,8]

Subsequently, we investigated the reactivity of $^{4,2}\mathbf{R}_1$ with selected substrates. Fig. 2 displays the potential energy surface of the reactions of $^{4,2}\mathbf{R}_1$ with xanthene, 1,4-cyclohexadiene, ethylbenzene, triphenylphosphine and dimethylsulfide as calculated at UB3LYP/BS2//UB3LYP/BS1 level of theory.[9] These substrates cover H-abstraction reactions and oxygen atom transfer reaction mechanisms, including heteroatom oxidation and aromatic hydroxylation. The reactions with xanthene (XA), cyclohexadiene (CHD) and the benzyl position of ethylbenzene (EB) give H-abstraction *via* a transition state $\mathbf{TS}_{HA}$, leading to a radical intermediate, $[Ni^{II}OOH(TMC)]^+\cdots C_8H_9^{\bullet}(\mathbf{I}_{HA})$. The H-abstraction barrier of xanthene is small (14.6 kcal mol^{-1}), but that for the benzyl position of ethylbenzene is much higher in energy (20.6 kcal mol^{-1}) for the doublet spin state barriers. The latter value is very high and the reaction is unlikely to proceed in experiment. This implies that $\mathbf{R}_1$ is a possible oxidant of substrates with weak C–H bonds, such as xanthene and cyclohexadiene, but will be a poor oxidant for substrates with intermediate and strong C–H bonds including ethylbenzene. Using $\mathbf{R}_2$ as an oxidant the H-abstraction barriers for xanthene are 14.7 (14.8) kcal mol^{-1} for the quartet (doublet) spin state surfaces and hence are virtually identical to those found for $\mathbf{R}_1$. This implies that the TMC ring has little effect on the reaction kinetics and barrier heights, which also follows from the singly occupied molecular orbitals in Fig. 1(b) that have little TMC occupation. Hence, Ni(II)-superoxo complexes with alternative TMC isomers are expected to give similar reactivity patterns as described here for the *trans* isomer.

We also tested other oxidative reactions including aromatic hydroxylation at the *para*-position of ethylbenzene, PPh_3 oxidation and dimethylsulfide sulfoxidation by $^{4,2}\mathbf{R}_1$. Aromatic hydroxylation starts with an electrophilic attack of the terminal oxygen atom of the superoxo group onto the *para*-carbon atom of ethylbenzene *via* a transition state $\mathbf{TS}_{Ar}$ and leads to a radical intermediate ($\mathbf{I}_{Ar}$). Finally, we investigated two heteroatom oxidation reactions, namely dimethylsulfide sulfoxidation by $\mathbf{R}_1$, which is a concerted reaction mechanism *via* a transition state $\mathbf{TS}_{SO}$ to form sulfoxide product ($\mathbf{P}_{SO}$), and PPh_3 oxidation *via* a transition state $\mathbf{TS}_{PO}$ to form O=PPh_3 product ($\mathbf{P}_{PO}$). As can be seen from Fig. 2, both aromatic hydroxylation and sulfoxidation by $^{4,2}\mathbf{R}_1$ are high energy processes with barriers well over 25 kcal mol^{-1}. By contrast, PPh_3 oxidation encounters a low barrier of 15.8 kcal mol^{-1} on the doublet spin state. Indeed, a previous experimental study showed a quantitative yield of O=PPh_3 formation for this reaction process.[2b] Clearly, it appears that $^{4,2}\mathbf{R}_1$ is a poor oxidant of electrophilic mechanisms including aromatic hydroxylation and sulfoxidation, but is a potent oxidant for PPh_3 oxidation.

So what is the reason that $\mathbf{R}_1$ can only activate weak C–H bonds and oxidize PPh_3 and why is it a poor oxidant for sulfoxidation and aromatic hydroxylation? We will try to answer these questions in the following section. Thermodynamically, a hydrogen atom abstraction from a substrate SubH by an oxidant ROO gives ROOH *via* a reaction as displayed in eqn (1) with energy described by eqn (2) and (3). It was shown

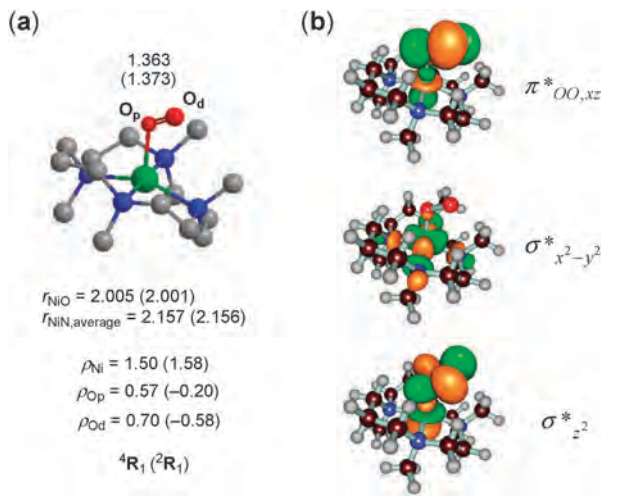

Fig. 1 (a) Optimized geometries with group spin densities of $^{4,2}\mathbf{R}_1$ with bond lengths in angstroms. O_p is the proximal oxygen atom and O_d is the distal oxygen atom. (b) Singly occupied orbitals of $^{4,2}\mathbf{R}_1$.

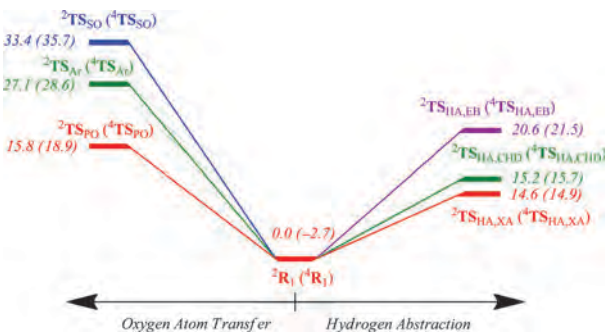

Fig. 2 Potential energy profile of substrate oxidation (H-abstraction, heteroatom oxidation and aromatic hydroxylation) by $^{4,2}\mathbf{R}_1$. Relative energies are in kcal mol^{-1} and obtained at UB3LYP/BS2//UB3LYP/BS1 and corrected for ZPE at UB3LYP/BS1. Quartet spin data is in parenthesis.

that the driving force for this reaction is proportional to the rate constant and consequently barrier height for the reaction, hence we will focus the discussion on the driving force for the reaction.[10]

$$ROO^{\bullet} + SubH \rightarrow ROOH + Sub^{\bullet} + \Delta H_{Eq1} \quad (1)$$

$$\Delta H_{Eq1} = BDE_{CH} - BDE_{OH} \quad (2)$$

$$ROOH \rightarrow ROO^{\bullet} + H^{\bullet} + BDE_{OH} \quad (3)$$

The calculated BDE_{CH} values of xanthene, 1,4-cyclohexadiene and ethylbenzene are 70.1, 69.7 and 82.4 kcal mol^{-1},[11] respectively, whereas we calculated a BDE_{OH} of $^{4}\mathbf{R}_1$ of 67.4 kcal mol^{-1}. The BDE_{OH} value of $^{4,2}\mathbf{R}_1$ is low as compared to that of a model of the active species of cytochrome P450 enzymes, *i.e.* $[Fe^{IV}{=}O(Por^{+\bullet})SH]$ with Por = porphyrin, where a BDE_{OH} = 88.9 kcal mol^{-1} was calculated using the same methods.[12] It is also well lower than the BDE_{OH} values for $[Fe^{IV}{=}O(Por^{+\bullet})L]$ and $[Fe^{IV}{=}O(TMC)L]^{n+}$, with L = Cl^{-} or $NCCH_3$, that are in the range of 82.8–88.6 kcal mol^{-1}.[13] Not surprisingly, these oxidants give much lower H-abstraction barriers from the benzyl position of ethylbenzene, and our recent studies showed a correlation between hydrogen abstraction barrier height and BDE_{OH} value of an oxidant.[14] Consequently, the low value of the BDE_{OH} of $^{4,2}\mathbf{R}_1$ implicates that only substrates with weak C–H bonds can be activated by this oxidant as indeed observed experimentally.[3]

Sulfoxidation is an electrophilic mechanism whereby two electrons are transferred from the substrate to the oxidant and a covalent S–O bond is formed.[15] As a result, the charge-transfer from the substrate to the oxidant in the transition state is large. The electron transfer processes that occur in the transition states, therefore, involve the filling of the $\pi^*_{OO,xz}$ orbital with a second electron. Consequently, the nickel unpaired spin density is hardly affected during the reaction mechanism and nickel acts as a spectator ion only by anchoring the superoxo group in a specific orientation. This contrasts the behaviour of iron(IV)-oxo porphyrin cation radical species, where the metal-porphyrin takes up the two electrons in an electrophilic mechanism and thereby lowers the reaction barriers.[11,13]

In summary, DFT calculations show that generally Ni(II)-superoxo is a poor oxidant of aliphatic and aromatic hydroxylation reactions. The calculations, however, implicate possible reactivity of $\mathbf{R}_1$ and $\mathbf{R}_2$ in H-abstraction reactions from xanthene and cyclohexadiene and in oxygen atom transfer to PPh_3. These studies are in support of experimental observation and rationalize the reactivity patterns.

The research was supported by CPU time provided by the National Service of Computational Chemistry Software (NSCCS). Financial support from KOSEF/MEST through the CRI and WCU (R31-2008-000-10010-0) programs is acknowledged. RL and LT thank the British Council for a Scholarship. DK holds a Ramanujan Fellowship from the Department of Science and Technology (DST), New Delhi (India), and acknowledges its financial support (Research Grants SR/S2/RJN-11/2008 and SR/S1/PC-58/2009). SdV thanks the Royal Society of Chemistry for a Journal Grant.

Notes and references

1 M. T. Kieber-Emmons and C. G. Riordan, *Acc. Chem. Res.*, 2007, **40**, 618.
2 (*a*) E. Szajna, A. M. Arif and L. M. Berreau, *J. Am. Chem. Soc.*, 2005, **127**, 17186; (*b*) M. T. Kieber-Emmons, J. Annaraj, M. S. Seo, K. M. Van Heuvelen, T. Tosha, T. Kitagawa, T. C. Brunold, W. Nam and C. G. Riordan, *J. Am. Chem. Soc.*, 2006, **128**, 14230; (*c*) M. Suzuki, *Acc. Chem. Res.*, 2007, **40**, 609; (*d*) S. Yao, E. Bill, C. Milsmann, K. Wieghardt and M. Driess, *Angew. Chem., Int. Ed.*, 2008, **47**, 7110; (*e*) S. Yao, C. Milsmann, E. Bill, K. Wieghardt and M. Driess, *J. Am. Chem. Soc.*, 2008, **130**, 13536; (*f*) S. Hikichi, H. Okuda, Y. Ohzu and M. Akita, *Angew. Chem., Int. Ed.*, 2009, **48**, 188; (*g*) T. D. Manuel and J.-U. Rohde, *J. Am. Chem. Soc.*, 2009, **131**, 15582; (*h*) A. Company, S. Yao, K. Ray and M. Driess, *Chem.–Eur. J.*, 2010, **16**, 9669.
3 (*a*) W. A. van der Donk, C. Krebs and J. M. Bollinger, Jr., *Curr. Opin. Struct. Biol.*, 2010, **20**, 673; (*b*) W. Lai and S. Shaik, *J. Am. Chem. Soc.*, 2011, **133**, 5444; (*c*) H. Hirao and K. Morokuma, *J. Am. Chem. Soc.*, 2010, **132**, 17901; (*d*) L. W. Chung, X. Li, H. Sugimoto, Y. Shiro and K. Morokuma, *J. Am. Chem. Soc.*, 2010, **132**, 11993; (*e*) H. Hirao and K. Morokuma, *J. Am. Chem. Soc.*, 2009, **131**, 17206; (*f*) J. M. Bollinger Jr. and C. Krebs, *Curr. Opin. Chem. Biol.*, 2007, **11**, 151.
4 (*a*) Y.-M. Lee, S. Hong, Y. Morimoto, W. Shin, S. Fukuzumi and W. Nam, *J. Am. Chem. Soc.*, 2010, **132**, 10668; (*b*) J. Cho, J. Woo and W. Nam, *J. Am. Chem. Soc.*, 2010, **132**, 5958; (*c*) A. Mukherjee, M. A. Cranswick, M. Chakrabarti, T. K. Paine, K. Fujisawa, E. Münck and L. Que, Jr., *Inorg. Chem.*, 2010, **49**, 3618.
5 J. Cho, R. Sarangi, J. Annaraj, S. Y. Kim, M. Kubo, T. Ogura, E. I. Solomon and W. Nam, *Nat. Chem.*, 2009, **1**, 568.
6 H. Kang, J. Cho and W. Nam, unpublished results.
7 (*a*) S. Shaik, D. Kumar, S. P. de Visser, A. Altun and W. Thiel, *Chem. Rev.*, 2005, **105**, 2279; (*b*) A. Bassan, T. Borowski, C. J. Schofield and P. E. M. Siegbahn, *Chem.–Eur. J.*, 2006, **12**, 8835.
8 R. Sarangi, J. Cho, W. Nam and E. I. Solomon, *Inorg. Chem.*, 2011, **50**, 614.
9 Basis set BS1/BS2 uses LACVP/LACV3P+ on Fe and 6-31G/6-311+G* on the rest of the atoms.
10 J. M. Mayer, *Acc. Chem. Res.*, 1998, **31**, 441.
11 (*a*) S. Shaik, D. Kumar and S. P. de Visser, *J. Am. Chem. Soc.*, 2008, **130**, 10128; (*b*) K. A. Prokop, S. P. de Visser and D. P. Goldberg, *Angew. Chem., Int. Ed.*, 2010, **49**, 5091.
12 S. P. de Visser and L. S. Tan, *J. Am. Chem. Soc.*, 2008, **130**, 12961.
13 (*a*) S. P. de Visser, *Chem.–Eur. J.*, 2006, **12**, 8168; (*b*) S. P. de Visser, L. Tahsini and W. Nam, *Chem.–Eur. J.*, 2009, **15**, 5577.
14 (*a*) S. P. de Visser, *J. Am. Chem. Soc.*, 2010, **132**, 1087; (*b*) D. Kumar, B. Karamzadeh, G. N. Sastry and S. P. de Visser, *J. Am. Chem. Soc.*, 2010, **132**, 7656.
15 (*a*) S. Shaik, Y. Wang, H. Chen, J. Song and R. Meir, *Faraday Discuss.*, 2010, **145**, 49; (*b*) D. Kumar, G. N. Sastry and S. P. de Visser, *Chem.–Eur. J.*, 2011, **17**, 6196.

 This journal is © The Royal Society of Chemistry 2011

CHAPTER 9

Drug Metabolism by Cytochrome P450: A Tale of Multistate Reactivity

DEVESH KUMAR

Molecular Modelling Group, Indian Institute of Chemical Technology, Hyderabad (A. P.) 500-607, India

9.1 Introduction

Cytochromes P450 (CYP 450 or P450) are heme based monoxygenases that form an iron(IV)-oxo heme cation radical in their catalytic cycle that is its active oxidant. They are named after the absorption band at 450 nm of the carbon-monoxide bound structure and essentially are a superfamily of cysteine thiolate-ligated heme enzymes that are responsible for most of phase I drug metabolism reactions. These enzymes are widespread in nature and have been identified in prokaryotic as well as eukaryotic cells.[1–7] The activity of CYP 450 enzymes determines the drug distribution in the human body, and as a consequence affects their pharmacological as well as toxic effects. There are many different isoforms of CYP 450 and these oxidize a wide range of chemical compounds although the substrate specificity does not correlate with their taxonomical classification. The CYP 450s catalyze various oxidation reactions, including aromatic and aliphatic hydroxylation, N-dealkylation, N-demethylation, O-dealkylation, O-demethylation, ester bond hydrolysis, dehalogenation, *etc*. A selection of substrates and products is given in Figure 9.1.[5] The CYP 450 enzymes play a central role in drug metabolism, which is likely evolved as an extension of the function of these enzymes in the metabolism of

Iron-Containing Enzymes: Versatile Catalysts of Hydroxylation Reactions in Nature
Edited by Samuel P de Visser and Devesh Kumar
© Royal Society of Chemistry 2012
Published by the Royal Society of Chemistry, www.rsc.org

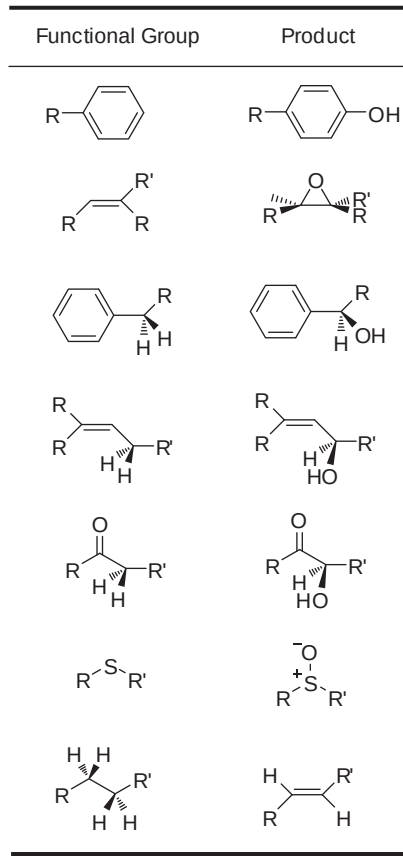

Figure 9.1 Reaction types catalyzed by CYP 450 enzymes.

endogenous substrates. The natural substrates, identified as endogenous compounds, for CYP 450 are classified as xenobiotic metabolizers.[8]

9.2 Nomenclature of Cytochrome P450 Enzymes

The Nomenclature Committee[9] has established a standardized system to name and assign individual genes of the CYP 450 superfamily into families and subfamilies. This is based on the level of amino acid sequence identity, phylogenetic association and gene organization as determined by the CYP 450. An italicized CYP is named for the root of all cytochrome P450 genomic and cDNA sequence, an Arabic numeral designates the individual family followed by the subfamily with letter. A pseudogene is a defective gene that often is a relic of gene duplications but does not produce a functional protein. The pseudogenes are designated by addition of the letter "P" immediately following the Arabic numeral family designation under the nomenclature rules for the cytochrome P450 superfamily.

With a large number of exceptions, CYP 450 sequences that have more than 40% amino acid identity are placed in the same family. Sequences that are more than 55% identical are placed in the same subfamily and those that are more than 97% identical are considered to represent alleles, unless there is evidence to the contrary.[2,10,11] On the basis of these rules, the first officially-named cytochrome P450 was CYP1A1. Since cytochrome P450 sequences are found throughout all domains of living organisms, the blocks of numbers that are reserved for the classification of new cytochrome P450 families, *i.e.*, CYP1–CYP49 and CYP301–CYP499 represent animal CYP 450s, whereas the CYP51–CYP69 and CYP501–CYP699 are CYP 450s found in lower eukaryotes, CYP71–CYP99 and CYP701–CYP999 are plant CYP 450s and finally the CYP101–CYP299 are bacterial CYP 450s.

With the aim to further organize the nomenclature of cytochrome P450s to reflect evolutionary history as well as better organization, the nomenclature committee has proposed to bundle the existing families into phylogenetically-relevant higher ordered clusters called "clans." A "clan" is defined as a group of gene families that evidently diverged from a single common ancestor based on commonalities among multiple phylogenetic assemblies of cytochrome P450 sequences.[12] These clans are then named either for the family with the lowest numerical CYP designation in the cluster or for the best-known family in the cluster. For example, the CYP3 (mammals), CYP5 (mammals), CYP6 (insects) and CYP9 (insects) families are part of the CYP3 clan. Enzyme derived from different gene is termed an isoform. Figure 9.2 presents the family tree of 60 sequenced genes of 18 families and 44 subfamilies of human cytochrome P450.[9]

9.3 Types of Drug Interactions

In the human body, the liver has been recognized as the major site for drug metabolism and, by the 1960s, the cytochrome P450 microsomal enzymes were characterized as key drug metabolizing enzymes. Adverse drug reactions happen if compounds that act as inducers or inhibitors of the enzymes disrupt the normal enzyme function. Enzyme induction can result in accelerated enzyme synthesis, faster drug metabolism and sub-therapeutic drug concentrations. Enzyme inhibition can lead to accumulation of a drug, in particular if the drug has a narrow therapeutic window, and serious toxicity may develop in a short time. Fortunately, because many drugs can be metabolized by more than one enzyme, inhibition of one pathway often brings an alternative pathway into play.[13]

9.3.1 Induction

Enzyme induction usually represents an absolute increase in enzyme synthesis, but phenobarbital, a well-known enzyme inducer, increases blood flow to the liver, and its use results in an increase of up to 50% in liver size.[14] Currently there are less than a dozen clinically important CYP 450 inducers that are

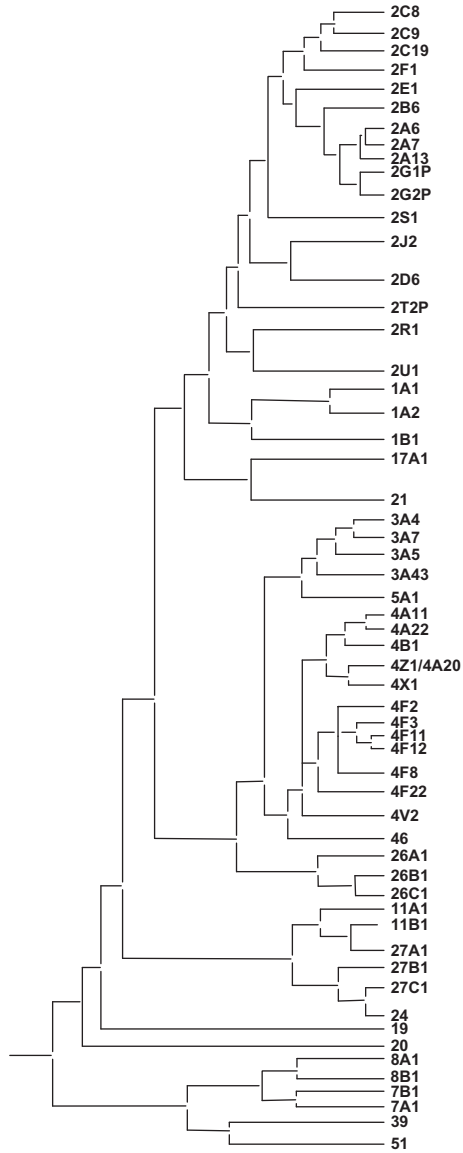

Figure 9.2 Family tree of human CYP 450 enzymes. All the names in the figure include the prefix CYP.

drugs. These include phenobarbital, other anticonvulsants and rifampin. One of the more serious recent examples is the induction of CYP3A4 by rifampin in HIV patients using protease inhibitors.[15] The onset and duration of the interaction depend both on the kinetics of the drug and of the half-life of the CYP enzyme, which ranges from 1–6 days.[14] Important non-pharmacologic inducers

include the polycyclic aromatic hydrocarbons in cigarette smoke, which cause the induction of CYP1A2 and result in higher dosing requirements of drugs like theophylline in smokers.[14] Chronic alcohol use induces CYP2E1, but its effects on metabolism of CYP2E1 substrates like acetaminophen are less predictable.

9.3.2 Inhibition

Enzyme inhibition usually represents an absolute decrease in enzyme metabolic activity because of the binding of an inhibitor can stop a substrate from entering into the active or binding site of enzyme. A good example is the inhibition of the metabolism of tricyclic antidepressants like desipramine by fluoxetine.[16] The substrate, desipramine, is metabolized by CYP2D6, and its metabolism is strongly inhibited by binding of fluoxetine to the same isozyme. Fluoxetine at a dose of 20 mg daily can produce a four-to-five-fold increase in the plasma concentration of desipramine, so that a decrease in desipramine dose is necessary to avoid unpleasant or toxic side effects. The duration of the interaction depends on the half-life of the inhibitor.[14] A drug can be both a substrate and an inhibitor for a particular isozyme. A drug that is not a substrate can also inhibit the activity of a non-substrate isozyme.[13] Quinidine is metabolized by CYP3A3/4, but powerfully inhibits CYP2D6.

Sometimes, detailed knowledge of metabolic pathways can predict the clinical significance of an interaction. For example, the potential drug interactions of tertiary tricyclic antidepressants like imipramine by inhibitors of CYP2D6 are limited, because oxidative metabolism can still go on through secondary pathways catalyzed by CYP1A2, CYP2C19, and CYP3A3/4.[13] Although it is helpful to know the extent of the theoretical possibilities, only clinical experience is able to prove which interactions are clinically significant.[17]

9.4 Important Isoforms of Human CYP

There are about 18 families and 43 subfamilies of CYP genes in humans, which comprise up to 60 cytochrome P450s and 58 pseudogenes. In terms of drug metabolism these enzymes mainly belong to the CYP1, CYP2 and CYP3 families. Table 9.1 summarizes the human CYP family with their primary function. In recent years significant numbers of crystal structures of various CYP 450 isoforms have been reported. As an example, Figure 9.3 shows the active site of three isoforms, CYP1A2, CYP2D6 and CYP3A4, as taken from the crystal structure coordinates from 2HI4,[18] 2F9Q,[19] and 3NXU[20] protein databank (pdb) files, respectively.

9.4.1 CYP1A2 Isoform

CYP1A2 mostly metabolizes chemicals and environmental toxins[21] and drug substrates for this isoform are caffeine, propranolol and theophylline[14] The drugs imetidine, fluvoxamine, erythromycin, clarithromycin, enoxacin,

Table 9.1 Diversity and function of human cytochrome P450 enzymes.

CYP family	*Primary function*	*Subfamily, genes, pseudogenes*
CYP1	Drug metabolism	3 Subfamilies, 3 genes, 1 pseudogene
CYP2	Drug and steroid metabolism	13 Subfamilies, 16 genes 16 pseudogenes
CYP3	Drug metabolism	1 Subfamily, 4 genes, 2 pseudogenes
CYP4	Arachidonic acid or fatty acid metabolisms	5 Subfamilies, 11 genes, 10 pseudogenes
CYP5	Thromboxane A2 synthase	1 Subfamily, 1 gene
CYP7A	Bile acid biosynthesis 7-α hydroxylase of steroid nucleus	1 Subfamily, 1 gene
CYP7B	Brain specific form of 7-α hydroxylase	1 Subfamily, 1 gene
CYP8A	Prostacyclin synthase	1 Subfamily, 1 gene
CYP8B	Bile acid biosynthesis	1 Subfamily, 1 gene
CYP11	Steroid biosynthesis	2 Subfamilies, 3 genes
CYP17	Steroid biosynthesis (17-α hydroxylase)	1 Subfamily, 1gene
CYP19	Steroid biosynthesis (aromatase forms estrogens)	1 Subfamily, 1 gene
CYP20	Unknown function	1 Subfamily, 1 gene
CYP21	Steroid biosynthesis	1 Subfamily, 1 gene, 1 pseudogene
CYP24	Vitamin D degradation	1 Subfamily, 1 gene
CYP26	Retinoic acid hydroxylase	3 Subfamily, 3 gene
CYP27A	Bile acid biosynthesis	1 Subfamily, 1 gene
CYP27B	Vitamin D3, 1-α hydroxylase activates vitamin D3	1 Subfamily, 1 gene
CYP27C	Unknown function	1 Subfamily, 1 gene
CYP39	7-α Hydroxylation of 24 hydroxy cholesterol	1 Subfamily, 1 gene
CYP46	Cholesterol 24-hydroxylase	1 Subfamily, 1 gene
CYP51	Cholesterol biosynthesis, lanosterol 14-alpha demethylase	1 Subfamily, 1 gene, 2 pseudogenes

Replace with new figur

Figure 9.3 Active site of three typical CYP 450 isoforms: (a) CYP1A2 as taken from the 2HI4 pdb file; (b) CYP2D6 as taken from the 2F9Q pdb file; (c) CYP3A4 as taken from the 3NXU pdb file.

AQ1

ciprofloxacin, isoniazid *etc*. are inhibitor whereas polycyclic aromatic hydrocarbons (cigarette smoke) and dioxin are inducers for CYP1A2.

9.4.2 CYP2C8, CYP2C9 and CYP2C19 Isoforms

CYP2C8, CYP2C9 and CYP2C19 are the most clinically important isoforms among the 2C subfamily. CYP2C8 is well known to catalyze the paclitaxel biosynthesis[22] and the bioconversion of arachidonic acid into epoxyeicosatrienoic acid in liver and kidney tissue.[23] CYP2C9 is highly expressed in hepatic tissue and displays strong metabolic activity towards numerous drugs, including the anticoagulant warfarin, the antidiabetic agent tolbutamide, and sedatives such as hexobarbital, ibuprofen, diclofen and several non-steroidal anti-inflammatory drugs. Drugs like phenobarbital and rifampin are its inducers, whereas other drugs such as amiodarone, fluconazole, fluoxetine, ticlopidine operate as inhibitors. CYP2C19 is known for the metabolism of the anticonvulsant agent mephenytoin and also shows significant activity towards various antidepressants such as diazepam and also towards anti-malarial drugs.

9.4.3 CYP2D6 Isoform

CYP2D6 can metabolize over 80 different clinically used drugs,[24] including most antidepressants, with the exception of fluvoxamine, nefazodone, citalopram and bupropion, which are either inhibitors of CYP2D6 or metabolized by CYP2D6.[25] The CYP2D6 inhibitors include drugs such as quinidine, paroxetine, fluoxetine, norfluoxetine, sertraline, desmethylsertraline, fluvoxamine, nefazodone, venlafaxine, erythromycin and ketoconazole. On the other hand, rifampin is induced by this CYP 450 isozyme.[14]

9.4.4 CYP3A4 Isoform

CYP3A4 metabolizes more than 150 different drugs and drug types, including most calcium channel blockers, benzodiazepines, cyclosporine and tacrolimus.[14] The CYP3A4 isoform does not exhibit polymorphism, but it shows large individual variations in isozyme levels[14,24] and this complicates predictions of drug interactions. About 70% of CYP3A4 isozymes are found in the gut, where they are involved in metabolism of substrates before they can reach the liver. Therefore, CYP3A4 is a major agent of the first-phase of drug metabolism. Commonly known drugs like rifampin, rifabutin and rifapentine act as inducer for CYP3A4 whereas drugs like cimetidine, erythromycin, grapefruit juice, ketoconazole and related species are well-known inhibitors.

Figure 9.4 shows contributions of different isoforms of CYP families towards drug metabolism of the 200 most frequently prescribed drugs in the United States of America. Obviously, from Figure 9.4, most (87%) of these drugs are metabolized by CYP families 1, 2 and 3, with major contributions from

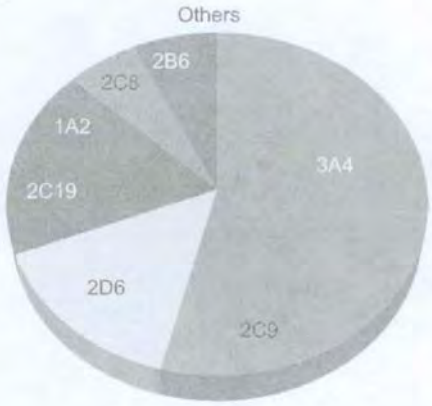

Figure 9.4 Contributions of CYP isoforms towards drug metabolism of the 200 most frequently prescribed drugs in the United States of America.

CYP3A4/5 (37% of drugs) followed by CYP2C9 (17%), CYP2D6 (15%), CYP2C19 (10%), CYP1A2 (9%), CYP2C8 (6%) and CYP2B6 (4%).[26]

9.5 Examples of Generation of Various Metabolites from a Single CYP 450

Several studies were carried out to identify which of the CYP 450 isoforms is responsible for the formation of the primary metabolites of drugs *in vitro* using human liver microsomes. Generally, only one CYP 450 isoform is responsible for formation of the different metabolites, while occasionally one other CYP 450 isoform generates one of the metabolites. For example, three CYP 450-mediated metabolites, namely, ziprasidone sulfoxide, ziprasidone sulfone and oxindole acetic acid, were identified using mass spectroscopy for ziprasidone (a FDA approved drug for the treatment of schizophrenia) *in vitro* using human liver microsomes (Figure 9.5). It was found that CYP3A4 is solely responsible for the formation of ziprasidone metabolites and that ziprasidone is not even a substrate for the other isoforms.[27–29]

Another example of different metabolites of a drug that are cleared by only one CYP 450 isoform is fluvastatin (lescol), which is a 3-hydroxy-3-methyl-glutaryl coenzyme A reductase inhibitor, and helps to lower the low density lipoprotein cholesterol levels by 20–30% at a daily dose of 20–40 mg.[30–32] Fluvastatin is metabolized by human liver microsomes into three metabolites, namely 5-hydroxy-, 6-hydroxy- and *N*-deisopropyl-fluvastatin (Figure 9.6). The HPLC and mass spectroscopy studies showed that although five CYP 450 isoforms can metabolize fluvastatin, actually all three metabolites are formed by CYP2C9 only, whereas CYP1A1, CYP2C8, CYP2D6 and CYP3A4 only produce 5-hydroxy-fluvastatin.[33]

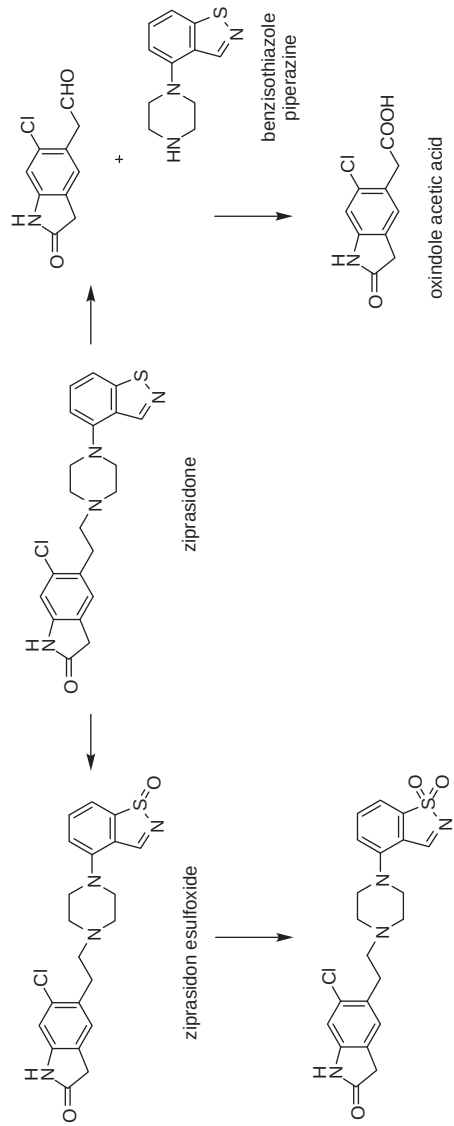

Figure 9.5 *In vitro* metabolic pathways of ziprasidone by human liver microsomes.

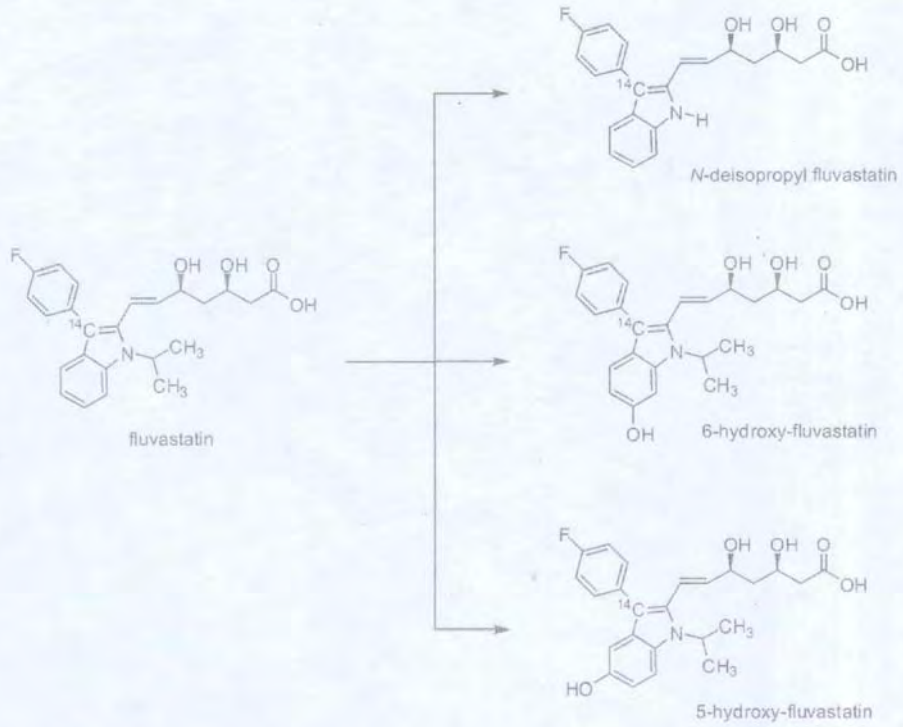

Figure 9.6 *In vitro* metabolic pathways of fluvastatin by human liver microsomes.

There are numerous drug compounds, such as rosiglitazone, thiazolidinedione, rifampicin, paracetamol, *etc.*,[34–36] whose various metabolites are cleared by only one specific CYP 450 isoform *via* various oxidation reactions such as aromatic and aliphatic hydroxylation, N-dealkylation, O-dealkylation, ester bond hydrolysis, dehalogenation, *etc*. These large varieties of catalytic reactions, however, seem to implicate the involvement of multiple oxidant species in CYP 450 enzymes that are responsible for these reactions. Detailed mechanistic studies, experimentally as well as computationally, have established that actually only one active species in the catalytic cycle of CYP 450 enzymes is responsible for all oxygen mediated reactions, namely Compound I (which will be discussed in detail later).

9.6 CYP 450 Structure

In 1985, Poulos and coworkers reported the first X-ray crystal structure of a CYP 450 isozyme using the soluble bacterial CYP 450_{cam} isolated from the bacterium *Pseudomonas putida*.[37] Now-a-days a range of different crystal structure coordinates are available for catalytic cycle intermediates, which have been characterized using spectroscopic techniques. More than 300 different crystal structures of various CYP 450 isozymes can be found in the protein

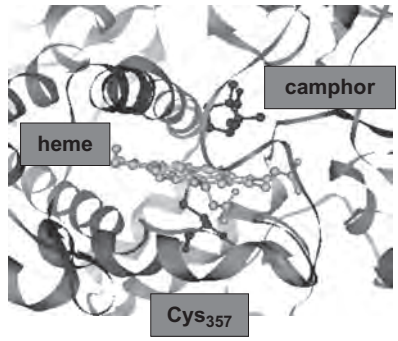

Figure 9.7 Active site of CYP 450_{cam} as taken from the 1DZ9 crystal structure, with axial cysteinate and substrate highlighted.

databank.[38] These isozymes show considerable homology and all contain a central heme *b* group (iron protoporphyrin IX), where the catalysis takes place. Generally, the heme is linked to a cysteine (Cys) amino acid *via* thiolate bonding to the metal, which is often termed the axial ligand of the metal.[39]

Figure 9.7 shows active site of CYP 450_{cam} (a bacterial enzyme that hydroxylates camphor) with the substrate molecule placed over the active site of the enzyme. In all CYP 450 isoforms, the active species of the enzyme is an iron ion ligated to a protoporphyrin IX macrocycle with two additional ligands: one labeled axial that is usually a thiolate group from a cysteinate residue (Cys_{357} in CYP 450_{cam}) of the protein and the other labeled distal, which is a variable ligand and the site of molecular oxygen binding. This distal ligand changes during the catalytic cycle of the enzyme and thereby activates the enzyme's main function.

9.7 Catalytic Cycle of CYP 450

The catalytic cycle of CYP 450 enzymes is schematically depicted in Figure 9.8 and starts from a resting state (**1**) where a distal water molecule is ligated to the sixth ligand position of a low spin ferric state. Entry of substrate into substrate binding pocket expels this distal water molecule and also triggers a spin state crossing from low-spin to high-spin[40] resulting in a five-coordinate high spin ferric state (**2**). In most CYP 450 isozymes, the substrate binds tightly to the substrate binding pocket in a locked position through electrostatic and hydrogen bonding interactions.[41] Density functional theory and combined quantum mechanics/molecular mechanics studies confirmed that a spin state crossing occurs with a different spin state ordering for **1** and **2**.[42–44] The change in spin state triggers an electron transfer process from the reductase domain and reduces the ferric complex to a ferrous complex (**3**).[40] Molecular oxygen then binds to **3** to form the ferric-superoxo heme complex (**4**, Fe^{III}-O_2^{-}). Upon addition of a second electron to the heme, **4** converts into **5**, which is assumed to be the rate-limiting step in the catalytic cycle,[45] and yields a ferric-peroxo species (**5**, Fe^{III}-O_2^{2-}).

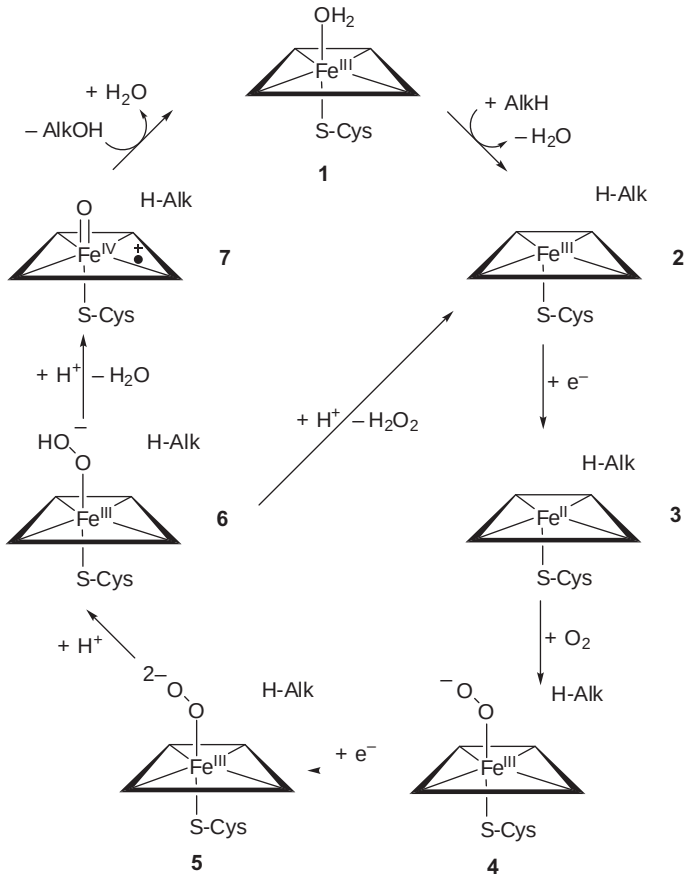

Figure 9.8 Catalytic cycle of cytochrome P450 enzymes.

A subsequent protonation step of **5** gives a ferric-hydroperoxo complex, **6**, also known as Compound 0 (Cpd 0). The delivery of the second proton onto the proximal oxygen atom of Cpd 0 will result in release of a hydrogen peroxide (H_2O_2) molecule to yield **2**, whereas delivery onto the distal oxygen atom of Cpd 0 results in heterolytic O–O bond cleavage to form a water molecule and generate the putative iron(IV)-oxo porphyrin π-cation radical intermediate (**7**). The latter is commonly known as Compound I (Cpd I) and is equivalent to Cpd I of horseradish peroxidase (HRP). The Cpd I (**7**) monoxygenates the substrate, for example, an alkane is converted into an alcohol and released from the binding pocket. The vacant binding site of the heme is then reoccupied with a water molecule that has re-entered the active site and restores the system to the resting state (**1**).

9.8 Compound I of CYP 450: The Active Species

Recently, Rittle and Green reported[46] spectroscopic and kinetic evidence of the existence of Cpd I in CYP119. In their study they found that the electronic

structure of P450 Cpd I has a triplet iron(IV)-oxo group ($S=1$) coupled to an $S=\frac{1}{2}$ ligand-base radical. The UV/visible and Mössbauer spectra of CYP119 Cpd I are similar to that found for Cpd I of chloroperoxidase, although the EPR signatures are different. They also investigated the rate constants and kinetic isotope effects (KIE) of substrate hydroxylation reactions for hexanoic acid, octanoic acid, dodecanoic acid and camphor. These studies confirm the existence of Cpd I of CYP 450 and also the capability of Cpd I to hydroxylate unactivated hydrocarbons.[46] Earlier studies inferred its presence from cryogenic and electronic absorption studies[47,48] as well as from cryogenic EPR/ENDOR spectroscopy of the alcohol product of camphor hydroxylation.[49–51] The analogous reactivity (similar product distribution and stereochemical scrambling) of synthetic Cpd I species and CYP 450 towards the same substrates provides strong but indirect support for the participation of Cpd I in the reaction mechanism.[52] Owing to problems in detecting and characterizing Cpd I, many suggestions of alternative oxidant species were made such as Cpd 0,[53–55] and Cpd II,[56–58] which is the one-electron reduced species of Cpd I. However, detailed biomimetic experimental studies showed that Cpd 0 is less reactive than Cpd I and, therefore, ruled out the ferric-hydroperoxo species as a possible oxidant. So far all studies (computational as well as experimental) agree that only one oxidant, namely Cpd I, is active in CYP 450 enzymes.[7,59–61] Since experimental studies failed to characterize Cpd I and were unable to resolve the uncertainty of the status as the primary oxidant of CYP 450 enzymes, theoretical studies have been performed with the main focus of establishing the active species of this enzyme.[62–78] It is generally agreed that Cpd I has two low-lying degenerate spin states, doublet and quartet, that can masquerade the activity of the oxidant and lead to the seeming involvement of multiple oxidants.

Figure 9.9(a) and (b) presents the geometry of Cpd I with two different axial ligands, SH^- and SMe^-, respectively, that mimic the cysteinate axial ligand in the enzyme. Also given are group spin densities (ρ) as obtained from DFT and DFT/MM.[79] These values are compared with those obtained from experimental EXAFS[80] and EPR-ENDOR[81] studies.

Figure 9.9(d) shows the high lying occupied and low lying virtual orbitals as well as the electronic configuration of Cpd I (**7**). In particular, the five metal 3d-type orbitals are shown and a high-lying mixed porphyrin-thiolate based orbital, labeled as a_{2u}. Since thiolate is a potent electron donor, the sulfur-porphyrin mixing in a_{2u} is significant,[71] but for weaker electron-donor ligands, such as imidazole,[82,83] this mixing is negligible and a_{2u} is a pure porphyrin orbital. The lowest three 3d-block orbitals are, in increasing order of energy, the nonbonding $\delta(3d_{x2-y2})$ orbital and the two π^*_{FeO} (π^*_{xz} and π^*_{yz}) orbitals; the other two involve antibonding interactions between the metal $3d_{xz,yz}$ and the oxygen $2p_{x,y}$ atomic orbitals and they are high-lying virtual orbitals of Cpd I (σ^* orbitals); the σ^*_{xy} orbital describes the Fe–N antibonding interactions whereas the σ^*_{z2} describes the interactions along the O–Fe–S axis. Their energy ordering is dominated by the length and consequently the strength of the Fe–O bond, and when the distance is short the σ^*_{z2} orbital rises above the σ^*_{xy}

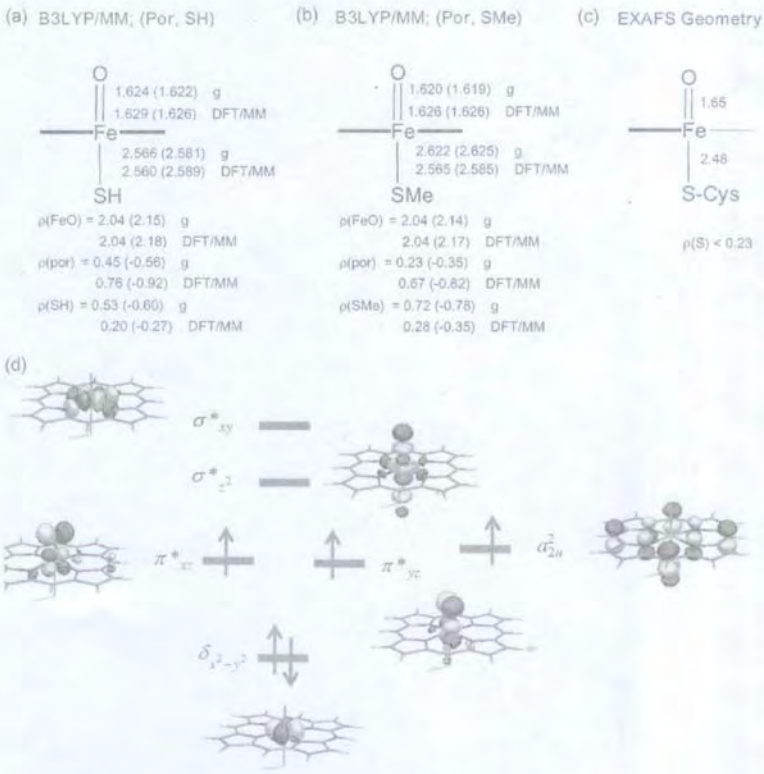

Figure 9.9 Structure of Cpd I (Å) with axial ligand (a) SH^- and (b) SMe^-, and spin group spin densities.[79] (c) Geometry (Å) as obtained from experimental EXAFS[80] and EPR-ENDOR spin densities.[81] (d) Key molecular orbitals of Cpd I. Data refer to ^{4}Cpd I (^{2}Cpd I). Here g stands for gas-phase and ρ is spin density.

orbital. In Cpd I with the $Por^{\bullet+}Fe^{IV}$ oxidation state, the 3d-block orbitals have four electrons whereas the porphyrin-based a_{2u} orbital is singly occupied. This occupation generates a pair of almost degenerate spin states: one quartet spin state ($S=\frac{3}{2}$) with occupancy $\delta^{\uparrow\downarrow}\ \pi^*_{xz}{}^{\uparrow}\ \pi^*_{yz}{}^{\uparrow}\ a_{2u}{}^{\uparrow}$ and a doublet spin state ($S=\frac{1}{2}$) with occupancy $\delta^{\uparrow\downarrow}\ \pi^*_{xz}{}^{\uparrow}\ \pi^*_{yz}{}^{\uparrow}\ a_{2u}{}^{\downarrow}$. Obviously, from Figure 9.9(a), in the gas phase the a_{2u} spin density is equally distributed over the porphyrin and sulfur groups whereas in a QM/MM calculated system more spin density is found on the porphyrin. There exists also some other possible spin states ($S=\frac{5}{2}$ and $\frac{3}{2}$) which are also relatively low lying and generated due to one-electron promotion from an electron in the δ orbital to the σ^*_{xy} orbital. These electronic states and their occupancy will be discussed below.[68,84]

9.8.1 Axial Ligand Effect of Compound I

Heme enzymes are common enzymes in nature, but not all heme enzymes have the heme linked to the protein *via* a thiolate bridge of a cysteinate residue. Thus, peroxidases have a central heme group, where the metal is bound to the imidazole ring of a histidine residue, while catalase is a heme enzyme with a tyrosinate axial ligand.[85–87] The differences in heme binding have been correlated with the functional differences of these enzymes, whereby peroxidases detoxify hydrogen peroxide to two water molecules and catalases convert hydrogen peroxide into molecular oxygen and water. The axial ligand of heme enzymes, therefore, seems to affect the function of the heme and it has been suggested that anionic ligands, such as cysteinate have electron-donating properties, *i.e.* entice a ''push''-effect on the heme, whereas a neutral histidine ligand will be electron-withdrawing, *i.e.* has a ''pull''-effect on the heme.[88,89] Since many computational studies addressed this ''push'' and ''pull'' effects, let us include a short summary of studies on peroxidases and catalases here.

Figure 9.10 displays the catalytic cycle of a typical peroxidase, namely cytochrome *c* peroxidase (C*c*P). As mentioned, the heme is linked to the protein *via* a histidine axial ligand.[90] This histidine ligand is part of a hydrogen bonded triad that includes a carboxylic acid group of an aspartic acid (Asp_{235}) and an axially located tryptophan group (Trp_{191}). On the distal site, substrate hydrogen peroxide binds, which is involved in hydrogen bonding interactions with a histidine group (His_{52}) and an arginine side chain (Arg_{48}). In the first step of the catalytic cycle, the substrate donates a proton to His_{52} to form an iron(III)-hydroperoxo complex, similar to Cpd 0 in the catalytic cycle of CYP 450. This complex abstracts a proton from His_{52} again and splits off a water molecule to form an iron(IV)-oxo $Trp(^{+\bullet})$ species, designated as Cpd I(C*c*P). In most other peroxidases, however, Cpd I has an electronic state similar to that found for CYP 450 with a heme cation radical rather than a tryptophan cation radical. Cpd I(C*c*P) after two reduction and two protonation steps releases a water molecule and returns back to the resting state.

Detailed computational studies using the QM/MM methodology on the enzyme horseradish peroxidase confirmed the first step in the catalysis as a proton relay where His_{52} initially abstracts the proximal proton of hydrogen peroxide that is relayed to the distal oxygen atom in a subsequent step to give Cpd I and a water molecule.[91]

C*c*P was one of the first heme peroxidases for which a crystal structure was determined and Cpd I was characterized with electron paramagnetic resonance (EPR) studies and as such it has become the template of peroxidases in general.[92–94] This is despite the formation of a Cpd I structure with an unusual radical site. Cpd I of CYP 450, designated as [Cpd I(P450)], as well as Cpd I of catalase, or [Cpd I(Cat)], and many heme-peroxidases all have the same electronic state with an iron(IV)-oxo group embedded into a singly-oxidized heme group, *i.e.* $[Fe^{IV}{=}O(heme^{+\bullet})L]$ with L being the axial ligand. By contrast, the electronic structure of Cpd I(C*c*P) is $[Fe^{IV}{=}O(heme)(Trp^{+\bullet})]$, where essentially an electron transfer from the axial tryptophan residue to the heme has

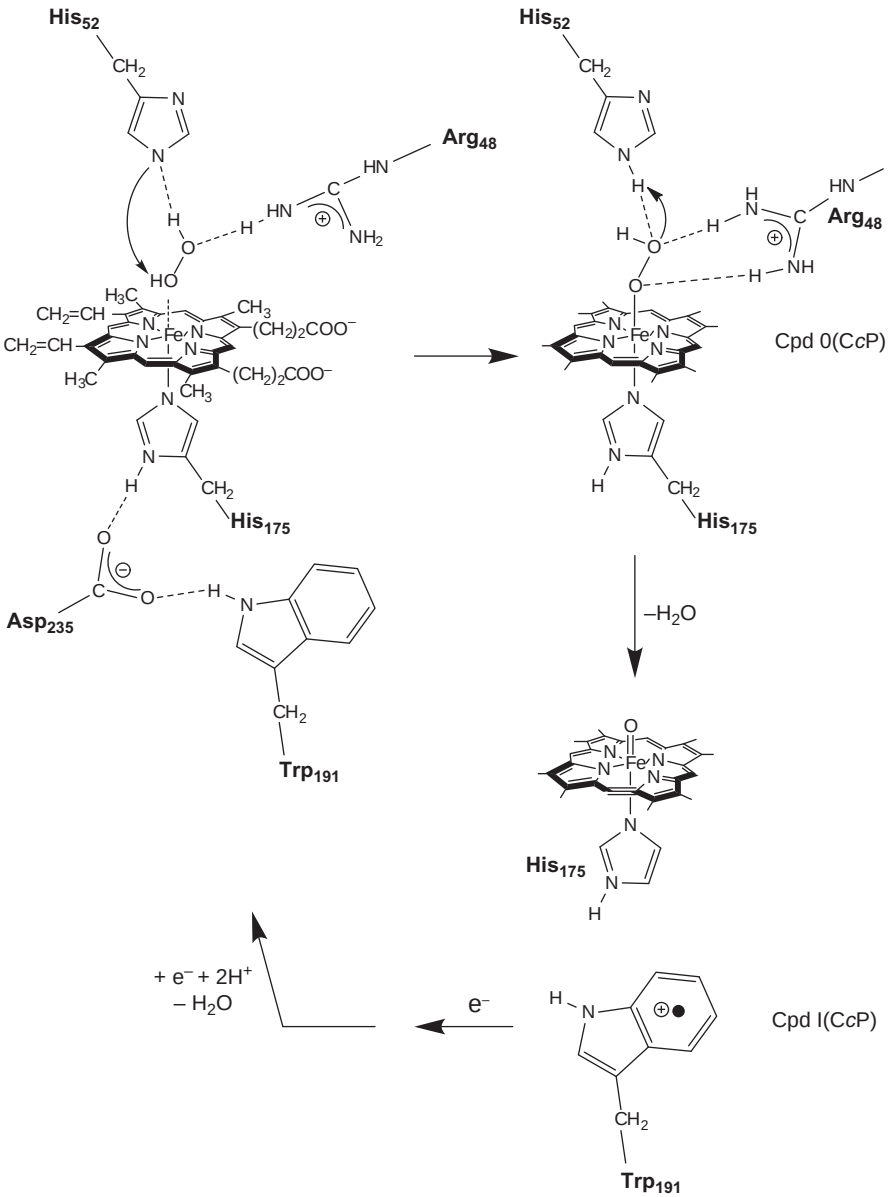

Figure 9.10 Catalytic cycle of cytochrome *c* peroxidase enzymes.

occurred. Structurally, the active site of C*c*P is not dramatically different from that obtained for, for example, horseradish peroxidase (HRP) and ascorbate peroxidase (APX).[95–97] In HRP and APX the heme is also linked to a histidine axial ligand of the protein that is hydrogen bonded to a carboxylic acid group of an aspartic acid residue. APX also has an axial tryptophan residue within

hydrogen bonding distance to the axial histidine, but it is missing in HRP and replaced by a phenylalanine residue. Nevertheless, Cpd I in both HRP and APX are characterized as [Fe^{IV}=O(heme$^{+\bullet}$)His].

A series of computational studies were performed to determine the origin of the differences in electronic configuration of Cpd I(C*c*P) and Cpd I(APX).[98–101] Figure 9.11 displays the optimized geometries of a Cpd I(C*c*P) model that is described as an iron(IV)-oxo group in protoporphyrin IX (without side chains) and bound to an axial imidazole group. In addition, Asp_{235} and Trp_{191} are included as acetate and indole groups, respectively. Crystal structure coordinates of the active site of C*c*P and APX reveal a cation binding site in APX that accommodates a K^+ ion.[94] Density functional theory studies included a point charge in the model in the cation binding site with a charge $Q = 0$, $+1$ or -1.[100] As follows from the group spin densities depicted in Figure 9.11, the FeO group has a total spin density (ρ) of about 2, implicating two unpaired electrons in FeO type orbitals. These can be assigned to the π^*_{FeO} (π^*_{xz} and π^*_{yz}) orbitals similar to those shown in Figure 9.9(d) for Cpd I(P450). The third unpaired electron spin

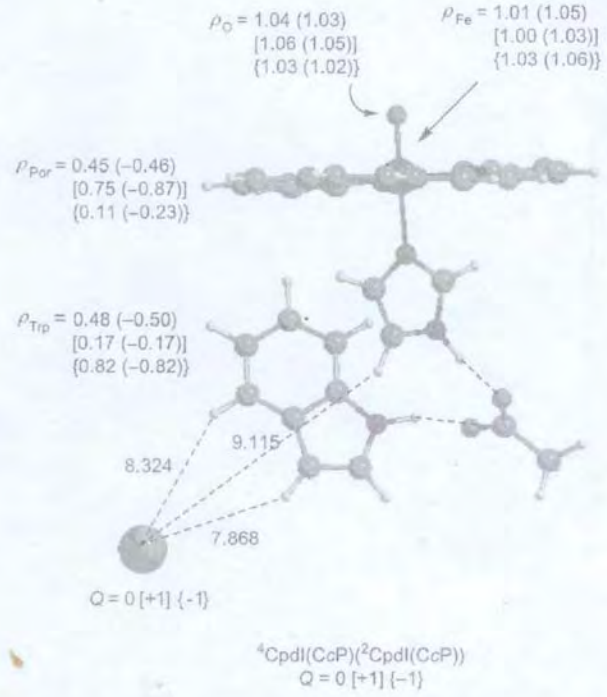

Figure 9.11 Group spin densities of quartet and doublet Cpd I(C*c*P) under the influence of an added point charge with magnitude $Q = 0$, $+1$ or -1. Group spin densities out of parentheses correspond to quartet and those in parentheses correspond to doublet spin state with $Q = 0$. Group spin densities in square brackets correspond to $Q = +1$ whereas those in curly brackets correspond to $Q = -1$ in the above fashion. Also given are distances (Å) between the point charge and atoms of the chemical model.

density is distributed over the heme (ρ_{Por}) and the tryptophan ligand (ρ_{Trp}). Without a point charge there is approximately equal spin density, *i.e.* radical character, on the heme and tryptophan units. This is in agreement with early studies of the Siegbahn group on peroxidases,[102] where also spin density on both groups was found. However, adding a point charge to the system dramatically changes the radical character of the heme and tryptophan groups, whereby a positive charge gives an [Fe^{IV}=O(heme$^{+\bullet}$)(Trp)] conformation, while a negative point charge an [Fe^{IV}=O(heme)(Trp$^{+\bullet}$)] situation. These studies, therefore, confirm the experimental observation of charge separation in the various Cpd I species and show the intricate balance charges in Cpd I. More recent QM/MM studies on the difference of C*c*P and APX enzymes revealed an induced electric field effect of the protein to affect the orbital energy levels of Cpd I, and hence the relative energies of [Fe^{IV}=O(heme$^{+\bullet}$)(Trp)] *versus* [Fe^{IV}=O(heme)(Trp$^{+\bullet}$)].[103,104]

Clearly, the axial ligand plays a vital role in controlling the electron affinity of Cpd I due to subtle charge/spin density relay from the heme to other groups in the vicinity. As a consequence, there have been many efforts to quantify the axial ligand effect of hemes. The first such study was performed by Gross and coworkers and relates to an experimental investigation using [Fe^{IV}=O(TMP$^{+\bullet}$)L] with L = F^-, Cl^-, CH_3COO^-, $CF_3SO_3^-$ and ClO_4^- (TMP = tetramesitylporphyrin).[105–107] Thus, ligating anionic ligands (F^-, Cl^-, CH_3COO^-) gave enhanced reactivities in styrene epoxidation as compared to nonligating ligands ($CF_3SO_3^-$ and ClO_4^-). In addition, a *trans*-influence on the spectroscopic parameters was identified, whereby the systems with strong "push"-effect ligands gave higher Fe–O vibrational frequencies. Nam and coworkers investigated [Fe^{IV}=O(TPFPP$^{+\bullet}$)L] with L = Cl^- or $NCCH_3$ [TPFPP = *meso*-tetrakis(pentafluorophenyl)porphyrin].[108] The axial ligand effect gave differences in *cis versus trans* product ratios in olefin epoxidation, differences in kinetic isotope effects and even regioselectivity changes from aliphatic to aromatic hydroxylation.

To understand the axial ligand effect on the catalysis of substrate activation by Cpd I models, many studies have investigated the electronic properties of Cpd I with variable axial ligand,[109–116] and the subsequent reactivity differences in oxygen atom transfer reactions.[117] Figure 9.12 displays a selection of calculated Cpd I type species that differ by the ligand *trans* to the oxo group as taken from refs 73, 83, 100, 113 and 118. These systems represent a CYP 450 Cpd I mimic, Cpd I(SH), where the cysteinate ligand is replaced by thiolate. It also has mimics of Cpd I of catalase, Cpd I(Cat), and cytochrome *c* peroxidase, Cpd I(C*c*P), where the axial ligands undergo hydrogen bonding interactions with nearby residues. Finally, Figure 9.12 displays a biomimetic model system with a chloride axial ligand, Cpd I(Cl). As follows from the optimized geometries in Figure 9.12, the average Fe–N distance falls within a narrow range of 2.017–2.022 Å. By contrast, much larger deviations are found for the Fe–O distances, which range from 1.648 Å for ^{2}Cpd I(SH) to 1.665 Å for ^{4}Cpd I(C*c*P). This will directly affect the stretch vibration for the Fe–O mode, but also implies that the bond is stronger for Cpd I(SH) as compared to Cpd I(C*c*P), for instance.

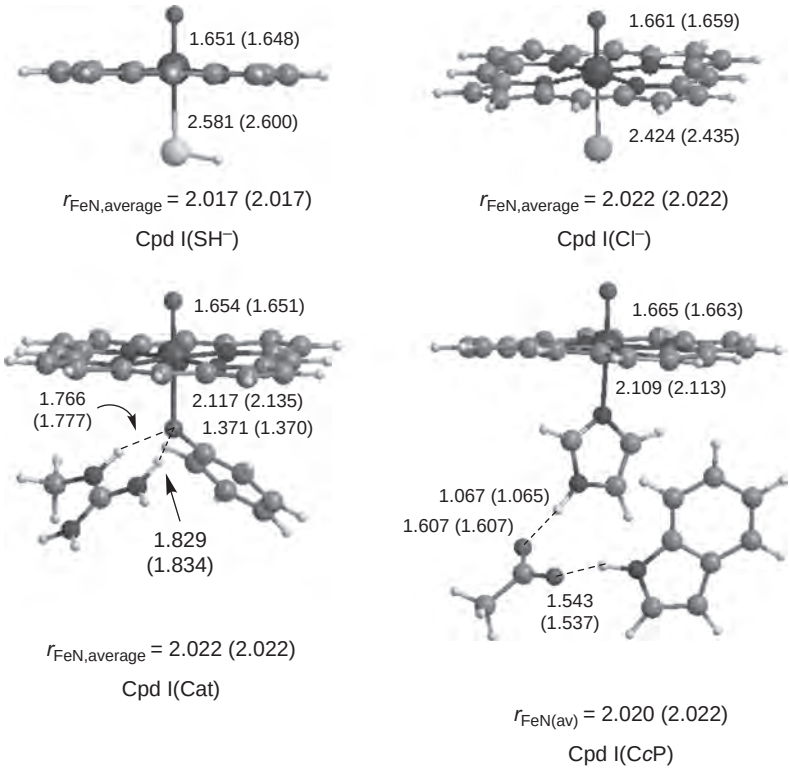

Figure 9.12 Optimized geometries of various Cpd I models with different axial ligand descriptions. Bond lengths are in ångströms.

Shaik, de Visser and coworkers estimated the axial ligand effect through investigating the electron affinity of Cpd I ($EA_{\text{Cpd I}}$) and compared the result with the electron affinity of a Cpd I system without axial ligand (EA_{NL}) and a model where the axial ligand is replaced by a point charge (EA_{PC}).[112,114] Figure 9.13 displays the calculated electron affinities for CYP 450 Cpd I and catalase Cpd I. A full geometry optimization of Cpd I(SH) and Cpd I(Cat) and their one-electron reduced forms, Compound II or Cpd II, was performed and subsequently single point calculations were carried out for the structures without axial ligand or with a point charge in the position of the atom that is bound to the metal. From these calculations, the effect of the axial ligand can be divided into an electric field effect (ΔE_{field}) and a quantum mechanical effect (ΔE_{QM}). The electric field effect induced by the axial ligand is estimated from the energy difference between EA_{NL} and EA_{PC}, whereas the quantum mechanical effect is estimated from the difference between EA_{PC} and $EA_{\text{Cpd I}}$. That way an electric field effect contribution of 76.7 kcal mol^{-1} is calculated for Cpd I(Cat) and 54.0 kcal mol^{-1} for Cpd I(SH). On the other hand, values of $\Delta E_{\text{QM}} = 1.8$ and 38.8 kcal mol^{-1} are found for Cpd I(Cat) and Cpd I(SH), respectively. Thus, in the case of catalase the dominant contribution is the

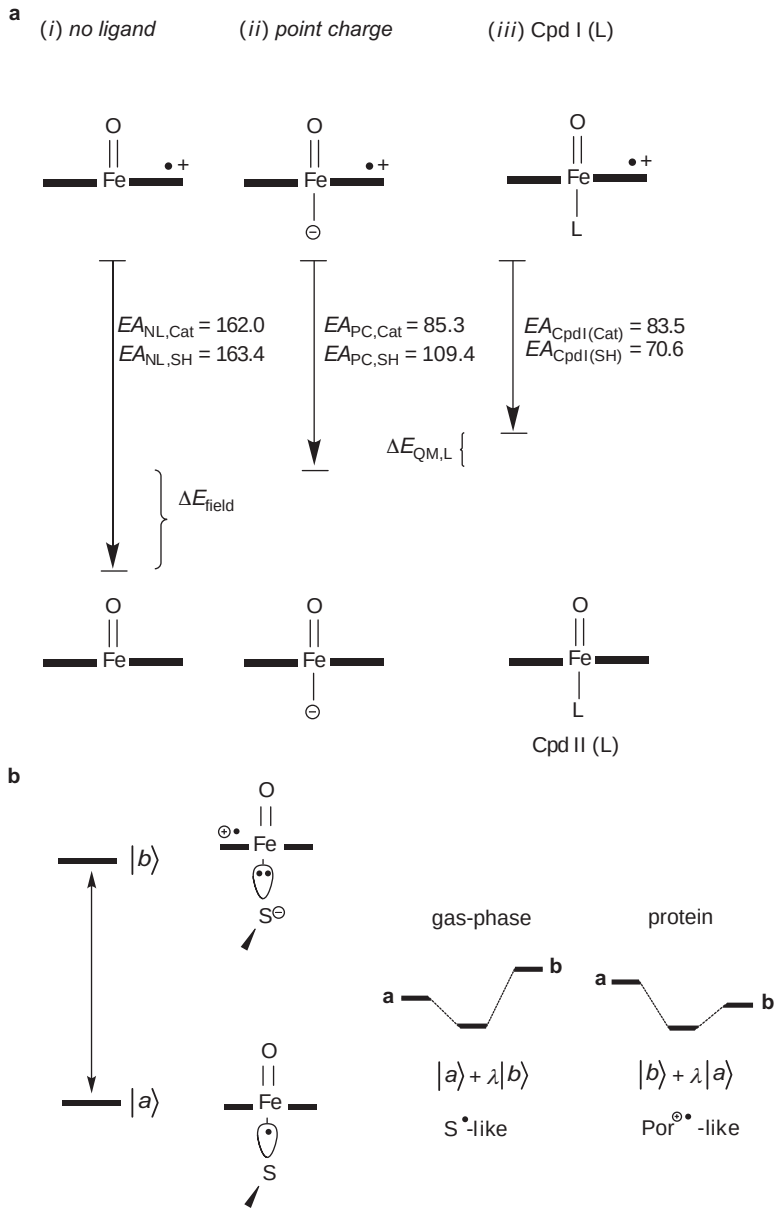

Figure 9.13 (a) Estimate of the ''push''-effect strength from quantum chemical calculations, with electron affinities in kcal mol^{-1}. (b) Orbital mixing of porphyrin and thiolate orbitals in Cpd I.

electric field effect, due to the short distance between the metal and the axial ligand: $r_{Fe-OTyr} = 2.117$ Å while r_{Fe-S} is 2.581 Å. In Cpd I(SH) the quantum mechanical effect is large as a result of orbital interactions between a porphyrin

type orbital with a lone pair on the axial ligand. Figure 9.13(b) explains the orbital mixing in Cpd I(SH) and the corresponding effect of this on the charge and spin density distribution. Cpd I has two high-lying molecular orbitals that are close in energy and mix, namely, a lone-pair on the thiolate axial ligand (π_S) and the porphyrin type a_{2u} orbital discussed and shown above in Figure 9.9(d). These orbitals are occupied by three electrons, which means a purely singly occupied π_S orbital will give a Por $S^{\bullet}$ electronic configuration, state $|a\rangle$, whereas a purely singly occupied a_{2u} orbital will result in a $Por^{+\bullet}$ S^{-} configuration, state $|b\rangle$. In Cpd I(SH) these two states mix and partial radical character on both porphyrin and axial ligand is found. However, it has been shown that hydrogen bonding interactions toward the thiolate group, for instance mimicked by two ammonia molecules, already shift the orbital mixing to a more dominant porphyrin cation radical situation.[67,71] Subsequent, quantum mechanics/molecular mechanics calculations indeed showed that Cpd I has a large radical component on the porphyrin and lesser on the axial ligand.[79]

9.9 Reactivity of Compound I

As discussed above, Compound I is an iron(IV)-oxo heme cation radical species with three unpaired electrons in π^*_{xz}, π^*_{yz} and a_{2u} orbitals (Figure 9.9). Owing to the small spin–orbit coupling between the unpaired electrons there are two electromers (doublet and quartet) that are close in energy. In the quartet spin state all spins are aligned (ferromagnetically coupled), whereas in the doublet spin state the a_{2u} electron has opposite spin to the two π^* electrons. In the following we give the spin multiplicity in superscript on the left-hand-side of the labels. The reactant states of Compound I, ^{2,4}R, involve the two low lying spin states ($S = \frac{1}{2}, \frac{3}{2}$) with two excited states ($S = \frac{3}{2}, \frac{5}{2}$), ^{4,6}R′, slightly higher in energy. The latter two states contain an excitation from the nonbonding δ_{x2-y2} orbital to the antibonding σ^*_{xy} orbital, which are two orbitals in the plane of the heme. In addition all states have a doubly occupied orbital, ϕ_{CH}, that represents the electron pair in the C–H bond. Technically, Cpd I can be assigned as an Fe^{IV} center with a hole in the porphyrin (*i.e.*, $Por^{+\bullet}$).

A substrate hydroxylation reaction gives products ^{2,4}P and ^{4,6}P′ that are described by an Fe^{III} center and a closed-shell porphyrin. Thus, any reaction catalyzed by Cpd I of CYP 450 will involve two formal electron "transfer" reactions from the substrate undergoing oxidation. Figure 9.14 shows these two electron transfer processes from reactants *via* intermediates leading to products. Each of these steps involves a single electron transfer, one into the a_{2u} orbital and the second into the π^*_{xz}(FeO) orbital, in the quartet and doublet spin states for tri-radicaloid state. On the other hand, starting from the ^{4,6}R′ states the first electron transfer is into the a_{2u} orbital, while the second electron transfer fills the σ^*_{xy} orbital with one electron. For the tri-radicaloid state, the first electron shift generates an Fe^{IV}-type intermediate with a closed-shell porphyrin, whereas for the penta-radicaloid state, the electron shift generates an Fe^{III}-type intermediate with a radical cationic situation on the porphyrin ring.

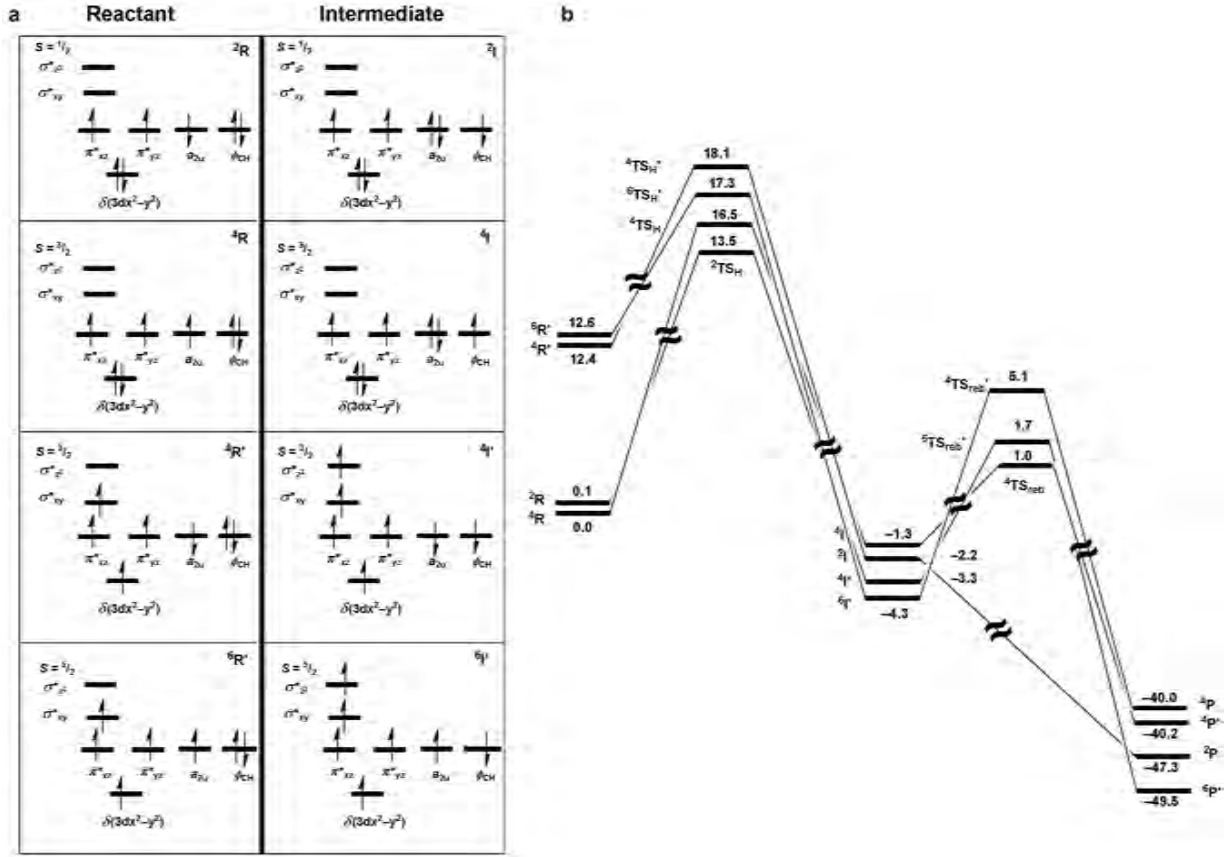

Figure 9.14 (a) Orbital occupancy evolution during substrate metabolism by CYP 450 Cpd I. (b) Reaction pathways for C–H hydroxylation of propene as obtained by the B3LYP/LACV3P+*//LACVP level of theory. The model includes two NH_3–S hydrogen bonds that mimic the interactions in the protein and a polarization effect through the addition of a medium with dielectric constant $\varepsilon = 5.7$. Relative energies are in kcal mol^{-1} and contain zero-point corrections calculated at B3LYP/LACVP.

In all cases, the substrate maintains a radical center with a singly occupied orbital (ϕ_{CH}). Therefore, we have four closely packed radical intermediates during the reactions.[119] The second electron is transferred from the substrate to fill either the a_{2u} orbital or one of the d-orbitals on the iron. Looking at Figure 9.14 it is obvious that there are several other possible electronic states, which can be obtained by redistribution of the electrons in this dense orbital manifold.[120–125] Therefore, the reaction catalyzed by Cpd I of P450 will involve at least two spin states, *i.e.* will proceed *via* two-state reactivity (TSR), and possibly involves many electromeric states or multistate reactivity (MSR).[126–128] The most intriguing feature of TSR and MSR is that the different spin states and/or electromers may lead to reaction *via* different mechanisms and thereby produce different intermediates and products. This spin-dependent mechanistic phenomenon has been observed during oxidation processes ranging from the simple reaction of FeO^+ [129,130] to the complex mechanisms of enzymes and synthetic catalysts.[120,129–134] Sometimes, significant energy differences between the LS and HS activation barriers lead to a spin-selective single-state reactivity (SSR).

9.10 Aliphatic C–H Hydroxylation by Compound I of CYP 450

Aliphatic hydroxylation is the most common reaction catalyzed by CYP 450 enzymes and it is known to perform this reaction on a broad range of chemical substrates. Since this is an important reaction in catalysis many efforts have been made to rationalize substrate hydroxylation reactions and predict the rate constant of substrate hydroxylation.[135–137] Generally, aliphatic substrates are activated by Cpd I *via* an initial hydrogen atom abstraction, which leads to a radical intermediate.[138] Alcohol products are formed after radical rebound of the hydroxyl group to the radical rest group. The hydrogen atom abstraction from a substrate RH by Cpd I to form the intermediate complex I_H is described in Equation (9.1) and the reaction enthalpy for this reaction (ΔH_{HA}) is dependent on the relative energies of reactants and products:

$$[Fe^{IV}{=}O(Por^{+\bullet})Cys] + RH \rightarrow [Fe^{IV}(OH)(Por)Cys] + R^{\bullet} + \Delta H_{HA} \qquad (9.1)$$

The reaction enthalpy (ΔH_{HA}) for the above reaction can be written as a function of the C–H bond dissociation energy (BDE_{C-H}) of the substrate and the BDE_{O-H} for the O–H bond dissociation energy of [Fe^{IV}(OH)(Por)Cys] through combination of Equations (9.1) and (9.2) to give Equation (9.3):

$$RH \rightarrow R^{\bullet} + H^{\bullet} + BDE_{C-H} \qquad (9.2)$$

$$\Delta H_{HA} = BDE_{C-H} - BDE_{O-H} \qquad (9.3)$$

In the case a series of calculations is performed on substrate hydroxylation by [Fe^{IV}=O($Por^{+\bullet}$)SH] as a mimic of Cpd I of CYP 450 this implies that the

BDE_{O-H} value will be the same for all reaction mechanisms studied. Therefore, the exo- or endothermicity of formation of the intermediate complexes ($^{4,2}I_H$) in the reaction should correlate linearly with the BDE_{C-H} value of the substrates RH. Indeed a linear correlation of reaction energy or driving force with BDE_{C-H} was found with $R^2 = 0.99$.[135] The standard deviation from linearity for this driving force is small and consequently the DFT calculated reaction energies are within a few kcal mol^{-1} error. These values are much smaller than the systematic error generally reported for DFT calculations of 3–5 kcal mol^{-1} with respect to experimentally determined enthalpies.[139–141]

Subsequently, the relationship of hydrogen abstraction barrier height with BDE_{C-H} was investigated and the obtained correlation is shown in Figure 9.15 for aliphatic hydroxylation of the following substrates by [Fe^{IV}=O($Por^{+\bullet}$)SH]: methane, ethane, propane, propene, toluene, ethylbenzene, *trans*-methylphenylcyclopropane, *trans*-*i*-propylphenylcyclopropane, *N*,*N*-dimethylaniline and camphor. The trend depicted in Figure 9.15(b) represents the raw data of calculated barrier height *versus* BDE_{C-H}, while the one displayed in Figure 9.15(c) includes a correction factor for the resonance energy ($RE_{Substrate}$). The resonance energy presents the geometric distortion of the radical with respect to the reactant conformation.

A valence bond (VB) curve crossing diagram has been used to explain the substrate hydroxylation trends and confirms the correlation between hydrogen abstraction barrier height and BDE_{C-H}. Figure 9.16 displays the VB curve crossing diagram from reactants (Cpd I + substrate, RH) *via* a radical intermediate leading to alcohol products. The curve crossing diagram starts bottom-left with the structure of Cpd I. In principle, the π-system in the Fe–O bond is occupied with six electrons ($\pi_{xz}^2\ \pi_{yz}^2\ \pi^*_{xz}{}^1\ \pi^*_{yz}{}^1$) each of those electrons is identified with a dot next to the atom in Figure 9.16. Since the π^*_{xz} and π^*_{yz} orbitals are singly occupied orbitals on the Fe–O bond, each of these orbitals gives about 50% spin density on the iron and 50% spin density on the oxygen atom. This results in the two electromers K_1 and K_2 depicted in Figure 9.16. Apart from the two unpaired electrons in the π^*_{xz} and π^*_{yz} orbitals there is also an unpaired electron in the porphyrin based a_{2u} orbital. The alcohol products by contrast have the metal in oxidation state Fe^{III} coupled to a closed-shell heme. The orbital occupation of ^2P is $\delta^2\ \pi^*_{xz}{}^2\ \pi^*_{yz}{}^1\ a_{2u}{}^2$, whereas that for ^4P is $\delta^2\ \pi^*_{xz}{}^1\ \pi^*_{yz}{}^1\ \sigma^*_{z2}{}^1\ a_{2u}{}^2$. In a VB diagram the electronic configuration of the reactants (with wave function Ψ_r) connects to an excited state in the products (with wave function Ψ_p*). Similarly, the product electronic configuration (with wave function Ψ_p) connects to an excited state in the reactants (with wave function Ψ_r*). At the point where the two curves cross, there will be an avoided crossing and a transition state leading from reactants to products. The direct barrier, *i.e.* concerted barrier, from reactants to products is high in energy,[142] but a lowering of the barrier is achieved thanks to the interception of an intermediate curve. This intermediate leads to the radical intermediate in the reaction mechanism, in this case with electronic configuration [Fe^{IV}(OH)(Por)Cys---R$^\bullet$]. In addition, there also will be an intermediate curve leading to the [Fe^{III}(OH)($Por^{+\bullet}$)Cys---R$^\bullet$] intermediate, but in most gas-phase studies this is high in energy.

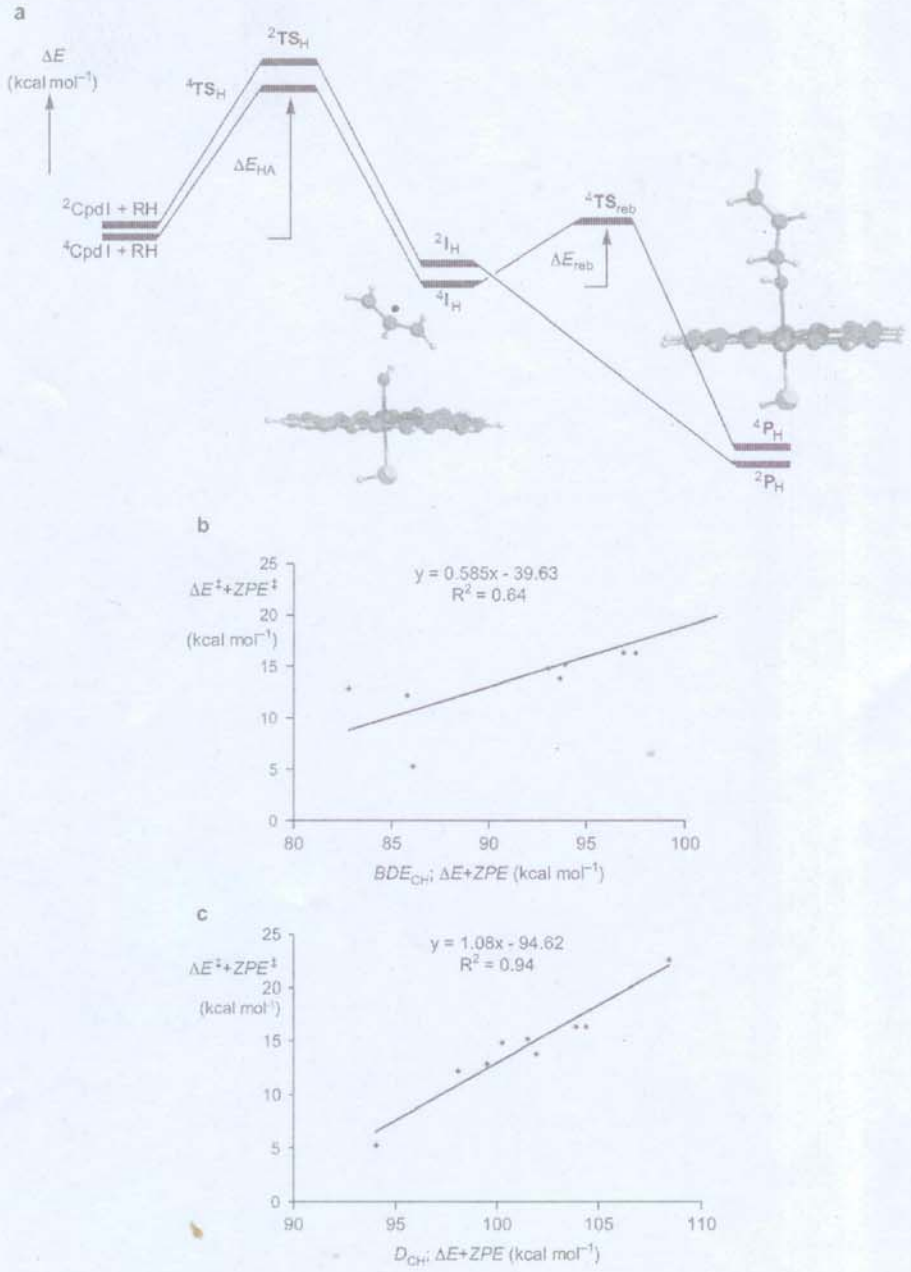

Figure 9.15 (a) General mechanism of substrate hydroxylation by Cpd I of CYP 450 in TSR. (b) Plot of the average barriers $\Delta E^{\ddagger}+ZPE^{\ddagger}$ (UB3LYP/LACV3P+*) for the quartet and doublet hydrogen abstraction steps *versus* BDE_{C-H} (UB3LYP/LACV3P+*). (c) Plot of the average barriers $\Delta E^{\ddagger}+ZPE^{\ddagger}$ (UB3LYP/LACV3P+*) for the quartet and doublet hydrogen abstraction steps *versus* D_{CH} ($D_{CH} = BDE_{C-H}+RE_{Substrate}^{\bullet}$) as calculated with UB3LYP/LACV3P + *. Substrates are methane (**1**), ethane (**2**), propane (**3**), *trans*-methylphenylcyclopropane (**5**), *trans-i*-propylphenylcyclopropane (**6**), *N*,*N*-dimethylaniline (**7**), toluene (**8**), ethylbenzene (**9**) and camphor (**10**).

AQ3

Replace figure with new attached one

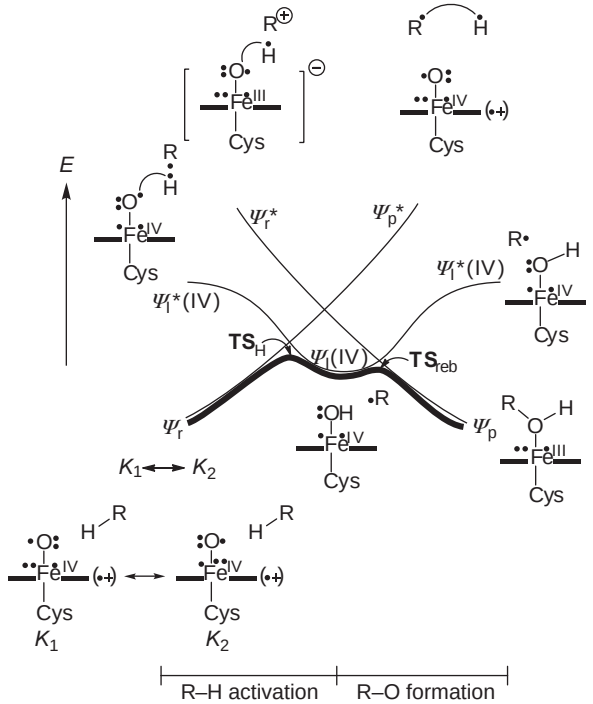

Figure 9.16 Valence bond curve crossing diagram for substrate hydroxylation by Cpd I of CYP 450 that takes place *via* an [Fe^{IV}(OH)(Por)Cys---R$^{\bullet}$] intermediate.

The intermediate curve (with wave function Ψ_I) crosses the reactant wave function and gives rise to a hydrogen atom abstraction barrier and crosses with the product wave function to generate a radical rebound barrier. This VB curve diagram, therefore, predicts a stepwise mechanism for substrate hydroxylation by CYP 450 enzymes that proceed *via* a radical intermediate. Moreover, it explains the electron transfer processes that proceed during the reaction mechanism.

The VB diagram not only is a quantitative way to explain the reaction mechanism, but can also be used to predict hydrogen atom abstraction barriers from empirical values. Thus, the barrier height $\Delta E^{\ddagger}$ for a hydrogen atom abstraction is a factor B below the curve crossing energy (ΔE_c).[143] Moreover, the curve crossing energy is a fraction (f) of the excitation energy (or promotion gap, $G_{H,r}$) between the ground state and the electronic state that represents the products. Consequently, the barrier height $\Delta E^{\ddagger}$ can be written as follows using Equation (9.4):

$$\Delta E^{\ddagger} = \Delta E_c - B = fG_H - B \tag{9.4}$$

As follows from Figure 9.17, the excitation energy or promotion gap $G_{H,r}$ refers to a singlet to triplet excitation in the C–H bond of the substrate plus an electron transfer from the oxygen atom into the a_{2u} orbital. A singlet–triplet excitation in a single bond essentially equals the bond dissociation energy for

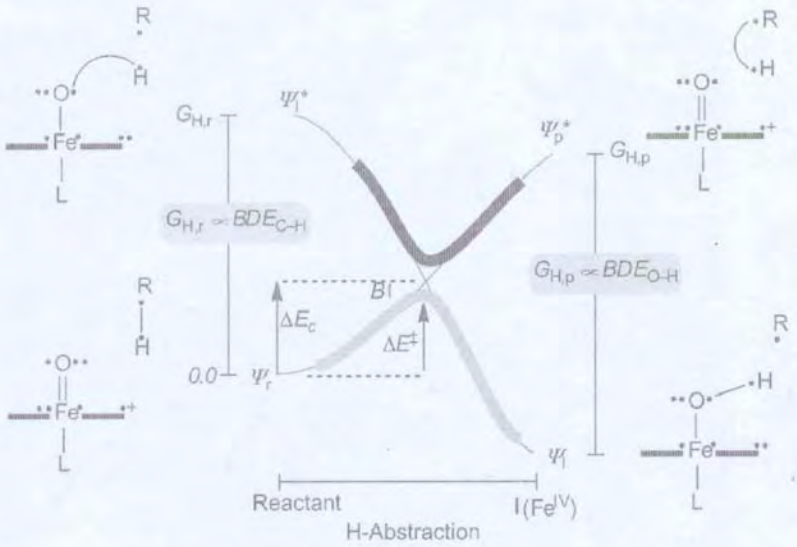

Figure 9.17 Rationalization of the correlation of barrier height with either BDE_{C-H} or BDE_{O-H}.

that bond, and hence is proportional to BDE_{C-H}. This VB curve crossing diagram, therefore, proves that the barrier height of substrate hydroxylation correlates linearly with BDE_{C-H}.

Recent studies also focused on the correlation of hydrogen atom abstraction barrier of propene with a range of different oxidants.[116] According to Equation (9.3), the reaction energy should correlate with BDE_{C-H} as well as with BDE_{O-H}. Changing the oxidant but keeping the substrate constant, therefore, will vary BDE_{O-H} and keep BDE_{C-H} constant. Indeed, linear correlations similar to those displayed in Figure 9.15 are found. The VB curve crossing diagram shown in Figure 9.17 explains the observed trends. Now, the relevant reaction mechanism is the backward reaction starting in products (the radical intermediates) and the barrier leading to Cpd I and substrate is investigated. For this process the barrier is proportional to an excitation energy ($G_{H,p}$) that is dependent on the singlet to triplet excitation in the O–H bond of the iron(IV)-hydroxo complex. Of course, the reverse barrier height is equal to the forward barrier height minus the driving force for the reaction. Consequently, both BDE_{C-H} and BDE_{O-H} connect to the hydrogen abstraction barrier.

Although the first hydrogen atom abstraction reactions by CYP 450 Cpd I model systems were studied using methane as a substrate,[144–146] in the past ten years many more realistic substrates have been studied as well. Special emphasis has always been on camphor hydroxylation by CYP 450_{cam}, because it is the natural substrate for hydroxylation by this CYP 450 isozyme. Initial studies used DFT methods but later also full QM/MM techniques were applied to investigate the complete enzyme.[147,148] CYP 450_{cam} regioselectively hydroxylates the C^5 position of camphor mostly because camphor is tightly bound to

the substrate binding pocket and only the C^5 position approaches the heme close enough to enable substrate hydroxylation. All these studies predict the same mechanistic trends, namely, starting with an initial hydrogen atom abstraction followed by radical rebound to form the alcohol products.

Table 9.2 summarizes substrate hydroxylation reactions calculated with DFT or QM/MM methods for Cpd I(L) with axial ligand $L = SH^-$, SMe^-.[136,137,148–155] Essentially the general mechanism of substrate hydroxylation as supported by all calculations is the one shown in Figure 9.15(a). In some cases; the rebound step leads to either N-dealkylation or dehydrogenation.[156] Nevertheless, the initial hydrogen atom abstraction barrier is the rate-determining step as well. On average the low-spin barriers are below the high-spin barriers by 0.9 ± 1.3 kcal mol^{-1}. Obviously, substrate hydroxylation phenomenon follows a two-state-reactivity pathway with competing spin state surfaces and reaction barriers.

9.10.1 Rearrangement Mechanisms of Aliphatic Hydroxylation Reactions

Owing to the transient lifetime of Cpd I and the failure to identify and characterize it as the active species, many experimental studies have been performed to find indirect evidence of its activity. In one of those experiments, so-called, radical-clocks substrates were used.[157–159] These radical clock substrates react with an oxidant *via* partial rearrangement processes, as displayed by the reaction in Figure 9.18, where an initial hydrogen atom abstraction gives rebound to form the unrearranged products (*U*) or the obtained radical (Alk$^\bullet$) can rearrange with rearrangement rate constant k_r to form a rearranged radical (Ãlk$^\bullet$) that rebounds the hydroxyl to form rearranged products (*R*). Based on the ratio of [*U*/*R*] Newcomb and coworkers[53,158] estimated the lifetime of the radicals. However, the obtained radical lifetimes of the radicals in the reaction mechanisms did not correlate with known lifetimes of these types of chemical systems. This made Newcomb and coworkers suggest that a "second-oxidant" is involved in the reaction that catalyzes the substrate hydroxylation. In particular, the precursor of Cpd I in the catalytic cycle was suggested to act as an oxidant either side-by-side with Cpd I or replacing Cpd I. This hypothesis has prompted many experimental and computational studies in the field and therefore we will dedicate this section to the mechanism of radical clock substrate and the involvement of Cpd 0 in substrate hydroxylation.

The potential energy profile for the reaction mechanism of *trans*-methylphenylcyclopropane hydroxylation by [Fe^{IV}=O($Por^{+\bullet}$)SH] was calculated using DFT models leading to unrearranged and rearranged products;[120,121] a summary of the results is given in Figure 9.18. The calculations predict Cpd I(SH) to exist in close-lying doublet and quartet spin states and as a consequence the reaction proceeds *via* two-state reactivity on competing doublet and quartet spin state surfaces. On both spin state surfaces there is a hydrogen atom abstraction *via* a transition state TS_H leading to an [Fe^{IV}(OH)(Por)(SH)---Alk$^\bullet$] radical intermediate (I_U). Radical rebound to give the unrearranged products

Table 9.2 DFT calculated aliphatic hydrogen atom abstraction barriers (kcal mol^{-1}) by Cpd I models. The description of the axial cysteinate ligand in the calculations is given as L.

L	*Substrate*	$\Delta E_{HA,HS}^{\ddagger}$	$\Delta E_{HA,LS}^{\ddagger}$	*Ref.*
SH^-	Methane	22.9	22.3	147
SH^-	Methane	22.9	24.7	170
SH^-	Ethane	17.4	15.3	147
SH^-	Ethanol: from C^1	11.7	10.3	175
SH^-	Ethanol: from OH	12.3	12.7	175
SH^-	Acetaldehyde	8.2	10	171
SH^-	Propane, 2° carbon	15.8	13.9	147
SH^-	Propane, 1° carbon	17.5	15.2	147
SH^-	Propane	20.6	19.5	167
SH^-	Propene	13	12.8	147
SH^-	*N*,*N*-Dimethylaniline	5.5	5	147
SH^-	Toluene	12.4	12.1	147
SH^-	Ethylbenzene	12.6	11.5	147
SH^-	Camphor	14.5	15.9	147
SH^-	*trans*-2-Phenyl-methylcyclopropane	14.5	13.1	147
SH^-	*trans*-2-Phenyl-isopropylcyclopropane	13.4	12.3	147
SH^-	Arginine	10.5	4.9	176
SH^-	*N*-Cyclopropyl-*N*-methylaniline	11.4	9.6	180
SH^-	*N*-Cyclopropyl-*N*-methylaniline	11.2	9.2	180
SH^-	Testosterone-β_1	13	11.4	177
SH^-	Testosterone-β_2	8.2	9.7	177
SH^-	Testosterone-β_6	6.1	5.3	177
SH^-	Testosterone-β_{15}	11.6	9.7	177
SMe^-	Trimethylamine	9.6	8.3	178
SMe^-	Morpholine	<1	<1	179
$SCys^-$	Camphor	21.8	21.1	167
SMe^-	Methane	20.7		160
SMe^-	Propane, 1° carbon	17.7		160
SMe^-	Propane, 2° carbon	14.8		160
SMe^-	Isobutane	14.3		160
SMe^-	Propene	12.9		160
SMe^-	Propionaldehyde	11.4		160
SMe^-	Toluene	13		160
SMe^-	Ethylbenzene, 2°	12.1		160
SMe^-	1-Methylethyl-benzene	13.3		160
SMe^-	Dimethyl ether	12.2		160
SMe^-	Dimethylsulfane	11		160
SMe^-	Methyl(phenyl)sulfane	10.8		160
SMe^-	Dimethylamine	7.6		160
SMe^-	Trimethylamine	6.7		160
SMe^-	Fluoroethane, 2°	18.4		160
SMe^-	Fluoroethane, 1°	14.7		160
SMe^-	Ethylbenzene, 1°	17.3		160
SMe^-	2-Fluoroprop-1-ene	13.2		160
SMe^-	Prop-1-en-2-ol	11.7		160
SMe^-	*p*-Xylene	12.7		160
SMe^-	1-Methyl-4-nitrosobenzene	11.8		160
SMe^-	Methoxybenzene	13		160
SMe^-	*N*-Methylaniline	7.6		160
SMe^-	*N*,*N*-Dimethylaniline	6.9		160

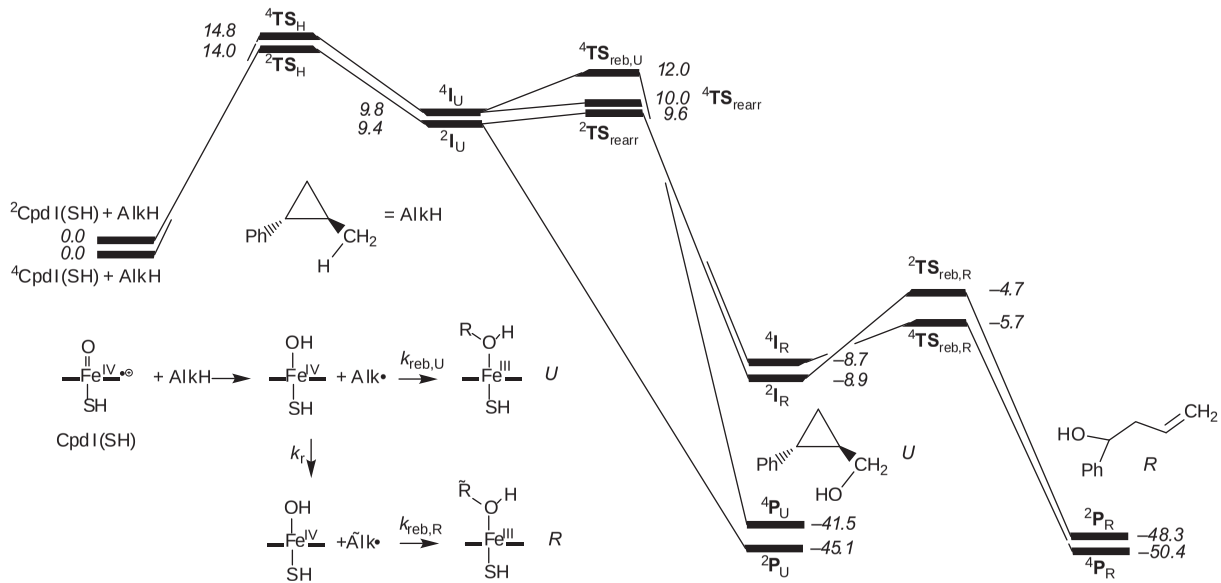

Figure 9.18 Calculated potential energy profile of *trans*-1-methyl-2-phenylcyclopropane hydroxylation by [Fe^{IV}=O($Por^{+\bullet}$)SH] with relative energies in kcal mol^{-1}. Also given is the reaction mechanism leading to unrearranged products (*U*) and rearranged products (*R*).

($\mathbf{P_U}$) encounters a barrier ($\mathbf{TS_{reb,U}}$) of 2.2 kcal mol^{-1} on the high-spin surface and is virtually barrier-free on the low-spin surface. An alternative mechanism leads to rearrangement within the radical intermediate to form the rearranged intermediate ($\mathbf{I_R}$). This reaction step has a small barrier ($\mathbf{TS_{rearr}}$) of about 0.2 kcal mol^{-1} on both spin state surfaces and large exothermicity, which implies that it will be an irreversible step. A final radical rebound barrier ($\mathbf{TS_{reb,R}}$) then leads to the rearranged product complexes ($\mathbf{P_R}$). As follows from the calculations depicted in Figure 9.18, on the low-spin surface $\mathbf{TS_{reb,U}} < \mathbf{TS_{rearr}}$, therefore, little rearranged product may be expected. On the other hand, on the high-spin surface $\mathbf{TS_{reb,U}} > \mathbf{TS_{rearr}}$, which indicates dominant rearrangement process. Consequently, the reaction mechanism displayed in Figure 9.18 indicates spin-selective product formation, whereby the high-spin gives rearrangement and the low-spin no rearranged products.

The spin-selective product formation will also have a crucial effect on kinetic isotope effect in the experiments. To test this, Kumar and coworkers[120,121] calculated product isotope effects (PIE) from kinetic isotope effects (KIE). They reasoned that the PIE ratio for products U/R, Equation (9.5), can be estimated from the KIE values obtained for the LS and HS surfaces only:

$$\mathrm{PIE}(U/R) = \mathrm{KIE}(U)/\mathrm{KIE}(R) = \mathrm{KIE(LS)}/\mathrm{KIE(HS)} \tag{9.5}$$

Kinetic isotope effects were calculated from the semi-classical Eyring equation ($\mathrm{KIE_{Eyring}}$), Equation (9.6), which is dependent on the free energy of activation ($\Delta G^{\ddagger}$) of the reaction of Cpd I with *trans*-methylphenylcyclopropane and that where one or more of the methyl hydrogen atoms are replaced by deuterium atoms. In Equation (9.6) the temperature is given by T and R is the gas constant:

$$\mathrm{KIE_{Eyring}} = \exp[(\Delta G^{\ddagger}_{\mathrm{D}} - \Delta G^{\ddagger}_{\mathrm{H}})/RT] \tag{9.6}$$

More advanced KIE calculations include the effect of tunneling as calculated with either the Wigner ($\mathrm{KIE_{Wigner}}$) or Bell ($\mathrm{KIE_{Bell}}$) models, Equations (9.7–9.9). These models take the shape of the potential energy curve around the transition state into effect through the value of the imaginary frequency in the **TS**, namely, ν. In Equations (9.7–9.9) the Boltzmann constant is given as k_{B} and Planck's constant as h:

$$\mathrm{KIE_{tunneling}} = \mathrm{KIE_{Eyring}} \times Q_{t,H}/Q_{t,D} \tag{9.7}$$

$$Q_{\mathrm{t,Wigner}} = 1 + u_{\mathrm{t}}^2/24 \text{ with } u_{\mathrm{t}} = h\nu/k_{\mathrm{B}}T \tag{9.8}$$

$$Q_{\mathrm{t,Bell}} = \frac{u_{\mathrm{t}}}{2\sin(0.5u_{\mathrm{t}})} - \sum_{n=1}^{\infty}(-1)^n \frac{\exp[(u_{\mathrm{t}} - 2n\pi)\Delta E/u_{\mathrm{t}}]}{(u_{\mathrm{t}} - 2n\pi)/u_{\mathrm{t}}} \tag{9.9}$$

For *trans*-methylphenylcyclopropane *versus trans*-d_1-methylphenylcyclopropane a product isotope ratio $\mathrm{PIE_{Eyring}} = 1.03$, $\mathrm{PIE_{Wigner}} = 1.07$ and $\mathrm{PIE_{Bell}} = 1.20$ at

298 K was calculated,[120,121] which compares favorably with the experimental value of 1.14.[160] The calculations, therefore, showed that the experimental product distributions and radical clock lifetimes can be explained with the two-state reactivity model, whereby Cpd I is the sole oxidant of substrate hydroxylation. The seeming observance of two active oxidants in the experimental studies, therefore, arises from the two spin states of Cpd I. Those two spin states of Cpd I lead to the masquerade of individual spin state processes and reactivities that are different on each spin state surface.

Further calculations on the relative activity of Cpd I and Cpd 0 in substrate epoxidation and sulfoxidation reactions gave evidence that Cpd 0 is a sluggish oxidant as compared to Cpd I and will not be able to activate substrates.[161–164] In support of this, Nam and coworkers carried out experimental studies in which they compared the reactivity of synthetic iron(IV)-oxo oxidants with iron(III)-hydroperoxo analogs.[165] No products were observed in the reaction of the iron(III)-hydroperoxo species with thioanisole and cyclohexene, therefore, Cpd 0 is unlikely to be an oxidant of aliphatic hydroxylation, epoxidation and sulfoxidation reactions.

9.11 C=C Epoxidation by Compound I of CYP 450

Substrate activation by CYP 450 enzymes commonly leads to oxygen atom transfer processes. When the substrate contains a double bond, the oxygen atom transfer will give epoxide product complexes. Figure 9.19 displays the common reaction products observed in double bond activation by CYP 450 enzymes. Thus, the dominant products will be epoxides, although stereochemical scrambling is possible, *i.e.* the production of *cis*-olefins from *trans*-alkenes. In addition, epoxidation reactions suffer from reactions leading to by-products. One type of by-products are the so-called suicidal complexes, where the olefin has formed bridging bonds with the oxo group of Cpd I and one of the nitrogen atoms of the porphyrin ring to form a five-membered ring.[166–169] This is a dead-end product and consequently terminates the activity of the enzyme. In addition, aldehyde by-products have been observed in the reaction mechanism. To gain insight into the mechanisms of olefin epoxidation by CYP 450 Cpd I and the formation of by-products (suicidal complexes and aldehydes), a series of computational studies were performed, which we briefly summarize here.[123,124,128,170–172]

A typical potential energy profile for substrate epoxidation is shown in Figure 9.20 and displays the results for ethene, propene and styrene as taken from ref. 124, 128 and 171. As follows, the reaction mechanism resembles that found for aliphatic hydroxylation closely, whereby an initial C–O bond formation leads to a radical intermediate prior to a ring-closure to form epoxide products.[172] DFT studies also investigated a possible concerted reaction mechanism where the oxo group inserts into the double bond and directly forms epoxide products. The latter mechanism, however, was found to proceed *via* a second-order transition state that is much higher in energy than the

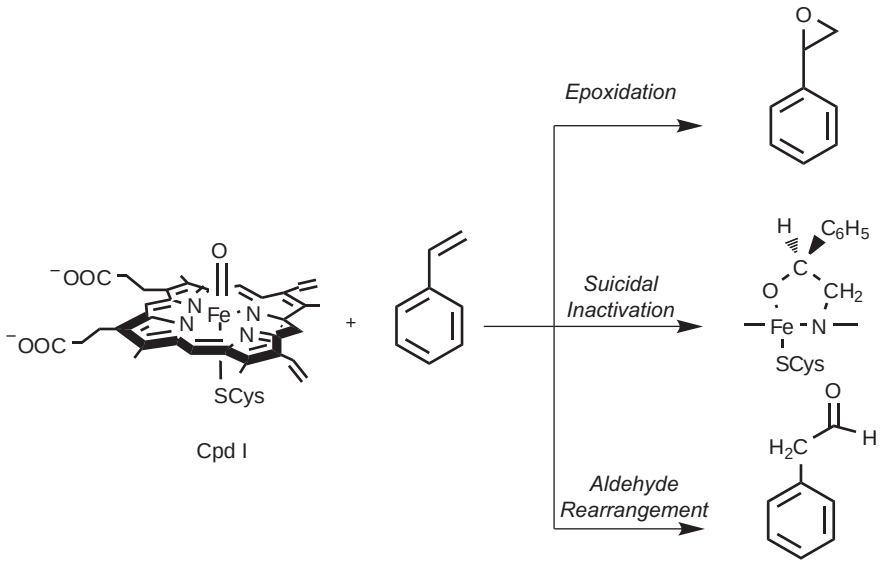

Figure 9.19 Olefin epoxidation by CYP 450 Cpd I leading to epoxide products, suicidal complexes and aldehyde by-products. Styrene is used as an example here.

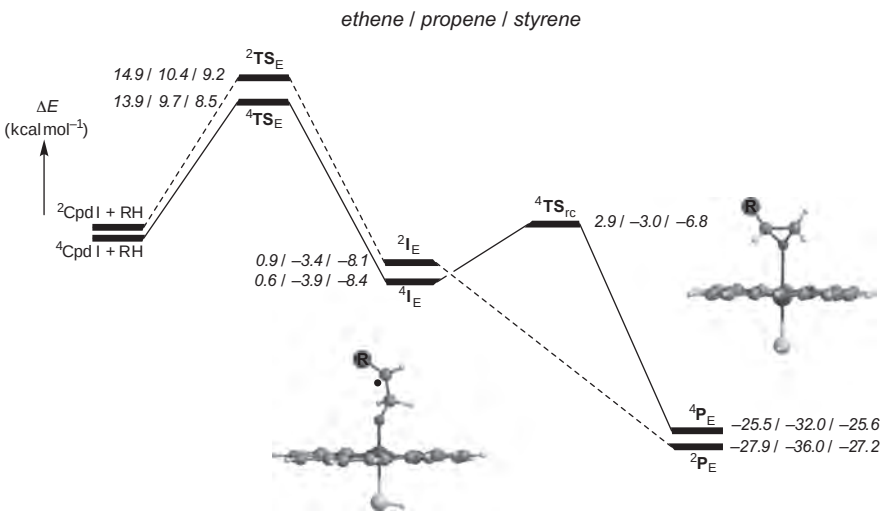

Figure 9.20 Potential energy profile of substrate (ethene/propene/styrene) epoxidation by Cpd I(SH). All energies are in kcal mol^{-1} relative to isolated reactants and taken from refs 124, 128 and 171.

stepwise barriers, hence substrate epoxidation will takes place *via* a stepwise mechanism.[173] Interestingly, if one starts with pure *cis* or *trans* olefins one often ends up with a mixture of *cis* and *trans* epoxides.[52] The DFT studies on five

different olefins (ethene, propene, cyclohexene, camphene and styrene)[124,125,128,174] revealed a multi-state reactivity (MSR) scenario in which electromers with different spin state take part in the product formation in a state specific manner.

As can be seen from Figure 9.20, the rate-determining step in the epoxidation mechanism is the first C–O bond formation step (*via* $\mathbf{TS}_{E}$) and generally the ring closure barrier ($\mathbf{TS}_{rc}$) is much lower. Thus, similarly to substrate hydroxylation the reaction takes place *via* two-state reactivity patterns on competing doublet and quartet spin states. Also in substrate epoxidation, the intermediates are of [Fe^{IV}(Por)O–$CH_2R^{\bullet}$] electronic configuration $^{4,2}\mathbf{I}_{rad,IV}$ with orbital occupation $\delta^2\ \pi^*_{xz}{}^1\ \pi^*_{yz}{}^1\ a_{2u}{}^2\ \phi_R{}^1$, while the corresponding Fe^{III} states are around 4 kcal mol^{-1} higher in energy.[171]

Substrate epoxidation has side reactions leading to suicidal complexes and aldehyde by-products. The origin of those two by-products was investigated using DFT methods and ethene and styrene as a substrate.[124,175] Both products were found to originate from cationic intermediates $^4\mathbf{I}_{cat,xy}$ and $^4\mathbf{I}_{cat,z2}$ with either a $\delta^2\ \pi^*_{xz}{}^1\ \pi^*_{yz}{}^1\ \sigma^*_{xy}{}^1\ a_{2u}{}^2\ \phi_R{}^0$ or $\delta^2\ \pi^*_{xz}{}^1\ \pi^*_{yz}{}^1\ \sigma^*_{z2}{}^1\ a_{2u}{}^2\ \phi_R{}^0$ configuration with orbitals defined as in Figure 9.9(d) and ϕ_R the radical on the substrate. Thus, in substrate epoxidation the mechanism is stepwise *via* a radical intermediate $^{4,2}\mathbf{I}_{rad,IV}$, which results in a C–O bond formation and a formal one-electron transfer from the substrate to oxidant. On the high-spin surface the radical intermediate has a finite lifetime due to the existence of a ring-closure transition state, but on the LS surface the radical lifetime will be short and quickly collapse to the epoxide product complexes. During the lifetime of the radical, the radical can rearrange leading to, for instance, stereochemical scrambling and the production of *cis*-epoxides from *trans*-olefins. This stereochemical scrambling, therefore, is likely on the HS surface and unlikely on the LS surface. In a similar vein, during the lifetime of the radical intermediate, the system can undergo a surface crossing from a radical to a cationic state giving either $^4\mathbf{I}_{cat,xy}$ or $^4\mathbf{I}_{cat,z2}$ intermediates. These states then give rise to the suicidal and aldehyde by-products.

To gain further insight into the mechanisms of substrate epoxidation, a systematic study was performed with the aim of rationalizing the rate constant, *i.e.* C–O bond formation barrier, in substrate epoxidation.[172] Thus, two sets of calculations were performed: firstly the epoxidation of seven different olefins by Cpd I(SH) was studied and secondly propene epoxidation by a range of iron(IV)-oxo porphyrin cation radical oxidants was investigated. The first studies used ethene, propene, 1-butene, *trans*-2-butene, 1,3-cyclohexadiene, 1,4-cyclohexadiene and styrene (Figure 9.21). The latter studies used a series of Cpd I models where the axial ligand was varied and a biomimetic nonheme iron(IV)-oxo complex and the iron(IV)-oxo active species of taurine/α-ketoglutarate dioxygenase.[176,177]

Since the highest occupied molecular orbital (HOMO) of an olefin is generally a π-orbital along a double bond, it was reasoned that a correlation between substrate epoxidation barrier height with double bond ionization could be expected. Indeed the trend of epoxidation barriers of Cpd I(SH) with these substrates corresponded to the strength of the double bond of the olefin,

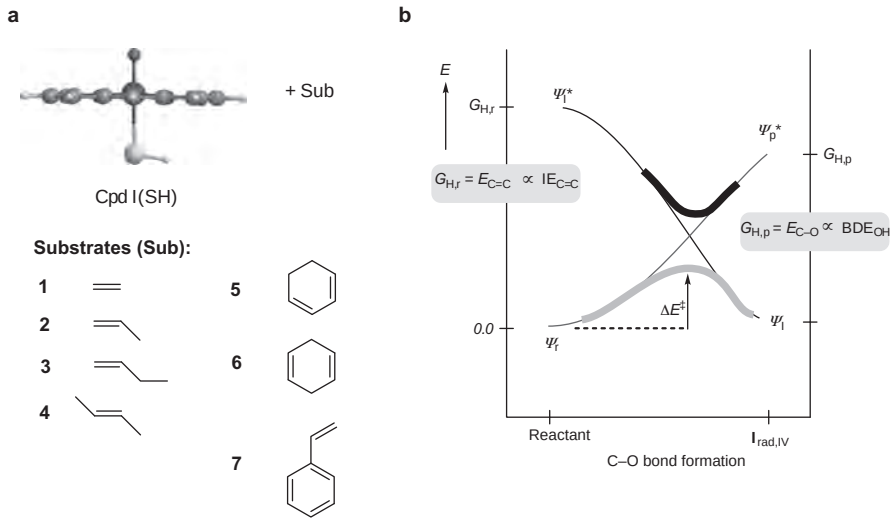

Figure 9.21 Systematic study of substrate epoxidation by Cpd I(SH). (a) Olefins investigated; (b) valence bond curve crossing diagram for C–O bond formation.

and hence ionization energy (IE) of the substrate. In fact the plot of barrier height with IE gave a correlation coefficient $R^2 = 0.80$. Subsequent studies using one substrate (propene) and a range of different oxidants showed that the formation of the O–C bond in substrate epoxidation can be modeled with the formation of an O–H bond and, consequently, a linear correlation between barrier height and BDE_{O-H} was found.

These observations of barrier height with either IE or BDE_{O-H} were rationalized with a valence bond curve crossing diagram as depicted in Figure 9.21(b). Thus, the forward barrier (from reactants to radical intermediates) is dependent on the singlet–triplet excitation energy in the double bond of the olefin that is broken, and can be estimated from IE values. On the other hand, using one substrate and multiple oxidants gives a correlation with BDE_{O-H}. The reverse epoxidation barrier, *i.e.* from radical intermediates to reactants, has a promotion gap that represents the singlet–triplet excitation in the C–O bond, which can be estimated from the excitation in an O–H bond and therefore is proportional to BDE_{O-H}. The valence bond curve crossing diagram, therefore, predicts that the mechanism is stepwise *via* a radical intermediate and confirms that the epoxidation barrier correlates with IE and BDE_{O-H}. This knowledge can also be used to predict barrier heights and rate constants of substrates where IE is known.

9.12 Sulfoxidation Reaction by Compound I of CYP 450

Sulfoxidation reactions are common in drug metabolism as well as substrate detoxification processes in the liver. For example, the metabolism of the

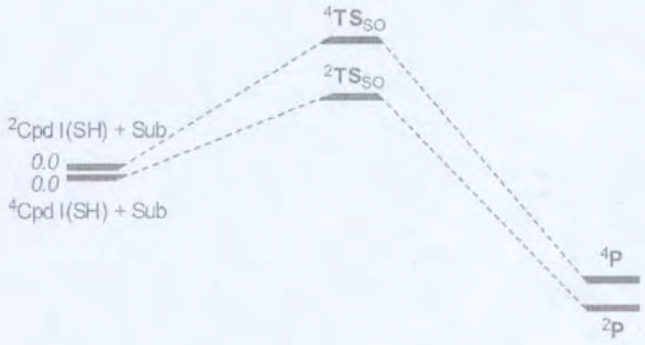

	$^2TS_{SO}$	$^4TS_{SO}$
1	20.9	27.0
2	14.6	19.0
3	9.8	13.4
4	13.5	18.8
5	7.7	13.8
6	7.3	14.4
7	7.9	13.3

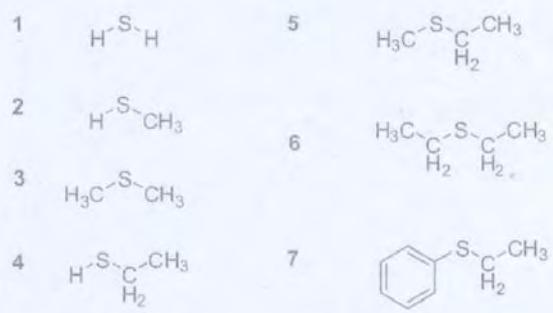

Cpd I(SH)

Figure 9.22 Reaction mechanism of substrate sulfoxidation by Cpd I(SH). Substrates studied are: H_2S (**1**), methyl sulfide (**2**), dimethyl sulfide (**3**), ethyl sulfide (**4**), methyl ethyl sulfide (**5**), diethyl sulfide (**6**) and ethyl phenyl sulfide (**7**). The barrier heights are given in kcal mol^{-1}.

pesticide aldicarb and the biodegradation of neuroleptic drugs in the liver is associated with substrate sulfoxidation by CYP 450 isozymes.[178–183] Detailed reaction mechanism studies on CYP 450 enzymes and biomimetic complexes for substrate sulfoxidation reactions have been carried out by several groups and the consensus mechanism for substrate sulfoxidation by CYP 450 enzymes is a concerted reaction mechanism as shown in Figure 9.22.[184–188]

The experimental observations are consistent with those obtained from density functional theory (DFT) and quantum mechanics/molecular mechanics (QM/MM) studies on substrate sulfoxidation by Cpd I of P450.[153,162,163,189,190] These studies confirmed a concerted reaction mechanism for substrate sulfoxidation in contrast to the stepwise mechanisms found for aliphatic hydroxylation and epoxidation reactions.

Experimental studies of the Watanabe group found a correlation between the rate constant of substrate sulfoxidation by CYP 450 enzymes and the ionization potential (IP) of the substrate.[191–193] Shaik and coworkers and Kumar and coworkers calculated substrate sulfoxidation by Cpd I of CYP 450 using a range of substrates. The obtained trends were explained with a valence bond curve crossing diagram including electron transfer processes.[194,195]

Using the series of substrates displayed in Figure 9.22, the barrier height of S–O bond formation was found to correlate linearly with the IP of the substrate. The correlation coefficient ($R^2 = 0.91$) supports the hypothesis of this relationship. Contrary to substrate epoxidation and aliphatic C–H hydroxylation by Cpd I of CYP 450, however, the inclusion of the reorganization energy (RE) on the obtained trends has very little effect and the correlation coefficient is virtually the same ($R^2 = 0.92$). The reason for this is that the RE values are very small, *i.e.* between 0.04 and 1.05 kcal mol^{-1} due to the attack of the oxo-group of Cpd I on a lone pair orbital on the sulfur atom of the substrate. Consequently, the geometry in the transition state will have distorted minimally with respect to the reactant conformation, resulting in a low value for the RE. Of course, thermodynamically the rate constant is connected to the free energy of activation; therefore, the rate constant of substrate sulfoxidation should connect with IP as well, as indeed observed by the Watanabe group.[191–193] Interestingly, since both substrate epoxidation and sulfoxidation barriers connect to the IP value of the substrate, this should imply that the regioselectivity of substrate epoxidation *versus* sulfoxidation will be dependent on the nature of the substrate only and not on the properties of the oxidant.

9.13 Aromatic Hydroxylation Reaction by Compound I of CYP 450

The final reaction mechanism for substrate activation by CYP 450 Cpd I that we will discuss is the aromatic hydroxylation. The mechanism of aromatic hydroxylation has long remained controversial and leads to the production of phenols often with ketones and/or epoxides as by-products. The production of ketones proceeds *via* the so-called NIH shift, where one of the hydrogen atoms from the aromatic ring undergoes a 1,2-shift.

Many computational studies on aromatic hydroxylation by CYP 450 Cpd I have been reported.[196–201] Figure 9.23 displays the computationally recommended reaction mechanism of aromatic hydroxylation by Cpd I of CYP 450 enzymes leading to phenol and cyclohexa-1,3-dienone products. Thus, the reaction starts with attack of the oxo group on one of the carbon atoms of the aromatic ring to form an intermediate complex *via* a transition state $\mathbf{TS_{CO}}$. In principle, C–O bond formation can lead to single electron transfer from the substrate to the heme to give a radical intermediate ($\mathbf{I_{rad}}$) or a double electron transfer to produce a cationic intermediate ($\mathbf{I_{cat}}$). Generally, these intermediates are close in energy and in the case of ethylbenzene hydroxylation the low-spin pathway gives a cationic intermediate, whereas the quartet spin state surface gives a radical intermediate instead. As a consequence, there are considerable energy differences between the doublet and quartet C–O bond formation barriers, which are in favor of the low-spin surface. Therefore, aromatic hydroxylation will take place on a dominant low-spin surface *via* single-state reactivity, in contrast to the two- or multi-state reactivity found for aliphatic hydroxylation and epoxidation.

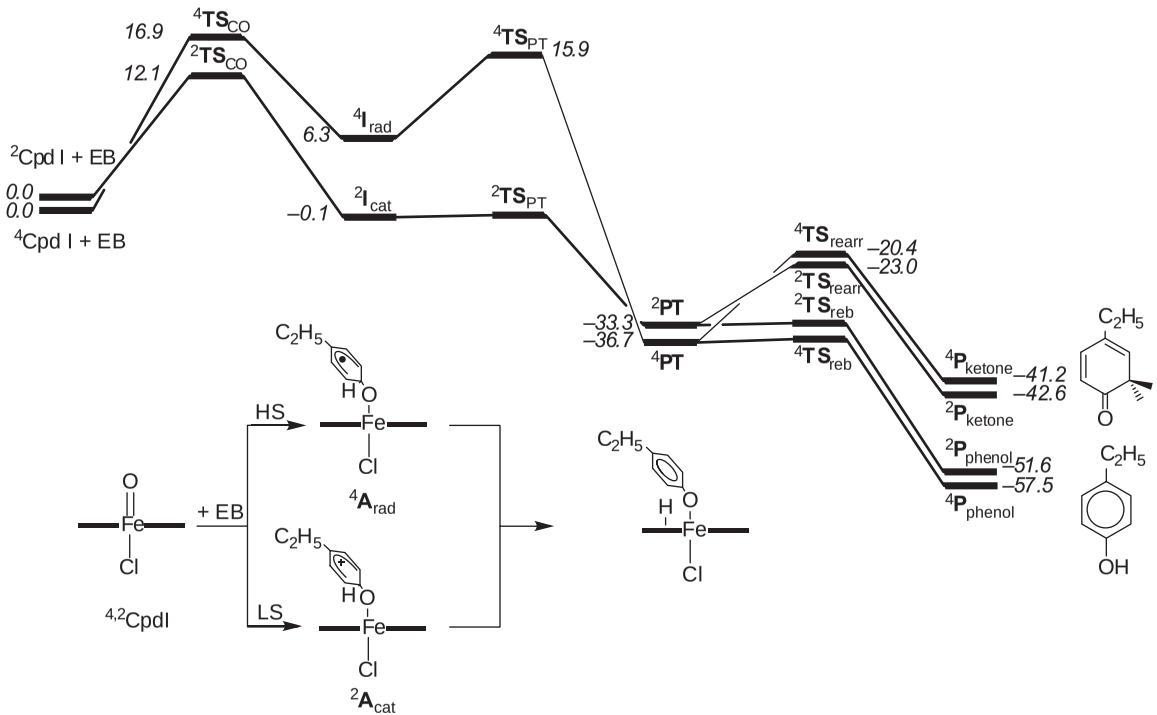

Figure 9.23 Aromatic hydroxylation of ethylbenzene (EB) at the *para*-position by Cpd I(Cl), passing through radical and cationic intermediates. Mechanisms leading to phenol and ketone products are given. All energies are in kcal mol^{-1} relative to isolated reactants in the quartet spin state.

In the next step of the reaction mechanism, the *ipso*-proton is transferred to one of the nitrogen atoms of the porphyrin ring to form the proton-transfer intermediate (**PT**). This essentially brings the aromaticity back in the benzene ring of the substrate and creates a protonated porphyrin group with one pyrrole group tilted out of the plane. This barrier is small and the process encounters a large exothermicity and, hence, will be an irreversible process. The proton from the protonation porphyrin group is transferred to the oxygen atom to form phenol products *via* rebound barrier ($\mathbf{TS}_{reb}$) or alternatively is reshuttled to the C^2 carbon atom to give cyclohexa-1,3-dienone products *via* the rearrangement barrier ($\mathbf{TS}_{rearr}$). In addition there is a mechanism leading to epoxide products that starts from the radical or cationic intermediates *via* a ring-closure barrier. For all calculations this ring-closure barrier was found to be larger than the proton-shuttle barrier to form **PT**.[196]

The mechanism displayed in Figure 9.23 explains the experimentally observed NIH effect and the by-product formation of ketones and epoxides. Studies on the regioselectivity of aliphatic *versus* aromatic hydroxylation of ethylbenzene by Cpd I(Cl) showed that the free energies of activation of the aromatic hydroxylation processes are just 1–2 kcal mol^{-1} higher in energy than those found for aliphatic hydroxylation. Since replacement of the hydrogen atoms of ethylbenzene by deuterium atoms raises the aliphatic hydroxylation barriers by several kcal mol^{-1} but not the aromatic hydroxylation barriers, this results in a regioselectivity switch from aliphatic hydroxylation for ethylbenzene-h_{10} to aromatic hydroxylation for ethylbenzene-d_{10}.[117]

9.14 Role of Water Molecule as Biocatalyst

Water is the medium in which the chemistry takes place in a biological system. Irrespective of its main role as bulk solvent, water also directly participates in biochemical reaction. In the catalytic cycle of CYP 450, Cpd I is formed by release of a water molecule after protonation of its precursor Cpd 0. This water molecule, however, forms a hydrogen bond with oxo atom of Fe(IV)-oxo moiety and may linger in the substrate binding pocket during catalysis.[202] A systematic QM/MM investigation by the Thiel group discovered the possible catalytic role of this water molecule.[203,204] In their study they found that increase in the hydrogen bond strength between this water molecule and the oxo atom during the process of the hydrogen abstraction in CYP 450_{cam} is because of a more negatively charged oxo atom in the transition state. The magnitude of lowering of the hydrogen abstraction barrier in CYP 450_{cam} is found to be about 4 kcal mol^{-1} at the B3LYP/CHARMM level of theory. On the basis of a classical electrostatic model (with interaction energies calculated using Mulliken charges), they concluded that the catalytic effect of the water molecule arises due to more favorable electrostatic interactions in the transition state.[203,204] They further extended their work with the aim of exploring the generality of this

effect by studying the hydrogen atom abstraction of nine substrates by Cpd I with a total of 12 different modes of abstraction, both in the doublet and quartet state using the DFT method. Table 9.3 summarizes the hydrogen atom abstraction barriers of these nine substrates in the presence and in the absence of this water molecule. Clearly, the magnitude in barrier lowering is correlated with the donor bond strength of the substrate and with the amount of charge transfer in the transition state.[205]

Table 9.3 B3LYP/LACVP barriers (kcal mol^{-1}) for hydrogen atom abstraction from substrates **1–9** by a Cpd I model system in the gas phase.

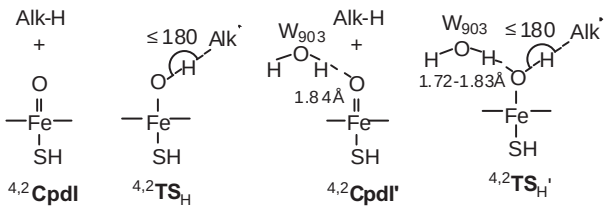

			B3LYP/LACVP barrier		
Substrate	*Label*[a]	*Spin state*[b]	*Without water molecule in model*	*With water molecule in model*	*Difference*
Ethane	**1**	D	20.32	18.13	2.19
		Q	21.28	18.71	2.57
Propane	**2n**	D	20.47	19.06	1.41
		Q	21.62	20.33	1.29
Propane	**2i**	D	18.02	16.61	1.41
		Q	19.26	16.63	2.63
Ethylbenzene	**3n**	D	19.96	17.70	2.26
		Q	21.16	18.30	2.86
Ethylbenzene	**3b**	D	14.30	10.53	3.77
		Q	14.57	10.81	3.76
trans-Methylphenylcyclopropane	**4**	D	17.43	14.85	2.58
		Q	18.46	14.20	4.26
Camphor	**5**	D	17.08	13.63	3.45
		Q	18.08	14.78	3.30
Propene	**6**	D	15.01	13.60	1.37
		Q	15.33	13.21	1.80
Toluene	**7**	D	15.78	12.66	2.67
		Q	15.15	12.05	3.01
trans-i-Propylphenylcyclopropane	**8**	D	13.68	13.39	0.29
		Q	14.33	12.92	1.41
N,*N*-Dimethylaniline	**9**	D	6.33	–1.57	7.90
		Q	7.79	2.27	5.52

[a]Substrates labeled as: ethane **1**, propane (abstraction of primary hydrogen atom) **2n**, propane (abstraction of secondary hydrogen atom) **2i**, ethylbenzene (abstraction of methyl hydrogen atom) **3n**, ethylbenzene (abstraction of benzyl hydrogen atom) **3b**, *trans*-methylphenylcyclopropane **4**, camphor **5**, propene **6**, toluene **7**, *trans-i*-propylphenylcyclopropane **8**, and *N*,*N*-dimethylaniline **9**.
[b]D, doublet spin state; Q, quartet spin state.

9.15 Conclusion

This chapter reviews the importance of heme enzymes CYP 450, which can be coupled to derive important structural and functional information on intermediates. Out of five subfamilies (1A, 2B, 2C, 2D, 3A) eight human cytochrome P450 enzymes are responsible for the vast majority of oxidative drug metabolisms of the most important clinical drugs. Out of the 200 most often prescribed drugs in the USA, about 80% are cleared primarily by these CYPs. The chapter also reviews the complexities that arise at the level of basic mechanisms such as substrate-dependent effects, linkage *etc*. Several metabolites of drugs like ziprasidone, fluvastatin, *etc*. are cleared by only one specific CYP 450 isozyme, such as CYP3A4, CYP2C9, respectively. This suggests that several alternative oxidant species of CYP 450, such as Cpd 0, Cpd II or Cpd I. On the basis of recent experimental as well theoretical studies this review suggests that Cpd 0 is less reactive than Cpd I. The chapter also focuses on the TSR/MSR concept, its occurrence in the reactions of high-valent metal-oxo reagents, and explains important features of TSR/MSR, that is, the different spin states and the different electromers that prefer different mechanisms and therefore produce different intermediates and products. Sometimes the reactivity is reduced to a spin-selective single-state reactivity (SSR) phenomenon when the low-spin state activation barrier is sufficiently lower than that for the high-spin state. This chapter clearly emphasizes that the enormous value of the pharmaceutical applications that can arise from *theoretical/computational* modeling of human drug metabolizing enzymes promises a drive toward another generation of research into the structure and catalytic activity of cytochrome P450s – one of the most ancient and versatile of all protein super families. The computational tools used to predicting drug metabolism will be crucial in rapidly growing drug discovery. Considerable challenges remain for drug metabolism prediction using structure-based methods, but apparently the opportunities for accurate prediction of drug metabolism using computational tools will become a mainstream component of drug design and will be an achievable goal in the near future.

Acknowledgements

D.K. is the Ramanujan Fellow of the Department of Science and Technology (New Delhi). The helpful scientific discussions with, and suggestions by, Dr Sam de Visser, University of Manchester, Manchester, United Kingdom to bring this chapter to its final shape are heartily acknowledged. The encouragement and support from Dr. J.S. Yadav, Director, IICT and scientific discussions with Dr. C.N. ~~Sastry~~ Sastry, MMG, IICT are also acknowledged

References

1. J. H. Dawson and M. Sono, *Chem. Rev.*, 1987, **87**, 1255.
2. D. R. Nelson, T. Kamataki, D. J. Waxman, F. P. Guengerich, R. W. Estabrook, R. Feyereisen, F. J. Gonzalez, M. J. Coon, I. C. Gunsalus, O. Gotoh, K. Okuda and D. W. Nebert, *DNA Cell Biol*, 1993, **12**, 1.

3. M. Sono, M. P. Roach, E. D. Coulter and J. H. Dawson, *Chem. Rev.*, 1996, **96**, 2841.
4. K. M. Kadish, K. M. Smith and R. Guilard (eds.), *The Porphyrin Handbook*, Academic Press, San Diego, 2000, vol. 4.
5. F. P. Guengerich, *Chem Res. Toxicol.*, 2001, **14**, 611.
6. P. R. Ortiz de Montellano (ed.), *Cytochrome P450: Structure, Mechanism and Biochemistry*, 3rd edn, Kluwer Academic/Plenum Publishers, New York, 2004.
7. Y. Watanabe, H. Nakajima and T. Ueno, *Acc. Chem. Res.*, 2007, **40**, 554.
8. P. B. Danielson, *Curr. Drug. Metab.*, 2002, **3**, 561.
9. http://drnelson.uthsc.edu/cytochromeP450.html (accessed 16 March 2011).
10. D. W. Nebert and D. R. Nelson, in *Methods in Enzymology. Cytochrome P450*, vol. 206, ed. M. R. Waterman and E. F. Johnson, Academic Press, New York, 1991, pp. 3–11.
11. M. R. Waterman and E. F. Johnson (eds.), *Methods in Enzymology. Cytochrome P450*, vol. 206, Academic Press, New York, 1991.
12. D. R. Nelson, *Comp. Biochem. Physiol. C. Pharmacol. Toxicol. Endocrinol.*, 1998, **121**, 15.
13. L. Ereshefsky, C. Riesenman and Y. W. Lam, *J. Clin. Psychiatry*, 1996, **57**, 17.
14. E. L. Michalets, *Pharmacotherapy*, 1998, **18**, 84.
15. V. Dixit, N. Hariparsad, F. Li, P. Desai, K. E. Thummel and J. D. Unadkat, *Drug Metab Dispos*, 2007, **35**, 1853.
16. M. L. Catterson, S. H. Preskorn and R. L. Martin, *Psychiatr. Clin. North Am.*, 1997, **20**, 205.
17. L. Goshman, J. Fish and K. Roller, *J. Pharmacy Soc. Wisconsin 1999*, May/June,23.
18. S. Sansen, J. K. Yano, R. L. Reynald, G. A. Schoch, K. J. Griffin, C. D. Stout and E. F. Johnson, *J. Biol. Chem.*, 2007, **282**, 14348.
19. P. Rowland, F. E. Blaney, M. G. Smyth, J. J. Jones, V. R. Leydon, A. K. Oxbrow, C. J. Lewis, M. G. Tennant, S. Modi, D. S. Eggleston, R. J. Chenery and A. M. Bridges, *J. Biol. Chem.*, 2006, **281**, 7614.
20. I. F. Sevrioukova and T. L. Poulos, *Proc. Natl. Acad. Sci. USA*, 2010, **107**, 18422.
21. K. E. Ketter, D. A. Flockhart and R. M. Post, *J. Clin. Psychopharmacol.*, 1995, **15**, 387.
22. J. W. Harris, A. Rahman, B. R. Kim, F. P. Guengerich and J. M. Collins, *Cancer Res.*, 1994, **54**, 4026.
23. M. A. Leo, J. M. Lasker, J. L. Raucy, C. I. Kim, M. Black and C. S. Lieber, *Arch. Biochem. Biophys.*, 1989, **269**, 305.
24. D. J. Waxman, *Adv. Mol. Cell Biol.*, 1996, **14**, 341.
25. B. G. Pollock, R. A. Sweet, M. Kirschner and C. F. Reynolds, *Ther. Drug. Monit.*, 1996, **18**, 581.
26. U. M. Zanger, M. Turpeinen, K. Klein and M. Schwab, *Anal. Bioanal. Chem.*, 2008, **392**, 1093.
27. C. Prakash, A. Kamel, D. Cui, R. D. Whalen, J. J. Miceli and D. Tweedie, *J. Clin. Pharmacol.*, 2000, **49**(Suppl. 1), 35S.

28. C. Prakash, A. Kamel, W. Anderson and H. Howard, *Drug Metab. Dispos.*, 1997, **25**, 206.
29. B. Testa, in *The Metabolism of Drugs and Other Xenobiotics*, ed. B. Testa, J. Caldwell, Academic Press, New York, 1995, pp. 203–234.
30. R. I. Levy, A. J. Troendle and J. M. Fattu, *Circulation*, 1993, **87**(Suppl. 4), III45.
31. T. K. Peters, J. Jewitt-Harris, M. Mehra and E. N. Muratti, *Am. J. Hypertens.*, 1993, **6**, S346.
32. M. H. Davidson, *Am. J. Med.*, 1994, **96**, S41.
33. V. Fischer, L. Johanson, F. Heitz, R. Tullman, E. Graham, J.-P. Baldeck and W. T. Robinson, *Drug Metabol. Dispos.*, 1999, **27**, 410.
34. P. J. Cox, D. A. Ryan, F. J. Hollis, A.-M. Harris, A. K. Miller, M. Vousden and H. Cowley, *Drug Metabol. Dispos.*, 2000, **28**, 772.
35. V. B. G. Reddy, B. V. Karanam, W. L. Gruber, M. A. Wallace, S. H. Vincent, R. B. Franklin and T. A. Baillie, *Chem. Res. Toxicol.*, 2005, **18**, 880.
36. B. Prasad and S. Singh, *J. Pharm. Biomed. Anal.*, 2009, **50**, 475.
37. T. L. Poulos, B. C. Finzel, I. C. Gunsalus, G. C. Wagner and J. Kraut, *J. Biol. Chem.*, 1985, **260**, 16122.
38. H. M. Berman, J. Westbrook, Z. Feng, G. Gilliland, T. N. Bhat, H. Wiessig, I. N. Shindylov and P. E. Bourne, *Nucleic Acids Res.*, 2000, **28**, 235.
39. I. G. Denisov, T. M. ~~Markis~~ Makris, S. G. Sligar and I. Schlichting, *Chem. Rev.*, 2005, **105**, 2253.
40. S. G. Sligar, *Biochemistry*, 1976, **15**, 5399.
41. M. Swart, A. R. Groenhof, A. W. Ehlers and K. Lammertsma, *Chem. Phys. Lett.*, 2005, **403**, 35.
42. A. Altun and W. Thiel, *J. Phys. Chem. A*, 2005, **109**, 1268.
43. A. R. Groenhof, M. Swart, A. W. Ehlers and K. Lammertsma, *J. Phys. Chem. A*, 2005, **109**, 3411.
44. P. R. Balding, C. S. Porro, K. J. McLean, M. J. Sutcliffe, J.-D. Maréchal, A. W. Munro and S. P. de Visser, *J. Phys. Chem. A*, 2008, **112**, 12911.
45. C. B. Brewer and J. A. Peterson, *J. Biol. Chem.*, 1988, **263**, 791.
46. J. Rittle and M. T. Green, *Science*, 2010, **330**, 933.
47. T. Hishiki, H. Shimada, S. Nagano, T. Egawa, Y. Kanamori, R. Makino, S.-Y. Park, S. Adachi, Y. Shiro and Y. Ishimura, *J. Biochem. (Tokyo)*, 2000, **128**, 965.
48. T. Egawa, H. Shimada and Y. Ishimura, *Biochem. Biophys. Res. Commun.*, 1994, **201**, 1464.
49. I. G. Denisov, T. M. Makris and S. G. Sligar, *J. Biol. Chem.*, 2001, **276**, 11648.
50. D. G. Kellner, S. C. Hung, K. E. Weiss and S. G. Sligar, *J. Biol. Chem.*, 2002, **277**, 9641.
51. R. Davydov, T. M. Makris, V. Kofman, D. E. Werst, S. G. Sligar and B. M. Hoffman, *J. Am. Chem. Soc.*, 2001, **123**, 1403.
52. J. T. Groves, in *Cytochrome P450: Structure, Mechanism, and Biochemistry*, 3rd edn, ed. P. R. Ortiz de Montellano, Kluwer Academic/Plenum Publishers, New York, 2005, ch. 1.

53. M. Newcomb and P. H. Toy, *Acc. Chem. Res.*, 2000, **33**, 449.
54. S. Jin, T. M. Makris, T. A. Bryson, S. G. Sligar and J. H. Dawson, *J. Am. Chem. Soc.*, 2003, **125**, 3406.
55. A. D. N. Vaz, D. F. McGinnity and M. J. Coon, *Proc. Natl. Acad. Sci. USA*, 1998, **95**, 3555.
56. W. Nam, H. J. Lee, S.-Y. Oh, C. Kim and H. G. Jang, *J. Inorg. Biochem.*, 2000, **80**, 219.
57. W. Nam, S.-E. Park, I. K. Lim, M. H. Lim, J. K. Hong and J. Kim, *J. Am. Chem. Soc.*, 2003, **125**, 14674.
58. J. Kaizer, E. J. Klinker, N. Y. Oh, J.-U. Rohde, W. J. Song, A. Stubna, J. Kim, E. Münck, W. Nam and L. Que Jr., *J. Am. Chem. Soc.*, 2004, **126**, 472.
59. Y. Ichikawa, H. Nakajima and Y. Watanabe, *ChemBioChem*, 2006, **7**, 1582.
60. A.-R. Han, Y. J. Jeong, Y. Kang, J. Y. Lee, M. S. Seo and W. Nam, *Chem. Commun.*, 2008, 1076.
61. A. Franke, C. Fertinger and R. van Eldik, *Angew. Chem., Int. Ed.*, 2008, **47**, 5238.
62. G. H. Loew and D. L. Harris, *Chem. Rev.*, 2000, **100**, 407.
63. M. T. Green, *J. Am. Chem. Soc.*, 1999, **121**, 7939.
64. M. T. Green, *J. Am. Chem. Soc.*, 2000, **122**, 9495.
65. M. T. Green, *J. Am. Chem. Soc.*, 2001, **123**, 9218.
66. T. Ohta, K. Matsuura, K. Yoshizawa and I. Morishima, *J. Inorg. Biochem.*, 2000, **82**, 141.
67. F. Ogliaro, S. Cohen, S. P. de Visser and S. Shaik, *J. Am. Chem. Soc.*, 2000, **122**, 12892.
68. J. C. Schöneboom, F. Neese and W. Thiel, *J. Am. Chem. Soc.*, 2005, **127**, 5840.
69. A. Altun, D. Kumar, F. Neese and W. Thiel, *J. Phys. Chem. A*, 2008, **112**, 12904.
70. P. Rydberg, E. Sigfridsson and U. Ryde, *J. Biol. Inorg. Chem.*, 2004, **9**, 203.
71. F. Ogliaro, S. P. de Visser, S. Cohen, J. Kaneti and S. Shaik, *ChemBioChem*, 2001, **2**, 848.
72. F. Ogliaro, S. Cohen, M. Filatov, N. Harris and S. Shaik, *Angew. Chem., Int. Ed.*, 2000, **39**, 3851.
73. F. Ogliaro, S. P. de Visser, J. T. Groves and S. Shaik, *Angew. Chem., Int. Ed.*, 2001, **40**, 2874.
74. D. L. Harris, G. H. Loew and L. Waskell, *J. Inorg. Biochem.*, 2001, **83**, 309.
75. M. Filatov, N. Harris and S. Shaik, *Angew. Chem., Int. Ed.*, 1999, **38**, 3510.
76. M. Filatov, N. Harris and S. Shaik, *J. Chem. Soc.*, Perkin Trans. 2, 1999, 399.
77. J. Antony, M. Grodzicki and A. X. Trautwein, *J. Phys. Chem. A*, 1997, **101**, 2692.

78. M. Radoń and E. Broclawik, *J. Chem. Theory Comput.*, 2007, **3**, 728.
79. J. C. Schöneboom, H. Lin, N. Reuter, W. Thiel, S. Cohen, F. Ogliaro and S Shaik, *J. Am. Chem. Soc.*, 2002, **124**, 8142.
80. K. L. Stone, R. K. Behan and M. T. Green, *Proc. Natl. Acad. Sci. USA*, 2005, **102**, 16563.
81. S. H. Kim, R. Perera, L. P. Hager, J. H. Dawson and B. M. Hoffman, *J. Am. Chem. Soc.*, 2006, **128**, 5598.
82. E. Derat, S. Cohen, S. Shaik, A. Altun and W. Thiel, *J. Am. Chem. Soc.*, 2005, **127**, 13611.
83. S. P. de Visser, S. Shaik, P. K. Sharma, D. Kumar and W. Thiel, *J. Am. Chem. Soc.*, 2003, **125**, 15779.
84. H. Hirao, D. Kumar, W. Thiel and S. Shaik, *J. Am. Chem. Soc.*, 2005, **127**, 13007.
85. P. R. Ortiz de Montellano, *Annu. Rev. Pharmacol. Toxicol.*, 1992, **32**, 89.
86. P. Nicholls, I. Fita and P. C. Loewen, *Adv. Inorg. Chem.*, 2000, **51**, 51.
87. N. G. Veitch and A. T. Smith, *Adv. Inorg. Chem.*, 2000, **51**, 107.
88. J. H. Dawson, R. H. Holm, J. R. Trudell, G. Barth, R. E. Linder, E. Bunnenberg, C. Djerasi and S. C. Tang, *J. Am. Chem. Soc.*, 1976, **98**, 3707.
89. T. L. Poulos, *J. Biol. Inorg. Chem.*, 1996, **1**, 356.
90. D. B. Goodin and D. E. McRee, *Biochemistry*, 1993, **32**, 3313.
91. E. Derat, S. Shaik, C. Rovira, P. Vidossich and M. Alfonso-Prieto, *J. Am. Chem. Soc.*, 2007, **129**, 6346.
92. M. Sivaraja, D. B. Goodin, M. Smith and B. M. Hoffman, *Science*, 1989, **245**, 738.
93. J. E. Huyett, P. E. Doan, R. Gurbriel, A. L. P. Houseman, M. Sivaraja, D. B. Goodin and B. M. Hoffman, *J. Am. Chem. Soc.*, 1995, **117**, 9033.
94. C. A. Bonagura, B. Bhaskar, H. Shimizu, H. Li, M. Sundaramoorthy, D. E. McRee, D. B. Goodin and T. L. Poulos, *Biochemistry*, 2003, **42**, 5600.
95. G. I. Berglund, G. H. Carlsson, A. T. Smith, H. Szöke, A. Henriksen and J. Hajdu, *Nature*, 2002, **417**, 463.
96. B. Bhaskar, C. A. Bonagura, H. Li and T. L. Poulos, *Biochemistry*, **41**, 2684.
97. E. L. Raven, *Nat. Prod. Rep.*, 2003, **20**, 367.
98. G. M. Jensen, S. W. Bunte, A. Warshel and D. B. Goodin, *J. Phys. Chem. B*, 1998, **102**, 8221.
99. D. K. Menyhárd and G. Náray-Szabó, *J. Phys. Chem. B*, 1999, **103**, 227.
100. S. P. de Visser, *J. Phys. Chem. A*, 2005, **109**, 11050.
101. S. P. de Visser, The axial ligand effect on substrate monoxygenation by the oxo-iron active species of heme enzymes. How does cytochrome c peroxidase compare to cytochrome P450?, in *Inorganic Biochemistry: Research Progress*, ed. J. G Hughes and A. J. Robinson, Nova Science Publishers, Inc., 2008, pp. 197–224.
102. M. Wirstam, M. R. A. Blomberg and P. E. M. Siegbahn, *J. Am. Chem. Soc.*, 1999, **121**, 10178.
103. C. M. Bathelt, A. J. Mulholland and J. N. Harvey, *Dalton Trans.*, 2005, 3470.

104. J. N. Harvey, C. M. Bathelt and A. J. Mulholland, *J. Comput. Chem.*, 2006, **27**, 1352.
105. Z. Gross and S. Nimri, *Inorg. Chem.*, 1994, **33**, 1731.
106. K. Czarnecki, S. Nimri, Z. Gross, L. M. Proniewicz and J. R. Kincaid, *J. Am. Chem. Soc.*, 1996, **118**, 2929.
107. Z. Gross, *J. Biol. Inorg. Chem.*, 1996, **1**, 368.
108. W. J. Song, Y. O. Ryu, R. Song and W. Nam, *J. Biol. Inorg. Chem.*, 2005, **10**, 294.
109. W. Nam, *Acc. Chem. Res.*, 2007, **40**, 522.
110. I. M. C. M. Rietjens, A. M. Osman, C. Veeger, O. Zakharieva, J. Antony, M. Grodzicki and A. X. Trautwein, *J. Biol. Inorg. Chem.*, 1996, **1**, 372.
111. H. Kuramochi, L. Noodleman and D. A. Case, *J. Am. Chem. Soc.*, 1997, **119**, 11442.
112. F. Ogliaro, S. P. de Visser and S. Shaik, *J. Inorg. Biochem.*, 2002, **91**, 554.
113. S. P. de Visser, *J. Biol. Inorg. Chem.*, 2006, **11**, 168.
114. R. Wang and S. P. de Visser, *J. Inorg. Biochem.*, 2007, **101**, 1464.
115. S. P. de Visser, L. Tahsini and W. Nam, *Chem. Eur. J.*, 2009, **15**, 5577.
116. S. P. de Visser, *J. Am. Chem. Soc.*, 2010, **132**, 1087.
117. S. P. de Visser, *Chem. Eur. J.*, 2006, **12**, 8168.
118. S. P. de Visser, *Inorg. Chem.*, 2006, **45**, 9551.
119. S. Shaik, H. Hirao and D. Kumar, *Acc. Chem. Res.*, 2007, **40**, 532.
120. D. Kumar, S. P. de Visser, P. K. Sharma, S. Cohen and S. Shaik, *J. Am. Chem. Soc.*, 2004, **126**, 1907.
121. D. Kumar, S. P. de Visser and S. Shaik, *J. Am. Chem. Soc.*, 2003, **125**, 13024.
122. D. Kumar, S. P. de Visser and S. Shaik, *J. Am. Chem. Soc.*, 2004, **126**, 5072.
123. E. Derat, D. Kumar, H. Hirao and S. Shaik, *J. Am. Chem. Soc.*, 2006, **128**, 473.
124. S. P. de Visser, D. Kumar and S. Shaik, *J. Inorg. Biochem.*, 2004, **98**, 1183.
125. D. Kumar, S. P. de Visser and S. Shaik, *Chem.Eur. J.*, 2005, **11**, 2825.
126. H. Hirao, D. Kumar and S. Shaik, *J. Inorg. Biochem.*, 2006, **100**, 2054.
127. S. Shaik, S. P. de Visser, F. Ogliaro, H. Schwarz and D. Schröder, *Curr. Opin. Chem. Biol.*, 2002, **6**, 556.
128. S. Shaik, D. Kumar, S. P. de Visser, A. Altun and W. Thiel, *Chem. Rev.*, 2005, **105**, 2279.
129. S. P. de Visser, F. Ogliaro, N. Harris and S. Shaik, *J. Am. Chem. Soc.*, 2001, **123**, 3037.
130. M. Filatov and S. Shaik, *J. Phys. Chem. A*, 1998, **102**, 3835.
131. D. Schröder, H. Schwarz, D. E. Clemmer, Y. Chen, P. B. Armentrout, V. I. Baranov and D. K. Bohme, *Int. J. Mass Spectrom. Ion Processes*, 1997, **161**, 175.
132. E. Derat and S. Shaik, *J. Am. Chem. Soc.*, 2006, **128**, 13940.
133. H. Hirao, D. Kumar, L. Que Jr. and S. Shaik, *J. Am. Chem. Soc.*, 2006, **128**, 8590.

AQ4

94 is now correct.

134. A. M. Khenkin, D. Kumar, S. Shaik and R. Neumann, *J. Am. Chem. Soc*., 2006, **128**, 15451.
135. S. Shaik, S. Cohen, Y. Wang, H. Chen, D. Kumar and W. Thiel, *Chem. Rev*., 2010, **110**, 949.
136. S. P. de Visser, D. Kumar, S. Cohen, R. Shacham and S. Shaik, *J. Am. Chem. Soc*., 2004, **126**, 8362.
137. L. Olsen, P. Rydberg, T. H. Rod and U. Ryde, *J. Med. Chem*., 2006, **49**, 6489.
138. S. Shaik, D. Kumar and S. P. de Visser, *J. Am. Chem. Soc*., 2008, **130**, 10128.
139. J. T. Groves and G. A. McClusky, *J. Am. Chem. Soc*., 1976, **98**, 859.
140. A. D. Becke, *J. Chem. Phys*., 1993, **98**, 5648.
141. M. Güell, J. M. Luis, M. Solà and M. Swart, *J. Phys. Chem. A*, 2008, **112**, 6384.
142. F. Neese, *Coord. Chem. Rev*., 2009, **253**, 526.
143. S. J. Kim, R. Latifi, H. Y. Kan, W. Nam and S. P. de Visser, *Chem. Commun*., 2009, 1562.
144. S. S. Shaik, *J. Am. Chem. Soc*., 1981, **103**, 3692.
145. F. Ogliaro, N. Harris, S. Cohen, M. Filatov, S. P. de Visser and S. Shaik, *J. Am. Chem. Soc*., 2000, **122**, 8977.
146. K. Yoshizawa, Y. Kagawa and Y. Shiota, *J. Phys. Chem. B*, 2000, **104**, 12365.
147. N. Harris, S. Cohen, M. Filatov, F. Ogliaro and S. Shaik, *Angew. Chem., Int. Ed*., 2000, **39**, 2003.
148. T. Kamachi and K. Yoshizawa, *J. Am. Chem. Soc*., 2003, **125**, 4652.
149. J. C. Schöneboom, S. Cohen, H. Lin, S. Shaik and W. Thiel, *J. Am. Chem. Soc*., 2004, **126**, 4017.
150. Y. Wang, H. Wang, C. Yang, L. Yang and K. J. Han, *J. Phys. Chem. B*, 2006, **110**, 6154.
151. Y. Wang, C. Yang, H. Wang, K. Han and S. Shaik, *ChemBioChem*, 2007, **8**, 277.
152. S. P. de Visser and L. S. Tan, *J. Am. Chem. Soc*., 2008, **130**, 12961.
153. Y. Zhang, P. Morisetti, J. Kim, L. Smith and H. Lin, *Theor. Chem. Acc*., 2008, **121**, 313.
154. P. Rydberg, U. Ryde and L. Olsen, *J. Chem. Theory Comput*., 2008, **4**, 1369.
155. A. R. Shaikh, R. Sahnoun, E. Broclawik, M. Koyama, H. Tsuboi, N. Hatakeyama, A. Endou, H. Takaba, M. Kubo, C. A. Del Carpio and A. Miyamoto, *J. Inorg. Biochem*., 2009, **103**, 20.
156. D. Li, Y. Wang, C. Yang and K. Han, *Dalton Trans*., 2009, 291.
157. D. Kumar, L. Tahsini, S. P. de Visser, H. Y. Kang, S. J. Kim and W. Nam, *J. Phys. Chem. A*, 2009, **113**, 11713.
158. P. R. Ortiz de Montellano and R. A. Stearns, *J. Am. Chem. Soc*., 1987, **109**, 3415.
159. M. Newcomb, R. Shen, S.-Y. Choi, P. H. Toy, P. F. Hollenberg, A. D. N. Vaz and M. J. Coon, *J. Am. Chem. Soc*., 2000, **122**, 2677.

160. M. Newcomb, D. Aebisher, R. Shen, R. Esala, P. Chandrasena, P. F. Hollenberg and M. J. Coon, *J. Am. Chem. Soc.*, 2003, **125**, 6064.
161. F. Ogliaro, S. P. de Visser, S. Cohen, P. K. Sharma and S. Shaik, *J. Am. Chem. Soc.*, 2002, **124**, 2806.
162. T. Kamachi, Y. Shiota, T. Ohta and K. Yoshizawa, *Bull. Chem. Soc. Jpn.*, 2003, **76**, 721.
163. P. K. Sharma, S. P. de Visser and S. Shaik, *J. Am. Chem. Soc.*, 2003, **125**, 8698.
164. C. S. Porro, M. J. Sutcliffe and S. P. de Visser, *J. Phys. Chem. A*, 2009, **113**, 11635.
165. M. J. Park, J. Lee, Y. Suh, J. Kim and W. Nam, *J. Am. Chem. Soc.*, 2006, **128**, 2630.
166. P. R. Ortiz de Montellano, H. S. Beilan, K. L. Kunze and B. A. Mico, *J. Biol. Chem.*, 1981, **256**, 4395.
167. K. L. Kunze, B. L. K. Mangold, C. Wheeler, H. S. Beilan and P. R. Ortiz de Montellano, *J. Biol. Chem.*, 1983, **258**, 4202.
168. P. R. Ortiz de Montellano, B. L. K. Mangold, C. Wheeler, K. L. Kunze and N. O. Reich, *J. Biol. Chem.*, 1983, **258**, 4208.
169. Z.-Q. Tian, J. Richards and T. G. Traylor, *J. Am. Chem. Soc.*, 1995, **117**, 21.
170. S. P. de Visser, F. Ogliaro, P. K. Sharma and S. Shaik, *Angew. Chem., Int. Ed.*, 2002, **41**, 1947.
171. S. P. de Visser, F. Ogliaro, P. K. Sharma and S. Shaik, *J. Am. Chem. Soc.*, 2002, **124**, 11809.
172. D. Kumar, B. Karamzadeh, G. N. Sastry and S. P. de Visser, *J. Am. Chem. Soc.*, 2010, **132**, 7656.
173. S. P. de Visser, F. Ogliaro and S. Shaik, *Chem. Commun.*, 2001, 2322.
174. S. Shaik, S. P. de Visser and D. Kumar, *J. Biol. Inorg. Chem.*, 2004, **9**, 661.
175. S. P. de Visser, F. Ogliaro and S. Shaik, *Angew. Chem., Int. Ed.*, 2001, **40**, 2871.
176. S. P. de Visser, *J. Am. Chem. Soc.*, 2006, **128**, 9813.
177. S. P. de Visser, *J. Am. Chem. Soc.*, 2006, **128**, 15809.
178. M. Werner, G. Birner and W. Dekant, *Chem. Res. Toxicol.*, 1996, **9**, 41.
179. A. Madan, A. Parkinson and M. D. Faiman, *Drug Metabol. Dispos.*, 1995, **23**, 1153.
180. K. A. Usmani, E. D. Karoly, E. Hodgson and R. L. Rose, *Drug Metabol. Dispos.*, 2004, **32**, 333.
181. B. Furnes and D. Schlenk, *Drug Metabol. Dispos.*, 2005, **33**, 214.
182. E. J. Perkins, A. El-Alfy and D. Schlenk, *Toxicol. Sci.*, 1999, **48**, 67.
183. J. Wójcikowski, P. Maurel and W. A. Daniel, *Drug Metabol. Dispos.*, 2006, **34**, 471.
184. Y. Goto, T. Matsui, S.-i. Ozaki, Y. Watanabe and S. Fukuzumi, *J. Am. Chem. Soc.*, 1999, **121**, 9497.
185. S. Kato, H.-J. Yang, T. Ueno, S.-i. Ozaki, G. N. Phillips Jr., S. Fukuzumi and Y. Watanabe, *J. Am. Chem. Soc.*, 2002, **124**, 8506.

186. T. J. Volz, D. A. Rock and J. P. Jones, *J. Am. Chem. Soc.*, 2002, **124**, 9724.
187. K.-B. Cho, Y. Moreau, D. Kumar, D. A. Rock, J. P. Jones and S. Shaik, *Chem. Eur. J.*, 2007, **13**, 4103.
188. J. Benet-Buchholz, P. Comba, A. Llobet, S. Roeser, P. Vadivelu and S. Wiesner, *Dalton Trans.*, 2010, **39**, 3315.
189. D. Kumar, S. P. de Visser, P. K. Sharma, H. Hirao and S. Shaik, *Biochemistry*, 2005, **44**, 8148.
190. C. Li, L. Zhang, C. Zhang, H. Hirao, W. Wu and S. Shaik, *Angew. Chem., Int. Ed.*, 2007, **46**, 8168.
191. Y. Watanabe, T. Iyanagi and S. Oae, *Tetrahedron Lett.*, 1980, **21**, 3685.
192. Y. Watanabe, T. Numata, T. Iyanagi and S. Oae, *Bull. Chem. Soc. Jpn.*, 1981, **54**, 1163.
193. Y. Watanabe, T. Iyanagi and S. Oae, *Tetrahedron Lett.*, 1982, **23**, 533.
194. S. Shaik, Y. Wang, H. Chen, J. Song and R. Meir, *Faraday Discuss.*, 2010, **145**, 49.
AQ5 195. D. Kumar, G. N. Sastry and S. P. de Visser, *Chem. Eur. J.*, 2011, ~~in press.~~ ASAP DOI: 10.1002/chem.201003187.
196. S. P. de Visser and S. Shaik, *J. Am. Chem. Soc.*, 2003, **125**, 7413.
197. C. Hazan, D. Kumar, S. P. de Visser and S. Shaik, *Eur. J. Inorg. Chem.*, 2007, 2966.
198. S. P. de Visser, L. Tahsini and W. Nam, *Chem. Eur. J.*, 2009, 5577.
199. C. M. Bathelt, L. Ridder, A. J. Mulholland and J. N. Harvey, *J. Am. Chem. Soc.*, 2003, **125**, 15004.
200. C. M. Bathelt, L. Ridder, A. J. Mulholland and J. N. Harvey, *Org. Biomol. Chem.*, 2004, **2**, 2998.
201. C. M. Bathelt, A. J. Mulholland and J. N. Harvey, *J. Phys. Chem. A*, 2008, **112**, 13149.
202. J. Zheng, D. Wang, W. Thiel and S. Shaik, *J. Am. Chem. Soc.*, 2006, **128**, 13204.
203. A. Altun, V. Guallar, R. A. Friesner, S. Shaik and W. Thiel, *J. Am. Chem. Soc.*, 2006, **128**, 3924.
204. A. Altun, S. Shaik and W. Thiel, *J. Comput. Chem.*, 2006, **27**, 1324.
205. D. Kumar, A. Altun, S. Shaik and W. Thiel, *Faraday Discuss.*, ~~2010, 145, in press.~~ 2011, 148, 373.

JOURNAL OF CHEMICAL INFORMATION AND MODELING

ARTICLE

pubs.acs.org/jcim

Comparison of Computational Methods to Model DNA Minor Groove Binders

Hemant Kumar Srivastava, Mukesh Chourasia, Devesh Kumar, and G. Narahari Sastry*

Molecular Modelling Group, Indian Institute of Chemical Technology, Taranaka, Hyderabad 500 607, India

Supporting Information

ABSTRACT: There has been a profound interest in designing small molecules that interact in sequence-selective fashion with DNA minor grooves. However, most in silico approaches have not been parametrized for DNA ligand interaction. In this regard, a systematic computational analysis of 57 available PDB structures of noncovalent DNA minor groove binders has been undertaken. The study starts with a rigorous benchmarking of GOLD, GLIDE, CDOCKER, and AUTODOCK docking protocols followed by developing QSSR models and finally molecular dynamics simulations. In GOLD and GLIDE, the orientation of the best score pose is closer to the lowest rmsd pose, and the deviation in the conformation of various poses is also smaller compared to other docking protocols. Efficient QSSR models were developed with constitutional, topological, and quantum chemical descriptors on the basis of B3LYP/6-31G* optimized geometries, and with this ΔT_m values of 46 ligands were predicted. Molecular dynamics simulations of the 14 DNA−ligand complexes with Amber 8.0 show that the complexes are stable in aqueous conditions and do not undergo noticeable fluctuations during the 5 ns production run, with respect to their initial placement in the minor groove region.

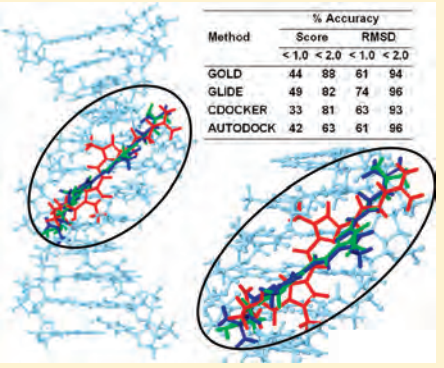

INTRODUCTION

The interaction of small molecules with DNA recently has drawn the attention of several researchers because DNA is generally the prime target of anticancer drugs. These interactions can cause DNA damage in cancer cells, which inhibits the growth of cancer cells by either inhibiting replication or transcription and results in cell death or apoptosis.[1] The B-form of the DNA right-handed double-helical structure, which is most common in cells under normal conditions, is biologically relevant because of its shallow wide major groove and deep minor groove and thus has been identified as an important target for cancer therapy. Drug−DNA interactions can be classified into two major categories: intercalation and groove binding. Both covalent and noncovalent binding modes are possible in these two categories. Intercalative and nonintercalative drugs represent the major classes of noncovalent binding with DNA.[2] Intercalators are typically made of a planar polyaromatic system, which bind between the layers of nucleic acid base pairs with less sequence specificity and disrupt the organization of the DNA double-helix.[3] The naphthalimides are a family of important DNA intercalators because of their antitumor properties. The DNA alkylating agents like nitrogen mustards,[4] cis-platin,[5] etc. fall into a covalent binding category. These compounds inhibit transcription, translation, and replication of DNA and block the progression of DNA polymerase.[6] The nitrogen mustards represent the extensively studied class of the DNA interstrand cross-linking agent, and mechlorethamine and chlorambucil are two important clinical anticancer agents from this class.[7] The major and minor grooves of DNA differ in very subtle ways in terms of hydrogen bonding characteristics, steric disposition, electrostatic environment, and microenvironmental polarity.[8] This leads to contrasting preferences for the incoming molecules to bind to DNA, with proteins and large molecules preferring the major groove.[9] However, small molecules were found to bind with both the major and minor groove regions of the double-helical DNA with a slight preference toward the later mode of binding.[9] The natural product azinomycin B is an antitumor agent, and its biological activity was traced to the formation of covalent interstrand cross-linking within the major groove via N7 alkylation of two purine bases.[10] Interest in delineating the details of the molecular mechanism of action and effective antitumor activity resulted in several studies involving synthetic, mechanistic, and molecular modeling studies of azinomycin and its derivatives.[11] Table 1 and Figure 1 together depict the various classes of DNA binders, their mode of binding, PDB-ID, and type of activity along with a representative chemical structure.

Minor groove binding agents have long and planar structures that allow them to adopt a crescent shape that fits into the groove. The small molecules bind at AT-rich region in the minor groove in a sequence-selective fashion. The DNA minor groove is the target for a large number of drugs such as the antiviral agents netropsin and distamycin, the antipneumocystis carinii drugs pentamidine and furamidines, the antiseptic and disinfectant propamidine, the trypanocidal drug berenil, the experimental antitumor agent and important DNA stain Hoechst dyes.[12] Moreover, several minor groove binders proved to have potent antitumor activity in

Received: October 11, 2010
Published: March 04, 2011

ACS Publications © 2011 American Chemical Society

Table 1. List of DNA Binding Drugs, Their Action, and Mode of Binding (Minor/Major Groove and Intercalators) with PDB ID

number	DNA binders	activity	mode of binding		PDB ID
1	netropsin	antitumor, antiviral	minor groove	noncovalent	121D, 195D, 1D86, 1DNE, 261D
2	hoechst	antitumor	minor groove	noncovalent	109D, 127D, 128D, 129D, 1D43, 1D44, 1D45, 1D46, 8BNA, 1DNH, 264D, 302D, 311D, 303D, 442D, 443D, 448D
3	distamycin	antitumor, antiviral	minor groove	noncovalent	2DND
4	DAPI	fluorescence	minor groove	noncovalent	1D30
5	bernil	antitrypanosomal	minor groove	noncovalent	1D63, 2DBE
6	pentamidine	against *Pneumocystis carinii*	minor groove	noncovalent	1D64
7	propamidine	antiseptic and disinfectant	minor groove	noncovalent	102D, 1PRP
8	CC1065	antitumor antibiotic	minor groove	covalent	1DSM
9	bisfuramidine	against *P. carinii*, antitumor	minor groove	noncovalent	1FMQ, 1FMS, 1EEL, 360D, 289D, 298D, 227D
10	SN7167	antitumor, antiviral	minor groove	noncovalent	328D
11	SN6999	against *P. falciparum*	minor groove	noncovalent	144D
12	mithramycin	anticancer antibiotic	minor groove	noncovalent	146D
13	plicamycin	anticancer antibiotic	minor groove	noncovalent	1BP8
14	chromomycin A3	anticancer antibiotic	minor groove	noncovalent	1EKH
15	PBDs	anticancer	minor groove	covalent	2K4L
16	cis-platin	anticancer antibiotic	cross-linking	covalent	1AU5
17	cis-{Pt(NH3)2(pyridine)}2+	anticancer	major groove	covalent	3CO3
18	aminoglycoside (NB33)	broad-spectrum antibacterial	major groove	noncovalent	454D
19	nogalamycin	antitumor	intercalation	noncovalent	182D
20	menogaril	antitumor- topoisomerase II poison	intercalation	covalent	202D

preclinical studies, and some of them are at an advanced stage of clinical trials. These include duocarmycin derivatives adozelesin,[13] carzelesin,[14] bizelesin,[15] KW-2189,[16] and a distamycin A-derivative tallimustine.[17] Distamycin A is a naturally occurring antibiotic agent isolated from *Streptomyces distallicus* that is active against a few viruses, gram-positive bacteria, and protozoa but inactive as an antitumor agent.[18] Recently, synthetic strategies have been developed to modify the distamycin scaffold to enhance the recognition efficiency together with mixed base-pair reading capacity.[18d] Pentamidine, a synthetic diamidine dication, was used against parasitic microorganisms and for the treatment of *Pneumocystis jiroveci* pneumonia (PCP) within infants.[19] A furan-based diamidine called furamidine (DB75, similar in structure to pentamidine) has shown promising therapeutic activity against a variety of parasitic microorganisms.[19] A prodrug of furamidine was in phase II clinical trials against malaria and phase III clinical trials against pneumocystis pneumonia and human African trypanosomiasis (HAT).[20] The antibiotic netropsin is a dicationic amidine−guanidine natural product that has been extremely useful in characterizing the full molecular basis for DNA minor groove recognition.[21] Bisguanidine and especially bis(2-aminoimidazoline)diphenyl compounds displayed potent antitrypanosomal activity in vitro and in vivo against *T. b. rhodesiense* (*Trypanosoma brucei rhodesiense*).[22]

Thus, it is evident that there is a tremendous interest to design the molecule with optimal binding to DNA minor groove. Lead optimization in this case requires a detail understanding of the way in which the small molecules bind to the minor groove. There are several well-established docking procedures for protein−ligand interactions;[23,24] however, in comparison, docking studies involving DNA−ligand interactions are not as popular.[25] This is because most docking methods were developed for targeting protein−ligand interactions. Developing force field or parametrization for scoring functions is often indispensable to a new class of molecules; however, such a practice is not desirable when the existing scoring function is adequate. Neidle et al. demonstrated that the parametrization is transferable from proteins to DNA in some selected cases.[25e] To the best of our knowledge, no systematic parametrization is available for complexes involving nucleic acid ligand binding (with the exception of DOCK).[26] However, there are a large number of studies in the literature that adopt existing docking protocols to model DNA ligand complexes very effectively.[25e−h,27] Tang et al.[27] in a recent paper have made an exhaustive study on the available RNA ligand complexes and demonstrated the applicability and reliability of GOLD[28] and GLIDE[29] methods. Neidle et al.[25e] evaluated DOCK and AUTODOCK[30] protocols on 28 DNA−ligand complexes and found 40% and 55% success, respectively, in predicting crystallographic poses within a 2.0 Å root-mean-square deviation (rmsd). Recently, Trent et al.[25g] have shown that AUTODOCK and Surflex[31] can reproduce the crystal structure of DNA minor groove binders (distamycin and pentamidine) and DNA intercalators (daunorubicin and ellipticine). Clearly, while the Neidle's study reveals the poor performance of adopted docking methods, Trent's study was far from exhaustive.

It appears to be extremely important to evaluate various popular docking protocols on a reasonable number of compounds for DNA−ligand interaction studies. Here, we present a systematic computational analysis of 57 noncovalent DNA minor groove binders (available in PDB)[32] using four popular docking protocols: GOLD, GLIDE, CDOCKER,[33] and AUTODOCK (Table 2). One of the main objectives of the current paper is to address the question, "Is it necessary to develop a new scoring function for nucleic acid ligand interaction or can one use the

dx.doi.org/10.1021/ci100474n |*J. Chem. Inf. Model.* 2011, 51, 558–571

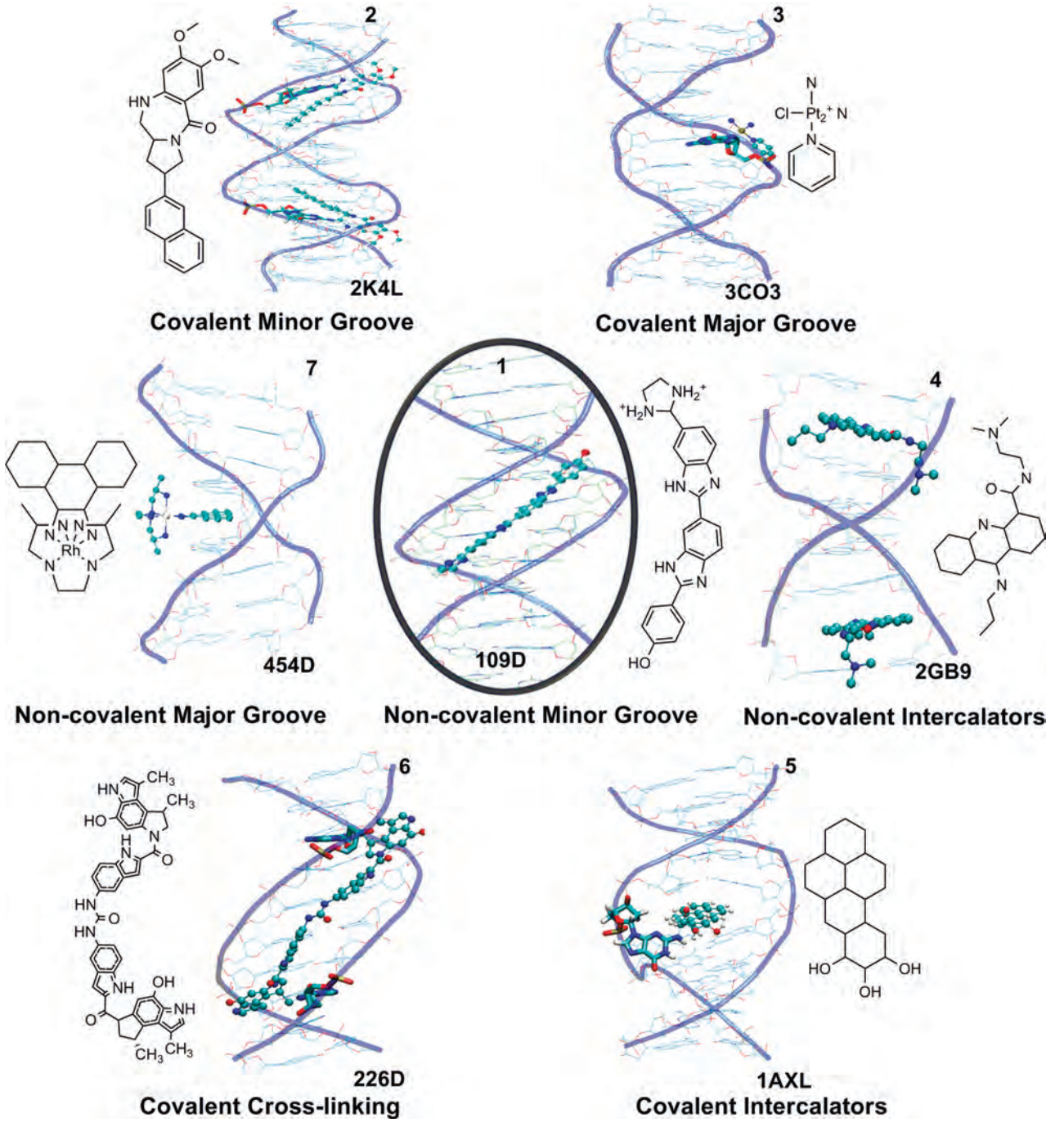

Figure 1. Representation of various classes of DNA binders and their mode of binding.

existing parameters?" Experimentally observed ΔT_m is an important parameter to measure the thermal stability of the DNA−ligand complex. The ΔT_m values of 11 available compounds (among the structures considered) were collected from the literature[34] for QSSR (quantitative structure stability relationship) studies. QSAR/QSPR/QSTR/QSSR methods are based on the axiom that the variance in the activities or physicochemical properties of chemical compounds is determined by the variance in their molecular structures.[35] QSAR has been widely used for the prediction of activities of diverse series of compounds.[36] In this work, we present a valuable method to predict ΔT_m values of DNA minor groove binders on the basis of QSSR approaches. To address the fundamental issues relating the DNA rigidity and structural deviations upon the ligand binding, we did an extensive 5 ns molecular dynamics simulation on a set of 14 selected complexes. The MD simulation provide useful information on the time-dependent behavior, including atomic level fluctuations and conformational changes of a macromolecule.[37] MM-PBSA based interaction energies derived from the MD simulation are broadly accepted to estimate interactions between small and large molecules.[38] The interaction energy of all the complexes were calculated by using the Poisson−Boltzmann continuum electrostatic method in which the influence of the solvent is incorporated implicitly.[39]

dx.doi.org/10.1021/ci100474n |J. Chem. Inf. Model. 2011, 51, 558–571

Table 2. Structure of All Ligands with Their PDB ID and Resolution, along with rmsd values of B3LYP/6-31G* Optimized Geometries with the Crystallographic Ligands[a]

Ligand, PDB-ID and Resolution	RMSD	Ligand, PDB-ID and Resolution	RMSD	Ligand, PDB-ID and Resolution	RMSD
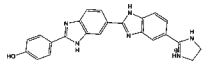	4.09	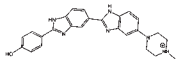	0.53	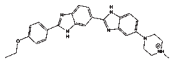	0.89
1. 109D, 2.00		**2.** 127D, 2.00		**3.** 129D, 2.25	
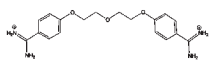	0.85	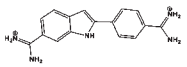	0.60	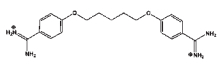	1.43
4. 166D, 2.20		**5.** 1D30, 2.40		**6.** 1D64, 2.10	
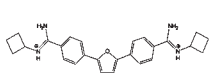	1.21	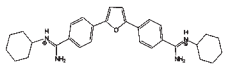	1.80	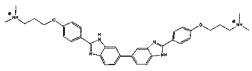	1.55
7. 1FMQ, 2.00		**8.** 1FMS, 1.90		**9.** 1FTD, 2.00	
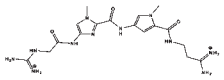	1.16	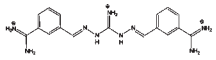	1.01	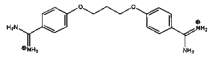	0.86
10. 1LEX, 2.25		**11.** 1M6F, 1.78		**12.** 1PRP, 2.10	
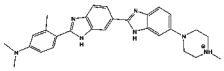	4.35	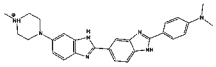	6.14	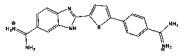	3.08
13. 1QV4, 2.50		**14.** 1QV8, 2.50		**15.** 1VZK, 1.77	
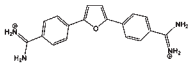	0.78	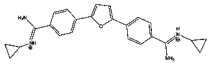	1.23	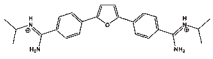	1.04
16. 227D, 2.20		**17.** 289D, 2.20		**18.** 298D, 2.20	
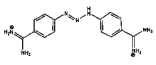	0.77	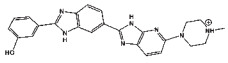	1.15	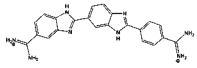	0.61
19. 2DBE, 2.50		**20.** 302D, 2.20		**21.** 311D, 2.20	
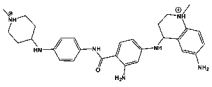	2.27	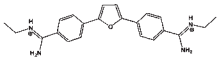	0.59	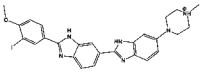	0.53
22. 328D, 2.60		**23.** 360D, 1.85		**24.** 442D, 1.60	
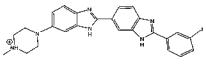	0.71	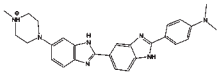	1.14	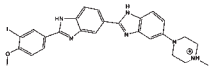	0.59
25. 443D, 1.60		**26.** 447D, 2.20		**27.** 448D, 2.20	
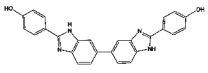	0.26	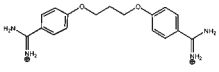	0.72	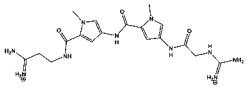	1.09
28. 453D, 1.80		**29.** 102D, 2.20		**30.** 121D, 2.20	
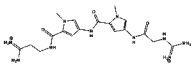	0.77	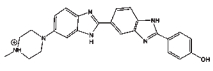	1.15	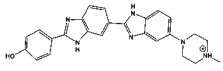	0.90
31. 195D, 2.30		**32.** 1D43, 2.00		**33.** 1D44, 2.00	
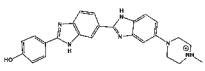	1.08	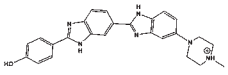	0.84	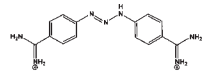	0.37
34. 1D45, 1.90		**35.** 1D46, 2.00		**36.** 1D63, 2.00	
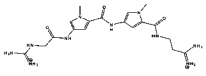	1.39	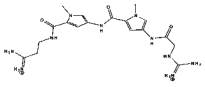	1.74	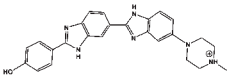	0.63
37. 1D86, 2.20		**38.** 1DNE, 2.40		**39.** 1DNH, 2.25	

dx.doi.org/10.1021/ci100474n |J. Chem. Inf. Model. 2011, 51, 558–571

Table 2. Continued

Ligand, PDB-ID and Resolution	RMSD	Ligand, PDB-ID and Resolution	RMSD	Ligand, PDB-ID and Resolution	RMSD
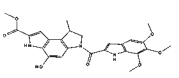	0.53	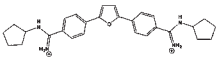	1.06	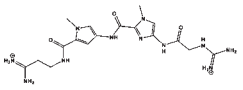	0.98
40. 1DSA, NA		**41.** 1EEL, 2.40		**42.** 1LEY, 2.25	
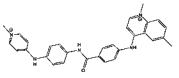	0.99	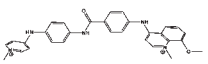	1.25	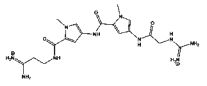	0.88
43. 1ZPH, 1.80		**44.** 1ZPI, 1.60		**45.** 261D, 2.40	
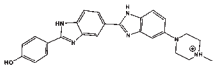	0.59	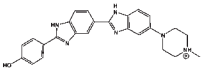	0.55	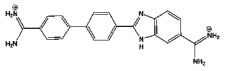	0.28
46. 264D, 2.44		**47.** 296D, 2.25		**48.** 2B0K, 1.64	
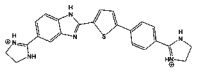	0.47	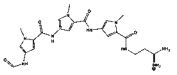	0.48	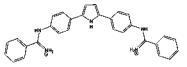	1.05
49. 2B3E, 1.36		**50.** 2DND, 2.20		**51.** 2GYX, 1.86	
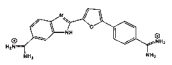	0.25	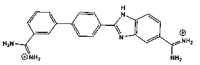	0.51	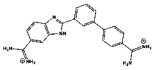	0.53
52. 2I2I, 1.63		**53.** 2I5A, 1.65		**54.** 2NLM, 2.05	
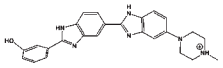	0.80	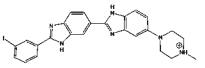	0.68	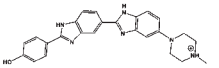	0.49
55. 303D, 2.20		**56.** 449D, 2.10		**57.** 8BNA, 2.20	

[a] Ligands from DNA sequences 5′-CGCGAATTCGCG-3′ (1-28, 32-35, 37, 39, 41-44, 48-49, 51-57), 5′-CGCAAATTTGCG-3′ (29, 30, 36, 46, 47, 50), 5′-GACTAATTGAC-3′ (40), 5′-CGCGTTAACGCG-3′ (31), 5′-CGCGATATCGCG-3′ (38), and 5′-CGCAATTCGC-3′ (45) have been collected (see references in the Supporting Information for citations of all the considered structures with PDB ID).

Thus, the current computational study rigorously examines the available popular modeling approaches for the DNA minor groove binding and compares them with experimental results where available. Finally, the paper provides important insights into the lead optimization of this class of compounds, which should be of high interest to medicinal chemists.

MATERIALS AND METHODS

A total of 57 crystal structures of DNA−ligand complexes were downloaded from the protein data bank (PDB). These 57 complexes are divided into six different groups on the basis of the extent of sequence similarity of DNA. Complexes **1**−**28**, **32**−**35**, **37**, **39**, **41**−**44**, **48**−**49**, and **51**−**57** have 5′-CGCGAATTCGCG-3′, complexes **29**, **30**, **36**, **46**, **47**, and **50** have 5′-CGCAAATTTGCG-3′, complex **40** has 5′-GACTAATTGAC-3′, complex **31** has 5′-CGCGTTAACGCG-3′, complex **38** has 5′-CGCGATATCGCG-3′, and complex **45** has 5′-CGCAATTCGC-3′ DNA sequences. Considering this, we used six different DNA sequences (PDB ID: 1VZK, 121D, 1DSA, 195D, 1DNE, and 261D) as receptors for docking of the respective group of complexes. Docking with the above-mentioned six different receptors does not show any significant variation in absolute rmsd values in comparison with that of a single receptor (see Table S13 of the Supporting Information). The four widely accepted docking protocols, GOLD, GLIDE, CDOCKER, and AUTODOCK, were considered for the docking study. The ability to reproduce a ligand pose close to crystallographic pose is a critical determinant for the effectiveness of the docking program. Constitutional, topological, and conceptual DFT-based descriptors were used to generate QSSR models for the prediction of ΔT_m values. Gaussian 03,[40] CODESSA,[41] and Scigress Explorer[42] programs were used for geometry optimization (B3LYP/6-31G* level), descriptor generation, and regression analysis, respectively. MD simulation was performed with the Amber 8.0[43] program, and interaction energies were calculated with MM-PBSA[39] calculations.

COMPUTATIONAL DETAILS

Ligands and Receptors Preparation. The ligands were extracted from DNA-bound crystal structures. Explicit hydrogens were added and were subjected to energy minimization on a Sybyl 6.9.2 (Tripos, Inc., St. Louis, MO) program by using MMFF94 force field and point charges.[44] The DNA was extracted from six considered complexes. Explicit hydrogens were added, and the energy minimization of hydrogens was carried out. Ligands were optimized by using 0.01 kcal mol^{-1}/Å, whereas hydrogens of all six receptors were optimized by using 0.1 kcal mol^{-1}/Å root-mean-squared gradient.

METHODOLOGY FOR DOCKING

GOLD. The entire conformational space of the DNA was scanned by selecting the central atom as the binding site for the molecular docking calculations in GOLD 3.2 software that uses

dx.doi.org/10.1021/ci100474n |J. Chem. Inf. Model. 2011, 51, 558–571

the genetic algorithm (GA) to perform flexible docking. For each of the 10 independent GA runs, a maximum number of 100,000 operations were performed with a population size of 100 individuals. Default values of niche size (2) and selection pressure (1.1) was used, and operator weights for crossover, mutation, and migration were set to 95, 95, and 10, respectively. Default cutoff values of 2.5 Å for hydrogen bonds and 4.0 Å for van der Waals distance were employed. The 10 best conformations were generated for each ligand without putting any constraints in the docking.

GLIDE. The Sybyl 6.9.2 generated receptors were optimized in gas phase in Maestro by using OPLS2005 force field before docking study using GLIDE 4.5. All heavy atoms were constrained to their original coordinates with the "Truncated Newton" algorithm, and 100 iterations were used with 0.01 gradient criterion. A receptor grid was generated using a 1.00 van der Waals (vdW) radius scaling factor and 0.25 partial charge cutoff. The radius of 30 Å from the central atom of DNA was defined as the binding site that covers the entire DNA. Ligands were docked using the standard precision mode without using any constraints and a 0.80 van der Waals (vdW) radius scaling factor and 0.15 partial charge cutoff. Twenty poses per ligand were generated, and post-docking minimization was carried out.

AUTODOCK. The binding site in AUTODOCK is defined by the grid of interaction points. The N3 atom of minor groove adenine was defined as the center of grid, and the grid was made up of the grid points 70(X), 80(Y), and 126(Z) with grid spacing of 0.375 Å. The central axis of DNA is along the Z-axis. The number of generations, energy evaluations, and individuals in the population are set to 27000, 5×10^6, and 150, respectively. The 50 deg/step was used for quaternion and torsion, while 2 Å/step was used for the translation during the docking run. The Lamarckian genetic algorithm was adopted for sampling ligand conformations in the minor groove of DNA. The default parameters of free energy scoring function were used for the docking studies. The best scoring and lowest rmsd solutions from 20 runs were considered as the predicted binding conformers. The rmsd values of each docked conformer were calculated from the corresponding crystal structure as reference to access the accuracy of poses with respect to their binding energy.

CDOCKER. CDOCKER has an all-atom CHARMm force field-based docking algorithm and uses soft-core potentials with an optional grid representation to dock ligands into active site of the receptor. The nucleotide falls within the 20 Å radius from the center atom of the DNA as defined in AUTODOCK and was considered an active site. CHARMm force field was applied to both DNA and ligands, and DNA was kept rigid during the docking study. CDOCKER generates the random ligand conformations through molecular dynamics simulation. A variable number of rigid-body rotations/translations are applied to each conformation to generate the initial ligand poses. The final poses of the ligands were then subjected to simulated annealing to refine the poses in the DNA minor groove. A total of 10 final poses were saved, and rmsd values were also calculated for the same.

rmsd Calculations. The all-atom rmsd values were calculated by superimposing all the docked poses obtained from various docking protocols on their respective crystallographic structure using the superimposition tool of the Maestro 8.5 package. While calculating the rmsd values of the ligands, the receptor of the docked structure was fitted on the receptor of the crystal structure employing least-squares fitting.

MOLECULAR DYNAMICS SIMULATION

Molecular dynamics simulations were carried out using the Amber 8.0 program on 14 DNA ligand complexes. The antechamber module of the program was used to generate parameters for the cocrystal from the GAFF force field using AM1-BCC charges. The "addions" command as implemented in "xleap" was used to add the Na^+ ions explicitly to neutralize the system. The TIP3P water box of 10 Å distance from the edge atom of the DNA−ligand complex was constructed. Equilibration of the solvated complex was completed by carrying out a short energy minimization (500 steps of each steepest descent and conjugate gradient method), 50 ps of heating, and 50 ps of density equilibration, with weak restraints on the complex followed by 500 ps of constant pressure equilibration at 300 K. Application of cutoffs to include noncovalent interactions is subjective, and

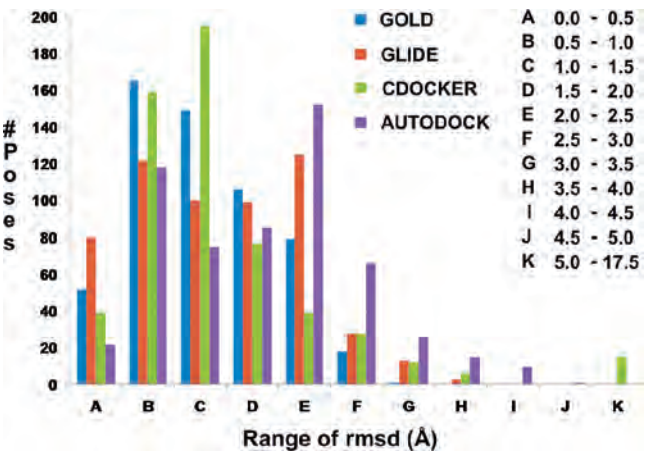

Figure 2. Comparison of rmsd values of all the generated ligand poses obtained from the GOLD, GILDE, CDOCKER, and AUTODOCK docking protocols from the crystallographic pose.

Table 3. Success Rate of Prediction of Crystallographic Poses within 2 Å rmsd by Various Docking Protocols, rmsd Variation, and Mean Average Deviations (MAD)

protocols	best score[a] (%)	lowest rmsd[b] (%)	rmsd variation[c]	MADb[d]	MADl[e]
GOLD	88	94	0.29−3.02	1.24	0.95
GLIDE	82	96	0.22−3.55	1.23	0.81
CDOCKER	81	93	0.24−17.65	1.44	0.95
AUTODOCK	63	96	0.23−4.97	1.57	0.92

[a] Success rate, while considering best score pose. [b] Success rate, while considering the pose having the lowest rmsd values. [c] The variation of rmsd values in different generated poses. [d] Average rmsd of the poses having the best score. [e] Average rmsd of the poses having the lowest rmsd from crystallographic poses.

dx.doi.org/10.1021/ci100474n |J. Chem. Inf. Model. 2011, 51, 558–571

Table 4. Regression Equations and Statistical Significance of Various QSSR Models Developed for the Prediction of ΔT_m Values[a]

model	regression equation	R^2	R^2_{cv}	AE	outliers
1	$\Delta T_m = -79.7666 \times \text{RNSB} + 1.49384 \times \text{SIC}_1 + 22.0308$	0.98	0.94	0.54	1
2	$\Delta T_m = 1.61315 \times \text{BIC}_1 + 84.8372 \times \text{RNAB} - 62.2725$	0.99	0.97	0.46	1
3	$\Delta T_m = 7.40497 \times \text{AIC}_2 - 5.80395 \times \eta - 3.64542$	0.84	0.71	1.56	0
4	$\Delta T_m = -71.3385 \times \text{RNSB} + 1.37832 \times \text{SIC}_1 + 19.7289$	0.95	0.87	0.76	0
5	$\Delta T_m = 1.47582 \times \text{BIC}_1 + 75.0745 \times \text{RNAB} - 55.1181$	0.95	0.89	0.77	0
6	$\Delta T_m = 0.454204 \times \text{GOLD} - 21.411$	0.74	0.53	1.82	0
7	$\Delta T_m = -3.35634 \times \text{GLIDE} - 25.8601$	0.57	0.56	2.52	0
8	$\Delta T_m = 0.159975 \times \text{CDOCKER} + 5.22858$	0.37	0.14	2.68	0
9	$\Delta T_m = -1.26609 \times \text{AUTODOCK} + 3.51885$	0.26	0.06	3.46	0
10	$\Delta T_m = 9.58562 \times \text{AIC}_1 - 16.1747$	0.72	0.59	1.95	0
11	$\Delta T_m = -0.83609 \times \omega + 33.4477$	0.79	0.68	2.40	1
12	$\Delta T_m = 7.2866 \times \text{AIC}_2 - 12.4702$	0.74	0.63	2.04	0

[a] RNSB is relative number of single bonds. SIC_1 is structural information content (order 1). BIC_1 is bonding information content (order 1). RNAB is relative number of aromatic bonds. AIC_2 is average information content (order 2). η is chemical hardness [$\eta = (E_{LUMO} - E_{HOMO})/2$]. GOLD is best fitness score obtained from GOLD docking protocols. GLIDE is best fitness score obtained from GLIDE docking protocols. CDOCKER is best fitness score obtained from CDOCKER docking protocols. AUTODOCK is best fitness score obtained from AUTODOCK docking protocols. AIC_1 is average information content (order 1). ω is electrophilicity index [$\omega = \mu^2/2\eta$, where μ is chemical potential, $\mu = (E_{LUMO} + E_{HOMO})/2$]. R^2 is correlation coefficient. R^2_{cv} is cross validation coefficient. AE is average of residuals (observed−predicted).

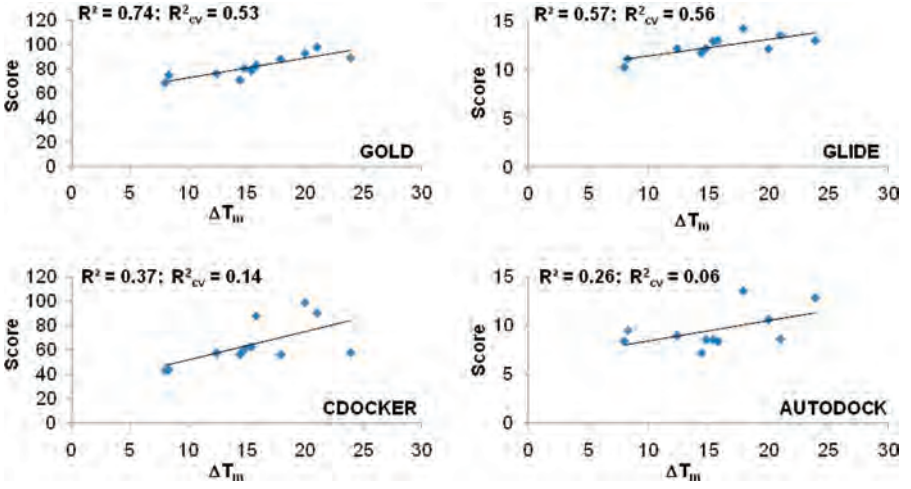

Figure 3. Comparison of various docking scores with experimental ΔT_m values.

adequate cutoff sizes are necessary to get reliable results. The larger cutoff sizes for the long-range nonbonded interactions are computationally more demanding, and a perusal of the available literature indicates that a cutoff size of 8.0 Å is more frequently used.[44] To verify the appropriate cutoff size, we performed a systematic study with 6.0, 8.0, 10.0, and 12.0 Å cutoff sizes on three different systems with 5 ns time period, and found a cutoff size of 8.0 Å is reasonable for these complexes. Therefore, a cutoff of 8.0 Å was used for MD simulations for all 14 complexes. All long-range electrostatics were included by means of a Particle−Mesh Ewald (PME) method. All hydrogen-heavy atom bonds were constrained by the SHAKE method, and simulations were performed with a 2 fs time step and langevin dynamics for temperature control. The same conditions as the final phase of equilibration are used for production run of 5 ns, and the coordinates are recorded in every 10 ps. The periodic boundary conditions (PBC) were used during MD simulations. MM-PBSA calculations were performed to extract 500 snapshots from production runs by using "extract_coords.mmpbsa" script, and the interaction energies were calculated by using "binding_energy.mmpbsa" script (see Table S14 of the Supporting Information for the details of the parameters used for the IE calculation). The reported interaction energies are the average of all 500 snapshots.

RESULTS AND DISCUSSION

Docking of Noncovalent Minor Groove Binders. This study was designed to evaluate four widely accepted docking protocols for the study of 57 available DNA minor groove binders in the PDB. From the investigation of the docked poses obtained from various docking protocols, in most cases it was found that the best score pose does not correspond to the lowest rmsd pose (see Tables S6 and S7 of the Supporting Information). Initially, 10 docked poses were generated in all the docking programs. In those cases where the success rate while evaluating docking protocols was found to be less than 95% on the basis of the first 10 docked poses, the number of poses has been increased to 20. An analysis of all the docked poses (irrespective to their docking

dx.doi.org/10.1021/ci100474n |J. Chem. Inf. Model. 2011, 51, 558–571

Table 5. Comparison of Experimental vs Predicted ΔT_m Values of Ligands by QSSR Models of Current Study with the Available Previous Data[a]

PDB ID	Exp. ΔT_m	charge	pred. ΔT_m (J1)	pred. ΔT_m (J2)	pred. ΔT_m (M2)	pred. ΔT_m (M5)	Res. (J1)	Res. (J2)	Res. (M2)	Res. (M5)
109D	23.9	2	22.5	25.5	23.73	22.49	1.40	−1.60	0.17	1.42
2DBE	8.0	1	5.00	5.60	8.55	8.57	3.00	2.40	−0.55	−0.57
121D	20.0	2	16.8	15.5	20.11	19.74	3.20	4.50	−0.11	0.26
2DND	21.0	1	21.3	22.6	21.18	20.72	−0.30	−1.60	−0.18	0.28
227D	8.3	2	5.2	7.1	7.69	7.76	3.10	1.20	0.61	0.54
298D	14.4	2	15.3	14.6	14.70	14.51	−0.90	−0.20	−0.30	−0.11
289D	12.4	2	13.5	13.5	13.53	13.41	−1.10	−1.10	−1.13	−1.01
127D	17.9	1	19.4	20.4	20.47	20.47	−1.50	−2.50	−	−2.57
1FMQ	14.8	2	15.8	15.2	14.23	14.13	−1.00	−0.40	0.57	0.67
1EEL	15.8	2	17.1	17.1	14.84	14.75	−1.30	−1.30	0.96	1.05
1FMS	15.4	2	19.5	18.2	15.45	15.36	−4.10	−2.80	−0.05	0.04
Avg.							1.90	1.78	0.46	0.77

[a] Exp. is experimental. Charge is formal charge on ligand. J1 and J2 are predicted values collected from reference 45. M2 is QSSR model-2 and M5 is QSSR model-5 of this work. Res. is the difference in experimental and predicted ΔTm values. Avg. is the average res. M5 is without any outlier. M2 is with 127D as outlier.

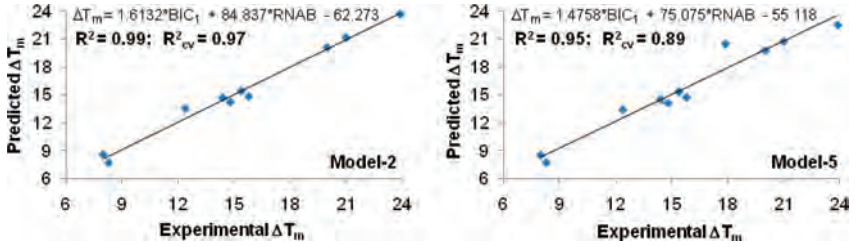

Figure 4. Plots of experimental versus predicted ΔT_m values of the DNA minor groove binders by two best QSSR models.

score) showed that GOLD, GLIDE, CDOCKER, and AUTODOCK have 30%, 63%, 36%, and 76% cases where at least one pose shows rmsd > 2.0 Å. This suggests that AUTODOCK and GLIDE generate diverse poses, whereas GOLD and CDOCKER generate similar poses. This is probably the reason for the requirement of 20 docked poses in the first two docking protocols. A success rate of 88%, 82%, 81%, and 63% has been obtained for GOLD, GLIDE, CDOCKER, and AUTODOCK protocols, respectively, with the best score pose (see Tables S1−S7of the Supporting Information). Encouragingly, the lowest rmsd score poses are within the acceptable deviations in all docking protocols employed (Table 3). Thus, all the docking protocols are able to produce at least one pose that is close to the crystallographic pose, although it may not be the one with the best score, which is reflected in most cases. In addition, all the docking protocols demonstrate similar results (GOLD 12%, GLIDE 9%, CDOCKER 11%, and AUTODOCK 14%) when we consider the cases where the best score pose and lowest rmsd pose are the same. Figure 2, which provides the graphical representation of rmsd values of all the generated poses obtained in various docking protocols, indicates that the performance of GLIDE and GOLD docking protocols is highly satisfactory. Lower rmsd variations were obtained in GOLD (0.29−3.02 Å) and GLIDE (0.22−3.55 Å) compared to those of CDOCKER (0.24−17.65 Å) and AUTODOCK (0.23−4.97 Å) as shown in Table 3. The summary of docking results in terms of mean values is also presented in Table 3. If we consider the mean average deviation in rmsd of the best score pose (MADb, the average rmsd, while considering the best score pose), GOLD (1.24 Å) and GLIDE (1.23 Å) provide better results compared to those of CDOCKER (1.44 Å) and AUTODOCK (1.57 Å) protocols. At the same time if we consider the mean average deviation on lowest rmsd pose (MADl, the average rmsd, while considering the poses have lowest rmsd values), similar results are observed in all docking protocols. The rmsd of the B3LYP/6-31G* optimized geometry with the crystal structure of ligands were calculated and are presented in Table 2. It has been observed that 37% (>2.0 Å 30%, >3.0 Å 2%, and >4.0 Å 5%) ligands show rmsd values higher than 2.0 Å.

QSSR Analysis for the Prediction of ΔT_m Values. We made an attempt to develop QSSR models with the experimental ΔT_m values of 11 available compounds. Twelve diverse QSSR models have been generated by using two different schemes. In the first scheme, docking scores obtained from various docking protocols were used as descriptors for making four different QSSR models. In the second scheme, descriptors generated from CODESSA program along with conceptual DFT-based descriptors were used for making eight different QSSR models. Table 4 summarizes the statistical significance of all 12 QSSR models (see Table S8 and S9 of the Supporting Information for the values of various descriptors and comparison of experimental and predicted ΔT_m values and Figure S1 for the plot of experimental vs predicted values obtained from all 12 QSSR models). GOLD docking scores (R^2 = 0.74 and R^2_{cv} = 0.53) show the best correlation with ΔT_m values, while the correlation for GLIDE docking scores (R^2 = 0.57 and R^2_{cv} = 0.56) is acceptable to a certain extent. No correlations were found for CDOCKER (R^2 = 0.37 and R^2_{cv} = 0.14) and AUTODOCK (R^2 = 0.26 and R^2_{cv} = 0.06) docking scores with the ΔT_m values (Figure 3). These QSSR studies validate our observations that GOLD and GLIDE

dx.doi.org/10.1021/ci100474n |J. Chem. Inf. Model. 2011, 51, 558–571

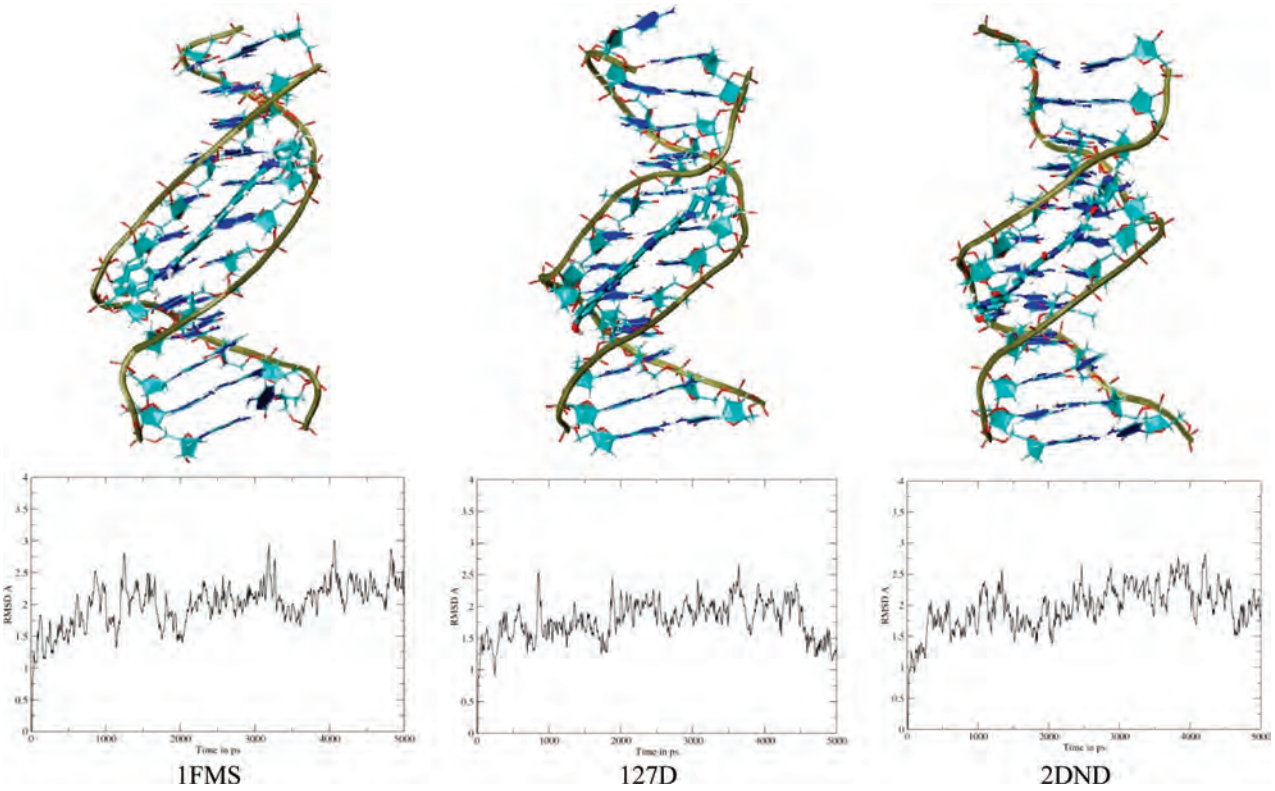

Figure 5. Snapshots of three different DNA−ligand complexes at 5 ns MD simulation, which show the highest, moderate, and lowest ΔT_m values and plots of rmsd vs time of their trajectory.

Table 6. Interaction Energies of DNA−Ligand Complexes at Various Time Scales and Comparison with Experimental ΔT_m Values

			IE[a]	IE	IE	IE	IE	IE	IE[b]
number	PDB ID	Exp. ΔT_m	0 −1 ns	1−2 ns	2−3 ns	3−4 ns	4−5 ns	0−5 ns	0−5 ns
1	2DBE	8.00	−43.38	−34.65	−38.09	−36.40	−35.22	−37.55	−44.77
2	227D	8.30	−36.76	−39.10	−39.54	−35.46	−36.07	−37.39	−45.57
3	289D	12.40	−39.71	−51.56	−51.51	−51.93	−47.59	−48.46	−55.01
4	298D	14.40	−51.04	−50.26	−49.42	−49.97	−51.41	−50.42	−56.71
5	1FMQ	14.80	−51.70	−51.25	−39.44	−38.60	−39.26	−44.05	−51.92
6	1FMS	15.40	−54.82	−54.08	−55.65	−51.47	−54.49	−54.10	−59.34
7	1EEL	15.80	−53.85	−51.95	−51.82	−51.45	−48.68	−51.55	−60.53
8	127D	17.90	−53.12	−54.64	−55.24	−57.46	−55.66	−55.22	−56.47
9	121D	20.00	−70.21	−71.00	−69.66	−67.65	−67.71	−69.25	−73.45
10	2DND	21.00	−63.29	−62.72	−64.79	−64.69	−62.12	−63.52	−64.74
11	109D	23.90	−47.76	−48.43	−47.14	−48.31	−47.55	−47.84	−53.61
12	1D86	99.89[c]	−70.00	−69.02	−69.13	−70.12	−68.88	−69.43	−73.29
13	1D63	76.70[c]	−36.07	−40.49	−45.01	−45.59	−45.11	−42.45	−47.20
14	1D46	36.45[c]	−45.91	−46.48	−47.01	−44.55	−41.65	−45.32	−46.23

[a] IE (interaction energy) is the final estimated binding free energy calculated by the MM-PBSA method at various time intervals. [b] Final estimated binding free energy calculated by the MM-GBSA method. [c] GOLD docking fitness score.

docking protocols are good for DNA−ligand complexes and provide reliable scores and poses. QSSR model-5 is the best model with correlation coefficient (R^2) of 0.95 and cross-validation coefficient (R^2_{cv}) of 0.89 along with an average residual (AE) of 0.77. Only two descriptors, BIC_1 (topological descriptor, bonding information content, order 1) and RNAB (constitutional descriptor, relative number of aromatic bonds), were used for making QSSR model-5. QSSR model-2 is the modification of model-5 by taking out one outlier. This model has very good regression summary with R^2 = 0.99, R^2_{cv} = 0.97, and AE = 0.46 only. The experimental and predicted ΔT_m values by using QSSR model-2 and model-5 are given in Table 5 along

dx.doi.org/10.1021/ci100474n |J. Chem. Inf. Model. 2011, 51, 558–571

with the residual values. The plot of experimental versus predicted ΔT_m values show the linear relationship (Figure 4). Table 4 clearly shows that the topological descriptors (SIC_1, AIC_1, and AIC_2) and conceptual DFT-based descriptors (η and ω) can also be used in different combinations for making valuable QSSR models. Some properties like ω, AIC_1, and AIC_2 even as a single descriptor provide good regression coefficients, but the average residual is on the higher side (models 10, 11, and 12, respectively). A systematic, swift all-atom energy-based computational protocol for the prediction of ΔT_m values has been presented earlier.[45] Clearly, the QSAR equations derived here are robust and have a high predictive ability compared to the earlier studies, as evidenced from the statistical parameters (Table 5). On the basis of three selected QSSR models, the ΔT_m values for the remaining 46 complexes used in this study are predicted (see Table S10 of the Supporting Information). We found that the ligands of 1FTD, 328D, and 1ZPI complexes may bind very strongly to the minor groove of DNA as these ligands have highest predicted ΔT_m values.

Molecular Dynamics Simulation. Following the validation of various docking protocols on 57 DNA−ligand complexes and QSSR analysis for the prediction of ΔT_m values, more rigorous MD simulations were performed on 14 selected complexes. These complexes were chosen on the basis of the availability of experimental ΔT_m values (11 complexes) and variation of GOLD scores (highest, moderate, and lowest score). MD simulations with explicit solvent involving around 8000 water molecules have been performed up to 5 ns time period. Snapshots at 5 ns for the selected complexes are presented in Figure 5, along with the rmsd variations during the simulation (see Figures S2 and S3 of the Supporting Information for rmsd values and snapshots at various time scales, respectively, for all the complexes considered for MD simulations). It is clear from Figure 5 that the ligands remain bound to the DNA near the preferential binding position and do not experience considerable deviations with respect to their initial placement in the minor groove region of DNA. A separate plot of rmsd versus time interval for each complex, DNA, and ligand (see Figure S2 of the Supporting Information for details) also indicate that all the complexes are stable and do not show any unusual fluctuations during the simulation. It has been observed that 1FMQ and 109D complexes show higher rmsd (~3.5 Å) variations. In the case of the 1FMQ complex, both DNA (3.5 Å) and ligand (2.0 Å) are responsible for the higher rmsd variation, while in the case of 109D complex, ligand (0.5 Å) is the most stable structure compared to all the complexes, and only DNA (3.5 Å) is responsible for the higher rmsd variation. Except for the 1FMQ and 109D complexes, all other complexes show rmsd variation less than 3.0 Å during a 5 ns production run. Further, there is no considerable deviation in the rmsd of complexes and DNA with an increase in time period. If we compare the rmsd variation of ligands separately, ligands for 1FMQ, 1FMS, and

Table 7. Comparison of Docking Scores with Binding Free Energies of DNA−Ligand Complexes That Have Experimental ΔT_m Values and Ligands, Showing Low, Moderate, and High GOLD Fitness Scores

		docking score				
PDB ID	Exp. ΔT_m	GOLD	GLIDE	CDOCKER	AUTODOCK	IE[a]
227D	8.3	74.52	−11.08	43.68	−9.53	−37.39
2DBE	8.0	68.05	−10.23	42.79	−8.40	−37.55
1D63	_	76.70	−10.16	70.28	−7.33	−42.45
1FMQ	14.8	80.13	−12.16	60.57	−8.56	−44.05
1D46	_	36.45	−8.21	77.08	−15.91	−45.32
109D	23.9	88.95	−12.97	57.75	−12.88	−47.84
289D	12.4	75.87	−12.15	57.48	−8.95	−48.46
298D	14.4	70.44	−11.72	56.10	−7.15	−50.42
1EEL	15.8	82.78	−12.97	88.15	−8.37	−51.55
1FMS	15.4	78.22	−12.89	62.54	−8.53	−54.10
127D	17.9	87.71	−14.18	56.16	−13.59	−55.22
2DND	21.0	97.73	−13.50	90.60	−8.61	−63.52
121D	20.0	92.60	−12.12	99.20	−10.64	−69.25
1D86	_	99.89	−12.13	99.74	−9.53	−69.43

[a] IE (interaction energy) is the final estimated binding free energy calculated by MM-PBSA method.

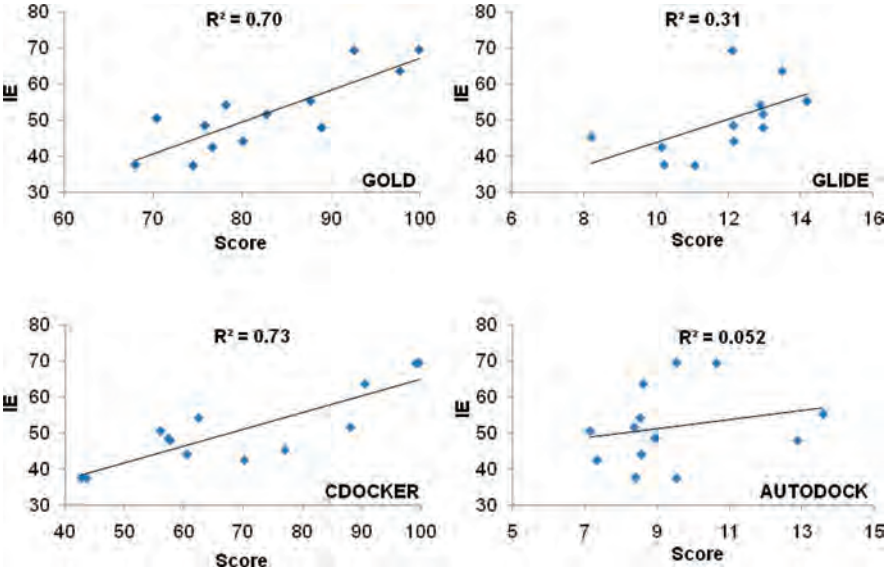

Figure 6. Regression analysis of docking scores of DNA minor groove binders obtained from various docking protocols with their IE (interaction energy) obtained from the MM-PBSA method.

dx.doi.org/10.1021/ci100474n |J. Chem. Inf. Model. 2011, 51, 558–571

Table 8. Interaction Eenergy (IE) Deviation Based on Different Cutoff Values Used in the Molecular Dynamics Simulation at 5 ns Time and Average IE Deviation for Three Complexes Considered for the Study

	cutoff Å/IE GB				cutoff Å/IE PB			
PDB ID	6	8	10	12	6	8	10	12
127D	54.29	56.47	58.55	57.53	51.51	55.22	57.49	55.67
298D	52.36	56.71	56.02	54.75	45.24	50.42	50.84	48.72
1FMQ	49.23	51.92	51.90	50.28	40.90	44.05	44.15	43.49
Avg.	51.96	55.03	55.49	54.19	45.88	49.90	50.83	49.29

127D complexes show higher rmsd variation (~2.0 Å), while other ligands show rmsd variation less than 2.0 Å.

Interaction Energy of DNA−Ligand Complexes. The IE values as obtained from MM-PBSA calculations are presented in Table 6 with the respective ΔT_m values. Higher deviation in IE values with respect to time was observed for ligands having lower ΔT_m values (<15.00). Ligands with higher ΔT_m values show consistent interaction until the 5 ns period without much deviation in the IE values. Table 6 clearly shows that the ligands with the lowest ΔT_m (2DBE, 227D complexes; ΔT_m < 10.0) have lowest IE values (~−37.0 kcal/mol), the ligands with moderate ΔT_m (289D, 298D, 1FMQ, 1FMS, 1EEL and 127D complexes; ΔT_m 10.0 to 20.0) have IE values in the range of −50.0 to −60.0 kcal/mol, and the ligands with the highest ΔT_m (121D, 2DND complexes; ΔT_m > 20.0) have highest IE values (~−70.0 kcal/mol). However, the ligand of the 109D complex is the only exception with ΔT_m = 23.9, and IE = −47.84 kcal/mol. The reason for the exceptional behavior of the 109D complex may be a consequence of a higher rmsd (3.5 Å during simulation in case of DNA; see Figure S2 of the Supporting Information) compared to those of all other ligands. However, the ligand of the 109D complex shows the lowest rmsd (0.5 Å), which correlates well with the highest ΔT_m of this compound. We have observed a moderate correlation between IE values and docking score for GOLD (R^2 = 0.70) and CDOCKER (R^2 = 0.73) protocols, where a docking score >90.00 is always associated with IE >−62.0 kcal/mol, though such a correlation is not observed in the case of GLIDE (R^2 = 0.31) and AUTODOCK (R^2 = 0.052) protocols (Table 7). Moreover a GOLD docking score of <80.00 is always associated with the IE values <−51.0 kcal/mol. An exception to this behavior is observed in the case of 109D complex probably because of the highest rmsd during simulation in the case of DNA (see Figure S2 of the Supporting Information). From the above discussion and Figure 6, it is clear that the GOLD and CDOCKER docking score correlates better than other docking scores with the IE values obtained from MM-PBSA calculations. The effect of various cutoff sizes (6.0, 8.0, 10.0, and 12.0 Å) on the IE values were also studied on three different DNA−ligand complexes (127D, 298D, 1FMQ) between the 0 and 5 ns time period. The deviation in IE values for the considered complexes with average values at 5 ns time is presented in Table 8 (see Table S12 of the Supporting Information for more details). Higher deviations in IE values were observed between 6.0 to 8.0 Å cutoff values (average deviation in IE value is 4.02 and 3.07 kcal/mol in PB and GB methods, respectively). However, the deviation in IE values is marginal from 8.0 Å and onward cutoff values as apparent from Table 8.

CONCLUSIONS

DNA minor groove binders are an important class of compounds with high therapeutic potential, and this class of compounds provided several FDA approved drugs and offers a great potential for structure-based computer-aided drug design methods. The present comprehensive computational study with 57 DNA minor groove binders reveals the strength and limitations of popular docking protocols. This study shows that GOLD and GLIDE docking protocols seem very reliable in modeling nucleic acid ligand complexes. Molecular dynamics studies suggest that the DNA duplex skeleton undergoes only a minor deviation upon ligand binding in most cases, and this provides the basis for employing the docking protocols in which the receptor is kept rigid. Therefore, the current exhaustive study consolidates the existing evidence to apply the currently available docking protocols to nucleic acid ligand binding, albeit they are not specifically parametrized for nucleic acids. While the studies are directed to the DNA minor groove noncovalent binders, further validation is required before generalization to intercalators, covalent binders, etc. Surprisingly, ΔT_m values, which are a measure of duplex stability, have shown good correlation with docking fitness scores and MM-PBSA based interaction energies. Considering that similar good correlations are reported earlier between the ΔT_m and binding affinity, it seems that the stronger binding of ligands to DNA impart higher stability to the duplex. The MM-PBSA based interaction energies calculated from the MD simulations are in good agreement with the experimental ΔT_m values and the GOLD docking fitness scores. While we observe subtle deviations in the backbone and cleft of DNA upon ligand binding, in most cases (except for the 109D complex) the dynamical nature of DNA does not affect the binding strength. Our attempts to build QSSR models based on the 11 available experimental ΔT_m values yielded robust statistical models using one (R^2 = 0.79; R^2_{cv} = 0.68) and two (R^2 = 0.99; R^2_{cv} = 0.97) descriptors. Considering the high pharmaceutical relevance of the minor groove binders and also the range of flexible options available for lead optimization, we feel that this will be a fertile ground for the interaction between molecular modeling and medicinal chemists. The present study illustrates and validates the performance of docking, molecular dynamics, and structure stability relationship approaches that should trigger the interplay further.

ASSOCIATED CONTENT

Supporting Information. The rmsd values corresponding to various generated poses for each of the cocrystals from GOLD3.2, GLIDE4.5, CDOCKER, and AUTODOCK docking protocols. Lowest and highest docking score from all the docking protocols. Descriptors and their values used to generate QSSR models. Experimental and predicted ΔT_m values of different QSSR models. Comparison of docking score with MD interaction energies and ΔT_m values. DNA sequence, DOI, NDB ID, PubMed ID, and chemical name of all the ligands. Interaction energy deviation on the basis of different cutoff values at various time scale for three DNA ligand complexes. Variation in lowest and highest rmsd values with respect to receptor. Details of parameters used for snapshot extraction and IE calculation. Plot of predicted versus experimental ΔT_m values. The rmsd variations with time in MD for complex, DNA, and ligand separately. Snapshots of the complexes at various time scales in the simulation process. Structural variations in the ligands considered for QSSR analysis.

References for all the PDB codes used in the study. This material is available free of charge via Internet at http://pubs.acs.org.

AUTHOR INFORMATION

Corresponding Author

*Phone: +91 40 27193016; fax: +91 40 27160512; e-mail: gnsastry@gmail.com.

ACKNOWLEDGMENT

H.K.S. and G.N.S. thank Department of Science and Technology (DST), New Delhi for Fast-Track, and Swarnajayanti projects, respectively. We thank the CSIR network program of Centre for Excellence (NWP0053) and Department of Biotechnology (DBT), New Delhi for financial assistance. Madhavi Sastry is thanked for critical reading of the manuscript.

ABBREVIATIONS

QM = quantum mechanical; QSSR = quantitative structure stability relationship; rmsd = root mean squared deviation, which is the measure of the average distance between the backbones of superimposed structures; MM-PBSA/GBSA = a postprocessing method to evaluate binding/interaction energies by using Poisson−Boltzmann or Generalized-Born methods; ΔT_m = the change in melting temperature of DNA upon drug binding (a standard for duplex stability); QSPR = quantitative structure property relationship; MD = molecular dynamics; Success rate = the rate of success in getting rmsd less than 2.0 Å, while superimposing docked poses obtained from various docking protocols on the crystallographic poses; IE (interaction energy) = the final estimated binding free energy calculated by MM-PBSA method after molecular dynamics simulations; CODESSA (comprehensive descriptors for structural and statistical analysis) = a software for descriptor calculation, regression and QSAR analysis; MMFF = Merck molecular force field (first published force field in this family is MMFF94); OPLS = optimized potential for liquid simulations (force field); GOLD = genetic optimization for ligand docking; GLIDE= a complete solution for ligand−receptor docking; CDOCKER = a CHARMm-based MD docking algorithm; AUTODOCK = suite of automated docking tools; PDB = protein data bank

REFERENCES

(1) (a) Song, Y.-M.; Wu, Q.; Yang, P.-J.; Luan, N.-N.; Wang, L.-F.; Liu, Y.-M. DNA Binding and cleavage activity of Ni(II) complex with all-trans retinoic acid. *J. Inorg. Biochem.* **2006**, *100*, 1685–1691. (b) Kožurková, M.; Sabolová, D.; Janovec, L.; Mikeš, J.; Koval', J.; Ungvarskcy′, J.; Stefanisinová, M.; Fedorocko, P.; Kristian, P.; Imrich, J. Cytotoxic activity of proflavine diureas: Synthesis, antitumor, evaluation and DNA binding properties of 1′,1′′-(acridin-3,6-diyl)-3′,3′′-dialkyldiureas. *Bioorg. Med. Chem.* **2008**, *16*, 3976–3984. (c) Reddy, B. S. P.; Sondhi, S. M.; Lown, J. W. Synthetic DNA minor groove-binding drugs. *Pharmacol. Ther.* **1999**, *84*, 1–111.

(2) Neidle, S. The molecular basis for the action of some DNA-binding drugs. *Prog. Med. Chem.* **1979**, *16*, 151–221.

(3) Hurley, L. H. DNA and its associated processes as targets for cancer therapy. *Nat. Rev. Cancer* **2002**, *2*, 188–200.

(4) Bauer, G. B.; Povrik, L. F. Specificity and kinetics of interstrand and intrastrand bifunctional alkylation by nitrogen mustards at a G-G-C sequence. *Nucleic Acids Res.* **1997**, *25*, 1211–1218.

(5) Wang, K.; Lu, J.; Li, R. The events that occur when cisplatin encounters cells. *Coord. Chem. Rev.* **1996**, *151*, 53–88.

(6) (a) Masta, A.; Gray, P. J.; Phillips, D. R. Nitrogen mustard inhibits transcription and translation in a cell free system. *Nucleic Acids Res.* **1995**, *23*, 3508–3515. (b) Fuertes, M. A.; Castilla, J.; Alonso, C.; Perez, J. M. Novel concepts in the development of platinum antitumor drugs. *Curr. Med. Chem.: Anti-Cancer Agents* **2002**, *2*, 539–551.

(7) Haskel, C. M. *Cancer Treatment*, 2nd ed.; Saunders: Philadelphia, PA, 1990.

(8) Blackburn, G. M. DNA and RNA Structure. In *Nucleic Acids in Chemistry and Biology*, 2nd ed.; Blackburn, G. M., Gait, M. J., Eds.; Oxford University Press: New York, 1996; pp 15−81

(9) Morávek, Z; Neidle, S; Schneider, B. Protein and drug interactions in the minor groove of DNA. *Nucleic Acids Res.* **2002**, *30*, 1182–1191.

(10) (a) Nagaoka, K.; Matsumoto, M.; Oono, J.; Yokoi, K.; Ishizeki, S.; Nakashima, T.; Azinomycins, A; New Antitumor, B. Antibiotics. I. Producing organism, fermentation, isolation and characterization. *J. Antibiot.* **1986**, *39*, 1527–1532. (b) Hodgkinson, T. J.; Shipman, M. Chemical synthesis and mode of action of the azinomycins. *Tetrahedron* **2001**, *57*, 4467–4488. (c) Rajski, S. R.; Williams, R. M. DNA cross-linking agents as antitumor drugs. *Chem. Rev.* **1998**, *98*, 2723–2795.

(11) (a) Fujiwara, T.; Saito, I.; Sugiyama, H. Highly efficient DNA interstrand cross-linking induced by an antitumor antibiotic, carzinophilin. *Tetrahedron Lett.* **1999**, *40*, 315–318. (b) Coleman, R. S. Issues of orthogonality and stability: Synthesis of the densely functionalized heterocyclic ring system of the antitumor agents azinomycins A and B. *Synlett* **1998**, *10*, 1031–1039. (c) Coleman, R. S.; Li, J.; Navarro, A. Total synthesis of azinomycin A. *Angew. Chem., Int. Ed.* **2001**, *40*, 1736–1739. (d) Coleman, R. S.; Kong, J. S.; Richardson, T. E. Synthesis of naturally occurring antitumor agents: Stereocontrolled synthesis of the azabicyclic ring system of the azinomycins. *J. Am. Chem. Soc.* **1999**, *121*, 9088–9095. (e) Alcaro, S.; Ortuso, F.; Coleman, R. S. Molecular modeling of DNA cross-linking analogues based on the azinomycin scaffold. *J. Chem. Inf. Model.* **2005**, *45*, 602–609.

(12) (a) Henderson, D.; Hurley, L. H. Molecular struggle for transcriptional control. *Nature Med.* **1995**, *1*, 525–527. (b) Thurston, D. E. Nucleic acid targeting: Therapeutic strategies for the 21st century. *Br. J. Cancer* **1999**, *80*, 65–85. (c) Marchini, S.; Ciro, M.; Gallinari, F.; Geroni, C.; Cozzi, P.; D'Incalci, M.; Broggini, M. α-Bromoacryloyl derivative of distamycin A (PNU 151807): A new non-covalent minor groove DNA binder with antineoplastic activity. *Br. J. Cancer* **1999**, *80*, 991–997.

(13) (a) Burris, H. A.; Dieras, V. C.; Tunca, M.; Earhart, R. H.; Eckardt, J. R.; Rodriguez, G. I.; Shaffer, D. S.; Fields, S. M.; Campbell, E.; Schaaf, L.; Kasunic, D.; Von Hoff, D. D. Phase I study with the DNA sequence-specific agent adozelesin. *Anticancer Drugs.* **1997**, *8*, 588–596. (b) Foster, B. J.; LoRusso, P. M.; Poplin, E.; Zalupski, M.; Valdivieso, M.; Wozniak, A.; Flaherty, L.; Kasunic, D. A.; Earhart, R. H.; Baker, L. H. Phase I trial of adozelesin using the treatment schedule of daily 35 every 3 weeks. *Invest. New Drugs.* **1996**, *13*, 321–326.

(14) (a) Li, L. H.; DeKoning, T. F.; Kelly, R. C.; Krueger, W. C.; McGovren, J. P.; Padbury, G. E.; Petzold, G. L.; Wallace, T. L.; Ouding, R. J.; Prairie, M. D.; Gebhard, I. Cytotoxicity and antitumor activity of carzelesin, a prodrug cyclopropylpyrroloindole analogue. *Cancer Res.* **1992**, *52*, 4904–4913. (b) Houghton, P. J.; Cheshire, P. J.; Hallman, J. D. N.; Houghton, J. A. Therapeutic efficacy of the cyclopropylpyrroloindole, carzelesin, against xenografts derived from adult and childhood solid tumors. *Cancer Chemother. Pharmacol.* **1995**, *36*, 45–52.

(15) (a) Carter, C. A.; Waud, W. R.; Li, L. H.; DeKoning, T. F.; McGovren, J. P.; Plowman, J. Preclinical antitumor activity of bizelesin in mice. *Clin. Cancer Res.* **1996**, *2*, 1143–1149. (b) Walker, D. L.; Reid, J. M.; Ames, M. M. Preclinical pharmacology of bizelesin, a potent bifunctional analog of the DNA-binding antibiotic CC-1065. *Cancer Chemother. Pharmacol.* **1994**, *34*, 317–322.

(16) Kobayashi, E.; Okamoto, A.; Asada, M.; Okabe, M.; Nagamura, S.; Asai, A.; Saito, H.; Gomi, K.; Hirata, T. Characteristics of antitumor activity of KW-2189, a novel water-soluble derivative of duocarmycin, against murine and human tumors. *Cancer Res.* **1994**, *54*, 2404–2410.

(17) Pezzoni, G.; Grandi, M.; Biasoli, G.; Capolongo, L.; Ballinari, D.; Giuliani, F. C.; Barbieri, B.; Pastori, A.; Pesenti, E.; Mongelli, N.;

Spreafico, F. Biological profile of FCE 24517, a novel benzoyl mustard analogue of distamycin A. *Br. J. Cancer* **1991**, *64*, 1047–1050.

(18) (a) Yang, F.; Belitsky, J. M.; Villanueva, R. A.; Dervan, P. B.; Roth, M. J. Inhibition of Moloney murine leukemia virus integration using polyamides targeting the long-terminal repeat sequences. *Biochemistry* **2003**, *42*, 6249–6258. (b) Dyatkina, N. B.; Roberts, C. D.; Keicher, J. D.; Dai, Y.; Nadherny, J. P.; Zhang, W.; Schmitz, U.; Kongpachith, A.; Fung, K.; Novikov, A. A.; Lou, L.; Vellingan, M.; Khorlin, A. A.; Chan, M. S. Minor groove DNA binders as antimicrobial agents. 1. Pyrrole tetraamides are potent antibacterials against vancomycin resistant *Enteroccoci* and methicillin resistant *Staphylococcus aureus*. *J. Med. Chem.* **2002**, *45*, 805–817. (c) Broyles, S. S.; Kremer, M.; Knutson, B. A. Antiviral activity of distamycin A against vaccinia virus is the result of inhibition of postreplicative mRNA synthesis. *J. Virol.* **2004**, *78*, 2137–2141. (d) Ghosh, S.; Usharani, D.; Paul, A.; De, S.; Jemmis, E. D.; Bhattacharya, S. Design, synthesis, and DNA binding properties of photoisomerizable azobenzene−distamycin conjugates: An experimental and computational study. *Bioconjugate Chem.* **2008**, *19*, 2332–2345.

(19) Tidwell, R. R.; Boykin, D. W. Dicationic, D. N. A. Minor groove binders as antimicrobial agents. *Small Molecule DNA and RNA Binders: From Synthesis to Nucleic Acid Complexes*; Wiley-VCH: New York, 2003; pp 416−460.

(20) (a) Fairlamb, A. H. Chemotherapy of human African trypanosomiasis: Current and future prospects. *Trends Parasitol.* **2003**, *19*, 488–494. (b) Bouteille, B.; Oukem, O.; Bisser, S.; Dumas, M. Treatment perspectives for human African trypanosomiasis. *Fundam. Clin. Pharmacol.* **2003**, *17*, 171–181. (c) Yeramian, P.; Meshnick, S. R.; Krudood, S.; Chalermurut, K.; Silachamroon, U.; Tangukdee, N.; Allen, J.; Brun, R.; Kweik, J. J.; Tidwell, R. R.; Looareesuwan, S. Efficacy of DB289 in Thai patients with *Plasmodium* vivax or acute, uncomplicated *Plasmodium falciparum* infections. *J. Infect. Dis.* **2005**, *192*, 319–322.

(21) (a) Wemmer, D. E. Designed sequence-specific minor groove ligands. *Annu. Rev. Biophys. Biomol. Struct.* **2000**, *29*, 439–461. (b) Wemmer, D. E. Ligands recognizing the minor groove of DNA: Development and applications. *Biopolymers* **1999**, *52*, 197–211. (c) Neidle, S. DNA minor-groove recognition by small molecules. *Nat. Prod. Rep.* **2001**, *18*, 291–309. (d) Bailly, C.; Chaires, J. B. Sequence-specific DNA minor groove binders. Design and synthesis of netropsin and distamycin analogues. *Bioconjugate Chem.* **1998**, *9*, 513–538.

(22) (a) Dardonville, C.; Barrett, M. P.; Brun, R.; Kaiser, M.; Tanious, F.; Wilson, W. D. DNA binding affinity of bisguanidine and bis(2-aminoimidazoline) derivatives with in vivo antitrypanosomal activity. *J. Med. Chem.* **2006**, *49*, 3748–3752. (b) Dardonville, C.; Brun, R. Bisguanidine, bis(2-aminoimidazoline), and polyamine derivatives as potent and selective chemotherapeutic agents against *Trypanosoma brucei rhodesiense*. Synthesis and in vitro evaluation. *J. Med. Chem.* **2004**, *47*, 2296–2307.

(23) (a) Moitessier, N.; Englebienne, P.; Lee, D.; Lawandi, J.; Corbeil, C. R. Towards the development of universal, fast and highly accurate docking/scoring methods: a long way to go. *Br. J. Pharmacol.* **2008**, *153*, S7–S26. (b) Sternberg, M. J. E.; Gabb, H. A.; Jackson, R. M. Predictive docking of protein−protein and protein−DNA complexes. *Curr. Opin. Struct. Biol.* **1998**, *8*, 250–256.

(24) (a) Bissantz, C.; Folkers, G.; Rognan, D. Protein-based virtual screening of chemical databases. 1. Evaluation of different docking/scoring combinations. *J. Med. Chem.* **2000**, *43*, 4759–4767. (b) Wang, R.; Lu, Y.; Wang, S. Comparative evaluation of 11 scoring functions for molecular docking. *J. Med. Chem.* **2003**, *46*, 2287–2303. (c) Warren, G.; Andrews, C.; Capelli, A.-M.; Clarke, B.; LaLonde, J.; Lambert, M.; Lindvall, M.; Nevins, N.; Semus, S.; Senger, S.; Tedesco, G.; Wall, I.; Woolven, J.; Peishoff, C.; Head, M. A. Critical assessment of docking programs and scoring functions. *J. Med. Chem.* **2006**, *49*, 5912–5931. (d) Reddy, A. S.; Pati, S. P.; Kumar, P. P.; Pradeep, H. N.; Sastry, G. N. Virtual screening in drug discovery: A computational perspective. *Curr. Protein Pept. Sci.* **2007**, *8*, 329–351.

(25) (a) Grootenhuis, P. D. J.; Kollman, P. A.; Seibel, G. L.; DesJarlais, R. L.; Kuntz, I. D. Computerized selection of potential DNA binding compounds. *Anti-Cancer Drug Des.* **1990**, *5*, 237–242. (b) Grootenhuis, P. D. J.; Roe, D. C.; Kollman, P. A.; Kuntz, I. D. Finding potential DNA-binding compounds by using molecular shape. *J. Comput.- Aided Mol. Des.* **1994**, *8*, 731–750. (c) Rohs, R.; Bloch, I.; Sklenar, H.; Shakked, Z. Molecular flexibility in ab initio drug docking to DNA: Binding-site and binding-mode transitions in all-atom Monte Carlo simulations. *Nucleic Acids Res.* **2005**, *33*, 7048–7057. (d) Tuttle, T.; Kraka, E.; Cremer, D. J. Docking, triggering and biological activity of dynemicin A in DNA: A computational study. *J. Am. Chem. Soc.* **2005**, *127*, 9469–9484. (e) Evans, D. A.; Neidle, S. Virtual screening of DNA minor groove binders. *J. Med. Chem.* **2006**, *39*, 4232–4238. (f) Yan, Z.; Sikri, S.; Beveridge, D. L.; Baranger, A. M. Identification of an aminoacridine derivative that binds to RNA tetraloops. *J. Med. Chem.* **2007**, *50*, 4096–4104. (g) Holt, P. A.; Chaires, J. B.; Trent, J. O. Molecular docking of intercalators and groove-binders to nucleic acids using AutoDock and Surflex. *J. Chem. Inf. Model.* **2008**, *48*, 1602–1615. (h) Kamal, A.; Bharathi, E. V.; Ramaiah, M. J.; Dastagiri, D.; Reddy, J. S.; Viswanath, A.; Sultana, F.; Pushpavalli, S. N. C. V. L.; Pal-Bhadra, M.; Srivastava, H. K.; Sastry, G. N.; Juvekar, A.; Sen, S.; Zingde, S. Quinazolinone linked pyrrolo[2,1-c][1,4]benzodiazepine (PBD) conjugates: Design, synthesis and biological evaluation as potential anticancer agents. *Bioorg. Med. Chem.* **2010**, *18*, 526–542.

(26) DOCK 5.1.1 Manual, 2003. http://dock.compbio.ucsf.edu.

(27) Li, Y.; Shen, J.; Sun, X.; Li, W.; Liu, G.; Tang, Y. *J. Chem. Inf. Model.* **2010**, *50*, 1134–1146.

(28) Jones, G.; Willett, P.; Glen, R. C.; Leach, A. R.; Taylor, R. Development and validation of a genetic algorithm for flexible docking. *J. Mol. Biol.* **1997**, *267*, 727–748.

(29) Friesner, R. A.; Banks, J. L.; Murphy, R. B.; Halgren, T. A.; Klicic, J. J.; Mainz, D. T.; Repasky, M. P.; Knoll, E. H.; Shelley, M.; Perry, J. K.; Shaw, D. E.; Francis, P.; Shenkin, P. S.; Glide, A New approach for rapid, accurate docking and scoring. 1. Method and assessment of docking accuracy. *J. Med. Chem.* **2004**, *47*, 1739–1749.

(30) Morris, G.; Goodsell, D.; Halliday, R.; Huey, R.; Hart, W.; Belew, R.; Olson, A. Automated docking using a lamarckian genetic algorithm and an empirical binding free energy function. *J. Comput. Chem.* **1998**, *19*, 1639–1662.

(31) *Surflex*, version 2.11; Tripos, Inc.: St. Louis, MO, 2007.

(32) PDB Web site, 2009. http://www.rcsb.org/pdb/.

(33) Wu, G.; Roberston, D. H.; Brooks, C. L., III; Vieth, M. Detailed analysis of grid-based molecular docking: A case study of CDOCKER − A CHARMm-based MD docking algorithm. *J. Comput. Chem.* **2003**, *24*, 549–562.

(34) (a) Brooijmans, N.; Kuntz, I. D. Molecular recognition and docking algorithms. *Annu. Rev. Biophys. Biomol. Struct.* **2003**, *32*, 335–373. (b) Warren, G. L.; Andrews, C. W.; Capelli, A; Clarke, B; LaLonde, J; Lambert, M. H.; Lindvall, M.; Nevins, N.; Semus, S. F.; Senger, S.; Tedesco, G.; Wall, I. D.; Woolven, J. M; Peishoff, C. E; Head, M. S. A critical assessment of docking programs and scoring functions. *J. Med. Chem.* **2006**, *49*, 5912–5931. (c) Ge, W.; Schneider, B.; Olson, W. K. Knowledge-based elastic potentials for docking drugs or proteins with nucleic acids. *Biophys. J.* **2005**, *88*, 1166–1190. (d) Shaikh, S. A.; Ahmed, S. R.; Jayaram, B. A molecular thermodynamic view of DNA-drug interactions: A case study of 25 minor-groove binders. *Arch. Biochem. Biophys.* **2004**, *429*, 81–99. (e) Beveridge, D. L.; McConnell, K. J. Nucleic acids: Theory and computer simulation, Y2K. *Curr. Opin. Struct. Biol.* **2000**, *10*, 182–196. (f) Orozco, M.; Perez, A.; Agnes, N.; Javier, L. F. Theoretical methods for the simulation of nucleic acids. *Chem. Soc. Rev.* **2003**, *6*, 350–364. (g) Cheatham, T. E. Simulation and modeling of nucleic acid structure, dynamics and interactions. *Curr. Opin. Struct. Biol.* **2004**, *14*, 360–367. (h) Young, M. A.; Jayaram, B.; Beveridge, D. L. Local dielectric environment of B-DNA in solution: Results from a 14 ns molecular dynamics trajectory. *J. Phys. Chem. B.* **1998**, *102*, 7666–7669. (i) Manning, G. S. The molecular theory of polyelectrolyte solutions with applications to the electrostatic properties of polynucleotides. *Q. Rev. Biophys.* **1978**, *11*, 179–246. (j) Cornell, W. D.; Cieplak, P.; Bayly, C. F.; Gould, I. R.; Kenneth, M. M.; Ferguson, D. M.; Spellmeyer, D. C.; Fox, T.; Caldwell, J. W.; Kollman, P. A. A second-generation force field for the simulation of proteins, nucleic acids

and organic molecules. *J. Am. Chem. Soc.* **1995**, *117*, 5179–5197. (k) Yu, Y. B.; Privalov, P. L.; Hodges, R. B. Contribution of translational and rotational motions to molecular association in aqueous solution. *Biophys. J.* **2001**, *81*, 1632–1642. (l) Ren, J.; Jenkins, T. C.; Chaires, J. B. Energetics of intercalation reactions. *Biochemistry* **2000**, *39*, 8439–8447.

(35) (a) Schultz, T. W.; Cronin, M. T. D.; Walker, J. D.; Aptula, A. O. Quantitative structure−activity relationships (QSARs) in toxicology: A historical perspective. *J. Mol. Struct. − THEOCHEM* **2003**, *622*, 1–22. (b) Karcher, W.; Devillers, J. SAR and QSAR in the Environmental Chemistry and Toxicology: Scientific Tool or Wishful Thinking? In *Practical Applications of Quantitative Structure−activity Relationships (QSAR) in Environmental Chemistry and Toxicology*; Karcher, W.; Devillers, J., Eds.; Kluwer Academic Publishers: Dordrecht, Boston, London, 1990; pp 1−12. (c) Singh, P. P.; Pasha, F. A.; Srivastava, H. K. Novel application of softness parameter for regioselectivity and reaction mechanism. *Indian J. Chem. B.* **2004**, *43*, 983–991. (d) Katritzky, A. R.; Petrukhin, R.; Tatham, D.; Basak, S.; Benfenati, E. Interpretation of Quantitative Structure-Property and -Activity Relationships. *J. Chem. Inf. Comput. Sci.* **2001**, *41*, 679–685.

(36) (a) Ravindra, G. K.; Achaiah, G.; Sastry, G. N. Molecular modeling studies of phenoxypyrimidinyl imidazoles as p38 kinase inhibitors using QSAR and docking. *Eur. J. Med. Chem.* **2008**, *43*, 830–838. (b) Janardhan, S; Srivani, P; Sastry, G. N. 2D and 3D quantitative structure−activity relationship studies on a series of bis-pyridinium compounds as choline kinase inhibitors. *QSAR Combi. Sci.* **2006**, *25*, 860–872. (c) Srivastava, H. K. A Comparative QSPR study of alkanes with the help of computational chemistry. *Bull. Korean Chem. Soc.* **2009**, *30*, 67–76. (d) Srivani, P.; Srinivas, E.; Raghu, R.; Sastry, G. N. Molecular modeling studies of pyridopurinone derivatives-potential phosphodiesterase 5 inhibitors. *J. Mol. Graph. Modell.* **2007**, *26*, 378–390. (e) Pasha, F. A.; Muddassar, M.; Cho, S. J. Molecular docking and 3D QSAR studies of Chk2 inhibitors. *Chem. Biol. Drug. Des.* **2009**, *73*, 292–300. (f) Srivastava, H. K.; Pasha, F. A.; Singh, P. P. Atomic softness based QSAR activity of testosterone derivatives. *Int. J. Quantum Chem.* **2005**, *103*, 237–245. (g) Srivani, P.; Sastry, G. N. Potential choline kinase inhibitors: A molecular modeling study of bis-quinolinium compounds. *J. Mol. Graph. Modell.* **2009**, *27*, 676–688. (h) de Jonge, M. R.; Koymans, L. M.; Vinkers, H. M.; Daeyaert, F. F.; Heeres, J.; Lewi, P. J.; Janssen, P. A. Structure based activity prediction of HIV-1 reverse transcriptase inhibitors. *J. Med. Chem.* **2005**, *48*, 2176–2183.

(37) (a) Karplus, M.; McCammon, J. A. Molecular dynamics simulations of biomolecules. *Nat. Struct. Biol.* **2002**, *9*, 646–652. (b) McDowell, S. E.; Spackova, N.; Sponer, J.; Walter, N. G. Molecular dynamics simulations of RNA: An in silico single molecule approach. *Biopolymers.* **2007**, *85*, 169–184.

(38) (a) Lu, N. D.; Kofke, D. A. Accuracy of free energy perturbation calculations in molecular simulation. I. Modeling. *J. Chem. Phys.* **2001**, *114*, 7303–7311. (b) Florian, J.; Goodman, M. F.; Warshel, A. Free energy perturbation calculations of DNA destabilization by base substitutions: The effect of neutral guanine thymine, adenine cytosine and adenine difluorotoluene mismatches. *J. Phys. Chem. B.* **2000**, *104*, 10092–10099. (c) Kamal, A.; Shankaraiah, N.; Reddy, C. R.; Prabhakar, S.; Markandeya, N.; Srivastava, H. K.; Sastry, G. N. Synthesis of bis-1,2,3-triazolo-bridged unsymmetrical pyrrolobenzodiazepine trimers via 'click' chemistry and their DNA-binding studies. *Tetrahedron.* **2010**, *66*, 5489–5506. (d) Brandsdal, B. O.; Smalas, A. O. Evaluation of protein−protein association energies by free energy perturbation calculations. *Protein Eng.* **2000**, *13*, 239–245. (e) Beveridge, D. L.; Dicapua, F. M. Free-energy via molecular simulation: Applications to chemical and biomolecular systems. *Annu. Rev. Biophys. Biol.* **1989**, *18*, 431–492.

(39) (a) Roux, B.; Simonson, T. Implicit solvent models. *Biophys. Chem.* **1999**, *78*, 1–20. (b) Honig, B.; Nicholls, A. Classical electrostatics in biology and chemistry. *Science* **1995**, *268*, 1144–1149.

(40) Frisch, M. J.; Trucks, G. W.; Schlegel, H. B.; Scuseria, G. E.; Robb, M. A.; Cheeseman, J. R.; Montgomery, J. A., Jr.; Vreven, T.; Kudin, K. N.; Burant, J. C.; Millam, J. M.; Iyengar, S. S.; Tomasi, J.; Barone, V.; Mennucci, B.; Cossi, M.; Scalmani, G.; Rega, N.; Petersson, G. A.; Nakatsuji, H.; Hada, M.; Ehara, M.; Toyota, K.; Fukuda, R.; Hasegawa, J.; Ishida, M.; Nakajima, T.; Honda, Y.; Kitao, O.; Nakai, H.; Klene, M.; Li, X.; Knox, J. E.; Hratchian, H. P.; Cross, J. B.; Adamo, C.; Jaramillo, J.; Gomperts, R.; Stratmann, R. E.; Yazyev, O.; Austin, A. J.; Cammi, R.; Pomelli, C.; Ochterski, J. W.; Ayala, P. Y.; Morokuma, K.; Voth, G. A.; Salvador, P.; Dannenberg, J. J.; Zakrzewski, V. G.; Dapprich, S.; Daniels, A. D.; Strain, M. C.; Farkas, O.; Malick, D. K.; Rabuck, A. D.; Raghavachari, K.; Foresman, J. B.; Ortiz, J. V.; Cui, Q.; Baboul, A. G.; Clifford, S.; Cioslowski, J.; Stefanov, B. B.; Liu, G.; Liashenko, A.; Piskorz, P.; Komaromi, I.; Martin, R. L.; Fox, D. J.; Keith, T.; Al-Laham, M. A.; Peng, C. Y.; Nanayakkara, A.; Challacombe, M.; Gill, P. M. W.; Johnson, B.; Chen, W.; Wong, M. W.; Gonzalez, C.; Pople, J. A. *Gaussian 03*, revision E.0.1; Gaussian, Inc.: Pittsburgh, PA, 2003.

(41) Katritzky, A. R.; Lobanov, V. S.; Karelson, M.*CODESSA 2.0, Comprehensive Descriptors for Structural and Statistical Analysis*; University of Florida: Gainesville, FL, 1994−1996.

(42) *Scigress Explorer*, version 7.7; Fujitsu: Tokyo, 2008.

(43) (a) Case, D. A.; Darden, T. A.; Cheatham, T. E., III; Simmerling, C. L.; Wang, J.; Duke, R. E.; Luo, R.; Merz, K. M.; Wang, B.; Pearlman, D. A.; Crowley, M.; Brozell, S.; Tsui, V.; Gohlke, H.; Mongan, J.; Hornak, V.; Cui, G.; Beroza, P.; Schafmeister, C.; Caldwell, J. W.; Ross, W. S.; Kollman, P. A. *AMBER 8*; University of California: San Francisco, 2004. (b) Jakalian, A.; Bush, B. L.; Jack, D. B.; Bayly, C. I. Fast, efficient generation of high-quality atomic charges. AM1-BCC Model: I. Method. *J. Comput. Chem.* **2000**, *21*, 132–146. (c) Wang, J.; Wolf, R. M.; Caldwell, J. W.; Kollman, A. P.; Case, D. A. Development and testing of a general Amber force field. *J. Comput. Chem.* **2004**, *25*, 1157–1174. (d) Jakalian, A.; Jack, D. B.; Bayly, C. I. Fast efficient generation of high-quality atomic charges. AM1-BCC model: II. Parametrization and validation. *J. Comput. Chem.* **2002**, *23*, 1623–1641.

(44) Beck, D. A. C.; Armen, R. S.; Daggett, V. Cutoff size need not strongly influence molecular dynamics results for solvated polypeptides. *Biochemistry* **2005**, *44*, 609–616.

(45) Shaikh, S. A.; Jayaram, B. A Swift all-atom energy-based computational protocol to predict DNA−ligand binding affinity and ΔT_m. *J. Med. Chem.* **2007**, *50*, 2240–2244.

JACS
JOURNAL OF THE AMERICAN CHEMICAL SOCIETY

ARTICLE

pubs.acs.org/JACS

Theoretical Study on the Mechanism of the Oxygen Activation Process in Cysteine Dioxygenase Enzymes

Devesh Kumar,*[,†,‡] Walter Thiel,[†] and Sam P. de Visser*[,§]

[†]Max-Planck-Institut für Kohlenforschung, Kaiser-Wilhelm-Platz 1, D-45470 Mülheim an der Ruhr, Germany

[‡]Molecular Modelling Group, Indian Institute of Chemical Technology, Hyderabad 500 607, India

[§]The Manchester Interdisciplinary Biocenter and School of Chemical Engineering and Analytical Science, University of Manchester, 131 Princess Street, Manchester M1 7DN, United Kingdom

Supporting Information

ABSTRACT: Cysteine dioxygenase (CDO) is a vital enzyme for human health involved in the biodegradation of toxic cysteine and thereby regulation of the cysteine concentration in the body. The enzyme belongs to the group of nonheme iron dioxygenases and utilizes molecular oxygen to transfer two oxygen atoms to cysteinate to form cysteine sulfinic acid products. The mechanism for this reaction is currently disputed, with crystallographic studies implicating a persulfenate intermediate in the catalytic cycle. To resolve the dispute we have performed quantum mechanics/molecular mechanics (QM/MM) calculations on substrate activation by CDO enzymes using an enzyme monomer and a large QM active region. We find a stepwise mechanism, whereby the distal oxygen atom of the iron(II)-superoxo complex attacks the sulfur atom of cysteinate to form a ring structure, followed by dioxygen bond breaking and the formation of a sulfoxide bound to an iron(IV)-oxo complex. A sulfoxide rotation precedes the second oxygen atom transfer to the substrate to give cysteine sulfinic acid products. The reaction takes place on several low-lying spin-state surfaces via multistate reactivity patterns. It starts in the singlet ground state of the iron(II)-superoxo reactant and then proceeds mainly on the quintet and triplet surfaces. The initial and rate-determining attack of the superoxo group on the cysteinate sulfur atom involves a spin-state crossing from singlet to quintet. We have also investigated an alternative mechanism via a persulfenate intermediate, with a realignment of hydrogen bonding interactions in the substrate binding pocket. However, this alternative mechanism of proximal oxygen atom attack on the sulfur atom of cysteinate is computed to be a high-energy pathway, and therefore, the persulfenate intermediate is unlikely to participate in the catalytic cycle of CDO enzymes.

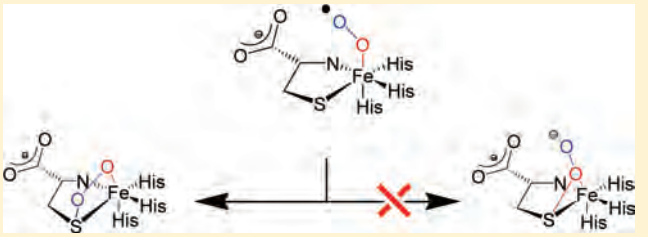

I. INTRODUCTION

Mononuclear nonheme iron-containing enzymes are common enzymes in the body involved in key biochemical processes for human health. Because of their large versatility of substrate activation they are implicated with a broad range of catalytic functions.[1] A large group of these mononuclear nonheme iron containing enzymes utilize α-ketoglutarate as a cosubstrate and act as dioxygenases (α-ketoglutarate-dependent dioxygenases)[2] with biochemical functions that, e.g., include DNA and RNA base repair, molecular responses to hypoxia, and oxygen sensing.[3,4] Generally, these enzymes bind α-ketoglutarate to an iron(II) center that is linked to the protein backbone via a 2His/1Asp facial triad ligand motif,[5] while substrate binds in the vicinity. Dioxygen binding to the iron center typically leads to decarboxylation of α-ketoglutarate to form succinate and an iron(IV)-oxo species that is the active oxidant of substrate hydroxylation reactions.[6] High-valent iron(IV)-oxo complexes have been identified as the active oxidant of many heme and nonheme mono- and dioxygenases and are known to efficiently abstract hydrogen atoms from aliphatic substrates.[1,7] The iron(IV)-oxo active species of two α-ketoglutarate dependent dioxygenases, namely, taurine/α-ketoglutarate dioxygenase (TauD) and prolyl-4-hydroxylase, have been trapped and characterized by resonance Raman, Mössbauer, and extended X-ray absorption fine structure (EXAFS) studies.[8]

Despite the fact that most mononuclear nonheme iron dioxygenases have a 2His/1Asp structural motif, there are several dioxygenases with different ligand binding motifs.[9] For example, acetylacetone Dke1 contains a transition metal active site where three histidine groups bind to the metal,[10] while in quercetin dioxygenase the metal is bound to the side chains of three histidine and one glutamic acid group via a 3His/1Glu structural motif.[11] Another mononuclear nonheme iron dioxygenase with a 3His metal binding motif is cysteine dioxygenase (CDO), which is a vital enzyme for human health involved in the metabolism of toxic cysteine in the body (Scheme 1).[12] Thus, a decline in CDO

Received: August 19, 2010
Published: February 23, 2011

ACS Publications © 2011 American Chemical Society

dx.doi.org/10.1021/ja107514f | J. Am. Chem. Soc. 2011, 133, 3869–3882

Scheme 1. Reaction Catalyzed by CDO Enzymes

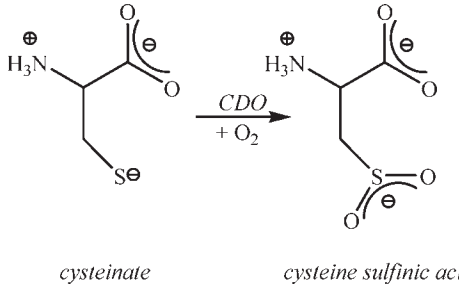

activity has been associated with neurological disorders,[13] including diseases such as Alzheimer's and Parkinson's.[14] Because of its importance for human health, many studies have been reported on the catalytic mechanism of cysteine dioxygenation by CDO enzymes.[15,16]

There are various enzymes in nature apart from CDO that catalyze *S*-oxygenation reactions, including heme enzymes, such as the cytochromes P450[7,17] and the nonheme iron enzyme nitrile hydratase.[18] The nitrile hydratases contain a cysteinate group ligated to the metal, which has been shown to be oxygenated in the reaction mechanism.[19] This discovery led to the synthesis and study of many biomimetic complexes containing an iron ligated to a thiolate group.[20] Indeed some of these complexes react with dioxygen to form oxygenated metal−ligands. Recently, a biomimetic model of CDO was created, which also reacted with molecular oxygen via a metal−ligand *S*-oxygenation.[21]

Figure 1 displays an extract of the active site of CDO as taken from the 2IC1 protein databank (pdb) file.[22] The metal is linked to three imidazole groups of His_{86}, His_{88}, and His_{140} that form a facial triad typical for nonheme iron dioxygenases. Substrate cysteinate binds as a bidentate ligand through the thiolate and amine groups that are located trans to the His_{140} and His_{88} ligands, respectively. The last binding site of iron is vacant in Figure 1 but is reserved for molecular oxygen. The carboxylic acid group of substrate cysteinate forms a salt bridge with the methylguanidinium group of Arg_{60}. Further hydrogen-bonding interactions that stabilize this salt bridge come from the phenol group of Tyr_{157} and the imidazole group of His_{155}. An interesting feature of the active site of CDO is the covalent linkage between the thiolate side chain of Cys_{93} with the aromatic ring of Tyr_{157}. It has been hypothesized[23] that substrate binding to the active center leads to the formation of this Cys_{93}−Tyr_{157} linkage. Site-directed mutations showed that this linkage improved the catalytic efficiency 10-fold but it is not clear how.[12b]

To gain insight into dioxygen activation by nonheme iron containing enzymes and their ligand systems, we performed a series of density functional theory (DFT) studies on TauD as well as on CDO enzymes.[16,24] These studies were focused on the oxygen activation mechanism for CDO and three of its active-site mutants, whereby one of the His ligands was replaced by a carboxylic acid group. The calculations highlighted the importance of the 3His ligand system in CDO enzymes to accommodate optimal substrate dioxygenation. Calculations on CDO mutants with a 2His/1Asp structural ligand system gave increased reaction barriers and in some cases a mechanism that stops after one oxygen atom is transferred.[16b] Our DFT study on the active site of CDO enzymes established a possible

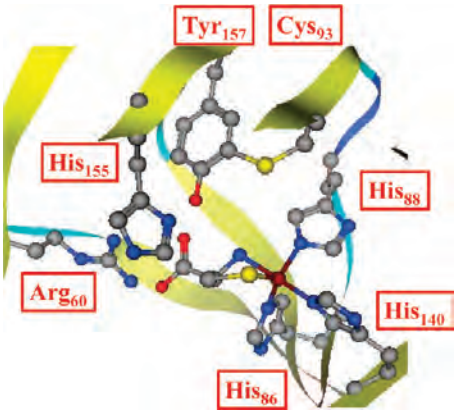

Figure 1. Active-site structure of CDO enzymes as taken from the 2IC1 pdb file.[22] All amino acids are labeled as in the corresponding pdb file.

mechanism of the oxygen activation process (mechanism I in Scheme 2).[16] It was proposed that the dioxygen molecule binds in an end-on fashion (**A**) and that the dioxygen activation process starts with attack of the distal oxygen atom (O_d) on the sulfur of the cysteinate side chain via a barrier $\mathbf{TS_A}$ to form a ring structure with an S−Fe−O−O four-membered ring (**B**). A subsequent dioxygen bond breakage via a barrier $\mathbf{TS_B}$ then leads to cysteine oxide and an iron(IV)-oxo species (**C**). The sulfoxide group undergoes an internal rotation via a barrier $\mathbf{TS_C}$ to make space for the second incoming oxygen atom (Structure **C′**). A fast rebound reaction via barrier $\mathbf{TS_D}$ leads to cysteine sulfinic acid products (**D**). DFT studies established that the rate-determining step in this process is the barrier via $\mathbf{TS_A}$ and that a conversion from a ground state singlet spin state to a quintet spin state precedes the barrier leading to the ring structure.[16]

This DFT-based mechanism was disputed by experimental X-ray studies on a CDO enzyme that detected a persulfenate intermediate.[25] These experimental studies were unable to resolve whether the persulfenate is an intermediate in the catalytic cycle or a dead-end product from a side reaction. However, an alternative mechanism was suggested (mechanism II in Scheme 2),[25] whereby a hydrogen bonding interaction of the phenol group of Tyr_{157} with the distal oxygen atom of the O_2 group in structure **A** facilitates the dioxygenation mechanism through an initial S−O bond formation between the cysteine sulfur atom and the proximal oxygen atom (O_p) to form the persulfenate intermediate (structure **E**). Subsequently, the distal oxygen atom forms a bond with sulfur to form a ring-structure **F** after which the dioxygen bond breaks to form a sulfoxide intermediate (**G**). A final oxygen atom transfer then gives cysteine sulfinic acid products.

Clearly, the mechanism of CDO enzymes is unresolved and surrounded by controversies that call for further studies, especially with regard to the impact of the protein environment on the mechanism and on the possible involvement of persulfenate intermediates. Since the earlier computational work had addressed only small gas-phase model systems and mechanism I, we decided to reinvestigate cysteine dioxygenation in CDO enzymes by performing quantum mechanics/molecular mechanics (QM/MM) calculations[26] on a realistic model of the full enzyme for both proposed mechanisms. Previous DFT and QM/MM studies on the enzyme cytochrome P450 have revealed differences in the mechanism and the electronic configuration of active oxidants when the protein environment is taken into account at the QM/MM level.[27] Moreover, Lundberg

dx.doi.org/10.1021/ja107514f |*J. Am. Chem. Soc.* 2011, 133, 3869–3882

Scheme 2. Suggested Mechanisms of Cysteine Metabolism by CDO Enzymes As Taken from Refs 16 and 23

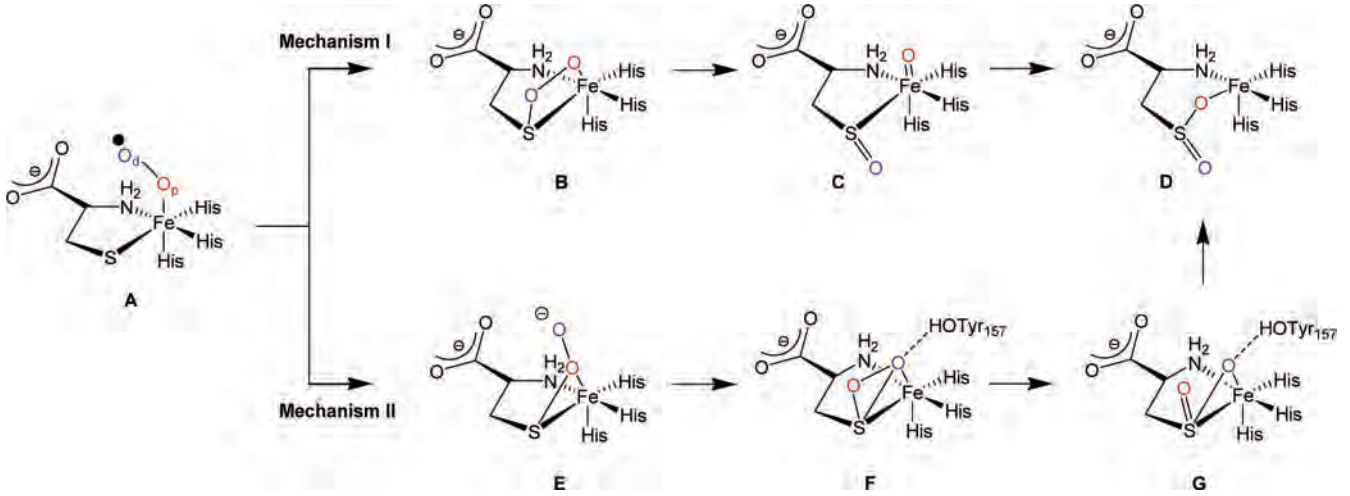

and Morokuma have shown in the case of isopenicillin *N* synthase that a QM/MM treatment is required for the dioxygen binding step in the catalytic cycle, since small model complexes failed to describe this step correctly.[28] In this work, we present the first QM/MM study on the oxygen activation mechanism in CDO enzymes via mechanisms I and II. The QM/MM calculations confirm the dioxygen activation mechanism proposed on the basis of DFT model calculations and assign the persulfenate structure as an intermediate of a side reaction. These findings may also be relevant for other dioxygenases.

II. COMPUTATIONAL METHODS

A. Setup of the System. Our calculations use methods and procedures previously applied in QM/MM studies of the cytochromes P450 and TauD enzymes.[29,30] The initial coordinates were taken from the pdb file 2IC1, which represents a substrate-bound CDO monomer.[22] Hydrogen atoms were added as well as an O_2 molecule to create an iron(II)-superoxo bound intermediate in the catalytic cycle of CDO. Solvation and protonation schemes were applied in an analogous manner as before.[27a,31] Briefly, the protonation states of most residues were determined from the pK_a values calculated with the PropKa program, except for the histidine side chains whose protonation states were assigned by visual inspection of their local environment as follows: His_{20}, His_{81}, His_{82}, His_{92}, His_{165}, and His_{173} were protonated at the NE atom and His_{86}, His_{88}, His_{140}, and His_{155} at the ND atom. The overall system was charge neutral and consisted of 24,779 atoms including 7,109 TIP3P water molecules. CDO was solvated in a pre-equilibrated water sphere of 40 Å and the solvated system was energy minimized followed by a molecular dynamics (MD) simulation at the MM level using the CHARMM22 force field[32] as implemented in the CHARMM program package.[33] The Fe atom, the dioxygen group, the cysteinate substrate, and the His_{86}, His_{88}, and His_{140} residues as well as the outer 8 Å of solvent layer were kept fixed during the classical energy minimizations and MD simulations. Energy-minimized snapshots from the MD trajectories were taken as starting structures for the QM/MM calculations. The CHARMM22 force field[32] served as MM component in all QM/MM calculations.

B. QM/MM Geometry Optimizations. The active region in QM/MM geometry optimizations comprised the QM region (see below) and all residues and water molecules within an 8 Å distance from Fe or any other active-site atom (dioxygen, His_{86}, His_{88}, His_{140}, or cysteinate substrate). Consequently, close to 1,500 atoms in the MM region were fully optimized in the individual snapshots during the QM/MM calculations, while the remaining MM atoms were fixed.

Transition-state structures were located as follows: Initially detailed geometry scans between the two local minima were performed in either direction. The maxima of these geometry scans were used as starting points of full transition state optimizations. Numerical frequency calculations were done at the QM/MM level to characterize the optimized structures as transition states with one imaginary frequency for the correct mode. Extensive geometry scans from reactants to products and vice versa on the singlet, triplet, and quintet spin states confirmed the proposed reaction mechanisms by establishing contiguous paths between the stationary points.

C. QM Part of the QM/MM Calculations. Following previous experience in the field,[34−36] our default QM treatment employed unrestricted hybrid density functional theory (UB3LYP)[37,38] in combination with a Los Alamos-type LACVP basis set on Fe (with a small core ECP) and 6-31G on the other atoms: basis set B1.[39] Full geometry optimizations were normally done with basis set B1 (unless otherwise noted). Subsequent single-point calculations on the optimized geometries made use of the Wachters all-electron basis set on iron and 6-31+G* on the remaining atoms in the QM region, basis set B2W.[40] To ascertain that our default level is sufficient, we performed additional geometry optimizations on **A**, $\mathbf{TS_A}$, and **B** (Scheme 2) using B3LYP/CHARMM in combination with a larger TZVP basis set,[41] which gave only slightly different results (see section III.A) and thus supported our choice of basis set B1 for geometry optimizations.

In our previous work on cytochrome P450 enzymes, the QM approach outlined above was found to reproduce experimental free energies of activation for aliphatic hydroxylation and epoxidation reactions within 3 kcal mol^{-1}.[34a,34b] Moreover, the errors in the barriers were systematic so that the relative values for a series of aliphatic hydroxylation reactions were accurate to within 1 kcal mol^{-1}.[34c,34d] Benchmark calculations for kinetic isotope effects[35] and spectroscopic (vibrational as well as electron paramagnetic resonance (EPR)) parameters[36] also reproduced the available experimental data very well. For further validation in the present CDO system, we tested the effect of the chosen density functional on the ordering and relative energies of the lowest-lying spin states in the iron(II)-superoxo complex by running single-point calculations using the BLYP,[38,42] BP86,[42,43] PBE0,[44] OLYP,[38,45] and OPBE[45,46] functionals with basis set B1 on the UB3LYP/B1 optimized geometries. Since the latter two density

dx.doi.org/10.1021/ja107514f |*J. Am. Chem. Soc.* 2011, 133, 3869–3882

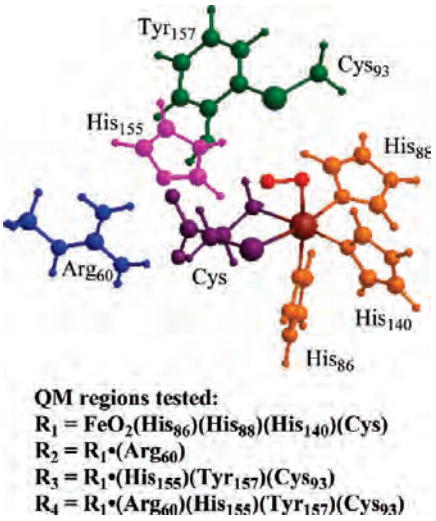

Figure 2. Definition of the four QM regions (R_1, R_2, R_3, and R_4) tested in the calculations.

functionals have not been implemented in TURBOMOLE yet, these calculations were done at the QM level using Gaussian 09.[47] In addition, we ran single-point calculations using a dispersion-corrected B3LYP method (B3LYP-D).[48]

The complete project generated a considerable amount of data (spin densities, charge distributions, detailed geometries, potential energy scans, etc.), which are documented in the Supporting Information that accompanies this paper.

An electronic embedding scheme[49] was adopted in the QM/MM calculations, whereby the interactions of the electrons in the QM region with charges in the MM region are incorporated into the one-electron Hamiltonian of the QM calculation. No cutoffs were introduced for the nonbonding MM and QM/MM interactions. The QM/MM boundary was treated with hydrogen link atoms through the charge shift model. The TURBOMOLE program package[50] was used for the QM treatment in the QM/MM as well as in the pure QM calculations. The CHARMM-22 force field was run through the DL_POLY[51] program to handle the MM part of the systems. The QM/MM calculations were performed with the ChemShell package[52] that integrates the TURBOMOLE and DL_POLY programs and performs geometry optimizations with the HDLC optimizer.[53]

D. Snapshots. Seven different snapshots were selected from an initial classical MD simulation after 0, 50, 100, 150, 200, 250, and 2000 ps and subjected to combined QM/MM calculations (full system).

E. QM Regions. We employed four different QM regions: R_1, R_2, R_3, and R_4, as defined in Figure 2. The smallest QM region, R_1, contains the metal, dioxygen, substrate cysteinate (Cys), and imidazole groups replacing the three histidine ligands. To test the effect of secondary sphere amino acids on the substrate dioxygenation mechanism, we enlarged the QM region with the methylguanidinium group of Arg_{60} in R_2, which also changes the total charge of the QM region from neutral to +1. QM region R_3, which is overall neutral in charge, consists of R_1 plus the phenol group of Tyr_{157}, its covalently linked Cys_{93} as methylsulfide and another imidazole group for His_{155}. Our largest QM region, R_4, contains R_1 and the amino acid side chains of Arg_{60}, His_{155}, Tyr_{157}, and Cys_{93} to account for the effects of all secondary amino acids. Consequently, QM region R_4 is also singly positively charged.

R_1 (42 atoms): Fe, O1, O2, Cys_{202}, His_{86}, His_{88}, His_{140}
R_2 (55 atoms): R_1, Arg_{60}
R_3 (68 atoms): R_1, His_{155}, Tyr_{157}, Cys_{93}
R_4 (81 atoms): R_1, Arg_{60}, His_{155}, Tyr_{157}, Cys_{93}

III. RESULTS

A. Benchmark Studies on Accuracy and Reproducibility of the Methods. Recent work of Lundberg and Morokuma on dioxygen binding to an iron center of the enzyme isopenicillin *N*-synthase showed that DFT calculations on small enzyme models can give rise to large systematic errors due to the fact that the interactions of the protein environment with the active center are not taken into consideration.[28] This is particularly essential for dioxygen binding processes, and therefore, QM/MM studies should give more reliable structures and energetics than those obtained with small DFT models. Consequently, we decided to investigate the catalytic mechanism of CDO enzymes using QM/MM techniques. Unfortunately, it is impossible to calibrate our calculations on CDO catalytic cycle intermediates against experiment due to the absence of spectroscopic data on dioxygen bound intermediates. Thus, we started our work with an extensive set of calibration calculations on the reactant, namely, the Fe(II)-superoxo bound complex of CDO. Specifically, we tested the reproducibility of the calculations by using a selection of different MD snapshots, QM regions, density functionals, and basis sets.

First, we computed the iron(II)-superoxo complex (**A**) in the lowest-lying singlet, triplet, and quintet spin states using seven different snapshots (Sn) from the MD simulations taken after 0, 50, 100, 150, 200, 250, and 2000 ps. These values are given in subscript to the snapshot label; for example, Sn_{100} denotes calculations starting from the snapshot taken after 100 ps. Figure 3 gives the ordering and relative energies of the lowest-lying spin states for these snapshots. Note that all optimized geometries of structure **A** refer to an end-on bound iron(II)-superoxo group. We made efforts to find a side-on bound structure which, however, did not succeed since the geometry optimizations always converged to end-on bound structures instead. In all cases, the singlet spin state is the ground state followed by the triplet and quintet spin states, respectively. These spin state orderings are in agreement with previous studies on iron(II)-superoxo complexes in taurine/α-ketoglutarate dioxygenase[24c] and cytochrome P450 enzymes.[54] The iron(II)-superoxo intermediate in the catalytic cycle of cytochrome P450 is known to have a singlet ground state, both computationally and experimentally (EPR).[54] Recent biomimetic studies on iron(II)-superoxo and iron(III)-peroxo complexes in porphyrin-ligated complexes showed a delicate balance between the two configurations.[55] Apparently, the local environment of the dioxygen moiety in CDO stabilizes the iron(II)-superoxo over the iron(III)-peroxo species.

The average value and standard deviation of the singlet−triplet energy gaps (ΔE_{ST}) of these snapshots are $\Delta E_{ST} = 4.0 \pm 0.6$ kcal mol^{-1} for the B1 data and $\Delta E_{ST} = 4.3 \pm 0.7$ kcal mol^{-1} for the B2W results. Therefore, within the error bars of the calculations, both basis sets give the same singlet−triplet energy gap. The singlet−quintet energy gap (ΔE_{SQ}), by contrast, shows somewhat larger fluctuations among the snapshots, covering a range of about 4.0 kcal mol^{-1} for each basis set, with an average value and standard deviation of $\Delta E_{SQ} = 10.8 \pm 1.6$ kcal mol^{-1} for basis set B1 and $\Delta E_{SQ} = 13.9 \pm 1.7$ kcal mol^{-1} for B2W. Hence, enlarging the basis set from B1 to B2W has only minor effects on the computed singlet−triplet energy gaps, whereas the singlet−quintet energy gaps are more sensitive and generally increase slightly upon basis set extension. Since all snapshots predict the same trends and spin state ordering, we decided to perform the

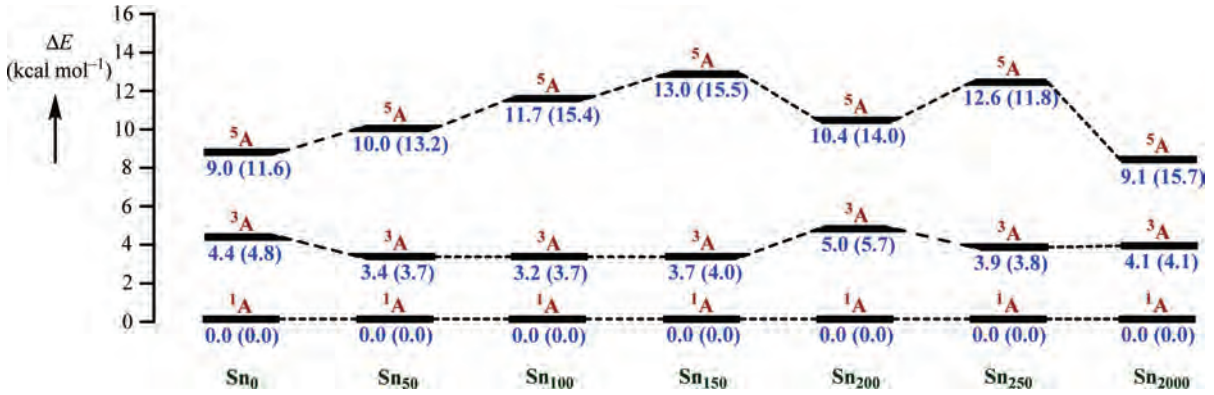

Figure 3. Relative energies (in kcal mol^{-1}) of the lowest-lying singlet, triplet, and quintet spin states of the iron(II)-superoxo complex (^{1,3,5}**A**) of CDO as calculated using seven different snapshots from the MD simulations and QM region R_4. All data were obtained with QM/MM using B3LYP/B1 optimizations and QM region R_4. Values in parentheses were calculated at the B3LYP/B2W//B3LYP/B1 level of theory.

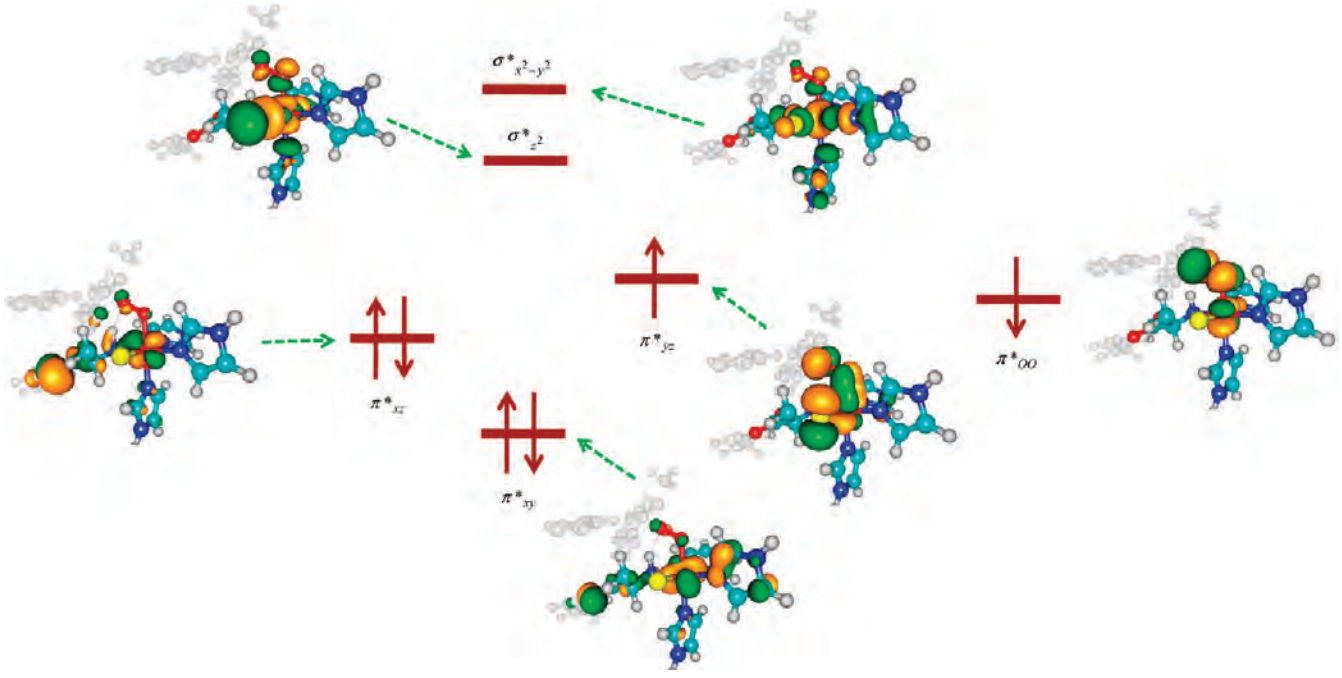

Figure 4. High-lying occupied and low-lying virtual molecular orbitals of ^{1}**A**.

dioxygen activation studies using two different snapshots only, namely, Sn_{100} and Sn_{200}, which are expected to provide a good representation of the actual system.

The DFT calculations on the iron(II)-superoxo complex ^{1,3,5}**A** from ref 16 are in good agreement with the QM/MM calculations presented here. They gave a singlet spin ground state with the triplet and quintet spin states higher in energy by ΔE_{ST} = 2.6 kcal mol^{-1} and ΔE_{SQ} = 5.9 kcal mol^{-1} at the B3LYP/B2//B3LYP/B1 level of theory, where B2 denotes an LACV3P+ basis set on iron and 6-311+G* on the other atoms. Inclusion of a dielectric continuum with ε = 5.7 in the DFT treatment raised ΔE_{SQ} to 8.4 kcal mol^{-1}, while a ΔE_{ST} was only marginally influenced (ΔE_{ST} = 2.0 kcal mol^{-1}).[16b] The previous DFT calculations give the same spin-state ordering as the present QM/MM results and are consistent with a small singlet−triplet energy gap of about 2−4 kcal mol^{-1}. The effect of the protein on the spin-state ordering and relative energies of the iron(II)-superoxo complex is thus rather small.

To understand the electronic differences between the various spin states, consider first the high-lying occupied and low-lying virtual orbitals of our reactant complex ^{1}**A** in Figure 4. The orbitals are dominated by metal 3d contributions. The lowest one depicted in Figure 4 is the doubly occupied π^*_{xy} orbital, a nonbonding orbital in the plane of the cysteinate ligand. Somewhat higher in energy is the doubly occupied π^*_{xz} orbital, which is parallel to the O−O bond and shows little interaction with the dioxygen moiety. There are two singly occupied orbitals in ^{1}**A** and ^{3}**A**, namely, the π^*_{yz} and π^*_{OO} orbitals. The former represents an antibonding interaction between the metal $3d_{yz}$ and a 3p orbital on sulfur and also interacts with the dioxygen group, while the latter is antibonding along the dioxygen bond. Finally, the virtual $\sigma^*_{z^2}$ orbital represents the antibonding combination of $3d_{z^2}$ on iron with distal and axial ligands as well as with a σ-orbital on sulfur, whereas the virtual $\sigma^*_{x^2-y^2}$ orbital involves interactions between iron $3d_{x^2-y^2}$ and orbitals on histidine and substrate amide groups. The orbitals shown in

dx.doi.org/10.1021/ja107514f |*J. Am. Chem. Soc.* 2011, 133, 3869–3882

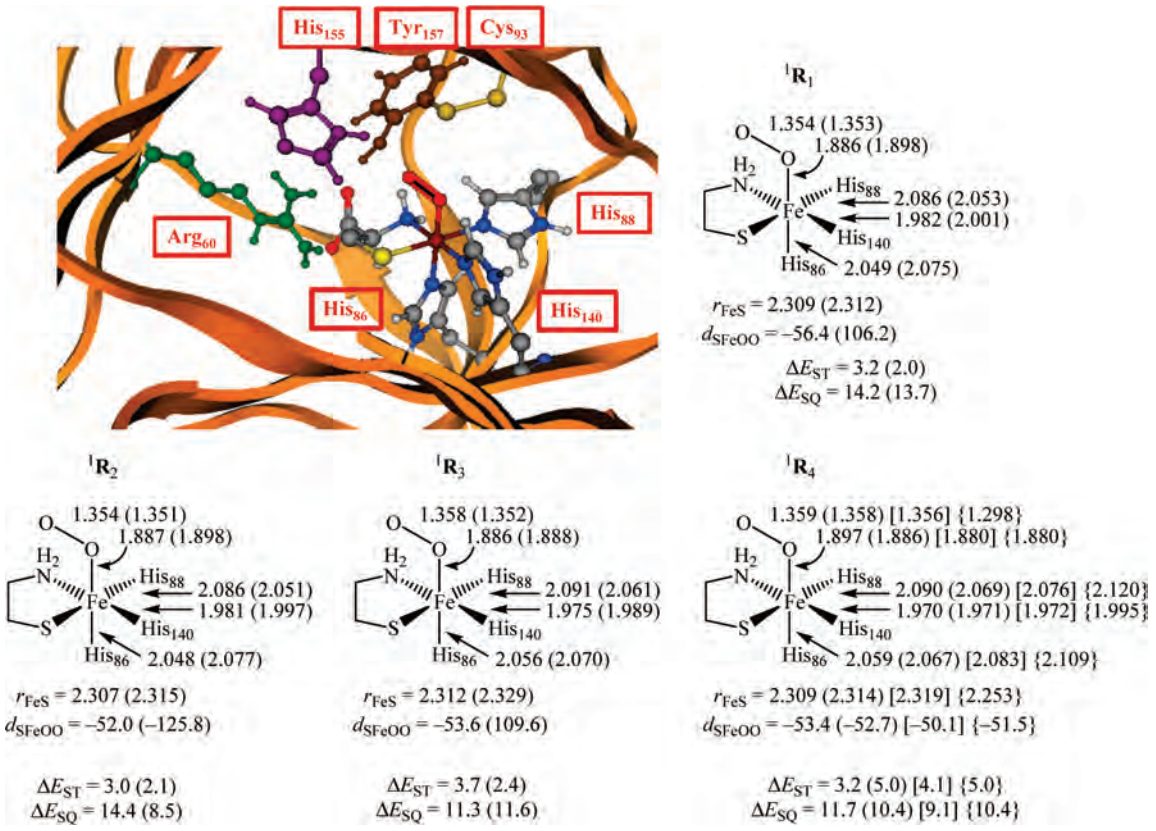

Figure 5. Optimized geometries of the singlet spin iron(II)-superoxo bound species (^{1}**A**) using different size QM regions (R_1, R_2, R_3, and R_4 as defined in Figure 2). Only the metal and its ligands are shown. All bond lengths are given in angstroms and the dihedral angle S−Fe−O−O (d_{SFeOO}) is given in degrees. Optimized geometries are obtained from snapshot Sn_{100} (Sn_{200}) [Sn_{2000}] {Sn_{200}-TZVP}. Relative energies (in kcal mol^{-1}) are based on the B1 results.

Figure 4 are occupied with six electrons and give an orbital occupation of $\pi^*_{xy}{}^2\,\pi^*_{xz}{}^2\,\pi^*_{yz}{}^1\,\pi^*_{OO}{}^1$ for ^{1}**A** as assigned with the arrows next to the orbitals. The triplet spin state (^{3}**A**) has the same orbital occupation as the singlet spin state, but the unpaired electrons are ferromagnetically rather than antiferromagnetically coupled. As a consequence, ^{3}**A** and ^{1}**A** are close in energy, with an average energy gap of 4.3 kcal mol^{-1} (B3LYP/B2W) for seven different MD snapshots (vide supra). The singlet and triplet spin states have the same orbital occupation in the present QM/MM and the previous DFT model calculations, and they can both be characterized as an iron(II)-superoxo complex. In ^{5}**A** the system is also described as a iron(II)-superoxo complex, but with orbital occupation $\pi^*_{xy}{}^2\,\pi^*_{xz}{}^1\,\pi^*_{yz}{}^1\,\sigma^*_{z^2}{}^1\,\pi^*_{OO}{}^1$.

As already shown by DFT model calculations,[16] the ^{5}**A** state is an excited state of the iron(II)-superoxo complex of CDO. Its energy relative to the singlet spin ground state (ΔE_{SQ}) is influenced by the protein environment, as indicated by the fluctuations in the computed singlet−quintet energy gaps for our seven QM/MM snapshots (vide supra). Electronically, in four of the seven snapshots, the ^{5}**A** state has group spin densities of $\rho_{Fe} = 3.72-3.76$, $\rho_{OO} = 0.42-0.56$, and $\rho_{Cys} = -0.31$ through -0.46 (B3LYP/B2W), which are similar to the DFT values obtained for the small model complex. These group spin densities reflect a dominant $\pi^*_{xy}{}^2\,\pi^*_{xz}{}^1\,\pi^*_{yz}{}^1\,\sigma^*_{z^2}{}^1\,\pi^*_{OO}{}^1$ configuration.[16] A natural orbital analysis of the QM/MM wave function shows some admixture of the $\pi^*_{xy}{}^2\,\pi^*_{xz}{}^1\,\pi^*_{yz}{}^1\,\sigma^*_{z^2}{}^1\,\sigma^*_{x^2-y^2}{}^1\,lp_S{}^1\,\pi^*_{OO}{}^1$ configuration, which is due to an electron transfer from a lone pair on the sulfur of cysteinate (lp_S orbital) into a virtual metal-based orbital ($\sigma^*_{x^2-y^2}$) with σ-type antibonding interactions along the Fe−S bond. As a consequence, the spin densities on the metal and the cysteinate ligand are somewhat larger than expected. Attempts to swap orbitals and create a configurationally more pure quintet state failed and converged back to this mixed state. Two of the seven snapshots give different group spin densities (B3LYP/B2W) with $\rho_{Fe} = 2.82$ or 2.84, $\rho_{OO} = 0.80$ or 0.79, and $\rho_{Cys} = 0.31$ or 0.30 for Sn_{150} and Sn_{250}, respectively. Attempts to swap orbitals in these two cases failed to converge to the type of quintet state found for the other snapshots and DFT model complexes. Energetically, there is no significant difference between the quintet state energies (ΔE_{SQ}) obtained for snapshots Sn_{150} and Sn_{250} as compared to the other snapshots. It thus seems that environmental perturbations affect the exact nature of the quintet spin state and may lead to a different mix of energetically close-lying configurations in the quintet spin-state wave function.

Subsequently, we tested the effect of the size of the QM region on the spin-state ordering, optimized geometries, and relative energies. Thus, we investigated two characteristic snapshots (Sn_{100} and Sn_{200}) and ran full geometry optimizations using four different QM regions (R_1, R_2, R_3, and R_4) as defined above in Figure 2. This was done to establish the effect of second sphere coordination atoms on the optimized geometries and the charge distributions. Additionally, we performed two more geometry optimizations on QM region R_4: one after a long 2000-ps MD run (Sn_{2000}) and one on Sn_{200} using the B3LYP/TZVP method for the QM region (Sn_{200}-TZVP). Figure 5 shows the optimized

dx.doi.org/10.1021/ja107514f |J. Am. Chem. Soc. 2011, 133, 3869–3882

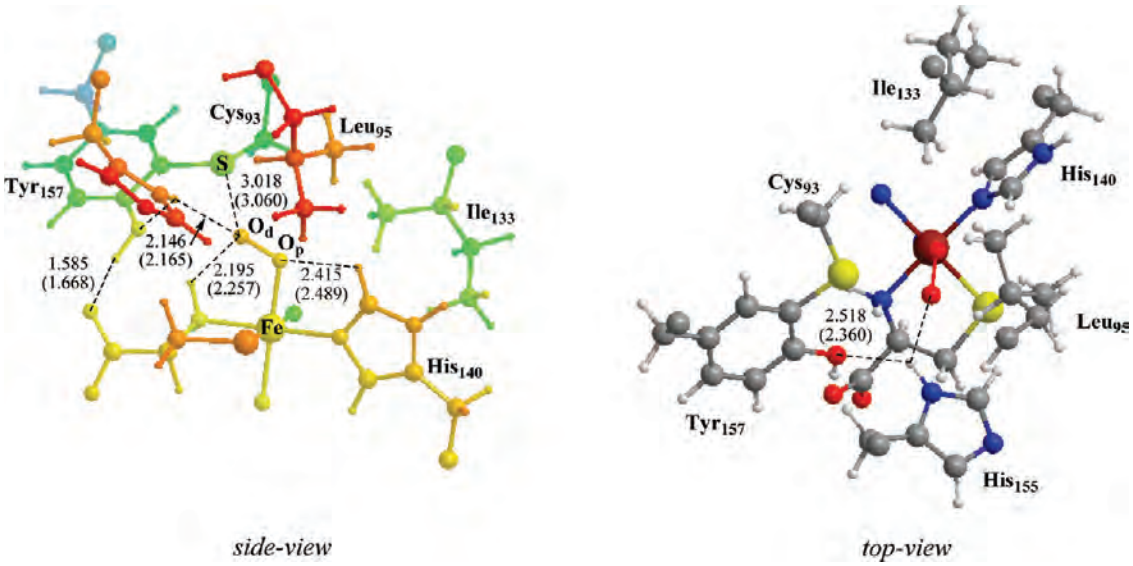

Figure 6. Extracts of optimized geometries, with focus on the dioxygen environment of ^{1}**A**, from QM(B3LYP/B1)/CHARMM and QM(B3LYP/TZVP)/CHARMM (data in parentheses). Bond lengths are given in angstroms. Calculations were done with QM region R_4, but only selected QM and MM atoms are shown.

geometries in the singlet spin ground state as well as the adiabatic excitation energy from the singlet to the lowest-lying triplet (ΔE_{ST}) and quintet (ΔE_{SQ}) spin states, respectively. Generally the optimized bond lengths (UB3LYP/B1) are very similar for the four QM regions (typically within 0.010 Å, maximum deviation of 0.030 Å). The same is true for the optimized geometries in the triplet and quintet spin states (see Supporting Information). The calculated singlet−triplet energy gaps with the four QM models lie within a few kcal mol^{-1}, while the singlet−quintet energy gaps show somewhat larger fluctuations ranging from 9.1 to 14.3 kcal mol^{-1}. It appears, therefore, that second coordination sphere effects are small and do not lead to significant changes in the geometry and electronic properties of the calculated species.

The optimized geometries in Figure 5 show features typical for a dioxygen bound complex. In all structures the Fe−O distance is 1.880−1.898 Å and hence somewhat shorter than found in a DFT model study (1.906 Å)[16a] and also shorter than typically calculated for iron(II)-superoxo complexes in cytochrome P450 enzymes, where values of 1.940 to 2.002 Å have been reported.[54c,56] On the other hand, the O−O distance calculated for the singlet spin DFT model complex from ref 16a is midway in the range of values from 1.298−1.359 Å shown in Figure 5. The O−O distances for the CDO optimized geometries are close to values reported for heme-based iron(II)-superoxo complexes.[57] Although the three histidine ligands are anchored to the protein backbone, surprisingly the three Fe−N distances are very much alike with a spread of maximally about 0.1 Å. The size of the QM region has very little effect on the optimized geometries of the iron with its direct ligands. Moreover, the QM/MM optimized geometries are very similar to those from a DFT model study[16a] which gave Fe−N_{His86}, Fe−N_{His88}, and Fe−N_{His140} distances of 2.090, 2.055, and 2.014 Å, respectively. The largest difference between the various QM regions and snapshots is found for the dihedral angle between S−Fe−O−O.

In summary, the size of the QM region has very little effect on the optimized geometries of the active-site region and minor effects on the relative energies, and the spin-state ordering is the same in all cases. Nevertheless, to make sure that the choice of the QM region will not affect the conclusions drawn in this paper, we decided to run the complete reaction mechanism calculations with the large QM region R_4.

As further test on basis set effects, we optimized the geometry of ^{1}**A** using QM region R_4 in Sn_{200} and the large TZVP basis set (instead of basis B1). The results displayed in Figure 5 show that identical spin-state energies between the lowest lying singlet, triplet, and quintet spin states are obtained from the QM/MM optimizations with the TZVP and B1 basis sets. Furthermore, the optimized geometries are very similar, without any dramatic differences. Consequently, for the remainder of the calculations, we restricted ourselves to basis set B1 for geometry optimizations. Previous studies on iron(IV)-oxo model complexes and their reactivity patterns reported similar trends in energetics from geometries optimized with a double-ζ quality basis set as compared to a triple-ζ basis set,[58] which further supports our choice of basis set for these types of calculations.

We now address the local environment of the superoxo moiety in ^{1}**A** as calculated with QM(B3LYP/B1)/CHARMM and QM-(B3LYP/TZVP)/CHARMM. Figure 6 shows the relevant parts of the corresponding optimized structures which exhibit similar hydrogen-bonding interactions of the superoxo group with its local environment. The superoxo group is located in a cavity surrounded by the amino acid side chains of Cys_{93}, Leu_{95}, Ile_{133}, His_{155}, Tyr_{157}, and substrate cysteinate. The hydrogen-bonding donor and acceptor groups of the second-sphere amino acids are included in the QM region of the calculations, while Leu_{95} and Ile_{133} are part of the MM region. The distal oxygen atom is involved in hydrogen-bonding interactions with the amine group of substrate cysteinate and with the imidazole group of His_{155} (distances of 2.146−2.257 Å). The sulfur atom of Cys_{93} is located about 3 Å away from the distal oxygen atom O_d, indicating non-negligible electrostatic interactions. Interestingly, the proximal oxygen atom forms a hydrogen bond with the imidazole group of the metal ligand His_{140}. This will force the proximal oxygen atom into a specific orientation, which may be

dx.doi.org/10.1021/ja107514f |*J. Am. Chem. Soc.* 2011, 133, 3869–3882

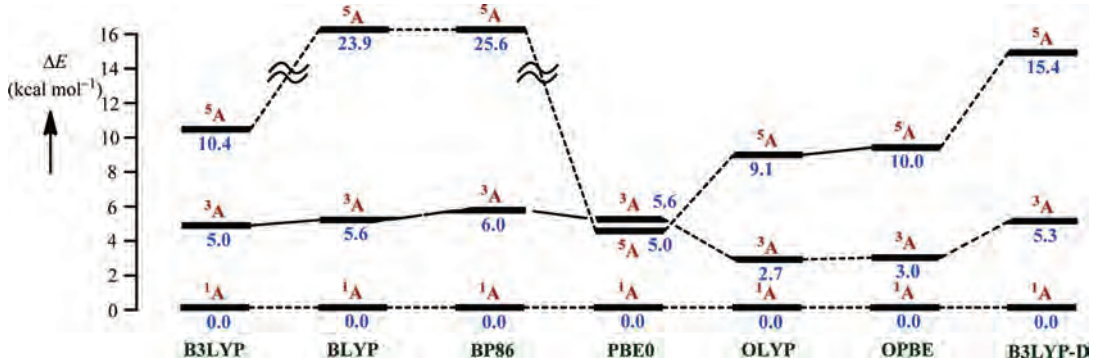

Figure 7. Relative energies (in kcal mol^{-1}) of the lowest-lying singlet, triplet, and quintet spin states of the iron(II)-superoxo complex of CDO (**A**) as calculated with seven different density functional methods. Single-point calculations using basis set B1 on optimized B3LYP/B1 structures were performed using snapshot Sn_{200} and QM region R_4.

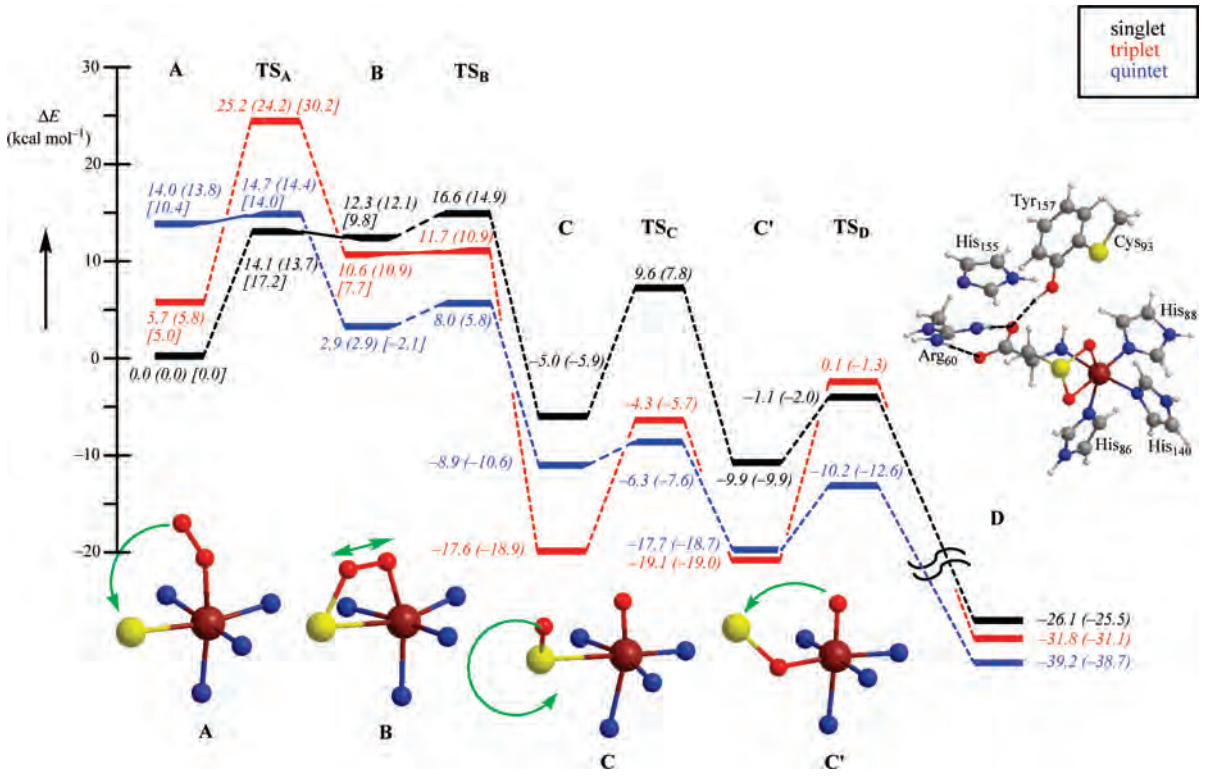

Figure 8. Potential energy profile of dioxygen activation by CDO enzymes starting from the iron(II)-superoxo complex (^{1,3,5}**A**) using QM region R_4. All energies are in kcal mol^{-1} relative to ^{1}**A**. The two values given for each structure represent ΔE and ΔE+ZPE. QM(B3LYP/B2W)/MM energies ΔE were obtained from single-point calculations on QM(B3LYP/B1)/MM optimized geometries, and zero-point energies ZPE were determined at the QM(B3LYP/B1)/MM level; the surface follows the ΔE+ZPE data. Values given in square brackets refer to QM(B3LYP/TZVP)/MM energies ΔE obtained after geometry optimizations at this level.

reason why we were unable to locate the side-on bound isomer of the iron(II)-superoxo or iron(III)-peroxo intermediate. Clearly, the superoxo group in ^{1}**A** is held in position by several moderately strong interactions and is thus expected to be fairly rigid in its local environment.

A final set of calibration calculations were done using seven different density functionals: B3LYP, BLYP, BP86, PBE0, B3LYP-D, OLYP, and OPBE. In transition metal complexes the choice of the density functional can sometimes influence spin-state orderings and relative energies dramatically and should therefore be thoroughly calibrated.[59] Thus, with hybrid functionals such as B3LYP high spin states are generally stabilized, whereas closed-shell configurations tend to be favored with pure density functionals such as BP86. Furthermore, it has been shown that dispersion-corrected density functional methods, such as B3LYP-D, give superior performance in calculating spin-state energetics.[60] To test the sensitivity of our QM/MM results with regard to the chosen functionals, we calculated the lowest-lying singlet, triplet, and quintet spin states of the iron(II)-superoxo bound structure (^{1,3,5}**A**) using seven commonly employed density functionals. Figure 7 displays the spin-state ordering and relative energies obtained on B3LYP/B1 optimized geometries.

All density functionals predict a singlet spin ground state that is separated from the other spin states by at least 2.7 kcal mol^{-1}.

dx.doi.org/10.1021/ja107514f |*J. Am. Chem. Soc.* 2011, 133, 3869–3882

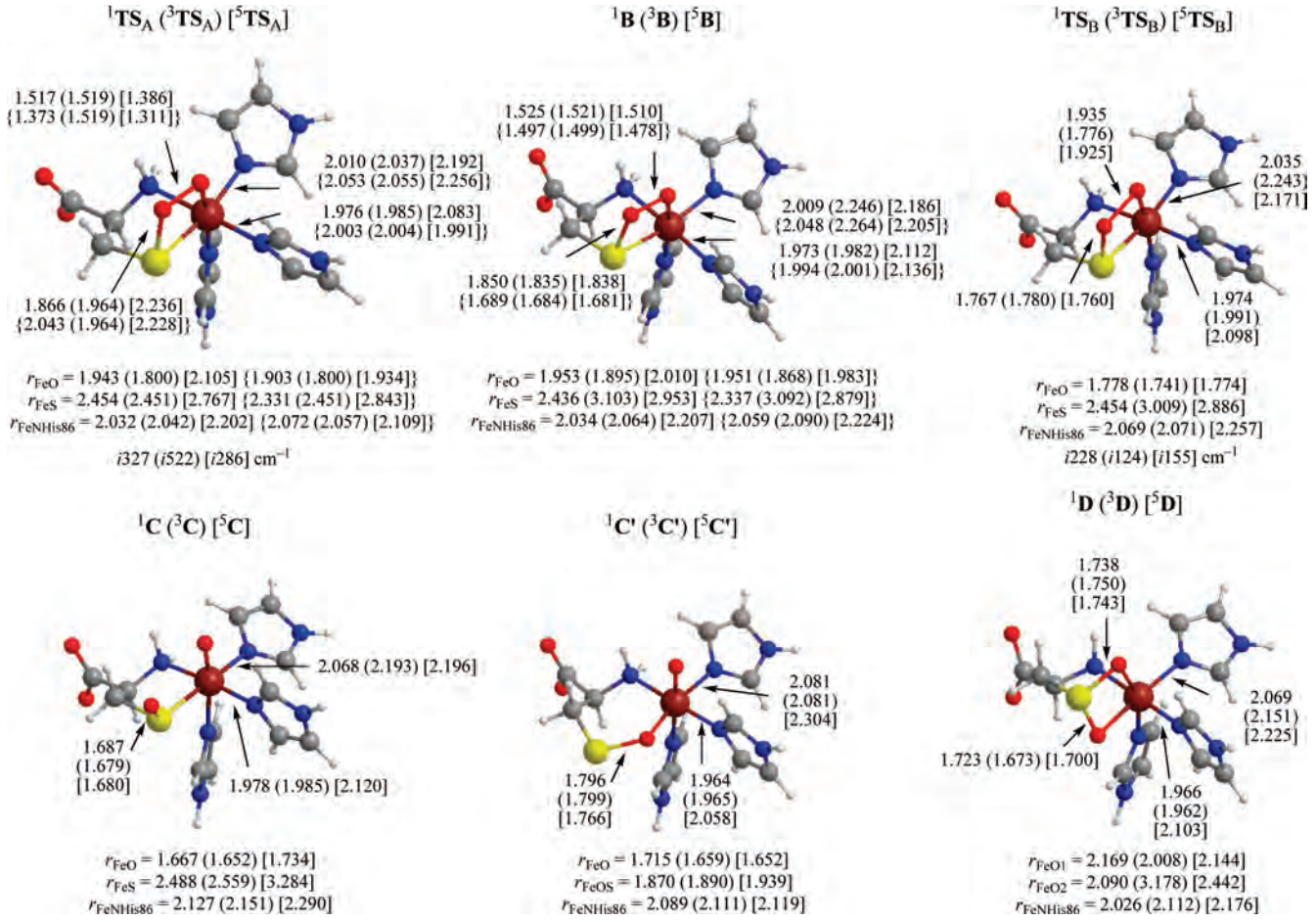

Figure 9. Extracts of the optimized geometries for mechanism I of cysteine dioxygenation by CDO as calculated by QM(B3LYP/B1)/MM using snapshot Sn_{200}. Values are given for the singlet (triplet) [quintet] spin states; the data in curly brackets come from QM(B3LYP/TZVP)/MM geometry optimizations. Bond lengths are given in angstroms and imaginary transition-state frequencies in wavenumbers. All structures depicted here were optimized using QM region R_4. The second-sphere amino acids in the QM region are not shown.

All give the triplet spin state well below the quintet spin state, except for PBE0, where the order is reversed and the energy difference between triplet and quintet is small (only 0.6 kcal mol^{-1}). Consequently, the PBE0 functional is probably least suitable for the studies presented here. On average the triplet state is 4.7 ± 1.3 kcal mol^{-1} above the singlet ground state, with the B3LYP result closest to the average. As expected, there is some fluctuation in the relative energy of the quintet spin state, which is destabilized when using pure density functionals, such as BLYP and BP86. This is a common feature for these types of DFT methods.[59] If we exclude the results obtained with BLYP and BP86, the average singlet−quintet energy gap is 10.0 ± 3.7 kcal mol^{-1}. Again, the B3LYP result seems to be closest to the average. In any event, all methods agree that the quintet spin state is an excited state that lies appreciably above the singlet ground state of the iron(II)-superoxo bound species. In the remainder of this article, we shall use the B3LYP functional exclusively, in view of the present validation and its well-established performance in computational studies of iron containing enzymes.[54c,56]

B. Dioxygen Activation via Mechanism I. Subsequently, we studied the dioxygen activation reaction by cysteinate via Mechanism I (Scheme 2) as calculated with QM/MM methods using snapshot Sn_{200} and the largest QM region R_4 (81 atoms). The calculated potential energy profile is shown in Figure 8, while optimized geometries of the critical points are given in Figure 9. The optimized geometries of the local minima and transition states show little geometric distortion in the second-sphere amino acids included in the QM region. Thus, the hydrogen bond distances between Tyr_{157} and the carboxylic acid group of cysteinate (or its derivative) range between 1.550 and 1.587 Å, and so do salt bridge distances between Arg_{60} and this carboxylate group. The hydrogen bonding between His_{155} and Tyr_{157} is somewhat more flexible, with pertinent distances ranging from 2.518 Å in ^{1}**A** via 2.672 Å in ^{5}**B** to 2.277 Å and 2.048 Å in ^{3}**C** and ^{3}**C**′, respectively. Given this situation, we only show the metal and its ligands in Figure 9, although it should be emphasized that the geometry optimizations were done with QM region R_4, which includes the side chains of Arg_{60}, His_{155}, Tyr_{157}, and Cys_{93}. In all optimized geometries, the proximal oxygen atom forms a hydrogen bond with the imidazole group of His_{140}, which remains twisted during the reaction.

As follows from Figure 8, the reaction takes place via multistate reactivity patterns on competing singlet, triplet, and quintet spin-state surfaces, similar to substrate hydroxylation by heme and nonheme iron(IV)-oxo oxidants.[61] Although the singlet spin state is the ground state for the iron(II)-superoxo complex (**A**), a spin-state crossing to the quintet spin state initiates the reaction

dx.doi.org/10.1021/ja107514f |J. Am. Chem. Soc. 2011, 133, 3869–3882

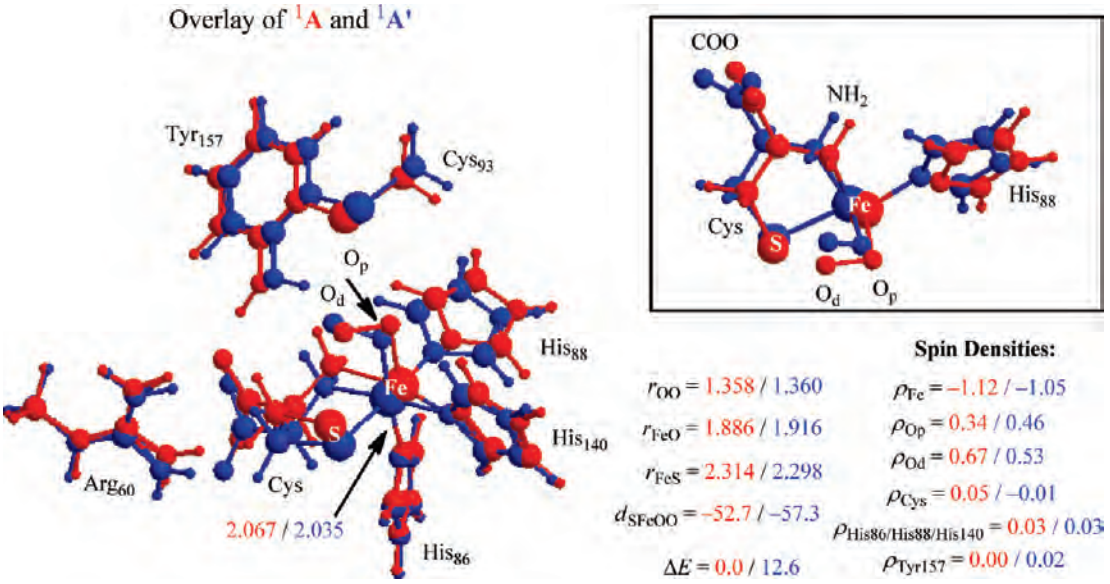

Figure 10. Overlay of the optimized geometries of ^{1}**A** (in red) and ^{1}**A**′ (in blue) obtained with QM region R_4. The inset shows the FeO_2 with cysteinate and opposing histidine ligands in a different view. Selected bond distances are in angstroms and dihedral angles in degrees. Also shown is the relative energy between ^{1}**A** and ^{1}**A**′ and the group spin densities calculated at the QM(B3LYP/B1)/MM level.

to form a quintet spin ring structure (^{5}**B**). This crossing occurs slightly before (after) the transition state ^{1}**TS**$_A$ for S−O bond formation when using the TZVP (B1) basis set for geometry optimization. The resulting quintet intermediate with a four-membered ring (^{5}**B**) undergoes dioxygen bond cleavage leading to a sulfoxide and an iron-oxo species (**C**) via a barrier of ΔE+ZPE = 2.9 kcal mol^{-1} (B3LYP/B2W). This reaction is highly exothermic at B3LYP/B2W level, and 13.5 kcal mol^{-1} of energy is released in the quintet spin state. Intermediate **C** has a lower-lying triplet state, that is, ^{3}**C** is below ^{5}**C** by 8.3 kcal mol^{-1} (B3LYP/B2W). The sulfoxide intermediate ^{5}**C** probably has a short lifetime since only a small reaction barrier ^{5}**TS**$_C$ of 3.0 kcal mol^{-1} separates it from the rotated sulfoxide structure ^{5}**C**′. During the rotation from **C** to **C**′ the Fe−S bond in **C** breaks, and a rotation around the C−C bond moves the sulfur atom away from the metal and gives the oxygen atom the opportunity to bind instead. In the resulting structure (**C**′) the sulfur atom is freely accessible for the second oxygen atom, while the sulfoxide oxygen atom binds to iron. On the triplet spin-state surface this barrier is substantially higher (13.2 kcal mol^{-1} via ^{3}**TS**$_C$). The rotated sulfoxide structure **C**′ also has a triplet spin ground state with the quintet spin state 0.3 kcal mol^{-1} higher in energy. Both **C** and **C**′ are thus iron(IV)-oxo complexes with a triplet spin ground state. This spin-state ordering is supported by experimental and computational studies of nonheme iron(IV)-oxo complexes that tend to give a triplet spin ground state.[62,63] By contrast, the iron(IV)-oxo species of TauD has a quintet spin ground state due to a 2His/1Asp ligand system that decreases the $\pi^*_{xy}/\sigma^*_{x^2-y^2}$ energy gap through strong ligand interactions and hence stabilizes the quintet state over the triplet.[63] The $\sigma^*_{x^2-y^2}$ orbital is lowered in energy when strong anionic ligands are bound to the metal in the *xy* plane of symmetry (perpendicular to the Fe(IV)═O axis). In structures **C** and **C**′ in CDO, the *xy* plane of symmetry contains two histidine ligands and a sulfoxide group, which are all neutral. By contrast, in TauD there are two carboxylic acid groups bound to the metal in the *xy* plane, and as a consequence, the $\sigma^*_{x^2-y^2}$ orbital is lowered in energy and a quintet ground state is created, while structures **C** and **C**′ in CDO have a triplet ground state. The final step leading to cysteine sulfinic acid products (**C**′ → **D**) has the smallest barrier on the quintet spin-state surface (6.1 kcal mol^{-1} at B3LYP/B2W). Previous DFT studies of the reactivity of nonheme iron(IV)-oxo complexes also gave lower reaction barriers in the quintet spin state as compared to the triplet spin state, in agreement with what is found here.[24,61b,63,64] The product complex has a quintet ground state. The overall reaction exothermicity is 38.7 kcal mol^{-1} with B3LYP/B2W. This value compares well with reaction exothermicities calculated for substrate hydroxylation and epoxidation by iron(IV)-oxo oxidants, where the reaction exothermicities were shown to be governed by the energies of the bonds that are broken and formed.[34c,34d,58c]

The overall reaction mechanism calculated with QM-(B3LYP)/MM is similar to that reported before using DFT model complexes,[16] although there are some significant differences. However, these differences do not affect the product distributions or the rate-determining steps in the mechanism. All our theoretical studies predict a singlet spin iron(II)-superoxo complex that undergoes S−O bond formation with cysteinate via a spin crossing to the quintet spin-state surface. The rate-determining barrier in all cases is this spin state crossing to ^{5}**TS**$_A$ on the path to the ring structure. In the following steps, we find multistate reactivity patterns on competing triplet and quintet spin-state surfaces with QM/MM, whereas the DFT model calculations[16] predict the quintet and triplet spin states of **C**, **C**′, and **D** to be well separated with a quintet spin ground state. On the quintet spin-state surface, each intermediate is computed to be lower in energy than its precursor, at both levels.

We note that full QM/MM geometry optimizations with UB3LYP/TZVP closely reproduce the results obtained with UB3LYP/B1 and confirm the corresponding mechanistic conclusions. Test calculations with QM regions R_1 and R_4 further

dx.doi.org/10.1021/ja107514f |*J. Am. Chem. Soc.* 2011, 133, 3869–3882

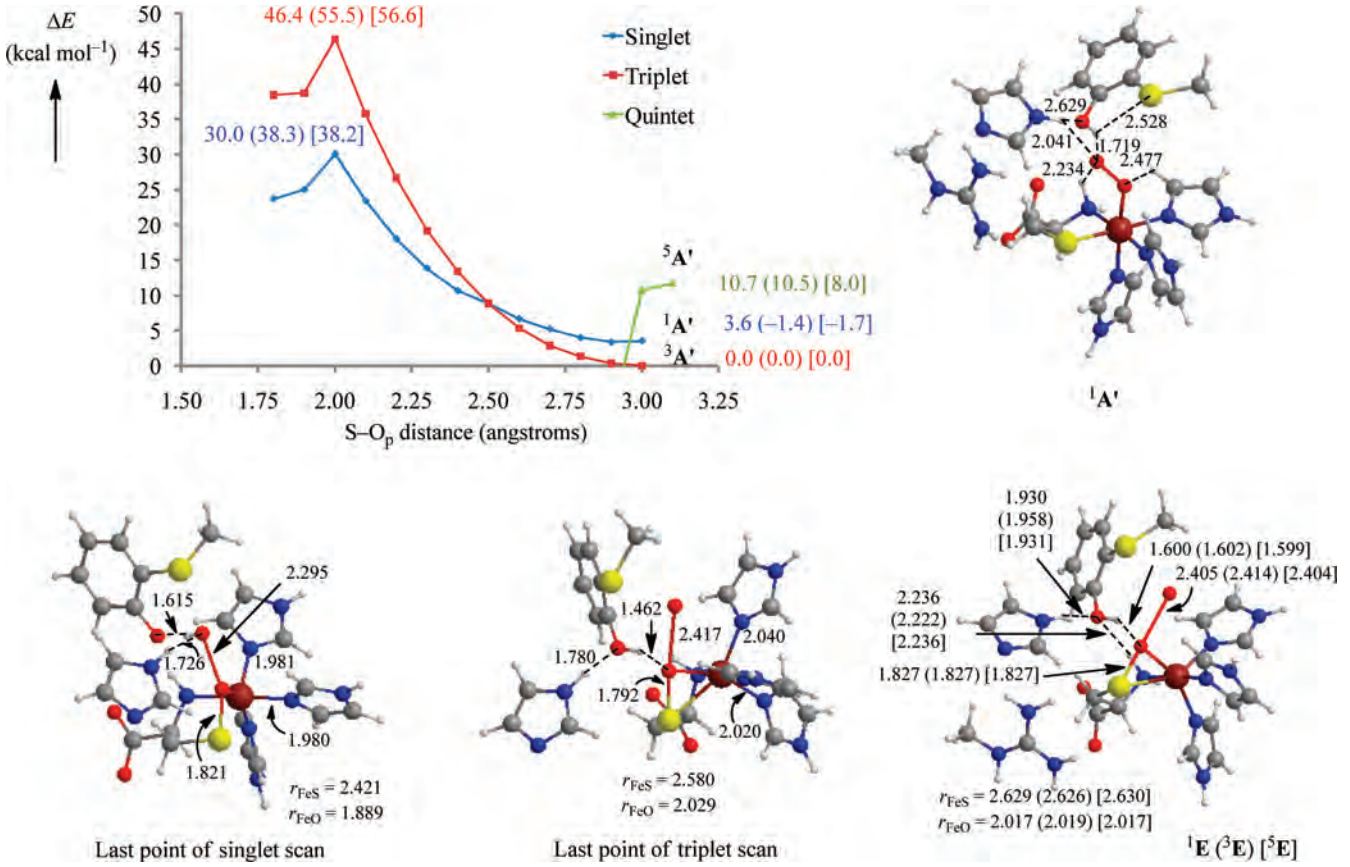

Figure 11. Geometry scans for attack of sulfur on the proximal oxygen atom. Single-point QM(B3LYP)/MM energies obtained with the B1 (B2W) [TZVP] basis set on QM(B3LYP/B1)/MM-optimized geometries using QM region R_4, given in kcal mol^{-1} relative to ^{3}**A**′. Also shown are the optimized geometries of ^{1}**A**′, of the last point of the singlet and triplet geometry scans, and of the "persulfenate"' structures ^{1,3,5}**E,** with bond lengths given in angstroms.

indicate that the results are not too sensitive with regard to the choice of the QM region (see Supporting Information for further details).

C. Dioxygen Activation via Mechanism II. Crystal structure analysis led to the proposal of an alternative mechanism for cysteine activation by CDO enzymes (mechanism II in Scheme 2), where the sulfur group of cysteinate attacks the proximal oxygen atom to form a persulfenate complex, facilitated through a hydrogen bonding interaction of the distal oxygen atom with the phenol proton of Tyr_{157}.[25] To test this hypothesis, we first optimized the geometries (using QM region R_4) of the rotated dioxygen bound complexes ^{1,3,5}**A**′, which contain a direct hydrogen bond between the phenol OH group of Tyr_{157} and the distal oxygen atom of O_2. These structures are significantly higher in energy than structure ^{1}**A**, by 12.5, 9.0, and 19.7 kcal mol^{-1} at the QM(B3LYP/B1)/MM level of theory. Figure 10 displays the overlay of optimized geometry of ^{1}**A**′ and ^{1}**A** as calculated with QM/MM using B3LYP/B1.

Obviously, ^{1}**A** and ^{1}**A**′ are very much alike in their geometric features. The Fe−S distance is somewhat shortened by 0.016 Å, while the Fe−O distance is slightly elongated by 0.030 Å when going from ^{1}**A** to ^{1}**A**′. The key difference, however, is the rotation of the phenol OH group of Tyr_{157}, with a switch of the hydrogen bond from the carboxylic acid group of the substrate in ^{1}**A** to the distal oxygen atom of the superoxo group in ^{1}**A**′. The corresponding QM(B3LYP/B1)/MM hydrogen bond distances are 1.585 Å in ^{1}**A** and 1.719 Å in ^{1}**A**′. The latter hydrogen bond is obviously weaker, and hence ^{1}**A**′ is less stable than ^{1}**A**. Because of the reorientation of the Tyr residue, the dioxygen moiety is bent toward the Tyr group and the dihedral angle S−Fe−O_p−O_d increases to −57.3°.

Electronically, the two isomers ^{1}**A** and ^{1}**A**′ are virtually identical with one unpaired electron each on a metal based orbital (π^*_{xz}) and an antibonding orbital along the O−O bond (π^*_{OO}), whereby the former orbital contains a β-spin electron and the latter an α-spin electron. Reorientation of the phenol OH group of Tyr_{157} results in sizable loss of polarization on the individual oxygen atoms in the dioxygen group, and the spin densities change from $\rho_{Op} = 0.34$ and $\rho_{Od} = 0.67$ in ^{1}**A** to $\rho_{Op} = 0.46$ and $\rho_{Od} = 0.53$ in ^{1}**A**′. At the same time, the iron loses some of its unpaired spin density (0.07 units) and so does the cysteinate substrate (0.06 units). This change in polarization may affect the reaction mechanism of cysteine activation.

Subsequently, we investigated the attack of the proximal oxygen atom (O_p) on the sulfur atom of substrate cysteinate. The computed geometry scans and the optimized geometries of the critical points are shown in Figure 11. They indicate high-energy mechanisms with reaction barriers well over 30 kcal mol^{-1} on the singlet and triplet spin-state surfaces. These barriers are much higher than those obtained for mechanism I (see Figure 8) which is thus clearly favored. In the case of the quintet spin state, the geometry scan failed and led to the formation of a ring structure similar to structure ^{5}**B** discussed in the previous section. The initial points of the scan on the quintet surface are, however, already higher in energy than the rate-limiting barriers of

dx.doi.org/10.1021/ja107514f |*J. Am. Chem. Soc.* 2011, 133, 3869–3882

Scheme 3. Proposed Mechanism of Cysteine Dioxygenation by CDO Enzymes As Elucidated by QM/MM Studies

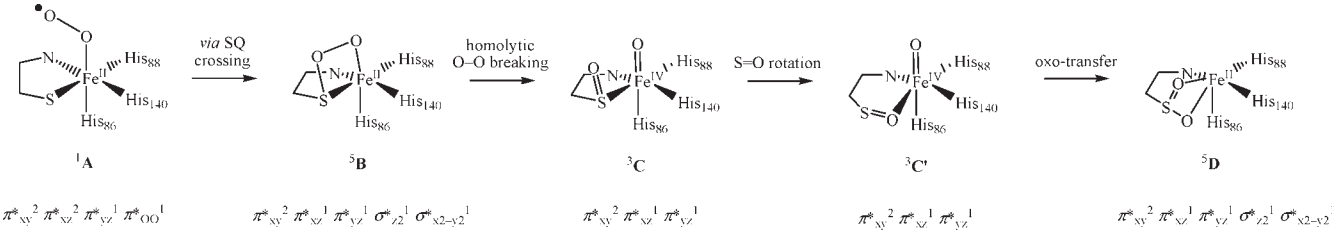

mechanism I. In conclusion, our QM/MM calculations thus rule out the persulfenate structure as an intermediate in the catalytic cycle of CDO enzymes.

Optimized geometries starting from the last points of these geometry scans are included at the bottom of Figure 11. These QM(B3LYP/B1)/MM geometry optimizations were done without geometric constraints. In both the singlet and the triplet, the dioxygen bond weakens dramatically to well over 2 Å. In the triplet spin state the dioxygen bond lengthens to 2.417 Å, so that this species is actually a sulfoxide with a nearby oxygen atom rather than the expected persulfenate structure. The proximal oxygen atom O_p is still held in position by a donating hydrogen bond from the phenol group of Tyr_{157}. The Fe−S distance of 2.580 Å and the S−O distance of 1.792 Å (Figure 11) indicate structural similarities with ^{3}**C** (Figure 9). In the singlet spin state, these distances are similar (r_{FeS} = 2.421 Å and r_{SO} = 1.821 Å), but the dioxygen distance is shorter (2.295 Å). In addition, the distal oxygen atom has abstracted a proton from Tyr_{157} to give an OH^- anion nearby a sulfoxide group. At the same time, the donating hydrogen bond from His_{155} is shifted from the phenolate oxygen atom in the triplet spin-state product to the OH^- group in the singlet spin state. It appears, therefore, that the singlet persulfenate structure is not a stable moiety and will abstract a proton readily from a nearby proton source.

To ascertain that there is no alternative persulfenate structure with an intact dioxygen bond, we manually created suitable starting geometries of a persulfenate bound complex, ^{1,3,5}**E**, which however collapsed upon unconstrained full optimization to structures similar to those found after a full geometry optimization of the last point of the geometry scans (see data given at the bottom right of Figure 11). The persulfenate-type structures ^{1,3,5}**E** thus rearrange in a barrierless process to sulfoxides with a nearby oxygen atom. Hence, according to the QM/MM calculations, persulfenate species are not stable in the CDO enzyme active-site environment, and the proposed mechanism II is therefore not supported. It seems likely the experimentally found "persulfenate" structure actually refers to a protonated species.

D. Electronic Characterization of Mechanism I. To summarize the QM/MM reaction mechanism of cysteine dioxygenation by CDO enzymes, we now address the changes in electronic structure during the reaction. The mechanism that emerges from the QM/MM calculations is given in Scheme 3, which specifies under each species the orbital occupation of the dominant electronic configuration. The reaction starts with a spin-state crossing from the singlet spin state to the quintet spin state with an electron transfer from π^*_{xz} to $\sigma^*_{z^2}$. This happens during attack of the distal oxygen atom on the sulfur atom of the substrate to form a dioxygen bridged structure **B**. On the quintet spin state this ring closure involves a homolytic S−O bond formation where the radical on the distal oxygen atom pairs up with one of the electrons from a lone-pair on sulfur, while the other electron from the lone-pair is transferred to the $\sigma^*_{x^2-y^2}$ orbital, hence ^{5}**B** has orbital occupation $\pi^*_{xy}{}^2\ \pi^*_{xz}{}^1\ \pi^*_{yz}{}^1\ \sigma^*_{z^2}{}^1\ \sigma^*_{x^2-y^2}{}^1$. Indeed, the conversion of ^{1}**A** to ^{5}**B** leads to an elongation of the Fe−S bond from 2.314 to 2.953 Å indicative of occupation of the $\sigma^*_{z^2}$ orbital with an extra electron (from ^{1}**A** to ^{5}**A**) and transfer of an electron from π^*_{OO} to $\sigma^*_{x^2-y^2}$ (from ^{5}**A** to ^{5}**B**). Accordingly, the radical character on the sulfur atom is reduced and the spin density of the cysteinate group changes from ρ_{Cys} = −0.44 in ^{5}**A** to ρ_{Cys} = −0.30 in ^{5}**TS**$_A$ to ρ_{Cys} = 0.09 in ^{5}**B** (B3LYP/B2W), whereas the spin density on the dioxygen group drops from ρ_{OO} = 0.51 in ^{5}**A** to ρ_{OO} = 0.11 in ^{5}**B**.

Dioxygen bond breaking in ^{5}**B** gives an iron(IV)-oxo complex with sulfoxide in the triplet spin state (^{3}**C**) with electronic configuration $\pi^*_{xy}{}^2\ \pi^*_{xz}{}^1\ \pi^*_{yz}{}^1$. By contrast, on the quintet spin-state surface ^{5}**C** is an iron(III)-oxo complex with a sulfoxide radical with orbital occupation $\pi^*_{xy}{}^1\ \pi^*_{xz}{}^1\ \pi^*_{yz}{}^1\ \sigma^*_{z^2}{}^1\ \sigma^*_{x^2-y^2}{}^1\ \pi^*_{SO}{}^1$. In the triplet manifold, ^{3}**C** carries considerable spin density on the sulfoxide moiety, ρ_{SO} = −0.51 (B3LYP/B2W). Rotation of the sulfoxide group gives pure iron(IV)-oxo sulfoxide complexes ^{3}**C**′ and ^{5}**C**′ with electronic configuration $\pi^*_{xy}{}^2\ \pi^*_{xz}{}^1\ \pi^*_{yz}{}^1$ and $\pi^*_{xy}{}^1\ \pi^*_{xz}{}^1\ \pi^*_{yz}{}^1\ \sigma^*_{x^2-y^2}{}^1$, respectively. In the final step of the mechanism, the oxygen atom is transferred to the sulfoxide, and two electrons are relayed from the sulfoxide to the metal, which is reduced to the iron(II) oxidation state with orbital occupation $\pi^*_{xy}{}^2\ \pi^*_{xz}{}^2\ \pi^*_{yz}{}^1\ \sigma^*_{z^2}{}^1$ and $\pi^*_{xy}{}^2\ \pi^*_{xz}{}^1\ \pi^*_{yz}{}^1\ \sigma^*_{z^2}{}^1\ \sigma^*_{x^2-y^2}{}^1$, respectively, for ^{3}**D** and ^{5}**D**.

In summary, the QM/MM calculations thus predict multistate reactivity patterns, with close-lying singlet, triplet, and quintet spin states participating in the reaction mechanism. The exact nature of the reaction mechanism will depend on the efficiency of spin-state crossings between these spin-state surfaces. If these crossings are facile such that the system can always access the lowest energy surface, the reaction will proceed along the sequence ^{1}**A**, ^{5}**TS**$_A$, ^{5}**B**, ^{5}**TS**$_B$, ^{3}**C**, ^{5}**TS**$_C$, ^{3}**C**′, and ^{5}**TS**$_D$ to give ^{5}**D**. In this mechanism the rate-determining step is the spin crossing from singlet to quintet around **TS**$_A$. If we assume that the initial singlet−quintet spin crossing is spin-forbidden such that the quintet state is not accessible, we arrive at an alternative mechanism where the ferric-dioxygen complex (^{1}**A**) reacts on the singlet spin-state surface to form ^{1}**B**, followed by a surface crossing to ^{3}**B**. The reaction then continues on the triplet spin-state surface via ^{3}**TS**$_B$, ^{3}**C**, ^{3}**TS**$_C$ and ^{3}**C**′ before a spin-state crossing to the quintet spin state gives ^{5}**D** products. In this alternative mechanism, the first step is again rate-determining (^{1}**TS**$_A$, 14.1 kcal mol^{-1}), although the subsequent transition state ^{3}**TS**$_C$ is only 0.8 kcal mol^{-1} lower in energy (B3LYP/B2W). In

dx.doi.org/10.1021/ja107514f |J. Am. Chem. Soc. 2011, 133, 3869–3882

both cases, mechanism I involves a rate-determining spin-state crossing during the conversion from **A** to **B**.

IV. CONCLUSIONS

Quantum mechanics/molecular mechanics calculations on cysteine activation by CDO enzymes are reported. We have considered two mechanisms starting from the dioxygen bound intermediate, namely, attack of the proximal or distal oxygen atoms of O_2 on the sulfur of cysteinate. In agreement with earlier DFT modeling of active-site structures, the QM/MM calculations favor mechanism I with an initial singlet−quintet crossing and subsequent transformations on the quintet surface that involve the transfer of the distal oxygen atom to yield a sulfoxide bound to an iron(IV)-oxo species followed by the formation of cysteine sulfinic acid bound to an iron(III) group. Calculations on mechanism II have identified only high-energy pathways that will not be able to compete with mechanism I.

■ ASSOCIATED CONTENT

Supporting Information. Ninety-four tables with group spin densities, charges, and relative energies of all complexes described in this work; eight figures with geometry scans and MD simulations; refs 32, 47, and 52 in full. This material is available free of charge via the Internet at http://pubs.acs.org.

■ AUTHOR INFORMATION

Corresponding Author
dkclcre@yahoo.com; sam.devisser@manchester.ac.uk

■ ACKNOWLEDGMENT

D.K. holds a Ramanujan Fellowship from the Department of Science and Technology (DST), New Delhi (India), and acknowledges its financial support (Research Grants SR/S2/RJN-11/2008 and SR/S1/PC-58/2009).

■ REFERENCES

(1) (a) Solomon, E. I.; Brunold, T. C.; Davis, M. I.; Kemsley, J. N.; Lee, S.-K.; Lehnert, N.; Neese, F.; Skulan, A. J.; Yang, Y.-S.; Zhou, J. *Chem. Rev.* **2000**, *100*, 235–349. (b) Bugg, T. D. H. *Curr. Opin. Chem. Biol.* **2001**, *5*, 550–555. (c) Costas, M.; Mehn, M. P.; Jensen, M. P.; Que, L., Jr. *Chem. Rev.* **2004**, *104*, 939–986. (d) Bruijnincx, P. C. A.; van Koten, G.; Klein Gebbink, R. J. M. *Chem. Soc. Rev.* **2008**, *37*, 2716–2744. (e) Bugg, T. D. H.; Ramaswamy, S. *Curr. Opin. Chem. Biol.* **2008**, *12*, 134–140.

(2) (a) Krebs, C.; Fujimori, D. G.; Walsh, C. T.; Bollinger, J. M., Jr. *Acc. Chem. Res.* **2007**, *40*, 484–492. (b) Schofield, C. J.; Zhang, Z. *Curr. Opin. Chem. Biol.* **1999**, *9*, 722–731. (c) Bugg, T. D. H. *Tetrahedron* **2003**, *59*, 7075–7101.

(3) (a) Trewick, S. C.; Henshaw, T. F.; Hausinger, R. P.; Lindahl, T.; Sedgwick, B. *Nature* **2002**, *419*, 174–178. (b) Falnes, P. Ø.; Johansen, R. F.; Seeberg, E. *Nature* **2002**, *419*, 178–182. (c) Duncan, T.; Trewick, S. C.; Koivisto, P.; Bates, P. A.; Lindahl, T.; Sedgwick, B. *Proc. Natl. Acad. Sci. U.S.A.* **2002**, *99*, 16660–16665. (d) Aas, P. A.; Otterlei, M.; Falnes, P. Ø.; Vågbø, C. B.; Skorpen, F.; Akbari, M.; Sundheim, O.; Bjørås, M.; Slupphaug, G.; Seeberg, E.; Krokan, H. E. *Nature* **2003**, *421*, 859–863. (e) Mishina, Y.; Duguid, E. M.; He, C. *Chem. Rev.* **2006**, *106*, 215–232.

(4) Chowdhury, R.; Hardy, A.; Schofield, C. J. *Chem. Soc. Rev.* **2008**, *37*, 1308–1319.

(5) Que, L., Jr. *Nat. Struct. Biol.* **2000**, *7*, 182–184.

(6) (a) Ryle, M. J.; Hausinger, R. P. *Curr. Opin. Chem. Biol.* **2002**, *6*, 193–201. (b) O'Brien, J. R.; Schuller, D. J.; Yang, V. S.; Dillard, B. D.; Lanzilotta, W. N. *Biochemistry* **2003**, *42*, 5547–5554. (c) Bollinger, J. M., Jr.; Price, J. C.; Hoffart, L. M.; Barr, E. W.; Krebs, C. *Eur. J. Inorg. Chem.* **2005**, 4245–4254. (d) Abu-Omar, M. M.; Loaiza, A.; Hontzeas, N. *Chem. Rev.* **2005**, *105*, 2227–2252.

(7) (a) Sono, M.; Roach, M. P.; Coulter, E. D.; Dawson, J. H. *Chem. Rev.* **1996**, *96*, 2841–2888.(b) *The Porphyrin Handbook*; Kadish, K. M., Smith, K. M., Guilard, R., Eds.; Academic Press: San Diego, CA, 2000. (c) Groves, J. T. *Proc. Natl. Acad. Sci. U.S.A.* **2003**, *100*, 3569–3574. (d) Guengerich, F. P. *Chem. Res. Toxicol.* **2001**, *14*, 611–650.(e) *Cytochrome P450: Structure, Mechanism and Biochemistry*, 3rd ed.; Ortiz de Montellano, P. R., Ed.; Kluwer Academic/Plenum Publishers: New York, 2004. (f) Munro, A. W.; Girvan, H. M.; McLean, K. J. *Nat. Prod. Rep.* **2007**, *24*, 585–609. (g) Nam, W. *Acc. Chem. Res.* **2007**, *40*, 522–531.

(8) (a) Proshlyakov, D. A.; Henshaw, T. F.; Monterosso, G. R.; Ryle, M. J.; Hausinger, R. P. *J. Am. Chem. Soc.* **2004**, *126*, 1022–1023. (b) Riggs−Gelasco, P. J.; Price, J. C.; Guyer, R. B.; Brehm, J. H.; Barr, E. W.; Bollinger, J. M., Jr.; Krebs, C. *J. Am. Chem. Soc.* **2004**, *126*, 8108–8109. (c) Hoffart, L. M.; Barr, E. W.; Guyer, R. B.; Bollinger, J. M., Jr.; Krebs, C. *Proc. Natl. Acad. Sci. U.S.A.* **2006**, *103*, 14738–14743.

(9) Straganz, G. D.; Nidetzky, B. *ChemBioChem.* **2006**, *7*, 1536–1548.

(10) Straganz, G. D.; Nidetzky, B. *J. Am. Chem. Soc.* **2005**, *127*, 12306–12314.

(11) Gopal, B.; Madan, L. L.; Betz, S. F.; Kossiakoff, A. A. *Biochemistry* **2005**, *44*, 193–201.

(12) (a) Stipanuk, M. H. *Annu. Rev. Nutr.* **2004**, *24*, 539–577. (b) Joseph, C. A.; Maroney, M. J. *Chem. Commun.* **2007**, 3338–3349.

(13) Perry, T. L.; Norman, M. G.; Yong, V. W.; Whiting, S.; Crichton, J. U.; Hansen, S.; Kish, S. *J. Ann. Neurol.* **1985**, *18*, 482–489.

(14) Heafield, M. T.; Fearn, S.; Steventon, G. B.; Waring, R. H.; Williams, A. C.; Sturman, S. G. *Neurosci. Lett.* **1990**, *110*, 216–220.

(15) (a) McCoy, J. G.; Bailey, L. J.; Bitto, E.; Bingman, C. A.; Aceti, D. J.; Fox, B. G.; Phillips, G. N., Jr. *Proc. Natl. Acad. Sci. U.S.A.* **2006**, *103*, 3084–3089. (b) Simmons, C. R.; Liu, Q.; Huang, Q.; Hao, Q.; Begley, T. P.; Karplus, P. A.; Stipanuk, M. H. *J. Biol. Chem.* **2006**, *281*, 18723–18733. (c) Pierce, B. D.; Gardner, J. D.; Bailey, L. J.; Brunold, T. C.; Fox, B. G. *Biochemistry* **2007**, *46*, 8569–8578. (d) Gardner, J. D.; Pierce, B. S.; Fox, B. G.; Brunold, T. C. *Biochemistry* **2010**, *49*, 6033–6041.

(16) (a) Aluri, S.; de Visser, S. P. *J. Am. Chem. Soc.* **2007**, *129*, 14846–14847. (b) de Visser, S. P.; Straganz, G. D. *J. Phys. Chem. A* **2009**, *113*, 1835–1846.

(17) (a) Werner, M.; Birner, G.; Dekant, W. *Chem. Res. Toxicol.* **1996**, *9*, 41–49. (b) Madan, A.; Parkinson, A.; Faiman, M. D. *Drug Metab. Dispos.* **1995**, *23*, 1153–1158. (c) Goto, Y.; Matsui, T.; Ozaki, S.-i.; Watanabe, Y.; Fukuzumi, S. *J. Am. Chem. Soc.* **1999**, *121*, 9497–9502. (d) Kato, S.; Yang, H.-J.; Ueno, T.; Ozaki, S.-i.; Phillips, G. N., Jr.; Fukuzumi, S.; Watanabe, Y. *J. Am. Chem. Soc.* **2002**, *124*, 8506–8507. (e) Usmani, K. A.; Karoly, E. D.; Hodgson, E.; Rose, R. L. *Drug Metab. Dispos.* **2004**, *32*, 333–339. (f) Furnes, B.; Schlenk, D. *Drug Metab. Dispos.* **2005**, *33*, 214–218.

(18) Kovacs, J. A. *Chem. Rev.* **2004**, *104*, 825–848.

(19) Heinrich, L.; Mary-Verla, A.; Li, Y.; Vaissermann, J.; Chottard, J.-C. *Eur. J. Inorg. Chem.* **2001**, 2203–2206.

(20) For examples on biomimetic nitrile hydratases, see: (a) Farmer, P. J.; Solouki, T.; Mills, D. K.; Soma, T.; Russell, D. H.; Reibenspies, J. H.; Darensbourg, M. Y. *J. Am. Chem. Soc.* **1992**, *114*, 4601–4605. (b) Farmer, P. J.; Verpeaux, J.-N.; Amatore, C.; Darensbourg, M. Y.; Musie, G. *J. Am. Chem. Soc.* **1994**, *116*, 9355–9356. (c) Grapperhaus, C. A.; Darensbourg, M. Y. *Acc. Chem. Res.* **1998**, *31*, 451–459. (d) Harrop, T. C.; Mascharak, P. K. *Acc. Chem. Res.* **2004**, *37*, 253–260. (e) Chohan, B. S.; Shoner, S. C.; Kovacs, J. A.; Maroney, M. J. *Inorg. Chem.* **2004**, *43*, 7726–7734. (f) Li, B.; Liu, T.; Singleton, M. L.; Darensbourg, M. Y. *Inorg. Chem.* **2009**, *48*, 8393–8403. (g) Rose, M. J.; Betterley, N. M.; Mascharak, P. K. *J. Am. Chem. Soc.* **2009**, *131*, 8340–8341. (h) McDonald, A. R.; Bukowski, M. R.; Farquhar, E. R.; Jackson, T. A.; Koehntop, K. D.; Seo, M. S.; De Hont, R. F.; Stubna, A.; Halfen, J. A.;

Münck, E.; Nam, W.; Que, L., Jr. *J. Am. Chem. Soc.* **2010**, *132*, 17118–17129.
(21) Jiang, Y.; Widger, L. R.; Kasper, G. D.; Siegler, M. A.; Goldberg, D. P. *J. Am. Chem. Soc.* **2010**, *132*, 12214–12215.
(22) Ye, S.; Wu, X.; Wei, L.; Tang, D.; Sun, P.; Bartlam, M.; Rao, Z. *J. Biol. Chem.* **2007**, *282*, 3391–3402.
(23) Dominy, J. E., Jr.; Hwang, J.; Guo, S.; Hirschberger, L. L.; Zhang, S.; Stipanuk, M. H. *J. Biol. Chem.* **2008**, *283*, 12188–12201.
(24) (a) de Visser, S. P. *Angew. Chem., Int. Ed.* **2006**, *45*, 1790–1793. (b) de Visser, S. P. *J. Am. Chem. Soc.* **2006**, *128*, 9813–9824. (c) de Visser, S. P. *Chem. Commun.* **2007**, 171–173. (d) de Visser, S. P. *Coord. Chem. Rev.* **2009**, *253*, 754–768.
(25) Simmons, C. R.; Krishnamoorthy, K.; Granett, S. L.; Schuller, D. J.; Dominy, J. E., Jr.; Begley, T. P.; Stipanuk, M. H.; Karplus, P. A. *Biochemistry* **2008**, *47*, 11390–11392.
(26) For a recent review on QM/MM methods, see: Senn, H. M.; Thiel, W. *Angew. Chem., Int. Ed.* **2009**, *48*, 1198–1229.
(27) (a) Schöneboom, J. C.; Lin, H.; Reuter, N.; Thiel, W.; Cohen, S.; Ogliaro, F.; Shaik, S. *J. Am. Chem. Soc.* **2002**, *124*, 8142–8151. (b) Schöneboom, J. C.; Cohen, S.; Lin, H.; Shaik, S.; Thiel, W. *J. Am. Chem. Soc.* **2004**, *126*, 4017–4034. (c) Bathelt, C. M.; Zurek, J.; Mulholland, A. J.; Harvey, J. N. *J. Am. Chem. Soc.* **2005**, *127*, 12900–12908.
(28) Lundberg, M.; Morokuma, K. *J. Phys. Chem. B* **2007**, *111*, 9380–9389.
(29) (a) Cohen, S.; Kumar, D.; Shaik, S. *J. Am. Chem. Soc.* **2006**, *128*, 2649–2653. (b) Altarsha, M.; Benighaus, T.; Kumar, D.; Thiel, W. *J. Am. Chem. Soc.* **2009**, *131*, 4755–4763. (c) Altarsha, M.; Benighaus, T.; Kumar, D.; Thiel, W. *J. Biol. Inorg. Chem.* **2010**, *15*, 361–372.
(30) Godfrey, E.; Porro, C. S.; de Visser, S. P. *J. Phys. Chem. A* **2008**, *112*, 2464–2468.
(31) (a) Schöneboom, J. C.; Thiel, W. *J. Phys. Chem. B* **2004**, *108*, 7468–7478. (b) Altun, A.; Thiel, W. *J. Phys. Chem. B* **2005**, *109*, 1268–1280.
(32) MacKerell, A. D.; et al. *J. Phys. Chem. B* **1998**, *102*, 3586–3616 (see the Supporting Information).
(33) Brooks, B. R.; Bruccoleri, R. E.; Olafson, B. D.; States, D. J.; Swaminathan, S.; Karplus, M. *J. Comput. Chem.* **1983**, *4*, 187–217.
(34) (a) Kumar, D.; de Visser, S. P.; Shaik, S. *Chem.—Eur. J.* **2005**, *11*, 2825–2835. (b) de Visser, S. P.; Oh, K.; Han, A.-R.; Nam, W. *Inorg. Chem.* **2007**, *46*, 4632–4641. (c) Shaik, S.; Kumar, D.; de Visser, S. P. *J. Am. Chem. Soc.* **2008**, *130*, 10128–10140. (d) de Visser, S. P. *J. Am. Chem. Soc.* **2010**, *132*, 1087–1097.
(35) (a) Kumar, D.; de Visser, S. P.; Shaik, S. *J. Am. Chem. Soc.* **2003**, *125*, 13024–13025. (b) Kumar, D.; de Visser, S. P.; Sharma, P. K.; Cohen, S.; Shaik, S. *J. Am. Chem. Soc.* **2004**, *126*, 1907–1920. (c) de Visser, S. P. *Chem.—Eur. J.* **2006**, *12*, 8168–8177.
(36) (a) de Visser, S. P. *Chem.—Eur. J.* **2008**, *14*, 4533–4541. (b) de Visser, S. P.; Tahsini, L.; Nam, W. *Chem.—Eur. J.* **2009**, *15*, 5577–5587. (c) Porro, C. S.; Kumar, D.; de Visser, S. P. *Phys. Chem. Chem. Phys.* **2009**, *11*, 10219–10226.
(37) Becke, A. D. *J. Chem. Phys.* **1993**, *98*, 5648–5652.
(38) Lee, C.; Yang, W.; Parr, R. G. *Phys. Rev. B* **1988**, *37*, 785–789.
(39) (a) Hay, P. J.; Wadt, W. R. *J. Chem. Phys.* **1985**, *82*, 299–310. (b) Hehre, W. J.; Ditchfield, K.; Pople, J. A. *J. Chem. Phys.* **1972**, *56*, 2257–2261.
(40) (a) Wachters, A. J. H. *J. Chem. Phys.* **1970**, *52*, 1033–1036. (b) Hay, P. J. *J. Chem. Phys.* **1977**, *66*, 4377–4384. (c) Bauschlicher, C. W., Jr.; Langhoff, S. R.; Partridge, H.; Barnes, L. A. *J. Chem. Phys.* **1989**, *91*, 2399–2411. (d) Krishnan, R.; Binkley, J. S.; Seeger, R.; Pople, J. A. *J. Chem. Phys.* **1980**, *72*, 650–654.
(41) Weigend, F.; Häser, M.; Patzelt, H.; Ahlrichs, R. *Chem. Phys. Lett.* **1998**, *294*, 143–152.
(42) Becke, A. D. *Phys. Rev. A* **1988**, *38*, 3098–3100.
(43) Perdew, J. P. *Phys. Rev. B* **1986**, *33*, 8822–8824.
(44) Adamo, C.; Barone, V. *J. Chem. Phys.* **1999**, *110*, 6158–6169.
(45) (a) Handy, N. C.; Cohen, A. J. *Mol. Phys.* **2001**, *99*, 403–412. (b) Hoe, W.-M.; Cohen, A.; Handy, N. C. *Chem. Phys. Lett.* **2001**, *341*, 319–328.
(46) Perdew, J. P.; Burke, K.; Ernzerhof, M. *Phys. Rev. Lett.* **1996**, *77*, 3865–3868.
(47) Frisch, M. J. et al. *Gaussian 09*, revision A.02; Gaussian, Inc., Wallingford CT, 2009 (see the Supporting Information).
(48) Schwabe, T.; Grimme, S. *Phys. Chem. Chem. Phys.* **2007**, *9*, 3397–3406.
(49) Bakowies, D.; Thiel, W. *J. Phys. Chem.* **1996**, *100*, 10580–10594.
(50) Ahlrichs, R.; Bär, M.; Häser, M.; Horn, H.; Kölmel, C. *Chem. Phys. Lett.* **1989**, *162*, 165–169.
(51) Smith, W.; Forester, T. R. *J. Mol. Graphics* **1996**, *14*, 136–141.
(52) Sherwood, P.; et al. *J. Mol. Struct.* **2003**, *632*, 1–28 (see the Supporting Information).
(53) Billeter, S. R.; Turner, A. J.; Thiel, W. *Phys. Chem. Chem. Phys.* **2000**, *2*, 2177–2186.
(54) (a) Chottard, G.; Schappacher, M.; Ricard, L.; Weiss, R. *Inorg. Chem.* **1984**, *23*, 4557–4561. (b) Harris, D. L.; Loew, G. H. *J. Am. Chem. Soc.* **1998**, *120*, 8941–8948. (c) Shaik, S.; Kumar, D.; de Visser, S. P.; Altun, A.; Thiel, W. *Chem. Rev.* **2005**, *105*, 2279–2328.
(55) Dürr, K.; Jux, N.; Zahl, A.; van Eldik, R.; Ivanović-Burmazović, I. *Inorg. Chem.* **2010**, *49*, 11265–11260.
(56) (a) Harris, D. L.; Loew, G. H.; Waskell, L. *J. Am. Chem. Soc.* **1998**, *120*, 4308–4318. (b) Kumar, D.; Hirao, H.; de Visser, S. P.; Zheng, J.; Wang, D.; Thiel, W.; Shaik, S. *J. Phys. Chem. B* **2005**, *109*, 19946–19951. (c) Shaik, S.; Cohen, S.; Wang, Y.; Chen, H.; Kumar, D.; Thiel, W. *Chem. Rev.* **2010**, *110*, 949–1017.
(57) (a) Park, M. J.; Lee, J.; Suh, Y.; Kim, J.; Nam, W. *J. Am. Chem. Soc.* **2006**, *128*, 2630–2634. (b) Emerson, J. P.; Farquhar, E. R.; Que, L., Jr. *Angew. Chem., Int. Ed.* **2007**, *46*, 8553–8556. (c) Solomon, E. I.; Wong, S. D.; Liu, L. V.; Decker, A.; Chow, M. S. *Curr. Opin. Chem. Biol.* **2009**, *13*, 99–113.
(58) (a) Ogliaro, F.; Cohen, S.; de Visser, S. P.; Shaik, S. *J. Am. Chem. Soc.* **2000**, *122*, 12892–12893. (b) Kumar, D.; Karamzadeh, B.; Sastry, G. N.; de Visser, S. P. *J. Am. Chem. Soc.* **2010**, *132*, 7656–7667.
(59) Ghosh, A.; Taylor, P. R. *Curr. Opin. Chem. Biol.* **2003**, *7*, 113–124.
(60) (a) Siegbahn, P. E. M.; Blomberg, M. R. A.; Chen, S.-L. *J. Chem. Theor. Comput.* **2010**, *6*, 2040–2044. (b) Lonsdale, R.; Harvey, J. N.; Mulholland, A. J. *J. Phys. Chem. Lett.* **2010**, *1*, 3232–3237.
(61) (a) Shaik, S.; de Visser, S. P.; Ogliaro, F.; Schwarz, H.; Schröder, D. *Curr. Opin. Chem. Biol.* **2002**, *6*, 556–567. (b) Kumar, D.; Hirao, H.; Que, L., Jr.; Shaik, S. *J. Am. Chem. Soc.* **2005**, *127*, 8026–8027.
(62) (a) Rohde, J.-U.; In, J.-H.; Lim, M. H.; Brennessel, W. W.; Bukowski, M. R.; Stubna, A.; Münck, E.; Nam, W.; Que, L., Jr. *Science* **2003**, *299*, 1037–1039. (b) Martinho, M.; Banse, F.; Bartoli, J.-F.; Mattioli, T. A.; Battioni, P.; Horner, O.; Bourcier, S.; Girerd, J.-J. *Inorg. Chem.* **2005**, *44*, 9592–9596. (c) Sastri, C. V.; Seo, M. S.; Park, M. J.; Kim, K. M.; Nam, W. *Chem. Commun.* **2005**, 1405–1407. (d) De Oliveira, F. T.; Chanda, A.; Banerjee, D.; Shan, X.; Mondal, S.; Que, L., Jr.; Bominaar, E. L.; Münck, E.; Collins, T. J. *Science* **2007**, *315*, 835–838. (e) Jackson, T. A.; Rohde, J.-U.; Seo, M. S.; Sastri, C. V.; DeHont, R.; Stubna, A.; Ohta, T.; Kitagawa, T.; Münck, E.; Nam, W.; Que, L., Jr. *J. Am. Chem. Soc.* **2008**, *130*, 12394–12407.
(63) (a) de Visser, S. P. *J. Am. Chem. Soc.* **2006**, *128*, 15809–15818. (b) Latifi, R.; Bagherzadeh, M.; de Visser, S. P. *Chem.—Eur. J.* **2009**, *15*, 6651–6662.
(64) (a) Hirao, H.; Kumar, D.; Que, L., Jr.; Shaik, S. *J. Am. Chem. Soc.* **2006**, *128*, 8590–8606. (b) Hirao, H.; Que, L., Jr.; Nam, W.; Shaik, S. *Chem.—Eur. J.* **2008**, *14*, 1740–1756.

CHEMISTRY
A EUROPEAN JOURNAL

DOI: 10.1002/chem.201003187

Effect of the Axial Ligand on Substrate Sulfoxidation Mediated by Iron(IV)–Oxo Porphyrin Cation Radical Oxidants

Devesh Kumar,*[a] G. Narahari Sastry,[a] and Sam P. de Visser*[b]

Abstract: Cytochromes P450 catalyze a range of different oxygen-transfer processes including aliphatic and aromatic hydroxylation, epoxidation, and sulfoxidation reactions. Herein, we have investigated substrate sulfoxidation mediated by models of P450 enzymes as well as by biomimetic oxidants using density functional-theory methods and we have rationalized the sulfoxidation reaction barriers and rate constants. We carried out two sets of calculations: first, we calculated the sulfoxidation by an iron(IV)–oxo porphyrin cation radical oxidant [Fe^{IV}=O($Por^{+\bullet}$)SH] that mimics the active site of cytochrome P450 enzymes with a range of different substrates, and second, we studied one substrate (dimethyl sulfide) with a selection of different iron(IV)–oxo porphyrin cation radical oxidants [Fe^{IV}=O($Por^{+\bullet}$)L] with varying axial ligands L. The study presented herein shows that the barrier height for substrate sulfoxidation correlates linearly with the ionization potential of the substrate, thus reflecting the electron-transfer processes in the rate-determining step of the reaction. Furthermore, the axial ligand of the oxidant influences the pK_a value of the iron(IV)–oxo group, and, as a consequence, the bond dissociation energy (BDE_{OH}) value correlates with the barrier height for the reverse sulfoxidation reaction. These studies have generalized substrate-sulfoxidation reactions and have shown how they fundamentally compare with substrate hydroxylation and epoxidation reactions.

Keywords: axial ligands · cytochrome P450 · dioxygen activation · heme proteins · enzyme models

Introduction

Iron(IV)–oxo oxidants are powerful oxygen-transfer catalysts and have been identified as the active species of several enzymes including the cytochromes P450.[1] They are involved in important biochemical transformations ranging from biodegradation of toxic compounds in the liver to the biosynthesis of hormones in the body. Furthermore, they catalyze vital drug-metabolism reactions and, as such, the understanding of their mechanism and function is of great interest to the biotechnology field and the pharmaceutical industry.[1e] These enzymes are highly versatile and catalyze oxygen-transfer reactions (monoxygenation), ranging from aliphatic and aromatic hydroxylation to epoxidation and sulfoxidation.

Sulfoxidation reactions are catalyzed by many P450 isozymes.[2] For instance, the metabolism of the pesticide aldicarb and the biodegradation of neuroleptic drugs in the liver are associated with substrate sulfoxidation by P450 isozymes.[3] Detailed studies of the reaction mechanism of P450 enzymes and biomimetic complexes for substrate-sulfoxidation reactions have been reported[4] and give evidence of a concerted reaction mechanism. These studies are supported by density functional theory (DFT) and quantum mechanics/molecular mechanics (QM/MM) studies that highlight the iron(IV)–oxo heme cation radical (Compound I; Cpd I in Figure 1) as the active oxidant.[5] Furthermore, the experimental studies of Watanabe et al. implicated a relationship between the rate constant of substrate sulfoxidation by P450 enzymes and the ionization potential (IE) of the substrate.[6] Indeed, recent computational-modeling studies explained this correlation with electron-transfer mechanisms and a valence bond (VB) curve-crossing model.[7]

However, the first enzymatic iron(IV)–oxo heme cation radical species that has been characterized spectroscopically by using a combination of X-ray crystallographic studies,[8] was not that of cytochrome P450, but of the related enzyme horseradish peroxidase (HRP). The fundamental difference in the structure of the active site of HRP and P450 enzymes is the nature of the axial ligand (*trans* to the oxo group in Cpd I), which is a histidine ligand in HRP (His_{170} in Figure 2), but a cysteinate ligand in the P450s. Experimental studies identified a strong axial-ligand effect on the reactivity of heme enzymes,[9] in which a cysteinate ligand causes a push effect, whereas a histidine axial ligand withdraws elec-

[a] Dr. D. Kumar, Dr. G. N. Sastry
Molecular Modelling Group
Indian Institute of Chemical Technology
Hyderabad 500-607 (India)
Fax: (+91) 40-27193016
E-mail: dkclcre@yahoo.com

[b] Dr. S. P. de Visser
The Manchester Interdisciplinary Biocentre
and the School of Chemical Engineering and Analytical Science
The University of Manchester, 131 Princess Street
Manchester M1 7DN (UK)
Fax: (+44) 161-3065201
E-mail: sam.devisser@manchester.ac.uk

Supporting information for this article is available on the WWW under http://dx.doi.org/10.1002/chem.201003187.

WILEY ONLINE LIBRARY
© 2011 Wiley-VCH Verlag GmbH & Co. KGaA, Weinheim

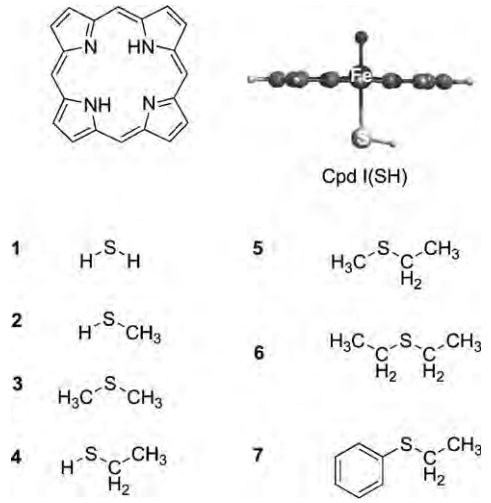

Figure 1. Oxidant and substrates used in this work.

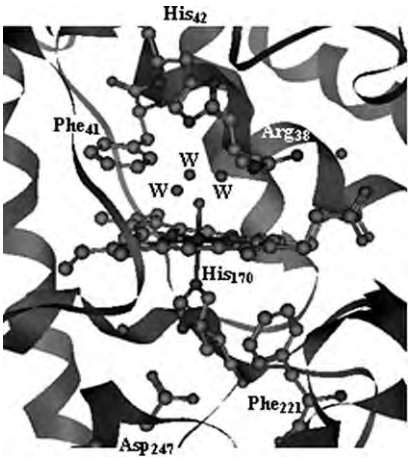

Figure 2. Structure of the active site of HRP (taken from the 1HCH pdb file). Amino acids labeled according to the pdb file, W = water molecules.

trons, thus resulting in a pull effect. As a consequence, this difference in push/pull effect of the axial ligand changes the central properties of the heme unit and results in functional differences. Further biomimetic studies by Gross and Nimri using iron(IV)–oxo tetramesitylporphyrin (TMP) cation radical oxidants with variable axial ligands showed a pronounced axial ligand effect on styrene epoxidation. These studies showed that electron-donating ligands lead to faster oxygen-transfer reactions, that is, higher rate constants, than systems with weaker electron-donating ligands.[10] More recent studies of Nam and co-workers[11] established a correlation between the reduction potential of the oxidant with the rate constant of hydrogen-atom abstraction. Additional computational studies[11b] showed that electron-donating axial ligands lower the triplet–quintet energy gap of the nonheme iron(IV)–oxo species, which thereby lowers the hydrogen-abstraction barriers of the substrates.

Figure 2 displays the structure of the active site of HRP as taken from the 1HCH protein databank (pdb) file.[12] The heme unit is linked to the protein through an interaction with a histidine axial ligand (His_{170}), which is involved in hydrogen-bonding interactions with a nearby carboxylic acid group of Asp_{247}. Also located on the axial site is an aromatic residue (Phe_{221}) that has been proposed to participate in electron-transfer processes from the reductase domain to the heme unit.[13] The amino acid residues Arg_{38} and His_{42} on the distal side are involved in proton-relay mechanisms in the catalytic cycle that generates Cpd I.

Electron nuclear double resonance (ENDOR) investigations on Cpd I of HRP revealed that the active species have an intriguing electronic configuration with three unpaired electrons: two in π^*_{FeO} orbitals located on the FeO group coupled to a heme-based cation radical in an orbital with a_{2u} symmetry.[14] This triplet pair of electrons on the Fe=O group is either ferromagnetically coupled to the heme radical into an overall quartet spin state or antiferromagnetically coupled into an overall doublet spin state. The nature of the electronic ground state, however, was shown to be sensitive to external conditions, whereby some experiments implicated a doublet-spin ground state, whereas others found a high-spin ground state.[15] Indeed, additional computational studies predicted the two spin states to be close in energy, that is, within about 1 kcal mol^{-1}.[16] Further computational studies showed that the degeneracy of the oxidant states also has consequences for substrate-activation mechanisms, which tend to lead to two-state reactivity (TSR) patterns with different rate constants and reaction mechanisms on both spin-state surfaces.[17] This TSR profile can result in the masquerade of kinetic isotope effects and the seemingly observance of multiple oxidants in the reaction mixture.

So far, most of the experimental and computational studies focused on the effect of the axial ligand on substrate hydroxylation and epoxidation by iron(IV)–oxo oxidants.[10,11,18,19] However, few studies have been reported on the effect of the axial ligand on substrate-sulfoxidation mechanisms by Cpd I species. Shaik and et al.[7] have recently reported substrate sulfoxidation by a Cpd I model of P450 using four *para*-substituted thioanisole compounds. The barrier heights of substrate sulfoxidation were found to be correlated to the IE of the substrate. Those studies, however, used only one oxidant and multiple substrates, whereas in this work we generalize the reactivity trends by investigating 1) one oxidant with multiple substrates and 2) one substrate with multiple oxidants. Thus, the primary focus of this paper is to investigate the fundamental properties that influence the barrier height of substrate-sulfoxidation reactions with a range of different oxidants.

Results and Discussion

We started our investigation with a detailed study of the reaction barriers of substrate sulfoxidation by Compound I of P450, which was modeled using a porphyrin unit without side chains and a thiolate axial ligand, [Fe^{IV}=O($Por^{+\bullet}$)SH] or designated Cpd I(SH). In contrast to the reported studies of Shaik et al.[7] we investigated a range of mainly aliphatic sul-

 © 2011 Wiley-VCH Verlag GmbH & Co. KGaA, Weinheim

fides that differ in the length of the alkyl chain and range from a hydrogen atom to an ethyl group. Our selected range of substrates covers a much larger spread in ionization potentials, although not all substrates are natural sulfoxidation substrates by the P450s. Nevertheless, this series of substrates enables us to determine the rate constants and the barrier heights of a broad range of sulfoxidation reactions. Figure 1 shows the oxidant and the sulfide reactants that were used in this investigation, namely the reaction of Cpd I(SH) with hydrogen sulfide (**1**), methylmercaptane (**2**), dimethyl sulfide (**3**), ethylmercaptane (**4**), ethyl methyl sulfide (**5**), diethyl sulfide (**6**), and ethyl phenyl sulfide (**7**).

Cpd I(SH) has a degenerate doublet and quartet spin state as the ground state with the same orbital occupation: $(\pi^*_{xz})^1(\pi^*_{yz})^1(a_{2u})^1$. The former two orbitals are orthogonal π^*_{FeO} orbitals for the antibonding interactions of the metal $3d_{xz}/3d_{yz}$ atomic orbitals with $2p_x/2p_y$ orbitals on the oxo group. The a_{2u} orbital is a nonbonding orbital on the heme that is singly occupied, so that the reactant formally has an electronic configuration: $[Fe^{IV}{=}O(Por^{+\bullet})SH]$. We find the doublet and quartet spin states to be within 0.1 kcal mol^{-1}, which is in agreement with previous studies.[20] This degeneracy of the doublet and quartet spin state surfaces leads to two-state reactivity patterns with barriers and mechanisms on both spin state surfaces.[21] Often in aliphatic hydroxylation and epoxidation reactions the doublet and quartet barrier heights are close in energy,[22–24] but in the case of aromatic hydroxylation and sulfoxidation, significant differences in barrier heights, and consequently rate constants, were found between the two spin-state surfaces, thereby reducing the mechanism from two-state reactivity to single-state reactivity.[5,25]

Figure 3 shows an example of a typical potential energy surface for a sulfoxidation reaction, which was observed for the reaction of Cpd I(SH) with substrates **1**–**7**, in which we give the mechanism for ethyl methyl sulfide (**5**) sulfoxidation as an example. The reaction mechanisms obtained using the other substrates are similar although the energies are different. The inset of Figure 3 gives the barrier heights of substrate sulfoxidation with the other substrates. Thus, the reaction is concerted with a single barrier ($\mathbf{TS}_{SO}$) that separates the reactants from sulfoxide products (**P**). In the following, we will give the substrate in parenthesis behind these labels, for instance $^2\mathbf{TS}_{SO}(\mathbf{5})$ is the low-spin barrier for the sulfoxidation reaction of substrate **5** (ethyl methyl sulfide). The lowest lying barrier for sulfoxidation of substrate **5** is on the doublet spin state surface, which is 5.1 kcal mol^{-1} lower in energy than that found for the quartet spin state surface. This means that the reaction will proceed faster on the doublet spin state surface than on the quartet spin state surface. Consequently, the doublet spin state will dominate the reactivity, that is, a single-state reactivity on a doublet spin state surface will be expected. In a similar fashion, the other substrates (inset of Figure 3) also give $^2\mathbf{TS}_{SO}$ below $^4\mathbf{TS}_{SO}$ with an average doublet-quartet energy gap of (5.4 ± 1.2) kcal mol^{-1}. This spin-state ordering is in line with recent substrate-sulfoxidation studies by models of Cpd I of P450, which also gave a single-state reactivity mechanism on a dominant low spin state.[7]

The product complexes give the same spin-state ordering as the transition states with low spin below high spin. Previous studies on substrate hydroxylation and epoxidation mechanisms also gave doublet products below quartet-spin products.[23,24] The overall reaction is accomplished by a double-electron transfer from the substrate to the iron-porphyrin to give an iron(III)-porphyrin product complex with electronic configuration $(\pi^*_{xz})^2(\pi^*_{yz})^1(a_{2u})^2$ in $^2\mathbf{P}$ and $(\pi^*_{xz})^1(\pi^*_{yz})^1(\sigma^*_{z^2})^1(a_{2u})^2$ configuration in $^4\mathbf{P}$. Therefore, the double-electron transfer leads to the filling of the a_{2u} orbital with a second electron, whereas the other electron transfer occurs into the metal 3d system. Because the π^*_{xz} orbital is lower in energy than the $\sigma^*_{z^2}$ orbital, the doublet spin state is the lowest in energy for the product complexes. It was shown that the barrier height of substrate sulfoxidation correlates with the electron-transfer processes for the reaction,[7] hence substrate sulfoxidation should give a $^2\mathbf{TS}_{SO}$ below $^4\mathbf{TS}_{SO}$ barrier as indeed observed here. Interestingly, a recent quantum mechanics/molecular mechanics study on dimethyl sulfide sulfoxidation by Cpd I of two P450 isozymes ($P450_{cam}$ and $P450_{BM3}$) gave a quartet below doublet barrier,[5e] which im-

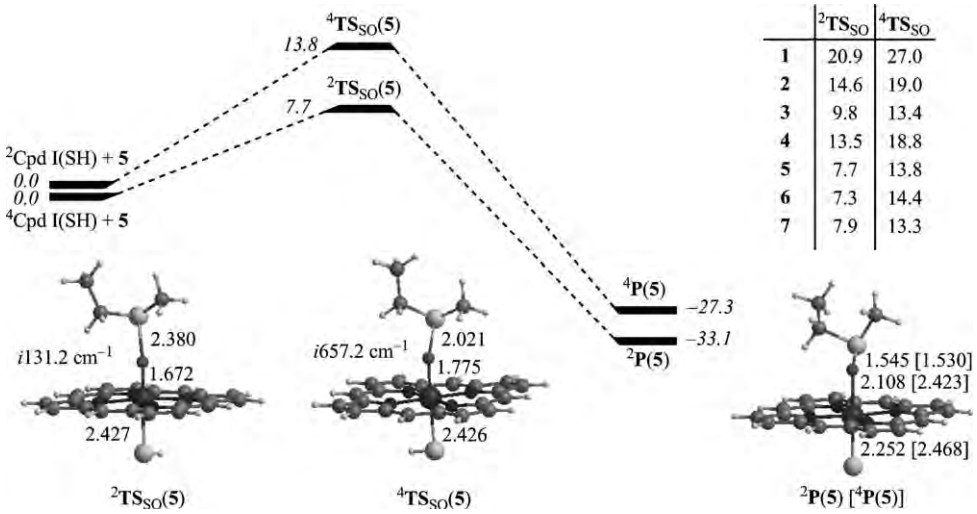

	$^2TS_{SO}$	$^4TS_{SO}$
1	20.9	27.0
2	14.6	19.0
3	9.8	13.4
4	13.5	18.8
5	7.7	13.8
6	7.3	14.4
7	7.9	13.3

Figure 3. Calculated potential-energy surface corresponding to the sulfoxidation of ethyl methyl sulfide (**5**) mediated by Cpd I(SH). All energies (kcal mol^{-1}) are relative to isolated reactants in the quartet spin state. Optimized geometries of $^{4,2}\mathbf{TS}_{SO}(\mathbf{5})$ and $^{4,2}\mathbf{P}(\mathbf{5})$ are also shown. Bond lengths are given in Ångstroms and the imaginary frequency in the transition state is in wave numbers. The table in the inset gives $^{4,2}\mathbf{TS}_{SO}$ barriers for the reaction of Cpd I(SH) with substrate **1**–**7** (kcal mol^{-1}).

© 2011 Wiley-VCH Verlag GmbH & Co. KGaA, Weinheim

plies that environmental perturbations, such as those in the substrate-binding pocket may influence the reactivity patterns and regioselectivity. This is particularly obvious from the differences in molecular geometry between ^{4}**TS**$_{SO}$ and ^{2}**TS**$_{SO}$ as can be seen in Figure 3. Thus, in most low-spin transition states in the gas phase the S–O bond is significantly longer than that found for the high-spin transition state, which may have consequences if the protein binding pocket was included in the model. In particular, inclusion of the protein binding pocket in the calculations as done in a QM/MM treatment may affect the relative energies of the low-spin and high-spin barriers because of their difference in interaction distance with nearby residues.

Optimized geometries of the doublet and quartet transition states of substrate **5** are shown in Figure 3, whereas the transition-state structures obtained using the other substrates are given in Figure 4. Figure 3 also displays the doublet and quartet product complexes, whereas the optimized geometries for the other complexes are summarized in the Supporting Information document. Generally, very little differences are observed among the various ^{2}**P** structures and similarly the ^{4}**P** structures are very much alike. Although we searched for correlations between bond distances and barrier height (Figure S12 in the Supporting Information), no obvious correlations were found. The best correlation coefficient ($R^2=0.78$) is found for the relationship between the low-spin barrier height and the O–S distance between oxidant and substrate. This trend implicates a low barrier for transition structures with long O–S distances and high barriers for transition structures with short O–S distances, which means that early transition states have the lowest barrier for the sulfoxidation reaction. The Fe–S distance in the transition states is very close for all structures with an average value of (2.432 ± 0.023) Å for ^{2}**TS**$_{SO}$ and (2.445 ± 0.015) Å for ^{4}**TS**$_{SO}$. The slightly longer distance obtained for the quartet spin state is due to electron transfer from the substrate into the $\sigma^*_{z^2}$ orbital that is antibonding along the Fe–S axis and therefore elongates the Fe–S bond. This effect is even more pronounced in the product complexes where the LS and HS Fe–S distances are separated by 0.216 Å. Furthermore, the Fe–O distances of the transition states are found in a narrow range with an average value of (1.700 ± 0.025) Å for ^{2}**TS**$_{SO}$ and (1.766 ± 0.033) Å for ^{4}**TS**$_{SO}$. Again, here the HS distance is slightly elongated with respect to the LS values owing to partial electron transfer from the substrate into the $\sigma^*_{z^2}$ orbital.

All transition states are characterized with a single imaginary frequency for the O–S stretch vibration. The ^{2}**TS**$_{SO}$ barriers have small imaginary frequencies ranging from *i*109.0 to *i*299.0 cm^{-1}, whereas the ^{4}**TS**$_{SO}$ barriers have much larger imaginary frequencies where values between *i*153.5–*i*771.9 cm^{-1} are found. These values imply that the shape of the potential-energy surface for substrate sulfoxidation on the doublet spin state surface is quite different from that found for the quartet spin state surface. Thus, the doublet spin state surface is broad and wide, whereas that for the quartet spin state surface is steeper and narrower around the barrier. In principle, this affects the amount of tunneling in the reaction.

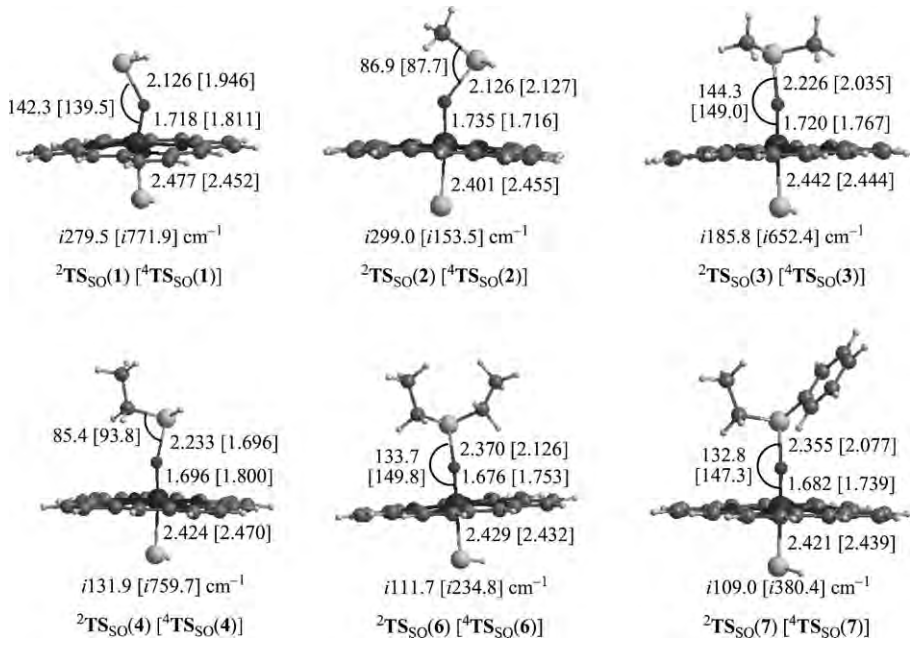

Figure 4. Optimized geometries of doublet and quartet transition states for the reaction of ^{4,2}Cpd I(SH) with substrates **1–4**, **6** and **7**. Bond lengths are in Ångstroms, angles in degrees and the imaginary frequency in the transition state is in wave numbers. For the structure of ^{4,2}**TS**$_{SO}$(**5**) see Figure 3.

Subsequently, we investigated the correlation between the height of the barrier for the sulfoxidation reaction (^{2}**TS**$_{SO}$) corresponding to the reaction of Cpd I(SH) with the series of substrates **1–7** and the IE of the substrate. The observed trends are displayed in Figure 5. The same trends were tested for the series of ^{4}**TS**$_{SO}$ barriers with ionization potential (Figure S11 in the Supporting Information), but the correlations are very similar, so we focused on the lowest lying barriers only, which proceed on the doublet spin potential energy surface. Calculated IE values of substrate correlate well with experimental data[26] with a systematic error of about 4 kcal mol^{-1}, as expected for DFT calculations at the B3LYP level of theory. As can be seen from Figure 5, the correlation coefficient is reasonable ($R^2=0.91$), which supports the hypothesis of a relationship between barrier height

 © 2011 Wiley-VCH Verlag GmbH & Co. KGaA, Weinheim

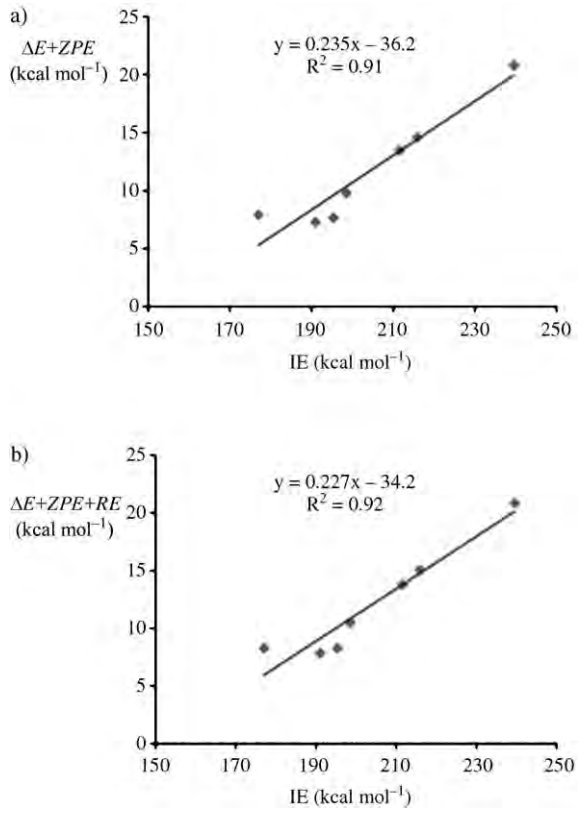

Figure 5. a) Correlation between the height of the barrier (^{2}**TS**$_{SO}$) for the reaction of ^{2}Cpd I(SH) with substrates **1**–**7** and the ionization energy of the substrate (IE). All values in kcal mol^{-1} and calculated with B3LYP. b) RE corrected barrier heights.

and IE. Following previous procedures,[23a] we also calculated the reorganization energy of the substrate (RE), which is defined as the energy of the substrate in the transition-state geometry minus that for the fully converged substrate structure. These RE values, however, are very small, that is, between 0.04 and 1.05 kcal mol^{-1} (Table S2 in the Supporting Information), so that an inclusion of its effect is minimal. The reason for these small values for RE come from the fact that substrate sulfoxidation is initiated by an attack of the oxo group of Cpd I on a lone pair of the sulfur atom of the substrate. This leads to very little geometric distortion in the transition-state geometry, hence the geometry of the substrate in the transition state is close to its fully relaxed structure, thus resulting in a small RE value. Inclusion of the RE value, (Figure 5b) therefore, gives only minor changes to the reactivity trends and the correlation coefficient between barrier height and IE changes slightly to $R^2 = 0.92$. Thus, our computational studies and reactivity trends are in perfect agreement with previous substrate sulfoxidation and epoxidation studies,[7,24] and implicate a linear correlation between barrier height and IE. Because rate constant and barrier heights are proportional to each other, also the rate constant of substrate sulfoxidation should connect with IE as indeed observed by Watanabe et al.[6] The correlation is consistent with the electron-transfer processes obtained from reactants to products that involve an electron transfer from substrate to oxidant. Moreover, the trend depicted in Figure 5 can be used to predict barrier heights of sulfide-sulfoxidation processes by [Fe^{IV}=O(Por$^{+\bullet}$)SH] using IE values of known substrates.

So far, we have reported the results obtained for one oxidant (Cpd I(SH)) with different sulfoxidation substrates. However, in a further set of calculations, we have searched for fundamental properties that correlate the barrier height of substrate sulfoxidation with a range of iron(IV)–oxo porphyrin cation radical oxidants Cpd I(L) with variable axial ligands L. Thermodynamically, in aliphatic hydroxylation reactions by iron(IV)–oxo oxidants, the reaction enthalpy and hence the driving force for the hydrogen atom abstraction by Cpd I(SH) or [Fe^{IV}=O(Por$^{+\bullet}$)SH] from substrates (SubH) is equal to the difference in strength of the C–H bond that is broken in the process and the O–H bond that is formed [Eqs. (1)–(3)].[27,28] However, apart from the driving force also the barrier height for the hydrogen-atom-abstraction reaction and consequently the rate constant is proportional to either BDE$_{CH}$ or BDE$_{OH}$.[23] These correlations have been rationalized by a VB curve crossing diagram that illustrated that the barrier heights of the reaction are connected to the electron-transfer processes involved in the reaction mechanism. In fact, these electron-transfer processes represent a singlet–triplet excitation in a C–H bond for aliphatic hydroxylation, which is proportional to BDE$_{CH}$, hence providing computational support for the observed trends. The computational studies revealed a correlation between barrier height of hydrogen-atom abstraction by Cpd I(SH) and BDE$_{CH}$,[23a] and a relationship between barrier height of hydrogen abstraction from propene by a range of iron(IV)–oxo oxidants proportional to the strength of the O–H bond formed in the process (BDE$_{OH}$).[23c]

$$[Fe^{IV}{=}O(Por^{+\bullet})SH]+SubH \rightarrow [Fe(OH)(Por)SH]+Sub^{\bullet} \quad (1)$$

$$\Delta H_{[Eq.\ (1)]} = BDE_{CH} - BDE_{OH} \quad (2)$$

$$AH \rightarrow A^{\bullet} + H^{\bullet} + BDE_{AH} \quad (3)$$

Recent studies of substrate-epoxidation reactions by metal–oxo oxidants found a correlation between the barrier height for the epoxidation reaction by Cpd I(SH) with the ionization energy of the substrate similar to what is shown here for substrate sulfoxidation.[25] This implies that the regioselectivity of substrate epoxidation versus sulfoxidation by Cpd I(SH) is determined by the IE of the substrate only. Accordingly, our studies implicate that the regioselectivity of epoxidation versus sulfoxidation in the enzyme can only be changed through favouring or disfavoring substrate binding processes in the substrate binding pocket.

Using a series of heme and nonheme Cpd I models with varying axial ligands, the substrate epoxidation reaction was studied computationally and was found to correlate with the BDE$_{OH}$ value of the oxidant.[24] Consequently, the formation of a C–O bond in a substrate epoxidation reaction was

 © 2011 Wiley-VCH Verlag GmbH & Co. KGaA, Weinheim

found to be proportional to the formation of a H–O bond (BDE_{OH}). Therefore, to mimic the formation of an S–O bond in substrate-sulfoxidation reactions we investigated the correlation between the height of the barrier for substrate sulfoxidation and the BDE_{OH}. In particular, sulfoxidation reactions mediated by iron(IV)–oxo complexes follow the same electron-transfer mechanisms found in substrate epoxidation, in which the reaction of Cpd I(SH) with substrates correlates with IE(substrate). Therefore, we used one substrate (dimethyl sulfide, **3**) and investigated the sulfoxidation reaction using a series of iron(IV)–oxo porphyrin cation radical oxidants with variable axial ligands (L): Cpd I(L) with $L = SH^-$, OH^-, Cl^-, ImH, and CF_3COO^-. ImH is an imidazole-based ligand and as such Cpd I(ImH) represents a peroxidase Cpd I mimic. This set of oxidants span over a range of almost 20 kcal mol^{-1} in BDE_{OH} values, thus highlighting the effect of the axial ligand, where [Fe^{IV}=O($Por^{+\bullet}$)OH] is the system with the largest BDE_{OH} value (98.8 kcal mol^{-1}) and [Fe^{IV}=O($Por^{+\bullet}$)ImH] the one with the smallest BDE_{OH} value (79.4 kcal mol^{-1}). Although we again calculated the complete reaction mechanism similarly to that displayed in Figure 3, we now focus on the sulfoxidation transition states ^{4,2}**TS**$_{SO}$ only (for the complete set of data see the Supporting Information).

Figure 6 shows the optimized geometries of ^{4}**TS**$_{SO}$(**3**$_L$) with $L = OH^-$, Cl^-, ImH, and CF_3COO^-, whereas the ^{4}**TS**$_{SO}$(**3**$_{SH}$) structure is given in Figure 4. Optimized geometries of ^{4}**TS**$_{SO}$(**3**$_L$) with $L = OH^-$, Cl^-, ImH, and CF_3COO^- are in good agreement with those observed and presented in Figure 3 and Figure 4 (see above). Also here the low-spin data follow the same trends and characteristics of the high-spin data, so that we will focus on the lowest lying barriers that pass ^{4}**TS**$_{SO}$ only. The Fe–O distance for ^{4}**TS**$_{SO}$(**3**$_{OH}$) and ^{4}**TS**$_{SO}$(**3**$_{Cl}$) is within the standard deviation of the values obtained in Figure 3 and Figure 4. The ^{4}**TS**$_{SO}$(ImH) structure, by contrast, has a very long Fe–O distance of 1.892 Å. Interestingly, the axial ligand has different effects on the transition state geometries than those discussed above regarding the mechanism of Cpd I(SH) with sulfides. No correlation between the length of the S–O bond and the barrier height is found for the axial-ligand studies presented in Figure 6. This implies that barrier height is determined by a set of intricate electron-transfer factors, which work in concordance or discordance as the substrate and oxidant varies, which precludes the correlation of barrier height with a single parameter.

Thus, the axial-ligand effect on substrate sulfoxidation manifests itself through differences in barrier height of the reaction processes that correlate with BDE_{OH}, Figure 6b. As follows from Figure 6b, the oxidant with the largest BDE_{OH} value reacts with dimethyl sulfide with the lowest reaction barriers, that is, highest rate constants, and therefore, will be the most effective oxidant of this series to perform substrate-sulfoxidation reactions. Although there is a bit of scatter in the data, the obtained correlation between barrier height and BDE_{OH} is reasonable ($R^2 = 0.90$) and is in good agreement with the trend of the axial-ligand effect found for

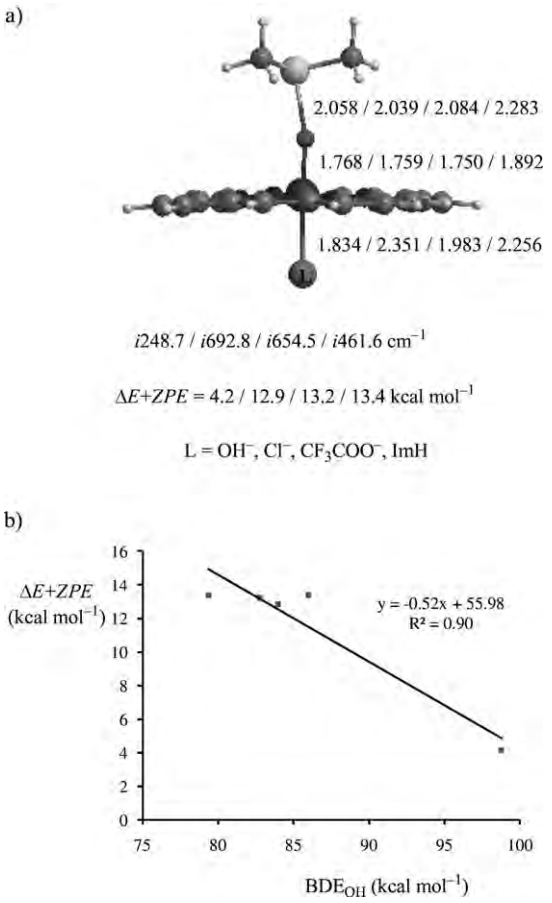

Figure 6. a) Optimized geometries of ^{4}**TS**$_{SO}$(**3**$_L$) with $L = OH^-$, Cl^-, ImH, and CF_3COO^-. Bond lengths are in Ångstroms and the imaginary frequencies are in wave numbers. b) Correlation between barrier height and BDE_{OH} value.

substrate epoxidation mediated by similar iron(IV)–oxo porphyrin cation radical oxidants.[24] Consequently, BDE_{OH} is a reasonably good representative of the axial-ligand effect in substrate sulfoxidation and the formation of a S–O bond can be faithfully mimicked with the formation of a H–O bond. Moreover, using known BDE_{OH} values for several oxidants, the catalytic potential in substrate sulfoxidation can be estimated (Figure 6b).

In addition to the correlations between the height of the barrier of a given reaction with the energetic properties (IE, BDE_{OH} etc), in the past we also established correlations between reaction enthalpy and reaction polarizability ($\Delta\alpha_r$).[28] Recent studies of reaction barriers of aliphatic hydroxylation and epoxidation mediated by iron(IV)–oxo complexes, reported a relationship between the barrier height and the change of polarizability volume between the reactant and the transition-state structures.[23c,24] To gain further insight into this unexpected relationship between polarizability difference and barrier height, we extracted the polarizability trace from the Gaussian frequency calculations and calculated the reaction polarizability ($\Delta\alpha_r$) using Equation (4). In this equation, the polarizability trace of the transition-state

 © 2011 Wiley-VCH Verlag GmbH & Co. KGaA, Weinheim

structure, Cpd I and the substrate are given by α_{TS}, $\alpha_{Cpd\,I}$, and α_{SubH}, respectively.

$$\Delta\alpha_r = \alpha_{TS} - \alpha_{Cpd\,I} - \alpha_{SubH} \quad (4)$$

Figure 7 displays the correlation between reaction polarizability and barrier height for the high-spin and low-spin sulfoxidation reactions by Cpd I(SH). It appears that both trends give a reasonable linear correlation with a negative

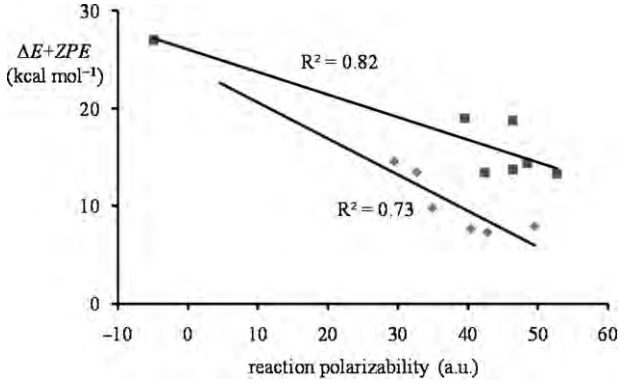

Figure 7. Correlation between the height of the barrier for substrate sulfoxidation and reaction polarizability for the high-spin (HS; ■) and low-spin (LS; ◆) mechanisms by Cpd I(SH).

slope, which implicates that high barriers are the result of larger changes in polarizability. Interestingly the reaction of ^{4}Cpd I(SH) with H_2S via ^{4}**TS**$_{SO}$(**1**) gives a negative reaction polarizability, which probably indicates that the reaction cannot take place on this spin-state surface. Note that polarizability does not correlate with the ionization potential,[29] so that the correlations shown in Figure 7 must have a different origin.

Experimental studies on substrate sulfoxidation by P450 enzymes gave a linear correlation between the log of the rate constant and the IE of the substrate.[6] Recent computational studies for the reaction of Cpd I(SH) with four *para*-substituted thioanisole substrates also gave a correlation between barrier height and substrate IE, which was rationalized by a VB curve-crossing diagram.[7,30] In this work, we found the same correlation between barrier height and substrate IE for the reaction of Cpd I(SH) with substrates. In addition, we show that the barrier height is proportional to the polarizability difference for the reaction and proportional to the barrier height for the reaction of dimethyl sulfide sulfoxidation mediated by metal–oxo oxidants and BDE_{OH}.

The observed trends are generalized in Figure 8 with a VB curve-crossing diagram for the sulfoxidation reaction.[7] The reaction starts from the left side with the wave function of the reactant (Ψ_r) and continues to the right to the wave function (Ψ_p) of the products. Thus, the reactant- and product-wave functions cross and lead to an avoided crossing and a transition state for substrate sulfoxidation ($\Delta E_{SO}^{\ddagger}$). The excited-state wave functions (Ψ_r* and Ψ_p*) are the re-

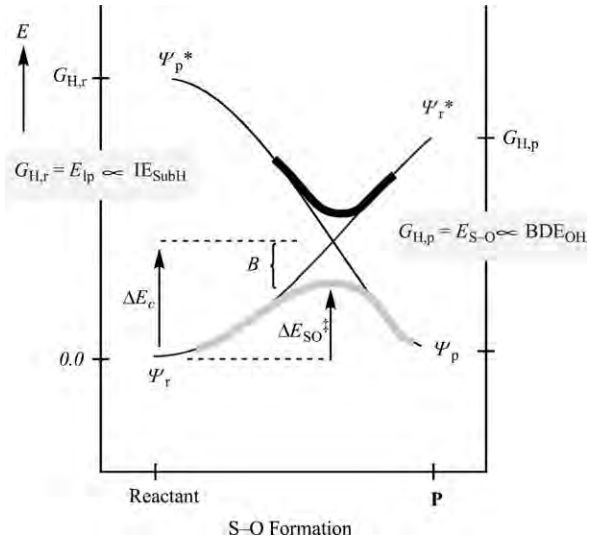

Figure 8. VB diagram for substrate sulfoxidation by Cpd I oxidants.

actant-wave function in the product geometry (Ψ_r*) and product-wave function in the reactant geometry (Ψ_p*). These wave functions are normally the electronic images of the states they correlate with, but here they represent the one-electron excitation energies.[30] Thus, the curve crossing between the reactant- and product-wave functions is located at a certain energy (ΔE_c), but the actual transition state ($\Delta E_{SO}^{\ddagger}$) for the sulfoxidation is lower in energy by a factor of *B*. It was further shown that the barrier height is proportional to a fraction (*f*) of the promotion gap in the reactant state ($G_{H,r}$) through

$$\Delta E_{SO}^{\ddagger} = f\,G_{H,r} - B \quad (5)$$

Thus, in the case of substrate sulfoxidation by iron(IV)–oxo complexes, the promotion gap $G_{H,r}$ represents the excitation energy of a lone pair of the substrate. Time dependent DFT calculations (TD-DFT) on the substrates showed that these excitation energies are proportional to the IE of the substrate, therefore, the VB diagram (Figure 8) predicts that IE should correlate with the height of the barrier for sulfoxidation as indeed shown in the described reactivity studies (Figure 5).

The reverse reaction from products to reactants has a barrier ($\Delta E_{SO,rev}^{\ddagger}$) that is proportional to $G_{H,p}$ rather than $G_{H,r}$ in Equation (5). The reverse sulfoxidation barrier is equal to the forward sulfoxidation barrier ($\Delta E_{SO}^{\ddagger}$) minus the reaction energy from reactants to products, that is, the driving force. Thus, $\Delta E_{SO,rev}^{\ddagger}$ involves two components: first, the one-electron oxidation of the heme group, in which the a_{2u} orbital is filled, and second, the energy for the S–O bond formation.[7] Hence, this step should correlate with the electron affinity of the oxidant, $EA_{Cpd\,I}$. The latter is connected to BDE_{OH} in combination with the pK_a value of Cpd I, [Eq. (6)].[31] The constant *C* constitutes factors including the ionization potential of a hydrogen atom as well as solvent corrections to the system.

 © 2011 Wiley-VCH Verlag GmbH & Co. KGaA, Weinheim

$$BDE_{OH} = 23.06\,EA_{Cpd\,I} + 1.37\,pK_a + C \quad (6)$$

Therefore, the trends depicted in this work show that formation of an O–H bond is proportional to the formation of an O–S bond through BDE_{OH}. Interestingly, previous reactivity studies of substrate hydroxylation and epoxidation by a range of iron(IV)–oxo porphyrin cation radical complexes also showed a correlation with BDE_{OH}.[23c,24] This implies, therefore, that the regioselectivity of substrate hydroxylation, epoxidation, and sulfoxidation is not depending on the nature of the oxidant, because all these reactions correlate with BDE_{OH}. As a consequence, changing the axial ligand should not affect the regioselectivity of the process and of the observed product distributions. In all three cases the correlation of the height of the barrier with BDE_{OH} gives a slope in the region −0.52 to −0.76 and an intercept of 56.0 (sulfoxidation, Figure 6 b), 76.5 (hydroxylation, Ref. [23c]) and 79.7 (epoxidation, Ref. [24]). Thus, the hydroxylation and epoxidation curves are almost parallel with an equal slope and intercept that are within the error of the fitted curves. The intercept for substrate sulfoxidation is somewhat smaller, because a S–O bond is weaker than a O–H or C–O bond.

It is interesting to compare the reactions of oxygen-atom transfer from an iron(IV)–oxo porphyrin cation radical oxidant that result in the hydroxylation, epoxidation, and sulfoxidation of the substrate (Table 1). By varying the substrates and keeping the oxidant constant, we have shown that the intrinsic properties of the substrate determine the reaction barrier, and therefore the reaction kinetics. In the case of substrate epoxidation and sulfoxidation, the ionization potential of the substrate is the key for the reaction process, whereas in substrate hydroxylation the key is in the C–H bond strength of the substrate. In a similar way, we also investigated the effect of the oxidant on substrate hydroxylation, epoxidation, and sulfoxidation. In all processes, the rate-determining barrier involves the formation of a bond between the oxygen atom and one atom of the substrate (O–H bond in substrate hydroxylation, O–C bond for epoxidation, and O–S bond in sulfoxidation). These bond-formation steps can be successfully mimicked by the BDE_{OH} value of the oxidant. These studies, therefore, highlight the axial-ligand effect on substrate oxidation by metal–oxo oxidants.

Table 1. Properties of substrate and oxidant that affect the reaction barrier in the oxygen-transfer reaction mediated by iron(IV)–oxo porphyrin cation radicals.

	Intrinsic property that determines barrier height	
process	variable substrate	variable oxidant
sulfoxidation	IE	BDE_{OH}
epoxidation	IE	BDE_{OH}
hydroxylation	BDE_{CH}	BDE_{OH}

Conclusion

We have presented a systematic study carried out by means of density-functional theory on substrate sulfoxidation by iron(IV)–oxo porphyrin cation radical complexes and we have focused on the effect obtained by changing the axial ligand of the oxidant. To quantify the axial-ligand effect, we investigated the correlations between the heights of the barrier for the sulfoxidation reactions with the intrinsic properties of substrate and oxidant. Thus, the barrier heights of the sulfoxidation reaction correlate with the ionization potential of the substrate as well as with the BDE_{OH} of the oxidant. It is shown that the axial-ligand affects the BDE_{OH} value strongly and, in turn, this influences the rate constant of substrate sulfoxidation. We set up a VB curve-crossing diagram to explain the correlations. Furthermore, we showed that substrate sulfoxidation follows the same trends as substrate epoxidation, that is, is connected to the IE of the substrate and to the BDE_{OH} of the oxidant, which implies that the regioselectivity of epoxidation versus sulfoxidation should be constant with varying axial ligands.

Experimental Section

The procedures and methods used in this work are well-tested and benchmarked and have been applied to many reactivity studies of iron(IV)–oxo oxidants.[17,32] All geometries were fully optimized with the Jaguar 7.0 program package without geometric constraints and characterized as local minima or first order saddle points using an analytical frequency in Gaussian 03.[33,34] All transition states described in this work have a single imaginary frequency for the S–O stretch vibration, whereas local minima had real frequencies only. A double-ζ quality LACVP basis set on iron that includes a core potential combined with 6-31G** on the rest of the atoms (basis set B1) was used for geometry optimizations, frequencies, and initial geometry scans.[35] To test the effect of the basis set on the relative energies, we ran single point calculations using a triple-ζ quality LACV3P+ basis set on iron that contains a set of diffuse basis functions as well as a core potential in combination with 6–311+G* on the rest of the atoms (basis set B2). We use the B3LYP hybrid density functional method throughout,[36] as previous studies showed it to give good agreement with experimental rate constants.[37]

Following previous studies we simplified the iron(IV)–oxo species of P450 enzymes as protoporphyrin IX, whereby all side chains were replaced by hydrogen atoms.[20b] A thiolate axial ligand was used as it was shown to give a BDE_{OH} value close to a large active-site model with a CysGlyGly ligand system.[23e] To test the effect of the axial ligand on the reactivity patterns and trends, we replaced the axial ligand with Cl^-, OH^-, CF_3COO^-, and imidazole. All calculations were performed for the doublet and quartet spin state surfaces, which give similar trends. However, owing to space limitation we focused on the major trends only (see the supporting information for details).

Ionization potentials and BDE_{OH} values were calculated for isolated reactants at the same level of theory as described above. TD-DFT calculations were performed in Gaussian.[38]

Acknowledgements

The research was supported by CPU time provided by the National Service of Computational Chemistry Software (NSCCS). D.K. is Ramanujan Fellow of the Department of Science and Technology (New Delhi).

 © 2011 Wiley-VCH Verlag GmbH & Co. KGaA, Weinheim

[1] a) M. Sono, M. P. Roach, E. D. Coulter, J. H. Dawson, *Chem. Rev.* **1996**, *96*, 2841–2888; b) F. P. Guengerich, *Chem. Res. Toxicol.* **2001**, *14*, 611–650; c) J. T. Groves, *Proc. Natl. Acad. Sci. USA* **2003**, *100*, 3569–3574; d) *Cytochrome P450: Structure, Mechanism and Biochemistry*, 3rd ed. (Ed.: P. R. Ortiz de Montellano), Kluwer Academic/Plenum Publishers, New York, **2004**; e) A. W. Munro, H. M. Girvan, K. J. McLean, *Nat. Prod. Rep.* **2007**, *24*, 585–609; f) *Handbook of Porphyrin Science* (Eds.. K. M. Kadish, K. M. Smith, R. Guilard), World Scientific, New Jersey, **2010**; g) P. R. Ortiz de Montellano, *Chem. Rev.* **2010**, *110*, 932–948.

[2] a) M. Werner, G. Birner, W, Dekant, *Chem. Res. Toxicol.* **1996**, *9*, 41–49; b) A. Madan, A. Parkinson, M. D. Faiman, *Drug Metab. Dispos.* **1995**, *23*, 1153–1158; c) K. A. Usmani, E. D. Karoly, E. Hodgson, R. L. Rose, *Drug Metab. Dispos.* **2004**, *32*, 333–339; d) B. Furnes, D. Schlenk, *Drug Metab. Dispos.* **2005**, *33*, 214–218.

[3] a) E. J. Perkins, A. El-Alfy, D. Schlenk, *Toxicol. Sci.* **1999**, *48*, 67–73; b) J. Wójcikowski, P. Maurel, W. A. Daniel, *Drug Metab. Disp.* **2006**, *34*, 471–476.

[4] a) Y. Goto, T. Matsui, S.-i. Ozaki, Y. Watanabe, S. Fukuzumi, *J. Am. Chem. Soc.* **1999**, *121*, 9497–9502; b) S. Kato, H.-J. Yang, T. Ueno, S.-i. Ozaki, G. N. Phillips, Jr., S. Fukuzumi, Y. Watanabe, *J. Am. Chem. Soc.* **2002**, *124*, 8506–8507; c) T. J. Volz, D. A. Rock, J. P. Jones, *J. Am. Chem. Soc.* **2002**, *124*, 9724–9725; d) K.-B. Cho, Y. Moreau, D. Kumar, D. A. Rock, J. P. Jones, S. Shaik, *Chem. Eur. J.* **2007**, *13*, 4103–4115; e) J. Benet-Buchholz, P. Comba, A. Llobet, S. Roeser, P. Vadivelu, S. Wiesner, *Dalton Trans.* **2010**, *39*, 3315–3320.

[5] a) P. K. Sharma, S. P. de Visser, S. Shaik, *J. Am. Chem. Soc.* **2003**, *125*, 8698–8699; b) D. Kumar, S. P. de Visser, P. K. Sharma, H. Hirao, S. Shaik, *Biochemistry* **2005**, *44*, 8148–8158; c) P. Rydberg, U. Ryde, L. Olsen, *J. Chem. Theory Comput.* **2008**, *4*, 1369–1377; d) C. Li, L. Zhang, C. Zhang, H. Hirao, W. Wu, S. Shaik, *Angew. Chem.* **2007**, *119*, 8316–8318; *Angew. Chem. Int. Ed.* **2007**, *46*, 8168–8170; e) C. S. Porro, M. J. Sutcliffe, S. P. de Visser, *J. Phys. Chem. A* **2009**, *113*, 11635–11642.

[6] a) Y. Watanabe, T. Iyanagi, S. Oae, *Tetrahedron Lett.* **1980**, *21*, 3685–3688; b) Y. Watanabe, T. Numata, T. Iyanagi, S. Oae, *Bull. Chem. Soc. Jpn.* **1981**, *54*, 1163–1170; c) Y. Watanabe, T. Iyanagi, S. Oae, *Tetrahedron Lett.* **1982**, *23*, 533–536.

[7] S. Shaik, Y. Wang, H. Chen, J. Song, R. Meir, *Faraday Discuss.* **2010**, *145*, 49–70.

[8] a) B. Chance, L. Powers, Y. Ching, T. L. Poulos, G. R. Schonbaum, I. Yamazaki, K. G. Paul, *Arch. Biochem. Biophys.* **1984**, *235*, 596–611; b) J. E. Penner-Hahn, K. Smith Eble, T. J. McMurry, M. Renner, A. L. Balch, J. T. Groves, J. H. Dawson, K. O. Hodgson, *J. Am. Chem. Soc.* **1986**, *108*, 7819–7825.

[9] J. H. Dawson, R. H. Holm, J. R. Trudell, G. Barth, R. E. Linder, E. Bunnenberg, C. Djerassi, S. C. Tang, *J. Am. Chem. Soc.* **1976**, *98*, 3707–3709.

[10] a) Z. Gross, S. Nimri, *Inorg. Chem.* **1994**, *33*, 1731–1732; b) Z. Gross, *J. Biol. Inorg. Chem.* **1996**, *1*, 368–371.

[11] a) C. V. Sastri, M. J. Park, T. Ohta, T. A. Jackson, A. Stubna, M. S. Seo, J. Lee, J. Kim, T. Kitagawa, E. Münck, L. Que Jr. , W. Nam, *J. Am. Chem. Soc.* **2005**, *127*, 12494–12495; b) C. V. Sastri, J. Lee, K. Oh, Y. J. Lee, J. Lee, T. A. Jackson, K. Ray, H. Hirao, W. Shin, J. A. Halfen, J. Kim, L. Que Jr. , S. Shaik, W. Nam, *Proc. Natl. Acad. Sci. USA* **2007**, *104*, 19181–19186; c) H. Hirao, L. Que Jr. , W. Nam, S. Shaik, *Chem. Eur. J.* **2008**, *14*, 1740–1756.

[12] G. I. Berglund, G. H. Carlsson, A. T. Smith, H. Szöke, A. Henriksen, J. Hajdu, *Nature* **2002**, *417*, 463–468.

[13] a) A. Morimoto, M. Tanaka, S. Takahashi, K. Ishimori, H. Hori, I. Morishima, *J. Biol. Chem.* **1998**, *273*, 14753–14760; b) B. D. Howes, N. C. Veitch, A. T. Smith, C. G. White, G. Smulevich, *Biochem. J.* **2001**, *353*, 181–191.

[14] a) J. E. Roberts, B. M. Hoffman, R. Rutter, L. P. Hager, *J. Am. Chem. Soc.* **1981**, *103*, 7654–7656; b) J. E. Roberts, B. M. Hoffman, R. Rutter, L. P. Hager, *J. Biol. Chem.* **1981**, *256*, 2118–2121.

[15] a) C. E. Schulz, R. Rutter, J. T. Sage, P. G. Debrunner, L. P. Hager, *Biochemistry* **1984**, *23*, 4743–4754; b) W.-J. Chuang, H. E. J. Van Wart, *J. Biol. Chem.* **1992**, *267*, 13293–13301; c) J. R. Kincaid, Y. Zheng, J. Al-Mustafa, K. Czarnecki, *J. Biol. Chem.* **1996**, *271*, 28805–28811.

[16] a) H. Kuramochi, L. Noodleman, D. A. Case, *J. Am. Chem. Soc.* **1997**, *119*, 11442–11451; b) R. J. Deeth, *J. Am. Chem. Soc.* **1999**, *121*, 6074–6075; c) M. T. Green, *J. Am. Chem. Soc.* **2000**, *122*, 9495–9499.

[17] a) S. Shaik, D. Kumar, S. P. de Visser, A. Altun, W. Thiel, *Chem. Rev.* **2005**, *105*, 2279–2328; b) S. Shaik, H. Hirao, D. Kumar, *Nat. Prod. Rep.* **2007**, *24*, 533–552.

[18] a) K. Czarnecki, S. Nimri, Z. Gross, L. M. Proniewicz, J. R. Kincaid, *J. Am. Chem. Soc.* **1996**, *118*, 2929–2935; b) T. Ohno, N. Suzuki, T. Dokoh, Y. Urano, K. Kikuchi, M. Hirobe, T. Higuchi, T. Nagano, *J. Inorg. Biochem.* **2000**, *82*, 123–125; c) W. J. Song, Y. O. Ryu, R. Song, W. Nam, *J. Biol. Inorg. Chem.* **2005**, *10*, 294–304; d) T. Yamane, K. Makino, N. Umezawa, N. Kato, T. Higuchi, *Angew. Chem.* **2008**, *120*, 6538–6540; *Angew. Chem. Int. Ed.* **2008**, *47*, 6438–6440; e) T. A. Jackson, J.-U. Rohde, M. S. Seo, C. V. Sastri, R. DeHont, A. Stubna, T. Ohta, T. Kitagawa, E. Münck, W. Nam, L. Que Jr, *J. Am. Chem. Soc.* **2008**, *130*, 12394–12407; f) A. Takahashi, T. Kurahashi, H. Fujii, *Inorg. Chem.* **2009**, *48*, 2614–2625; g) S. Fukuzumi, H. Kotani, T. Suenobu, S. Hong, Y.-M. Lee, W. Nam, *Chem. Eur. J.* **2009**, *15*, 354–361; h) M. E. Crestoni, S. Fornarini, F. Lanucara, *Chem. Eur. J.* **2009**, *15*, 7863–7866; i) Y. Kang, H. Chen, Y. J. Jeong, W. Lai, E. H. Bae, S. Shaik, W. Nam, *Chem. Eur. J.* **2009**, *15*, 10039–10046; j) K. A. Prokop, S. P. de Visser, D. P. Goldberg, *Angew. Chem.* **2010**, *122*, 5217–5221; *Angew. Chem. Int. Ed.* **2010**, *49*, 5091–5095; k) S. P. de Visser, R. Latifi, L. Tahsini, W. Nam, *Chem. Asian J.* **2011**, *6*, 493–504.

[19] a) T. Kamachi, T. Kouno, W. Nam, K. Yoshizawa, *J. Inorg. Biochem.* **2006**, *100*, 751–754; b) D. Kumar, S. P. de Visser, P. K. Sharma, E. Derat, S. Shaik, *J. Biol. Inorg. Chem.* **2005**, *10*, 181–189; c) S. P. de Visser, *J. Biol. Inorg. Chem.* **2006**, *11*, 168–178; d) S. P. de Visser, *J. Phys. Chem. B* **2006**, *110*, 20759–20761; e) S. P. de Visser, *J. Am. Chem. Soc.* **2006**, *128*, 15809–15818; f) S. P. de Visser, *J. Phys. Chem. B* **2007**, *111*, 12299–12302; g) S. P. de Visser, L. Tahsini, W. Nam, *Chem. Eur. J.* **2009**, *15*, 5577–5587.

[20] a) M. T. Green, *J. Am. Chem. Soc.* **1999**, *121*, 7939–7940; b) F. Ogliaro, S. P. de Visser, S. Cohen, J. Kaneti, S. Shaik, *ChemBioChem* **2001**, *2*, 848–851; c) S. P. de Visser, S. Shaik, P. K. Sharma, D. Kumar, W. Thiel, *J. Am. Chem. Soc.* **2003**, *125*, 15779–15788.

[21] S. Shaik, S. P. de Visser, F. Ogliaro, H. Schwarz, D. Schröder, *Curr. Opin. Chem. Biol.* **2002**, *6*, 556–567.

[22] a) T. Kamachi, K. Yoshizawa, *J. Am. Chem. Soc.* **2003**, *125*, 4652–4661; b) S. P. de Visser, D. Kumar, S. Cohen, R. Shacham, S. Shaik, *J. Am. Chem. Soc.* **2004**, *126*, 8362–8363.

[23] a) S. Shaik, D. Kumar, S. P. de Visser, *J. Am. Chem. Soc.* **2008**, *130*, 10128–10140; b) R. Latifi, M. Bagherzadeh, S. P. de Visser, *Chem. Eur. J.* **2009**, *15*, 6651–6662; c) S. P. de Visser, *J. Am. Chem. Soc.* **2010**, *132*, 1087–1097.

[24] D. Kumar, B. Karamzadeh, G. N. Sastry, S. P. de Visser, *J. Am. Chem. Soc.* **2010**, *132*, 7656–7667.

[25] S. P. de Visser, S. Shaik, *J. Am. Chem. Soc.* **2003**, *125*, 7413–7424.

[26] a) S. G. Lias, *Ionization Energy evaluation* in *NIST Chemistry Webbook* (Eds.: P. J. Linstrom, W. G. Mallard), National Institute of Standards and Technology, Gaithersburg, http://webbook.nist.gov, **2009**; b) K. Kimura, S. Katsumata, Y. Achiba, T. Yamazaki, S. Iwata, *Ionization Energies, ab initio Assignments, and Valence Electronic Structure for 200 Molecules in Handbook of HeI Photoelectron Spectra of Fundamental Organic Compounds*, Scientific Society Press, Tokyo, **1981**.

[27] a) J. M. Mayer, *Acc. Chem. Res.* **1998**, *31*, 441–450; b) J. M. Mayer, *Annu. Rev. Phys. Chem.* **2004**, *55*, 363–390; c) E. A. Mader, V. W. Manner, T. F. Markle, A. Wu, J. A. Franz, J. M. Mayer, *J. Am. Chem. Soc.* **2009**, *131*, 4335–4345; d) J. Kaizer, E. J. Klinker, N. Y. Oh, J.-U. Rohde, W. J. Song, A. Stubna, J. Kim, E. Münck, W. Nam, L. Que, Jr., *J. Am. Chem. Soc.* **2004**, *126*, 472–473; e) J. Yoon, S. A. Wilson, Y. K. Jang, M. S. Seo, K. Nehru, B. Hedman, K. O. Hodgson, E. Bill, E. I. Solomon, W. Nam, *Angew. Chem.* **2009**, *121*, 1283–

 © 2011 Wiley-VCH Verlag GmbH & Co. KGaA, Weinheim

1286; *Angew. Chem. Int. Ed.* **2009**, *48*, 1257–1260; f) D. E. Lansky, D. P. Goldberg, *Inorg. Chem.* **2006**, *45*, 5119–5125; g) S. R. Bell, J. T. Groves, *J. Am. Chem. Soc.* **2009**, *131*, 9640–9641.
[28] S. P. de Visser, *Phys. Chem. Chem. Phys.* **1999**, *1*, 749–753.
[29] S. P. de Visser, unpublished results.
[30] S. Shaik, W. Lai, H. Chen, Y. Wang, *Acc. Chem. Res.* **2010**, *43*, 1154–1165.
[31] a) L. E. Friedrich, *J. Org. Chem.* **1983**, *48*, 3851–3852; b) F. G. Bordwell, J.-P. Cheng, *J. Am. Chem. Soc.* **1991**, *113*, 1736–1743; c) F. G. Bordwell, J.-P. Cheng, G.-Z. Ji, A. V. Satish, X. Zhang, *J. Am. Chem. Soc.* **1991**, *113*, 9790–9795.
[32] S. P. de Visser, W. Nam, *High-Valent Iron–Oxo Porphyrins in Oxygenation Reactions in Handbook of Porphyrin Science, Vol. 10* (Eds.: K. M. Kadish, K. M. Smith, R. Guilard), World Scientific Publishing, New Jersey, **2010**, Chapter 44, pp. 85–140.
[33] Jaguar 7.0, Schrödinger, LLC., New York **2007**.
[34] Gaussian 03, Revision C.01, M. J. Frisch, G. W. Trucks, H. B. Schlegel, G. E. Scuseria, M. A. Robb, J. R. Cheeseman, J. A. Montgomery, Jr., T. Vreven, K. N. Kudin, J. C. Burant, J. M. Millam, S. S. Iyengar, J. Tomasi, V. Barone, B. Mennucci, M. Cossi, G. Scalmani, N. Rega G. A. Petersson, H. Nakatsuji, M. Hada, M. Ehara, K. Toyota, R. Fukuda, J. Hasegawa, M. Ishida, T. Nakajima, Y. Honda, O. Kitao, N. Nakai, M. Klene, X. Li, J. E. Knox, H. P. Hratchian, J. B. Cross, C. Adamo, J. Jaramillo, R. Gomperts, R. E. Stratmann, O. Yazyev, A. J. Austin, R. Cammi, C. Pomelli, J. W. Ochterski, P. Y. Ayala, K. Morokuma, G. A., Voth, P. Salvador, J. J. Dannenberg, V. G. Zakrzewski, S. Dapprich, A. D. Daniels, M. C. Strain, O. Farkas, D. K. Malick, A. D. Rabuck, K. Raghavachari, J. B. Foresman, J. V. Ortiz, Q. Cui, A. G. Baboul, S. Clifford, J. Cioslowski, B. B. Stefanov, G. Liu, A. Liashenko, P. Piskorz, I. Komaromi, R. L. Martin, D. J. Fox, T. Keith, M. A. Al-Laham, C. Y. Peng, A., Nanayakkara, M. Challacombe, P. M. W. Gill, B. Johnson, W. Chen, M. W. Wong, C. Gonzalez, J. A. Pople, Gaussian, Inc., Wallingford CT, **2004**.
[35] a) P. J. Hay, W. R. Wadt, *J. Chem. Phys.* **1985**, *82*, 270–283; b) W. J. Hehre, R. Ditchfield, J. A. Pople, *J. Chem. Phys.* **1972**, *56*, 2257–2261.
[36] a) A. D. Becke, *J. Chem. Phys.* **1993**, *98*, 5648–5652; b) C. Lee, W. Yang, R. G. Parr, *Phys. Rev. B* **1988**, *37*, 785–789.
[37] S. P. de Visser, K. Oh, A.-R. Han, W. Nam, *Inorg. Chem.* **2007**, *46*, 4632–4641.
[38] R. Bauernschmitt, R. Ahlrichs, *Chem. Phys. Lett.* **1996**, *256*, 454–464.

Received: November 5, 2010
Published online: April 5, 2011

 © 2011 Wiley-VCH Verlag GmbH & Co. KGaA, Weinheim

Water as biocatalyst in cytochrome P450†

Devesh Kumar,[a] Ahmet Altun,[a] Sason Shaik[b] and Walter Thiel*[a]

Received 7th April 2010, Accepted 21st April 2010
DOI: 10.1039/c004950f

Published on 14 December 2010 on http://pubs.rsc.org | doi:10.1039/C004950F
Downloaded by Hebrew University of Jerusalem on 18 December 2010

According to previous quantum mechanics/molecular mechanics (QM/MM) studies, camphor hydroxylation in cytochrome P450 is catalysed by a single water molecule which lowers the computed B3LYP/CHARMM barrier by about 4 kcal mol^{-1}. Gas-phase B3LYP model studies for a variety of different substrates show the generality of this effect. Its origin is an electrostatic enhancement of hydrogen bonding in the transition state for hydrogen abstraction. Attempts are made to correlate the slight variations in the calculated barrier lowerings with substrate properties. Individual water molecules also have a decisive influence on other reactions in cytochrome P450cam, for instance, on the relative propensity for coupling and uncoupling upon protonation of Compound 0 in the wild-type enzyme and its mutants. These and other examples are reviewed briefly. Finally, we address some methodological issues on how to handle the possible involvement of water molecules in biocatalysis at the QM/MM level.

1. Introduction

Water is ubiquitous in biological systems. It is the medium in which the chemistry of life takes place. Apart from its role as bulk solvent, water can also directly participate in biochemical transformations. The biocatalytic function of individual water molecules is addressed in this contribution, using enzymatic reactions in cytochrome P450 as examples.

The cytochrome P450 enzymes are a superfamily of heme-containing oxygenases that catalyse the regio- and stereoselective oxidation of a wide variety of xenobiotics, including numerous drugs. Recent theoretical work on the structure, reactivity, and selectivity of these enzymes has been summarised in two comprehensive reviews.[1,2] The commonly accepted active species in cytochrome P450 enzymes is a high-valent iron(IV)-oxo π-cation radical intermediate called Compound I (Cpd I), which is the most powerful electrophilic oxidant of all the intermediates in the catalytic cycle. The prototypical reaction in P450cam is the hydroxylation of the non-activated C^5–H^{5exo} bond of camphor by Cpd I. The consensus mechanism of this reaction involves an initial hydrogen abstraction from camphor and a subsequent recombination (rebound) of the formed radical pair. The reaction can occur both on the doublet and quartet spin state (two-state reactivity) which have rate-limiting barriers of similar magnitude for hydrogen abstraction, whereas the rebound step is intrinsically more facile especially in the doublet state.[1,2]

[a]*Max-Planck-Institut für Kohlenforschung, Kaiser-Wilhelm-Platz 1, 45470 Mülheim, Germany. E-mail: thiel@mpi-muelheim.mpg.de*
[b]*The Institute of Chemistry and The Lise Meitner-Minerva Center for Computational Quantum Chemistry, Hebrew University of Jerusalem, Givat Ram Campus, 91904 Jerusalem, Israel*

† Electronic supplementary information (ESI) available: Detailed numerical results (Tables S1–S51) as well as optimised structures and correlation plots (Figures S1–S24). See DOI: 10.1039/c004950f

View Online

Published on 14 December 2010 on http://pubs.rsc.org | doi:10.1039/C004950F
Downloaded by Hebrew University of Jerusalem on 18 December 2010

Several groups have studied the hydrogen abstraction step in P450cam theoretically[1,2] using combined quantum mechanics/molecular mechanics (QM/MM) methods,[3,4] typically describing the QM region by density functional theory (DFT, *e.g.*, B3LYP functional) and the MM region by a standard protein force field (*e.g.*, CHARMM). The initially computed QM/MM barriers were mostly higher than expected, considering the fact that it has not yet been possible to characterise Cpd I in P450cam experimentally. This problem was at least partially resolved in later systematic QM/MM investigations,[5,6] that discovered the catalytic role of a single active-site water molecule. When forming Cpd I by protonation of its precursor (Cpd 0), a water molecule is generated next to the oxo atom of the Fe(IV)=O moiety.[7] The strength of the hydrogen bond between this water molecule and the oxo atom increases during the course of the hydrogen abstraction in P450cam simply because the oxo atom becomes more negatively charged. The associated barrier lowering in P450cam amounts to about 4 kcal mol^{-1} at the B3LYP/CHARMM level. This change can be rationalized in an almost quantitative fashion by a classical electrostatic model (with interaction energies computed on the basis of Mulliken charges), thus confirming that the catalytic effect of the water molecule arises from more favorable electrostatic interactions in the transition state.[5,6]

In this article, we explore the generality of this effect by studying the hydrogen abstraction by Cpd I for 9 substrates and a total of 12 different modes of abstraction, both in the doublet and quartet state. This computational survey is done at the DFT level for suitable gas-phase model systems since corresponding systematic QM/MM work would be much more expensive. Section 2 describes the chosen computational approach. Section 3 presents the essential results from this model study, while detailed numerical results and evaluations are documented in the electronic supplementary information (ESI†). Section 4 provides a brief overview over other enzymatic reactions in cytochrome P450 where water plays a decisive mechanistic role. Section 5 addresses the general question of how to treat water in QM/MM studies of enzymatic reactions.

2. Computational details

Cpd I was represented by iron-oxo-porphyrin without heme side chains and with an axial SH ligand to represent the coordinating cysteine (40 atoms, corresponding to QM region R1 in our previous QM/MM work[5,6]). The following substrates were considered: ethane **1**, propane **2**, phenylethane **3**, *trans*-methyl-phenyl-cyclopropane **4** (known as Me-probe), camphor **5**, propene **6**, toluene **7**, *trans*-isopropyl-phenyl-cyclopropane **8** (known as iPr-probe), and N,N-dimethylaniline **9**. The DFT calculations were carried out for systems consisting of Cpd I and substrate, either with or without an additional water molecule hydrogen bonded to the oxo atom of Cpd I.

The QM calculations employed the B3LYP hybrid functional[8–10] with the VWN5-LDA correlation as implemented in the Turbomole code.[11] In our standard basis set B1,[5,6] the iron atom was described by a small-core effective core potential together with the associated double-zeta quality LACVP basis,[12] while the other atoms were described by the 6-31G basis.[13] Three larger basis sets were mainly used for single-point calculations: B2W[6] combines Wachters' all-electron basis at iron[14–16] with Pople-type basis sets[13] elsewhere (6-31+G* on the six atoms coordinated to iron and the O atom of water, 6-31++G** at the migrating H atom and the H atoms of water, 6-31G on the remaining atoms). B3 denotes the all-electron TZVP basis.[17,18] B4 consists of a polarized all-electron dzpdf basis at iron[19,20] and Pople-type basis sets[13] elsewhere (6-31+G* on first-row atoms, 6-31G at all hydrogen atoms). All QM calculations were performed using Turbomole.[11]

In the case of camphor, starting geometries were extracted from the available QM/MM optimized structures.[5,6] In the other systems, camphor was manually replaced, and the respective substrate was added in a suitable orientation. The geometries of all reactants and transition states were fully optimised at the B3LYP/B1 level using

 This journal is © The Royal Society of Chemistry 2011

View Online

the HDLC optimiser[21] as implemented in the ChemShell package.[22] For some of the substrates, optimisations were also done at the B3LYP/B4 level.

3. Results

The optimised B3LYP/B1 transition structures for the systems without and with an additional water molecule are shown in Fig. 1 and 2, respectively, which also specify the values of some key distances (for more detailed data see ESI,† Tables S46 and S47). In propane, there is a separate transition state (TS) for hydrogen abstraction from the primary (**2n**) and secondary (**2i**) carbon atoms, respectively. Likewise, in phenylethane, there are separate TS structures for the transfer of a primary (**3n**) and benzylic (**3b**) hydrogen atom.

In the water-free systems (Fig. 1), the overall shape of the transition states is similar for all substrates (both in the doublet and the quartet), with an essentially linear O···H···C arrangement at the migrating hydrogen atom (angles of 166–175°). In the presence of an additional water molecule (W903, notation as in P450cam), this shape is generally retained (O···H···C angles of 163–177°): W903

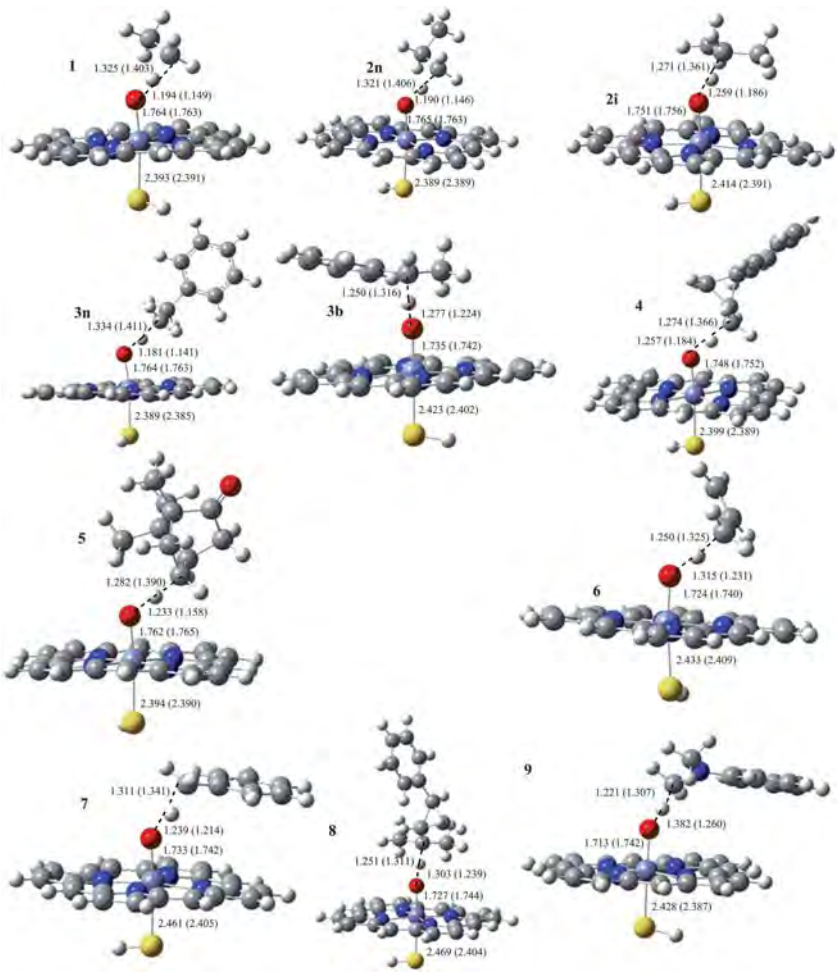

Fig. 1 B3LYP/B1 optimized transition structures in the absence of W903 (see text). Key distances for the doublet (quartet) state are given in Å.

Published on 14 December 2010 on http://pubs.rsc.org | doi:10.1039/C004950F
Downloaded by Hebrew University of Jerusalem on 18 December 2010

View Online

Published on 14 December 2010 on http://pubs.rsc.org | doi:10.1039/C004950F
Downloaded by Hebrew University of Jerusalem on 18 December 2010

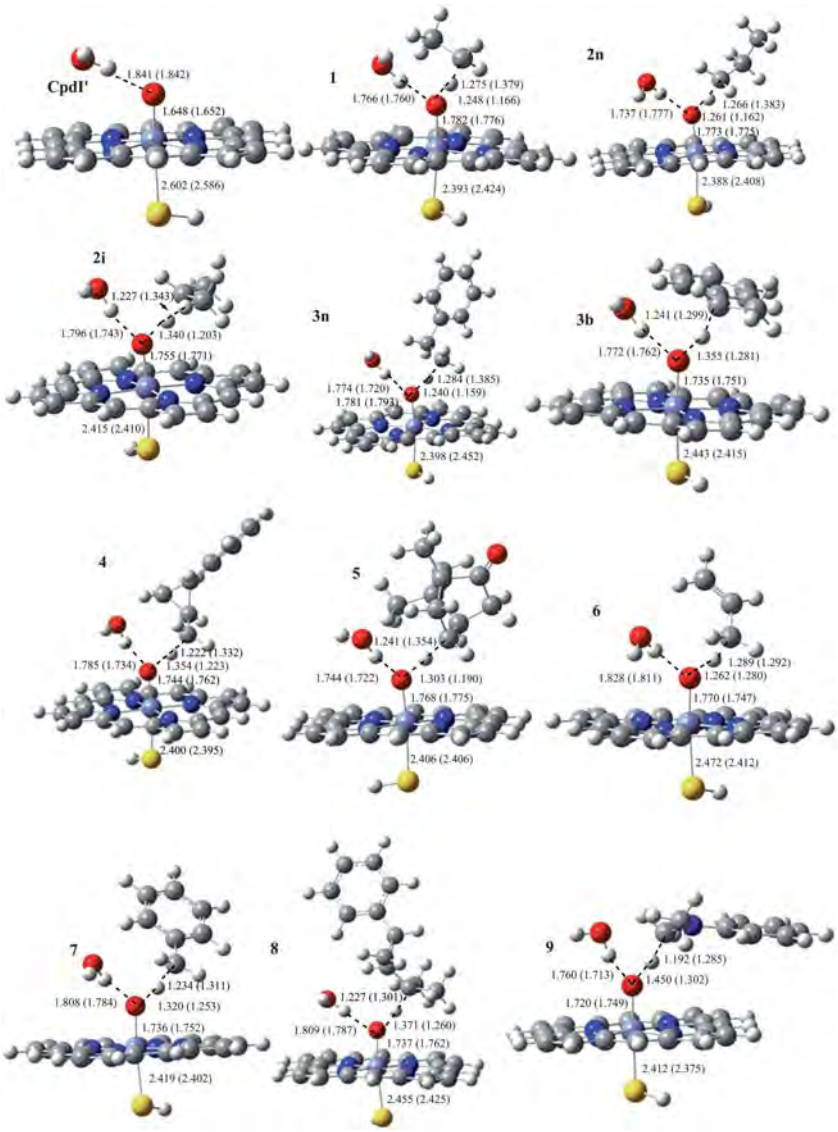

Fig. 2 B3LYP/B1 optimized structure for the Cpd I–W903 complex and for the transition structures in the presence of W903 (see text). Key distances for the doublet (quartet) state are given in Å.

is normally hydrogen bonded to the oxo atom such that it does not interfere with the substrate (see Fig. 2), except in the case of N,N-dimethylaniline **9** (see further discussion below). The optimised distances in the O···H···C moiety indicate that the transition state in the doublet always occurs somewhat earlier along the reaction coordinate than that in the quartet. Comparing the systems without and with W903, the transition state is always earlier in the latter case: in the presence of W903, the optimised C···H distance is shorter, typically by 0.03–0.08 (0.02–0.06) Å in the doublet (quartet), while the optimised O···H distance is longer, typically by 0.05–0.10 (0.02–0.06) Å in the doublet (quartet).

 This journal is © The Royal Society of Chemistry 2011

View Online

Published on 14 December 2010 on http://pubs.rsc.org | doi:10.1039/C004950F
Downloaded by Hebrew University of Jerusalem on 18 December 2010

Table 1 lists the computed B3LYP/B1 barriers for hydrogen abstraction by the chosen Cpd I model, both in the doublet (D) and quartet (Q) spin state. The barriers in the water-free systems correspond to the differences in the energies of the transition state and the separated reactants. The barriers in the systems with W903 are obtained as the difference between the energy of the transition state and the sum of the energies of the substrate and the Cpd I–W903 complex. The energies of all species involved (see ESI,† Tables S1–S14) are evaluated at their optimised B3LYP/B1 geometries. The quoted barriers do not include any zero-point vibrational energy corrections nor any other corrections.

It should be noted that the substrates may initially form reactant complexes with Cpd I (or Cpd I–W903). The existence of such a reactant complex is the reason for the negative barrier obtained for dimethylaniline (D, with W903, see Table 1): in this case, the transition state lies above the reactant complex, but below the dissociation limit (with N,N-dimethylaniline at infinite distance). In the following, we disregard such reactant complexes.

The barriers computed in the absence of W903 cover a large range between 6 and 22 kcal mol^{-1}. For a given substrate, the values for the doublet and quartet state are usually quite close to each other, typically within 1 kcal mol^{-1}, with the barrier being normally lower in the doublet state. The strong substrate dependence of the barrier to hydrogen abstraction has been examined previously, and it has been shown that

Table 1 B3LYP/B1 barriers (kcal mol^{-1}) for hydrogen abstraction from substrates **1–9** by a Compound I model system in the gas phase[a]

			B3LYP/B1 barrier		
Substrate	Label[b]	Spin[c]	Without W903	With W903	Difference
Ethane	**1**	D	20.32	18.13	2.19
		Q	21.28	18.71	2.57
Propane	**2n**	D	20.47	19.06	1.41
		Q	21.62	20.33	1.29
Propane	**2i**	D	18.02	16.61	1.41
		Q	19.26	16.63	2.63
Phenylethane	**3n**	D	19.96	17.70	2.26
		Q	21.16	18.30	2.86
Phenylethane	**3b**	D	14.30	10.53	3.77
		Q	14.57	10.81	3.76
Me-Probe	**4**	D	17.43	14.85	2.58
		Q	18.46	14.20	4.26
Camphor	**5**	D	17.08	13.63	3.45
		Q	18.08	14.78	3.30
Propene	**6**	D	15.01	13.60	1.37
		Q	15.33	13.21	1.80
Toluene	**7**	D	15.78	12.66	2.67
		Q	15.15	12.05	3.01
iPr-Probe	**8**	D	13.68	13.39	0.29
		Q	14.33	12.92	1.41
Dimethylaniline	**9**	D	6.33	−1.57	7.90
		Q	7.79	2.27	5.52
Dimethylaniline	**9c**	D	6.33	3.38	2.95
		Q	7.79	5.28	2.51

[a] See text for definition of basis B1 and barrier evaluation. [b] **2n** (**2i**): abstraction of primary (secondary) hydrogen atom in propane; **3n** (**3b**): abstraction of methyl (benzyl) hydrogen atom in phenylethane; **9c**: W903 constrained to be *trans* to substrate. [c] D doublet, Q quartet.

View Online

Downloaded by Hebrew University of Jerusalem on 18 December 2010
Published on 14 December 2010 on http://pubs.rsc.org | doi:10.1039/C004950F

the bond dissociation energy (BDE) of the breaking CH bond is the decisive factor that governs the barrier.[1,2,23] Good correlations are available between computed BDEs and barriers which allow fast reactivity predictions for substrates.[24,25] Hence there is no need for further analysis of these data.

For a given substrate, the barriers computed in the presence of W903 are generally somewhat lower than those computed without W903. The B3LYP/B1 barrier lowerings for substrates **1–8** range between 0.3 and 4.3 kcal mol^{-1}, while those for N,N-dimethylaniline **9** are significantly larger (5.5–7.9 kcal mol^{-1}). The reason is obvious when looking at the optimised TS structures (see Fig. 2): **9** is the only substrate engaged in direct interactions with W903 which can provide additional TS stabilization. To assess the magnitude of this side effect, we have performed a constrained TS optimization, with the W903 oxygen atom in *trans*-position to the aniline nitrogen atom, to enforce a non-interfering arrangement of W903: the resulting barrier lowerings of 3.0 (2.5) kcal mol^{-1} for the doublet (quartet) of **9c** now lie in the usual range (Table 1). Whether the extra TS stabilization afforded by W903 in the unconstrained gas-phase optimization (**9** *vs.* **9c**) is a real effect in the enzymatic environment remains an open question at this point. This could be resolved by a QM/MM study which is, however, beyond the scope of this article. Preliminary docking tests suggest that TS structure **9** (Fig. 2) might actually fit into the active site of P450 BM3.

The B3LYP/B1 gas-phase data presented so far show that W903 indeed acts as a catalyst for hydrogen abstraction by Cpd I in all cases (substrates **1–9**, both doublet and quartet). The barrier lowerings are moderate, typically of the order of 2–4 kcal mol^{-1}, and the optimised TS structures indicate earlier transition states in the presence of W903 that are consistent with the smaller barriers. Applying the same type of classical electrostatic modelling as in our previous work on cytochrome P450cam,[5,6] we have confirmed that the calculated barrier lowering is of electrostatic origin in all cases (for detailed numerical data see ESI,† Tables S44 and S45). In qualitative terms, the hydrogen bond between W903 and the oxo atom of Cpd I is stronger in the transition state than in the reactant because of the increase of the negative charge at the oxo atom. This suggests that the amount of barrier lowering might be correlated with the donor strength of the substrate or with the amount of charge transfer in the transition state. We have attempted several such correlations, but without much success. There is practically no correlation between the computed (B3LYP/B1) barrier lowerings and ionisation potentials. The calculated net charges of the substrate in the transition state (as a measure of charge transfer) correlate reasonably well at first sight with the barrier lowerings for substrates **1–9**. However, closer inspection shows that these net charges are generally around 0.30–0.35 *e* for **1–8** and around 0.50 *e* for **9** and **9c** so that the correlation coefficient crucially depends on the barrier lowering for N,N-dimethylaniline (**9** or **9c**). As discussed above, this value is quite different in unconstrained (**9**) and constrained (**9c**) optimisations in spite of the fact that the charge transfer is essentially the same in both cases. Hence, the seemingly good correlation obtained with the data for **9** cannot be regarded as trustworthy (for detailed data and correlation plots see ESI,† Tables S50–S51 and Figures S23–S24).

We now address basis set issues. We have carried out single-point B3LYP calculations at the B3LYP/B1 geometries using three larger basis sets (B2W, B3, and B4, see section 2). The corresponding results are documented in the ESI† (Tables S16–S37). The barrier lowerings obtained with these three sets tend to be smaller than the B3LYP/B1 values and are generally similar to each other. Therefore we have performed additional geometry optimisations only at the B3LYP/B4 level for four representative substrates (*i.e.*, **1**, **4**, **5**, and **9**). The B3LYP/B4 optimised geometries are given in the ESI† (see Figures S17–S21 and Tables S48 and S49), while the corresponding barriers are listed in Table 2. The catalytic effect of W903 is also apparent from the B3LYP/B4 results, with earlier TS geometries and smaller barriers in the presence of W903. The trends are qualitatively the same as at the B3LYP/B1 level, but less pronounced overall. The B3LYP/B4 barrier reductions amount to

 This journal is © The Royal Society of Chemistry 2011

View Online

Table 2 B3LYP/B4 barriers (kcal mol^{-1}) for hydrogen abstraction from substrates **1**, **4**, **5** and **9** by a Compound I model system in the gas phase[a]

			B3LYP/B4 barrier		
Substrate	Label	Spin[b]	Without W903	With W903	Difference
Ethane	**1**	D	19.49	18.10	1.39
		Q	21.67	20.02	1.67
Me-Probe	**4**	D	16.99	15.06	1.93
		Q	19.15	16.83	2.32
Camphor	**5**	D	16.45	14.22	2.23
		Q	18.71	16.32	2.39
Dimethylaniline	**9**	D	6.79	0.51	6.28
		Q	8.77	5.22	3.55

[a] See text for definition of basis B4 and barrier evaluation. [b] D doublet, Q quartet.

Published on 14 December 2010 on http://pubs.rsc.org | doi:10.1039/C004950F
Downloaded by Hebrew University of Jerusalem on 18 December 2010

typically 60–70% of the corresponding B3LYP/B1 values for these substrates (see Tables 1 and 2).

In the case of camphor **5**, additional data on the basis set dependence are available from our previous QM/MM work on the quartet state.[5,6] The reported barrier lowerings (QM = B3LYP/B1, MM = CHARMM) are around 4 kcal mol^{-1}, with slight variations depending on the chosen snapshot and the protonation state of Asp297. Using QM region R1′[6] which is equivalent to our current QM model system, QM/MM optimisations yield barrier lowerings of 4.4 and 3.7 kcal mol^{-1} for basis sets B1 and B2W, respectively. Gas-phase single-point B3LYP/B1 calculations at QM/MM optimised geometries of R1′ lead to a somewhat smaller value of 3.0 kcal mol^{-1},[6] which is reasonably close to the current result of 3.3 kcal mol^{-1} at re-optimised QM geometries (see Table 1). Judging from these data, the catalytic effect of W903 on the hydrogen abstraction barrier appears to be somewhat larger in the enzyme than in the gas phase. This is related to the electronic character of the transition state:[1,2] the Fe(IV) electromer that is favored in the gas phase is expected to be less polarisable than the Fe(III) electromer predominant in the enzyme, which suggests that it should be somewhat less susceptible to the influence of W903. In any event, the basic mechanism of differential electrostatic TS stabilisation by hydrogen bonding to W903 will operate in both cases.

In summary, the present QM model study shows that a single water molecule (W903) indeed acts as a general biocatalyst for hydrogen abstraction by Cpd I, in the doublet and the quartet state of each of the substrates considered (**1–9**). According to the B3LYP/B1 results, the barriers are reduced typically by 2–4 kcal mol^{-1} in the presence of W903. This catalytic effect tends to be diminished when using larger QM basis sets, but should be enhanced when going from the gas phase into the protein environment (see above). Due to these counteracting trends, the computed B3LYP/B1 barrier lowerings may well be realistic estimates for the situation in the enzyme.

4. Brief survey of the role of water in P450 chemistry

One might suspect that the discussed biocatalytic effect of water during hydrogen abstraction by Cpd I is something odd or unusual. To put this into perspective, we briefly comment on other examples in P450 chemistry where an individual water molecule makes the difference.

Water is directly involved in several steps of the catalytic cycle in cytochrome P450cam (Fig. 3).[1,2] In the resting state (**S1**), one water molecule serves as an axial

View Online

ligand. Upon entry of the substrate, it is replaced along with other water molecules that are present in the binding pocket. This replacement gates the catalytic cycle because the redox potential of the resulting pentacoordinate intermediate (**S2**) is such that it can be reduced (unlike the resting state) by the nearby reductase enzyme. After oxygen uptake and another reduction step, the formed ferric peroxo species (**S5**) is protonated to yield the hydroperoxo intermediate (**S6**, Cpd 0). According to QM/MM calculations,[26] the proton delivery is very facile in the wild-type enzyme, because of the presence of a hydrogen-bond network in the Asp251 channel (from protonated Asp251 *via* crystallographic water W901 and Thr252 to the FeOO

Downloaded by Hebrew University of Jerusalem on 18 December 2010
Published on 14 December 2010 on http://pubs.rsc.org | doi:10.1039/C004950F

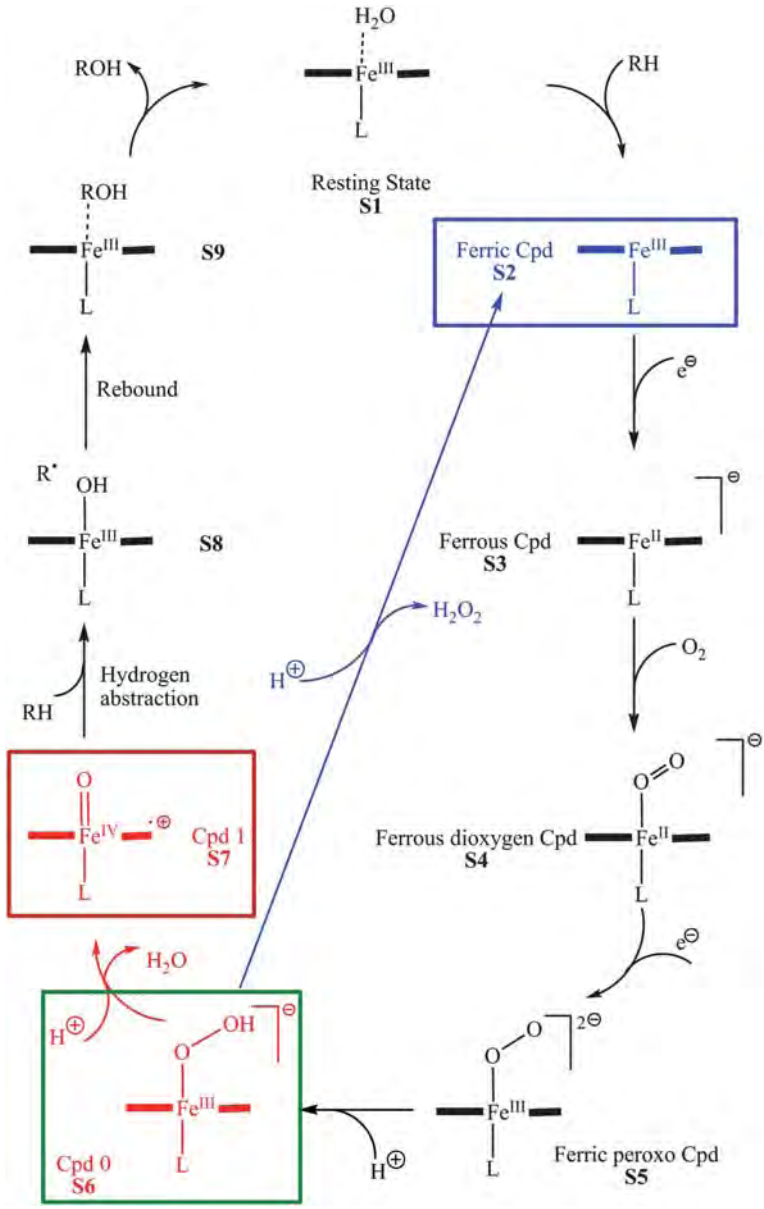

Fig. 3 Catalytic cycle of cytochrome P450cam.

 This journal is © The Royal Society of Chemistry 2011

View Online

Published on 14 December 2010 on http://pubs.rsc.org | doi:10.1039/C004950F
Downloaded by Hebrew University of Jerusalem on 18 December 2010

moiety). In the D251N mutant, the Asn251 side chain flips into a different conformation (thus disrupting the hydrogen-bond network and the proton-transfer pathway), and the entry of an additional water molecule into the active site of D251N is needed to regenerate the network and to enable proton delivery in the mutant.[26] Protonation of the distal oxygen atom in Cpd 0 produces water and Cpd I (**S7**) in wild-type P450cam, again by proton transfer in the Asp251 channel after initial O–O cleavage.[7] The alternative protonation at the proximal oxygen atom in Cpd 0 leads to the formation of hydrogen peroxide and the pentacoordinated ferric intermediate (**S2**) (uncoupling, see Fig. 3). This unproductive side reaction is not observed in wild-type P450cam, but is the only reaction seen in the Thr252Ala and Thr252Gly mutants. This experimental finding has been rationalized in a QM/MM study by showing for these mutants that the entry of an additional water molecule in the Asp251 channel generates an ideal hydrogen-bond network for uncoupling and makes this reaction more favorable than Cpd I formation.[27] This extra water molecule is not present in wild-type P450cam for steric reasons, since threonine is larger than alanine or glycine. The protonation of Cpd 0 in the wild-type and the mutant enzymes is thus an example where the presence of a single water molecule can tip the balance between two competing pathways.[27] The next step in the catalytic cycle of P450cam is substrate hydroxylation (**S7** → **S8** → **S9**) which is catalysed by W903 both in the quartet[5,6] and the doublet[28] state; we have shown in this article that the catalytic effect of W903 is general and also applies to other substrates (see section 3). The catalytic cycle of P450cam is closed by the release of the product alcohol and re-entry of water into the binding pocket to regenerate the resting state (**S1**).

It is obvious from this brief survey that individual water molecules play a crucial mechanistic role in cytochrome P450cam and its mutants. This is also true in other P450-mediated reactions.[1,2] To quote just one striking example, P450 StaP (CYP245A1) catalyses the formation of staurosporine from chromopyrrolic acid by an intricate mechanism that has been unravelled through DFT(B3LYP)/MM calculations.[29] Three of the ten elementary steps involve the relocation of individual water molecules that make the subsequent hydrogen shifts feasible. These water molecules have therefore been called the "working bees" of this mechanism. They act as biocatalysts that enable a very complex transformation.

5. Methodological considerations

Having shown that individual water molecules can make a difference in enzymatic reaction mechanisms, it is of obvious importance not to miss them in theoretical investigations, for example, in QM/MM calculations. Concerning the present case study, the catalytic effect of W903 on hydrogen abstraction in P450cam had not been recognised in our early QM/MM work,[30] simply because W903 had moved away from its initial position near the iron-oxo moiety during the classical molecular dynamics (MD) simulations performed as part of the usual QM/MM setup procedure. The catalytic effect became obvious only in systematic later work[5,6] where the starting geometries for QM/MM optimisation included arrangements with W903 hydrogen bonded to the oxo atom.

This experience motivated a thorough study of the influence of the chosen QM/MM setup procedures on the QM/MM results for P450cam.[31] In particular, different geometry-based hydration procedures were tested, the resulting setups were subjected to classical MD runs to check their feasibility, and twelve of the thus prepared systems were optimised at the QM/MM level to assess the dependence of the QM/MM results on the degree of hydration. Without going too much into details,[31] it was found that saturating the protein interior with water on purely geometry-based criteria is detrimental and leads to high structural flexibility and catalytically inefficient active-site geometries. Classical MD simulations were confirmed to be useful tools for selecting starting geometries with reasonable water content. The

View Online

QM/MM results for the preferred hydration schemes thus obtained turned out to be rather similar, indicating that slight differences in the solvation close to the active site are not critical as long as the substrate and the crystallographic water molecules preserve their positions from the experimental X-ray structure.[31]

During the QM/MM setup phase, it may also be advisable to apply more sophisticated methods such as free-energy calculations, in order to determine whether water is present in a protein cavity that is large enough, but is not occupied by a crystallographic water molecule. It may, of course, be thermodynamically more favorable for a hydrophobic cavity to be empty rather than filled with water,[32] but on the other hand, it is also possible that a mobile water molecule is present, but not detected by X-ray analysis. In practice, one may not be able to decide this issue unambiguously. If one expects such a putative water molecule close to the active site to be relevant mechanistically, it is inevitable in QM/MM optimisation work to perform the calculations with and without this molecule in order to explore all likely possibilities.[26–31]

Part of the QM/MM setup is the partitioning of the system into the QM and MM regions. The safe choice is to include any mechanistically important species into the QM region, of course. For the sake of analysis, it can be worthwhile, however, to consider alternative partitionings. Concerning the current case study, separate QM/MM calculations on camphor hydroxylation by Cpd I have been done with W903 included either in the QM region or in the MM region.[5,6] W903 was found to act as a catalyst in both cases, with comparable barrier lowerings, thus indicating the electrostatic origin of the catalysis (that is also captured when treating W903 at the MM level).

Published on 14 December 2010 on http://pubs.rsc.org | doi:10.1039/C004950F
Downloaded by Hebrew University of Jerusalem on 18 December 2010

Acknowledgements

The research at the Hebrew University is supported in part by an Israeli-Science Foundation (ISF) grant (10/06) and the Ministry of Education and Research within the framework of the German–Israeli Project Cooperation (DIP-G7.1).

References

1 S. Shaik, D. Kumar, S. P. de Visser, A. Altun and W. Thiel, *Chem. Rev.*, 2005, **105**, 2279.
2 S. Shaik, S. Cohen, Y. Wang, H. Chen, D. Kumar and W. Thiel, *Chem. Rev.*, 2010, **110**, 949.
3 H. M. Senn and W. Thiel, *Top. Curr. Chem.*, 2007, **268**, 173.
4 H. M. Senn and W. Thiel, *Angew. Chem., Int. Ed.*, 2009, **48**, 1198.
5 A. Altun, V. Guallar, R. A. Friesner, S. Shaik and W. Thiel, *J. Am. Chem. Soc.*, 2006, **128**, 3924.
6 A. Altun, S. Shaik and W. Thiel, *J. Comput. Chem.*, 2006, **27**, 1324.
7 J. Zheng, D. Wang, W. Thiel and S. Shaik, *J. Am. Chem. Soc.*, 2006, **128**, 13204.
8 A. D. Becke, *J. Chem. Phys.*, 1988, **38**, 3098.
9 C. Lee, W. Yang and R. G. Parr, *Phys. Rev. B: Condens. Matter*, 1988, **37**, 785.
10 A. D. Becke, *J. Chem. Phys.*, 1993, **98**, 5648.
11 R. Ahlrichs, M. Bär, M. Häser, H. Horn and C. Kölmel, *Chem. Phys. Lett.*, 1989, **162**, 165.
12 J. P. Hay and W. R. Wadt, *J. Chem. Phys.*, 1985, **82**, 299.
13 W. J. Hehre, L. Radom, P. v. R. Schleyer and J. A. Pople, *Ab Initio Molecular Orbital Theory*, John Wiley & Sons, New York, 1986.
14 A. J. H. Wachters, *J. Chem. Phys.*, 1970, **52**, 1033.
15 P. J. Hay, *J. Chem. Phys.*, 1977, **66**, 4377.
16 C. W. Bauschlicher, Jr., S. R. Langhoff and L. A. Barnes, *J. Chem. Phys.*, 1989, **91**, 2399.
17 A. Schäfer, H. Horn and R. Ahlrichs, *J. Chem. Phys.*, 1992, **97**, 2571.
18 A. Schäfer, C. Huber and R. Ahlrichs, *J. Chem. Phys.*, 1994, **100**, 5829.
19 E. Sigfridsson and U. Ryde, *J. Biol. Inorg. Chem.*, 1999, **4**, 99.
20 K. P. Jensen and U. Ryde, *J. Biol. Chem.*, 2004, **279**, 14561.
21 S. R. Billeter, A. J. Turner and W. Thiel, *Phys. Chem. Chem. Phys.*, 2000, **2**, 2177.
22 P. Sherwood, A. H. de Vries, M. F. Guest, G. Schreckenbach, C. R. A. Catlow, S. A. French, A. A. Sokol, S. T. Bromley, W. Thiel, J. Turner, S. Billeter, F. Terstegen,

 This journal is © The Royal Society of Chemistry 2011

View Online

S. Thiel, J. Kendrick, S. C. Rogers, J. Casci, M. Watson, F. King, E. Karlsen, M. Sjovoll, A. Fahmi, A. Schäfer and C. Lennartz, *THEOCHEM*, 2003, **632**, 1.
23 See section 4.7 in Ref. 1 and section 5.1 in Ref. 2.
24 S. P. de Visser, D. Kumar, S. Cohen, R. Shacham and S. Shaik, *J. Am. Chem. Soc.*, 2004, **126**, 8362.
25 L. Olsen, P. Rydberg, T. H. Rod and U. Ryde, *J. Med. Chem.*, 2006, **49**, 6489.
26 D. Wang, J. Zheng, S. Shaik and W. Thiel, *J. Phys. Chem. B*, 2008, **112**, 5126.
27 M. Altarsha, T. Benighaus, D. Kumar and W. Thiel, *J. Am. Chem. Soc.*, 2009, **131**, 4755.
28 A. Altun, S. Shaik and W. Thiel, *J. Am. Chem. Soc.*, 2007, **129**, 8978.
29 Y. Wang, H. Chen, M. Makino, S. Shiro, S. Nagano, H. Onaka and S. Shaik, *J. Am. Chem. Soc.*, 2009, **131**, 6748.
30 J. C. Schöneboom, S. Cohen, H. Lin, S. Shaik and W. Thiel, *J. Am. Chem. Soc.*, 2004, **126**, 4017.
31 J. Zheng, A. Altun and W. Thiel, *J. Comput. Chem.*, 2007, **28**, 2147.
32 V. Helms and R. C. Wade, *Biophys. J.*, 1995, **69**, 810.

Published on 14 December 2010 on http://pubs.rsc.org | doi:10.1039/C004950F
Downloaded by Hebrew University of Jerusalem on 18 December 2010

Steric Factors Override Thermodynamic Driving Force in Regioselectivity of Proline Hydroxylation by Prolyl-4-hydroxylase Enzymes

Baharan Karamzadeh,[†] Devesh Kumar,*[,‡] G. Narahari Sastry,[‡] and Sam P. de Visser*[,†]

The Manchester Interdisciplinary Biocenter and the School of Chemical Engineering and Analytical Science, The University of Manchester, 131 Princess Street, Manchester M1 7DN, United Kingdom, and Molecular Modelling Group, Indian Institute of Chemical Technology, Hyderabad 500-607, India

Received: September 20, 2010; Revised Manuscript Received: November 4, 2010

Prolyl-4-hydroxylase is an important nonheme iron-containing dioxygenase in humans involved in the regioselective hydroxylation of a proline residue in a peptide chain on the C^4 position. In biosystems this process is important to create collagen cross-linking and cellular responses to hypoxia. We have performed a series of density functional theory (DFT) studies into the origin of the regioselectivity of proline hydroxylation by P4H enzymes using a minimal active site model (where substrate is unhindered in the binding site) and a larger active site model that incorporates steric hindrance of the substrate by several secondary sphere aromatic residues. Our studies show that thermodynamically the most favorable hydrogen atom abstraction position of proline is from the C^5 position; hence, the small model gives a low reaction barrier and large exothermicity for this process. However, stereochemical repulsions of the substrate with aromatic residues of Tyr_{140} and Trp_{243} in the second coordination sphere prevent C^5 hydroxylation and make C^4 hydroxylation the dominant mechanism, despite a lesser driving force for the reaction. These studies explain the remarkable regioselectivity of proline hydroxylation by P4H enzymes and show that the regioselectivity is kinetically controlled but not thermodynamically. In addition, we calculated spectroscopic parameters and found good agreement with experimental data.

Introduction

Mononuclear nonheme iron-containing enzymes are versatile enzymes in nature that catalyze important reaction processes in many biosystems, including the human body.[1] These enzymes often share a common motif, whereby the metal is bound to the protein via interactions with two histidine and one carboxylic acid group of either an Asp or a Glu amino acid side chain to form a characteristic facial metal binding triad.[2] A large group of mononuclear nonheme iron-containing enzymes utilize α-ketoglutarate (αKG) as a cofactor and catalyze aliphatic hydroxylation reactions as well as substrate halogenation, desaturation, and ring-closure reactions.[1,3] In nature, these enzymes, for instance, are involved in the biosynthesis of vancomycin and fosfomycin in antibiotics,[4] as well as in DNA and RNA base repair mechanisms in mammals.[5] In addition, the α-ketoglutarate-dependent dioxygenases are also involved in cross-linking of collagen and responses to hypoxia.[6]

The most extensively studied α-ketoglutarate-dependent dioxygenase is taurine/α-ketoglutarate dioxygenase (TauD) found in *Escherichia coli*. TauD is involved in the hydroxylation of taurine and is highly soluble and relatively stable.[7] Thanks to this, it was the first enzyme where a high-valent iron(IV)−oxo species was characterized with resonance Raman, Mössbauer, and X-ray absorption spectroscopy.[8] As a consequence, TauD has become the template for mononuclear nonheme iron enzymes and has prompted many additional studies. The catalytic cycle of TauD enzymes is well-established[9,10] and starts with αKG binding to an Fe center and substrate in its vicinity.

SCHEME 1: Proline Hydroxylation by P4H Enzymes

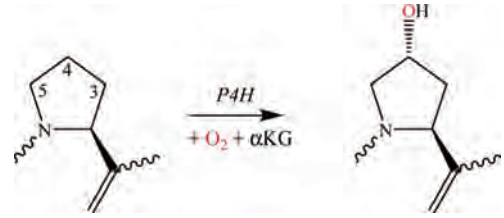

Subsequently, dioxygen binds to the last binding site of the metal, which attacks αKG at the α-keto position to form a bicyclic ring structure. Subsequently, decarboxylation leads to succinate and a high-valent iron(IV)−oxo species, which has been spectroscopically characterized with various methods for TauD.[8] The final steps in the catalytic cycle start with a hydrogen atom abstraction from the substrate by the iron(IV)−oxo oxidant followed by rebound of the hydroxyl group to form alcohol products.

Another α-ketoglutarate-dependent dioxygenase with importance for human health is prolyl-4-hydroxylase (P4H), involved in the regioselective hydroxylation of proline groups on the C^4 position (Scheme 1).[11] This is an important reaction in biosystems due to cross-linking collagen helices, oxygen sensing, and cellular response to hypoxia through the hypoxia inducible factor (HIF).[12,13] Thus, the cross-linking strand in collagen contains a series of repeated triads, where the first residue usually is proline, the second is often 4-hydroxyproline, while the last residue typically is a glycine.[14] A combination of spectroscopic and kinetic studies on substrate hydroxylation by P4H using a small peptide $(Pro\text{-}Ala\text{-}Pro\text{-}Lys)_3$ showed that the proline residues are readily hydroxylated by the enzyme.[15] Studies using $^{18}O_2$ showed that one oxygen atom of molecular oxygen is incorporated into

* To whom correspondence should be addressed. E-mail: sam.devisser@manchester.ac.uk (S.P.d.V.), dkclcre@yahoo.com (D.K.).
[†] The University of Manchester.
[‡] Indian Institute of Chemical Technology.

10.1021/jp1089855 © 2010 American Chemical Society
Published on Web 11/29/2010

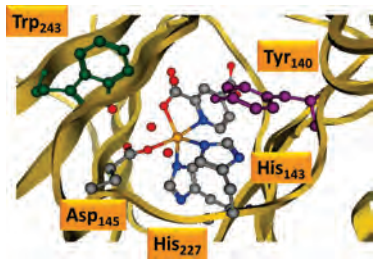

Figure 1. Active site of P4H enzyme as taken from the 2JIG Protein Databank file. Amino acids labeled as in the crystal structure.

hydroxo−proline products.[16] Further stopped-flow absorption and Mössbauer experiments provided evidence of an iron(IV)−oxo intermediate with features similar to those detected for the iron(IV)−oxo oxidant of TauD above. Moreover, a large kinetic isotope effect was measured for replacement of the 2,3,3,4,4,5,5-positions by deuterium atoms. Mechanistic studies using 5-oxaproline-containing peptides as a substrate found evidence of a Groves-type radical rebound mechanism.[17] By contrast, studies of the reaction of P4H with fluorinated proline residues gave no reaction products, due to the strength of the C−F bond.[15] On the other hand, with a sulfide group in this position, substrate sulfoxidation was observed.

Figure 1 displays the active site structure of P4H enzymes as taken from the 2JIG Protein Databank file.[18] The metal is bound to a 2His-1Asp binding motif through interactions with His_{143}, Asp_{145}, and His_{227} similar to other nonheme iron dioxygenases. Instead of αKG, the PDB contains pyridine-2,4-dicarboxylate, which binds as a bidentate ligand to the metal similarly to αKG. Currently no substrate-bound crystal structures are available. The metal center is closely located to the protein surface, and a water channel is seen above the metal, and it has been proposed that the substrate will bind here.[19] Directly above the metal are located a series of aromatic residues, such as Tyr_{140} and Trp_{243}, that may restrict substrate approach to the binding site. At the moment, the origin of the substrate selectivity of P4H enzymes is unclear. Thus, the enzyme regioselectively hydroxylates a proline residue at the C^4 position exclusively, and so far there is no evidence of products from hydroxylation of the C^3 and C^5 positions. To gain insight into the substrate hydroxylation mechanism of this important enzyme for human health and the factors that determine the regioselectivity of substrate hydroxylation, we have performed a density functional theory (DFT) study on models of the active site of P4H enzymes. In principle, the origin of this regioselectivity can arise from thermodynamic factors, i.e., the relative strength of the C^4−H bond with respect to the C^3−H and C^5−H bonds or, alternatively, through electrostatic interactions such as substrate approach to the active center. In this study, we investigated both possibilities and show that stereochemical factors within the substrate binding pocket favor C^4 hydroxylation over C^3 and C^5 hydroxylation.

Methods

The mechanism of proline hydroxylation by P4H enzymes was modeled using density functional theory using methods tested and benchmarked on nonheme iron enzyme models in our group.[20] We use the hybrid density functional method B3LYP[21] combined with a double-ζ quality basis set containing LACVP on iron and 6-31G on the rest of the atoms (H, C, O, N), the basis set BS1.[22] Geometry optimizations were done with Jaguar 7.6,[23] while analytical frequencies were calculated with Gaussian 03.[24] Energetics were improved through single-point calculations with a triple-ζ quality LACV3P+ basis set on iron and 6-311+G* on H, C, O, N atoms, the basis set BS2. The effect of the environment was tested through single-point calculations in Jaguar using the self-consistent reaction field model with a dielectric constant of $\varepsilon = 5.7$ and a probe radius of 2.72 Å; however, these single-point calculations had little effect on the overall energetics of the process; see Supporting Information, Table S6 and S7. In the past, the methods have been extensively benchmarked against experimental data and it was shown that free energies of activation are reproduced within 3 kcal mol^{-1},[25] although this is a systematic error and generally barrier heights have standard deviations between 1 and 2 kcal mol^{-1}.[20,26] In addition, extensive calibration studies were done on related systems in which spectroscopic parameters as well as kinetic isotope effects were calculated.[27] These studies generally reproduced experimental data well and confirm that the methods are reliable and suitable for these types of systems.

Kinetic isotope effects (KIE) were calculated from the semiclassical Eyring equations (eq 1) using the free energy of activation ($\Delta G_H^{\ddagger}$) of the reference structure and those where one or more hydrogen atoms of the substrate were replaced by deuterium atoms. In eq 1, R represents the gas constant and T the estimated temperature (298 K).

$$KIE_{Eyring} = \exp[(\Delta G_D^{\ddagger} - \Delta G_H^{\ddagger})/RT] \quad (1)$$

Further corrections to the isotope effect due to tunneling were applied by multiplying KIE_{Eyring} with the tunneling ratio (Q_{tH}/Q_{tD}) (eq 2). Two methods to estimate the tunneling ratio were used due to Wigner and Bell as given in eqs 3 − 6.[28] In these equations h is Planck's constant, k_B is the Boltzmann constant, and ν the imaginary frequency in the transition state.

$$KIE_{tunneling} = KIE_{Eyring} \times Q_{tH}/Q_{tD} \quad (2)$$

$$Q_{t,Wigner} = 1 + u_t^2/24 \quad \text{with} \quad u_t = h\nu/k_BT \quad (3)$$

$$Q_{t,Bell} = Q_1 + Q_2 \quad (4)$$

$$Q_1 = \frac{u_t}{2\sin\left(\frac{1}{2}u_t\right)} \quad (5)$$

$$Q_2 = -\sum_{n=1}^{\infty}(-1)^n \frac{\exp(v_t\Delta G_H)}{v_t} \quad \text{with} \quad v_t = \frac{u_t - 2n\pi}{u_t} \quad (6)$$

In addition to replacing hydrogen atoms by deuterium atoms, we also investigated the effects of replacing $^{16}O_2$ by $^{18}O_2$ on the IR frequencies of the iron(IV)−oxo species. The geometry was optimized as described above and followed by a frequency calculation at the UB3LYP/BS1 level of theory in the Gaussian 03 suits of programs. A single-point calculation was performed on this structure with isotopic substitution of $^{16}O_2$ by $^{18}O_2$ and the obtained frequencies were analyzed. All frequencies were scaled by a factor of 0.9257.[29]

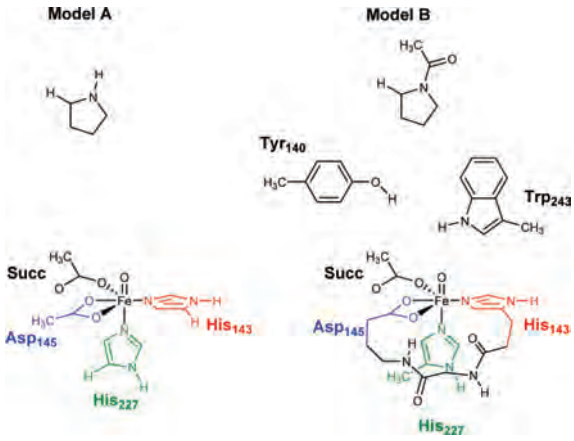

Figure 2. Models of P4H studied in this work.

Results and Discussion

Our models were based on the crystal structure coordinates (PDB file 2JIG) of P4H.[18] We selected strand A of the dimer, since its peptide chain is longer. Subsequently, we added hydrogen atoms, replaced the metal by iron and pyridine-2,4-dicarboxylate by αKG, and inserted an oxo group trans to His_{227}. Two different models of the active site of P4H enzymes were set up; see Figure 2. Model A is a minimal model analogous to the one we used in our earlier studies of TauD[33] and comprises of an iron(IV)−oxo group that is linked to two imidazole groups that mimic the His_{143} and His_{227} ligands, while the two carboxylic acid ligands of Asp_{145} and succinate (Succ) are abbreviated to acetate groups and proline as a saturated five-membered ring without side chains. A more elaborate model B was built by inclusion of the peptide chain between His_{143} and Asp_{145}, whereby amino acid 144 is modeled by Gly. Furthermore, His_{227} is mimicked as methylimidazole, and two distal aromatic amino acids (Tyr_{140} and Trp_{243}) are included as *p*-cresol and indole groups, respectively. Finally, substrate proline is extended with a peptide bond on the *N*-terminus. To prevent the individual groups from reorienting from the original positions in the crystal structure, during the geometry optimization we constrained the position of the carbon atom of the methyl group of Tyr_{140} and Trp_{243} with respect to the metal center as well as the angle and dihedral of its neighboring carbon atom. However, no constraints were placed on the metal ligands or the substrate.

The active species of P4H enzymes is a high-valent iron(IV)−oxo species, which is one of the few iron(IV)−oxo species of enzymatic systems that has been spectroscopically characterized with resonance Raman, EPR, and Mössbauer spectroscopic methods.[15] In order to benchmark our methods and procedures, we started our work with a detailed analysis of the iron(IV)−oxo species (**1**) using models A and B as depicted in Figure 2. Here, for each considered species, the spin multiplicity is given as a superscript and model as a subscript before and after the species label, respectively. We ran a full geometry optimization on the lowest lying singlet, triplet, quintet, and septet spin states and subsequently calculated IR spectra as well as EPR and Mössbauer spectroscopic parameters.

The high-lying occupied and low-lying virtual orbitals of the iron(IV)−oxo species of P4H (**1**) are shown in Figure 3. For simplicity, we only show the orbitals for the small model; those for the large model are essentially the same. The metal 3d type

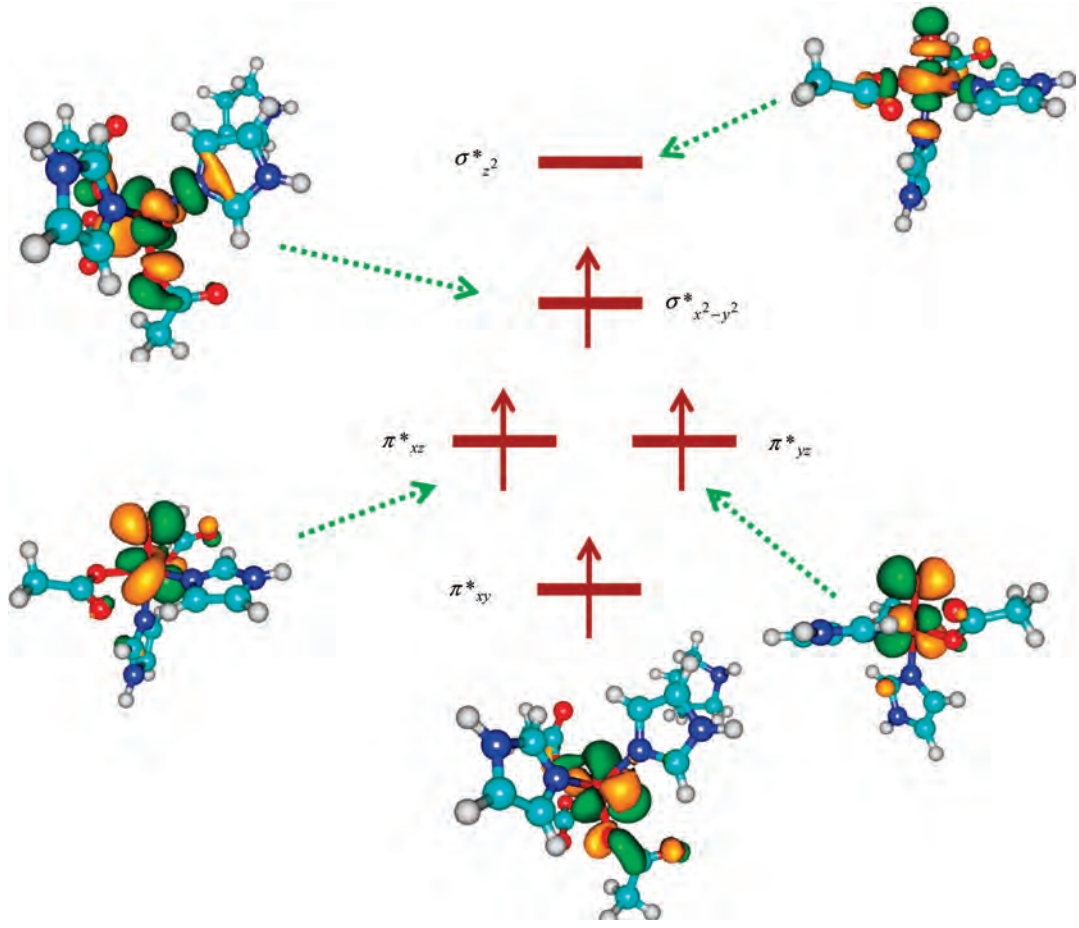

Figure 3. High-lying occupied and virtual orbitals of the iron(IV)−oxo species of P4H.

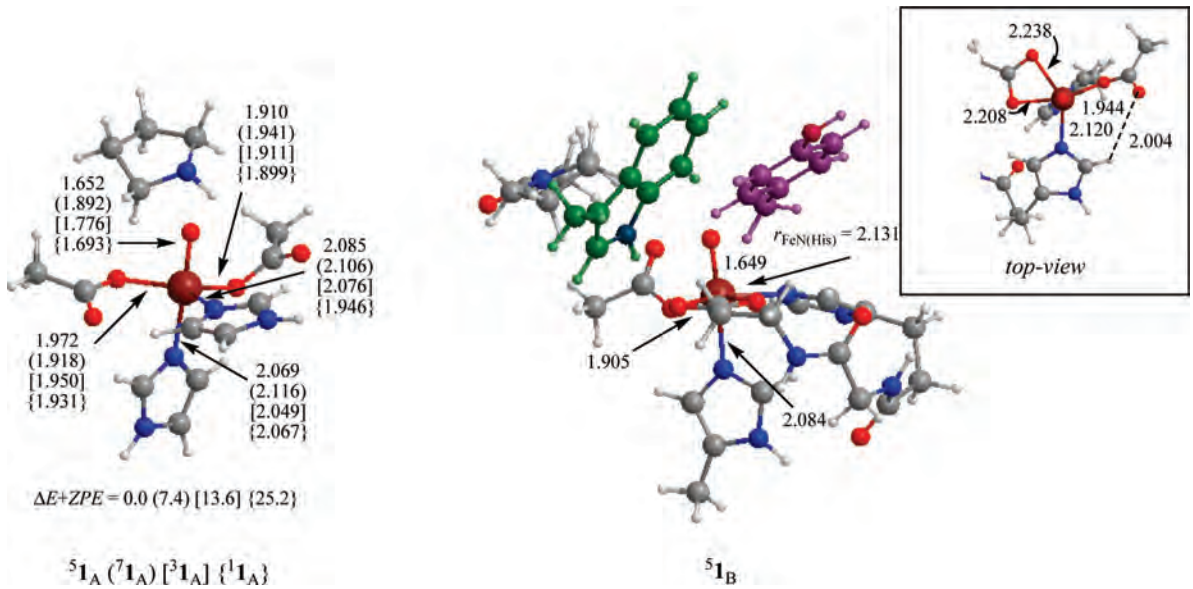

Figure 4. Optimized geometries of the iron(IV)−oxo species of P4H models A and B with bond lengths given in angstroms. Also given are relative energies of the quintet, septet, triplet, and singlet spin states. The inset gives a top view of the metal and its direct ligands for $^5\mathbf{1}_B$.

orbitals split into three lower lying π^* orbitals and two higher lying σ^* orbitals. The lowest one is the π^*_{xy} orbital that is orthogonal to the Fe−O bond and interacts with the His_{143}, Asp_{145}, and succinate ligands. Slightly higher in energy are two π^*_{FeO} orbitals (labeled as π^*_{xz} and π^*_{yz}) for the antibonding interactions of the metal $3d_{xz,yz}$ with corresponding 2p orbitals on the oxygen atom. Higher in energy are two σ^* type orbitals for the antibonding interactions along the O−Fe−$NHis_{227}$ axis ($\sigma^*_{z^2}$) and one in the plane of the His_{143}, Asp_{145}, and succinate ligands ($\sigma^*_{x^2-y^2}$). This set of orbitals is occupied by four electrons to give the metal oxidation state Fe(IV). DFT calculations on the iron(IV)−oxo species of TauD predicted a quintet spin ground state with $\pi^*_{xy}{}^1\ \pi^*_{xz}{}^1\ \pi^*_{yz}{}^1\ \sigma^*_{x^2-y^2}{}^1$ occupation.[30] In biomimetic nonheme iron(IV)−oxo species, on the other hand, usually a triplet spin ground state is found with $\pi^*_{xy}{}^2\ \pi^*_{xz}{}^1\ \pi^*_{yz}{}^1$ occupation.[31,32] DFT calculations showed that electron-donating axial ligands tend to reduce the energy gap between the π^*_{xy} and $\sigma^*_{x^2-y^2}$ orbitals and thereby lower the triplet−quintet energy gap in favor of a triplet spin ground state in biomimetic systems.[33]

Subsequently, we did a full geometry optimization of the lowest lying spin state structures of models A and B and the results are shown in Figure 4, which clearly demonstrates that both models predict the ground state of **1** to be a quintet spin state with orbital occupation $\pi^*_{xy}{}^1\ \pi^*_{xz}{}^1\ \pi^*_{yz}{}^1\ \sigma^*_{x^2-y^2}{}^1$. The triplet spin state has $\pi^*_{xy}{}^2\ \pi^*_{xz}{}^1\ \pi^*_{yz}{}^1$ occupation, whereas the septet spin state has $\pi^*_{xy}{}^1\ \pi^*_{xz}{}^1\ \pi^*_{yz}{}^1\ \sigma^*_{x^2-y^2}{}^1\ \sigma^*_{z^2}{}^1\ lp_O{}^1$ occupation. The latter orbital refers to a lone pair on the oxo group. Finally, the singlet spin state has $\pi^*_{xy}{}^2\ \pi^*_{xz}{}^1\ \pi^*_{yz}{}^1$ occupation with the two unpaired electrons having opposing spin direction. Our assignment supports experimental EPR studies[15] that indicated a quintet spin ground state. DFT and quantum mechanics/molecular mechanics (QM/MM) studies on the active species of the related nonheme iron enzyme TauD predicted a similar spin state ordering to that obtained for P4H here with a quintet spin state as the molecular ground state.[10,34]

The quintet spin ground state is well-separated from the septet, triplet, and singlet spin states by 7.4, 13.6, and 25.2 kcal mol^{-1} for Model A. For the iron(IV)−oxo intermediate in the catalytic cycle of TauD, Siegbahn and co-workers[10] found a quintet spin ground state that was 6.0 kcal mol^{-1} lower in energy than the lowest septet spin state, in perfect agreement with our calculations here. This spin state ordering is similar to previous studies of nonheme iron(IV)−oxo complexes in enzymatic systems,[30,34,35] where also large quintet−triplet and quintet−singlet energy gaps were obtained. In the nonheme iron enzyme isopenicillin *N*-synthase the iron(IV)−oxo intermediate is in a quintet spin ground state with the triplet and septet spin states 5.2 and 10.3 kcal mol^{-1} higher in energy.[36] It appears therefore that the relative energy of the quintet and triplet spin states is very sensitive to the ligands bound to the metal, and minor changes lead to major shifts in the quintet−triplet energy gap. This is also apparent from studies on biomimetic nonheme iron(IV)−oxo complexes that tend to have a triplet spin ground state with the lowest lying quintet spin state several kcal mol^{-1} higher in energy.[32,37] Usually in biomimetic nonheme iron(IV)−oxo complexes the septet spin state is high in energy and does not play a role of importance. Obviously, this is quite different from the situation in enzymatic systems such as TauD and P4H, where the septet spin state is significantly lower in energy, sometimes within 5 kcal mol^{-1} of the quintet spin ground state. Clearly, in P4H the triplet and singlet spin states are so high in energy in the reactants that they will not contribute significantly to the reaction mechanism; therefore, in the remainder of the paper, we will focus on the lowest lying quintet and septet spin states only. Extensive DFT studies on nonheme iron-containing enzymes such as TauD and α-ketoglutarate-dependent halogenase showed that the singlet and triplet spin state surfaces stay high in energy along the substrate hydroxylation mechanism.[10,30,35,38]

Interestingly, the optimized geometries do not seem dramatically affected by the size of the model. For instance, an iron−oxo bond length in the quintet spin state of 1.652 and 1.649 Å is found for $^5\mathbf{1}_A$ and $^5\mathbf{1}_B$, respectively. In addition, the calculated metal−ligand bond distances between Fe and His_{143}, Asp_{145}, His_{227}, and Succ give only small differences between the two models. It appears, therefore, that the optimized geometry is very little affected by increasing the size of the model through addition of mainly secondary sphere amino acids. The calculated iron(IV)−oxo distances are in excellent agreement with those calculated for complexes of heme and nonheme systems before.[32,39] An Fe−O distance ranging from 1.62 to 1.65 Å was found for heme-based iron(IV)−oxo complexes

dependent on the axial ligand. Our calculated Fe−O stretch vibration of 811 cm^{-1} for $^5\mathbf{1}_B$ is in line with previously determined values for iron(IV)−oxo complexes.

Resonance Raman experiments of Hausinger et al.[8b] on TauD supplied with $^{16}O_2$ and $^{18}O_2$ provided a difference spectrum with oxygen sensitive peaks at 583, 821, and 859 cm^{-1} in the $^{16}O_2$ spectrum. The latter vibration, however, coincided with a strong solvent band, so its identification was not unambiguous. To find the corresponding vibrations for the iron(IV)−oxo species of P4H, we analyzed the frequencies of $^5\mathbf{1}_B$ and its $^{18}O_2$ substituted spectrum. Thus, in the catalytic cycle of P4H and TauD, molecular oxygen donates one oxygen atom to αKG to form succinate and an iron(IV)−oxo species. Therefore, we replaced the oxo group and one of the oxygen atoms of the carboxylic acid group of succinate that binds iron by ^{18}O atoms to calculate the $^{18}O_2$ spectrum. Vibrational frequency analysis of $^5\mathbf{1}_B[^{16}O_2]$ gives an Fe═O stretch vibration at $\nu_{Fe=O} = 811$ cm^{-1}, while the stretch vibration along the Fe−O bond between the metal and the succinate group is located at $\nu_{Fe-OSucc} = 857$ cm^{-1}. Our calculations, therefore, support the experimental assignment of an Fe═O stretch vibration at 811 cm^{-1} and confirm that there indeed is an oxygen-sensitive band at 857 cm^{-1}, which originates from the first oxygen atom transfer process in the catalytic cycle where succinate is formed. Two bending vibrations in the carboxylic acid group of succinate are identified at 557 cm^{-1} (out-of-plane) and 583 cm^{-1} (in-plane). Substitution of $^{16}O_2$ by $^{18}O_2$ in $^5\mathbf{1}_B$ downshifts $\nu_{Fe=O}$ by 33 cm^{-1} and the $\nu_{Fe-OSucc}$ by 18 cm^{-1}. Much smaller frequency shifts are obtained for the two bending vibrations of −11 cm^{-1} for the in-plane vibration and −4 cm^{-1} for the out-of-plane vibration. However, these two bending vibrations give sharp differences in the calculated Raman intensities, whereby the higher vibration is more Raman active in the $^{16}O_2$ spectrum, whereas the lower vibration is more active in the $^{18}O_2$ spectrum. As a consequence of this, they implicate a single peak that shifts by about 30 cm^{-1} but in fact represent two peaks with different Raman intensities in the $^{16}O_2$ and $^{18}O_2$ spectra.

In addition, we calculated Mössbauer spectroscopic parameters of **1** and focused on the electric field splitting (ΔE_Q), the asymmetry parameter of the nuclear quadrupole tensor (η), and the isomer shift (δ) (Supporting Information, Table S8). Although the error bars for these types of calculations are high, a modest agreement between the calculated values of ΔE_Q for $^5\mathbf{1}$ with the experimental data from ref 15 is found. Hence, DFT calculations on the iron(IV)−oxo species of P4H support the spectroscopic assignments in the literature in favor of a quintet spin as the ground state. The benchmark calculations of spectroscopic parameters on models A and B give good agreement with experimental data and support the use of these models for our calculations.

Substrate Hydroxylation by P4H Enzymes. The general mechanism of substrate hydroxylation by the iron(IV)−oxo species of P4H is shown in Scheme 2. Thus, the iron(IV)−oxo species (**1**) picks up a hydrogen atom from the substrate via a hydrogen atom abstraction barrier (TS_{HA}) to form an iron(III)−hydroxo complex with a nearby prolyl radical (**2**). A radical rebound barrier (TS_{reb}) separates this radical intermediate from the alcohol product complex (**3**). This mechanism is similar to the rebound mechanism proposed for substrate hydroxylation reactions by the iron(IV)−oxo heme(+•) active species of cytochrome P450 enzymes and confirmed by biomimetic and computational studies.[40]

Theoretically, substrate hydroxylation by P4H enzymes should lead to products originating from hydroxylation at the

SCHEME 2: General Mechanism of Substrate Hydroxylation by P4H Enzymes

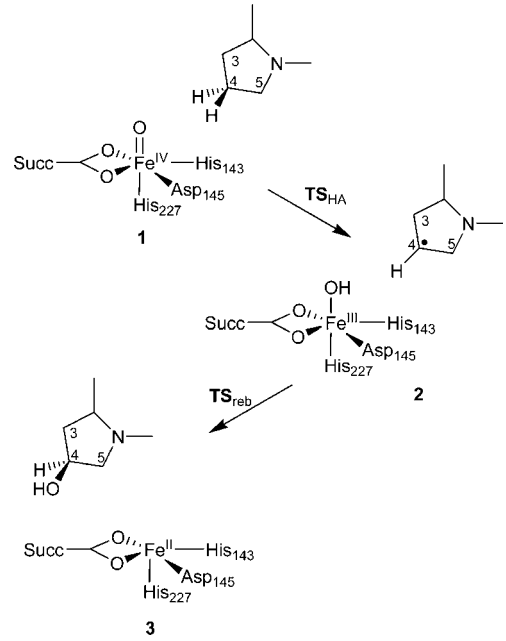

C^3, C^4, and C^5 positions of proline; however, in the enzyme only the C^4 position is activated. To find out what the most likely hydroxylation site of a proline molecule is, we did a series of DFT calculations to determine the bond dissociation energies (BDE_{CH}) of the various C−H bonds of proline; see Figure 5. The C−H bond strength or BDE_{CH} was calculated from eq 7:

$$\text{Pro}-\text{H} \rightarrow \text{Pro}^{\bullet} + \text{H}^{\bullet} + \text{BDE}_{\text{CH}} \qquad (7)$$

Experimental studies of hydrogen abstraction reactions by metal(IV)−oxo oxidants showed that the rate constants and hence free energies of activation correlated with the strength of the C−H bond that is broken in the process.[41] Recent DFT studies in combination with valence bond modeling rationalized these hydrogen abstraction reactions and showed that the correlation follows from electron transfer processes from reactants to radical intermediates.[26c] In the case of testosterone hydroxylation by the iron(IV)−oxo species of cytochrome P450, the barrier heights of hydrogen atom abstraction for four different C−H positions of the substrate correlated to the strength of these C−H bonds.[42]

Figure 5 displays the calculated BDE_{CH} values of the C^3−H, C^4−H, and C^5−H positions of proline. As follows, H-abstraction from the C^5 position from proline should be the easiest because it has the weakest C−H bond strength ($BDE_{CH} = 85.4$ kcal mol^{-1}). Furthermore, the C^4−H bond strength of proline apparently is the strongest of these C−H bonds and, therefore, the least likely position for hydroxylation with a $BDE_{CH} = 92.4$

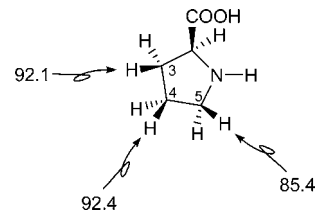

Figure 5. Calculated BDE_{CH} values of proline C−H bonds with energies in kcal mol^{-1}.

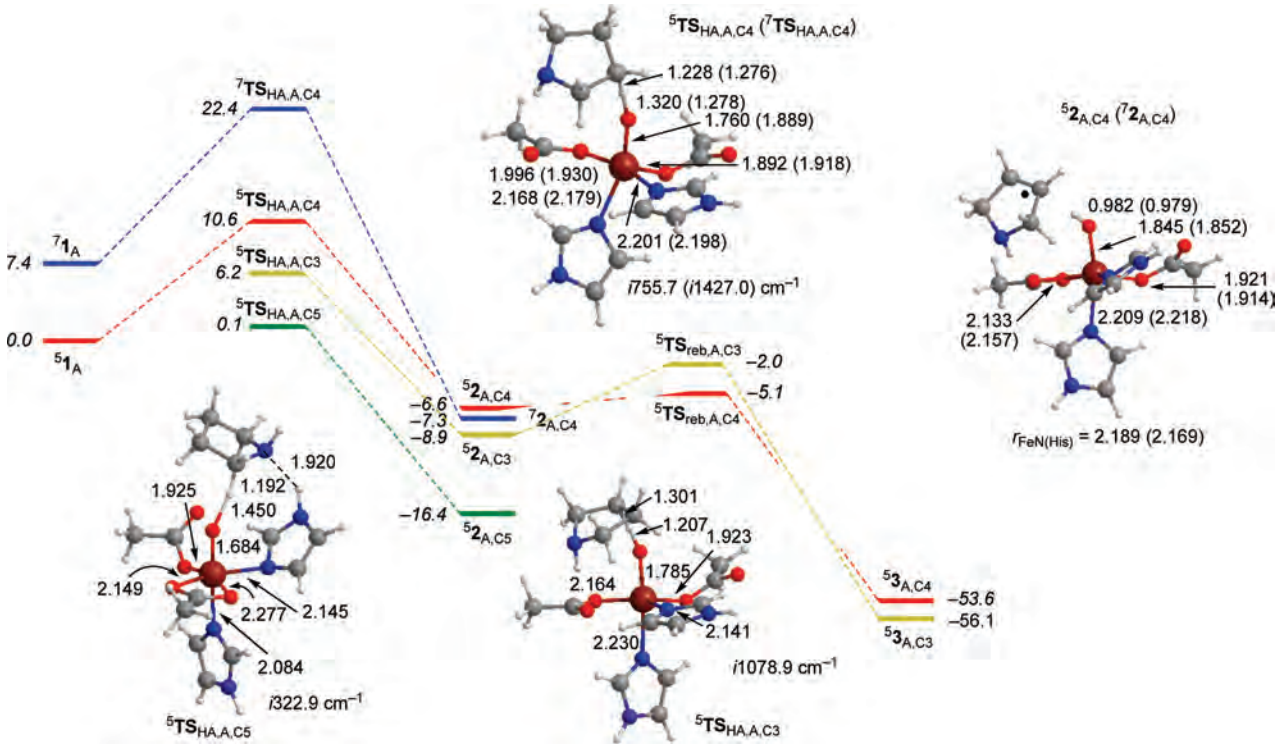

Figure 6. Potential energy landscape of proline hydroxylation at the C^5, C^4, and C^3 positions using model A. Relative energies are in kcal mol^{-1}, obtained with basis set BS2, while ZPE corrections are calculated with basis set BS1. Optimized geometries contain bond lengths in angstroms and the imaginary frequency in wavenumbers.

kcal mol^{-1}. Therefore, our BDE_{CH} calculations show that proline hydroxylation on the C^4 position is thermodynamically the least expected hydroxylation site, despite the fact that this is the targeted site in the enzyme. Using a small Ala-Pro-Ala peptide, the calculated BDE_{CH} values at the C^3, C^4, and C^5 positions of proline are 93.5, 92.9, and 86.7 kcal mol^{-1}, respectively, which indicates that these BDE_{CH} values give little sensitivity regarding the size of the substrate. In order to find out why P4H enzymes hydroxylate proline on the C^4 position while the driving force for the reaction is the smallest at this position, we ran a series of DFT calculations to establish environmental (stereochemical) effects on the reaction mechanism and barriers.

Subsequently, we investigated the mechanism of proline hydroxylation at the C^5, C^4, and C^3 positions using the minimal model (model A), and the results are shown in Figure 6. Proline hydroxylation at the C^4 position was calculated on the lowest lying singlet, triplet, quintet, and septet spin states. The singlet and triplet reactants, however, are well higher in energy than $^5\mathbf{1}_A$ (Figure 4) by 25.2 and 13.6 kcal mol^{-1}, respectively, and so are their corresponding hydrogen atom abstraction barriers leading to an iron−hydroxo intermediate (>28 kcal mol^{-1}). Therefore, we will focus in the main text on the quintet and septet states only; details of the other spin states can be found in the Supporting Information. Proline hydroxylation at the C^3 and C^5 positions was only calculated on the quintet spin state surface.

Although the reactant state has a quintet spin ground state, after hydrogen abstraction close-lying iron(III)−hydroxo complexes (**2**) in the quintet and septet spin states, $^5\mathbf{2}_{A,C^4}$ and $^7\mathbf{2}_{A,C^4}$, are found within 1 kcal mol^{-1}. These two states have the same orbital occupation ($\pi^*_{xy}{}^1\ \pi^*_{xz}{}^1\ \pi^*_{yz}{}^1\ \sigma^*_{z^2}{}^1\ \sigma^*_{x^2-y^2}{}^1\ \pi_{Sub}{}^1$) with a singly occupied metal d-block coupled to an unpaired electron on the proline rest-group; this interaction is ferromagnetic in the septet spin state and antiferromagnetic in the quintet spin state. Even though the intermediate has close-lying quintet and septet spin states, as a matter of fact, in the H-abstraction transition states, the quintet state is well-separated from the septet by more than 10 kcal mol^{-1} for the C^4-hydroxylation mechanism. Consequently, P4H hydroxylation will proceed via single-state reactivity on a dominant quintet spin state surface only. The energy gap between $^5TS_{HA}$ and $^7TS_{HA}$ is in contrast to substrate hydroxylation by TauD models, where two-state reactivity patterns on close lying quintet and septet spin states were found.[26b,30] Nevertheless, the H-abstraction step is rate-determining as the radical rebound barrier is much smaller.

In agreement with the thermodynamic analysis mentioned above, the relative energies of the H-abstraction transition states and radical intermediates follow the trend in BDE_{CH} with $^5TS_{HA,A,C^5} < {}^5TS_{HA,A,C^3} < {}^5TS_{HA,A,C^4}$. Hydrogen abstraction of a H-atom from the C^5 position ($^5TS_{HA,A,C^5}$) is 10.5 kcal mol^{-1} lower in energy than that for H-atom abstraction from position C^4 ($^5TS_{HA,A,C^4}$), whereas the energy difference between the two radical intermediates ($^5\mathbf{2}_{A,C^4}$ and $^5\mathbf{2}_{A,C^5}$) is 9.8 kcal mol^{-1}. The difference in energy between the BDE_{CH} values for H-abstraction at the C^5 and C^4 positions (Figure 5) is calculated to be 7.0 kcal mol^{-1}, which is comparable to the difference obtained between $^5\mathbf{2}_{A,C^5}$ and $^5\mathbf{2}_{A,C^4}$. Thermodynamically, the exothermicity of formation of $^5\mathbf{2}_A$ from $^5\mathbf{1}_A$ is the difference in energy between BDE_{CH} of the C−H bond of the substrate that is broken and the BDE_{OH} of the FeO−H bond that is formed (eq 8).[41a,b]

$$\Delta H = BDE_{CH} - BDE_{OH} \qquad (8)$$

For a small model of TauD that closely resembles model A here, a BDE_{OH} of 95.7 kcal mol^{-1} was calculated.[26b] Combination of this BDE_{OH} value with the BDE_{CH} values from Figure 5 gives predicted reaction exothermicities ΔH using eq 8 for formation of intermediate complexes for H-abstraction at the C^4 and C^5 position of −3.3 and −10.3 kcal mol^{-1}. These values

are a few kcal mol^{-1} less exothermic than those calculated for $^5\mathbf{2}_{A,C^4}$ and $^5\mathbf{2}_{A,C^5}$. The reason for this is the close proximity of the radical to the iron(III)−hydroxo complex. As a matter of fact, the hydrogen atom of the amide group of the radical forms a hydrogen bond with the carboxylic acid ligand of the metal and thereby lowers the energy of this radical intermediate. Nevertheless, the trends in relative energies of $^5\mathbf{2}_{A,C^4}$ and $^5\mathbf{2}_{A,C^5}$ in Figure 6, therefore, reflect the differences in BDE_{CH} of the C−H bonds of the substrate that are broken. Consequently, thermodynamically and kinetically one would expect P4H enzymes to hydroxylate the C^5 position of proline rather than the C^4 position, which was found in the enzyme. To find out whether stereochemical interactions change this regioselectivity preference, we calculated also a larger model of the P4H active site, vide infra.

Recent studies of hydrogen abstraction trends by iron(IV)−oxo species of heme and nonheme oxidants showed that the barrier height from reactants to iron(III)−hydroxo intermediates correlates linearly with BDE_{CH}, whereas the reverse reaction barrier correlates with BDE_{OH} instead.[20,26] The calculated BDE_{CH} values in Figure 5, therefore, support the ordering of the hydrogen abstraction barriers calculated for the small P4H model complex with ordering $^5TS_{HA,A,C^5} < {}^5TS_{HA,A,C^3} < {}^5TS_{HA,A,C^4}$. The hydrogen abstraction barrier $^5TS_{HA,A,C^4}$ of 10.6 kcal mol^{-1} is slightly higher in energy than the barrier obtained before for toluene (7.6 kcal mol^{-1})[26b] hydroxylation by the iron(IV)−oxo species of TauD, where a C−H bond of BDE_{CH} = 85.8 kcal mol^{-1} is broken. The C^4−H bond strength in proline, actually, compares to the BDE_{CH} value for hydrogen abstraction from the secondary carbon atom of propane (BDE_{CH} = 93.0 kcal mol^{-1}), which would imply that the active oxidant of P4H enzymes is a powerful enough oxidant to hydroxylate very strong C−H bonds like in propane.

Thermodynamically, one would expect a similar barrier height for hydrogen atom abstraction from the C^3 and C^4 positions. The TS_{HA} barrier for abstraction of a hydrogen atom from the C^3 position, however, is lowered with respect to that of the C^4 position due to more stabilizing hydrogen-bonding interactions. The structure is stabilized by a short hydrogen bond of 2.231 Å between the amide proton of the substrate to one of the carboxylic acid oxygen atoms of the succinate residue, while the complementary hydrogen bond in the C^4 mechanism is 2.650 Å long. This stronger O···H−N interaction in the C^3 mechanism lowers the barrier height significantly with respect to that obtained for the C^4 mechanism.

Geometrically, $^5TS_{HA,A,C^4}$ is in a more upright position than $^5TS_{HA,A,C^3}$ with an Fe−O−$C_{proline}$ angle of 150.8° compared to 140.8°, respectively. Furthermore, $^5TS_{HA,A,C^4}$ is early with short C−H and long O−H distances (r_{CH} = 1.228 Å, r_{OH} = 1.320 Å) in comparison to those found for the $^5TS_{HA,A,C^3}$ (r_{CH} = 1.301 Å, r_{OH} = 1.207 Å). The magnitude of the imaginary frequency in the transition state for all H-abstraction barriers are large, which is indicative of narrow and steep barriers, which will result in a significant amount of tunneling in the H-abstraction process. The final H-abstraction transition state, $^5TS_{HA,A,C^5}$, is well lower than that expected based on the BDE_{CH} of the C^5−H bond that is broken. Thus, a BDE_{CH} for H-abstraction from proline at the C^5 position of 85.4 kcal mol^{-1} compares to the value obtained for aliphatic hydrogen abstraction from toluene, which gave a H-abstraction barrier of 7.6 kcal mol^{-1} using a similar nonheme iron-containing oxidant.[26b] The substantial lowering of the barrier height is due to the geometric distortion of the oxidant, whereby the imidazole group of His_{143} bends upward and donates a hydrogen bond to the amide group of the substrate and hence is lowered in energy.

This considerable distortion of the orientation of the histidine group may not be possible in the actual enzyme due to steric interactions. The small model (A), therefore, may not be an appropriate model for the studies of proline hydroxylation by P4H enzymes, and in particular, the C^5 hydroxylation mechanism is disturbed due to artificial bonding patterns that cannot happen in the actual enzyme configuration. We, therefore, decided to study a larger enzyme model of P4H enzymes instead.

Figure 7 shows the potential energy profile of proline hydroxylation using the large active site model of P4H (model B) as calculated on the quintet spin state surface. Similarly to the results shown above using the smaller model, the reaction is stepwise via a radical intermediate with a rate-determining hydrogen atom abstraction barrier. Substrate hydroxylation at the C^4 position gives energies in line with those obtained with the small model above. The H-abstraction barrier ($^5TS_{HA,B,C^4}$) is 12.6 kcal mol^{-1} higher in energy than reactants and is only slightly raised with respect to the small model system (10.6 kcal mol^{-1}), where the substrate has no stereochemical interactions with second sphere amino acids. Hydrogen atom abstraction from the C^3 position is raised by 7.3 kcal mol^{-1} in model B with respect to model A and is now slightly higher in energy to that obtained for the C^4 position: $^5TS_{HA,C,C^3}$ = 13.5 kcal mol^{-1}.

In addition to the mechanisms for hydrogen abstraction from proline at the C^3 and C^4 positions for model B, we also made efforts to find the C^5−H abstraction mechanism. Although we were able to locate the radical intermediate ($^5\mathbf{2}_{B,C^5}$), we did not manage to find its corresponding H-abstraction transition state ($^5TS_{HA,B,C^5}$). Thus, a geometry scan for the hydrogen transfer step starting from $^5\mathbf{2}_{B,C^5}$ led to a high-energy pathway (>30 kcal mol^{-1}), which implies that the steric hindrance of the two aromatic residues (Tyr_{140} and Trp_{243}) included in the model block the hydrogen atom abstraction from the C^5 position effectively. Although, the substrate approach leading to H-abstraction from the C^5 position gave favorable hydrogen-bonding interactions and lowering of the barrier for the small model, as a matter of fact for the larger and more realistic model these hydrogen-bonding interactions are not possible and instead the approach is hampered and the barrier considerably raised in energy. This is important for the enzyme due to the weak C^5−H bond strength of proline and prevention of hydroxylation at that position. It appears, therefore, that the substrate approach to the active center is aligned in such a way as to favor the C^4 hydroxylation mechanism and stereochemically disfavor hydroxylation on the other positions of proline. Furthermore, it may be anticipated that mutants whereby the Tyr_{140} and/or Trp_{243} amino acids are replaced by smaller size amino acids should give substantial hydroxylation at the C^3 and C^5 positions. Recent experimental studies on an α-ketoglutarate-dependent halogenase highlighted the intricate involvement of the active site amino acid residues by favoring a regioselective halogenation over hydroxylation of the substrate, which could be reversed by active site mutations.[43]

Geometrically, $^5TS_{HA,B,C^4}$ is quite different from $^5TS_{HA,A,C^4}$ (compare Figures 6 and 7) with a relatively long C−H distance of 1.326 Å (compared to 1.228 Å in $^5TS_{HA,A,C^4}$) and short O−H distance of 1.194 Å (compared to 1.320 Å in $^5TS_{HA,A,C^4}$). Thus, $^5TS_{HA,B,C^4}$ is late with a geometry close to intermediate, whereas $^5TS_{HA,A,C^4}$ has a more symmetrical C−H−O orientation.

The hydrogen atom abstraction process leading to radical intermediates is slightly exothermic and has the largest exother-

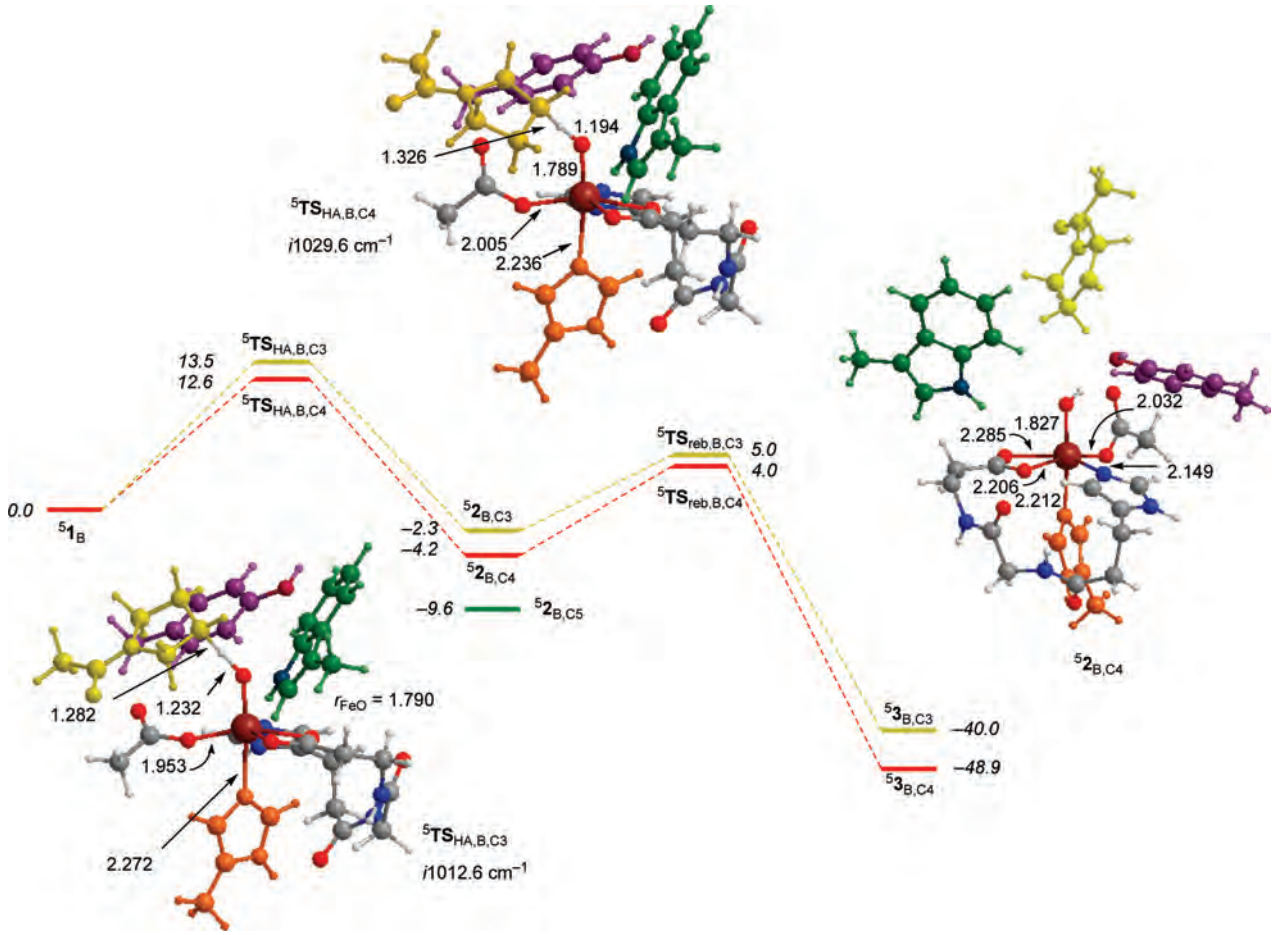

Figure 7. Potential energy landscape of proline hydroxylation at the C^4 and C^3 positions using model B. Relative energies are in kcal mol^{-1}, obtained with basis set BS2, while ZPE corrections are calculated with basis set BS1. Optimized geometries contain bond lengths in angstroms and the imaginary frequency in wavenumbers.

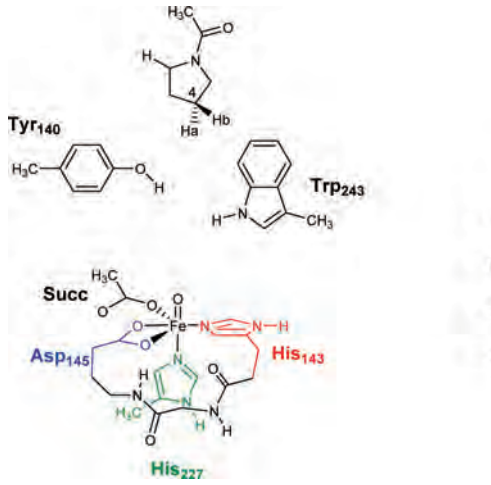

		KIE$_{Eyring}$	KIE$_{Wigner}$	KIE$_{Bel}$
HaHb	i1030			
DaHb	i778	7.74	9.89	15.98
HaDb	i1009	1.10	1.12	1.19
DaDb	i765	8.68	11.23	18.39

Figure 8. Kinetic isotope effects (KIE) as calculated with the Eyring, and Wigner and Bell models for the replacement of one or both of the hydrogen atoms at the C^4 position of proline with deuterium atoms. Also given are the imaginary frequencies in the transition states. H_a is the transferring hydrogen atom, and replacement of H_b with a deuterium atom gives the secondary kinetic isotope effect.

micity for H-abstraction from the C^5 position. This is in agreement with the discussion above that the energy difference between reactants and radical intermediates equals the $BDE_{CH} - BDE_{OH}$ difference of substrate and oxidant (eq 8). The reaction energy for formation of the radical intermediates in model A is significantly larger than that obtained for model B due to the formation of hydrogen-bonding interactions of the amide group of proline with hydrogen-bonding donors of the metal ligands. Due to stereochemical interactions of the aromatic residues in model B, the substrate cannot approach the iron center closely and therefore these hydrogen-bonding interactions are not possible; hence, those structures are somewhat higher in energy. The reaction energies for formation of $^5\mathbf{2}_{B,C^4}$ and $^5\mathbf{2}_{B,C^5}$ are within 1 kcal mol^{-1} of the ΔH values calculated from eq 8 and hence follow thermodynamic principles.

A comparison of Figures 6 and 7 reveals a further effect of the stereochemical interactions of the aromatic residues, namely, on the radical rebound barriers that increase from 1.5 kcal mol^{-1}

in model A ($^5TS_{reb,A,C^4}$) to 8.2 kcal mol^{-1} in model B ($^5TS_{reb,B,C^4}$). Similar trends are observed for proline hydroxylation at the C^3 position. These enlarged radical rebound barriers will increase the lifetime of the radical intermediates significantly during which, for instance, rearrangement of the radical can take place, leading to side products.[44] Despite the rise in rebound barrier, however, the H-atom abstraction barrier is still the rate-determining step in the reaction mechanism. The reaction exothermicities found for the large models are similar to those found for the smaller models (compare Figures 6 and 7). These large values for reaction exothermicities follow thermodynamic principles and are comparable to values obtained before for substrate hydroxylation by iron(IV)−oxo complexes.[45] In particular, for substrate dehydrogenation, which also starts with an initial hydrogen atom abstraction step, it was shown that the reaction energy can be written as a sum of bond dissociation energies of the bonds that are broken and formed during the reaction process.[46] That way, reaction energies of 50 kcal mol^{-1} were rationalized.

Subsequently, we calculated the kinetic isotope effect for replacement of one or two of the hydrogen atoms at the C^4 position of substrate proline by deuterium atoms using model B, and the results are shown in Figure 8. These procedures use the semiclassical kinetic isotope effect due to Eyring and are based on the free energies of activation of the hydrogen and deuterium-substituted reactions (eq 1). Subsequently, two methods to estimate the difference in tunneling properties of a hydrogen versus a deuterium atom were used, namely, via the methods of Wigner and Bell.[28] The Eyring kinetic isotope effect for replacement of the transferring hydrogen atom by deuterium is substantial (7.7) and increases to 9.9 when tunneling corrections due to Wigner are included and to 16.0 using the Bell model. Interestingly, the secondary isotope effect is larger than 1, although only slightly, which contrast the typical value of 0.9 obtained before.[44] As a consequence, the KIE value for substitution of both hydrogen atoms by deuterium atoms increases to 11.2 and 18.4 with tunneling corrections included due to Wigner and Bell, respectively. These values point to a substantial kinetic isotope effect and considerable tunneling corrections, which are as expected for hydrogen atom transfer processes. Nevertheless, the values obtained here are somewhat smaller than those observed experimentally for the native substrate, where a KIE = 60 was obtained.[15] This may have to do with the difference in substrate used or due to interactions of the rest of the protein with the substrate−oxidant complex.

Conclusions

In this work, the regioselectivity of proline hydroxylation by P4H enzymes is investigated using density functional theory methods. It is shown that thermodynamically substrate hydroxylation at the C^5 position should be favorable over that on the C^4 position with significantly larger H-abstraction exothermicity. Stereochemical interactions, in particular, of two aromatic amino acid residues (Tyr_{140} and Trp_{243}) hamper H-abstraction from the C^3 and C^5 positions and thereby lead to a regioselectivity preference of C^4 hydroxylation. These stereochemical interactions affect the hydrogen abstraction as well as radical rebound barriers, but the former remains the rate-determining step in the reaction mechanism. Thus, these stereochemical interactions are essential for the enzyme activity and make sure that proline is regioselectively hydroxylated at the unfavorable C^4 position. We validated the models by matching the computed spectroscopic values with experimental ones (IR spectra, Mössbauer and EPR spectroscopy). The iron(IV)−oxo model gives good agreement between experimental and DFT calculated spectroscopic parameters.

Acknowledgment. The research was supported by CPU time provided by the National Service of Computational Chemistry Software (NSCCS). D.K. holds a Ramanujan Fellowship from the Department of Science and Technology (DST), New Delhi (India), and acknowledges its financial support (Research Grants SR/S2/RJN-11/2008 and SR/S1/PC-58/2009).

Supporting Information Available: Cartesian coordinates of all structures, tables with group spin densities, charges, and absolute energies of all structures calculated in this work, and figures with optimized geometries and geometry scans. This material is available free of charge via the Internet at http://pubs.acs.org.

References and Notes

(1) (a) Solomon, E. I.; Brunold, T. C.; Davis, M. I.; Kemsley, J. N.; Lee, S.-K.; Lehnert, N.; Neese, F.; Skulan, A. J.; Yang, Y.-S.; Zhou, J. *Chem. Rev.* **2000**, *100*, 235–349. (b) Bugg, T. D. H. *Curr. Opin. Chem. Biol.* **2001**, *5*, 550–555. (c) Ryle, M. J.; Hausinger, R. P. *Curr. Opin. Chem. Biol.* **2002**, *6*, 193–201. (d) Costas, M.; Mehn, M. P.; Jensen, M. P.; Que, L., Jr. *Chem. Rev.* **2004**, *104*, 939–986. (e) Abu-Omar, M. M.; Loaiza, A.; Hontzeas, N. *Chem. Rev.* **2005**, *105*, 2227–2252. (f) Bruijnincx, P. C. A.; van Koten, G.; Klein Gebbink, R. J. M. *Chem. Soc. Rev.* **2008**, *37*, 2716–2744. (g) Bugg, T. D. H.; Ramaswamy, S. *Curr. Opin. Chem. Biol.* **2008**, *12*, 134–140.

(2) Que, L., Jr. *Nat. Struct. Biol.* **2000**, *7*, 182–184.

(3) (a) Krebs, C.; Fujimori, D. G.; Walsh, C. T.; Bollinger, J. M., Jr. *Acc. Chem. Res.* **2007**, *40*, 484–492. (b) Schofield, C. J.; Zhang, Z. *Curr. Opin. Chem. Biol.* **1999**, *9*, 722–731. (c) Bugg, T. D. H. *Tetrahedron* **2003**, *59*, 7075–7101.

(4) (a) Choroba, O. W.; Williams, D. H.; Spencer, J. B. *J. Am. Chem. Soc.* **2000**, *122*, 5389–5390. (b) Higgins, L. J.; Yan, F.; Liu, P.; Liu, H.-W.; Drennan, C. L. *Nature* **2005**, *437*, 838–844.

(5) (a) Mishina, Y.; Duguid, E. M.; He, C. *Chem. Rev.* **2006**, *106*, 215–232. (b) O'Brien, P. J. *Chem. Rev.* **2006**, *106*, 720–752. (c) Simmons, J. M.; Müller, T. A.; Hausinger, R. P. *Dalton Trans.* **2008**, 5132–5142. (d) Yi, C.; Yang, C. G.; He, C. *Acc. Chem. Res.* **2009**, *42*, 519–529.

(6) Chowdhury, R.; Hardy, A.; Schofield, C. J. *Chem. Soc. Rev.* **2008**, *37*, 1308–1319.

(7) Muthukumaran, R. B.; Grzyska, P. K.; Hausinger, R. P.; McCracken, J. *Biochemistry* **2007**, *46*, 5951–5959.

(8) (a) Price, J. C.; Barr, E. W.; Tirupati, B.; Bollinger, J. M., Jr.; Krebs, C. *Biochemistry* **2003**, *42*, 7497–7508. (b) Proshlyakov, D. A.; Henshaw, T. F.; Monterosso, G. R.; Ryle, M. J.; Hausinger, R. P. *J. Am. Chem. Soc.* **2004**, *126*, 1022–1023. (c) Riggs-Gelasco, P. J.; Price, J. C.; Guyer, R. B.; Brehm, J. H.; Barr, E. W.; Bollinger, J. M., Jr.; Krebs, C. *J. Am. Chem. Soc.* **2004**, *126*, 8108–8109. (d) Grzyska, P. K.; Appelman, E. H.; Hausinger, R. P.; Proshlyakov, D. A. *Proc. Natl. Acad. Sci. U.S.A.* **2010**, *107*, 3982–3987.

(9) (a) Bollinger, J. M., Jr.; Price, J. C.; Hoffart, L. M.; Barr, E. W.; Krebs, C. *Eur. J. Inorg. Chem.* **2005**, 4245–4254. (b) Clifton, I. J.; McDonough, M. A.; Ehrismann, D.; Kershaw, N. J.; Granatino, N.; Schofield, C. J. *J. Inorg. Biochem.* **2006**, *100*, 644–669.

(10) Borowski, T.; Bassan, A.; Siegbahn, P. E. M. *Chem.*−*Eur. J.* **2004**, *10*, 1031–1041.

(11) (a) Winter, A. D.; Page, A. P. *Mol. Cell. Biol.* **2000**, 4084–4093. (b) Kivirikko, K. I.; Myllyla, R.; Pihlajaniemi, T. *FASEB J.* **1989**, *3*, 1609–1617.

(12) (a) Bruick, R. K.; McKnight, S. L. *Science* **2001**, *294*, 1337–1340. (b) Berra, E.; Benizri, E.; Ginouvès, A.; Volmat, V.; Roux, D.; Pouysségur, J. *EMBO J.* **2003**, *22*, 4082–4090. (c) Lee, K. A.; Lynd, J. D.; O'Reilly, S.; Kiupel, M.; McCormick, J. J.; LaPres, J. J. *Mol. Cancer Res.* **2008**, *6*, 829–842. (d) Seifert, A.; Katschinski, D. M.; Tonack, S.; Fischer, B.; Santos, A. N. *Chem. Res. Toxicol.* **2008**, *21*, 341–348.

(13) West, C. M.; van der Wel, H.; Wang, Z. A. *Development* **2007**, *134*, 3349–3358.

(14) Gorres, K. L.; Edupuganti, R.; Krow, G. R.; Raines, R. T. *Biochemistry* **2008**, *47*, 9447–9455.

(15) Hoffart, L. M.; Barr, E. W.; Guyer, R. B.; Bollinger, J. M., Jr.; Krebs, C. *Proc. Natl. Acad. Sci. U.S.A.* **2006**, *103*, 14738–14743.

(16) Fujimoto, D.; Tamiya, N. *Biochem. J.* **1962**, *84*, 333–335.

(17) Wu, M.; Moon, H.-S.; Begley, T. P.; Myllyharju, J.; Kivirikko, K. I. *J. Am. Chem. Soc.* **1999**, *121*, 587–588.

(18) Koski, M. K.; Hieta, R.; Böllner, C.; Kivirikko, K. I.; Myllyharju, J.; Wierenga, R. K. *J. Biol. Chem.* **2007**, *282*, 37112–37123.

(19) (a) McDonough, M. A.; McNeill, L. A.; Tilliet, M.; Papamicaël, C. A.; Chen, Q.-Y.; Banerji, B.; Hewitson, K. S.; Schofield, C. J. *J. Am. Chem. Soc.* **2005**, *127*, 7680–7681. (b) Pappalardi, M. B.; Martin, J. D.; Jiang, Y.; Burns, M. C.; Zhao, H.; Ho, T.; Sweitzer, S.; Lor, L.; Schwartz, B.; Duffy, K.; Gontarek, R.; Tummino, P. J.; Copeland, R. A.; Luo, L. *Biochemistry* **2008**, *47*, 11165–11167. (c) Culpepper, M. A.; Scott, E. E.; Limburg, J. *Biochemistry* **2010**, *49*, 124–133.

(20) (a) Aluri, S.; de Visser, S. P. *J. Am. Chem. Soc.* **2007**, *129*, 14846–14847. (b) de Visser, S. P. *J. Am. Chem. Soc.* **2010**, *132*, 1087–1097.

(21) (a) Becke, A. D. *J. Chem. Phys.* **1993**, *98*, 5648–5652. (b) Lee, C.; Yang, W.; Parr, R. G. *Phys. Rev. B* **1988**, *37*, 785–789.

(22) (a) Hay, P. J.; Wadt, W. R. *J. Chem. Phys.* **1985**, *82*, 270–283. (b) Hehre, W. J.; Ditchfield, R.; Pople, J. A. *J. Chem. Phys.* **1972**, *56*, 2257–2261.

(23) *Jaguar 7.6*;Schrödinger, LLC.: New York, 2007.

(24) Frisch, M. J. ; Trucks, G. W.; Schlegel, H. B.; Scuseria, G. E.; Robb, M. A.; Cheeseman, J. R.; Montgomery, J. A.; Jr., Vreven, T.; Kudin, K. N.; Burant, J. C.; Millam, J. M.; Iyengar, S. S.; Tomasi, J.; Barone, V.; Mennucci, B.; Cossi, M.; Scalmani, G.; Rega, N.; Petersson, G. A.; Nakatsuji, H.; Hada, M.; Ehara, M.; Toyota, K.; Fukuda, R.; Hasegawa, J.; Ishida, M.; Nakajima, T.; Honda, Y.; Kitao, O.; Nakai, N.; Klene, M.; Li, X.; Knox, J. E.; Hratchian, H. P.; Cross, J. B.; Adamo, C.; Jaramillo, J.; Gomperts, R.; Stratmann, R. E.; Yazyev, O.; Austin, A. J.; Cammi, R.; Pomelli, C.; Ochterski, J. W.; Ayala, P. Y.; Morokuma, K.; Voth, G. A.; Salvador, P.; Dannenberg, J. J.; Zakrzewski, V. G.; Dapprich, S.; Daniels, A. D.; Strain, M. C.; Farkas, O.; Malick, D. K.; Rabuck, A. D.; Raghavachari, K.; Foresman, J. B.; Ortiz, J. V.; Cui, Q.; Baboul, A. G.; Clifford, S.; Cioslowski, J.; Stefanov, B. B.; Liu, G.; Liashenko, A.; Piskorz, P.; Komaromi, I.; Martin, R. L.; Fox, D. J.; Keith, T.; Al-Laham, M. A.; Peng, C. Y.; Nanayakkara, A.; Challacombe, M.; Gill, P. M. W.; Johnson, B.; Chen, W.; Wong, M. W.; Gonzalez, C.; Pople, J. A. *Gaussian 03, Revision C.01*; Gaussian, Inc.: Wallingford, CT, 2004.

(25) (a) Kumar, D.; de Visser, S. P.; Shaik, S. *Chem.—Eur. J.* **2005**, *11*, 2825–2835. (b) de Visser, S. P.; Oh, K.; Han, A.-R.; Nam, W. *Inorg. Chem.* **2007**, *46*, 4632–4641.

(26) (a) de Visser, S. P.; Kumar, D.; Cohen, S.; Shacham, R.; Shaik, S. *J. Am. Chem. Soc.* **2004**, *126*, 8362–8363. (b) Latifi, R.; Bagherzadeh, M.; de Visser, S. P. *Chem.—Eur. J.* **2009**, *15*, 6651–6662. (c) Shaik, S.; Kumar, D.; de Visser, S. P. *J. Am. Chem. Soc.* **2008**, *130*, 10128–10140.

(27) (a) Kumar, D.; de Visser, S. P.; Shaik, S. *J. Am. Chem. Soc.* **2003**, *125*, 13024–13025. (b) de Visser, S. P. *Chem.—Eur. J.* **2006**, *12*, 8168–8177. (c) de Visser, S. P. *Chem.—Eur. J.* **2008**, *14*, 4533–4541. (d) Porro, C. S.; Kumar, D.; de Visser, S. P. *Phys. Chem. Chem. Phys.* **2009**, *11*, 10219–10226. (e) Heyes, D. J.; Sakuma, M.; de Visser, S. P.; Scrutton, N. S. *J. Biol. Chem.* **2009**, *284*, 3762–3767.

(28) Melander, L.; Saunders, W. H., Jr. *Reaction Rates of Isotopic Molecules*; Robert, E. Krieger Publishing Co.: Malabar, FL, 1987.

(29) de Visser, S. P. *Coord. Chem. Rev.* **2009**, *253*, 754–768.

(30) (a) de Visser, S. P. *J. Am. Chem. Soc.* **2006**, *128*, 9813–9824. (b) de Visser, S. P. *Chem. Commun.* **2007**, 171–173.

(31) (a) Rohde, J.-U.; In, J.-H.; Lim, M. H.; Brennessel, W. W.; Bukowski, M. R.; Stubna, A.; Münck, E.; Nam, W.; Que, L., Jr. *Science* **2003**, *299*, 1037–1039. (b) Martinho, M.; Banse, F.; Bartoli, J.-F.; Mattioli, T. A.; Battioni, P.; Horner, O.; Bourcier, S.; Girerd, J.-J. *Inorg. Chem.* **2005**, *44*, 9592–9596. (c) Sastri, C. V.; Seo, M. S.; Park, M. J.; Kim, K. M.; Nam, W. *Chem. Commun.* **2005**, 1405–1407. (d) De Oliveira, F. T.; Chanda, A.; Banerjee, D.; Shan, X.; Mondal, S.; Que, L., Jr.; Bominaar, E. L.; Münck, E.; Collins, T. J. *Science* **2007**, *315*, 835–838. (e) Jackson, T. A.; Rohde, J.-U.; Seo, M. S.; Sastri, C. V.; DeHont, R.; Stubna, A.; Ohta, T.; Kitagawa, T.; Münck, E.; Nam, W.; Que, L., Jr. *J. Am. Chem. Soc.* **2008**, *130*, 12394–12407.

(32) (a) Kumar, D.; Hirao, H.; Que, L., Jr.; Shaik, S. *J. Am. Chem. Soc.* **2005**, *127*, 8026–8027. (b) Hirao, H.; Kumar, D.; Que, L., Jr.; Shaik, S. *J. Am. Chem. Soc.* **2006**, *128*, 8590–8606.

(33) Hirao, H.; Que, L., Jr.; Nam, W.; Shaik, S. *Chem.—Eur. J.* **2008**, *14*, 1740–1756.

(34) Godfrey, E.; Porro, C. S.; de Visser, S. P. *J. Phys. Chem. A* **2008**, *112*, 2464–2468.

(35) (a) Sinnecker, S.; Svensen, N.; Barr, E. W.; Ye, S.; Bollinger, J. M., Jr.; Neese, F.; Krebs, C. *J. Am. Chem. Soc.* **2007**, *129*, 6168–6179. (b) Topol, I. A.; Nemukhin, A. V.; Salnikow, K.; Cachau, R. E.; Abashkin, Y. G.; Kasprzak, K. S.; Burt, S. K. *J. Phys. Chem. A* **2006**, *110*, 4223–4228. (c) Nemukhin, A. V.; Topol, I. A.; Cachau, R. E.; Burt, S. K. *Theor. Chem. Acc.* **2006**, *115*, 348–353.

(36) Lundberg, M.; Siegbahn, P. E. M.; Morokuma, K. *Biochemistry* **2008**, *47*, 1031–1042.

(37) For examples of computational studies on biomimetic nonheme iron(IV)−oxo complexes, see the following:(a) Bautz, J.; Comba, P.; Lopez de Laorden, C.; Menzel, M.; Rajaraman, G. *Angew. Chem., Int. Ed.* **2007**, *46*, 8067–8070. (b) de Visser, S. P. *J. Am. Chem. Soc.* **2006**, *128*, 15809–15818. (c) Decker, A.; Rohde, J.-U.; Klinker, E. J.; Wong, S. D.; Que, L., Jr.; Solomon, E. I. *J. Am. Chem. Soc.* **2007**, *129*, 15983–15996. (d) Bernasconi, L.; Baerends, E. J. *Eur. J. Inorg. Chem.* **2008**, 1672–1681. (e) de Visser, S. P.; Nam, W. *J. Phys. Chem. A* **2008**, *112*, 12887–12895. (f) Comba, P.; Maurer, M.; Vadivelu, P. *Inorg. Chem.* **2009**, *48*, 10389–10396.

(38) (a) Nemukhin, A. V.; Grigorenko, B. L.; Topol, I. A.; Burt, S. K. *Int. J. Quantum Chem.* **2006**, *106*, 2184–2190. (b) de Visser, S. P.; Latifi, R. *J. Phys. Chem. B* **2009**, *113*, 12–14. (c) Ye, S.; Price, J. C.; Barr, E. W.; Green, M. T.; Bollinger, J. M., Jr.; Krebs, C.; Neese, F. *J. Am. Chem. Soc.* **2010**, *132*, 4739–4751. (d) Borowski, T.; Noack, H.; Radoń, M.; Zych, K.; Siegbahn, P. E. M. *J. Am. Chem. Soc.* **2010**, *132*, 12887–12898.

(39) (a) Green, M. T. *J. Am. Chem. Soc.* **1999**, *121*, 7939–7940. (b) Ogliaro, F.; de Visser, S. P.; Cohen, S.; Kaneti, J.; Shaik, S. *ChemBioChem* **2001**, *2*, 848–851. (c) Schöneboom, J. C.; Lin, H.; Reuter, N.; Thiel, W.; Cohen, S.; Ogliaro, F.; Shaik, S. *J. Am. Chem. Soc.* **2002**, *124*, 8142–8151. (d) de Visser, S. P.; Shaik, S.; Sharma, P. K.; Kumar, D.; Thiel, W. *J. Am. Chem. Soc.* **2003**, *125*, 15779–15788. (e) Behan, R. K.; Hoffart, L. M.; Stone, K. L.; Krebs, C.; Green, M. T. *J. Am. Chem. Soc.* **2006**, *128*, 11471–11474.

(40) (a) Groves, J. T. Models and Mechanisms of Cytochrome P450 Action. In *Cytochrome P450: Structure, Mechanism and Biochemistry*, 3rd ed.; Ortiz de Montellano, P. R., Ed.; Kluwer Academic/Plenum Publishers: New York, 2005; Chapter 1, pp 1−44. (b) Nam, W. *Acc. Chem. Res.* **2007**, *40*, 522–531. (c) Sono, M.; Roach, M. P.; Coulter, E. D.; Dawson, J. H. *Chem. Rev.* **1996**, *96*, 2841–2888.

(41) (a) Bordwell, F. G.; Cheng, J.-P.; Ji, G.-Z.; Satish, A. V.; Zhang, X. *J. Am. Chem. Soc.* **1991**, *113*, 9790–9795. (b) Mayer, J. M. *Acc. Chem. Res.* **1998**, *31*, 441–450. (c) Kaizer, J.; Klinker, E. J.; Oh, N. Y.; Rohde, J.-U.; Song, W. J.; Stubna, A.; Kim, J.; Münck, E.; Nam, W.; Que, L., Jr. *J. Am. Chem. Soc.* **2004**, *126*, 472–473. (d) Yoon, J.; Wilson, S. A.; Jang, Y. K.; Seo, M. S.; Nehru, K.; Hedman, B.; Hodgson, K. O.; Bill, E.; Solomon, E. I.; Nam, W. *Angew. Chem., Int. Ed.* **2009**, *48*, 1257–1260. (e) Lansky, D. E.; Goldberg, D. P. *Inorg. Chem.* **2006**, *45*, 5119–5125. (f) Bell, S. R.; Groves, J. T. *J. Am. Chem. Soc.* **2009**, *131*, 9640–9641. (g) Prokop, K. A.; de Visser, S. P.; Goldberg, D. P. *Angew. Chem., Int. Ed.* **2010**, *49*, 5091–5095.

(42) Zhang, Y.; Morisetti, P.; Kim, J.; Smith, L.; Lin, H. *Theor. Chem. Acc.* **2008**, *121*, 313–319.

(43) Matthews, M. L.; Neumann, C. S.; Miles, L. A.; Grove, T. L.; Booker, S. J.; Krebs, C.; Walsh, C. T.; Bollinger, J. M., Jr. *Proc. Natl. Acad. Sci. U.S.A.* **2009**, *106*, 17723–17728.

(44) (a) de Visser, S. P.; Ogliaro, F.; Shaik, S. *Angew. Chem., Int. Ed.* **2001**, *40*, 2871–2874. (b) Kumar, D.; de Visser, S. P.; Sharma, P. K.; Cohen, S.; Shaik, S. *J. Am. Chem. Soc.* **2004**, *125*, 1907–1920. (c) Kumar, D.; de Visser, S. P.; Shaik, S. *J. Am. Chem. Soc.* **2004**, *126*, 5072–5073.

(45) (a) Ogliaro, F.; Harris, N.; Cohen, S.; Filatov, M.; de Visser, S. P.; Shaik, S. *J. Am. Chem. Soc.* **2000**, *122*, 8977–8989. (b) Kamachi, T.; Yoshizawa, K. *J. Am. Chem. Soc.* **2003**, *125*, 4652–4661. (c) de Visser, S. P.; Kumar, D.; Cohen, S.; Shacham, R.; Shaik, S. *J. Am. Chem. Soc.* **2004**, *126*, 8362–8363.

(46) Kumar, D.; Tahsini, L.; de Visser, S. P.; Kang, H. Y.; Kim, S. J.; Nam, W. *J. Phys. Chem. A* **2009**, *113*, 11713–11722.

JP1089855

J|A|C|S ARTICLES

Published on Web 05/18/2010

What Factors Influence the Rate Constant of Substrate Epoxidation by Compound I of Cytochrome P450 and Analogous Iron(IV)-Oxo Oxidants?

Devesh Kumar,*[,†] Baharan Karamzadeh,[‡] G. Narahari Sastry,[†] and Sam P. de Visser*[,‡]

Molecular Modelling Group, Indian Institute of Chemical Technology, Hyderabad 500-607, India, and The Manchester Interdisciplinary Biocenter and the School of Chemical Engineering and Analytical Science, The University of Manchester, 131 Princess Street, Manchester M1 7DN, United Kingdom

Received December 16, 2009; E-mail: sam.devisser@manchester.ac.uk; dkclcre@yahoo.com

Abstract: The cytochromes P450 are a versatile range of mono-oxygenase enzymes that catalyze a variety of different chemical reactions, of which the key reactions include aliphatic hydroxylation and C=C double bond epoxidation. To establish the fundamental factors that govern substrate epoxidation by these enzymes we have done a systematic density functional theory study on substrate epoxidation by the active species of P450 enzymes, namely the iron(IV)-oxo porphyrin cation radical oxidant or Compound I. We show here, for the first time, that the rate constant of substrate epoxidation, and hence the activation energy, correlates with the ionization potential of the substrate as well as with intrinsic electronic properties of the active oxidant such as the polarizability volume. To explain these findings we present an electron-transfer model for the reaction mechanism that explains the factors that determine the barrier heights and developed a valence bond (VB) curve crossing mechanism to rationalize the observed trends. In addition, we have found a correlation for substrate epoxidation reactions catalyzed by a range of heme and nonheme iron(IV)-oxo oxidants with the strength of the O−H bond in the iron-hydroxo complex, i.e. BDE_{OH}, which is supported by the VB model. Finally, the fundamental factors that determine the regioselectivity change between substrate hydroxylation and epoxidation are discussed. It is shown that the regioselectivity of aliphatic hydroxylation versus double bond epoxidation is not influenced by the choice of the oxidant but is purely substrate dependent.

Introduction

The cytochromes P450 (P450s) are important heme based mono-oxygenases that take part in key biomolecular processes in the body that include detoxification processes in the liver, the biosynthesis of hormones, and metabolism of drugs.[1] The P450s bind molecular oxygen on a heme center and transfer one of its oxygen atoms to a substrate, while the second oxygen atom originating from O_2 is reduced to a water molecule. A versatile range of oxygen atom transfer reactions is catalyzed by the P450s that consists of aliphatic and aromatic hydroxylation, heteroatom oxidation, and double bond epoxidation.[2] For instance, unsaturated fatty acids are epoxidized by bacterial as well as human liver P450 enzymes.[3] Thus, the biosynthesis of hormones in cockroaches involves the epoxidation of methyl farnesoate, a reaction that is catalyzed by P450 15A1.[4] The fundamental factors that determine the mechanism and kinetics of substrate epoxidation by P450 enzymes are currently unknown. To gain insight into the factors that govern the epoxidation process, we present a systematic study on double bond epoxidation mechanisms by metal-oxo oxidants such as those that appear in P450 enzymes for the first time and investigate the intrinsic features of substrate and oxidant that determine the reaction kinetics.

The active site of P450 enzymes is a heme group that is linked to the protein via a thiolate bridge of a cysteinate residue of the protein. Figure 1 shows the active site of a well-studied P450 enzyme, namely $P450_{cam}$.[5] P450 enzymes undergo a complicated catalytic cycle that starts from the resting state where a water molecule fills the sixth binding site of iron. Upon substrate entrance into the binding pocket, this water molecule is displaced; the heme is reduced and binds molecular oxygen.

[†] Indian Institute of Chemical Technology.
[‡] The University of Manchester.

(1) (a) Sono, M.; Roach, M. P.; Coulter, E. D.; Dawson, J. H. *Chem. Rev.* **1996**, *96*, 2841–2888. (b) Kadish, K. M.; Smith, K. M.; Guilard, R., Eds. *The Porphyrin Handbook*; Academic Press: San Diego, CA, 2000; Vol. 4. (c) Guengerich, F. P. *Chem. Res. Toxicol.* **2001**, *14*, 611–650. (d) Groves, J. T. *Proc. Natl. Acad. Sci. U.S.A.* **2003**, *100*, 3569–3574. (e) Ortiz de Montellano, P. R., Ed. *Cytochrome P450: Structure, Mechanism and Biochemistry*, 3rd ed.; Kluwer Academic/Plenum Publishers: New York, 2004. (f) Munro, A. W.; Girvan, H. M.; McLean, K. J. *Nat. Prod. Rep.* **2007**, *24*, 585–609.

(2) (a) Groves, J. T. Models and Mechanisms of Cytochrome P450 Action. In *Cytochrome P450: Structure, Mechanism and Biochemistry*, 3rd ed.; Ortiz de Montellano, P. R., Ed.; Kluwer Academic/Plenum Publishers: New York, 2005; Chapter 1, pp 1−44. (b) Nam, W. *Acc. Chem. Res.* **2007**, *40*, 522–531. (c) Nam, W. In *Comprehensive Coordination Chemistry II*; Que, L., Jr., Tolman, W. B., Eds.; Elsevier Ltd.: New York, 2004; Vol. 8, pp 281−307.

(3) (a) Daikh, B. E.; Lasker, J. M.; Raucy, J. L.; Koop, D. R. *J. Pharmacol. Exp. Therap.* **1994**, *271*, 1427–1433. (b) Çelik, A.; Sperandio, D.; Speight, R. E.; Turner, N. J. *Org. Biomol. Chem.* **2005**, *3*, 2688–2690.

 10.1021/ja9106176 © **2010 American Chemical Society**

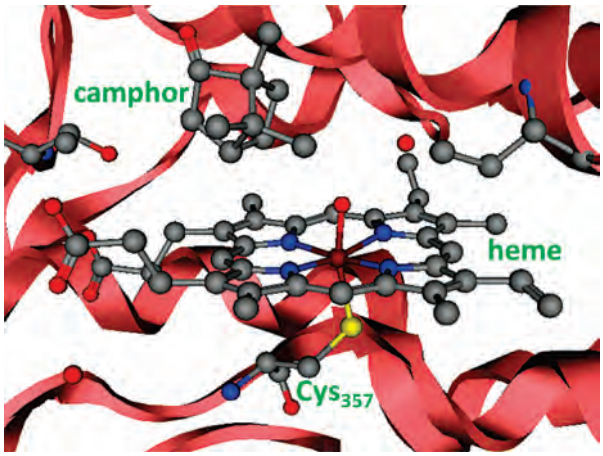

Figure 1. Active site of $P450_{cam}$ as taken from the 1DZ9 pdb file[3] with residues labeled as in the pdb file.

Thereafter, a second reduction followed by two protonation steps gives an iron(IV)-oxo heme cation radical species that is also known as Compound I (Cpd I). This species reacts with substrates via oxygen atom transfer to give oxygenated products. Indirect evidence of Cpd I through kinetic isotope effects and product distributions has implicated it to be the key oxidant involved in mono-oxygenase reactions with substrates.[6] More recent low pressure mass spectrometric studies[7] on biomimetic iron-porphyrins and computational modeling[8] have shown it to be a very efficient oxidant of substrate hydroxylation and epoxidation reactions.

Iron(IV)-oxo oxidants are the active species of mononuclear heme as well as nonheme iron containing enzymes, and recently spectroscopic evidence of the iron(IV)-oxo species of the nonheme enzymes of taurine/α-ketoglutarate dioxygenase (TauD), prolyl-4-hydroxylase, and α-ketoglutarate dependent halogenase was found.[9] In addition, several biomimetic nonheme iron(IV)-oxo species were detected and characterized with a range of spectroscopic techniques.[10] These biomimetic oxidants have been shown to react with substrates via aliphatic hydroxylation as well as epoxidation reactions very efficiently. The key features that influence the epoxidation mechanism and kinetics are unknown as well as what determines the regioselectivity of aliphatic hydroxylation versus epoxidation.

Substrate epoxidation by P450 enzymes has been extensively studied.[11] For instance, palmitoleic acid and related monounsaturated fatty acids were found to be oxidized by P450 enzymes to hydroxylated and epoxidized products.[12] These studies implicated a common oxidant for the reaction products, presumably an iron(IV)-oxo heme cation radical species such as Cpd I. $P450_{cam}$ studies using *cis*-β-methyl styrene as a substrate gave strong enantioselectivity with an 89:11 preference of the 1*S*,2*R* epoxide product over the 1*R*,2*S* form.[13] Molecular dynamics docking calculations predicted the substrate binding orientation to be responsible for this product ratio. Several studies reported epoxidation of non-natural substrates, such as propene, styrene, and cyclohexene.[14] Interestingly, the kinetics of styrene epoxidation by two P450 isozymes, CYP119 and CYP102HD, was found to be very similar,[14d] and so was the kinetics of aliphatic hydroxylation of benzyl alcohol by these isozymes. The regioselectivity of substrate hydroxylation versus epoxidation was investigated with two P450 isozymes and two of its mutants using cyclohexene and *cis*- and *trans*-2-butene as substrates.[15] The results on cyclohexene gave a relatively constant alcohol versus epoxide product ratio between 1.0 and 2.4, whereas with the other substrates large differences in the product ratios were observed.

Substrate epoxidation by biomimetic iron−porphyrin complexes has been extensively studied over the past 30 years.[16,17] For instance, it was shown that the axial ligand *trans* to the oxo group in biomimetic Cpd I complexes affects the oxidative power of the active species that correlated with the rate constant of styrene epoxidation.[18] More recent studies of Nam et al.[19] also showed an axial ligand effect for aliphatic hydroxylation and phosphorylation reactions by nonheme iron(IV)-oxo species. In the case of aliphatic hydroxylation reactions by metal-oxo oxidants Mayer et al. showed that the rate constant of hydrogen atom abstraction is related to the energy required to break the

(4) Helvig, C.; Koener, J. F.; Unnithan, G. C.; Feyereisen, R. *Proc. Natl. Acad. Sci. U.S.A.* **2004**, *101*, 4024–4029.
(5) Schlichting, I.; Berendzen, J.; Chu, K.; Stock, A. M.; Maves, S. A.; Benson, D. E.; Sweet, R. M.; Ringe, D.; Petsko, G. A.; Sligar, S. G. *Science* **2000**, *287*, 1615–1622.
(6) (a) Egawa, T.; Shimada, H.; Ishimura, Y. *Biochem. Biophys. Res. Commun.* **1994**, *201*, 1464–1469. (b) Kellner, D. G.; Hung, S.-C.; Weiss, K. E.; Sligar, S. G. *J. Biol. Chem.* **2002**, *277*, 9641–9644.
(7) (a) Chiavarino, B.; Cipollini, R.; Crestoni, M. E.; Fornarini, S.; Lanucara, F.; Lapi, A. *J. Am. Chem. Soc.* **2008**, *130*, 3208–3217. (b) Crestoni, M. E.; Fornarini, S.; Lanucara, F. *Chem.—Eur. J.* **2009**, *15*, 7863–7866.
(8) (a) Meunier, B.; de Visser, S. P.; Shaik, S. *Chem. Rev.* **2004**, *104*, 3947–3980. (b) Shaik, S.; Kumar, D.; de Visser, S. P.; Altun, A.; Thiel, W. *Chem. Rev.* **2005**, *105*, 2279–2328. (c) Shaik, S.; Cohen, S.; Wang, Y.; Chen, H.; Kumar, D.; Thiel, W. *Chem. Rev.* **2010**, *110*, 949–1017.
(9) (a) Proshlyakov, D. A.; Henshaw, T. F.; Monterosso, G. R.; Ryle, M. J.; Hausinger, R. P. *J. Am. Chem. Soc.* **2004**, *126*, 1022–1023. (b) Riggs-Gelasco, P. J.; Price, J. C.; Guyer, R. B.; Brehm, J. H.; Barr, E. W.; Bollinger, J. M., Jr.; Krebs, C. *J. Am. Chem. Soc.* **2004**, *126*, 8108–8109. (c) Hoffart, L. M.; Barr, E. W.; Guyer, R. B.; Bollinger, J. M., Jr.; Krebs, C. *Proc. Natl. Acad. Sci. U.S.A.* **2006**, *103*, 14738–14743. (d) Galonić, D. P.; Barr, E. W.; Walsh, C. T.; Bollinger, J. M., Jr.; Krebs, C. *Nat. Chem. Biol.* **2007**, *3*, 113–116.
(10) For example, see: (a) Rohde, J.-U.; In, J.-H.; Lim, M. H.; Brennessel, W. W.; Bukowski, M. R.; Stubna, A.; Münck, E.; Nam, W.; Que, L., Jr. *Science* **2003**, *299*, 1037–1039. (b) Bukowski, M. R.; Koehntop, K. D.; Stubna, A.; Bominaar, E. L.; Halfen, J. A.; Münck, E.; Nam, W.; Que, L., Jr. *Science* **2005**, *310*, 1000–1002. (c) Jensen, M. P.; Costas, M.; Ho, R. Y. N.; Kaizer, J.; Mairate i Payeras, A.; Münck, E.; Que, L., Jr.; Rohde, J.-U.; Stubna, A. *J. Am. Chem. Soc.* **2005**, *127*, 10512–10525. (d) De Oliveira, F. T.; Chanda, A.; Banerjee, D.; Shan, X.; Mondal, S.; Que, L., Jr.; Bominaar, E. L.; Münck, E.; Collins, T. J. *Science* **2007**, *315*, 835–838.
(11) (a) Guengerich, F. P. *Arch. Biochem. Biophys.* **2003**, *409*, 59–71. (b) McLean, K. J.; Munro, A. W. *Drug Metabol. Rev.* **2008**, *40*, 427–446.
(12) Ruettinger, R. T.; Fulco, A. J. *J. Biol. Chem.* **1981**, *256*, 5728–5734.
(13) Ortiz de Montellano, P. R.; Fruetel, J. A.; Collins, J. R.; Camper, D. L.; Loew, G. H. *J. Am. Chem. Soc.* **1991**, *113*, 3195–3196.
(14) (a) Groves, J. T.; Avaria-Neisser, G. E.; Fish, K. M.; Imachi, M.; Kuczkowski, R. L. *J. Am. Chem. Soc.* **1986**, *108*, 3837–3838. (b) Alcalde, M.; Farinas, E. T.; Arnold, F. H. *J. Biomol. Screen.* **2004**, *9*, 141–146. (c) Dansette, P. M.; Bertho, G.; Mansuy, D. *Biochem. Biophys. Res. Commun.* **2005**, *338*, 450–455. (d) Yuan, X.; Wang, Q.; Horner, J. H.; Sheng, X.; Newcomb, M. *Biochemistry* **2009**, *48*, 9140–9146.
(15) Vaz, A. D. N.; McGinnity, D. F.; Coon, M. J. *Proc. Natl. Acad. Sci. U.S.A.* **1998**, *95*, 3555–3560.
(16) For example, see: (a) Groves, J. T.; Subramanian, D. V. *J. Am. Chem. Soc.* **1984**, *106*, 2177–2181. (b) Solomon, E. I.; Brunold, T. C.; Davis, M. I.; Kemsley, J. N.; Lee, S.-K.; Lehnert, N.; Neese, F.; Skulan, A. J.; Yang, Y.-S.; Zhou, J. *Chem. Rev.* **2000**, *100*, 235–349. (c) Costas, M.; Mehn, M. P.; Jensen, M. P.; Que, L., Jr. *Chem. Rev* **2004**, *104*, 939–986. (d) Bruijnincx, P. C. A.; van Koten, G.; Klein Gebbink, R. J. M. *Chem. Soc. Rev.* **2008**, *37*, 2716–2744.

C−H bond, i.e. BDE_{CH}, as defined by eq 1.[20] This relationship was later found for substrate hydroxylation by a range of different iron- and manganese-oxo oxidants.[21]

$$SubH \rightarrow Sub^{\cdot} + H^{\cdot} + BDE_{CH} \quad (1)$$

In contrast to this, no correlations are known that relate the rate constant of substrate epoxidation by metal-oxo complexes as a function of substrate and/or oxidant properties. To understand the regioselectivity difference of substrate epoxidation versus hydroxylation, it is important to characterize the fundamental factors that determine the rate constant and hence the free energy of activation of substrate epoxidation and hydroxylation by metal-oxo oxidants. That will enable one to predict barrier heights and rate constants from empirical values. Currently, very little is known on the factors that influence the rate constant of substrate epoxidation and no systematic studies have been reported yet. Therefore, in this work we present models that link a range of substrate epoxidation reactions by metal-oxo oxidants with intrinsic chemical and physical properties of the reactants. In principle, substrate epoxidation requires the conversion of a double bond of an olefin into a single bond concomitant with the abstraction of an oxygen atom to bridge this bond. As will be seen in this work, the energy of the π-bond of the olefin is correlated to the ionization potential of the substrate, which subsequently relates to the barrier height of an epoxidation reaction. Using thermodynamic cycles and a valence bond curve crossing diagram, we generalize substrate epoxidation by iron(IV)-oxo oxidants and explain what the electronic factors are that determine the reactivity patterns. Thus, we explain the fundamental differences of substrate epoxidation versus aliphatic hydroxylation based on the electronic properties of the individual reactants, substrate, and oxidant. The studies show what intrinsic electronic properties of the substrate determine the regioselectivity of epoxidation over hydroxylation.

Methods

The calculations described in this work utilize density functional theory (DFT) as implemented in the *Jaguar* 7.6 and *Gaussian*-03 program packages.[22,23] All geometries were fully optimized (without any constraints) in *Jaguar* followed by an analytical frequency in *Gaussian*. Local minima had real frequencies only, whereas transition state structures were characterized by a single imaginary frequency that corresponds to the appropriate mode. All calculations reported here were performed with the B3LYP hybrid density functional method,[24] since this method is capable of reproducing free energies of activation of substrate epoxidation and hydroxylation reactions by iron(IV)-oxo complexes within ~3 kcal mol^{-1} with respect to experiment.[25] Recent studies of a series of hydrogen abstraction reactions by P450 enzyme models showed[26,27] that this is a systematic error and a linear correlation with the bond dissociation energy of the C−H bond of the substrate was found with a standard deviation of ~1 kcal mol^{-1}. Furthermore, these computational methods were shown to accurately reproduce experimentally determined kinetic isotope effects,[28] electron paramagnetic resonance parameters,[29] and vibrational spectra.[30] The methods, therefore, should be suitable for calculations on trends in substrate epoxidation mechanisms as well. Extensive test calculations with alternative density functional methods predicted trends similar to those obtained with B3LYP.[31]

Geometry optimizations and frequency calculations were performed with a double-ζ quality LACVP basis set on iron (including an Effective Core Potential) coupled to 6-31G on the remaining atoms, basis set B1.[32] Subsequently, single-point calculations were performed in *Jaguar* utilizing a triple-ζ quality LACV3P+ basis

(17) For example, see: (a) Groves, J. T.; Myers, R. S. *J. Am. Chem. Soc.* **1983**, *105*, 5791–5796. (b) Groves, J. T.; Watanabe, Y. *J. Am. Chem. Soc.* **1986**, *108*, 507–508. (c) Collman, J. P.; Kodadek, T.; Brauman, J. I. *J. Am. Chem. Soc.* **1986**, *108*, 2588–2594. (d) Ostović, D.; Bruice, T. C. *J. Am. Chem. Soc.* **1989**, *111*, 6511–6517. (e) Collman, J. P.; Brauman, J. I.; Hampton, P. D.; Tanaka, H.; Bohle, D. S.; Hembre, R. T. *J. Am. Chem. Soc.* **1990**, *112*, 7980–7984. (f) Groves, J. T.; Gross, Z.; Stern, M. K. *Inorg. Chem.* **1994**, *33*, 5065–5072. (g) Nam, W.; Lim, M. H.; Lee, H. J.; Kim, C. *J. Am. Chem. Soc.* **2000**, *122*, 6641–6647. (h) Stephenson, N. A.; Bell, A. T. *Inorg. Chem.* **2006**, *45*, 2758–2766. (i) Collman, J. P.; Zeng, L.; Wang, H. J. H.; Lei, A.; Brauman, J. I. *Eur. J. Org. Chem.* **2006**, 2707–2714. (j) Song, W. J.; Sun, Y. J.; Choi, S. K.; Nam, W. *Chem.—Eur. J.* **2006**, *12*, 130–137. (k) Song, W. J.; Seo, M. S.; DeBeer George, S.; Ohta, T.; Song, R.; Kang, M.-J.; Tosha, T.; Kitagawa, T.; Solomon, E. I.; Nam, W. *J. Am. Chem. Soc.* **2007**, *129*, 1268–1277. (l) Hessenauer-Ilicheva, N.; Franke, A.; Meyer, D.; Woggon, W.-D.; van Eldik, R. *J. Am. Chem. Soc.* **2007**, *129*, 12473–12479. (m) Hull, J. F.; Sauer, E. L. O.; Incarvito, C. D.; Faller, J. W.; Brudvig, G. W.; Crabtree, R. H. *Inorg. Chem.* **2009**, *48*, 488–495. (n) McGown, A. J.; Kerber, W. D.; Fujii, H.; Goldberg, D. P. *J. Am. Chem. Soc.* **2009**, *131*, 8040–8048. (o) Company, A.; Feng, Y.; Guell, M.; Ribas, X.; Luis, J. M.; Que, L., Jr.; Costas, M. *Chem.—Eur. J.* **2009**, *15*, 3359–3362. (p) Franke, A.; Wolak, M.; van Eldik, R. *Chem.—Eur. J.* **2009**, *15*, 10182–10198. (q) Hessenauer-Ilcheva, N.; Franke, A.; Wolak, M.; Higuchi, T.; van Eldik, R. *Chem.—Eur. J.* **2009**, *15*, 12447–12459.

(18) (a) Gross, Z.; Nimri, S. *Inorg. Chem.* **1994**, *33*, 1731–1732. (b) Czarnecki, K.; Nimri, S.; Gross, Z.; Proniewicz, L. M.; Kincaid, J. R. *J. Am. Chem. Soc.* **1996**, *118*, 2929–2935. (c) Gross, Z. *J. Biol. Inorg. Chem.* **1996**, *1*, 368–371. (d) Gross, Z.; Nimri, S.; Barzilay, C. M.; Simkhovich, L. *J. Biol. Inorg. Chem.* **1997**, *2*, 492–506.

(19) (a) Nam, W.; Lim, M. H.; Oh, S.-Y.; Lee, J. H.; Lee, H. J.; Woo, S. K.; Kim, C.; Shin, W. *Angew. Chem., Int. Ed.* **2000**, *39*, 3646–3649. (b) Sastri, C. V.; Park, M. J.; Ohta, T.; Jackson, T. A.; Stubna, A.; Seo, M. S.; Lee, J.; Kim, J.; Kitagawa, T.; Münck, E.; Que, L., Jr.; Nam, W. *J. Am. Chem. Soc.* **2005**, *127*, 12494–12495. (c) Sastri, C. V.; Lee, J.; Oh, K.; Lee, Y. J.; Lee, J.; Jackson, T. A.; Ray, K.; Hirao, H.; Shin, W.; Halfen, J. A.; Kim, J.; Que, L., Jr.; Shaik, S.; Nam, W. *Proc. Natl. Acad. Sci. U.S.A.* **2007**, *104*, 19181–19186. (d) Kang, Y.; Chen, H.; Jeong, Y. J.; Lai, W.; Bae, E. H.; Shaik, S.; Nam, W. *Chem.—Eur. J.* **2009**, *15*, 10039–10046.

(20) (a) Mayer, J. M. *Acc. Chem. Res.* **1998**, *31*, 441–450. (b) Mayer, J. M. *Annu. Rev. Phys. Chem.* **2004**, *55*, 363–390. (c) Mader, E. A.; Manner, V. W.; Markle, T. F.; Wu, A.; Franz, J. A.; Mayer, J. M. *J. Am. Chem. Soc.* **2009**, *131*, 4335–4345.

(21) (a) Kaizer, J.; Klinker, E. J.; Oh, N. Y.; Rohde, J.-U.; Song, W. J.; Stubna, A.; Kim, J.; Münck, E.; Nam, W.; Que, L., Jr. *J. Am. Chem. Soc.* **2004**, *126*, 472–473. (b) Yoon, J.; Wilson, S. A.; Jang, Y. K.; Seo, M. S.; Nehru, K.; Hedman, B.; Hodgson, K. O.; Bill, E.; Solomon, E. I.; Nam, W. *Angew. Chem., Int. Ed.* **2009**, *48*, 1257–1260. (c) Lansky, D. E.; Goldberg, D. P. *Inorg. Chem.* **2006**, *45*, 5119–5125. (d) Bell, S. R.; Groves, J. T. *J. Am. Chem. Soc.* **2009**, *131*, 9640–9641.

(22) *Jaguar 7.6*; Schrödinger, LLC.: New York, NY, 2007.

(23) Frisch, M. J.; et al. *Gaussian 03*, revision C.02; Gaussian, Inc.: Wallingford, CT, 2004.

(24) (a) Becke, A. D. *J. Chem. Phys.* **1993**, *98*, 5648–5652. (b) Lee, C.; Yang, W.; Parr, R. G. *Phys. Rev. B* **1988**, *37*, 785–789.

(25) (a) Kumar, D.; de Visser, S. P.; Shaik, S. *Chem.—Eur. J.* **2005**, *11*, 2825–2835. (b) de Visser, S. P.; Oh, K.; Han, A.-R.; Nam, W. *Inorg. Chem.* **2007**, *46*, 4632–4641.

(26) Shaik, S.; Kumar, D.; de Visser, S. P. *J. Am. Chem. Soc.* **2008**, *130*, 10128–10140.

(27) Olsen, L.; Rydberg, P.; Rod, T. H.; Ryde, U. *J. Med. Chem.* **2006**, *49*, 6489–6499.

(28) (a) Kumar, D.; de Visser, S. P.; Shaik, S. *J. Am. Chem. Soc.* **2003**, *125*, 13024–13025. (b) Kumar, D.; de Visser, S. P.; Sharma, P. K.; Cohen, S.; Shaik, S. *J. Am. Chem. Soc.* **2004**, *126*, 1907–1920. (c) de Visser, S. P. *Chem.—Eur. J.* **2006**, *12*, 8168–8177.

(29) Porro, C. S.; Kumar, D.; de Visser, S. P. *Phys. Chem. Chem. Phys.* **2009**, *11*, 10219–10226.

(30) (a) de Visser, S. P. *Chem.—Eur. J.* **2008**, *14*, 4533–4541. (b) de Visser, S. P. *Coord. Chem. Rev.* **2009**, *253*, 754–768.

(31) (a) de Visser, S. P.; Tahsini, L.; Nam, W. *Chem.—Eur. J.* **2009**, *15*, 5577–5587. (b) Kumar, D.; Tahsini, L.; de Visser, S. P.; Kang, H. Y.; Kim, S. J.; Nam, W. *J. Phys. Chem. A* **2009**, *113*, 11713–11722.

(32) (a) Hay, P. J.; Wadt, W. R. *J. Chem. Phys.* **1985**, *82*, 270–283. (b) Hehre, W. J.; Ditchfield, R.; Pople, J. A. *J. Chem. Phys.* **1972**, *56*, 2257–2261.

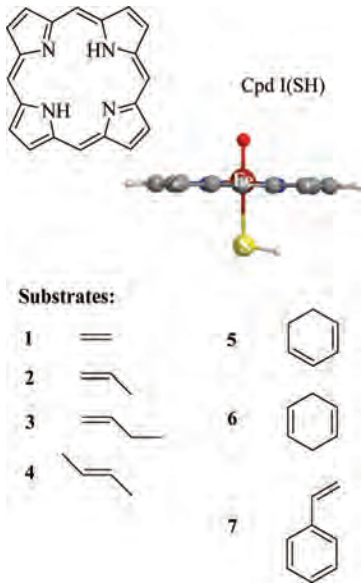

Figure 2. Model oxidant [Cpd I(SH)] and epoxidation substrates studied in this work.

set on iron (including Effective Core Potential) and 6-311+G* on the remaining atoms, basis set B2. Energies reported in this work were obtained with basis set B2 and corrected with zero-point energies from basis set B1 unless otherwise noted. To test whether the basis set affects the optimized geometries and/or energies, we reoptimized the 1-butene epoxidation mechanism by ^{4,2}Cpd I(SH) using basis set B2 followed by an analytical frequency calculation at this level. These studies gave only minor geometric and energetic differences from those done with the smaller basis set; hence basis set B1 was used for geometry optimizations and frequencies for the remaining work, while single-point calculations were done with basis set B2.

The effect of the environment was investigated by single-point calculations in *Jaguar* at UB3LYP/B2 with the self-consistent reaction field model using a dielectric constant of $\varepsilon = 5.7$ and a probe radius of 2.72 Å. These studies did not affect the trends presented in this work (Supporting Information Figure S7); therefore, we will focus in the main text on the gas-phase results only.

Cpd I of P450 was abbreviated as iron-protoporphyrin IX with a distal oxo group and axial thiolate ligand, designated Cpd I(SH);[33] see Figure 2. In this work we studied the substrate epoxidation by a model of Cpd I of P450 using a range of typical substrates. Furthermore, a comparison is made with other heme and nonheme iron(IV)-oxo oxidants. To distinguish the different iron(IV)-oxo oxidants, we will give the axial ligand of the oxidant in parentheses of Cpd I; i.e. Cpd I(SH) is designated as the iron(IV)-oxo porphyrin cation radical species of a P450 model described by a thiolate axial ligand. Cpd I(SH) appears in almost degenerate doublet and quartet spin states; therefore, all calculations were done for both spin state surfaces. We studied substrate epoxidation by Cpd I(SH) with seven olefins: ethene (**1**), propene (**2**), 1-butene (**3**), *trans*-2-butene (**4**), 1,3-cyclohexadiene (**5**), 1,4-cyclohexadiene (**6**), and styrene (**7**). Although ethene epoxidation by Cpd I(SH) was studied before,[34] we redid these calculations using the methods described above. Data for propene and styrene epoxidation by Cpd I(SH) were taken from the literature.[25a,35]

Ionization energies of substrates (IE_{Sub}) represent adiabatic ionization energies and were calculated with the same procedures mentioned above, namely geometry optimizations using basis set B1, while energies are taken from single-point calculations with basis set B2 corrected for ZPE with basis set B1. These calculated values reproduce experimentally determined IE values excellently; see Supporting Information.[36]

Reorganization energies (RE) were calculated as before from the difference in energy of the substrate in the transition state geometry and its fully relaxed structure.[26] The bond dissociation energy of the O−H bond in the iron(IV)-hydroxo complex with ligand L (BDE_{OH}) was calculated from eq 2 using fully optimized geometries at the B3LYP/B1 level of theory and energies from B3LYP/B2//B3LYP/B1 including ZPE at basis set B1.

$$\text{Cpd I(L)} + \text{H}^{\bullet} \rightarrow \text{Fe}^{\text{IV}}\text{OH(L)} + \text{BDE}_{\text{OH}} \qquad (2)$$

In addition, we also tested trends of epoxidation reactions with varying oxidants but with the same substrate (propene), namely Cpd I(SH), Cpd I(OH), Cpd I(Cl), Cpd I(ImP), Cpd I(C*c*P), Cpd I(TauD), and Fe^{IV}═O$(TMCS)^+$; see Figure 3. The first four of these oxidants are iron(IV)-oxo porphyrin cation radical models with the axial ligand of these systems written in parentheses. Cpd I(C*c*P) and Cpd I(TauD) represent enzyme active site models of the iron(IV)-oxo species of the enzymes cytochrome *c* peroxidase (C*c*P) and taurine/α-ketoglutarate dioxygenase (TauD). Data for propene epoxidation by Cpd I(Cl), Cpd I(ImP), Cpd I(TauD), and Fe^{IV}═O$(TMCS)^+$ were taken from the literature.[37] Cpd I(ImP) is an iron(IV)-oxo porphyrin cation radical oxidant with an imidazole ligand whereby the atom bound to the metal is replaced by phosphorus, whereas Fe^{IV}═O$(TMCS)^+$ represents a nonheme iron(IV)-oxo complex with TMCS = 1-mercaptoethyl-4,8,11-trimethyl-1,4,8,11-tetraaza cyclotetradecane as a pentadentate ligand.

To find out whether a thiolate axial ligand correctly mimics the cysteinate ligand in P450 enzymes, we ran an extra set of calculations where we calculated the BDE_{OH} value for three different models, namely using SH^-, SCH_3^-, and a large model containing a peptide chain of cysteinate connected to two glycine amino acids, $CysGlyGly^-$. In the latter structure the hydrogen bonding interactions of amide protons to the sulfur atom of cysteinate [NH---S interactions] in the enzyme are included that determine the electron-donating ability of the axial ligand. BDE_{OH} values of 88.9, 87.4, and 88.95 kcal mol^{-1} were obtained for Cpd I(SH), Cpd I(SCH_3), and Cpd I(CysGlyGly), respectively. Therefore, thiolate is a faithful mimic of the active species of P450 enzymes. Further calculations on the relative BDE_{OH} values of Cpd I(OH) and Cpd I(OCH_3) predicted values of 97.4 versus 99.5 kcal mol^{-1}, respectively, which implies that these two axial ligand systems will show similar reactivity patterns with the substrates discussed in this work.

Results and Discussion

Substrate Epoxidation by Cpd I(SH). The active species of P450 enzymes is elusive but is expected to resemble that of chloroperoxidase enzymes, which is well characterized spec-

(33) de Visser, S. P.; Shaik, S.; Sharma, P. K.; Kumar, D.; Thiel, W. *J. Am. Chem. Soc.* **2003**, *125*, 15779–15788.
(34) de Visser, S. P.; Ogliaro, F.; Harris, N.; Shaik, S. *J. Am. Chem. Soc.* **2001**, *123*, 3037–3047.
(35) (a) de Visser, S. P.; Ogliaro, F.; Sharma, P. K.; Shaik, S. *Angew. Chem., Int. Ed.* **2002**, *41*, 1947–1951. (b) de Visser, S. P.; Ogliaro, F.; Sharma, P. K.; Shaik, S. *J. Am. Chem. Soc.* **2002**, *124*, 11809–11826.
(36) (a) Lias, S. G. Ionization energy evaluation. In *NIST Chemistry Webbook, NIST Standard Reference Database Number 69*; Linstrom, P. J., Mallard, W. G., Eds.; National Institute of Standards and Technology: Gaithersburg, MD. 20899 (http://webbook.nist.gov, 2009). (b) Kimura, K.; Katsumata, S.; Achiba, Y.; Yamazaki, T.; Iwata, S. *Handbook of HeI photoelectron spectra of fundamental organic molecules: ionization energies, ab initio assignments, and valence electronic structure for 200 molecules*; Japan Scientific Society Press: Tokyo, 1981.
(37) (a) de Visser, S. P. *J. Biol. Inorg. Chem.* **2006**, *11*, 168–178. (b) de Visser, S. P. *J. Am. Chem. Soc.* **2006**, *128*, 9813–9824. (c) de Visser, S. P. *J. Am. Chem. Soc.* **2006**, *128*, 15809–15818. (d) de Visser, S. P. *J. Phys. Chem. B* **2007**, *111*, 12299–12302. (e) de Visser, S. P. *Angew. Chem., Int. Ed.* **2006**, *45*, 1790–1793.

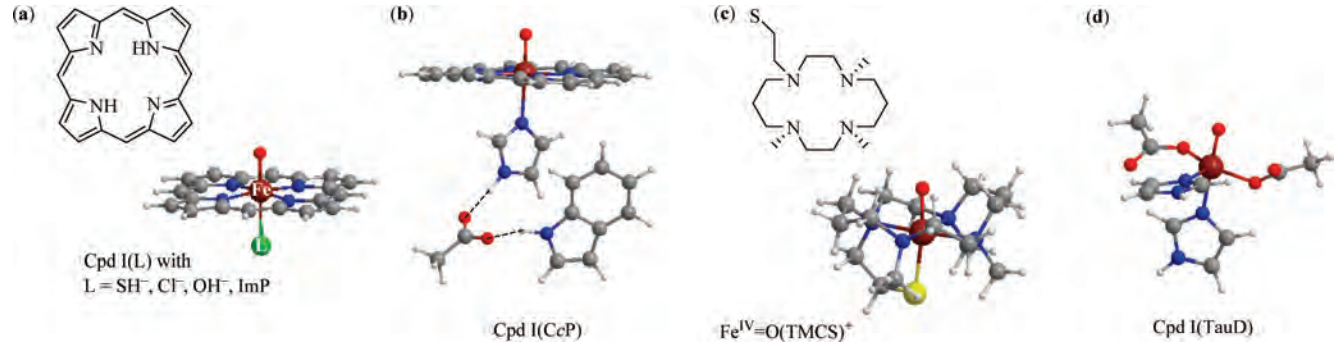

Figure 3. Iron(IV)-oxo oxidants studied in the reaction with propene.

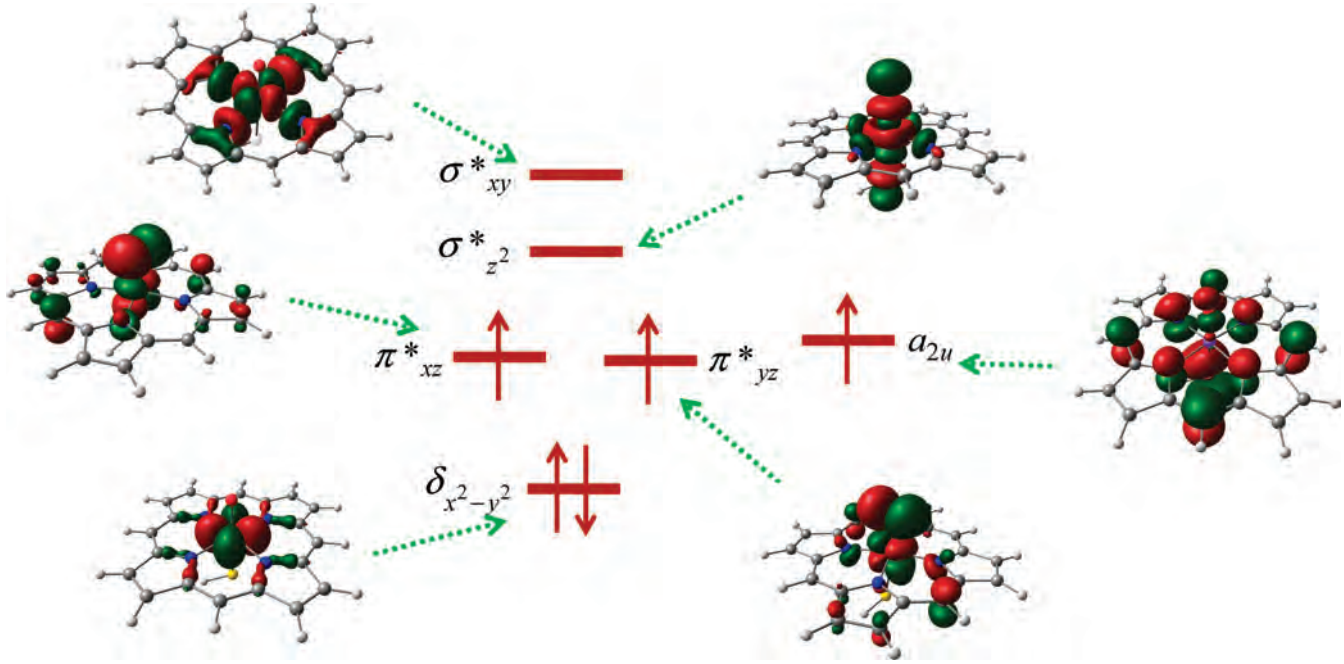

Figure 4. High-lying occupied and low-lying virtual orbitals of Cpd I(SH).

troscopically and computationally.[38] Substrate epoxidation by Cpd I of P450 takes place via two-state-reactivity patterns on competing doublet and quartet spin state surfaces[39] with electronic configuration $\delta_{x^2-y^2}{}^2\ \pi^*_{xz}{}^1\ \pi^*_{yz}{}^1\ a_{2u}{}^1$ as shown in Figure 4. These orbitals are dominated by the 3*d* metal contributions, whereby the lowest one of those is the nonbonding $\delta_{x^2-y^2}$ orbital in the plane of the heme that is doubly occupied in all structures discussed in this work. Higher in energy and singly occupied is a pair of orthogonal π^*_{xz} and π^*_{yz} orbitals for the antibonding combination of a 3*d* orbital on iron with a 2*p* orbital on the oxo group. The lowest two virtual orbitals with metal contributions are the σ^*_{xy} orbital for the antibonding interactions of the metal with the porphyrin nitrogen atoms and the $\sigma^*_{z^2}$ orbital for the antibonding interactions with the axial and distal ligands. Also singly occupied is a porphyrin based orbital that in D_{4h} symmetry has the label a_{2u}. Since the interaction between the two π^* orbitals and the a_{2u} orbital is small, the doublet and quartet spin states are close in energy and lead to reactivity patterns on the two spin state surfaces with different reaction barriers.[39]

The other oxidants given in Figure 3 have similar sets of valence orbitals, and all heme oxidants, apart from Cpd I(C*c*P), have the same orbital occupation. Cpd I(C*c*P) has a singly occupied π-orbital on the axial Trp residue rather than a porphyrin radical. The nonheme iron(IV)-oxo oxidants, Fe^{IV}═O(TMCS)$^+$ and Cpd I(TauD), were calculated in the quintet spin state with $\delta_{x^2-y^2}{}^1\ \pi^*_{xz}{}^1\ \pi^*_{yz}{}^1\ \sigma^*_{xy}{}^1$ occupation.

A typical example of a reaction profile of substrate epoxidation by Cpd I(SH) is given in Figure 5 for the epoxidation of 1-butene (**3**) by Cpd I(SH); all other epoxidation reactions studied in this work gave similar reaction profiles; see Supporting Information. The reaction starts from ^{4,2}Cpd I(SH), whereby both states are within 0.1 kcal mol^{-1}. The initial and rate-determining step in the reaction mechanism is C−O bond formation to give a radical intermediate (**I**) via a transition state $\mathbf{TS}_E$. A subsequent ring-closure barrier ($\mathbf{TS}_{rc}$) separates the intermediate complexes from products (**P**). Generally, the ring-

(38) (a) Rutter, R.; Hager, L. P.; Dhonau, H.; Hendrich, M.; Valentine, M.; Debrunner, P. *Biochemistry* **1984**, *23*, 6809–6816. (b) Palcic, M. M.; Rutter, R.; Araiso, T.; Hager, L. P.; Dunford, H. B. *Biochem. Biophys. Res. Commun.* **1980**, *94*, 1123–1127. (c) Egawa, T.; Proshlyakov, D. A.; Miki, H.; Makino, R.; Ogura, T.; Kitagawa, T.; Ishimura, Y. *J. Biol. Inorg. Chem.* **2001**, *6*, 46–54. (d) Hosten, C. M.; Sullivan, A. M.; Palaniappan, V.; Fitzgerald, M. M.; Terner, J. *J. Biol. Chem.* **1994**, *269*, 13966–13978. (e) Kim, S. H.; Perera, R.; Hager, L. P.; Dawson, J. H.; Hoffman, B. M. *J. Am. Chem. Soc.* **2006**, *128*, 5598–5599. (f) Stone, K. L.; Behan, R. K.; Green, M. T. *Proc. Natl. Acad. Sci. U.S.A.* **2006**, *103*, 12307–12310.
(39) Shaik, S.; de Visser, S. P.; Ogliaro, F.; Schwarz, H.; Schröder, D. *Curr. Opin. Chem. Biol.* **2002**, *6*, 556–567.

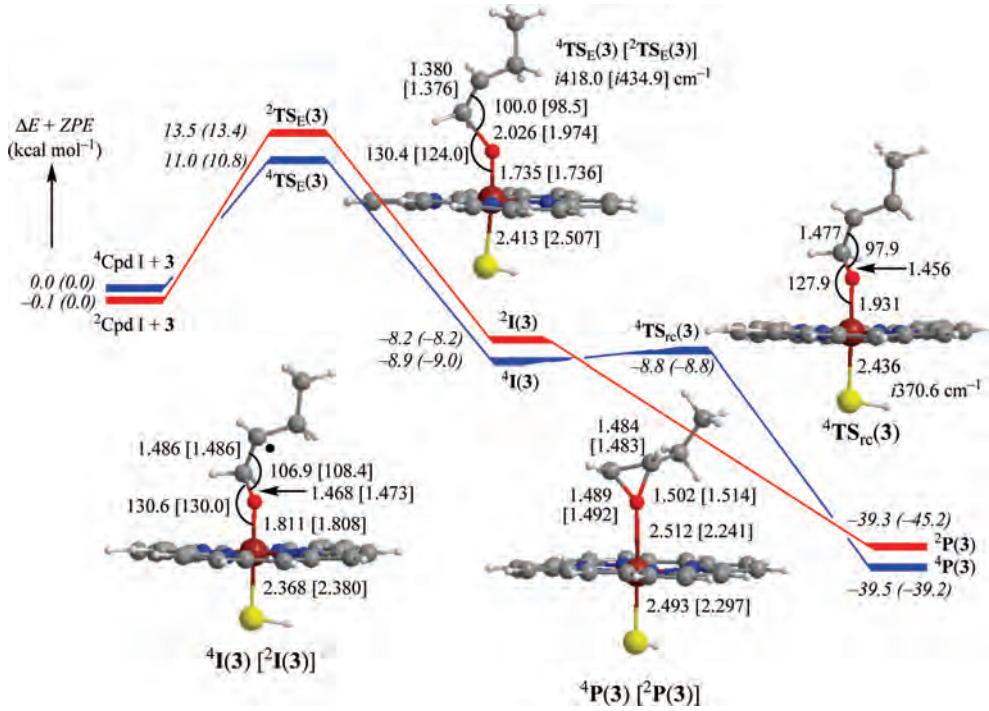

Figure 5. Reaction profile of 1-butene (**3**) epoxidation by ^{4,2}Cpd I(SH) with energies in kcal mol^{-1}. Also shown are optimized geometries of the critical points along the reaction mechanism obtained at UB3LYP/B1 with distances in angstroms, angles in degrees, and the value of the imaginary frequency in the transition state in wave numbers. Energies reported outside parentheses are obtained with basis set B2 on UB3LYP/B1 optimized geometries and contain ZPE corrections with basis set B1. Inside parentheses are reported energies (including ZPE) calculated at UB3LYP/B2 after a UB3LYP/B2 geometry optimization and frequency.

Table 1. Relative Energies of Critical Points along the Mechanism of Epoxidation of Substrates by Cpd I(SH) and Calculated Values of the Reorganization Energy (RE) and Ionization Energy (IE) of the Substrates[a]

	Substrate	^{4}TS$_E$	^{4}I	^{2}TS$_E$	^{2}I	RE$_{HS}$	IE$_{Sub}$
1	ethene	14.13	−5.95	14.29	−5.52	2.80	238.9
2	propene	13.13	−6.48	12.60	−6.27	2.93	219.7
3	1-butene	11.06	−8.86	13.52	−8.21	1.29	214.8
4	*trans*-2-butene	10.85	−6.80	10.03	*b*	2.96	203.7
5	1,3-cyclohexadiene	7.90	−19.29	9.42	*b*	2.91	181.4
6	1,4-cyclohexadiene	11.94	−3.96	13.12	*b*	5.15	194.5
7	styrene	8.95	−15.13	9.53	−14.70	3.25	187.7

[a] All energies are in kcal mol^{-1}, relative to isolated reactants and obtained with basis set B2 including ZPE with basis set B1. [b] No low-spin intermediate found; instead the reaction gives products directly.

closure barrier is small or negligible on the low-spin surface and somewhat higher on the high-spin surface.[34] This mechanism shows similarities to aliphatic hydroxylation mechanisms discussed before that gave a stepwise mechanism with an initial and rate-determining hydrogen abstraction step.[8] Similar to the epoxidation mechanism, in aliphatic hydroxylation reactions the rebound step is either negligible or barrierless on the low-spin surface, whereas it proceeds with a significantly higher barrier on the high-spin surface.[40] To ascertain that the optimized geometries and relative energies are not influenced by the choice of the basis set in the calculations, we repeated the geometry optimizations for the complete reaction mechanism shown in Figure 5 using the UB3LYP/B2 method followed by an analytical frequency at this level. As follows, the energies of the various steps in the reaction mechanism are generally within 0.2 kcal mol^{-1} of those obtained at UB3LYP/B2//UB3LYP/B1 with ZPE included from the UB3LYP/B1 results. Moreover, the optimized geometries are very similar to those found with the smaller basis set generally with deviations well below 0.010 Å for distances and less than 1° for angles and dihedrals (Supporting Information). It appears, therefore, that relative energies obtained from geometry and frequency calculations at UB3LYP/B1 are reliable and single-point energy calculations at the UB3LYP/B2 level of theory give sufficiently accurate results. Accordingly, we have used the latter method for the remaining calculations described in this work.

Table 1 summarizes the relative energies of ^{4,2}**TS**$_E$ and ^{4,2}**I** for all substrate epoxidation reactions calculated with Cpd I(SH), while optimized geometries of ^{4,2}**TS**$_E$ are shown in Figure 6. The lowest epoxidation barriers are obtained with 1,3-cyclohexadiene and styrene, while the highest barriers are found for ethene (**1**). The values of ^{4,2}**TS**$_E$(**1**) are in good agreement with those reported in the literature[34] although calculated with slightly different methods. In three cases we were unable to locate a radical intermediate in the low-spin state (^{2}**I**), namely using *trans*-2-butene, 1,3-cyclohexadiene, and 1,4-cyclohexadiene as substrates, where the geometry optimization fell to the product complexes instead. In all other cases an optimized geometry

(40) (a) Shaik, S.; Cohen, S.; de Visser, S. P.; Sharma, P. K.; Kumar, D.; Kozuch, S.; Ogliaro, F.; Danovich, D. *Eur. J. Inorg. Chem.* **2004**, 207–226. (b) Siegbahn, P. E. M.; Borowski, T. *Acc. Chem. Res.* **2006**, *39*, 729–738.

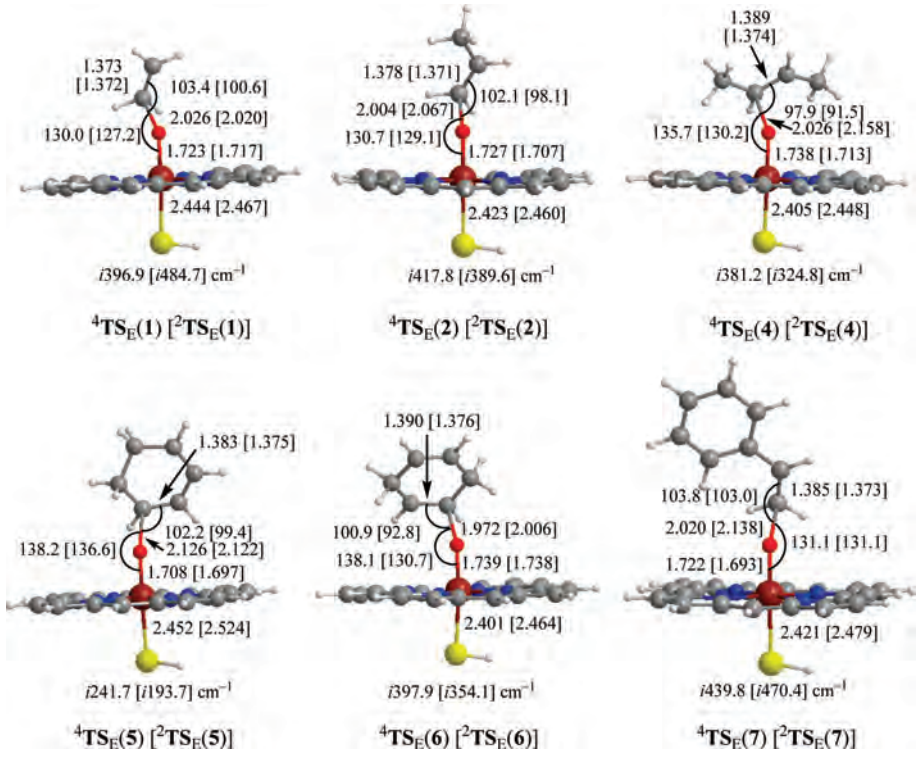

Figure 6. Optimized transition state geometries, ^{4,2}**TS**$_E$, as obtained with *Jaguar* with B3LYP for substrates: ethene (**1**), propene (**2**), *trans*-2-butene (**4**), 1,3-cyclohexadiene (**5**), 1,4-cyclohexadiene (**6**), and styrene (**7**). Bond lengths are in angstroms, angles in degrees, and the imaginary frequency in the transition state in wave numbers. Structures for 1-butene are displayed in Figure 5 above.

for a doublet spin intermediate was found, but these structures are short-lived with negligible ring-closure barriers leading to products. Therefore, the low-spin mechanism can be regarded as concerted via ^{2}**TS**$_E$, although this is not a symmetric transition state since it contains significant radical character and unequal C−O distances.

Generally the quartet and doublet spin transition state structures are close in energy, typically within 2 kcal mol^{-1}, which is not surprising since the same electron transfer processes take place, whereby an electron is transferred from the substrate into the a_{2u} orbital to give a radical intermediate with the metal in oxidation state Fe(IV) and a closed shell porphyrin macrocycle. Earlier epoxidation studies showed that in the gas phase the barriers leading to intermediates with an iron(III) coupled to a porphyrin cation radical are higher in energy.[35] Optimized geometries of epoxidation barriers in Figure 6 show typical features observed before. In most cases the transition state is early with relatively long C−O distances of ∼2 Å and short C−C bonds of 1.37−1.39 Å. Attempts to correlate the geometric features of the transition states with barrier height gave no clear relationships (see Supporting Information Figures S1−S6).

In principle, the highest occupied molecular orbital of an olefin is typically a π-orbital along a double bond; hence ionizing an electron from this bond should correspond to the strength of this double bond. To test whether the barrier heights of substrate epoxidation by Cpd I(SH) are connected to the ionization potential of the substrate, we calculated epoxidation mechanisms and substrate ionization potentials. In Figure 7, we display the correlation between epoxidation barrier height in the quartet spin state with substrate ionization energy (IE) for the reactions with Cpd I(SH) as an oxidant. The correlation between barrier height and substrate IE is fair with a correlation coefficient $R^2 = 0.80$. In previous studies we showed that a

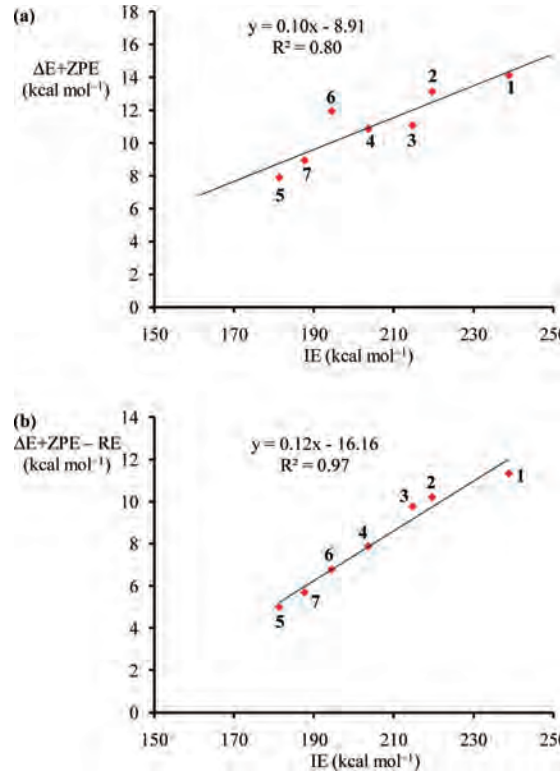

Figure 7. Correlation of epoxidation barrier height with the IE of the substrate without inclusion of the reorganization energy (a) or with inclusion of the RE (b). Substrates studied are: ethene (**1**), propene (**2**), 1-butene (**3**), *trans*-2-butene (**4**), 1.3-cyclohexadiene (**5**), 1,4-cyclohexadiene (**6**), and styrene (**7**).

better correlation can be achieved through inclusion of an RE contribution.[26] Indeed, a significant improvement is found

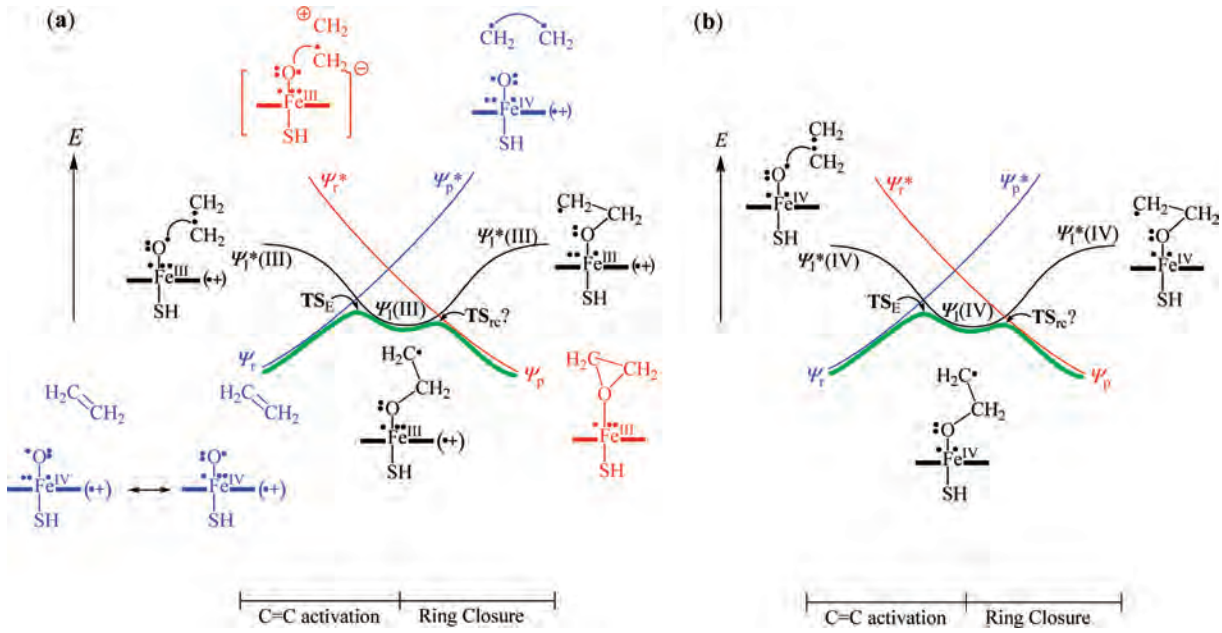

Figure 8. Valence bond curve crossing diagram of ethene epoxidation by Cpd I of P450 via **I**(Fe^{III}) (a) or **I**(Fe^{IV}) (b).

(Figure 7b) and the correlation coefficient rises to $R^2 = 0.97$, which proves that substrate epoxidation reactions are connected to the ionization potential of the substrates and that IE is a good representation of the π-bond strength of the olefin. To test the effect of a local environment on the barrier heights we recalculated the energies in a dielectric constant of $\epsilon = 5.7$ (Figure S7); however, the displayed trend only shows minor differences with the one reported in Figure 7a.

Origin of Correlation between Epoxidation Barrier and Ionization Energy (IE). The trends displayed in Figure 7 show that the barrier of olefin epoxidation by Cpd I(SH) correlates with the ionization energy of the substrate. Since, the highest occupied molecular orbital (HOMO) in all substrates is a π-orbital representing the double bond of the olefin, this implies that the energy of converting the double bond of the olefin into a single bond determines the barrier height of epoxidation. Recently, we explained substrate hydroxylation by heme and nonheme iron(IV)-oxo oxidants with a valence bond (VB) curve crossing diagram and thermodynamic cycles, and here we will follow an analogous approach to describe substrate epoxidation.[26,41]

Figure 8 displays the VB curve crossing diagram for substrate epoxidation by Cpd I(SH), where we use ethene as the olefin, but for other substrates analogous diagrams can be drawn. The relevant valence π-electrons in Figure 8 are displayed with a dot. The VB curve crossing diagram starts bottom left (in blue) with the reactants that appear in a reactant wave function Ψ_r. Thus, Cpd I(SH) has orbital occupation $\delta_{x^2-y^2}{}^2\ \pi_{xz}{}^2\ \pi_{yz}{}^2\ \pi^*_{xz}{}^1\ \pi^*_{yz}{}^1\ a_{2u}{}^1$, which gives rise to a spin density of approximately one on the iron, one on the oxygen atom, and one spread out over the porphyrin and axial ligands; hence we depict one unpaired electron next to the iron, one next to the oxo group, and one on the porphyrin macrocycle. In addition there are two electrons in the π-bond of the double bond of the substrate. This wave function connects to an excited state in the product geometry (Ψ_p*). In a similar way, the product wave function is represented by Ψ_p and has orbital occupation $\delta_{x^2-y^2}{}^2\ \pi^*_{xz}{}^2\ \pi^*_{yz}{}^1\ a_{2u}{}^2$ for $^2\mathbf{P}_E$ or $\delta_{x^2-y^2}{}^2\ \pi^*_{xz}{}^1\ \pi^*_{yz}{}^1\ \sigma^*_{z^2}{}^1\ a_{2u}{}^2$ for $^4\mathbf{P}_E$. The product wave function connects to an excited state wave function Ψ_r* in the geometry of the reactants. Thus, the point where the Ψ_r and Ψ_p wave functions cross leads to an avoided crossing and a transition state for the reaction. However, the reactant and product wave function are crossed by a third wave function curve that represents the intermediate complexes. In principle, there are two possibilities of an intermediate complex, namely one with the $Fe^{III}(Por^{+\bullet})(SH)OCH_2CH_2^{\bullet}$ configuration, designated **I**(Fe^{III}), and the other with the $Fe^{IV}(Por)(SH)OCH_2CH_2^{\bullet}$ configuration or **I**(Fe^{IV}). Gas-phase DFT calculations usually predict the Fe^{IV} complexes to be the lowest in energy,[34,35] but in enzymatic models often the Fe^{III} complexes are lowest lying.[42] Nevertheless, we show both VB diagrams in Figure 8, and the calculated trends on the Fe^{III} and Fe^{IV} surfaces should be similar. The crossing of the intermediate wave function, that is Ψ_I(III) or Ψ_I(IV), with the reactant wave function gives rise to a C−O bond formation barrier ($\mathbf{TS}_E$), while its crossing with the product wave function leads to the ring-closure transition state ($\mathbf{TS}_{rc}$). Thus, these VB curve crossing diagrams shown in Figure 8 explain why the reactions are stepwise via a radical intermediate. This quantitative model supports the reaction mechanisms calculated for the structures shown in Table 1 and the landscape depicted in Figure 5.

In VB theory the height of the avoided crossing can be determined from the excitation energy values in the reactant geometry;[43] see Figure 9. Thus, the crossing of reactant and intermediate wave functions Ψ_r and Ψ_I leads to an avoided crossing and a transition state for C−O bond formation in the epoxidation reaction. The curve crossing takes place at ΔE_c above the energy of the reactants, but the barrier height $\mathbf{TS}_E$ is a factor B below this crossing point at an energy $\Delta E^{\ddagger}$. This factor B represents the resonance energy of the molecule in the

(41) (a) Latifi, R.; Bagherzadeh, M.; de Visser, S. P. *Chem.—Eur. J.* **2009**, *15*, 6651–6662. (b) de Visser, S. P. *J. Am. Chem. Soc.* **2010**, *132*, 1087–1097.

(42) Schöneboom, J. C.; Cohen, S.; Lin, H.; Shaik, S.; Thiel, W. *J. Am. Chem. Soc.* **2004**, *126*, 4017–4034.

(43) (a) Shaik, S. S. *J. Am. Chem. Soc.* **1981**, *103*, 3692–3701. (b) Shaik, S.; Shurki, A. *Angew. Chem., Int. Ed.* **1999**, *38*, 586–625.

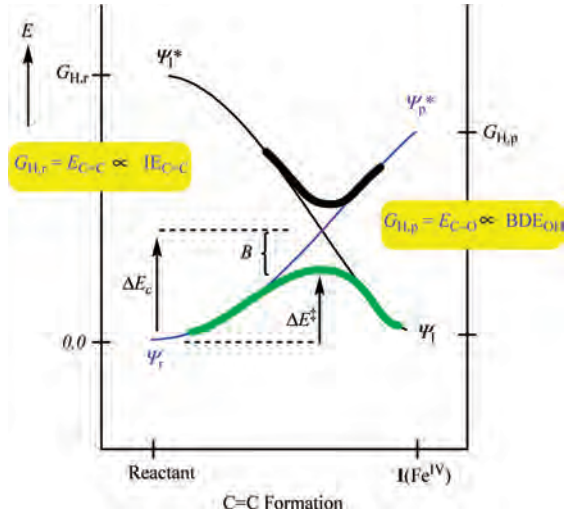

Figure 9. VB curve crossing diagram for the C−O bond formation step in the epoxidation reaction.

Table 2. DFT and VB Calculated Epoxidation Barrier Heights[a]

substrate	^{4}**TS**$_E$	RE$_{HS}$	$\Delta E_{DFT}^{\ddagger}$ [b]	$\Delta E_{VB}^{\ddagger}$
ethene	14.13	2.80	11.33	9.10
propene	13.13	2.93	10.21	9.07
1-butene	11.06	1.29	9.78	8.62
trans-2-butene	10.85	2.96	7.89	8.55
1,3-cyclohexadiene	7.90	2.91	5.00	5.50
1,4-cyclohexadiene	11.94	5.15	6.78	8.87
styrene	8.95	3.25	5.70	6.34

[a] All values in kcal mol^{-1}. [b] $\Delta E_{DFT}^{\ddagger} = \Delta E + ZPE(^4\mathbf{TS}_E) - RE_{HS}$.

transition state. The promotion gap (G_H) or excitation energy from the reactant wave function to the intermediate wave function in the reactants geometry is proportional to a fraction f of the curve crossing point via $\Delta E_c = f G_H$ to give

$$\Delta E^{\ddagger} = fG_H - B \qquad (3)$$

As follows from Figures 8 and 9, the promotion gap G_H is proportional to the energy to break the π-bond of the olefin. Since the IE of the olefins studied here is correlated with the expulsion of an electron from the double bond, this implies that the barrier height $\mathbf{TS}_E$ should correlate with IE as well, as indeed shown above in Figure 7. Therefore, the VB curve crossing diagram explains the correlation of barrier height with IE. This makes substrate epoxidation fundamentally different from aliphatic hydroxylation, where the VB curve crossing diagram connected the barrier with the strength of the C−H bond of the substrate.

To test whether the VB method described in Figure 9 can predict epoxidation barrier heights from empirical data, we used eq 3 above together with estimated values for G_H and B. The promotion gap was estimated as twice the first excitation energy of the substrate, which corresponds to a $\pi-\pi^*$ excitation in the double bond, i.e. is proportional to the dissociation energy of the double bond, $D_{C=C}$. Excitation energies were calculated using time-dependent DFT on the optimized reactant geometries using basis set B2. The resonance energy (B) was taken as half the energy of the C=C bond energy. Together with the RE corrected barrier heights, f was calculated using the values for G_H and B. The average value of f ($f_{AV} = 0.299 \pm 0.008$) together with G_H and B gave the VB calculated barrier heights ($\Delta E_{VB}^{\ddagger}$); see Table 2. For comparison we also give the DFT calculated barrier height ($\Delta E_{DFT}^{\ddagger}$), which is the difference between $^4\mathbf{TS}_E$ and RE. In general, the agreement between $\Delta E_{DFT}^{\ddagger}$ and $\Delta E_{VB}^{\ddagger}$ is fair with a standard deviation of 1.4 kcal mol^{-1}; hence the VB estimated barriers reproduce DFT calculated barriers well and predict the correct trends.

Scheme 1. Thermodynamic Cycle for the Reaction of Cpd I(SH) with Olefin To Form a Radical Intermediate

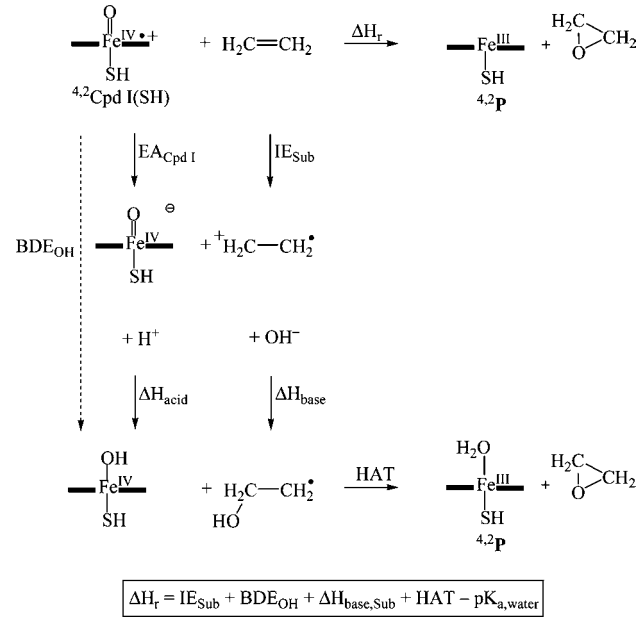

The VB diagram in Figure 9 predicts that the barrier height of substrate epoxidation is connected to the IE of the substrate through the reactant promotion gap ($G_{H,r}$), whereas the promotion gap in the radical intermediate is proportional to the energy required to form the C−O bond ($G_{H,p}$). To predict substrate epoxidation barriers, we have investigated thermodynamic cycles that ultimately correlate the C−O bond formation with barrier height. Thermodynamically, the reaction between oxidant and olefin leading to epoxide products is described in Scheme 1 and has reaction enthalpy ΔH_r. This enthalpy can be split into several components, such as the ionization energy of the substrate (IE_{Sub}) and the electron affinity of Cpd I(SH), EA_{CpdI}. As shown in eq 2, the latter is connected to the value of BDE_{OH} of Fe^{IV}(OH)(Por)(SH) via the sum of EA_{CpdI} and ΔH_{acid} (or pK_a).[44] In a similar way the OH affinity of substrate (ethene) is the sum of the IE of ethene and ΔH_{base}, Scheme 1. A final hydrogen atom transfer (HAT) between $HOCH_2CH_2^{\bullet}$ and Fe^{IV}(OH)(Por)(SH) followed by ring closure then gives an iron(III)−porphyrin complex with bound water and epoxide products. Energetically, the overall epoxidation reaction of olefins by metal-oxo complexes, therefore, is dependent on IE_{Sub}, BDE_{OH}, $\Delta H_{base}({}^+CH_2-CH_2^{\bullet})$, and the HAT energy. If this thermodynamic scheme is correct, then both aliphatic hydroxylation and double bond epoxidation reactions by metal-oxo oxidants are dependent on BDE_{OH}. To test this hypothesis, we calculated a series of propene epoxidation reactions using a range of iron(IV)-oxo oxidants and compared the epoxidation barrier heights with BDE_{OH}, as described in the next section.

Propene Epoxidation by Iron(IV)-Oxo Oxidants. So far, only studies using one particular oxidant have been discussed;

(44) (a) Friedrich, L. E. *J. Org. Chem.* **1983**, *48*, 3851–3852. (b) Bordwell, F. G.; Cheng, J.-P. *J. Am. Chem. Soc.* **1991**, *113*, 1736–1743. (c) Bordwell, F. G.; Cheng, J.-P.; Ji, G.-Z.; Satish, A. V.; Zhang, X. *J. Am. Chem. Soc.* **1991**, *113*, 9790–9795.

Table 3. DFT Calculated Propene Epoxidation Barriers Using a Range of Iron(IV)-Oxo Oxidants and Calculated Values for the Electron Affinity of Cpd I($EA_{Cpd\ I}$) and BDE_{OH}

	oxidant	$^{HS}TS_E$	$EA_{Cpd\ I}$	BDE_{OH}
A	Cpd I(SH)	13.13	70.6	88.9
B	Cpd I(OH)	5.67	76.2	99.5
C	Cpd I(Cl)	12.72	79.3	87.5
D	Cpd I(ImP)	13.58	151.0	85.4
E	Cpd I(C*c*P)	15.78	147.8	83.5
F	Fe^{IV}═O(TMCS)$^+$	17.90	124.6	84.1
G	Cpd I(TauD)	4.82	53.0	95.8

[a] All data in kcal mol^{-1} obtained with basis set B2 and with ZPE included with basis set B1.

however, to generalize the trends and to prove the thermodynamic model shown in Scheme 1, we calculated a series of substrate epoxidation reactions using propene as a substrate and varying iron(IV)-oxo oxidants with heme as well as nonheme ligand systems. In principle, the VB diagram shown above predicts that the barrier height of substrate epoxidation by iron(IV)-oxo oxidants should also correlate with the energy to form the C−O bond. In principle, however, the formation of a C−O bond between a substrate and an iron(IV)-oxo complex should be proportional to the formation of an O−H bond in a reaction of an iron(IV)-oxo species with a hydrogen atom, i.e. BDE_{OH} as predicted by the thermodynamic cycle in Scheme 1. To test this hypothesis, we ran an extra set of calculations on propene epoxidation by a range of different Cpd I models, using the iron(IV)-oxo complexes shown in Figure 3 above. Propene epoxidation data for Cpd I(Cl), Cpd I(ImP), Cpd I(TauD), and Fe^{IV}═O(TMCS)$^+$ were taken from the literature.[34] Subsequently, we took the various Cpd I reactants and added a hydrogen atom to give the iron-hydroxo complexes and calculated the bond dissociation energy of the O−H bond (BDE_{OH}) for the iron-hydroxo complex using reaction 2. Calculated barrier heights, BDE_{OH}, and EA_{CpdI} data are summarized in Table 3. These oxidants have different BDE_{OH} strengths with a range spread of more than 16 kcal mol^{-1}. The lowest epoxidation barriers are obtained with Cpd I(TauD) and Cpd I(OH), which are also the oxidants with the largest BDE_{OH} values. Interestingly, no correlation between electron affinity of the oxidant (EA_{CpdI}) and barrier height is found.

Figure 10 shows propene epoxidation barriers as a function of BDE_{OH} for the seven oxidants shown in Figure 3. The correlation is reasonable and improves to $R^2 = 0.92$ when corrections for the RE are applied. Therefore, in support of the electron transfer mechanisms shown in Figure 8 and the thermodynamic cycle in Scheme 1, we have established a method to correlate the barrier height to the strength of the C−O bond formed in an epoxidation reaction through the use of BDE_{OH}. Interestingly, also aliphatic hydroxylation reactions correlate with BDE_{OH}, which means that the regioselectivity of substrate epoxidation versus hydroxylation is not determined by the oxidant but only by the electronic properties of the substrate.

The trends observed in Table 2 and Figure 10 are in excellent agreement with previous axial ligand studies of styrene epoxidation by Fe^{IV}═O(TMP$^{+\bullet}$)L, with L = F^-, $HOCH_3$, Cl^-, OAc^-, $CF_3O_2SO^-$, and ClO_4^- and with TMP = tetramesitylporphyrin.[18] Thus, calculations on Fe^{IV}═O(Por$^{+\bullet}$)L with L = F^-, Cl^-, OAc^-, and ClO_4^- give BDE_{OH} values of 93.7, 87.5, 89.5, and 83.2 kcal mol^{-1}, respectively. For the set of Fe^{IV}═O(TMP$^{+\bullet}$)L with L = F^-, Cl^-, and OAc^-, Gross and co-workers measured rate constants of styrene epoxidation of 706, 149, and 114 × 10^{-3} M^{-1} min^{-1} at −78 °C, while Fe^{IV}═O(TMP$^{+\bullet}$)ClO_4 was found to be unreactive. The trends in BDE_{OH} values are, therefore, in good agreement with the styrene epoxidation rate constants of the Gross group, where the highest rate constant was found for Fe^{IV}═O(Por$^{+\bullet}$)F and no reactivity with Fe^{IV}═O(Por$^{+\bullet}$)ClO_4. Furthermore, Fe^{IV}═O(TMP$^{+\bullet}$)Cl and Fe^{IV}═O(TMP$^{+\bullet}$)OAc have very similar BDE_{OH} values and their rate constants of styrene epoxidation are close. Consequently, experimental data support the conclusions drawn from the DFT calculations excellently.

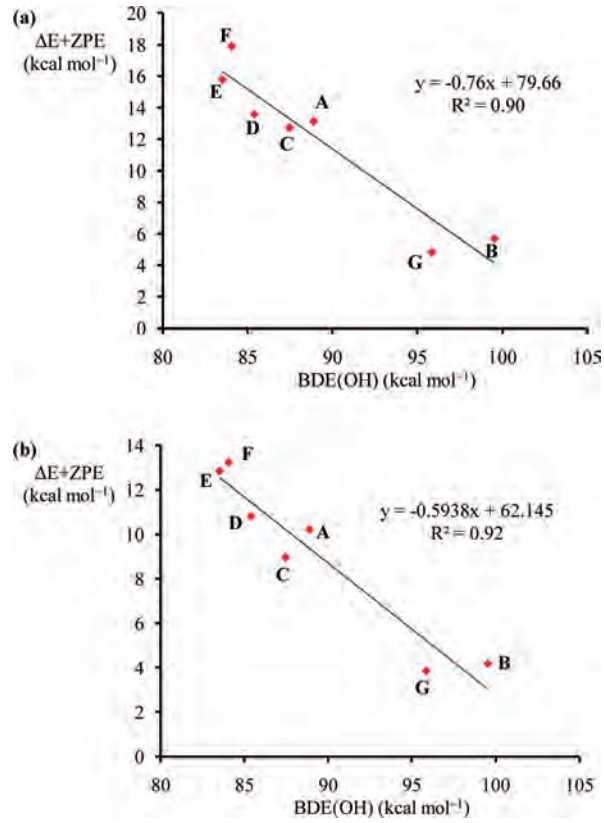

Figure 10. Correlation of propene epoxidation barrier height with BDE_{OH} of Cpd I without inclusion of the RE (a) or with inclusion of the RE (b). Oxidants studied are as follows: Cpd I(SH) (**A**), Cpd I(OH) (**B**), Cpd I(Cl) (**C**), Cpd I(ImP) (**D**), Cpd I(C*c*P) (**E**), Fe^{IV}═O(TMCS)$^+$ (**F**), and Cpd I(TauD) (**G**).

Correlation of Barrier Height with Polarizability. In the past we showed that atomization enthalpies of analogous molecules are linearly related with the difference in polarizability volume ($\Delta\alpha_{AV}$) for atomization,[45] whereby this polarizability difference was defined as the polarizability of molecule *M* (α_M) minus the sum of the atomic polarizabilities of its contents (α_{atoms}), eq 4.

$$\Delta\alpha_{AV} = \alpha_M - \sum \alpha_{atoms} \qquad (4)$$

To test whether the barrier height of substrate epoxidation reactions follows a similar correlation with polarizability volume, we took the polarizability trace from the Gaussian frequency calculations and estimated the polarizability difference for the process from reactants to transition state geometry. The polarizability difference ($\Delta\alpha_{AV}$) is calculated as the difference in polarizability trace between that for the transition state (α_{TS}) with respect to that for isolated reactants, i.e. Cpd I and substrate (Sub) as follows:

(45) de Visser, S. P. *Phys. Chem. Chem. Phys.* **1999**, *1*, 749–753.

$$\Delta\alpha_{AV} = \alpha_{TS} - \alpha_{CpdI} - \alpha_{Sub} \quad (5)$$

A plot of the polarizability difference against barrier height of substrate epoxidation by Cpd I(SH) using the data from Table 1 is given in Figure 11. The correlation is reasonable and implicates the polarizability volume change as indeed being proportional to the energy change during the reaction. This change is the largest for systems with small reaction barriers. Therefore, the charge distribution in the transition state will influence the polarizability volume, and the more dramatic the change encountered is the lower the barrier heights will be.

Nature of the Ring-Closure Barrier. So far, this work was focused only on the rate determining C−O bond formation step. However, in two-state reactivity the ring-closure step cannot be neglected. The reason for that is because in porphyrin ligated iron complexes Cpd I appears in close lying doublet and quartet spin states, whereby the initial C−O bond activation is on close lying spin state surfaces. However, as shown above in Figure 4, after the intermediate the doublet and quartet spin state surfaces bifurcate due to differences in electron transfer mechanisms. As a consequence, the low-spin surface gives retention of the stereochemistry, whereas on the high-spin surface the intermediate has a finite lifetime and may give rearrangement or side reactions.

The ring-closure barrier in all cases discussed in this work is small and generally much lower in energy than the C−O bond activation transition state. In addition, in several cases it was shown that no radical intermediate exists and the reaction collapses to products immediately. This has important consequences, since the lifetime of the radical intermediate may, for instance, lead to stereochemical scrambling and the formation of e.g. *cis*-epoxides from *trans*-olefins. In cases where no intermediate was found, the reaction will retain its stereochemical preference and no scrambling will occur. Figure 12 explains the ring-closure processes on the quartet and doublet spin state surfaces starting from the radical intermediates in the Fe(IV) electronic configuration, i.e. with orbital occupation $\delta_{x^2-y^2}{}^2\,\pi^*_{xz}{}^1\,\pi^*_{yz}{}^1\,a_{2u}{}^2\,\phi_{Sub}{}^1$. Thus, on the low-spin surface there is a radical on the terminal CH_2 group with a down-spin and an up-spin unpaired electron on the oxo group. These two electrons will pair up and form the C−O bond. Since these two electrons are already aligned in the intermediate complex, it will cost very little energy to close the bond, which is in agreement with the calculated potential energy surfaces. The promotion gap in the low-spin state is proportional to the IE of the substrate and the electron affinity of Cpd I.

In the high-spin state the situation is slightly different, whereby an electron has to transfer from the oxo group into a $\sigma^*_{z^2}$ orbital to create a product electronic configuration $\delta_{x^2-y^2}{}^2\,\pi^*_{xz}{}^1\,\pi^*_{yz}{}^1\,\sigma^*_{z^2}{}^1\,a_{2u}{}^2$. As a consequence, the promotion gap is larger in the high-spin ring closure than it is for the low-spin, and as a result also the ring-closure barrier is widened. Therefore, the high-spin surface is expected to proceed via a radical intermediate with a finite lifetime, while on the low-spin surface its lifetime is ultrashort and lead to products instantaneously. Consequently, the low-spin mechanism will retain its stereochemical preference, whereas stereochemical scrambling may occur on the high-spin surface, so that the two spin state surfaces are expected to lead to different product distributions. The epoxidation ring-closure mechanism follows similar electron transfer mechanisms to the rebound mechanism in aliphatic hydroxylation reactions, where also the doublet spin mechanism is barrierless or small, while the quartet spin rebound encounters significantly higher rebound barriers.[40]

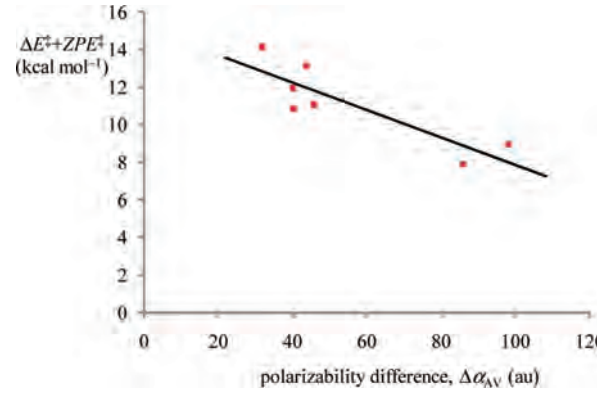

Figure 11. Correlation of epoxidation barrier height with polarizability difference for substrate epoxidation by Cpd I(SH).

In experimental work often stereochemical scrambling occurs, where *cis*-olefins give *trans*-epoxides, although the product ratios of *cis*- and *trans*-epoxides appear to be dependent on the reaction conditions and the nature of the oxidant.[46] For instance, experimental studies of *cis*-β-methylstyrene epoxidation using biomimetic iron porphyrins, such as Fe^{IV}═O($TMP^{+\bullet}$)L with L = F^-, Cl^-, or ClO_4^-, found retention of the stereochemistry when the experiment was performed at 0 °C or room temperature (>96% *cis*-epoxide products), whereas at lower temperatures (−78 °C) the *trans*-epoxide products were dominant.[18d] These studies support our general mechanism shown in Figures 5 and 12 that predict the intermediate complex to be in a shallow minimum that is separated from products by a small ring-closure barrier. At lower temperatures, the lifetime of the intermediate complex will be longer during which an internal rotation within the radical intermediate can take place that leads to stereochemical scrambling and the conversion of *cis*-olefins into *trans*-epoxides.

In addition, the studies of Gross et al.[18d] suggested that with strong electron-withdrawing axial ligands the radical intermediate has the Fe^{IV}(Por)OCH_2CHR conformation, whereas with weaker axial ligands the Fe^{III}($Por^{+\bullet}$)OCH_2CHR conformation is the lowest in energy. Indeed, in the case of propene epoxidation by Cpd I(CcP) the lowest lying C−O activation barrier is of the Fe^{III}-form, with the Fe^{IV} state 1.1 kcal mol^{-1} higher in energy.[47] Previous studies showed the difference between these two states to be close in energy for Cpd I(SH),[35] and environmental perturbations, such as solvent, influence their state ordering.

Other experimental studies showed that the nature of the olefin determined the rate constants for a set of olefin epoxidation studies by a biomimetic iron−porphyrin system.[48] This observation is in agreement with our correlation shown above between barrier height and ionization energy.

Differences and Comparisons between Substrate Epoxidation and Hydroxylation by Iron(IV)-Oxo Oxidants. So what are the fundamental differences between substrate epoxidation and substrate hydroxylation? First, as shown above the rate constant,

(46) Collman, J. P.; Brauman, J. I.; Meunier, B.; Hayashi, T.; Kodadek, T.; Raybuck, S. A. *J. Am. Chem. Soc.* **1985**, *107*, 2000–2005.
(47) de Visser, S. P. The axial ligand effect on substrate monoxygenation by the oxo-iron active species of heme enzymes. How does cytochrome c peroxidase compare to cytochrome P450? In *Inorganic Biochemistry: Research Progress*; Hughes, J. G., Robinson, A. J., Eds.; Nova Science Publishers, Inc.: New York, 2008; Chapter 7, pp 197−224.
(48) Collman, J. P.; Kodadek, T.; Raybuck, S. A.; Brauman, J. I.; Papazian, L. M. *J. Am. Chem. Soc.* **1985**, *107*, 4343–4345.

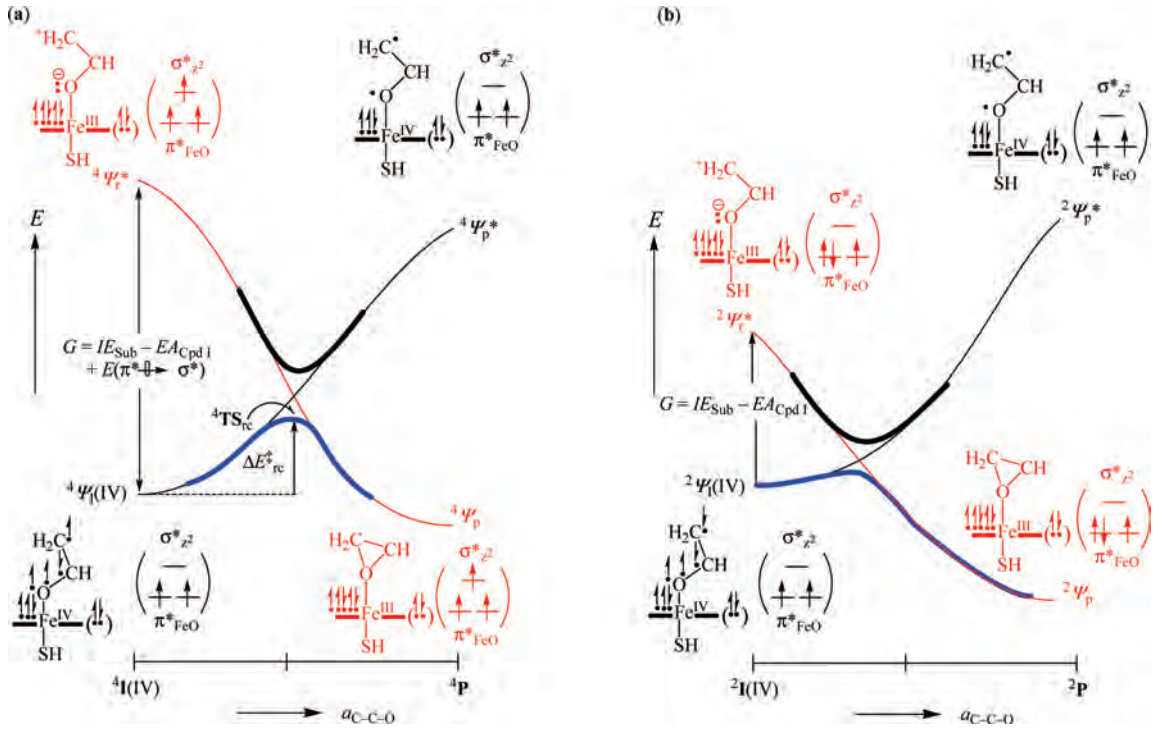

Figure 12. VB curve crossing diagram for high-spin and low-spin ring-closure mechanisms starting from ^{4,2}**I**(Fe^{IV}).

and hence the free energy of activation, of an epoxidation reaction correlates with the IE of the substrate as well as with the BDE_{OH} value of the iron-hydroxo complex and the polarizability change for the reaction. By contrast, a substrate hydroxylation has a rate-determining hydrogen atom abstraction whereby the barrier is related to BDE_{CH} and BDE_{OH}.[20,21,26] Since, aliphatic hydroxylation and double bond epoxidation both correlate with BDE_{OH}, this implies that the regioselectivity of aliphatic hydroxylation versus epoxidation is determined by the difference in IE of the substrate and the strength of the C−H bond of the substrate *but not by the intrinsic properties of the oxidant*. Propene epoxidation and aliphatic hydroxylation were studied with DFT using all oxidants shown in Figure 3, which enables us to calculate the ratio of epoxidation versus hydrogen atom abstraction barriers for a selection of different oxidants. Thus an average ratio of hydrogen atom abstraction over double bond epoxidation of $\mathbf{TS}_H/\mathbf{TS}_E = 1.17 \pm 0.17$ was found, with generally a preference of substrate hydroxylation over double bond epoxidation in the gas phase. Within the error of the calculations this ratio supports our observation that the nature of the oxidant does not affect the regioselectivity of substrate hydroxylation over epoxidation. This hydroxylation/epoxidation product ratio is in excellent agreement with that found by Vaz et al.[15] for cyclohexene epoxidation by P450 Δ2B4 and Δ2E1 isozymes. Moreover, the free energy of activation for styrene epoxidation[25a] by Cpd I(SH) calculated at 298 K is within 3 kcal mol^{-1} of the experimentally determined value of Vaz et al. More recent studies of the Newcomb group[14d] of styrene epoxidation and benzyl alcohol hydroxylation by CYP119 and CYP102HD isozymes showed similar kinetics and thermodynamics for each substrate, hence supporting our hypothesis that the regioselectivity of substrate hydroxylation versus epoxidation is dependent on the substrate only.

It should be realized, however, that BDE_{CH} is essentially the sum of an electron and a proton transfer. Nevertheless, the electron and proton transfers usually happen simultaneously so that the BDE_{CH} cannot be split into separate electron and proton transfer mechanisms. Therefore, the regioselectivity of substrate epoxidation versus hydroxylation is determined by the IE of the substrate relative to the BDE_{CH} value.

Conclusions

In this study we delineate the fundamental factors responsible for substrate epoxidation by an iron(IV)-oxo heme and nonheme systems through computational and VB methods. Substrate epoxidation by the iron(IV)-oxo system depends on the IE of the substrate and not on the oxidants. We show that the reactions are stepwise via a radical intermediate. The rate -determining step is the initial C−O bond formation transition state, which is found to correlate with the ionization energy of the substrate, the BDE_{OH} of the oxidant, and the polarizability change for the reaction. These properties are explained with a VB curve crossing diagram that identifies the electron transfer mechanisms in the process. It is further shown that the regioselectivity of substrate epoxidation versus hydroxylation is not dependent on the choice of the oxidant, but the thermodynamics of the reaction is.

Acknowledgment. The research was supported by CPU time provided by the National Service of Computational Chemistry Software (NSCCS). D.K. is the Ramanujan Fellow of the Department of Science and Technology (New Delhi). Prof Sason Shaik is acknowledged for helpful discussions regarding the Valence Bond diagram and critical proofreading of our manuscript.

Supporting Information Available: Cartesian coordinates of all structures, tables with group spin densities, charges and absolute energies of all structures calculated in this work. Also given are seven figures with correlations of geometric parameters with barrier height as well as complete ref 23. This material is available free of charge via the Internet at http://pubs.acs.org.

JA9106176

J Biol Inorg Chem (2010) 15:361–372
DOI 10.1007/s00775-009-0608-3

ORIGINAL PAPER

Coupling and uncoupling mechanisms in the methoxythreonine mutant of cytochrome P450cam: a quantum mechanical/molecular mechanical study

Muhannad Altarsha · Tobias Benighaus · Devesh Kumar · Walter Thiel

Received: 6 August 2009 / Accepted: 4 November 2009 / Published online: 20 November 2009
© The Author(s) 2009. This article is published with open access at Springerlink.com

Abstract The Thr252 residue plays a vital role in the catalytic cycle of cytochrome P450cam during the formation of the active species (Compound I) from its precursor (Compound 0). We investigate the effect of replacing Thr252 by methoxythreonine (MeO-Thr) on this protonation reaction (coupling) and on the competing formation of the ferric resting state and H_2O_2 (uncoupling) by combined quantum mechanical/molecular mechanical (QM/MM) methods. For each reaction, two possible mechanisms are studied, and for each of these the residues Asp251 and Glu366 are considered as proton sources. The computed QM/MM barriers indicate that uncoupling is unfavorable in the case of the Thr252MeO-Thr mutant, whereas there are two energetically feasible proton transfer pathways for coupling. The corresponding rate-limiting barriers for the formation of Compound I are higher in the mutant than in the wild-type enzyme. These findings are consistent with the experimental observations that the Thr252MeO-Thr mutant forms the alcohol product exclusively (via Compound I), but at lower reaction rates compared with the wild-type enzyme.

Keywords Cytochrome P450 · Methoxythreonine · *O*-Methylthreonine · Proton transfer · Quantum mechanics/Molecular mechanics

Electronic supplementary material The online version of this article (doi:10.1007/s00775-009-0608-3) contains supplementary material, which is available to authorized users.

M. Altarsha · T. Benighaus · D. Kumar · W. Thiel (✉)
Max-Planck-Institut für Kohlenforschung,
Kaiser-Wilhelm-Platz 1,
45470 Mülheim, Germany
e-mail: thiel@mpi-muelheim.mpg.de

Introduction

Cytochrome P450 is one of the most versatile enzymes in nature [1, 2]. It uses dioxygen to catalyze a great variety of stereospecific and regioselective processes of oxygen insertion into organic compounds [3–8]. These processes are of vital importance in biosystems, where the enzyme participates in detoxification and in biosyntheses [1]. Since the activation of inert C–H bonds is one of the holy grails of chemistry [9], the facility to carry out this process makes the P450 enzyme superfamily a model for creative mimetic chemistry [10] designed to generate novel catalysts that can perform C–H activation.

The bacterial enzyme P450cam (CYP101) is the workhorse of P450 research which has generated much insight into the role of the protein in regulating the activity of the enzyme and the effects of site-directed mutations [4, 11–14]. Its active site contains a heme unit that consists of an iron protoporphyrin IX complex with Cys as the proximal axial ligand. The active catalytic species, with an Fe(IV)–oxo moiety, is commonly denoted as Compound I. It has been observed in a related chloroperoxidase, but is still elusive for P450 enzymes, where it has only been identified by transient spectroscopy [8].

Site-directed mutagenesis studies [15–18] in combination with X-ray structural analyses [19, 20] indicate that the conserved P450 residue Thr252 at the active site plays a crucial role in the catalysis, in particular during the formation of Compound I [21, 22]. Hence, it was no surprise that Thr252 became an early target for mutagenesis [23, 24]. Several mutants such as Thr252Ala and Thr252Gly show an uncoupling of O_2 consumption from D-camphor hydroxylation, most of the O_2 consumed being converted to H_2O_2 without cleaving the O–O bond (Scheme 1), whereas Thr252Ser retains significant coupling of O_2

consumption with D-camphor hydroxylation [15]. When Thr252 is replaced by methoxythreonine (MeO-Thr), the resulting Thr252MeO-Thr mutant gives 100% formation of 5-*exo*-hydroxycamphor (no uncoupling), but the rate of reaction is slowed down to one third compared with that for the wild-type enzyme [25]. None of the other Thr252X mutants studied preserves the coupling activity to a similar extent [25]. It is generally assumed that site-directed Thr252X mutagenesis will disrupt the proton relay that converts Compound 0 to Compound I in P450 enzymes [26, 27].

Several theoretical studies have addressed the protonation reactions that generate Compound I [28–37]. The commonly formulated mechanism is protonation of Compound 0 at the distal oxygen atom followed by O–O bond cleavage. Recent density functional theory calculations on a large gas-phase active-site model (96 atoms) indeed gave a stable protonated Compound 0 species with significant barriers for the conversion toward both Compound 0 and Compound I [32]. However, subsequent quantum mechanical/molecular mechanical (QM/MM) calculations showed that such an intermediate is quite instable in the enzyme (more than 20 kcal/mol above Compound 0) and mechanistically irrelevant (barriers of only 3–4 kcal/mol for the decay to Compound 0 and Compound I) [37]. An alternative mechanism was proposed that involves an initial O–O bond cleavage followed by a proton transfer to the OH species formed (via a hydrogen-bonding network in the Asp251 channel), with a concomitant electron transfer from the heme (yielding Compound I and water) [37]. A similar mechanistic scenario was considered in heme oxygenase and chloroperoxidase [38, 39]. The latest QM/MM work [40] on this topic investigated both the coupling and the uncoupling reactions of Compound 0 in the wild-type P450cam enzyme and in four Thr252X mutants (X = Ser, Val, Ala, Gly). It was found that the formation of Compound I (coupling) always proceeds through the two-step mechanism with initial O–O bond cleavage [40]. By contrast, the uncoupling reaction is always concerted. Its barrier is always higher than that of the coupling reaction if the Asp251 channel contains only residue 252, the crystallographic water molecule Wat901, and protonated Asp251. Molecular dynamics (MD) simulations indicate, however, that an additional water molecule is stable in the Asp251 channel for X = Val, Ala, and Gly, which leads to much smaller barriers for uncoupling owing to a much more favorable hydrogen-bonding network. Including this extra water molecule in the QM region makes uncoupling competitive with coupling in the case of X = Val and renders it more facile for X = Ala and Gly [40], in qualitative agreement with experiment [15].

Here, we extend our previous QM/MM work by considering the effect of the Thr252MeO-Thr mutation. We address both the coupling and the uncoupling reactions and attempt to answer the question whether the Thr252MeO-Thr mutation will indeed disrupt the proton relay channel that is commonly viewed as being an essential prerequisite for the conversion of Compound 0 to Compound I.

Computational methods and proposed mechanisms

The initial structure was taken from the MD trajectory of the native enzyme studied earlier [37]. Thr was mutated into MeO-Thr by manually replacing the OH group in the Thr252 residue by OCH_3. The same solvation and protonation schemes were applied as in previous studies [41–43]. Glu366 and Asp251 were considered as possible proton sources [17, 31, 44], and the corresponding two

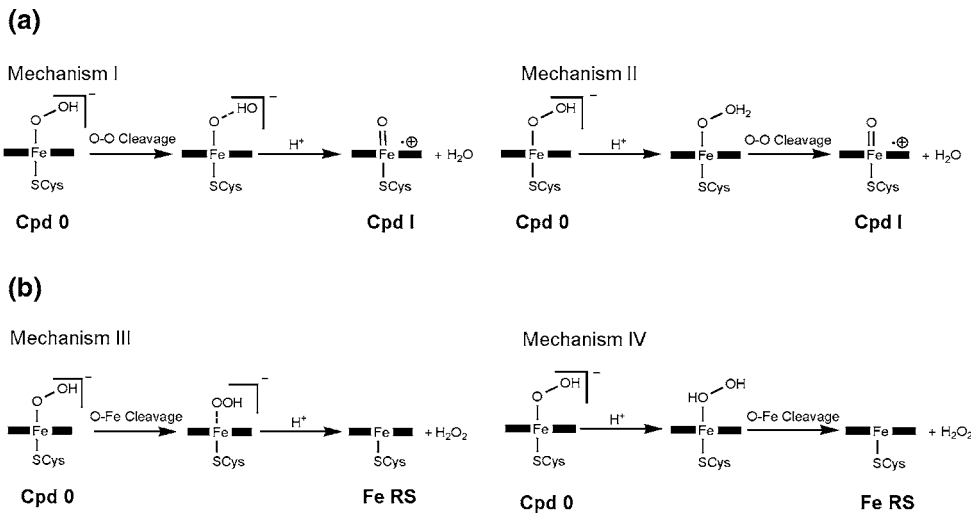

Scheme 1 **a** Two mechanisms for the conversion of Compound 0 (*Cpd 0*) to Compound I (*Cpd I*, coupling reaction). **b** Two mechanisms for ferric resting state (*Fe RS*) formation (uncoupling reaction)

protonation schemes were adopted as in the standard setup used previously [41–43] (i.e., protonated Glu366 and deprotonated Asp251 in the Glu366 channel, and deprotonated Glu366 and protonated Asp251 in the Asp251 channel). Both setups consisted of 24,988 atoms in total, including 5,891 TIP3P water molecules [45]. The solvated systems were relaxed by performing classical energy minimizations and MD simulations at the MM level using the CHARMM22 force field [46] as implemented in the CHARMM program [47]. The heme units with the Cys357 and OOH ligands as well as the outer 8 Å of the solvent layer were kept fixed during these initial runs.

The QM/MM method chosen was analogous to that used in our previous studies [41–43]. Here, we briefly mention some aspects relevant to the present work. Minimized snapshots from the MD trajectories were taken as initial structures for QM/MM optimizations. In the QM/MM calculations, the QM part was treated by unrestricted hybrid density functional theory (UB3LYP) [48] with the LACVP [49] small-core effective core potential basis set on iron and 6-31G [50] on the remaining atoms (B1) for geometry optimizations, while the MM part was described by the CHARMM22 force field. Single-point calculations were carried out with the TZVP [51, 52] basis set (B2).

An electronic embedding scheme [53] was adopted in the QM/MM calculations, i.e., interactions with MM charges were incorporated into the one-electron Hamiltonian of the QM calculation. No cutoffs were introduced for the nonbonding MM and QM/MM interactions. Hydrogen link atoms with the charge shift model were employed to treat the QM/MM boundary. The TURBOMOLE program [54] was used for the QM treatment in the QM/MM calculations as well as in pure QM calculations. The CHARMM22 force field was run through the DL_POLY [55] program to handle the MM part of the systems. The QM/MM calculations were performed with the ChemShell package [56], which integrates the TURBOMOLE and DL_POLY programs and performs geometry optimization with the HDLC optimizer [57].

Possible proton transfer pathways

Scheme 1 shows the four proposed mechanisms that were investigated for both protonation channels (Glu366 and Asp251).

In mechanism I, initially the O–O bond is cleaved to generate an OH radical and one-electron-reduced Compound I. Subsequently, a proton is transferred to the OH radical with a concomitant electron transfer from the heme that yields Compound I and water [37].

In mechanism II, a proton is transferred to the distal oxygen atoms of the hydroperoxo group to form protonated Compound 0 (containing $FeOOH_2$), followed by heterolytic O–O bond cleavage that generates Compound I and water.

Mechanisms I and II both give Compound I and correspond to the coupling reaction (Scheme 1a).

In mechanism III, initially the Fe–O bond is cleaved to generate an OOH radical, followed by a proton transfer to the OOH group that yields the ferric resting state and hydrogen peroxide.

In mechanism IV, a proton is transferred to the proximal oxygen atom of the hydroperoxo group to form an FeH_2O_2 moiety, followed by heterolytic cleavage of the O–Fe bond generating the ferric resting state and hydrogen peroxide.

Mechanisms III and IV both yield the ferric resting state and hydrogen peroxide (uncoupling reaction, Scheme 1b).

QM region

In the QM/MM calculations, we employed QM regions analogous to those adopted for the wild-type enzyme in our previous work [37] (Fig. 1), except that the Thr252 residue was replaced by MeO-Thr. In both channels (Asp251 and Glu366), the QM region included: iron porphine (without heme side chains), the sulfur atom of Cys357, the axial OOH moiety, and MeO-Thr (represented by $CH_3OCH_2CH_3$). In addition, the QM region also contained Wat901 and Asp251 (represented by CH_3COOH) in the case of the Asp251 channel, and Wat523, Wat566, Wat687, Wat902, and Glu366 (represented by CH_3COOH) in the case of the Glu366 channel (Fig. 1). Hence, the water molecules that may be involved in the proton transfer are part of the QM region for each channel.

Compound 0 can exist in a doublet, quartet or sextet state. It has a doublet ground state both in the wild-type P450cam enzyme and in the Thr252X mutants. According to the QM/MM calculations, the lowest quartet and sextet states lie 8.3 and 9.0 kcal/mol above the doublet ground state of the Thr252MeO-Thr mutant, respectively. Therefore, we only studied the reactions in the doublet state of the mutant, as was done previously in the case of the wild-type enzyme [37].

Results

Figures 2, 3, 4, 5, 6, 7, and 8 show the optimized QM/MM geometries of the QM regions for all relevant minima and transition states (Thr252MeO-Thr mutant, mechanisms I–IV, Glu366 and Asp251 channels). The computed relative QM/MM energies of the stationary points are summarized for basis sets B1/B2 in Table 1 (coupling reaction, mechanisms I and II) and Table 2 (uncoupling reaction, mechanisms III and IV). The single-point energies obtained

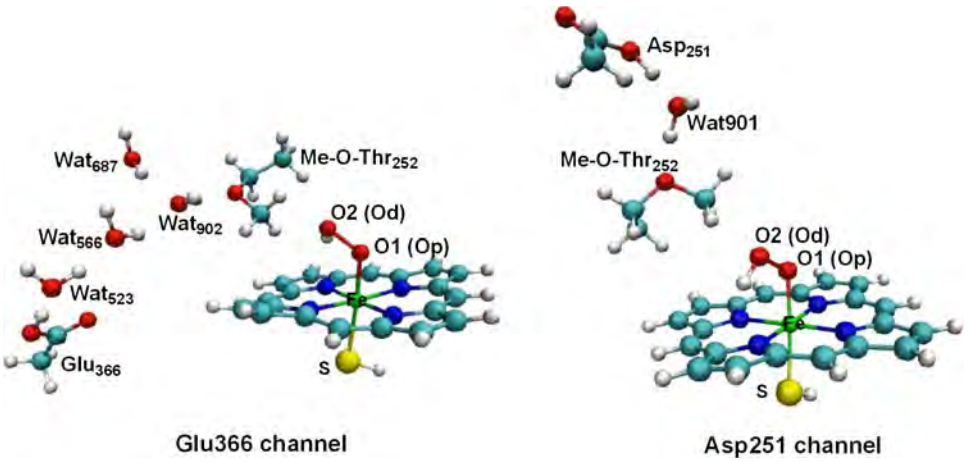

Fig. 1 Quantum mechanical region for the Thr252MeO-Thr mutant in the Glu366 and Asp251 channels

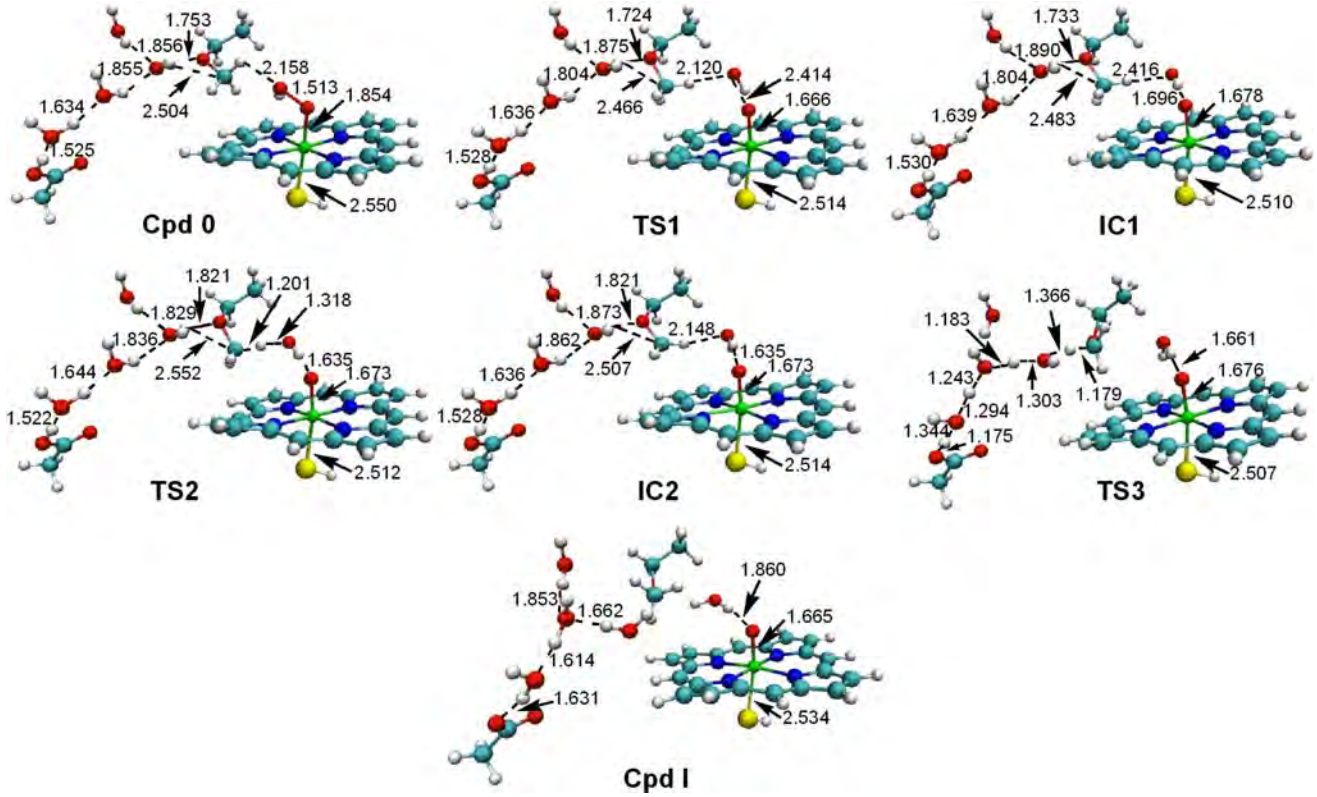

Fig. 2 Optimized geometries (UB3LYP/B1/CHARMM) for mechanism I (coupling reaction) in the Glu366 channel

with the larger TZVP basis (B2) at the corresponding optimized QM/MM geometries (B1) are generally quite similar to those obtained with the smaller basis (B1), although they are consistently slightly higher relative to Compound 0, typically by 1–3 kcal/mol. A similar behavior was also observed for the wild-type enzyme [37]. In the following discussion, we shall only quote B1 results for the sake of consistency (energies, geometries, etc.). Formation of the correct intermediates and products was verified by analysis of the spin densities and Mulliken charges. These data and selected geometrical parameters are documented in the electronic supplementary material.

Mechanism I: homolytic O–O bond cleavage followed by coupled proton–electron transfer

Glu366 channel

The first step passes over a barrier of 18.1 kcal/mol and leads to an intermediate (IC1), in which the OH moiety

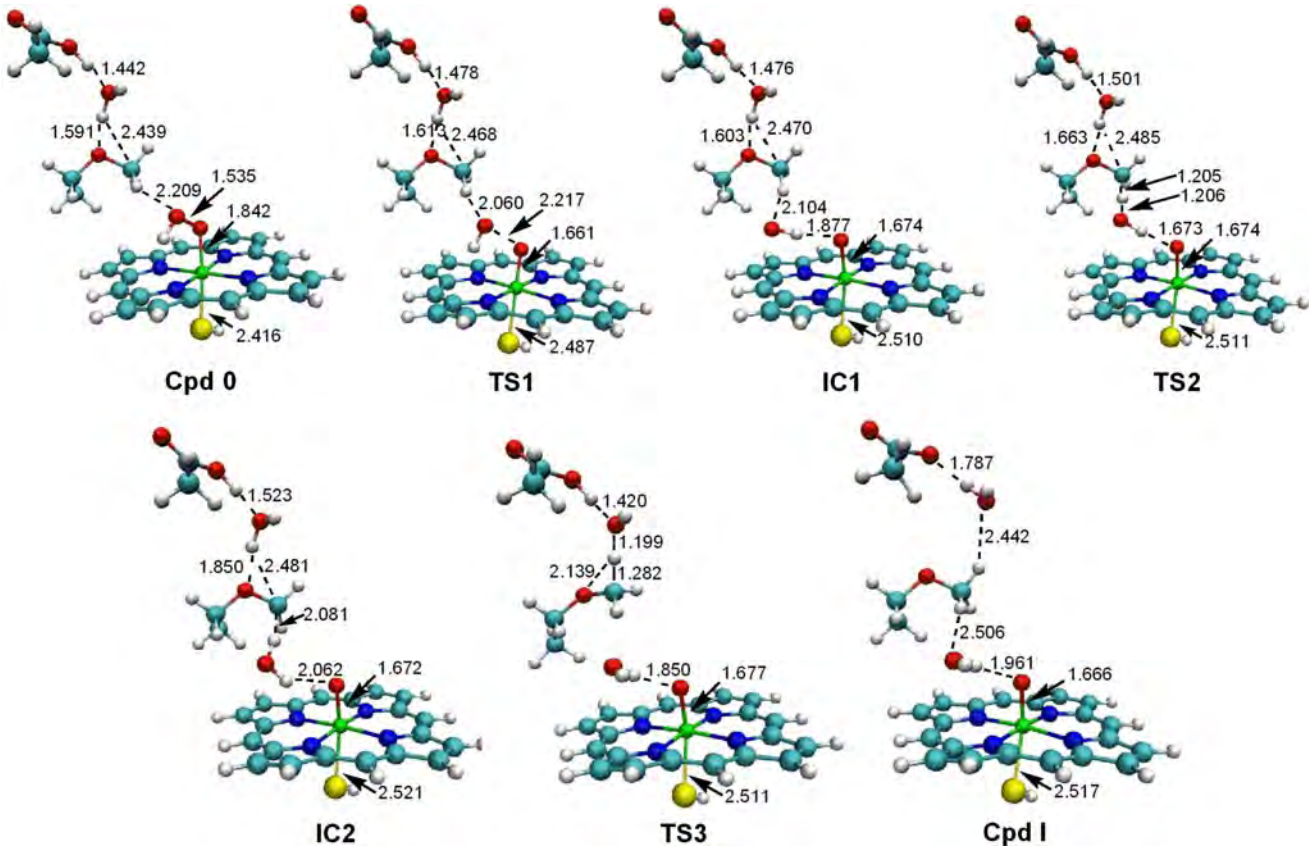

Fig. 3 Optimized geometries (UB3LYP/B1/CHARMM) for mechanism I (coupling reaction) in the Asp251 channel

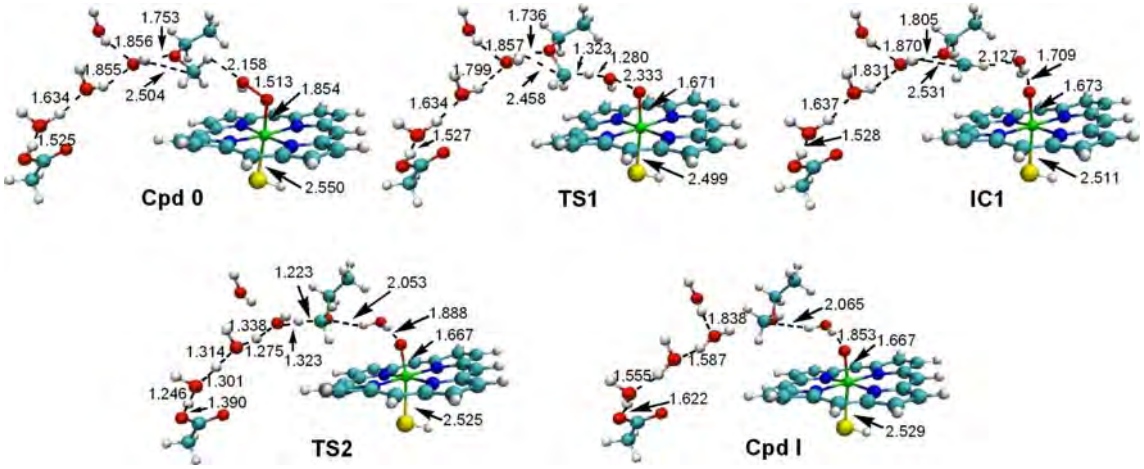

Fig. 4 Optimized geometries (UB3LYP/B1/CHARMM) for mechanism II (coupling reaction) in the Glu366 channel

forms two hydrogen bonds with MeO-Thr and with Fe=O (Fig. 2). During this step, the Fe–O bond shortens to 1.67 Å in TS1 and then remains at 1.68 Å in IC1. These structural features are similar to those reported for the wild-type enzyme [37]. The spin density and partial charge of the OH group in the first intermediate (IC1) are −0.93 and −0.04, indicating that IC1 contains an OH radical and one-electron-reduced Compound I. This suggests that the O–O bond cleavage is homolytic: the Fe=O moiety carries two unpaired electrons, and the third unpaired electron is mainly located on the OH moiety. IC1 is stabilized by hydrogen-bonding interactions of OH with FeO and MeO-Thr252, and therefore lies only 10.3 kcal/mol above the reactant.

The second step is a hydrogen transfer from the MeO-Thr group to the OH moiety which yields Compound I and

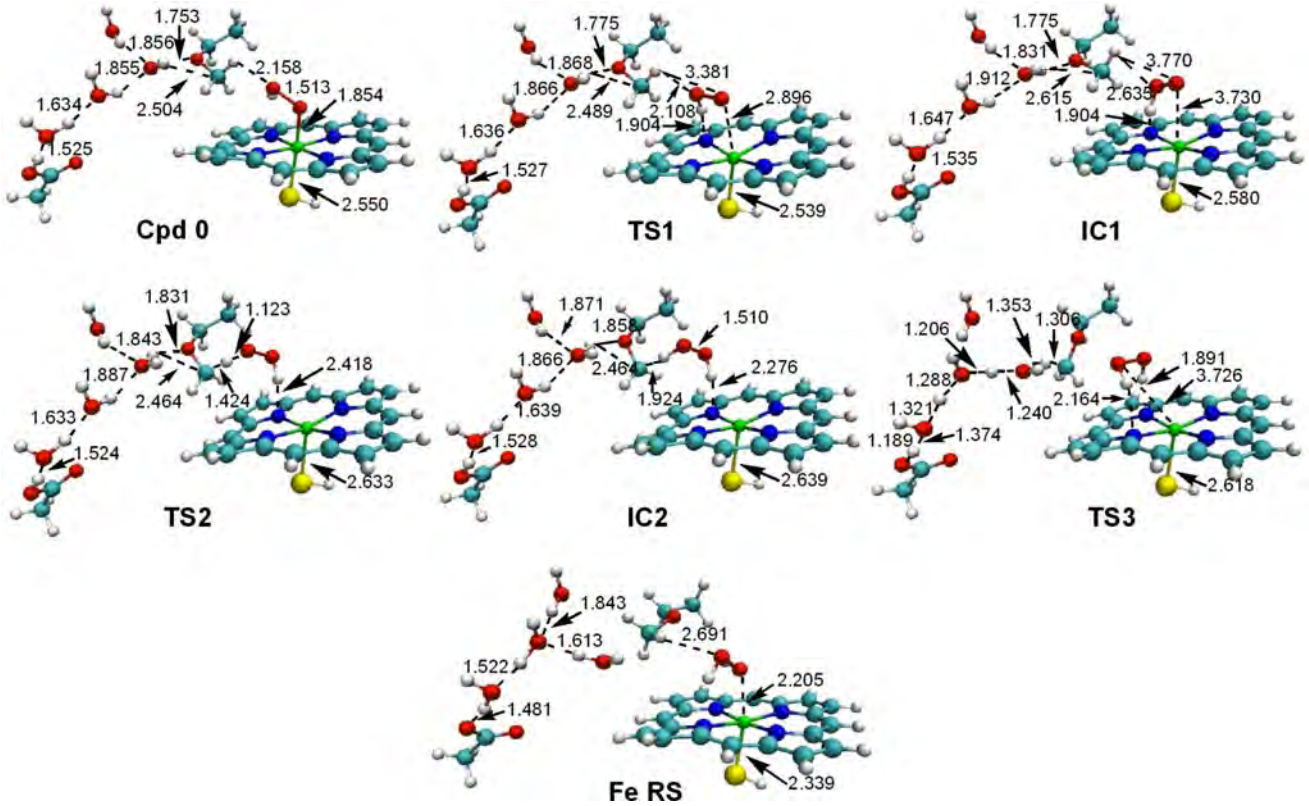

Fig. 5 Optimized geometries (UB3LYP/B1/CHARMM) for mechanism III (uncoupling reaction) in the Glu366 channel

water. The corresponding transition state (TS2) lies 18.5 kcal/mol above Compound 0, and the intermediate complex of CH_2O-Thr radical with Compound I (IC2) is quite stable, with an energy of 1.1 kcal/mol relative to Compound 0. The OH moiety is obviously reactive enough to abstract a proton from the methoxy group, and the resulting intermediate (IC2) is stabilized by Wat902 and the water molecule formed via two hydrogen bonds.

In the last step, a proton is transported from Glu366 to MeO-Thr in a concerted process via three bridging water molecules. Simultaneously, an electron is transferred from the heme to the methylene group to regenerate the MeO-Thr and form a π cation radical at the heme. The transition state (TS3) and the product (Compound I) lie 17.2 and 8.0 kcal/mol above Compound 0, respectively. The hydrogen-bonding network between Glu366 and MeO-Thr is reoriented after the proton transfer. Overall, the rate-limiting step is the hydrogen abstraction from the methoxy group with a barrier of 18.5 kcal/mol (TS2).

Asp251 channel

In this channel, the barrier of O–O bond cleavage is 18.6 kcal/mol (TS1 in Fig. 3), similar to the corresponding barrier in the Glu366 channel (18.1 kcal/mol). The intermediate (IC1, OH moiety and one-electron-reduced Compound I) is rather high in energy (14.4 kcal/mol). For the conversion of IC1 to Compound I, a proton needs to be transported from the Asp251 carboxyl group via Wat901 and MeO-Thr to OH, with a concomitant electron transfer from the heme. The spin density and partial charge of the OH group in IC1 are −0.79 and −0.12, indicating that OH will not behave as a "perfect" radical in IC1 owing to the strong hydrogen-bonding interactions with the methoxy group (2.10 Å) and the FeO unit (1.88 Å). In contrast to the wild-type enzyme [37], the subsequent proton delivery proceeds in two steps. As in the Glu366 channel, a hydrogen atom is first transferred from the methoxy group of MeO-Thr (TS2 at 22.6 kcal/mol, i.e., 8.2 kcal/mol above IC1). The intermediate formed (IC2 at 11.4 kcal/mol) then receives a proton through the Asp251 channel and an electron from the heme in a simultaneous process (TS3 at 23.0 kcal/mol). After releasing its proton, the side chain of Asp251 rotates back into a salt bridge with Arg186, as shown in Fig. 3.

Comparison

In each channel, the three transition states lie at similar energies relative to Compound 0. The highest point in the reaction profile is TS2 (TS3) in the Glu366 (Asp251)

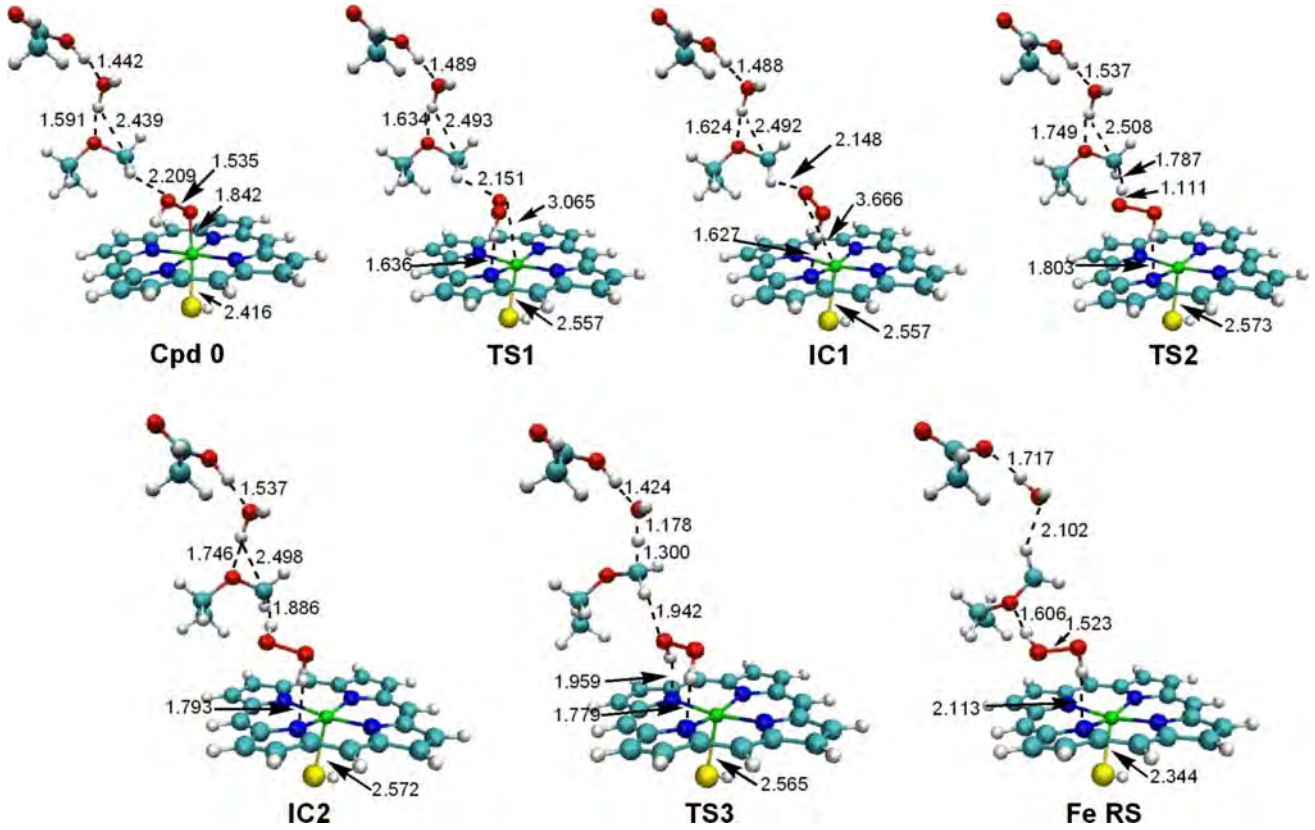

Fig. 6 Optimized geometries (UB3LYP/B1/CHARMM) for mechanism III (uncoupling reaction) in the Asp251 channel

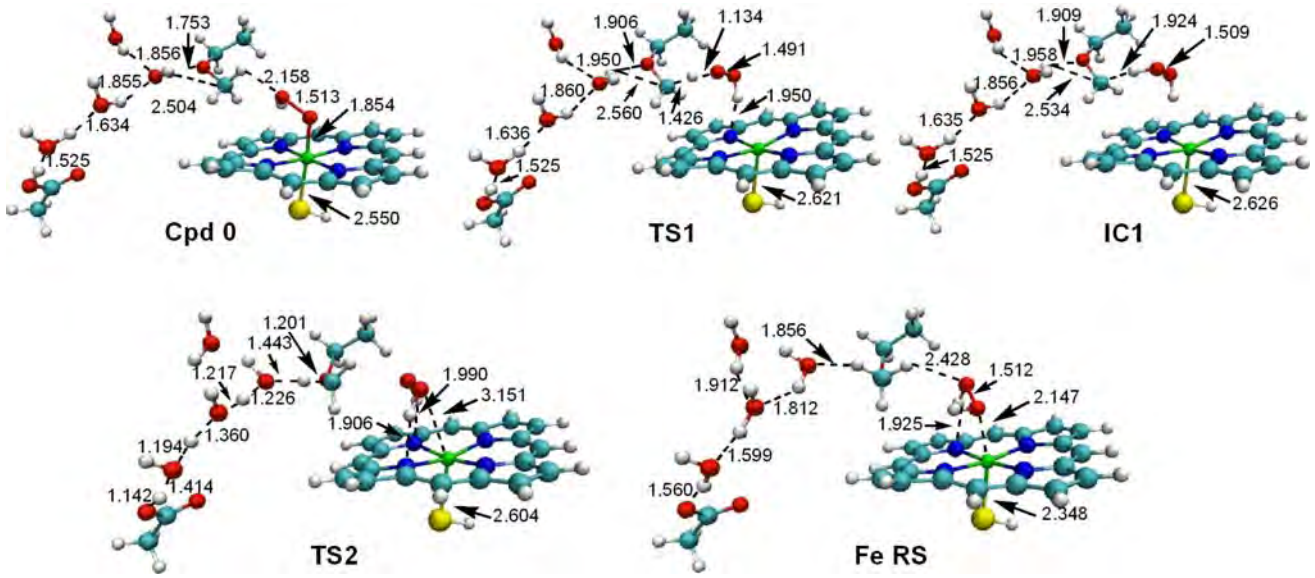

Fig. 7 Optimized geometries (UB3LYP/B1/CHARMM) for mechanism IV (uncoupling reaction) in the Glu366 channel

channel at 18.5 (23.0) kcal/mol (see Table 1), i.e., about 4–8 kcal/mol higher than in the wild-type enzyme [37]. The conversion of Compound 0 to Compound I via mechanism I should thus be much slower in the Thr252MeO-Thr mutant compared with the wild-type enzyme.

Additional snapshot

To ensure that the snapshot used in this study is representative for the system, reaction mechanism I in the Asp251 channel was also studied in an analogous manner

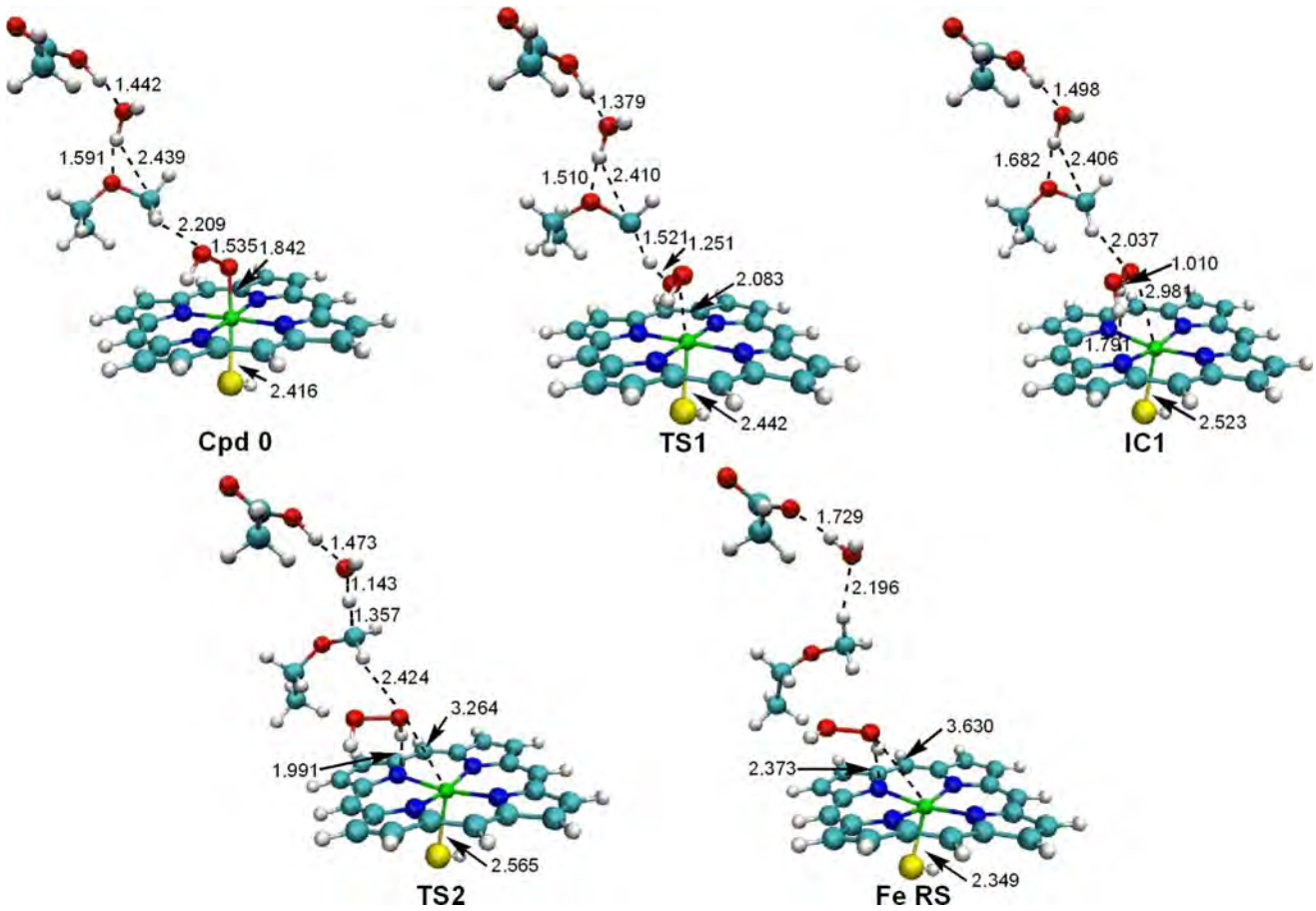

Fig. 8 Optimized geometries (UB3LYP/B1/CHARMM) for mechanism IV (uncoupling reaction) in the Asp251 channel

Table 1 Quantum mechanical/molecular mechanical (QM/MM) relative energies (kcal/mol) for optimized structures of mechanisms I and II of the coupling reaction for the Glu366 and Asp251 channels using basis sets B1/B2 (relative to Compound 0)

	Mechanism I						Mechanism II			
	TS1	IC1	TS2	IC2	TS3	Compound1	TS1	IC1	TS2	Compound I
Glu366 channel	18.1/20.7	10.3/13.0	18.5/21.2	1.1/4.5	17.2/20.3	8.0/12.2	20.8/23.8	0.8/2.3	20.0/24.5	8.0/13.5
Asp251 channel	18.6/19.0	14.4/15.4	22.6/23.6	11.4/14.0	23.0/25.9	7.7/11.3				

TS transition state, *IC* intermediate compound

Table 2 QM/MM relative energies (kcal/mol) for optimized structures of mechanisms III and IV of the uncoupling reaction for the Glu366 and Asp251 channels using basis sets B1/B2 (relative to Compound 0)

	Mechanism III						Mechanism IV			
	TS1	IC1	TS2	IC2	TS3	Fe RS	TS1	IC1	TS2	Fe RS
Glu366 channel	30.3/32.2	17.7/20.0	42.4/43.8	40.6/41.7	60.7/64.0	28.4/30.0	40.3/42.0	38.0/36.1	58.3/59.6	25.2/27.7
Asp251 channel	28.1/30.0	25.7/28.6	47.6/50.1	47.4/49.0	58.4/61.5	28.8/30.9	52.9/55.1	47.6/50.7	54.9/55.8	26.4/29.1

Fe RS ferric resting state

with a different snapshot which was drawn after 1,500 ps of MD simulation. The computed relative energies of all stationary points (Table S23) agree with those from the first snapshot (Table 1) to within 1 kcal/mol. The highest point in the reaction profile (TS3) is at 23.2 kcal/mol, very close to the value of 23.0 kcal/mol from the first snapshot (see earlier). The results from both snapshots are thus entirely consistent with each other.

Mechanism II: proton-assisted heterolytic O–O bond cleavage

Glu366 channel

The energy barrier for direct hydrogen atom transfer from MeO-Thr to FeOOH is 20.8 kcal/mol, and the resulting intermediate (IC1, Fig. 4) lies 0.8 kcal/mol above Compound 0. The unpaired electron is mainly located on the iron atom (iron spin density of 1.37). In contrast to the reaction in the wild-type enzyme, IC1 is not a protonated Compound 0 species, since the O–O bond is cleaved in the first step [37]. However, mechanism II differs from mechanism I, since the hydrogen transfer is part of the first step. In the second step, the concomitant transport of one proton (from Glu366) and one electron (from the heme) leads to formation of Compound I. The relative energies of TS2 and Compound I are 20.0 and 8.0 kcal/mol, respectively.

Asp251 channel

In the Asp251 channel, we chose several different reaction coordinates to convert Compound 0 to protonated Compound 0 by proton transfer from Asp251 to the distal oxygen atom of the hydroperoxo group. However, all energy scans led to continuously increasing energy profiles, and we were unable to locate protonated Compound 0. Similar problems have also been reported in previous QM/MM calculations for the wild-type enzyme [37].

Mechanism III: homolytic O_1–Fe bond cleavage followed by coupled proton–electron transfer

Glu366 channel

The optimized geometries are presented in Fig. 5. The barrier (TS1) for homolytic breaking of the O_1–Fe bond is 30.3 kcal/mol, and the intermediate (IC1) consisting of iron-bound heme and the OOH radical lies 17.7 kcal/mol above Compound 0. The subsequent hydrogen transfer from MeO-Thr to OOH is very difficult (TS2 at 42.4 kcal/mol, thus 24.7 kcal/mol above IC1), and the second intermediate (IC2) with iron-bound heme and the CH_2O-Thr radical is a shallow minimum (IC2 at 40.6 kcal/mol). The barrier for final proton transfer from Glu366 to CH_2O-Thr with concomitant electron transfer from the heme is prohibitively high (TS3 at 60.7 kcal/mol). The overall reaction is endothermic by 28.4 kcal/mol.

Asp251 channel

Figure 6 shows the optimized geometries. In general, the barriers are quite similar to those in the Glu366 channel. The barrier (TS1) for homolytic cleavage of the O_1–Fe bond is 28.1 kcal/mol. In the resulting intermediate (IC1 at 25.7 kcal/mol), the spin densities of OOH (−0.97) and iron (1.98) indicate that iron has two unpaired electrons and that OOH is present as a radical. The following hydrogen transfer from MeO-Thr to OOH is again difficult (TS2 at 47.6 kcal/mol, hence 21.9 kcal/mol above IC1) and leads to a very shallow intermediate (IC2 at 47.4 kcal/mol) with a CH_2O-Thr radical (spin density of −0.92). The final proton transfer from Asp251 to CH_2O-Thr requires much activation (TS3 at 58.4 kcal/mol, i.e., 11.0 kcal/mol above IC2). At the end of the reaction, Asp251 rotates to rebuild the salt bridge with Arg186, as also found in mechanism I. The overall reaction is endothermic by 28.8 kcal/mol.

Mechanism IV: proton-assisted heterolytic O–Fe bond cleavage

Glu366 channel

As can be seen from Fig. 7, the first step involves O–Fe bond cleavage combined with a hydrogen transfer from MeO-Thr to the proximal oxygen atom. The corresponding barrier is high (TS1 at 40.3 kcal/mol), and the shallow intermediate (IC1 at 38.0 kcal/mol) contains essentially neutral hydrogen peroxide with almost zero spin density and an O_1–O_2 distance of 1.51 Å; the Fe–O_1 distance increases from 1.85 Å (Compound 0) to 3.75 Å (IC1). The subsequent proton transfer from Glu366 to CH_2O-Thr again needs much activation (TS2 at 58.3 kcal/mol, thus 20.3 kcal/mol above IC1). The product (ferric resting state and hydrogen peroxide) lies 25.2 kcal/mol above Compound 0.

Asp251 channel

Figure 8 presents the optimized geometries. The O–Fe bond cleavage with formation of hydrogen peroxide again occurs in the first step, which has a very high barrier (TS1 at 52.9 kcal/mol). The intermediate (IC1 at 47.6 kcal/mol) contains hydrogen peroxide and a CH_2O-Thr radical (spin density of −0.90). The transition state for proton transfer from Asp251 to CH_2O-Thr (TS2 at 54.9 kcal/mol) lies 7.3 kcal/mol above IC1. The overall reaction is endothermic by 26.4 kcal/mol.

Discussion and conclusions

In this work, the coupling and uncoupling reactions in the Thr252MeO-Thr mutant of cytochrome P450cam were investigated for two proton delivery channels (Glu366 and Asp251) and four possible mechanisms by means of

QM/MM calculations. It is obvious from the QM/MM results that the uncoupling reaction (formation of the ferric resting state and hydrogen peroxide) is strongly disfavored. Regardless of mechanistic details, it suffers from high endothermicities of 25–30 kcal/mol and extremely high overall activation energies of 55–61 kcal/mol. We note in this context that our previous QM/MM study [37] of the uncoupling reaction in the wild-type enzyme yielded a barrier of 27 kcal/mol in the Asp251 channel, with the required proton being provided via the Asp251–Wat901–Thr252 network (mechanism similar to mechanism IV). Such proton delivery is expected to be more facile in the wild-type enzyme than the corresponding process in the Thr252MeO-Thr mutant since the hydroxyl group in Thr is a much better proton donor than the methyl group in MeO-Thr, and it is thus not surprising that the uncoupling reaction requires more activation in the Thr252MeO-Thr mutant.

In our recent QM/MM study [40], we discovered that the barrier for uncoupling is dramatically reduced in the Thr252X mutants (X = Val, Ala, Gly) when an extra water molecule enters the Asp251 channel and becomes part of a well-connected hydrogen-bonding network that provides a good proton delivery pathway. In these mutants, the extra water molecule remains present in 2-ns MD simulations, whereas it escapes from the channel for X = Ser and X = Thr. Also in the Thr252MeO-Thr mutant, the stability of an additional water molecule was tested by means of 2-ns MD simulations. It was observed that the additional water molecule escapes from the active site in both channels in the course of the MD simulations (Figs. S2, S3). This is in agreement with our previous findings for the wild-type enzyme, since MeO-Thr is sterically more demanding than Thr.

According to the present QM/MM results for the Thr252MeO-Thr mutant, the coupling reaction (mechanisms I and II) is endothermic by about 8 kcal/mol and requires an overall activation of 18–23 kcal/mol, depending on the channel and mechanism. It thus seems feasible and is clearly preferred over the uncoupling reaction. For both the coupling reaction and the uncoupling reaction, the highest point on the computed QM/MM energy profiles corresponds to hydrogen abstraction by OH and OOH species that are present in the intermediates formed. It is well known, e.g., from QM studies on small model systems [58], that such reactions are intrinsically more facile and more exothermic with OH than with OOH. For example, at the UB3LYP/6-31+G* level, the barrier (reaction energy) for hydrogen abstraction from ethyl methyl ether is 2.1 (−15.0) kcal/mol for OH and 12.6 (10.0) kcal/mol for OOH (Fig. S1). These intrinsic preferences are reflected in the QM/MM energies (Tables 1, 2).

Experimentally, the Thr252MeO-Thr mutant gives 100% coupling reaction and no uncoupling reaction [25], consistent with our QM/MM results. Furthermore, the observed rate constant for the formation of 5-*exo*-hydroxycamphor is one third of that of the wild-type enzyme [25]. This is in qualitative agreement with the QM/MM finding that the rate-limiting barriers for the coupling reaction are higher in the Thr252MeO-Thr mutant than in the wild-type enzyme. There are two caveats, however; first, it is not certain that the differences in the observed rate constants are actually due to different rates of Compound I formation; second, a factor 3 in the rate constant translates to a rather small difference in free-energy barriers of 0.7 kcal/mol (much smaller than the differences of 4–9 kcal/mol in the rate-limiting QM/MM barriers for the wild-type enzyme and the Thr252MeO-Thr mutant).

We finally address the question of the preferred coupling mechanism in the Thr252MeO-Thr mutant. At face value, the rate-limiting barriers are somewhat lower in the Glu366 channel than in the Asp251 channel (Table 1). One should keep in mind, however, that the Asp251 channel is in contact with bulk water, so it should be rather facile to reprotonate Asp251 after each coupling reaction that involves proton transfer in the Asp251 channel. This is not true for Glu366, which resides in a hydrophobic pocket and is thus difficult to reprotonate. Protonation via the Asp251 channel may thus actually be a more realistic scenario for the coupling reaction, as in the case of the wild-type enzyme. In this scenario, the barrier for the initial homolytic cleavage is predicted to rise from 14.3 kcal/mol in the wild-type enzyme to 18.6 kcal/mol in the mutant. This increase in activation energy can be rationalized by an analysis of the hydrogen-bonding network. In the wild-type enzyme, the OH radical is stabilized in the transition state by hydrogen bonds to Thr252 and the FeO unit with distances of 1.64 and 2.06 Å, respectively [37]. Stabilization is less effective in the Thr252MeO-Thr mutant, where these distances increase to 2.06 and 2.22 Å, respectively (mechanism I in the Asp251 channel). The subsequent protonation, with concomitant electron transfer from the heme, is essentially downhill in the wild-type enzyme and requires some activation in the mutant (Table 1). This is not surprising, and gas-phase QM modeling of this process indeed confirms the qualitative expectation that the hydroxyl group in Thr252 is a better proton donor than the methoxy group in MeO-Thr252 (see Sect. 9 in the electronic supplementary material). In the mutant enzyme, this process is split into two steps (hydrogen transfer from the methoxy group to OH followed by a simultaneous proton and electron transfer in the Asp251 channel, see mechanism I) which make it energetically feasible, through the stabilization of the resulting intermediates by strong hydrogen bonds to two water molecules. Regardless of their limited quantitative accuracy, the present QM/MM results thus raise the possibility that residue 252 may play

an active role in the proton delivery mechanism both for the wild-type enzyme and for the Thr252MeO-Thr mutant, whereas previous interpretations of the experimental data view this residue mainly as a structural factor for coordinating water molecules that deliver protons to the FeOOH unit [25].

We end with a cautionary note. The favored mechanism I in the Asp251 channel involves an incipient OH radical in the initial intermediate (IC1) that might be expected to undergo competing side reactions such as attack at the *meso* position of the porphyrin to affect heme degradation or demethylation of the methoxy group to regenerate Thr252. We note again in this context that the initially formed OH species is stabilized by hydrogen-bonding interactions with surrounding partners which lead to reduced OH spin density and hence presumably also to lower radical reactivity, in analogy to the situation in the wild-type enzyme [37]. A more reliable assessment will require QM/MM studies of the competing side reactions which are beyond the scope of this article.

Open Access This article is distributed under the terms of the Creative Commons Attribution Noncommercial License which permits any noncommercial use, distribution, and reproduction in any medium, provided the original author(s) and source are credited.

References

1. Ortiz de Montellano PR (1998) Cytochrome P450: structure, mechanism and biochemistry. Plenum Press, New York
2. Ortiz de Montellano PR (1986) In: Ortiz de Montellano PR (ed) Cytochrome P450: structure, mechanism and biochemistry. Plenum Press, New York, pp 216–271
3. Dawson JH, Sono M (1987) Chem Rev 87:1255–1276
4. Sono M, Roach MP, Coulter ED, Dawson JH (1996) Chem Rev 96:2841–2888
5. Woggon WD (1997) Top Curr Chem 184:39–96
6. Ortiz de Montellano PR, De Voss JJ (2002) Nat Prod Rep 19:471–499
7. Watanabe Y (2001) J Biol Inorg Chem 8:846–856
8. Denisov IG, Makris TM, Sligar SG, Schlichting I (2005) Chem Rev 105:2253–2278
9. Schröder D, Schwarz H, Shaik S (2000) Struct Bond 97:91–123
10. Groves JT (2000) J Porphyrins Phthalocyanines 4:350–352
11. Meunier B (2000) J Porphyrins Phthalocyanines 4:353
12. Woggon WD, Wagenknecht HA, Claude C (2001) J Inorg Biochem 83:289–300
13. Costas M, Mehn MP, Jensen MP, Que L Jr (2004) Chem Rev 104:939–986
14. Rohde JU, In JH, Lim MH, Brennessel WW, Bukowski MR, Stubna A, Münck E, Nam W, Que L Jr (2003) Science 299:1037–1039
15. Imai M, Shimada H, Watanabe Y, Matsuhima-Hibiya Y, Makino R, Koga H, Horiuchi T, Ishimura Y (1989) Proc Natl Acad Sci USA 86:7823–7827
16. Martinis SA, Atkins WM, Stayton PS, Sligar SG (1989) J Am Chem Soc 111:9252–9253
17. Gerber NC, Sligar SG (1994) J Biol Chem 269:4260–4266
18. Gerber NC, Sligar SG (1992) J Am Chem Soc 114:8742–8743
19. Loew GH, Rohmer MM (1980) J Am Chem Soc 102:3655–3657
20. Poulos TL, Anthony-Cahill SJ, Griffith MC, Schultz PG (1989) Science 244:182–188
21. Harris DL, Loew GH (1994) J Am Chem Soc 116:11671–11674
22. Makris TM, Denisov IG, Sligar SG (2003) Biochem Soc Trans 31:516–519
23. Davydov R, Kappl R, Huttermann J, Peterson JA (1991) FEBS Lett 295:113–115
24. Davydov R, Macdonald IDG, Makris TM, Sligar SG, Hoffman BM (1999) J Am Chem Soc 121:10654–10655
25. Kimata Y, Shimada H, Hirose T, Ishimura Y (1995) Biochem Biophys Res Commun 208:96–102
26. Newcomb M, Toy PH (2000) Acc Chem Res 33:449–455
27. Vaz ADN, McGinnity DF, Coon MJ (1998) Proc Natl Acad Sci USA 95:3555–3560
28. Harris DL, Loew GH (1998) J Am Chem Soc 120:8941–8948
29. Guallar V, Friesner RA (2004) J Am Chem Soc 126:8501–8508
30. Kamachi T, Shiota Y, Ohta T, Yoshizawa K (2003) Bull Chem Soc Jpn 76:721–732
31. Taraphder S, Hummer G (2003) J Am Chem Soc 125:3931–3940
32. Kumar D, Hirao H, de Visser SP, Zheng J, Wang D, Thiel W, Shaik S (2005) J Phys Chem B 109:19946–19951
33. Shaik S, Kumar D, de Visser SP, Altun A, Thiel W (2005) Chem Rev 105:2279–2328
34. Ogliaro F, de Visser SP, Cohen S, Sharma PK, Shaik S (2002) J Am Chem Soc 124:2806–2817
35. Derat E, Shaik S (2006) J Phys Chem B 110:10526–10533
36. Sen K, Hackett JC (2009) J Phys Chem B 113:8170–8182
37. Zheng J, Wang D, Thiel W, Shaik S (2006) J Am Chem Soc 128:13204–13215
38. Chen H, Moreau Y, Derat E, Shaik S (2008) J Am Chem Soc 130:1953–1965
39. Chen H, Hirao H, Derat E, Schlichting I, Shaik S (2008) J Phys Chem B 112:9490–9500
40. Altarsha M, Benighaus T, Kumar D, Thiel W (2009) J Am Chem Soc 131:4755–4763
41. Schöneboom JC, Lin H, Reuter N, Thiel W, Cohen S, Ogliaro F, Shaik S (2002) J Am Chem Soc 124:8142–8151
42. Schöneboom JC, Thiel W (2004) J Phys Chem B 108:7468–7478
43. Altun A, Thiel W (2005) J Phys Chem B 109:1268–1280
44. Vidakovic M, Sligar SG, Li H, Poulos TL (1998) Biochemistry 37:9211–9219
45. Jorgensen WL, Chandrasekhar J, Madura JD, Impey RW, Klein ML (1983) J Chem Phys 79:926–935
46. MacKerell AD Jr, Bashford D, Bellott M, Dunbrack RL Jr, Evanseck JD, Field MJ, Fischer S, Gao J, Guo H, Ha S, Joseph-McCarthy D, Kuchnir L, Kuczera K, Lau FTK, Mattos C, Michnick S, Ngo T, Nguyen DT, Prodhom B, Reiher WE III, Roux B, Schlenkrich M, Smith JC, Stote R, Straub J, Watanabe M, Wiórkiewicz-Kuczera J, Yin D, Karplus M (1998) J Phys Chem B 102:3586–3616
47. Brooks BR, Bruccoleri RE, Olafson BD, States DJ, Swaminathan S, Karplus M (1983) J Comput Chem 4:187–217
48. Becke AD (1993) J Chem Phys 98:5648–5652
49. Hay PJ, Wadt WR (1985) J Chem Phys 82:299–310
50. Hehre WJ, Ditchfield K, Pople JA (1972) J Chem Phys 56:2257–2261
51. Schäfer A, Horn H, Ahlrichs R (1992) J Chem Phys 97:2571–2577
52. Schäfer A, Huber C, Ahlrichs R (1994) J Chem Phys 100:5829–5835
53. Bakowies D, Thiel W (1996) J Phys Chem 100:10580–10594
54. Ahlrichs R, Bär M, Häser M, Horn H, Kölmel C (1989) Chem Phys Lett 162:165–169
55. Smith W, Forester TR (1996) J Mol Graph 14:136–141

56. Sherwood P, De Vries AH, Guest MF, Schreckenbach G, Catlow CRA, French SA, Sokol AA, Bromley ST, Thiel W, Turner AJ, Billeter S, Terstegen F, Thiel S, Kendrick J, Rogers SC, Casci J, Watson M, King F, Karlsen E, Sjøvoll M, Fahmi A, Schäfer A, Lennartz C (2003) J Mol Struct 632:1–28
57. Billeter SR, Turner AJ, Thiel W (2000) Phys Chem Chem Phys 2:2177–2186
58. Siegbahn PEM, Blomberg MRA, Crabtree RH (1997) Theor Chem Acc 97:289–300

P450 Enzymes: Their Structure, Reactivity, and Selectivity—Modeled by QM/MM Calculations

Sason Shaik,*,† Shimrit Cohen,† Yong Wang,† Hui Chen,† Devesh Kumar,‡,§ and Walter Thiel*,‡

Institute of Chemistry and the Lise-Meitner-Minerva Center for Computational Quantum Chemistry, The Hebrew University of Jerusalem, 91904 Jerusalem, Israel, and Max-Planck-Institut für Kohlenforschung, Kaiser-Wilhelm-Platz 1, D-45470 Mülheim an der Ruhr, Germany

Received March 30, 2009

Contents

1. Introduction 950
2. Theoretical Methods 952
   2.1. Methodological Issues in QM/MM Studies 953
      2.1.1. QM/MM Partitioning 953
      2.1.2. Choice of QM Method 953
      2.1.3. Choice of MM Method 954
      2.1.4. Subtractive versus Additive Schemes 954
      2.1.5. Electrostatic QM/MM Interactions 954
      2.1.6. Boundary Treatments 954
      2.1.7. QM/MM Geometry Optimization 954
      2.1.8. QM/MM Molecular Dynamics 955
      2.1.9. QM/MM Energy versus Free Energy Calculations 955
   2.2. Practical Issues in QM/MM Studies 955
      2.2.1. QM/MM Software 955
      2.2.2. QM/MM Setup 955
      2.2.3. Accuracy of QM/MM Results 956
      2.2.4. QM/MM Geometry Optimization 956
   2.3. Conventions and Notations 956
   2.4. Coverage and Sources of Computational Results 957
3. The Catalytic Cycle of P450 Enzymes 957
   3.1. Models of the Enzyme 958
   3.2. Oxidation States and Key Orbitals of Species in the Catalytic Cycle 958
   3.3. The Resting State (**1**) and the Pentacoordinate Intermediates (**2**, **3**) 959
      3.3.1. The Resting State 959
      3.3.2. The Pentacoordinated States 960
      3.3.3. Gating of the Catalytic Cycle 961
      3.3.4. DFT/MM Study of the Electron Transfer Event 962
   3.4. The Oxy-Ferrous (**4**) and Ferric Peroxo (**5**) Complexes 962
      3.4.1. Bonding Features of Oxy-Ferrous (**4**) and Ferric Peroxo (**5**) Complexes 962
   3.5. Cpd 0: The Ferric-Hydroperoxide Complex (**6**) and its Formation from **5** 964
   3.6. The Protonation Mechanism and Generation of the Ultimate Oxidant, Cpd I (**7**) 964
      3.6.1. First Protonation Step: Conversion of (**5**) into Cpd 0 (**6**) 965
      3.6.2. Second Protonation Step: Conversion of Cpd 0 (**6**) into Cpd I (**7**) 966
      3.6.3. Conversion of Cpd 0 (**6**) into Cpd I (**7**) in the T252X Mutants 967
      3.6.4. Conversion of Cpd 0 (**6**) into Cpd I (**7**) in the D251N Mutant 968
   3.7. Cpd I (**7**): The Ultimate Active Species 969
      3.7.1. A Model for the Chameleon Behavior of Cpd I 971
      3.7.2. Cpd I Species in Human P450 Isoforms 972
      3.7.3. Effect of Substrate Binding on Cpd I of CYP3A4 973
      3.7.4. Description of Cpd I by Highly Correlated QM Levels 974
      3.7.5. Low-Lying Excited States of Cpd I 975
      3.7.6. Se-Cpd I for an in-Silico Designed Mutant of P450 975
   3.8. Concluding Remarks on the Catalytic Cycle of P450 975
4. QM/MM and QM-Only Studies of P450 Reactivity 976
   4.1. Coverage of Reactivity and Mechanistic Issues 976
   4.2. Reactivity of Cpd I: Counting Electrons, Spin States, and Electromeric Situations 977
   4.3. DFT/MM and DFT-Only Studies of C−H Hydroxylation by Cpd I of P450 978
      4.3.1. Camphor Hydroxylation by CYP101 and the Controversial Role of Spin Density on the Propionate Side Chains 978
      4.3.2. Camphor Hydroxylation by CYP101—How Does Wat_{903} Catalyze the Reactions? 979
      4.3.3. Camphor Hydroxylation by CYP101—More States than Just Two 980
      4.3.4. Camphor Hydroxylation by CYP101—The Product Release Step 981
      4.3.5. Camphor Hydroxylation by CYP101—Can Cpd II Compete with Cpd I? 982
      4.3.6. Allylic Hydroxylation of Cyclohexene by CYP101 982
      4.3.7. Why is Cpd I Elusive in CYP101? 983
   4.4. DFT/MM Studies of C=C Epoxidation by Cpd I of P450 984
   4.5. DFT/MM and DFT-Only Studies of Aromatic Hydroxylation by Cpd I of P450 985

* E-mail: S.S., sason@yfaat.ch.huji.ac.il; W.T., thiel@mpi-muelheim.mpg.de. Further contact information for S.S.: phone, +972-2-6585909; fax, +972-2-6584680/6585345.
† The Hebrew University of Jerusalem.
‡ Max-Planck-Institut für Kohlenforschung.
§ Current address: Molecular Modeling Group, Indian Institute of Chemical Technology, Hyderabad 500 607, India.

10.1021/cr900121s © 2010 American Chemical Society
Published on Web 10/08/2009

4.5.1. DFT/MM Studies of Benzene Hydroxylation by CYP2C9 987
4.5.2. DFT-Only Studies of Oxidative Dehalogenation of Perhalogenated Benzenes by P450 988
4.6. DFT-Only Studies of *N*-Dealkylation of *N*,*N*-Dimethylaniline Derivatives 989
4.6.1. KIE is a Reliable Probe of Spin State Selectivity in Oxidation of DMAs 993
4.6.2. Decomposition of the Carbinolaniline Initial Product 993
4.6.3. Summary of the Mechanistic Findings on Dealkylation of DMAs by Cpd I 994
4.7. DFT-Only Studies of Sulfur and Nitrogen Oxidation 994
4.7.1. Sulfur Oxidation 994
4.7.2. Nitrogen Oxidation 996
4.8. A DFT-Only Study of Ethanol Oxidation by P450 996
4.9. DFT/MM Study of the C−C Bond Forming Reactivity of P450 997
4.10. DFT-Only and DFT/MM Calculations of Regioselectivity in the Reactions of Cpd I 998
4.10.1. Competitive Heteroatom Oxidation vs C−H Hydroxylation 998
4.10.2. DFT-Only Studies of the Competition between Epoxidation and Allylic Hydroxylation in Propene and Cyclohexene by Cpd I 999
4.10.3. DFT/MM Studies of the Competition between Epoxidation and Allylic Hydroxylation in Propene and Cyclohexene by Cpd I 999
4.10.4. DFT-Only Studies of the Metabolic Switching from Benzylic C−H Hydroxylation to Phenyl Hydroxylation in Toluene by Cpd I 1001
4.11. Miscellaneous Reactions: Carbocation Intermediates 1001
5. Predictive Models for P450 Reactivity Patterns 1001
5.1. Predictive Pattern of C−H Hydroxylation Barriers Based on Bond Dissociation Energies 1001
5.2. Valence Bond Modeling of Reactivity Patterns in C−H Hydroxylation 1002
5.2.1. Valence Bond Diagrams for C−H Hydroxylation 1002
5.2.2. Quantitative Aspects of Valence Bond Modeling for C−H Hydroxylation 1005
5.2.3. Comments on the VB Modeling of the Rebound Step 1008
5.3. Summary of Valence Bond Modeling of P450 Reactivity 1009
6. Summary of Reactivity Patterns 1009
7. Concluding Remarks 1009
8. Abbreviations 1010
9. Acknowledgments 1012
10. Note Added in Proof 1012
11. References 1012

1. Introduction

The introduction of oxygen into biochemical processes has brought about an evolutionary leap in the history of life, whereby many organisms have evolved to use oxygen as part of the life sustaining process and at the same time invented means to lower its toxic effects.[1] One of these means is the enzyme cytochrome P450 (CYP), which is a heme protein that was scientifically discovered by Omura and Sato a few decades ago.[2] Within a short time, it has become clear that this is a superfamily of isoforms present in a diverse array of organisms and performing biosyntheses of hormones and detoxifications of *xenobiotics* by utilizing oxygen and two reducing equivalents, and thereby oxidizing a variety of organic compounds.[3−21]

Scheme 1 shows the great diversity in the chemical reactivity of P450s. The most common reaction involves a single oxygen insertion into an organic molecule, such as C−H hydroxylation, sulfoxidation, C=C epoxidation, etc.; hence, the name "monooxygenase" is given to this enzyme. However, as can be seen in the scheme, the enzyme performs

Sason Shaik was born in Iraq. His family immigrated to Israel in the Exodus of the Iraqi Jewry. He received his B.Sc. and M.Sc. degrees in chemistry from Bar-Ilan University and his Ph.D. from the University of Washington under Nicholaos D. Epiotis. In 1978/9 he spent a Post Doctoral year with Roald Hoffmann at Cornell University. In 1980 he started his first academic position as a Lecturer at Ben-Gurion University, where he became a Professor in 1988. He subsequently moved to the Hebrew University, where he is currently the director of The Lise Meitner-Minerva Center for Computational Quantum Chemistry. Among the awards he received are the Lise-Meitner-Alexander von Humboldt Senior Award in 1996−1999, the 2001 Israel Chemical Society Prize, the 2001 Kolthoff Award, and the 2006 Schrödinger Medal. He is an AAAS fellow and a WATOC fellow. His research interests are in the use of quantum chemistry, and in particular of valence bond theory, to develop paradigms which can pattern data and lead to the generation and solution of new problems. He started his P450 research in 1998 and has been fascinated ever since!

Shimrit Cohen was born in Ashdod, Israel, in 1978. She received her B.Sc. in chemistry from the Hebrew University in 2000. She joined the group of Prof. Sason Shaik while she was an undergraduate student, and she is currently completing her Ph.D. in quantum chemistry. In 2005 she received the Wolf scholarship for excellent Ph.D. students. Her research involves applications of QM/MM methodology for understanding the mechanism and catalysis of cytochrome P450.

Yong Wang was born in Anhui, China, in 1975. He received his B.Sc. degree in theoretical physics at Anhui University in 1999, his M.Sc. degree in atomic and molecular physics at Henan Normal University in 2002, and his Ph.D degree (supervised by Prof. Keli Han) in physical chemistry at Dalian Institute of Chemical Physics, CAS, in 2007. During his Ph.D. research, he has been fortunate to cooperate with Prof. Shaik since 2005. He then joined Shaik's group as a postdoctoral fellow. He was awarded by the Hebrew University the 2008−2009 Lady-Davis Postdoctoral Fellowship. His current research interests are focused on the mechanisms of biotransformations catalyzed by P450, by means of QM, QM/MM, and MD methods.

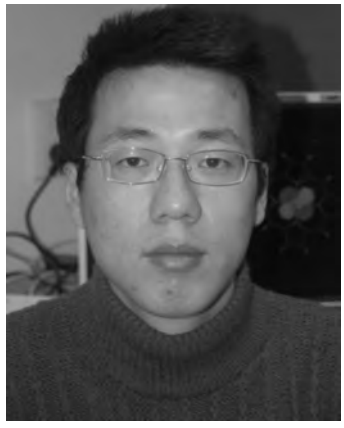

Hui Chen was born in China in 1978. He received his B.Sc. (2001) degree in chemistry from Nanjing University (China) and his Ph.D. (2006) degree in physical chemistry from Nanjing University, under the supervision of Prof. Shuhua Li at the Institute of Theoretical and Computational Chemistry. Since then he has been working with Prof. Sason Shaik at the Hebrew University as a postdoctoral fellow until now. He is the recipient of a Golda Meir Fellowship (2007−2009) of the Hebrew University and won the Lise Meitner Prize of the Lise-Meitner-Minerva Center (2007) for computational quantum chemistry. His main research interests are theoretical studies of reaction mechanisms and chemical bonding in chemistry and biochemistry.

a variety of other transformations, such as desaturation, oxidative dehalogenation, reductive dehalogenation, deformylation, N-dealkylation, O-dealkylation, C−C coupling, and so on. The immense biological impact of this enzyme may be appreciated from the fact that more than 70% of the drugs taken orally by humans are metabolized by the P450 isozymes CYP3A4 and CYP2D6.[21]

Due to this chemical versatility and the biological importance of P450, the area has become a target of intense research both practical and fundamental. An exciting branch of the basic research is related to the structure and mechanism of the enzyme, and attempts *to understand how it performs its reactions so fast and so efficiently*, albeit not in all the isoforms. Experimental mechanistic studies have uncovered important modes of reaction, such as the rebound mechanism

Devesh Kumar was born in India in 1965. He received his B.Sc. from the L. N. Mithla University and his M.Sc. and Ph.D. in Physics from the D. D. U. Gorakhpur University. He worked at the Centre for Liquid Crystal Research and Education, Nagarjuna University, as a research associate (July 2001−March 2002) before joining Prof. Sason Shaik at the Hebrew University of Jerusalem as a postdoc in May 2002. Subsequently, he joined Professor Walter Thiel at the Max-Planck-Institut für Kohlenforschung in Mülheim an der Ruhr, Germany, as a postdoc (June 2006−March 2009). At present he is Ramanujan Fellow at the Indian Institute of Chemical Technology, Hyderabad. His main research interests are QM and QM/MM studies of conformations and interactions of mesogens and enzyme catalysis.

Walter Thiel was born in Treysa, Germany, in 1949. He studied chemistry at the University of Marburg and received his Ph.D. degree in 1973. After two postdoctoral years at the University of Texas at Austin with Michael Dewar, he returned to Marburg and obtained the Habilitation in 1981. He was Professor at the University of Wuppertal from 1983 to 1992, Visiting Professor at the University of California at Berkeley in 1987, and Full Professor of Chemistry at the University of Zürich from 1992 to 1999. He is now Director at the Max-Planck-Institut für Kohlenforschung in Mülheim an der Ruhr, and affiliated with the University of Düsseldorf as an Honorary Professor. He received the Heisenberg Fellowship in 1982, the Alfried-Krupp-Award in 1988, and the WATOC Schrödinger Medal in 2002. His research area is theoretical and computational chemistry, both method development and applications.

in C−H hydroxylation,[3,8,22] but at the same time have raised many questions and interesting puzzles.[18,23,24]

It is very difficult to prove a mechanism and to characterize unstable intermediates with very short lifetimes, such as the active species, Cpd I, of the enzyme shown at the top of Scheme 1, and this is where theory comes into play and offers a complementary tool to aid experiment. Indeed, the allure of P450 has attracted many theoretical studies[25−32] designed to understand these fundamental aspects of P450. Most of the initial studies were done on model iron-porphine systems using primarily density functional theory (DFT) as the quantum mechanical (QM) tool.[25,26,33−52] These DFT calcula-

Scheme 1. Chemical Transformations Achieved by P450s, Shown along with the Putative Active Species, Compound I (Cpd I)

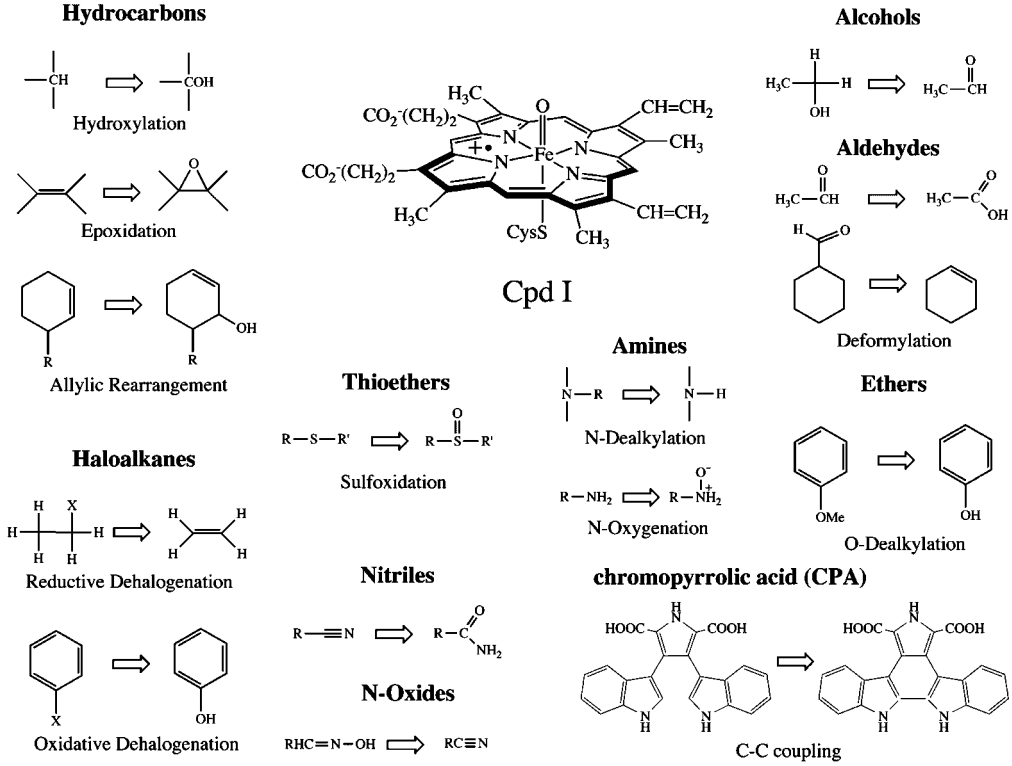

tions have contributed a great deal to the understanding of the electronic structure of the active species of the enzyme, the iron-oxo porphyrin species shown in Scheme 1, and to its reactivity patterns, including its high sensitivity to the environment, such as the bulk polarity or the hydrogen bonding to the axial cysteine ligand.

It was however recognized that part of the versatility of P450s must be attributed to the fact that while all the isoforms share the same active species, they differ by the identity of their proteins. Therefore, a more suitable level to study these isoforms is the hybrid QM/MM (quantum mechanical/molecular mechanical) method (see section 2), which treats the active species within its native protein environment. The first QM(DFT)/MM study[53] of the active species in 2002 revealed the utility of this method. It was followed by an increasing number of QM/MM studies of all the species in the catalytic cycle in CYP101, known also as $P450_{cam}$,[54] the active species of human isoforms,[55,56] and some of the reaction mechanisms initiated by this active species with a variety of organic molecules.[57−61] In-silico mutants were designed,[62,63] and in one case, the design of a selenocysteine mutant[62] even preceded its experimental preparation.[64,65] Species and reactivity patterns of related heme enzymes, such as chloroperoxidase (CPO),[66,67] nitric oxide synthase (NOS),[68,69] and horseradish peroxidase (HRP),[70−74] were also investigated. Some of these studies were done in collaboration with experimentalists[58,66,67] or were used by experimentalists as benchmarks,[75] thus demonstrating the usefulness of QM-(DFT)/MM as a companion to experiment. Recent advances in computing hardware and software have allowed large-scale calculations, e.g., on the mechanism of electron transfer from the reductase to the ferric-heme in CYP101,[76] as well as sophisticated QM/MM calculations with correlated ab initio QM methods using MR-CI (multireference configuration interaction)[77,78] and CASSCF (complete-active-space self-consistent field)[79] approaches. Over the past few years, there has been an increasing number of QM/MM studies dedicated to P450 that reveal many exciting new insights about the role of the protein in shaping the structures and reactivity patterns of these enzymes. All these studies have had a considerable impact on the field and led to an ever-growing surge of theoretical activity. It was therefore deemed timely to review the theoretical results provided in recent years by QM/MM methods, *especially on the issues of P450 reactivity and selectivity*. The main goal is to project the new insight gained on the bonding and reactivity of P450s, including studies of novel mechanisms whereby P450 functions as a peroxidase and participates in proton-coupled electron transfer (PCET).[58,80]

Some of the material covered in previous reviews[28−32,81−83] is included here too in order to create a unified survey. We start with a brief summary of the available QM/MM methods (section 2), and then we describe the various species in the catalytic cycle (section 3), the principal mechanisms by which the enzyme catalyzes oxygenation reactions (section 4), and predictive models of mechanisms and reactivity (section 5).

2. Theoretical Methods

Combined QM/MM theory has emerged as the method of choice for modeling local electronic events in large biomolecular systems. The basic idea is to describe the active site (where chemical reactions or electronic excitations occur) by quantum mechanics, as accurately as needed, while capturing the effects of the biomolecular environment by molecular mechanics, i.e., at the classical force field level. The QM/MM concept was introduced, as early as 1976, by Warshel and Levitt, who presented a semiempirical QM/MM treatment for a chemical reaction in lysozyme.[84] The QM/MM approach has become ever more popular over the past two decades, and numerous reviews have addressed both the development of the QM/MM methodology and its application in the biomolecular area. Here we cite only a

Scheme 2. Different Model Systems and Their Abbreviations

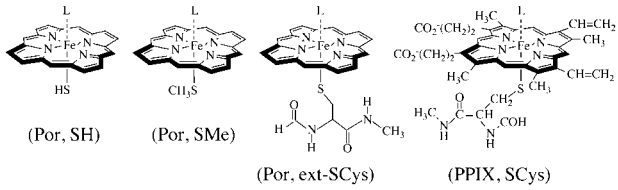

few of these[85−97] and refer to two recent reviews[93,97] for an up-to-date coverage of the field with a comprehensive survey of the literature (755 and 627 references, respectively). In this section, we address theoretical issues relevant for QM/MM studies of enzymes (section 2.1), discuss some practical issues that arise during such QM/MM calculations (section 2.2), and introduce notations and conventions for the following sections (section 2.3).

2.1. Methodological Issues in QM/MM Studies

In composite theoretical approaches such as QM/MM, a guiding principle is to retain the formalism of the methods that are being combined (as far as possible) and to adopt well-defined rules for their coupling. In the following, we address the methodological choices that need to be made, both in general and specifically in the case of QM/MM studies on cytochrome P450 enzymes.

2.1.1. QM/MM Partitioning

Inherent to the QM/MM concept is the division of the system into the inner QM region (active site) that is treated quantum-mechanically and the outer MM region (protein environment) that is described by a force field. In the boundary region at the interface, the standard QM and MM procedures may be modified in some way (e.g., by adding link atoms; see below). The choice of the QM region is usually made by consideration of the chemical problem: chemical arguments normally suggest a minimum-size QM region which can then be enlarged to check the sensitivity of the QM/MM results with regard to such an extension. In the case of cytochrome P450, the minimum-size QM region will contain the heme (iron-porphine without side chains) and the axial ligands (with SH being the smallest model to represent the cysteinate ligand; see Scheme 2). Enlarged QM regions may include the heme side chains, larger representations of the cysteinate ligand, selected residues of the protein environment, and water molecules close to the active site, depending on the problem under study. The actual choice requires care because the QM/MM system needs to be electronically balanced and properly screened with regard to electrostatic interactions.

Standard QM/MM applications employ a fixed QM/MM partitioning which is defined once and for all at the outset. It is possible to allow the boundary to move during QM/MM simulations (adaptive partitioning).[98] In another generalization of the QM/MM approach, one may go from two-layer to three-layer approaches, for example by using a continuum solvation model as a third layer[99,100] or by adopting an ONIOM-type scheme with two different inner QM layers and an outer MM layer.[101] Such more involved QM/MM treatments have not yet been applied to P450 enzymes.

2.1.2. Choice of QM Method

The selection follows the same criteria as in pure QM studies (accuracy and reliability versus computational effort). In the case of metalloproteins such as P450 enzymes, DFT is the natural choice which has been used in the vast majority of QM-only model studies[32] and also in most recent QM/MM work. There is a myriad of density functionals available, ranging from simple local functionals (LDA, local density approximation) via gradient-corrected functionals (GGA, generalized gradient approximation), meta-GGA functionals (with second derivative terms), and hybrid functionals (with admixture of HF exchange) to more advanced forms. The various functionals with their shorthand notations have been described amply, and the reader may consult a recent review for a brief survey.[102] Some of these functionals are derived from first principles and are thus parameter-free, while others involve a semiempirical calibration against theoretical or experimental reference data. In practice, gradient-corrected functionals such as BP86 are normally considered suitable for metalloenzymes, but the preferred choices are hybrid functionals such as B3LYP. Generally speaking, B3LYP is known to perform well for a number of properties,[103] even though the more recent, highly parametrized functionals such as those from the M06 series[102] show smaller overall deviations in various standard benchmarks, especially with respect to relative energies and reaction barriers. On the other hand, it has been established that B3LYP reproduces relative spin state energies in heme systems quite well, apparently since it has the "right" admixture of Hartree−Fock exchange, which is an essential prerequisite for realistic studies on P450 enzymes. Many other successful B3LYP applications have been reported early on in the P450 area,[32] and it is thus no surprise that B3LYP has become by far the most popular QM component in DFT/MM studies of heme enzymes. Nevertheless, in view of several documented shortcomings of B3LYP, one must remain critical and refrain from expecting too much accuracy, in particular with regard to the absolute values of barriers. While B3LYP is dominant at present,[103] we anticipate an increasing use of more advanced density functionals and of correlated ab initio methods in future QM/MM work.

Ab initio QM methods can in principle provide a convergent path to the correct solution of the nonrelativistic Schrödinger equation and are thus indispensable for accurate theoretical work. It has recently been demonstrated in the case of *p*-hydroxybenzoate hydroxylase (PHBH) and chorismate mutase that QM/MM calculations can reproduce the barriers of enzymatic reactions to within 1−2 kcal mol^{-1} when applying high-level correlated ab initio QM treatments (i.e., local coupled cluster methods).[104,105] These single-reference examples are however easier to handle than the multireference situations that are commonly encountered in heme enzymes. Ab initio MR-CI/MM and CASSCF/MM calculations have been reported for some P450 intermediates and analogous heme enzymes recently,[77−79] but entire P450 reactions have not yet been treated at this level because of technical limitations that prevent the use of a balanced active space along the complete reaction path. The ab initio MR-CI/MM results for relative spin state energies[77,78] are quite similar to those from B3LYP/MM and thus provide further justification for the latter approach. Such ab initio QM/MM calculations are expected to gain importance for validating crucial DFT/MM predictions.

2.1.3. Choice of MM Method

MM force field methods express the total energy of a molecular system as a sum of bonded energy terms, electrostatic terms, and van der Waals interactions. The bonded energy terms normally consist of harmonic stretching and bending potentials and periodic torsion potentials. The nonbonded electrostatic interactions are commonly treated as Coulomb interactions between fixed point charges. The van der Waals interactions are normally represented by a Lennard-Jones potential with attractive $1/r^6$ and repulsive $1/r^{12}$ terms. Established force fields of this kind are available for proteins (e.g., CHARMM, AMBER, GROMOS, and OPLS). These standard force fields are generally considered suitable for biomolecular applications, although their relative merits have not yet been studied systematically at the QM/MM level. In QM/MM work on P450 enzymes, CHARMM has been most widely used as the MM component.

The use of fixed MM point charges in the standard protein force fields neglects polarization effects. The logical next step toward higher accuracy should thus be the transition to polarizable force fields, which are currently developed in the biomolecular simulation community using various classical models (e.g., induced dipoles, fluctuating charges, or charge-on-spring models). The QM/MM formalism has been adapted to handle such polarizable force fields,[93,106] and one may expect corresponding QM/MM applications once these new force fields are widely accepted. In the meantime, essential polarization effects in residues close to the active site may be taken into account in QM/MM studies by a suitable extension of the QM region.

2.1.4. Subtractive versus Additive Schemes

Subtractive QM/MM schemes are interpolation procedures. The QM/MM energy is obtained from three separate calculations: the MM energy of the entire system is corrected by adding the QM energy of the QM region and subtracting the MM energy of the QM region. In this approach, the QM/MM interactions are handled entirely at the MM level. This may be problematic for the electrostatic interactions, which will then typically be computed from fixed atomic charges in the QM and MM regions (neglecting the polarization of the QM region by the MM charges).

In additive QM/MM schemes, the QM/MM energy is the sum of the QM energy of the QM region, the MM energy of the MM region, and the QM/MM coupling terms. The latter normally include bonded terms across the QM/MM boundary and nonbonded van-der-Waals terms (both generally handled at the MM level) as well as electrostatic interaction terms which are modeled explicitly and can thus be described realistically using QM-based treatments (allowing for polarization of the QM region by the MM charges). This is probably the reason why most of the published QM/MM studies on P450 enzymes employ an additive scheme.

2.1.5. Electrostatic QM/MM Interactions

There are several strategies for handling these interactions ranging from simple mechanical to electronic and polarized embedding.[107] In the case of the polar protein environment, an electronic embedding is generally considered necessary. Thus, the electrostatic interactions are incorporated into the QM calculations by including the MM charges into the QM Hamiltonian, so that the QM subsystem is polarized in response to the electric field of the protein environment. The resulting QM density should be much closer to reality than that from a gas-phase model calculation. Electronic embedding is the standard choice in current QM/MM studies of enzymes.

The most refined embedding scheme is polarized embedding where the back-polarization of the MM region by the QM region is included as well, preferably in a fully self-consistent manner. This approach has been applied only rarely up to now (and not at all for P450 enzymes). It is expected to become more popular when more QM/MM studies with polarized force fields appear, because polarized embedding is the natural coupling scheme in this case.

2.1.6. Boundary Treatments

It is often unavoidable that the QM/MM boundary cuts through a covalent bond. The resulting dangling bond must be capped to satisfy the valency at the frontier, and in the case of electronic or polarized embedding, one must prevent overpolarization of the QM density by the charges close to the cut. To cope with these problems, there are several options. The most common approach is to introduce a link atom, typically hydrogen,[108,109] but it is also possible to use specifically parametrized boundary atoms[110] or pseudobonds[111] or specifically tailored pseudopotentials[112] or frozen orbitals.[113−115] All of these options seem to work well if proper care is exercised, especially with regard to the treatment of electrostatics at the QM/MM boundary.[116−118] In practice, the link atom approach is used most widely in QM/MM studies of P450 enzymes, often in combination with a charge shift scheme at the boundary.[118,119] It is common to fix the link atom in the bond being cut, at some well-defined distance from the QM frontier atom, and to redistribute the forces acting on it to the two neighbor atoms,[120] which effectively removes the artificial degrees of freedom of the link atom.

2.1.7. QM/MM Geometry Optimization

Special techniques are available to optimize the structures of large biomolecules with thousands of atoms at the QM/MM level that exploit the partitioning into a QM region, where energy and gradient evaluation are computationally expensive, and an MM region, where these calculations are almost for free. These techniques include a linear-scaling fragment-based divide-and-conquer optimizer[121] and microiterative strategies with alternating geometry relaxation in the core region (containing the QM region) and the environment.[122] Their combined use allows the efficient optimization of minima and transition states at the QM/MM level, also in the case of electronic or polarized embedding.[123] However, QM/MM geometry optimizations of the stationary points along a single reaction path are of limited significance, since there are many closely related paths in large biomolecules because of their conformational flexibility. It is thus advisable to determine at least several representative transition states with their corresponding minima in order to assess the influence of the conformational diversity of the environment. This strategy is often followed in DFT/MM studies of P450 enzymes.

2.1.8. QM/MM Molecular Dynamics

The vast configuration space that is accessible to large molecules can be sampled using molecular dynamics (MD) or related techniques. Straightforward QM/MM MD calculations are computationally demanding, however, and routinely affordable only at the semiempirical QM/MM level. For higher-level QM/MM approaches, approximate techniques are required that reduce the computational cost, e.g., by exploiting the QM/MM partitioning. One strategy is to avoid the expensive direct sampling of the QM region while fully sampling the MM configuration. An early example of this approach[124] keeps the QM region fixed and uses ESP (electrostatic potential)-derived charges for the QM atoms to evaluate the electrostatic QM/MM interactions during the MD run, in the context of free energy perturbation theory.[124,125] Using this procedure, it has recently been shown that the effects of sampling on the computed DFT/MM reaction profile are minor in the case of hydrogen abstraction in cytochrome $P450_{cam}$.[126]

2.1.9. QM/MM Energy versus Free Energy Calculations

In principle, theoretical studies should aim at free energy calculations, since chemical thermodynamics and kinetics are governed by free energy differences. These can be determined by statistical mechanics through sampling procedures (e.g., using thermodynamic integration, umbrella sampling, or free energy perturbation theory). Recent advances in this area have been summarized in an excellent review.[96] It is straightforward to perform free energy calculations at the semiempirical QM/MM level using any of these techniques (as demonstrated in several recent applications[125−128]), but the necessary sampling tends to become expensive with ab initio or DFT QM components. This is the reason why QM/MM free energy studies on P450 enzymes are still very rare. Judging from the available evidence, however, the differences between QM/MM energy and free energy profiles in enzymatic reactions tend to be small as long as local chemical events are investigated (e.g., hydrogen abstraction in $P450_{cam}$, OH transfer in PHBH, and nucleophilic substitution in fluorinase).[126] For reactions of this kind, one can thus expect to gain valuable mechanistic information by the less demanding DFT/MM geometry optimization studies that are commonly performed for P450 enzymes.

2.2. Practical Issues in QM/MM Studies

QM/MM methods have matured over the past two decades, but canonical "black-box" procedures have not yet been established. It would thus seem worthwhile to address briefly some of the practical problems and choices that are encountered in QM/MM work.

2.2.1. QM/MM Software

QM/MM calculations require efficient programs with wide-ranging functionality. Several of the standard QM and MM packages offer QM/MM capabilities as an add-on. The alternative is to interface independent external QM and MM programs to a central control module that supplies the QM/MM coupling as well as routines for standard tasks such as geometry optimization and molecular dynamics. In the long run, the latter modular approach is expected to be more flexible, since it can provide access to more QM/MM functionality (e.g., facilitating the combination of many different QM and MM methods). An example for such a modular implementation is the ChemShell package.[118,129]

2.2.2. QM/MM Setup

Realistic starting structures for QM/MM work will normally be derived from experiment (typically from an X-ray crystal structure). Small modifications of experimental structures are common in the setup phase, e.g., replacement of an inhibitor by substrate or substitution of selected residues to generate a specific mutant. The available structural information from experiment is generally incomplete and often not error-free. It is thus usually checked and processed employing the protocols developed by the classical simulation community. This includes, for example, adding missing hydrogen atoms, adding water molecules in "empty" spots, assigning the protonation states of titrable residues (e.g., His, Asp, Glu), and checking the orientation of residues in ambiguous cases (e.g., His, Asn, Gln). The correct choice of protonation states can often be crucial in QM/MM work; the assignments may be guided by empirical rules, structural considerations (e.g., via visual inspection of local hydrogen-bonding networks), empirical algorithms for pK_a predictions (e.g., PROPKA[130]), and explicit pK_a calculations (e.g., of Poisson−Boltzmann type). A related issue concerns the overall neutrality of the entire system, which may be achieved by suitable placement of counterions or by neutralization of charged residues at the surface of the protein.

After these initial setup choices are made, the enzyme is put into a water box and relaxed by a series of constrained energy minimizations and MD runs at the MM level (which may necessitate the derivation of missing force field parameters for the "nonstandard" parts of the system). After equilibration, the system is subjected to a classical production run from which several (5−10) snapshots are taken as starting geometries for the QM/MM work (often supplemented by an "initial" snapshot that resembles the available X-ray structure as much as possible). The starting structures generated in this manner for a P450 enzyme in a droplet of water typically contain around 20,000−25,000 atoms.

It is obvious that the setup phase requires a lot of work prior to the actual QM/MM calculations, and it should be emphasized that errors and wrong choices during setup can normally not be recovered at a later stage. These issues have been discussed in more detail in a recent review.[93] For the specific case of cytochrome $P450_{cam}$, there is a systematic QM/MM investigation of how the barrier to hydrogen abstraction from camphor is affected by the choices made during setup.[131] In this context, it should be noted that early QM/MM work on different $P450_{cam}$ intermediates and on different steps of the catalytic cycle employed separate setups that had been generated independently, which raises the question whether it is possible to handle the whole cycle with the same QM/MM setup. This is indeed the case: following a standard protocol that starts from the X-ray structure of the ferrous dioxygen complex and that involves careful assignment of protonation states and hydration, one can generate a common setup that gives QM/MM results for $P450_{cam}$ which are generally consistent with those obtained previously with individual setups.[54] This confirms that setup issues can be resolved in a consistent manner if proper care is exercised.

2.2.3. Accuracy of QM/MM Results

Given the large number of choices in QM/MM work, it is very difficult to converge the QM/MM results with regard to all computational options. Typical QM/MM studies on P450 enzymes may employ DFT/MM calculations with a standard protein force field such as CHARMM, electronic embedding, and a link atom boundary treatment. In practice, the sensitivity of the QM/MM results with regard to the chosen force field, embedding scheme, and boundary treatment is normally not checked (even though the results will depend on these choices). On the other hand, since the QM treatment influences the outcome rather directly, it is quite common to use different basis sets and different density functionals, at least in single-point energy calculations, to assess the reliability and robustness of the QM/MM results within DFT. Systematic convergence studies with high-level ab initio QM components are still rare, however,[104,105] and the most that has been achieved up to now for $P450_{cam}$ are single-point ab initio MR-CI/MM calculations to validate relative spin state energies for selected intermediates.[77,78] Finally, it is advisable to check the convergence of the results also with regard to the QM/MM approach itself. This can be done by QM/MM calculations with QM regions of increasing size, since extension of the QM region should decrease the influence of the QM/MM coupling and MM force field terms and, thus, make the QM/MM treatment more realistic overall. Such checks are often performed in QM/MM studies on P450 enzymes.

2.2.4. QM/MM Geometry Optimization

For systems with 20,000−30,000 atoms, it is usually sufficient to allow only around 1000 atoms to move during optimization (i.e., the active site and its environment) while the outer part remains fixed at the initially prepared snapshot geometry. It is essential in QM/MM work on reaction profiles to retain the same conformation of the optimized active region in order to ensure a smooth and continuous reaction path. If this requirement is not satisfied (e.g., by the flip of a distant hydrogen bond or some other remote conformational change), the QM/MM results from geometry optimization become spurious.[131] Experience shows that such problems can normally be avoided with an optimized active region up to about 1000 atoms (as typically used in QM/MM studies on P450 enzymes).

2.3. Conventions and Notations

It is obvious from the preceding discussion that there are not yet "canonical" black-box procedures for QM/MM methods and that one must decide on a large number of choices in QM/MM studies. Therefore, QM/MM calculations cannot be characterized by a short label, in contrast to QM studies on small molecules, where it is often sufficient to quote the acronyms for the QM method and basis set. A full specification of the chosen QM/MM options is impractical in the context of a review, and in this regard, the readers will thus normally be referred to the original literature in the following sections.

In spite of this general caveat, it is still possible to outline a "consensus" QM/MM approach that has emerged in the computational P450 community over the past years. This approach employs DFT(B3LYP)/MM calculations with an established protein force field (mostly CHARMM, sometimes OPLS or AMBER), electronic embedding, and a link atom boundary treatment. Open-shell systems are normally described by an unrestricted B3LYP treatment; this is implied when we use the label B3LYP while a restricted open-shell treatment will be denoted by ROB3LYP (analogous conventions apply for other functionals). The QM/MM setup usually starts from a crystal structure and involves initial classical MD calculations for system preparation. The actual QM/MM studies normally employ geometry optimization of the active site and its surroundings. Readers should envision this kind of QM/MM approach when we review QM/MM studies in the following sections.

There are two factors that affect the outcome of QM/MM calculations on P450 enzymes rather directly and that will therefore often be mentioned in the following sections, namely the QM region and the basis set for the QM calculation. The QM region needs to be adapted to the problem under investigation, but there are a few standard choices that will be introduced in section 3.1 (see Scheme 2, which also gives the corresponding notation). The commonly used basis sets show a greater diversity. Many of them include Pople-type basis sets[132] on the nonmetal atoms, such as 6-31G, 6-31G*, etc. Based on the experience with QM model calculations, the earliest QM/MM work on P450[53] employed a basis set (B1) of double ζ (DZ) quality that describes iron by an effective core potential and the LACVP basis[133] and the other atoms by the 6-31G basis. The B1 basis is often applied for geometry optimization, while subsequent single-point QM/MM calculations normally use larger basis sets to determine more reliable energies. Early examples for such larger sets are the B2 basis, which differs from B1 by including polarization functions (6-31G*) on the six ligands to iron (four pyrrole nitrogen atoms, the oxo atom, and the sulfur atom of the coordinating cysteine), and the B2W basis,[134] which differs from B2 by describing iron by an all-electron Wachters basis with an additional diffuse d function and a set of f polarization functions.[135−137] More recent QM/MM work often employs more extended basis sets for single-point calculations, typically of triple ζ (TZ) quality with one or more sets of polarization (P) functions. One such example is the B′ basis for $P450_{cam}$,[54,78] composed of the Wachters all-electron basis for iron, polarized triple ζ valence basis sets[138] for the six atoms coordinated to iron (TZVP), the C^5 atom of camphor (TZVP), the H^{5exo} atom of camphor (TZVPP), and the smaller SV basis[139] for the remaining atoms. Special basis sets are needed for special purposes, e.g., for the computation of Mössbauer parameters, which requires a flexible uncontracted basis in the core region of iron.[77] It is clearly impractical to specify in this review all the basis sets that have been used in recent QM and QM/MM studies on P450 enzymes. In the following sections, we shall refer to the labels introduced above (B1, B2, B2W, B′) when deemed appropriate, using a notation of the type DFT(B3LYP/B1)/MM. We shall explicitly specify other basis sets when necessary, but we shall also quote results from the literature in more general terms (e.g., those obtained with the largest basis set) and refer the reader to the original paper for technical details. As a general caveat, we note that the label B2 has been used in the literature also for larger basis sets than the one introduced above; in the following sections, such usage will be indicated either explicitly or by reference to the original paper.

2.4. Coverage and Sources of Computational Results

Most of the older theoretical literature on P450 up to the year 2000 can be found in the reviews of Loew and Harris[28] and Loew.[140] Studies that have appeared between 2000 and 2004 and during part of 2005 were summarized in our 2005 review.[32] These studies include complete QM(DFT)-only modeling of the catalytic cycle of P450 by Rydberg et al.,[141] Shaik et al.,[31,142,143] and Hata et al.[144] In addition, the 2005 *Chemical Review* article covers extensively the two-state reactivity (TSR) concept in P450 enzymes[25,30,37,83,145−147] and discusses a variety of mechanistic studies, using QM(DFT)-only methods, e.g., of C−H hydroxylation,[39−43,45,146−153] double bond epoxidation,[35−37,44,149,150] benzene and arene hydroxylation,[33,34,38] and sulfoxidation.[154] These studies will be mentioned in passing but will not be covered thoroughly in the present review.

The 2005 *Chemical Review* article included only a few QM(DFT)/MM studies.[53,59,134,155−157] However, since that review has been published, there have appeared a variety of QM(DFT)/MM studies, as well as single-point QM(CI)/MM calculations. Many of these studies concern the entire catalytic cycle of CYP101 and of selected species in human isoforms, e.g., CYP3A4.[54−56,77,78,158−162] Some of these studies describe analogous species in the selenocysteine mutant, the Mn mutant, the D251N and L358P mutants of CYP101, as well as the CPO and NOS enzymes.[62,63,66−69,160,161] In addition, QM(DFT)/MM has also been used to study the mechanisms of C−H hydroxylation, C=C epoxidation, aromatic hydroxylation, and C−C coupling.[57−61,131,163,164] Mechanistic studies since 2005 using QM-only methods addressed dehalogenation of aromatic compounds,[165] N-dealkylation in *N*,*N*-dimethylanilines,[166,167] ethanol oxidation,[168] and sulfoxidation.[169] QM-only methods were also used for computational investigations of C−H hydroxylation, aromatic hydroxylation, and heteroatom oxygenation,[170−173] as well as for valence bond modeling of the mechanism and reactivity patterns in C−H hydroxylation.[174] These QM/MM and QM-only studies will form the core of the present review.

3. The Catalytic Cycle of P450 Enzymes

To understand P450 reactivity, one must first understand the catalytic cycle of CYP enzymes, since, in many of the isoforms of this enzyme, the rate-determining event is not substrate oxidation; this poses obvious difficulties to mechanistic investigations of these reactions. It is established by now that CYP enzymes operate by means of the generic catalytic cycle drawn in Figure 1,[175,176] where, except for **1**, the heme is depicted by two bold horizontal lines, and the cysteinate proximal ligand is abbreviated as CysS. The resting state (**1**) of the enzyme generally involves a ferric-protoporphyrin complex, coordinated to the proximal cysteine residue and to a water molecule at the distal side; in some isoforms, such as CYP2D6, the water ligand is missing.[177] This hexacoordinated Fe^{III} complex (**1**) exists largely in a low-spin doublet state, and as long as this is the case, the enzyme will remain inactive.[175,178] When the substrate (for example, an alkane, AlkH) enters, it displaces the water molecule, leaving a pentacoordinated ferric-porphyrin (**2**), and changes the spin state to a sextet. Due to the loss of the water ligand, the ferric complex (**2**) is a slightly better electron acceptor than the resting state (by approximately 130−300 mV), and this is sufficient to trigger an electron

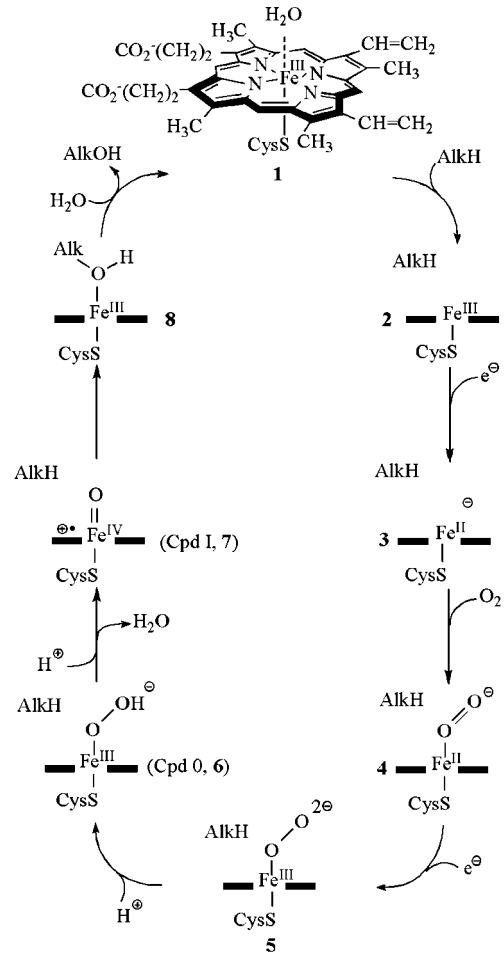

Figure 1. Schematic representation of the catalytic cycle of P450. Reprinted with permission from ref 32. Copyright 2005 American Chemical Society.

transfer from a reductase protein (which operates at 200 mV), leading to a high-spin ferrous complex (**3**), which is a good dioxygen binder. The binding of molecular oxygen yields the oxy-ferrous complex (**4**), which has a singlet spin state and is a good electron acceptor. This, in turn, triggers a second reduction of the system to generate the ferric-peroxo anion species (**5**). This second reduction is in some cases, albeit not always,[179] the rate determining step in the catalytic cycle.[180] Since the reduced dioxygen-complex (**5**) is a good base, it gets quickly protonated to form the ferric-hydroperoxide species (**6**) that is called Compound 0 (Cpd 0). Thereafter, Cpd 0 abstracts another proton, and a water molecule splits off to generate the high-valent iron-oxo species (**7**), so-called Compound I (Cpd I). In the common case, Cpd I monooxygenates the substrate; for example, the alkane in Figure 1 is converted to an alcohol (**8**), which exits the pocket, thereby allowing water molecules to re-enter and restore the resting state (**1**).

Note that a single water molecule is used to gate the cycle in Figure 1; however, the enzyme also requires a protonation machinery to come full cycle. The protonation machinery is believed to involve an acid−alcohol pair (in the case of CYP101, the Asp_{251} and Thr_{252} residues shown in Figure 2).[175,178,181] It is thought that these residues, and perhaps also Glu_{366} that is not shown in the drawing,[182] shuttle the protons to the dioxygen moiety in **4**−**6**, via water molecules.[182] Indeed, mutation of Asp_{251} reduces the rate of camphor hydroxylation, while mutation of Thr_{252} can virtually stop

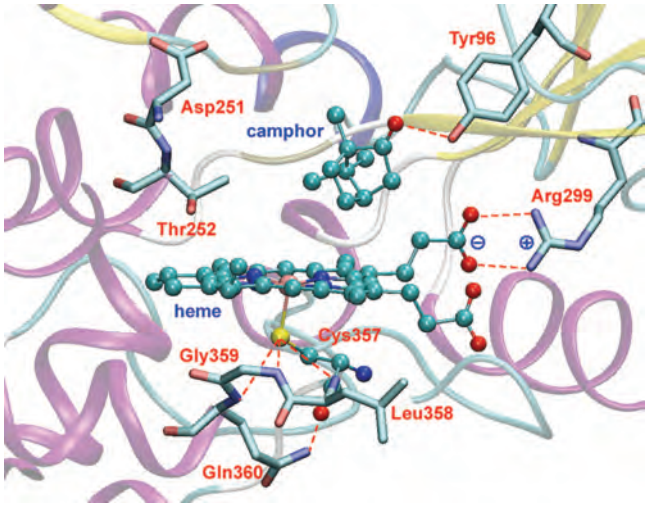

Figure 2. Close-up of the active site of CYP101 as taken from the X-ray structure (pdb code: 1DZ8) of Schlichting et al.[178] with some essential groups highlighted.

the process:[175,178,181] the T252A mutant performs only C═C epoxidation, presumably via Cpd 0.[183] Oddly, the double mutant, with both Asp_{251} and Thr_{252} mutated to residues that do not shuttle protons, shows significant camphor hydroxylation activity,[184] thereby implying that proton shuttle can occur through water networks with no need for the alcohol−acid pair of residues. The role of water is like a two-edged sword: On the one hand, water molecules are important for protonation,[182] but on the other hand, too much water leads to formation of hydrogen peroxide and other uncoupling products that waste the oxygen and the reducing equivalents.[185−187] Thus, the enzyme has to function in a middle road: having some water molecules and at the same time denying them free access to the neighborhood of the Fe-OO moiety, in order to be able to activate bonds and to produce oxidized products efficiently. Although some isoforms, especially the human ones,[21] are promiscuous and have large pockets, which can accommodate many water molecules[188] and more than one substrate molecule,[189] nonetheless, the control of water is influenced in part by the tightness of substrate binding by the enzyme.[190,191] For example, in the case of CYP101 (Figure 2), this is achieved by a substrate-binding domain made from Tyr_{96}, which forms a hydrogen bond (H-bond) with the carbonyl group of camphor and holds the substrate steady in place just above the FeO moiety. In addition to this feature, as shown in Figure 2, the sulfur atom of the cysteinate ligand interacts with the three amidic groups of Gln_{360}, Gly_{359}, and Leu_{358} (only one of these has the geometry of a classical H-bond), while the carbonyl group of the cysteine interacts with Gln_{360}.[178,192] These interactions appear to be essential for the stability and activity of the enzyme.[193,194] These issues have all been studied by QM/MM and will be addressed in the next subsections that summarize the theoretical studies of the different species in the catalytic cycle (structures **1**−**8**).

Concerning reactivity, there is uncertainty about the details of the cycle starting from **6** and onward back to **1**; Cpd I is elusive in the native cycle, and its mechanism of formation is still putative. The reason for its elusiveness is thought to be its fast formation and fast consumption, but this is not yet clear. Furthermore, the range of reactivity patterns of Cpd I is still not fully understood. Thus, while the normal activity involves monooxygenation as in C−H hydroxylation (Scheme 1), the enzyme seems to be much more versatile. For example, in the bacterial enzyme CYP245A1 (P450 StaP),[195] the enzyme seems to function more like cytochrome *c* peroxidase,[196] while, in CYP3A4, the enzyme often requires a few substrate molecules to operate efficiently.[189] As we shall show, QM/MM theory provides very useful insight into some of these major questions by considering the properties of Cpd I and its reactivity patterns.

3.1. Models of the Enzyme

Since the complete enzyme cannot be described by QM(DFT), one usual practice among the workers in the field is either to truncate the active species and calculate the model system by QM only or to embed it in the protein and use QM/MM. Generally, the heme is treated as porphine by removing all side chains of the protoporphyrin IX (PPIX) macrocycle. In some cases, these side chains were included in the calculation.[59,68,131,155,157,163] The cysteinate ligand is modeled either as thiolate (SH^-), as methyl mercaptide (SCH_3^-), or as cysteinate anion ($SCys^-$), and in some cases as an extended cysteinate (ext-SCys), augmented by the peptide bonds of the adjacent Leu_{358} and Leu_{356} residues. DFT(B3LYP)/MM calculations[53] showed that gas-phase DFT(B3LYP) calculations using SH^- give generally better agreement with the DFT/MM results than SCH_3^-, or even the full cysteinate ligand. Many of the calculations, especially those on reaction mechanisms, used the simplest model with porphine and SH^- as the thiolate ligand, or porphine and SCH_3^-. The most recurring model systems and their notations are summarized above in Scheme 2. There are however, quite a few other models, which incorporate porphyrin substituents, and specific key residues in the active site; these will be mentioned specifically wherever deemed necessary.

3.2. Oxidation States and Key Orbitals of Species in the Catalytic Cycle

Since the species in the cycle (Figure 1) possess a dense orbital manifold that is only partially filled, this gives rise to many closely lying spin and electromeric states, which differ in the oxidation states on the iron and the ligands.[25] It is, therefore, important to establish a common language by beginning with the oxidation state formalism of these P450 species and then describing a generic orbital picture, which describes at least most of the species in the cycle. More orbital diagrams will be presented as we proceed along with the discussion of various specific issues and reactivity patterns.

The oxidation state of iron is given as Roman numerals near the iron atom in the species in Figure 1; note that the total charge of the species is indicated in a circle near the species. We must remember that the oxidation state formalism is a heuristic device, which assumes that all metal−ligand bonds are "ionic". It turns out that this assumption is useful to keep track of the "number of d-electrons" that remain on the metal ion in redox processes; however, the oxidation number is not identical to and may be even remote from the charge distribution in the molecule (or from the real integrated d-population altogether). In this formalism, the porphyrin ligand has an oxidation number of 2−, while the cysteine ligand is 1−. Any molecular ligand that has already an electronic octet like water is counted as zero (0), while, for any other ligand, which does not possess an electronic octet, the assigned oxidation number is determined by the number of electrons that this ligand "takes from iron" to fill

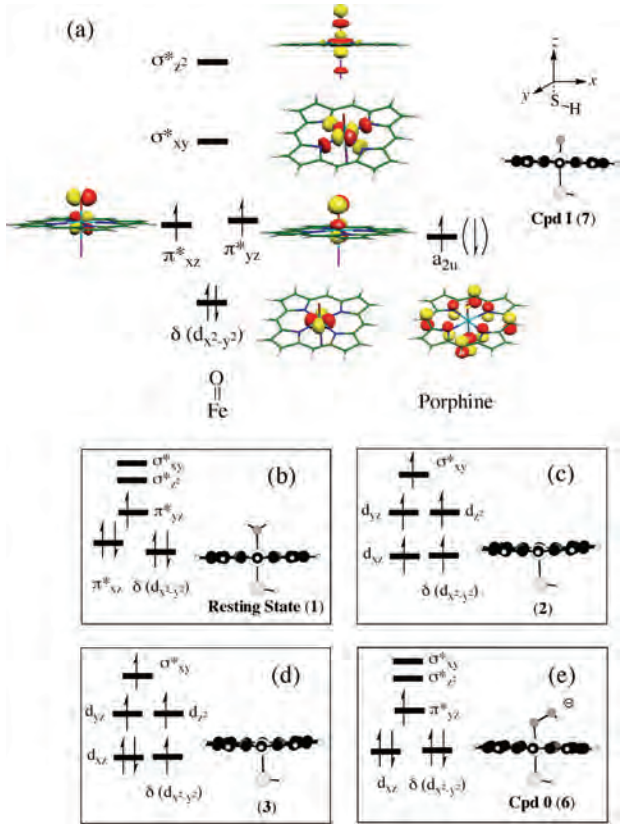

Figure 3. (a) Orbitals and their occupations in Cpd I (**7**). (b−e) Orbital occupations for the resting state (**1**), the pentacoordinated complexes (**2** and **3**), and Cpd 0 (**6**).

its octet; for example, an oxo ligand is 2−, while an OOH ligand is 1−. Thus, for all the neutral complexes, with and without a water ligand, the oxidation number of iron will be 3+, which is labeled in Figure 1 as Fe^{III}. This corresponds to the resting state (**1**) and the pentacoordinated complex (**2**). After accepting one electron from the reductase, the pentacoordinate complex (**3**) becomes negatively charged and iron is in the ferrous state Fe^{II}. This complex (**4**) has an O_2 molecule that possesses an octet, and hence it can be formally written as $Fe^{II}O_2$. It is thus referred to as oxy-ferrous; as we shall see later, the bonding features of **4** are more appropriately represented by $Fe^{III}O_2^{-}$.[79] In the reduced complex (**5**) with an additional electron, it is customary to assign the dioxygen ligand oxidation number of 2−, and hence, **5** is a ferric-peroxy species, $Fe^{III}O_2^{2-}$, with a total charge of 2−. After protonation, Cpd 0 (**6**) is a ferric-hydroperoxide, Fe^{III}−OOH, with a total charge of 1−. In Cpd I (**7**), which is neutral, the formal oxidation state of the entire heme is 5+, and this is assigned partly to the iron as Fe^{IV} and partly to the porphyrin ring, which becomes a π-cation-radical $Por^{\bullet+}$. This assignment is not part of the rules of the oxidation-state formalism but is based on knowledge of the electronic structure (see Figure 3). Finally, the product complex (**8**) is a neutral Fe^{III} species, and as such, Cpd I has two-oxidation equivalents above those of the resting state and of the product complex.

The oxidation states in Figure 1 provide some rationale for comprehending the electronic structure of the P450 species. The orbital labels and ground state configurations are shown in Figure 3 for **1**−**3**, **6**, and **7**, whereas, for **4** and **5**, the bonding features are more complex and will be described separately. Thus, each species in the figure has five d-type orbitals, which differ from species to species depending on the interaction of the d-orbitals with the ligand orbitals. In addition, a porphyrin-based orbital is drawn for **7** alongside the d-type orbitals, in Figure 3a. The total oxidation state on iron and porphyrin determines the occupancy of these orbitals, while the interaction strength with the ligand will determine the spread of these orbitals and hence the propensity for high-spin ground states.

In Figure 3a we show the orbitals and electronic configuration of Cpd I (**7**), on the left-hand side the five metal d-type orbitals, and near them the high-lying mixed porphyrin-thiolate orbital, so-called a_{2u}. The sulfur−porphyrin mixing in a_{2u} is significant, since thiolate is a powerful electron donor,[197,198] but with weaker donor ligands, such as imidazole,[74,199] this mixing is negligible and a_{2u} is a pure porphyrin orbital. As we shall see, the singly occupied a_{2u} orbital is sensitive to the donor capability of the thiolate, and in fact to any good donor that may participate in the electronic structure of Cpd I.[199]

The d-block in Figure 3a is split into the characteristic three-below-two sets, which are nascent from the purely octahedral t_{2g} and e_g sets with an additional splitting of t_{2g} into one-below-two. The lowest three orbitals are, in increasing energy order, the nonbonding $\delta(d_{x^2-y^2})$ orbital and the two π^*_{FeO} (π^*_{xz} and π^*_{yz}) orbitals; the latter two involve antibonding interactions between the metal $3d_{xz,yz}$ and the oxygen $2p_{x,y}$ atomic orbitals. The two high-lying virtual orbitals of Cpd I are σ^* orbitals; one (σ^*_{xy}) describes the Fe−N antibonding interactions and the other ($\sigma^*_{z^2}$) those along the O−Fe−S axis; the ordering of the σ^* orbitals is dominated by the length of the Fe−O bond, and when it is short as in Cpd I, $\sigma^*_{z^2}$ rises above σ^*_{xy}. With the $Por^{\bullet+}Fe^{IV}$ oxidation state, there are four electrons in the d-block, and the porphyrin-based orbital is singly occupied. This occupation gives rise to a pair of almost degenerate spin states, one quartet ($S = {}^3/_2$) with all single electrons being up-spin, and one doublet state with a spin flip in the porphyrin-based orbital. Some other spin states ($S = {}^5/_2$ and ${}^3/_2$) are also relatively low lying and involve 1e-promotion from δ to σ^*_{xy}.[77,200]

In those species where the Fe−O bond is longer than that in Cpd I (**1**, **6**) or where the complex loses its sixth ligand altogether (**2**, **3**), two orbitals exhibit weaker antibonding interactions; these are $\sigma^*_{z^2}$ and one of the π^* orbitals, which undergo significant stabilization, as indicated in Figures 3b−d. In **2** and **3**, both orbitals become nonbonding d orbitals, d_{z^2} and d_{xz}, while, in **1** and **6**, the $\sigma^*_{z^2}$ orbital gets stabilized and descends below σ^*_{xy}, whereas the π^*_{xz} orbital is almost a nonbonding d_{xz} orbital. The weakening of the ligand field shrinks the spacing of the d-orbitals, thus giving rise to low lying high-spin states as ground states.

3.3. The Resting State (1) and the Pentacoordinate Intermediates (2, 3)

3.3.1. The Resting State

The resting state (**1**) is the most thoroughly studied species. According to electron spin echo envelope modulation (ESEEM) spectroscopy, it has a doublet ground state.[201] Other experimental observations show spin equilibrium between the doublet ground state and a sextet state[202−204] and indicate thereby that these two states are closely lying within 2 kcal mol^{-1} or less. QM-only calculations do not reproduce this trend[32] and exhibit particular sensitivity to the representation of the cysteine ligand. Thus, in some studies the ground state

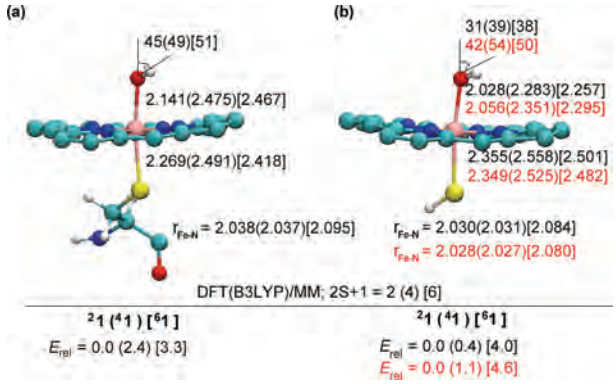

Figure 4. Bond lengths (in Å), angles (in degree), and relative energies (in kcal mol^{-1}) of the spin states of the resting state (**1**). The spin states are indicated by left-hand superscripts. r_{Fe-N} is the average distance of the four Fe−N bonds. (a) DFT(B3LYP/B2)/MM results (Por,ext-SCys model).[156] (b) DFT(B3LYP/B1)/MM results (Por,SH model) from ref 156 (first line) and ref 54 (second line) which employ slightly different QM/MM setups; the relative energies are average values from six snapshots, respectively.

is the sextet state,[141] and in others, the Fe−O bond lengths of the quartet and sextet states are virtually dissociated.[156]

The two most recent DFT/MM studies[54,156] investigated the resting state thoroughly, in order to establish the most reliable computational levels and procedures. The earlier one[156] compared two different QM regions for the thiolate ligand (SH and ext-SCys), two different protonation states (for Asp_{297}), three different density functionals (BLYP, B3LYP, and BHLYP), two different basis sets, and six different snapshots as starting points for QM/MM optimizations. The relative energies of the spin states were strongly affected by the choice of the functional, consistent with previous computational experience[205,206] on other iron complexes: BLYP overestimates the stability of the low-spin states, BHLYP artificially favors high-spin states, and only B3LYP gives realistic multiplet splittings. The results were less dependent on the other choices (such as protonation state or snapshot). The more recent study[54] used DFT(B3LYP)/MM only on the small QM model (SH) but performed the calculations of the entire cycle in a common setup that enables comparison of the various QM/MM energies.

Some representative DFT(B3LYP)/MM data for the resting state[54,156] are summarized in Figure 4. In agreement with experiment, the DFT(B3LYP)/MM calculations[54,156] predict a doublet ground state and closely lying quartet and sextet states. As can be seen from the energy differences, the three states are packed within 3−5 kcal mol^{-1} or so, depending on the proximal ligand representation. Comparison of the most recent results[54] to the previous ones[156] in Figure 4b reveals virtually identical features, so that the results are not too dependent on the system setup. A dense spin-state manifold was found also in single-point DFT/MM calculations by Scherlis et al.[207,208] on a fixed geometry of the resting state. Thus, although their doublet-sextet gap is a bit higher, the spin states are still close energetically, in line with the experimental observation of spin equilibrium.[204]

The geometric features in parts a and b of Figure 4 are also similar. In both cases, the optimized geometries show a tilt of the water ligand by 31−54°, because of hydrogen bonding interactions with the other water molecules in the pocket. The calculated tilt in the doublet ground state is in excellent agreement with ESEEM measurements[201] of the distances between the iron and the protons of the bound water ligand (computed 2.646 and 2.620 Å, ESEEM 2.62 Å).

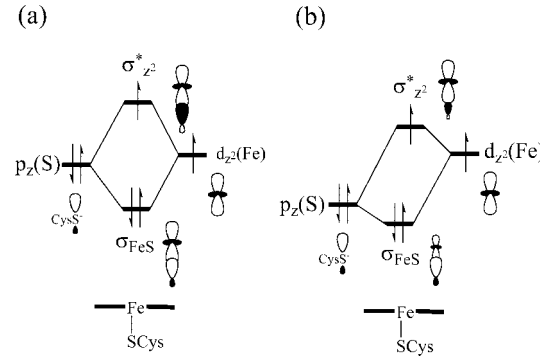

Figure 5. Orbital interactions that generate the Fe−S bond orbital (σ_{FeS}) and the $\sigma^*_{z^2}$ orbital: (a) in the gas phase where the interaction is strong, and (b) in the protein where the interaction is weakened due to stabilization of the p_z(S) orbital.

Furthermore, the predicted Fe−O (2.141 Å) and Fe−S (2.269 Å) distances (Figure 4a) for the ground state are shorter and longer, respectively, than the corresponding gas-phase values and are in reasonable agreement with the X-ray data of 2.28 ± 0.2 Å and 2.25 ± 0.2 Å (pdb file: 1PHC).[209]

The impact of the protein environment is moderate on the doublet ground state but significant on the higher spin states. Thus, in the gas phase, the Fe−O bonds of both quartet and sextet states are almost dissociated (3.6−3.7 Å),[156] but in the protein, this bond is significantly shorter (2.26−2.48 Å). Furthermore, the energy gaps in Figure 4 are smaller than the corresponding gas-phase DFT(B3LYP)-only values; especially affected is the quartet state that is greatly stabilized by the protein. These two trends are connected and are both associated with the effect of the protein on the orbital mixing in Figure 5. Thus,[156] the mixing of the d_{z^2} orbital on iron and the p_z(S) orbital generates a bonding and an antibonding combination; the latter is the $\sigma^*_{z^2}$ orbital of the water complex. In the gas phase (Figure 5a), the p_z(S) orbital is high lying and close to d_{z^2}(Fe), and hence, the mixing is strong, leading to a high-energy $\sigma^*_{z^2}$ orbital with significant S−Fe antibonding character. On the other hand, in the protein (Figure 5b), the hydrogen bonding to the sulfur (see the NH···S interaction above in Figure 2) and the bulk polarity lower the sulfur orbital and weaken its mixing with d_{z^2}, resulting in a lower lying $\sigma^*_{z^2}$ orbital, with less antibonding character. Since $\sigma^*_{z^2}$ is populated in both the quartet and sextet states, the protein stabilizes both states relative to the doublet ground state. Furthermore, the strong Fe−S interaction in the gas phase raises the $\sigma^*_{z^2}$ orbital, and this weakens significantly any potential p(O)−d_{z^2}(Fe) interaction, leading to very long Fe−O bonds in the gas phase and short Fe−S bonds. By contrast, the weaker S−Fe interaction in the protein results in a long Fe−S bond and enables the formation of a short Fe−O bond.

3.3.2. The Pentacoordinated States

The conversion of **1** to **2** is the crucial event that enables the gating of the cycle via reduction of **2** to **3**. Experimental work shows that **2** has a sextet ground state, ($d_{x^2-y^2}{}^1 d_{xz}{}^1 d_{yz}{}^1 \sigma^*_{z^2}{}^1 \sigma^*_{xy}{}^1$; see orbitals in Figure 3c), which is in spin equilibrium with a doublet state, in a manner that reflects sensitivity to the protein environment.[204,210] The doublet state, ^{2}**2**, corresponds to $d_{x^2-y^2}{}^2 d_{xz}{}^2 \pi^*_{yz}{}^1$, and the intermediate spin state, ^{4}**2**, to $d_{x^2-y^2}{}^2 d_{xz}{}^1 d_{yz}{}^1 \sigma^*_{z^2}{}^1$. Much like the pentacoordinated ferric complex, the reduced ferrous complex **3**, obtained after electron uptake by ^{6}**2**, is known

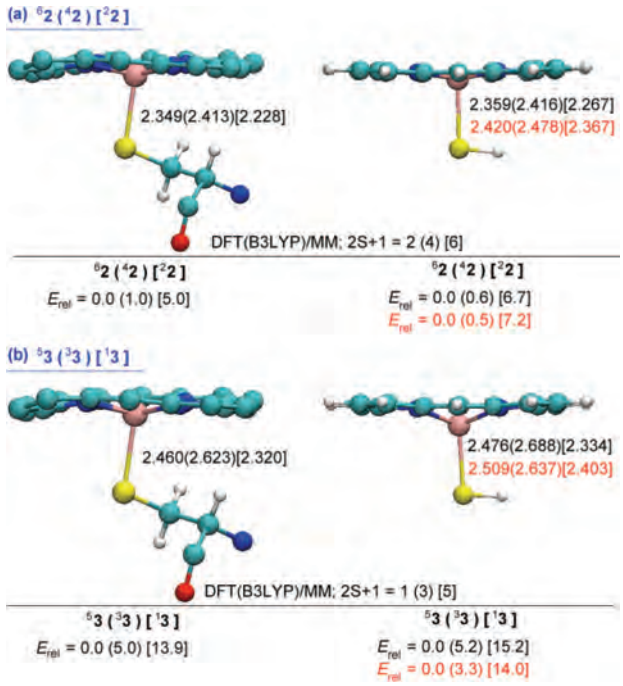

Figure 6. Optimized Fe−S bond lengths (in Å) and relative energies of the various spin states (in kcal mol^{-1}) of the pentacoordinated complexes **2** and **3**. The superscripts on the left-hand side refer to the spin multiplicity ($2S + 1$) of the state. (a) DFT(B3LYP)/MM results for the small and large QM subsystems for **2**. (b) DFT(B3LYP)/MM results for the small and large QM subsystems for **3**. The data in parts a and b correspond to different basis sets and setups. They are taken from ref 134 (first line, basis B2W, snapshot 31) and from ref 54 (second line, basis B1 for geometry optimization, basis B′ for energies, snapX).

to have a high-spin quintet state, ^{5}**3**.[203,211] Two alternative electronic configurations are possible, $d_{x^2-y^2}{}^2 d_{xz}{}^1 d_{yz}{}^1 \sigma^*_{z^2}{}^1 \sigma^*_{xy}{}^1$ and $d_{x^2-y^2}{}^1 d_{xz}{}^2 d_{yz}{}^1 \sigma^*_{z^2}{}^1 \sigma^*_{xy}{}^1$ (see Figure 3); these may be labeled as $^5\mathbf{3}_{xz}$ and $^5\mathbf{3}_{x^2-y^2}$.[143] Closely lying states are the triplet state, ^{3}**3**, with the $d_{x^2-y^2}{}^2 d_{xz}{}^2 d_{yz}{}^1 \sigma^*_{z^2}{}^1$ configuration, and a singlet state, ^{1}**3**, with $d_{x^2-y^2}{}^2 d_{xz}{}^2 d_{yz}{}^2$ occupation.

Early QM(B3LYP)-only studies[134,141,143] for the low-lying spin states of **2** and **3**, with sufficiently large basis sets and different ligand representations, gave remarkably good results. High-spin ground states are found in all these gas-phase model calculations, and the ferrous complex has a $^5\mathbf{3}_{xz}$ ground state, with the $^5\mathbf{3}_{x^2-y^2}$ state lying only ca. 2 kcal mol^{-1} higher.[134,143] The various sets of results show some scatter, of course, but they agree with regard to the trends, and the computed geometries were in reasonable accord with the experimental X-ray data.[178]

The pentacoordinated complexes **2** and **3** have been studied recently by means of DFT(B3LYP)/MM in different QM/MM setups and with large basis sets.[54,134] Key geometric data and spin-state energy gaps are given in Figure 6 for the two extreme ligand representations.

The geometric parameters in Figure 6 are in basic accord with the experimental data.[178] A recent DFT(B3LYP)/MM study of **3** with and without the reductase (putidaredoxin) by Freindorf et al.[212] gave similar structural data and further showed that the Fe−S bond distance gets shorter upon binding of the reductase, to the proximal side of the active site. This bond shortening (by 0.05−0.10 Å) is accompanied by an increase of the stretching frequency of the Fe−S bond in qualitative accord with experimental findings.[213]

The data in Figure 6 show that DFT(B3LYP)/MM also reproduces the precise identity of the ground states of ^{6}**2** and ^{5}**3** in accord with experimental data. Thus, while the smallest ^{2}**2**−^{6}**2** energy difference of 5 kcal mol^{-1} (for the Por,ext-SCys model) is still on the high side for spin equilibrium, this value is sufficiently low to suggest this phenomenon.[214] Furthermore, according to the DFT(B3LYP/B2W)/MM results for the larger QM region,[134] the protein inverts the relative ordering of the quintet electromers of the ferrous complex ^{5}**3**: a $^5\mathbf{3}_{x^2-y^2}$ ground state is predicted in the enzyme (one electron in the $d_{x^2-y^2}$ orbital; see Figure 3), which is preferred by 0.5 kcal mol^{-1} over the $^5\mathbf{3}_{xz}$ electromer. Indeed, the comparison of calculated[134] Mössbauer parameters with the measured quadrupole splitting and asymmetry parameter[203,211,215] unequivocally assigns the ground state as $^5\mathbf{3}_{x^2-y^2}$.

The experimental values of the reduction potentials of free and putidaredoxin-bound ^{6}**2** are −170 and −173 mV, respectively.[180,215] Using the potential of the standard hydrogen electrode (−4.43 V)[216] as reference, this implies that the free energy change ΔG for the reduction $\mathbf{2} + e^- \rightarrow \mathbf{3}$ is −98 kcal mol^{-1}. Approximating ΔG by the energy change ΔE, QM(B3LYP)-only calculations predict the conversion of ^{6}**2** into ^{5}**3** to be exothermic by −85.5 kcal mol^{-1} with a dielectric constant of $\varepsilon = 5.7$,[143] and by −80.2 kcal mol^{-1} with $\varepsilon = 80$.[141] DFT(B3LYP)/MM calculations[54,134] show a strong dependence on the protonation state of the protein. Thus, when the total charge of the protein is 9−, the reaction energy is endothermic by 53.8 kcal mol^{-1}, while a neutral protein leads to an overall reduction energy of −81.6 kcal mol^{-1} (QM region: Por,SH; basis B1). However, the most recent DFT(B3LYP/B′)/MM calculations[54] reveal that this accuracy was obtained at the expense of unrealistically doubly protonating all the His residues; when using more realistic protonation states, of an otherwise neutral protein, the exothermicity of reduction is underestimated by 30−50 kcal mol^{-1}. Free energy calculations on reduction potentials in enzymes[217,218] have emphasized the importance of proper sampling and derived QM/MM-based reorganization energies,[218] which are substantial and will only partly be captured in an approach relying on geometry optimization.

3.3.3. Gating of the Catalytic Cycle

DFT(B3LYP/LACV3P+*) calculations[143] including bulk polarity ($\varepsilon = 5.7$) demonstrated that the reduction $^6\mathbf{2} \rightarrow {}^5\mathbf{3}$ is 10.7 kcal mol^{-1} more exothermic than the reduction of the resting state ($\mathbf{1} \rightarrow \mathbf{1}^-$), compared with an experimental value of about 3 kcal mol^{-1}. This result supports the experimentally accepted gating mechanism[180,219] and can be understood based on the orbital picture of the resting state and of **2** and **3**. Thus, as shown in Figure 3b, reducing the resting state adds an electron into a π^* orbital, which exhibits antibonding interactions with the water ligand. By contrast, during the reduction of **2**, an electron is added to a low-lying orbital at iron (d_{xz} in Figure 3c). Of course, electron−electron repulsion of the excess electron with the water ligand in $\mathbf{1}^-$ must also contribute to the resistance of the resting state to accept an electron from the reductase, and as such, **1** is the off-state in the cycle.

Another conclusion from the theoretical study[143] concerns the role of the thiolate ligand in this gating mechanism. Thus, it was demonstrated that upon removal of the thiolate ligand both **1** and **2** could be easily reduced by most reductants. It is therefore the thiolate ligand that controls the gating of the catalytic cycle by making the system a poorer electron

acceptor *so that only the pentacoordinated ferric porphyrin can be reduced by the reductase*.

3.3.4. DFT/MM Study of the Electron Transfer Event

A DFT/MM study of the electron transfer mechanism in the complex of CYP101 and putidaredoxin (PDX) has recently appeared.[76] Starting from crystal structures of the two components, protein−protein docking and refinement procedures were used to generate four CYP101−PDX complexes that were then subjected to a QM/MM electron transfer path search algorithm. In this algorithm, the geometry and atomic charges of the donor (Fe_2S_2 cluster) and the acceptor (heme) are first obtained from QM/MM energy minimizations and held fixed thereafter. The QM region in the following QM/MM calculation includes the entire transfer region between donor and acceptor. A receptor in the QM region is identified by injecting an extra electron and allowing it to localize at a given residue, which is then excluded from the QM region in the subsequent QM/MM calculation. This procedure is iterated until the entire electron transfer path between PDX and the heme has been mapped.

The key findings of this study are the following: (a) The binding of the negative Fe_2S_2 cluster of PDX to CYP101 is maintained by the $Arg_{112}^{CYP}-Asp_{38}^{PDX}$ salt bridge between the two proteins. The minimum Fe−Fe distance between the two redox centers in the different complexes varies between 12.7 Å and 14.4 Å. (b) In all four complexes, Arg_{112}^{CYP} acts as mediator of the electron transfer, either through its carbonyl group or its side chain. On the PDX side, the carbonyl group of Asp_{38}^{PDX} is involved in three cases and Gly_{41}^{PDX} in one case. (c) The so identified electron transfer pathways are *not connected to the propionate side chain* of the heme but rather pass through the Cys_{357} ligand. This unimportance of the 6-propionate side chain is in accord with experimental findings[220,221] that replacement of this side chain by a methyl group has little effect on the consumption of NADH.

3.4. The Oxy-Ferrous (4) and Ferric Peroxo (5) Complexes

The oxy-ferrous (**4**) and ferric peroxo (**5**) complexes are crucial for the propagation of the cycle. The oxy-ferrous species is remarkable, since the two constituents ^{5}**2** and $^3O_2$ have a total of six unpaired spins to begin with, and all these spins couple in **4**, which is known to be a singlet-state species.[222] Its geometry has been determined by X-ray crystallography to be an end-on complex with a bent O_2 moiety (132°) and Fe−O/Fe−S distances of 1.8/2.3 Å, respectively.[178] The ferric-peroxo complex of CYP101 has been detected by EPR/ENDOR (electron paramagnetic resonance/ electron−nuclear double resonance) studies in cryogenic experiments and is known to have a doublet spin state.[176] Its structure has not been determined yet, but its resonance Raman spectrum was recorded in the D251N mutant.[223] A structural investigation of the analogous CPO enzyme revealed spontaneous protonation to Cpd 0 (**6**).[67] However, the structure of the corresponding ferric peroxo complex of myoglobin (Mb) was recently determined in a combined X-ray and DFT(B3LYP)/MM study, and was found to possess an Fe−O bond of 1.85 Å (1.90 Å by DFT/MM).[224]

QM(DFT)-only calculations[31,141,225,226] correctly predict the spin states of the ground states for the two species and the end-on bent geometry but tend to give a somewhat longish Fe−O bond, ca. 0.15 Å longer[141] than the experimental values.[178] Adding the H-bonding protonation machinery to the Fe-OO moiety further elongates the Fe−O distances by 0.05 Å and shortens the Fe−S distances.[226] Thus, the electrostatic interactions of the dioxygen ligand with the water molecules and the peptide groups apply a *trans*-effect; the Fe−S bond gets shorter due to the weakening of the Fe−O bond. This might well be an artifact of B3LYP, which tends to undermine the $Fe-O_2$ bonding.[103] Indeed, a recent CASPT2 study shows that the only functional that reproduces the binding energy is OLYP.[227]

Both **4** and **5** have recently been investigated by means of DFT(B3LYP)/MM calculations, using different protonation states, different basis sets, and different representations of the proximal ligand.[161,162] The results are shown in Figure 7. Once again, the calculations correctly predict the end-on bent geometry of the Fe−OO moiety but seem to exaggerate the Fe−OO bond length, while the Fe−S bond length is in line with experimental data for **4**.[178] Furthermore, irrespective of the model used in the DFT(B3LYP)/MM calculations, the ground state of **4** is found to be an open-shell singlet state with a very low lying triplet state. An intact ferric peroxo complex **5** is only found in the doublet state, whereas the quartet and sextet states dissociate upon QM/MM optimization into **2**(Fe^{II}) and a superoxide ion, $O_2^{\bullet-}$. Reduction of the singlet ground state of **4** will generate **5** in its doublet state. If intersystem crossing to higher spin states of **5** occurs, one would expect dissociation; such uncoupling is indeed observed.[175] Recent resonance Raman data for the Fe−O stretching mode indicate that the Fe−O bond of **4** is weaker than that in **5**,[223] which does not correlate with the relative bond lengths computed at the DFT(B3LYP)/MM level (see Figure 7).

The calculated reduction potential for the conversion **4** → **5** is sensitive to the chosen model, QM region, and protonation state. The DFT(B3LYP)/CHARMM values range between −2.28 and −1.04 V, relative to a standard hydrogen electrode,[161,162] and are comparable to the values obtained by QM(DFT)-only calculations.[141,143,226] While the mechanism of electron transfer was studied,[76] the barrier for this process has not yet been calculated due to the immense complexity of the problem. However, judging from the significant protein reorganization during reduction, one may conclude that the process cannot be facile,[162] thus conforming to experimental inferences that this is the rate controlling step in the CYP101 cycle.[228]

3.4.1. Bonding Features of Oxy-Ferrous (4) and Ferric Peroxo (5) Complexes

As mentioned above, the bonding in **4** and **5** is more complex than the orbital diagrams in Figure 3 suggest. Indeed, the Fe−OO bonding in type-**4** complexes has been a focus of a longstanding debate, ever since Pauling and Coryell[229] measured the magnetic susceptibility of the oxy-ferrous complex of hemoglobin and found it to be diamagnetic. Pauling suggested a model whereby $PorFe^{II}$, in a singlet state, binds $^1O_2(^1\Delta_g)$ in a coordinative dative bond, involving the lone pair on O_2 and the empty d_{z^2} orbital of the ferrous ion. On the other hand, Weiss[230] proposed another model based on spectroscopic and chemical behavior of model oxy complexes, especially their tendency to dissociate to $Fe^{III} + O_2^-$. In his model, Fe^{II} donates one electron to O_2 and the two radicals couple to a singlet pair. A third model that was

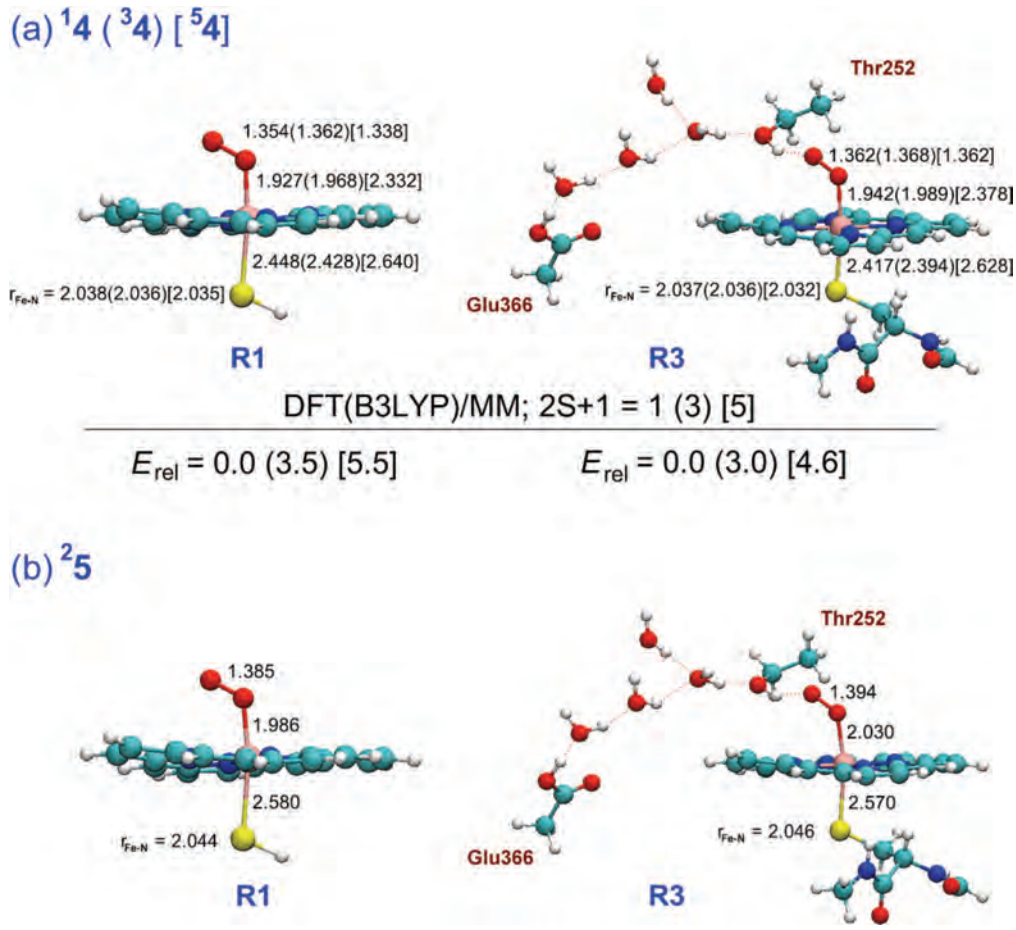

Figure 7. DFT (B3LYP/B1)/MM optimized geometries (Å) of **4** (oxy-ferrous) and ^{2}**5** (ferric peroxo) using the Por,SH (R1) and Por,ext-SCys (R3) models.[161,162] Relative energies for the spin states of **4** are given in kcal mol^{-1}.

initially suggested by McClure[231,232] involves singlet coupling of the triplet PorFe^{II} and $^3O_2$ moieties into a double Fe═O bond.

The DFT(B3LYP) and DFT(B3LYP)/MM calculations for **4** yield an open-shell singlet state configuration, with two unpaired electrons, one in a π_{yz}(FeO) orbital with a dominant iron character and the other one in a π^*_{yz}(FeO) orbital largely on the dioxygen ligand,[161,162] as shown in Figure 8a. As such, the DFT results seem to support the Weiss model for bonding: PorFe^{II} donates one electron to the π^*_{xz}(OO) orbital which becomes doubly occupied and coordinates to Fe via a dative σ-bond, maintained by overlap between the filled 2p AO on oxygen and the vacant d_{z^2} orbital on iron. At the same time, the single electron in the d_{yz} orbital of PorFe^{III} couples with the single electron in the π^*_{yz}(OO) orbital to form a singlet-pair: a weakly coupled π-type bond (described by an open-shell singlet with single electron occupancy in both a π_{yz}(FeO) and a π^*_{yz}(FeO)). The weakness of the bond is further appreciated from the fact that the corresponding triplet state is only 3.5 kcal mol^{-1} higher in energy than the open-shell singlet ground state.

Since open-shell singlet states in DFT have to be considered with some care (the open-shell singlet formulation of DFT involves one determinant and refers to an indefinite spin state), it is advisable to test the DFT results by using correlated ab initio wave function theory. This has been done recently through CASSCF/MM calculations of the oxy-Mb complex which demonstrated indeed that all the properties calculated with DFT/MM and CASSCF/MM were virtually identical and that spin projection of the DFT/MM wave

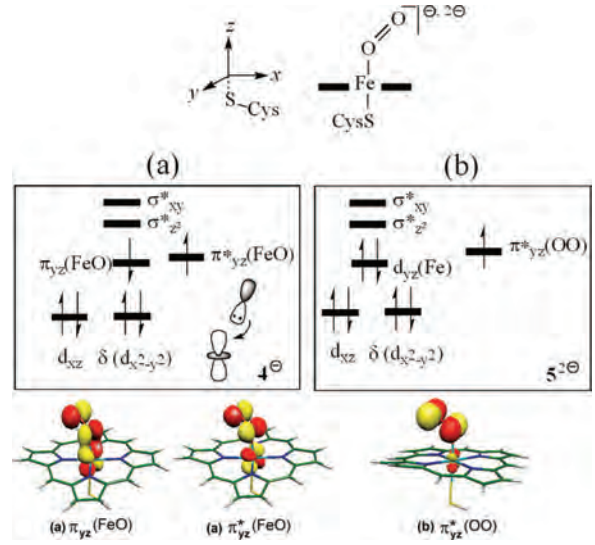

Figure 8. (a) Orbitals and their occupancies in ^{1}**4**. Shown are the singly occupied π-type orbitals and a scheme of the dative σ_{FeO} bond, made by donation from the oxygen filled p orbital to the vacant d_{z^2} iron orbital. (b) Orbitals and their occupancies in ^{2}**5** formed by reduction of **4**. Shown is the singly occupied π^*(OO) orbital.[161,162]

function gives the same singlet-to-triplet energy gap as CASSCF/MM. Furthermore, the CASSCF/MM wave function could be transformed[79] to an open-shell singlet configuration analogous to the DFT result in Figure 8a. In fact, using natural Kohn−Sham orbitals for the DFT(B3LYP)/MM species gives rise to virtually the same electronic

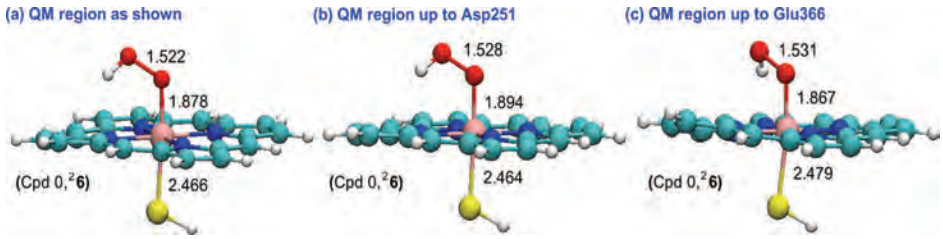

Figure 9. DFT(B3LYP/B1)/MM optimized structures (Å) of Cpd 0 in the doublet ground state, ^{2}**6**:[78,159] (a) QM region as shown; (b) QM region, which includes Thr_{252}, W_{901}, and Asp_{251}; (c) QM region, which includes Thr_{252}, W_{523}, W_{566}, W_{687}, W_{902}, and Glu_{366}.

population as the CASSCF/MM wave function,[79] thus further showing that DFT(B3LYP) captures the chemical essence of the oxy-ferrous complex. Hence, the best description of this species in terms of oxidation states is indeed $Fe^{III}-O_2^-$, with a σ_{FeO} bond and a weakly coupled electron pair in the π^*(OO)-d_{yz} orbitals, precisely as in the Weiss model. The σ_{FeO} bond is formed by electron pair donation from the doubly occupied orbital of the coordinated oxygen atom to the vacant d_{z^2} orbital on Fe, as schematized in Figure 8a. Furthermore,[79] the CASSCF/MM results were found to differ significantly from the gas-phase CASSCF results, highlighting the impact of the protein on the electronic structure. Thus, in the gas phase the oxy-ferrous complex is quite far from the Weiss model, exhibiting more covalency as in the McClure model, and it is the protein and its bulk polarity that drive the structure increasingly more toward the $Fe^{III}-O_2^-$ direction by stabilizing the negative charge on the terminal H-bonded oxygen. This sensitivity to the protein environment suggests that oxy-ferrous complexes of different heme proteins (and model systems) may have different characters of the Weiss-type bonding, thus behaving like an "electronic chameleon".

Once the orbital diagram for **4** in Figure 8a is admitted, the electronic structure of **5** is simple and corresponds to Figure 8b, with one unpaired electron in the π^*_{yz}(OO) orbital. This singly occupied orbital has an antibonding interaction with the d_{yz} orbital, which should be sensitive to H-bonding and bulk polarity effects, even more so than in the oxy-ferrous case. Indeed, a very recent DFT(B3LYP)/MM investigation showed that the ferric-peroxo species of nitric oxide synthase (NOS) forms a very strong H-bond with the positively charged arginine substrate which strongly modifies its electronic structure—the singly occupied orbital is now an almost pure iron d_{yz} orbital while the filled orbital made from the bonding combination of π^*_{yz}(OO) and d_{yz} (labeled as d_{yz}(Fe) in Figure 8b) becomes a low lying orbital describing the partially formed O···H bond.[69]

3.5. Cpd 0: The Ferric-Hydroperoxide Complex (6) and its Formation from 5

Cpd 0 (**6**) has been generated as a transient by cryoradiolytic reduction of the oxy-ferrous complex of CYP101 and detected by EPR[176] and more recently also by resonance Raman spectroscopy.[223,233] The structure of Cpd 0 was determined for the analogous CPO enzyme, by means of a combined X-ray crystallography and DFT(B3LYP/B1)/MM study.[67] The corresponding Cpd 0 in a mutant (M69A) of Cyt c552 was also recently identified by EPR and electronic spectroscopy.[234] The EPR studies indicate that the ground state is a $^2\Pi_{yz}$ state, ^{2}**6**, with a single electron in the π^*_{yz} orbital (Figure 3e), and the combined experimental-theoretical study of CPO Cpd 0 also shows that the observed structural parameters fit only those of the doublet spin state. A doublet ground state ^{2}**6** was in fact anticipated by early DFT(B3LYP)-only calculations[225] and confirmed by subsequent similar work[44,140,142,226] and an early DFT(ROB3LYP)/MM study.[157] A key feature of ^{2}**6** in all DFT-only calculations is the characteristic hydrogen bond between the proton of the distal OH group and one of the nitrogen atoms of the porphyrin ring. However, larger QM models, which include Glu_{366}, Asp_{251}, Thr_{252}, and crystal water molecules (Wat_{901}, Wat_{902}, Wat_{903}), revealed that this internal hydrogen bond can be replaced by an external one where the OH group points upward, donating a hydrogen bond to a water molecule (W_{901}) and accepting one from Thr_{252}. The same conformations were reported in the DFT(ROB3LYP)/MM study[157] and in more recent DFT(B3LYP)/MM studies.[78,159]

The DFT(B3LYP/B1)/MM geometry of ^{2}**6** for CYP101 is shown in Figure 9 for three different QM regions, i.e., the bare heme moiety (Figure 9a), the heme moiety plus the residues and crystallographic water molecules of the Asp_{251} channel (Figure 9b), and the Glu_{366} channel (Figure 9c). The QM/MM calculations of these three QM regions yield quite similar distances, Fe−O (1.878; 1.894; 1.867 Å), O−O (1.522; 1.528; 1.531 Å), and Fe−S (2.466; 2.464; 2.479 Å), which are in good accord with the experimentally determined parameters for CPO Cpd 0 (1.82, 1.50, and 2.4 Å, respectively).[67] Interestingly, the computed Fe−O bond length in Cpd 0 is shorter than that in the corresponding oxy-ferrous complex (Figure 7), and here this is in accord with the conclusion from resonance Raman spectroscopy that the Fe−O bond is stronger in Cpd 0.[223,233] The three structures in Figure 9 show internal H-bonding between the OH group of the Fe-OOH moiety and one nitrogen atom of the porphyrin ring. However, according to a recent DFT(B3LYP)/MM study of CPO Cpd 0,[66] the conformation wherein the OH group maintains a strong H-bond with Glu_{183} is more stable in CPO, and the barrier between the two conformations is rather small (<7 kcal mol^{-1} with the larger basis set).

Figure 9 does not show the geometries of higher spin states. As already reviewed,[32] the quartet and sextet states are significantly higher in energy than the doublet state. The most recent extensive MR-CI/MM calculations[78] of Cpd 0 for CYP101 give a doublet-quartet separation of 10.6 kcal mol^{-1}, in close agreement with the DFT(B3LYP)/MM results[159] and with earlier studies.[142,235]

3.6. The Protonation Mechanism and Generation of the Ultimate Oxidant, Cpd I (7)

Formation of Cpd I requires two protonations (**5** → **6** → **7**). This involves translocation of the proton from the bulk solvent into the active site and reorientation of the hydrogen-bond network to facilitate the migration of the proton. It is thus important to identify the aqueducts in the enzyme, along with the titratable amino acids that can adopt different protonation states, and thereby facilitate the proton transfer.

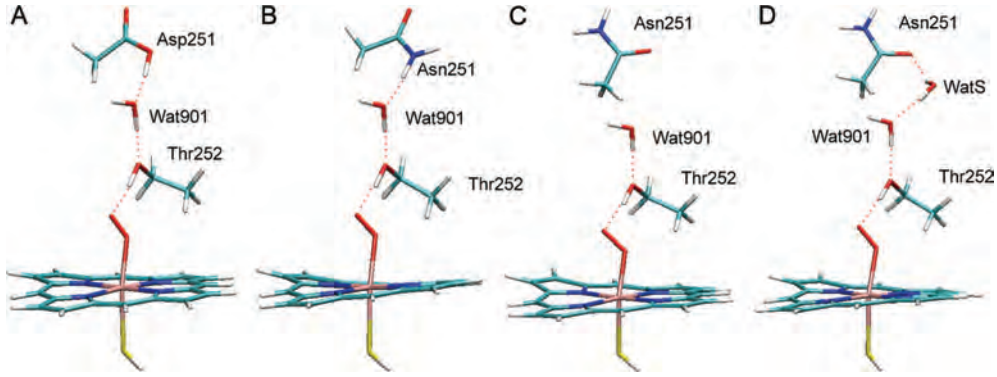

Figure 10. QM-models A−D for DFT/MM studies of the protonation of ^{2}**5** to ^{2}**6**, in the wild type (A) and the D251N mutant of CYP101 with the different Asn_{251} conformations (B−D). WatS is an added water molecule. Reprinted with permission from ref 161. Copyright 2008 American Chemical Society.

As already discussed, the protonation machinery of P450 enzymes is generally thought to involve an acid−alcohol pair and a water network, which shuttles the proton in a Grotthuss type mechanism.[236] In the case of CYP101, possible candidates are Asp_{251}-Thr_{252} and/or Glu_{366}-Thr_{252}, along with active-site water molecules (Wat_{523}, Wat_{566}, Wat_{687}, Wat_{901}, and Wat_{902}).[175,182,219,237] An alternative path involves Arg_{299}, which participates in a salt bridge with the propionate-A side chain (7-propionate) of the heme; it has been postulated to function as a gate that opens wide by a conformational change and thereby allows water molecules in.[238] These many potential channels make the problem very complex. Adding to this complexity is the coupling between reduction and protonation, as indicated by significant kinetic solvent isotope effects (KSIE) that are observed already for the reduction of ^{1}**4**.[182,239−241] The D251N mutant exhibits a very large KSIE of 10,[182] which implies Asp_{251} as a key acid in the protonation process. Indeed, Asp_{251} has access to the bulk water, and it can control the proton shuttle through a "carboxylate switch": deprotonated Asp_{251} blocks the water entry, since it is engaged in salt bridges (Arg_{186}; Lys_{178}), but upon protonation, it may flip to the inside of the active site and open the channel to water molecules.[178,182] The relevance of Glu_{366} does not seem as compelling, considering the fact that mutation experiments[242] showed little change of activity when replacing Glu_{366} by Met. Moreover, the Glu_{366} residue does not have direct connection with the bulk solvent, such that there is no obvious mechanism of reprotonating this residue after transferring its proton to the heme-oxy moiety.

*3.6.1. First Protonation Step: Conversion of (***5***) into Cpd 0 (***6***)*

Early DFT-only studies of the protonation of ^{2}**5** to form ^{2}**6**[45,235,243,244] provided insight into the mechanism but also showed that protonation cannot be studied with simple model systems; different models yield disparate results for the exothermicity/endothermicity of the process and its barriers. Thus, with a calculated proton affinity of 422 kcal mol^{-1}, ^{2}**5** would even accept a proton from a nearby water molecule,[235] but the energy of the process highly depends on the number of water molecules, as well as a correct choice of the residues near the water molecules.[243,244] A DFT(ROB3LYP)/MM study[157] considered only the process originating from Glu_{366} and reported a small barrier of 4.0 kcal mol^{-1}.

As outlined above, however, the Asp_{251} channel provides the most likely pathway for proton delivery. Therefore, a recent DFT(B3LYP)/MM study focused on this channel in the wild type (WT) and mutant CYP101 enzymes.[161] The four models A−D that were investigated are shown in Figure 10. According to MD calculations in an earlier study,[159] Asp_{251} can rotate rather easily out of its salt bridge with Arg_{186} (at an energetic cost of less than 4 kcal mol^{-1} for twists up to 40°), and it should thus be dynamically accessible to protonate it from bulk solvent. The wild-type enzyme model A thus employed protonated Asp_{251} as proton source. Three models B−D were used for the D251N mutant: B was generated from A by manually replacing Asp by Asn, C was taken from the MD trajectory of B showing a flip of the Asn side chain within 45 ps to the outside of the pocket (due to repulsion with Arg_{186}), while D was generated from C by adding a water molecule, WatS, to the space generated by the flipped Asn.

The mechanism for the WT enzyme is depicted in Figure 11, along with relative energies of the "reactant complex" ($\mathbf{5}_{RC}$), transition state ($\mathbf{5}_{TS}$), and "product complex" ($\mathbf{6}_{PC}$). The barrier for protonation is very small and hardly sensitive to the basis set used, being 2.5 kcal mol^{-1} with the largest basis set (def2-TZVP, 6-311++G(2d,2p)) and 1.2 kcal mol^{-1} with the lowest basis set (B1). The small barrier agrees well with the short lifetime of this species and with the fact that the reduction of the oxy-ferrous complex **4** exhibits KSIE, which means that the formation of **5** and its protonation are almost simultaneous.[239] The generation of Cpd 0, **6**, is seen to be exothermic by 33.6 kcal mol^{-1}, quite close to the result of a large-model DFT-only calculation reviewed before.[32] Indeed, the transition state, $\mathbf{5}_{TS}$, which involves a synchronous proton shuttle from Asp_{251} all the way to the Fe-OO moiety, is "early", in accord with the highly exothermic reaction and low barrier. Interestingly, **5** has been implicated as an additional oxidant in deformylation reactions (see review of mechanistic aspects[22]). However, with a barrier of only 2.5 kcal mol^{-1} for collapse to Cpd 0, it is unlikely that **5** can be responsible for deformylation in the WT enzyme, unless this barrier is significantly larger, due to conformational changes in the protein.

For the D251N mutant, model B yields a very low barrier (2.2 kcal mol^{-1} with the largest basis set) for proton transfer from the NH_2 side chain of Asn_{252} to the FeOO moiety via Wat_{901} and Thr_{252} (see Figure 10), which was attributed to the acidifying effect of the Arg_{186} residue.[161] However, model B is hardly realistic, since classical MD simulations give a very low barrier (<2 kcal mol^{-1}) for the flip of the Asn_{251} side chain that leads to model C. The results for model C are given in Figure 12. Since the flipped Asn_{251} has no good way to deliver a proton, the transfer occurs from Thr_{252}, which becomes an anion: the corresponding barrier is

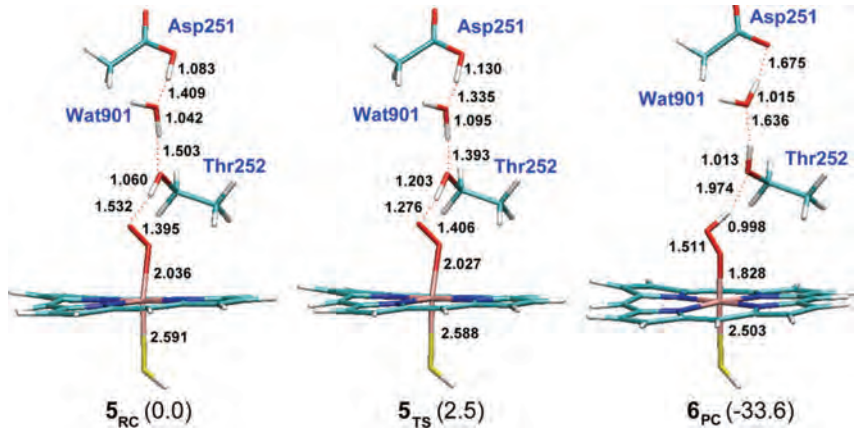

Figure 11. DFT(B3LYP/B1)/MM optimized geometries (Å) and relative energies (kcal mol^{-1}) of $\mathbf{5}_{RC}$, $\mathbf{5}_{TS}$, and $\mathbf{6}_{PC}$, for the proton transfer that leads to the formation of Cpd 0 (**6**) in the WT enzyme (model A in Figure 10).[161] Relative energies refer to the largest basis, def2-TZVP(Fe)/6-311++G(2d,2p) (rest).

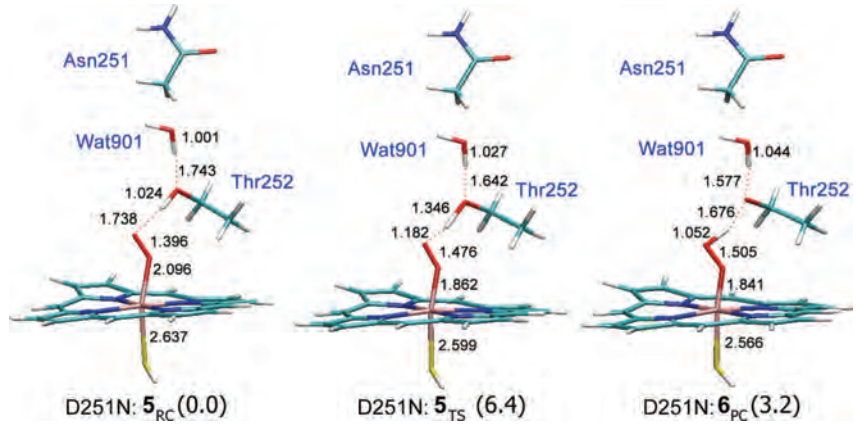

Figure 12. DFT(B3LYP/B1)/MM optimized geometries (Å) and relative energies (kcal mol^{-1}) of $\mathbf{5}_{RC}$, $\mathbf{5}_{TS}$, and $\mathbf{6}_{PC}$, for the proton transfer that leads to the formation of Cpd 0 (**6**) in the D251N mutant (model C in Figure 10).[161] Relative energies refer to the largest basis, def2-TZVP(Fe)/6-311++G(2d,2p) (rest).

significant (6.4 kcal mol^{-1}), the reaction is endothermic, and the transition state is advanced. No facile path for reprotonation of the Thr_{252} anion was found, however, and it may thus well be that an alternative route is actually preferred for model C, namely back-flip to B and subsequent proton transfer in B, which requires an overall activation of ca. 10 kcal mol^{-1}.[161]

A variant of C is D, where an additional water molecule (WatS, Figure 10) can enter the pocket from the bulk and mediate the proton transfer. This process is mildly exothermic (−6.3 kcal mol^{-1} at the highest level), but the barrier remains significant, 7.5 kcal mol^{-1}.[161] It is conceivable that the resulting system with an OH^- anion (from WatS, stabilized by H-bonds) can be reprotonated from bulk solvent without undue activation (not studied). In summary, the DFT(B3LYP)/MM study of several realistic models of the D251N mutant indicates sizable overall barriers for the proton transfer **5** → **6**. Hence, the lifetime of **5** will be significant in the D251N mutant, and the KSIE might be large, especially for model D, where the generated hydroxide anion of WatS will have to be reprotonated from bulk water.

*3.6.2. Second Protonation Step: Conversion of Cpd 0 (**6**) into Cpd I (**7**)*

EPR/ENDOR studies of the T252A mutant of $P450_{cam}$ by Davydov et al.[176] showed that Cpd 0 is still formed but no camphor hydroxylation occurs, thus suggesting that this mutation prevents the protonation of Cpd 0 and the formation

Scheme 3. Schematic Consensus Mechanism of the Conversion of Cpd 0 (6) to Cpd I (7)

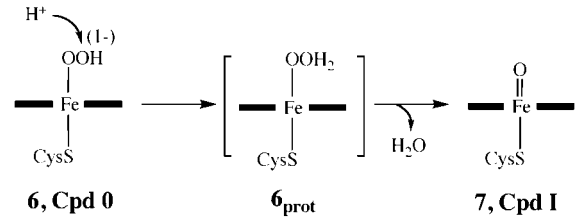

of the ultimate oxidant, presumably Cpd I. The Cpd I formation in P450 enzymes is generally assumed to follow the Poulos−Kraut mechanism that is well established in peroxidases,[245] where the proton is added to the distal oxygen of Cpd 0 followed by water splitting (see Scheme 3). The species labeled as $\mathbf{6}_{prot}$ is not necessarily considered to be stable but perhaps a transition state en route to Cpd I (**7**).

Early attempts to study this second protonation process by means of DFT-only calculations of the isolated molecule suggested that Cpd 0 (**6**) is a very strong base with a proton affinity of 334 kcal mol^{-1},[235] or 330.1 kcal mol^{-1},[142,143] and that it is thus expected to accept a proton and collapse to Cpd I without a barrier.[45,144] A somewhat larger model[45] also gave a highly exothermic reaction and no definite barrier. An early DFT(ROB3LYP)/MM study[157] indicated a highly exothermic process as well, but no precise data appear in the paper to assess the cause of the exothemicity. By contrast, a more recent study of a large model of 96 atoms, which

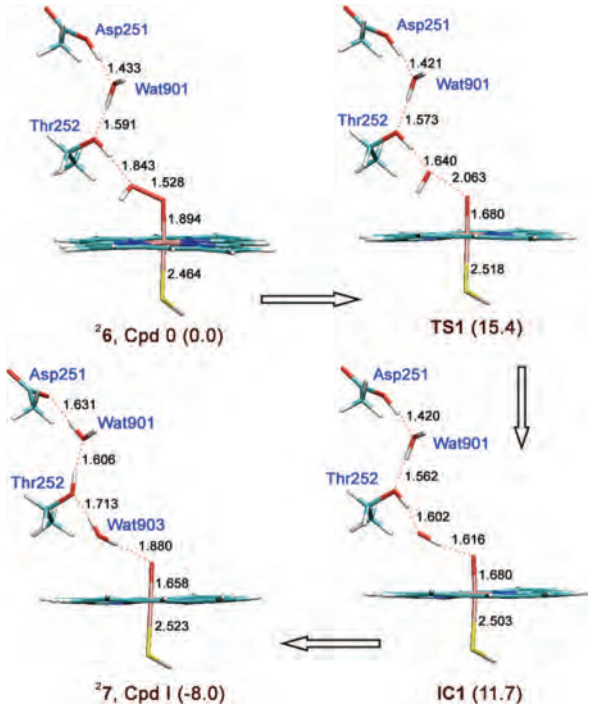

Figure 13. DFT(B3LYP/B1)/MM optimized geometries (Å) of Cpd 0 (^{2}**6**), TS1, IC1, and Cpd I (^{2}**7**). Relative energies (kcal mol^{-1}) refer to the largest basis set employed: LACV3P++**(Fe)/6-311++G** (rest). Reprinted with permission from ref 159. Copyright 2006 American Chemical Society.

included Asp_{251}, Thr_{252}, Glu_{366}, and the water networks connecting the two acids to the FeOOH moiety,[226] suggested for the first time that the process is almost thermoneutral and that $\mathbf{6}_{prot}$ may be a true intermediate. A significant barrier was found for the formation of $\mathbf{6}_{prot}$ as well as for its subsequent water splitting step.

This spectrum of results was clearly confusing and motivated a recent DFT(B3LYP)/MM study of CYP101[159] that addressed both the Glu_{366}-Thr_{252} and Asp_{251}-Thr_{252} channels. The Glu_{366}-Thr_{252} channel indeed gave the mechanism shown in Scheme 3 and located in the preceding model study.[226] However, the $\mathbf{6}_{prot}$ intermediate was found to be unstable at the DFT(B3LYP)/MM level, lying >20 kcal mol^{-1} above Cpd 0 and having a very small barrier (3−4 kcal mol^{-1}) for collapse to Cpd I. The Asp_{251}-Thr_{252} channel did not yield this mechanism at all. In any event, with such energetics, this mechanism does not seem to be the likely candidate for the formation of Cpd I.

The second mechanism considered originates from the Asp_{251}-Thr_{252} channel, and its key features are shown in Figure 13. It is not driven by initial protonation but rather starts with homolysis of the O−OH bond. As OH departs (see IC1), two events happen simultaneously: (i) an electron from the porphyrin a_{2u} orbital is shifted to the departing OH radical, converting it to OH^-, and (ii) simultaneously Thr_{252} protonates the hydroxide anion and gets itself protonated by Wat_{901}. Thus, the mechanism involves proton-coupled electron transfer (PCET), which is made possible by the facile proton delivery along the hydrogen bonding network in the Asp_{251}-Thr_{252} channel and the "push effect" of the thiolate that promotes the electron shift. The barrier for the O−OH cleavage was calculated to be 15.4 kcal mol^{-1} (at the highest level). The intermediate IC1 is a shallow minimum with standard QM/MM options (using the QM region shown in Figure 13). Inclusion of Arg_{186} into the QM region facilitates the protonation by acidifying Wat_{901}, and as a result, the IC1 minimum disappears in the largest QM/MM model considered. The analogous mechanism in the Glu_{366}-Thr_{252} channel gives a similar initial barrier but proceeds in a stepwise manner. It was not pursued further because Glu_{366} is not connected to the bulk water and can thus not easily be reprotonated (see above) which would be necessary in a complete catalytic cycle. In both mechanisms, the formation of Cpd I from Cpd 0 is either almost thermoneutral or slightly exothermic, with a "best" estimated reaction energy of about −8 kcal mol^{-1}. At this stage we cannot say whether the small exothermicity is a general feature or one that is specific to $P450_{cam}$. Nevertheless, the PCET mechanism seems to carry over to other enzymes. Thus, in subsequent QM/MM work, the synchronous PCET mechanism for Cpd I formation has also been found in CPO[66] and in NOS.[69] In all these cases, PCET proceeds by a hybrid homolytic−heterolytic mechanism, and this hybrid nature lowers the O−O cleavage barrier well below that of the pure homolytic mechanism.[66]

What remains to be studied for the wild-type $P450_{cam}$ enzyme is the process for generating the higher spin states of Cpd I, ^{4,6}**7**. Corresponding DFT(B3LYP)/MM calculations for CPO gave large barriers of the order of 20 kcal·mol^{-1}.[66] If this is true also for P450, then we might conclude that the ^{4,6}**7** species are not formed directly but must be generated by intersystem crossing from ^{2}**7**.

*3.6.3. Conversion of Cpd 0 (**6**) into Cpd I (**7**) in the T252X Mutants*

The mutation of Thr_{252} is known to have an adverse effect on the activity of CYP101.[175] Replacement of Thr_{252} by a small aliphatic residue in mutants such as T252A and T252G leads to an uncoupling of O_2 consumption from camphor hydroxylation, since most of the consumed O_2 is converted to H_2O_2 (95% or more). Both hydroxylation and uncoupling are observed in the T252V mutant, to a similar extent, whereas hydroxylation is the dominant channel in the T252S mutant (85%) and the only channel in the wild-type enzyme (100%). The latter trend remains true when the Thr_{252} side-chain OH group is replaced by a methoxyl group (which, however, slows down the reaction significantly). The double mutant D251N/T252A as well as the single mutant D251N also perform hydroxylation, albeit at a reduced rate compared with the wild-type enzyme. These experimental findings clearly indicate that the Thr_{252} residue plays a crucial mechanistic role and influences the ratio of hydroxylation vs uncoupling products. It is also known that some T252X mutants retain partial oxygenation activity. For example, the T252A mutant is still capable of epoxidizing the double bond of 5-methylenylcamphor,[183] which has been interpreted to arise from reactivity of Cpd 0, acting as an oxidant toward the more reactive substrates if Cpd I formation is suppressed (recall the more favorable uncoupling in the T252A mutant, see above). Since the crystal structure of the T252A mutant contains a water molecule near the O_2 binding site that is not present in the wild-type enzyme,[184,185] it has been suggested that solvent participation affects the reactivity, in particular the competition between Cpd I formation and uncoupling.

To address these issues, the T252X mutants with X = serine, valine, alanine, and glycine were studied by DFT(B3LYP)/MM calculations.[246] Starting geometries for Cpd 0 were taken from a crystal structure of the wild-type enzyme (pdb: 1DZ8) that had been used in previous QM/

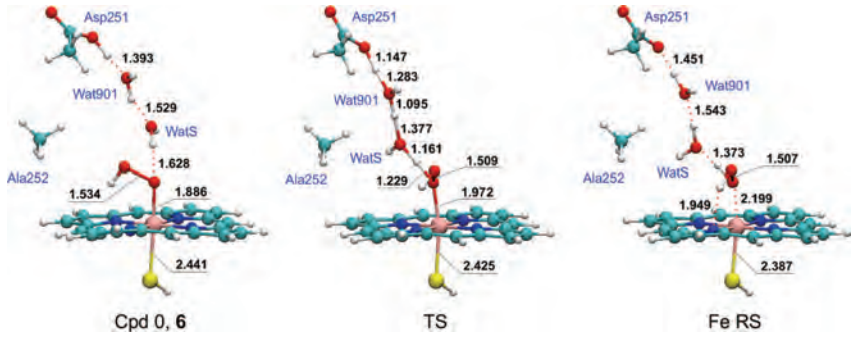

Figure 14. DFT(B3LYP/B1)/MM optimized geometries (Å) for the species in the uncoupling reaction of the T252A mutant in the presence of an extra water molecule, WatS. Reprinted with permission from ref 246. Copyright 2009 American Chemical Society.

MM work, and mutant structures were generated by manually replacing the threonine residue by the desired amino acid X and subsequent relaxation and equilibration. The crystal water molecule Wat_{901} that is located in the X-ray structure, of the wild type (WT) enzyme, between Thr_{252} and Asp_{251} remains in this position during classical 2 ns MD simulations, both in the WT enzyme and in each of the four mutants. By contrast, an additional water molecule, WatS, placed manually into the vicinity of residue 252 quickly escapes from this region during classical MD in the case of the WT enzyme and the T252S mutant, whereas it remains put during the full 2 ns simulation in the case of the T252V, T252A, and T252G mutants. The corresponding substitutions obviously generate enough "empty space" to accommodate an extra water molecule so that the latter three mutants should be modeled with inclusion of WatS.

The conversion of Cpd 0 to Cpd I is computed to proceed by essentially the same mechanism in the WT enzyme and in the four mutants. As discussed above (see section 3.6.2), the first and rate-limiting step involves a homolytic−heterolytic cleavage of the O−O bond followed by a proton-coupled electron transfer. The computed barrier is in the range of 14−17 kcal mol^{-1} for all five systems and is not affected much by the presence or absence of WatS in the T252V, T252A, and T252G mutants. The uncoupling reaction (formation of hydrogen peroxide) is found to be a concerted reaction in the WT enzyme, with a rather high barrier of 27 kcal mol^{-1}, which reflects the large distortions that are necessary to establish a proton delivery path from Asp_{251} via Wat_{901} and Thr_{252} to the proximal (rather than the closer distal) oxygen atom of the FeOOH moiety. The alternative two-step mechanism (Fe−O cleavage first followed by proton transfer) is even less favorable because of the strength of the Fe−O bond. In the mutants, in the absence of WatS, the uncoupling reactions remain concerted and difficult to achieve, with barriers between 23 and 29 kcal mol^{-1}. However, in the presence of WatS, a much more favorable hydrogen bond network is established in the Asp_{251} channel for the T252V, T252A, and T252G mutants, with uncoupling barriers of 19, 12, and 12 kcal mol^{-1}, respectively. The corresponding optimized geometries and reaction profiles are illustrated for the T252A mutant in Figures 14 and 15, respectively.

In summary, the DFT(B3LYP)/MM calculations for the T252X mutants agree with the experimental findings and offer a consistent mechanistic scenario. In the WT enzyme, Cpd I formation is favored, since its rate-limiting barrier is 13 kcal mol^{-1} lower than that for uncoupling. The difference is reduced to 7 kcal mol^{-1} in the T252S mutant. In the case of the other three mutants, an extra water molecule enters

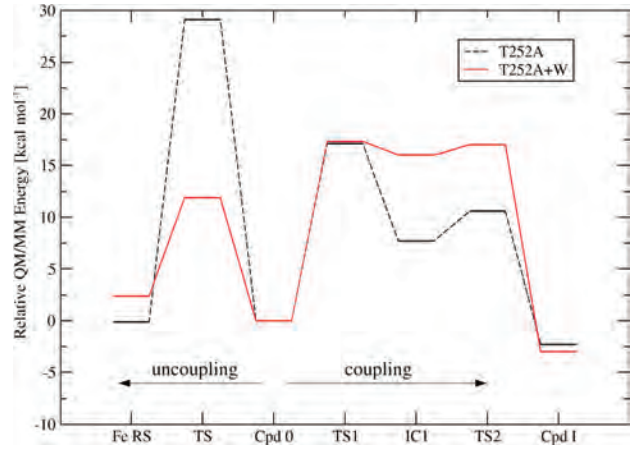

Figure 15. DFT(B3LYP/TZVP)/MM energy profile for coupling and uncoupling reactions with and without an extra water molecule in the T252A mutant. Reprinted with permission from ref 246. Copyright 2009 American Chemical Society.

the active site and lowers the activation energy for uncoupling significantly. With the additional water molecule, Cpd I formation and uncoupling have similar barriers in the T252V mutant, and uncoupling becomes favored in the T252A and T252G mutants. These DFT(B3LYP)/MM thus confirm the hypothesis that proton delivery by solvent water is responsible for the uncoupling reaction in some mutants.

*3.6.4. Conversion of Cpd 0 (**6**) into Cpd I (**7**) in the D251N Mutant*

As mentioned above, it is known experimentally[182] that the D251N mutant does not undergo uncoupling but performs hydroxylation of camphor, albeit at a reduced rate (lower by a factor of 30 compared with wild-type $P450_{cam}$). This suggests that the mutant forms Cpd I, but more slowly than the wild-type enzyme. DFT(B3LYP)/MM calculations[247] on the D251N mutant confirm that the barriers for uncoupling are indeed always significantly higher than those for coupling, in agreement with experiment. As in the case of the first proton transfer that leads to Cpd 0 (see section 3.6.1), three models of the D251N active site were used to study the second proton transfer that converts Cpd 0 into Cpd I: the mutated Asn_{251} residue can be directed toward the heme (model I, no flip) or away from the heme (model II, flip), and in the latter case, the reorientation of the Asn_{251} side chain generates enough empty space to hold an extra water molecule (model III, flip with WatS). Classical MD simulations show that model I rearranges spontaneously to model II within less than 400 ps and that the extra water molecule of model III remains stable in the active site during 2 ns of

MD simulation. For all three models, Cpd I formation in the D251N mutant follows the same basic mechanism as in the wild-type case (see section 3.6.2), with initial O−O cleavage followed by proton transfer. The barrier for the initial step is similar in all D251N models (around 14 kcal/mol), but the proton transfer is most facile in model III (not feasible in model II, significantly higher barriers in model I). The proton transfer in model III generates a hydroxide anion (at Wat_{901}) that is not reprotonated easily by neighboring residues (Arg_{186}); however, proton delivery from bulk solvent seems possible by a Grotthuss mechanism via a water network that remains intact during 2 ns of classical MD simulation. In summary, the DFT(B3LYP)/MM calculations show that Cpd I formation in the D251N mutant is feasible only when extra water molecules enter the active site (model III). They reproduce the experimentally observed preference of the mutant for coupling, and the lower hydroxylation activity can be tentatively ascribed to a less facile proton transfer (since the initial O−O cleavage has similar barriers in the wild-type enzyme and in the D251N mutant).

3.7. Cpd I (7): The Ultimate Active Species

As mentioned above, Cpd I is elusive in the native working cycle. X-ray structural evidence for the existence of Cpd I[178] seemed initially very convincing but has subsequently been cast in doubt,[176] although not definitely ruled out. The presence of Cpd I as a transient species was inferred by cryogenic and electronic absorption studies[184,248−250] and from cryogenic EPR/ENDOR spectroscopy of the alcohol product of camphor hydroxylation starting from deuterated camphor at the C^5−H position.[176] Attempts to generate Cpd I using oxygen surrogates such as iodosylbenzene or peracids led usually to the one-electron reduced species, so-called Compound II (Cpd II), and a Tyr radical.[251−254] More recent experiments[250,255] showed how one can optimize the formation of Cpd I, before the heme bleaches due to destruction by the peracid, and observe the characteristic chemistry of Cpd I. Strong but indirect support for the participation of Cpd I was provided by the analogous reactivity of synthetic Cpd I species and P450 toward the same substrates (similar product distribution and stereochemical scrambling).[22] A recent study by Dowers et al.[256] used a surrogate oxygen atom donor to generate the N-oxide derivative of *N*,*N*-dimethyl amines and demonstrated that this leads to hydroxylation of the methyl group of the *N*,*N*-dimethyl amines, thereby strongly implying that the only competent oxidant in the reaction was Cpd I. Nevertheless, the elusiveness of Cpd I, in the working cycle, prompted suggestions for alternative oxidant species, such as Cpd 0,[23,183,257] Cpd II,[258−260] and recently also the perferryl PorFe(V)═O species.[261,262] However, recent experiments, which directly compared the reactivity of Cpd 0 and Cpd I in enzymes and in model systems showed Cpd 0 to be far less reactive than Cpd I, so that in all likelihood the latter is the only oxidant in a working P450 enzyme.[234,263−265] According to computational work (described in more detail below), the same applies to the reactivity of Cpd II,[164] while the perferryl proposal seems at present untenable because of the high energy of this species.[164,266] Furthermore, in a more recent study of Newcomb et al.,[262] Cpd I of the thermophilic enzyme CYP119 was generated by laser flash photolysis (LFP) from Cpd II and was allowed to react with a variety of substrates, thus providing rate constants for substrate oxidations by a P450 Cpd I. The so obtained rate constants were generally 2−3 orders of magnitude larger than the rate constants for the reactions of model Cpd I species with the same set of substrates.[267] While the reaction rate for CYP119 Cpd I, generated in the native working cycle, is still not known, these results already show that a P450 Cpd I generated by LFP is a competent oxidant. As such, the weight of evidence seems to be in favor of Cpd I being the primary if not the sole oxidant species in the P450 cycle.

Because of the uncertainty regarding Cpd I, and because of its status as the primary oxidant of P450, theoretical studies have tended to focus primarily on this species, using QM-only models[28,46−50,141,197,198,266,268−271] and DFT/MM studies of many P450 isoforms[53,55,56,77,78,157,160] and other thiolate enzymes such as CPO[66] and NOS,[68,69] as well as other heme enzymes.[74,272,273] All these DFT-based studies as well as the available correlated ab initio studies[77,78,274] agree on one feature, namely, that the species has two low-lying spin states, doublet and quartet, which are almost degenerate, as already discussed by reference to Figure 3a.

Early DFT-only studies of Cpd I models in vacuum led to controversial results about the electronic ground state.[28,46−50,53,141,197,198,266,268−271] In particular, the results were very sensitive to the choice of the axial ligand. Still, all calculations agreed that Cpd I possesses three singly occupied orbitals, two of which are the π^*_{xz} and π^*_{yz} orbitals (Figure 3a). However, the nature of the third singly occupied orbital appeared to depend on the chosen thiolate model and on the interactions of the sulfur atom with the environment.[28,46−50,53,141,197,198,266,268−271] In cases where the cysteinate was modeled by SMe[46,141,271] or SCys without internal hydrogen bonding,[49] the third unpaired electron resides in a lone-pair orbital on the sulfur, leading to a very large spin density located on the sulfur ligand and hardly any on the porphyrin ring. By contrast, the choice of SH^- or cysteinate with internal hydrogen bonding leads to $^{4,2}A_{2u}$ electronic states where the a_{2u} porphyrin orbital is singly occupied ($\pi^*_{xz}{}^1\pi^*_{yz}{}^1a_{2u}{}^1$), with spin densities distributed evenly between porphyrin and sulfur.[29,50,198] Furthermore, the Fe−S distance was found to depend on the nature of the ligand model used for cysteine and to vary as a result of environmental perturbations, which were modeled by NH···S hydrogen bonding and a dielectric constant to mimic the effect of the electric field of the protein.[50,197,266] The environmental effects on the geometry and spin densities of Cpd I are depicted in Figure 16, which shows results of Ogliaro et al.[50] and Shaik et al.[26] for the system (Por,SH) and those of Rydberg et al.[141] for the system (Por,SMe).

It is seen from Figure 16 that, generally, the FeO moiety bears a spin density (ρ) of around 2, indicative of singly occupied π^*_{xz} and π^*_{yz} orbitals (see Figure 3a). The third spin is distributed on the sulfur and porphyrin groups, in a manner sensitive to the environment and ligand representation. Thus, in the gas phase and without any external interactions, the species has a predominant thiolate radical character; for example, for $^4A_{2u}$ 54% (Figure 16a) or 72% (Figure 16b) of the spin density is on the thiolate ligand. External interactions with a dielectric medium ($\varepsilon = 5.7$) or NH···S hydrogen bonding (Figure 16a) shift spin density from sulfur to porphyrin; in the case of the Por,SH model, the species acquires a predominant porphyrin radical cationic character (74−89% in Figure 16a).[26,50] Further inspection of Figure 16 reveals that, while the Fe═O and Fe−N bonds are not sensitive to the environment, the Fe−S distance is significantly affected by the external perturbation. Thus,

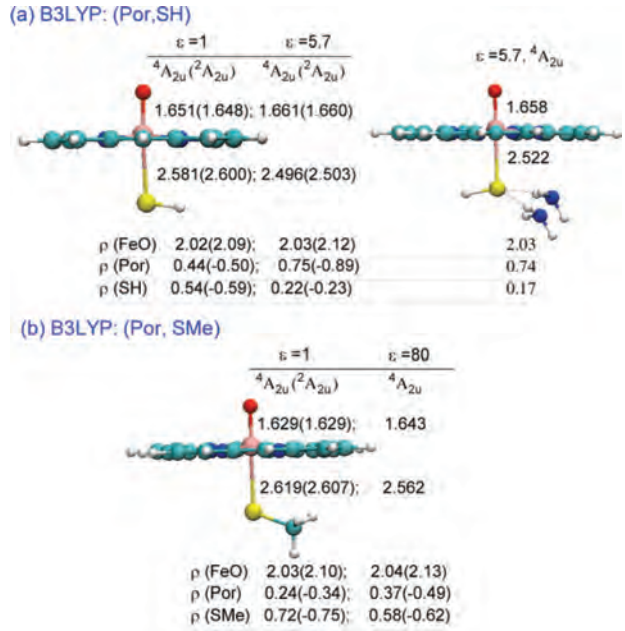

Figure 16. Environmental effects on geometrical parameters (Å) and group spin densities ρ of Cpd I: (a) Model calculations[26,50] with different dielectric constants ε and with hydrogen bonding (NH···S); (b) model calculations[141] with different dielectric constants ε.

relative to the gas phase, the Fe−S distance is shortened, in some cases by almost 0.1 Å.[50,197] In view of this sensitivity of the electronic structure and Fe−S bond length of Cpd I, Ogliaro et al.[197] characterized Cpd I *as a chameleon species* that can change its nature depending on external conditions.[50,197] Later it was shown that an external electric field (EEF) oriented along the S−Fe−O axis can induce these changes or create an exclusive sulfur radical by simply switching the direction of the EEF, thereby further supporting the chameleon nature of the species.[275]

These geometric and electronic changes exerted by the environment, noted initially in DFT model studies that accounted for the environment,[50,197] were confirmed by the DFT(B3LYP)/MM study of Cpd I in the native protein.[53] The first DFT(B3LYP)/MM calculation on Cpd I of CYP101 was published in 2002.[53] It employed three QM regions with different cysteine parts (labeled in Scheme 2 as SH, SMe, and ext-SCys), a few snapshots from equilibrated MD simulations, and three different basis sets. Representative DFT(B3LYP)/MM results obtained for the 29 ps snapshot and the largest basis set are shown in Figure 17a−c and compared with the corresponding gas-phase data. It is apparent that for all QM regions the protein shortens the Fe−S bond and converts the species from a predominantly sulfur radical to a porphyrin cation radical. Thus, irrespective of the ligand model, all the species in the protein environment look very similar to one another. This picture did not change with subsequent studies of CYP101, which all gave Fe═O/Fe−S distances of approximately 1.64/2.55 Å and an electronic structure that is typified by a porphyrin cation radical with some thiolate spin density ≤0.23.[56,77,78,160] As shown in Figure 17d, these results are in general agreement with recent EXAFS (extended X-ray absorption fine structure) structural data[276] and ENDOR spin density data[75] for CPO Cpd I.

Another impact of the protein environment can be seen from Table 1, which summarizes Mössbauer spectroscopic

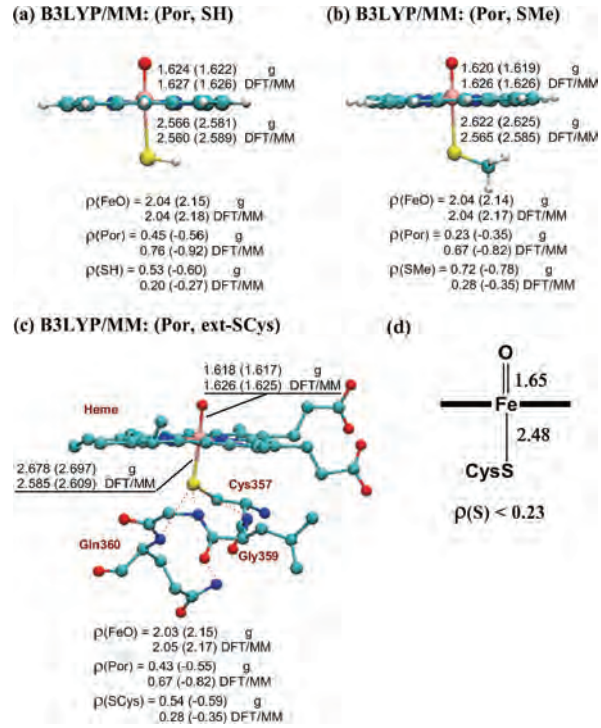

Figure 17. (a−c) Gas-phase and DFT(B3LYP/B1)/MM optimized structures (Å) and group spin density data for three different QM regions.[53] Data refer to $^4A_{2u}(^2A_{2u})$ states. (d) Experimental EXAFS geometry[276] (Å) and EPR-ENDOR spin densities[75] for the analogous CPO Cpd I.

Table 1. DFT(B3LYP)/MM and DFT(B3LYP)-Only Computed[a] Mössbauer Properties—Isomer Shift δ, Quadrupole Splitting ΔE_Q, and Asymmetry Parameter η—of Cpd I Species of CYPs and Analogous Thiolate Enzymes, Including Available Experimental Data for CPO

Cpd I species	δ (mm/s)	ΔE_Q (mm/s)	η	source
CYP101-enzyme	0.10	0.58	0.19	ref 160
CYP101-enzyme	0.13	0.67	0.09	ref 77
CYP101-model	0.09	1.34	0.06	ref 77
CYP3A4	0.11	1.36	0.17	ref 55
Se-CYP101	0.11	1.19	0.08	ref 62
CPO	0.11	0.73	0.32	ref 160
NOS	0.08	1.00	0.21	ref 160
CPO expt	0.15	1.02	n/a	ref 422

[a] DFT-only data refer to gas-phase calculations for a CYP101 model system.

parameters of Cpd I in the gas phase and in the protein. The first two entries correspond to the Por,ext-SCys model of CYP101,[77] while other entries refer to the Por,SH model of CYP3A4[55] and of CYP101, its L358P mutant, and the analogous CPO and NOS enzymes.[160] The largest difference between the protein and the gas phase (see the first three entries) is seen in the quadrupole splitting parameter. However, some changes are also apparent in the isomer shift and asymmetry parameters. The changes of the quadrupole splitting and isomer shift parameters reflect the reduced charge density on the iron center in the protein environment, in line with the increased porphyrin cation radical character, while the larger asymmetry parameter reflects the greater off-planar doming distortion of the porphyrin moiety from planarity in the protein. Similar differences were noted for other spectral properties, such as zero field splitting parameters and EPR/ENDOR parameters.[77] Interestingly, the enzymes that are closer than others to the gas-phase environment are CYP3A4 (4th entry) and NOS (7th entry).

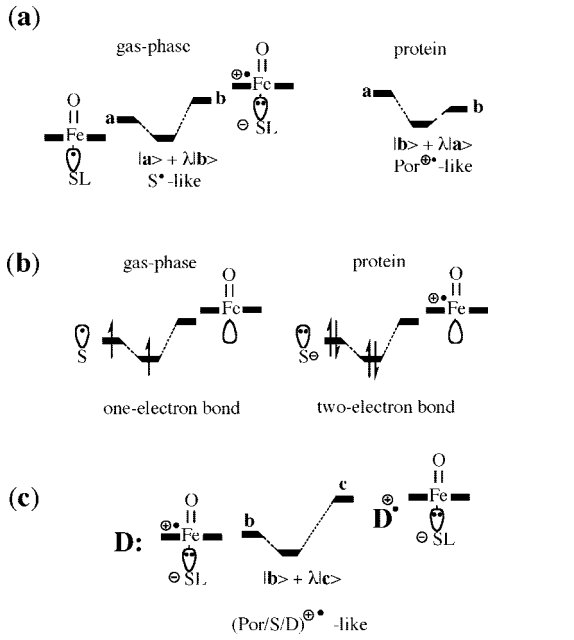

Figure 18. Valence bond modeling of the influence of the protein environment on the electronic structure of Cpd I: (a) Valence bond mixing of the contributing structures. (b) The Fe−S bond orbital, its occupancy, and the type of the Fe−S bond, depending of the environment. (c) The valence bond mixing situation in which an additional electron donor, **D:**, contributes to the electronic structure and participates in the cation-radical manifold.[50,53,198,199] Reprinted with permission from ref 32. Copyright 2005 American Chemical Society.

In the case of NOS vs the CYP and CPO enzymes, this difference was found[160] to correlate with the differences in the orientation of the EEF vector of the protein vis-à-vis Cpd I in a manner analogous to the model study of the EEF effect;[275] thus, whereas, in most enzymes, the EEF vector is aligned approximately with the S−Fe−O axis, in the case of NOS it lies in the porphyrin plane. This finding highlights the importance of the protein field in shaping the properties of Cpd I.

The protein-field effect also has energetic consequences that were reviewed before.[32] Thus, the range of QM energetic stabilization (within the QM/MM energy) of Cpd I by the protein relative to the gas-phase species, for the three ligand models (Por,SH; Por,SMe; Por,ext-SCys), is of the order of 100−150 kcal mol^{-1}. Recalling that the QM energy component in QM/MM includes the effect of the MM charges, these stabilization energies reflect the field effect exerted by the protein on Cpd I, due to the interaction of the partial charges and H-bonding with the active species. Interestingly, the same quantity in CYP3A4 was calculated to be significantly lower (85 kcal mol^{-1}), in accord with the similarity of the corresponding Mössbauer data to the gas phase noted above in Table 1.

3.7.1. A Model for the Chameleon Behavior of Cpd I

The importance of the protein field effect, and its effect on the properties of Cpd I, can be rationalized most simply using the valence bond (VB) models shown in Figure 18.[31,50,53,198,199] The main idea in this model is that the iron-oxo porphyrin cation-radical moiety is a powerful electron acceptor, and therefore, any good electron donor can donate electrons into the porphyrin hole and participate in the electronic structure as part of the cation-radical moiety. In the Cpd I species itself, the good electron donor is the thiolate ligand, and therefore, we can view Cpd I as a composite of the two resonance structures in Figure 18a, one in which the porphyrin is closed-shell and the thiolate is a radical (state $|\mathbf{a}\rangle$) while the other (state $|\mathbf{b}\rangle$) is an ion-pair with a cation radical on the porphyrin and a thiolate anion. In the gas-phase $|\mathbf{a}\rangle$ is below $|\mathbf{b}\rangle$ and the energy separation depends mainly on the choice of the axial ligand, e.g., thiolate or methyl mercaptide, etc. However, a dielectric medium and/or hydrogen bonding interactions will stabilize the ion-pair state $|\mathbf{b}\rangle$, to the extent that it moves below $|\mathbf{a}\rangle$, as evident from the large energetic protein-field effect discussed above. In this case, the mixed state becomes more $|\mathbf{b}\rangle$-like, having more spin density on the porphyrin. This is indeed what the above calculations show in Figures 16 and 17. An alternative way to understand the change in Figure 18a is by noting that the singly occupied "a_{2u}" orbital of Cpd I changes its character from a sulfur-dominated orbital in the gas phase to a porphyrin cation radical in the protein or in the condensed phase.[26,77,197] Generally speaking, the electronic structure in this picture is expected to show sensitivity to nearby additives, which are polar, such as water molecules[50] or charged residues.[160] Moreover, as shown in Figure 18b, the Fe−S bond changes from a weak and long one-electron bond in the gas phase to a stronger and shorter two-electron bond in the protein. Therefore, Cpd I is a mixed-valent state and as such, its Fe−S distance and electronic properties depend on the hydrogen-bonding network and polarity of the surrounding enzyme.

However, as shown in Figure 18c, thiolate is not the only donor in the protein environment. There may be other electron donors, labeled generally as D: (with an electron pair in a donor orbital). These donors may be other protein residues or the substrate itself.[199] In such an event, we can think of an additional resonance structure, where the external donor molecule/moiety donates one electron to Cpd I, leading to D$^{\bullet+}$/Cpd II. The mixing of the two structures now creates a new hybrid state, where the cation radical moiety will be spread over the sulfur, the porphyrin, and the D moieties, i.e., (S/Por/D)$^{\bullet+}$. Alternatively, if the donor moiety is a powerful one and there is no delocalization path that allows mixing, the *electronic* structure will tend to localize as D$^{\bullet+}$/Cpd II, altogether. Such an electronic situation is known among peroxidases, where cytochrome *c* peroxidase (C*c*P) involves a Cpd II and Trp$^{\bullet+}$, whereas ascorbate peroxidase (APX) has a normal Cpd I, due to subtle changes in the proximal side of the active site.[196,272] By contrast, the chameleon-like behavior with delocalization of the cation radical species over a few moieties has recently been observed computationally in NOS, where Cpd I, the arginine substrate, and the cofactor H_4B seem to share the cation radical.[69] Moreover, this phenomenon has recently been postulated to occur in the P450 isoform called P450 StaP (CYP245A1),[195] which has been confirmed by DFT(B3LYP)/MM computations.[58]

The DFT(B3LYP)/MM spin density distributions and singly occupied orbitals of the complex of P450 StaP Cpd I with the substrate chromopyrollic acid (CPA) are shown in Figure 19. It is seen that, in all three situations considered, the cation radical is distributed over Por, sulfur, and CPA. CPA participates through the indolic moiety, while the Por/sulfur moieties participate through the normal a_{2u} orbital. When the His_{250} residue is protonated in its distal side, in Figure 19a, the spin density on CPA is small (0.23), and when it is protonated at the proximal side, in Figure 19b,

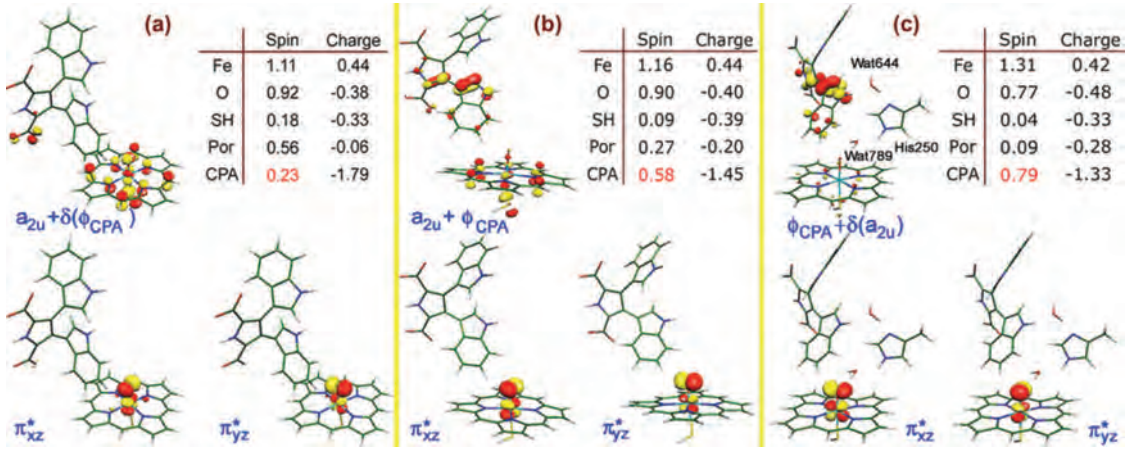

Figure 19. Electronic structures and spin densities of Cpd I of P450 StaP with the substrate, chromopyrrolic acid (CPA) in three situations: (a) His_{250} protonated at the N atom distal to Cpd I and Wat_{789} absent; (b) His_{250} protonated at the N atom proximal to Cpd I and Wat_{789} absent; (c) His_{250} protonated at the N atom proximal to Cpd I and Wat_{789} present. Note that the third unpaired electron is initially (a) almost completely in the a_{2u} porphyrin orbital and finally (c) almost completely on the indole group of CPA. Reprinted with permission from ref 58. Copyright 2008 American Chemical Society.

the CPA spin density rises to 0.58 and the singly occupied orbital acquires significant indolic character. Finally, in Figure 19c, when Wat_{789} (the water molecule that splits off during the formation of Cpd I; see above) is added, the CPA spin density rises to 0.79 and the singly occupied orbital looks virtually indolic. This delocalization of the cation radical species over to CPA is determined by the fact that the protein causes double deprotonation of CPA and holds it by an extensive array of H-bonds. However, in the dianionic state, CPA becomes a powerful enough donor to participate in the cation-radical species, and at the same time, the hybrid $(Por/S/CPA)^{\bullet+}$ character arises due to the delocalization path that involves CPA-Wat_{644}-His_{250}-Wat_{789} moieties and the interaction of the CPA carboxylate with the propionic acid side chain on the porphyrin. Thus, while the chameleon property varies with protein fluctuation, it is still apparent in all conformations.

At the same time, we must recall that not every interaction will make a difference. For example, recent calculations[160] on the L358P mutant of CYP101,[194] where the NH···S interaction due to the NH group of Leu_{358} is severed by mutating it to Pro, showed that the removal of the H-bonding-like interaction has hardly any effect on the geometry and spin density of Cpd I. Similarly, in CYP3A4, the analogous NH···S interaction with the Met_{445} residue was shown to be insignificant.[55] However, the other NH···S interactions (in CYP101 with Gly_{459} and Gln_{360}, and in CYP3A4 with Gly_{444} and Ile_{443}) are important[55] and are responsible for the shifting of the spin density from sulfur to porphyrin, as shown in Figures 16 and 17.

Another case in point is the early DFT(ROB3LYP)/MM study of Cpd I of CYP101,[157] which reported considerable spin density on the propionate side chain A (propionates 7). However, in this case, extensive test calculations using DFT(B3LYP)/MM[55,59,131,163,277] did not find any significant spin density at the propionate groups whenever these are properly screened by the neighboring arginines, *both in the gas phase and in the protein*. This screening makes the propionates poor electron donors, and therefore, they do not participate in the electronic structure, as initially proposed.[157] However, it may well be that, under the conformational fluctuations of the protein, Cpd I may acquire transitory spin density on the propionate side chains[74] and provide a delocalization path as found in NOS, where the H_4B cofactor

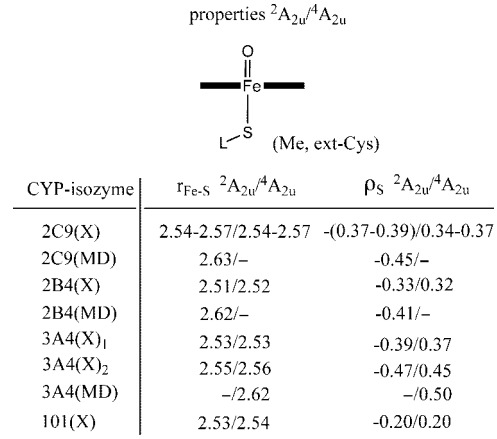

CYP-isozyme	r_{Fe-S} $^2A_{2u}/^4A_{2u}$	ρ_S $^2A_{2u}/^4A_{2u}$
2C9(X)	2.54-2.57/2.54-2.57	-(0.37-0.39)/0.34-0.37
2C9(MD)	2.63/–	-0.45/–
2B4(X)	2.51/2.52	-0.33/0.32
2B4(MD)	2.62/–	-0.41/–
$3A4(X)_1$	2.53/2.53	-0.39/0.37
$3A4(X)_2$	2.55/2.56	-0.47/0.45
3A4(MD)	–/2.62	–/0.50
101(X)	2.53/2.54	-0.20/0.20

Figure 20. DFT(B3LYP)/MM optimized Fe−S distances (Å) and sulfur spin densities for the doublet and quartet spin states of Cpd I for different CYP isozymes. X and MD denote the snapshots derived from the X-ray structure and from the preparatory MD simulations, respectively. Reprinted with permission from ref 56. Copyright 2005 American Chemical Society.

acquires spin density (partially as $H_4B^{\bullet+}$) due to the interaction with the propionate side chain.[69]

3.7.2. Cpd I Species in Human P450 Isoforms

An extensive DFT(B3LYP)/MM study of Cpd I in the human isoforms CYP2C9, 2B4, and 3A4, with comparison to CYP101,[56] involved the Por,SMe and Por,ext-SCys models and several other variants, with residues in the distal and proximal sides as well as on the porphyrin ring. The starting geometries for QM/MM optimization were mostly taken from an X-ray structure (snapX), and in some cases from snapshots of an MD run (snapMD). The results are shown in Figure 20; there are changes from one isozyme to the other, but they are not larger than the changes due to fluctuations within a given isozyme. The authors concluded, therefore, that while the electronic structure of Cpd I, in the human isoforms tested, is somewhat dependent on the environment, the differences are not larger than those found for a given isoform in different snapshots. This is clearly true for the Cpd I species of the limited human isoform group used in this study but not valid for the entire range of Cpd I structures investigated since then (see below).

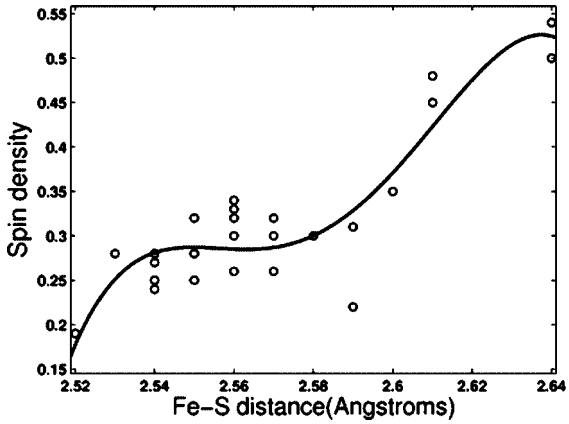

Figure 21. The variation of spin densities on sulfur as a function of the Fe−S distance in CYP3A4 Cpd I in 28 DFT(B3LYP)/MM structures optimized along the MD trajectory. Reprinted with permission from ref 55. Copyright 2007 American Chemical Society.

3.7.3. Effect of Substrate Binding on Cpd I of CYP3A4

An extensive DFT(B3LYP)/MM study[55] focused on CYP3A4 in order to understand the observation of cooperative binding, whereby substrate oxidation follows faster kinetics when two or more molecules of substrate are admitted into the active site, which is large in this isoform. Seven substrate-free models of Cpd I were used, with different thiolate ligand representations and with propionate substituents on the porphyrin ring and the corresponding arginines that form salt bridges, as well as distal and proximal residues (in the latter cases those substituents that form NH···S interactions with the proximal Cys_{442} ligand). Two starting structures (PDB: 1TQN and 1W0E) were chosen and subjected to a 0.5 ns MD simulation. Optimizations starting from the initial X-ray structures produced DFT(B3LYP)/MM geometries and spin densities similar to those obtained in the above study of Bathelt et al.[56] Changes occurred, however,[55] in the human isoforms tested, when the optimizations started from the snapshots along the MD trajectory. The results are summarized in Figure 21 for 28 different QM/MM optimized structures. It is seen that as long as the Fe−S bond is shorter than 2.61 Å, the spin density on sulfur remains approximately at 0.25, whereas, for longer Fe−S bonds, the spin density reaches values larger than 0.50; the maximum occurs for the structures optimized after 0.5 ns MD. Thus, within 0.5 ns, the substrate-free active species tends to elongate its Fe−S bond and to localize the radical on the sulfur; both aspects may signal instability of the species (possibly by sulfur-based radical abstraction of a hydrogen atom from neighboring residues).

In a second set of calculations, Fishelovitch et al.[55] interrogated the effect of the substrate by studying the three different models shown in Figure 22. The substrate is a drug molecule called diazepam (Dia), known to exhibit cooperative binding with two molecules inside the pocket. As shown in Figure 22, the first model (Dia_far) includes a single unrestricted diazepam molecule that was QM/MM optimized starting from the 5.5 ns snapshot from the MD simulation trajectory;[189] here, the diazepam molecule drifted away from Cpd I, reaching a distance of 9 Å. In the second model (Dia_prox), one diazepam molecule was docked and constrained to the same position it has when the other diazepam molecule is present, but in the absence of the second molecule (the effector, see below). And finally, in the third model (Dia_CB),

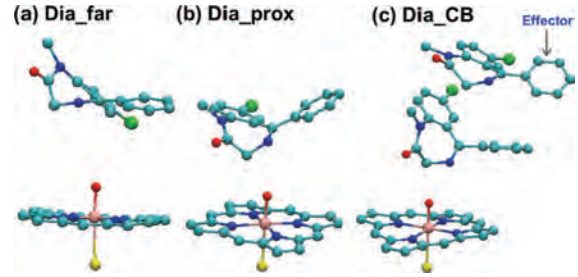

Figure 22. Three models used for studying the effect of cooperative binding (CB) on Cpd I of CYP3A4 with the drug molecule called diazepam (Dia). From left to right: (a) Dia-far, Cpd I with one diazepam after 5.9 ns of MD; the diazepam is far away. (b) Dia-prox, Diazepam docked with the methylene group undergoing activation near the oxo group of Cpd I. (c) Dia_CB, Cpd I with two diazepam molecules; the farthest one is labeled as "the effector". Reprinted with permission from ref 55. Copyright 2007 American Chemical Society.

there are two diazepam molecules, simulating cooperative binding (CB); one close to Cpd I is called the "substrate"; the other one, far away, is called "the effector".

All three models were subjected to MM optimization and 0.5 ns MD prior to QM/MM optimization; the results are depicted in Figure 23. Figure 23a and b shows the situation of Cpd I in the former model (Dia_far) where the substrate was allowed to drift away. It is seen that the Fe−S bond here is long, and this elongation is attended by spin density localization on the sulfur. Moreover, the oxo group of Cpd I is H-bonded over short distances to nearby protein residues, T309 (Thr_{309}) and A305 (Ala_{305}) (Figure 23a and b). Thus, when the substrate is not in the proximity of the active site, Cpd I will be surrounded by abstractable H-bonds from the protein residues and will be consumed before it can react with the substrate. This is reminiscent of attempts to generate Cpd I by shunting the catalytic cycle with peracid, which generally results in Cpd II and a protein radical.[253] The long Fe−S bond and the high S-radical content further aggravate the situation, since sulfur itself may abstract hydrogen and convert P450 to the inactive form known as P420.[7]

By contrast, the situation in Figure 23c is very different: in the presence of the substrate, the Fe−S bond remains short even after 0.5 ns, the sulfur spin density is well below 0.5, and the only C−H bond close to Cpd I is the one of the diazepam molecule; all other H-bonds from the adjacent residues are either displaced or elongated. Adding the effector diazepam to the calculations has no noticeable effects on the geometry or electronic structure of Cpd I, other than what we just mentioned. As such, the role of the effector is simply to push the substrate mechanically and hold it close to Cpd I. Therefore, when the substrate is close to Cpd I, the only abstractable hydrogen will be the one from the substrate. Thus, the effect of cooperative binding in a wide-mouthed isoform such as CYP3A4 is to optimize substrate oxidation by preventing the destabilization of Cpd I (via Fe−S elongation) and by ensuring that no other abstractable hydrogens are in the vicinity of the active species. A detailed analysis showed that this robustness of Cpd I was associated also with the stabilization of the Fe−S bond by the two NH···S interactions (from Ile_{443} and Gly_{444}) with the proximal ligand.

Interestingly, a substrate effect on the lifetime of the oxidizing species was noted experimentally in CYP101.[176,241,278] Thus, in the substrate-free case, the last dioxygen-containing species (Cpd 0) has an extremely short lifetime.[278] When

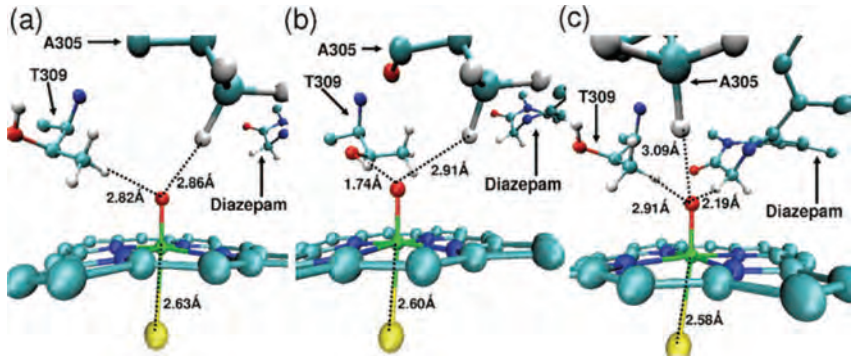

Figure 23. DFT(B3LYP/B1)/MM optimized geometries of the three models in Figure 22: Parts a and b are two snapshots of Dia_far; note that the closest hydrogens to Cpd I are those in the CH group of A305, and the OH or CH groups of T309 (A is Ala; T is Thr). (c) Snapshot from Dia_prox; note that diazepam displaces the interacting H-moieties of the A305 and T309 residues, and its own C−H bond is now closest to Cpd I with an O···H distance of 2.19 Å. Note also the short Fe−S bond in part c compared with those in parts a and b. Reprinted with permission from ref 55. Copyright 2007 American Chemical Society.

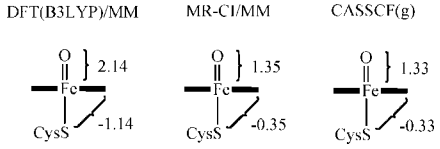

Figure 24. Spin densities obtained from DFT(B3LYP)/MM, MR-CI/MM, and CASSCF(g) studies of the doublet state of CYP101 Cpd I.[77,78,274]

camphor was added, the lifetime of the oxidant species increased 20-fold, while using a bulkier substrate increased the lifetime 80-fold. As such, the substrate stabilizes Cpd I, allowing it to live longer near the substrate so it can optimize substrate oxidation. In the absence of the substrate, Cpd I gets consumed all too quickly by the protein residues. In CYP101, with its tight binding pocket, one molecule of substrate is sufficient to achieve the effect, but in CYP3A4, with a very large pocket, the same effect requires cooperative binding.

3.7.4. Description of Cpd I by Highly Correlated QM Levels

Three studies of Cpd I by highly correlated levels have appeared between 2005 and 2008.[77,78,274] All three studies used initial CASSCF wave functions of varying sizes, which were augmented subsequently by accounting for dynamic correlation; in the first two by MR-CI methods[77,78] and in the third one by CASPT2.[274] Furthermore, the first two studies included the effect of the protein, hence MR-CI/MM, while the third one employed a gas-phase model, hence CASPT2(g). The three studies agree that Cpd I has two virtually degenerate doublet and quartet states, and while the MR-CI/MM results show conclusively a doublet ground state,[77,78] the CASPT2(g) results are less decisive, reflecting probably the lack of the protein environment, as was reasoned before from model studies.[198]

In both sets of studies, the quartet state properties closely resemble the DFT(B3LYP)/MM results. However, the doublet state comes out quite different. Figure 24 shows the spin density distribution from DFT(B3LYP)/MM, MR-CI/MM, and CASPT2(g) calculations for the doublet state. The difference is apparent: while the DFT method yields two spins on the FeO moiety, one with spin-up and one spin-down on the combined Por/S moiety, the correlated calculations give a spin density of 1.33−1.35 on FeO and a total of −(0.33−0.35) on the Por/S moieties.

Scheme 4. (a) Spin Arrangements of the π^*_{xz}, π^*_{yz}, and a_{2u} Orbitals in the Three Determinants (D_1−D_3) That Are Required To Obtain a Spin-Adapted Doublet-State Wave Function $^2\Phi_{111}$ and (b) Covalent Configuration $^2\Phi_{111}$ and the "Ionic" Ones, $^2\Phi_{210}$ and $^2\Phi_{012}$, Which Contribute to the Doublet $^2A_{2u}$ State

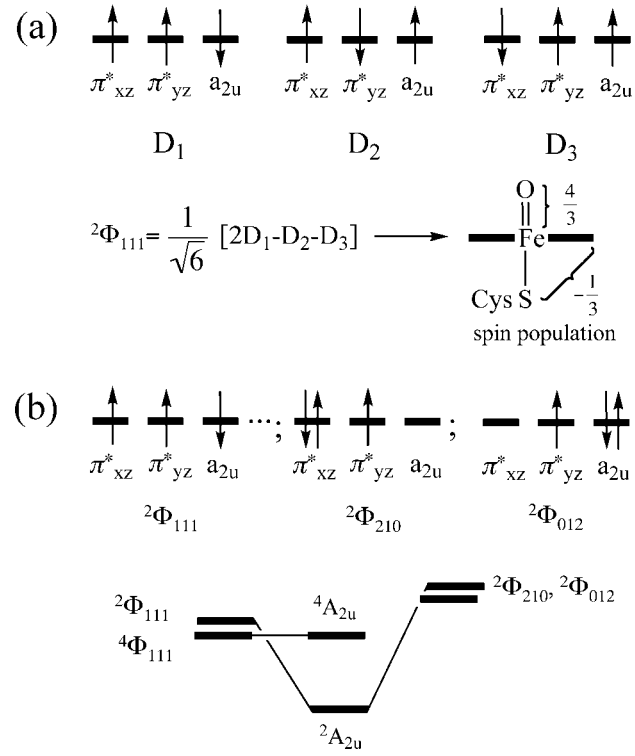

One of the problems of DFT is the use of a single Kohn−Sham determinant to describe the doublet state. This leads to a broken symmetry solution, since the single determinant is not a definitive spin state and does not properly describe the open-shell singlet coupling of the a_{2u} and π^* electrons; therefore, the spin distribution of the $^2A_{2u}$ state is incorrectly evaluated by DFT. However, this can be easily remedied by constructing from the DFT determinant a spin-adapted wave function that describes properly the doublet spin, as shown in Scheme 4a. Thus, since the electron in the a_{2u} orbital is singlet-coupled to each one of the electrons in the π^* orbitals, the corresponding wave function will involve a combination of spin arrangements as shown in Scheme 4a. Therefore, if we order the orbitals as $\pi^*_{xz}\pi^*_{yz}a_{2u}$, the spin arrangements will be $D_1 = |\uparrow\uparrow\downarrow\rangle$, $D_2 =$

$|\uparrow\downarrow\uparrow\rangle$, and $D_3 = |\downarrow\uparrow\uparrow\rangle$, with the former having a double coefficient and hence a quadrupled weight compared with the latter two. Since the spin of the a_{2u} electron has a spin down with a relative weight of 4 and a spin up with a relative weight of 2, the sum is a spin down weight of 2. When we normalize the wave function, the spin distribution in the doublet states should be $^2/_3$ in each of the π^*_{xz} and π^*_{yz} orbitals and $-^1/_3$ in a_{2u}. This distribution in Scheme 4 is close to the MR-CI/MM and CASPT2(g) distributions, and we may conclude that spin adaptation is sufficient to retrieve these high level results. As such, the $^2A_{2u}$ state is described at the correlated level as a triradicaloid with singly occupied π^*_{xz}, π^*_{yz}, and a_{2u} orbitals.

The recent MR-CI/MM study[78] emphasizes that the wave function of the $^2A_{2u}$ state has a multireference character, more so than the $^4A_{2u}$ state, which is dominated by a single configuration analogous to the DFT/MM Kohn−Sham determinant. As shown in Scheme 4b, in addition to the triradicaloid configuration, $^2\Phi_{111}$, with a single electron in each one of the occupied π^*_{xz}, π^*_{yz}, and a_{2u} orbitals, the $^2A_{2u}$ state wave function has contributions from $^2\Phi_{210}$ and $^2\Phi_{012}$. The latter two are obtained from $^2\Phi_{111}$ by back-and-forth single electron shifts between the π^*_{xz} and a_{2u} orbitals. This configuration mixing is analogous to the covalent-ionic mixing that stabilizes singlet diradicals in valence bond (VB) theory.[279] By analogy, if we refer to $^2\Phi_{111}$ as a covalent electronic structure, then the other two configurations are simply the corresponding ionic ones. This "covalent-ionic" mixing stabilizes the $^2A_{2u}$ state below the $^4A_{2u}$ state, as shown in Scheme 4b. Interestingly, these configurations were not found in the CASPT2(g) study,[274] which reported a close analogy of the $^2A_{2u}$ state to the corresponding DFT description, presumably just the triradicaloid structure $^2\Phi_{111}$. The mixing found in the MR-CI/MM study, of course, cannot be very stabilizing, since the two states remain very close (within <1 kcal mol^{-1}) to each other. Nevertheless, the presence of the "ionic configurations" is sufficient to lower $^2A_{2u}$ below $^4A_{2u}$ and may reflect the effect of the protein on the electronic structure, discussed in model studies.[198]

3.7.5. Low-Lying Excited States of Cpd I

Here we restrict ourselves to excited states that may have some impact on the reactivity of Cpd I, while excited states that are useful for spectroscopic identification (e.g., the split Soret band) of Cpd I species have been discussed by Harris et al.[268] The $^{4,2}A_{1u}$ excited states have been considered either as ground or low-lying excited states in Cpd I and other metalloporphyrin species.[280] DFT and DFT/MM calculations usually predict these states of P450 Cpd I to lie 7−10 kcal mol^{-1} higher than the corresponding $^{4,2}A_{2u}$ pair.[78,266] However, as noted recently for HRP Cpd I,[74] the distortion of the porphyrin ring by the protein causes mixing of these states, such that the ground states have $A_{2u}-A_{1u}$ mixed character. Furthermore, a recent treatment[280] showed how to analyze a variety of metalloporphyrin systems and obtain the $A_{2u}-A_{1u}$ contents in the ground states. Having said that, the state with dominant $^{4,2}A_{1u}$ character is still predicted by DFT to lie well above the $^{4,2}A_{2u}$ ground states. However, a recent MR-CI/MM treatment[78] gave a rather small $^2A_{1u}-^2A_{2u}$ gap of only 1.9 kcal mol^{-1}, a feature which merits further investigation.

The other pair of states, which are interesting from the point of view of chemical reactivity,[200] are the pentaradicaloid $^{6,4}A_{2u}$ states, which arise from electron promotion from the δ to the σ^*_{xy} orbital in Figure 3a. Early DFT(B3LYP) calculations[266] predicted this state to lie only 14 kcal mol^{-1} higher than the $^{4,2}A_{2u}$ ground states. Subsequent DFT/MM calculations[277] verified that these states are indeed low lying, ca. 11 kcal mol^{-1} above the ground state. The major factor that stabilizes these pentaradicaloid states is the increased number of d−d exchange interactions generated by the excitation. This stabilization may lower the transition states nascent from these states sufficiently to make them relevant for the reactivity of Cpd I.

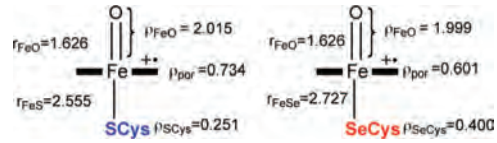

Figure 25. Key geometric features (Å) and spin densities obtained in the quartet state of the Cpd I species of the wild type CYP101 (S-Cpd I) and the selenocysteine mutant (Se-Cpd I) from DFT(B3LYP)/MM calculations.[62]

3.7.6. Se-Cpd I for an in-Silico Designed Mutant of P450

The recently discovered 21st amino acid is selenocysteine, in which selenium replaces the sulfur atom. It was therefore interesting to find out whether an in-silico DFT(B3LYP)/MM designed mutant would be stable and what kind of properties the corresponding Se-Cpd I would have compared with the wild-type (WT) S-Cpd I.[57,277] The in-silico mutation was done by simply replacing the sulfur by Se in the DFT(B3LYP)/MM calculated[53,156] resting state, **1**, and in Cpd I of the WT enzyme, taking a few snapshots from the MD trajectory and optimizing them by DFT(B3LYP)/MM.[57,277] The resting state Se-**1** was found to be stable and sufficiently close to WT-**1** (having a doublet ground state), with an Fe−Se distance close to that in known organometallic Fe/Se complexes. The geometric and spin density features of Se-Cpd I are shown in Figure 25 alongside the S-Cpd I analogue. It is seen that the major difference is the greater radical character of Se-Cpd I, which is almost identical to the gas-phase spin density in S-Cpd I. Indeed, the calculated Mössbauer parameters of Se-Cpd I are quite close to the gas-phase parameters of S-Cpd I.[57] Thus, the increased donor ability of CysSe vis-à-vis CysS causes a greater mixing of the Cys-Se$^{\bullet}$/Cpd II state into the Cys-Se$:^-$/Cpd I state in terms of the VB mixing model in Figure 18a.

Once again we see how the powerful electron acceptor property of the Por$^{\bullet+}$FeO moiety results in a chameleonic behavior of the Cpd I species. In the meantime, the mutant was made experimentally using different techniques.[64,65]

3.8. Concluding Remarks on the Catalytic Cycle of P450

The cycle of P450 has many subtle factors that influence the function of the enzyme. As discussed before,[143] and further argued above based on DFT(B3LYP)/MM calculations, the gating of the cycle by a single water molecule is enabled by the negative charge and electron donor property of the thiolate (cysteinate) ligand, i.e., "push"-effect. In the absence of axial thiolate, the resting state would have been

reduced too, while in its presence there is a narrow window of redox potential that applies only to the pentacoordinate intermediate **2** and the oxy-ferrous species **4**. Further into the catalytic cycle, the "push"-effect increases the proton basicity of the species **5** and Cpd 0 (**6**), thereby affecting their efficient protonation, while at the same time preventing the reduction of these species. In the last step of the catalytic cycle, the "push"-effect generally prevents reduction of Cpd I so *that it preferentially reacts by hydrogen abstraction or bond formation*.[143,281] However, as the example of P450 StaP above shows, this is not a firm rule, since in some cases the substrate is a good enough donor to partly reduce Cpd I and to participate in the electronic structure of this species. This brings us to the chameleon nature of Cpd I, which originates in the electron acceptor capability of the iron-oxo porphyrin cation radical moiety that tends to accept electron density from its internal donor, the cysteine, as well as from any sufficiently good donor around, be this protein residue or a substrate. The potential implications of the chameleon nature may be far reaching but have not yet been fully explored.

There are still unresolved issues with regard to other steps in the catalytic cycle, for example, concerning the role of the reductase, the participation of individual water molecules, and the mechanism of the proton transfers, which may be different in different mutants.[282] What is also missing is a way to assess the cycle as a whole based on the integration of its many features. Preliminary MD studies by Fishelovitch et al.[283] suggest that the reductase plays a role in regulating the cycle, not only by providing the electrons needed for reduction but also by the conformational changes it induces in the protein such that formerly closed water pathways[178] can open and assist the function of the enzyme. The MD simulations in CYP3A4 show that the arginine residue that forms the salt bridge with propionate 7 (propionate A) is flexible and functions as a gate. When the substrate (e.g., testosterone) is in the pocket, the gate is closed. However, as soon as the reductase is attached to the heme from the proximal side close to the cysteine ligand, it causes the Arg residue to rotate and open the gate. When the gate opens up, water molecules flow into the pocket and form a water chain that connects with the acid−alcohol pair (Glu and Thr).[283] Some support for the specific status of the salt bridge to propionate 7 was recently demonstrated by the work of Hayashi et al., who showed that severing the propionate substituent has an adverse effect on the functionality of the enzyme and its efficiency of electron uptake.[221] If these conclusions are general for the P450 family, then the catalytic cycle is completely regulated by the attachment of the reductase to the heme. Thus, upon substrate binding, water molecules including the aqua ligand leave the site,[178] thereby making the heme a better electron acceptor and causing an attachment of the electron donor reductase. Once the reductase is attached, it causes both reduction of the heme and a timely entrance of water molecules that can shuttle protons required for the O−O bond cleavage and the formation of Cpd I. In this manner, P450 enzymes possess a functional catalytic cycle that drives off water molecules, when these are not necessary, and lets them in when they are required. Quite an ingeneous cycle!

4. QM/MM and QM-Only Studies of P450 Reactivity

4.1. Coverage of Reactivity and Mechanistic Issues

Let us start with issues that have been reviewed before and will thus receive only minor coverage herein. Then we shall address new reactivity issues that will be discussed here at some length.

One of the key features of reactivity derives from the nearly degenerate spin states of Cpd I, which brings about a hybrid reactivity pattern, so-called two-state reactivity (TSR), that affects product distributions, kinetic isotope effects (KIEs), and other reactivity aspects through the interplay of the two reactive spin states of Cpd I.[30,145,284] This has been reviewed amply, by some of us[25,26,31,32,83] as well as by others,[18,22,285−287] focusing on how the interplay of the two spin states in TSR elucidates the controversial radical-clock lifetimes, the rearrangement patterns, and other features in C−H hydroxylation. We shall therefore not cover these topics as such, although the notion of TSR and multistate reactivity (MSR) will be mentioned throughout the following discussions.

Another important issue that has been prominent in mechanistic discussions is the putative presence of a second oxidant species in the cycle of P450, which until recently was assumed to be Cpd 0.[24] The evidence for the participation of Cpd 0 in substrate oxidation arose from the observation that mutants in which the proton relay that converts Cpd 0 to Cpd I is disrupted by site-directed mutagenesis[23,183,257] exhibit different reactivity patterns compared with the WT enzyme. For example, the T252A mutant of $P450_{cam}$ does not hydroxylate camphor but is capable of epoxidizing the double bond of 5-methylenylcamphor, albeit more sluggishly than the WT enzyme.[183] Since the catalytic cycle of T252A is thought to terminate at Cpd 0, this necessarily means that Cpd 0 should be involved in the epoxidation of an activated double bond but that its reactivity is smaller than that of Cpd I. Curiously, the double mutant of $P450_{cam}$, T252A/D251N, in which the protonation machinery has been disrupted by mutations of both Thr_{252} and Asp_{251}, shows partial activity in camphor hydroxylation,[184] which indicates that Cpd I might after all be present even in these mutants. Moreover, a mechanistic study[256] reports that oxidation reactions, thought before to involve Cpd 0, are caused in fact by Cpd I. As we already mentioned, there are now direct experimental data showing that Cpd 0 is orders of magnitudes less reactive than Cpd I, and that in WT P450 it should be silent in the presence of Cpd I.[234,263−265] Thus, while the reactivity of Cpd 0 in the "absence" of Cpd I seems to be generally accepted, the very recent QM/MM calculations of the T252X mutants (section 3.6.3) show that even in these mutants Cpd I is formed, albeit somewhat more slowly than in the WT enzyme, and might be the actual oxidant (it will possess a smaller steady-state concentration due to increased uncoupling). Be this as it may, the simultaneous reactivity of Cpd I and Cpd 0 in the WT enzyme is hardly considered to be viable anymore, with a few exceptions.[288,289] Since this Cpd I/Cpd 0 conundrum has been reviewed by some of us before,[26] it will not be covered here.

Another but similar issue is the recent suggestion that the only oxidant in P450 is the perferryl PorFe(V)═O species and not at all Cpd I, since model Cpd I species react much slower than the assumed reaction rate in $P450_{cam}$.[261,267] As discussed above (section 3.7), however, both QM-only and

QM/MM calculations show that the perferryl species lies too high in energy to react and that the electromeric conversion of PorFe(V)═O to Por$^{\bullet+}$Fe(IV)═O should be virtually barrier free. In fact, the more recent study of Newcomb et al.[262] actually shows that an in situ generated CYP119 Cpd I, by means of LFP,[267,290] is more reactive than model Cpd I species in bimolecular reactions and is, hence, a viable oxidant.

Two comments might be in order here: (a) The use of bimolecular reaction rates vs rates in the enzyme is an insecure grounds for deducing mechanistic conclusions on the enzymatic reaction: A factor that slows down bimolecular reactions is the entropic contribution due to the loss of translational and rotational degrees of freedom in the transition state, which raises the free energy barrier, by up to 12 kcal mol^{-1}, where these degrees of freedom are completely lost, or less if they are only partially lost (this loss enters the $T\Delta S^{\ddagger}$ term that raises the free energy barrier).[26,291] This factor does not play a role in P450 enzymes, because here, the loss of degrees of freedom in the formation of an enzyme−substrate reaction complex is compensated by an increase of the degrees of freedom as the water molecules leave the pocket upon substrate entrance; another factor is the enthalpy of substrate binding (e.g., in CYP101, there is a $Tyr_{96}\cdots O{=}C$ hydrogen bond with camphor).[59,180] The enzymatic reaction then starts from a "complex" that has already lost two rotational and all translational degrees of freedom, and hence, the free-energy barrier for the reaction from this complex should be lower than that of the bimolecular models by a quantity that can reach up to a maximum of 12 kcal mol^{-1} if the translational and rotational degrees of freedom are completely lost. Thus, the complexation effect accounts for a large part, if not all, of the difference observed between the rate constants of the bimolecular reactions vis-à-vis the enzymatic process. (b) Deducing mechanistic conclusions by comparing reaction rates for an LFP generated Cpd I of CYP119[262] to the reaction rate in $P450_{cam}$ estimated by extrapolation from the cryogenic temperature[176] is also insecure, since one has to assume a certain rate constant for these cryogenic experiments and to extrapolate this assumed value from a very low temperature to ambient temperature, which is a questionable procedure. An ultimate resolution of this mechanistic conundrum will come by comparing the reaction rates of the LFP generated Cpd I with the native reaction of the same enzyme toward a given substrate.

Based on the above considerations, Cpd I emerges as the most important if not the sole oxidant of P450s. Therefore, although we shall present some DFT(B3LYP)/MM results that compare the reactivity of Cpd I to other possible oxidants such as Cpd II, etc., the discussion in the following sections will focus on the reactivity patterns of Cpd I. Accordingly, we shall cover DFT/MM results on C−H hydroxylation,[59,61,131,163,164,277] C═C epoxidation,[277] aromatic hydroxylation,[60] and C−C coupling.[58,80] In addition, we shall describe DFT-only results for N-dealkylation,[166,167] ethanol oxidation,[168] hydroxylation of arenes,[172] dehalogenation of polyhalogenated benzene derivatives,[165] and heteroatom (N,S) oxidations.[170,171,292,293] In the following section (section 5), we shall discuss attempts to correlate P450 barriers,[170,172] as well as the recent valence bond approach to the modeling of the barriers and mechanisms for C−H hydroxylations.[174]

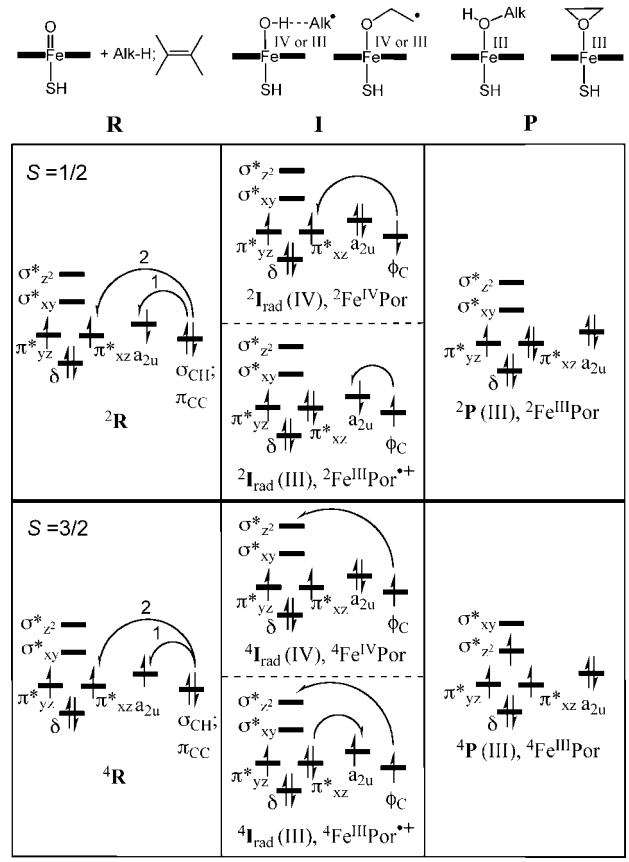

Figure 26. Orbital occupancy evolution diagrams during C−H hydroxylation and/or C═C epoxidation by Cpd I, in the doublet ($S = {}^1/_2$) and quartet ($S = {}^3/_2$) states. Reprinted with permission from ref 25. Copyright 2007 American Chemical Society.

4.2. Reactivity of Cpd I: Counting Electrons, Spin States, and Electromeric Situations

As we argued at the outset, the "oxidation state formalism" has been used fruitfully in inorganic chemistry, as a heuristic device for following the electronic reorganization and for assigning the "right number of electrons" to the d-block orbitals of the metal. Here we use it in Figure 26 in terms of orbital occupancy evolution during C−H hydroxylation and/or C═C epoxidation.

The reactant states, ^{2,4}**R**, involve the two spin states ($S = {}^1/_2, {}^3/_2$) of Cpd I, having the orbital picture already shown in Figure 3a, and the substrate, which is represented here by a doubly occupied orbital, σ_{CH} or π_{CC}. The heme of Cpd I effectively contains an Fe^{IV} center and a hole in the porphyrin (i.e., Por$^{\bullet+}$) and thus has two oxidation equivalents more than the product state complexes ^{2,4}**P** that have an Fe^{III} center and a closed-shell porphyrin. Thus, any reaction of Cpd I will ultimately involve two formal electron "transfer" events from the substrate undergoing oxidation to the heme. Starting from the left-hand side, Figure 26 shows two of these electron shift events, one to the a_{2u} orbital and the second to the π^*_{xz}(FeO) orbital, in the quartet and doublet spin states. The first electron shift generates an Fe^{IV}-type intermediate with a closed-shell porphyrin, while the second shift generates an Fe^{III}-type intermediate with a radical cationic situation on the porphyrin ring. In both cases, the substrate retains a radical center with a singly occupied orbital labeled ϕ_C. In addition, each of these two electromers will come in two

spin varieties, so we might expect involvement of at least four radical intermediate states during the reactions.[83] During the second bond formation step, an additional electron is "transferred" from the substrate to fill either the a_{2u} orbital or one of the d-orbitals of the iron. Filling the π_{xz}* orbital generates the doublet-spin ferric product, whereas the filling of the $\sigma^*_{z^2}$ orbital leads to the quartet-spin ferric product. Of course, in synchronous reactions, both "electron transfer" events will transpire in one step (see later the sulfoxidation mechanism).

It is apparent already from Figure 26 that there are other possible states, which are obtained by redistribution of the electrons in this dense orbital manifold. For example, shifting electrons from the ϕ_C orbital of the radical intermediate center into one of the d-orbitals will generate a variety of states in which the substrate is a cationic species, as described in studies of the clock substrates.[147,152,294] Additionally, there are low-lying sextet and quartet states (section 3.7.5), which may generate intermediates of sufficiently low energy that can participate in the reaction.[200,277] As such, the reactivity of Cpd I will involve at least two spin states, and possibly many electromeric states, hence TSR and MSR.

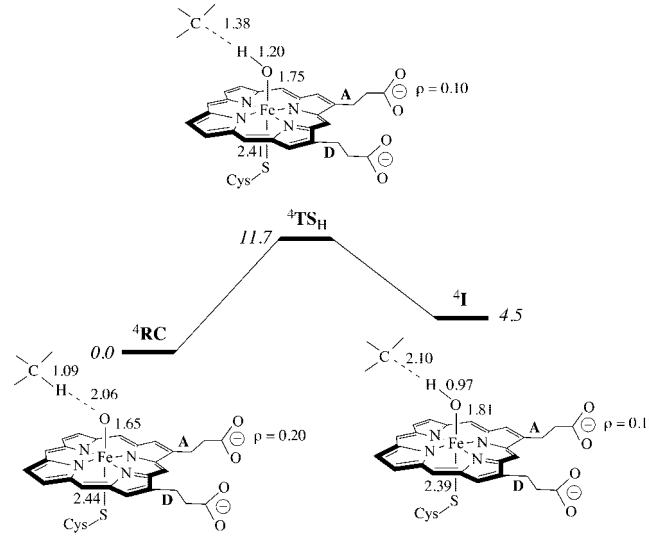

Figure 27. DFT(ROB3LYP)/MM results[155,157] for geometries (Å) and spin densities (ρ values) during H-atom abstraction from camphor by CYP101. Energies in kcal mol^{-1}.

4.3. DFT/MM and DFT-Only Studies of C−H Hydroxylation by Cpd I of P450

Many DFT-only studies were performed to elucidate the mechanism of C−H hydroxylation and to resolve the controversy around the radical clock data.[45,146−153,295] The more recent studies involve DFT/MM modeling of camphor hydroxylation by $P450_{cam}$.[59,61,131,155,157,163,164,277,296] The nature of the iron-hydroxo intermediate during the reaction was recently studied by means of MR-CI/MM calculations.[78] The DFT and DFT/MM studies cover more than 10 different substrates, which has led to a general and unified mechanistic picture that involves TSR and MSR, as reviewed before.[32]

4.3.1. Camphor Hydroxylation by CYP101 and the Controversial Role of Spin Density on the Propionate Side Chains

An early DFT(ROB3LYP)/MM(OPLS) study[155] of camphor hydroxylation by CYP101 yielded a surprisingly low barrier of 11.7 kcal mol^{-1} for the quartet state reaction, as shown in Figure 27. The low barrier which could have potentially explained the elusiveness of Cpd I was ascribed to a drift of spin density to the propionate side chain (propionate-A); thus, the propionate spin density, which starts as 0.2 at the reactant complex, diminished to 0.10 at the transition state. It was argued[155,157] that the diminishment of the propionate spin density at ^{4}**TS**$_H$ causes an increase of the propionate negative charge, which is stabilized by the salt bridge to the neighboring arginine, thereby lowering the barrier and stabilizing the intermediate ^{4}**I**. However, subsequent studies did not find support for this attractive mechanism.

The first comprehensive DFT(B3LYP)/MM study of camphor hydroxylation by CYP101[59,277,296] employed four different snapshots after MD equilibration, using two different models of the QM subsystem (Por,SH and Por,ext-SCys), and two different basis sets. The results are depicted in Figure 28, where it is seen that the reaction coordinate exhibits a hydrogen abstraction phase (bond activation) and a reorientation of the alkyl moiety attended by a rebound process that generates the ferric-alcohol complexes. The bond activation phase involves the quartet high-spin (HS) and doublet low-spin (LS) bond activation transition states (^{4,2}**TS**$_H$), which originate in the two spin states of Cpd I. The LS species, ^{2}**TS**$_H$, lies slightly below the HS one; generally, the two bond activation transition states are close in energy to within 2 kcal mol^{-1} or less. This phase generates the clusters **I**, which involve an alkyl radical (CAM$^\bullet$) weakly coordinated to the iron-hydroxo species; the ^{2,4}**I** intermediates appear in the Fe^{III}Por$^{\bullet+}$ and Fe^{IV}Por varieties discussed above (Figure 26), but in the figure we show generically the two lowest ^{4,2}**I** states (for a discussion of all the states, see later). Subsequently, the rebound on the HS manifold encounters a significant barrier, while from the LS manifold the barrier is negligible, *ca.* <0.3 kcal mol^{-1}. The scenario is extremely similar to the findings in the corresponding gas-phase process,[59,277,296] as well as in all the gas-phase reactions studied thereafter.[32,174] Thus, this study confirms the TSR picture that emerged from gas-phase model calculations using the small model representation, Por,SH.[146]

However, comparison of the DFT(B3LYP)/MM barriers to those in Figure 27 shows that while the transition state geometries are similar, the barriers in the DFT(B3LYP)/MM study are significantly higher. Since the DFT(ROB3LYP)/MM calculations (Figure 27) included also the propionate side chains, while the DFT(B3LYP)/MM calculations (Figure 28) did not, it was deemed necessary to test the putative appearance of the spin density on the propionate, by including these side chains in the DFT(B3LYP)/MM calculations and performing single-point calculations on the so optimized structures.[59,277,296] These tests show that as long as the propionates are properly screened by Arg_{299}, these side chains have zero spin density. Furthermore, the presence or absence of propionate spin density does not lower the barriers in these calculations, and DFT(B3LYP)/MM geometry optimization did not change these conclusions.[277]

Since then, three other comprehensive studies were carried out to benchmark the barrier for the camphor hydroxylation reaction and to test the propionate spin density hypothesis.[61,131,163] Thus, Zurek et al.[163] used DFT(B3LYP)/MM, different setups of the system, different MD procedures, and different QM models. The results are shown in Figure 29, and it is apparent that, despite the differences in the two DFT(B3LYP)/MM approaches, the results are very similar to those of Schöne-

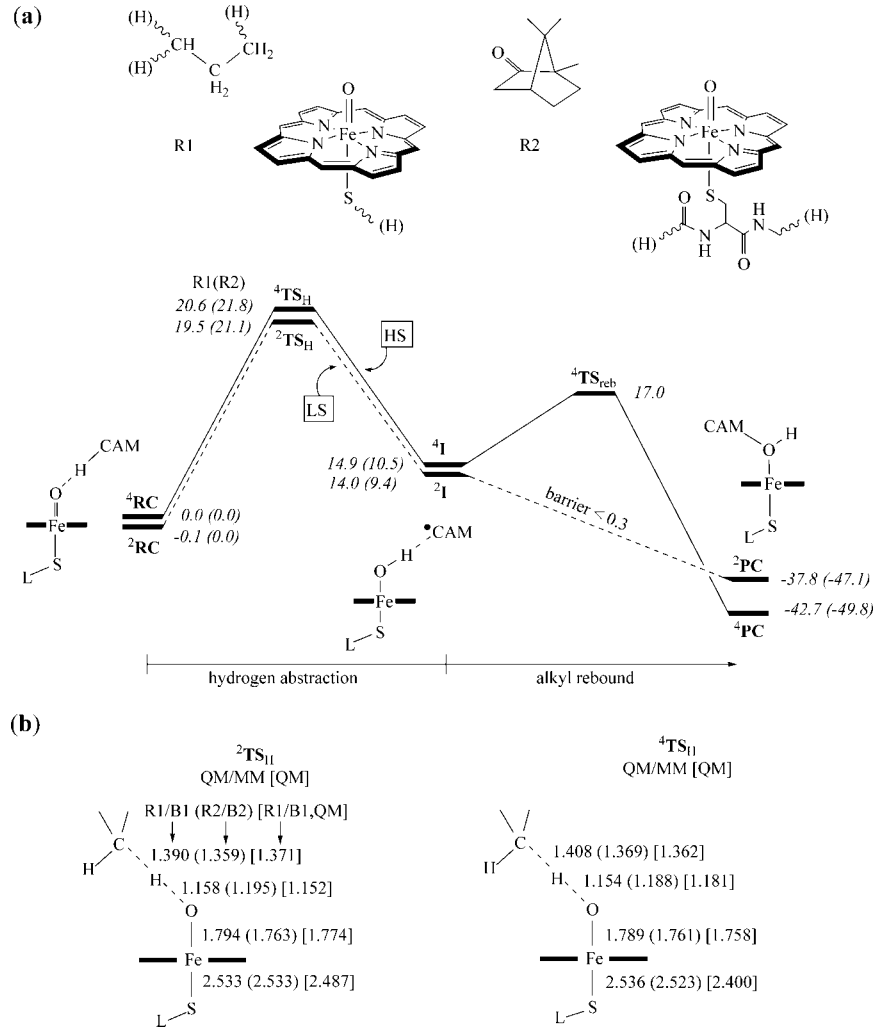

Figure 28. Representative DFT(B3LYP/B2)/MM energy profiles for camphor (CAM-H) hydroxylation calculated for the equilibrated 40 ps snapshot. The QM regions are labeled as R1 (Por,SH; truncated CAM-H) and R2 (Por,ext-SCys; full CAM-H). Data correspond to R1 (R2), respectively. Energies (a) in kcal mol^{-1}, distances (b) in Å. Reprinted with permission from ref 59. Copyright 2004 American Chemical Society.

boom et al.[59,296] in Figure 28, in the sense that the two studies lead to barriers of 15−20 kcal mol^{-1} depending on models and basis sets. The largest barriers were obtained for QM region R2 when the Asp_{297} residue adjacent to propionate-A is deprotonated. Zurek et al.[163] carefully studied the role of propionate spin density, which appears with deprotonated Asp_{297} and then actually raises the barrier. Furthermore, the observed short O···O distance of 2.4−2.8 Å between the oxygen atoms of Asp_{297} and propionate-A[178] could not be reproduced with deprotonated Asp_{297}, in which case both QM/MM optimizations and MD runs result in O···O distances of up to 4 Å. By contrast, with protonated Asp_{297} the O···O distance is stable at 2.7 Å.

The source of the differences between the published DFT(B3LYP)/MM and DFT(ROB3LYP)/MM results[59,155,157] for the hydrogen abstraction barrier in the HS state was traced through systematic calculations[61,131] that employed a variety of QM models ranging from 51 atoms for the simplest one (the Por,SH model in Scheme 2) up to 170 atoms (with full camphor, ext-SCys ligand, all porphyrin substituents, and their salt bridges, as well as a crystal water molecule, Wat_{903}). It was found that (i) the two procedures gave essentially the same barriers *as long as one used the same geometries*, (ii) no spin density appeared on the propionate side chains *as long as these groups were properly screened*, (iii) *the barriers were raised somewhat whenever spin density appeared on the propionate side chains*, and (iv) reoptimization of the DFT(ROB3LYP)/MM **RC** and $\mathbf{TS}_H$ species,[155,157] *with a consistent protein environment*, gave a barrier about 5 kcal mol^{-1} higher than reported originally.[155,157] The latter point (iv) serves as a reminder that QM/MM optimizations require great technical care to avoid artifacts and that it is actually easier to determine technically reliable barriers with the smallest QM-model (Por,SH), which poses less technical difficulties during optimization. Overall, these systematic comparisons have resolved the noted discrepancies and have shown that the different DFT/MM approaches yield compatible results when applied in a consistent manner.

4.3.2. Camphor Hydroxylation by CYP101—How Does Wat_{903} Catalyze the Reactions?

Another important finding of these systematic studies[61,131] is shown in Figure 30, which depicts the ^{4}**RC** and $^4\mathbf{TS}_H$ species of a representative model, along with the HS barrier and the charges on the oxygen atom of the FeO bond. There is a nearby water molecule, labeled as Wat_{903}, which is seen in the X-ray structure (1DZ9)[178] and presumably represents the water molecule liberated during the formation of Cpd I from Cpd 0 (see Figure 1). During

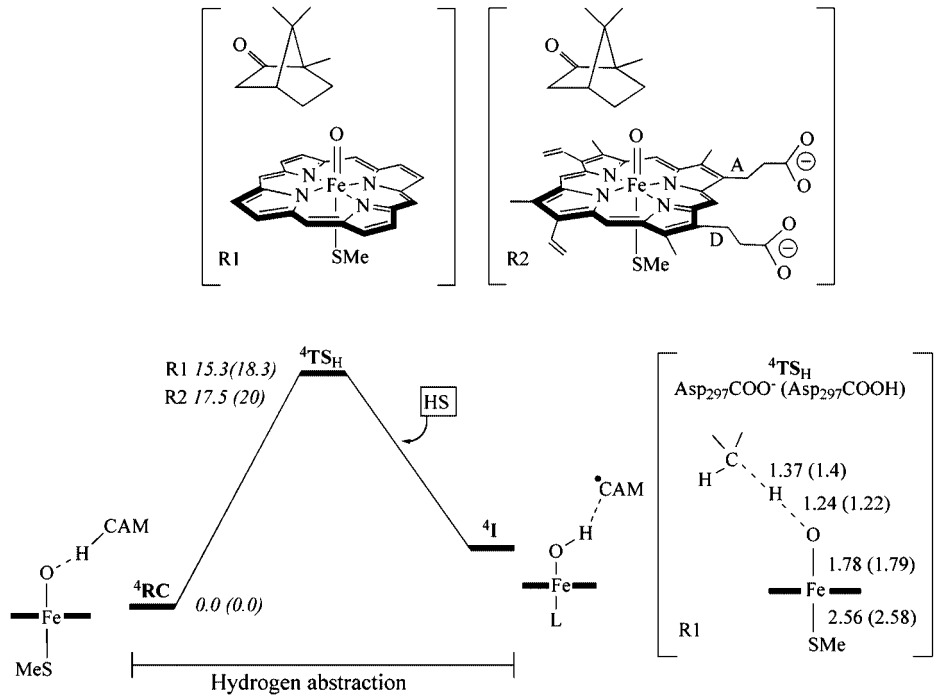

Figure 29. DFT(B3LYP/B2)/MM energy profiles for camphor hydroxylation in the high-spin state of Cpd I, for two models, R1 (Por,SMe; full CAM-H) and R2 (ext-Por,SMe with heme side chains; full CAM-H). Relative energies (kcal mol^{-1}) and distances (Å) are given for setups with deprotonated Asp_{297} (protonated Asp_{297}).[163]

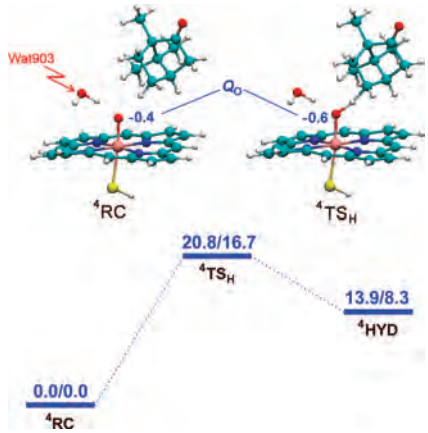

Figure 30. DFT(B3LYP/B1)/MM relative energies (kcal mol^{-1}) of the stationary points for hydrogen abstraction from camphor by quartet Cpd I, in the absence/presence of Wat_{903}. Shown are the ^{4}**RC** and ^{4}**TS**$_H$ species and the Mulliken charge of the oxo ligand in the presence of Wat_{903}.[61,131]

the preparatory MD runs in our original QM/MM work,[296] Wat_{903} moved to the cavity around camphor and thus did not directly participate in the reaction.[59] By contrast, the QM/MM calculations of Guallar and Friesner[157] started from the X-ray structure and followed the QM/MM reaction path without prior MD runs, with Wat_{903} remaining near the oxo group. The presence of this water molecule lowers the hydrogen abstraction barrier; when it is included near the oxo group in our original setup, the barrier goes down by 4 kcal mol^{-1} [61,131] and the endothermicity of the intermediate, ^{4}**I**, is reduced by 6 kcal mol^{-1}. Virtually the same energy changes are obtained whether the Wat_{903} molecule is part of the QM region or the MM region, which suggests that the effect of Wat_{903} is primarily electrostatic. The same effect is observed on isolated gas-phase models, with and without the Wat_{903} molecule; in each case, the water molecule lowers the barrier and the endothermicity of ^{4}**I**. Furthermore, simple electrostatic calculations using the Mulliken charges reproduce the barrier lowering of the Wat_{903} molecule. As can be seen from Figure 30, the favorable interaction of the Wat_{903} molecule with ^{4}**TS**$_H$ arises because the negative charge on its oxo group increases compared with the reactant complex, ^{4}**RC**, due to the charge transfer (∼0.3−0.4*e*) that occurs from camphor to the Cpd I moiety in the transition state. This autocatalytic effect of the Wat_{903} molecule is intriguing; since Wat_{903} is liberated during the conversion of Cpd 0 to Cpd I, it catalyzes the consumption of its own creation.

A subsequent DFT(B3LYP)/MM study[164] further explored the role of Wat_{903} on the barriers as well as on the TSR feature of C−H hydroxylation. The study used three different QM models, a few snapshots, and three different basis sets. Figure 31 shows representative results for the R1 model (Por,SH) using the B1 basis set. The results confirm that the presence of Wat_{903} does not affect the TSR feature; at the bond activation transition state, ^{2}**TS**$_H$ is still below ^{4}**TS**$_H$, the LS rebound is still almost barrier free, while the HS rebound has a significant barrier. Additionally, Figure 31 shows that the barriers without Wat_{903} are 4 kcal mol^{-1} higher than those calculated in its presence, and similarly, the intermediates ^{4,2}**I** are stabilized by 6 kcal mol^{-1} or so.

Therefore, a water molecule that is present near the oxo group of Cpd I will play a biological role as a catalyst. These results imply that the C−H hydroxylation barrier will be susceptible to additives present near the reaction center (water molecules, ions, positive residues, etc), as suggested in the past on the basis of DFT-only model calculations.[150,275,292]

4.3.3. Camphor Hydroxylation by CYP101—More States than Just Two

As already discussed above, there are more states that can be involved in the C−H hydroxylation (as well as other reactions) by Cpd I: (a) the pentaradicaloid states,[200] which

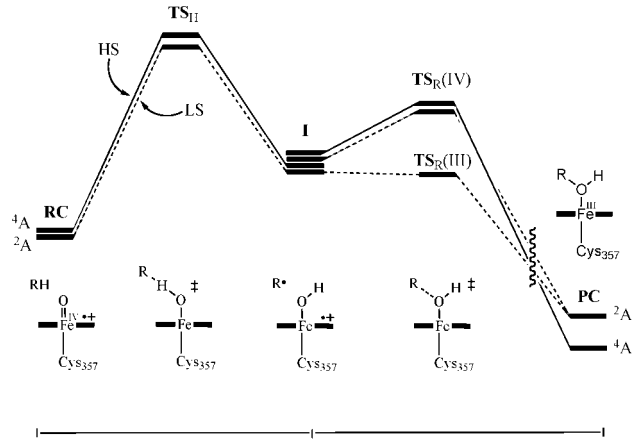

	RC	TS_H	TS_{II}^W	I(III)/I(IV)	$[I(III)/I(IV)]^W$	$[TS_R(III)/TS_R(IV)]^W$	PC^W
^{2}A B1	0.0	19.5	15.8	(14.0/15.2)	9.0/11.7	9.2/13.8	-40.3
^{4}A B1	0.1	20.6	17.1	(14.9/16.0)	10.1/12.5	-/13.9	-45.6

Figure 31. DFT(B3LYP/B1)/MM energy profiles for camphor hydroxylation using the R1 model (Por,SH; truncated-CAM-H) with and without Wat_{903}. The relative energies (kcal mol^{-1}) are given below the drawing. Species with W_{903} are labeled with a superscripted "W", e.g., $\mathbf{TS}_H^W$, etc. Reprinted with permission from ref 164. Copyright 2007 American Chemical Society.

originate by promotion of an electron from the δ to the σ^*_{xy} orbital (see Figure 3a), and (b) the two electromeric varieties of the intermediates, ^{4,2}**I**(IV) and ^{4,2}**I**(III).[32,59,83] In fact, as previously suggested,[32,59,83] all these states may contribute to reactivity and product distribution during the oxidation by Cpd I. The role of these states was examined by Altun et al.[78,164] using DFT(B3LYP)/MM calculations for all these extra states, and MR-CI/MM calculations for the intermediate states ^{4,2}**I**(IV) and ^{4,2}**I**(III) states.

Figure 32 shows the energy profiles of the pentaradicaloid states and the orbital occupancy evolution diagram. While, at the reaction onset, these states are 12 kcal mol^{-1} above the ground states, the gap decreases to less than 5 kcal mol^{-1} at the $\mathbf{TS}_H$ stage and further goes down to 4 kcal mol^{-1} at the intermediate state **I** (see Figure 32a), quite similar to a DFT-only study done before.[200] The reason for the low energy of these states at the intermediate stage can be understood from the orbital occupation diagrams shown in Figure 32b. It is seen that going from the reactant state to the intermediate, ^{6}**I**, the spin-up electron that is shifted from the substrate orbital (σ_{CH}) to the $\sigma^*_{z^2}$ d-orbital on iron adds four new d-d exchange interactions (which can contribute as much as 10−20 kcal mol^{-1} per interaction), and this exchange stabilization overrides the orbital energy gap and lowers the energy of the intermediate, which is now a heptaradicaloid. The reduction of the energy gap between the ^{6}**I** and the lower ^{2,4}**I** states comes from these increased exchange interactions, and the small gaps imply that all these states may be accessible for rebound.

The energy spacing of all the intermediates is shown in detail in Figure 33, for the Por,SH model (R1) using two basis sets, B1 and B2W. With B1, the lowest states are the ^{2,4}**I**(III) electromers, and the entire energy spread is 4.9 kcal mol^{-1}. In the larger B2W basis set, the four ^{2,4}**I**(III) and ^{2,4}**I**(IV) states are condensed into 1.5 kcal mol^{-1}.[164] ^{6}**I** was not computed at this level, but most likely it will go down as well.[200] As shown in Figure 33, MR-CI/MM calculations give rise to similar results, even though the wave functions of all these species show some multireference character.[78] The match between MR-CI/MM and DFT(B3LYP)/MM

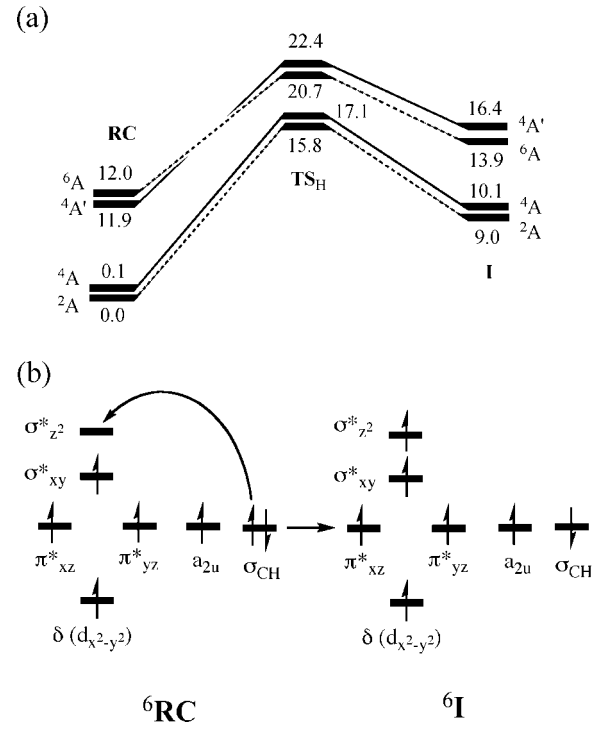

Figure 32. (a) DFT(B3LYP/B1)/MM energy profiles (kcal mol^{-1}) for hydrogen abstraction from camphor by the triradicaloid (doublet and quartet) and pentaradicaloid (sextet and quartet) of Cpd I. (b) Orbital occupancy evolution diagram showing the transformation from ^{6}**RC** to ^{6}**I**. Reprinted with permission from ref 164. Copyright 2007 American Chemical Society.

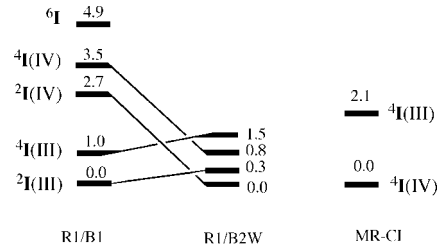

Figure 33. (a) DFT(B3LYP)/MM relative energies (kcal mol^{-1}) of the various intermediate states during camphor hydroxylation, ^{2,4,6}**I**, for R1 (Por,SH; truncated-Por) with two basis sets, B1 and B2W.[164] Shown are also some corresponding MR-CI/MM results with basis B′.[78]

shows once again that the latter method is reliable for P450 species. Finally, the small energy spacing of all the states in the intermediate stage argues for MSR, where the various intermediates exhibit complex dynamics due to their different rebound barriers and possible interconversions.

4.3.4. Camphor Hydroxylation by CYP101—The Product Release Step

According to detailed low temperature electron nuclear double resonance (ENDOR) studies at 200 K, product formation occurs through three distinct hydroxycamphor-bound conformations.[176] The spectroscopic results suggest that the immediate product after hydroxylation corresponds to a nonequilibrium state, involving a more or less normal Fe−O distance (≈2 Å) and that the heme pocket then relaxes in two detectable steps to accommodate the anomalously long Fe−O bond of 2.67 Å, found in the crystal structure.[297]

The product release was reviewed before[32] and will thus only be summarized here briefly. Thus, DFT(B3LYP/B1)/MM calculations[158] on the ferric complex of hydroxy

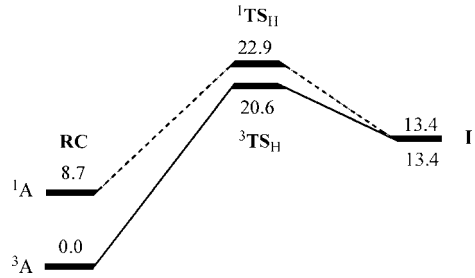

Figure 34. DFT(B3LYP/B1)/MM energy profiles (kcal mol^{-1}) for hydrogen abstraction from camphor by Cpd II in the presence of Wat_{903}.[164]

camphor in its different spin states indicate a doublet minimum at an Fe−O distance of ca. 2.2 Å, and a flat, barrierless potential for the dissociation of the Fe−O bond. Comparisons with analogous calculations on the isolated QM system in the gas phase show that inclusion of the protein/solvent environment lowers the activation energy for bond dissociation in the doublet state because of interactions within the binding pocket and accounts for a significant stabilization of the quartet and sextet states. The DFT(B3LYP)/MM results support the interpretation of the low-temperature ENDOR data[176] that the initially observed nonequilibrium species with a short Fe−O distance is a hexacoordinated product complex in the doublet state. The other two observed species with longer Fe−O distances could well correspond to pentacoordinated quartet and doublet minima with a relaxed protein environment, but a conclusive assignment is not possible in view of the flatness of the computed potential curves.[158]

4.3.5. Camphor Hydroxylation by CYP101—Can Cpd II Compete with Cpd I?

As mentioned above, all attempts to generate Cpd I by shunting the cycle with, e.g., peracids resulted in Cpd II and a radical on a protein residue. To recall, Cpd II is the 1-electron reduced form of Cpd I, with a filled a_{2u} orbital and a triplet ground state, ^3A (see orbitals in Figures 3a and 26). Theoretical considerations of reactivity factors during C−H hydroxylation[174] suggest that Cpd II should be less reactive than Cpd I for two major reasons that are associated with the much poorer electron acceptor capability of Cpd II compared with Cpd I; one is the diminished charge transfer from camphor to the iron-oxo moiety in the transition state, which denies the transition states of Cpd II the stabilization contributed by the polar character of the TS, and the other is the lesser stability of the H-abstracted PorFe(III)−OH/CAM• intermediates. Experimentally it has been shown indeed that synthetic models of Cpd II are able to carry out C−H hydroxylation as well as other oxidation reactions, albeit more slowly than the corresponding Cpd I species.[258] In order to gauge the relative reactivities, Altun et al.[164] explored by means of DFT(B3LYP)/MM the reactivity of Cpd II toward camphor hydroxylation in CYP101, and the energy profiles are depicted in Figure 34. It is seen that, with the same QM model, R1 (Por,SH; truncated-CAM-H), and with the same basis set (B1), the barrier for H-abstraction by Cpd II is 5 kcal mol^{-1} higher than the corresponding one for Cpd I in Figure 31. This sluggish reactivity of Cpd II is in accord with known experimental data.[258] Interestingly, the reaction of Cpd II involves TSR too, since the singlet state of the species (with spin-up and spin-down electrons in the π^* orbitals in Figures 3a and 26) leads to a transition state

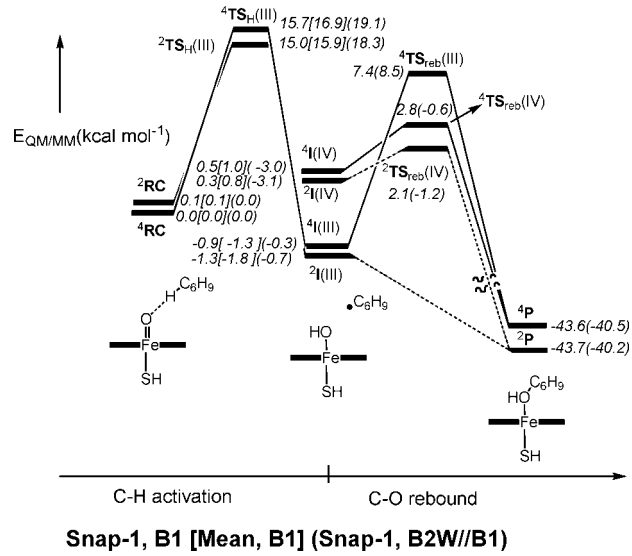

Figure 35. DFT(B3LYP)/MM results for the allylic hydroxylation of cyclohexene, using the R1 model (Por,SH; C_6H_{10}). Each data line contains relative energies for Snap-1, B1 [Mean, B1] (Snap-1, B2W), where the second datum refers to the mean value of seven snapshots (see text).[57,277]

not much higher than ^{3}**TS**$_H$ and a degenerate ^{1,3}**I** intermediate state. While the rebound was not studied, it is clear that the two states, which connect to different electronic structures of the Fe^{II} product complex, will possess different rebound barriers. Additionally, it was found that the H-abstraction barrier of Cpd II is not affected much by the local environment of the propionate side chains (e.g., by the protonation state of Asp_{297}).[164]

4.3.6. Allylic Hydroxylation of Cyclohexene by CYP101

The allylic hydroxylation of cyclohexene by CYP101 was studied by means of DFT(B3LYP)/MM using the simplest QM model R1 (Por,SH) with Wat_{903} (Snap-X) and without it, for altogether eight different snapshots from the MD trajectory.[57,277] The energy profile for the C−H hydroxylation is depicted in Figure 35, for a representative snapshot (Snap-1) and reveals the same biphasic behavior, common to all C−H hydroxylations studied so far, with a bond activation phase and a rebound phase. The relative energies in Figure 35 are given for three different situations (i.e., values for snap-1 and basis B1, mean values for the seven snapshots and basis B1, values for snap-1 and basis B2W). As in camphor hydroxylation, here too, the four electromeric and spin states participate in the rebound. The highest rebound barrier is again[277,296] found for the ^{4}**I**(III) intermediate, while the ^{2}**I**(III) state possesses a barrier free rebound. Unlike in gas-phase models, the ^{2,4}**I**(IV) states both exhibit small barriers to rebound, perhaps due to steric constraints. But the overall picture is similar as in the camphor hydroxylation case; namely, the HS intermediates will possess longer lifetimes than the LS ones.

The role of the pentaradicaloid state of Cpd I ($^6A_{2u}$) was tested for one of the snapshots (Snap-6), and the relative spacing of the transition states, ^{2,4,6}**TS**$_H$, for allylic hydroxylation is shown in Figure 36. It is seen that the energy gap between the lowest of the two transition states, ^{2,4}**TS**$_H$, nascent from the ground triradicaloid state of Cpd I, and the sextet state, ^{6}**TS**$_H$, species is only 2.0 kcal mol^{-1} at the highest level. Thus, as in camphor hydroxylation, here too DFT(B3LYP)/MM predicts that the pentaradicaloid states

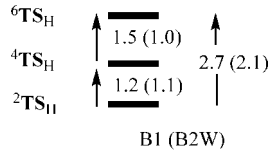

Figure 36. DFT(B3LYP)/MM $^{2,4,6}TS_H$ relative energies (kcal mol^{-1}) for the allylic hydroxylation of cyclohexene, using the R1 model (Por,SH; C_6H_{10}) and the B1 (B2W) basis sets.[277]

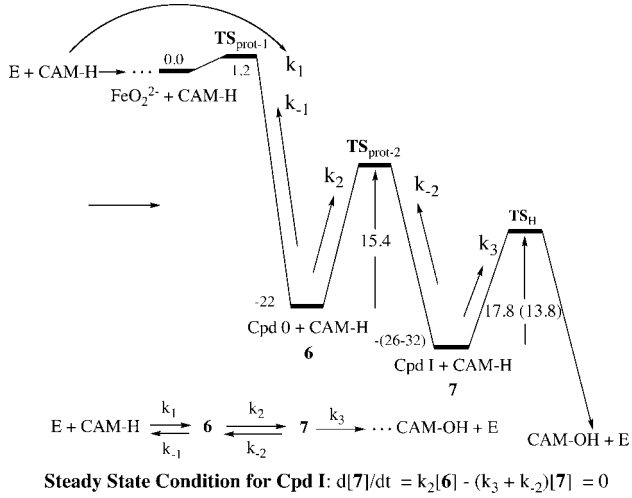

Figure 37. Mechanistic scheme for camphor (CAM-H) hydroxylation by Cpd I (**7**), starting from the enzyme−camphor complex (E+CAM-H) and going via Cpd 0 and Cpd I to the product complex. The relative energies (kcal mol^{-1}) are taken from DFT(B3LYP)/MM calculations.[61,164] The H-abstraction barrier during hydroxylation is given without and with ZPE correction (4 kcal mol^{-1}, as determined from gas-phase calculations[59]). At the bottom is the corresponding kinetic scheme with rate constants, and the steady-state condition for the concentration of Cpd I.

of Cpd I may play a role in C−H hydroxylation reactivity, thus making this a multistate scenario, MSR.

Finally, the H-abstraction barriers in the presence of Wat_{903} (Snap-X) are lower than the Snap-1 barriers for the B1 (B2W) basis by 2.5 (1.7) kcal mol^{-1} in the LS state and by 1.5 (0.5) kcal mol^{-1} in the HS state.[277] Thus, in principle, Wat_{903} still catalyzes the H-abstraction process, but only to a minor extent. Moreover, for B2W, there is one snapshot that has equal barriers with and without Wat_{903}, and therefore the status of the Wat_{903} effect here is not clear without further sampling. As we shall see later, however, the effect on the C=C epoxidation barriers is clear-cut and rate-enhancing. It might thus be that catalysis by Wat_{903} is substrate and reaction dependent.

4.3.7. Why is Cpd I Elusive in CYP101?

As mentioned before, Cpd I of $P450_{cam}$ continues to be an elusive species, which has not yet been detected experimentally in the native working cycle. Under steady-state conditions, the detectability of Cpd I will depend on a few rate constants that involve this species as well as Cpd 0. By now, the relevant energetics are available from DFT(B3LYP)/MM calculations, and we may therefore attempt to tackle this issue better than we did in the past.[32] Figure 37 shows a schematic DFT(B3LYP)/MM potential energy profile for the process from the enzyme camphor complex ES at the peroxo stage (FeO_2^{2-}) through Cpd 0 and Cpd I up to the hydroxycamphor product. The corresponding kinetic scheme is included below the energy profile. Assuming steady state conditions (applied to the concentration of Cpd I), the ratio of Cpd 0 to Cpd I is given by the following expression:

$$d[\text{Cpd I}]/dt = 0 \rightarrow [\text{Cpd 0}]/[\text{Cpd I}] = (k_3 + k_{-2})/k_2 \quad (1)$$

Here k_3 is the rate constant for camphor hydroxylation, k_2 for the formation of Cpd I, and k_{-2} for the reverse process, going back from Cpd I to Cpd 0.

Using the Eyring expression, these rate constants are given as exponentials of the corresponding free energies of activation. While we do not have these free energies, computations of hydrogen abstraction in $P450_{cam}$ indicate a negligible entropic effect.[126] Thus, the computed DFT(B3LYP)/MM barriers with ZPE correction are expected to be good approximations to the corresponding free energies. These barriers and relative energies are presented in Figure 37 for the simplest model R1 (Por,SH) with the largest basis set available for the two processes.[61,159,164] The best estimate of the barrier for O−O bond heterolysis is 15.4 kcal mol^{-1} (LACV3P++**/6-311++G**), while the reaction exothermicity is in the range of 4−10 kcal mol^{-1}.[159] The experimental activation energy for O−O cleavage in the FeOOR complex of CYP119, obtained by shunting the reaction with *m*-chloroperbenzoic acid, is 14.1 kcal mol^{-1};[250] a value which is close to the computational datum and is slightly lower, as would be expected when the departing moiety is *m*-chlorobenzoic acid. The LS H-abstraction barrier from camphor at the highest level is 17.8 kcal mol^{-1} (for the large QM region labeled as R2s).[164] One should not forget, however, that zero-point energy (ZPE) correction reduces this latter value by about 4 kcal mol^{-1} because the contribution from one C−H stretching mode is lost at the transition state.[32] This will lower the H-abstraction barrier down to about 13.8 kcal mol^{-1} ($k_3 \sim 10^3$ s^{-1}); at the same time, the ZPE correction for the O−O cleavage should be significantly smaller. Taking the ZPE correction and the range of calculated exothermicity into account, the reverse barrier for going back to Cpd 0 is 6.4−10.4 kcal mol^{-1} higher than the barrier for H-abstraction. This means that Cpd I will be consumed (k_3) 10^4−10^7 faster than it can revert to Cpd 0 (with k_{-2}). Hence, eq 1 can be simplified to:

$$[\text{Cpd 0}]/[\text{Cpd I}] = k_3/k_2 = \exp[(\Delta E^{\ddagger}_2 - \Delta E^{\ddagger}_3)/RT] \quad (2)$$

While the limited accuracy of our computational data suggests some caution, it is still interesting to describe the scenario that follows from the mechanistic scheme with this data. Thus, if we ignore the tunneling contribution to k_3, the ratio of k_3/k_2 at room temperature will be >10, and at 200 K, which is the cryogenic temperature used to probe the various intermediates in the cycle,[176] this ratio is 55:1, already reaching the detection limit of the experiment. Moreover, if tunneling is important during H-abstraction, this could further lower the effective barrier, maybe by as much as 3 kcal mol^{-1},[298] which would then lead to a value of ca. 10.8 kcal mol^{-1}. In this case, the ratio of concentration becomes 40,000:1, which is clearly way beyond the detection limits. In fact, even a small tunneling correlation that cuts only 1 kcal mol^{-1} from the barrier would place the ratio at 600:1, again outside the detection limit. One should note, however, that the measured kinetic isotope effects (KIEs) do not provide conclusive evidence for tunneling in $P450_{cam}$: the KIE values for camphor hydroxylation (ca. 4−5)[299] are lower

than those for norbornane hydroxylation (ca. 11)[300] and thus less indicative of tunneling. Be this as it may, the scenario in Figure 37 seems already sufficient to rationalize the elusiveness of Cpd I. Furthermore, in the case of the T252X mutants (section 3.6.3), where the barrier for the conversion of Cpd 0 to Cpd I can rise up to 17 kcal mol^{-1}, the likelihood of probing Cpd I is even smaller than in the WT enzyme. One can also include in the steady state derivation of eq 1 other reactions which consume Cpd I, e.g., the reduction of Cpd I to the resting state (the oxidase reaction)[180] or its autoxidation etc. In such a case, eq 1 will include in the numerator a sum of all the rate constants corresponding to the consuming reactions. For the WT enzyme, all these rate constants are smaller than k_3 (the rate constant for oxidation) and hence eq 2 is still valid. Of course, this scenario predicts that Cpd I can be observed in cases where k_3 is made very small, e.g., by using a perfluorinated derivative of camphor, or in cases where k_2 is large, e.g., by the design of an appropriate mutant. The experiment with 5,5-difluorocamphor led to exclusive hydroxylation at C-9.[12] To the best of our knowledge, experiments with perfluorinated substrates have not been carried out.

4.4. DFT/MM Studies of C═C Epoxidation by Cpd I of P450

Alkene epoxidation by P450 and other Cpd I reagents has many of the puzzling mechanistic features that have been discussed for C−H hydroxylation.[8,301] Several experimental observations, such as occasional *cis*/*trans* isomerization,[302] sensitivity of the reaction to the donor capability of the olefin,[303] production of aldehydes,[302,304] and formation of heme-alkylated products ("suicidal complexes"),[10,18] indicate that the mechanism involves intermediates which are very likely of different nature. Indeed, the proposed mechanistic schemes[8,301] suggest the incursion of radicals, cations, and radical cationic intermediates. Theory was used to shed light on these mechanistic puzzles.

DFT(B3LYP)-only calculations have been carried out on the epoxidation of ethene,[36,305] propene,[150] cyclohexene,[277] styrene,[306] and 5-methylenylcamphor.[26,307] Most of these studies have been reviewed already[32] and will not be discussed here in detail; we shall only mention the essential features. The reaction profile is very similar to the one found for C−H hydroxylation; the mechanism follows a nonsynchronous MSR with competing HS and LS pathways and a few electromeric varieties, as shown in Scheme 5. An initial C═C bond activation step proceeds via nonsynchronous transition states, to the iron alkoxy radical species, $^{4,2}\mathbf{I}_{rad}$ (i.e., PorFeO-CR′H-CRH$^{\bullet}$), which are of the $\mathbf{I}_{rad}$(III) and $\mathbf{I}_{rad}$(IV) varieties. In addition, there are cationic situations, $\mathbf{I}_{cat}$ (e.g., PorFeO-CR′H-CRH^{+}), that are generated by electron transfer from the carbon radical moiety into the heme. In all the cases, the LS species, be they radicals or cations, collapse in a barrier-free manner to the epoxide with conserved stereochemistry of the alkene, while all the HS state electromers give rise to epoxide with scrambled stereochemistry or to aldehyde and suicidal byproduct (^{4}**AC**, ^{4}**SC**). The choice depends on the barriers for epoxide-ring closure; thus, $^4\mathbf{I}_{rad}$(IV) with the lowest ring closure barrier gives epoxides with scrambled stereochemistry, while $^4\mathbf{I}_{rad}$(III) with the highest ring closure barrier crosses (and/or mixes) with the HS cationic states and leads to the aldehyde complex and the suicidal complex.

Scheme 5. DFT-Only Computed Mechanistic Schemes of Alkene Epoxidation by Cpd I and of Byproduct Formation in the High-Spin (HS) and Low-Spin (LS) Manifolds

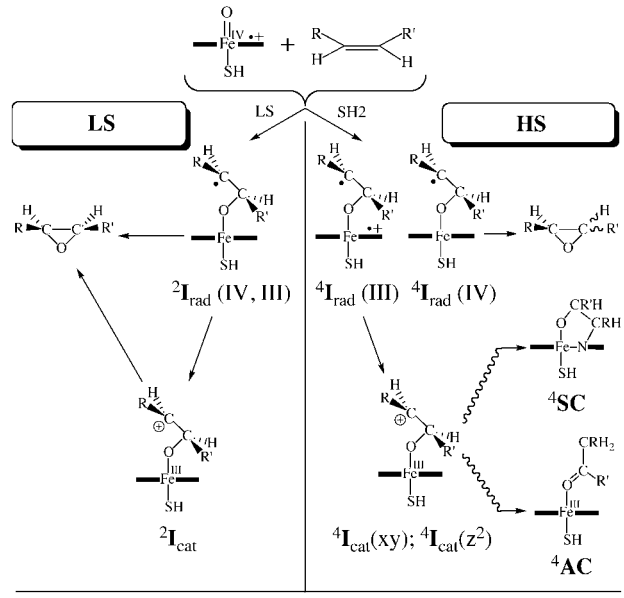

To complement the picture, two DFT(B3LYP)/MM studies of C═C epoxidation have been carried out by the Jerusalem group, using propene and cyclohexene as substrates.[57,277] The two substrates were chosen because they have been used amply in P450 chemistry.[194,308] The focus of the study was on the mechanistic details of epoxidation and the effects of the protein on these mechanisms; no attempt was made to explore the side product formation, as was done in the DFT(B3LYP)-only studies. In the following we discuss only the reactions of cyclohexene, since propene exhibits essentially similar trends.

Figure 38a shows the energy profiles in the gas phase.[57,277] The mechanism displays MSR whereby different electromers and spinomers participate in two phases, C═C bond activation followed by ring closure. The gas-phase profile reveals rather small bond activation barriers, which increase by 2−3 kcal mol^{-1} with the larger basis set (B2W). ZPE corrections are negligible, and we can assume that this will also be the case in the protein. As expected, the $^{2,4}\mathbf{TS}_C$ transition states are essentially of Fe^{IV} character and lead to ^{2,4}**I**(IV) intermediates. Using TDDFT, $^4\mathbf{TS}_C$(III) was found to lie ca. 15 kcal mol^{-1} above the $^4\mathbf{TS}_C$(IV) species. The ring closure exhibits barrier-free LS processes and a moderate barrier for the ^{4}**I**(IV) species. The ^{4}**I**(III) species was located and had a much higher barrier to ring closure, as expected from results for other model systems.[26,37,306,307]

The situation within the protein is shown in Figure 38b, which depicts the DFT(B3LYP)/MM energy profile for one of the snapshots (Snap-5, others are similar) selected from the MD trajectory, as well as the mean relative energies for all snapshots. Since cyclohexene is a symmetric molecule, one might expect similar bond activation barriers for an attack on either carbon atom of the double bond C$^{\alpha}$═C$^{\beta}$. However, in the protein environment, these two carbon atoms are no longer equivalent, and therefore, the reacting carbon atom in each snapshot was selected as the one having the shortest C···O distance in the initial complex.

Inspection of Figure 38b shows that the lowest-energy transition states are $^2\mathbf{TS}_C$(III) and $^4\mathbf{TS}_C$, with the latter having mixed Fe^{IV} and Fe^{III} character (as judged from the spin density). However, in other snapshots (Snaps-X, 1, 2, and

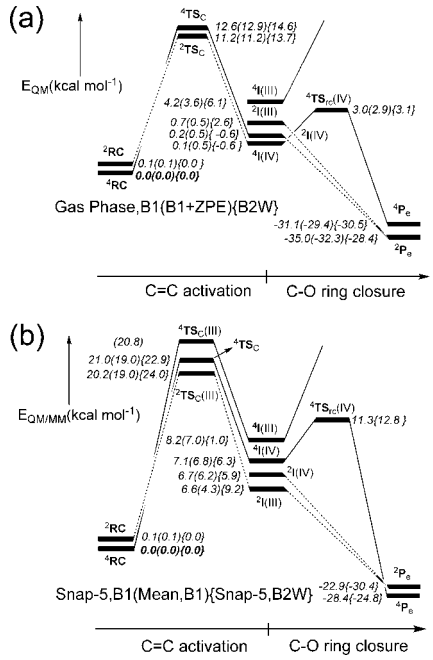

Figure 38. (a) Gas-phase DFT(B3LYP)-only energy profiles during cyclohexene epoxidation, using the R1 model (Por,SH; C_6H_{10}); energy data are given for B1 (B1+ZPE) {B2W}. (b) DFT(B3LYP)/MM results for cyclohexene epoxidation using the R1 model (Por,SH; C_6H_{10}). Each data line contains relative energies for Snap-5,B1 (Mean,B1) {Snap-5,B2W}, where the second datum refers to the mean value of seven snapshots (see text).[57,277]

6), ^{4}**TS**$_C$ is of Fe^{III} type; this underscores the fact that the electromeric states tend to be very close in the protein. TDDFT calculations were performed on all transition states and confirmed that the quartet transition states are the ground state in each snapshot. Similar to the gas phase, in the protein too, the ring-closure phase involves the two electromers in two spin-state varieties; the LS species exhibit a barrier-free process, while the HS ones have significant barriers, and the longest lived intermediate is the ^{4}**I**(III) species. This confirms the conclusions derived from DFT(B3LYP)-only studies[306] that the stereorandomization (*cis* and *trans*) of the epoxide is due to ^{4}**I**(IV) and ^{4}**I**(III), while the suicidal and aldehyde complexes will be nascent from the ^{4}**I**(III) type intermediate (see Scheme 5).

The bond activation barriers in the enzyme (Figure 38b) are seen to be significantly higher than those in the gas phase (Figure 38a), and this is reflected in the corresponding TS energies. The transition state geometries for the bond activation phase are depicted in Figure 39 for both the gas phase and the protein. In all these structures, the cyclohexene assumes an upright position; the parallel position was not explored because the corresponding initial ^{2,4}**RC** complexes were higher in energy. Figure 39 displays structures typical for epoxidation TSs,[37,150] showing elongation of the C═C and Fe—O bonds and shortening of the Fe—S bond. The gas-phase species have earlier "reactant like" structures compared with the in-protein species, i.e., longer C···O distances, shorter C═C distances, and longer Fe—S distances. This shift of the transition state by the protein is no doubt the origin of the increased barriers within the protein. As discussed before,[150] the electromeric nature of the species is apparent by comparing ^{4}**TS**$_C$ and ^{4}**TS**$_C$(III); the latter has shorter C···O bonds and longer Fe—O and Fe—S bonds, caused by the electron transfer from the $\pi_{C=C}$ orbital to the antibonding π^*_{xz} orbital of the Fe═O moiety (see Figure 26). The corresponding snapshot-averaged geometrical properties of ^{4}**TS**$_C$ and ^{4}**TS**$_C$(III) are similar to those of Snap-5.

Finally, we note that, as in the camphor hydroxylation study,[61] the lowest barriers in the protein are again found for Snap-X, which includes the Wat_{903} molecule. This barrier is invariant to whether Wat_{903} is part of the QM or MM region, which indicates that the influence of Wat_{903} is largely electrostatic, as noted before. For the mean barrier over all snapshots, the energy-lowering effect of Wat_{903} amounts to 4.0 (3.5) kcal mol^{-1} for B1 (B2W), thus once again highlighting the biological role of water as a catalytic species. This effect is somewhat less prominent in the allylic hydroxylation case (see above), suggesting that the catalytic role of water is reaction and substrate dependent.

4.5. DFT/MM and DFT-Only Studies of Aromatic Hydroxylation by Cpd I of P450

Arene hydroxylation by cytochrome P450 enzymes still poses tantalizing questions, concerning both the reaction mechanism and the toxicity of some of the metabolites.[10,12] The reaction yields typically three types of products, phenol, cyclohexenone, and arene oxide, which are shown in Scheme 6 using the reaction of benzene as an example.

The P450 mediated conversion of arene to phenol (**P**) has traditionally been viewed as a means of detoxification and excretion of the toxic arene by the biosystem. By contrast, arene oxide (**AO**) is carcinogenic and mutagenic through its interaction with, e.g., DNA and other cellular material.[309−312] The relationship between the two products became intriguing, when mechanistic investigations[311,312] led to the conclusion that the arene oxide is an intermediate in this reaction and the phenol is one of its byproducts. Further studies indicated that arene oxide is an obligatory intermediate in arene hydroxylation.[313,314] However, in the course of time, new evidence appeared that questioned these conclusions and served to propose alternative pathways proceeding through radical and/or cationic Meisenheimer intermediates.[10,12,315,316] However, based on the detailed analysis of Ortiz de Montellano,[10] it is fair to say that as yet there is no consensus mechanism that is unequivocally established or that can rule out all others. Scheme 7 summarizes the main mechanistic hypotheses for arene hydroxylation by Cpd I.

A universal feature of arene hydroxylation[10,12,311,312] is the migration of the substituent from the site of hydroxylation to the adjacent carbon (so-called "NIH-shift"). The substituent migration results in a partial skeletal retention of the original hydrogen of the activated C−H bond. This observation leaves in Scheme 7 those hypotheses that account for the NIH-shift. For clarity we labeled in the scheme the migrating hydrogen atom with D to identify the position of this atom in all intermediates.[12] In mechanism a, everything is channeled through the arene oxide,[312] which is postulated to be the primary product of the enzymatic reaction. In a subsequent nonenzymatic step, the epoxide ring opens to the zwitterionic species, which can further react in two different manners: A hydrogen/deuterium exchange will produce phenol (**P**, **P′**) whereas a 1,2-hydride (deuteride) shift to the carbocationic center (NIH-shift) will give rise to cyclohexenone (**K**), which can, in turn, enolize to the phenol.[10,12,311,312] Mounting experimental evidence, of various kinds, has revealed, however, that phenol and ketone formation is unlikely to proceed through arene oxide.[315,316] Hence, in the alternative mechanistic hypothesis b, all products are generated from the tetrahedral intermediate σ-complexes; the

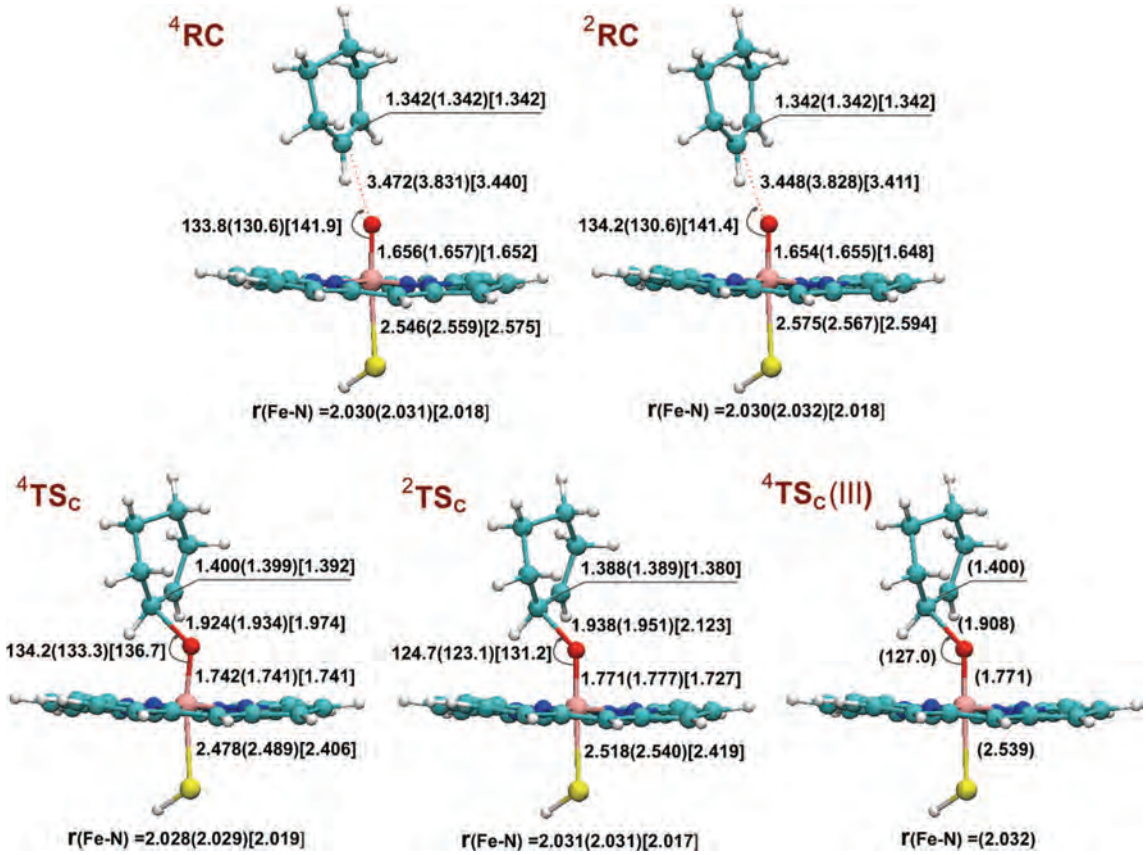

Figure 39. DFT(B3LYP/B1)-only and DFT(B3LYP/B1)/MM optimized key distances (Å) and angles (degree) of the stationary points during cyclohexene epoxidation (see Figure 38). Each data line reports three values, Snap-5 (mean) [gas-phase]. The mean values for the eight snapshots studied are always found to be rather similar to those for Snap-5 (see text).[57,277]

Scheme 6. Observed Products during Arene Hydroxylation by P450

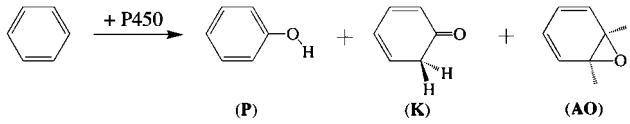

phenol and ketone are formed directly from the intermediate cationic σ-complex (***σ*-C$^+$**) (Scheme 7),[315−317] while arene oxide formation is suggested[316] to transpire from the radical σ-complex intermediate (***σ*-C$^\bullet$**). Parts of scheme b have gained indirect support from kinetic isotope effect measurements,[316] regiochemical studies,[316] frontier orbital theoretical arguments, and local density Xα type calculations that ruled out concerted epoxidation as the initial activation step of substituted benzene by Cpd I.[318,319] A related mechanism c that involves an initial electron transfer,[6,10,12,320] followed by collapse to the σ-complexes, was suggested too, but the existence of a free (diffusive) radical cation of the arene has not been demonstrated yet.[10,12,315] The role of charge transfer from the arene to the iron porphyrin has nevertheless been inferred from kinetic isotope effects, e.g., for the *meta* hydroxylation of chlorobenzene.[315] Clearly, the catalysis of arene hydroxylation by P450 offers a rich and complex mechanistic puzzle. Despite the support accumulated thus far for the σ-complex based mechanism b, there still exist counterarguments and compelling evidence for the intermediacy of benzene oxide, as in mechanism a.[10,12] Furthermore, the postulated pathways that lead to arene oxide vis-à-vis phenol/ketone products are still under debate. Is the arene oxide intermediary tenable? Are there really both radicalar and carbocationic σ-complexes?[315] And if they exist, how precisely do they rearrange to yield ketone and phenol products?

Initial DFT(B3LYP)-only calculations, by de Visser and Shaik,[38] and subsequently by Bathelt et al.,[33,34] addressed the reaction mechanism and concluded, in agreement with the mechanisms proposed by Korzekwa et al.[315] and Rietjens et al.,[316] that the process involves initial electrophilic attack on the π-system of benzene, to form Meisenheimer complexes of hybrid character, i.e., σ-C$^+$ with a substantial admixture of σ-C$^\bullet$[38] (see mechanism b in Scheme 7). Incorporation of bulk polarity and amidic H-bonds to the thiolate[38] was found to increase the cationic nature of the intermediate, raising the positive charge on the benzene moiety to >0.5. These studies[33,34,38] also found that the lowest pathway occurs preferentially via the doublet spin state. Bathelt et al.[34] demonstrated that the same LS mechanism operates for an extended series of arenes, and they derived useful structure−reactivity correlations. There was also consensus[33,34,38] that the σ-C$^+$ Meisenheimer complex leads to all the products in Scheme 6, and de Visser and Shaik[38] further demonstrated that the epoxide product (**AO**) is a dead-end product that does not transform to phenol (**P**) or ketone (**K**). Many of these features were confirmed in the most recent DFT-only study of 17 arene hydroxylation reactions.[172]

Theory also revealed some novel aspects of the mechanism, which are shown in Scheme 8. Thus, de Visser and Shaik[38] found that, starting from the hybrid $^2\sigma$-C$^+$/$^2\sigma$-C$^\bullet$ Meisenheimer complex, the oxygenated benzene moiety transfers a proton from the *ipso* carbon to one of the nitrogen atoms of the porphyrin ring to form the protonated porphyrin intermediate, ^{2}**I**$_{NH}$ (path a in Scheme 8). This is possible since

Scheme 7. Alternative Mechanistic Hypotheses for Arene Oxidation by P450 (Reprinted with Permission from ref 38. Copyright 2003 American Chemical Society)

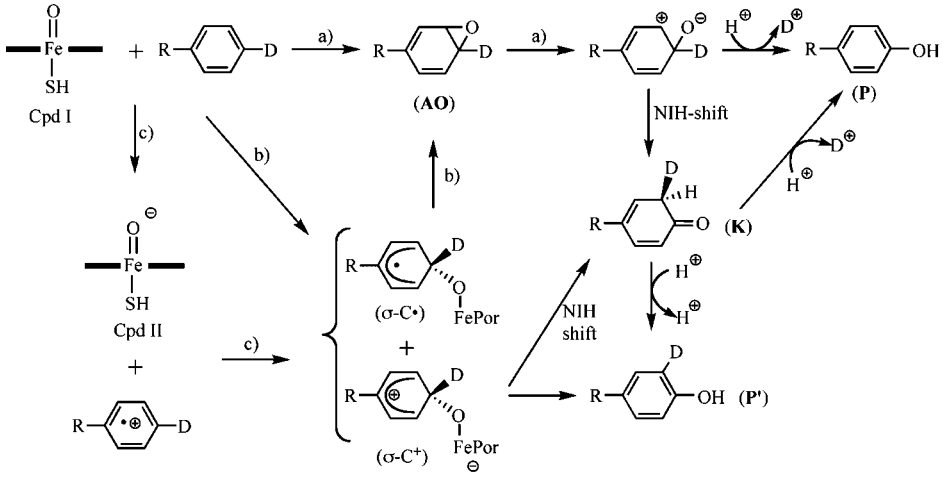

Scheme 8. Theoretically Derived Mechanisms of Phenol (P) and Ketone (K) Formation from the Hybrid Meisenheimer Complexes in Side-on and Face-on Conformations[33,34,38]

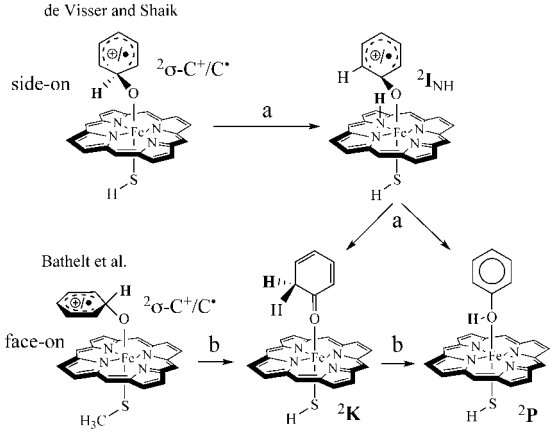

The original "H" that migrates during the processes is indicated in bold.

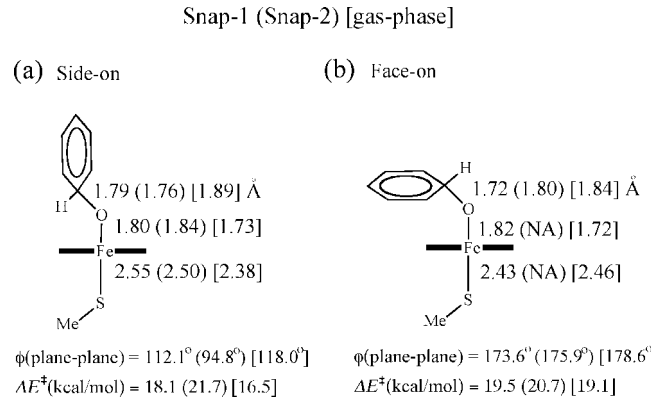

Figure 40. DFT(B3LYP/B1)-only and DFT(B3LYP/B1)/MM optimized transition state structures and barriers (in kcal mol^{-1}), for the (a) side-on and (b) face-on conformations. Reprinted with permission from ref 60 using new data from the author (J. N. Harvey). Copyright 2007 American Chemical Society.

the nitrogens in the porphyrin are basic. The intermediate then reprotonates the oxo group to form phenol (^{2}**P**) and the *ortho* carbon to produce the ketone (^{2}**K**). In contrast to this proton-shuttle mechanism, Bathelt et al.[33,34] found that the Meisenheimer $^2\sigma$-C$^+$/C$^\bullet$ intermediate undergoes a 1,2-H shift (path b in Scheme 8) from the *ipso* to the *ortho* carbon and generates ^{2}**K**, which can subsequently undergo further rearrangement to the phenol, ^{2}**P**.

Thus, while the two mechanisms in Scheme 8 are different, they both account for the NIH shift, whereby the original "H" from the arene ends on either the ketone or phenol products. The reason for the two different mechanisms is obvious from Scheme 8, where it is seen that, in the study of de Visser and Shaik,[38] the phenyl plane is perpendicular to the porphyrin (side-on) and the *ipso* C−H bond is in direct contact with one of the nitrogen atoms of the porphyrin, thus leading to an instantaneous proton transfer and reshuttle mechanism as described in mechanism a in Scheme 8. By contrast, in the initial study of Bathelt et al.[33] the phenyl ring is parallel to the porphyrin plane (face-on), and the *ipso* C−H bond points away, thus being prone to skeletal rearrangement by 1,2 hydride shifts, as in mechanism b in Scheme 8. In a subsequent study, Bathelt et al.[34] confirmed the proton-shuttle mechanism a for the NIH shift, and the results of the two groups converged. Indeed, in the protein pocket both conformations may exist and contribute to the NIH shift.

4.5.1. DFT/MM Studies of Benzene Hydroxylation by CYP2C9

The mechanism was recently reinvestigated by Bathelt et al.[60] using DFT(B3LYP)/MM calculations for benzene hydroxylation by CYP2C9, starting from an X-ray structure (pdb: 1OG2), which lacked a substrate and hence could be used to accommodate benzene without conformational bias due to the presence of another substrate. After a short MD equilibration, two snapshots were selected for each of the benzene conformations of Scheme 8, the face-on and the side-on structures. The calculations were restricted to the LS state.

Figure 40 depicts transition state geometries for the two bond activation transition states and provides additional data as well as comparison with the gas-phase structures of Bathelt et al.[60] The calculations show that the two conformations, face-on and side-on, are competitive inside the protein, as postulated before.[32] The computed barriers of 18.1−21.0 kcal mol^{-1} are in good accord with experimental data in CYP2E1,[321] obtained by conversion of the rate constants to free energy barriers. The barriers in the protein are slightly larger than those in the gas phase, and the corresponding

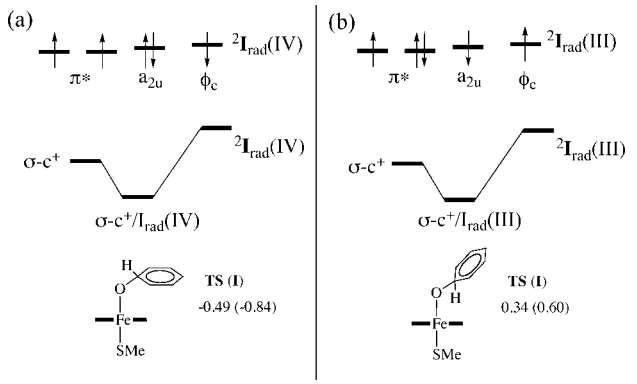

Figure 41. VB mixing diagrams showing the cationic/radicalar hybrid character, as well as the generation of (a) negative and (b) positive spin density on the phenyl moiety in the radical. DFT(B3LYP)/MM computed spin densities[60] in the transition state (**TS**) and intermediate (**I**) are shown beneath the mixing diagrams.

TSs occur somewhat earlier (see the C···O distances). It was noted[60] that the Meisenheimer complexes are destabilized in the protein relative to the gas phase, and hence, this behavior follows the Hammond principle.

Another interesting feature is the electronic structure of the transition states and the Meisenheimer hybrid $^2\sigma$-C$^+$/C$^\bullet$ intermediate. Thus, while, in both the DFT-only and DFT/MM calculations, the transition states and intermediates have a hybrid cationic/radicalar nature, with spin density as well as charge (+0.3 to +0.57) residing on the benzene moiety, the computed spin density was positive in both face-on species, while it was positive in one and negative in the other snapshot of the side-on species. This hybrid nature and the sign of spin densities on the phenyl moiety can be understood by reference to the orbital occupancy diagrams for the Meisenheimer intermediates in Figure 41. Thus, in Figure 41a, we show a mixing of the cationic state with a radicalar state, corresponding to ^{2}**I**(IV). We recall from Figure 26 that this radicalar state arises from a shift of a spin-up electron to the a$_{2u}$ orbital of the heme, thus resulting in a negative spin density on the benzene moiety (see the ϕ_C orbital); the mixing of this radicalar state with the cationic state will lead to some negative spin density on the benzene moiety in the hybrid state. This is precisely the spin density computed in the transition state and the intermediate Meisenheimer complex, shown underneath the mixing diagram. By comparison, in Figure 41b, we show a similar mixing but now with the ^{2}**I**(III) electromer, which by reference to Figure 26 arises by shifting a spin-down electron to one of the π*(FeO) orbitals of the heme and, hence, generating now a positive spin density on the benzene moiety, as shown underneath the mixing diagram. Clearly, therefore, benzene hydroxylation may involve MSR as well with different electromeric states, which may be addressed in future studies.

Finally, the DFT(B3LYP)/MM calculations support the proton-shuttle mechanism with an N-protonated intermediate (^{2}**I**$_{NH}$) as a viable pathway for phenol production. Figure 42 shows in a schematic manner the various barriers nascent from the collapse of the side-on (SO) and face-on (FO) Meisenheimer $^2\sigma$-C$^+$/C$^\bullet$ intermediates to the various products. Considering these barriers, it seems that the side-on complex leads preferentially to epoxide and to phenol, the latter via the N-protonated porphyrin species (the proton shuttle mechanism in Scheme 8). The ketone is generated from both face-on and side-on pathways with approximately the same barriers.

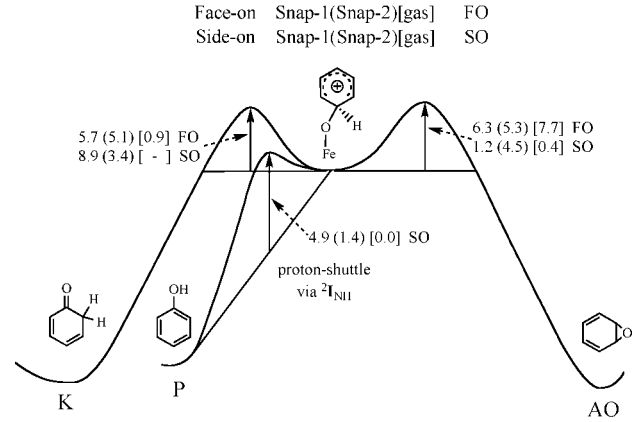

Figure 42. DFT(B3LYP)/MM and DFT(B3LYP)-only computed barriers (kcal mol^{-1}) for the collapse of the face-on (FO) and side-on (SO) Meisenheimer complexes to the three products of arene oxidation by P450.[60] The energy profiles are featureless; note, however, that the SO path proceeds to the phenol product via ^{2}I$_{NH}$.

Scheme 9. Products Formed during Oxidative P450 Dehalogenation of Polyhalogenated Benzene[165]

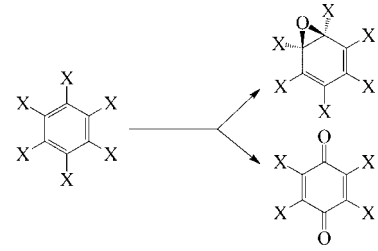

In conclusion, the DFT(B3LYP)/MM study of Bathelt et al.[60] recovers the basic features of the DFT(B3LYP)-only studies,[33,34,38] while accounting in detail for the role of the protein.

4.5.2. DFT-Only Studies of Oxidative Dehalogenation of Perhalogenated Benzenes by P450

Polyhalogenated aromatics are persistent hazardous environmental pollutants.[322,323] While partially halogenated arenes are degradable by some organisms,[324−327] more extensively halogenated species are degraded at a very slow rate.[328] P450 enzymes have the potential to oxidatively metabolize halogenated benzenes, so much so, that a considerable effort has been put into engineering of bacterial P450s with enhanced dehalogenation kinetics.[329−335] P450-catalyzed dehalogenation generally produces 1,4-diquinones and arene oxides, as shown in Scheme 9. The mechanism of formation of these and other species during P450 dehalogenation has been a topic of extensive debate.[336]

In order to elucidate the mechanism of dehalogenation and to identify potential primary products, Hackett et al.[165] performed DFT-only calculations of a few polyhalogenated benzene derivatives. The authors used the PBE functional with the resolution-of-identity approximation to expedite geometry optimization, hence RI-PBE, and complemented this by single-point energy calculations using B3LYP. Despite the different geometry of Cpd I compared with B3LYP, the triradicaloid nature of Cpd I is apparent even at the RI-PBE level, so that the mechanisms deduced by this study are most likely reliable.

The reaction of Cpd I with hexachlorobenzene (HCB) is shown in Figure 43. It is seen that the reaction is concerted,

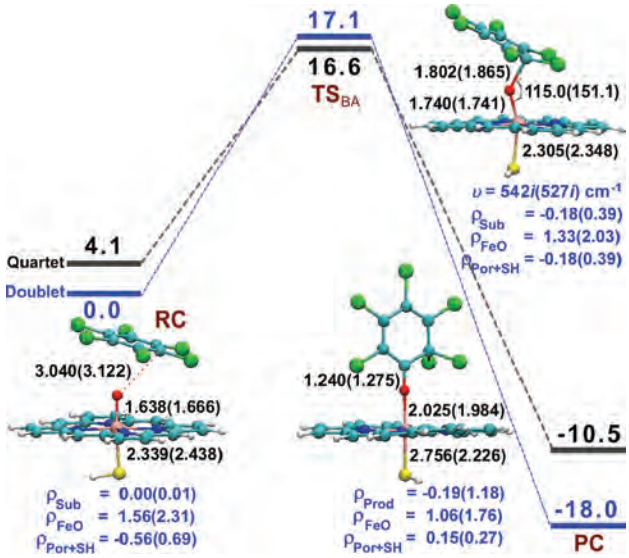

Figure 43. DFT-only calculations of the first step in the oxidative dehalogenation of hexachlorobenzene by P450 Cpd I. Numerical results for bond lengths (Å), angles (degree), and spin densities ρ refer to the doublet (quartet) state. The energy profiles (kcal mol^{-1}) come from RI-PBE/TZVPP calculations at RI-PBE/TZVP,SV(P) optimized geometries. Reprinted with permission from ref 165. Copyright 2007 American Chemical Society.

involving π-attack of Cpd I on the hexachlorobenzene, with concomitant 1,2-Cl shift. The transition states are virtually degenerate for the doublet and quartet spin states, but in the product complex, the doublet state is significantly lower than the quartet at the RI-PBE level, which tends to overstabilize low-spin states. The final organic product in the reaction is 2,2,3,4,5,6-hexachloro-3,5-cyclohexadienone.

Even though the Meisenheimer intermediates are not formed in this concerted process, inspection of the spin density (ρ) data for the transition states (^{2,4}**TS**$_{BA}$) reveals a similar electronic structure as during benzene hydroxylation (see above). The negative spin density on the HCB moiety of ^{2}**TS**$_{BA}$ indicates an Fe^{IV} type species, and the small charge development on the same moiety reveals a primary radical nature, and not cationic or hybrid ones, as in the benzene hydroxylation case.

The concerted nature of the transition states depends however on the halogen, and in the case of hexafluorobenzene (HFB), shown in Figure 44, there are two well separated TSs: a bond activation **TS**$_{BA}$ species, going to a Meisenheimer-type intermediate, **I**$_{\sigma\text{-C}}$·, followed by a 1,2-F-shift **TS**$_{shift}$ species. The final product is a 2,2,3,4,5,6-hexafluoro-3,5-cyclohexadienone. The similarity to the benzene hydroxylation is apparent; the spin density on the HFB moiety in the ^{2}**I**$_{\sigma\text{-C}}$· intermediate is large and negative (−0.50), while the charge is small, thus indicating a mostly radicalar mechanism nascent from the Fe^{IV} electromer (see Figure 41a). Interestingly, the bond activation barrier for the reaction of Cpd I with HFB is substantially lower (5.3 (RI-PBE) and 13.8 kcal mol^{-1} (B3LYP)) than that with HCB. While Hackett et al.[165] did not account for this difference, we propose tentatively that the effect is associated with the well-known fluoro effect of stabilizing radical species.[337]

2,2,3,4,5,6-Hexahalo-3,5-cyclohexadienones, which are the primary products in Figures 43 and 44, have not been observed experimentally but could well be key intermediates for the formation of tetrahaloquinones during P450 oxidation. The experimentally observed product from hexachlorobenzene is pentachlorophenol. Hackett et al.[165] suggested that this product is obtained from 2,2,3,4,5,6-hexacholoro-3,5-cyclohexadienones by electron capture from the reductase followed by a loss of chloride ion, another reduction, and formation of pentachlorophenol as shown in Scheme 10. Alternatively, the reduction can arise from nonenzymatic soluble biological factors in aqueous solution. Hackett et al. have verified that the 2,2,3,4,5,6-hexahalo-3,5-cyclohexadienones have sufficiently large electron affinities to be easily reducible.

Once the pentachlorophenol is formed, another Cpd I-mediated oxidation by π-attack would lead, in a mechanism analogous to the one shown in Figure 43, to 4-hydroxy-2,2,3,5,6-pentachloro-3,5-hexadienone (and the corresponding *meta*- and *ortho*-attack products), as sketched in Scheme 11. At physiological pH, deprotonation of 4-hydroxy-2,2,3,5,6-pentachloro-3,5-hexadienone and Cl^{-} expulsion will predominate and yield the tetrachloroquinone. This mechanism is general, only in that, in the perfluoro case, the F^{-} expulsion requires incorporation of bulk solvation in the calculations.

With mixed chloro−fluoro derivatives, the calculations reproduce the experimentally observed preferential oxidation at the fluorinated sites. The calculations predict a barrier that is substantially smaller, by 4−6 kcal mol^{-1}, for the π-attack on the fluorinated site compared with a chlorinated site. Once again, this intriguing fact may reflect effects of radical stabilization by fluorine.[337] However, confirmation of this effect will require a close analysis of the spin density distribution on fluorine vs chlorine to assess the role of hyperconjugative interactions between the developing radical in the benzenic moiety and the COF vs COCl moieties in the **TS**$_{BA}$ species.

In summary, the study of Hackett et al.[165] on oxidative dehalogenation and the above studies on benzene hydroxylation demonstrate that activation of aromatic substrates generally proceeds by π-attack on the aromatic ring. The low barriers for oxidative defluorination suggest that P450s can be very effective in detoxification of fluorinated aromatics. Of course, without further DFT/MM studies or at least DFT-only studies augmented with bulk polarity effects, this conclusion should be considered tentative.

4.6. DFT-Only Studies of *N*-Dealkylation of *N*,*N*-Dimethylaniline Derivatives

The mechanism of *N*-demethylation of *N*,*N*-dimethylanilines (DMAs) by cytochrome P450 is a highly debated topic in mechanistic bioinorganic chemistry. Scheme 12 describes the two rival mechanistic hypotheses. Thus, one mechanism labeled as (i) in Scheme 12 suggests that the reaction starts by the usual H-atom abstraction (HAT) reaction, followed by rebound to form the carbinolamine, which decomposes subsequently in a nonenzymatic reaction to give rise to formaldehyde and a dealkylated amine.[338−342] The alternative mechanistic hypothesis, labeled as (ii), starts with a single electron transfer (SET) from the amine to Cpd I,[343−354] followed by proton transfer to the Cpd II species and proceeding with a rebound to form the carbinolamine, which then decomposes as outlined above.

The HAT-first mechanism has been supported by kinetic isotope effect (KIE) profiles, which showed that the KIEs measured for P450 oxidation of a series of *para*-substituted *N*,*N*-dimethylanilines (*p*-X-DMAs), by a few isoforms, correlate linearly with the KIEs measured for the same *p*-X-

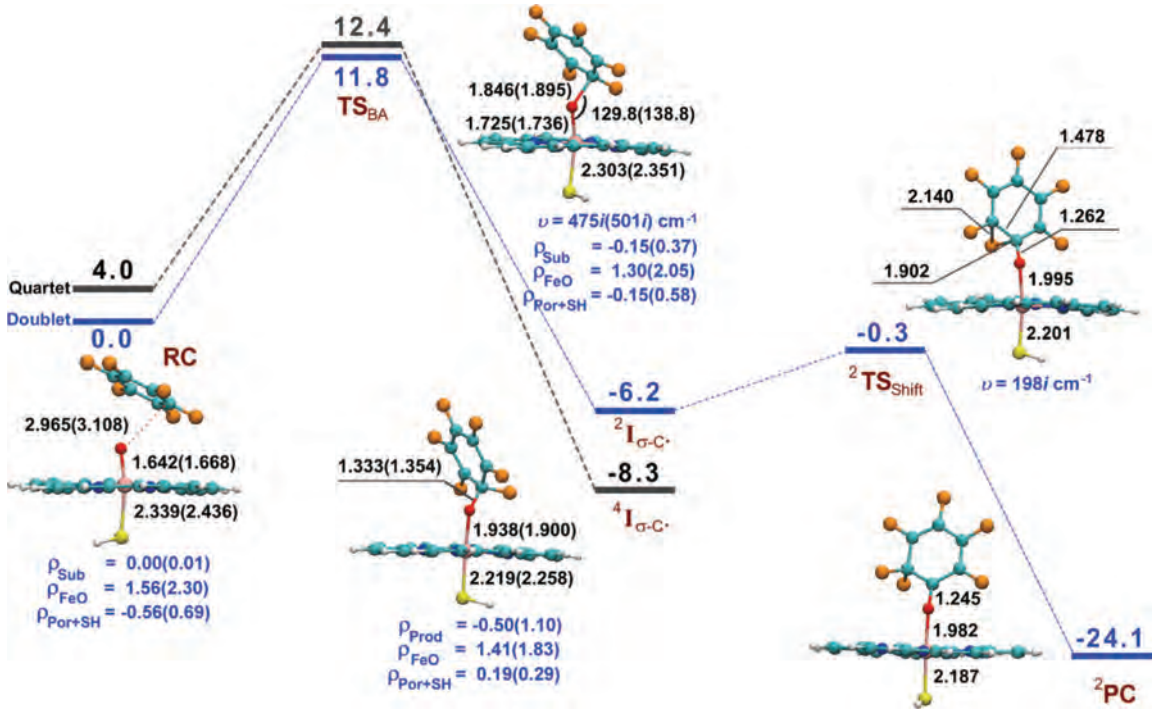

Figure 44. DFT-only calculations of the first step in the oxidative dehalogenation of hexafluorobenzene by P450 Cpd I. Numerical results for bond lengths (Å), angles (degree), and spin densities ρ refer to the doublet (quartet) state. The energy profiles (kcal mol^{-1}) come from RI-PBE/TZVPP calculations at RI-PBE/TZVP,SV(P) optimized geometries. Reprinted with permission from ref 165. Copyright 2007 American Chemical Society.

Scheme 10. Proposed Mechanism for the Formation of the Ferric-Phenolate Complex by Electron Transfers from the Reductase, Followed by Cl$^-$ Expulsion[165]

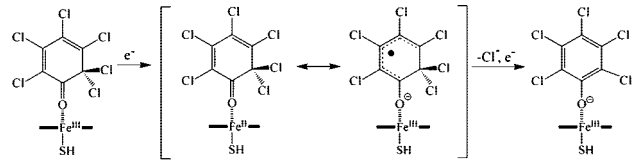

Scheme 11. Proposed Mechanism for the Formation of the Tetrachloroquinone Product, Starting with Cpd I Oxidative Dehalogenation of Pentachlorophenol and Followed by Nonenzymatic Elimination of HCl[165]

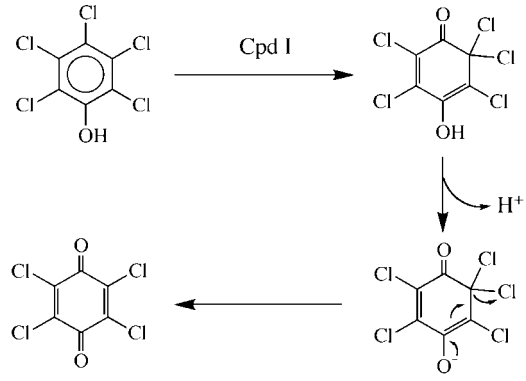

Scheme 12. Mechanistic Hypotheses for *N*-Dealkylation of Amines: Mechanism (i) Involves Hydrogen Atom Transfer (HAT) First, While Mechanism (ii) Involves Single Electron Transfer (SET) First[a]

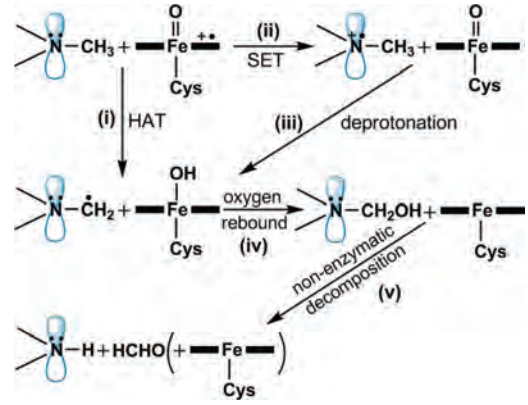

[a] The two mechanisms converge at the carbinolamine decomposition, which is proposed to occur nonenzymatically. Reprinted with permission from ref 167. Copyright 2007 American Chemical Society.

DMAs series in a real HAT reaction with the *t*BuO$^\bullet$ radical.[338−341] In addition, use of clock substrates[355−359] and other experimental criteria[342,360−363] seemed to rule out amine cation radical formation. The SET-first mechanism has been supported by the facts that (a) the KIE values are low and seem atypical of HAT reactions[343,344,346,352,353] and (b) the reaction rates for N-demethylation of *p*-X-DMAs correlate nicely with Hammett substituent parameters (which are negative)[345,347−351,354,364−367] and with the redox potential $E_{1/2}$ values of the *p*-X-DMAs.[345,347−351,354,364−367]

Since all these pieces of evidence are more or less circumstantial, it was essential to study the *N*-dealkylation by theoretical means. This was done using DFT(B3LYP)-only calculations of the reactions of Cpd I with four *para*-(H, Cl, CN, NO_2) substituted DMAs used in the experimental research.[167] An initial study of the unsubstituted DMA itself with Cpd I[166] showed that the SET-first hypothesis, at least for this substrate, is less likely, since the electron-transferred DMA$^{\bullet+}$/Cpd II species are significantly higher in energy than the DMA/Cpd I pair, both at the cluster geometry and at the corresponding TS geometry (without and with inclusion of bulk polarity effects). The second study[167] showed also a

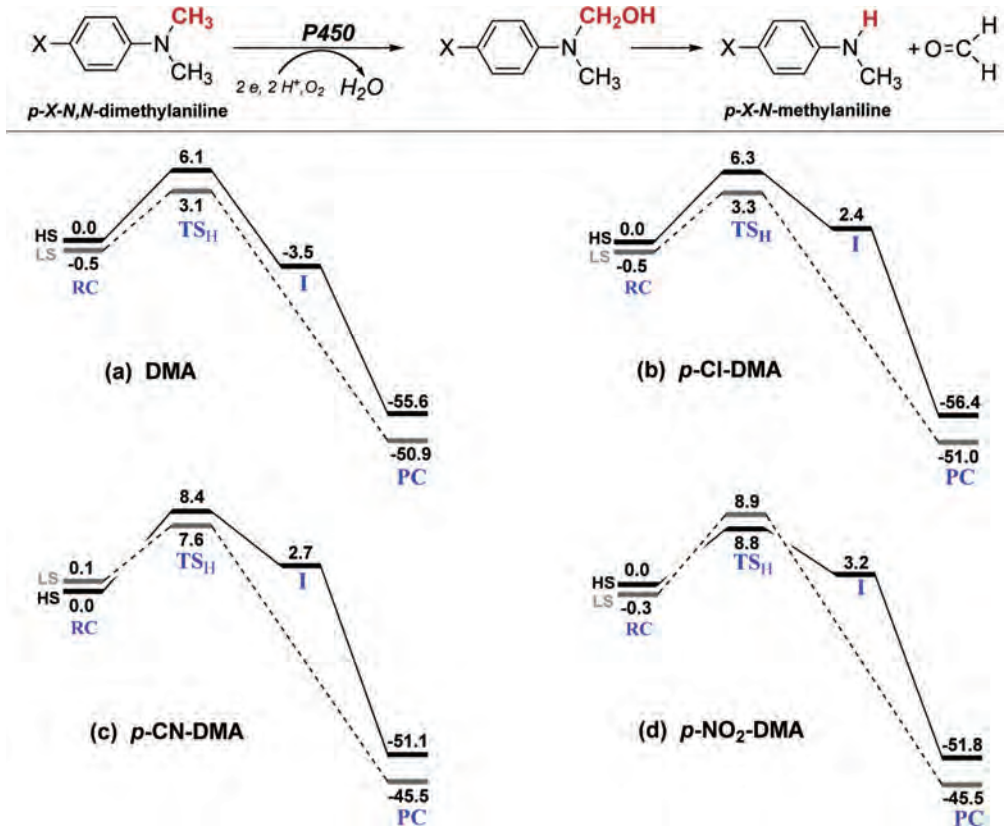

Figure 45. DFT(B3LYP)-only energy profiles (kcal mol^{-1}) for C−H hydroxylation of *p*-X-DMA (X = H, Cl, CN, NO_2). Geometries were optimized with the B1 basis, while the relative energies were determined using a larger basis, LACV3P+(Fe)/6-31+G*(rest), with inclusion of ZPE, bulk polarity (ε = 5.6), and NH···S corrections. Reprinted with permission from ref 167. Copyright 2007, American Chemical Society.

HAT mechanism. In addition, the calculated KIE_{LS} for the low-spin (LS) HAT reaction of the pristine DMA (X = H) agrees closely with experiment. These results then led to the conclusion that all the reactions proceed by HAT-first, and it remained to understand the various structure−reactivity correlations and low KIEs that implied SET-first, using the HAT-first mechanism.

Figure 45 shows the energy profiles for the reactions of Cpd I with the *para*-(H, Cl, CN, NO_2) substituted DMAs, at the highest level, with the LACV3P+*(Fe)/6-311+G*(rest) basis set, including bulk polarity (ε = 5.7) and two NH···S amidic H-bonds to the thiolate ligand.[167] Both the LS and HS profiles exhibit a transition state for HAT, ^{2,4}**TS**$_H$; there are no intermediates, and the "^{4}**I**" feature in the figure is a shoulder and not a real intermediate. It is seen that the energy difference between the ^{2}**TS**$_H$ and ^{4}**TS**$_H$ species depends on the *para* substituent: the gap is largest for *p*-H and *p*-Cl, ca. 3.0 kcal mol^{-1}, and smaller in the other cases, 0.8 kcal mol^{-1} for *p*-CN and 0.1 kcal mol^{-1} for *p*-NO_2. As a whole, there is a switch from a single-state mechanism (SSM) in the *p*-H and *p*-Cl case, which will proceed preferentially via the LS state, to TSR in the *p*-CN and *p*-NO_2 case.

The structures of ^{2,4}**TS**$_H$ are displayed in Figure 46. They exhibit some interesting trends with regard to the progress along the H-transfer coordinate, C···H···O. In the LS species, ^{2}**TS**$_H$, the pristine case (*p*-H) has the shortest C−H and longest O−H bond and is hence the "earliest". As the substituent becomes more electron withdrawing, from *p*-Cl to *p*-NO_2, the transition state occurs progressively later. In the HS species, ^{4}**TS**$_H$, the transition states are more advanced along the H-transfer coordinate but exhibit a smaller amount of variation in the series, compared with the LS species.

The calculated KIE values are collected in Table 2, together with the experimental KIE values. The KIE_{LS} values are smaller than the corresponding KIE_{HS} values, and they exhibit a variation consistent with the Melander−Westheimer postulate that the KIE value reflects the position of the TS along the H-transfer coordinate; the earlier the position, the smaller is the KIE—much the same as in the experimental data. The small values for *p*-H and *p*-Cl reflect the early nature of the corresponding TSs, as reasoned by Dinnocenzo and co-workers.[338−341] By contrast, the KIE_{HS} values are almost constant, in line with the smaller variation in geometry of these species (Figure 46), and the larger values manifest the more "central" position of the respective TSs, precisely as expected from the Melander−Westheimer postulate. Furthermore, the absolute magnitudes of the KIEs correlate with the reaction barriers and with the extent of the C−H elongation in the **TS**$_H$ species. It is apparent that the KIE values and the KIE profile are entirely congruent with the HAT nature of the reaction.

Figure 47 shows plots of computed $KIE_{HS,LS}$ values against experimental values, KIE_{expt}. Obviously, the KIE_{HS} values do not correlate with the experimental data, while the KIE_{LS} values do so quite well (see Figure 47a and b). Finally, Figure 47c presents the correlation of a blended KIE with the experimental values. The blending coefficient was determined by fitting the KIE differences in the series to the experimental ones.[167] As can be seen, the computational data match experiment perfectly, such that, in the case of *p*-H and *p*-Cl with a large energetic preference for the LS state, the reactivity is exclusively LS, and as the electron withdrawing power of the substituent increases and the LS preference decreases, there is a shift to TSR. This blending fits also

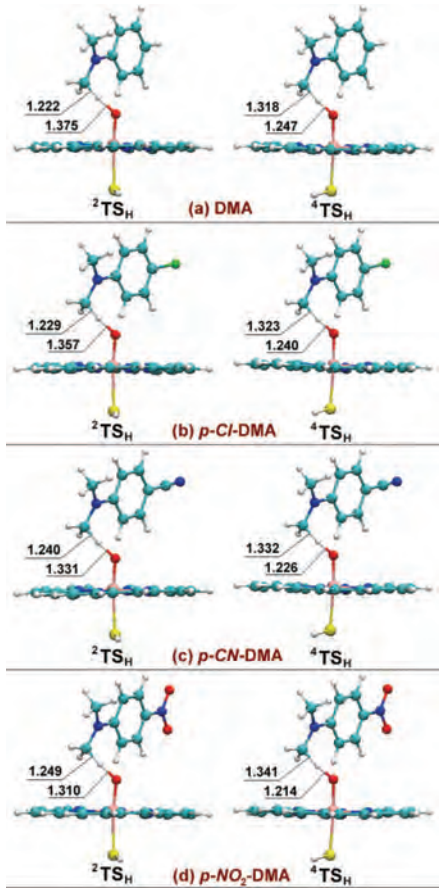

Figure 46. DFT(B3LYP/B1) optimized transition states (Å) for C−H hydroxylation of *p*-X-DMA (X = H, Cl, CN, NO_2). Reprinted with permission from ref 167. Copyright 2007 American Chemical Society.

Table 2. DFT(B3LYP/B1)-Only Computed[a] KIE Values for *p*-X-DMA, along with Experimental Values

	DMA	*p*-Cl-DMA	*p*-CN-DMA	*p*-NO_2-DMA
KIE_{HS}	5.5	5.4	5.5	5.6
KIE_{LS}	3.6	3.8	4.2	4.4
KIE_{exp}	2.6	2.8	3.6	4.0

[a] From ref 167.

nicely with the change in the computed $^4\mathbf{TS}_H-{}^2\mathbf{TS}_H$ energy gaps in Figure 45, where initially the LS TS is significantly lower and finally becomes virtually degenerate with the HS TS for the electron withdrawing substituents.

Since the KIEs fit a HAT-first mechanism, then, what about the observed Hammett correlations and the correlation with the redox potentials of the DMAs, discussed above? Figure 48a shows the computed barriers for the LS states plotted against the Hammett substituent parameters. The correlation is linear and has a negative slope, in perfect agreement with the experimentally observed negative Hammett slope value. Figure 48b indicates that the LS barriers for HAT correlate nicely with the redox potential $E_{1/2}$ of the *p*-X-DMAs. Clearly, therefore, the computed barriers for a HAT-first mechanism reproduce the experimental correlations and demonstrate thereby that these correlations cannot serve as a proof for a SET-first mechanism.

Having seen that all the experimental trends are reproduced by the DFT(B3LYP) calculations using a HAT-first mechanism, the question to ask is: what is the mechanistic information of the experimentally observed correlations?

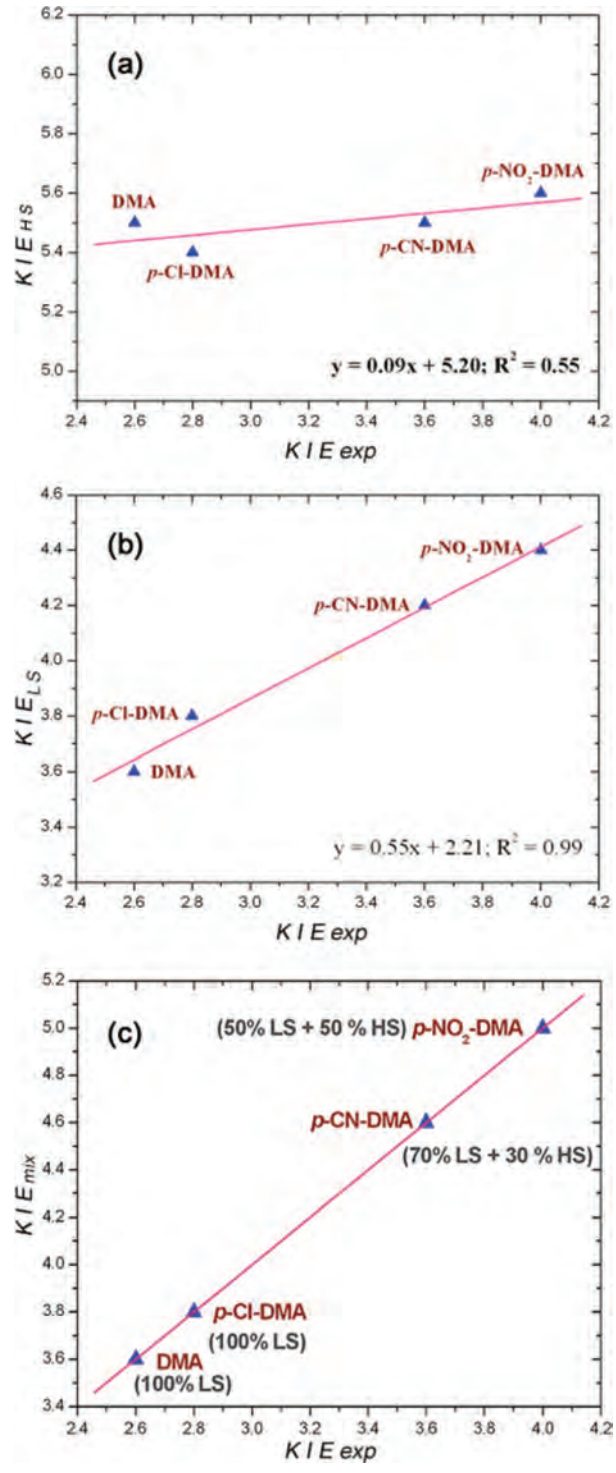

Figure 47. DFT(B3LYP/B1) calculated $KIE_{HS,LS}$ values and experimental data, KIE_{exp}, for C−H hydroxylation of *p*-X-DMA (X = H, Cl, CN, NO_2): (a) KIE_{HS} plotted against KIE_{exp}, (b) KIE_{LS} plotted against KIE_{exp}, and (c) KIE_{mixed} plotted against KIE_{exp}. Reprinted with permission from ref 167. Copyright 2007 American Chemical Society.

Some clue is given by Figure 49, which shows linear correlations of the spin density, ρ(N), on the nitrogen adjacent to the CH_3 group being activated, for the HS and LS $\mathbf{TS}_H$ species, with the Hammett substituent constants. The nitrogen atom accumulates spin density during the reaction because its lone pair can conjugate with the nascent radical on the carbon as the C−H bond is being cleaved and stabilize it. Thus, as the *para* substituent becomes increasingly more electron withdrawing, the nitrogen lone pair is "sucked" by

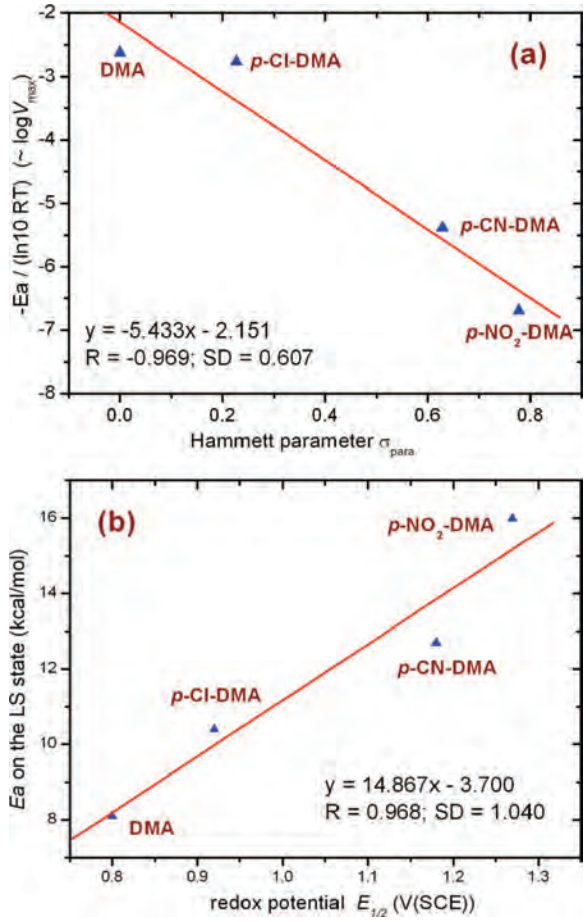

Figure 48. Plots of calculated LS barriers for *p*-X-DMAs against (a) the Hammett substituent parameter of *p*-X and (b) the redox $E_{1/2}$ values of *p*-X-DMAs. Reprinted with permission from ref 167. Copyright 2007 American Chemical Society.

the substituent and the spin density on N decreases. Hence, the *para* substituent X communicates with the TS by changing the accessibility of the nitrogen lone pair to interact with the activated C−H bond, as well as by transferring charge to the Cpd I moiety. The less electron withdrawing the substituent, the more accessible is the lone pair, and the larger is the stabilization of the nascent radical, since more charge will be transferred from the aryl group to the C---H---O(FePor) moiety in the TS. This is the main reason for the good correlation of the barriers with the Hammett substituent constants and with the redox potential of the DMA. All these correlations reflect the "polar" character of the process; it is not an SET process but an HAT process that involves "partial charge transfer character". Indeed, all the cases exhibit a positive charge accumulation on the *p*-X-DMA moiety in the TS.

This stabilization mechanism endowed by the nitrogen lone pair is shown in Scheme 13 using three resonance VB structures (**R**1−**R**3) which represent the formation of a new covalent O−H bond (**R**1), the three-electron resonance stabilization of the $CH_2^{\bullet}$ moiety by the nitrogen lone pair (**R**2), and polar contributions to the TS (**R**3). As the *para* substituent X becomes more electron withdrawing, the resonance structures **R**2 and **R**3 become less important and the TS stabilization diminishes. The correlation with the Hammett substituent constants thus reflects the attenuation of the conjugation between the nitrogen lone-pair and the cleaving C−H bond in the TS by the ring substituent. One can witness in fact this weakening of the conjugation due to the electron withdrawal of X = CN and NO_2, by inspecting the orbitals of the $\mathbf{TS}_H$ species.[167] The impaired delocalization causes in turn destabilization of the $\mathbf{TS}_H$ species for the more electron withdrawing substituents and requires a higher degree of C−H bond cleavage, and hence also a larger KIE value.

4.6.1. KIE is a Reliable Probe of Spin State Selectivity in Oxidation of DMAs

The correlation of computed and experimental KIE values in Figure 47 as well as the results of the preliminary study for the pristine DMA[166] show that in fact KIE can serve as a reliable probe of the spin state selectivity of Cpd I. Thus, with the pristine DMA and the *p*-Cl-DMA, where the H-abstraction $^2\mathbf{TS}_H$ has a significantly lower energy than the corresponding HS species, the observed low KIE values reflect the LS-only reactivity. As the substituent becomes increasingly more electron withdrawing, the electronic advantage of the LS mechanism diminishes, causing $^2\mathbf{TS}_H$ and $^4\mathbf{TS}_H$ to approach one another in energy, and as a result the observed KIE becomes a blended mixture of KIE_{LS} and KIE_{HS}. The use of KIE as a probe for spin state reactivity has been demonstrated before for the gas-phase activation of norbornane by FeO^+, where the exo-CH and endo-CH bonds exhibited very different KIEs that turned out to correspond to the LS and HS process, respectively.[368] This idea found use in other C−H bond activation processes as well, e.g., in the observation of KIE jumps during the oxidation of DMA by the native Cpd I vis-à-vis Cpd I prepared using the PhI═O oxygen surrogate.[292] As shown in that study, the use of PhI═O leads preferentially to the HS Cpd I species, and when the oxidation barrier is as small as in DMA, the latter gets oxidized by the HS spin state before spin interconversion can occur.

4.6.2. Decomposition of the Carbinolaniline Initial Product

After methyl hydroxylation of DMA, the so formed carbinolaniline decomposes as shown in Scheme 14. The conventional wisdom is that this process occurs in a nonenzymatic manner after the carbinolaniline is released and most likely leaves the active site. The DFT(B3LYP) calculations[167] confirm this supposition; thus, the binding energies of the carbinolaniline to the heme are very small (8.5 kcal mol^{-1} for the doublet ferric complex), whereas the decomposition barriers are much larger (≥30.3 kcal mol^{-1} for the doublet state complex). Furthermore, as shown in Figure 50, the decomposition reaction is assisted by water molecules, which are abundant on the protein surface. Thus, the barrier for decomposition is 29.6 kcal mol^{-1} without water assistance and drops to 14.8 kcal mol^{-1} after the addition of a single water molecule. The reason for this large effect is clear from the structure of the decomposition transition state, $\mathbf{TS}_{decomp}$, in Figure 50. Thus, in the absence of a water molecule, the hydroxyl H migrates to the nitrogen atom via a strained four-membered cyclic structure, while in the presence of a water molecule the water mediates the H-migration via a six-membered cyclic TS which is strain-free. We have not pursued further whether more water molecules will reduce the barrier even more.

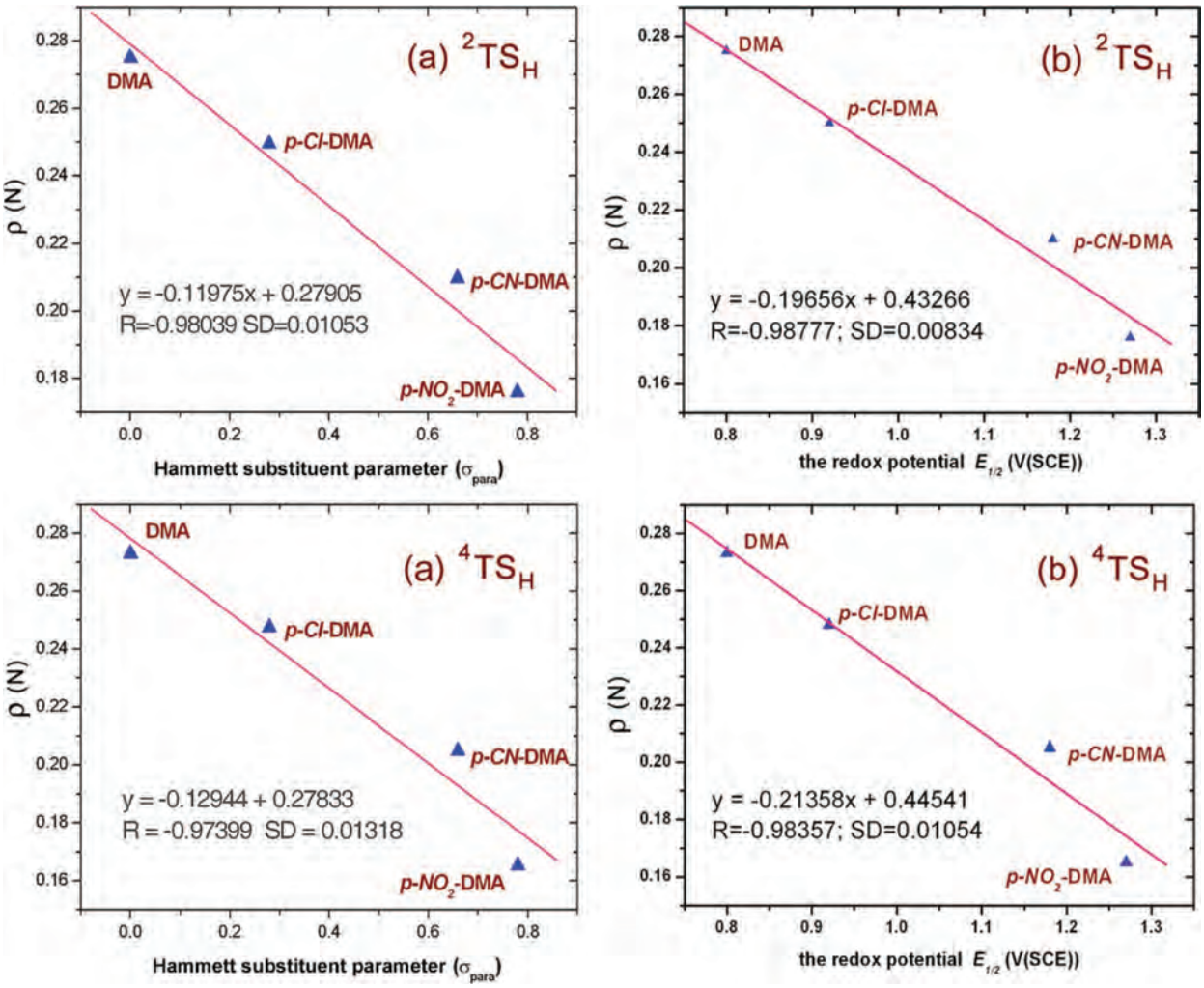

Figure 49. Plots of calculated spin density, ρ(N), on the nitrogen atom adjacent to the activated C−H bond of $^2\mathbf{TS}_H$ and $^4\mathbf{TS}_H$, against the (a) Hammett substituent parameter of *p*-X, and (b) redox $E_{1/2}$ values of *p*-X-DMAs. Reprinted with permission from ref 167. Copyright 2007 American Chemical Society.

Scheme 13. Three of the Resonance Structures That Contribute to the Stabilization of TS_H for C−H Hydroxylation in *p*-X-DMA[a]

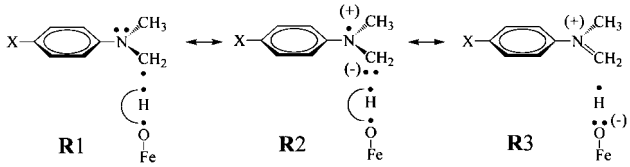

[a] The curved lines connecting the electrons signify spin-paired electrons (covalent bonding).

Scheme 14. Decomposition Reaction of Carbinolanilines

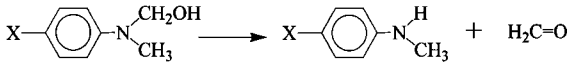

4.6.3. Summary of the Mechanistic Findings on Dealkylation of DMAs by Cpd I

The DFT(B3LYP) calculations resolve mechanistic controversies, offer a consistent mechanistic view, and reveal the following features. (a) The reaction pathways involve C−H hydroxylation by Cpd I followed by a nonenzymatic carbinolamine decomposition, which is assisted by water molecules. (b) C−H hydroxylation is initiated by a hydrogen atom transfer (HAT) step that possesses a "polar" character. As such, the HAT energy barriers correlate with the $E_{1/2}$ values and the HOMO energies of the DMAs. (c) The series exhibits a switch from spin-selective reactivity for DMA and *p*-Cl-DMA to two-state reactivity, with low- and high-spin states, for *p*-CN-DMA and *p*-NO_2-DMA. (d) The computed kinetic isotope effect profiles for these scenarios match the experimentally determined profiles. Furthermore, KIEs and TS structures vary in a manner predicted by the Melander−Westheimer postulate: as the substituent becomes more electron withdrawing, the TS is shifted to a later position along the H-transfer coordinate and the corresponding KIE increases. (e) Theory shows that a KIE can serve as a reliable probe of the spin-state selectivity of Cpd I.

4.7. DFT-Only Studies of Sulfur and Nitrogen Oxidation

4.7.1. Sulfur Oxidation

An early DFT(B3LYP) investigation of sulfoxidation of dimethyl sulfide (DMS) from 2003[52] has already been reviewed.[32] In this initial work, it was found that the sulfoxidation of DMS involves a single step that occurs preferentially from the HS quartet state. The LS TS turned out to be higher in energy and distorted as though performing porphyrin oxidation. Subsequently, two independent studies showed that there is indeed a lower-energy TS[169,171,293] that

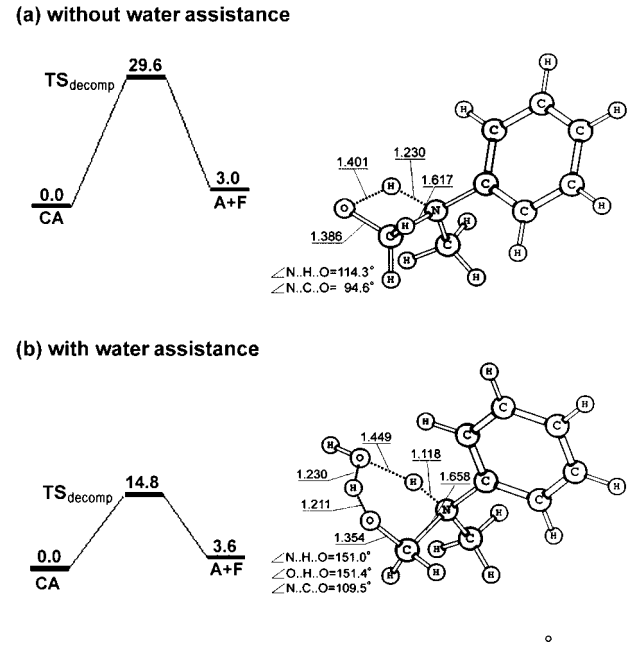

Figure 50. DFT(B3LYP) calculated transition states (distances in Å) and energy profiles (kcal mol^{-1}) for the carbinolaniline (CA) decomposition reaction to aniline (A) and formaldehyde (F): (a) without water assistance, and (b) with water assistance. Relative energies were determined using a large basis, LACV3P+(Fe)/6-31+G*(rest), and including ZPE, bulk polarity (ε = 5.6), and NH···S corrections.[167]

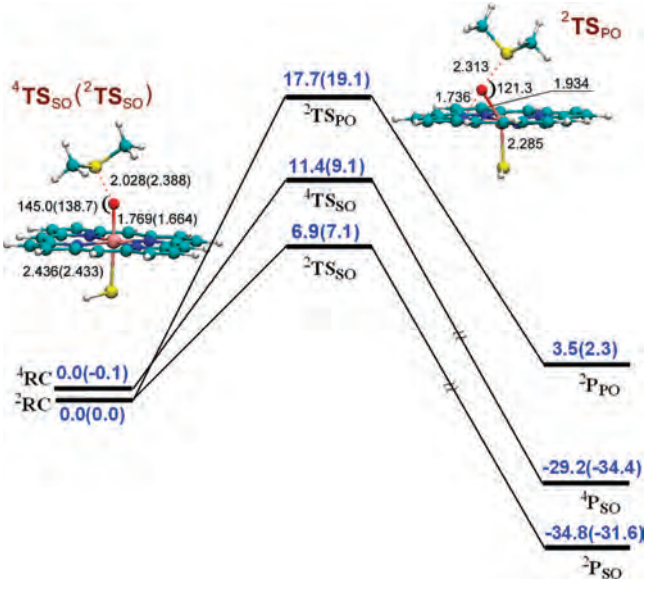

Figure 51. DFT(B3LYP/LACVP**) optimized transition states during sulfoxidation of dimethyl sulfide by Cpd I in the doublet and quartet state (^{2,4}**TS**$_{SO}$) and corresponding energy profiles. The ^{2}**TS**$_{PO}$ species corresponds to porphyrin self-oxygenation by Cpd I. The relative energies (kcal mol^{-1}) in each line come from single-point calculations with the LACV3P+(Fe)/6-311++G**(rest) basis (in parentheses: with inclusion of ZPE, bulk solvation (ε = 5.7), and NH···S hydrogen bonding corrections). Reproduced with permission from ref 169. Copyright 2007 Wiley-VCH Verlage GmbH & Co KGaA.

was missed in the original study because of the extreme flatness of the energy surface.

Figure 51 shows the results obtained by Li et al.[169,293] using DFT(B3LYP/LACV3P++**) and including ZPE corrections and the effects of bulk polarity and NH···S hydrogen

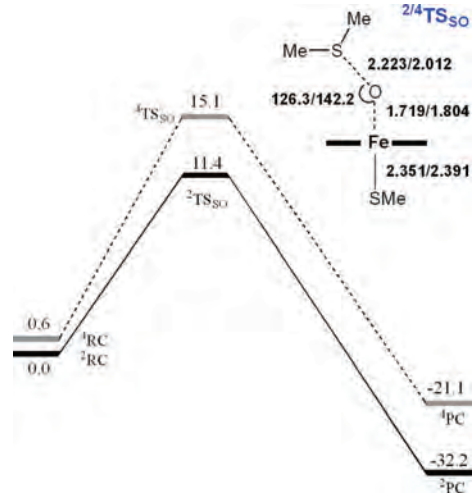

Figure 52. DFT(B3LYP/DZP) transition states for the sulfoxidation of dimethyl sulfide by Cpd I in the doublet and quartet states, and corresponding energy profiles (kcal mol^{-1}). Relative energies from single-point calculations using a large basis set with double polarization and diffuse functions. Reprinted with permission from ref 171. Copyright 2008 American Chemical Society.

Scheme 15. Different Electronic Reorganization Events Leading to ^{2}TS$_{SO}$ and ^{4}TS$_{SO}$ during Sulfoxidation by Cpd I

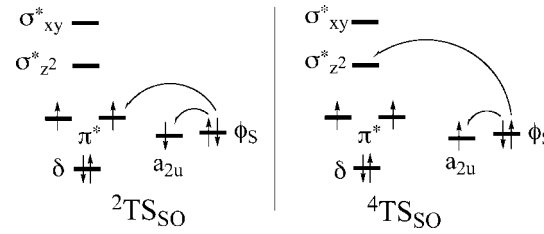

bonding. It is seen that the lowest-energy **TS**$_{SO}$ species is the doublet with a barrier of merely 7.1 kcal mol^{-1}, somewhat higher than the bond activation barrier in DMA but still very small, showing that sulfoxidation is facile. About 2.0 kcal mol^{-1} higher is a quartet ^{4}**TS**$_{SO}$ species. When neglecting bulk polarity, H-bonding, and ZPE corrections, the ^{4}**TS**$_{SO}$ species lies 4.5 kcal mol^{-1} above ^{2}**TS**$_{SO}$. Still considerably higher in energy is the distorted LS transition state, labeled as ^{2}**TS**$_{PO}$, which was wrongly assigned in 2003 as a sulfoxidation TS.[52] The label ^{2}**TS**$_{PO}$ signifies that this is a transition state for porphyrin oxidation, leading to N−O porphyrin adducts found experimentally.[16]

Figure 52 shows the DFT(B3LYP)-only results of Olsen and Ryde[171] using a large basis set. While the numerical values of the barriers and the key geometric features of the ^{2,4}**TS**$_{SO}$ species are different from those in Figure 51, the trends are similar, showing preference for the LS pathways.

In retrospect, the preference for the LS process should have been clear all along, for the same reasons that have been discussed for the HS and LS rebound processes during C−H hydroxylation. Thus, as shown in the orbital occupancy diagrams in Scheme 15, a LS state can be generated by shifting an electron from the sulfur lone-pair orbital (ϕ_S) to one of the low-lying π^* orbitals of the oxo-heme. By contrast, in the HS process, one electron must be shifted to the high lying $\sigma^*_{z^2}$ orbital, which raises the energy of the ^{4}**TS**$_{SO}$ species, compared with ^{2}**TS**$_{SO}$.

4.7.2. Nitrogen Oxidation

DFT(B3LYP) studies of oxo-transfer to aminic nitrogen have been reported by two groups,[171,292,369] using DMA and trimethylamine (TMA). They arrive at a mechanism similar to the one discussed above for sulfoxidation: the reaction is a synchronous oxo-transfer from Cpd I to the nitrogen atom, and it occurs preferentially on the LS surface, with the HS mechanism having barriers that are higher by 7 kcal mol^{-1} for DMA[292,369] and by 4−5 kcal mol^{-1} for TMA.[171,369]

Interestingly, the reverse reaction whereby the N−O compound transfers an oxygen to the heme to form Cpd I has been used by Dowers et al.[256] to study the mechanism of N-dealkylation of DMA derivatives by Cpd I. The feasibility of the oxo-transfer from the N-oxide derivative of DMA to the heme has been addressed in two recent studies,[292,369] which found a barrier of the order of 17−18 kcal mol^{-1} (or 13.6 kcal mol^{-1} after including bulk polarity and NH···S H-bonding effects). The complete energy profile[369] is shown in Figure 53 for only the LS state. It is seen that if one starts from the LS ferric complex of the N-oxo-DMA ($^2\mathbf{P}_{NO}$), the oxo-transfer to the heme is the rate controlling step, followed by a very fast step of C−H hydroxylation of one of the CH_3 groups of DMA. In such a scenario, Cpd I is not observable, but one might think about using the same technique with the N-oxide of hexafluorinated *p*-NO_2-DMA-F_6, in which case the subsequent reaction of Cpd I will become competitive or faster.

4.8. A DFT-Only Study of Ethanol Oxidation by P450

Lieber and DeCarli have suggested already in the late 1960s that the microsomal CYP2E1 is responsible for alcohol dehydrogenation activity in the liver.[370−372] This suggestion was followed by a surge of studies of toxicology aspects, such as acidosis and fatty liver disease, associated with

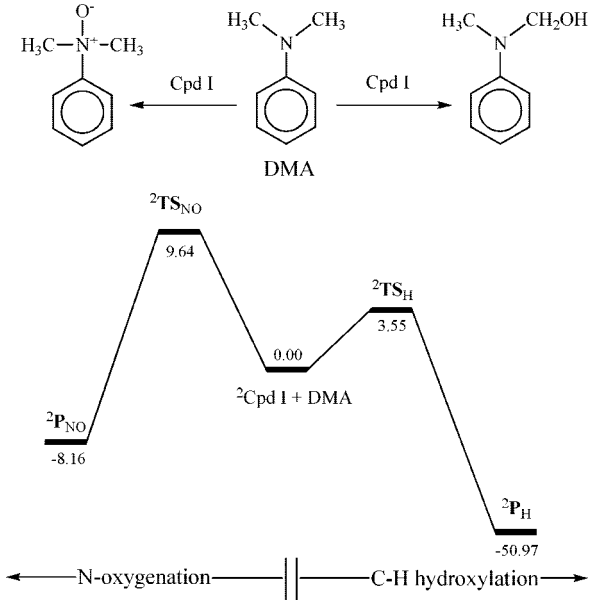

Figure 53. DFT(B3LYP/B1) optimized transition states and energy profiles for C−H hydroxylation and N-oxidation of *N*,*N*-dimethylaniline (DMA) by Cpd I in the LS state. Relative energies from single-point calculations using the LACV3P+(Fe)/6-311+G*(rest) basis, and including ZPE, bulk polarity ($\varepsilon = 5.7$), and NH···S H-bonding corrections. Reproduced with permission from ref 369. Copyright 2009 Wiley-VCH Verlage GmbH & Co KGaA.

Scheme 16. Three Mechanistic Hypotheses for Ethanol Dehydrogenation by CYP2E1 (Reproduced with Permission from Ref 168. Copyright 2007 Wiley-VCH Verlage GmbH & Co KGaA)

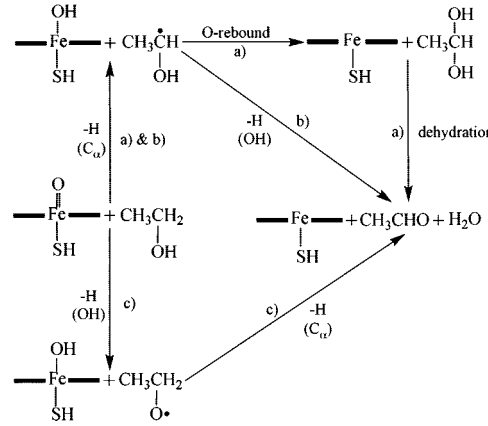

CYP2E1 malfunction, and of the mechanism of alcohol dehydrogenation.[373−383] Three mechanisms have been proposed and are shown in Scheme 16. The consensus mechanism is the gem-diol mechanism a, in which the rate-determining step is H-abstraction from the α-carbon atom of the alcohol, followed by radical rebound to form the diol, which then undergoes dehydration and produces acetaldehyde.[374−376,378−382] The second mechanistic hypothesis b starts with the same H-abstraction step from C_α as in mechanism a but follows with a second H-abstraction from the radical and is hence called the dual hydrogen abstraction (DHA) mechanism.[373,377,379,383] Finally, the third hypothesis c, so-called reverse dual hydrogen abstraction (R-DHA), involves an initial H-abstraction from the hydroxyl group of the alcohol, followed by a second H-abstraction from the α-carbon atom. This is the one discovered by computational means, using B3LYP(LACVP**/6-31G**) and corrections to account for basis set (LACV3P+*/6-311+G*) and bulk polarity effects.[168]

The computational study explored all three mechanistic hypotheses. Figure 54 shows the DHA and gem-diol mechanisms, which both start with an initial H-abstraction step (Figure 54a). As usual, this step involves TSR, leading to the iron-hydroxo/ethanolyl radical complexes, $^{2,4}\mathbf{I}$. These $^{2,4}\mathbf{I}$ complexes are not stable intermediates but appear as shoulders on the potential energy surface (the reason for the missing rebound barrier is the low ionization potential of the radical; see discussion later); and collapse in a barrier-free fashion to the products of mechanisms a and b, as shown in Figure 54b for $^4\mathbf{I}$. Thus, a rotation of the iron-hydroxo OH group, on the left side of Figure 54b, leads directly to the gem-diol product, while combining this rotation with the enol radical rotation, as on the right side of Figure 54b, gives rise to a second and barrier-free H-abstraction that generates the acetaldehyde complex.

The H-abstraction barrier in Figure 54a is affected by bulk polarity, by as much as 1.5−4.1 kcal mol^{-1} when the bulk polarity is taken to be that of ethanol; the barriers are 13.2/14.4 kcal mol^{-1} for the HS/LS states.[168]

Figure 55 shows the energy profile calculated for the R-DHA mechanism in the gas phase and with bulk polarity effects taken into account. It is seen that the mechanism starts in a regular TSR scenario, leading to an iron-hydroxo/ethanoyl radical complex, $^{2,4}\mathbf{I}$. This complex then undergoes a second H-abstraction from the α-methylene group of the ethanoyl radical. In this step, the LS state has a tiny barrier,

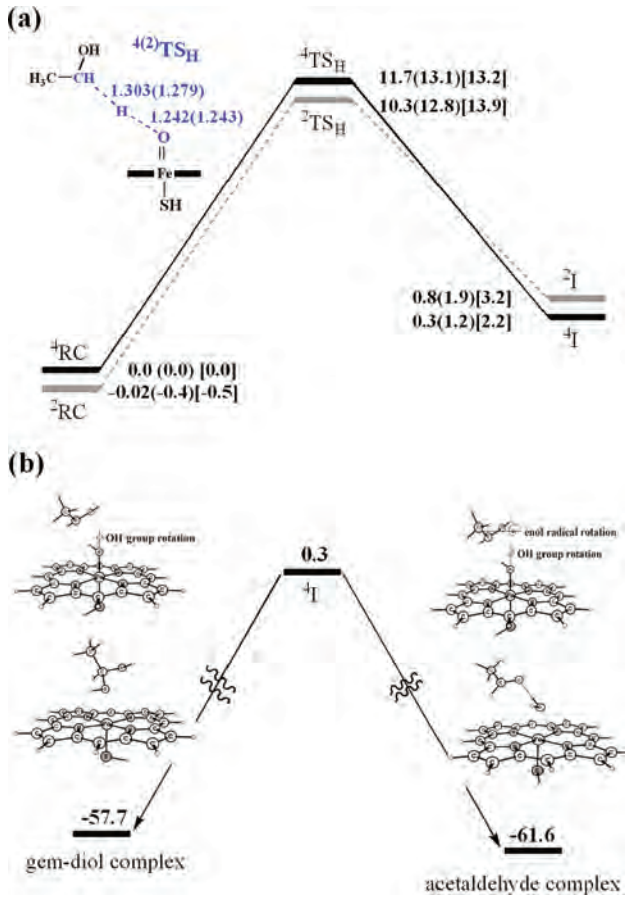

Figure 54. DFT(B3LYP/LACVP**) optimized transition states and energy profiles (kcal mol^{-1}) for ethanol dehydrogenation by Cpd I in the DHA and gem-diol mechanisms. (a) H-abstraction step and (b) collapse of **^{4}I** to the gem-diol or acetaldehyde complexes. In part a, the relative energies refer to the LACV3P+(Fe)/6-311+G*(rest) basis, labeled as B. In part a, the three relative energy values in each line correspond to B+ZPE (B+ZPE; ε = 5.62) [B+ZPE; ε = 24.55]. Reproduced with permission from ref 168. Copyright 2007 Wiley-VCH Verlage GmbH & Co KGaA.

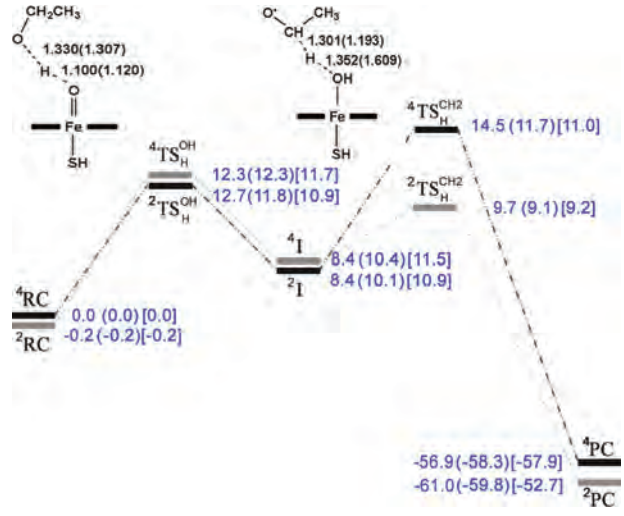

Figure 55. DFT(B3LYP/LACVP**) optimized transition states and energy profiles (kcal mol^{-1}) for ethanol dehydrogenation by Cpd I in the R-DHA mechanism. The three relative energy values in each line correspond to B+ZPE (B+ZPE; ε = 5.62) [B+ZPE; ε = 24.55], where B denotes the LACV3P+(Fe)/6-311+G*(rest) basis. Reproduced with permission from ref 168. Copyright 2007 Wiley-VCH Verlage GmbH & Co KGaA.

Scheme 17. Orbital Occupancy Evolution during the Second H-Abstraction Step of the R-DHA Mechanism in Figure 55[a]

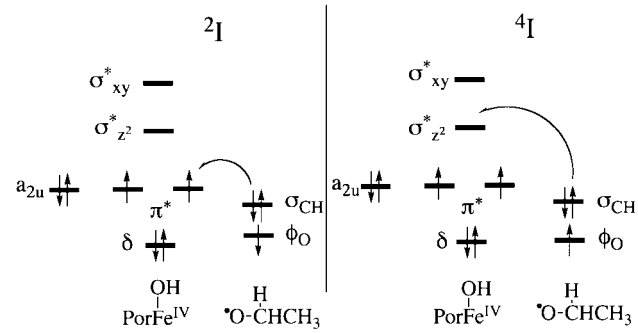

[a] Note that the electron shift to a_{2u} occurs en-route from ^{2,4}**TS**$_H^{OH}$ down to the intermediate complexes.

while the HS state has a large barrier. The reason for this spin-selective second H-abstraction can be understood from the orbital occupancy evolution diagrams in Scheme 17. Thus, the H-abstraction involves a one-electron shift from the σ_{CH} orbital of the methylene group to the iron hydroxo complex; in the LS case, the electron is shifted to the low lying π^* orbital, while in the HS case, the shift occurs to the high lying $\sigma^*_{z^2}$ orbital (that is 18 kcal mol^{-1} higher than the π^* orbital).

Assuming a fast spin crossover from quartet to doublet in the second H-abstraction event (see reasoning in the original paper[168]), the rate controlling step during the R-DHA mechanism in Figure 55 is the first H-abstraction from the hydroxyl group of ethanol. Comparison of Figures 54a and 55 reveals that, in the gas phase, the consensus mechanisms (DHA and gem-diol) possesses a slightly smaller barrier than the R-DHA mechanism. However, with bulk polarity included, the reverse is true; the barriers for R-DHA are 11.7/11.1 vis-à-vis 13.2/14.4 kcal mol^{-1} (for HS/LS, respectively). Thus, the R-DHA mechanism competes with the traditional DHA or gem-diol mechanism in a weakly polar environment (ε = 5.62), which reflects the hydrophobic heme pocket of CYP2E1. However, under stronger polarity (ε = 24.55), corresponding to that of ethanol, the R-DHA mechanism should prevail. This might explain the adaptive response of CYP2E1 to high ethanol concentration in the blood, resulting in the acceleration of ethanol dehydrogenation.[370−372] The influence of ethanol concentration on the CYP2E1 pocket has in fact been observed by changes in the Fe−CO bond of the ferrous−carbon monoxide complex, which are in line with the expected modulation of the polarity of the pocket.[384] A reasonable scenario was proposed whereby the increased ethanol concentration in the blood modifies the pocket polarity and induces a mechanistic shift from a competitive gem-Diol-DHA/R-DHA situation to a dominant R-DHA mechanism, which offers a faster alcohol dehydrogenation path and thereby accounts for the observed acceleration of ethanol dehydrogenation.[370−372]

4.9. DFT/MM Study of the C−C Bond Forming Reactivity of P450

P450 StaP (CYP245A1) catalyzes the formation of staurosporine (STA) from chromopyrrolic acid (CPA) as depicted in Scheme 18.[195,385] Staurosporines are natural products that possess strong inhibitory activity on protein kinase, which makes them therapeutically important anticancer agents. The staurosporine indolocarbazole cores are derived from L-

Scheme 18. Conversion of L-Trp to Staurosporine (STA) via CPA[a]

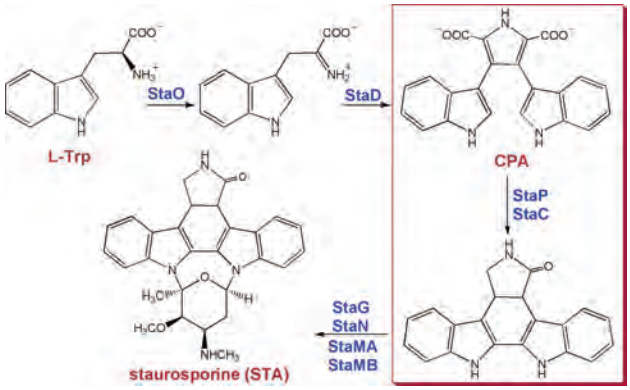

[a] The oxidation of CPA by P450 StaP in the frame involves C−C formation and loss of two H atoms. Acronyms on the arrows refer to the enzymes that catalyze the specific steps. Reprinted with permission from ref 80. Copyright 2009 American Chemical Society.

tryptophan (L-Trp) via a series of oxidative transformations catalyzed by a series of enzymes that are indicated on the arrows in Scheme 18. The most remarkable transformation is the fusion of the two indole rings of CPA by cytochrome P450 StaP and its coenzyme StaC, to generate a six-ring indolocarbazole scaffold that undergoes subsequent *N*-glycosylation, followed by methyl transfer steps leading in the end to STA. How does an enzyme that regularly monooxygenates organic compounds perform this remarkable transformation that involves C−C bond formation and a loss of two H atoms? This transformation becomes all the more puzzling in view of the fact that CPA is held steadfast in the crystal structure by an array of H-bonds quite distant from Cpd I, as shown in Figure 56. As such, there is no chance of moving the CPA closer to enable Cpd I to abstract hydrogens or affect CPA directly in any other manner. The action must be from a distance and/or mediated by water molecules and active residues.

The electronic structure of Cpd I of P450 StaP was already discussed above in Figure 19, based on DFT(B3LYP)/MM calculations.[58,80] In this Cpd I species, the cation-radical moiety is distributed over Por, sulfur, and CPA in an orbital that has a mixed character, made from a_{2u} for the Por/S ligand and ϕ_{CPA} that is localized in the proximal indolic moiety of CPA. Furthermore, the DFT(B3LYP)/MM calculations[58] show that when the His_{250} residue is protonated in the proximal side to the FeO moiety of Cpd I, there is an H-bond triad consisting of Wat_{789} (the water molecule that is liberated during the formation of Cpd I), Wat_{644}, and His_{250} that connects the indolic NH of CPA to the oxo group of Cpd I. As shown in Figure 57, this provides a nice Grotthuss-type proton transfer pathway[236] for proton delivery from NH to the oxo group, which occurs simultaneously to an electron transfer from CPA to Cpd I. This proton-coupled electron transfer (PCET) event results in a net H-atom transfer from the indole NH to Cpd I, without bringing CPA close to Cpd I. In this mechanism P450 StaP functions much like a peroxidase.[58,71] Three elements join to provide this remarkable functionality: (i) the protein environment deprotonates the two carboxylic acid groups of CPA and immobilizes the substrate via an array of H-bonds that claw the carboxylate groups (see Figure 56), (ii) the so created CPA^{2-} dianion is an excellent electron donor, while Cpd I is a powerful electron acceptor, which together promote electron transfer from a distance, and (iii) the Wat_{644}-His_{250}-Wat_{789} triad enables us to shuttle protons from the CPA to the Cpd I species.

However, the PCET step in Figure 57 just initiates the mechanism of CPA oxidation, which was recently elucidated by means of extensive DFT(B3LYP)/MM calculations.[80] The entire computed mechanism is shown in Scheme 19. It involves 10 steps labeled as **s1**−**s10**. In addition to the PCET step (**s1**), there is another key element, a bond-formation coupled electron transfer (BFCET) step (**s4**) that involves the second electron transfer from the substrate to the heme along with the C−C bond formation. There are also four proton transfer (PT) events; in the first one, PT1 (**s3**), the proton from the distal indolic N−H group of CPA, is transferred to the proximal N, while thereafter (**s6**) this proton is relayed to the iron hydroxo to form the ferric-aqua complex of the resting state. Steps PT3 and PT4 (**s8** and **s10**) rearrange the protons from the C−H groups of the HC−CH moiety of the indole back to the indolic bare nitrogen atoms, thus completing the transformation and coming full cycle.

However, recalling that the CPA substrate is immobilized, none of these events could have happened without the water relocation steps (**s2**, **s5**, **s7**, and **s9**) in Scheme 19. As an example, **s2** is shown in Figure 58. Here, after the PCET event, **s1** in Scheme 19, Wat_{789} and Wat_{644} migrate to establish together with His_{250} a new triad that can relay the proton from the distal indolic N−H group to the proximal bare N atom. Similarly, the hydrogen shifts from the carbons to the N positions in the indole (**s8** and **s10**) are mediated by water molecules that have to migrate initially to the correct positions to effect these rearrangements. Without the water molecules, these H-rearrangements have large barriers, which become smaller than 12 kcal mol^{-1} in their presence.

Indeed, the water molecules are the "working-class bees" of this complex mechanism. By moving around, they tend to "nurture" the immobilized CPA, allowing it to undergo a most complex transformation. *They act as biocatalysts.*

4.10. DFT-Only and DFT/MM Calculations of Regioselectivity in the Reactions of Cpd I

An important function of an enzyme is its ability to carry out regioselective reactions of substrates that have two functionalities. P450 enzymes fulfill this role quite well: they may perform C−H hydroxylations in the presence of double bonds, or sulfur, or phenyl groups, and vice versa (oxidation of these groups in the presence of C−H bonds). A few of these regiochemical problems have been addressed by theory and are discussed below.

4.10.1. Competitive Heteroatom Oxidation vs C−H Hydroxylation

For substrates such as *N*,*N*-dimethylaniline (DMA), trimethylamine (TMA), and dimethylsulfide (DMS), there is a possibility for competitive C−H hydroxylation of the α-methyl group and oxo-transfer to the heteroatom. Interestingly, amines such as DMA and TMA prefer C−H hydroxylation (eventually leading to *N*-demethylation; see section 4.6), while sulfur containing compounds such as DMS prefer sulfoxidation.[18,287,386] The former issue has been addressed by DFT(B3LYP)-only calculations by Li et al.[369] and Cho et al.,[292] who showed that C−H hydroxylation is preferred over oxo-transfer to nitrogen, by as much as 3 kcal mol^{-1} for TMA and 6 kcal mol^{-1} for DMA. Rydberg et al.[171]

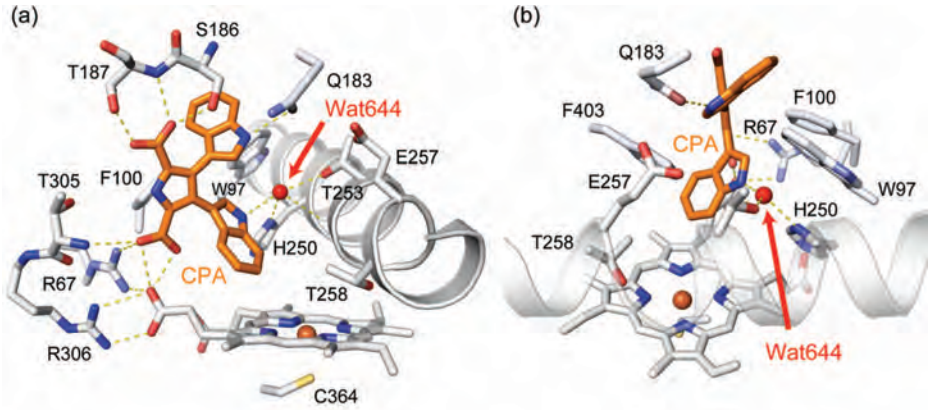

Figure 56. X-ray structure showing the binding of chromopyrrolic acid (CPA) by P450 StaP via an array of H-bonds, which are indicated by dotted lines. (a) and (b) represent two different perspectives; (b) shows His_{250} being H-bonded to CPA via a water molecule.[195] Reprinted with permission from ref 80. Copyright 2009 American Chemical Society.

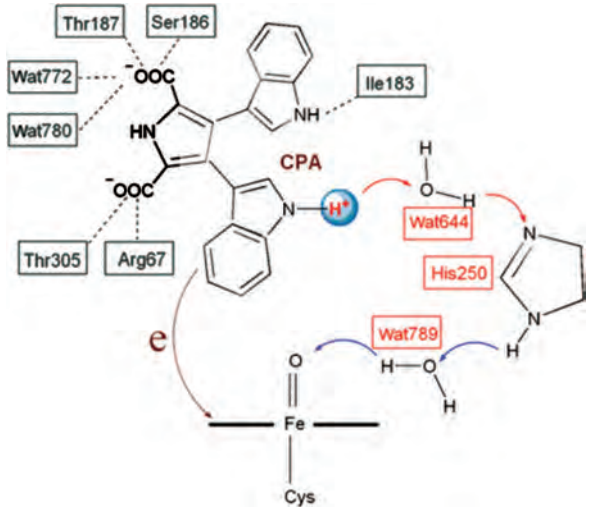

Figure 57. Schematic representation of the proton-coupled electron transfer (PCET) event involving a proton relay from the indole group of CPA to the iron-oxo moiety of Cpd I, via the Wat_{644}-His_{250}-Wat_{789} triad, with concomitant electron transfer from CPA to Cpd I. Reprinted with permission from ref 58. Copyright 2008 American Chemical Society.

studied both types of competition for TMA and DMS as substrates, using DFT(B3LYP)-only calculations, and they reported a preference of 4.4 kcal mol^{-1} for C−H hydroxylation in TMA and of 4 kcal mol^{-1} for oxo transfer to sulfur in DMS. The slightly different values of the two groups reflect differences in basis sets and in the incorporation or neglect of bulk polarity corrections. Notwithstanding these minor differences, these results show that DFT(B3LYP)-only calculations are capable of addressing the regiochemical problem in heteroatom containing compounds.

4.10.2. DFT-Only Studies of the Competition between Epoxidation and Allylic Hydroxylation in Propene and Cyclohexene by Cpd I

The competition of C−H hydroxylation and C═C epoxidation in olefins that possess allylic hydrogens, such as cyclohexene and propene in Scheme 20, is a fundamental problem in P450 selectivity. Experimentally, with liver microsomal P450, propene gives products that are exclusively related to C═C activation,[8,387] while cyclohexene yields a roughly 1:1 ratio of the two products with a variety of P450s.[194,308] Other olefins give different values, generally with preference to C═C activation, but not always.[257,388] Interestingly, using synthetic Cpd I reagents, one can get with cyclohexene a variable C−H/C═C activation ratio that ranges from the typical 1:1 ratio of the enzymatic reaction up to 100% C−H activation, depending on conditions such as solvent polarity and small amounts of water in the solvent.[389,390] Thus, the model studies show that a single oxidant (Cpd I) may yield different C−H/C═C regioselectivity ratios under different conditions of polarity, water content, axial ligand, and so on.

Early DFT(B3LYP) studies with propene as a model substrate by de Visser et al.[149,150] addressed the C−H/C═C competition. In the gas phase, Cpd I was found to be nonselective, yielding C−H/C═C ratios close to 1. However, inclusion of the effects of bulk polarity and hydrogen bonding to the sulfur ligand led to a clear preference for C−H activation, by as much as 7 kcal mol^{-1}, thus predicting exclusive allylic hydroxylation. For cyclohexene, DFT(B3LYP) calculations show a preference for C−H hydroxylation already in the gas phase, which is augmented by polarity.[57] Another recent study of propene oxidation indicates[275] that an electric field alone can achieve selectivity in this reaction and that, by simply reversing the field direction along the S−Fe−O-olefin axis, one could control the selectivity at will to give C═C or C−H activation. This is an exciting result, and studies of synthetic models seem to suggest that it is also a viable one.[389,390]

4.10.3. DFT/MM Studies of the Competition between Epoxidation and Allylic Hydroxylation in Propene and Cyclohexene by Cpd I

The results of the model studies,[149,150] which show a preference for C−H hydroxylation for both propene and cyclohexene, are in discord with the experimental results in the enzyme. Clearly, the enzymatic regioselection issue must be studied by means of QM/MM calculations within the native protein. However, before discussing the results of such calculations, it is important to clarify the conditions whereby experimental selectivity can be studied in P450 enzymes. Experimentally, the rate controlling step in these enzymes is not at all substrate oxidation but rather the second electron transfer step[180] in the catalytic cycle (see Figure 1), at least for quite a few of the isozymes, albeit not for all.[391] Thus, a regioselectivity that reflects the relative barriers for C═C and C−H activations, under experimental conditions, requires a rapid equilibrium between the two reactant complexes of

Scheme 19. DFT(B3LYP)/MM-Elucidated Mechanism of CPA Oxidation by P450 StaP Involving 10 Steps, Labeled as s1−s10 (Reprinted with Permission from Ref 80. Copyright 2009 American Chemical Society)

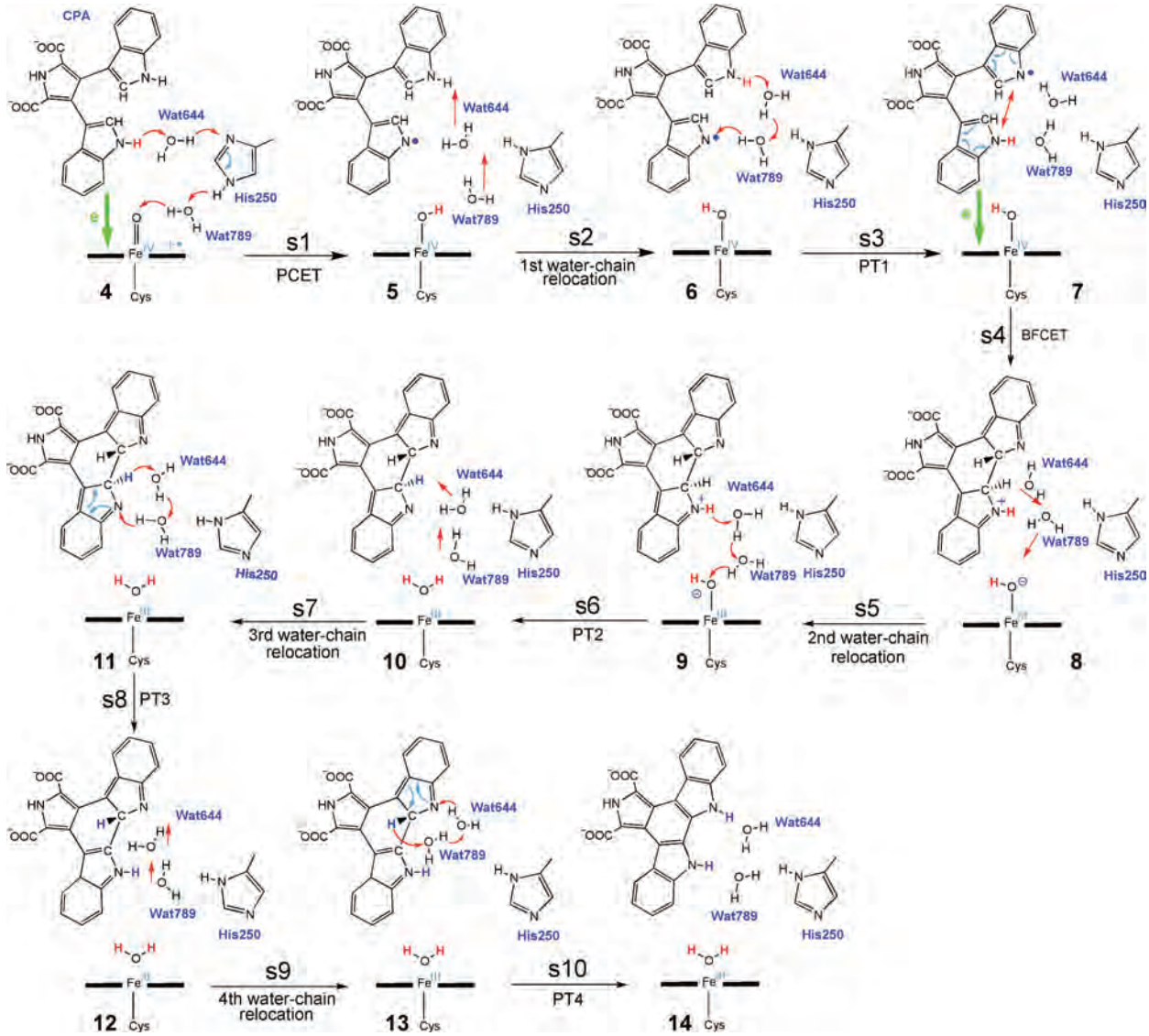

Cpd I with the C═C and C−H moieties. In such a case, the C−H/C═C ratio is determined by the relative energies of the corresponding bond activation TSs. Otherwise, the measured regioselection ratio will not reflect the actual oxidation process. Therefore, any QM/MM calculation of regioselectivity must ascertain this condition of free tumbling of the substrate. Under these conditions, the relative barriers will be determined solely by the difference in TS energies, while the relative energies of the reactant complexes do not matter.

The C−H/C═C regioselection problem was tackled by Cohen et al.[57,277] using DFT(B3LYP)/MM calculations for both propene and cyclohexene in CYP101. Initial MD simulations showed that, unlike camphor, which is bound by Tyr_{96} and Val_{295}, both cyclohexene and propene tumble freely within the pocket and have no favored conformation of binding by the residues of the enzyme. This means that, in principle, there should be a rapid equilibrium between the reactant complexes of Cpd I and the two regiochemical sites, i.e. Cpd I/C−H and Cpd I/C═C. Under these conditions, the reactant complexes do not influence the regioselectivity, and *the relevant comparison is between the QM/MM energies of the respective transition states.*

The results of the DFT(B3LYP)/MM calculations[57] for two different basis sets were very similar for the two olefins. In both cases, the protein environment was shown to prefer the C−H activation by as much as 7−8 kcal mol^{-1} for cyclohexene and 3−5 kcal mol^{-1} for propene. These results are clearly still in discord with experimental reports on the two reactions in P450 enzymes. To tackle this disparity, the original paper[57] suggested a model based on the kinetics of the full catalytic cycle. The model seemed successful in predicting the C−H/C═C ratio for the two olefins and others. However, in retrospect, it was recognized that the suggested model described two disconnected cycles, with no free tumbling between the reactant complexes, and as such was inappropriate for addressing this problem, since the MD simulations clearly showed free tumbling. Evidently, DFT(B3LYP)/MM calculations are still incapable of treating this delicate problem. At the time of writing of this review, this problem remains unresolved. Another pending issue is the fact that the results from synthetic model studies of C═C/C−H competition[389,390] are different from those in the enzyme, at least with respect to the regioselectivity of cyclohexene oxidation.

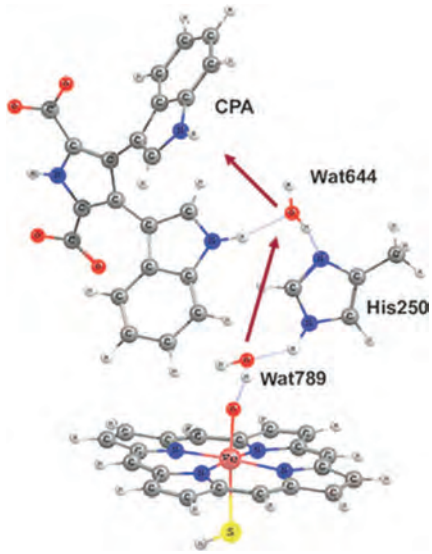

Figure 58. DFT(B3LYP/LACVP) optimized product of the PCET event (**s1** in Scheme 19) with arrows indicating the movements of Wat_{644} and Wat_{789} in the water relocation step (**s2** in Scheme 19). Reprinted with permission from ref 80. Copyright 2009 American Chemical Society.

Scheme 20. Regiochemical Pathways of Cyclohexene and Propene Epoxidation, as Representatives of the Competition of C=C Epoxidation vis-à-vis Allylic C−H Hydroxylation (Reprinted with Permission from Ref 57. Copyright 2006 American Chemical Society)

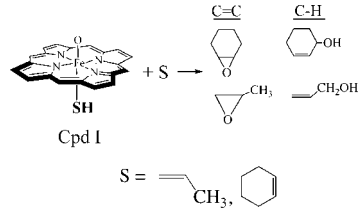

4.10.4. DFT-Only Studies of the Metabolic Switching from Benzylic C−H Hydroxylation to Phenyl Hydroxylation in Toluene by Cpd I

Metabolic switching is the name given to the changes in regioselectivity induced by replacement of hydrogen by deuterium.[317,357,391−394] This is exemplified in the case of toluene in Scheme 21. Thus, while the pristine toluene gives mostly benzyl alcohol, deuteration of the methyl group results in "metabolic switching" to phenyl hydroxylation products.[317,392,394] This of course depends on the magnitude of the KIE during benzylic H-atom abstraction, as well as on bulk polarity and environmental effects (H-bonds to sulfur, etc.) that might differentiate the radicalar mechanism for H-abstraction from the polar π-attack mechanism of the phenyl activation (see section 4.5). Indeed, DFT(B3LYP)-only calculations[395] show that, in the pristine toluene, the H-abstraction from the benzylic position has a free energy barrier which is 5.6 kcal mol^{-1} lower than that of phenyl activation, whereas, for deuterated toluene and with the inclusion of bulk polarity and NH···S H-bonding effects, the C−H hydroxylation preference went down by a significant amount to only 0.4 kcal mol^{-1}. Thus, while these results do not accurately reproduce the experimental data, due to the limited accuracy of DFT, they still give the correct trend, namely, that the combination of deuteration and bulk polarity effects tends to favor phenyl over C−H hydroxylation, as also observed in model systems.[389]

Scheme 21. Regiochemical Pathways of Toluene Oxidation by Cpd I, Showing the Metabolic Switching upon Methyl Deuteration (Reproduced with Permission from Ref 395. Copyright 2007 Wiley-VCH Verlage GmbH & Co KGaA)

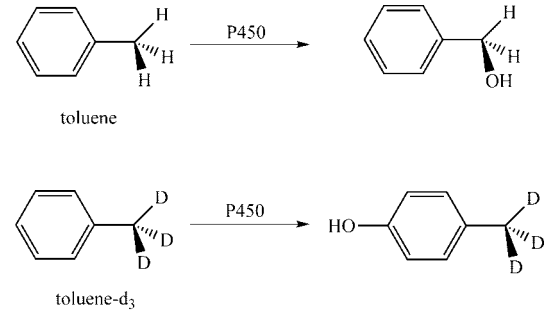

	o-cresol	*m*-cresol *p*-cresol	benzyl alcohol
toluene	14.8	16.2	69.0
toluene-d_3	34.7	41.0	24.3
toluene-d_8	35.2	45.2	19.6

A recent DFT(B3LYP)-only study by Lin et al.[173] shows that gas-phase calculations can predict the regioselectivity trend in testosterone hydroxylation by CYP3A4. The regioselectivity follows the bond dissociation energies of the various C−H bonds undergoing hydroxylation, much as demonstrated previously by de Visser et al.[153]

4.11. Miscellaneous Reactions: Carbocation Intermediates

The incursion of carbocations during P450 bond activation has been reviewed before.[32,152] It involves an electron shift from the radical center, initially formed by bond activation, to the iron-hydroxo or iron-alkoxy complex. This was shown to be the main mechanism of the dehydrogenase-oxidase activity often observed in P450 enzymes.[380,396,397] The same mechanism was found recently by DFT(B3LYP)-only calculations to be responsible for the last of the aromatization steps in the catalytic conversion of androgens to estrogen products by CYP19 aromatase.[381]

5. Predictive Models for P450 Reactivity Patterns

Predictive models for P450 reactivity are sought for two main reasons. One reason is pragmatic, since finding correlative relationships for P450 reactivity should be extremely useful for fast predictions of drug metabolism.[170,172,398] Another reason is fundamental, trying to achieve understanding and predictive ability from first principles. In reviewing this activity, we shall focus mainly on models that relate reactivity to a few fundamental properties of the molecules and are based on an underlying physical model behind the correlation. We do not consider schemes such as QSAR (quantitative structure−activity relation) that use a multitude of molecular descriptors, and we refer readers interested in such schemes to recent reviews in the field of drug metabolism.[399,400]

5.1. Predictive Pattern of C−H Hydroxylation Barriers Based on Bond Dissociation Energies

As reviewed previously,[32] there have been a number of studies that attempt to correlate hydrogen abstraction barriers

with the corresponding bond dissociation energies (BDE_{CH}),[401−403] which were reasonably successful for P450 hydroxylation.[404,405] Notably, de Visser et al.[153] used DFT(B3LYP) calculations with two different basis sets (B1 and LACV3P+/6-311++G**) and studied the barriers for C−H hydroxylation by Cpd I for 10 different substrates, ranging from methane through camphor to toluene and phenyl ethane. The use of ZPE corrected BDE_{CH} values led to very good correlation with ZPE corrected barriers:[153]

$$\Delta E(\mathrm{ZPE})^{\ddagger} = 0.5887\mathrm{BDE}_{\mathrm{CH}} - 39.418\ (\mathrm{kcal\ mol^{-1}}) \quad (3)$$

More recently,[174] the same authors took a different set of reactions and used a different basis set and different software to run the DFT(B3LYP)-only calculations (GAUSSIAN instead of JAGUAR, which have small differences). Interestingly, while the quality of the correlation was less good than the one found in the past, the equation for the correlation remained essentially the same:

$$\Delta E(\mathrm{ZPE})^{\ddagger} = 0.5849\mathrm{BDE}_{\mathrm{CH}} - 39.625\ (\mathrm{kcal\ mol^{-1}}) \quad (4)$$

The utility of this correlation can be illustrated for the case of camphor hydroxylation by $P450_{cam}$. The computed low-spin $\Delta E(\mathrm{ZPE})^{\ddagger}$ barrier (LACV3P+), relative to the gas-phase reactant complex, is 15.1 kcal mol^{-1}, and the corresponding $\Delta H^{\ddagger}$ value is within 0.4−0.6 kcal mol^{-1}.[277] A similar $\Delta E(\mathrm{ZPE})^{\ddagger}$ barrier is obtained from DFT(B3LYP)/MM calculations[59] that do not include the barrier lowering effect of Wat_{903}.[61] The computed BDE_{CH} value (6-311++G**) for camphor is 93.7 kcal mol^{-1}, close to the experimental estimate of 98 ± 4 kcal mol^{-1}.[281] Using the computed BDE_{CH} value of 93.7 kcal mol^{-1} in eq 4 yields an estimate of 15.2 kcal mol^{-1} for the barrier, almost identical to the actually computed value of 15.1 kcal mol^{-1} (see above). Furthermore, a single turnover kinetics datum for camphor hydroxylation[406] by $P450_{cam}$ yields an upper limit of the free energy barrier as $\Delta G^{\ddagger} < 15$ kcal mol^{-1} ($k > 200\ s^{-1}$). The estimated DFT(B3LYP)/MM barrier in Figure 37, with the Wat_{903} effect and ZPE correction included, is 13.8 kcal mol^{-1} and is not too far from these correlation-based estimates. This match supports the utility of the correlations given in eqs 3 and 4.

Recently, Olsen et al.[170] calculated the C−H abstraction barriers for a larger set of 24 molecules with sp^3 and sp^2 hybridizations, as well as primary, secondary and tertiary carbons. They found good correlations of the HS barriers with BDE_{CH} values. They further showed that one could use computationally cheaper methods and obtain reasonable correlations. Based on these correlations, the authors were able to derive qualitative bracketing rules for the various C−H abstraction barriers (excluding methane), depending on the chemical environment of the carbon atom: (i) Primary sp^3 hybridized carbons, ∼17−18 kcal mol^{-1}, (ii) secondary and tertiary sp^3 hybridized carbons, 14−15 kcal mol^{-1}, (iii) carbons adjacent to aromatic and C=C moieties (e.g., allylic), 12−13 kcal mol^{-1}, (iv) carbons with a heteroatom O or S in an α-position, 11−12 kcal mol^{-1}, and (v) carbons with an N heteroatom in the α-position, 7 kcal mol^{-1}. These qualitative rules were used subsequently to predict the regiochemistry in the metabolism of progesterone and dextromethorphan by CYP3A4, once again attesting to the utility of these correlations. The authors noted that even the high barriers in these series correspond to a rate constant of 0.1 s^{-1} and thereby illustrate the high reactivity of Cpd I. Furthermore, for metabolic purposes, these high rates reduce the predictive task to locating the C−H sites that are most reactive and sterically most accessible to the reactive species. The second factor, in the authors' opinion, depends on the P450 isozyme and can be studied by means of docking and MD simulations. Similar ideas were shown to apply for 17 cases of arene hydroxylation by Cpd I.[172]

5.2. Valence Bond Modeling of Reactivity Patterns in C−H Hydroxylation

Among the most successful chapters in theoretical chemistry have been those that involved constructions of quantum chemical models for conceptualizing the reactivity and mechanism of complex organic reactions. Such theories, like the Woodward−Hoffmann rules[407−411] and Fukui's frontier orbital theory,[412] have formed an extremely useful interface between experiment and numerical calculations. As such, these models enable chemists to design better experiments and to benefit from the interplay between theoretical calculations and experiments. The field of P450 certainly involves a great deal of complexity on the experimental side, but it is equally complex on the computational side. Here too we need simpler models that can bridge the two disciplines and provide a conceptual framework for understanding the P450 reactivity patterns from a few first principles. Some progress along these lines has been made in recent years, and these attempts are described in this subsection.[26,83,174]

During the studies of correlation of reactivity with BDE_{CH},[170,174] it was noted that using in situ bond strengths, which do not allow for structural relaxation of the radical after bond dissociation, generally gave a better correlation than the experimental BDE_{CH} values. Moreover, in C−H activation by nonheme iron-oxo reagents, where the correlation with the BDE_{CH} values was successful,[260] one could find an equally good correlation with the ionization potential of the alkane (IP_{AlkH}).[413] This means that the BDE_{CH} and IP_{AlkH} values are internally correlated, and the correlation with BDE_{CH} is not necessarily fundamental, albeit very useful. Indeed, a correlation by itself cannot imply a causal relationship, and this recognition formed an incentive to seek a more fundamental principle than the Bell−Evans−Polanyi (BEP) one that is responsible for these correlations. Such a model should deal not only with C−H activation but also with the rebound step and its spin-state selectivity, and it should be sufficiently general to deal with other reactions such as C=C epoxidation, heteroatom oxidation, and so on. This principle was derived using the valence bond (VB) diagram model of reactivity, which explains the origins of barriers and of the incursion of reaction intermediates.[402,414,415]

5.2.1. Valence Bond Diagrams for C−H Hydroxylation

As already noted, there are two electromeric intermediates that may be involved during the reactions: these are the $Por^{\bullet+}Fe^{III}OH$ and $PorFe^{IV}OH$ species. In addition, there are two spin states, doublet and quartet, which lead to distinct reaction profiles. In order to economize the discussion, we shall start by modeling the mechanisms for the two electromeric states, without specifying spin states, and then comment on the spin-state effect mainly by reference to the rebound step.[26,83]

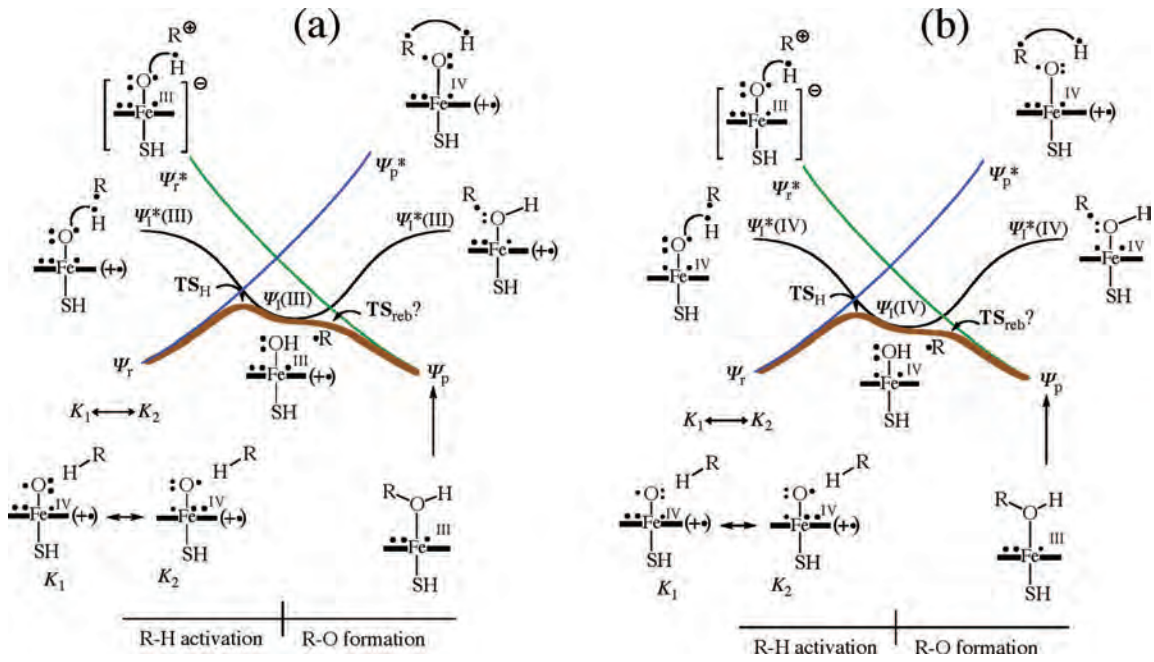

Figure 59. Valence bond (VB) diagrams describing the mechanistic scenarios for C−H hydroxylation by Cpd I, for the two electromeric pathways, without specifying a spin state. In each case, an intermediate curve cuts through the high barrier of the reactants' and products' curves. In part a, the intermediate curve corresponds to the Por$^{\bullet+}$Fe(III)OH electromer, and in part b, it corresponds to the PorFe(IV)OH electromer. The VB mixing and avoided crossing creates the reaction profile, which is shown in both cases by the bold curve. The question mark alongside **TS**$_{reb}$ signifies that the existence of this species depends on the spin-state variety. The various species are illustrated in more detail in Scheme 22. Reprinted with permission from ref 174. Copyright 2008 American Chemical Society.

Figure 59 shows the VB diagrams for the hydroxylation reactions involving the two electromeric intermediates; the alkane is symbolized as R−H, and the porphyrin ring by the bold lines flanking the iron. The two diagrams involve two major curves that correspond to reactant and product states shown in blue and green, respectively. A third curve (in black) that cuts through the high energy ridge of the two major curves provides a low energy pathway for the transformation.[402,416] Looking at the wave functions of reactants and products, labeled as Ψ_r and Ψ_p at the lower two ends of each diagram, it is seen that the overall process of conversion of the alkane, R−H, to an alcohol involves also a two-electron reduction of iron-oxo porphyrin, which changes from Por$^{\bullet+}$Fe^{IV}═O to PorFe^{III}(alcohol). This however is mediated by the intermediate curve that describes an H-abstraction process, whereby the electron of the abstracted H$^{\bullet}$ reduces either the oxidation state on iron to Fe^{III} (Figure 59a) or the oxidation state of the porphyrin from a cation-radical to a closed-shell species (Figure 59b). This step is followed by radical rebound, where an electron shift from the alkyl radical (R$^{\bullet}$) to the iron-porphyrin moiety generates the alcohol and the ferric porphyrin, which is twice reduced vis-à-vis the reactant state. *This three-curve VB diagram is a typical case, where an intermediate state internally facilitates the otherwise more difficult transformation of* Ψ_r *directly to* Ψ_p.[402,416]

To facilitate understanding of the state correlation in the VB diagram, we have to translate the VB representation of the various anchor states to the molecular orbital picture and the language of oxidation state formalism, used throughout this review. The two major curves describe the transformation of reactants to products and are anchored in two ground states, Ψ_r and Ψ_p, for the reactants and products, and the two corresponding excited states, Ψ_r* and Ψ_p*. Each state-curve represents a single bonding scheme: Thus Ψ_r describes the bonding pattern in the reactants, and so does Ψ_p*, only that the latter state represents the reactant-type bonding in the geometry of the products. Similarly, Ψ_r* involves the product-type bonding but in the geometry of the reactants. As a result of these bonding features, as we move along the reaction coordinate, by stretching the C−H bond and shrinking the O···H and R···O distances and thereby changing the geometry from reactants to products, the Ψ_r state connects to Ψ_p* and, at the same time, Ψ_r* connects to Ψ_p. Let us now inspect these four states in terms of electronic structure cartoons in detail.

Starting with the reactants state, Ψ_r (Figure 59), we depict in Scheme 22 the VB-MO representations of Ψ_r for ^{4}Cpd I and R−H. In the VB formulation (Scheme 22a), Cpd I has six π-electrons, distributed in two perpendicular planes, across the Fe−O moiety, and coupled to produce a triplet spin state.[417] This state is described by a resonance mixture of the two forms (K_1 and K_2) that lead to formation of two three-electron bonds in the two perpendicular planes; the line connecting the Fe and O atoms in Figure 59 and in Scheme 22 represents the σ_{Fe-O} bond. The porphyrin is open-shell, as indicated by a cation−radical sign. In the MO formulation (Scheme 22b) these six π-electrons on the FeO moiety occupy two bonding π_{FeO} orbitals and two singly occupied antibonding π^*_{FeO} orbitals. The third unpaired electron of Cpd I resides on the porphyrin in an a_{2u} type orbital, and its spin is either ferromagnetically or antiferromagnetically coupled to the triplet FeO pair, thereby yielding two spin states: overall quartet or doublet. Note that the doubly occupied δ orbital on iron and two virtual antibonding orbitals (σ^*_{xy} and $\sigma^*_{z^2}$) are not shown explicitly in Scheme 22. The alkane R−H is represented in VB diagrams by the corresponding Lewis structure and in MO representations by the bond orbital σ_{CH} of the R−H bond undergoing activation.

The excited state Ψ_r* in Figure 59 is a charge transfer state in which one electron is transferred from the R−H

Scheme 22. (a) Valence Bond (VB) Scheme Describing the FeO Bonding in Cpd I in Terms of the Two Resonance Structures, K_1 and K_2, That Account for π-Bonding. (b) Corresponding MO Representation Showing That the Six π-Electrons Occupy the π and π^* Manifold of Perpendicular Orbitals, While the Cation-Radical State Is Described by the a_{2u} Orbital[a]

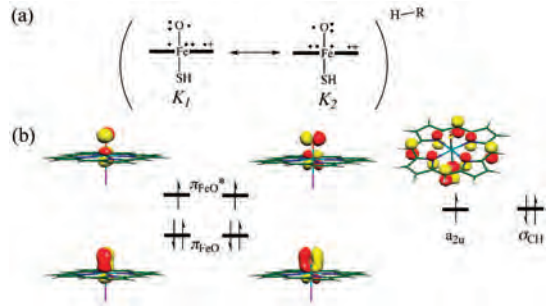

[a] In part a, the heavy dots represent the π-electrons in two perpendicular planes, while the line connecting Fe−O represents the Lewis σ_{FeO} bond. The (•+) sign near the porphyrin represents the cation-radical state of this moiety. The alkane is represented by the R−H bond. In part b, the alkane is represented by the corresponding σ_{CH} orbital. Reprinted with permission from ref 174. Copyright 2008 American Chemical Society.

alkane to fill the "hole" in the a_{2u} orbital of the porphyrin radical cation of Cpd I, while at the same time the H• moiety is spin-paired to the odd electron on the oxo group. This spin pairing[418] is shown in Figure 59a by the curved line connecting the single electrons on H• and on the oxo group of Cpd I; the RH moiety in this state is a cation radical. With these bonding changes, the oxidation state of iron in Ψ_r* is reduced from Fe^{IV} to Fe^{III}. The assignment of oxidation state for Ψ_r* is based on the electron counting formalism explained in section 3.2. Thus, in Ψ_r*, the oxo is spin-paired to H•, and as an "OH" group its oxidation state becomes HO^{1-} so that iron changes to oxidation state Fe^{III}. As such, by linking the H• atom to the iron-oxo, the oxo group accepts formally one electron from the H-atom, and hence, it "releases" back one of the two electrons it took from Fe in Cpd I. This in addition to the actual charge transfer from R−H in Ψ_r* makes this state "twice reduced" relative to the reactant state, Ψ_r. As such, along the reaction coordinate, which involves R···H bond elongation, and O···H and O···R shortening, the Ψ_r* state gets stabilized by forming O−H and O−R bonds and becomes the ground state of the ferric-alcohol product, Ψ_p, which involves three electrons in iron dπ orbitals (drawn as heavy dots on iron). Thus, Ψ_r* is the electronic image state of Ψ_p and, hence, the two states correlate along the reaction coordinate. The same applies in fact to the relationship between the states Ψ_r and Ψ_p*, with the latter being the electronic image of the former, with spin pairing between R and H, but with the geometry of the product. As such, the two states correlate with one another along the reaction coordinate.

Let us turn now to the intermediate curves, which are labeled as Ψ_I*(III) in Figure 59a and Ψ_I*(IV) in Figure 59b. In the VB representation, the C−H bond in R−H is unpaired into a triplet spin,[402,416,419] and the H• atom is spin-paired to the odd electron on the oxo group. As already discussed above, this spin pairing changes the oxidation state of the OH moiety to −1 and "releases" one electron to the heme. In the case of Ψ_I*(III), this electron is given to iron that is reduced to Fe^{III}, while, in Ψ_I*(IV), the electron shifts from the iron into the porphyrin hole, while the iron keeps two unpaired electrons in the dπ orbitals, thereby remaining in oxidation state Fe^{IV}. In each case, the entire intermediate curve corresponds to a single VB structure with energy changes reflecting the geometric changes along the reaction coordinate. Thus, at the intermediate stage, it corresponds to an H-abstraction intermediate (for example, **I** in Figure 35), composed of an iron-hydroxo/R• species, where the iron-porphyrin is in two electromeric states ($Por^{•+}Fe^{III}OH$ or $PorFe^{IV}OH$). Similarly, at the product geometry, this state involves a charge transfer from porphyrin to the R−O linkage in Figure 59a or from the iron d-electrons to the same linkage in Figure 59b.

The final energy profile for the mechanism in Figure 59 involves VB mixing of the three curves. The mixing that is shown by the bold-brown lines leads to an avoided crossing and generates the corresponding transition states; initially for the H-abstraction step, $\mathbf{TS}_H$, and subsequently for the radical rebound via $\mathbf{TS}_{reb}$. The latter transition state exists only on the quartet energy profile (see above in section 4.3, and discussion below), as has already been rationalized using VB diagrams.[26,83] To denote the spin-state condition on the existence of this particular barrier, a question mark is attached to the symbol $\mathbf{TS}_{reb}$ in Figure 59.

The $\mathbf{TS}_H$ species is expected to have a polar character, with some charge transfer, Q_{CT}, from the alkane moiety to the iron-oxo species, due to the secondary VB mixing of the Ψ_r* curve into $\mathbf{TS}_H$. Indeed, the many transition states calculated so far possess Q_{CT} values between 0.32 and 0.49.[174] All other qualitative features, which are predicted by the diagram, are apparent in the computational results of P450 hydroxylation, summarized in papers and reviews.[26,30,32,83] Furthermore, it is seen from Figure 59 that *the intermediate curve catalyzes the two-electron oxidation process by cutting through the high barrier*, which would have been encountered otherwise due to the crossing of the main curves that emanate from reactants and products, Ψ_r and Ψ_p. Therefore, in addition to revealing the source of the polar effect in $\mathbf{TS}_H$, the VB diagram accounts nicely and simply for the findings, both experimentally[420] and computationally,[32] of a stepwise rather than a concerted process. Additionally, the model predicts that there should exist a correlation between the degrees of C−H bond breaking and O−H bond formation in $\mathbf{TS}_H$, on the one hand, and the corresponding reaction barriers on the other hand. Such correlations have been observed before (see section 5.1),[170,174] and they reflect the mechanism of an avoided crossing that leads to the transition states: Thus, the crossing of the reactant (Ψ_r) and intermediate (Ψ_I*(III) or (Ψ_I*(IV)) curves, to establish $\mathbf{TS}_H$, is caused by C−H stretching and O−H approach, and hence the barrier correlates with the progress of these geometric features compared with the reactants state.

Let us next discuss the spin-state effect on the rebound process.[26,83] The VB diagrams for the rebound step on the two spin states of the $PorFe^{IV}OH/R•$ electromer are shown in Figure 60. They start from the center of Figure 59b, where the intermediate curve Ψ_I(IV) has to cross the Ψ_r* curve that descends toward the product state Ψ_p. To clarify the argument, we show small orbital occupation diagrams in Figure 60 describing the three upper orbitals of the d-block. Figure 60 shows the situation for the quartet spin state on the left and for the doublet spin curve on the right. At the intermediate geometry, the Ψ_r* state includes an electron transfer from the radical moiety R• to the iron-hydroxo complex. To maintain the quartet spin state, the electron is transferred into the high lying $\sigma^*_{z^2}$ orbital, while, for the

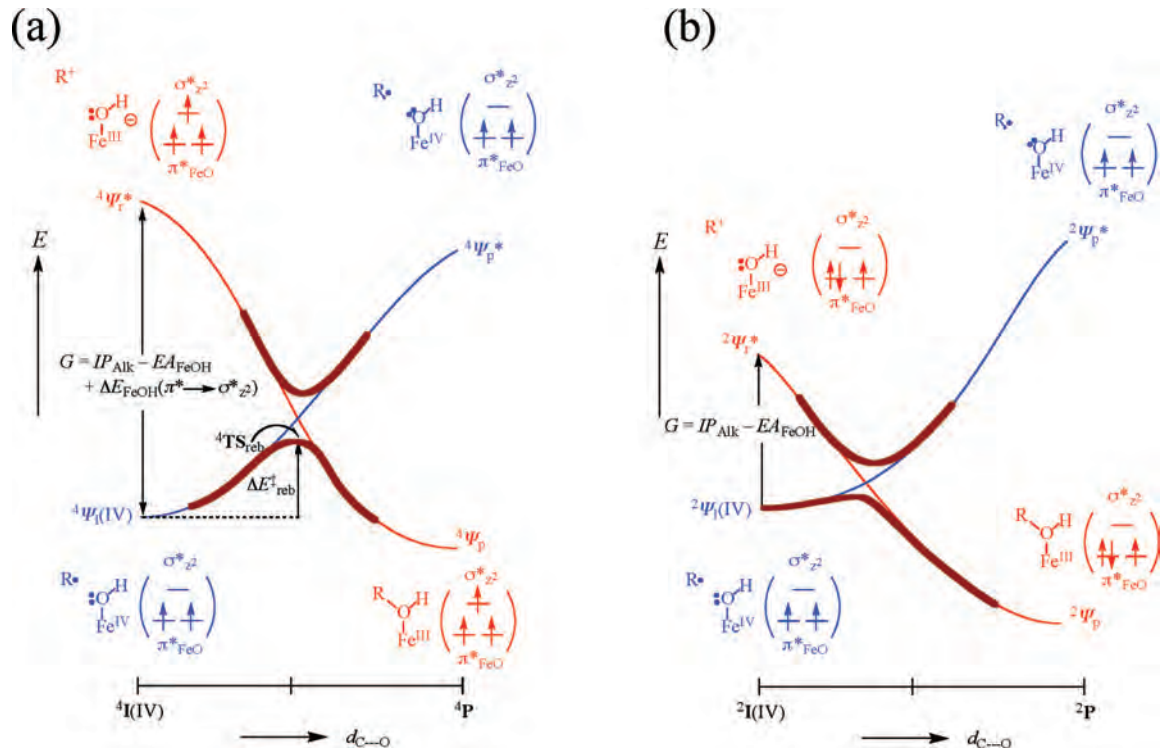

Figure 60. VB diagrams showing the energy profiles of the rebound process for the PorFe(IV)FeOH/R$^{\bullet}$ intermediates in the quartet (a) and doublet (b) spin states. It is seen that the promotion gap, G, for the quartet rebound is larger than that for the doublet by the promotion energy of an electron from the π^* orbital to the $\sigma^*_{z^2}$ orbital, labeled in part a as $\Delta E_{FeOH}(\pi^* \rightarrow \sigma^*)$. As a result of the larger gap, the quartet state will generally exhibit a barrier for rebound, while the doublet state will rebound in a barrier-free manner. These scenarios are shown by the bold energy profile that reflects the VB mixing of the two curves. Reprinted with permission from ref 174. Copyright 2008 American Chemical Society.

doublet state, it goes into a lower lying π^* orbital. The height of the crossing point depends on the initial gap between the two curves: the larger this energy gap, the higher the crossing point. Consequently, in the quartet spin state, where the gap is large[26,83] the VB mixing will generate a barrier for rebound. On the other hand, in the doublet spin state, the gap is much smaller (by 26 kcal mol^{-1}) so that the avoided crossing yields a barrier-free radical rebound. This trend has been observed so far in all computational studies of this reaction.[26,32,83]

The reason why the quartet rebound barrier is significantly higher for the $^4\Psi_I$(III) electromer compared with the $^4\Psi_I$(IV) electromer has been analyzed before in VB terms.[26,83] The chief reason is the amount of mixing between the VB-state curves (the avoided crossing energy) at the crossing point of Figure 59. Thus, in the case shown in Figure 60, the $^4\Psi_I$(IV) and $^4\Psi_r$* states differ by a single electron transfer from the radical to the $\sigma^*_{z^2}$ orbital, whereas, in the case of the ^{4}**I**(III) rebound, the $^4\Psi_I$(III) and $^4\Psi_r$* states differ by two electron transfers, one from the radical to $\sigma^*_{z^2}$ and the other from the filled π^*_{FeO} orbital to the singly occupied a_{2u} orbital. Therefore, the avoided crossing energy for the ^{4}**I**(IV) rebound is large, since the two states mix strongly, while for the ^{4}**I**(III) rebound the two states mix weakly and the avoided crossing energy is small;[418] the result is a small barrier for the ^{4}**I**(IV) rebound and a significantly larger one for the ^{4}**I**(III) rebound. It is apparent from the various C−H hydroxylation (and C═C epoxidation) cases in this review that these trends are manifest in all the computations, showing that the ^{4}**I**(III) intermediate is the longest-lived species during the reaction.

All in all, the VB diagram model provides a good rationale for the computational and experimental findings on various aspects of P450 hydroxylation.

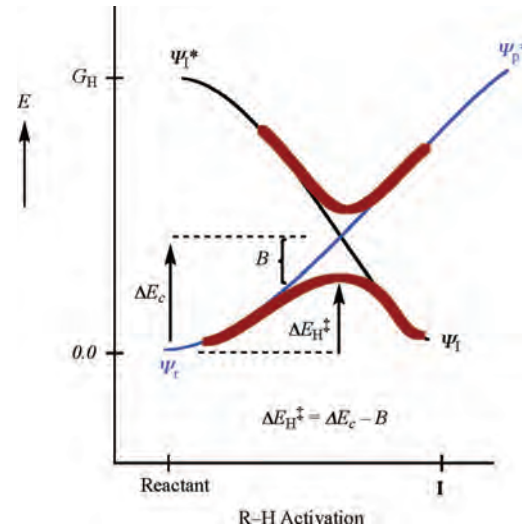

Figure 61. A VB state-correlation diagram (VBSCD) showing the formation of the barrier for the H-abstraction step of alkane hydroxylation by P450, without specifying the spin state. G_H is the promotion energy gap, B is the resonance energy of the transition state due to VB mixing, and $\Delta E_H^{\ddagger}$ is the resulting barrier. Reprinted with permission from ref 174. Copyright 2008 American Chemical Society.

5.2.2. Quantitative Aspects of Valence Bond Modeling for C−H Hydroxylation

Let us now turn to a more quantitative aspect of the modeling. Figure 61 shows the VB diagram for the first step in the reaction mechanism, i.e., C−H bond activation. The two curves (Ψ_r and Ψ_I*) are initially separated by an energy gap G_H (the so-called promotion gap[402,416]) and cross one

another along the reaction coordinate to generate a transition state ($\mathbf{TS}_H$) through VB mixing and avoidance of the crossing.

The barrier for the reaction, $\Delta E_H^{\ddagger}$, can be expressed as the height of the crossing point, ΔE_c, minus the avoided crossing or resonance energy (B) of $\mathbf{TS}_H$ due to the VB mixing:

$$\Delta E_H^{\ddagger} = \Delta E_c - B \quad (5)$$

The height of the crossing point in turn can be expressed as a fraction (f) of the promotion gap (G_H):

$$\Delta E_c = fG_H \quad (6)$$

Combining these two equations, an expression for the barrier heights is derived:

$$\Delta E_H^{\ddagger} = fG_H - B \quad (7)$$

This effective equation includes the BEP effect of the reaction energy difference (between Ψ_r and Ψ_1* in Figure 61) directly into the f factor, and although there exist explicit expressions which depend on all the variables in the diagram,[402,416,419] eq 7 is the most convenient one to use.

Based on previous modeling of the barrier for H-abstraction processes, it has been established[419] that f is approximately 0.3, while B is given by eq 8:

$$B \approx {}^1/_2(\mathrm{BDE_W}) \quad (8)$$

Here BDE_W stands for the bond dissociation energy of the weakest bond among the two that are formed and broken during the reaction: either the C−H or FeO−H bond. Thus, B can be estimated from the raw data of BDEs.

Finally, the promotion gap G_H, which is related to the triplet unpairing of the C−H bond,[174,415] was shown to be well approximated by eq 9, as twice the in situ bond strength, D_{CH}, of the activated C−H bond:

$$G_H = 2D_{CH} = 2(\mathrm{BDE_{CH}} + \mathrm{RE_{Alk\cdot}}) \quad (9)$$

The in situ bond strength is given as the sum of the BDE and the reorganization energy of the alkyl radical, $RE_{Alk\cdot}$, from its equilibrium geometry to its geometry in the alkane. The only missing quantity is $RE_{Alk\cdot}$, which can be calculated easily for a given radical. Thus, in principle, once we define the various alkane substrates, all the quantities necessary for calculating the barriers for C−H activation from raw fundamental data are available for the VB scheme outlined above.

This model was applied to a series of alkanes, depicted in Scheme 23, which are the same substrates used in eq 4 to find a correlation between barriers and BDE_{CH} properties. The computed BDE_{CH} and $RE_{Alk\cdot}$ values are collected in Table 3, while the corresponding barriers are given in Table 4.[174] It is seen that the BDE_{CH} values and the associate barriers range over 20 and 17 kcal mol^{-1}, respectively, and hence these substrates form a good test set to attempt a quantitative evaluation of the barrier from raw data.

To this end, one could use eqs 6−9 to calculate the barriers or to correlate the barriers, e.g., with D_{CH}. At the outset, it should be clear from the above discussion that neither f nor B can be constant for all the alkanes. Nevertheless, it would be interesting to ascertain whether the proposed values of f $\sim$ 0.3 and B (eq 8) will emerge from barriers by applying eq 7 in conjunction with eq 9. There are two ways to do so: Either one can use the equations and find the f values that reproduce the calculated barriers, or one can apply the equations with $f = 0.3$ for all the reactions and find the corresponding B values that are required to reproduce the barriers. This was done and is discussed here only for the barriers at the highest level (DFT(B3LYP/B2)).

Scheme 23. Alkane Substrates, 1−10, Used for the Application of the VB Model To Predict H-Abstraction Barriers

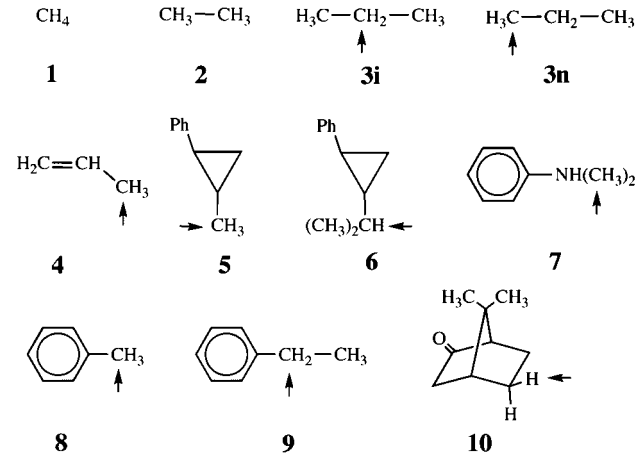

In the first method of modeling, the B values based on eq 8 are all $\leq$44.45 kcal mol^{-1}, with the smallest value being 41.4 kcal mol^{-1}. Using these values and G_H according to eq 9, one obtains an average value of $f_{av} = 0.285 \pm 0.015$. Thus, while f is not constant, its values cluster around the theoretical value of 0.3. The largest deviations are found for substrates **1** and **7**. Using $f_{av} = 0.285$ to calculate barriers, the resulting values are within 2.4 kcal mol^{-1} of the B3LYP/B2 computed ones.

In the second method of modeling, the computed B values cluster around an average $B_{av} = 46.39$ kcal mol^{-1} with a scatter of $\pm$2.24 kcal mol^{-1}. The largest deviations are for the substrates **1** and **7**, for which the so found B values are 3.97 kcal mol^{-1} smaller and 4.76 kcal mol^{-1} larger than the average quantity. Thus, once again, while the B values are not constant, they still cluster around an average value with a moderate scatter, as suggested by eq 8.

It is clear therefore that the two ways of modeling the barriers lead to f and B values that are not too far from each other. Therefore, we calculated all the barriers obtained with eq 7 using $f = 0.3$ and $B_{av} = 46.39$ kcal mol^{-1}. A plot of the resulting barriers against the computed ones gives a correlation coefficient $r \approx 0.9$. Table 5 displays the DFT and VB-derived barriers. The correlation coefficient between the two sets is modest, but considering the fact that only raw data were used, the correlation is good. We may therefore conclude that the VB models can predict barrier heights of P450-catalyzed reactions in the gas phase quite well.

The VB-derived barriers are close to the DFT-computed ones, with an average deviation of 1.53 kcal mol^{-1}. The greatest deviations (Table 5) are found for methane (**1**), where the VB equation underestimates the barrier by 4.0 kcal mol^{-1}, and *N*,*N*-dimethylaniline (**7**), for which the barrier is overestimated by 4.7 kcal mol^{-1}. Without these outliers, the VB equation predicts the computed barriers to within 0.90 kcal mol^{-1} (rms). The two outliers have clear physical origins, which are explained below.

Table 3. Calculated BDE_{CH}, BDE_{OH}, and RE_{Alk}. Data for the Alkanes 1−10 in Scheme 23 and for the PorFeO−H Species[a]

	BDE_{CH}				$RE_{Alk\bullet}$[b]	
	B1		B2		ΔE	
	ΔE	ΔE + ZPE	ΔE	ΔE + ZPE	B1	B2
methane (**1**)	112.45	102.77	111.29	101.62	7.42	6.79
ethane (**2**)	107.51	97.70	106.67	96.87	7.45	7.00
isopropane (**3i**)	103.39	93.55	102.87	93.03	7.56	7.21
n-propane (**3n**)	107.98	98.37	107.09	97.49	7.23	6.87
propene (**4**)	91.48	82.89	91.39	82.80	17.69	16.69
trans-methylphenylcyclopropane (**5**)	103.66	94.32	102.96	93.62	9.00	8.30
trans-isopropylphenylcyclopropane (**6**)	95.92	86.56	95.95	86.60	9.04	8.60
N,*N*-dimethylaniline (**7**)	95.72	86.99	94.81	86.08	8.14	7.94
toluene (**8**)	94.45	86.08	94.16	85.80	13.15	12.27
phenylethane (**9**)	91.30	82.44	91.31	82.45	19.32	18.38
camphor (**10**)	104.08	94.58	103.39	93.89	7.90	7.61
PorFeO−H	88.59[c]	81.81	95.69	88.91		

[a] All data in kcal mol^{-1} and calculated with basis set B1 or B2.[174] ZPE data with basis set B1. B1 is LACVP(Fe)/6-31G(rest); B2 is LACV3P+(Fe)/6-311+G*(rest). [b] These are absolute magnitudes. [c] BDE_{FeO-H}.

Table 4. DFT(B3LYP)-Only Barriers, $\Delta E^{\ddagger}$ and $(\Delta E + ZPE)^{\ddagger}$, Relative to Separated Reactants, ^{4,2}Cpd I + Alk-H, for TS_H[a,b]

		B1		B2	
		$\Delta E^{\ddagger}$	$(\Delta E + ZPE)^{\ddagger}$	$\Delta E^{\ddagger}$	$(\Delta E + ZPE)^{\ddagger}$
HS Data					
1	methane	26.77	22.81	26.87	22.91
2	ethane	21.32	17.71	21.02	17.41
3i	isopropane	19.05	15.39	19.46	15.80
3n	*n*-propane	21.47	17.84	21.12	17.48
4	propene	14.68	11.70	15.93	12.95
5	*trans*-methyl phenylcyclopropane	18.28	14.73	18.09	14.53
6	*trans*-isopropylphenylcyclopropane	16.03	12.46	17.03	13.46
7	*N*,*N*-dimethylaniline	7.66	5.04	8.17	5.54
8	toluene	14.81	11.79	15.45	12.43
9	phenylethane	14.57	11.19	15.93	12.55
10	camphor	17.96	14.21	18.27	14.51
LS Data					
1	methane	25.87	22.24	25.97	22.34
2	ethane	20.23	16.65	18.88	15.30
3i	isopropane	17.68	14.17	17.36	13.85
3n	*n*-propane	20.36	16.70	18.85	15.19
4	propene	15.15	12.13	15.85	12.82
5	*trans*-methyl phenylcyclopropane	17.31	13.90	16.54	13.13
6	*trans*-isopropylphenylcyclopropane	15.05	11.64	15.68	12.27
7	*N*,*N*-dimethylaniline	6.65	4.53	7.11	4.99
8	toluene	14.78	11.73	15.10	12.05
9	phenylethane	14.21	10.69	15.00	11.47
10	camphor	18.39	14.02	20.25	15.88

[a] All energies are in kcal mol^{-1}. Basis sets B1 and B2 are defined in Table 3.[174] [b] HS, quartet (high-spin); LS, doublet (low-spin).

Table 5. B3LYP/B2//B1 Barriers (kcal mol^{-1}), $\Delta E^{\ddagger}_{(DFT)}$, and Barriers Modeled by VB Theory, $\Delta E^{\ddagger}_{(VB)}$

alkane	$\Delta E^{\ddagger}_{(DFT)}$[a]	$\Delta E^{\ddagger}_{(VB)}$[b]
1	22.63	18.66
2	16.35	15.93
3i	14.82	13.75
3n	16.34	16.23
4	12.89	13.31
5	13.83	14.76
6	12.86	10.73
7	5.27	10.02
8	12.24	12.45
9	12.01	14.10
10	15.20	14.51

[a] These are averaged HS and LS barriers.[174] [b] The barriers were calculated using eq 6: $\Delta E^{\ddagger}(VB) = 0.3G_H - B_{AV}$; $B_{AV} = 46.39$ kcal mol^{-1}.

5.2.2.1. Deviations for Methane. As shown by the spin density distribution,[174] the ^{2,4}**TS**$_H$ transition states for methane hydroxylation are the only ones in the computed series with a clear ^{2,4}**TS**$_H$(III) character, having a porphyrin cation radical moiety; all other substrates exhibit ^{2,4}**TS**$_H$(IV) species. Referring back to Figure 59, we can see that while G_H is virtually the same in both cases, the two states Ψ_l*(IV) and Ψ_l*(III), which cross Ψ_r and generate the corresponding intermediate, are different. In Figure 59b, the state, Ψ_l*(IV), that crosses Ψ_r down to the $PorFe^{IV}OH/R^{\bullet}$ intermediate, has an odd electron that is localized on the oxo group. By contrast, Ψ_l*(III) in Figure 59a has two resonance structures that delocalize the odd electron on the oxo group between two planes. Therefore, the bond coupling interaction of the spin paired moieties, H•−•O, in Ψ_l*(IV) is strong, while in Ψ_l*(III) the same interaction is weak. The result is that Ψ_l*(IV) establishes a low energy crossing point (smaller *f* in eq 6), while Ψ_l*(III) establishes a higher crossing point (larger *f* in eq 6). Consequently, the barrier for the Fe^{III} electromer will be generally higher than the one for the Fe^{IV} electromer in the gas phase. Furthermore, this higher barrier is expected to be attended by **TS**$_H$(III) species that lie later

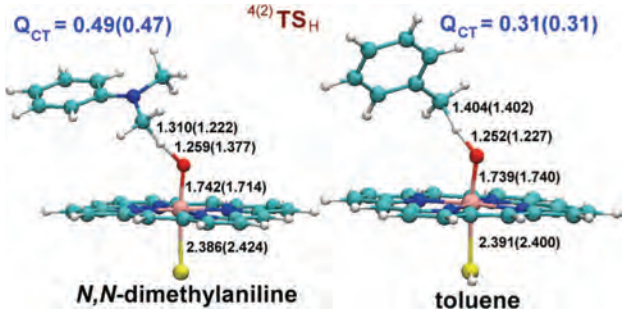

Figure 62. DFT(B3LYP/LAVCP) transition state structures (Å) and degree of charge transfer from the alkane to Cpd I, Q_{CT}, for *N*,*N*-dimethylaniline vs toluene. Q_{CT} is determined from NBO charges computed with the LACV3P+(Fe)/6-311+G*(rest) basis.[174] The charges are given in the quartet (doublet) states, respectively.

on the H-transfer coordinate, having greater extents of elongations of the R−H and Fe−O bonds than the corresponding $\mathbf{TS}_H$(IV) species. Coming back to methane, we note that since the strength of the C−H bond in methane is the largest in the series, it requires extensive bond stretching to reach the **TS**. And indeed, the computed C−H bond lengths in the $^2\mathbf{TS}_H$ ($^4\mathbf{TS}_H$) species of methane are highly stretched, being 1.489 (1.499) Å, respectively. With such a stretched C−H bond, the transition states will always be of $\mathbf{TS}_H$(III)-type.[174] This in turn means that a larger *f* value is required in the VB model to reproduce more accurately the corresponding barrier for methane hydroxylation, and this is the reason why the use of $f = 0.3$ (in Table 5) underestimates the barrier; an *f* value of 0.318 would have given a perfect barrier.

We note that, notwithstanding methane, in the gas phase we seldom expect to find the $\mathbf{TS}_H$(III) species being lower than the $\mathbf{TS}_H$(IV) species. However, in a polarizing medium such as the protein, the Fe^{III} electromeric states are stabilized compared with the Fe^{IV} states and become the lower energy species. Indeed, the **TS** geometries in the protein show larger extents of C···H stretching and O···O formation than the corresponding gas-phase species. Camphor is a case in point, where the QM/MM optimized transition states are of the $^{4,2}\mathbf{TS}_H$(III) variety; their C−H bonds are longer compared with those of the corresponding gas-phase species.[59]

5.2.2.2. Deviations for *N*,*N*-Dimethylaniline—Polar Effects in P450 Hydroxylation. We recall that the DFT computed barrier for C−H bond activation of *N*,*N*-dimethylaniline (DMA, **7**) is very small and deviates from the VB barriers of the other substrates. In fact, looking at Tables 3 and 5, it is seen that the BDE_{CH} value of **7** is much like that in toluene, **8**, but the corresponding barrier is 7−8 kcal mol^{-1} lower! The reason is a strong polar effect in the corresponding $\mathbf{TS}_H$ species, which was discussed above by reference to Figure 59 and which in the specific case of DMA is apparent in Scheme 13.

Indeed, Figure 62 shows side by side the $\mathbf{TS}_H$ species of toluene and DMA along with the corresponding Q_{CT} values (calculated with the NBO method), i.e., the charge transferred from the alkane to Cpd I in the transition state. It is seen that the Q_{CT} value for DMA is close to 0.5 and is significantly larger than the one for toluene. Such a large Q_{CT} value means a very strong mixing of the radical cation state into the $\mathbf{TS}_H$ species (see Ψ_r* in Figure 59). As already discussed in Scheme 13, this mixing is enhanced by the conjugation between the lone pair and the empty orbital on carbon in the $N-CH_2^+$ moiety.

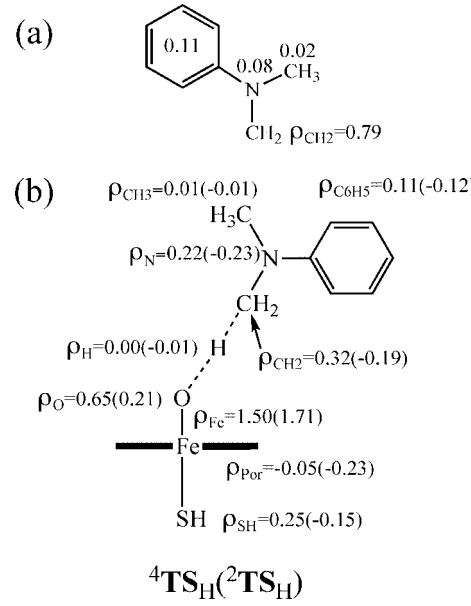

Figure 63. DFT(B3LYP/LACV3P+/6-311+G*) computed spin densities for the *N*-methylene-*N*-methylaniline radical and the $\mathbf{TS}_H$ species for hydrogen abstraction by Cpd I.[174] The spin densities are given in the quartet (doublet) states, respectively.

The extensive lone pair conjugation in the $\mathbf{TS}_H$ species can be deduced also by inspecting the amount of radical development at the nitrogen atom in Figure 63. It can be seen that the nitrogen develops spin density (ρ) in the $\mathbf{TS}_H$ species to an extent that is even larger than that in the isolated radical species, the *N*-methylene-*N*-methylaniline radical. This enhanced conjugation increases the resonance energy of the transition state[166] and thereby lowers the barrier. Thus, the deviation of **7** in Table 5 is caused by the *B* factor that gets larger (ca. 51 kcal mol^{-1} vs 46.39 kcal mol^{-1}) due to the enhanced conjugation of the nitrogen lone pair in the transition state. Indeed, as discussed above in the *p*-X-DMA series,[167] the H-abstraction barriers exhibit a Hammett correlation that reflects the *para* substituent effect on the ability of the nitrogen to conjugate with the stretched C−H bond in $\mathbf{TS}_H$. In fact, in the absence of this conjugation for $X = NO_2$,[167] the barrier for H-abstraction is close to the one calculated here for **7**, using the standard *B* value of 46.39 kcal mol^{-1} for the series.

5.2.3. Comments on the VB Modeling of the Rebound Step

A quantitative modeling of the rebound has not been attempted yet. However, the utility of the model was demonstrated in its ability to predict the observed rearrangement patterns, notably in the series of radical clock substrates studied by Newcomb[26,30,32,83] but not only in this series. Thus, the VB model of the rebound in Figure 60 was used[83] to predict and rationalize the variation of the rebound barrier with the change of the proximal axial ligand from thiolate to imidazole and to $PhSO_3$, and for the change of the metal from Fe to Ru. As can be seen from Figure 60, the promotion gap for the HS rebound depends also on the energy difference between the low lying π^*_{FeO} orbital and the higher lying $\sigma^*_{z^2}$ orbital. The latter orbital is affected by the antibonding interaction of the metal with the axial ligand. Therefore, in heme complexes, the $\sigma^*_{z^2}$ orbital is less antibonding and lower in energy, thus lowering the rebound

barrier, while, in the Ru-Cpd I, the $\sigma^*_{z^2}$ orbital lies very high, since Ru is a much stronger binder of ligand than Fe, and hence the rebound barrier is much larger. Another prediction of the model in Figure 60 is that different P450 isozymes should exhibit different amounts of rearrangement for a given substrate as a result of the stronger or weaker binding strength between iron and the cysteine ligand of the particular isozyme. There is ample evidence in the literature that the amount of rearrangement for a given probe substrate depends on the identity of the P450 isozyme, and while this does not prove the correctness of the prediction, still the prediction is clearly testable by a combination of QM/MM calculations and experimental means.

5.3. Summary of Valence Bond Modeling of P450 Reactivity

All in all, the VB diagram model provides a good rationale for the computational and experimental findings on various aspects of P450 hydroxylation. VB modeling of the H-abstraction barrier shows, according to eqs 6−9, that the promotion gap depends on BDE_{CH}, which can be used to estimate barriers quickly from experimental BDE values, without having to compute the $RE_{Alk\cdot}$ quantities. In fact, eq 3 has the form of the barrier equation, eq 6, with $f = 0.293$ and $B = 39.6$ kcal mol^{-1}, except that the promotion gap will here simply be 2 BDE_{CH}. In any event, the barrier equation shows the usefulness of BDE_{CH}, but the correlation with these quantities has little to do with the original BEP correlation; it is a correlation with the promotion gap that leads to the barrier.

While this has not yet been done, the diagrams in Figures 59 and 60 can be used with small modifications (using the π-charge transfer state for Ψ_r* and a triplet excited state for the intermediate curve) to discuss the reactivity and mechanistic aspects of C═C epoxidation. The mechanism of arene hydroxylation can also find a rationale in the VB diagram of Figure 59, with the modification that the excited state Ψ_r* is a charge transfer state involving an electron transfer from the π-system of the arene to Cpd I and is thus likely to be sufficiently low-lying to lead to a transition state with a hybrid radicalar-cationic character in the arene, as discussed above (section 4.5) in conjunction with the corresponding DFT(B3LYP) and DFT(B3LYP)/MM calculations.[33,34,38,60] Similarly, heteroatom oxidation, which involves a concerted mechanism dominated by the LS state, can be accommodated with a two-state scenario, involving the reactants curve and the curve that starts at the charge transfer state, Ψ_r*, which will be low-lying for sulfides and amines. As such, the VB method can provide a unified framework for the reactivity of P450 enzymes.

6. Summary of Reactivity Patterns

Theory shows that Cpd I is a versatile reagent with uncanny solutions for complex reactions. On the one hand, it is a two-state triradicaloid reagent (or even a four-state reagent if one counts the pentaradicaloid states in section 3.7.5), and therefore, it participates in radical-type reactions that involve bond activation processes on at least two spin states, with state-specific chemistry, known as TSR or MSR.[26,32,146] At the same time, Cpd I is highly electron deficient, having an effective overall oxidation state of V. As such, it participates also in electrophilic reactions, electron transfer reactions, and bond-reorganization coupled electron transfer reactions, such as the proton-coupled electron transfer (PCET) mechanism of P450 StaP.[58] Taken together, Cpd I is a chameleon species that adapts its electronic structure to the protein environment, to additives such as water molecules,[61,131] ions, etc., and to the substrate with which it reacts.[58] These features are revealed by both QM-only and QM/MM calculations. Theory shows that kinetic isotope effect (KIE) measurements can probe TSR and the reactive spin states of Cpd I, at least for C−H hydroxylation.[166,167] In addition, VB modeling provides an understanding of the mechanism and reactivity patterns. This has been demonstrated for C−H hydroxylation,[174] but the principles of this model can clearly be applied to other reactions as well.

An important aspect that is revealed by the QM/MM calculations is the biological role of small molecules that may affect the reactivity of the enzyme. Chief among these is the water molecule. Placed in strategic positions inside the enzyme cavity[58,61,131] or coming from the surface or the deep of the protein,[73] water molecules act as promoters of otherwise difficult transformations by lowering reaction barriers[58,61,131] or by bridging the distance separation between the immobilized substrate and Cpd I reactants.[58]

7. Concluding Remarks

With current computational capabilities, QM(DFT)-only and QM(DFT)/MM calculations can be used to investigate models of cytochrome P450 systems, with typically around 50−100 and up to about 200 atoms (including heme and substrate, plus a few neighboring residues and water molecules) in the QM region and with thousands of atoms (typically around 25000) in the MM region. It has become apparent by extensive validation studies in several groups that the current technology is good enough for meaningful investigations of metalloenzymes such as cytochrome P450, when using B3LYP as QM(DFT) component, with medium-size basis sets for geometry optimization and larger basis sets for single-point energy evaluations; realistic QM/MM calculations employ electronic embedding and established protein force fields as MM component. Higher accuracies are expected by QM/MM methods with high-level correlated ab initio QM methods (e.g., MR-CI). Currently, only a few such calculations have been published, on Cpd I and other intermediates[77,78] in the catalytic cycle of $P450_{cam}$ and related enzymes.[79] This limited set of calculations has given results that are rather similar to those from DFT(B3LYP)/MM, but of course more tests are required to properly assess the quantitative accuracy of DFT/MM methods in this area.

The QM/MM methods have advanced to the point that the complete catalytic cycle of a metalloenzyme can now be studied. In fact, QM/MM calculations have been carried out for all intermediates of cytochrome $P450_{cam}$ and for most of the reactions in the catalytic cycle, including the mechanism of electron transfer,[76] the formation of Cpd 0 and of Cpd I in the wild-type and various mutant enzymes,[159,161,246] and the various reactions catalyzed by the active species, Cpd I, for example in bond activation (C−H, C═C, aryl, etc), oxo-transfer (sulfoxidation, N-oxidation, etc.), and C−C bond coupling reactions. Furthermore, they have addressed the in-silico design of new mutants, such as the selenocysteine mutant of P450,[61] which has already received attention

by the experimental community.[64] Coupled with MD simulations, it is now possible to probe the role of the reductase and to pinpoint the factors that may regulate and make for a functional catalytic cycle.[283]

There remain open-ended issues, of course, that will require further improvements in the theoretical tools. The DFT(B3LYP)/MM data in Figure 37 seem to suggest a solution for one of the puzzling open problems, i.e., the inability to observe the active species Cpd I in $P450_{cam}$. The proposed explanation depends on the difference between the barriers for formation of Cpd I from Cpd 0 and for H-abstraction from camphor. However, since a question mark still looms over the accuracy of DFT barriers, these two reactions should be investigated by more accurate ab initio QM(MR-CI)/MM calculations, which will hopefully provide reliable barriers for Figure 37 and allow us to draw more definitive conclusions on the elusive nature of Cpd I in $P450_{cam}$.

Another key aspect is the role of additives on the reactivity of P450 enzymes. DFT(B3LYP)/MM calculations have so far demonstrated nicely that Cpd I is a chameleon species and that various additives and different substrates can dramatically affect its reactivity patterns (see, for example, the role of Wat_{903} in $P450_{cam}$[61,131] and of Wat_{789} in P450 StaP[58]). The potential of the latter concept is far-reaching and awaits exploration by further theoretical and experimental studies.

The issue of selectivity is still a sore point, since it is still hard to understand, e.g., the regioselectivity of C−H vs C═C activation or of N-demethylation vs sulfoxidation. As pointed out above, the DFT(B3LYP)/MM results for the C−H/C═C competition in propene and cyclohexene oxidation do not reproduce the experimental data.[57] This might require QM(MR-CI)/MM calculations to ascertain whether the problem is associated with the inaccuracy of B3LYP barriers or with the lack of sufficient conformational sampling.

The DFT(B3LYP) and DFT(B3LYP)/MM calculations invariably find two or more low-lying spin states, which contribute to reactivity and product formation (in a state-specific manner). It has indeed been shown that TSR and MSR scenarios can rationalize many puzzling experimental observations on P450 reactivity.[18,32,285,286] The actual kinetics of these processes will depend on the probability of spin crossover. There is a clear need for more quantitative theoretical studies of spin crossover in order to better assess the role of TSR and MSR in P450 chemistry. There is a further need for studying spin-state perturbations, e.g., by external magnetic and/or electric fields, that may affect the stereospecificity and selectivity of P450 enzymes.[25] This requires development of DFT(MR-CI)/MM methods to handle such external fields, as well as experimental studies of these phenomena.

Dynamical aspects in P450 have generally only been addressed at the classical force-field level up to now, and it would certainly be of interest to study them also at higher QM/MM levels, for example with regard to the biological role of water molecules in the various proton-relay mechanisms during Cpd 0 and Cpd I formation and in the reactions of Cpd I (e.g., with regard to the catalytic effect of Wat_{903} in $P450_{cam}$ reactions[61,131] and the mechanistic role of the two water molecules during aryl−aryl coupling by P450 StaP[58,80]). In addition, there is a need for a thorough thermodynamical analysis of the whole catalytic cycle in P450 enzymes that includes the reduction steps and their dependence on the protonation state of the enzyme.

Finally, a treatment of plant P450s is still missing. Some of these P450 enzymes are interesting because they do not use exogenous oxygen, but rather activate hydroperoxides of polyunsaturated fatty acids to catalyze several remarkable reactions.[421] Investigation of these mechanisms may provide more insight into the uncanny ability of P450 enzymes to find solutions for performing complex transformations.

8. Abbreviations

AC	aldehyde complex
Alk	alkyl
AlkH	alkane
AO	arene oxide
APX	ascorbate peroxidase
Arg	arginine
Asn	asparagine
Asp	aspartic acid
B2W	a basis set consisting of Wachters basis (with polarization and diffuse f) on iron, and 6-31G* on the atoms of the first coordination shell
B3LYP	a hybrid functional used in DFT consisting of 20% Hartree−Fock and 80% Becke88 exchange combined with the Lee−Yang−Parr correlation functional
BDE	bond dissociation energy
BEP	Bell−Evans−Polanyi
BFCET	bond-formation coupled electron transfer
BHLYP	a hybrid functional used in DFT, consisting of half Hartree−Fock and half Becke88 exchange combined with the Lee−Yang−Parr correlation functional
BLYP	a pure gradient functional used in DFT, consisting of Becke88 exchange combined with the Lee−Yang−Parr correlation functional
BO	ferric benzene oxide complex
BP86	a pure gradient corrected functional used in DFT consisting of Becke88 exchange and Perdew86 correlation functional
CAM	camphor
CASSCF	complete active space self-consistent field method
CASPT2	multiconfigurational second-order perturbation theory
CB	cooperative binding
C*c*P	cytochrome *c* peroxidase
CCSD(T)	coupled cluster method with single and double excitations, and a perturbative treatment of triple excitations
CI	configuration interaction
CPA	chromopyrrolic acid
Cpd 0	ferric hydroperoxide species in heme protein
Cpd I	the active species of heme enzymes, Compound I, involving Fe(IV)O and a porphyrin radical cation
Cpd II	one-electron reduced species of Cpd I
CPO	chloroperoxidase
CYP	cytochrome P450
Cys	cysteine
D251N	a mutant of $P450_{cam}$ in which Asp_{251} is replaced by asparagine (N)
def2-TZVP	a triple ζ quality basis set of Ahlrichs and coworkers (TURBOMOLE notation)
DFT	density functional theory
DFT/MM	a density functional/molecular mechanical method, a variant of QM/MM
DHA	dual hydrogen transfer
Dia	diazepam

DMA	*N*,*N*-dimethylaniline
DMS	dimethyl sulfide
DNA	deoxyribonucleic acid
DZ	double ζ basis set
DZP	double ζ basis set with polarization
EC	ferric epoxide complex
EEF	external electric field
EPR/ENDOR	electron paramagnetic resonance/electron−nuclear double resonance
ESEEM	electron spin echo envelope modulation spectroscopy
ESP	electrostatic potential
EXAFS	extended X-ray absorption fine structure
ext-SCys	extended cysteinate
FO	face-on
fs	femtosecond
GGA	generalized gradient approximation
Gln	glutamine
Glu	glutamic acid
Gly	glycine
H_4B	tetrahydrobiopterin
HAT	H-atom abstraction
HCB	hexachlorobenzene
HF	Hartree−Fock
HFB	hexafluorobenzene
His	histidine
HO	heme oxygenase
HOMO	highest occupied molecular orbital
HRP	horseradish peroxidase
HS	high spin
I	intermediate
Ile	isoleucine
IP	ionization potential
K	ketone
KIE	kinetic isotope effect
KSIE	kinetic solvent isotope effect
L358P	a P450 mutant created by replacement of leucine 358 (Leu_{358}) by proline
LACV3P++**	a triple ζ basis set augmented with diffuse and polarization functions describing the valence orbitals on the transition metal (the core is described by an effective core potential), combined with 6-311++G** for other atoms
LACV3P+*	a triple ζ basis set augmented with diffuse and polarization functions describing the valence orbitals on the transition metal (the core is described by an effective core potential), combined with 6-311+G* for other atoms
LACVP	a double ζ basis set describing the valence orbitals on the transition metal (the core is described by an effective core potential), combined with 6-31G on all other atoms
LDA	local density approximation
Leu	leucine
LFP	laser flash photolysis
LS	low spin
Lys	lysine
M06	M06 suite of density functionals of Truhlar and co-workers
Mb	myoglobin
MD	molecular dynamics
MM	molecular mechanics
MR-CI	multireference configuration interaction
MSR	multistate reactivity
NADH	reduced nicotinamide adenine dinucleotide
NIH shift	a chemical rearrangement where a hydrogen atom on an aromatic ring undergoes an intramolecular migration, primarily during a hydroxylation relation
NOS	nitric oxide synthase
ns	nanosecond
OLYP	a pure gradient functional used in DFT, consisting of Handy's OPTX modification of Becke's exchange combined with the Lee−Yang−Parr correlation functional
P	products (in benzene hydroxylation, P also refers to phenol)
P450	cytochrome P450 enzymes
PBE	Perdew, Burke, and Ernzerhof exchange-correlation functional
PCET	proton-coupled electron transfer
PDX	putidaredoxin
PHBH	*p*-hydroxybenzoate hydroxylase
pK_a	$pK_a = -\log K_a$, K_a is the dissociation constant of an acid
Por	porphyrin or porphine
PPIX	protoporphyrin IX, the native porphyrin for heme enzymes
ps	picosecond
PT	proton transfer
Q_{CT}	charge transfer
QM	quantum mechanics
QM/MM	a hybrid method that couples a quantum mechanical (QM) method and a molecular mechanical (MM) method. The QM method can be DFT, hence QM(DFT)/MM.
QSAR	quantitative structure−activity relationship
R	reactant state
RC	reactant complex
RE	reorganization energy
RI	resolution of identity
ROB3LYP	restricted open-shell B3LYP
SC	suicidal complex
SCys	cysteinate
SET	single electron transfer
SMe	methyl mercaptide
SO	side-on
SSM	single-state mechanism
STA	staurosporine
SV(P)	split-valence basis set with valence polarization of Ahlrichs and co-workers
T252A	a P450 mutant created by replacement of threonine 252 (Thr_{252}) by alanine
T252G	a P450 mutant created by replacement of threonine 252 (Thr_{252}) by glycine
T252S	a P450 mutant created by replacement of threonine 252 (Thr_{252}) by serine
T252V	a P450 mutant created by replacement of threonine 252 (Thr_{252}) by valine
T252X	a P450 mutant created by replacement of threonine 252 (Thr_{252}) by amino acid X
Thr	threonine
TMA	trimethylamine
Trp	tryptophan
TS	transition state
TS_E	epoxidation transition state
TS_H	hydroxylation transition state
TSR	two-state reactivity
Tyr	tyrosine
TZ	triple ζ basis set
TZVP	a valence triple ζ with valence polarization basis set of Ahlrichs and co-workers
TZVPP	a valence triple ζ with valence multiple polarization basis set of Ahlrichs and co-workers, including 2p, 1d polarization functions for H, and 2d, 1f polarization functions for heavy atoms
UB3LYP	unrestricted B3LYP
VB	valence bond
Wat	water molecule
WT	wild type (native enzyme)
ZPE	zero point energy

9. Acknowledgments

The research at the Hebrew University is supported in part by an Israeli-Science Foundation (ISF) grant (10/06) and a German Israeli Project Cooperation (DIP-G7.1). The authors are indebted to J. P. Dinnocenzo for his insightful advice regarding Figure 37.

10. Note Added in Proof

A recent paper used DFT/MM calculations for the mechanism of Cpd I formation in CYP51. The authors found a heterolytic mechanism like the one described in ref. 70 for HRP, alongside an energetically close hybrid homolytic-heterolytic mechanism like the one presented here. See: Sen, K.; Hackett, J. C. *J. Phys. Chem. B* **2009**, *113*, 8170-8182.

11. References

(1) Raymond, J.; Segrè, D. *Science* **2006**, *311*, 1764–1767.
(2) Omura, T.; Sato, R. *J. Biol. Chem.* **1962**, *237*, 1375–1376.
(3) Groves, J. T. *J. Chem. Educ.* **1985**, *62*, 928–931.
(4) Dawson, J. H.; Sono, M. *Chem. Rev.* **1987**, *87*, 1255–1276.
(5) Ortiz de Montellano, P. R. *Trends Pharmacol. Sci.* **1989**, *10*, 354–359.
(6) Guengerich, F. P.; MacDonald, T. L. *FASEB J.* **1990**, *4*, 2453–2459.
(7) *Cytochrome P450: Structure, Mechanism, and Biochemistry*, 2nd ed.; Ortiz de Montellano, P. R., Ed.; Plenum Press: New York, 1995.
(8) Groves, J. T.; Han, Y.-Z. In *Cytochrome P450: Structure, Mechanism, and Biochemistry*, 2nd ed.; Ortiz de Montellano, P. R., Ed.; Plenum Press: New York, 1995; Chapter 1, pp 3−48.
(9) Guengerich, F. P. In *Cytochrome P450: Structure, Mechanism, and Biochemistry*, 2nd ed.; Ortiz de Montellano, P. R., Ed.; Plenum Press: New York, 1995; Chapter 14, pp 473−535.
(10) Ortiz de Montellano, P. R. In *Cytochrome P450: Structure, Mechanism, and Biochemistry*, 2nd ed.; Ortiz de Montellano, P. R., Ed.; Plenum Press: New York, 1995; Chapter 8, pp 245−303.
(11) Poulos, T. L.; Cupp-Vickery, J.; Li, H. In *Cytochrome P450: Structure, Mechanism, and Biochemistry*, 2nd ed.; Ortiz de Montellano, P. R., Ed.; Plenum Press: New York, 1995; Chapter 4, pp 125−150.
(12) Sono, M.; Roach, M. P.; Coulter, E. D.; Dawson, J. H. *Chem. Rev.* **1996**, *96*, 2841–2887.
(13) Woggon, W.-D. *Top. Curr. Chem.* **1996**, *184*, 39–96.
(14) Guengerich, F. P. *Annu. Rev. Pharmacol. Toxicol.* **1999**, *39*, 1–17.
(15) Sligar, S. G. *Essays Biochem.* **1999**, *34*, 71–83.
(16) Watanabe, Y. *J. Biol. Inorg. Chem.* **2001**, *6*, 846–856.
(17) Lewis, D. F. V. *Guide to Cytochromes P450*; Taylor and Francis: New York, 2001.
(18) Ortiz de Montellano, P. R.; de Voss, J. J. *Nat. Prod. Rep.* **2002**, *19*, 477–493.
(19) *Cytochrome P450: Structure, Mechanism, and Biochemistry*, 3rd ed.; Ortiz de Montellano, P. R., Ed.; Kluwer Academic/Plenum Publishers: New York, 2005.
(20) *The Ubiquitous Role of Cytochrome P450 Proteins In Metal Ions in Life Sciences*; Sigel, A., Sigel, H., Sigel, R. K. O., Eds.; John Wiley & Sons Ltd: Chichester, England, 2007; Vol. 3.
(21) Guengerich, F. P. In *Cytochrome P450: Structure, Mechanism, and Biochemistry*, 3rd ed.; Ortiz de Montellano, P. R., Ed.; Kluwer Academic/Plenum Publishers: New York, 2005; Chapter 10, pp 377−530.
(22) Groves, J. In *Cytochrome P450: Structure, Mechanism, and Biochemistry*, 3rd ed.; Ortiz de Montellano, P. R., Ed.; Kluwer Academic/Plenum Publishers: New York, 2005; Chapter 1, pp 1−43.
(23) Newcomb, M.; Toy, P. H. *Acc. Chem. Res.* **2000**, *33*, 449–455.
(24) Newcomb, M.; Shen, R.; Choi, S.-Y.; Toy, P. H.; Hollenberg, P. F.; Vaz, A. D. N.; Coon, M. J. *J. Am. Chem. Soc.* **2000**, *122*, 2677–2686.
(25) Shaik, S.; Hirao, H.; Kumar, D. *Acc. Chem. Res.* **2007**, *40*, 532–542.
(26) Shaik, S.; Hirao, H.; Kumar, D. *Nat. Prod. Rep.* **2007**, *24*, 533–552.
(27) Yamamoto, S.; Kashiwagi, H. *Chem. Phys. Lett.* **1989**, *161*, 85–89.
(28) Loew, G. H.; Harris, D. L. *Chem. Rev.* **2000**, *100*, 407–419.
(29) Harris, D. L. *Curr. Opin. Chem. Biol.* **2001**, *5*, 724–735.
(30) Shaik, S.; de Visser, S. P.; Ogliaro, F.; Schwarz, H.; Schröder, D. *Curr. Opin. Chem. Biol.* **2002**, *6*, 556–567.
(31) Shaik, S.; de Visser, S. P. In *Cytochrome P450: Structure, Mechanism, and Biochemistry*, 3rd ed.; Ortiz de Montellano, P. R., Ed.; Kluwer Academic/Plenum Publishers: New York, 2005; Chapter 2, pp 45−85.
(32) Shaik, S.; Kumar, D.; de Visser, S. P.; Altun, A.; Thiel, W. *Chem. Rev.* **2005**, *105*, 2279–2328.
(33) Bathelt, C. M.; Ridder, L.; Mulholland, A. J.; Harvey, J. N. *J. Am. Chem. Soc.* **2003**, *125*, 15004–15005.
(34) Bathelt, C. M.; Ridder, L.; Mulholland, A. J.; Harvey, J. N. *Org. Biomol. Chem.* **2004**, *2*, 2998–3005.
(35) de Visser, S. P.; Ogliaro, F.; Shaik, S. *Angew. Chem., Int. Ed.* **2001**, *40*, 2871–2874.
(36) de Visser, S. P.; Ogliaro, F.; Shaik, S. *Chem. Commun.* **2001**, 2322–2323.
(37) de Visser, S. P.; Ogliaro, F.; Harris, N.; Shaik, S. *J. Am. Chem. Soc.* **2001**, *123*, 3037–3047.
(38) de Visser, S. P.; Shaik, S. *J. Am. Chem. Soc.* **2003**, *125*, 7413–7424.
(39) Yoshizawa, K.; Ohta, T.; Eda, M.; Yamabe, T. *Bull. Chem. Soc. Jpn.* **2000**, *73*, 401–407.
(40) Yoshizawa, K.; Shiota, Y.; Kagawa, Y. *Bull. Chem. Soc. Jpn.* **2000**, *73*, 2669–2673.
(41) Yoshizawa, K.; Kagawa, Y.; Shiota, Y. *J. Phys. Chem. B* **2000**, *104*, 12365–12370.
(42) Yoshizawa, K.; Kamachi, T.; Shiota, Y. *J. Am. Chem. Soc.* **2001**, *123*, 9806–9816.
(43) Yoshizawa, K. *Coord. Chem. Rev.* **2002**, *226*, 251–259.
(44) Kamachi, T.; Shiota, Y.; Ohta, T.; Yoshizawa, K. *Bull. Chem. Soc. Jpn.* **2003**, *76*, 721–732.
(45) Kamachi, T.; Yoshizawa, K. *J. Am. Chem. Soc.* **2003**, *125*, 4652–4661.
(46) Green, M. T. *J. Am. Chem. Soc.* **1999**, *121*, 7939–7940.
(47) Green, M. T. *J. Am. Chem. Soc.* **2000**, *122*, 9495–9499.
(48) Green, M. T. *J. Am. Chem. Soc.* **2001**, *123*, 9218–9219.
(49) Ohta, T.; Matsuura, K.; Yoshizawa, K.; Morishima, I. *J. Inorg. Biochem.* **2000**, *82*, 141–152.
(50) Ogliaro, F.; Cohen, S.; de Visser, S. P.; Shaik, S. *J. Am. Chem. Soc.* **2000**, *122*, 12892–12893.
(51) de Visser, S. P.; Ogliaro, F.; Gross, Z.; Shaik, S. *Chem.—Eur. J.* **2001**, *7*, 4954–4960.
(52) Sharma, P. K.; de Visser, S. P.; Ogliaro, F.; Shaik, S. *J. Am. Chem. Soc.* **2003**, *125*, 2291–2300.
(53) Schöneboom, J. C.; Lin, H.; Reuter, N.; Thiel, W.; Cohen, S.; Ogliaro, F.; Shaik, S. *J. Am. Chem. Soc.* **2002**, *124*, 8142–8151.
(54) Zheng, J. J.; Altun, A.; Thiel, W. *J. Comput. Chem.* **2007**, *28*, 2147–2158.
(55) Fishelovitch, D.; Hazan, C.; Hirao, H.; Wolfson, H. J.; Nussinov, R.; Shaik, S. *J. Phys. Chem. B* **2007**, *111*, 13822–13832.
(56) Bathelt, C. M.; Zurek, J.; Mulholland, A. J.; Harvey, J. N. *J. Am. Chem. Soc.* **2005**, *127*, 12900–12908.
(57) Cohen, S.; Kozuch, S.; Hazan, C.; Shaik, S. *J. Am. Chem. Soc.* **2006**, *128*, 11028–11029.
(58) Wang, Y.; Hirao, H.; Chen, H.; Onaka, H.; Nagano, S.; Shaik, S. *J. Am. Chem. Soc.* **2008**, *130*, 7170–7171.
(59) Schöneboom, J. C.; Cohen, S.; Lin, H.; Shaik, S.; Thiel, W. *J. Am. Chem. Soc.* **2004**, *126*, 4017–4034.
(60) Bathelt, C. M.; Mulholland, A. J.; Harvey, J. N. *J. Phys. Chem. A* **2008**, *112*, 13149–13156.
(61) Altun, A.; Guallar, V.; Friesner, R. A.; Shaik, S.; Thiel, W. *J. Am. Chem. Soc.* **2006**, *128*, 3924–3925.
(62) Cohen, S.; Kumar, D.; Shaik, S. *J. Am. Chem. Soc.* **2006**, *128*, 2649–2653.
(63) Hirao, H.; Cho, K.-B.; Shaik, S. *J. Biol. Inorg. Chem.* **2008**, *13*, 521–530.
(64) (a) Jiang, Y.; Ortiz de Montellano, P. R. *Inorg. Chem.* **2008**, *47*, 3480–3482. (b) Jiang, Y.; Sivaramakrishnan, S.; Hayashi, T.; Cohen, S.; Moënne-Loccoz, P.; Shaik, S.; Ortiz de Montellano, P. R. *Angew. Chem., Int. Ed.* **2009**, *48*, 7193–7195.
(65) Aldag, I.; Gromov, I.; García-Rubio, I.; von Koenig, K.; Schlichting, I.; Jaun, B.; Hilvert, D. *Proc. Natl. Acad. Sci. U. S. A.* **2009**, *106*, 5481–5486.
(66) Chen, H.; Hirao, H.; Derat, E.; Schlichting, I.; Shaik, S. *J. Phys. Chem. B* **2008**, *112*, 9490–9500.
(67) Kühnel, K.; Derat, E.; Terner, J.; Shaik, S.; Schlichting, I. *Proc. Natl. Acad. Sci. U. S. A.* **2007**, *104*, 99–104.
(68) Cho, K.-B.; Derat, E.; Shaik, S. *J. Am. Chem. Soc.* **2007**, *129*, 3182–3188.
(69) Cho, K.-B.; Carvajal, M. A.; Shaik, S. *J. Phys. Chem. B* **2009**, *113*, 336–346.
(70) Derat, E.; Shaik, S. *J. Phys. Chem. B* **2006**, *110*, 10526–10533.
(71) Derat, E.; Shaik, S. *J. Am. Chem. Soc.* **2006**, *128*, 13940–13949.
(72) Derat, E.; Shaik, S. *J. Am. Chem. Soc.* **2006**, *128*, 8185–8198.
(73) Derat, E.; Shaik, S.; Rovira, C.; Vidossich, P.; Alfonso-Prieto, M. *J. Am. Chem. Soc.* **2007**, *129*, 6346–6347.

(74) Derat, E.; Cohen, S.; Shaik, S.; Altun, A.; Thiel, W. *J. Am. Chem. Soc.* **2005**, *127*, 13611–13621.
(75) Kim, S. H.; Perera, R.; Hager, L. P.; Dawson, J. H.; Hoffman, B. M. *J. Am. Chem. Soc.* **2006**, *128*, 5598–5599.
(76) Wallrapp, F.; Masone, D.; Guallar, V. *J. Phys. Chem. A* **2008**, *112*, 12989–12994.
(77) Schöneboom, J. C.; Neese, F.; Thiel, W. *J. Am. Chem. Soc.* **2005**, *127*, 5840–5853.
(78) Altun, A.; Kumar, D.; Neese, F.; Thiel, W. *J. Phys. Chem. A* **2008**, *112*, 12904–12910.
(79) Chen, H.; Ikeda-Saito, M.; Shaik, S. *J. Am. Chem. Soc.* **2008**, *130*, 14778–14790.
(80) Wang, Y.; Chen, H.; Makino, M.; Shiro, S.; Nagano, S.; Onaka, H.; Shaik, S. *J. Am. Chem. Soc.* **2009**, *131*, 6748–6762.
(81) Harris, D. L. *Curr. Opin. Drug Discovery Dev.* **2004**, *7*, 43–48.
(82) Meunier, B.; de Visser, S. P.; Shaik, S. *Chem. Rev.* **2004**, *104*, 3947–3980.
(83) Shaik, S.; Cohen, S.; de Visser, S. P.; Sharma, P. K.; Kumar, D.; Kozuch, S.; Ogliaro, F.; Danovich, D. *Eur. J. Inorg. Chem.* **2004**, 207–226.
(84) Warshel, A.; Levitt, M. *J. Mol. Biol.* **1976**, *103*, 227–249.
(85) Gao, J. L. In *Reviews in Computational Chemistry*; Lipkowitz, K., Boyd, D., Eds.; VCH: Weinheim, 1996; Vol. 7, pp 119−185.
(86) Sherwood, P. In *Modern Methods and Algorithms of Quantum Chemistry*; NIC Series; Grotendorst, J., Ed.; John von Neumann Institute for Computing: Jülich, 2000; Vol. 1, pp 257−277.
(87) Gao, J. L.; Truhlar, D. G. *Annu. Rev. Phys. Chem.* **2002**, *53*, 467–505.
(88) Field, M. J. *J. Comput. Chem.* **2002**, *23*, 48–58.
(89) Warshel, A. *Annu. Rev. Biophys. Biomol. Struct.* **2003**, *32*, 425–443.
(90) Monard, G.; Prat-Resina, X.; González-Lafont, A.; Lluch, J. M. *Int. J. Quantum Chem.* **2003**, *93*, 229–244.
(91) Ridder, L.; Mulholland, A. J. *Curr. Top. Med. Chem.* **2003**, *3*, 1241–1256.
(92) Friesner, R. A.; Guallar, V. *Annu. Rev. Phys. Chem.* **2005**, *56*, 389–427.
(93) Senn, H. M.; Thiel, W. *Top. Curr. Chem.* **2007**, *268*, 173–290.
(94) Senn, H. M.; Thiel, W. *Curr. Opin. Chem. Biol.* **2007**, *11*, 182–187.
(95) Lin, H.; Truhlar, D. G. *Theor. Chem. Acc.* **2007**, *117*, 185–199.
(96) Hu, H.; Yang, W. T. *Annu. Rev. Phys. Chem.* **2008**, *59*, 573–601.
(97) Senn, H. M.; Thiel, W. *Angew. Chem., Int. Ed.* **2009**, *48*, 1198–1229.
(98) Heyden, A.; Lin, H.; Truhlar, D. G. *J. Phys. Chem. B* **2007**, *111*, 2231–2241.
(99) Riccardi, D.; Schaefer, P.; Cui, Q. *J. Phys. Chem. B* **2005**, *109*, 17715–17733.
(100) Benighaus, T.; Thiel, W. *J. Chem. Theory Comput.* **2008**, *4*, 1600–1609.
(101) Svensson, M.; Humbel, S.; Froese, R. D. J.; Matsubara, T.; Sieber, S.; Morokuma, K. *J. Phys. Chem.* **1996**, *100*, 19357–19363.
(102) Zhao, Y.; Truhlar, D. G. *Theor. Chem. Acc.* **2008**, *120*, 215–241.
(103) Siegbahn, P. E. M. *J. Biol. Inorg. Chem.* **2006**, *11*, 695–701.
(104) Claeyssens, F.; Harvey, J. N.; Manby, F. R.; Mata, R. A.; Mulholland, A. J.; Ranaghan, K. E.; Schütz, M.; Thiel, S.; Thiel, W.; Werner, H.-J. *Angew. Chem., Int. Ed.* **2006**, *45*, 6856–6859.
(105) Mata, R. A.; Werner, H.-J.; Thiel, S.; Thiel, W. *J. Chem. Phys.* **2008**, *128*, 025104/1−025104/8.
(106) Geerke, D. P.; Thiel, S.; Thiel, W.; van Gunsteren, W. F. *J. Chem. Theory Comput.* **2007**, *3*, 1499–1509.
(107) Bakowies, D.; Thiel, W. *J. Phys. Chem.* **1996**, *100*, 10580–10594.
(108) Singh, U. C.; Kollman, P. A. *J. Comput. Chem.* **1986**, *7*, 718–730.
(109) Field, M. J.; Bash, P. A.; Karplus, M. *J. Comput. Chem.* **1990**, *11*, 700–733.
(110) Antes, I.; Thiel, W. *J. Phys. Chem. A* **1999**, *103*, 9290–9295.
(111) Zhang, Y. K.; Lee, T.-S.; Yang, W. T. *J. Chem. Phys.* **1999**, *110*, 46–54.
(112) Laio, A.; VandeVondele, J.; Rothlisberger, U. *J. Chem. Phys.* **2002**, *116*, 6941–6947.
(113) Théry, V.; Rinaldi, D.; Rivail, J.-L.; Maigret, B.; Ferenczy, G. G. *J. Comput. Chem.* **1994**, *15*, 269–282.
(114) Gao, J. L.; Amara, P.; Alhambra, C.; Field, M. J. *J. Phys. Chem. A* **1998**, *102*, 4714–4721.
(115) Murphy, R. B.; Philipp, D. M.; Friesner, R. A. *J. Comput. Chem.* **2000**, *21*, 1442–1457.
(116) Reuter, N.; Dejaegere, A.; Maigret, B.; Karplus, M. *J. Phys. Chem. A* **2000**, *104*, 1720–1735.
(117) Lennartz, C.; Schäfer, A.; Terstegen, F.; Thiel, W. *J. Phys. Chem. B* **2002**, *106*, 1758–1767.
(118) Sherwood, P.; de Vries, A. H.; Guest, M. F.; Schreckenbach, G.; Catlow, C. R. A.; French, S. A.; Sokol, A. A.; Bromley, S. T.; Thiel, W.; Turner, A. J.; Billeter, S.; Terstegen, F.; Thiel, S.; Kendrick, J.; Rogers, S. C.; Casci, J.; Watson, M.; King, F.; Karlsen, E.; Sjøvoll, M.; Fahmi, A.; Schäfer, A.; Lennartz, C. *THEOCHEM* **2003**, *632*, 1–28.
(119) Sherwood, P.; de Vries, A. H.; Collins, S. J.; Greatbanks, S. P.; Burton, N. A.; Vincent, M. A.; Hillier, I. H. *Faraday Discuss.* **1997**, *106*, 79–92.
(120) Eichler, U.; Kölmel, C. M.; Sauer, J. *J. Comput. Chem.* **1997**, *18*, 463–477.
(121) Billeter, S. R.; Turner, A. J.; Thiel, W. *Phys. Chem. Chem. Phys.* **2000**, *2*, 2177–2186.
(122) Maseras, F.; Morokuma, K. *J. Comput. Chem.* **1995**, *16*, 1170–1179.
(123) Kästner, J.; Thiel, S.; Senn, H. M.; Sherwood, P.; Thiel, W. *J. Chem. Theory Comput.* **2007**, *3*, 1064–1072.
(124) Zhang, Y. K.; Liu, H. Y.; Yang, W. T. *J. Chem. Phys.* **2000**, *112*, 3483–3492.
(125) Kästner, J.; Senn, H. M.; Thiel, S.; Otte, N.; Thiel, W. *J. Chem. Theory Comput.* **2006**, *2*, 452–461.
(126) Senn, H. M.; Kästner, J.; Breidung, J.; Thiel, W. *Can. J. Chem.* **2009**, *87*, 1322−1337.
(127) Senn, H. M.; Thiel, S.; Thiel, W. *J. Chem. Theory Comput.* **2005**, *1*, 494–505.
(128) Kästner, J.; Thiel, W. *J. Chem. Phys.* **2005**, *123*, 144104/1–144104/5.
(129) http://www.chemshell.org.
(130) Li, H.; Robertson, A. D.; Jensen, J. H. *Proteins* **2005**, *61*, 704–721.
(131) Altun, A.; Shaik, S.; Thiel, W. *J. Comput. Chem.* **2006**, *27*, 1324–1337.
(132) Hehre, W. J.; Radom, L.; Schleyer, P. v. R.; Pople, J. A. *Ab Initio Molecular Orbital Theory*; Wiley-Interscience: New York, 1986.
(133) Hay, P. J.; Wadt, W. R. *J. Chem. Phys.* **1985**, *82*, 299–310.
(134) Altun, A.; Thiel, W. *J. Phys. Chem. B* **2005**, *109*, 1268–1280.
(135) Wachters, A. J. H. *J. Chem. Phys.* **1970**, *52*, 1033–1036.
(136) Hay, P. J. *J. Chem. Phys.* **1977**, *66*, 4377–4384.
(137) Bauschlicher, C. W.; Langhoff, S. R.; Partridge, H.; Barnes, L. A. *J. Chem. Phys.* **1989**, *91*, 2399–2411.
(138) Ahlrichs, R.; May, K. *Phys. Chem. Chem. Phys.* **2000**, *2*, 943–945.
(139) Schäfer, A.; Horn, H.; Ahlrichs, R. *J. Chem. Phys.* **1992**, *97*, 2571–2577.
(140) Loew, G. H. *Int. J. Quantum Chem.* **2000**, *77*, 54–70.
(141) Rydberg, P.; Sigfridsson, E.; Ryde, U. *J. Biol. Inorg. Chem.* **2004**, *9*, 203–223.
(142) Ogliaro, F.; de Visser, S. P.; Cohen, S.; Sharma, P. K.; Shaik, S. *J. Am. Chem. Soc.* **2002**, *124*, 2806–2817.
(143) Ogliaro, F.; de Visser, S. P.; Shaik, S. *J. Inorg. Biochem.* **2002**, *91*, 554–567.
(144) Hata, M.; Hirano, Y.; Hoshino, T.; Nishida, R.; Tsuda, M. *J. Phys. Chem. B* **2004**, *108*, 11189–11195.
(145) Shaik, S.; Filatov, M.; Schröder, D.; Schwarz, H. *Chem.—Eur. J.* **1998**, *4*, 193–199.
(146) Ogliaro, F.; Harris, N.; Cohen, S.; Filatov, M.; de Visser, S. P.; Shaik, S. *J. Am. Chem. Soc.* **2000**, *122*, 8977–8989.
(147) Kumar, D.; de Visser, S. P.; Sharma, P. K.; Cohen, S.; Shaik, S. *J. Am. Chem. Soc.* **2004**, *126*, 1907–1920.
(148) Ogliaro, F.; Filatov, M.; Shaik, S. *Eur. J. Inorg. Chem.* **2000**, 2455–2458.
(149) de Visser, S. P.; Ogliaro, F.; Sharma, P. K.; Shaik, S. *Angew. Chem., Int. Ed.* **2002**, *41*, 1947–1951.
(150) de Visser, S. P.; Ogliaro, F.; Sharma, P. K.; Shaik, S. *J. Am. Chem. Soc.* **2002**, *124*, 11809–11826.
(151) Kumar, D.; de Visser, S. P.; Shaik, S. *J. Am. Chem. Soc.* **2003**, *125*, 13024–13025.
(152) Kumar, D.; de Visser, S. P.; Shaik, S. *J. Am. Chem. Soc.* **2004**, *126*, 5072–5073.
(153) de Visser, S. P.; Kumar, D.; Cohen, S.; Shacham, R.; Shaik, S. *J. Am. Chem. Soc.* **2004**, *126*, 8362–8363.
(154) Sharma, P. K.; de Visser, S. P.; Shaik, S. *J. Am. Chem. Soc.* **2003**, *125*, 8698–8699.
(155) Guallar, V.; Baik, M.-H.; Lippard, S. J.; Friesner, R. A. *Proc. Natl. Acad. Sci. U. S. A.* **2003**, *100*, 6998–7002.
(156) Schöneboom, J. C.; Thiel, W. *J. Phys. Chem. B* **2004**, *108*, 7468–7478.
(157) Guallar, V.; Friesner, R. A. *J. Am. Chem. Soc.* **2004**, *126*, 8501–8508.
(158) Lin, H.; Schöneboom, J. C.; Cohen, S.; Shaik, S.; Thiel, W. *J. Phys. Chem. B* **2004**, *108*, 10083–10088.
(159) Zheng, J. J.; Wang, D.; Thiel, W.; Shaik, S. *J. Am. Chem. Soc.* **2006**, *128*, 13204–13215.
(160) Cho, K.-B.; Hirao, H.; Chen, H.; Carvajal, M. A.; Cohen, S.; Derat, E.; Thiel, W.; Shaik, S. *J. Phys. Chem. A* **2008**, *112*, 13128–13138.
(161) Wang, D.; Zheng, J. J.; Shaik, S.; Thiel, W. *J. Phys. Chem. B* **2008**, *112*, 5126–5138.
(162) Wang, D.; Thiel, W. *THEOCHEM* **2009**, *898*, 90–96.
(163) Zurek, J.; Foloppe, N.; Harvey, J. N.; Mulholland, A. J. *Org. Biomol. Chem.* **2006**, *4*, 3931–3937.

(164) Altun, A.; Shaik, S.; Thiel, W. *J. Am. Chem. Soc.* **2007**, *129*, 8978–8987.
(165) Hackett, J. C.; Sanan, T. T.; Hadad, C. M. *Biochemistry* **2007**, *46*, 5924–5940.
(166) Li, C. S.; Wu, W.; Kumar, D.; Shaik, S. *J. Am. Chem. Soc.* **2006**, *128*, 394–395.
(167) Wang, Y.; Kumar, D.; Yang, C. L.; Han, K. L.; Shaik, S. *J. Phys. Chem. B* **2007**, *111*, 7700–7710.
(168) Wang, Y.; Yang, C. L.; Wang, H. M.; Han, K. L.; Shaik, S. *ChemBioChem* **2007**, *8*, 277–281.
(169) Li, C. S.; Zhang, L.; Zhang, C.; Hirao, H.; Wu, W.; Shaik, S. *Angew. Chem., Int. Ed.* **2007**, *46*, 8168–8170.
(170) Olsen, L.; Rydberg, P.; Rod, T. H.; Ryde, U. *J. Med. Chem.* **2006**, *49*, 6489–6499.
(171) Rydberg, P.; Ryde, U.; Olsen, L. *J. Chem. Theory Comput.* **2008**, *4*, 1369–1377.
(172) Rydberg, P.; Ryde, U.; Olsen, L. *J. Phys. Chem. A* **2008**, *112*, 13058–13065.
(173) Zhang, Y.; Morisetti, P.; Kim, J.; Smith, L.; Lin, H. *Theor. Chem. Acc.* **2008**, *121*, 313–319.
(174) Shaik, S.; Kumar, D.; de Visser, S. P. *J. Am. Chem. Soc.* **2008**, *130*, 10128–10140.
(175) Denisov, I. G.; Makris, T. M.; Sligar, S. G.; Schlichting, I. *Chem. Rev.* **2005**, *105*, 2253–2277.
(176) Davydov, R.; Makris, T. M.; Kofman, V.; Werst, D. E.; Sligar, S. G.; Hoffman, B. M. *J. Am. Chem. Soc.* **2001**, *123*, 1403–1415.
(177) Rowland, P.; Blaney, F. E.; Smyth, M. G.; Jones, J. J.; Leydon, V. R.; Oxbrow, A. K.; Lewis, C. J.; Tennant, M. G.; Modi, S.; Eggleston, D. S.; Chenery, R. J.; Bridges, A. M. *J. Biol. Chem.* **2006**, *281*, 7614–7622.
(178) Schlichting, I.; Berendzen, J.; Chu, K.; Stock, A. M.; Maves, S. A.; Benson, D. E.; Sweet, R. M.; Ringe, D.; Petsko, G. A.; Sligar, S. G. *Science* **2000**, *287*, 1615–1622.
(179) Guengerich, F. P.; Miller, G. P.; Hanna, I. H.; Sato, H.; Martin, M. V. *J. Biol. Chem.* **2002**, *277*, 33711–33719.
(180) Mueller, E. J.; Loida, P. J.; Sligar, S. G. In *Cytochrome P450: Structure, Mechanism, and Biochemistry*, 2nd ed.; Ortiz de Montellano, P. R., Ed.; Plenum Press: New York, 1995; Chapter 3, pp 83−124.
(181) von Köning, K.; Schlichting, I. In *Metal Ions in Life Sciences*; Sigel, A., Sigel, H., Sigel, R. K. O., Eds.; John Wiley & Sons Ltd: Chichester, England, 2007; Vol. 3; Chapter 8, pp 235−266.
(182) Vidakovic, M.; Sligar, S. G.; Li, H.; Poulos, T. L. *Biochemistry* **1998**, *37*, 9211–9219.
(183) Jin, S.; Makris, T. M.; Bryson, T. A.; Sligar, S. G.; Dawson, J. H. *J. Am. Chem. Soc.* **2003**, *125*, 3406–3407.
(184) Hishiki, T.; Shimada, H.; Nagano, S.; Egawa, T.; Kanamori, Y.; Makino, R.; Park, S.-Y.; Adachi, S.; Shiro, Y.; Ishimura, Y. *J. Biochem. (Tokyo, Jpn.)* **2000**, *128*, 965–974.
(185) Raag, R.; Martinis, S. A.; Sligar, S. G.; Poulos, T. L. *Biochemistry* **1991**, *30*, 11420–11429.
(186) Bell, S. G.; Sowden, R. J.; Wong, L.-L. *Chem. Commun.* **2001**, 635–636.
(187) Jung, C. In *Metal Ions in Life Sciences*; Sigel, A., Sigel, H., Sigel, R. K. O., Eds.; John Wiley & Sons Ltd: Chichester, England, 2007; Vol. 3; Chapter 7, pp 187−234.
(188) Rydberg, P.; Rod, T. H.; Olsen, L.; Ryde, U. *J. Phys. Chem. B* **2007**, *111*, 5445–5457.
(189) Fishelovitch, D.; Hazan, C.; Shaik, S.; Wolfson, H. J.; Nussinov, R. *J. Am. Chem. Soc.* **2007**, *129*, 1602–1611.
(190) Atkins, W. M.; Sligar, S. G. *J. Biol. Chem.* **1988**, *263*, 18842–18849.
(191) Bell, S. G.; Hoskins, N.; Whitehous, C. J. C.; Wang, L.-L. In *Metal Ions in Life Sciences*; Sigel, A., Sigel, H., Sigel, R. K. O., Eds.; John Wiley & Sons Ltd: Chichester, England, 2007; Vol. 3, pp 437−476.
(192) Poulos, T. L. *J. Biol. Inorg. Chem.* **1996**, *1*, 356–359.
(193) Suzuki, N.; Higuchi, T.; Urano, Y.; Kikuchi, K.; Uekusa, H.; Ohashi, Y.; Uchida, T.; Kitagawa, T.; Nagano, T. *J. Am. Chem. Soc.* **1999**, *121*, 11571–11572.
(194) Yoshioka, S.; Takahashi, S.; Ishimori, K.; Morishima, I. *J. Inorg. Biochem.* **2000**, *81*, 141–151.
(195) Makino, M.; Sugimoto, H.; Shiro, Y.; Asamizu, S.; Onaka, H.; Nagano, S. *Proc. Natl. Acad. Sci. U. S. A.* **2007**, *104*, 11591–11596.
(196) Poulos, T. L. *Nat. Prod. Rep.* **2007**, *24*, 504–510.
(197) Ogliaro, F.; de Visser, S. P.; Cohen, S.; Kaneti, J.; Shaik, S. *ChemBioChem* **2001**, *2*, 848–851.
(198) Ogliaro, F.; Cohen, S.; Filatov, M.; Harris, N.; Shaik, S. *Angew. Chem., Int. Ed.* **2000**, *39*, 3851–3855.
(199) de Visser, S. P.; Shaik, S.; Sharma, P. K.; Kumar, D.; Thiel, W. *J. Am. Chem. Soc.* **2003**, *125*, 15779–15788.
(200) Hirao, H.; Kumar, D.; Thiel, W.; Shaik, S. *J. Am. Chem. Soc.* **2005**, *127*, 13007–13018.
(201) Thomann, H.; Bernardo, M.; Goldfarb, D.; Kroneck, P. M. H.; Ullrich, V. *J. Am. Chem. Soc.* **1995**, *117*, 8243–8251.
(202) Tsai, R.; Yu, C. A.; Gunsalus, I. C.; Peisach, J.; Blumberg, W.; Orme-Johnson, W. H.; Beinert, H. *Proc. Natl. Acad. Sci. U. S. A.* **1970**, *66*, 1157–1163.
(203) Sharrock, M.; Debrunner, P. G.; Schulz, C.; Lipscomb, J. D.; Marshall, V.; Gunsalus, I. C. *Biochim. Biophys. Acta* **1976**, *420*, 8–26.
(204) Sligar, S. G. *Biochemistry* **1976**, *15*, 5399–5406.
(205) Reiher, M.; Salomon, O.; Hess, B. A. *Theor. Chem. Acc.* **2001**, *107*, 48–55.
(206) Salomon, O.; Reiher, M.; Hess, B. A. *J. Chem. Phys.* **2002**, *117*, 4729–4737.
(207) Scherlis, D. A.; Cymeryng, C. B.; Estrin, D. A. *Inorg. Chem.* **2000**, *39*, 2352–2359.
(208) Scherlis, D. A.; Marti, M. A.; Ordejon, P.; Estrin, D. A. *Int. J. Quantum Chem.* **2002**, *90*, 1505–1514.
(209) Poulos, T. L.; Finzel, B. C.; Howard, A. J. *Biochemistry* **1986**, *25*, 5314–5322.
(210) Auclair, K.; Moënne-Loccoz, P.; Ortiz de Montellano, P. R. *J. Am. Chem. Soc.* **2001**, *123*, 4877–4885.
(211) Champion, P. M.; Lipscomb, J. D.; Münck, E.; Debrunner, P.; Gunsalus, I. C. *Biochemistry* **1975**, *14*, 4151–4158.
(212) Freindorf, M.; Shao, Y.; Kong, J.; Furlani, T. R. *J. Inorg. Biochem.* **2008**, *102*, 427–432.
(213) Unno, M.; Christian, J. F.; Benson, D. E.; Gerber, N. C.; Sligar, S. G.; Champion, P. M. *J. Am. Chem. Soc.* **1997**, *119*, 6614–6620.
(214) Lipscomb, J. D. *Biochemistry* **1980**, *19*, 3590–3599.
(215) Debrunner, P. G. In *Iron Porphyrins Part 3: Physical Bioinorganic Chemistry Series*; Lever, A. B. P., Gray, H. B., Eds.; VCH: New York, 1989; Vol. 4; Chapter 2, pp 137−234.
(216) Reiss, H.; Heller, A. *J. Phys. Chem.* **1985**, *89*, 4207–4213.
(217) Olsson, M. H. M.; Hong, G. Y.; Warshel, A. *J. Am. Chem. Soc.* **2003**, *125*, 5025–5039.
(218) Li, G. H.; Zhang, X. D.; Cui, Q. *J. Phys. Chem. B* **2003**, *107*, 8643–8653.
(219) Makris, T. M.; Denisov, I. G.; Schlichting, I.; Sligar, S. In *Cytochrome P450: Structure, Mechanism and Biochemistry*, 3rd ed.; Ortiz de Montellano, P. R., Ed.; Kluwer Academic/Plenum Publishers: New York, 2005; Chapter 5, pp 149−182.
(220) Harada, K.; Sakurai, K.; Ikemura, K.; Ogura, T.; Hirota, S.; Shimada, H.; Hayashi, T. *J. Am. Chem. Soc.* **2008**, *130*, 432–433.
(221) Hayashi, T.; Harada, K.; Sakurai, K.; Shimada, H.; Hirota, S. *J. Am. Chem. Soc.* **2009**, *131*, 1398–1400.
(222) Chottard, G.; Schappacher, M.; Ricard, L.; Weiss, R. *Inorg. Chem.* **1984**, *23*, 4557–4561.
(223) Denisov, I. G.; Mak, P. J.; Makris, T. M.; Sligar, S. G.; Kincaid, J. R. *J. Phys. Chem. A* **2008**, *112*, 13172–13179.
(224) Unno, M.; Chen, H.; Kusama, S.; Shaik, S.; Ikeda-Saito, M. *J. Am. Chem. Soc.* **2007**, *129*, 13394–13395.
(225) Harris, D. L.; Loew, G. H.; Waskell, L. *J. Am. Chem. Soc.* **1998**, *120*, 4308–4318.
(226) Kumar, D.; Hirao, H.; de Visser, S. P.; Zheng, J. J.; Wang, D.; Thiel, W.; Shaik, S. *J. Phys. Chem. B* **2005**, *109*, 19946–19951.
(227) Radoń, M.; Pierloot, K. *J. Phys. Chem. A* **2008**, *112*, 11824–11832.
(228) Benson, D. E.; Suslick, K. S.; Sligar, S. G. *Biochemistry* **1997**, *36*, 5104–5107.
(229) Pauling, L.; Coryell, C. D. *Proc. Natl. Acad. Sci. U.S.A* **1936**, *22*, 210–216.
(230) Weiss, J. J. *Nature* **1964**, *202*, 83–84.
(231) McClure, D. S. *Radiat. Res. Suppl.* **1960**, *2*, 218–242.
(232) Harcourt, R. D. *Chem. Phys. Lett.* **1990**, *167*, 374–377.
(233) Mak, P. J.; Denisov, I. G.; Victoria, D.; Makris, T. M.; Deng, T. J.; Sligar, S. G.; Kincaid, J. R. *J. Am. Chem. Soc.* **2007**, *129*, 6382–6383.
(234) Ichikawa, Y.; Nakajima, H.; Watanabe, Y. *ChemBioChem* **2006**, *7*, 1582–1589.
(235) Harris, D. L.; Loew, G. H. *J. Am. Chem. Soc.* **1998**, *120*, 8941–8948.
(236) de Grotthuss, C. J. T. *Anal. Chim.* **1806**, *58*, 54–73.
(237) Taraphder, S.; Hummer, G. *J. Am. Chem. Soc.* **2003**, *125*, 3931–3940.
(238) Oprea, T. I.; Hummer, G.; García, A. E. *Proc. Natl. Acad. Sci. U. S. A.* **1997**, *94*, 2133–2138.
(239) Aikens, J.; Sligar, S. G. *J. Am. Chem. Soc.* **1994**, *116*, 1143–1144.
(240) Purdy, M. M.; Koo, L. S.; Ortiz de Montellano, P. R.; Klinman, J. P. *Biochemistry* **2006**, *45*, 15793–15806.
(241) Kim, S.-H.; Yang, T.-C.; Perera, R.; Jin, S.-X.; Bryson, T. A.; Sono, M.; Davydov, R.; Dawson, J. H.; Hoffman, B. M. *Dalton Trans.* **2005**, 3464–3469.
(242) Shimada, H.; Makino, R.; Unno, M.; Horiuchi, T.; Ishimura, Y. In *8th International Conference on Cytochrome P450: Biochemistry, Biophysics and Molecular Biology*, Lisbon, Portugal, 1994; pp 299−306.

(243) Guallar, V.; Harris, D. L.; Batista, V. S.; Miller, W. H. *J. Am. Chem. Soc.* **2002**, *124*, 1430–1437.
(244) Harris, D. L. *J. Inorg. Biochem.* **2002**, *91*, 568–585.
(245) Poulos, T. L. In *The Porphyrin Handbook*; Kadish, K. M., Smith, K. M., Guilard, R., Eds.; Academic Press: San Diego, 2000; Vol. 4, pp 189−218.
(246) Altarsha, M.; Benighaus, T.; Kumar, D.; Thiel, W. *J. Am. Chem. Soc.* **2009**, *131*, 4755–4763.
(247) Altarsha, M.; Wang, D.; Benighaus, T.; Kumar, D.; Thiel, W. *J. Phys. Chem. B* **2009**, *113*, 9577–9588.
(248) Egawa, T.; Shimada, H.; Ishimura, Y. *Biochem. Biophys. Res. Commun.* **1994**, *201*, 1464–1469.
(249) Denisov, I. G.; Makris, T. M.; Sligar, S. G. *J. Biol. Chem.* **2001**, *276*, 11648–11652.
(250) Kellner, D. G.; Hung, S. C.; Weiss, K. E.; Sligar, S. G. *J. Biol. Chem.* **2002**, *277*, 9641–9644.
(251) Jung, C. *J. Mol. Recognit.* **2000**, *13*, 325–351.
(252) Jung, C. *Biochim. Biophys. Acta, Proteins Proteomics* **2002**, *1595*, 309–328.
(253) Schünemann, V.; Jung, C.; Terner, J.; Trautwein, A. X.; Weiss, R. *J. Inorg. Biochem.* **2002**, *91*, 586–596.
(254) Meilleur, F.; Contzen, J.; Myles, D. A. A.; Jung, C. *Biochemistry* **2004**, *43*, 8744–8753.
(255) Spolitak, T.; Dawson, J. H.; Ballou, D. P. *J. Biol. Chem.* **2005**, *280*, 20300–20309.
(256) Dowers, T. S.; Rock, D. A.; Jones, J. P. *J. Am. Chem. Soc.* **2004**, *126*, 8868–8869.
(257) Vaz, A. D. N.; McGinnity, D. F.; Coon, M. J. *Proc. Natl. Acad. Sci. U. S. A.* **1998**, *95*, 3555–3560.
(258) Nam, W.; Lee, H. J.; Oh, S.-Y.; Kim, C.; Jang, H. G. *J. Inorg. Biochem.* **2000**, *80*, 219–225.
(259) Nam, W.; Park, S.-E.; Lim, I. K.; Lim, M. H.; Hong, J. K.; Kim, J. *J. Am. Chem. Soc.* **2003**, *125*, 14674–14675.
(260) Kaizer, J.; Klinker, E. J.; Oh, N. Y.; Rohde, J.-U.; Song, W. J.; Stubna, A.; Kim, J.; Münck, E.; Nam, W.; Que, L., Jr. *J. Am. Chem. Soc.* **2004**, *126*, 472–473.
(261) Newcomb, M.; Zhang, R.; Chandrasena, R. E.; Halgrimson, J. A.; Horner, J. H.; Makris, T. M.; Sligar, S. G. *J. Am. Chem. Soc.* **2006**, *128*, 4580–4581.
(262) Sheng, X.; Horner, J. H.; Newcomb, M. *J. Am. Chem. Soc.* **2008**, *130*, 13310–13320.
(263) Watanabe, Y.; Nakajima, H.; Ueno, T. *Acc. Chem. Res.* **2007**, *40*, 554–562.
(264) Han, A.-R.; Jeong, Y. J.; Kang, Y.; Lee, J. Y.; Seo, M. S.; Nam, W. *Chem. Commun.* **2008**, 1076–1078.
(265) Franke, A.; Fertinger, C.; van Eldik, R. *Angew. Chem., Int. Ed.* **2008**, *47*, 5238–5242.
(266) Ogliaro, F.; de Visser, S. P.; Groves, J. T.; Shaik, S. *Angew. Chem., Int. Ed.* **2001**, *40*, 2874–2878.
(267) Pan, Z.; Zhang, R.; Newcomb, M. *J. Inorg. Biochem.* **2006**, *100*, 524–532.
(268) Harris, D. L.; Loew, G. H.; Waskell, L. *J. Inorg. Biochem.* **2001**, *83*, 309–318.
(269) Filatov, M.; Harris, N.; Shaik, S. *Angew. Chem., Int. Ed.* **1999**, *38*, 3510–3512.
(270) Filatov, M.; Harris, N.; Shaik, S. *J. Chem. Soc., Perkin Trans. 2* **1999**, 399–410.
(271) Antony, J.; Grodzicki, M.; Trautwein, A. X. *J. Phys. Chem. A* **1997**, *101*, 2692–2701.
(272) Harvey, J. N.; Bathelt, C. M.; Mulholland, A. J. *J. Comput. Chem.* **2006**, *27*, 1352–1362.
(273) Alfonso-Prieto, M.; Borovik, A.; Carpena, X.; Murshudov, G.; Melik-Adamyan, W.; Fita, I.; Rovira, C.; Loewen, P. C. *J. Am. Chem. Soc.* **2007**, *129*, 4193–4205.
(274) Radoń, M.; Broclawik, E. *J. Chem. Theory Comput.* **2007**, *3*, 728–734.
(275) Shaik, S.; de Visser, S. P.; Kumar, D. *J. Am. Chem. Soc.* **2004**, *126*, 11746–11749.
(276) Stone, K. L.; Behan, R. K.; Green, M. T. *Proc. Natl. Acad. Sci. U. S. A.* **2005**, *102*, 16563–16565.
(277) Cohen, S. Ph.D. Thesis, Hebrew University of Jerusalem, Israel, in preparation.
(278) Davydov, R.; Perera, R.; Jin, S.-X.; Yang, T.-C.; Bryson, T. A.; Sono, M.; Dawson, J. H.; Hoffman, B. M. *J. Am. Chem. Soc.* **2005**, *127*, 1403–1413.
(279) Shaik, S.; Hiberty, P. C. *A Chemist's Guide to Valence Bond Theory*; John Wiley & Sons Inc.: 2007; Chapter 2, pp 26−33.
(280) Hirao, H.; Shaik, S.; Kozlowski, P. M. *J. Phys. Chem. A* **2006**, *110*, 6091–6099.
(281) Green, M.; Dawson, J.; Gray, H. *Science* **2004**, *304*, 1653–1656.
(282) Kimata, Y.; Shimada, H.; Hirose, T.; Ishimura, Y. *Biochem. Biophys. Res. Commun.* **1995**, *208*, 96–102.
(283) Fishelovitch, D. Ph.D. Thesis, Tel-Aviv University, Israel, 2009.
(284) Schröder, D.; Shaik, S.; Schwarz, H. *Acc. Chem. Res.* **2000**, *33*, 139–145.
(285) Cryle, M. J.; Stuthe, J. M.; Ortiz de Montellano, P. R.; de Voss, J. J. *Chem. Commun.* **2004**, 512–513.
(286) He, X.; Ortiz de Montellano, P. R. *J. Biol. Chem.* **2004**, *279*, 39479–39484.
(287) Ortiz de Montellano, P. R.; de Voss, J. J. In *Cytochrome P450: Structure, Mechanism and Biochemistry*, 3rd ed.; Ortiz de Montellano, P. R., Ed.; Kluwer Academic/Plemun Publishers: New York, 2005; Chapter 6, pp 183−245.
(288) Bach, R. D.; Dmitrenko, O. *J. Am. Chem. Soc.* **2006**, *128*, 1474–1488.
(289) Groenhof, A. R.; Ehlers, A. W.; Lammertsma, K. *J. Am. Chem. Soc.* **2007**, *129*, 6204–6209.
(290) Zhang, R.; Chandrasena, R. E. P.; Martinez, E.; Horner, J. H.; Newcomb, M. *Org. Lett.* **2005**, *7*, 1193–1195.
(291) Page, M. I.; Jencks, W. P. *Proc. Natl. Acad. Sci. U. S. A.* **1971**, *68*, 1678–1683.
(292) Cho, K.-B.; Moreau, Y.; Kumar, D.; Rock, D. A.; Jones, J. P.; Shaik, S. *Chem.−Eur. J.* **2007**, *13*, 4103–4115.
(293) Li, C. S.; Zhang, L.; Zhang, C.; Hirao, H.; Wu, W.; Shaik, S. *Angew. Chem., Int. Ed.* **2008**, *47*, 8148.
(294) Derat, E.; Kumar, D.; Hirao, H.; Shaik, S. *J. Am. Chem. Soc.* **2006**, *128*, 473–484.
(295) Harris, N.; Cohen, S.; Filatov, M.; Ogliaro, F.; Shaik, S. *Angew. Chem., Int. Ed.* **2000**, *39*, 2003–2007.
(296) Schöneboom, J. C. Ph.D. Thesis, University of Düsseldorf, Germany, 2003.
(297) Li, H. Y.; Narasimhulu, S.; Havran, L. M.; Winkler, J. D.; Poulos, T. L. *J. Am. Chem. Soc.* **1995**, *117*, 6297–6299.
(298) Truhlar, D. G.; Gao, J. L.; Alhambra, C.; Garcia-Viloca, M.; Corchado, J.; Sánchez, M. L.; Villà, J. *Acc. Chem. Res.* **2002**, *35*, 341–349.
(299) Gelb, M. H.; Heimbrook, D. C.; Malkonen, P.; Sligar, S. G. *Biochemistry* **1982**, *21*, 370–377.
(300) Groves, J. T.; McClusky, G. A.; White, R. E.; Coon, M. J. *Biochem. Biophys. Res. Commun.* **1978**, *81*, 154–160.
(301) Guengerich, F. P.; Macdonald, T. L. *Acc. Chem. Res.* **1984**, *17*, 9–16.
(302) Groves, J. T.; Gross, Z.; Stern, M. K. *Inorg. Chem.* **1994**, *33*, 5065–5072.
(303) Groves, J. T.; Nemo, T. E. *J. Am. Chem. Soc.* **1983**, *105*, 5786–5791.
(304) Gross, Z.; Nimri, S.; Barzilay, C. M.; Simkhovich, L. *J. Biol. Inorg. Chem.* **1997**, *2*, 492–506.
(305) de Visser, S. P.; Kumar, D.; Shaik, S. *J. Inorg. Biochem.* **2004**, *98*, 1183–1193.
(306) Kumar, D.; de Visser, S. P.; Shaik, S. *Chem.−Eur. J.* **2005**, *11*, 2825–2835.
(307) Hirao, H.; Kumar, D.; Shaik, S. *J. Inorg. Biochem.* **2006**, *100*, 2054–2068.
(308) White, R. E.; Groves, J. T.; McClusky, G. A. *Acta Biol. Med. Ger.* **1979**, *38*, 475–482.
(309) Boyland, E. *Biochem. Soc. Symp.* **1950**, *5*, 40−54.
(310) Boyland, E.; Sims, P. *Biochem. J.* **1965**, *95*, 780–787.
(311) Jerina, D.; Daly, J.; Witkop, B.; Zaltzman-Nirenberg, P.; Udenfriend, S. *Arch. Biochem. Biophys.* **1968**, *128*, 176–183.
(312) Jerina, D.; Daly, J. *Science* **1974**, *185*, 573–582.
(313) Jerina, D.; Daly, J.; Witkop, B.; Zaltzman-Nirenberg, P.; Udenfriend, S. *J. Am. Chem. Soc.* **1968**, *90*, 6525–6527.
(314) Jerina, D.; Daly, J.; Witkop, B.; Zaltzman-Nirenberg, P.; Udenfriend, S. *Biochemistry* **1970**, *9*, 147–156.
(315) Korzekwa, K. R.; Swinney, D. C.; Trager, W. F. *Biochemistry* **1989**, *28*, 9019–9027.
(316) Rietjens, I.; Soffers, A.; Veeger, C.; Vervoort, J. *Biochemistry* **1993**, *32*, 4801–4812.
(317) Hanzlik, R.; Hogberg, K.; Judson, C. *Biochemistry* **1984**, *23*, 3048–3055.
(318) Zakharieva, O.; Grodzicki, M.; Trautwein, A. X.; Veeger, C.; Rietjens, I. *J. Biol. Inorg. Chem.* **1996**, *1*, 192–204.
(319) Zakharieva, O.; Grodzicki, M.; Trautwein, A.; Veeger, C.; Rietjens, I. *Biophys. Chem.* **1998**, *73*, 189–203.
(320) Burka, L. T.; Plucinski, T. M.; Macdonald, T. L. *Proc. Natl. Acad. Sci. U. S. A.* **1983**, *80*, 6680–6684.
(321) Nedelcheva, V.; Gut, I.; Soucek, P.; Tichavska, B.; Tynkova, L.; Mraz, J.; Guengerich, F. P.; Ingelman-Sundberg, M. *Arch. Toxicol.* **1999**, *73*, 33–40.
(322) Kimbrough, R. D. *Crit. Rev. Toxicol.* **1995**, *25*, 133–163.
(323) Evangelista de Duffard, A. M.; Duffard, R. *Environ. Health Perspect.* **1996**, *104*, 353–360.
(324) Janssen, D. B.; Oppentocht, J. E.; Poelarends, G. J. *Curr. Opin. Biotechnol.* **2001**, *12*, 254–258.

(325) Lee, M. D.; Odom, J. M.; Buchanan, R. J., Jr. *Annu. Rev. Microbiol.* **1998**, *52*, 423–452.
(326) Fetzner, S. *Appl. Microbiol. Biotechnol.* **1998**, *50*, 633–657.
(327) Commandeur, L. C. M.; Parsons, J. R. *Biodegradation* **1990**, *1*, 207–220.
(328) Motosugi, K.; Soda, K. *Cell. Mol. Life Sci.* **1983**, *39*, 1214–1220.
(329) Bell, S. G.; Chen, X.; Xu, F.; Rao, Z.; Wong, L.-L. *Biochem. Soc. Trans.* **2003**, *31*, 558–562.
(330) England, P. A.; Harford-Cross, C. F.; Stevenson, J.-A.; Rouch, D. A.; Wong, L.-L. *FEBS Lett.* **1998**, *424*, 271–274.
(331) Nickerson, D. P.; Harford-Cross, C. F.; Fulcher, S. R.; Wong, L.-L. *FEBS Lett.* **1997**, *405*, 153–156.
(332) Stevenson, J.-A.; Westlake, A. C. G.; Whittock, C.; Wong, L.-L. *J. Am. Chem. Soc.* **1996**, *118*, 12846–12847.
(333) Jones, J. P.; O'Hare, E. J.; Wong, L.-L. *Eur. J. Biochem.* **2001**, *268*, 1460–1467.
(334) Harford-Cross, C. F.; Carmichael, A. B.; Allan, F. K.; England, P. A.; Rouch, D. A.; Wong, L.-L. *Protein Eng.* **2000**, *13*, 121–128.
(335) Chen, X.; Christopher, A.; Jones, J. P.; Bell, S. G.; Guo, Q.; Xu, F.; Rao, Z.; Wong, L.-L. *J. Biol. Chem.* **2002**, *277*, 37519–37526.
(336) Rietjens, I.; den Besten, C.; Hanzlik, R. P.; van Bladeren, P. J. *Chem. Res. Toxicol.* **1997**, *10*, 629–635.
(337) Bernardi, F.; Cherry, W.; Shaik, S.; Epiotis, N. D. *J. Am. Chem. Soc.* **1978**, *100*, 1352–1356.
(338) Dinnocenzo, J. P.; Karki, S. B.; Jones, J. P. *J. Am. Chem. Soc.* **1993**, *115*, 7111–7116.
(339) Karki, S. B.; Dinnocenzo, J. P.; Jones, J. P.; Korzekwa, K. R. *J. Am. Chem. Soc.* **1995**, *117*, 3657–3664.
(340) Karki, S. B.; Dinnocenzo, J. P. *Xenobiotica* **1995**, *25*, 711–724.
(341) Manchester, J. I.; Dinnocenzo, J. P.; Higgins, L.; Jones, J. P. *J. Am. Chem. Soc.* **1997**, *119*, 5069–5070.
(342) Jurva, U.; Bissel, P.; Isin, E. M.; Igarashi, K.; Kuttab, S.; Castagnoli, N. *J. Am. Chem. Soc.* **2005**, *127*, 12368–12377.
(343) Abdel-Monem, M. M. *J. Med. Chem.* **1975**, *18*, 427–430.
(344) Miwa, G.; Garland, W.; Hodshon, B.; Lu, A.; Northrop, D. *J. Biol. Chem.* **1980**, *255*, 6049–6054.
(345) Shono, T.; Toda, T.; Oshino, N. *J. Am. Chem. Soc.* **1982**, *104*, 2639–2641.
(346) Miwa, G.; Walsh, J.; Kedderis, G.; Hollenberg, P. *J. Biol. Chem.* **1983**, *258*, 14445–14449.
(347) Galliani, G.; Rindone, B.; Dagnino, G.; Salmona, M. *Eur. J. Drug Metab. Pharmacokinet.* **1984**, *9*, 289–293.
(348) Burka, L. T.; Guengerich, F. P.; Willard, R. J.; Macdonald, T. L. *J. Am. Chem. Soc.* **1985**, *107*, 2549–2551.
(349) Galliani, G.; Nali, M.; Rindone, B.; Tollari, S.; Rocchetti, M.; Salmona, M. *Xenobiotica* **1986**, *16*, 511–517.
(350) Macdonald, T. L.; Gutheim, W. G.; Martin, R. B.; Guengerich, F. P. *Biochemistry* **1989**, *28*, 2071–2077.
(351) Parker, V. D.; Tilset, M. *J. Am. Chem. Soc.* **1991**, *113*, 8778–8781.
(352) Hollenberg, P. F.; Miwa, G. T.; Walsh, J. S.; Dwyer, L. A.; Rickert, D. E.; Kedderis, G. L. *Drug Metab. Dispos.* **1985**, *13*, 272–275.
(353) Guengerich, F. P.; Yun, C.-H.; Macdonald, T. L. *J. Biol. Chem.* **1996**, *271*, 27321–27329.
(354) Goto, Y.; Watanabe, Y.; Fukuzumi, S.; Jones, J. P.; Dinnocenzo, J. P. *J. Am. Chem. Soc.* **1998**, *120*, 10762–10763.
(355) Shaffer, C. L.; Morton, M. D.; Hanzlik, R. P. *J. Am. Chem. Soc.* **2001**, *123*, 349–350.
(356) Shaffer, C. L.; Morton, M. D.; Hanzlik, R. P. *J. Am. Chem. Soc.* **2001**, *123*, 8502–8508.
(357) Shaffer, C. L.; Harriman, S.; Koen, Y. M.; Hanzlik, R. P. *J. Am. Chem. Soc.* **2002**, *124*, 8268–8274.
(358) Cerny, M. A.; Hanzlik, R. P. *Arch. Biochem. Biophys.* **2005**, *436*, 265–275.
(359) Cerny, M. A.; Hanzlik, R. P. *J. Am. Chem. Soc.* **2006**, *128*, 3346–3354.
(360) Bhakta, M. N.; Wimalasena, K. *J. Am. Chem. Soc.* **2002**, *124*, 1844–1845.
(361) Bhakta, M. N.; Wimalasena, K. *Eur. J. Org. Chem.* **2005**, 4801–4805.
(362) Bhakta, M.; Hollenberg, P. F.; Wimalasena, K. *Chem. Commun.* **2005**, 265–267.
(363) Bhakta, M. N.; Hollenberg, P. F.; Wimalasena, K. *J. Am. Chem. Soc.* **2005**, *127*, 1376–1377.
(364) Baciocchi, E.; Lanzalunga, O.; Lapi, A.; Manduchi, L. *J. Am. Chem. Soc.* **1998**, *120*, 5783–5787.
(365) Baciocchi, E.; Gerini, M. F.; Lanzalunga, O.; Lapi, A.; Mancinelli, S.; Mencarelli, P. *Chem. Commun.* **2000**, 393–394.
(366) Baciocchi, E.; Gerini, F. M.; Lanzalunga, O.; Lapi, A.; Grazia Lo Piparo, M.; Mancinelli, S. *Eur. J. Org. Chem.* **2001**, 2305–2310.
(367) Baciocchi, E.; Bietti, M.; Gerini, M. F.; Lanzalunga, O. *J. Org. Chem.* **2005**, *70*, 5144–5149.
(368) Harris, N.; Shaik, S.; Schröder, D.; Schwarz, H. *Helv. Chim. Acta* **1999**, *82*, 1784–1797.
(369) Li, C. S.; Wu, W.; Cho, K.-B.; Shaik, S. *Chem.—Eur. J.* **2009**, *15*, 8492−8503.
(370) Lieber, C. S.; Decarli, L. M. *Science* **1968**, *162*, 917–918.
(371) Lieber, C. S. *Physiol. Rev.* **1997**, *77*, 517–544.
(372) Lieber, C. S. *Drug. Metab. Rev.* **2004**, *36*, 511–529.
(373) Cheng, K.; Schenkman, J. *J. Biol. Chem.* **1983**, *258*, 11738–11744.
(374) Ekstrom, G.; Norsten, C.; Cronholm, T.; Ingelmansundberg, M. *Biochemistry* **1987**, *26*, 7348–7354.
(375) Wood, A. W.; Swinney, D. C.; Thomas, P. E.; Ryan, D. E.; Hall, P. F.; Levin, W.; Garland, W. A. *J. Biol. Chem.* **1988**, *263*, 17322–17332.
(376) Vaz, A. D. N.; Coon, M. J. *Biochemistry* **1994**, *33*, 6442–6449.
(377) Bellucci, G.; Chiappe, C.; Pucci, L.; Gervasi, P. G. *Chem. Res. Toxicol.* **1996**, *9*, 871–874.
(378) Bell, L. C.; Guengerich, F. P. *J. Biol. Chem.* **1997**, *272*, 29643–29651.
(379) Bell-Parikh, L. C.; Guengerich, F. P. *J. Biol. Chem.* **1999**, *274*, 23833–23840.
(380) Guengerich, F. P. *Chem. Res. Toxicol.* **2001**, *14*, 611–650.
(381) Hackett, J. C.; Brueggemeier, R. W.; Hadad, C. M. *J. Am. Chem. Soc.* **2005**, *127*, 5224–5237.
(382) Han, J. H.; Yoo, S. K.; Seo, J. S.; Hong, S. J.; Kim, S. K.; Kim, C. *Dalton Trans.* **2005**, 402–406.
(383) Oh, N. Y.; Suh, Y.; Park, M. J.; Seo, M. S.; Kim, J.; Nam, W. *Angew. Chem., Int. Ed.* **2005**, *44*, 4235–4239.
(384) Smith, S. V.; Koley, A. P.; Dai, R.; Robinson, R. C.; Leong, H.; Markowitz, A.; Friedman, F. K. *Biochemistry* **2000**, *39*, 5731–5737.
(385) Howard-Jones, A. R.; Walsh, C. T. *J. Am. Chem. Soc.* **2007**, *129*, 11016–11017.
(386) Seto, Y.; Guengerich, F. P. *J. Biol. Chem.* **1993**, *268*, 9986–9997.
(387) Groves, J. T.; Avarianeisser, G. E.; Fish, K. M.; Imachi, M.; Kuczkowski, R. L. *J. Am. Chem. Soc.* **1986**, *108*, 3837–3838.
(388) Ruettinger, R. T.; Fulco, A. J. *J. Biol. Chem.* **1981**, *256*, 5728–5734.
(389) Song, W.-J.; Ryu, Y.-O.; Song, R.; Nam, W. *J. Biol. Inorg. Chem.* **2005**, *10*, 294–304.
(390) Agarwala, A.; Bandyopadhyay, D. *Chem. Commun.* **2006**, 4823–4825.
(391) Yun, C.-H.; Miller, G. P.; Guengerich, F. P. *Biochemistry* **2001**, *40*, 4521–4530.
(392) Hanzlik, R. P.; Hogberg, K.; Moon, J. B.; Judson, C. M. *J. Am. Chem. Soc.* **1985**, *107*, 7164–7167.
(393) Atkins, W. M.; Sligar, S. G. *J. Am. Chem. Soc.* **1987**, *109*, 3754–3760.
(394) Hanzlik, R. P.; Ling, K.-H. J. *J. Org. Chem.* **1990**, *55*, 3992–3997.
(395) Hazan, C.; Kumar, D.; de Visser, S. P.; Shaik, S. *Eur. J. Inorg. Chem.* **2007**, 2966–2974.
(396) Wand, M. D.; Thompson, J. A. *J. Biol. Chem.* **1986**, *261*, 14049–14056.
(397) Rettie, A. E.; Boberg, M.; Rettenmeier, A. W.; Baillie, T. A. *J. Biol. Chem.* **1988**, *263*, 13733–13738.
(398) Lewis, D. F. V.; Sams, C.; Loizou, G. D. *J. Biochem. Mol. Toxicol.* **2003**, *17*, 47–52.
(399) Bugrim, A.; Nikolskaya, T.; Nikolsky, Y. *Drug Discovery Today* **2004**, *9*, 127–135.
(400) Afzelius, L.; Arnby, C. H.; Broo, A.; Carlsson, L.; Isaksson, C.; Jurva, U.; Kjellander, B.; Kolmodin, K.; Nilsson, K.; Raubacher, F.; Weidolf, L. *Drug. Metab. Rev.* **2007**, *39*, 61–86.
(401) Mayer, J. M. *Acc. Chem. Res.* **1998**, *31*, 441–450.
(402) Shaik, S.; Shurki, A. *Angew. Chem., Int. Ed.* **1999**, *38*, 586–625.
(403) Mayer, J. M. In *Biomimetic Oxidations Catalyzed by Transition Metal Complexes*; Meunier, B., Ed.; Imperial College Press: London, 2000; Chapter 1, pp 1−45.
(404) Korzekwa, K. R.; Jones, J. P.; Gillette, J. R. *J. Am. Chem. Soc.* **1990**, *112*, 7042–7046.
(405) Park, J.-Y.; Harris, D. *J. Med. Chem.* **2003**, *46*, 1645–1660.
(406) Brewer, C. B.; Peterson, J. A. *J. Biol. Chem.* **1988**, *263*, 791–798.
(407) Hoffmann, R.; Woodward, R. B. *J. Am. Chem. Soc.* **1965**, *87*, 2046–2048.
(408) Hoffmann, R.; Woodward, R. B. *J. Am. Chem. Soc.* **1965**, *87*, 4388–4389.
(409) Hoffmann, R.; Woodward, R. B. *J. Am. Chem. Soc.* **1965**, *87*, 4389–4390.
(410) Woodward, R. B.; Hoffmann, R. *J. Am. Chem. Soc.* **1965**, *87*, 395–397.
(411) Woodward, R. B.; Hoffmann, R. *J. Am. Chem. Soc.* **1965**, *87*, 2511–2513.
(412) Fukui, K.; Yonezawa, T.; Shingu, H. *J. Chem. Phys.* **1952**, *20*, 722–725.
(413) Sydora, O. L.; Goldsmith, J. I.; Vaid, T. P.; Miller, A. E.; Wolczanski, P. T.; Abruña, H. D. *Polyhedron* **2004**, *23*, 2841–2856.
(414) Shaik, S. *J. Am. Chem. Soc.* **1981**, *103*, 3692–3701.
(415) Shaik, S.; Hiberty, P. C. *A Chemist's Guide to Valence Bond Theory*; John Wiley & Sons Inc.: Hoboken, NJ, 2007.

(416) Shaik, S.; Hiberty, P. C. In *A Chemist's Guide to Valence Bond Theory*; John Wiley & Sons Inc.: 2007; Chapter 6, pp 116.
(417) Shaik, S.; Danovich, D.; Fiedler, A.; Schröder, D.; Schwarz, H. *Helv. Chim. Acta* **1995**, *78*, 1393–1407.
(418) Shaik, S.; Hiberty, P. C. In *A Chemist's Guide to Valence Bond Theory*; John Wiley & Sons Inc.: 2007; Chapter 3, pp 40−74.
(419) Su, P.; Song, L.; Wu, W.; Hiberty, P. C.; Shaik, S. *J. Am. Chem. Soc.* **2004**, *126*, 13539–13549.
(420) Groves, J. T.; McClusky, G. A. *J. Am. Chem. Soc.* **1976**, *98*, 859–861.
(421) Lee, D.-S.; Nioche, P.; Hamberg, M.; Raman, C. S. *Nature* **2008**, *455*, 363–370.
(422) Rutter, R.; Hager, L. P.; Dhonau, H.; Hendrich, M.; Valentine, M.; Debrunner, P. *Biochemistry* **1984**, *23*, 6809–6816.

CR900121S

THE JOURNAL OF PHYSICAL CHEMISTRY A

© Copyright 2009 by the American Chemical Society VOLUME 113, NUMBER 43, OCTOBER 29, 2009

Downloaded by INDIAN INST OF CHEMICAL TECH on October 30, 2009 | http://pubs.acs.org
Publication Date (Web): October 22, 2009 | doi: 10.1021/jp907271c

A Tribute to Walter Thiel

The 60th birthday of a scientist is a reason for celebration—advanced enough for the life's work to shape up, yet so early in time that there is plenty of opportunity for more to come. This is especially true for someone with the activity and creativity of Walter Thiel. It is a pleasure to introduce this Special Issue in his honor.

An important leitmotif throughout his career has been the development and application of semiempirical quantum-chemical methods. In his postdoctoral time with Michael Dewar in the early 1970s, Walter almost single-handedly implemented the godfather of all modern semiempirical methods, MNDO (modified neglect of differential overlap). Enticed by its potential in the application to large systems, he has continued to develop and refine the underlying models and methodologies ever since. These developments are based on a philosophy of designing and fitting parameters with well-defined physical meanings, rather than tweaking results by massive parametrization. By introducing orthogonalization corrections, for instance, fundamental flaws of semiempirical methods in describing molecular conformations can be overcome. Using know-how from sophisticated multireference ab initio techniques, Walter continues to push the development of MNDO-based approaches into terrain that is yet too difficult for other theoretical methods, such as excited states of large molecules.

Theory is at its best when it can enable experimentalists to interpret their results sensibly. In many collaborations with spectroscopists, Walter and his co-workers have provided highly accurate ab initio data for small molecules, which have guided

10.1021/jp907271c CCC: $40.75 © 2009 American Chemical Society
Published on Web 10/22/2009

the assignment of high-resolution rovibrational spectra in the gas phase and the spectroscopic identification of previously unknown reactive species. Stimulated by the vibrant environment of a Max Planck Institute devoted to catalysis research, he has used state-of-the-art density-functional theory (DFT) methods to shed light on the complicated mechanisms of homogeneous catalytic processes involving transition-metal complexes. In the heyday of fullerene chemistry, when Buckyballs were still frighteningly large for quantum-chemical calculations, Walter's group helped expand the limits of semiempirical and ab initio methods by applying them to ever larger fullerenes, providing new insights into their structures and reactions.

Walter's vision is not one of competition, but of complement. Nothing illustrates this point better than his activities in the area of hybrid quantum-mechanical/molecular-mechanical (QM/MM) methods, which are designed to bring together the best of the two worlds, namely, high accuracy and applicability to large systems. Walter was not the first to invent these methods, but recognizing their potential, seizing the opportunities for their implementation and their further development, and applying them to hot topics has made him one of the world's leading authorities in the QM/MM field. He has always pursued a strategy of flexible integration of the constituent QM and MM parts, so that almost any of them can now be seamlessly wielded together, tailoring the resulting hybrid for specific applications. One particularly fruitful area for such applications is biocatalysis by enzymes, for example, cytochrome P450 chemistry. In collaboration with Sason Shaik, he has used QM/MM methods to characterize the active species of P450 and its electronic structure. By elucidating the reaction mechanisms of P450cam in the wild type as well as in mutants, he is helping to resolve the controversies concerning the catalytic cycles of this important group of enzymes.

Chemistry is not only about the interaction between particles but also about the interaction between people. Respected for his competent, open, and unpretentious way, Walter has long become a renowned scientist, friend, and colleague within the scientific community. He would rather laugh with people than quarrel with them. This also includes the members of his group, whom he tries to motivate by leading instead of pushing.

Walter's big picture of theoretical chemistry is that of a versatile toolbox to complement, precede, and guide experiments in all branches of chemistry. In the concert of theory and experiment, he knows how to play the keys on all the instruments from computational chemistry, including those he himself has helped to shape and design. We hope he will like the multivoiced choir of papers assembled in this issue. Happy birthday, Walter!

Michael Bühl

University of St. Andrews

Devesh Kumar

Indian Institute of Chemical Technology

JP907271C

Downloaded by INDIAN INST OF CHEMICAL TECH on October 30, 2009 | http://pubs.acs.org
Publication Date (Web): October 22, 2009 | doi: 10.1021/jp907271c

Effect of Porphyrin Ligands on the Regioselective Dehydrogenation versus Epoxidation of Olefins by Oxoiron(IV) Mimics of Cytochrome P450†

Devesh Kumar,*,‡ Laleh Tahsini,§ Sam P. de Visser,*,§ Hye Yeon Kang,|| Soo Jeong Kim,|| and Wonwoo Nam*,||

Contribution from Molecular Modeling Group, Indian Institute of Chemical Technology, Hyderabad 500-607, India, The Manchester Interdisciplinary Biocenter and the School of Chemical Engineering and Analytical Science, The University of Manchester, 131 Princess Street, Manchester M1 7DN, United Kingdom, and Department of Chemistry and Nano Science, Department of Bioinspired Science, Centre for Biomimetic Systems, Ewha Womans University, Seoul 120-750, Korea

Received: March 30, 2009; Revised Manuscript Received: June 29, 2009

The cytochromes P450 are versatile enzymes involved in various catalytic oxidation reactions, such as hydroxylation, epoxidation and dehydrogenation. In this work, we present combined experimental and theoretical studies on the change of regioselectivity in cyclohexadiene oxidation (i.e., epoxidation vs dehydrogenation) by oxoiron(IV) porphyrin complexes bearing different porphyrin ligands. Our experimental results show that meso-substitution of the porphyrin ring with electron-withdrawing substituents leads to a regioselectivity switch from dehydrogenation to epoxidation, affording the formation of epoxide as a major product. In contrast, electron-rich iron porphyrins are shown to produce benzene resulting from the dehydrogenation of cyclohexadiene. Density functional theory (DFT) calculations on the regioselectivity switch of epoxidation vs dehydrogenation have been performed using three oxoiron(IV) porphyrin oxidants with hydrogen atoms, phenyl groups, and pentachlorophenyl ($ArCl_5$) groups on the meso-position. The DFT studies show that the epoxidation reaction by the latter catalyst is stabilized because of favorable interactions of the substrate with halogen atoms of the meso-ligand as well as with pyrrole nitrogen atoms of the porphyrin macrocycle. Hydrogen abstraction transition states, in contrast, have a substrate-binding orientation further away from the porphyrin pyrrole nitrogens, and they are much less stabilized. Finally, the regioselectivity of dehydrogenation versus hydroxylation is rationalized using thermodynamic cycles.

Downloaded by INDIAN INST OF CHEMICAL TECH on October 30, 2009 | http://pubs.acs.org
Publication Date (Web): August 6, 2009 | doi: 10.1021/jp9028694

Introduction

Cytochromes P450 (P450) are oxygen-activating enzymes involved in key processes in biosystems ranging from drug metabolism, to the biosynthesis of hormones, to the detoxification processes in the liver.[1,2] Figure 1 shows an extract of the active site of a typical P450 enzyme, namely, $P450_{cam}$,[3] which is a bacterial P450 that regioselectively hydroxylates camphor at the C^5 position.[4] The enzyme active site is a heme group with a metal (iron) embedded in its center and that is linked to the protein via a sulfur bridge of a cysteinate residue (Cys_{357} in $P450_{cam}$).[5] The active center binds molecular oxygen, which is converted into an oxoiron(IV) active species, Compound I (Cpd I), via a series of reduction and protonation steps. Cpd I, however, is elusive, but kinetic isotope effects and product distributions implicate it to be involved in substrate monooxygenation reactions.[6]

P450 enzymes catalyze a range of different reaction mechanisms; for instance, aliphatic C−H hydroxylation, aromatic C−H hydroxylation, C═C double bond epoxidation, sulfoxidation, *N*-dealkylation, and dehydrogenation.[2] As a consequence, some substrates react at the active center of P450 enzymes to give competing reaction mechanisms leading to one or more different products. Mutagenesis studies, whereby key active site residues are replaced, occasionally give a regioselectivity switch from one product to another. Furthermore, it has been shown that a regioselectivity switch can also occur through the replacement of hydrogen atoms in the substrate by deuterium atoms, which is termed metabolic switching.[7] In particular, hydroxylation took place at the C^3 position with deuterated 5,6-*exo*-*exo*-norcamphor at the C^5 and C^6 positions, whereas in the nondeuterated substrate, the C^5 position was activated. Similar regioselectivity switches were observed for toluene hydroxylation by P450 enzymes.[8]

These subtle changes in regioselectivity preference by P450 enzymes have triggered many studies to try to establish factors that drive reaction mechanisms. In biomimetic studies, it was

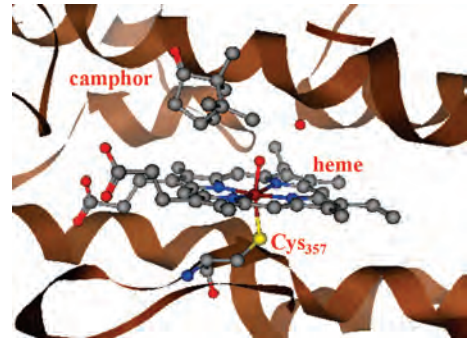

Figure 1. Extract of the active site of $P450_{cam}$ as taken from the 1DZ9 pdb file with substrate (camphor), heme, and its axial ligand (Cys_{357}) highlighted.

† Part of the "Walter Thiel Festschrift".

* Corresponding authors. E-mail: dkclcre@yahoo.com (D.K.); sam.devisser@manchester.ac.uk (S.P.d.V.); wwnam@ewha.ac.kr (W.N.).
‡ Indian Institute of Chemical Technology.
§ The University of Manchester.
|| Ewha Womans University.

10.1021/jp9028694 CCC: $40.75 © 2009 American Chemical Society
Published on Web 08/06/2009

shown that the meso-substituent on the porphyrin ring influences the oxidative power of the oxoiron(IV) oxidant.[9] In particular, electron-deficient iron(III) porphyrins afforded a much higher yield of epoxide products in comparison with oxidants with fewer electron-deficient substituents.[10] Moreover, studies on a series of metal−oxo porphyrin complexes with electron-withdrawing meso-substituents showed a strong ^{17}O NMR shift to higher frequencies that correlated linearly with the force constant of the metal−oxo bond as well as with the rate constant of triphenylphosphine oxidation, which implicates a direct correlation between meso-substitution and the strength of the Fe−O bond of the oxidant.[11] However, the exact nature of the meso-substituent and its influence on the reaction mechanisms has never been studied in depth. To gain insight into the meso-substituent effect on the electronic and catalytic properties of the oxoiron(IV) center, we have performed combined experimental and theoretical studies on cyclohexadiene (CHD) activation by oxoiron(IV) porphyrin oxidants with variable substituents on the meso-position. Earlier studies of us and others have established procedures to generate oxoiron(IV) porphyrin cation radical species using single oxygen atom donors such as iodosylbenzene (PhIO) and *m*-chloroperbenzoic acid (*m*-CPBA). These oxoiron(IV) porphyrin complexes have been shown to react readily with aliphatic groups by hydrogen atom abstraction and with C=C double bonds to give epoxide products.[12] As such, CHD reacts with Cpd I to form epoxide products or alternatively lead to dehydrogenation to form benzene.[13] The studies presented in this work show that a substituent on the meso-position changes the electronic properties of the porphyrin ring leading to subtle differences in electron affinities of the oxidant. Moreover, bulky groups on the meso-position influence substrate binding processes and access to the oxoiron(IV) group.

Downloaded by INDIAN INST OF CHEMICAL TECH on October 30, 2009 | http://pubs.acs.org
Publication Date (Web): August 6, 2009 | doi: 10.1021/jp9028694

Methods

Experimental Section. Commercially available reagents were of the best available purity and were used without further purification unless otherwise noted. Acetonitrile (CH_3CN) and dichloromethane (CH_2Cl_2) were dried according to literature procedures and distilled under Argon prior to use.[13] *m*-CPBA was purified by washing with phosphate buffer (pH 7.4) first, followed by water and then dried under reduced pressure.[14] PhIO was prepared by a literature method.[15] Fe(TPFPP)Cl (TPFPP = *meso*-tetrakis(pentafluorophenyl)porphyrin) was purchased from Aldrich Chemical Co., whereas Fe(TMP)Cl (TMP = *meso*-tetramesitylporphyrin) and Fe(TDCPP)Cl (TDCPP = *meso*-tetrakis(2,6-dichlorophenyl)porphyrin) were obtained from Frontier Scientific Inc. (Logan, UT). Fe(TF4TMAP)$(CF_3SO_3)_5$ (TF4TMAP = *meso*-tetrakis(2,3,5,6-tetrafluoro-4-*N*,*N*,*N*-trimethylaniliniumyl)porphyrin) was synthesized using commonly known procedures.[16] Figure 2 shows geometries and labels of the various substituted porphyrin macrocycles at the meso-position studied in this work.

Oxidant (0.10 mmol), either PhIO or *m*-CPBA, was added to a reaction solution containing iron(III) porphyrin chloride (2 mM) and 1,4-cyclohexadiene (0.10 mmol) in a solvent mixture (2 mL) of CH_3CN and CH_2Cl_2 (3:1) at 25 °C. After stirring for 10 min and filtering through an 0.45 μM filter, the reaction mixture was analyzed with Agilent Technologies 6890N gas chromatography equipped with a FID detector (GC) and Thermo Finnigan (Austin, TX) FOCUS DSQ (dual stage quadrupole) mass spectrometer interfaced with a Finnigan FOCUS gas chromatograph (GC-MS). We identified products by comparing retention times and mass patterns with those of known authentic samples. We determined product yields by comparison against

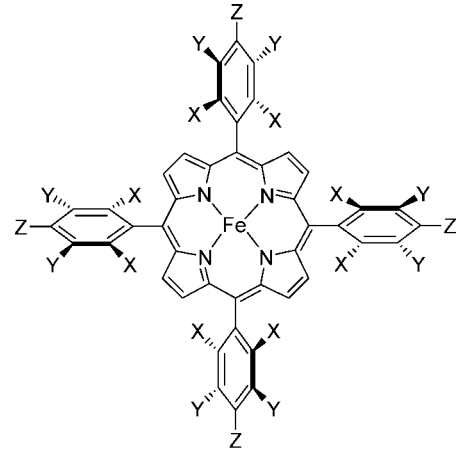

	X	Y	Z
TPP:	H	H	H
TMP:	Me	H	Me
TDCPP:	Cl	H	H
TPFPP:	F	F	F
TPCPP:	Cl	Cl	Cl
TF4TMAP:	F	F	TMA

Figure 2. Definition of the oxidants studied in this work. TMA stands for trimethylaniliniumyl.

standard curves prepared with authentic samples and by using *n*-decane as an internal standard.

Density Functional Theory Calculations. The calculations presented in this work were all obtained from density functional theory (DFT) calculations on biomimetic oxoiron(IV) porphyrin complexes using previously described procedures.[17] Our model is iron−protoporphyrin IX, whereby all side chains of the porphyrin were initially abbreviated with hydrogen atoms (Por). The active species (Cpd I) is an oxoiron(IV) porphyrin cation radical system with a chloride axial ligand similar to that of previous studies of ours in the field: $[Fe^{IV}{=}O(Por^{+\bullet})Cl]$.[18] We studied the regioselective epoxidation and dehydrogenation of 1,3-cyclohexadiene and 1,4-cyclohexadiene as model substrates using DFT with the unrestricted B3LYP method[19] because earlier work of ours on related systems predicted rate constants and kinetic isotope effects in good agreement with experiment.[20] Initial geometry optimizations employed a modest double-ζ quality LACVP basis set on iron and 6-31G on the rest of the atoms (basis set B1).[21] All structures were subjected to a full geometry optimization in Gaussian-03, followed by an analytical frequency calculation.[22] Subsequent, single-point calculations on the optimized geometries with a triple-ζ LACV3P+ basis set on iron and 6-311+G* on the rest of the atoms were done in Jaguar 7.0 to improve the energetics (basis set B2).[23] Local minima described here had real frequencies only, whereas the transition states were characterized by a single imaginary frequency for the correct mode. All charges reported in this work were taken from the atomic polar tensor (APT) charges from the Gaussian frequency calculations. The effect of the environment was tested via single-point calculations at B3LYP/B1 in Jaguar in a continuum solvent with a dielectric constant of ε = 5.7 and a probe radius of 2.72 Å.

In a second set of calculations, we studied the effect of meso-substitution on the electronic and catalytic properties of the oxoiron(IV) species. First, we studied the electronic properties of doublet and quartet oxoiron(IV) species with phenyl, pen-

SCHEME 1

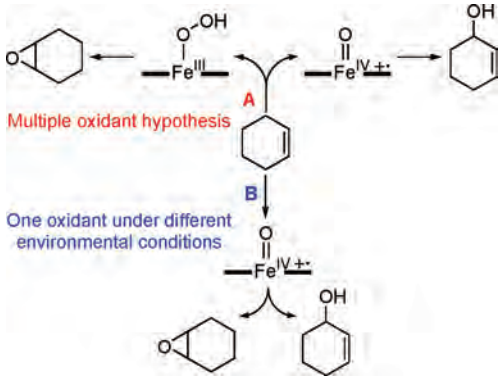

tachlorophenyl ($ArCl_5$), and methoxy substituents on the four meso-positions to give *meso*-tetraphenylporphyrin (TPP), *meso*-tetrakis(pentachlorophenyl)porphyrin (TPCPP), and *meso*-tetramethoxyporphyrin. In addition, using Fe^{IV}=O($TPP^{+\bullet}$)Cl and Fe^{IV}=O($TPCPP^{+\bullet}$)Cl, we re-evaluated the reaction mechanisms for epoxidation and dehydrogenation of 1,3-cyclohexadiene using Jaguar. Full optimizations were done in Jaguar with basis set B1, followed by single-point calculations with basis set B2 in the gas phase and in a continuum solvent with dielectric constant of $\varepsilon = 5.7$. Because of the size of these systems, we only ran frequency calculations on the optimized geometries for the mechanism using Fe^{IV}=O($TPP^{+\bullet}$)Cl as an oxidant and the transition-state structures ^{4}**TS**$_H$(TPCPP) and ^{4}**TS**$_E$(TPCPP).

To test the effect of the density functional method on the relative energies, we ran single-point calculations with the OPBE and PW91B95 density functional methods for the reaction mechanism of $^{4,2}Fe^{IV}$=O($Por^{+\bullet}$)Cl with 1,3-cyclohexadiene.[24,25] The trends are reproduced with alternative density functionals (Supporting Information) so that we do not expect major changes because of the choice of the density functional method.

Results and Discussion

Dehydrogenation versus Epoxidation in Iron Porphyrin-Catalyzed Oxidation Reactions. It has been shown in enzymatic and biomimetic reactions that products formed in the epoxidation of olefins are different depending on reaction conditions.[26−31] For example, Coon and coworkers examined the effect of site-directed mutagenesis of threonine to alanine on the epoxidation of olefins with cytochromes P450 and their mutants and observed the regioselectivity change from epoxide formation to allylic oxidation.[27] The authors proposed that the formation of different products in the reactions of cytochromes P450 and their mutants was due to the involvement of two different active oxidants with electrophilic properties in the oxidation of cyclohexene, such as a ferric−hydroperoxo and an iron(IV)−oxo porphyrin π-cation radical for the epoxidation and allylic hydroxylation, respectively (Scheme 1, pathway A).[27] Contrary to the proposal derived from enzymatic studies, Groves and coworkers have shown in biomimetic studies that the epoxidation of cyclohexene by $[Fe^{III}(TMP)]^+$ and oxidants such as *m*-CPBA and PhIO yielded products derived from both epoxidation (e.g., cyclohexene oxide) and allylic hydroxylation (e.g., cyclohexen-3-ol and cyclohexen-3-one) and that the amounts of epoxidation and allylic hydroxylation products changed significantly depending on reaction temperatures, choice of the selected oxidants, and axial ligands of the iron porphyrin catalyst.[28] Nam and coworkers supported the assertion of Groves and coworkers by showing that the regioselectivity of C=C epoxidation versus allylic C−H hydroxylation in the oxygenation of olefins by in situ-generated oxoiron(IV) porphyrin π-cation radicals depends significantly on the reaction conditions such as reaction temperature, the electronic nature of iron porphyrins, and substrates.[29] These results demonstrated that the regioselectivity of C=C epoxidation versus C−H hydroxylation in the oxygenation of cyclohexene by a single oxidant, ($TMP^{+\bullet}$)Fe^{IV}=O(X), can be altered depending on the reaction conditions (Scheme 1B). The results further suggest that the regioselectivity change does not implicate the participation of two distinct intermediates in olefin oxidations. Very recently, Fujii and coworkers interpreted the change of the regioselectivity with that where the epoxidation reaction is enthalpy-controlled, whereas the allylic hydroxylation reaction is entropy-controlled.[30] In the present study, we extended the study of the porphyrin ligand effect on the regioselectivity change to elucidate the origin of the regioselectivity change depending on the reaction conditions and the substituent effect of the porphyrin ligand.

SCHEME 2

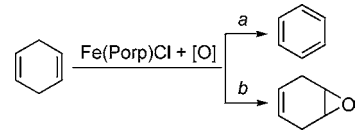

TABLE 1: Oxidation of 1,4-Cyclohexadiene by Iron(III) Porphyrin Complexes and Oxidants[a]

			products (%)[b,c]	
entry	catalyst	oxidant	benzene	4-cyclohexadiene oxide
1	Fe(TMP)Cl	PhIO	37 ± 4	2 ± 1
		m-CPBA	34 ± 4	3 ± 1
2	Fe(TDCPP)Cl	PhIO	14 ± 3	27 ± 3
		m-CPBA	17 ± 3	29 ± 3
3	Fe(TPFPP)Cl	PhIO	<1	32 ± 3
		m-CPBA	<1	30 ± 3
4	Fe(TF4TMAP)$(CF_3SO_3)_5$	PhIO	<1	35 ± 3
		m-CPBA	<1	32 ± 3

[a] See Experimental Section for detailed reaction conditions. [b] Yields (%) are calculated on the basis of the amounts of oxidant added. [c] Product distributions did not change depending on reaction temperatures (e.g., at −20 °C).

The regioselectivity of dehydrogenation versus epoxidation in the oxidation of olefins by iron(III) porphyrin complexes and oxidants was examined using 1,4-cyclohexadiene (CHD) as a substrate. The oxidation of CHD by PhIO or *m*-CPBA catalyzed by an iron(III) porphyrin complex afforded the formation of benzene and 4-cyclohexadiene oxide (Scheme 2) depending on the electron-richness of porphyrin ligands. The results shown in Table 1 show that Fe(TMP)Cl, which is an electron-rich iron(III) porphyrin catalyst, yielded benzene as the major product with the formation of a trace amount of epoxide product (entry 1). In contrast, 4-cyclohexadiene oxide was the major product in the reactions of electron-deficient iron porphyrin complexes, such as Fe(TPFPP)Cl and Fe(TF4TMAP)$(CF_3SO_3)_5$ (entries 3 and 4). We have also observed the formation of benzene and 4-cyclohexadiene oxide in the reaction of Fe(TDCPP)Cl (entry 2); the electron-richness of this iron porphyrin complex was between the electron-rich and -deficient iron porphyrins. These results indicate that electron-rich iron porphyrins prefer C−H bond activation to give olefin dehydrogenation (Scheme 2, pathway a), whereas oxygen atom transfer to a double bond is the preferred pathway in the reaction of electron-deficient iron porphyrin catalysts (Scheme 2, pathway b).[9,31] Furthermore, the product distributions were identical irrespective of oxidants,

Downloaded by INDIAN INST OF CHEMICAL TECH on October 30, 2009 | http://pubs.acs.org
Publication Date (Web): August 6, 2009 | doi: 10.1021/jp9028694

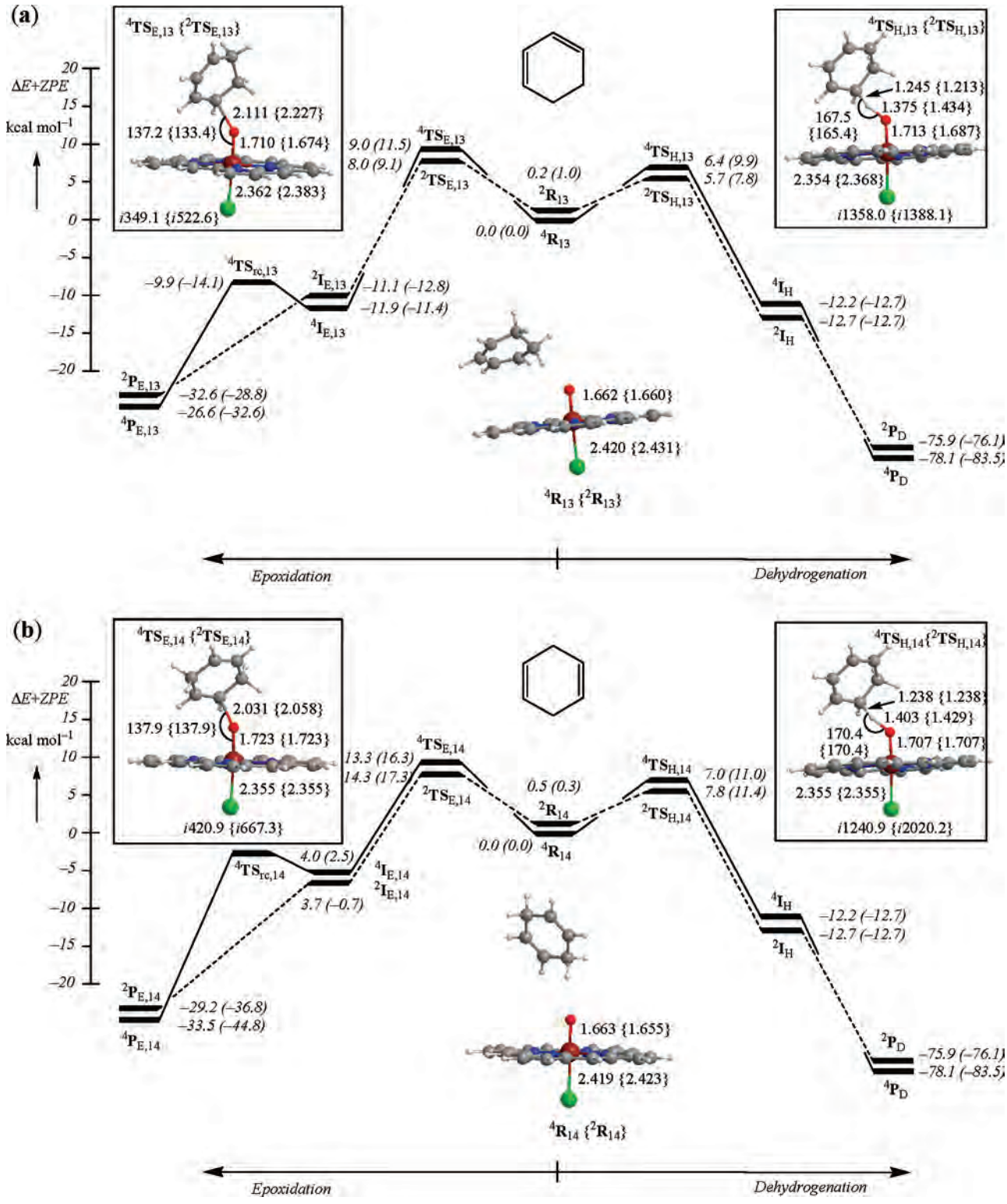

Figure 3. Potential energy profiles of (a) 1,3-cyclohexadiene and (b) 1,4-cyclohexadiene epoxidation and dehydrogenation by ^{4,2}**R**, as calculated with UB3LYP. Energies contain ZPE and are obtained with basis set B1, whereas values in parentheses were calculated with basis set B2 and include solvent corrections. Also given are geometries of the reactants and rate-determining transition states with bond lengths in angstroms, angles in degrees, and the value of the imaginary frequency in wavenumbers.

suggesting that a common intermediate (for example, a high-valent iron(IV)−oxo porphyrin π-cation radical species) was generated as reactive species responsible for the dehydrogenation and epoxidation reactions.[32]

Theoretical Modeling of the Reaction Mechanism. Because our experimental studies on the reaction of oxoiron(IV) porphyrins with 1,4-cyclohexadiene (CHD) show that a mixture of dehydrogenation and epoxidation products are formed depending on the nature of the group on the meso-position (Table 1), we decided to do a series of DFT calculations to trace the origins of this regioselectivity switch. Let us first start with a description of the simplest chemical system, whereby the porphyrin ring (Por) has no side chains and the reaction of the oxoiron(IV) species is with CHD, that is, Fe^{IV}═O($Por^{+\bullet}$)-

Downloaded by INDIAN INST OF CHEMICAL TECH on October 30, 2009 | http://pubs.acs.org
Publication Date (Web): August 6, 2009 | doi: 10.1021/jp9028694

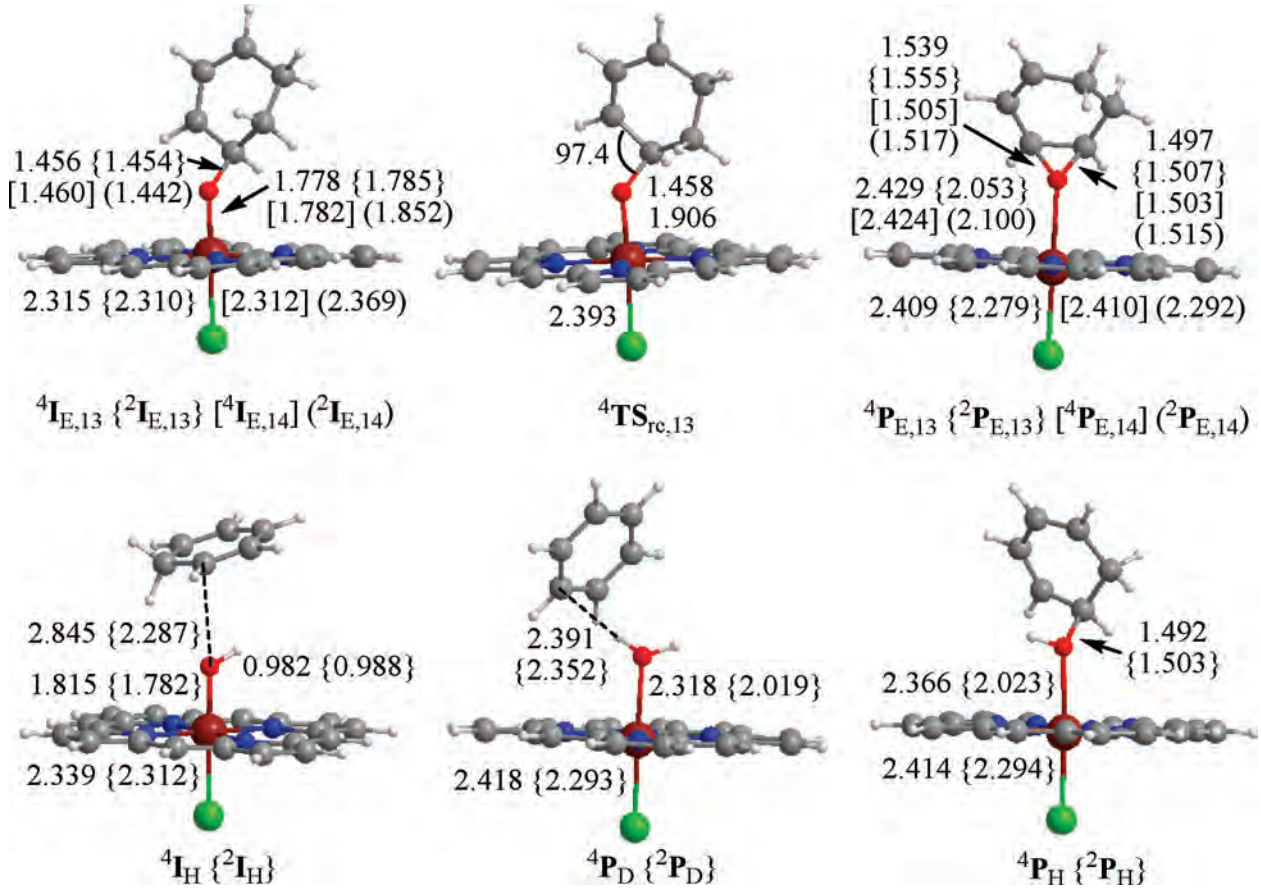

Figure 4. Optimized geometries of critical points along the reaction coordinates shown in Figure 3. All structures optimized with UB3LYP/B1 with bond lengths given in angstroms and angles in degrees.

Downloaded by INDIAN INST OF CHEMICAL TECH on October 30, 2009 | http://pubs.acs.org
Publication Date (Web): August 6, 2009 | doi: 10.1021/jp9028694

Cl−C_6H_8. Figure 3 shows the potential energy profile of 1,3-cyclohexadiene and 1,4-cyclohexadiene epoxidation and dehydrogenation by [Fe^{IV}═O($Por^{+\bullet}$)Cl] (designated **R**) on the doublet and quartet spin-state surfaces as calculated with DFT.

The reactions are stepwise starting from the degenerate spin states of Cpd I, doublet (^{2}**R**) and quartet (^{4}**R**). As shown before, Cpd I has close-lying doublet and quartet spin states with the same orbital occupation, that is, $\pi^*_{xz}{}^1$ $\pi^*_{yz}{}^1$ $a_{2u}{}^1$, leading to an electronic configuration of [Fe^{IV}═O($Por^{+\bullet}$)Cl].[33] The π^* set of orbitals are antibonding orbitals for the Fe−O interaction through atomic orbital interactions between the $3d_{xz,yz}$ on iron and $2p_{x,y}$ on oxygen. The third unpaired electron is on a heme-type orbital that has an a_{2u} label in D_{4h} symmetry.[34] Because the interactions of the $\pi^*_{xz,yz}$, on one hand, with a_{2u}, on the other hand, are small, the three unpaired electrons can be ferromagnetically coupled into an overall quartet spin state or antiferromagnetically coupled into a doublet spin state. It has been shown that in oxoiron(IV) species of heme enzymes these two states are close in energy and environmental perturbations and the nature of the axial ligand determine the ordering and relative energy of the two spin states.[35] As a consequence, Cpd I reacts with substrates via two-state-reactivity patterns on competing doublet and quartet spin state surfaces.[36]

The reaction in Figure 3 starts from the center with ^{2,4}**R**. Whereas the mechanism to the left leads to epoxide products, the mechanism to the right affords dehydrogenation products. The epoxidation reaction passes a C−O bond activation barrier (^{4,2}**TS**$_E$) to form a radical intermediate (^{4,2}**I**$_E$), followed by a ring-closure barrier (^{4,2}**TS**$_{rc}$) to give epoxide products. This mechanism is similar to the one that we and others observed before for alkene epoxidation by Cpd I of P450.[37] The barrier ^{4,2}**TS**$_E$ is the rate-determining step in the reaction mechanism, and only on the quartet spin-state surface was a significant ring-closure barrier found. On the doublet spin-state surface, the ring-closure barrier was found to be negligible, similar to radical rebound studies of alkane hydroxylation reactions.[38] Optimized geometries of ^{4,2}**TS**$_E$ are characteristic of epoxidation transition states with long C−O bonds and an imaginary frequency representing a C−O stretch vibration. Optimized geometries for epoxidation of 1,3-cyclohexadiene and 1,4-cyclohexadiene are very similar, and the only differences are related to the relative energies. Because of more π-system stabilization of the radical intermediates, ^{4,2}**I**$_{E,13}$ are significantly lower in energy than ^{4,2}**I**$_{E,14}$, and so are the epoxidation barriers. Optimized geometries of subsequent structures in the epoxidation mechanism (^{4,2}**I**$_E$, ^{4}**TS**$_{rc}$, and ^{4,2}**P**$_E$) are shown in Figure 4. These structures show typical features of epoxidation intermediate, ring-closure transition state, and product complexes and resemble geometries of substrate epoxidation of smaller molecules previously published.[37]

The dehydrogenation mechanism proceeds from the center in Figure 3 starting with ^{2,4}**R** by a hydrogen abstraction transition state (^{4,2}**TS**$_H$) that leads to a hydroxo−iron(IV) complex, ^{4,2}**I**$_H$. In a subsequent step, a second hydrogen atom is abstracted to give benzene (i.e., a dehydrogenated product, ^{4,2}**P**$_D$). Note that the mechanisms for hydrogen abstraction by both 1,3-cyclohexadiene and 1,4-cyclohexadiene give the same hydroxo−iron(IV) complex (^{4,2}**I**$_H$), and as a consequence, the rebound/second hydrogen abstraction mechanisms are also the same. Accordingly, the relative energies of the hydrogen abstraction transition states for 1,3-cyclohexadiene and 1,4-cyclohexadiene are within a few kilocalories per mole. In contrast, the epoxidation barriers for 1,3-cyclohexadiene and 1,4-cyclohexa-

Downloaded by INDIAN INST OF CHEMICAL TECH on October 30, 2009 | http://pubs.acs.org
Publication Date (Web): August 6, 2009 | doi: 10.1021/jp9028694

diene are much wider apart; therefore, Fe^{IV}═O($Por^{+\bullet}$)Cl will react with 1,4-cyclohexadiene via exclusive dehydrogenation, whereas with 1,3-cyclohexadiene, minor epoxidation products may be formed.

Extensive geometry scans show that the second hydrogen abstraction from $^{4,2}\mathbf{I}_H$ is essentially barrierless on both spin-state surfaces. Alternatively, the hydroxo group can rebound to the radical rest group to form alcohol products ($^{4,2}\mathbf{P}_H$); however, geometry scans for the radical rebound show it to proceed by a much larger barrier than substrate dehydrogenation so that the reaction will generate dehydrogenation rather than hydroxylation products. Later in this work, we will give a thermodynamic explanation for the preference of dehydrogenation over hydroxylation using this substrate. The hydrogen abstraction barriers for 1,3-cyclohexadiene are favored over epoxidation by 2.3 (2.6) kcal mol^{-1} for the doublet (quartet) spin states with a small basis set, whereas improvement of the basis set and solvent corrections decreases these gaps to 1.3 (1.6) kcal mol^{-1}. Although the energy differences are small, they support the experimental studies discussed above, where electron-donating substituents on the meso-position give dehydrogenation products rather than epoxidation products.

Hydrogen abstraction leads to electron transfer into the a_{2u} orbital to generate an iron(IV)−hydroxo complex with orbital occupation of $\pi^*_{xz}{}^1\ \pi^*_{yz}{}^1\ a_{2u}{}^2\ \phi_{Alk}{}^1$, whereby the latter orbital represents the substrate radical. The intermediate complex in the dehydrogenation mechanism, therefore, is an Fe^{IV}(OH)(Por)Cl···Alk$^\bullet$ system with Alk$^\bullet$ as the substrate radical rest group. This is similar to earlier studies of substrate hydroxylation by P450 models, whereby the hydrogen abstraction reaction proceeds with electron transfer from the substrate into the a_{2u} orbital.[39] Optimized geometries show features characteristic of this mechanism with bond lengths in good agreement with the literature. In the hydrogen abstraction transition states ($^{4,2}\mathbf{TS}_{H,13}$ and $^{4,2}\mathbf{TS}_{H,14}$), the transferrable hydrogen atom is slightly closer to the donor-carbon atom than to the acceptor-oxygen atom; for example, r_{CH} = 1.245 (1.213) Å and r_{OH} = 1.375 (1.434) Å for $^4\mathbf{TS}_{H,13}$ ($^2\mathbf{TS}_{H,13}$), respectively, which indicates that the transition-state structures are reactantlike. These transition states are characterized by a large imaginary frequency of *i*1358.0 (*i*1388.1) cm^{-1} for $^4\mathbf{TS}_{H,13}$ ($^2\mathbf{TS}_{H,13}$) and *i*1240.9 (*i*2020.2) cm^{-1} for $^4\mathbf{TS}_{H,14}$ ($^2\mathbf{TS}_{H,14}$), implying that an elevated kinetic isotope effect may be expected upon replacement of the transferrable hydrogen atom with deuterium. After hydrogen abstraction and the formation of the radical intermediate, there are two possible mechanisms to product formation, namely, radical rebound to the hydroxo group to form alcohol products or a second hydrogen abstraction to give benzene and water products (dehydrogenation). Geometrically, the dehydrogenation product is a water molecule interacting with benzene and is essentially a resting state system with an interacting substrate. The structure resembles that of an azole molecule bound to a resting state structure of P450.[40]

Subsequently, we extended our chemical system with either four phenyl or four pentachlorophenyl ($ArCl_5$) groups on the meso-positions of the porphyrin macrocycle to create Cpd I(TPP) and Cpd I(TPCPP) and re-evaluated the epoxidation and dehydrogenation reactions. Before describing these results, let us first make a comparison of Cpd I with three meso-substituted porphyrins in Figure 5, whereby Cpd I(OMe) contains four methoxy groups on the meso-positions. Geometrically, ^{4,2}Cpd I and the meso-substituted structures are almost identical with differences in bond lengths well below 0.01 Å. The Fe−O stretch vibration (ν_{FeO}) of ^{4}Cpd I shifts from 848 to 840 cm^{-1} upon the addition of $ArCl_5$ substituents to the meso-position, which implies that a small change on the strength of the Fe−O bond is incurred. A similar pattern is observed for the group spin densities, where only minor differences are found. Therefore, an extra group on the meso-position does not alter the orbital levels and electronic ground state of Cpd I. The group charges, by contrast, show somewhat larger variations between the different Cpd I structures: The overall charge (Q) on the porphyrin ring decreases from Q_{Por} = 0.21 (0.20) in the unsubstituted system ^{4}Cpd I (^{2}Cpd I) to Q_{Por} = 0.09 (0.10) for ^{4}Cpd I(TPCPP) (^{2}Cpd I(TPCPP)). This decrease in the total charge of the porphyrin ring is mainly due to a decreased charge on the *meso*-carbon atoms to an average from $Q_{C\text{-}meso}$ = 0.40 (0.41) in ^{4}Cpd I (^{2}Cpd I) to 0.67 (0.68) for ^{4}Cpd I(TPCPP) (^{2}Cpd I(TPCPP)). A substituent on the meso-position also has an effect on the charge of the oxygen atom, although the difference is not as dramatic in comparison with the *meso*-carbon atom, but it will influence the electron affinity of the oxidant and its ability to transfer the oxygen atom to substrates. Indeed, a calculation of the one-electron reduced form of these Cpd I complexes, that is, ^{3}Cpd II and ^{3}Cpd II(TPCPP), reveals that the electron affinity (EA) has increased from 3.09 to 4.02 eV for the large system.

Finally, we calculated some key structures in the epoxidation and dehydrogenation reaction mechanisms of 1,3-cyclohexadiene activation by ^{4,2}Cpd I(TPCPP), and the results are given in Figure 6. The mechanisms are similar to those shown above in Figure 3, and so is the labeling of the structures. Because of the size of the chemical system, geometry scans and transition state searches for the hydrogen abstraction and C−O activation in the epoxidation reactions were run only for the quartet spin state. We do not expect dramatic changes for the doublet spin state because the same electron transfer processes occur there. In general, doublet and quartet aliphatic hydrogen abstraction barriers are within a few kilocalories per mole and so are epoxidation barriers.[37,39] Intermediates were calculated for both spin-state structures, although attempts to calculate the iron(IV)−hydroxo complex in the doublet spin state failed and converged to the dehydrogenation product complex instead ($^2\mathbf{P}_D$(TPCPP)).

The potential energy profile shown in Figure 6 predicts dominant epoxidation over hydroxylation by 4.9 kcal mol^{-1} in the gas phase. This regioselectivity is in agreement with the data shown in Table 1, where a switch from dehydrogenation to epoxidation is observed through the addition of electron-withdrawing groups to the meso-position. Because of the size of the chemical system, we ran frequency calculations on only the transition-state geometries of Figure 6. With zero-point energy corrections included, barriers of $^4\mathbf{TS}_E$ = 6.4 kcal mol^{-1} and $^4\mathbf{TS}_H$ = 7.4 kcal mol^{-1} are obtained at the ΔE_{B2} + ZPE_{B1} level of theory, whereas corrections to a dielectric constant change these barriers to 6.8 and 6.9 kcal mol^{-1}, respectively. Therefore, ZPE corrections bring $^4\mathbf{TS}_E$(TPCPP) and $^4\mathbf{TS}_H$(TPCPP) in a dielectric constant within 1 kcal mol^{-1} of each other. These values are in perfect agreement with the product ratios observed for the reaction of Fe═O(TDCPP)Cl with cyclohexadiene (entry 2 in Table 1). Energetically, the epoxidation mechanism shows close similarities to the small model complex depicted in Figure 3 with a slightly lower epoxidation barrier of 7.2 kcal mol^{-1}, whereas the hydrogen abstraction barrier is considerably destabilized with basis set B1.

In addition, we calculated the intermediate complexes in the reaction mechanism ($^{4,2}\mathbf{I}_E$ and $^{4,2}\mathbf{I}_H$) for the reaction of $^{4,2}Fe^{IV}$═O($TPP^{+\bullet}$)Cl with 1,3-cyclohexadiene. At the ΔE_{B2} +

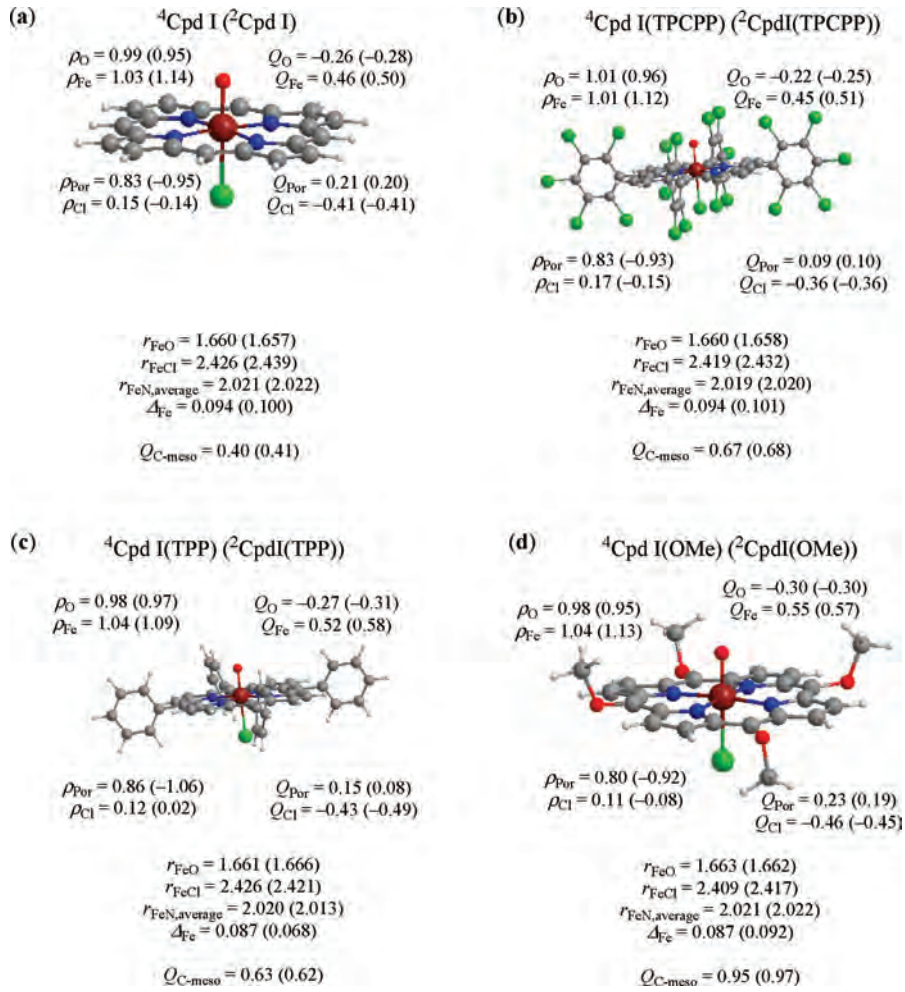

Figure 5. Optimized geometries, group charges (Q), and group spin densities (ρ) of ^{4,2}Cpd I, ^{4,2}Cpd I(TPCPP), ^{4,2}Cpd I(TPP), and ^{4,2}Cpd I(OMe) with bond lengths in angstroms. The $r_{FeN,average}$ distance is the average Fe−N distance between the metal and the pyrrole nitrogen atoms, and Δ_{Fe} is the displacement of the metal from the plane of the porphyrin ring.

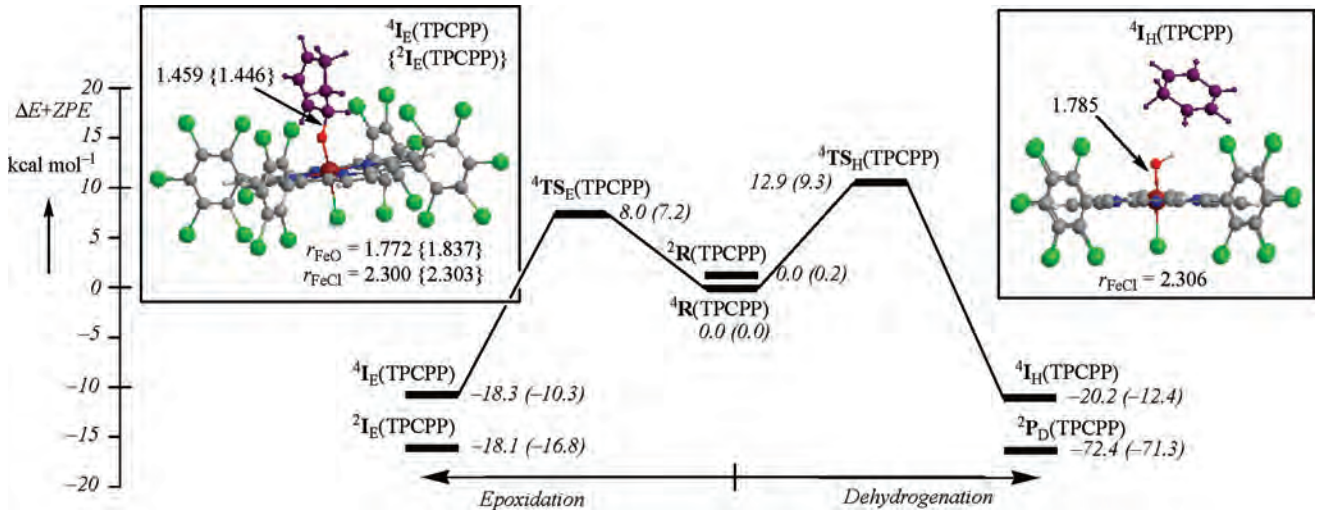

Figure 6. Potential energy profile of 1,3-cyclohexadiene epoxidation and dehydrogenation by ^{4,2}Cpd I(TPCPP), as calculated with UB3LYP. Energies are obtained with basis set B1, whereas values in parentheses are obtained with basis set B2 and solvent corrections. Also given are geometries of the intermediates along the epoxidation and dehydrogenation mechanism with bond lengths in angstroms and angles in degrees.

ZPE_{B1} level of theory, we find energies of −13.8, −13.7, −15.5, and −15.2 kcal mol^{-1} relative to isolated reactants for ^{4}**I**$_E$(TPP), ^{2}**I**$_E$(TPP), ^{4}**I**$_H$(TPP), and ^{2}**I**$_H$(TPP), respectively. These values are a few kilocalories per mole more exothermic than those observed for the unsubstituted porphyrin in Figure 3a. Moreover, the difference in energy between epoxidation and hydrogen abstraction intermediates is about 1.5 kcal mol^{-1} in favor of hydrogen abstraction, which is of the same order of magnitude as that observed for unsubstituted porphyrin. Therefore, the reaction exothermicity for formation of the intermediate complexes is close in energy for Cpd I(Por) and Cpd I(TPP), whereas the reaction is more exothermic for Cpd I(TPCPP). Therefore,

Downloaded by INDIAN INST OF CHEMICAL TECH on October 30, 2009 | http://pubs.acs.org
Publication Date (Web): August 6, 2009 | doi: 10.1021/jp9028694

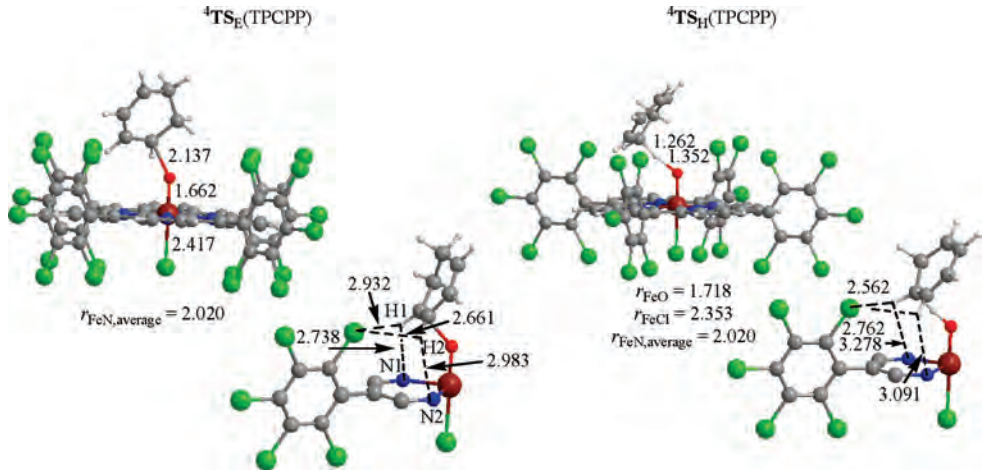

Figure 7. Optimized geometries of ^{4}**TS**$_E$(TPCPP) and ^{4}**TS**$_H$(TPCPP) with bond lengths in angstroms.

Downloaded by INDIAN INST OF CHEMICAL TECH on October 30, 2009 | http://pubs.acs.org
Publication Date (Web): August 6, 2009 | doi: 10.1021/jp9028694

the halogen ligands of the meso-substituent influence the reaction mechanism by stabilizing the intermediate complexes of epoxidation. In the following, we will give a geometric explanation for this regioselectivity switch.

Optimized geometries of ^{4}**TS**$_E$(TPCPP) and ^{4}**TS**$_H$(TPCPP) are given in Figure 7. Geometrically, there are no dramatic differences between the structures in Figures 3 and 7. The Fe−Cl and Fe−O distances are slightly elongated for ^{4}**TS**$_E$(TPCPP) by about 0.05 Å. Moreover, the C−O bond in ^{4}**TS**$_E$(TPCPP) is enhanced by 0.026 Å with respect to ^{4}**TS**$_E$, whereas the O−H distance is shorter by 0.03 Å in ^{4}**TS**$_H$(TPCPP) compared with ^{4}**TS**$_H$. The main cause of destabilization of the hydrogen abstraction barrier, however, is due to the interactions of the substrate with the halogen ligands on the meso-substituents. Therefore, in the C−O activation barrier, the substrate approaches the oxo group with the double bond perpendicular to the C−O bond parallel to the porphyrin ring. As a consequence, the two hydrogen atoms attached to the carbon atoms of this double bond form hydrogen bonding interactions with the nitrogen atoms of the porphyrin ring as well as with a chloride atom of the $ArCl_5$ group. These hydrogen bond lengths are between 2.66 and 2.99 Å and will stabilize the structure in this conformation. In line with this, olefin epoxidation reactions by hydrogen peroxide in fluorinated alcohols were shown to be enhanced because of favorable interactions of the fluoride atoms through template-catalysis.[41] The hydrogen abstraction in ^{4}**TS**$_H$-(TPCPP) takes place with the substrate further away from the oxo group as compared with ^{4}**TS**$_H$ because the transferring hydrogen atom is located in between the substrate and the oxo group. As a result, the substrate is too far away to form favorable hydrogen bonding interactions with the porphyrin pyrrole nitrogen atom with CH−N distances well over 3 Å, and only hydrogen bonding occurs between C−H groups of the substrate with a chloride atom of the $ArCl_5$ ligand. Therefore, the hydrogen abstraction transition state is much less stabilized by polar interactions than the epoxidation transition state, and hence ^{4}**TS**$_E$(TPCPP) is considerably lower in energy than ^{4}**TS**$_H$-(TPCPP). Alternatively, the approach of the substrate to the oxo group from the top, that is, along the *z* axis or Fe−O axis, whereby the interactions between substrate and metal ligands are minimal, is not possible in heme systems because the electron transfer processes in the transition states favor a bent conformation for the Fe−O−substrate group.[42,43] The regioselectivity of epoxidation versus hydrogen atom abstraction by [Fe^{IV}=O(TPCPP$^{+\bullet}$)Cl], therefore, is determined by substrate binding to the oxidant, which favors the epoxidation mechanism.

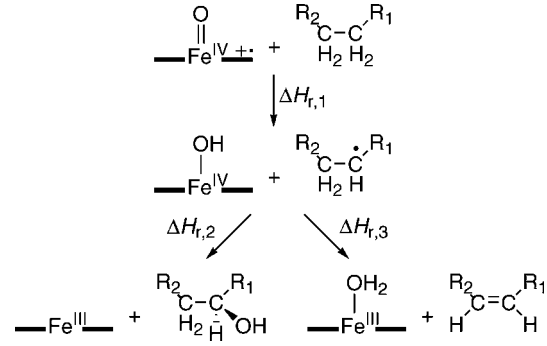

Figure 8. Mechanisms of hydrogen atom abstraction, hydroxylation, and dehydrogenation derived from DFT calculations.

Thermodynamic Factors That Determine Dehydrogenation versus Hydroxylation Regioselectivity. The cytochromes P450 generally react with substrates by hydrogen atom abstraction that leads to the formation of alcohol products, although occasionally, dehydrogenation reactions also occur. In the following, we will discuss factors that influence the regioselectivity of substrate dehydrogenation versus hydroxylation. Consider the overall reaction mechanism for both substrate dehydrogenation and hydroxylation in Figure 8. The reaction starts at the top with Cpd I and a molecule with two neighboring CH_2 groups and substituents R_1 and R_2 that determine whether the total molecule is an alkane or cycloalkane. The initial reaction is a hydrogen atom abstraction to form a hydroxo−iron(IV) complex and an alkyl radical with reaction enthalpy, $\Delta H_{r,1}$. It has been shown that this reaction enthalpy for the hydrogen atom abstraction is proportional to the difference in bond dissociation energy (BDE) between the C−H bond that is broken and the O−H bond that is formed in the process.[44] The BDE to split AH into A$^\bullet$ and a hydrogen atom is defined in eq 1. The energy to break the O−H bond in the hydroxo−iron(IV) complex is BDE_{FeOH}, and the energy to break the C−H bond in $R_2CH_2CH_2R_1$ is BDE_{CH2}. Combining these values of BDE_{FeOH} and BDE_{CH2} with $\Delta H_{r,1}$ gives eq 2.

$$AH \rightarrow A^\bullet + H^\bullet + BDE_{AH} \quad (1)$$

$$\Delta H_{r,1} = BDE_{CH_2} - BDE_{FeOH} \quad (2)$$

To make a prediction on regioselective substrate dehydrogenation versus hydroxylation, we calculated the C−H bond

TABLE 2: Calculated Bond Dissociation Energies and Reaction Energies for the Reactions Shown in Figure 8 from Isolated Species[a]

substrate	BDE_{CH_2}	$\Delta H_{r,1}$	BDE_{rad}	$\Delta H_{r,3}$	BDE_{COH}	$\Delta H_{r,2}$
ethane	96.2	9.5	36.7	−34.0	85.8	−55.5
trans-butane	92.6	5.9	33.5	−37.3	85.4	−55.2
cyclohexane	93.0	6.4	33.6	−37.2	85.8	−55.6
cyclohexene	77.7	−9.0	47.5	−23.3	69.1	−38.9
cyclohexadiene	69.0	−17.6	21.8	−49.0	59.7	−29.5

[a] All values are in kilocalories per mole.

strengths of several substrates, namely, ethane, *trans*-butane, cyclohexane, cyclohexene, and 1,3-cyclohexadiene. The calculated values of BDE_{CH_2} together with the value of BDE_{FeOH} = 86.6 kcal mol^{-1} from ref 17b give an estimate of the expected $\Delta H_{r,1}$ for hydrogen abstraction, and these data have been accumulated in Table 2. As follows, the hydrogen abstraction reaction is more exothermic with substrates with weak C−H bonds, and as a consequence, lower hydrogen abstraction barriers may also be expected. The reaction exothermicity of hydrogen abstraction from CHD is estimated to be −17.6 kcal mol^{-1} (Table 2). Using the same methods and basis sets, this value compares excellently with that calculated for the formation of $^4\mathbf{I}_H$ ($^2\mathbf{I}_H$) from isolated reactants where exothermicities of −18.2 (−18.2) kcal mol^{-1} were found in the gas phase.

The next step in the reaction mechanism is either hydroxyl rebound to the radical to form alcohol products with exothermicity, $\Delta H_{r,2}$, or a second hydrogen abstraction to form water and olefin with exothermicity, $\Delta H_{r,3}$. Analogous to eq 2 above, the latter reaction exothermicity ($\Delta H_{r,3}$) can be written as the difference in bond dissociation energy of the C−H bond of $R_2CH_2C^{\bullet}R_1$ (designated BDE_{rad}) and the bond dissociation energy of the O−H bond in the water−iron(III) complex (designated BDE_{FeOH_2}), eq 3. A value of 70.8 kcal mol^{-1} for BDE_{FeOH_2} is calculated, whereas the values for BDE_{rad} and $\Delta H_{r,3}$ are given in Table 2. Saturated alkanes give very similar dehydrogenation reaction energies, but the most exothermic reaction is found for 1,3-cyclohexadiene, which is due to the increased resonance stabilization of product benzene.

$$\Delta H_{r,3} = BDE_{rad} - BDE_{FeOH_2} \quad (3)$$

The alternative reaction from the hydroxo−iron(IV) intermediate is substrate hydroxylation that involves hydroxyl rebound to the radical and formation of alcohol products via $\Delta H_{r,2}$. The bond dissociation energy to break the Fe−O bond in the hydroxo−iron(IV) complex (BDE_{FeOH}) is defined as in eq 4 and is calculated to be 30.2 kcal mol^{-1}.

$$Fe(IV)OH(Por)Cl \rightarrow Fe(III)(Por)Cl + OH^{\bullet} + BDE_{FeOH} \quad (4)$$

In a similar way, the hydroxyl affinities of the radical intermediates were estimated from the BDE_{COH} energies, as defined in eq 5.

$$AOH \rightarrow A^{\bullet} + OH^{\bullet} + BDE_{COH} \quad (5)$$

The reaction enthalpy for the hydroxylation reaction ($\Delta H_{r,2}$) is estimated using the values for BDE_{FeOH} and BDE_{COH}, and the results are given in Table 2. As follows, saturated alkanes have a large value of BDE_{COH}, and as a consequence, the hydroxylation rebound is highly exothermic. By contrast, the hydroxyl affinity of the radical obtained after hydrogen abstraction of CHD is very small (BDE_{COH} = 59.7 kcal mol^{-1}), which gives an overall hydroxylation rebound exothermicity of only $\Delta H_{r,2}$ = −29.5 kcal mol^{-1}. However, the competing dehydrogenation reaction is much more exothermic ($\Delta H_{r,3}$ = −49.0 kcal mol^{-1}), and hence a reaction of Cpd I with CHD gives dehydrogenated products rather than hydroxylated products. The other substrates given in Table 2 all have a more exothermic hydroxylation reaction as compared with the dehydrogenation reaction; therefore, these substrates will react with Cpd I to give hydroxylated products, except CHD, which has a lower energy dehydrogenation pathway because of the formation of the much more stable benzene product. Indeed, experimental studies on cyclohexene activation by a oxoiron(IV)porphyrin complex gave a mixture of epoxide and cyclohexenol products but no evidence of dehydrogenation.[45] The reaction exothermicities shown in Table 2, therefore, explain trends in product yields and explain the preference of substrate dehydrogenation by CHD.

Conclusions

Combined experimental and density functional studies of the reactions of cyclohexadiene with oxoiron(IV) porphyrin oxidants with variable meso-substituents are reported. It is shown that oxidants with electron-rich meso-substituents give benzene product, whereas electron-deficient meso-substituents react to form epoxide as a major product. Our DFT studies show that in the gas phase, the two processes are competitive with a small preference of hydrogen abstraction over epoxidation. However, a chemical system with pentachlorophenyl substituents (TPCPP) influences substrate binding and sterically hinders hydrogen atom abstraction, whereas the epoxidation transition state is stabilized. The present results give insight into the effect and influence of ligands on reaction mechanisms and regioselectivity of substrate monoxygenation by oxoiron(IV) porphyrins.

Acknowledgment. The research was supported by CPU time provided by the National Service of Computational Chemistry Software (NSCCS). Financial support from KOSEF/MEST through the CRI and WCU (R31-2008-000-10010-0) Programs is acknowledged. L.T. acknowledges the British Council for a Scholarship, and D.K. is a Ramanujan Fellow of the Department of Science and Technology (New Delhi).

Supporting Information Available: Cartesian coordinates of all structures described in this work and group spin densities and charges. This material is available free of charge via the Internet at http://pubs.acs.org.

References and Notes

(1) (a) Sono, M.; Roach, M. P.; Coulter, E. D.; Dawson, J. H. *Chem. Rev.* **1996**, *96*, 2841–2888. (b) Guengerich, F. P. *Chem. Res. Toxicol.* **2001**, *14*, 611–650. (c) Groves, J. T. *Proc. Natl. Acad. Sci. U.S.A.* **2003**, *100*, 3569–3574. (d) *Cytochrome P450: Structure, Mechanism, and Biochemistry*, 3rd ed.; Ortiz de Montellano, P. R., Ed.; Kluwer Academic/Plenum Publishers: New York, 2004. (e) Munro, A. W.; Girvan, H. M.; McLean, K. J. *Nat. Prod. Rep.* **2007**, *24*, 585–609.

(2) (a) van Eldik, R. *Coord. Chem. Rev.* **2007**, *251*, 1649–1662. (b) Makris, T. M.; von Koenig, K.; Schlichting, I.; Sligar, S. G. *J. Inorg. Biochem.* **2006**, *100*, 507–518. (c) Groves, J. T. *J. Inorg. Biochem.* **2006**, *100*, 434–447. (d) Woggon, W.-D. *Acc. Chem. Res.* **2005**, *38*, 127–136.

(3) Schlichting, I.; Berendzen, J.; Chu, K.; Stock, A. M.; Maves, S. A.; Benson, D. E.; Sweet, R. M.; Ringe, D.; Petsko, G. A.; Sligar, S. G. *Science* **2000**, *287*, 1615–1622.

(4) (a) Sligar, S. G.; Gunsalus, I. C. *Proc. Natl. Acad. Sci. U.S.A.* **1976**, *73*, 1078–1082. (b) Poulos, T. L. *Biochem. Biophys. Res. Commun.* **2003**, *312*, 35–39. (c) Kuznetsov, V. Y.; Poulos, T. L.; Sevrioukova, I. F.

Downloaded by INDIAN INST OF CHEMICAL TECH on October 30, 2009 | http://pubs.acs.org
Publication Date (Web): August 6, 2009 | doi: 10.1021/jp9028694

Biochemistry **2006**, *45*, 11934–11944. (d) Purdy, M. M.; Koo, L. S.; Ortiz de Montellano, P. R.; Klinman, J. P. *Biochemistry* **2006**, *45*, 15793–15806. (e) Denisov, I. G.; Makris, T. M.; Sligar, S. G.; Schlichting, I. *Chem. Rev.* **2005**, *105*, 2253–2277.

(5) Poulos, T. L.; Finzel, B. C.; Howard, A. J. *J. Mol. Biol.* **1987**, *195*, 687–700.

(6) (a) Egawa, T.; Shimada, H.; Ishimura, Y. *Biochem. Biophys. Res. Commun.* **1994**, *201*, 1464–1469. (b) Kellner, D. G.; Hung, S. C.; Weiss, K. E.; Sligar, S. G. *J. Biol. Chem.* **2002**, *277*, 9641–9644. (c) Chiavarino, B.; Cipollini, R.; Crestoni, M. E.; Fornarini, S.; Lanucara, F.; Lapi, A. *J. Am. Chem. Soc.* **2008**, *130*, 3208–3217.

(7) Atkins, W. M.; Sligar, S. G. *J. Am. Chem. Soc.* **1987**, *109*, 3754–3760.

(8) (a) Hanzlik, R. P.; Hogberg, K.; Judson, C. M. *Biochemistry* **1984**, *23*, 3048–3055. (b) Hanzlik, R. P.; Hogberg, K.; Moon, J. B.; Judson, C. M. *J. Am. Chem. Soc.* **1985**, *107*, 7164–7167.

(9) (a) Dolphin, D.; Traylor, T. G.; Xie, L. Y. *Acc. Chem. Res.* **1997**, *30*, 251–259. (b) Nam, W. *Acc. Chem. Res.* **2007**, *40*, 522–531.

(10) Traylor, T. G.; Kim, C.; Richards, J. L.; Xu, F.; Perrin, C. L. *J. Am. Chem. Soc.* **1995**, *117*, 3468–3474.

(11) Fujii, H.; Kurahashi, T.; Tosha, T.; Yoshimura, T.; Kitagawa, T. *J. Inorg. Biochem.* **2006**, *100*, 533–541.

(12) (a) Wolak, M.; van Eldik, R. *Chem.—Eur. J.* **2007**, *13*, 4873–4883. (b) Hessenauer-Ilicheva, N.; Franke, A.; Meyer, D.; Woggon, W.-D.; van Eldik, R. *J. Am. Chem. Soc.* **2007**, *129*, 12473–12479. (c) Song, W. J.; Sun, Y. J.; Choi, S. K.; Nam, W. *Chem.—Eur. J.* **2006**, *12*, 130–137. (d) Nehru, K.; Seo, M. S.; Kim, J.; Nam, W. *Inorg. Chem.* **2007**, *46*, 293–298. (e) Park, M. J.; Lee, J.; Suh, Y.; Kim, J.; Nam, W. *J. Am. Chem. Soc.* **2006**, *128*, 2630–2634. (f) Song, W. J.; Seo, M. S.; DeBeer George, S.; Ohta, T.; Song, R.; Kang, M.-J.; Tosha, T.; Kitagawa, T.; Solomon, E. I.; Nam, W. *J. Am. Chem. Soc.* **2007**, *129*, 1268–1277.

(13) *Purification of Laboratory Chemicals*; Armarego, W. L. F., Perrin, D. D., Eds.; Pergamon Press: Oxford, U.K., 1997.

(14) (a) Traylor, T. G.; Miksztal, A. R. *J. Am. Chem. Soc.* **1987**, *109*, 2770–2774. (b) Bortolini, O.; Campestrini, S.; Di Furia, F.; Modena, G. *J. Org. Chem.* **1987**, *52*, 5093–5095.

(15) *Organic Syntheses*; Saltzman, H., Sharefkin, J. G., Eds.; Wiley: New York, 1973; Vol. *V*, p 658.

(16) La, T.; Miskelly, G. M.; Bau, R. *Inorg. Chem.* **1997**, *36*, 5321–5328.

(17) (a) de Visser, S. P. *J. Am. Chem. Soc.* **2006**, *128*, 9813–9824. (b) de Visser, S. P.; Tan, L. S. *J. Am. Chem. Soc.* **2008**, *130*, 12961–12974.

(18) de Visser, S. P. *Chem.—Eur. J.* **2006**, *12*, 8168–8177.

(19) (a) Becke, A. D. *J. Chem. Phys.* **1993**, *98*, 5648–5652. (b) Lee, C.; Yang, W.; Parr, R. G. *Phys. Rev. B* **1988**, *37*, 785–789.

(20) (a) Kumar, D.; de Visser, S. P.; Sharma, P. K.; Cohen, S.; Shaik, S. *J. Am. Chem. Soc.* **2004**, *126*, 1907–1920. (b) Kumar, D.; de Visser, S. P.; Shaik, S. *Chem.—Eur. J.* **2005**, *11*, 2825–2835. (c) de Visser, S. P.; Oh, K.; Han, A.-R.; Nam, W. *Inorg. Chem.* **2007**, *46*, 4632–4641. (d) Kim, S. J.; Latifi, R.; Kang, H. Y.; Nam, W.; de Visser, S. P. *Chem. Commun.* **2009**, 1562–1564.

(21) (a) Hay, P. J.; Wadt, W. R. *J. Chem. Phys.* **1985**, *82*, 270–283. (b) Hehre, W. J.; Ditchfield, R.; Pople, J. A. *J. Chem. Phys.* **1972**, *56*, 2257–2261.

(22) Frisch, M. J., Trucks, G. W.; Schlegel, H. B.; Scuseria, G. E.; Robb, M. A.; Cheeseman, J. R.; Montgomery, J. A., Jr.; Vreven, T.; Kudin, K. N.; Burant, J. C.; Millam, J. M.; Iyengar, S. S.; Tomasi, J.; Barone, V.; Mennucci, B.; Cossi, M.; Scalmani, G.; Rega N.; Petersson, G. A.; Nakatsuji, H.; Hada, M.; Ehara, M.; Toyota, K.; Fukuda, R.; Hasegawa, J.; Ishida, M.; Nakajima, T.; Honda, Y.; Kitao, O.; Nakai, N.; Klene, M.; Li, X.; Knox, J. E.; Hratchian, H. P.; Cross, J. B.; Adamo, C.; Jaramillo, J.; Gomperts, R.; Stratmann, R. E.; Yazyev, O.; Austin, A. J.; Cammi, R.; Pomelli, C.; Ochterski, J. W.; Ayala, P. Y.; Morokuma, K.; Voth, G. A.; Salvador, P.; Dannenberg, J. J.; Zakrzewski, V. G.; Dapprich, S.; Daniels, A. D.; Strain, M. C.; Farkas, O.; Malick, D. K.; Rabuck, A. D.; Raghavachari, K.; Foresman, J. B.; Ortiz, J. V.; Cui, Q.; Baboul, A. G.; Clifford, S.; Cioslowski, J.; Stefanov, B. B.; Liu, G.; Liashenko, A.; Piskorz, P.; Komaromi, I.; Martin, R. L.; Fox, D. J.; Keith, T.; Al-Laham, M. A.; Peng, C. Y.; Nanayakkara, A.; Challacombe, M.; Gill, P. M. W.; Johnson, B.; Chen, W.; Wong, M. W.; Gonzalez, C.; Pople, J. A. *Gaussian 03*, revision C.02; Gaussian, Inc.: Wallingford, CT, 2004.

(23) *Jaguar 7.0*; Schrödinger, LLC.: New York, 2007.

(24) (a) Hoe, W.-M.; Cohen, A.; Handy, N. C. *Chem. Phys. Lett.* **2001**, *341*, 319–328. (b) Perdew, J. P.; Burke, K.; Ernzerhof, M. *Phys. Rev. Lett.* **1996**, *77*, 3865–3868.

(25) (a) Perdew, J. P.; Chevary, J. A.; Vosko, S. H.; Jackson, K. A.; Pederson, M. R.; Singh, D. J.; Fiolhais, C. *Phys. Rev. B* **1992**, *46*, 6671–6687. (b) Becke, A. D. *J. Chem. Phys.* **1996**, *104*, 1040–1046.

(26) (a) Farinas, E. T.; Alcalde, M.; Arnold, F. *Tetrahedron* **2004**, *60*, 525–528. (b) Ruettinger, R. T.; Fulco, A. J. *J. Biol. Chem.* **1981**, *256*, 5728–5734.

(27) (a) Vaz, A. D. N.; McGinnity, D. F.; Coon, M. J. *Proc. Natl. Acad. Sci. U.S.A.* **1998**, *95*, 3555–3560. (b) Vaz, A. D. N.; Pernecky, S. J.; Raner, G. M.; Coon, M. J. *Proc. Natl. Acad. Sci. U.S.A.* **1996**, *93*, 4644–4648.

(28) Groves, J. T.; Gross, Z. In *Bioinorganic Chemistry: An Inorganic Perspective of Life*; Kessissoglon, D. P., Ed.; NATO Advanced Study Institute Series *459*; Kluwer Academic Publishers: Dordrecht, The Netherlands, 1995; pp 39−47.

(29) Song, W. J.; Ryu, Y. O.; Song, R.; Nam, W. *J. Biol. Inorg. Chem.* **2005**, *10*, 294–304.

(30) Takahashi, A.; Kurahashi, T.; Fujii, H. *Inorg. Chem.* **2007**, *46*, 6227–6229.

(31) Lim, M. H.; Jin, S. W.; Lee, Y. J.; Jhon, G. J.; Nam, W.; Kim, C. *Bull. Korean Chem. Soc.* **2001**, *22*, 93–96.

(32) Nam, W. In *Comprehensive Coordination Chemistry II*; Que, L., Jr., Tolman, W. B., Eds.; Elsevier: Oxford, U.K., 2003; Vol *8*, pp 281−307.

(33) (a) Ogliaro, F.; de Visser, S. P.; Groves, J. T.; Shaik, S. *Angew. Chem., Int. Ed.* **2001**, *40*, 2874–2878. (b) Schöneboom, J. C.; Neese, F.; Thiel, W. *J. Am. Chem. Soc.* **2005**, *127*, 5840–5853. (c) Groenhof, A. R.; Ehlers, A. W.; Lammertsma, K. *J. Am. Chem. Soc.* **2007**, *129*, 6204–6209. (d) Bathelt, C. M.; Zurek, J.; Mulholland, A. J.; Harvey, J. N. *J. Am. Chem. Soc.* **2005**, *127*, 12900–12908.

(34) Ghosh, A. *Acc. Chem. Res.* **1998**, *31*, 189–191.

(35) Green, M. T. *J. Am. Chem. Soc.* **1999**, *121*, 7939–7940.

(36) Shaik, S.; de Visser, S. P.; Ogliaro, F.; Schwarz, H.; Schröder, D. *Curr. Opin. Chem. Biol.* **2002**, *6*, 556–567.

(37) (a) de Visser, S. P.; Ogliaro, F.; Harris, N.; Shaik, S. *J. Am. Chem. Soc.* **2001**, *123*, 3037–3047. (b) de Visser, S. P.; Ogliaro, F.; Sharma, P. K.; Shaik, S. *J. Am. Chem. Soc.* **2002**, *124*, 11809–11826. (c) Kamachi, T.; Shiota, Y.; Ohta, T.; Yoshizawa, K. *Bull. Chem. Soc. Jpn.* **2003**, *76*, 721–732.

(38) Shaik, S.; Cohen, S.; de Visser, S. P.; Sharma, P. K.; Kumar, D.; Kozuch, S.; Ogliaro, F.; Danovich, D. *Eur. J. Inorg. Chem.* **2004**, 207–226.

(39) (a) Ogliaro, F.; Harris, N.; Cohen, S.; Filatov, M.; de Visser, S. P.; Shaik, S. *J. Am. Chem. Soc.* **2000**, *122*, 8977–8989. (b) Yoshizawa, K.; Kamachi, T.; Shiota, Y. *J. Am. Chem. Soc.* **2001**, *123*, 9806–9816. (c) Kamachi, T.; Yoshizawa, K. *J. Am. Chem. Soc.* **2003**, *125*, 4652–4661. (d) de Visser, S. P.; Kumar, D.; Cohen, S.; Shacham, R.; Shaik, S. *J. Am. Chem. Soc.* **2004**, *126*, 8362–8363. (e) Shaik, S.; Kumar, D.; de Visser, S. P. *J. Am. Chem. Soc.* **2008**, *130*, 10128–10140. (f) Balcells, D.; Raynaud, C.; Crabtree, R. H.; Eisenstein, O. *Chem. Commun.* **2008**, 744–746.

(40) Balding, P. R.; Porro, C. S.; McLean, K. J.; Sutcliffe, M. J.; Maréchal, J.-D.; Munro, A. W.; de Visser, S. P. *J. Phys. Chem. A* **2008**, *112*, 12911–12918.

(41) (a) de Visser, S. P.; Kaneti, J.; Neumann, R.; Shaik, S. *J. Org. Chem.* **2003**, *68*, 2903–2912. (b) Berkessel, A.; Adrio, J. A. *J. Am. Chem. Soc.* **2006**, *128*, 13412–13420.

(42) (a) Sharma, P. K.; de Visser, S. P.; Shaik, S. *J. Am. Chem. Soc.* **2003**, *125*, 8698–8699. (b) Kumar, D.; de Visser, S. P.; Sharma, P. K.; Hirao, H.; Shaik, S. *Biochemistry* **2005**, *44*, 8148–8158.

(43) de Visser, S. P. *J. Am. Chem. Soc.* **2006**, *128*, 15809–15818.

(44) Mayer, J. M. *Acc. Chem. Res.* **1998**, *31*, 441–450.

(45) Agarwala, A.; Bandyopadhyay, D. *Chem. Commun.* **2006**, 4823–4825.

JP9028694

Downloaded by INDIAN INST OF CHEMICAL TECH on October 30, 2009 | http://pubs.acs.org
Publication Date (Web): August 6, 2009 | doi: 10.1021/jp9028694

Electronic properties of pentacoordinated heme complexes in cytochrome P450 enzymes: search for an Fe(I) oxidation state

Cristina S. Porro,[a] Devesh Kumar[b] and Sam P. de Visser*[a]

Received 18th June 2009, Accepted 2nd September 2009
First published as an Advance Article on the web 22nd September 2009
DOI: 10.1039/b911966c

The cytochrome P450s are versatile enzymes that catalyze a range of monoxygenation reactions. Their catalytic cycle includes molecular oxygen binding and two reduction and protonation steps to create the active species, Compound I. In an anaerobic environment, however, only two reduction steps starting from the resting state can take place. Currently, very little information is known on this doubly-reduced species; therefore, we have performed a detailed density functional theory (DFT) and combined quantum mechanics/molecular mechanics (QM/MM) study on this complex. In principle, the doubly-reduced pentacoordinated heme can exist in two possible electronic configurations, namely an Fe(I) with closed-shell heme or an Fe(II) coupled to a heme anion radical [Fe^{II} $Por^{-\bullet}$]. Our calculations show that there are several close-lying spin states with a [Fe^{II} $Por^{-\bullet}$] configuration and these states are much lower in energy than the alternative [Fe^{I} Por^{0}] situation. We have calculated spectroscopic parameters of the lowest lying sextet spin state, including IR spectra and EPR parameters.

A. Introduction

The cytochrome P450s are ubiquitous heme enzymes involved in important bioprocesses in the body, such as the metabolism of drugs, the biosynthesis of hormones and detoxification processes in the liver.[1–4] As such, a lot of work has been devoted to the understanding of the mechanism of substrate oxidation by these enzymes. Generally, the P450s are heme enzymes that bind and utilize molecular oxygen and react with substrates as a monoxygenase.[1,5,6] However, despite extensive searches, its active oxidant remains elusive, although indirect evidence through kinetic isotope effects and product distributions point to an iron(IV)–oxo porphyrin cation radical (Compound I, Cpd I) as the most likely oxidant.[7,8] These studies are supported by theoretical modeling that indeed predicted the iron(IV)–oxo porphyrin cation radical intermediate in the catalytic cycle as an efficient oxidant of C–H hydroxylation, epoxidation and sulfoxidation reactions.[9–12] The P450s undergo a complicated catalytic cycle that starts from the resting state, where a water molecule is bound to the heme (Scheme 1). However, this water molecule is displaced after substrate (SubH) binding, which triggers a low-spin to high-spin transition of the heme to form structure **R**.[13] Subsequently, the heme is reduced to give an Fe(II) pentacoordinated heme (**S**). Under normal aerobic conditions this intermediate binds molecular oxygen, followed by another reduction step and two protonation processes to give Cpd I, the active oxidant.[14–16] However, under anaerobic conditions the catalytic cycle cannot proceed beyond **S**, although the heme can be reduced further to structure **D**, the doubly-reduced pentacoordinated complex. Recently, **D** was identified with electron paramagnetic resonance (EPR) and electron–nuclear double resonance (ENDOR) techniques.[17] It has been proposed that it may consist of either an Fe(II) coupled to a heme anion radical, [Fe^{II} $Por^{-\bullet}$] (**D**), or alternatively as an Fe^{I} with a closed-shell heme, [Fe^{I} Por^{0}] (**D′**).

Currently, it is unclear which of these electronic configurations corresponds to the pentacoordinated structure. However, if it is the [Fe^{II} $Por^{-\bullet}$], it would be the only P450 structure apart from Cpd I that contains a heme-based radical. Thus, to gain insight into this doubly-reduced pentacoordinated system and establish its spectroscopic properties, we have performed a series of density functional theory (DFT) and quantum mechanics/molecular mechanics (QM/MM) calculations on its structure and properties which we report in this work.

$P450_{BM3}$ has been used as a template for our DFT and QM/MM studies that focus on intermediates of the catalytic cycle of the enzyme under anaerobic conditions. $P450_{BM3}$ is a bacterial P450 enzyme that closely resembles human P450s and, as such, has been the focus of many experimental studies.[18,19] $P450_{BM3}$ catalyzes the hydroxylation of long chain fatty acids, such as *N*-palmitoylglycine and its active site is characterized by a central iron atom embedded in a heme group that is linked to the protein backbone *via* a thiolate linkage with a cysteinate group (Cys_{400}). Our studies focused on the following questions: (a) what is the electronic state of the doubly reduced pentacoordinated system, is it Fe(I) heme or an Fe(II) heme anion radical? (b) How does the surrounding protein influence spin state ordering and spectroscopic parameters?

[a] *The Manchester Interdisciplinary Biocenter and the School of Chemical Engineering and Analytical Science, The University of Manchester, 131 Princess Street, M1 7DN, Manchester, United Kingdom. E-mail: sam.devisser@manchester.ac.uk; Fax: +44-1613065201; Tel: +44-1613064882*
[b] *Molecular Modelling Group, Organic Division – I, Indian Institute of Chemical Technology, Hyderabad 500 607, India*

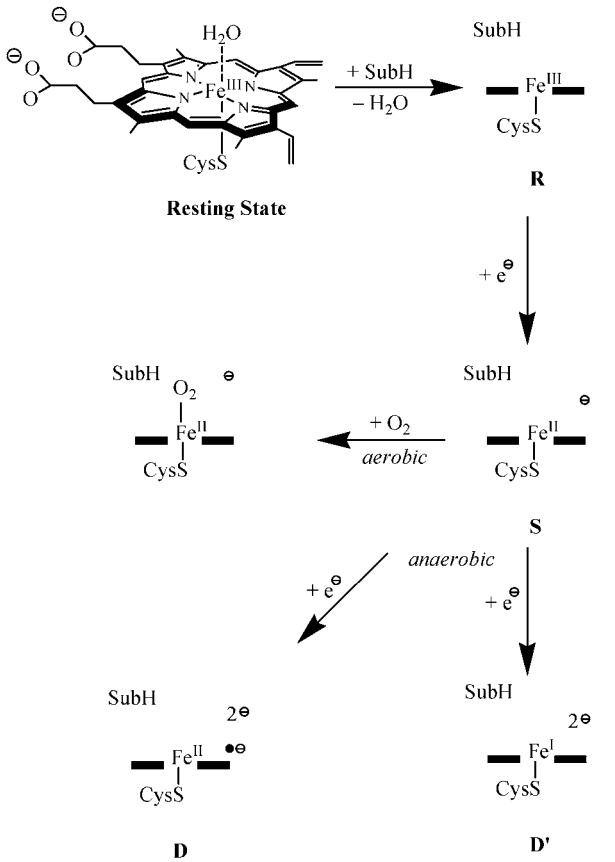

Scheme 1 Formation of **D** and **D′** from the resting state of P450.

B. Methods

The work contains two sets of calculations, one set utilizing DFT calculations on active site models of P450 enzymes, and another one consisting of full QM/MM calculations on the complete enzyme. For consistency, the DFT and QM/MM calculations use similar descriptions of the active site region and use the same DFT methods and basis sets throughout.

B1. DFT model calculations

Initial DFT studies were done on a small active site model of cytochrome P450 comprising iron–protoporphyrin IX (without side chains) and the axial cysteinate ligand replaced by thiolate, similar to previous studies of ours and others in the field.[20–23] This minimal model of **D** has the stoichiometry $FeC_{20}H_{13}N_4S$, overall charge −2 and spin multiplicity doublet, quartet or sextet. Full geometry optimizations were performed in Jaguar 7.0 with the unrestricted hybrid density functional method (UB3LYP).[24–26] These studies used a modest Los Alamos-type double-ζ quality basis set LACVP on iron that includes a core potential, while all other atoms are described by a 6-31G basis set: basis set B1.[27] Subsequent single point calculations with LACV3P+ on iron and 6-311++G** on the rest of the atoms confirmed the electronic situations and relative energies, designated LACV3P++** or basis set B2. Analytical frequency calculations at the UB3LYP/B1 level of theory confirmed the structures as local minima and were performed in GAUSSIAN 03.[28] All frequencies reported in this work were scaled with a factor of 0.9614 as proposed by Scott and Radom.[29] To test the effect of the basis set on the optimized geometries, all structures were reoptimized in GAUSSIAN using the LACVP** basis set, basis set B3.

To test the effects of the environment on the relative energies and spin state ordering of the structures, we carried out additional single point calculations on the optimized gas phase geometries using (i) a dielectric constant, (ii) the addition of two hydrogen bonded ammonia molecules pointing toward the thiolate that mimic the interactions in the protein, (iii) a combination of the effects described in (i) and (ii), and (iv) full quantum mechanics/molecular mechanics (QM/MM) optimizations (see next section for details). The calculations done with a dielectric constant follow similar procedures as we used before in Jaguar 7.0, using the self-consistent reaction field model,[30–32] whereby three different dielectric constants with values of $\varepsilon = 5.708$ (probe radius = 2.72 Å), $\varepsilon = 35.74$ (probe radius = 2.73 Å) and $\varepsilon = 80.37$ (probe radius = 1.40 Å) were employed. Our previous work showed that the electronic description of the thiolate ligand, in particular of Cpd I, is strongly influenced by hydrogen bonding interactions as they appear in the protein.[33] In the past, we mimicked these interactions faithfully by the addition of two hydrogen-bonded ammonia molecules pointing toward the thiolate group.[34,35] To test the effect of hydrogen bonding toward the thiolate in the studies presented here, we took the geometries of these ammonia molecules from ref. 33 and added those to our optimized geometries and ran a single point calculation at the UB3LYP/B1 level of theory.

In addition, we tested the effect of an applied electric field on the spin state ordering and electronic descriptions. This was done using literature procedures[36–38] by the addition of an electric field along one of the principal axes of the molecule. Here, applied electric fields in the range of ±0.015 au (±77 MV cm^{-1}) are used, whereas typical values of induced electric fields by a protein are 10 MV cm^{-1}. The applied electric field effects studied here should therefore be seen as upper values to what may be expected in the protein.

These methods have been commonly used in our groups and were carefully benchmarked against experimental data. Thus, for a range of hydrogen abstraction barriers by iron(IV)–oxo oxidants, a linear correlation with C–H bond dissociation energy of the substrate was found, with a spread of energies of 1–2 kcal mol^{-1}.[39,40] Moreover, experimentally-determined free energies of activation were reproduced within 3 kcal mol^{-1} with B3LYP calculations.[41–44] Further assessment of the computational data against experimentally-determined kinetic isotope effects of hydrogen abstraction reactions and spectroscopic data were favourable.[45,46]

In addition, we ran a series of benchmark studies using alternative density functional methods to ascertain whether B3LYP can correctly reproduce spin state ordering and relative energies of these iron–porphyrin complexes. Single point calculations were performed on the B3LYP/B1 optimized geometries using GAUSSIAN 03, employing either the BP86,[47,48] OPBE,[49,50] PW91B95,[51,52] B3P86,[25,48] B3PW91,[25,51] or B3LYP with 15% exchange included. It has been suggested that, for transition metal complexes, 15% exchange provides more accurate energetics.[53,54] However, in

 This journal is © the Owner Societies 2009

our calculations only minor differences from the B3LYP results are found. Thus, all methods predict the doublet spin state below the quartet while doublet–quartet energy gaps of ΔE_{DQ} = 3.6, 7.4, 6.0, 7.8, 1.6, 2.1 and 4.3 kcal mol^{-1} are found for B3LYP, BP86, OPBE, PW91B95, B3P86, B3PW91 and B3LYP(15% exchange), respectively. Furthermore, the doublet–sextet energy difference is −5.6, −1.8, −6.8, −9.3 and −2.9 kcal mol^{-1} for B3LYP, OPBE, B3P86, B3PW91 and B3LYP(15% exchange) in favor of the sextet spin state. Thus, alternative DFT methods reproduce the spin state ordering and give the same low-lying electronic states with the same orbital occupation. Moreover, the B3LYP result is the closest to the median value in most cases and therefore the most appropriate to use.

B2. QM/MM calculations

Full QM/MM calculations started from a substrate-free $P450_{BM3}$ structure[55] and followed previous procedures in the field.[56–58] The starting point of the calculations was taken from ref. 58, which includes monomer A of the 1JPZ pdb file, and where the substrate *N*-palmitoylglycine is replaced by dimethylsulfide and hydrogen atoms added to the protein. The protonation state of all histidine residues was carefully checked: His_{66}, His_{123}, His_{210}, His_{287} were protonated at the ND1 atom only, His_{397} was protonated on the NE2 atom only, and all other histidine amino acids were taken as doubly protonated. The system was solvated in a 15 Å layer of water molecules in a truncated octahedral box with a total of about 52 000 atoms and a net charge of −9. Subsequently, a molecular dynamics equilibration at 300 K was carried out for 400 ps in AMBER using the FF94 force field.[59,60] After equilibration, structures were analyzed and low energy snapshots were selected from the molecular dynamics simulations and used as a starting point for the QM/MM calculations. The protein and a 5 Å layer of solvent (water) molecules was selected to create a system with a total of 10 179 atoms. The QM region contains the heme without side chains, iron and thiolate for cysteinate. Full geometry optimizations on all atoms in the system (QM as well as MM region) were performed in the doublet, quartet and sextet spin states using the ONIOM program package[61] as implemented in GAUSSIAN 03.[28] The QM region was described with UB3LYP/LANL2DZ, and the MM region with a UFF force field.[62] We also tested the use of Amber for the MM region but very little difference was found with respect to the UFF results.[58] Initial calculations used the LANL2DZ basis set (basis set B1), but additional single point calculations with an LACVP** basis set (basis set B3) were performed to confirm the energetics. These calculations did not change the spin state ordering and relative energies. ONIOM uses the link-atom method that replaces a covalent bond on the boundary between the QM and MM regions with a C–H bond,[63] and includes mechanical embedding of the protein into the QM region. We ran single point calculations on the optimized doublet, quartet and sextet spin state structures, including electronic embedding of the MM region into the QM Hamiltonian. Relative energies obtained were 0.0, 1.2 and −4.8 kcal mol^{-1} for the doublet, quartet and sextet, respectively, whereas values of 0.0, 2.5 and −4.1 kcal mol^{-1} were found with mechanical embedding only. Therefore, electronic embedding has very little effect on the relative energies of the individual spin states and the spin state ordering.

In addition, we calculated zero-field splitting parameters and EPR *g*-parameters of our models using methods taken from the literature.[64,65]

C. Results and discussion

Substrate binding to the active site of P450 enzymes releases the water molecule from the sixth binding site of the active site heme to give a pentacoordinated iron(III)-heme, **R**. This process is accomplished with a doublet to sextet spin state crossing that triggers an electron transfer process from the reductase domain to the active center to form **S**.[13,66] In our system, the pentacoordinated system is doubly-reduced, **D**. Let us first start with a description of the electron transfer processes in these reduction mechanisms. Fig. 1 shows the high-lying occupied and low-lying virtual orbitals of the pentacoordinated iron–heme systems as they appear in *e.g.* cytochrome P450 enzymes, as well as the electron transfer processes for the two reduction steps starting from **R**, *via* the singly reduced pentacoordinated species (**S**) leading to **D**.

On the right-hand-side of Fig. 1 we show the orbitals originating from the 3d metal orbitals, which split into the typical $3t_{2g} - 2e_g$ pattern of orbitals with three low-lying nonbonding orbitals on the metal ($3d_{xy}$, $3d_{xz}$ and $3d_{yz}$) and two higher lying antibonding orbitals ($\sigma^*_{x^2-y^2}$ and $\sigma^*_{z^2}$). The two σ* orbitals result from the antibonding combination of the mixing of the $3d_{x^2-y^2}$ orbital on iron with 2p orbitals on the four nitrogen atoms of the heme (in $\sigma^*_{x^2-y^2}$) and through mixing of the $3d_{z^2}$ orbital on iron with a lone pair orbital on the thiolate (in $\sigma^*_{z^2}$). On the top, we show one of the virtual heme-type orbitals of **R**, with e_g symmetry labeled as e_g*. This pair of e_g* orbitals is virtual in the resting state (**R**) and its reduced form (**S**) but these orbitals become accessible for **D**. This set of orbitals is occupied by five electrons in **R** in an overall sextet, quartet or doublet spin state with either configuration ^{6}**R** = $3d_{xy}^1\ 3d_{xz}^1\ 3d_{yz}^1\ \sigma^*_{z^2}{}^1\ \sigma^*_{x^2-y^2}{}^1$, ^{4}**R** = $3d_{xy}^2\ 3d_{xz}^1\ 3d_{yz}^1\ \sigma^*_{z^2}{}^1$ or ^{2}**R** = $3d_{xy}^2\ 3d_{xz}^2\ 3d_{yz}^1$ (Fig. 1). In all three spin states, the metal 3d block is occupied by five electrons, hence the metal is in oxidation state Fe^{III}, regardless of the overall spin state. EPR spectroscopy studies showed that, with a water molecule in the sixth binding site, the ground state is doublet spin state (^{2}**R**), but in the pentacoordinated form, the sextet state is the ground state.[13,66] DFT and QM/MM studies confirmed this spin state ordering.[67–69]

Also given in Fig. 1 are the electron transfer processes from ^{2,4,6}**R** to form ^{1,3,5}**S**. A one-electron reduction of ^{6}**R** gives a quintet spin state structure, and filling of the $3d_{xy}$ orbital with a second electron results in occupation ^{5}**S** = $3d_{xy}^2\ 3d_{xz}^1\ 3d_{yz}^1\ \sigma^*_{z^2}{}^1\ \sigma^*_{x^2-y^2}{}^1$. By contrast, reduction of ^{4}**R** can also give this ^{5}**S** state or, alternatively, the ^{3}**S** state with occupation $3d_{xy}^2\ 3d_{xz}^2\ 3d_{yz}^1\ \sigma^*_{z^2}{}^1$. Reduction of ^{2}**R** connects to the ^{3}**S** state as well or gives a closed-shell singlet (^{1}**S**) with occupation $3d_{xy}^2\ 3d_{xz}^2\ 3d_{yz}^2$. DFT and QM/MM calculations[67,68] both predict a

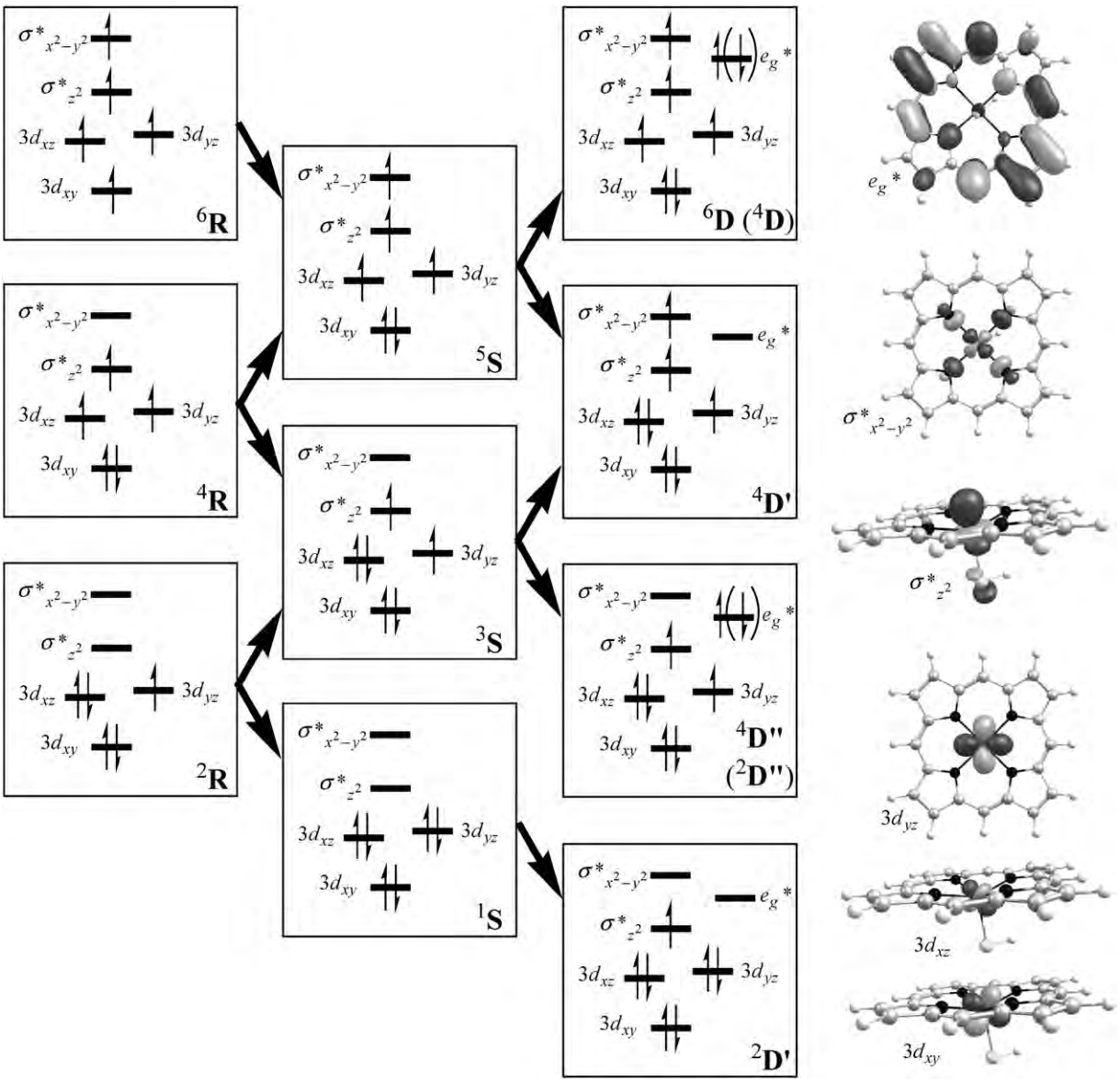

Fig. 1 Orbital occupation of the low-lying spin states of **R**, **S** and **D**, their electron transfer processes, and drawings of the relevant orbitals.

quintet spin ground state for **S** with Mössbauer parameters in good agreement with experimentally measured ones.[70]

In this work, we studied systems that are reduced further with one more electron to give **D**, which gives a multitude of possible electronic configurations and some of these are given in Fig. 1. For example, a one-electron reduction of ^{5}**S** can lead to an electron transfer into a low-lying virtual heme orbital, such as e_g*, to give ^{4,6}**D** = $3d_{xy}^2\ 3d_{xz}^1\ 3d_{yz}^1\ \sigma^*_{z^2}{}^1\ \sigma^*_{x^2-y^2}{}^1\ e_g{}^{*1}$. In this case, the spin in the e_g* orbital is ferromagnetically coupled to the metal based spins into an overall sextet spin state (in ^{6}**D**) or antiferromagnetically coupled into an overall quartet spin state (in ^{4}**D**). These two electronic states have the metal in oxidation state Fe^{II} and the porphyrin group singly-reduced (Fe^{II} $Por^{-\bullet}$). Alternatively, the extra electron can be donated into the 3d metal system (into $3d_{xz}$) to create an electronic situation with the metal in oxidation state Fe^{I} and a neutral heme (^{4}**D**′ = Fe^{I} Por^0). This state is also accessible through the reduction of ^{3}**S**. In addition, reduction of ^{3}**S** can give rise to a pair of degenerate doublet and quartet spin states with occupation ^{2,4}**D**′′ = $3d_{xy}^2\ 3d_{xz}^2\ 3d_{yz}^1\ \sigma^*_{z^2}{}^1\ e_g{}^{*1}$.

DFT and QM/MM optimized geometries of **D** of the lowest-lying doublet, quartet, and sextet spin states are shown in Fig. 2. In all cases, the sextet spin state is the ground state with the doublet and quartet spin states at least 5.5 kcal mol^{-1} higher. With the small DFT model, ^{6}**D** is considerably more stable than the doublet and quartet spin state structures. The latter two states are characterized as ^{2,4}**D**′′ with $3d_{xy}^2\ 3d_{xz}^2\ 3d_{yz}^1\ \sigma^*_{z^2}{}^1\ e_g{}^{*1}$ configuration. This assignment is supported by the group spin densities (ρ) shown in Fig. 2. The relative energies between ^{6}**D** and ^{4,2}**D**′′ are equally perturbed by the MM region and the energy difference from an MM calculation on the full structure and an MM calculation on the QM region is less than 0.6 kcal mol^{-1}.

Using the DFT model complex, we also located ^{4}**D** with electronic configuration $3d_{xy}^2\ 3d_{xz}^1\ 3d_{yz}^1\ \sigma^*_{z^2}{}^1\ \sigma^*_{x^2-y^2}{}^1\ e_g{}^{*1}$ that was found to be isoenergetic to ^{6}**D**, however, attempts to

 This journal is © the Owner Societies 2009

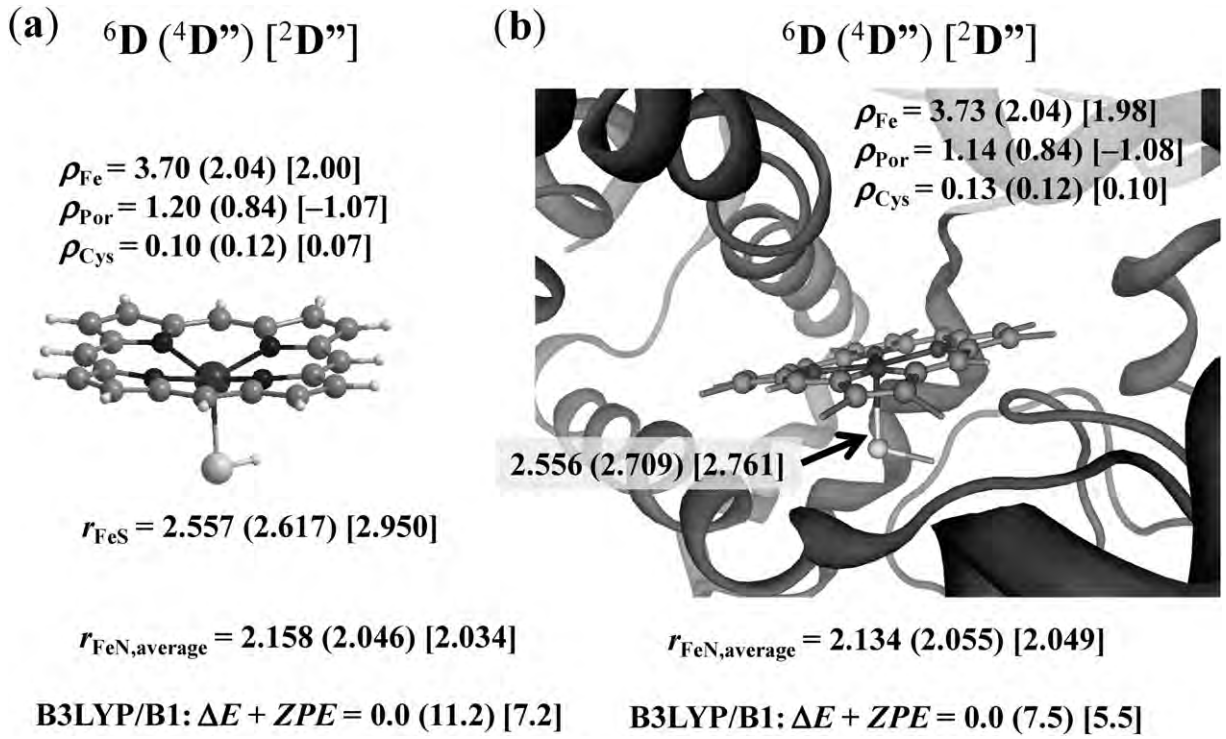

Fig. 2 Optimized geometries of ^{2,4,6}**D** as calculated with a gas-phase DFT model (part a) or QM/MM (part b). Bond lengths are in Å and relative energies in kcal mol^{-1}.

locate ^{4}**D** in QM/MM failed and converged back to ^{4}**D**′′ instead. Nevertheless, it is clear from both DFT and QM/MM that the ground state of **D** is an [Fe^{II} Por$^{-\bullet}$]. All attempts to find an electronic state with overall quartet or doublet spin with the metal in oxidation state Fe^I as in ^{4,2}**D**′ (Fig. 1) failed and each time converged back to one of the [Fe^{II} Por$^{-\bullet}$] situations described above. A time-dependent density functional theory (TD-DFT) calculation on the optimized doublet and quartet spin state geometries implicated that the excitations from the [Fe^{II} Por$^{-\bullet}$] state to the lowest lying Fe^I solution requires 52.3 and 53.4 kcal mol^{-1}, respectively, and represents an excitation of a β-spin electron from e_g* to $\sigma^*_{x^2-y^2}$ (quartet) to form ^{4}**D**′ or an excitation to $3d_{yz}$ (doublet) to form ^{2}**D**′. Although TD-DFT may considerably overestimate these relative energies, it is clear that the [Fe^I Por^0] solution is a high-lying excited state that will not be accessible to the protein. Note that no low-lying sextet spin state can form an Fe^I solution due to an already fully occupied 3d metal block. Thus, the Fe^I oxidation states are high-lying electronic states that will not be accessible in the gas phase.

Optimized geometries obtained with the small DFT model compare well with full QM/MM calculations. As can be seen from Fig. 2, the Fe–S distance is relatively long (>2.5 Å) and the iron is significantly displaced from the plane of the heme. This is presumably due to the fact that the sixth ligand site of the metal is vacant and the thiolate pulls the iron below the plane of the heme, a fact that has been shown before in pentacoordinated systems.[10,68,69,71,72] Thus, Altun and Thiel[69] find QM/MM optimized geometries with Fe–S distances of 2.349 and 2.413 Å for ^{6,4}**R**. Our system, however, has two extra electrons in the 3d metal system and, in particular, filling of the $\sigma^*_{z^2}$ orbital with one electron enhances the Fe–S bond significantly. Therefore, our optimized geometries are in good agreement with related structures from the literature. The sextet spin state has considerably smaller Fe–S distances of 2.557 (DFT) and 2.556 (QM/MM) Å than those obtained in the doublet and quartet spin states, where values around 2.7 Å (QM/MM) are found. These differences in Fe–S bond length lead to a shift of the Fe–S stretch vibration that shifts from 223.7 cm^{-1} for the sextet spin structure to 137.3 (quartet) and 131.5 (doublet) cm^{-1}.

In order to find out what the effect of the environment is on the relative energies of the various spin states and whether a system with an Fe^I oxidation state, such as ^{4,2}**D**′, can be stabilized in a more polar environment, we did an extensive set of extra calculations that take the perturbation due to the local environment into effect. Firstly, we studied the doublet, quartet and sextet spin state structures in a dielectric constant (ε) ranging in magnitude from 5.7 to 80. Fig. 3 shows the group spin densities (ρ) and relative energies of the doubly-reduced pentacoordinated systems in the doublet, quartet and sextet spin states as obtained in dielectric constants ranging from ε = 5.7 to 80.3 (water). As follows from Fig. 3, the group spin densities are virtually the same regardless of the dielectric constant and imply that the electronic state and orbital occupation stays the same regardless of whether a polar environment is applied to the system. Moreover, the spin densities obtained from the dielectric constant calculations are close to the gas phase and QM/MM data reported above in Fig. 2. Note that in a dielectric constant, ^{2}**D**′′ is stabilized with respect to the gas phase and QM/MM energies shown above in Fig. 2. Interestingly, in a dielectric constant mimicking a water

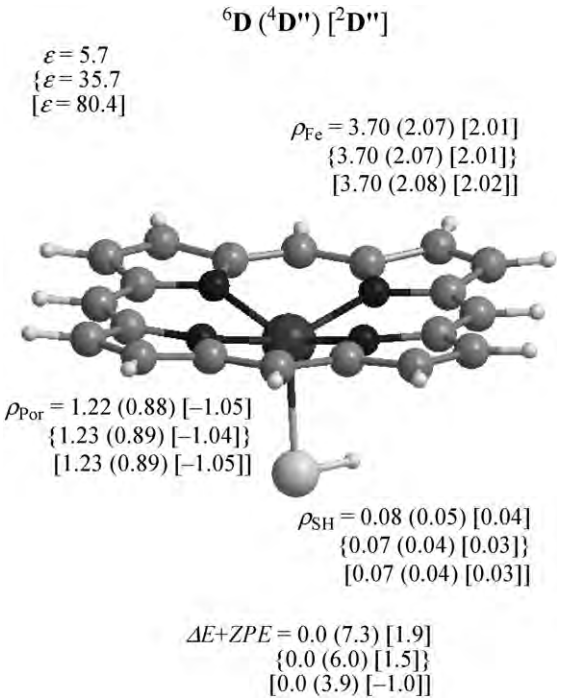

Fig. 3 Single point calculations on ^{6}**D** and ^{4,2}**D**′′ with a dielectric constant included. Data reported are group spin densities (ρ) and relative energies.

solution, ^{2}**D**′′ becomes the ground state, although only by a small margin. Therefore, a dielectric constant changes the spin state ordering of the individual electronic states. However, the protein in the enzyme will induce a dielectricum on the active site that is far below that of water, so that a sextet spin state is more likely in the enzyme, in agreement with the QM/MM studies reported above.

Further studies with the addition of two hydrogen-bonded ammonia molecules that mimic the hydrogen bonding interactions toward the thiolate ligand in the protein environment were performed for the sextet spin state. The thus-obtained group spin densities in the gas phase, as well as with an additional dielectric constant specified, gave group spin densities that are virtually identical to those shown in Fig. 3 for the systems without hydrogen-bonded ammonia molecules. This is not surprising because the thiolate ligand is closed shell in all systems studied here and only participates in the singly occupied $\sigma^*_{z^2}$ orbital. Calculations on CpdI of P450 showed that it has a singly-occupied molecular orbital with mixed heme and thiolate character.[33] Hydrogen bonding interactions toward the thiolate in the case of CpdI change the ratio of heme *versus* thiolate character of this singly occupied orbital and thereby change the group spin densities and charges.[33] Here, the effect of these hydrogen bonding interactions is negligible, as also follows from the difference between the DFT and QM/MM optimized geometries shown in Fig. 2.

Subsequently, we tested the effect of an applied electric field on the charge and spin distributions of the systems, see Fig. 4. It was shown that an applied electric field effect can change the charge and spin distributions of heme systems and thereby influence the regioselectivity of C=C double bond epoxidation

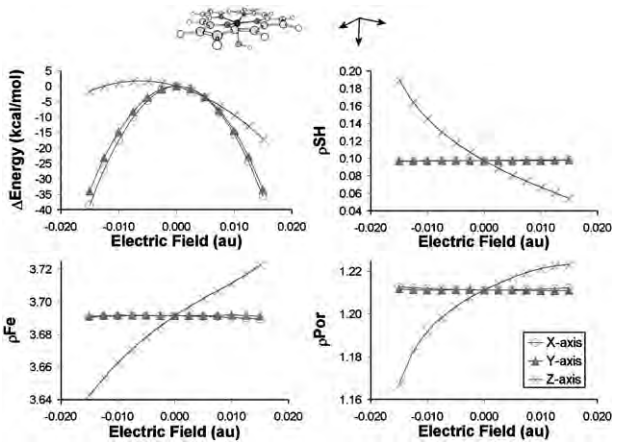

Fig. 4 Effect of an external electric field on the group spin densities and energies of ^{6}**D**.

versus C–H hydroxylation.[36] Moreover, DFT calculations on cytochrome c peroxidase (CcP) CpdI predicted a situation in the gas phase with two unpaired electrons on the metal coupled to a protein radical on a nearby tryptophan residue.[37] However, the calculations showed that with an applied electric field on CcP CpdI, the system changed from a tryptophan radical to a heme radical due to these perturbations.[37]

The calculations on ^{6}**D** with an external electric field along the molecular *x*-, *y*-, or *z*-axis changes the group spin densities and charges by less than 5% (see Fig. 4). In particular, an applied electric field along the *x*- or *y*-axis has negligible effect on the group spin densities and relative energies. Although some minor changes in spin densities are observed with a field along the *z*-axis, this does not change the electronic state of any of the spin states studied. A field along the *z*-axis displaces spin density from the thiolate to the heme and iron groups. Therefore, in the gas phase, as well as under environmental perturbations, the lowest lying configuration is [Fe^{II} $Por^{-\bullet}$], generally with a ^{6}**D** ground state. Perturbations through an external electric field, a dielectric constant or hydrogen bonding do not change the nature of the electronic ground state and this orbital occupation and oxidation state are retained. Furthermore, no evidence of a low-lying electronic state with the metal in oxidation state Fe(I) is found.

Finally, to check that the nature of the density functional method does not influence the results, we reoptimized the structures with the PBE0 and BP86 density functionals instead.[48,50] The spin state ordering obtained with PBE0 is similar to that found with the B3LYP density functional, but with BP86 the ordering of the spin states is reversed and the doublet spin state is the ground state. Nevertheless, all methods predict an [Fe^{II} $Por^{-\bullet}$] ground state with close-lying spin states.

In summary, we performed an extensive set of calculations on DFT model complexes with various external perturbations included (see above). Addition of a dielectric constant or hydrogen bonding interactions to the thiolate group do not change the spin state ordering or give evidence of a low-lying [Fe^{I} Por^{0}] complex. Subsequent calculations with an applied electric field along the molecular *x*-, *y*- or *z*-axis also did not lead to an [Fe^{I} Por^{0}] solution. It appears, therefore, that the

 This journal is © the Owner Societies 2009

Table 1 Excitation energies (Δ_i) from the sextet spin ground state to higher lying states. Orbital occupation, total spin multiplicity (S) and zero-field splitting parameters (D_i) are given

	Orbital occupation							
S	$3d_{xy}$	$3d_{xz}$	$3d_{yz}$	$\sigma^*_{z^2}$	$\sigma^*_{x^2-y^2}$	e_g*	Δ_i/cm^{-1}	D_i [a]/cm^{-1}
5/2	2	1	1	1	1	1		
5/2	1	2	1	1	1	1	2433	16.4
5/2	1	1	2	1	1	1	2433	16.4
5/2	1	1	1	2	1	1	5063	7.9
3/2	2	2	1	1	0	1	2623	9.5
3/2	2	1	2	1	0	1	2623	9.5

[a] Estimated using eqn (1).

[Fe^{I} Por^{0}] solution is a high-lying excited state that will not be accessible in the protein.

Subsequently, we decided to calculate several spectroscopic parameters of our ground state structures. First, we focused on the zero-field splitting (ZFS), which can be described as a function of spin–orbit coupling factors arising from excited state contributions with equal overall spin to the ground state or one spin unit higher or lower than the ground state.[64] In our case, the ground state is the sextet spin state and all orbitals shown in Fig. 1 above are occupied with at least one electron. As a consequence, excitations from the sextet to the lowest-lying octet spin state require an excitation to a high-lying orbital and its contribution to the ZFS value will be negligible. Therefore, only excitations from the ground state sextet and higher-lying sextet and quartet spin states have been considered here. The ZFS value D_i is estimated using a common literature procedure,[64,65] which we will briefly summarize here. Thus, D_i contains contributions of one-electron excitations to other sextet spin states or quartet spin states as described by eqn (1). In eqn (1), Δ_i is the vertical excitation energy from the sextet ground state. The sextet spin state values were determined from TD-DFT calculations on the ground state. The lowest excitation leading to a quartet spin state gives the ^{4}**D**′′ structure described above in Fig. 1 and 2 and has Δ_i = 7.5 kcal mol^{-1} (2623 cm^{-1}). All other quartet spin excitations were determined from a TD-DFT calculation on ^{4}**D**′′. The covalency factors (γ_i) for each of the orbitals shown above in Fig. 1 are determined from orbital occupations of the natural orbital analysis and the spin–orbit coupling constant (ζ) is taken as 500 cm^{-1}.[73]

$$D_i = D^{S=\frac{5}{2}} + D^{S=\frac{3}{2}} = \frac{1}{S^2}\sum_{ij}\gamma_i\gamma_j\frac{\zeta^2}{\Delta_i} + \frac{1}{S(2S-1)}\sum_{ij}\gamma_i\gamma_j\frac{\zeta^2}{\Delta_i} \quad (1)$$

Thus, the lowest sextet spin excitations correspond to $3d_{xy} \rightarrow 3d_{xz}/3d_{yz}$, and somewhat higher in energy is the $3d_{xy} \rightarrow \sigma^*_{z^2}$ excitation. All other sextet spin excitations were found to be well above 10 000 cm^{-1} and were therefore ignored. One electron excitations from a sextet to a quartet spin state correspond to $\sigma^*_{x^2-y^2} \rightarrow 3d_{xz}/3d_{yz}$, whereas all other excitations are much higher in energy. In this way, the sum of all D_i values in Table 1 enables us to estimate a ZFS value of 58.8 cm^{-1} for structure ^{6}**D**.

In a similar fashion, we determined EPR parameters for the sextet spin ground state. Thus, the in-plane components of the magnetic g-tensor are affected by spin–orbit coupling due to excitations from the ground state to higher lying sextet spin states *via* $g_x = g_y = g_\perp = g_e + \Delta g_\perp$ with g_e being the value for the free electron. Similarly to eqn (1) above, the term $\Delta g_\perp$ can be estimated using TD-DFT from the vertical excitation energies, Δ_i, as described by eqn (2). In this particular case, excitations from a half-filled orbital into an empty one have a negative sign, while those from a filled to a half-filled orbital have positive sign. All transitions shown in Table 1 correspond to transitions from a filled to a half-filled orbital and give a value $\Delta g_\perp$ = 0.20 and $g_\perp$ = 2.20. This value is in excellent agreement with the experimentally-determined EPR value of Davydov and Hoffman[17] on this species, who reported a value $g_\perp$ = 2.25.

$$\Delta g_\perp = \frac{1}{S}\sum_{ij}\gamma_i\gamma_j\frac{\zeta}{\Delta_i} \quad (2)$$

D. Conclusions

In summary, DFT and QM/MM calculations have been performed on a doubly-reduced pentacoordinated complex. This complex has a large manifold of accessible spin states and the lowest of these have an [Fe^{II} $Por^{-\bullet}$] configuration. Our calculations show that an alternative [Fe^{I} Por^{0}] state is high in energy and will not be an accessible spin state structure. Our calculated EPR parameters confirm ^{6}**D** as the ground state.

Acknowledgements

The research was supported by a studentship to C.S.P. from a Doctoral Training Award (DTA) from the Engineering and Physical Sciences Research Council (EPSRC, UK). In addition, calculations were done with CPU time provided by the National Service of Computational Chemistry Software (NSCCS). D.K. is the Ramanujan Fellow of the Department of Science and Technology (New Delhi, India). Prof Roman Davydov, Prof Frank Neese and Dr Stephen Rigby are acknowledged for fruitful discussions about the paper.

References

1 M. Sono, M. P. Roach, E. D. Coulter and J. H. Dawson, *Chem. Rev.*, 1996, **96**, 2841.
2 J. T. Groves, *Proc. Natl. Acad. Sci. U. S. A.*, 2003, **100**, 3569.
3 *Cytochrome P450: Structure, Mechanism and Biochemistry*, ed. P. R. Ortiz de Montellano, 3rd edn, Kluwer Academic/Plenum Publishers, New York, 2004.
4 A. W. Munro, H. M. Girvan and K. J. McLean, *Nat. Prod. Rep.*, 2007, **24**, 585.
5 F. P. Guengerich, *Chem. Res. Toxicol.*, 2001, **14**, 611.
6 W. Nam, *Acc. Chem. Res.*, 2007, **40**, 522.
7 T. Egawa, H. Shimada and Y. Ishimura, *Biochem. Biophys. Res. Commun.*, 1994, **201**, 1464.
8 D. G. Kellner, S. C. Hung, K. E. Weiss and S. G. Sligar, *J. Biol. Chem.*, 2002, **277**, 9641.
9 B. Meunier, S. P. de Visser and S. Shaik, *Chem. Rev.*, 2004, **104**, 3947.
10 S. Shaik, D. Kumar, S. P. de Visser, A. Altun and W. Thiel, *Chem. Rev.*, 2005, **105**, 2279.
11 E. Derat, D. Kumar, H. Hirao and S. Shaik, *J. Am. Chem. Soc.*, 2005, **128**, 473.

12 S. Shaik, H. Hirao and D. Kumar, *Nat. Prod. Rep.*, 2007, **24**, 533.
13 S. G. Sligar, *Biochemistry*, 1976, **15**, 5399.
14 G. H. Loew and D. L. Harris, *Chem. Rev.*, 2000, **100**, 407.
15 M. T. Green, J. H. Dawson and H. B. Gray, *Science*, 2004, **304**, 1653.
16 A. R. Groenhof, A. W. Ehlers and K. Lammertsma, *J. Am. Chem. Soc.*, 2007, **129**, 6204.
17 R. Davydov and B. M. Hoffman, *J. Biol. Inorg. Chem.*, 2008, **13**, 357.
18 H. Y. Li and T. L. Poulos, *Nat. Struct. Biol.*, 1997, **4**, 140.
19 I. F. Sevrioukova, H. Y. Li, H. Zhang, J. A. Peterson and T. L. Poulos, *Proc. Natl. Acad. Sci. U. S. A.*, 1999, **96**, 1863.
20 M. T. Green, *J. Am. Chem. Soc.*, 1999, **121**, 7939.
21 S. P. de Visser, S. Shaik, P. K. Sharma, D. Kumar and W. Thiel, *J. Am. Chem. Soc.*, 2003, **125**, 15779.
22 C. M. Bathelt, J. Zurek, A. J. Mulholland and J. N. Harvey, *J. Am. Chem. Soc.*, 2005, **127**, 12900.
23 S. P. de Visser and L. S. Tan, *J. Am. Chem. Soc.*, 2008, **130**, 12961.
24 Jaguar 7.0, Schrödinger, LLC., New York, NY, 2007.
25 A. D. Becke, *J. Chem. Phys.*, 1993, **98**, 5648.
26 C. Lee, W. Yang and R. G. Parr, *Phys. Rev. B*, 1988, **37**, 785.
27 P. J. Hay and W. R. Wadt, *J. Chem. Phys.*, 1985, **82**, 270.
28 M. J. Frisch, G. W. Trucks, H. B. Schlegel, G. E. Scuseria, M. A. Robb, J. R. Cheeseman, J. A. Montgomery, Jr, T. Vreven, K. N. Kudin, J. C. Burant, J. M. Millam, S. S. Iyengar, J. Tomasi, V. Barone, B. Mennucci, M. Cossi, G. Scalmani, N. Rega, G. A. Petersson, H. Nakatsuji, M. Hada, M. Ehara, K. Toyota, R. Fukuda, J. Hasegawa, M. Ishida, T. Nakajima, Y. Honda, O. Kitao, N. Nakai, M. Klene, X. Li, J. E. Knox, H. P. Hratchian, J. B. Cross, C. Adamo, J. Jaramillo, R. Gomperts, R. E. Stratmann, O. Yazyev, A. J. Austin, R. Cammi, C. Pomelli, J. W. Ochterski, P. Y. Ayala, K. Morokuma, G. A. Voth, P. Salvador, J. J. Dannenberg, V. G. Zakrzewski, S. Dapprich, A. D. Daniels, M. C. Strain, O. Farkas, D. K. Malick, A. D. Rabuck, K. Raghavachari, J. B. Foresman, J. V. Ortiz, Q. Cui, A. G. Baboul, S. Clifford, J. Cioslowski, B. B. Stefanov, G. Liu, A. Liashenko, P. Piskorz, I. Komaromi, R. L. Martin, D. J. Fox, T. Keith, M. A. Al-Laham, C. Y. Peng, A. Nanayakkara, M. Challacombe, P. M. W. Gill, B. Johnson, W. Chen, M. W. Wong, C. Gonzalez and J. A. Pople, *GAUSSIAN03 (Revision C.01)*, Gaussian, Inc., Wallingford, CT, 2004.
29 A. P. Scott and L. Radom, *J. Phys. Chem.*, 1996, **100**, 16502.
30 S. P. de Visser, *Chem.–Eur. J.*, 2006, **12**, 8168.
31 S. P. de Visser, *J. Am. Chem. Soc.*, 2006, **128**, 15809.
32 S. P. de Visser, *Chem.–Eur. J.*, 2008, **14**, 4533.
33 F. Ogliaro, S. Cohen, S. P. de Visser and S. Shaik, *J. Am. Chem. Soc.*, 2000, **122**, 12892.
34 S. P. de Visser, F. Ogliaro, P. K. Sharma and S. Shaik, *J. Am. Chem. Soc.*, 2002, **124**, 11809.
35 S. P. de Visser and S. Shaik, *J. Am. Chem. Soc.*, 2003, **125**, 7413.
36 S. Shaik, S. P. de Visser and D. Kumar, *J. Am. Chem. Soc.*, 2004, **126**, 11746.
37 S. P. de Visser, *J. Phys. Chem. A*, 2005, **109**, 11050.
38 S. P. de Visser, *Inorg. Chem.*, 2006, **45**, 9551.
39 S. Shaik, D. Kumar and S. P. de Visser, *J. Am. Chem. Soc.*, 2008, **130**, 10128.
40 R. Latifi, M. Bagherzadeh and S. P. de Visser, *Chem.–Eur. J.*, 2009, **15**, 6651.
41 D. Kumar, S. P. de Visser and S. Shaik, *Chem.–Eur. J.*, 2005, **11**, 2825.
42 S. P. de Visser, K. Oh, A.-R. Han and W. Nam, *Inorg. Chem.*, 2007, **46**, 4632.
43 S. P. de Visser, L. Tahsini and W. Nam, *Chem.–Eur. J.*, 2009, **15**, 5577.
44 L. Tahsini, M. Bagherzadeh, W. Nam and S. P. de Visser, *Inorg. Chem.*, 2009, **48**, 6661.
45 D. Kumar, S. P. de Visser, P. K. Sharma, S. Cohen and S. Shaik, *J. Am. Chem. Soc.*, 2004, **126**, 1907.
46 S. P. de Visser and R. Latifi, *J. Phys.Chem. B*, 2009, **113**, 12.
47 A. D. Becke, *Phys. Rev. A*, 1988, **38**, 3098.
48 J. P. Perdew, *Phys. Rev. B*, 1986, **33**, 8822.
49 N. C. Handy and A. J. Cohen, *Mol. Phys.*, 2001, **99**, 403.
50 J. P. Perdew, K. Burke and M. Ernzerhof, *Phys. Rev. Lett.*, 1996, **77**, 3865.
51 J. P. Perdew, J. A. Chevary, S. H. Vosko, K. A. Jackson, M. R. Pederson, D. J. Singh and C. Fiolhaus, *Phys. Rev. B*, 1992, **46**, 6671.
52 A. D. Becke, *J. Chem. Phys.*, 1996, **104**, 1040.
53 M. Reiher, O. Salomon and B. A. Hess, *Theor. Chim. Acta*, 2001, **107**, 48.
54 P. E. M. Siegbahn and F. Himo, *J. Biol. Inorg. Chem.*, 2009, **14**, 643.
55 D. C. Haines, D. R. Tomchick, M. Machius and J. A. Peterson, *Biochemistry*, 2001, **40**, 13456.
56 J. C. Schöneboom, H. Lin, N. Reuter, W. Thiel, S. Cohen, F. Ogliaro and S. Shaik, *J. Am. Chem. Soc.*, 2002, **124**, 8142.
57 E. Godfrey, C. S. Porro and S. P. de Visser, *J. Phys. Chem. A*, 2008, **112**, 2464.
58 C. S. Porro, M. J. Sutcliffe and S. P. de Visser, *J. Phys. Chem. A*, 2009, **113**, DOI: 10.1021/jp9023926, in press.
59 D. A. Case, T. A. Darden, T. E. Cheatham III, C. L. Simmerling, J. Wang, R. E. Duke, R. Luo, K. M. Merz, D. A. Pearlman, M. Crowley, R. C. Walker, W. Zhang, B. Wang, S. Hayik, A. Roitberg, G. Seabra, K. F. Wong, F. Paesani, X. Wu, S. Brozell, V. Tsui, H. Gohlke, L. Yang, C. Tan, J. Mongan, V. Hornak, G. Cui, P. Beroza, D. H. Mathews, C. Schafmeister, W. S. Ross and P. A. Kollman, *AMBER 9*, University of California, San Francisco, 2006.
60 W. D. Cornell, P. Cieplak, C. I. Bayly, I. R. Gould, K. M. Merz, Jr, D. M. Ferguson, D. C. Spellmeyer, T. Fox, J. W. Caldwell and P. A. Kollman, *J. Am. Chem. Soc.*, 1995, **117**, 5179.
61 T. Vreven, K. S. Byun, I. Koma′romi, S. Dapprich, J. A. Montgomery, Jr, K. Morokuma and M. J. Frisch, *J. Chem. Theory Comput.*, 2006, **2**, 815.
62 A. K. Rappé, C. J. Casewit, K. S. Colwell, W. A. Goddard III and W. M. Skiff, *J. Am. Chem. Soc.*, 1992, **114**, 10024.
63 U. C. Singh and P. A. Kollman, *J. Comput. Chem.*, 1986, **7**, 718.
64 J. C. Schöneboom, F. Neese and W. Thiel, *J. Am. Chem. Soc.*, 2005, **127**, 5840.
65 A. Chanda, X. Shan, M. Chakrabarti, W. C. Ellis, D. L. Popescu, F. T. de Oliveira, D. Wang, L. Que Jr, T. J. Collins, E. Münck and E. L. Bominaar, *Inorg. Chem.*, 2008, **47**, 3669.
66 K. Auclair, P. Moënne-Loccoz and P. R. Ortiz de Montellano, *J. Am. Chem. Soc.*, 2001, **123**, 4877.
67 F. Ogliaro, S. P. de Visser and S. Shaik, *J. Inorg. Biochem.*, 2002, **91**, 554.
68 A. Altun and W. Thiel, *J. Phys. Chem. B*, 2005, **109**, 1268.
69 P. R. Balding, C. S. Porro, K. J. McLean, M. J. Sutcliffe, J.-D. Maréchal, A. W. Munro and S. P. de Visser, *J. Phys. Chem. A*, 2008, **112**, 12911.
70 P. M. Champion, J. D. Lipscomb, E. Münck, P. G. Debrunner and I. C. Gunsalus, *Biochemistry*, 1975, **14**, 4151.
71 D. Harris and G. Loew, *J. Am. Chem. Soc.*, 1993, **115**, 5799.
72 D. Harris and G. Loew, *J. Am. Chem. Soc.*, 1993, **115**, 8775.
73 J. Bendix, M. Brorson and C. E. Schäffer, *Inorg. Chem.*, 1993, **32**, 2838.

 This journal is © the Owner Societies 2009

QM/MM Study of the Second Proton Transfer in the Catalytic Cycle of the D251N Mutant of Cytochrome P450cam

Muhannad Altarsha, Dongqi Wang,† Tobias Benighaus, Devesh Kumar, and Walter Thiel*

Max-Planck-Institut für Kohlenforschung, Kaiser-Wilhelm-Platz 1, D-45470 Mülheim an der Ruhr, Germany

Received: November 7, 2008; Revised Manuscript Received: May 20, 2009

Protonation of Compound 0 in the catalytic cycle of cytochrome P450cam may lead to the formation of either the reactive Compound I (coupling) or the ferric resting state (uncoupling). In this work, we investigate the effect of the D251N mutation on the coupling and uncoupling reaction by combined quantum mechanics/molecular mechanics (QM/MM) calculations. The mutated Asn251 residue has two possible orientations, i.e. directed toward the active site (no flip) or away from the active site (flip), with the latter one being preferred in classical molecular dynamics (MD) simulations. The possible proton transfer mechanisms in the coupling and uncoupling reaction were studied for three models of the D251N mutant, i.e. no flip (model I), flip (model II), and flip with an extra water (model III). According to the QM/MM calculations, the uncoupling reaction is always less favorable than the coupling reaction. The coupling reaction in the D251N mutant follows the same mechanism as in the wild-type enzyme, with initial O−O cleavage followed by proton transfer. The barrier for the initial step is similar in all D251N models, but the proton transfer is most facile in model III. The hydroxide anion formed in model III is not reprotonated easily by neighboring residues, while proton delivery from bulk solvent seems possible via a water network that remains intact during 2 ns classical MD simulation. The computational results are consistent with the experimental findings that the coupling reaction dominates the consumption of dioxygen in the D251N mutant, but with lower activity than in the wild-type enzyme.

Downloaded by MPI KOHLENFORSCH / BIOANORG CH on July 9, 2009
Published on June 19, 2009 on http://pubs.acs.org | doi: 10.1021/jp809838k

I. Introduction

Cytochromes P450 (P450s),[1] a ubiquitous family of heme containing monooxygenases, utilize dioxygen to insert an oxygen atom into inert hydrocarbon substrates. They play an important role in the biosynthesis of steroids, drug metabolism, and detoxification of xenobiotics.[2] Many studies of P450 have focused on the bacterial P450cam[3] with a camphor substrate, the first soluble P450 protein whose sequence and X-ray structure were determined.[4]

The catalytic cycle of P450cam is shown in Scheme 1.[3] The essential steps up to the formation of the active species involve (1) binding of the substrate, (2) reduction of the ferric cytochrome P450 to the ferrous state, (3) binding of molecular oxygen leading to the ferrous dioxygen complex, (4) second electron transfer and formation of the peroxo-iron(III) complex, (5) protonation of the distal oxygen, which leads to the formation of the ferric hydroperoxo complex (Compound 0, Cpd 0), and (6) second protonation of the distal oxygen with O−O bond cleavage, which generates the putative oxoferryl species (Compound I, Cpd I). Alternatively, protonation of the proximal oxygen in Cpd 0 leads to the uncoupling reaction that yields the ferric resting state and hydrogen peroxide instead of the hydroxylated product. Hence, a well-targeted proton transfer is indispensable for cleavage of the iron-bound dioxygen and formation of Cpd I.

Two proton delivery pathways have been proposed for P450cam that involve the highly conserved residues Asp251[5−10] and Glu366.[3,11,12] The crystallographic structure published by Schlichting et al.[3] indicated that there could be a Glu366 channel composed of Glu366, the bridging water molecules 687, 566,

SCHEME 1: Cytochrome P450cam Catalytic Cycle

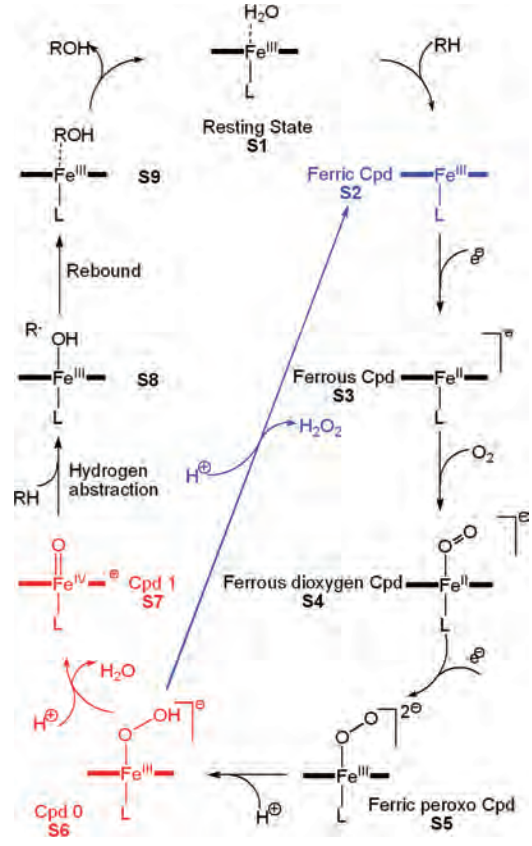

* To whom correspondence should be addressed. E-mail: thiel@mpi-muelheim.mpg.de.
† Current address: Laboratory of Physical Chemistry, Swiss Federal Institute of Technology Zürich, ETH, CH-8093 Zürich, Switzerland.

10.1021/jp809838k CCC: $40.75 © 2009 American Chemical Society
Published on Web 06/19/2009

523, and 902 (numbering as in PDB structure 1DZ8[3]), and the hydroxyl group of Thr252. The hydrogen bond network between the carboxyl group of Glu366 and the distal oxygen atom remains stable throughout molecular dynamics (MD) simulation.[13] However, this chain terminates at Glu366 without any connection to the protein surface,[10] and mutations of Glu366 show little influence on catalytic activity. These findings suggest that Glu366 does not play a major role in catalysis.[9,10,14]

Closer inspection of the Asp251 channel renders this a better candidate. First, the crystallographic structure indicates that the Asp251 residue may serve as a proton shuttle between the solvent accessible Lys178/Asp182/Arg186 triad and Thr252.[6,10,15,16] This is supported by MD simulations that confirm the flexibility of the Asp251 residue.[17−19] Second, extensive site-directed mutation studies clearly indicate that Asp251 and Thr252 play a vital role in the catalytic cycle.[6,10,20,21] Therefore, it has been suggested that the Asp251 and Thr252 residues are important in constituting a controlled proton delivery pathway that involves solvent water and provides an active-site H-bond donor. This may be a trapped water molecule or Thr252.[6,10]

An alternative proposal[22] assumes that the proton transfer from the solvent into the active site of P450 may proceed through the hydration cluster close to the heme propionates in the resting state. However, after the entry of the substrate, this pathway is blocked and will therefore not be considered.[3]

The D251N mutation causes a structural change in the vicinity of the active site. The new Asn251 amide side chain no longer favors the hydrogen bonds with Thr185 and Lys178 that keep Asp251 in an orientation toward the active site. Instead, Asn251 forms a new hydrogen bond with Asp182 and rotates away from the active site. This makes the active site more accessible for the solvent, such that an alternative solvent-based proton delivery channel may be established, as indicated by solvent kinetic isotope effect measurements.[4,10] Overall, the D251N mutant exhibits a greatly diminished rate of O_2 consumption for the coupling reaction. The product formation rate decreases by a factor of more than 30 from 820 nmol/min/nmol heme in the wild-type enzyme to 26 nmol/min/nmol heme in the D251N mutant; this has been interpreted in terms of a slower proton transfer to the iron-linked dioxygen.[10]

Mutation of the Thr252 residue by amino acids without hydrogen-bonding side chains virtually suppresses camphor hydroxylation in favor of the uncoupled reduction of O_2 to H_2O_2.[5,8,10,23] The crystal structure of the pentacoordinated ferric complex of the Thr252Ala mutant indicates that the solvent may be responsible for the observed uncoupling of the enzyme turnover from camphor hydroxylation in this mutant, since it contains a water molecule near the O_2 binding site, which is not present in the wild-type enzyme.[11,23]

Although the formation of Cpd I from Cpd 0 has been the subject of numerous theoretical studies, their results were partly inconsistent and mechanistic details such as the stability of a protonated Cpd 0 intermediate (prot-Cpd 0) depended strongly on the chosen model system.[11,17,24−28] Therefore, Zheng et al.[19] studied the formation of Cpd I in the full P450cam enzyme using a hybrid quantum mechanical/molecular mechanical (QM/MM) approach. They found that protonated Cpd 0 is an intermediate only in the Glu366 channel. It is very high in energy (more than 20 kcal/mol above Cpd 0) and the barrier for its decay is only 3−4 kcal/mol toward either Cpd 0 or Cpd I. In the Asp251 channel, protonated Cpd 0 was found to be unstable. Therefore, a novel mixed homolytic−heterolytic mechanism was proposed as the most favored pathway in both channels,[19] with the rate-limiting step being the initial O−O bond cleavage with a barrier of about 13−14 kcal/mol. The same methodology was used to study the effect of mutations at the Thr252 position to explain the important role of this residue in the proton delivery pathway and to rationalize the preference for coupling or uncoupling in the Thr252 mutants.[29]

Wang et al.[30] compared the role of the Asp251 and Asn251 residues during formation of Cpd 0 in the wild-type enzyme and the D251N mutant, respectively. In the D251N mutant, the Asn251 side chain was observed to be flexible during MD simulations and to flip from an orientation toward the active site to an orientation away from the active site, which generates some empty space between Arg186 and Wat901 that may be filled by an extra water molecule. QM/MM calculations on the resulting no flip, flip, and flip with extra water models led to the conclusion that the proton transfer in the Asn251 channel requires either a back-flip of the Asn251 side chain or the participation of an extra water molecule in the active site, and even then the barriers are higher than those in wild-type P450cam.

Until now, the effect of the D251N mutation on the coupling and uncoupling reactions of Cpd 0 has not been studied by QM/MM methods that account for the full enzyme. This article reports QM/MM calculations on both reaction pathways for the D251N mutant and the wild-type enzyme to elucidate the mechanistic role of the Asp251 residue and solvent molecules. In section II we briefly describe the computational methods employed. In section III we present and discuss the results of classical MD simulations and of QM/MM calculations for the different D251N models and compare them to results for the wild-type enzyme and to experimental data. Finally, section IV offers conclusions.

II. Computational Methodology and Proposed Mechanisms

QM/MM Setup. The available experimental X-ray structure of cytochrome P450cam (PDB code, 1DZ8;[3] resolution, 1.9 Å) was used as a starting point in our work. The same protonation and solvation protocol was employed as in previous studies.[31−33] Glu366 remains deprotonated, since we do not consider the Glu366 channel. Asn251 is neutral in the D251N mutant while Asp251 was protonated in our related previous QM/MM work on the wild-type enzyme.[19,30]

Both the wild-type and mutant system contain around 25000 atoms including 5895 TIP3P water molecules.[34] The initially prepared systems were relaxed by energy minimizations and MD simulations using the CHARMM22 force field[35] as implemented in the CHARMM program.[36] During the MD simulation, the heme unit, Cys357, and the outer 8 Å of the solvent layer were kept fixed.

The chosen QM/MM methodology is analogous to that used in previous studies.[19,30−33] Therefore, only those aspects relevant to the present work are mentioned here. Minimized snapshots from classical MD simulation trajectories were taken as the initial structures for QM/MM calculations. The QM region was described by unrestricted hybrid DFT (UB3LYP)[37] using the LACVP[38] small-core ECP basis set on Fe and 6-31G[39] on the rest of all atoms (B1) for geometry optimizations. Single-point calculations were carried out with the TZVP[40,41] basis set (B2) applied to all atoms. The CHARMM force field was run through the DL_POLY[42] code to treat the MM part of the system. All QM/MM calculations were performed with the ChemShell package[43] that integrates the TURBOMOLE[44] and DL_POLY programs and also provides the HDLC optimizer[45] for geometry optimizations. An electronic embedding scheme[46] was adopted

Downloaded by MPI KOHLENFORSCH / BIOANORG CH on July 9, 2009
Published on June 19, 2009 on http://pubs.acs.org | doi: 10.1021/jp809838k

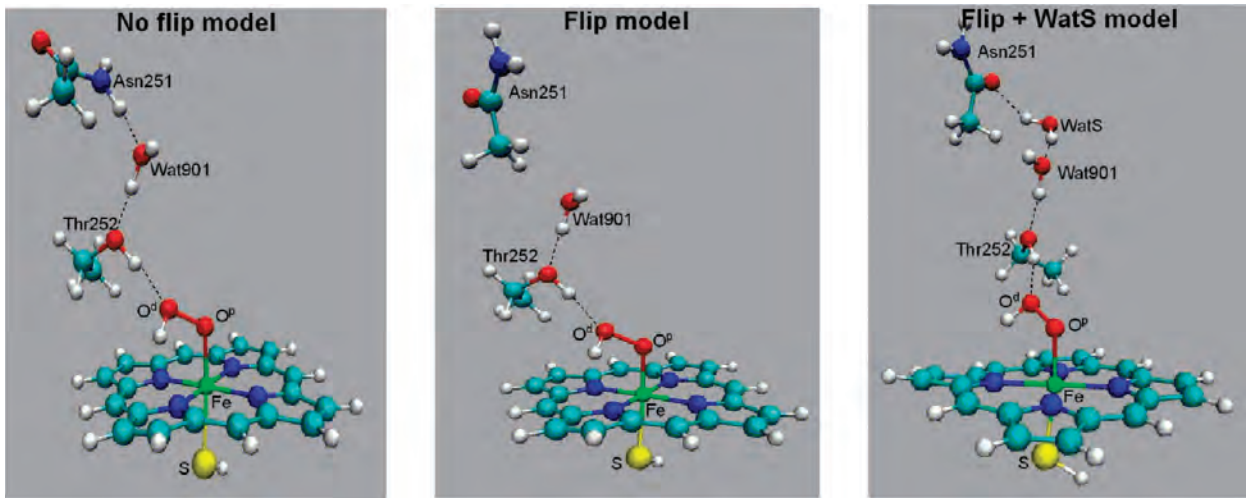

Figure 1. QM models for the Asn251 mutant: Model I represents the no flip configuration of the Asn251 side chain, model II represents the flip configuration, and model III extends model II with an extra water molecule (WatS).

SCHEME 2: (a) Two Proposed Reaction Mechanisms for Cpd I Formation (Coupling Reaction), and (b) Two Proposed Reaction Mechanisms for Ferric Resting State Formation (Uncoupling Reaction)

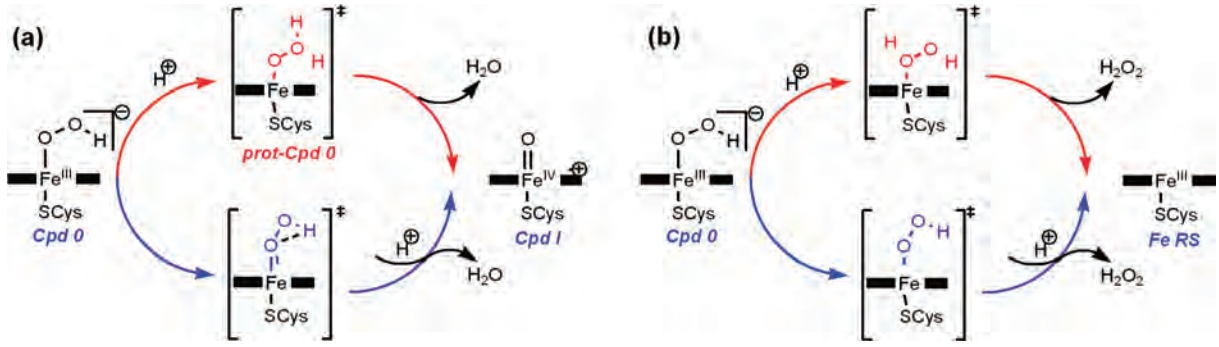

in the QM/MM calculations; that is, the MM charges were included in the one-electron Hamiltonian of the QM part, and QM/MM electrostatic interactions were evaluated as interaction of the QM electrostatic potential with MM partial charges. Hydrogen link atoms in combination with a charge shift model[47] were employed to treat the QM/MM boundary. All minima (reactants, products, and intermediates) and transition states (TS) reported in this paper were fully optimized.

The active region was defined to include all residues and water molecules within 6 Å of any non-hydrogen atom of the core region which contains the heme unit, Cys357, Glu366, Asn251, Thr252, Wat523, Wat566, Wat687, Wat901, and WatS. This results in ca. 1400 atoms to be optimized.

QM Region. We used an analogous QM region as in previous work on the wild-type enzyme.[19] In the D251N mutant, the Asp251 residue was manually replaced by Asn, and the QM region thus includes the following: porphyrin-FeOOH without side chains, SH ligand, Asn251 (CH_2CONH_2), Thr252 (CH_3CHOH), and Wat901. This QM region is shown in Figure 1 for models I and II, which represent the no flip and flip conformations encountered during 2 ns classical MD simulations (see below). In model III an extra water molecule (WatS) was manually placed in the empty space between Arg186 and Wat901. The stability of WatS in the active site was confirmed by means of classical MD simulation, and therefore, model II was extended to model III by including WatS. The three models are illustrated in Figure 1.

Possible Proton Transfer Pathways. Scheme 2 presents possible pathways that yield two different products through proton transfer, respectively. In the first two pathways (coupling reactions, Scheme 2a), the proton is transferred from the hydroxy group of threonine to the distal oxygen (O^d), while in the other two pathways (uncoupling, Scheme 2b), the proton is transferred to the proximal oxygen (O^p). In both cases, Wat901 bridges Asn251 and Thr252 (and WatS in model III) to construct the proton transfer channel. The details of these mechanisms are as follows.

In the coupling reaction (Scheme 2a), which leads to the formation of Cpd I and one water molecule, the proton is transferred to the proximal oxygen via two possible pathways. The first pathway represents the conventional mechanism (in red, Scheme 2a), in which the coupling reaction is initiated by proton transfer to the distal oxygen atom of the O_2H moiety and protonated Cpd 0 is formed, followed by a heterolytic O−O bond cleavage that yields Cpd I and water.[19] In the second mechanism, an initial O−O bond cleavage generates an OH species hydrogen-bonded to the FeO moiety. A subsequent proton transfer to this OH species with a concomitant electron transfer from the heme yields Cpd I and water[19] (blue pathway in Scheme 2a).

The uncoupling reaction (Scheme 2b) leads to the formation of the ferric resting state and hydrogen peroxide. Two possible mechanisms have been investigated also for this reaction. The first one (red pathway in Scheme 2b) starts with a proton transfer to the proximal oxygen to form Fe−O_2H_2, followed by heterolytic Fe−O bond cleavage that generates the ferric resting state and hydrogen peroxide. In the second mechanism, the

Downloaded by MPI KOHLENFORSCH / BIOANORG CH on July 9, 2009
Published on June 19, 2009 on http://pubs.acs.org | doi: 10.1021/jp809838k

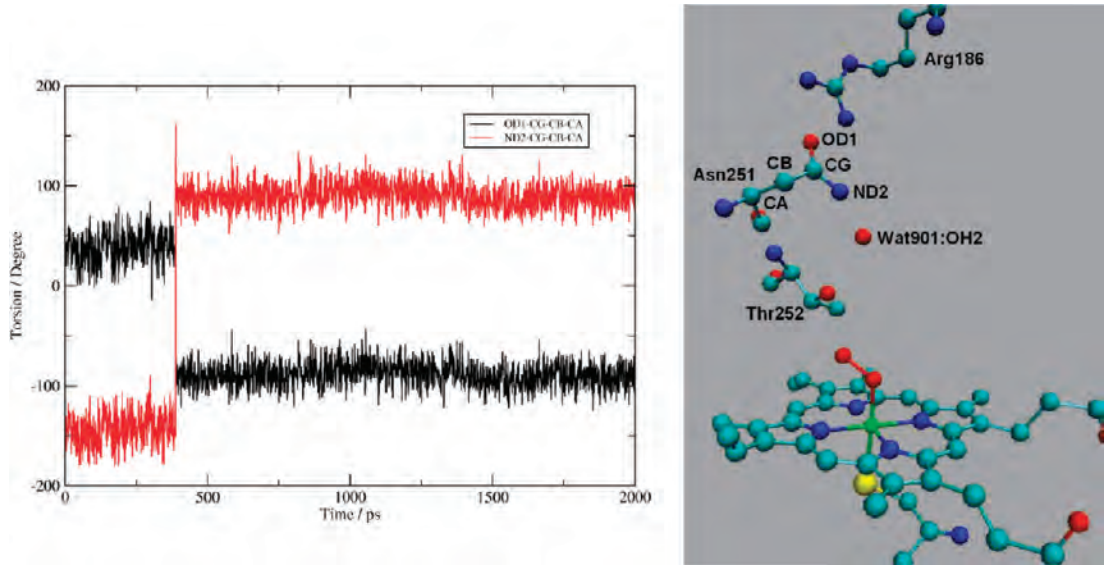

Figure 2. Motion of the Asn251 side chain during the MD simulation. Left: results for torsion angles OD1−CG−CB−CA and ND2−CG−CB−CA. Right: definition of atom labels.

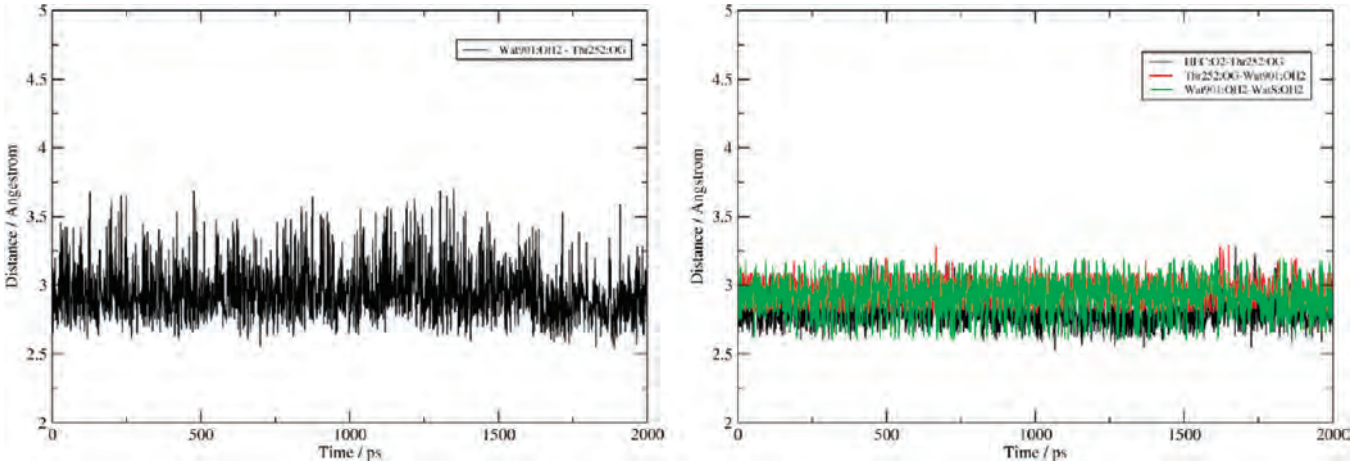

Figure 3. Monitoring the mobility of the crystallographic water molecule (Wat901) and the extra water molecule (WatS) during the MD simulation (for atom labels, see Figure 2). Left: Wat901 in model II. Right: Wat901 and WatS in model III.

Downloaded by MPI KOHLENFORSCH / BIOANORG CH on July 9, 2009
Published on June 19, 2009 on http://pubs.acs.org | doi: 10.1021/jp809838k

Fe−O bond is cleaved first and a hydroperoxo radical is formed, which is then converted to hydrogen peroxide.

III. Results and Discussion

MD Simulation Results. The crystal structure of the D251N mutant (2A1N)[48] is a dimer which contains the Asn251 residue in two different orientations in the two units (normal and flipped orientation). In the former case, the Asn251 side chain shows a 25° rotation toward Wat901, thus establishing a connection to the active site.[48] This suggests that there is no strong interaction between Asn251 and Arg186, unlike the salt bridge which exists between Asp251 and Arg186 in the crystal structure of the wild-type enzyme (1DZ8). Consequently, a direct interaction between Asn251 and Wat901 is possible, and a proton transfer channel from Asn251 via the only crystallographic water molecule in this region (Wat901) to the active site may be formed.[10,18]

We performed a 2 ns classical MD simulation of the D251N mutant of Cpd 0 starting from model I (no flip) to study the stability of the Asn251 amide group. Its conformation is characterized by two torsion angles with the backbone (OD1−CG−CB−CA and ND2−CG−CB−CA). During the simulation (see Figure 2), the OD1−CG−CB−CA torsion angle decreases from 70° to −90°, whereas the ND2−CG−CB−CA angle increases from −108° to 88°. In the no flip conformation, the Asn251 residue forms hydrogen bonds with nearby residues, i.e. Arg186 and Wat901 (relevant average distances: Arg186:HH22−Asn251:OD1, 1.809 Å; Arg186:HH12−Asn251:OD1, 1.779 Å; Wat901:OH2−Asn251:HD22, 1.656 Å). After the flip of the Asn251 side chain (model II), the amide group of Asn251 retains its hydrogen bond with Arg186 and forms new hydrogen bonds with Thr181 and Asp182 (average distances: Thr181:OG1−Asn251:HD22, 2.049 Å; Asp182:OD1−Asn251:HD21, 1.651 Å).

Wat901 and WatS play a critical role in the proton delivery, and we have therefore checked their mobility by additional MD simulations. Figure 3 shows the results for Cpd 0 in model II (left) and model III (right). The connection between Wat901 and the side chain of Asn251 is interrupted in model II (flip) of the Asn251 mutant. However, since Wat901 keeps its hydrogen bond with the Thr252:OH group, it does not escape from the protein pocket during the 2 ns simulation but stays close to Thr252 (see Figure 3). Likewise, in model III (flip with extra water), Wat901 remains stable next to the Thr252 amino acid: the average value and the standard deviation for the distance between Wat901:OH2 and Thr252:OG1 is 2.955 ± 0.224 Å,

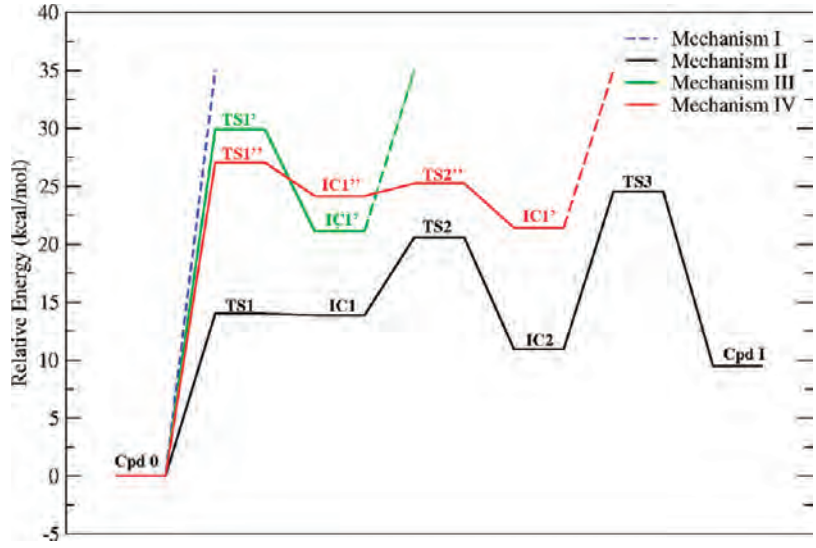

Figure 4. Energy profiles for the four possible mechanisms in the no flip conformation of the D251N mutant (I and II for coupling, III and IV for uncoupling). Relative energies are given in kcal/mol with respect to Cpd 0.

Downloaded by MPI KOHLENFORSCH / BIOANORG CH on July 9, 2009
Published on June 19, 2009 on http://pubs.acs.org | doi: 10.1021/jp809838k

indicating that the hydrogen bond between Thr252 and Wat901 is conserved. The extra water molecule that is inserted in model III (WatS) does not escape from the distal pocket during the MD simulation: the average value and the standard deviation for the distances HEC:O2−Thr252:OG1, Thr252:OG1−Wat901:OH2, and Wat901:OH2−WatS:OH2 are 2.803 ± 0.102 Å, 2.940 ± 0.096 Å, and 2.925 ± 0.127 Å, respectively. These results confirm that both water molecules are stable in the distal pocket of the enzyme.

QM/MM Results. In the following, we present the results from QM/MM geometry optimizations and reaction path calculations for models I−III. Since previous work on the native enzyme and several mutants has established that the doublet state of Cpd 0 is more stable than the quartet state both in gas phase models[7,26] and in the actual enzyme environment,[19] we focus on the doublet spin state in this study. The QM/MM optimized structures of the QM region of the D251N mutant have already been shown in Figure 1 for Cpd 0 in models I−III. The figures in this section will present QM/MM optimized structures of all relevant stationary points (with data for selected geometrical parameters) as well as energy profiles (with relative energies obtained from the B1/B2 basis sets). Since the computed relative energies are not too sensitive to extension of the basis set, we shall discuss the B1 values in the text (B1 is the basis used for geometry optimization). Other computational results (such as spin densities, Mulliken charges, and additional reaction profiles) are documented in the Supporting Information (SI), which also provides an overview picture of the active-site structure (Figure S38).

A. No Flip Model. As already mentioned, four different reaction mechanisms were studied for the coupling and uncoupling reactions of Cpd 0. The coupling mechanisms I and II yield Cpd I and water, while the uncoupling mechanisms III and IV lead to the formation of the ferric resting state and hydrogen peroxide. Figure 4 shows the energy profiles of all mechanisms for the no flip model. In the case of mechanism I (blue line in Figure 4), the energy profile goes uphill only, and we were unable to locate a stable prot-Cpd 0 intermediate. In previous QM/MM studies by our group on the native enzyme and the Thr252X (X = Ser, Ala, Val, Gly) mutants in the Asp251 channel, prot-Cpd 0 was also found to be unstable.[19,29] Mechanism II proceeds in three steps (black line in Figure 4). The first one is O−O bond cleavage with an energy barrier of 14.0 kcal/mol. In the second step, the hydrogen on Thr252 is transferred to the OH moiety with an energy barrier of 8.0 kcal/mol followed by the deprotonation of Asn251 with a barrier of 13.6 kcal/mol relative to IC2.

In contrast to mechanism II, mechanisms III and IV give the ferric resting state and hydrogen peroxide. Mechanism III (green line in Figure 4) starts with a direct proton transfer from the Thr252 residue to the proximal oxygen (O1) of the FeOOH moiety, accompanied by a spontaneous O−Fe bond cleavage. This step has an energy barrier of 29.9 kcal/mol. After this proton transfer, the first intermediate (IC1′), comprising the ferric resting state and hydrogen peroxide with an O-Thr252 anion, is calculated to be 21.1 kcal/mol above the reactant. The recovery of the natural state of Thr252 by abstracting a proton from Asn251 seems to be unrealistic in this model, since deprotonated Asn251 is a significantly stronger base than deprotonated Thr252 in IC1′. Therefore, the proton channel is interrupted and this mechanism does not lead to the desired product.

In mechanism IV (red line in Figure 4), the initial step is O−Fe bond cleavage with a barrier of 27.1 kcal/mol. The resulting intermediate IC1″ contains an OOH moiety and has an energy of ca. 24 kcal/mol. In the next step, a proton is transferred from Thr252 to the proximal oxygen of the OOH moiety with a tiny barrier of only around 1 kcal/mol relative to IC1″. This step leads to an intermediate that is very similar to the one of mechanism III and has an energy of 21.4 kcal/mol. However, in mechanism IV the product of the final proton transfer from Asn251 to the deprotonated Thr252 is again not stable.

In summary, we find that mechanism I is not a realistic pathway, since the formation of its first intermediate (prot-Cpd 0) is difficult. Mechanisms III and IV involve significantly higher activation energies than mechanism II already in the initial stage of the reaction. Qualitatively similar results were also obtained for models II and III. Hence, mechanism II emerges as the most favorable pathway, and we will discuss only this mechanism in detail for all three models. Further information about the other mechanisms is given in the Supporting Information.

Figure 5 presents the QM/MM optimized structures and the energy profile of mechanism II in the no flip model of the D251N mutant. In this conformation, the hydrogen bonding

Downloaded by MPI KOHLENFORSCH / BIOANORG CH on July 9, 2009
Published on June 19, 2009 on http://pubs.acs.org | doi: 10.1021/jp809838k

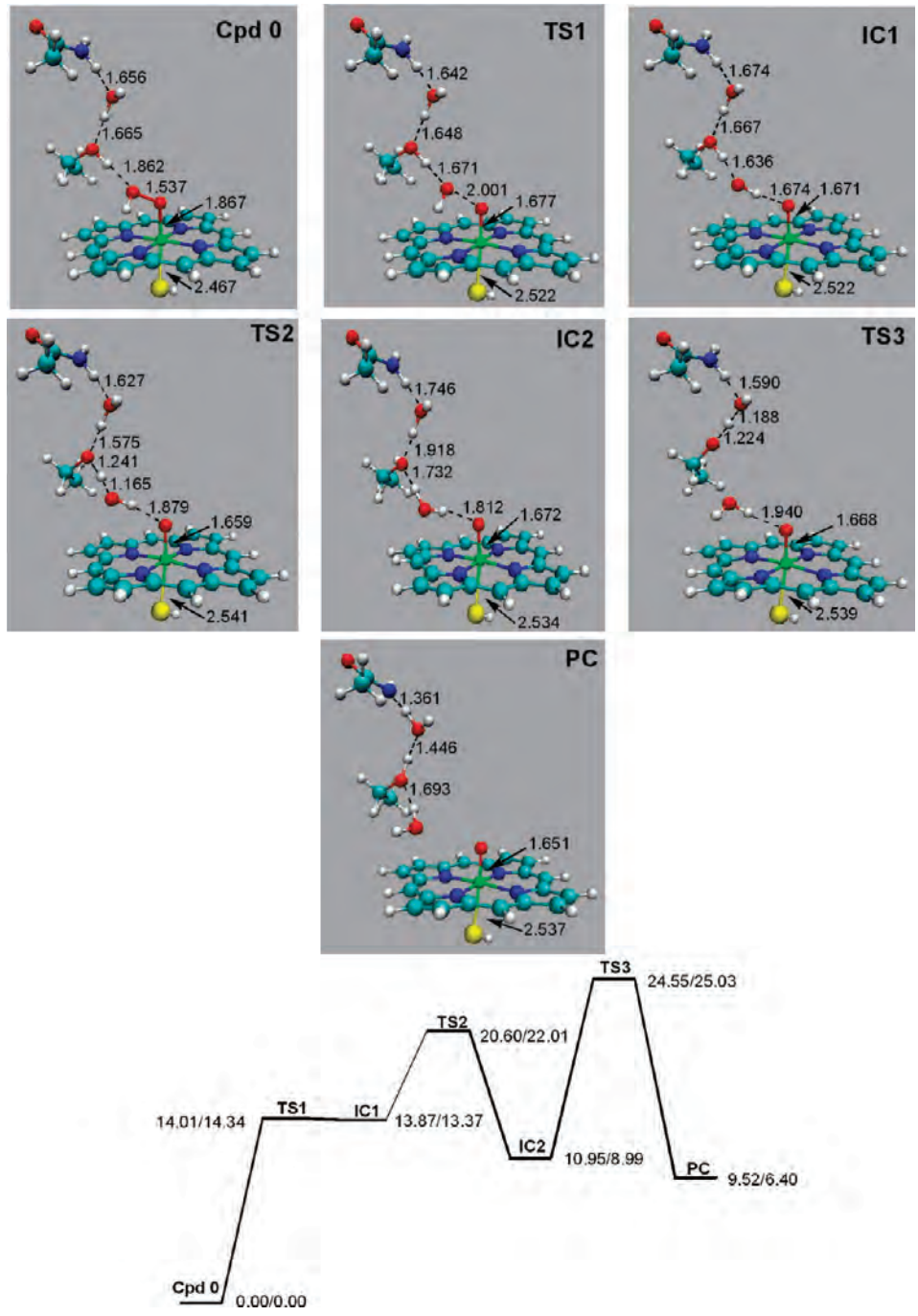

Figure 5. Asn251 mutant, no flip model. (a) Optimized geometries of Cpd 0, TS1, IC1, TS2, IC2, TS3, and PC (UB3LYP/B1/CHARMM). Only the QM region is shown. (b) Energy profile of mechanism II. Energies in kcal/mol relative to Cpd 0 (B1/B2).

network between the proton source (Asn251) and the distal oxygen (O^d) is conserved. The O^d-O^p bond cleavage has a barrier of 14.0 kcal/mol (i.e., very similar to the wild-type enzyme) and leads to the first intermediate (IC1) with an energy of 13.9 kcal/mol. During the first step, the O^d-O^p distance increases from 1.537 (Cpd 0) to 2.001 (TS1) and 2.524 Å (IC1), indicating cleavage of the O−O bond. Meanwhile, the $Fe-O^p$ distance decreases noticeably from 1.867 to 1.677 Å from reactant to first transition state, and the Fe−S distance elongates from 2.467 (Cpd 0) to 2.522 Å (TS1, IC1).

During the reaction, the hydrogen bond between Thr252 and the distal oxygen atom becomes stronger due to the displacement of the OH moiety toward the Thr252 residue. In IC1, a new strong FeO−HO hydrogen bond with a distance of 1.674 Å is formed. The spin density and charge of the OH moiety in IC1 are −0.7 and −0.1, respectively, which indicates that OH will not behave as a "perfect" radical in IC1. This is due to the strong hydrogen-bonding interactions of the OH moiety with both the heme (through FeO) and the protein environment (through Thr252). A similar spin density was reported previously for the wild-type enzyme.[19]

The subsequent proton transfer from Asn251 to the distal oxygen proceeds in two steps. First, a hydrogen atom is transferred from Thr252 to the OH moiety, and then Thr252 is reprotonated via Wat901 by Asn251 with a concomitant electron transfer from the heme. During the first step, the system has to pass over a high energy barrier (TS2) of 20.6 kcal/mol to reach a stable intermediate (IC2) with an energy of 11.0 kcal/mol. In IC2, the spin density of the OH group reduces to almost zero and the hydrogen atom of Thr252 is transferred to the distal

Downloaded by MPI KOHLENFORSCH / BIOANORG CH on July 9, 2009
Published on June 19, 2009 on http://pubs.acs.org | doi: 10.1021/jp809838k

oxygen (0.997 Å) to form a water molecule. The spin density and Mulliken charge on Thr252 are −1.0 and −0.2, respectively. The radical character of Thr252 in IC2 is confirmed by QM/MM calculations with different QM regions, functionals, basis sets, and initial guesses for the density matrix (see Tables S27−S29 of the Supporting Information). The occurrence of such an IC2 radical intermediate in the D251N mutant contrasts with the situation in the wild-type enzyme where the proton transfer from Asp251 is more facile (due to the much higher acidity of Asp251 compared with Asn251) and proceeds in a concerted manner. The transition state of the last step (TS3) in the mutant has an energy of 24.6 kcal/mol above Cpd 0, representing the highest point of the whole pathway. The overall process is endothermic by 9.5 kcal/mol. Reaction path calculations indicate that a concerted proton transfer in the mutant requires an activation of about 39 kcal/mol relative to Cpd 0 (see the Supporting Information).

It is also worthwhile to discuss the nature of IC1 and TS1. In a previous study that employed the same model of the wild-type enzyme, we found a similar reactive high-energy species whose stability depends on the size of the QM region.[19] In view of the energetic similarities of TS1 and IC1 (IC1 is about 0.2 kcal/mol more stable than TS1) and the geometric similarities of IC1 and TS2, it seems probable that TS1 and IC1 are artifacts resulting from the limited size of the QM region and the absence of conformational sampling. Hence, it is more realistic to regard the no flip mechanism in the mutant as a two-step process. The first step then corresponds to O−O bond cleavage, hydrogen transfer, and water formation with an overall barrier of 20.6 kcal/mol. The second step is the deprotonation of the mutated Asn251 residue with a barrier of 13.6 kcal/mol.

The major difference between the wild-type enzyme and the D251N mutant is 2-fold: (1) The barrier of the rate-determining step increases from 14.4 kcal/mol in the wild-type enzyme to 20.6 kcal/mol in the D251N mutant. (2) The formation of Cpd I is a one-step process in the wild-type enzyme, while it becomes a two-step reaction in the D251N mutant with a stable deprotonated Thr252 radical intermediate. Both effects result from the much higher pK_a value of the mutated Asn251 residue compared to Asp251 that acts as the proton source in the wild-type enzyme.

Finally, we tested if an extension of the QM region has a significant effect on the relative energies by including the Arg186 residue into the QM region. We found only very minor changes in relative energies and geometries (see the Supporting Information).

B. Flip Model. In the flipped conformer, rotation of the Asn251 residue causes an interruption of the hydrogen bond network so that it cannot serve as a proton source. Figure 6 shows the QM/MM optimized structures with selected geometric parameters and the energy profile of mechanism II in the flip model. The first step, cleavage of the O−O bond, remains unaffected by the Asn251 flip: the transition state (TS1) and the first intermediate (IC1) have energies of 14.0 and 9.0 kcal/mol relative to Cpd 0, respectively. The spin densities of OH (−1.0) and Fe═O (2.1) in IC1 indicate that the Fe═O moiety carries two unpaired electrons, and the third unpaired electron is mainly located at the OH moiety. The hydrogen bond interactions with the proximal oxygen of the heme and Thr252 that stabilize the OH radical are structurally similar to those of model I but provide a more efficient energetic stabilization of ca. 5 kcal/mol (relative to TS1). Subsequently, the reaction follows a radical mechanism as in the no flip model. The second step is the hydrogen transfer from Thr252 to the OH radical with a transition state (TS2) energy of 17.6 kcal/mol and an intermediate complex (IC2) at 12.4 kcal/mol. The computed spin densities and charges confirm that the proton transfer leads to the formation of a water molecule and the O-Thr radical species (see Tables S6 and S28 of the Supporting Information). Finally, a proton from water (Wat901) and an electron from the heme are transported to the O-Thr252 radical. The corresponding transition state (TS3) and the product complex lie 21.1 and 19.2 kcal/mol above Cpd 0, respectively.

The resulting product complex contains a negatively charged OH species with weak radical character, as indicated by the computed spin density and Mulliken charge (−0.2 and −0.5, respectively). This species is stabilized by strong hydrogen bonds with Thr252 and Asn251 (distances of 1.427 and 1.888 Å, respectively). The reaction pathway is blocked at this stage, since the Asn251 residue does not act as a proton source in the flip model and no other proton source exists in the vicinity. We have also included the Arg186 side chain into the QM region to check if Arg186 may serve as an alternative proton source but found that the distance to the OH anion is too large to enable proton transfer (details see in the Supporting Information). We thus have to conclude that flip conformations of this kind are unlikely to contribute to the formation of Cpd I in the D251N mutant.

C. Flip Model with an Extra Water WatS. As mentioned before, an extra water fits into the space which is released by the flip of the Asn251 side chain (see Figure 1). The introduction of WatS improves the hydrogen bond network with the Arg186 residue that is a potential proton source. Figure 7 presents the QM/MM optimized geometries and the energy profile for the flip model in the presence of the WatS molecule. In this pathway, the O^d-O^p bond cleavage has an energy barrier of 14.0 kcal/mol, similar to cases of the no flip and flip models. The energy of the first intermediate complex (IC1) is 11.8 kcal/mol relative to that of Cpd 0. The spin densities and Mulliken charges of the OH group and the proximal oxygen atom also confirm the cleavage of the O−O bond. The OH group in IC1 forms two strong hydrogen bonds with the heme and the Thr252 residue (distances of 1.447 and 1.690 Å, respectively).

The energy barrier of the second step which involves proton transfer from Wat901 to the OH moiety via Thr252 and concomitant electron transfer from the heme is 0.3 kcal/mol. The whole reaction is endothermic, with the product lying 7.7 kcal/mol above Cpd 0. Both the OH spin density (−0.2) and Mulliken charge (−0.5) indicate that an anionic OH species with only weak radical character is formed, which is stabilized by two hydrogen bonds with Thr252 and WatS (distances of 1.236 and 1.638 Å, respectively). Evidently, the proton transfer is facilitated by the additional water molecule, and the overall endothermicity decreases from 19.2 kcal/mol in model II to 7.7 kcal/mol in model III. Since the barrier for proton transfer is reduced to less than 0.5 kcal/mol, it is appropriate to regard the overall process essentially as a one-step reaction similar to model I.

Starting from the product complex, we tried to move one proton from WatS to the OH anion of Wat901. However, this proton always moved back to the emerging hydroxide anion upon full QM/MM optimization, indicating that WatS is an even weaker Brönsted acid than Wat901 in the given environment (see SI for detailed information). Closer inspection of these structures indicates that WatS also forms a hydrogen bond with the Arg186 residue, thus making Arg186 a potential proton source. To explore the role that Arg186 plays in the presence of WatS, we included the side chain of the Arg186 residue into

Downloaded by MPI KOHLENFORSCH / BIOANORG CH on July 9, 2009
Published on June 19, 2009 on http://pubs.acs.org | doi: 10.1021/jp809838k

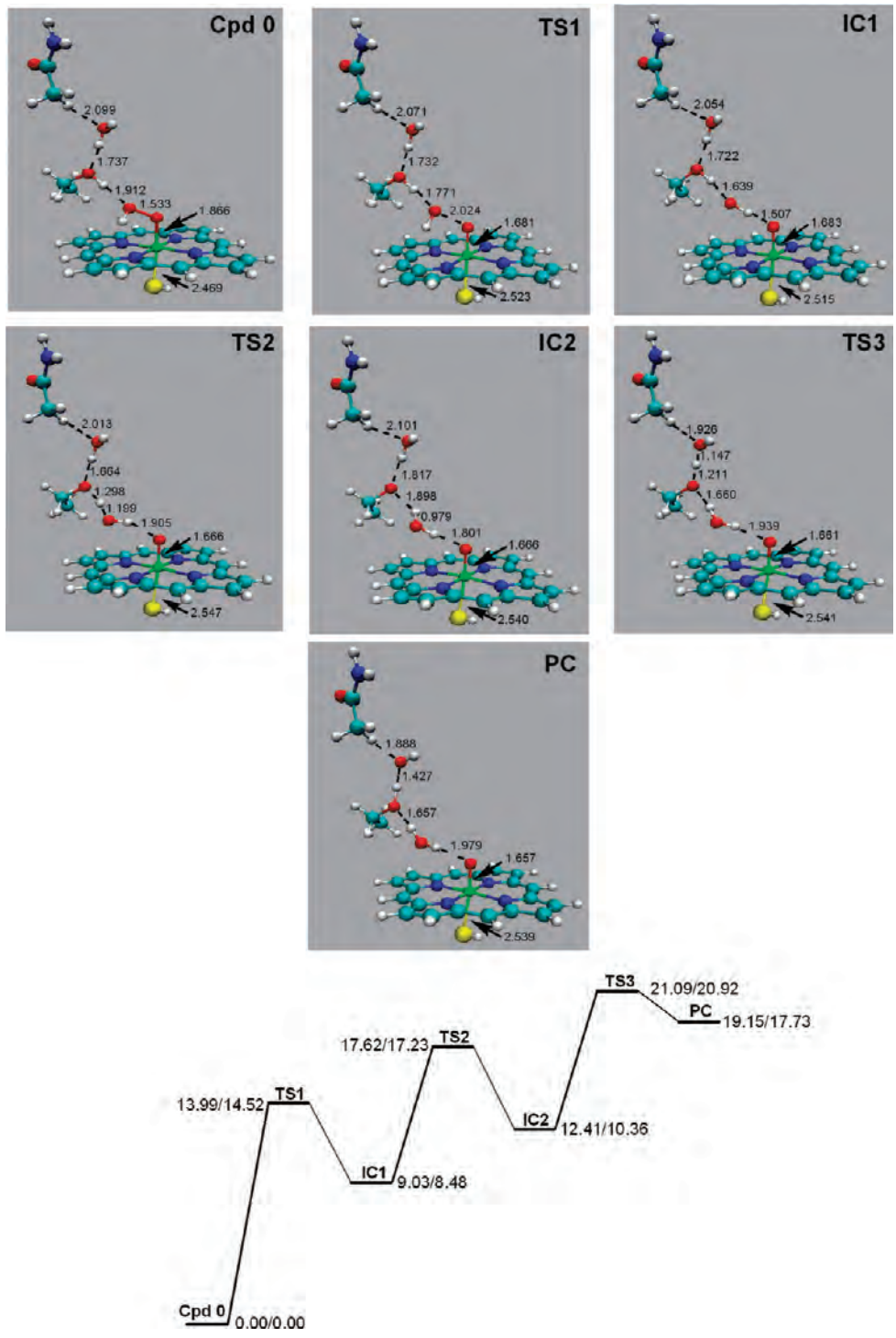

Figure 6. Asn251 mutant, flip model. (a) Optimized geometries of Cpd 0, TS1, IC1, TS2, IC2, TS3, and PC (UB3LYP/B1/CHARMM). Only the QM region is shown. (b) Energy profile of mechanism II. Energies in kcal/mol relative to Cpd 0 (B1/B2).

the QM region and tested if it can act as a proton source. Figure 8 presents the QM/MM optimized geometries of the reactant, first intermediate, and product complex of the flip model with an extra water molecule and Arg186 included in the QM region. The product complex (PC) contains an OH anion (Wat901) that is stabilized by strong hydrogen bonds to Thr252 (1.334 Å) and Wat901 (1.549 Å). We tried to locate the alternative product complex (PC′) with deprotonated Arg186 and two water molecules that would be formed by proton transfer from Arg186 to the OH anion (Wat901). However, constrained geometry optimizations indicate that PC′ is less stable than PC by about 8 kcal/mol and that the rearrangement from PC′ to PC is barrierless. This implies that in the given environment Wat901 is a better proton donor than Arg186 due to the favorable stabilization of the formed OH anion through hydrogen bond interactions. We have to conclude that deprotonated Wat901 will not be replenished by proton transfer via Arg186.

Further inspection of the structure of the product complex (PC) reveals that the hydroxide anion of Wat901 may be connected to the bulk solvent via WatS and three crystallographic water molecules (Wat149, Wat148, and Wat133) and that this network can further be improved by including an additional water molecule in the vacant space between WatS and Wat149. We have confirmed that this extended water

Downloaded by MPI KOHLENFORSCH / BIOANORG CH on July 9, 2009
Published on June 19, 2009 on http://pubs.acs.org | doi: 10.1021/jp809838k

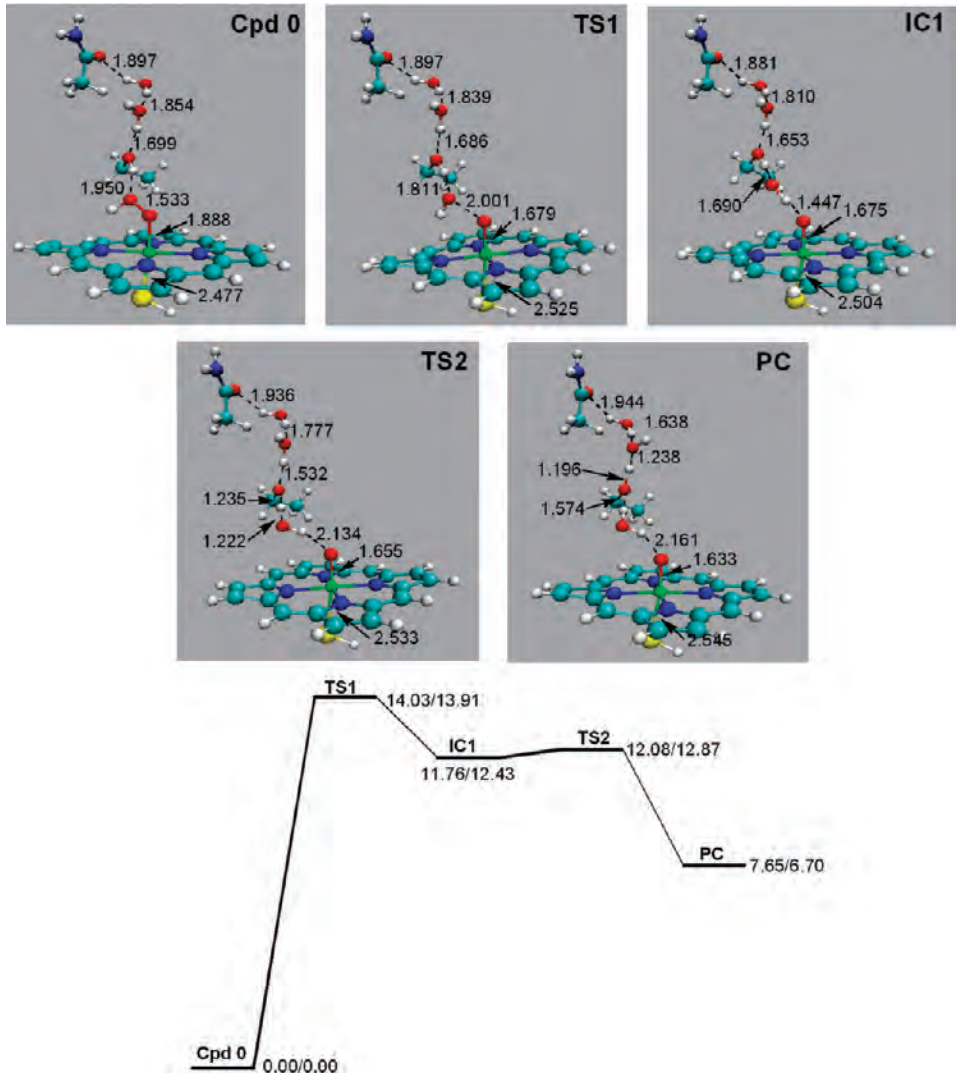

Figure 7. Asn251 mutant, flip model with an extra water. (a) Optimized geometries of Cpd 0, TS1, IC1, TS2, and PC (UB3LYP/B1/CHARMM). Only the QM region is shown. (b) Energy profile of mechanism II. Energies in kcal/mol relative to Cpd 0 (B1/B2).

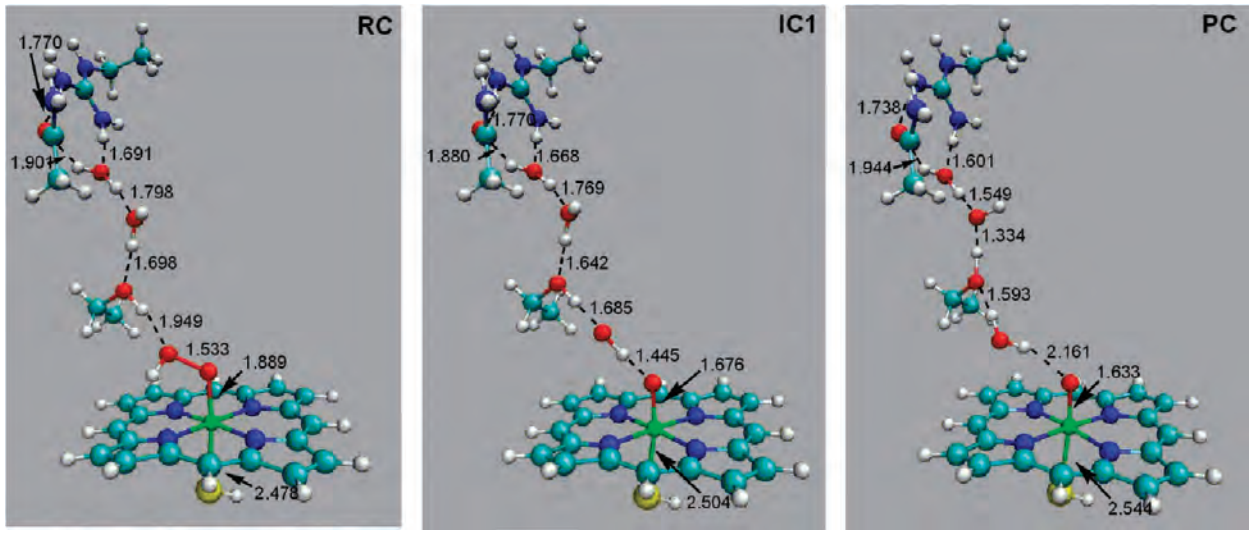

Figure 8. Asn251 mutant, flip model with an extra water and the Arg186 residue included in the QM region: Optimized geometries of Cpd 0, IC1, and PC (UB3LYP/B1/CHARMM). Only the QM region is shown.

network remains intact during 2 ns of classical MD simulation (see Figures S36−S37 and Table S26 in the Supporting Information). This suggests that the formed hydroxide anion may be reprotonated from the bulk solvent by a Grotthuss-type mechanism. It is well-known[49] that the free energy barriers for such proton transfers are quite low in liquid water, for the migration both of excess protons and of proton holes (involving hydroxide anions),[49−51] and similarly low barriers have recently

also been reported for the proton transfer along a wirelike water network in bacteriorhodopsin.[52] We thus consider it likely that such a low-barrier mechanism operates also in our case, but in view of the conformational complexity, we have not attempted to locate any of the corresponding transition states for reprotonation from bulk solvent.

IV. Discussion

In previous QM/MM work,[30] we have investigated the first proton transfer in the catalytic cycle of wild-type P450cam and its D251N mutant that leads to the formation of Cpd 0. In the mutant, the Asn251 side chain was found to be flexible in MD simulations and to flip to an orientation away from the active site, thus generating some empty space that can be occupied by an extra water molecule. Participation of this additional water molecule in the hydrogen-bonding network between Arg186/Asn251 and the heme was shown to provide a viable proton-transfer path in the D251N mutant, even though the resulting rate-limiting barrier remained higher than that in the wild-type enzyme.

In the present QM/MM study we address the second proton transfer in the catalytic cycle that converts Cpd 0 into Cpd I. As in the case of wild-type P450cam,[19] we find that the textbook mechanism with initial protonation of the distal oxygen atom of the FeOOH moiety and subsequent heterolytic O−O cleavage does not operate in the mutant. Instead a mixed homolytic−heterolytic mechanism is again more favorable, with initial O−O cleavage followed by proton transfer in the Asp251/Asn251 channel. The initial step is thus the same in both cases, and the corresponding barriers are indeed almost identical in the wild-type enzyme and the D251N mutant (ca. 14 kcal/mol). This is not surprising, since the cleavage of the O−O bond in the FeOOH moiety should not be influenced much by the Asp251/Asn251 replacement.

This substitution does however affect the subsequent proton transfer step. In wild-type P450cam, protonated Asp251 can act as a proton source, and there is a rather facile concerted pathway for proton delivery to the initially formed, hydrogen-bonded OH species. In the D251N mutant, this path requires significant activation according to the current QM/MM calculations for model I (no flip), and it is not available for models II (flip) and III (flip+WatS), where Asn251 does not serve as a proton donor. As in our previous QM/MM work on the first proton transfer,[30] the preferred arrangement in the mutant involves a flipped Asn251 conformation with an extra water molecule (WatS) that bridges the Asn251 residue and the crystallographic water molecule (Wat901) close to Thr252. The hydrogen-bonding network thus formed facilitates the second proton transfer, and the corresponding transition state lies indeed only about 12−13 kcal/mol above Cpd 0 (i.e., slightly below the transition state for O−O cleavage). However, the resulting product complex (ca. 7−8 kcal/mol above Cpd 0) still contains an OH anion (Wat901) which cannot be protonated by the Arg186 residue (via WatS). This is in contrast to the mechanism of the first proton transfer in the D251N mutant, where such reprotonation was found to be feasible. We note in this context that the two heme species being protonated in the catalytic cycle differ in their total charge (−2 for the reduced oxyheme complex and −1 for Cpd 0) so that one may expect from general electrostatic arguments that reprotonation from the bulk should be less facile in the case of Cpd 0.

In summary, we have identified one viable path for the second proton transfer in the D251N mutant which terminates at Wat901 and is thus not complete, since it does not provide a route for reprotonating the formed OH anion (Wat901). We anticipate, however, that reprotonation may be achieved through a water network that connects this OH anion with the bulk solvent. Inspection of the active-site geometry reveals that there is enough space between the residues Arg186, Asn251, and Asn255 to accommodate another water molecule which could form a stable network connecting WatS and Wat149 (at the boundary to the bulk). Classical MD simulations support this idea and reveal that the hydrogen-bonded network remains intact during 2 ns simulations. Proton delivery along such a network via a Grotthuss-type mechanism seems feasible but has not been studied at present.

Experimentally, the D251N mutant catalyzes the hydroxylation of camphor, but it is significantly less active than wild-type P450cam. The observed decrease in the product formation rate by a factor of 30 implies that the rate-limiting barrier should be about 2 kcal/mol higher in the D251N mutant compared with the wild-type enzyme. It is not clear which step in the catalytic cycle is responsible for this reduced activity. Concerning the conversion from Cpd 0 to Cpd I, we find similar barriers for the initial O−O cleavage in both systems, suggesting that the subsequent proton transfer makes the difference. The QM/MM calculations indicate that the active-site proton transfer events are rather facile both in the wild-type enzyme (from Asp251) and in the flip+WatS model of the D251N mutant (from Wat901). It is thus conceivable that a more difficult reprotonation from bulk solvent contributes to the reduced activity of the mutant.

Experimental solvent kinetic isotope effects (SKIEs) provide further mechanistic information. A recent study[53] reported an SKIE value (H/D) of 1.8 at 190 K (corresponding roughly to 1.6−1.7 at ambient temperature) for the second proton transfer (Cpd 0 → Cpd I) in wild-type P450cam, indicating some solvent participation in this process. Measurements of the turnover rates in various protium−deuterium mixtures gave SKIE values (H/D) of 1.8 for wild-type P450cam and of 10 for the D251N mutant.[10] These steady-state data do not refer to well-defined elementary reaction steps and can thus not be directly related to our computational results, but the dramatic increase for the D251N mutant suggests that solvent water molecules are more heavily involved in the reactions of this mutant compared with the wild-type enzyme. According to proton inventory analysis, the number of protons involved in the rate-limiting step appears to be far larger in the mutant (five to seven) than in wild-type P450cam.[10] These experimental findings are not at odds with the mechanistic scenario outlined above for the D251N mutant (i.e., proton delivery from bulk solvent to the formed OH anion through a water network).

In general, Cpd 0 can undergo two different protonation reactions, namely coupling (formation of Cpd I and water) and uncoupling (formation of the ferric resting state and hydrogen peroxide). According to the present QM/MM calculations, coupling is favored over uncoupling by a large margin in the D251N mutant. This is consistent with the experimental result that hydroxylation is the dominant reaction also in the D251N mutant, which implies the formation of Cpd I as the crucial reactive species in the P450cam consensus mechanism.

V. Conclusion

The present QM/MM study of the D251N mutant of cytochrome P450cam addresses the mechanism of the protonation reactions involving Cpd 0. The QM/MM calculations were performed at the UB3LYP/CHARMM level with two different

Downloaded by MPI KOHLENFORSCH / BIOANORG CH on July 9, 2009
Published on June 19, 2009 on http://pubs.acs.org | doi: 10.1021/jp809838k

Downloaded by MPI KOHLENFORSCH / BIOANORG CH on July 9, 2009
Published on June 19, 2009 on http://pubs.acs.org | doi: 10.1021/jp809838k

basis sets. For all reactions, only minor differences in the computed relative energies were observed upon basis set extension.

Classical MD simulations indicate that the side chain of the Asn251 residue can adopt two conformations: pointing toward the active site (no flip) and pointing toward the protein surface (flip). The flip of the Asn251 side chain breaks the H-bond network that connects the FeOOH moiety and Asn251, and releases enough space to accommodate an additional water molecule. The stability of the extra water molecule (WatS) was confirmed by MD simulation. Hence, three models were considered for the D251N mutant: no flip, flip, and flip with an extra water molecule.

We investigated two mechanisms that correspond to the formation of Cpd I and water (coupling reaction) and two mechanisms that lead to the formation of hydrogen peroxide and the ferric resting state (uncoupling reaction). The results clearly show, in agreement with experimental[54] findings, that the uncoupling reaction is unfavorable in the D251N mutant. Likewise, the mechanism that involves initial protonation of Cpd 0 in the coupling reaction is less likely, since the formation of protonated Cpd 0 is difficult. The coupling reaction in the D251N mutant is thus predicted to follow a stepwise mechanism that involves initial cleavage of the O−O bond and subsequent proton transfer to the distal oxygen. As this initial step does not require the participation of a proton source, there is no significant effect due to the D251N mutation.

The course of the subsequent protonation is found to be model-dependent. In model I (no flip), the Asn251 residue serves as the proton source, in spite of its high pK_a value. The first hydrogen transfer has an effective barrier of 20.6 kcal/mol and leads to the formation of Cpd I and deprotonated Thr252, which is then restored in a second step by accepting a proton from Asn251 via Wat901 and an electron from the heme (transition state 24.5 kcal/mol above Cpd 0). The reprotonation of Asn251 is expected to be facile, since Asn251 is in close contact with the bulk solvent.

In model II (flip) the protonation requires three steps. The path is blocked after the protonation of the Thr252 residue, however, since the Asn251 residue does not act as proton source and there is no other proton source in the vicinity. The corresponding product complex lies 19.2 kcal/mol above Cpd 0. Including the Arg186 residue in this model does not help, since it is too far away to enable proton transfer.

In model III (flipped with an extra water molecule in the active site), there is a well-connected H-bond network that facilitates the formation of Cpd I and the reprotonation of Thr252 from Wat901. The proton transfer is effectively concerted with a barrier of around 14 kcal/mol and an endothermicity of 7.7 kcal/mol. The presence of an extra water thus lowers the barrier appreciably and makes model III most realistic. However, we were unable to reprotonate the formed hydroxide anion (Wat901) from Arg186, so that the most likely scenario is reprotonation from the bulk solvent via a water network that remains intact during 2 ns of classical MD simulation. This process has not been studied at the QM/MM level, but it may well require additional activation and thus increase the effective barrier for Cpd I formation.

Acknowledgment. This work was supported by the Max Planck Society.

Supporting Information Available: Energies, spin densities, group charges, and optimized geometries for mechanisms II, III, and IV. QM/MM energy profiles from pathway calculations. Relative QM/MM energies for mechanism II (with partitioning into QM and MM contributions). MD simulation of the water network in the product complex (mechanism II, model III). Spin densities and group charges of intermediate IC2 in models I and II for different combinations of functional, basis set, and QM region. An overview figure showing all relevant residues. This material is available free of charge via the Internet at http://pubs.acs.org.

References and Notes

(1) Omura, T.; Sato, R. *J. Biol. Chem.* **1962**, *237*, 1375–1376.
(2) Ortiz de Montellano, P. R. *Cytochrome P450: Structure, Mechanism and Biochemistry*, 3rd ed.; Plenum Press: New York, 2005.
(3) Schlichting, I.; Berendzen, J.; Chu, K.; Stock, A. M.; Maves, S. A.; Benson, D. E.; Sweet, R. M.; Ringe, D.; Petsko, G. A.; Sligar, S. G. *Science* **2000**, *287*, 1615–1622.
(4) Poulos, T. L.; Finzel, B. C.; Howard, A. J. *J. Mol. Biol.* **1987**, *195*, 687–700.
(5) Aikens, J.; Sligar, S. G. *J. Am. Chem. Soc.* **1994**, *116*, 1143–1144.
(6) Gerber, N. C.; Sligar, S. G. *J. Biol. Chem.* **1994**, *269*, 4260–4266.
(7) Kamachi, T.; Shiota, Y.; Ohta, T.; Yoshizawa, K. *Bull. Chem. Soc. Jpn.* **2003**, *76*, 721–732.
(8) Martinis, S. A.; Atkins, W. M.; Stayton, P. S.; Sligar, S. G. *J. Am. Chem. Soc.* **1989**, *111*, 9252–9253.
(9) Shimada, H.; Makino, R.; Unno, M.; Horiuchi, T.; Ishimura, Y. In *Cytochrome P450cam 8th International Conference*; Libbey, J., Ed.; Eurotext:Paris, 1994, p 299.
(10) Vidakovic, M.; Sligar, S. G.; Li, H.; Poulos, T. L. *Biochemistry* **1998**, *37*, 9211–9219.
(11) Guallar, V.; Friesner, R. A. *J. Am. Chem. Soc.* **2004**, *126*, 8501–8508.
(12) Harris, D. L.; Loew, G. H. *J. Am. Chem. Soc.* **1996**, *118*, 6377–6387.
(13) Harris, D. L.; Loew, G. H. *J. Am. Chem. Soc.* **1994**, *116*, 11671–11674.
(14) Sligar, S. G.; Markis, T. M. Private communications, February 2005.
(15) Gerber, N. C.; Sligar, S. G. *J. Am. Chem. Soc.* **1992**, *114*, 8742–8743.
(16) Lounnas, V.; Wade, R. C. *Biochemistry* **1997**, *36*, 5402–5417.
(17) Harris, D. L.; Loew, G. H. *J. Am. Chem. Soc.* **1998**, *120*, 8941–8948.
(18) Taraphder, S.; Hummer, G. *J. Am. Chem. Soc.* **2003**, *125*, 3931–3940.
(19) Zheng, J.; Wang, D.; Thiel, W.; Shaik, S. *J. Am. Chem. Soc.* **2006**, *128*, 13204–13215.
(20) Benson, D. E.; Suslick, K. S.; Sligar, S. G. *Biochemistry* **1997**, *36*, 5104–5107.
(21) Imai, M.; Shimada, H.; Watanabe, Y.; Matsuhima-Hibiya, Y.; Makino, R.; Koga, H.; Horiuchi, T.; Ishimura, Y. *Proc. Natl. Acad. Sci. U. S. A.* **1989**, *86*, 7823–7827.
(22) Oprea, T. I.; Hummer, G.; Garcïa, A. E. *Proc. Natl. Acad. Sci. U. S. A.* **1997**, *94*, 2133–2138.
(23) Raag, R.; Martinis, S. A.; Sligar, S. G.; Poulos, T. L. *Biochemistry* **1997**, *36*, 5104–5107.
(24) Kamachi, T.; Yoshizawa, K. *J. Am. Chem. Soc.* **2003**, *125*, 4652–4661.
(25) Kumar, D.; Hirao, H.; De Visser, S. P.; Zheng, J.; Wang, D.; Thiel, W.; Shaik, S. *J. Phys. Chem. B* **2005**, *109*, 19946–19951.
(26) Ogliaro, F.; De Visser, S. P.; Cohen, S.; Sharma, P. K.; Shaik, S. *J. Am. Chem. Soc.* **2002**, *124*, 2806–2817.
(27) Shaik, S.; Kumar, D.; de Visser, S. P.; Altun, A.; Thiel, W. *Chem. Rev.* **2005**, *105*, 2279–2328.
(28) Hishiki, T.; Shimada, H.; Nagano, S.; Egawa, T.; Kanamori, Y.; Makino, R.; Park, S. Y.; Adachi, S. I.; Shiro, Y.; Ishimura, Y. *J. Biochem.* **2000**, *128*, 965–974.
(29) Altarsha, M.; Benighaus, T.; Kumar, D.; Thiel, W. *J. Am. Chem. Soc.* **2009**, *131*, 4755–4763.
(30) Wang, D.; Zheng, J.; Shaik, S.; Thiel, W. *J. Phys. Chem. B* **2008**, *112*, 5126–5138.
(31) Altun, A.; Thiel, W. *J. Phys. Chem. B* **2005**, *109*, 1268–1280.
(32) Schöneboom, J. C.; Lin, H.; Reuter, N.; Thiel, W.; Cohen, S.; Ogliaro, F.; Shaik, S. *J. Am. Chem. Soc.* **2002**, *124*, 8142–8151.
(33) Schöneboom, J. C.; Thiel, W. *J. Phys. Chem. B* **2004**, *108*, 7468–7478.
(34) Jorgensen, W. L.; Chandrasekhar, J.; Madura, J. D.; Impey, R. W.; Klein, M. L. *J. Chem. Phys.* **1983**, *79*, 926–935.
(35) MacKerell, A. D., Jr.; Bashford, D.; Bellott, M.; Dunbrack, R. L., Jr.; Evanseck, J. D.; Field, M. J.; Fischer, S.; Gao, J.; Guo, H.; Ha, S.; Joseph-McCarthy, D.; Kuchnir, L.; Kuczera, K.; Lau, F. T. K.; Mattos, C.;

Michnick, S.; Ngo, T.; Nguyen, D. T.; Prodhom, B.; Reiher, W. E., III; Roux, B.; Schlenkrich, M.; Smith, J. C.; Stote, R.; Straub, J.; Watanabe, M.; Wiórkiewicz-Kuczera, J.; Yin, D.; Karplus, M. *J. Phys. Chem. B* **1998**, *102*, 3586–3616.

(36) Brooks, B. R.; Bruccoleri, R. E.; Olafson, B. D.; States, D. J.; Swaminathan, S.; Karplus, M. *J. Comput. Chem.* **1983**, *4*, 187–217.

(37) Becke, A. D. *J. Chem. Phys.* **1993**, *98*, 5648–5652.

(38) Hay, P. J.; Wadt, W. R. *J. Chem. Phys.* **1985**, *82*, 299–310.

(39) Hehre, W. J.; Ditchfield, K.; Pople, J. A. *J. Chem. Phys.* **1972**, *56*, 2257–2261.

(40) Schäfer, A.; Horn, H.; Ahlrichs, R. *J. Chem. Phys.* **1992**, *97*, 2571–2577.

(41) Schäfer, A.; Huber, C.; Ahlrichs, R. *J. Chem. Phys.* **1994**, *100*, 5829–5835.

(42) Smith, W.; Forester, T. R. *J. Mol. Graphics* **1996**, *14*, 136–141.

(43) Sherwood, P.; De Vries, A. H.; Guest, M. F.; Schreckenbach, G.; Catlow, C. R. A.; French, S. A.; Sokol, A. A.; Bromley, S. T.; Thiel, W.; Turner, A. J.; Billeter, S.; Terstegen, F.; Thiel, S.; Kendrick, J.; Rogers, S. C.; Casci, J.; Watson, M.; King, F.; Karlsen, E.; Sjøvoll, M.; Fahmi, A.; Schäfer, A.; Lennartz, C. *THEOCHEM* **2003**, *632*, 1–28.

(44) Ahlrichs, R.; Bär, M.; Häser, M.; Horn, H.; Kälmel, C. *Chem. Phys. Lett.* **1989**, *162*, 165–169.

(45) Billeter, S. R.; Turner, A. J.; Thiel, W. *Phys. Chem. Chem. Phys.* **2000**, *2*, 2177–2186.

(46) Bakowies, D.; Thiel, W. *J. Phys. Chem.* **1996**, *100*, 10580–10594.

(47) Sherwood, P.; De Vries, A. H.; Collins, S. J.; Greatbanks, S. P.; Burton, N. A.; Vincent, M. A.; Hillier, I. H. *Faraday Discuss.* **1997**, *106*, 79–92.

(48) Nagano, S.; Poulos, T. L. *J. Biol. Chem.* **2005**, *280*, 31659–31663.

(49) Marx, D. *ChemPhysChem* **2006**, *7*, 1848–1870.

(50) Muller, R. P.; Warshel, A. *J. Phys. Chem.* **1995**, *99*, 17516–17524.

(51) Tuckerman, M. E.; Chandra, A.; Marx, D. *Acc. Chem. Res.* **2006**, *39*, 151–158.

(52) Mathias, G.; Marx, D. *Proc. Natl. Acad. Sci. U. S. A.* **2007**, *104*, 6980–6985.

(53) Kim, S. H.; Yang, T.-C.; Perera, R.; Jin, S.; Bryson, T. A.; Sono, M.; Davydov, R.; Dawson, J. H.; Hoffman, B. M. *Dalton Trans.* **2005**, 3464–3469.

(54) Markis, T. M.; Denisov, I. G.; Schlichting, I.; Sligar, S. G. In *Cytochrome P450: Sturcture, Mechanism and Biochemistry*, 2nd ed.; Plenum Press: New York, 1995.

JP809838K

Downloaded by MPI KOHLENFORSCH / BIOANORG CH on July 9, 2009
Published on June 19, 2009 on http://pubs.acs.org | doi: 10.1021/jp809838k

J|A|C|S ARTICLES

Published on Web 03/12/2009

How is the Reactivity of Cytochrome P450cam Affected by Thr252X Mutation? A QM/MM Study for X = Serine, Valine, Alanine, Glycine

Muhannad Altarsha, Tobias Benighaus, Devesh Kumar, and Walter Thiel*

Max-Planck-Institut für Kohlenforschung, Kaiser-Wilhelm-Platz 1, D-45470 Mülheim an der Ruhr, Germany

Received November 7, 2008; E-mail: thiel@mpi-muelheim.mpg.de

Abstract: Proton transfer reactions play a vital role in the catalytic cycle of cytochrome P450cam and are responsible for the formation of the iron-oxo species called Compound I (Cpd I) that is supposed to be the active oxidant. Depending on the course of the proton transfer, protonation of the last observable intermediate (ferric hydroperoxo complex, Cpd 0) can lead to either the formation of Cpd I (coupling reaction) or the ferric resting state (uncoupling reaction). The ratio of these two processes is drastically affected by mutation of the Thr252 residue. In this work, we study the effect of Thr252X (X = serine, valine, alanine, glycine) mutations on the formation of Cpd I by means of hybrid quantum mechanical/molecular mechanical (QM/MM) calculations and classical simulations. In the wild-type enzyme, the coupling reaction is favored since its rate-limiting barrier is 13 kcal/mol lower than that for uncoupling. This difference is reduced to 7 kcal/mol in the serine mutant. In the case of valine, alanine, and glycine mutants, an additional water molecule enters the active site and lowers the activation energy of the uncoupling reaction significantly. With the additional water molecule, coupling and uncoupling have similar barriers in the valine mutant, and the uncoupling reaction becomes favored in the alanine and glycine mutants. These findings agree very well with experimental results and thus confirm the assumption that uncontrolled proton delivery by solvent water networks is responsible for the uncoupling reaction. The present study provides a detailed mechanistic understanding of the role of the Thr252 residue.

I. Introduction

The heme protein monooxygenases known as cytochrome P450 play a vital role in the metabolism of xenobiotic substances in plants, fungi, bacteria, insects, and mammals.[1−3] They catalyze a variety of reactions including hydroxylation, epoxidation, and heteroatom oxidation. The consensus mechanism of P450 hydroxylation is shown in Scheme 1, where the proximal cysteinate ligand is abbreviated as L, and the porphyrin macrocycle is symbolized by the two bold lines flanking the iron.[4] The catalytic cycle begins with the resting state (**S1**) in which a water molecule is bound to the ferric ion in the distal side. When a substrate enters the protein pocket, the water molecule is displaced from the reactive center, leaving a ferric substrate-bound state (ferric resting state, **S2**). This complex is a slightly better electron acceptor than the resting state and can therefore take up an electron from reductase protein, leading to a high-spin ferrous complex (**S3**). Subsequent binding of molecular oxygen produces the oxyferrous state (**S4**). Addition of a second electron yields a peroxo-ferric derivative (**S5**) that, upon protonation of the distal oxygen, forms a hydroperoxo-ferric intermediate which is also known as Compound 0 (Cpd 0, **S6**). A second protonation then leads to O−O bond cleavage with loss of a water molecule and generates the "active oxygen" in the putatively active oxoferryl species Compound I (Cpd I, **S7**). Alternatively, protonation of the proximal oxygen of Cpd 0 (**S6**) leads to release of hydrogen peroxide and regenerates the ferric resting state (**S2** in Scheme 1).

In recent years, much attention has focused on possible mechanisms for the required proton delivery to the active site. On the basis of extensive site-directed mutation studies,[5−10] it has been suggested that the Asp251 and Thr252 residues participate in a controlled proton delivery pathway that involves solvent water and provides an active-site H-bond donor, which may be a trapped water molecule rather than Thr252.[5,8] The Thr252 residue is highly conserved in P450cam crystal structures and is believed to play an important role in the dioxygen activation machinery.[11]

(1) Guengerich, F. P. *J. Biol. Chem.* **1991**, *266*, 10019–10022.
(2) Porter, T. D.; Coon, M. J. *J. Biol. Chem.* **1991**, *266*, 13469–13472.
(3) (a) Ortiz de Montellano, P. R. *Cytochrome P450: Structure, Mechanism and Biochemistry*, 2nd ed.; Plenum Press: New York, 1995. (b) Ortiz de Montellano, P. R. *Cytochrome P450: Structure, Mechanism and Biochemistry*, 3rd ed.; Plenum Press: New York, 2005.
(4) Davydov, R.; Macdonald, I. D. G.; Makris, T. M.; Sugar, S. G.; Hoffman, B. M. *J. Am. Chem. Soc.* **1999**, *121*, 10654–10655.
(5) Vidakovic, M.; Sligar, S. G.; Li, H.; Poulos, T. L. *Biochemistry* **1998**, *37*, 9211–9219.
(6) Martinis, S. A.; Atkins, W. M.; Stayton, P. S.; Sligar, S. G. *J. Am. Chem. Soc.* **1989**, *111*, 9252–9253.
(7) Imai, M.; Shimada, H.; Watanabe, Y.; Matsuhima-Hibiya, Y.; Makino, R.; Koga, H.; Horiuchi, T.; Ishimura, Y. *Proc. Natl. Acad. Sci. U.S.A.* **1989**, *86*, 7823–7827.
(8) Gerber, N. C.; Sligar, S. G. *J. Biol. Chem.* **1994**, *269*, 4260–4266.
(9) Gerber, N. C.; Sligar, S. G. *J. Am. Chem. Soc.* **1992**, *114*, 8742–8743.
(10) Benson, D. E.; Suslick, K. S.; Sligar, S. G. *Biochemistry* **1997**, *36*, 5104–5107.

 © 2009 American Chemical Society

Scheme 1. Cytochrome P450cam Reaction Cycle

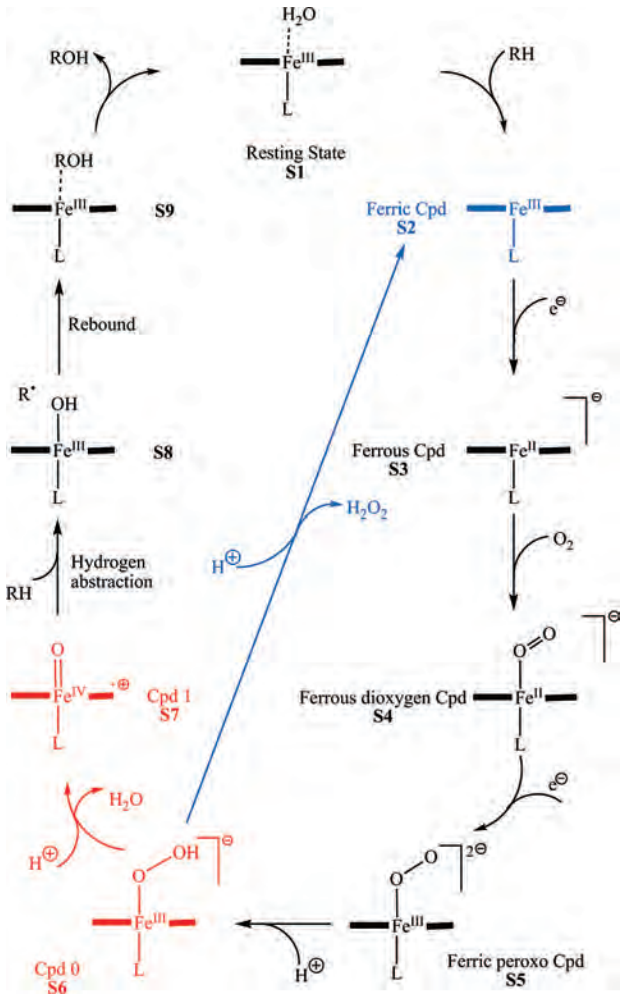

Site-directed mutagenesis studies[6−9] indicate that the presence of Thr252 is essential for the formation of Cpd I in P450cam. Upon replacement by an aliphatic residue in mutants such as Thr252Ala (T252A)[7,12] and Thr252Gly (T252G),[7] there is an uncoupling of O_2 consumption from camphor hydroxylation: most of O_2 consumed is converted to H_2O_2 without O−O bond cleavage,[7] and only 5% (3%) of the T252A (T252G) mutants undergo hydroxylation. By contrast, in the wild-type enzyme, the coupling ratio of O_2 consumption and hydroxylation is 100%. According to a low-temperature EPR and ENDOR study, both wild-type P450cam and the T252A mutant form Cpd 0 at 77 K, but only the former gives hydroxylation upon warming while the latter shows uncoupling, thus confirming the key role of Thr252 during the delivery of the second proton in the catalytic cycle (from **S6** to **S7**).[4] Given that Cpd I formation is suppressed in the T252A mutant, the observed reactivity toward other substrates may suggest the existence of more than one oxidant in P450 enzymes.[13] For example, the T252A mutant is capable of epoxidizing the double bond of olefins such as 5-methylenylcamphor, presumably with Cpd 0 being the active species in this case.[14] However, Cpd 0 is generally found to be a sluggish oxidant that is not competitive with Cpd I and may only function as such in the absence of Cpd I.[14−17]

Substitution of Thr252 with valine (T252V) also causes a considerable uncoupling of oxygen consumption and hydroxylation, with about 30−40% of hydrogen peroxide formation.[7,18] Substitution with serine (T252S), a hydroxyamino acid, has a smaller effect: only approximately 15% of O_2 consumed is recovered as H_2O_2.[7,18,19] Replacing the Thr252 side-chain hydroxyl (OH) with a methoxy (OCH_3) group slows the hydroxylation reaction significantly, but the yield of 5-exohydroxycamphor is still 100% (no uncoupling).[19]

Taken together, these experimental findings indicate that the Thr252 residue plays a crucial mechanistic role and influences the ratio of hydroxylation versus uncoupling products. Although a free hydroxy group at position 252 is not a prerequisite for O−O bond cleavage in P450cam, the replacement of Thr252 by amino acids with non-hydrogen-bonding side chains virtually suppresses camphor hydroxylation in favor of the uncoupled reduction of O_2 to H_2O_2.[7,18,20]

In the crystal structure of the T252A mutant, there is a water molecule near the O_2 binding site of the mutant which is not present in the wild-type enzyme.[11,21] This suggests that the solvent may be responsible for the observed uncoupling of the enzyme turnover from camphor hydroxylation in the mutant:[12,21] solvent in contact with dioxygen may supply protons in an uncontrolled manner, promoting H_2O_2 production, rather than substrate hydroxylation.

The available crystal structures[22] of wild-type P450cam indicate three possible proton delivery pathways through the Asp251,[5,23,24] Glu366,[22,25] and Arg299[26] channels. The latter has been characterized through a combined site-directed mutagenesis and molecular dynamics study[27] but is blocked when substrate is present. In the Glu366 channel, the bridging water molecules (nos. 687, 566, 523, and 902 in PDB structure 1DZ8[22]) and the hydroxyl group of Thr252 form a network connecting the carboxyl group of Glu366 and the distal oxygen atom, which however terminates at Glu366 without any connection to the surface.[5] In this paper, we shall therefore focus on the Asp251 channel only.

(11) Raag, R.; Martinis, S. A.; Sligar, S. G.; Poulos, T. L. *Biochemistry* **1991**, *30*, 11420–11429.
(12) Nagano, S.; Cupp-Vickery, J. R.; Poulos, T. L. *J. Biol. Chem.* **2005**, *280*, 22102–22107.
(13) Denisov, I. G.; Makris, T. M.; Sligar, S. G.; Schlichting, I. *Chem. Rev.* **2005**, *105*, 2253–2278.
(14) Jin, S.; Makris, T. M.; Bryson, T. A.; Sligar, S. G.; Dawson, J. H. *J. Am. Chem. Soc.* **2003**, *125*, 3406–3407.
(15) De Visser, S. P.; Kumar, D.; Shaik, S. *J. Inorg. Biochem.* **2004**, *98*, 1183–1193.
(16) Li, C.; Zhang, L.; Zhang, C.; Hirao, H.; Wu, W.; Shaik, S. *Angew. Chem., Int. Ed.* **2007**, *46*, 8168–8170.
(17) Hirao, H.; Kumar, D.; Shaik, S. *J. Inorg. Biochem.* **2006**, *100*, 2054–2068.
(18) Shimada, H.; Makino, R.; Imai, M.; Horiuchi, T.; Ishimura, Y. Mechanism of Oxygen Activation by Cytochrome P-450cam. *International Symposium on Oxygenases and Oxygen Activation*; Yamada Science Foundation, 1990; pp 133−136.
(19) Kimata, Y.; Shimada, H.; Hirose, T.; Ishimura, Y. *Biochem. Biophys. Res. Commun.* **1995**, *208*, 96–102.
(20) Aikens, J.; Sligar, S. G. *J. Am. Chem. Soc.* **1994**, *116*, 1143–1144.
(21) Hishiki, T.; Shimada, H.; Nagano, S.; Egawa, T.; Kanamori, Y.; Makino, R.; Park, S. Y.; Adachi, S. I.; Shiro, Y.; Ishimura, Y. *J. Biochem.* **2000**, *128*, 965–974.
(22) Schlichting, I.; Berendzen, J.; Chu, K.; Stock, A. M.; Maves, S. A.; Benson, D. E.; Sweet, R. M.; Ringe, D.; Petsko, G. A.; Sligar, S. G. *Science* **2000**, *287*, 1615–1622.
(23) Taraphder, S.; Hummer, G. *J. Am. Chem. Soc.* **2003**, *125*, 3931–3940.
(24) Kamachi, T.; Yoshizawa, K. *J. Am. Chem. Soc.* **2003**, *125*, 4652–4661.
(25) Guallar, V.; Friesner, R. A. *J. Am. Chem. Soc.* **2004**, *126*, 8501–8508.
(26) Oprea, T. I.; Hummer, G.; García, A. E. *Proc. Natl. Acad. Sci. U.S.A.* **1997**, *94*, 2133–2138.
(27) Loida, P. J.; Sligar, S. G.; Paulsen, M. D.; Arnold, G. E.; Ornstein, R. L. *J. Biol. Chem.* **1995**, *270*, 5326–5330.

Previous theoretical studies have addressed the formation of Cpd I from Cpd 0 in the wild-type enzyme using gas-phase model systems.[23,25,28−32] In the most elaborate such work, density functional theory (DFT) calculations on a large active site model with 96 atoms predict the existence of a protonated Cpd 0 species with significant barriers for the conversion both toward Cpd 0 and Cpd I.[30] According to a later quantum mechanics/molecular mechanics (QM/MM) study,[33] protonation of Cpd 0 by Glu366 via a hydrogen-bonding network may indeed generate such an intermediate, which however is very high in energy (more than 20 kcal/mol above Cpd 0) and mechanistically irrelevant since the barrier for its decay is only 3−4 kcal/mol both toward Cpd 0 and Cpd I. The QM/MM calculations suggest another mechanism instead: an initial homolytic O−O bond cleavage generates an OH species and one-electron reduced Cpd I, and subsequent proton transfer to this OH species with concomitant electron transfer from the heme yields Cpd I and water. The rate-limiting step at the QM/MM level is O−O cleavage with a barrier of about 13−14 kcal/mol in both the Asp251 and Glu366 channels.

Here, we extend this previous QM/MM work to address the effect of Thr252 mutations on the formation of Cpd I and on the competition between coupling and uncoupling reactions, that is, conversion of Cpd 0 to Cpd I and water as opposed to the ferric resting state and hydrogen peroxide. We cover the wild-type P450cam enzyme and its mutants T252S, T252V, T252A, and T252G. We also consider the effect of an extra water molecule in the active site by means of classical MD simulations and QM/MM calculations for different mutants.

II. Computational Details

Starting from a crystallographic structure (pdb file: 1DZ8), we generated a Cpd 0 model for the T252S, T252V, T252A, and T252G mutants by manually replacing the threonine residue in the wild-type enzyme with serine, valine, alanine, and glycine, respectively. Solvation and protonation procedures followed standard protocols used previously in our group.[34−36] Asp251 was protonated since it serves as proton source in the present study. The resulting model with a net charge of −8*e* was neutralized by protonating selected ionic residues at the surface of the enzyme without affecting salt bridges or hydrogen bonds.

The system was solvated using 5891 TIP3P water molecules[37] (yielding a total of ca. 25 000 atoms). It was relaxed by energy minimizations and classical molecular dynamics (MD) simulations using the CHARMM22 force field[38] as implemented in the CHARMM[39] program. Throughout all MD simulations, the coordinates of the entire heme unit and the coordinating Cys357 as well as the outer 8 Å of the solvent layer were kept fixed.

The applied QM/MM methodology is analogous to that used in our group in related studies.[33−36] Therefore, only some aspects relevant to the present work are presented here. An electronic embedding scheme[40] was adopted in the QM/MM calculations; that is, the MM charges were included in the one-electron Hamiltonian of the QM part, and the QM/MM electrostatic interactions were evaluated from the QM electrostatic potential and MM partial charges. No cutoffs were introduced for the nonbonding MM and QM/MM interactions. Hydrogen link atoms and the charge shift model[41] were employed to treat the QM/MM boundary. The TURBOMOLE[42] program was used for the QM calculations, while the CHARMM22 force field was run through the DL_POLY[43] code for the treatment of the MM part. The QM/MM calculations were performed with the ChemShell package[44] that integrates the TURBOMOLE and DL_POLY programs, and geometry optimizations were carried out using the HDLC optimizer[45] implemented in ChemShell.

The QM part was treated by the UB3LYP[46] density functional method with a LACVP[47] small-core ECP basis set (B1), that is, double ζ on Fe and 6-31G[48] on the rest of the atoms. The MM part was described by the CHARMM22 force field. For improved accuracy, all calculations were repeated using the larger TZVP[49,50] basis set (B2) on all atoms.

The optimized active region was defined to include all residues and water molecules within 6 Å of any atom of the core region. This results in ca. 1400 atoms to be optimized, which belong to the iron−dioxygen−porphyrin complex, camphor, and the amino acid residues and water molecules around the active site. All minima and transition states (TS) reported in this paper were fully optimized.

QM Region: For our present QM/MM calculations, we employed QM regions analogous to those adopted for the wild-type enzyme in our previous work[33] (see Figure 1). For the wild-type enzyme (model A): iron−porphine (without heme side chains), sulfur atom of Cys357, distal O_2H moiety, the $C^{\beta}H-O^{\mu 1}H$ unit of Thr252, Wat901, and the $C^{\beta}H_2-C^{\mu}(=O^{\delta 1})(-O^{\delta 2}H)$ unit of Asp251 (Figure 1). For the serine mutant (model B), the threonine side chain was replaced by the serine side chain, and hence only the $C^{\mu 2}H_3-O^{\mu 1}H$ unit was included in the QM region. The QM regions for the valine, alanine, and glycine mutants were obtained analogously (see models C, E, and G in Figure 1), with the $C^{\mu 2}H_3-C^{\beta}H-C^{\mu 2}H_3$ unit (C) and the $C^{\mu 2}H_4$ unit (E) being part of the QM region. Finally, an extra water molecule (WatS) in the QM region extends models C, E, and G to models D, F, and H, respectively.

III. Results and Discussion

1. Classical MD Results. Classical MD simulations were performed to check whether the Asp251 channel can support an additional water molecule (WatS) to form a more extended hydrogen-bonding network. The native enzyme has been studied

(28) Shaik, S.; Kumar, D.; de Visser, S. P.; Altun, A.; Thiel, W. *Chem. Rev.* **2005**, *105*, 2279–2328.
(29) Ogliaro, F.; De Visser, S. P.; Cohen, S.; Sharma, P. K.; Shaik, S. *J. Am. Chem. Soc.* **2002**, *124*, 2806–2817.
(30) Kumar, D.; Hirao, H.; De Visser, S. P.; Zheng, J.; Wang, D.; Thiel, W.; Shaik, S. *J. Phys. Chem. B* **2005**, *109*, 19946–19951.
(31) Kamachi, T.; Shiota, Y.; Ohta, T.; Yoshizawa, K. *Bull. Chem. Soc. Jpn.* **2003**, *76*, 721–732.
(32) Harris, D. L.; Loew, G. H. *J. Am. Chem. Soc.* **1998**, *120*, 8941–8948.
(33) Zheng, J.; Wang, D.; Thiel, W.; Shaik, S. *J. Am. Chem. Soc.* **2006**, *128*, 13204–13215.
(34) Schöneboom, J. C.; Thiel, W. *J. Phys. Chem. B* **2004**, *108*, 7468–7478.
(35) Schöneboom, J. C.; Lin, H.; Reuter, N.; Thiel, W.; Cohen, S.; Ogliaro, F.; Shaik, S. *J. Am. Chem. Soc.* **2002**, *124*, 8142–8151.
(36) Altun, A.; Thiel, W. *J. Phys. Chem. B* **2005**, *109*, 1268–1280.
(37) Jorgensen, W. L.; Chandrasekhar, J.; Madura, J. D.; Impey, R. W.; Klein, M. L. *J. Chem. Phys.* **1983**, *79*, 926–935.
(38) MacKerell, A. D., Jr.; et al. *J. Phys. Chem. B* **1998**, *102*, 3586–3616.
(39) Brooks, B. R.; Bruccoleri, R. E.; Olafson, B. D.; States, D. J.; Swaminathan, S.; Karplus, M. *J. Comput. Chem.* **1983**, *4*, 187–217.
(40) Bakowies, D.; Thiel, W. *J. Phys. Chem.* **1996**, *100*, 10580–10594.
(41) Sherwood, P.; De Vries, A. H.; Collins, S. J.; Greatbanks, S. P.; Burton, N. A.; Vincent, M. A.; Hillier, I. H. *Faraday Discuss.* **1997**, *106*, 79–92.
(42) Ahlrichs, R.; Bär, M.; Häser, M.; Horn, H.; Kölmel, C. *Chem. Phys. Lett.* **1989**, *162*, 165–169.
(43) Smith, W.; Forester, T. R. *J. Mol. Graph.* **1996**, *14*, 136–141.
(44) Sherwood, P.; et al. *J. Mol. Struct.* **2003**, *632*, 1–28.
(45) Billeter, S. R.; Turner, A. J.; Thiel, W. *Phys. Chem. Chem. Phys.* **2000**, *2*, 2177–2186.
(46) Becke, A. D. *J. Chem. Phys.* **1993**, *98*, 5648–5652.
(47) Hay, P. J.; Wadt, W. R. *J. Chem. Phys.* **1985**, *82*, 299–310.
(48) Hehre, W. J.; Ditchfield, K.; Pople, J. A. *J. Chem. Phys.* **1972**, *56*, 2257–2261.
(49) Schäfer, A.; Huber, C.; Ahlrichs, R. *J. Chem. Phys.* **1994**, *100*, 5829–5835.
(50) Schäfer, A.; Horn, H.; Ahlrichs, R. *J. Chem. Phys.* **1992**, *97*, 2571–2577.

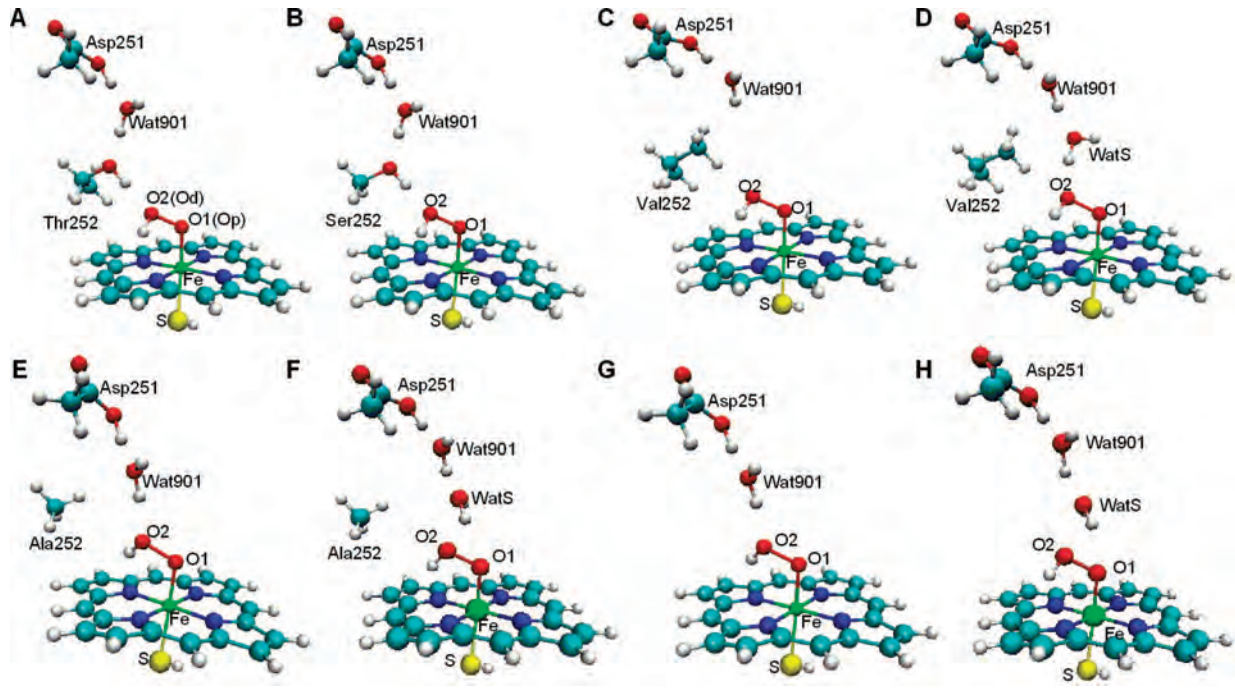

Figure 1. QM regions for the wild-type enzyme and its mutants. Models A, B, C, E, and G represent the native enzyme of P450cam, the T252S mutant, the T252V mutant, the T252A mutant, and the T252G mutant, respectively. Models D, F, and H extend models C, E, and G, respectively, with an extra water molecule (WatS).

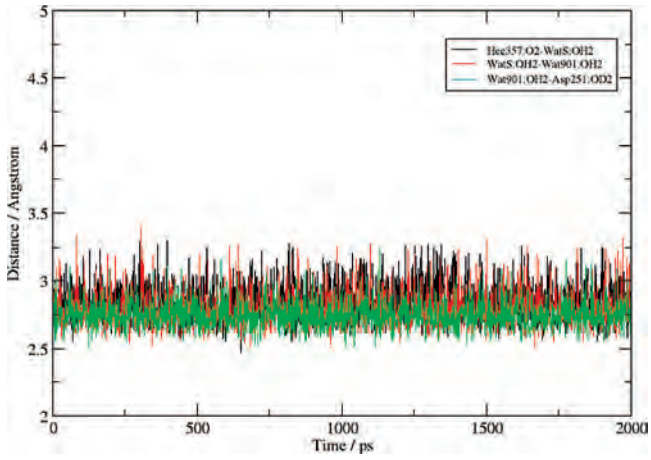

Figure 2. Monitoring the mobility of the extra water molecule (WatS) in the T252A mutant (for atom labels, see Figure 1F; Hec is the porphine-FeO2 unit).

previously in this regard, and it was found that the extra water molecule leaves the active site.[51] In the present MD simulations on the serine, valine, alanine, and glycine mutants of Cpd 0, we checked the mobility of WatS and, at the same time, tested the stability of the hydrogen-bonding network between Asp251 and the FeO_2H moiety.

Substitution of threonine by alanine generates some empty space in the distal pocket so that WatS can find a stable position between Wat901 and the FeO_2H moiety. The classical MD results for the alanine mutant in Figure 2 show that Wat901 and WatS do not escape from the protein pocket during the 2 ns simulation. WatS stays close to the FeO_2H moiety for most of the time, whereas Wat901 forms two hydrogen bonds with WatS and the Asp251 residue (confirmed by average distances of 2.80 ± 0.13 and 2.75 ± 0.10 Å for WatS:OH2-Wat901:OH2 and Wat901:OH2-Asp251:OD2, respectively). The distance between the O_2H moiety and the oxygen atom of WatS also remains around 3 Å (2.85 ± 0.13 Å). Hence all these hydrogen bonds are conserved in the alanine mutant. This is consistent with the crystal structure of the T252A mutant which shows an extra water molecule (not present in the wild-type enzyme) near the O2 (distal oxygen) binding site of the mutant.[11,21] Likewise, the 2 ns MD simulations for the valine and glycine mutants confirm the stability of the additional water molecule (see Figures S2 and S3 in the Supporting Information). By contrast, the extra water molecule is not stable in the serine mutant since it escapes from the distal pocket very early in the MD simulation (see Figure S1 in the Supporting Information), in analogy to the behavior of the wild-type enzyme.

2. Survey of Possible Reaction Mechanisms. Scheme 2 shows the four mechanisms that were considered in the QM/MM calculations. In each case, the crystallographic water molecule W901 (in combination with WatS in models D, F, and H) supports proton transfer from Asp251 to the X252 residue (X = threonine, serine, valine, alanine, and glycine). The proton transferred to the FeO_2H moiety comes from the hydroxy group of threonine in the WT enzyme or serine in the T252S mutant. In the absence of a hydroxy group, such as in the valine, alanine, and glycine mutants, it is transferred from the closest water molecule, which is Wat901 in models C, E, and G, and WatS in models D, F, and H. The proton-donating sites are replenished by proton transfer along the hydrogen-bonding network in the Asp251 channel. The following mechanisms were studied for coupling (I,II) and uncoupling (III,IV).

Mechanism I: Initially, the O−O bond is cleaved homolytically to generate an OH species and a one-electron reduced Cpd

(51) Zheng, J.; Altun, A.; Thiel, W. *J. Comput. Chem.* **2007**, *28*, 2147–2158.

Scheme 2. Mechanisms for (a) Cpd I Formation (Coupling Reaction) and (b) Ferric Resting State Formation (Uncoupling Reaction)

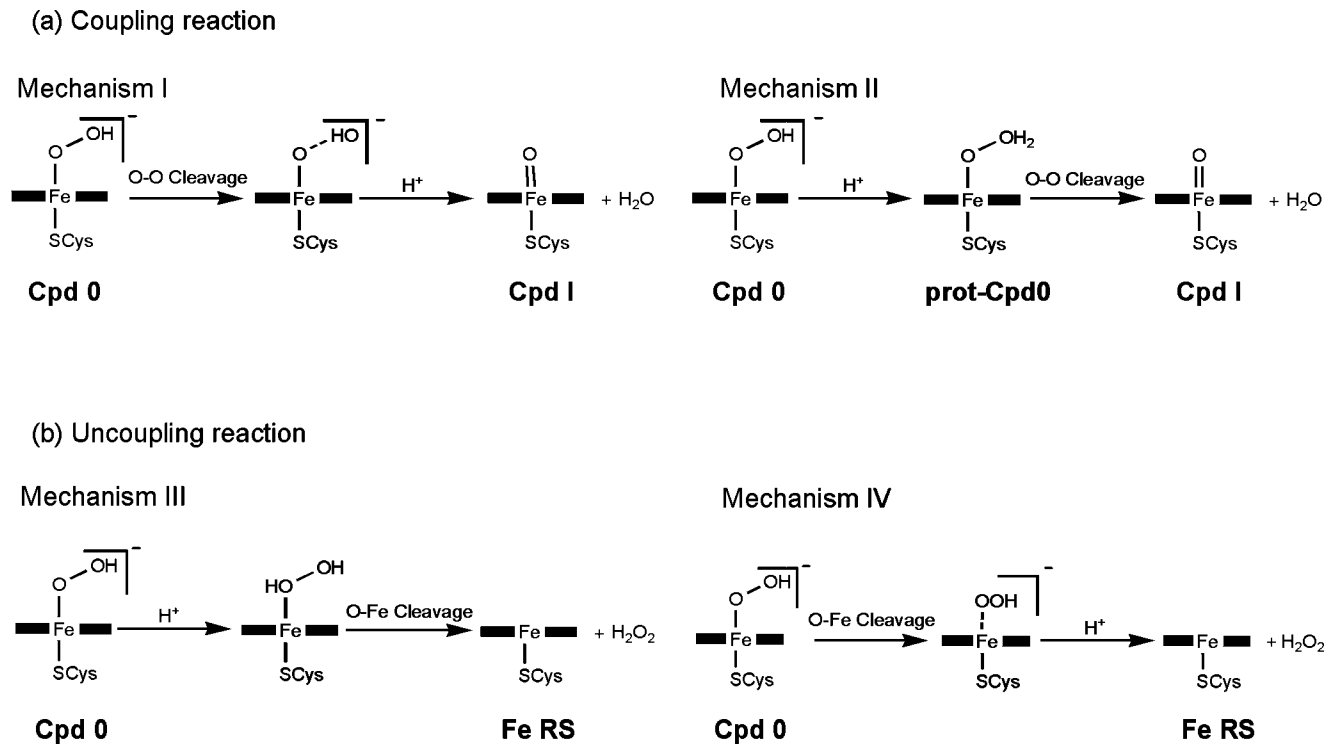

I. A subsequent proton transfer to the OH species with a concomitant electron transfer from the heme yields Cpd I and water.[33]

Mechanism II: A proton is transferred to the distal oxygen atoms of the hydroperoxo group to form protonated Cpd 0 (prot-Cpd 0: $FeOOH_2$), followed by heterolytic O−O bond cleavage that generates Cpd I and water.[33] In the Asp251 channel, we were unable to locate a stable prot-Cpd 0 minimum for any of the mutants, as in the case of the native enzyme.[33] We thus conclude that mechanism I is preferred and only discuss this mechanism for the coupling reaction.

Mechanism III: A proton is transferred to the proximal oxygen atom of the hydroperoxo group to form FeH_2O_2, accompanied by heterolytic O−Fe bond cleavage that generates the ferric resting state and hydrogen peroxide.

Mechanism IV: Initially, the O−Fe bond is cleaved homolytically to generate an OOH radical, followed by a proton transfer to the OOH group to yield the ferric resting state and hydrogen peroxide. Mechanism IV is calculated to be much less favorable than mechanism III for the uncoupling reaction since the O−Fe cleavage reaction always requires much activation. Inclusion of an extra water molecule in the T252V, T252A, and T252G mutants has only a minor effect on this barrier which remains high. Therefore, we do not discuss the corresponding results here but only document them in the Supporting Information.

3. QM/MM Results. The QM/MM optimized structures for the QM region of Cpd 0 are shown in Figure 1 for the native enzyme and its mutants. In the native enzyme, Cpd 0 has a doublet ground state which is more stable than the quartet state both in the gas phase[29,31] and the enzyme environment.[33] The same also holds for the T252X mutants, and we shall therefore only discuss the doublet state in this paper. We have carried out full QM/MM optimizations for all relevant doublet species using both the B1 and B2 basis set. The geometries and energies obtained with the two basis sets are generally similar. Optimized geometries are shown in Figures 3 and 4 and in Figures S4−S16 of Supporting Information. Table 1 lists the relative energies of all optimized stationary points (both B1 and B2 values, relative to Cpd 0). In the text, we shall quote energy values computed with the larger B2 basis set (unless noted otherwise).

In addition, we have also performed full QM/MM optimizations for the lowest quartet and sextet states of Cpd 0 in the wild-type enzyme and each mutant using the B1 basis set. The Supporting Information documents the corresponding results along with those for the doublet ground state in detail, providing QM, MM, and QM/MM energies, spin densities, group charges, and selected geometric parameters (Tables S2−S13). The Supporting Information also contains spin densities and group charges for the doublet states of the optimized stationary points of mechanisms I, III, and IV (B1 basis).

3.1. Wild-Type Enzyme. Coupling Reaction: We have previously investigated the conversion of Cpd 0 to Cpd I in the wild-type enzyme at the QM/MM level using the B1 basis.[33] We have now reoptimized the stationary points using the B2 basis, which leads to minor changes only. The transition states for the initial O−O cleavage and the subsequent proton transfer lie 14.3 and 11.7 kcal/mol above Cpd 0, respectively, and the overall reaction energy is calculated to be −3.7 kcal/mol.

Uncoupling Reaction: In the favored mechanism III, the proton is transferred through the Asp251−Wat901−Thr252−HOOFe hydrogen-bonding chain to O1 (proximal oxygen) which triggers O−Fe bond cleavage and generates the ferric resting state and hydrogen peroxide. Figure 3 shows the corresponding QM/MM optimized structures. According to the QM/MM calculations, the reaction proceeds in a single step, with an activation barrier of 27.0 kcal/mol, and is endothermic by 6.4 kcal/mol. The formed hydrogen peroxide has almost zero spin density (see Supporting Information) in the product (ferric resting state, FeRS). The Fe−O1 distance increases from 1.87 Å in Cpd 0 to

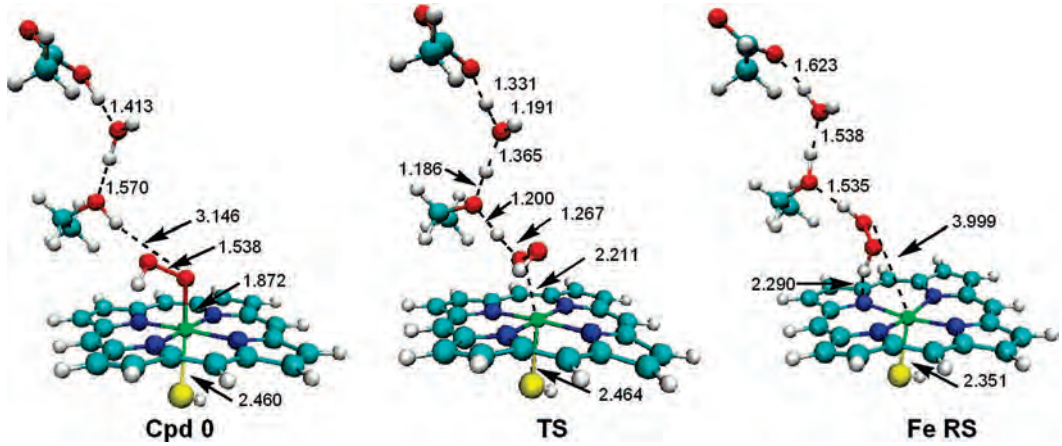

Figure 3. Optimized geometries (UB3LYP/B1/CHARMM) for the uncoupling reaction in the wild-type enzyme. Only the QM region is shown.

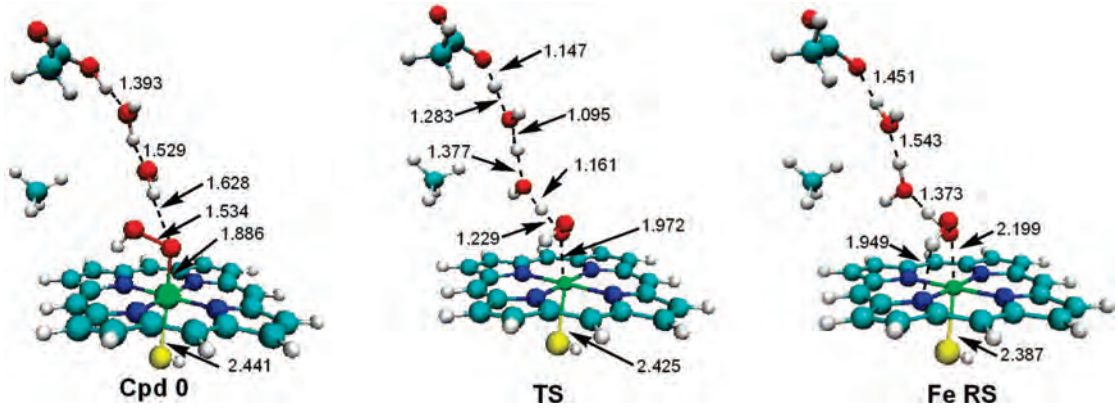

Figure 4. Optimized geometries (UB3LYP/B1/CHARMM) for the uncoupling reaction in the T252A mutant in the presence of an extra water molecule (WatS). Only the QM region is shown.

Table 1. Computed Relative Energies (kcal/mol) for Optimized Stationary Points Using Basis Sets B1/B2 (with respect to Cpd 0)[a]

mechanism	species	model A WT	model B T252S	model C T252V	model D T252V+W	model E T252A	model F T252A+W	model G T252G	model H T252G+W
I	TS1	14.4/14.3	15.8/15.6	17.1/17.1	19.0/18.9	17.4/17.1	17.5/17.3	18.8/17.9	19.3/18.9
	IC1	11.7/10.9	9.4/8.4	11.4/11.0	16.0/15.4	9.5/7.7	15.2/16.0	5.7/5.9	11.5/11.5
	TS2	14.3/11.7	11.4/11.6	14.6/15.0	18.1/18.1	12.3/10.6	16.7/17.0	7.1/7.8	11.7/11.9
	Cpd I	−0.2/−3.7	−0.4/−3.8	−0.2/−2.6	7.1/−0.6	−2.0/−2.3	2.5/−3.0	−2.6/−3.4	2.0/−5.0
III	TS	26.6/27.0	22.3/23.1	24.5/26.5	19.4/19.5	27.6/29.1	11.7/11.9	28.8/28.2	11.4/12.0
	Fe RS	7.2/6.4	11.8/8.0	7.5/6.4	13.4/7.2	5.6/−0.1	4.3/2.4	4.4/−1.0	4.8/1.7

[a] For notation see text; for models A−H, see Figure 1; +W denotes the presence of an extra water molecule. All energies refer to geometries that are fully optimized using the corresponding basis set (B1/B2).

4.00 Å in FeRS, and the O1−O2 distance is 1.51 Å, as expected for hydrogen peroxide.

In the native P450cam enzyme, the coupling reaction is thus computed to be much more facile than uncoupling, and there should be no release of hydrogen peroxide. This agrees with experiment where 5-exohydroxycamphor is found as the only product.[18]

3.2. T252S Mutant. In this mutant, there is only one water molecule (Wat901) in the distal pocket of the enzyme since a manually added water molecule (WatS) quickly leaves the pocket during MD simulation (see above and Figure S1 in Supporting Information). However, like threonine in the wild-type enzyme, serine has a hydroxyl group and can thus form a proton transfer channel from Asp251 to the FeOOH moiety through Wat901 and its hydroxyl group.

Coupling Reaction: Figure S4 in the Supporting Information presents the QM/MM optimized structures for the coupling reaction of the serine mutant. The barrier for O−O bond cleavage is 15.6 kcal/mol, and the energy of the first intermediate (IC1) is 8.4 kcal/mol. The transition state for the subsequent proton transfer from Asp251 via the water molecule (Wat901) to serine lies at 11.6 kcal/mol. The overall reaction is exothermic by −3.8 kcal/mol. After proton release, the side chain of Asp251 rotates back to form a salt bridge with Arg186 as shown in Figure S4 in Supporting Information. The spin density and charge of the OH group in the first intermediate (IC1) are −0.6 and −0.2, indicating that OH will not behave as a "perfect" radical in IC1 due to the strong hydrogen-bonding interactions with Ser252 and the FeO unit (as in the case of the wild-type enzyme[33]). Overall, the coupling reaction is very similar in the T252S mutant and the wild-type enzyme, both electronically and mechanistically. The rate-limiting barrier is slightly higher in the T252S mutant (15.6 vs 14.3 kcal/mol in the wild-type enzyme).

Uncoupling Reaction: The optimized structures are shown in Figure S5 in Supporting Information. Like in the wild-type enzyme, the reaction proceeds in one step, with an energy barrier of 23.1 kcal/mol, and is endothermic by 8.0 kcal/mol. In the transition state and the product, Ser252 and Asp251 have zero spin density, consistent with a proton-assisted heterolytic O−Fe bond cleavage. The O−O distance stays at around 1.5 Å during the reaction, whereas the Fe−O1 distance increases from 1.87 Å in Cpd 0 to 2.24 Å in TS1 and to 3.71 Å in the product, thus reflecting the formation of hydrogen peroxide and the cleavage of the O−Fe bond.

A comparison of the computed rate-limiting barriers for the T252S mutant shows that the coupling reaction is favored over the uncoupling reaction by 7.5 kcal/mol, less so than in the wild-type enzyme where the difference in the computed barriers is 12.8 kcal/mol. Experimentally, the serine mutant retains a high ratio in the coupling of oxygen consumption to *d*-camphor hydroxylation with some H_2O_2 formation being observed (15% of oxygen consumption relates to hydrogen peroxide and 85% to *d*-camphor hydroxylation).[7,19] The QM/MM calculations thus give the correct qualitative trend that uncoupling becomes more facile in the T252S mutant compared with the wild-type enzyme, but they are not accurate enough to provide quantitative predictions.

3.3. T252V Mutant. As noted before, the T252V mutant has enough space to accommodate an extra water molecule (WatS) in the distal pocket of the enzyme (see above and Figure S2 in Supporting Information). We have therefore studied its reactions without and with WatS (see models C and D in Figure 1). Figures S6−S9 in the Supporting Information show the QM/MM optimized structures (QM region only).

Coupling Reaction without WatS: Similar to the wild-type enzyme and the T252S mutant, the coupling reaction starts with O−O cleavage followed by proton transfer from Asp251 to the formed OH species either directly through Wat901 or through the methyl group of valine. The latter path through the methyl group is unfavorable (transition state at 26 kcal/mol) and will thus not be discussed. On the preferred path through Wat901, the transition states for the two steps lie at 17.1 and 15.0 kcal/mol, respectively, and the intermediate (IC1) is 11.0 kcal/mol above Cpd 0. Judging from the computed spin density (−0.97) IC1 contains an almost "pure" OH radical. After the proton transfer, Asp251 moves back to form a hydrogen bond with Arg186; in this product conformation, Asp251 has zero spin density and a Mulliken group charge of almost −0.5 e.

Coupling Reaction with WatS: The introduction of WatS extends the hydrogen-bonding network in the Asp251 channel. It does not affect the computed energy profile much. The two transition states are raised in energy slightly, to 18.9 and 18.1 kcal/mol, respectively. The intermediate again contains an OH radical (spin density of −0.98), and the formation of Cpd I is again roughly thermoneutral (−0.6 kcal/mol). The presence of an extra water molecule (WatS) in the protein pocket of the T252V mutant thus does not have a significant influence on the coupling reaction.

Uncoupling Reaction without WatS: As in the case of the T252V mutant, only a concerted process is found, with a barrier of 26.5 kcal/mol and an endothermicity of 6.4 kcal/mol. The O−Fe distance increases from 1.86 Å in Cpd 0 to 2.10 Å in the transition state and 4.04 Å in the product. The H_2O_2 moiety has zero spin density and a total charge of −0.1 in the product, consistent with the formation of hydrogen peroxide.

Uncoupling Reaction with WatS: The incorporation of an extra water molecule into the Asp251 channel lowers the computed barrier appreciably, by 7.0 to 19.5 kcal/mol, while the endothermicity changes only slightly to 7.2 kcal/mol. In the product, the spin density and Mulliken charge on H_2O_2 are 0.0 and −0.4 e, respectively.

Comparing the different mechanistic scenarios for the T252V mutant, we find similar barriers for coupling and uncoupling in the presence of WatS (18.9 vs 19.5 kcal/mol) and a slightly lower rate-limiting barrier for coupling in the absence of WatS (17.1 kcal/mol). Considering the limited accuracy of our calculations, we can only conclude qualitatively that these reactions should be competitive and that one should expect both *d*-camphor hydroxylation and H_2O_2 formation in the T252V mutant.

3.4. T252A Mutant. As in the case of the T252V mutant, we have studied the coupling and uncoupling reactions both in the absence and presence of an additional water molecule (WatS). The QM/MM optimized structures are shown in Figure 4 and Figures S10−S12 in the Supporting Information (QM regions only).

Coupling Reaction without WatS: The transition states for the two steps are located at 17.1 and 10.6 kcal/mol above Cpd 0. The rate-limiting barrier for the initial O−O cleavage is 2.8 kcal/mol higher than in the wild-type enzyme. The O−O distance increases from 1.53 Å in Cpd 0 to 2.60 Å in the intermediate (IC1), reflecting cleavage of the O−O bond. The O−Fe distance is 1.66 Å in the product, confirming the formation of Cpd I.

Coupling Reaction with WatS: Inclusion of an extra water molecule (i.e., going from model E to model F in Figure 1) has a negligible effect on the rate-limiting barrier for the initial O−O cleavage (17.3 kcal/mol) but raises the energies of the intermediate and the transition state for proton transfer appreciably. The overall exothermicity is also not affected much (−3.0 kcal/mol). After proton release, the side chain of Asp251 rotates back to form a salt bridge with Arg186 in the product.

Uncoupling Reaction without WatS: The proton transfer and the O−Fe bond cleavage occur in a concerted manner, with an activation barrier of 29.1 kcal/mol, which is about 12 kcal/mol higher than that for the coupling reaction in this mutant.

Uncoupling Reaction with WatS: Upon extension of the hydrogen-bonding network by WatS, the reaction remains concerted, but its barrier is reduced dramatically to 11.9 kcal/mol. The reaction energy does not change much (endothermic by 2.4 kcal/mol).

Comparing the computed barriers for the T252A mutant, we conclude that the uncoupling reaction is favored over the coupling reaction by about 5 kcal/mol, provided that an additional water molecule can enter the Asp251 channel close to the active site. If this is the case, the QM/MM results imply that formation of hydrogen peroxide should be dominant. This is consistent with the available experimental evidence.[12,21] Since Cpd I is not formed under these conditions, the experimentally observed epoxidation in the T252A mutant must be due to another oxidant, with Cpd 0 being an obvious candidate.[14] DFT calculations for gas-phase model systems indicate that Cpd 0 can indeed act as an oxidant for epoxidation, even though it is far less reactive than Cpd I.[17] It would seem worthwhile to address the possible competition between epoxidation and uncoupling in the T252A mutant in future QM/MM work.

3.5. T252G Mutant. Since the T252G mutant also provides sufficient space for an extra water molecule (WatS) close to

the active site, we studied the coupling and uncoupling reactions again in the absence and in the presence of WatS. Figures S13−S16 in the Supporting Information show the optimized QM/MM structures (QM regions only). Glycine is part of the MM region since it has no side chain that could be included in the QM region.

Coupling Reaction without WatS: The rate-limiting barrier for the initial O−O cleavage is 17.9 kcal/mol, that is, of similar magnitude as in the T252V and T252A mutants, but higher than in the wild-type enzyme. The intermediate (IC1) and the transition state for proton transfer from Asp251 to the OH radical lie 5.9 and 7.8 kcal/mol above Cpd 0, respectively. The overall reaction is exothermic by −3.4 kcal/mol.

Coupling Reaction with WatS: As in the other mutants, the presence of WatS molecule does not have much effect on the coupling reaction. Its inclusion raises the barrier for the initial O−O cleavage slightly to 18.9 kcal/mol and also increases the relative energies of the intermediate (11.5 kcal/mol) and the second transition (11.9 kcal/mol). The reaction remains exothermic (−5.0 kcal/mol).

Uncoupling Reaction without WatS: As in the case of the T252A mutant, the proton transfer from Asp251 via Wat901 to O1 and the cleavage of the Fe−O1 bond occur in a concerted reaction. The activation energy for the formation of H_2O_2 is 28.2 kcal/mol and thus about as high as that of the T252A mutant.

Uncoupling Reaction with WatS: The inclusion of WatS allows the formation of a more extended hydrogen-bonding network that provides a much better path for proton transfer between the proton source (Asp251) and the proton acceptor (O1). The barrier is thus reduced drastically to 12.0 kcal/mol, without affecting the reaction energy much (endothermic by 1.7 kcal/mol).

At first sight, it seems surprising that the uncoupling reaction with WatS has a significantly lower barrier in the T252A and T252G mutants than in the T252V mutant. Closer inspection of the QM/MM optimized structures of Cpd 0 offers an explanation: In the alanine and glycine mutants, WatS is hydrogen-bound to both oxygen atoms of the FeO_2 unit with distances of 1.5 to 1.7 Å. In the T252V mutant, however, the steric demands of the valine residue change the hydrogen-bonding network such that WatS is hydrogen-bound to the distal oxygen only so that the proton transfer to the proximal oxygen is hindered and requires more activation. As a consequence, a clear preference for uncoupling results only for the T252A and T252G mutants.

IV. Summary and Conclusions

Four mutants (Thr252Ala, Thr252Val, Thr252Gly, Thr252Ser) of P450cam have been targeted to investigate mutation effects on the formation of Cpd I. We have studied two competing reactions at the QM/MM level, which both originate from Cpd 0 and require proton transfer toward Cpd 0: the conversion of Cpd 0 to Cpd I and water (coupling reaction), and the regeneration of the ferric resting state with concomitant formation of hydrogen peroxide (uncoupling reaction). For each reaction, we have considered two mechanisms: either first bond cleavage in the FeOOH moiety followed by proton transfer in the Asp251 channel, or both steps in reverse order. Only the more facile of these two pathways has been discussed in the text for each reaction (mechanisms I and III), while the other results are only presented as Supporting Information.

The stability of an additional water molecule in the distal pocket has been tested for all four mutants by classical MD simulations. This extra water molecule quickly escapes from the distal pocket of the T252S mutant (as in the case of the native enzyme) but remains stable during 2 ns simulations of the T252A, T252G, and T252V mutants. Hence, for these three mutants, the reactions have been studied both without and with an additional water molecule.

In the coupling reaction, the initial and rate-limiting step is a homolytic O−O bond cleavage followed by a concomitant proton and electron transfer that yields Cpd I and water. In the wild-type enzyme, the O−O bond cleavage has a barrier of 14 kcal/mol that increases slightly to 16 kcal/mol in the T252S mutant and 17−18 kcal/mol in the T252A, T252V, and T252G mutants. The presence of the extra water molecule (WatS) in the T252A, T252V, and T252G mutants has only marginal effects on this barrier. The transition state for the initial O−O cleavage is rate-limiting in all five enzymes considered. Since the mutations as well as the additional water molecule mainly affect the subsequent proton transfer, it is reasonable that neither of these modifications causes any significant effect on the rate-limiting step of the coupling reaction.

The uncoupling reaction involves a proton transfer from Asp251 via a hydrogen-bonding network to the distal oxygen atom (O1) accompanied by O−Fe bond cleavage that leads to the ferric resting state and hydrogen peroxide. An alternative two-step mechanism with initial O−Fe bond cleavage is less favorable. Without the extra water molecule, the energy barrier of the concerted mechanism is 25−28 kcal/mol in the wild-type enzyme and the valine, alanine, and glycine mutants. The presence of an extra water molecule (WatS) drastically reduces this barrier to 11 kcal/mol for the T252A and T252G mutants and to 19 kcal/mol for the T252V mutant.

According to the experimental data, the coupling reaction is more favorable in the wild-type enzyme and the serine mutant, with 100 and 85% coupling (formation of Cpd I), respectively. In the serine mutant, uncoupling (formation of hydrogen peroxide) accounts for 15% of the O_2 consumption. The uncoupling reaction dominates in the T252A and T252G mutants, where only 3−5% of the O_2 is consumed to form Cpd I. In the T252V mutant, both reactions occur with similar probability.

If the effect of an additional water molecule is not taken into account, the present QM/MM calculations would disagree with experimental results; that is, all mutants would behave like the wild-type enzyme and prefer coupling over uncoupling. An additional water molecule in the Asp251 channel has only a minor influence on the formation of Cpd I. However, consistent with experimental observations that direct contact between solvent water and the heme active site is responsible for uncoupling, an extra water molecule has a significant effect on the uncoupling reaction. In case of the T252A and T252G mutants, the barrier of the uncoupling reaction is reduced dramatically such that the coupling reaction becomes disfavored, in line with experiment. For the T252V mutant, both reactions are observed experimentally, which can again only be rationalized if an additional water molecule is taken into account. The competition between the coupling and uncoupling reactions and the effects of the extra water molecule are illustrated by the energy profiles for the wild-type enzyme (Figure 5) and the T252A mutant (Figure 6). It is conceivable that there are other P450 systems (e.g., with other substrates and/or other mutations) where a single additional water molecule may also play a

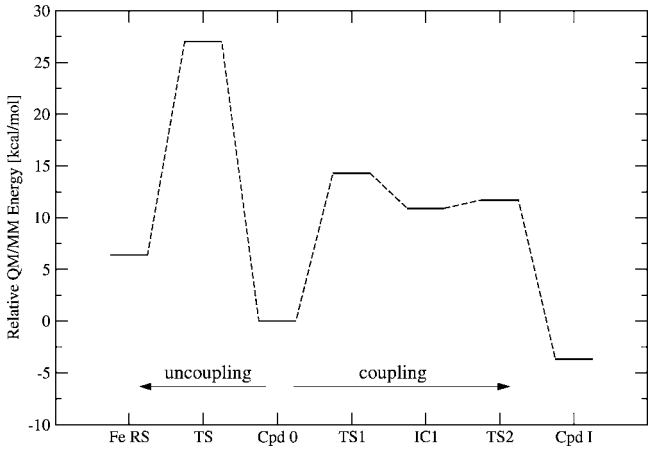

Figure 5. Energy profile (UB3LYP/B2/CHARMM) of the coupling and uncoupling reaction in the wild-type enzyme.

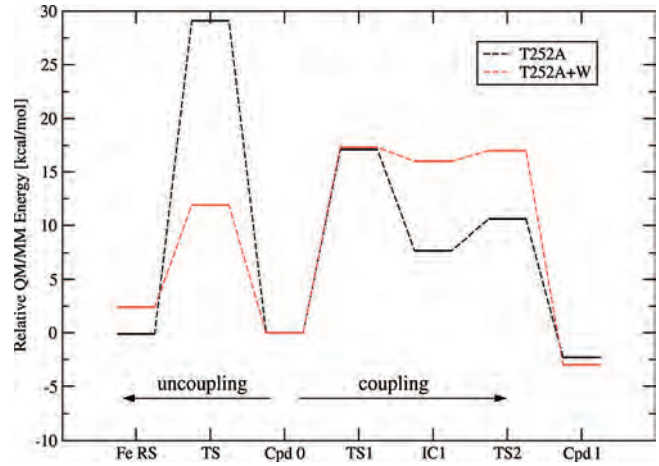

Figure 6. Energy profiles (UB3LYP/B2/CHARMM) of the coupling and uncoupling reaction with and without an extra water in the T252A mutant.

decisive mechanistic role, and it is therefore generally advisable in theoretical work to check this possibility by explicit simulation.

The present QM/MM results agree with the available experimental evidence and thus offer an atomistic explanation for the role of the Thr252 residue in the reactions of Cpd 0. Thr252 is a highly specific proton donor to the distal oxygen atom of Cpd 0, and the preference for the coupling reaction in the wild-type enzyme is based on this specificity. If Thr252 is replaced by small aliphatic residues, an additional water molecule can enter the active site and establish proton transfer channels to both oxygen atoms of the FeOOH moiety. Optimum hydrogen-bonding networks can be formed in the T252A and T252G mutants, which lower the barriers to proton transfer substantially and lead to a preference for uncoupling. This effect is less pronounced in the T252V mutant with the sterically more demanding valine residue, and hence both reactions can occur in this case. Replacing Thr252 with a structurally similar serine residue causes only relatively minor changes since the required proton transfer can make use of the OH group that is present in both residues, without the need to involve an extra water molecule. The difference between the computed rate-limiting barriers for coupling and uncoupling is smaller in the T252S mutant than in the wild-type enzyme, which is qualitatively consistent with the slight decrease in the observed specificity.

Acknowledgment. This work was supported by the Max Planck Society.

Supporting Information Available: MD results for the T252S, T252V, and T252G mutants. Energies, spin densities, and group charges for mechanisms I, III, and IV. Geometric parameters for mechanisms I and III. Optimized geometries of the stationary points of mechanisms I, III, and IV. Complete references 38 and 44. This material is available free of charge via the Internet at http://pubs.acs.org.

JA808744K

THE JOURNAL OF PHYSICAL CHEMISTRY A

© Copyright 2008 by the American Chemical Society VOLUME 112, NUMBER 50, DECEMBER 18, 2008

A Tribute to Sason Shaik[†]

It is a pleasure and honor for us to introduce a special issue dedicated to the scientific achievements of our mentor, guide and former supervisor, Professor Sason S. Shaik. Although the official date of birth of Sason has been lost in history, it is predicted that his 60th birthday will commence somewhere in 2008. We thought this would be the ideal time to celebrate his birthday with a special issue in the *Journal of Physical Chemistry* dedicated to his broad and exceptional accomplishments to the Physical, Organic and Bioinorganic Chemistry communities. We are delighted that the Editorial Board of the *Journal of Physical Chemistry* has approved this and thank them for the opportunity this has given us to acknowledge the work of Sason together with a long list of former and present co-workers as well as many scientific friends.

During his already highly successful and fruitful scientific career, which we hope will continue for many more years to come, Sason put a firm stamp on theoretical chemistry and functioned as an ambassador of the field toward the general science community. Thus, although theoreticians often work on fundamental problems, with sometimes-limited practical value, Sason has always tried to make the work accessible to a large general audience. This, for instance, has resulted in (co)-authorship of 93 publications in the *Journal of the American Chemical Society* (at the time of writing of this Tribute). Consequently, his work has influenced not only theoretical chemists, but also inorganic-, organic-, and biochemists (among many others). This influence is also reflected in the broad range of contributions, which this special issue has attracted, from authors with a wide spectrum of backgrounds ranging from experimental biochemists and inorganic chemists to mass spectrometrists, physical chemists and, of course, theoretical chemists and physicists.

In this short Tribute it is impossible to describe all scientific achievements and breakthroughs of Sason in detail. We have therefore chosen to focus on a few key highlights that have established him as a world leader in his field.

Valence Bond Modeling

Sason's earliest successes are associated with valence bond (VB) modeling of reaction processes. During his Ph.D. with Nicholaos D. Epiotis, he "discovered" this largely forgotten theory and had a short flirt with it. Subsequently, during his postdoctoral period with Roald Hoffman, he saw the benefit

[†] The former name used in publication is Sason S. Shaik.

10.1021/jp8063454 CCC: $40.75 © 2008 American Chemical Society
Published on Web 12/11/2008

of using both localized and delocalized electronic structures and developed the technical means to project molecular orbital (MO) wave function with or without configuration interaction (CI) into VB structures, based on fragment orbitals or atomic hybrid orbital, as deemed necessary for the particular problem. At that time, the VB methodology was out of fashion and only a few people in the world were actively engaged in the use of its techniques. Sason immediately recognized the potential of this theory to describe basic reaction mechanisms in a simple and straightforward way. Mainly thanks to his and his many co-workers' tremendous efforts in the field, the VB methodology has survived and is gaining interest and momentum ever again.

He applied the VB technique to explain and predict reaction mechanisms of polar reactions, electron transfer processes, cycloadditions and many bond reactions.[1] Thus, it was shown that an elementary reaction from reactants to products can be described with a curve crossing diagram, whereby the avoided crossing provides the transition state of the reaction, and an important excited state surface that is crucial for the photochemical transformation. It can be shown, therefore, that the wave function in the transition state is a mixed VB wave function of reactants and products. The work on VB modeling has been done in collaboration, initially with Pross, and later with the Hiberty and Wu groups. The tools developed by Sason and co-workers have given great understanding of basic reaction mechanisms in organic and inorganic chemistry.

Two-State Reactivity

In the mid 1990s, Sason Shaik and Helmut Schwarz of the Technical University of Berlin (Germany) began a collaborative project on gas phase reactions of transition-metal-oxo species. The mass spectrometric studies of the Schwarz group produced conflicting results and a model was needed to explain the reaction mechanisms and observed rate constants. A collaborative project of the two groups resulted in the hypothesis of two-state-reactivity (TSR), whereby an active oxidant has an electronic ground state with two close lying spin states.[2] It was predicted that the oxidant would be able to react with substrates on both spin state surfaces that would give different rate constants and different products on each spin state surface. This seminal discovery of Shaik and Schwarz et al. was later shown to be common in transition metal containing oxides.[3] In particular, it explained the reactivity patterns of a key enzyme for human health, the cytochromes P450, whereby the active form is an iron(IV)−oxo heme(+•) called Compound I.[4] Thus, Compound I is described as a triradical species, with two electrons in orthogonal π^*_{FeO} orbitals and a third one located on a heme orbital called a_{2u}. It was shown that ferromagnetic coupling of these three orbitals gives a quartet spin state, whereas the antiferromagnetic coupling gives a doublet spin state. The quartet and doublet spin states of Compound I of P450 enzymes are close in energy and, as a consequence, give rise to different reaction barriers on each spin state surface. This has been termed two-state-reactivity (TSR) and explains the experimentally observed product distributions and kinetic isotope effects. These scientific discoveries have set the scene for many future projects in the Shaik group and focused on the elucidation of reaction mechanisms of short-lived oxidants in enzymatic systems. Sason was one of the first people to realize that a challenging system like the cytochromes P450 needed more advanced methods and techniques than the commonly used model calculations on extracts of enzyme active sites. In collaboration with Walter Thiel from the Max Planck Institut für Kohlenforschung in Mülheim an der Ruhr, the two groups started working with quantum mechanics/molecular mechanics (QM/MM) techniques. Indeed, for the complicated description of the electronic ground state of Compound I of cytochrome P450, for instance, it was quickly seen that the protein environment added a crucial perturbation to the model that influenced the electronic properties of the metal center considerably. In the past six years or so, the QM/MM methodology has been further developed and optimized for many transition metal containing systems. The work has given tremendous insight into fast processes that happen in enzymes and have led to many predictions for experimental studies, such as the elucidation of reaction mechanisms, the identification of the active oxidant in the reaction process and the origins of byproducts.

Bonding

The most recent seminal contribution of Sason Shaik we highlight is his work on bonding, charge-shift bonds and ferromagnetic bonds. Especially intriguing are the ferromagnetic bonds, which bind atoms without any electron pairing. Thus, calculations on alkali metal dimers in a triplet spin state ($^3Li_2$, $^3Na_2$ etc.) showed that these clusters are stable albeit with a small bonding energy.[5] This is quite surprising because $^3Li_2$ has only one electron in a σ-bonding type orbital but another one in a σ^*-antibonding orbital, which should make the system dissociative. The work of Shaik et al., however, showed that despite the fact that these systems lack bonding electron pairs they are stable clusters due to ferromagnetic coupling of electrons in the maximum spin state. Thus, it was shown through valence bond modeling that the ferromagnetic bonding comprises delocalized covalent-ionic fluctuations that spread over and bind the high-spin cluster. The bonding energy per atom in a cluster increases and converges to a limiting value, at around 10−12 atoms. This ferromagnetic bonding is particularly large for lithium and copper clusters and decreased for elements down the periodic table.

Summary

The previous three sections only highlight three major contributions of Sason to science in general, which represent only a fraction of the actual work he has done. Despite the fact that Sason always has had a modest size research group with limited resources, he has been doing exceptional high-quality research and made major scientific contributions. We are proud and honored to have had the opportunity to work with him for several years. He has been a fantastic supervisor. It should be mentioned here that he is very demanding and precise, but he demands the same of himself, all in the pursuit of the best possible science. We all remember the numerous hours he spent with us to explain a concept. Redrawing Figures for publications a couple of dozen times until perfection is one of the things you will have to get used to when you work for Sason, but in hind-side these modifications always improved the quality of the work. We have learnt very much from his guidance and working style and congratulate him again with this Special Issue and hope readers will enjoy the contributions.

References and Notes

(1) Shaik, S. S. *J. Am. Chem. Soc.* **1981**, *103*, 3692–3701.

(2) Shaik, S.; Danovich, D.; Fiedler, A.; Schröder, D.; Schwarz, H. *Helv. Chim. Acta* **1995**, *78*, 1393–1407.

(3) (a) Shaik, S.; de Visser, S. P.; Ogliaro, F.; Schwarz, H.; Schröder, D. *Curr. Opin. Chem. Biol.* **2002**, *6*, 556–567. (b) Shaik, S.; Hirao, H.; Kumar, D. *Acc. Chem. Res.* **2007**, *40*, 532–542.

(4) (a) Meunier, B.; de Visser, S. P.; Shaik, S. *Chem. Rev.* **2004**, *104*, 3947–3980. (b) Shaik, S.; Kumar, D.; de Visser, S. P.; Altun, A.; Thiel, W. *Chem. Rev.* **2005**, *105*, 2279–2328.

(5) (a) Danovich, D.; Wu, W.; Shaik, S. *J. Am. Chem. Soc.* **1999**, *121*, 3165–3174. (b) de Visser, S. P.; Danovich, D.; Wu, W.; Shaik, S. *J. Phys. Chem. A* **2002**, *106*, 4961–4969. (c) de Visser, S. P.; Kumar, D.; Danovich, M.; Nevo, N.; Danovich, D.; Sharma, P. K.; Wu, W.; Shaik, S. *J. Phys. Chem. A* **2006**, *110*, 8510–8518.

Sam P. de Visser
The University of Manchester

Etienne Derat
Université Pierre et Marie Curie

Devesh Kumar
Max-Planck-Institut für Kohlenforschung

JP8063454

Multireference Ab Initio Quantum Mechanics/Molecular Mechanics Study on Intermediates in the Catalytic Cycle of Cytochrome $P450_{cam}$†

Ahmet Altun,‡ Devesh Kumar,‡ Frank Neese,§ and Walter Thiel*,‡

Max-Planck-Institut für Kohlenforschung, Kaiser-Wilhelm-Platz 1, D-45470 Mülheim an der Ruhr, Germany, and Institut für Physikalische und Theoretische Chemie, Universität Bonn, Wegelerstrasse 12, D-53115 Bonn, Germany

Received: March 10, 2008; Revised Manuscript Received: April 7, 2008

We have investigated the elusive reactive species of cytochrome $P450_{cam}$ (Compound I), the hydroxo complex formed during camphor hydroxylation, and the ferric hydroperoxo complex (Compound 0) by combined quantum mechanical/molecular mechanical (QM/MM) calculations, employing both density functional theory (DFT) and correlated ab initio methods. The first two intermediates appear multiconfigurational in character, especially in the doublet state and less so in the quartet state. DFT(B3LYP)/MM calculations reproduce the relative energies from correlated ab initio QM/MM treatments quite well, except for the splitting of the lowest $A_{1u}-A_{2u}$ radical states. The inclusion of dynamic correlation is crucial for the proper ab initio treatment of these intermediates.

I. Introduction

Cytochrome P450 enzymes are a ubiquitous monooxygenase superfamily of hemoproteins which are of vital importance for regulation of drug metabolism, detoxification of xenobiotics, and biosynthesis of metabolites.[1–3] They catalyze regio- and stereoselective C−H bond hydroxylation in many organic substances. For example, $P450_{cam}$ (CYP101) hydroxylates camphor at the C^5 position, leading to 5-*exo*-hydroxycamphor as the sole product.[4] Scheme 1 shows three key intermediates in the catalytic cycle of $P450_{cam}$. The ferric hydroperoxo complex called Compound 0 (Cpd 0) is the last species that is observed experimentally before the hydroxycamphor product. It can be converted to an oxyferryl−porphyrin cation called Compound I (Cpd I) which is generally believed to be the active oxidant of P450 enzymes. Cpd I of the thermostable cytochrome CYP119 was recently identified by its characteristic spectral features[5,6] and appeared to be relatively stable in kinetic studies,[6] whereas Cpd I of chloroperoxidase was found to be stable enough to be characterized by electron paramagnetic resonance and Mössbauer spectroscopy.[7,8] However, Cpd I of $P450_{cam}$ has never been detected, and its hydroxylation mechanism is still controversial.[1–11] The most common assumption is that Cpd I abstracts a hydrogen atom from camphor to yield a hydroxo intermediate (HYD) followed by a rebound that generates the product complex.[1–11]

Theoretical model studies (see ref 3 and references therein) as well as combined quantum mechanical/molecular mechanical (QM/MM) calculations,[12–16] which consider the complete $P450_{cam}$ enzyme, find barriers for the rate-determining H-abstraction reaction during camphor hydroxylation that seem too high to explain the elusiveness of Cpd I. Density functional theory (DFT) is the method of choice in almost all of these theoretical studies on high-valent metalloporphyrins and related molecules.[3] The question thus arises whether DFT is accurate enough for calculations of this kind, which calls for a careful calibration of DFT against high-level ab initio calculations.[17–22]

SCHEME 1: Key Intermediates in the Catalytic Cycle of P450 Enzymes

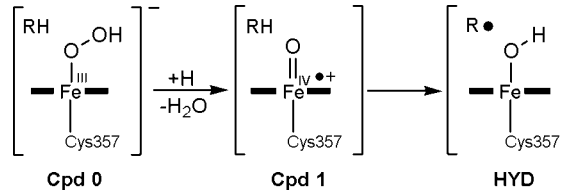

In this paper, we investigate the Cpd 0, Cpd I, and HYD intermediates of $P450_{cam}$ (see Scheme 1) by QM/MM calculations. The QM part is treated both with DFT and ab initio multireference configuration interaction (MR−CI) methods to allow for direct comparisons. In our previous QM/MM study on Cpd I of $P450_{cam}$ with MR−CI methods,[21] only the three singly occupied orbitals were included in the active space, which is sufficient for calculating the separation between the lowest doublet and quartet states. Here we use larger active spaces to assess the electronic structure of these species in more detail and to compute excitation energies to some lower-lying excited states. We examine doublet and quartet states in these intermediates but focus mainly on the quartet species. We do not address reaction energies and activation barriers presently, because an even-handed MR−CI treatment of all relevant species would be very demanding.

II. Computational Methods

The system used in this study for Cpd I and HYD corresponds to the snapX setup with protonated Asp297, as defined in refs 13–15. Cpd 0 is represented by the setup described in ref 23. Details of the adopted QM/MM methodology and protocols are given in refs 13–15 and 21. In the following, we only address some aspects relevant to the present study.

B3LYP/CHARMM geometry optimizations were performed by using the ChemShell[24] package and included all residues

† Part of the "Sason S. Shaik Festschrift".

* To whom correspondence should be addressed. E-mail: thiel@mpi-muelheim.mpg.de. Phone: +49-208-306-2150. Fax: +49-208-306-2996.

‡ Max-Planck-Institut für Kohlenforschung.

§ Universität Bonn.

10.1021/jp802092w CCC: $40.75 © 2008 American Chemical Society
Published on Web 06/11/2008

TABLE 1: $^2A/^4A$ B3LYP/CHARMM Relative Energies (kcal/mol)

	R1/B1	R1/B′//R1/B1
Cpd I	0.0/0.1	0.0/0.3
HYD(III)[a]	9.0/10.1	6.7/7.8
HYD(IV)[a]	11.7/12.5	4.9/5.5
Cpd 0	0.0/8.3	0.0/7.5

[a] Energies relative to the ^2A state of Cpd I.

and water molecules that have atoms within a distance of 4 Å to any atom of the heme, coordinating Cys357, or camphor. All ab initio QM/MM calculations were carried out using the ORCA 2.4.44 program package[25] and R1/B1 B3LYP/CHARMM-optimized geometries. As in our previous work, QM region R1 consists of the heme (without side chains) and the axial ligands (SH and OOH for Cpd 0; SH and oxo plus propane to represent camphor in the case of Cpd I and HYD). Basis set B1 describes iron by a small-core effective core potential (ECP) together with the associated double-ζ quality LACVP basis[26] and all other atoms by 6-31G.[27] The ab initio R1/B′ QM/MM calculations employ the following basis (B′): Wachters all-electron basis set[28] in the contraction [8s6p4d2f] for iron; TZVP[29] for the six atoms coordinated to iron and for C^5; TZVPP[29] for H^{5exo}; SV[30] for the remaining atoms. The auxiliary basis set used is TZVPP/C for iron and TZV/C for the other atoms.[31] Throughout this paper, the oxidation state of iron will be specified in parenthesis (e.g., HYD(III)).

The zero-order wave function in all MR ab initio calculations was chosen to be the complete active-space self-consistent field (CASSCF)[32] wave function determined with quasi-restricted DFT(B3LYP) orbitals as initial guess; Hartree−Fock (HF) orbitals cannot be used for this purpose since HF calculations

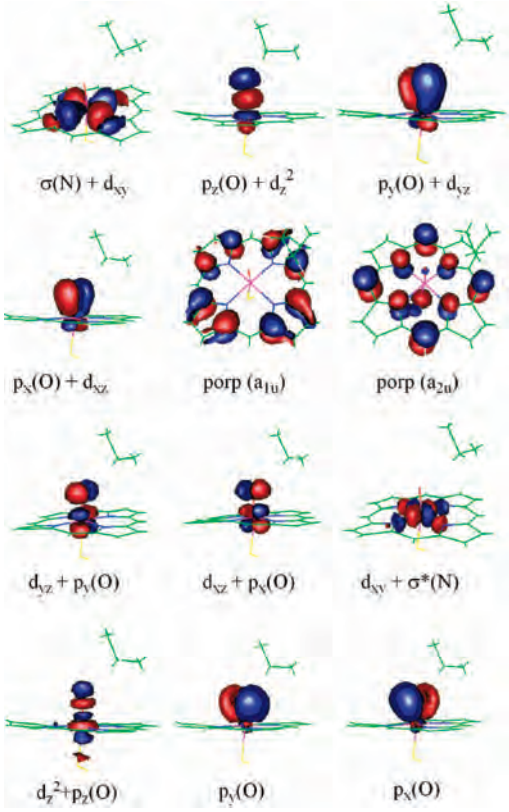

Figure 1. Active-space CASSCF(13,12) orbitals of Cpd I in the quartet state and their approximate descriptions.

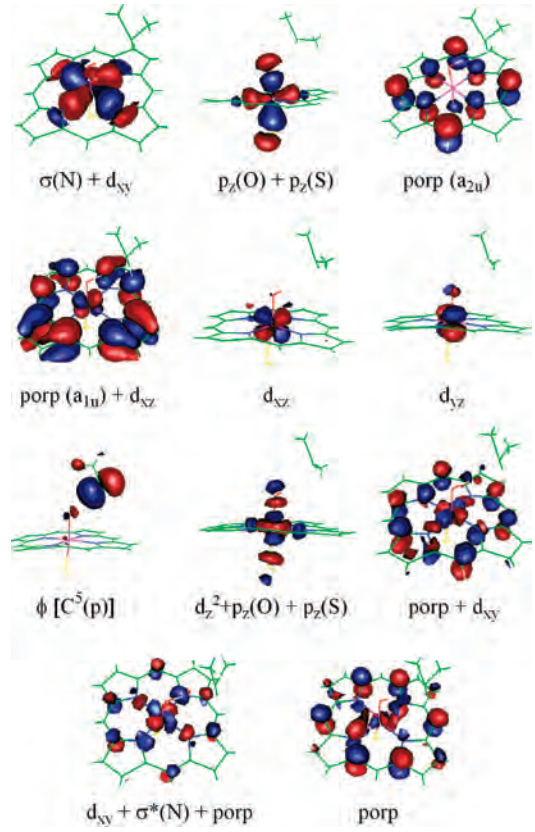

Figure 2. Active-space CASSCF(11,11) orbitals of HYD(IV) in the quartet state and their approximate descriptions.

predict the porphyrin a_{1u} and a_{2u} orbitals to be singly occupied for Cpd I and HYD. CASSCF captures the major part of the nondynamical correlation energy by mixing the active-space configurations at the full CI level. The subsequent ab initio MR−CI/MM calculations were carried out with a natural orbital iterative difference dedicated CI scheme (DDCI2)[33,34] that includes all single excitations as well as double excitations which involve either two holes in the occupied inactive orbitals or two particles in the inactive empty orbitals. The MR−Davidson correction (Q) for the effect of unlinked quadruple substitutions was applied to account for the fact that the DDCI2 method is not size consistent. Hence, the reported MR−CI/MM energies refer to DDCI2+Q.[34] To enhance computational efficiency without significant loss of accuracy, the ORCA thresholds T_{sel}, T_{pre}, and T_{nat} were set to 10^{-6} E_h, 10^{-4}, and 10^{-5}, respectively.[34,35] In a recent validation study on the model reaction $Fe^+ + H_2 \rightarrow FeO^+ + H_2O$, the DDCI2+Q approach was found to reproduce the energy profiles from higher-level ab initio MR methods quite well,[36] and it was therefore considered appropriate for the present study on larger related systems.

CAS calculations for Cpd I and HYD were performed both using a minimal active space of 3 electrons in 3 orbitals, and a large active space with 13 electrons in 12 orbitals for Cpd I and 11 electrons in 11 orbitals for HYD which was designed to properly describe the axial and equatorial ligand fields. These active spaces will be described in the next section in more detail. As a general guideline, we included all orbitals into the large active space that affect the computed relative energies significantly. For lower transition metal oxidation states, a second d shell (4d) is often essential for obtaining reliable correlated ab initio results.[37] Since this radial correlation effect becomes less pronounced as the metal oxidation state increases,[18] our active spaces do not include this unoccupied 4d shell at iron. It has

TABLE 2: Most Important DDCI2+Q Configuration State Functions of the Quartet State Cpd I in the Two Lowest Roots

root	ΔE (kcal/mol)	weight (%)	σ(N)	p_z(O)	p_y(O)	p_x(O)	a_{1u}	a_{2u}	d_{yz}	d_{xz}	d_{xy}	d_{z^2}	p_y(O)	p_x(O)
1	0.0	77.6	2	2	2	2	2	1	1	1	0	0	0	0
		2.0	2	1	2	1	2	1	2	1	0	1	0	0
		1.9	2	2	1	1	2	1	2	2	0	0	0	0
		1.8	2	1	1	2	2	1	1	2	0	1	0	0
		1.2	2	0	2	2	2	1	1	1	0	2	0	0
		1.0	2	2	2	1	2	1	2	1	0	0	0	0
		0.9	2	2	1	2	2	1	1	2	0	0	0	0
		0.6	1	2	2	2	2	1	1	1	1	0	0	0
		0.6	2	1	2	2	2	1	1	1	0	1	0	0
		0.5	2	2	2	2	1	0	1	1	0	0	1	1
		0.3	2	2	2	2	1	2	1	1	0	0	0	0
2	1.9	77.0	2	2	2	2	1	2	1	1	0	0	0	0
		2.0	2	1	2	1	1	2	2	1	0	1	0	0
		1.9	2	2	1	1	1	2	2	2	0	0	0	0
		1.8	2	1	1	2	1	2	1	2	0	1	0	0
		1.2	2	2	2	1	1	2	2	1	0	0	0	0
		1.1	2	0	2	2	1	2	1	1	0	2	0	0
		1.0	2	2	1	2	1	2	1	2	0	0	0	0
		0.7	2	1	2	2	1	2	1	1	0	1	0	0
		0.6	1	2	2	2	1	2	1	1	1	0	0	0
		0.4	2	2	2	2	0	1	1	1	0	0	1	1
		0.3	2	2	2	2	2	1	1	1	0	0	0	0

been noted previously for $Fe^{III}(P)Cl$ and $[Fe(P)Cl]^+$ (P^{2-} = porphinato)[18] that CASSCF calculations erroneously predict the A_{1u} porphyrin radical states to be lower in energy than the A_{2u} radical states (by ca. 5 kcal/mol). It is thus possible that 1-root calculations with our large active space may not produce the lowest-energy configuration, and therefore we performed 6-root CASSCF calculations. This led to convergence for the quartet, but not for the doublet states. Hence, with the large active space, we can only present results for the quartet states for Cpd I and HYD. These complications are absent in Cpd 0 where the porphyrin a_{1u} and a_{2u} orbitals are doubly occupied both in the quartet and the doublet so that both spin states can be converged in 1-root calculations with a large active space comprising 13 electrons in 11 orbitals.

In all QM/MM calculations, an electronic embedding scheme[38] was applied, in which the fixed MM point charges are included in the one-electron Hamiltonian of the QM calculation and the QM/MM electrostatic interactions are evaluated from the QM electrostatic potential and the MM atomic charges. The electrostatic interactions between the QM region and the MM point charges were included in the QM energy. No cutoffs were introduced for the nonbonding MM and QM/MM interactions. Hydrogen link atoms[39] were used at the QM/MM boundary along with the charge shift model.[40]

III. Results

III.A. B3LYP/CHARMM Results. B3LYP/CHARMM optimizations indicate that Cpd I has almost degenerate quartet and doublet states with a slight preference (0.1−0.3 kcal/mol) for the doublet (see Table 1). Upon basis set extension from B1 to B′, HYD(III) [HYD(IV)] is stabilized by ca. 2 [7] kcal/mol relative to Cpd I, and the energy ordering changes such that HYD(IV) becomes more stable. The doublet ground state of HYD lies ca. 1 kcal/mol below the quartet for both oxidation states and both basis sets. Cpd 0 also has a doublet ground state, with a larger doublet−quartet gap of ca. 8 kcal/mol.

III.B. MR Ab Initio QM/MM Results. ***Compound I.*** The minimal active space for Cpd I consists of the three singly occupied orbitals, i.e., the antibonding π^*_{xz} and π^*_{yz} molecular orbitals (MOs) built from the iron d_{xz}/d_{yz} and oxygen p_x/p_y orbitals, and the porphyrin a_{2u} orbital. CASSCF(3,3)-DDCI2+Q/MM calculations yield a doublet−quartet splitting of −1.8 kcal/mol in state-specific calculations at separately optimized geometries and of −1.2 kcal/mol in state-averaged calculations at the quartet state geometry. The previous[21] CAS(3,3) DDCI2+Q/MM result of −0.1 kcal/mol on top of spin-restricted DFT orbitals generated with the BP86 functional is closer to the B3LYP/CHARMM result of −0.3 kcal/mol (see Table 1). The previous calculations[21] differ from the present ones in the choice of orbitals for the DDCI2+Q treatment [DFT(BP86) vs CASSCF] and in the use of tighter ORCA thresholds (see section II) which affects the relative spin state energies by ca. 1 kcal/mol in this case (see also footnote 60 of ref 21).

The CASSCF(3,3) calculations for Cpd I predict a multiconfigurational doublet state, with major contributions from three configurations with the following occupancies of $\pi^*_{xz}\pi^*_{yz}a_{2u}$: 210 (38%), 012 (30%), and 111 (22%). The CAS(3,3) DDCI2+Q Mulliken spin populations on FeO (1.35 e), sulfur (−0.03 e), and pyrrolic nitrogens (average, −0.04 e) are considerably lower than the B3LYP values (2.14, −0.24, and −0.18 e, respectively). Hence, broken-symmetry DFT treatments cannot be used to calculate spin-dependent properties of doublet Cpd I without applying a spin projection scheme. The spin populations of the quartet state with a dominant 111 configuration (90%) are analogous in DDCI2+Q (1.99, 0.07, and 0.14 e) and B3LYP (2.05, 0.21, and 0.16 e).

It should be noted that the quartet 111 configuration will be lower in energy than the corresponding doublet 111 configuration built from the same set of MOs. The doublet can be stabilized by mixing in the ionic 210 and 120 configurations (not available in the quartet case), and it depends on the extent of this admixture whether the doublet becomes the ground state. This is the case in our present and previous[21] CASSCF(3,3)-DDCI2+Q calculations, even though the doublet and quartet were more nearly degenerate previously. The actual numerical results depend on subtle factors (see above), but in a qualitative sense it is the multiconfigurational character of the doublet (i.e., the mixing between the 111, 210, and 120 configurations) which provides the mechanism for bringing the doublet below the quartet (when using symmetry-adapted rather than symmetry-broken MOs).

TABLE 3: Most Important DDCI2+Q Configuration State Functions in the Lowest Six Quartet States of HYD

root	ΔE (kcal/mol)	weight (%)	σ(N)	p_z(O, S)	a_{2u}	a_{1u}	d_{xz}	d_{yz}	ϕ	d_{z^2}	porp	d_{xy}	Porp
1	0.00	67.6	2	2	2	2	1	1	1	0	0	0	0
		15.5	2	2	2	1	2	1	1	0	0	0	0
		2.2	2	2	2	1	1	1	1	1	0	0	0
		0.5	2	2	1	2	0	1	1	0	1	1	0
		0.4	2	2	2	2	1	1	1	0	1	0	0
		0.3	2	0	2	2	1	1	1	2	0	0	0
		0.3	2	2	2	2	1	1	1	0	0	1	0
2	2.1	82.3	2	2	1	2	2	1	1	0	0	0	0
		1.2	2	2	2	1	1	2	1	0	0	0	0
		1.0	2	2	1	1	2	1	1	1	0	0	0
		0.5	2	2	0	2	1	1	1	0	1	1	0
		0.4	2	0	1	2	2	1	1	2	0	0	0
		0.4	2	2	1	2	2	1	1	0	1	0	0
		0.4	2	2	1	2	2	1	1	0	0	1	0
3	7.6	82.8	2	2	2	1	1	2	1	0	0	0	0
		1.2	2	2	1	2	2	1	1	0	0	0	0
		0.6	2	2	1	1	0	2	1	0	1	1	0
		0.5	2	2	2	1	1	2	1	1	0	0	0
		0.4	2	0	2	1	1	2	1	2	0	0	0
		0.4	2	2	2	1	1	2	1	0	1	0	0
		0.3	2	2	2	1	1	0	1	0	0	0	2
		0.3	2	2	0	1	1	2	1	0	2	0	0
		0.3	2	2	2	1	1	2	1	0	0	1	0
4	12.8	66.7	2	2	1	1	2	1	1	1	0	0	0
		16.3	2	2	1	2	1	1	1	1	0	0	0
		1.5	2	2	1	2	2	1	1	0	0	0	0
		0.6	2	2	0	1	1	1	1	1	1	1	0
		0.4	2	2	2	1	2	1	1	0	0	0	0
		0.4	2	2	1	2	2	1	0	1	0	0	0
		0.4	2	2	1	1	2	1	2	0	0	0	0
		0.4	2	2	1	1	0	1	1	1	2	0	0
		0.4	2	2	1	1	2	1	1	1	1	0	0
		0.3	2	2	1	1	0	1	1	1	0	2	0
		0.3	1	2	1	1	2	1	1	1	0	0	1
		0.3	2	2	1	1	2	1	1	1	0	1	0
5	14.2	82.0	2	2	2	1	1	1	1	1	0	0	0
		1.7	2	2	2	2	1	1	1	0	0	0	0
		0.9	2	2	2	1	1	1	2	0	0	0	0
		0.7	2	2	1	1	0	1	1	1	1	1	0
		0.6	2	2	2	2	1	1	0	1	0	0	0
		0.5	2	2	2	1	2	1	1	0	0	0	0
		0.5	1	2	2	1	1	1	1	1	0	0	1
		0.4	2	2	2	1	1	1	1	1	1	0	0
		0.4	2	2	2	1	1	1	1	1	0	1	0
		0.3	2	2	0	1	1	1	1	1	2	0	0
6	14.7	51.6	2	2	2	1	1	1	1	1	0	0	0
		17.5	2	2	2	0	2	1	1	1	0	0	0
		16.9	2	2	2	2	0	1	1	1	0	0	0
		0.7	2	2	1	1	0	1	1	1	1	1	0
		0.5	2	2	2	1	1	1	1	1	1	0	0
		0.4	2	2	2	1	1	1	1	1	0	1	0
		0.3	1	2	2	1	1	1	1	1	0	0	1

In addition to the three singly occupied orbitals, the large active space for Cpd I includes the bonding π_{xz} and π_{yz} MOs of the iron−oxo moiety, the axial σ and σ^* MOs composed of iron d_{z^2}, oxygen p_z, and sulfur p_z orbitals, the equatorial σ and σ^* MOs derived from iron d_{xy} and nitrogen orbitals, the porphyrin a_{1u} orbital, and the strongly correlating unoccupied oxygen $3p_x$ and $3p_y$ orbitals. The iron d_{xy} and the sulfur lone-pair p orbital were not put into the active space because doing so in test calculations did not affect the CASSCF excitation energies significantly. The 6-root CASSCF(13,12) orbitals of Cpd I in the quartet state are shown in Figure 1. The calculations yield roots that contain strong contributions from configurations with singly occupied a_{1u} and a_{2u} porphyrin orbitals, respectively. The lowest "A_{1u} root" lies 6.3 kcal/mol below the lowest "A_{2u} root" at the CASSCF/MM level, which is reversed at the DDCI2+Q/MM level where the "A_{2u} root" is more stable by 1.9 kcal/mol. Hence, dynamic correlation is crucial for obtaining the correct ground state. As B3LYP accounts for dynamic correlation, it is not surprising that the lowest-energy Kohn−Sham determinant contains singly occupied π^*_{xz}, π^*_{yz}, and a_{2u} orbitals as in DDCI2+Q. The DDCI2+Q configuration state functions (CSF) with weights of more than 0.3% are given in Table 2 for the lowest two roots. The DDCI2+Q/MM excitation energies to the other four roots, which are mainly made up of configurations that have one electron in each of the d_{xy}, d_{xz} (or d_{yz}), and a_{2u} (or a_{1u}) orbitals, are 31−35 kcal/mol. If the equatorial σ and σ^* MOs are not included in the active space, the excitation energy to the first accessible state remains essentially the same (1.9 vs 1.6 kcal/mol) but the energies of the other four roots are underestimated by ca. 10 kcal/mol as the corresponding

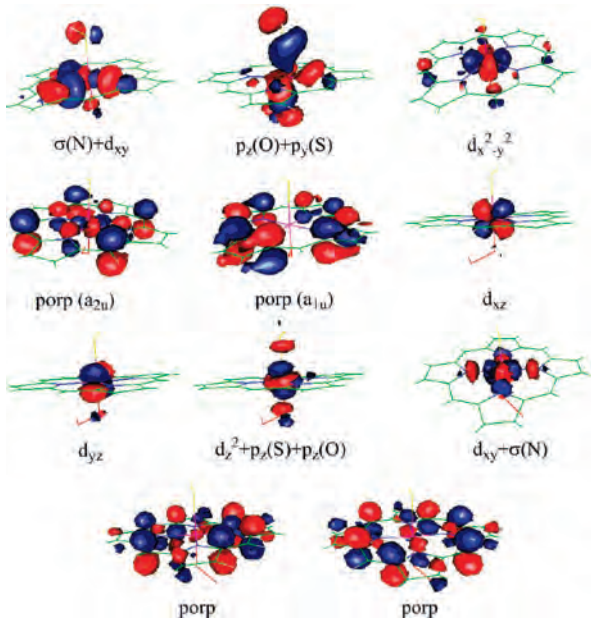

Figure 3. Active-space CASSCF(13,11) orbitals of Cpd 0 from a spin-averaged treatment and their approximate descriptions (see text).

excitations involve the iron d_{xy} orbital (see Figure 1, notation according to ref 3 throughout this paper).

In the CASSCF(13,12)-DDCI2+Q wave function of the two lowest quartet states (Table 2), the most important configuration in the ground state (weight 78%) has one electron in each of π^*_{xz}, π^*_{yz}, and a_{2u} orbitals, in agreement with the CASSCF(3,3) and B3LYP calculations. Enlarging the active space from CAS(3,3) to CAS(13,12) reduces the weight of the dominant configuration by ca. 12%, indicating some multiconfigurational character also for the quartet ground state. The first excited quartet state is characterized by a configuration with one electron in each of π^*_{xz}, π^*_{yz}, and a_{1u} orbitals (weight 77%). Since it lies only 1.9 kcal/mol above the ground state (according to the DDCI2+Q/MM results), it might even play a role in the reactivity of Cpd I. By contrast, TDDFT(B3LYP)/MM calculations predict an energy of 12.3 kcal/mol for this "A_{1u} root" which should then be hardly accessible in reactions. The Mulliken spin populations of the quartet ground state are qualitatively comparable in DDCI2+Q/MM (FeO, 2.02 e; S, 0.00 e; N, −0.02 e; porphyrin, 0.97 e) and B3LYP/MM (FeO, 2.05 e; S, 0.21 e; N, 0.16 e; porphyrin, 0.74 e), as expected since the same configuration is dominant in both treatments.

Hydroxo Intermediate HYD. The minimal active space for HYD(IV) contains the three singly occupied orbitals, i.e., the iron d_{xz} and d_{yz} orbitals and the radical p orbital of the C^5 atom of camphor (abbreviated as ϕ). CASSCF(3,3)-DDCI2+Q/MM calculations yield a doublet−quartet splitting of −2.0 kcal/mol in state-specific calculations at separately optimized geometries and of −1.8 kcal/mol in state-averaged calculations at the quartet state geometry, similar to the B3LYP/MM result of −0.6 kcal/mol (see Table 1). The doublet−quartet splitting of HYD(III) species is similar in CASSCF(3,3)-DDCI2+Q/MM (−2.4 kcal/mol in state-specific calculations at separate geometries; −0.6 kcal/mol in state-averaged calculations at the quartet state geometry; active space: $d_{xz} + \phi$, d_{yz}, and $\phi + \pi^*_{xz}$ orbitals) and B3LYP/MM (−1.1 kcal/mol, see Table 1). The ab initio calculations for the hydroxo complex again give a multiconfigurational doublet state, as in the case of Cpd I. For the HYD(IV) reference function of the doublet, the dominant CSFs have the following occupancies of the d_{xz}, d_{yz}, and ϕ orbitals: 210 (45%), 012 (29%), and 111 (23%); hence, the ferryl configuration contributes less than the ferric configuration. For the HYD(III) reference function of the doublet, the dominant CSFs show the following occupancies of the $d_{xz} + \phi$, d_{yz}, and $\phi + \pi^*_{xz}$ orbitals: 210 (49%), 012 (41%), and 111(2%). In view of the multiconfigurational character of the doublet in both oxidation states, it is remarkable that the relative spin state energies from B3LYP/MM agree with the ab initio QM/MM results within 2 kcal/mol.

The CASSCF(3,3)-DDCI2+Q Mulliken spin populations of FeO, S, camphor, porphyrin, and pyrrolic nitrogens for the doublet state of HYD(III) {0.98, 0.00, −0.14, 0.16, and 0.02 e} and HYD(IV) {1.40, −0.04, −0.32, −0.04, and −0.09 e} are significantly different from the B3LYP values for HYD(III) {1.15, −0.16, 0.88, −0.86 e, and −0.18 e} and for HYD(IV) {2.15, −0.11, −0.91, −0.14, and −0.05 e}, which again emphasizes the inappropriateness of broken-symmetry DFT solutions for spin-dependent properties. As the CAS(3,3) quartet wave function is dominated by the 111 configuration (>90%), the DDCI2+Q Mulliken spin populations for HYD(IV) {2.16, −0.07, 0.99, −0.07, and −0.02 e} and for HYD(III) {0.99, 0.03, 0.99, 0.99, and 0.13 e} are analogous to the B3LYP results for HYD(IV) {2.27, −0.08, 0.96, −0.14, and −0.05 e} and for HYD(III) {1.08, 0.17, 0.96, 0.79, and 0.16 e}, respectively.

In addition to the three singly occupied orbitals, the large active space for HYD(IV) includes the axial and equatorial σ and σ^* MOs (as in the case of Cpd I), the porphyrin a_{1u} and a_{2u} orbitals, and two correlating unoccupied porphyrin orbitals. The 6-root CASSCF(11,11) orbitals of HYD(IV) in the quartet state are shown in Figure 2. The lowest "A_{1u} root" is again 5.3 kcal/mol more stable than the next lowest root at the CASSCF/MM level. The inclusion of dynamic correlation in the DDCI2+Q/MM calculations reverses this order and makes the "A_{2u} root" the lowest one in energy, as in case of B3LYP/MM.

The most important contribution to the quartet ground-state wave function of HYD (see Table 3) comes from an Fe(IV) configuration with a weight of 68% (singly occupied orbitals: d_{xz}, d_{yz}, and ϕ), but there is also a notable contribution of 16% from an Fe(III) configuration (singly occupied orbitals: a_{1u}, d_{yz}, and ϕ). The next quartet state (at 2.1 kcal/mol) is mainly of Fe(III) character (configuration with singly occupied orbitals a_{2u}, d_{yz}, and ϕ: weight of 82%). Although both these HYD(III) and HYD(IV) species are to some extent multiconfigurational, the B3LYP-based estimates of their separation (adiabatic QM/MM energy difference of 2.7 kcal/mol; vertical QM energy difference of 3.2 kcal/mol at HYD(IV) geometry) agree well with the vertical DDCI2+Q/MM energy difference (2.1 kcal/mol).

The second excited quartet state of HYD, with an excitation energy of 7.6 kcal/mol, corresponds to an "A_{1u} root" of HYD(III) character (leading configuration with singly occupied orbital a_{1u}, d_{xz}, and ϕ, weight of 83%). The DDCI2+Q/MM excitation energies to the other three roots, which involve a_{1u} (or d_{xz}) → d_{z^2} excitations, are very similar to each other (between 12.8 and 14.7 kcal/mol, see Table 3). The third excited state of HYD (at 12.8 kcal/mol) features $a_{1u} \rightarrow d_{z^2}$ (67%) and $d_{xz} \rightarrow d_{z^2}$ (16%) excitations in HYD(III) configurations with single occupation of a_{2u}. The next one (at 14.2 kcal/mol) involves $a_{1u} \rightarrow d_{z^2}$ (82%) excitations on HYD(IV). The fifth one (at 14.7 kcal/mol) is characterized by an $a_{1u} \rightarrow d_{z^2}$ (52%) excitation on HYD(IV), with additional contributions from a $d_{xz} \rightarrow d_{z^2}$ (15%) single excitation and from double excitations from a_{1u} to d_{z^2} and d_{xz} (18%).

TABLE 4: Most Important DDCI2+Q Configuration State Functions of the Doublet (^{2}A) and Quartet (^{4}A) State Cpd 0

state	weight (%)	σ(N)	p_z(O, S)	$d_{x^2-y^2}$	A_{2u}	a_{1u}	d_{xz}	d_{yz}	d_{z^2}	d_{xy}	porp	porp
^{2}A	86.5	2	2	2	2	2	2	1	0	0	0	0
	0.8	2	2	1	2	2	1	1	0	0	1	1
	0.4	2	2	2	2	2	0	1	0	0	2	0
^{4}A	86.8	2	2	2	2	2	1	1	1	0	0	0
	1.5	2	2	2	1	1	1	1	1	0	1	1
	0.4	2	2	1	2	2	1	1	1	1	0	0
	0.4	2	2	2	2	0	1	1	1	0	0	0
	0.4	2	2	2	2	0	1	1	1	0	0	2

Compound 0. The minimal active space for the doublet state of Cpd 0 consists of three electrons in the two π^*_{xz} and π^*_{yz} antibonding MOs (doubly and singly occupied, respectively, in the leading ground-state configuration), whereas the minimal description of the quartet state requires three electrons in the three antibonding π^*_{xz}, π^*_{yz}, and $\sigma^*_{z^2}$ MOs (all singly occupied). Separate CAS-based calculations with these minimal spaces are unbalanced and do not yield reliable doublet−quartet splittings for Cpd 0. We thus consider only a common large active space with 13 electrons in 11 orbitals. In addition to the antibonding π^*_{xz}, π^*_{yz}, and $\sigma^*_{z^2}$ MOs (see above), it contains the axial σ MO, the equatorial σ and σ^* MOs, the porphyrin a_{1u} and a_{2u} orbitals, and two correlating unoccupied porphyrin orbitals (as in the case of HYD) as well as the doubly occupied iron $d_{x^2-y^2}$ (δ) orbital. The active-space (13,11) orbitals of Cpd 0 from a state-averaged treatment are shown in Figure 3. State-specific calculations yield analogous active-space orbitals with more pronounced mixing between nearly degenerate doubly occupied MOs. Contrary to the situation in Cpd I and HYD, the wave functions for the lowest doublet and quartet states of Cpd 0 are always dominated by the leading CASSCF configuration so that 1-root calculations are sufficient for each spin state (which converge without problems).

CAS(13,11) DDCI2+Q calculations yield a doublet−quartet splitting of 10.6 kcal/mol in state-specific calculations at separately optimized geometries and of 3.7 kcal/mol in state-averaged calculations at the quartet state geometry. These values bracket the B3LYP doublet−quartet splitting of 7.5 kcal/mol (Table 1) which is closer to the former DDCI2+Q value. The CAS(13,11) DDCI2+Q spin populations (doublet/quartet values) on the FeOOH (1.02 e/2.91 e), SH (−0.01 e/0.06 e), and porphyrin (−0.01 e/0.03 e) moieties are consistent with the corresponding B3LYP values (FeOOH, 1.09 e/2.93 e; SH, −0.03 e/0.15 e; porphyrin, −0.06 e/−0.06 e). This is not surprising since the leading configuration corresponds to the Kohn−Sham determinant in both states, with a weight of 86−87% (compared with less than 2% for the next most important configurations, see Table 4). The lowest doublet and quartet state of Cpd 0 are thus of single-reference character, and they are qualitatively well described by the leading monoradicaloid and triradicaloid configurations, respectively.

IV. Discussion and Conclusions

Compound 0, Compound I, and the hydroxo intermediate in the catalytic cycle of cytochrome $P450_{cam}$ have been studied by B3LYP/CHARMM and correlated ab initio CASSCF-DDCI2+Q/CHARMM calculations. According to the ab initio results, all species have a doublet ground state which has a pronounced multiconfigurational character in the case of Cpd I and HYD. The B3LYP/CHARMM calculations also give a doublet ground state and reproduce the doublet−quartet splitting well (typically within ca. 2 kcal/mol). However, the broken-symmetry DFT solution for the doublet Cpd I and HYD does not capture the multiconfigurational nature of this state and can thus not be used for the calculation of any spin-dependent property without applying a spin projection scheme.

The CASSCF calculations with the larger active space for Cpd I [CAS(13,12)] and for HYD [CAS(11,11)] converged only for the quartet state. For both species, the lowest CASSCF root corresponds to a state with A_{1u} porphyrin radical character. Inclusion of dynamic correlation in 6-root CASSCF-DDCI2+Q calculations reverses the order of states such that the most stable quartet state has A_{2u} character. Dynamic correlation is thus crucial for obtaining the correct lowest-energy quartet state. Similar findings have been reported in porphyrin model systems with an axial Cl ligand,[18] where CASSCF (CASPT2) calculations gave an A_{1u} (A_{2u}) ground state. We conclude that 1-root multireference ab initio calculations on top of CASSCF orbitals may yield erroneous results for heme systems containing porphyrin radicals and that several roots should always be computed in such calculations. This caveat does not apply to systems with a neutral porphyrin ring, such as the previously studied oxy- and oxo-heme complexes,[18,41] where the porphyrin a_{1u} and a_{2u} orbitals are both doubly occupied. Likewise, and for the same reason, Cpd 0 can be described with 1-root calculations which converge for both spin states with the large active space [CAS(13,11)], leading to solutions that are dominated a single configuration (i.e., the Kohn−Sham determinant).

Both for Cpd I and HYD, the lowest-energy states from the B3LYP/MM and CASSCF-DDCI2+Q/MM calculations with basis B′ always correspond to ferryl [Fe(IV)] A_{2u} radical states. The computed $A_{1u}-A_{2u}$ splitting between the lowest quartet states of Cpd I is only 1.9 kcal/mol at the CASSCF(13,12)-DDCI2+Q/MM level, significantly smaller than the value of 12.3 kcal/mol from TDDFT(B3LYP)/MM calculations. In the case of HYD, the DFT and ab initio treatments both yield small values of 2 kcal/mol or less for this splitting.

In summary, the present comparisons show that B3LYP reproduces the relative spin state energies and excitation energies from the correlated ab initio treatment quite well (except for the $A_{1u}-A_{2u}$ splitting in Cpd I), in spite of the multiconfigurational character of some of the states considered (especially the doublet states). Further calibration studies with comparisons against high-level multireference ab initio results are desirable to check the performance of DFT (and particularly B3LYP) for other electronically demanding species in heme chemistry.

Acknowledgment. This work was supported by the Volkswagenstiftung (Grant I/80540).

References and Notes

(1) (a) Ortiz de Montellano, P. R. Ed. *Cytochrome P450: Structure, Mechanisms, and Biochemistry*, 2nd ed.; Plenum Presss: New York, 1995. (b) Ortiz de Montellano, P. R. Ed. *Cytochrome P450: Structure, Mechanism, and Biochemistry*, 3rd ed.; Kluwer Academic/Plenum Publishers: New York, 2004.

(2) Denisov, I. G.; Makris, T. M.; Sligar, S. G.; Schlichting, I. *Chem. Rev.* **2005**, *105*, 2253.

(3) Shaik, S.; Kumar, D.; de Visser, S. P.; Altun, A.; Thiel, W. *Chem. Rev.* **2005**, *105*, 2279.

(4) Mueller, E. J.; Lioda, P. J.; Sligar, S. G. In *Cytochrome P450: Structure, Mechanism, and Biochemistry*, 2nd ed.; Ortiz de Montellano, P. R. Ed.; Plenum Press: New York, 1995; Vol. 2, Chapter 3.

(5) (a) Egawa, T.; Shimada, H.; Ishimura, Y. *Biochem. Biophys. Res. Commun.* **1994**, *201*, 1464. (b) Kellner, D. G.; Hung, S.-C.; Weiss, K. E.; Sligar, S. G. *J. Biol. Chem.* **2002**, *277*, 9641. (c) Spolitak, T.; Dawson, J. H.; Ballou, D. P. *J. Biol. Chem.* **2005**, *280*, 20300.

(6) Newcomb, M.; Zhang, R.; Chandrasena, R. E. P.; Halgrimson, J. A.; Horner, J. H.; Makris, T. M.; Sligar, S. G. *J. Am. Chem. Soc.* **2006**, *128*, 4580.

(7) Rutter, R.; Hager, L. P.; Dhonau, H.; Hendrich, M.; Valentine, M.; Debrunner, P. *Biochemistry* **1984**, *23*, 6809.

(8) Kim, S. H.; Perera, R.; Hager, L. P.; Dawson, J. H.; Hoffman, B. M. *J. Am. Chem. Soc.* **2006**, *128*, 5598.

(9) Groves, J. T.; Watanabe, Y. *J. Am. Chem. Soc.* **1988**, *110*, 8443.

(10) Dunford, H. B. *Heme Peroxidases*; Wiley-VCH: New York, 1999.

(11) Messerschmidt, A., Huber, R., Poulos, T. L., Wieghardt, K. Eds. *Handbook of Metalloproteins*; John-Wiley and Sons: New York, 2001; Vol. 1.

(12) Schöneboom, J. C.; Cohen, S.; Lin, H.; Shaik, S.; Thiel, W. *J. Am. Chem. Soc.* **2004**, *126*, 4017.

(13) Altun, A.; Guallar, V.; Friesner, R. A.; Shaik, S.; Thiel, W. *J. Am. Chem. Soc.* **2006**, *128*, 3924.

(14) Altun, A.; Shaik, S.; Thiel, W. *J. Comput. Chem.* **2006**, *27*, 1324.

(15) Altun, A.; Shaik, S.; Thiel, W. *J. Am. Chem. Soc.* **2007**, *129*, 8978.

(16) Zheng, J. J.; Altun, A.; Thiel, W. *J. Comput. Chem.* **2007**, *28*, 2147.

(17) Koch, W.; Holthausen, M. C. *A Chemist's Guide to Density Functional Theory*; Wiley-VCH: New York, 2000.

(18) Ghosh, A.; Persson, B. J.; Taylor, P. R. *J. Biol. Inorg. Chem.* **2003**, *8*, 507.

(19) Ghosh, A.; Taylor, P. R. *Curr. Opin. Chem. Biol.* **2003**, *7*, 113.

(20) Neese, F. *J. Biol. Inorg. Chem.* **2006**, *100*, 716.

(21) Schöneboom, J. C.; Neese, F.; Thiel, W. *J. Am. Chem. Soc.* **2005**, *127*, 5840.

(22) Radon, M.; Broclawik, E. *J. Chem. Theory Comput.* **2007**, *3*, 728.

(23) Zheng, J.; Wang, D.; Thiel, W.; Shaik, S. *J. Am. Chem. Soc.* **2006**, *128*, 13204.

(24) (a) ChemShell is a modular QM/MM program developed in the European QUASI project under the coordination of P. Sherwood. See: http://www.chemshell.org. (b) Sherwood, P.; de Vries, A. H.; Guest, M. F.; Schreckenbach, G.; Catlow, C. R. A.; French, S. A.; Sokol, A. A.; Bromley, S. T.; Thiel, W.; Turner, A. J.; Billeter, S.; Terstegen, F.; Thiel, S.; Kendrick, J.; Rogers, S. C.; Casci, J.; Watson, M.; King, F.; Karlsen, E.; Sjovoll, M.; Fahmi, A.; Schäfer, A.; Lennartz, C. *J. Mol. Struct. (THEOCHEM)* **2003**, *632*, 1.

(25) Neese, F. *ORCA*, an ab initio, DFT and semiempirical electronic structure package, version 2.4, revision 44; Max-Planck-Institut für Bioanorganische Chemie: Mülheim an der Ruhr, Germany, 2005.

(26) Hay, J. P.; Wadt, W. R. *J. Chem. Phys.* **1985**, *82*, 299.

(27) (a) Ditchfield, R.; Hehre, W. J.; Pople, J. A. *J. Chem. Phys.* **1971**, *54*, 724. (b) Hehre, W. J.; Ditchfield, R.; Pople, J. A. *J. Chem. Phys.* **1972**, *56*, 2257. (c) Hariharan, P. C.; Pople, J. A. *Theor. Chim. Acta* **1973**, *28*, 213. (d) Clark, T.; Chandrasekhar, J.; Spitznagel, G. W.; Schleyer, P. v. R. *J. Comput. Chem.* **1983**, *4*, 294.

(28) (a) Wachters, A. J. H. *J. Chem. Phys.* **1970**, *52*, 1033. (b) Hay, P. J. *J. Chem. Phys.* **1977**, *66*, 4377. (c) Bauschlicher, C. W., Jr.; Langhoff, S. R.; Barnes, L. A. *J. Chem. Phys.* **1989**, *91*, 2399.

(29) (a) Ahlrichs, R.; May, K. *Phys. Chem. Chem. Phys.* **2000**, *2*, 943. (b) Schäfer, A.; Huber, C.; Ahlrichs, R. *J. Chem. Phys.* **1994**, *100*, 5829.

(30) Schäfer, A.; Horn, H.; Ahlrichs, R. *J. Chem. Phys.* **1992**, *97*, 2571.

(31) (a) The auxiliary basis sets were obtained from the TURBOMOLE basis set library under ftp.chemie.uni-karlsruhe.de/pub/cbasen. (b) Eichkorn, K.; Weigend, F.; Treutler, O.; Ahlrichs, R. *Theor. Chem. Acc.* **1997**, *97*, 119. (c) Weigend, F.; Häser, M. *Theor. Chem. Acc.* **1997**, *97*, 331.

(32) Roos, B. O.; Taylor, P. R. *Chem. Phys.* **1980**, *48*, 157.

(33) Miralles, J.; Castell, O.; Caballol, R.; Malrieu, J. P. *Chem. Phys.* **1993**, *172*, 33.

(34) Neese, F. *J. Chem. Phys.* **2003**, *119*, 9428.

(35) Wanko, M.; Hoffman, M.; Strodel, P.; Koslowski, A.; Thiel, W.; Neese, F.; Frauenheim, T.; Elstner, M. *J. Phys. Chem. B* **2005**, *109*, 3606.

(36) Altun, A.; Neese, F.; Thiel, W. **2008**, to be submitted for publication.

(37) Roos, B. O.; Andersson, K.; Fülscher, M. P.; Malmqvist, P.-A.; Serrano-Andrés, L.; Pierloot, K.; Merchán, M. *Adv. Chem. Phys.* **1996**, *93*, 219.

(38) Bakowies, D.; Thiel, W. *J. Phys. Chem.* **1996**, *100*, 10580.

(39) Antes, I.; Thiel, W. *Hybrid Quantum Mechanical and Molecular Mechanical Methods*; Gao, J. Ed.; ACS Symposium Series 712; American Chemical Society: Washington, DC, 1998; p 50.

(40) de Vries, A. H.; Sherwood, P.; Collins, S. J.; Rigby, A. M.; Rigutto, M.; Kramer, G. J. *J. Phys. Chem. B* **1999**, *103*, 6133.

(41) Yamamoto, S.; Teraoka, J.; Kashiwagi, H. *J. Chem. Phys.* **1988**, *88*, 303.

JP802092W

J|A|C|S
ARTICLES

Published on Web 07/11/2008

A Valence Bond Modeling of Trends in Hydrogen Abstraction Barriers and Transition States of Hydroxylation Reactions Catalyzed by Cytochrome P450 Enzymes

Sason Shaik,*,† Devesh Kumar,†,$ and Sam P. de Visser*,‡

Institute of Chemistry and the Lise Meitner-Minerva Center for Computational Quantum Chemistry, The Hebrew University of Jerusalem, 91904 Jerusalem, Israel, and The Manchester Interdisciplinary Biocenter and School of Chemical Engineering and Analytical Science, University of Manchester, 131 Princess Street, Manchester M1 7DN, United Kingdom

Received March 17, 2008; E-mail: sason@yfaat.ch.huji.ac.il (S.S.); sam.devisser@manchester.ac.uk (S.P.d.V.)

Abstract: The paper outlines the fundamental factors that govern the mechanisms of alkane hydroxylation by cytochrome P450 and the corresponding barrier heights during the hydrogen abstraction and radical rebound steps of the process. This is done by a combination of density functional theory calculations for 11 alkanes and valence bond (VB) modeling of the results. The energy profiles and transition states for the various steps are reconstructed using VB diagrams (Shaik, S. S. *J. Am. Chem. Soc.* **1981**, *103*, 3692–3701. Shaik, S.; Shurki, A. *Angew. Chem. Int. Ed.* **1999**, *38*, 586–625.) and the DFT barriers are reproduced by the VB model from raw data based on C−H bond energies. The model explains a variety of other features of P450 hydroxylations: (a) the nature of the polar effect during hydrogen abstraction, (b) the difference between the activation mechanisms leading to the Fe^{IV} vs the Fe^{III} electromers, (c) the difference between the gas phase and the enzymatic reaction, and (d) the dependence of the rebound barrier on the spin state. The VB mechanism shows that the active species of the enzyme performs a complex reaction that involves multiple bond making and breakage mechanisms by utilizing *an intermediate VB structure that cuts through the high barrier of the principal transformation between reactants and products, thereby mediating the process at a low energy cost*. The correlations derived in this paper create order and organize the data for a process of a complex and important enzyme. This treatment can be generalized to the reactivity patterns of nonheme systems and synthetic iron−oxo porphyrin reagents.

Introduction

Hydroxylation of nonactivated C−H bonds is one of the most difficult to achieve chemical transformations. Nevertheless, several enzymes that use high valent iron−oxo active species, such as the heme enzymes called cytochromes P450 (P450s) (Scheme 1)[1] and nonheme enzymes, like taurine/α-ketoglutarate dioxygenase (TauD),[2] are known to be efficient catalysts of this reaction. Moreover, many synthetic analogues of P450 and of nonheme enzymes having high-valent metal−oxo complexes have been made and demonstrated to perform C−H hydroxylation reactions.[3] This study focuses on P450 with the aim of generating a general theoretical framework that organizes the reactivity patterns of C−H hydroxylation.

Scheme 1 illustrates the active site of the enzyme $P450_{cam}$, which is a bacterial enzyme that regioselectively hydroxylates camphor at the C^5 position.[4,5] It is seen that the iron ion is bound to a protoporphyrin IX macrocycle and linked to the protein backbone via a thiolate linkage of a cysteinate residue (Cys_{357} in $P450_{cam}$). Here and in P450s in general, the binding of the substrate to the active site triggers a series of events that include a reduction of the heme, dioxygen binding, a second reduction step, and finally two protonation events leading to the iron−oxo active species, the so-called compound I (Cpd I).[6] Despite the

† The Hebrew University of Jerusalem.
‡ University of Manchester.
$ Present Address: Max-Planck-Institut für Kohlenforschung, Kaiser-Wilhelm-Platz 1, D45470 Mülheim an der Ruhr, Germany.

(1) (a) Sono, M.; Roach, M. P.; Coulter, E. D.; Dawson, J. H. *Chem. Rev.* **1996**, *96*, 2841–2887. (b) Guengerich, F. P. *Chem. Res. Toxicol.* **2001**, *14*, 611–650. (c) Ortiz de Montellano, P. R.; De Voss, J. J. *Nat. Prod. Rep.* **2002**, *19*, 477–494. (d) Groves, J. T. *Proc. Natl. Acad. Sci. U.S.A.* **2003**, *100*, 3569–3574. (e) *Cytochrome P450: Structure, Mechanism and Biochemistry*, 3rd ed.; Ortiz de Montellano, P. R., Ed.; Kluwer Publishers/Plenum Press: New York, 2005.
(2) (a) Ryle, M. J.; Hausinger, R. P. *Curr. Opin. Chem. Biol.* **2002**, *6*, 193–201. (b) Costas, M.; Mehn, M. P.; Jensen, M. P.; Que, L., Jr *Chem. Rev.* **2004**, *104*, 939–986. (c) Abu-Omar, M. M.; Loaiza, A.; Hontzeas, N. *Chem. Rev.* **2005**, *105*, 2227–2252. (d) Krebs, C.; Fujimori, D. G.; Walsh, C. T.; Bollinger, J. M., Jr *Acc. Chem. Res.* **2007**, *40*, 484–492.
(3) See, for example: (a) Groves, J. T. *J. Inorg. Biochem.* **2006**, *100*, 434−447. (b) Rohde, J.-U.; In, J.-H.; Lim, M. H.; Brennessel, W. W.; Bukowski, M. R.; Stubna, A.; Münck, E.; Nam, W.; Que, L., Jr. *Science* **2003**, *299*, 1037–1039. (c) Lim, M. H.; Rohde, J.-U.; Stubna, A.; Bukowski, M. R.; Costas, M.; Ho, R. Y. N.; Münck, E.; Nam, W.; Que, L., Jr *Proc. Natl. Acad. Sci. U.S.A.* **2003**, *100*, 3665–3670.
(4) (a) Schlichting, I.; Berendzen, J.; Chu, K.; Stock, A. M.; Maves, S. A.; Benson, D. E.; Sweet, R. M.; Ringe, D.; Petsko, G. A.; Sligar, S. G. *Science* **2000**, *287*, 1615–1622. (b) Davydov, R.; Makris, T. M.; Kofman, V.; Werst, D. E.; Sligar, S. G.; Hoffman, B. M. *J. Am. Chem. Soc.* **2001**, *123*, 1403–1415.
(5) Poulos, T. L.; Finzel, B. C.; Howard, A. J. *J. Mol. Biol.* **1987**, *195*, 687–700.
(6) Meunier, B.; de Visser, S. P.; Shaik, S. *Chem. Rev.* **2004**, *104*, 3947–3980.

 10.1021/ja8019615 CCC: $40.75 © **2008 American Chemical Society**

Scheme 1. An Illustration of the Iron−Oxo Active Species of Cytochrome $P450_{cam}$ That Regioselectively Hydroxylates the C^5-H_{exo} Bond of Camphor (taken from PDB file 1DZ9)[4a]

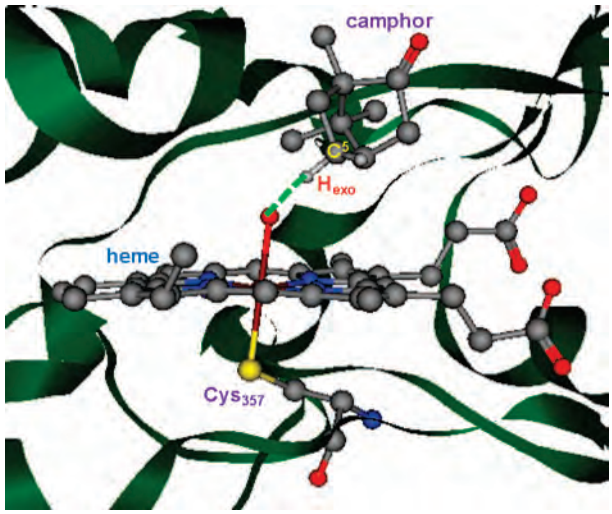

Scheme 2. The Groves Rebound Mechanism of Alkane (Alk−H) Hydroxylation by Iron−Oxo Species

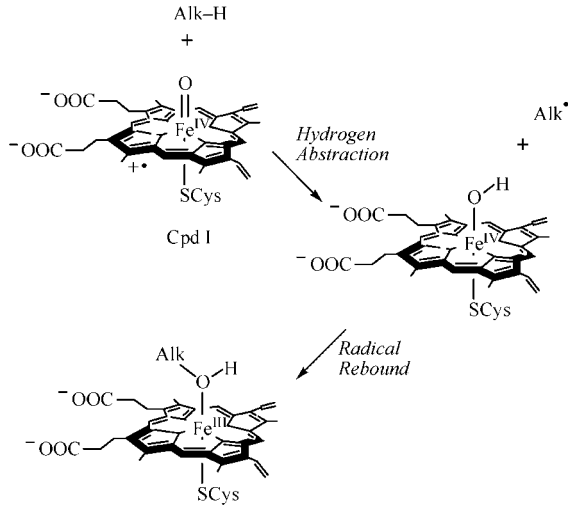

elusiveness of Cpd I in the working cycle of the enzyme, its presence can be inferred in a variety of ways, and it is generally assumed to be the species that performs the hydroxylation.[4b,7]

The net reaction between Cpd I and an alkane (AlkH) involves, in addition to the C−H bond activation, lowering of the oxidation state of the heme by two oxidation equivalents. Thus, as shown in Scheme 2, Cpd I, labeled $Por^{+\bullet}Fe^{IV}$=O with Por = protoporphyrin IX, changes its oxidation state during the reaction to $PorFe^{III}O(H)Alk$ in the products. As such, the metal and the protoporphyrin groups are both reduced by one oxidation equivalent. This reduction is common to other oxidation reactions, e.g., in the nonheme dioxygenases, where the oxidation state changes from Fe^{IV} to Fe^{II}.[2b] The question is, how is this interplay of bond activation and "redox" property, inherent to the net reaction, being expressed in the reactivity patterns of the hydroxylation reactions?

Recently there have appeared a number of publications that demonstrated computationally in P450s,[8] experimentally in synthetic heme,[9] and both experimentally and computationally in nonheme complexes[10] and in other metal−oxo reagents[11] that the reactivity ordering follows the bond dissociation energy (BDE) of the C−H bond in the alkane as well as the BDE of the forming O−H bond of the metal−oxo reagent.[8a,11] The origin of these correlations is usually interpreted by invoking the Brønsted−Bell−Evans−Polanyi (BBEP) principle,[11a,12] whereby one might expect that the barrier would decrease as the hydrogen-abstraction reaction becomes more exothermic (exoergic). But we must recall that even in the first step of the reaction the iron−oxo reagent undergoes a redox reaction and its oxidation state is lowered by one oxidation equivalent (see Scheme 2). Indeed, at least in the case of nonheme iron−oxo reagents, the reactivity of the series of alkanes correlates nicely not only with the BDE_{C-H},[10a] but also with the corresponding ionization potential (IP) of the alkane, IP(AlkH).[13] Similar dual correlations exist in P450 hydroxylation, where a good correlation was reported between the reaction rate and the redox properties of the alkanes, such as in the *N*,*N*-dimethylaniline series.[14] It is arguable that this "dual" correlation exists because in some series of alkanes the two molecular properties correlate with each other. Still, this raises a few questions. One question concerns the causality relationship: Does the correction with BDE_{C-H} or with IP(AlkH) imply a causal relationship, or are these just useful correlations with no causal implication? And, second, why does one often get these extended correlations with BDE_{C-H} in such oxidative reactions? Another set of questions concerns the mechanism, beautifully termed by Groves as the rebound mechanism:[15] why is it stepwise and not concerted? What are the factors that control the final alcohol formation step?

A clear answer to these questions can emerge from a quantum chemical modeling of the reaction mechanism and barrier formation in each mechanistic step. This is the main goal of the present paper, which seeks to pattern the reactivity trends by focusing on P450 hydroxylation as a general paradigm for these reactions. As such, we approach the problem in a two-pronged manner: We first perform an extended series of calculations for P450 C−H activation of alkanes, as in Scheme

(7) Perera, R.; Jin, S.; Sono, M.; Dawson, J. H. Cytochrome P450-Catalyzed Hydroxylations and Epoxidations. In *Metal Ions in Life Sciences: The Ubiquitous Roles of Cytochrome P450 Proteins*; Sigel, A., Sigel, H., Sigel, R. K. O., Eds.; Wiley: New York, 2007; Vol. 3, Chapter 11, p 319.

(8) (a) Korzekwa, K. R.; Jones, J. P.; Gillette, J. R. *J. Am. Chem. Soc.* **1990**, *112*, 7042–7046. (b) de Visser, S. P.; Kumar, D.; Cohen, S.; Shacham, R.; Shaik, S. *J. Am. Chem. Soc.* **2004**, *126*, 8362–8363. (c) Olsen, L.; Rydberg, P.; Rod, T. H.; Ryde, U. *J. Med. Chem.* **2006**, *49*, 6489–6499. (d) Kamachi, T.; Yoshizawa, K. *J. Am. Chem. Soc.* **2003**, *125*, 4652–4661.

(9) Jin, N.; Bourassa, J. L.; Tizio, S. C.; Groves, J. T. *Angew. Chem., Int. Ed.* **2000**, *39*, 3849–3851.

(10) (a) Kaizer, J.; Klinker, E. J.; Oh, N. Y.; Rohde, J.-U.; Song, W. J.; Stubna, A.; Kim, J.; Münck, E.; Nam, W.; Que, L., Jr. *J. Am. Chem. Soc.* **2004**, *126*, 472–473. (b) Hirao, H.; Kumar, D.; Que, L., Jr.; Shaik, S. *J. Am. Chem. Soc.* **2006**, *128*, 8590–8606.

(11) (a) Mayer, J. M. *Acc. Chem. Res.* **1998**, *31*, 441–450. (b) MayerJ. M. In *Biomimetic Oxidations Catalyzed by Transition Metal Complexes*; Meunier, B., Ed.; Imperial College Press: London, 1999; 1−43.

(12) (a) Bell, R. P. *Proc. R. Soc. London Ser. A* **1936**, *154*, 414–421. (b) Evans, M. G.; Polanyi, M. *Trans. Faraday Soc.* **1938**, *34*, 11–24. (c) See comments: Pross, A.; Shaik, S. S. *Nouv. J. Chim.* **1989**, *13*, 427−433.

(13) Sydora, O. L.; Goldsmith, J. I.; Vaid, T. P.; Miller, A. E.; Wolczanski, P. T.; Abruña, H. D. *Polyhedron* **2004**, *23*, 2841–2856.

(14) (a) Okazaki, O.; Guengerich, F. P. *J. Biol. Chem.* **1993**, *268*, 1546–1552. (b) Wang, Y.; Kumar, D.; Yang, C.; Han, L.; Shaik, S. *J. Phys. Chem. B* **2007**, *111*, 7700–7710. (c) Li, C.; Wu, W.; Kumar, D.; Shaik, S. *J. Am. Chem. Soc.* **2006**, *128*, 394–395.

(15) Groves, J. T.; McClusky, G. A. *J. Am. Chem. Soc.* **1976**, *98*, 859–861.

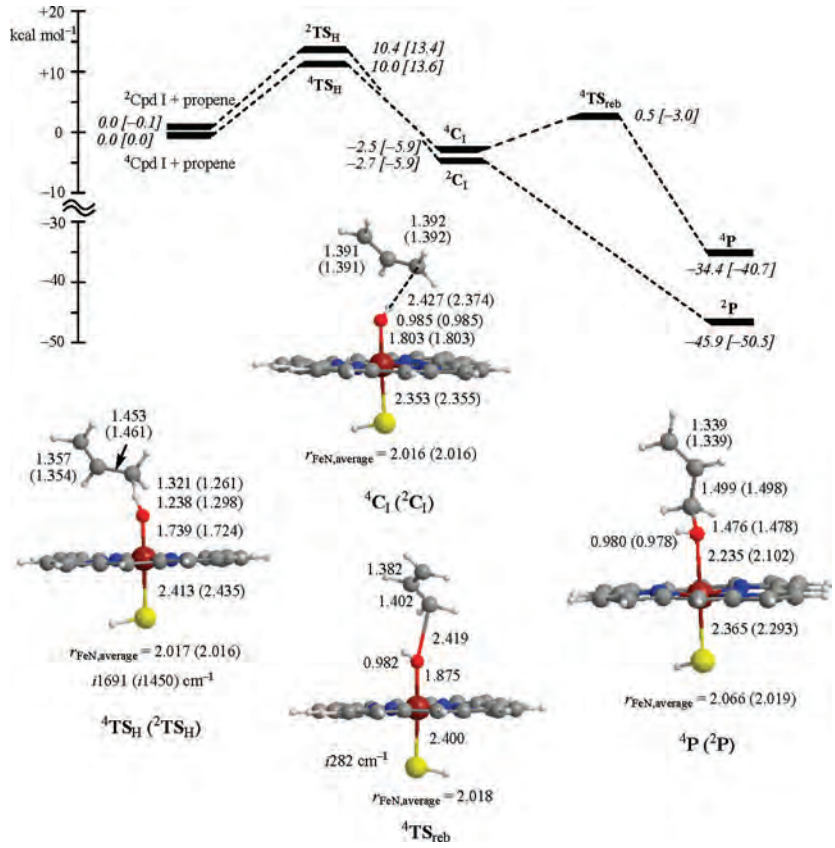

Figure 1. Potential energy profiles and optimized geometries of the critical points for the allylic hydroxylation of propene by ^{4,2}Cpd I. All energies ($\Delta(E+ZPE)$) are in kcal mol^{-1} relative to isolated ^{4}Cpd I and propene reactants with energies calculated with basis set B1 (B2 data in square brackets). Bond lengths are in Å and the value of the imaginary frequency of the transition state is in cm^{-1}.

2, where Alk−H corresponds to methane (**1**),[16] ethane (**2**),[8b] propane (**3**),[8b] propene (**4**),[17] *trans*-methylphenylcyclopropane (**5**),[18] *trans*-isopropylphenylcyclopropane (**6**),[18] *N*,*N*-dimethylaniline (**7**),[14b] toluene (**8**),[19] phenylethane (**9**), and camphor (**10**). *N*,*N*-Dimethylaniline belongs to a series whose reactivity does not follow the trend in BDE.[14b,c] Subsequently, we use valence bond theory[20] to model computational results and elucidate the origins of the various barriers and transition state (TS) structures.

Methods

Software. In order to calculate a series of hydrogen abstraction barriers as catalyzed by a Cpd I model of P450 enzymes, with small nonsystematic errors, we decided to reoptimize all transition states that appeared in our previous set of calculations.[8b,14b,16–19] That way we are able to create a data set of which all systems are calculated using the same methods, procedures, and basis sets. This should remove any nonsystematic errors from the calculations and enable us to describe trends of barrier heights and establish a VB correlation for the series. All the calculations were previously[8b] done using the Jaguar 4.2 program package[21] for geometry optimization and Gaussian 98[22] for frequency calculations. Since we have noticed that occasionally Jaguar and Gaussian yield slightly different transition state structures,[23] it was deemed necessary to repeat all the geometry optimizations and frequencies with Gaussian 03,[24] which possesses a robust geometry optimization routine. Although, small differences in transition state geometries, imaginary frequencies, and energies between the Jaguar and Gaussian 03 data sets (see Supporting Information for details) were found, the reaction barriers themselves did not change significantly, so all previous conclusions based on the Jaguar optimizations remain valid. The changes in geometries and frequencies are not large but nevertheless affected the zero point energy (ZPE) corrections and, as a result, introduced significant error bars on kinetic isotope effect values for the two spin state processes (see Table S1 in the Supporting Information). However, the calculated energy differences ranged between 0 and 1.5 kcal mol^{-1} and did not affect the correlations that are discussed in the text. Both barrier data sets correlated perfectly with each other (Figure S12 of the Supporting Information) and exhibit similar correlations with BDEs. Therefore, we will focus on the newly generated Gaussian 03 data in this paper, while all other data is relegated to the Supporting Information.

Functional and Basis Sets. All the calculations presented here were performed using the unrestricted hybrid density functional method UB3LYP.[25] Geometry optimizations (without constraints) followed by analytical frequency calculations were performed in Gaussian 03 with an LACVP basis set on iron and a 6-31G basis

(16) Ogliaro, F.; Harris, N.; Cohen, S.; Filatov, M.; de Visser, S. P.; Shaik, S. *J. Am. Chem. Soc.* **2000**, *122*, 8977–8989.
(17) (a) de Visser, S. P.; Ogliaro, F.; Sharma, P. K.; Shaik, S. *Angew. Chem. Int. Ed* **2002**, *41*, 1947–1951. (b) de Visser, S. P.; Ogliaro, F.; Sharma, P. K.; Shaik, S. *J. Am. Chem. Soc.* **2002**, *124*, 11809–11826.
(18) (a) Kumar, D.; de Visser, S. P.; Shaik, S. *J. Am. Chem. Soc.* **2003**, *125*, 13024–13025. (b) Kumar, D.; de Visser, S. P.; Sharma, P. K.; Cohen, S.; Shaik, S. *J. Am. Chem. Soc.* **2004**, *126*, 1907–1920.
(19) Hazan, C.; Kumar, D.; de Visser, S. P.; Shaik, S. *Eur. J. Inorg. Chem.* **2007**, 2966–2974.
(20) (a) Shaik, S. S. *J. Am. Chem. Soc.* **1981**, *103*, 3692–3701. (b) Shaik, S.; Shurki, A. *Angew. Chem., Int. Ed.* **1999**, *38*, 586–625.
(21) *Jaguar 4.2*; Schrödinger, LLC: Portland, OR, 2000.
(22) Frisch, M. J. *Gaussian 98*; Gaussian: Wallingford, CT, 1998.
(23) (a) Sharma, P. K.; de Visser, S. P.; Shaik, S. *J. Am. Chem. Soc.* **2003**, *125*, 8698–8699. (b) de Visser, S. P. *J. Am. Chem. Soc.* **2006**, *128*, 9813–9824. (c) Godfrey, E.; Porro, C. P.; de Visser, S. P. *J. Phys. Chem. A* **2008**, *112*, 2464–2468.
(24) Frisch, M. J. *Gaussian 03*; Gaussian: Wallingford, CT, 2003.

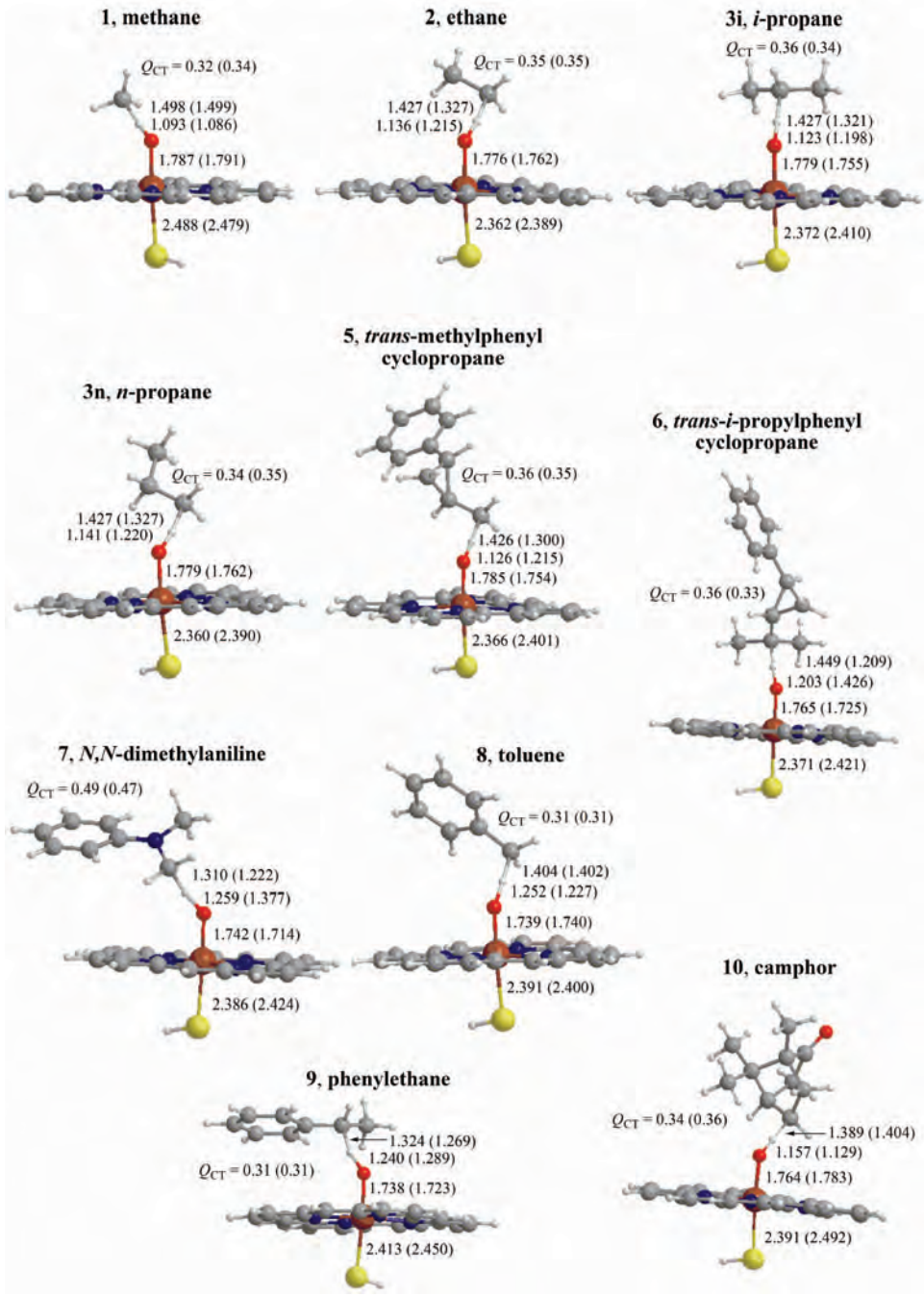

Figure 2. Key geometric features of H-abstraction transition states obtained at the UB3LYP/B1 level for **1**−**3i** and **5**−**10**. The data is displayed respectively as ^4TS_H (^2TS_H) with bond lengths in Å. The Q_{CT} data correspond to the amounts of charge transferred from the alkane to Cpd I in the transition state calculated at the NBO/B3LYP/B2 level.

set on the rest of the atoms (basis set B1).[26,27] Subsequent, single-point calculations were done on the optimized geometries in Jaguar 7.0 using a triple-ζ quality LACV3P+ basis set on iron and 6-311+G* on the rest of the atoms (basis set B2), which were done to correct the energies, but essentially gave the same trends as the double-ζ basis set.[28] All ZPE values reported in this work are taken from the UB3LYP/B1 frequency calculations. These methods and procedures were shown to reproduce experimental free energies of activation and kinetic isotope effects.[29]

Models and Systems. To model Cpd I of P450, the species was truncated as an iron−oxo porphine with HS^- as axial ligand, since it was shown to be a good representation of the actual cysteinate

(25) (a) Becke, A. D. *J. Chem. Phys.* **1992**, *96*, 2155–2160. (b) Becke, A. D. *J. Chem. Phys.* **1992**, *97*, 9173–9177. (c) Becke, A. D. *J. Chem. Phys.* **1993**, *98*, 5648–5652. (d) Lee, C.; Yang, W.; Parr, R. G. *Phys. Rev. B* **1988**, *37*, 785–789.
(26) Hay, P. J.; Wadt, W. R. *J. Chem. Phys.* **1985**, *82*, 299–308.
(27) Hehre, W. J.; Ditchfield, R.; Pople, J. A. *J. Chem. Phys.* **1972**, *56*, 2257–2261.
(28) Jaguar 7.0, Schrödinger, LLC, New York, NY, 2007.
(29) de Visser, S. P.; Oh, K.; Han, A.-R.; Nam, W. *Inorg. Chem.* **2007**, *46*, 4632–4641.
(30) (a) Ogliaro, F.; de Visser, S. P.; Cohen, S.; Kaneti, J.; Shaik, S. *ChemBioChem.* **2001**, *7*, 848–851. (b) Schöneboom, J. C.; Lin, H.; Reuter, N.; Thiel, W.; Cohen, S.; Ogliaro, F.; Shaik, S. *J. Am. Chem. Soc.* **2002**, *124*, 8142–8151. (c) de Visser, S. P.; Shaik, S.; Sharma, P. K.; Kumar, D.; Thiel, W. *J. Am. Chem. Soc.* **2003**, *125*, 15779–15788.

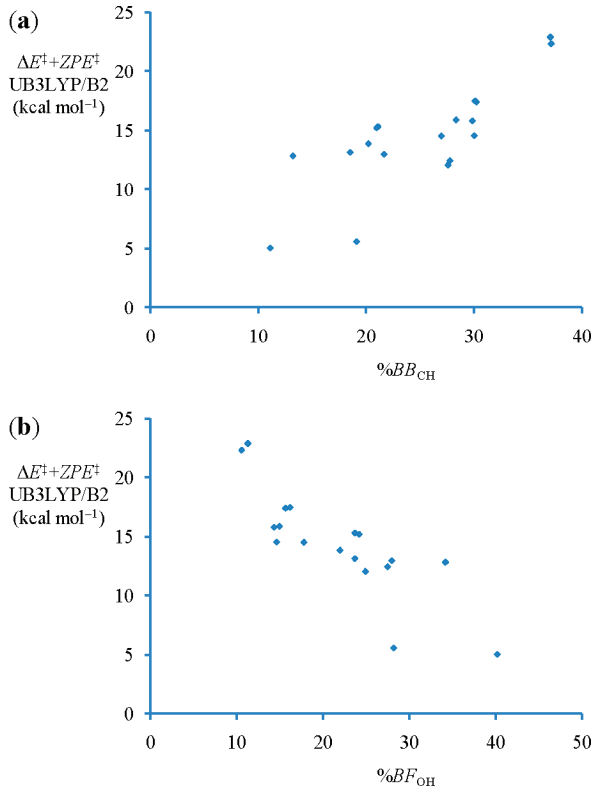

Figure 3. Plots of the barriers for the C−H bond activation of **1**−**10**, against the percentage of bond breaking, $\%BB_{CH}$ (a), and of bond formation, $\%BF_{OH}$ (b).

ligand.[30] Typically, Cpd I is a two-state reagent with close-lying doublet and quartet ground states (^{4,2}Cpd I), which react via different pathways with substrates.[31] Generally, the doublet (low spin, LS) spin surface gives an effectively concerted reaction path, whereas the quartet (high spin, HS) spin surface is stepwise. Thus ^{4,2}Cpd I reacts via two-state reactivity (TSR) with substrates with different HS and LS reaction barriers.[31,32] As indicated in the Introduction, the hydrogen-abstraction transition states for the reaction with ^{4,2}Cpd I were calculated for the following substrates: methane (**1**), ethane (**2**), propane (**3**), propene (**4**), *trans*-methylphenylcyclopropane (**5**), *trans*-isopropylphenylcyclopropane (**6**), *N*,*N*-dimethylaniline (**7**), toluene (**8**), phenylethane (**9**), and camphor (**10**). The set of substrates covers a large range of hydrogen-abstraction barriers with a large variation in the C−H bond strengths that are activated in the process. In the case of propane, both hydrogen abstraction from the primary and secondary carbon atoms were studied, which we labeled **3n** and **3i**, respectively. In our previous work,[8b] we reported the phenylethane hydroxylation from the primary carbon atom, but here we focused on the realistic process of C−H activation in the benzylic position. In total, this set generated 22 hydrogen abstraction reactions that are calculated with the same models, same methods, same basis sets, and the same software packages. This should remove many systematic errors and enable us to find trends in the data set and to model it by use of valence bond diagrams.[20b] Charges were obtained with the natural bond orbital analysis (NBO) program[33] at UB3LYP/B1 in Gaussian 03 and at UB3LYP/B2 in Jaguar 7.0. To test the effect of the environment on the barrier heights, single-point calculations using the UB3LYP/B2 method were performed with Jaguar using a solvent with a dielectric constant of $\varepsilon = 5.7$ and a probe radius of 2.72 Å.

Auxiliary Data. The bond dissociation energies (BDE_{CH} and BDE_{OH}) of the aliphatic C−H bond of the substrates (Alk−H) and of the O−H bond in the iron−hydroxo complexes (see Figure 1) were calculated and defined from the energy difference of the following reactions:

$$\text{Alk}-\text{H} \rightarrow \text{Alk}\bullet + \text{H}\bullet + \text{BDE}_{\text{CH}} \quad (1)$$

$$\text{PorFeO}-\text{H} \rightarrow \text{PorFe}{=}\text{O(Cpd I)} + \text{H}\bullet + \text{BDE}_{\text{OH}} \quad (2)$$

For completeness and consistency with the hydrogen abstraction barriers, we recalculated these BDE values using Gaussian 03 with basis set B1 followed by a single-point calculation with basis set B2 so that all data discussed here is calculated using the same methods and procedures. In our previous study, we showed that BDEs calculated with Gaussian 98 and the B3LYP/6-31G (B1) or B3LYP/6-311++G** (B3) basis sets give similar correlations with reaction barriers.[8b] BDE_{CH} is calculated for the isolated reactants while BDE_{OH} is for the substrate free reaction in eq 2.

From the geometry of the Alk residue in the substrate and in the Alk• radical, we estimated the reorganization energy of the radical ($RE_{Alk\bullet}$) as the energy difference of the Alk• rest group in the free substrate and in the fully relaxed geometry of the Alk• radical.[34] The combination of BDE_{CH} and $RE_{Alk\bullet}$ in eq 3 defines the bond strength (D_{CH}), which is a more faithful measure of the interaction strength between the bonded Alk and H moieties in the alkane:[8b]

$$D_{\text{CH}} = \text{BDE}_{\text{CH}} + \text{RE}_{\text{Alk}} \quad (3)$$

All the data generated in this study are shown in the Supporting Information. For space economy, the following sections will focus on the key data only.

Results

Energy Profiles. Figure 1 shows an example of a typical two-state reactivity (TSR) mechanism of an alkane hydroxylation reaction by Cpd I,[32] in this case for the C−H activation of the methyl group of propene. All the substrates studied follow essentially the same reaction mechanism as displayed in Figure 1 and only the relative energies vary. The energetics of the reaction are similar to those obtained previously with slightly different methods and techniques.[17] The initial step involves a hydrogen abstraction by ^{4,2}Cpd I from the substrate via barrier $^{4,2}TS_H$ leading to an intermediate ($^{4,2}C_I$) consisting of an iron−hydroxo group and a nearby allyl radical. Since Cpd I has a degenerate quartet and doublet ground state,[31,32] there are reaction barriers on both spin surfaces, with the ^4TS_H barrier being slightly higher in energy than the one passing via ^2TS_H (13.6 vs 13.4 kcal mol^{-1}, using basis set B2). Within the intermediate complex, the radical rebounds onto the hydroxo group via $^{4,2}TS_{reb}$ to form the ferric−propenol products ($^{4,2}P$). On the HS surface, a small but significant barrier ($\Delta E^{\ddagger} + \text{ZPE}^{\ddagger}$ for $^4TS_{reb}$ is 2.9 kcal mol^{-1}, with basis set B2) separates intermediates from products, while the LS pathway is essentially barrier free. Thus, the HS intermediate (^4C_I) will have a finite lifetime in which, for instance, rearrangement leading to side reactions can take place.[35] We recall from previous publications that the iron−hydroxo complexes in the $^{4,2}C_I$ intermediates come in two electromeric varieties: ^{4,2}Por$^{+\bullet}$Fe^{III}OH and ^{4,2}Por-

(31) Shaik, S.; de Visser, S. P.; Ogliaro, F.; Schwarz, H.; Schröder, D. *Curr. Opin. Chem. Biol.* **2002**, *6*, 556–567.
(32) Shaik, S.; Kumar, D.; de Visser, S. P.; Altun, A.; Thiel, W. *Chem. Rev.* **2005**, *105*, 2279–2328.
(33) Reed, A. E.; Curtiss, L. A.; Weinhold, F. *Chem. Rev.* **1988**, *88*, 899–926.
(34) Bernardi, F.; Cherry, W.; Shaik, S.; Epiotis, N. D. *J. Am. Chem. Soc.* **1978**, *100*, 1352–1356.
(35) (a) de Visser, S. P.; Ogliaro, F.; Shaik, S. *Angew. Chem., Int. Ed.* **2001**, *40*, 2871–2874. (b) de Visser, S. P.; Kumar, D.; Shaik, S. *J. Inorg. Biochem.* **2004**, *98*, 1183–1193. (c) Kumar, D.; de Visser, S. P.; Shaik, S. *Chem. Eur. J.* **2005**, *11*, 2825–2835.

Table 1. Barriers, $\Delta E^{\ddagger}$, and $\Delta E^{\ddagger} + \mathrm{ZPE}^{\ddagger}$ relative to separated reactants, ^{4,2}Cpd I + Alk-H[a,b]

		TS_H(B1)		TS_H(B2)	
		$\Delta E^{\ddagger}$	$\Delta E^{\ddagger} + \mathrm{ZPE}^{\ddagger}$	$\Delta E^{\ddagger}$	$\Delta E^{\ddagger} + \mathrm{ZPE}^{\ddagger}$
		High-Spin (Quartet) Data			
1	methane	26.77	22.81	26.87	22.91
2	ethane	21.32	17.71	21.02	17.41
3i	*i*-propane	19.05	15.39	19.46	15.80
3n	*n*-propane	21.47	17.84	21.12	17.48
4	propene	14.68	11.70	15.93	12.95
5	*trans*-methylphenylcyclopropane	18.28	14.73	18.09	14.53
6	*trans*-isopropylphenylcyclopropane	16.03	12.46	17.03	13.46
7	*N*,*N*-dimethylaniline	7.66	5.04	8.17	5.54
8	toluene	14.81	11.79	15.45	12.43
9	phenylethane	14.57	11.19	15.93	12.55
10	camphor	17.96	14.21	18.27	14.51
		Low-Spin (Doublet) Data			
1	methane	25.87	22.24	25.97	22.34
2	ethane	20.23	16.65	18.88	15.30
3i	*i*-propane	17.68	14.17	17.36	13.85
3n	*n*-propane	20.36	16.70	18.85	15.19
4	propene	15.15	12.13	15.85	12.82
5	*trans*-methylphenylcyclopropane	17.31	13.90	16.54	13.13
6	*trans*-isopropylphenylcyclopropane	15.05	11.64	15.68	12.27
7	*N*,*N*-dimethylaniline	6.65	4.53	7.11	4.99
8	toluene	14.78	11.73	15.10	12.05
9	phenylethane	14.21	10.69	15.00	11.47
10	camphor	18.39	14.02	20.25	15.88

[a] All energies are in kcal mol^{-1}. [b] Data obtained after full optimization and frequency in Gaussian 03 using UB3LYP/B1 and after additional single-point UB3LYP/B2 calculation in Jaguar 7.0.

Table 2. Calculated BDE_{CH}, BDE_{OH}, and $RE_{Alk\bullet}$ Data of All the Species Mentioned in the Text[a]

	BDE_{CH}				$RE_{Alk\bullet}$	
	B1		B2		ΔE	
	ΔE	ΔE + ZPE	ΔE	ΔE + ZPE	B1	B2
methane	112.45	102.77	111.29	101.62	−7.42	−6.79
ethane	107.51	97.70	106.67	96.87	−7.45	−7.00
i-propane	103.39	93.55	102.87	93.03	−7.56	−7.21
n-propane	107.98	98.37	107.09	97.49	−7.23	−6.87
propene	91.48	82.89	91.39	82.80	−17.69	−16.69
trans-methylphenylcyclopropane	103.66	94.32	102.96	93.62	−9.00	−8.30
trans-isopropylphenylcyclopropane	95.92	86.56	95.95	86.60	−9.04	−8.60
N,*N*-dimethylaniline	95.72	86.99	94.81	86.08	−8.14	−7.94
toluene	94.45	86.08	94.16	85.80	−13.15	−12.27
phenylethane	91.30	82.44	91.31	82.45	−19.32	−18.38
camphor	104.08	94.58	103.39	93.89	−7.90	−7.61
FeOH	88.59	81.81	95.69	88.91		

[a] All data are in kcal mol^{-1} and calculated with basis set B1 or B2. ZPE data calculated with basis set B1.

$Fe^{IV}OH$.[36] The latter are lower in energy than the former in the gas phase, while in the protein both state varieties are very close in energy. The same patterns apply to the $^{4,2}TS_H$ and $^{4}TS_{reb}$ species.[32] We shall address the processes for the two electromers and delineate their similarities and differences below.

The rate-determining step in most systems studied for both HS and LS surfaces is the initial hydrogen abstraction step via $^{4,2}TS_H$. The hydrogen abstraction transition states ($^{4,2}TS_H$) for all systems studied are characterized by an almost linear O−H−C angle. While we shall attempt to model the entire mechanism using VB diagrams,[20] a major focus of this paper is going to be the hydrogen-abstraction step. The rebound step has been discussed in great detail elsewhere[37] and will receive here somewhat less attention.

Structures and Trends in the Transition States for H-Abstraction. The key geometric features of the H-abstraction transition states, for the substrates **1**−**3i** and **5**−**10** are depicted

(36) de Visser, S. P.; Ogliaro, F.; Harris, N.; Shaik, S. *J. Am. Chem. Soc.* **2001**, *123*, 3037–3047.

(37) (a) Shaik, S.; Cohen, S.; de Visser, S. P.; Ogliaro, F.; Sharma, P. K. *Eur. J. Inorg. Chem.* **2004**, 207–226. (b) Shaik, S.; Hirao, H.; Kumar, D. *Nat. Prod. Rep.* **2007**, *24*, 533–552.

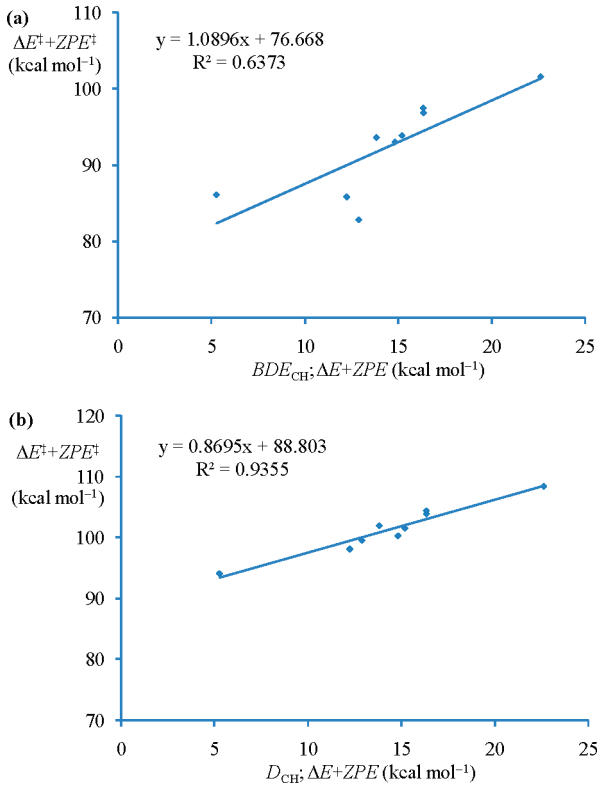

Figure 4. (a) A plot of the average barriers $\Delta E^{\ddagger} + ZPE^{\ddagger}$ (B2) for the quartet and doublet H-abstraction steps vs BDE_{CH} (B2). (b) A plot of the average barriers $\Delta E^{\ddagger} + ZPE^{\ddagger}$ for the quartet and doublet H-abstraction steps vs D_{CH} (defined by eq 3) as calculated with basis set B2.

in Figure 2 (for **4**, see Figure 1), where the data is given in respective order for ^4TS_H (^2TS_H). Also indicated in the figure are the amounts of charge transfer, Q_{CT}, from the substrate to Cpd I, using the NBO/B2 method for charge partition. It is seen that, generally, the quartet spin state structures involve a greater extent of C−H bond cleavage, in accord with the general trend discussed above with reference to Figure 1. The O−H bond is quite short in all the transition states. Another common feature is the O−H−C angle, which is close to 180° in all the computed species. The charge distribution shows that in the transition state the alkane transfers approximately 0.31−0.36 e$^-$ (NBO/B2) to Cpd I, with the exception of **7** (*N*,*N*-dimethylaniline), where the Q_{CT} corresponds to 0.49 (0.47) for ^4TS_H (^2TS_H), respectively. This charge transfer is in accord with the notion from the oxidation state formalism that the process involves also a change in the oxidation state of Cpd I. In this respect, the spin density distribution (Table S4 in the Supporting Information) shows that all the transition states (with the exception of **1**) are more of the Fe^{IV} type rather than of the $Por^{\bullet+}Fe^{III}$ type. We recall that in the protein the latter electromers are more stable.[38]

Figure 3 depicts the barriers plotted against the percentages of bond breaking (%BB) and bond formation (%BF) for all transition states calculated here. Thus, the percentage of bond breaking of the C−H bond ($\%BB_{CH}$) is defined as the elongation of the C−H distance in the transition state relative to the one in the reactants. Similarly, the percentage of bond formation of the O−H bond ($\%BF_{OH}$) is the distance in the transition state relative to that in the iron−hydroxo intermediate. As can be seen from Figure 3, the $\%BB_{CH}$ and $\%BF_{OH}$ are generally correlated with the height of the barrier for the C−H bond activation. In particular, the C−H bond elongation in the transition state is longer for the transition states with higher barriers, i.e. the structures are of product-like geometry. By contrast, when the barrier is low, the respective transition states show reactant-type geometries with short C−H and long O−H distances. It appears, therefore, that the nature of all these transition states is similar and that a common electronic effect determines the height of the hydrogen abstraction barrier. Later in this paper we will explain these functions through VB modeling of the barriers.

Reaction Barriers and Bond Dissociation Energies during H-Abstraction. The barriers for the H-abstraction processes for all the systems are collected in Table 1 for the UB3LYP/B1 and UB3LYP/B2 results. These barriers are close to the ones computed before with slightly different methods and basis sets and follow similar trends.[8b,17–19] The Supporting Information provides detailed comparisons of the Jaguar and Gaussian 03 optimized structures, but since the barrier heights are similar, we focus only on the trends of the barriers here. Furthermore, test calculations using the effect of a bulk polarity showed that the barriers are influenced to a similar extent, with a standard deviation of ±1.2 kcal mol^{-1}. Therefore, the trends as obtained from the gas-phase calculations can be extrapolated to situations in the protein or other environments.

Table 2 shows the corresponding BDE_{CH} (B1 and B2) values and the reorganization energies RE_{Alk} of the radical species. The last entry in Table 2 gives the corresponding BDE_{OH} datum for the iron−hydroxo species. Using these BDE_{CH} data and the BDE_{OH} values, one can calculate the thermodynamic driving forces of the processes.

BBEP Correlations of Barriers with Bond Dissociation Energies. The correlation of activation barriers (logarithms of reaction rates) with BDEs derives from the Brønsted−Bell−Evans−Polanyi (BBEP) principle,[12] which relates the barrier to the reaction exothermicity (exoergicity). The reaction energy (ΔE in energy or free energy units) for the H-abstraction step in Figure 1, is given by eq 4,

$$\Delta E = BDE_{CH} - BDE_{OH} \quad (4)$$

in terms of the bond dissociation energy difference of the C−H bond undergoing abstraction and the O−H bond being made in the iron−hydroxo complex of the $^{4,2}C_I$ intermediates in Figure 1. Since BDE_{OH} is a constant value throughout the series of H-abstraction reactions discussed in this work, and the interaction energies of the radical with the iron−hydroxo are small and virtually constant,[37a] this implies that the variation in the reaction energy will depend on the BDE_{CH} quantity only.

Figure 4a shows the correlation of the averaged doublet and quartet spin state barriers vis-à-vis the corresponding BDE_{CH} (correlations for the individual spin-state barriers are shown in Figures S13−S20 of the Supporting Information). It is seen that the correlation is relatively poor, with a correlation coefficient of 0.64. Figure 4b shows the corresponding correlation with the bond strength quantity, D_{CH} (eq 3). This correlation is much better, thus indicating that the strength of the interaction in the C−H bond has to be considered rather than merely the BDE_{CH} that dominates the thermodynamic driving force. Many other correlations, shown in the Supporting Information, for example, the barrier height with ZPE correction, lead to the same

(38) (a) Schöneboom, J. C.; Cohen, S.; Lin, H.; Shaik, S.; Thiel, W. *J. Am. Chem. Soc.* **2004**, *126*, 4017–4034. (b) Altun, A.; Shaik, S.; Thiel, W. *J. Am. Chem. Soc.* **2007**, *129*, 8978–8987. (c) Harvey, J. N.; Bathelt, C. M.; Mulholland, A. J. *J. Comput. Chem.* **2006**, *27*, 1352–1362.

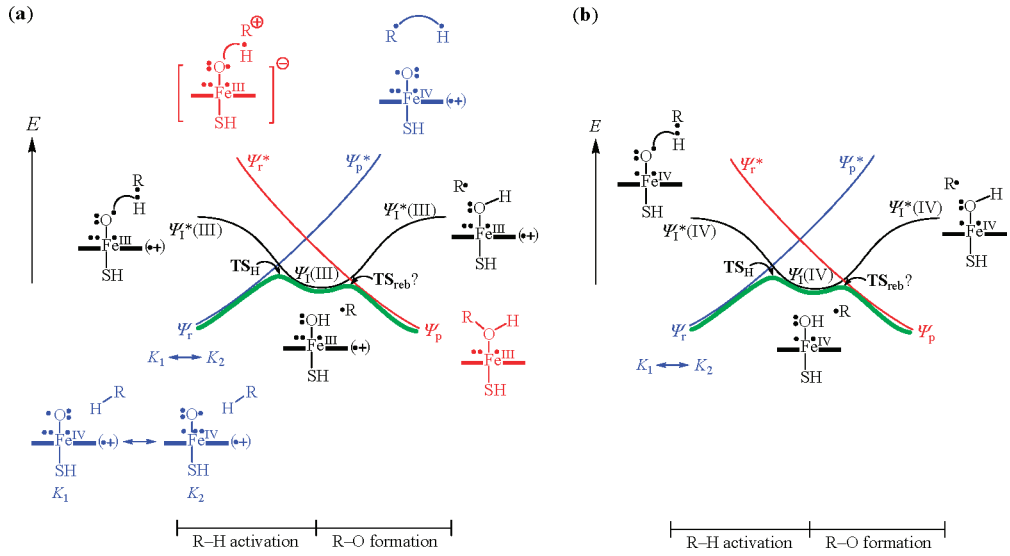

Figure 5. VB diagrams describing the mechanisms of C−H hydroxylation of an alkane (R−H) by Cpd I (the porphyrin is symbolized by the two bold lines flanking the iron) for two electromeric states: (a) formation of the $Por^{+\bullet}Fe^{III}OH/R\bullet$ intermediate, and (b) formation of the $PorFe^{IV}OH/R\bullet$ intermediate. The diagrams can represent either quartet or doublet spin states. The spin pairing in the excited state is indicated by a curved line connecting electrons on two different atoms.[20b] The reactant curve with its relevant structures is shown in blue and the product curve in red. The bold green profile shows the state curve during the reaction process.

conclusion. The D_{CH} values of **6** and **9** deviated significantly from the line due to underestimated RE values in comparison with our previous studies and have been omitted from the correlation.[8b] These deviations will be explained during the VB modeling.

Discussion

The above results show some interesting patterns that require understanding: First, why is the entire hydroxylation process stepwise, with H-abstraction and rebound steps, and not a concerted oxygen atom transfer? Second, what factors govern the barriers for H-abstraction in a fundamental manner that does not rely on correlations? Then there is a host of related questions: What is the source of the polar effect, which is apparent from the charge transfer data in Figure 2? Finally, what factors govern the barrier for the rebound? In order to achieve the requisite insight, we shall use the VB approach to model the mechanism and the origins of the various barriers.[20] In the end, we shall show that the barriers can be calculated from raw data based on the VB state correlation diagram (VBSCD) model.[39]

Modeling the Mechanism of C−H Hydroxylation Using Valence Bond Diagrams. As we already noted, there are two electromeric intermediates[36] that may be involved during the reactions: $Por^{+\bullet}Fe^{III}OH$ and $PorFe^{IV}OH$ species. In addition, there are two spin states, with doublet and quartet spins, which lead to distinct reaction profiles.[32] In order to economize the discussion, we shall model the mechanisms for the two electromeric states and comment on the spin-state effect only by reference to the rebound step.[37a]

Figure 5 shows the VB diagrams for the hydroxylation reactions involving the two electromeric intermediates; the alkane is symbolized as R−H and the porphyrin ring by the bold lines flanking the iron. The two diagrams involve two major curves that correspond to reactants and products states shown in blue and red, respectively. A third curve that cuts through the high-energy ridge of the other two major curves provides a low-energy pathway for the transformation.[20b] Looking at the wave functions of reactants and products, labeled as Ψ_r and Ψ_p at the lower two ends of each diagram, it is seen that the overall process of conversion of the alkane, R−H, to an alcohol involves also a two-electron reduction of iron−oxo porphyrin, which changes from $Por^{+\bullet}Fe^{IV}{=}O$ to $PorFe^{III}$(alcohol). This, however, is mediated by the intermediate curve that describes a H-abstraction process, whereby the electron of the abstracted H• reduces either the oxidation state on iron to Fe^{III} (Figure 5a) or the oxidation state of the porphyrin from a cation-radical to a closed-shell species (Figure 5b). This step is followed by radical rebound, where an electron shift from the alkyl radical (R•) to the iron−porphyrin moiety generates the alcohol and the ferric−porphyrin, which is twice-reduced vis-à-vis the reactants state. *This three-curve VB diagram is a typical case, where an intermediate state internally facilitates the otherwise more difficult transformation of Ψ_r directly to Ψ_p.*

To facilitate understanding of the state correlation in the VB diagram, we have to digress and translate the VB representation of the various anchor states [Ψ_r, Ψ_r*, Ψ_p, Ψ_p*, Ψ_1*(III), and Ψ_1*(IV)] to the more commonly used molecular orbital (MO) diagram and the language of oxidation state formalism.[32,37] The two major curves describe the transformation of reactants to products and are anchored in two ground states, Ψ_r and Ψ_p, for the reactants and products and two corresponding excited states, Ψ_r* and Ψ_p*. Each state-curve represents a single bonding scheme: Thus, Ψ_r describes the bonding pattern in the reactants, and so does Ψ_p*, only that the latter state represents the reactant-type bonding in the geometry of the products. Similarly, Ψ_r* involves the product-type bonding but in the geometry of the reactants. As a result of these bonding features, as we move along the reaction coordinate, by stretching the C−H bond and shrinking the O−H and R−O distances and thereby changing the geometry from reactants to products, the Ψ_r state connects to Ψ_p* and, at the same time, Ψ_r* connects to Ψ_p. Let us now inspect these four states in terms of electronic structure cartoons in detail.

(39) Su, P.; Song, L.; Wu, W.; Hiberty, P. C.; Shaik, S. *J. Am. Chem. Soc.* **2004**, *126*, 13539–13549.

Scheme 3. Electronic Structure of Cpd I: (a) VB Representation[a] and (b) MO Representation

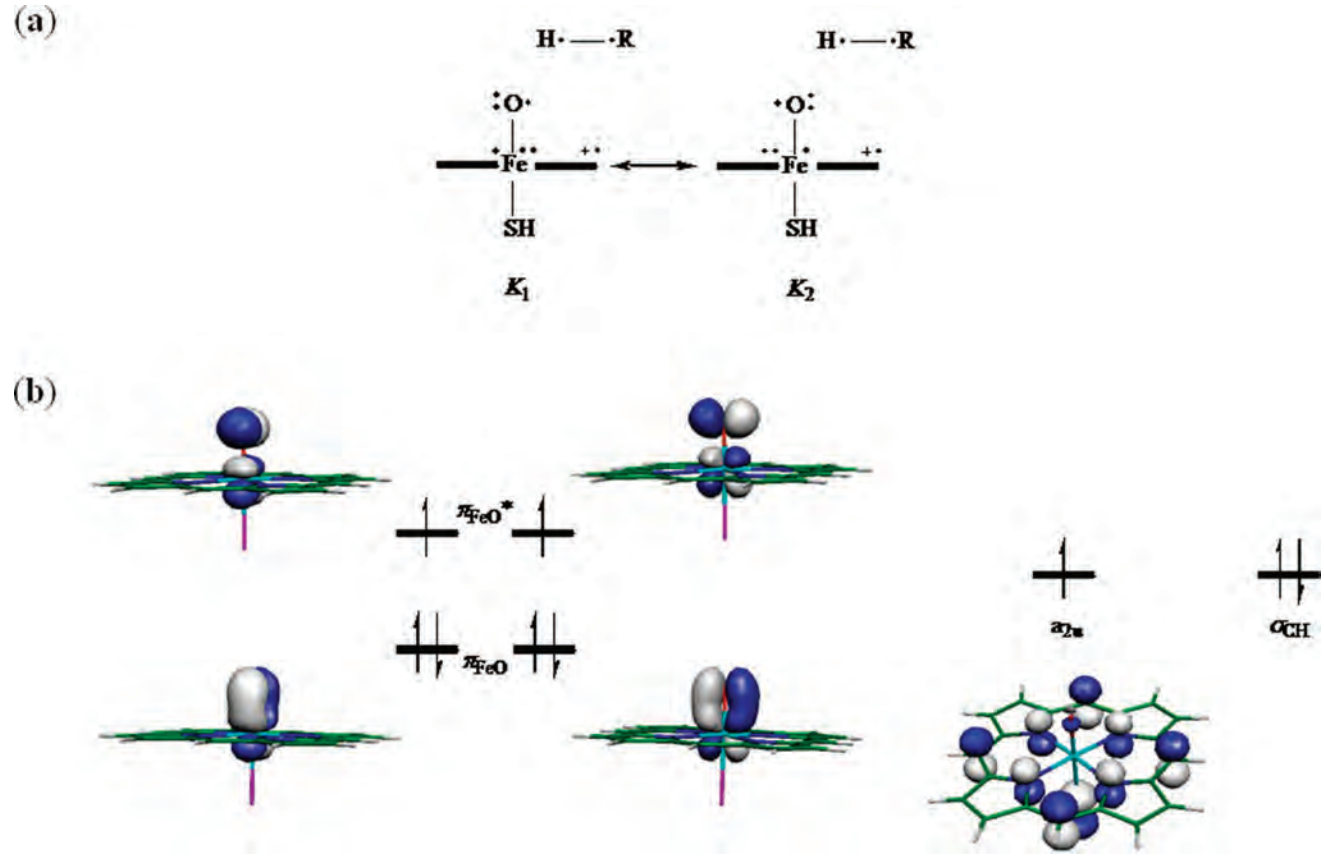

[a] Here the dots on both sides of Fe represent the π-electrons in two perpendicular planes, and the Fe−O line represents the σ-bond.

Starting with the reactants state, Ψ_r (Figure 5), we depict in Scheme 3 the VB-MO representation of Ψ_r for ^{4}Cpd I and R−H. In the VB formulation (Scheme 3a), Cpd I has six π-electrons, distributed in two perpendicular planes, across the Fe−O moiety, and are coupled to produce a triplet spin state.[40] This is described by a resonance mixture of the two forms (K_1 and K_2) that lead to formation of two three-electron bonds in the two perpendicular planes; the line connecting the Fe and O atoms in Figure 5 and here in Scheme 3 represents the σ-bond. The porphyrin is open shell, as indicated with a cation−radical sign. In the MO formulation (Scheme 3b) these six π-electrons on the FeO moiety occupy two bonding π_{FeO} orbitals and two singly occupied antibonding π^*_{FeO} orbitals.[32] The third unpaired electron of Cpd I resides on the porphyrin in an a_{2u} type orbital, and its spin is either ferromagnetically or antiferromagnetically coupled to the triplet FeO pair, thereby yielding two spin states: overall quartet or doublet. In addition, there are three more orbitals originating from the 3d metal atomic orbitals, namely one doubly occupied d(δ) orbital on iron and two virtual antibonding orbitals (σ^*_{xy} and $\sigma^*_{z^2}$), which are not shown explicitly in Scheme 3. The alkane R−H is represented in VB by the corresponding Lewis structure and in MO in terms of the bond orbital σ_{CH} of the R−H bond undergoing activation.

The excited state Ψ_r* in Figure 5 is a charge transfer state in which one electron is transferred from the R−H alkane to fill the "hole" in the a_{2u} orbital of the porphyrin radical cation of Cpd I, while at the same time the H• moiety is spin-paired to the odd electron on the oxo group. This spin-pairing[41] is shown in Figure 5a by the curved line connecting the single electrons on H• and on the oxo group of Cpd I; the RH moiety in this state is a cation−radical. With these bonding changes, the oxidation state of iron in Ψ_r* is reduced from Fe^{IV} to Fe^{III}. The assignment of oxidation state for Ψ_r* is based on an electron counting formalism, which needs a brief explanation. Thus, in Ψ_r, the oxo group of Cpd I is counted as O^{2-}, the four nitrogen ligands of the porphyrin as N_4^{2-}, and the sulfur of the cysteine as S^{1-}. Since Cpd I is neutral, these oxidation states require the iron to be Fe^{IV} and the porphyrin a cation−radical species. However, in Ψ_r*, the oxo is spin-paired to H•, and as an "OH" group its oxidation state becomes HO^{1-}, so the iron ion changes to oxidation state Fe^{III}. Thus, by linking the H• atom to the iron−oxo, the oxo group accepts formally one electron from the H-atom, and hence it "releases" back one of the two electrons it took from Fe in Cpd I. This, in addition to the actual charge transfer from R−H to the heme Ψ_r*, makes this state "twice reduced" relative to the reactant state, Ψ_r. As such, along the reaction coordinate, which involves R−H bond elongation and O−H and O−R shortening, the Ψ_r* state gets stabilized by forming O−H and O−R bonds and becomes the ground state of the ferric−alcohol product, Ψ_p, which involves three electrons in iron d_π orbitals (drawn as heavy dots on iron). Thus, Ψ_r* is the electronic image state of Ψ_p and hence the two states correlate along the reaction coordinate. The same applies in fact to the relationship between the states Ψ_r and Ψ_p*; the latter being the electronic image of the former, with spin-pairing

(40) Shaik, S.; Danovich, D.; Fiedler, A.; Schröder, D.; Schwarz, H. *Helv. Chim. Acta* **1995**, *78*, 1393–1407.

(41) Shaik, S.; Hiberty, P. C. *A Chemist's Guide to Valence Bond Theory*; Wiley-Interscience: New York, 2007; see, in particular, Chapter 3.

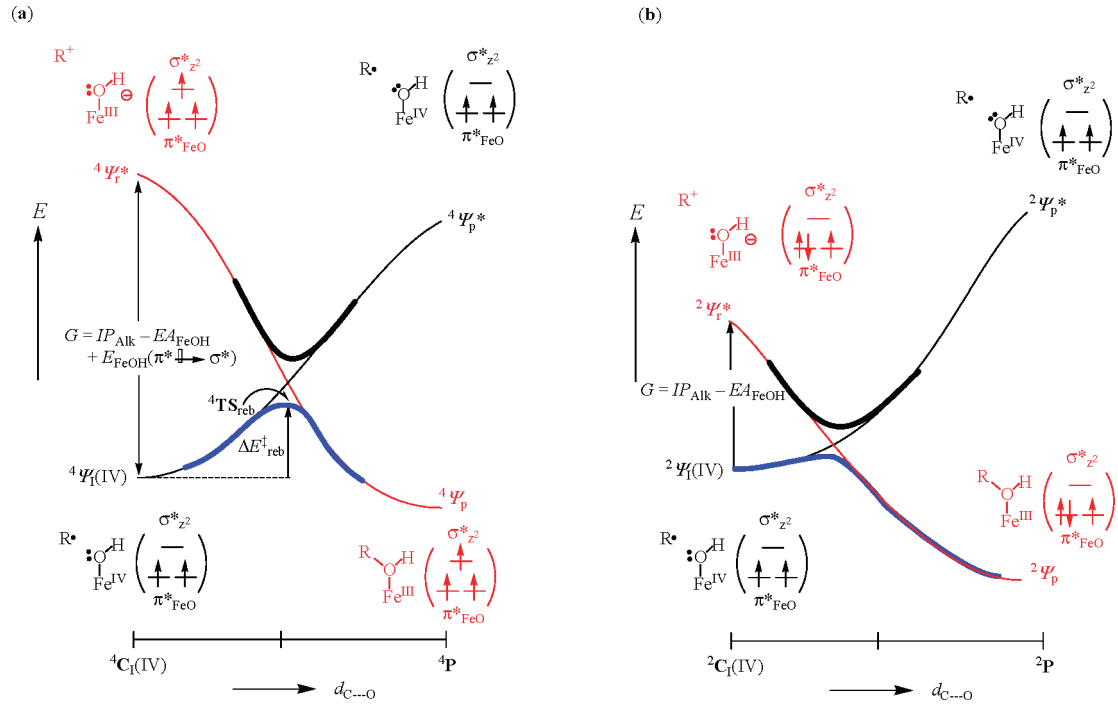

Figure 6. VB mixing and avoided crossing during the rebound processes of the quartet (a) and doublet (b) spin states of the PorFe^{IV}OH/R• intermediate.

between R and H, but with the geometry of the product. As such, the two states correlate with one another along the reaction coordinate.

Let us turn now to the intermediate curves, which are labeled as Ψ_I*(III) in Figure 5a and Ψ_I*(IV) in Figure 5b. In the VB representation, the C−H bond in R−H is unpaired into a triplet spin,[20b,39] and the H• atom is spin-paired to the odd electron on the oxo group. As already discussed above, this spin-pairing changes the oxidation state of the OH moiety to −1 and "releases" one electron to the heme. In the case of Ψ_I*(III), this electron is given to iron, which is reduced to Fe^{III}, while in Ψ_I*(IV), the electron shifts from the iron into the porphyrin hole and the iron keeps two unpaired electrons in the dπ orbitals, thereby remaining in oxidation state Fe^{IV}. In each case, the entire intermediate curve corresponds to a single VB structure but in different geometries. Thus, at the intermediate stage, it corresponds to an H-abstraction intermediate (C_I in Figure 1), composed of an iron−hydroxo/R• species, where the iron−porphyrin is in two electromeric states (Por$^{\bullet+}$Fe^{III}OH or PorFe^{IV}OH). Similarly, at the product geometry, this state involves a charge transfer from porphyrin to the R−O linkage in Figure 5a, or from the iron d-electrons to the same linkage in Figure 5b.

The final energy profile for the mechanism in Figure 5 involves VB mixing of the three curves. The mixing that is shown by the bold green lines leads to avoidance of the crossing and generates the corresponding transition states, initially, for the H-abstraction step, TS_H, and subsequently for the radical rebound via TS_{reb}. The latter transition state exists only on the quartet energy profile (see analysis below), as has already been rationalized using VB diagrams.[37] To denote the spin-state condition on the existence of this particular barrier, we marked the symbol TS_{reb} in Figure 5 with a question mark.

The polar character of the TS_H species, defined above in Figure 2 as the degree of charge transfer, Q_{CT}, arises from the secondary VB mixing of the Ψ_r* curve into TS_H. All these features are apparent in the computational results discussed above by reference to Figures 1 and 2 and analogous findings summarized in papers and reviews.[31,32,37] Furthermore, it is seen from Figure 5 that the intermediate curve catalyzes the two-electron oxidation process by cutting through the high barrier, which would have been encountered otherwise due to the crossing of the main curves that emanate from reactants and products, Ψ_r and Ψ_p. Therefore, in addition to revealing the source of the polar effect (see Q_{CT} in Figure 2), the VB diagram accounts nicely and simply for the findings, both experimentally,[15] and computationally,[32,37] of a stepwise rather than a concerted process. Additionally, the geometric characteristics of the H-abstraction transition states, and the correlations of %BB and %BF with the corresponding energy barriers (see Figure 3), reflect the mechanism of an avoided crossing that leads to the transition states. Thus, the crossing of the reactant (Ψ_r) and intermediate [Ψ_I*(III)] curves, to establish TS_H, is caused by C−H stretching and O−H approach, and hence, the barrier correlates with the progress of these geometric features compared with the reactants state.

Let us discuss the spin-state effect on the rebound process.[37] The VB diagram for the rebound step on the two spin states of the PorFe^{IV}OH/R• electromer is shown in Figure 6. This figure starts from the center of Figure 5b, where the intermediate curve Ψ_I(IV) has to cross the Ψ_r* curve that descends toward the product state Ψ_p. To clarify the argument, we show compact MO occupation diagrams in Figure 6 describing the three upper MOs of the d-block. Figure 6a shows the situation for the quartet spin state, while the doublet spin curve is depicted in part b. At the intermediate geometry, the Ψ_r* state includes an electron transfer from the radical moiety R• to the iron−hydroxo complex. To maintain a quartet-spin, the electron is transferred into the high-lying $\sigma^*_{z^2}$ orbital, while for the doublet state in Figure 6b the electron is transferred into a lower-lying π* orbital. The height of the crossing point depends on the initial gap between the two curves: the larger this gap, the higher the crossing point. Consequently, in the quartet spin state, where

the gap is large (the difference is 26 kcal mol^{-1}),[37a] the VB mixing will generate a barrier for rebound. On the other hand, in the doublet spin state the gap is much smaller (by 26 kcal mol^{-1}) so that the avoided crossing yields a barrier-free radical rebound. This trend has been observed so far in all the calculations done by our groups.[31,32,37] An explanation why the quartet rebound barrier is significantly higher for the $^4\Psi_I$(III) electromer compared with the $^4\Psi_I$(IV) electromer has been given before in VB terms and will not be repeated here.[35,37]

All in all, the VB diagram model provides a good rationale for the computational and experimental findings on various aspects of P450 hydroxylation. Let us turn now to a more quantitative aspect of the modeling.

Modeling of the Barriers for H-Abstraction Using the Valence Bond Diagram. Figure 7 shows the VB diagram for only the first step in the reaction mechanism, namely the one representing the C−H bond activation. The two curves (Ψ_r and Ψ_I*) are initially separated by an energy gap G_H (the so-called promotion gap[20b,41]) and cross one another along the reaction coordinate to generate a transition state (TS_H) through VB mixing and avoidance of the crossing.

The barrier for the reaction, $\Delta E^{\ddagger}$ can be expressed as the height of the crossing point, ΔE_c, minus the resonance energy (B) of TS_H due to the VB mixing:

$$\Delta E^{\ddagger} = \Delta E_c - B \tag{5}$$

The height of the crossing point in turn can be expressed as a fraction (f) of the promotion gap (G_H):

$$\Delta E_c = fG_H \tag{6}$$

Combining these two equations, an expression for the barrier heights is derived:

$$\Delta E^{\ddagger} = fG_H - B \tag{7}$$

This effective equation includes the BBEP effect of the reaction driving force directly into the f factor and is the most convenient one to use.[42]

On the basis of previous modeling of the barrier for H-abstraction process, we have established[39] that f is approximately 0.3, while B is given by eq 8:

$$B = \frac{1}{2}\mathrm{BDE_W} \tag{8}$$

Here BDE_W stands for the bond dissociation energy of the weakest bond among the two that are formed and broken during the reaction: either the C−H or FeO−H bond. Restricting ourselves to the highest level calculations (with basis set B2), all the BDE_{CH} values in our series (**1**−**10**), except those for propene (**4**), *trans*-isopropylphenylcyclopropane (**6**), *N*,*N*-dimethylaniline (**7**), toluene (**8**), and phenylethane (**9**), are larger than BDE_{OH}. Thus, B can be estimated from the raw data of BDEs tabulated in the Supporting Information and in Table 2.

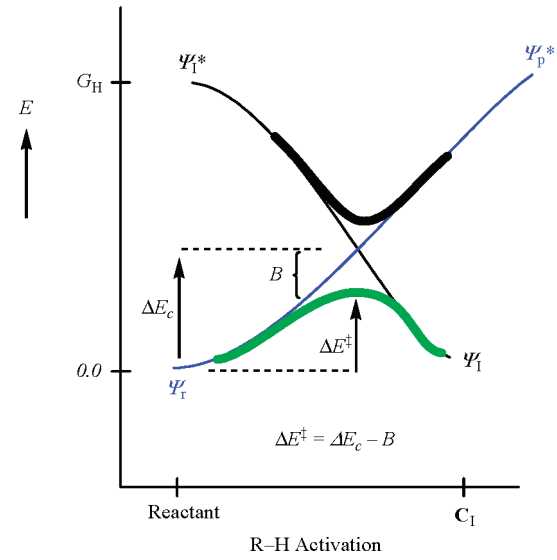

Figure 7. VB diagram showing the barrier formation for the H-abstraction step and the factors controlling its height.

Finally, the promotion gap G_H was shown[20b,39,41] to involve ca. 75% of the corresponding singlet-to-triplet promotion of the C−H bond that undergoes activation[43] and to be given to a good approximation by eq 9 as twice the bond strength of the activated C−H bond:

$$G_H = 2D_{CH} = 2(\mathrm{BDE_{CH}} + \mathrm{RE_{Alk}}) \tag{9}$$

Using the data in Table 2, we can quantify all the corresponding $G_H$factors.

Thus, in principle, all the quantities necessary for calculating the barriers for C−H activation from raw fundamental data are available. However, it would be more interesting to show that the barriers themselves produce the proposed values of $f \sim 0.3$ and B values (eq 8). There are two ways to do so: in one, we use eqs 7–9 and find the f values that reproduce the calculated barriers, while in the second, using eqs 7 and 9 with $f = 0.3$ for all the reactions we find the corresponding B values that are required to produce the barriers. Subsequently, we shall compare the so obtained f and B quantities to the values proposed above from previous theoretical modeling.[39] To economize the data, we model only the highest level barriers at B2 averaged over the doublet and quartet spin states. The data are collected in Table 3 along with the calculated B2 barriers in the first column.

In the first method of modeling, we used the B values according to eq 8 and found the f values that would be required to reproduce the computed barrier. For all the substrates except for **4**, **6**, **7**, **8**, and **9**, the weakest bond is FeO−H, giving B = 44.45 kcal mol^{-1}, whereas for the other substrates, the weakest bond is C−H, leading to B < 44.45 kcal mol^{-1}. Using these values and G_H according to eq 9, the so obtained f values gave an average value of $f_{av} = 0.285 \pm 0.015$; i.e., they all cluster around the theoretical value of 0.3. The barrier data in the second column shows the barriers computed with eq 7 and $f_{av} = 0.285$. The so reproduced barriers are close to the B3LYP/B2 computed ones within a scatter of ±2.4 kcal mol^{-1}.

In the second method of modeling, we use $f = 0.3$ and find those B values that reproduce the barriers. That way, the values cluster around an average B_{av} = 46.39 kcal mol^{-1} with a scatter of ±2.24 kcal mol^{-1}. The largest deviations are for the substrates **1** and **7**, for which the B values are 3.97 kcal mol^{-1} smaller and 4.76 kcal mol^{-1} larger than the average quantity. The same

(42) See Chapter 6 in ref 41. Using the gaps and f factors on both sides of the diagram, one obtains an equation that involves explicitly the effect of the driving force on the barriers. However, this equation requires knowledge of the two gaps and individual f factors and is therefore less convenient to use.

(43) The G value for the Fe^{IV} electromer includes also the promotion energy of an electron from π^*_{FeO} to the a_{2u} orbital. This is a constant quantity, previously evaluated to be ~5−6 kcal mol^{-1}. See: Ogliaro, F.; de Visser, S. P.; Groves, J. T.; Shaik, S. *Angew. Chem. Int. Ed* **2001**, *40*, 2874−2878.

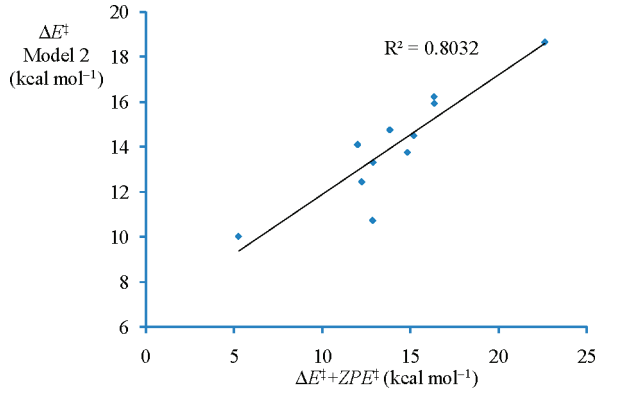

Figure 8. A plot of the VB barriers (last column in Table 3) against the DFT calculated barrier heights.

two substrates also deviate in the first method. With these two substrates excluded, the estimated barrier heights (column 3 in Table 3) show a deviation of ±1.80 kcal mol^{-1} from the DFT calculated values. We shall account for these deviations later.

The last column of Table 3 collects the barriers obtained with eq 7 using $f = 0.3$ and $B_{av} = 46.39$ kcal mol^{-1}. These barriers are close to the computed ones with a scatter of ±1.53 kcal mol^{-1}, which improves to ±0.90 kcal mol^{-1} when the outliers for methane and *N*,*N*-dimethylaniline are removed from the data set. The two deviations have clear physical origins, which are explained in the following sections. Just to provide a pictorial representation, we show in Figure 8 a plot of the so estimated VB barrier vis-à-vis the DFT calculated values; the correlation is reasonably good. We may therefore conclude that the VB models can predict barrier heights quite well of P450-catalyzed reactions in the gas phase.

It is important to comment here on the relationship of the VB model to the often used BBEP correlation with the BDE_{CH} quantity. Thus, while eq 9 shows that the gap in the VB diagram (Figure 7) is related to BDE_{CH}, it also shows that this relation does not derive from the BBEP principle.[12] The actual correlation is between the barrier and the promotion gap that originates it. Thus, the correlation per se cannot invoke causality unless one reveals the mechanism of the correlation, as done, for example, in the VB diagram.

Barriers for H-Abstraction for the Fe^{IV} vs Fe^{III} Electromeric State. Thus, while the values of G_H in both cases are virtually the same,[43] the two states $^4\Psi_l$*(IV) and $^4\Psi_l$*(III), which cross $^4\Psi_r$ or generate the corresponding intermediate, are different and their energy descent is different as well. In Figure 5b, the state, Ψ_l*(IV), that crosses Ψ_r down to the $PorFe^{IV}OH/R\bullet$ intermediate has an odd electron that is localized on the oxo group. By contrast, Ψ_l*(III) in Figure 5a has two resonance structures that delocalize the odd electron on the oxo group between two planes. Therefore, the bond coupling interaction of the spin-paired moieties, H•−•O, in Ψ_l*(IV) is strong, while in Ψ_l*(III) the same interaction is weaker. The result is that Ψ_l*(IV) establishes a low-energy crossing point (smaller *f* in eq 7), while Ψ_l*(III) establishes a higher crossing point (larger *f* in eq 7). Consequently, the barrier for the Fe^{III} electromer will be generally higher than the one for the Fe^{IV} electromer. Furthermore, this higher barrier is expected to be attended by TS_H(III) species that lie later on the H-transfer coordinate, having greater extents of elongations of the R−H and Fe−O bonds than the corresponding TS_H(IV) species. An example for an TS_H(III) species is the case of methane (**1**) activation, where the spin density distribution (in Tables S5 and S6 of the Supporting Information) clearly shows that it has $Fe^{III}Por^{+\bullet}$ character. Figure 2 shows that indeed the C−H bond is extensively cleaved in the TS, being 1.489 (1.499) Å. The strength of the C−H bond in methane being the largest in the series requires extensive bond stretching to achieve the TS. With such a TS geometry, the lowest electromer is of the $Fe^{III}Por^{+\bullet}$ variety and the transition states are $^{4,2}TS_H$(III) types. This in turn means that a larger *f* value is required in the VB model to reproduce more accurately the corresponding barrier for methane hydroxylation, and this is the reason why use of $f = 0.3$ underestimates the barrier in Table 3.

Table 3. B3LYP/B2//B1 Barriers (kcal mol^{-1}) [$\Delta E^{\ddagger}$(DFT)] and Barriers Modeled by VB Theory [$\Delta E^{\ddagger}$(VB)]

		$\Delta E^{\ddagger}$(VB)	
system	$\Delta E^{\ddagger}$(DFT)	model 1[a]	model 2[b]
1	22.63	17.41	18.66
2	16.35	14.82	15.93
3i	14.82	12.75	13.75
3n	16.34	15.10	16.23
4	12.89	15.38	13.31
5	13.83	13.71	14.76
6	12.86	11.03	10.73
7	5.27	10.61	10.02
8	12.24	13.07	12.45
9	12.01	16.31	14.10
10	15.20	13.47	14.51

[a] Use of eq 7 leads to $f = 0.285 \pm 0.015$. All the barriers were calculated with eq 7 as follows: $\Delta E^{\ddagger}(VB) = 0.285\ G_H - B$; $B = 44.45$ kcal mol^{-1} (0.5 BDE_{OH}) with the exception of **4**, **6**, **7**, **8**, and **9**. [b] Use of eq 7 and $f = 0.3$ leads to $B_{AV} = 46.39 \pm 2.24$ kcal mol^{-1}. The barriers were calculated using eq 7 as follows: $\Delta E^{\ddagger}(VB) = 0.3\ G_H - B_{AV}$.

However, notwithstanding methane, in the gas phase we seldom expect to find the TS_H(III) species being lower than the TS_H(IV) species. The same applies to the corresponding intermediates, where invariably the lowest state is for the $PorFe^{IV}OH/R\bullet$ electromer. However, the Fe^{III} electromers, which possess a porphyrin cation−radical moiety, are more polarizable compared with the Fe^{IV} electromers.[36] Consequently, in a strongly polarizing medium like the protein, the Fe^{III} electromeric states are stabilized compared with the Fe^{IV} states and generally become the lower energy species. All the QM/MM calculations show these trends.[37,38] Indeed, the TS geometries in the protein show larger extents of C−H stretching and greater O−O formation than the corresponding gas-phase species. Camphor (**10**) is a case in point, where the QM/MM-optimized transition state species are of the $^{4,2}TS_H$(III) variety and their C−H bonds are longer compared with the corresponding gas-phase species.[38a]

Polar Effects in P450 Hydroxylation−The Case of *N*,*N*-Dimethylaniline (7). We recall that the C−H bond activation barrier for this substrate is very small and it deviates from the VB barriers of the other substrates. Inspection of Table 2 shows that the BDE_{CH} of **7** is much like that in toluene (**8**), but the corresponding barrier is 7−8 kcal mol^{-1} lower! The reason for this is a strong polar effect in the corresponding TS_H species.[14b,c] The polar effect is apparent from the amount of charge transfer, Q_{CT}, which is close to 0.5, which indicates a very strong mixing of the radical−cation state into the TS_H species (see Ψ_r* in Figure 5). This mixing is enhanced by the conjugation between the lone pair and the empty orbital on carbon in the $N-CH_2^+$. In fact, the extensive lone pair conjugation in the TS_H species can be deduced also by inspecting the amount of radical development on the nitrogen atom in TS_H of **7** in Scheme 4. It

Scheme 4. B3LYP/B2 Spin Density Distribution on the Nitrogen and on the CH_2 Moiety (top) in the Free *N*-Methyl-*N*-methylenylaniline radical and (bottom) in the TS_H species of *N*,*N*-Dimethylaniline (**7**)

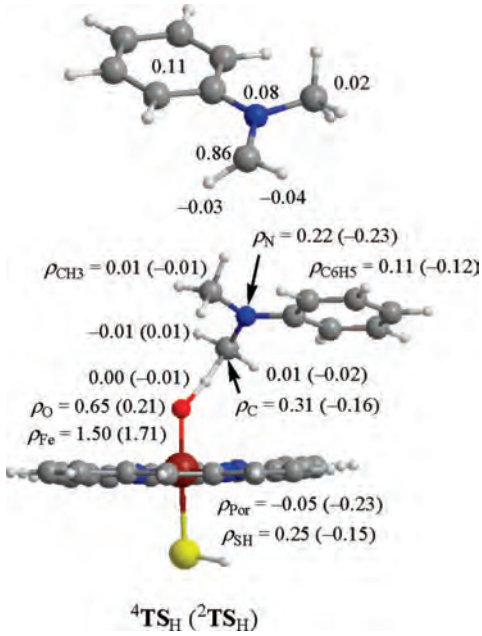

$^4\mathbf{TS}_H$ ($^2\mathbf{TS}_H$)

can be seen that the nitrogen develops spin density in the TS_H species to an extent larger than in the isolated radical species *N*-methyl-*N*-methylenylaniline radical. This enhanced conjugation increases the resonance energy of the transition state[14c] and thereby lowers the barrier. Thus, the deviation of **7** in Table 3 is caused by the *B* factor that gets larger (compared with eq 8) due to the enhanced conjugation of the nitrogen lone pair in the transition state. Indeed, as shown recently by Wang et al.,[14b] the H-abstraction barriers in a series of para-substituted *N*,*N*-dimethylaniline derivatives exhibit a Hammett correlation that reflects the substituent effect due to the ability of the nitrogen lone pair to conjugate with the stretched C−H bond in the TS.

Conclusions

Density functional theoretic studies on a series of hydrogen abstraction barriers of cytochrome P450 reactions show that the barriers correlate linearly with the bond strength (D_{CH}) of the C−H bond that is broken, rather than with the corresponding bond dissociation energy (BDE_{CH}). Structurally, the trends show that high barriers are associated with product-type TS geometries with long C−H bonds and short O−H bonds, while the low-barrier processes have reactant-type structures. These structural and energetic trends of hydrogen-bond energies are accounted for by the valence bond model of chemical reactivity.[20] The model shows that the correlation between the barrier and the corresponding D_{CH} quantities is the promotion energy gap (G_H, Figure 6) that has to be overcome by molecular distortions in order to establish the transition state. Using these promotion gaps, the valence bond model can predict quantitatively the barriers with reasonable reproducibility. The model explains other features of P450 hydroxylations as well: (a) the nature of the polar effect, (b) the difference between the activation mechanisms leading to the Fe^{IV} vs the Fe^{III} electromers, (c) the difference between the gas phase and enzymatic reaction, and (d) the dependence of the rebound barrier on the spin state.

The valence bond mechanism in Figure 5 shows that compound I can perform a complex reaction that involves multiple bond making−breakage by utilizing an intermediate valence bond structure that cuts through the high barrier of the principal transformation between reactions and products, thereby mediating the process at a lower energy cost (Figure 5). The correlations derived in this paper, along with previous treatment of the rebound process,[37] create order and organize the data for a process of a complex and important enzyme. While this treatment has obvious bearing also on the reactivity patterns in the nonheme systems,[2] a straightforward extrapolation is not possible due to the existence of triplet and quintet spin state surfaces with different barrier heights.[44] A preliminary VB model for C−H activation by nonheme reagents was described in ref 23b.

Acknowledgment. S.P.d.V. acknowledges the National Service of Computational Chemistry Software (NSCCS) for providing CPU time. S.S. acknowledges the DFG for funding within DIP-G 7.1.

Supporting Information Available: Detailed comparison of Jaguar- and Gaussian-optimized geometries, Cartesian coordinates of all structures described in this work, tables with group spin densities and charges, figures with various correlations, as well as complete refs 22 and 24. This material is available free of charge via the Internet at http://pubs.acs.org.

JA8019615

(44) (a) Hirao, H., Jr.; Nam, W.; Shaik, S. *Chem. Eur. J.* **2008**, *14*, 1740–1756. (b) de Visser, S. P. *J. Am. Chem. Soc.* **2006**, *128*, 15809–15818.

Theoretical Study of *N*-Demethylation of Substituted *N,N*-Dimethylanilines by Cytochrome P450: The Mechanistic Significance of Kinetic Isotope Effect Profiles

Yong Wang,[†] Devesh Kumar,[‡] Chuanlu Yang,[†,§] Keli Han,*[,†,§] and Sason Shaik*[,‡]

State Key Laboratory of Molecular Reaction Dynamics, Dalian Institute of Chemical Physics, Chinese Academy of Sciences, Dalian 116023, People's Republic of China, Institute of Chemistry and the Lise Meitner-Minerva Center for Computational Quantum Chemistry, The Hebrew University of Jerusalem, 91904 Jerusalem, Israel, and Department of Physics, Yantai Normal University, Yantai 264025, People's Republic of China

Received: March 25, 2007

The mechanism of *N*-demethylation of *N,N*-dimethylanilines (DMAs) by cytochrome P450, a highly debated topic in mechanistic bioinorganic chemistry (Karki, S. B.; Dinnocenczo, J. P.; Jones, J. P.; Korzekwa, K. R. *J. Am. Chem. Soc.* **1995**, *117*, 3657), is studied here using DFT calculations of the reactions of the active species of the enzyme, Compound I (Cpd I), with four *para*-(H, Cl, CN, NO_2) substituted DMAs. The calculations resolve mechanistic controversies, offer a consistent mechanistic view, and reveal the following features: (a) the reaction pathways involve C−H hydroxylation by Cpd I followed by a nonenzymatic carbinolamine decomposition. (b) C−H hydroxylation is initiated by a hydrogen atom transfer (HAT) step that possesses a "polar" character. As such, the HAT energy barriers correlate with the energy level of the HOMO of the DMAs. (c) The series exhibits a switch from spin-selective reactivity for DMA and *p*-Cl-DMA to two-state reactivity, with low- and high-spin states, for *p*-CN-DMA and *p*-NO_2-DMA. (d) The computed kinetic isotope effect profiles (KIEPs) for these scenarios match the experimentally determined KIEPs. Theory further shows that the KIEs and TS structures vary in a manner predicted by the Melander−Westheimer postulate: as the substituent becomes more electron withdrawing, the TS is shifted to a later position along the H-transfer coordinate and the corresponding KIEs increases. (e) The generated carbinolaniline can readily dissociate from the heme and decomposes in a nonenzymatic environment, which involves water assisted proton shift.

1. Introduction

The ubiquitous cytochrome P450 (CYP450) enzymes, are considered to be among "the most versatile biological catalysts known",[1] owing to their vital roles in the metabolism of xenobiotics, such as drugs, and in the biosynthesis of endogenous compounds, such as steroids. A wide variety of chemical transformations including hydroxylation of inert C−H bonds, epoxidation of C═C bonds, dealkylations, etc., are all catalyzed by these monooxygenase enzymes. Despite the extensive mechanistic explorations of these processes by experimental means, there remain many intriguing questions on which theory can offer the missing insight and reveal new features. This is precisely the case for the mechanism of the amine *N*-dealkylation mediated by cytochrome P450,[2] which is targeted in the present theoretical study.

The overall reaction of CYP450-catalyzed *N*-dealkylation of amines involves two processes as outlined in Scheme 1. The initial process, catalyzed by CYP450, involves the conversion of the amine to the corresponding carbinolamine (**i**, **iv**, or **ii**−**iv** in Scheme 1), and the second one, thought to be nonenzymatic, involves decomposition of the carbinolamine to a secondary amine and formaldehyde (process **v** in Scheme 1). The mechanistic debates concern the initial process, with two

SCHEME 1: Alternative Mechanistic Hypotheses for *N*-Demethylation of *N,N*-Dimethylanilines

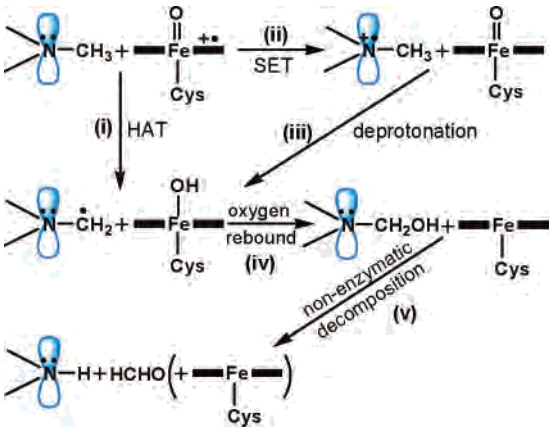

alternative mechanisms that have survived more than 30 years of discourse and are shown in **i** vs **ii**−**iii** in Scheme 1. One is the single electron transfer (SET) mechanism,[3] involving an initial one-electron oxidation of the amine, followed by deprotonation of the cation radical to produce an α-amino radical (**ii**−**iii** in Scheme 1), which rebounds to produce the ferric-carbinolamine complex that follows onward with decomposition of the carbinolamine. The second mechanism (**i** in Scheme 1) begins with direct hydrogen atom transfer (HAT)[4] and then proceeds via the same series of steps.

* To whom correspondence should be addressed. E-mail: klhan@dicp.ac.cn (K.H.); sason@yfaat.ch.huji.ac.il (S.S.).
[†] Chinese Academy of Sciences.
[‡] The Hebrew University of Jerusalem.
[§] Yantai Normal University.

10.1021/jp072347v CCC: $37.00 © 2007 American Chemical Society
Published on Web 06/09/2007

The evidence for SET has been mainly based on the following experimental observations: (a) the oxidative dealkylations generally exhibit low deuterium kinetic isotope effect (KIE);[5] (b) the free energy relationship of *N*-demethylation for a series of para-substituted *N*,*N*-dimethylanilines by CYP450 and its model analogs features large negative Hammett ρ value, and the reaction rates correlate with substrate redox potentials $E_{1/2}$;[6−7] and (c) 1,4-dihydropyridine Hantzsch esters[8] and cyclopropylamines[9] are suicide inactivators of CYP450.

The HAT mechanism is supported by the following facts: (a) the KIE profile (KIEP), found by Dinnocenzo and co-workers for a series of DMA oxidation reactions by cytochrome P450s, correlates linearly with the KIEP measured in a genuine HAT by the *t*-butoxyl radical reacting with the same DMA series;[4] (b) Model electrochemical-mass spectrometric studies by Jurva et al.[10] showed that amino radical cations were unlikely to be obligatory intermediates in the P450-catalyzed oxidations of *N*-cyclopropyl cyclic tertiary allylamines; (c) Bhakta and Wimalasena[11] reported that the C_α−H's of both cyclopropyl and alkyl substituents were removed at isotopically sensitive steps without producing detectable amounts of cyclopropyl ring opened products; (d) Hanzlik et al.[12] demonstrated that the CYP450-catalyzed oxidation of *N*-benzyl-*N*-cyclopropylamine fitted only a HAT mechanism; (e) DFT calculations by Li et al.[13] on the C−H hydroxylation of DMA oxidation supported a HAT mechanism. However, the DFT calculations showed also significant differences between the C−H hydroxylation of DMA vis-à-vis alkanes.

It is apparent from the above introduction that the mechanism of DMA dealkylations poses some challenging puzzles. On the one hand, the facts that the reaction rates are related to the redox potentials of the amines[2a,6d] and that a large negative Hammett ρ parameter is observed in free energy relationship studies[6a,c] could be taken to indicate a SET mechanism. On the other hand, the extended correlation of the KIEPs for the oxidations catalyzed by CYP450 and the HAT reactions with the *t*-BuO• radical, favors a HAT mechanism for the CYP450-catalyzed DMA oxidations. Therefore, one obvious question to answer is: HAT or SET? Second, since theory was found[13] to favor a HAT mechanism for DMA oxidation by P450, why does this HAT proceed in a spin-selective manner (SSM), whereas the HAT in the alkane hydroxylation proceeds by two-state reactivity (TSR)?[14a−b] If DMA oxidation involves indeed initial HAT, why then is there a good correlation of the reaction rates with the substrate redox potential, and what is the cause for the large negative Hammett ρ parameters observed in free energy relationship studies? Can theory reconstruct the KIEP found by Dinnocenzo and co-workers[4b,d] in the series of *p*-substituted DMAs? Since Li et al.[13] have reported that higher energy was required for a SET process than a HAT process, for the best electron donor in the series, DMA, thus the SET mechanism was excluded. The present work tries to answer the aforementioned questions to resolve mechanistic controversies and to offer a consistent mechanistic view, by use of density functional theoretic (DFT) calculations of the P450 oxidation reactions of the series of *p*-*X*−$C_6H_4N(CH_3)_2$ (*X* = H, Cl, CN, and NO_2) in Scheme 2.

SCHEME 2: Net Reaction of Oxidation of *N*,*N*-Dimethylanilines by P450

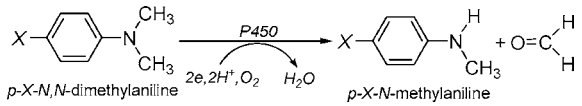

2. Computational Methodology

A recent study by Dowers et al. provided compelling evidence for the reactivity of Compound I (Cpd I).[15] Therefore, to model Cpd I of CYP450, we employed a six-coordinate oxo−ferryl species, $Fe^{4+}O^{2-}(C_{20}N_4H_{12})^-(SH)^-$ [14b,c,16] and used it with the series of *para* (H, Cl, CN, NO_2) substituted DMAs in Scheme 2. The DFT calculations were carried out with the Gaussian 03 suit of programs.[17] The spin-unrestricted B3LYP[18] was employed using two basis sets: (a) LACVP(Fe)/6-31G(H, C, N, O, S, Cl), henceforth B1, was used to optimize transition states and minima without symmetry constraint. (b) A single-point energy was performed with a higher basis set, LACV3P+*(Fe)/6-311+G*(the rest), B2 in brief.[19] The model and computational method were tested extensively and proved to be reliable.[2c,d,13]

Transition states were ascertained by vibrational frequency analysis to possess only one mode with an imaginary frequency. Bulk polarity effects of the active site in the protein environment were evaluated with the PCM solvation model using a nonpolar solvent, chlorobenzene ($\epsilon = 5.62$). The carbinolamine decomposition in the polar nonenzymatic environment was studied using aqueous medium (water, $\epsilon = 78.39$). The effect of hydrogen bonding to the sulfur ligand was mimicked by adding two ammonia molecules that point toward the sulfur of the proximal ligand at fixed distances of $r_{S-HN} = 2.660$ Å.[13,14c] All of the energy corrections due to solvent and NH−S hydrogen bonds were evaluated with B2. All of the data are collected in the Supporting Information (SI) document, whereas the text discusses the highest-level results, UB3LYP/B2//B1. Thus, the single-point energy B2//B1 values will refer to hereafter as E1, whereas E2 will include in addition also the zero-point energy (ZPE) correction, the NH−S hydrogen bonding and the bulk polarity effects ($\epsilon = 5.6$), whereas E3 will correspond to the case with $\epsilon = 78.39$.[13,14c]

The kinetic isotope effect (KIE) of the HAT process was determined using the Gaussian frequency data based on two expressions.[20] The first one is the semi-classical Eyring equation, where the KIE is given as

$$\left(\frac{k_H}{k_D}\right)_s = \exp\left[-\frac{(G_H^{\#} - G_H^R) - (G_D^{\#} - G_D^R)}{RT}\right] \quad (1)$$

The second expression uses a simple "quantum correction" by multiplying the semiclassical $(k_H/k_D)_s$ with the Wigner quantum correction Q^{corr} factor

$$\left(\frac{k_H}{k_D}\right)_w = Q_w^{corr}\left(\frac{k_H}{k_D}\right)_s \quad (2)$$

$$Q_w^{corr} = (1 + u_t^2/24)/(1 + u_t'^2/24) \quad (3)$$

with $u_t = h\nu_H/k_BT$ and $u_t' = h\nu_D'/k_BT$, where ν is the imaginary frequency of the transition state. Detailed formulation and the corresponding Fortran codes are presented in the Supporting Information (SI).

3. Results and Discussion

3.1. Substituent Effects on Reaction Mechanisms and the Origins of Spin-Selective Reactivity. Figure 1 shows the calculated energy profiles for the formation of carbinolanilines for the pristine *N*,*N*-dimethylaniline substrate (Figure 1a) and its three *para* substituted derivatives (Figure 1b−d), whereas the geometric information of the corresponding ^{2,4}**TS**$_H$ species

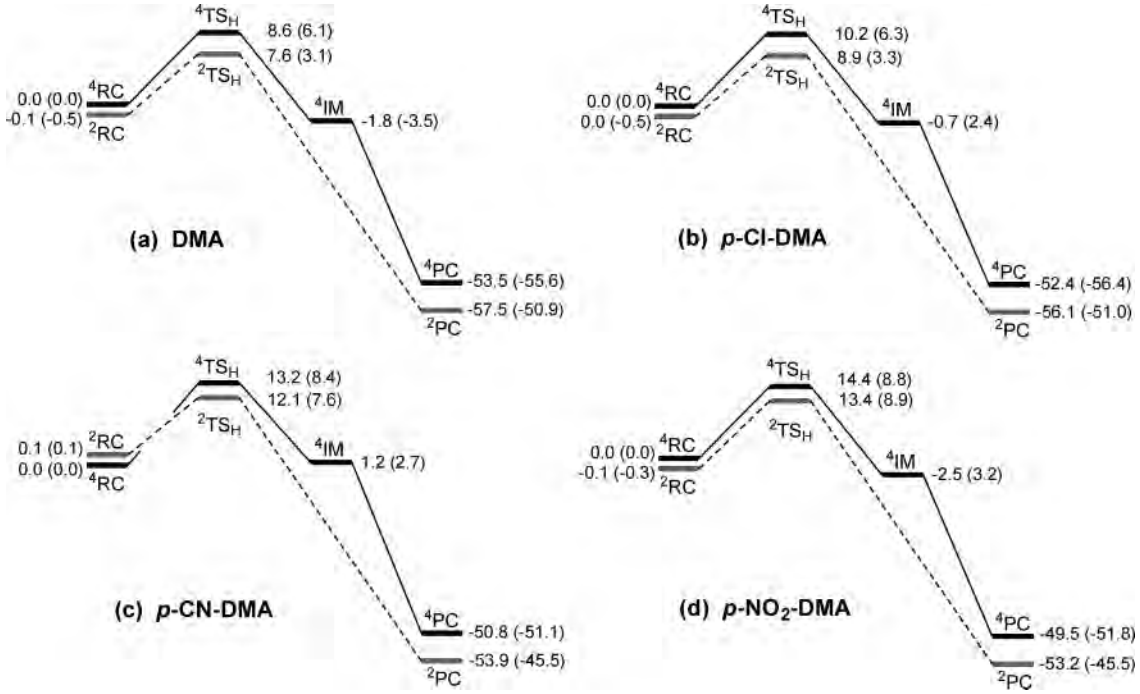

Figure 1. Energy profiles (in kcal/mol) for C−H hydroxylation of *p*-(H, Cl, CN, NO_2)-DMAs by Cpd I on the quartet and doublet states. Relative energies are given at the E1 (UB3LYP/B2//B1) level out of parentheses and the E2 (UB3LYP/B2//B1; ZPE, NH−S, $\epsilon = 5.6$) level in parentheses.

is displayed in Figure 2. As usual for P450 reactions, the mechanism involves two states nascent from the degenerate states of Cpd I. In both states, the rate-determining step involves C−H bond activation, namely a HAT process followed by the usual O-rebound[21] to form the carbinolaniline complexes, ^{2,4}**PC**. The barrier data in the figure correspond to UB3LYP/B2//B1 values (E1 and E2), whereas the corresponding UB3LYP/B1//B1 data are given in the SI document (Tables S1−S4).

Figure 1a shows the energy profile for C−H hydroxylation of the pristine DMA. At the E1 level, the barrier difference is within 1 kcal/mol for the two states, 7.7/8.6 kcal/mol for the LS/HS states, respectively. When the ZPE correction, the bulk polarity effects, and the NH···SH hydrogen bond interactions are incorporated (E2 level), the energy difference between ^{2}**TS**$_H$ and ^{4}**TS**$_H$ increases to about 3.0 kcal/mol, which means that reaction should proceed in a spin-selective manner (SSM), predominantly via the LS reaction route, as found before.[13] The **TS**$_H$ geometries (Figure 2a) reveal that the LS species is earlier than the HS on the H-transfer coordinate. Large spin density accumulation along with nearly zero charge on the generated organic moiety in the HS intermediate,^{4}**IM** (see Table S1 in the SI), provide further support for a HAT process. The LS route is concerted and follows to the ferric-carbinolaniline complex without a distinct rebound step. The high-spin ^{4}**IM** species behave like a shoulder and not a genuine minimum and fall in a barrier-free rebound to the corresponding ferric−carbinolaniline complex. Thus, on the two states, the C−H hydroxylation is an effectively concerted HAT process. These results are in agreement with a recent work by Li et al.[13] and follow earlier predictions.[14b]

For the remaining substrates, *p*-Cl-DMA, *p*-CN-DMA, and *p*-NO_2-DMA (Figure 1b−d), the reactions proceed similarly, with an initial HAT followed by a barrier-free rebound to form the corresponding ferric-carbinolaniline complexes. The para substituent induces differences in the transition state structures (Figure 2b−d) and in the energy barriers (Figure 1b−d), but it does not change the "chemical mechanism" as such. From Figure 1a−d, we can see that the activation energies (both E1 and E2) for H-abstraction keep increasing as the electron-withdrawing power of the substituent becomes stronger. At the E1 level, the LS/HS activation energies are 7.7/8.6 kcal/mol for DMA, 8.9/10.2 kcal/mol for *p*-Cl-DMA, 12.0/13.2 kcal/mol for *p*-CN-DMA, and 13.5/14.4 kcal/mol for *p*-NO_2-DMA. At the E2 level, the activation energies are 3.6/6.1 kcal/mol for DMA, 3.8/6.3 kcal/mol for *p*-Cl-DMA, 7.5/8.4 kcal/mol for *p*-CN-DMA, and 8.8/9.2 kcal/mol for *p*-NO_2-DMA. The energy gaps between ^{2}**TS**$_H$ and ^{4}**TS**$_H$ are high (ca. 3 kcal/mol) for DMA and *p*-Cl-DMA and as low as 0.1−0.8 for the other two substrates. For these four reactions, the ratios of the reaction rates on the LS:HS route are DMA, 57.8:1; *p*-Cl-DMA, 57.8:1; *p*-CN-DMA, 4.3:1; *p*-NO_2-DMA, 0.5:1. Therefore, with the large gaps for DMA and *p*-Cl-DMA, the mechanism is SSM; however, with the small gaps for *p*-CN-DMA and *p*-NO_2-DMA, the mechanism is the traditional TSR.[14,16] As a whole, there is a mechanistic switch from SSM to TSR in these four oxidation processes of the substituted DMAs. This trend also exists even when entropic contributions are taken into account. Table 1 shows that the corrected energy gaps for DMA and *p*-Cl-DMA are 1.9∼2.2 kcal/mol, whereas those for *p*-CN-DMA and *p*-NO_2-DMA are as small as 0.1∼0.4 kcal/mol.

Table 2 presents further information on the roots of this mechanistic switch. At the UB3LYP/LACVP level, the energy gap decreases gradually, starting with 1.7 and down to 0.9 kcal/mol, when the substrate changes in the series DMA, *p*-Cl-DMA, *p*-CN-DMA, and *p*-NO_2-DMA. ZPE corrections decrease the energy gaps for all these four substrates. At the higher E1 level, the energy differences between ^{2}**TS**$_H$ and ^{4}**TS**$_H$ are 1.0∼1.3 kcal/mol. However, taking into account the protein bulk polarity effects produces a quantitative difference between, on the one hand, DMA and *p*-Cl-DMA and, on the other, *p*-CN-DMA and *p*-NO_2-DMA oxidations. Now the barrier difference between the spin states is different for the two subgroups, 2.6−3.3 kcal/mol for the DMA and *p*-Cl-DMA and half as much, 1.1−1.9 kcal/mol, for *p*-CN-DMA and *p*-NO_2-DMA. Further addition of the ZPE correction and the effect of NH···S H-bond interaction sharpen the division between the two pairs of

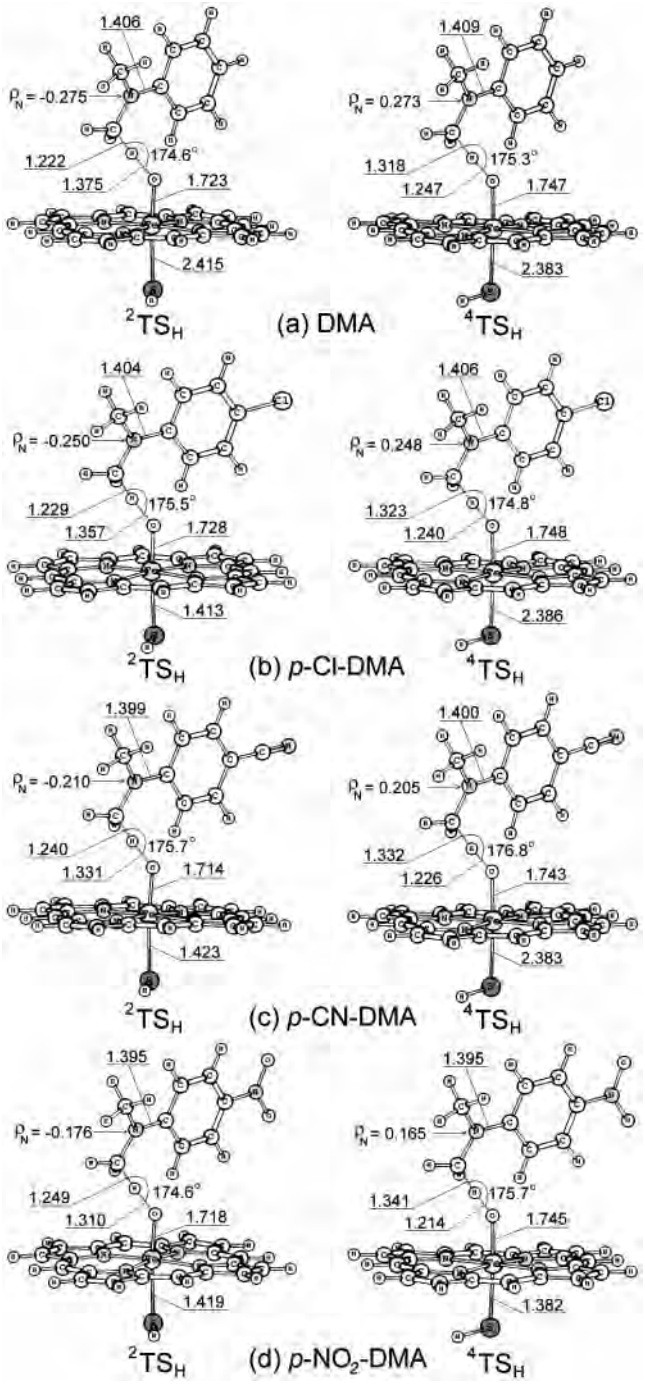

Figure 2. Key geometric features (lengths in Å and angles in degree) of UB3LYP/LACVP optimized ^{2,4}**TS**$_H$ species for C−H hydroxylation of *p*-(H, Cl, CN, NO_2)-DMAs with Cpd I.

TABLE 1: Relative Free Energies (in kcal/mol) for the H-Abstraction Reactions of *p*-(H, Cl, CN, NO_2)−DMAs with Cpd I

	DMA	p-Cl−DMA	p-CN−DMA	p-NO_2−DMA
^{4}**RC**	0.0	0.0	0.0	0.0
^{2}**RC**	−0.8	−0.4	−0.9	−0.3
^{4}**TS**$_H$	9.1	10.6	11.5	10.6
^{2}**TS**$_H$	6.4	8.0	11.0	10.7
ΔE_{HS}	9.1	10.6	11.5	10.6
ΔE_{LS}	7.2	8.4	11.9	11.0

substrates. Now, in the first two reactions, the barrier on the LS surface is significantly smaller than the one on the high spin surface, by ca. 3 kcal/mol. By contrast, in the latter two cases, the difference is small, ca. 0.1∼0.8 kcal/mol.

TABLE 2: Breakdown of the Contributions of the Activation Energies (in kcal/mol) for the H-Abstraction Reactions of *p*-(H, Cl, CN, NO_2)-DMAs with Cpd I

	DMA	*p*-Cl−DMA	*p*-CN−DMA	*p*-NO_2−DMA
		(a) UB3LYP/B1		
^{4}**TS**$_H$	9.8	11.8	14.2	16.9
^{2}**TS**$_H$	8.2	10.4	13.0	16.0
		(b) UB3LYP/B1+ZPE		
^{4}**TS**$_H$	6.8	8.7	11.1	13.3
^{2}**TS**$_H$	5.8	7.9	10.3	12.7
		(c) UB3LYP/B2//B1 (E1)		
^{4}**TS**$_H$	8.6	10.2	13.2	14.4
^{2}**TS**$_H$	7.6	8.9	12.1	13.4
		(d) UB3LYP/B2//B1 + Bulk Polarity		
^{4}**TS**$_H$	7.3	7.8	10.8	11.9
^{2}**TS**$_H$	4.7	4.5	8.9	10.8
		(e) UB3LYP/B2//B1 + Bulk Polarity + NH−S H-Bonding		
^{4}**TS**$_H$	9.1	9.4	11.5	12.4
^{2}**TS**$_H$	5.6	5.8	10.2	12.3
		(f) UB3LYP/B2//B1 + Bulk Polarity + NH−S H-Bonding + ZPE (E2)		
^{4}**TS**$_H$	6.1	6.3	8.4	8.8
^{2}**TS**$_H$	3.1	3.3	7.6	8.9

TABLE 3: Dipole Moments (in Debye) of the ^{2,4}TS$_H$ Species for the H-Abstraction Reactions of *p*-(H, Cl, CN, NO_2)−DMAs with Cpd I

	DMA	Cl−DMA	CN−DMA	NO_2−DMA
^{2}**TS**$_H$	7.5613	6.9605	7.6924	8.1441
^{4}**TS**$_H$	6.4658	6.1014	7.2511	8.0968
$\Delta\mu$ (D)	1.0955	0.8591	0.4413	0.0473

These barrier differences that are caused by the external effects (bulk polarity and NH−S hydrogen bonding) are not mere artifacts and arise from the electric properties of the TSs. Table 3 makes this point by showing the dipole moments for ^{2,4}**TS**$_H$. It is seen that dipole moments of ^{2}**TS**$_H$ are larger than those of ^{4}**TS**$_H$ for all four DMAs, which means that ^{2}**TS**$_H$ will be more stabilized than ^{4}**TS**$_H$ by bulk polarity. However, as the para substituent becomes more electron-withdrawing, the dipole moment difference is reduced and for *p*-NO_2-DMA, the difference is just 0.0473 Debye. These substituent-dependent dipole moments account at least in part for the finding that at the E2 level, the energy gap between ^{2}**TS**$_H$ and ^{4}**TS**$_H$ for the DMA and *p*-Cl-DMA oxidations is as large as ca. 3.0 kcal/mol, whereas for *p*-CN-DMA and *p*-NO_2-DMA oxidations, the difference is small, 0.1∼0.8 kcal/mol.

The structures of the ^{2,4}**TS**$_H$ displayed in Figure 2 show some interesting variations along the H-transfer coordinate, C−H−O. The ^{2}**TS**$_H$ species of the pristine DMA is "early" with a rather short C−H distance and a long H−O distance. As the para substituent becomes more electron withdrawing, the corresponding ^{2}**TS**$_H$ species progresses along the H-transfer coordinate and becomes less and less early; in the entire series, the C−H distances change from 1.222 to 1.249 Å, whereas the H−O distances change from 1.375 to 1.310 Å. However, the ^{4}**TS**$_H$ species of the pristine DMA is more "central" with a long C−H of 1.318 Å, and as the para substituent on DMA becomes more electron withdrawing the transition state lies increasingly "later" along the H-transfer coordinate; in the entire series the C−H distances change from 1.318 to 1.341 Å, and the H−O distances change from 1.247 to 1.214 Å. Interestingly, the barriers for both the LS and the HS processes increase as the C−H bond undergoes more stretching in the TS. In short, the transition states of P450-catalyzed oxidation of substituted DMAs are all

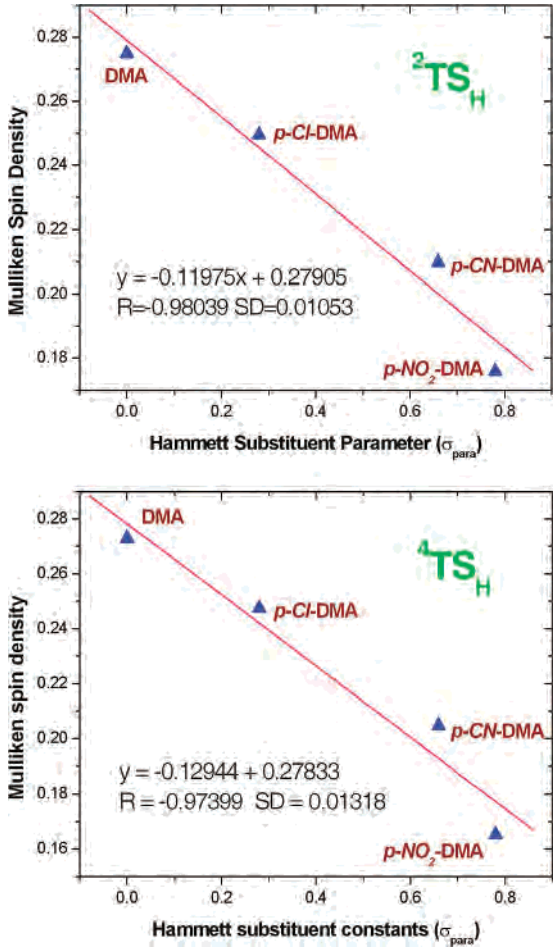

Figure 3. Plot of Mulliken spin density on the N atom of ^{2,4}**TS**$_H$ vs Hammett substituent constants σ_{para} (from ref 22) of the *p*-*X* (*X* = H, Cl, CN, NO_2) substituents.

asymmetric, which results in relativly low KIE values, following the Melander−Westheimer postulate and as originally reasoned by Dinnocenzo and co-workers.[4]

To obtain some insights into the changes in geometries and barriers, we plotted in Figure 3 the Mulliken spin density on the N atom of the **TS**$_H$ species against the Hammett σ parameter of the four para substituents.[22] It is seen that as the substituent becomes more electron-withdrawing, the spin density on N decreases. This in turn means that, as electron-withdrawing power of the substituent increases, the lone pair on the nitrogen is "sucked" into the phenyl ring and becomes less accessible for delocalization toward the developing radial center on the carbon atom of the C−H moiety. This impaired delocalization causes in turn destabilization of the TSs for the cases with the more electron-withdrawing substituents and requires a higher degree of C−H bond cleavage. Consequently, along the series, as the substituent becomes more electron withdrawing, the barriers increase and the corresponding **TS**$_H$ species lie later on the H-transfer coordinate. Thus, the various computational sets of the data are consistent and are based on clear physical effects.

As we already mentioned, the free energy relationship of a series of para-substituted *N*,*N*-dimethylaniline oxidations by CYP450 and its model analogs feature a large negative Hammett ρ value,[6a,c,7] which indicates that the rate-determining step is facilitated by electron-donating substituents,[6a] as expected if positive charge accumulates on the substrate during the reaction.[2a] This fact was originally used as evidence for the operation of a SET mechanism. However, our calculated results demonstrate

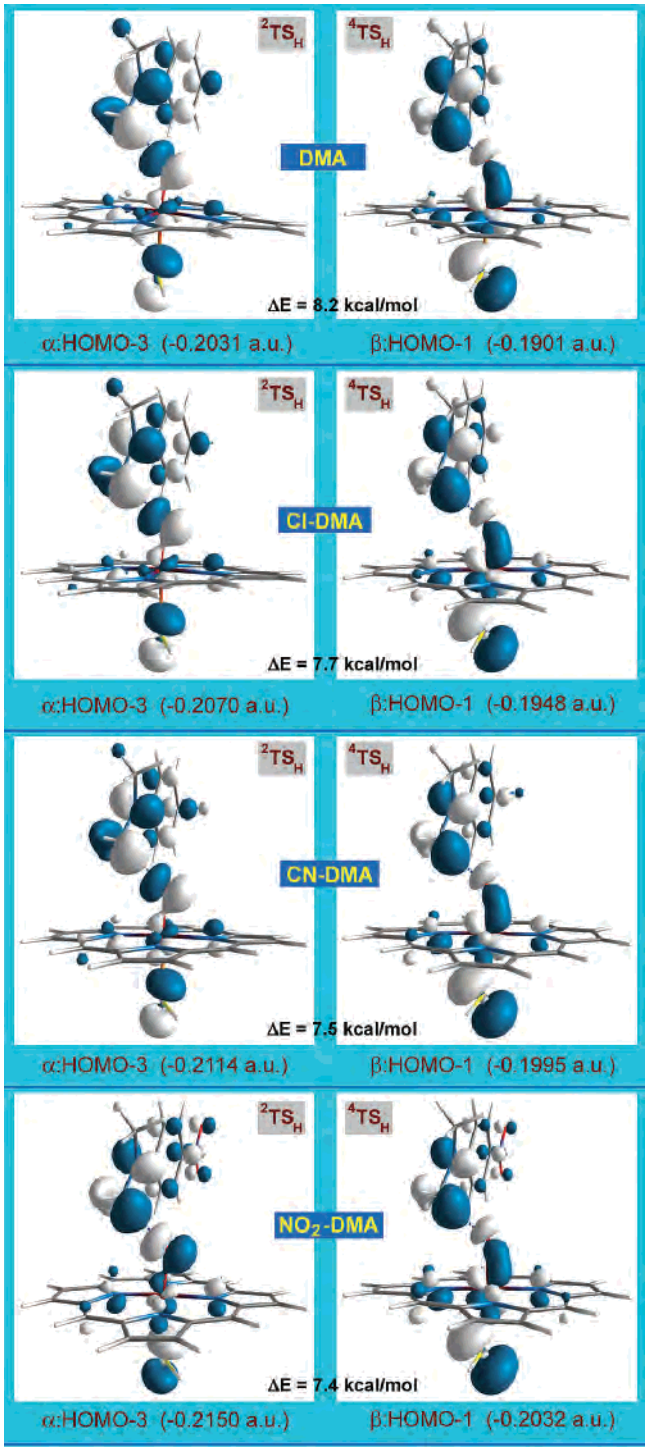

Figure 4. Some high lying occupied orbitals showing electronic delocalization in the ^{2,4}**TS**$_H$ species, in the H-abstraction reactions of *p*-(H, Cl, CN, NO_2)-DMAs with Cpd I.

the mechanism is HAT, and one must therefore find an alternative explanation for the observed free energy relationships. A few molecular orbitals shown in Figure 4 provide some insight into the nature of the transition state. The C−H hybrid orbital is coupled with the lone pair p orbital of N so as to form a π_{C-N} orbital, which is in turn conjugated with the π orbital on the phenyl group and forms a conjugated $\pi_{ph}-\pi_{C-N}$ orbital; this is the reason why spin density was found above on the nitrogen (other sets of delocalized orbitals, which reveal this conjugation are given in the SI document). By virtue of this conjugative interaction, the electronic features of the

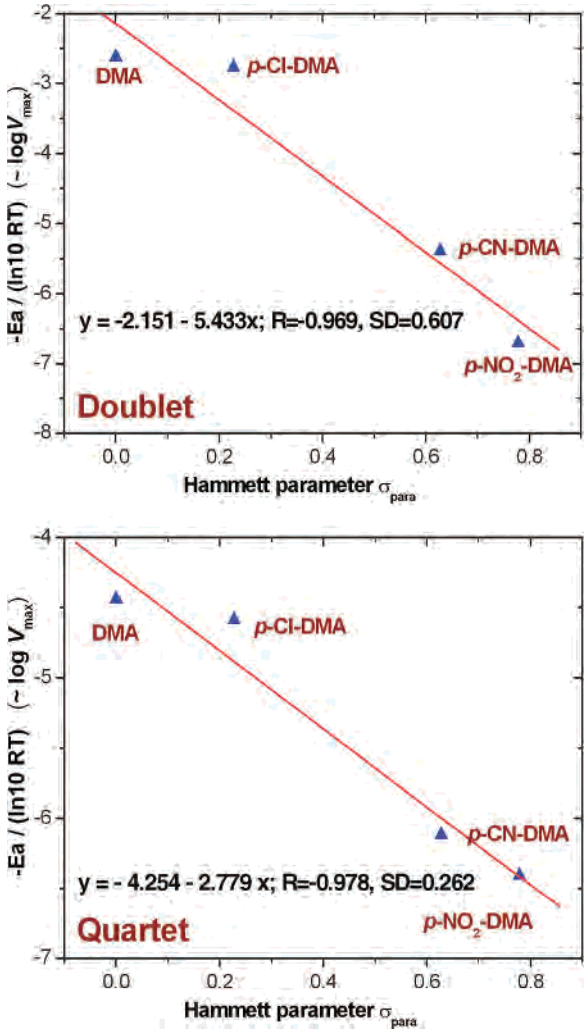

Figure 5. Plot of $-E_a/(\ln 10RT)$ against Hammett substituent constants σ_{para} (from ref 22) of *p*-*X* (X = H, Cl, CN, NO_2) substituents.

substituents exert influence on the nature of the $C_\alpha-H$ bond. Electron-withdrawing substituents will weaken this electron delocalization and will decrease the charge transfer from the substrate to Cpd I. The charges on the *p*-X−Ph−N-$(CH_3)(CH_2)$ moieties are listed in Tables S1−S4 in the SI, which illustrate that the accumulated positive charges on TSs are 0.10−0.13 for Ph−N−$(CH_3)(CH_2)$ and *p*-Cl−Ph−N−$(CH_3)(CH_2)$, 0.07−0.11 for *p*-CN−Ph−N−$(CH_3)(CH_2)$, and 0.03−0.06 for *p*-NO_2−Ph−N−$(CH_3)(CH_2)$. These diminishing charges are precisely in line with the conclusions reached above on the role of the substituent on the ability of the N-lone pair to stabilize the developing radical-center (Figure 3).

Let us further elaborate this point by reproducing the negative Hammett slope observed in the experimental free energy relationship of log V_{max} against the Hammett parameter σ_{para}. According to the classic Arrhenius formula, the rate constant for the catalysts is given by

$$k_{cat} = A \exp\left(-\frac{E_a}{RT}\right) \qquad (4)$$

Since $-E_a/RT = \ln k_{cat} - \ln A$, and since the reaction rate k_{cat} approximates to V_{max} (of the Michaelis−Menten equation), the following relationship holds: log V_{max} approximates to $-E_a/\ln 10RT$. Figure 5 shows the plot of the $-E_a/\ln 10RT$ variable against the Hammett σ constants of the substituents. One can see a linear correlation with a negative slope (quartet, −5.4; double,: −2.8) that corresponds to a large negative ρ value, as reported experimentally.[6a,6c] However, since our calculations show a HAT process with a development of a radical on the substrate, the observed large negative Hammett ρ parameter cannot be used as evidence for a SET mechanism.

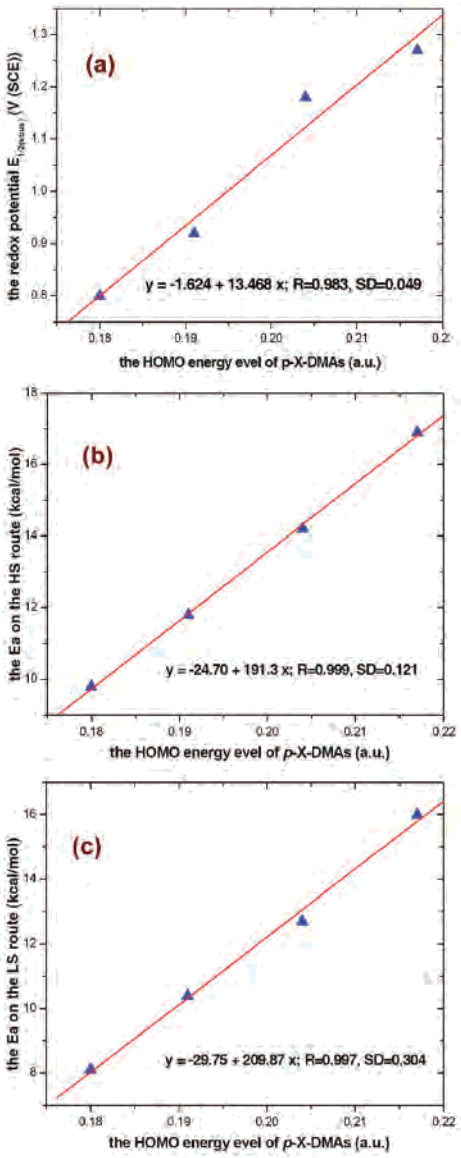

Figure 6. Plots of (a) the substrate redox potentials $E_{1/2}$ (from ref 6d) against the HOMO energy levels of *p*-*X*−DMAs (X = H, Cl, CN, NO_2); (b and c) the activation energies, E_a, for the HS and LS mechanisms, against the HOMO energy levels of *p*-*X*−DMAs (X = H, Cl, CN, NO_2).

Furthermore, the conjugated $\pi_{ph}-\pi_{C-N}$ orbital in the TS evolves from the highest occupied molecular orbital (HOMO) of *p*-X-DMA substrates (see Figure S1 in the SI), and the energy level of this HOMO is related, in turn, to the one-electronic redox potential, $E_{1/2}$, of the substrate. Figure 6a shows indeed a linear correlation of $E_{1/2}$ vs E(HOMO). Thus, the observed correlation between the reaction rates and the substrate redox potentials reveals that the reactivity is correlated with the energy level of the substrate's HOMO. From Figure 6b,c we can see that indeed there is a very good correlation between the HAT barriers and the HOMO energies (HS, R = 0.999; LS, R = 0.997). Clearly therefore, the experimentally observed correlation is not associated with SET and reflects simply the polar character of the TS in an otherwise H-abstraction process.

TABLE 4: Comparison of the Calculated Kinetic Isotope Effects (KIEs) with Experimental Values for the *N*-Demethylation of *p*-(H, Cl, CN, NO_2)−DMA with Cpd I[a]

	DMA ($KIE_{exp} = 2.6$)[a]	*p*-Cl−DMA ($KIE_{exp} = 2.8$)[a]	*p*-CN−DMA ($KIE_{exp} = 3.6$)[a]	*p*-NO_2−DMA ($KIE_{exp} = 4.0$)[a]
KIE_{LS}[b]	3.6 (3.7)	3.8 (4.1)	4.2 (4.7)	4.4 (5.1)
KIE_{HS}[b]	5.5 (7.3)	5.4 (7.3)	5.5 (7.6)	5.6 (7.8)

[a] Experimental KIE values from refs 4b and 4d. [b] Theoretical KIEs. Figures outside of the parenthesis are semiclassical Eyring KIEs, and those inside the parenthesis are Wigner-corrected ones.

3.2. Substituent Effect on Kinetic Isotope Effect. Table 4 shows the calculated KIEs (KIE_{LS} and KIE_{HS}) for both the HS and LS reaction routes, alongside the experimental KIEs determined by Dinnocenzo, Jones et al., using intramolecular KIE determination that is free of masking.[4] Figure 7 shows various plots of the computed and experimental KIE values. The computed values, in Table 4, are consistently higher than experimental ones. However, the trends in the computational KIE_{LS} and experimental KIE data are similar, namely, there is a gradual increase in the KIE value as the substitutent becomes more electron-withdrawing. This relationship is shown pictorially in Figure 7a,b, where the KIE values are plotted against the Hammett σ parameters of the substituents. By contrast to the well-behaved KIE_{LS}, the KIE_{HS} values are almost constant, irrespective of the substituent variation. Furthermore, as shown in Figure 7c the KIE_{HS} values have no correlation with the Hammett σ parameters, and they also do not match the experimental trends.

Although KIE_{LS} correlates nicely with the experimental values, the theory−experimental match can be further improved by considering the SSM and TSR scenarios based on the computed barrier differences, discussed above (see, e.g., E2 values in Table 2 and Figure 1). Thus, in accord with the SSM nature of the reactions of DMA and *p*-Cl-DMA, only the KIE_{LS} values match the experimental data both in the variation trends and in the incremental increase of 0.2 in the values, as the substituent changes from H to Cl. The corresponding KIE_{HS} values are much too high and virtually constant. On the other hand, in accord with the TSR nature of the reactions of *p*-CN-DMA and *p*-NO_2-DMA, the experimental KIE increments can be matched well only if a combination of KIE_{LS} and KIE_{HS} is assumed in line with the TSR scenario revealed by the computations. Indeed, the incremental differences of the KIE_{LS} values for *p*-CN-DMA and *p*-NO_2-DMA relative to DMA are too small compared with the experimental values. Thus, taking the DMA oxidations as the reference reaction, and assuming that the percentage of KIE_{LS} in KIE_{obs} is x, we can then derive the following relationships by comparing the experimental KIEs and the calculated KIE_{LS} and KIE_{HS} for the entire series:

$$KIE^{i}_{exp} - KIE^{DMA}_{exp} = (KIE^{i}_{doublet} - KIE^{DMA}_{doublet})x + (KIE^{i}_{quartet} - KIE^{DMA}_{doublet})(1 - x)$$

where i = *p*-Cl-DMA, *p*-CN-DMA, *p*-NO_2-DMA (5)

Substituting the relative values of Table 4 into this formula, we can obtain mechanistically averaged KIE values. The equation shows that *p*-Cl-DMA oxidation is also SSM, in accord with the computed HS and LS barriers in Figure 1, whereas for *p*-CN-DMA and *p*-NO_2-DMA, the reactions involve TSR; for *p*-CN-DMA, 70% LS + 30% HS; for *p*-NO_2-DMA, 50% LS + 50% HS. These percentages match reasonably well the ratio of reaction rates calculated with the activation energy differences between the HS and LS processes. Figure 7d shows a plot of these mechanistically averaged KIEs against corresponding experimental values, and the match is very good. Thus, all in all, the kinetic isotope effect profile study demonstrates that there is a mechanistic switch from SSM to TSR, the latter occurring for the *p*-CN-DMA and *p*-NO_2-DMA oxidations.

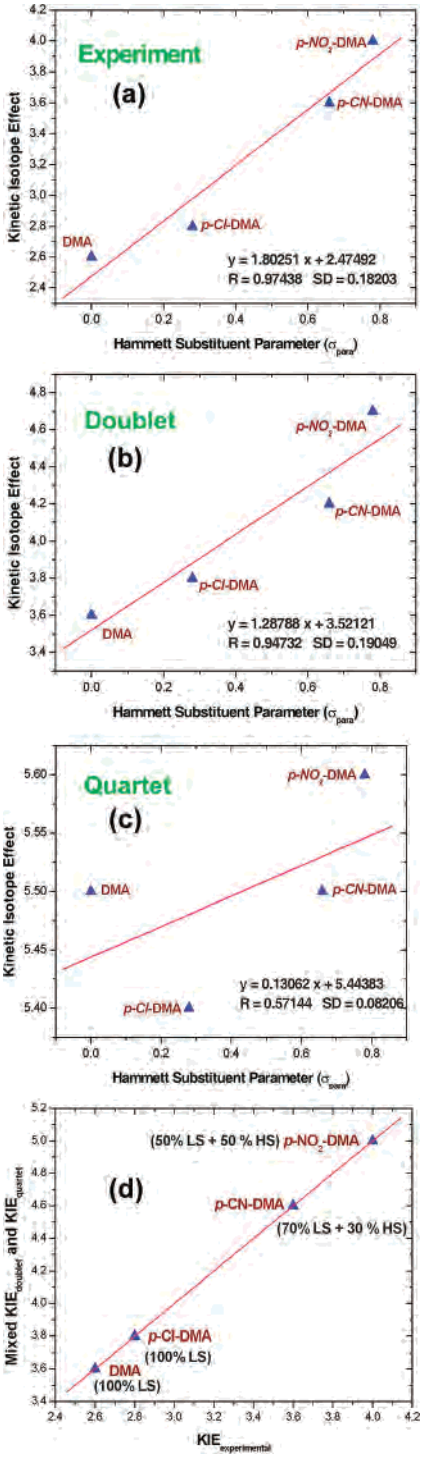

Figure 7. Plots of [2,4]KIEs and KIE(exp) against Hammett substituent parameters σ_{para} of para substituents: (a) KIE(experimental) vs the Hammett parameter, (b) KIE_{LS} vs the Hammett parameter, (c) KIE_{HS} vs the Hammett parameter, and (d) mixed HS-LS KIE vs $KIE_{experimental}$.

To sum up, our calculated results on the geometric structure of the transition states demonstrate that the low KIE values just reflect the asymmetry of HAT transition states (Figure 2), and do not emerge from a SET mechanism. Furthermore, the trends in the KIEP reveal a mechanistic switch from spin-selective

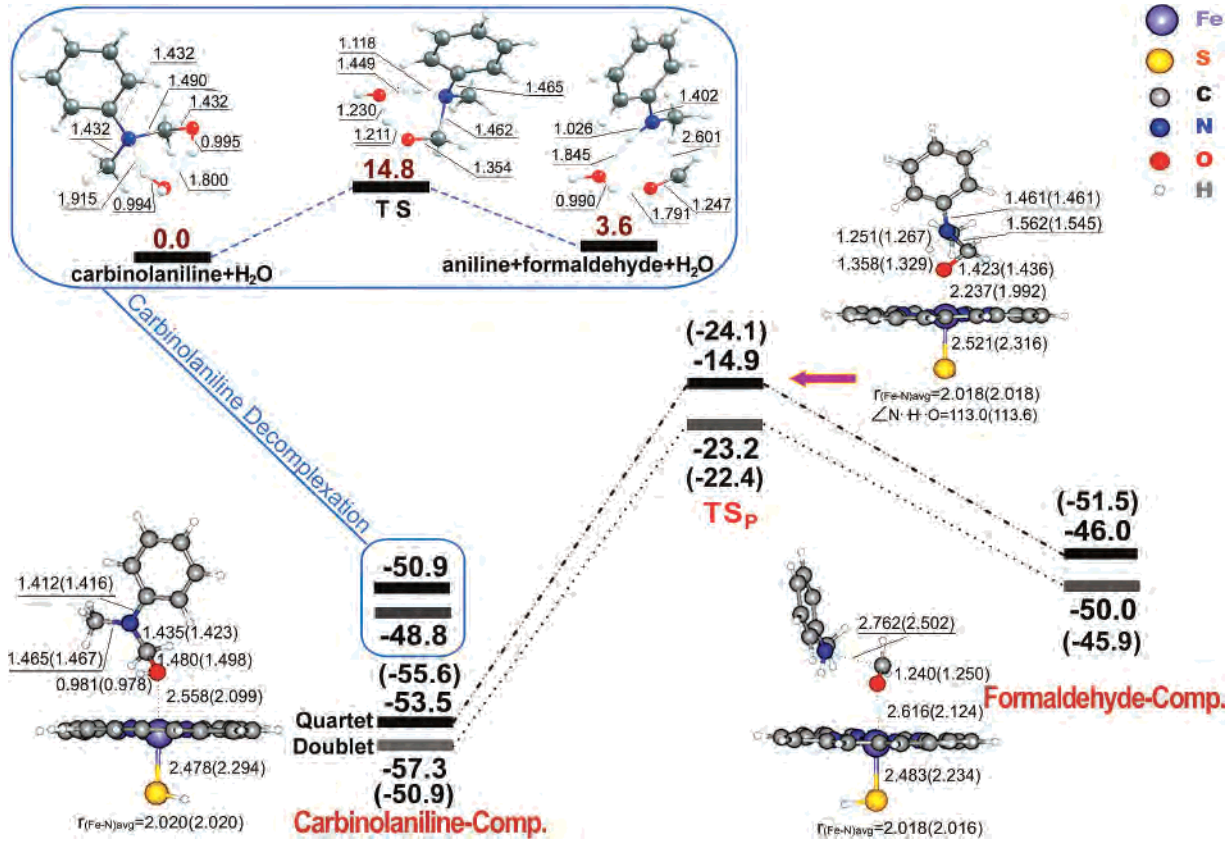

Figure 8. Energy profiles for the carbinolaniline decomposition in the enzymatic (bottom) and nonenzymatic (top) environments. Relative energies for the enzymatic process are given at the E1 (UB3LYP/B2//B1) level out of parentheses and the E2 (UB3LYP/B2//B1; ZPE, NH−S, $\epsilon = 5.6$) level in parentheses. For the nonenzymatic processes, the relative energies are at the E3 (UB3LYP/B2//B1; ZPE, $\epsilon = 78.39$) level. Energies are in kcal/mol, bond length in Å, and angles in degree.

reactivity to two-state reactivity, and reinforce the validity of the results obtained from energy profile studies (Figure 1).

3.3. Carbinolaniline Decomposition Process in the Enzymatic and Nonenzymatic Environments. Before summarizing the mechanistic picture, we must ascertain the nature of the carbinolaniline decomposition after C−H hydroxylation. The conventional concept about this process is that carbinolaniline decomposition proceeds in the nonenzymatic environment; therefore, our first study aim is that which factor causes this process proceeding in the nonenzymatic environment. Figure 8 shows the energy profiles for the carbinolaniline decomposition for the pristine DMA in the enzymatic and nonenzymatic environments. The process starts from the ferric complex that is ca. 50 kcal/mol lower than the reactants channel in Figure 1a. In the enzymatic environment, the activation energy for carbinolaniline decomposition is about 31.5 (28.5) kcal/mol for the quartet (doublet) route. No significant spin density change occurs, so this process involves proton transfer with simultaneous bond cleavage. In the gas phase, the excess energy of the carbinolamine would have been sufficient to lead to decomposition. However, in the protein environment, this excess energy is distributed very fast, and therefore, the process will encounter a very large barrier, > 30 kcal/mol. Since the binding energy of carbinolaniline to the heme is quite small (quartet, 2.6 kcal/mol; doublet, 8.5 kcal/mol), the carbinolaniline can readily dissociate from the heme and be released outside of the enzyme's pocket. In such a case, the carbinolaniline will decompose in a nonenzymatic route, which is shown at the top left side of Figure 8. Since the process involves a proton shift from the O−H moiety to the nitrogen, we considered the assistance by a single water molecule. Thus as can be seen, when the effects of water assistance, bulk solvation (water), and ZPE correction are taken into account, the activation energy for carbinolaniline decomposition in the nonenzymatic environment drops to 14.8 kcal/mol.

Figure 9 shows the energetic effect brought about by one water molecule on the carbinolaniline decomposition in the enzymatic and nonenzymatic environments, whereas Figure 10 depicts the corresponding TSs. As seen from Figure 9, in both enzymatic and nonenzymatic processes, the water molecule lowers the barrier. However, the barriers in the enzymatic environment are consistently larger than in the nonenzymatic processes by 0.6−11.3 kcal/mol. Comparison of these data with the low binding energy (2.6−8.5 kcal/mol) of carbinolaniline to the heme provides further support for the hypothesis that the carbinolaniline decomposition proceeds in the nonenzymatic environment.

The energetic effect induced by one water molecule is based on the fact that the carbinolaniline decomposition is a pericyclic reaction, as shown in Figure 10. Thus, without the water molecule, the transition state is a strained rhomboidal structure (∠N...C...O = 93.9° ∼ 94.6°). When one water molecule is added, the transition state becomes hexagonal and relatively strain free (∠N...C...O = 108.4° ∼ 109.5°). This reduces the energy barrier significantly.

We also calculate KIE values for the proton shift in the *p*-(H, Cl, CN, NO_2)-DMA decomposition processes in the nonenzymatic environment. The KIEs for cabinolaniline decompositions are as follow: for carbinolaniline, 3.0 (3.4); for *p*-Cl-carbinolaniline, 2.2 (2.5); for *p*-CN-carbinolaniline, 2.2 (2.5); for *p*-NO_2-carbinolaniline, 2.1 (2.4) (figures outside of the parenthesis are values of the semiclassical Eyring KIEs and those in the

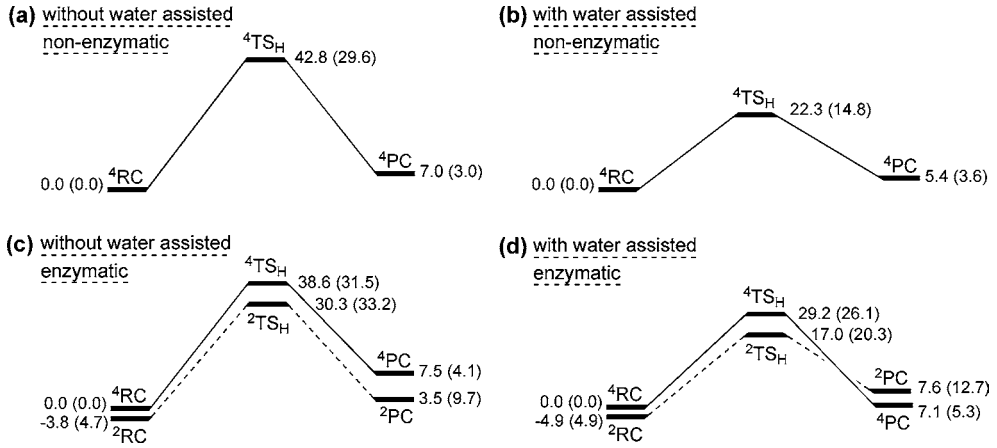

Figure 9. Effect of one water molecule on the carbinolaniline decomposition barriers in the nonenzymatic (a and b) and enzymatic environments (c and d). Relative energies (in kcal/mol) in parts a and b are given at the E1 level out of parentheseses and the E3 (UB3LYP/B2//B1; ZPE, $\epsilon = 78.39$) level in parentheses, whereas in parts c and d at the E1 (UB3LYP/B2//B1) level out of parentheses at the E2 (UB3LYP/B2//B1; ZPE, NH−S, $\epsilon = 5.6$) level in parentheses.

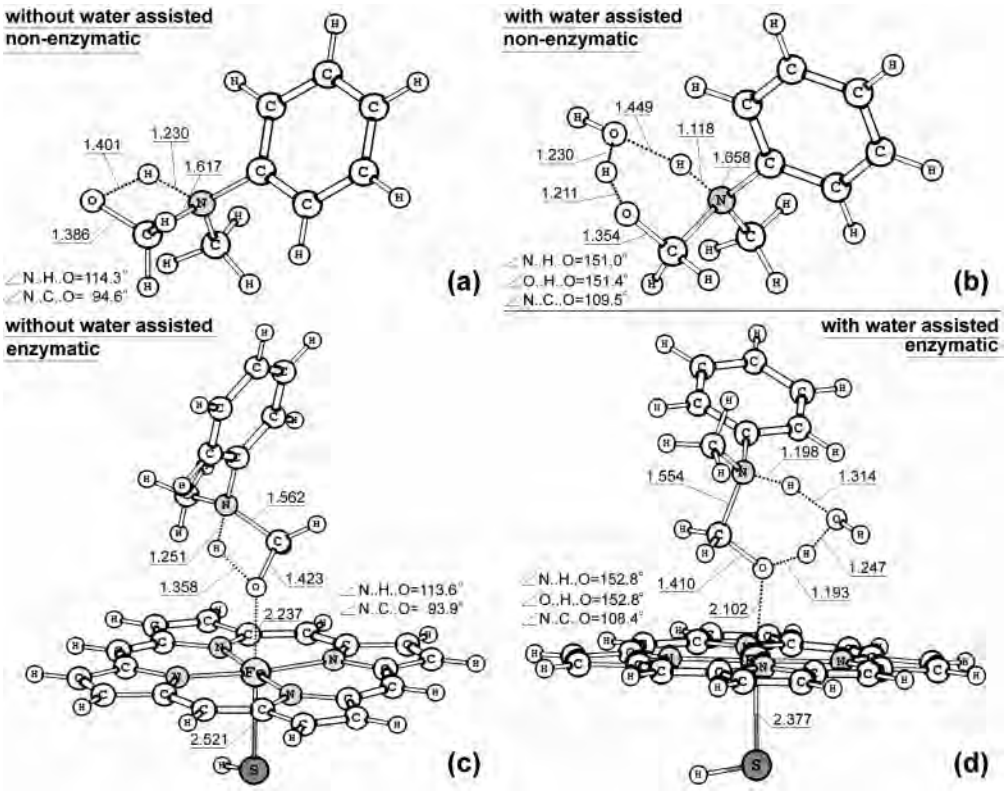

Figure 10. Geometric properties (length in Å, and angle in degree) of the transition states of the carbinolaniline decomposition process in the enzymatic/nonenzymatic environment with/without one water molecular assistance.

parenthesis are values of the Wigner-corrected ones). These values are not consistent with the observed KIEs for the *N*-demethylation reactions. We may therefore conclude that the carbinolaniline decomposition step does not affect the KIE determination of the C−H hydroxylation process in the DMA *N*-demethylation by cytochrome P450.

3.4. Mechanistic Overview of the *N*-Demethylation Process and the Significance of the Kinetic Isotope Effect Profiles. As we mentioned in the introduction, one of the arguments in favor of a SET mechanism (Scheme 1) was the low KIE value (1.78) obtained for the demethylation reactions of *N*-methyl-*N*-(trideuteriomethyl)anilines.[5a] In their response, Dinnocenzo and co-workers[4] showed that the KIEs determined with *N*-methyl-*N*-(trideuteriomethyl)anilines were masked. They further pointed out that the proposed HAT and SET mechanisms could not be distinguished by the magnitude of the isotope effect as such, and instead they proposed that kinetic isotope effect profiles (KIEP) correlations can be more diagnostic. In so doing these authors demonstrated that the KIEP obtained from P450 oxidation of the DMAs was virtually identical to the KIEP obtained for a model HAT reaction with *t*-BuO• radical. This correlation provided compelling evidence in support of the HAT mechanism. Furthermore, Donnocenzo and Jones showed also that different P450 isoforms, covering four different P450 families, gave the same KIEPs; a fact which means that all of the P450 isoforms metabolize the anilines via a common reaction mechanism.

The large negative Hammett ρ value obtained from the free energy relationship of a series of para-substituted *N*,*N*-dimethylanilines by CYP450 and model analogs,[6a,c,7] served as additional

evidence for a SET mechanism. However, as argued by Donnocenzo et al.,[4c] the ρ value of -0.6 was remarkably similar to the value of -0.4, which was obtained for the HAT reactions from DMAs by the OBu^t radical,[23] thus reflecting a polar effect in an otherwise HAT process.

Following the calculations by Li et al.,[13] the present study provides systemic calculations of the mechanisms and the KIEs of the entire series of reactions between Cpd I and para substituted *N*,*N*-dimethylanilines (DMAs). All of the mechanisms are found to be exclusively HAT types. Moreover, the computed energy profiles reveal that the HAT process proceeds in a spin-selective manner (SSM) for the pair DMA and *p*-Cl-DMA but switches to two-state reactivity (TSR) for the pair *p*-CN-DMA and *p*-NO_2-DMA. There is a very good match between the calculated KIE values and the experimental ones. The calculated geometries of the transition states reveal significantly asymmetric structures, which are expected to yield low isotope effects. Our calculations show that as the substituent becomes more electron-withdrawing, the transition state moves to a less early position along the H-transfer coordinate, and the KIE as well as the barrier increase. The observed[6a,ac] large negative Hammett ρ parameter in free energy relationships, and the correlation of the reaction rates with the substrate redox potentials, are reproduced by theory and shown to reveal the evolution of the delocalized $\pi_{ph}-\pi_{C-N}$ orbitals of the transition states, from the corresponding HOMOs of the DMA substrate. Thus, the more electron-withdrawing substituents suck the lone pair orbital on N into the aromatic moiety and inhibit conjugation with the developing radical in the TS. As such, the HAT process has some polar character that is substituent-dependent and is revealed by all of the free energy correlations. However, these correlations are not causal, and we found no evidence for a SET mechanism.

Finally, the calculations of the carbinolaniline decomposition process demonstrated that the generated carbinolaniline can readily dissociate from the heme and decomposes in a nonenzymatic environment, which involves water assisted proton shift.

4. Conclusions

This study which addressed the mechanism of *N*-demethylation of four *N*,*N*-dimethylanilines (DMAs) by Cpd I of P450, vis-à-vis the experimental data,[2,4] led to the following conclusions: (a) Both mechanistic and kinetic isotope effect profiles (KIEPs) reveal that all of the reactions proceed in a HAT mechanism, with a mechanistic switch from spin-selective reactivity for the DMA and *p*-Cl-DMA substrates to two-state reactivity for the *p*-CN-DMA and *p*-NO_2-DMA substrates. (b) The computed KIEPs for these scenarios match the experimentally determined KIEPs. Theory shows that the low-spin KIEs are sensitive to the nature of the substrates and vary in a manner predicted by the Melander−Westheimer postulate: the TSs are "early" along the H-transfer coordinate for DMA and become progressively less early as the electron-withdrawing ability of the para substituent increases. By contrast, the KIE values for the high-spin route remain almost constant ($\sim$5.5) and the corresponding TSs are all "central" or "late" along the H-transfer coordinate. (c) The electronic features of the para substituents exert influence on the nature of the $C_\alpha-H$ bond via a conjugated $\pi_{ph}-\pi_{C-N}$ orbital that stretches to the aromatic moiety and is sensitive to the substituent; this is the route cause for the observation of a negative Hammett ρ parameter. (d) The observed correlation between reaction rates and the substrate redox potentials just reflects the polar character of the HAT process and the sensitivity of HAT energy barriers to the energy level of the highest occupied molecular orbital of the substituted DMAs. (e) The generated carbinolaniline can readily dissociate from the heme and decomposes in a nonenzymatic environment, which involves water assisted proton shift.

Acknowledgment. The research in the Dalian Insititute is supported by NSFC (Grants 20373071, 20333050) to K.H. Y.W. acknowledges the advice of Dr. Sam de Visser on polarizability calculations. The research in the HU is supported by an ISF grant to S.S.

Supporting Information Available: KIE expressions based on the theory of absolute reaction rates and the corresponding Fortran source code, 4 figures and 27 tables for detailed electronic and geometric features of various reaction species, reference 17 in full, and *x*, *y*, *z*, coordinates. This material is available free of charge *via* the Internet at http://pubs.acs.org.

References and Notes

(1) (a) Porter, T. D.; Coon, M. J. *J. Biol. Chem.* **1991**, *266*, 13469. (b) Coon, M. J. *Annu. Rev. Pharmacol. Toxicol.* **2005**, *45*, 1.

(2) (a) de Montellano, P. R. O. in *Cytochrome P450: Structure, Mechanism and Biochemistry*, 2nd ed.; Ortiz de Montellano, P. R., Ed.; Plenum Press: New York, 1995; Chapter 8. (b) Ortiz de Montellano, P. R.; De Voss, J. J. *Nat. Prod. Rep.* **2002**, *19*, 477. (c) Meunier, B.; de Visser, S. P.; Shaik, S. *Chem. Rev.* **2004**, *104*, 3947. (d) Shaik, S.; Kumar, D.; de Visser, S. P.; Altun, A.; Thiel, W. *Chem. Rev.* **2005**, *105*, 2279. (e) Sono, M.; Roach, M. P.; Coulter, E. D.; Dawson, J. H. *Chem. Rev.* **1996**, *96*, 2841. (f) Guengerich, F. P. *Chem. Res. Toxic.* **2001**, *14*, 611.

(3) (a) Guengerich, F. P.; Macdonald, T. L. *FASEB J.* **1990**, *4*, 2453. (b) Guengerich, F. P.; Macdonald, T. L. *Adv. Electron Transfer Chem.* **1993**, *3*, 191.

(4) (a) Dinnocenzo, J. P.: Karki, S. B.: Jones, J. P. *J. Am. Chem. Soc.* **1993**, *115*, 7111. (b) Karki, S. B.; Dinnocenczo, J. P.; Jones, J. P.; Korzekwa, K. R. *J. Am. Chem. Soc.* **1995**, *117*, 3657. (c) Karki, S. B.; Dinnocenzo, J. P. *Xenobiotica* **1995**, *25*, 711. (d) Manchester, J. I.; Dinnocenzo, J. P.; Higgins, L. A.; Jones, J. P. *J. Am. Chem. Soc.* **1997**, *119*, 5069.

(5) (a) Miwa, G. T.; Walsh, J. S.; Kedderis, G. L.; Hollenberg, P. F. *J. Biol. Chem.* **1983**, *258*, 14445. (b) Miwa, G. T.; Garland, W. A.; Hodshon, B. J.; Lu, A. Y. H.; Northrop, D. B. *J. Biol. Chem.* **1980**, *255*, 6049. (c) Abdel-Monem, M. M. *J. Med. Chem.* **1975**, *18*, 427. (d) Hollenberg, P. F.; Miwa, G. T.; Walsh, J. S.; Dwyer, L. A.; Kedderis, G. L. *Drug Metab. Dispos.* **1985**, *13*, 272. (e) Guengerich, F. P.; Yun, C.-H.; Macdonald, T. L. *Biochemistry* **1996**, *271*, 27321.

(6) (a) Burka, L. T.; Guengerich, F. P.; Willard, R. J.; Macdonald, T. L. *J. Am. Chem. Soc.* **1985**, *107*, 2549. (b) Galliani, G.; Rindone, B.; Dagnino, G.; Salmona, M. *Eur. J. Drug Metab. Pharmacokin.* **1984**, *9*, 289. (c) Galliani, G.; Nali, M.; Rindone, B.; Tollari, S.; Rocchetti, M.; Salmona, M. *Xenobiotica* **1986**, *16*, 511. (d) Macdonald, T. L.; Gutheim, W. G.; Martin, R. B.; Guengerich, F. P. *Biochemistry* **1989**, *28*, 2071. (e) Shono, T.; Toda, T.; Oshino, N. *J. Am. Chem. Soc.* **1982**, *104*, 2639. (f) Parker, V. D.; Tilset, M. *J. Am. Chem. Soc.* **1991**, *113*, 8778. (g) Goto, Y.; Watanabe, Y.; Fukuzumi, S.; Jones, J. P.; Dinnocenzo, J. P. *J. Am. Chem. Soc.* **1998**, *120*, 10762.

(7) (a) Baciocchi, E.; Lanzalunga, O.; Lapi, A.; Manduchi, L. *J. Am. Chem. Soc.* **1998**, *120*, 5783. (b) Baciocchi, E.; Gerini, M. F.; Lanzalunga, O.; Lapi, A.; Mancinelli, S.; Mencarelli, P. *Chem. Commun.* **2000**, 393. (c) Baciocchi, E.; Gerini, M. F.; Lanzalunga, O.; Lapi, A.; Piparo, M. G. L.; Mancinelli, S. *Eur. J. Org. Chem.* **2001**, 2305. (d) Baciocchi, E.; Bietti, M.; Gerini, M. F.; Lanzalunga, O. *J. Org. Chem.* **2005**, *70*, 5144.

(8) (a) Augusto, O.; Beilan, H. S.; Ortiz de Montellano, P. R. *J. Biol. Chem.* **1982**, *257*, 11288. (b) Lee, J. S.; Jacobsen, N. E.; Ortiz de Montellano, P. R. *Biochemistry* **1988**, *27*, 7703. (c) Guengerich, F. P.; Brian, W. R.; Iwasaki, M.; Sari, M.-A.; Bäärnhielm, C.; Berntsson, P. *J. Med. Chem.* **1991**, *34*, 1838. (d) Okazaki, O.; Guengerich, F. P. *J. Biol. Chem.* **1993**, *268*, 1546. (e) Cuppoletti, A.; Dagostin, C.; Florea, C.; Galli, C.; Gentili, P.; Lanzalunga, O.; Petride, A.; Petride, H. *Chem. Eur. J.* **1999**, *5*, 2993. (f) Bietti, M.; Cuppoletti, A.; Dagostin, C.; Florea, C.; Galli, C.; Gentili, P.; Petride, H.; Caia, C. R. *Eur. J. Org. Chem.* **1998**, *2425*.

(9) (a) Hanzlik, R. P.; Kishore, V.; Tullman, R. *J. Med. Chem.* **1979**, *22*, 759. (b) Hanzlik, R. P.; Tullman, R. *J. Am. Chem. Soc.* **1982**, *104*, 2048. (c) Macdonald, T. L.; Zirvi, K.; Burka, L. T.; Peyman, P.; Guengerich, F. P. *J. Am. Chem. Soc.* **1982**, *104*, 2050. (d) Bondon, A.; Macdonald, T. L.; Harris, T. M.; Guengerich, F. P. *J. Biol. Chem.* **1989**, *64*, 1988. (e) Chen, H.; deGroot, M. J.; Vermeulen, N. P. E.; Hanzlik, R. P. *J. Org. Chem.* **1997**, *62*, 8227.

(10) Jurva, U.; Bissel, P.; Isin, E. M.; Igarashi, K.; Kuttab, S.; Castagnoli, N. *J. Am. Chem. Soc.* **2005**, *127*, 12368.

(11) (a) Bhakta, M. N.; Wimalasena, K. *J. Am. Chem. Soc*. **2002**, *124*, 1844. (b) Bhakta, M. N.; Hollenberg, P. F.; Wimalasena, K. *Chem. Commun*. **2005**, 265. (c) Bhakta, M. N.; Wimalasena, K. *Eur. J. Org. Chem*. **2005**, 4801. (d) Bhakta, M. N.; Hollenberg, P. F.; Wimalasena, K. *J. Am. Chem. Soc*. **2005**, *127*, 1376.

(12) (a) Cerny, M. A.; Hanzlik, R. P. *J. Am. Chem. Soc.* **2006**, *128*, 3346. (b) Cerny, M. A.; Hanzlik, R. P. *Arch. Biochem. Biophys.* **2005**, *436*, 265. (c) Shaffer, C. L.; Harriman, S.; Koen, Y. M.; Hanzlik, R. P. *J. Am. Chem. Soc.* **2002**, *124*, 8268. (d) Shaffer, C. L.; Morton, M. D.; Hanzlik, R. P. *J. Am. Chem. Soc.* **2001**, *123*, 8502. (e) Shaffer, C. L.; Morton, M. D.; Hanzlik, R. P. *J. Am. Chem. Soc.* **2001**, *123*, 349.

(13) Li, C.; Wu, W.; Kumar, D.; Shaik, S. *J. Am. Chem. Soc.* **2006**, *128*, 394.

(14) (a) Shaik, S.; Filatov, M.; Schroder, D.; Schwarz, H. *Chem. Eur. J.* **1998**, *4*, 193. (b) Ogliaro, F.; Harris, N.; Cohen, S.; Filatov, M.; de Visser, S. P.; Shaik, S. *J. Am. Chem. Soc.* **2000**, *122*, 8977. (c) de Visser, S. P.; Ogliaro, F.; Sharma, P. K.; Shaik, S. *J. Am. Chem. Soc.* **2002**, *124*, 11809.

(15) (a) Dowers, T. S.; Rock, D. A.; Jones, J. P. *J. Am. Chem. Soc.* **2004**, *126*, 8868. (b) Volz, T. J.; Rock, D. A.; Jones, J. P. *J. Am. Chem. Soc.* **2002**, *124*, 9724.

(16) (a) Filatov, M.; Harris, N.; Shaik, S. *Angew. Chem. Int. Ed.* **1999**, *38*, 3510. (b) Harris, N.; Cohen, S.; Filatov, M.; Ogliaro, F.; Shaik, S. *Angew. Chem. Int. Ed.* **2000**, *39*, 2003. (c) Ogliaro, F.; Cohen, S.; de Visser, S. P.; Shaik, S. *J. Am. Chem. Soc.* **2000**, *122*, 12892. (d) de Visser, S. P.; Ogliaro, F.; Harris, N.; Shaik, S. *J. Am. Chem. Soc.* **2001**, *123*, 3037. (e) Kumar, D.; de Visser, S. P.; Shaik, S. *J. Am. Chem. Soc.* **2004**, *126*, 5072. (f) Schoneboom, J. C.; Cohen, S.; Lin, H.; Shaik, S.; Thiel, W. *J. Am. Chem. Soc.* **2004**, *126*, 4017. (g) Wang, Y.; Wang, H.; Wang, Y.; Yang, C.; Yang, L.; Han, K. *J. Phys. Chem. B* **2006**, *110*, 6154.

(17) Frisch, M. J.; et al. *Gaussian 03*, revision C.02; Gaussian, Inc.: Wallingford, CT, 2004.

(18) (a) Becke, A. D. *J. Chem. Phys.* **1993**, *98*, 5648. (b) Lee, C.; Yang, W.; Parr, R. G. *Phys. Rev. B* **1988**, *37*, 785.

(19) (a) Hay, J. P.; Wadt, W. R. *J. Chem. Phys.* **1985**, *82*, 99. (b) Friesner, R. A.; Murphy, R. B.; Beachy, M. D.; Ringlanda, M. N.; Pollard, W. T.; Dunietz, B. D.; Cao, Y. X. *J. Phys. Chem. A* **1999**, *103*, 1913.

(20) Melander, L.; Saunders, W. H., Jr. In *Reaction rates of isotopic molecules.*; Robert E. Krieger Publishing Company: Malabar, FL, 1987; Chapter 2.

(21) (a) Groves, J. T.; McClusky, G. A. *J. Am. Chem. Soc.* **1976**, *98*, 859. (b) Groves, J. T. *J. Chem. Educ.* **1985**, *62*, 928.

(22) Jaffe, H. H. *Chem. Rev.* **1953**, *53*, 191.

(23) Uneyama, K.; Namba, H.; Oae, S. *Bull. Chem. Soc. Jpn.* **1968**, *41*, 1928.

DOI: 10.1002/ejic.200700117

A Density Functional Study of the Factors That Influence the Regioselectivity of Toluene Hydroxylation by Cytochrome P450 Enzymes

Carina Hazan,[a] Devesh Kumar,[a] Sam P. de Visser,*[b] and Sason Shaik*[a]

Keywords: Density functional calculations / Enzyme catalysis / Enzyme models / Isotope effects / Metalloenzymes

Density functional theory calculations have been performed to elucidate the factors that influence the regioselectivity of toluene hydroxylation by a model of the active species of cytochrome P450 enzymes, so-called Compound I (Cpd I). Cpd I can hydroxylate the benzylic C–H and generate benzyl alcohol, or it can activate the phenyl group and produce *p*-cresol and *p*-methylcyclohexanone products. The reactions take place via two-state reactivity on competing doublet and quartet spin state surfaces. In the gas phase, the benzyl alcohol is preferred over *p*-cresol by more than three orders of magnitude. Environmental perturbations, namely, NH···S hydrogen bonding to the thiolate ligand and bulk polarity of the protein, lower this preference to roughly 10:1 in favour of benzyl alcohol. Substitution of methyl hydrogen atoms by deuterium atoms raises the barriers that lead to benzyl alcohol without affecting those leading to *p*-cresol. Therefore combining toluene deuteration with the effects of NH···S hydrogen bonding and bulk polarity lowers the free energy difference between the two processes to only 0.4 kcal mol^{-1}, and the two processes become competitive. These results as well as the calculated kinetic isotope effects are in good general agreement with experimental data.
(© Wiley-VCH Verlag GmbH & Co. KGaA, 69451 Weinheim, Germany, 2007)

1. Introduction

The cytochromes P450 (P450s) form a large family of heme-enzymes that are involved in drug metabolism as well as the detoxification of foreign substances in aerobic biosystems.[1] As such, P450s catalyze a large variety of chemical reactions ranging from alkyl and aromatic hydroxylation to sulfoxidations and dealkylations. This catalytic versatility makes these enzymes of great interest to the biotechnological industry. However, although a lot of scientific research has been devoted to this class of enzymes, the mechanisms of their reactions are still shrouded in controversies. The active center of P450 contains an iron embedded into a porphyrin macrocycle and connected to the protein backbone via a thiolate ligand.[2] This thiolate group elicits a "push"-effect on the iron-heme that gauges the oxidative properties of the system.[3] Thus, the enzyme utilizes molecular oxygen which is activated by reduction and protonation steps, and is converted into water and an iron-oxo species. This iron-oxo species (Compound I, Cpd I) has been postulated as the active species that performs the monoxygenation reactions of the enzyme although there are also suggestions that the precursor of Cpd I, i.e. the hydroperoxo-iron complex (Compound 0, Cpd 0) can act too as an alternative oxidant.[4] Theoretical studies of the catalytic properties of Cpd I vis-à-vis Cpd 0, however, indicate that Cpd 0 is a sluggish oxidant that will not be able to compete with Cpd I.[5]

Although Cpd I appears to be elusive and has never been detected experimentally, there is indirect evidence that confirm its existence.[6] These studies have led to the suggestion that the hydroxylation of aliphatic substrates by Cpd I proceeds via the "hydrogen abstraction/oxygen rebound" mechanism.[7] Many experimental studies on product distribution of substrate hydroxylations by the P450s are known. Of particular interest to us are the ones that involve metabolic switching, i.e. which lead to a product distribution change when hydrogenated substrates are replaced by the deuterated ones.[8,9] For instance, toluene hydroxylation by rat liver cytochrome P450 produced along with benzyl alcohol also significant amounts of cresol by-products (Scheme 1); the benzyl alcohol was the preponderant product.[9] Moreover, substitution of the methyl hydrogen atoms by deuterium atoms led to a regioselectivity change from benzyl hydroxylation to phenyl hydroxylation. By contrast, substitution of the ring hydrogen atoms by deuterium atoms in toluene only changed the product distributions slightly (Scheme 1). Further studies show that specific P450 isozymes give different product ratios: $P450_{1A1}$ and $P450_{2B1/2}$ produce dominant *o*-cresol products, while $P450_{2B1/2}$ and $P450_{2E1}$ mainly give *p*-cresol products and $P450_{2C11/2C6}$

[a] Department of Organic Chemistry and The Lise Meitner-Minerva Center for Computational Quantum Chemistry,
The Hebrew University of Jerusalem, 91904 Jerusalem, Israel
E-mail: sason@yfaat.ch.huji.ac.il
[b] The Manchester Interdisciplinary Biocenter and the School of Chemical Engineering and Analytical Science, The University of Manchester,
131 Princess Street, Manchester M1 7DN, United Kingdom
E-mail: sam.devisser@manchester.ac.uk
Supporting information for this article is available on the WWW under http://www.eurjic.org or from the author.

 © 2007 Wiley-VCH Verlag GmbH & Co. KGaA, Weinheim

mostly benzyl alcohol.[10] Thus, for example, the oxidation reaction of toluene by cytochrome $P450_{2E}$ produces 96% benzyl alcohol and 4% cresol products.[11] Another example from the study of metabolism of toluene by human cytochrome P450 isozymes of Asian and Caucasian livers reveals that there is a significant difference in the ratio of the benzylic/aromatic oxidation products in the two groups caused by the different concentrations of the isozymes for each group.[12] The regioselectivity of toluene oxidation by P450 is the focus of this paper, which utilizes density functional theory (DFT) to elucidate the main electronic factors that contribute to the choice between C–H and phenyl activations.

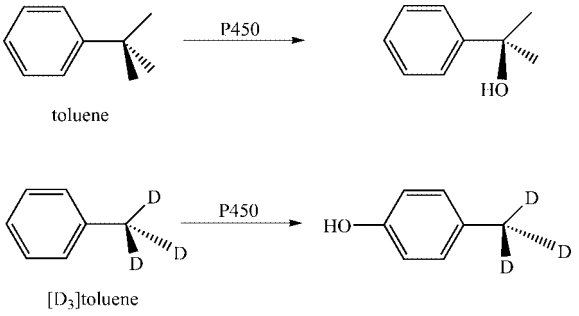

	o-cresol	*m*-cresol *p*-cresol	benzyl alcohol
toluene	14.8	16.2	69.0
[D_3]toluene	34.7	41.0	24.3
[D_8]toluene	35.2	45.2	19.6

Scheme 1. Dominant reaction products obtained for toluene, [D_3]-toluene and [D_8]toluene hydroxylation by rat liver P450s, and the product distributions (in mol-%) of *o*-, *m*-, and *p*-cresol and benzyl alcohol (data taken from ref.[9c]).

Toluene hydroxylation is an archetype of many similar problems in P450 chemistry. Thus, for example, the hydroxylation of ethylbenzene by P450 enzymes also gives metabolic switching after hydrogen atoms are replaced by deuterium atoms.[13] These studies demonstrated that the hydrogen abstraction from ethylbenzene is stereospecific and it occurs mainly at the benzylic position where the pro-*S* hydrogen is favoured 4 to 1 with respect to the pro-*R* bond. This pro-*S* C–H activation of ethylbenzene was proposed to occur due to the shape of the active site pocket, which applies chiral constraints on the binding of ethylbenzene. A very small amount of 2-phenylethanol and ethylphenol byproducts were found and their product distribution increased when the benzylic hydrogens were replaced with deuterium.

Substrate oxidation by Cpd I proceeds generally via stepwise mechanisms with discrete intermediates.[1d,7] Scheme 2 shows as an example the mechanism of alkane hydroxylation, whereby Cpd I abstracts a hydrogen atom from the substrate (AlkH), and subsequently the alkyl radical (Alk) intermediate rebounds onto the hydroxy group to form the alcohol product.[7] Theoretical studies of alkene epoxidation[14] and alkane[15] hydroxylation confirm this general mechanistic feature, but reveal that these processes transpire by a two state reactivity (TSR) scenario originating from the closely lying doublet and quartet spin states of the active species, Cpd I. The quartet state process is truly stepwise, as in Scheme 2, whereas the doublet state process is effectively concerted, with no discrete intermediates.[15,16]

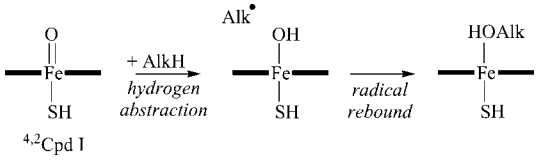

Scheme 2. Reaction mechanism of alkane hydroxylation by Cpd I of P450 enzymes. AlkH is an aliphatic substrate. The superscripts in Cpd I indicate the spin multiplicity of the state.

As revealed by theory, the aromatic hydroxylation reaction[17,18] by Cpd I has additional features. Here the oxoiron group attacks one of the ring carbon atoms of the substrate thereby forming a tetrahedral intermediate σ complex, which can be carbocation-like or radical-like (structures **C** and **R** in Scheme 3). Previous results[17,18] on benzene hydroxylation by a P450 mimic showed that aromatic hydroxylation proceeds on a dominant low-spin state surface (the doublet state) that corresponds to electrophilic attack of Cpd I on benzene leading to a cationic Meisenheimer complex intermediate. Although, with benzene, the corresponding radical intermediate is a few kcal mol^{-1} higher in energy, with ethylbenzene as a substrate the energy separation between **C** and **R** is much larger. From the σ complexes the *ipso* proton is shuttled to one of the nitrogen atoms of the porphyrin ring and is reshuttled to either the oxygen atom to form phenol products or to the *ortho*-carbon atom to form the ketone.

The regioselectivity of benzylic hydroxylation vs. aromatic hydroxylation in substrates having both moieties usually favours the alkyl hydroxylation.[19] In many cases, the hydroxylation reactions catalyzed by the P450s are regio- and stereoselective due either to electronic factors, or to the arrangement of the shape of the active site which provides multiple van der Waals interactions between enzyme and substrate and depends on the mode of binding of the substrate to the enzyme active site.[20] Kinetic isotope effect studies (*KIE*) showed that the benzylic position is more reactive than the aromatic ring whereas the release of the benzyl alcohol is much slower than the release of cresol and furthermore is partially rate limiting in turnover.[9c] A large number of *KIE* studies have been done in order to understand the kinetics and the mechanism of arene[21] hydroxylation by P450 enzymes. Since experimental studies supported the notion that the oxidant in most cytochrome P450 isozymes is Cpd I, this information could be used to construct a single electronic model that describes many P450 enzymes.[22] Jones et al.[23] developed an electronic model for aromatic oxidation with the aim of predicting the binding affinity related to steric features. Using a kinetic study, they found that the step prior to the substrate oxidation is rate limiting in the catalytic cycle whereas product

 © 2007 Wiley-VCH Verlag GmbH & Co. KGaA, Weinheim

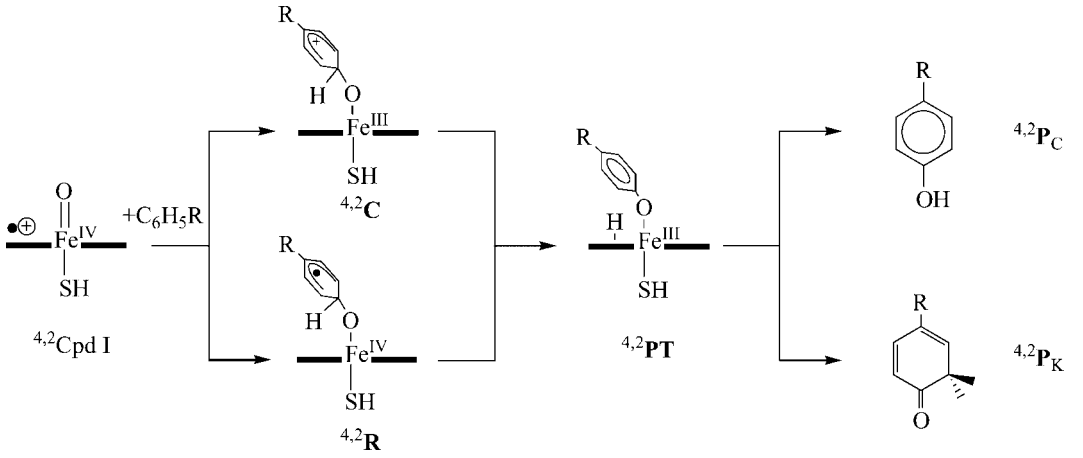

Scheme 3. Reaction mechanism of arene (C_6H_5R) hydroxylation by a model Cpd I of P450. The superscripts indicate the spin multiplicity of the state.

formation is not. Clearly, therefore the regioselectivity of P450 oxidation is still an unresolved issue, and theory can contribute to such an eventual resolution.

Our goal in this paper is to elucidate the electronic factors of regioselectivity and of metabolic switching upon substrate deuteration by focusing on toluene oxidation (see Scheme 1 above). To this end, we performed DFT calculations of the reaction mechanisms of toluene hydroxylation by an iron-oxo porphyrin catalyst leading to *p*-cresol and benzyl alcohol products. As we will show in this work, subtle external perturbations (e.g. hydrogen bonding and bulk polarity) change the relative energies of the rate-determining barriers to the various products and thereby contribute to the observed metabolic switching when toluene is deuterated.

2. Methods

The methods used here were similar to those described in previous studies.[24] The calculations were carried out using the hybrid density functional theory UB3LYP[25] combined with a double zeta LACVP basis set[26] on iron and a 6-31G basis set on the remaining atoms (hence UB3LYP/LACVP). Single point calculations were done with a triple zeta basis set, which includes diffuse functions on iron and polarization and diffuse functions on all other non-hydrogen atoms (hence B3LYP/LACV3P+*). Previous studies on similar systems showed that geometry optimizations performed with the LACVP or LACVP+* basis sets give similar geometries and vibrational frequencies, therefore, optimizations were done with LACVP, while single point calculations used the larger basis set.[27] All calculations were performed using Jaguar 4.5[28] for geometry optimizations and GAUSSIAN 98[29] for frequency analysis. All structures were fully optimized without geometric constraints. The single imaginary frequency of the transition state was examined and confirmed the nature of the transition state. The study generated a considerable amount of data (spin densities, charge distributions, detailed geometries, potential energy scans, etc.), which are useful but cannot be included in the paper for space economy and therefore are relegated to the Supplementary material. All calculations were performed on the doublet (low-spin, LS) and quartet (high-spin, HS) spin state surfaces.

Cpd I was modelled as a porphyrin-iron-oxo complex, where the proximal thiolate ligand was truncated to SH^-, as in previous studies.[30] The hydrogen bonding to the thiolate ligand, as found in the enzyme, was mimicked by adding two ammonia molecules each pointing an N–H bond at the sulfur of the SH^- ligand at fixed distances of r_{NH-S} = 2.660 Å.[30,31] The distances and angles of the atoms in the ammonia molecules were initially fully optimized for ^{4}Cpd I and subsequently exported to the other structures.[31] The effects of NH···S hydrogen bonding and solvation by a dielectric medium were obtained by single point energy calculations on the optimized structures. The effect of protein bulk polarity was studied using the self-consistent reaction field (SCRF) model as implemented in Jaguar with a dielectric constant of ε = 5.7 and probe radius 2.72 Å. We used a typical dielectric constant of ε = 5.7 that is in the range of values expected for enzymatic systems.

The geometry scans were performed by taking one variable as the "reaction coordinate", while all the remaining degrees of freedom were fully optimized. These geometry scans were used as starting points for the transition state searches and are included in the supporting information as Figures S1, S2, S6–S9 (electronic supporting information; see also the footnote on the first page of this paper).

Finally, kinetic isotope effects (*KIE*) were calculated using the semi-classical Eyring model (KIE_E) and the Wigner tunnelling corrected value (KIE_W), based on Equation (1), (2), (3).[14c,15c] The Eyring isotope effect reflects the differences in free energies of activation ($\Delta G^{\dagger}$) of the deuterium substituted and reference all-hydrogenic substrates. The free energy of activation was taken from the Gaussian frequency files and includes the electronic energy with ZPE, entropic and thermal corrections (at 298.15 K). In the past we calculated many free energies of reactions of

 © 2007 Wiley-VCH Verlag GmbH & Co. KGaA, Weinheim

porphyrin-iron-oxo systems for a range of substrates and generally found good agreement with experimental rate constants and free energies.[14d,15d,32] Further corrections to the KIE_E using the tunnelling ratio Q_{tH}/Q_{tD} between the hydrogen and deuterium substituted systems gives the Wigner isotope effect.

$$KIE_E = k_H/k_D = \exp[(\Delta G^{\dagger}_D - \Delta G^{\dagger}_H)/RT] \quad (1)$$

$$KIE_W = KIE_E \times Q_{tH}/Q_{tD} \quad (2)$$

$$Q_t = 1 + (h\nu/kT)^2/24 \quad (3)$$

In Equations 1–3, R is the gas constant, T the temperature, h is the Planck constant, k is the Boltzmann constant and ν the imaginary frequency in the transition state.

3. Results and Discussion

We have studied the competitive hydroxylations, benzylic and aromatic, of toluene by P450 model Cpd I and essentially followed the reaction mechanisms of alkyl and aromatic hydroxylations as depicted in Scheme 2 and Scheme 3 above. Thus, the reaction starts from Cpd I, which is a triradicaloid species with singly occupied π^*_{xz}, π^*_{yz} and a_{2u} orbitals.[24] The former two orbitals are the Fe–O antibonding orbitals, while the latter one is a nonbonding orbital on the porphyrin. The three electrons can be ferromagnetically coupled into an overall quartet spin state or antiferromagnetically coupled into an overall doublet spin state. These two states are close in energy, hence the system reacts via two-state reactivity (TSR) patterns.[33] All reaction mechanisms, therefore, come in two varieties: one for the doublet spin and one for the quartet spin. The spin multiplicity, $2S+1$, is indicated by a superscript on the left hand side of the label of the structure.

3.1 Benzyl Hydroxylation

Because, experimentally, the dominant reaction is benzyl hydroxylation, we will start with the discussion of this reaction mechanism first. Figure 1 shows the potential energy surface of benzylic hydroxylation of toluene by Cpd I in the quartet and doublet spin states. The rate-determining step is the hydrogen abstraction (via ^{4,2}**TS**$_B$) that leads to an iron-hydroxo complex with a nearby $C_7H_7^{\cdot}$ radical (^{4,2}**B**) that rebounds onto the hydroxo group via a barrier **TS**$_{reb}$ to generate the benzyl alcohol product complex (^{4,2}**P**$_B$). On the doublet spin surface the rebound barrier is negligible, but on the quartet spin surface we located a small barrier of 1.8 kcal mol^{-1}. This is a common observation in aliphatic hydroxylations by P450 enzymes, and it means that the ^{4}**B** intermediate will have a finite lifetime, whereas ^{2}**B** will instantaneously react to form products.[14,15]

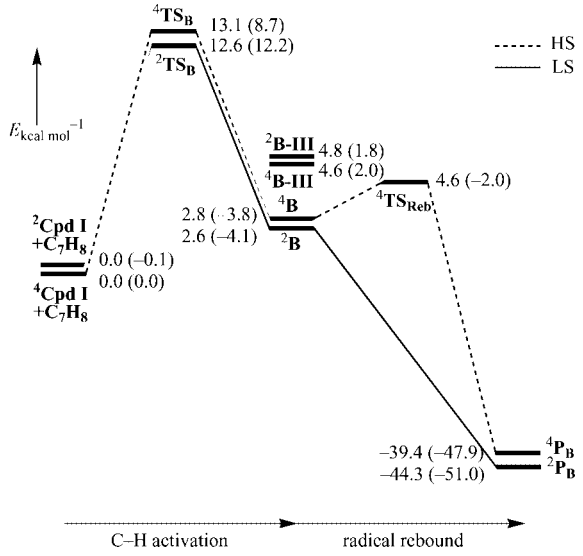

Figure 1. Potential energy profile for the benzyl hydroxylation of toluene by ^{4,2}Cpd I. All data refer to energies obtained at the UB3LYP/LACVP (UB3LYP/LACV3P+*) level with *ZPE* corrections at the LACVP level of theory. Energies are in kcal mol^{-1} relative to isolated reactants in the quartet spin state.

The hydrogen abstraction step is accomplished with a simultaneous electron shift from the substrate into the singly occupied a_{2u} orbital whereby the metal stays in oxidation state Fe^{IV} to create ^{4,2}**B**. Alternatively, this electron shift can fill one of the singly occupied π^* orbitals to create an intermediate with the metal in oxidation state Fe^{III} and a cation radical on the heme.[14a] We tested these states (labelled as ^{4,2}**B**-III), but they are well higher in energy than ^{4,2}**B**, i.e. the intermediates with the metal in oxidation state Fe^{IV}. Thus, although the Fe^{III} states will play a role, their radical rebound patterns[24] from intermediates to products is similar to the one exhibited here for the Fe^{IV} state.[14d] Therefore we did not follow the rebound behaviour of ^{4,2}**B**-III further.

The rate-determining transition states ^{4,2}**TS**$_B$ lie 8.7 (HS) and 12.2 (LS) kcal mol^{-1} above the isolated reactants at the UB3LYP/LACV3P+* level of theory with ZPE included (calculated at the LACVP level). Interestingly, the barriers for ethylbenzene hydroxylation are of the same order of magnitude as the ones for toluene but the order of the transition states is reversed, namely ^{2}**TS**$_B$ is 9.1 kcal mol^{-1} and ^{4}**TS**$_B$ is 11.7 kcal mol^{-1}, above the reactants, using the same methods and basis sets.[17b] We recall that the ethylbenzene project[17b] used an porphyrin-iron-oxo catalyst with a chloride axial ligand, whereas the present study uses a thiolate axial ligand. As such, differences in axial ligand of the models (SH^- vs. Cl^-) may cause a different "push" effect (release of electron density) toward the iron-oxo group and thereby change the doublet-quartet energy splitting along the reaction path. In sum: benzylic hydroxylation reactions of toluene and ethylbenzene take place on competing quartet and doublet spin surfaces via TSR that possess radical intermediates with the metal in oxidation state Fe^{IV}.

 © 2007 Wiley-VCH Verlag GmbH & Co. KGaA, Weinheim

Optimized geometries of $^{4,2}\mathbf{TS_B}$ are shown in Figure 2. As can be seen, the transition states are late with longer C–H distances than O–H distances. As expected the O–H–C angle is almost linear. These results match perfectly earlier studies on hydrogen abstraction transition states.[15] Note as well that the benzene group is not pointing upwards, i.e. away from the heme, but is bent with an O–C^1–C^2 angle of 104.8° (HS) and 103.5° (LS). The imaginary frequency of the transition state is large (i1949.9 cm^{-1} for $^{4}\mathbf{TS_B}$ and i1617.6 cm^{-1} for $^{2}\mathbf{TS_B}$), which is typical for a hydrogen abstraction barrier.

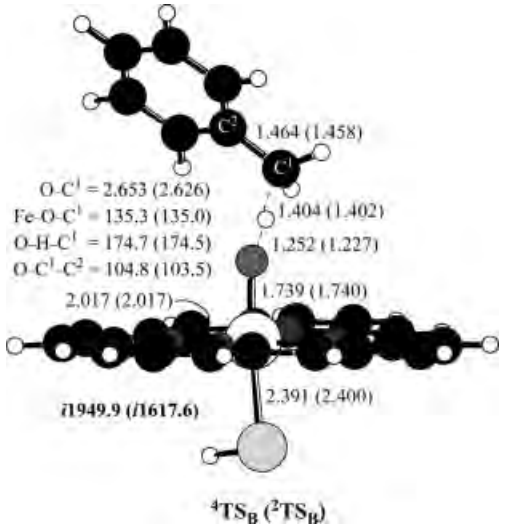

Figure 2. UB3LYP/LACVP optimized geometries of $^{4,2}\mathbf{TS_B}$. All bond lengths are given in Å and all angles in degrees. The Fe–N distance is the average bond length of all four Fe–N bonds. Also given is the imaginary frequency of the transition state in cm^{-1}.

3.2 Phenyl Hydroxylation

Commonly observed by-products in benzyl hydroxylation reactions by toluene are cresols. We have studied the mechanisms leading to *p*-cresol and *p*-methylcyclohexanone by-products in Figure 3. The mechanisms are essentially the same as the ones obtained for phenyl hydroxylation in benzene and ethylbenzene by oxo-iron porphyrins and follows the mechanism shown in Scheme 3 above.[17] The initial reaction step is phenyl activation leading to a C–O bond formation and a cationic (**C**) or radicalar (**R**) σ adducts via the transition states $^{4,2}\mathbf{TS_C}$ and $^{4,2}\mathbf{TS_R}$ respectively. Subsequently, the *ipso* proton is shuttled toward one of the nitrogen atoms of the porphyrin group to create the proton-transfer complex ($^{4,2}\mathbf{PT}$), which essentially is a cresolate anion adjacent to a protonated porphyrin group. The barriers separating $^{4,2}\mathbf{C}$ from $^{4,2}\mathbf{PT}$ via the transition states $^{4,2}\mathbf{TS_{PT}}$, and the ones in between $^{4,2}\mathbf{R}$ and $^{4,2}\mathbf{PT}$ via $^{4,2}\mathbf{TS_{PTR}}$, lead to the corresponding $^{4,2}\mathbf{PT}$ intermediates. From the $^{4,2}\mathbf{PT}$ complexes the proton can be shuttled back to the oxygen atom to create the cresol products ($^{4,2}\mathbf{P_C}$) via $^{4,2}\mathbf{TS_{PTC}}$, or alternatively the proton can be reshuttled to the aromatic ring to generate *p*-methylcyclohexanone products ($^{4,2}\mathbf{P_K}$) via $^{4,2}\mathbf{TS_{PTK}}$. This electrophilic substitution reaction mechanism of aromatic hydroxylation by iron-oxo

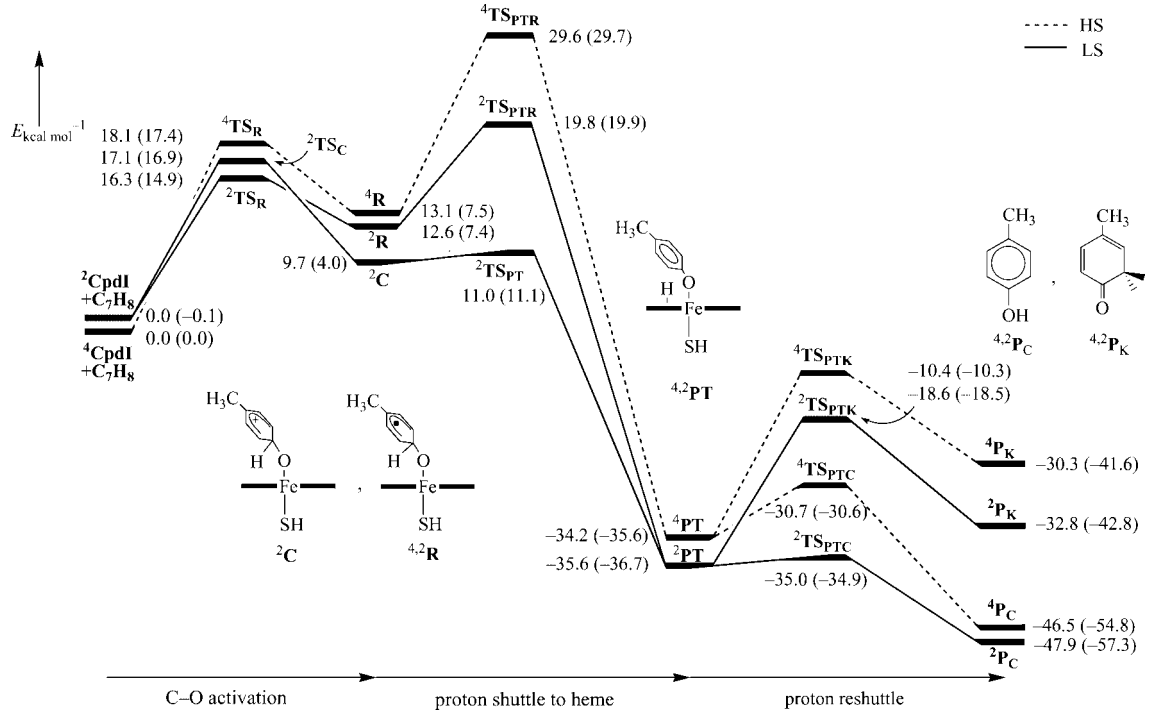

Figure 3. Potential energy profile for the aromatic hydroxylation of toluene by ^{4,2}Cpd I leading to *p*-cresol ($\mathbf{P_C}$) and *p*-methylcyclohexanone ($\mathbf{P_K}$) products. All data refer to energies obtained at the UB3LYP/LACVP (UB3LYP/LACV3P+*) level with *ZPE* corrections at the LACVP level of theory. The energies for the $\mathbf{TS_{PT}}$ structures at UB3LYP/LACV3P+* level are estimated. Energies are in kcal mol^{-1} relative to isolated reactants in the quartet spin state.

 © 2007 Wiley-VCH Verlag GmbH & Co. KGaA, Weinheim

complexes has been corroborated by experimental studies of anthracene hydroxylation by a nonheme iron-oxo complex. Thus, a large negative Hammett ρ value and an inverse kinetic isotope effect of 0.9 for the replacement of all hydrogen atoms in the substrate by deuterium atoms implied that the reaction proceeds via an electrophilic substitution reaction similarly to the one shown here in Scheme 3 and Figure 3.[32]

As follows from Figure 3 we located three transition states leading to σ-type intermediates: ^{2}**C** and ^{4,2}**R**. Attempts to calculate ^{4}**C** failed and converged back to the much lower lying state ^{4}**R**. In the gas phase, the lowest barrier leads to a radicalar intermediate (^{2}**R**) and is 14.9 kcal mol^{-1} above reactants, while the barriers leading to ^{4}**R** and ^{2}**C** are higher by 2.5 and 2.0 kcal mol^{-1}, respectively at the LACV3P+* level. Therefore, at least in the gas phase the phenyl hydroxylation takes place via TSR with a dominant LS mechanism via ^{2}**TS**$_{R}$. Below we discuss the factors that influence the relative energies of ^{2}**TS**$_{C}$ and ^{4,2}**TS**$_{R}$ in detail.

The next step in the reaction mechanism is the proton transfer from the *ipso* position to the porphyrin ring leading to formation of the proton transfer intermediates (^{4,2}**PT**). From the radical intermediates this pathway requires overcoming of a significant barrier; at the UB3LYP/LACV3P+* level, ^{2}**TS**$_{PTR}$ is 12.5 kcal mol^{-1} above ^{2}**R** and ^{4}**TS**$_{PTR}$ is 22.2 kcal mol^{-1} above ^{4}**R**, while from the cationic intermediate ^{2}**C** the corresponding barrier is significantly smaller (7.1 kcal mol^{-1}). The reason for this is that for the radical complexes a proton as well as an electron are transferred in the process, whereas ^{2}**C** already has the correct electronic configuration and only a proton is transferred in the process.[17a] Thus, ^{4,2}**R** have an electronic configuration $\pi^{*1}_{xz}\ \pi^{*1}_{yz}\ \phi^{1}_{Ph}$, wherein the two π* orbitals are the antibonding orbitals across the Fe–O bond and ϕ_{Ph} is a singly occupied orbital on the phenyl moiety. By contrast, ^{2}**C** has orbital occupation $\pi^{*2}_{xz}\ \pi^{*1}_{yz}\ \phi^{0}_{Ph}$, which is identical to the orbital occupation of ^{2}**PT**. Therefore, the process from ^{2}**C** to ^{2}**PT** does not involve any electronic rearrangement, while the process from ^{2}**R** to ^{2}**PT** leads to the transfer of an electron from ϕ_{Ph} into π^{*}_{xz}.[17] On the cationic surface, therefore, the rate-determining step is ^{2}**TS**$_{C}$, whereas on the radical surfaces the rate-determining steps are the second **TS**s (via ^{4,2}**TS**$_{PTR}$). The proton transfer intermediates (^{4,2}**PT**) are significantly more stable than the σ complexes (^{4,2}**R**, ^{2}**C**) by more than 40 kcal mol^{-1}. Therefore, the proton transfer is irreversible and the reaction will proceed with reshuttling of the proton from the heme to the substrate to form the product complexes. On the LS surface only a tiny barrier separates ^{2}**PT** from ^{2}**P**$_{C}$, but a larger barrier has to be surmounted to form methylcyclohexanone products (^{2}**P**$_{K}$). Therefore, cyclohexanone products are unlikely to be formed on the LS surface. On the HS surface the barrier leading to cyclohexanone products is still considerable, but since the barrier is well lower than the energy of ^{4}**R** there is a possibility that some cyclohexanone by-products may be observed. Although most structures give relative energies within a few kcal mol^{-1} with the two basis sets, the product complexes are all stabilized by around 10 kcal mol^{-1} using the LACV3P+* basis set. This has no influence what-soever on the final conclusions drawn in this paper.

Figure 4 shows the optimized geometries of ^{2}**TS**$_{C}$ and ^{4,2}**TS**$_{R}$. Generally, the transition state occurs later in the HS spin state than in the LS spin state, with shorter C–O and longer Fe–O distances. As can be seen from the structures in Figure 4 the substrate attacks the oxo group from the top and the benzene group points away from the heme. As a result the *ipso* hydrogen atom is in a hydrogen-bonding distance from one of the nitrogen atoms of the porphyrin group. Optimized geometries are in good agreement with ones obtained earlier for benzene and ethylbenzene hydroxylation by iron-oxo porphyrin catalysts.[17] Even the absolute values of the imaginary frequency in the transition states for toluene and ethylbenzene hydroxylation are of the same order of magnitude, which implies that the shapes of the potential energy surfaces around the transition states are very similar.

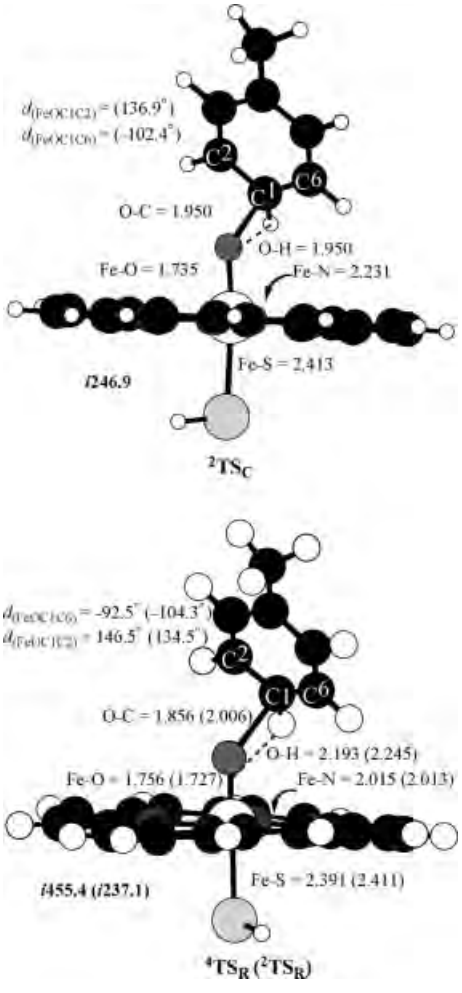

Figure 4. UB3LYP/LACVP optimized geometries of ^{2}**TS**$_{C}$ and ^{4,2}**TS**$_{R}$. All bond lengths are given in Å and all angles in degrees. Fe–N is the average bond length of all four Fe–N bonds. Also shown is the imaginary frequency of the transition state in cm^{-1}.

 © 2007 Wiley-VCH Verlag GmbH & Co. KGaA, Weinheim

3.3 Factors That Influence the Ordering of the Transition States

Table 1 shows the relative energies of the five bond activation transition states (^{4,2}**TS**$_B$, ^{4,2}**TS**$_R$ and ^{2}**TS**$_C$) for the competing benzyl and phenyl hydroxylation mechanisms, calculated using various methods and under different environmental conditions. Thus, the LACVP basis set gives four out of five transition states within 1 kcal mol^{-1} of each other. Adding polarization and diffuse basis functions to the basis set stabilizes ^{4}**TS**$_B$ by 4 kcal mol^{-1} and ^{2}**TS**$_R$ by 1 kcal mol^{-1}, with respect to the other three **TS**s. As shown before, here too *ZPE* corrections further stabilize the C–H hydroxylation **TS** over C–O bond activation **TS**,[14c] by about 3 kcal mol^{-1}. Therefore, at the most reliable level [ΔE(LACV3P+*) + *ZPE*], in the gas-phase benzyl hydroxylation is preferred over phenyl hydroxylation by 6.1 kcal mol^{-1}.

Table 1. Relative energies of the rate-determining transition states calculated with different methods and models.[a,b]

	Gas-phase			ε = 5.7	+2NH···S in ε = 1	+2NH···S in ε = 5,7
	ΔE	ΔE	ΔE+*ZPE*	ΔE_{solv}+*ZPE*	ΔE+*ZPE*	ΔE_{solv}+*ZPE*
Basis set:[c]	B1	B2	B2	B2	B2	B2
^{4}**TS**$_B$	0.27	–3.77	–3.53	–1.91	–0.81	–0.43
^{2}**TS**$_B$	0.00	0.00	0.00	0.00	0.00	0.00
^{4}**TS**$_R$	2.19	1.76	5.10	5.89	5.36	6.78
^{2}**TS**$_R$	0.49	–0.66	2.57	2.82	1.28	1.75
^{2}**TS**$_C$	0.78	0.89	4.61	4.05	0.76	1.10

[a] The ΔE terms were calculated with the indicated basis set. All *ZPE* and E_{solv} corrections are LACVP calculated values. [b] All energies are in kcal mol^{-1} relative to ^{2}**TS**$_B$. [c] B1 refers to an LACVP basis set and B2 to an LACV3P+* basis set.

Table 1 further shows the effects of the local environment on the ordering and relative energies of the rate-determining transition states. Bulk polarity, corresponding to a dielectric constant of ε = 5.7, destabilizes ^{4}**TS**$_B$ but does not change the ordering of the transition states. Since, phenyl hydroxylation transpires via a cationic intermediate the corresponding ^{2}**TS**$_C$ species is stabilized to some extent (by 0.5 kcal mol^{-1}), but this is not sufficient to create a preference for phenyl activation by Cpd I. The energy gap between ^{4}**TS**$_B$ and ^{2}**TS**$_R$ is reduced from 6.1 kcal mol^{-1} to 4.7 kcal mol^{-1}, therefore the bulk polarity has a small effect on the relative energies of the benzyl vs. phenyl hydroxylation transition states.

Finally, we mimicked the enzyme environment by adding two NH···S hydrogen bonding interactions with the thiolate axial ligand, using procedures described before.[31] Combined density functional theory/molecular mechanics (DFT/MM) calculations showed that the model with hydrogen-bonded ammonia molecules gives a correct orbital representation of Cpd I compared with the actual enzyme.[34] The results in Table 1 show that ^{4}**TS**$_B$ is destabilized due to the hydrogen bonding interactions and that ^{4}**TS**$_B$ and ^{2}**TS**$_B$ approach each other to within 1 kcal mol^{-1}. Small changes are also observed for the relative energies between ^{2}**TS**$_B$ and ^{4,2}**TS**$_R$, whereby the high-spin species is destabilized and the low-spin stabilized. Most noteworthy, however, is the considerable stabilization (by almost 4 kcal mol^{-1}) of ^{2}**TS**$_C$ when hydrogen-bonding interactions are added to the model. Addition of bulk polarity (ε = 5.7) to the calculations does not modify the trends set by the hydrogen bonding effect. In conclusion, the calculations show that toluene hydroxylation by P450 enzyme models is expected to yield more benzyl hydroxylation products compared with phenyl hydroxylation. The predicted ratio (roughly 10:1 based on 1.53 kcal/mol free energy difference) is not too far from the experimental data in Scheme 1.

3.4 Kinetic Isotope Effects

Table 2 shows the kinetic isotope effects (*KIE*) for the replacement of one or several hydrogen atoms of toluene by deuterium atoms. Since ^{4,2}**TS**$_B$ are transition states for hydrogen abstraction, the corresponding processes show considerable sensitivity to replacement by deuterium atoms and lead to *KIE* values of 8.2 (KIE_E) and 12.7 (KIE_W). These values are in excellent agreement with the experimental observations of Hanzlik et al.[9] and are also of similar order of magnitude to theoretical results obtained with propene and methyl-phenyl-cyclopropane as substrates.[14c,15c] Replacement of ring hydrogen atoms by deuterium atoms has little effect on the *KIE*s (*KIE* ≈ 1.0) because phenyl hydroxylation involves a rate-determining C–O activation step.

Table 2. Kinetic isotope effects (*KIE*) as calculated with the Eyring (KIE_E) or Wigner (KIE_W) models for the replacement of one or more hydrogen atoms of toluene by deuterium atoms.[a]

	C_6H_5–CH_2–D		C_6H_5–CD_3		C_6D_5–CH_3		C_6D_5–CD_3	
	KIE_E	KIE_W	KIE_E	KIE_W	KIE_E	KIE_W	KIE_E	KIE_W
^{4}**TS**$_B$	6.5	10.0	7.4	11.4	1.0	1.0	8.2	12.7
^{2}**TS**$_B$	6.7	9.7	7.6	11.2	0.9	0.9	8.2	12.1
^{4}**TS**$_R$	1.0	1.0	1.0	1.0	0.9	0.9	1.0	1.0
^{2}**TS**$_R$	1.0	1.0	1.0	1.0	0.9	0.9	1.0	1.0
^{2}**TS**$_C$	1.0	1.0	1.0	1.0	0.9	0.9	1.0	1.0

[a] All data are for k_H/k_D and relative to [H_8]toluene.

Figure 5 displays the relative free energies of the ^{4,2}**TS**$_B$, ^{4,2}**TS**$_R$ and ^{2}**TS**$_C$ species for [H_8]toluene and [D_8]-toluene as calculated under various environmental conditions: namely (i) in the gas-phase (ε = 1), (ii) with bulk polarity effects (ε = 5.7), (iii) with two additional hydrogen-bonded ammonia molecules in the gas phase and (iv) with two additional hydrogen-bonded ammonia molecules and with ε = 5.7. The free energies of activation for the hydrogen- and deuterium-substituted systems were taken from the Gaussian frequency calculations at LACVP level of theory with energies corrected to the LACV3P+* level, and with additions of environmental corrections at the LACVP level of theory. Because the kinetic isotope effect for the substitution of hydrogen by deuterium is similar for the HS and LS processes, the relative free energies of ^{4}**TS**$_B$ vs. ^{2}**TS**$_B$ stay virtually the same independent from isotopic substitution. These species are destabilized by 1–2 kcal mol^{-1} upon

 © 2007 Wiley-VCH Verlag GmbH & Co. KGaA, Weinheim

replacement of methyl hydrogen atoms by deuterium atoms. As a result, the free energy gap between ^{4}**TS**$_B$ and ^{2}**TS**$_R$ drops from 5.6 kcal mol^{-1} for [H_8]toluene in the gas phase to 0.4 kcal mol^{-1} for [D_8]toluene with inclusion of hydrogen-bonded interactions and bulk polarity effects. Thus, deuteration of toluene disfavours benzyl hydroxylation because it requires more energy to break a C–D bond than a C–H bond. In addition, as we saw above in Table 1, the hydrogen bonding and polarity effects tend to stabilize the phenyl hydroxylation **TS**s. These two factors combine to reduce considerably the energy difference between the benzyl and phenyl hydroxylation TSs, thus bringing ^{4}**TS**$_B$ and ^{2}**TS**$_R$ to within 0.4 kcal mol^{-1}. Consequently, a deuterated toluene in an environment that mimics the bulk polarity and hydrogen-bonding machinery of the enzyme, is expected to produce significant amount of cresol by-products in agreement with experimental observations.[9] The experimental preference of 5:1 (Scheme 1) would correspond to less than 1 kcal/mol on the free energy scale in favour of phenyl hydroxylation, whereas the calculations predict 0.4 kcal/mol in favour of benzyl hydroxylation. Clearly, within the accuracy of DFT and of the procedures used here, these differences are too small, and the calculations may be considered to predict at least the correct trend, if not an actual regioselectivity reversal.

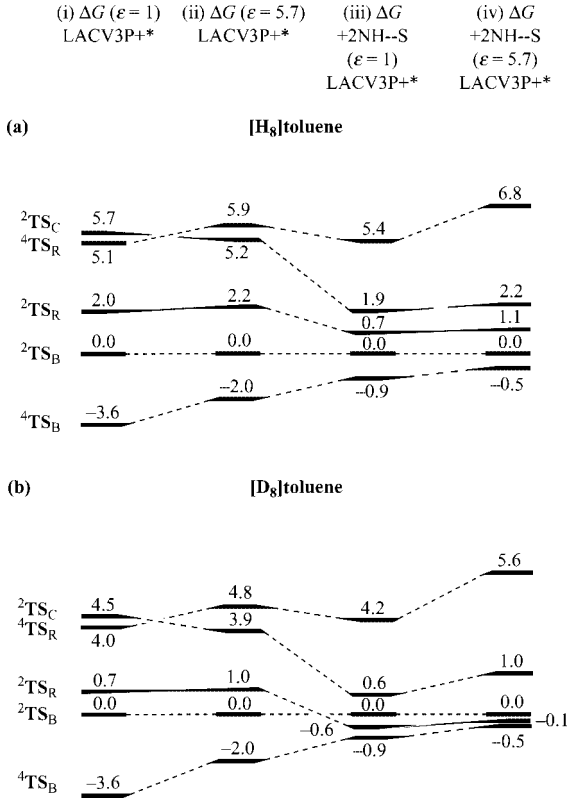

Figure 5. Relative free energies of ^{4,2}**TS**$_B$, ^{4,2}**TS**$_R$ and ^{2}**TS**$_C$ under different environmental conditions for [H_8]toluene (part a) and [D_8]toluene (part b). All energies are in kcal mol^{-1} relative to ^{2}**TS**$_B$.

Needless to say, our model system is not an enzyme. Firstly, it lacks the steric constraints that might operate in the enzyme pocket. Secondly, its does not consider the regioselectivity as a result of the kinetics of a whole catalytic cycle as done recently.[35] Third, it does not consider product release as a regioselectivity factor. Thus, experimental studies[9c] show that product release is partly rate limiting in turnover, i.e. deuterium-induced metabolic switching directs the substrate to ring hydroxylation although it has higher barriers but the product releases faster from the enzyme active site. Thus, while our theoretical study does not include these effects, it nevertheless clearly shows that for the deuterated toluene the two processes become competitive, in line with experiment, thus underscoring the importance of the electronic factors in determining the regioselectivity.

4. Conclusion

The hydroxylation of toluene by a P450 enzyme model has been studied using DFT calculations. Several possible reaction mechanisms leading to various products (benzyl alcohol, *p*-cresol and *p*-methyl-cyclohexanone) were tested. The studies show that the benzylic hydroxylation proceeds via two-state reactivity on competing HS and LS spin state surfaces via radical type intermediates. The phenyl hydroxylation can pass either to a radical or a cationic intermediate, which are close in energy. In the gas-phase the benzyl hydroxylation barriers are significantly lower in energy than the ones leading to cresol by-products, but the barriers become rather similar in an enzyme mimicked environment where the NH···S hydrogen bonding to the thiolate ligand and bulk polarity effects are taken into account. The KIE calculations show that the benzyl hydroxylation has a large isotope effect, while the phenyl hydroxylation exhibits no isotope sensitivity. Thus, the combination of the environmental perturbations and the isotopic substitution lowers the barriers for phenyl hydroxylation considerably, thereby making the process competitive with benzyl hydroxylation. As such, the theoretical results are in good agreement with experimental work on toluene and [D_8]toluene hydroxylation by P450 enzymes.

Other factors, which may affect the regioselectivity are the shape and size of the substrate binding pocket, and the product release in the actual enzyme. However, fuller elucidation of these factors,[35] must await a DFT/MM study of the project on the complete enzyme.

Supporting Information (see also the footnote on the first page of this article): The SI provides absolute and relative energies as well as group spin densities and charges of all optimized structures as calculated with basis sets B1 and B2, but also under different environmental conditions (12 Tables). In addition, the document provides detailed geometry scans that connect the reactants from intermediates and products and optimized geometries of all structures mentioned in the text (14 Figures).

Acknowledgments

The research of S. S. was supported by the German Federal Ministry of Education and Research (BMBF) within the framework of the German-Israeli Project Cooperation (DIP), and the Israeli Sci-

 © 2007 Wiley-VCH Verlag GmbH & Co. KGaA, Weinheim

ence Foundation (ISF). C. H. thanks the Lady Davis Fellowship Trust for support.

[1] a) F. P. Guengerich, *Chem. Res. Toxicol.* **2001**, *14*, 611–650; b) P. R. Ortiz de Montellano (Ed.), *Cytochrome P450: Structure, Mechanism and Biochemistry*, 3rd ed.; Kluwer Academic/Plenum Publishers, New York, **2005**; c) I. G. Denisov, T. M. Makris, S. G. Sligar, I. Schlichting, *Chem. Rev.* **2005**, *105*, 2253–2277; d) J. T. Groves, *J. Inorg. Biochem.* **2006**, *100*, 434–447; e) T. M. Makris, K. von Koenig, I. Schlichting, S. G. Sligar, *J. Inorg. Biochem.* **2006**, *100*, 507–518.

[2] a) T. L. Poulos, B. C. Finzel, A. J. Howard, *Biochemistry* **1986**, *25*, 5314–5322; b) I. Schlichting, J. Berendzen, K. Chu, A. M. Stock, S. A. Maves, D. E. Benson, R. M. Sweet, D. Ringe, G. A. Petsko, S. G. Sligar, *Science* **2000**, *287*, 1615–1622.

[3] a) J. H. Dawson, R. H. Holm, J. R. Trudell, G. Barth, R. E. Linder, E. Bunnenberg, C. Djerassi, S. C. Tang, *J. Am. Chem. Soc.* **1976**, *98*, 3707–3709; b) T. L. Poulos, *J. Biol. Inorg. Chem.* **1996**, *1*, 356–359.

[4] a) A. D. N. Vaz, D. F. McGinnity, M. J. Coon, *Proc. Natl. Acad. Sci. USA* **1998**, *95*, 3555–3560; b) S. Jin, T. M. Makris, T. A. Bryson, S. G. Sligar, J. H. Dawson, *J. Am. Chem. Soc.* **2003**, *125*, 3406–3407.

[5] a) F. Ogliaro, S. P. de Visser, S. Cohen, P. K. Sharma, S. Shaik, *J. Am. Chem. Soc.* **2002**, *124*, 2806–2817; b) P. K. Sharma, S. P. de Visser, S. Shaik, *J. Am. Chem. Soc.* **2003**, *125*, 8698–8699.

[6] a) T. Egawa, H. Shimada, Y. Ishimura, *Biochem. Biophys. Res. Commun.* **1994**, *201*, 1464–1469; b) D. G. Kellner, S. C. Hung, K. E. Weiss, S. G. Sligar, *J. Biol. Chem.* **2002**, *277*, 9641–9644.

[7] J. T. Groves, G. A. McCluskey, *J. Am. Chem. Soc.* **1976**, *98*, 859–861.

[8] For examples on metabolic switching in P450 enzymes, see, for example a) W. M. Atkins, S. G. Sligar, *J. Am. Chem. Soc.* **1987**, *109*, 3754–3760; b) C.-H. Yun, G. P. Miller, F. P. Guengerich, *Biochemistry* **2001**, *40*, 4521–4530; c) C. L. Shaffer, S. Harriman, Y. M. Koen, R. P. Hanzlik, *J. Am. Chem. Soc.* **2002**, *124*, 8268–8274.

[9] a) R. P. Hanzlik, K. Hogberg, C. M. Judson, *Biochemistry* **1984**, *23*, 3048–3055; b) R. P. Hanzlik, K. Hogberg, J. B. Moon, C. M. Judson, *J. Am. Chem. Soc.* **1985**, *107*, 7164–7167; c) R. P. Hanzlik, K. H. J. Ling, *J. Org. Chem.* **1990**, *55*, 3992–3997.

[10] W. Yuan, D. J. Sequeira, G. F. Cowlew, C. S. Eyer, W. L. Backes, *Arch. Biochem. Biophys.* **1997**, *339*, 55–63.

[11] W. Tassaneeyakul, D. J. Birkett, J. W. Edwards, M. E. Veronese, W. Tassaneeyakul, R. H. Tukey, J. O. Miners, *J. Pharmacol. Exp. Ther.* **1996**, *276*, 101–108.

[12] H. Kim, R. S. Wang, E. Elovaara, H. Raunio, O. Pelkonen, T. Aoyome, H. Vainio, T. Nakayima, *Xenobiotica* **1997**, *27*, 657–665.

[13] R. E. White, J. P. Miller, L. V. Favreau, A. Bhattacharyya, *J. Am. Chem. Soc.* **1986**, *108*, 6024–6031.

[14] a) S. P. de Visser, F. Ogliaro, N. Harris, S. Shaik, *J. Am. Chem. Soc.* **2001**, *123*, 3037–3047; b) S. P. de Visser, F. Ogliaro, P. K. Sharma, S. Shaik, *Angew. Chem. Int. Ed.* **2002**, *41*, 1947–1951; c) S. P. de Visser, F. Ogliaro, P. K. Sharma, S. Shaik, *J. Am. Chem. Soc.* **2002**, *124*, 11809–11826; d) D. Kumar, S. P. de Visser, S. Shaik, *Chem. Eur. J.* **2005**, *11*, 2825–2835.

[15] a) F. Ogliaro, N. Harris, S. Cohen, M. Filatov, S. P. de Visser, S. Shaik, *J. Am. Chem. Soc.* **2000**, *122*, 8977–8989; b) T. Kamachi, K. Yoshizawa, *J. Am. Chem. Soc.* **2003**, *125*, 4652–4661; c) D. Kumar, S. P. de Visser, P. K. Sharma, S. Cohen, S. Shaik, *J. Am. Chem. Soc.* **2004**, *126*, 1907–1920; d) S. P. de Visser, D. Kumar, S. Cohen, R. Shacham, S. Shaik, *J. Am. Chem. Soc.* **2004**, *126*, 8362–8363; e) N. Harris, S. Cohen, M. Filatov, F. Ogliaro, S. Shaik, *Angew. Chem. Int. Ed.* **2000**, *39*, 2003–2007.

[16] a) H. Hirao, D. Kumar, L. Que Jr, S. Shaik, *J. Am. Chem. Soc.* **2006**, *128*, 8590–8606; b) S. P. de Visser, *Angew. Chem. Int. Ed.* **2006**, *45*, 1790–1793; c) S. P. de Visser, *J. Am. Chem. Soc.* **2006**, *128*, 9813–9824; d) S. P. de Visser, *J. Am. Chem. Soc.* **2006**, *128*, 15809–15818.

[17] a) S. P. de Visser, S. Shaik, *J. Am. Chem. Soc.* **2003**, *125*, 7413–7424; b) S. P. de Visser, *Chem. Eur. J.* **2006**, *12*, 8168–8177.

[18] a) C. M. Bathelt, L. Ridder, A. J. Mulholland, J. N. Harvey, *J. Am. Chem. Soc.* **2003**, *125*, 15004–15005; b) C. M. Bathelt, L. Ridder, A. J. Mulholland, J. N. Harvey, *Org. Biomol. Chem.* **2004**, *2*, 2998–3005.

[19] P. J. Loida, S. G. Sligar, *Biochemistry* **1993**, *32*, 11530–11538.

[20] L. Flitsch, S. J. Aitken, C. S. Y. Chow, G. Grogan, A. Staines, *Bioorg. Chem.* **1999**, *27*, 81–90.

[21] K. R. Iyer, J. P. Jones, J. F. Darvyshire, W. F. Trager, *Biochemistry* **1997**, *36*, 7136–7147.

[22] L. Higgins, G. A. Bennett, M. Shimoji, J. P. Jones, *Biochemistry* **1998**, *37*, 7039–7046.

[23] K. R. Korzekwa, J. P. Jones, J. R. Gillette, *J. Am. Chem. Soc.* **1990**, *112*, 7042–7046.

[24] S. Shaik, D. Kumar, S. P. de Visser, A. Altun, W. Thiel, *Chem. Rev.* **2005**, *105*, 2279–2328.

[25] a) A. D. Becke, *J. Chem. Phys.* **1992**, *96*, 2155–2160; b) A. D. Becke, *J. Chem. Phys.* **1992**, *97*, 9173–9177; c) A. D. Becke, *J. Chem. Phys.* **1993**, *98*, 5648–5652; d) C. Lee, W. Yang, R. G. Parr, *Phys. Rev. B* **1988**, *37*, 785–789.

[26] a) P. J. Hay, W. R. Wadt, *J. Chem. Phys.* **1985**, *82*, 299–310; b) R. A. Friesner, R. B. Murphy, M. D. Beachy, M. N. Ringlanda, W. T. Pollard, B. D. Dunietz, Y. X. Cao, *J. Phys. Chem. A* **1999**, *103*, 1913–1928.

[27] P. K. Sharma, S. P. de Visser, S. Shaik, *J. Am. Chem. Soc.* **2003**, *125*, 8698–8699.

[28] *Jaguar 4.5*; Schrödinger, Inc.: Portland, Oregon, **2000**.

[29] M. J. Frisch, G. W. Trucks, H. B. Schlegel, G. E. Scuseria, M. A. Robb, J. R. Cheeseman, V. G. Zakrzewski, J. A. Montgomery Jr, R. E. Stratmann, J. C. Burant, S. Dapprich, J. M. Millam, A. D. Daniels, K. N. Kudin, M. C. Strain, O. Farkas, J. Tomasi, V. Barone, M. Cossi, R. Cammi, B. Mennucci, C. Pomelli, C. Adamo, S. Clifford, J. Ochterski, G. A. Petersson, P. Y. Ayala, Q. Cui, K. Morokuma, D. K. Malick, A. D. Rabuck, K. Raghavachari, J. B. Foresman, J. Cioslowski, J. V. Ortiz, A. G. Baboul, B. B. Stefanov, G. Liu, A. Liashenko, P. Piskorz, I. Komaromi, R. Gomperts, R. L. Martin, D. J. Fox, T. Keith, M. A. Al-Laham, C. Y. Peng, A. Nanayakkara, C. Gonzalez, M. Challacombe, P. M. W. Gill, B. Johnson, W. Chen, M. W. Wong, J. L. Andres, C. Gonzalez, M. Head-Gordon, E. S. Replogle, J. A. Pople, *Gaussian 98*, Revision A.7, Gaussian Inc., Pittsburgh, PA, **1998**.

[30] a) F. Ogliaro, S. P. de Visser, S. Cohen, J. Kaneti, S. Shaik, *ChemBioChem* **2001**, *2*, 848–851; b) F. Ogliaro, S. P. de Visser, J. T. Groves, S. Shaik, *Angew. Chem. Int. Ed.* **2001**, *40*, 2874–2878.

[31] F. Ogliaro, S. Cohen, S. P. de Visser, S. Shaik, *J. Am. Chem. Soc.* **2000**, *122*, 12892–12893.

[32] S. P. de Visser, K. Oh, A.-R. Han, W. Nam, *Inorg. Chem.* **2007**, in press.

[33] a) S. Shaik, M. Filatov, D. Schröder, H. Schwarz, *Chem. Eur. J.* **1988**, *4*, 193–199; b) S. Shaik, S. P. de Visser, F. Ogliaro, H. Schwarz, D. Schröder, *Curr. Opin. Chem. Biol.* **2002**, *6*, 556–567.

[34] a) J. C. Schöneboom, H. Lin, N. Reuter, W. Thiel, S. Cohen, F. Ogliaro, S. Shaik, *J. Am. Chem. Soc.* **2002**, *124*, 8142–8151; b) C. M. Bathelt, J. Zurek, A. J. Mulholland, J. N. Harvey, *J. Am. Chem. Soc.* **2005**, *127*, 12900–12908.

[35] S. Cohen, S. Kozuch, C. Hazan, S. Shaik, *J. Am. Chem. Soc.* **2006**, *128*, 11028–11029.

Received: January 29, 2007
Published Online: May 22, 2007

 © 2007 Wiley-VCH Verlag GmbH & Co. KGaA, Weinheim

Reactivity patterns of cytochrome P450 enzymes: multifunctionality of the active species, and the two states–two oxidants conundrum†

Sason Shaik,* Hajime Hirao and Devesh Kumar

Received (in Cambridge, UK) 16th March 2007
First published as an Advance Article on the web 23rd April 2007
DOI: 10.1039/b604192m

Covering: up to 2006 but not exhaustively

This focused review discusses mechanisms of oxygenation of organic compounds by cytochrome P450, based on density functional theory (DFT) and hybrid DFT and molecular mechanics (DFT/MM). The reactivity of the active species, Compound I, generally involves two-state reactivity (TSR) and sometimes multi-state reactivity (MSR). The reactivity of the ferric-hydroperoxide species (Compound 0) is reviewed too. According to DFT calculations, Compound 0 must be silent in the presence of Compound I. Much of the experimental mechanistic data is shown to be accounted for by the TSR/MSR concept.

1 Introduction
2 The catalytic cycle of the enzyme
3 Unresolved issues in the chemistry of P450 enzymes
3.1 How many reactive oxidant species does the P450 have?
3.2 Unresolved issues in the mechanism of hydroxylation and epoxidation
4 Properties of Cpd I of P450
4.1 Electronic structure and geometries of low-lying states of Cpd I
4.2 Origins of two- and multi-state reactivity
5 Reactivity of Cpd I towards alkanes and olefins
5.1 The mechanism of C–H hydroxylation
5.2 The mechanism of double bond epoxidation
5.3 The mechanism of desaturation
6 Gauging the reactivity of Cpd 0
6.1 A computational assessment of the electrophilic reactivity of Cpd 0
6.2 A computational assessment of the reactivity of Cpd 0 *via* initial O–O homolysis
6.3 An assessment of the reactivity of the two oxidant of P450
7 Conclusions
8 Acknowledgements
9 References

1 Introduction

Cytochromes P450 (P450s) are heme enzymes that are present in all aerobic species and carry out vital oxidative processes, namely, detoxification of foreign compounds and biosynthesis of hormones and other essential molecules.[1-22] As such, P450s are extremely versatile enzymes which perform a great variety of stereoselective transformations that are otherwise difficult to achieve, *e.g.*, hydroxylation of strong C–H bonds, epoxidation of C=C bonds, heteroatom oxidation (sulfoxidation), and desaturation reactions. With all these features, it is no wonder that P450s have become the focus of intense research that has led to important insights and generated lively debates that may sometimes remind one of the intellectually-laden heyday of physical organic chemistry.

Many of the experimental, mechanistic and structural aspects have been covered in two monographs,[1,2] and in a variety of other reviews.[3-22] Three recent articles in *Chemical Reviews*,[16,17,20] one micro-review in *European Journal of Inorganic Chemistry*,[18] a chapter in the *P450 Monograph*[19] and three shorter reviews,[15,21,22] provide exhaustive coverage of density functional theoretical (DFT) studies and hybrid DFT/molecular mechanical (MM) investigations of the structure and reactivity of $P450_{cam}$. Therefore, the present manuscript is an updated focused summary of the insights obtained from theory regarding controversial electronic structure and mechanistic aspects associated with the active species of the enzyme.

2 The catalytic cycle of the enzyme

The consensus catalytic cycle of the enzyme, based on experimental spectroscopic and structural data, is illustrated in Fig. 1.[5,9,23,24] All of the species have also been computed by DFT and DFT/MM methods, as outlined in extensive reviews of the topic.[16,19] The cycle begins with the resting state (**1**), in which a heme is bound to a water molecule on the distal side and to the thiolate side chain of a cysteine residue (abbreviated as CysS) on the proximal side. The entrance of the substrate (*e.g.*, an alkane, AlkH) displaces the water molecule, causes a change of the spin state, and triggers the transfer of an electron from a reductase protein. The resulting ferrous complex (**3**) binds molecular oxygen, which gets activated by an additional electron transfer from the reductase followed by protonation from a suitable proton-relay system on the distal side of the protein, thereby generating the ferric-hydroperoxide species (**6**), also called Compound 0 (Cpd 0). The resulting Cpd 0

Department of Organic Chemistry and The Lise Meitner-Minerva Center for Computational Quantum Chemistry, The Hebrew University of Jerusalem, Givat Ram, 91904 Jerusalem, Israel. E-mail: sason@yfaat.ch.huji.ac.il; Fax: +972-2-6584680; Tel: +972-2-6585909

† This paper was published as a part of a special issue on the chemistry and biochemistry of heme proteins.

Sason Shaik was born in 1948 in Iraq. His family immigrated to Israel in the Exodus of the Iraqi Jewry. He received his BSc and MSc in chemistry from Bar-Ilan University, and his PhD from the University of Washington under Nicholaos D. Epiotis. In 1978/9 he spent a postdoctoral year with Roald Hoffmann at Cornell University. In 1980 he started his first academic position as a Lecturer at Ben-Gurion University where he became Professor in 1988. He subsequently moved in 1992 to the Hebrew University, where he is currently the director of The Lise Meitner-Minerva Center for Computational Quantum Chemistry. Among the awards he received are the Lise-Meitner-Alexander von Humboldt Senior Award in 1996–1999, the 2001 Israel Chemical Society Prize, the 2001 Kolthoff Award and he is the recipient of the Schrödinger Medal of WATOC for 2007. He is an AAAS Fellow. His research interests are in the use of quantum chemistry, and in particular of molecular orbital and valence bond theories, to develop paradigms which can pattern data and lead to the generation and solution of new problems. In 1994, he entered the field of oxidation and bond activation by metal oxo catalysts and enzymes. The P450 research started in 1998, and has been fascinating ever since!

Hajime Hirao was born in Hyogo, Japan in 1975. He received his BSc (1998) and MSc (2000) degrees in chemistry from Kyoto University. In 2004, he obtained his PhD from The University of Tokyo with Professor T. Ohwada. After three years of work on computer-assisted molecular modeling (CAMM) at the Novartis Tsukuba Research Institute, he moved in 2005 to The Hebrew University of Jerusalem, where he has since worked with Professor S. Shaik as a postdoctoral fellow, and as a JSPS fellow since April 2007. His research interests include application of computer chemistry to reactions and interactions of chemical and biochemical molecules, as well as development of new methods for analyzing chemical reactivity based on molecular orbital and valence bond theories.

Devesh Kumar was born in India in 1965. He received his BSc from the L. N. Mithla University and his MSc and PhD in Physics from the D. D. U. Gorakhpur University, India. He worked at the Centre for Liquid Crystal Research and Education, Nagarjuna University, India as a research associate (July 2001–March 2002) before joining the group of Professor Sason Shaik at the Hebrew University of Jerusalem as a postdoc in May 2002. He is currently pursuing postdoctoral research in the laboratory of Professor Walter Thiel in the Max Planck Institute in Mülheim. His main research interests are theoretical studies of conformations and interactions of mesogens and enzyme catalysis.

Sason Shaik

Hajime Hirao

Devesh Kumar

accepts an additional proton and splits off a water molecule to form **7**, the so-called Compound I (Cpd I) species. Cpd I possesses a high-valent ferryl moiety, Fe^{IV}=O, and a radical cationic state in the porphyrin, *i.e.*, Por$^{\bullet+}Fe^{IV}$=O. Cpd I is known from studies of synthetic models and from the related chloroperoxidase (CPO) enzyme, to be a competent oxidant[3,5,25,26] and as such, it is thought that P450 Cpd I is the ultimate oxidant species that transfers an oxygen atom to the substrate leading to the product (*e.g.*, ferric-alcohol) complex, **8**. The cycle is restored by release of the oxidized substrate (*e.g.*, the alcohol, Alk-OH) and the binding of a water molecule to the heme to regenerate the resting state.

As already mentioned, all of the species in the cycle have been computed,[16,19,20,21] and there is a general agreement between experiment and theory on most aspects of the cycle. Two features have, however, remained controversial to this day. Firstly, Cpd I of P450 is still not fully characterized by experiment, and secondly, the reactivity patterns of P450 suggest that in addition to Cpd I, the enzyme utilizes "other species" in the cycle to oxidize organic molecules.[6] This is an intellectually challenging problem for theory. And it is this challenge that has been the main trigger for generating new mechanistic ideas, such as two-state reactivity (TSR) and multi-state reactivity (MSR), which may shed light on these unresolved issues.[15,18] Let us first follow with a more detailed description of the major problems.

3 Unresolved issues in the chemistry of P450 enzymes

3.1 How many reactive oxidant species does the P450 have?

Cpd I appears to be the consensus primary oxidant, but as it has *never* been directly characterized, under native turnover conditions, the fuzziness in its status has left room for speculations on the nature of the active species of the enzyme. A recent tentative characterization of Cpd I under conditions of cryogenic X-ray crystallography,[24] has since been cast in doubt.[23] Even the consensus technique of generating Cpd I species using the oxygen surrogate iodosylbenzene has been questioned recently.[27] Attempts to generate Cpd I using other oxygen surrogates such as peracids

This journal is © The Royal Society of Chemistry 2007

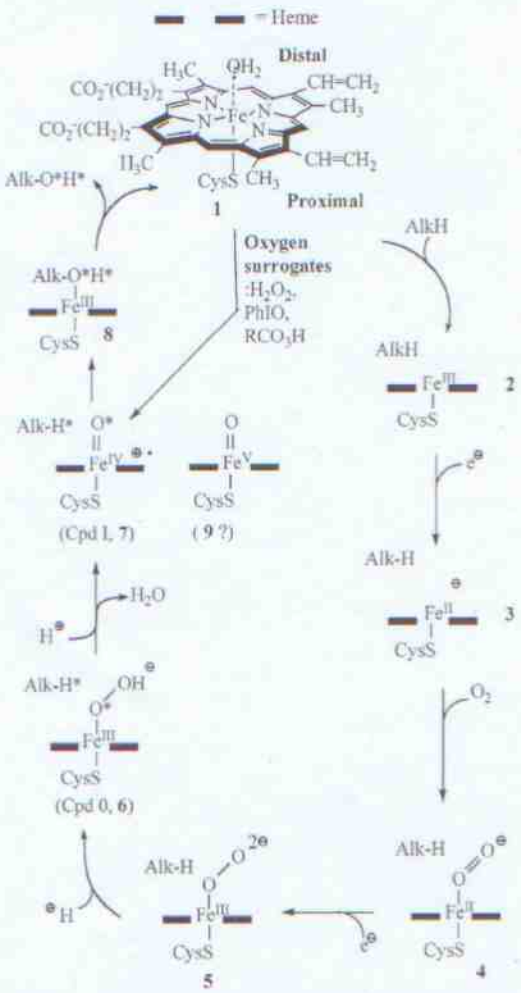

Fig. 1 Schematic representation of the catalytic cycle of P450 (adapted from Fig. 2.2 in ref. 19, with permission from Springer Science and Business Media).

(see Fig. 1) led to the one-electron reduced species, $PorFe^{IV}=O$, so-called Compound II (Cpd II), and a Tyr radical.[28] While this repeated generation of Cpd II has usually been taken as an alarming sign that Cpd I may not exist, more recent experiments[29] showed how one could optimize the formation of Cpd I before it converts to Cpd II or before the heme bleaches due to destruction by the peracid; these findings may make it possible to observe some of the characteristic chemistry of Cpd I. Strong but indirect support for the participation of Cpd I has been provided by determining the reactivity of synthetic Cpd I species and P450 towards the same substrates, where both sets of reactions led to similar product distributions and stereochemical scrambling information.[5] Similarly, a recent mechanistic study[30] used the *N*-oxo derivative of a series of substituted *N*,*N*-dimethylanilines to generate the Cpd I species of $P450_{cam}$ and P4502E1 *in situ*, and to measure the resulting kinetic isotope effect (*KIE*) due to the subsequent reactions of these Cpd I species with the *N*,*N*-dimethylaniline substrates. The obtained *KIE* values were virtually the same as those measured for the reaction of the P450 enzymes when the same series of *N*,*N*-dimethylanilines were oxygenated *via* the normal route of catalysis (reduction, addition of O_2, and protonation, see Fig. 1). This result provided compelling evidence for the reactivity of P450 Cpd I in the C–H hydroxylation of *N*,*N*-dimethylanilines. Similarly, the action of Cpd I was also inferred for camphor hydroxylation, where the product alcohol was found to be formed with its oxygen atom coordinated to the iron center and with the substrate-derived proton attached to the product alcohol,[23] as shown by the asterisks on the Alk-OH moiety, **8**, in Fig. 1.

While Cpd I has never been observed in a native turnover system, its existence was detected by the use of exogenous oxygen surrogates in $P450_{cam}$ (CYP101)[29] and in the thermostable isozyme, CYP119,[31] from *Sulfolobus solfataricus*. Ballou *et al.*,[29] using transient electronic spectroscopy and decay kinetics methods, also confirmed the high reactivity of Cpd I and Cpd II/tyrosyl radical species (Cpd ES), with several reductants. Further support for this assignment of the active species came from theoretical calculations,[32] which reproduced the split Soret band that was blue shifted relative to the resting state. There are also close analogies between P450 Cpd I and the Cpd I species of the enzyme chloroperoxidase (CPO) in spectroscopic features,[25] and in the patterns of reactivity towards a variety of organic molecules.[26] Recent EXAFS[33] and ENDOR[34] studies further refined the structural and electronic features of CPO Cpd I, and affirmed close correspondence between the experimental data for CPO Cpd I and the DFT/MM calculated values[35,36] for CYP101 Cpd I. Thus, despite the lingering uncertainty, the inferences that Cpd I exists and is responsible for the native oxidation processes of the enzyme in the cycle are quite strong. Accordingly, in the following sections we shall review the computed reactivity patterns of Cpd I.

The evidence for a second oxidant species in the cycle of P450 is indirect; it derives from reactivity studies, lifetime measurements of putative intermediates, and product distributions of P450s and their mutants. Thus, mutant enzymes, in which the proton relay that converts Cpd 0 to Cpd I is disrupted by site-directed mutagenesis,[6,37] exhibit reactivity patterns different from those of the wild type (WT) enzyme. For example, with *cis* and *trans* 2-butene, the mutant enzyme yields more epoxidation products compared with C–H hydroxylation products.[37] Similarly, the T252A mutant of CYP101,[38] in which Thr252, which plays a key role in the conversion of Cpd 0 to Cpd I, is replaced by Ala, does not hydroxylate camphor, but is capable of epoxidation of the double bond of camphene, albeit more sluggishly than the WT enzyme. Since during catalysis, the T252A mutant is thought to be trapped at Cpd 0, this and the reactivity of the mutant toward camphene derivatives constituted evidence that Cpd 0 is involved in the epoxidation of an activated double bond. Curiously, however, the double mutant of $P450_{cam}$, T252A/D251N, in which the protonation machinery has been disrupted by mutations of both Thr252 and Asp251, is able to hydroxylate camphor,[39] despite the T252A mutation that should have hypothetically blocked the formation of Cpd I. This implies either that Cpd 0 has a variable reactivity in different mutants (that include the T-to-A mutation) or that variable quantities of Cpd I may be present even in the case of the different T → A mutant. Thus, while the participation of Cpd 0 in oxidation is still a clouded issue, the data behave as though more than one oxidant is available to P450. This pattern confronts both theory and experiment with a tantalizing mechanistic enigma. We shall review here some of the DFT calculations associated with the reactivity of Cpd 0 towards substrates.

Another species that has been invoked as the reactive oxidant of P450 is the perferryl, **9** (Fig. 1), in which the porphyrin has a closed-shell and iron is in oxidation state +5, hence, $PorFe^{V}=O$. This species, that was postulated by Murakami *et al.* some time ago in reactions of some model systems,[40] has recently been hypothetically invoked as the species responsible for the high reactivity of the enzyme itself.[41] There is however no concrete evidence for the actual presence of $PorFe^{V}=O$ in P450, other than the following conjectures. Thus, based on a new technique, Cpd II has been reported to photo-oxidatively convert to Cpd I, and the decay of the latter species can be observed in the presence of substrates.[42] It was thus observed that the so-generated Cpd I species of model iron-porphyrin systems are orders of magnitude less reactive[43] than with the corresponding $PorMn^{V}=O$ species.[44] When the technique was applied to CYP119,[41] the so-generated species, thought to be Cpd I, was rather inactive in the presence of laurate, a native substrate of the enzyme. Since CYP101 hydroxylates camphor with a rate constant exceeding 1000 s^{-1} at ambient temperature,[41] it was conjectured that the reactive species in CYP119 and CYP101 must be the $PorFe^{V}=O$ species **9** (Fig. 1). In contrast to this result, the use of *meta*-chloroperbenzoic acid to generate Cpd I for CYP119 led to the formation of Cpd I, which reacted with laurate to give hydroxylaurate within the dead-time of the experiment.[31] Apparently, the two experiments are at odds with each other, and one may wonder if the photo-oxidative experiment indeed gave rise to Cpd I. Furthermore, close inspection of the spectrum of the photo-oxidatively produced species in CYP119, shows it to be more compatible with Cpd ES, which is Cpd II and a protein radical that was reported for CYP101.[29,45] Cpd II is known to be less reactive than Cpd I in hydroxylation and epoxidation reactions from both experimental[46,47] and computational results.[48]

A process of reasoning that is often used in mechanistic research is based on the comparison of reactivities in model bimolecular reactions to those of P450. This however requires some careful scrutiny as we shall now argue. Thus, with a rate constant $k \geq 200$–1000 s^{-1} (at ambient temperatures) for the reaction of CYP101 with camphor,[41,49] the free energy barrier at room temperature is *ca.* 13.4–14.3 kcal mol^{-1}. If we take even a very high rate of 10^{6} s^{-1} the barrier would be *ca.* 9.3 kcal mol^{-1}. By comparison, for the bimolecular reactions of the model systems,[43] the free energy barriers are 14.1–17.5 kcal mol^{-1} (rate constants of 1–300 M^{-1} s^{-1}). Thus, with this comparison of the barriers, one may be led to deduce that the reactive species of the enzyme is not Cpd I, since the model Cpd I species have higher barriers than the enzymatic species. However, this deduction neglects to consider the different entropic factors for bimolecular and enzymatic reactions. In bimolecular reactions, the transition state is established with a loss of rotational and translational degrees of freedom compared with the reactants. The loss of these degrees of freedom in the TS raises the free energy barrier by *ca.* 6–12 kcal mol^{-1} (ref. 50 assumes a loss of 40 eu,[50] which translates to 12 kcal mol^{-1}, but the actual number depends on the strength of the interaction). By contrast, in the enzyme, this loss of degrees of freedom is compensated by a gain of degrees of freedom when molecules of water leave the pocket as the substrate goes in and binds *e.g.*, as camphor does in CYP101 due to hydrogen bonding with Tyr96 and hydrophobic interactions with Val295.[16,19] The enzymatic reaction then starts from a "complex" that has lost already the rotational and translational degrees of freedom, and hence the free-energy barrier for the reaction from this complex should be lower than the bimolecular models by 6–12 kcal mol^{-1}. This effect by itself accounts for a large part, if not all, of the observed differences between the bimolecular and the P450 enzymatic process. As such, it is not really necessary to invoke $PorFe^{V}=O$ as the species that is responsible for the high reactivity of P450s; this can be reasonably extrapolated from the reactivity of model Cpd I systems.

The energetics of the $PorFe^{V}=O$ species were computed recently by DFT,[51] and all of its possible electromeric states were found to be higher in energy, by 17–26 kcal mol^{-1}, than the normal Cpd I species. It is therefore doubtful that this species can be generated in the enzyme under turnover conditions, considering the fact that the barrier to the formation of Cpd I in CYP101 was calculated recently to be 12–15 kcal mol^{-1},[52] and in CYP119 the experimentally determined barrier was 14.1 kcal mol^{-1}.[31] Thus, the combined energy increase needed to reach the $PorFe^{V}=O$ species in CYP119 could well be 31–40 kcal mol^{-1}. Indeed, DFT/MM calculations in our group designed to find transition states that are associated with $Fe^{V}=O$ show that these species lie much higher than the lowest transition states.[8] Therefore, it is not very likely that $PorFe^{V}=O$ is the species that accounts for the reactivity of P450s, unless there is some yet unknown basis for that, *e.g.*, crossing of the potential energy profile for generating the species on the excited state surface (starting from $PorFe^{V}=O$) below the transition state separating Cpd 0 and Cpd I.

We are well aware of the fact that Fe^{V} species are acessible in nonheme systems, *e.g.*, among the Que reagents,[53,54] the recent Wieghardt complexes,[55] and the oxo-iron of polyoxometalate.[56] However, the Fe^{V} species exist in these cases because they all lack the easily oxidizable porphyrin. Furthermore, DFT calculations show[51,57] that the Cpd I analog with ruthenium replacing iron, has a $PorRu^{V}=O$ ground state. Here the reason is more subtle; as discussed in the original literature,[51,57] it is associated with the orbital energy levels and exchange interactions that facilitate the transfer of an electron to the porphyrin cation radical to create $PorRu^{V}=O$ much more easily than with $PorFe^{V}=O$. To avoid further speculation, the $PorFe^{V}=O$ species will not be considered in this review.

3.2 Unresolved issues in the mechanism of hydroxylation and epoxidation

The above uncertainties in the identity of the oxidant, led to controversies regarding the mechanism of C–H hydroxylation by P450.[5,6,11,37] The consensus mechanism of C–H hydroxylation by Cpd I is the "rebound" mechanism proposed by Groves and McClusky[58] and depicted in Fig. 2a. The first step in the mechanism involves an initial hydrogen abstraction from the alkane by Cpd I. Subsequently the alkyl radical ($Alk^{\bullet}$) is partitioned between two competing processes. It can either instantly undergo rebound to form an alcohol complex, where the alcohol is unrearranged (***U***), keeping the original stereochemical information possessed by the alkane, or it can first undergo skeletal rearrangement and then rebound to give a rearranged (***R***) alcohol product. The rebound mechanism accounts for the key experimental data: the partial loss of stereochemistry and geometrical rearrangement data, as well as the observed large kinetic isotope effect (*KIE*)[3,5,10,31] when the activated C–H bond is replaced by C–D.

This journal is © The Royal Society of Chemistry 2007

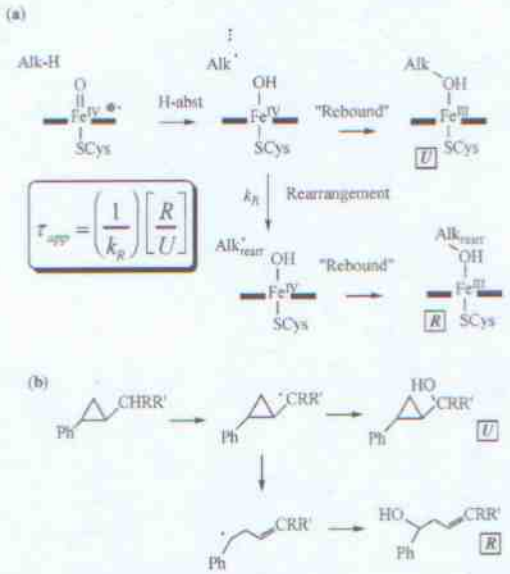

Fig. 2 (a) The rebound mechanism[58] and the apparent lifetime (τ_{app}) of the radical. (b) *U* and *R* products of ultrafast clock substrates.

Based on Fig. 2a, the apparent radical lifetime (τ_{app}) is approximately given by the ratio of rearranged (*R*) product yield to unrearranged (*U*) product yield, divided by the rate constant for rearrangement of the free radical clock (k_R). Using this approach, an initial study of the lifetime of the radical intermediate[59] indicated a short but finite lifetime, of the order of 50 ps. Other data gave a range of lifetimes from nanoseconds to picoseconds.[5,60] However, studies[6] using ultrafast radical clocks such as the ones depicted in Fig. 2b, questioned the presence of the radical intermediate and the validity of the rebound mechanism. Determination of [*R*/*U*] for these probe substrates led to the conclusion *that if one assumes that there is a radical during P450 oxidation*, then the lifetime of this species would be the order of 100 fs or less, which is too short to support the existence of a real intermediate species. Such unrealistically short lifetimes question the validity of the rebound mechanism. Furthermore, in mutant P450s, in which Cpd I was presumably absent, the ratio [*R*/*U*] was generally larger in comparison to the WT enzyme.[6] This in turn suggested that the rearranged products arose from non-radical intermediates that were generated due to the presence of another oxidant species that became prominent in the mutants. Probe substrates, which can distinguish between radical and carbocationic rearrangement patterns, were used to support this hypothesis;[6] the corresponding results suggested that the major reaction intermediate is in fact a carbocation and not a radical. Therefore, Newcomb *et al.*[6,61] proposed that C–H hydroxylation proceeds *via* multiple and competing oxidant species (Scheme 1); Cpd I that leads to concerted oxygen insertion into the C–H bond, and Cpd 0 or ferric hydrogen peroxide that transfers an OH^+ species and generates a protonated alcohol that subsequently undergoes rearrangements typical of a carbocationic species. In the mutant enzymes (*e.g.*, T252A CYP101) the amount of Cpd 0 presumably grew at the expense of Cpd I and therefore led to more carbocationic rearrangment, as well as to more of the marker products of, *e.g.*, double bond epoxidation[57] and phenyl hydroxylation.[6] Interestingly, similar Cpd 0 species in heme

The multiple-oxidant hypothesis:

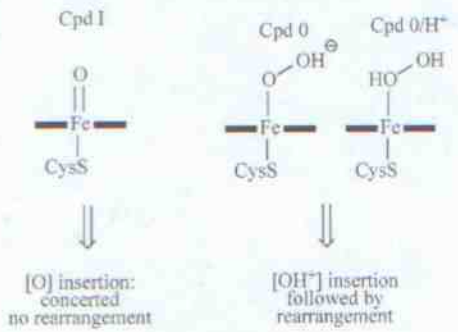

Scheme 1 Postulated multiple oxidants in P450.

oxygenase (HO) and in mutants of *e.g.*, myoglobin (Mb) are known to insert a hydroxyl group into the *meso* position of the heme.[62,63] The key question in our eyes is not whether Cpd 0 can ever effect C–H hydroxylation and epoxidation, but rather *does it ever act in competition with Cpd I during these oxidation processes*? Theory can provide some answers to this question.

In summary: the evidence on P450 reactivity has so far been indirect; the primary oxidant species is still not fully characterized, its identity is cast into doubt, and the reactivity patterns behave as though more than one oxidant is responsible for the product distribution. The identity of this second oxidant is however still shrouded. This is an intellectually intriguing scenario that calls for the involvement of theory. Theoretical analyses since 1998[64] offered a possible reconciliation of the controversy based on the two-state reactivity (TSR) paradigm. Subsequently, the Jerusalem group used DFT to study the mechanism of C–H hydroxylation reactions between Cpd I and a variety of alkanes, by now more than 10.[16,65] In collaboration with the Mülheim group, the two groups explored the mechanism of camphor hydroxylation by Cpd I of $P450_{cam}$ using hybrid quantum mechanical (QM)/molecular mechanical (MM) calculations.[66] The reactivity of Cpd 0 was explored in C–H hydroxylation,[67,68] double-bond epoxidation,[48,69,70] and sulfoxidation reactions, without and with acid catalysis.[71] The possibility of C–H hydroxylation by the ferric hydrogen peroxide complex, $PorFe^{III}(H_2O_2)$, was also studied.[67] These extensive computational studies[16] have revealed that: (a) Cpd 0 is much less reactive than Cpd I, and cannot be invoked as an oxidant in the presence of Cpd I, unless the barriers to oxidation by Cpd 0 are smaller than the one to the conversion of Cpd 0 to Cpd I,[52] (b) ferric-hydrogen peroxide is less reactive than Cpd I, (c) the reactivity of Cpd I involves at least two productive states, and can be described as TSR, or more accurately as multi-state reactivity (MSR), and (d) TSR and MSR reconcile the major mechanistic questions raised above. These features are briefly reviewed herein in an updated form.

4 Properties of Cpd I of P450

4.1 Electronic structure and geometries of low-lying states of Cpd I

Before discussing the electronic structure of Cpd I, it is important to assess the quality of the calculations of Cpd I against some

experimental data. Fig. 3 compares the DFT(B3LYP)/MM geometries and spin densities (ρ) calculated for CYP101 Cpd I[16,18,19,35,36,74] alongside those obtained experimentally for the characterized species of CPO.[33,34] The computational studies[35,36] employed different models of the thiolate ligand, starting from the simple representation ($L = HS^-$) through $L = CH_3S^-$ and all the way to the more extended cysteinate representation ($L = CysS^-$). Since all the models gave similar DFT(B3LYP)/MM results,[35] for the sake of economy we present only the simplest model in the figure. It is seen (Fig. 3a) that the calculated bond lengths[35] for the two lowest spin states of CYP101 Cpd I are in reasonable accord with experimental EXAFS values for Cpd I of CPO.[33] Similarly, the spin density distribution (for the quartet state) on sulfur and porphyrin, Fig. 3b, matches the results obtained from recent EPR/ENDOR experiments.[34] Quite a few other spectroscopic features were shown to match the experimental data, and the correspondence between DFT(B3LYP)/MM and high-level configuration interaction calculations was noted.[36] Additional DFT(B3LYP)/MM calculations for Cpd I of human P450s[72,73] further reinforce this match between theory and experiment.

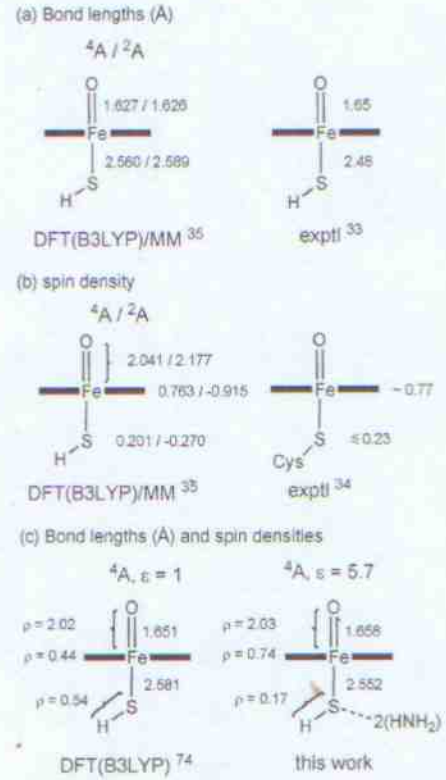

Fig. 3 DFT(B3LYP/B3)/MM computed properties of CYP101 Cpd I (for snapshot 29 fs) *vs.* experimental data for CPO Cpd I; B3 is LACVP(Fe)/6–31 + G* on the immediate coordination sphere/6–31G on all other atoms: bond lengths in (a) and spin densities (ρ) in (b); computed values correspond to quartet/doublet. (c) DFT(B3LYP/LACVP) data of model systems; on the left is the gas phase species ($\varepsilon = 1$) and on the right is the species with two NH–S interactions and bulk polarity ($\varepsilon = 5.7$).

As was argued originally by the Jerusalem group,[74] Cpd I is a "*chameleon species*"; its geometric and electronic features are shaped by the polarity in the protein pocket and hydrogen bonding (H-bonding) of the protein residues to the thiolate ligand. Simple DFT calculations with two NH–S H-bonds and bulk polarity corresponding to a dielectric constant (ε) of 5.7 could in fact reproduce both the DFT/MM and EPR/ENDOR results, as shown in Fig. 3c; it is apparent that the two H-bonds and bulk polarity effects (evaluated by single point calculations on the optimized Cpd I·($2NH_3$) structures), incorporated into the model, cause a shortening of the Fe–S bond and a shift of spin density from the thiolate to the porphyrin. These external perturbations gauge the donor ability of the thiolate ligand *vis-à-vis* the porphyrin cation-radical center, and thereby control the spin density on the sulfur/porphyrin and the Fe–S bond lengths (see an orbital-based explanation below).

The data in Fig. 3 show that Cpd I is a tri-radicaloid species with three unpaired electrons, this and other features as well can be understood by a simple orbital picture. Fig. 4 shows the six higher-lying orbitals of P450 Cpd I. Five orbitals (left hand) constitute the d-block; four of these orbitals contain antibonding interactions between iron atomic d orbitals and the appropriate orbitals of the ligands, while the fifth orbital, δ, is a pure d orbital on iron. The sixth orbital, labelled as a_{2u}, is a porphyrin-based orbital that also involves an antibonding interaction between the atomic lobes on the nitrogen atoms of the porphyrin and the hybrid orbital on thiolate. The effects of polarity and H-bonding are expressed through the nature of the latter orbital, as shall be immediately analyzed.[16,35,74,75]

Based on DFT[74,75] and DFT/MM calculations (for CYP101 and human P450s)[16,35,36,72,73] using the B3LYP functional and a variety of basis sets, the ground state of Cpd I is a pair of doublet and quartet spin-states, which are labeled in Fig. 4 as $^{4,2}\Psi_g$ and which possess three unpaired electrons in the π^* and a_{2u} orbitals that are coupled ferromagnetically (to generate a quartet spin) or antiferromagnetically (to generate a doublet spin); the superscript to the left of the state symbol signifies the spin multiplicity, $2S + 1$. Since the π^* and a_{2u} orbitals are disjointed, the coupling is weak and the quartet and doublet states are virtually degenerate, the doublet lies *ca.* 10–21 cm^{-1} below the quartet.[35,36]

The effects of polarity and H-bonding capability of the protein are expressed through the nature of the singly occupied a_{2u} orbital, as shown in Scheme 2, where we construct the orbital of Cpd I from the fragment orbitals of oxo-iron porphyrin and the thiolate fragments. In the gas phase, the $CysS^-$ center is a good electron donor; its hybrid orbital h_z(g) lies closer to the porphyrin's a_{2u}(Por) orbital, and therefore the orbitals of the two fragments mix strongly. Consequently, the $CysS^-$ center releases more electron density towards the porphyrin cation radical, and hence, the sulfur becomes more radical-like, it acquires a higher spin density, and the Fe–S bond gets longer and weaker.[16,51,74] Changing the environment from the gas phase to the protein pocket, the H-bonding and polarity effects in the protein pocket reduce the donation power of the thiolate ligand and its hybrid orbital h_z(p) gets stabilized. Consequently, the orbital gap and the mixing of the sulfur hybrid with the porphyrin a_{2u}(Por) fragment orbital will diminish compared with the situation in the gas phase. The result is that within the protein environment, the orbital of Cpd I becomes more porphyrin centered, the thiolate has a smaller radical character and the Fe–S bond gets shorter and stronger compared with the gas phase.[16,35,74,75] Since the state of Cpd I depends so critically on the donor ability of the thiolate, the

This journal is © The Royal Society of Chemistry 2007

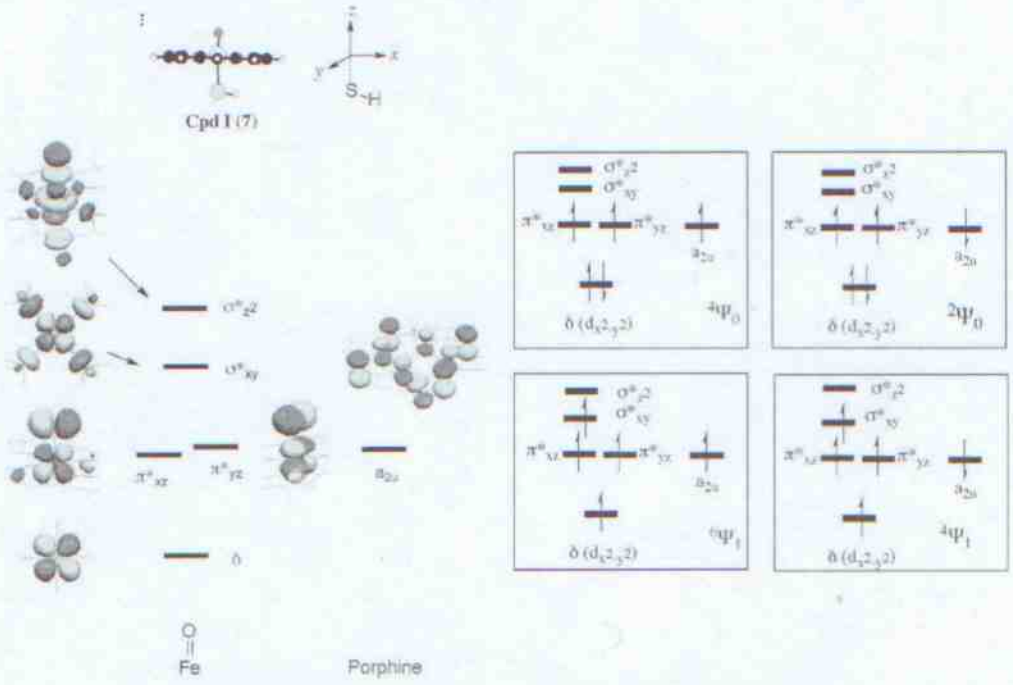

Fig. 4 Key orbitals of Cpd I and occupation diagrams in the low-lying states.

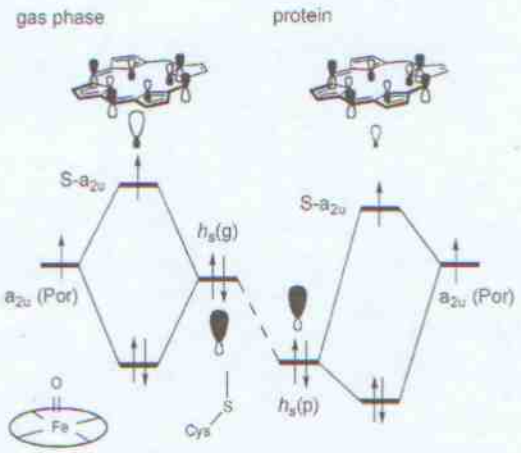

Scheme 2 Construction of the mixed S-a_{2u} orbital from fragment orbitals of the porphyrin and the thiolate ligand (S) in the gas phase and in the protein.

simplest ligand representation HS^- in the gas phase is the closest to the actual state of the cysteinate ligand ($CysS^-$) in the protein; the gas-phase CH_3S^- representation gives a wrong electronic state and geometry of Cpd I.[75]

Another pair of states, labelled as $^{6,4}\Psi_1$ in Fig. 4, can be generated from the $\delta^1\pi^{*2}\sigma^{*}_{xy}{}^1a_{2u}{}^1$ configuration that has five unpaired electrons coupled to generate sextet and quartet spin states. Although the δ-σ^{*}_{xy} orbital gap is quite large, these states enjoy significant stabilization due to the multiple exchange interactions of the d-block electrons, and as a result, they are expected to be not much higher than the pair of ground states. Both DFT[51,76] and DFT(B3LYP)/MM calculations[80] show that the $^{6,4}\Psi_1$ states lie only *ca.* 12 kcal mol^{-1} above the doublet and quartet states with the $\delta^2\pi^{*2}a_{2u}{}^1$ configuration. With such a small energy gap to the $^{6,4}\Psi_1$ states, it is not surprising that DFT[76] and DFT/MM[77] calculations show that *all the four states in* Fig. 4 *potentially contribute to the reactivity of the enzyme.*

4.2 Origins of two- and multi-state reactivity

Based on the above discussion, Cpd I is an oxidant that has a degenerate pair of ground states and two more easily accessible states. However, even more states become accessible along the oxidation pathways, as the bonds of substrates are activated, and as Cpd I, which has Fe(IV) and a porphyrin cation radical, gets reduced by the substrate and finally becomes a ferric (Fe(III)) porphyrin state. Thus, any reaction of Cpd I will ultimately involve two formal "electron transfer" events from the substrate being oxidized to the heme (or a single event with a "double electron transfer"). To facilitate the discussion we show in Fig. 5 the changes in orbital occupancy along the reaction paths for C–H hydroxylation and C=C epoxidation by the degenerate state, $^{4,2}\Psi_0$, of Cpd I. The Cpd I species is represented by the d-block and the a_{2u} orbitals, while the substrate is represented by a single orbital; *i.e.* π_{CC} is the orbital for the π-bond, activated during epoxidation, and σ_{CH} is the orbital for the C–H bond that is broken during hydroxylation. In the triradicaloid states in panels (a) and (b), the doublet spin state is indicated using an inversed electron spin within parentheses.

Starting from the first set of panels, $^{4,2}\Psi_0$, the initial bond activation step (a → b) involves an electron "transfer" event from the substrate into Cpd I. Two of the possibilities for this "transfer" are: (1) into the porphyrin hole (a_{2u}-orbital) to generate in (b) the $^{4,2}I_{rad}$(IV) doublet and quartet Fe^{IV}-type intermediates, with a closed-shell porphyrin, *i.e.*, the PorFe(IV) electromers, and (2) into the π^{*}_{xz}-orbital to generate $^{4,2}I_{rad}$(III), the Fe(III)-type intermediates with a radical cationic situation on the porphyrin

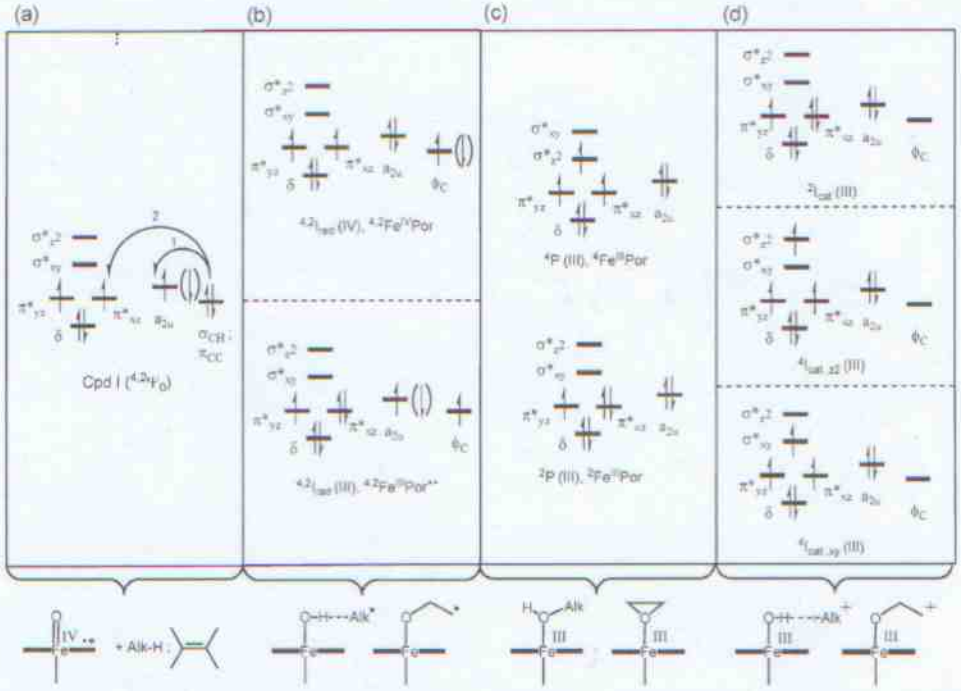

Fig. 5 Orbital occupancy evolution during C–H hydroxylation and C=C epoxidation. (a)–(c) constitute the radical pathways, while the transition from (b) to (d) shows the cationic path.

ring, *i.e.* the Por$^{\bullet+}$Fe(III) electromers. In both cases, the substrate retains a radical center with a singly occupied orbital labelled ϕ_C. During the second bond formation (b → c), an additional electron is "transferred" from the substrate to fill, either the a_{2u} orbital of Por$^{\bullet+}$Fe^{III} or one of the d-orbitals of PorFe(IV). Filling the π^*_{xz} orbital generates the doublet-spin ferric product ^{2}**P**(III), whereas the filling of the $\sigma^*_{z^2}$ orbital leads to the quartet-spin ferric product ^{4}**P**(III).

In addition to the above intermediate states, there are other possible species where the organic moiety becomes carbocationic, as shown in the set of panels in Fig. 5(d). Thus, shifting electrons from the ϕ_C orbital of the radical intermediate center (in b) into one of the d-orbitals or into a_{2u} generate ^{2,4}**I**$_{cat}$, namely, *carbocationic species* coordinated to a heme complex in the doublet or the quartet spin state. For simplicity we do not show the states that are nascent from $^{6,4}\Psi_1$. The latter states are close in energy to the other intermediate states in Fig. 5, and the interested reader can consult the original literature.[76] Clearly therefore, the reactivity of Cpd I will involve at least two spin states, and possibly also a few electromeric states where the iron atom and the porphyrin ring are in different oxidation states. This multitude of states typifies TSR and MSR. In the following section we show two examples, one for C–H hydroxylation where TSR accounts for the salient features, and the other C=C epoxidation where MSR is required to account for the reactivity patterns.

5 Reactivity of Cpd I towards alkanes and olefins

5.1 The mechanism of C–H hydroxylation

More than 10 cases of C–H hydroxylation have been studied by now,[16,65] and some of the substrates are depicted in Scheme 3. A few

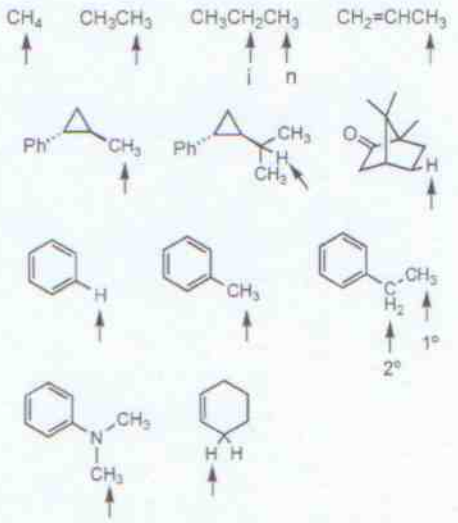

Scheme 3 Substrates studied for their C–H hydroxylation by Cpd I using DFT(B3LYP) and/or DFT(B3LYP)/MM. The arrows indicate the reaction sites.

of these were studied by DFT(B3LYP) only, while others with both DFT(B3LYP) and DFT(B3LYP)/MM.[66,77,78,79] The DFT(B3LYP) and DFT(B3LYP)/MM results revealed differences, which are relatively small as long as the DFT(B3LYP) calculations include polarity and NH–S H-bonding effects. All of these cases were found to exhibit a TSR scenario, with two energy profiles nascent from the degenerate ground state of Cpd I. The mechanism is biphasic; the initial phase involves C–H bond activation and the second phase a rebound. The C–H bond activation is the rate-determining step of the mechanism and the averaged barriers

This journal is © The Royal Society of Chemistry 2007

(over the two spin states) correlate well with the corresponding bond energies (D_{CH}), according to the expression in eqn 1:[65]

$$\Delta E\ (\text{kcal mol}^{-1}) = 0.5887 D_{CH} - 39.418 \quad (1)$$

Thus, while a correlation between two variables may not necessarily also mean a causal relationship, still, the correlation, together with the structures of the TSs, which all virtually possess a linear O–H–C triad of atoms, and the large computed *KIE*s mean that the first step involves H-abstraction. However, the interesting story begins in the rebound phase as shown below.

The computed TSR scenario is displayed schematically in Fig. 6, where the quartet state surface nascent from $^4\Psi_0$ is designated as the high-spin (HS) state, while the doublet surface nascent from $^2\Psi_0$ is labeled as the low-spin (LS) state. The two reaction profiles remain close throughout the C-H bond activation phase, up to the iron-hydroxo/radical complexes ($^{4,2}\mathbf{I}_{rad}$), where the radical moieties are bound to iron-hydroxo by a weak OH–Alk interaction. After snapping out of the weak OH–Alk interaction, the alkyl radical assumes a rebound position ($^{4,2}\mathbf{I}_{reb}$, which are not real intermediates), and thereafter the two states bifurcate. On the HS manifold, there is a significant barrier (3–10 kcal mol^{-1} or so[16,18,66,77]) for rebound *en route* to the HS ferric-alcohol complex (^{4}**P**). By contrast, the rebound on the LS surface is barrier free, leading spontaneously to the LS ferric-alcohol complex (^{2}**P**). Thus, the DFT calculations support the rebound mechanism,[58] but modify it by introducing into the mechanistic picture the TSR phenomenon and the multitude of intermediates that give rise to different products.

Fig. 6 presents only two generic intermediates, $^{4,2}\mathbf{I}_{rad}$, but, as we argued above, there are quite a few more. Fig. 7 shows a typical situation exemplified by the case of camphor hydroxylation, with four radical intermediates of the Por$^{\bullet+}$Fe^{III} and PorFe^{IV} electromer varieties.[16,18,66,77] It is seen that the four states are condensed within 2 kcal mol^{-1} or less, and hence, all the four species are accessible and will generate products. For each electromer type, the LS intermediate collapses to the product complexes without a barrier,

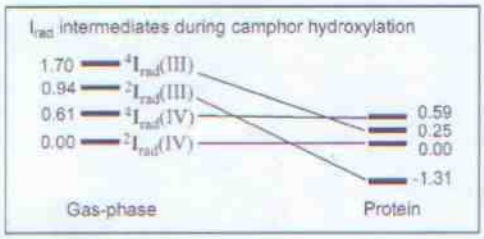

Fig. 7 Intermediates during camphor hydroxylation in the gas phase and in the protein of CYP101 (adapted from Fig. 22 in ref. 16, with permission from the American Chemical Society).

while the HS intermediate has a significant barrier to rebound. Therefore, generally speaking, C–H hydroxylation proceeds *via* two competing processes on different spin-state manifolds; *one on the LS manifold is effectively concerted with an ultrashort radical lifetime, the other on the HS manifold is stepwise with a significant lifetime for the intermediate.*

It is this feature of TSR that creates *the likeness of two different oxidants* and, in our view, is the cause of the controversial conclusions which were derived from the clock experiments.[6] In a typical clock experiment (Fig. 2) the apparent lifetime (τ_{app}) of the radical intermediate, during P450 hydroxylation, is determined from the extent of skeletal rearrangement observed in the alcohol product [*R*/*U*] and the known speed of rearrangement of the free radical (k_X). This expression for the apparent lifetime is based on the assumption that there is a single intermediate that is branching out to give the two products. However, using the TSR scheme, it is apparent that *R* and *U* do not originate from the same intermediate; *R* arising only from the HS manifold and *U* mostly, if not only, from the LS manifold. As such, the apparent lifetime of the clock experiments, *e.g.*, in Fig. 2, is not the real lifetime, since it reflects the relative importance of the HS and LS pathways. Furthermore, since the LS H-abstraction barrier is generally lower than the corresponding HS quantity[16] (see Fig. 6), the measured [*R*/*U*] quantity will generally lead to apparent lifetimes that are

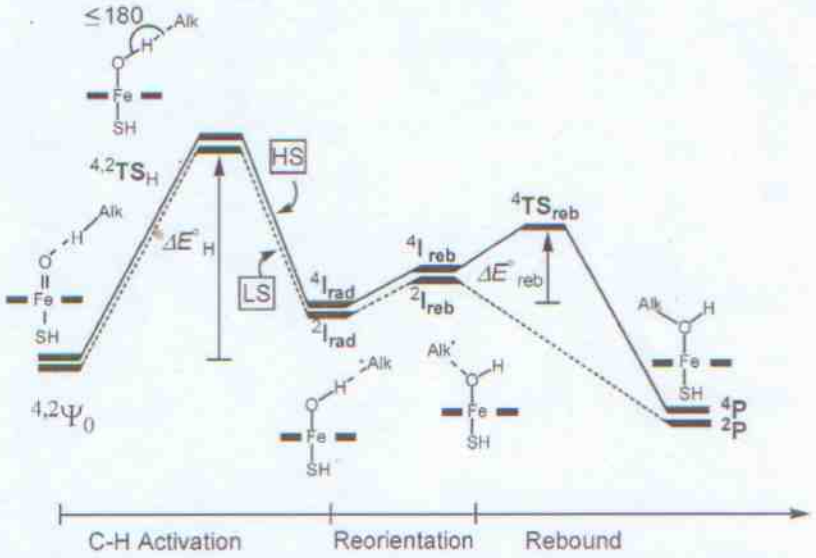

Fig. 6 A two-state reactivity (TSR) scenario in the mechanism of C–H hydroxylation by the quartet (HS) and doublet (LS) states of Cpd I ($^{4,2}\Psi_0$) (adapted from Fig. 2 in ref. 18, with permission from Wiley-VCH GmbH & Co KG).

too short. In the cases of C–H hydroxylation where the yield of the HS process is particularly small, the great majority of the product will be the unrearranged variety, and the apparent lifetime will be artificially ultrashort. In reality, however, radicals exist on the HS manifold and have normal lifetimes, while the ultrashort apparent lifetimes originate from the assumption that the two products arise from a single state of the radical complex.

Analysis of the barrier to rebound on the HS manifold,[18] in terms of a general model of barrier formation,[80] creates some order in the experimental data coming from the clocks. Fig. 8 shows the formation of the barrier to the HS rebound for the Alk•/Fe^{IV}OH species due to the states that interchange along the reaction coordinate and mix to give the rebound transition state, $^4TS_{reb}$. As shown already in Fig. 5(b → c), in order to establish the Alk–OH bond, in the quartet state, the Alk• radical has to shift an electron to the high-lying σ^*_{z2} orbital. If we shift the electron without changing the geometry of the $^4I_{cat}$(IV) ground state, we get as in Fig. 8 a vertical excited state $^4I_{cat}$*(III) that contains an Alk$^+$ cation and an excited ferric-hydroxo anion complex. The total energy gap, G, of this state relative to the ground state $^4I_{cat}$(IV) is given by the ionization potential, $IP_{Alk^\bullet}$, of the Alk• radical (within the gas phase or protein environments of the process), minus the electron attachment energy, EA_{FeOH}, of the Fe(IV)-hydroxo complex, and plus the excitation energy of the attached electron from the low-lying π^* orbital to the higher-lying σ^*_{z2} orbital, $E_{FeOH}(\pi^* \rightarrow \sigma^*)$. Along the rebound coordinate (shortening the C–O distance from **I** to **P**) this $^4I_{cat}$*(III) excited state will be stabilized by Alk–O bond-making and become the ground state of the ferric-alcohol product, ^{4}**P**(III); at the same time the $^4I_{cat}$(IV) state correlates to an excited state of the product, ^{4}**P***(IV). The barrier that results from the mixing of these two electronic states, will depend on G. For the doublet-state process, the corresponding G is smaller since the electron is shifted to the low-lying π^* orbital, and since $E_{FeOH}(\pi^* \rightarrow \sigma^*)$ makes for a major fraction of G,[18] the barrier to LS rebound will be either very small or nil, as indeed it is. The calculations show a barrier-free LS rebound (in camphor hydroxylation[66] the calculated LS barrier was 0.29 kcal mol^{-1}),[16,18,66] and what remains is to consider the HS rebound.

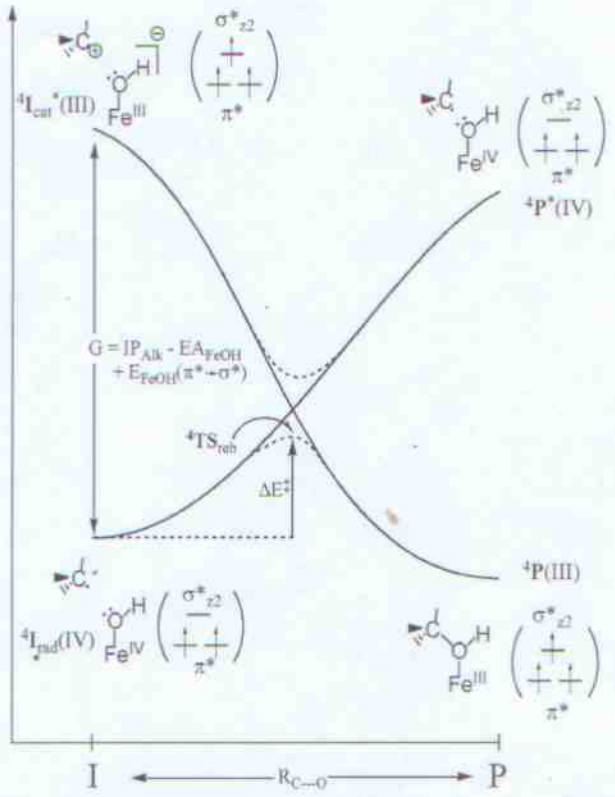

Fig. 8 A valence bond curve-crossing model for the barrier formation during the HS rebound process. The state mixing is shown by the dashes (adapted from Fig. 9 in ref. 18, with permission from Wiley-VCH GmbH & Co KG).

Looking at a series of substrates with the common iron-hydroxo complex of P450, leads to the simple prediction that as the radical becomes a better electron donor (lower ionization potential, IP, or oxidation potential), so should the rebound barrier decrease until it would altogether disappear. This prediction is manifested in the series of probe substrates used by Newcomb and Toy,[6] as shown in Scheme 4. Thus, probes **1a** and **1b** lead to significant amounts of the rearranged product, while probe **1e** that produces the radical with the lowest IP_{Alk} exhibits virtually no rearrangement (below the detection limit). Recent DFT calculations,[81] show that indeed **1b** should yield significant amount of the rearranged product, estimated as 20–30% based on the relative HS and LS barriers, while **1e** should produce no rearranged products, since *its LS and HS pathways are both effectively concerted.*

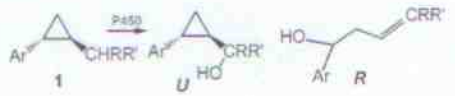

probe	Ar	R,R'	IP_{Alk}	[U/R]
1a	pCF_3	H, H	highest	4
1b	*p*H	H, H		4.3
1c	pCF_3	H, CH_3		12
1d	*p*H	H, CH_3		25
1e	*p*H	CH_3, CH_3	lowest	> 100

Scheme 4 Probe substrates and their relative unrearranged/rearranged ([*U*/*R*]) alcohol product yields as a function of the ionization potential of the corresponding radical.

In addition, the TSR model predicts the dependence of [*R*/*U*] on the strength of the Fe–S bond and the polarity of the pocket; the stronger the bond and the more polar the pocket, in a given P450 isozyme, the more rearranged products are expected.[18] To the best of our knowledge, different P450 isozymes give rise to different [*R*/*U*] values for a given clock. Another prediction of the TSR model is that since the *KIE*(H/D) reflects the HS and LS transition states for H-abstraction, and these transition states are different, then the [*R*/*U*] value would be subject to product isotope effect (PIE), namely different *KIE* values are expected for *U* and *R*. Our most current results,[77,78] show that the protein changes the TS geometries, compared with gas phase calculations, and therefore in cases where the TS structures for the HS and LS states are close, the derivation of exact PIE values from model gas-phase DFT calculations, as we proposed in the past,[81] is not reliable. Nevertheless, the reason why PIE should be different than 1 in TSR is quite evident. Moreover, an observation of PIE ≠ 1 cannot arise from a single intermediate that branches into *U* and *R*. Therefore, until a better explanation is found for the observation

This journal is © The Royal Society of Chemistry 2007

of PIE, PIE values different than unity indicate the operation of TSR.

5.2 The mechanism of double bond epoxidation

As shown in Scheme 5, double bond epoxidation is normally attended by formation of aldehydes and suicidal complexes, in which the olefin alkylates the heme through one of its nitrogen atoms.[1–3] In addition, if one starts with pure *cis* or *trans* olefins one observes a mixture of *cis* and *trans* epoxides, although the scrambling of this isomeric information is not large.[3] The mechanistic details of C=C activation by P450 have been the subject of debate, albeit not as intense as in the case of C–H hydroxylation. Our studies of five different olefins (ethene, propene, cyclohexene, camphene and styrene)[15,16,48,77,79,82] revealed a multi-state reactivity (MSR) scenario, where different spin states and electromers participate in the product formation in a state-specific manner.

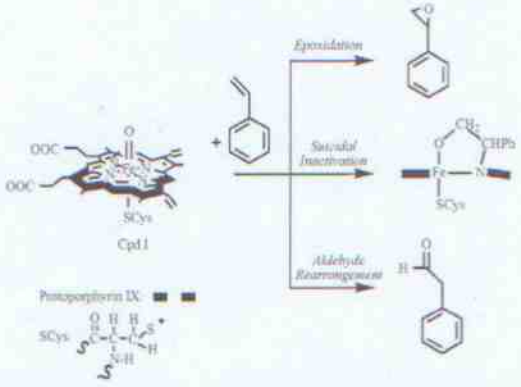

Scheme 5 C=C epoxidation- and by-products formed during styrene epoxidation (adapted from Scheme 1 in ref. 82, with permission from Wiley-VCH GmbH & Co KG).

A representative example is the epoxidation of styrene in Fig. 9.[82] It is seen that here, in addition to the usual pair of LS and HS transition states, $^{2,4}TS_{rad}$, which lead to the radical intermediates, $^{2,4}I_{rad}$, there is also a LS cationic transition state $^{2}TS_{cat,yz}$ that leads to the cationic intermediate, $^{2}I_{cat,yz}$, having a $\delta^2\pi^{*2}_{xz}\pi^{*1}_{yz}$ configuration on the porphyrin iron-oxo moiety and a carbocationic center on the benzylic carbon of styrene. The bond activation here leads to five low-lying intermediate states (during the self-consistent-field procedure $^{2}I_{rad}$(III) became one of the cationic states), of the radical and cationic varieties. All the LS intermediates undergo ring closure to give the LS epoxide product, ^{2}P, without a barrier and hence, give rise to effectively concerted LS processes.

In contrast to the LS species, the HS intermediates encounter barriers to ring closure, and therefore give rise to a stepwise mechanism with sufficiently long-lived intermediates that can participate in a variety of side product formations and in scrambling of

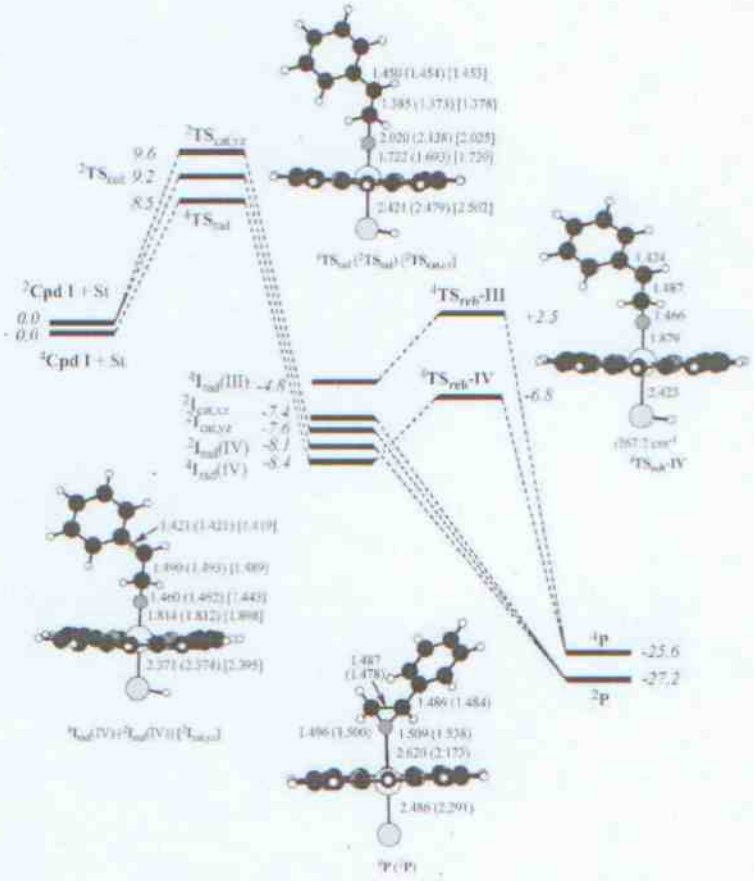

Fig. 9 A multi-state reactivity (MSR) scenario during styrene epoxidation by Cpd I (adapted from Fig. 6 in ref. 82, with permission from Wiley-VCH GmbH & Co KG). More states are shown in Fig. 10.

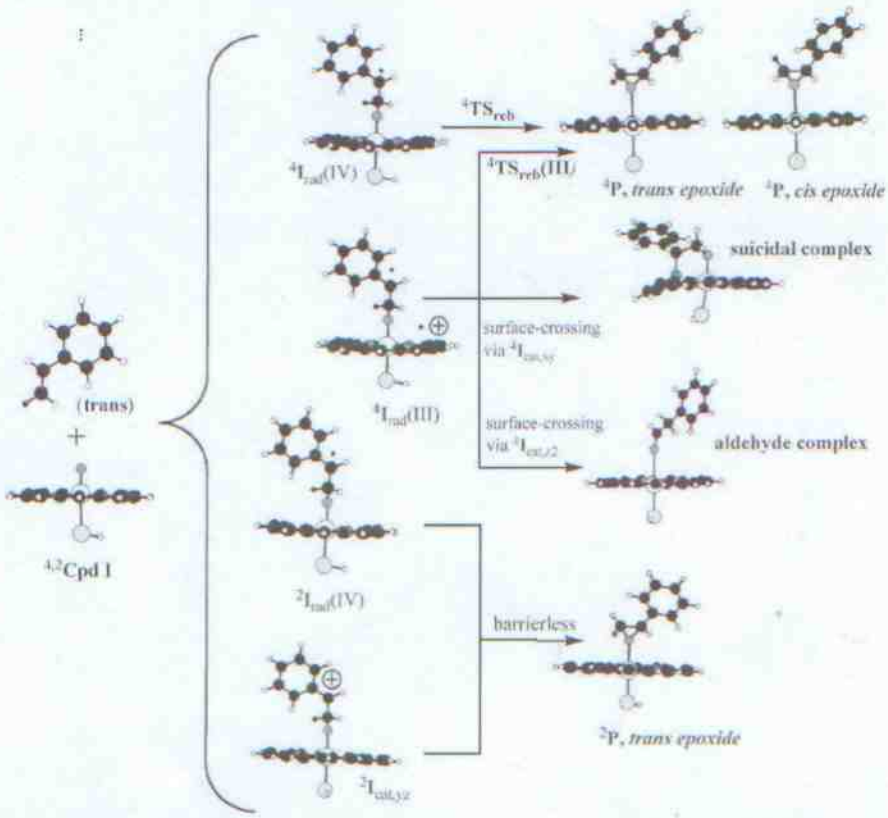

Fig. 10 The MSR scenario and the state origins of the various products obtained during the oxidation of *trans*-2-deuterio-styrene (adapted from Fig. 9 in ref. 82, with permission from Wiley-VCH GmbH & Co KG).

stereochemistry (*e.g.*, if one starts with *trans*-2-deuterio-styrene) to yield a mixture of *cis* and *trans* epoxide products.

Fig. 10 shows the MSR scheme for the reaction of Cpd I with *trans*-2-deuterio-styrene (two hydrogen atoms are labeled in white, while the deuterium atom is in black). This is a state-specific scheme, where the spin states and the electromers participate in specific reactions. The LS intermediates undergo ring closure to form *trans*-epoxides and conserve the initial stereochemistry. By contrast, the HS intermediates participate in stereochemical scrambling and in side-product formation. The rotational barrier around the C–C bond of the radical intermediate is only 1.3 kcal mol^{-1}, which is smaller than the barriers to ring closure for both HS intermediates. Therefore, both $^4\mathbf{I}_{rad}$(IV) and $^4\mathbf{I}_{rad}$(III) will have sufficient lifetimes to lose stereochemistry and undergo ring closure to produce a mixture of *cis* and *trans* epoxide products.

The suicidal and aldehyde complexes, which are side products in the reaction, were found to originate only from the HS cationic states; one state, $^4\mathbf{I}_{cat,z2}$, with configuration $a_{2u}{}^2\delta^2\pi^*_{xz}{}^1\pi^*_{yz}{}^1\ \sigma^*_{z2}{}^1$ correlates in a barrier-free fashion to the aldehyde complex, and the other, $^4\mathbf{I}_{cat,xy}$, with the configuration $a_{2u}{}^2\delta^2\pi^*_{xz}{}^1\pi^*_{yz}{}^1\ \sigma^*_{xy}{}^1$ correlates similarly to the suicidal complex. The formation of these side-product complexes requires crossover from the HS radical states to the HS cationic states. The barriers to these crossovers are of the order of 10 kcal mol^{-1}. Consequently, $^4\mathbf{I}_{rad}$(IV), which possesses a much smaller barrier to ring closure will give a scrambled epoxide but will not produce a suicidal complex or aldehyde. By contrast, the $^4\mathbf{I}_{rad}$ (III) intermediate possesses a sufficiently large barrier to ring closure to also be able to participate in the production of the suicidal complex and aldehyde side products.[82]

5.3 The mechanism of desaturation

Scheme 6 shows the P450 mechanisms studied by the Jerusalem group. It is apparent that not all the reactions involve TSR and/or MSR. There are a few reactions that proceed on a single spin-state surface. For example, benzene hydroxylation,[83] as well as a variety of substituted benzenes,[84] occurs preferentially on the LS surface, and mostly *via* a cationic Meisenheimer complex. Sulfur oxidation was originally found to prefer a HS oxygenation.[71] But recently, our collaborators[85] identified an additional low-energy pathway for the LS states, and therefore we label the character of this process, in Scheme 6, with a question mark until we satisfactorily resolve the identities of different pathways in this reaction.

As can be seen in the scheme, desaturation is another process that proceeds on the LS *via* a cationic intermediate state.[86] Since this reaction bears a relationship to the mechanism whereby P450 aromatase, CYP19, converts androgens to estrogen products,[87] we discuss below the mechanism of desaturation to demonstrate *the versatility of Cpd I as an MSR reagent.*

Thus, in its normal activity, P450 catalyzes the "insertion" of an oxygen atom into substrates by utilizing two reduction equivalents ($2e^-$), one mole of O_2, and two proton equivalents; the other [O] equivalent is converted to water, eqn 2. Occasionally, the O_2 consumption follows eqn 3, where the enzyme converts all the

This journal is © The Royal Society of Chemistry 2007

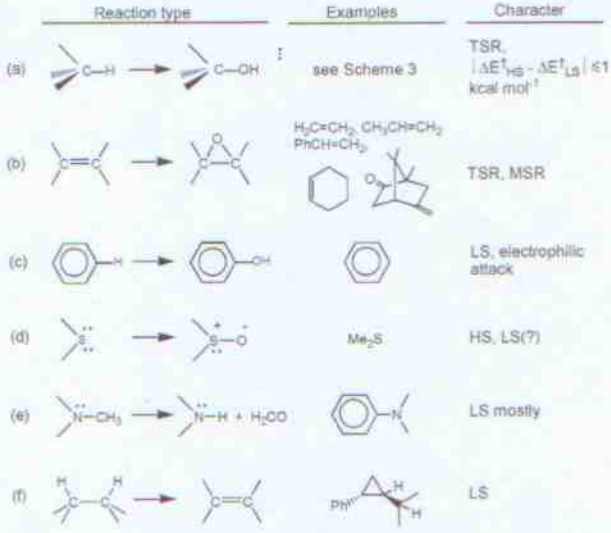

Scheme 6 Mechanisms of P450 oxidation studied by DFT(B3LYP) and/or DFT(B3LYP)/MM, and their characterization in terms of TSR, MSR or a single-state reactivity.

dioxygen into water, thereby acting as an oxidase, but at the same time it dehydrogenates the substrate,[12,88] creating a double bond.

$$O_2 + 2e^- + 2H^+ + R_2C\text{–}CR'_2H \rightarrow R_2C\text{–}CR'_2OH + H_2O \quad (2)$$

$$O_2 + 2e^- + 2H^+ + HR_2C\text{–}CR'_2H \rightarrow R_2C{=}CR'_2 + 2H_2O \quad (3)$$

A seminal study[88] of C–H hydroxylation of valproic acid (an anti-epileptic drug) showed that the desaturation activity and the normal monooxygenation function branch from the same oxidation mechanism that involves Cpd I. Since mechanistic alternatives exist for the desaturation reaction, involving either radicals or cations,[12] theoretical calculations by the Jerusalem group[86] were used to establish the preferred mechanism. The model alkane (Alk–H) chosen for the calculations is *trans*-2-phenyl-1-*iso*-propylcyclopropane (probe substrate **1e** in Scheme 4). Despite the fact that there are no clear experimental data that show oxidase/dehydrogenase reactivity for this substrate, it was selected because it leads to both radical and cationic species *en route* to rebound; these species were postulated to be involved in the desaturation/oxygenation dichotomy.[12,88,89]

Fig. 11a shows the radical, $^2\mathbf{I}_{rad}$ and the cation, $^2\mathbf{I}_{cat}$; it is seen that the C–O distance in $^2\mathbf{I}_{cat}$ is longer than in $^2\mathbf{I}_{rad}$ (2.587 Å *vs.* 2.142 Å). But in $^2\mathbf{I}_{cat}$ the hydrogens of the methyl groups of the isopropyl moiety are close to the iron-hydroxo anion. As shown by the arrows in Fig. 11a, $^2\mathbf{I}_{rad}$ undergoes C–O bond making (barrier-free, as in Fig. 6) to yield the alcohol Alk-OH, while $^2\mathbf{I}_{cat}$ spontaneously loses a proton, from the $[(CH_3)_2C\text{–}H]^+$ moiety to the ferric-hydroxo anion, to form the corresponding alkene and the ferric-water complex.

In fact, the $^2\mathbf{I}_{cat}$ species is on the downhill slope *en route* to the alkene product complex; once the electron shifts from the Alk$^\bullet$ radical to the iron(IV)-hydroxo complex, the latter becomes a strong base and abstracts a proton from the carbocation to give rise to an olefin. Thus, theory reveals that the dehydrogenase activity is associated not with radicals of the substrates but rather with the corresponding carbocations. This is indeed one of the possibilities postulated in the experimental literature.[12,89]

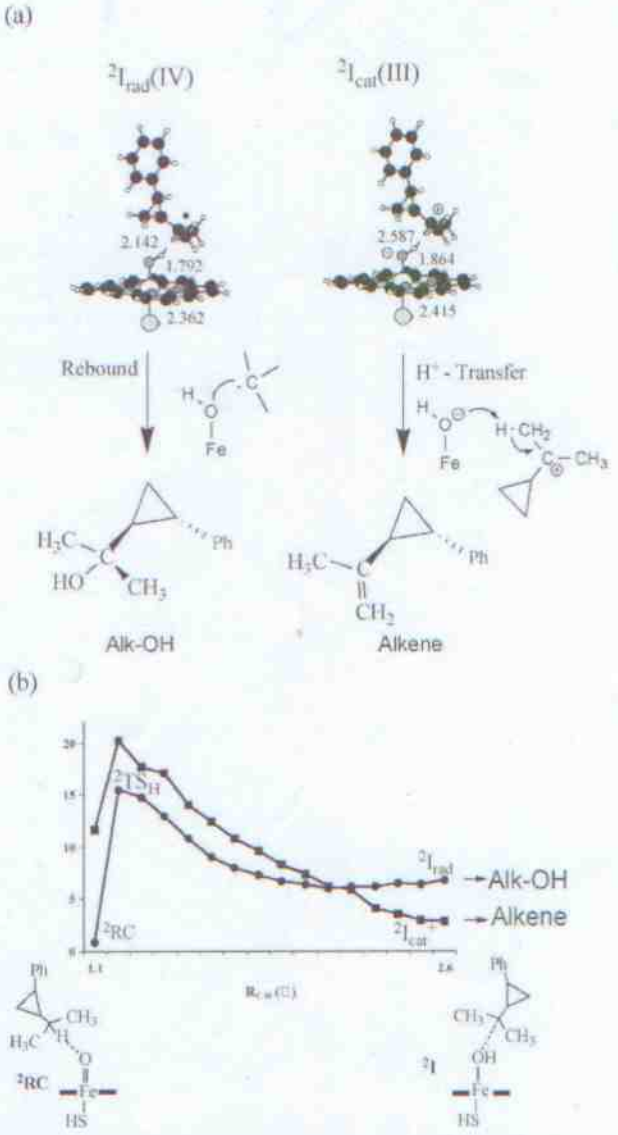

Fig. 11 The DFT(B3LYP) computed mechanism of desaturation occurring in competition with C–H hydroxylation (adapted from Fig. 35 in ref. 16, with permission from the American Chemical Society).

Furthermore, as shown in Fig. 11b,[86] the electron transfer from the alkyl radical to the iron-hydroxo complex occurs by surface crossing, between the radical and cationic manifolds, during the initial C–H abstraction phase, wherefrom the reaction proceeds further to the alkene. A very similar mechanism was demonstrated, using DFT(B3LYP) and molecular dynamics, to be responsible for the third "mysterious" step during aromatase catalysis that results in androgen aromatization.[87]

What is the reason for the oxidase-dehydrogenase mode of $^2\mathbf{I}_{cat}$? Inspection of the geometry of the species in Fig. 11a shows that the C–O distance is 2.59 Å compared with 2.14 Å for the corresponding radical $^2\mathbf{I}_{rad}$. The reason for the longish C–O distance is rooted in the steric bulk of the isopropyl group and the charges of the two moieties of $^2\mathbf{I}_{cat}$. Thus, on the one hand, the steric bulk of the isopropyl prevents the necessary close approach

for instantaneous C–O bond making and alcohol formation. This distance is further augmented by electrostatic preference: in the cationic species, $^2\mathbf{I}_{cat}$, the iron-hydroxo is negatively charged, and it prefers to maintain O^-–H^+ interaction with the close-by positively charged hydrogen ends of the CH_3 groups of the Alk cation moiety; this facilitates proton abstraction. Thus, the electro-steric factor causes a spontaneous proton transfer from the radical to the iron-hydroxo complex, and results in the dehydrogenase activity.

The electro-steric factor links the theoretically studied process to the "pure" oxidase activity of P450, which converts the two oxygen atoms in O_2 to water, by using an extra mole of reductase in the course of the reaction (*i.e.*, $O_2 + 4e^- + 4H^+ \rightarrow 2H_2O$). As has been shown,[90] the "decoupling" of oxygen consumption from substrate oxidation occurs when Cpd I accepts two electrons from the reductase. Mueller *et al.*[91] have further demonstrated that whenever the protein pocket is sufficiently encumbered to prevent an approach of the substrate C–H bond to the FeO moiety of Cpd I, one also observes increased "decoupling" and heightened "pure" oxidase activities. The theoretical study[86] shows similarly that, whenever the substrate is sterically encumbered, thus hindering the C–O approach, the cationic intermediate will lead to a mixed oxidase–dehydrogenase reaction. Thus, the oxidase–dehydrogenase function requires substrates that combine steric inhibition of rebound and stable carbocationic complexes. Such conditions are met in the third step of aromatization of androgens, where the ferric-hydroxo anion deprotonates a *gem*-diol, thereby causing deformylation and aromatization of the *A* ring of androgens.[87] It is further reasonable to speculate that in the protein environment, release of the carbocation, away from the iron-hydroxo anion, may compete with dehydrogenation. In such an event, the carbocation will either be hydroxylated (*e.g.*, by rebound from a long C–O distance [Fig. 11b], or simply by water), or mediate "pure" oxidase activity by accepting electrons from the reductase, while restoring the substrate by hydrogen abstraction.

6 Gauging the reactivity of Cpd 0

The reactivity of the T252A mutant of CYP101 towards the camphene analogs of camphor[38] has created a tantalizing problem for both experiment and theory: Must we invoke Cpd 0 as a secondary oxidant in P450, or could the data still be interpreted by Cpd I as the sole oxidant? Let us see how theory attempted to tackle this question.

6.1 A computational assessment of the electrophilic reactivity of Cpd 0

Since C=C epoxidation is thought to be a marker of Cpd 0 reactivity, this reaction was the first to be studied by DFT(B3LYP) calculations, performed independently by two groups.[69,70] The two studies concluded that the barriers to electrophilic epoxidation by Cpd 0 are exceedingly high. Furthermore, the computed barriers to epoxidation by Cpd 0, through either one of the two oxygen atoms of the OOH moiety, were much higher than the corresponding barriers to ethene epoxidation by Cpd I, for example, >36 kcal mol^{-1} *vs.* 14–15 kcal mol^{-1}.[69]

It is well known from model compounds that Cpd I is capable of oxygenating sulfur.[92] Nonheme $Fe^{IV}O$ type complexes can also achieve this transformation, whereas the corresponding nonheme $Fe^{III}OOH$ species fail to produce any reaction under the same conditions where $Fe^{IV}O$ was reactive.[93] To gauge the sulfoxidation reactivity of Cpd 0 *vs.* Cpd I, the Jerusalem group studied the sulfoxidation of Me_2S, dimethyl sulfide (DMS), by these two species.[71,85] The reaction of Cpd I in Fig. 12a (energies include corrections due to the bulk polarity effect) involves a concerted oxo transfer from Cpd I to the sulfur atom; the lowest barrier is 16.0 kcal mol^{-1} *via* $^4\mathbf{TS}_1$ (unpublished results[85] show an even lower barrier on the LS surface, *ca.* 12.5 kcal mol^{-1}, and assign the LS path in Fig. 12a to a porphyrin oxygenation reaction). Fig. 12b

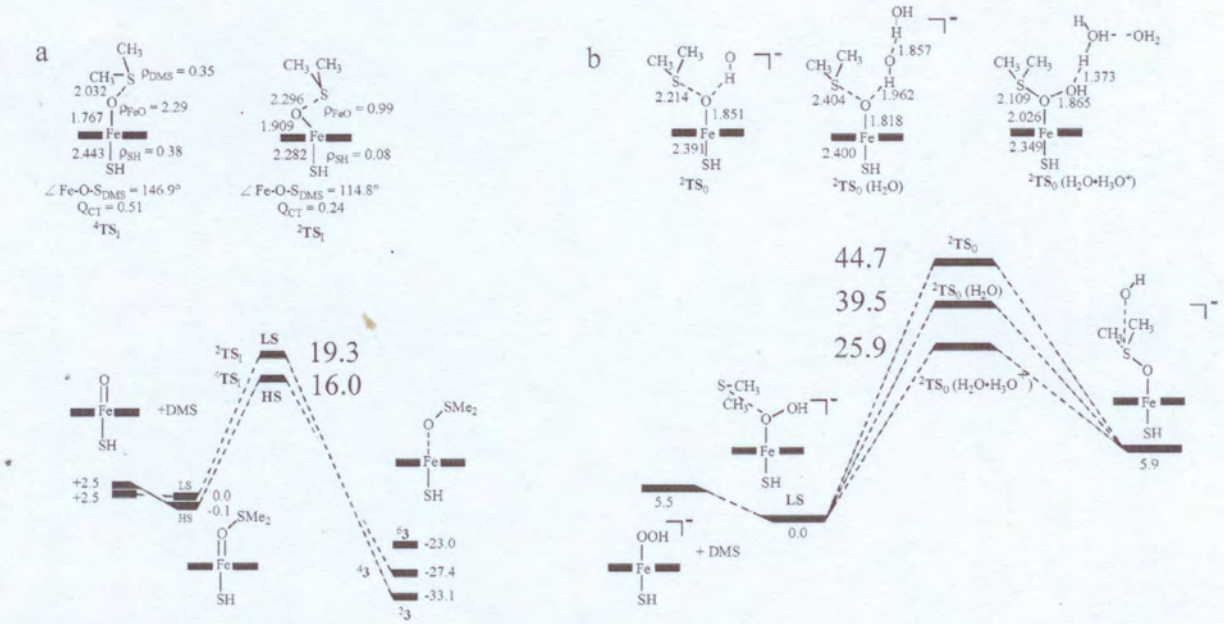

Fig. 12 DFT(B3LYP) results for the sulfoxidation of $(CH_3)_2S$ by (a) Cpd I, and (b) Cpd 0 (see ref. 71). Work in progress (ref. 85) shows the existence of an additional $^2\mathbf{TS}_1$ species 6.8 kcal mol^{-1} lower than the one shown in (a).

This journal is © The Royal Society of Chemistry 2007

shows the monooxygenation reaction of Me_2S *via* the proximal oxygen of Cpd 0. With a bulk polarity correction, but without acid catalysis, the barrier is exceedingly high. Hydrogen bonding by a molecule of water lowers this barrier by *ca.* 5 kcal mol^{-1}, while assistance from a potent proton source, $H_3O^+(H_2O)$ further lowers the barrier. If we take the $H_3O^+(H_2O)$ species to represent a limiting acidity, this would mean that even under these limiting conditions, the barrier to sulfur oxygenation by Cpd 0 remains at the very least 10 kcal mol^{-1} higher compared to sulfoxidation by Cpd I.

The lowering of the barrier to oxygen transfer by Cpd 0 due to acid catalysis is in line with the experimental observation that oxo-transfer reactions by $MOOH^{n+}$ species (M-transition metal) to dialkyl sulfides and triarylphosphines require acid catalysis, even for positively charged metallo-hydroperoxide reagents.[94] It should be kept in mind though that Cpd 0 of P450 carries a negative charge and this does not favor electrophilic reactivity. While the effect of the negative charge of Cpd 0 is partially offset by the acid catalysis, the sulfoxidation study shows that this does not make Cpd 0 competitive with Cpd I. Furthermore, since the barrier[31,52] to conversion of Cpd 0 to Cpd I is smaller than the barrier to sulfur oxygenation by Cpd 0, theory does not favor participation of Cpd 0 in monooxygenation in the WT enzyme.

In conclusion, based on the present computational picture, Cpd 0 is *a sluggish electrophilic oxidant* that cannot compete, as such, with Cpd I. This conclusion is similar to the one drawn recently in the nonheme catalysts where the $LFe^{III}OOH^{2+}$ species were shown to be silent under conditions where the corresponding ferryl species $LFe^{IV}=O^{2+}$ were reactive.[93]

6.2 A computational assessment of the reactivity of Cpd 0 *via* initial O–O homolysis

The interplay of homolytic and heterolytic O–O bond cleavages in Cpd 0 species is well known.[95–97] For example, the peroxide dependent P450 hydroxylation of cyclohexane,[95] gave a small *KIE* value ($[C_6H_{12}/C_6D_{12}]$) of ~2, which was diagnostic of the HO• radical reactivity due to the homolysis of the O–O bond of the ferric-hydroperoxide. Indeed, the Jerusalem group[98] showed recently that Cpd 0 undergoes relatively facile O–O bond homolysis and generates a bound OH• radical, which then performs hydroxylation of the *meso* position of the porphyrin, in a manner analogous to the reaction of heme-oxygenase (HO) enzymes.[99] As such, in the presence of an oxidizable substrate, one may expect a competition between substrate oxidation and *meso* heme-hydroxylation by the bound OH• radical, as shown in Scheme 7. The Jerusalem group has studied this competition for the two substrates **1** and **2** shown in the scheme;[48,67] **1** is a probe substrate (see Scheme 7) that undergoes C–H hydroxylation giving rise to results that were interpreted[6] in terms of the "two oxidant hypothesis" in Scheme 1, above, while substrate **2** was shown to undergo expoxidation by the T252A mutant of CYP101, implying Cpd 0 as an oxidant.[38]

C–H hydroxylation by Cpd 0: Fig. 13 shows the DFT(B3LYP) computed mechanism[67] of hydroxylation of **1** by Cpd 0. It is seen that the first step involves O–O bond homolysis, leading to an intermediate $^2\mathbf{I}_{O\text{-}O}$ in which the OH• radical is bound to a Cpd II moiety. Subsequently, the OH• radical abstracts a hydrogen atom from **1**, and then the alkyl radical rebounds on the ferryl to give rise

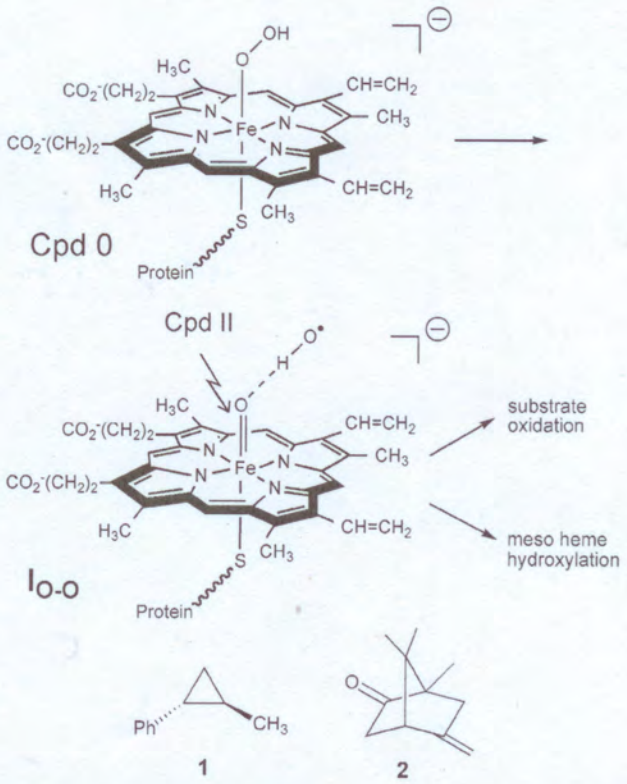

Scheme 7 Homolytic cleavage of the O–O bond in Cpd 0, the ensuing chemical reactions induced by the bound OH• radical, and the two substrates studied by DFT(B3LYP) to explore the hydroxylation and oxidation capabilities of Cpd 0 *via* this mechanism.

to a ferric-alkoxy complex, $^2\mathbf{P}_{AC}$, of the alkoxide derived from **1**. An alternative process whereby the radical derived from **1** rebounds on the water molecule, while the ferryl abstracts a hydrogen atom from the water, has a much higher barrier (40 kcal mol^{-1}) and is therefore not shown in Fig. 13.[67]

In the insets of Fig. 13, we show two other events: inset (a) shows the *meso* hydroxylation process nascent from $^2\mathbf{I}_{O\text{-}O}$, while inset (b) shows the rearrangement barrier of the free radical derived from **1**, and is labelled as $^2\mathbf{I}_U$ in the figure. Two conclusions can be drawn: (i) the bound OH• radical will carry out *meso* hydroxylation of the heme in preference to H-abstraction from **1**, since the H-abstraction barrier is larger than the barrier to *meso* attack, and (ii) the radical derived from **1** will rearrange faster than it can rebound to give the hydroxylation product (the rebound barrier is 5.2 kcal mol^{-1}; see Fig. 13 insets).

Since the hydroxylation of **1** by Cpd I was studied before at the same computational level,[81] it is possible to compare the barriers for the rate-controlling steps in the two mechanisms. The data shown in Table 1 involve corrections due to the zero point energy (ZPE), bulk solvation (a dielectic constant of 5.7) and NH–S hydrogen-bonding effects. It is seen that the C–H hydroxylation barrier by Cpd 0 is *ca.* 9.9 kcal mol^{-1} higher than the corresponding barrier of Cpd I. Clearly, therefore, *Cpd 0 is a sluggish hydroxylation reagent that will be silent in the presence of Cpd I.* If Cpd I is not present, Cpd 0 may lead to a limited amount of hydroxylation due to the competition with *meso*-heme hydroxylation.

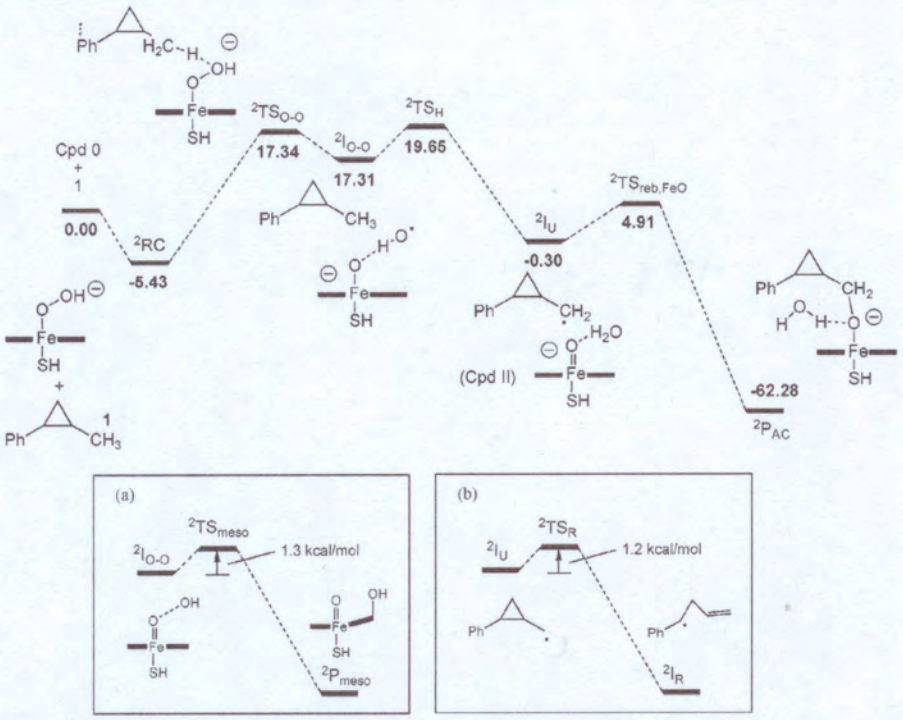

Fig. 13 DFT(B3LYP/LACV3P+*) energies during hydroxylation of **1** by Cpd 0 (see ref. 67). Shown in the insets are (a) the barrier to heme hydroxylation starting from $^2I_{O\text{-}O}$, (data taken from ref. 48) and (b) the barrier to rearrangement of the radical derived from ^2I_U. (from ref. 81).

Table 1 Energy barriers (in kcal mol^{-1}) for C–H hydroxylation of **1** by Cpd I and Cpd 0

Computational level	$\Delta E^{\ddagger}$, kcal mol^{-1} [a]	
	Cpd I[b]	Cpd 0[c]
(1) LACVP	19.4	22.9
(2) LACVP + ZPE	15.2	18.3
(3) LACV3P+(d)	17.0	25.1
(4) LACVP + ZPE + 2NH$\cdots$S + ε = 5.7	18.3	23.8
(5) LACV3P+(d)+ZPE + 2NH$\cdots$S + ε = 5.7	16.0	25.9

[a] Barriers relative to the clusters of the substrate with Cpd I or Cpd 0. [b] See refs. 67 and 81. [c] See ref. 67.

Another DFT (B3LYP) study of the reactivity of Cpd 0 in C–H hydroxylations[68] reached the conclusion that all the P450 chemistry can be understood in terms of the chemistry of Cpd 0, without a need to invoke Cpd I. These conclusions were based on the computational results of the hydroxylation reactions of CH_4 and isobutane by Cpd 0. The case of CH_4 is of course academically interesting; P450 does not hydroxylate methane. In the case of isobutane, the authors obtained a barrier of 19.5 kcal mol^{-1}. However, using analogous substrates with secondary and tertiary C–H bonds, shows that Cpd I is more reactive.[16,65] Thus, the barrier to H-abstraction of the isopropylic C-H of propane is 16.9 kcal mol^{-1} (12.9 kcal mol^{-1} after ZPE correction), while for a tertiary C–H of the probe substrate **1e** in Scheme 4, the barrier is 16.6 (12.7) kcal mol^{-1}.[81] Therefore, the barriers for Cpd I are at least 3 kcal mol^{-1} lower than the value obtained for Cpd 0 (if ZPE were included, most likely the difference would be significantly larger, but no ZPE was reported in ref. 68). Furthermore, considering the fact that the barrier of Cpd 0 is raised by 2.5 kcal mol^{-1} more than the barrier of Cpd I, when the effects of polarity and NH–S hydrogen bonding are taken into account (see entries 2 *vs.* 4 in Table 1), the difference in the barrier becomes at least 5.5 kcal mol^{-1} in favor of Cpd I.

Other inconsistencies of the C–H hydroxylation by Cpd 0 are mechanistic. Thus, suppose that Cpd 0 was indeed the ultimate oxidant also in the wild type (WT) enzyme, then one would not have expected to find the original hydrogen of the C–H bond in the alcohol product as was reported to be the case in the cryogenic EPR/ENDOR study of camphor hydroxylation by CYP101.[23] In addition, H-abstraction by OH$^{\bullet}$ radical is expected to lead to small *KIE* values,[95] whereas the experimental ones for Cpd I are 8–12.[5,11,67] Furthermore, if it were true that Cpd 0 was the only oxidant of P450, *this should have rendered the T252A mutant of CYP101 considerably more reactive than the WT enzyme*, which is obviously not the case. The minimally drawn conclusion at this point in time is that Cpd 0 may lead to C–H hydroxylation only in the absence of Cpd I. In the case of T252A reacting with camphor, no C–H hydroxylation was observed. So it remains to be proven that P450 Cpd 0 can indeed participate in C–H hydroxylation.

C=C epoxidation by Cpd 0 will proceed by TSR: Fig. 14 shows the DFT(B3LYP) energy profile for the oxidation of 5-methylenylcamphor, **2**, by Cpd 0 in its two lowest spin states.[48] The relative energies include corrections due to ZPE, NH–S H-bonds, and bulk polarity (using a dielectric constant $\varepsilon = 5.7$). Thus, as described above, the initial step involves O–O bond homolysis to give rise to the $\mathbf{I}_{o\text{-}o}$ intermediate, which involves Cpd II and a bound OH$^{\bullet}$ radical. The OH$^{\bullet}$ radical then attacks the double bond and in a barrier-free fashion gives rise to the hydroxylated intermediate $\mathbf{I}_d$. Being barrier free, the attack on the double bond

This journal is © The Royal Society of Chemistry 2007

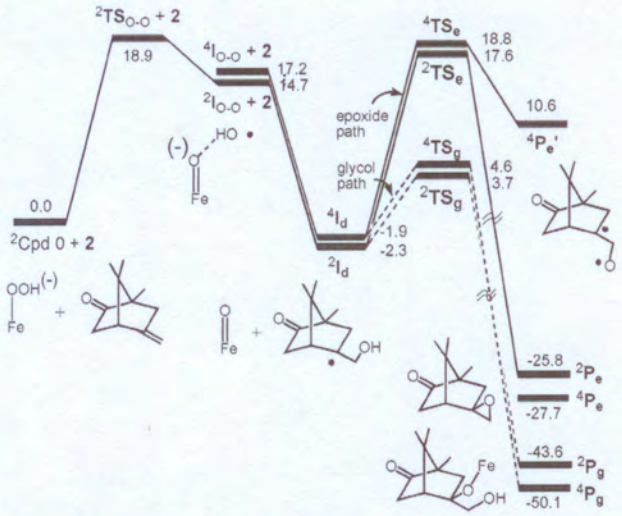

Fig. 14 DFT(UB3LYP/LACV3P+* + NH–S + ε = 5.7 + ZPE) results (adapted from ref. 48, with permission from Elsevier) for the mechanism of the epoxidation of **2** by Cpd 0 *via* the mechanism starting with O–O bond homolysis. Please note the competition between the epoxidation and glycol pathways.

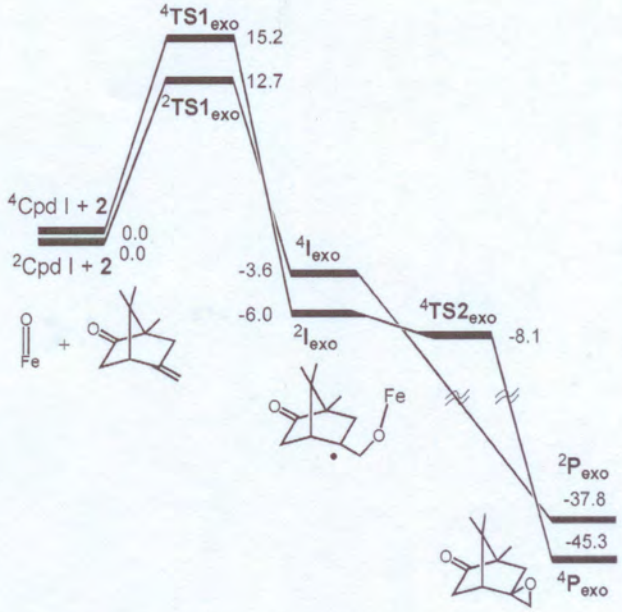

Fig. 15 DFT(UB3LYP/LACV3P+* + NH–S + ε = 5.7 + ZPE) results (adapted from ref. 48, with permission from Elsevier) for the mechanism of the epoxidation of **2** by Cpd I.

will compete favorably with heme degradation *via meso* attack (see Fig. 13 inset (a)).

Subsequent to the attack on the double bond, the $\mathbf{I}_d$ intermediate can undergo a radical coupling reaction, whereby the radical, derived from the hydroxyl attack on **2**, couples with the oxo group of Cpd II (recall Cpd II is a diradical like $^3O_2$), and leads to a ferric-glycol complex, $\mathbf{P}_g$. Being a radical coupling process, this reaction has a small barrier *ca.* 6 kcal mol^{-1}.

Alternatively, Cpd II can abstract a hydrogen atom from the hydroxyl group of the radical intermediate in $\mathbf{I}_d$, and cause ring closure to form the epoxide product. This latter step involves significant electronic reorganization (C–H bond breaking, Fe=O bond breaking, C–O bond formation, and electron shift from the organic moiety to convert the Fe(IV) to Fe(III)), and therefore the corresponding barrier is large, *ca.* 20 kcal mol^{-1}. As such, it is clear that Cpd 0 will not lead to epoxidation of **2**, but would rather generate the corresponding glycol (1,2-diol). Nevertheless, the glycol path may be less plausible within the enzymatic environment due to the steric restraints of the substrate in the active site of $P450_{cam}$, where Tyr96 can hold the carbonyl by a hydrogen bond and restricts its movements.[48] We can tentatively deduce that were Cpd 0 the reactive species in the T252A mutant of CYP101, one would have expected to find alongside the epoxide of **2** also some of the corresponding 1,2-diol. Finding the glycol product is important because its formation is a clearer signature of Cpd 0 reactivity than having merely an epoxide product, especially since the latter can be easily formed with Cpd I.

Indeed, as shown in Fig. 15, epoxidation of **2** by Cpd I,[48] leads to a barrier of 12.7 kcal mol^{-1} for the LS state; 6.2 kcal mol^{-1} lower than the barrier to the rate-controlling step for Cpd 0 (Fig. 14). Once again we conclude that *in the presence of Cpd I, Cpd 0 will be silent towards the epoxidation of* **2**. However, *in the absence of Cpd I*, Cpd 0 may become a by-default oxidant *via* the mechanism that starts with O–O bond homolysis. Without the observation of the glycol, and having no definitive proof that Cpd 0 is the reactive species of the mutant, there will remain a lingering question: can Cpd I still be present in the mutant but be formed slowly and with too poor a juxtaposition to perform hydroxylation, but still in a favorable position to allow some epoxidation?

Interestingly, like Cpd I, one can see from Fig. 14 that *Cpd 0 is predicted to react by the two-state reactivity* (*TSR*) *scenario* and to lead to some loss of stereochemistry in cases where the double bond carries some stereochemical *cis* or *trans* information. However, a much greater loss is predicted for Cpd 0, since the quartet transition state $^4\mathbf{TS}_e$ which is almost at the same energy as the doublet species, leads to the triplet diradical substrate in $^4\mathbf{P}_e'$.[48]

Sulfoxidation by Cpd 0: We tried to apply the same homolytic mechanism to the sulfoxidation of DMS. All our attempts showed that the OH$^\bullet$ radical cannot transfer an oxygen atom to sulfur, the energy expense is simply too high (>25 kcal mol^{-1}). It may well be that the sulfoxidation can proceed *via* the Cpd II moiety after O–O bond homolysis, but this was not explored further since it seemed to be the same process that was already studied in Fig. 12b, where the proximal oxygen of Cpd 0 is transferred to DMS.

Acid catalysis of the oxidation reactions by Cpd 0: All attempts to study the effect of acid catalysis on the reactivity of Cpd 0, resulted in the $Fe^{III}(H_2O_2)$ complex,[67,48] once the proton was given freedom and was not constrained to remain in the proton source (*e.g.*, $NH_4^+(H_2O)_2$). We therefore studied also the reactivity of ferric-hydrogen peroxide in C–H hydroxylation,[67] and performed preliminary calculations for C=C epoxidation.[48] Indeed, the presence of a second proton on the proximal oxygen lowered the barriers (but the overall barrier for the processes were still higher than those of Cpd I). However, the binding energy of H_2O_2 to the ferric porphyrin is rather small (*ca.* 10 kcal mol^{-1}) and smaller than the barrier to C–H hydroxylation. This in turn means that the $Fe^{III}(H_2O_2)$ complex will lead to uncoupling (H_2O_2 release) in preference to substrate oxidation.[67] The ratio of uncoupling to substrate oxidation will depend greatly on the

substrate; reactive ones will exhibit higher substrate oxidation yields. Thus, establishing the role of the $Fe^{III}(H_2O_2)$ in substrate oxidation merits future attention.

6.3 An assessment of the reactivity of the two oxidant of P450

Theory shows that in the presence of Cpd I, Cpd 0 would not be a competent oxidant, unless the barrier separating Cpd 0 and Cpd I is larger than the barrier to oxidation by Cpd 0, which does not seem to be the case.[31,52] This statement is in line with experimental observations that the Fe^{III}–OOH species in the T252A mutant of CYP101 is incapable of camphor hydroxylation.[38] This is also in line with the demonstration that in nonheme systems the Fe^{III}–OOH species is silent under the conditions where the Fe^{IV}=O species is reactive.[93] As such, at present, the reactivity patterns of C–H hydroxylation by the WT enzymes are best understood in terms of TSR (MSR[15,76,82]) of Cpd I in its various spin states. The interpretations that the reactivity of the WT enzyme arises from a competition of Cpd I and Cpd 0,[6,37,61] or that Cpd 0 is the only oxidant,[68] do not seem tenable.

In mutant enzymes, it is conceivable that if indeed Cpd I is absent, then Cpd 0 can do the job, albeit more sluggishly.[38,48] What is missing in P450 research is a direct characterization of the reactivity of Cpd 0 in the mutant: Which oxygen in the Fe–OOH moiety is transferred to the substrate? What are the *KIE* patterns for *e.g.*, C–H hydroxylation? These are some of the questions that need to be addressed before a fruitful discussion can go on, on this topic. An experimental study like the one recently conducted for nonheme systems[93] is sorely missing in the P450 field. Another nagging question is whether Cpd I really does not exist in the mutant? What is the precise mechanism of the conversion of Cpd 0 to Cpd I, and what are the energetic aspects of the process? Here theory can play a more active role than it has done so far. But this would require a Herculean effort using DFT/MM studies of the Cpd 0 → Cpd I conversion in WT,[52] T252A and T252A/D251N mutants.

7 Conclusions

The role of theory is not to merely generate "accurate" numbers (something which is anyway still impossible for systems like P450), but rather to paint global pictures and generate new ideas that can hopefully lead to new and more meaningful experiments. The present review highlights this role of theory and shows that the accessiblity of the spin states of Cpd I, its electron deficiency and dense orbital manifold *lead to TSR and MSR scenarios, which describe the simultaneous reactivity of many states.* These scenarios lead to intriguing consequences, and generate, in some cases, reactivity patterns as though belonging to two or more different oxidants. So far, many of the experimental data can be understood in terms of the TSR paradigm without a need to invoke the reactivity of Cpd 0 for the WT enzymes.[7,16,18,60,100–103] The spin states of Cpd I emerge from generally trustworthy computational procedures,[36] and their degeneracy can be reasoned *a priori* also by theoretical considerations of the nature of Cpd I.[22,64] Model Cpd I systems are abundant,[5,103] and are known to have two closely lying spin states. As such, if Cpd I is the active species of P450, as is indeed suggested by experiment, then these spin states also exist "in the flasks" of the experimentalist.

The problem is: how precisely can one probe these states? An essential element, which is still missing in the TSR (MSR) scheme, is some quantitative information on the rate of spin crossover between the two spin states *vis-à-vis* the radical rearrangment and rebound rates. Understanding this factor may provide the mechanistic chemists with additional means to articulate the concept and design experiments for testing it. Based on previous experience[104] the spin–orbit coupling that is needed to induce spin-state transitions should be small in cases like the doublet and quartet states of Cpd I and of the radical complex intermediates, $^{2,4}\mathbf{I}_{rad}$ (Fig. 6). In such a case, the interconversion of the ^{4}Cpd I and ^{2}Cpd I will still be competitive with the slower process of H-abstraction. However, the interconversion of the $^4\mathbf{I}_{rad}$ and $^2\mathbf{I}_{rad}$ species will be slow compared with rebound, and will be competitive with rearrangement for very slow clocks, but incompetitive with the rearrangement of the ultrafast clocks (Fig. 2b). Thus, the TSR scenario is likely to have different features/manifestations depending on the competition of all these events. The advent of spin–orbit calculations and a proper rate theory will be needed to make further progress on this issue.

As we showed above for benzene hydroxylation, and desaturation reactions, *the enzyme sometimes uses one of the spin states selectively.* Recently, it was shown that *N*-dealkylation proceeds only *via* the low-spin state.[105] It was further demonstrated that the spin-state degeneracy in Cpd I and in its species along both C–H hydroxylation and C=C epoxidation pathways, can be affected dramatically by external electric fields.[106] These results along with the recent demonstration of magnetic-field effects in oxidative reactions by horseradish peroxidase[107] pose some exciting prospects of probing and affecting spin-selective chemistry by P450s.

Our attempts to gauge the reactivity of Cpd 0 led to a clear conclusion: *Cpd 0 is less reactive than Cpd I for* C=C *epoxidation*, C–H *hydroxylation and sulfoxidation.* Thus, when Cpd I is present in the cycle, Cpd 0 will be silent, unless of course, the barrier for the conversion of Cpd 0 to Cpd I is higher than the barriers to oxidation by Cpd 0. Since this does not seem to be the case,[31,52] theory does not support a scenario whereby Cpd 0 and Cpd I compete for oxidation of substrates. We are aware of the most recent study of Cryle and De Voss,[108] with $P450_{BM3}$, which strongly implies that sulfur oxidation is effected by Cpd 0 in both the WT and T268A mutant. However, all our studies so far exclude this interpretation. Electrophilic reactivity of Cpd 0 is deemed to be very low since the species is an anion.[69] The reactivity through the proximal oxygen atom of Cpd 0 may be promoted by general acid catalysis ("pull" by water molecules) and/or by nucleophilic substrates, like reactive olefins.[5,71] Alternatively, Cpd 0 may react *via* initial O–O bond homolysis and generation of a reactive OH$^\bullet$ radical, in which case one would expect to find the distal oxygen of Cpd 0 in the oxidized substrate. In the case of Cpd 0 reacting with an olefin, *via* the homolytic mechanism, we find that a most likely product is the *gem*-diol; *its presence can be a marker reaction of Cpd 0, if the latter were reactive.* Despite these possibilities for the reactivity of Cpd 0, there is still a lingering question: do the P450 mutants really lack Cpd I?

The status of Cpd I in the WT and mutant enzymes, the precise mechanism of conversion of Cpd 0 to Cpd I in P450s and the complete characterization of Cpd I are still the major unknowns in the P450 field. The field, by now distraught by controversies,

This journal is © The Royal Society of Chemistry 2007

is begging for a focused effort to resolve these unknowns. Theory might be a helpful partner to experiment in this endeavor, *e.g.*, in designing new mutants with promising properties, as the recently postulated selenocysteine mutant,[109] or by careful scrutiny of the effects of side chains, residues and additives on the structure and reactivity of P450 species.[72,110,111] Recent experimental observations of Cpd I in $P450_{cam}$ (CYP101) and $P450_{BM3}$, using oxygen surrogate donors,[112,113] will hopefully also enable the study of the substrate oxidation processes by these enzymes.

8 Acknowledgements

The research was supported in part by a DIP grant (DIP-G.7.1) and an ISF grant (16/06). HH is a JSPS Postdoctral Fellow for Research Abroad. SS thanks D. Ballou, I. Denisov and S. G. Sligar for critical reading of the section on Cpd I, and J. H. Dawson, J. T. Groves, and J. P. Jones, for many helpful discussions. Special thanks go to all the coworkers in the P450 field: H. Schwarz, D. Schröder, N. Harris, M. Filatov, F. Ogliaro, S. P. de Visser, P. K. Sharma, S. Cohen, S. Kozuch, E. Derat, C. Hazan, K. Cho, C. Li, W. Wu, W. Thiel, A. Altun, J. Schöneboom, H. Lin, J. Zheng, D. Wang, and N. Reuter.

9 References

1 *Cytochrome P450: Structure, Mechanism and Biochemistry*, ed. P. R. Ortiz de Montellano, Plenum Press, New York, 2nd edn, 1995.
2 *Cytochrome P450: Structure, Mechanism and Biochemistry*, ed. P. R. Ortiz de Montellano, Plenum Press, New York, 3rd edn, 2005.
3 M. Sono, M. P. Roach, E. D. Coulter and J. H. Dawson, *Chem. Rev.*, 1996, **96**, 2841.
4 T. M. Makris, I. G. Denisov, I. Schlichting and S. G. Sligar, Activation of Molecular Oxygen by Cytochrome P450, in *Cytochrome P450: Structure, Mechanism and Biochemistry*, ed. P. R. Ortiz de Montellano, Plenum Press, New York, 3rd edn, 2005, ch. 5, pp. 149–181.
5 J. T. Groves, Models and Mechanisms of Cytochrome P450 Action, in *Cytochrome P450: Structure, Mechanism and Biochemistry*, ed. P. R. Ortiz de Montellano, Plenum Press, New York, 3rd edn, 2005, ch. 1, pp. 1–44.
6 M. Newcomb and P. H. Toy, *Acc. Chem. Res.*, 2000, **33**, 449.
7 P. R. Ortiz de Montellano and J. J. De Voss, *Nat. Prod. Rep.*, 2002, **19**, 477.
8 W.-D. Woggon, *Top. Curr. Chem.*, 1996, **184**, 39.
9 I. G. Denisov, T. M. Makris, S. G. Sligar and I. Schlichting, *Chem. Rev.*, 2005, **105**, 2253.
10 Y. Watanabe, *J. Biol. Inorg. Chem.*, 2001, , **6**, 846.
11 J. T. Groves, *Proc. Natl. Acad. Sci. U. S. A.*, 1998, **95**, 3555.
12 F. P. Guengerich, *Chem. Res. Toxicol.*, 2001, **14**, 611.
13 T. L. Poulos and E. F. Johnson, Structure of Cytochrome P450 Enzymes, in *Cytochrome P450: Structure, Mechanism and Biochemistry*, ed. P. R. Ortiz de Montellano, Plenum Press, New York, 3rd edn, 2005, ch. 3, pp. 87–114.
14 T. M. Makris, K. von Koenig, I. Schlichting and S. G. Sligar, *J. Inorg. Biochem.*, 2006, **100**, 507.
15 S. Shaik, S. P. de Visser and D. Kumar, *J. Biol. Inorg. Chem.*, 2004, **9**, 661.
16 S. Shaik, D. Kumar, S. P. de Visser, A. Altun and W. Thiel, *Chem. Rev.*, 2005, **105**, 2279.
17 B. Meunier, S. P. de Visser and S. Shaik, *Chem. Rev.*, 2004, **104**, 3947.
18 S. Shaik, S. Cohen, S. P. de Visser, P. K. Sharma, D. Kumar, S. Kozuch, F. Ogliaro and D. Danovich, *Eur. J. Inorg. Chem.*, 2004, **35**, 207.
19 S. Shaik and S. P. de Visser, Computational Approaches to Cytochrome P450 Function, in *Cytochrome P450: Structure, Mechanism and Biochemistry*, ed. P. R. Ortiz de Montellano, Plenum Press, New York, 3rd edn, 2005, ch. 2, pp. 45–85.
20 G. H. Loew and D. L. Harris, *Chem. Rev.*, 2000, **100**, 407.
21 D. L. Harris, *Curr. Opin. Chem. Biol.*, 2001, **5**, 724.
22 S. Shaik, S. P. de Visser, F. Ogliaro, H. Schwarz and D. Schröder, *Curr. Opin. Chem. Biol.*, 2002, **6**, 556.
23 R. Davydov, T. M. Makris, V. Kofman, D. E. Werst, S. G. Sligar and B. M. Hoffman, *J. Am. Chem. Soc.*, 2001, **123**, 1403.
24 I. Schlichting, J. Berendzen, K. Chu, A. M. Stock, S. A. Maves, D. E. Benson, R. M. Sweet, D. Ringe, G. A. Petsko and S. G. Sligar, *Science*, 2000, **287**, 1615.
25 R. Rutter, L. P. Hager, H. Dhonau, M. Hendrich, M. Valentine and P. Debrunner, *Biochemistry*, 1984, **23**, 6809.
26 A. Zaks and D. R. Dodds, *J. Am. Chem. Soc.*, 1995, **117**, 10419.
27 M. N. Bhakta, P. F. Hollenberg and K. Wimalasena, *J. Am. Chem. Soc.*, 2005, **127**, 1376.
28 V. Schünemann, C. Jung, J. Terner, A. X. Trautwein and R. Weiss, *J. Inorg. Biochem.*, 2002, **91**, 586.
29 T. Spolitak, J. H. Dawson and D. P. Ballou, *J. Biol. Chem.*, 2005, **280**, 20300.
30 T. S. Dowers, D. A. Rock, D. A. Rock and J. P. Jones, *J. Am. Chem. Soc.*, 2004, **126**, 8868.
31 D. G. Kellner, S.-C. Hung, K. E. Weiss and S. G. Sligar, *J. Biol. Chem.*, 2002, **277**, 9641.
32 D. L. Harris, G. Loew and L. Waskell, *J. Inorg. Biochem.*, 2001, **83**, 309.
33 K. L. Stone, R. K. Behan and M. T. Green, *Proc. Natl. Acad. Sci. U. S. A.*, 2005, **102**, 16563.
34 S. H. Kim, R. Perera, L. P. Hager, J. H. Dawson and B. M. Hoffman, *J. Am. Chem. Soc.*, 2006, **128**, 5598.
35 J. C. Schöneboom, H. Lin, N. Reuter, W. Thiel, S. Cohen, F. Ogliaro and S. Shaik, *J. Am. Chem. Soc.*, 2002, **124**, 8142.
36 J. C. Schöneboom, F. Neese and W. Thiel, *J. Am. Chem. Soc.*, 2005, **127**, 5840.
37 A. D. N. Vaz, D. F. McGinnity and M. J. Coon, *Proc. Natl. Acad. Sci. U. S. A.*, 1998, **95**, 3555.
38 S. Jin, T. M. Makris, T. A. Bryson, S. G. Sligar and J. H. Dawson, *J. Am. Chem. Soc.*, 2003, **125**, 3406.
39 T. Hishiki, H. Shimada, S. Nagano, T. Egawa, Y. Kanamori, R. Makino, S.-Y. Park, S. Adachi, Y. Shiro and Y. Ishimiura, *J. Biochem.*, 2000, **128**, 965.
40 T. Murakami, K. Yamaguchi, Y. Watanabe and I. Morishima, *Bull. Chem. Soc. Jpn.*, 1998, **71**, 1343.
41 M. Newcomb, R. Zhang, R. E. P. Chandrasena, J. A. Halgrimson, J. H. Horner, T. M. Makris and S. G. Sligar, *J. Am. Chem. Soc.*, 2006, **128**, 4580.
42 R. Zhang, R. E. P. Chandrasena, E. Martinez, II, J. H. Horner and M. Newcomb, *Org. Lett.*, 2005, **7**, 1193.
43 Z. Pan, P. R. Zhang and M. Newcomb, *J. Inorg. Biochem.*, 2006, **100**, 524.
44 R. Zhang and M. Newcomb, *J. Am. Chem. Soc.*, 2003, **125**, 12418.
45 D. Ballou, private communication.
46 J. T. Groves, Z. Gross and M. K. Stearns, *Inorg. Chem.*, 1994, **33**, 5065.
47 W. Nam, S.-E. Park, I. K. Lim, M. H. Lim, J. Hong and J. Kim, *J. Am. Chem. Soc.*, 2003, **125**, 14674.
48 H. Hirao, D. Kumar and S. Shaik, *J. Inorg. Biochem.*, 2006, **100**, 2054.
49 C. B. Brewer and J. A. Peterson, *J. Biol. Chem.*, 1988, **263**, 791.
50 M. I. Page and W. P. Jencks, *Proc. Natl. Acad. Sci. U. S. A.*, 1971, **68**, 1678.
51 F. Ogliaro, S. P. de Visser, J. T. Groves and S. Shaik, *Angew. Chem., Int. Ed.*, 2001, **40**, 2874.
52 J. Zheng, D. Wang, W. Thiel and S. Shaik, *J. Am. Chem. Soc.*, 2006, **128**, 13204.
53 A. Bassan, M. R. A. Blomberg, P. E. M. Siegbahn and L. Que, Jr., *Angew. Chem., Int. Ed.*, 2005, **44**, 2939.
54 P. T. de Oliveira, A. Chanda, D. Banerjee, X. Shan, S. Mondal, L. Que, Jr., E. L. Bominaar, E. Münck and T. J. Collins, *Science*, 2007, **315**, 835.
55 J. F. Berry, E. Bill, E. Bothe, S. D. George, B. Mienert, F. Neese and K. Wieghardt, *Science*, 2006, **312**, 1937.
56 S. P. de Visser, D. Kumar, R. Newmann and S. Shaik, *Angew. Chem., Int. Ed.*, 2004, **43**, 5661.
57 P. K. Sharma, S. P. de Visser, F. Ogliaro and S. Shaik, *J. Am. Chem. Soc.*, 2003, **125**, 2291.
58 J. T. Groves and G. A. McClusky, *J. Am. Chem. Soc.*, 1976, **98**, 859.
59 P. R. Ortiz de Montellano and R. A. Stearns, *J. Am. Chem. Soc.*, 1987, **109**, 3415.

60 P. R. de Montellano and J. J. De Voss, Substrate Oxidation by Cytochrome P450 Enzymes, in *Cytochrome P450: Structure, Mechanism and Biochemistry*, ed. P. R. Ortiz de Montellano, Plenum Press, New York, 3rd edn, 2005, ch. 6, pp. 183-245.
61 M. Newcomb, D. Aebisher, R. Shen, R. E. P. Chandrasena, P. F. Hollenberg and M. J. Coon, *J. Am. Chem. Soc.*, 2003, **125**, 6064.
62 P. R. Ortiz de Montellano, *Acc. Chem. Res.*, 1998, **31**, 543.
63 L. Avila, H.-w. Huang, C. O. Damaso, S. Lu, P. Möenne-Loccoz and M. Rivera, *J. Am. Chem. Soc.*, 2003, **125**, 4103.
64 S. Shaik, M. Filatov, D. Schröder and H. Schwarz, *Chem.–Eur. J.*, 1998, **4**, 193.
65 S. P. de Visser, D. Kumar, S. Cohen, R. Shacham and S. Shaik, *J. Am. Chem. Soc.*, 2004, **126**, 8362.
66 J. C. Schöneboom, S. Cohen, H. Lin, S. Shaik and W. Thiel, *J. Am. Chem. Soc.*, 2004, **126**, 4017.
67 E. Derat, D. Kumar, H. Hirao and S. Shaik, *J. Am. Chem. Soc.*, 2006, **128**, 473.
68 R. D. Bach and O. Dmitrenko, *J. Am. Chem. Soc.*, 2006, **128**, 1474.
69 F. Ogliaro, S. P. de Visser, S. Cohen, P. K. Sharma and S. Shaik, *J. Am. Chem. Soc.*, 2002, **124**, 2806.
70 T. Kamachi, Y. Shiota, T. Ohta and K. Yoshizawa, *Bull. Chem. Soc. Jpn.*, 2003, **76**, 721.
71 P. K. Sharma, S. P. de Visser and S. Shaik, *J. Am. Chem. Soc.*, 2003, **125**, 8698.
72 J. Harvey, C. M. Bathelt and A. J. Mulholland, *J. Comput. Chem.*, 2006, **27**, 1352.
73 C. M. Bathelt, J. Zurek, A. J. Mulholland and J. N. Harvey, *J. Am. Chem. Soc.*, 2005, **127**, 12900.
74 F. Ogliaro, S. Cohen, S. P. de Visser and S. Shaik, *J. Am. Chem. Soc.*, 2000, **122**, 12892.
75 F. Ogliaro, S. Cohen, M. Filatov, N. Harris and S. Shaik, *Angew. Chem., Int. Ed.*, 2000, **39**, 3851.
76 H. Hirao, D. Kumar, W. Thiel and S. Shaik, *J. Am. Chem. Soc.*, 2005, **127**, 13007.
77 S. Cohen, PhD Thesis, The Hebrew University of Jerusalem, in preparation.
78 S. Cohen, S. Kozuch, C. Hazan and S. Shaik, *J. Am. Chem. Soc.*, 2006, **128**, 11028.
79 S. P. de Visser, F. Ogliaro, P. K. Sharma and S. Shaik, *J. Am. Chem. Soc.*, 2002, **124**, 11809.
80 S. Shaik and A. Shurki, *Angew. Chem., Int. Ed.*, 1999, **38**, 586.
81 D. Kumar, S. P. de Visser, P. K. Sharma, S. Cohen and S. Shaik, *J. Am. Chem. Soc.*, 2004, **126**, 1907.
82 D. Kumar, S. P. de Visser and S. Shaik, *Chem.–Eur. J.*, 2005, **11**, 2825.
83 S. P. de Visser and S. Shaik, *J. Am. Chem. Soc.*, 2003, **125**, 7413.
84 C. M. Bathelt, L. Ridder, J. Mulholland and J. N. Harvey, *J. Am. Chem. Soc.*, 2003, **125**, 15004.
85 C. Li, C. Zhang, W. Wu and S. Shaik, yet unpublished data.
86 D. Kumar, S. P. de Visser and S. Shaik, *J. Am. Chem. Soc.*, 2004, **126**, 5072.
87 J. C. Hackett, R. W. Brueggemeier and C. M. Hadad, *J. Am. Chem. Soc.*, 2005, **127**, 5224.
88 A. E. Rettie, M. Boberg, W. A. Rettenmeier and T. A. Baillie, *J. Biol. Chem.*, 1988, **263**, 13733.
89 M. D. Wand and J. A. Thompson, *J. Biol. Chem.*, 1986, **261**, 14049.
90 W. M. Atkins and S. G. Sligar, *J. Am. Chem. Soc.*, 1987, **109**, 3754.
91 E. J. Mueller, P. J. Loida and S. G. Sligar, Twenty-five Years of P450cam Research, in *Cytochrome P450: Structure, Mechanism and Biochemistry*, ed. P. R. Ortiz de Montellano, Plenum Press, New York, 2nd edn, 1995, ch. 3, pp. 83–124.
92 Y. Goto, T. Matsui, S. Ozaki, Y. Watanabe and S. Fukuzumi, *J. Am. Chem. Soc.*, 1999, **121**, 9497.
93 M. J. Park, J. Lee, Y. Suh, J. Kim and W. Nam, *J. Am. Chem. Soc.*, 2006, **128**, 2630.
94 K. Lemma and A. Bakac, *Inorg. Chem.*, 2004, **43**, 6224.
95 R. E. White, S. G. Sligar and M. J. Coon, *J. Biol. Chem.*, 1980, **255**, 11108.
96 A. J. Allentoff, J. L. Bolton, A. Wilks, J. A. Thompson and P. R. Ortiz de Montellano, *J. Am. Chem. Soc.*, 1992, **114**, 9744.
97 J. T. Groves and Y. Watananbe, *J. Am. Chem. Soc.*, 1988, **110**, 8443.
98 P. K. Sharma, R. Kevorkiants, S. P. de Visser, D. Kumar and S. Shaik, *Angew. Chem., Int. Ed.*, 2004, **116**, 1129.
99 C. Colas and P. R. Ortiz de Montellano, *Chem. Rev.*, 2003, **103**, 2305.
100 X. He and P. R. Ortiz de Montellano, *J. Biol. Chem.*, 2004, **279**, 39479.
101 M. J. Cryle, J. M. U. Stuthe, P. R. Ortiz de Montellano and J. J. De Voss, *Chem. Commun.*, 2004, 512.
102 K. Auclair, Z. Hu, D. M. Littlê, P. R. Ortiz de Montellano and J. T. Groves, *J. Am. Chem. Soc.*, 2002, **124**, 6020.
103 J. T. Groves, *J. Inorg. Biochem.*, 2006, **100**, 434.
104 D. Danovich and S. Shaik, *J. Am. Chem. Soc.*, 1997, **119**, 1173.
105 C. Li, W. Wu, D. Kumar and S. Shaik, *J. Am. Chem. Soc.*, 2006, **128**, 394.
106 S. Shaik, S. P. de Visser and D. Kumar, *J. Am. Chem. Soc.*, 2004, **125**, 11746.
107 M. S. Afanasyeva, M. B. Taraban, P. A. Purtov, T. V. Leshina and C. B. Grissom, *J. Am. Chem. Soc.*, 2006, **128**, 8651.
108 M. J. Cryle and J. J. De Voss, *Angew. Chem., Int. Ed.*, 2006, **45**, 8221.
109 S. Cohen, D. Kumar and S. Shaik, *J. Am. Chem. Soc.*, 2006, **128**, 2649.
110 A. Altun, S. Shaik and W. Thiel, *J. Comput. Chem.*, 2006, **27**, 1324.
111 J. Zurek, N. Foloppe, J. N. Harvey and A. J. Mulholland, *Org. Biomol. Chem.*, 2006, **4**, 3931.
112 T. Spolitak, J. H. Dawson and D. P. Ballou, *J. Inorg. Biochem.*, 2006, **100**, 2034.
113 G. M. Raner, J. I. Thompson, A. Haddy, V. Tangham, N. Bynum, G. R. Reddy, D. P. Ballou and J. H. Dawson, *J. Inorg. Biochem.*, 2006, **100**, 2045.

This journal is © The Royal Society of Chemistry 2007

Reactivity of High-Valent Iron–Oxo Species in Enzymes and Synthetic Reagents: A Tale of Many States

SASON SHAIK,* HAJIME HIRAO, AND DEVESH KUMAR†

Department of Organic Chemistry and The Lise Meitner-Minerva Center for Computational Quantum Chemistry, The Hebrew University of Jerusalem, Givat Ram Campus, 91904 Jerusalem, Israel

Received December 18, 2006

ABSTRACT

The Account discusses the phenomenon of two-state reactivity (TSR) or multistate reactivity (MSR) in high-valent metal–oxo reagents, projecting its wide-ranging applicability starting from the bare species, through the reagents made by Que, Nam, and collaborators, to the Mn(V)–oxo substituted polyoxometalate, all the way to Compound I species of heme enzymes. The Account shows how the behaviors of all these variegated species derive from a simple set of electronic structure principles. Experimental trends that demonstrate TSR and MSR are discussed. Diagnostic mechanistic probes are proposed for the TSR/MSR scenario, based on kinetic isotope effect, stereochemical studies, and magnetic- and electric-field effects.

Introduction

High-valent metal–oxo complexes are ubiquitous species used in nature and in the laboratory for the purpose of oxygenation of organic compounds. While iron is the most common metal in these species, there are also complexes with manganese–oxo, copper–oxo, and other moieties.[1] These species are formed in enzymes by O–O bond activation of O_2 or H_2O_2, depending on the class of enzymes, or synthetically by use of oxygen donors, e.g., PhI=O, which transfer oxygen to the transition metal (Scheme 1).[2]

These species, in heme and non-heme systems,[2] seem to share mechanistic features; they cause bond activation leading to unstable intermediates, e.g., by abstraction of hydrogen from alkanes, proton abstraction coupled with electron transfer (PCET) from phenols,[3] π-cleavage of C=C double bonds, etc. The initial bond activation is then followed by oxygen transfer from the transition metal–oxygen species to the organic intermediate, as in alkane hydroxylation by cytochrome P450,[4] or the radical itself will undergo oligomerization reactions as in plant peroxidases.[3]

The importance of metal–oxo species cannot be overstated, and the interest in their reaction mechanisms matches this distinction. Since an experimental proof of mechanism is not a simple matter, mechanistic bioinorganic chemistry has evolved with significant interplay of experiment and theory. In this sense, theoretical chemistry, specifically density functional theory (DFT) and hybrid DFT/molecular mechanics (DFT/MM) calculations,[4,5] has been playing an essential role in providing mechanistic data and structures of unstable intermediates and in deriving useful concepts.

An important role of theory is to provide insight and paint global pictures. In this sense, the two-state reactivity (TSR) and multistate reactivity (MSR) concepts[4,6] have emerged in response to intriguing experimental data, which have indicated that oxygenation reactions by enzymes like P450 and synthetic transition metal–oxo reagents behave as though more than one oxidant species were involved in the process. This apparent observation has generated lively mechanistic debates,[4,7] which are reminiscent of the heydays of physical organic chemistry, where intellectual chemistry figured prominently. In oxygenation reactions by P450, the recognition of TSR and MSR in 1998[8] eventually led to resolution of enigmatic issues and to predictions of novel mechanistic features.[4,7] Since, in the meantime, the TSR/MSR scenario has been repeatedly produced by theory in a variety of processes, including enzymes[3] and synthetic reagents,[9] our purpose here is to highlight the wide-ranging applicability of the concept and its insight into reactivity, to draw generalities, and to suggest mechanistic probes of TSR/MSR scenarios.

TSR/MSR Scenarios in Bond Activation Reactions

Figures 1–5 show TSR/MSR scenarios in five different systems. All these cases share one common feature; they involve energy profiles of at least two spin states that either criss-cross or remain in proximity. This is the fundamental feature of the TSR/MSR scenario, whereby different states coproduce different reaction intermediates and products in a given process. The figures also exhibit differences, which we would like to understand and generalize.

Figure 1 depicts the energy profiles for the gas-phase conversion of H_2 to water by FeO^+.[10] The figure exhibits doubling of the energy profile into sextet [high-spin (HS)] and quartet processes [low-spin (LS)], where the LS state crosses below the HS transition state and hence potentially mediates the transformation. This figure is an archetype

Sason Shaik is a quantum chemist, a former student of Nicolaos Epiotis, and a former postdoc of Roald Hoffmann. His current interests are in developing general concepts for bonding and reactivity and in modeling of metalloenzymes and bioinorganic reactions.

Hajime Hirao is a native of Japan and a student of Tomohiko Ohwada. He is at present a JSPS postdoc of S. Shaik. His interests are in method development and in structure and reactivity in bioinorganic chemistry.

Devesh Kumar is a native of India and a student of Mihir Roychoudhury. He was a postdoc of S. Shaik and is currently a postdoc of W. Thiel. His present interests are in modeling cytochrome P450.

* To whom correspondence should be addressed. Telephone: +972 (0)2 658 5909. Fax: +972 (0)2 658 4033. E-mail: sason@yfaat.ch.huji.ac.il.

† Current address: Max-Planck-Institut für Kohlenforschung, Kaiser-Wilhelm-Platz 1, D-45470 Mülheim an der Ruhr, Germany.

10.1021/ar600042c CCC: $37.00 © 2007 American Chemical Society
Published on Web 05/09/2007

Scheme 1. O–O Bond Activation in Iron-Based Complexes and Enzymes

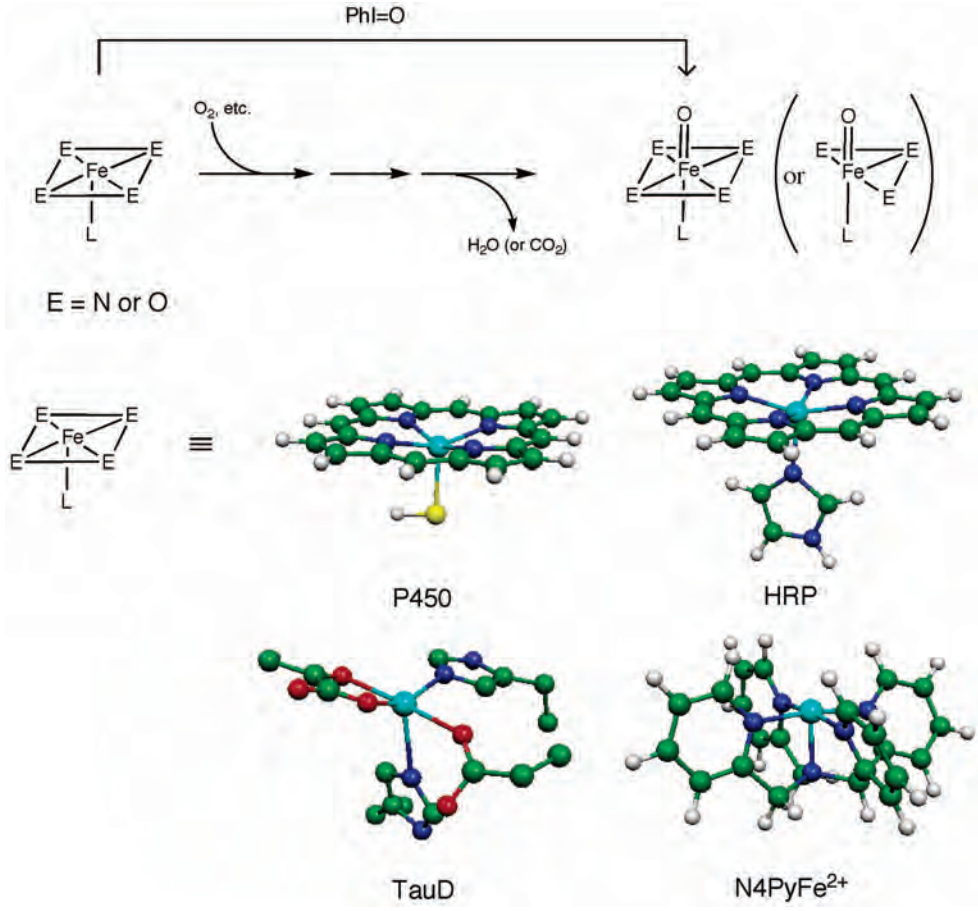

of the energy profiles corresponding to the activation of alkanes by transition metal–oxo cations.[6a,c,11,12]

Figure 2 shows a C–H hydroxylation reaction by the active species of the enzyme cytochrome P450, so-called Compound I (Cpd I). Panel (a) shows the gas-phase mechanism,[13,14] while panel (b) shows the mechanism by which the bulk polarity of the protein is mimicked using a low dielectric constant ($\varepsilon = 5.7$) and the amidic NH–S interactions with the thiolate ligand of Cpd I in P450s[15] are modeled by addition of two NH_3 molecules.[4,14] Figure 2a exhibits doublet- and quartet-state profiles that are roughly parallel throughout the H-abstraction step. Subsequently, the doublet intermediate "rebounds" and forms an alcohol complex in a barrier-free manner, while the quartet intermediate faces a barrier to rebound. There is also a low-lying sextet-state surface that behaves like the quartet surface. Notably, the H-abstraction transition states ($\mathbf{TS}_{\mathrm{H}}$) carry Roman numerals that indicate the different oxidation states of the iron center. Figure 2b shows that the interactions of Cpd I with the "environment" bring more states into the act,[14] some with Fe(III) others with Fe(IV). The doublet states exhibit effectively concerted processes with barrier-free rebounds, while the quartet states have stepwise mechanisms with barriers to rebound. This reactivity scenario was termed MSR to signify the multitude of states that contribute to product formation.

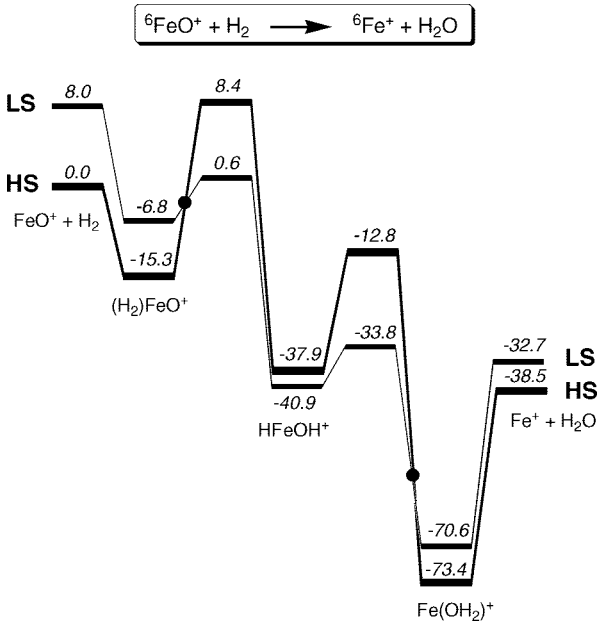

FIGURE 1. DFT(B3LYP)-calculated TSR scenario in the gas-phase oxygenation of H_2 by FeO^+.[10] The labels HS and LS indicate the relative spin quantum number.

Figure 3 shows the MSR scenario in styrene epoxidation by Cpd I.[16] Here too, a few states run parallel through the C=C activation phase and then produce HS quartet and LS doublet organic radical and cationic complexes. Thus,

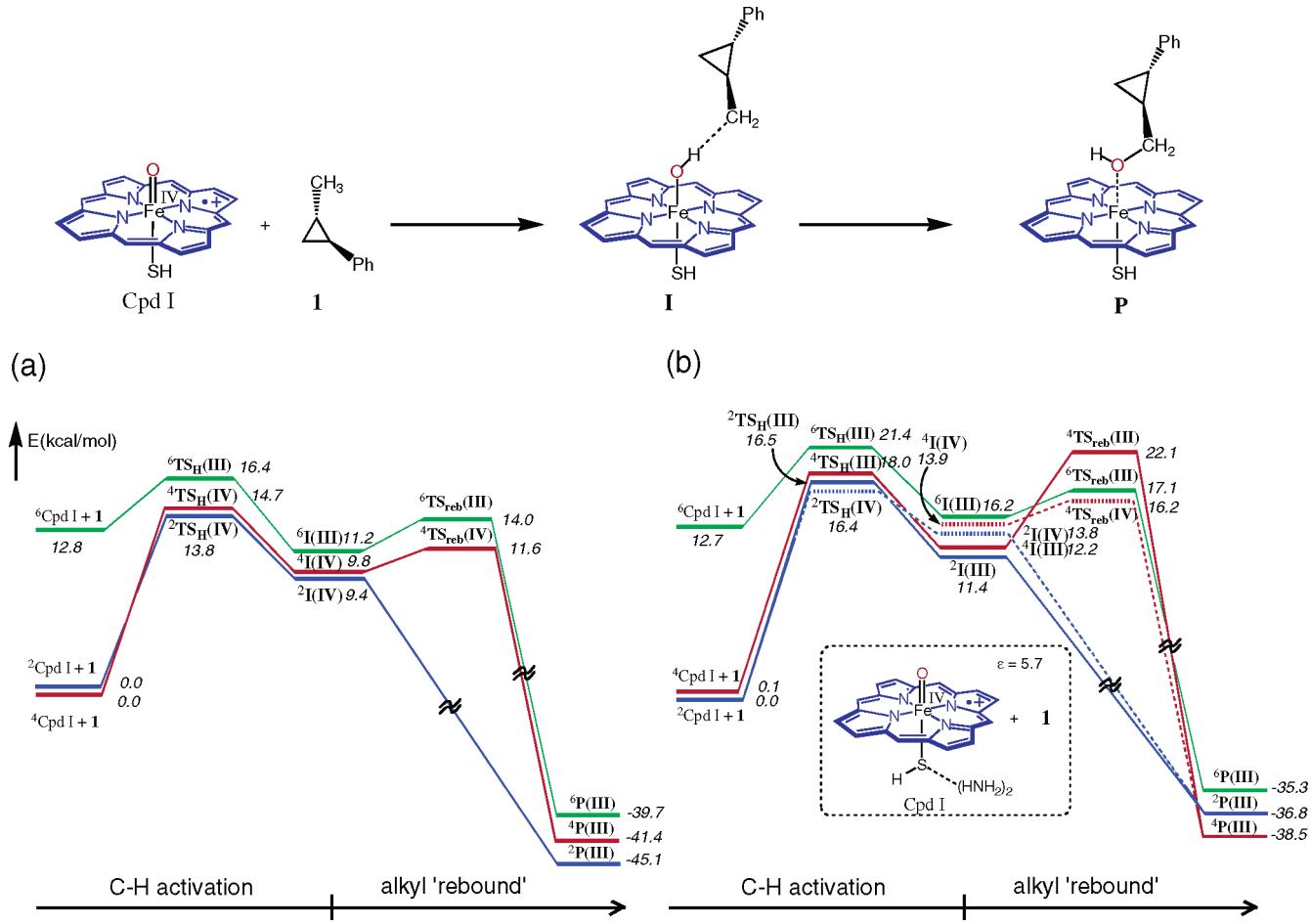

FIGURE 2. DFT(B3LYP/LACVP)-calculated TSR/MSR scenarios in the C–H hydroxylation of **1** by Compound I of P450: (a) in the gas phase and (b) with NH–S interactions (included in geometry optimization) and bulk polarity effect. Relative energies include ZPEs.

Figures 2 and 3 share a common behavior: the HS mechanisms are stepwise with sufficiently long lived intermediates, while the LS mechanisms are effectively concerted with ultrashort lived intermediates. All heme systems investigated by us possess similar features irrespective of the axial ligand (thiolate as in P450 or imidazole as in HRP or microperoxidases).

Figure 4 shows a manganese–oxo complex, made from the polyoxometalate cage $[PW_{12}O_{40}]^{3-}$ via replacement of one W=O moiety with a Mn^{V}=O moiety. Such a reagent was recently characterized by NMR and shown to possess a singlet ground state, and to perform C–H and C=C activations.[17] The figure exhibits an MSR scenario in the allylic hydroxylation of propene, which is mediated by the triplet and quintet states that cut through the high singlet-state barrier.

By now we have calculated the reactivity of some 10 different L_5Fe^{IV}=O reagents made[18] with the polydentate nitrogenous ligands. Figure 5 shows a typical TSR/MSR scenario, with C–H activation and rebound, in the hydroxylation of cyclohexane (**CH**) by $[N4Py]Fe^{IV}O^{2+}$.[9] It is seen that the quintet state cuts below the barrier of the ground triplet state and mediates the transformation. Note that, unlike before, here the HS process is effectively concerted.

Taken together, Figures 1–5 exhibit an impressive collage of processes that share the common feature of spin-state crossing and entanglement. Can we make sense of these features and generalize the picture? Do these features have characteristic mechanistic impact? In the following sections, we address these questions.

Origins of TSR/MSR Scenarios

Transition metals have five d orbitals that are close in energy, with energy spacing depending on the strengths of the ligand–metal interactions. Sometimes the ligands have high-lying orbitals close to the d block orbitals.[4] Additionally, during bond activation, the organic substrate develops high-lying orbitals close to the d block. As such, the number of closely lying orbitals that are not doubly occupied is large and becoming larger as the reaction progresses, hence giving rise to a dense manifold of states. The other factor is the exchange interaction between the electrons in d orbitals, e.g., 20 kcal/mol on Fe, which favors high-spin situations.[9,19] Taken together, metal–oxo reagents involve a dense manifold of states differing in orbital occupancy, transition metal and ligand oxidation states, and spin quantum numbers. In general, these states will remain close along the reaction pathways, and as their

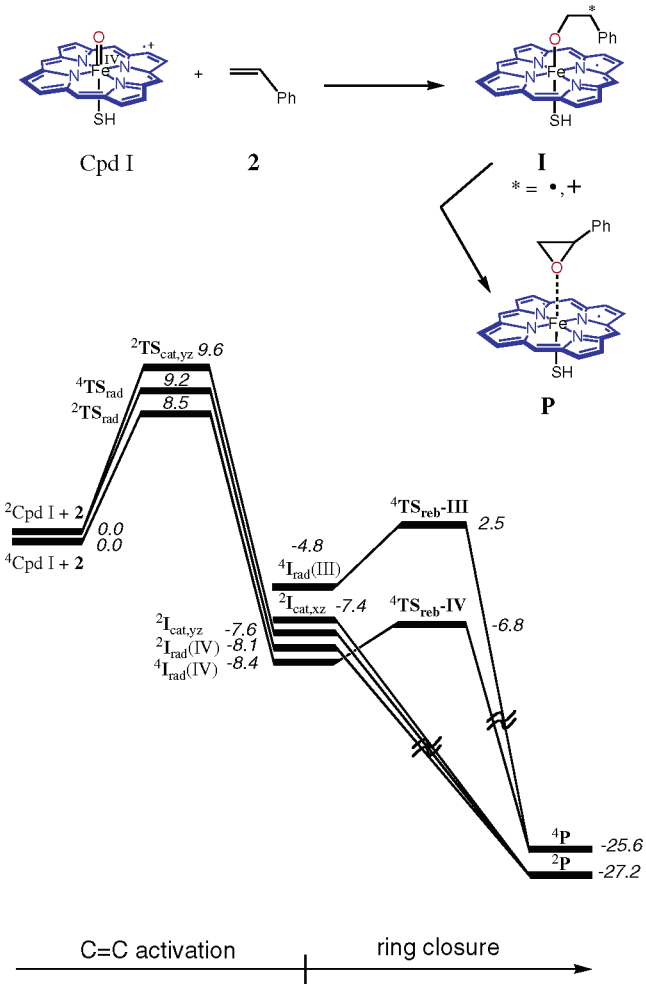

FIGURE 3. B3LYP/LACVP(+ZPE)-calculated MSR scenario during styrene epoxidation by Compound I.[16]

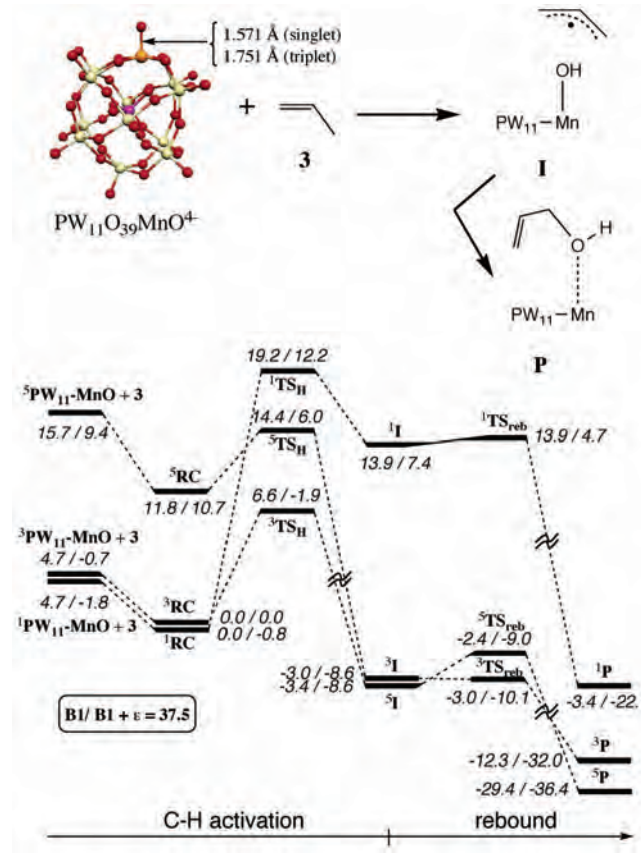

FIGURE 4. BLYP-calculated MSR scenario during allylic hydroxylation of propene by $[PW_{11}O_{39}\text{-}Mn^{V}{=}O]^{4-}$ ($PW_{11}MnO$). Energies are reported for a gas phase and an acetonitrile solution ($\varepsilon = 37.5$).[17] RC is the reactant complex.

number increases, when orbitals of the molecule undergoing oxidation become accessible, one obtains the TSR/MSR scenarios as in Figures 1–5. The following analyses illustrate these factors.

Figure 6a shows orbitals and low-lying states of $[N4Py]Fe^{IV}{=}O^{2+}$.[9] This d block spreads into the three-below-two pattern typical of distorted octahedra; the group of three has a low-lying δ orbital and two π^* orbitals with antibonding $Fe(d_\pi)-O(p_\pi)$ character, while the group of two involves σ^* antibonding orbitals, one with the equatorial nitrogen lone pairs and one with the two axial ligands. With oxidation state IV, the d block contains four electrons; the ground state has the $\delta^2\pi^{*1}\pi^{*1}$ configuration with a triplet spin quantum number ($S = 1$), and the corresponding singlet state ($S = 0$) lies higher by 8.4 kcal/mol. These states are analogues of the triplet and singlet states of O_2, and this is common to all iron–oxo complexes, which maintain the stable triplet $\pi^{*1}\pi^{*1}$ FeO configuration.[1,3,4,6,8,9,12,19] A low-lying state is the quintet ($S = 2$)[18] $\delta^1\pi^{*1}\pi^{*1}\sigma^*_{xy}{}^1$ configuration; its energy relative to $S = 1$ is a balance between the large $\delta \rightarrow \sigma^*_{xy}$ orbital energy gap, determined by the N–Fe interaction strength, favoring $S = 1$, and the five new d–d exchange interactions[19] (20 kcal/mol each) that favor $S = 2$.[9] On balance, this creates a small energy gap between the two states and sets the stage for TSR.

The transformation of these two states along the reaction pathway is represented by the orbital diagram[9] in Figure 6b. It depicts the changes in orbital occupancy using the oxidation-state formalism; in this formalism, the substrate undergoing oxidation donates two electrons to the iron–oxo complex. These diagrams are represented in three panels, corresponding, from left to right, to the reactants, the intermediate ($^{2S+1}$**I**), and the product ($^{2S+1}$**P**). Thus, with the triplet state as the beginning, as H-abstraction occurs, one electron shifts from the σ_{CH} orbital of the alkane to a π^*(FeO) orbital, and a spin develops on the alkyl radical due to the singly occupied orbital, ϕ_C, in intermediate ^{3}**I**. Subsequently, as the alkyl radical rebounds, the electron shifts from ϕ_C to the $\sigma^*_{z^2}$ orbital and generates the alcohol complex, ^{3}**P**. On the quintet surface, the H-abstraction is attended by an electron shift from σ_{CH} to $\sigma^*_{z^2}$. Now an electron with spin up is shifted to increase the rate of exchange on the iron by four new d–d interactions.[9] This large exchange stabilization lowers the quintet barrier below the triplet state and leads to their crossing (Figure 5). In the rebound step, starting from ^{5}**I**, the electron shifts from ϕ_C to the δ orbital of the iron–hydroxo complex. Since the δ orbital is low-lying, there will be no barrier to rebound on the quintet surface. By contrast, on the triplet surface, the

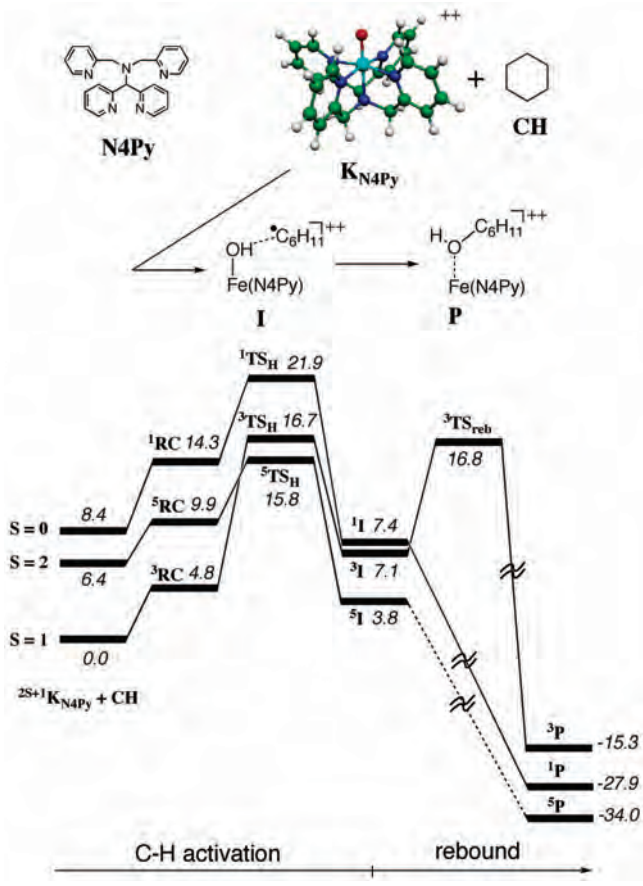

FIGURE 5. B3LYP/LACV3P++**//LACVP-calculated TSR/MSR scenario during hydroxylation of cyclohexane by $[N4Py]Fe^{IV}O^{2+}$.[9] Relative energies include ZPEs and solvation energies in acetonitrile (ε = 37.5).

electron shifts, during rebound, to the high-lying $\sigma^*_{z^2}$ orbital (without much gain of exchange), and therefore, the triplet state features a significant barrier. As such, we obtain in Figure 5 a TSR scenario, with a triplet-state mechanism that has a large H-abstraction barrier and a significant rebound barrier, and an effectively concerted quintet mechanism that cuts through the triplet barrier.

The orbital diagram in Figure 6a can be used to explain also the MSR scenario of the Mn(V)=O complex in Figure 4. Now, the ground state is a singlet with two electrons on the lowest-lying δ orbital. With no electrons in the π^*(MnO) orbitals, the Mn=O bond of this state is short and strong (Figure 4).[17] Therefore, the singlet state will have a high barrier to bond activation. The process will be mediated by higher-spin states, which possess long and hence activated Mn=O bonds.

Figure 7 shows the orbitals and low-lying states of Cpd I of P450.[4,14,20] Here, two porphyrin orbitals, a_{2u} and a_{1u}, are sufficiently high in energy (recall, the porphyrin periphery is "antiaromatic") to intermingle with the d block orbitals. Since the total oxidation state of the complex is V, the iron will be Fe^{IV}, while the porphyrin will assume the remaining oxidation equivalent as a cation radical. With a d^4 configuration, and one unpaired electron on porphyrin, the ground state, nascent from the $\delta^2\pi^{*1}\pi^{*1}a_{2u}{}^1$ configuration, has two spin states: quartet ($S = {}^3/_2$) and doublet ($S = {}^1/_2$), labeled as $^{4,2}A_{2u}$. However, the dense orbital block generates a manifold of states squeezed within 26 kcal/mol, e.g., $^2A_{2u}$ where the two electrons in the $\pi^{*1}\pi^{*1}$ configuration are paired into a singlet state, $^{2,4}A_{1u}$ states,[21] and Fe^V=O states, where one electron from the $\delta^2\pi^{*1}\pi^{*1}$ configuration goes to fill the a_{2u} orbital of the porphyrin. In addition, the exchange d–d interaction plays its role and generates $^{6,4}A_{2u}$ states with a $\delta^1\pi^{*1}\pi^{*1}a_{2u}{}^1\sigma^*_{xy}{}^1$ configuration, and within 14 kcal/mol of the ground states. What a rich manifold of states!

The orbital evolution diagram in Figure 8 focuses on the species nascent from the doubly degenerate ground state, $^{2,4}A_{2u}$, during C–H hydroxylation (C=C epoxidation).[4,7] In the course of H-abstraction (C=C activation), an electron shifts from the σ_{CH} (π_{CC}) orbital to one of the singly occupied orbitals of Cpd I and generates four intermediates. Shifting the electron to a_{2u} creates the $^{2,4}\mathbf{I}_{rad}$(IV) intermediates having Fe^{IV} centers, while shifting it to π^*(FeO) generates the $^{2,4}\mathbf{I}_{rad}$(III) intermediates with Fe^{III} centers and porphyrin radical cations.

In the rebound (ring closure) steps, the electron will shift from ϕ_C to the heme to form the ferric–alcohol (epoxide) complexes [^{2,4}**P**(III)]. In the $^2\mathbf{I}_{rad}$(III) intermediate, the electron will shift to a_{2u}, while in $^2\mathbf{I}_{rad}$(IV), the electron will shift to $\pi_{xz}{}^*$(FeO), both cases leading to ^{2}**P**(III). By contrast, in the ^{4}**I** intermediates, spin conservation requires shifting electron(s) to higher-lying orbitals. In $^4\mathbf{I}_{rad}$(IV), the electron will shift to the $\sigma^*_{z^2}$ orbital, whereas in $^4\mathbf{I}_{rad}$(III), two electrons must shift to avoid spin frustration: one electron from ϕ_C to $\sigma^*_{z^2}$ while another, with spin down, from the filled π^*(FeO) to a_{2u}.[6b,7]

Since in the doublet manifold the electron is shifted to low-lying orbitals, these rebound (ring closure) processes are barrier-free, whereas the quartet-state processes which involve shifting electrons to the higher-lying $\sigma^*_{z^2}$ orbital face significant rebound barriers.[7] Furthermore, since the electronic reorganization involving $^4\mathbf{I}_{rad}$(III) rebound is more complex than that of $^4\mathbf{I}_{rad}$(IV), the rebound (ring closure) barriers nascent from $^4\mathbf{I}_{rad}$(III) will be higher than those from $^4\mathbf{I}_{rad}$(IV).[7] Reviewing Figures 2 and 3 shows that these are the computed patterns. Thus, the LS states proceed via effectively concerted mechanisms, while the HS states have stepwise mechanisms, with radical intermediates whose lifetimes depend on the oxidation state of iron in the complex; the radical in the $^4\mathbf{I}_{rad}$(III) intermediate is longer-living than the one in the $^4\mathbf{I}_{rad}$(IV) intermediate.

Note that shifting the second electron without creating the O–C bond would leave behind alkyl cations. Here again, the resultant doublet $^2\mathbf{I}_{cat}$(III) species collapses to the alcohol (epoxide) without a barrier (e.g., Figure 3). The quartet-spin intermediate will be higher in energy and longer-living and may lead to free carbocations[7,13] and other products as well.[16] As such, the reactivity scheme is rich with radicals and cations, in two spin manifolds and with different mechanistic behaviors.

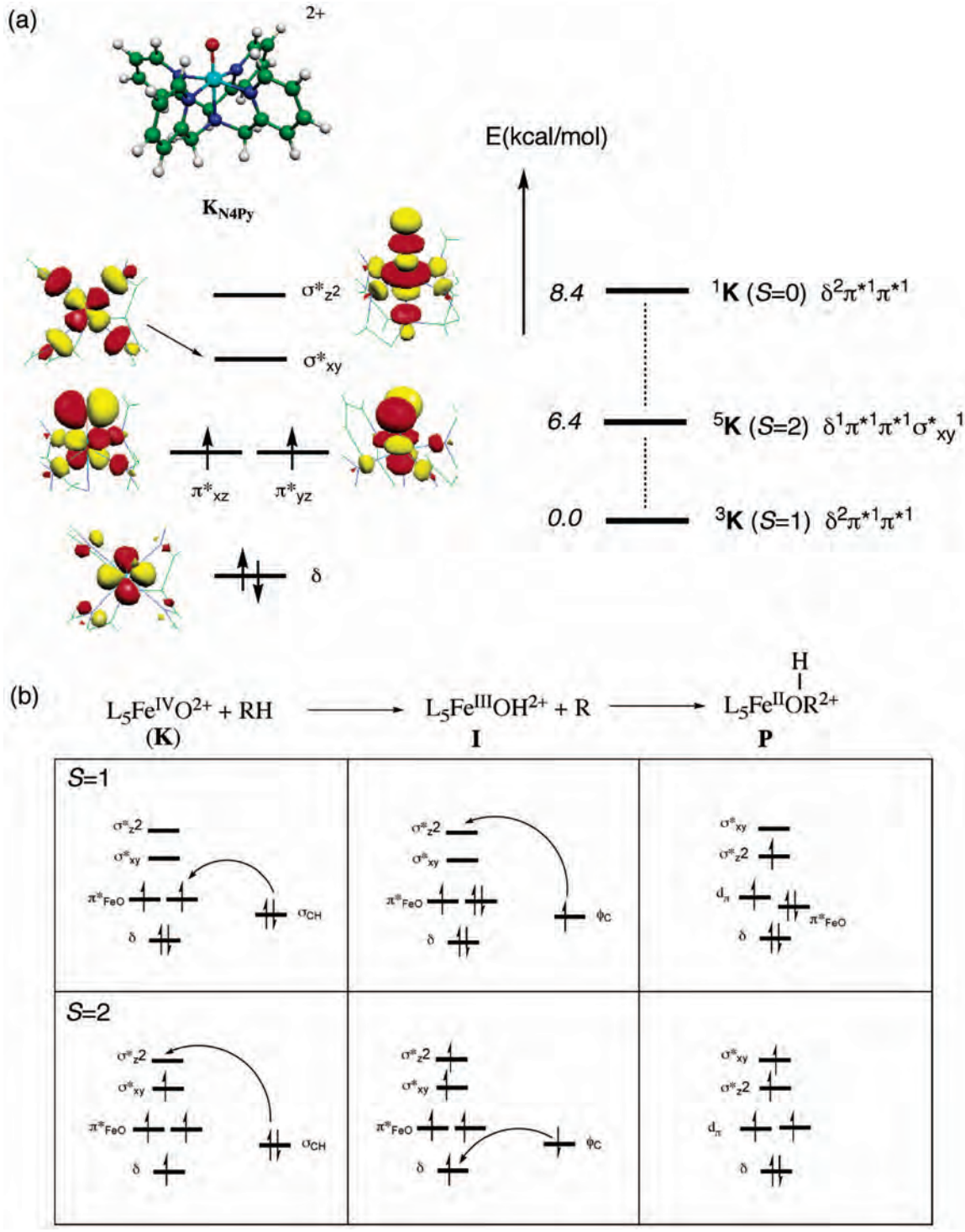

FIGURE 6. (a) Energy diagram of d block orbitals of [N4Py]Fe^{IV}=O^{2+} (**K**) and the low-lying spin states (S = 1, 2, or 0), with their B3LYP/LACV3P++**//LACVP relative energies in solution (ε = 37.5). (b) Orbital occupancy evolution during C–H hydroxylation.

Features of TSR/MSR Scenarios

While the effect of spin-state crossing on rates is occasionally important,[22,23] there are key aspects of TSR/MSR which arise from the fact that the participating states have different transition-state structures, different stereochemical or regiochemical preferences, and intermediates with different lifetimes. As discussed below, these scenarios will pose a challenge in mechanistic studies based on single-state reactivity concepts.

Catalysis by Spin Crossover. An example of this effect is the reaction in Figure 1.[6a,c;10–12] Thus, since the HS TS lies well above the threshold energy of the reactants, the HS reaction is in fact gas-phase "forbidden" at ambient temperatures. What enables oxidation of H_2 to water, at all, is the LS surface that cuts through the HS surface and mediates the bond activation process.[6a,c;10] What limits the efficiency of the reaction is the poor spin-orbit coupling interaction at the spin-inversion junctions in

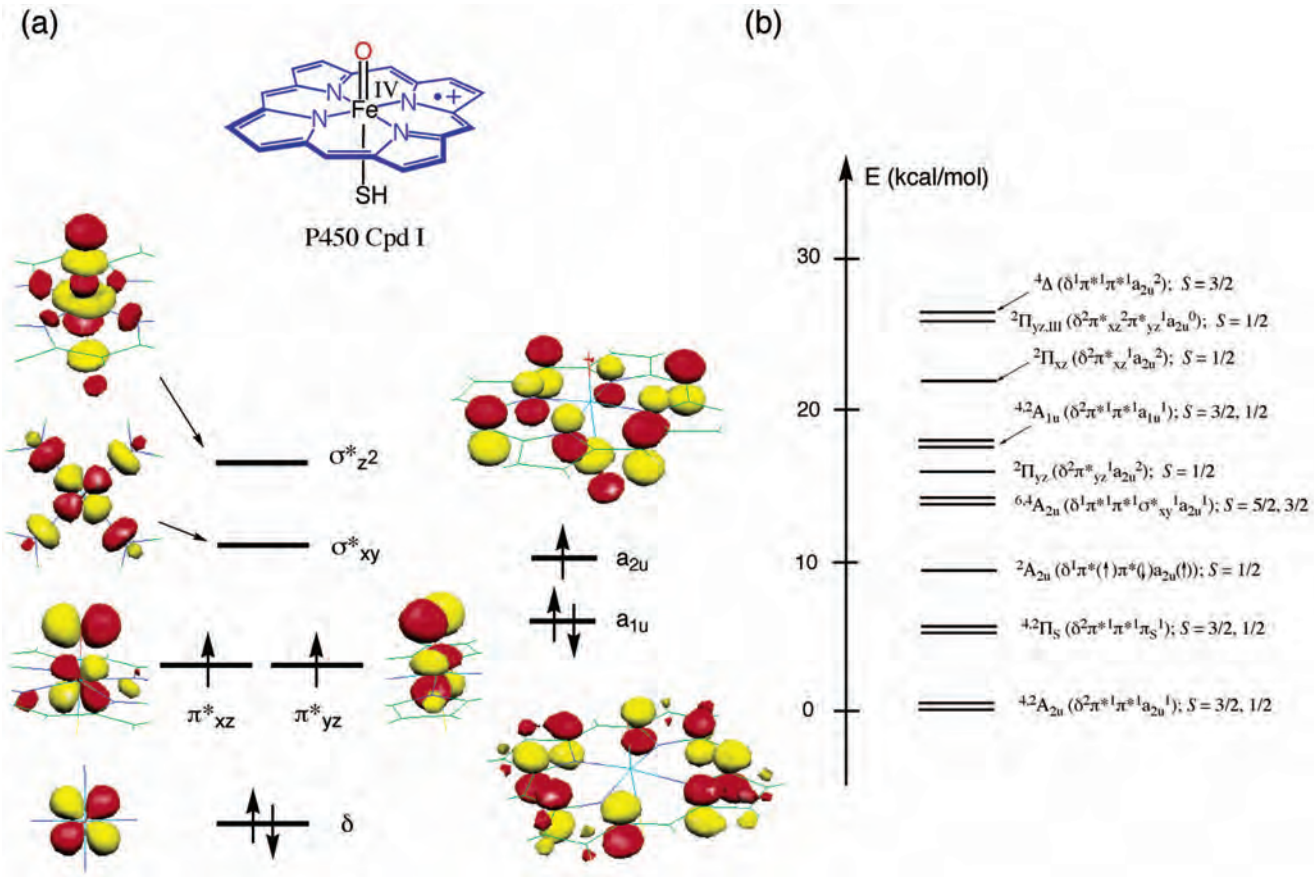

FIGURE 7. (a) Energy diagram of key orbitals of Cpd I of P450. (b) Low-lying states and their relative B3LYP energies in the gas phase.

Figure 1.[10,23] Nevertheless, without the LS–HS crossing, no oxidation would have occurred at ambient temperatures! Note that the hydroxylation reactions mediated by [N4Py]–Fe^{IV}=O^{2+} (Figure 5),[9] $PW_{11}O_{39}$–Mn^{V}=O^{4-} (Figure 4),[17] etc.,[9] also exhibit "catalysis" by spin crossover.

Different Products from Different States. Another intriguing TSR feature is the fact that the two spin states prefer different mechanisms that produce different intermediates and products. This spin-dependent mechanistic phenomenon has been observed throughout the gamut of oxidation processes; from the simple reaction of FeO^{+} [10,24] to the complex mechanisms of enzymes and synthetic catalysts.[3,4,9,13,17]

In P450 oxygenation (Figures 2 and 3), the LS states lead to products via effectively concerted pathways while the HS states proceed by stepwise mechanisms with sufficiently long lived intermediates. As argued,[4,7] this dichotomy is behind the controversial lifetimes of the radical intermediates quantified by assuming product formation via a single reactive state. Thus, as illustrated in Figure 9a, in a single-state scenario the alkyl radical formed by H-abstraction can either rebound to give an unrearranged alcohol (***U***) or first rearrange and then rebound to form a rearranged alcohol (***R***). The apparent lifetime (τ_{app}) of the radical is then determined from the branching ratio [***R***/***U***] of the radical and the speed (k_R) of its rearrangement. However, the use of ultrafast radical probes (Figure 9b) for quantifying τ_{app} [25] produced unrealistically short lifetimes that could not support the presence of intermediates. Nevertheless, radical intermediates abound in this reaction,[2b,26] so what could be the source of this contradiction?

Figure 2 reveals that TSR is the source of these unrealistic apparent lifetimes. Thus, since the LS doublet state is effectively concerted, it will produce only unrearranged (***U***) products. By contrast, the stepwise HS processes will mainly produce the rearranged product (***R***). Therefore, the quantity [***R***/***U***] is a measure of the relative yields of the HS and LS processes and not a true measure of the branching of a single radical species into two products as required by the equation in Figure 9a. As such, for very fast radical clocks (as in Figure 9b), the [***R***/***U***] ratio will be determined primarily by the relative H-abstraction barriers on the HS-quartet and LS-doublet surfaces. Since ^{2}**TS$_H$** is lower than ^{4}**TS$_H$**,[4,7] the yield of the LS reaction is higher than the HS yield, and hence, [***R***/***U***] will predict a τ_{app} shorter than the real lifetime of the radical on the HS surfaces. Furthermore, modeling the rebound barrier predicts that[4,7] the HS barrier will gradually diminish as the radical center becomes a better electron donor; at some limiting donor capability, the barrier will vanish, thus making both HS and LS processes effectively concerted. Figure 10[4,7] depicts the TSR for the substrate where the methyl group is replaced with an isopropyl group, making the resulting radical a powerful donor. Now, the two states generate ferric–alcohol products in effectively concerted manners and are therefore predicted to produce

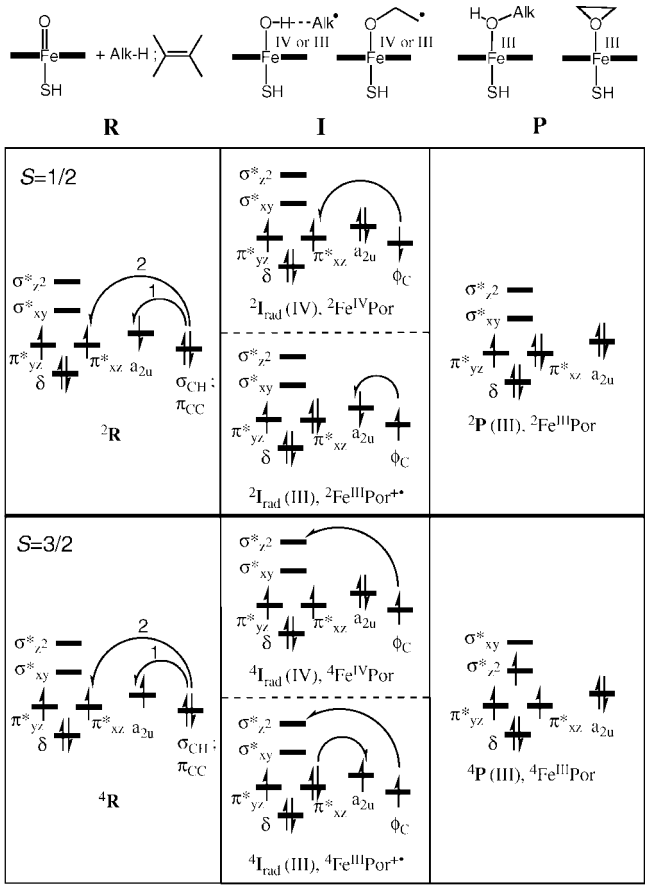

FIGURE 8. Orbital occupancy evolution during C–H hydroxylation (C=C epoxidation) by P450 Cpd I.

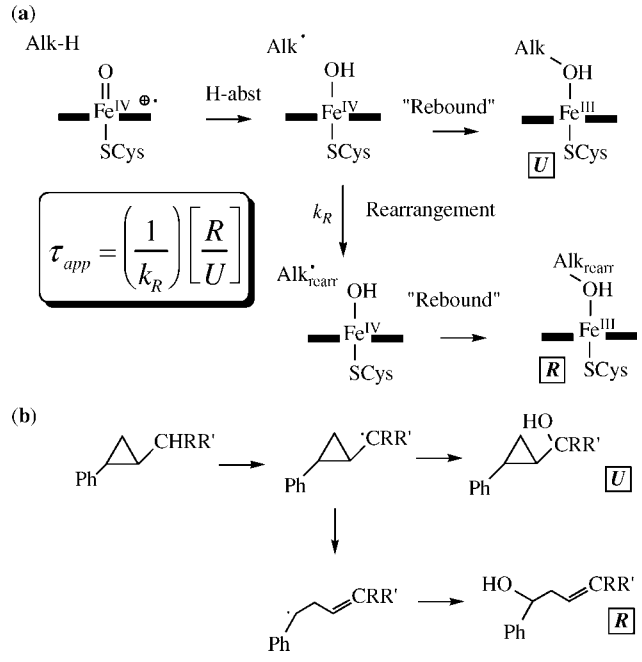

FIGURE 9. (a) Rebound mechanism and the apparent radical lifetime. (b) ***U*** and ***R*** products of ultrafast radical clocks.

no rearranged alcohols. Experimentally, the [***R***/***U***] quantity for this probe is <0.01.[25]

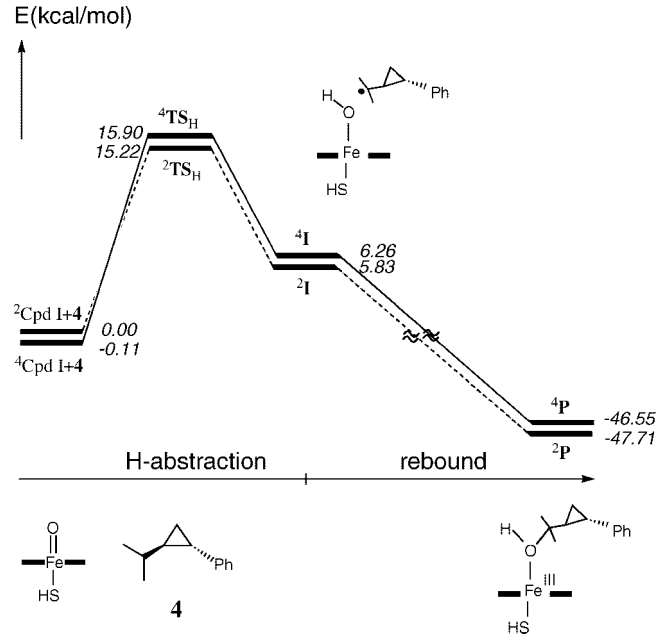

FIGURE 10. B3LYP/LACVP results for C–H hydroxylation of **4**.[13]

Scheme 2. TSR and SSR in Two Ends of a Single Molecule

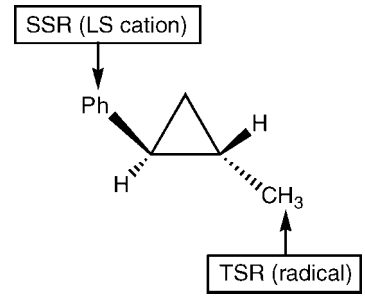

Let us highlight two more consequences of TSR/MSR scenarios. Thus, during C=C epoxidation (Figure 3), there are radical intermediates in the HS manifold with two different oxidation states on iron, namely, ^{4}**I**$_{rad}$(IV) and ^{4}**I**$_{rad}$(III). As reasoned above, the ring-closure barrier for ^{4}**I**$_{rad}$(III) is much larger. With a small barrier, the ^{4}**I**$_{rad}$(IV) state will lead mostly to epoxide products with scrambled stereochemistry [due to almost free C–C bond rotation in ^{4}**I**$_{rad}$(IV)], whereas the ^{4}**I**$_{rad}$(III) state will have sufficient lifetime to produce heme-alkylated and aldehyde complexes that require surmounting significant barriers.[4,16]

Sometimes, the energy difference between the LS and HS activation barriers is significant, leading therefore to a spin-selective single-state reactivity (SSR). An amusing case is the probe substrate *trans*-2-phenylmethanecyclopropane in Scheme 2. This substrate leads to hydroxylation of both the methyl and phenyl groups.[13] As we showed in Figure 2, the methyl group hydroxylation proceeds by TSR and MSR with radical intermediates. By contrast, the phenyl oxidation proceeds via a LS cationic Meisenheimer complex.[27]

Prospective: Probes of TSR and MSR

Experimental probing of TSR/MSR scenarios is challenging and would require the interplay of experiment and theory.

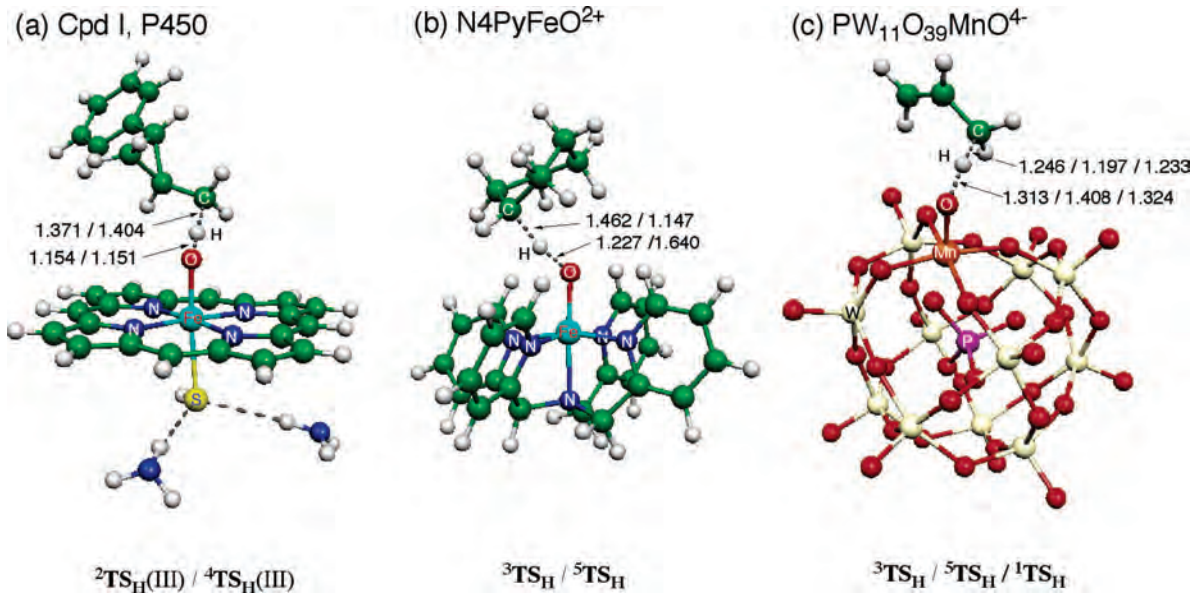

FIGURE 11. O–H–C distances (B3LYP/LACVP) for the $^{2S+1}$**TS**$_H$ species of (a) Figure 2b, (b) Figure 5, and (c) Figure 4.

Devising mechanistic probes for TSR/MSR or spin-selective chemistry requires both traditional and unconventional methods:

Measurements of [*R*/*U*]. Consider the C–H bond hydroxylation by the synthetic iron–oxo reagent in Figure 5. Here and in all other related reagents,[9] only the triplet-state surface exhibits a barrier to rebound while the quintet state features an effectively concerted process. This means that a fast radical probe (large rearrangement rate constant) on the triplet manifold will give rise only to ***R*** products, while the quintet-state reaction will lead exclusively to ***U***, thus enabling one to quantify the $[S = 1]/[S = 2]$ reactivity ratio.

Kinetic Isotope Effect Probes. In 1998, we showed that HS and LS processes for C–H bond activation exhibit different semiclassical kinetic isotope effect (KIE) values due to different TS geometries.[10] Figure 11 displays the spin-dependent O–H–C distances in $^{2S+1}$**TS**$_H$ species for C–H bond activation by three different metal–oxo species.[9,14,17] In fact, all the cases we studied possess spin-dependent O–H–C distances.[28] Since the KIE is sensitive to the location of the transition state along the H-transfer coordinate,[28] we expect different KIEs for different spin sates. This feature of the $^{2S+1}$**TS**$_H$ species can serve as a probe of spin-state reactivity.

Scheme 3 shows two examples of spin-dependent KIEs. In the gas-phase C–H bond activation of norbornane by FeO^+ (Scheme 3a), the activation of the C–H$_{endo}$ bond was found to involve a KIE value much smaller than that of the C–H$_{exo}$ bond.[29] This difference was demonstrated[29] to result from two different spin states: the LS quartet activating the *endo* C–H bond and the HS doublet the *exo* C–H bond. In the case of C–H bond hydroxylation of *N*,*N*-dimethylaniline by P450 Cpd I (Scheme 3b),[28] the computed KIE$_{LS}$ value is smaller than the corresponding KIE$_{HS}$. Only the KIE$_{LS}$ value fits the experimental KIE.[30] Theory shows[28] also that ^{2}**TS**$_H$ is 3.7 kcal/mol lower than ^{4}**TS**$_H$, and hence, the reaction will proceed exclusively via the

Scheme 3. KIEs in Two Examples of HS and LS C–H Bond Activations

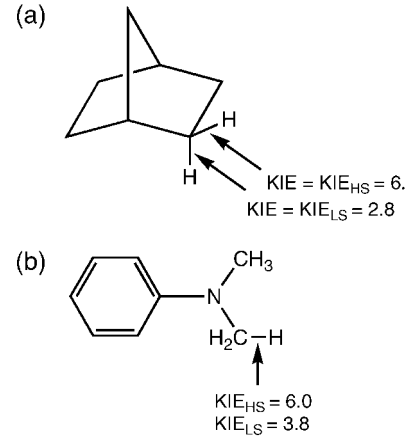

LS state. Similar, yet unpublished, results were obtained for C–H bond hydroxylation of trimethylamine and the series of para-substituted *N*,*N*-dimethylanilines discussed in ref 30. All these examples show that KIE measurement can be a probe of spin-selective chemistry.

A system that should exhibit spectacular KIE features is the C–H bond hydroxylation by the $L_5Fe(IV)$═O reagents (Figure 5).[18] Here, for most iron–oxo complexes,[9] the quintet state cuts below the triplet barrier and will participate in product formation. As predicted recently,[9] the extent of participation of the quintet state should decrease as the strength of the C–H bond increases. From the analogous non-heme enzyme TauD, where the C–H bond activation proceeds on the quintet state,[31] the observed KIE value is >30.[31a] This tunneling-like value occurs since the quintet barrier (for cases with weak C–H bonds) is small, on the order of the C–H vibration energy that can propagate the system across the barrier within the amplitude of a single vibration.[9] Therefore, the measurements[32] of KIE values of 30–50 in C–H bond activations of triphenylmethane and ethylbenzene by, for

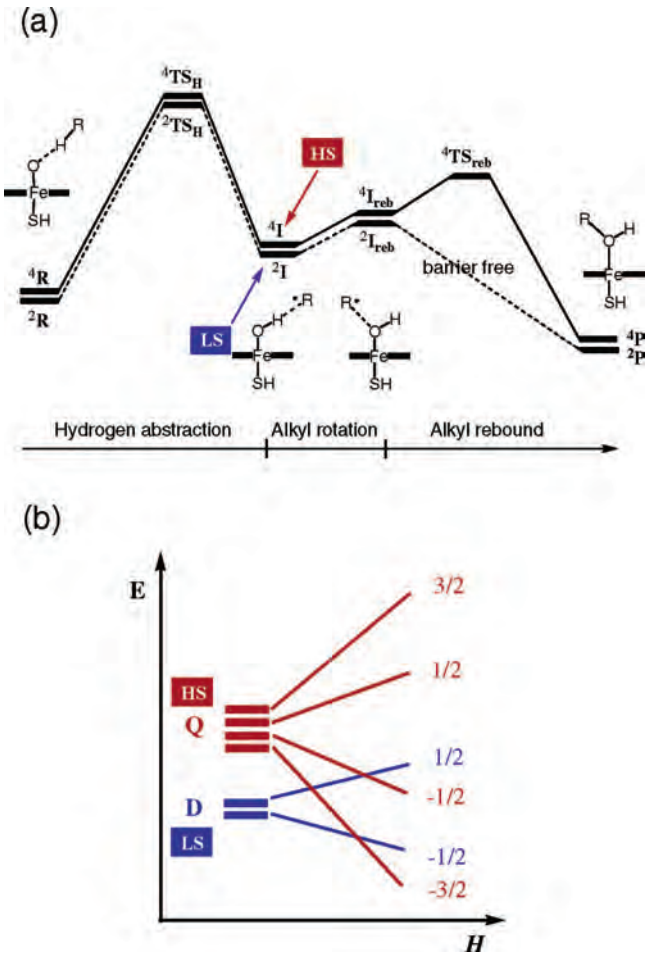

FIGURE 12. (a) Generic TSR in P450 hydroxylation. (b) Effect of magnetic field strength on the spin sublevel energies of the HS and LS intermediates.

example, [N4Py]FeO^{2+} originated in fact in TSR. The TSR prediction[9] that the KIE values should be very large for weaker C–H bonds but normal for cases with stronger C–H bonds is still awaiting a test. Furthermore, using fast radical clocks and measuring KIEs for the rearranged and unrearranged products should reveal major differences in the KIE values for the ***R*** and ***U*** products, differences that are expected to vary also with the strength of the C–H bond.

Magnetic Field Effects in TSR and MSR. As shown in Figures 2,3, and 5, the HS and LS species at the intermediate junction are close in energy. Had the spin inversion in this junction been faster than the rearrangement, all the intermediates would have crossed over to the lowest-energy surface where the reaction is effectively concerted, resulting in complete stereospecificity. The observation of rearranged products, for example, in P450 hydroxylations[2b,26] suggests that spin inversion is slower than rearrangement and rebound. As exemplified in Figure 12, for P450 hydroxylation, a magnetic field will lift the degeneracy of the spin sublevels of the HS-quartet and LS-doublet states, and hence will induce crossings between the spin states, and may thereby affect the spin crossover rates. In such an event, the extent of stereochemical scrambling will vary with the strength of the applied field. Magnetic field effects were demonstrated recently for an oxidation reaction of horseradish peroxidase.[33]

Electric Field and Double-Field Effects in TSR and MSR. External electric fields affect the relative energies of spin states.[34a] For example, when Cpd I reacts with propene, the electric field strength, its direction, and its orientation have selective stabilization effects on the HS and LS transition states of both hydroxylation and epoxidation reactions, as well as on the regiochemical preference for epoxidation versus hydroxylation.[34a] The application of electric fields will also change the relative stability of HS and LS intermediates.[34b] Therefore, double-field experiments, combining electric and magnetic fields, can be utilized to modulate the stereoselectivity and regioselectivity. Electric-field effects, demonstrated in principle for P450,[34a] will be truly spectacular[34b] in highly charged reagents, such as [N4Py]FeO^{2+}, [TMC(L)]$FeO^{1,2+}$, etc.,[2a,18,35] and the functionalized polyoxometalates, e.g., PW_{11}-MnO^{4-}.[17]

Concluding Remarks

This Account focuses on the TSR/MSR concept, its occurrence in the reactions of high-valent metal–oxo reagents, and its manifestations and potential probes. The concept applies well beyond. Our ongoing studies reveal TSR/MSR situations in aziridination and amidation by heme and non-heme iron–nitrido complexes[34b] and in oxidation by vanadium-substituted polyoxometalates. TSR/MSR is also prevalent in a variety of gas-phase and organometallic processes.[22,36]

Concepts are generators of our worlds and the creative means whereby these worlds may change and evolve. The TSR/MSR concept can fashion a mechanistic territory in the surging field of chemical and enzymatic reactivity.

S.S. is supported by the Israel Science Foundation. S.S. thanks his many co-workers in TSR and especially H. Schwarz and D. Schröder with whom this odyssey started. The Account is dedicated to Sigrid Peyerimhoff on her 70th birthday.

References

(1) (a) Ghosh, A. High-Valent Iron Intermediates in Biology. *J. Inorg. Biochem.* **2006**, *100*, 419–880. (b) van Eldik, R. Inorganic and Bioinorganic Mechanisms. *Chem. Rev.* **2005**, *105*, 1917–2722.
(2) (a) Shan, X.; Que, L., Jr. High-Valent Nonheme Iron-Oxo Species in Biomimetic Oxidations. *J. Inorg. Biochem.* **2006**, *100*, 421–433. (b) Groves, J. T. High-Valent Iron in Chemical and Biological Oxidations. *J. Inorg. Biochem.* **2006**, *100*, 434–447.
(3) Derat, E.; Shaik, S. An Efficient Proton-Coupled Electron Transfer Process during Oxidation of Ferulic Acid by Horseradish Peroxidase: Coming Full Cycle. *J. Am. Chem. Soc.* **2006**, *128*, 13940–13949.
(4) Shaik, S.; Kumar, D.; de Visser, S. P.; Altun, A.; Thiel, W. Theoretical Perspective on Structure and Mechanisms of Cytochrome P450 Enzymes. *Chem. Rev.* **2005**, *105*, 2279–2328.
(5) (a) Siegbahn, P. E. M.; Borowski, T. Modeling Enzymatic Reactions Involving Transition Metals. *Acc. Chem. Res.* **2006**, *39*, 729–738. (b) Ryde, U. Combined Quantum and Molecular Mechanics Calculations on Metalloproteins. *Curr. Opin. Chem. Biol.* **2003**, *7*, 136–142.
(6) (a) Shaik, S.; Danovich, D.; Schröder, D.; Schwarz, H. Two-State Reactivity in Organometallic Gas-Phase Ion Chemistry. *Helv. Chim. Acta* **1995**, *78*, 1393–1407. (b) de Visser, S. P.; Ogliaro, F.; Harris,

N.; Shaik, S. Multi-State Epoxidation of Ethene by Cytochrome P450: A Quantum Chemical Study. *J. Am. Chem. Soc.* **2001**, *123*, 3037–3047. (c) Schröder, D.; Shaik, S.; Schwarz, H. Two-State Reactivity as a New Concept in Organometallic Chemistry. *Acc. Chem. Res.* **2000**, *33*, 139–145.

(7) Shaik, S.; Cohen, S.; de Visser, S. P.; Sharma, P. K.; Kumar, D.; Kozuch, S.; Ogliaro, F.; Danovich, D. The "Rebound Controversy": An Overview and Theoretical Modeling of the Rebound Step in C-H Hydroxylation by Cytochrome P450. *Eur. J. Inorg. Chem.* **2004**, *207*, 207–226.

(8) Shaik, S.; Filatov, M.; Schröder, D.; Schwarz, H. Electronic Structure Makes a Difference: Cytochrome P-450 Mediated Hydroxylation of Hydrocarbons as a Two-State Reactivity Paradigm. *Chem.—Eur. J.* **1998**, *4*, 193–199.

(9) Hirao, H.; Kumar, D.; Que, L., Jr.; Shaik, S. Two-State Reactivity in Alkane Hydroxylation by Nonheme Iron-Oxo Complexes. *J. Am. Chem. Soc.* **2006**, *128*, 8590–8606.

(10) Filatov, M.; Shaik, S. Theoretical Investigation of Two-State Reactivity Pathways of H-H Activation by FeO^+: Addition-Elimination, "Rebound" and Oxene-Insertion Mechanisms. *J. Phys. Chem. A* **1998**, *102*, 3835–3846.

(11) (a) Clemmer, D. E.; Chen, Y.-M.; Kahn, F. A.; Armentrout, P. B. State-Specific Reactions of Fe^+ (a^6D,a^4F) with D_2O and Reactions of FeO^+ with D_2. *J. Phys. Chem.* **1994**, *98*, 6522–6529. (b) Fiedler, A.; Schröder, D.; Shaik, S.; Schwarz, H. Electronic Structures and Gas-Phase Reactivities of Cationic Late-Transition-Metal Oxides. *J. Am. Chem. Soc.* **1994**, *116*, 10734–10741.

(12) (a) Yoshizawa, K. Nonradical Mechanism for Methane Hydroxylation by Iron-Oxo Complexes. *Acc. Chem. Res.* **2006**, *39*, 375–382. (b) Shiota, Y.; Yoshizawa, K. Methane-to-Methanol Conversion by First-Row Transition-Metal Oxide Ions: ScO^+, TiO^+, VO^+, CrO^+, MnO^+, FeO^+, CoO^+, NiO^+, and CuO^+. *J. Am. Chem. Soc.* **2000**, *122*, 12317–12326.

(13) Kumar, D.; de Visser, S. P.; Sharma, P. K.; Cohen, S.; Shaik, S. Radical Clock Substrates, Their C-H Hydroxylation Mechanism by Cytochrome P450 and Other Reactivity Patterns: What Does Theory Reveal about Clocks' Behavior. *J. Am. Chem. Soc.* **2004**, *126*, 1907–1920.

(14) Hirao, H.; Shaik, S. Unpublished data .

(15) Poulos, T. L. The Role of the Proximal Ligand in Heme Enzymes. *J. Biol. Inorg. Chem.* **1996**, *1*, 356–359.

(16) Kumar, D.; de Visser, S. P.; Shaik, S. Multi-State Reactivity in the Epoxidation of Styrene by Compound I of Cytochrome P450: Mechanisms of Products and Side Products Formation. *Chem.—Eur. J.* **2005**, *11*, 2825–2835.

(17) Khenkin, A. M.; Kumar, D.; Shaik, S.; Neumann, R. Characterization of Mn(V)-Oxo Polyoxometalate Intermediates and Their Properties in Oxygen Transfer Reactions. *J. Am. Chem. Soc.* **2006**, *128*, 15451–15460.

(18) Bukowski, M. R.; Koehntop, K. D.; Stubna, A.; Bominaar, E. L.; Halfen, J. A.; Münck, E.; Nam, W.; Que, L., Jr. A Thiolate-Ligated Nonheme Oxoiron(IV) Complex Relevant to Cytochrome P450. *Science* **2005**, *310*, 1000–1002.

(19) (a) Carter, E. A.; Goddard, W. A., III. Relationships between Bond Energies in Coordinatively Unsaturated and Coordinatively Saturated Transition-Metal Complexes: A Quantitative Guide for Single, Double, and Triple Bonds. *J. Phys. Chem.* **1988**, *92*, 5679–5683. (b) Carter, E. A.; Goddard, W. A., III. Early- versus Late-Transition-Metal-Oxo Bonds: The Electronic Structure of VO^+ and RuO^+. *J. Phys. Chem.* **1988**, *92*, 2109–2115.

(20) Ogliaro, F.; de Visser, S. P.; Groves, J. T.; Shaik, S. Chameleon States: The High-Valent Metal-Oxo Species of Cytochrome P450 and its Ruthenium Analog. *Angew. Chem., Int. Ed.* **2001**, *40*, 2874–2878.

(21) Hirao, H.; Shaik, S.; Koslowski, P. M. Theoretical Analysis of Structural and Electronic Properties of Metalloporphyrin π-Cation Radicals. *J. Phys. Chem. A* **2006**, *110*, 6091–6099.

(22) Poli, R.; Harvey, J. N. Spin Forbidden Chemical Reactions of Transition Metal Compounds. New Ideas and New Computational Challenges. *Chem. Soc. Rev.* **2003**, *32*, 1–8.

(23) Danovich, D.; Shaik, S. Spin-Orbit Coupling in the Oxidative Activation of H-H by FeO^+. Selection Rules and Reactivity Effects. *J. Am. Chem. Soc.* **1997**, *119*, 1773–1786.

(24) Schröder, D.; Schwarz, H.; Clemmer, D. E.; Chen, Y.; Armentrout, P. B.; Baranov, V. I.; Bohme, D. K. Activation of Hydrogen and Methane by Thermalized FeO^+ in the Gas Phase as Studied by Multiple Mass Spectrometric Techniques. *Int. J. Mass Spectrom. Ion Processes* **1997**, *161*, 175–192.

(25) Newcomb, M.; Toy, P. H. Hypersensitive Radical Probes and the Mechanisms of Cytochrome P450-Catalyzed Hydroxylation Reactions. *Acc. Chem. Res.* **2000**, *33*, 449–455.

(26) For example: (a) Ortiz de Montellano, P. R.; De Voss, J. Oxidizing Species in the Mechanism of Cytochrome P450. *Nat. Prod. Rep.* **2002**, *19*, 477–493. (b) He, X.; Ortiz de Montellano, P. R. Radical Rebound Mechanism in Cytochrome P450-Catalyzed Hydroxylation of the Multifaceted Radical Clocks α- and β-Thujone. *J. Biol. Chem.* **2004**, *279*, 39479–39484.

(27) (a) Bathelt, C. M.; Ridder, L.; Mulholland, A. J.; Harvey, J. N. Mechanism and Structure-Reactivity Relationships for Aromatic Hydroxylation by Cytochrome P450. *Org. Biomol. Chem.* **2004**, *2*, 2998–3005. (b) de Visser, S. P.; Shaik, S. Proton-Shuttle Mechanism Mediated by the Porphyrin in Benzene Hydroxylation by Cytochrome P450 Enzymes. *J. Am. Chem. Soc.* **2003**, *125*, 7413–7425.

(28) Li, C.; Wu, W.; Kumar, D.; Shaik, S. Kinetic Isotope Effect is a Sensitive Probe of Spin State Reactivity in C-H Hydroxylation of *N,N*-dimethylaniline by Cytochrome P450. *J. Am. Chem. Soc.* **2006**, *128*, 394–395.

(29) Harris, N.; Shaik, S.; Schröder, D.; Schwarz, H. Single- and Two-State Reactivity in the Gas Phase C-H Bond Activation of Norbornane by Bare FeO^+. *Helv. Chim. Acta* **1999**, *82*, 1784–1797.

(30) Manchester, J. I.; Dinnocenzo, J. P.; Higgins, L. A.; Jones, J. P. A New Mechanistic Probe for Cytochrome P450: An Application of Isotope Effect Profiles. *J. Am. Chem. Soc.* **1997**, *119*, 5069–5070.

(31) (a) Price, J. C.; Barr, E. W.; Glass, T. E.; Krebs, C.; Bollinger, J. M., Jr. Evidence for Hydrogen Abstraction from C1 of Taurine by High-Spin Fe(IV) Intermediate Detected during Oxygen Activation by Taurine:α-Ketoglutarate Dioxygenase (TauD). *J. Am. Chem. Soc.* **2003**, *125*, 13008–13009. (b) de Visser, S. P. Propene Activation by the Iron-Oxo Active Species of Taurine/α-Ketoglutarate Dioxygenase (TauD) Enzyme. How Does the Catalysis Compare to Heme-Enzymes? *J. Am. Chem. Soc.* **2006**, *128*, 9813–9824.

(32) Kaizer, J.; Klinker, E. J.; Oh, N. Y.; Rhode, J.-U.; Song, W. J.; Stubna, A.; Kim, J.; Münck, E.; Nam, W.; Que, L., Jr. Noneheme $Fe^{IV}O$ Complexes That Can Oxidize the C-H Bonds of Cyclohexane at Room Temperature. *J. Am. Chem. Soc.* **2004**, *126*, 472–473.

(33) Afanasyeva, M. S.; Taraban, M. B.; Purtov, P. A.; Leshina, T. V.; Grissom, C. B. Magnetic Spin Effects in Enzymatic Reactions: Radical Oxidation of NADPH by Horseradish Peroxidase. *J. Am. Chem. Soc.* **2006**, *128*, 8651–8658.

(34) (a) Shaik, S.; de Visser, S. P.; Kumar, D. An External Electric Field Will Control the Selectivity of an Enzymatic-Like Bond Activations. *J. Am. Chem. Soc.* **2004**, *126*, 11746–11749. (b) Hirao, H.; Shaik, S. Unpublished data .

(35) Bukowski, M. R.; Comba, P.; Lienke, A.; Limberg, C.; Lopez De Lardon, C.; Merz, M.; Que, L., Jr. Catalytic Epoxidation and 1,2-Dihydroxylation of Olefins with Bispidine Iron(II)/H_2O_2 Systems. *Angew. Chem., Int. Ed.* **2006**, *45*, 3446–3449.

(36) A tiny sample: (a) Harvey, J. N.; Poli, R.; Smith, K. M. Understanding of Transition Metal Complexes Involving Multiple Spin States. *Coord. Chem. Rev.* **2003**, *238–239*, 347–361. (b) Schwarz, H. On the Spin-Forbiddeness of Gas Phase Ion-Molecule Reactions: A Fruitful Intersection of Experimental and Computational Studies. *Int. J. Mass Spectrom.* **2004**, *237*, 75–105. (c) Hess, J. S.; Leelasubcharoen, S. L.; Rheingold, A. L.; Doren, D. J.; Theopold, K. H. Spin Surface Crossing in Chromium-Mediated Olefin Epoxidation with O_2. *J. Am. Chem. Soc.* **2002**, *124*, 2454–2455. (d) Döhring, A.; Jensen, V. R.; Jolly, P. W.; Thiel, W.; Weber, J. C. Donor-Ligand-Substituted Cyclopentadienylchromium(III) Complexes: A New Class of Alkene Polymerization Catalyst. 2. Phosphinoalkyl-Substituted Systems. *Organometallics* **2001**, *20*, 2234–2245. (e) Strassner, T.; Houk, K. N. Predictions of Geometries and Multiplicities of the Manganese-Oxo Intermediates in the Jacobsen Epoxidation. *Org. Lett.* **1999**, *1*, 419–422. (f) Linde, C.; Koliaï, N.; Norrby, P.-O.; Åkermark, B. Experimental Evidence for Multiple Oxidation Pathways in the (Salen)Mn-Catalyzed Epoxidation of Alkene. *Chem.—Eur. J.* **2002**, *8*, 2568–2573. (g) Jin, N.; Groves, J. T. Unusual Kinetic Stability of a Ground-State Singlet Oxomanganese(V) Porphyrin. Evidence for a Spin State Crossing Effect. *J. Am. Chem. Soc.* **1999**, *121*, 2923–2924.

AR600042C

The Electronic Structure of Reduced Phosphovanadomolybdates and the Implications on Their Use in Catalytic Oxidation Initiated by Electron Transfer

Hajime Hirao,[†] Devesh Kumar,[†] Hui Chen,[†] Ronny Neumann,*[,‡] and Sason Shaik*[,†]

Department of Organic Chemistry and the Lise Meitner-Minerva Center for Computational Quantum Chemistry, The Hebrew University, Jerusalem, Israel 91904, and Department of Organic Chemistry, Weizmann Institute of Science, Rehovot, Israel 76100

Received: December 18, 2006; In Final Form: March 23, 2007

The geometries and electronic structures of the five isomers of $[PV_2Mo_{10}O_{40}]^{5-}$ and its mono- and direduced species were theoretically investigated by means of B3LYP calculations, with an attempt to understand their role as oxidative catalysts in electron-transfer-initiated processes. The calculations reveal the following features: (a) Either in the gas phase or in a solvent, the reduction of the $[PV_2Mo_{10}O_{40}]^{5-}$ produces $[PV_2Mo_{10}O_{40}]^{6,7-}$ ions in which the excess electrons are localized on the vanadium atoms in the corresponding δ orbitals. By contrast, the direduced $[PV_2Mo_{10}O_{40}]^{7-}$ isomers where the one electron is localized on molybdenum are high in energy. Consequently, whereas the five isomers of $[PV_2Mo_{10}O_{40}]^{5-}$ have roughly a statistical distribution, in the direduced species, the 1,4-$[PV_2Mo_{10}O_{40}]^{7-}$ isomer becomes more stable than others. (b) The gas-phase reduction of the parent $[PMo_{12}O_{40}]^{3-}$ anion is exceedingly more favorable (by ca. 250 kcal/mol) than the reduction of $[PV_2Mo_{10}O_{40}]^{5-}$. By contrast, contribution of the solvent exerts a strong leveling effect and makes the reduction potentials of the two species very similar. (c) Since the reduction of $[PV_2Mo_{10}O_{40}]^{5-}$ concentrates high negative charge near the O═VO_4 moiety, this negative charge accumulation will act as an attractor that binds the organic radical cation (cation), which causes a subsequent proton transfer to an oxo ligand of the vanadium. As such, in terms of an electron-transfer catalytic effect, the presence of vanadium in $[PV_2Mo_{10}O_{40}]^{5-}$ creates function for the catalyst. (d) The computations reveal that $[PV_2Mo_{10}O_{40}]^{7-}$ is a diradicaloid that possesses two virtually degenerate states, with singlet and triplet spins. Thus, we may expect two-state reactivity (TSR) in the catalytic reactions of $[PV_2Mo_{10}O_{40}]^{5-}$. Some predictions are made based on these features.

Introduction

Polyoxometalates are versatile compounds that have been investigated as oxidation catalysts for the past twenty five years or so.[1] Research within the field of homogeneous oxidation catalysis on aerobic oxidation catalyzed by phosphovanadomolybdates, $[PV_xMo_{12-x}O_{40}]^{(3+x)-}$ ($x = 0-6$ but most often 2), has attracted considerable attention. The $[PV_2Mo_{10}O_{40}]^{5-}$ compound is a polyoxometalate of the α-Keggin-type structure, and due to the presence of two vanadium centers, it has five isomers that are depicted in Figure 1. To date, it has not been possible to separate these isomers and to study them individually. The literature also indicates that the isomer distribution may well be a function of the solvent.[2] Also, depending on the ratio of Mo/V used in its synthesis, $[PV_2Mo_{10}O_{40}]^{5-}$ may contain varying small amounts (usually <5 mol %) of $[PVMo_{11}O_{40}]^{4-}$ and $[PV_3Mo_9O_{40}]^{6-}$ as impurities.

Despite the unresolved isomer distribution and exact purity in each investigation, $[PV_2Mo_{10}O_{40}]^{5-}$ has extensively and successfully been used in catalysis.[3] Reactions described include the oxidative hydration of alkenes,[4] the oxidation of bromide and iodide coupled with electrophilic aromatic substitution,[5] the oxidation of organic and inorganic sulfur compounds,[6] and the oxydehydrogenation of cyclic dienes,[7] alcohols, amines,[8] and phenols.[9] It has been also shown that, with $[PV_2Mo_{10}O_{40}]^{5-}$, electron-transfer oxygenation reactions for the oxidation of hydrocarbons at moderate temperatures were possible.[10] Additional interesting findings are that $[PV_2Mo_{10}O_{40}]^{5-}$ appears to catalyze the formation of hydroxyl radicals in the presence of CO and O_2, leading to the oxidation of methane and benzene[11] and, together with palladium salts, catalyzes the oxidative coupling of benzene with acrylates.[12]

Often, the defining mechanistic motif of most of the above reactions is that $[PV_2Mo_{10}O_{40}]^{5-}$ functions as an oxidase-type catalyst. As such, the reaction is perceived to proceed through a redox mechanism, whereby the $[PV_2Mo_{10}O_{40}]^{5-}$ oxidizes the inorganic or organic substrates (H_2Donor) by a series of proton-coupled electron transfers (PCETs), leading to oxidation of the substrate with concomitant reduction of the polyoxometalate, Scheme 1.

There is significant experimental support for this mechanism, and in certain cases, such as the oxidation of anthracene and α-terpinene, the radical-cation intermediate formed by the initial electron transfer (H_2Donor molecule to $[PV_2Mo_{10}O_{40}]^{5-}$) has been directly observed by EPR.[7b,10b] Molecular oxygen is used to reoxidize the reduced polyoxometalate. Despite the fact that the general mechanistic scheme has rather broad experimental support, there are considerable gaps in our understanding of various features. (i) The PCET mechanism can be stepwise, initially generating a reduced polyoxometalate anion that abstracts a proton from the organic cation radical. Alternatively, when the H_2Donor is not a good electron donor, the process

* To whom correspondence should be addressed. E-mail: sason@yfaat.ch.huji.ac.il (S.S.); Ronny.Neumann@weizmann.ac.il (R.N.).
† The Hebrew University.
‡ Weizmann Institute of Science.

10.1021/jp068673c CCC: $37.00 © 2007 American Chemical Society
Published on Web 05/05/2007

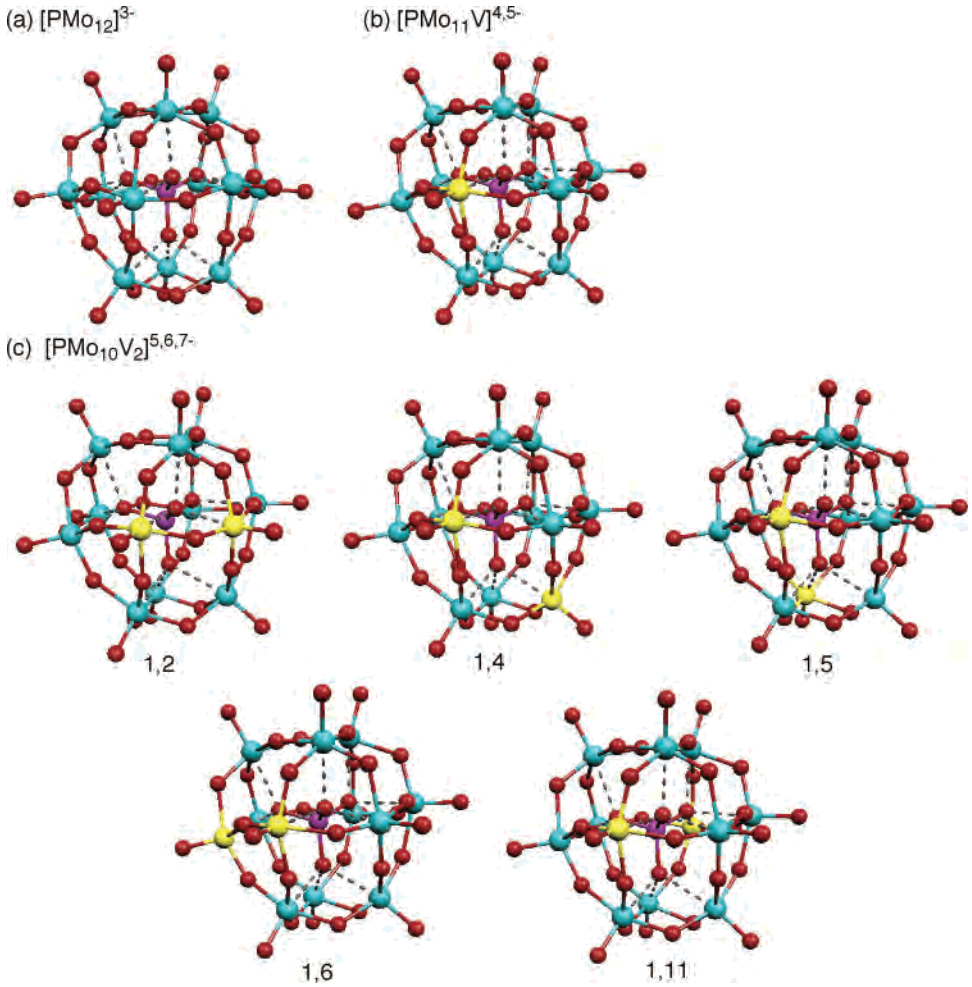

Figure 1. MOLEKEL[19] drawings of (a) the parent $[PMo_{12}]^{3-}$, (b) the monovanadate $[PMo_{11}V]^{(4,5)-}$, and (c) divanadate $[PMo_{10}V_2]^{(5-7)-}$ species explored in this study. Phosphorus, oxygen, molybdenum, and vanadium atoms are colored purple, red, light blue, and yellow, respectively.

SCHEME 1: A Mechanistic Scheme for Oxidase Catalysis by $[PV_2Mo_{10}O_{40}]^{5-}$

$$[PV^{V}_{2}Mo_{10}O_{40}]^{5-} + H_2Donor \xrightarrow{-e^-,\,-H^+} [PV^{IV}V^{V}Mo_{10}O_{40}]^{6-} + H^+ + HDonor^{\bullet}$$

$$[PV^{v}_{2}Mo_{10}O_{40}]^{5-} \text{ or } [PV^{IV}V^{V}Mo_{10}O_{40}]^{6-} + HDonor^{\bullet} \xrightarrow{-e^-,\,-H^+} [PV^{IV}V^{V}Mo_{10}O_{40}]^{6-} \text{ or } [PV^{IV}_{2}Mo_{10}O_{40}]^{7-} + H^+ + Donor$$

$$\Big\| \text{ Product}$$

$$2\,[PV^{IV}V^{V}Mo_{10}O_{40}]^{6-} \text{ or } [PV^{IV}_{2}Mo_{10}O_{40}]^{7-} + 2\,H^+ + 1/2\,O_2 \longrightarrow [PV^{V}_{2}Mo_{10}O_{40}]^{5-} + H_2O$$

may be concerted, namely, the electron and proton are transferred from the substrate in one step, albeit to different sites of the $[PV_2Mo_{10}O_{40}]^{5-}$ molecule. This mechanistic question has an added allure since peroxidases oxidize phenols and anilines by PCET mechanisms, which are concerted.[13] (ii) The electronic structures of the parent $[PV_2Mo_{10}O_{40}]^{5-}$ polyoxometalate and the reduced $[PV_2Mo_{10}O_{40}]^{6,7-}$ species after one- and two-electron transfers are not known.[14] (iii) Since $[PV_2Mo_{10}O_{40}]^{5-}$ is an intractable mixture of isomers, it is unknown if all of the isomers are equally reactive. Further, it is also not established whether one- and/or two-electron reduced species are formed and which isomers are reduced because it has not been possible to definitively differentiate the various species by means of UV−vis, NMR, or EPR spectroscopy.

Obviously, answering these questions will have important implications toward our understanding of the oxidase catalytic activity of $[PV_2Mo_{10}O_{40}]^{5-}$. Although the various isomers of $[PV_2Mo_{10}O_{40}]^{5-}$ and the corresponding one- and two-electron-reduced species are not experimentally accessible as pure compounds, they are computationally accessible. Therefore, as a first step, the objective of this research was to augment our understanding of catalytic oxidation by this class of polyoxometalate compounds by computationally studying the relative stability and electron structures of the oxidized and one- and two-electron-reduced species, $[PV_2Mo_{10}O_{40}]^{5,6,7-}$ and by comparing these results with the corresponding parent polyoxometalate, $[PMo_{12}O_{40}]^{3,4-}$, and the monovanadium-substituted compounds, $[PVMo_{11}O_{40}]^{4,5-}$. To describe these species henceforth, we shall use a shorthand notation, $[PMo_{12-x}V_x]^{q-}$, where x signifies the number of V atoms and can vary between 0 and 2 and q is the value of the negative charge of the polyoxometalate. Figure 1 shows all of the structures investigated in this study. The labels of the isomers of $[PMo_{10}V_2]^{q-}$ follow the nomenclature proposed by Pope and Scully.[15]

Theoretical Methods

All calculations were performed with Jaguar 5.5[16] and Gaussian 03[17] using the unrestricted UB3LYP density functional theoretic (DFT) method.[18a] Geometry optimization was per-

formed with the LACVP basis set,[18b] henceforth, B1. Structure drawings were done with MOLEKEL,[19] while orbital drawings were generated by MOLDEN.[20] DFT calculations[21] of polyoxometalate systems have been actively pursued, and specifically, B3LYP has proven to be a practically reliable level.

Frequency calculations with B3LYP/B1 were performed for the $[PMo_{10}V_2]^{5-}$ species. Since every frequency job takes a significant amount of CPU resources, the entire characterization is beyond our current means, and hence, the rest of the structures were optimized without symmetry constraints but were not tested by frequency calculations. Single-point calculations were subsequently performed with LACV3P* (B2).[16] The importance of solvation on this highly charged species is well recognized in the field.[14b,21i−k] Thus, to mimic acetic acid and acetonitrile solvents often used in catalytic applications, we corrected the gas-phase energies using the self-consistent reaction field (SCRF) model implemented in Jaguar 5.5 with the B1 basis set at the gas-phase geometry.[16] The two solvents were specified by dielectric constant (ϵ) and probe radius (r) values, that is, $\epsilon = 6.15$ and $r = 2.247$ Å for acetic acid (Solv1 or S1) and $\epsilon = 37.5$ and $r = 2.183$ Å for acetonitrile (Solv2 or S2). The solvation calculations do not take into consideration any ion pairing or effects of the counterions. Inclusion of counterions will make the calculation much too complicated and time consuming and, therefore, impractical.

All of the detailed data are summarized in the Supporting Information (SI), while the text discusses key results. The textual data correspond to B2//B1 energies corrected by solvation energies, E_{solv}. Thus, E(B2//B1) + E_{solv}(Solv1) is indicated in the text as $E1$, while E(B2//B1) + E_{solv}(Solv2) is denoted as $E2$. Since ZPE correction for the cases where the data were available negligibly affected the relative energies, it was decided to waive the frequency calculations for some of the reduced species. Therefore, the reported relative energies do not include ZPE correction.

Results

Following the oxidation state formalism, in the oxidized forms of $[PMo_{12-x}V_x]^{q-}$, all of the transition-metal ions are devoid of d electrons. The reduced anions have one or two d electrons for the monoreduced or doubly reduced species, respectively. Thus, we computed the singlet spin states for $[PMo_{10}V_2]^{5-}$, the doublet states for $[PMo_{10}V_2]^{6-}$, and both the singlet and triplet states for $[PMo_{10}V_2]^{7-}$, for all possible isomers (in total, 20 species, with structural and energy data summarized in the SI).

A. Isomers of $[PMo_{10}V_2]^{5-}$. Figure 2 shows key optimized geometric parameters for the various isomers of $[PMo_{10}V_2]^{5-}$, alongside the parent $[PMo_{12}]^{3-}$ compound. The labels in Figure 2 specify the oxygen atoms according to their positions in the polyoxometalate, bridging (O_b), terminal (O_t), and internal (O_i) ones. The relative $E1$ and $E2$ energies of the $[PMo_{10}V_2]^{5-}$ isomers are indicated underneath of the corresponding structures. It is seen that the average bridging Mo−O_b distances are 1.946−1.947 Å, while the terminal ones, Mo−O_t, are 1.747 Å; all values are quite close to the distances in the parent Keggin salt, $[PMo_{12}]^{3-}$. The V−O distances are 1.900−1.908 Å for the bridging positions and 1.609−1.611 Å for the terminal ones. These are slightly shorter than the corresponding Mo−O distances. There are no unusual features that typify one isomer over the other in the $[PMo_{10}V_2]^{5-}$ series. This indicates that the polyoxometalate structure is not susceptible to large distortions.

Electronically, the five isomers of $[PMo_{10}V_2]^{5-}$ were verified to possess closed-shell singlet electronic structures (Table S1);

(a) $[PMo_{12}]^{3-}$

r(P-O_i) = 1.639
r(Mo-O_b) = 1.947
r(Mo-O_t) = 1.728
r(Mo-O_i) = 2.444

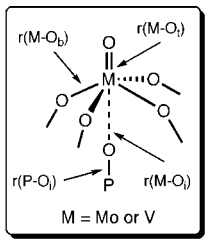

(b) $[PMo_{10}V_2]^{5-}$

	(1,2)	(1,4)	(1,5)	(1,6)	(1,11)
r(P-O_i)	1.639	1.639	1.639	1.639	1.639
r(Mo-O_b)	1.947	1.947	1.947	1.947	1.946
r(V-O_b)	1.905	1.900	1.906	1.906	1.908
r(Mo-O_t)	1.747	1.747	1.747	1.747	1.747
r(V-O_t)	1.611	1.609	1.610	1.611	1.611
r(Mo-O_i)	2.431	2.421	2.426	2.425	2.431
r(V-O_i)	2.389	2.445	2.411	2.433	2.387
E1	1.41	0.00	1.17	1.17	0.78
E2	1.33	0.00	1.04	0.98	0.59

Figure 2. Averaged key geometric parameters of (a) $[PMo_{12}]^{3-}$ and (b) the five isomers of $[PMo_{10}V_2]^{5-}$. The relative energies, $E1$ and $E2$ (in kcal/mol), are given beneath the structures.

$[PMo_{10}V_2]^{6-}$

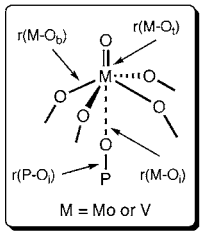

	(1,2)	(1,4)	(1,5)	(1,6)	(1,11)
r(P-O_i)	1.643	1.643	1.643	1.643	1.643
r(Mo-O_b)	1.946	1.947	1.948	1.947	1.947
r(V-O_b)	1.952	1.943	1.947	1.949	1.945
r(Mo-O_t)	1.758	1.758	1.758	1.758	1.758
r(V-O_t)	1.621	1.620	1.621	1.622	1.620
r(Mo-O_i)	2.442	2.433	2.442	2.435	2.444
r(V-O_i)	2.410	2.462	2.431	2.460	2.391
E1	1.16	0.00	0.58	1.04	1.30
E2	1.29	0.00	0.60	1.04	1.27
ρ(V)	1.06	1.06	1.07	1.05	1.07

Figure 3. Key geometric parameters of $[PMo_{10}V_2]^{6-}$. The figures beneath the structures correspond to the $E1$ and $E2$ relative energies in the two solvents. The ρ(V) values are the spin densities on V.

no stable open-shell singlet states were found. As can be seen from the $E1$ and $E2$ values, in Figure 2, the five isomers are almost equally stable and are condensed within 1.33−1.41 kcal/mol depending on the solvent (see also Table S5). Since the statistical ratio of the positional isomers of $[PMo_{10}V_2]^{5-}$ (2:2:2:4:1 for the 1,2; 1,4; 1,5; 1,6; and 1,11 compounds, respectively) was not taken into account in the calculations, we expect an entropic effect on the equilibrium mixture. Experimental data by Petterson et al. show that in aqueous solution, there is a statistical distribution of the isomers and that the 1,6 isomer with the highest degeneracy dominates the mixture.[2a] Neumann et al., on the other hand, found in organic solvents that the ratio of isomers was different than the statistically expected ratio and was solvent dependent.[2b] Considering the complexity of the problem, and the size of the species, the data in Figure 2 are in general accord with the experimental data that show the coexistence of all isomers of $[PMo_{10}V_2]^{5-}$ in a given solvent.

B. Isomers of $[PMo_{10}V_2]^{6-}$. Addition of a single electron to $[PMo_{10}V_2]^{5-}$ generates the $[PMo_{10}V_2]^{6-}$ isomers, which are depicted in Figure 3. Addition of a single electron is seen to increase the V−O_b distances from 1.900−1.908 (Figure 2) to 1.943−1.952 Å (Figure 3). This indicates that the additional electron is located near the V ions (see also below). The rest of the geometric parameters show only small changes; thus, the Mo−O_b distance remains 1.946−1.948 Å. One may notice also a slight lengthening of both the Mo−O_t and V−O_t distances, respectively, from 1.747 to 1.758 Å and from 1.609−1.611 Å to 1.620−1.622 Å, which indicates that part of the negative charge density in the polyoxometalate shifted toward the surface of the cage, that is, terminal oxygen atoms (see also Tables S2

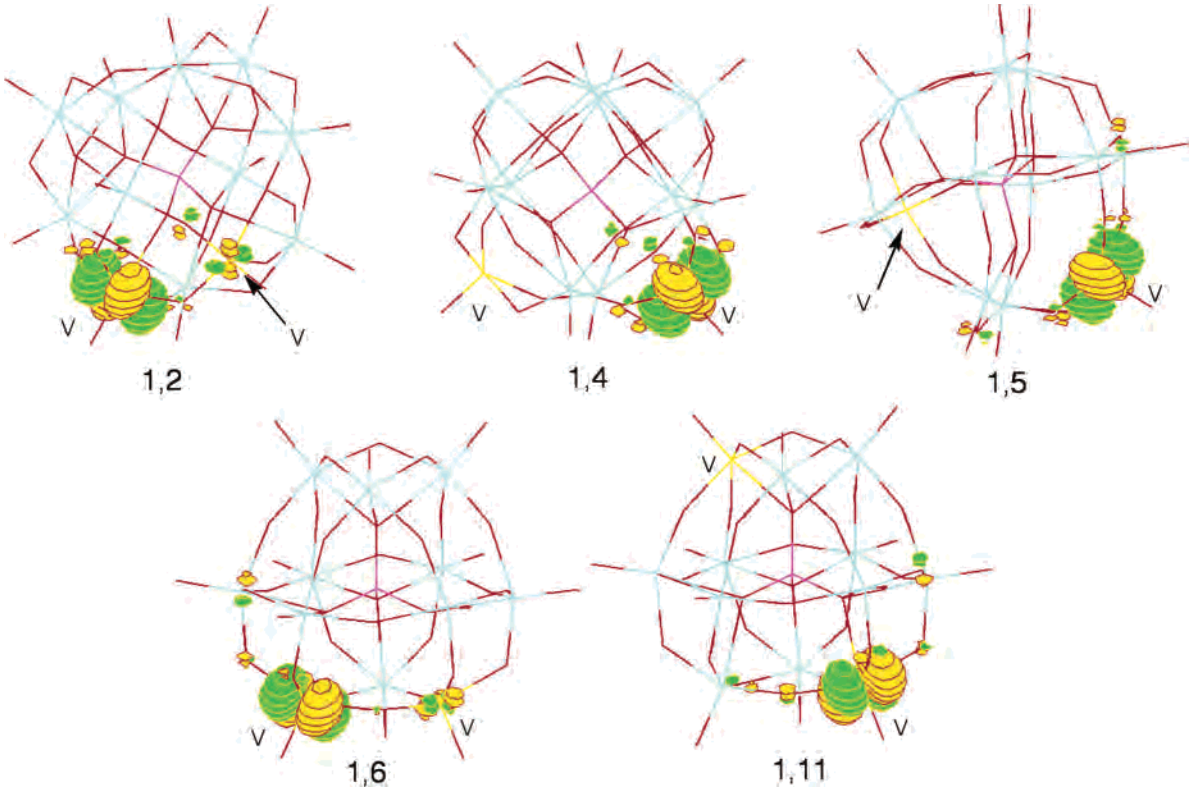

Figure 4. Singly occupied natural orbitals of $[PMo_{10}V_2]^{6-}$ isomers (drawn by MOLDEN[20]).

and S3 and Figure S6). It is valuable to note that there has been discussion in the literature on the position of the vanadyl moiety after reduction, with two contrasting views that argue for vanadyl to be either retained in the polyoxometalate unit or disassociated from it.[22] The computations support the former view, with only a limited shift of the $V-O_i$ moiety; $V-O_i$ is only 0.01−0.02 Å longer in $[PMo_{10}V_2]^{6-}$ versus in $[PMo_{10}V_2]^{5-}$. Also as may be seen, not taking into account the isomeric degeneracy of each species, energetically, the most stable isomer is the 1,4 in both solvents, but as for the reduced species, the entire energy scale is condensed to 1.29−1.30 kcal/mol.

The spin density distribution (ρ) in Figure 3 shows that in all of the isomers, the spin is exclusively localized on one of the vanadium atoms (see also Table S2). Figure 4 shows the singly occupied natural orbital of the $[PMo_{10}V_2]^{6-}$ isomers. It is seen that, invariably, this is a δ-type orbital localized on one V ion, with small tails to adjacent atoms. In contrast, in the monoreduced parent species $[PMo_{12}]^{4-}$ (Table S1), the electron is not localized completely on a single Mo ion, but some of the spin density is delocalized toward the adjacent atoms. Interestingly, while generally the identity of the lowest unoccupied orbital (LUMO) predicts the site of reduction,[14b] the LUMOs of the $[PMo_{10}V_2]^{5-}$ clusters in either the gas phase or in a solvent do not predict the electronic structure of the $[PMo_{10}V_2]^{6-}$ isomers (see Figure S5 in the SI). A way to understand the electronic structure will be discussed below.

C. Isomers of $[PMo_{10}V_2]^{7-}$. The geometries of the doubly reduced species, $[PMo_{10}V_2]^{7-}$, are shown in Figure 5 for both the singlet and triplet states. Again, the structure of the polyoxometalate is retained with only small changes in its geometry compared to the oxidized compound. For the 1,4, 1,5, and 1,11 isomers of $[PMo_{10}V_2]^{7-}$, the two additional electrons for both the singlet and triplet states are located in the δ orbitals of the two vanadium atoms (see also Tables S4 and S5). For the 1,2 and 1,6 isomers, however, one of the electrons is localized at a vanadium atom, while the other resides on a molybdenum atom. In these two isomers, the shorter distance between the two vanadium atoms apparently forces one of the electrons to be located at a more distal molybdenum center due to electron−electron repulsion. Since electrons inherently prefer to be localized at vanadium, the location of the second electron at a molybdenum center significantly raises the energy (13−14 kcal/mol) of these isomers compared to that of the others. Interestingly, the results in Figure 5 also show that the 1,4 isomer of $[PMo_{10}V_2]^{7-}$ is more stable than all other isomers; the 1,5 and 1,11 isomers are about 2.60−3.27 kcal/mol higher in energy than the singlet 1,4 isomer. Thus, under thermodynamic control, it is expected that the 1,4-$[PMo_{10}V_2]^{7-}$ species will be predominant in the reaction mixture after two-electron reduction. The results of this computational study concerning the likelihood of reduction of the various isomers are in contrast to a previous hypothesis wherein it was suggested that it would be easiest to reduce the 1,2 and 1,6 isomers by two electrons, while the two-electron reduction of the 1,11 isomer would be the most difficult.[2b]

Finally, since the two additional electrons lead to "diradicaloid" species, there are two closely lying singlet and triplet states. As shown in Table 1, our calculations show that, in all cases, with the exception of the 1,5 isomer, the singlet state is lower in energy (see also Tables S10 and S11). The energy differences are small enough to suggest that both states are accessible in a reaction according to Scheme 1.

D. Mono-Vanadium-Substituted and the Parent Compounds: $[PMo_{11}V]^{4,5-}$ and $[PMo_{12}]^{3,4-}$. The reduction of $[PMo_{12}]^{3-}$ to $[PMo_{12}]^{4-}$ leads to a highly delocalized electron in the anion. By contrast, upon reduction of $[PMo_{11}V]^{4-}$, the additional electron in $[PMo_{11}V]^{5-}$ is found to be localized on the vanadium atom. The geometry of the species and the spin density distribution are given in Figure 6 (see also Table S1).

E. Comparison of Reduction Energies of $[PMo_{12}]^{3-}$, $[PMo_{11}V]^{4-}$, and $[PMo_{10}V_2]^{5-}$. One of the important issues is, what actually does the substitution of vanadium into the

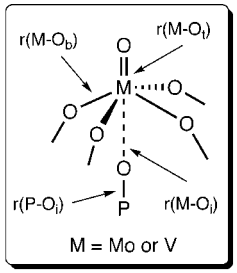

(a) $[PMo_{10}V_2]^{7-}$ (singlet)

	(1,2)	(1,4)	(1,5)	(1,6)	(1,11)
r(P-O$_i$)	1.647	1.648	1.648	1.647	1.648
r(Mo-O$_b$)	1.952	1.952	1.950	1.953	1.950
r(V-O$_b$)	1.960	1.982	1.985	1.956	1.990
r(Mo-O$_t$)	1.768	1.770	1.770	1.768	1.769
r(V-O$_t$)	1.633	1.630	1.632	1.633	1.631
r(Mo-O$_i$)	2.451	2.446	2.452	2.443	2.462
r(V-O$_i$)	2.428	2.492	2.449	2.484	2.398
E1	13.63	0.00	3.09	13.90	3.18
E2	13.28	0.00	2.90	13.63	2.91
ρ(V)	0.76 [a]	1.06	1.06	1.04	1.06
	-1.04	-1.06	-1.06	-0.74 [a]	-1.06

(b) $[PMo_{10}V_2]^{7-}$ (triplet)

	(1,2)	(1,4)	(1,5)	(1,6)	(1,11)
r(P-O$_i$)	1.648	1.648	1.647	1.647	1.648
r(Mo-O$_b$)	1.955	1.951	1.950	1.953	1.950
r(V-O$_b$)	1.962	1.985	1.985	1.962	1.990
r(Mo-O$_t$)	1.768	1.770	1.769	1.768	1.769
r(V-O$_t$)	1.633	1.630	1.631	1.633	1.631
r(Mo-O$_i$)	2.454	2.446	2.452	2.444	2.462
r(V-O$_i$)	2.428	2.493	2.445	2.483	2.398
E1	15.30	0.78	2.93	15.17	3.27
E2	15.04	0.67	2.60	14.82	2.96
ρ(V)	1.07	1.07	1.06	1.07	1.06
	0.80 [a]	1.07	1.05	0.79 [a]	1.06

[a] spin density on Mo

Figure 5. Averaged key geometric parameters of $[PMo_{10}V_2]^{7-}$. The figures beneath the structures correspond to the *E*1 and *E*2 relative energies (relative to the singlet (1,4)) in the two solvents and are given in each line for the two spin states. The value labeled as ρ(V) corresponds to the spin density on V, except in a few cases.

TABLE 1: Singlet Triplet Energy Differences (ΔE_{ST} in kcal/mol) for the Isomers of $[PMo_{10}V_2]^{7-}$

isomers of $[PMo_{10}V_2]^{7-}$	ΔE_{ST} (B2//B1)	$\Delta E_{ST}(E1)^a$	$\Delta E_{ST}(E2)^b$
1,2	0.98	1.66	1.76
1,4	0.60	0.78	0.67
1,5	−0.25	−0.16	−0.29
1,6	0.94	1.27	1.19
1,11	0.09	0.09	0.05

[a] With Solv1. [b] With Solv2.

α-Keggin polyoxomolybdate structure contribute to the catalytic function of the polyoxometalate? To answer this question, we inspected the reduction energies for all of the species starting from the parent, $[PMo_{12}]^{3-}$. Figure 7 shows the results in a pictorial manner, where one can discern the significant difference between the gas-phase and solution behavior (see also Table S13). In the gas phase, all of the reduction processes are highly endothermic, and the one- and two-electron reductions of $[PMo_{10}V_2]^{5-}$ to $[PMo_{10}V_2]^{7-}$ are both more endothermic than the respective reductions of the parent $[PMo_{12}]^{3-}$ species. This

(a) $[PMo_{12}]^{4-}$

r(P-O$_i$)	1.641
r(Mo-O$_b$)	1.949
r(Mo-O$_t$)	1.736
r(Mo-O$_i$)	2.449
ρ(Mo)	0.75

(b) $[PMo_{11}V]^{5-}$

r(P-O$_i$)	1.642
r(Mo-O$_b$)	1.946
r(V-O$_b$)	1.981
r(Mo-O$_t$)	1.747
r(V-O$_t$)	1.611
r(Mo-O$_i$)	2.443
r(V-O$_i$)	2.457
ρ(V)	1.06

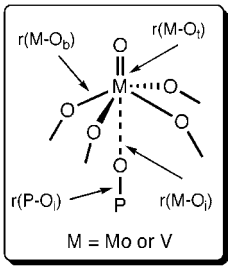

Figure 6. Key geometric parameters and the spin density distribution in $[PMo_{12}]^{4-}$ and $[PMo_{11}V]^{5-}$. The ρ(Mo) in $[PMo_{12}]^{4-}$ corresponds to the spin density on the Mo ion possessing the largest spin density.

trend makes sense since charge−charge repulsion dominates in the gas phase and will strongly disfavor the additional charging of the already quintuply negative $[PMo_{10}V_2]^{5-}$ species. In fact, the two-electron reduction of the $[PMo_{12}]^{3-}$ species is favored over that of the $[PMo_{10}V_2]^{5-}$ species by about 250 kcal/mol! However, as can be seen in Figure 7, in solution, all of the reduction processes are exothermic. The data for the two-electron reduction of $[PMo_{10}V_2]^{5-}$ to $[PMo_{10}V_2]^{7-}$ show a highly exothermic process of 103−116 kcal/mol in acetic acid and of 195−208 kcal/mol in acetonitrile, comparable with the process in the parent compound $[PMo_{12}]^{3-}$ to $[PMo_{12}]^{5-}$, where the two-electron reduction is also exothermic, ranging from ∼160 kcal/mol in acetic acid to ∼223 kcal/mol in acetonitrile. Thus, as has been recognized before, solvation exerts a strong impact on this highly charged species,[21i,j] and in the present case, the solvent levels the reduction potentials of all of the species by preferentially stabilizing the more highly charged $[PMo_{10}V_2]^{7-}$ species. Experimentally, it should be pointed out that cyclic voltammetry measurement indeed shows that $H_5PMo_{10}V_2O_{40}$ and $H_3PMo_{12}O_{40}$ have similar oxidation potentials.[23] This still does not explain the catalytic function of vanadium in these compounds, but as we shall see in the Discussion section below, the root cause of the catalytic electron-transfer activity of $[PMo_{10}V_2]^{5-}$ compared with that of $[PMo_{12}]^{3-}$ may, after all, be the higher negative charge of the vanadium-substituted polyoxometalates.

F. Charge Distribution in the Reduced Species. To gain insight into the position where a proton might be positioned upon proton-coupled electron transfer (see Scheme 1), we calculated the partial atomic charges (see Tables S1−S6 in the SI). Invariably, in all species, before and after the reduction, the highest negative charges are located on the bridging oxygen sites, but upon reduction, terminal oxygen sites also attain larger negative charges (see, e.g., Figure S9 in the SI). However, since the negative charge is extensively dispersed, it is not possible to pinpoint a single site or two sites that will bind the protons. Therefore, we summed, for all of the isomers of $[PMo_{10}V_2]^{6,7-}$, the total charge over the two vanadium ions and their closest neighboring oxygen atoms (discounting the oxygen atom of the central phosphate). These data are shown in Figure 8 as $Q(V_2O_9$ or $V_2O_{10})$. It is seen that a large fraction of the total negative charge of the polyoxometalate resides near the vanadium atoms that are also the sites that accept the excess electrons. On the basis of this, we may surmise that the radical cation of the organic substrate will be anchored in the vicinity of the vanadium atoms, and the protonation will take place at one of the oxygen atoms bound to vanadium.

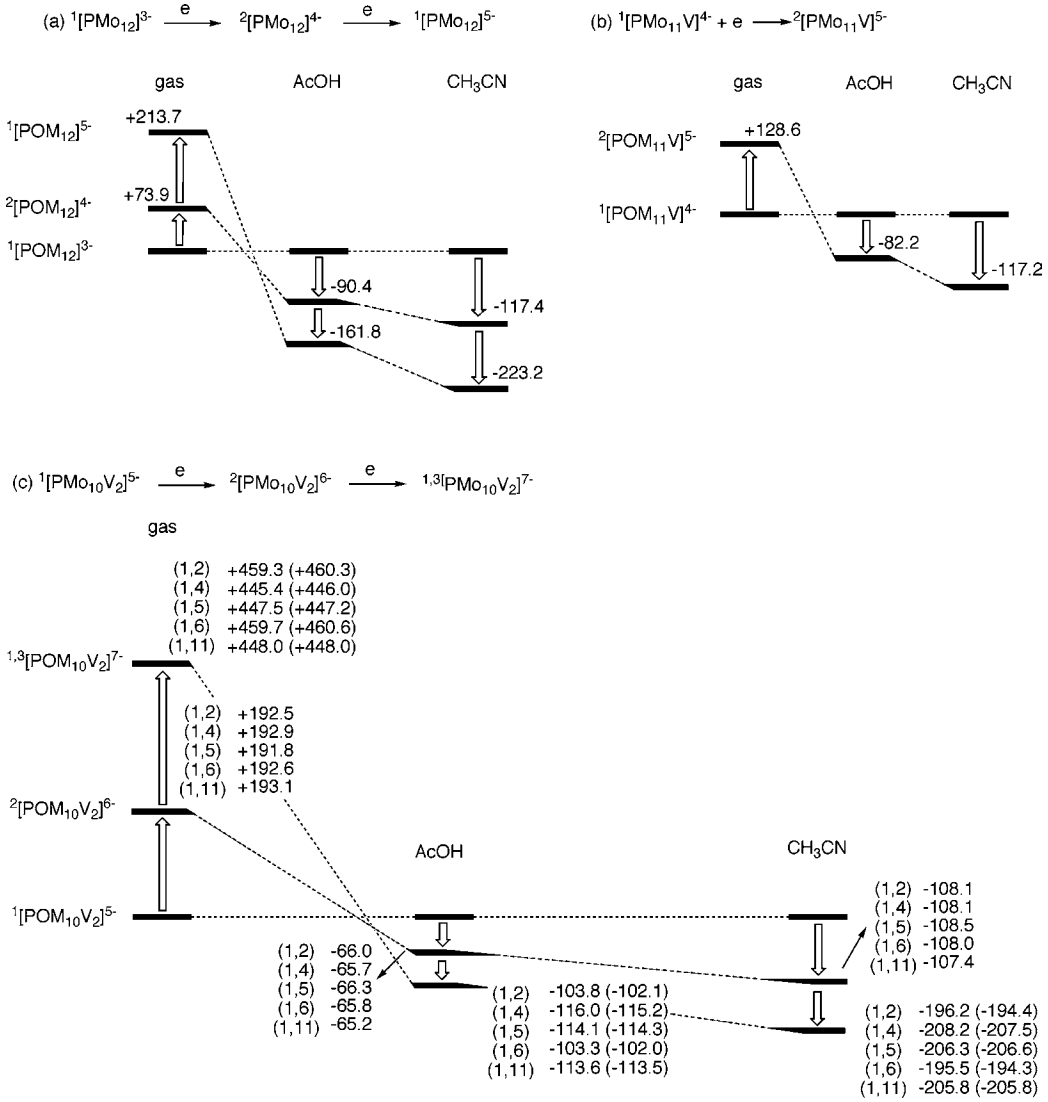

Figure 7. Schematic representation of solvent effect on reduction potentials in kcal/mol (values in parentheses are for the triplet state).

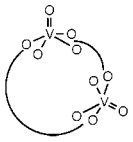

	1,2	1,4	1,5	1,6	1,11
$^2[PMo_{10}V_2]^{6-}$	-3.17	-3.84	-3.79	-3.12	-3.83
$^1[PMo_{10}V_2]^{7-}$	-3.32	-4.19	-4.16	-3.31	-4.18
$^3[PMo_{10}V_2]^{7-}$	-3.34	-4.20	-4.17	-3.31	-4.18

Figure 8. Charge distribution in the isomers of $[PMo_{10}V_2]^{6-}$ and $[PMo_{10}V_2]^{7-}$. The charge is given as $Q(V_2O_{10})$ and is summed over the immediate coordination sphere of the vanadium ions in the cage. The two values for $[PMo_{10}V_2]^{7-}$ correspond to the singlet/triplet states. In the 1,2 and 1,6 isomers, one bridging oxygen atom is shared by two vanadium atoms.

Discussion

The above calculations raise a few issues that require discussion. (i) What is the origin of the preferred site of reduction in the vanadium-substituted polyoxometalates and the ensuing electronic structures described by the occupied orbitals in Figures 4 and 9? (ii) What is the origin of the leveling effect of the solvent on the reduction potentials? (iii) Why are the $[PMo_{12-x}V_x]^{(3+x)-}$ species good catalysts, and what are the mechanistic implications for the proton-coupled electron-transfer (PCET) mechanism described in Scheme 1?

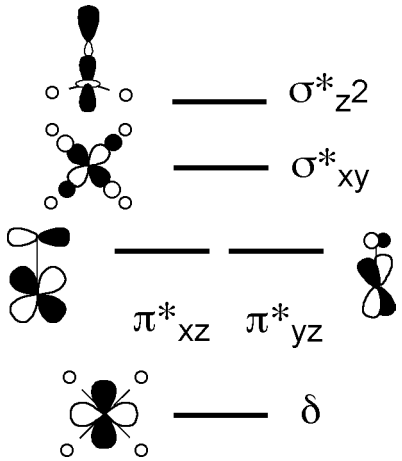

Figure 9. The d-block energy levels of vanadium in the local environment ($O{=}VO_{4/2}O_{1/3}$) in $[PMo_{10}V_2]^{5-}$, for which all of the orbitals are vacant.

A. Electronic Structure Considerations and Understanding the Preferred Reduction Sites in $[PMo_{12-x}V_x]^{(3+x)-}$ Species. As can be concluded from the above results, in almost all cases that we calculated, with the exception of the direduced 1,2- and 1,6-$[PMo_{10}V_2]^{5-}$ species, the excess electrons resided on the vanadium atom and in a δ-type orbital.[14b,21k,l] Considering

first the electronic structure issues, each vanadium is octahedrally coordinated by one terminal oxygen, four bridging oxygens shared with adjacent transition-metal ions, and one phosphate oxygen shared with three other transition-metal ions, hence, $O{=}VO_{4/2}O_{1/3}$. In this local environment, the d-block orbitals of vanadium within the cage will spread in a typical manner to a distorted octahedral environment, as shown in Figure 9. Thus, the three-below-two splitting undergoes additional subsplitting. The lowest three orbitals split into a δ and two $\pi_{xz,yz}$*(VO) orbitals, and the two higher orbitals are the corresponding σ^*_{xy} and $\sigma^*_{z^2}$ orbitals that are strongly antibonding. As vanadium in $[PMo_{10}V_2]^{5-}$ is in oxidation state of +5, all of the orbitals are vacant, and the excess electron will reside in the lowest d orbital, namely, the δ orbital. Similar conclusions were reached before by Poblet et al. [14b,21i,k] We note that the δ orbital in the reduced species is almost a pure nonbonding $d_{x^2-y^2}$ orbital since, in the reduced species, the O−V−O bond angles in the bridging positions are close to 90° (∼82−92°).

Of course, the molybdenum ion will have a corresponding d-block splitting, and the question is, why does the excess electron prefer to be located on vanadium? It was already mentioned that, at least for the present systems (see, however, ref 14b), the calculation of the LUMO of the corresponding oxidized species does not provide a correct directive of the sites of oxidation and predicts, invariably, that the excess electron will be distributed over the molybdenum ions in the cage, which is obviously not the case.[24] One possible rationale for the computational findings is the location of the vanadium and molybdenum atoms in the periodic table. Thus, since vanadium is located in an earlier period in the periodic table compared with molybdenum, we might expect that the d orbitals of vanadium will be lower than those of molybdenum, but this is not so straightforward since molybdenum is located to the right of vanadium, and the ionization potential of the isolated ions suggests that the reduction site should be at the Mo^{VI} atom.[14b] However, when the Mo^{VI} and V^V ions are put in the cage structure of the Keggin salt, they draw charge density from the electron-rich oxygen ions, which modify their electron accepting capabilities. Thus, the Mulliken charges in the $[PMo_{10}V_2]^{5-}$ are 1.6 (Mo) versus 1.3 (V) (Table S3); while the oxidation state of Mo is +6, its actual charge of +1.6 means that it gained a charge of $4.4e^-$ from the oxygen ions, whereas V gained only $3.7e^-$. Taken together, the two factors make V effectively a better electron sink within the $[PMo_{10}V_2]^{5-}$ complex. Thus, even though one may question the absolute values of the Mulliken charges, the relative ones are reliable, and this means that, in the oxidation states corresponding to the change $[PMo_{10}V_2]^{6-}$/$[PMo_{10}V_2]^{5-}$, the 3d level of vanadium would be effectively lower in energy than the 4d level of molybdenum. As such, the electron will go to vanadium. If this rationale is valid, one can then predict that replacement of vanadium by niobium will create a molybdenum-centered reduced species, possibly with different reactivity patterns than that of $[PMo_{10}V_2]^{5-}$. This appears, indeed, to be the case during the reduction of the related $SiW_9Nb_3O_{40}^{8-}$ Keggin ion.[14b]

B. The Effect of the Initial Charge on the Reduction of $[POM_{12-x}V_x]^{(3+x)-}$ Species. We recall that, in the gas phase, the reduction of the parent $[PMo_{12}]^{3-}$ species is considerably more facile than that of the highly charged $[PMo_{10}V_2]^{5-}$, but the solvent levels off the reduction potentials so that the one- and two-electron reduction energies are comparable for the two systems, Figure 7. The gas-phase results are dominated by electron−electron repulsion, and therefore, the reduction of $[PMo_{10}V_2]^{5-}$ species is highly disfavored due to the excess repulsion brought about by the addition of one and two electrons to the system.

A general treatment of the redox properties of polyoxometalates of any size and charge has appeared before.[21k] However, our problem here is more focused on a specific Keggin polyoxometalate with variable charge and its response to the solvent. We shall, therefore, focus only on the solvent effect, which can be understood by reference to the Born expression for solvation of an ion with charge Q_{ion} and effective radius R_{ion} in a solvent with a dielectric medium ϵ

$$\Delta G_S = [1/\epsilon - 1]Q^2_{ion}/R_{ion} \quad (1)$$

If we consider now changing the charge of the ion by a quantity, ΔQ_{ion}, the equation shows that the solvation energy will vary approximately by an amount that is proportional to the initial charge of the ion, namely,

$$\Delta\Delta G_S \sim 2[1/\epsilon - 1]Q_{ion}\cdot\Delta Q_{ion}/R_{ion} \quad (2)$$

Thus, for an ion with an initial charge of $Q_{ion} = -5$, the solvation energy increases by a factor of 5/3 compared with an ion with an initial charge of $Q_{ion} = -3$. Clearly, the initial charge of the anion amplifies the oxidative capability of the ion, and for this reason, a poorer gas-phase oxidant like $[PMo_{10}V_2]^{5-}$ can become a powerful oxidant in a solvent. As was mentioned above, the like $[PMo_{12}]^{3-}$ and $[PMo_{10}V_2]^{5-}$ have similar reduction potentials in electrochemical reduction.

C. The Effect of Vanadium on the Mechanism of Oxidation of Organic Substrates by $[PMo_{10}V_2]^{5-}$. As already discussed by one of us,[10b] the electron-transfer reaction is followed by an ion-pairing complex formation between the reduced $[PMo_{10}V_2]^{6,7-}$ species and the organic radical cation or cation species (Scheme 1), and the process is coupled to a proton transfer from the organic radical cation (cation) to the reduced catalyst. As shown in Figure 8, the vanadium plays a key role here since it concentrates the excess charge near its own coordination sphere. This charge concentration forms an anchor site for the positively charged organic moiety; the reduced $[PMo_{10}V_2]^{6-}$ or $[PMo_{10}V_2]^{7-}$ species will attract the cation radical/cation species to the site of the vanadium atoms, where the negative charge is maximal. Thus, the charge concentration will have a double effect, (a) it will stabilize the complex with the organic species compared with the parent $[PMo_{12}]^{4-}/[PMo_{12}]^{5-}$ species, where the excess negative charge is delocalized, and part of this stabilization will be expressed also in transition-state stabilization during the preceding electron-transfer events, and (b) the excess negative charge near the vanadium ions will facilitate the proton transfer from the coordinated radical cation or cation species to one of the oxo ligands of the vanadium center. Clearly therefore, the vanadium creates the function of the $[PMo_{10}V_2]^{5-}$ catalysts.

Conclusion

Our B3LYP calculations of the five isomers of the vanadium-substituted Keggin salts, $[PV_2Mo_{10}O_{40}]^{5-}$, and their mono- and direduced species show a few trends.

The first interesting trend is that either in the gas phase or in a solvent, the reduction of the $[PV_2Mo_{10}O_{40}]^{5-}$ produces $[PV_2Mo_{10}O_{40}]^{6,7-}$ ions in which the excess electrons are localized on the V ions in the corresponding δ orbitals, as found[14b] also by others. By contrast, the direduced $[PV_2Mo_{10}O_{40}]^{7-}$ isomers, where the one electron is localized on Mo, are high in energy. Thus, while the five isomers of $[PV_2Mo_{10}O_{40}]^{5-}$ and $[PV_2Mo_{10}O_{40}]^{6-}$ are very close in energy (within 1.5 kcal/mol

or less), in the direduced species, the 1,4-$[PV_2Mo_{10}O_{40}]^{7-}$ species is the most stable isomer.

The second feature is that, while in the gas phase, the reduction of the parent $[PMo_{12}O_{40}]^{3-}$ anion is exceedingly more favorable (by ca. 250 kcal/mol) than the reduction of $[PV_2Mo_{10}O_{40}]^{5-}$; the solvent applies a strong leveling effect and makes the reduction potentials of the two species very similar. In addition, since the reduction of $[PV_2Mo_{10}O_{40}]^{5-}$ concentrates high negative charge near the O═VO_4 moiety, this negative charge accumulation will act as an attractor that binds the organic radical cation (cation), which causes a subsequent proton transfer to an oxo ligand of the vanadium. As such, in terms of an electron-transfer catalytic effect, the presence of vanadium in $[PV_2Mo_{10}O_{40}]^{5-}$ creates function for the catalyst. Since the localization of the charge is so crucial, one might be tempted to predict that the kinetically most viable catalyst for one-electron reduction is the 1,2 isomer of $[PV_2Mo_{10}O_{40}]^{7-}$, which localizes more charge in the vicinity of the V_2O_{10} moiety. Furthermore, our reasoning on the effect of the transition-metal substituent in $[PMo_{12}O_{40}]^{3-}$ suggests that changing vanadium to niobium will create a molybdenum-centered reduced species $[PNb_2Mo_{10}O_{40}]^{6,7-}$ with very different catalytic properties than the vanadium-substituted species.

Finally, the computations reveal that $[PV_2Mo_{10}O_{40}]^{7-}$ is a diradicaloid that possesses two virtually degenerate states, with singlet and triplet spins. Thus, if this anion is effective in catalysis, as suggested by Scheme 1, we may expect two-state reactivity (TSR) in this reaction.[25] One way to probe the TSR scenario is to perform the reaction in a magnetic field, which will change the yield of oxidation products.[26]

Acknowledgment. This research was supported by the German Federal Ministry of Education and Research (BMBF) within the framework of the German−Israeli Project Cooperation (DIP-G7.1) and the Helen and Martin Kimmel Center for Molecular Design. R. N. is the Rebbeca and Israel Sieff Professor of Organic Chemistry. H.H. is a JSPS Postdoctoral Fellow for Research Abroad.

Supporting Information Available: Additional experimental and computational details. This material is available free of charge via the Internet at http://pubs.acs.org.

References and Notes

(1) Pope, M. T. *Heteropoly and Isopoly Oxometalates*; Springer: Berlin, Germany, 1983. (b) *Polyoxometalate: Chemistry From Topology via Self-Assembly to Applications*; Pope, M. T., Müller, A., Eds.; Kluwer: Dordrecht, The Netherlands, 2001. (c) Kozhevnikov, I. V. *Catalysis by Polyoxometalates*; Wiley: Chichester, England, 2002. (d) Hill, C. L.; Prosser-McCartha, C. M. *Coord. Chem. Rev.* **1995**, *143*, 407−455. (e) Mizuno, N.; Misono, M. *Chem. Rev.* **1998**, *98*, 199−218. (f) Neumann, R. *Prog. Inorg. Chem.* **1998**, *47*, 317−370.

(2) (a) Pettersson, L.; Andersson, I.; Grate, J. H.; Selling, A. *Inorg. Chem.* **1994**, *33*, 982−993. (b) Khenkin, A. M.; Rosenberger, A.; Neumann, R. *J. Catal.* **1999**, *182*, 82−91.

(3) Neumann, R.; Khenkin, A. M. *Chem. Commun.* **2006**, 2529−2538 and references therein.

(4) (a) Matveev, K. I. *Kinet. Catal.* **1977**, *18*, 716−728. (b) Matveev, K. I.; Kozhevnikov, I. V. *Kinet. Catal.* **1980**, *21*, 855−863. (c) Grate, J. H.; Hamm, D. R.; Mahajan, S. *Mol. Eng.* **1993**, *3*, 205−229. (d) Grate, J. H.; Hamm, D. R.; Mahajan, S. *Catal. Org. React.* **1993**, *53*, 213−264. (e) Grennberg, H.; Bergstad, K.; Bäckvall, J.-E. *J. Mol. Catal. A: Chem.* **1996**, *113*, 355−358. (f) Yokota, T.; Fujibayashi, S.; Nishiyama, Y.; Sakaguchi, S.; Ishii, Y. *J. Mol. Catal. A: Chem.* **1996**, *114*, 113−122. (g) Bergstad, K.; Grennberg, H.; Bäckvall, J.-E. *Organometallics* **1998**, *17*, 45−50.

(5) (a) Neumann, R.; Assael, I. *J. Chem. Soc., Chem. Commun.* **1998**, 1285−1287. (b) Branytska, O. V.; Neumann, R. *J. Org. Chem.* **2003**, *68*, 9510−9512.

(6) (a) Kozhevnikov, I. V.; Simagina, V. I.; Varnakova, G. V.; Matveev, K. I. *Kinet. Katal.* **1979**, *20*, 506−510. (b) Jumakaeva, B. S.; Golodov, V. A. *J. Mol. Catal.* **1986**, *35*, 303−307. (c) Karbanko, V. E.; Sidelnikov, V. N.; Kozhevnikov, I. V.; Matveev, K. I. *React. Kinet. Catal. Lett.* **1982**, *21*, 209−212. (d) Harrup, M. K.; Hill, C. L. *Inorg. Chem.* **1994**, *33*, 5448−5455. (e) Harrup, M. K.; Hill, C. L. *J. Mol. Catal. A: Chem.* **1996**, *106*, 57−66. (f) Hill, C. L.; Gall, R. D. *J. Mol. Catal. A: Chem* **1996**, *114*, 103−111.

(7) (a) Neumann, R.; Lissel, M. *J. Org. Chem.* **1989**, *54*, 4607−4610. (b) Neumann, R.; Levin, M. *J. Am. Chem. Soc.* **1992**, *114*, 7278−7286.

(8) (a) Neumann, R.; Levin, M. *J. Org. Chem.* **1991**, *56*, 5707−5710. (b) Ben-Daniel, R.; Alsters, P.; Neumann, R. *J. Org. Chem.* **2001**, *66*, 8650−8653. (c) Neumann, R.; Khenkin, A. M.; Vigdergauz, I. *Chem.—Eur. J.* **2000**, *6*, 875−882.

(9) Lissel, M.; Jansen in de Wal, H.; Neumann, R. *Tetrahedron Lett.* **1992**, *33*, 1795−1798.

(10) (a) Khenkin, A. M.; Neumann, R. *Angew. Chem., Int. Ed.* **2000**, *39*, 4088−4090. (b) Khenkin, A. M.; Weiner, L.; Wang, Y.; Neumann, R. *J. Am. Chem. Soc.* **2001**, *123*, 8531−8542.

(11) (a) Nizova, G. V.; Shulpin, G. B.; Süss-Fink, G.; Stanislas, S. *Chem. Commun.* **1998**, 1885−1886. (b) Tani, M.; Sakamoto, T.; Mita, S.; Sakaguchi, S.; Ishii, Y. *Angew. Chem., Int. Ed.* **2005**, *44*, 2586−2588.

(12) Yokota, T.; Tani, M.; Sakaguchi, S.; Ishii, Y. *J. Am. Chem. Soc.* **2003**, *125*, 1476−1477.

(13) See, for example, (a) Gajhede, M. In *Handbook of Metalloproteins*; Messerschmidt, A., Huber, R., Poulos, T. L., Wieghardt, K., Eds.; John-Wiley and Sons: New York, 2001; Vol. 1, pp 193−328. (b) Derat, E.; Shaik, S. *J. Am. Chem. Soc.* **2006**, *128*, 13940−13949.

(14) (a) For O3LYP calculations, with symmetry constraints, of the oxidized forms of the $[PV_xMo_{12-x}O_{40}]^{(3+x)-}$ polyoxometalates, see: Wang, J.; Hu, C.; Jian, M.; Zhang, J.; Li, G. *J. Catal.* **2006**, *240*, 23−30. (b) For a related study using a GGA functional, see: López, X.; Bo, C.; Poblet, J. M. *J. Am. Chem. Soc.* **2002**, *124*, 12574−12582.

(15) Pope, M. T.; Scully, T. F. *Inorg. Chem.* **1975**, *14*, 953−954.

(16) *Jaguar 5.5*; Schrödinger, Inc.: Portland, Oregon, 2004.

(17) Frisch, M. J.; Trucks, G. W.; Schlegel, H. B.; Scuseria, G. E.; Robb, M. A.; Cheeseman, J. R.; Montgomery, J. A., Jr.; Vreven, T.; Kudin, K. N.; Burant, J. C.; Millam, J. M.; Iyengar, S. S.; Tomasi, J.; Barone, V.; Mennucci, B.; Cossi, M.; Scalmani, G.; Rega, N.; Petersson, G. A.; Nakatsuji, H.; Hada, M.; Ehara, M.; Toyota, K.; Fukuda, R.; Hasegawa, J.; Ishida, M.; Nakajima, T.; Honda, Y.; Kitao, O.; Nakai, H.; Klene, M.; Li, X.; Knox, J. E.; Hratchian, H. P.; Cross, J. B.; Bakken, V.; Adamo, C.; Jaramillo, J.; Gomperts, R.; Stratmann, R. E.; Yazyev, O.; Austin, A. J.; Cammi, R.; Pomelli, C.; Ochterski, J. W.; Ayala, P. Y.; Morokuma, K.; Voth, G. A.; Salvador, P.; Dannenberg, J. J.; Zakrzewski, V. G.; Dapprich, S.; Daniels, A. D.; Strain, M. C.; Farkas, O.; Malick, D. K.; Rabuck, A. D.; Raghavachari, K.; Foresman, J. B.; Ortiz, J. V.; Cui, Q.; Baboul, A. G.; Clifford, S.; Cioslowski, J.; Stefanov, B. B.; Liu, G.; Liashenko, A.; Piskorz, P.; Komaromi, I.; Martin, R. L.; Fox, D. J.; Keith, T.; Al-Laham, M. A.; Peng, C. Y.; Nanayakkara, A.; Challacombe, M.; Gill, P. M. W.; Johnson, B.; Chen, W.; Wong, M. W.; Gonzalez, C.; Pople, J. A. *Gaussian 03*, revision C.02; Gaussian, Inc.: Wallingford, CT, 2004.

(18) (a) Becke, A. D. *J. Chem. Phys.* **1992**, *96*, 2155−2160. (b) Becke, A. D. *J. Chem. Phys.* **1992**, *97*, 9173−9177. (c) Becke, A. D. *J. Chem. Phys.* **1993**, *98*, 5648−5652. (d) Lee, C.; Yang, W.; Parr, R. G. *Phys. Rev. B* **1988**, *37*, 785−789. (e) The LACVP series is derived from LANL2DZ, see: Hay, J. P.; Wadt, W. R. *J. Chem. Phys.* **1985**, *82*, 299−310; Friesner, R. A.; Murphy, R. B.; Beachy, M. D.; Ringnalda, M. N.; Pollard, W. T.; Dunietz, B. D.; Cao, Y. *J. Phys. Chem. A* **1999**, *103*, 1913−1928.

(19) (a) Flükiger, P.; Lüthi, H. P.; Portmann, S.; Weber, J. *MOLEKEL 4.3*; Swiss Center for Scientific Computing: Manno, Switzerland, 2000−2002. (b) Portmann, S.; Lüthi, H. P. *Chimia* **2000**, *54*, 766−770.

(20) Schaftenaar, G.; Noordik, J. H. *J. Comput.-Aided Mol. Des.* **2000**, *14*, 123−134.

(21) For example, (a) Musaev, D. G.; Morokuma, K.; Geletii, Y. V.; Hil, C. L. *Inorg. Chem.* **2004**, *43*, 7702−7708. (b) For a recent interplay of DFT and experiment, see: Anderson, T. M.; Cao, R.; Skolnikna, E.; Hedman, B.; Hodgson, K. O.; Hardcastle, K. I.; Neiwert, W. A.; Wu, S.; Kirk, M. L.; Knottenbelt, S.; Depperman, E. C.; Keita, B.; Nadjo, L.; Musaev, D. G.; Morokuma, K.; Hill, C. L. *J. Am. Chem. Soc.* **2005**, *127*, 11948−11949. (c) Bagno, A.; Bonchio, M.; Sartorel, A.; Scorrano, G. *ChemPhysChem* **2003**, *4*, 517−519. (d) Maestre, J. M.; Lopez, X.; Bo, C.; Poblet, J.-M.; Casan-Pastor, N. *J. Am. Chem. Soc.* **2001**, *123*, 3749−3758. (e) Tsipis, A. C.; Tsipis, C. A. *J. Phys. Chem. A* **2000**, *104*, 859−865. (f) Duclusaud, H.; Borshch, S. A. *Inorg. Chem.* **1999**, *38*, 3489−3493. (g) Duclusaud, H.; Borshch, S. A. *J. Am. Chem. Soc.* **2001**, *123*, 2825−2829. (h) Bridgeman, A. J. *Chem. Eur.—J.* **2004**, *10*, 2935−2941. (i) López, X.; Fernández, J. A.; Romo, S.; Paul, J. F.; Kazansky, L.; Poblet, J. P. *J. Comput. Chem.* **2004**, *25*, 1542−1549. (j) De Visser, S. P.; Sharma, P. K.; Kumar, D.; Neumann, R.; Shaik, S. *Angew. Chem., Int. Ed.* **2004**, *42*, 5661−5665. (k) López, X.; Fernández, J. A.; Poblet, J. M. *J. Chem. Soc., Dalton Trans.* **2006**, 1162−1167.

(22) (a) For aqueous solutions, see: Selling, A.; Andersson, I.; Grate, J. H.; Pettersson, L. *Eur. J. Inorg. Chem.* **2000**, 743−749. (b) For solids, see: Pöppl, A.; Manikandan, P.; Köhler, K.; Maas, P.; Strauch, P.; Böttcher, R.; Goldfarb, D. *J. Am. Chem. Soc.* **2001**, *123*, 4577−4584.

(23) Fruchart, J. M.; Souchay, P. *C. R. Acad. Sci., Ser. C* **1968**, *266*, 1571−1574.

(24) One should note that early EPR measurements indeed indicate a delocalized electron for $[PMo_{12}]^{4-}$ and a vanadium localized electron for $[PMo_{10}V_2]^{6-}$. (a) Che, M.; Fournier, M.; Launay, J. P. *J. Chem. Phys.* **1979**, *71*, 1954−1960. (b) Maksimovskaya, R. I.; Fedotov, M. A.; Kuznetsova, L. I.; Mastikhin, V. M.; Matveev, K. I. *Dokl. Akad. Nauk SSSR* **1975**, *223*, 385−388.

(25) (a) Shaik, S.; Danovich, D.; Schröder, D.; Schwarz, H. *Helv. Chim. Acta* **1995**, *78*, 1393−1407. (b) Schroder, D.; Shaik, S.; Schwarz, H. *Acc. Chem. Res.* **2000**, *33*, 139−145.

(26) Afanasyeva, M. S.; Taraban, M. B.; Purtov, P. A.; Leshina, T. V.; Grissom, C. B. *J. Am. Chem. Soc.* **2006**, *128*, 8651−8658.

Electronic-Structure Calculations

DOI: 10.1002/ange.200700297

Singlet Diradical Character of an Oxidized Ruthenium Trithiolate: Electronic Structure and Reactivity**

Craig A. Grapperhaus, Pawel M. Kozlowski,* Devesh Kumar, Holly N. Frye, Kiran B. Venna, and Selma Poturovic*

The nucleophilicity of transition-metal thiolates has been attributed to a metal–sulfur d–p π interaction, which results in high sulfur character for the occupied frontier orbitals.[1–3] Consequently, oxidation of metal thiolates may be either sulfur- or metal-centered. Recent studies have focused on the stabilization and characterization of metal-coordinated phenylthiyl radicals and related complexes.[4–17] Unlike their phenoxide counterparts, phenylthiyl radicals tend to localize unpaired spin density on the heteroatom, yielding complexes with a potentially rich sulfur-based reactivity that is fundamentally different than the nucleophilicity of their reduced derivatives.

Elucidation of the electronic structure of metal-coordinated thiyl radicals is instrumental to unlocking their reactive potential. When spectroscopic methods alone are insufficient, density functional theory (DFT) is a vital tool. The spectroscopically observable thiyl-radical intermediate $[Ru(dppbt)_3]^+$ (dppbt = 2-diphenylphosphinothiaphenolate) displays sulfur-centered reactivity (Scheme 1) and is ideal for DFT investigations.[18,19]

Figure 1 shows atom positions and coordinates for the family of complexes in this study. To avoid formal oxidation states, a $\{Ru\text{-}(SR)_3\}^n$ convention, similar to the Enemark–Feltham notation, is used.[20,21] The anionic, neutral, and cationic complexes are here referred to as $\{Ru\text{-}(SR)_3\}^{12}$, $\{Ru\text{-}(SR)_3\}^{11}$, and $\{Ru\text{-}(SR)_3\}^{10}$, respectively. The $\{Ru\text{-}(SR)_3\}^{12}$ and $\{Ru\text{-}(SR)_3\}^{11}$ complexes were analyzed as a singlet ($S = 0$) and doublet ($S = 1/2$), consistent with experiment.[18,19] The reactive intermediate, $\{Ru\text{-}(SR)_3\}^{10}$, possesses a nearly degenerate electronic ground state with respect to frontier orbitals. Consequently, its electronic structure was considered as a singlet diradical, which is consistent with experimental data. This description is in line with oxidized nickel dithiolenes.[13]

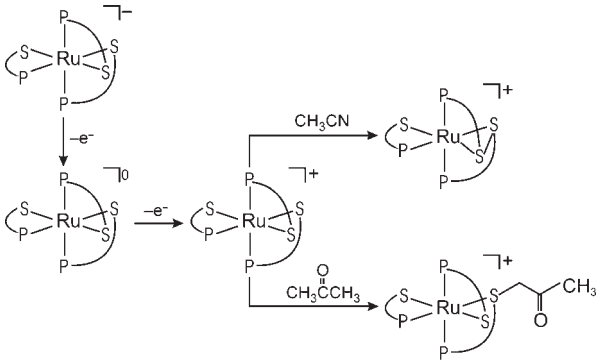

Scheme 1. Solvent-dependent reactivity of the $[Ru(dppbt)_3]^+$ ion. $\widehat{SP}$ = 2-diphenylphosphinothiaphenolate (dppbt).

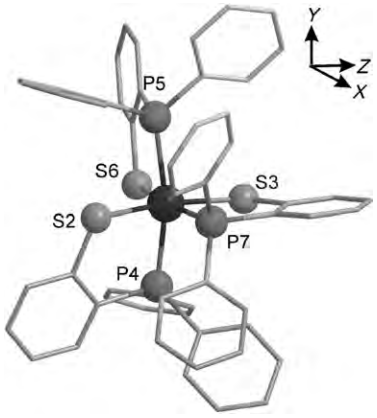

Figure 1. Structure of $[Ru(dppbt)_3]^n$ ($n = -1, 0, +1$) with numbering scheme and coordinate system.

Insight into the complex ground state of $\{Ru\text{-}(SR)_3\}^{10}$ can be gained from the qualitative MO diagram of $\{Ru\text{-}(SR)_3\}^{12}$ (Figure 2). The HOMO and HOMO−1 have π* character with significant ruthenium and sulfur contributions. Oxidation to $\{Ru\text{-}(SR)_3\}^{11}$ removes an electron from the Ru d_{yz}/S3 p_y π* orbital, while further oxidation to $\{Ru\text{-}(SR)_3\}^{10}$ removes an electron from the three-center π interaction between Ru d_{xz}, S2 p_x, and S6 p_z. In each case, the oxidation cannot be considered as strictly metal- or ligand-centered.

[*] Prof. Dr. C. A. Grapperhaus, Prof. Dr. P. M. Kozlowski, H. N. Frye, K. B. Venna, Dr. S. Poturovic
Department of Chemistry
University of Louisville
Louisville, KY 40292 (USA)
Fax: (+1) 502-852-8149
E-mail: grapperhaus@louisville.edu
pawel@louisville.edu
Dr. D. Kumar
Department of Organic Chemistry and
The Lise Meitner-Minerva Center for Computational Quantum Chemistry
Hebrew University
91904 Jerusalem (Israel)

[**] This research was supported in part by the National Science Foundation (CHE-0238137) and by the National Center for Supercomputing Applications utilizing the University of Kentucky High Performance Computing System. Acknowledgment is made to the Donors of the American Chemical Society Petroleum Research Fund (43917-AC3) for partial support of this work.

Supporting information for this article is available on the WWW under http://www.angewandte.org or from the author.

© 2007 Wiley-VCH Verlag GmbH & Co. KGaA, Weinheim

These are not the final page numbers!

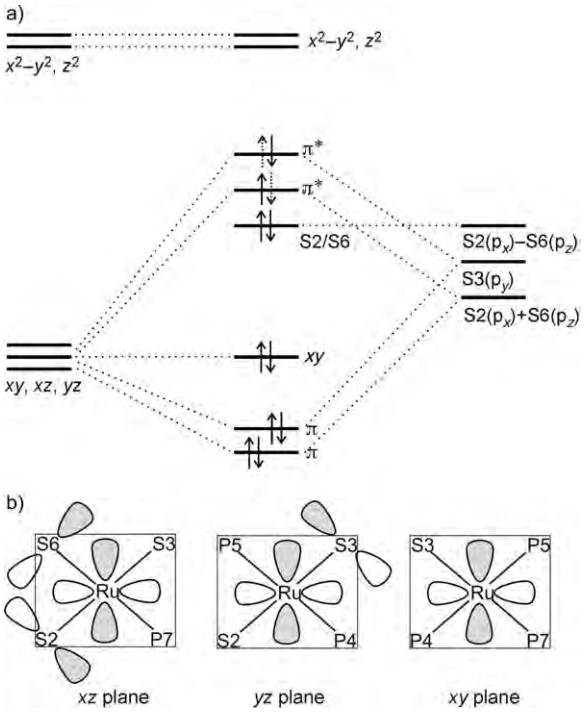

Figure 2. a) Qualitative MO diagram for $[Ru(dppbt)_3]^n$ ($n=-1$, 0, +1) showing π interacations of Ru d orbitals and S p orbitals. b) Views of the *xz*, *yz*, and *xy* planes highlighting π interactions between Ru d orbitals and S p orbitals.

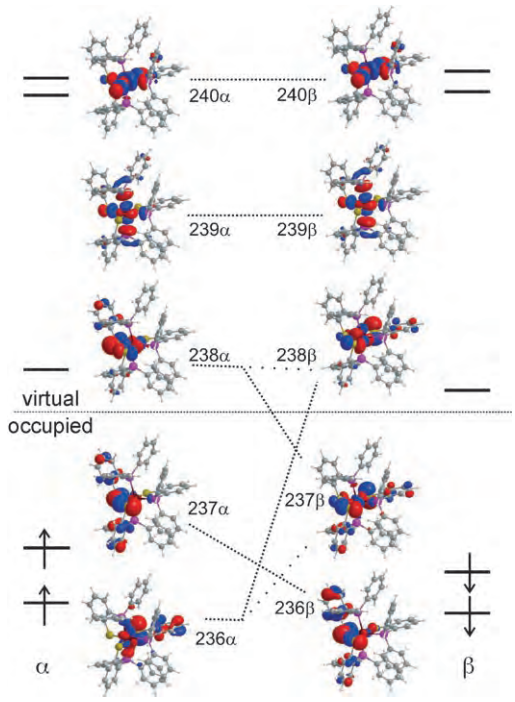

Figure 3. Partial MO diagram of $\{Ru\text{-}(SR)_3\}^{10}$.

Mulliken atomic spin densities are consistent with these expectations (Table 1). For $\{Ru\text{-}(SR)_3\}^{11}$, large spin densities at Ru (0.62), S2 (0.17), and S6 (0.20) are observed, suggesting

Table 1: Mulliken atomic spin densities.

Complex (total spin)[a]	Ru	S2	S3	S6
$\{Ru\text{-}(SR)_3\}^{10}$ ($S=0$)[b]	0.84	0.21	0.47	0.31
$\{Ru\text{-}(SR)_3\}^{11}$ ($S=1/2$)	0.62	0.17	0.02	0.20
$\{Ru\text{-}(SR)_3\}^{12}$ ($S=0$)	0.19	0.10	0.03	−0.06

[a] The total spin includes additional ligand contributions not included in the table. [b] Values reported were calculated for the triplet ground state and are assumed to represent the absolute value of the spin density for the singlet diradical ground state.[13]

that the ground state is best described as a resonance of Ru^{III} thiolate and Ru^{II} thiyl radical. The location and magnitude of spin densities for the singlet diradical $\{Ru\text{-}(SR)_3\}^{10}$ were taken from calculations for the triplet ground state as in previous studies.[13] Spin localization is observed on Ru (0.84), S2 (0.21), S3 (0.47), and S6 (0.31). These results are consistent with a delocalized Ru^{III} thiyl radical with contributions from states including Ru^{IV} thiolate and Ru^{II} dithiyl radical.

Partial quantitative molecular orbital diagrams for $\{Ru\text{-}(SR)_3\}^{10}$ and $\{Ru\text{-}(SR)_3\}^{11}$ are shown in Figure 3 and Figure S1 in the Supporting Information, respectively. For both complexes, orbitals 239 and 240 are metal-centered ($d_{x^2-y^2}$ and d_{z^2}) virtual orbitals. Both complexes also have occupied S-centered orbitals (out-of-phase S2 p_x and S6 p_z); in $\{Ru\text{-}(SR)_3\}^{10}$, these are 237α and 236β. The α π* orbitals Ru d_{yz}/S3 p_y and Ru d_{xz}/S2 p_x/S6 p_z are identified as 236α (occupied) and 238α (virtual). The β π* orbitals are linear combinations of their α counterparts. The Ru d_{xz}/S2 p_x/S6 p_z contribution is largest in 237β (occupied), while 238β (virtual) is predominately Ru d_{yz}/S3 p_y in character. Thus, orbitals 236α and 238α (or a linear combination of the two) represent magnetic orbitals of the $\{Ru\text{-}(SR)_3\}^{10}$ diradical. The partial overlap of the magnetic orbitals may be responsible for the preference for a singlet, rather than triplet, ground state. For $\{Ru\text{-}(SR)_3\}^{11}$, the odd electron lies in orbital 237α, a π* orbital (Figure S1 in the Supporting Information).

Metal-coordinated thiyl radicals typically display a low-energy charge-transfer band in solution.[13] The lowest 20 excited states of singlet $\{Ru\text{-}(SR)_3\}^{10}$ were determined by time-dependent DFT (Table S3 in the Supporting Information). Excitation 4 is the most intense band, with large contributions from 237α to 238α and 236β to 238β at an energy of 9200 cm^{-1}. A pair of intense transitions with large ligand-to-ligand contributions are also observed at 11300 and 12100 cm^{-1} (excitations 6 and 7). Experimentally, $\{Ru\text{-}(SR)_3\}^{10}$ displays a band at 11600 cm^{-1} in acetonitrile or acetone.[18,19]

The electronic structure of $\{Ru\text{-}(SR)_3\}^{10}$ is best described as a diradical with unpaired electrons delocalized about Ru d_{yz}/S3 p_y and Ru d_{xz}/S2 p_x/S6 p_z, as shown in Scheme 2. The half-occupied orbitals overlap slightly, but the major components are orthogonal. This orientation precludes rapid combination to the disulfide. In fact, decay of $\{Ru\text{-}(SR)_3\}^{10}$ to disulfide is slow with a large entropic barrier,[18] facilitating reactivity with other substrates.

When $\{Ru\text{-}(SR)_3\}^{10}$ is generated in the presence of methyl ketones, C–S bond formation occurs.[19] The reaction is presumed to involve the enol tautomer; S-based reactivity

© 2007 Wiley-VCH Verlag GmbH & Co. KGaA, Weinheim

These are not the final page numbers!

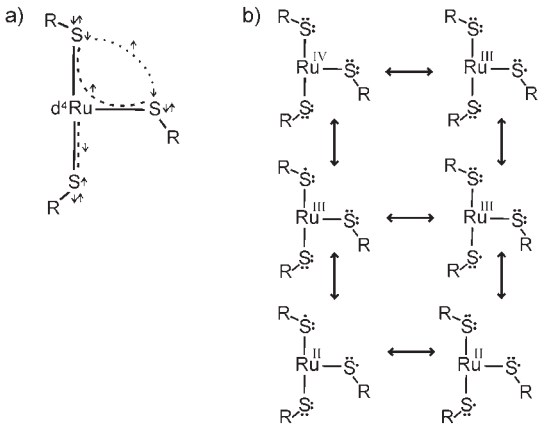

Scheme 2. a) Representation of the singlet diradical ground state of $\{Ru\text{-}(SR)_3\}^{10}$. Electrons on the dashed lines are delocalized between Ru and S. The electron on the dotted line is delocalized between S2 and S6. b) Resonance depictions of the singlet diradical ground state of $\{Ru\text{-}(SR)_3\}^{10}$.

of oxidized Ru thiolates with alkenes was reported by Goh, Webster, and co-workers.[22] As such, $\{Ru\text{-}(SR)_3\}^{11}$ was oxidized in the presence of styrene by bulk electrolysis. The voltammogram after oxidation (1 e^-; Figure S2 in the Supporting Information) reveals a product with a single redox event at +800 mV, assigned as Ru^{III}/Ru^{II}. This is a shift of +1150 mV from $[Ru(dppbt)_3]$ and is consistent with a Ru^{II} dithioether.[23] Electrospray ionization mass spectrometry (ESI-MS) of the product (Figure S3 in the Supporting Information) reveals a parent-ion peak at *m*/*z* 1085.132 with an isotopic envelope consistent with the anticipated 1-phenylethyl dithiother product, $[Ru(dppbt)(dppbt_2)\text{-}\{CH_2CH(Ph)\}]^+$. Alkene addition to oxidized nickel dithiolenes has been reported, although recent studies indicate intraligand as opposed to interligand alkene addition.[24,25] In our system, only interligand addition is possible.

Based on the current analysis, the singlet diradical ground state of $\{Ru\text{-}(SR)_3\}^{10}$ is akin to the generally accepted ground state of ozone. To a first approximation, the Ru^{II} dithiyl radical fragment and O_3 are isoelectronic. Ozone reacts with alkenes to initially generate a primary ozonide,[26] whereas $\{Ru\text{-}(SR)_3\}^{10}$ adds alkenes to generate a dithioether (Scheme 3).

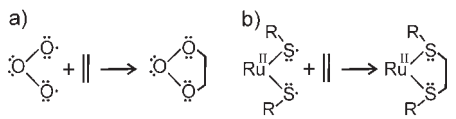

Scheme 3. a) Ozonolysis of alkenes to the initial primary ozonide. b) Alkene addition to $\{Ru\text{-}(SR)_3\}^{10}$.

Experimental Section

Calculations: The initial structure analysis was performed by using Jaguar[27] and the LACVP(Fe)/6-31G(d)(rest) basis set. The final geometry optimization and analysis of electronic states were carried out with the B3LYP functional and the mixed basis set (6-31g(d) for carbon and hydrogen atoms, 6-311g(d,p) for sulfur and phosphorus atoms, and LanL2DZ for ruthenium) as implemented in Gaussian 03.[28] Initial Cartesian coordinates were taken from the crystallographic coordinates of the anionic complex, $[PPN][Ru(dppbt)_3]$ ($PPN^+ = (PPh_3)_2N^+$)

Synthetic methods: Solutions of $[Ru(dppbt)_3]$ were prepared as described previously.[23] Mass spectra were recorded at the Mass Spectrometry Application and Collaboration Facility in the Chemistry Department at Texas A&M University.

$[PPN][Ru(dppbt)(dppbt_2)\{CH_2CH(Ph)\}]$: Styrene(2.0 ml) was added to a solution of freshly prepared $[Ru(DPPBT)_3]$ in acetonitrile (2 mM, 10 ml) containing *n*-tetrabutylhexafluorophosphate (0.100 M) chilled to −20 °C in a foil-wrapped spectroelectrochemical cell. Bulk oxidation at +0.620 V resulted in a one-electron oxidation and formation of the desired product as an air- and thermally stable yellow solution. ESI-MS obsd (calcd): *m*/*z*: 1085.132 (1085.133). $E_{1/2} = +0.80$ V vs. Ag/Ag^+.

Received: January 22, 2007
Published online: ■■ ■■, ■■■■

Keywords: density functional calculations · diradicals · electronic structure · oxidation · sulfur

[1] M. T. Ashby, J. H. Enemark, D. L. Lichtenberger, *Inorg. Chem.* **1988**, *27*, 191.
[2] C. A. Grapperhaus, M. Y. Darensbourg, *Acc. Chem. Res.* **1998**, *31*, 451.
[3] C. A. Grapperhaus, C. S. Mullins, P. M. Kozlowski, M. S. Mashuta, *Inorg. Chem.* **2004**, *43*, 2859.
[4] K. Ray, A. Begum, T. Weyhermuller, S. Piligkos, J. van Slageren, F. Neese, K. Wieghardt, *J. Am. Chem. Soc.* **2005**, *127*, 4403.
[5] K. Ray, E. Bill, T. Weyhermuller, K. Wieghardt, *J. Am. Chem. Soc.* **2005**, *127*, 5641.
[6] K. Ray, T. Weyhermuller, F. Neese, K. Wieghardt, *Inorg. Chem.* **2005**, *44*, 5345.
[7] K. Ray, T. Weyhermuller, A. Goossens, M. W. J. Craje, K. Wieghardt, *Inorg. Chem.* **2003**, *42*, 4082.
[8] P. Ghosh, E. Bill, T. Weyhermuller, F. Neese, K. Wieghardt, *J. Am. Chem. Soc.* **2003**, *125*, 1293.
[9] P. Ghosh, A. Begum, D. Herebian, E. Bothe, K. Hildenbrand, T. Weyhermuller, K. Wieghardt, *Angew. Chem.* **2003**, *115*, 581; *Angew. Chem. Int. Ed.* **2003**, *42*, 563.
[10] P. Ghosh, E. Bill, T. Weyhermuller, K. Wieghardt, *J. Am. Chem. Soc.* **2003**, *125*, 3967.
[11] P. Ghosh, A. Begum, E. Bill, T. Weyhermuller, K. Wieghardt, *Inorg. Chem.* **2003**, *42*, 3208.
[12] D. Herebian, P. Ghosh, H. Chun, E. Bothe, T. Weyhermuller, K. Wieghardt, *Eur. J. Inorg. Chem.* **2002**, 1957.
[13] V. Bachler, G. Olbrich, F. Neese, K. Wieghardt, *Inorg. Chem.* **2002**, *41*, 4179.
[14] S. Kimura, E. Bill, E. Bothe, T. Weyhermuller, K. Wieghardt, *J. Am. Chem. Soc.* **2001**, *123*, 6025.
[15] H. Chun, C. N. Verani, P. Chaudhuri, E. Bothe, E. Bill, T. Weyhermuller, K. Wieghardt, *Inorg. Chem.* **2001**, *40*, 4157.
[16] D. Herebian, E. Bothe, E. Bill, T. Weyhermuller, K. Wieghardt, *J. Am. Chem. Soc.* **2001**, *123*, 10012.
[17] C. H. Hsieh, I. J. Hsu, C. M. Lee, S. C. Ke, T. Y. Wang, G. H. Lee, Y. Wang, J. M. Chen, J. F. Lee, W. F. Liaw, *Inorg. Chem.* **2003**, *42*, 3925.
[18] C. A. Grapperhaus, S. Poturovic, *Inorg. Chem.* **2004**, *43*, 3292.
[19] S. Poturovic, C. A. Grapperhaus, M. S. Mashuta, *Angew. Chem.* **2005**, *117*, 1917; *Angew. Chem. Int. Ed.* **2005**, *44*, 1883.
[20] The value *n* represents the total number of metal d electrons plus the number of sulfur electrons available for p interactions. Thiolate sulfur atoms donate two electrons to the p network,

 © 2007 Wiley-VCH Verlag GmbH & Co. KGaA, Weinheim

thiyl radicals donate one electron, and sulfenylium cations donate zero electrons.
[21] J. H. Enemark, R. D. Feltham, *Coord. Chem. Rev.* **1974**, *13*, 339.
[22] R. Y. C. Shin, M. E. Teo, W. K. Leong, J. J. Vittal, J. H. K. Yip, L. Y. Goh, R. D. Webster, *Organometallics* **2005**, *24*, 1483.
[23] C. A. Grapperhaus, S. Poturovic, M. S. Mashuta, *Inorg. Chem.* **2002**, *41*, 4309.
[24] W. E. Geiger, *Inorg. Chem.* **2002**, *41*, 136.
[25] D. J. Harrison, N. Nguyen, A. J. Lough, U. Fekl, *J. Am. Chem. Soc.* **2006**, *128*, 11026.
[26] J. March, *Advanced Organic Chemistry: Reactions, Mechanisms, and Structure*, 4th ed., Wiley, New York, **1992**.
[27] Jaguar 5.0, L. L. C. Schrödinger, Portland, OR, 1991 – 2003.
[28] Gaussian 03, Revision A.1, M. J. Frisch, G. W. Trucks, H. B. Schlegel, G. E. Scuseria, M. A. Robb, J. R. Cheeseman, J. A. Montgomery, Jr., T. Vreven, K. N. Kudin, J. C. Burant, J. M. Millam, S. S. Iyengar, J. Tomasi, V. Barone, B. Mennucci, M. Cossi, G. Scalmani, N. Rega, G. A. Petersson, H. Nakatsuji, M. Hada, M. Ehara, K. Toyota, R. Fukuda, J. Hasegawa, M. Ishida, T. Nakajima, Y. Honda, O. Kitao, H. Nakai, M. Klene, X. Li, J. E. Knox, H. P. Hratchian, J. B. Cross, C. Adamo, J. Jaramillo, R. Gomperts, R. E. Stratmann, O. Yazyev, A. J. Austin, R. Cammi, C. Pomelli, J. W. Ochterski, P. Y. Ayala, K. Morokuma, G. A. Voth, P. Salvador, J. J. Dannenberg, V. G. Zakrzewski, S. Dapprich, A. D. Daniels, M. C. Strain, O. Farkas, D. K. Malick, A. D. Rabuck, K. Raghavachari, J. B. Foresman, J. V. Ortiz, Q. Cui, A. G. Baboul, S. Clifford, J. Cioslowski, B. B. Stefanov, G. Liu, A. Liashenko, P. Piskorz, I. Komaromi, R. L. Martin, D. J. Fox, T. Keith, M. A. Al-Laham, C. Y. Peng, A. Nanayakkara, M. Challacombe, P. M. W. Gill, B. Johnson, W. Chen, M. W. Wong, C. Gonzalez, J. A. Pople, Gaussian, Inc., Pittsburgh, PA, **2003**.

 © 2007 Wiley-VCH Verlag GmbH & Co. KGaA, Weinheim

These are not the final page numbers!

Zuschriften

Berechnung elektronischer Strukturen

C. A. Grapperhaus,* P. M. Kozlowski,*
D. Kumar, H. N. Frye, K. B. Venna,
S. Poturovic ——— ■■■■–■■■■

Singlet Diradical Character of an Oxidized Ruthenium Trithiolate: Electronic Structure and Reactivity

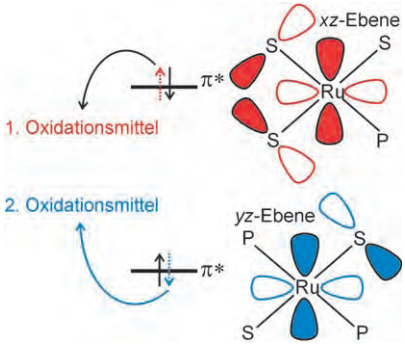

Ganz allein: Nach Rechnungen ist der Grundzustand des oxidierten reaktiven Intermediats $[Ru(dppbt)_3]^+$ (dppbt = 2-Diphenylphosphanylthiaphenolat) ein Singulettdiradikal. Die ungepaarten Elektronen in den π*-Orbitalen sind über das Metallatom und die S-Atome der Liganden delokalisiert. Die relative Orientierung der halbbesetzten Orbitale verhindert die Disulfidbildung und begünstigt die Addition ungesättigter Kohlenwasserstoffe an benachbarte Schwefelatome.

© 2007 Wiley-VCH Verlag GmbH & Co. KGaA, Weinheim

DOI: 10.1002/chem.200601704

Formation of the Active Species of Cytochrome P450 by Using Iodosylbenzene: A Case for Spin-Selective Reactivity

Kyung-Bin Cho,[a] Yohann Moreau,[a] Devesh Kumar,[a, b] Dan A. Rock,[c, d] Jeffrey P. Jones,*[c] and Sason Shaik*[a]

Abstract: The generation of the active species for the enzyme cytochrome P450 by using the highly versatile oxygen surrogate iodosylbenzene (PhIO) often produces different results compared with the native route, in which the active species is generated through O_2 uptake and reduction by NADPH. One of these differences that is addressed here is the deuterium kinetic isotope effect (KIE) jump observed during N-dealkylation of *N*,*N*-dimethylaniline (DMA) by P450, when the reaction conditions change from the native to the PhIO route. The paper presents a theoretical analysis targeted to elucidate the mechanism of the reaction of PhIO with heme, to form the high-valent iron–oxo species Compound I (Cpd I), and define the origins of the KIE jump in the reaction of Cpd I with DMA. It is concluded that the likely origin of the KIE jump is the spin-selective chemistry of the enzyme cytochrome P450 under different preparation procedures. In the native route, the reaction proceeds via the doublet spin state of Cpd I and leads to a low KIE value. PhIO, however, diverts the reaction to the quartet spin state of Cpd I, which leads to the observed high KIE values. The KIE jump is reproduced here experimentally for the dealkylation of *N*,*N*-dimethyl-4-(methylthio)aniline, by using intramolecular KIE measurements that avoid kinetic complexities. The effect of PhIO is compared with *N*,*N*-dimethylaniline-*N*-oxide (DMAO), which acts both as the oxygen donor and the substrate and leads to the same KIE values as the native route.

Keywords: cytochromes · density functional calculations · heme proteins · kinetic isotope effects · spin selectivity

Introduction

The cytochrome P450 family of enzymes is well known for mediating oxygenation reactions on a plethora of diverse chemical structures.[1–5] Targeting a range of substrates, the enzyme utilizes a heme group for its catalysis, normally with consumption of O_2 and reducing equivalents supplied ultimately from NADPH (hereafter, the "native route"). Central to this reaction is an oxidizing species that is subject to many ongoing studies today.[3–5] In the late 1970s, it was shown that this oxidizing species, or at least one that functions like it, could be generated by oxygen atoms derived from $NaIO_4$ and $NaClO_2$ that serve as "oxygen surrogates" in the absence of O_2 and NADPH.[6–8] Subsequently, Lichtenberger et al.[9] reported on iodosylbenzene (PhIO)-supported liver microsomal O-dealkylation of 7-ethoxycoumarin without NADPH or O_2. Around the same time, Gustafsson and Bergman[10] showed that PhIO is an efficient oxygen donor that supports hydroxylation of fatty acids. PhIO was thus found to be a very efficient oxygen donor for the reaction, and the formation of the oxidizing species. Due to the nature of the oxygen donors, it could be assumed that

[a] Dr. K.-B. Cho, Dr. Y. Moreau, Dr. D. Kumar, Prof. S. Shaik
Department of Organic Chemistry and
The Lise Meitner-Minerva Center for Computational Quantum Chemistry
Hebrew University, 91904 Jerusalem (Israel)
Fax: (+972) 2-6584680
E-mail: sason@yfaat.ch.huji.ac.il

[b] Dr. D. Kumar
Current address:
Max-Planck-Institut für Kohlenforschung
Kaiser-Wilhelm-Platz 1, 45470 Mülheim an der Ruhr (Germany)

[c] Dr. D. A. Rock, Prof. J. P. Jones
Department of Chemistry, Washington State University
PO BOX 644630, Pullman, WA 99164-4630 (USA)
Fax: (+1) 509-335-8867
E-mail: jpj@wsu.edu

[d] Dr. D. A. Rock
Current address:
Amgen, Pharmacokinetics & Drug Metabolism
1201 Amgen Court West, Seattle, WA 98119 (USA)

Supporting information for this article is available on the WWW under http://www.chemeurj.org/ or from the author.

 © 2007 Wiley-VCH Verlag GmbH & Co. KGaA, Weinheim WILEY InterScience

the P450 oxidizing species contained only one oxygen atom, thereby strengthening the conjecture that this species was related to Compound I (Cpd I) found in horseradish peroxidase (HRP).[6,7] Recently, Dowers et al.[11] have shown that the single oxygen atom donated from *N*-oxide of three different substituted *N*,*N*-dimethylanilines (DMAs) gives identical isotope effects for N-dealkylation as the enzyme system supported by NADPH and O_2, supporting the idea that a single oxygen atom is the oxidizing species for this reaction. Thus, there is a general consensus today that the active species is indeed the high-valent iron–oxo species Cpd I, which is directly responsible for the oxygenation of substrates in P450 oxidations. Indeed, while the active-oxygen species has evaded experimental detection, since the rate-limiting step precedes its formation leading to low steady-state levels of Cpd I under the native conditions, its involvement in the reaction has been strongly inferred.[4,11] The similarity between the oxidizing species generated with PhIO and the NADPH/O_2-generated Cpd I has been documented,[12,13] and Cpd I is now presumed to be formed with PhIO as well. Moreover, given that the rate-limiting step in the generation of Cpd I by NADPH and O_2 is the second electron transfer from P450 reductase, the iodosylbenzene procedure bypasses this step and is thus better suited for studies of the reaction of Cpd I with substrates. As such, PhIO has become an important mechanistic tool in the study of heme enzymes in both substrate oxidation and inhibition mechanisms.[14,15]

For instance, given the ability of PhIO to circumvent any dioxygen species in the catalytic cycle of P450, the reagent has been used to distinguish between oxidations by Cpd 0 (an iron–peroxy species) and Cpd I.[16–18] Since Cpd 0 has been suggested as an additional P450 oxidant,[19] the detection of differences between surrogate single oxygen donors and the native route have often been taken as evidence for the functioning of Cpd 0 (or a similar species) alongside Cpd I. As such, PhIO has also been used to circumvent the rate-limiting second electron reduction, and by difference with the native route, served to pin down the effects of steps prior to oxidation, and their contribution to the preexponential factor.[20] Furthermore, since PhIO eliminates the need for P450 reductase, its utilization provided an assessment of the role of protein–protein interactions in altering reaction regioselectivity through conformational changes in the P450 enzyme.[21] Finally, its utility is wide-ranging and stretches beyond the heme system to nonheme mimetic systems in bioinorganic chemistry, in which it can be utilized to synthesize novel high-valent metal–oxo reagents.[22] PhIO is often used to generate Cpd I in model systems that are compared with the P450 enzyme native route. All of these applications depend on the Cpd I species that is generated by the native route and by PhIO being identical.

In light of this widespread use, it has become important to understand the differences in Cpd I species generated by PhIO and other oxygen donors with respect to the NADPH/O_2-generated Cpd I. Minor differences were noted early on,[13,23] but more recently, evidence has been accumulating that the oxidant generated by the reaction of PhIO with P450 behaves differently compared with the Cpd I generated by the native route. Guengerich et al.[24] showed that the application of PhIO generated an oxidizing species that leads to considerably higher kinetic isotope effect (KIE) compared with the natively generated Cpd I, and much more like the KIE observed from the reaction with HRP. This was attributed to a possible formation of a PhI-O-Fe complex[25] that generated a protonated Cpd I less capable of abstracting the proton from the substrate. The notion of a PhI-O-Fe oxidizing complex was supported by Collman et al.,[26,27] who used different iodosylarenes as oxygen donors, and showed that these reagents gave different product ratios for epoxidation of substrates. This was inconsistent with the view that beyond the formation of Cpd I, the initial source of oxygen did not matter for the reactions. A PhI-O-Fe complex was indeed found by Nam et al.[28,29] to be in equilibrium with Cpd I, but whether or not this complex was an oxidizing species could not be ascertained by the experimental data. Recently, Bhakta et al.[18] have shown that the PhIO-generated oxidant differs from the normal Cpd I in dealkylating *N*-cyclopropyl-*N*-alkyl-*p*-chloroaniline derivatives, yielding different products. In fact, the PhIO-generated Cpd I produced the same products as HRP.

Taken together, there is enough evidence to conclude that the Cpd I formation from oxygen donors such as PhIO is not well understood, and experiments may have been conducted for some time under the potentially inaccurate assumption that PhIO-generated Cpd I would behave the same way as the native Cpd I. Along with the fleeting existence of Cpd I, this situation creates an ideal situation for computational research directed at understanding the mechanism of formation of Cpd I from oxygen donors or surrogates. We have therefore conducted a theoretical investigation of the reactions of the two oxygen surrogates, outlined in Scheme 1, in

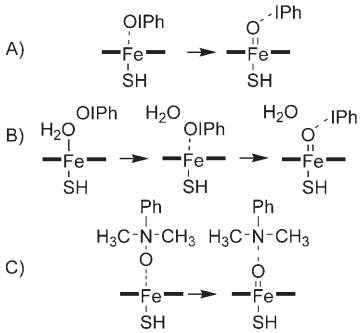

Scheme 1. The three reactions investigated in this study.

an attempt to understand the reason why the use of PhIO (reactions A and B) leads to a KIE jump,[24] while the use of *N*,*N*-dimethylaniline-*N*-oxide (DMAO), in reaction C, leads to low KIE values, identical to those obtained from the native route of the enzyme, for a few different P450 isoforms.[11] To rule out that the KIE jumps originated in "kinetic complexity", we also carried out experiments with PhIO to ascertain the KIE jump by determining intramolec-

 © 2007 Wiley-VCH Verlag GmbH & Co. KGaA, Weinheim

ular KIE values for N-dealkylation of *N*,*N*-dimethyl-4-(methylthio)aniline. Since we have shown in the past that *N*-methyl-*N*-(trideuteromethyl)anilines exhibit kinetic complexity ("masking") and do not provide a good estimate of the intrinsic isotope effect for some P450 enzymes,[30] we adapted here a special experimental design. The deutrium content of the formaldehyde produced from *N*,*N*-bis(dideuteromethyl-^{13}C)-4-(methylthio)aniline is used to determine the intramolecular isotope effect; thereby evading the masking issue (see more later).

Results

Three model reactions were investigated in this study. In all of the models, the heme is represented by an iron–porphine ring, and an SH group replaces the axial cysteine ligand which is present in P450. In the first reaction (reaction A, Scheme 1), we studied the simple process in which PhIO binds to pentacoordinate heme and Cpd I is formed through oxygen transfer. In the second reaction (reaction B, Scheme 1), this system was extended to include a water ligand to represent the aqua–ferric resting state of the P450 enzyme (note that in the enzyme there is a spin equilibrium between low- and high-spin species; the latter is pentacoordinated). Thus in the second case the reaction involves the displacement of the water ligand from the heme before the binding of PhIO. In the third reaction (reaction C, Scheme 1), DMAO has been used as the oxygen donor in order to further confirm and correlate the conclusions obtained from reactions A and B to experimental results. The energy values mentioned throughout this study include big basis set, solvent, and zero-point vibration energy (Z_0) corrections unless explicitly otherwise stated. Thermal effects, that is, entropy and enthalpy corrections, are only included where specifically mentioned.

Reaction A: The ground state of the pentacoordinate heme was found to be the sextet spin state, with the valence-electron orbital configuration of $(\delta)^1(\pi^*_{yz})^1(\pi^*_{xz})^1(\sigma^*_{z^2})^1(\sigma^*_{xy})^1$, all electrons having a spin-up configuration. These results have previously been obtained for the pentacoordinated heme models tested before.[31–33] The energy difference to the quartet state, with the configuration $(\pi^*_{xz})^1(\pi^*_{yz})^1(\sigma^*_{z^2})^1$ is 3.1 kcal mol^{-1} higher. The doublet state $(\pi^*_{yz})^1$, in contrast, lies considerably higher in energy at 7.3 kcal mol^{-1} over the sextet. The energies for reaction A are collected in Table 1.

Table 1. Relative energies[a] for the different structures in reaction A [data in kcal mol^{-1}].

	Heme +OIPh	**1**	**TS1**	**2**	Cpd I +IPh
doublet	7.15	0.00	5.06	−5.44	−3.98
quartet	2.95	2.11	7.72	−5.75	−3.75
sextet	−0.18	2.10	7.91	3.39	5.74

[a] These energies are obtained at B3LYP/LACV3P*$^+$(ERMLER2*$^+$ on I)//LACVP level, including Z_0 and solvent effects (see Computational methods).

However, upon PhIO binding to the heme (structure **1** in Figure 1a), all three states are now close to each other, within 2.1 kcal mol^{-1}, with the doublet state (^{2}**1**) being lowest. The various spin-states have the same orbital electronic configurations as in the pentacoordinate heme complex. Figure 1a shows the geometrical parameters for **1**. Consistent with the small binding energy, the O–Fe distance ranges from 1.9 to 2.2 Å. The I–O distance barely changes compared to the free PhIO (Table S17 in the Supporting Information), confirming the view that this species is more correctly described as a weak PhIO···heme complex and is not a PhI–Cpd I complex (i.e., PhI···O=FePor).

The transfer of the oxygen from PhIO to the heme and formation of Cpd I is found to occur through a transition

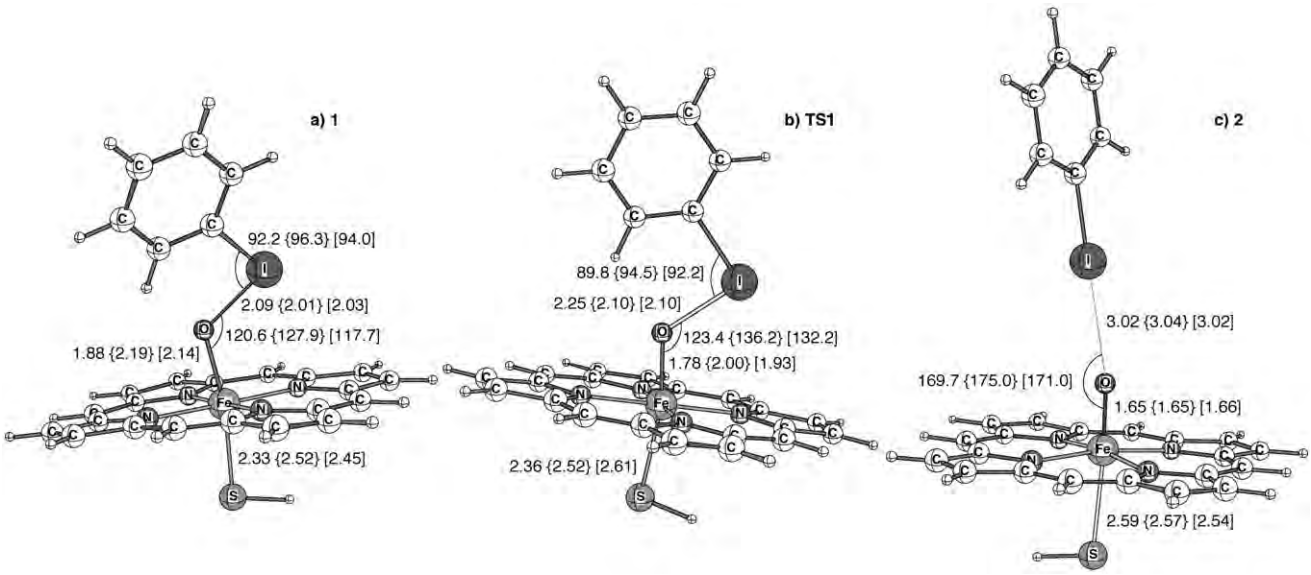

Figure 1. Optimized structure a) **1**, b) **TS1**, and c) **2** for reaction A. Values with two decimals are distances in Å. Values with one decimal are angles in degrees. The values for each species are in order doublet, {quartet}, and [sextet].

 © 2007 Wiley-VCH Verlag GmbH & Co. KGaA, Weinheim

state (**TS1**, Figure 1b) with a moderate energy barrier ranging from 5.1 to 7.9 kcal mol^{-1}. This confirms that this reaction is faster than the normal generation of Cpd I, in which the O_2 bond breaking in general has a barrier in the range of 10–15 kcal mol^{-1}, and the rate-limiting electron-transfer step from the P450 reductase should correspond to an even higher barrier. The spin and charge distributions for this transition-state structure resemble more the corresponding features in **1** rather than **2** (compare Tables S5, S8, and S11), but the critical O–Fe distance half way between these two structures and the imaginary frequencies of 103.4*i*, 223.8*i*, and 184.6*i* cm^{-1}, in respective spin states, confirm that this is indeed a transition-state structure.

The product of this reaction (**2**) is shown in Figure 1c. The oxygen has now undergone bonding to the heme, forming Cpd I. The Cpd I state with Fe^{V} oxidation number on iron was not produced by the process, in accord with previous calculations showing this species to lie about 20 kcal mol^{-1} above the Por(+•)$Fe^{IV}O$ states.[34] As may be seen by inspection of structure **2**, the PhI moiety is bound very weakly to the oxygen with the I–O distance at around 3 Å. The PhI–Cpd I complexation energies are in the range 1.5–2.4 kcal mol^{-1} within respective multiplicities. Structures ^{2}**2** and ^{4}**2** are virtually degenerate and ^{6}**2** is 9.1 kcal mol^{-1} higher in energy than ^{4}**2**. These energy differences between the spin states of Cpd I are known from earlier calculations.[35–37]

A couple of interesting results relating to these calculations are worth mentioning. First, upon releasing **TS1** in the direction of the product **2**, the freed PhI would find a position alongside the porphine plane, where the protons of the porphine macrocycle can weakly hold it. In fact, the LACVP energies were virtually the same as **2**. Therefore, this distinction between **2** and the obtained complexed product was insignificant, other than to confirm that the I–O interaction at this stage is extremely weak, and that the surface may have multiple local minima. The weakness of the complexation interaction between PhI and Cpd I casts serious doubts on the suggestions that this is the root cause of the differences in the reactivity between the native route and the PhIO route.[24–27]

A second feature is that the sextet ^{6}**TS1** species found here in fact led to an iron–oxo product in which the sulfur ligand was detached from the iron atom. It should be noted, that this iron–sulfur bond disruption may or may not really happen in the real enzyme, for which the sextet state was found by QM/MM calculations to have a normal Fe–S bond.[35] In the current theoretical model, we assume that the detached sulfur returns to the axial ligand position. Indeed, by varying the Fe–S bond length, it is found that the Fe–S bond once again can form over a negligible barrier lying lower than ^{6}**TS1** (Figure S7 in the Supporting Information). Therefore, **TS1** is here presented as the transition state connecting **1** with **2**. Nevertheless, to be cautious we shall consider later also the putative consequences of this heme dissociation in the sextet state.

The main conclusions drawn from reaction A are that the energy barrier **TS1** is overall relatively low, and the differences are small between the different multiplicities at this point. Inclusion of thermal effects to the reaction reduces this gap even further (Table S28), and the higher multiplicities will even be lower in the presence of hydrogen bonds to sulfur (see below). The final energy graph of reaction A is shown in Figure 2.

Theoretical results on the effects of hydrogen bonds on sulfur: To investigate the effect of hydrogen bonds to the sulfur ligand on the overall energy, single-point calculations were carried out on **1**, **TS1**, and **2**, with two NH_3 molecules hydrogen bonded to the sulfur at a distance of 2.66 Å. No frequency calculations were done on these structures since they were not optimized; hence Z_0 is not included in any of the values quoted in this section, including those without the NH_3 molecules. The relative energy values are presented in Table 2.

The effect on the order of the different states was negligible for **2**, but it was more pronounced for **1** and **TS1**. Relative to ^{2}**1**, the relative energy of ^{4}**1** dropped from 3.3 to −2.2 kcal mol^{-1}, while ^{6}**1** went from 4.2 to 1.8 kcal mol^{-1}.

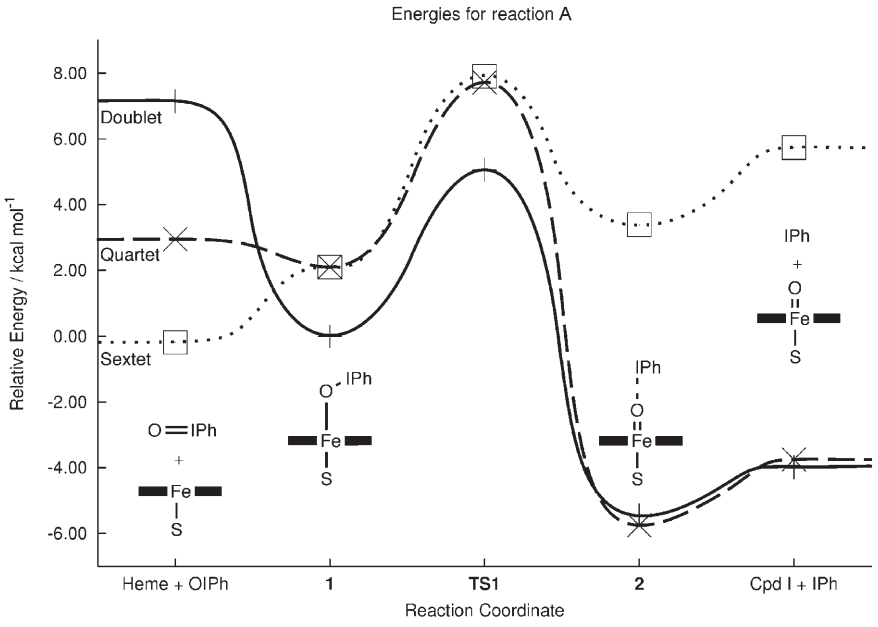

Figure 2. Energy changes of reaction A taken from Table 1. The values include single-point energies using the large basis set, solvation, and Z_0.

 © 2007 Wiley-VCH Verlag GmbH & Co. KGaA, Weinheim

Table 2. Influence on the relative energies[a] by NH···S hydrogen bonding to SH ligand [data in kcal mol^{-1}].

	Without NH···S			With 2 NH···S		
	1	**TS1**	**2**	**1**	**TS1**	**2**
doublet	0.00	5.28	−5.35	0.00	3.73	−8.75
quartet	3.30	9.27	−5.58	−2.17	3.45	−8.50
sextet	4.22	10.54	5.01	1.77	4.97	1.62

[a] The relative energies correspond to B3LYP/LACV3P*$^{+}$ (ERMLER2*$^{+}$ on I)//LACVP and include solvent correction but not Z_0 correction.

This would reflect the hydrogen-bond effect on the populated $\sigma^*_{z^2}$ orbital for ^{4}**1** and ^{6}**1**,[33,37–39] which is not populated in the case of ^{2}**1** or **2**. This trend was continued in **TS1**. Specifically, it now predicts ^{4}**TS1** to be the lowest by 0.3 kcal mol^{-1} lower than ^{2}**TS1**. Comparing the relative energies of **1**, **TS1** , and **2** to each other, the extra hydrogen bonds increase the exothermicity for the doublet surface (from 5.4 to 8.8 kcal mol^{-1}), but this increase is largely compensated by the stabilization of ^{4}**1** and ^{6}**1** in the quartet and sextet surface. The barriers are also lowered by a small amount.

Based on these observations, it is clear that environmental factors play a role in this reaction. The important observation here is that hydrogen bonds to the thiolate ligand stabilize the higher multiplicities of **1** and **TS1** more than they stabilize the doublet state, as discussed later.

Reaction B: Adding a water molecule to the heme, the reaction starts with the resting state model of the enzyme with a water molecule ligated in the previously vacant axial position. Therefore, the reaction now includes a water dislocation step that occurs before the main reaction, the oxygen transfer to the iron, takes place. At the resting state, the heme–H_2O, all the spin states are energetically within 1.4 kcal mol^{-1} from each other. Upon complexation (structure **0**, Figure 3a) PhIO forms a hydrogen bond to the water. Energetically, ^{2}**0** is now lowest, but the states remain close to each other. The complexation energies are in the range 4.6–6.0 kcal mol^{-1} relative to ^{2}**0** (Table 3).

The dislocation of the water ligand occurs over a transition state **TS0** (Figure 3b). The water is now completely dissociated from the heme, and PhIO is about to bind to Fe. The region around this transition state is flat, with imaginary frequencies of 33.0*i*, 27.7*i*, and 25.9*i* cm^{-1} for the various spin states. The doublet state ^{2}**TS0** is now clearly the highest state at 9.2 kcal mol^{-1} (relative to ^{2}**1**), while ^{4}**TS0** is 3.3 kcal mol^{-1} (relative to ^{2}**0**). The sextet ^{6}**TS0** state on the other hand is associated with a very small barrier, only 0.6 kcal mol^{-1} above ^{2}**0**, which is also 0.6 kcal mol^{-1} lower than ^{6}**0**. Thus with such differences between the spin states, it can be concluded that the high energy ^{2}**TS0** acts as a "filter" that allows the reaction to go on in higher multiplicities in general, and hindering the reaction to occur at the doublet state in particular. The reason for the low energy of the sextet state at **TS0** and for the high energy of the doublet state is associated with the relative strength of Fe–OH_2 binding and is not particularly affected by PhIO, which is only loosely coordinated to the heme. Therefore, the energy profile for water dislocation is quite general, irrespective of the identity of the oxygen donor.

Table 3. Relative energies [in kcal mol^{-1}][a] for the different structures in reaction B.

	[H_2O–heme] +PhIO	**0**	**TS0**	**1**	**TS1**	**2**	[H_2O-Cpd I] +PhI
doublet	6.90	0.85	9.18	0.00	6.25	−3.21	−3.09
quartet	6.37	2.32	4.17	1.84	8.29	−2.74	−3.88
sextet	5.48	2.04	1.42	1.75	8.68	4.87	4.70

[a] Energies obtained as in Table 1.

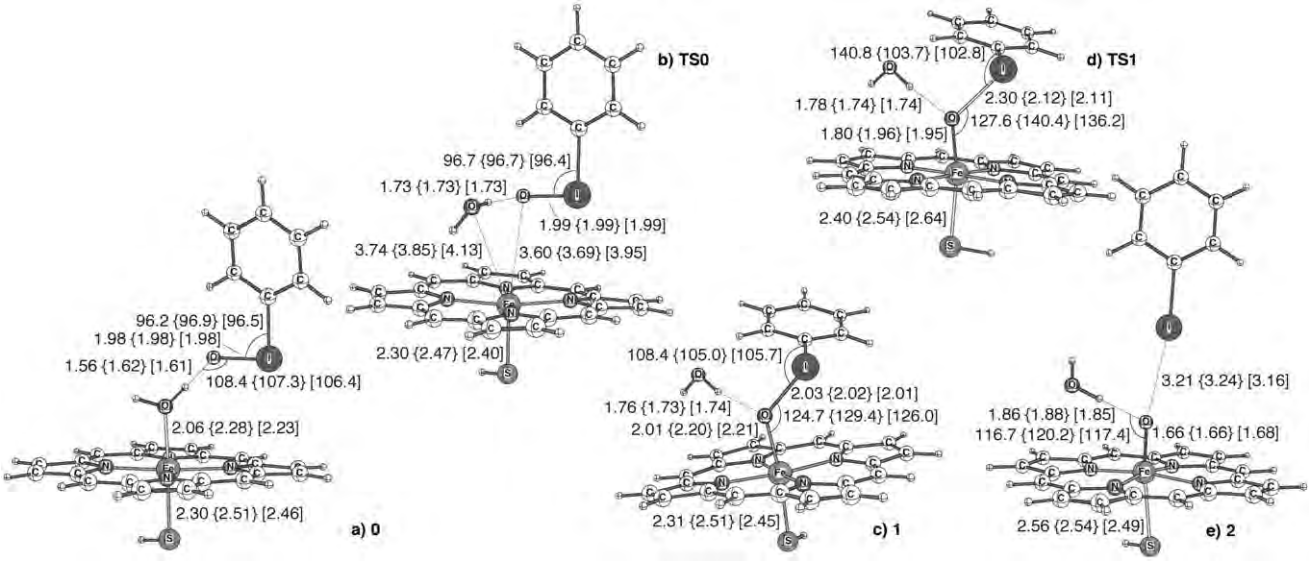

Figure 3. Optimized structure a) **0**, b) **TS0**, c) **1**, d) **TS1**, and e) **2** for reaction B. See legend of Figure 1 for explanation of the numbers.

 © 2007 Wiley-VCH Verlag GmbH & Co. KGaA, Weinheim

The structures for **1** (Figure 3c), **TS1** (Figure 3d) and **2** (Figure 3e) in reaction B are largely as described for reaction A. Geometrically, the water is hydrogen bonded to the oxygen, and the only notable difference to reaction A is in **2**, in which the I–O distance is elongated by 0.1–0.2 Å; that is, the introduction of H_2O further weakens the I–O bond. Energetically, the internal energy changes (that is, the changes in the energy differences within each structure) are less than 1 kcal mol^{-1} with no internal order changes, with the sole exception of **2**, for which the difference between ^{4}**2** and ^{6}**2** drops from 9.1 to 7.6 kcal mol^{-1} and the order of preference changes between ^{2}**2** and ^{4}**2**. Looking at the changes of energy differences between the structures, once again **2** stands out by having their energies raised by 1.5–3.0 kcal mol^{-1}, reflecting the weaker I–O bond. Also here, relaxation of ^{6}**TS1** leads to the Fe–S bond break as described in reaction A.

For **TS1**, the barriers for different states remain close to each other as in reaction A. It can now be concluded that in the case of PhIO the crucial energy barrier in determining the final spin state of the product is the dislocation of water via **TS0**, due to the large energy difference between the doublet and the others, rather than **TS1**. The final energies for reaction B are shown in a graph in Figure 4.

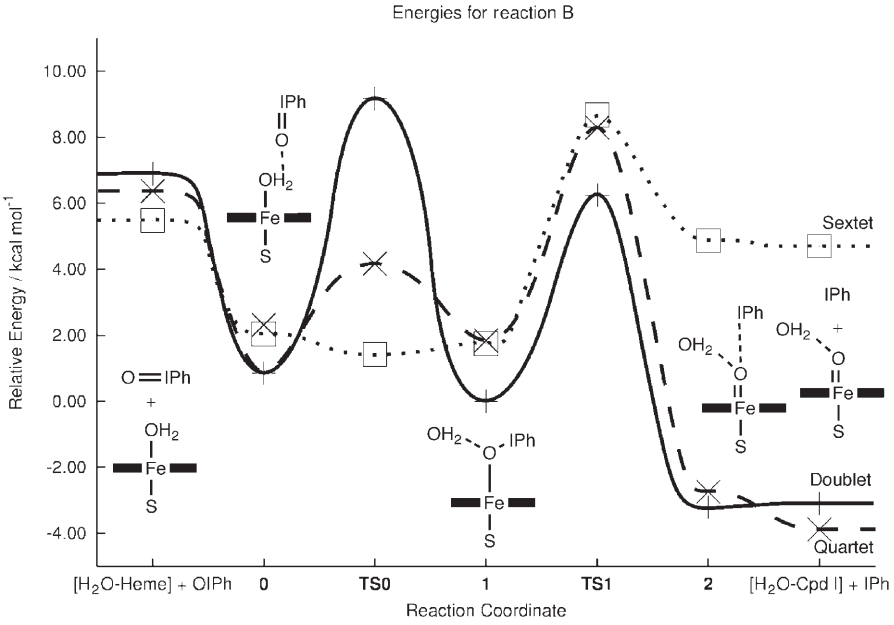

Figure 4. B3LYP energy profile for reaction B. The values are taken from Table 3.

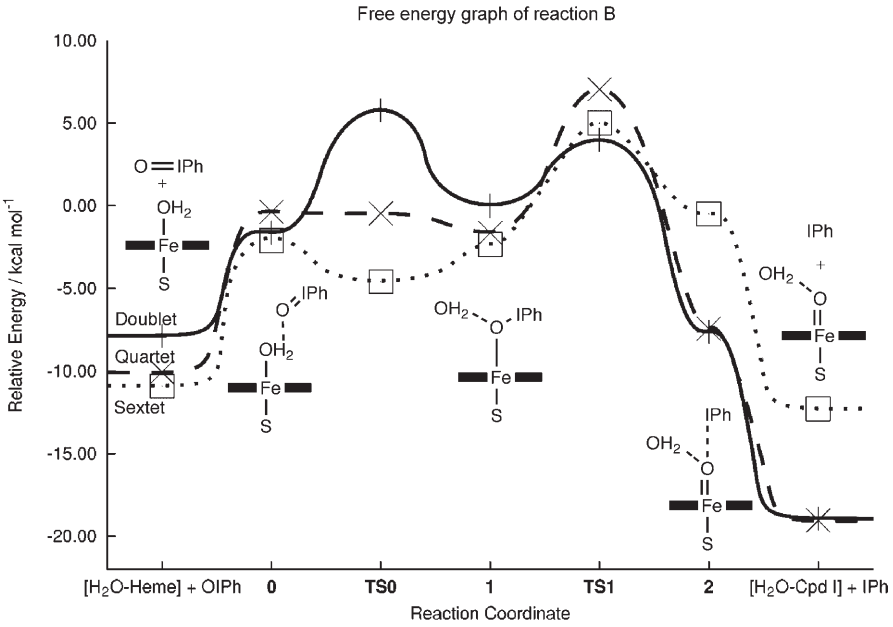

Figure 5. Free-energy profile for reaction B. The values are taken from Table S61.

Free energy changes for reaction B: It is instructive to consider also the free energy of this reaction (Figure 5). It should be stressed here that the endpoint free energies might not be reliable (resulting in large entropy effects due to the loss of translational and rotational degrees of freedom upon encounter). The free-energy comparisons from **0** to **2** are, however, reliable. The most interesting feature is that on the free-energy scale, the sextet surface is the lowest one for the range of structures **0**, **TS0**, and **1**. The quartet surface is also stabilized, ^{4}**1** being lower than ^{2}**1**. In addition, the gap between ^{2}**TS1** and ^{6}**TS1** is reduced from 2.4 to 1.0 kcal mol^{-1}, although the gap between ^{2}**TS1** and ^{4}**TS1** increases from 2.0 to 3.1 kcal mol^{-1}. Thus the inclusion of the thermal effects works favorably for the higher multiplicities with the sole exception of ^{4}**TS1**, something that is only reinforced if the sulfur ligand is hydrogen bonded as presented earlier.

Reaction C: Since the above results on reaction B indicate that the dislocation of water is independent of the oxygen donor, and that the presence of a water molecule does not

 © 2007 Wiley-VCH Verlag GmbH & Co. KGaA, Weinheim

affect the subsequent step of Cpd I formation (see reaction A versus **1** to **2** in reaction B), we restricted the study of reaction C to the oxygen transfer from DMAO to the heme (Figure 6). In **1** (Figure 6a), DMAO is bound to heme in a similar manner as in reaction A. Also here, the lowest energy state is a doublet state, although the differences to the other states are within 1.4 kcal mol^{-1} (Table 4). However,

Table 4. Relative energies[a] for the different structures in reaction C [data in kcal mol^{-1}].

	Heme +DMAO	**1**	**TS1**	**2**	Cpd I +DMA
doublet	2.24	0.00	21.07	9.82	7.87
quartet	−1.96	1.41	28.10	9.37	8.09
sextet	−5.09	0.98	30.34	18.58	17.59

[a] Energies obtained as in Table 1.

the decisive difference to the PhIO reaction is seen in **TS1** (Figure 6b), which lies significantly higher in the case of DMAO. The energy barrier at **TS1**, while being in the range of 6.3–8.7 kcal mol^{-1} for PhIO (Table 3), is now in the range of 21.1–30.3 kcal mol^{-1} (Table 4), roughly four times higher. Furthermore, it can be seen in Table 4 that ^{2}**TS1** for reaction C is more than 7 kcal mol^{-1} lower than that for ^{4,6}**TS1**; hence the reaction will continue in a doublet state and produce a doublet product ^{2}**2** (Figure 6c). This confirms that unlike the PhIO case in which water dislocation makes the spin-state selection, for DMAO the oxygen-atom transfer process is the spin-selecting step. This high barrier in reaction C should provide ample time for spin relaxation at **1** from an initial high-spin heme, pentacoordinated state. According to earlier theoretical predictions,[40] this will generate a low KIE, as further documented in the next section.

The issue of the Fe–S bond breakage in the sextet state was found here too, with an extremely long Fe–S bond of 3.2 Å at the transition state ^{6}**TS1**. However, the energy landscape around this transition state was found to be relatively insensitive to the Fe–S bond length; it could vary down to 2.8 Å without significant energy changes. As in the case of PhIO, re-formation of the Fe–S bond was found to occur through a negligible barrier here as well (Figure S24 in the Supporting Information). We therefore present ^{6}**2** here as a structure in which the Fe–S bond is intact, in the same manner as in reactions A and B.

Theoretical KIE values for DMA hydroxylation by Cpd I: We calculate here the transition state ($\mathbf{TS_H}$) of DMA hydroxylation by Cpd I in the doublet, quartet, and the sextet states from which we can calculate the energies and KIE. This would enable us to see whether the generation of Cpd I from PhIO versus DMAO may affect the spin-state selection. In addition to the doublet and quartet states, we found two possible electronic states for the sextet structure. One was a pentaradical state with valence electron orbitals $(\delta)^1(\pi^*_{xz})^1(\pi^*_{yz})^1(a_{2u})^1(\sigma^*_{xy})^1$, and the other a heptaradical state with the orbitals $(\delta)^1(\pi^*_{xz})^1(\pi^*_{yz})^1(a_{2u})^1(\sigma^*_{xy})^1(\sigma^*_{z^2})^1(\varphi_{subs})^1$, the last orbital being a spin-down orbital on the substrate. The heptaradical state was found to be lower in energy than the pentaradical state by 4.2 kcal mol^{-1} at the transition state, and features a long Fe–S distance of 3.3 Å, indicating that the Fe–S bond is broken. Comparisons with the doublet and quartet values are shown in Table 5.

The doublet and quartet KIE values are in line with earlier published values;[40] that is, low for the doublet and high for the quartet. Looking at the energy barriers for this step, both the sextet steps are high, with the pentaradical sextet state definitively ruled out. The 4.9 kcal mol^{-1} energy difference from the quartet also rules out the heptaradical sextet route, especially considering the efficient spin-orbit coupling between the sextet and quartet states,[41–43] which will serve to channel the sextet species to the quartet manifold. The doublet–quartet spin-orbit coupling is small, however, and

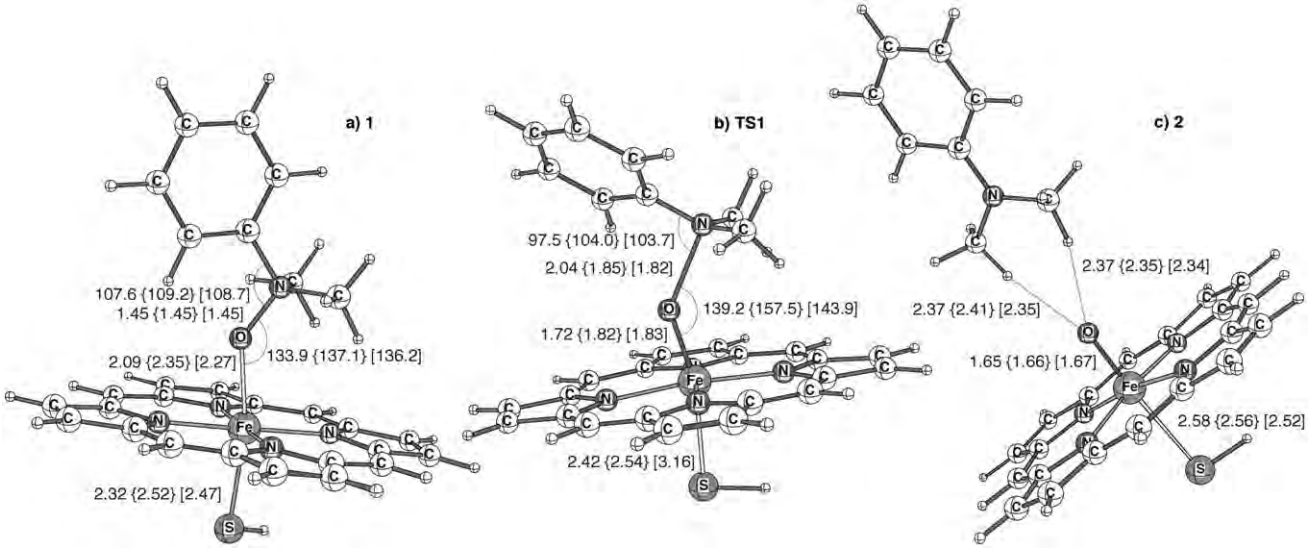

Figure 6. Optimized structures for reaction C. a) **1** b) **TS1**, and c) **2**. See legend of Figure 1 for explanation of the numbers.

 © 2007 Wiley-VCH Verlag GmbH & Co. KGaA, Weinheim

Table 5. Theoretically calculated $\mathbf{TS_H}$ energies and average KIE values for hydrogen atom abstraction by ^{2,4,6}CpdI from deuterium substituted *N*,*N*-$(CD_2H)_2$-aniline at $T = 298.15$ K.[a]

	Doublet	Quartet	Sextet[e]	Sextet[f]
KIE1[b]	3.79	5.78	5.59	2.34
KIE2[c]	4.06	7.75	7.53	2.34
energy[d]	6.44	8.78	17.95	13.72

[a] Note that experimental KIEs in reference [24] and here are at $T = 310$ K. [b] Eyring model. [c] Wigner correction with scaled frequency by scale factor 0.9704. [d] Energy in kcal mol^{-1} relative to ^{4}**2** in reaction C. [e] Pentaradical. [f] Heptaradical.

with such a small doublet–quartet energy difference as 2.3 kcal mol^{-1}, the quartet barrier should be small enough to allow reactions to continue in the quartet state given favorable conditions. It has been suggested earlier that this difference in the spin states may give rise to different KIE values,[40] and applied to the current case, the KIE jump observed when using PhIO-generated CpdI may be due to the reactions occurring in the quartet state (see Discussion below). Since the calculations show that on the sextet surface the thiolate may be detached for the porphyrin–iron–oxo moiety (PorFeO) during the formation of CpdI, we have also considered the hydroxylation of the DMA by PorFeO devoid of the SH ligand. These results are presented in Supporting Information (Part 4).

Experimental determination of KIE for *N*,*N*-dimethyl-4-(methylthio)aniline dealkylation: Guengerich et al.[24] reported that the KIE for N-dealkylation of *N*,*N*-dimethylaniline was 1.7 and 6.7 for dealkylation of *N*-methyl-*N*-(trideuteromethyl)aniline by the native route and with PhIO, respectively. Since KIE values for *N*-methyl-*N*-(trideuteromethyl)aniline have been determined to be masked and give smaller KIE values for some P450 enzymes than when *N*,*N*-bis(dideuteromethyl-^{13}C)aniline is used to determine the isotope effect,[30] we decided to test the KIE jump using this more sophisticated experimental design. Thus, the experimental KIE was determined for the N-dealkylation of *N*,*N*-dimethyl-^{13}C-4-(methylthio)aniline to ascertain if the KIE jump observed by Guengerich et al.[24] for PhIO with respect to the native route could be reproduced, or if it was a result of differences in the masking of the intrinsic isotope effect for the two systems. A KIE jump was also observed for *N*,*N*-dimethyl-^{13}C-4-(methylthio)aniline, which gave a KIE of 2.2 for the NADPH/O_2/P450 system and a KIE of 4.2 for the PhIO-supported system, confirming that the KIE differences are not a result of differing kinetics, but instead reflect a change in transition-state structure. It is important to recognize that intramolecular KIE values reported here are free of masking from other rate-limiting steps ("kinetic complexity"). This has been shown by using a detailed kinetics model[44] and a number of arguments further support this statement:

1) The KIEs determined for substituted anilines in the native P450 system are the same in six different P450 enzymes; this would require every enzyme to show the same amount of masking, which is not too probable.[45]
2) The native P450 system gives identical KIEs as the enzyme in which CpdI is generated by using DMAO analogues as the oxygen donor; this identity of the KIEs is inconsistent with masking effects in the native enzyme, since the rate-limiting steps are different in these two systems.[11]
3) In a series of *N*,*N*-dimethylanilines, the changes in intramolecular KIEs reflect a change in reaction energies consistent with the Melander–Westheimer postulate and inconsistent with masking.[11]

Thus, our KIE data above for the native route and the PhIO routes are reliable data free of kinetic complexities. As such, the observation of Guengerich et al.[24] carries over to another substrate, showing that the use of PhIO leads to a higher KIE value, which can be as high as 6–7 for DMA itself.

Discussion

Our theoretical results show that while PhIO will generate CpdI in its higher spin multiplicities due to water dislocation barriers (Table 3), N−O surrogates such as DMAO will generate the species exclusively in its doublet state due to oxygen-transfer barriers (Table 4). As outlined below, these results can provide a consistent rationale for experimental observations of the KIE jump in the PhIO route, compared with the constant KIE in the DMAO route. Figure 7 shows the computational scenario for the generation of CpdI from a DMAO surrogate followed by the hydrogen abstraction from DMA.

As we argued in the results section, the water dislocation step from the resting state will be identical for different oxygen surrogates. Therefore, we start the DMAO reaction at **TS0**; the data for **TS0** was taken from reaction B (modified with respect to different oxygen–heme binding energies). Following the release of water, which has relatively low barriers compared with those in the rate-determining step for this surrogate, complex C**1** (Figure 7) has to surmount a very high barrier, to transfer the oxygen from the N–oxo moiety of DMAO to the iron and generate CpdI, followed by much smaller barriers for hydrogen abstraction. Since the oxygen-transfer barrier via ^{2}**TS1** is the lowest (by 7.0 and 9.2 kcal mol^{-1}, compared with the other states), the reaction will proceed selectively from the doublet state, thereby forming doublet CpdI. This will be followed by a very fast step of hydrogen abstraction from DMA, which again has the lowest barrier on the doublet surface, via $^2\mathbf{TS_H}$. Therefore, CpdI will perform mostly a doublet state reaction when formed from DMAO. Furthermore, it follows that CpdI prepared in the native route will also perform hydrogen abstraction mostly via $^2\mathbf{TS_H}$, even if ^{2}CpdI and ^{4}CpdI undergo spin equilibration, since the $^2\mathbf{TS_H}$ species is lower than $^4\mathbf{TS_H}$. For this reason, the experimental KIE

 © 2007 Wiley-VCH Verlag GmbH & Co. KGaA, Weinheim

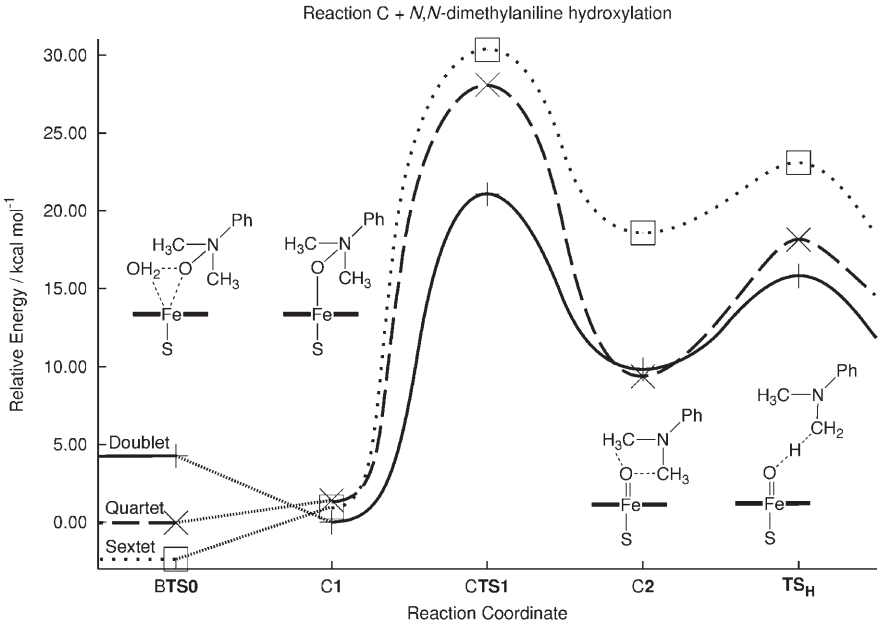

Figure 7. Full energy profile from heme resting state with DMAO to CpdI followed by H-abstraction from DMA. The water dislocation **TS0** of reaction B has been patched to reaction C, in which the relative energies of **TS0** have been adjusted accounting for the different oxygen-donor binding energy to heme according to Tables 1 and 4. At the end, the energy profile results for DMA hydroxylation have been added to reaction C. The reaction coordinate axis labels starting with "B" or "C" refer to the reactions B or C, respectively. The exact values for this graph are found in Table S85.

values measured in the process in which CpdI is nascent from the N–O surrogate are virtually identical to the ones measure from the native process of the enzyme, using NADPH and O_2.[11] Both sets of the measured KIE values are low for the entire series of *N*,*N*-dimethylanilines, in agreement with the theoretical prediction that the doublet state leads to a low KIE value. Thus, the calculated barrier scenario and KIE values lead to the same conclusion that the use of the N–O surrogate results in a selective doublet-state reaction.

The corresponding scenario for PhIO is depicted in Figure 8 and is seen to be entirely different than the case of DMAO. Here the water dislocation step is rate limiting for the doublet state. The corresponding barrier (via **TS0**) is 5.0 kcal mol^{-1} higher than the quartet and 7.8 kcal mol^{-1} higher than the sextet (Table 3). Therefore, this barrier could act as a filter that produces preferentially quartet and sextet species of the Fe-O-IPh complex, **1** (B**1** in Figure 8). In the absence of water as a ligand the ^{6}**1** species is produced directly from the ground state of the pentacoordinate complex (Figure 2 and Table S28). An analogous sextet-state complex (devoid of a proximal ligand to the iron) was identified by Nam et al,[28] based on changes in UV/VIS, EPR, and X-ray absorption spectra. As can be further seen from Figure 8, during the formation of CpdI (B**2**) the quartet surface goes down in energy, while the sextet state rises high. Since the quartet and sextet states of **1** and **TS1** maintain strong spin-orbit coupling,[41–43] the most likely outcome of this scenario is a spin flip from the sextet to the quartet, to generate CpdI in its quartet state. Since at this stage the spin-orbit coupling between the quartet and doublet states is small, the quartet state can then abstract a hydrogen atom from DMA via ^{4}**TS$_H$** before spin flip to a doublet state can occur. Thus, the KIE for the PhIO-supported hydroxylation process will correspond to the quartet-state

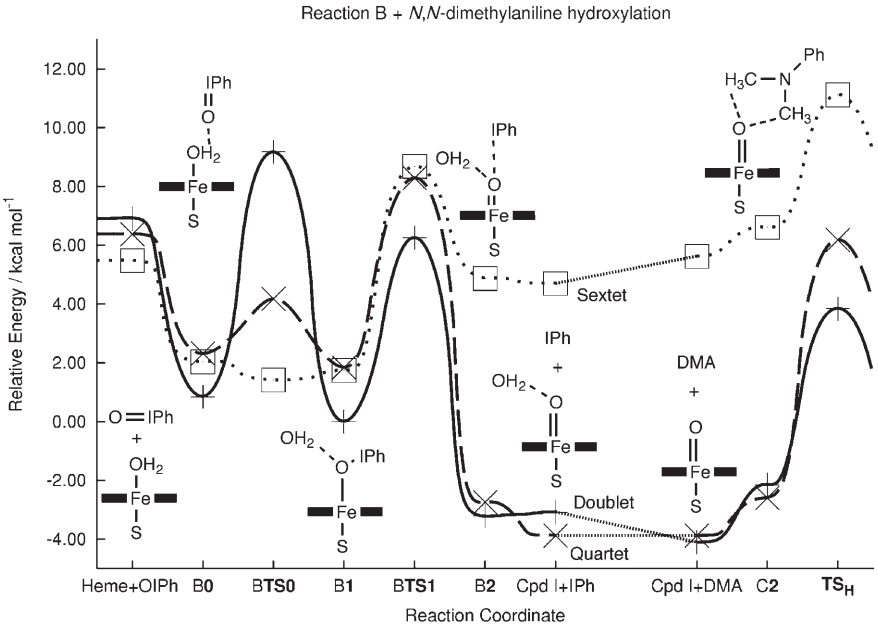

Figure 8. Full energy profile from heme resting state with PhIO to CpdI followed by hydrogen abstraction from DMA. Reaction B has been patched at CpdI+IPh stage with the profiles for CpdI+DMA results. The reaction coordinate axis labels starting with "B" or "C" refer to the reactions B or C, respectively. The exact values for this graph are found in Table S62.

 © 2007 Wiley-VCH Verlag GmbH & Co. KGaA, Weinheim

process. It follows therefore that, the N-dealkylation reaction of DMA may occur through different spin states under different conditions (native, N−O or PhI=O route).

As already mentioned, the KIE of the native route is low. The N-dealkylation of DMA in $P450_{2B1}$ has been experimentally shown to occur with a KIE of 2.5,[45] while the PhIO-supported reaction yields a KIE of 6.7.[24] We confirmed experimentally in this study that a larger KIE is observed for *N*-dealkylation reactions with another substrate, *N*,*N*-dimethyl-4-(methylthio)aniline, and a different enzyme, $P450_{BM3}$, when the NADPH/O_2-supported reaction is compared to that of PhIO (2.2 versus 4.2, respectively). The theoretically calculated KIE values for the doublet and quartet states fit these values (Table 5); the doublet state leads to a low value (3.79/4.06), while the quartet state leads to a high one (5.78/7.75).

The scenario described above for the PhIO-supported reaction versus the native process provides a logical explanation for a very enigmatic experimental result. What strengthens and lends credibility to this scenario is the contrasting outcome using the N−O oxygen surrogate. Indeed, here for the same substrate, *N*,*N*-dimethyl-4-(cyano)aniline, as well as others,[11] the KIE values obtained using the N−O surrogate and the native route are now virtually identical and low. Thus, the theoretical data in terms of energetics and KIE scenarios of the processes for the two oxygen surrogates match experimental results and provide a unified description for the two sets of data. Other scenarios (e.g., the thiolate dissociation scenario) that were considered and discarded are given in full in the Supporting Information.

A key element in the scenario is the reactivity of the substrate undergoing hydroxylation. Thus, fast-reacting substrates like DMA[24] or *N*,*N*-dimethyl-4-(methylthio)aniline (as shown in the present study) exhibit a jump when the CpdI species is generated with PhIO relative to the values obtained in the "native route" (O_2/NADPH) of the enzyme. However, for slow reactions (i.e. high $^{2,4}\mathbf{TS_H}$ with close-lying spin states) such as allylic oxidation of cyclohexene, the spin states will have sufficient time to equilibrate and the KIE values should always correspond to two-state reactivity of CpdI. In most of the cases with less reactive C−H bonds, the KIE(doublet) and KIE(quartet) values are both high and quite close to each other (KIE(doublet) ≈ KIE(quartet)).[37,46] Indeed, virtually identical KIE values have been measured when either cumene hydroperoxide or NADPH/O_2 are used for cyclohexene,[47] and Gelb et al.[48] found that PhIO-supported hydrogen-atom abstractions with $P450_{cam}$ gave identical isotope ratios as the NADPH/O_2-supported reaction of camphor. Scheme 2 shows a summarized view of these conclusions, and Table 6 collects known experimental KIE values for comparisons.

The relative energies are, as we have shown here, subject to additional factors such as hydrogen bonds and entropy effects, among others. Therefore, few kcal mol^{-1} variations in the relative energies are expected, and one should be careful drawing conclusions based on close-lying differences. In this study, however, the main conclusions derive from two large differences that should be outside any error margins: one is the **TS0** water-displacing step, in which the doublet–sextet energy difference is 7.8 kcal mol^{-1}, and **TS1** in reaction C, in which the doublet–quartet difference is 7.0 kcal mol^{-1}. This coupled to the small doublet–quartet energy difference in $\mathbf{TS_H}$ (2.3 kcal mol^{-1}) should enable the hydroxylation reaction to proceed in either spin state, as determined by the preceding barriers. This is one possible, simple interpretation of our current data, in an attempt to explain the measured KIE differences in what is likely to be a complicated reaction. As with all theoretical model calculations, however, this may be in need of further experimental verifications. Furthermore, a sober note of caution is necessary to emphasize that our study did not rule out the possibility that **1** will undergo protonation on the oxo group, which upon release

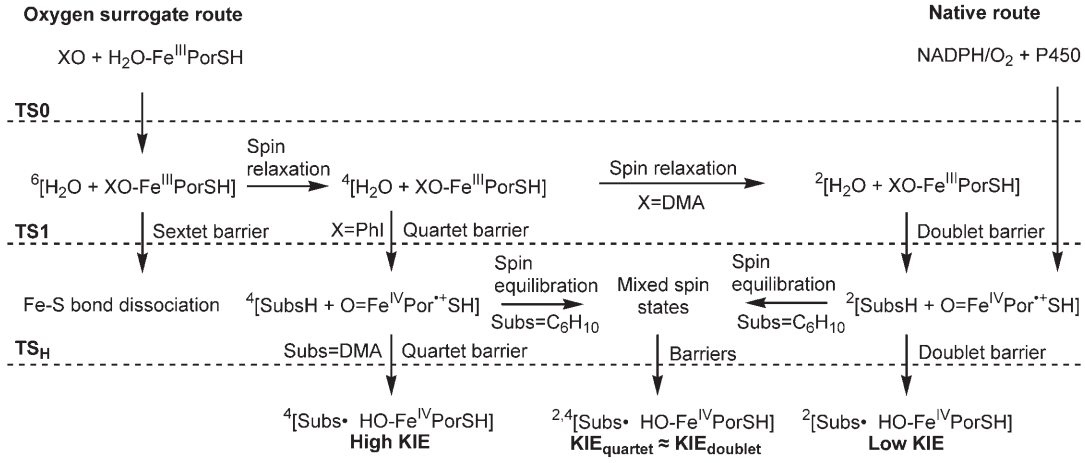

Scheme 2. Possible pathways of induced CpdI by the oxygen surrogate route (XO = PhIO/DMAO) versus the native route (NADPH/O_2). The labels **TS0**, **TS1**, and $\mathbf{TS_H}$ correspond to the transition states of water dislocation, CpdI formation, and hydrogen abstraction from the substrate, respectively (see text). For the oxygen surrogate route, passing the **TS0** barrier generates a sextet; spin relaxation will allow the complex to pass **TS1** as a doublet or quartet to form ^{2,4}CpdI. The final predicted KIE ranges depend on the spin state of the complex when passing $\mathbf{TS_H}$, and are shown in bold. Left-hand superscripts denote system spin multiplicity.

 © 2007 Wiley-VCH Verlag GmbH & Co. KGaA, Weinheim

Table 6. Experimental KIE values.

Substrate	Enzyme	Oxygen donor	KIE	Reference
DMA and/or analogues	$P450_{cam}$	$NADPH/O_2$	2.23–3.1	[11]
	$P450_{cam}$	DMAO analogues	2.53–3.07	[11]
	$P450_{2E1}$	$NADPH/O_2$	2.92–3.65	[11]
	$P450_{2E1}$	DMAO analogues	2.87–3.66	[11]
	$P450_{2B1}$	$NADPH/O_2$	1.56–3.56	[24]
	$P450_{2B1}$	PhIO	6.7–7.3	[24]
	Porphine[a]	DMAO	3.79/4.06	this study
	Porphine[a]	PhIO	5.78/7.75	this study
	$P450_{BM3}$	$NADPH/O_2$	2.2	this study
	$P450_{BM3}$	PhIO	4.2	this study
	6 P450 species	$NADPH/O_2$	2.4–4.1	[45]
cyclohexene[b]	$P450_{LM2}$	$NADPH/O_2$	4.1–4.9	[47]
	$P450_{LM2}$	Cum-OOH	4.8–5.1	[47]
camphor[c]	$P450_{cam}$	$NADPH/O_2$	1.18/4.51/4.39	[48]
	$P450_{cam}$	PhIO	1.48/3.76/4.69	[48]

[a] Theoretical model used in this study with calculated Eyring/Wigner KIE values assigned to DMAO and PhIO supported reactions according to the Discussion section. [b] Cum-OOH is cumeme peroxide. The values varied slightly depending on the equation used. [c] These three sets are hydrogen/deuterium isotope ratios in the product alcohol but are not KIE values. The values were measured where the camphor was deuterized at 5-*exo*/5,6-*endo*/5-*endo* positions.

of PhI, will give rise to a protonated Cpd I species that leads to substrate oxidation. This would, however, require the observation of KIE jumps/variation, compared with the native route, for all substrates; something which is not observed.

Conclusion

In conclusion, it is clear that the seemingly simple reaction in Scheme 1 becomes intriguingly complex due to the different available spin states, and the energetics may very well be sensitive to the kind of systems used, both for the porphyrin and the oxygen donor, as has been found experimentally.[26–29] Nevertheless, the present study at least shows that the existence of a PhIO–heme complexed system **1** is indeed possible, and so is the incursion of **2**, the PhI–Cpd I complex. However, the weakness of the complexation interaction between PhIO and the Fe(Por) in **1** and between PhI and Cpd I in **2** casts doubts on the suggestions that, for example, **2** is the root cause of the differences in the reactivity between the native route and the PhIO route. While a protonated Cpd I generated from **1** cannot be ruled out, it remains unclear how such a species can explain the KIE jump that is observed in DMA and similar substrates but not in others.

At the same time, our results regarding the importance of different spin states provide a reasonable explanation, hitherto unconsidered, for the observed experimental KIE jumps. In the case of PhIO, the energy barrier of going from **1** to **2** is only marginal for the higher spin states (Figure 8). This makes it possible that ^{4}Cpd I could be the oxidizing species, at least for a finite time before relaxing to a doublet, hence giving a high KIE. Moreover, the calculations also show that DMAO-supported Cpd I formation should occur exclusively on the doublet surface (Figure 7), consistent with available experiments showing low KIE for this reaction.[11] The KIE jump observed here experimentally for *N*,*N*-dimethyl-4-(methylthio)aniline when using PhIO compared with the native route, and the identical KIE for the N–O route and the native route for the same substrate (and others) further support the theoretical model. In our view, this correlation between the spin states and measured KIE is not coincidental. However, the general applicability of this requires an extensive systematic investigation of theory and experiment involving a variety of oxygen surrogates.

Experimental Section

Computational methods: All the calculations were done with the density functional theory (DFT) formalism[49] by using the B3LYP hybrid functional.[50–53] Even though there is criticism on the accuracy of B3LYP for reproducing spin-state ordering, there is ample evidence that it is reliable for heme complexes of the type studied here. As has been shown for Cpd I,[35] the UB3LYP spin state ordering is in good agreement with the results of extensive configuration interaction calculations. More relevant evidence is provided in the Supporting Information. Ground-state geometry optimizations were done with Jaguar 5.5,[54] while transition state optimizations and frequency calculations were done by Gaussian 03.[55] The basis set used here was LACVP, a basis set of double-ζ quality with an effective core potential (ECP) on iron, as defined in Jaguar. Single-point solvent and larger basis set calculations were done on the LACVP-optimized geometries with Jaguar. In the solvent calculations, the dielectric constant of $\varepsilon = 5.71$ and the probe molecule radius of 2.721 Å was used, corresponding to chlorobenzene. Calculations with a large basis set used ERMLER2^{*+} on iodine[56,57] and LACV3P^{*+} on the rest (corresponding to LACV3P^{+} on Fe), to obtain more accurate energies (see below). The ERMLER2^{*+} basis set involves, on iodine, a small core relativistic ECP with scalar and spin orbit correction. In the Jaguar implementation, the 4d, 5s, and 5p valence shells are outside of the core.[56] The basis set is of double-ζ quality augmented with diffuse and polarization functions taken from the relativistic all-electron double-ζ basis set of Dyall.[57]

Basis-set calibration: Since two of our reactions included the heavy atom iodine, it was necessary to validate the use of our usual protocol LACV3P^{*+}//LACVP, especially since in the case of iodine the LACV3P^{*+} basis set is per definition the same as LAV3P in Jaguar. To this end, comparisons were made with the basis set ERMLER2^{*+} as implemented in Jaguar. In the first test suite, the I_2 dissociation energy was used as a benchmark system. Here, LACV3P^{*+} yielded an I_2 bond energy of 60.7 kcal mol^{-1}, while the single-point ERMLER2^{*+} yielded 21.4 kcal mol^{-1}. Experimental values put the energy at 36.1 kcal mol^{-1}.[58] The large discrepancy, with experiment, was in part due to the poor optimized geometry produced by LACVP. Looking at the structure, the calculated bond length was at 3.37 Å, compared to 2.70 Å found experimentally. Indeed, optimizing I_2 using ERMLER2^{*+} instead yielded a bond length of 2.78 Å, and a much more accurate bond dissociation energy value of 39.5 kcal mol^{-1}. Thus, LACVP yields an extremely poor geometry in the case of I_2, whereas ERMLER2^{*+} proved to be a reliable basis set for iodine, both with regards to the geometry and the energy of I_2. Another benchmark test was then performed, this time on the IO$^{\bullet}$ radical. Optimization with LACVP and subsequent single-point calculation with LACV3P^{*+} yielded a bond energy of 46.1 kcal mol^{-1}. Replacing the

 © 2007 Wiley-VCH Verlag GmbH & Co. KGaA, Weinheim

basis set on I with ERMLER2*+ in a single-point calculation gives 53.5 kcal mol^{-1}. Re-optimizing the structure with the latter basis set combination changed only slightly the bond length from 2.01 to 1.95 Å and the bond dissociation energy to 54.4 kcal mol^{-1}. Available experimental values put this energy to 59.5 kcal mol^{-1}.[58] Thus the geometry was accurately treated with LACVP, but a more than 7 kcal mol^{-1} energy discrepancy between LACV3P*+ with ERMLER2*+ was still apparent in the bond dissociation energies. The discrepancy was worse when the I–O bond strength was examined in PhIO, for which LACV3P*+ gave a bond strength of 13.3 kcal mol^{-1}, but single-point ERMLER2*+ gave 27.3 kcal mol^{-1}. However, geometry optimizations with ERMLER2*+ on iodine and LACV3P*+ on the rest of the atoms changed the relevant geometries by less than 0.1 Å (and the bond-energy difference less than 2 kcal mol^{-1} compared to the single point), confirming that the geometry was sufficiently reproduced at LACVP level. The selected procedure employed therefore LACVP for optimization, and the LACV3P*+ basis set in combination with ERMLER2*+ on iodine (when present) for the single-point energy evaluation.

Theoretical KIE calculations: KIE calculations were carried out for the reaction of DMA hydroxylation with Cpd I, following established procedures.[46] Since calculations indicated that during the formation of Cpd I in the sextet state the Fe–S bond may dissociate, we deemed it necessary to explore also the KIE results with the thiolate ligand-free Cpd I, in order to ascertain the consistency of the conclusions (see the Supporting Information).

Experimental KIE measurements: Intramolecular KIE values were determined for the N-dealkylation of *N,N*-dimethyl-4-(methylthio)aniline as described by Volz et al.[59] For enzymatic incubations, 10 mL scintillation vials were charged with substrate (1.6 μmol in 9 μL methanol), purified $P450_{BM3}$ enzyme (200 pmol), glucose-6-phosphate (9.2 μmol), glucose-6-phosphate dehydrogenase (0.40 nmol), catalase (0.34 nmol), and magnesium chloride (4.2 μmol) in phosphate buffer (0.1 M, pH 7.4) to give a total volume of 990 μL. The incubations were initiated by adding NADP (1.2 μmol in 110 μL of the phosphate buffer) and placed in a shaker bath at 30°C for 25 min. The incubations were terminated by adding methanol (300 μL) and filtered through a 0.45 μm filter. Enzymatic products were analyzed by liquid chromatography mass spectrometry (LC-MS) using electrospray ionization as described by Dowers et al.[11] For the PhIO-supported reactions the glucose-6-phosphate, glucose-6-phosphate dehydrogenase, and NADP were left out of the reaction and PhIO was added to a final concentration of 2 mM.

Acknowledgements

S.S. acknowledges support by the German Federal Ministry of Education and Research (BMBF) within the framework of the German–Israeli Project Cooperation (DIP) and by the Israel Science foundation (ISF). J.P.J. acknowledges the National Institute of Environmental and Health Sciences Grant 09122.

[1] G. H. Loew, D. L. Harris, *Chem. Rev.* **2000**, *100*, 407–419.
[2] B. M. Meunier, S. P. de Visser, S. Shaik, *Chem. Rev.* **2004**, *104*, 3947–3980.
[3] P. R. Ortiz de Montellano in *Cytochrome P450, 3rd ed.* (Ed.: P. R. Ortiz de Montellano), Kluwer Academic/Plenum, New York, **2005**.
[4] T. Spolitak, J. H. Dawson, D. P. Ballou, *J. Biol. Chem.* **2005**, *280*, 20300–20309.
[5] M. Newcomb, R. Zhang, R. E. P. Chandrasena, J. A. Halgrimson, J. H. Horner, T. M. Makris, S. G. Sligar, *J. Am. Chem. Soc.* **2006**, *128*, 4580–4581.
[6] E. G. Hrycay, J.-Å. Gustafsson, M. Ingelman-Sundberg, L. Ernster, *FEBS Lett.* **1975**, *56*, 161–165.
[7] E. G. Hrycay, J.-Å. Gustafsson, M. Ingelman-Sundberg, L. Ernster, *Biochem. Biophys. Res. Commun.* **1975**, *66*, 209–216.
[8] A. Berg, K. Carlström, J.-Å. Gustafsson, M. Ingelman-Sundberg, *Biochem. Biophys. Res. Commun.* **1975**, *66*, 1414–1423.
[9] F. Lichtenberger, W. Nastainczyk, V. Ullrich, *Biochem. Biophys. Res. Commun.* **1976**, *70*, 939–946.
[10] J.-Å. Gustafsson, J. Bergman, *FEBS Lett.* **1976**, *70*, 276–280.
[11] T. S. Dowers, D. A. Rock, J. P. Jones, *J. Am. Chem. Soc.* **2004**, *126*, 8868–8869.
[12] R. C. Blake II, M. J. Coon, *J. Biol. Chem.* **1989**, *264*, 3694–3701.
[13] J.-Å. Gustafsson, L. Rondahl, J. Bergman, *Biochemistry* **1979**, *18*, 865–870.
[14] U. M. Kent, S. Yanev, P. F. Hollenberg, *Chem. Res. Toxicol.* **1999**, *12*, 317–322.
[15] U. M. Kent, E. S. Roberts-Kirchhoff, N. Moon, W. R. Dunham, P. F. Hollenberg, *Biochemistry* **2001**, *40*, 7253–7261.
[16] A. D. N. Vaz, E. A. Roberts, M. J. Coon, *J. Am. Chem. Soc.* **1991**, *113*, 5886–5887.
[17] F. P. Guengerich, A. D. N. Vaz, G. N. Raner, S. J. Pernecky, M. J. Coon, *Mol. Pharmacol.* **1997**, *51*, 147–151.
[18] M. N. Bhakta, P. F. Hollenberg, K. Wimalasena, *J. Am. Chem. Soc.* **2005**, *127*, 1376–1377.
[19] M. Newcomb, P. H. Toy, *Acc. Chem. Res.* **2000**, *33*, 449–455.
[20] T. L. Macdonald, W. G. Gutheim, R. B. Martin, F. P. Guengerich, *Biochemistry* **1989**, *28*, 2071–2077.
[21] S. Modi, D. E. Gilham, M. J. Sutcliffe, L.-Y. Lian, W. U. Primrose, C. R. Wolf, G. C. K. Roberts, *Biochemistry* **1997**, *36*, 4461–4470.
[22] X. Shan, L. Que, Jr. *J. Inorg. Biochem.* **2006**, *100*, 421–433.
[23] A. Berg, M. Ingelman-Sundberg, J.-Å. Gustafsson, *J. Biol. Chem.* **1979**, *254*, 5264–5271.
[24] F. P. Guengerich, C.-H. Yun, T. L. Macdonald, *J. Biol. Chem.* **1996**, *271*, 27321–27329.
[25] P. R. Ortiz de Montellano in *Cytochrome P450, 1st ed.* (Ed.: P. R. Ortiz de Montellano), Plenum, New York, **1987**, pp. 217–271.
[26] J. P. Collman, A. S. Chien, T. A. Eberspacher, J. I. Brauman, *J. Am. Chem. Soc.* **2000**, *122*, 11098–11100.
[27] J. P. Collman, L. Zeng, R. A. Decréau, *Chem. Commun.* **2003**, 2974–2975.
[28] W. Nam, S. K. Choi, M. H. Lim, J. U. Rohde, I. Kim, J. Kim, C. Kim, L. Que Jr, *Angew. Chem.* **2003**, *115*, 113–115; *Angew. Chem. Int. Ed.* **2003**, *42*, 109–111.
[29] For the use of PhIO in nonheme complexes, see: Y. Suh, M. S. Seo, K. M. Kim, Y. S. Kim, H. G. Jang, T. Tosha, T. Kitagawa, J. Kim, W. Nam, *J. Inorg. Biochem.* **2006**, *100*, 627–633.
[30] J. P. Dinnocenzo, S. B. Karki, J. P. Jones, *J. Am. Chem. Soc.* **1993**, *115*, 7111–7116.
[31] F. Ogliaro, S. P. de Visser, S. Shaik, *J. Inorg. Biochem.* **2002**, *91*, 554–567.
[32] P. Rydberg, E. Sigfridsson, U. Ryde, *J. Biol. Inorg. Chem.* **2004**, *9*, 203–223.
[33] A. Altun, W. Thiel, *J. Phys. Chem. B* **2005**, *109*, 1268–1280.
[34] F. Ogliaro, S. P. de Visser, J. T. Groves, S. Shaik, *Angew. Chem.* **2001**, *113*, 3612–3612; *Angew. Chem. Int. Ed.* **2001**, *40*, 2874–2878; .
[35] J. Schöneboom, F. Neese, W. Thiel, *J. Am. Chem. Soc.* **2005**, *127*, 5840–5853.
[36] F. Ogliaro, S. Cohen, S. P. de Visser, S. Shaik, *J. Am. Chem. Soc.* **2000**, *122*, 12892–12893.
[37] H. Hirao, D. Kumar, W. Thiel, S. Shaik, *J. Am. Chem. Soc.* **2005**, *127*, 13007–13018.
[38] J. Schöneboom, W. Thiel, *J. Phys. Chem. B*, **2004**, *108*, 7468–7478.
[39] S. Shaik, D. Kumar, S. P. de Visser, A. Altun, W. Thiel, *Chem. Rev.* **2005**, *105*, 2279–2328.
[40] C. Li, W. Wu, D. Kumar, S. Shaik, *J. Am. Chem. Soc.* **2006**, *128*, 394–395.
[41] D. Danovich, S. Shaik, *J. Am. Chem. Soc.* **1997**, *119*, 1773–1786.
[42] Y. Shiota, K. Yoshizawa, *J. Chem. Phys.* **2003**, *118*, 5872–5879.
[43] Going from quartet to sextet in Cpd I involves a shift of an electron from the doubly occupied $\delta_{x^2-y^2}$ to the σ^*_{xy} orbital, the latter is delocalized over the iron and the nitrogen atoms of the heme. Such delocalization will reduce the spin-orbital coupling, although the value may still be high enough to induce fast spin inversion. The spin-orbit coupling between the quartet and doublet states is much less

 © 2007 Wiley-VCH Verlag GmbH & Co. KGaA, Weinheim

efficient, since the two states differ simply by the direction of the spin in the a_{2u} orbital of the porphyrin.
[44] L. Higgins, G. A. Bennett, M. Shimoji, J. P. Jones, *Biochemistry*, **1998**, *37*, 7039–7046.
[45] S. B. Karki, J. P. Dinnocenzo, J. P. Jones, K. R. Korzekwa, *J. Am. Chem. Soc.* **1995**, *117*, 3657–3664.
[46] D. Kumar, S. P. de Visser, P. K. Sharma, S. Cohen, S. Shaik, *J. Am. Chem. Soc.* **2004**, *126*, 1907–1920.
[47] J. Groves, *Adv. Chem. Ser.* **1980**, *191*, 227–289.
[48] M. H. Gelb, D. C. Heimbrook, P. Malkonen, S. G. Sligar, *Biochemistry* **1982**, *21*, 370–377.
[49] W. Kohn, L. J. Sham, *Phys. Rev. A* **1965**, *140*, 1133–1138.
[50] A. D. Becke, *Phys. Rev. A* **1988**, *38*, 3098–3100.
[51] A. D. Becke, *J. Chem. Phys.* **1993**, *98*, 1372–1377.
[52] A. D. Becke, *J. Chem. Phys.* **1993**, *98*, 5648–5652.
[53] C. Lee, W. Yang, R. G. Parr, *Phys. Rev. B* **1988**, *37*, 785–789.
[54] Jaguar 5.5, Schrodinger, LLC, Portland, OR (USA), **2003**.
[55] Gaussian 03, Revision B.05, M. J. Frisch, G. W. Trucks, H. B. Schlegel, G. E. Scuseria, M. A. Robb, J. R. Cheeseman, J. A. Montgomery, Jr., T. Vreven, K. N. Kudin, J. C. Burant, J. M. Millam, S. S. Iyengar, J. Tomasi, V. Barone, B. Mennucci, M. Cossi, G. Scalmani, N. Rega, G. A. Petersson, H. Nakatsuji, M. Hada, M. Ehara, K. Toyota, R. Fukuda, J. Hasegawa, M. Ishida, T. Nakajima, Y. Honda, O. Kitao, H. Nakai, M. Klene, X. Li, J. E. Knox, H. P. Hratchian, J. B. Cross, V. Bakken, C. Adamo, J. Jaramillo, R. Gomperts, R. E. Stratmann, O. Yazyev, A. J. Austin, R. Cammi, C. Pomelli, J. W. Ochterski, P. Y. Ayala, K. Morokuma, G. A. Voth, P. Salvador, J. J. Dannenberg, V. G. Zakrzewski, S. Dapprich, A. D. Daniels, M. C. Strain, O. Farkas, D. K. Malick, A. D. Rabuck, K. Raghavachari, J. B. Foresman, J. V. Ortiz, Q. Cui, A. G. Baboul, S. Clifford, J. Cioslowski, B. B. Stefanov, G. Liu, A. Liashenko, P. Piskorz, I. Komaromi, R. L. Martin, D. J. Fox, T. Keith, M. A. Al-Laham, C. Y. Peng, A. Nanayakkara, M. Challacombe, P. M. W. Gill, B. Johnson, W. Chen, M. W. Wong, C. Gonzalez, J. A. Pople, Gaussian, Inc., Wallingford CT, **2004**.
[56] L. A. LaJohn, P. A. Christiansen, R. B. Ross, T. Atashroo, W. C. Ermler, *J. Chem. Phys.* **1987**, *87*, 2812–2824.
[57] K. G. Dyall, *Theor. Chem. Acc.* **1998**, *99*, 366–371.
[58] J. A. Kerr in *Handbook of Chemistry and Physics, 81st ed.* (Ed.: D. R. Lide), CRC, Boca Raton, **2000**.
[59] T. J. Volz, D. A. Rock, J. P. Jones, *J. Am. Chem. Soc.* **2002**, *124*, 9724–9725.

Received: November 28, 2006
Published online: March 19, 2007

 © 2007 Wiley-VCH Verlag GmbH & Co. KGaA, Weinheim

ChemPubSoc Europe

DOI: 10.1002/chem.201604361

CHEMISTRY A European Journal Full Paper

Reaction Mechanisms

A Systematic Account on Aromatic Hydroxylation by a Cytochrome P450 Model Compound I: A Low-Pressure Mass Spectrometry and Computational Study

Fabián G. Cantú Reinhard[+],[a] Mala A. Sainna[+],[a] Pranav Upadhyay,[b] G. Alex Balan,[a] Devesh Kumar,[b] Simonetta Fornarini,*[c] Maria Elisa Crestoni,*[c] and Sam P. de Visser*[a]

Abstract: Cytochrome P450 enzymes are heme-containing mono-oxygenases that mainly react through oxygen-atom transfer. Specific features of substrate and oxidant that determine the reaction rate constant for oxygen atom transfer are still poorly understood and therefore, we did a systematic gas-phase study on reactions by iron(IV)-oxo porphyrin cation radical structures with arenes. We present herein the first results obtained by using Fourier transform-ion cyclotron resonance mass spectrometry and provide rate constants and product distributions for the assayed reactions. Product distributions and kinetic isotope effect studies implicate a rate-determining aromatic hydroxylation reaction that correlates with the ionization energy of the substrate and no evidence of aliphatic hydroxylation products is observed. To further understand the details of the reaction mechanism, a computational study on a model complex was performed. These studies confirm the experimental hypothesis of dominant aromatic over aliphatic hydroxylation and show that the lack of an axial ligand affects the aliphatic pathways. Moreover, a two-parabola valence bond model is used to rationalize the rate constant and identify key properties of the oxidant and substrate that drive the reaction. In particular, the work shows that aromatic hydroxylation rates correlate with the ionization energy of the substrate as well as with the electron affinity of the oxidant.

Introduction

Aromatic hydroxylation is a challenging catalytic reaction because a very strong C–H bond of a substrate needs to be broken in the process. Several enzymes in nature have developed procedures to enable an aromatic hydroxylation or even a dioxygenation.[1] Among those are the nonheme iron dioxygenases that regio- and stereospecifically dihydroxylate an aromatic substrate into a catechol.[2] Highly relevant for environmental purposes are, for instance, the naphthalene dioxygenases that have functions in biotechnology that include the cleaning up of oil-spills and removal of aromatic compounds from soil.[3] Also, in the human body applications of heme and nonheme iron dioxygenases are found, for instance, for the biodegradation of aromatic amino acids starting with a mono- or dihydroxylation reaction.[4] Further arene-activating enzymes in the body include the thiolate-ligated heme mono-oxygenases called cytochromes P450 (P450) that have been shown to hydroxylate arenes to phenols as a means to metabolize drugs as well as xenobiotic molecules in the liver.[5]

The full details of the mechanism of the latter processes are still shrouded in many mysteries and so far, no experimental reaction rates have been obtained. Progress in understanding the P450-type reaction mechanisms has been made in the fields of computational chemistry and low-pressure mass spectrometry.[6,7] In particular, recently, Fourier transform-ion cyclotron resonance mass spectrometry (FT-ICR MS) has been used by us to trap and characterize a pentacoordinated model complex of the active species of P450 enzymes (Compound I, CpdI).[8] We have utilized this experience and measured low-pressure thermal rate constants of aromatic hydroxylation by this CpdI model for the first time and present these results here.

P450 CpdI is a high-valent iron(IV)-oxo heme cation radical, which is bound to the enzyme through a thiolate bridge of a conserved cysteinate residue. It has been spectroscopically

[a] F. G. Cantú Reinhard,[+] Dr. M. A. Sainna,[+] G. A. Balan, Dr. S. P. de Visser
Manchester Institute of Biotechnology and School of Chemical Engineering and Analytical Science
The University of Manchester, 131 Princess Street
Manchester M1 7DN (UK)
E-mail: sam.devisser@manchester.ac.uk

[b] P. Upadhyay, Dr. D. Kumar
Department of Applied Physics, School for Physical Sciences
Babasaheb Bhimrao Ambedkar University, Vidya Vihar
Rae Bareilly Road, Lucknow (UP) 226025, (India)

[c] Prof. Dr. S. Fornarini, Prof. Dr. M. E. Crestoni
Dipartimento di Chimica e Tecnologie del Farmaco
Università di Roma "La Sapienza", P.le A. Moro 5
00185, Roma, (Italy)
E-mail: simonetta.fornarini@uniroma1.it
mariaelisa.crestoni@uniroma1.it

[+] Both authors contributed equally to this work.

Supporting information and the ORCID identification number(s) for the author(s) of this article can be found under http://dx.doi.org/10.1002/chem.201604361.

© 2016 Wiley-VCH Verlag GmbH & Co. KGaA, Weinheim

trapped and characterized at low temperature for one specific isozyme, but experimental rate constants could be determined for only very few substrates due to its short lifetime.[9] As such, much is to be gained from understanding the reactivity patterns of CpdI with substrates and particularly on the regioselectivity and bifurcation patterns leading to a variety of products. On the other hand, CpdI and its reactivity patterns with substrates have been extensively studied with computational methods and detailed mechanisms of aromatic and aliphatic hydroxylation as well as sulfoxidation were established.[10]

Figure 1 shows the active site description of P450 CYP120 A1 with the heme and its link to Cys_{391} highlighted. These crystal structure coordinates contain retinoic acid as a substrate in the vicinity of the heme on its distal site.[11] CpdI was shown to be a versatile oxidant and to react efficiently with a variety of different substrates. In our previous work we reported a combined mass spectrometric and computational study on a biomimetic model of CpdI, in which the protoporphyrin IX was replaced by 5,10,15,20-tetrakis(pentafluorophenyl) porphyrin (TPFPP), Figure 1 b.[12] The ensuing $[Fe^{IV}(O)(TPFPP^{+\bullet})]^+$ cation was trapped in the cell of an FT-ICR mass spectrometer and its reactivity studied with a selection of olefins.

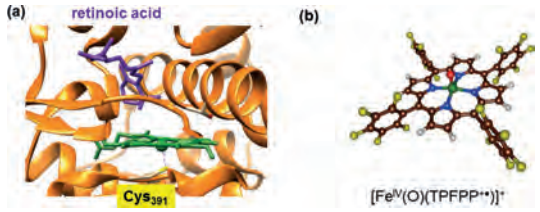

Figure 1. Enzymatic and biomimetic models of cytochrome P450 CpdI. (a) Active site structure as taken of substrate bound-resting state P450 from the 2VE3 pdb file. (b) Biomimetic model investigated here.

These studies established rate constants for olefin epoxidation, showing them to correlate with the ionization energy (IE) of the substrate that is activated. Subsequently, DFT calculations confirmed the observed trend and using a valence bond (VB) scheme highlighted the major components of the oxidant and substrate that contribute to the free energy of activation. To gain further insight into the reactivity patterns of CpdI model complexes using a combined FT-ICR MS and DFT approach, we decided to follow up our studies with work on aromatic hydroxylation. We propose a nucleophilic addition pathway as the rate determining reaction step, whereby the rate is determined by the ionization potential of the substrate and the π/π^* energy splitting of the CpdI models as well as electron reorganization energies within the complex. Furthermore, it is found that the removal of the axial cysteinate ligand as in the FT-ICR MS model used here raises the energies of the aliphatic hydroxylation pathways dramatically and prevents these product channels. The studies, therefore, give evidence of the axial ligand to be crucial in determining the activity and potential of the reactive oxidant of P450 enzymes.

Results

Experiment

In previous work, we established working procedures for the trapping of high-valent transition-metal-oxo intermediates in an FT-ICR MS.[7,12] These studies identified structures with *m/z* 1044 in the mass spectrum representing $[Fe^{IV}(O)(TPFPP^{+\bullet})]^+$ ions in good abundance and with long enough lifetime to enable ion-molecule reactions in the gas-phase. These procedures enabled us to do a systematic study into olefin epoxidation by these ions,[12] which established reactivity trends and a model that accounts for the observed reactivity. We decided to follow the study up with a systematic account on arene hydroxylation processes. In particular, a series of 16 aromatic substrates were investigated and their second-order rate constants (k_{exp}) determined in a reaction with $[Fe^{IV}(O)(TPFPP^{+\bullet})]^+$. Note that due to bifurcation processes, multiple reaction channels and products are possible, leading to aromatic and aliphatic hydroxylation products. Using the Average Dipole Orientation (ADO) theory (see Methods), the experimental rate constants were converted into reaction efficiencies (Φ) that represent the fraction of reactive collisions.

Table 1 summarizes the experimentally determined reaction rates for all substrates as well as their individual product distributions. Also included are ionization energies (IE) taken from the NIST database.[13] Thus, the reaction of $[Fe^{IV}(O)(TPFPP^{+\bullet})]^+$ with arenes typically gives two reaction channels, namely oxygen atom transfer (OAT) and an addition process (Add), see Scheme 1. The OAT reaction leads to the formation of $[Fe^{III}(TPFPP)]^+$ ions with *m/z* 1028 and consequently release of oxygenated substrate. In addition, in several cases an adduct

Table 1. FT-ICR MS reactivity of $[Fe^{IV}(O)(TPFPP^{+\bullet})]^+$ with arenes: Second-order rate constants, reaction efficiencies and product distributions for OAT and Add.

Substrate	IE[a]	k_{exp}[b,c]	k_{ADO}[b]	Φ_{OAT}	Φ_{Add}	[%] OAT	[%] Add
benzaldehyde	9.50	0.15	11.4	–	1.3	0	100
α-[D_1]-benzaldehyde	9.50	0.14	11.4	–	1.2	0	100
benzene	9.20	0.012	8.8	0.14	–	100	–
toluene	8.80	0.36	9.2	3.1	0.78	80	20
ethylbenzene	8.77	0.58	9.5	4.3	1.8	70	30
[D_5]-ethylbenzene	8.77	0.56	9.5	4.2	1.7	72	28
[D_{10}]-ethylbenzene	8.77	0.57	9.5	4.4	1.6	73	27
i-propylbenzene	8.73	1.2	10.0	7.8	4.2	65	35
tert-butylbenzene	8.68	1.0	10.0	9.5	0.5	95	5
o-xylene	8.56	1.4	9.5	9.5	5.2	65	35
[D_4]-*o*-xylene	8.56	1.4	9.5	9.1	5.6	62	38
[D_6]-*o*-xylene	8.56	1.3	9.5	8.9	4.8	65	35
m-xylene	8.55	1.6	9.5	15.8	1.2	93	7
p-xylene	8.44	1.3	8.9	9.4	5.1	65	35
mesitylene	8.40	1.9	9.0	12.6	8.4	60	40
naphthalene	8.14	0.93	9.1	7.6	2.4	76	24

[a] from NIST database, in eV. [b] second-order rate constants (k_{exp}) in units of 10^{-10} cm^3 $molecule^{-1}$ s^{-1}, at the temperature of the FT-ICR cell (300 K). [c] The estimated error is ±30%; the internal consistency of the data is within ±10%.

© 2016 Wiley-VCH Verlag GmbH & Co. KGaA, Weinheim

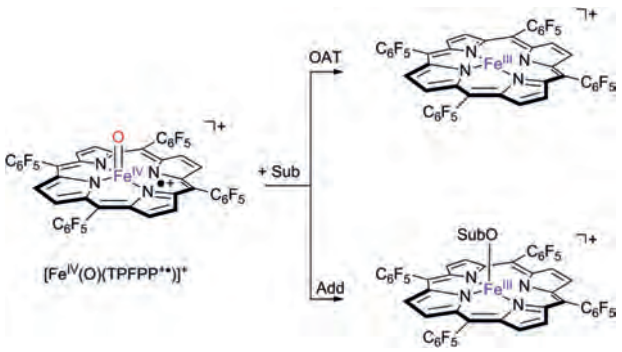

Scheme 1. Reaction products observed from the reaction of $[Fe^{IV}(O)(TPFPP^{+\bullet})]^+$ with arenes (Sub).

complex is observed with mass corresponding to $[Fe^{III}(TPFPP)(SubO)]^+$, whereby Sub represents the substrate.

Figure S1 in the Supporting Information shows an example of a mass spectrum recorded along the kinetic run for the reaction of $[Fe^{IV}(O)(TPFPP^{+\bullet})]^+$ with toluene at 3.8×10^{-8} mbar and displays signals at 120 s reaction time for the reactant $[Fe^{IV}(O)(TPFPP^{+\bullet})]^+$ centered at *m/z* 1044, product ions $[Fe^{III}(TPFPP)]^+$ at *m/z* 1028, and $[Fe^{III}(TPFPP)(SubO)]^+$ at *m/z* 1136.

The actual formation of an oxidation product remaining in the coordination sphere of $[Fe^{III}(TPFPP)]^+$ assigned to the $[Fe^{III}(TPFPP)(SubO)]^+$ ion at *m/z* 1136 has been verified by isolating the complex and submitting it to low-energy collision induced dissociation. As shown in Figure S2 (Supporting Information), the ion at *m/z* 1136 undergoes fragmentation, releasing $[Fe^{III}(TPFPP)]^+$ by loss of SubO, namely the oxidation product of toluene. Additional evidence for the formation of a SubO ligand is inferred from a reaction that is observed at longer reaction times whereby the $[Fe^{III}(TPFPP)(SubO)]^+$ ion undergoes a ligand substitution process by a Sub molecule, the neutral present in the FT-ICR cell, to give $[Fe^{III}(TPFPP)(Sub)]^+$. This process is clearly observed for the reaction of benzaldehyde. In this case, one finds that the efficiency for the $[Fe^{III}(TPFPP)(SubO)]^+ + Sub \rightarrow [Fe^{III}(TPFPP)(Sub)]^+ +$ SubO reaction is less than 1.3% (this value represents the efficiency for the $[Fe^{IV}(O)(TPFPP^{+\bullet})]^+ + Sub \rightarrow [Fe^{III}(TPFPP)(SubO)]^+$ reaction, with Sub equal to benzaldehyde).

On this basis, an indirect probe for the structure of $[Fe^{III}(TPFPP)(SubO)]^+$ ions has been sought by forming distinct model complexes and studying their gas phase reactivity towards benzaldehyde. In methanol solution $[Fe^{III}(TPFPP)]^+$ reacts with both (*m*/*p*)-hydroxy-benzaldehyde and benzoic acid to give an addition complex which is delivered by electrospray ionization (ESI) into the gas phase, led into the ICR cell and tested for bimolecular reactivity with benzaldehyde. The complex with benzoic acid is found to be substantially more reactive in the ligand transfer process than both complexes with (*m*/*p*)-hydroxy-benzaldehyde (reaction efficiencies are equal to 14% and around 0.60%, respectively, Equations 1–3). This result is indicative that the gas phase oxidation of benzaldehyde by $[Fe^{IV}(O)(TPFPP^{+\bullet})]^+$ is directed at the aromatic ring rather than at the formyl group. The same experiment could not be extended to other substrates, given the scant ligand transfer reactivity typically displayed by arenes, but this outcome in the favorable case of benzaldehyde suggests that $[Fe^{IV}(O)(TPFPP^{+\bullet})]^+$ prefers attack at the aromatic ring rather than at a side chain substituent.

$$[Fe^{III}(TPFPP)(C_6H_5COOH)]^+ + C_6H_5CHO \rightarrow [Fe^{III}(TPFPP)(C_6H_5CHO)]^+ + C_6H_5COOH \quad (1)$$
$$\Phi = 14\,\%$$

$$[Fe^{III}(TPFPP)(p\text{-}OH\text{-}C_6H_4CHO)]^+ + C_6H_5CHO \rightarrow [Fe^{III}(TPFPP)(C_6H_5CHO)]^+ + p\text{-}OH\text{-}C_6H_4CHO \quad (2)$$
$$\Phi = 0.64\,\%$$

$$[Fe^{III}(TPFPP)(m\text{-}OH\text{-}C_6H_4CHO)]^+ + C_6H_5CHO \rightarrow [Fe^{III}(TPFPP)(C_6H_5CHO)]^+ + m\text{-}OH\text{-}C_6H_4CHO \quad (3)$$
$$\Phi = 0.56\,\%$$

As follows from Table 1, the rate constant ranges from 0.012×10^{-10} $cm^3\,molecule^{-1}\,s^{-1}$ for the reaction of $[Fe^{IV}(O)(TPFPP^{+\bullet})]^+$ with benzene increasing to a value of 1.9×10^{-10} $cm^3\,molecule^{-1}\,s^{-1}$ for the reaction with mesitylene. As such, a spread of two orders of magnitude in rate constant is found for the series of substrates investigated here. In all cases (except for benzaldehyde) the dominant product complex obtained is the $[Fe^{III}(TPFPP)]^+$ ion representing the OAT channel. However, addition products are obtained in significant amounts with percentages of up to 40% (with mesitylene), whereas for benzaldehyde this is the sole reaction channel. Figure 2 displays the reactant and product abundancies as

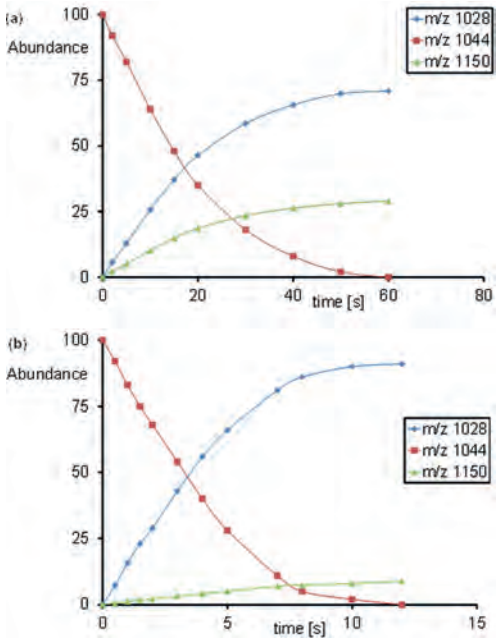

Figure 2. Ion distributions as a function of time for the reaction of $[Fe^{IV}(O)(TPFPP^{+\bullet})]^+$ with (a) ethylbenzene and (b) *m*-xylene.

© 2016 Wiley-VCH Verlag GmbH & Co. KGaA, Weinheim

a function of time for the reaction of $[Fe^{IV}(O)(TPFPP^{+\bullet})]^+$ with ethylbenzene and *m*-xylene. The reactant ion abundance decays according to pseudo first-order kinetics as expected for a bimolecular reaction in the gas-phase. Thus, the ion abundance at *m/z* 1044 decays slowly as a function of time as the $[Fe^{IV}(O)(TPFPP^{+\bullet})]^+$ reacts away and the decay patterns were used to establish the experimental second-order rate constants k_{exp}. In the case of ethylbenzene as a substrate (Figure 2a) two products are formed with *m/z* 1028 and *m/z* 1150 representing the OAT and Add channels. The shape of the curves shown in Figure 2 is used to determine the efficiencies Φ_{OAT} and Φ_{Add} described in Table 1. As follows the ratio of the abundancies of the OAT and Add channels are constant as a function of time for ethylbenzene as well as *m*-xylene with ratios of *m/z* 1028: *m/z* 1150 ion abundancies of 2.5 and 13, respectively. This implies that these products originate from the same source and most probably, product release from the iron(III) complex and, most probably, is a slow process.

To find out whether the reactivities and, in particular, the product distributions relate to aromatic or aliphatic hydroxylation pathways, we repeated some of the reactions with deuterated substrates. Thus, we tested ethylbenzene with all aliphatic hydrogen atoms replaced by deuterium ($[D_5]$-ethylbenzene) and fully deuterated ethylbenzene ($[D_{10}]$-ethylbenzene). As can be seen from Table 1, the substrate deuteration has a small but nonsignificant effect on the reaction efficiencies and product distributions. Therefore, it can be concluded that the reaction between $[Fe(O)(TPFPP^{+\bullet})]^+$ and ethylbenzene does not proceed with a rate-determining hydrogen atom abstraction. The indication is rather that these reactions with deuterated substrates strongly implicate an aromatic hydroxylation of substrates. The product ratios also suggest that an ethylphenol product (as obtained from ethylbenzene) is more strongly bound to the iron(III) complex than the dimethylphenol product obtained from *m*-xylene.

To further confirm the reactions as aromatic hydroxylation, we investigated *o*-xylene with all aromatic hydrogen atoms replaced by deuterium ($[D_4]$-*o*-xylene) and all aliphatic hydrogen atoms replaced by deuterium ($[D_6]$-*o*-xylene). Table 1 gives the product distributions and reaction efficiencies for *o*-xylene, $[D_4]$-*o*-xylene and $[D_6]$-*o*-xylene. Within our experimental error margin all reaction efficiencies, rate constants and product distributions are the same, which gives evidence that in the reaction of $[Fe(O)(TPFPP^{+\bullet})]^+$ with *o*-xylene no rate determining hydrogen atom abstraction takes place.

Theory

To support the experiments and gain insight into the details of the reaction mechanism, we followed the work up with an extensive DFT study to establish reactivity trends. Our initial work was aimed at the aromatic hydroxylation mechanism of arenes by [4,2]$[Fe^{IV}(O)(TPFPP^{+\bullet})]^+$, although we utilized a model without porphyrin substituents here, that is, porphyrin (Por). The investigated arenes in this work were mesitylene (**1**), toluene (**2**), ethylbenzene (**3**), fluorobenzene (**4**), chlorobenzene (**5**), naphthalene (**6**), *iso*-propylbenzene (**7**) and *tert*-butylbenzene (**8**). Test calculations with the full TPFPP model were also performed but found to give only minor differences in structure and reactivity with respect to the smaller porphyrin complex without side groups (see Supporting Information). Figure 3 shows the aromatic hydroxylation reaction of the *para*-position of toluene (PhMe; henceforth indicated with the subscript 2 beside the label of the structure) by the doublet and quartet spin states of $[Fe^{IV}(O)(Por^{+\bullet})]^+$ as calculated with DFT as an example. Thus, the reaction starts with an electrophilic attack of the oxo group on the *para*-carbon atom of the substrate that

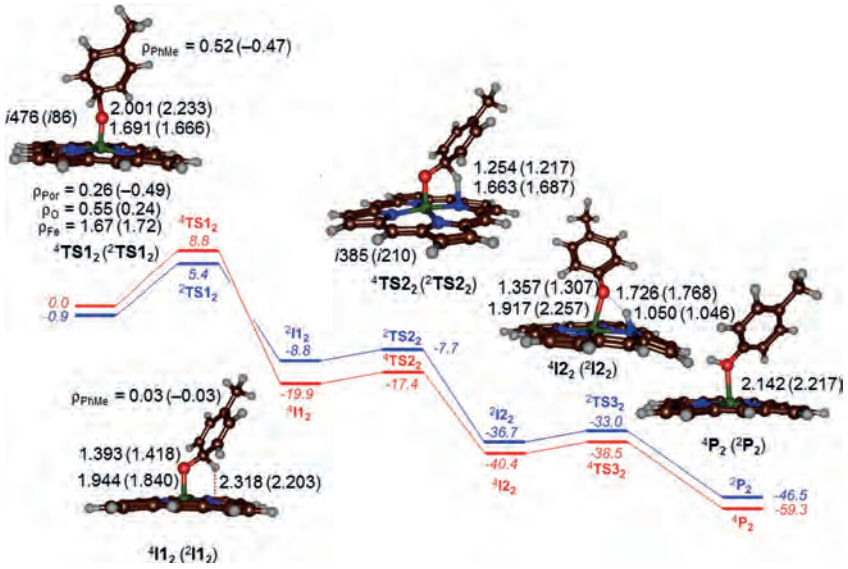

Figure 3. Potential energy profile (in kcal mol^{-1}) of aromatic hydroxylation of toluene (PhMe) by $[Fe^{IV}(O)(Por^{+\bullet})]^+$ as calculated with DFT at UB3LYP/BS2//UB3LYP/BS1 level of theory. All data include ZPE corrections and are calculated relative to isolated reactants. Bond lengths are given in angstroms and group spin densities (ρ) in atomic units.

© 2016 Wiley-VCH Verlag GmbH & Co. KGaA, Weinheim

via a transition state **TS1** leads to the intermediate **I1**. As shown previously by calculations on P450 model complexes, the *ipso*-proton is abstracted by the porphyrin group via transition state **TS2** to form the protonated porphyrin structure **I2**. Finally, the proton is relayed to the phenolate group via transition state **TS3** to form phenol products (**P**).[14]

An analysis of the group spin densities and charges establishes the intermediates **I1** as cationic on the substrate moiety ($\rho_{PhMe} = 0.03/-0.03$ in ^{4}**I1**$_2$/^{2}**I1**$_2$), which implies that two electrons have transferred from substrate to oxidant. We made several attempts to find radical intermediates through the swapping of molecular orbitals, but in all of these cases the wave functions converged back to the cationic intermediates instead. Recent experimental studies of Asaka and Fujii found experimental evidence of fast electron transfer during the C–O bond formation step and hence support the formation of a cationic intermediate.[15]

After the cationic intermediates (**I1**) the substrate loses its *ipso*-proton to the porphyrin ring via a small reaction barrier of 2.5 kcal mol^{-1} on the quartet spin state and 1.1 kcal mol^{-1} on the doublet spin surface. This proton-transfer intermediate (**I2**) then relays the proton back to the phenolate oxygen atom to form phenol products via another transition state **TS3** lying close in energy to **I2**.

The rate determining step in the reaction mechanism, however, is the electrophilic addition step via **TS1**, which elongates the Fe–O bond to 1.691/1.666 Å in ^{4,2}**TS1**$_2$ and has the substrate in an almost upright position. An analysis of the group spin densities (ρ) establishes it as a radical-type transition state with spin densities of 2.22 (1.96), 0.26 (−0.49) and 0.52 (−0.47) on the FeO, Por and PhMe groups, respectively, in ^{4}**TS1**$_2$ (^{2}**TS1**$_2$). As the reactant state has an electronic configuration $\pi^*_{xz}{}^1\ \pi^*_{yz}{}^1\ a_{1u}{}^1$ with spin density of about 2 on the FeO group and 1 on the porphyrin ring, this implies that radical character on the porphyrin manifold is lost in the transition state. In particular, an electron transfer from substrate into the a_{1u} orbital has occurred to create a transition state with configuration approximating $\pi^*_{xz}{}^1\pi^*_{yz}{}^1 a_{1u}{}^2\ \phi_{PhMe}{}^1$.

After the transition state the system relaxes to the cationic intermediate **I1**, which involves a second electron transfer from the substrate to the metal to generate an intermediate with orbital occupation $\pi^*_{xz}{}^1\pi^*_{yz}{}^1\sigma^*_{z2}{}^1 a_{1u}{}^2\ \phi_{PhMe}{}^0$. Geometrically, this second electron transfer and the single occupation of the σ^*_{z2} orbital results in considerable lengthening of the Fe–O bond from 1.691 Å in ^{4}**TS1**$_2$ to 1.944 Å in ^{4}**I1**$_2$. At the same time the C–O distance shortens from 2.001 Å in the transition state to 1.393 Å in the intermediate.

In the subsequent step we located transition states for proton transfer from the *ipso*-position to one of the nitrogen atoms of the porphyrin ligand in the doublet and quartet spin states. These proton transfer barriers have relatively small imaginary frequencies, i385 cm^{-1} (^{4}**TS2**$_2$) and i210 cm^{-1} (^{2}**TS2**$_2$), as compared to typical hydrogen atom abstraction transition states where values of well over i1000 cm^{-1} were found.[16] From the **I2** intermediates another proton transfer leads to the phenol product complexes with high exothermicity. A small barrier **TS3** is obtained in both spin states.

Overall, the aromatic hydroxylation reaction is stepwise with a rate determining electrophilic addition step with a barrier of $\Delta E^{\neq} + ZPE = 8.8$ (5.4) kcal mol^{-1} on the quartet (doublet) spin states. These values compare well with previous studies of aliphatic and aromatic hydroxylation by iron(IV)-oxo porphyrin cation radical complexes.[12,16–18]

Thereafter, we completed the investigation of ^{4,2}[Fe^{IV}(O)(Por$^{+\bullet}$)]$^+$ and its aromatic hydroxylation of a range of arenes and initially calculated the full landscape for chlorobenzene hydroxylation by ^{4,2}[Fe^{IV}(O)(Por$^{+\bullet}$)]$^+$, see Supporting Information for details. The landscape gives the same pattern as that seen for toluene in Figure 3 with a rate-determining electrophilic addition barrier **TS1**$_5$ leading to a cationic intermediate **I1**$_5$. Similarly to the toluene data reported above, ^{2}**TS1**$_5$ is below ^{4}**TS1**$_5$ as seen before in aromatic hydroxylation by P450 CpdI models.[14]

In addition, we calculated ^{4,2}**TS1** and ^{4,2}**I1** for the following substrates: mesitylene, ethylbenzene, fluorobenzene, naphthalene, *iso*-propylbenzene and *tert*-butylbenzene, whereby we give the label as a subscript after the structure name. In general, the same structural trends are observed in the quartet and doublet spin states and the mechanism is the same.

As can be seen strong geometric differences are found upon changing the *para*-substituent of the arene, whereby the ^{4}**TS1** structure for fluorobenzene gives Fe–O and O–C distances of 1.703 and 1.942 Å, while with ethylbenzene these distances change to 1.689 and 2.005 Å, respectively. Similar differences are seen for the other complexes as well as in the value of the imaginary frequency in the transition state. Nevertheless, all **TS1** structures shown in Figure 4 represent the same electronic transition of electron transfer from arene to a_{1u} and the accumulation of radical character on the arene group. Moreover, the transition state structures are geometrically alike with the substrate in virtually the same orientation in all cases. The occurrence of an electron transfer equilibrium preceding aromatic hydroxylation by a compound I model within a solvent cage has been highlighted.[15] The electrophilic addition transition states shown in Figure 4 differ strongly in the barrier height and values of $\Delta E^{\neq} + ZPE$ range from 1.8 kcal mol^{-1} for ^{2}**TS**$_6$ (naphthalene) to 12.4 kcal mol^{-1} for ^{4}**TS1**$_4$ (fluorobenzene). Nevertheless, all of them are radical type transition states with group spin densities similar to those reported for ^{4,2}**TS1**$_2$ above in Figure 3.

To ascertain that the lowest energy pathway indeed is aromatic hydroxylation rather than aliphatic hydroxylation, we also calculated the aliphatic hydroxylation mechanisms of toluene and ethylbenzene by ^{4}[Fe^{IV}(O)(Por$^{+\bullet}$)]$^+$, see Figure 5. These reactions are also stepwise with an initial hydrogen atom abstraction via transition state ^{4}**TS**$_H$ that leads to a radical intermediate ^{4}**I**$_H$. In both aliphatic hydrogen atom abstraction transition states significant radical character ($\rho = -0.52$ for both) is obtained. In a subsequent radical rebound barrier the OH group is transferred to substrate to form alcohol product complexes ^{4}**P**$_H$. The hydrogen atom abstraction is rate determining and has a relatively central transition state with elongated C–H distances of 1.202 Å for both toluene and ethylbenzene. In both structures the Fe–O bond has elongated to well over 1.7 Å.

© 2016 Wiley-VCH Verlag GmbH & Co. KGaA, Weinheim

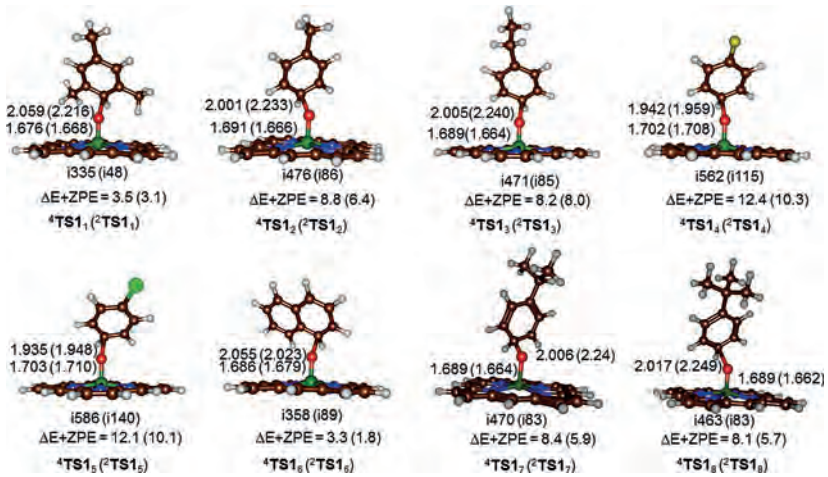

Figure 4. Optimized electrophilic addition transition states for the reaction of $^{4,2}[Fe^{IV}(O)(Por^{+\bullet})]^{+}$ with arenes. Barrier heights (in kcal mol^{-1}) given are relative to isolated reactants and calculated at UB3LYP/BS2//UB3LYP/BS1 level of theory. Bond lengths are in angstroms and imaginary frequencies in wave numbers.

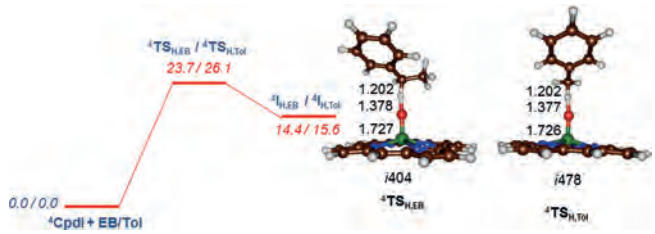

Figure 5. Aliphatic hydroxylation potential energy landscape as calculated at UB3LYP/BS2//UB3LYP/BS1 level of theory. Energies are in kcal mol^{-1} and include ZPE correction, while geometries give bond distances in angstroms and the imaginary frequency in wave numbers.

Energetically, the hydrogen atom abstraction barriers are higher than the arene activation barriers **TS1** shown in Figure 4 by well over 15 kcal mol^{-1}. Therefore, the dominant pathway is expected to be aromatic hydroxylation of arenes by $[Fe^{IV}(O)(Por^{+\bullet})]^{+}$ and little or no aliphatic hydroxylation products should be observed. The $[Fe^{IV}(O)(Por^{+\bullet})]^{+}$ system, as a consequence, reacts sluggishly with aliphatic groups, in contrast to iron(IV)-oxo porphyrins with an anionic axial ligand. Previously, we and others showed that the barrier heights of aliphatic hydroxylation reactions correlate with the bond dissociation energy (BDE_{OH}) for the formation of the iron(IV)-hydroxo species from the iron(IV)-oxo species and a hydrogen atom.[19] This implies that the BDE_{OH} of the $[Fe^{IV}(O)(Por^{+\bullet})]^{+}$ system will be considerably smaller than that of P450 CpdI and unable to react via hydrogen atom abstraction. Indeed, we calculate a BDE_{OH} for the reaction of $^{3}[Fe^{III}(OH)(Por^{+\bullet})]^{+}$ into CpdI and a hydrogen atom of $\Delta E + ZPE = 66.3$ kcal mol^{-1}, whereas for a P450 CpdI model a value of 88.9 kcal mol^{-1} was obtained.[20] In aliphatic hydroxylation the energy of the hydrogen atom abstraction step is equal to the difference in BDE_{CH} of the substrate and the BDE_{OH} of the oxidant. The BDE_{CH} of ethylbenzene is 82.5 kcal mol^{-1}.[14b] In the case of $[Fe^{IV}(O)(Por^{+\bullet})]^{+}$, therefore, hydrogen atom abstraction from ethylbenzene will be endothermic by 16.2 kcal mol^{-1}, whereas the P450 CpdI model should give an exothermic hydrogen atom abstraction by −6.4 kcal mol^{-1}. Indeed, the radical intermediate $^{4}\mathbf{I}_{H}$ for ethylbenzene as a substrate is 14.4 kcal mol^{-1} higher in energy than reactants and therefore matches the difference in energy between BDE_{OH} and BDE_{CH} of oxidant and substrate. The endothermicity for the hydrogen atom abstraction reactions of substrates by $[Fe^{IV}(O)(Por^{+\bullet})]^{+}$ is too high and, therefore; this process will not be able to compete with lower energy reaction channels, such as substrate epoxidation and aromatic hydroxylation.

Thus, the efficiency and reaction rate constant of aliphatic hydroxylation was shown to be linearly correlated with BDE_{OH},[19b] hence the system without axial ligand, that is $[Fe^{IV}(O)(Por^{+\bullet})]^{+}$, has reduced catalytic efficiency for aliphatic hydroxylation. Clearly, the axial cysteinate ligand in P450 enzymes affects the reactivity properties of the oxo group and thereby makes it a better oxidant. Electrophilic reactions, such as aromatic hydroxylation and epoxidation, however, tend to connect with the ionization energy of the substrate and the electron affinity of the oxidant,[21] which is appropriate for $[Fe^{IV}(O)(Por^{+\bullet})]^{+}$ to perform these reactions.

Discussion

In this work a comprehensive overview of arene activation by $[Fe^{IV}(O)(Por^{+\bullet})]^{+}$ and $[Fe^{IV}(O)(TPFPP^{+\bullet})]^{+}$ is given as mimics of P450 CpdI reactivity with substrates. As some of the substrates have aliphatic substituents to the arene, our initial work focused on establishing the nature of the reaction products. Unfortunately, aliphatic and aromatic hydroxylation of arenes gives products with equal mass and as such cannot be distinguished by mass spectrometry. Moreover, the fragmentation patterns of the products did not give direct evidence of what pathway was followed either. Hence, FT-ICR MS cannot distinguish the two products directly. We, therefore, repeated the experiments with deuterium-labelled compounds, which gave only minor changes to the rate constants and implicated that

© 2016 Wiley-VCH Verlag GmbH & Co. KGaA, Weinheim

the rate determining step does not include a hydrogen atom abstraction.

To gain further insight into the details of the reaction mechanism and the bifurcation processes, computational modelling was performed. In particular, DFT studies on the relative barriers for aliphatic versus aromatic hydroxylation reactions were performed (Figures 4 and 5) and confirmed the latter to be well lower in energy. As such, in the gas-phase the $[Fe^{IV}(O)(TPFPP^{+\bullet})]^+$ complex will preferentially react via aromatic hydroxylation over aliphatic hydroxylation with substrates. Nam et al.[22] studied the aliphatic versus aromatic hydroxylation of ethylbenzene by $[Fe^{IV}(O)(TPFPP^{+\bullet})(X)]$ with $X = Cl^-$/$CF_3SO_3^-$ in dichloromethane. Aliphatic hydroxylation products were obtained with $[Fe^{IV}(O)(TPFPP^{+\bullet})(Cl)]$ as an oxidant, whereas aromatic hydroxylation products were detected in a reaction with $[Fe^{IV}(O)(TPFPP^{+\bullet})(CF_3SO_3)]$. Subsequent computational modelling showed that the axial ligand affects the electron affinity and O–H bond strength (bond dissociation energy, BDE_{OH}) and hence affected the relative barriers of aliphatic versus aromatic hydroxylation.[14b,23] To gain further insight into the intricate details of the bifurcation processes, below, a molecular orbital and valence bond interpretation of the mechanisms is shown. First, however, a discussion of the experimental reaction trends is presented.

To find trends and a rationale in the obtained rate constants and particularly find evidence on the properties of the catalyst/oxidant that determines the reaction process, we decided to search for physicochemical properties of substrate and oxidant in correlation with the rate constant. These analyses should give insight into the fundamental properties of P450 CpdI and how it is able to activate arenes. To this end, we decided to plot the natural logarithm of the rate constant against physical chemical properties of the substrate and oxidant, including the ionization energy of the substrate. Thus, previously it was shown that reactions starting with a rate-determining hydrogen atom abstraction generally correlate with the strength of the C–H bond that is broken, that is, the bond dissociation energy (BDE_{CH}).[24,25] However, aromatic hydroxylation pathways by metal-oxo complexes were shown to connect to the ionization energy (IE) of the substrate.[25]

Figure 6 displays plots of the natural logarithm of the experimentally determined rate constant versus the ionization energy of the substrate (part a) and the BDE_{CH} value of the aliphatic group of the substrate (part b). As can be seen from Figure 6, the ionization energy of the substrate follows a linear correlation with the ln k_{exp} value with an R^2 value of 0.88. Interestingly, the rate constants for benzene and naphthalene activation by $[Fe^{IV}(O)(TPFPP^{+\bullet})]^+$ do not fit the trend. This may be due to the fact that these substrates approach the oxidant differently and give extra interactions with the oxidant. Aromatic hydroxylation, similarly to double bond epoxidation, therefore, gives rate constants that are proportional to the IE of the substrate involved.[25] This means that any oxidant reacting with a substrate containing an arene and a double bond as a separate group will give preferential aromatic hydroxylation rather than double bond epoxidation.

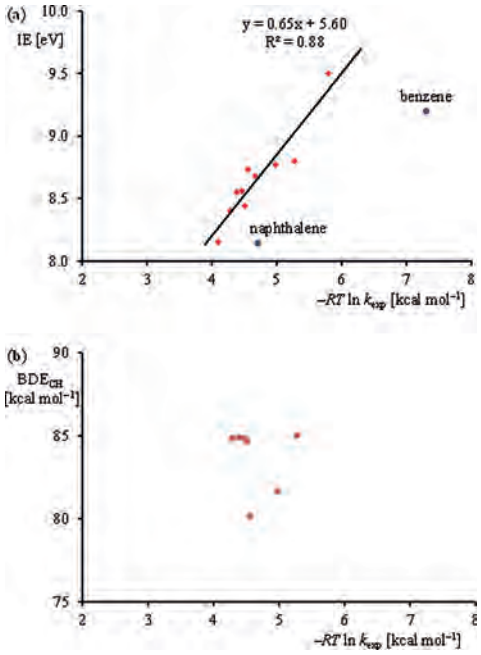

Figure 6. Correlation of the natural logarithm of the rate constant with (a) ionization energy from the substrate. (b) BDE_{CH} value of the aliphatic group of the substrate. Ionization energies taken from the NIST Database.[13] BDE_{CH} values calculated with DFT at B3LYP/BS2//UB3LYP/BS1 including ZPE corrections.

For the set of substrates with aliphatic substituents also a plot of ln k_{exp} versus BDE_{CH} was attempted (Figure 6b), however, no clear linear correlation is found. Based on this evidence the aliphatic hydroxylation pathway can be ruled out as a viable mechanism for arene activation by $[Fe^{IV}(O)(TPFPP^{+\bullet})]^+$ and, based on the reactivity trends as well as the kinetic isotope effect (KIE) values, the dominant pathway is aromatic hydroxylation.

Figure 7 gives the corresponding plot for the correlation between the ionization energy and the computationally determined aromatic hydroxylation free energy of activation calculated for the various ^{4,2}**TS1** structures for the substrates in Figure 4. In agreement with the experimental result, a linear correlation between barrier height and ionization energy is found with an $R^2 = 0.91$ (quartet) and 0.93 (doublet). As such, both experimental reaction rates and computational barrier heights implicate a linear correlation between the natural logarithm of the rate constant and ionization energy. As both experiment and theory give the same correlation, of course, the experimental rates also correlate linearly with the computational barrier heights. Moreover, using the found trends, this enables us to predict reaction rates of alternative substrates. For instance, the rate constants for aromatic hydroxylation of chlorobenzene and fluorobenzene could not be measured. However, the trend from Figure 6a and Figure 7a enable us to predict their values as 4.8 and 5.0×10^{-11} $cm^3\,molecule^{-1}\,s^{-1}$, respectively. Similarly, we predict barrier heights at B3LYP level of theory from the experimental trend in Figure 6a of $\Delta G^{\neq} = 19.5$, 19.9 and 24.4 kcal mol^{-1} for *iso*-propylbenzene, *tert*-butylbenzene and benzaldehyde, respectively, whereas values of $\Delta G^{\neq} =$

© 2016 Wiley-VCH Verlag GmbH & Co. KGaA, Weinheim

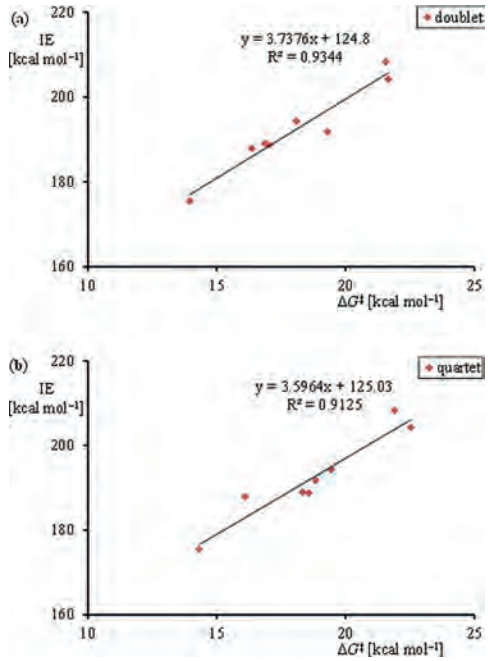

Figure 7. Correlation of the computationally determined free energy of activation of aromatic hydroxylation (**TS1**) with calculated ionization energy of the substrate.

18.8, 19.2 and 19.3 kcal mol^{-1} are expected for *m*-, *o*-, and *p*-xylene. As such the two plots from Figure 6 and Figure 7 enable one to predict experimental rates from computational trends or computational barriers from experimental trends. To verify the accuracy of this procedure we predicted the DFT barriers for toluene, ethylbenzene and mesitylene from the trend in Figure 6a and find values of $\Delta G^{\ddagger}=22.3$, 21.2 and 16.4 kcal mol^{-1}, respectively, which are within a mean error of 2.8 kcal mol^{-1} of the DFT calculated results (Supporting Information).

Electronically, the fact that the trends correlate with ionization energy implicate that the electron transfer from substrate to oxidant will determine the reaction rate. The trends in reactivity also imply that none of the products observed in the mass spectra can correlate with aliphatic hydroxylation products. Therefore, the product ions with *m/z* 1028 and *m/z* 1150 (Figure 2) originate from the aromatic hydroxylation of substrates. Clearly, product release from the iron(III) complex is a slow process and a mixture of metal-ligated and free phenol products are obtained.

Evidently, the rate constant and reactivity patterns of the iron(IV)-oxo porphyrin complex with arenes is dependent on key properties of the oxidant and substrate. In order to improve catalyst design and find novel oxidants for this reaction process, we delineated the transition-state barrier into fundamental properties of oxidant and substrate. This analysis identifies the origin of the reaction mechanism and explains how the oxidant can be further improved for better catalysis.

To understand the obtained trends and correlations we used a parabolic approximation of previously described VB models to explain the reaction barrier.[26] Figure 8 displays the basic

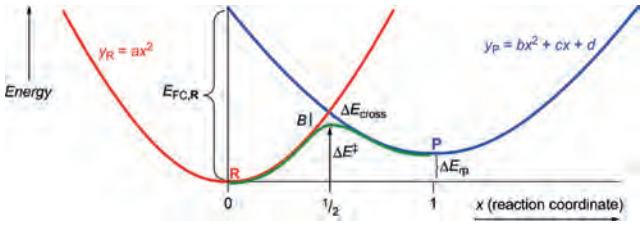

Figure 8. Two-parabola curve crossing model for the prediction of barrier heights.

features of the two-parabola crossing model, where we assume the reactant complex (**R**) to reside in a local minimum that can be described by a parabola with function $y_R=ax^2$ with y_R being the energy function of the reactant complex, x the reaction coordinate and a is a constant that describes the curvature of the reaction coordinate function. The reactant complex is defined as the starting point of the reaction with coordinates $x_R=0$ and $y_R=0$. For the product complex we describe the potential energy surface with another parabola that is shifted from the reactant parabola and hence has function $y_P=bx^2+cx+d$ with b, c, and d being some constants that describe the curvature and extremes of the parabola. We now assume that the product local minimum is located at a reaction coordinate with value $x=1$ and the transition state at the half-way point ($x={}^1/_2$). That means the two curves for y_R and y_P will cross at $x_{cross}={}^1/_2$ and create a crossing point, at energy $y_P({}^1/_2)=\Delta E_{cross}$, which will ultimately lead to an avoided crossing and a transition state for the reaction. One can see from Figure 8 that $y_P(0)=d=E_{FC,R}$, whereby $E_{FC,R}$ represents the Franck–Condon energy at the reactant geometry. Furthermore, $y_P(1)$ is equal to the driving force for the reaction (ΔE_{rp}). Using the information for the first derivative of y_P at the point $x=1$, that is, $y_P'(1)=0$, we can now derive Equation 4 for $y_P({}^1/_2)$ as a function of the driving force for the reaction and the Franck–Condon energy at the reactants geometry.

$$y_P({}^1/_2)=\Delta E_{cross}=\frac{1}{4}E_{FC,R}+\frac{3}{4}\Delta E_{rp} \quad (4)$$

The actual transition state, however, with energy $\Delta E^{\ddagger}$ will be below the crossing point by an amount B that represents the resonance energy, Equation 5.

$$\Delta E^{\ddagger}=\Delta E_{cross}-B \quad (5)$$

Using Equations 4 and 5 we can predict the barrier height for the reaction in terms of the driving force for the reaction (ΔE_{rp}), the change in electronic configuration between the reactant and product state in the geometry of the reactants ($E_{FC,R}$) and the resonance energy B. Values for the driving force are taken as the difference in energy ($\Delta E+ZPE$) between reactant complex (**R**) of ^{4}CpdI and substrate with the radical intermediate ^{4}**I1**.

Figure 9 shows the curve crossing diagram with key valence bond (VB) structures of critical points along the reaction mechanism. The difference in VB structure between the reactant and product structures in the geometry of the reactants will

© 2016 Wiley-VCH Verlag GmbH & Co. KGaA, Weinheim

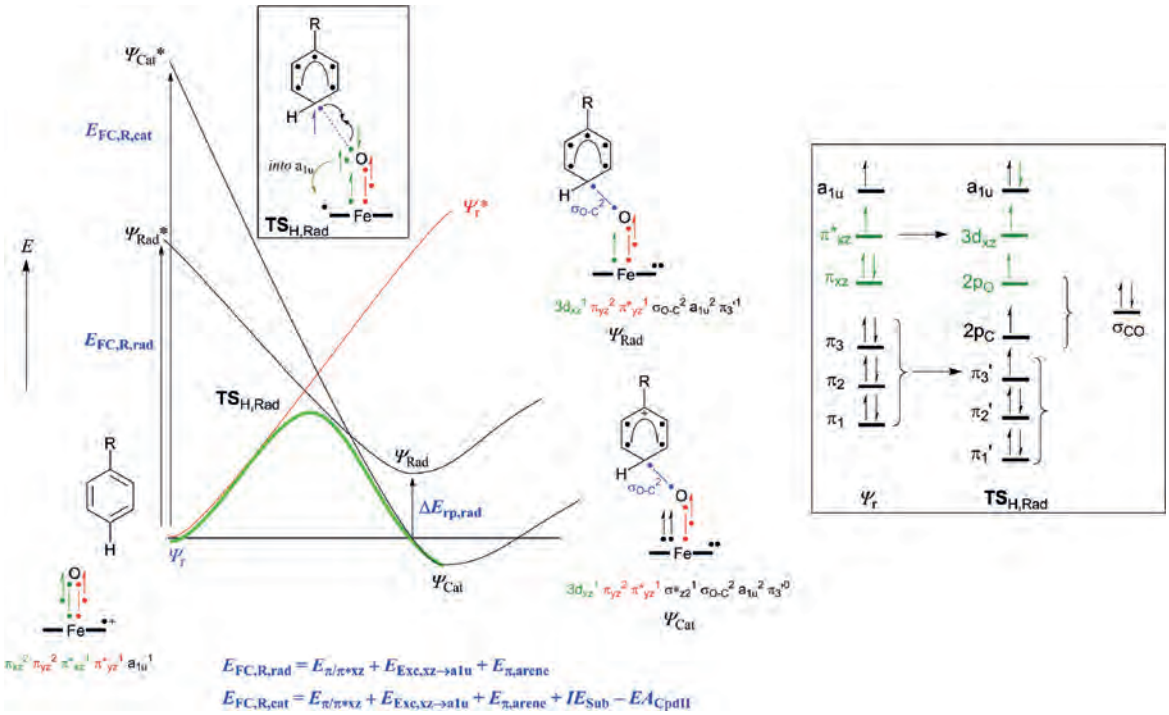

Figure 9. Valence bond curve crossing diagram and orbital/bonding changes along the electrophilic addition pathway of arene activation by $[Fe^{IV}(O)(Por^{+\bullet})]^+$. Valence bond structures give electrons as dots. Orbital occupation and hybridization changes are indicated with the orbital diagram.

determine the value of $E_{FC,R}$. These diagrams have been used previously to rationalize barrier heights of chemical reactions and explain what features of substrate and oxidant affect the value of the barrier height.[21,27]

The diagram starts on the bottom-left with the reactant configuration of $[Fe^{IV}(O)(Por^{+\bullet})]^+$ and arene. Thus, in the ground state the system has three unpaired electrons distributed over the π^*_{xz}, π^*_{yz} and a_{1u} molecular orbitals. The π_{xz}/π^*_{xz} and π_{yz}/π^*_{yz} molecular orbitals represent the bonding and antibonding combinations of 3d orbitals on Fe with 2p orbitals on oxygen.

The a_{1u} orbital is a nonbonding π-orbital on the porphyrin ring and is close in energy to the a_{2u} orbital. In previous work on $[Fe^{IV}(O)(Por^{+\bullet})]^+$ we found several close-lying electronic states with either doublet or quartet spin and single occupation of a_{1u} or a_{2u}.[12] The three green dots along the Fe–O bond in Figure 9 represent the π_{xz}/π^*_{xz} electrons, while the ones in red are the π_{yz}/π^*_{yz} electrons. Both sets of π/π^* orbitals form a three-electron bond along the Fe–O group. Upon formation of the intermediate complex either a radical or cationic structure is formed. In both cases the C–O bond is formed from one of the electrons of the π-cloud of the substrate plus an electron from the π_{xz}/π^*_{xz} system. This means that electrophilic addition will result in the breaking of the π-system of the substrate and the set of six electrons in the substrate π-system (π_1, π_2 and π_3 orbitals), will be split into a $2p_C$ atomic orbital for one carbon and a conjugated π-system over the remaining five carbon atoms with orbitals π_1', π_2' and π_3'. Breaking the π-cloud of the substrate, will cost the system an energy $E_{\pi,arene}$. Of course, the breaking of the π-cloud will also be correlated to the excitation energy in the π-system as well as the ionization energy for removal of an electron from one of the π-orbitals.

As such, the barrier height and the driving force for the reaction are likely to correlate with the ionization energy of the substrate as indeed shown in Figure 6a and Figure 7 . By contrast, the cationic pathway will more likely be connected to the second ionization energy of the substrate as apart from the breaking of the π-orbitals of the substrate and also an electron will have to transfer to the oxidant.

In the calculations presented in Figures 3 and 4 the intermediates are of a cationic nature with an electronic configuration of $3d_{xz}{}^1 \pi_{yz}{}^2 \pi^*_{yz}{}^1 \sigma^*_{z2}{}^1 a_{1u}{}^2 \pi'_3{}^0$ with spin density of less than 0.1 on the aromatic ring and a value of about 3 on the FeO unit. Interestingly, the transition states give significant radical character on the aromatic ring, typically 0.50–0.70, so that these transition states should be considered as radical-type transition states connecting the reactants with the radical intermediates. For the estimation of the barrier heights from the VB structures, therefore, we will use the driving force to reach the radical intermediates, $\Delta E_{rp,rad}$. On the oxidant side of the reaction, a number of electron transfer and orbital reorganizations happen, which enable us to predict the value for $E_{FC,R,rad}$. Firstly, the π_{xz}/π^*_{xz} set of orbitals (highlighted in green in the VB structures for the reactant and the transition state) split back into atomic orbitals ($3d_{xz}$ and $2p_O$), which will cost the system E_{π/π^*xz} in energy. One of the electrons of $2p_O$ pairs up with the single electron in $2p_C$ and forms the new C–O bonding orbital σ_{CO}. The value of E_{π/π^*xz} is determined from the relative energies of the two orbitals in the reactant complex and is 85.2 kcal mol^{-1}. The remaining two electrons stay on the metal-

© 2016 Wiley-VCH Verlag GmbH & Co. KGaA, Weinheim

porphyrin side of the system and one of those electrons is promoted into the a_{1u} orbital to fill it with a second electron with excitation energy $E_{Exc,xz\rightarrow a1u}$. From the relative energies of the π_{xz} and a_{1u} orbitals in the reactant complex a value of 51.5 kcal mol^{-1} is obtained. Finally, the Franck–Condon energy between the reactant and the radical state is dependent on the breaking of the π-system of the arene, $E_{\pi,arene}$. The overall Franck–Condon energy for the transition from the reactant to the radical state is given in Equation 6.

$$E_{FC,\mathbf{R},rad} = E_{\pi/\pi*xz} + E_{Exc,xz\rightarrow a1u} + E_{\pi,arene} \quad (6)$$

Using Equations 4–6 we have estimated VB predicted barrier heights of $\Delta E + ZPE = 12.5$, 12.1, 5.1 and 6.2 kcal mol^{-1} for the reaction of $[Fe^{IV}(O)(Por^{+\bullet})]^{+}$ with chlorobenzene, fluorobenzene, toluene and ethylbenzene, respectively. These values are in good quantitative agreement with those obtained from full DFT optimizations and shown in Figure 3 and 4 above. As such, the two-parabola curve crossing diagram gives a good quantitative representation of the reaction mechanism and the kinetics obtained. Moreover, the model gives hints on the key electronic properties of oxidant and substrate that determine the rate determining reaction step.

Equation 6 shows that the barrier height for aromatic hydroxylation should be proportional to the excitation energy of the π-cloud of the substrate arene, which, of course, is proportional to the ionization energy. Indeed that is what we observe above in Figure 6 and Figure 7. The fact that the rate constants for benzene and naphthalene do not fit the trend displayed in Figure 6 could be explained as those systems following a cationic pathway rather than a more radical pathway and hence should correlate with $E_{FC,\mathbf{R},cat}$ rather than $E_{FC,\mathbf{R},rad}$.

In the case of electrophilic addition, however, there is also a pathway leading to a cationic intermediate with wave function Ψ_{Cat}. This electronic configuration can be formed from the radical intermediate through an electron transfer from the substrate π-system into the σ^*_{z2} orbital of the metal. As such, we expect there to be a direct transition state leading to the radical intermediate as well as one to form the cationic intermediate, although the latter is higher in energy. These transition states will be proportional to the Franck–Condon energy from the reactant state to the excited state representing the product electronic configuration. Figure 8 gives descriptions for the Franck–Condon energies reaching the radical state ($E_{FC,\mathbf{R},rad}$) and the one leading to the cationic state ($E_{FC,\mathbf{R},cat}$). Based on the electronic differences between ground and excited state configurations, we established the individual contributions determining these excitation energies. As it happens, the excitation energy leading to the cationic state contains all features of the one leading to the radical state plus two additional terms, namely the ionization energy of the substrate (IE_{Sub}) and the electron affinity of the metal in the radical intermediate, which is the reduced form of the iron(IV)-oxo species, namely EA_{CpdII}. Therefore, in the transition state the cationic process is higher in energy and only after the barrier a crossover from radical to cationic pathway will be observed leading to the cationic intermediate and fast conversion to phenol products. The DFT and VB models, therefore, implicate a rate determining electrophilic addition step with a radical-type transition state. However, upon C–O bond formation en route to the intermediate a state crossing occurs to the lower lying cationic intermediate.

In summary, the VB diagram highlights the factors of the substrate and oxidant that affect the barrier height and predicts that the rate constant is proportional to the ionization energy of the substrate regarded that the oxidant stays the same.

Conclusion

A combined FT-ICR MS and DFT study is performed on the reactivity of arenes with a model of P450 CpdI without axial ligand. It is shown that removal of the axial ligand gives a dominant aromatic hydroxylation pathway and no evidence of aliphatic hydroxylation is found. In general, the natural logarithm of the rate constant of aromatic hydroxylation links linearly with the ionization energy of the substrate. The explanation of this finding is supported within the framework of a Valence Bond model.

Experimental Section

Materials

All chemicals and solvents used for this work were research grade and purchased from commercial sources. Iodosylbenzene was used as a terminal oxidant for the synthesis of the iron(IV)-oxo complex and was generated according to a literature procedure,[29] and subsequently stored at −20 °C prior to usage.

Instrumental

A Bruker BioApex FT-ICR mass spectrometer was used for all experiments described here, which includes a cylindrical infinity cell, a 4.7 T superconducting magnet and an Apollo I electrospray ionization (ESI) source. Analyte solutions of reactants were infused into the mass spectrometer through a fused-silica capillary with internal diameter of 50 μm at a continuous flow rate of 120 μL h^{-1} by a syringe pump. Ions were desolvated by applying an N_2 counter current drying gas heated at 380 K and then accumulated for 0.8 seconds in a radiofrequency-only hexapole ion guide. Thereafter, the ions were pulsed into the ICR cell that is held at room temperature (300 K). The ions of interest, $[Fe^{IV}(O)(TPFPP^{+\bullet})]^{+}$ at *m/z* 1044, were mass selected by ion ejection procedures and ion-molecule reactions were studied by inserting neutral collision gases and monitoring the abundance of product ions as a function of time. Neutral reagents were admitted into the FT-ICR cell at stationary pressures (in the range from 1.0–15×10^{-8} mbar) by a needle valve. The pressure in the FT-ICR cell was measured with a cold-cathode sensor (IKR Pfeiffer Balzers S.p.A., Milan, Italy) and calibrated against the rate constant of proton transfer from methane cation radical to methane, Eq 7, which is known to have a rate constant $k = 1.1\times 10^{-9}$ cm^3 s^{-1}.[29]

$$CH_4^{+\bullet} + CH_4 \rightarrow CH_5^{+} + CH_3^{\bullet} \quad (7)$$

In the mass spectra, corrections for ^{13}C isotopic contributions were applied in order to reveal possible species deriving from a hydro-

© 2016 Wiley-VCH Verlag GmbH & Co. KGaA, Weinheim

gen atom transfer channel, namely $[Fe^{IV}(OH)(TPFPP)]^+$ ions at *m/z* 1045, presenting a formally protonated ferryl unit.

Ion abundances were monitored as a function of time and pseudo first-order rate constants were obtained from the slope of the semi-logarithmic plots. These values, determined at least in triplicate, were then converted into second-order rate constants (k_{exp}) by dividing the parent ion abundances by the substrate concentration at 300 K. Reaction efficiencies (Φ) were calculated from the ratio of the second-order rate constant and the collision rate constant (k_{ADO}), Equation 8. Values for k_{ADO} were calculated using the parametrized trajectory theory.[30]

$$\Phi = k_{exp}/k_{ADO} \times 100\,\% \quad (8)$$

Product ion branching ratios and reaction efficiencies were found to be independent of the pressure in the ICR cell. The error in the estimated second-order rate constants (k_{exp}) is to within 10% with an absolute error of $\pm 30\%$, caused largely by the uncertainty affecting the pressure of the neutral.[31]

Sample preparation

The $[Fe^{IV}(O)(TPFPP^{+\bullet})]^+$ ion was synthesized in a methanol/dichloromethane (1:1) mixture by adding iodosylbenzene (0.5 mM) to the corresponding iron(III)chloride complex, 10 μM of $[Fe^{III}(TPFPP)Cl]$, and cooled to −40 °C. The iron(IV)-oxo complex remained stable at this temperature for at least 1 hour. The ESI FT-ICR mass analysis of the reaction mixture gave a prominent peak centered at *m/z* 1044 with isotopic pattern conforming to an iron(IV)-oxo complex, $[Fe^{IV}(O)(TPFPP^{+\bullet})]^+$, together with the reduced form $[Fe^{III}(TPFPP)]^+$ at *m/z* 1028. Nonetheless, the ion population at *m/z* 1044 comprises a fraction of isomeric species, likely corresponding to an isobaric ion oxidized on the porphyrin ring, and unable to attain any oxidation process. This fraction was titrated by its complete trapping by NO yielding the $[Fe^{III}(TPFPP{-}O)(NO)]^+$ adduct, in analogy with the reduced form, $[Fe^{III}(TPFPP)]^+$. The presence of this unreactive form was taken into account in treating the kinetic data.

Computation

To support the experimental observations and determine further trends and features of the reaction mechanism, we did a detailed DFT study on aromatic hydroxylation by $[Fe^{IV}(O)(Por^{+\bullet})]^+$, where Por represents an unsubstituted porphyrin ligand. We also tested the full $[Fe^{IV}(O)(TPFPP^{+\bullet})]^+$ system but found very little differences in geometry, electronic description and reactivity with respect to the $[Fe^{IV}(O)(Por^{+\bullet})]^+$ system (Supporting Information Figure S4), hence the latter was used here. All calculations were performed in Gaussian-09,[32] and implemented DFT methods. Test calculations with a range of density functional methods show little sensitivity of the amount of exchange and correlation to optimized geometries and the potential energy landscape gives the same pattern (Supporting Information Tables S1–S20), therefore, we will show results obtained with the B3LYP[33] density functional method only as that will enable a direct comparison with our previous work.[12]

Initial geometry optimizations and constraint geometry scans were performed at the UB3LYP/BS1 level of theory: BS1 is LACVP on iron (with core potential) and 6–31G on the rest of the atoms.[34] The maxima of the geometry scans were then used as starting points for the transition state searches, which established first-order saddle points with a single imaginary frequency for the correct mode. Improved energies were obtained through single point calculations at the UB3LYP/BS2 level of theory: BS2 is LACV3P+ on iron (with core potential) and 6–311+G* on the rest of the atoms. Free energies are reported at a temperature of 298 K and 1atm pressure and include zero-point, thermal and entropic corrections under standard conditions. Although the experiments were performed in the gas-phase, we also tested the effect of solvent on the obtained rate constants from single point calculations using the polarized continuum model in Gaussian with a dielectric constant mimicking acetonitrile. All structures represent full geometry optimizations without constraints and were characterized with a frequency calculation as either a local minimum (real frequencies only) or a first-order saddle point.

Acknowledgements

M.A.S. and F.G.C.R. thank the Petroleum Technology Development Fund and the Conacyt Mexico for a studentship. SdV acknowledges CPU time support from the National Service of Computational Chemistry Software (NSCCS). The EU-COST Network Explicit Control Over Spin-states in Technology and Biochemistry (ECOSTBio, CM1305) is acknowledged for support. M.E.C. and S.F. are grateful to the Università di Roma "La Sapienza" for funding of the FT-ICR MS work.

Keywords: arenes · density functional theory · fourier transform-ion cyclotron resonance · mass spectrometry · oxygen atom transfer

[1] a) M. Costas, M. P. Mehn, M. P. Jensen, L. Que Jr, *Chem. Rev.* **2004**, *104*, 939–986; b) M. M. Abu-Omar, A. Loaiza, N. Hontzeas, *Chem. Rev.* **2005**, *105*, 2227–2252; c) W. Nam, *Acc. Chem. Res.* **2007**, *40*, 522–531; d) P. Comba, M. Kerscher, *Coord. Chem. Rev.* **2009**, *253*, 564–574; e) *Iron-containing enzymes: Versatile catalysts of hydroxylation reaction in nature* (Eds.: S. P. de Visser, D. Kumar), RSC Publishing, Cambridge (UK), **2011**.

[2] a) E. I. Solomon, T. C. Brunold, M. I. Davis, J. N. Kemsley, S. K. Lee, N. Lehnert, F. Neese, A. J. Skulan, Y. S. Yang, J. Zhou, *Chem. Rev.* **2000**, *100*, 235–349; b) S. V. Kryatov, E. V. Rybak-Akimova, S. Schindler, *Chem. Rev.* **2005**, *105*, 2175–2226; c) P. C. A. Bruijnincx, G. van Koten, R. J. M. Klein Gebbink, *Chem. Soc. Rev.* **2008**, *37*, 2716–2744; d) M. Costas, *Coord. Chem. Rev.* **2011**, *255*, 2912–2932; e) A. R. McDonald, L. Que Jr, *Coord. Chem. Rev.* **2013**, *257*, 414–428; f) W. Nam, Y.-M. Lee, S. Fukuzumi, *Acc. Chem. Res.* **2014**, *47*, 1146–1154.

[3] A. Karlsson, J. V. Parales, R. E. Parales, D. T. Gibson, H. Eklund, S. Ramaswamy, *Science* **2003**, *299*, 1039–1042.

[4] a) T. D. H. Bugg, *Tetrahedron* **2003**, *59*, 7075–7101; b) E. G. Kovaleva, J. D. Lipscomb, *Science* **2007**, *316*, 453–457; c) S. Fetzner, R. A. Steiner, *Appl. Microbiol. Biotechnol.* **2010**, *86*, 791–804.

[5] a) M. Sono, M. P. Roach, E. D. Coulter, J. H. Dawson, *Chem. Rev.* **1996**, *96*, 2841–2888; b) J. T. Groves, *Proc. Natl. Acad. Sci. USA* **2003**, *100*, 3569–3574; c) B. Meunier, S. P. de Visser, S. Shaik, *Chem. Rev.* **2004**, *104*, 3947–3980; d) *Cytochrome P450: Structure, Mechanism and Biochemistry* (Ed.: P. R. Ortiz de Montellano) 3rd Ed., Kluwer Academic/Plenum Publishers, New York, **2005**; e) A. W. Munro, H. M. Girvan, K. J. McLean, *Nat. Prod. Rep.* **2007**, *24*, 585–609; f) G. Grogan, *Curr. Opin. Chem. Biol.* **2011**, *15*, 241–248; g) *Handbook of Porphyrin Science* (Eds.: K. M. Kadish, K. M. Smith, R. Guilard), World Scientific Publishing Co., New Jersey, **2010**; h) T. L. Poulos, *Chem. Rev.* **2014**, *114*, 3919–3962.

[6] a) S. Shaik, D. Kumar, S. P. de Visser, A. Altun, W. Thiel, *Chem. Rev.* **2005**, *105*, 2279–2328; b) M. R. A. Blomberg, T. Borowski, F. Himo, R.-Z. Liao, P. E. M. Siegbahn, *Chem. Rev.* **2014**, *114*, 3601–3658.

[7] a) F. Lanucara, M. E. Crestoni, *Chem. Eur. J.* **2011**, *17*, 12092–12100; b) M. E. Crestoni, S. Fornarini, F. Lanucara, J. J. Warren, J. M. Mayer, *J. Am. Chem. Soc.* **2010**, *132*, 4336–4343; c) B. Chiavarino, R. Cipollini, M. E. Crestoni, S. Fornarini, F. Lanucara, A. Lapi, *J. Am. Chem. Soc.* **2008**,

© 2016 Wiley-VCH Verlag GmbH & Co. KGaA, Weinheim

130, 3208 – 3217; d) M. E. Crestoni, S. Fornarini, F. Lanucara, *Chem. Eur. J.* **2009**, *15*, 7863 – 7866; e) M. E. Crestoni, S. Fornarini, *Inorg. Chem.* **2005**, *44*, 5379 – 5387.
[8] M. E. Crestoni, S. Fornarini, *Inorg. Chem.* **2007**, *46*, 9018 – 9020.
[9] J. Rittle, M. T. Green, *Science* **2010**, *330*, 933 – 937.
[10] a) M. T. Green, *J. Am. Chem. Soc.* **1999**, *121*, 7939 – 7940; b) F. Ogliaro, N. Harris, S. Cohen, M. Filatov, S. P. de Visser, S. Shaik, *J. Am. Chem. Soc.* **2000**, *122*, 8977 – 8989; c) D. Li, Y. Wang, K. Han, *Coord. Chem. Rev.* **2012**, *256*, 1137 – 1150; d) S. P. de Visser, *Adv. Inorg. Chem.* **2012**, *64*, 1 – 31.
[11] K. Kühnel, N. Ke, M. J. Cryle, S. G. Sligar, M. A. Schuler, I. Schlichting, *Biochemistry* **2008**, *47*, 6552 – 6559.
[12] M. A. Sainna, S. Kumar, D. Kumar, S. Fornarini, M. E. Crestoni, S. P. de Visser, *Chem. Sci.* **2015**, *6*, 1516 – 1529.
[13] NIST Chemistry WebBook, *NIST Standard Reference Database*, Number 69 (Eds.: P. J. Linstrom, W. G. Mallard) National Institute of Standards and Technology, Gaithersburg MD, 20899, http://webbook.nist.gov.
[14] a) S. P. de Visser, S. Shaik, *J. Am. Chem. Soc.* **2003**, *125*, 7413 – 7424; b) S. P. de Visser, R. Latifi, L. Tahsini, W. Nam, *Chem. Asian J.* **2011**, *6*, 493 – 504.
[15] M. Asaka, H. Fujii, *J. Am. Chem. Soc.* **2016**, *138*, 8048 – 8051.
[16] S. Kumar, A. S. Faponle, P. Barman, A. K. Vardhaman, C. V. Sastri, D. Kumar, S. P. de Visser, *J. Am. Chem. Soc.* **2014**, *136*, 17102 – 17115.
[17] L. Ji, A. S. Faponle, M. G. Quesne, M. A. Sainna, J. Zhang, A. Franke, D. Kumar, R. van Eldik, W. Liu, S. P. de Visser, *Chem. Eur. J.* **2015**, *21*, 9083 – 9092.
[18] S. M. Pratter, C. Konstantinovics, C. L. M. DiGiuro, E. Leitner, D. Kumar, S. P. de Visser, G. Grogan, G. D. Straganz, *Angew. Chem. Int. Ed.* **2013**, *52*, 9677 – 9681; *Angew. Chem.* **2013**, *125*, 9859 – 9863.
[19] a) J. M. Mayer, *Acc. Chem. Res.* **1998**, *31*, 441 – 450; b) S. P. de Visser, *J. Am. Chem. Soc.* **2010**, *132*, 1087 – 1097.
[20] S. P. de Visser, L.-S. Tan, *J. Am. Chem. Soc.* **2008**, *130*, 12961 – 12974.
[21] D. Kumar, B. Karamzadeh, G. N. Sastry, S. P. de Visser, *J. Am. Chem. Soc.* **2010**, *132*, 7656 – 7667.
[22] W. J. Song, Y. O. Ryu, R. Song, W. Nam, *J. Biol. Inorg. Chem.* **2005**, *10*, 294 – 304.
[23] S. P. de Visser, *Chem. Eur. J.* **2006**, *12*, 8168 – 8177.
[24] a) J. M. Mayer, *Annu. Rev. Phys. Chem.* **2004**, *55*, 363 – 390; b) J. Kaizer, E. J. Klinker, N. Y. Oh, J.-U. Rohde, W. J. Song, A. Stubna, J. Kim, E. Münck, W. Nam, L. Que Jr., *J. Am. Chem. Soc.* **2004**, *126*, 472 – 473; c) J. Yoon, S. A. Wilson, Y. K. Jang, M. S. Seo, K. Nehru, B. Hedman, K. O. Hodgson, E. Bill, E. I. Solomon, W. Nam, *Angew. Chem. Int. Ed.* **2009**, *48*, 1257 – 1260; *Angew. Chem.* **2009**, *121*, 1283 – 1286; d) D. P. Goldberg, *Acc. Chem. Res.* **2007**, *40*, 626 – 634; e) Y. Kang, H. Chen, Y. J. Jeong, W. Lai, E. H. Bae, S. Shaik, W. Nam, *Chem. Eur. J.* **2009**, *15*, 10039 – 10046.
[25] a) S. Shaik, P. Milko, P. Schyman, D. Usharani, H. Chen, *J. Chem. Theory Comput.* **2011**, *7*, 327 – 339; b) D. Kumar, G. N. Sastry, S. P. de Visser, *J. Phys. Chem. B* **2012**, *116*, 718 – 730.
[26] a) S. S. Shaik, *J. Am. Chem. Soc.* **1981**, *103*, 3692 – 3701; b) S. Shaik, *Phys. Chem. Chem. Phys.* **2010**, *12*, 8706 – 8720.
[27] a) S. Shaik, D. Kumar, S. P. de Visser, *J. Am. Chem. Soc.* **2008**, *130*, 10128 – 10140; b) D. Kumar, R. Latifi, S. Kumar, E. V. Rybak-Akimova, M. A. Sainna, S. P. de Visser, *Inorg. Chem.* **2013**, *52*, 7968 – 7979.
[28] H. Saltzman, J. G. Sharefkin, *Organic Syntheses*, Wiley, Hoboken, **1973**, Collect. Vol. 5, p 658.
[29] a) M. Meot-Ner in *Gas Phase Ion Chemistry*, (Ed.: M. T. Bowers), Academic Press, New York, **1979**, Vol. 1; b) J. E. Bartmess, R. M. Georgiadis, *Vacuum* **1983**, *33*, 149 – 154.
[30] T. Su, W. J. Chesnavich, *J. Chem. Phys.* **1982**, *76*, 5183 – 5185.
[31] F. Angelelli, B. Chiavarino, M. E. Crestoni, S. Fomarini, *J. Am. Soc. Mass Spectrom.* **2005**, *16*, 589 – 598.
[32] M. J. Frisch, *Gaussian* 09, revision D.01; M. J. Frisch, G. W. Trucks, H. B. Schlegel, G. E. Scuseria, M. A. Robb, J. R. Cheeseman, G. Scalmani, V. Barone, B. Mennucci, G. A. Petersson, H. Nakatsuji, M. Caricato, X. Li, H. P. Hratchian, A. F. Izmaylov, J. Bloino, G. Zheng, J. L. Sonnenberg, M. Hada, M. Ehara, K. Toyota, R. Fukuda, J. Hasegawa, M. Ishida, T. Nakajima, Y. Honda, O. Kitao, H. Nakai, T. Vreven, J. A. Montgomery, Jr., J. E. Peralta, F. Ogliaro, M. Bearpark, J. J. Heyd, E. Brothers, K. N. Kudin, V. N. Staroverov, T. Keith, R. Kobayashi, J. Normand, K. Raghavachari, A. Rendell, J. C. Burant, S. S. Iyengar, J. Tomasi, M. Cossi, N. Rega, J. M. Millam, M. Klene, J. E. Knox, J. B. Cross, V. Bakken, C. Adamo, J. Jaramillo, R. Gomperts, R. E. Stratmann, O. Yazyev, A. J. Austin, R. Cammi, C. Pomelli, J. W. Ochterski, R. L. Martin, K. Morokuma, V. G. Zakrzewski, G. A. Voth, P. Salvador, J. J. Dannenberg, S. Dapprich, A. D. Daniels, O. Farkas, J. B. Foresman, J. V. Ortiz, J. Cioslowski, D. J. Fox, Gaussian, Inc., Wallingford, CT, 2004.
[33] a) A. D. Becke, *J. Chem. Phys.* **1993**, *98*, 5648 – 5652; b) C. Lee, W. Yang, R. G. Parr, *Phys. Rev. B* **1988**, *37*, 785 – 789.
[34] a) P. J. Hay, W. R. Wadt, *J. Chem. Phys.* **1985**, *82*, 270 – 283; b) W. J. Hehre, R. Ditchfield, J. A. Pople, *J. Chem. Phys.* **1972**, *56*, 2257 – 2261.

Received: September 14, 2016
Published online on November 15, 2016

© 2016 Wiley-VCH Verlag GmbH & Co. KGaA, Weinheim

Biomimetic Models Very Important Paper

International Edition: DOI: 10.1002/anie.201604412
German Edition: DOI: 10.1002/ange.201604412

Deformylation Reaction by a Nonheme Manganese(III)–Peroxo Complex via Initial Hydrogen-Atom Abstraction

Prasenjit Barman, Pranav Upadhyay, Abayomi S. Faponle, Jitendra Kumar, Sayanta Sekhar Nag, Devesh Kumar, Chivukula V. Sastri,* and Sam P. de Visser**

Abstract: *Metal–peroxo intermediates are key species in the catalytic cycles of nonheme metalloenzymes, but their chemical properties and reactivity patterns are still poorly understood. The synthesis and characterization of a manganese(III)–peroxo complex with a pentadentate bispidine ligand system and its reactivity with aldehydes was studied. Manganese(III)–peroxo can react through hydrogen-atom abstraction reactions instead of the commonly proposed nucleophilic addition reaction. Evidence of the mechanism comes from experiments which identify a primary kinetic isotope effect of 5.4 for the deformylation reaction. Computational modeling supports the established mechanism and identifies the origin of the reactivity preference of hydrogen-atom abstraction over nucleophilic addition.*

The chemistry of metal–dioxygen intermediates has attracted interest in the field of biological as well as bioinorganic chemistry communities for many decades. These complexes are key intermediates in the catalytic cycles of metalloenzymes that activate and utilize molecular oxygen for vital biological processes in the human body, including the metabolism of drugs and the biosynthesis of hormones.[1] Although many metalloenzymes use iron as the central cofactor, several actually use manganese instead. Biologically active manganese ions are included, for instance, in the oxygen-evolving complex of photosystem II,[2] but also in superoxide dismutase that catalyzes the detoxification of superoxide and hydrogen peroxide to water.[3] The manganese–peroxo intermediate has been postulated as an important intermediate in these catalytic cycles; however, as it is short-lived, there currently is no experimental evidence available. Therefore, synthetic biomimetic models have been developed that have a ligand architecture suitable for studies in solution but have a coordination sphere that resembles enzyme analogues and consequently may give insight into the chemical and spectroscopic properties of enzymatic intermediates and their reactivity patterns.[4]

In the past few years, several biomimetic metal–peroxo adducts of iron and manganese have been prepared and characterized with UV/Vis, electronic absorption, electron paramagnetic resonance (EPR), and X-ray absorption spectroscopy techniques.[5,6] Furthermore, reactivity patterns with model substrates were studied, which showed that these metal–peroxo species mainly react through nucleophilic addition reactions.[7,8] Recently, a nonheme manganese(III)–peroxo complex with cyclam-type ligand was spectroscopically characterized with electronic absorption, EPR, and X-ray absorption techniques. Moreover, the complex was shown to react with manganese(II) chloride to form manganese(IV)–oxo and manganese(III)–hydroxo complexes.[9]

Synthetic metal–peroxo complexes are known to react with aldehydes efficiently in a proposed nucleophilic reaction mechanism. However, an alternative mechanism, not considered previously, concerns a rate determining hydrogen-atom abstraction from the α-position prior to oxygen-atom transfer. Recent work on metal–bispidine ligand systems showed that these complexes react efficiently with substrates through hydrogen-atom abstraction, owing to their rigid ligand framework, and reaction rates could be monitored effectively over a broad temperature and concentration range.[10] Therefore, we decided to investigate the relative reactivity of the $[Mn^{III}(L^1)(O_2)]^+$ complex (Scheme 1) with aldehydes and study the possible nucleophilic addition versus hydrogen-atom abstraction mechanisms. In particular, we report the synthesis and characterization of a novel side-on manganese(III)–peroxo complex with a pentadentate bispidine N5 ligand, $[Mn^{III}(L^1)(O_2)]^+$ (**1**),[11] Scheme 1, and study its reactivity patterns with 2-phenylpropionaldehyde (2-PPA) and its α-deuterated form.

The starting manganese(II) complex, $[Mn^{II}(L^1)(ClO_4)_2]^{2+}$ (**2**), was synthesized by reacting $Mn^{II}(ClO_4)_2{\cdot}2CH_3CN$ with the pentadentate bispidine ligand (L^1) in CH_3CN under an argon atmosphere, in analogy to previously reported procedures.[12] Addition of 10 equivalents of H_2O_2 to a colorless solution containing $[Mn^{II}(L^1)(ClO_4)_2]^{2+}$ (**2**; 2 mM) and triethylamine (TEA; 2.5 equivalents) in an acetonitrile solution at 15 °C afforded a blue intermediate (**1**) with an absorption band at 605 nm ($\varepsilon = 270\ L\,mol^{-1}\,cm^{-1}$; with a half-life of about 60 minutes (Figure 1a; see the Supporting Information for experimental details). The blue intermediate is characterized with various spectroscopic techniques including UV/Vis, high-

[*] P. Barman, S. S. Nag, Dr. C. V. Sastri
Department of Chemistry, Indian Institute of Technology Guwahati
Assam, 781039 (India)
E-mail: sastricv@iitg.ernet.in
P. Upadhyay, J. Kumar, Dr. D. Kumar
Department of Applied Physics, School of Physical Sciences
Babasaheb Bhimrao Ambedkar University
Lucknow, 226025 (India)
E-mail: dkclcre@yahoo.com
A. S. Faponle, Dr. S. P. de Visser
Manchester Institute of Biotechnology and School of Chemical Engineering and Analytical Science, The University of Manchester
131 Princess Street, Manchester M1 7DN (UK)
E-mail: sam.devisser@manchester.ac.uk
Supporting information and the ORCID identification number(s) for the author(s) of this article can be found under http://dx.doi.org/10.1002/anie.201604412.

 © 2016 Wiley-VCH Verlag GmbH & Co. KGaA, Weinheim

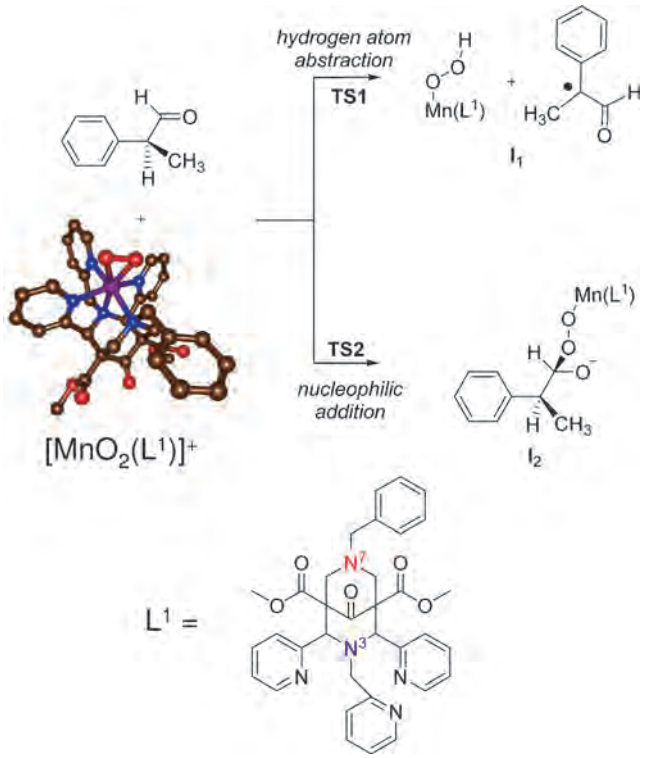

Scheme 1. Reactant complex $[Mn^{III}(L^1)(O_2)]^+$ and the possible reactivity patterns with 2-PPA substrate.

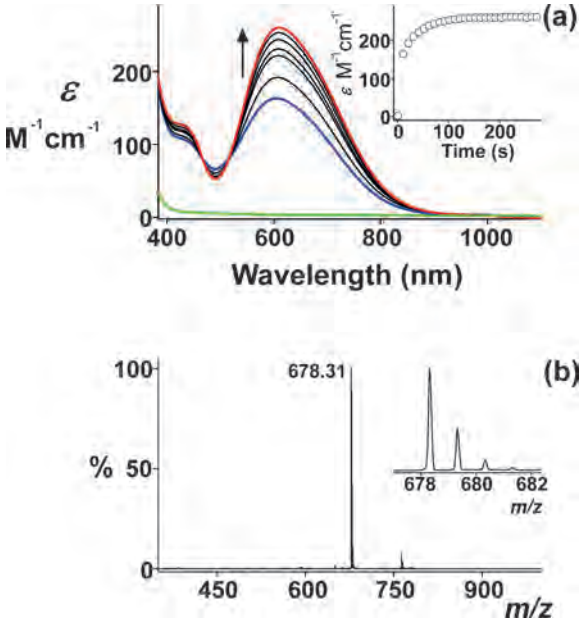

Figure 1. a) UV/Vis spectra of formation of **1** (2 mM) upon addition of $[Mn(L^1)]^{2+}$ (**2**; green line) in the presence of TEA (5 mM) and H_2O_2 (20 mM) in CH_3CN at 15 °C. Inset: the time trace for the formation the **1**. b) ESI-MS spectrum of **1**. Inset: the observed isotope distribution patterns for $[Mn(L^1)(O_2)]^+$.

resolution electrospray ionization-mass spectrometry (ESI-MS), and DFT. The ESI mass spectra of **1** exhibit a prominent ion peak with *m*/*z* 678.31, its isotopic distribution pattern

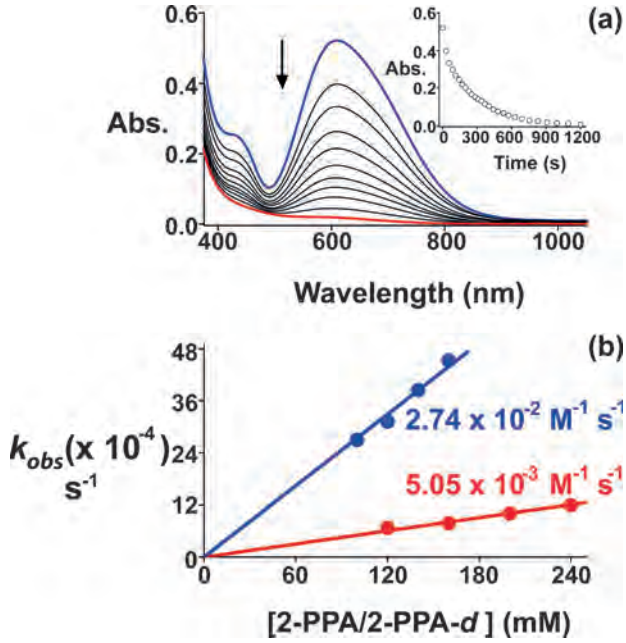

Figure 2. Kinetics of the reaction of **1** with 2-PPA: a) UV/Vis spectral changes of **1** (2 mM) upon addition of 2-PPA (160 mM) in the presence of TEA (5 mM) and hydrogen peroxide (20 mM) in CH_3CN at 15 °C. Inset: time course of the absorbance at 605 nm. b) Plot of k_{obs} against the concentration of 2-PPA and α-[D_1]-PPA (ca. 90%, D-enriched) and the derived second-order rate constant for the reaction of 2 mM **1** with substrate at various concentrations in CH_3CN at 15 °C for 2-PPA (●, blue) and α-[D_1]-PPA (●, red).

corresponds to $[Mn^{III}(L^1)(O_2)]^+$ (Figure 1b). These spectra are similar to those found by Jackson et al. on an analogous manganese(III)–peroxo complex.[9]

The nucleophilic and electrophilic character of **1** was then investigated in a reaction with 2-PPA as a substrate. Previous work showed that manganese(III)–peroxo complexes react with aldehydes to give the corresponding deformylated products by attacking the carbonyl group in a nucleophilic reaction.[6c,d] Upon addition of 2-PPA to **1** in CH_3CN at 15 °C, the intermediate decayed immediately and led to acetophenone as product (Figure 2a). The pseudo first-order rate constant of the decay of **1** increased linearly with increasing 2-PPA concentration, thus giving a second-order rate constant of 2.74×10^{-2} L mol^{-1} s^{-1}.

To establish whether the mechanism proceeds through a nucleophilic attack on the carbonyl group we used 2-methyl-2-phenylpropionaldehyde (2-Me-2-PPA) as a mechanistic probe. Upon addition of 2-Me-2-PPA to **1** at 15 °C, the intermediate decays at the rate of its natural decay. However, when the reaction solutions were analyzed with ESI-MS no deformylated products were observed. These results demonstrate that the manganese(III)–peroxo does not react with 2-PPA through a nucleophilic attack on the carbonyl group. As such, the work contradicts previous studies on the reactivity of nonheme and heme metal–peroxo complexes with aldehydes, that all reported a nucleophilic mechanism.[5b,6a,13]

To find out whether an alternative pathway was possible starting with an initial hydrogen-atom abstraction, we decided to investigate the reaction with α-[D_1]-PPA. Thus, upon

 © 2016 Wiley-VCH Verlag GmbH & Co. KGaA, Weinheim

addition of α-[D_1]-PPA (ca. 90%, D-enriched) to **1** in CH_3CN at 15 °C we determined a second-order rate constant of 5.05×10^{-3} L mol^{-1} s^{-1} (Figure 2b). Therefore, our kinetics studies establish the manganese(III)–peroxo complex to react with 2-PPA via a rate determining hydrogen-atom abstraction reaction from the α-position with a kinetic isotope effect (KIE) of 5.4.

To find further evidence of this novel reaction mechanism, we performed a radical trapping experiment with bromotrichloromethane using procedures reported previously.[14] Addition of 2-PPA to intermediate **1** in the presence of excess CCl_3Br (or CBr_4) in CH_3CN at 15 °C, leads to the formation of α-brominated product of the 2-PPA exclusively, which was confirmed by NMR analysis (Supporting Information). Consequently, our kinetics and reactivity studies clearly reveal a novel reaction mechanism between manganese(III)–peroxo complexes with aldehydes starting from an α-hydrogen-atom abstraction step.

To gain further insight into the rate determining step for the reaction of manganese(III)–peroxo with aldehydes, we decided to follow the experimental work up with a set of density functional theory calculations using previously reported procedures.[15] Two pathways were investigated, namely 1) hydrogen-atom abstraction by **1** from the α-position of 2-PPA; and 2) nucleophilic attack of the peroxo group on the carbonyl moiety of 2-PPA. The optimized geometries of the hydrogen-atom abstraction (^{5}**TS**$_{HA}$) and nucleophilic transition state (^{5}**TS**$_{NA}$) are given in the Supporting Information, Figures S15 and S18. Herein, we will focus on the analysis of the results and the understanding as to why the hydrogen-atom abstraction pathway is favorable. The hydrogen-atom abstraction barrier is relatively central with close values of the C–H and H–O distances and as expected happens with a large imaginary frequency for the C–H–O stretch typical for hydrogen-atom abstraction reactions.[16] In agreement with experimental observation the lowest barrier is ^{5}**TS**$_{HA}$ ($\Delta E + ZPE^{\ddagger} = 23.9$ kcal mol^{-1}). By contrast, the nucleophilic transition state (^{5}**TS**$_{NA}$) is well higher in energy ($\Delta E + ZPE^{\ddagger} = 28.7$ kcal mol^{-1}).

To understand the mechanistic preference of hydrogen-atom abstraction over nucleophilic addition, we devised a novel two-parabola curve crossing diagram to explain the reaction mechanism, which shows analogy to the valence bond curve crossing diagrams of Shaik.[17] Figure 3 shows details of the two-parabola curve crossing model. Thus, we consider the reaction along the reaction coordinate (x) that starts in the reactants (at $x = 0$) that is connected to another local minimum at $x = 1$ via a reaction barrier. We assume that the potential energy curve (y) can be described with a parabola with function $y_R = ax^2$ for the reactant complex and $y_P = bx^2 + cx + d$ for the products. If we assume that the transition state for the reaction happens at a reaction coordinate $x = {}^1/_2$ then these two curves will cross at $x = {}^1/_2$ and using the values for $y_P(0)$, $y_P({}^1/_2)$, $y_P(1)$, and $y_P'(1)$, we can derive an equation for the curve crossing energy (ΔE_{cross}) as a function of the Franck-Condon energy in the reactants

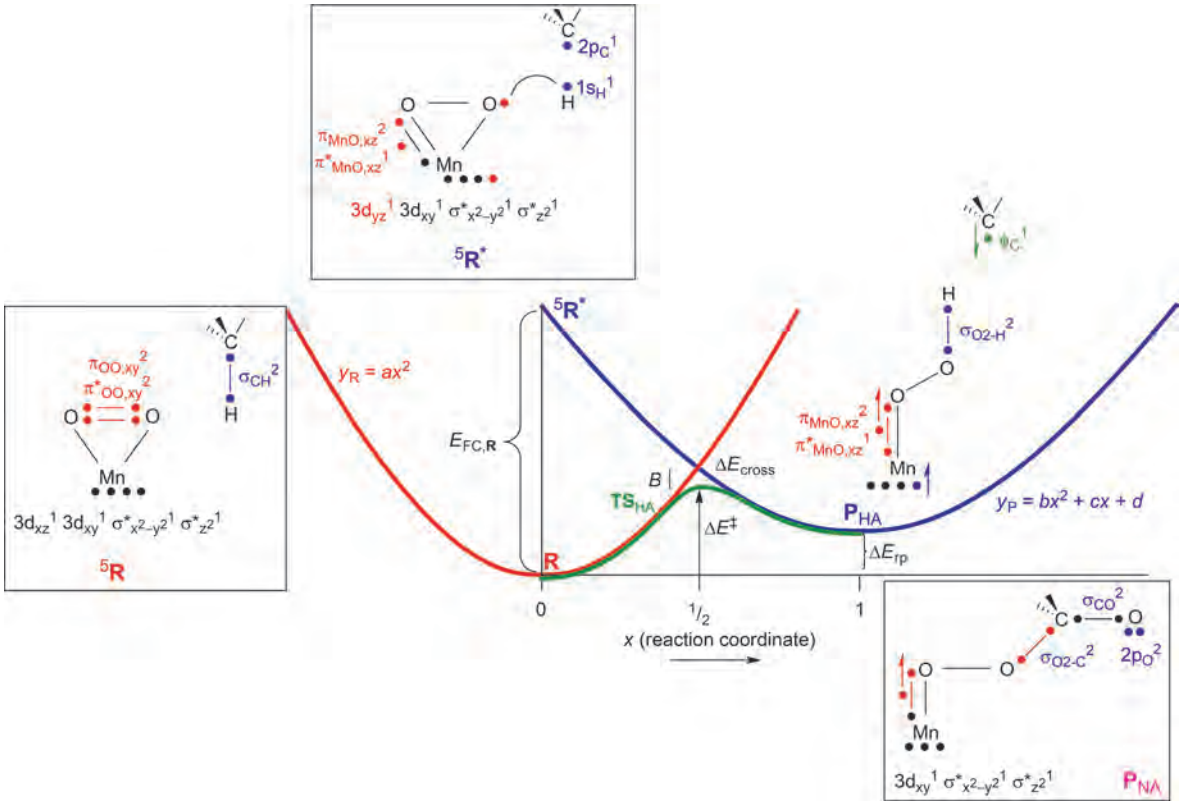

Figure 3. Two-parabola curve-crossing rationalization of the hydrogen-atom abstraction pathway in the reaction of **1** with 2-PPA. Bond orbital changes along the pathways highlighted. Dots represent electrons, and a line between two dots is a bond occupied by two electrons. Straight arrows indicate spin orbitals. Also shown is the VB representation of the alternative nucleophilic intermediate **P**$_{NA}$.

 © 2016 Wiley-VCH Verlag GmbH & Co. KGaA, Weinheim

($E_{FC,\mathbf{R}}$) and the driving force for the reaction (ΔE_{rp}), Equation (1), as defined in Figure 3.

$$\Delta E_{cross} = {}^1\!/_4 E_{FC,R} + {}^3\!/_4 \Delta E_{rp} \quad (1)$$

As shown previously using valence-bond curve-crossing diagrams,[17] the actual transition state is below the curve crossing energy by an amount B (the resonance energy), so that we can predict the value of the transition state based on estimates for $E_{FC,\mathbf{R}}$, ΔE_{rp}, and B with Equation (2).

$$\Delta E^{\neq}_{VB,HAT} = \Delta E_{cross} - B \quad (2)$$

We then analyzed the bond breaking and orbital changes between reactants, transition states and intermediates for the rate determining reaction step to predict the Franck–Condon energy between $^5\mathbf{R}$ and $^5\mathbf{R}$* and give details in Figure 3 in a valence bond format. These VB schemes were used previously to predict reactivities and rationalize reactivity trends.[18,19] Thus, the hydrogen-atom abstraction is accomplished through the breaking of the σ_{CH} bond of the substrate leading to atomic $2p_C$ and $1s_H$ orbitals, which energetically is equal to the bond dissociation energy of the C–H bond (BDE_{CH}). On the oxidant side of the reaction the $\pi_{OO,xy}{}^2$ $\pi^*_{OO,xy}{}^2$ pair of orbitals revert back to atomic orbitals and will cost an energy $E_{O=O}$. This will generate two doubly occupied 2p atomic orbitals, one on each oxygen atom. One of those 2p electrons on the terminal oxygen atom will form a bond with the incoming hydrogen atom, while the other electron is transferred to the $3d_{yz}$ orbital on Mn. Finally, the other 2p orbital on oxygen atom O1 will form a three-electron bond with the $3d_{xz}$ orbital on manganese and form the $\pi_{MnO,xz}$ and $\pi^*_{MnO,xz}$ pair of orbitals. The Franck–Condon energy, therefore, can be described as the sum of BDE_{CH}, $E_{O=O}$, and E_{ET}. We calculate a BDE_{CH} value for the α-position of 2-PPA of 80.3 kcal mol^{-1}, while the energy difference between the $\pi_{OO,xy}$ and $\pi^*_{OO,xy}$ was found to be 129.1 kcal mol^{-1} in the side-on manganese(III)–peroxo complex. Finally, the excitation energy from $\pi^*_{OO,xy}$ to $3d_{yz}$ was estimated to be 96.6 kcal mol^{-1}. The resonance energy, as before,[17] was taken as one half of the weakest bonds that are either broken or formed, which in this case is the sum of the O–H and Mn–O bond. As such, we estimate a hydrogen-atom abstraction barrier of 24.5 kcal mol^{-1}, which is in excellent agreement with the DFT barrier reported above.

Subsequently, we investigated the bond breaking and electron rearrangements for the nucleophilic addition reaction of which we show the VB representation of the product configuration in Figure 3. The reaction is initiated with the breaking of the carbonyl π-bond ($E_{PPA,\pi}$) as well as the splitting of the $\pi_{OO,xy}{}^2$ $\pi^*_{OO,xy}{}^2$ pair of orbitals on the peroxo group into atomic orbitals, that is, $E_{O=O}$. Similarly to the hydrogen-atom abstraction process the $2p_{O1}$ pair of electrons form a three-electron bond with the $3d_{xz}$(Mn) electron. Finally, a C–O bond is formed between peroxo and carbonyl. However, in contrast to the hydrogen-atom abstraction process no electron transfer from peroxo to manganese takes place. Instead, two electrons from the peroxo are donated into the C–O bond and the two electrons from the C=O π-bond move to the carbonyl oxygen atom. The resonance energy for the nucleophilic pathway is one-half of the sum of the C–O and Mn–O bonds that are formed, while a value of $E_{PPA,\pi=}$184.7 kcal mol^{-1} was estimated. Based on first principles, we estimate the nucleophilic barrier to be $\Delta E^{\neq}_{VB,NA} = 44.9$ kcal mol^{-1}.

The VB modeling, therefore, predicts that the side-on manganese–peroxo will react with 2-PPA through preferential α-hydrogen-atom abstraction rather than via nucleophilic addition. This is possible thanks to its small redox potential that enables efficient electron transfer from peroxo to manganese, which is a lower energy pathway than transferring an electron from peroxo to substrate carbonyl. Furthermore, the C–H bond strength of the substrate is only 80.3 kcal mol^{-1} and despite the fact that the side-on peroxo will give a weaker O–H bond, actually a strong Mn–O three-electron bond is formed, which gives the reaction to large driving force. By contrast, the nucleophilic pathway gains a rather weak C–O bond probably due to stereochemical repulsions of the ligand substituents interfering with the bond formation, so that this process overall will cost more energy. Therefore, the side-on manganese–peroxo with bispidine ligand system will preferentially react via hydrogen-atom abstraction rather than nucleophilic addition with aldehydes through its availability of low-energy metal 3d orbitals that can pick up an electron from the peroxo group. Further research will need to be done on synthetic and enzymatic manganese and iron–peroxo complexes, such as the aldehyde deformylating dioxygenases,[20] to find out whether this is a general mechanism.

Acknowledgements

Research support was provided by the Department of Science and Technology (SERB), India (EMR/2014/000279) to C.V.S. The National Service of Computational Chemistry Software (NSCCS) is acknowledged for CPU time to S.d.V. A.S.F. thanks the Tertiary Education Trust Fund Nigeria for a studentship. D.K. is the Ramanujan Fellow of the Department of Science and Technology, New Delhi (India).

Keywords: biomimetic models · density functional theory · enzyme models · hydrogen-atom abstraction · reaction mechanisms

How to cite: *Angew. Chem. Int. Ed.* **2016**, *55*, 11091–11095
Angew. Chem. **2016**, *128*, 11257–11261

[1] a) *Biomimetic Oxidations Catalyzed by Transition Metal Complexes* (Ed.: B. Meunier), Imperial College Press, London, **2000**; b) *Cytochrome P450: Structure, Mechanism, and Biochemistry*, 3rd ed. (Ed.: P. R. Ortiz de Montellano), Kluwer Academic/Plenum Publishers, New York, **2005**.

[2] a) D. J. Vinyard, G. M. Ananyev, G. C. Dismukes, *Annu. Rev. Biochem.* **2013**, *82*, 577–606; b) G. Renger, T. Renger, *Photosynth. Res.* **2008**, *98*, 53–80; c) J. Barber, *Q. Rev. Biophys.* **2003**, *36*, 71–89; d) P. E. M. Siegbahn, *Chem. Eur. J.* **2008**, *14*, 8290–8302.

[3] a) T. A. Jackson, T. C. Brunold, *Acc. Chem. Res.* **2004**, *37*, 461–470; b) B. R. Streit, B. Blanc, G. S. Lukat-Rodgers, K. R. Lukat-Rodgers, J. L. Dubois, *J. Am. Chem. Soc.* **2010**, *132*, 5711–5724;

 © 2016 Wiley-VCH Verlag GmbH & Co. KGaA, Weinheim

c) S. Hofbauer, C. Gruber, K. F. Pirker, A. Sündermann, I. Schaffner, C. Jakopitsch, C. Oostenbrink, P. G. Furtmüller, C. Obinger, *Biochemistry* **2014**, *53*, 3145 – 3157.
[4] a) M. Costas, M. P. Mehn, M. P. Jensen, L. Que, Jr., *Chem. Rev.* **2004**, *104*, 939 – 986; b) P. C. A. Bruijnincx, G. van Koten, R. J. M. Klein Gebbink, *Chem. Soc. Rev.* **2008**, *37*, 2716 – 2744; c) M. M. Abu-Omar, A. Loaiza, N. Hontzeas, *Chem. Rev.* **2005**, *105*, 2227 – 2252; d) S. V. Kryatov, E. V. Rybak-Akimova, S. Schindler, *Chem. Rev.* **2005**, *105*, 2175 – 2226.
[5] a) G. Roelfes, V. Vrajmasu, K. Chen, R. Y. N. Ho, J.-U. Rohde, C. Zondervan, R. M. la Crois, E. P. Schudde, M. Lutz, A. L. Spek, R. Hage, B. L. Feringa, E. Münck, L. Que, Jr., *Inorg. Chem.* **2003**, *42*, 2639 – 2653; b) J. Annaraj, Y. Suh, M. S. Seo, S. O. Kim, W. Nam, *Chem. Commun.* **2005**, 4529 – 4531; c) A. Thibon, J.-F. Bartoli, S. Bourcier, F. Banse, *Dalton Trans.* **2009**, 9587 – 9594; d) A. Mukherjee, M. A. Cranswick, M. Chakrabarti, T. K. Paine, K. Fujisawa, E. Münck, L. Que, Jr., *Inorg. Chem.* **2010**, *49*, 3618 – 3628; e) J. Cho, S. Jeon, S. A. Wilson, L. V. Liu, E. A. Kang, J. J. Braymer, M. H. Lim, B. Hedman, K. O. Hodgson, J. S. Valentine, E. I. Solomon, W. Nam, *Nature* **2011**, *478*, 502 – 505.
[6] a) J. Annaraj, J. Cho, Y.-M. Lee, S. Y. Kim, R. Latifi, S. P. de Visser, W. Nam, *Angew. Chem. Int. Ed.* **2009**, *48*, 4150 – 4153; *Angew. Chem.* **2009**, *121*, 4214 – 4217; b) D. F. Leto, S. Chattopadhyaay, V. W. Day, T. A. Jackson, *Dalton Trans.* **2013**, *42*, 13014 – 13025; c) M. Zlatar, M. Gruden, O. Y. Vassilyeva, E. A. Buvaylo, A. N. Ponomarev, S. A. Zvyagin, J. Wosnitza, J. Krzystek, P. Garcia-Fernandez, C. Duboc, *Inorg. Chem.* **2016**, *55*, 1192 – 1201; d) C.-M. Lee, C.-H. Chuo, C.-H. Chen, C.-C. Hu, M.-H. Chiang, Y.-J. Tseng, C.-H. Hu, G.-H. Lee, *Angew. Chem. Int. Ed.* **2012**, *51*, 5427 – 5430; *Angew. Chem.* **2012**, *124*, 5523 – 5526.
[7] W. Nam, *Acc. Chem. Res.* **2007**, *40*, 522 – 531.
[8] a) M. K. Coggins, J. A. Kovacs, *J. Am. Chem. Soc.* **2011**, *133*, 12470 – 12473; b) M. K. Coggins, V. Martin-Diaconescu, S. DeBeer, J. A. Kovacs, *J. Am. Chem. Soc.* **2013**, *135*, 4260 – 4272.
[9] H. E. Colmer, A. W. Howcroft, T. A. Jackson, *Inorg. Chem.* **2016**, *55*, 2055 – 2069.
[10] a) P. Comba, M. Kerscher, W. Schiek, *Prog. Inorg. Chem.* **2007**, *55*, 613 – 704; b) P. Comba, S. Fukuzumi, H. Kotani, S. Wunderlich, *Angew. Chem. Int. Ed.* **2010**, *49*, 2622 – 2625; *Angew. Chem.* **2010**, *122*, 2679 – 2682.
[11] L^1 = dimethyl-2,4-di(2-pyridyl)3-(pyridin-2-ylmethyl)-7-benzyl-3,7-diaza-bicyclo[3.3.1] nonan-9-one-1,5-dicarboxylate.
[12] P. Barman, A. K. Vardhaman, B. Martin, S. J. Wörner, C. V. Sastri, P. Comba, *Angew. Chem. Int. Ed.* **2015**, *54*, 2095 – 2099; *Angew. Chem.* **2015**, *127*, 2123 – 2127.
[13] a) M. S. Seo, J. Y. Kim, J. Annaraj, Y. Kim, Y.-M. Lee, S.-J. Kim, J. Kim, W. Nam, *Angew. Chem. Int. Ed.* **2007**, *46*, 377 – 380; *Angew. Chem.* **2007**, *119*, 381 – 384; b) R. A. Geiger, S. Chattopadhyay, V. W. Day, T. A. Jackson, *Dalton Trans.* **2011**, *40*, 1707 – 1715; c) Y. Goto, S. Wada, I. Morishima, Y. Watanabe, *J. Inorg. Biochem.* **1998**, *69*, 241 – 247; d) J. Cho, R. Sarangi, J. Annaraj, S. Y. Kim, M. Kubo, T. Ogura, E. I. Solomon, W. Nam, *Nat. Chem.* **2009**, *1*, 568 – 572; e) R. L. Shook, W. A. Gunderson, J. Greaves, J. W. Ziller, M. P. Hendrich, A. S. Borovik, *J. Am. Chem. Soc.* **2008**, *130*, 8888 – 8889; f) J. Cho, R. Sarangi, H. Y. Kang, J. Y. Lee, M. Kubo, T. Ogura, E. I. Solomon, W. Nam, *J. Am. Chem. Soc.* **2010**, *132*, 16977 – 16986; g) R. V. Ottenbacher, D. G. Samsonenko, E. P. Talsi, K. P. Bryliakov, *ACS Catal.* **2016**, *6*, 979 – 988; h) J. A. Kovacs, *Acc. Chem. Res.* **2015**, *48*, 2744 – 2753; i) C.-M. Lee, C.-H. Chuo, C.-H. Chen, C.-C. Hu, M.-H. Chiang, Y.-J. Tseng, C.-H. Hu, G.-H. Lee, *Angew. Chem. Int. Ed.* **2012**, *51*, 5427 – 5430; *Angew. Chem.* **2012**, *124*, 5523 – 5526.
[14] a) J. T. Groves, T. E. Nemo, *J. Am. Chem. Soc.* **1983**, *105*, 6243 – 6248; b) S. Rana, A. Dey, D. Maiti, *Chem. Commun.* **2015**, *51*, 14469 – 14472.
[15] a) A. K. Vardhaman, P. Barman, S. Kumar, C. V. Sastri, D. Kumar, S. P. de Visser, *Angew. Chem. Int. Ed.* **2013**, *52*, 12288 – 12292; *Angew. Chem.* **2013**, *125*, 12514 – 12518; b) S. P. de Visser, M. G. Quesne, B. Martin, P. Comba, U. Ryde, *Chem. Commun.* **2014**, *50*, 262 – 282; c) S. Kumar, A. S. Faponle, P. Barman, A. K. Vardhaman, C. V. Sastri, D. Kumar, S. P. de Visser, *J. Am. Chem. Soc.* **2014**, *136*, 17102 – 17115.
[16] L. Ji, A. S. Faponle, M. G. Quesne, M. A. Sainna, J. Zhang, A. Franke, D. Kumar, R. van Eldik, W. Liu, S. P. de Visser, *Chem. Eur. J.* **2015**, *21*, 9083 – 9092.
[17] a) S. S. Shaik, *J. Am. Chem. Soc.* **1981**, *103*, 3692 – 3701; b) S. Shaik, *Phys. Chem. Chem. Phys.* **2010**, *12*, 8706 – 8720.
[18] a) D. Kumar, B. Karamzadeh, G. N. Sastry, S. P. de Visser, *J. Am. Chem. Soc.* **2010**, *132*, 7656 – 7667; b) D. Kumar, R. Latifi, S. Kumar, E. V. Rybak-Akimova, M. A. Sainna, S. P. de Visser, *Inorg. Chem.* **2013**, *52*, 7968 – 7979.
[19] A. S. Faponle, M. G. Quesne, S. P. de Visser, *Chem. Eur. J.* **2016**, *22*, 5478 – 5483.
[20] L. J. Rajakovich, H. Nørgard, D. M. Warui, W.-C. Chang, N. Li, S. J. Booker, C. Krebs, J. M. Bollinger, Jr., M.-E. Pandelia, *J. Am. Chem. Soc.* **2015**, *137*, 11695 – 11709.

Received: May 6, 2016
Revised: June 3, 2016
Published online: July 8, 2016

 © 2016 Wiley-VCH Verlag GmbH & Co. KGaA, Weinheim

This is an open access article published under a Creative Commons Attribution (CC-BY) License, which permits unrestricted use, distribution and reproduction in any medium, provided the author and source are cited.

ACS Catalysis

Research Article

pubs.acs.org/acscatalysis

Origin of the Enhanced Reactivity of μ-Nitrido-Bridged Diiron(IV)-Oxo Porphyrinoid Complexes over Cytochrome P450 Compound I

Matthew G. Quesne,[†] Dhurairajan Senthilnathan,[‡,$] Devendra Singh,[&] Devesh Kumar,[&] Pascale Maldivi,[*,‡,◇] Alexander B. Sorokin,[*,⊥] and Sam P. de Visser[*,†]

[†]Manchester Institute of Biotechnology and School of Chemical Engineering and Analytical Science, The University of Manchester, 131 Princess Street, Manchester M1 7DN, United Kingdom

[‡]Univ. Grenoble Alpes, INAC-SCIB, Reconnaissance Ionique et Chimie de Coordination, F-38000 Grenoble, France

[◇]CEA, INAC-SCIB, F-38000 Grenoble, France

[$]Center for Computational Chemistry, CRD, PRIST University, Vallam, Thanjavur, Tamilnadu 613403, India

[&]Department of Applied Physics, Babasaheb Bhimrao Ambedkar University, School for Physical Sciences, Vidya Vihar, Rae Bareilly Road, Lucknow, Uttar Pradesh 226025, India

[⊥]Institut de Recherches sur la Catalyse et l'Environnement de Lyon (IRCELYON), UMR 5256, CNRS-Université Lyon 1, 2, av. A. Einstein, 69626 Villeurbanne, France

Supporting Information

ABSTRACT: μ-Nitrido-bridged diiron porphyrins and phthalocyanines are known to be efficient oxidants that are able to oxidize some of the strongest C−H bonds in nature, such as the one in methane. The origin of their catalytic efficiency is poorly understood, and in order to gain insight into the structural and electronic features of this chemical system, we performed a detailed and systematic study into their chemical properties and reactivities using density functional theory. Our work shows that μ-nitrido-bridged diiron porphyrins and phthalocyanines are highly active catalytic oxidants, which react with methane with very low reaction barriers and a rate-determining hydrogen-atom-abstraction step. Furthermore, the μ-nitrido-bridged diiron porphyrin and phthalocyanine complexes react with a free energy of activation that is more than 10 kcal mol^{-1} lower in energy than that found for cytochrome P450 Compound I, which is known to be one of the most efficient C−H hydroxylating agents in Nature. We have analyzed the electronic configuration of reactants and transition states in detail and have identified the key properties of the oxidants that lead to this rate enhancement. In particular, the potency of the oxidant is related to the orbital mixing patterns along the Fe−O axis, whereby the axial iron(IV)-nitrido group donates sufficient electron density to affect the pK_a of the oxo group as well as the strength of the O−H bond formed in the iron(IV)-hydroxo complex. The studies confirm that μ-nitrido diiron-oxo complexes should react via oxygen atom transfer readily even with strong C−H bonds as in methane. The results are analyzed with orbital diagrams, valence bond, and thermochemical cycles and explain the intricate details of the mechanism and the properties of the oxidant.

KEYWORDS: *biomimetic models, hydrogen abstraction, hydroxylation, iron, ligand effects*

INTRODUCTION

Cytochrome P450 enzymes are versatile enzymes in human physiology that mainly react with compounds through oxygen atom transfer, including the hydroxylation of C−H bonds. P450s activate their substrates with the aim to initiate their metabolism and detoxification but, on the other hand, also assist in biosynthetic pathways of e.g., hormones.[1] Thus, the biodegradation of long chain fatty acids and xenobiotics is catalyzed by P450 liver isozymes through a mechanism that is considered to proceed via an iron(IV)-oxo heme cation radical intermediate called Compound I (CpdI). To understand the fundamental features of the oxidant in the P450-enzyme-catalyzed reaction mechanism, synthetic models have been prepared that model the enzyme active site composition and coordination.[2] These so-called biomimetic model complexes enable one to study the reactivity patterns and the intrinsic chemical properties of iron porphyrins and gain understanding into the intricate structural and electronic features of the active site. Biomimetic work indeed confirmed a high-valent iron(IV)-oxo porphyrin cation radical to be the active oxidant in chemical transformations of substrates and ruled out many alternative suggestions.[3]

Recent biochemical studies isolated and characterized Compound I in a P450 isozyme and established the electronic

Received: November 30, 2015
Revised: January 11, 2016
Published: February 19, 2016

 © 2016 American Chemical Society

DOI: 10.1021/acscatal.5b02720
ACS Catal. 2016, 6, 2230−2243

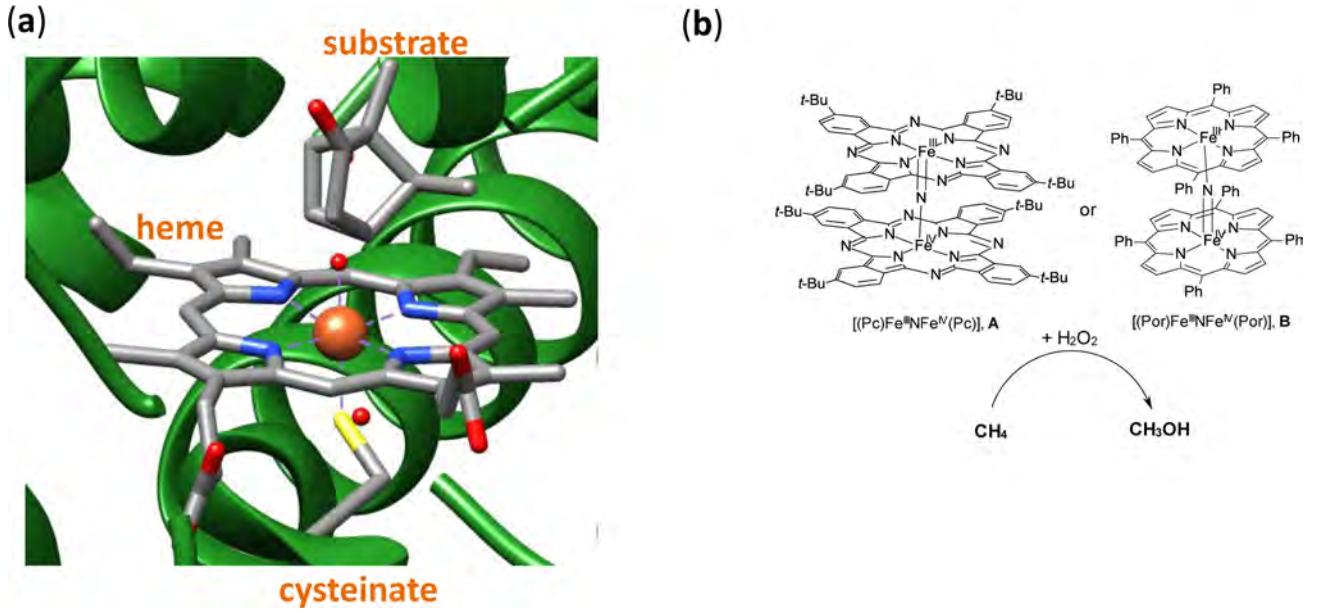

Figure 1. Comparative structural features of the active site of $P450_{cam}$ (a) and μ-nitrido-bridged diiron-oxo porphyrin and phthalocyanine complexes (b).

configuration with spectroscopic methods.[4] Although the P450s are known to be efficient and powerful oxidants in nature, native enzymes do not catalyze the conversion of methane to methanol, which requires the breaking of a very strong C−H bond with a bond dissociation energy (BDE) of 104.9 kcal mol^{-1}. However, using iodosylbenzene as an oxidant, it was shown that CYP153A6 is able to oxidize methane at room temperature, although very low turnover numbers of 0.02−0.05 were obtained.[5] On the other hand, guest/host activation of $P450_{BM3}$ with perfluorocarboxylic acids as decoy molecules enabled the oxidation of all short alkanes tested except for methane.[6,7]

Structurally, the P450s all contain an active heme group (Figure 1a) linked to the protein through a cysteinate bridge. To mimic the active site features of P450 CpdI, over the years, work on synthetic iron porphyrins has been performed with the aim of improving the oxidative power of the active species through modifications of the porphyrin scaffold. In particular, research was done to find a metal porphyrin system able to hydroxylate methane, but so far, only a few of these studies have been successful. Thus, several μ-nitrido-bridged diiron-oxo phthalocyanines and porphyrin (**A** and **B**, Figure 1b) complexes prepared using H_2O_2 or *m*-chloroperbenzoic acid (m-CPBA) are able to oxidize methane to methanol efficiently.[8,9] Experimental and computational studies on these exciting catalysts also show that these μ-nitrido-bridged systems are stable and maintain their dimerization throughout the reactions that they catalyze, unlike many of the μ-oxo dimers.[8]

It appears, therefore, that these diiron complexes are more potent oxidants than the active species of P450 enzymes, an example of which is shown using the active site structure from $P450_{cam}$ as taken from the protein databank[10] for structural comparison in Figure 1. The question is, then, what makes **A**/**B** a stronger oxidant than the enzyme, and what is the effect of the bridging μ-nitrido group on the chemical properties of the oxidant and the catalysis?

The origin of the reactivity differences between μ-nitrido-bridged diiron complexes and P450 CpdI may derive from a range of chemical and structural differences. First, some P450 isozymes have a tight substrate binding pocket and selectively activate substrates,[11] and the pocket may not be setup to hydroxylate methane efficiently, resulting in an uncoupling reaction. However, the use of decoy molecules, such as inert perfluorocarboxylic acids, makes it possible to accommodate methane into the cavity, but this did not lead to the oxidation of methane.[7] On the other hand, there are clear structural differences between **A**/**B** and P450 CpdI and particularly related to the axial ligand (i.e., cysteinate versus nitrido-iron(IV)-phthalocyanine).

It is known that the axial ligand of iron-porphyrins has a major effect on catalysis as well as on the spectroscopic properties (e.g., Fe−O vibrations) of the oxidant.[12] These biomimetic studies on axial ligand effects in iron(IV)-oxo complexes are in analogy to those derived from biochemical work on enzymes including heme-peroxidases and heme-monoxygenases. Thus, peroxidases generally have a histidine axial ligand coordinating the heme, whereas heme-monooxygenases such as the P450s have a cysteinate axial ligand. The axial ligand incurs a push- or a pull effect of electron density and thereby gives fundamental differences between the two heme enzyme classes.[13] This difference in function of P450 monoxygenases, heme peroxidases, and catalases has been assigned to the axial ligand bound to the heme.[14] In addition, biomimetic work has shown equatorial ligand may also have an effect on reactivity patterns but usually to a lesser extent than the axial ligand.[15]

Clearly, the reactivity and electronic properties of iron porphyrin/heme complexes is sensitive to the axial ligand bound and, in particular, experimental evidence appears to suggest that an axial μ-nitrido iron(IV) makes the oxidant so powerful that it can even hydroxylate methane. Therefore, we decided to investigate the electronic properties and reactivity patterns of μ-nitrido-bridged diiron-oxo complexes and find out the key factors that influence their catalytic activity with strong C−H bonds. The work shows that the axial μ-nitrido iron(IV) group has π and π^* orbitals that mix with the iron(IV)-oxo π/π^* orbitals and thereby make the oxidant more reactive.

DOI: 10.1021/acscatal.5b02720
ACS Catal. 2016, 6, 2230−2243

Scheme 1. Models of μ-Nitrido-Bridged Diiron Porphyrazine (1) and Porphyrin (2) as well as P450 CpdI (3) Investigated in This Work

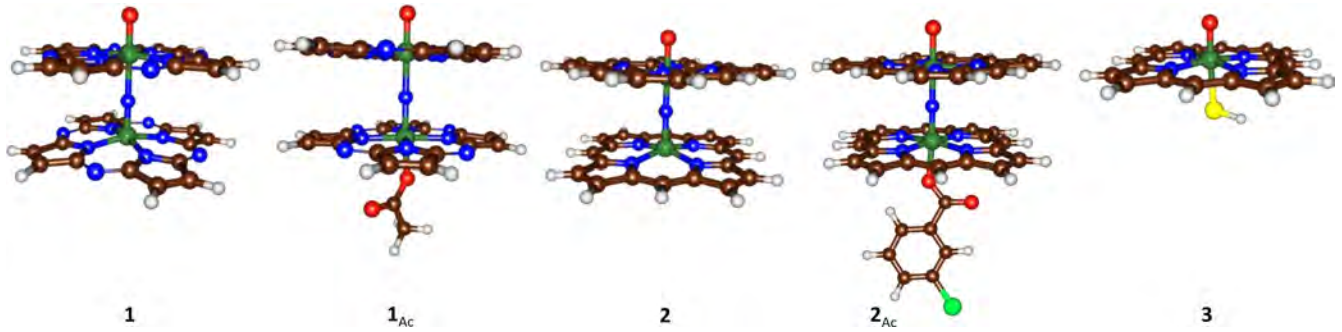

METHODS

Models. To understand the chemical properties of **A**/**B**, we created a number of models with different equatorial and axial ligands included, see Scheme 1. First, we created a "small" μ-nitrido-bridged diiron-oxo chemical structure of 68 atoms, whereby the phthalocyanine units were abbreviated to porphyrazine macrocycles (**1**). However, experimental Mössbauer studies indicated the possible presence of an anionic axial ligand in μ-nitrido-bridged high-valent diiron porphyrin oxo species,[9] when a concentrated solution of the complex and m-CPBA was used at very low temperatures. Although the presence of the axial ligand could not be ascertained under catalytic conditions in the experiments, we decided to include a model with an axial acid anion ligand and investigated its possible influence on the oxidizing properties of the oxo species in model $\mathbf{1}_{Ac}$. As a comparison, we also investigated the properties of μ-nitrido-bridged diiron-oxo porphyrin without an anionic axial ligand attached to Fe_2 (structure **2**) and with 3-chlorobenzoate ligated (structure $\mathbf{2}_{Ac}$) to reflect the use of m-CPBA experimentally. Structures **1** and **2** are overall charge neutral, whereas $\mathbf{1}_{Ac}$ and $\mathbf{2}_{Ac}$ have a total charge of −1.

A complete model with tetraphenylporphyrin (TPP) ligands ($\mathbf{2}_{TPP}$) was also studied, but the addition of substituents to the *meso*-position of the porphyrin had little effect on the optimized geometries and electronic configuration of the reactant complexes, see Supporting Information for details.

All structures and reactivities were compared with model complexes of P450 CpdI, which was modeled, as before,[16] as an iron(IV)-oxo-porphyrin cation radical ($\mathbf{3}_{SH}$, [Fe^{IV}(O) ($Por^{+\bullet}$)-SH]) but also with an elaborate cysteinate axial ligand description ($\mathbf{3}_{Cys}$, [Fe^{IV}(O) ($Por^{+\bullet}$)Cys]). In previous work, we extensively tested various enzyme models and compared those to results obtained from QM/MM studies and experiment.[17] Indeed, in recent work, model clusters were compared to QM/MM results with increasing QM size.[17b] The energy differences upon the barrier heights fluctuated within a range of a few kcal mol^{-1} and did not affect the shape of the landscape or the overall conclusions. The models discussed here were shown to reproduce QM/MM obtained results well and gave similar electronic configuration as well as reactivity patterns with barrier heights reproduced within 1.1 kcal mol^{-1}.[17a] For example, the charge and spin distributions of CpdI and the spin-state ordering and relative energies follow similar trends. In addition, studies on product isotope effects through bifurcation pathways gave excellent agreement with experimentally determined values.[18] The small model complexes used here enable one to understand the fundamental chemical differences between the active site of P450 and the synthetic μ-nitrido-bridged diiron-oxo complexes described here by elimination of the protein interactions. The P450 models were overall charge neutral and were calculated in the lowest-lying doublet and quartet spin states. Our study produced a comprehensive set of data of which the highlights are presented here, and all the details can be found in the Supporting Information.

Computational Procedures. The studies presented in this work used density functional theory methods as implemented in the Gaussian-09, Jaguar 7.8, and ORCA program packages.[19] The potential energy surfaces of the reaction of methane with **1**, $\mathbf{1}_{Ac}$, $\mathbf{2}_{TPP}$, and **3** on all low-lying spin states were initially explored at the UB3LYP level of theory[20] in Gaussian-09 in combination with a double-ζ quality LACVP basis set on iron with core potential and 6-31G on the rest of the atoms: basis set BS1.[21] Subsequently, full geometry optimizations of local minima and transition states were calculated at UB3LYP[20] and UBP86[22] level of theory and followed by an analytical frequency, see Supporting Information for details. Transition states were characterized with a single imaginary frequency for the correct mode, while local minima had real frequencies only. Subsequently, single-point calculations were done using a triple-ζ type LACV3P+ basis set on iron with core potential and 6-311+G* on the rest of the atoms: basis set BS2. Test calculations, whereby the geometries were optimized with UB3LYP/BS2 gave a potential energy profile of substrate hydroxylation that was within a few tenths of a kcal mol^{-1} from those obtained with UB3LYP/BS2//UB3LYP/BS1;[23] therefore, the rest of the systems were geometry optimized with UB3LYP/BS1.

As the experimental work used acetonitrile as a solvent, we performed solvent calculations using the polarized continuum model (PCM) with a dielectric constant of ε = 37.5 and a probe radius of 2.183 Å as implemented in Jaguar using a triple-ζ or better basis set on all atoms. Test calculations, whereby the geometry was optimized with a solvent model included, were performed (see Supporting Information Figure S19). However, this did not lead to changes in the electronic structure of the local minima and gave very similar optimized geometries.

Detailed geometry scans along one degree of freedom were performed between reactants and intermediates as well as between intermediates and products. These constrained geometry optimizations had one degree of freedom fixed, while all other coordinates were optimized. Geometry scans confirmed the reaction mechanisms and electron-transfer processes. Due to the size of the chemical systems investigated here, we only were able to run Intrinsic Reaction Coordinate (IRC) scans for a selection of systems. Those studies confirmed

DOI: 10.1021/acscatal.5b02720
ACS Catal. 2016, 6, 2230−2243

the mechanism and did not give results that were dramatically different from the geometry scans. The methods and procedures used in this work were extensively tested and benchmarked. For instance, in previous work, we reproduced experimental free energies of activation within 3 kcal mol^{-1},[24] but also experimental rate enhancements,[25] as well as kinetic isotope effects.[26]

The calculations of the reaction mechanism of methane with **2** and $\mathbf{2}_{Ac}$ were explored at the UB3LYP/BS1 level of theory in Jaguar with basis set BS1, and with Orca using a basis set that contains LANL2DZ on iron and 6-31G on the rest of the atoms. As for the porphyrazine species, stationary points were characterized with a frequency calculation with minima and transition states having all real or one imaginary frequency, respectively. In the latter case, the imaginary mode was displayed using the Orca Pltvib utility[19c] and GOpenMol[19d] to check its nature. Solvent effects were incorporated through the Conductor-like Screening Model (Cosmo) as implemented in Orca using a dielectric constant of 37 mimicking acetonitrile. Optimizations for both minima and transition states were done in solvent at the UB3LYP/BS1 level of theory, but the resulting structures, spin densities, and energy differences were very similar to the gas-phase results. Single points at the UB3LYP/BS2 level of theory were also performed on stationary points. Natural bond order analysis calculations were performed in Gaussian-09.

Structure **1** and $\mathbf{1}_{Ac}$ were investigated in Gaussian-09 on all low lying spin states: doublet, quartet, sextet and octet. As before,[27] we tested a range of ferromagnetically and antiferromagnetically coupled spin-state occupations of the reactant complexes. In particular, we attempted to create a P450 CpdI-type electronic configuration with a metal radical coupled to a ligand radical. However, all our attempts to generate an electronic state with ligand radical failed, and converted back to a state with only radical character on the OFe_1NFe_2 atoms. The same efforts were also done for **2** and $\mathbf{2}_{Ac}$ in Orca and Jaguar with the same effects: namely, no radical character on the macrocycle was obtained. Although several spin states were investigated, the doublet spin state was found to be the ground state and well separated from the nearest quartet, sextet, and octet spin states. Therefore, the other models were calculated in the doublet spin state only.

To test the reproducibility of the work, we did a range of single-point calculations on the UB3LYP/BS1 optimized geometries in Gaussian using a number of (unrestricted) density functional methods with basis set BS2, namely B3LYP,[20] BP86,[22] B3LYP* (B3LYP with 15% HF),[28] dispersion-corrected B3LYP (B3LYP-D3),[29] M06-L,[30] and PBE0.[31] In general, the same spin-state ordering is obtained regardless of the density functional method, and all chemical trends are reproduced. For clarity, we will focus in the main text on the B3LYP results, but all other results can be found in the Supporting Information.

Multireference perturbation theory of the N-electron valence type (NEVPT2) was applied to test the electronic configuration of the reactant and radical intermediate complexes. These calculations were done in Orca using procedures described previously.[32]

Kinetic Isotope Effects. We estimated the kinetic isotope effect (KIE) for the hydrogen-atom-abstraction reactions by replacing one or more of the hydrogen atoms of the substrate by deuterium atoms. Thus, the ratio of the rate constants of the substrate and the deuterated substrate (k_H/k_D) is a measure of the KIE, whereby we estimated the primary KIE for replacing the transferring hydrogen atom by deuterium as well as the secondary KIE, where the other hydrogen atoms of the substrate were replaced.[33] Semiclassical KIEs (eq 1) were estimated from the Eyring equation using the free energies of activation ($\Delta G^{\ddagger}_H$) of the deuterium substituted and reference systems.

$$KIE_E = k_H/k_D = \exp\{(\Delta G^{\ddagger}_D - \Delta G^{\ddagger}_H)/RT\} \quad (1)$$

In this equation, R is the gas constant, and T the temperature (298.15 K). Further corrections due to tunneling were obtained from the Wigner model (KIE_W, eq 2) by multiplying KIE_E with the tunneling ratio (Q_{tH}/Q_{tD}, eq 3) as follows:

$$KIE_W = KIE_E \times Q_{tH}/Q_{tD} \quad (2)$$

$$Q_t = 1 + (h\nu/k_BT)^2/24 \quad (3)$$

Here, k_B is Boltzmann's constant, h is Planck's constant, and ν is the magnitude of the imaginary frequency in the transition state. Kinetic isotope effects were calculated using the data from the Gaussian frequency calculations for the hydrogen-atom-abstraction process from methane by **1**, $\mathbf{1}_{Ac}$ and **3**.

Thermochemistry. The O−H and C−H bond dissociation energies (BDE_{OH} and BDE_{CH}) were determined from the relative energy (ΔE + ZPE + E_{solv}) for the following two equations:

$$Fe^{IV} = O(L) + H^{\bullet} \rightarrow Fe^{III}OH(L) + BDE_{OH} \quad (4)$$

$$A^{\bullet} + H^{\bullet} \rightarrow A - H + BDE_{CH} \quad (5)$$

Electron affinities (EA) and ionization energies (IE) reported here are adiabatic values calculated with UB3LYP/BS2 with ZPE and solvent included.

RESULTS

In this work, we focus on the chemical properties of the μ-nitrido bound diiron complexes and their reactivity with methane and, in particular, aim to elucidate why **A**/**B** react faster by hydrogen atom abstraction than P450 CpdI. We used extensively benchmarked and calibrated methods, which on analogous chemical systems are known to give the correct spin-state ordering and kinetics.[34] Subsequently, the electronic properties and the origin of the reactivity differences of **1**/**2** versus **3** were elucidated through thermochemical cycles, valence bond schemes and electronic properties of the various species involved.

Substrate Hydroxylation Mechanism. Let us start with evaluating the reactivity differences of methane hydroxylation by **1**, $\mathbf{1}_{Ac}$, **2**, $\mathbf{2}_{Ac}$, and **3** as obtained with B3LYP. We investigated the methane hydroxylation by **1**, $\mathbf{1}_{Ac}$, **2**, and $\mathbf{2}_{Ac}$ and compare the obtained result with those calculated previously for $[Fe^{IV}(O)(Por^{+\bullet})SH]$ or **3**.[35] We initially created a long-range complex (**Re**) of structures **1**, $\mathbf{1}_{Ac}$, **2**, and $\mathbf{2}_{Ac}$ with methane and optimized the geometries in the doublet, quartet, sextet, and octet spin states. However, the doublet spin state was the ground state in isolated reactants as well as the reactant complexes and remained the lowest-lying spin state along the full reaction mechanism. The results of the alternative spin states are given in the Supporting Information Figures S2−S4 and S6−S8, Tables S5 and S9−S16.

The reaction is stepwise with an initial hydrogen atom abstraction via transition state $\mathbf{TS}_{HA}$ to form the radical

DOI: 10.1021/acscatal.5b02720
ACS Catal. 2016, 6, 2230−2243

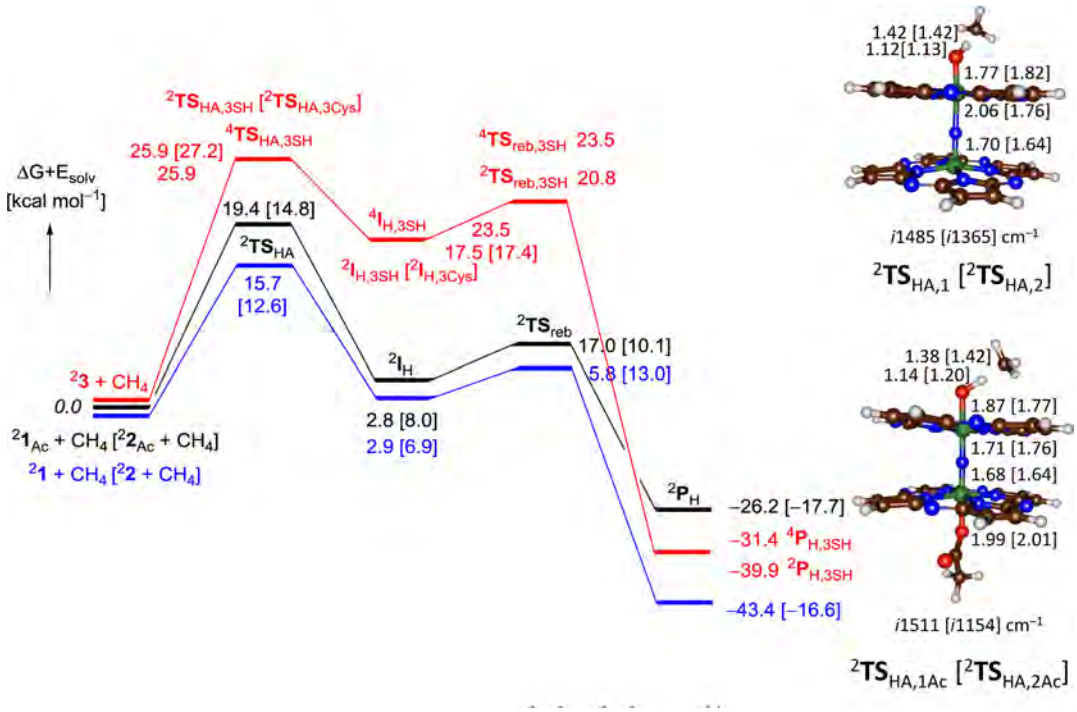

Figure 2. DFT calculated methane hydroxylation pathway by $^{2}\mathbf{1}$, $^{2}\mathbf{1}_{Ac}$, $^{2}\mathbf{2}$, $^{2}\mathbf{2}_{Ac}$, and $^{2,4}\mathbf{3}$. Data for $\mathbf{1}/\mathbf{1}_{Ac}$ and **3** were calculated in Gaussian at the UB3LYP/BS2//UB3LYP/BS1 level of theory, whereas the values for $\mathbf{2}/\mathbf{2}_{Ac}$ are obtained in Orca at UB3LYP/BS2//UB3LYP/BS1. Free energies are in kcal mol^{-1} and include ZPE, entropic, thermal, and solvent corrections. Also shown are optimized geometries of the rate-determining transition states with bond lengths in Å and the imaginary frequency of the **TS** in wave numbers. Data for model $\mathbf{1}/\mathbf{2}$ are given in blue, $\mathbf{1}_{Ac}/\mathbf{2}_{Ac}$ in black and values for complex **3** are shown in red.

intermediate $\mathbf{I}_{H}$, which is a complex of iron(IV)-hydroxo with $CH_3^{\bullet}$. In the next step, the OH rebounds to the $CH_3^{\bullet}$ group via transition state $\mathbf{TS}_{reb}$ to form the methanol-bound product complex $\mathbf{P}_{H}$. In all cases, $\mathbf{TS}_{HA}$ is the rate-determining reaction step, and $\mathbf{TS}_{reb}$ is smaller. This is in agreement with previous aliphatic hydroxylation mechanisms for iron(IV)-oxo complexes.[36]

Figure 2 shows the free energy landscape for methane hydroxylation by $^{2}\mathbf{1}$, $^{2}\mathbf{1}_{Ac}$, $^{2}\mathbf{2}$, $^{2}\mathbf{2}_{Ac}$, and $^{2,4}\mathbf{3}$. For comparison, in previous work, a free energy of activation of 25.9 kcal mol^{-1} in solvent using the same computational methods was obtained for the reaction of $[Fe^{IV}(O)(Por^{+\bullet})SH] + CH_4$.[35b] However, the free energy of activation of hydrogen atom abstraction from methane by **1**, in contrast, only has a value of $\Delta G^{\ddagger}$ = 15.7 kcal mol^{-1}, which raises to 19.4 kcal mol^{-1} when acetate binds as an axial ligand. The ratio of the rate constants for methane hydroxylation by **3** versus **1** would imply a rate enhancement of about 10^7 for this reaction. As such, it appears that μ-nitrido-bridged diiron-oxo complexes are highly effective oxidants of substrate hydroxylation reactions and should be able to hydroxylate methane at ambient temperatures and pressures. Indeed, experimental work of Sorokin and co-workers confirmed methanol products from the reaction of μ-nitrido-bridged diiron phthalocyanine with methane.[8b,c] To further ascertain that this rate enhancement is not due to the choice of the density functional method, we repeated the calculations of all rate-determining steps with alternative density functional methods (see Supporting Information Tables S9, S10, and S60−S63 for details). However, in all cases, the free energy of activation for the reaction of methane with $\mathbf{1}/\mathbf{1}_{Ac}$ was considerably lower than that with a P450 CpdI model.

In order to test whether the rate enhancement from **3** to $\mathbf{1}/\mathbf{1}_{Ac}$ is due to the phthalocyanine ligand or the μ-nitrido-bridged diiron arrangement, we decided to also investigate the reactivity of the analogous porphyrin complexes $\mathbf{2}/\mathbf{2}_{Ac}$. As follows from the data shown in Figure 2, the same trend is obtained for the couple $^{2}\mathbf{2}/^{2}\mathbf{2}_{Ac}$, where the hydrogen-atom-abstraction barrier is raised by 2.2 kcal mol^{-1} for the latter. Consequently, all μ-nitrido-bridged diiron-oxo complexes (**1**, $\mathbf{1}_{Ac}$, **2**, $\mathbf{2}_{Ac}$) give low free energies of activation for methane hydroxylation, which implies that they should catalyze the reaction at room temperature, which is in agreement with experimental data.[8b]

Geometrically, all transition states are product-like with considerably longer C−H than O−H distances. Previous studies on aliphatic hydrogen abstraction reactions by iron(IV)-oxo complexes showed that methane hydroxylation generally proceeds with a barrier characterized by a short O−H distance, a much longer C−H distance, and a geometry resembling the radical intermediate.[35,36] The two Fe_1−N and Fe_2−N distances for the bridging nitrido group in $\mathbf{TS}_{HA,1}$ and $\mathbf{TS}_{HA,1Ac}$ are considerably different due to the electron-donating properties of the acetate ligand that pull Fe_2 into the plane of the phthalocyanine/porphyrin ring.

All hydrogen-atom-abstraction transition states are characterized with a single large imaginary frequency of well over i1100 cm^{-1} that reflects a mode for the asymmetrical stretch vibration along the O−H−C bond and hence corresponds to a hydrogen atom transfer. These values are typical of hydrogen-atom-abstraction barriers by metal-oxo oxidants and implicate a narrow barrier with potentially significant amount of tunneling.[37] The nature of the barrier and its connection to reactants and radical intermediates was further established by initially running constraint geometry scans (with one degree of freedom

DOI: 10.1021/acscatal.5b02720
ACS Catal. 2016, 6, 2230−2243

fixed) as well as IRCs, see Supporting Information for details, which confirmed the mechanism shown in Figure 2.

Interestingly, we find a considerably larger dipole moment for $\mathbf{TS}_{HA,1}$ of 4.7 D versus that for $\mathbf{TS}_{HA,3}$ [0.8 D], and additionally, it points in the opposite direction. Similar dipole moments are found for the reactant complexes. Obviously, an enlarged dipole moment will lead to stabilization of the complex in solution and interactions with polar solvent molecules, which may affect the relative reactivities through their environment. To find further electronic factors that contribute to the transition state energy, we calculated the change in polarizability volume ($\delta\alpha$) for the geometric change from reactants to $\mathbf{TS}_{HA}$, eq 6.[38] The value $\delta\alpha$ was calculated from the difference in polarizability volume between the transition state structure and those of the isolated reactants.

$$\delta\alpha_i = \alpha_{TS} - \alpha_i - \alpha_{CH4},\ \mathbf{i} = \mathbf{1}, \mathbf{1}_{Ac} \quad (6)$$

Previously, we showed that the polarizability change correlates linearly with enthalpy change for chemical reactions as well as for transition state formation.[23,39] This polarizability change is then plotted as a function of barrier height for a range of hydrogen-atom-abstraction reactions by [Fe^{IV}(O) ($Por^{+\bullet}$)-SH] in the doublet and quartet spin states (Figure 3). As can be

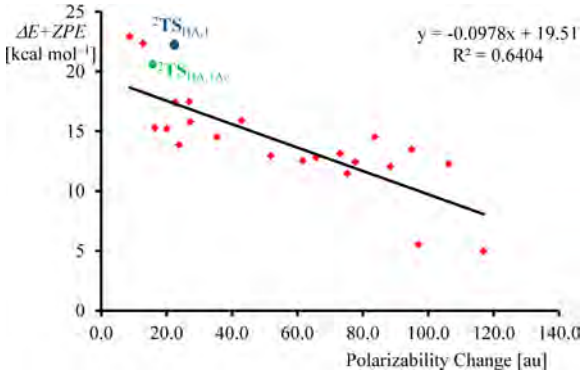

Figure 3. Plot of the change in polarizability volume ($\delta\alpha$) as a function of barrier height (ΔE + ZPE) for the reaction of [Fe^{IV}(O) ($Por^{+\bullet}$)SH] with aliphatic substrates.

seen, the correlation is reasonably linear, which implies that all transition states are characterized as electronically similar and are connected through the same electron-transfer processes. The calculated values for $^2\mathbf{TS}_{HA,1}$ and $^2\mathbf{TS}_{HA,1Ac}$ fit the trend and support the obtained correlation.

As the rate-determining step in the reaction mechanism is a hydrogen atom abstraction, we investigated the kinetic isotope effects (KIE) by replacing one or more hydrogen atoms of the CH_4 reactant with deuterium atoms. Thus, we replaced the transferring hydrogen atom of methane by deuterium to get the primary KIE but also the three other hydrogen atoms (secondary KIE); lastly, we replaced all hydrogen atoms of CH_4 by deuterium atoms and the obtained results for reactions with **1**, $\mathbf{1}_{Ac}$, and **3** are given in Table 1. We calculated KIE values using the semiclassical Eyring model but also the Wigner model with tunneling corrections included. The KIE values are dependent on the magnitude of the imaginary frequency in the transition state and the free energy of activation, see Methods section for details. Although a considerably larger imaginary frequency in the transition state for $^2\mathbf{TS}_{HA,1}$ (i1485 cm^{-1}) is found as compared to $^{2,4}\mathbf{TS}_{HA,3}$ (values of i946 and i791 cm^{-1} for doublet and quartet spin states, respectively), actually, the

Table 1. Calculated Kinetic Isotope Effects Using the Eyring (Wigner) Models for Replacing Hydrogen Atoms in Methane by Deuterium Atoms[a]

oxidant	O−D−CH_3	O−H−CD_3	O−D−CD_3
1	7.0 (9.9)	2.2 (2.3)	16.3 (23.4)
$\mathbf{1}_{Ac}$	7.1 (10.1)	1.4 (1.4)	10.3 (14.9)
3	5.7 (9.2)	1.4 (2.3)	8.6 (13.7)

[a]Data from Gaussian frequency calculation at 298 K for doublet spin states.

Wigner KIE effects are not dramatically different for the two complexes. Nevertheless, replacement of the transferring hydrogen atom by deuterium leads to major differences in KIE values. We calculated KIE values of 7.0 (9.9) using the Eyring (Wigner) models for **1** for replacement of the transferring hydrogen atom by deuterium. Note that a significant secondary KIE value of about 1.4−2.3 for replacing the nontransferrable hydrogen atoms by deuterium atoms is obtained for all systems. The results in Table 1 show that **1** should give a considerably larger KIE value than $\mathbf{1}_{Ac}$ and **3** for hydrogen atom abstraction from unactivated, sp^3 hybridized, carbon centers.

DISCUSSION

As shown in the previous section and in agreement with experimental observation, μ-nitrido-bridged diiron-oxo complexes are efficient oxidants of aliphatic hydroxylation reactions and can even hydroxylate methane at room temperature. To understand the origin of these reactivity differences with P450 CpdI, which does not hydroxylate methane at room temperature, we did a detailed analysis of the physicochemical properties of the reactants and an evaluation of the obtained transition states, which will be covered in detail in the following.

Electronic Configuration of the Reactants. To gain insight into the nature of the reactivity differences observed above, let us start our analysis with an evaluation of the electronic configuration of the isolated reactants (i.e., without methane) and compare $\mathbf{1}/\mathbf{1}_{Ac}/\mathbf{2}/\mathbf{2}_{Ac}$ on the one hand with **3** on the other hand.

Figure 4 displays the orbital energy levels of P450 CpdI, that is, [Fe^{IV}(O) ($Por^{+\bullet}$)Cys], and how the mixing with an axial iron(IV)-nitrido group of [Fe^{IV}(N) (Por)] gives the new orbital energy levels for the μ-nitrido diiron-oxo complexes **1** and **2**. Thus, P450 CpdI is a triradical system with two unpaired electrons in π^*_{FeO} orbitals and a third one in a heme orbital with a_{2u} symmetry (Figure 4: left-hand-side). These three orbitals are either ferromagnetically coupled into a quartet spin state or antiferromagnetically coupled into a doublet spin state and usually DFT calculations find the two states within 1 kcal mol^{-1}.[17,40]

The π_{FeO}/π^*_{FeO} orbitals reflect the interaction of the $3d_{xz}/3d_{yz}$ atomic orbitals on iron with the $2p_x/2p_y$ orbitals on oxygen, whereas the a_{2u} orbital is a nonbonding heme orbital. Addition of an axial ligand to CpdI leads to mixing of orbitals on the ligand with both the a_{2u} and π^*_{FeO} orbitals. In particular, a cysteinate axial ligand results in mixing of the $3p_z$ orbital of the sulfur atom with the a_{2u} orbital on the porphyrin and the antibonding combination ($3p_z-a_{2u}$) is raised in energy with respect to the original a_{2u} orbital.[41] This change in orbital energy lowers the electron affinity of CpdI and it has been

DOI: 10.1021/acscatal.5b02720
ACS Catal. 2016, 6, 2230−2243

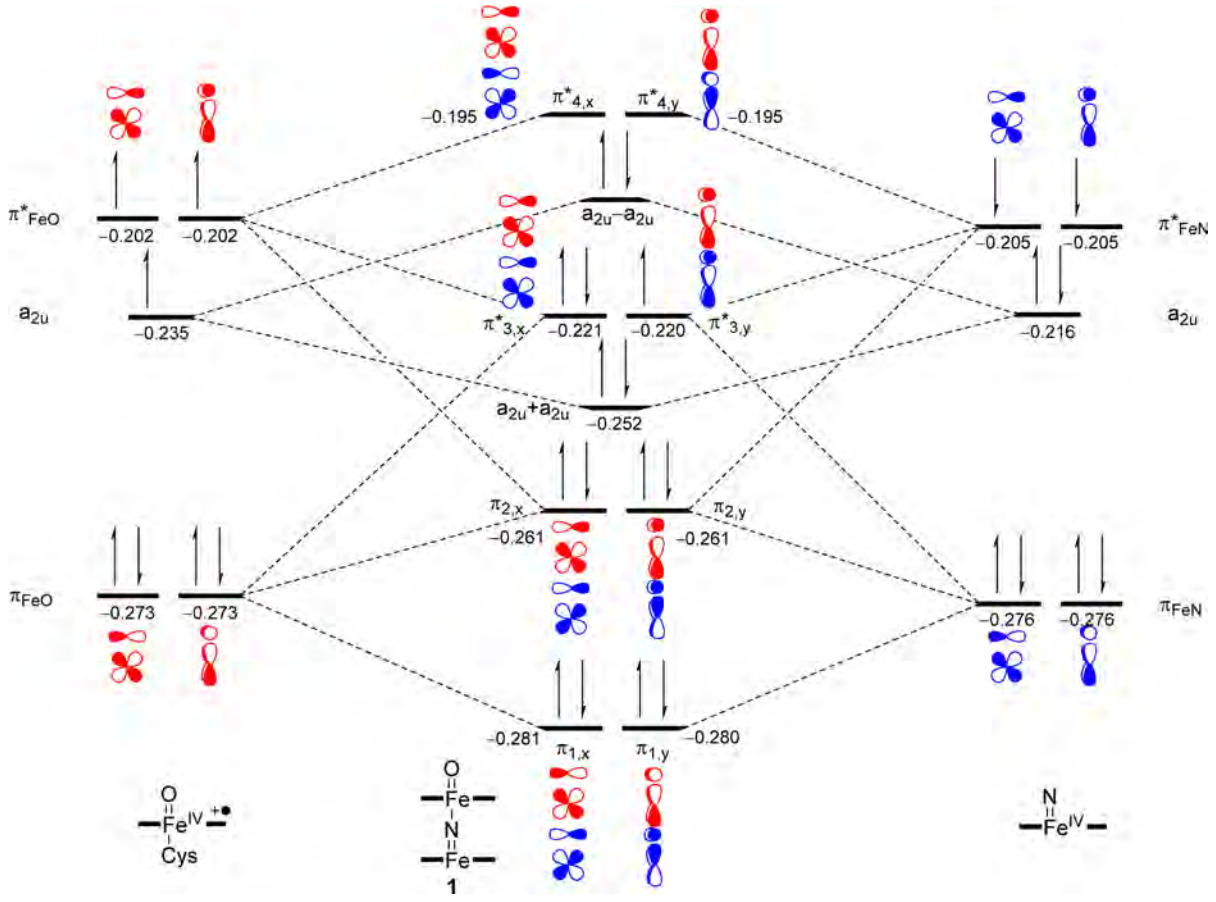

Figure 4. Orbital energy splitting of μ-nitrido-bridged diiron(IV)-oxo phthalocyanine and porphyrin species and how the orbital mixing originates from iron(IV)-oxo porphyrin cation radical (left-hand-side) and iron(IV)-nitrido (right-hand-side). Orbital energies are given for ^{2}**2** in au.

proposed that this could make it a better oxidant than an iron(IV)-oxo porphyrin without axial ligand.[26,41]

On the right-hand-side of Figure 4, we give the orbital occupation of the iron(IV)-nitrido group, which is essentially the one-electron reduced form of CpdI with orbital occupation $\pi_{FeN,xz}^{2}\ \pi_{FeN,yz}^{2}\ a_{2u}^{2}\ \pi^*_{FeN,xz}^{1}\ \pi^*_{FeN,yz}^{1}$. The iron(IV)-nitrido group has the same orbital shapes as the iron(IV)-oxo species with a pair of π_{FeN}/π^*_{FeN} orbitals and a close-lying a_{2u} orbital.

Upon formation of a μ-nitrido-bridged diiron-oxo complex, the orbitals along the molecular z-axis (i.e., along the O−Fe_1−N−Fe_2 axis) will mix and form a new set of orbitals, as shown in the middle panel of Figure 4. Thus, addition of an axial iron(IV)-nitrido group to an iron(IV)-oxo porphyrin cation radical changes the orbital interactions and energies along the z-axis dramatically. Due to alignment of the O, Fe_1, N, and Fe_2 atoms along the molecular z-axis in **1**, their atomic orbitals interact and form new molecular orbitals that span the complete molecular z-axis. The orbital interactions of the two iron $3d_{xz}/3d_{yz}$ atomic orbitals with the $2p_x/2p_y$ orbitals on the oxo and bridging nitrido groups leads to a set of bonding and antibonding combinations; namely four sets of molecular orbitals along the x and y-axis labeled as $\pi_{1,x}/\pi_{1,y}$, $\pi_{2,x}/\pi_{2,y}$, $\pi^*_{3,x}/\pi^*_{3,y}$, and $\pi^*_{4,x}/\pi^*_{4,y}$. In addition, the porphyrin π-orbitals, such as the a_{1u} and a_{2u} orbitals, mix and form bonding and antibonding sets of orbitals due to π-stacking interactions as well as the mixing with the $\sigma_{z2}/\sigma^*_{z2}$ orbitals on Fe_1 and Fe_2.

The orbital diagram in Figure 4 shows that complexes **1**/**2** should have a dominant doublet spin state with a singly occupied $\pi^*_{3,y}$ orbital and a closed-shell ligand system. This contrast of the orbital occupation and energy levels of P450 CpdI, where the high-lying π^*_{FeO} orbitals are close in energy to the a_{2u} orbital, so that a combination of ferromagnetically and antiferromagnetically coupled spin states are possible. In structures **1**/$\mathbf{1}_{Ac}$/**2**/$\mathbf{2}_{Ac}$, the separation between the a_{2u} and π^*_3 orbitals is large, and no low-lying states were found with radical character spread over metal and ligands. In particular, antiferromagnetic (or ferromagnetic) coupling of spin states where unpaired electrons on the metal(s) is coupled to an unpaired electron on the porphyrazine group was attempted but did not converge to stable, low-energy conformations. Furthermore, the spin-state ordering, relative energies, and group spin densities of the calculated doublet, quartet, sextet, and octet spin states of **1** and $\mathbf{1}_{Ac}$ all show little radical character on the porphyrazine ligand (see Supporting Information, Tables S11 and S15).

Experimental Mössbauer spectra implicated a doublet spin ground state, which is reproduced excellently by our calculations. We attempted to create an electronic state with porphyrazine or porphyrin radical by swapping molecular orbitals or imposing local spin polarizations. Therefore, an extensive series of additional calculations were done to locate the alternative $^2A_{2u}$ state with occupation (core) $\pi^*_{3,x}{}^2\ \pi^*_{3,y}{}^2\ \pi^*_{4,x}{}^0\ (a_{2u}-a_{2u})^1$. However, in all cases during the SCF convergence the system reverted back to the $^2\Pi$ state described in Figure 4. Test calculations with a range of unrestricted density functional theory methods, i.e. B3LYP, B3LYP-D3, BP86, M06, PBE0 and B3LYP*, either after a full geometry optimization or a single-point calculation at the UB3LYP/BS1

DOI: 10.1021/acscatal.5b02720
ACS Catal. 2016, 6, 2230−2243

geometry consistently gave the same spin state ordering and predicted the $^2\Pi$ state as the ground state, Supporting Information Table S17. Group spin densities obtained with these methods show small differences as seen in Table 2. In all cases the spin density on the equatorial ligand, i.e. porphyrazine or porphyrin, is negligible and all radical character is dominantly located on the OFeNFe group. The spin density contributions in Table 2 characterize all structures as a $^2\Pi$ state with a single unpaired electron in the $\pi^*_{3,y}$ orbital.

Table 2. Group Spin Densities of Reactant Configurations of 1, 1_{Ac}, 2, and 2_{Ac} As Calculated with Various Computational Methods[a]

oxidant	method	ρ_{OFeNFe}	ρ_{Por}/ρ_{Pz}
1	UB3LYP	1.16	−0.10
	UBP86	1.01	0.00
	UB3LYP*	1.11	−0.01
	UB3LYP-D3	0.85	0.02
	M06-L	1.12	−0.12
$\mathbf{1}_{Ac}$	UB3LYP	1.18	−0.04
	UBP86	1.02	−0.01
	UB3LYP*	1.20	−0.04
	UB3LYP-D3	1.20	−0.04
	NEVPT2	1.00	0.00
2	UB3LYP	1.16	−0.05
	UBP86	1.01	0.00
	UB3LYP*	1.11	−0.01
	UB3LYP-D3	0.86	0.01
$\mathbf{2}_{Ac}$	UB3LYP	1.18	−0.02
	UBP86	1.02	0.00
	UB3LYP*	1.20	−0.02
	UB3LYP-D3	1.21	−0.02

[a]Data obtained for $\mathbf{1}/\mathbf{1}_{Ac}$ are from a Gaussian single-point calculation with basis set BS2 on a UB3LYP/BS1 optimized geometry, whereas data for $\mathbf{2}/\mathbf{2}_{Ac}$ were calculated in Orca.

The optimized geometries appear reasonably consistent between the various density functional theory methods (Supporting Information, Table S17). Thus, without an axial ligand bound, the Fe_1−O and Fe_2−N bond lengths are short (most values are between 1.62 and 1.66 Å) and implicate a double bond for both the Fe_1═O and Fe_2═N groups. Interestingly, upon addition of an acetate ligand to **1**, the nitrido group moves more to the center of the Fe_1−Fe_2 atoms at distances of 1.81 and 1.88 Å. Although to a much lesser extent, the same is true for structure **2**, where binding of an chlorobenzoate axial ligand leads to Fe_2−N bond elongation. Optimized geometries of **1** and **2** are virtually the same for each density functional method and implicate little changes upon replacing the porphyrin ligand with porphyrazine. This is in line with previous studies on *meso*-substituted metal-oxo porphyrinoid systems that showed little changes upon ligand substitution.[12d,32,42] The BP86 optimized geometries of the *μ*-nitrido diiron oxo species supported by phthalocyanine ligands provided the following distances: Fe_1−O = 1.73 Å, Fe_1−N = 1.77 Å, and Fe_2−N = 1.61 Å.[42b] These values are very close to those obtained for **1** and **2** with the same BP86 functional.

To test the effect of the environment on the spin state ordering and the nature of the electronic state of $^2\mathbf{1}_{Ac}$, we performed a full UB3LYP/BS2 optimization in solvent, for structure $^2\mathbf{1}_{Ac}$; however, there was very little structural or spin density change during the optimization as compared to the structure minimized in the gas-phase with basis set BS1 (Supporting Information Figure S19).

In a final attempt to unequivocally establish the molecular ground state of complexes **1** and $\mathbf{1}_{Ac}$, we performed a NEVPT2 single-point calculation on these chemical systems. In support of the DFT studies, a molecular ground state with $^2\Pi$ configuration with no radical character on the porphyrin/porphyrazine ligands observed. Therefore, the most likely ground state of complexes **1**, $\mathbf{1}_{Ac}$, **2**, and $\mathbf{2}_{Ac}$ is the $^2\Pi$ state in the gas-phase. However, the presence of explicit solvent molecules, electric, and/or magnetic fields as well as the inclusion of entropy and interactions of the oxidant with ions and solvent may change the ordering of the electronic states.[43] Thus, DFT calculations of P450 CpdI models showed that hydrogen bonding interactions toward the thiolate ligand, or an electric field effect changed the electronic description of CpdI and moved radical character from the axial ligand to the porphyrin manifold.[43b] Furthermore, CpdI models of both of cytochrome *c* peroxidase and ascorbate peroxidase, showed that the addition of a point charge at 12 Å distance from the iron center changed the electronic configuration from a heme cation radical to a tryptophan radical.[44] As such, environmental

Scheme 2. Electron-Transfer Pathways for the Hydrogen Atom Abstraction from Methane by CpdI (top) and *μ*-Nitrido-Bridged Diiron-Oxo Species (bottom)

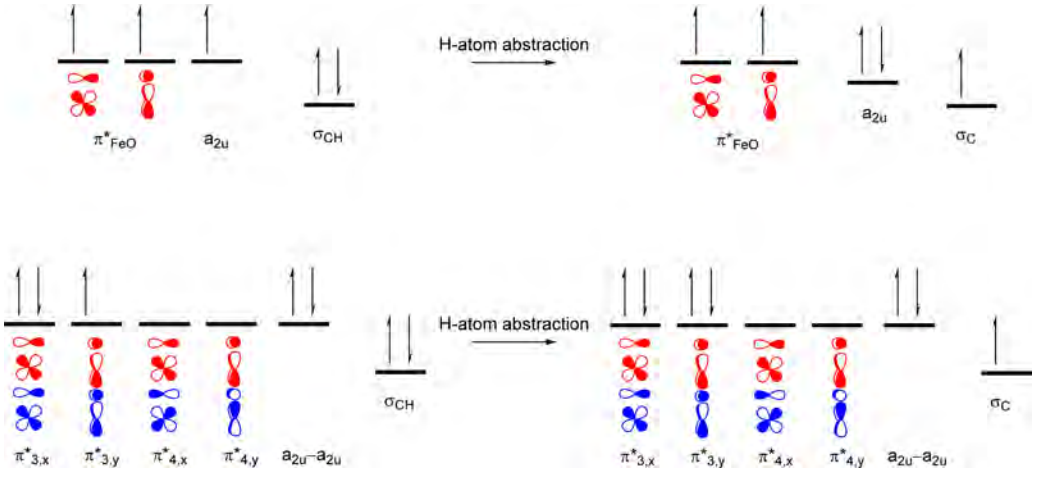

DOI: 10.1021/acscatal.5b02720
ACS Catal. 2016, 6, 2230−2243

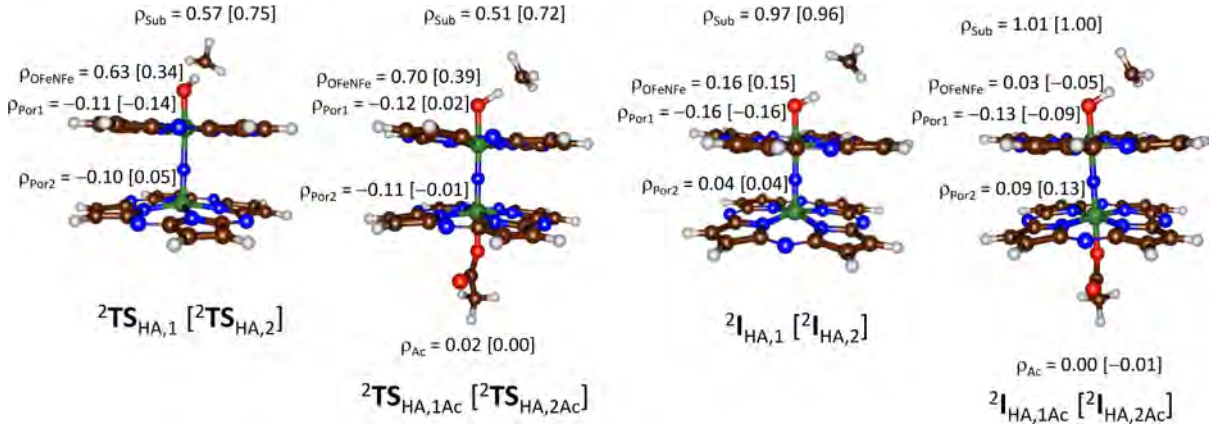

Figure 5. Group spin densities of hydrogen-atom-abstraction barriers and radical intermediates as taken from the B3LYP/BS2 results.

perturbations can have a major effect on spin-state ordering and relative energies. However, single-point calculations using the conductor-like polarized continuum model (CPCM) on species **1**, $\mathbf{1}_{Ac}$, **2**, and $\mathbf{2}_{Ac}$ did not change the electronic ground states.

Our DFT studies on **1** are in good agreement with calculations reported in the literature.[45] All these reports predict a doublet spin ground state, in agreement with experiment, with most unpaired spin density located on the O−Fe_1−N−Fe_2 group. Interestingly, Anasari et al.[45b] report an electronic ground state of ^{2}**1** with spin densities of 3.78 and −2.92 on Fe_1 and Fe_2, respectively, which implicates a state with four unpaired electrons on Fe_1 antiferromagnetically coupled to three unpaired electrons on Fe_2. This state is different from the state proposed on the basis of experimental Mössbauer and EPR spectra[9,46] and also to the considerably larger chemical model studied here.

Electron Transfer during the Mechanism. The hydrogen-atom-abstraction reaction from a substrate leads to formation of a hydroxo bond and the transfer of an electron from the oxo group into the metal−ligand system. Scheme 2 summarizes the main electron-transfer pathways that were observed in the hydrogen-atom-abstraction step from methane by **3** (top) and **1**/$\mathbf{1}_{Ac}$ (bottom). Thus, the breaking of the C−H bond leads to the splitting of the σ_{CH} orbital into an atomic hydrogen orbital ($1s_H$) and a substrate radical orbital (σ_C). The $1s_H$ orbital then mixes with a 2p orbital on oxygen to form the σ_{OH} bond with two electrons. This process results in the one electron transferred from the oxo group into a metal or ligand type orbital and in P450 it moves into the a_{2u} orbital.

In the μ-nitrido-bridged diiron-oxo species the electron transfer is different from P450 CpdI due to a closed-shell a_{2u} orbital in the reactant state. As a result the electron moves into the $\pi^*_{3,y}$ orbital to fill it with a second electron. Indeed, the group spin densities of the hydrogen-atom-abstraction transition states (Figure 5) give a considerable reduction of the spin on the OFe_1NFe_2 group, which drops to almost zero in the radical intermediates. At the same time, a spin density of about +1 on the substrate rest-group is obtained.

We tested several possibilities for alternative radical intermediates and electron-transfer pathways with ferromagnetically and antiferromagnetically coupled states, but all those attempts gave higher energy structures. Therefore, the lowest-lying electron transfer appeared to lead to a radical intermediate with configuration $\pi^*_{3,x}{}^2\ \pi^*_{3,y}{}^2\ \sigma_C{}^{\uparrow}$. A subsequent NEVPT2 single-point calculation gave spin density contributions corresponding to the same electronic state and confirms it to be the lowest-lying radical intermediate and hydrogen-atom-abstraction barrier. Attempts to swap molecular orbitals were done to generate the electronic state with occupation $\pi^*_{3,x}{}^2\ \pi^*_{3,y}{}^{\uparrow}\ \pi^*_{4,x}{}^{\uparrow}\ \sigma_C{}^{\downarrow}$; however, during the SCF convergence, they fell back to the state shown in Scheme 2, and hence, it is an excited state. Similarly, attempts to swap orbitals and generate a state with the (a_{2u}−a_{2u}) orbital singly occupied failed and led to the radical intermediate described above.

Group spin densities of the hydrogen abstraction transition states and radical intermediates are given in Figure 5. As can be seen, significant radical character on the CH_3 group is accumulating already in the transition state, which grows to a value of around 1 for the radical intermediates. The growth in spin density on the CH_3 group happens simultaneously with the loss of total spin density on the OFe_1NFe_2 group. The radical character on both porphyrin or porphyrazine groups remains small and never grows beyond a value of 0.2. Therefore, the calculations, in contrast to those on P450 CpdI, give no porphyrin radical in the oxidant and also not along the calculated reaction mechanism.

Physicochemical Properties of Reactant Complexes. The above studies show that structures **1** and **2** have well-separated electronic states, which are fundamentally different from the electronic ground state ($^{2,4}A_{2u}$ state) found in P450 Cpd I with three unpaired electrons and $\pi^*_{FeO,x}{}^1\ \pi^*_{FeO,y}{}^1\ a_{2u}{}^1$ occupation. Therefore, the difference in molecular valence orbitals between **1** or **2**, on the one hand, with **3**, on the other hand, will affect the relative energies of the molecular orbitals, such as the HOMO−LUMO energy gap, and as a consequence also the ionization potential, the electron affinity and pK_a values of the oxidant. This means that the spectroscopic and catalytic properties of the oxidants will be dramatically different as well as the H atom abstraction reaction, which involves a combined proton and electron transfer.[47] These factors influence the reactivity patterns with substrates and in this particular case enhance the reactivity. In addition, the potential energy landscapes shown in Figure 2 above shows that the binding of an axial ligand raises the hydrogen-atom-abstraction barriers by several kcal mol^{-1} and hence make it a weaker oxidant.

To understand how the intricate details of individual components can cause a change in the electron affinity of **1** and $\mathbf{1}_{Ac}$ as compared to P450 CpdI, we dissected the electron affinities into several factors, namely the electric field effect due to the axial ligand (E_{field}), a quantum mechanical effect from orbital overlap between the oxidant and the axial ligand (E_{QM}) and a π-stacking effect of the two porphyrazine groups (E_{π_π}),

DOI: 10.1021/acscatal.5b02720
ACS Catal. 2016, 6, 2230−2243

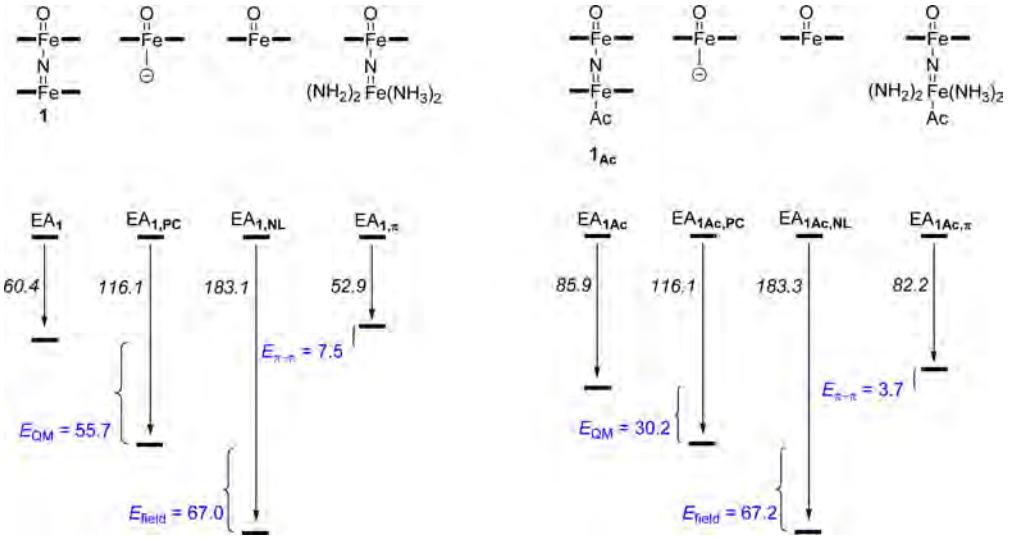

Figure 6. Axial ligand effects contributing to the electron affinity of **1** (left) and $\mathbf{1}_{Ac}$ (right). All values represent ΔE + ZPE + E_{solv} energies (in kcal mol^{-1}) and contain solvent corrections.

see Figure 6. Thus, we took the optimized structures of **1** and $\mathbf{1}_{Ac}$ and in one set of calculations removed the axial nitrido-iron(IV)porphyrazine group (no ligand, NL) and did a single-point electron affinity calculation to give EA_{NL}.

Subsequently, we did another set of single-point electron affinity calculations on these systems without axial ligand, where a point charge (PC) was placed in the position of the nitrido group (EA_{PC}). The difference in energy between EA and EA_{PC}, represents the quantum mechanical effect (E_{QM}) of the axial ligand group due to mixing of axial ligand orbitals with the iron(IV)-oxo group, eq 7. On the other hand, the difference in energy between EA_{PC} and EA_{NL} gives the electric field effect of the interaction of the charges of the axial ligand with the iron(IV)-oxo group, eq 8.

$$E_{QM} = EA - EA_{PC} \quad (7)$$

$$E_{field} = EA_{PC} - EA_{NL} \quad (8)$$

In a final set of calculations we attempted to estimate the π-stacking contribution for the two porphyrazine ligands. To this end, we replaced the porphyrazine group of the iron(IV)-nitrido group by $(NH_3)_2(NH_2^-)_2$, which keeps the same charge and coordination number but lacks the second porphyrazine unit, and calculated the electron affinity of [O═Fe(Pz)−N═$Fe(NH_3)_2(NH_2^-)_2$] with and without Ac axial ligand. We call this electron affinity, the π-stacking electron affinity, EA_π, as it lacks the π-stacking interactions. The resulting data on EA, EA_{PC}, EA_{NL}, and EA_π as well as the values of E_{QM} and E_{field} are depicted in Figure 6 for comparison. On the basis of the orbital energy levels above, we predict an increased EA upon axial ligand binding, which indeed is confirmed with the calculations in Figure 2. This contrasts the behavior of P450 CpdI that sees a decrease in electron affinity upon addition of an axial ligand (cysteinate) or replacing it with a neutral molecule or solvent molecule.[23] The reason for this disparity comes from the orbital interactions that raise the antibonding a_{2u}-axial ligand interaction in P450 CpdI, whereas the π^*_3 orbitals are stabilized (and π^*_4 orbitals destabilized) in $\mathbf{1}_{Ac}$ with respect to **1** due to the additional acetate ligand.

The latter also is highlighted from our dissection of the electron affinity contributions, where **1** has a much larger quantum mechanical contribution of the axial ligand than $\mathbf{1}_{Ac}$ (E_{QM} is 55.7 kcal mol^{-1} for **1** and 30.2 kcal mol^{-1} for $\mathbf{1}_{Ac}$). As such, binding of an acetate group has a major influence on the electron distribution within the oxidant and changes the orbital interactions so drastically that the electron affinity is raised by about 25 kcal mol^{-1}, which will affect its oxidation potential with substrates. Needless to say, the electric field effect due to the iron(IV)-nitrido porphyrazine group is virtually the same for $\mathbf{1}/\mathbf{1}_{Ac}$ at a value of 67.0/67.2 kcal mol^{-1}. By contrast, the π-stacking energy (E_{π_π}) is small, and only in the order of 3.7−7.5 kcal mol^{-1}, and hence will not be the dominant factor. However, the electron affinity of both complexes **1** and $\mathbf{1}_{Ac}$ are larger with a porphyrazine group attached to the iron(IV)-nitrido unit (compare $EA_{1,\pi}$ vs EA_1), which confirms an important interaction between the axial ligand and the porphyrazine moiety exists.

The values of E_{field} and E_{QM} calculated previously for the axial ligand effect of [Fe^{IV}(O) ($Por^{+\bullet}$)SH] were 54.0 and 38.8 kcal mol^{-1}, respectively.[48] The field effect calculated here is somewhat larger as the point charge was placed in the position of the bridging nitrogen atom at 2.06 Å, whereas in P450 CpdI, it was in the position of the sulfur atom at 2.49 Å.[48] Obviously, a shorter distance will lead to a larger Coulomb interaction and a larger field effect. In addition to an increased field effect, a comparison of **1** and [Fe^{IV}(O) ($Por^{+\bullet}$)SH] also gives an increased quantum chemical effect by 16.9 kcal mol^{-1} due to better orbital interactions along the O−Fe_1−N−Fe_2 system. However, most of this benefit is lost when acetate binds to Fe_2. Nevertheless, **1** has a considerably lower electron affinity than P450 CpdI (EA_{CpdI} = 92.9 kcal mol^{-1}), which is partially due to a larger electric field effect and partially as a result of a quantum mechanical effect. Based on the much smaller electron affinity of **1** versus **3**, one would expect the former to be a much weaker oxidant in hydrogen-atom-abstraction reactions. Nevertheless, as will be shown later in this work, system **1** has also a decreased pK_a value, which makes it more basic and leads to a larger driving force for hydrogen atom abstraction as shown previously.[25]

Thermochemical Properties Affecting Reactivities. In order to assign the origin of reactivity differences one has to take the thermochemical properties of the oxidant and substrate

DOI: 10.1021/acscatal.5b02720
ACS Catal. 2016, 6, 2230−2243

into consideration. Experimental studies on hydrogen-atom-abstraction reactivities showed that the rate constant generally correlates with the strength of the C−H bond of the substrate that is broken (BDE_{CH}) as well as with the strength of the O−H bond that is formed (BDE_{OH}).[49] The BDE_{OH} and BDE_{CH} values are defined for the reactions described in eq 4 and 5 above. However, the BDE_{OH} value can be split into an electron transfer (electron affinity, EA of the oxidant), a proton affinity of the reduced oxidant (ΔG_{acid}) and the ionization energy (IE_H) of a hydrogen atom as described in eqs 9−11.

$$AH \rightarrow A^- + H^+ + \Delta G_{acid} \quad (9)$$

$$A \rightarrow A^- + EA_A \quad (10)$$

$$H \rightarrow H^+ + IE_H \quad (11)$$

Combination of reactions 9−11 adds up to reaction 4 and will give a BDE_{OH} description as given in eq 12.

$$-BDE_{OH} = \Delta G_{acid} - EA_{FeO} - IE_H \quad (12)$$

The ionization energy of a hydrogen atom is taken here from the NIST database.[50] Subsequently, we calculated the EA, ΔG_{acid}, and BDE_{OH} values of **1**, $\mathbf{1}_{Ac}$, and **3** and give the results graphically in Figure 7 but also tabulate the results in Table 3.

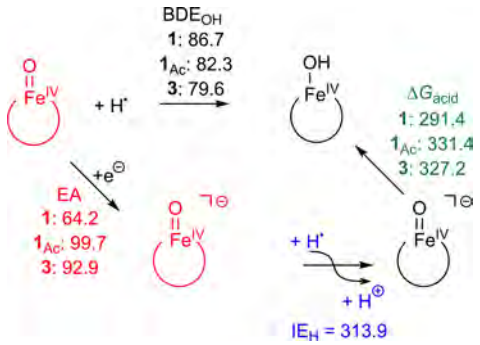

Figure 7. Calculated thermochemical variables for **1** and $\mathbf{1}_{Ac}$. Data represents $\Delta G + E_{solv}$ values with free energies that include solvent, thermal, and entropic corrections (in kcal mol^{-1}).

Table 3. Calculated Thermochemical Variables for 1, $\mathbf{1}_{Ac}$, and 3[a]

oxidant	BDE_{OH}	ΔG_{acid}	EA
1	86.7	291.4	64.2
$\mathbf{1}_{Ac}$	82.3	331.4	99.7
$\mathbf{3}_{SH}$	79.6	327.2	92.9

[a]Free energies with solvent corrections given in kcal mol^{-1}.

Extensive experimental studies implicated that the dominant component to the BDE_{OH} trends relates to the acidity of the oxo group (i.e., ΔG_{acid}).[51] With a solvent model included, we calculated a value of $BDE_{OH}(\mathbf{1}) = 86.7$ kcal mol^{-1}, which is only slightly higher in energy than the value we calculated before for $\mathbf{1}_{Ac}$, $BDE_{OH}(\mathbf{1}_{Ac}) = 82.3$ kcal mol^{-1} and the one for $\mathbf{3}_{SH}$, $BDE_{OH}(\mathbf{3}_{SH}) = 79.6$ kcal mol^{-1}.[43a] This change is likely due to the push-effect of electron density from the axial ligand to the metal-oxo group, which affects the orbital energies and consequently the electron affinity as well as the acidity of the iron(IV)-hydroxo group. However, **1** has an electron affinity that is about 35 kcal mol^{-1} lower in energy than that for $\mathbf{1}_{Ac}$, and as a consequence, **1** has a 40 kcal mol^{-1} lower ΔG_{acid} value. It is this acidity change that will make **1** a much better oxidant than either $\mathbf{1}_{Ac}$ or $\mathbf{3}_{SH}$ for substrate hydroxylation reactions.

Therefore, **1** is found to be a more powerful oxidant of hydrogen-atom-abstraction reactions than **3** due to an increased basicity of the iron(IV)-hydroxo complex that is formed, which is mainly due to orbital reorganization that affects the electron affinity of the oxidant. Figure 7 breaks down this basicity change into BDE_{OH} and EA components for species **1**, $\mathbf{1}_{Ac}$, and **3**.

In summary, the μ-nitrido diiron(IV)-oxo complexes have dramatically altered electronic configurations with respect to P450 CpdI, which is mainly due to charge and orbital delocalization along the O−Fe_1−N−Fe_2 axis. Because of this, the electron affinity of **1** is much lower than that of P450 CpdI; however, its interaction with ligands bound to the iron(IV)-nitrido group is also less. These orbital interactions lower the ability to abstract hydrogen atoms efficiently and make **1** a considerably better oxidant of hydrogen-atom-abstraction reactions than P450 CpdI. In addition, these electronic effects also influence the pK_a value of the corresponding iron(IV)-hydroxo group. As such, both thermochemical and electronic analysis point to the reasons for the reactivity differences of μ-nitrido-bridged diiron oxo complexes with respect to P450 CpdI.

Valence Bond Rationalization of the Reaction Mechanism. Finally, we have tried to understand the reaction mechanism obtained and rationalize why structures **1** and **2** are better oxidants than P450 CpdI in methane hydroxylation processes by setting up a valence bond (VB) curve crossing diagram, see Figure 8. These diagrams were used previously to rationalize hydrogen-atom-abstraction barriers and double bond epoxidation barriers by iron(IV)-oxo complexes and explained the obtained rate constant trends, but also identified the origin of the stepwise processes.[23,36,37,39] The figure starts on the bottom left with the reactant states, and in the case of **1** and **2**, the system has orbital occupation (core) $\pi^*_{3,x}{}^2\ \pi^*_{3,y}{}^1\ (a_{2u}-a_{2u})^2$ in a doublet spin ground state, which essentially implicates an iron(V)-oxo that is connected to an iron(IV)-nitrido group. This system has electrons in the $\pi_{1,x}$, $\pi_{2,x}$, and $\pi^*_{3,x}$ orbitals as identified by the dots next to the O, Fe_1, N, and Fe_2 atoms. The dots on the right-hand-side of the labels refer to the six electrons in $\pi_{1,x}{}^2\ \pi_{2,x}{}^2\ \pi^*_{3,x}{}^2$, and those on the left-hand-side of the labels represent the five electrons in $\pi_{1,y}{}^2\ \pi_{2,y}{}^2\ \pi^*_{3,y}{}^1$. In the VB structures, the equatorial ligand is given as a bold horizontal bar and both doubly occupied a_{2u} orbitals on each of the porphyrazine groups are identified with two dots next to these bars. Lastly, the C−H bond is occupied with two electrons and is given as a bar connected with two dots.

In the transition state for hydrogen atom abstraction, the C−H bond splits back into atomic orbitals, whereby the up-spin electron is retained by the CH_3 radical, while the down-spin electron leaves as a $1s_H$ orbital with hydrogen. In addition, in the transition state the $\pi_{1,x}/\pi_{2,x}/\pi^*_{3,x}/\pi^*_{4,x}$ set of orbitals is rehybridized and separated into a $2p_y$ orbital on oxygen with two electrons and three new orbitals for the interaction between Fe_1, N, and Fe_2 ($\pi'_{1,x}/\pi'_{2,x}/\pi^{*\prime}_{3,x}$). One of the electrons of the $2p_x$ orbital forms a bond (σ_{OH}) with the incoming $1s_H$ orbital of hydrogen, whereas the other electron is transferred into the $\pi'_{1,x}/\pi'_{2,x}/\pi^{*\prime}_{3,x}$ that ends up with five electrons. In the subsequent step in the reaction mechanism, namely, the OH rebound step (not shown in Figure 8), the set of $\pi_{1,y}/\pi_{2,y}/\pi^*_{3,y}/\pi^*_{4,y}$ orbitals is split into a $2p_y$ and a set of new π'_y orbitals. The radical on the substrate then forms a bond

DOI: 10.1021/acscatal.5b02720
ACS Catal. 2016, 6, 2230−2243

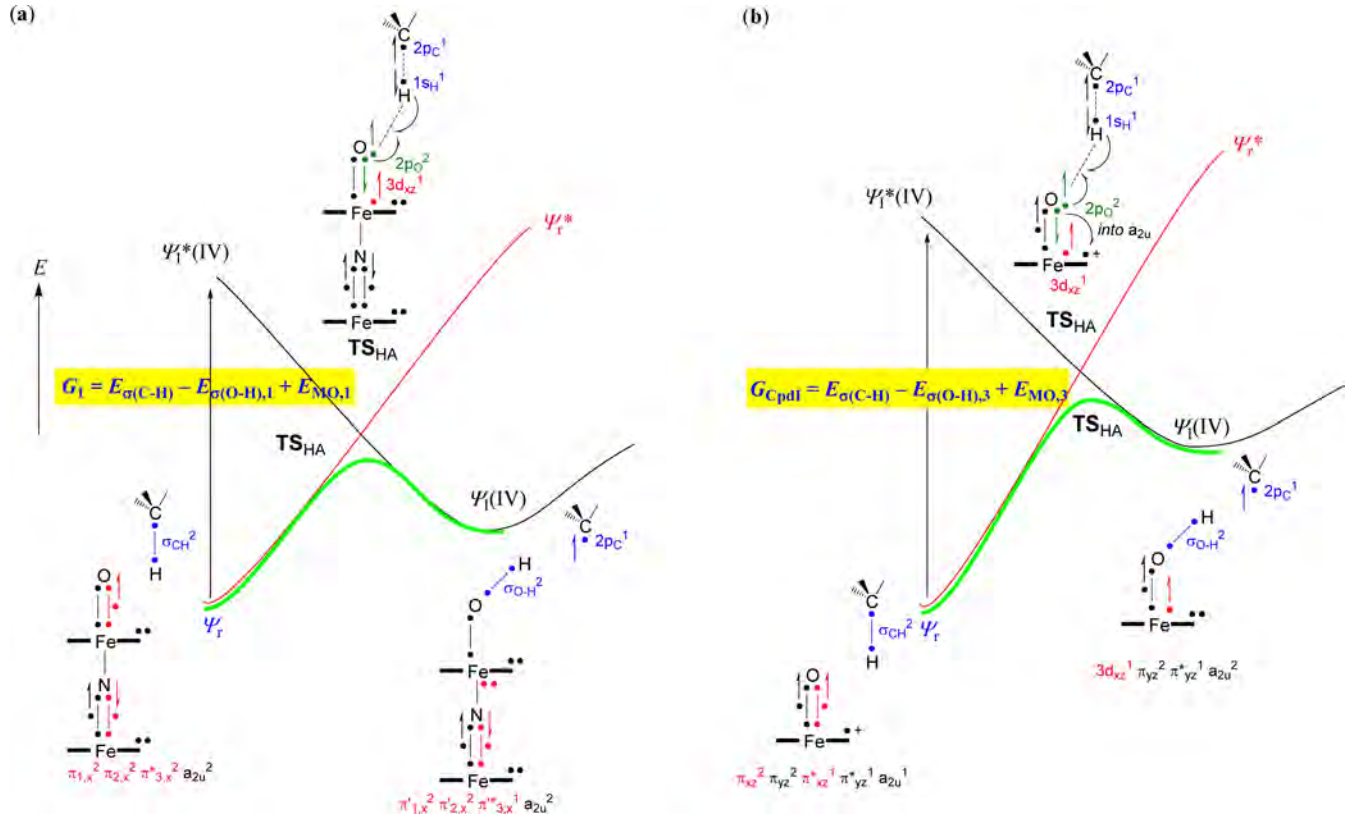

Figure 8. Valence bond curve crossing diagram for the methane hydroxylation by **1** (panel a) and P450 Cpd I (panel b). Dots represent valence electrons and lines (curved or straight) implicate chemical bonds.

with the electron in $2p_y$ to form the methanol product complex. These electron-transfer pathways and orbital occupations agree with the spin densities reported above.

The reactant configuration can be described quantum mechanically with a reactant wave function (Ψ_r) and the radical intermediate with the intermediate wave function Ψ_I. In valence bond theory, the reactant wave function represents an excited state in the intermediate geometry (i.e., Ψ_r*), whereas the intermediate configuration links to an excited state in the reactant geometry (i.e., Ψ_I*).

It has been shown that the barrier height from reactants to products is proportional to the excitation energy (or promotion gap G) from Ψ_r to Ψ_I*.[52] A comparison of the VB structures of the Ψ_r and Ψ_I* (i.e., TS) configurations gives insight into the chemical and physical components that determine the transition state for the reaction and enable us to estimate the promotion gap of **1** or **2**. Thus, the barrier is determined by the energy of the σ_{CH} bond of the substrate that is broken into atomic orbitals (i.e., $E_{\sigma(C-H)}$). In addition, it is based on the energy of the σ_{OH} bond that is formed (i.e., $E_{\sigma(O-H)}$). As discussed above, the barrier height is also dependent on molecular orbital changes (E_{MO}) in the oxidant and particularly on the electron-transfer energies and rehybridization of some of the orbitals due to bond formation and breaking. For instance, the E_{MO} value contains the energy to split the $\pi_{1,x}/\pi_{2,x}/\pi^*_{3,x}/\pi^*_{4,x}$ set of orbitals into a $2p_x$ on oxygen and a $\pi'_{1,x}/\pi'_{2,x}/\pi^{*\prime}_{3,x}$ set of orbitals along the Fe_1-N-Fe_2 axis. The overall value of the promotion gap of **1** or **2** is given in eq 13.

$$G_{\mathbf{1}} = E_{\sigma(C-H)} - E_{\sigma(O-H),\mathbf{1}} + E_{MO,\mathbf{1}} \quad (13)$$

On the right-hand-side of Figure 8, we show the analogous VB curve crossing diagram for methane hydroxylation by P450 CpdI. Thus, the dots along the Fe−O bond represent the three electrons in the π_{xz}/π^*_{xz} (in red) and the three electrons in the π_{yz}/π^*_{yz} (in black) orbitals. Similarly, as discussed above for **1** and $\mathbf{1}_{Ac}$, the $\pi_{xz}^2\,\pi^*_{xz}{}^1$ orbitals split into atomic orbitals with two electrons in $2p_x(O)$ and one in the metal $3d_{xz}$. One of the electrons of $2p_x(O)$ forms the σ_{OH} bond with the incoming $1s_H$ hydrogen atom, whereas the other atom of $2p_x(O)$ is promoted to the nearest available electronic orbital, namely, the a_{2u} orbital. The promotion gap for this reaction ($G_{\mathbf{CpdI}}$) is described in eq 14. Obviously, since we use the same substrate (methane) as in the reaction with **1**, the value $E_{\sigma(C-H)}$ will be the same for **1** and **3**.

$$G_{\mathbf{CpdI}} = E_{\sigma(C-H)} - E_{\sigma(O-H),\mathbf{3}} + E_{MO,\mathbf{3}} \quad (14)$$

In principle, the $E_{\sigma(O-H)}$ represents the strength of the O−H bond that is formed and will be proportional to the BDE_{OH} value. As shown above in Table 3, the BDE_{OH} value for **1** is about 4.4 kcal mol^{-1} larger than that for $\mathbf{1}_{Ac}$ and 7.1 kcal mol^{-1} larger than that found for **3**. Therefore, we expect a smaller promotion gap for **1** than for $\mathbf{1}_{Ac}$ and **3**, which should result in a lower hydrogen-atom-abstraction barrier for **1** than for **3**. Indeed, the potential energy profiles (Figure 2) show a $\mathbf{TS}_{HA}$ ordering of $\mathbf{TS}_{HA,1} < \mathbf{TS}_{HA,1Ac} < \mathbf{TS}_{HA,3}$ in agreement with the promotion gap differences. Thus, part of the differences in BDE_{OH} values relate to differences in the acidity of the iron-hydroxo complex. However, part of this benefit is canceled out by changes in the electron affinity of the oxidants, Table 3.

The major difference between complex **1** and **3** is related to the rehybridization energy or E_{MO}, which is determined by the

DOI: 10.1021/acscatal.5b02720
ACS Catal. 2016, 6, 2230−2243

difference in electron affinity of **1** versus **3**. Thus, in **3**, the π_{xz}/π^*_{xz} couple is rehybridized into atomic orbitals $2p_x(O)$ and $3d_{xz}(Fe)$ of which the $2p_x(O)$ mixes with the $1s_H$ orbital to form the new σ_{CH} orbital. By contrast, in **1** the set of four coupled orbitals $(\pi_{1,x}/\pi_{2,x}/\pi^*_{3,x}/\pi^*_{4,x})$ is reduced to a set of three coupled orbitals and the atomic $2p_x(O)$ orbital, which amounts to a much lesser orbital reorganization and consequently a much smaller E_{MO} value. Therefore, **1** will have a smaller E_{MO} value than **3** and hence also a smaller excitation energy as well as higher reactivity in H atom abstraction reactions. Because of the larger quantum chemical changes upon reduction of **3** versus the reduction of **1** and the increased stability of the product, it is evident that **3** will be a lesser good oxidant of hydrogen-atom-abstraction reactions. Indeed, that is what is observed by the relative methane hydrogen-atom-abstraction reactions when **1** and **3** are compared.

CONCLUSION

The calculations presented in this work highlight how small external perturbations, such as those of an axially coordinated nitrido iron porphyrin ligand can lead to dramatic changes in molecular orbital interactions of the metal(IV)-oxo group with aligned ligand-orbitals as well as the dipole moment of the oxidant. In particular, an μ-nitrido-bridged diiron-oxo complex, with either porphyrin or phthalocyanine, has an increased basicity of the oxo group that is highly susceptible to hydrogen atom abstraction. This explains the enhanced reactivity observed for **A**/**B** over P450 Compound I. Moreover, these insights will assist in the design of efficient and powerful oxidants of hydrogen-atom-abstraction reactions. A detailed thermochemical, valence bond, and orbital analysis has given insight into the intricate details of μ-nitrido-bridged diiron(IV) complexes and gives hints on how this complex can be further modified to improve its catalytic properties.

ASSOCIATED CONTENT

Supporting Information

The Supporting Information is available free of charge on the ACS Publications website at DOI: 10.1021/acscatal.5b02720.

Computational details, including tables with absolute and relative energies, group spin densities and charges, as well as figures with geometry scans, IRCs, and Cartesian coordinates of optimized geometries (PDF)

AUTHOR INFORMATION

Corresponding Authors

*E-mail: sam.devisser@manchester.ac.uk.
*E-mail: alexander.sorokin@ircelyon.univ-lyon1.fr.
*E-mail: pascale.maldivi@cea.fr.

Notes

The authors declare no competing financial interest.

ACKNOWLEDGMENTS

The National Service of Computational Chemistry Software (NSCCS) is thanked for CPU time provided. M.G.Q. thanks the BBSRC for a studentship. D.K. holds the Ramanujan Fellowship (SR/S2/RJN-11/2008) from the Department of Science and Technology (DST), New Delhi (India). A.B.S. is indebted to ANR (France) for financial support (grant ANR-08-BLANC-0183-01). P.M. is grateful to the French National Agency for Research (ANR) "Programme Labex" (ARCANE project no. ANR-11-LABX-003) for partial funding. D.S. wishes to thank Prof Sason Shaik for fruitful discussions and support in this study. S.d.-V. and P.M. also thank Prof Jean-Marc Latour for useful discussions on the structure and spectroscopy of the reactant complex. The COST action CM1305 ECostBio is acknowledged for support. This work was partially performed using HPC resources from GENCI- CINES (Grant 2015-089173).

REFERENCES

(1) (a) Sono, M.; Roach, M. P.; Coulter, E. D.; Dawson, J. H. *Chem. Rev.* **1996**, *96*, 2841−2888. (b) Groves, J. T. *Proc. Natl. Acad. Sci. U. S. A.* **2003**, *100*, 3569−3574. (c) Ortiz de Montellano, P. R., Ed., *Cytochrome P450: Structure, Mechanism and Biochemistry*, 3rd ed.; Kluwer Academic/Plenum Publishers: New York, 2005. (d) Munro, A. W.; Girvan, H. M.; McLean, K. J. *Nat. Prod. Rep.* **2007**, *24*, 585−609. (e) Kadish, K. M., Smith, K. M., Guilard, R., Eds.; *Handbook of Porphyrin Science*; World Scientific Publishing Co.: Singapore, 2010. (f) de Visser, S. P., Kumar, D., Eds.; *Iron-containing enzymes: Versatile catalysts of hydroxylation reaction in nature*; RSC Publishing: Cambridge, U.K., 2011. (g) Grogan, G. *Curr. Opin. Chem. Biol.* **2011**, *15*, 241−248. (h) Poulos, T. L. *Chem. Rev.* **2014**, *114*, 3919−3962. (i) Blomberg, M. R. A.; Borowski, T.; Himo, F.; Liao, R.-Z.; Siegbahn, P. E. M. *Chem. Rev.* **2014**, *114*, 3601−3658.

(2) (a) Costas, M. *Coord. Chem. Rev.* **2011**, *255*, 2912−2932. (b) Bruijnincx, P. C. A.; van Koten, G.; Klein Gebbink, R. J. M. *Chem. Soc. Rev.* **2008**, *37*, 2716−2744. (c) Kryatov, S. V.; Rybak-Akimova, E. V.; Schindler, S. *Chem. Rev.* **2005**, *105*, 2175−2226. (d) McDonald, A. R.; Que, L., Jr *Coord. Chem. Rev.* **2013**, *257*, 414−428. (e) Nam, W.; Lee, Y.-M.; Fukuzumi, S. *Acc. Chem. Res.* **2014**, *47*, 1146−1154.

(3) (a) Groves, J. T. Models and Mechanisms of Cytochrome P450 Action. In *Cytochrome P450: Structure, Mechanism and Biochemistry*, 3rd ed.; Ortiz de Montellano, P. R., Ed.; Kluwer Academic/Plenum Publishers: New York, 2005; Chapter 1, pp 1−44. (b) Nam, W. *Acc. Chem. Res.* **2007**, *40*, 522−531. (c) Denisov, I. G.; Makris, T. M.; Sligar, S. G.; Schlichting, I. *Chem. Rev.* **2005**, *105*, 2253−2277.

(4) Rittle, J.; Green, M. T. *Science* **2010**, *330*, 933−937.

(5) Chen, M. M.; Coelho, P. S.; Arnold, F. H. *Adv. Synth. Catal.* **2012**, *354*, 964−968.

(6) Zilly, F. E.; Acevedo, J. P.; Augustyniak, W.; Deege, A.; Häusig, U. W.; Reetz, M. T. *Angew. Chem., Int. Ed.* **2011**, *50*, 2720−2724; Corrigendum: *Angew. Chem., Int. Ed.* **2013**, *52*, 13503.

(7) (a) Kawakami, N.; Shoji, O.; Watanabe, Y. *Angew. Chem., Int. Ed.* **2011**, *50*, 5315−5318. (b) Kawakami, N.; Shoji, O.; Watanabe, Y. *Chem. Sci.* **2013**, *4*, 2344−2348.

(8) (a) Sorokin, A. B.; Mangematin, S.; Pergrale, C. *J. Mol. Catal. A: Chem.* **2002**, *182-183*, 267−281. (b) Sorokin, A. B.; Kudrik, E. V.; Bouchu, D. *Chem. Commun.* **2008**, 2562−2564. (c) Sorokin, A. B.; Kudrik, E. V.; Alvarez, L. X.; Afanasiev, P.; Millet, J. M. M.; Bouchu, D. *Catal. Today* **2010**, *157*, 149−154. (d) Sorokin, A. B. *Chem. Rev.* **2013**, *113*, 8152−8191. (e) Afanasiev, P.; Kudrik, E. V.; Millet, J-M. M.; Bouchu, D.; Sorokin, A. B. *Dalton Trans.* **2011**, *40*, 701−740. (f) Colomban, C.; Kudrik, E. V.; Afanasiev, P.; Sorokin, A. B. *J. Am. Chem. Soc.* **2014**, *136*, 11321−11330.

(9) Kudrik, E. V.; Afanasiev, P.; Alvarez, L. X.; Dubourdeaux, P.; Clémancey, M.; Latour, J.-M.; Blondin, G.; Bouchu, D.; Albrieux, F.; Nefedov, S. E.; Sorokin, A. B. *Nat. Chem.* **2012**, *4*, 1024−1029.

(10) Berman, H. M.; Westbrook, J.; Feng, Z.; Gilliland, G.; Bhat, T. N.; Weissig, H.; Shindyalov, I. N.; Bourne, P. E. *Nucleic Acids Res.* **2000**, *28*, 235−242.

(11) (a) Butler, C. F.; Peet, C.; Mason, A. E.; Voice, M. W.; Leys, D.; Munro, A. W. *J. Biol. Chem.* **2013**, *288*, 25387−25399. (b) Batabyal, D.; Poulos, T. L. *Biochemistry* **2013**, *52*, 8898−8906. (c) Müller, C. S.; Knehans, T.; Davydov, D. R.; Bounds, P. L.; von Mandach, U.; Halpert, J. R.; Caflisch, A.; Koppenol, W. H. *Biochemistry* **2015**, *54*, 711−721. (d) Xu, K.; Wang, Y.; Hirao, H. *ACS Catal.* **2015**, *5*, 4175−4179.

DOI: 10.1021/acscatal.5b02720
ACS Catal. 2016, 6, 2230−2243

(12) (a) Gross, Z.; Nimri, S. *Inorg. Chem.* **1994**, *33*, 1731−1732. (b) Czarnecki, K.; Nimri, S.; Gross, Z.; Proniewicz, L. M.; Kincaid, J. R. *J. Am. Chem. Soc.* **1996**, *118*, 2929−2935. (c) Song, W. J.; Ryu, Y. O.; Song, R.; Nam, W. *JBIC, J. Biol. Inorg. Chem.* **2005**, *10*, 294−304. (d) Takahashi, A.; Yamaki, D.; Ikemura, K.; Kurahashi, T.; Ogura, T.; Hada, M.; Fujii, H. *Inorg. Chem.* **2012**, *51*, 7296−7305.
(13) For examples, see the following: (a) Alfonso-Prieto, M.; Biarnés, X.; Vidossich, P.; Rovira, C. *J. Am. Chem. Soc.* **2009**, *131*, 11751−11761. (b) Colin, J.; Wiseman, B.; Switala, J.; Loewen, P. C.; Ivancich, A. *J. Am. Chem. Soc.* **2009**, *131*, 8557−8563. (c) Raven, E. L. *Nat. Prod. Rep.* **2003**, *20*, 367−381. (d) Veitch, N. C. *Phytochemistry* **2004**, *65*, 249−259.
(14) (a) Dawson, J. H.; Holm, R. H.; Trudell, J. R.; Barth, G.; Linder, R. E.; Bunnenberg, E.; Djerassi, C.; Tang, S. C. *J. Am. Chem. Soc.* **1976**, *98*, 3707−3709. (b) Poulos, T. L. *JBIC, J. Biol. Inorg. Chem.* **1996**, *1*, 356−359.
(15) (a) Zhou, Y.; Shan, X.; Mas-Ballesté, R.; Bukowski, M. R.; Stubna, A.; Chakrabarti, M.; Slominski, L.; Halfen, J. A.; Münck, E.; Que, L., Jr *Angew. Chem., Int. Ed.* **2008**, *47*, 1896−1899. (b) de Visser, S. P.; Nam, W. *J. Phys. Chem. A* **2008**, *112*, 12887−12895. (c) Takahashi, A.; Kurahashi, T.; Fujii, H. *Inorg. Chem.* **2011**, *50*, 6922−6928.
(16) Shaik, S.; Kumar, D.; de Visser, S. P.; Altun, A.; Thiel, W. *Chem. Rev.* **2005**, *105*, 2279−2328.
(17) (a) Porro, C. S.; Sutcliffe, M. J.; de Visser, S. P. *J. Phys. Chem. A* **2009**, *113*, 11635−11642. (b) Hernández-Ortega, A.; Quesne, M. G.; Bui, S.; Heyes, D. J.; Steiner, R. A.; Scrutton, N. S.; de Visser, S. P. *J. Am. Chem. Soc.* **2015**, *137*, 7474−7487. (c) Quesne, M. G.; Borowski, T.; de Visser, S. P. *Chem. - Eur. J.* **2016**, *22*, 2562−2581.
(18) (a) de Visser, S. P.; Quesne, M. G.; Martin, B.; Comba, P.; Ryde, U. *Chem. Commun.* **2014**, *50*, 262−282. (b) Kumar, D.; de Visser, S. P.; Sharma, P. K.; Cohen, S.; Shaik, S. *J. Am. Chem. Soc.* **2004**, *126*, 1907−1920. (c) Kumar, D.; de Visser, S. P.; Shaik, S. *J. Am. Chem. Soc.* **2004**, *126*, 5072−5073.
(19) (a) Frisch, M. J. et al. *Gaussian 09*, revision D.01; Gaussian, Inc.: Wallingford, CT, 2009. (b) *Jaguar*, version 8.4; Schrodinger, Inc.: New York, NY, 2013. (c) Neese, F. *ORCA − an ab initio, DFT and semiempirical SCF-MO package*, version 2.9; University of Bonn: Bonn, Germany, 2009. (d) Visualizing Molecules with gOpenMol. http://www.chem.utah.edu/directory/anderson/research-group/gopen/ (accessed January 2016).
(20) (a) Becke, A. D. *J. Chem. Phys.* **1993**, *98*, 5648−5652. (b) Lee, C.; Yang, W.; Parr, R. G. *Phys. Rev. B: Condens. Matter Mater. Phys.* **1988**, *37*, 785−789.
(21) (a) Hay, P. J.; Wadt, W. R. *J. Chem. Phys.* **1985**, *82*, 299−310. (b) Hehre, W. J.; Ditchfield, K.; Pople, J. A. *J. Chem. Phys.* **1972**, *56*, 2257−2261.
(22) (a) Becke, A. D. *Phys. Rev. A: At., Mol., Opt. Phys.* **1988**, *38*, 3098−3100. (b) Perdew, J. P. *Phys. Rev. B: Condens. Matter Mater. Phys.* **1986**, *33*, 8822−8824.
(23) de Visser, S. P. *J. Am. Chem. Soc.* **2010**, *132*, 1087−1097.
(24) (a) Vardhaman, A. K.; Sastri, C. V.; Kumar, D.; de Visser, S. P. *Chem. Commun.* **2011**, *47*, 11044−11046. (b) Vardhaman, A. K.; Barman, P.; Kumar, S.; Sastri, C. V.; Kumar, D.; de Visser, S. P. *Angew. Chem., Int. Ed.* **2013**, *52*, 12288−12292. (c) Vardhaman, A. K.; Barman, P.; Kumar, S.; Sastri, C. V.; Kumar, D.; de Visser, S. P. *Chem. Commun.* **2013**, *49*, 10926−10928.
(25) Prokop, K. A.; de Visser, S. P.; Goldberg, D. P. *Angew. Chem., Int. Ed.* **2010**, *49*, 5091−5095.
(26) de Visser, S. P. *Chem. - Eur. J.* **2006**, *12*, 8168−8177.
(27) (a) Sainna, M. A.; Kumar, S.; Kumar, D.; Fornarini, S.; Crestoni, M. E.; de Visser, S. P. *Chem. Sci.* **2015**, *6*, 1516−1529. (b) Sainna, M. A.; Sil, D.; Sahoo, D.; Martin, B.; Rath, S. P.; Comba, P.; de Visser, S. P. *Inorg. Chem.* **2015**, *54*, 1919−1930.
(28) Reiher, M.; Salomon, O.; Hess, B. A. *Theor. Chem. Acc.* **2001**, *107*, 48−55.
(29) Grimme, S.; Antony, J.; Ehrlich, S.; Krieg, H. *J. Chem. Phys.* **2010**, *132*, 154104−154104.
(30) Zhao, Y.; Truhlar, D. G. *J. Chem. Phys.* **2006**, *125*, 194101−194101.
(31) Adamo, C.; Barone, V. *J. Chem. Phys.* **1999**, *110*, 6158−6169.
(32) Neu, H. M.; Quesne, M. G.; Yang, T.; Prokop-Prigge, K. A.; Lancaster, K. M.; Donohoe, J.; DeBeer, S.; de Visser, S. P.; Goldberg, D. P. *Chem. - Eur. J.* **2014**, *20*, 14584−14588.
(33) Heyes, D. J.; Sakuma, M.; de Visser, S. P.; Scrutton, N. S. *J. Biol. Chem.* **2009**, *284*, 3762−3767.
(34) For examples, see the following: Neu, H. M.; Yang, T.; Baglia, R. A.; Yosca, T. H.; Green, M. T.; Quesne, M. G.; de Visser, S. P.; Goldberg, D. P. *J. Am. Chem. Soc.* **2014**, *136*, 13845−13852.
(35) (a) Yoshizawa, K.; Kamachi, T.; Shiota, Y. *J. Am. Chem. Soc.* **2001**, *123*, 9806−9816. (b) de Visser, S. P.; Kumar, D.; Cohen, S.; Shacham, R.; Shaik, S. *J. Am. Chem. Soc.* **2004**, *126*, 8362−8363.
(36) Shaik, S.; Kumar, D.; de Visser, S. P. *J. Am. Chem. Soc.* **2008**, *130*, 10128−10140.
(37) For examples, see the following: Kumar, S.; Faponle, A. S.; Barman, P.; Vardhaman, A. K.; Sastri, C. V.; Kumar, D.; de Visser, S. P. *J. Am. Chem. Soc.* **2014**, *136*, 17102−17115.
(38) de Visser, S. P. *Phys. Chem. Chem. Phys.* **1999**, *1*, 749−754.
(39) (a) Kumar, D.; Karamzadeh, B.; Sastry, G. N.; de Visser, S. P. *J. Am. Chem. Soc.* **2010**, *132*, 7656−7667. (b) Kumar, D.; Sastry, G. N.; de Visser, S. P. *Chem. - Eur. J.* **2011**, *17*, 6196−6205.
(40) de Visser, S. P.; Shaik, S.; Sharma, P. K.; Kumar, D.; Thiel, W. *J. Am. Chem. Soc.* **2003**, *125*, 15779−15788.
(41) Ogliaro, F.; de Visser, S. P.; Cohen, S.; Kaneti, J.; Shaik, S. *ChemBioChem* **2001**, *2*, 848−851.
(42) (a) Kumar, D.; Tahsini, L.; de Visser, S. P.; Kang, H. Y.; Kim, S. J.; Nam, W. *J. Phys. Chem. A* **2009**, *113*, 11713−11722. (b) Colomban, C.; Kudrik, E. V.; Briois, V.; Shwarbrick, J. C.; Sorokin, A. B.; Afanasiev, P. *Inorg. Chem.* **2014**, *53*, 11517−11530.
(43) (a) de Visser, S. P.; Tan, L. S. *J. Am. Chem. Soc.* **2008**, *130*, 12961−12974. (b) Shaik, S.; de Visser, S. P.; Kumar, D. *J. Am. Chem. Soc.* **2004**, *126*, 11746−11749.
(44) de Visser, S. P. *J. Phys. Chem. A* **2005**, *109*, 11050−11057.
(45) (a) Silaghi-Dumitrescu, R.; Makarov, S. V.; Uta, M.-M.; Dereven'kov, I. A.; Stuzhin, P. A. *New J. Chem.* **2011**, *35*, 1140−1145. (b) Ansari, M.; Vyas, N.; Ansari, A.; Rajaraman, G. *Dalton Trans.* **2015**, *44*, 15232−15243. (c) İşci, Ü.; Faponle, A. S.; Afanasiev, P.; Albrieux, F.; Briois, V.; Ahsen, V.; Dumoulin, F.; Sorokin, A. B.; de Visser, S. P. *Chem. Sci.* **2015**, *6*, 5063−5075.
(46) Bocian, D. F.; Findsen, E. W.; Hofmann, J. A., Jr; Schick, G. A.; English, D. R.; Hendrickson, D. N.; Suslick, K. S. *Inorg. Chem.* **1984**, *23*, 800−807.
(47) For examples, see the following: (a) Latifi, R.; Bagherzadeh, M.; de Visser, S. P. *Chem. - Eur. J.* **2009**, *15*, 6651−6662. (b) Faponle, A. S.; Quesne, M. G.; Sastri, C. V.; Banse, F.; de Visser, S. P. *Chem. - Eur. J.* **2015**, *21*, 1221−1236.
(48) Ogliaro, F.; de Visser, S. P.; Shaik, S. *J. Inorg. Biochem.* **2002**, *91*, 554−567.
(49) (a) Friedrich, L. E. *J. Org. Chem.* **1983**, *48*, 3851−3852. (b) Bordwell, F. G.; Cheng, J.-P. *J. Am. Chem. Soc.* **1991**, *113*, 1736−1743. (c) Mayer, J. M. *Acc. Chem. Res.* **1998**, *31*, 441−450.
(50) *NIST Chemistry WebBook*, NIST Standard Reference Database, Number 69; Linstrom, P. J., Mallard, W. G., Eds.; National Institute of Standards and Technology: Gaithersburg, MD, 2016. http://webbook.nist.gov.
(51) (a) Green, M. T.; Dawson, J. H.; Gray, H. B. *Science* **2004**, *304*, 1653−1656. (b) Parsell, T. H.; Yang, M.-Y.; Borovik, A. S. *J. Am. Chem. Soc.* **2009**, *131*, 2762−2763.
(52) Shaik, S. S. *J. Am. Chem. Soc.* **1981**, *103*, 3692−3701.

DOI: 10.1021/acscatal.5b02720
ACS Catal. 2016, 6, 2230−2243

Chemical Physics 456 (2015) 41–46

Contents lists available at ScienceDirect

Chemical Physics

journal homepage: www.elsevier.com/locate/chemphys

Polarizability study of nematic liquid crystal 4-cyano-4′-pentylbiphenyl (5CB) and its nitrogen derivatives

Pranav Upadhyay, Manoj Kumar Rastogi, Devesh Kumar *

Department of Applied Physics, Babasaheb Bhimrao Ambedkar University, Lucknow 226025, U.P., India

ARTICLE INFO

Article history:
Received 22 January 2015
In final form 25 March 2015
Available online 16 April 2015

Keywords:
Liquid crystal
Polarizability
Density functional theory
5CB

ABSTRACT

The effect of electric field on the molecular polarizability and HOMO–LUMO gap for 4-cyano-4′-pentylbiphenyl (**1**) and its nitrogen derivatives 2-cyano-5-(4-pentylphenyl)pyridine (**2**), 2-(4-cyanophenyl)-5-pentylpyrimidine (**3**) and 5-cyano-2-(4-pentylphenyl)pyrimidine (**4**) has been studied using density functional theory (DFT). The effect on polarizability and HOMO–LUMO gap due to presence of substituent in the molecules is also investigated by comparing results obtained from two different DFT approaches B3LYP and M062X. It was observed that variation of polarizability with change in electric field for all molecules show a common feature that is stabilization of polarizability between two values of electric field (or for a range of electric field). 4-cyano-4′-pentylbiphenyl (**1**) polarizes more in comparison to all other derivatives and has widest stability region among all.

© 2015 Published by Elsevier B.V.

1. Introduction

Now-a-days liquid crystals (LC) are widely used for commercial applications such as electro-optical flat panel display devices for consumer audio-visual and office equipment. Among the all type of liquid crystals, nematic phase is characterized by long range orientational order, i.e. the long axis of the molecule tend to align along a preferred direction and its orientational order can also be altered by an applied magnetic or electric field [1–3].

Williams et al. [4] studied the effect of dc field on nematic liquid crystal by confining it between two electrodes and observed a convective instability beyond a threshold voltage (∼5 V) resulting in breakdown of the nematic phase and formation of regular patterns or domains. These domains become visible in polarized light with direction of polarization parallel to the direction of initial molecular alignment [5]. It was also observed that the electro-convection and flexo-electric pattern was formed upon application of superimposed dc and ac electric fields [6].

The effect of electric field on liquid crystals can be studied by analyzing an important parameter known as polarizability, which is a crucial property responsible for dispersion as well as induction forces in molecules and materials. Depending on the polarizability of a material, an applied electric field causes its polarization so that material can be used for a desired purpose. In liquid crystals, the molecular polarizability and its anisotropy are important inherent molecular properties because the intermolecular interaction energies depend on them [7].

To measure polarizability and other physical properties, different theoretical models and approaches have been proposed over past few decades; Vuks [8], Neugebauer [9], Lippincott δ-function model [10] and their modifications are the methods to name a few.

As dielectric anisotropy ($\Delta\varepsilon = \varepsilon_{||} - \varepsilon_{\perp}$, $\varepsilon_{||}$ and $\varepsilon_{\perp}$ are the permittivity parallel and perpendicular to the director respectively) dominates the reorientation of liquid crystal molecules under an external electric field, so it becomes critical for most of the electro-optic applications [11]. Maier–Meier theory [12] either with some alterations or hybridizing it with other methods [13–15] had been used by many researchers for determining dielectric anisotropy. Semi-empirical molecular orbit (MO) methods to calculate the dielectric anisotropy was first used by Bremer and Tarumi [16] in which they were successful in finding reasonable correlation between $\Delta\varepsilon$ and dipole moment with some scatter. *ab initio* method (B3LYPD/6-31G(d)) was compared with semi-empirical method (MOPAC/AM1) by Demus and Inukai [17,18] with different conformers and they found latter was more near to experiments. Aver'yanov studied the influence of the orientational order of molecules in a nematic liquid crystal on the average dielectric permittivity and anisotropy of the molecular polarizability in the framework of the molecular statistical approach with a perturbation of the electronic structure of molecules due to the change in the conformation of their aromatic core and intermolecular interactions [19].

* Corresponding author.
E-mail address: dkclcre@yahoo.co.in (D. Kumar).

http://dx.doi.org/10.1016/j.chemphys.2015.03.011
0301-0104/© 2015 Published by Elsevier B.V.

Presently liquid crystals are experiencing a revolutionary phase of research in which aspects other than display properties are brought forward by studying the applicability of liquid crystalline states of matter in the field of organic electronics [20,21], nanoparticle organization [22,23]. Photonics [24], polymers [25,26], complexes [27], biology [28,29], pharmacology [30] and food science [31] as well [32]. Electro-optical properties of liquid crystals after being doped with different kind of dopants have been analyzed [23,33]. Materials like graphene oxide [34,35], active matter [36] possessing liquid crystalline phase have been demonstrated.

In this paper we present a comparative study of polarizability of 4-cyano-4′-pentylbiphenyl (**1**) (commonly known as 5CB) and its nitrogen derivatives 2-cyano-5-(4-pentylphenyl)pyridine (**2**), 2-(4-cyanophenyl)-5-pentylpyrimidine (**3**) and 5-cyano-2-(4-pentylphenyl)pyrimidine (**4**), which are nematic liquid crystal. 5CB is about 20 Å long and exhibit liquid crystal phases near room temperature. The molecular structure along with transition temperatures and dielectric constants of these molecules is summarized in Table I. They have positive dielectric anisotropy ($\Delta\varepsilon$) and are useful for parallel or twist alignment.

2. Geometry optimization and methodology

Geometry optimization and total-energy calculations were carried out by using density-functional theory which is proven good for characterization/correlation/explanation of properties of various types of molecules [41–43]. The structures were created using GaussView 5.0. The molecular structures were fully optimized without any constrain and frequency were calculated with B3LYP [44,45] hybrid functional for Gaussian type orbitals (GTOs) and 6-31G** [46] basis set using Gaussian 09 [47]. Inter-ring distance and inter-ring twist after optimization is given in Table 2. Effect of electric field along the long axis (*x*-axis) on polarizability (α) was calculated using B3LYP and M062X [48] methods with 6-31G** basis set using Gaussian 09. These methods are already proven in the area of intramolecular interactions, conformational studies [49], enzymatic reaction mechanism [50–53], investigations on molecular structure, spectroscopy [54], and studies of clusters [55].

M06-2X belongs to M06-class functional which relies on spin densities, spin density gradients, spin kinetic energy densities, and for nonlocal hybrid functionals, Hartree–Fock exchange. M06-2X, is hybrid meta functional, has excellent performance for main group chemistry. It is quite accurate in predicting valence and Rydberg electronic excitation energies, including dispersion corrections and provide excellent results for aromatic–aromatic stacking interactions [48].

Table 2
Inter-ring distance and inter-ring twist of compounds.

Compound	Inter-ring distance (Å)	Inter-ring twist (°)
1	1.48276	143.581
2	1.47949	143.227
3	1.48557	180.262
4	1.47469	180.084

Table 3
Showing the conversion factor for atomic unit to SI unit.

Physical parameter	Atomic unit (a.u.)	SI unit
Electric field	1	5.142206×10^{11} Vm^{-1}
Polarizability	1	1.648777×10^{-41} C^2 m^2 J^{-1}
Energy	1 hartree	4.3597×10^{-18} J

Calculation of effect of field as implemented in Gaussian 09 is well explained by Jensen [56]. Molecular geometry was not allowed to change during calculation of polarizability. The field was varied from 0.000 a.u. to 0.050 a.u. with an increment of 0.002 a.u. Polarizability was calculated from the trace of polarizability tensor. Table 3 presents conversion different parameters from atomic unit to SI unit.

3. Results

Fig. 1 presents the optimized geometry of the molecules **1**, **2**, **3**, and **4**.

3.1. 4-cyano-4′-pentylbiphenyl

Fig. 2 presents the variation of polarizability and HOMO–LUMO band gap with the electric field for molecule **1**. The polarizability varies exponentially with respect to electric field till it reaches a point (0.018 a.u. for B3LYP and 0.022 a.u. for M062X) where it gets stabilized and remains constant till 0.042 a.u. for both B3LYP and M062X. HOMO–LUMO gap also varies with electric field as shown in Fig. 2. It gets stabilized after continuous decrement at the same field value for which polarizability gets stabilized.

3.2. 2-cyano-5-(4-pentylphenyl)pyridine

Replacement of carbon at *ortho* position with nitrogen in second benzene ring from the chain side has pushed the stability range by 0.006 a.u. Starting points of stability region is 0.022 a.u. for B3LYP and 0.024 a.u. for M062X and stability region ends at 0.038 a.u. for

Table 1
List of molecules studied with their transition temperature and values for dielectric anisotropy (measured at $0.98 \times T_{N-I}$, where T_{N-I} is nematic clearing point) (Ref. [37]).

Compound	Molecular structure	Transition temperature (crystal) (°C)	Transition temperature (nematic) (°C)[a]	Dielectric anisotropy ($\Delta\varepsilon$)	References
1		22.5	35	+8.5	[38]
2	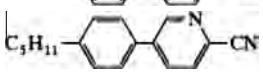	73	[31]	+9.4	[39]
3	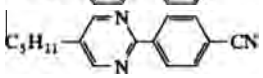	71	(52)	+21	[40]
4	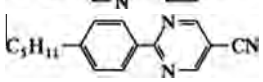	96	109[b]	+3.4	[41]

[a] The parenthesis represent a monotropic transition temperature and square bracket represent an extrapolated "virtual" transition temperature.
[b] Smectic A phase at 93.5 °C.

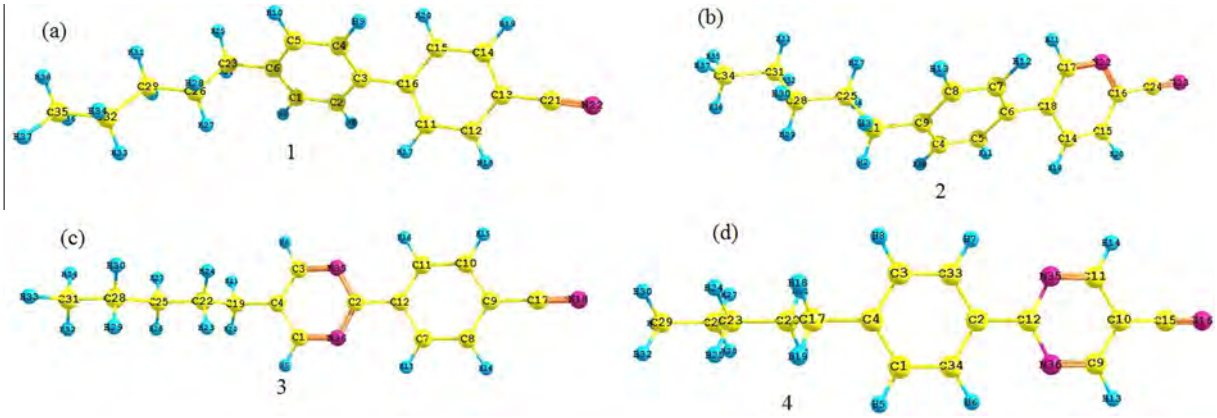

Fig. 1. The optimized geometry for the molecules (a) 4-cyano-4′-pentylbiphenyl (b) 2-cyano-5-(4-pentylphenyl)pyridine, (c) 2-(4-cyanophenyl)-5-pentylpyrimidine, (d)5-cyano-2-(4-pentylphenyl)pyrimidines. Atoms labelled are used for finding inter-ring twist.

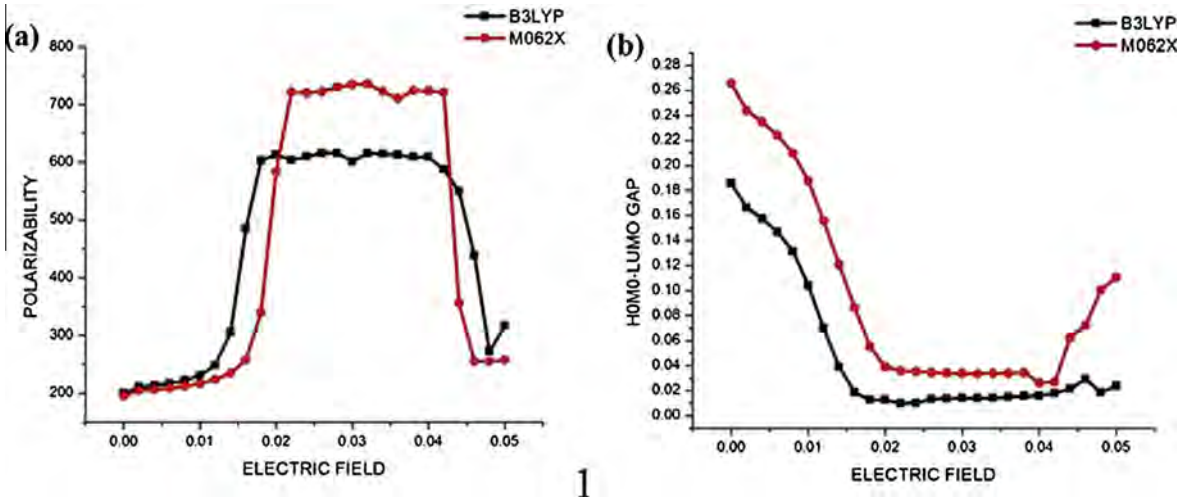

Fig. 2. (a) Variation of polarizability with electric field and (b) variation of HOMO–LUMO gap for molecule 1.

B3LYP and 0.040 a.u. for M062X. HOMO–LUMO gap variation gets modified accordingly with electric field as shown in Fig. 3.

3.3. 2-(4-cyanophenyl)-5-pentylpyrimidine

From Fig. 4, it can be observed that on replacing both *ortho* carbons with nitrogen in the first ring from chain side, the stability range achieves nearly the same value as that of molecule **1** for both B3LYP and M062X. The starting point for B3LYP is 0.02 a.u. and 0.024 a.u. for M062X, while dropping value is 0.04 a.u. For B3LYP and 0.044 a.u. for M062X. Stability of HOMO–LUMO gap is also between the same ranges of field values.

3.4. 5-cyano-2-(4-pentylphenyl) pyrimidine

Replacement of both *meta* carbons in the second ring with nitrogen gives us a stability range similar to molecule **2**.Stability starts at 0.022 a.u. for B3LYP and 0.024 a.u. for M062X which ends at 0.038 a.u. for B3LYP and 0.042 for M062X (Fig. 5). Plot for HOMO–LUMO gap follows accordingly.

3.5. Effect of high field on charge distribution

There is fall of polarizability on field above 0.42 a.u. in most cases. Tables 4 and 5 shows the Mullikan charge distribution for all compounds at 0.46 a.u. electric field. At this field even few hydrogen atoms also bears negative charge.

4. Discussion and conclusions

Polarizability versus electric field plot for all molecules shows a common feature of stabilized polarizability between two values of electric field (or for a range of electric field values). 5CB (**1**) polarizes more in comparison to all other derivatives and has widest stability region among all.

For 5CB, stability region always remains above the level of 600 a.u. but for its nitrogen derivatives, stability region is below 600 a.u. Similarly for M062X, 5CB has more polarizability than its nitrogen derivatives (**2**, **3**, **4**).

Initially both M062X and B3LYP start with similar values of polarizability. M062X gives higher value in comparison to B3LYP. Fall for M062X is sharper while for B3LYP it is quite smooth. For all the molecules, HOMO–LUMO gap is flat in the stability region of the respective molecule.

To conclude, we found that the polarizability as well as HOMO–LUMO gap remains stable within a particular range of electric field and around a certain level. The possible reason is that the increase in magnitude of field results in conjugation effect whereby electrons prefer to delocalize instead of being localized. The mobile electrons which are available as a result of this conjugation (delocalization) are responsible for an increased polarizability.

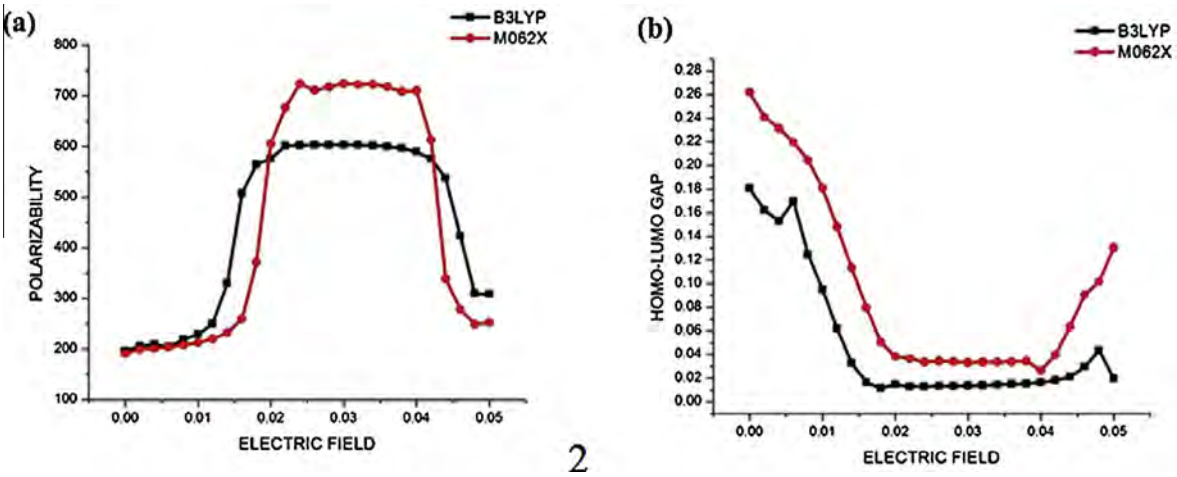

Fig. 3. (a) Variation of polarizability with electric field and (b) variation of HOMO–LUMO gap for molecule 2.

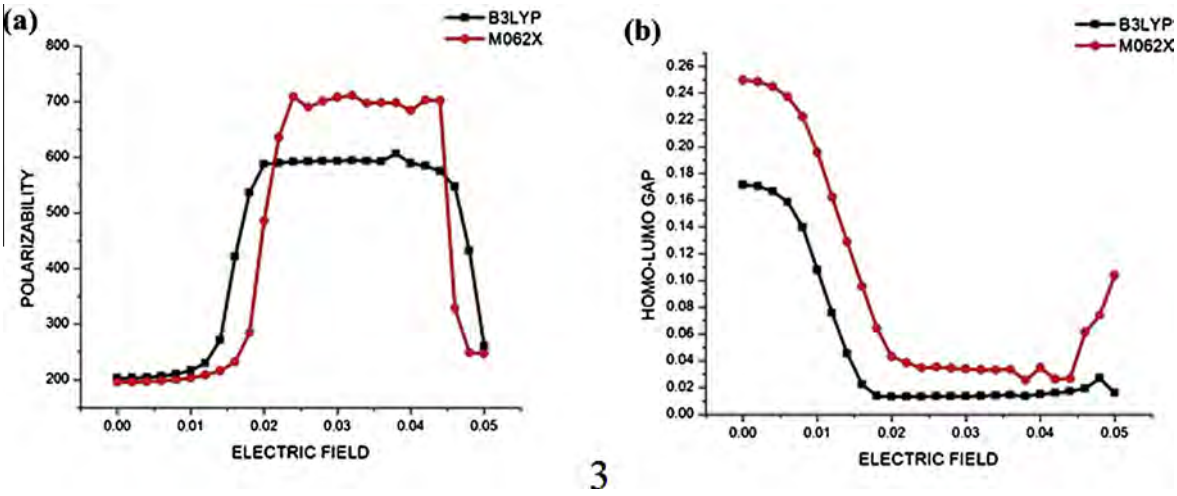

Fig. 4. (a) Variation of polarizability with electric field and (b) variation of HOMO–LUMO gap for molecule 3.

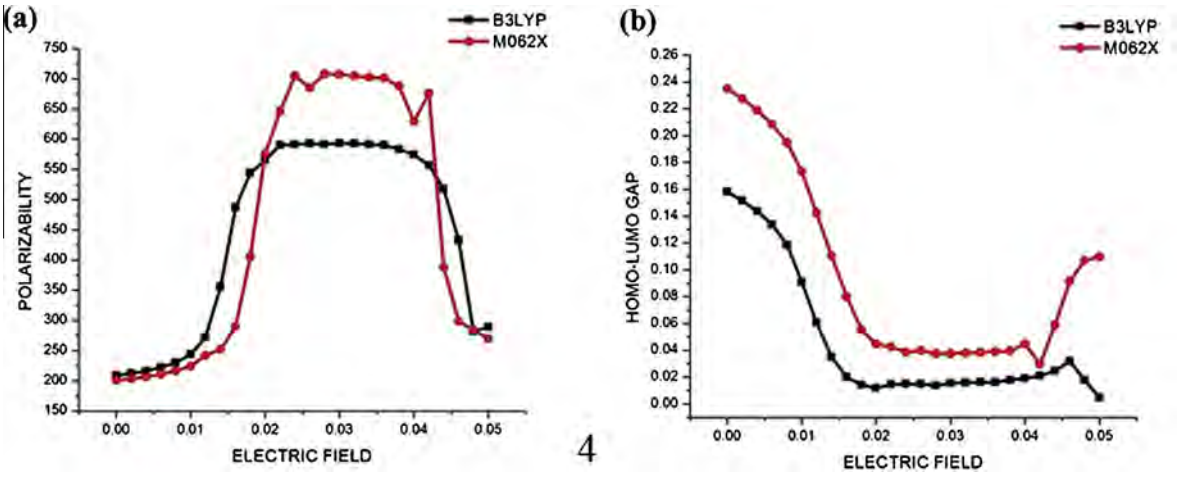

Fig. 5. (a) Variation of polarizability with electric field and (b) variation of HOMO–LUMO gap for molecule 4.

Table 4
Below is the charge on the atoms (along with number showing their label as per Fig. 1) of molecule **1** and molecule **2** at an electric field 0.46 a.u. At this field even few hydrogen atoms also bears negative charge.

Molecule 1				Molecule 2			
B3LYP		M062X		B3LYP		M062X	
Atom	Charge	Atom	Charge	Atom	Charge	Atom	Charge
1 C	−0.106952	1 C	−0.133739	1 C	−0.272783	1 C	−0.305298
2 C	−0.130472	2 C	−0.151885	2 H	0.194829	2 H	0.215619
3 C	0.071506	3 C	0.041636	3 H	0.188529	3 H	0.209565
4 C	−0.129848	4 C	−0.151047	4 C	−0.108535	4 C	−0.131893
5 C	−0.108796	5 C	−0.135126	5 C	−0.130910	5 C	−0.151430
6 C	0.111276	6 C	0.072510	6 C	0.069187	6 C	0.042380
7 H	0.162151	7 H	0.190161	7 C	−0.128521	7 C	−0.149455
8 H	−0.002686	8 H	0.021733	8 C	−0.107823	8 C	−0.131457
9 H	0.003350	9 H	0.027779	9 C	0.110871	9 C	0.068179
10 H	0.160909	10 H	0.189030	10 H	0.166995	10 H	0.198928
11 C	−0.106311	11 C	−0.123124	11 H	0.010615	11 H	0.038237
12 C	−0.173103	12 C	−0.193774	12 H	−0.008761	12 H	0.018861
13 C	0.080857	13 C	0.044794	13 H	0.154694	13 H	0.186753
14 C	−0.156672	14 C	−0.177652	14 C	−0.080025	14 C	−0.097778
15 C	−0.101844	15 C	−0.119514	15 C	−0.134952	15 C	−0.159389
16 C	−0.015856	16 C	−0.045458	16 C	0.140832	16 C	0.126896
17 H	0.085379	17 H	0.118690	17 C	−0.011578	17 C	−0.010253
18 H	−0.167330	18 H	−0.136005	18 C	−0.033042	18 C	−0.064789
19 H	−0.244051	19 H	−0.212995	19 H	0.034833	19 H	0.069156
20 H	0.035047	20 H	0.068118	20 H	−0.253879	20 H	−0.218983
21 C	−0.477575	21 C	−0.480141	21 H	0.086766	21 H	0.117889
22 N	−0.867158	22 N	−0.876627	22 N	−0.578246	22 N	−0.601324
23 C	−0.273206	23 C	−0.306147	23 N	−0.867764	23 N N	−0.877294
24 H	0.195485	24 H	0.207441	24 C	−0.411950	24 C	−0.410744
25 H	0.193595	25 H	0.207229	25 C	−0.209482	25 C	−0.244894
26 C	−0.209470	26 C	−0.249957	26 H	0.143177	26 H	0.157444
27 H	0.139028	27 H	0.143048	27 H	0.137423	27 H	0.150286
28 H	0.137051	28 H	0.144271	28 C	−0.243577	28 C	−0.294578
29 C	−0.243058	29 C	−0.314832	29 H	0.303379	29 H	0.322739
30 H	0.297745	30 H	0.333861	30 H	0.292126	30 H	0.311233
31 H	0.302180	31 H	0.335331	31 C	−0.316701	31 C	−0.383574
32 C	−0.317298	32 C	−0.424723	32 H	0.333522	32 H	0.367202
33 H	0.358611	33 H	0.426065	33 H	0.358460	33 H	0.399700
34 H	0.327459	34 H	0.427253	34 C	−0.224698	34 C	−0.265855
35 C	−0.225756	35 C	−0.298803	35 H	0.482233	35 H	0.513851
36 H	0.432923	36 H	0.535205	36 H	0.486310	36 H	0.525778
37 H	0.478920	37 H	0.460534	37 H	0.428442	37 H	0.458291
38 H	0.483968	38 H	0.536863				

Table 5
Below is the charge on the atoms (along with number showing their label as per Fig. 1) of molecule **3** and molecule **4** at an electric field 0.46 a.u. At this field even few hydrogen atoms also bears negative charge.

Molecule 3				Molecule 4			
B3LYP		M062X		B3LYP		M062X	
Atom	Charge	Atom	Charge	Atom	Charge	Atom	Charge
1 C	0.052251	1 C	0.047005	1 C	−0.110861	1 C	−0.136575
2 C	0.281837	2 C	0.309511	2 C	0.106206	2 C	0.059961
3 C	0.050341	3 C	0.045206	3 C	−0.110666	3 C	−0.136314
4 C	0.070346	4 C	0.021892	4 C	0.113301	4 C	0.070232
5 H	0.164444	5 H	0.192650	5 H	0.156254	5 H	0.187345
6 H	0.147118	6 H	0.175596	6 H	0.021837	6 H	0.052943
7 C	−0.107216	7 C	−0.122112	7 H	0.026949	7 H	0.057955
8 C	−0.166211	8 C	−0.188420	8 H	0.161162	8 H	0.191650
9 C	0.072714	9 C	0.031567	9 C	−0.021188	9 C	−0.025511
10 C	−0.161262	10 C	−0.183348	10 C	0.045060	10 C	0.011418
11 C	−0.105618	11 C	−0.120957	11 C	−0.020985	11 C	−0.025098
12 C	0.013114	12 C	−0.045675	12 C	0.167624	12 C	0.179625
13 H	0.083775	13 H	0.118593	13 H	−0.170911	13 H	−0.139818
14 H	−0.164968	14 H	−0.139052	14 H	−0.163626	14 H	−0.132425
15 H	−0.189966	15 H	−0.164631	15 C	−0.479875	15 C	−0.473988
16 H	0.066921	16 H	0.101590	16 N	−0.842733	16 N	−0.852825
17 C	−0.407839	17 C	−0.414523	17 C	−0.272401	17 C	−0.305030
18 N	−0.819774	18 N	−0.838138	18 H	0.194590	18 H	0.213245
19 C	−0.266471	19 C	−0.294839	19 H	0.189653	19 H	0.211739

(*continued on next page*)

Table 5 (*continued*)

Molecule 3				Molecule 4			
B3LYP		M062X		B3LYP		M062X	
Atom	Charge	Atom	Charge	Atom	Charge	Atom	Charge
20 H	0.160755	20 H	0.180367	20 C	−0.209472	20 C	−0.244972
21 H	0.146005	21 H	0.168852	21 H	0.143992	21 H	0.155411
22 C	−0.206873	22 C	−0.245119	22 H	0.136339	22 H	0.152619
23 H	0.172722	23 H	0.190895	23 C	−0.242904	23 C	−0.293905
24 H	0.156828	24 H	0.177794	24 H	0.297779	24 H	0.321026
25 C	−0.245983	25 C	−0.298120	25 H	0.296551	25 H	0.313544
26 H	0.262488	26 H	0.290181	26 C	−0.315986	26 C	−0.382781
27 H	0.251999	27 H	0.275287	27 H	0.361464	27 H	0.362879
28 C	−0.303373	28 C	−0.369811	28 H	0.324875	28 H	0.399101
29 H	0.390503	29 H	0.398197	29 C	−0.227147	29 C	−0.267586
30 H	0.347346	30 H	0.427873	30 H	0.433362	30 H	0.522136
31 C	−0.233901	31 C	−0.269783	31 H	0.480015	31 H	0.512308
32 H	0.412778	32 H	0.510140	32 H	0.479391	32 H	0.459210
33 H	0.506401	33 H	0.541933	33 C	−0.130594	33 C	−0.151148
34 H	0.455606	34 H	0.436625	34 C	−0.130287	34 C	−0.150612
35 N	−0.447741	35 N	−0.477812	35 N	−0.342514	35 N	−0.356970
36 N	−0.439096	36 N	−0.469415	36 N	−0.344255	36 N	−0.358793

As the field is increased gradually, the polarizability attains nearly constant value due to availability of large number of mobile electrons. Further, availability of mobile electrons due to conjugation results in decrease of HOMO–LUMO separation.

When the applied electric field is increased further, it results in drop of polarizability due to excessive and random distribution of electrons (negative charge). As we can see from the Tables 4 and 5 that even hydrogen of benzene ring (near to CN group) and carbon of CN group bears some negative charge.

Replacement of carbon with nitrogen has not only reduced the stability range but has also pushed it further. Presence of more electronegative nitrogen makes derivatives less polarizable by countering the effect of cyano group hence higher field is required to reach the stability region.

Conflict of interest

No conflict of interest.

Acknowledgments

Authors are thankful to Mr. Ankur Trivedi for scientific discussions and suggestions. DK is DST-Ramanujan Fellow (SR/S2/RJN-11/2008).

References

[1] P.G. de Gennes, J. Prost, The Physics of Liquid Crystals, second ed., Oxford University Press, Oxford, 1993.
[2] S. Chandrasekhar, Liquid Crystals, second ed., Cambridge University Press, Cambridge, 1992.
[3] M.J. Stephen, J.P. Straley, Rev. Mod. Phys. 46 (1974) 617.
[4] R. Williams, J. Chem. Phys. 39 (1963) 384.
[5] D.T. Teaney, A. Migliori, J. Appl. Phys. 41 (1970) 998.
[6] K. Alexei, Phys. Rev. E 89 (2014) 052507.
[7] P.R. Alapati, D. Bhuyan, D. Madhavilatha, P. Pardhasaradhi, V.G.K.M. Pisipati, P.V. Datta Prasad, K.N. Singh, World J. Condens. Matter Phys. 1 (2011) 167.
[8] M.F. Vuks, Opt. Spectrosc. 20 (1966) 361.
[9] H.E.J. Neugebauer, Can. J. Phys. 18 (1950) 292.
[10] E.R. Lippincott, J.M. Stutman, J. Phys. Chem. 68 (1964) 2926.
[11] Z. Ran, H. Jun, P. Zeng-Hui, X. Li, Chin. Phys. Soc. 18 (2009) 7.
[12] W. Maier, G.Z. Meier, Naturforschung 16 (1961) 262.
[13] G. Saitoh, M. Satoh, E. Hasegawa, Mol. Cryst. Liq. Cryst. 301 (1997) 13.
[14] M. Klasen, M. Bremer, A. Gäotz, S. Manabe, S. Naemura, K. Tarumi, Jpn. J. Appl. Phys. 37 (1998) 945.
[15] A. Fujita, M. Ushioda, H. Takeuchi, T. Inukai, D. Demus, Mol. Cryst. Liq. Cryst. 331 (1999) 305.
[16] M. Bremer, K. Tarumi, Adv. Mater. 5 (1993) 842.
[17] D. Demus, T. Inukai, Liq. Cryst. 26 (1999) 1257.
[18] D. Demus, T. Inukai, Mol. Liq. Cryst. 400 (2003) 39.
[19] E.M. Aver'yanov, Phys. Solid State 56 (2014) 1058.
[20] M. O'Neill, S. Kelly, Adv. Mater. 23 (2011) 566.
[21] J. Harden, M. Chambers, R. Verduzco, P. Luchette, J.T. Gleeson, S. Sprunt, A. Jakli, Appl. Phys. Lett. 96 (2010) 102907.
[22] H. Chen, W. Lee, Opt. Rev. 12 (2005) 223.
[23] P. van der Schoot, V. Popa-Nita, S. Kralj, J. Phys. Chem. B 112 (2008) 4512.
[24] R. Won, Nat. Photon 5 (2011) 133.
[25] J. Clapper, S. Iverson, C. Guymon, Biomacromolecules 8 (2007) 2104.
[26] C. Mock-knoblauch, O.S. Enger, U.D. Schalkowsky, SID Dig. (2006) 1673.
[27] A.P. Kovshika, E.S. Krainyukova, S.A. Kovshika, A.A. Knyazevb, Yu.G. Galyametdinovb, E.I. Ryumtsev, Opt. Spectrosc. 116 (2014) 56.
[28] S. Sivakumar, K.L. Wark, J.K. Gupta, N.L. Abbott, F. Caruso, Adv. Funct. Mater. 19 (2009) 2260.
[29] C. Jang, L. Cheng, C. Olsen, N. Abbott, Nano Lett. 6 (2006) 1053.
[30] C. Muller-goymann, Eur. J. Pharm. Biopharm. 58 (2004) 343.
[31] L. Sagalowicz, M. Leser, H. Watzke, M. Michel, Trends Food Sci. Technol. 17 (2006) 204.
[32] J.P.F. Lagerwall, G. Scalia, Curr. Appl. Phys. 12 (2012) 1387.
[33] M. Urbanski, J. Mirzaei, T. Hegmann, H.S. Kitzerow, ChemPhysChem 15 (2014) 1395.
[34] J.E. Kim, T.H. Han, S.H. Lee, J.Y. Kim, Chi Won Ahn, Je Moon Yun, Sang Ouk Kim, Angew. Chem. Int. Ed. 50 (2011) 3043.
[35] J.Y. Kim, S.O. Kim, Nat. Mater. 32 (2014) 325.
[36] S. Zhoua, A. Sokolovb, O.D. Lavrentovicha, I.S. Aranson, PNAS 111 (2014) 1265.
[37] S.M. Kelly, M. O'Neill, Liquid Crystals, Display and Laser Materials, vol. 7, Academic Press, U.K., 2000. Chapter 1.
[38] G.W. Gray, K.J. Harrison, J.A. Nash, Electron. Lett. 9 (1973) 130.
[39] L.A. Karamysheva, E.I. Kovshev, A.I. Pavluchenko, K.V. Roitman, V.V. Titov, S.I. Torgova, M.F. Grebyonkin, Mol. Cryst. Liq. Cryst. 67 (1981) 241.
[40] A. Boller, M. Cereghetti, M. Schadt, H. Scherrer, Mol. Cryst. Liq. Cryst. 42 (1977) 1225.
[41] S. Kumar, A.S. Faponle, P. Barman, A.K. Vardhaman, C.V. Sastri, D. Kumar, S.P. de Visser, J. Am. Chem. Soc. 136 (2014) 17102.
[42] A.K. Vardhaman, P. Barman, S. Kumar, C.V. Sastri, D. Kumar, S.P. de Visser, Angew. Chem. Int. Ed. 52 (2013) 12288.
[43] D. Umadevi, S. Panigrahi, G.N. Sastry, Acc. Chem. Res. 47 (2014) 2574.
[44] A.D. Becke, J. Chem. Phys. 1993 (98) (1993) 5648.
[45] C. Lee, W. Yang, R.G. Parr, Phys. Rev. B 37 (1988) 785.
[46] P.J. Hay, W.R. Wadt, J. Chem. Phys. 82 (1985) 270.
[47] M.J. Frisch, G.W. Trucks, H.B. Schlegel, G.E. Scuseria, M.A. Robb, J.R. Cheeseman, G. Scalmani, V. Barone, B. Mennucci, G.A. Petersson, H. Nakatsuji, M. Caricato, X. Li, H.P. Hratchian, A.F. Izmaylov, J. Bloino, G. Zheng, J.L. Sonnenberg, M. Hada, M. Ehara, K. Toyota, R. Fukuda, J. Hasegawa, M. Ishida, T. Nakajima, Y. Honda, O. Kitao, H. Nakai, T. Vreven, J.A. Montgomery Jr., J.E. Peralta, F. Ogliaro, M. Bearpark, J.J. Heyd, E. Brothers, K.N. Kudin, V.N. Staroverov, T. Keith, R. Kobayashi, J. Normand, K. Raghavachari, A. Rendell, J.C. Burant, S.S. Iyengar, J. Tomasi, M. Cossi, N. Rega, J.M. Millam, M. Klene, J.E. Knox, J.B. Cross, V. Bakken, C. Adamo, J. Jaramillo, R. Gomperts, R.E. Stratmann, O. Yazyev, A.J. Austin, R. Cammi, C. Pomelli, J.W. Ochterski, R.L. Martin, K. Morokuma, V.G. Zakrzewski, G.A. Voth, P. Salvador, J.J. Dannenberg, S. Dapprich, A.D. Daniels, O. Farkas, J.B. Foresman, J.V. Ortiz, J. Cioslowski, D.J. Fox, Gaussian-09, Revision B.01, Gaussian Inc., Wallingford CT, 2010.
[48] Y. Zhao, D.G. Truhlar, Theor. Chem. Acc. 120 (2008) 215.
[49] U. Yadava, M. Singh, M. Roychaudhury, Comput. Theor. Chem. 977 (2011) 134.
[50] S. Shaik, S.P. de Visser, D. Kumar, J. Am. Chem. Soc. 126 (2004) 11746.
[51] S.P. de Visser, J. Phys. Chem. A 109 (2005) 11050.
[52] S.P. de Visser, Inorg. Chem. 45 (2006) 9551.
[53] Rong-Zheng Liao, Jian-Guo Yu, F. Himo, J. Phys. Chem. B 114 (2010) 2533.
[54] U. Yadava, D.K. Gupta, M. Roychoudhury, J. Mol. Liq. 156 (2010) 187.
[55] A. Sorkin, D.G. Truhlar, E.A. Amin, J. Chem. Theory Comput. 5 (2009) 1254.
[56] F. Jensen, Introduction to Computational Chemistry, second ed., John Wiley & Sons Ltd, UK, 2006. Chapter 10, p. 315.

ChemPubSoc Europe

DOI: 10.1002/chem.201500329

CHEMISTRY A European Journal Full Paper

Reaction Mechanisms |*Hot Paper*|

Drug Metabolism by Cytochrome P450 Enzymes: What Distinguishes the Pathways Leading to Substrate Hydroxylation Over Desaturation?

Li Ji,[a] Abayomi S. Faponle,[b] Matthew G. Quesne,[b] Mala A. Sainna,[b] Jing Zhang,[a] Alicja Franke,[c] Devesh Kumar,[e] Rudi van Eldik,[c, d] Weiping Liu,*[a] and Sam P. de Visser*[b]

Abstract: Cytochrome P450 enzymes are highly versatile biological catalysts in our body that react with a broad range of substrates. Key functions in the liver include the metabolism of drugs and xenobiotics. One particular metabolic pathway that is poorly understood relates to the P450 activation of aliphatic groups leading to either hydroxylation or desaturation pathways. A DFT and QM/MM study has been carried out on the factors that determine the regioselectivity of aliphatic hydroxylation over desaturation of compounds by P450 isozymes. The calculations establish multistate reactivity patterns, whereby the product distributions differ on each of the spin-state surfaces; hence spin-selective product formation was found. The electronic and thermochemical factors that determine the bifurcation pathways were analysed and a model that predicts the regioselectivity of aliphatic hydroxylation over desaturation pathways was established from valence bond and molecular orbital theories. Thus, the difference in energy of the O–H versus the O–C bond formed and the π-conjugation energy determines the degree of desaturation products. In addition, environmental effects of the substrate binding pocket that affect the regioselectivities were identified. These studies imply that bioengineering P450 isozymes for desaturation reactions will have to include modifications in the substrate binding pocket to restrict the hydroxylation rebound reaction.

Introduction

The cytochrome P450s (P450s) are key drug metabolizing enzymes in the human body,[1] and are widely distributed in living organisms, such as eukaryotic animals, but also in plants, fungi and bacteria. As of January 2015, more than 20000 different sequences had been identified, making the P450s one of the major biological enzyme classes.[2] In the human body, P450s are predominantly found in the liver, where they catalyse the biodegradation of xenobiotics but are also involved in the biosynthesis of hormones.[3] As such the P450s have multiple functions in the body, which also shows their versatility in substrate activation. For instance, the $P450_{BM3}$ subclass hydroxylates long-chain fatty acids,[4] and has a substrate binding pocket that accommodates long and thin substrates. By contrast, $P450_{cam}$ is a bacterial isozyme that regioselectively hydroxylates camphor at the carbon-5 position and has a fit-for-purpose substrate binding pocket.[5] A key drug metabolizing P450 isozyme is $P450_{2D6}$, which has a more open substrate binding pocket and can activate a large range of different substrate shapes and sizes. As P450 isozymes are highly efficient in substrate activation, they have gained interest from the biotechnology industry for the regioselective and/or stereospecific activation of substrates.[6] Despite decades of extensive scientific research into P450 chemistry, there are still major gaps in our understanding of its reactivity and activity, in particular related to the metabolism of drug molecules and xenobiotics, which is important for drug development and the pharmaceutical industry.

The name cytochrome P450 derives from the fact that the CO bound heme complex has an absorption band at 450 nm.[7] Their heme active site is linked to the protein via a thiolate linkage of a cysteinate residue covalently bound to the iron

[a] *Dr. L. Ji, J. Zhang, Prof. Dr. W. Liu*
College of Environmental and Resource Sciences
Zhejiang University, Yuhangtang Road 866, Hangzhou 310058 (China)
E-mail: wliu@zju.edu.cn

[b] *A. S. Faponle, Dr. M. G. Quesne, M. A. Sainna, Dr. S. P. de Visser*
Manchester Institute of Biotechnology and School of
Chemical Engineering and Analytical Science
The University of Manchester, 131 Princess Street
Manchester M1 7DN (UK)
E-mail: sam.devisser@manchester.ac.uk

[c] *Dr. A. Franke, Prof. Dr. R. van Eldik*
Inorganic Chemistry, Department of Chemistry and Pharmacy
University of Erlangen-Nuremberg
Egerlandstrasse 1, 91058 Erlangen (Germany)

[d] *Prof. Dr. R. van Eldik*
Faculty of Chemistry, Jagiellonian University
Ingardena 3, 30-060 Krakow (Poland)

[e] *Dr. D. Kumar*
Department of Applied Physics, School for Physical Sciences
Babasaheb Bhimrao Ambedkar University, Vidya Vihar
Rai Bareilly Road, Lucknow 226 025 (India)

Supporting information for this article is available on the WWW under http://dx.doi.org/10.1002/chem.201500329.

© 2015 Wiley-VCH Verlag GmbH & Co. KGaA, Weinheim

centre,[8] while the substrate binding pocket varies in shape and size for the different P450 isozymes. As an example we show in Figure 1 the active site of $P450_{2C19}$ with substrate warfarin bound as taken from the 4GQS protein databank (PDB) file.[9] The heme is linked to the protein through an iron–thiolate linkage with Cys435 and *trans* to this ligand the substrate (warfarin) binds.

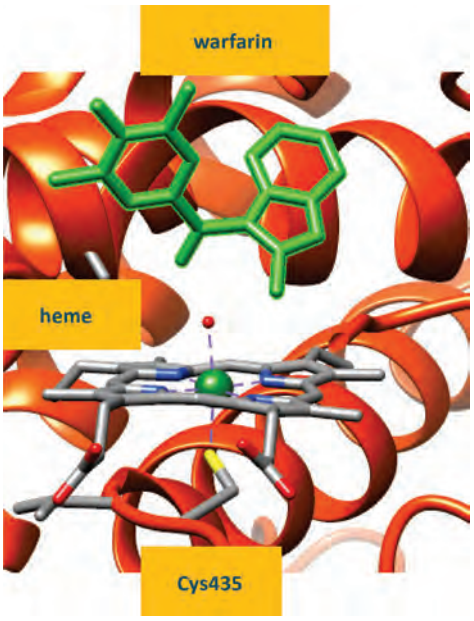

Figure 1. Extract of the active site of $P450_{2C19}$ as taken from the 4GQS PDB file.

The active species of P450 enzymes is an iron(IV)–oxo heme cation radical species called Compound I (Cpd I).[10] Due to its transient nature, Cpd I is short-lived and difficult to study with experimental means and as a consequence many details of its catalytic mechanism with substrates are unknown. The most common reaction mechanism performed by the P450s is aliphatic hydroxylation of substrates,[11] which was experimentally revealed as a stepwise process leading to alcohol product complexes.[12] Computational modelling confirmed the general mechanism and showed that the oxidation actually contains two close-lying spin states that lead to two-state reactivity patterns, each with an individual rate constant of the reaction.[13] Moreover, the two-state reactivity pattern also predicted that the lifetime of the radical intermediate could lead to a bifurcation of the potential energy profile, thereby generating, for instance, rearrangement patterns on one spin-state surface but not on the other.[14]

A key reaction mechanism in P450 chemistry with great relevance to drug metabolism is the desaturation of aliphatic groups to form olefins. As shown in Scheme 1 desaturation is a reaction mechanism that shows similarities to aliphatic hydroxylation, whereby both processes start with an initial hydrogen atom abstraction. However, thereafter the reaction bifurcates into two possible product channels: one giving OH rebound to form alcohol products (aliphatic hydroxylation) and the other leading to a second hydrogen atom abstraction to give an olefin and water (desaturation). Although the basic mechanism of substrate desaturation has been studied previously,[15] the origin and consequences of the bifurcation pathways in P450 catalysis are currently unknown and no predictive model exists that gives product distributions as a function of substrate chemical properties.

Several drug molecules have been shown to produce desaturation metabolites by P450 enzymes. Namely, valproic acid, an antiepileptic drug, is converted by P450 enzymes to form both alcohol and olefin products.[16] Another example is ethylcarbamate,[17] that in a reaction with $P450_{2E1}$ enzymes leads to a small amount of vinyl carbamate as a precursor to its epoxide.[18] The latter is considered the ultimate carcinogen[19] and its biosynthesis requires an essential desaturation step. Over the years a range of substrates of P450 isozymes have been identified that are desaturated to form olefins, including lauric acid,[20] but also a step in the biosynthesis of ergosterol includes a desaturation.[21]

Clearly, the mechanistic pathways surrounding drug metabolism by the P450s produce a large versatility of product patterns and currently it is not clear why certain substrates lead to desaturation, whereas others solely give hydroxylation products. To gain insight into the origin of the regioselectivity of desaturation versus hydroxylation processes by P450 enzymes, we decided to carry out a comprehensive computational study that includes density functional theory (DFT) modelling, quantum mechanics/molecular mechanics (QM/MM) and valence

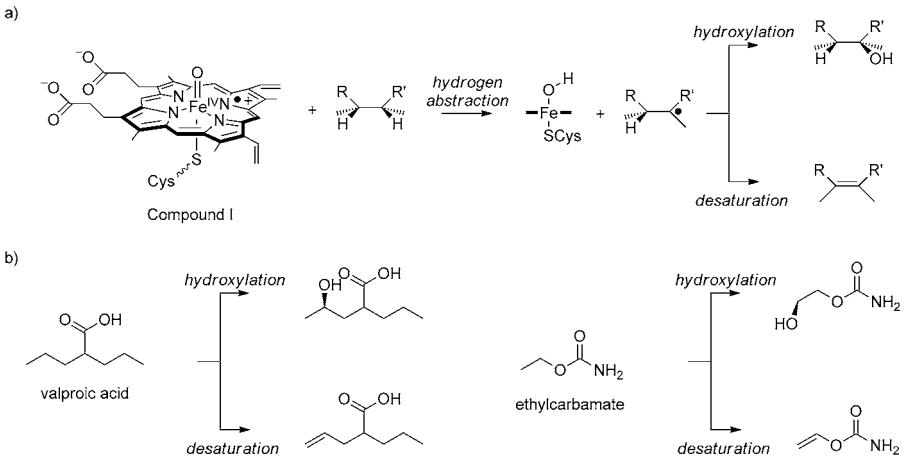

Scheme 1. a) Competitive hydroxylation and desaturation metabolism pathways of drug molecules by P450 Cpd I. b) Reaction products observed for valproic acid and ethylcarbamate.

© 2015 Wiley-VCH Verlag GmbH & Co. KGaA, Weinheim

bond (VB) theory. The overall study gives an electronic structure description on the metabolism of a variety of drug molecules and enables us to provide a predictive pattern that anticipates desaturation versus hydroxylation product distributions. Our studies explain the experimentally observed bifurcation reactions and may be used to develop computer-aided toxic risk assessment of potential carcinogens resulting from desaturation reactions catalysed by P450 isozymes.

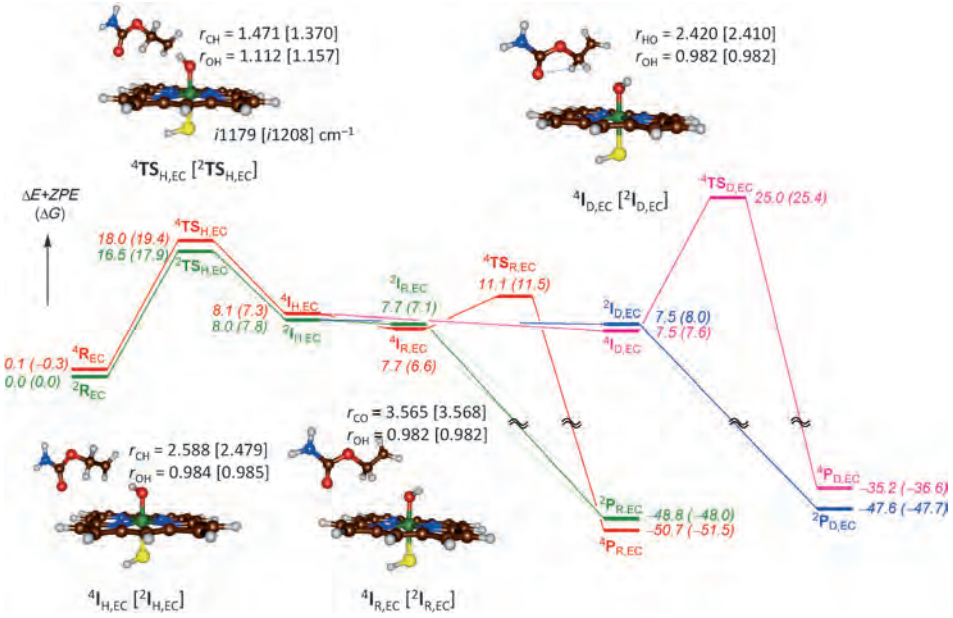

Figure 2. Potential energy profile of ethylcarbamate activation by ^{4,2}Cpd I of P450 as calculated with DFT. Energies are given in kcal mol^{-1} and are calculated at UB3LYP/BSII//UB3LYP/BSI level of theory with *ZPE* and solvent corrections included. Values in parenthesis are free energies in solvent. Optimized geometries give bond lengths in Å and the imaginary frequency in the transition states in wave numbers.

Results and Discussion

DFT model reactions

Before going into detail of the mechanism of drug metabolism by P450 enzymes, let us first go through a typical reaction mechanism of substrate activation leading to desaturation and hydroxylation products by taking ethylcarbamate (EC) as an example. Scheme 2 displays the calculated reaction mechanisms of EC activation by Cpd I of P450 and the bifurcation mechanism leading to desaturation and hydroxylation products.

We calculated the reaction between Cpd I and ethylcarbamate, as shown in Figure 2, starting from a reactant complex (^{4,2}**R**$_{EC}$), which exists in close-lying doublet and quartet spin states, both with electronic configuration $\delta_{x^2-y^2}{}^2\pi^*_{xz}{}^1\pi^*_{yz}{}^1a_{2u}{}^1$. Attack of the oxo group of Cpd I on the substrate leads to a hydrogen atom abstraction via a transition state ^{4,2}**TS**$_{H,EC}$ to form a radical intermediate (^{4,2}**I**$_{H,EC}$) with electronic configuration $\delta_{x^2-y^2}{}^2\pi^*_{xz}{}^1\pi^*_{yz}{}^1a_{2u}{}^2\ \phi_{Rad}{}^1$. During the lifetime of the radical intermediate it can isomerize to structures ^{4,2}**I**$_{D,EC}$, whereby the C–H group of the substrate forms a hydrogen-bonding interaction with the oxygen atom of the OH group as a precursor to the second hydrogen atom abstraction step via transition state ^{4,2}**TS**$_{D,EC}$ to form desaturated products ^{4,2}**P**$_{D,EC}$. The alternative mechanism from ^{4,2}**I**$_{H,EC}$ gives an isomerization to form the pro-hydroxylation radical intermediate ^{4,2}**I**$_{R,EC}$, where the radical is aligned to the oxygen atom for rebound via transition state ^{4,2}**TS**$_{R,EC}$ to give the alcohol product complexes ^{4,2}**P**$_{R,EC}$. Our calculations were focused on establishing whether isomerization barriers exist from **I**$_H$ to **I**$_D$ and **I**$_R$, and what the factors are that determine the height of these barriers and consequently the regioselectivity of the reaction.

As shown in Figure 2, the hydrogen atom abstraction step is endergonic by $\Delta G^{\neq} = 19.4$ (17.9) kcal mol^{-1} in the quartet (doublet) spin states, respectively. Addition of dispersion corrections to the calculated relative energies lowers ^{4,2}**TS**$_{H,EC}$ in energy by about 4 kcal mol^{-1}, which is in accord with analogous previous findings for transition metal complexes.[22] The hydrogen atom abstraction transition states are characterized by an almost linear O–H–C configuration and a large imaginary frequency (HS: *i*1179 cm^{-1}; LS: *i*1208 cm^{-1}), and consequently a considerable kinetic isotope effect (KIE) for the reaction may be expected.[23]

We then investigated the OH rebound to form alcohol products and the second hydrogen atom abstraction to give desaturation products. We propose this to happen (Scheme 2) by an initial isomerization of the radical intermediate from ^{4,2}**I**$_{H,EC}$ to ^{4,2}**I**$_{R,EC}$, which sets up the molecular orientation for the OH rebound leading to the 2-hydroxyethyl-carbamate product. Similarly to previous studies,[24]

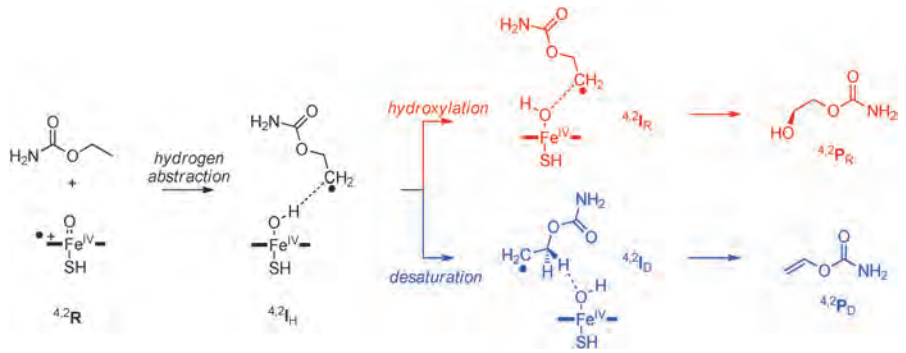

Scheme 2. Reaction mechanism of ethylcarbamate activation by Cpd I of P450.

© 2015 Wiley-VCH Verlag GmbH & Co. KGaA, Weinheim

a small but significant rebound barrier ($\Delta G = 4.9$ kcal mol^{-1}) is found on the quartet spin surface, while the doublet spin pathway is barrier free. Dispersion corrections lower the rebound barriers by about 1 kcal mol^{-1}, which is a significant smaller change than that found for the hydrogen atom abstraction step. The radical rebound pathway from $^{4,2}\mathbf{I}_{H,EC}$ is exergonic by $\Delta G = 58.8$ (55.8) kcal mol^{-1} on the quartet (doublet) spin state surfaces as expected for the formation of a stable alcohol product complex.

The alternative isomerization pathway from $^{4,2}\mathbf{I}_{H,EC}$, leads to a substrate rotation to form $^{4,2}\mathbf{I}_{D,EC}$, whereby the oxygen atom of the OH group is aligned with a hydrogen atom of the substrate to enable a second hydrogen atom abstraction. Note that the difference in orientation between $^{4,2}\mathbf{I}_{R,EC}$ and $^{4,2}\mathbf{I}_{D,EC}$ is similar to those reported for a synthetic manganese–hydroxo porphyrin complex.[25] The DFT calculations give negligible isomerization barriers between structures $\mathbf{I}_H$, $\mathbf{I}_R$ and $\mathbf{I}_D$, however, as shown below the effect of the protein changes this dramatically.

The doublet spin radical intermediate $^{2}\mathbf{I}_{D,EC}$ collapses to the desaturation product complex virtually barrier-free, whereas the quartet spin complex $^{4}\mathbf{I}_{D,EC}$ encounters a large activation barrier ($^{4}\mathbf{TS}_{D,EC}$) of $\Delta G^{\ddagger} = 17.8$ kcal mol^{-1} instead. Similarly to the above-mentioned rebound process, the activation barrier only decreases by 1.5 kcal mol^{-1} after dispersion corrections are added. The large $^{4}\mathbf{TS}_{D,EC}$ barrier implicates that desaturation is an unlikely process on the quartet spin-state surface. Moreover, the difference in kinetics between the quartet and doublet spin desaturation routes suggests that the doublet spin state surface is the only viable pathway responsible for vinyl carbamate formation. Consequently, the regioselectivity of desaturation versus hydroxylation is a spin-selective reaction process, whereby the high-spin pathway gives solely hydroxylation products whereas a mixture of products may be expected on the low-spin surface instead.

Experimental reports on ethylcarbamate activation by $P450_{2E1}$ isozymes reveal only a small but significant proportion of biotransformation leading to desaturation reactions.[18] The DFT calculations presented in Figure 2, therefore, are in line with these experimental product distributions of hydroxylation versus desaturation, which predict a mixture of products. Moreover, when we look at the driving force for desaturation versus hydroxylation, both pathways on the low-spin surface have similar exergonicity, that is, $\Delta G = -48.0$ versus -47.7 kcal mol^{-1}. As such, P450s should exhibit mixed hydroxylase/desaturase activity toward EC as indeed observed experimentally.

To find a general trend in desaturation versus hydroxylation regioselectivity preferences, we did a further set of calculations using alternative substrates that should give the chemical extremes of the two processes. In Figure 3 we display studies on desaturation versus hydroxylation mechanisms using valproic acid (VA), ethane (ET) and 9,10-dihydroanthracene (DHA) as substrates. Thus, experimentally, DHA in a reaction with P450 enzymes is known to lead to anthracene as major product, whereas ethane leads solely to alcohol products instead. For all chemical systems the full potential energy profile like the one shown in Figure 2 is calculated on both spin-state surfaces, and mechanisms are analogous to those reported above; for details see the Supporting Information. Thus, for valproic acid as a substrate the DFT calculations predict mixed desaturase/hydroxylase activity on a low-spin surface (Figure S1 in the Supporting Information). Key optimized geometries of the hydrogen atom abstraction transition states are given in Figure 3. In general, all substrates reveal the same catalytic mechanism as calculated above and previously reported in the literature[13,26] with a rate determining hydrogen-atom abstraction leading to a radical intermediate. Differences, however, are found for the relative energies for radical rebound versus desaturation.

On the quartet spin-state surface a small but significant radical rebound barrier exists (0.8–4.9 kcal mol^{-1}), whereas all low-spin rebound pathways are essentially barrier-free. Details of the rebound and desaturation barriers for all substrates are given in Table 1. By contrast to the radical rebound process, the desaturation barriers ($\mathbf{TS}_D$) show considerably more variation in relative energies. Similarly to the ethylcarbamate mechanism from Figure 2, a substantial desaturation barrier of 4.2–35.6 kcal mol^{-1} is required for valproic acid, ethane and DHA desaturation on the quartet spin state. Note as well that there is a significant desaturation barrier on the low-spin pathway for ethane, which is further evidence that desaturation is an unlikely process for a substrate like ethane.

The barrier heights displayed in Table 1 implicate competitive hydroxylation and desaturation on the doublet spin-state surface for all substrates except ethane. On the high-spin surface, on the other hand, there appears to be a clear preference for radical rebound. This is similar to previous studies on the

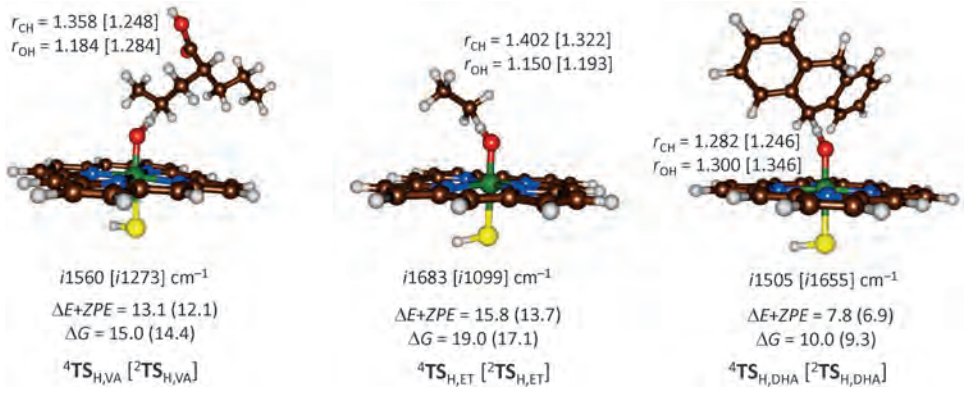

Figure 3. Optimized geometries of hydrogen-atom abstraction transition states of VA, ET and DHA by ^{4,2}CpdI of P450 as calculated with DFT. Bond lengths are in Å, the imaginary frequency is in wave numbers and (free) energies are given in kcal mol^{-1} and are calculated at UB3LYP/BSII//UB3LYP/BSI level of theory with *ZPE* and solvent corrections included.

© 2015 Wiley-VCH Verlag GmbH & Co. KGaA, Weinheim

Table 1. Free energies of activation of hydrogen-atom abstraction, rebound and desaturation barriers and the overall free energies for the hydroxylation and desaturation reactions.[a]

Substrate	TS_H[b]	TS_R[c]	TS_D[d]	P_R/P_D[b]
LS				
ethylcarbamate	17.9	0.0	0.0	−48.0/−47.7
valproic acid	14.4	0.0	0.0	−51.5/−49.1
ethane	17.1	0.0	14.7	−49.1/−43.0
DHA	9.3	0.0	0.0	−47.1/−61.5
HS				
ethylcarbamate	19.4	4.9	17.8	−51.5/−36.6
valproic acid	15.0	1.3	23.0	−56.0/−49.7
ethane	19.0	1.7	35.6	−51.9/−32.3
DHA	10.0	0.8	4.2	−50.8/−64.7

[a] ΔG values at 298 K in kcal mol^{-1}. [b] ΔG relative to **R**. [c] ΔG relative to $\mathbf{I}_H$. [d] ΔG relative to $\mathbf{I}_D$.

regioselectivity of substrate epoxidation versus suicidal complex formation in olefin activation by P450 isozymes that was predicted to only lead to by-products on the high-spin surface.[14] It should be noted, however, that the driving force for hydroxylation as compared to desaturation is larger for EC, VA and ethane as substrates, whereas it is favourable for desaturation for DHA. Thermodynamically, therefore, DHA should preferentially undergo the desaturation pathway, in accord with experimental studies on iron(IV)–oxo porphyrins that observed anthracene as the major product.[27] It seems the precursor leading to the aromatic species on the desaturation pathway gives the highest desaturase activity, because of its increased resonance stabilization of the benzene product.[28] By contrast, VA gives a thermodynamically dominant hydroxylase activity in analogy to EC. This is in agreement with experiment, where the ratio of desaturated to hydroxylated metabolites produced during P450-mediated VA activation is 1:37 for $P450_{2B1}$, and 1:2 for $P450_{4B1}$.[16c] Regardless of the external factors, we conclude that the P450-catalyzed desaturation reaction can occur, but is competitive with hydroxylation reactions on the low-spin state. However, as seen in the P450-mediated VA case, the proportion of desaturated metabolites also depends on the P450 isoforms and hence the substrate binding pocket must incur a significant effect on the regioselectivity of the reaction.

To further assess the calculated results, we estimated kinetic isotope effects for the replacement of the transferring hydrogen atom by deuterium using the semi-classical Eyring equation as well as the tunnelling-corrected Wigner isotope effect.[29] We re-evaluated the free energy and imaginary frequency for the hydrogen-atom abstraction step for $[D_2]$VA-4,4 and based on a comparison with the fully hydrogenated system establish a KIE = 6.4 (8.4) using the Eyring model and a KIE = 7.2 (12.1) at the doublet (quartet) spin states with tunnelling corrections included. These values compare well with the experimentally determined KIE value of 5.58 for the same substrate.[16b]

QM/MM studies of desaturation

As follows from the DFT model calculations in the previous section, both the radical rebound and second hydrogen-atom abstraction processes are barrierless on the doublet spin-state surface, whereas a substantial barrier on the quartet spin state surface is found. This implies that the mechanistic switch from substrate hydroxylation to desaturation by P450-catalyzed drug metabolism reactions is not kinetically controlled by the properties of the oxidant and/or substrate, but must be affected—at least in part—by external influences, such as the substrate binding into the substrate binding pocket. Therefore, we followed up our study by a set of QM/MM calculations on a system that is known to desaturate its natural substrate. These calculations take the size and shape of the substrate binding pocket into consideration and should give a realistic picture of the regioselectivity switch from hydroxylation to desaturation.

The $OleT_{JE}$ P450 isozyme binds long-chain fatty acids, such as eicosanoic acid (EA), and converts them to olefins, CO_2 and water on an iron(IV)–oxo heme cation radical system. We calculated the potential energy landscape as obtained by QM/MM for the hydrogen-atom abstraction by Cpd I from the C^{β}–H group of eicosanoic acid. The pathways leading to desaturation and hydroxylation starting from the radical intermediate ($^4\mathbf{I}_{H\beta,EA}$) are given in Figure 4. The hydrogen-atom abstraction barrier is low and of the same order of magnitude as those reported above for the DFT models as well as to previous hydrogen-atom abstraction barriers from the literature.[13,24,26]

The hydrogen-atom abstraction leads, as above, to an iron(IV)–hydroxo intermediate and substrate radical ($^{4,2}\mathbf{I}_{H\beta,EA}$) with electronic configuration $\delta^2\pi^*_{xz}{}^1\pi^*_{yz}{}^1\ \phi_{Sub}{}^1$. These structures have the O–H–C atoms aligned with an angle close to linearity. Subsequently, we investigated the pathways leading to desaturation and hydroxylation. We initially ran stepwise geometry

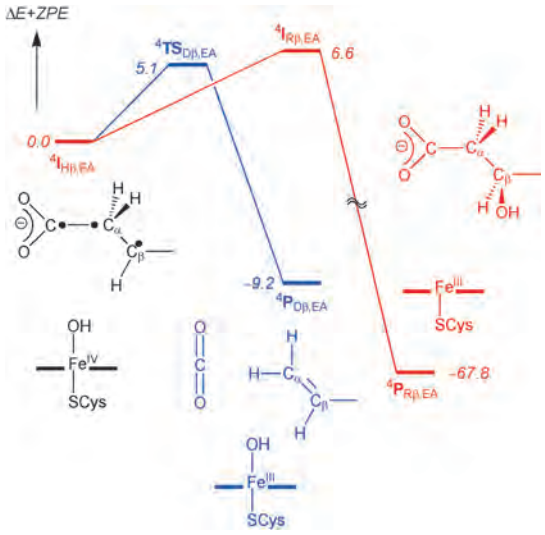

Figure 4. Potential energy profile of eicosanoic acid activation by ^{4}Cpd I of P450 as calculated with QM/MM. Energies are given in kcal mol^{-1} and are calculated at UB3LYP/BSIV//UB3LYP/BSIII level of theory with *ZPE* corrections included relative to $^4\mathbf{I}_{H\beta,EA}$.

© 2015 Wiley-VCH Verlag GmbH & Co. KGaA, Weinheim

scans, whereby one degree of freedom (the reaction coordinate) was fixed and all other parameters were minimized. However, all local minima and maxima of the scans were subjected to geometry optimizations and characterized with a frequency. The geometry of $\mathbf{TS}_{H\beta,EA}$ (see the Supporting Information) is analogous to the hydrogen atom abstraction barriers of ethylcarbamate, valproic acid and ethane, where long C–H and short H–O distances are found to be 1.33 and 1.18 Å, respectively. At the same time, the Fe–O bond elongates from about 1.602 Å in $\mathbf{R}_{EA}$ to 1.730 Å in $\mathbf{TS}_{H\beta,EA}$, which is indicative of electron rearrangement within the Fe–O bond (see below).

The energy landscape starting from $^4\mathbf{I}_{H\beta,EA}$ is shown in Figure 4. We located a small barrier ($^4\mathbf{TS}_{D\beta,EA}$) of $\Delta E + ZPE = 5.1$ kcal mol^{-1} for desaturation and the formation of a terminal olefin and CO_2 as reaction products ($^4\mathbf{P}_{D\beta,EA}$) with a modest exothermicity of -9.2 kcal mol^{-1}. Optimized geometries of local minima are shown in Figure 5. The desaturation transition state results in elongation of the OOC–$C_\alpha H_2 C_\beta$ bond to 1.874 Å with an imaginary frequency for the C–C_α stretch vibration of *i*541.3 cm^{-1}. This results in heterolytic splitting of the C–C bond and the formation of a double bond between C_α and C_β by pairing of the radical on C_β with the electron from the C–C_α bond. At the same time an electron is transferred from the carboxylate group to the iron(IV)–hydroxo group to form an iron(III)–hydroxo complex and enables the carboxylate group to leave as CO_2 and desaturate the fatty acid to a terminal olefin. In the iron(III)–hydroxo complex the metal has $\delta^2\pi^*_{xz}{}^1\pi^*_{yz}{}^1\sigma^*_{z^2}{}^1$ orbital occupation, whereby the latter orbital is antibonding along the S–Fe–O axis and hence elongates the Fe–S and Fe–O distances, as seen in Figure 5.

The alternative pathway starting with a rotation of the OH group around the Fe–O axis is, in contrast to the DFT calculations reported above, endothermic by 6.6 kcal mol^{-1}. Analysis of the chemical structure of $^4\mathbf{I}_{R\beta,EA}$ shows stereochemical clashes of the OH proton with a proline (Pro246) residue that blocks the rotation process.

In addition, a network of water molecules and polar groups force the iron(IV)–hydroxo group in $^4\mathbf{I}_{H\beta,EA}$ in a tight conformation. Several water molecules (three are shown in Figure 5) bridge the iron(IV)–hydroxo to the salt bridge of Arg245 with the carboxylate group of the substrate, but also links the water network to the propionate side chains of the heme. By contrast, the substrate binding pocket of $P450_{cam}$ is very tight and has few water molecules present.[8] Clearly, the subtle network of hydrogen bonding interactions affects the regioselectivity of the reaction and destabilizes the OH rebound pathway. A geometry scan for the C^α–COO dissociation in the substrate and subsequent transition-state characterization leads to release of CO_2 and the formation of olefin as shown in Figure 4. This pathway has a lower barrier than the alternative OH rotation and therefore, the desaturation degree of freedom will be C–C cleavage here rather than OH rotation. The regioselectivity of hydroxylation versus desaturation, therefore, in $OleT_{JE}$ is guided by the hydrogen-bonding network in the substrate binding pocket that destabilizes the rebound pathways that are barrierless in the gas-phase and in model complexes. This is the first example of a P450 isozyme that has accommodated its substrate binding pocket with polar residues to enable a substrate desaturation reaction.

Valence bond rationalization of rebound and desaturation mechanisms

To understand the origin of the regioselectivity of desaturation over hydroxylation, we set up valence bond (VB) curve-crossing diagrams that rationalize the kinetics of the reactions. These curve-crossing diagrams were used previously to rationalize oxygen-atom transfer reactions to heme and nonheme metal–oxo and metal–nitrido complexes.[30] Figure 6 shows the VB curve-crossing diagrams for the radical rebound and desaturation pathways leading to the competitive hydroxylation and desaturation products. These curve-crossing diagrams

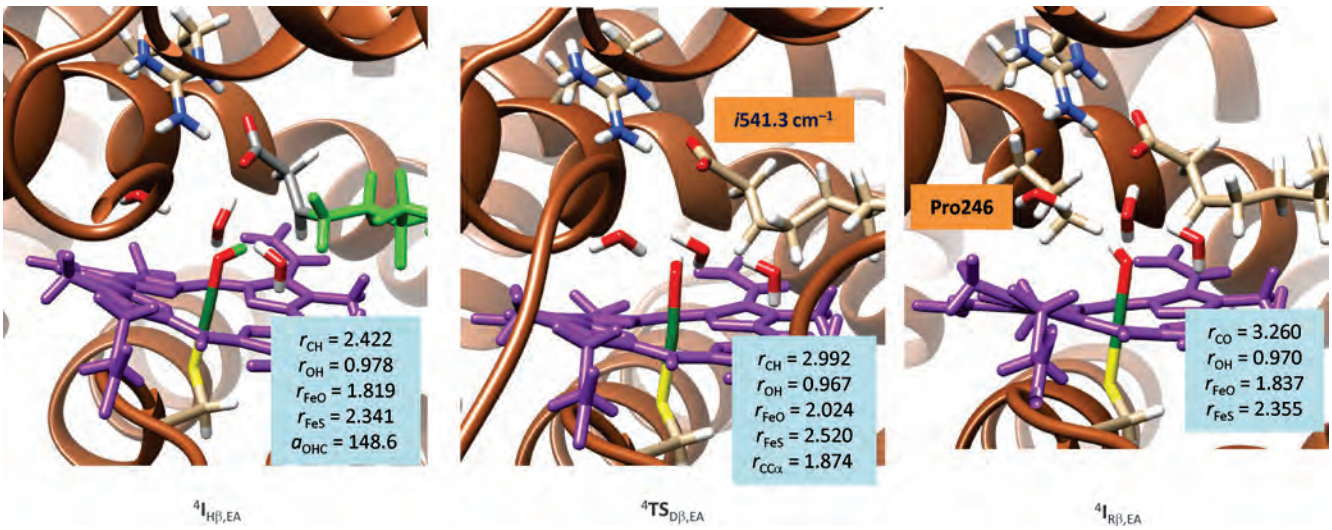

Figure 5. QM/MM optimized geometries (B3LYP/Charmm) of local minima along the reaction profile from Figure 4. Bond lengths (*r*) are in Å, angles (*a*) in degrees and the imaginary frequency in the transition state in wave numbers.

© 2015 Wiley-VCH Verlag GmbH & Co. KGaA, Weinheim

start on the left-hand side with the radical intermediates, that is, $^{4,2}\mathbf{I}_H$, which are described as an iron(IV)–hydroxo (porphyrin) complex with a nearby radical. The wave function Ψ_I represents structure $^{4,2}\mathbf{I}_H$ and corresponds to an electronic configuration $\delta_{x^2-y^2}{}^2\pi^*_{xz}{}^1\pi^*_{yz}{}^1\ \phi_{Rad}{}^1$ with two unpaired electrons along the Fe–O bond and a third on the substrate in the ϕ_{Rad} orbital. On the bottom right-hand side of each Figure the product complexes are drawn, which are either alcohol products or olefin products. The product complexes $^{4,2}\mathbf{P}_R$ and $^{4,2}\mathbf{P}_D$ have wave function Ψ_P and Ψ_D, respectively, whereby the doublet spin states have configuration $\delta_{x^2-y^2}{}^2\pi^*_{xz}{}^2\pi^*_{yz}{}^1$ and the quartet spin states $\delta_{x^2-y^2}{}^2\pi^*_{xz}{}^1\pi^*_{yz}{}^1\sigma^*_{z^2}{}^1$. In a curve-crossing diagram, as displayed in Figure 6, the reactant wave function (Ψ_I) connects with an excited-state wave function (Ψ_P* in part a and Ψ_D* in part b) in the product geometry. At the same time, the ground state product wave function connects to an excited state in the reactant geometry ($\Psi_{I,reb}$* in part a and $\Psi_{I,D}$* in part b). These two curves cross and lead to an avoided crossing and hence a transition state for the reaction pathway from intermediate to products.

Mathematically, the height of the barrier ($\Delta E^{\neq}$) can be determined from a VB curve-crossing diagram by estimating the excitation energy (or promotion gap G) in the reactant geometry from Ψ_I to Ψ_I*. Thus, as has been shown previously,[31] the barrier height is equal to the curve-crossing energy (ΔE_X) minus the resonance energy (B). Since, ΔE_X is proportional to a fraction (f) of the promotion gap, the barrier height can be estimated from Equation (1):

$$\Delta E^{\neq} = \Delta E_X - B = fG - B \qquad (1)$$

A careful look at the VB structures in the reactant geometry for the hydroxylation pathway shows that upon excitation the two electrons on the carbon of the substrate and the donor oxygen atom in $\Psi_{I,reb}$* have formed a bond and at the same time an electron has transferred from the OH group to iron. The rebound excitation energy G_{reb}, therefore, depends on the strength of the CO bond formed, that is, the bond-dissociation energy of the CO bond (BDE_{CO}), but also on the excitation energy ($E_{ex,FeOH}$) within the iron–hydroxo complex from $2p_z$(OH) into the iron 3d-block [Eq. (2)].

This excitation energy will fill the π^*_{xz} orbital with a second electron in the doublet spin state and the $\sigma^*_{z^2}$ orbital in the quartet spin state.

$$G_{reb} = BDE_{CO} + E_{ex,FeOH} \qquad (2)$$

The desaturation pathway, by contrast, shows somewhat different electron-transfer mechanisms as compared to the hydroxylation pathway (Figure 6b). Thus, in the excited state $\Psi_{I,D}$* the secondary hydrogen atom forms a chemical bond with the hydroxo moiety, whereas this bond is missing but it forms a bond with the carbon atom of the substrate instead. Therefore, the excitation energy is proportional to the difference in strength of the O–H bond that is formed (BDE_{OH}) and the C–H bond that is broken (BDE_{CH}). In addition, the two radicals on the adjacent carbon atoms in $\Psi_{I,D}$* have formed a π-bond with energy E_π. Obviously, π-conjugation will have a major effect on the excitation energy and lower it dramatically in value. Similarly to the radical rebound also in the desaturation pathway there is an internal electron transfer from the hydroxo group to the metal ($E_{ex,FeOH}$) [Eq. (3)]:

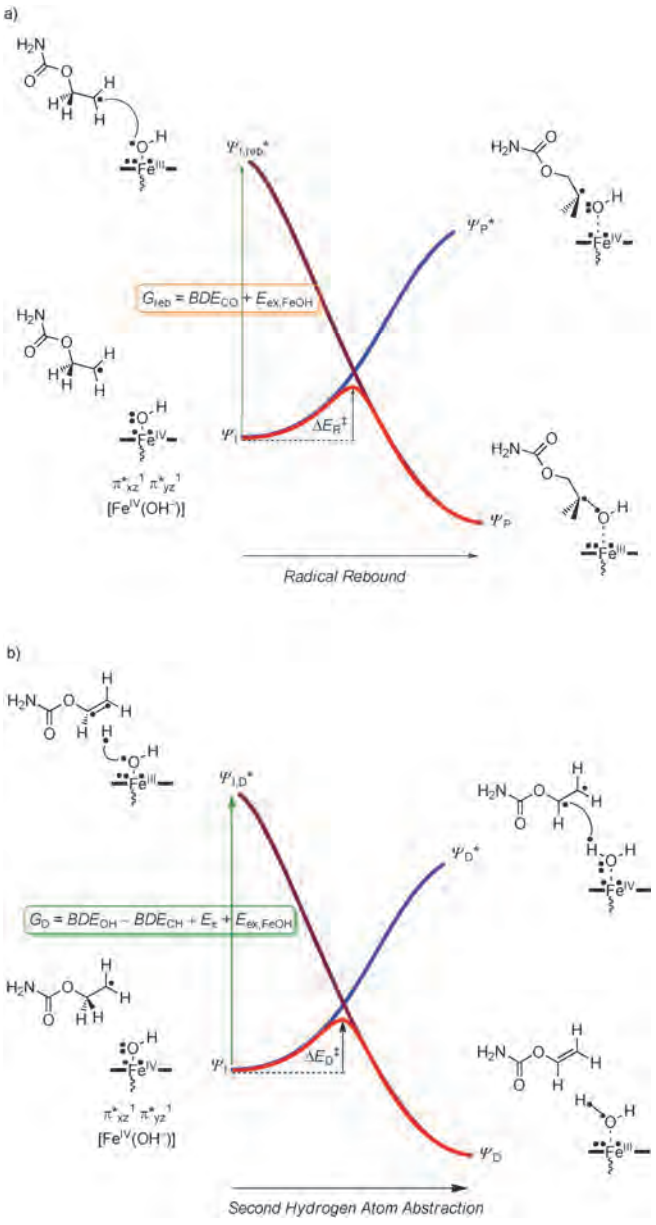

Figure 6. Valence bond curve-crossing diagrams for product formation from radical intermediates. a) Radical rebound leading to hydroxylation products. b) Hydrogen-atom transfer to give desaturation products.

In order to stabilize a desaturation pathway over a hydroxylation pathway the barrier for the latter should be higher in energy than that for the desaturation mechanism, that is, $\Delta E_{reb}{}^{\neq} > \Delta E_D{}^{\neq}$. Considering Equation (1) above, the difference in barrier height of radical rebound versus desaturation then depends on the promotion gap values, G, of the two processes

© 2015 Wiley-VCH Verlag GmbH & Co. KGaA, Weinheim

and the resonance energies, *B*. Generally, *f* is found to have a constant value of 0.30.[32] Therefore, if both pathways incur similar resonance energy values, *B*, the change in product distributions will only depend on the relative values of G_{reb} versus G_D [Eq. (4)]:

$$G_{reb} - G_D = BDE_{CO} - BDE_{OH} + BDE_{CH} - E_\pi \quad (4)$$

The BDE_{OH} value was calculated from the iron(III)–water complex and iron(IV)–hydroxo intermediate to be 70.8 kcal mol^{-1} for the iron–porphyrin model used here.[28] The corresponding C–H bond strength of the substrate that is broken ranges from 36.7 kcal mol^{-1} for $C_2H_5^\bullet$ to 21.8 kcal mol^{-1} for cyclo-$C_6H_7^\bullet$. By contrast, the C–O bond strength of the alcohol product that is formed ranges from BDE_{CO} = 85.8 kcal mol^{-1} for ethane to 59.7 kcal mol^{-1} for cyclohexadiene. Furthermore, DFT calculations predicted a π-conjugation energy of about 36 kcal mol^{-1} for a benzene molecule.[33] Based on this, we calculate a difference $G_{reb} - G_D = +16$ kcal mol^{-1} for a molecule like ethane, whereas a value of −25 kcal mol^{-1} is found for cyclohexadiene. This implies that a regioselective hydroxylation of ethane may be expected, whereas the desaturation will be favourable for cyclohexadiene. These values, therefore, implicate strong effects of the nature of the substrate on the regioselectivity of hydroxylation over desaturation, which is determined by a much stronger C–O bond formed in ethanol (by 26 kcal mol^{-1}) than the corresponding alcohol of cyclohexadiene and in addition has a stronger C–H bond for the second hydrogen atom that is abstracted in the desaturation process (by another 15 kcal mol^{-1}).

As the difference $G_{reb} - G_D$ for ethane is calculated to be +16 kcal mol^{-1} in favour of substrate hydroxylation, this implies that perturbations through binding of the substrate in the enzyme binding pocket will have to overcome 16 kcal mol^{-1} in order to change the regioselectivity of hydroxylation over desaturation for this particular substrate. As seen in Figures 4 and 5, a substrate with an aliphatic chain like eicosanoic acid can be desaturated by P450 enzymes due to a tight substrate binding pocket that through hydrogen-bonding networks prevent the OH rotation and, thereby, blocks the OH-rebound process efficiently.

Subsequently, we calculated the difference $G_{reb} - G_D$ for the drug molecules EC and VA as well as for DHA and find values of 10, 13 and −4 kcal mol^{-1}, respectively. This implies that the DHA reaction will naturally be driven towards desaturation and the formation of anthracene products. However, in the case of EC and VA the balance in the isolated system is in favour of hydroxylation rather than desaturation. The P450 isozymes involved in detoxification of EC and VA, therefore, have a specific substrate binding pocket that will change the balance in favour of desaturation rather than hydroxylation due to environmental perturbations affecting the rebound process. Consequently, subtle perturbations in the substrate binding pocket can have a major effect on the regioselectivity of substrate activation by P450 isozymes and are necessary to change the preference from hydroxylation to desaturation. This may be an important point to consider in bioengineering P450s for commercial purposes.

Conclusion

We present here a detailed set of computational results on the potential regioselectivity of aliphatic hydroxylation versus desaturation. We identify key steps in the mechanisms that both are initiated by a hydrogen atom abstraction step followed by OH isomerization to form either the pro-hydroxylation radical intermediate or the pro-desaturation radical intermediate. A VB and molecular orbital analysis (Supporting Information) identifies the electron-transfer processes for both reaction steps and highlights the substrate-specific factors and orbitals that drive the regioselectivity to hydroxylation or desaturation. Further evidence from QM/MM calculations shows that the regioselectivity can be modified through external perturbations that block one of the isomerization pathways.

Experimental Section

Our work uses two main computational approaches, namely DFT calculations on model complexes and QM/MM on a full P450 isozyme.

DFT model calculations

As in previous studies of our groups,[34] Cpd I of P450 was modelled as a six-coordinated iron(IV)–oxo porphyrin (Por) cation radical complex, [Fe^{IV}(O)($Por^{+\cdot}$)(SH)]. For simplicity, the heme is replaced by protoporphyrin IX, whereby all side chains are abbreviated with hydrogen atoms and the axial cysteinate ligand is changed to thiolate. All geometries were optimized using the unrestricted hybrid B3LYP density functional[35] in combination with an LACVP basis set on iron and 6–31G on the rest of the atoms;[36] basis set BSI. A subsequent analytical frequency calculation was run to confirm that all ground states had no imaginary frequencies, and all transition states had a single one for the correct mode. The computed vibrational frequencies were then used further for quantifying the zero-point energy (*ZPE*), and enabled us to calculate thermal and entropic corrections to the free energy at 298.15 K and 101.325 kPa. More accurate energies were determined by single-point calculations with the SDD basis set on iron coupled to 6–311++G** on the rest of the atoms; basis set BSII. To test the effect of the basis set on the optimized geometries, we calculated a full potential energy profile of 1-butene epoxidation by Cpd I using different basis sets. However, a single point calculation with a triple-ζ quality basis set on all atoms performed on a geometry that was optimized with either a double-ζ or a triple-ζ quality basis set did only give minor differences in the relative energies to within 0.1 kcal mol^{-1} of each other,[37] hence the former procedure was used in this work.

Bulk protein environment was simulated with the polarized continuum-solvation model with a dielectric constant of $\varepsilon = 5.62$. Dispersion interactions were added to the energy at the UB3LYP-D3 level of theory with zero damping.[38] All calculations were carried out using the Gaussian 09 program package.[39]

As density functional theory occasionally struggles with the correct description of spin-state ordering of transition metal complexes,[40] we tested the effect of the density functional method on the spin-state ordering and relative energies of the rebound versus desatu-

© 2015 Wiley-VCH Verlag GmbH & Co. KGaA, Weinheim

ration reactions. We did full geometry optimizations at the UBLYP/BSI,[35b,41] UB3PW91/BSI[35a,42] and TPSS/BSI[43] levels of theory. However, no change in spin state ordering was observed and only minor differences in the relative energies of the barrier heights were obtained (see the Supporting Information). Therefore, the same qualitative picture is obtained with alternative DFT methods and we will focus on the B3LYP results only.

QM/MM calculations

To support the DFT calculations and gain insight into whether the model would be applicable to realistic systems, we did a further set of calculations using an actual P450 isozyme that is known to desaturate its natural substrate. $OleT_{JE}$ was recently identified as a P450 isozyme that converts long-chain fatty acids into terminal olefins.[44] We investigated the pathways of β-hydroxylation and desaturation of eicosanoic acid by the P450 isozyme $OleT_{JE}$ using QM/MM methods. The starting coordinates for the calculations were taken from crystal structure data.[45] We followed the set-up procedures of the QM/MM system as reported and benchmarked before, which we will briefly summarize here.[46]

Starting from the crystal structure coordinates, hydrogen atoms and oxo group were added to the structure using the PDB2PQR program package[47] and the active site was manually modified from a resting state iron(III)–water(heme) complex into an iron(IV)–oxo heme cation radical (Cpd I) structure. We did a careful and visual analysis of all acidic and basic amino acid side chains for their protonation states, whereby we chose all glutamic and aspartic acid residues to be deprotonated at the carboxylic acid group and all arginine and lysine residues protonated. All histidine groups were visually inspected for proton-donor and -acceptor possibilities. The histidine residues His120 and His210 were doubly protonated, whereas the other six (His85, His92, His222, His259, His325 and His363) were singly protonated. The overall structure was neutralized with counter-ions (Mg^{2+} and Cl^{-}). Solvent water (with a sphere of radius of 35 Å) was added to this structure, and equilibrated, followed by a molecular dynamics minimization and heating procedure to 298 K of the full structure using the CHARMM force field.[48] The thus obtained QM/MM model had a total number of 32992 atoms including 8739 TIP3P water molecules.

In these QM/MM calculations the inner core including all residues and water molecules within a radius of 8 Å from the heme iron were fully geometry optimized, whereas all other atoms were fixed in the MD simulated coordinates. The iron(IV)–hydroxo species was geometry optimized in the doublet and quartet spin states and a frequency calculation on the QM region established these structures as stationary points.

QM/MM calculations employed the Turbomole program package[49] for the calculations of the QM region and Charmm as implemented in DL-Poly[50] for the MM region all linked through the ChemShell interface.[51] For consistency with the DFT studies reported above, we selected the UB3LYP[35] density functional for the QM region in combination with the Turbomole built-in basis set SVP, BSIII.[49] The QM region contained the iron(IV)–oxo group, the heme (without side chains), thiolate for the axial cysteinate group and the butanoate group of the substrate. To improve the energetics, single-point calculations were performed with a Wachters all electron basis set on iron and 6–311+G** on the rest of the atoms; basis set BSIV.[52] These methods and basis sets are of similar quality to those used for the model complexes and have been shown to give comparable results for analogous systems.[46] Electronic embedding procedures were implemented,[53] thereby taking into consideration to electronic interactions of electrons in the QM region with charges in the MM region.

The QM region selected in the QM/MM calculations contains the heme (without side chains) and its ligands and part of the substrate. As the substrate has a terminal carboxylate group that is linked through a salt bridge with an arginine residue, we kept the methylguanidinium component of Arg245 in the QM region and terminated the substrate at the sixth carbon atom. All side chains of the heme were in the MM region and the axial cysteinate residue was abbreviated by methylmercaptane. Subsequently, we investigated hydrogen atom abstraction from the C^{β} position of the substrate and the pathways leading to desaturation and hydroxylation.

Acknowledgements

L.J. and W.L. gratefully thank support from the National Natural Science Foundation of China (Grant No. 21307107 and 21320102007). A.F. and R.v.E. gratefully acknowledge financial support from the Deutsche Forschungsgemeinschaft and the National Science Centre of Poland (grant no. 2012/05/B/ST5/00389). The China National Supercomputing Centre in Shenzhen (Shenzhen Cloud Computing Centre, Contract No. S13037 and S14011) and the National Service of Computational Chemistry Software UK are acknowledged for providing computational resource and CPU time to L.J. and S.d.V. A.S.F., M.G.Q. and M.A.S. thank the Tertiary Education Trust Fund, the BBSRC and the Petroleum Technology Development Fund, respectively, for studentships. D.K. is the Ramanujan Fellow of the DST, New Delhi (India).

Keywords: compound I · density functional calculations · enzyme catalysis · reaction mechanisms · oxygen atom transfer

[1] a) M. Sono, M. P. Roach, E. D. Coulter, J. H. Dawson, *Chem. Rev.* **1996**, *96*, 2841–2888; b) J. T. Groves, *Proc. Natl. Acad. Sci. USA* **2003**, *100*, 3569–3574; c) *Cytochrome P450: Structure, Mechanism and Biochemistry* (Ed.: P. R. Ortiz de Montellano), 3rd ed., Kluwer, New York, **2004**; d) I. G. Denisov, T. M. Makris, S. G. Sligar, I. Schlichting, *Chem. Rev.* **2005**, *105*, 2253–2277; e) B. Meunier, S. P. de Visser, S. Shaik, *Chem. Rev.* **2004**, *104*, 3947–3980; f) *Handbook of Porphyrin Science* (Eds.: K. M. Kadish, K. M. Smith, R. Guilard) World Scientific, New Jersey, **2010**; g) P. R. Ortiz de Montellano, *Chem. Rev.* **2010**, *110*, 932–948.

[2] D. R. Nelson, *Human Genomics* **2009**, *4*, 59–65.

[3] a) F. P. Guengerich, *Chem. Res. Toxicol.* **2001**, *14*, 611–650; b) G. H. Posner, P. M. O'Neill, *Acc. Chem. Res.* **2004**, *37*, 397–404; c) A. W. Munro, H. M. Girvan, K. J. McLean, *Nat. Prod. Rep.* **2007**, *24*, 585–609.

[4] a) M. H. Gelb, D. C. Heimbrook, P. Mälkönen, S. G. Sligar, *Biochemistry* **1982**, *21*, 370–377; b) W. M. Atkins, S. G. Sligar, *J. Am. Chem. Soc.* **1987**, *109*, 3754–3760.

[5] a) R. T. Ruettinger, L. P. Wen, A. J. Fulco, *J. Biol. Chem.* **1989**, *264*, 10987–10995; b) D. R. Davydov, G. H. Bon Hoa, J. A. Peterson, *Biochemistry* **1999**, *38*, 751–761.

[6] a) E. O'Reilly, V. Koehler, S. Flitsch, N. Turner, *Chem. Commun.* **2011**, *47*, 2490–2501; b) G. Grogan, *Curr. Opin. Chem. Biol.* **2011**, *15*, 241–248.

[7] T. Omura, R. Sato, *J. Biol. Chem.* **1962**, *237*, 1375–1376.

[8] a) T. L. Poulos, B. C. Finzel, I. C. Gunsalus, G. C. Wagner, J. Kraut, *J. Biol. Chem.* **1985**, *260*, 6122–6130; b) I. Schlichting, J. Berendzen, K. Chu, A. M. Stock, S. A. Maves, D. E. Benson, R. M. Sweet, D. Ringe, G. A. Petsko, S. G. Sligar, *Science* **2000**, *287*, 1615–1622; c) K. Auclair, P. Moënne-Loccoz, P. R. Ortiz de Montellano, *J. Am. Chem. Soc.* **2001**, *123*, 4877–4885.

© 2015 Wiley-VCH Verlag GmbH & Co. KGaA, Weinheim

[9] R. L. Reynald, S. Sansen, C. D. Stout, E. F. Johnson, *J. Biol. Chem.* **2012**, *287*, 44581 – 44591.
[10] J. Rittle, M. T. Green, *Science* **2010**, *330*, 933 – 937.
[11] a) J. T. Groves, *Models and Mechanisms of Cytochrome P450 Action, in Cytochrome P450: Structure, Mechanism and Biochemistry* (Ed.: P. R. Ortiz de Montellano), 3rd ed., Kluwer, New York, **2005**, Chapter 1, pp. 1 – 44; b) Y. Watanabe, H. Nakajima, T. Ueno, *Acc. Chem. Res.* **2007**, *40*, 554 – 562.
[12] J. T. Groves, G. A. McClusky, *J. Am. Chem. Soc.* **1976**, *98*, 859 – 861.
[13] a) T. Kamachi, K. Yoshizawa, *J. Am. Chem. Soc.* **2003**, *125*, 4652 – 4661; b) S. Shaik, D. Kumar, S. P. de Visser, A. Altun, W. Thiel, *Chem. Rev.* **2005**, *105*, 2279 – 2328.
[14] a) S. P. de Visser, F. Ogliaro, S. Shaik, *Angew. Chem. Int. Ed.* **2001**, *40*, 2871 – 2874; *Angew. Chem.* **2001**, *113*, 2955 – 2958; b) D. Kumar, S. P. de Visser, P. K. Sharma, S. Cohen, S. Shaik, *J. Am. Chem. Soc.* **2004**, *126*, 1907 – 1920.
[15] a) D. Kumar, S. P. de Visser, S. Shaik, *J. Am. Chem. Soc.* **2004**, *126*, 5072 – 5073; b) W. Lai, H. Chen, S. Cohen, S. Shaik, *J. Phys. Chem. Lett.* **2011**, *2*, 2229 – 2235.
[16] a) A. E. Rettie, A. W. Rettenmeier, W. N. Howald, T. A. Baillie, *Science* **1987**, *235*, 890 – 893; b) A. E. Rettie, M. Boberg, A. W. Rettenmeier, T. A. Baillie, *J. Biol. Chem.* **1988**, *263*, 13733 – 13738; c) A. E. Rettie, P. R. Sheffels, K. R. Korzekwa, F. J. Gonzalez, R. M. Philpot, T. A. Baillie, *Biochemistry* **1995**, *34*, 7889 – 7895; d) A. J. M. Sadeque, M. B. Fisher, K. R. Korzekwa, F. J. Gonzalez, A. E. Rettie, *J. Pharmacol. Exp. Ther.* **1997**, *283*, 698 – 703; e) X. Wen, J. S. Wang, K. T. Kivistö, P. J. Neuvonen, J. T. Backman, *Br. J. Clin. Pharmacol.* **2001**, *52*, 547 – 553; f) A. Gunes, E. Bilir, H. Zengil, M. O. Babaoglu, A. Bozkurt, U. Yasar, *Pharmacol. Toxicol.* **2007**, *100*, 383 – 386.
[17] a) J. M. Loch, J. Potter, K. A. Bachmann, *Pharmacol.* **1995**, *50*, 146 – 153; b) P. G. Forkert, R. P. Lee, *Toxicol. Appl. Pharmacol.* **1997**, *146*, 245 – 254; c) R. P. Lee, A. Parkinson, P.-G. Forkert, *Drug Metabol. Disp.* **1998**, *26*, 60 – 65; d) F. P. Guengerich, *Chem. Res. Toxicol.* **2008**, *21*, 70 – 83.
[18] F. P. Guengerich, D. H. Kim, *Chem. Res. Toxicol.* **1991**, *4*, 413 – 421.
[19] M. T. Leithauser, A. Liem, B. C. Stewart, E. C. Miller, J. A. Miller, *Carcinogenesis* **1990**, *11*, 463 – 473.
[20] X. Guan, M. B. Fisher, D. H. Lang, Y. M. Zheng, D. R. Koop, A. E. Rettie, *Chem. Biol. Interact.* **1998**, *110*, 103 – 121.
[21] S. L. Kelly, D. C. Lamb, D. E. Kelly, *FEBS Lett.* **1997**, *412*, 233 – 235.
[22] a) R. Lonsdale, J. N. Harvey, A. J. Mulholland, *J. Phys. Chem. Lett.* **2010**, *1*, 3232 – 3237; b) A. K. Vardhaman, P. Barman, S. Kumar, C. V. Sastri, D. Kumar, S. P. de Visser, *Angew. Chem. Int. Ed.* **2013**, *52*, 12288 – 12292; *Angew. Chem.* **2013**, *125*, 12514 – 12518.
[23] S. P. de Visser, *Chem. Eur. J.* **2006**, *12*, 8168 – 8177.
[24] S. Shaik, D. Kumar, S. P. de Visser, *J. Am. Chem. Soc.* **2008**, *130*, 10128 – 10140.
[25] J. F. Hull, D. Balcells, E. L. O. Sauer, C. Raynaud, G. W. Brudvig, R. H. Crabtree, O. Eisenstein, *J. Am. Chem. Soc.* **2010**, *132*, 7605 – 7616.
[26] See, for example: a) F. Ogliaro, N. Harris, S. Cohen, M. Filatov, S. P. de Visser, S. Shaik, *J. Am. Chem. Soc.* **2000**, *122*, 8977 – 8989; b) S. P. de Visser, D. Kumar, S. Cohen, R. Shacham, S. Shaik, *J. Am. Chem. Soc.* **2004**, *126*, 8362 – 8363; c) R. Latifi, M. Bagherzadeh, S. P. de Visser, *Chem. Eur. J.* **2009**, *15*, 6651 – 6662; d) L. Ji, G. Schüürmann, *Angew. Chem. Int. Ed.* **2013**, *52*, 744 – 748; *Angew. Chem.* **2013**, *125*, 772 – 776.
[27] a) Y. J. Jeong, Y. Kang, A. R. Han, Y. M. Lee, H. Kotani, S. Fukuzumi, W. Nam, *Angew. Chem. Int. Ed.* **2008**, *47*, 7321 – 7324; *Angew. Chem.* **2008**, *120*, 7431 – 7434; b) L. Ji, A. Franke, M. Brindell, M. Oszajca, A. Zahl, R. van Eldik, *Chem. Eur. J.* **2014**, *20*, 14437 – 14450.
[28] D. Kumar, L. Tahsini, S. P. de Visser, H. Y. Kang, S. J. Kim, W. Nam, *J. Phys. Chem. A* **2009**, *113*, 11713 – 11722.
[29] D. J. Heyes, M. Sakuma, S. P. de Visser, N. S. Scrutton, *J. Biol. Chem.* **2009**, *284*, 3762 – 3767.
[30] a) S. Kumar, A. S. Faponle, P. Barman, A. K. Vardhaman, C. V. Sastri, D. Kumar, S. P. de Visser, *J. Am. Chem. Soc.* **2014**, *136*, 17102 – 17115; b) M. A. Sainna, S. Kumar, D. Kumar, S. Fornarini, M. E. Crestoni, S. P. de Visser, *Chem. Sci.* **2015**, *6*, 1516 – 1529.
[31] S. Shaik, P. C. Hiberty, *A Chemist's Guide to Valence Bond Theory*, Wiley-Interscience, New York, **2007**.
[32] D. Usharani, W. Lai, C. Li, H. Chen, D. Danovich, S. Shaik, *Chem. Soc. Rev.* **2014**, *43*, 4968 – 4988.
[33] I. Fernández, G. Frenking, *Chem. Commun.* **2006**, 5030 – 5032.
[34] a) S. P. de Visser, L. S. Tan, *J. Am. Chem. Soc.* **2008**, *130*, 12961 – 12974; b) L. Ji, J. Zhang, W. Liu, S. P. de Visser, *Chem. Asian J.* **2014**, *9*, 1175 – 1182.
[35] a) A. D. Becke, *J. Chem. Phys.* **1993**, *98*, 5648 – 5652; b) C. Lee, W. Yang, R. G. Parr, *Phys. Rev. B* **1988**, *37*, 785 – 789.
[36] a) P. J. Hay, W. R. Wadt, *J. Chem. Phys.* **1985**, *82*, 299 – 310; b) W. J. Hehre, K. Ditchfield, J. A. Pople, *J. Chem. Phys.* **1972**, *56*, 2257 – 2261.
[37] a) D. Kumar, B. Karamzadeh, G. N. Sastry, S. P. de Visser, *J. Am. Chem. Soc.* **2010**, *132*, 7656 – 7667; b) A. S. Faponle, M. G. Quesne, C. V. Sastri, F. Banse, S. P. de Visser, *Chem. Eur. J.* **2015**, *21*, 1221 – 1236.
[38] S. Grimme, *J. Comput. Chem.* **2006**, *27*, 1787 – 1799.
[39] Gaussian 09, Revision D.01, M. J. Frisch, G. W. Trucks, H. B. Schlegel, G. E. Scuseria, M. A. Robb, J. R. Cheeseman, G. Scalmani, V. Barone, B. Mennucci, G. A. Petersson, H. Nakatsuji, M. Caricato, X. Li, H. P. Hratchian, A. F. Izmaylov, J. Bloino, G. Zheng, J. L. Sonnenberg, M. Hada, M. Ehara, K. Toyota, R. Fukuda, J. Hasegawa, M. Ishida, T. Nakajima, Y. Honda, O. Kitao, H. Nakai, T. Vreven, J. A. Montgomery, Jr., J. E. Peralta, F. Ogliaro, M. Bearpark, J. J. Heyd, E. Brothers, K. N. Kudin, V. N. Staroverov, T. Keith, R. Kobayashi, J. Normand, K. Raghavachari, A. Rendell, J. C. Burant, S. S. Iyengar, J. Tomasi, M. Cossi, N. Rega, J. M. Millam, M. Klene, J. E. Knox, J. B. Cross, V. Bakken, C. Adamo, J. Jaramillo, R. Gomperts, R. E. Stratmann, O. Yazyev, A. J. Austin, R. Cammi, C. Pomelli, J. W. Ochterski, R. L. Martin, K. Morokuma, V. G. Zakrzewski, G. A. Voth, P. Salvador, J. J. Dannenberg, S. Dapprich, A. D. Daniels, O. Farkas, J. B. Foresman, J. V. Ortiz, J. Cioslowski, D. J. Fox, Gaussian, Inc., Wallingford CT, **2013**.
[40] S. P. de Visser, M. G. Quesne, B. Martin, P. Comba, U. Ryde, *Chem. Commun.* **2014**, *50*, 262 – 282.
[41] A. D. Becke, *Phys. Rev. A* **1988**, *38*, 3098 – 3100.
[42] J. P. Perdew, Y. Wang, *Phys. Rev. B* **1992**, *45*, 13244 – 13249.
[43] J. Tao, J. P. Perdew, V. N. Staroverov, G. E. Scuseria, *Phys. Rev. Lett.* **2003**, *91*, 146401.
[44] M. A. Rude, T. S. Baron, S. Brubaker, M. Alibhai, S. B. Del Cardayre, A. Schirmer, *Appl. Environ. Microbiol.* **2011**, *77*, 1718 – 1727.
[45] J. Belcher, K. J. McLean, S. Matthews, L. S. Woodward, K. Fisher, S. E. J. Rigby, D. R. Nelson, D. Potts, M. T. Baynham, D. A. Parker, D. Leys, A. W. Munro, *J. Biol. Chem.* **2014**, *289*, 6535 – 6550.
[46] a) D. Kumar, W. Thiel, S. P. de Visser, *J. Am. Chem. Soc.* **2011**, *133*, 3869 – 3882; b) M. G. Quesne, R. Latifi, L. E. Gonzalez-Ovalle, D. Kumar, S. P. de Visser, *Chem. Eur. J.* **2014**, *20*, 435 – 446.
[47] T. J. Dolinsky, P. Czodrowski, H. Li, J. E. Nielsen, J. H. Jensen, G. Klebe, N. A. Baker, *Nucl. Acids Res.* **2007**, *35*, W522 – W531.
[48] B. R. Brooks, R. E. Bruccoleri, B. D. Olafson, D. J. States, S. Swaminathan, M. Karplus, *J. Comput. Chem.* **1983**, *4*, 187 – 217.
[49] R. Ahlrichs, M. Bär, M. Häser, H. Horn, C. Kölmel, *Chem. Phys. Lett.* **1989**, *162*, 165 – 169.
[50] W. Smith, T. R. Forester, *J. Mol. Graphics* **1996**, *14*, 136 – 141.
[51] P. Sherwood, *J. Mol. Struct.* **2003**, *632*, 1 – 28.
[52] A. J. H. Wachters, *J. Chem. Phys.* **1970**, *52*, 1033 – 1036.
[53] D. Bakowies, W. Thiel, *J. Phys. Chem.* **1996**, *100*, 10580 – 10594.

Received: January 26, 2015
Published online on April 29, 2015

© 2015 Wiley-VCH Verlag GmbH & Co. KGaA, Weinheim

ORGANOMETALLICS

Article

pubs.acs.org/Organometallics

A Trimetal Carbene with Reactivity Reminiscent of Fischer–Tropsch Catalysis

Mala A. Sainna,[†,§] Devendra Singh,[‡,§] Devesh Kumar,*[,‡] and Sam P. de Visser*[,†]

[†]Manchester Institute of Biotechnology and School of Chemical Engineering and Analytical Science, The University of Manchester, 131 Princess Street, Manchester M1 7DN, United Kingdom

[‡]Department of Applied Physics, School for Physical Sciences, Babasaheb Bhimrao Ambedkar University, Vidya Vihar, Rae Bareilly Road, Lucknow (U. P.) 226 025, India

Supporting Information

ABSTRACT: Metal-carbenes are common reaction intermediates in chemical catalysis; however, very few catalysts are known with a trimetal-carbene active center. In this work, we describe a computational study into the chemical and catalytic properties of a unique trimetal carbene containing a Ru_2Pt-carbene core, $[(CpRu)_2(\mu_2\text{-}CH_2)(\mu_3\text{-}NCH_3)Pt(P(CH_3)_3)_2]$, with and without bound CO. The chemical structure and individual orbital interactions are identified from a natural bond orbital analysis, and the reaction pathways for consecutive intramolecular CH_3 and H transfer (or vice versa) are investigated. The studies show that CO binding has dramatic effects on the reaction mechanism and weakens the Ru–H bond strength. The reaction processes are rationalized by valence bond models and thermochemical bond strength studies. The work leads to suggestions on how to improve this chemical system for enhanced alkane synthesis.

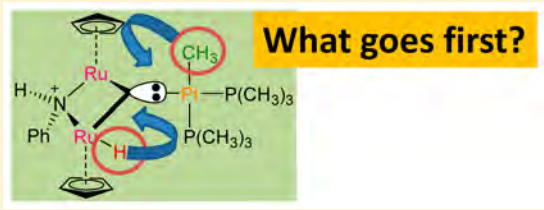

INTRODUCTION

In industrial Fischer–Tropsch catalysis, alkanes are being synthesized from H_2 and CO gas on a metal surface, which is a process that was developed and exploited in Germany in the 1920s and 1930s as an alternative to fossil fuels.[1] With dwindling supplies of fossil fuels, urgent alternative sources are needed; however, the Fischer–Tropsch process is energetically demanding and usually requires high pressures and/or temperatures as well as expensive heterogeneous catalysts.[2] Research on improving Fischer–Tropsch catalysis is hampered due to the lack of knowledge of details of the reaction mechanism and the properties played by the metal surface. In addition, few homogeneous catalysts are known that perform a Fischer–Tropsch-type reaction.[3]

Recently, the Matsuzaka group[4] reported the synthesis and spectroscopic characterization of $[(Cp^*Ru)_2(\mu_2\text{-}CH_2)(\mu_3\text{-}NPh)Pt(P(CH_3)_3)_2]$, which was treated with CH_3OTf in diethyl ether and, after heating in toluene, produced a unique structure (labeled as **3** in ref 4) with a trigonal sp^2 hybridized carbon atom linked to three transition-metal atoms. It was reported that structure **3** reacted via a Fischer–Tropsch-type reaction via H and CH_3 migration from the RuH and $PtCH_3$ ligands to form μ_2-$CHCH_3$ products (Scheme 1). Therefore, structure **3** catalyzes the C–C and C–H bond formation reactions for the synthesis of alkanes alike to the Fischer–Tropsch process, which are thermodynamically difficult processes. As such, structure **3** is one of the few homogeneous Fischer–Tropsch catalysts available currently. However, little is known of the reaction process and the overall potential of this type of chemical system. In order to explore its possibilities further, it is important to fully understand the origin of the reaction mechanism and the chemical properties that drive the process. Currently, there is limited knowledge on the chemical system displayed in Scheme 1, and experimental studies failed to identify intermediates along the reaction mechanism. Hence, it is unclear how and why this chemical system operates and how it can be further improved. Moreover, there are very few examples in the literature of analogous processes, and this chemical system may pose a novel synthetic route for the generation of alkanes on a carbene center.

Scheme 1. Chemical Reaction Investigated in This Work

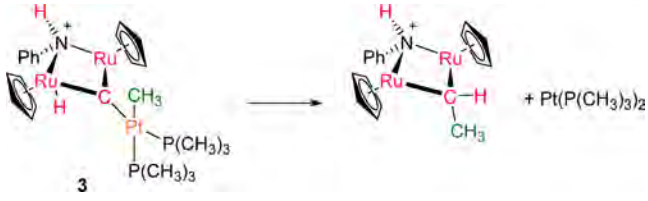

The aim of the studies in this work, therefore, is focused on establishing the reaction mechanism of alkyl chain growth on the carbene center and the chemical properties of the reaction center shown in Scheme 1. First, the chemical properties of the trimetal carbene center are poorly understood, and theory may give insight into whether it would be a suitable catalytic center. Second, it is unclear whether there is an initial H transfer, followed by a CH_3 transfer or the reverse. Moreover, it may very well be that both mechanisms are kinetically and thermodynamically possible. Third, as shown in iron-porphyrin

Received: February 7, 2015
Published: April 30, 2015

ACS Publications © 2015 American Chemical Society

DOI: 10.1021/acs.organomet.5b00305
Organometallics 2015, 34, 1651–1660

Scheme 2. Definition of the Chemical Model, and Nomenclature of Structures along the Reaction Mechanism

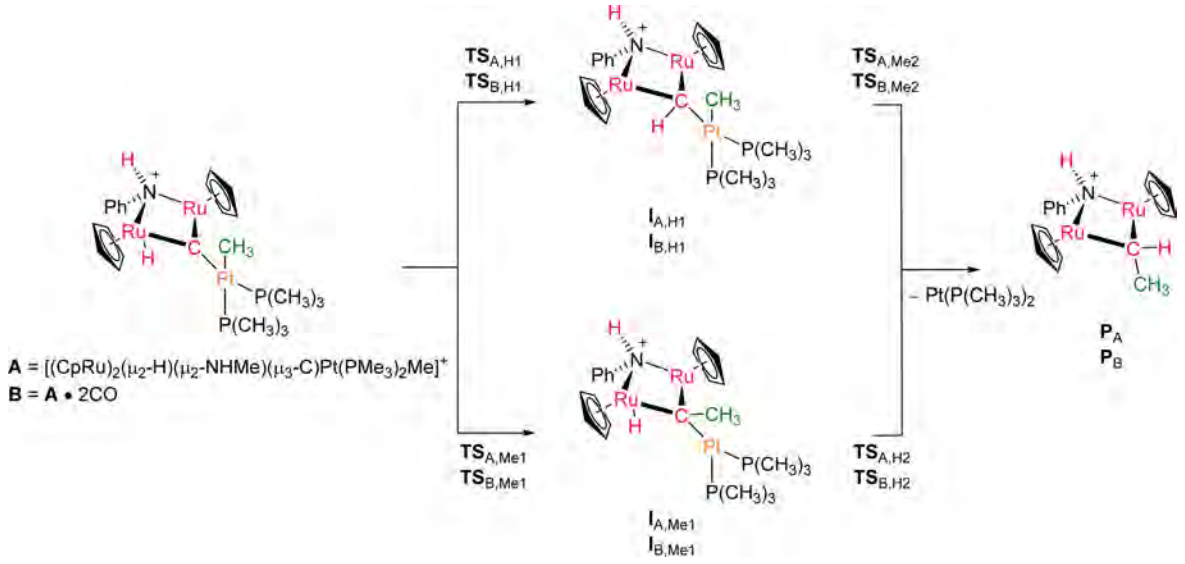

chemistry, for many examples, the reaction can take place via proton transfer, hydrogen atom transfer, or hydride transfer.[5] Furthermore, hydrogen atom and hydride transfer processes may happen via proton-coupled electron transfer (PCET), whereby the electrons move to a different donor site than the protons involved in the reaction. Theory is the ideal tool to distinguish between these mechanistic pathways and to establish the electronic features that drive this important mechanism. In addition to the reactivity questions and the synthesis of alkyl groups on this carbon center, there are also questions related to the chemical structure of the central carbon atom in **3** itself. Thus, an sp^2 hybridized carbon atom would make **3** a carbocation with a planar conformation, which is unlikely given the fact that the carbon atom is surrounded by positively charged metal ions. On the other hand, if the carbon atom is negatively charged, i.e., a carbanion, it would have a pyramidal structure because of its sp^3 hybridization, which is in disagreement with the experimental crystal structure coordinates. Clearly, the structural and reactivity features of this complex are poorly understood, and theory may provide insight into its electronic and structural features.

The Ru_2PtC core of structure **3** is an unusual structure in chemical catalysis but shows some resemblance to Grubbs catalyst,[6] where the metal is covalently linked to a carbon atom through either a single, a double, or a triple bond. However, as far as we know, there are no reported catalysts in the literature, where the carbon atom is ligated to two Ru atoms and a Pt atom. There are several examples in the literature of carbido centered structures, where the carbon atom is bound to three or more metal atoms,[7] but very few of these show catalytic activity. It, therefore, remains unclear why structure **3** is reactive for the formation of alkyl groups from individual methyl, hydrogen, and carbon groups. In order to gain insight into the peculiar structure and reactivity of **3**, we decided to do a computational study and establish the electronic and thermochemical features. As we will show here, our studies give fundamental insight into the nature of the metal−carbon bond and characterizes structure **3** as a trimetal carbene that can react via sequential methyl and hydrogen atom transfer to form μ_2-$CHCH_3$. These results may have direct relevance to heterogeneous catalysis on metal surfaces.

METHODS

The calculations reported in this work were performed using density functional theory (DFT) methods as used previously on transition-metal complexes by our groups,[8] and are implemented in the Jaguar 7.7[9] and Gaussian 09[10] program packages. Initial geometries were optimized (without constraints) in Jaguar using the hybrid density functional theory method B3LYP[11] coupled with an LACVP basis set (including a core potential) on ruthenium and platinum and 6-31G on the rest of the atoms: basis set BS1.[12] A subsequent analytical frequency in Gaussian confirmed the structures as local minima with real frequencies only or first-order saddle points with one imaginary frequency for the correct mode. Energies were then improved by running a single point calculation in Jaguar using a triple-ζ quality LACV3P+ basis set on iron and 6-311+G* on the rest of the atoms: basis set BS2. We also tested the effect of dispersion on the reaction energies by doing a UB3LYP-D3 single point calculation in Jaguar using the model of Grimme and co-workers.[13] For a selection of chemical systems, i.e., reactants and transition states, we did geometry optimizations at UB3LYP/BS2 and UB3LYP-D3/BS2, but found very little changes with respect to those obtained at UB3LYP/BS1. Since transition-metal complexes often react via multistate reactivity,[14] we calculated the complete potential energy profile on the lowest-lying singlet, triplet, and quintet spin states; however, in all cases, the singlet spin state was the ground state and well separated from the other spin states. Energies reported in this work contain B3LYP/BS2 energies and include zero-point and solvent corrections (calculated with B3LYP/BS2 using the polarized continuum model with a dielectric constant mimicking toluene).

As occasionally DFT calculations on spin state ordering and relative energies of transition-metal complexes show fluctuations depending on the choice of the density functional method,[15] we decided to do a series of test calculations with alternative DFT methods, namely, B3LYP-D3,[13] BP86,[16] M06,[17] OPBE, and PBE0; see the Supporting Information.[18] Similar to previously reported calculations on analogous systems,[19] these studies confirmed the trends and did not change the conclusions.

The methods described here were benchmarked previously on transition-metal-containing systems and compared with experimentally determined data, which gave free energies of activation within 4 kcal mol^{-1} from experiment,[20] but also gave reasonable agreement for spectroscopic data, where they reproduced resonance Raman, EXAFS, and Mössbauer data excellently.[21] To locate transition-state structures, we ran extensive geometry scans between the various local minima and used the maximum of those scans as a starting point for the actual transition state searches. Moreover, these scans confirmed that

DOI: 10.1021/acs.organomet.5b00305
Organometallics 2015, 34, 1651−1660

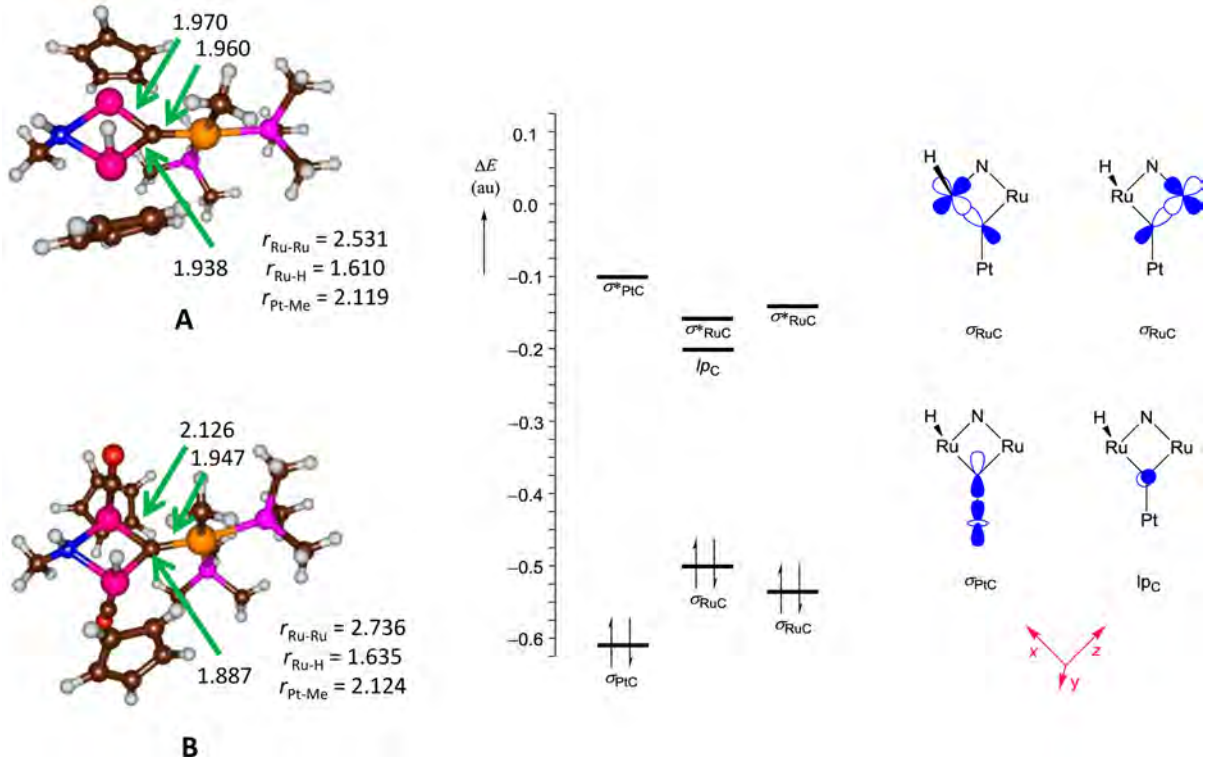

Figure 1. Optimized geometry of **A** and **B** as calculated with B3LYP with bond lengths given in angstroms. The right-hand side displays relative energies of the natural orbitals of **A** and gives drawings of the metal-carbon interactions.

reactants and products indeed connect via the reported transition state.

Our chemical model (Scheme 2) is based on the crystal structure coordinates of $[(Cp^*Ru)_2(\mu_2\text{-}H)(\mu_2\text{-}NHPh)(\mu_3\text{-}C)PtCH_3(P(CH_3)_3)_2]^+$,[4] whereby we replaced the Cp* groups with Cp and phenyl by methyl: Structure **A**. The stereochemical effects of the methyl groups of the $P(CH_3)_3$ groups on the reaction mechanism were investigated by replacement of the $P(CH_3)_3$ groups with PH_3. The latter structures are identified as **A′**, $\mathbf{I}_{A,Me}'$, and $\mathbf{I}_{A,H}'$. As the chemical system is saturated in carbon monoxide, we also created a model with two CO molecules bound (one on each Ru center): Structure **B**. We investigated the pathways starting from structures **A** and **B** for hydrogen atom abstraction to form $\mathbf{I}_{A,H1}/\mathbf{I}_{B,H1}$ intermediates via transition state $\mathbf{TS}_{A,H1}/\mathbf{TS}_{B,H1}$ as well as the alternative pathway for initial methyl transfer via transition states $\mathbf{TS}_{A,Me1}/\mathbf{TS}_{B,Me1}$ to form intermediates $\mathbf{I}_{A,Me1}/\mathbf{I}_{B,Me1}$. Subsequently, the methyl group is transferred to $\mathbf{I}_{A,H1}/\mathbf{I}_{B,H1}$ via transition state $\mathbf{TS}_{A,Me2}/\mathbf{TS}_{B,Me2}$ to form products. Alternatively, in the reactant, a methyl group is relayed to form $\mathbf{I}_{A,Me1}/\mathbf{I}_{B,Me1}$, followed by a hydrogen atom migration via transition state $\mathbf{TS}_{A,H2}/\mathbf{TS}_{B,H2}$ to form products (Scheme 2).

Charges reported in this work were obtained from a natural bond occupation (NBO) calculation as implemented in the Gaussian program package at the B3LYP/BS2 level of theory.[22]

In order to fully understand the thermodynamics and kinetics of the mechanism of the overall chemical reaction, we calculated the bond dissociation free energies (BDFEs) of key Ru/C−H and Pt/C−CH_3 bonds in complexes **A**, **B**, $\mathbf{I}_{A,Me1}$, $\mathbf{I}_{B,Me1}$, $\mathbf{I}_{A,H1}$, $\mathbf{I}_{B,H1}$, $\mathbf{P}_{A,H}$, and $\mathbf{P}_{B,H}$. The release of either $H^\bullet$, H^+, $CH_3^\bullet$, or CH_3^+ from these four complexes as described by eqs 1−4, whereby each individual structure was calculated through a full geometry optimization to give the adiabatic bond dissociation free energies. In addition, we calculated the methylenium transfer Gibbs free energy (MTFE) and the proton transfer Gibbs free energy (PTFE). The latter was calculated through the use of the H_2O/H_3O^+ couple to balance the equation. As there were large structural changes upon H/CH_3 bond breaking on the various complexes, we also calculated the diabatic bond dissociation free energies, or vertical bond dissociation free energies, whereby we took the optimized geometries of **A**, **B**, $\mathbf{I}_{A,Me1}$, $\mathbf{I}_{B,Me1}$, $\mathbf{I}_{A,H1}$, $\mathbf{I}_{B,H1}$, $\mathbf{P}_{A,H}$, and $\mathbf{P}_{B,H}$ and ran single point calculations with either $H^\bullet$, H^+, $CH_3^\bullet$, or CH_3^+ removed.

$$\mathbf{A}^+ \rightarrow [\mathbf{A} - H]^+ + H^\bullet + BDFE_H \quad (1)$$

$$\mathbf{A}^+ \rightarrow [\mathbf{A} - CH_3]^+ + CH_3^\bullet + BDFE_{Me} \quad (2)$$

$$\mathbf{A}^+ + H_2O \rightarrow [\mathbf{A}{-}H]^0 + H_3O^+ + PTFE \quad (3)$$

$$\mathbf{A}^+ \rightarrow [\mathbf{A} - CH_3]^0 + CH_3^+ + MTFE \quad (4)$$

RESULTS AND DISCUSSION

Before we discuss our calculated reaction mechanisms, let us briefly summarize the main results on our reactant structures, **A** and **B**, and establish their chemical properties. The optimized geometries of **A** and **B** are shown in Figure 1. The obtained bond distances of **A** are to within 0.011 Å of the crystal structure coordinates reported in ref 4, and as such, the DFT calculations give reasonable chemical structures. The Pt−C bond of 1.960/1.947 Å in **A**/**B** represents a single bond and is in good agreement with several reported Pt−C containing crystal structures from the literature.[23] The two Ru−C bonds are very close in bond length in **A**, and the fact that one of the two atoms is protonated, therefore, appears to have little effect on its interaction with carbon. However, addition of two CO molecules strongly affects the Ru−C bond lengths, and one of those is elongated to 2.126 Å in **B**. Ru−C bond lengths found here are typical for a single bond and compare to analogous structures reported before.[24] Therefore, addition of two CO molecules to structure **A** does not appear to have drastically changed the molecular geometry and keeps its original features.

The experimental studies of ref 4 implicate the hydride to bind as a bridging ligand to both Ru atoms, whereas Figure 1 gives a terminal-hydride atom that is linked to a single Ru atom.

DOI: 10.1021/acs.organomet.5b00305
Organometallics 2015, 34, 1651−1660

We created starting structures for a geometry optimization using both a bridging hydride atom as well as a terminal hydride atom. However, both of these calculations (whether CO was used as ligands or not) converged to the structure with a terminal hydride atom. This implies that a structure with a bridging hydride atom will be a higher energy state and possibly inaccessible.

As transition-metal complexes containing iron or ruthenium generally contain close-lying spin states and often react via multistate reactivity patterns,[14] structure **A** was optimized in the singlet, triplet, and quintet spin states. The closed-shell singlet spin state is the ground state and is well separated from the triplet and quintet spin states by ΔG_{gas} = 17.1 and 44.8 kcal mol^{-1}, respectively. These values change by less than 1 kcal mol^{-1} when solvent corrections are included. Clearly, structure **A** is a closed-shell species that will react via single-state reactivity in contrast to metal(IV)-oxo and metal(IV)-nitrido complexes from the literature.[25]

In order to shed light on the bonding pattern of the central carbon atom, we did a natural bond orbital (NBO) analysis of structure **A**. Thus, the NBO analysis reveals three bonding type orbitals for the central carbon atom, namely, three single bonds for the interaction with the two Ru atoms and the Pt atom. The σ_{PtC} orbital represents the σ-bonding orbital between Pt and C and is built up from the interaction of the $5d_{z^2}$ orbital on Pt with the $2p_z$ orbital on C. In addition, there are two single bonds between the carbido atom and the two Ru atoms, which result from the mixing of the 2s, $2p_x$, and $2p_z$ atomic orbitals on C with the $4d_{z^2}$ orbital on Ru or the $4d_{x^2-z^2}$ on Ru(H). As such, the central carbon atom is sp^2 hybridized. However, the fourth valence orbital on carbon is a virtual $2p_y$ atomic orbital. The NBO analysis, therefore, assigns the central carbon atom as a carbene with three sp^2 hybridized orbitals that are occupied with two electrons in an orbital donating to Pt (σ_{PtC}), and two bonding orbitals where both C and Ru donate one electron each into the bond (σ_{RuC}, σ_{RuC}). This hybridization scheme gives the central carbon atom its planar structure (Scheme 3).

Scheme 3. Hybridization Scheme of A and B

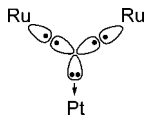

As such, the chemical structure of Ru_2CPt represents a Fischer-carbene, where the lone pair of the carbon atom interacts with an empty Pt orbital and the π-type Pt orbitals give backbonding into the empty $2p_y$ orbital of the carbene.[26] The NBO charges displayed in Figure 1 reveal a charge-neutral carbon atom (Q_C = 0.04) that is surrounded by slightly negatively charged metal atoms. Consequently, there is very little charge built up in this chemical system.

Subsequently, we calculated the potential energy profile for μ_2-$CHCH_3$ formation starting from **A** and **B**. We tested two mechanisms as shown in Figure 2: (i) initial hydrogen transfer from RuH to the carbene, followed by methyl abstraction, and (ii) initial methyl transfer from $PtCH_3$, followed by hydrogen/proton transfer. Figure 2 starts from the center with **A**/**B** and follows the two possible reaction mechanisms: The initial H transfer (mechanism to the right) and the initial CH_3 transfer (mechanism to the left). The two mechanisms are described as follows: In the first case, the metal-carbene group abstracts a hydrogen atom from the RuH group via a transition state $\mathbf{TS}_{H1}$ to form the H-transfer intermediate $\mathbf{I}_{H1}$. A subsequent CH_3 transfer from the $PtCH_3$ group via a barrier $\mathbf{TS}_{Me2}$ gives the μ_2-$CHCH_3$ bound product **P**. We also tested the alternative pathway starting with an initial CH_3 abstraction by the metal-carbene group via transition state $\mathbf{TS}_{Me1}$ leading to the methyl transfer intermediate $\mathbf{I}_{Me1}$. This intermediate then reacts further by H abstraction from RuH via a transition state $\mathbf{TS}_{H2}$ to form product **P**.

We attempted to also locate the alternative synchronous transfer of both hydrogen and methyl group at the same time to the carbene atom; however, all calculations converged to one of the lower-lying transition states (or local minima) described in this work. Previously, we calculated the concerted epoxidation reaction of an olefin by an iron(IV)-oxo heme cation radical system and found it to be a second-order saddle point that is well higher in energy than the stepwise transition states.[27]

Dramatic differences in relative energies and optimized structures are found for the pathways starting from **A** or **B**; however, in both cases, the H-atom transfer reaction has the lowest Gibbs free energy of activation of $\Delta G^{\ddagger}$ = 19.6 (3.1) kcal mol^{-1} for **A** (**B**). Nevertheless, in both cases, it is not the rate-determining step as the subsequent CH_3 transfer to form products gives an additional barrier with a maximum of 23.1 (24.2) kcal mol^{-1}. Therefore, the reaction that is initiated with H-atom transfer from **A** has an unfeasible Gibbs free energy of activation of 42.7 kcal mol^{-1} for $\mathbf{TS}_{A,Me2}$ with respect to **A** and will not be able to proceed through that pathway. On the other hand, this barrier for structure **B** is much lower in energy, but still would imply a relatively slow reaction process. This is in agreement with experimental observation that found evidence of a structure with analogy to $\mathbf{I}_H$, but the methyl group bound to one of the Ru atoms, which would imply a fast hydrogen abstraction, followed by a much slower methyl transfer. The origin of the enhanced stabilization of CO bound intermediate $\mathbf{I}_{B,H1}$ with respect to $\mathbf{I}_{A,H1}$ comes from the structural differences. Thus, without CO bound, the carbene carbon atom pyramidalizes much more and the dihedral angle $d_{CRuRuPt}$ = 43.3° in $\mathbf{I}_{A,H1}$, whereas it is 25.7° in $\mathbf{I}_{B,H1}$. The large pyramidalization causes contraction of the chemical system and more stereochemical repulsions of the $P(CH_3)_3$ groups with the RuCp groups that destabilize the structure.

The alternative pathway with an initial CH_3 transfer, on the other hand, has a calculated Gibbs free energy of activation of $\Delta G^{\ddagger}$ = 21.5 (25.4) kcal mol^{-1} for **A** (**B**) and, therefore, is disfavored over the initial H-atom transfer process. However, this reaction leads to a very stable intermediate $\mathbf{I}_{A,Me1}$ with an exergonicity of almost 10 kcal mol^{-1}, whereas the reaction is endothermic for the formation of $\mathbf{I}_{B,Me1}$. Its subsequent H-atom transfer leading to products only has a Gibbs free energy of activation of 18.3 (6.2) kcal mol^{-1} from intermediates for **A** (**B**). Therefore, product formation is a viable, but kinetically slow, pathway through this channel for both structures **A** and **B**, whereby it is the dominant mechanism for **A** and competitive with initial hydrogen atom abstraction for **B**. Binding of CO molecules to the reaction center, therefore, changes the regioselectivity of the chemical reaction in favor of initial hydrogen atom abstraction. In previous work on the regioselectivity of substrate epoxidation versus hydroxylation by iron(IV)-oxo complexes, we showed that changes to the ligand system of the iron or even replacing hydrogen atoms of the substrate by deuterium atoms can reverse a regioselectivity, and as such, the Ru_2Pt-carbene complex is another example of a

DOI: 10.1021/acs.organomet.5b00305
Organometallics 2015, 34, 1651−1660

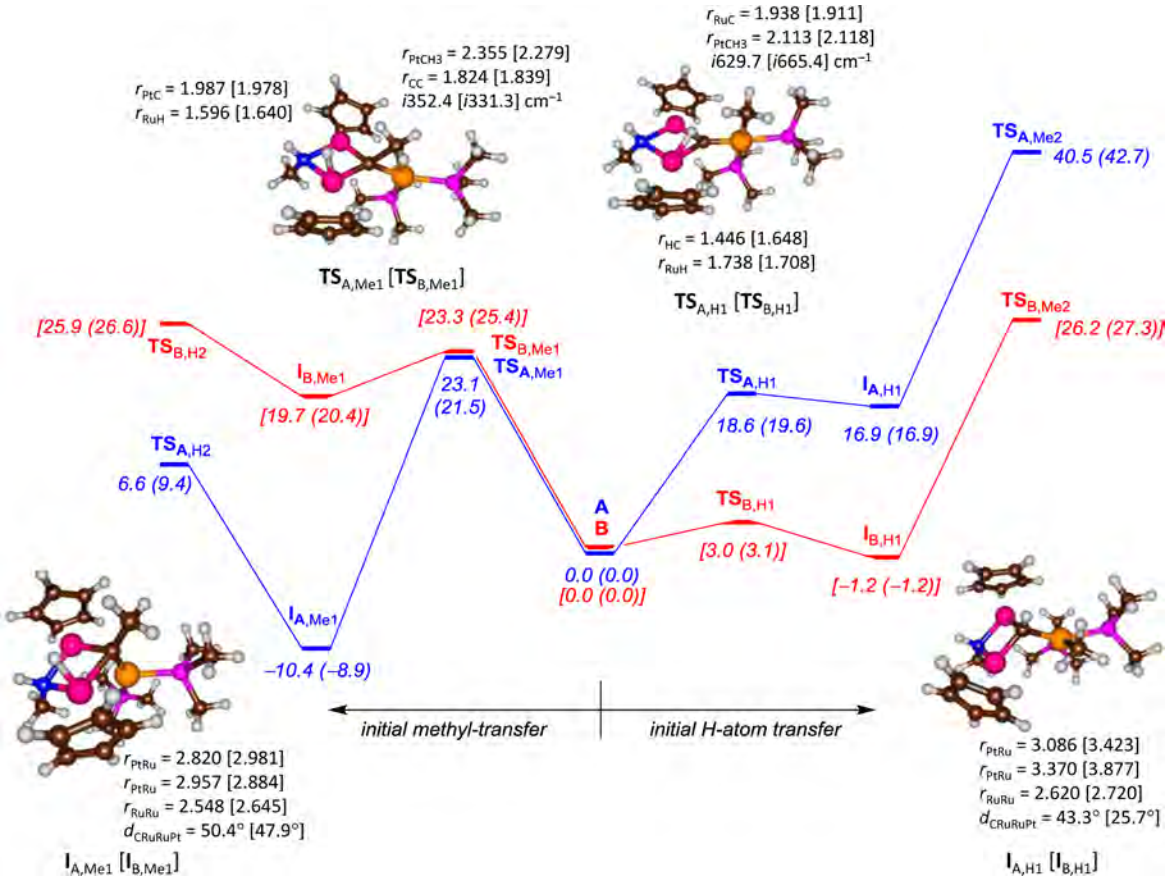

Figure 2. Gibbs free energy profile of alkyl chain growth on **A** and **B** via either (i) CH_3 transfer, followed by H transfer (mechanism from the center to the left), or (ii) H transfer, followed by CH_3 transfer (mechanism from the center to the right). Energies (ΔE + ZPE) and free energies (ΔG, in parentheses) obtained with B3LYP/BS2 with values in kcal mol^{-1}. All data include solvent corrections to the energy. Optimized geometries report bond lengths in angstroms, angles in degrees, and the imaginary frequency of the transition states in wavenumbers.

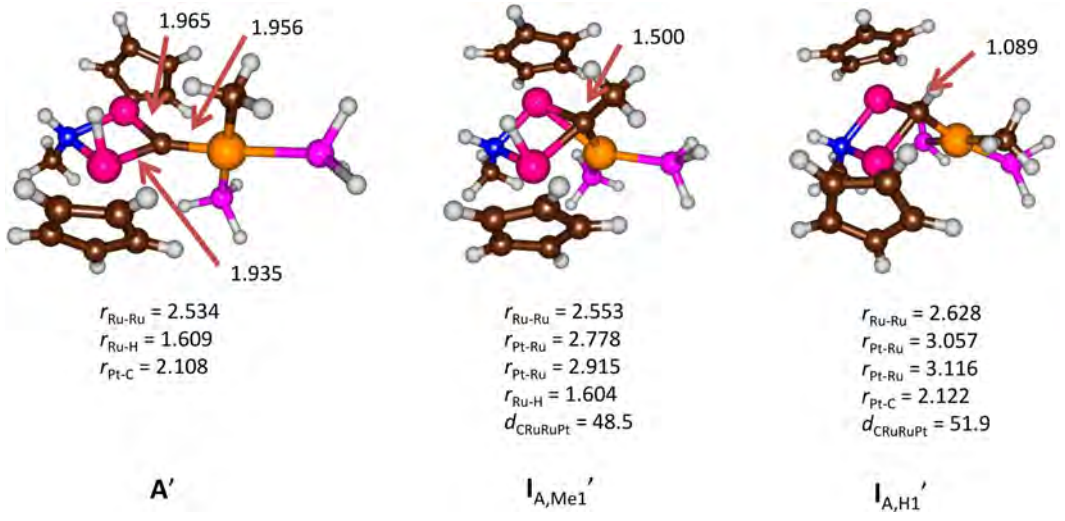

Figure 3. Optimized geometries of **A**′, $I_{A,Me1}$′, and $I_{A,H1}$′ with bond lengths in angstroms.

chemical catalyst that changes its reactivity upon ligand modifications.[28]

The origin of the differences in stability of $I_{A,Me1}$ versus $I_{B,Me1}$ stems from differences in location of the transferring hydrogen atom. Thus, in $I_{A,Me1}$, the hydrogen atom is located close to one Ru atom with Ru1−H and Ru2−H distances of 1.604 and 2.521 Å, whereas they change to 1.736 and 1.943 Å, respectively, in $I_{B,Me1}$. The structure with the bridging proton is considerably destabilized with respect to singly protonated Ru atom.

In summary, DFT establishes a possible alkyl synthesis mechanism for **A** as a stepwise mechanism with an initial CH_3 transfer, followed by H-atom transfer, whereas structure **B** proceeds with competitive mechanisms via either initial CH_3-

DOI: 10.1021/acs.organomet.5b00305
Organometallics 2015, 34, 1651−1660

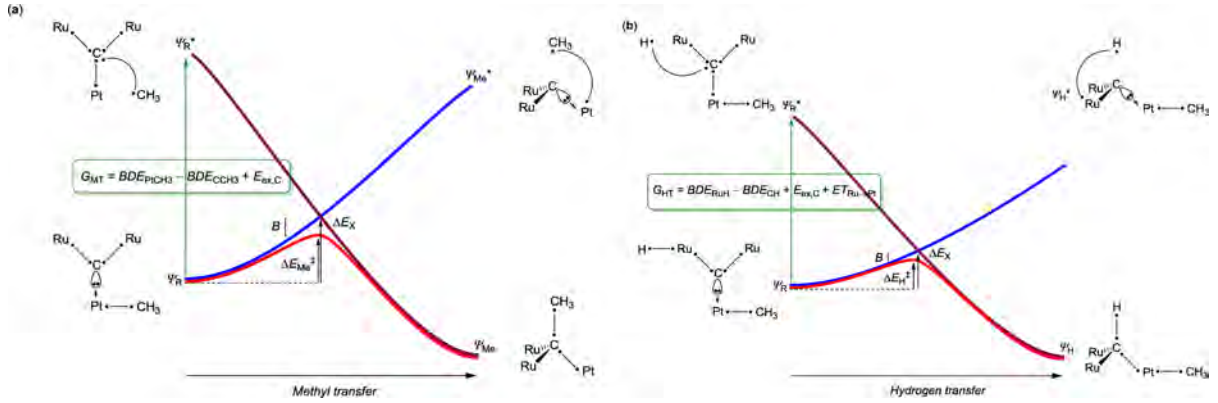

Figure 4. Valence bond curve crossing diagrams for methyl transfer (part a) and hydrogen atom transfer (part b) from reactants (**A** or **B**). Valence electrons are identified with a dot.

or H-transfer processes. An analysis of the group spin densities and charges (Supporting Information) along the complete reaction mechanism shows that all local minima and transition states are closed-shell singlet species with no radical built up during the reaction. Accordingly, the reaction starts with either proton transfer or CH_3^+ transfer.

So, why is the reaction displayed in Figure 2 stepwise with consecutive CH_3- or H-transfer processes, and what is the function of the Ru_2Pt scaffold? These questions will be answered in the following discussion. Structurally, there are major changes happening at the Ru_2Pt-carbene center during the reaction mechanism. Although **A** and **B** have an sp^2 hybridized carbon atom that lies in the plane of the Ru_2Pt atoms, upon H/CH_3 transfer, the planarity is distorted and the carbon atom relaxes to a pyramidal conformation due to sp^3 hybridization. The pyramidalization is considerably more pronounced for the CH_3-transfer process than in the H-atom transfer pathway as dihedral angles C−Ru−Ru−Pt of 50.4° for $\mathbf{I}_{A,Me1}$ and 43.3° for $\mathbf{I}_{A,H1}$ are found. At the same time, the Pt−Ru distances in $\mathbf{I}_{A,Me1}$ shorten by as much as 0.8 Å with respect to **A** to well below 3 Å, while, in $\mathbf{I}_{A,H1}$, they stay considerably longer: r_{PtRu} = 3.086 and 3.370 Å. These large structural changes for the CH_3-transfer pathway will have an effect on the reaction energetics and kinetics as well as on the relative stability of $\mathbf{I}_{A,Me1}$ versus $\mathbf{I}_{A,H1}$. Thus, the Pt atom in $\mathbf{I}_{A,Me1}$ only has three ligands due to CH_3 transfer to the carbon atom, which means limited stereochemical interactions between the two $P(CH_3)_3$ groups and the rest of the molecule so that the Pt atom can approach the two Ru atoms closely. In $\mathbf{I}_{A,H1}$, the Pt atom remains tetracoordinated and the stereochemical interactions between all ligands and the rest of the molecule prevent a close approach to the Ru_2C center. As a consequence of the stereochemical repulsions, $\mathbf{I}_{A,H1}$ is considerably destabilized over $\mathbf{I}_{A,Me1}$ and the reaction pathway with initial H-atom transfer is energetically disfavored.

To further establish these stereochemical interactions in $\mathbf{I}_{A,H1}$ versus $\mathbf{I}_{A,Me1}$, we did a subsequent set of calculations on these structures, but with the $P(CH_3)_3$ groups replaced by PH_3: structures $\mathbf{I}_{A,H1}'$ and $\mathbf{I}_{A,Me1}'$ (Figure 3). The optimized geometry of **A′** (Figure 3) is very close to that reported above for **A** in Figure 1, and only minor changes in bond lengths are obtained. Clearly, the $P(CH_3)_3$ groups have little effect on the structure of the Ru_2PtC core of our chemical system. A similar situation occurs for $\mathbf{I}_{A,Me1}'$, which has large structural similarities with $\mathbf{I}_{A,Me}$ reported in Figure 2. Major changes, however, are seen when $\mathbf{I}_{A,H1}$ is compared to $\mathbf{I}_{A,H1}'$. Thus, one of the Ru−Pt distances decreases from 3.370 to 3.116 Å, and as a consequence, the pyramidality of the carbon center changes from $d_{CRuRuPt}$ = 43.3° in $\mathbf{I}_{A,H1}$ to a value of 51.9° in $\mathbf{I}_{A,H1}'$. This has a major effect on the stability of $\mathbf{I}_{A,H1}'$, and it is stabilized by 6.0 kcal mol^{-1} with respect to **A′**; however, the $\mathbf{I}_{A,Me1}'$ remains the most stable conformation. This implies that the $P(CH_3)_3$ groups incur a destabilizing effect on the reaction mechanism, but will not reverse the preference of initial CH_3 transfer over H-atom transfer.

To gain insight into the electronic changes during the reaction mechanism, a NBO analysis was also performed on the intermediate and product complexes. The NBO calculation reveals a configuration on the central carbon atom of $2s^{1.08}2p^{2.92}$ for $\mathbf{I}_{A,Me1}$ and $2s^{1.18}2p^{3.10}$ for $\mathbf{I}_{A,H1}$. Both intermediate complexes, therefore, have an electronic configuration close to sp^3 hybridization, and as a consequence, their geometries have changed from planar to pyramidal, in agreement with the optimized structures.

In order to fully understand the thermodynamics and kinetics of the mechanism displayed in Figure 2, and, in particular, gain insight into the electron transfer mechanisms during the reaction processes, we set up valence bond (VB) curve crossing diagrams (Figure 4) for the methyl transfer and hydrogen atom transfer steps. We applied these VB curve crossing diagrams previously to rationalize the reaction mechanisms of substrate activation (hydroxylation, epoxidation, desaturation, and sulfoxidation) by Compound I of cytochrome P450 enzymes as well as the nonheme iron(IV)-oxo species of dioxygenases.[29] These studies rationalized reaction mechanisms and, for instance, explained why a reaction was stepwise via a radical intermediate rather than synchronous (concerted). Furthermore, in the case of P450 Compound I, several possible electron transfer pathways in substrate hydroxylation by Compound I were identified via either an iron(IV)-hydroxo intermediate or an iron(III)-hydroxo heme cation radical, and different activation barriers (and consequently rate constants) were identified that passed these individual intermediates.[30] VB diagrams explained the differences in electron transfer pathways and rationalized the ordering of the various electronic and spin states. Finally, the VB diagrams were used to find patterns in activation energies/rate constants and create predictive models. As such, these VB curve crossing diagrams may also find their use in organometallic chemistry, and therefore, we applied it to the chemical system described here.

The VB curve crossing diagrams start at the bottom-left with the reactant electronic configuration and wave function (Ψ_R) of

DOI: 10.1021/acs.organomet.5b00305
Organometallics 2015, 34, 1651−1660

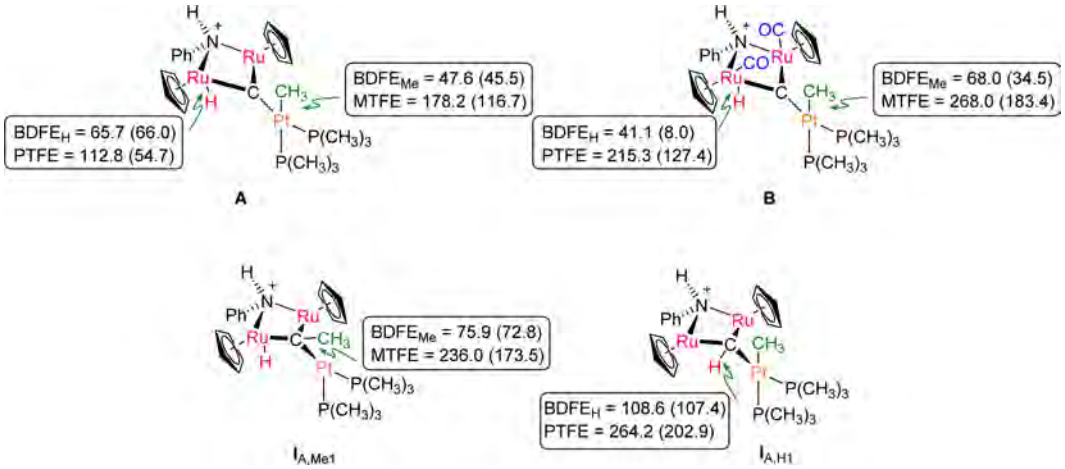

Figure 5. Bond dissociation free energies (BDFEs in kcal mol^{-1}) of key bonds in structures **A**, **B**, $\mathbf{I}_{A,Me1}$, and $\mathbf{I}_{A,H1}$. Reactions calculated according to eqs 1−4. Values in parentheses are solvent-corrected free energies, whereas those out of parentheses are gas-phase data. PTFE and MTFE are the proton and methyl transfer Gibbs free energies, respectively.

A/**B**, which is a carbene where two sp^2 electrons form bonding orbitals with electrons on the two ruthenium atoms and the other two electrons represent a lone pair orbital that donates a bond to Pt. Each of the dots in Figure 4 represents one of these valence electrons. In part (a) in Figure 4, the reaction follows the methyl transfer from Pt to carbene and the structure on the right-hand side gives the electronic configuration of $\mathbf{I}_{Me}$ with wave function Ψ_{Me}. In $\mathbf{I}_{Me}$, the central carbon atom is sp^3 hybridized and forms a single bond with Ru, Ru, Pt, and CH_3. In VB theory, the wave functions of the reactant and product complexes cross, i.e., Ψ_R and Ψ_{Me} in Figure 4a, and lead to an avoided crossing and a transition state for the reaction from reactants to intermediates.[31] Thus, the curve crossing energy (ΔE_X) is above the actual transition state ($\Delta E_{Me}^{\ddagger}$) by a factor *B*, which is called the resonance energy. It has been shown that the barrier height can be described by the difference in energy by a fraction (f) of the promotion gap (G) and the resonance energy *B*: $\Delta E_{Me}^{\ddagger} = fG_{MT} - B$. The promotion gap signifies the excitation energy from the ground state wave function to the product wave function in the geometry of the reactants; i.e., G_{MT} is the energy difference between Ψ_R and Ψ_R* in the reactant geometry. The VB diagrams also give chemical structures of the reactant and product wave functions of the ground and excited state species with valence electrons identified with a dot.

A close inspection of the VB diagrams in Figure 4 shows that the promotion gap for methyl transfer (G_{MT}) represents the breaking of the Pt−CH_3 bond and the formation of a new C−CH_3 bond. In addition, the VB structures of Ψ_R and Ψ_R* show that the carbene carbon is rehybridized from sp^2 to sp^3 hybridization and one electron of the lone pair orbital pointing toward Pt is promoted into the new sp^3 orbital. At the same time, the electron from the broken Pt−CH_3 bond moves into the carbene−Pt bond. Thus, the promotion gap also contains a component for the excitation energy of the carbene from sp^2 to sp^3 hybridization ($E_{ex,C}$), which essentially requires a promotion of an electron from the σ_{PtC} orbital to the virtual 2p$_y$ molecular orbital on carbon. Energetically, G_{MT} can be described in terms of the bond dissociation energies (BDEs) of the respective bonds that are broken and formed in the reaction process (eq 5), whereby BDE_{PtCH_3} represents the Gibbs free energy to break the Pt−CH_3 bond in **A**/**B** and BDE_{CCH_3} is the Gibbs free energy to form the C−CH_3 bond in $\mathbf{I}_{A,Me1}$/$\mathbf{I}_{B,Me1}$.

$$G_{MT} \propto BDE_{PtCH_3} - BDE_{CCH_3} + E_{ex,C} \quad (5)$$

The situation is dramatically different for hydrogen atom transfer from **A**/**B**, as shown in Figure 4b. Thus, the barrier height for hydrogen atom transfer ($\Delta E_H^{\ddagger}$) is proportional to the promotion gap for hydrogen atom transfer (G_{HT}), which correlates with the strength of the Ru−H bond that is broken (BDE_{RuH}), the strength of the C−H bond that is formed (BDE_{CH}), and again the excitation energy for the carbene to change from sp^2 to sp^3 hybridization. In addition to these three terms, the promotion gap G_{HT} also contains a component for the electron transfer energy from Ru to Pt ($ET_{Ru\rightarrow Pt}$). The hydrogen atom transfer process, therefore, incurs extra electron reorganization energy in the Ru_2Pt-carbene scaffold, which is not necessary for the methyl transfer step. The overall preference of hydrogen atom transfer versus methyl transfer will depend on the relative strengths of the bonds that are broken and formed in the process and the electron reorganization energy. To find out whether there are major differences between the BDE values in eq 5 and those in eq 6, we decided to calculate their values with DFT.

$$G_{HT} \propto BDE_{RuH} - BDE_{CH} + E_{ex,C} + ET_{Ru\rightarrow Pt} \quad (6)$$

As the VB drawings in Figure 4 only give qualitative analysis of electron transfer processes and no actual quantitative values, we decided to calculate BDEs and bond dissociation free energies (BDFEs) of key Ru/C−H and Pt/C−CH_3 bonds in complexes **A**, **B**, $\mathbf{I}_{A,Me1}$, and $\mathbf{I}_{A,H1}$ by calculating the release of a H$^{\bullet}$, H$^+$, $CH_3^{\bullet}$, and CH_3^+ from these four complexes according to eqs 1−4 above. Figure 5 displays the diabatic driving forces for H/CH_3 release from complexes **A**, **B**, $\mathbf{I}_{A,H1}$, and $\mathbf{I}_{A,Me1}$. We initially calculated the adiabatic BDFE calculations, whereby we did a full geometry optimization of all individual chemical structures in eqs 1−4 and then took the difference in Gibbs free energy for each of these reactions. However, due to considerable rehybridization of the central carbon atom and, as a consequence, large geometrical changes in some of the structures, the adiabatic BDFE values gave unrealistic results. For instance, the adiabatic bond dissociation energy for the breaking of the Ru−H bond in **A** appears negative, which

DOI: 10.1021/acs.organomet.5b00305
Organometallics 2015, 34, 1651−1660

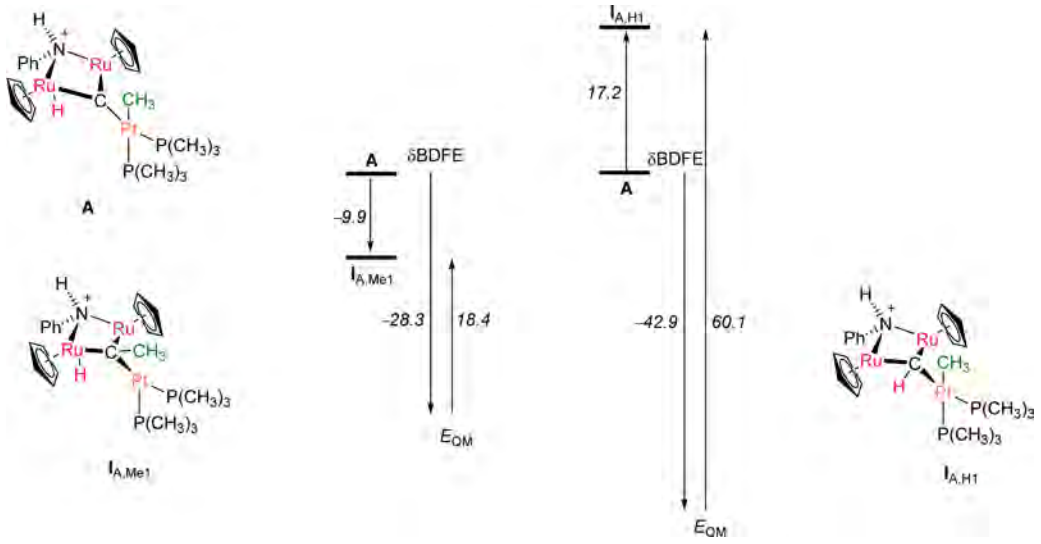

Figure 6. Energy decomposition of the methyl and hydrogen atom transfer reaction from **A**. Gibbs free energies given are in kcal mol^{-1}.

would imply spontaneous dissociation, in disagreement with the experimental crystal structure. However, this did not happen during the geometry optimization, and consequently, there is a significant barrier for this process. Another reason the adiabatic energies give unrealistic results is the dramatic structural changes upon removal of one ligand, i.e., H or CH_3, which changes systems from hexacoordination to pentacoordination, i.e., from an octahedral to a trigonal bipyramical structure, which leads to major changes in electronic structure.[32] Conversely, when we calculate the diabatic Gibbs free energy change by taking the H and [**A**−H] products in the geometry of **A**, then the BDFE is positive. The same is found for the dissociation of a methyl group from **A**. By contrast to structure **A**, the adiabatic and diabatic bond energies in structures $\mathbf{I}_{A,Me1}$ and $\mathbf{I}_{A,H1}$ are very similar and vary by less than 6 kcal mol^{-1}. In the following, however, we will focus on the diabatic bond dissociation free energies.

As can be seen, the strength of the C−H bond in **A** is considerably different from that obtained for **B**. Thus, the $BDFE_H$ for **A** is 45.5 kcal mol^{-1} in solvent, whereas a value of 34.5 kcal mol^{-1} is found for **B**, and as a consequence, the hydrogen atom transfer should be much easier with the CO bound complex then with complex **A**. Indeed, the potential energy landscape in Figure 2 shows that formation of $\mathbf{I}_{B,H1}$ is exergonic by −1.2 kcal mol^{-1}, whereas it is endergonic for $\mathbf{I}_{A,H1}$. Thus, CO binding affects the chemical structure of the Ru centers and weakens the Ru−H bond and makes it more susceptible for hydrogen atom transfer. Despite the fact that the subsequent methyl transfer still has a barrier of about 28 kcal mol^{-1} (virtually unchanged with respect to **A**), it is now sufficiently low to cross at ambient temperatures and pressures. On the other hand, the platinum−methyl bond is much stronger in the CO bound structures and results in a considerable raise in the $\mathbf{I}_{B,Me1}$ energy.

Thermodynamically, the driving force to form $\mathbf{I}_{A,Me1}/\mathbf{I}_{A,H1}$ from **A** represents the breaking of a weak Pt−CH_3 or Ru−H bond and the formation of a much stronger C−CH_3/C−H bond. Hence, the reaction should be strongly exergonic, which is seen for the reaction via $\mathbf{I}_{A,Me1}$ in Figure 2, but not for the one via $\mathbf{I}_{A,H1}$. Thus, the hydrogen atom transfer from Ru in **A** to the carbene to form $\mathbf{I}_{A,H1}$ results in the breaking of the Ru−H bond of $BDFE_H$ = 65.7 kcal mol^{-1} in the gas phase and the formation of a C−H bond with a diabatic value of 108.6 kcal mol^{-1}, and if the driving force was solely dependent on the change in bond strength, the reaction would have been exergonic by 42.9 kcal mol^{-1}. As shown in Figure 2, however, this reaction is endergonic by 17.2 kcal mol^{-1}, which implies that the stereochemical and electronic effects, i.e., the sp^2 to sp^3 rehybridization ($E_{ex,C}$) and the Ru → PT electron transfer ($ET_{Ru\rightarrow Pt}$), account for a destabilization of $\mathbf{I}_{A,H1}$ by about 60 kcal mol^{-1} in Gibbs free energy. This is explained schematically in Figure 6, where we deconvolute the processes from **A** to $\mathbf{I}_{A,Me1}$ and from **A** to $\mathbf{I}_{A,H1}$ into factors for bond breaking and formation (δBDFE) and quantum mechanical effects (E_{QM}). Thus, the methyl transfer reaction from **3** results in the breaking of the Pt−CH_3 bond, which requires a $BDFE_{Me,diabatic}$ = 47.6 kcal mol^{-1}, and, at the same time, the formation of the C−CH_3 bond ($BDFE_{Me,diabatic}$ = 75.9 kcal mol^{-1}). Therefore, the change in bond dissociation Gibbs free energy for the methyl transfer is −28.3 kcal mol^{-1}. The reaction mechanism in Figure 2 found the methyl transfer process to be exergonic by 9.9 kcal mol^{-1}, which implies that the quantum mechanical effect of the process accounts for 18.4 kcal mol^{-1}. The quantum mechanical effect includes the rehybridization energy of the carbene group and the geometric and stereochemical factors associated with the methyl transfer. By comparison, the hydrogen atom transfer shows a much larger change in bond dissociation energy due to the strong C−H bond that is formed ($\delta BDFE_{H,diabatic}$ = −42.9 kcal mol^{-1}). However, this reaction incurs a large quantum mechanical effect of 60.1 kcal mol^{-1} and thereby makes the overall process highly endergonic. The quantum mechanical effect includes the rehybridization of the carbon atom, which will probably be of the same order of magnitude as that found for the methyl transfer process, i.e., about 18 kcal mol^{-1}. In addition, there are the above-mentioned stereochemical repulsions of the methyl groups of the $P(CH_3)_3$ moieties that raise $\mathbf{I}_{A,H1}$ by about 6 kcal mol^{-1}. Finally, the electronic effects (E_{QM}) for the hydrogen atom transfer reaction include the electron transfer energy from Ru to Pt, as described in the VB diagram in Figure 4.

In addition to removal of H/CH_3 from our reactant complexes and intermediates, the breaking of the bond into two ions was also investigated and is described as the proton transfer Gibbs free energy (PTFE) and methyl transfer Gibbs

DOI: 10.1021/acs.organomet.5b00305
Organometallics 2015, 34, 1651−1660

free energy (MTFE). As follows from the data in Figure 5, it requires considerably more energy to break the Ru−H and Pt−CH_3 bonds than a homogeneous splitting into $Ru^{\bullet}$ + $H^{\bullet}$ and $Pt^{\bullet}$ + $CH_3^{\bullet}$. The thermodynamic analysis confirms the results described above in Figure 2, where either an $H^{\bullet}$ or $CH_3^{\bullet}$ is transferred rather than H^+ and CH_3^+.

So what about the next step for the formation of μ_2-$CHCH_3$ products? The reaction from $\mathbf{I}_{A,Me1}$ to products results in the breaking of the Ru−H bond and the formation of a new C−H bond. By contrast, the pathway from $\mathbf{I}_{A,H1}$ leads to the breaking of the Pt−CH_3 bond and the transfer of the methyl group to carbon. However, this process breaks the C−Pt bond and the $Pt(P(CH_3)_3)_2$ group is left behind with two unpaired electrons. Thus, an electron on Pt is promoted into a virtual orbital and the reaction proceeds via a high energy pathway. Indeed, the DFT calculated potential energy profile in Figure 2 gives a high barrier for $\mathbf{TS}_{A,Me2}$, in agreement with this.

In summary, DFT calculations presented here show a novel pathway for the synthesis of linear alkanes on a trimetal-carbene center. The chemical system discussed here, however, is inefficient as the lowest-lying initial barrier is for hydrogen atom transfer, which leads to a dead-end reaction intermediate. By contrast, the initial methyl transfer can be followed by hydrogen atom transfer to lead to products. The question is how this catalyst may be improved for alkane synthesis. The thermodynamic and VB schemes above give some clear indication to this. As shown in eqs 5 and 6, above, the barrier heights $\mathbf{TS}_{H1}$ and $\mathbf{TS}_{Me1}$ are dependent on the Ru−H and Pt−CH_3 bonds that are broken and the C−H and C−CH_3 bonds being formed. Consequently, a chemical system with a weaker metal−CH_3 bond should react predominantly via initial methyl transfer and may be more efficient. The work described here may have relevance to biological and heterogeneous catalysis for the synthesis of alkanes. In particular, in heterogeneous catalysis, linear alkanes are generated on a metal surface using often CO and H_2 as reactants. It may very well be that the trimetal-carbene structure discussed here is a common type intermediate in heterogeneous catalysis, but further research will have to be performed to establish this.

CONCLUSIONS

In summary, our calculations establish the key features of a synthetic homogeneous catalyst for alkyl chain growth. A combination of DFT, NBO, VB, and thermochemical studies has been performed and establish the intrinsic chemical properties of **A** or **B**. First, we characterize reactants as having a Ru_2Pt-carbene core where the lone pair is donated to Pt via a bonding/backbonding configuration. Second, we find a low energy mechanism of alkyl formation through consecutive $CH_3^{\bullet}$ and $H^{\bullet}$ transfer to the carbene with low Gibbs free energy of activation and exergonic driving force. We show that the reverse process is thermochemically hampered and would lead to an excited triplet configuration.

Overall, our work identifies a novel reaction for the synthesis of alkanes that starts from a trimetal carbene. This unique structure is shown to be capable of intramolecular methyl and hydrogen atom transfer to the carbene to form μ_2-$CHCH_3$ products as precursor to alkanes.

ASSOCIATED CONTENT

Supporting Information

Supporting Information with Cartesian coordinates as well as tables with group spin densities, charges, and absolute and relative energies is provided. The Supporting Information is available free of charge on the ACS Publications website at DOI: 10.1021/acs.organomet.5b00305.

AUTHOR INFORMATION

Corresponding Authors

*E-mail: Sam.devisser@manchester.ac.uk (S.P.d.V.).
*E-mail: dkclcre@yahoo.com (D.K.).

Author Contributions

§These authors contributed equally.

Notes

The authors declare no competing financial interests.

ACKNOWLEDGMENTS

The National Service of Computational Chemistry Software is thanked for CPU time provided. D.K. holds the Ramanujan Fellowship (SR/S2/RJN-11/2008) from the Department of Science and Technology (DST), New Delhi (India). M.A.S. thanks the Petroleum Technology Development Fund in Nigeria for a studentship.

REFERENCES

(1) (a) Rofer-de Poorter, C. K. *Chem. Rev.* **1981**, *81*, 447−474. (b) Schulz, H. *Appl. Catal., A* **1999**, *186*, 3−12. (c) Khodakov, A. Y.; Chu, W.; Fongarland, P. *Chem. Rev.* **2007**, *107*, 1692−1744. (d) Maitlis, P. M.; Zanotti, V. *Chem. Commun.* **2009**, 1619−1634.

(2) See, e.g.: (a) Tsakoumis, N. E.; Rønning, M.; Borg, Ø.; Rytter, E.; Holmen, A. *Catal. Today* **2010**, *154*, 162−182. (b) Shetty, S.; van Santen, R. A. *Catal. Today* **2011**, *171*, 168−173. (c) Inderwildi, O. R.; Jenkins, S. J. *Chem. Soc. Rev.* **2008**, *37*, 2274−2309.

(3) (a) Perkins, P.; Vollhardt, K. P. C. *J. Am. Chem. Soc.* **1979**, *101*, 3985−3987. (b) Inderwildi, O. R.; King, D. A.; Jenkins, S. J. *Phys. Chem. Chem. Phys.* **2009**, *11*, 11110−11112.

(4) Takemoto, S.; Morita, H.; Karitani, K.; Fujiwara, H.; Matsuzaka, H. *J. Am. Chem. Soc.* **2009**, *131*, 18026−18027.

(5) (a) Mayer, J. M. *Acc. Chem. Res.* **1998**, *31*, 441−450. (b) Weinberg, D. R.; Gagliardi, C. J.; Hull, J. F.; Murphy, C. F.; Kent, C. A.; Westlake, B. C.; Paul, A.; Ess, D. H.; McCafferty, D. G.; Meyer, T. J. *Chem. Rev.* **2012**, *112*, 4016−4093.

(6) See, e.g.: (a) Love, J. A.; Sanford, M. S.; Day, M. W.; Grubbs, R. H. *J. Am. Chem. Soc.* **2003**, *125*, 10103−10109. (b) Alcaide, B.; Almendros, P.; Luna, A. *Chem. Rev.* **2009**, *109*, 3817−3858. (c) Bernal, M. J.; Torres, O.; Martín, M.; Sola, E. *J. Am. Chem. Soc.* **2013**, *135*, 19008−19015.

(7) (a) Miller, R. L.; Wolczanski, P. T.; Rheingold, A. L. *J. Am. Chem. Soc.* **1993**, *115*, 10422−10423. (b) Su, C.-J.; Su, P.-C.; Chi, Y.; Peng, S.-M.; Lee, G.-H. *J. Am. Chem. Soc.* **1996**, *118*, 3289−3290. (c) Peters, J. C.; Odom, A. L.; Cummins, C. C. *Chem. Commun.* **1997**, 1995−1996. (d) Caselli, A.; Solari, E.; Scopelliti, R.; Floriani, C. *J. Am. Chem. Soc.* **2000**, *122*, 538−539. (e) Buchowicz, W.; Herbaczyńska, B.; Jerzykiewicz, L. B.; Lis, T.; Pasynkiewicz, S.; Pietrzykowski, A. *Inorg. Chem.* **2012**, *51*, 8292−8297. (f) Harding, D. J.; Kerpal, C.; Meijer, G.; Fielicke, A. *J. Phys. Chem. Lett.* **2013**, *4*, 892−896. (g) Borren, E. S.; Hill, A. F.; Shang, R.; Sharma, M.; Willis, A. C. *J. Am. Chem. Soc.* **2013**, *135*, 4942−4945. (h) Li, X.; Wang, L.-S.; Boldyrev, A. I.; Simons, J. *J. Am. Chem. Soc.* **1999**, *121*, 6033−6038.

(8) (a) de Visser, S. P.; Tan, L. S. *J. Am. Chem. Soc.* **2008**, *130*, 12961−12974. (b) Latifi, R.; Bagherzadeh, M.; de Visser, S. P. *Chem.—Eur. J.* **2009**, *15*, 6651−6662.

(9) *Jaguar 7.7*, version 7.9; Schrodinger, LLC: New York, NY, 2011.

(10) Frisch, M. J.; Trucks, G. W.; Schlegel, H. B.; Scuseria, G. E.; Robb, M. A.; Cheeseman, J. R.; Scalmani, G.; Barone, V.; Mennucci, B.; Petersson, G. A.; Nakatsuji, H.; Caricato, M.; Li, X.; Hratchian, H. P.; Izmaylov, A. F.; Bloino, J.; Zheng, G.; Sonnenberg, J. L.; Hada, M.; Ehara, M.; Toyota, K.; Fukuda, R.; Hasegawa, J.; Ishida, M.; Nakajima, T.; Honda, Y.; Kitao, O.; Nakai, H.; Vreven, T.; Montgomery, J. A., Jr.;

DOI: 10.1021/acs.organomet.5b00305
Organometallics 2015, 34, 1651−1660

Peralta, J. E.; Ogliaro, F.; Bearpark, M.; Heyd, J. J.; Brothers, E.; Kudin, K. N.; Staroverov, V. N.; Kobayashi, R.; Normand, J.; Raghavachari, K.; Rendell, A.; Burant, J. C.; Iyengar, S. S.; Tomasi, J.; Cossi, M.; Rega, N.; Millam, J. M.; Klene, M.; Knox, J. E.; Cross, J. B.; Bakken, V.; Adamo, C.; Jaramillo, J.; Gomperts, R.; Stratmann, R. E.; Yazyev, O.; Austin, A. J.; Cammi, R.; Pomelli, C.; Ochterski, J. W.; Martin, R. L.; Morokuma, K.; Zakrzewski, V. G.; Voth, G. A.; Salvador, P.; Dannenberg, J. J.; Dapprich, S.; Daniels, A. D.; Farkas, Ö.; Foresman, J. B.; Ortiz, J. V.; Cioslowski, J.; Fox, D. J. *Gaussian 09*, Revision A.1; Gaussian, Inc.: Wallingford, CT, 2009.

(11) (a) Becke, A. D. *J. Chem. Phys.* **1993**, *98*, 5648−5652. (b) Lee, C.; Yang, W.; Parr, R. G. *Phys. Rev. B* **1988**, *37*, 785−789.

(12) Hay, P. J.; Wadt, W. R. *J. Chem. Phys.* **1985**, *82*, 299−310.

(13) Grimme, S.; Antony, J.; Ehrlich, S.; Krieg, H. *J. Chem. Phys.* **2010**, *132*, 154104.

(14) (a) Shaik, S.; de Visser, S. P.; Ogliaro, F.; Schwarz, H.; Schröder, D. *Curr. Opin. Chem. Biol.* **2002**, *6*, 556−567. (b) de Visser, S. P. *Angew. Chem., Int. Ed.* **2006**, *45*, 1790−1793.

(15) (a) de Visser, S. P.; Quesne, M. G.; Martin, B.; Comba, P.; Ryde, U. *Chem. Commun.* **2014**, *50*, 262−282. (b) Quesne, M. G.; Latifi, R.; Gonzalez-Ovalle, L. E.; Kumar, D.; de Visser, S. P. *Chem.—Eur. J.* **2014**, *20*, 435−446.

(16) (a) Becke, A. D. *Phys. Rev. A* **1988**, *38*, 3098−3100. (b) Perdew, J. P. *Phys. Rev. B* **1986**, *33*, 8822−8824.

(17) Zhao, Y.; Truhlar, D. G. *Theor. Chem. Acc.* **2008**, *120*, 215−241.

(18) (a) Adamo, C.; Barone, V. *J. Chem. Phys.* **1999**, *110*, 6158−6169. (b) Perdew, J. P.; Burke, K.; Ernzerhof, M. *Phys. Rev. Lett.* **1996**, *77*, 3865−3868.

(19) (a) Sainna, M. A.; Kumar, S.; Kumar, D.; Fornarini, S.; Crestoni, M. E.; de Visser, S. P. *Chem. Sci.* **2015**, *6*, 1516−1529. (b) Sainna, M. A.; Sil, D.; Sahoo, D.; Martin, B.; Rath, S. P.; Comba, P.; de Visser, S. P. *Inorg. Chem.* **2015**, *54*, 1919−1930.

(20) (a) Vardhaman, A. K.; Sastri, C. V.; Kumar, D.; de Visser, S. P. *Chem. Commun.* **2011**, *47*, 11044−11046. (b) Kumar, S.; Faponle, A. S.; Barman, P.; Vardhaman, A. K.; Sastri, C. V.; Kumar, D.; de Visser, S. P. *J. Am. Chem. Soc.* **2014**, *136*, 17102−17115.

(21) (a) Karamzadeh, B.; Kumar, D.; Sastry, G. N.; de Visser, S. P. *J. Phys. Chem. A* **2010**, *114*, 13234−13243. (b) Kumar, D.; Latifi, R.; Kumar, S.; Rybak-Akimova, E. V.; Sainna, M. A.; de Visser, S. P. *Inorg. Chem.* **2013**, *52*, 7968−7979. (c) Draksharapu, A.; Angelone, D.; Quesne, M. G.; Padamati, S. K.; Gómez, L.; Hage, R.; Costas, M.; Browne, W. R.; de Visser, S. P. *Angew. Chem., Int. Ed.* **2015**, *54*, 4357−4361. (d) Sallmann, M.; Kumar, S.; Chernev, P.; Nehrkorn, J.; Schnegg, A.; Kumar, D.; Dau, H.; Limberg, C.; de Visser, S. P. *Chem.—Eur. J.* **2015**, DOI: 10.1002/chem.201500644.

(22) Weinhold, F.; Carpenter, J. E. The Natural Bond Orbital Lewis Structure Concept for Molecules, Radicals, and Radical Ions. In *The Structure of Small Molecules and Ions*; Naaman, R., Vager, Z., Eds.; Plenum Press: New York, 1988; pp 227−236.

(23) (a) de Quadras, L.; Bauer, E. B.; Stahl, J.; Zhuravlev, F.; Hampel, F.; Gladysz, J. A. *New. J. Chem.* **2007**, *31*, 1594−1604. (b) Che, C.-M.; Huang, J.-S. *Coord. Chem. Rev.* **2002**, *231*, 151−164. (c) Das, R. K.; Saha, B.; Rahaman, S. M. W.; Bera, J. K. *Chem.—Eur. J.* **2010**, *16*, 14459−14468. (d) Algarra, A. G.; Grushin, V. V.; MacGregor, S. A. *Organometallics* **2012**, *31*, 1467−1476.

(24) (a) Mutter, S. T.; Platts, J. A. *J. Phys. Chem. A* **2011**, *115*, 11293−11302. (b) Conner, D.; Jayaprakash, K. N.; Wells, M. B.; Manzer, S.; Gunnoe, T. B.; Boyle, P. D. *Inorg. Chem.* **2003**, *42*, 4759−4772. (c) Patra, S. K.; Sadhukhan, N.; Bera, J. K. *Inorg. Chem.* **2006**, *45*, 4007−4015. (d) Patra, S. K.; Bera, J. K. *Organometallics* **2006**, *25*, 6054−6060. (e) MacGregor, S. A.; McKay, D.; Panetier, J. A.; Whittlesey, M. K. *Dalton Trans.* **2013**, *42*, 7386−7395. (f) Sharma, P. K.; de Visser, S. P.; Ogliaro, F.; Shaik, S. *J. Am. Chem. Soc.* **2003**, *125*, 2291−2300.

(25) (a) Latifi, R.; Sainna, M. A.; Rybak-Akimova, E. V.; de Visser, S. P. *Chem.—Eur. J.* **2013**, *19*, 4058−4068. (b) Vardhaman, A. K.; Barman, P.; Kumar, S.; Sastri, C. V.; Kumar, D.; de Visser, S. P. *Angew. Chem., Int. Ed.* **2013**, *52*, 12288−12292.

(26) See, e.g.: (a) Diver, S. T. *Coord. Chem. Rev.* **2007**, *251*, 671−701. (b) Barluenga, J.; Fernández-Rodríguez, M. A.; Aguilar, E. *J. Organomet. Chem.* **2005**, *690*, 539−587. (c) Bernasconi, C. F. *Chem. Soc. Rev.* **1997**, *26*, 299−307.

(27) (a) de Visser, S. P.; Ogliaro, F.; Shaik, S. *Angew. Chem., Int. Ed.* **2001**, *40*, 2871−2874. (b) de Visser, S. P.; Ogliaro, F.; Shaik, S. *Chem. Commun.* **2001**, 2322−2323.

(28) (a) de Visser, S. P. *Chem.—Eur. J.* **2006**, *12*, 8168−8177. (b) de Visser, S. P.; Tahsini, L.; Nam, W. *Chem.—Eur. J.* **2009**, *15*, 5577−5587.

(29) Previous work that used VB diagrams to explain reaction mechanisms: (a) Shaik, S.; Kumar, D.; de Visser, S. P. *J. Am. Chem. Soc.* **2008**, *130*, 10128−10140. (b) de Visser, S. P. *J. Am. Chem. Soc.* **2010**, *132*, 1087−1097. (c) Kumar, D.; Karamzadeh, B.; Sastry, G. N.; de Visser, S. P. *J. Am. Chem. Soc.* **2010**, *132*, 7656−7667. (d) Ji, L.; Faponle, A. S.; Quesne, M. G.; Sainna, M. A.; Zhang, J.; Franke, A.; Kumar, D.; van Eldik, R.; Liu, W.; de Visser, S. P. *Chem. Eur. J.* **2015**, DOI: 10.1002/chem.201500329.

(30) de Visser, S. P.; Ogliaro, F.; Sharma, P. K.; Shaik, S. *J. Am. Chem. Soc.* **2002**, *124*, 11809−11826.

(31) Shaik, S.; Hiberty, P. C. *A Chemist's Guide to Valence Bond Theory*; Wiley-Interscience: New York, NY, 2007.

(32) Quesne, M. G.; de Visser, S. P. *J. Biol. Inorg. Chem.* **2012**, *17*, 841−852.

DOI: 10.1021/acs.organomet.5b00305
Organometallics 2015, 34, 1651−1660

ChemPubSoc Europe

DOI: 10.1002/chem.201500644

CHEMISTRY A European Journal Full Paper

Enzyme Models

Structure and Mechanism Leading to Formation of the Cysteine Sulfinate Product Complex of a Biomimetic Cysteine Dioxygenase Model

Madleen Sallmann,[a] Suresh Kumar,[b] Petko Chernev,[c] Joscha Nehrkorn,[d] Alexander Schnegg,[d] Devesh Kumar,*[b] Holger Dau,*[c] Christian Limberg,*[a] and Sam P. de Visser*[e]

Abstract: Cysteine dioxygenase is a unique nonheme iron enzyme that is involved in the metabolism of cysteine in the body. It contains an iron active site with an unusual 3-His ligation to the protein, which contrasts with the structural features of common nonheme iron dioxygenases. Recently, some of us reported a truly biomimetic model for this enzyme, namely a trispyrazolylborato iron(II) cysteinato complex, which not only has a structure very similar to the enzyme–substrate complex but also represents a functional model: Treatment of the model with dioxygen leads to cysteine dioxygenation, as shown by isolating the cysteine part of the product in the course of the work-up. However, little is known on the conversion mechanism and, so far, not even the structure of the actual product complex had been characterised, which is also unknown in case of the enzyme. In a multidisciplinary approach including density functional theory calculations and X-ray absorption spectroscopy, we have now determined the structure of the actual sulfinato complex for the first time. The Cys-SO_2^- functional group was found to be bound in an η^2-*O*,*O*-coordination mode, which, based on the excellent resemblance between model and enzyme, also provides the first support for a corresponding binding mode within the enzymatic product complex. Indeed, this is again confirmed by theory, which had predicted a η^2-*O*,*O*-binding mode for synthetic as well as the natural enzyme.

Introduction

Mononuclear nonheme iron dioxygenases (MNHID) are found in all forms of life and catalyse vital reactions in biosystems.[1] These nonheme iron dioxygenases are highly versatile in nature and are involved in biodegradation pathways, for example, in the metabolism of cysteine in the body, as well as biosynthesis functions, for example, antibiotics synthesis in microbes, and in DNA and RNA repair mechanisms.[2] They utilise molecular oxygen on a nonheme iron centre and transfer both oxygen atoms to either one or two substrate molecules. Thus, in the α-ketoglutarate dioxygenases, which is a common and well-studied nonheme iron dioxygenase, an α-ketoglutarate co-substrate binds to the iron centre, which is converted into succinate, CO_2 and a high-valent iron(IV)-oxo species.[3] The latter has been characterised spectroscopically for a number of α-ketoglutarate dioxygenases and halogenases and was shown to react with aliphatic groups with a large kinetic isotope effect through C–H abstraction.[4] A common theme within the α-ketoglutarate dependent dioxygenases, and also in other MNHID, is the active site structural features, whereby the metal is linked to the protein through a conserved 2-His/1-Asp (or Glu) ligand system in a facial orientation.[5] However, there are a handful of representatives of the MNHID enzyme family that show a different organisation. The cysteine dioxygenase (CDO) belongs to those because it features an iron centre bound by

[a] *M. Sallmann,[+] Prof. Dr. C. Limberg*
Humboldt-Universität zu Berlin, Institut für Chemie
Brook-Taylor-Strasse 2, 12489 Berlin (Germany)
Fax: (+49) 30-2093-6966
E-mail: christian.limberg@chemie.hu-berlin.de

[b] *S. Kumar,[+] Dr. D. Kumar*
Department of Applied Physics
Babasaheb Bhimrao Ambedkar University
School for Physical Sciences, Vidya Vihar
Rae Bareilly Road, Lucknow, UP (India)
E-mail: dkclcre@yahoo.com

[c] *Dr. P. Chernev, Prof. Dr. H. Dau*
Freie Universität Berlin, FB Physik
Arnimallee 14, 14195 Berlin (Germany)
E-mail: holger.dau@fu-berlin.de

[d] *Dr. J. Nehrkorn, Dr. A. Schnegg*
Helmholtz-Zentrum Berlin für Materialien und Energie GmbH
Institut für Silizium-Photovoltaik, Kekuléstrasse 5
12489 Berlin (Germany)

[e] *Dr. S. P. de Visser*
Manchester Institute of Biotechnology
and School of Chemical Engineering and Analytical Science
The University of Manchester
131 Princess Street, Manchester M1 7DN (UK)
E-mail: sam.devisser@manchester.ac.uk

[+] *These authors contributed equally to this work.*

Supporting information for this article is available on the WWW under http://dx.doi.org/10.1002/chem.201500644.

© 2015 Wiley-VCH Verlag GmbH & Co. KGaA, Weinheim

three histidine ligands.[6] The origin and demand for this structural arrangement is still poorly understood[7] and has led to much speculation on the function of the 3-His ligand binding, triggering interest from a range of disciplines including biomimetic chemistry.

CDO catalyses the metabolism of cysteine with molecular oxygen to yield cysteine sulfinic acid (Scheme 1), which is

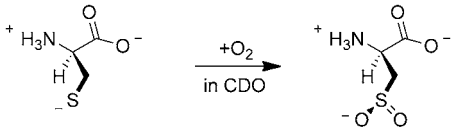

Scheme 1. Catalytic reaction mechanism of cysteine oxygenation by CDO enzymes.

needed for the assembly of central metabolites in the human organism.[8] A CDO structure has been known since 2006,[6] and a substrate-bound structure was also characterised: the substrate cysteine coordinates to the 3-His Fe^{II} centre through the sulfur atom and the nitrogen atom, so that a pentagonal coordination sphere results for the iron(II) ion and one coordination site remains open for the potential coordination and activation of O_2. However, little information is available on the events that take place after dioxygen binding. The exact mechanism of cysteine oxidation is thus still controversial and several possible intermediates and reaction pathways have been suggested.[9] One particular problem in CDO enzymes comes from the fact that most dioxygen-bound structures are short-lived and, for instance, no product complex has ever been characterised.

Whereas the functions of many oxygenating iron enzymes have been successfully imitated within the last decades by using molecular model compounds, such as biomimetic complexes,[1,10] only in the past three years have major advances with respect to the modelling of CDO been made.[11] Some of us have recently reported the successful coordination and dioxygenation of a protected cysteinato ligand at a $(His)_3Fe^{II}$ analogue with three facially arranged *N*-heterocyclic donor functions coordinating to iron(II) and thus about a truly biomimetic model system for CDO had been developed.[11d] For the simulation of the His_3 coordination sphere at the iron centre of CDO, the well-known trispyrazolylborato (Tp) ligand system was chosen, with phenyl residues at the 3-positions of the pyrazole units to create a protective reaction pocket imitating the one in the actual enzyme. L-Cysteine ethyl ester was employed as the substrate ligand, which coordinated to the TpFe unit in a fashion very similar to that found for the CDO-cysteinate complex (Scheme 2). O_2 treatment led to dioxygenation, as evidenced by the results of electrospray ionisation/mass spectrometry (ESI/MS). Unfortunately, due to the instability of the actual product, so far, all attempts to grow single crystals that might have allowed a characterisation through X-ray diffraction, failed. However, aqueous work-up (Scheme 2) provided the cysteine sulfinic acid derivative, suggesting a constitution $[Tp^{Me,Ph}Fe(O_2S\text{-}CH_2\text{-}CH(NH_2)CO_2Et)]$, **1**, for the initially formed product complex.

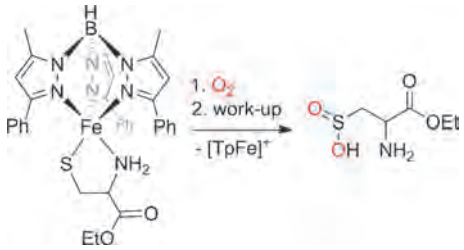

Scheme 2. Reactivity of $[Tp^{Me,Ph}Fe(CysOEt)]$ towards O_2.

With this knowledge, the structure of the dioxygenated compound **1** is of high interest, especially bearing in mind that no experimental data is available for the product complex of the natural enzyme. It can be safely assumed that the cysteine sulfinate will bind as a chelating ligand, but there are several possibilities: The SO_2 unit can bind through one oxygen atom, through two oxygen atoms or—as recently found in an experimental model study—through the sulfur atom.[11f] Given that no experimental data has been reported on the product complex of the enzyme, a quantum mechanics/molecular mechanics (QM/MM) study was performed, which provided insight into the enzymatic reaction mechanism leading to the cysteine sulfinic product complex, of which we highlight the active site structure in Figure 1.[9g] These calculations led to the conclu-

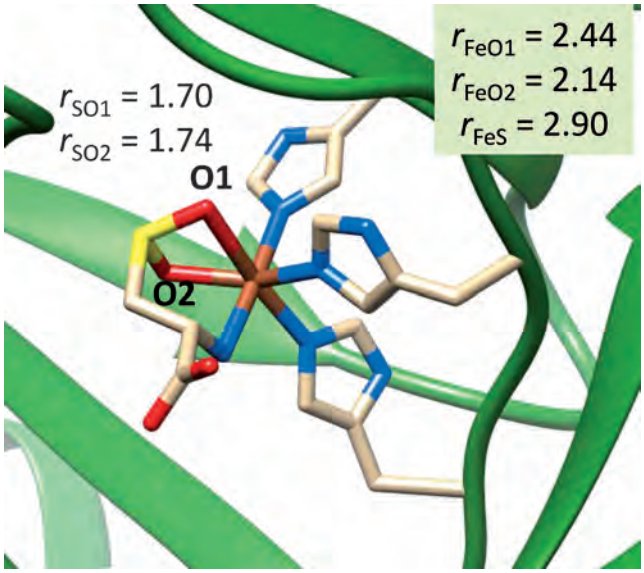

Figure 1. QM/MM optimised structure of the quintet spin product complex as taken from Reference [9g]. Bond lengths are given in angstroms.

sion that the coordination proceeds through a η^2-*O*,*O*-binding mode. However, until today there has been no experimental support for this finding, and hence we hoped to gain such evidence through the investigation of the biomimetic model system **1**, which is sufficiently stable to allow investigations in solutions.

Herein, we present the results of a combined theoretical and experimental study on the product structure of our realistic

© 2015 Wiley-VCH Verlag GmbH & Co. KGaA, Weinheim

model of the CDO and propose a catalytic mechanism for the formation of this complex starting from the reactants. This multidisciplinary approach leads to the conclusion that the biomimetic model truly reflects the enzymatic system with a closely related catalytic cycle and a product complex that binds through η^2-*O*,*O*-coordination.

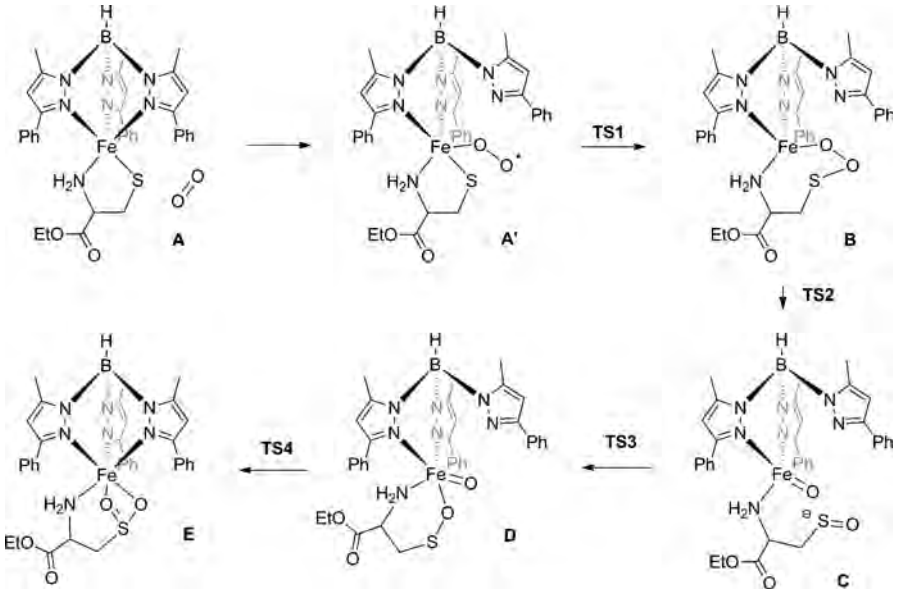

Scheme 3. Mechanism and nomenclature of cysteine dioxygenation by a biomimetic model complex.

Results and Discussion

At the outset of this work, we initiated a computational study on the mechanism of substrate dioxygenation within the biomimetic CDO complex leading to the product complex. The optimised geometries were then compared with the results of experimental spectroscopic analysis. Before we discuss the latter, we will highlight the major computational results on the conversion of our biomimetic CDO complex and underline the key differences and similarities with respect to the enzymatic system.

Computational studies on the oxygen activation process of [Tp^{Me,Ph}Fe(CysOEt)] with O_2

We calculated the complete dioxygenation reaction starting from an iron(II) complex, [Tp^{Me,Ph}Fe(CysOEt)], with a nearby dioxygen molecule, as described in detail in Scheme 3. We set out from a long-range complex of [Tp^{Me,Ph}Fe(CysOEt)] and O_2, designated **A**. Subsequently, we allowed the oxygen to approach the iron centre to form iron(III)-superoxo complex **A′**. The terminal oxygen atom attacks the sulfur atom to form ring-structure **B**, via transition-state **TS1**, followed by O–O breaking via transition-state **TS2** to give an iron(IV)-oxo complex and sulfoxide **C**. A subsequent barrier via **TS3** leads to binding of the sulfoxide to the iron centre, structure **D**, followed by transfer of the second oxygen atom via transition-state **TS4** to give cysteine sulfinate complex **E**.

This mechanism shows analogy to that calculated for CDO enzymes and biomimetic models published previously,[9c,g,12] although we will highlight some critical differences below. The postulated mechanism proceeds stepwise via multiple local minima for the sequential oxygen atom transfer, on several close-lying potential energy surfaces. Although, we calculated the full mechanism on the singlet, triplet, quintet and septet spin state surfaces, actually the ground state of all local minima in Scheme 3 is either triplet or quintet spin. Full details of all calculations on the alternative (singlet and septet) spin states are given in the Supporting Information; we focus herein on the triplet and quintet spin state structures only.

Let us start with a detailed analysis of the reactant structures **A** and **A′** as depicted schematically in Figure 2. Thus, without oxygen bound to the iron centre (as in **A**) the metal is pentacoordinated with the Tp^{Me,Ph} ligand bound as a tripodal tridentate ligand and cysteinate as a bidentate ligand that binds through the amine and thiolate groups to the metal. The ground state of **A** is a triplet spin state with the septet, open-shell singlet and quintet spin states higher in energy by $\Delta G_d =$ 9.2, 11.0 and 11.8 kcal mol^{-1}, respectively, whereby the free energy was calculated with UB3LYP-D/BS2 energies and corrected with zero-point, thermal and entropic corrections at UB3LYP/BS1 in the gas-phase. The optimised geometry and the resulting bond parameters are in reasonable agreement with those determined by a single-crystal X-ray analysis for [Tp^{Me,Ph}Fe(CysOEt)]. Whereas the Fe–S bond revealed by XRD (Fe–S 2.3122(8) Å) is somewhat shorter than that in the calculated structure, all Fe–N bonds are somewhat longer (experiment: Fe–N_{Cys} 2.290(3) Å, Fe–N_{Pz} 2.106(2), 2.112(2), 2.275(2) Å;

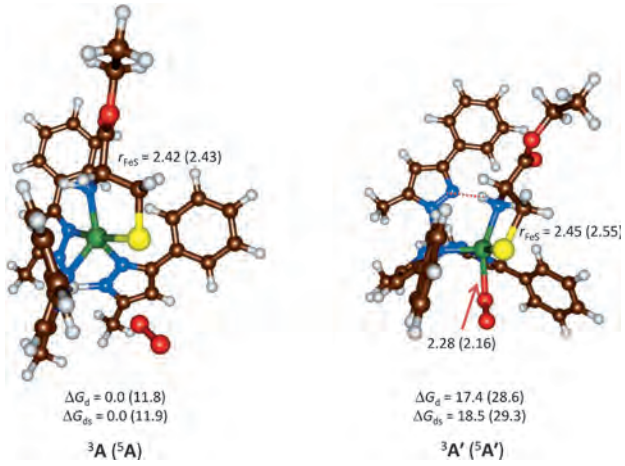

Figure 2. DFT optimised geometries of ^{3,5}**A** and ^{3,5}**A′** with Fe–O and Fe–S bond lengths in angstroms and free energies in the gas phase (ΔG_d) and in solvent (ΔG_{ds}) in kcal mol^{-1}.

© 2015 Wiley-VCH Verlag GmbH & Co. KGaA, Weinheim

calculations: Fe–N_{Cys} 2.182 [2.179] Å; Fe–N_{Pz} 2.082 [2.085], 2.092 [2.089], 2.216 [2.212] Å). The three pyrazole groups form a facial triad in close analogy to the 3-His ligand system in CDO enzymes. In addition, substrate cysteinate in the enzyme also binds as a bidentate ligand; therefore, structure **A** faithfully mimics the active sites of CDO enzymes. To test the effect of the basis set on the structure, we also performed a B3LYP/BS2 geometry optimisation (see the Supporting Information, Figure S10), however, only small changes in bond lengths were found.

The bulky phenyl substituents of the $Tp^{Me,Ph}$ ligand, however, prevent binding of a sixth ligand to the metal centre. Thus, approach of molecular oxygen to the iron centre with formation of the iron(III)-superoxo complex **A′** is accompanied by the release of one of the pyrazole groups from the iron centre in a barrierless process. While the pyrazole group loses a covalent linkage with the iron, it forms a new hydrogen bond with the amine group of the cysteinate residue. Thus, dioxygen binding to our biomimetic CDO model contrasts with the dioxygen binding process in CDO enzymes, in which all original metal–ligand and metal–substrate interactions remain intact. Another difference of the iron(III)-superoxo complex **A′** with respect to the analogous system calculated for CDO enzymes relates to the orientation of the substrate with respect to the superoxo group: In CDO, both amine and thiolate groups are *cis* with respect to the superoxo group, whereas in structure **A′**, the thiolate is in the *cis* position and the amine is *trans* to the superoxo group.

The loss of one of the iron-pyrazole interactions has little effect on the spin-state ordering, and the triplet spin state remains the ground state, although an open-shell singlet spin state approaches it to within 2 kcal mol^{-1}. However, on the singlet spin state surface, the rest of the mechanism is at least 15 kcal mol^{-1} higher in energy. The large structural changes upon dioxygen binding to the iron centre means that this O_2-binding step of the mechanism is strongly endergonic.

The spin-state ordering for structures **A** and **A′** contrast with the one found in calculations on CDO enzymes, for which an open-shell singlet spin state was found as the ground state.[9c,g] However, test calculations using the BP86, PBE0 and B3LYP-D3 methods gave the same spin state ordering for **A** and **A′** as the one found for B3LYP with a triple-ζ quality basis set. Calculations on $[Fe^{III}(LN_3S)O_2]$, for which LN_3S was a bis(imino)pyridine ligand with a pendant thiolate arm, gave an open-shell singlet ground state, too, although both the triplet and the quintet spin states were located within 5.5 kcal mol^{-1}.[12a] The origin of the triplet spin ground state for the iron(III)-superoxo complex probably stems from the fact that complexes **A** and **A′** are pentacoordinated iron(III) complexes, whereas the CDO enzymatic and reported model systems have the metal in an environment of six ligands. Given that iron(III)-superoxo complexes are known to have a large variety of close-lying electronic and spin states, it is reasonable that subtle changes in the coordination environment and electrostatic interactions will lead to changes in the spin state energy.[13] In a similar vein, we recently showed that iron(IV)-oxo complexes in a pentacoordinated environment stabilise structures in a high-spin state, whereas hexacoordination favours the intermediate (triplet) spin state instead.[14]

After dioxygen binding and the formation of the iron(III)-superoxo structure **A′**, the reaction continues with attack of the terminal oxygen atom of the superoxo group on the sulfide group of cysteinate. The formation of the S–O bond leads to ring-structure **B** via a rate-determining transition state **TS1** of $\Delta G_d = 12.3$ and $\Delta G_{ds} = 11.3$ kcal mol^{-1} with respect to **A′**, whereby the latter represents the free energies with solvent corrections included (Figure 3). This is similar to the mechanism of CDO and other nonheme iron dioxygenases for which the iron(III)-superoxo group attacks with the terminal oxygen atom to form a bicyclic ring-structure.[9c,g,15] The barriers are of the same order of magnitude as those obtained for the enzymatic system. Similar to the mechanism calculated for CDO enzymes and model complexes, here also the reaction from ^{3}**A′** to ^{3}**B** is endothermic, whereas it is exothermic on the quintet spin state surface.[9c,g,15] It is expected that a spin-state-crossing from the triplet to the quintet spin state will occur either en route from ^{3}**TS1** to **B** or during the lifetime of ^{3}**B**.

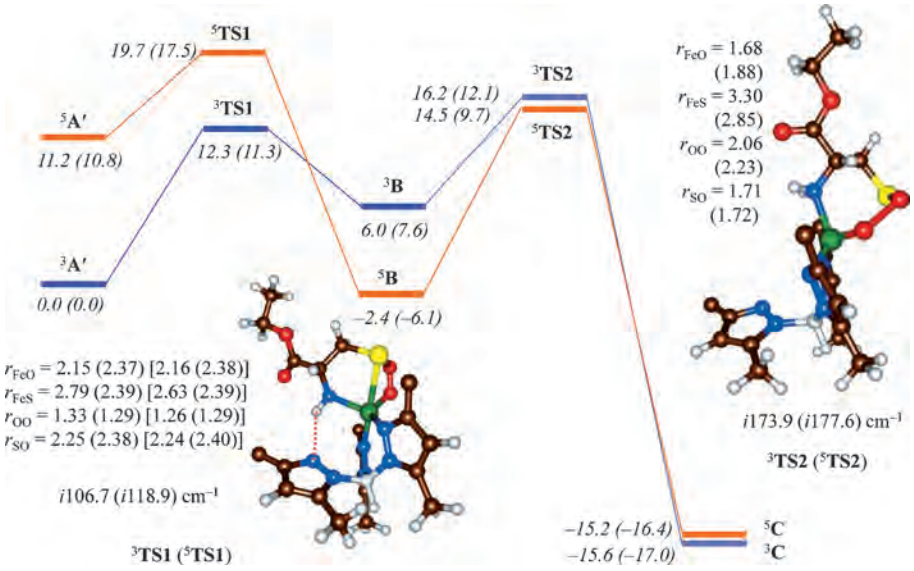

Figure 3. Potential energy landscape for the mechanism of the first oxygen atom transfer from O_2 to cysteinate with free energies in the gas phase and in solvent (in parenthesis) in kcal mol^{-1}. Optimised geometries of ^{3,5}**TS1** and ^{3,5}**TS2** with bond lengths in angstroms; the imaginary frequency in wave numbers are also shown. UB3LYP/BS2 optimised geometries are given in square brackets. Phenyl substituents have been removed for clarity.

© 2015 Wiley-VCH Verlag GmbH & Co. KGaA, Weinheim

Formation of the cyclic ring structure **B** leads to weakening of the O–O bond and it formally changes from a bond order of 1.5 in the iron(III)-superoxo complex (1.26 Å in ^{3}**A**′ and 1.28 Å in ^{5}**A**′) to a single bond in **B** (1.38 Å in ^{3}**B** and 1.46 Å in ^{5}**B**). The dioxygen bond subsequently breaks in **TS2** and an iron(IV)-oxo complex with dangling cysteine sulfoxide is formed (**C**) in a highly exothermic and possibly irreversible process. The exothermicity is as expected and is consistent with the results of previous computational studies of oxygen activation by nonheme iron dioxygenases.[9c,g,15] However, in all these previous studies it was found that the formation of iron(IV)-oxo and sulfoxide units keeps the sulfur atom bound to the iron centre, whereas in the complex studied here the Fe–S bond is broken and the sulfoxide is dangling away from the metal centre. Nevertheless, this moiety is still bound to the iron through the amine group, and sulfoxide products cannot be released at this stage. Instead, the sulfoxide rebinds to the iron centre to form structure **D** later in the mechanism.

The spin-state ordering of the iron(IV)-oxo complex **C** gives the triplet spin in close energy to the quintet spin state and their ordering depends on whether relative enthalpies or free energies, or gas-phase versus solvent models are chosen. Previous computational studies of iron(IV)-oxo complexes also showed close-lying triplet and quintet spin states, whereby the spin-state ordering and relative energies were found to be sensitive to the ligand binding, environmental effects and to the computational methods used.[14,16]

Optimised geometries of the triplet and quintet spin states of **B**, **C** and **D** are given in Figure 4. The cyclic structure **B** has

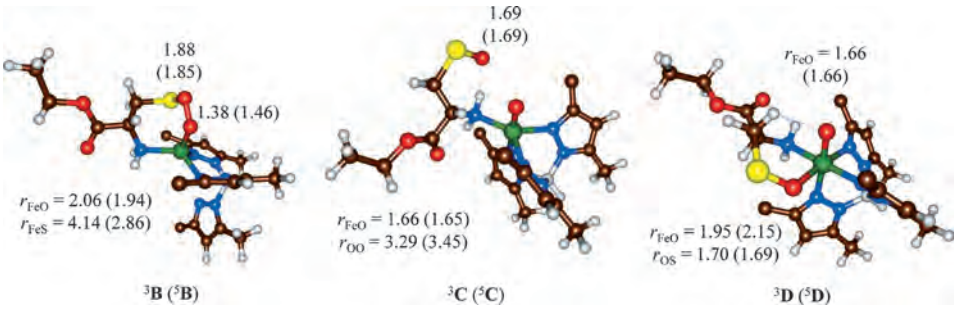

Figure 4. Optimised geometries of ^{3,5}**B**, ^{3,5}**C** and ^{3,5}**D** with bond lengths in angstroms. Phenyl substituents have been removed for clarity.

a sulfur atom that is not bound to the metal and is located at a distance of 2.86 Å in ^{5}**B** and well over 4 Å in ^{3}**B**. In ^{3}**B**, the $Tp^{Me,Ph}$ binds again as a tridentate ligand, thus keeping the metal pentacoordinated. In ^{5}**B**, one arm of the $Tp^{Me,Ph}$ ligand remains unbound, so that the metal is coordinated by only four donor ligands, probably because low-coordination favours high-spin states. In fact the stabilisation reached in this way is considerable, so that the quintet state drops below the triplet spin state, whereas the two spin states are isoenergetic in **C**. The first oxygen atom transfer to form cysteine sulfoxide **C** brings the $Tp^{Me,Ph}$ ligand back in its original position as a tridentate ligand also in the case of ^{5}**B**; **C** contains the sulfoxide group as a free dangling group in hydrogen-bonding interaction with the amine group of cysteinate. Rebound of the sulfoxide group to the iron centre via **TS3** has a negligible barrier on all spin state surfaces and gives structure **D**, which is a hexacoordinated iron complex. This chemical structure resembles the optimised geometries calculated for the iron(IV)-oxo-sulfoxide intermediates in CDO enzymes and model complexes closely.[9c,g,15,17] Energetically, there is no dramatic stabilisation upon sulfoxide binding to the iron centre and we find ^{3}**D** to be more stable than ^{3}**C** by $\Delta G_d = 2.3$ kcal mol^{-1} and $\Delta G_{ds} = 1.3$ kcal mol^{-1}. Similarly, we calculate ^{5}**D** to be more stable than ^{5}**C** by $\Delta G_d = 6.5$ kcal mol^{-1} and $\Delta G_{ds} = 6.6$ kcal mol^{-1}.

The oxygen atom transfer within the iron(IV)-oxo-sulfoxide complex **D** to give the product complex **E**, with both oxygen atoms bound to the iron, was then investigated. A small barrier ^{3}**TS4** was characterised on the triplet spin state, whereas the quintet spin pathway had a negligible barrier. The optimised geometries of ^{3}**TS3** and ^{3}**TS4** are given in Figure 5. At the ΔG_d (ΔG_{ds}) levels of theory, we find ^{3}**TS3** to be 3.4 (3.5) kcal mol^{-1} above ^{3}**C**, and ^{3}**TS4** was located at less than 0.5 kcal mol^{-1} above ^{3}**D**. Therefore, the conversion of ^{3}**C** into ^{3}**D** and conversion from ^{3}**D** into ^{3}**E** are fast processes, and complexes **C** and **D** are expected to have a short lifetime. These small barriers also have an effect on the imaginary frequencies in the transition states, which also tend to be small. These barriers are also small on the quintet spin state and we were unable to fully characterise these transition states. Therefore, the second oxygen atom transfer is a facile and fast process. This part of the mechanism shows good resemblance to the enzymatic reaction mechanism in which an exothermic second oxygen atom transfer with small individual barriers was calculated, too.

We also investigated an alternative mechanism, whereby molecular oxygen attacks the sulfur atom of the substrate directly, that is, without binding to iron and the formation of an iron(III)-superoxo structure first. A mechanism of this type was suggested for a cofactor-independent dioxygenase, in which molecular

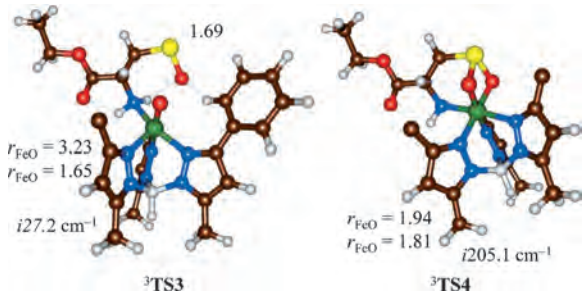

Figure 5. Optimised geometries of ^{3}**TS3** and ^{3}**TS4** with bond lengths in angstroms and the imaginary frequency in wave numbers. Phenyl substituents have been removed for clarity.

© 2015 Wiley-VCH Verlag GmbH & Co. KGaA, Weinheim

oxygen attacks the (1*H*)-3-hydroxy-4-oxoquinaldine substrate directly without involvement of a metal centre.[18] All geometry scans for closing the distance between the O_2 moiety and the sulfur atom, however, led to binding of O_2 to the iron centre upon close approach. Clearly, direct attack of O_2 on sulfur is a high-energy pathway that cannot compete with the formation of an iron(III)-superoxo structure. Previous calculations on CDO model complexes as well as synthetic model complexes for intradiol catechol dioxygenases established similar conclusions that O_2 needs to bind the iron first.[12b,19]

Structure and electronic properties of the product complex

The product complex obtained by following the mechanism as described in Scheme 3 leads to chemical structures with η^2-*O*,*O*-coordination, but, in principle, binding of the cysteine sulfinic acid in alternative orientations could be conceivable. Therefore, we undertook a detailed study into all possible cysteine sulfinic acid binding orientations. These calculations were then used to interpret the results of experimental spectroscopic measurements, which will be discussed in the next section.

Firstly, the triplet and quintet geometries that followed the final step in the mechanism described in the previous section were optimised. This led to the structures ^{3}**E** and ^{5}**E** shown on the left of Figure 6. The optimised geometries give relatively short Fe–O distances of 1.92 (2.05) Å for ^{3}**E** (^{5}**E**), which is somewhat shorter than the distances found for the enzymatic product complex with QM/MM, for which a value of 2.30 Å was obtained. A similar shortening of the Fe–S distance was found from 2.90 Å in the QM/MM structure to 2.80 Å for ^{5}**E**. Note that a geometry optimisation at the BP86 and PBE0 density functional level of theory (see the Supporting Information) gives structures that are similar to those located with B3LYP, as can be seen from the central panel in Figure 6. Furthermore, a geometry optimisation at UB3LYP/BS2 rather than UB3LYP/BS1 (see the Supporting Information) also did not lead to dramatic changes in the optimised geometry: *r*(Fe–O, average) = 2.15 Å and *r*(Fe–S) = 2.75 Å. Therefore, the geometric differences observed between the structures in Figure 1 and Figure 6 are the result of electronic differences between the enzymatic and biomimetic product complexes. Furthermore, they may also highlight the effect of the protein as a ligand. At the ΔG_d level of theory, triplet and quintet spin states are almost degenerate, with the quintet spin state slightly more stable by 0.4 kcal mol^{-1}. Solvent corrections to the structures, however, reverse the order and make the triplet slightly more stable by 2.6 kcal mol^{-1}. A subsequent solvent optimisation gives the same spin state ordering with the triplet lower in energy than the quintet by 1.6 kcal mol^{-1}, and, hence, gives a qualitatively similar result.

In addition, we investigated alternative cysteine sulfinate binding modes and attempted to optimise the geometries of product complexes with coordination through just one oxygen atom to the metal centre. All these attempts, however, converged to structure ^{3,5}**E**, as displayed in Figure 6, with the cysteine sulfinate bound to iron as a tridentate ligand in a facial *N*,*O*,*O*-coordination mode.

We tested one more possible product complex orientation with the iron bound to one oxygen atom and the sulfur atom by taking the ^{5}**E** optimised structure with the SO_2 group rotated by 180°. Although the optimisation yielded structures with one C–O and one Fe–O bond (**E′**, Figure 6, right), close inspection of the optimised geometries revealed that it is not a product complex as such. Thus, the oxygen atom that forms the Fe–O bond has attacked the *ortho*-carbon position of one of the phenyl substituents in an aromatic-type electrophilic addition step. In particular, the *ortho*-carbon atom in ^{3,5}**E′** is in sp^3 hybridisation and forms four bonding interactions. The resulting structure has the iron in oxidation state +II, with four unpaired electrons, and no radical character is found on the Tp ligand or cysteine sulfinate unit. Consequently, a product complex with η^2-*S*,*O*-coordination mode is not a likely intermediate due to stereochemical constraints of the three phenyl groups of the $Tp^{Me,Ph}$ ligand. To test whether ^{3,5}**E′** are dead-end products or not, we investigated the S–O bond breakage leading to a sulfoxide and oxidised phenyl ring of the $Tp^{Me,Ph}$ unit. We calculated the electrophilic attack on the *ortho*-carbon atom and located transition states (^{3,5}**TS5**) and electrophilic oxidation products (^{3,5}**F**). The barriers were found to be considerable, however, with values of ΔG_d (ΔG_{ds}) = 20.8 (28.9) kcal mol^{-1} above ^{5}**E′** on the quintet spin state surface, although the reaction is exergonic by 12.5 (8.0) kcal mol^{-1} leading to ^{5}**F**, which is

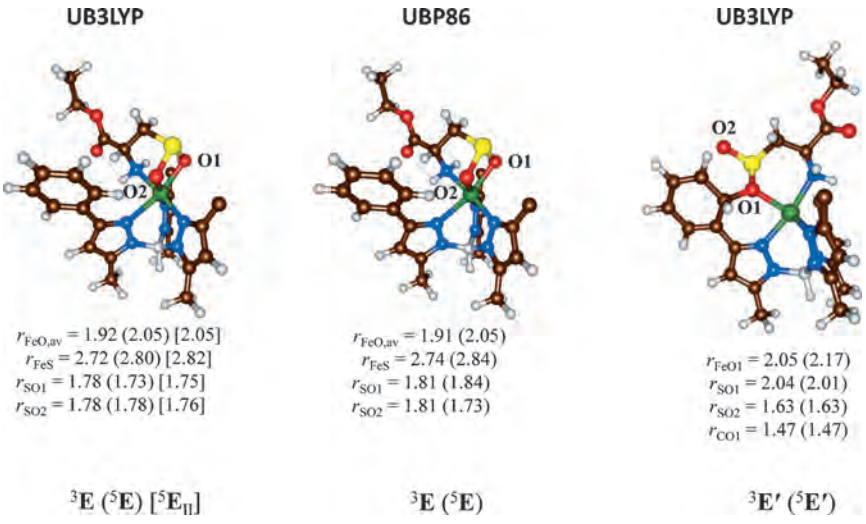

Figure 6. Optimised geometries of ^{3,5}**E** and ^{3,5}**E′** as obtained with either B3LYP or BP86 with bond lengths given in angstroms. Phenyl substituents have been removed for clarity.

© 2015 Wiley-VCH Verlag GmbH & Co. KGaA, Weinheim

a cysteine sulfoxide ligated to an iron(II) centre with the $Tp^{Me,Ph}$ ligand hydroxylated at the phenyl group. Therefore, electrophilic attack of the cysteine sulfinic acid group on one of the aromatic rings of the ligand is a high-energy pathway that is unlikely to occur in the real system. It should also be noted that formation of ^{3,5}**E**′ itself from either ^{3,5}**D** or ^{3,5}**E** is energetically costly because it will lead to the destruction of aromaticity in one of the Ph ligands.

In summary, the computational studies on model **1**, similar to the calculations on the CDO product complex, predict a η^2-*O*,*O*-binding mode for cysteine sulfinate product complex, which underlined the model character of **1** and encouraged us to continue with attempts to confirm the structure experimentally.

Comparison of the theoretical results with experimental findings

Given that the product complex **1** eluded crystallisation (see above), we performed solution X-ray absorption spectroscopy (XAS) at the KMC1 beamline of the BESSY synchrotron in Berlin (see the Supporting Information for details). The spectrum in the X-ray absorption near-edge structure (XANES) region of the starting material in comparison with the oxygenated product is shown in Figure 7. The pre-edge feature (insets in Figure 7) is lower in the product complex than in the precursor

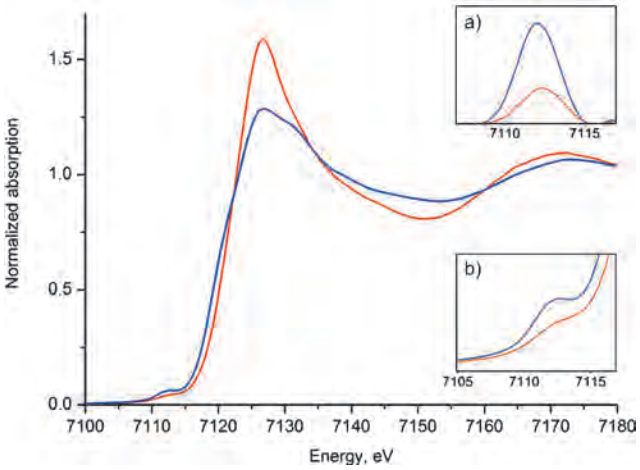

Figure 7. Normalised Fe *K*-edge XANES of [$Tp^{Me,Ph}$Fe(CysOEt)] (dark blue) and **1** (red). The insets shows magnified pre-edge features a) extracted by background subtraction and b) expanded (without background subtraction).

[$Tp^{Me,Ph}$Fe(CysOEt)]; furthermore, the principal edge maximum (white line) is much sharper and higher. Both these observations suggest that oxygenation results in an increase of the coordination number from five, in the precursor, to six, in **1**. The observed spectral changes are prototypical for transformation to an octahedrally coordinated compound, as discussed elsewhere, in the framework of molecular orbital and scattering theory.[20,21] After oxygenation, the white-line height of **1** reaches an especially high value (more than 1.5) typically observed only for octahedral $Fe(N/O)_6$ coordination in the absence of any sulfur ligation.[22] This already argues in favour of an η^2-*O*,*O*-binding mode of the sulfinate unit, and the extended X-ray absorption fine-structure (EXAFS) data were also consistent with this conclusion.

The position of the edge jump is indicative of the oxidation state of the absorbing atom. The edge position of complex **1** shifted up only slightly (by ca. 0.6 eV) compared with [$Tp^{Me,Ph}$Fe(CysOEt)]. This shift can also be partly attributed to the change from five- to six-coordinated iron. We conclude therefore that complex **1**, as the precursor [$Tp^{Me,Ph}$Fe(CysOEt)], contained mostly iron(II) species.

The EXAFS spectrum of the precursor and that of the product of O_2 treatment are compared in Figure 8. Comparison of

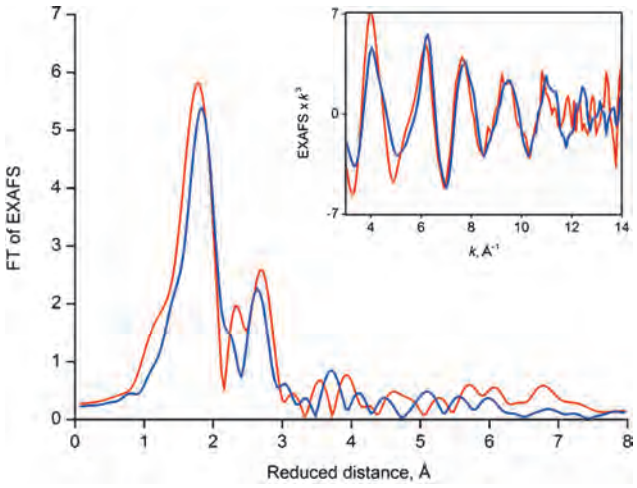

Figure 8. Overlay of the Fourier transforms of the EXAFS data for [$Tp^{Me,Ph}$Fe(CysOEt)] (blue) and **1** (red). The inset shows *k*-space data for [$Tp^{Me,Ph}$Fe(CysOEt)] (blue) and **1** (red). The distances between ligands of the first, second and third coordination sphere were determined by EXAFS simulations and typically exceed the indicated "reduced distance" by 0.4 Å.

the bond distances obtained for [$Tp^{Me,Ph}$Fe(CysOEt)], **A**, with those determined by X-ray diffraction shows relatively small differences (one Fe–N shell with coordination number four at 2.13 Å from EXAFS vs. four Fe–N distances between 2.11 and 2.29 Å from XRD; Fe–S at 2.30 Å from EXAFS vs. Fe–S at 2.31 Å from XRD, see the Supporting Information, Figure S1 and Table S1). In the product of O_2 treatment, the most notable feature is a new peak at a reduced distance of 2.32 Å. Indeed, setting out from the DFT-optimised geometry, a very good fit of the EXAFS data could be reached, which indicated two scattering O atoms at 2.08 Å and an S atom at 2.70 Å (Figure 9 and Table 1). These distances are in reasonable agreement with those calculated and reported for **E** in Figure 6 above, with EXAFS favouring the quintet, although the Fe–O/N distances determined by DFT calculations are somewhat shorter than suggested by EXAFS. Note however that a geometry optimisation at UB3LYP/BS2 rather than UB3LYP/BS1 gives minor differences with respect to the structure displayed in Figure 6, but with Fe–O distances of 2.12 and 2.18 Å in the quintet spin state that are instead slightly longer than those determined by EXAFS. Generally, the B3LYP method gives reasonable energies

© 2015 Wiley-VCH Verlag GmbH & Co. KGaA, Weinheim

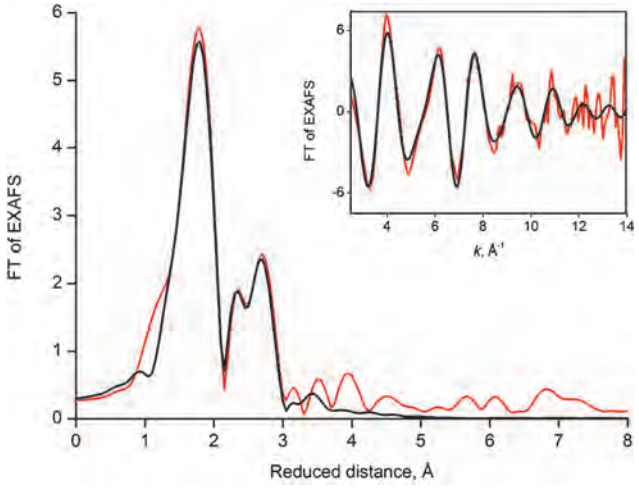

Figure 9. Fourier-transformed Fe *K*-edge EXAFS spectra of **1** (experiment: red; simulation: black). Goodness-of-fit parameters: $\chi^2 = 75$, $R_f = 9.1$.

Table 1. Parameters obtained by simulation of the k^3-weighted EXAFS spectrum of **1** shown in Figure 9. The errors represent the 68% confidence interval of the respective fit parameter (*N*, coordination number; *R*, absorber-backscatter distance; σ, Debye–Waller parameter). The coordination numbers were not fitted but were fixed to the values suggested by the structure.

Shell	*N*	*R* [Å]	σ [Å]
Fe–O	2	2.08 ± 0.01	0.06 ± 0.01
Fe–N	4	2.22 ± 0.01	0.06 ± 0.01
Fe–S	1	2.70 ± 0.02	0.09 ± 0.01
Fe–N	3	3.06 ± 0.01	0.05 ± 0.01

for calculations of reaction mechanisms, but tends to be weak at reproducing experimental geometries.[23] Therefore, we re-optimised ^{3,5}**E** by using the BP86 density functional method. We calculate an average Fe–O distance of 1.91 (2.05) Å in the triplet (quintet) spin states and an Fe–S separation of 2.74 (2.84) Å. These optimised geometries are not dramatically different from those observed at the B3LYP level of theory. Clearly, for this particular case, the agreement between experimental and computational Fe–S distances is very good, which is not always the case for distances between second-row elements, for which the differences can be quite large.[24] In conclusion, the experimental data on the structure of product complex **1** match nicely the findings made on **E** in the theoretical analysis. Other aspects of the calculated structures and reaction barriers also rationalise the experimental findings:

i) A $S = 2$ ground state was predicted for **A** and, indeed, investigations on the magnetic properties of the precursor complex [Tp^{Me,Ph}Fe(S-CH$_2$-CH(NH$_2$)(CO$_2$Et)] confirmed that: The magnetic moment for the precursor complex in solution at room temperature ($\mu_{eff} = 5.05\ \mu_B$), as determined by using the Evans method, is in accordance with the spin only (s.o.) value for four unpaired electrons with a total spin quantum number of $S = 2$ ($\mu_{s.o.} = 4.90\ \mu_B$). The isolated solid exhibits a magnetic moment of $\mu_{eff} = 4.96\ \mu_B$. We also tried to monitor the course of the reaction with O_2 by EPR. However, because this is an even-spin system, such studies are far from routine. Measurements in the parallel mode were performed but they were further complicated by the fact that the system is highly sensitive towards both O_2 and water, and at the same time had to be investigated at rather low concentrations. Hence, no reproducible results were obtained.

ii) The calculated mechanism shows why all of our attempts to detect the iron(III) superoxo species failed: Its formation is endergonic and the barrier back to **A** is virtually nonexistent.

iii) The comparatively high barrier for the rate-determining step, the further reaction to **B**, explains why the model reaction is comparatively slow and takes hours to reach completion.

Conclusion

Taken together, the theoretical results of the CDO product complex as well as the combined computational and experimental results on a closely related biomimetic model complex strongly suggest that the cysteine sulfinate also binds in a η^2-*O*,*O*-binding mode in the product complex of the CDO. Moreover, calculations were performed with the aim of further clarifying mechanistic details, and the results have helped rationalise the experimental observations. Finally, the results have revealed how to proceed to achieve an even closer resemblance between enzyme and model: The steric demand of residues at the Tp ligand (or at least one of the residues) has to be decreased to an extent that avoids intermediate dissociation of one of the pyrazole donors. At the same time, as before, it has to be sufficiently large to allow for the isolation of [TpFe(S-CH$_2$-CH(NH$_2$)CO$_2$Et)] and prohibit Fe^{III}-O-Fe^{III} formation in the oxygenation process; that is, a subtle balance has to be found. Corresponding investigations are underway.

Experimental Section

Preparation of a sample of 1 for XAS

All manipulations were carried out in a glove box, or by using Schlenk techniques under a dry argon atmosphere. [Tp^{Me,Ph}Fe(CysOEt)] was prepared and crystallised as described earlier.[11d] The preparation of complex **1** proceeded by the direct reaction of a solution of [Tp^{Me,Ph}Fe(CysOEt)] in dichloromethane with dioxygen. Below we give information on how this sample was treated for XAS studies.

XAS measurements and simulations

X-ray absorption spectroscopy at the K-edge of iron was performed at the KMC-1 beamline at the BESSY-II synchrotron (Helmholtz-Zentrum Berlin, Germany) at 20 K in a liquid-helium cryostat as described elsewhere.[25] Spectra were recorded in fluorescence mode using a 13-element Ge detector (Canberra). The extracted spectrum was weighted by k^3 and simulated in *k*-space; an E_0 value of 7112 eV was used for conversion of the energy scale to a *k*-scale. All EXAFS simulations were performed by using in-house software (SimX) after calculation of the phase functions with the FEFF program[26,27] (version 8.4, self-consistent field option activated). Atomic coordinates of the FEFF input files were generated for

© 2015 Wiley-VCH Verlag GmbH & Co. KGaA, Weinheim

several reasonable structural models; the EXAFS phase functions did not depend strongly on the details of the used model. An amplitude reduction factor S_0^2 of 0.94 was used. The data range used in the simulation was 15–750 eV (2–14 $Å^{-1}$). The EXAFS simulation was optimised by a minimisation of the error sum obtained by summation of the squared deviations between measured and simulated values (least-squares fit). The fit was performed by using the Levenberg–Marquardt method with numerical derivatives. The error ranges of the fit parameters were estimated from the covariance matrix of the fit, and indicate the 68% confidence intervals of the corresponding fit parameters. The fit error was calculated as in ref.[28]

Simulation of the EXAFS spectrum of [$Tp^{Me,Ph}$Fe(CysOEt)]

A simulation using only three shells (shown in Table S1) readily reproduces the experimental spectrum (Figure S1) and is in agreement with the known structure of [$Tp^{Me,Ph}$Fe(CysOEt)].

Computational studies

All calculations reported here were performed by using DFT as implemented in the Jaguar 7.7[29] and Gaussian 09[30] program packages. Initial geometries were optimised in Jaguar at the UB3LYP level of theory[31] coupled with an LACVP basis set on iron and 6–31G on the rest of the atoms: basis set BS1.[32] A subsequent analytic frequency in Gaussian confirmed the structures as local minima with real frequencies only or first order saddle points with one imaginary frequency for the correct mode. Energies were then improved by running a single-point calculation in Jaguar using a triple-ζ quality LACV3P+ basis set on iron and 6–311+G* on the rest of the atoms: basis set BS2. We also tested the effect of dispersion on the reaction energies by performing a UB3LYP-D3 single-point calculation in Jaguar by using the model of Grimme and coworkers.[33] The complete potential energy profile was calculated on the singlet, triplet, quintet and septet spin states. Previously, we used these methods for analogous systems and they reproduced free energies of activation within 4 kcal mol^{-1},[34] but also gave reasonable agreement for spectroscopic data.[35] We also showed previously that energies obtained at UB3LYP/BS2//UB3LYP/BS1 were within 0.1 kcal mol^{-1} of those obtained after a geometry optimisation at UB3LYP/BS2 level of theory.[36]

The product complex was investigated as a structure with the two oxygen atoms bound to the metal (structure **E**), as well as with the sulfur bound to the metal (structure **E′**). Although the latter structure was started without Fe–O bonding interactions, during the optimisation the sulfinic acid group rotated onto structure **E′** with one Fe–S and one Fe–O bond. To test the effect of solvent, we reoptimised ^{3,5}**E** in a solvent model (^{3,5}$\mathbf{E}_{solvopt}$) but this had only minor effects on the final structure. We used the polarised continuum model as implemented in Jaguar with a dielectric constant of 37.5 and a probe radius of 2.183 Å.

To test the effect of the density functional method and the basis set on the optimised geometries and spin-state ordering of the product complexes, we performed a further set of test calculations. First, we reoptimised ^{3,5}**A**, ^{3,5}**TS1** and ^{3,5}**E** at the UB3LYP/BS2 level of theory. In addition, we calculated ^{3,5}**E** by using the pure density functional method BP86.[37] These test calculations gave only minor changes in the structural features of the complexes and did not affect the conclusions.

Acknowledgements

We are grateful to the Humboldt-Universität zu Berlin and to UniCat (Unifying Concepts in Catalysis, Cluster of Excellence, Berlin) for financial support. We thank the Helmholtz-Zentrum Berlin for the allocation of synchrotron radiation beamtime. The National Service of Computational Chemistry Software (NSCCS) is acknowledged for cpu time to S.d.V. D.K. acknowledges the Department of Science and Technology (New Delhi) for a Ramanujan Fellowship. The EU-COST Network (CM1305) on spin state reactivity is acknowledged for support.

Keywords: density functional calculations · enzyme catalysis · enzyme models · oxygenation · reaction mechanisms

[1] a) E. I. Solomon, T. C. Brunold, M. I. Davis, J. N. Kemsley, S.-K. Lee, N. Lehnert, F. Neese, A. J. Skulan, Y.-S. Yang, J. Zhou, *Chem. Rev.* **2000**, *100*, 235–349; b) T. D. H. Bugg, *Curr. Opin. Chem. Biol.* **2001**, *5*, 550–555; c) M. J. Ryle, R. P. Hausinger, *Curr. Opin. Chem. Biol.* **2002**, *6*, 193–201; d) M. Costas, M. P. Mehn, M. P. Jensen, L. Que Jr, *Chem. Rev.* **2004**, *104*, 939–986; e) M. M. Abu-Omar, A. Loaiza, N. Hontzeas, *Chem. Rev.* **2005**, *105*, 2227–2252; f) P. C. A. Bruijnincx, G. van Koten, R. J. M. Klein Gebbink, *Chem. Soc. Rev.* **2008**, *37*, 2716–2744; g) S. V. Kryatov, E. V. Rybak-Akimova, S. Schindler, *Chem. Rev.* **2005**, *105*, 2175–2226.

[2] a) R. Chowdhury, A. Hardy, C. J. Schofield, *Chem. Soc. Rev.* **2008**, *37*, 1308–1319; b) J. M. Simmons, T. A. Müller, R. P. Hausinger, *Dalton Trans.* **2008**, 5132–5142; c) C. Loenarz, C. J. Schofield, *Nat. Chem. Biol.* **2008**, *4*, 152–156.

[3] a) A. Bassan, T. Borowski, P. E. M. Siegbahn, *Dalton Trans.* **2004**, 3153–3162; b) C. Krebs, D. Galonić Fujimori, C. T. Walsh, J. M. Bollinger Jr., *Acc. Chem. Res.* **2007**, *40*, 484–492; c) *Iron-Containing Enzymes: Versatile Catalysts of Hydroxylation Reaction in Nature* (Eds.: S. P. de Visser, D. Kumar), RSC Publishing, Cambridge, **2011**.

[4] a) D. A. Proshlyakov, T. F. Henshaw, G. R. Monterosso, M. J. Ryle, R. P. Hausinger, *J. Am. Chem. Soc.* **2004**, *126*, 1022–1023; b) P. J. Riggs-Gelasco, J. C. Price, R. B. Guyer, J. H. Brehm, E. W. Barr, J. M. Bollinger Jr, C. Krebs, *J. Am. Chem. Soc.* **2004**, *126*, 8108–8109.

[5] a) L. Que Jr, *Nat. Struct. Biol.* **2000**, *7*, 182–184; b) E. G. Kovaleva, J. D. Lipscomb, *Nat. Chem. Biol.* **2008**, *4*, 186–193.

[6] a) C. R. Simmons, Q. Liu, Q. Q. Huang, Q. Hao, T. P. Begley, P. A. Karplus, M. H. Stipanuk, *J. Biol. Chem.* **2006**, *281*, 18723–18733; b) S. Ye, X. Wu, L. Wei, D. Tang, P. Sun, M. Bartlam, Z. Rao, *J. Biol. Chem.* **2007**, *282*, 3391–3402.

[7] D. Buongiorno, G. D. Straganz, *Coord. Chem. Rev.* **2013**, *257*, 541–563.

[8] a) M. H. Stipanuk, *Annu. Rev. Nutr.* **2004**, *24*, 539–577; b) G. D. Straganz, B. Nidetzky, *ChemBioChem* **2006**, *7*, 1536–1548; c) C. A. Joseph, M. J. Maroney, *Chem. Commun.* **2007**, 3338–3349.

[9] a) J. G. McCoy, L. J. Bailey, E. Bitto, C. A. Bingman, D. J. Aceti, B. G. Fox, G. N. Phillips Jr., *Proc. Natl. Acad. Sci. USA* **2006**, *103*, 3084–3089; b) B. S. Pierce, J. D. Gardner, L. J. Bailey, T. C. Brunold, B. G. Fox, *Biochemistry* **2007**, *46*, 8569–8578; c) S. Aluri, S. P. de Visser, *J. Am. Chem. Soc.* **2007**, *129*, 14846–14847; d) C. R. Simmons, K. Krishnamoorthy, S. L. Granett, D. J. Schuller, J. E. Dominy Jr., T. P. Begley, M. H. Stipanuk, P. A. Karplus, *Biochemistry* **2008**, *47*, 11390–11392; e) T. Kleffmann, S. A. K. Jongkees, G. Fairweather, S. M. Wilbanks, G. N. L. Jameson, *J. Biol. Inorg. Chem.* **2009**, *14*, 913–921; f) J. D. Gardner, B. S. Pierce, B. G. Fox, T. C. Brunold, *Biochemistry* **2010**, *49*, 6033–6041; g) D. Kumar, W. Thiel, S. P. de Visser, *J. Am. Chem. Soc.* **2011**, *133*, 3869–3882; h) E. P. Tchesnokov, S. M. Wilbanks, G. N. L. Jameson, *Biochemistry* **2012**, *51*, 257–264; i) R. J. Souness, T. Kleffmann, E. P. Tchesnokov, S. M. Wilbanks, G. B. Jameson, G. N. L. Jameson, *Biochemistry* **2013**, *52*, 7606–7617.

[10] a) W. Nam, *Acc. Chem. Res.* **2007**, *40*, 522–531; b) I. Siewert, C. Limberg, *Chem. Eur. J.* **2009**, *15*, 10316–10328; c) S. Friedle, E. Reisner, S. J. Lippard, *Chem. Soc. Rev.* **2010**, *39*, 2768–2779.

[11] a) Y. Jiang, L. R. Widger, G. D. Kasper, M. A. Siegler, D. P. Goldberg, *J. Am. Chem. Soc.* **2010**, *132*, 12214–12215; b) A. R. McDonald, M. R. Bukowski,

 © 2015 Wiley-VCH Verlag GmbH & Co. KGaA, Weinheim

E. R. Farquhar, T. A. Jackson, K. D. Koehntop, M. S. Seo, R. F. De Hont, A. Stubna, J. A. Halfen, E. Münck, W. Nam, L. Que, Jr., *J. Am. Chem. Soc.* **2010**, *132*, 17118 – 17129; c) Y. M. Badiei, M. A. Siegler, D. P. Goldberg, *J. Am. Chem. Soc.* **2011**, *133*, 1274 – 1277; d) M. Sallmann, I. Siewert, L. Fohlmeister, C. Limberg, C. Knispel, *Angew. Chem. Int. Ed.* **2012**, *51*, 2234 – 2237; *Angew. Chem.* **2012**, *124*, 2277 – 2280; e) A. C. McQuilken, D. P. Goldberg, *Dalton Trans.* **2012**, *41*, 10883 – 10899; f) A. C. McQuilken, Y. Jiang, M. A. Siegler, D. P. Goldberg, *J. Am. Chem. Soc.* **2012**, *134*, 8758 – 8761; g) A. C. McQuilken, Y. Ha, K. D. Sutherlin, M. A. Siegler, K. O. Hodgson, B. Hedman, E. I. Solomon, G. N. L. Jameson, D. P. Goldberg, *J. Am. Chem. Soc.* **2013**, *135*, 14024 – 14027.

[12] a) D. Kumar, G. N. Sastry, D. P. Goldberg, S. P. de Visser, *J. Phys. Chem. A* **2012**, *116*, 582 – 591; b) L. E. Gonzalez-Ovalle, M. G. Quesne, D. Kumar, D. P. Goldberg, S. P. de Visser, *Org. Biomol. Chem.* **2012**, *10*, 5401 – 5409.

[13] S. P. de Visser, *Chem. Commun.* **2007**, 171 – 173.

[14] R. Latifi, M. A. Sainna, E. V. Rybak-Akimova, S. P. de Visser, *Chem. Eur. J.* **2013**, *19*, 4058 – 4068.

[15] a) T. Borowski, A. Bassan, P. E. M. Siegbahn, *Chem. Eur. J.* **2004**, *10*, 1031 – 1041; b) V. Georgiev, T. Borowski, P. E. M. Siegbahn, *J. Biol. Inorg. Chem.* **2006**, *11*, 571 – 585.

[16] a) D. Kumar, H. Hirao, L. Que Jr, S. Shaik, *J. Am. Chem. Soc.* **2005**, *127*, 8026 – 8027; b) H. Hirao, L. Que Jr, W. Nam, S. Shaik, *Chem. Eur. J.* **2008**, *14*, 1740 – 1756; c) S. Ye, F. Neese, *Proc. Natl. Acad. Sci. USA* **2011**, *108*, 1228 – 1233; d) S. P. de Visser, J.-U. Rohde, Y.-M. Lee, J. Cho, W. Nam, *Coord. Chem. Rev.* **2013**, *257*, 381 – 393.

[17] a) D. Kumar, G. N. Sastry, S. P. de Visser, *Chem. Eur. J.* **2011**, *17*, 6196 – 6205; b) A. K. Vardhaman, P. Barman, S. Kumar, C. V. Sastri, D. Kumar, S. P. de Visser, *Angew. Chem. Int. Ed.* **2013**, *52*, 12288 – 12292; *Angew. Chem.* **2013**, *125*, 12514 – 12518.

[18] A. Hernandez-Ortega, M. G. Quesne, S. Bui, D. P. H. M. Heuts, R. A. Steiner, D. J. Heyes, S. P. de Visser, N. S. Scrutton, *J. Biol. Chem.* **2014**, *289*, 8620 – 8632.

[19] R. Jastrzebski, M. G. Quesne, B. M. Weckhuysen, S. P. de Visser, P. C. A. Bruijnincx, *Chem. Eur. J.* **2014**, *20*, 15686 – 15691.

[20] H. Dau, P. Liebisch, M. Haumann, *Anal. Bioanal. Chem.* **2003**, *376*, 562 – 583.

[21] H. Dau, P. Liebisch, M. Haumann, *Phys. Scr.* **2005**, *T115*, 844 – 846.

[22] M. Haumann, A. Porthun, T. Buhrke, P. Liebisch, W. Meyer-Klaucke, B. Friedrich, H. Dau, *Biochemistry* **2003**, *42*, 13786 – 13786.

[23] M. G. Quesne, R. Latifi, L. E. Gonzalez-Ovalle, D. Kumar, S. P. de Visser, *Chem. Eur. J.* **2014**, *20*, 435 – 446.

[24] a) S. P. de Visser, S. Shaik, P. K. Sharma, D. Kumar, W. Thiel, *J. Am. Chem. Soc.* **2003**, *125*, 15779 – 15788; b) D. Kumar, R. Latifi, S. Kumar, E. V. Rybak-Akimova, M. A. Sainna, S. P. de Visser, *Inorg. Chem.* **2013**, *52*, 7968 – 7979.

[25] M. Barra, M. Haumann, P. Loja, R. Krivanek, A. Grundmeier, H. Dau, *Biochemistry* **2006**, *45*, 14523 – 14532.

[26] J. J. Rehr, R. C. Albers, *Rev. Mod. Phys.* **2000**, *72*, 621 – 654.

[27] A. L. Ankudinov, B. Ravel, J. J. Rehr, S. D. Conradson, *Phys. Rev. B* **1998**, *58*, 7565 – 7576.

[28] M. Risch, K. Klingan, J. Heidkamp, D. Ehrenberg, P. Chernev, I. Zaharieva, H. Dau, *Chem. Commun.* **2011**, *47*, 11912 – 11914.

[29] Jaguar 7.7, version 7.9, Schrodinger, LLC, New York, NY, **2011**.

[30] Gaussian 09, Revision B.01, M. J. Frisch, G. W. Trucks, H. B. Schlegel, G. E. Scuseria, M. A. Robb, J. R. Cheeseman, G. Scalmani, V. Barone, B. Mennucci, G. A. Petersson, H. Nakatsuji, M. Caricato, X. Li, H. P. Hratchian, A. F. Izmaylov, J. Bloino, G. Zheng, J. L. Sonnenberg, M. Hada, M. Ehara, K. Toyota, R. Fukuda, J. Hasegawa, M. Ishida, T. Nakajima, Y. Honda, O. Kitao, H. Nakai, T. Vreven, J. A. Montgomery, Jr., J. E. Peralta, F. Ogliaro, M. Bearpark, J. J. Heyd, E. Brothers, K. N. Kudin, V. N. Staroverov, T. Keith, R. Kobayashi, J. Normand, K. Raghavachari, A. Rendell, J. C. Burant, S. S. Iyengar, J. Tomasi, M. Cossi, N. Rega, J. M. Millam, M. Klene, J. E. Knox, J. B. Cross, V. Bakken, C. Adamo, J. Jaramillo, R. Gomperts, R. E. Stratmann, O. Yazyev, A. J. Austin, R. Cammi, C. Pomelli, J. W. Ochterski, R. L. Martin, K. Morokuma, V. G. Zakrzewski, G. A. Voth, P. Salvador, J. J. Dannenberg, S. Dapprich, A. D. Daniels, O. Farkas, J. B. Foresman, J. V. Ortiz, J. Cioslowski, and D. J. Fox, Gaussian, Inc., Wallingford CT, **2010**.

[31] a) A. D. Becke, *J. Chem. Phys.* **1993**, *98*, 5648 – 5652; b) C. Lee, W. Yang, R. G. Parr, *Phys. Rev. B* **1988**, *37*, 785 – 789.

[32] P. J. Hay, W. R. Wadt, *J. Chem. Phys.* **1985**, *82*, 299 – 310.

[33] S. Grimme, J. Antony, S. Ehrlich, H. Krieg, *J. Chem. Phys.* **2010**, *132*, 154104.

[34] a) D. Kumar, S. P. de Visser, S. Shaik, *Chem. Eur. J.* **2005**, *11*, 2825 – 2835; b) K. A. Prokop, S. P. de Visser, D. P. Goldberg, *Angew. Chem. Int. Ed.* **2010**, *49*, 5091 – 5095; *Angew. Chem.* **2010**, *122*, 5217 – 5221; c) A. K. Vardhaman, C. V. Sastri, D. Kumar, S. P. de Visser, *Chem. Commun.* **2011**, *47*, 11044 – 11046.

[35] a) B. Karamzadeh, D. Kumar, G. N. Sastry, S. P. de Visser, *J. Phys. Chem. A* **2010**, *114*, 13234 – 13243; b) P. Leeladee, G. N. L. Jameson, M. A. Siegler, D. Kumar, S. P. de Visser, D. P. Goldberg, *Inorg. Chem.* **2013**, *52*, 4668 – 4682.

[36] a) S. P. de Visser, *J. Am. Chem. Soc.* **2010**, *132*, 1087 – 1097; b) S. P. de Visser, M. G. Quesne, B. Martin, P. Comba, U. Ryde, *Chem. Commun.* **2014**, *50*, 262 – 282.

[37] a) A. D. Becke, *Phys. Rev. A* **1988**, *38*, 3098 – 3100; b) J. P. Perdew, *Phys. Rev. B* **1986**, *33*, 8822 – 8824.

Received: February 15, 2015
Published online on March 30, 2015

© 2015 Wiley-VCH Verlag GmbH & Co. KGaA, Weinheim

Computational and Theoretical Chemistry 1061 (2015) 1–5

Contents lists available at ScienceDirect

Computational and Theoretical Chemistry

journal homepage: www.elsevier.com/locate/comptc

On copper–copper bond in hydrated cupric acetate

Nirmal K. Shee [a], Ravi Verma [b], Devesh Kumar [b], Dipankar Datta [a,*]

[a] Department of Inorganic Chemistry, Indian Association for the Cultivation of Science, Calcutta 700 032, India
[b] Department of Applied Physics, Babasaheb Bhimrao Ambedkar University, Vidya Vihar, Lucknow 226 025, India

ARTICLE INFO

Article history:
Received 6 February 2015
Received in revised form 3 March 2015
Accepted 3 March 2015
Available online 20 March 2015

Keywords:
Copper(II)acetate
DFT
Broken symmetry
Copper–copper bond
Wiberg's bond index

ABSTRACT

Broken symmetry (BS) calculations within the framework of density functional theory are performed on hydrated copper(II)acetate and its anhydrous variety using LACVP*(Cu)/6-31G*(rest) and LACVP*(Cu)/6-311G++**(rest) basis sets. The experimentally known Cu—Cu distance of 2.617 Å in hydrated copper(II)acetate is reproduced well as 2.619 Å. Using the second basis set, the singlet–triplet separations in both the compounds come out as 497 cm^{-1}. The Cu—Cu distance in anhydrous copper(II)acetate is calculated as 2.480 Å. Bader's AIM calculations show presence of a bond critical point (BCP) of the type (3, −1) between the two copper atoms in both the compounds indicating the existence of a chemical bond between the metal atoms. The sign of the Laplacian associated with the electron density at the BCP is found to be negative indicating a covalent bond between the two copper centers. For the Cu—Cu bond in both the compounds, Wiberg's bond index comes out as ~0.3 suggesting a reasonably strong metal–metal bond in cupric acetate. Calculations of the energies of the BS and the triplet states around the Cu—Cu distance of 2.6 Å (to be specific, in the range of 2.4–2.9 Å) reveal that the observed magnetic behavior of hydrated cupric acetate is the resultant of two opposing pathways for the interaction between the two unpaired metal electrons – (1) through the ligand framework and (2) through a direct Cu—Cu bond. The Cu—Cu bond results in an antiferromagnetic exchange while the acetato framework provides a means of ferromagnetic interactions.

© 2015 Elsevier B.V. All rights reserved.

1. Introduction

Copper(II)acetate monohydrate (abbreviated as $Cu(OAc)_2H_2O$) plays a lead role in magnetochemistry and related studies. Understanding the magnetic properties of this compound is very crucial, which is still not fully clear. Lifschitz and Rosenbohm [1] first observed in 1915 that the molar magnetic susceptibility of $Cu(OAc)_2H_2O$ at room temperature is much lower than expected. This has been corroborated by several subsequent studies [2]. First variable temperature (83–304 K) magnetic susceptibility measurements on a single crystal of $Cu(OAc)_2H_2O$ have been reported by Guha [3] in 1951. In the following year, Bleany and Bowers [4] have explained the experimental data of Guha by assuming direct magnetic exchange coupling between a pair of copper(II) atoms with the exchange coupling constant J of $-315\ cm^{-1}$. Later on many such measure-ments [5] have been made lowering the temperature much below 83 K. J value obtained by Elmali [5] in 2000 in the temperature range 4.2–300 K, is $-292.2\ cm^{-1}$ by using Bleany–Bowers equation [6]. The X-ray crystal structure of $Cu(OAc)_2H_2O$ was first determined by Niekerk and Schoening [7] in 1953 to show that it is an acetato bridged dimer with a Cu—Cu distance of 2.64 Å, a bit longer than the interatomic distance of 2.556 Å in metallic copper at 293 K. This substantiated the idea of Bleany and Bowers. It is interesting to note that a search of CCDC shows that the X-ray crystal structure of $Cu_2(OAc)_4{\cdot}2H_2O$ has been determined at least thirteen times after Niekerk and Schoening, the latest one [8] being in 2012 where the Cu—Cu distance is found to be 2.6107(4) Å. From neutron-diffraction [9], Cu—Cu separation comes out as 2.614(2) Å. The number of times the variable temperature magnetic susceptibility and the crystal structure of $Cu_2(OAc)_4{\cdot}2H_2O$ have been repeated only shows the importance of this very compound in the magnetic studies of inorganic complexes.

Variable temperature magnetic susceptibility studies show that in $Cu_2(OAc)_4{\cdot}2H_2O$, singlet is the ground state, i.e. the unpaired electrons on the two copper(II) centers are antiferromagnetically coupled. MO studies of Malrieu and co-workers [10] in 1982 indicate that the observed magnetic behavior of $Cu(OAc)_2H_2O$ is a resultant of direct exchange (ferromagnetic), super-exchange (antiferromagnetic), double-spin polarization (overall antiferromagnetic) and some higher order effects (antiferromagnetic). Earlier in 1975 Hoffman and co-workers [11] have ruled

* Corresponding author. Tel.: +91 33 2473 5374; fax: +91 33 2473 2805.
E-mail address: icdd@iacs.res.in (D. Datta).

http://dx.doi.org/10.1016/j.comptc.2015.03.003
2210-271X/© 2015 Elsevier B.V. All rights reserved.

out the possibility of copper–copper bond in $Cu_2(OAc)_4{\cdot}2H_2O$ saying that the Cu—Cu distance is too long for a direct overlap between the d_x^2–y^2 orbitals on the metal (from EPR studies it is known that the unpaired electron of each copper atom remains in the respective d_x^2–y^2 orbital). Herein we re-examine this aspect by Bader's theory [12–14] of Atoms-in-Molecule (AIM). For comparison, we have done the same calculations for anhydrous copper(II) acetate, $Cu_2(OAc)_4$ also.

2. Computational

All calculations were done by using the hybrid density functional BP86 in Jaguar 7.9 program package [15]. Analytical frequency calculations were done using Gaussian 09 [16]. One set of basis (**1**) used is LACVP*(Cu)/6-31G*(rest) [17,18]. Single point calculations were done using basis set **2** comprising LACVP*(Cu)/6-311G++**(rest) on the geometry optimized by basis set **1**, to generate the wave function necessary for AIM calculations, as implemented in AIM 2000 program package [19]. Deviations from these protocols have been specified on appropriate occasions.

3. Results and discussion

To apply Bader's theory, one has to know the ground state wave function. Theoretically for two interacting spins S_1 and S_2, J is calculated from the energies of the low spin (LS) and high spin (HS) state. As mentioned above, singlet i.e. the LS state is the ground state in $Cu_2(OAc)_4{\cdot}2H_2O$ and $Cu_2(OAc)_4$ [2]. While the HS state can be readily described by single determinant wave function, LS state requires extensive treatment of electron–electron correlation. The LS state can be easily approximated by "broken symmetry" (BS) state in BS-DFT approach of Ginsberg, Noodleman and Yamaguchi [20–23]. Alvarez and co-workers [24,25] have shown that for $S_1 \geqslant S_2$,

$$J = \frac{E_{BS} - E_{HS}}{2S_1S_2 + S_2} \quad (1)$$

For $S_1 = S_2 = 1/2$ as in $Cu_2(OAc)_4{\cdot}2H_2O$ and $Cu_2(OAc)_4$, Eq. (1) becomes

$$J = E_{BS} - E_{HS} \quad (2)$$

One way to test whether the wave function for the BS state truly represent the singlet states in $Cu_2(OAc)_4{\cdot}2H_2O$ and $Cu_2(OAc)_4$ is to calculate the expectation value of total spin squared $\langle S_{BS}^2 \rangle$. It should be close to unity for a system where two unpaired electrons interact [26,27]. Our values for $Cu_2(OAc)_4{\cdot}2H_2O$ is 0.95 and for $Cu_2(OAc)_4$ 0.93 when basis set **1** is used. For basis set **2**, $\langle S_{BS}^2 \rangle$ for $Cu_2(OAc)_4{\cdot}2H_2O$ is 0.90 and for $Cu_2(OAc)_4$ 0.89. Thus in our calculations the singlet state has been simulated by the BS states quite satisfactorily.

From our calculations, the triplet state for $Cu_2(OAc)_4{\cdot}2H_2O$ is found to be higher than the singlet one by 528 and 497 cm^{-1} for basis set **1** and basis set **2** respectively. These are much higher than the experimental values. On the other hand, the experimental Cu—Cu distance in $Cu_2(OAc)_4{\cdot}2H_2O$ is very well reproduced in our calculations (Table 1). In the case of $Cu_2(OAc)_4$, the triplet state is higher than the singlet state by 574 and 497 cm^{-1} for the basis set **1** and basis set **2** respectively. Figgis and Martin [2] have experimentally determined the J for anhydrous copper(II)acetate as 286 cm^{-1}.

Figs. 1 and 2 present Bader's bond critical points (BCP) of (3, −1) type and Tables 1 and 2 summarize calculated bond distances as well as the electron density ρ at the BCP and its associated Laplacian, $\nabla^2\rho$, of some representative bonds in $Cu_2(OAc)_4{\cdot}2H_2O$ and $Cu_2(OAc)_4$ respectively. In Bader's theory, existence of a BCP between two atoms ensures chemical bonding between them. From the figures, it is clear that BCP is centrally located on the Cu—Cu bonds. The magnitude of the corresponding ρ and the sign of $\nabla^2\rho$ suggest a weak covalent bond [28] between the two Cu atoms. The topological analysis of the experimental charge density maps of $Cu_2(OAc)_4{\cdot}2H_2O$ at 100 K, performed by Bertolotti et al. in 2012, shows the expected bond critical points with the corresponding bond paths, including Cu—Cu bond [8]. The magnitudes of experimental ρ and $\nabla^2\rho$ for the Cu—Cu bond are somewhat higher than those obtained here (Table 1). Further, the sign of $\nabla^2\rho$ obtained experimentally is positive [8], while that obtained by us theoretically is negative. An interesting consequence of our BS calculations is presented in Fig. 3 where the orbitals of the two Cu(II) are different despite the D_{4h} symmetry of $Cu_2(OAc)_4{\cdot}2H_2O$. This indicates a breakdown of the simple molecular orbital picture, which is just a limiting case of BS calculations.

Existence of a bond between two copper atoms in $Cu_2(OAc)_4{\cdot}2H_2O$ and $Cu_2(OAc)_4$ is further supported by Wiberg's

Table 1
Lengths r, the electron density ρ at bond critical point and its associated Laplacian $\nabla^2\rho$ for some bonds in $Cu_2(CH_3COO)_4{\cdot}2H_2O$ as obtained from BP86/LACVP*(Cu)/6-311G++**(rest)//BP86/LACVP*(Cu)/6-31G*(rest) calculations on the BS state and comparison with the experimental data.[a]

Bond	r (Å)		ρ (e Å^{-3})		$\nabla^2\rho$ (e Å^{-5})		WBI
	calc	exp	calc	exp	calc	exp	
Cu_1—Cu_2	2.619	2.617	0.202	0.182(1)	−0.24	1.68(1)	0.31
Cu_1—Ow_1	2.378	2.157	0.202	0.378(6)	−0.96	6.07(1)	0.16
Cu_2—Ow_2	2.366	2.157	0.202	0.378(6)	−0.96	6.07(1)	0.16
Cu_1—O_1	2.013	1.947	0.472	0.521(1)	−2.65	9.22(1)	0.29
Cu_1—O_2	1.980	1.954	0.472	0.512(4)	−3.13	9.06(1)	0.31
Cu_2—O_3	2.050	1.954	0.472	0.512(4)	−2.65	9.06(1)	0.29
Cu_2—O_4	2.019	1.947	0.472	0.521(1)	−3.13	9.22(1)	0.31
Cu_1—O_5	2.027	1.996	0.405	0.558(1)	−2.65	9.86(1)	0.28
Cu_1—O_6	1.981	1.987	0.472	0.595(1)	−3.13	10.47(1)	0.30
Cu_2—O_7	2.050	1.987	0.405	0.595(1)	−2.41	10.47(1)	0.27
Cu_2—O_8	2.005	1.996	0.472	0.558(1)	−2.89	9.86(1)	0.28

[a] For atom labeling scheme, see Fig. 1. The experimental (exp) bond lengths are quoted from Ref. 5 and those for ρ and $\nabla^2\rho$ at 100 K are from Ref. 8.

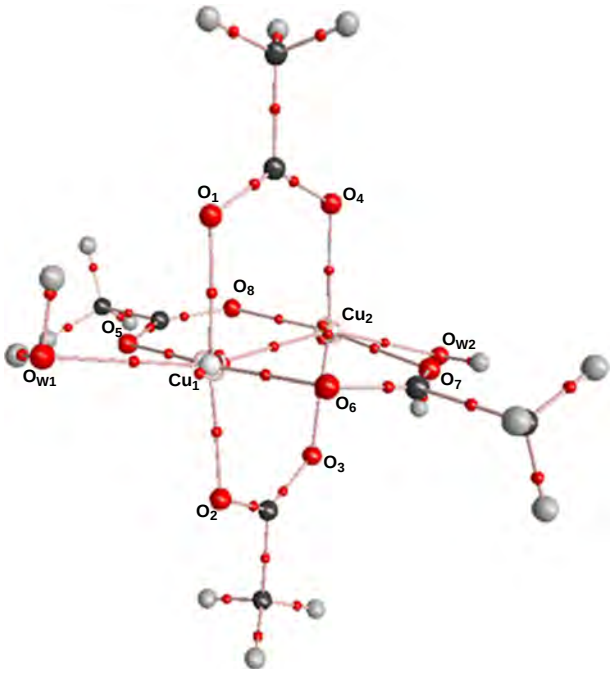

Fig. 1. Calculated bond critical points of $Cu_2(CH_3COO)_4{\cdot}2H_2O$.

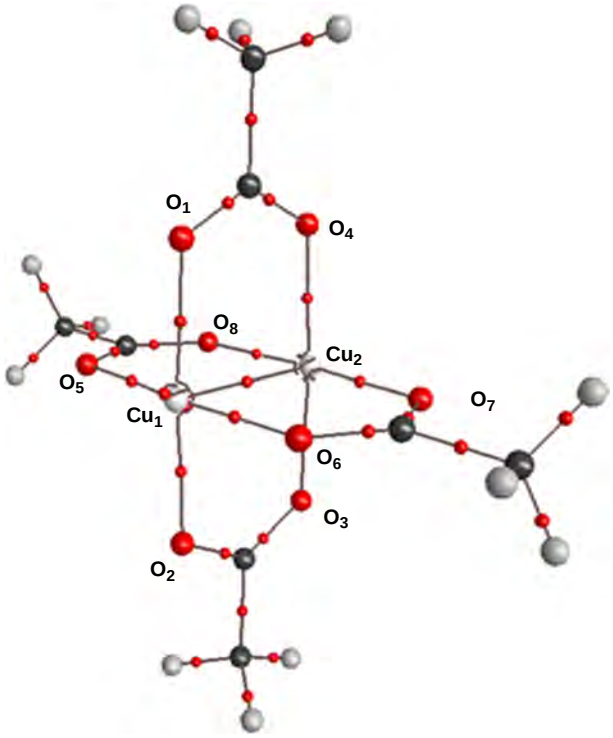

Fig. 2. Calculated bond critical points of $Cu_2(CH_3COO)_4$.

bond index (WBI) which is "the sum of the squares of the bond orders between any one atomic orbital and all other orbitals in a molecule" [29]. WBI of the Cu—Cu bond in $Cu_2(OAc)_4{\cdot}2H_2O$ is 0.31. It is one of the highest among all the bonds listed in Table 1. For anhydrous copper(II)acetate also, similar conclusion is drawn (Table 2). In the anhydrous variety, Cu—Cu distance comes out as somewhat smaller than that in the hydrated one with WBI remaining the same.

An interesting scenario emerges when we try to estimate the energies of the BS state and the triplet states for $Cu_2(OAc)_4{\cdot}2H_2O$ around the Cu—Cu distance of 2.6 Å – specifically in the range of 2.4–2.9 Å (Table 3, Fig. 4). For this purpose and to generate the wave functions in these cases necessary for AIM analyses, a single point calculation was done with B3LYP/6-31++G** after geometry optimization of $Cu_2(OAc)_4{\cdot}2H_2O$ with B3LYP/6-31G at a given Cu—Cu distance for each multiplicity. At Cu—Cu distances below 2.85 Å, the BS state is lower than the triplet state (*J* value negative). At 2.85 Å, the value of *J* is 0. Beyond that, the *J* value becomes positive indicating surfacing of ferromagnetic interaction. There are actually two opposing pathways in $Cu_2(OAc)_4{\cdot}2H_2O$ for the intramolecular magnetic interaction – (i) copper–copper bond and (ii) the acetato bridge. The van der Waals radius of copper, according to Bondi [30], is 1.4 Å. Consequently, beyond 2.8 Å, there should not be any Cu—Cu bond. An indirect support for this argument is provided by the alkoxo bridged dinuclear 3-amino-propanolato Cu(II) complexes of Farrugia et al. [31] where no bond path is found between the two copper(II) nuclei which are at a distance of 2.96 Å. The WBI values at the different Cu—Cu bond distances given in Table 3 show that as the distance between the two copper(II) centers approaches 2.9 Å, the Cu—Cu bond weakens very much. Our calculations reveal that the geometric parameters of the ligand framework remain more or less unperturbed (Table 4) in the explored vicinity of Cu—Cu distance of 2.6 Å. Thus the point is when Cu—Cu distance >2.85, the anti-ferromagnetic exchange interaction in $Cu_2(OAc)_4{\cdot}2H_2O$ through the Cu—Cu bond is much diminished or lost. But there remains the exchange interactions through the acetato bridge which is evidently ferromagnetic. Factorisation of magnetic exchange in a dinulear compound through different bridges has been attempted earlier [32].

Table 2
Lengths *r*, the electron density ρ at the bond critical point and its associated Laplacian $\nabla^2\rho$ of some bonds in $Cu_2(CH_3COO)_4$ as obtained from BP86/LACVP*(Cu)/6-311G++**(rest)//BP86/LACVP*(Cu)/6-31G*(rest) calculations on the BS state.[a]

Bond	*r* (Å)	ρ (e Å^{-3})	$\nabla^2\rho$ (e Å^{-5})	WBI
Cu_1—Cu_2	2.480	0.20	−0.48	0.30
Cu_1—O_1	1.987	0.47	−2.89	0.28
Cu_1—O_2	1.986	0.47	−2.89	0.28
Cu_2—O_3	1.994	0.47	−2.89	0.28
Cu_2—O_4	1.993	0.47	−2.89	0.28
Cu_1—O_5	1.987	0.47	−2.89	0.28
Cu_1—O_6	1.990	0.47	−2.89	0.28
Cu_2—O_7	1.995	0.47	−2.89	0.28
Cu_2—O_8	1.997	0.47	−2.89	0.28

[a] For atom labeling scheme, see Fig. 2.

Table 3
Variation of B3LYP BS-DFT energies of the BS (i.e. singlet; S) and the triplet (T) states and electron density ρ at the bond critical point and its associated Laplacian $\nabla^2\rho$ as obtained from B3LYP/6-31++G**//B3LYP/6-31G calculations on $Cu_2(CH_3COO)_4{\cdot}2H_2O$ with Cu—Cu distance.

Cu—Cu distance (Å)	Spin multiplicity	Energy (a.u.)	ρ (e Å^{-3})	$\nabla^2\rho$ (e Å^{-5})	WBI
2.4	S	−4348.311476	0.34	−0.48	0.13
	T	−4348.310571	0.34	−0.48	0.13
2.5	S	−4348.314778	0.27	−0.48	0.11
	T	−4348.313812	0.27	−0.48	0.11
2.6	S	−4348.315976	0.20	−0.48	0.09
	T	−4348.314948	0.20	−0.48	0.02
2.7	S	−4348.315458	0.13	−0.48	0.08
	T	−4348.314362	0.13	−0.48	0.02
2.8	S	−4348.313102	0.13	−0.24	0.06
	T	−4348.311926	0.13	−0.24	0.01
2.9	S	−4348.309734	0.13	−0.24	0.05
	T	−4348.310720	0.13	−0.24	0.01

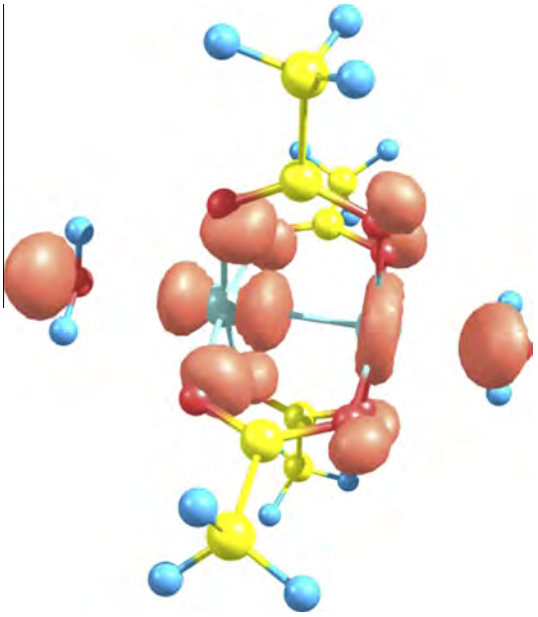

Fig. 3. An orbital picture of the interaction between the oxygen atoms of the water molecules with Cu(II) in $Cu_2(CH_3COO)_4{\cdot}2H_2O$ complex emerging out of our BS-DFT calculations.

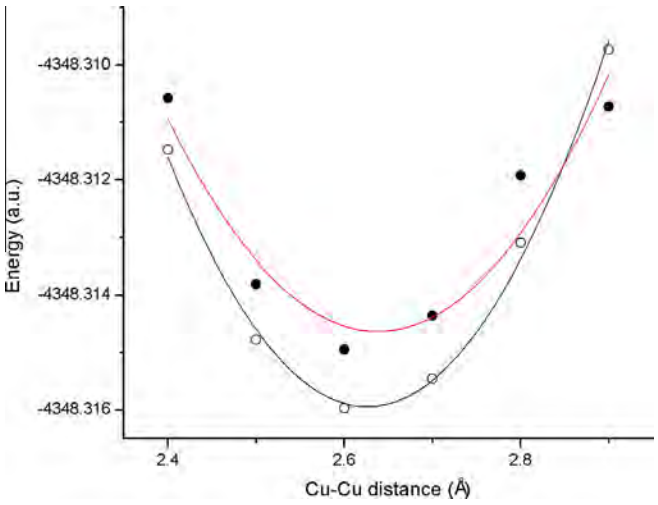

Fig. 4. Variation of the energies of the BS (black line, open circles) and the triplet (red line, filled circles) states in $Cu_2(CH_3COO)_4{\cdot}2H_2O$ with Cu—Cu distance. For data, see Table 3. Curves drawn are least squares fitted. Correlation coefficient *r*: black, 0.995; red, 0.914. (For interpretation of the references to color in this figure legend, the reader is referred to the web version of this article.)

Table 4
Variation of some structural parameters of $Cu_2(CH_3COO)_4{\cdot}2H_2O$ in the BS (i.e. singlet; S) and the triplet (T) states with Cu—Cu distance as obtained from B3LYP/6-31G optimization.[a]

Cu—Cu (Å)	Spin multiplicity	⟨C=O⟩ (Å)	⟨Cu—O⟩ (Å)	⟨Cu—O—C⟩ (°)	⟨O—C—O⟩ (°)
2.4	S	1.29	1.98	119.7	122.8
	T	1.29	1.98	119.7	122.7
2.5	S	1.29	1.98	120.8	123.2
	T	1.29	1.98	120.8	123.2
2.6	S	1.29	1.98	121.9	123.7
	T	1.29	1.98	121.9	123.6
2.7	S	1.29	1.98	123.0	124.1
	T	1.29	1.98	123.0	124.0
2.8	S	1.29	1.99	124.4	124.5
	T	1.29	1.99	124.5	124.4
2.9	S	1.29	1.99	126.2	124.8
	T	1.29	1.96	119.3	123.8

[a] Experimental data [5]: ⟨C=O⟩, 1.26 Å; ⟨Cu—O⟩, 1.97 Å; ⟨Cu—O—C⟩, 122.8°; ⟨O—C—O⟩, 125.2°.

4. Concluding remarks

Here we have shown that the interaction between the two spins on the two copper atoms in cupric acetate is actually a resultant of two pathways of counteracting nature. One path is through the ligand framework and another through the direct Cu—Cu bond. The Cu—Cu bond induces an antiferromagnetic exchange while the acetato framework provides a pathway for ferromagnetic interactions. Incidentally, presence of a Cu—Cu bond in cupric acetate was first proposed by Figgis and Martin in 1956 [2]. They envisaged a δ bonding between the two $d_{x^2-y^2}$ orbitals of the two copper atoms. Actually a $\delta \rightarrow \delta^*$ transition is observed in complexes of second-row and third row transition metals having metal–metal quadruple bonds [33]. Gray and co-workers have estimated this transition to be around 100 nm in $Cu_2(OAc)_4{\cdot}2H_2O$ [33], which they consider as "the archetypal weakly metal–metal-interacting dimer". It is mentioned that there is no correlation between the $\delta \rightarrow \delta^*$ transition energy and metal–metal bond strength.

Here we have relied on AIM. Alternative bonding pictures can be obtained from more rigorous methods like Domain Average Fermi Hole approach and delocalization indices [34]. Of these, Bertolotti et al. [8] have attempted to calculate the delocalization index for the Cu—Cu bond to conclude that there is a rather small amount of electron delocalization in the internuclear metallic region in $Cu_2(OAc)_4{\cdot}2H_2O$. It is cautioned that delocalization indices cannot be related to bond order.

Acknowledgement

Thanks are due to a reviewer for various help.

References

[1] J. Lifschitz, E. Rosenbohm, Magneto-chemistry of Internally Complex Compounds, Z. Electrochem. 21 (1915) 499–501.
[2] B.N. Figgis, R.L. Martin, Magnetic studies with copper(II) salts. Part I. Anomalous pasramagnetism and δ-bonding in anhydrous and hydrated copper(II) acetates, J. Chem. Soc. (1956) 3837–3846.
[3] B.C. Guha, Magnetic properties of some paramagnetic crystals at low temperature, Proc. Roy. Soc. Ser. A (London) 206 (1951) 353–373.
[4] B. Bleaney, K.D. Bowers, Anomalous paramagnetism of copper acetate, Proc. Roy. Soc. Ser. A (London) 214 (1952) 451–465.
[5] A. Elmali, The magnetic super-exchange coupling in copper(II) acetate monohy-drate and a redetermination of the crystal structure, Turk. J. Phys. 24 (2000) 667–672.
[6] G. Mostafa, G.K. Patra, J.M. Jana, D. Datta, A ferromagnetically coupled acetato bridged copper(II) dimer, Ind. J. Chem. 39A (2000) 1174–1176.
[7] J.N. van Niekerk, F.R.L. Schoening, A new type of copper complex as found in the crystal structure of cupric acetate, $Cu_2(CH_3COO)_4{\cdot}2H_2O$, Acta Cryst. 6 (1953) 227–232.
[8] F. Bertolotti, A. Forni, G. Gervasio, D. Marabello, E. Diana, Experimental and theoretical charge density of hydrated cupric acetate, Polyhedron 42 (2012) 118–127.
[9] G.M. Brown, R. Chidambaram, Dinuclear copper(II) acetate monohydrate: a redetermination of the structure by neutron-diffraction analysis, Acta Cryst. B29 (1973) 2393–2403.
[10] P. de Loth, P. Cassoux, J.P. Daudey, J.P. Malrieu, Ab initio direct calculation of the singlet-triplet separation in cupric acetate hydrate dimer, J. Am. Chem. Soc. 103 (1981) 4007–4016.
[11] P.J. Hay, J.C. Thibeault, R. Hoffmann, Orbital interactions in metal dimer complexes, J. Am. Chem. Soc. 97 (1975) 4884–4899.
[12] R.F.W. Bader, A quantum theory of molecular structure and its applications, Chem. Rev. 91 (1991) 893–928.
[13] S. Hati, D. Datta, Electronegativity and Bader's bond critical point, J. Comput. Chem. 13 (1992) 912–918.
[14] A.K. Samanta, D. Datta, A DFT and AIM study of the interactions of pyridine and pyrazine with alkali hydrides. Identification of dihydrogen bonds involving aromatic C–H hydrogen, Ind. J. Chem. 49A (2010) 176–179.
[15] Jaguar, version 7.9, Schrodinger, LLC, New York, NY, 2011.
[16] Gaussian-09, Revision C.01, M.J. Frisch, G.W. Trucks, H.B. Schlegel, G.E. Scuseria, M.A. Robb, J.R. Cheeseman, G. Scalmani, V. Barone, B. Mennucci, G.A. Petersson, H. Nakatsuji, M. Caricato, X. Li, H.P. Hratchian, A.F. Izmaylov, J. Bloino, G. Zheng, J.L. Sonnenberg, M. Hada, M. Ehara, K. Toyota, R. Fukuda, J. Hasegawa, M. Ishida, T. Nakajima, Y. Honda, O. Kitao, H. Nakai, T. Vreven, J.A. Montgomery, Jr., J.E. Peralta, F. Ogliaro, M. Bearpark, J.J. Heyd, E. Brothers, K.N. Kudin, V.N. Staroverov, T. Keith, R. Kobayashi, J. Normand, K. Raghavachari, A. Rendell, J.C. Burant, S.S. Iyengar, J. Tomasi, M. Cossi, N. Rega, J.M. Millam, M. Klene, J.E. Knox, J.B. Cross, V. Bakken, C. Adamo, J. Jaramillo, R. Gomperts, R.E. Stratmann, O. Yazyev, A.J. Austin, R. Cammi, C. Pomelli, J.W. Ochterski, R.L. Martin, K. Morokuma, V.G. Zakrzewski, G.A. Voth, P. Salvador, J.J. Dannenberg, S. Dapprich, A.D. Daniels, O. Farkas, J.B. Foresman, J.V. Ortiz, J. Cioslowski, D.J. Fox, Gaussian Inc., Wallingford CT, 2010.
[17] P.J. Hay, W.R. Wadt, Ab initio effective core potentials for molecular calculations. Potentials for the transition metal atoms Sc to Hg, J. Chem. Phys. 82 (1985) 270–283.
[18] W.J. Hehre, R. Ditchfield, J.A. Pople, Self-consistent molecular orbital methods. XII. Further extensions of Gaussian-type basis sets for use in molecular orbital studies of organic molecules, J. Chem. Phys. 56 (1972) 2257–2261.
[19] F. Biegler-König, J. Schönbohm, D. Bayles, AIM2000 – A program to analyze and visualize atoms in molecules, J. Comp. Chem. 22 (2001) 545–559.
[20] A.P. Ginsberg, Magnetic exchange in transition metal complexes. 12. Calculation of cluster exchange coupling constants with the X. alpha.-scattered wave method, J. Am. Chem. Soc. 102 (1980) 111–117.
[21] L. Noodleman, Valence bond description of antiferromagnetic coupling in transition metal dimers, J. Chem. Phys. 74 (1981) 5737–5743.
[22] K. Yamaguchi, Y. Takahara, T. Fueno, K.N. Houk, Extended Hartree-Fock (EHF) theory of chemical reactions, Theor. Chim. Acta 73 (1988) 337–364.
[23] F. Neese, Prediction of molecular properties and molecular spectroscopy with density functional theory: from fundamental theory to exchange-coupling, Coord. Chem. Rev. 253 (2009) 526–563.
[24] E. Ruiz, J. Cano, S. Alvarez, P. Alemany, Broken symmetry approach to calculation of exchange coupling constants for homobinuclear and heterobinuclear transition metal complexes, J. Comput. Chem. 20 (1999) 1391–1400.

[25] E. Ruiz, S. Alvarez, J. Cano, V. Polo, About the calculation of exchange coupling constants using density-functional theory: the role of the self-interaction error, J. Chem. Phys. 123 (2005) 164110.
[26] K. Yamaguchi, Y. Takahara, T. Fueno, in: J.V.H. Smith, H.F. Schaefer III, K. Morokuma (Eds.), Ab-initio molecular orbital studies of structure and reactivity of transition metal-oxo compounds, Appl. Quantum Chem., D. Reidel, Dordrecht, 1986, pp. 155–184.
[27] A. Bencini, Some considerations on the proper use of computational tools in transition metal chemistry, Inorg. Chim. Acta 361 (2008) 3820–3831.
[28] L. Zhang, F. Ying, W. Wu, P.C. Hiberty, S. Shaik, Topology of electron charge density for chemical bonds from valence bond theory: a probe of bonding types, Chem. Eur. J. 15 (2009) 2979–2989.
[29] K.B. Wiberg, Application of the Pople-Santry-Segal CNDO method to the cyclopropylcarbinyl and cyclobutyl cation and to bicyclobutane, Tetrahedron 24 (1968) 1083–1096.
[30] A. Bondi, Van der Waals volumes and radii, J. Phys. Chem. 68 (1964) 441–451.
[31] L.J. Farrugia, D.S. Middlemiss, R. Sillanpää, P. Seppälä, A combined experimental and theoretical charge density study of the chemical bonding and magnetism in 3-amino-propanolato Cu(II) complexes containing weakly coordinated anions, J. Phys. Chem. A 112 (2008) 9050–9067.
[32] S. Sarkar, A. Datta, A. Mondal, D. Chopra, J. Ribas, K.K. Rajak, S.M. Sairam, S.K. Pati, Competing magnetic interactions in a dinuclear Ni(II) complex: antiferromagnetic O–H···O moiety and ferromagnetic N_3^- ligand, J. Phys. Chem. B 110 (2006) 12–15.
[33] V.M. Miskowski, M.D. Hopkins, J.R. Winkler, H.B. Gray, Multiple metal–metal bonds, in: E.I. Solomon, A.B.P. Lever (Eds.), Inorganic Electronic Structure and Spectroscopy, vol. II, John Wiley & Sons, Inc., New York, 1999, (chapter 6).
[34] R. Ponec, C. Gatti, Do the structural changes defined by the electron density topology necessarily affect the picture of the bonding?, Inorg Chem. 48 (2009) 11024–11031.

Author's personal copy

J Mol Model (2015) 21:96
DOI 10.1007/s00894-015-2631-3

ORIGINAL PAPER

Pyrazolo[3,4-*d*]pyrimidines as novel inhibitors of O-acetyl-L-serine sulfhydrylase of *Entamoeba histolytica*: an in silico study

Umesh Yadava · Bindesh Kumar Shukla · Mihir Roychoudhury · Devesh Kumar

Received: 20 June 2014 / Accepted: 22 February 2015
© Springer-Verlag Berlin Heidelberg 2015

Abstract Amoebiasis, a worldwide explosive epidemic, caused by the gastrointestinal anaerobic protozoan parasite *Entamoeba histolytica*, infects the large intestine and, in advance stages, liver, kidney, brain and lung. Metronidazole (MNZ)—the first line medicament against amoebiasis—is potentially carcinogenic to humans and shows significant side-effects. Pyrazolo[3,4-*d*]pyrimidine compounds have been reported to demonstrate antiamoebic activity. In silico molecular docking simulations on nine pyrazolo[3,4-*d*]pyrimidine molecules without linkers (molecules **1–9**) and nine pyrazolo[3,4-*d*]pyrimidine molecules with a trimethylene linker (molecules **10–18**) along with the reference drug metronidazole (MNZ) were conducted using the modules of the programs Glide-SP, Glide-XP and Autodock with O-acetyl-L-serine sulfhydrylase (OASS) enzyme—a promising target for inhibiting the growth of *Entamoeba histolytica*. Docking simulations using Glide-SP demonstrate good agreement with reported biological activities of molecules **1**–**9** and indicate that molecules **2** and **4** may act as potential high affinity inhibitors. Trimethylene linker molecules show improved binding affinities among which molecules **15** and **16** supersede. MD simulations on the best docked poses of molecules **2, 4, 15, 16** and **MNZ** were carried out for 20 ns using DESMOND. It was observed that the docking complexes of molecules **4, 15** and **MNZ** remain stable in aqueous conditions and do not undergo noticeable fluctuations during the course of the dynamics. Relative binding free energy calculations of the ligands with the enzyme were executed on the best docked poses using the molecular mechanics generalized Born surface area (MM-GBSA) approach, which show good agreement with the reported biological activities.

Keywords *Entamoeba histolytica* · Glide docking · Schrodinger · ADME · Molecular dynamics

Introduction

Amoebiasis, the most aggressive disease of the human intestine, is caused by the anaerobic protozoan parasite *Entamoeba histolytica*, and is the third most common cause of death from parasitic infections, surpassing Schistosomiasis and malaria [1, 2]. It is more common in the young but may affect people of any age. It has a very high incidence in tropical countries like India, Mexico, Central and South America etc. and spreads commonly through contaminated water, feces and from food served with contaminated hands. The *E. histolytica* parasite penetrates the human gastrointestinal tract and burrows deep into the intestinal walls, which can cause abscesses and ulcers and may infect the bowel. Without treatment, it can travel to the other parts of the body, such as the liver, through the veins of the intestines. Other body parts that are reached by this protozoa may also become infected and adorned with abscesses and ulcers. The formation of pus in the liver (liver abscess), lungs (lung abscess), and brain (brain abscess), is a sign of advanced stage of amoebiasis, which may be highly fatal to a person. When the cyst of *E. histolytica* enters the small intestine, active amoebic parasites (trophozoites) are released, which can invade the epithelial cells of the large intestines, causing flask-shaped ulcers. Cysteine is an

Electronic supplementary material The online version of this article (doi:10.1007/s00894-015-2631-3) contains supplementary material, which is available to authorized users.

U. Yadava (✉) · B. K. Shukla · M. Roychoudhury
Department of Physics, D.D.U. Gorakhpur University, Gorakhpur 273009, India
e-mail: u_yadava@yahoo.com

D. Kumar
Department of Applied Physics, Babasaheb Bhimrao Ambedkar University, Vidya Vihar, Rae Bareilly Road, Lucknow 226025, India

Published online: 25 March 2015

Author's personal copy

important amino acid for the attachment and growth of trophozites of *E. histolytica* [3]. In this organism, the condensation of O-acetylserine with sulfide is the major route of cysteine biosynthesis, which involves two key enzymes: O-acetyl-L-serine sulfhydrylase (OASS) and serine acetyl transferase (SAT). These enzymes can act as promising targets for inhibiting the growth of *E. histolytica* [4, 5]. Metronidazole (MNZ)—the first line medicament against amoebiasis—produces significant side effects and is potentially carcinogenic to human cells on account of its genotoxicity [6]. Moreover, resistance of *E. histolytica* to MNZ and relapses of intestinal and hepatic amoebiasis have also been reported [7]. Because of multidrug resistance and the significant side effects of an assortment of available antiamoebic drugs, the development of novel effective antiamoebic drugs that produce fewer or no side effects is required.

Development of inhibitors of OASS using in silico docking methods and their in vitro testing have been reported in the literature [8]. Pyrazolo[3,4-d]pyrimidines constitute a class of naturally occurring fused uracils that exhibit diverse biological activities. These compounds are reported as potential anti-inflammatory agents [9], anti-coagulation inhibitors [10], xanthine oxidase inhibitors [11], antiproliferative and proapoptotic agents in several tumor types [12]. They are also known as SRC kinase inhibitors [13] and are useful in the treatment of human cancers sustaining oncogenic activation of RET [14]. Due to the structural similarity of pyrazolo[3,4-d]pyrimidine cores with almost all the antiamoebic drugs, e.g., metronidazole, tinidazole, and ornidazole (Fig. 1), pyrazolo[3,4-d]pyrimidine analogues were synthesized and found to be endowed with antiamoebic activity [15–18]. The in vitro antiamoebic activity of compounds **1**–**9** (Fig. 2a) against HM1:IMSS strain of *E. histolytica*, indicates that these compounds may have better inhibitor activity in comparison to the reference drug metronidazole [18]. Further, these compounds are also found to have low cytotoxicity against the human breast cancer cell line MCF-7. These preliminary results illustrate that pyrazolo[3,4-d]pyrimidine analogues could help in designing better molecules with improved antiamoebic activity. Pyrazolo[3,4-d]pyrimidine molecules having trimethylene linkers; the flexible models to facilitate aromatic π–π interactions also possess useful pharmaceutical properties [10, 19]. It is fascinating to consider these trimethylene linker molecules to investigate their potential as anti-amoebic agents in addition to molecules without this linker. The in silico molecular docking studies of nine pyrazolo[3,4-d]pyrimidine molecules with no linker (molecules **1**–**9**) and nine molecules with a trimethylene linker (molecules **10**–**18**) along with the reference molecule metronidazole (MNZ) (Fig. 2a, b) were carried out with the O-acetyl-L-serine sulfhydrylase (OASS) enzyme—the prime target for inhibiting the growth of *E. histolytica*. In order to study the stability and dynamic changes of predicted binding conformations, molecular dynamics (MD) simulations were performed on the best docking complexes. Molecular mechanics-generalized Born/surface area (MM-GB/SA) analysis was carried out to estimate the relative binding free energies of the ligands with OASS. To ensure success at clinical trial level, we carried out ADME (absorption, distribution, metabolism and excretion) predictions on ligand molecules.

Methods

GLIDE docking

The three-dimensional crystal structure of O-acetyl-L-serine sulfhydrylase enzyme complexed with cysteine and pyridoxal-5′-phosphate (PLP) ligands (PDB ID: 3BM5) determined by X-ray crystallography was retrieved from the Protein Data Bank (http://www.rcsb.org). This crystal structure was inspected carefully and processed in order to overcome a variety of potential problems, e.g., missing atoms, bond orders, added waters, chain breaks, alternate binding locations, etc. Preparations of protein and ligands were carried out and an electron affinity grid was subsequently generated. Docking of ligands with the receptor has been carried out using GLIDE5.2 module with standard precision (SP) and extra precision (XP) protocols both, as implemented in the SCHRÖDINGER Suite [20]. During docking, the receptor was kept rigid while ligands were treated as flexible, which enables generation of multiple poses of the receptor–ligand complexes. Each pose includes unique structural conformation of the ligand that

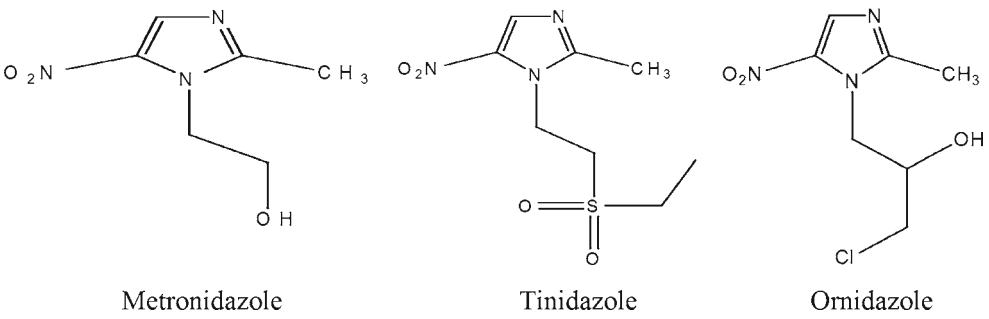

Fig. 1 Chemical structure of antiamoebic drugs bearing a nitrogen-containing heterocyclic ring

Author's personal copy

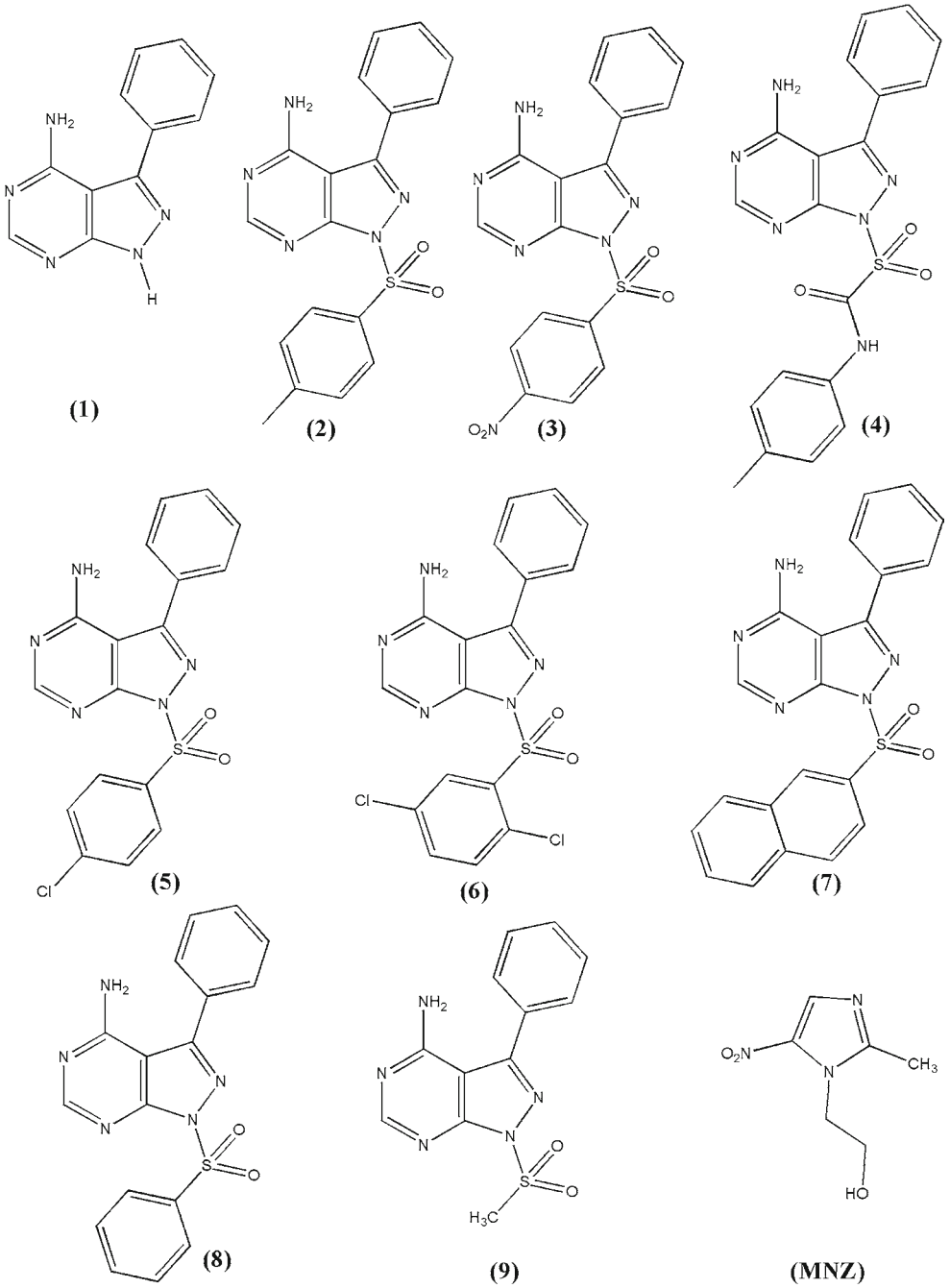

Fig. 2 **a** Chemical structures of pyrazolo[3,4-d]pyrimidines with no linker: **1** 3-phenyl-1H-pyrazolo[3,4-d]pyrimidin-4-amine, **2** 3-phenyl-1-tosyl-1H-pyrazolo[3,4-d]pyrimidin-4-amine, **3** 1-[(4-nitrophenyl)sulfonyl]-3-phenyl-1H-pyrazolo[3,4-d]pyrimidine-4-amine, **4** N-{4-[(4-amino-3-phenyl-1H-pyrazolo[3,4-d]pyrimidin-1-yl)sulfonyl]phenyl}acetamide, **5** 1-[(4-Chlorophenyl)sulfonyl]-3-phenyl-1H-pyrazolo[3,4-d]pyrimidine-4-amine, **6** 1-[(2,5-Dichlorophenyl)sulfonyl]-3-phenyl-1Hpyrazolo[3,4-d]pyrimidine-4-amine, **7** 1-(2-Naphthylsulfonyl)-3-phenyl-1H-pyrazolo[3,4-d]pyrimidin-4-amine, **8** 3-Phenyl-1-(phenylsulfonyl)-1H-pyrazolo[3,4-d]pyrimidine-4-amine, **9** 3-Phenyl-1-(methylsulfonyl)-1H-pyrazolo[3,4-d]pyrimidine-4-amine and Metronidazole (MNZ). **b** Chemical structures of pyrazolo[3,4-d]pyrimidines with trimethylene linkers: **10** 1,3-bis(4,6-diethylthio-1H-pyrazolo[3,4-d]pyrimidin-1-yl)propane; **11** 1,3-bis(4-ethoxy-6-methyl-sulfanyl-1H-pyrazolo[3,4-d]pyrimidin-1-yl)propane; **12** 1,10-(1,3-propanediyl)bis(5-methyl-6-methylthio-4,5-dihydro-1H-pyrazolo[3,4-d]pyrimidin-4-one); **13** 1,10-(1,3-propanediyl)bis(5-ethyl-6-methylthio-4,5-dihydro-1H-pyrazolo[3,4-d]pyrimidin-4-one); **14** 1,10-(1,3-propanediyl)bis(5-benzyl-6-methylsulfanyl-4,5-dihydro-1H-pyrazolo[3,4-d]pyrimidin-4-one); **15** 1-(4,6-dimethylsulfanyl-1H-pyrazolo[3,4-d]pyrimidin-1-yl)-3-(5-methyl-6-methylsulfanyl-4-oxo-1,5-dihydropyrazolo[3, 4-d]pyrimidin-1-yl)propane; **16** 4,6-bis(methylsulfanyl)-1-phthalimidopropyl-1H-pyrazolo[3,4-d]-pyrimidine; **17** 6-methylsulfanyl-1-phthalimidopropyl-4(pyrrolidin-1-yl)-1H-pyrazolo[3,4-d]pyrimidine; **18** and 6-methylsulfanyl-1-(3-phenylpropyl)-4,5-dihydro-1H-pyrazolo[3,4-d]pyrimidin-4-one

Author's personal copy

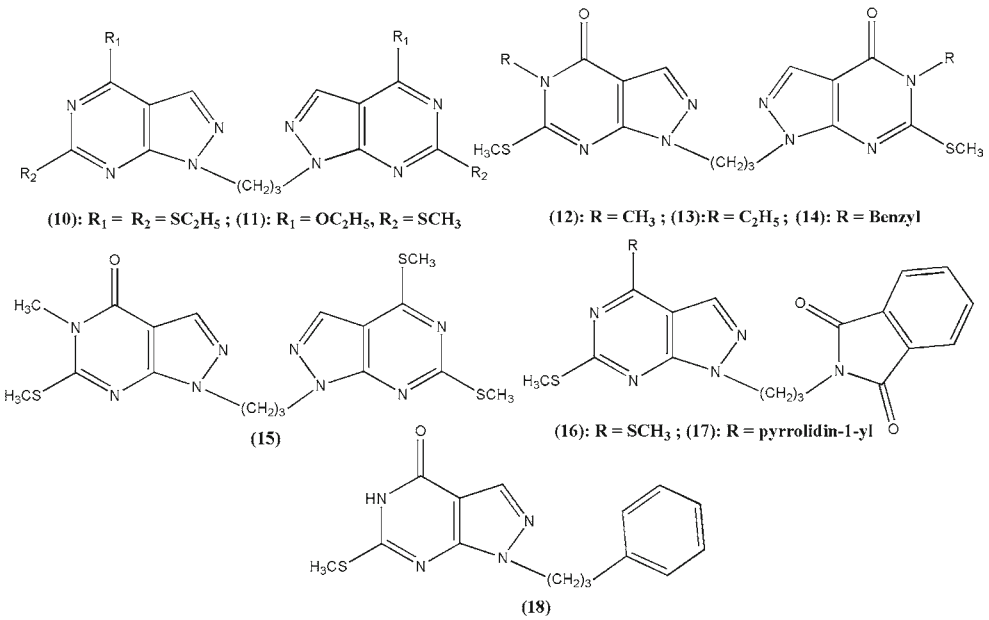

Fig. 2 (continued)

fit in the binding site of the receptor. Docking complexes were ranked by Glide scores (G-score). G-Score is an empirical scoring function that uses the combination of various parameters like hydrogen bonds, hydrophobic contacts, van der Waals, coulombic, polar interactions in the binding site, a metal binding term, penalties for buried polar groups and freezing rotatable bonds, etc. [21].

Ligand preparation

Geometries of all the ligands (molecules **1**–**18** and MNZ) were optimized using density functional theory (DFT) B3LYP method in conjunction with the 6-31G** basis set as implemented in GAUSSIAN03 [22]. Optimized coordinates of the ligands were prepared using the LIGPREP module, bond orders were modified according to their data and different conformers were generated using CONFGEN. Each generated conformer was subjected to a full minimization in the gas phase with the OPLS-2005 (optimized potential for liquid simulations) force field [23] to eliminate the bond length and bond angles biased from the crystal structure. LIGPREP produced the structures with various ionization states, tautomers, stereo-chemistries, and ring conformations.

Protein preparation

The three dimensional (3D) structure of OASS complexed with PLP was prepared using protein preparation wizard, where hydrogens were added automatically and subsequent refinement of the structure was carried out. Water molecules in the crystallographic complex are not critical to the functioning of the protein–ligand interaction, hence all the crystallographic waters were deleted and the bond orders were re-assigned. Further, the whole system was minimized to a root mean square deviation (RMSD) of 0.30 Å. Missing residues were added through the PRIME application of the SCHRODINGER Suite [24].

Receptor grid generation

The affinity and electrostatic potential grid for each type of atoms in ligands at different grid points, at the active site of the receptor were calculated. The position of PLP was taken as the center of the active site of the protein for all ligands. During the grid generation, no van der Waals radius sampling was done and the partial charge cutoff was taken as 0.25.

Ligand docking

SP and XP modes of Glide were used for flexible molecular docking of the prepared ligands within the active site of the receptor. For the minimization of ligands, the distance-dependent dielectric constant with a value of 2.0 and a conjugate gradient algorithm with 1,000 steps were used. All of the inhibitors were passed through a scaling factor of 0.80 and partial charge cutoff of 0.15 Å. After docking, post-docking minimization was performed to improve the geometry of the poses, which specifies a full force-field minimization of those poses that are considered for final scoring. After minimization, the results were used for binding energy calculations and docking scores.

Author's personal copy

Autodock docking

Docking simulations were also performed through Autodock4.2 [25], which hits upon favorable docking in a protein-binding site. Autodock tools were used to prepare the protein and the ligands. During preparation of the macromolecule, polar hydrogens were added in the crystal structure of OASS and Kollman United atom charges and atomic solvation parameters were then allocated. Autogrid4 was employed for the calculation of electron affinity and electrostatic potential grid. The grid center was taken as the location of the co-crystallized ligand PLP. The grid map was generated with 70×70×70 points with a grid spacing of 0.625 Å using distance-dependent dielectric constants. Molecular docking was performed using the GA–LS method, with the parameters defined in our earlier paper [10]. After docking, all the generated structures were assigned to clusters based on a tolerance of 1.0 Å all-atom RMSD from the lowest-energy structure. Hydrogen bonding and hydrophobic interactions between docked potent agents and the macromolecule were analyzed using ADT [25].

MD simulation

The coordinates of the best docking poses were subjected to MD simulation using DESMOND software [26, 27]. Each complex was neutralized using 3-sodium counter-ions. The complexes and the counter ions were "immersed" in a Monte-Carlo-equilibrated, periodic TIP3P water bath, such that the whole system was surrounded by a periodic box of transferable intermolecular potential (TIP3P) waters, which extended approximately 10 Å in each direction. The system thus constructed, had one protein molecule (solute), 3-sodium ions and water molecules in the box. The Verlet-leap-frog algorithm [28] was used in numerical integration with a 1.0 fs time step length for minimization and 2.0 fs for dynamics [29]. Hydrogen-atom bonds were constrained to "ideal" lengths using SHAKE. A cut-off of 9.0 Å was applied to the Lennard-Jones interactions, and constant pressure was maintained with isotropic-molecule-based scaling. Water molecules and counter-ions were first energy minimized by steps of steepest descent until gradient threshold 25 kcal mol^{-1} $Å^{-2}$ and then by conjugate-gradient energy minimization with a satisfactory convergence of rms gradient of 0.1 kcal mol^{-1} $Å^{-2}$. The entire system was subjected to 10, 000 steps of steepest-descent minimization followed by conjugate-gradient minimization. The velocities were assigned at 100 K to all the atoms according to Boltzmann's distribution. The temperature of the system was raised from 100 to 298 K over 2.0 ps by scaling velocities according to Berendsen algorithm followed by a constant-pressure-dynamics run over 25 ps. After initial equilibration, MD production run was performed over 20.0 ns.

Binding free energy calculation

The Prime/MM-GB/SA approach [24] was used to calculate the relative binding free energies of the ligands to the receptor. The best docked poses were minimized and energies of the complexes were computed using the OPLS-AA(2005) force field and GB/SA continuum solvent model as implemented in PRIME. The binding free energies were calculated as the sum of three terms: (1) ΔE, the difference of the minimized energies of the complex and ligand plus receptor ($\Delta E = E_{complex} - E_{ligand} - E_{protein}$); (2) ΔG_{solv}, the difference of solvation free energies of complex and ligand plus receptor ($\Delta G_{solv} = G_{solv(complex)} - G_{solv(ligand)} - G_{solv(protein)}$); and (3) ΔG_{SA}, the difference of surface area energies of the complex and ligand plus receptor ($\Delta G_{SA} = G_{SA(complex)} - G_{SA(ligand)} - G_{SA(protein)}$) [30].

ADME prediction

In order to ensure success at the clinical testing level [31, 32], ADME parameters and other pharmaceutically important properties of the ligands were also predicted using QikProp3.5 module [33]. The program was processed in normal mode and predicted 44 properties for all the molecules, consisting of principal descriptors and physiochemical properties with a detailed analysis of the logP (octanol/water), QP %, and logHERG etc. It also evaluates the acceptability of the analogues based on Lipinski's rule of 5, which is essential for rational drug design [34]. The rule describes the molecular properties important for a drug's pharmacokinetics in the human body, including its ADME. However, the rule does not predict whether a compound is pharmacologically active [35].

Results and discussion

Analysis of the crystal structure of O-acetyl-L-serine sulfhydrylase (OASS)—the prime target for the inhibition of *E. histolytica*—revealed that the polypeptide folds into two subunits comprising α and β domains. Each domain consists of a relatively small mobile N-terminal domain (residues 57–164) and a large rigid C-terminal domain (residues 1–56 and 165–336) [36]. The cofactor PLP is linked covalently to Lys-58, which is conserved in all OASS structures and is positioned in between these two domains. Other highly conserved residues, such as Gly236, Ser280 and Pro307, interact with the aromatic ring of PLP. These observations prompt us to view the position of PLP as the center of the active site.

GLIDE docking

Ligand docking of different pyrazolo[3,4-d]pyrimidines with OASS revealed a large variation in their binding energies.

Author's personal copy

Initially, five poses of each ligand were selected from the docking results, out of which the poses with better glide scores, better hydrogen bonding and better non-covalent interactions with lower glide energy values were chosen as the best poses for each molecule. Although the predicted free energy of binding is a useful descriptor of ligand–receptor complementarities, the choice of the 'best' docking model was ultimately dictated by various parameters of the ADME study. These best docked complexes were considered for further analysis and the results were compared.

Standard precision docking

Docking calculations of pyrazolo[3,4-d]pyrimidine molecules without linkers (molecules **1**–**9** and MNZ) through Glide-SP revealed that molecules **2** and **4** have better glide scores (−6.305 and −6.104 kcal mol^{-1}, respectively) than the reference drug MNZ, which has a socre of −5.934 (Table S1a). These results are consistent with the experimental results predicted on the basis of IC50 values [17], which proves the validity of the method used. The electron withdrawing group ($-NO_2$) in compound **3** causes it to have a lower glide score than **2**, **4** and MNZ. Molecules **7**, **1** and **6**, which contain planar aromatic moieties, exhibit the next best glide scores, while others have poorer scores. SP docking further demonstrates that almost all the molecules exhibit better glide energies than MNZ. Molecule **4** is the best, while molecule **7** exhibits the next best binding energy value. The electrostatic energy contribution of molecule **4** is most appreciable, followed by MNZ and molecule **2** (Table S1a). Other molecules have lower electrostatic contributions. The value of cross-correlation function of glide scores with IC50 values was found to be relatively good (R^2=0.631).

The hydrogen bonding interactions in the best poses of the docking of these ligands (without linkers) show that most of the molecules have same type of interactions as the reference molecule MNZ (Table S1b). Evidence for hydrogen bonding interactions with residue Lys58 is displayed by molecules **2**, **4**, **5**, **7** and MNZ, which is important from the molecular recognition point of view. Molecule **8** shows π-cation interaction with Lys58. Since PLP is linked covalently to residue Lys58 in all the structures of OASS, interactions with Lys58 play an important role in amoebiasis inhibition. Molecules **2**, **3**, **4**, **6**, **8** and **9** display hydrogen bonding interactions with residue Thr85. Hydrophobic interactions are exhibited by ligands with conserved residues of both the N– and C-terminal domains of the active site like Tyr313, Ile237, Pro307, Ala190, Val191, Val197, Val61, Val57, Met136, Phe160, Met112 and Ala239. Polar interactions with residues Asn88, Gln159, Gln235, Hie232, Ser113, Ser280, Ser308, Ser86, Ser56, Thr111, Thr193, Thr196, Thr85 and Thr89 were also observed. On the basis of Glide scores, Glide energies and non-covalent interactions as obtained through Glide SP docking and corresponding IC50 values, it can be concluded that compounds **2**, **3** and **4** might be better inhibitors than MNZ against amoebic histolytica disease.

Inspired by the successes with pyrazolo[3,4-d]pyrimidines without linker, SP docking studies with the target OASS were also performed using pyrazolo[3,4-d]pyrimidine molecules containing trimethylene linkers (molecules **10**–**18**). These molecules—well known flexible models for aromatic π–π interactions—have either two pyrazolo[3,4-d]pyrimidine moieties (molecules **10**–**15**) or one pyrazolo[3,4-d]pyrimidine moiety and another aromatic moiety connected through a trimethylene linker (molecules **16**–**18**). Interestingly, some of these molecules (**12**, **15**, **16** and **18**) show better glide scores than molecule **2**, which received the top glide score among the molecules without a linker. Molecule **16** showed the best glide score at −7.800 kcal mol^{-1}. It was observed that, when one of the thiomethyl substituents at the 4th position was replaced by a non-aromatic moiety pyrrolidin-1-yl (**17**), the glide score was reduced significantly to −5.266 kcal mol^{-1}, probably because of steric hindrance. Compound **15**, which belongs to the dissymmetric class of molecules containing two pyrazolo[3,4-d]pyrimidine moieties and a methyl substituent at the 5th position of one moiety, established the second best glide score of −7.404 kcal mol^{-1}. The symmetrical class of molecule **12**, containing a methyl group at the 5th position of both pyrazolo[3,4-d]pyrimidine moities, exhibited the third best glide score of −7.172 kcal mol^{-1}. However, replacing the methyl group with an ethyl group (**13**) or a benzyl group (**14**) reduces the glide scores. Molecules **10**, **11** and **18** have lower modulus of glide scores but higher than the originally crystallized molecule MNZ. Glide energies of all the ligands with the trimethylene linker were higher than those of both molecules without linker and MNZ.

Hydrogen bonding interactions in the best docking poses, revealed by ligands **2**, **4**, **12**, **15**, **16** and MNZ, as obtained through Glide-SP docking with target OASS are shown in Fig. 3. Both molecules **12** and **16** demonstrate four hydrogen bonding interactions whereas molecule **18** shows three. It can be observed from Fig. 3 and Table S1b, that molecules **10**, **11**, **12**, **14**, **16** and **18** demonstrate hydrogen bonding interactions with the residue Lys58—vital for the inhibition of OASS. Other residues that take part in hydrogen bonding interactions with different ligands are Arg116, Tyr313, Ser280, Thr85, Asn88, Gln159, Ser86, Gly236 and Thr193. Hydrophobic and polar interactions are also exhibited by ligands with different residues. Non covalent π–π interactions and cation–π interactions are exhibited by molecules **17** and **18** with residues His232 and Lys58, respectively.

Extra precision docking

In the XP module of GLIDE, protein–ligand structural motifs leading to enhanced binding affinity were included in addition

Author's personal copy

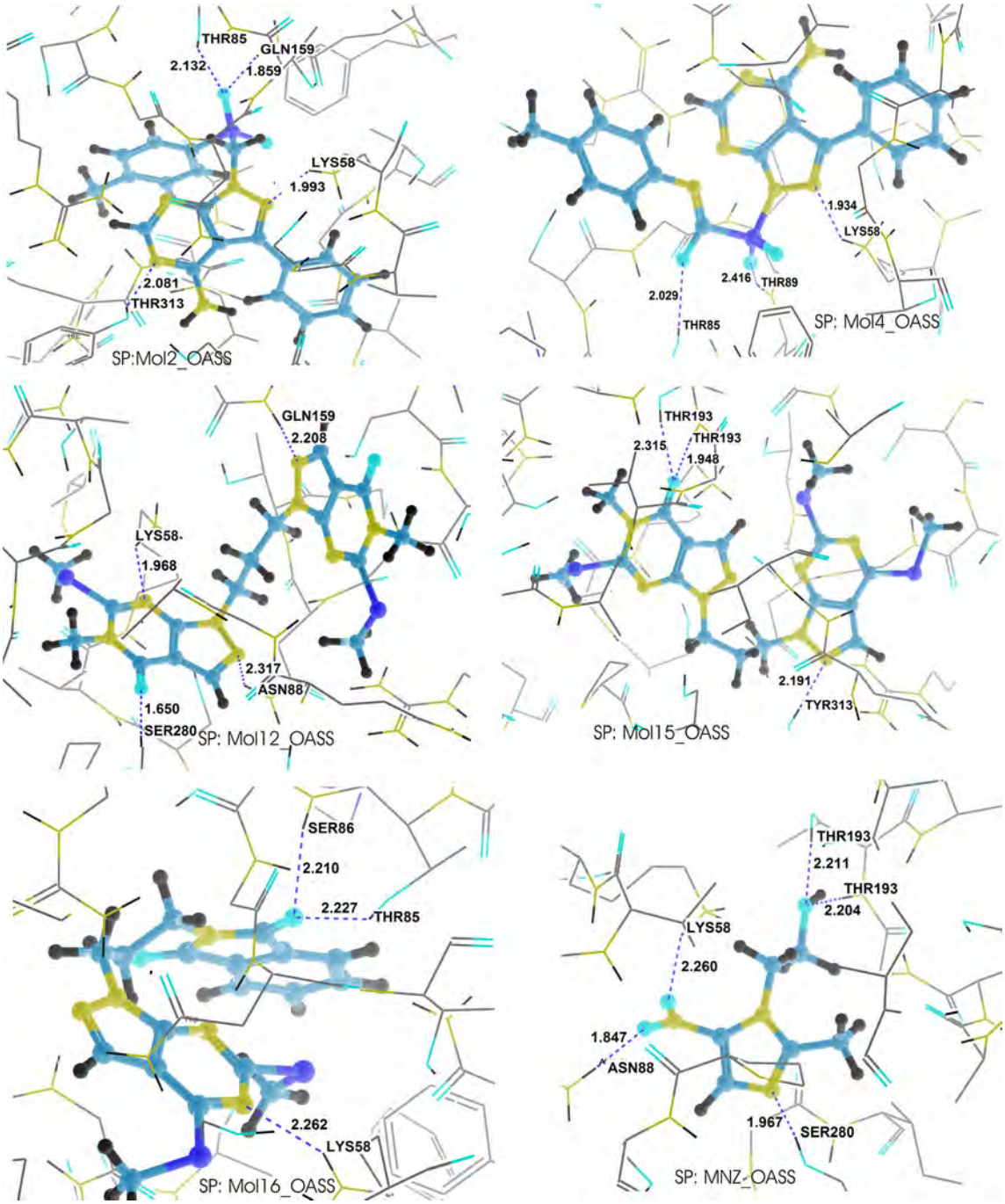

Fig. 3 Hydrogen bonding interactions in the best docking poses of molecules **2**, **4**, **12**, **15**, **16** and MNZ as obtained through Glide-SP docking

to unique water desolation energy terms. The Glide docking results of the XP protocol are summarized in Tables S2a, S2b and Fig. 4. It was observed that the Glide scores and docking energies differ from those of the SP mode. Glide scores of XP docking were reduced in comparison to SP docking. XP docking of the ligands without linker revealed that molecule **4** has the best glide score of −5.190 kcal mol^{-1}. Molecules **7** and **2** have the next best glide scores of −4.573 and −4.290 kcal mol^{-1}, respectively. It was further observed that all the ligands except molecule **3** exhibit better glide scores than MNZ. Comparison of glide energies divulge that molecule **4** has the minimum value of glide energy −51.232 kcal mol^{-1}. Molecules **2**, **6** and **8** received the next best values of glide energies. Binding energies of molecules **1**–**8** were better than MNZ, while molecule **9** had the lowest magnitude of binding energy. The relative strength of compounds **2** and **4** were reversed compared to SP docking. Overall, the performance of Glide SP is better than Glide XP and extended funnel does not advance the results, as reported by other authors [37]. The cross-correlation between XP_Glide

Author's personal copy

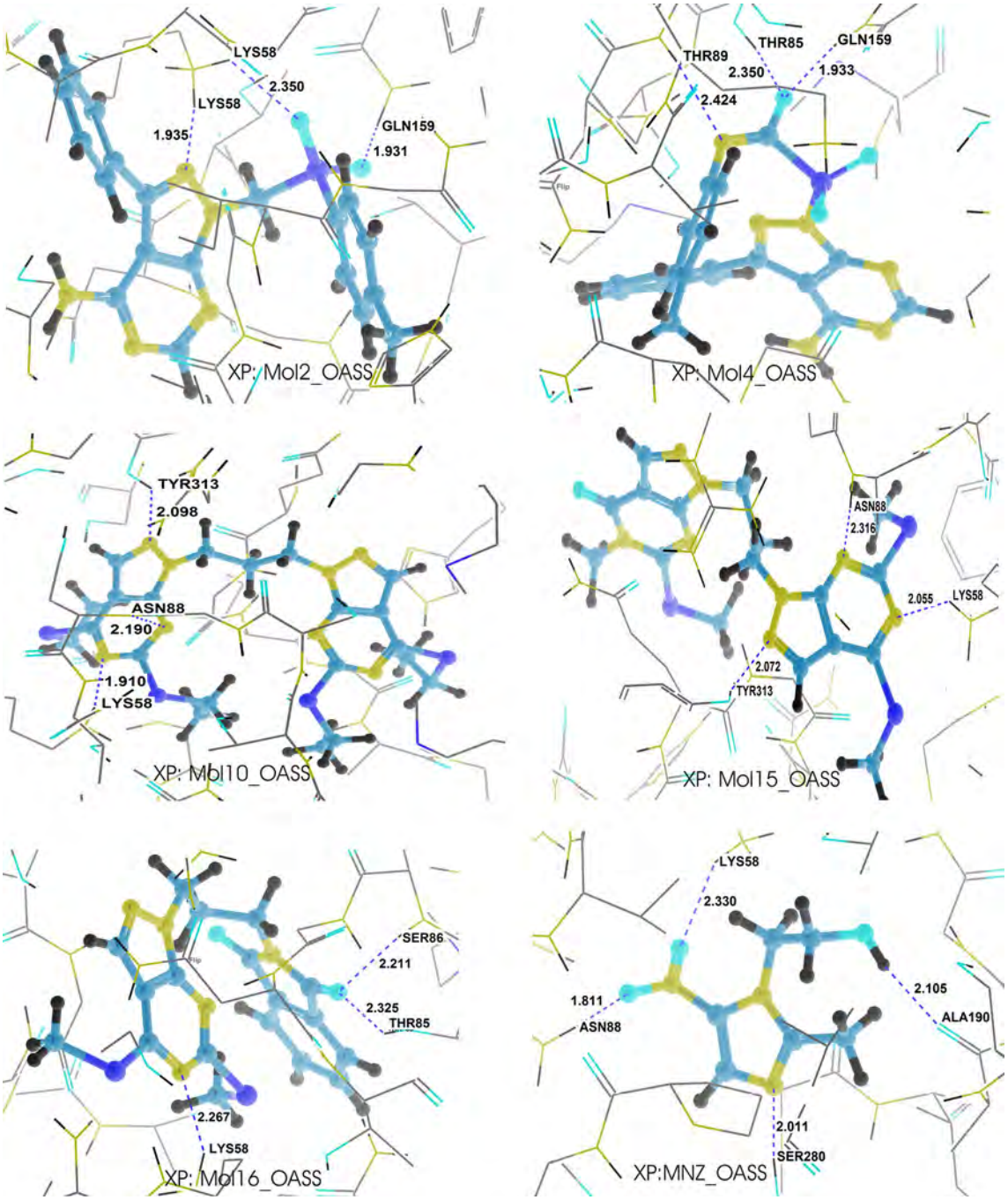

Fig. 4 Hydrogen bonding interactions in the best docking poses of molecules **2**, **4**, **10**, **15**, **16** and MNZ as obtained through Glide-XP docking

score and IC50 values was found to be relatively poor (R^2= 0.180).

The hydrogen bonding interactions as obtained through XP docking of pyrazolo[3,4-d]pyrimidine ligands containing no linkers with the target OASS were almost same as the reference molecule MNZ (Fig. 4 and Table S2b). Hydrogen bonding interactions with residue Lys58 were exhibited by molecules **1**, **2**, **5**, **8**, **9** and MNZ. Most of the ligands also exhibited interactions with residue Thr85. Non-covalent π–π stacking interactions with residue Phe160 were shown by molecule **6**, while molecule **8** revealed cation–π interactions with Lys58. Ligands **2** and **7** interact with different residues of the active site of the target each through five hydrogen bonding interactions, whereas each of the molecules **4**, **9** and MNZ exhibits four hydrogen bonding interactions. The residues Tyr313, Ile237, Pro307, Ala190, Val57, Met136, Phe160, Phe241, Ala239, Met112, Val191 in the active site of the protein form a hydrophobic packet. Polar interactions also exist between ligands and these residues. The residues that interact through polar interactions are Ser86, Ser308, Gln235, Ser280, Asn88,

Author's personal copy

Thr89, Gln159, Thr85, Gln159, Ser113, Thr193, Thr196, Ser56, His232 and Ser56.

XP docking of pyrazolo[3,4-d]pyrimidine molecules having trimethylene linker (molecules **10**–**18**) with target OASS shows that all these molecules in their best docked poses, except molecule **18**, have better glide scores than MNZ. In this respect, molecules **16** and **14** can be placed at the first and second place globally, i.e., they have the highest scores among all the ligands. Molecule **16** has a less aromatic phthallimide moiety whereas molecule **14** has a less aromatic pyrazolo[3,4-d]pyrimidine moiety and bulky benzyl substituent. Through SP docking, molecule **14** had a poorer glide score due to steric hindrance but showed better glide scores after inclusion of a hydrophobic enclosure. However, the glide score of molecule **15** was reduced in XP docking, and showed a better glide score through SP docking. The glide score of molecule **17**, obtained through replacement of the methylsulfanyl substituent at the 4th position of molecule **16** by a pyrollidin-1-yl moiety, was greatly reduced in the case of XP docking. Molecules **10**, **11**, **12** and **15** have comparatively better glide scores. However, molecules **13** and **18** had poorer scores than that of molecule **2**. Glide energies for molecules **10**, **11**, **13**, **14** and **15** were more negative than the highest negative value of glide energy of the ligands without linker. The glide energy value of molecule **16** was nearly the same as that of molecule **4**.

The hydrogen bonding and other non-covalent interactions of ligands with the residues of the active site, as obtained through XP docking, are presented in Table S2b. The hydrogen bonding interactions in the best docked poses of molecules **2**, **4**, **10**, **15**, **16** and MNZ are shown in Fig. 4. It can be seen that molecule **18** shows a cation–π interaction with Lys58 and molecule **17** exhibits an aromatic π–π interaction with residue His232. Hydrogen bonding interactions with backbone amino acids exist with residues Thr193, Gly236 and Ser86 bonded with molecules **15**, **16** and **17**, respectively. Side chain hydrogen bonding interactions in the conserved active site were displayed by all the molecules. Molecules **16** and **12** have four hydrogen bonds in each case, while molecule **18** have three hydrogen bonds. Hydrophobic and electrostatic interactions were similar to the case of molecules without linkers.

Autodock docking

The various energies and inhibitory coefficients (KI) as obtained through Autodock docking of the ligands with OASS (Table S3a) indicate the important role played by electronic interactions in ligand docking. The docking of molecules with no linker showed that molecule **2** has the best docking energy(−8.13 kcal mol^{-1}) and inhibition coefficient as obtained through Glide-SP and experimental observations. Molecules **7** and **4** have the next best energies, and show better results with Glide XP. Also, molecule **4** was found to have second best preference on the basis of experimental as well as Glide-SP calculations. Among the top five molecules, four (**2**, **4**, **7** and **6**) show agreement with Glide-SP results. Calculations further depict that the minimum inhibitory concentrations have the lowest docking energy. Intermolecular interaction energies also display parallel preferences. Docking simulations through Autodock on molecules with the trimethylene linker with OASS demonstrate that molecule **15** has the best docking energy followed by molecules **12** and **16**. Consequently, molecules **12**, **15** and **16** are common among the top three molecules as obtained through Glide SP. Also, as discussed, molecule **16** shows the best docking score through Glide-XP.

The noncovalent hydrogen bonding interactions in the best docking complexes are depicted in Table S3b and Figure S1. Intermolecular N–H···O and O–H···O type hydrogen bonding interactions, flanked by the ligands and residues of the active site, assist in stabilizing the complexes. Residues that are involved in N–H···O type hydrogen bonding interactions with ligands are Ser315, Glu311, Ala98, Glu34, Lys121, Arg312, Glu115, Arg10, Ser8, Arg116, Ser315, Asp317, Ser7, Thr111, Gly233, Gln235, Leu314, Ser113 etc. Also, in the best docking complexes, molecule **9** and MNZ exhibit O–H···O type hydrogen bonding interactions involving Tyr14 and Ser315 residues, respectively. Molecules **17** and **18** do not show any significant hydrogen bonding interactions.

ADME prediction

The ADME properties inspected using QIKPROP3.5 (Table S4) indicate that the molecules without linker (molecules **1**–**9**) do not exhibit any violation of Lipinski's rule of '5' while MNZ shows one violation. It has also been reported that molecules **10** and **14** have two violations and molecule **11** has one [13]. Molecules violating more than one or two of these rules may have problems with bioavailability. Molecules **1**–**9**, MNZ and molecule **10** of the linker-containing molecules have an octanol-water partition coefficient (LogP) greater than that of the range of 95 % of drugs while molecules **11**–**18** have LogP values within the range. Higher logP values are associated with poor absorption. ADME calculations and docking results suggest that pyrazolo[3,4-d]pyrimidine molecules may be good inhibitors of OASS, and molecules with trimethylene linker may have improved activity over molecules without linker.

Molecular dynamics simulation

On the basis of docking and ADME predictions, better docked complexes of the two molecules without linker (molecules **2** and **4**) and better docked complexes of the two molecules with trimethylene linkers (molecules **15** and **16**) along with the best

Author's personal copy

docked complex of MNZ, were subjected to MD simulation for 20.0 ns to ensure the stability of the ligands in the enzyme active site. In many cases, even the best docked structure flies away from the enzyme active site within a few picoseconds of MD simulations; consequently, a long MD run was carried out. The MD simulation was performed in water and neutralized with Na^+ counter ions to come close to the real situation. The average RMSDs of heavy atoms during MD simulation of each complex are plotted in Fig. 5. Small fluctuations and constant heavy atom RMSD is a good indication of system stability. The results indicate that the complexes OASS_Mol4, OASS_Mol15 and OASS_MNZ show small fluctuations in the beginning but transit quickly to nearly constant average RMSDs, with reasonably small oscillations centered around them. However, RMS deviations increase with simulation time in the case of OASS_Mol2 and OASS_Mol16 complexes, indicating that these complexes are not able to sustain stability in aqueous medium. The range of oscillation of each dynamic structure around the MD average is about ±0.30 Å. The OASS_Mol2 complex shows fluctuations at 3.6 ns with an RMSD of 5.6 Å; afterwards, it turned out to be centered around 2.5 Å at 5.0 ns. The RMSD of the complex OASS_Mol2 increased smoothly after 5.0 ns and approached a value of 5.6 Å at the end of 20.0 ns dynamics. The smoothed average RMSD of 3.6 Å was exhibited by OASS_Mol4 complex for dynamics over 3.0 ns. Although complex OASS_Mol15 showed smaller fluctuations in the beginning, with RMSDs 2.2 Å and 2.8 Å for 1.0 ns to 4.8 ns and 4.8 ns to 5.2 ns dynamics, respectively, a constant RMSD of 2.5 Å was seen for the rest of the dynamics. During the course of MD, increasing average RMSD behavior was displayed by OASS_Mol16 complex as it increased from 2.5 Å at 1.0 ns to 5.5 Å at 19.0 ns. After initially exhibiting small fluctuations, the heavy atom average RMSD of the complex with MNZ attained a constant value of 4.4 Å over 5.0 ns dynamics.

The average RMS fluctuations of individual residue positions from their mean positions indicate that residue Lys58 has very small fluctuations in almost all structures, indicating the possibility of non-covalent interactions. The RMS fluctuations of residues His79, Tyr168, Phe177 and Trp221 were smaller. It was also observed that the main contribution to the total energy in all cases comes from the electrostatic energy (receptor, complex and ligand), while the difference in van der Waals energy was more negative with respect to electrostatic energy. Strong van der Waals interactions also imply a reasonable geometry for binding with the receptor. High contributions of polar groups indicate that enzyme inhibition is supported mostly by hydrophilic interactions. The negative binding energy is a sign of the strong binding of the ligand with its receptor (Fig. S2). Small fluctuations in total energy specify that hydrogen bonding and other non-covalent interactions alternate among the residues of the active site, as no constraint was applied to the hydrogen bonding. It is noteworthy that the fluctuations in the total energy of the complexes falls within 10 kcal mol^{-1} for molecules **2**, **15**, **16** and MNZ and 50 kcal mol^{-1} for molecule **4**.

Protein–ligand interactions throughout the simulation exhibited four types of interaction: hydrogen bonds, hydrophobic, ionic and water bridges. Cation–π, aromatic π–π and other non-specific interactions fall into the category of

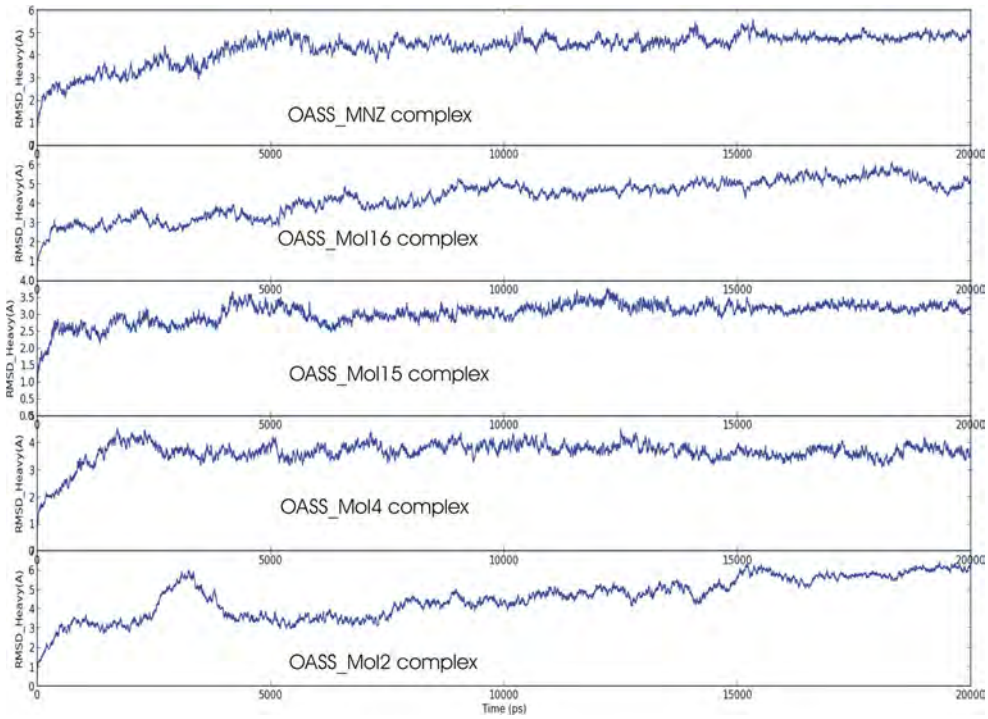

Fig. 5 **a**–**e** Average root mean square deviation (RMSD) of heavy atoms of the complexes during molecular dynamics (MD) simulation. **a** OASS_Mol2 complex, **b** OASS_Mol4 complex, **c** OASS_Mol15 complex, **d** OASS_Mol16 complex, **e** OASS_MNZ complex

Author's personal copy

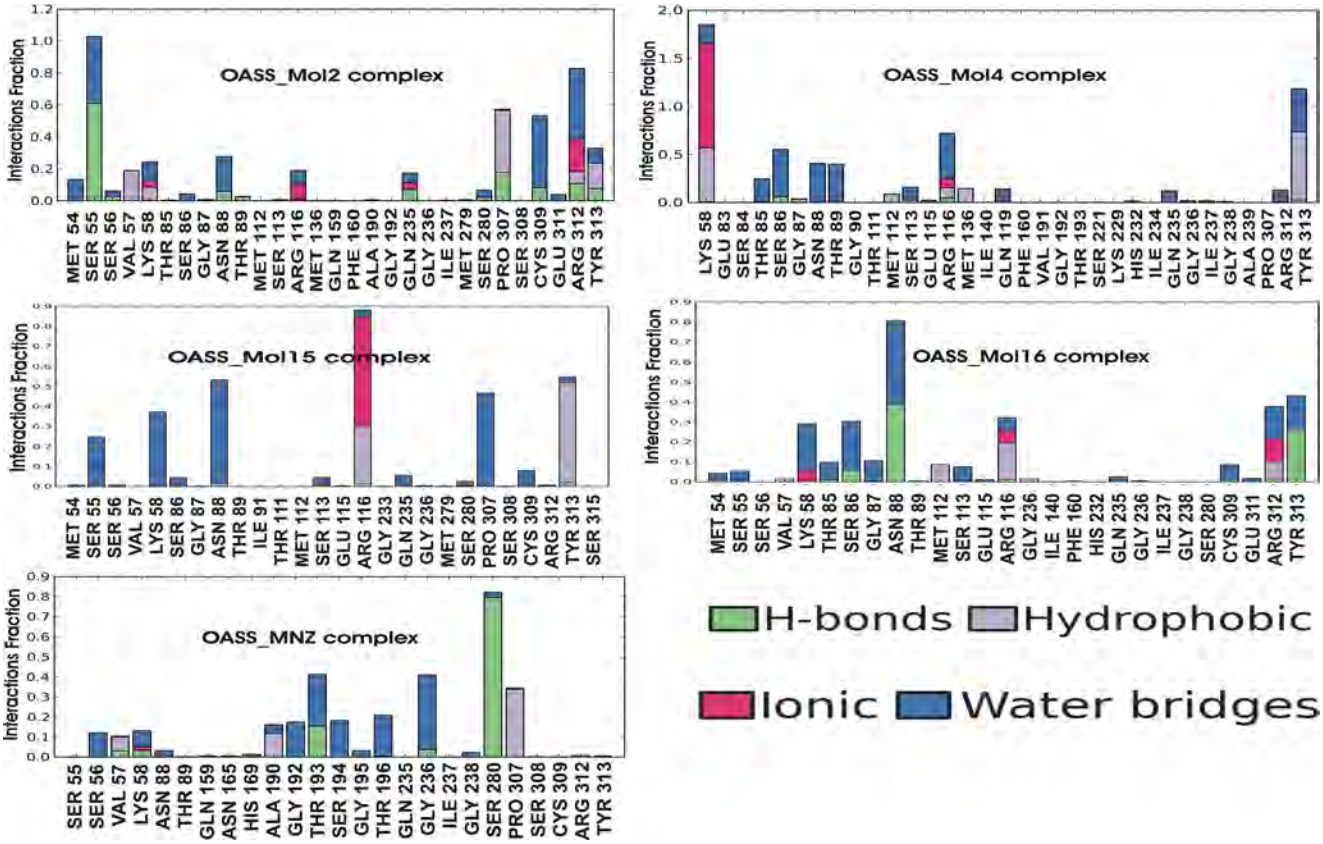

Fig. 6 Normalized stacked bar chart representation of interactions and contacts over the course of the MD trajectory. Values > 1.0 are possible as some residues make multiple contacts of the same subtype with ligands

hydrophobic interactions. These interactions were monitored throughout the MD (Fig. 6). It was observed, in the MD simulation of OASS_Mol2 complex, that H-bonding, hydrophobic, ionic and water bridge interactions of Arg312 with the ligand, were maintained at about 12 %, 8 %, 20 % and 40 %, respectively, of the simulation time, while hydrogen bonding and water bridge interactions of Ser55 were maintained about 60 and 40 %, respectively, of the simulation time. The interactions fraction diagram of the OASS_Mol4 complex revealed multiple ionic, hydrophobic and water bridge interactions of Lys58 with the ligand during 100 %, 55 % and 30 % of the simulation time. Ionic interactions were the major

Table 1 IC50 and relative binding free binding energy differences along with Glide SP, Glide XP and Autodock scores. *MM/GBSA* Molecular mechanics generalized Born surface area, *SP* standard precision, *XP* extra precision

Molecule	IC50 (μg/ml)	Relative Binding free energy difference (MM/GBSA) (kcal mol^{-1})	Best glide score (SP) (kcal mol^{-1})	Best Glide score (XP) (kcal mol^{-1})	Autodock score (kcal mol^{-1})
1	4.73	16.73	−5.722	−4.546	−5.85
2	0.57	−0.44	−6.305	−4.257	−8.13
3	2.52	2.87	−5.399	−3.590	−6.80
4	0.68	−4.84	−6.104	−5.190	−7.84
5	3.23	2.95	−5.399	−4.139	−6.98
6	2.37	1.75	−5.720	−3.620	−7.11
7	3.11	−1.51	−5.885	−4.573	−7.92
8	4.24	8.58	−5.363	−3.762	−7.67
9	5.15	8.97	−5.211	−3.868	−6.82
MNZ	1.80	0.00	−5.934	−3.824	−4.81
15	NA	−5.93	−7.404	−5.456	−7.16
16	NA	−22.66	−7.800	−7.811	−6.28

Author's personal copy

interactions in the OASS_Mol4 complex and were strong enough to be maintained throughout the dynamics. Strong electrostatic and hydrophobic interactions of the ligands with Arg116 remained prominent during the dynamics of the OASS_Mol15 complex for 52 % and 30 % of the simulation time, respectively. Other residues that maintained interactions over 50 % simulation time in OASS_Mol15 were Asn88 and Tyr313. On the other hand, Lys58 showed interactions during 40 % of the simulation time. Although molecule16_OASS and MNZ_OASS complexes made a major contribution to hydrogen bonding interactions, other interactions, also present within the binding site, were interchangeable in nature. A timeline representation of the interactions between residues of the active site and ligands revealed that the number of specific contacts varies between 1 and 9 in each complex over the course of the trajectory (Fig. S3). The alteration in the number of hydrogen bonds clearly demonstrates the flexibility of binding site residues. Lys58 forms more than four contacts in OASS_Mol4 and more than two contacts in the OASS_Mol16 complex. More than three contacts are exhibited by residues Arg116 and Ser280 in OASS_Mol15 and OASS_MNZ complexes, respectively, throughout the dynamics. In the OASS_Mol16 complex, Lys58 and Asn88 have more than three interactions up to 4.0 ns. Later interactions evolved with Arg312, Arg116 and Tyr313 with two or more interactions.

MM/GBSA binding free energy analysis

The MM/GBSA approach was undertaken in order to correlate relative binding free energies ($\Delta\Delta G_{binding}$) of the MD-optimized complexes with the corresponding IC50 values of compounds with the intention of predicting the relative activity of compounds with unknown activities. The MM/GBSA estimation of relative free energies on the representative structures was carried out with a partially flexible protein structure within 12 Å of the center of the ligand in the binding site. Table 1 depicts the relative binding free energies and glide scores, with corresponding IC50 values of the molecules. These calculations were performed on ten molecules (molecule **1** to **9** and MNZ) of known IC50 values to compare the results, and two molecules **15** and **16** to predict the relative binding affinity. The value of cross correlation coefficient R^2 (=0.702) between relative binding free energies and IC50 values was found to be excellent. Results also indicate that molecules **15** and **16** exhibit better relative binding free energies compared to other molecules, which is in good agreement with Glide scores.

Conclusions

Molecular docking studies of 18 pyrazolo[3,4d]pyrimidine analogues and MNZ were carried out with OASS enzyme, using Glide-SP, Glide-XP and Autodock docking protocols. Docking simulation and reported IC50 values of the ligands without linker indicate that molecules **2** and **4** may be better inhibitors than molecules **1**, **3**, **5**, **6**, **7**, **8** and **9**. The trimethylene linker pyrazolo[3,4-d]pyrimidine molecules had improved glide scores and binding energies over the molecules without linker. Docking simulation and ADME limitation demonstrate that linker-containing molecules **15** and **16** have better binding capabilities with the target than any other molecule under study. SP docking further indicates that the methyl substituents have enhanced glide scores, while bulky substitutions of the benzyl group reduces the score. It has also been observed that inclusion of a non-aromatic pyrollidin-1-yl moiety reduces the glide score significantly. On the basis of docking simulation, ADME calculation and reported IC50 values; molecules **2** and **4** without linkers, and trimethylene linker molecules **15** and **16** were screened as potential high affinity inhibitors. MD simulation of the best docked complexes of these molecules (molecules **2**, **4**, **15**, **16**, MNZ) demonstrated that the docking complexes of molecules **4**, **15** and MNZ remained stable during the course of dynamics. Timeline simulation interaction studies demonstrated several interactions (polar, hydrophobic and water bridges) of binding site residues with ligands that were maintained throughout the course of the trajectory. MM/GBSA estimation of relative binding free energies showed good agreement with experimental observations. These studies indicate that pyrazolo[3,4-d]pyrimidine analogues can act as lead molecules for the development of high affinity inhibitors of OASS enzyme—a promising target for inhibiting the growth of *E. histolytica* disease.

Acknowledgments U. Y. is thankful to DST, New Delhi, India for financial support through SERC Fast Track Young Scientist scheme(SR/FT/CS-78/2010) and UGC, New Delhi, India for the award of a Raman Fellowship for postdoctoral studies in the United States [F.No. 5-1/2013(IC)].

References

1. Lejeune M, Rybicka JM, Chadee K (2009) Recent discoveries in the pathogenesis and immense response towards *Entamoeba histolytica*. Future Microbiol 4:105–118
2. Salles JM, Moraes LA, Salles MC (2003) Hepatic amebiasis. Braz J Infect Dis 7:96–100
3. Takeuchi T, Weinbach EC, Gottlieb M, Diamond LS (1979) Mechanism of L-serine oxidation in *Entamoeba histolytica*. Comp Biochem Physiol B 62:281–285
4. Kumar S, Raj I, Nagpal I, Subbarao N, Gourinath S (2011) Structural and biochemical studies of serine acetyltransferase reveal why the parasite *Entamoeba histolytica* cannot form a cysteine synthase complex. J Biol Chem 286:12533–12541
5. Chinthalapudi K, Kumar M, Kumar S, Jain S, Alam N (2008) Crystal structure of native O-acetyl-serine sulfhydrylase from *Entamoeba histolytica* and its complex with cysteine: structural evidence for

Author's personal copy

cysteine binding and lack of interactions with serine acetyl transferase. Proteins 72:1222–1232
6. Bendesky A, Menendez D, Ostosky-Wegman P (2002) Is metonidazole carcinogenic? Mutat Res 511:134–144
7. Becker S, Hoffman P, Houpt ER (2011) Efficiency of antiamoebic drugs in a mouse model. Am J Trop Med Hyg 84:581–586
8. Nagpal I, Raj I, Subbarao N, Gourinath S (2012) Virtual screening, identification and in vitro testing of novel inhibitors of O-acetyl-L-serine sulfhydrylase of *Entamoeba histolytica*. PLoS ONE 7(2): e30305. doi:10.1371/journal.pone.0030305
9. Bekhit AA, Abdel-Azeim T (2004) Design, synthesis and biological evaluation of some pyrazole derivatives as anti-inflammatory-antimicrobial agents. Bioorg Med Chem 12:1935–1945
10. Yadava U, Singh M, Roychoudhury M (2013) Pyrazolo[3,4-d]pyrimidines as inhibitor of anti-coagulation and inflammation activities of phospholipase A2: insight from molecular docking studies. J Biol Phys 39:419–438
11. Elion GB, Callahan SW, Nathan H, Bieber S, Rundles RW, Hilching GH (1963) Pontetiation by inhibition of drug degradation:6-substituted purines and xanthine oxidase. Biochem Pharmacol 12:85–93
12. Schenone S, Brullo C, Musumeci F, Botta M (2010) Novel dual Src/Abl inhibitors for hematologic and solid malignancies. Expert Opin Investig Drugs 19:931–945
13. Indovina P, Giorgi F, Rizzo V, Khadang B, Schenone S, Marzo D, Forte IM, Tomei V, Mattioli E, Urso VD, Grilli B, Botta M, Giordano A, Pentimalli F (2012) New pyrazolo[3,4-d]pyrimidiine SRC inhibitors induce apoptosis in mesothelioma cell lines through p 27 nuclear nuclear stabilization. Oncogenes 31:929–938
14. Carlomagno F, Vitagliano D, Guida T, Basolo F, Castellone MD, Melillo RM, Fusco A, Santro M (2003) Efficient inhibition of RET/papillary thyroid carcinoma oncogenic kinases by 4-amino-5-(4-chloro-phenyl)-7-(t-Butyl)Pyrazolo[3,4-d]Pyrimidine (PP2). J Clin Endocrinol Metab 88:1897–1902
15. Hayat F, Salahudin A, Ummar S, Azam A (2010) Synthesis charasterization, antiamoebic activity and cytotoxicity of novel series of pyrazoline derivatives bearing quinoline tail. Eur J Med Chem 45: 4669–4675
16. Budakoti A, Abid M, Azam A (2007) Synthesis, characterization and in vitro antiamoebic activity of new Pd(II) complexes with 1-N-substituted thiocarbonyl1-3,5-dimethyl-2-pyrazoline derivatives. Eur J Med Chem 42:544–551
17. Parveen H, Hayat F, Mukhtar S, Salahudin A, Khan A, Islam F, Azam A (2011) Synthesis, characterization and biological evaluation of novel 2,4, 6 trisubstituted bis-pyrimidine derivatives. Eur J Med Chem 46:4669–4675
18. Siddiqui SM, Salahudin A, Azam A (2013) Pyrazolo[3,4-d]pyrimidine analogues: synthesis, characterization and their in-vitro antiamoebic activity. Med Chem Res 22:775–781
19. Yadava U, Singh M, Roychoudhury M (2011) Gas-phase conformational and intramolecular π-π interaction studies on some pyrazolo[3,4-d]pyrimidine derivatives. Comput Theo Chem 977:134–139
20. (2012) Glide: version 5.2 Schrödinger. LLC, New York
21. Friesner RA, Banks JL, Murphy RB, Halgren TA, Kliclic JJ, Mainz DT, Repasky MP, Knoll EH, Shelley M, Perry JK, Shaw DE, Francis P, Shenkin PS (2004) Glide: a new approach for rapid accurate docking and scoring, method and assessment of docking accuracy. J Med Chem 47:1739–1749
22. Frisch MJ, Trucks GW, Schlegel HB, Scuseria GE, Robb MA, Cheeseman JR, Montgomery JA, Vreven JT, Kudin KN, Burant JC, Millam JM, Iyengar SS, Tomasi J, Barone V, Mennucci B, Cossi M, Scalmani G, Rega N, Petersson GA, Nakatsuji H, Hada M, Ehara M, Toyota K, Fukuda R, Hasegawa J, Ishida M, Nakajima T, Honda Y, Kitao O, Nakai H, Klene M, Li X, Knox JE, Hratchian HP, Cross JB, Adamo C, Jaramillo J, Gomperts R, Stratmann RE, Yazyev O, Austin AJ, Cammi R, Pomelli C, Ochterski JW, Ayala PY, Morokuma K, Voth GA, Salvador P, Dannenberg JJ, Zakrzewski VG, Dapprich S, Daniels AD, Strain MC, Farkas O, Malick DK, Rabuck AD, Raghavachari K, Foresman JB, Ortiz JV, Cui Q, Baboul AG, Clifford S, Cioslowski J, Stefanov BB, Liu G, Liashenko A, Piskorz P, Komaromi I, Martin RL, Fox DJ, Keith T, Al-Laham MA, Peng CY, Nanayakkara A, Challacombe M, Gill PMW, Johnson B, Chen W, Wong MW, Gonzalez C, Pople JA (2003) GAUSSIAN 03, revision B.04. Gaussian, Inc, Pittsburgh
23. Jorgenson WL, Maxwell DS, Tirado-Rives J (1996) Development and testing of the OPLS all atom force field on conformational energetic and properties of organic liquids. J Am Chem Soc 118:11225–11236
24. (2012) Prime, version 3.1. Schrödinger, LLC, New York
25. Morris GM, Huey R, Lindstrom W, Sanner MF, Belew RK, Goodsell DS, Olson AJ (2009) Autodock 4 and Autodock Tools 4: automated docking with selective receptor flexibility. J Comput Chem 30:2785–2791
26. (2012) DESMOND molecular dynamics system, version 3.1. Shaw, New York
27. Bowers KJ, Chow E, Xu H, Dror RO, Eastwood MP, Gregersen BA, Klepeis JL, Kolossvary I, Moraes MA, Sacerdoti FD, Salmon JK, Shan Y and Shaw DE (2006) Scalable algorithms for molecular dynamics simulations on commodity clusters. Proc ACM/IEEE Conf Supercomp (SC06), Tampa, FL
28. Verlet L (1967) Computer "Experiments" on classical fluids I. Thermodynamical properties of Lennard–Jones molecules. Phys Rev 159:98–103
29. Swegat W, Schlitter JR, Kruger P, Wollmer A (2003) MD simulation of protein-ligand interaction: formation and dissociation of an insulin-phenol complex. Biophys J 84:1493–1506
30. Tripathi SK, Muttineni R, Singh SK (2013) Extra precision docking, free energy calculation and molecular dynamics simulation studies of CDK2 inhibitors. J Theor Biol 334:87–100
31. Kennedy T (1997) Managing the discovery/development interface. Drug Discov Today 2:436–444
32. DiMassi JA (1995) Success rates for new drugs entering clinical testing in the Unites States. Clin Pharmacol Ther 58:1–14
33. (2012) QikProp: version 3.5. Schrödinger, LLC, New York
34. Lipinski CA (2000) Drug-like properties and the causes of poor solubility and poor permeability. J Pharmacol Toxicol Methods 44:235–249
35. Lipinski CA, Lombardo F, Dominy BW, Feeney PJ (1997) Experimental and computational approaches to estimate solubility and permeability in drug discovery and development settings. Adv Drug Deliv Rev 23:3–25
36. Krishna C, Jain R, Kashav T, Wadhwa D, Alam N (2007) Crystallization and preliminary crystallographic analysis of cysteine synthase from *Entamoeba histolytica*. Acta Crystallogr F63:512–515
37. Kawatkar S, Wang H, Czerminski R, Joseph-McCarthy D (2009) Virtual fragment screening: an exploration of various docking and scoring protocols for fragments using glide. J Comput Aided Mol Des 23:527–539

Chemical Science

EDGE ARTICLE

View Article Online
View Journal | View Issue

CrossMark click for updates

Cite this: *Chem. Sci.*, 2015, **6**, 1516

Open Access Article. Published on 08 December 2014. Downloaded on 22/01/2015 17:11:53.
This article is licensed under a Creative Commons Attribution 3.0 Unported Licence.

A comprehensive test set of epoxidation rate constants for iron(IV)–oxo porphyrin cation radical complexes†

Mala A. Sainna,[a] Suresh Kumar,[b] Devesh Kumar,*[b] Simonetta Fornarini,*[c] Maria Elisa Crestoni*[c] and Sam P. de Visser*[a]

Cytochrome P450 enzymes are heme based monoxygenases that catalyse a range of oxygen atom transfer reactions with various substrates, including aliphatic and aromatic hydroxylation as well as epoxidation reactions. The active species is short-lived and difficult to trap and characterize experimentally, moreover, it reacts in a regioselective manner with substrates leading to aliphatic hydroxylation and epoxidation products, but the origin of this regioselectivity is poorly understood. We have synthesized a model complex and studied it with low-pressure Fourier transform-ion cyclotron resonance (FT-ICR) mass spectrometry (MS). A novel approach was devised using the reaction of $[Fe^{III}(TPFPP)]^+$ (TPFPP = *meso*-tetrakis(pentafluorophenyl) porphinato dianion) with iodosylbenzene as a terminal oxidant which leads to the production of ions corresponding to $[Fe^{IV}(O)(TPFPP^{+\bullet})]^+$. This species was isolated in the gas-phase and studied in its reactivity with a variety of olefins. Product patterns and rate constants under Ideal Gas conditions were determined by FT-ICR MS. All substrates react with $[Fe^{IV}(O)(TPFPP^{+\bullet})]^+$ by a more or less efficient oxygen atom transfer process. In addition, substrates with low ionization energies react by a charge-transfer channel, which enabled us to determine the electron affinity of $[Fe^{IV}(O)(TPFPP^{+\bullet})]^+$ for the first time. Interestingly, no hydrogen atom abstraction pathways are observed for the reaction of $[Fe^{IV}(O)(TPFPP^{+\bullet})]^+$ with prototypical olefins such as propene, cyclohexene and cyclohexadiene and also no kinetic isotope effect in the reaction rate is found, which suggests that the competition between epoxidation and hydroxylation – in the gas-phase – is in favour of substrate epoxidation. This notion further implies that P450 enzymes will need to adapt their substrate binding pocket, in order to enable favourable aliphatic hydroxylation over double bond epoxidation pathways. The MS studies yield a large test-set of experimental reaction rates of iron(IV)–oxo porphyrin cation radical complexes, so far unprecedented in the gas-phase, providing a benchmark for calibration studies using computational techniques. Preliminary computational results presented here confirm the observed trends excellently and rationalize the reactivities within the framework of thermochemical considerations and valence bond schemes.

Received 4th September 2014
Accepted 8th December 2014

DOI: 10.1039/c4sc02717e

www.rsc.org/chemicalscience

Introduction

The cytochromes P450 are part of the body's natural defence mechanism in the liver and perform vital functions for human health that include the biodegradation of xenobiotic and drug molecules.[1] Due to this broad chemical function the P450s can bind and activate a large range of substrates with varying shapes and sizes. Generally, the P450s act as monoxygenases, whereby they bind and utilize molecular oxygen *via* a heme centre and transfer one of the oxygen atoms of O_2 to a substrate, while the second oxygen atom leaves the process as a water molecule. The P450s react with substrates activating aliphatic and aromatic hydroxylation, epoxidation and sulfoxidation reactions, but have also been reported to catalyse desaturation and *N*-dealkylation reactions.[2] There are many different P450 isozymes and until early 2014 thousands of different structures had been characterized.[3] All P450s share common features which include a catalytically active heme group with a central iron atom that is linked to the protein by the thiolate sulphur atom of a cysteinate side chain.[4]

[a]*Manchester Institute of Biotechnology and School of Chemical Engineering and Analytical Science, The University of Manchester, 131 Princess Street, Manchester M1 7DN, UK. E-mail: sam.devisser@manchester.ac.uk*

[b]*Department of Applied Physics, School for Physical Sciences, Babasaheb Bhimrao Ambedkar University, Vidya Vihar, Rai Bareilly Road, Lucknow 226 025, India. E-mail: dkclcre@yahoo.com*

[c]*Dipartimento di Chimica e Tecnologie del Farmaco, Università di Roma "La Sapienza", P.le A. Moro 5, 00185, Roma, Italy. E-mail: mariaelisa.crestoni@uniroma1.it; simonetta.fornarini@uniroma1.it*

† Electronic supplementary information (ESI) available: Details of the computational results, including Tables with group spin densities, charges, absolute and relative energies as well as structures and Cartesian coordinates is provided. See DOI: 10.1039/c4sc02717e

This journal is © The Royal Society of Chemistry 2015

Open Access Article. Published on 08 December 2014. Downloaded on 22/01/2015 17:11:53.
This article is licensed under a Creative Commons Attribution 3.0 Unported Licence.

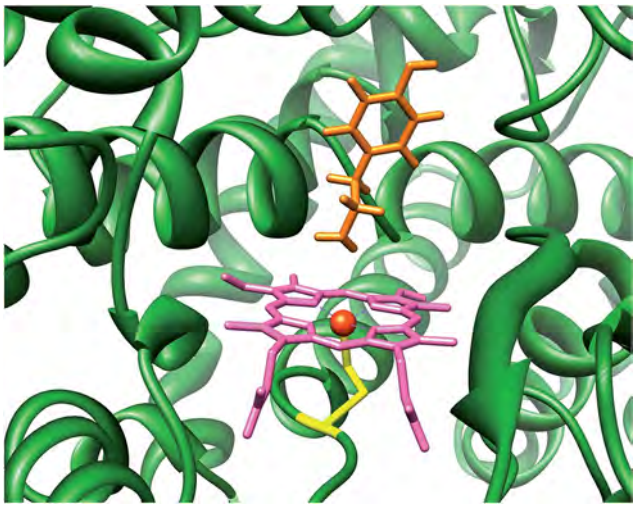

Fig. 1 Active site of P450 as taken from the 2WM4 pdb file. Substrate tyramine is highlighted in orange.

Fig. 1 displays the structure of a typical P450 active site, namely the one belonging to the CYP124 isozyme as taken from the 2WM4 protein databank (pdb) file.[5] As shown in Fig. 1 the substrate (tyramine) is located in a cleft nearby the heme, the substrate binding pocket, which is in a tight orientation with stabilizing hydrogen bonding interactions by several residues. The vacant sixth coordination site of iron is the position where molecular oxygen will bind during the catalytic cycle. The process includes two reduction and two protonation steps to synthesize the active species of P450 called Compound I (Cpd I).[6] Cpd I is highly reactive and therefore difficult to study experimentally, however, a few reports on its spectroscopic properties have appeared in the literature.[7]

Due to the short lifetime of Cpd I, studying catalytic mechanisms and reaction rates of P450 catalysed reactions is challenging;[8] therefore, many studies have focused on biomimetic iron–porphyrin complexes instead.[9] These studies gave detailed insight into the effect of axial and equatorial ligands,[10] but also on the local environment such as the substrate binding pocket. A particularly useful method to establish the properties and reactivity patterns of short-lived complexes, such as catalytic intermediates, is Fourier transform – ion cyclotron resonance (FT-ICR) mass spectrometry (MS).[11] In FT-ICR MS, the charged species of interest (either positive or negative ion) is trapped in a collision cell for a specific time during which reactions with neutral gases can occur and be studied at the prevailing low pressure of the instrument. FT-ICR MS allows one to measure the ion distributions and fragmentation patterns at varying trapping time, thereby yielding insight into reactivities, and enabling one to calculate rate constants and thermochemical properties. In recent work, Crestoni, Fornarini and co-workers have succeeded in trapping and characterizing the Cpd I analogues of iron and manganese porphyrin complexes and studied their reactivity with a selection of substrates.[12] Thus, the $[Mn^{V}(O)(TPFPP)]^{+}$ complex (TPFPP = *meso*-tetrakis (pentafluorophenyl)porphinato dianion) was found to react with model substrates through oxygen atom transfer (OAT), electron transfer (ET), hydride transfer and ligand addition. However, no direct hydrogen atom transfer (HAT) with any tested substrate took place.

In order to find out what drives the OAT reaction of Cpd I with olefins, we decided to investigate the properties and reactivities of $[Fe^{IV}(O)(Por^{+\bullet})]^{+}$ (Por = porphine dianion) and $[Fe^{IV}(O)(TPFPP^{+\bullet})]^{+}$ with FT-ICR MS and with density functional theory (DFT) methods. These studies represent the first comprehensive – experimental and computational – study on olefin epoxidation by iron(IV)–oxo porphyrin cation radical models and allow correlations to be established between the OAT rate constant and the ionization energy (IE) of the olefin. These correlations are further supported and rationalized by computational modelling.

Methods

Materials

All chemicals used in the experiments, including (5,10,15,20-tetrakis(pentafluorophenyl)porphinato)iron(III) chloride, $[Fe^{III}(TPFPP)]Cl$, were research grade products purchased from commercial sources and used as received. All the solvents were analytical grade. Ethylene, propylene, and *E*-2-butene were high purity gases from Matheson Gas Products Inc. Iodosylbenzene (C_6H_5IO) was prepared according to a published procedure and stored at −20 °C.[13]

Instrumental

All experiments were run on a Bruker BioApex Fourier transform-ion cyclotron resonance (FT-ICR) mass spectrometer equipped with an Apollo I electrospray ionization source, a 4.7 T superconducting magnet, and a cylindrical infinity cell. Analyte solutions were continuously infused through a 50 μm internal diameter fused-silica capillary at a flow rate of 120 μL h^{-1} by a syringe pump and ions were accumulated in a radiofrequency-only hexapole ion guide for 0.8 s. The ion population, desolvated by a heated (380 K) N_2 counter current drying gas, was pulsed into the ICR cell at room temperature (300 K), where the ion of interest was isolated by ion ejection procedures and allowed to react with the selected neutral reagent (L) admitted by a needle valve at stationary pressures in the range of 1.0–15 × 10^{-8} mbar. The pressure was measured with a cold-cathode sensor (IKR Pfeiffer Balzers S.p.A., Milan, Italy) calibrated by using the rate constant, $k_{methane} = 1.1 \times 10^{-9}$ cm^3 s^{-1}, for the reference reaction $CH_4^{+\bullet} + CH_4 \rightarrow CH_5^{+} + CH_3^{\bullet}$ and corrected for different response factors.[14]

Pseudo-first order rate constants were obtained from the slope of the semi-logarithmic decrease of the parent ion abundance as a function of time and divided by the substrate concentration to determine the second-order rate constants (k_{exp}) at 300 K. The reaction efficiencies (Φ) are percentages of the second-order rate constant with respect to the collision rate constant (k_{ADO}), *i.e.* $\Phi = k_{exp}/k_{ADO}$, calculated by the parametrized trajectory theory.[15] These values and product ion branching ratios were found to be independent of the pressure

Open Access Article. Published on 08 December 2014. Downloaded on 22/01/2015 17:11:53.
This article is licensed under a Creative Commons Attribution 3.0 Unported Licence.

of the neutral and of the additional presence of an inert bath gas, *i.e.* argon. The reproducibility of the k_{exp} values was within 10%, while the error of the absolute rate constants is estimated to be ±30%.

Sample preparation

The $[Fe^{IV}(O)(TPFPP^{+\bullet})]^+$ ion of interest was prepared by adding iodosylbenzene (0.5 mM) to $[Fe^{III}(TPFPP)]Cl$ (10 μM) in a CH_3OH/CH_2Cl_2 (1 : 1) solvent mixture cooled at −40 °C. The so-formed $[Fe^{IV}(O)(TPFPP^{+\bullet})]^+$ ion persisted at this temperature for about 1 h. The high-resolution electrospray ionization FT-ICR mass analysis shows the presence of ions $[Fe^{IV}(O)(TPFPP^{+\bullet})]^+$ as a prominent cluster centered at *m*/*z* 1044, along with the resting form $[Fe^{III}(TPFPP)]^+$, characterized by the same isotopic pattern, and centered at *m*/*z* 1028.

As already pointed out,[16] the synthetic method yields a portion of an isomeric species, likely oxidized on the porphyrin ligand and ineffective in any OAT reaction to reductants. This OAT-unreactive fraction of the overall ion population at *m*/*z* 1044 has been identified as a four-coordinate iron(III) complex incorporating an O-atom on the porphyrin ligand, henceforth denoted as $[Fe^{III}(TPFPP\text{-}O)]^+$.[16] Its relative amount has been evaluated exploiting the characteristic reaction with NO, displaying different paths from the two isomeric species. In fact, while $[Fe^{III}(TPFPP\text{-}O)]^+$ yields a ligand addition product, $[Fe^{III}(TPFPP\text{-}O)(NO)]^+$, the genuine iron(IV)–oxo complex $[Fe^{IV}(O)(TPFPP^{+\bullet})]^+$ undergoes an OAT process by releasing $[Fe^{III}(TPFPP)]^+$.

Computation

All calculations discussed here utilize density functional theory (DFT) methods as implemented in the Jaguar and Gaussian-09 program packages.[17] Two different models were investigated: (i) $[Fe^{IV}(O)(Por^{+\bullet})]^+$ (**A**) that includes a porphyrin (Por) ring with all side-chains abbreviated to hydrogen atoms, and (ii) $[Fe^{IV}(O)(TPFPP^{+\bullet})]^+$ (**B**), Scheme 1. Similar to previous work of ours in the field,[18] we use the unrestricted hybrid density functional method UB3LYP[19] as it was shown to reproduce the kinetics of metal(iv)–oxo oxidants well.[20] Initial exploratory calculations employed a modest LANL2DZ basis set on iron and 6-31G on the rest of the atoms (basis set BS1)[21] for geometry optimizations, analytical frequencies and geometry scans. These studies explored the potential energy surfaces involving reactants, intermediates and products on different spin states in detail and generated starting structures for the transition state optimizations. All local minima reported here had real frequencies only and the transition states were characterized by a single imaginary frequency for the correct mode. To improve the energetics of these structures we did single point calculations in the gas-phase with a triple-ζ quality basis set on iron (LACV3P+) and 6-311+G* on the rest of the atoms, basis set BS2. Subsequently, all geometries (local minima and transition states) were reoptimized at the UB3LYP/BS2 and UB3LYP-D3/BS2 levels of theory[19,22] and characterized by an analytical frequency analysis. Barrier heights reported in this work were calculated relative to isolated reactants, although using reactant complexes instead only minor changes are observed (ESI†).

The effect of solvent on the rate constants was tested through single point calculations using the self-consistent reactant field model as implemented in Gaussian with a dielectric constant representing chloroform ($\varepsilon = 4.7113$).

Ionization energies and bond dissociation energy (BDE_{OH}) values were calculated as before[23] and represent adiabatic values for reaction 1 and 2, respectively and report UB3LYP/BS2//UB3LYP/BS1 energies including ZPE and dispersion corrections.

$$A \rightarrow A^{+\bullet} + e^- + IE_A \quad (1)$$

$$[Fe^{IV}(OH)(Por)]^+ \rightarrow [Fe^{IV}(O)(Por^{+\bullet})]^+ + H^\bullet + BDE_{OH} \quad (2)$$

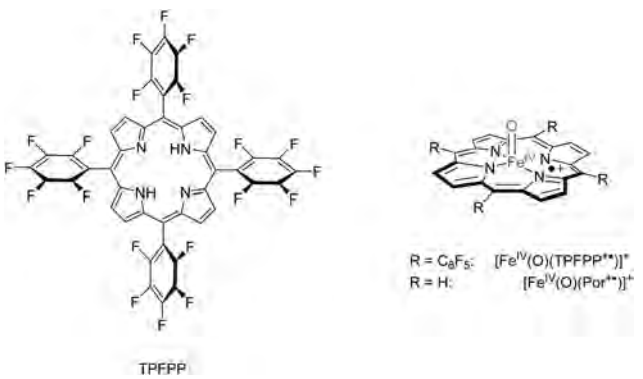

Scheme 1 Models investigated in this work.

Results

Gas phase reactivity with FT-ICR MS

Formation and characterization of naked $[Fe^{IV}(O)(TPFPP^{+\bullet})]^+$ ions. In an early survey, the preparation of a high-valent iron(IV)–oxo porphyrin cation radical was achieved by controlled oxidation of $[Fe^{III}(TPFPP)]Cl$ with H_2O_2 in a methanol solution. This solution was then sampled by electrospray ionization FT-ICR MS.[12a] However, under the selected experimental conditions, in addition to the heterolytic cleavage of the peroxide bond also a homolytic pathway is observed that yields a high-valent iron(IV)–hydroxo porphyrin complex $[Fe^{IV}(OH)(TPFPP)]^+$. Because the latter complex differs by one mass unit only from the species of interest, this presence complicates the ion distribution and the assignment of the oxidant in the reaction mixture. Therefore, we aimed to synthesize $[Fe^{IV}(O)(TPFPP^{+\bullet})]^+$ through an alternative, neater mechanism. A methanol/dichloromethane solution of $[Fe^{III}(TPFPP)]Cl$ was treated with iodosylbenzene (PhIO) as oxygen atom donor. The reaction mixture, assayed by electrospray ionization and high resolution mass measurements by FT-ICR mass spectrometry, displays an ion cluster centered at *m*/*z* 1044.0116, which corresponds to the acquisition of just one oxygen atom by the reactant species $[Fe^{III}(TPFPP)]^+$.

 This journal is © The Royal Society of Chemistry 2015

Open Access Article. Published on 08 December 2014. Downloaded on 22/01/2015 17:11:53.
This article is licensed under a Creative Commons Attribution 3.0 Unported Licence.

The thus generated, naked five-coordinate species proves to be resistant with respect to any unimolecular dissociation process ($k_{diss} \leq 0.001$ s^{-1}). However, when the ion-molecule reactivity of the ion cluster at *m*/*z* 1044 is examined through the addition of NO into the FT-ICR cell, two reaction products are observed: (i) a major fraction of ions reacts by OAT and forms $[Fe^{III}(TPFPP)]^+$ and NO_2 as the likely neutral product, (ii) a significant percentage of the starting ions undergo a ligand addition reaction to give a product with *m*/*z* 1074.

The product formed in the latter pathway has been sampled by collision induced dissociation (CID), and displays the loss of NO as unique fragmentation channel thus suggesting that NO has become part of the complex as intact ligand at a formerly vacant axial position. Note here that ligand addition is typical for the reactivity of tetracoordinate $[Fe^{III}(TPFPP)]^+$ ions.[12a] This finding provides circumstantial evidence for an ion population of the same elemental composition as $[Fe^{IV}(O)(TPFPP^{+\bullet})]^+$, that may correspond to an isomeric structure oxidized on the porphyrin ligand, designated as $[Fe^{III}(TPFPP\text{-}O)]^+$.

The chemical titration reaction with NO is a way to resolve the isomeric distribution of electrosprayed ions at *m*/*z* 1044 and allowed us to establish the relative amount of $[Fe^{IV}(O)(TPFPP^{+\bullet})]^+$ in each experiment, which is consistently found to be equal to or larger than 60% of the total ion population at *m*/*z* 1044.

Reactivity of naked $[Fe^{IV}(O)(TPFPP^{+\bullet})]^+$ ions with olefins. Our initial studies focused on experimentally determining the reactivity of $[Fe^{IV}(O)(TPFPP^{+\bullet})]^+$ with the selected olefins depicted in Scheme 2, and the results are summarized in Table 1. These olefins vary in molecular size and structure and their reported ionization energies span from 8.1 to 10.51 eV.[24] The $[Fe^{IV}(O)(TPFPP^{+\bullet})]^+$ ion was prepared from the reaction of iodosylbenzene with $[Fe^{III}(TPFPP)]Cl$ in methanol/dichloromethane solution and transferred by electrospray ionization into the mass spectrometer as described above. Subsequently, the $[Fe^{IV}(O)(TPFPP^{+\bullet})]^+$ ion was mass selected and trapped in the FT-ICR cell. The chosen olefin (Sub) was present at constant pressure in the cell and mass spectra were recorded at regular time intervals after isolation of the parent ion. Over time, all $[Fe^{IV}(O)(TPFPP^{+\bullet})]^+$ was found to react and new peaks corresponding to product ions appeared in the spectrum. Three different reaction paths were observed and monitored, namely oxygen atom transfer (OAT), hydride transfer (HT) and charge transfer (CT), as illustrated in Scheme 3.

These three pathways lead to different product ions in the recorded spectra: (i) $[Fe^{III}(TPFPP)]^+$ ions are the products of the OAT channel; (ii) ions at *m*/*z* corresponding to $[Sub\text{-}H]^+$ are obtained from the HT processes; (iii) ions corresponding to $Sub^{+\bullet}$ arise from a CT reaction. Interestingly, no evidence of hydrogen atom abstraction (HAT) is observed with any of the selected olefins listed in Table 1. In the case of two substrates, cyclohexene and 1,4-cyclohexadiene, molecular addition (Add) to the complex is also observed, leading to an ion with *m*/*z* value formally corresponding to $[Fe(O)(TPFPP)(Sub)]^+$. It is possible that these addition complexes are products from a hydrogen atom abstraction reaction but currently this cannot be established from the product ions. However, experiments with fully deuterated cyclohexene (cyclohexene-d_{10}) *versus* that of cyclohexene-h_{10} gave a rate constant ratio k_H/k_D very close to 1. Reactions starting with an initial hydrogen atom abstraction reaction normally encounter a large kinetic isotope effect (KIE = k_H/k_D) of well greater than 1, hence these KIE experiments implicate that no rate determining hydrogen atom abstraction takes place here.

Because the selected ions at *m*/*z* 1044 comprise isomeric species as described in the previous paragraph, it is important to mention that in all experiments with the selected substrates (olefins and unsaturated hydrocarbons) an unreactive fraction

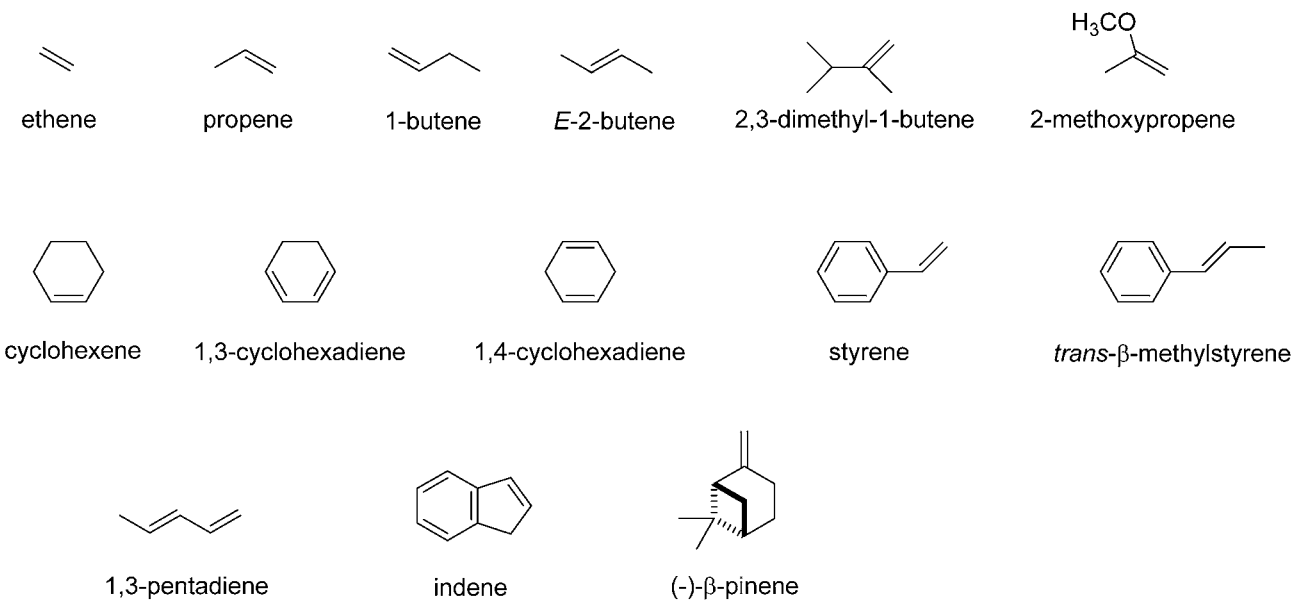

Scheme 2 Substrates investigated in this work.

Open Access Article. Published on 08 December 2014. Downloaded on 22/01/2015 17:11:53.
This article is licensed under a Creative Commons Attribution 3.0 Unported Licence.

Table 1 Kinetic data and product distributions obtained for the gas phase reaction of $[Fe^{IV}(O)(TPFPP^{+\bullet})]^+$ with selected olefins as determined by FT-ICR MS

Substrate	IE[a]	k_{exp}[b]	k_{ADO}[c]	Φ[d]	HT	CT	OAT	Add
Ethene	10.51	8.5×10^{-5}	8.5	1×10^{-3}	—	—	100	—
Propene	9.73	7.6×10^{-3}	9.45	0.080	—	—	100	—
1-Butene	9.55	0.029	9.6	0.30	—	—	100	—
E-2-Butene	9.10	0.080	10.8	0.74	—	—	100	—
2,3-Dimethyl-1-butene	9.07	0.145	9.5	1.5	—	—	100	—
Cyclohexene[e]	8.95	0.194–0.291	9.7	2–3	—	—	75	25
1,4-Cyclohexadiene	8.82	0.511	9.29	5.5	—	—	90	10
2-Methoxy-1-propene	8.64	0.819	10.5	7.8	—	—	100	—
1,3-Pentadiene	8.60	0.826	9.6	8.6	—	—	100	—
Styrene	8.46	1.40	9.26	15	—	—	100	—
1,3-Cyclohexadiene	8.25	1.58	9.29	17	—	—	100	—
trans-β-Methylstyrene	8.1–8.2	2.97	11.9	25	4	—	96	—
Indene	8.14	3.18	8.6	37	2	12	86	—
β-Pinene[f]	N/A	4.32–4.7	9.4	46–50	—	—	100	—

[a] Ionization energies (IE, eV) are from ref. 24. N/A stands for not available. [b] Second-order rate constants (k_{exp}) in units of 10^{-10} cm^3 molecule^{-1} s^{-1} are measured at a temperature of 300 K in the FT-ICR cell. The estimated error in k_{exp} is ±30%, although the internal consistency of the data is within ±10%. [c] Collision rate constants (k_{ADO}) evaluated with the parameterized trajectory theory. [d] Reaction efficiency (%), $\Phi = k_{exp}/k_{ADO} \times 100$. [e] The reaction with cyclohexene-d_{10} gave a rate constant within experimental error of that for cyclohexene-h_{10}. [f] The IE for α-pinene is 8.07 eV.

is observed in a corresponding relative amount as the species yielding the NO addition product in the probe reaction with nitric oxide. This species has been assigned the features of a porphyrin-oxidized complex and its contribution to the experiments has been thoroughly subtracted, an operation allowed by the distinctly different (un)reactivity of the two isomeric

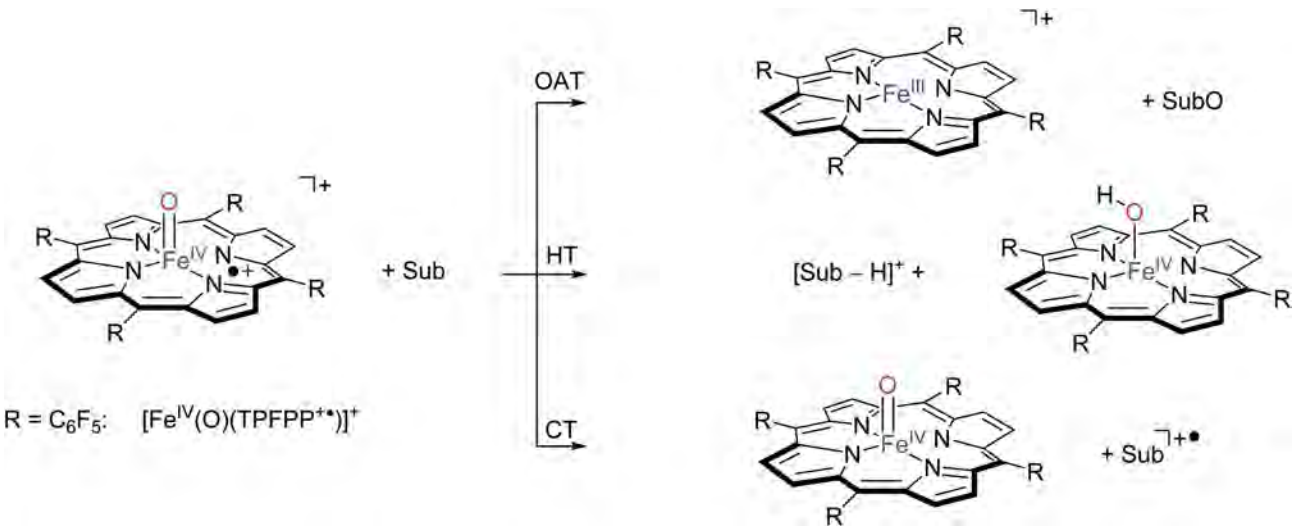

Scheme 3 Pathways observed for the reaction of $[Fe^{IV}(O)(TPFPP^{+\bullet})]^+$ ions (R = C_6F_5) with selected substrates (Sub) as studied with FT-ICR MS.

 This journal is © The Royal Society of Chemistry 2015

Open Access Article. Published on 08 December 2014. Downloaded on 22/01/2015 17:11:53.
This article is licensed under a Creative Commons Attribution 3.0 Unported Licence.

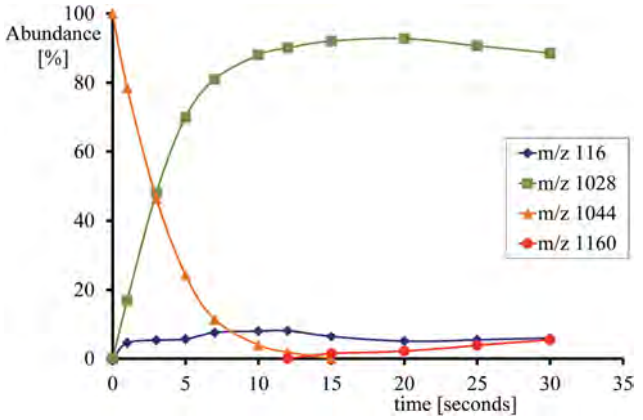

Fig. 2 Time dependence of relative ion abundancies for the reaction of $[Fe^{IV}(O)(TPFPP^{+\bullet})]^+$ (*m*/*z* 1044) with indene. Product ions are $[Fe^{III}(TPFPP)]^+$ (*m*/*z* 1028), $[Fe(TPFPP)(C_9H_8)O]^+$ (*m*/*z* 1160) and $C_9H_8^{+\bullet}$ (*m*/*z* 116). Experiments were performed in the presence of indene at 5.2×10^{-8} mbar in the FT-ICR cell.

complexes $[Fe^{IV}(O)(TPFPP^{+\bullet})]^+$ and $[Fe^{III}(TPFPP\text{-}O)]^+$. Henceforth, the implication of this species will not be further discussed.

Fig. 2 gives an example of the time dependence of the relative ion abundance of reactant and product ions as a function of time for the reaction of $[Fe^{IV}(O)(TPFPP^{+\bullet})]^+$ with indene. In general, the ion abundance of $[Fe^{IV}(O)(TPFPP^{+\bullet})]^+$ follows an exponential decay as a function of time, as illustrated by its reaction with indene in Fig. 2. The pseudo-first order decay of the reactant ion abundance as a function of time was then converted into a bimolecular rate constant, k_{exp}, which was normalized by the respective collision rate constant (k_{ADO}) to give the relative efficiency ($\Phi = k_{exp}/k_{ADO} \times 100$).[15] The gas phase reactivity of $[Fe^{IV}(O)(TPFPP^{+\bullet})]^+$ spans a wide range of reaction efficiencies, with values varying from 0.001% to 0.08% for terminal olefins, like ethene and propene, up to *ca.* 50% for electron-rich monoterpenes.

With most substrates a clean OAT conversion from reactants to products is observed without production of by-products and the time dependence shows a pattern like that displayed in Fig. 2. In the case of cyclohexene, about 25% addition occurs with the formation of an ion formally corresponding to $[Fe(TPFPP)(c\text{-}C_6H_{10})O]^+$. The formation of a long-lived complex with this substrate suggests that, within the metal coordination sphere, the olefin is activated to form an O-containing species endowed with appreciable affinity for the metal. Ligand binding to iron porphyrin complexes has been found to correlate with the gas phase basicity of the ligand.[25] It may thus be inferred that the olefin has turned into a more basic species, either an epoxide by O-addition across the double bond or an alcohol by allylic C–H bond activation. The nature of the adduct complex has been further probed and confirmed by low-energy CID, and reveals the formation of the reduced species $[Fe^{III}(TPFPP)]^+$ through the release of SubO. The so-formed complex from the reaction of $[Fe^{IV}(O)(TPFPP^{+\bullet})]^+$ with the olefin substrate may then be depicted as $[Fe^{III}(TPFPP)(SubO)]^+$. Similar product complexes have been observed previously from other substrates through oxygen atom-acceptor properties such as sulphides, amines, and phosphorus containing complexes.[12a,16]

In addition, substrates with low ionization potential are found to react *via* hydride transfer (*trans*-β-methylstyrene, and indene) and/or charge transfer reactions (indene) as side-reactions. We examined whether a charge-transfer (CT) reaction occurs between $[Fe^{IV}(O)(TPFPP^{+\bullet})]^+$ and sampled substrates. As in FT-ICR MS only exothermic reactions are able to occur due to the low number of collisions in the gas, the data in Table 1 show that the charge-transfer reaction is exothermic with indene as a substrate (eqn (3)), but endothermic with other substrates. Thus, the enthalpy change for the charge-transfer between $[Fe^{IV}(O)(TPFPP^{+\bullet})]^+$ and indene should be equal to the difference between the ionization energy of the substrate and the electron affinity (EA) of $[Fe^{IV}(O)(TPFPP^{+\bullet})]^+$. Since, no charge-transfer reaction occurs with substrates with an ionization energy above 8.2 eV (Table 1), this implies that the EA of gaseous $[Fe^{IV}(O)(TPFPP^{+\bullet})]^+$ ions must be lower than 8.2 eV. Previous FT-ICR MS studies predicted a lower limit of 7.5 eV for the EA of $[Fe^{IV}(O)(TPFPP^{+\bullet})]^+$,[16] which is in good general agreement with the data in Table 1. DFT calculations on $[Fe^{IV}(O)(Por^{+\bullet})X]$ with different axial ligands X have yielded electron affinities of 3.06 eV for $X = SH^-$, whereas values of 6.41 and 6.12 eV are found for systems with an imidazole or tyrosinate axial ligand, respectively.[26] Clearly, removal of the axial ligand is expected to raise the EA of the iron(IV)–oxo porphyrin cation radical substantially with respect to axially ligated systems due to the loss of interaction between the a_{2u} molecular orbital with axial ligand orbitals, *vide infra*.

$$[Fe^{IV}(O)(TPFPP^{+\bullet})]^+ + \text{indene} \rightarrow [Fe^{IV}(O)(TPFPP)] + \text{indene}^{+\bullet} \quad (3)$$

$$\Delta H_{Eq3} = IE_{indene} - EA_{[Fe^{IV}(O)(TPFPP^{+})]} < 0 \text{ kcal mol}^{-1} \quad (4)$$

Interestingly, although cytochrome P450 isozymes react with typical olefins, such as propene, cyclohexene and *Z*- and *E*-butene, to give a mixture of epoxide and enol products, actually the precise product distributions depend on the specific P450 isozyme.[27] Clearly, the substrate binding pocket and substrate orientation within the enzyme play a key role in determining the regioselectivity of the enzymatic reaction. In fact, enzymes manage to control the regioselectivity of substrate activation probably by binding the substrate under a specific orientation, which raises the epoxidation barriers and/or lowers the hydrogen atom abstraction barriers. Unfortunately, the FT-ICR MS results are unable to unequivocally distinguish hydroxylation products from epoxidation products as both have the same mass and are released as neutral molecules. As such, the experiments do not provide direct evidence supporting olefin epoxidation over a C–H activation channel in the reactions of $[Fe^{IV}(O)(TPFPP^{+\bullet})]^+$ with the selected olefins. However, we are able to show indirect evidence, *vide infra*. Computational studies on the regioselectivity of propene epoxidation *versus* hydroxylation by $[Fe^{IV}(O)(Por^{+\bullet})(SH)]$ gave lower epoxidation barriers in the gas-phase reaction,[28] but solvent and

Open Access Article. Published on 08 December 2014. Downloaded on 22/01/2015 17:11:53.
This article is licensed under a Creative Commons Attribution 3.0 Unported Licence.

environmental effects reversed the ordering. The computational studies from ref. 28, therefore, confirm the experimental trends in Table 1. This finding underlines the benchmark role played by a mechanistic study in the gas phase.

Theoretically derived reaction paths, energetics and structures. The experimental studies reported above present a comprehensive test set of model reactions of iron(IV)–oxo porphyrin cation radical complexes with olefins for the first time and enable extensive benchmarking and calibration of computational methods and procedures against gas-phase (Ideal Gas conditions) rate constants. We decided to take the opportunity and calibrate previously used methods and procedures for DFT studies on these chemical systems and compare to the results of the FT-ICR rates from Table 1. In addition, the computational studies were performed to further understand the substrate activation patterns by $[Fe^{IV}(O)(TPFPP^{+\bullet})]^{+}$ with olefins, and rationalize the obtained trends. Before we discuss details of the reaction mechanism and possible reactivity trends, let us start with a detailed analysis of the reactant species, namely $[Fe^{IV}(O)(Por^{+\bullet})]^{+}$, ^{4,2}**A**, and $[Fe^{IV}(O)(TPFPP^{+\bullet})]^{+}$, ^{4,2}**B**.

Fig. 3 displays the high-lying occupied and low-lying virtual orbitals of ^{4,2}**A**; the orbitals for ^{4,2}**B** look very similar. These orbitals are dominated by the interactions of the metal 3d orbitals with its ligands and several π-type porphyrin orbitals. Lowest in energy are a pair of σ-type orbitals (σ_{z2} and σ_{xy}): σ_{z2} represents the σ-interactions of the $3d_{z2}$ orbital on iron with the $2p_z$ orbital on oxygen, whereas the σ_{xy} gives the interactions of the $3d_{xy}$ orbital on iron with $2p_{x,y}$ orbitals on the four nitrogen atoms of the porphyrin ligand. The antibonding combinations of these two orbitals (σ^*_{z2} and σ^*_{xy}) are high in energy and virtual. Also doubly occupied is the δ_{x2-y2} orbital, which is a lone-pair orbital located in the plane of the porphyrin ring. Finally, the interaction of the metal $3d_{xz}/3d_{yz}$ with the $2p_x/2p_y$ on the oxygen atom leads to a pair of π_{xz}/π_{yz} and a pair of π^*_{xz}/π^*_{yz} set of orbitals. The σ_{z2}, σ_{xy}, π_{xz} and π_{yz} bonding orbitals are doubly occupied and low-lying in all calculations reported here. In addition to the metal-type orbitals there are also two porphyrin-type π-orbitals that in D_{4h} symmetry have the labels a_{1u} and a_{2u}. With a thiolate as axial ligand the a_{2u} orbital strongly mixes with a $3p_z$ orbital on sulphur and hence is destabilized in energy,[29] which strongly affects the electron affinity of the oxidant and consequently is responsible for its push-effect.[30]

The set of orbitals displayed in Fig. 3 is occupied with 15 electrons and as several of these orbitals are close in energy there are a number of possibilities to distribute the electrons

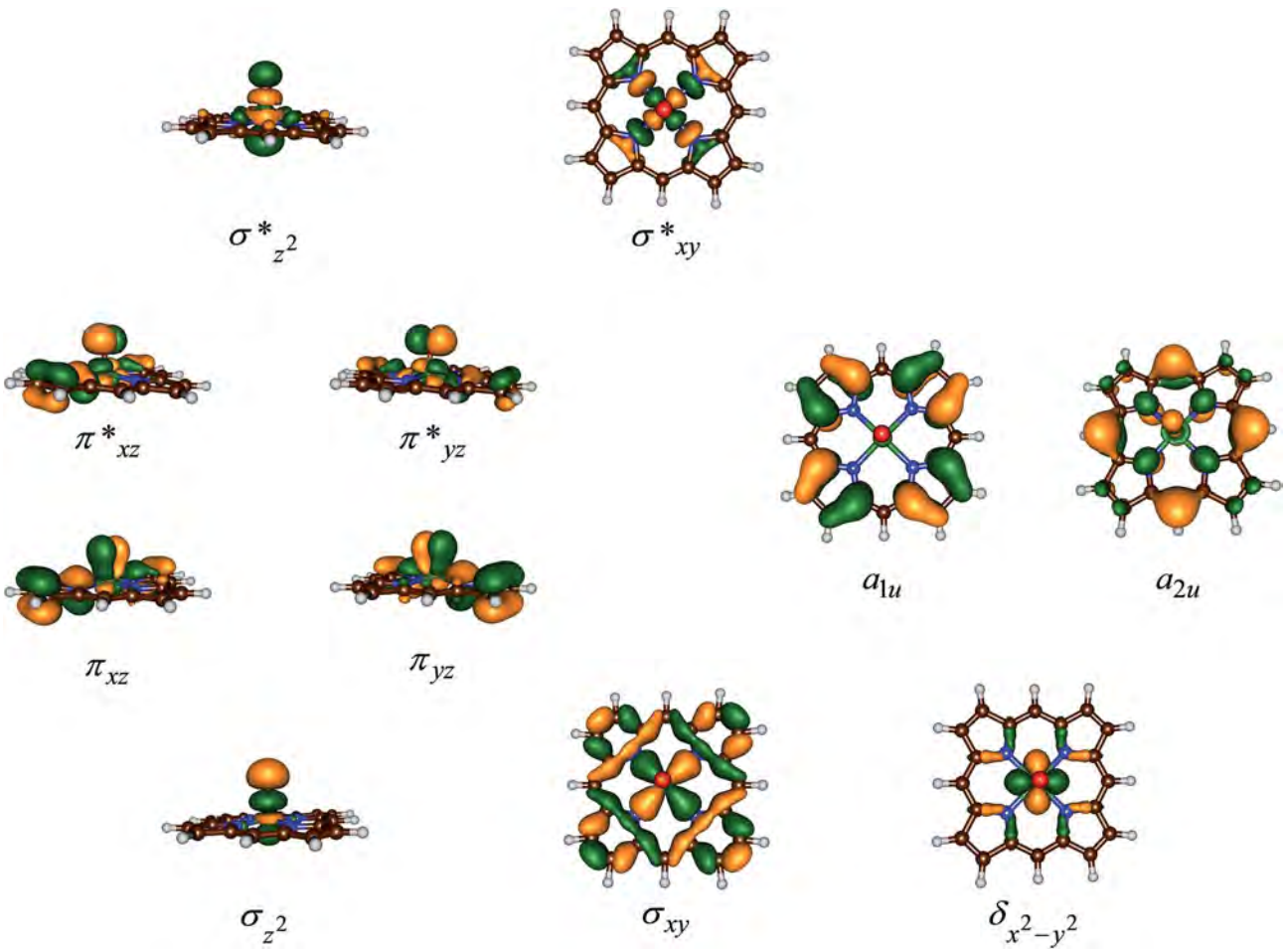

Fig. 3 Molecular valence orbitals of ^{4}A.

This journal is © The Royal Society of Chemistry 2015

Open Access Article. Published on 08 December 2014. Downloaded on 22/01/2015 17:11:53.
This article is licensed under a Creative Commons Attribution 3.0 Unported Licence.

over the orbitals. In addition, states can also be found in various spin states ranging from doublet to quartet and sextet, where we identify the spin state with a superscript in front of the electronic state label. Thus, the electronic state labelled as $^4A_{2u}$ has an overall quartet spin state and singly occupied a_{2u} molecular orbital with overall electronic configuration: $\sigma_{z2}^2\ \sigma_{xy}^2\ \pi_{xz}^2\ \pi_{yz}^2\ \delta_{x2-y2}^2\ \pi_{xz}^{*1}\ \pi_{yz}^{*1}\ a_{1u}^2\ a_{2u}^1$ or in short [core] $\delta_{x2-y2}^2\ \pi_{xz}^{*1}\ \pi_{yz}^{*1}\ a_{1u}^2\ a_{2u}^1$. Similarly, we calculated the doublet spin state ($^2A_{2u}$ state), where the unpaired electron in the a_{2u} orbital is antiferromagnetically coupled to the unpaired electrons in the two π* orbitals: $^2A_{2u}$ = [core] $\delta_{x2-y2}^2\ \pi_{xz}^{*\uparrow}\ \pi_{yz}^{*\uparrow}\ a_{1u}^2\ a_{2u}^{\downarrow}$.

Previous studies with either imidazole, acetonitrile or thiolate as axial ligand,[29,31] showed the $^{4,2}A_{2u}$ states to be close in energy and well below alternative states. However, this was due to considerable mixing of the a_{2u} orbital with the axial ligand orbitals, which obviously is not possible in our chemical system that lacks an axial ligand. However, in an isolated porphyrin macrocycle, the a_{1u} and a_{2u} orbitals are degenerate;[32] therefore, we decided to investigate a range of possible electronic states for the pentacoordinated iron(IV)–oxo porphyrin cation radical system, $[Fe^{IV}(O)(Por^{+\bullet})]^+$. Firstly, we tested the stability of the $^{4,2}A_{2u}$ states and the alternative $^{4,2}A_{1u}$ states with [core] $\delta_{x2-y2}^2\ \pi_{xz}^{*1}\ \pi_{yz}^{*1}\ a_{1u}^1\ a_{2u}^2$ orbital occupation. In addition, we attempted to generate models with the iron in oxidation state iron(V), *i.e.* $^2\Pi_{xz}$ state with occupation [core] $\delta_{x2-y2}^2\ \pi_{xz}^{*1}\ a_{1u}^2\ a_{2u}^2$, or the iron in oxidation state iron(III), *i.e.* the ^4A state with orbital occupation [core] $\delta_{x2-y2}^2\ \pi_{xz}^{*2}\ \pi_{yz}^{*1}\ a_{1u}^1\ a_{2u}^1$ and the $^6\Sigma_{xy,III}$ state with [core] $\delta_{x2-y2}^2\ \pi_{xz}^{*1}\ \pi_{yz}^{*1}\ \sigma_{xy}^{*1}\ a_{1u}^1\ a_{2u}^1$ occupation. However, all our attempts to calculate iron(III) or iron(V) states failed and converged back to lower lying solutions with four electrons on the metal in a formal iron(IV) oxidation state, hence the $^2\Pi_{xz}$, ^4A and $^6\Sigma_{xy,III}$ states are high in energy and inaccessible to our chemical system.

Table 2 summarizes relative energies of optimized geometries of the various electronic spin states as calculated with different DFT methods for ^{2,4,6}**A**. As follows from Table 2 all calculations of **A** give a $^2A_{1u}$ ground state that is nearly degenerate with the corresponding quartet spin state. In general, calculations done at UB3LYP/BS2 and UB3LYP-D3/BS2 give almost identical spin state orderings and relative energies, which shows that dispersion is not a critical component for these chemical structures. Nevertheless, the $^{4,2}A_{2u}$ and $^{4,2}A_{1u}$ states are close in energy and all four states could have a finite lifetime.

Optimized geometries of the $^{4,2}A_{2u}$ and $^{4,2}A_{1u}$ states are given in Fig. 4. Geometrically, no dramatic changes in bond lengths are obtained between the three optimization techniques. A small basis set gives slightly longer Fe–O distances than those found with a triple-ζ basis set. The effect of dispersion is negligible on the optimized geometries: UB3LYP/BS2 and UB3LYP-D3/BS2 give virtually the same chemical structures. Addition of *meso*-substituents to the porphyrin ring such as pentafluorophenyl groups is not expected to dramatically change key bond lengths in the optimized geometries and relative energies of individual spin states.[33] Thus, recent work of the Goldberg group showed that *meso*-substituted manganese–oxo porphyrinoid complexes retained the spin state ordering and converged to a closed-shell singlet manganese(V)–oxo state in all cases.[33a]

The calculations on the low-lying $^{4,2}A_{2u}$ and $^{4,2}A_{1u}$ states reported in Table 2 and Fig. 4 show that geometrically there are very little differences between these states, but the spin state ordering and relative energies are sensitive to the method and basis set. Recent complete active site (CASSCF) and restricted active site (RASSCF) calculations of Pierloot and co-workers[34] calculated the $^{4,2}A_{2u}$ and $^{4,2}A_{1u}$ states of **A** within 1 kcal mol^{-1} of each other with a small preference for the A_{1u} states. However, they also located two low-lying iron(V) states, which we were unable to characterize and for which no experimental evidence exist. Unfortunately, our chemical systems (in particular structure **B**) are too large to attempt calculations using the CASSCF and RASSCF methods; therefore, we decided to continue with UB3LYP instead.

Subsequently, we investigated the substrate epoxidation by $[Fe^{IV}(O)(Por^{+\bullet})]^+$, *i.e.* ^{4}**A**. We find the lowest lying barriers to proceed from the $^4A_{2u}$ state and will focus on those in the following. Previous studies on the epoxidation of olefins by $[Fe^{IV}(O)(Por^{+\bullet})(L)]$ with L = $NCCH_3$ or Cl^- showed that the same trends in reactivity are observed when the Por ligand is replaced by TPFPP,[35] hence the smaller model was used in this study. We investigated substrate epoxidation with a range of olefins:

Table 2 Relative energies of several low-lying electronic states of $[Fe(O)(Por^{+\bullet})]^+$ (**A**)[a]

		A[b]	**A**[c]	**A**[d]
State	Configuration	Δ*E* + ZPE	Δ*E* + ZPE	Δ*E* + ZPE
$^2A_{1u}$	$\delta^2\ \pi_{xz}^{*\uparrow}\ \pi_{yz}^{*\uparrow}\ a_{1u}^{\downarrow}$	0.00	0.00	0.00
$^4A_{1u}$	$\delta^2\ \pi_{xz}^{*\uparrow}\ \pi_{yz}^{*\uparrow}\ a_{1u}^{\uparrow}$	0.71	0.19	0.21
$^2A_{2u}$	$\delta^2\ \pi_{xz}^{*\uparrow}\ \pi_{yz}^{*\uparrow}\ a_{2u}^{\downarrow}$	1.65	3.75	3.80
$^4A_{2u}$	$\delta^2\ \pi_{xz}^{*\uparrow}\ \pi_{yz}^{*\uparrow}\ a_{2u}^{\uparrow}$	1.25	3.42	3.47
$^6A_{2u}$	$\delta^{\uparrow}\ \pi_{xz}^{*\uparrow}\ \pi_{yz}^{*\uparrow}\ \sigma_{xy}^{*\uparrow}\ a_{2u}^{\uparrow}$	9.25	18.68	19.38
$^4\Delta_{xy}$	$\delta^{\uparrow}\ \pi_{xz}^{*\uparrow}\ \pi_{yz}^{*\uparrow}\ \sigma_{xy}^{*\uparrow}\ a_{1u}^{\downarrow}$	9.69	ND	ND
$^4\Delta_{zz}$	$\delta^{\uparrow}\ \pi_{xz}^{*\uparrow}\ \pi_{yz}^{*\uparrow}\ \sigma_{z2}^{*\uparrow}\ a_{2u}^{\downarrow}$	19.53	ND	ND

[a] Relative energies in kcal mol^{-1} with respect to the $^2A_{1u}$ state, ND stands for not determined. [b] Energies obtained at UB3LYP/BS2//UB3LYP/BS1 level of theory. [c] Energies and geometries calculated at UB3LYP/BS2 level of theory. [d] Energies and geometries calculated at UB3LYP-D3/BS2 level of theory.

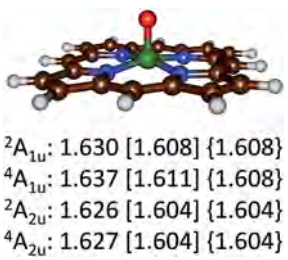

Fig. 4 Optimized geometries of the $^{4,2}A_{2u}$ and $^{4,2}A_{1u}$ states of ^{4,2}**A** as calculated with UB3LYP/BS1 [UB3LYP/BS2] {UB3LYP-D3/BS2} with Fe–O bond lengths in angstroms.

Open Access Article. Published on 08 December 2014. Downloaded on 22/01/2015 17:11:53.
This article is licensed under a Creative Commons Attribution 3.0 Unported Licence.

ethene (**1**), propene (**2**), 1-butene (**3**), *E*-2-butene (**4**), cyclohexene (**5**), 1,3-cyclohexadiene (**6**), styrene (**7**), *trans*-β-methylstyrene (**8**), *Z*-2-butene (**9**) and 2-pinene (**10**). For all substrates we calculated the full potential energy profile from reactants to epoxide products, see ESI,† but for space restrictions we will focus on the rate determining C–O bond formation transition states ($\mathbf{TS}_{CO}$) only. All reactions are concerted with a single C–O activation barrier leading to epoxide product complexes $\mathbf{P}_E$. This is unusual as previous calculations on substrate epoxidation by Cpd I models gave a stepwise mechanism *via* a radical intermediate that *via* a ring-closure barrier was separated from epoxide product complexes.[36] The orientation of the substrate and the strong displacement of the metal from the porphyrin plane are the likely reason for the fact that radical intermediates are saddlepoints here. Thus, the ring-closure barrier on the quartet spin state surface involves an electron transfer from substrate into σ^*_{z2}. The latter orbital in iron–porphyrin complexes with axial ligand, *e.g.* thiolate, contains a strong contribution from axial ligand orbitals ($3p_z$) and therefore is high in energy. Since our particular system lacks an axial ligand, the σ^*_{z2} orbital is considerably lower in energy and as a consequence the lifetime of the radical intermediate is reduced and the reaction to form products is now concerted.

Fig. 5 gives the optimized geometries of the C–O activation transition states ($\mathbf{TS}_{CO}$) for all substrates. Generally, the transition states occur early with a long C–O distance and relatively short Fe–O distance that has not dramatically changed from what it was in the iron(IV)–oxo porphyrin cation radical state. As expected the metal is considerably displaced from the plane through the four nitrogen atoms of the porphyrin ring by as much as 0.268–0.299 Å. These transition states bear resemblance to substrate epoxidation barriers calculated previously for P450 Cpd I reactions with olefins.[36] Electronically, all transition states are accomplished by single electron transfer from the substrate into the a_{2u} orbital and the formation of an $[Fe^{IV}(OSub)(TPFPP)]^+$ transition state with orbital occupation [core] $\delta_{x2-y2}^2\ \pi^{*1}_{xz}\ \pi^{*1}_{yz}\ a_{1u}^2\ a_{2u}^2\ \phi_{Sub}^1$ with ϕ_{Sub} a radical on the substrate group.

Discussion

The present work gives a detailed and extensive overview on the reactivity of iron(IV)–oxo porphyrin cation radical systems with a test-set of olefins. We determined rate constants and measured product ion distributions in the gas phase using FT-ICR MS. This comprehensive set of transition metal containing reactivities is unique and will enable computation to benchmark and calibrate its methods effectively. This is particularly important for transition metal complexes, such as iron(IV)-oxo species, where the reproducibility of the computational (DFT) methods sometimes varies strongly depending on the density functional method used, the basis set, environmental perturbations, dispersion effects *etc.*[37] In this work, we supplemented the experimental studies with a series of preliminary DFT calculations for two reasons: (i) to validate and calibrate computational methods against experiment; (ii) to establish the physicochemical properties that influence the rate constant of the chemical reaction.

Let us first start with a comparison of the experimental and computational reaction rates. As FT-ICR MS experiments are being performed at very low pressures, these experimental conditions are close to Ideal Gas conditions with very few

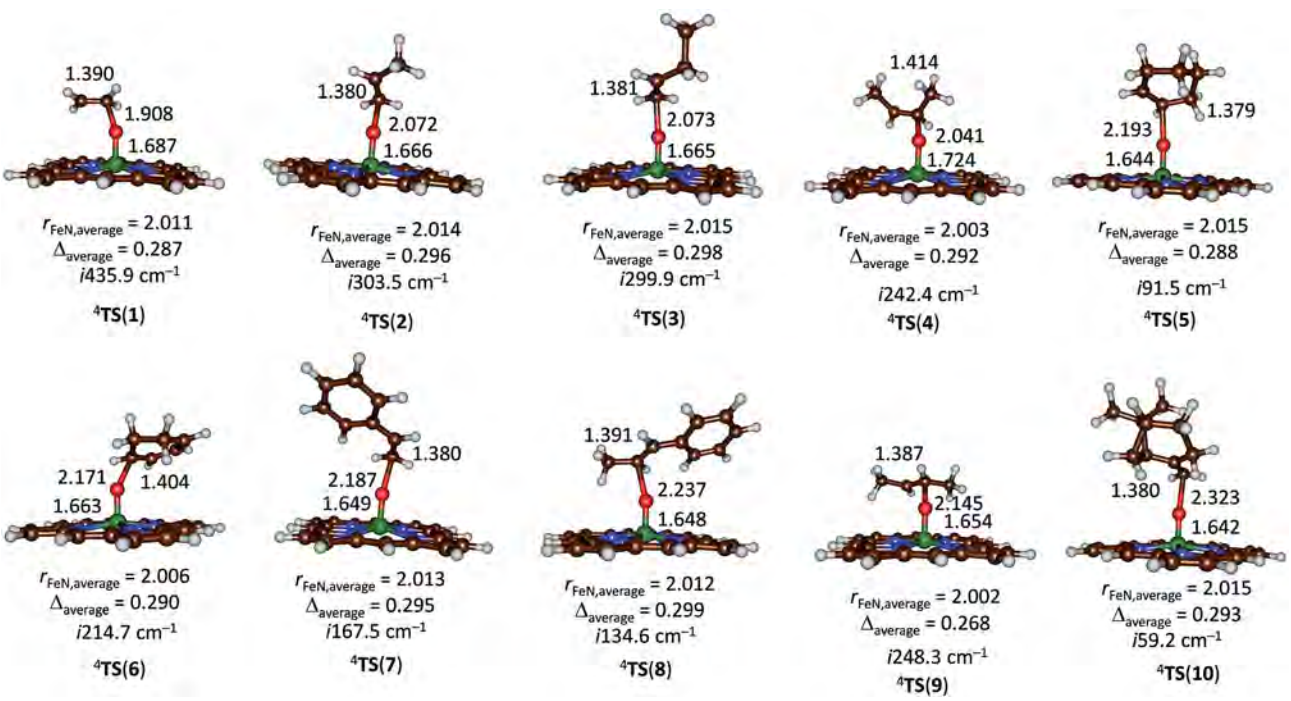

Fig. 5 UB3LYP/BS1 optimized geometries of epoxidation transition states with bond lengths in angstroms.

 This journal is © The Royal Society of Chemistry 2015

Open Access Article. Published on 08 December 2014. Downloaded on 22/01/2015 17:11:53.
This article is licensed under a Creative Commons Attribution 3.0 Unported Licence.

molecular collisions per second. In the kinetic study of ion-molecule reactions in the gas phase one needs to consider that thermal equilibration of the reacting system with the environment is in general not granted. On the contrary, when small species react at low pressures, the absence of thermalizing collisions leads to non-equilibrium energy distributions. In the absence of solvation, the double-well potential model first proposed by Brauman in 1977 to account for the kinetic behaviour of displacement reactions by anionic nucleophiles predicts that the energy of the intermediate and transition state must lie below the energy of the combined reactants.[38] Because at low pressure the intermediates cannot be stabilized by unreactive collisions, determining the transition state energy is less straightforward than in solution. However, the kinetics results presently reported deal with a relatively large reactant ion that effectively establishes thermal equilibrium with the environment through coupling with the background radiation field allowed by the several low frequency infrared modes of the iron(IV)–oxo macrocyclic ligand complex. This condition is responsible, for example, for the consistency between the kinetics of NO ligand addition to iron(II/III) porphyrin complexes and the equilibrium data independently established through equilibrium measurements.[25] Because of these considerations, the notion can be adopted that the presently investigated systems are in prevailing thermal equilibrium with the environment and reaction kinetics can be interpreted within the framework of transition state theory. Consequently, reaction rates represent bimolecular reactions and as such they should compare to computationally determined reaction rates well.

The experimental rate constants (Table 1) were converted into free energy units *via* $-RT \ln k_{exp}$, with R the gas constant and T the temperature, using transition state theory and plotted against the calculated enthalpy of activation for the same substrates, see Fig. 6. Although only a limited computational study is reported here, when we calculate the deviation between experiment and theory for each data point, we find an average difference between experiment and theory of 1.5 kcal mol^{-1} with a standard deviation of 3.4 kcal mol^{-1}. As such, the DFT methods used here reproduce the trends obtained from experimental enthalpies of activation well and the linearity and reproducibility of the calculations is well within the typical error reported for DFT calculations using this method of about 5 kcal mol^{-1}.[39] There is, however, a large systematic error as well as a relatively large standard deviation that require further studies. Note that the experimental data in Fig. 6 refers to free energies of activation, whereas the computational results are enthalpy changes instead. The systematic error between experiment and theory contains entropic corrections to the energy.

Subsequently, we investigated the origin of the rate constant, and in particular, the physical and chemical properties of the substrate and oxidant that determine the reaction mechanism and the enthalpy of activation of an epoxidation reaction. Previous studies on heteroatom oxidation and double bond epoxidation by P450 enzymes implicated a correlation between the natural logarithm of the rate constant with the ionization energy of the substrate.[12d,e,28,40] To find out whether the data in Table 1 follow these trends as well, we plot $RT \ln k_{exp}$ *versus* experimentally known ionization energies,[24] in Fig. 7. The set of data shown in Table 1 and Fig. 7 gives a linear correlation between the natural logarithm of the rate constant and the ionization energy of the substrate with an $R^2 = 0.96$. Fig. 7b displays the correlation between the DFT calculated enthalpy of

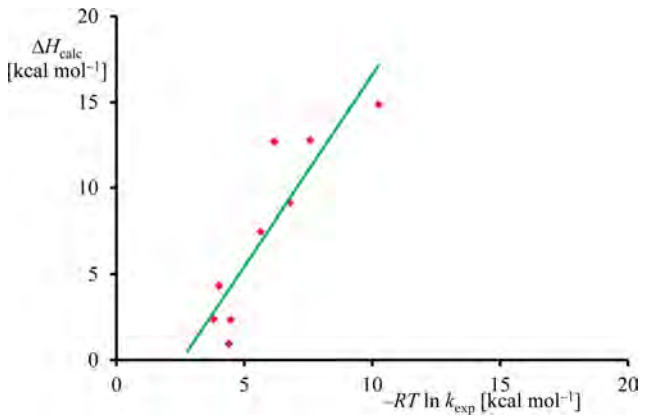

Fig. 6 Correlation between experimental and computational barrier heights.

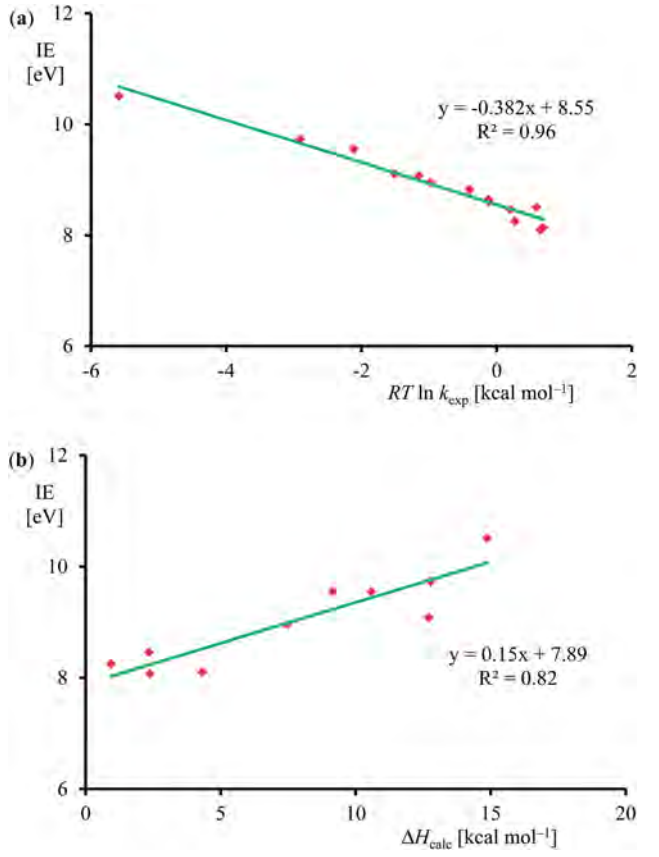

Fig. 7 (a) Correlation between experimentally determined $RT \ln k_{exp}$ (for raw data, see Table 1) *versus* known ionization energies (IE). (b) Correlation between calculated epoxidation activation enthalpy (in kcal mol^{-1}) and experimental ionization energy for the substrates in Fig. 5.

Open Access Article. Published on 08 December 2014. Downloaded on 22/01/2015 17:11:53.
This article is licensed under a Creative Commons Attribution 3.0 Unported Licence.

activation of the reaction of $[Fe^{IV}(O)(Por^{+\bullet})]^+$ with olefins. In agreement with the experimental trends given in part (a) of Fig. 7 also the computational trends link the natural logarithm of the rate constant to the ionization energy of the substrate. Clearly, the key physicochemical property that drives the reaction mechanism and affects the rate constant of substrate epoxidation by iron(IV)–oxo porphyrin cation radical complexes is the ionization energy of the substrate.

In order to explain the experimental and computational trends in the reaction mechanisms, we devised a valence bond (VB) curve crossing diagram, which is schematically depicted in Fig. 8. This diagram starts bottom left with the reactant configuration of $[Fe^{IV}(O)(TPFPP^{+\bullet})]^+$ in electronic configuration $\pi_{xz}^2\,\pi_{yz}^2\,\delta_{x2-y2}^2\,\pi_{xz}^{*1}\,\pi_{yz}^{*1}\,a_{2u}^1$. The π and π* electrons along the FeO bond are identified with dots in the VB diagram and due to occupation of $\pi_{xz}^2\,\pi_{xz}^{*1}$ there are three dots on the left-hand-side of the Fe–O bond. In addition, there are three electrons in the π_{yz} and π_{yz}^* orbitals, which are identified with the other three dots on the right-hand-side of the Fe–O bond. Furthermore, the oxidant has a radical on the porphyrin ring for single occupation of the a_{2u} molecular orbital. The substrate double bond is also highlighted with four electrons spread out over the interaction. Upon approach of the substrate on the iron(IV)–oxo species a radical intermediate is formed that has a single bond between the oxygen and carbon atoms and a doubly occupied a_{2u} orbital.

In VB theory the electronic configuration in the reactant complex (Ψ_R) connects to an excited state in the product geometry (Ψ_P^*) as shown with the blue line in Fig. 8. At the same time the product electronic configuration (Ψ_P) connects to an excited state in the reactant geometry (Ψ_R^*), black line in Fig. 8. These two VB curves cross and lead to an avoided crossing and a transition state for the C–O bond formation with barrier $\Delta E^{\ddagger}$. The barrier height is linearly proportional to the curve crossing energy, which in its own right is a fraction of the excitation energy (G_H) from the reactant wave function to the product wave function in the geometry of the reactants, *i.e.* for $\Psi_R \rightarrow \Psi_R^*$. The difference in VB structures for Ψ_R and Ψ_R^* thereby should give a reflection of the key electron transfer/migrations upon product formation. Moreover, based on the excitation energy, the factors that determine the barrier height can be predicted.

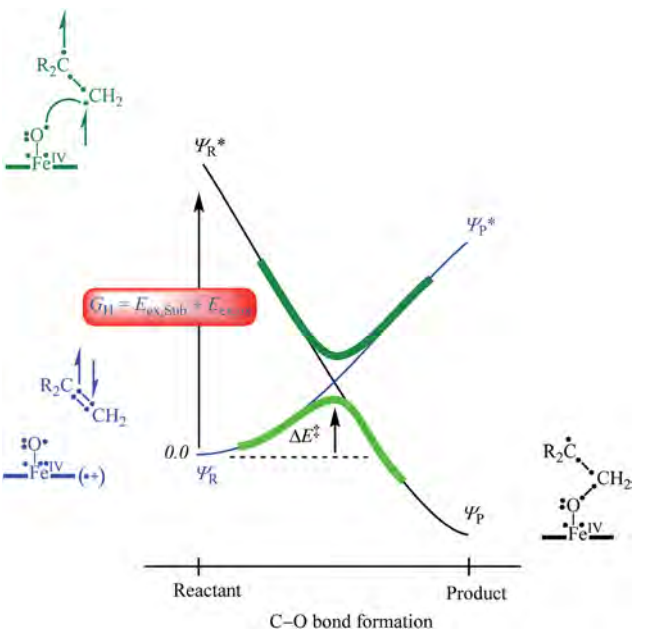

Fig. 8 VB curve crossing diagram for the C–O bond formation step in olefin epoxidation ($R_2C{=}CH_2$) by $[Fe^{IV}(O)(TPFPP^{+\bullet})]^+$. Valence electrons are identified with a dot and lines (curved and straight) in the VB structures represent bonds.

An analysis of the differences between the reactant and product wave functions in the reactant geometry reveals the following information: First of all, a comparison of the VB structures of Ψ_R and Ψ_R^* shows that the electrons in the π-bond of the olefin are singlet paired in the ground state and triplet coupled in the excited state, hence the excitation energy G_H includes the π–π* electron excitation in the substrate, $E_{ex,Sub}$. Generally, the first ionization potential of an olefin corresponds to the removal of an electron from a π-orbital, and, hence, is proportional to the π–π* excitation energy. Indeed, our experimentally and computationally determined barrier heights correlate linearly with the ionization energy of the olefin, and therefore support the VB model.

One of the electrons originating from the π-bond of the olefin forms a bond with the π_{xz}^* electron along the FeO bond, to create the C–O bonding pair of electrons. This means that the π_{xz}/π_{xz}^* pair of orbitals during the reaction splits back into individual atomic orbitals namely $3d_{xz}$(Fe) and $2p_x$(O). The $2p_x$(O) electron pairs with the electron from the substrate, while one of the electrons of the $3d_{xz}$(Fe) orbital is transferred into the a_{2u} orbital through internal excitation/rehybridization of the oxidant, $E_{ex,ox}$. The promotion gap, G_H, therefore, will be proportional to the π–π* excitation in the substrate and the $3d_{xz}$ to a_{2u} electron transfer in the oxidant: $G_H = E_{ex,Sub} + E_{ex,ox}$. Obviously, since the ionization energy represents the energy to remove an electron from a π-type orbital of an olefin, this will imply a linear correlation between the first excited state and the ionization energy of the substrate.[28] The VB diagram, therefore, confirms a linear correlation between the ionization energy of the substrate and the C–O bond formation enthalpy of activation as shown above.

Although, the oxygen atom transfer reaction between $[Fe^{IV}(O)(TPFPP^{+\bullet})]^+$ and an olefin could lead to either epoxide or hydroxylated products, unfortunately the FT-ICR MS experiments cannot distinguish the two. Thus, several substrates in Scheme 2 and Table 1 contain aliphatic groups that in a reaction with an iron(IV)–oxo group can be converted into an alcohol. A correlation between the rate constant of oxygen atom transfer and the ionization energy, Fig. 7a, of the olefin provides indirect experimental evidence that all reactions lead to epoxidation products. In fact, hydrogen atom abstraction reactions should not correlate with the ionization potential of the substrate, but were shown to be proportional to the strength of the C–H bond of the substrate that is formed.[12e,40] To test that the rate constants do not correlate with the bond dissociation energy (BDE_{CH}) of the C–H bond of the substrate that is broken, we plot

 This journal is © The Royal Society of Chemistry 2015

Open Access Article. Published on 08 December 2014. Downloaded on 22/01/2015 17:11:53.
This article is licensed under a Creative Commons Attribution 3.0 Unported Licence.

in Fig. 9 calculated BDE_{CH} and barrier heights of selected olefins, namely propene, *Z*-2-butene, *E*-2-butene, cyclohexene and 1,3-cyclohexadiene. As can be seen from Fig. 9, no correlation between BDE_{CH} and barrier height exists, and, therefore, hydrogen atom abstraction is not the rate determining step in the reaction mechanism. Further evidence that hydrogen atom abstraction reactions can be ruled out here comes from kinetic isotope effect (KIE) studies. We measured the rate constant of oxygen atom transfer with cyclohexene and cyclohexene-d_{10} and determined a KIE $= k_H/k_D \sim 1$ (Table 1). Consequently, the oxygen atom transfer is unlikely to proceed with an initial hydrogen atom abstraction and double bond epoxidation will be the dominant pathway.

The experimental trends, therefore, provide the first indirect experimental evidence that in the gas-phase the regioselectivity of double bond epoxidation *versus* aliphatic hydroxylation will be in favour of the epoxidation pathway. This implies that in enzymatic systems, such as the cytochromes P450, the shape and size of the substrate binding pocket will influence the regioselectivity of hydroxylation over epoxidation and can change the natural preference away from epoxidation.

Finally, the calculations presented in this work obviously refer to gas-phase results and hence correlate well with gas-phase mass spectrometric data. In order to further establish that the work can be extrapolated to solution phase, we did a series of single point calculations using the polarized continuum model with a dielectric constant of $\varepsilon = 4.7$ to mimic a solution. The obtained correlation between solvent corrected free energies of activation of epoxidation reactions by $[Fe^{IV}(O)(Por^{+\bullet})]^+$ is plotted against the solvent corrected ionization energy of all substrates in Fig. S1, ESI.† Even in solvent, the linear trend in the correlation between free energy of activation and ionization energy is retained, therefore, we expect to be able to extrapolate our results to the solution phase as well.

Conclusions

In this work we report a comprehensive combined mass spectrometric and computational study on substrate epoxidation by iron(IV)–oxo porphyrin cation radical complexes in the gas phase. We present a novel method to synthesize $[Fe^{IV}(O)(TPFPP^{+\bullet})]^+$ in the gas phase at low pressure. Furthermore, we report a large set of experimentally derived rate constants and product distributions. All olefins undergo oxygen atom transfer, whereas compounds with low ionization energy also give a certain degree of hydride transfer and charge transfer reactions. Our experimentally determined reaction rates correlate linearly with the ionization potential of the substrate and show that the electron transfer from substrate to oxidant is rate determining. A thorough computational survey has confirmed the suggested mechanism and provides a rationale for the observed trend in the rate constants. Moreover, the work highlights a regioselective epoxidation over hydroxylation in the gas phase.

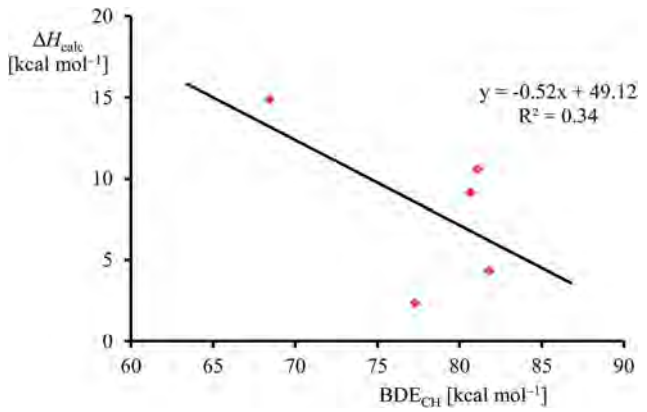

Fig. 9 Correlation between calculated epoxidation activation enthalpy (in kcal mol^{-1}) and BDE_{CH} for the substrates.

Acknowledgements

MAS thanks the Petroleum Technology Development Fund for a studentship. The National Service of Computational Chemistry Software (NSCCS) is thanked for providing valuable cpu time to SdV. DK acknowledges the Department of Science and Technology (New Delhi) for a Ramanujan Fellowship. MEC and SF thank the Università degli Studi di Roma La Sapienza for support.

Notes and references

1 (*a*) M. Sono, M. P. Roach, E. D. Coulter and J. H. Dawson, *Chem. Rev.*, 1996, **96**, 2841; (*b*) J. T. Groves, *Proc. Natl. Acad. Sci. U. S. A.*, 2003, **100**, 3569; (*c*) *Cytochrome P450: Structure, Mechanism and Biochemistry*, ed. P. R. Ortiz de Montellano, Kluwer Academic/Plenum Publishers, New York, 3rd edn, 2004; (*d*) I. G. Denisov, T. M. Makris, S. G. Sligar and I. Schlichting, *Chem. Rev.*, 2005, **105**, 2253; (*e*) *Handbook of Porphyrin Science*, ed. K. M. Kadish, K. M. Smith and R. Guilard, World Scientific, New Jersey, 2010; (*f*) P. R. Ortiz de Montellano, *Chem. Rev.*, 2010, **110**, 932; (*g*) E. O'Reilly, V. Koehler, S. Flitsch and N. Turner, *Chem. Commun.*, 2011, **47**, 2490; (*h*) G. Grogan, *Curr. Opin. Chem. Biol.*, 2011, **15**, 241.

2 (*a*) J. T. Groves, Models and Mechanisms of Cytochrome P450 Action, in *Cytochrome P450: Structure, Mechanism and Biochemistry*, ed. P. R. Ortiz de Montellano, Kluwer Academic/Plenum Publishers, New York, 3rd edn, 2005, ch. 1, pp. 1–44; (*b*) Y. Watanabe, H. Nakajima and T. Ueno, *Acc. Chem. Res.*, 2007, **40**, 554.

3 D. R. Nelson, *Methods Mol. Biol.*, 2006, **320**, 1.

4 (*a*) T. L. Poulos, B. C. Finzel, I. C. Gunsalus, G. C. Wagner and J. Kraut, *J. Biol. Chem.*, 1985, **260**, 6122; (*b*) T. L. Poulos, B. C. Finzel and A. J. Howard, *Biochemistry*, 1986, **25**, 5314.

5 J. B. Johnston, P. M. Kells, L. M. Podust and P. R. Ortiz de Montellano, *Proc. Natl. Acad. Sci. U. S. A.*, 2009, **106**, 20687.

6 (*a*) B. Meunier, S. P. de Visser and S. Shaik, *Chem. Rev.*, 2004, **104**, 3947; (*b*) *Iron-containing enzymes: Versatile catalysts of hydroxylation reaction in nature*, ed. S. P. de Visser and D. Kumar, RSC Publishing, Cambridge, UK, 2011.

7 J. Rittle and M. T. Green, *Science*, 2010, **330**, 9337.

Open Access Article. Published on 08 December 2014. Downloaded on 22/01/2015 17:11:53.
This article is licensed under a Creative Commons Attribution 3.0 Unported Licence.

8 (*a*) K. Auclair, Z. Hu, D. M. Little, P. R. Ortiz de Montellano and J. T. Groves, *J. Am. Chem. Soc.*, 2002, **124**, 6020; (*b*) P. Lafite, F. André, D. C. Zeldin, P. M. Dansette and D. Mansuy, *Biochemistry*, 2007, **46**, 10237; (*c*) T. S. Dowers, D. A. Rock, D. A. Rock and J. P. Jones, *J. Am. Chem. Soc.*, 2004, **126**, 8868; (*d*) H. L. R. Cooper and J. T. Groves, *Arch. Biochem. Biophys.*, 2011, **507**, 111; (*e*) K. M. Roberts and J. P. Jones, *Chem.–Eur. J.*, 2010, **16**, 8096.

9 See, *e.g.*, (*a*) J. T. Groves and R. S. Myers, *J. Am. Chem. Soc.*, 1983, **105**, 5791; (*b*) J. T. Groves and Y. Watanabe, *J. Am. Chem. Soc.*, 1986, **108**, 507; (*c*) D. Ostović and T. C. Bruice, *J. Am. Chem. Soc.*, 1989, **111**, 6511; (*d*) J. T. Groves, Z. Gross and M. K. Stern, *Inorg. Chem.*, 1994, **33**, 5065; (*e*) N. Stephenson and A. T. Bell, *Inorg. Chem.*, 2006, **45**, 2758; (*f*) N. Hessenauer-Ilicheva, A. Franke, D. Meyer, W.-D. Woggon and R. van Eldik, *J. Am. Chem. Soc.*, 2007, **129**, 12473; (*g*) R. Mas-Balleste and L. Que Jr, *J. Am. Chem. Soc.*, 2007, **129**, 15964; (*h*) P. Comba and G. Rajaraman, *Inorg. Chem.*, 2008, **47**, 78; (*i*) P. C. A. Bruijnincx, I. L. C. Buurmans, S. Gosiewska, M. A. H. Moelands, M. Lutz, A. L. Spek, G. van Koten and R. J. M. Klein Gebbink, *Chem.–Eur. J.*, 2008, **14**, 1228; (*j*) J. F. Hull, E. L. O. Sauer, C. D. Incarvito, J. W. Faller, G. W. Brudvig and R. H. Crabtree, *Inorg. Chem.*, 2009, **48**, 488; (*k*) A. McGown, W. D. Kerber, H. Fujii and D. P. Goldberg, *J. Am. Chem. Soc.*, 2009, **131**, 8040; (*l*) A. Company, Y. Feng, M. Güell, X. Ribas, J. M. Luis, L. Que Jr and M. Costas, *Chem.–Eur. J.*, 2009, **15**, 3359; (*m*) A. Franke, M. Wolak and R. van Eldik, *Chem.–Eur. J.*, 2009, **15**, 10182; (*n*) N. Hessenauer-Ilicheva, A. Franke, M. Wolak, T. Higuchi and R. van Eldik, *Chem.–Eur. J.*, 2009, **15**, 12447.

10 (*a*) Z. Gross and S. Nimri, *Inorg. Chem.*, 1994, **33**, 1731; (*b*) Z. Gross, *J. Biol. Inorg. Chem.*, 1996, **1**, 368; (*c*) K. Czarnecki, S. Nimri, Z. Gross, L. M. Proniewicz and J. R. Kincaid, *J. Am. Chem. Soc.*, 1996, **118**, 2929.

11 (*a*) A. G. Marshall, C. L. Hendrickson and G. S. Jackson, *Mass Spectrom. Rev.*, 1998, **17**, 1; (*b*) J. Roithová and D. Schröder, *Chem. Rev.*, 2010, **110**, 1170; (*c*) N. M. M. Nibbering, *Mass Spectrom. Rev.*, 2006, **25**, 962.

12 (*a*) M. E. Crestoni and S. Fornarini, *Inorg. Chem.*, 2005, **44**, 5379; (*b*) M. E. Crestoni and S. Fornarini, *Inorg. Chem.*, 2007, **46**, 9018; (*c*) M. E. Crestoni, S. Fornarini, F. Lanucara, J. J. Warren and J. M. Mayer, *J. Am. Chem. Soc.*, 2010, **132**, 4336; (*d*) M. E. Crestoni, S. Fornarini and F. Lanucara, *Chem.–Eur. J.*, 2009, **15**, 7863; (*e*) F. Lanucara and M. E. Crestoni, *Chem.–Eur. J.*, 2011, **17**, 12092.

13 H. Saltzman and J. G. Sharefkin, *Organic Syntheses*, Wiley, New York, 1973, vol. 5, p. 658, Collect.

14 (*a*) M. Meot-Ner, in *Gas Phase Ion Chemistry*, ed. M. T. Bowers, Academic Press, New York, 1979, vol. 1; (*b*) J. E. Bartmess and R. M. Georgiadis, *Vacuum*, 1983, **33**, 149.

15 T. Su and W. J. Chesnavich, *J. Chem. Phys.*, 1982, **76**, 5183.

16 B. Chiavarino, R. Cipollini, M. E. Crestoni, S. Fornarini, F. Lanucara and A. Lapi, *J. Am. Chem. Soc.*, 2008, **130**, 3208.

17 (*a*) Schrodinger, *Jaguar, version 7.9*, LLC, New York, NY, 2011; (*b*) M. J. Frisch, *Gaussian 09, revision D.01*, Gaussian, Inc., Wallingford, CT, 2004.

18 (*a*) R. Latifi, M. A. Sainna, E. V. Rybak-Akimova and S. P. de Visser, *Chem.–Eur. J.*, 2013, **19**, 4058; (*b*) M. G. Quesne, R. Latifi, L. E. Gonzalez-Ovalle, D. Kumar and S. P. de Visser, *Chem.–Eur. J.*, 2014, **20**, 435.

19 (*a*) A. D. Becke, *J. Chem. Phys.*, 1993, **98**, 5648; (*b*) C. Lee, W. Yang and R. G. Parr, *Phys. Rev. B: Condens. Matter Mater. Phys.*, 1988, **37**, 785.

20 (*a*) A. K. Vardhaman, C. V. Sastri, D. Kumar and S. P. de Visser, *Chem. Commun.*, 2011, **47**, 11044; (*b*) A. K. Vardhaman, P. Barman, S. Kumar, C. V. Sastri, D. Kumar and S. P. de Visser, *Angew. Chem., Int. Ed.*, 2013, **52**, 12288; (*c*) S. Kumar, A. S. Faponle, P. Barman, A. K. Vardhaman, C. V. Sastri, D. Kumar and S. P. de Visser, *J. Am. Chem. Soc.*, 2014, **136**, 17102.

21 P. J. Hay and W. R. Wadt, *J. Chem. Phys.*, 1985, **82**, 270.

22 S. Grimme, J. Antony, S. Ehrlich and H. Krieg, *J. Chem. Phys.*, 2010, **132**, 154104.

23 S. P. de Visser, *J. Am. Chem. Soc.*, 2010, **132**, 1087.

24 S. G. Lias, J. E. Bartmess, J. F. Liebman, J. L. Holmes, R. D. Levin and W. G. Mallard, in *Ion Energetics Data in NIST Chemistry WebBook*, ed. P. J. Linstrom and W. G. Mallard, National Institute of Standards and Technology, Gaithersburg, MD, 20899, http://webbook.nist.gov, NIST Standard Reference Database Number 69, retrieved in September 2014.

25 F. Angelelli, B. Chiavarino, M. E. Crestoni and S. Fornarini, *J. Am. Soc. Mass Spectrom.*, 2005, **16**, 589.

26 S. P. de Visser, *Inorg. Chem.*, 2006, **45**, 9551.

27 (*a*) R. E. White, J. T. Groves and G. A. McClusky, *Acta Biol. Med. Ger.*, 1979, **38**, 475; (*b*) R. T. Ruettinger and A. J. Fulco, *J. Biol. Chem.*, 1981, **256**, 5728; (*c*) J. T. Groves and D. V. Subramanian, *J. Am. Chem. Soc.*, 1984, **106**, 2177; (*d*) J. T. Groves, G. E. Avaria-Neisser, K. M. Fish, M. Imachi and R. L. Kuczkowski, *J. Am. Chem. Soc.*, 1986, **108**, 3837; (*e*) J. F. Bartoli, O. Brigaud, P. Battioni and D. Mansuy, *J. Chem. Soc., Chem. Commun.*, 1991, 440; (*f*) T. Ohno, N. Suzuki, T. Dokoh, Y. Urano, K. Kikuchi, M. Hirobe, T. Higuchi and T. Nagano, *J. Inorg. Biochem.*, 2000, **82**, 123; (*g*) S. Yoshioka, S. Takahashi, K. Ishimori and I. Morishima, *J. Inorg. Biochem.*, 2000, **81**, 141.

28 S. P. de Visser, F. Ogliaro, P. K. Sharma and S. Shaik, *J. Am. Chem. Soc.*, 2002, **124**, 11809.

29 (*a*) M. T. Green, *J. Am. Chem. Soc.*, 1999, **121**, 7939; (*b*) F. Ogliaro, S. P. de Visser, S. Cohen, J. Kaneti and S. Shaik, *ChemBioChem*, 2001, **11**, 848.

30 J. H. Dawson, R. H. Holm, J. R. Trudell, G. Barth, R. E. Linder, E. Bunnenberg, C. Djerassi and S. C. Tang, *J. Am. Chem. Soc.*, 1976, **98**, 3707.

31 (*a*) S. P. de Visser, S. Shaik, P. K. Sharma, D. Kumar and W. Thiel, *J. Am. Chem. Soc.*, 2003, **125**, 15779; (*b*) T. Kamachi and K. Yoshizawa, *J. Am. Chem. Soc.*, 2003, **125**, 4652; (*c*) C. M. Bathelt, J. Zurek, A. J. Mulholland and J. N. Harvey, *J. Am. Chem. Soc.*, 2005, **127**, 12900; (*d*) S. P. de Visser, *J. Phys. Chem. A*, 2005, **109**, 11050; (*e*) S. P. de Visser, L. Tahsini and W. Nam, *Chem.–Eur. J.*, 2009, **15**, 5577; (*f*) R. Lonsdale, J. Oláh, A. J. Mulholland and J. N. Harvey, *J. Am. Chem. Soc.*, 2011, **133**, 15464; (*g*)

 This journal is © The Royal Society of Chemistry 2015

Open Access Article. Published on 08 December 2014. Downloaded on 22/01/2015 17:11:53.
This article is licensed under a Creative Commons Attribution 3.0 Unported Licence.

H. Isobe, S. Yamanaka, M. Okumura, K. Yamaguchi and J. Shimada, *J. Phys. Chem. B*, 2011, **115**, 10730.

32 A. Ghosh, *Acc. Chem. Res.*, 1998, **31**, 189.

33 (*a*) H. M. Neu, M. G. Quesne, T. Yang, K. A. Prokop-Prigge, K. M. Lancaster, J. Donohoe, S. DeBeer, S. P. de Visser and D. P. Goldberg, *Chem.–Eur. J.*, 2014, **20**, 14584; (*b*) F. Lanucara, B. Chiavarino, M. E. Crestoni, D. Scuderi, R. K. Sinha, P. Maitre and S. Fornarini, *Inorg. Chem.*, 2011, **50**, 4445.

34 M. Radoń, E. Broclawic and K. Pierloot, *J. Chem. Theory Comput.*, 2011, **7**, 898.

35 (*a*) D. Kumar, L. Tahsini, S. P. de Visser, H. Y. Kang, S. J. Kim and W. Nam, *J. Phys. Chem. A*, 2009, **113**, 11713; (*b*) D. Kumar, R. Latifi, S. Kumar, E. V. Rybak-Akimova, M. A. Sainna and S. P. de Visser, *Inorg. Chem.*, 2013, **52**, 7968.

36 (*a*) S. P. de Visser, F. Ogliaro, N. Harris and S. Shaik, *J. Am. Chem. Soc.*, 2001, **123**, 3037; (*b*) S. P. de Visser, F. Ogliaro and S. Shaik, *Angew. Chem., Int. Ed.*, 2001, **40**, 2871; (*c*) S. P. de Visser, F. Ogliaro, P. K. Sharma and S. Shaik, *Angew. Chem., Int. Ed.*, 2002, **41**, 1947; (*d*) D. Kumar, B. Karamzadeh, G. N. Sastry and S. P. de Visser, *J. Am. Chem. Soc.*, 2010, **132**, 7656; (*e*) D. Kumar, S. P. de Visser and S. Shaik, *Chem.–Eur. J.*, 2005, **11**, 2825.

37 See, *e.g.*, (*a*) A. Ghosh and P. R. Taylor, *Curr. Opin. Chem. Biol.*, 2003, **7**, 113; (*b*) M. Swart, A. R. Groenhof, A. W. Ehlers and K. Lammertsma, *J. Phys. Chem. A*, 2004, **108**, 5479; (*c*) S. P. de Visser, M. G. Quesne, B. Martin, P. Comba and U. Ryde, *Chem. Commun.*, 2014, **50**, 262.

38 M. L. Chabinyc, S. L. Craig, C. K. Regan and J. I. Brauman, *Science*, 1998, **279**, 1882.

39 (*a*) Y. Zhao and D. G. Truhlar, *Acc. Chem. Res.*, 2008, **41**, 157; (*b*) T. Schwabe and S. Grimme, *Acc. Chem. Res.*, 2008, **41**, 569; (*c*) T. Weymuth, E. P. A. Couzijn, P. Chen and M. Reiher, *J. Chem. Theory Comput.*, 2014, **10**, 3092.

40 Y. Watanabe, T. Iyanagi and S. Oae, *Tetrahedron Lett.*, 1980, **21**, 3685.

JACS
JOURNAL OF THE AMERICAN CHEMICAL SOCIETY
Article
pubs.acs.org/JACS

Long-Range Electron Transfer Triggers Mechanistic Differences between Iron(IV)-Oxo and Iron(IV)-Imido Oxidants

Suresh Kumar,[†] Abayomi S. Faponle,[‡] Prasenjit Barman,[⊥] Anil Kumar Vardhaman,[⊥] Chivukula V. Sastri,*[,⊥] Devesh Kumar,*[,†] and Sam P. de Visser*[,‡]

[†]Department of Applied Physics, School for Physical Sciences, Babasaheb Bhimrao Ambedkar University, Vidya Vihar, Rae Bareilly Road, Lucknow, 226025 Uttar Pradesh, India

[⊥]Department of Chemistry, Indian Institute of Technology Guwahati, Assam 781039, India

[‡]Manchester Institute of Biotechnology and School of Chemical Engineering and Analytical Science, The University of Manchester, 131 Princess Street, Manchester M1 7DN, United Kingdom

Supporting Information

ABSTRACT: Nature often utilizes molecular oxygen for oxidation reactions through monoxygenases and dioxygenases. In many of these systems, a high-valent iron(IV)-oxo active species is found. In recent years, evidence has accumulated of possible iron(IV)-imido and iron(V)-nitrido intermediates in enzymatic catalysis, although little is known about their activity. In this work, we report a detailed combined kinetics and computational study on the difference in reactivity and chemical properties of nonheme iron(IV)-oxo compared with iron(IV)-tosylimido. We show here that iron(IV)-tosylimido complex is much more reactive with sulfides than the corresponding iron(IV)-oxo complex; however, the reverse trend is obtained for hydrogen atom abstraction reactions. The latter proceed with a relatively small kinetic isotope effect of k_H/k_D = 7 for the iron(IV)-tosylimido complex. Moreover, a Hammett analysis of hydrogen atom abstraction from para-X-benzyl alcohol reveals a slope of close to zero for the iron(IV)-oxo, whereas a strong negative slope is found for the iron(IV)-tosylimido complex. These studies implicate dramatic changes in the reaction mechanisms and suggest a considerable charge transfer in the transition states. Density functional theory calculations were performed to support the experiments and confirm an initial long-range electron transfer for the iron(IV)-tosylimido complex with substrates, due to a substantially larger electron affinity compared with the iron(IV)-oxo species. As a consequence, it also reacts more efficiently in electrophilic addition reactions such as those with sulfides. By contrast, the long-range electron transfer for the iron(IV)-tosylimido complex results in a rate constant that is dependent on the $\pi^*_{xz} \rightarrow \sigma^*_{z^2}$ excitation energy, which raises the hydrogen atom abstraction barrier above that found for the iron(IV)-oxo. On the other hand, sulfimidation has much earlier electron transfer steps with respect to sulfoxidation. All data has been analyzed and rationalized with valence bond models and thermochemical cycles. Our studies highlight the catalytic potential of iron(IV)-tosylimido complexes in chemistry and biology.

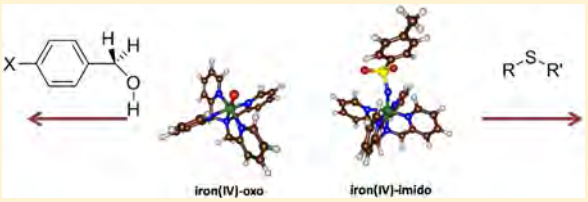

INTRODUCTION

Monoxygenases and dioxygenases are common enzymes in biology that utilize molecular oxygen usually on a transition metal center that can be bound into either a heme or nonheme environment.[1,2] A well-studied class of monoxygenases are the cytochromes P450 (P450s) that are found in all forms of life and catalyze the regioselective and stereospecific hydroxylation and epoxidation of substrates. These reactions have important functions in biology that include the biosynthesis of hormones in the liver, as well as the detoxification of metabolites and xenobiotics, such as drug molecules, in the body.[3] As such there is interest in understanding their function and mechanism from a pharmaceutical as well as biotechnological viewpoint. The P450s form a high-valent iron(IV)-oxo heme cation radical species in the catalytic cycle that is called compound I (Cpd I),[4] which is a highly reactive oxidant that reacts with substrates through aliphatic and aromatic hydroxylation, N-dealkylation, and sulfoxidation reactions.[5]

Despite the fact that much research has been devoted to P450 catalysis and synthetic model complexes there are still major gaps in our understanding of its catalytic mechanism and function. For instance, why does nature use molecular oxygen in the catalytic cycle of P450 enzymes and not, for instance, nitrogen, which is more abundant in the atmosphere? Technically, an iron(IV)-imido (Fe^{IV}═NR, R = alkyl) or iron(V)-nitrido (Fe^{V}≡N) complex should be a stable intermediate in P450 catalyzed reactions. Moreover, an iron(IV)-imido or iron(V)-nitrido could be reactive in NR group reactivity to substrates analogous to Cpd I. Indeed, over the years several examples in P450 catalysis, for example, in

Received: August 16, 2014
Published: November 12, 2014

ACS Publications © 2014 American Chemical Society

dx.doi.org/10.1021/ja508403w | J. Am. Chem. Soc. 2014, 136, 17102−17115

aziridation and imidation reactions, have been reported that include an iron(IV)-nitrido intermediate.[6] For example, the reaction of iron(III)-porphyrin complexes with *N*-tosyliminophenyliodinane (PhINTs) in the presence of olefins led to efficient aziridination of the substrate. More recent work on the amination of substrates by engineered $P450_{BM3}$ enzymes gave several examples of efficient nitrogen group transfer reactions.[7]

Despite being relatively rare in enzymology, actually in inorganic chemistry there are many examples of high-valent metal-imido and metal-nitrido complexes, where they have been shown to be reactive in various processes.[8] Bioinspired P450 analogues have been developed to understand the chemical and physical properties of the active species of P450 enzymes.[9] In a number of these synthetic complexes an iron-nitrido or iron-imido complex could be formed, spectroscopically characterized, and studied for reactivity with selected substrates.[10] In addition, studies have been reported on high-valent ruthenium-nitrido porphyrin complexes, which were shown to efficiently activate sp^3 hybridized C−H bonds of substrates.[11]

In more recent work, attention has shifted to nonheme iron and ruthenium based nitrido and imido complexes. These structures range from pentacoordinated to heptacoordinated iron complexes and have been spectroscopically characterized.[12] The studies showed that aliphatic substrates with a C−H bond strength analogous to that of cyclohexane could be activated efficiently. In addition to mononuclear iron and ruthenium complexes, evidence of diiron(III,IV)-tosylimido complexes has also been reported.[13] Thus, Latour and coworkers[13] observed hydrogen atom abstraction and nitrene transfer reactions by the diiron(III,IV)-tosylimido complex efficiently, whereby the sulfimidation of *para*-substituted thioanisoles was found to correlate linearly with the Hammett constant in an electrophilic pathway.

The iron(IV)-tosylimido (NTs) complex, tosylimido = NTs, with pentadentate N4Py ligand (N4Py = *N*,*N*-bis(2-pyridylmethyl)-*N*-bis(2-pyridyl) methylamine) was synthesized by Klinker et al.[14] and spectroscopically characterized with UV−vis, NMR, EPR, EXAFS, and Mössbauer spectroscopies. Because the analogous iron(IV)-oxo species is also known, we used the opportunity to study the reactivity of $[Fe^{IV}(O)(N4Py)]^{2+}$ (**1**) versus $[Fe^{IV}(NTs)(N4Py)]^{2+}$ (**2**), Figure 1, against selected substrates.[15] It is found that the iron(IV)-oxo oxidant is more effective in hydrogen atom abstraction reactions, but the iron(IV)-tosylimido species, surprisingly, is seen to be much more reactive with sulfides. The intricate details of the catalysts that are responsible for these reactivity differences between **1** and **2** could not be established in detail in our previous study; therefore, we decided to follow up our original study with a broader substrate range, as well as a comprehensive computational study on the reactivity of **1** and **2** with either sulfides (dimethylsulfide, DMS) or hydrogen abstraction donors. We show here, for the first time, that iron(IV)-oxo and iron(IV)-tosylimido have different valence orbital shapes, which lead to differences in electron affinity values that trigger reactivity changes.

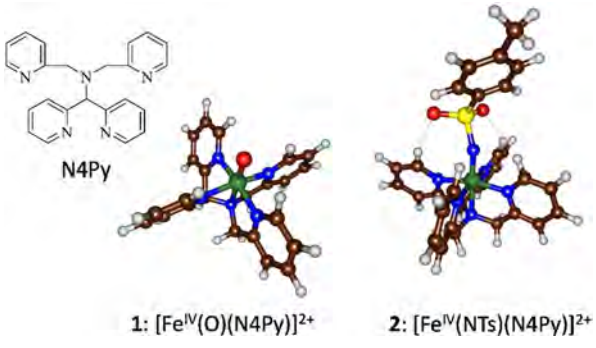

Figure 1. Iron(IV)-oxo and iron(IV)-tosylimido complexes studied in this work.

METHODS

Materials. All chemicals were obtained at the best available purity from Aldrich Chemical Co. and used as specified. Solvents were dried according to published procedures and distilled under argon prior to use.[16] Iodosylbenzene (PhIO) and *N*-tosyliminophenyliodinane (PhINTs) were prepared following literature procedures.[17] Iron(II) complex $[Fe^{II}(N4Py)](CF_3SO_3)_2$ was prepared in a glovebox as reported before.[18] Iron(IV) complexes, $[Fe^{IV}(O)(N4Py)]^{2+}$ and $[Fe^{IV}(NTs)(N4Py)]^{2+}$, were synthesized at ambient temperatures in acetonitrile by reacting the corresponding iron(II) complex with PhIO and PhINTs, respectively.[14,19] The oxidants (**1** and **2**) were characterized with UV−vis spectrophotometry and electrospray ionization mass spectrometry (ESI-MS) methods that confirmed their purity, see Figures S1 and S2 (Supporting Information).[15,19b] Benzyl alcohol-d_7 ($C_6D_5CD_2OH$) was purchased from C/D/N Isotopes Inc. (Pointe-Claire, Quebec, Canada).

Instrumentation. UV−vis spectra and kinetic measurements were recorded on a Hewlett-Packard 8453 spectrophotometer equipped with either a constant temperature circulating water bath or a liquid nitrogen cryostat (Unisoku) with a temperature controller. High resolution ESI-MS spectra of $[Fe^{IV}(O)(N4Py)]^{2+}$ and $[Fe^{IV}(NTs)(N4Py)]^{2+}$ were recorded on a Waters (Micromass MS Technologies) Q-TOF Premier mass spectrometer by infusing precooled (233 K) samples directly into the source at 15 μL min^{-1} using a syringe pump. The spray voltage was set at 2 kV, and the capillary temperature was set at 80 °C. Product analysis was done using NMR (^1H and ^{13}C), whereby the spectra were recorded with a Varian 400/100 MHz spectrometer and LCMS with WATERS ACQUITY UPLC equipped with a variable wavelength UV-200 detector.

Reactivity Studies. All reactions were run in a 10 mm path length UV cuvette by monitoring the UV−vis spectral changes of reaction solutions. Rate constants were determined by fitting the changes in absorbance of the intermediates under study. Their values were measured in triplicate and averaged, which gave a standard deviation of less than 10% of the given values.

Computation. The studies presented in this work use density functional theory (DFT) methods as implemented in the *Jaguar* 7.9 and *Gaussian*-09 program packages.[20] Calculations were performed on $[Fe^{IV}(O)(N4Py)]^{2+}$ (**1**) and $[Fe^{IV}(NTs)(N4Py)]^{2+}$ (**2**) as shown in Figure 1, and their reactivity patterns with 1,3-cyclohexadiene (CHD), benzyl alcohol (BA), and dimethylsulfide (DMS) as model substrates for hydrogen atom abstraction and sulfoxidation processes were investigated. Although calculations have been reported on the reaction mechanism of $[Fe^{IV}(NTs)(N4Py)]^{2+}$ with CHD and DMS,[15] those studies were based on gas-phase geometry optimizations and the effect of solvent was only treated at the single point level. However, because our chemical systems are multiply charged ions, we repeated all studies, whereby full geometry optimizations were performed using a solvent model (polarized continuum model) included that mimics an acetonitrile solution.[21]

Because the spin state ordering of transition metal complexes occasionally varies with the density functional method in the calculations,[22] we tested geometry optimizations with a range of DFT functionals, but all methods converged to very similar spin state orderings and relative energies. Initial studies utilized the unrestricted hybrid density functional method UB3LYP[23] in combination with a double-ζ quality LACVP basis set on iron and 6-31G on the rest of the atoms, basis set BS1.[24] With UB3LYP/BS1, the full potential energy

dx.doi.org/10.1021/ja508403w | J. Am. Chem. Soc. 2014, 136, 17102−17115

landscape from reactants to products on all possible low-lying spin and electronic states was investigated, and local minima and transition states were characterized. Furthermore, intrinsic reaction coordinate scans established the connectivity of the reactants with products via transition states. An analytical frequency calculation at this level of theory confirmed the structures as local minima (with real frequencies only) or first-order saddle points with a single imaginary frequency for the correct mode.

Subsequently all local minima and transition states were reoptimized with a triple-ζ quality basis set that contains an LACV3P+ basis set on iron coupled to 6-311+G* on the rest of the atoms, BS2. To test the reliability of the density functional method, we ran a series of single point calculations at the UB3LYP optimized structures using B3LYP-D3,[25] BP86,[26] PBE0,[27] and M06.[28] These studies did not change the spin state ordering (see Supporting Information) and confirmed the reactivity patterns and the conclusions drawn here.

Kinetic isotope effects (KIEs) were calculated using two models, namely, the semiclassical Eyring model (KIE_E) and the Wigner model (KIE_W), which includes tunneling corrections.[29] KIEs for the hydrogen atom abstraction step of substrates were evaluated from the frequency calculations, whereby the analytical frequencies of the reactants and transition states were recalculated with one or more of the hydrogen atoms of the substrate replaced by deuterium atoms. This led to a change in free energy of activation ($\Delta G^{\ddagger}$) for the original substrate versus that of the deuterium substituted one. The rate constant ratio (k_H/k_D) is then equal to the Eyring KIE, KIE_E, at a specific temperature T (298 K) via eq 1. Further corrections for tunneling are included in the Wigner KIE, KIE_W, which multiplies the KIE_E with the tunneling correction Q_{tH}/Q_{tD}, eqs 2 and 3. In eqs 1−3, R is the gas constant, h is Planck's constant, k_B is the Boltzmann constant, and ν is the imaginary frequency in the transition state.

$$KIE_E = k_H/k_D = \exp[(\Delta G_D^{\ddagger} - \Delta G_H^{\ddagger})/(RT)] \quad (1)$$

$$KIE_W = KIE_E Q_{tH}/Q_{tD} \quad (2)$$

$$Q_t = 1 + \frac{1}{24}\left(\frac{h\nu}{k_B T}\right)^2 \quad (3)$$

The free energy of activation for electron transfer ($\Delta G_{ET}^{\ddagger}$) was calculated using previously described methods,[30] from the driving force for the electron transfer reaction (ΔG_{ET}) and the solvent reorganization energy, λ_0, via eqs 4 and 5. These equations use Avogadro's number (N_A), the elementary charge (e), and the permittivity of vacuum (ε_0). The static and optical dielectric constants (ε_s and ε_{op}) were taken from the Gaussian calculation and had values of 35.688 (acetonitrile) and 1.807, respectively. The hard sphere radii (in Å) of the donor and acceptor molecules of the electron are labeled with r_1 and r_2.

$$\Delta G_{ET}^{\ddagger} = \frac{\lambda_0}{4}\left(1 + \frac{\Delta G_{ET}}{\lambda_0}\right)^2 \quad (4)$$

$$\lambda_0 = \frac{N_A e^2}{4\pi\varepsilon_0}\left(\frac{1}{\varepsilon_{op}} - \frac{1}{\varepsilon_s}\right)\left(\frac{1}{2r_1} + \frac{1}{2r_2} - \frac{1}{r_1 + r_2}\right) \quad (5)$$

RESULTS AND DISCUSSION

Experiment. The reactivity of high valent iron(IV)−oxo complexes has been extensively studied over the past few decades,[2,9,31] but, by contrast, only very few studies have been reported on its closely related iron(V)−nitrido ($Fe^V{\equiv}N$) or the iron(IV)−imido ($Fe^{IV}{=}NR$) species. The origin and chemical details of the reaction mechanism of iron(IV)-oxo compared with iron(IV)-imido with substrates are poorly understood; therefore, we decided to do a comparative kinetics study on the two complexes. Two of the most common reaction mechanisms found for enzymatic iron(IV)-oxo intermediates include hydrogen atom abstraction (HAT) and heteroatom oxidation; therefore, we studied the reactivity of **1** and **2** with *para*-X-benzyl alcohol and fluorene as models for HAT and *para*-X-thioanisole as models for heteroatom oxidation.

Complexes **1** and **2** were generated in an acetonitrile solution *in situ*, and subsequently substrate was added. Upon addition of substrate to a solution of **1** and **2**, the intermediates decayed by pseudo-first-order kinetics and the d−d transitions were monitored in the UV−vis spectrum (Figure 2a). The first-order rate constants were then plotted as a function of substrate concentration to obtain the second-order rate constants (k_2) of which we show the example for *para*-H-benzyl alcohol in Figure 2b. Table 1 summarizes the thus obtained second-order rate constants for all substrates discussed here.

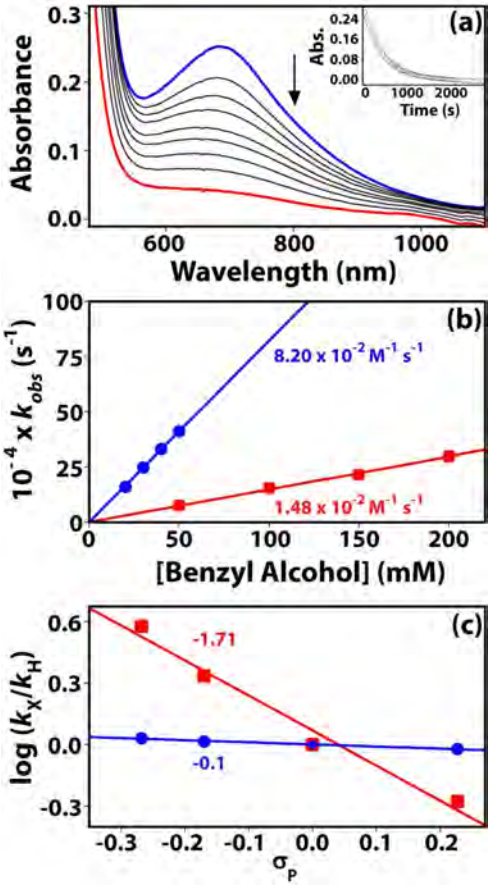

Figure 2. (a) UV−vis spectral changes of **2** (1 mM, blue line) upon the addition of *para*-H-benzyl alcohol (150 equiv diluted in 50 μL of CH_3CN) at 298 K. Inset shows decay profile of 660 nm band. (b) Second-order rate constants determined in the reactions of 1 mM of **1** (●) and **2** (■) in CH_3CN solution against various concentrations of benzyl alcohol at 298 K. (c) Plot of $\log(k_X/k_H)$ against σ_p values of *para*-X-benzyl alcohol in reaction with **1** (●) and **2** (■) at 298 K. The k_X and k_H are the second order rate constants of *para*-X-benzyl alcohol at 298 K.

The second-order rate constant, k_2, obtained for benzyl alcohol at 25 °C was determined to be 1.48×10^{-2} M^{-1} s^{-1} for $[Fe^{IV}(NTs)(N4Py)]^{2+}$, whereas a value of 8.20×10^{-2} M^{-1} s^{-1} was found for $[Fe^{IV}(O)(N4Py)]^{2+}$. Therefore, the $[Fe^{IV}(O)(N4Py)]^{2+}$ complex reacts with benzyl alcohol with rate

dx.doi.org/10.1021/ja508403w | J. Am. Chem. Soc. 2014, 136, 17102−17115

Table 1. Second-Order Rate Constants for the Reaction of 1 and 2 with Selected Substrates

	1			2		
substrate	k_2 (M^{-1} s^{-1})	KIE	Hammett (ρ)	k_2 (M^{-1} s^{-1})	KIE	Hammett (ρ)
thioanisole[a,b]	5.00×10^{-2}		−0.87	2.60×10^{-1}		−3.35
fluorene[b,c]	6.97×10^{-1}	30		1.16×10^{-1}	7	
para-X-benzyl alcohol[c]						
X = OCH_3	8.8×10^{-2}			5.6×10^{-2}		
X = CH_3	8.5×10^{-2}			3.2×10^{-2}		
X = H	8.20×10^{-2}	48[d]	−0.10	1.48×10^{-2}	7	−1.71
X = Cl	7.8×10^{-2}			7.8×10^{-3}		

[a]At 273 K. [b]From ref 15. [c]At 298 K. [d]From ref 32.

constants that are almost six times larger than those found for the $[Fe^{IV}(NTs)(N4Py)]^{2+}$ complex. Similar rate enhancements were found for fluorene, for example, by **1** and **2**.[15] As such the rate enhancement is not dependent on the HAT donor in these cases and most likely proceeds via the same mechanism for both oxidants.

To gain more insight into the details of the hydrogen atom abstraction mechanism, we repeated the experiments with benzyl alcohol-d_7 ($C_6D_5CD_2OH$) and give the comparative second-order rate plots in Figure S6, Supporting Information. These studies established a kinetic isotope effect (KIE) of 7.0, which is relatively low for typical hydrogen atom abstraction reactions but can still be considered as a rate determining HAT step in the reaction mechanism. In the case of HAT of fluorene by **1** and **2**, also a KIE = 7 for the iron(IV)-tosylimido complex was established, whereas a value of 30 was obtained for the iron(IV)-oxo species. Clearly, there are fundamental differences in reactivity between iron(IV)-oxo and iron(IV)-tosylimido that lead to this dramatic lowering of the kinetic isotope effects. Our studies, reported here, are in line with those reported on hydrogen atom abstraction from benzyl alcohol by $[Fe^{IV}(O)(N4Py)]^{2+}$, which also found a large KIE of 48 at 0 °C.[32]

To further understand the intrinsic details of the reaction mechanism of benzyl alcohol with **1** and **2**, we decided to study *para*-substituted benzyl alcohols and create a Hammett plot, see Figure 2c. Reaction of $[Fe^{IV}(O)(N4Py)]^{2+}$ with *para*-substituted benzyl alcohol indicates that the reaction rates are not greatly dependent on the *para*-substituent and whether it is electron-withdrawing or electron-donating gives similar reaction rates. When we plot the reaction rate as a function of σ_p of the substituent, a small Hammett ρ value, approximately −0.1, is found in agreement with the literature.[32] This clearly indicates that there is no substituent effect in the reaction of $[Fe^{IV}(O)(N4Py)]^{2+}$ with benzyl alcohol.

By contrast to the reaction of **1** with benzyl alcohol, the same reaction with **2** gives a dramatic change in substituent effect with a Hammett ρ value of approximately −1.71. This large Hammett value indicates that during the hydrogen atom abstraction from the substrate, there is a considerable amount of positive charge built-up in the transition state. Most likely it originates from additional stabilization of positive charge on the substrate in the transition state by electron-donating groups in the *para*-position of benzyl alcohol and thereby enhances the overall rate of oxidation. The large Hammett value and low KIE indicates that there is a large amount of charge transfer in the rate-determining step.[33]

To unequivocally establish that the rate-determining step is indeed one-electron transfer, we did a subsequent set of experiments with cyclobutanol as mechanistic probe. It has been shown previously that the oxidation of cyclobutanol proceeds through either an initial one-electron or two-electron transfer process, which leads to different products.[32,34] Thus, the one-electron transfer reaction is followed by ring-opening of the substrate to give 4-hydroxybutyraldehyde products, whereas the reaction initiated by a two-electron transfer results in the formation of cyclobutanone products. In the oxidation of cyclobutanol by **2**, we observe 4-hydroxybutyraldehyde as the major products; hence the reaction of **2** with aliphatic substrates proceeds via a dominant radical pathway. By contrast, cyclobutanol reacts with **1** to yield cyclobutanone products after a specific C−H bond cleavage.[32] This observation is in agreement with our earlier observation for the oxidation reaction of fluorene by **1** and **2**, where the latter gives 9,9′-bifluorene as the major product, while with the former fluorenone was obtained.[15]

In addition to the HAT mechanism of **1** versus **2** with selected substrates, we also investigated the sulfoxidation or sulfimidation reaction with *para*-X-thioanisole substrates, X = OCH_3, CH_3, H, and Cl.[15] A plot of the logarithm of the rate constant ratio k_X/k_H gave a linear correlation with the σ_p Hammett parameter with a slope of −0.87 for **1** and −3.35 for **2**, which implicated differences in reaction mechanism. This was assigned as a possible group transfer for the reaction of sulfides with $[Fe^{IV}(O)(N4Py)]^{2+}$ and electron transfer for the reaction with $[Fe^{IV}(NTs)(N4Py)]^{2+}$.

Computation. To gain further insight into the chemical differences between **1** and **2** in hydrogen atom abstraction and heteroatom transfer reactions, we decided to do a detailed density functional theory (DFT) study. To this end, we calculated the catalytic reaction mechanism of hydrogen atom abstraction from 1,3-cyclohexadiene (CHD) and benzyl alcohol (BA) by these oxidants as well as the reaction of **1** and **2** with dimethylsulfide (DMS). Full details of the calculations and the benchmarking of the computational methods are given in the Supporting Information, while we focus on the major trends in the paper here.

Before we discuss the substrate activation by **1** and **2**, let us first do an in-depth analysis of the reactant complexes with and without substrate. Figure 3 displays optimized geometries of $[Fe^{IV}(O)(N4Py)]^{2+}$ (**1**) and $[Fe^{IV}(NTs)(N4Py)]^{2+}$ (**2**) in the lowest lying singlet, triplet, and quintet spin states as obtained after a geometry optimization in a polarized continuum model. In both systems, the triplet spin state is the ground state by more than 4 kcal mol^{-1} over the nearest singlet and quintet spin states.

Optimized geometries of ^{1,3,5}**1** are similar to structures reported previously for gas-phase optimized structures and also to analogous iron(IV)-oxo intermediates from the literature.[35,36] Dramatic geometric differences are found between **1** and **2**. In particular, the Fe−O distance is short, about 1.65−

dx.doi.org/10.1021/ja508403w | J. Am. Chem. Soc. 2014, 136, 17102−17115

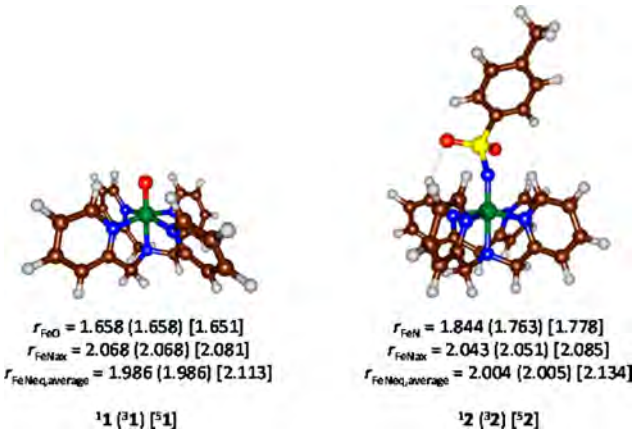

Figure 3. UB3LYP optimized geometries in a dielectric constant mimicking acetonitrile of **1** and **2** with bond lengths in angstroms. The distance between the iron and amide nitrogen atom is labelled as r_{FeNax}, whereas $r_{FeNeq,average}$ represents the average distance of the four iron-pyridine interactions.

1.66 Å in all spin states, typical for a double bond. By contrast, much longer Fe−N bonds are found for structure **2** that range from 1.763 Å for ^{3}**2** to 1.844 Å for ^{1}**2**. Similar bond lengths were obtained from a gas-phase geometry optimization.[15] Despite these differences, structures **1** and **2** have the same electronic configuration with orbital occupation of $\pi^*_{xy}{}^2\pi^*_{xz}{}^1\pi^*_{yz}{}^1$ in the triplet spin state. However, the interactions of the NTs group with the metal differs from that of an oxo group with the metal, and as a result changes in orbital energy levels, orbital ordering, and orbital stability is found.

Figure 4 displays the orbital energy levels of the π^*_{xy}, π^*_{xz}, π^*_{yz}, $\sigma^*_{z^2}$ and $\sigma^*_{x^2-y^2}$ molecular orbitals of ^{3}**1** and ^{3}**2**. The π^*_{xy} orbital is the lowest in energy typical for hexacoordinated iron complexes and its lobes are placed between the nitrogen atoms of the N4Py ligand. However, because the pyridine ligands are orthogonal to the four Fe−N axes, the equatorial nitrogen atoms can still form bonding and antibonding overlap interactions of $2p_x/2p_y$ orbitals with the $3d_{xy}$ orbital on the metal, and hence the π^*_{xy} orbital is higher in energy than in corresponding porphyrin complexes.

The $3d_{xz}$ and $3d_{yz}$ atomic orbitals on Fe interact with a pair of $2p_x/2p_y$ atomic orbitals on the oxo group and form a degenerate pair of π_{xz}/π^*_{xz} and π_{yz}/π^*_{yz} molecular orbitals in **1**. In $[Fe^{IV}(NTs)(N4Py)]^{2+}$, by contrast, the donating nitrogen atom also binds the tosyl group, and as a consequence, the π^*_{xz} and π^*_{yz} are not degenerate anymore. As seen in Figure 4, the $3d_{xz}$ orbital on Fe interacts with the σ_{SN} bonding orbital along the S−N bond to form the π_{xz}/π^*_{xz} set of orbitals, whereas the

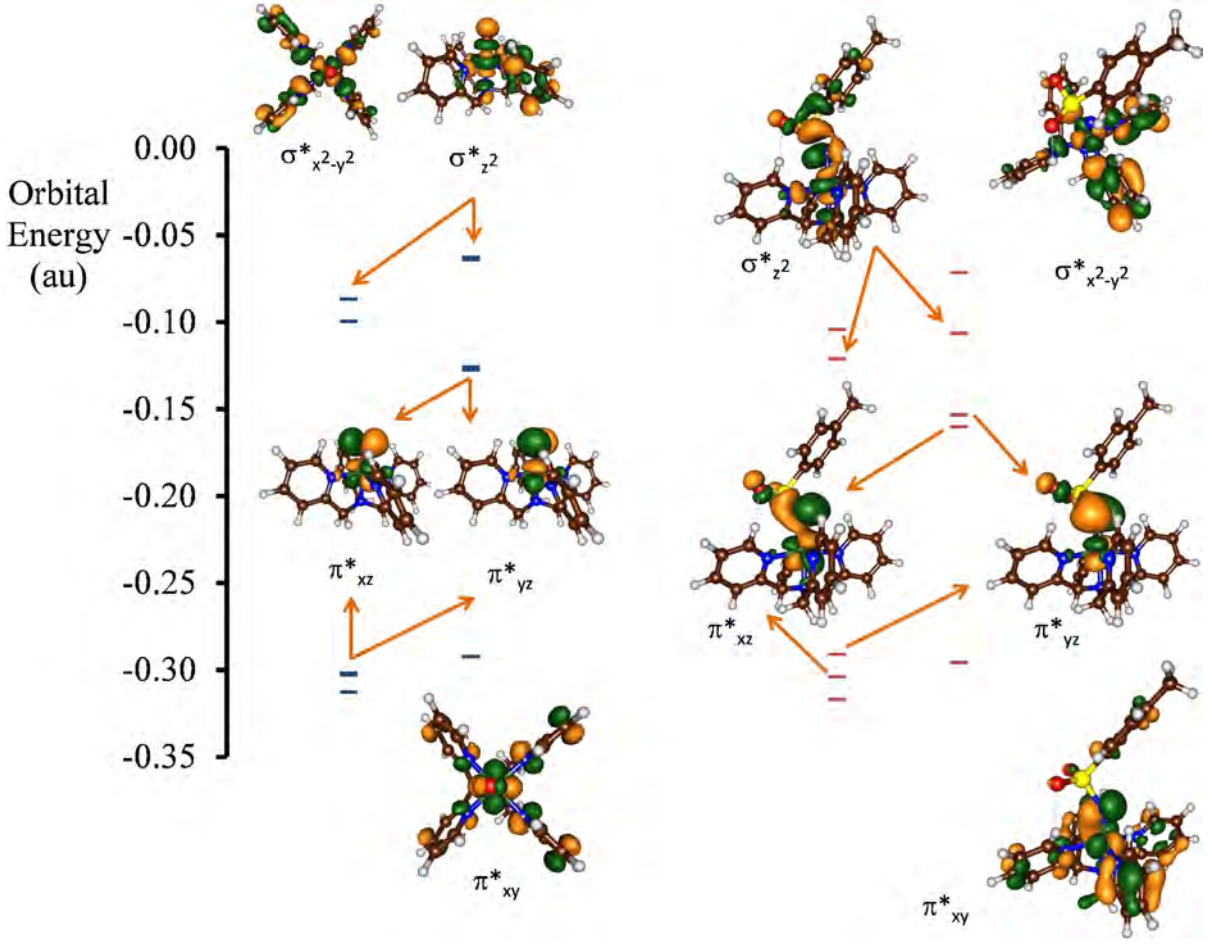

Figure 4. Orbital diagram of $[Fe^{IV}(O)(N4Py)]^{2+}$ (**1**) on the left-hand-side and $[Fe^{IV}(NTs)(N4Py)]^{2+}$ (**2**) on the right-hand-side. The energy levels of the α- and β-set of molecular valence orbitals are given (with energies in au) of both complexes. Also shown are orbital drawings of the relevant molecular orbitals.

dx.doi.org/10.1021/ja508403w | J. Am. Chem. Soc. 2014, 136, 17102−17115

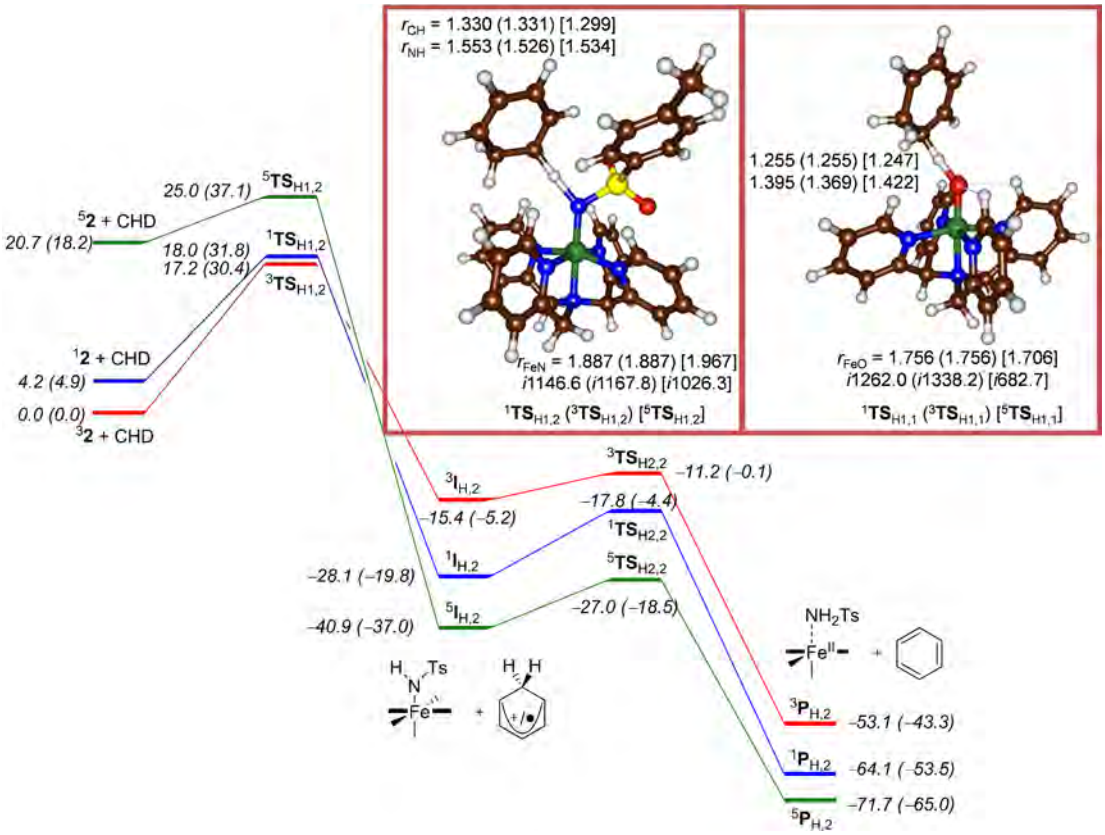

Figure 5. Potential energy landscape of dehydrogenation of CHD by $[Fe^{IV}(NTs)(N4Py)]^{2+}$ with energies relative to isolated reactants in kcal mol^{-1}. Out of parentheses are given ΔE + ZPE values in solvent, whereas free energies with solvent and entropic and thermal corrections are given in parentheses. Also shown are optimized geometries of $\mathbf{TS}_{H1,1}$ and $\mathbf{TS}_{H1,2}$ with bond lengths in angstroms and the imaginary frequency in wave numbers.

$3d_{yz}$ orbital pairs up with a lone pair ($2p_y$) on the nitrogen atom to form π_{yz}/π^*_{yz}.

Two virtual orbitals, $\sigma^*_{z^2}$ and $\sigma^*_{x^2-y^2}$, complement the set of valence orbitals in Figure 4. The $\sigma^*_{x^2-y^2}$ orbital is in the plane of the N4Py ligand and is similar in shape and orbital energy in **1** and **2**. The major orbital differences between **1** and **2** are found along the Fe−O/Fe−N axis. Thus, the $\sigma^*_{z^2}$ molecular orbital for the antibonding interactions of the $3d_{z^2}$ atomic orbital on Fe with the $2p_z$ orbital on O/N is affected strongly.

In **1**, the $\sigma^*_{z^2}$ orbital in $[Fe^{IV}(O)(N4Py)]^{2+}$ is the result of the interaction of the $3d_{z^2}$ orbital on iron with the $2p_z$ atomic orbital on oxygen. By contrast, the $\sigma^*_{z^2}$ orbital in $[Fe^{IV}(NTs)(N4Py)]^{2+}$ is built up from the $3d_{z^2}$ orbital on iron with the $2p_y$ orbital on nitrogen but also includes the $3p_z$ orbital on sulfur. These differences in molecular orbital interactions of the $\sigma^*_{z^2}$ orbital in **1** and **2** affect the energy level dramatically and change the ordering of $\sigma^*_{x^2-y^2}$ over $\sigma^*_{z^2}$, whereby the latter is lower in energy in **2**. The changes in orbital energies affect the HOMO−LUMO gaps, which are reduced in **2** with respect to **1** and thereby increase the electrophilicity of **2** as well. As such, based on the orbital diagrams, differences in chemical reactivity are expected between **1** and **2**.

Hydrogen Atom Abstraction Mechanisms. We then calculated the dehydrogenation of CHD by **1** and **2** with DFT methods, as well as the hydrogen atom abstraction of benzyl alcohol (Supporting Information). As an example of a typical potential energy profile of C−H activation by iron(IV)-tosylimido complexes, we display the dehydrogenation of CHD by ^{1,3,5}**2** in Figure 5. The reaction is stepwise with an initial hydrogen atom abstraction via a transition state $\mathbf{TS}_{H1}$ to form a radical intermediate $\mathbf{I}_H$. A second hydrogen atom abstraction then via transition state $\mathbf{TS}_{H2}$ gives dehydrogenated products, that is, benzene and water/H_2NTs. The labels in superscript refer to the spin multiplicity and the subscript label to the reactant, that is, either **1** or **2**. Thus, $^3\mathbf{TS}_{H1,1}$ is the initial hydrogen atom abstraction transition state from CHD by **1** on the triplet spin state surface.

Note that in the case of the iron(IV)-tosylimido system, actually the reaction starts with an electron transfer from substrate to oxidant prior to the hydrogen atom abstraction. Therefore, we first estimated the electron transfer barrier for reaction 6 using the Marcus equation described with eq 4 above. We estimate the electron transfer free energy of activation ($\Delta G^{\ddagger}_{ET}$) to be 3.4 kcal mol^{-1}, and hence it is well lower than the hydrogen atom abstraction barrier. Note that long-range electron transfer of high-valent iron(IV)-oxo complexes has been calculated before in the reaction of $[Fe(O)(BQEN)(NCCH_3)]^{3+}$, BQEN = *N*,*N*′-dimethyl-*N*,*N*′-bis(8-quinolyl)ethane-1,2-diamine, in a reaction with ethylbenzene as well as in a reaction of Cpd I of P450 with an arginine substrate.[37]

$$^3\mathbf{2} + \text{CHD} \rightarrow [Fe^{III}(NTs)(N4Py)]^+ + \text{CHD}^{\bullet+} + \Delta G_{ET} \quad (6)$$

The initial hydrogen atom abstraction barrier, $\mathbf{TS}_{H1}$, is rate determining in all cases and leads to very stable intermediates $\mathbf{I}_H$ with large exothermicity. The lowest lying barrier, $\mathbf{TS}_{H1,2}$, is on the triplet spin state surface with an energy of $\Delta E^{\ddagger}$ + ZPE =

dx.doi.org/10.1021/ja508403w | J. Am. Chem. Soc. 2014, 136, 17102−17115

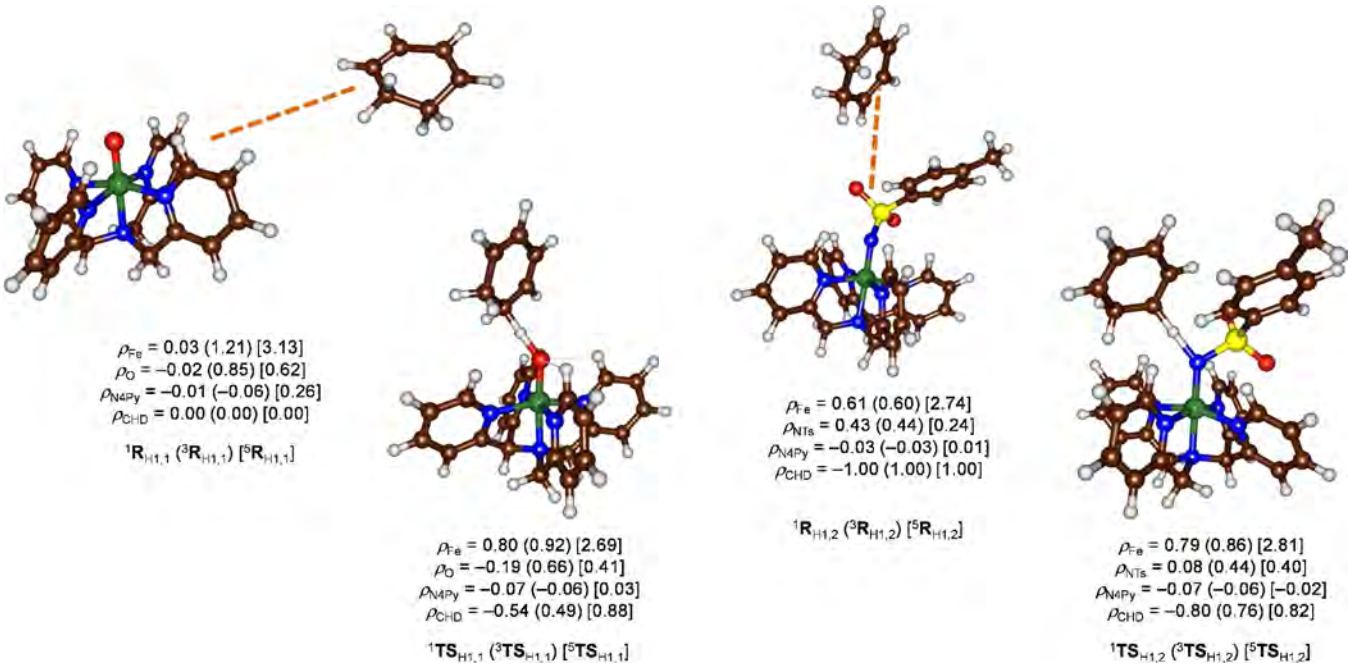

Figure 6. Group spin densities of $\mathbf{R}_{H1,1}$, $\mathbf{TS}_{H1,1}$, $\mathbf{R}_{H1,2}$, and $\mathbf{TS}_{H1,2}$ as obtained at UB3LYP/BS2 in a dielectric constant of 35.688.

17.2 kcal mol^{-1}. By contrast, the reaction of ^{3}**1** with CHD has a hydrogen atom abstraction barrier of 15.7 kcal mol^{-1} at the same level of theory (Supporting Information, Table S31). A change in enthalpy of 1.5 kcal mol^{-1} between the reaction of CHD with **1** and of CHD with **2** leads to a rate enhancement of about 11, which compares well with the one reported experimentally of 6 for *para*-H benzyl alcohol (Table 1), as well as with our previously reported reaction rates for CHD and fluorene.[15]

Although the absolute error of DFT calculated barrier heights is typically several kcal mol^{-1},[38] actually extensive reactivity trends showed that the error is mostly systematic. Thus, for a series of oxygen atom transfer reactions from Cpd I of P450 to substrates, a linear correlation was found with the strength of the C−H bond broken (in the case of HAT) or the ionization potential of the olefin (for epoxidation reactions) with a standard deviation of less than 2 kcal mol^{-1}.[39] Furthermore, DFT calculations on the reaction of ^{4,2}Cpd I with *trans*-2-phenylmethylcyclopropane gave a mixture of rearrangement and nonrearrangement pathways, which enabled the calculation of product isotope effect.[40] The calculated product isotope effect of 1.11 was very close to the experimental value of 1.14; hence DFT can calculate small regioselectivity differences of a few kcal mol^{-1} with good accuracy.

Past the transition state, $\mathbf{TS}_{H1,2}$, a spin crossing to a higher spin state occurs to form $\mathbf{I}_{H,2}$ in the quintet spin state. In the transition state, however, the triplet is well below the quintet spin. With iron(IV)-oxo as an oxidant, the second hydrogen atom abstraction has negligible barriers, but for [Fe^{IV}(NTs)(N4Py)]$^{2+}$, significant barriers, for example, ΔE + ZPE = 13.9 kcal mol^{-1} for $^{5}\mathbf{TS}_{H2,2}$, are found. This will imply that the radical intermediates have a finite lifetime during which rearrangement processes may occur leading to side reactions and byproducts.[41]

Geometrically, $\mathbf{TS}_{H1,1}$ is different from $\mathbf{TS}_{H1,2}$, although the value of the imaginary frequency is of the same order of magnitude. In particular, the N−H bond in $\mathbf{TS}_{H1,2}$ is rather long with values well over 1.5 Å, whereas the O−H distance in $\mathbf{TS}_{H1,1}$ is between 1.369 and 1.422 Å for the three spin states. Optimized geometries of intermediates and products are in line with previous studies on dehydrogenation processes by iron(IV)-oxo and iron(IV)-tosylimido complexes.[42,43]

To understand the differences between $\mathbf{TS}_{H1,1}$ and $\mathbf{TS}_{H1,2}$, we plot in Figure 6 the group spin densities of these transition states as well as the reactant complexes. At first glance, the two sets of spin densities for the transition states look very similar: In the triplet spin state there is about 1.5 spin density on the FeO/FeNTs group and considerable radical character on the substrate. However, a careful look at the reactant complexes $\mathbf{R}_{H1,1}$ and $\mathbf{R}_{H1,2}$ shows that the iron(IV)-tosylimido complex has undergone an electron transfer upon approach of the substrate, and $^{1,3,5}\mathbf{R}_{H1,2}$ all show a spin density of approximately 1 at the CHD unit. This may affect the spin densities and charge distributions in the transition states as well.

The group spin densities of the iron(IV)-oxo species in ^{1,3,5}**1** and $^{1,3,5}\mathbf{R}_{H1,1}$ are very similar, and little spin density has accumulated on the substrate moiety in $\mathbf{R}_{H1,1}$. Therefore, approach of the substrate on the iron(IV)-oxo species has little effect on the charge distributions, and in $\mathbf{R}_{H1,1}$ the oxidant is still an iron(IV)-oxo species. A comparison of the group spin densities of ^{1,3,5}**2** and $^{1,3,5}\mathbf{R}_{H1,2}$, on the other hand, shows that an electron transfer has occurred at relatively large distance and in $\mathbf{R}_{H1,2}$ the metal is reduced and the substrate is a cation radical, that is, [Fe^{III}(NTs)(N4Py)]$^{+}$···CHD$^{+\bullet}$ rather than [Fe^{IV}(NTs)(N4Py)]$^{2+}$···CHD. Hence the actual oxidant that performs the hydrogen atom abstraction is the iron(III)-tosylimido species rather than an iron(IV)-tosylimido species. Because experimental rate constants were measured after addition of substrate, this implies that we cannot use the reactant complex $\mathbf{R}_{H1,2}$ as a comparison with experiment but have to use isolated reactants instead. Clearly, the electron affinity of [Fe^{IV}(NTs)(N4Py)]$^{2+}$ is large, and the electron transfer happens prior to the substrate activation step. In recent work, we showed that binding of Zn^{2+} to a manganese-porphyrinoid system resulted in valence tautomerism and changes in electronic configuration

dx.doi.org/10.1021/ja508403w | J. Am. Chem. Soc. 2014, 136, 17102−17115

Scheme 1. Reaction Mechanisms Established for Iron(IV)-oxo and Iron(IV)-tosylimido Complexes

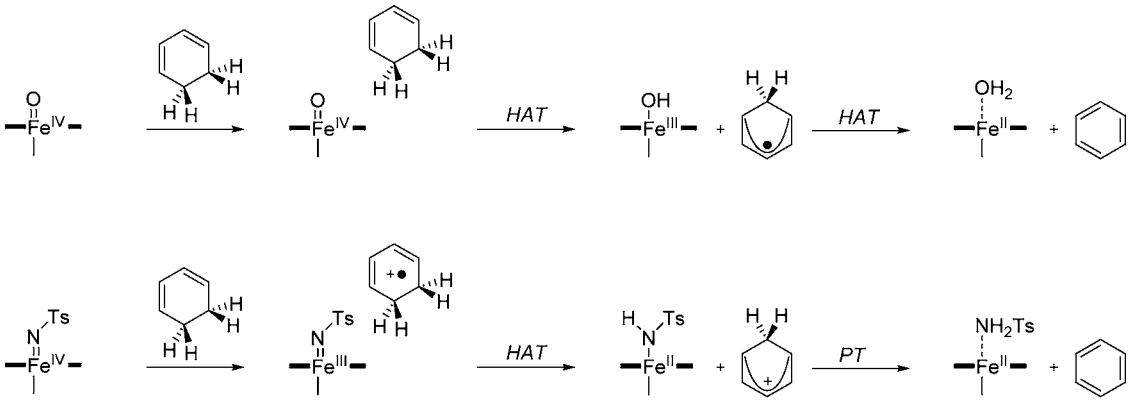

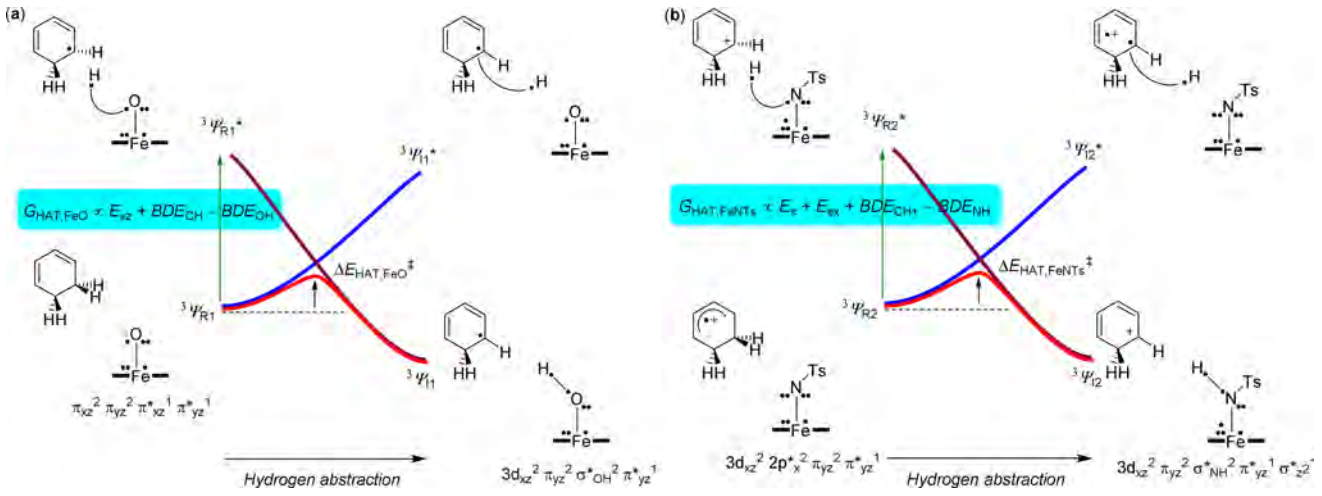

Figure 7. Valence bond curve crossing diagrams for hydrogen atom abstraction from substrate by $[Fe^{IV}(O)(N4Py)]^{2+}$ (a) and $[Fe^{III}(NTs)(N4Py)]^{+}$ (b). Valence electrons are identified with a dot, and lines (straight or bent) in chemical structures refer to bonds.

and consequently catalysis.[44] The $[Fe^{IV}(NTs)(N4Py)]^{2+}$ system, therefore, is another example of a catalyst where its activity is strongly dependent on environmental variables.

Note that the spin densities on the quintet spin state surface for $\mathbf{R}_{H1,2}$ and $\mathbf{TS}_{H1,2}$ implicate the ferromagnetic coupling of three electrons on iron with one on the substrate rest group. Previous studies on nonheme iron(IV)-oxo reactivity[35,36] found quintet spin states with five unpaired electrons on the iron(IV)-oxo antiferromagnetically coupled to a radical on the substrate rest group as the most stable radical intermediate. In these systems, the hydrogen atom typically attacks from the top and aligns itself with the Fe−O axis. In iron(IV)-tosylimido, this site is blocked by the tosylimido group, and the substrate attacks along an angle, thus stabilizing the π-pathway. We made attempts to swap molecular orbitals and create alternative quintet spin states with five unpaired electrons on the metal antiferromagnetically coupled to a substrate radical for transition states and intermediate complexes. However, all these calculations failed and led to high energy structures only.

The group spin densities and, in particular, the differences between $\mathbf{R}_{H1,1}$ and $\mathbf{TS}_{H1,1}$ and between $\mathbf{R}_{H,2}$ and $\mathbf{TS}_{H1,2}$ show that in both cases between the reactant complex and the **TS** a hydrogen atom abstraction takes place. The differences between the two processes are that in the iron(IV)-tosylimido already one electron had transferred upon formation of a long-range complex **R**, thereby generating a triplet ground state with $\pi^{*}_{xy}{}^{2}\pi^{*}_{xz}{}^{2}\pi^{*}_{xz}{}^{1}\pi_{CHD}{}^{1}$ configuration representing a state corresponding to $[Fe^{III}(NTs)(N4Py)]^{+}\cdots CHD^{+\bullet}$. Therefore, the subsequent hydrogen atom abstraction includes a second electron to be transferred and the formation of a $[Fe^{II}(NHTs)(N4Py)]$ intermediate. This complex then abstracts a proton to form the product complex. The $^{3}\mathbf{TS}_{H1,2}$ structure, therefore, has an electronic configuration closely resembling the product complexes, where the aromaticity in the benzene group is starting to form and an electron transfer from substrate into $\sigma^{*}_{z^2}$ takes place.

The singlet spin state reactant complex has the same electronic configuration as $^{3}\mathbf{R}_{H1,2}$, and its transition state is very close in energy to $^{3}\mathbf{TS}_{H1,2}$ and leads through an electron transfer to the closed-shell singlet intermediate $^{1}\mathbf{I}_{H,2}$ with configuration $\pi^{*}_{xy}{}^{2}\pi^{*}_{xz}{}^{2}\pi^{*}_{yz}{}^{2}$. The most stable intermediate, however, is $^{5}\mathbf{I}_{H,2}$ with configuration $\pi^{*}_{xy}{}^{2}\pi^{*}_{xz}{}^{1}\pi^{*}_{yz}{}^{1}\sigma^{*}_{z^2}{}^{1}\sigma^{*}_{x^2-y^2}{}^{1}$. Scheme 1 summarizes the mechanisms that we obtained for dehydrogenation of olefins, such as CHD, by **1** and **2**. The $\sigma^{*}_{z^2}$ orbital in $^{3}\mathbf{TS}_{H1,2}$ mixes strongly with a π-orbital on the aromatic substrate and hence is strongly affected in shape and energy level by the *para*-substituent on the ring. We can anticipate a large Hammett effect upon changing the *para*-H substituent by a more electron donating or withdrawing group.

The reaction mechanisms shown in Scheme 1 also explain the Hammett plot for benzyl alcohol in Figure 2c. Thus, the iron(IV)-oxo complex reacts with little charge accumulation on

dx.doi.org/10.1021/ja508403w | J. Am. Chem. Soc. 2014, 136, 17102−17115

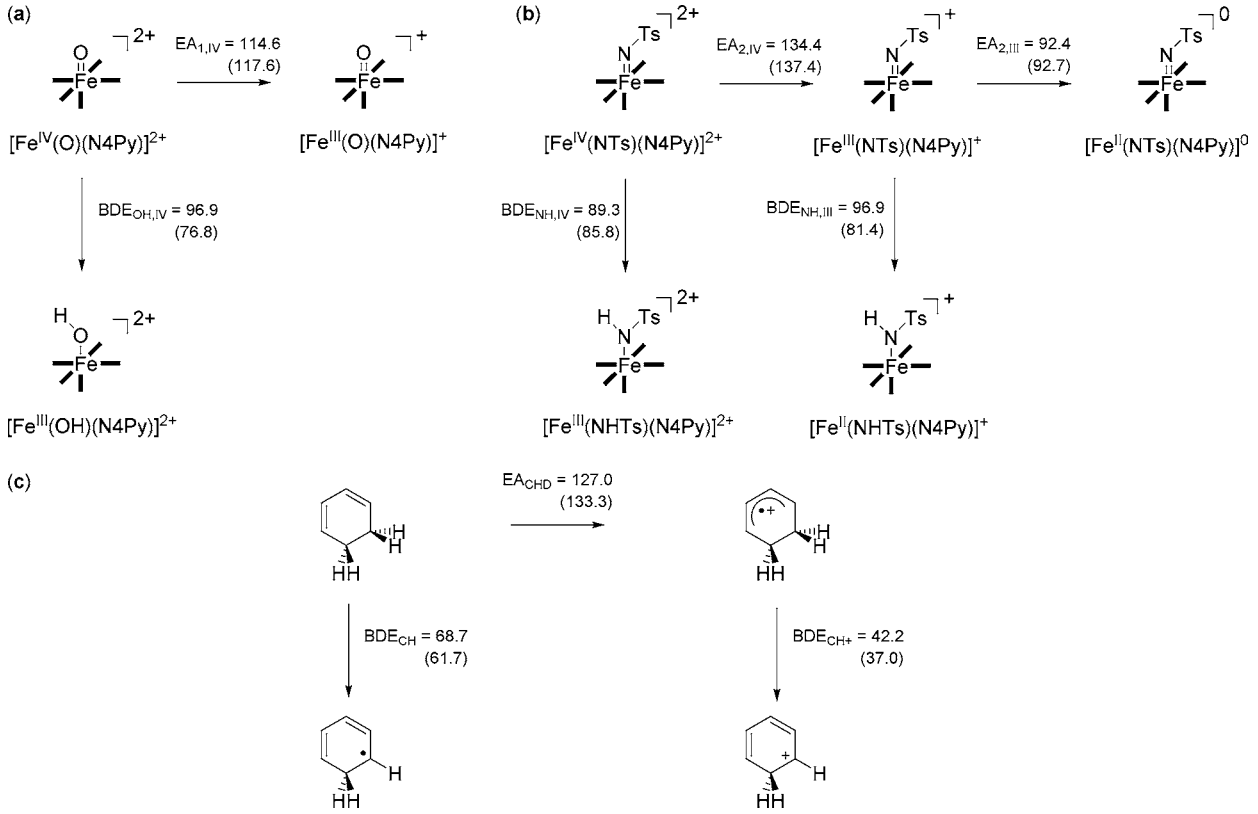

Figure 8. Thermochemical cycles for electron and hydrogen atom transfer from $[Fe^{IV}(O)(N4Py)]^{2+}$ (a), $[Fe^{IV}(NTs)(N4Py)]^{2+}$ (b), and cyclohexadiene (c). All data obtained after a UB3LYP/BS2//UB3LYP/BS1 calculation in a dielectric constant. Data out of parentheses are ΔE + ZPE values in solvent, whereas free energies are in parentheses.

the substrate and hence has an almost zero Hammett ρ value. By contrast, the iron(IV)-tosylimido complex starts the reaction with an electron transfer and the formation of a substrate cation radical. This large charge accumulation on the substrate has a strong effect on the Hammett parameter and as a result a value of $\rho = -1.71$ is obtained.

To further understand the intricate details of HAT reaction mechanisms by $[Fe^{IV}(O)(N4Py)]^{2+}$ versus $[Fe^{IV}(NTs)(N4Py)]^{2+}$, we did a valence bond (VB) and thermochemical analysis on the basic chemical properties of oxidants and substrates. Figure 7 displays the curve crossing diagrams of hydrogen atom abstraction by the reactant complexes $\mathbf{R}_{H1,1}$ and $\mathbf{R}_{H1,2}$. As discussed above, approach of CHD on an iron(IV)-oxo species gives $\mathbf{R}_{H1,1}$ or $[Fe^{IV}(O)(N4Py)]^{2+}\cdots$CHD. However, when CHD approaches the $[Fe^{IV}(NTs)(N4Py)]^{2+}$ complex instead, an electron transfer takes place to form $\mathbf{R}_{H1,2}$ or $[Fe^{III}(NTs)(N4Py)]^{+}\cdots CHD^{+\bullet}$. Figure 7 reflects these starting conditions and discusses the hydrogen atom abstraction mechanism from the reactant complexes.

The valence bond (VB) curve crossing diagrams start at the bottom left with the reactant complexes, that is, $\mathbf{R}_{H1,1}$ or $\mathbf{R}_{H1,2}$, which have a reactant wave function Ψ_{R1} and Ψ_{R2}, respectively. We then consider the hydrogen atom abstraction leading to intermediates $\mathbf{I}_{H1}/\mathbf{I}_{H2}$, which are described on the bottom right-hand-side of the figure with product wave function Ψ_{I1}/Ψ_{I2}. The crossing of the reactant and product wave functions leads to an avoided crossing and a hydrogen atom abstraction barrier with energy $\Delta E^{\ddagger}_{HAT}$. Previously, it has been shown that $\Delta E^{\ddagger}_{HAT}$ is proportional to a fraction of the excitation energy (G) for the excitation from Ψ_R to Ψ_R* in the reactant geometry.[45] In order to understand the factors that determine the actual value of G in the reaction of $[Fe^{IV}(O)(N4Py)]^{2+}$ and $[Fe^{IV}(NTs)(N4Py)]^{2+}$ with CHD, we display the VB structures of the ground and excited states corresponding to the Ψ_R and Ψ_R* wave functions. Note that upon approach of the substrate to $[Fe^{IV}(NTs)(N4Py)]^{2+}$ an electron transfer has taken place; therefore, we use $[Fe^{III}(NTs)(N4Py)]^{+}\cdots CHD^{+\bullet}$ as a reactant configuration instead.

The iron(IV)-oxo complex has electronic configuration $\pi_{xz}{}^2\pi_{yz}{}^2\pi^*_{xy}{}^2\pi^*_{xz}{}^1\pi^*_{yz}{}^1$ in a ground state triplet. The π_{xz}/π^*_{xz} and π_{yz}/π^*_{yz} pair of orbitals are located along the Fe−O bond, and the electrons in these orbitals are identified with dots, while the π^*_{xy} electrons have been omitted from Figure 7 for clarity. Hydrogen atom abstraction splits the π_{xz}/π^*_{xz} pair of orbitals back into atomic orbitals with two electrons in $3d_{xz}$ and a single electron in $2p_x$. The latter electron pairs up with the electron of the incoming hydrogen atom to form a σ_{OH} bond.

A comparison between the VB structures representing Ψ_{R1} and Ψ_{R1}* should give information on the components that affect the excitation energy and consequently the hydrogen atom abstraction barrier. The difference between the two VB structures highlights the breaking of the C−H bond of the substrate, the formation of the O−H bond, and the dehybridization of the π_{xz}/π^*_{xz} pair of orbitals. The excitation energy, $G_{HAT,FeO}$, therefore, includes the energy to break the C−H bond of the substrate, that is, BDE_{CH}, the energy to form an O−H bond, that is, BDE_{OH}, and finally the energy to split the π_{xz}/π^*_{xz} pair of molecular orbitals into atomic orbitals, E_{xz}, eq 7.

$$G_{HAT,FeO} = E_{xz} + BDE_{CH} - BDE_{OH} \quad (7)$$

dx.doi.org/10.1021/ja508403w | J. Am. Chem. Soc. 2014, 136, 17102−17115

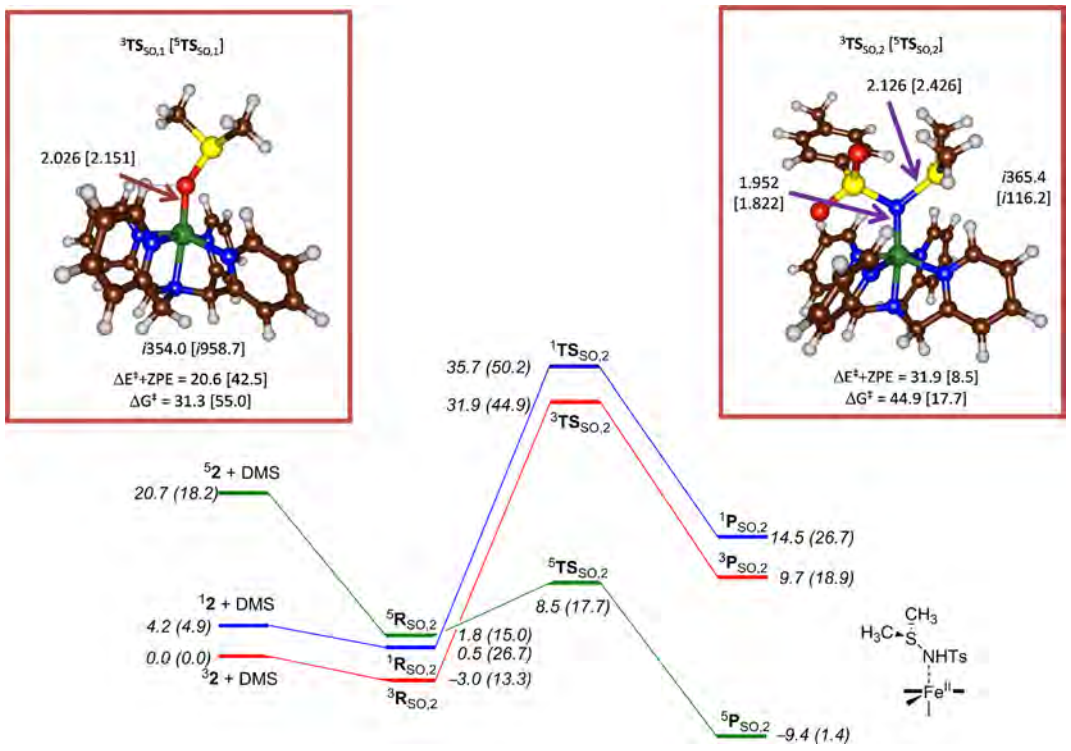

Figure 9. Potential energy landscape of dehydrogenation of CHD by $[Fe^{IV}(NTs)(N4Py)]^{2+}$ with energies relative to isolated reactants in kcal mol^{-1}. Out of parentheses are given ΔE + ZPE values in solvent, whereas free energies with solvent and entropic and thermal corrections are given in parentheses. Also shown are optimized geometries of $\mathbf{TS}_{SO,1}$ and $\mathbf{TS}_{SO,2}$ with bond lengths in angstroms and the imaginary frequency in wave numbers.

The situation is radically different for the reaction of $[Fe^{IV}(NTs)(N4Py)]^{2+}$ with CHD, where prior to the formation of the reactant complex an electron transfer has taken place. Figure 7b, therefore, starts bottom left with the $[Fe^{III}(NTs)(N4Py)]^{+}$ in close approach with CHD cation radical. The reactant wave function for this system is $3d_{xz}{}^{2}2p_{x}{}^{2}\pi_{yz}{}^{2}\pi^{*}_{xy}{}^{2}\pi^{*}_{yz}{}^{1}$. In the hydrogen atom abstraction, the C−H bond of the substrate ($CHD^{+\bullet}$) is broken, which will cost BDE_{CH+}. Note that with the iron(IV)-oxo species a hydrogen atom abstraction is from CHD, whereas with the iron(III)-tosylimido group it is from $CHD^{+\bullet}$. The values of BDE_{CH} and BDE_{CH+} are different, *vide infra*.

The hydrogen atom attacks the $2p_x$ orbital and forms a new σ_{NH} bond; however, since there are three electrons in the interaction, one of those is promoted into the $\sigma^{*}_{z^2}$ orbital, and therefore the bond formation energy is equal to the energy to form the N−H bond, that is, BDE_{NH}, plus the excitation energy from $2p_x$ to $\sigma^{*}_{z^2}$, E_{ex}. In addition, the radical left behind on the carbon atom, which originally bound the hydrogen atom conjugates with the remaining electrons of the $CHD^{+\bullet}$ π-system with energy E_{π}, eq 8.

$$G_{HAT,FeNTs} = E_{\pi} + E_{ex} + BDE_{CH+} - BDE_{NH} \quad (8)$$

To get a feeling for the magnitude of $G_{HAT,FeO}$ versus $G_{HAT,FeNTs}$, we calculated the various bond dissociation energies (BDEs) and ionization energies (IEs) as summarized in the thermochemical cycles in Figure 8. We calculate values ΔE + ZPE of 68.7 kcal mol^{-1} for BDE_{CH} and 96.9 kcal mol^{-1} for BDE_{OH}. The value of E_{xz} in eq 7 is estimated from the energy gap between the π_{xz} and π^{*}_{xz} α-orbitals in $^{3}[Fe^{IV}(O)(N4Py)]^{2+}$ for which we find 76.7 kcal mol^{-1}. Therefore, $G_{HAT,FeO}$ is estimated to have a value of 48.5 kcal mol^{-1}. Generally, the barrier height is about one-third of the height of the excitation energy G,[46] which in our case would lead to a VB predicted barrier height of $\Delta E^{\ddagger}_{HAT,FeO}$ = 16.2 kcal mol^{-1} for the reaction between **1** and CHD. The VB predicted barrier matches the DFT calculated one of 15.7 kcal mol^{-1} (Supporting Information, Table S31) perfectly.

Using a similar approach, we estimate the excitation energy $G_{HAT,FeNTs}$: the bond energy of the C−H bond in $CHD^{+\bullet}$ is BDE_{CH+} = 42.2 kcal mol^{-1}, whereas the N−H bond formation energy between $[Fe^{III}(NTs)(N4Py)]^{+}$ and a hydrogen atom is BDE_{NH} = 96.9 kcal mol^{-1} (Figure 8).

The $2p_x \rightarrow \sigma^{*}_{z^2}$ excitation energy is taken from the difference in energy of these orbitals in $[Fe^{III}(NTs)(N4Py)]^{+}$ and estimated to be 72.9 kcal mol^{-1}. The π-conjugation energy of olefins was previously reported to be about 32 kcal mol^{-1}.[47] As such, a value of $G_{HAT,FeNTs}$ = 50.2 kcal mol^{-1} is predicted from VB theory. A fraction of one-third of this value would give a $\Delta E^{\ddagger}_{HAT,FeNTs}$ = 16.7 kcal mol^{-1} again in good agreement with the DFT calculations reported in Figure 5. Furthermore, the VB estimated barriers reproduce the experimentally observed and DFT calculated ordering.

In conclusion, the VB curve crossing diagrams predict the iron(IV)-oxo species to be more reactive with CHD than the corresponding iron(III)-tosylimido system, because of a large contribution to the excitation energy for $2p_x$ to $\sigma^{*}_{z^2}$ promotion. Even though the driving force of the reaction for $[Fe^{III}(NTs)(N4Py)]^{+}$ with $CHD^{+\bullet}$ is larger than the one for $[Fe^{IV}(O)(N4Py)]^{2+}$ with CHD as also follows from the differences in BDE values.

The data in Figure 8 also shows that the electron affinity of **2** is considerably larger than that of **1** by about 20 kcal mol^{-1}. As

dx.doi.org/10.1021/ja508403w | J. Am. Chem. Soc. 2014, 136, 17102−17115

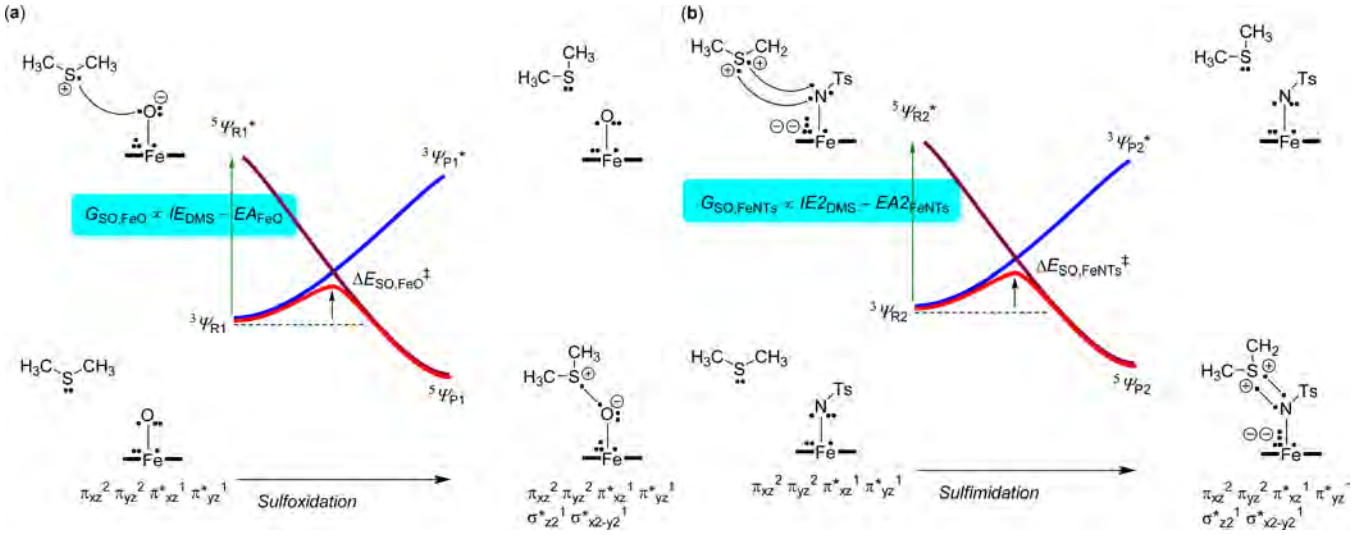

Figure 10. Valence bond curve crossing diagrams for sulfoxidation/sulfimidation from substrate by $[Fe^{IV}(O)(N4Py)]^{2+}$ (a) and $[Fe^{III}(NTs)(N4Py)]^{+}$ (b). Valence electrons are identified with a dot, and lines (straight or bent) in chemical structures refer to bonds.

a result of this, the electron transfer reaction of **1** with CHD is endergonic, whereas it is exergonic with **2**, eqs 9 and 10.

$$\mathbf{1} + \mathrm{CHD} \rightarrow [Fe^{III}(O)(N4Py)]^{+} + \mathrm{CHD}^{+\bullet} \qquad \Delta G = 15.8\ \mathrm{kcal\ mol^{-1}} \tag{9}$$

$$\mathbf{2} + \mathrm{CHD} \rightarrow [Fe^{III}(NTs)(N4Py)]^{+} + \mathrm{CHD}^{+\bullet} \qquad \Delta G = -4.1\ \mathrm{kcal\ mol^{-1}} \tag{10}$$

Indeed, a geometry optimization of the reactant complexes $\mathbf{R}_{H1,1}$ and $\mathbf{R}_{H1,2}$ shows that the iron(IV)-tosylimido group is reduced to an iron(III) species, whereas no electron transfer has occurred for the iron(IV)-oxo intermediate. As a consequence, the hydrogen atom abstraction in $\mathbf{TS}_{H1,1}$ is from CHD, whereas it is from $\mathrm{CHD}^{+\bullet}$ in $\mathbf{TS}_{H1,2}$. The C−H bond strength in $\mathrm{CHD}^{+\bullet}$ is considerably weaker than that in CHD by ΔG = 24.7 kcal $\mathrm{mol^{-1}}$, which should lower the barrier as well.

In order to find out whether the thermodynamics and kinetics of eq 10 is affected by the tosyl group bound to the iron(IV)-imido, we decided to calculate the same reaction for $[Fe^{IV}(NCH_3)(N4Py)]^{2+}$ and $[Fe^{IV}(NC_6H_5)(N4Py)]^{2+}$ as possible oxidants. We find free energy values (ΔG with solvent corrections) for eq 10 of 25.1 kcal $\mathrm{mol^{-1}}$ for $[Fe^{IV}(NCH_3)(N4Py)]^{2+}$ and 20.1 kcal $\mathrm{mol^{-1}}$ for $[Fe^{IV}(NC_6H_5)(N4Py)]^{2+}$. Consequently, the tosylimido group is strongly electron-withdrawing and enables a long-range electron transfer, while this is not possible with the alternative $[Fe^{IV}(NCH_3)(N4Py)]^{2+}$ and $[Fe^{IV}(NC_6H_5)(N4Py)]^{2+}$ complexes.

A HAT reaction of a substrate with **1** or **2** will lead to radical intermediates **I** with a reaction (free) energy equal to the difference in BDE_{CH} and BDE_{NH}/BDE_{OH}. Moreover, often the natural logarithm of the rate constant for HAT also is proportional to either BDE_{CH} or BDE_{OH} as seen in several examples of metal-oxo complexes.[48] Technically, however, the BDE_{OH} value essentially represents an electron and a proton transfer, which do not necessarily transfer to the same place. The BDE_{OH} is described in eq 11 into individual components for the electron affinity (EA), the acidity of the hydroxo group (ΔG_{acid}), and the ionization energy of an isolated hydrogen atom (IE_H).[49]

$$BDE_{OH} = -EA - \Delta G_{acid} - IE_H \tag{11}$$

The ionization energy of a hydrogen atom is 13.598 eV,[50] and together with our reported values of BDE_{OH}/BDE_{NH} and EA from Figure 8, we calculate a ΔG_{acid} = 211.8 kcal $\mathrm{mol^{-1}}$ for $[Fe^{IV}(O)(N4Py)]^{2+}$, whereas values of 262.1 and 343.5 kcal $\mathrm{mol^{-1}}$ are found for $[Fe^{IV}(NTs)(N4Py)]^{2+}$ and $[Fe^{III}(NTs)(N4Py)]^{2+}$. Thus, based on the acidity values, one would expect the iron(IV)-tosylimido and iron(III)-tosylimido complexes to be much better oxidants of HAT reactions. Indeed, the DFT calculated reaction energy for the HAT reaction is well larger for **2** than it is for **1** in agreement with the relative acidity values. The fact that the barrier heights do not follow this trend is due to stereochemical interactions of the approaching substrate with the bulky tosylimido group. The iron(IV)-oxo group, on the other hand, experiences very little stereochemical interactions with the approaching substrate.

Sulfoxidation Mechanisms. Subsequently, we investigated the sulfoxidation and sulfimidation of dimethylsulfide (DMS) by **1** and **2**, respectively, and the calculated potential energy profile for $[Fe^{IV}(NTs)(N4Py)]^{2+}$ is given in Figure 9, as well as the rate determining transition states for all systems calculated. The collision of DMS with oxidant leads to the formation of a reactant complex $\mathbf{R}_{SO}$, and heteroatom oxidation proceeds via barrier $\mathbf{TS}_{SO}$ to form the product complexes $\mathbf{P}_{SO}$. In both sets of calculations, the substrate approaches the oxidant from the side and reacts in a concerted pathway by insertion of the sulfide into the O/N system. Optimized geometries of the transition states give an FeN−SMe_2 distance that is only slightly longer than the FeO−SMe_2 distance, and in both cases it is longer in the quintet than in the triplet spin state.

The imaginary frequencies found for the $\mathbf{TS}_{SO}$ barriers are significantly lower than the ones reported above for the hydrogen atom abstraction barriers because heavier atoms are involved in the motion. The geometries and imaginary frequencies are in good agreement with previous substrate sulfoxidation transition states from the literature.[51]

In both chemical systems, the product complexes are most stable in the quintet spin state, whereas reactants (**1** and **2**) have a triplet spin ground state. This indicates that a spin crossover from triplet to quintet will need to take place on the potential energy surface during the course of the reaction. In

dx.doi.org/10.1021/ja508403w | J. Am. Chem. Soc. 2014, 136, 17102−17115

the sulfimidation reaction, the quintet spin transition state is well below the triplet in energy ($\Delta G^{\ddagger}$ = 17.7 kcal mol^{-1} for ^{5}**TS**$_{SO,2}$ and $\Delta G^{\ddagger}$ = 44.9 kcal mol^{-1} for ^{3}**TS**$_{SO,2}$), and consequently the spin state crossing happens well before the sulfimidation barrier.

The opposite is found for the reaction starting with the iron(IV)-oxo species, where ^{3}**TS**$_{SO,1}$ is lower in energy than ^{5}**TS**$_{SO,1}$. Furthermore, the absolute value of the barrier height for sulfoxidation is well higher than the sulfimidation reaction. Therefore, DFT predicts dimethylsulfide to react faster with [Fe^{IV}(NTs)(N4Py)]$^{2+}$ than with [Fe^{IV}(O)(N4Py)]$^{2+}$ in agreement with experimental observation (compare with Table 1).

Note that in the corresponding reactant complexes (**R**$_{SO,1}$ and **R**$_{SO,2}$) no charge transfer has occurred from substrate to oxidant in contrast to the results described in Figure 6 for **R**$_{H,2}$. This implies that the reactivities of **1** as well as the sulfimination by **2** start from an iron(IV) species, whereas the reaction of hydrogen atom abstraction by **2** is performed by its reduced species, that is, [Fe^{III}(NTs)(N4Py)]$^{+}$, and ionized CHD. Because of this difference the reactivity pattern has changed.

To further understand the heteroatom oxidation mechanism by **1** and **2** and to find the origin of the reactivity differences, we developed the corresponding VB curve crossing diagrams (Figure 10). These diagrams are similar to those reported above for the HAT processes but now connect the reactant wave function ($^{3}\Psi_{R}$) with the product wave function ($^{5}\Psi_{P}$) directly in a concerted reaction step. The sulfoxidation by iron(IV)-oxo complexes follows a VB diagram as reported before,[45c,52] whereby essentially a single electron transfer in the transition state for S−O bond formation occurs.

One of the electrons from one of the lone-pairs of the DMS substrate is transferred to the iron (into the $\sigma^{*}_{z^2}$ orbital), and a new S−O bond is formed between the singly occupied orbital on S with the singly occupied 2p$_x$ orbital on oxygen. The corresponding promotion gap for the sulfoxidation of DMS by **1** will, therefore, be proportional to the ionization potential of DMS (IE$_{DMS}$) as well as the electron affinity of **1** (EA$_{FeO}$). Indeed previous studies on trends in substrate sulfoxidation by iron(IV)-oxo complexes showed a linear correlation between the barrier height (**TS**$_{SO}$) and the IE of the substrate.[51c]

In the case of the reaction of DMS with **2**, the orbital occupation and group spin densities in the transition state implicate a double electron transfer and the formation of an electronic state that resembles the product complex. Thus, the double electron transfer with **2** occurs early on the potential energy surface and both electrons are transferred in the **TS**, while with **1** only one electron has moved yet in **TS**$_{SO}$. Because of this, the barrier height according to the VB curve crossing diagram will be dependent on the second ionization potential of DMS (IE2$_{DMS}$) for the removal of two electrons (from both lone pairs on sulfur) from DMS. At the same time, the oxidant accepts two electrons (into $\sigma^{*}_{x^2-y^2}$ and $\sigma^{*}_{z^2}$), and hence the double electron affinity (EA2$_{FeNTs}$) will determine the barrier height. The free energy (ΔG_{solv}) for conversion of [Fe^{IV}(NTs)(N4Py)]$^{2+}$ into [Fe^{III}(NTs)(N4Py)]$^{+}$ is 137.4 kcal mol^{-1} and the subsequent electron abstraction another 92.7 kcal mol^{-1} (Figure 8).

By contrast, the first electron affinity for [Fe^{IV}(O)(N4Py)]$^{2+}$ is 117.6 kcal mol^{-1}, and the addition of a second electron is 74.8 kcal mol^{-1}. Consequently, the two electron abstraction by **2** is 37.7 kcal mol^{-1} more favorable than that by **1**, which makes the two-electron transfer process for the heteroatom oxidation thermochemically favorable for the [Fe^{IV}(NTs)(N4Py)]$^{2+}$ complex, and as a result **TS**$_{SO,1}$ is higher in energy than **TS**$_{SO,2}$. Therefore, the iron(IV)-tosylimido complex will react with higher rate constants with sulfides than the corresponding iron(IV)-oxo complex.

The DFT and VB analyses, therefore, highlight the differences in chemical properties of [Fe^{IV}(NTs)(N4Py)]$^{2+}$ versus [Fe^{IV}(O)(N4Py)]$^{2+}$ that enable differences in reactivity patterns.

CONCLUSIONS

A combined kinetics and computational study is presented on the relative oxidative power of iron(IV)-oxo and iron(IV)-tosylimido. The experimental studies show that the iron(IV)-tosylimido reacts faster in heteroatom oxidation reactions, such as sulfimidation, compared with the iron(IV)-oxo species. However, the opposite trend is found for HAT reactions from, for example, *para*-X-benzyl alcohol and fluorene. Subsequent DFT calculations confirmed the experimentally observed trends and gave smaller barriers for HAT by iron(IV)-oxo complexes relative to iron(IV)-imido, whereas the reverse trend is found for heteroatom transfer. The origin of the rate reversal was investigated through a thermochemical analysis of the bond breaking and electron transfer processes. It was found that the electron affinity of [Fe^{IV}(NTs)(N4Py)]$^{2+}$ is so high that it accepts electrons from HAT substrates at a large distance, which was due to differences in orbital interactions compared with the iron(IV)-oxo species. As a result of that, the actual HAT is performed by its reduced species, that is, [Fe^{III}(NTs)(N4Py)]$^{+}$, which is catalytically much less potent than an iron(IV)-oxo species. On the other hand, heteroatom transfer reactions do not start with a long-range electron transfer but proceed via a rate determining group transfer, whereby two-electrons are transferred to the iron(IV)-imido, whereas only one electron is transferred yet at the same point along the potential energy profile in the reaction with the iron(IV)-oxo complex. A thermochemical and valence bond analysis has identified the key components that drive the reaction mechanism and cause a reactivity preference switch from preferred heteroatom transfer for iron(IV)-tosylimido to hydrogen atom transfer for iron(IV)-oxo.

ASSOCIATED CONTENT

Supporting Information

Detailed description of methods and techniques as well as full data of the calculations, including optimized geometries and Cartesian coordinates, as well as tables with group spin densities, group charges, absolute (free) energies, and relative (free) energies. This material is available free of charge via the Internet at http://pubs.acs.org.

AUTHOR INFORMATION

Corresponding Authors

sam.devisser@manchester.ac.uk
dkclcre@yahoo.com
sastricv@iitg.ernet.in

Notes

The authors declare no competing financial interest.

ACKNOWLEDGMENTS

The National Service of Computational Chemistry Software (NSCCS) is thanked for providing generous CPU time. Research support was provided by the Department of Science

and Technology, India (SR/S1/IC-02/2009), and Council for Scientific & Industrial Research (01(2527)/11/EMR-II) to C.V.S. D.K. acknowledges Department of Science and Technology (New Delhi) for a Ramanujan Fellowship. A.S.F. thanks the Tertiary Education Trust Fund for a studentship.

REFERENCES

(1) (a) Sono, M.; Roach, M. P.; Coulter, E. D.; Dawson, J. H. *Chem. Rev.* **1996**, *96*, 2841−2888. (b) Groves, J. T. *Proc. Natl. Acad. Sci. U.S.A.* **2003**, *100*, 3569−3574. (c) Ortiz de Montellano, P. R., Ed. *Cytochrome P450: Structure, Mechanism and Biochemistry*, 3rd ed.; Kluwer Academic/Plenum Publishers: New York, 2004. (d) Denisov, I. G.; Makris, T. M.; Sligar, S. G.; Schlichting, I. *Chem. Rev.* **2005**, *105*, 2253−2277. (e) Kadish, K. M., Smith, K. M., Guilard, R., Eds. *Handbook of Porphyrin Science*; World Scientific: Hackensack, NJ, 2010. (f) Ortiz de Montellano, P. R. *Chem. Rev.* **2010**, *110*, 932−948. (g) O'Reilly, E.; Koehler, V.; Flitsch, S.; Turner, N. *Chem. Commun.* **2011**, *47*, 2490−2501. (h) Grogan, G. *Curr. Opin. Chem. Biol.* **2011**, *15*, 241−248.

(2) (a) Solomon, E. I.; Brunold, T. C.; Davis, M. I.; Kemsley, J. N.; Lee, S.-K.; Lehnert, N.; Neese, F.; Skulan, A. J.; Yang, Y.-S.; Zhou, J. *Chem. Rev.* **2000**, *100*, 235−349. (b) Bugg, T. D. H. *Curr. Opin. Chem. Biol.* **2001**, *5*, 550−555. (c) Costas, M.; Mehn, M. P.; Jensen, M. P.; Que, L., Jr. *Chem. Rev.* **2004**, *104*, 939−986. (d) Bruijnincx, P. C. A.; van Koten, G.; Klein Gebbink, R. J. M. *Chem. Soc. Rev.* **2008**, *37*, 2716−2744. (e) Bugg, T. D. H.; Ramaswamy, S. *Curr. Opin. Chem. Biol.* **2008**, *12*, 134−140. (f) Abu-Omar, M. M.; Loaiza, A.; Hontzeas, N. *Chem. Rev.* **2005**, *105*, 2227−2252. (g) Kryatov, S. V.; Rybak-Akimova, E. V.; Schindler, S. *Chem. Rev.* **2005**, *105*, 2175−2226. (h) Kovaleva, E. G.; Lipscomb, J. D. *Nat. Chem. Biol.* **2008**, *4*, 186−193. (i) He, P.; Moran, G. R. *Curr. Opin. Chem. Biol.* **2009**, *13*, 443−450.

(3) (a) Guengerich, F. P. *Chem. Res. Toxicol.* **2001**, *14*, 611−650. (b) Munro, A. W.; Girvan, H. M.; McLean, K. J. *Nat. Prod. Rep.* **2007**, *24*, 585−609.

(4) (a) Rittle, J.; Green, M. T. *Science* **2010**, *330*, 933−937. (b) de Visser, S. P.; Kumar, D., Eds., *Iron-Containing Enzymes: Versatile Catalysts of Hydroxylation Reactions in Nature*. RSC Publishing: Cambridge, U.K., 2011.

(5) (a) Groves, J. T. *J. Inorg. Biochem.* **2006**, *100*, 434−447. (b) Meunier, B.; de Visser, S. P.; Shaik, S. *Chem. Rev.* **2004**, *104*, 3947−3980.

(6) (a) White, R. E.; McCarthy, M. B. *J. Am. Chem. Soc.* **1984**, *106*, 4922−4926. (b) Svastits, E. W.; Dawson, J. H.; Breslow, R.; Gellman, S. H. *J. Am. Chem. Soc.* **1985**, *107*, 6427−6428. (c) Mahy, J.-P.; Bedi, G.; Battioni, P.; Mansuy, D. *J. Chem. Soc., Perkin Trans. II* **1988**, 1517−1524.

(7) (a) McIntosh, J. A.; Coelho, P. S.; Farwell, C. C.; Wang, Z. J.; Lewis, J. C.; Brown, T. R.; Arnold, F. H. *Angew. Chem., Int. Ed.* **2013**, *52*, 9309−9312. (b) Singh, R.; Bordeaux, M.; Fasan, R. *ACS Catal.* **2014**, *4*, 546−552.

(8) (a) Eikey, R. A.; Abu-Omar, M. M. *Coord. Chem. Rev.* **2003**, *243*, 83−124. (b) Berry, J. F. *Comments Inorg. Chem.* **2009**, *30*, 28−66. (c) Saouma, C. T.; Peters, J. C. *Coord. Chem. Rev.* **2011**, *255*, 920−937.

(9) (a) Bukowski, M. R.; Koehntop, K. D.; Stubna, A.; Bominaar, E. L.; Halfen, J. A.; Münck, E.; Nam, W.; Que, L., Jr. *Science* **2005**, *310*, 1000−1002. (b) Rohde, J.-U.; In, J.-H.; Lim, M. H.; Brennessel, W. W.; Bukowski, M. R.; Stubna, A.; Münck, E.; Nam, W.; Que, L., Jr. *Science* **2003**, *299*, 1037−1039. (c) Martinho, M.; Banse, F.; Bartoli, J.-F.; Mattioli, T. A.; Battioni, P.; Horner, O.; Bourcier, S.; Girerd, J.-J. *Inorg. Chem.* **2005**, *44*, 9592−9596. (d) Sastri, C. V.; Seo, M. S.; Park, M. J.; Kim, K. M.; Nam, W. *Chem. Commun.* **2005**, 1405−1407.

(10) (a) Che, C.-M.; Lo, V. K.-Y.; Zhou, C.-Y.; Huang, J.-S. *Chem. Soc. Rev.* **2011**, *40*, 1950−1975. (b) Lu, H.; Zhang, X. P. *Chem. Soc. Rev.* **2011**, *40*, 1899−1909. (c) Long, Z.; Liang, D. *Chin. Sci. Bull.* **2012**, *57*, 2352−2360. (d) Zdilla, M. J.; Dexheimer, J. L.; Abu-Omar, M. M. *J. Am. Chem. Soc.* **2007**, *129*, 11505−11511.

(11) See, for example, Zardi, P.; Caselli, A.; Macchi, P.; Ferretti, F.; Gallo, E. *Organometallics* **2014**, *33*, 2210−2218.

(12) (a) Scepaniak, J. J.; Bontchev, R. P.; Johnson, D. L.; Smith, J. M. *Angew. Chem., Int. Ed.* **2011**, *50*, 6630−6633. (b) Hohenberger, J.; Ray, K.; Meyer, K. *Nat. Commun.* **2012**, *3*, 1−13. (c) Torres-Alacan, J.; Das, U.; Filippou, A. C.; Vöhringer, P. *Angew. Chem., Int. Ed.* **2013**, *52*, 12833−12837. (d) Liu, Y.; Guan, X.; Wong, E. L.-M.; Liu, P.; Huang, J.-S.; Che, C.-M. *J. Am. Chem. Soc.* **2013**, *135*, 7194−7204. (e) Man, W.-L.; Xie, J.; Pan, Y.; Lam, W. W. Y.; Kwong, H.-K.; Ip, K.-W.; Yiu, S.-M.; Lau, K.-C.; Lau, T.-C. *J. Am. Chem. Soc.* **2013**, *135*, 5533−5536. (f) Man, W.-L.; Lam, W. W. Y.; Kwong, H.-K.; Yiu, S.-M.; Lau, T.-C. *Angew. Chem., Int. Ed.* **2012**, *51*, 9101−9104.

(13) Gouré, E.; Avenier, F.; Dubourdeaux, P.; Sénèque, O.; Albrieux, F.; Lebrun, C.; Clémancey, M.; Maldivi, P.; Latour, J.-M. *Angew. Chem., Int. Ed.* **2014**, *53*, 1580−1584.

(14) Klinker, E. J.; Jackson, T. A.; Jensen, M. P.; Stubna, A.; Juhász, G.; Bominaar, E. L.; Münck, E.; Que, L., Jr. *Angew. Chem., Int. Ed.* **2006**, *45*, 7394−7397.

(15) Vardhaman, A. K.; Barman, P.; Kumar, S.; Sastri, C. V.; Kumar, D.; de Visser, S. P. *Angew. Chem., Int. Ed.* **2013**, *52*, 12288−12292.

(16) Perrin, D. D., Ed., *Purification of Laboratory Chemicals*; Pergamon Press: Oxford, U.K., 1997.

(17) (a) Sharefkin, J. G., Ed. *Organic Syntheses*; Wiley: New York, 1973; Vol. *5*, p 658. (b) Taylor, S.; Gullick, J.; McMorn, P.; Bethell, D.; Bulman Page, P. C.; Hancock, F. E.; King, F.; Hutchings, G. J. *J. Chem. Soc., Perkin Trans. II* **2001**, 1714−1723.

(18) (a) Lubben, M.; Meetsma, A.; Wilkinson, E. C.; Feringa, B.; Que, L., Jr. *Angew. Chem., Int. Ed.* **1995**, *34*, 1512−1515. (b) Vardhaman, A. K.; Barman, P.; Kumar, S.; Sastri, C. V.; Kumar, D.; de Visser, S. P. *Chem. Commun.* **2013**, *49*, 10926−10928.

(19) (a) Kaizer, J.; Klinker, E. J.; Oh, N. Y.; Rohde, J.-U.; Song, W. J.; Stubna, A.; Kim, J.; Münck, E.; Nam, W.; Que, L., Jr. *J. Am. Chem. Soc.* **2004**, *126*, 472−473. (b) Vardhaman, A. K.; Sastri, C. V.; Kumar, D.; de Visser, S. P. *Chem. Commun.* **2011**, *47*, 11044−11046.

(20) (a) *Jaguar*, version 7.9, Schrodinger, LLC: New York, NY, 2011. (b) Frisch, M. J. et al. *Gaussian 09*, revision C.01; Gaussian, Inc.: Wallingford, CT, 2010.

(21) Cossi, M.; Barone, V.; Cammi, R.; Tomasi, J. *Chem. Phys. Lett.* **1996**, *255*, 327−335.

(22) See, for example, (a) Latifi, R.; Sainna, M. A.; Rybak-Akimova, E. V.; de Visser, S. P. *Chem.—Eur. J.* **2013**, *19*, 4058−4068. (b) Quesne, M. G.; Latifi, R.; Gonzalez-Ovalle, L. E.; Kumar, D.; de Visser, S. P. *Chem.—Eur. J.* **2014**, *20*, 435−446. (c) de Visser, S. P.; Quesne, M. G.; Martin, B.; Comba, P.; Ryde, U. *Chem. Commun.* **2014**, *50*, 262−282.

(23) (a) Becke, A. D. *J. Chem. Phys.* **1993**, *98*, 5648−5652. (b) Lee, C.; Yang, W.; Parr, R. G. *Phys. Rev. B* **1988**, *37*, 785−789.

(24) Hay, P. J.; Wadt, W. R. *J. Chem. Phys.* **1985**, *82*, 270−283.

(25) Grimme, S. *J. Chem. Phys.* **2006**, *124*, No. 034108.

(26) (a) Becke, A. D. *Phys. Rev. A* **1988**, *38*, 3098−3100. (b) Perdew, J. P. *Phys. Rev. B* **1986**, *33*, 8822−8824.

(27) Adamo, C.; Barone, V. *J. Chem. Phys.* **1999**, *110*, 6158−6169.

(28) Zhao, Y.; Truhlar, D. G. *Theor. Chem. Acc.* **2008**, *120*, 215−241.

(29) (a) de Visser, S. P. *Chem.—Eur. J.* **2006**, *12*, 8168−8177. (b) Heyes, D. J.; Sakuma, M.; de Visser, S. P.; Scrutton, N. S. *J. Biol. Chem.* **2009**, *284*, 3762−3767.

(30) Ji, L.; Zhang, J.; Liu, W.; de Visser, S. P. *Chem.—Asian J.* **2014**, *9*, 1175−1182.

(31) Nam, W.; Lee, Y.-M.; Fukuzumi, S. *Acc. Chem. Res.* **2014**, *47*, 1146−1154.

(32) Oh, N. Y.; Suh, Y.; Park, M. J.; Seo, M. S.; Kim, J.; Nam, W. *Angew. Chem., Int. Ed.* **2005**, *44*, 4235−4239.

(33) Cheng, W.-C.; Yu, W.-Y.; Li, C.-K.; Che, C.-M. *J. Org. Chem.* **1995**, *60*, 6840−6846.

(34) See, for example, (a) Meyer, K.; Roček, J. *J. Am. Chem. Soc.* **1972**, *94*, 1209−1214. (b) Pestovsky, O.; Bakac, A. *J. Am. Chem. Soc.* **2004**, *126*, 13757−13764. (c) Hanson, S. K.; Baker, R. T.; Gordon, J. C.; Scott, B. L.; Silks, L. A.; Thorn, D. L. *J. Am. Chem. Soc.* **2010**, *132*, 17804−17816.

(35) (a) Kumar, D.; Hirao, H.; Que, L., Jr.; Shaik, S. *J. Am. Chem. Soc.* **2005**, *127*, 8026−8027. (b) Hirao, H.; Kumar, D.; Que, L., Jr; Shaik, S. *J. Am. Chem. Soc.* **2006**, *128*, 8590−8606.
(36) (a) de Visser, S. P. *J. Am. Chem. Soc.* **2006**, *128*, 15809−15818. (b) de Visser, S. P. *Angew. Chem., Int. Ed.* **2006**, *45*, 1790−1793. (c) Ye, S.; Neese, F. *Proc. Natl. Acad. Sci. U.S.A.* **2011**, *108*, 1228−1233.
(37) (a) Karamzadeh, B.; Singh, D.; Nam, W.; Kumar, D.; de Visser, S. P. *Phys. Chem. Chem. Phys.* **2014**, *16*, 22611−22622. (b) de Visser, S. P.; Tan, L. S. *J. Am. Chem. Soc.* **2008**, *130*, 12961−12974.
(38) (a) Zhao, Y.; Truhlar, D. G. *Acc. Chem. Res.* **2008**, *41*, 157−167. (b) Schwabe, T.; Grimme, S. *Acc. Chem. Res.* **2008**, *41*, 569−579. (c) Weymuth, T.; Couzijn, E. P. A.; Chen, P.; Reiher, M. *J. Chem. Theory Comput.* **2014**, *10*, 3092−3103.
(39) (a) de Visser, S. P. *J. Am. Chem. Soc.* **2010**, *132*, 1087−1097. (b) Kumar, D.; Karamzadeh, B.; Sastry, G. N.; de Visser, S. P. *J. Am. Chem. Soc.* **2010**, *132*, 7656−7667. (c) Kumar, D.; Latifi, R.; Kumar, S.; Rybak-Akimova, E. V.; Sainna, M. A.; de Visser, S. P. *Inorg. Chem.* **2013**, *52*, 7968−7979.
(40) Kumar, D.; de Visser, S. P.; Sharma, P. K.; Cohen, S.; Shaik, S. *J. Am. Chem. Soc.* **2004**, *126*, 1907−1920.
(41) de Visser, S. P.; Ogliaro, F.; Shaik, S. *Angew. Chem., Int. Ed.* **2001**, *40*, 2871−2874.
(42) Kumar, D.; Tahsini, L.; de Visser, S. P.; Kang, H. Y.; Kim, S. J.; Nam, W. *J. Phys. Chem. A* **2009**, *113*, 11713−11722.
(43) (a) Conradie, J.; Ghosh, A. *Inorg. Chem.* **2010**, *49*, 243−248. (b) Jaccob, M.; Rajaraman, G. *Dalton Trans.* **2012**, *41*, 10430−10439.
(44) Leeladee, P.; Baglia, R. A.; Prokop, K. A.; Latifi, R.; de Visser, S. P.; Goldberg, D. P. *J. Am. Chem. Soc.* **2012**, *134*, 10397−10400.
(45) (a) Shaik, S.; Kumar, D.; de Visser, S. P. *J. Am. Chem. Soc.* **2008**, *130*, 10128−10140. (b) Shaik, S. *Phys. Chem. Chem. Phys.* **2010**, *12*, 8706−8720. (c) Shaik, S.; Lai, W.; Chen, H.; Wang, Y. *Acc. Chem. Res.* **2010**, *43*, 1154−1165.
(46) Shaik, S. S. *J. Am. Chem. Soc.* **1981**, *103*, 3692−3701.
(47) Fernández, I.; Frenking, G. *Chem. Commun.* **2006**, 5030−5032.
(48) See, for example, (a) Bordwell, F. G.; Cheng, J.-P.; Ji, G.-Z.; Satish, A. V.; Zhang, X. *J. Am. Chem. Soc.* **1991**, *113*, 9790−9795. (b) Mayer, J. M. *Acc. Chem. Res.* **1998**, *31*, 441−450. (c) Goldberg, D. P. *Acc. Chem. Res.* **2007**, *40*, 626−634. (d) Kang, Y.; Chen, H.; Jeong, Y. J.; Lai, W.; Bae, E. H.; Shaik, S.; Nam, W. *Chem.—Eur. J.* **2009**, *15*, 10039−10046.
(49) Green, M. T.; Dawson, J. H.; Gray, H. B. *Science* **2004**, *304*, 1653−1656.
(50) Lias, S. G. Ionization energy evaluation. In *NIST Chemistry Webbook*; Linstrom, P. J., Mallard, W. G., Eds.; NIST Standard Reference Database Number 69; National Institute of Standards andTechnology: Gaithersburg, MD, 2009; 20899 (http://webbook.nist.gov).
(51) (a) Sharma, P. K.; de Visser, S. P.; Shaik, S. *J. Am. Chem. Soc.* **2003**, *125*, 8698−8699. (b) Prokop, K. A.; Neu, H. M.; de Visser, S. P.; Goldberg, D. P. *J. Am. Chem. Soc.* **2011**, *133*, 15874−15877. (c) Kumar, D.; Sastry, G. N.; de Visser, S. P. *Chem.—Eur. J.* **2011**, *17*, 6196−6205.
(52) Shaik, S.; Wang, Y.; Chen, H.; Song, J.; Meir, R. *Faraday Discuss.* **2010**, *145*, 49−70.

PCCP

PAPER

Cite this: *Phys. Chem. Chem. Phys.*, 2014, **16**, 22611

Properties and reactivities of nonheme iron(IV)–oxo *versus* iron(V)–oxo: long-range electron transfer *versus* hydrogen atom abstraction†

Baharan Karamzadeh,[a] Devendra Singh,[b] Wonwoo Nam,*[c] Devesh Kumar*[b] and Sam P. de Visser*[a]

Received 11th July 2014,
Accepted 8th September 2014

DOI: 10.1039/c4cp03053b

www.rsc.org/pccp

Recent work of Nam and co-workers [J. Yoon, S. A. Wilson, Y. K. Jang, M. S. Seo, K. Nehru, B. Hedman, K. O. Hodgson, E. Bill, E. I. Solomon and W. Nam, *Angew. Chem., Int. Ed.*, 2009, **48**, 1257] on a biomimetic iron complex implicated a mixture of iron(IV)–oxo and iron(V)–oxo intermediates but the latter could not be spectroscopically characterized, hence its involvement was postulated. To gain insight into the relative activity of these iron(IV)–oxo *versus* iron(V)–oxo intermediates, we have performed an extensive density functional theory (DFT) study on the chemical properties of the chemical system of Nam *et al.*, namely $[Fe(O)(BQEN)(NCCH_3)]^{2+/3+}$ with BQEN = *N*,*N*′-dimethyl-*N*,*N*′-bis(8-quinolyl)ethane-1,2-diamine and their reactivity in hydrogen atom abstraction from ethylbenzene. We show that the perceived iron(V)–oxo species actually is an iron(IV)–oxo ligand cation radical, similar to cytochrome P450 compound I. Moreover, this intermediate has an extremely large electron affinity and therefore can abstract electrons from substrates readily. In our particular system, this means that prior to the hydrogen atom abstraction, an electron is abstracted to form an iron(IV)–oxo species, which subsequently abstracts a hydrogen atom from the substrate. Thus, our calculations show for the first time how some nonheme iron complexes react by long-range electron transfer and others directly *via* hydrogen atom abstraction. We have rationalized our results with detailed thermochemical cycles that explain the observed reactivity patterns.

Introduction

Nonheme iron dioxygenases are important enzymes for human health with essential functions that include DNA base repair mechanisms and oxidative cleavage of carotenoids.[1] In several organisms, natural product biosynthesis is catalysed by nonheme iron dioxygenases, and, therefore, they have important functions in biology as well as in biotechnology. In order to understand enzymatic reaction processes, synthetic model complexes have been developed and designed.[2] These biomimetic model complexes of nonheme iron oxidants are well studied and many biomimetic high-valent catalytic intermediates have been characterized in recent years.[3] For instance, to tackle the controversy in Rieske dioxygenases regarding the active oxidant in the reaction process, several biomimetic model complexes with iron(V)–oxo(hydroxo) as reactive features have been studied and their reactivity patterns established.[4]

All biomimetic Rieske dioxygenase models contain a hydroxo group in a *cis*-position of the iron(IV/V)–oxo group. Only few examples exist of biomimetic iron(V)–oxo intermediates without this *cis*-hydroxo ligand and spectroscopic studies gave indirect evidence of its existance.[5] Thus, McKenzie and co-workers reported the structural characterization of an iron(V)–oxo species with a monoionic multidentate ligand and found it to react with thioanisole efficiently.[6] Kim and co-workers used a tetradentate ligand system and formed the corresponding iron(V)–oxo species by heterolytic cleavage of an iron–acylperoxo intermediate.[7] They determined kinetic isotope effects (KIE, k_H/k_D), $H_2{}^{18}O$ exchange reactions and measured product distributions. Using a tetraamido macrocyclic ligand, Collins and co-workers studied the sulfoxidation of substrates by an iron(V)–oxo species and compared the rates with analogous iron(IV)–oxo species.[8] Finally, Nam and co-workers studied the reaction of $[Fe^{II}(BQEN)]^{2+}$, BQEN = *N*,*N*′-dimethyl-*N*,*N*′-bis(8-quinolyl) ethane-1,2-diamine, with CH_3CO_3H and found evidence of competing reaction mechanisms originating from

[a] *Manchester Institute of Biotechnology and School of Chemical Engineering and Analytical Science, the University of Manchester, 131 Princess Street, Manchester M1 7DN, UK. E-mail: sam.devisser@manchester.ac.uk; Fax: +44 (0)1613065201; Tel: +44 (0)1613064882*

[b] *Department of Applied Physics, School for Physical Sciences, Babasaheb Bhimrao Ambedkar University, Vidya Vihar, Rai Bareilly Road, Lucknow 226 025, India. E-mail: dkclcre@yahoo.com*

[c] *Department of Chemistry and Nano Science, Ewha Womans University, Seoul 120-750, Korea. E-mail: wwnam@ewha.ac.kr*

† Electronic supplementary information (ESI) available: Tables with absolute and relative energies as well as group spin densities and charges. See DOI: 10.1039/c4cp03053b

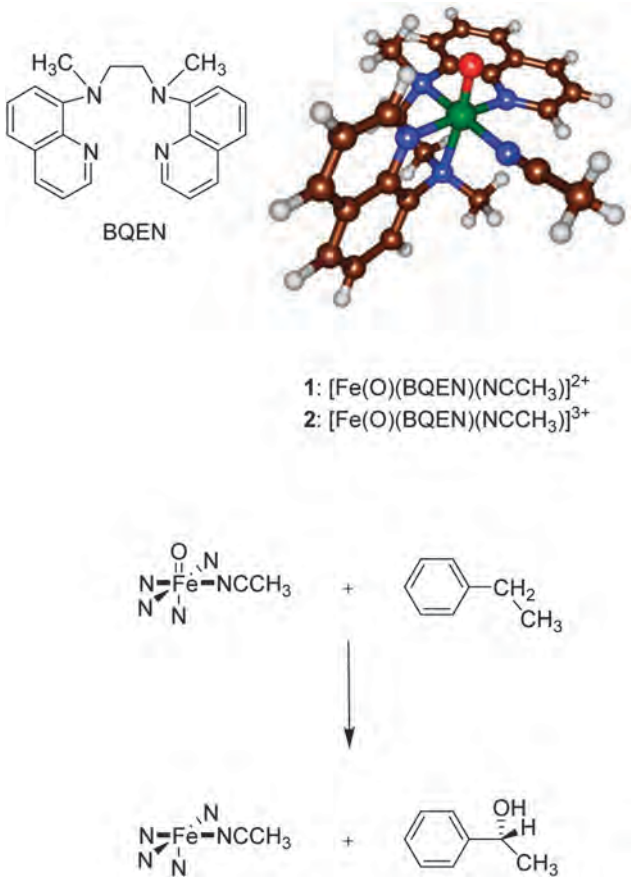

Scheme 1 Iron–oxo oxidants and ligand system studied in this work.

two oxidants in the reaction mixture that were tentatively assigned as $[Fe^{IV}(O)(BQEN)]^{2+}$ and $[Fe^{V}(O)(BQEN)]^{3+}$.[9] Their studies failed to unequivocally assign the active oxidant in the reaction mechanism, and therefore could not determine the relative reactivity of iron(IV)–oxo *versus* iron(V)–oxo. In order to resolve this dichotomy and gain general insight into the relative reactivity of iron(IV)–oxo *versus* iron(V)–oxo with nonheme ligand systems a computational study was conducted using the $[Fe^{IV}(O)(BQEN)(NCCH_3)]^{2+}$ (**1**) and $[Fe^{V}(O)(BQEN)(NCCH_3)]^{3+}$ (**2**) systems, Scheme 1.

Currently, very little is known regarding the catalytic activity of iron(V)–oxo intermediates and to the best of our knowledge, no direct comparison in reactivity between iron(IV)–oxo and iron(V)–oxo has been reported. We present here a DFT study to gain insight into the potential use of iron(V)–oxo intermediates as catalytic oxidants with ethylbenzene as the selected substrate. We present the first comparative study on the aliphatic hydroxylation by iron(IV)–oxo *versus* iron(V)–oxo using the BQEN ligand system shown in Scheme 1 and follow the mechanism of ethylbenzene activation leading to benzyl alcohol product complexes.

Methods

All studies reported here utilize density functional theory (DFT) methods as implemented in the Jaguar and Gaussian program packages.[10] We initially did exploratory gas-phase optimizations on $[Fe(O)(BQEN)(NCCH_3)]^{3+/2+}$ in Jaguar at the UB3LYP level of theory[11] and explored the catalytic mechanism of ethylbenzene hydroxylation. However, as most of our chemical systems are multiply charged ions we decided to do a subsequent set of calculations, where the complete project was done using a polarized continuum solvent model included during the geometry optimizations. These studies gave considerable differences from the gas-phase results and therefore we will focus on the solvent optimized calculations mainly. Details of the gas-phase calculations can be found in the ESI.† Thus, all geometry optimizations and frequencies were performed with a solvent model included with a dielectric constant mimicking acetonitrile. All local minima are characterized with a frequency calculation and have real frequencies only, whereas the transition states have one imaginary frequency for the correct mode. As transition metal containing complexes give close-lying electronic and spin states,[12] we calculated the $[Fe(O)(BQEN)(NCCH_3)]^{3+}$ complexes in the lowest lying doublet, quartet and sextet spin states and the $[Fe(O)(BQEN)(NCCH_3)]^{2+}$ complexes in the singlet, triplet and quintet spin states.

We tested the reproducibility and reliability of the density functional method by applying a range of unrestricted DFT methods, including B3LYP,[11] B3LYP-D3,[13] B3LYP*,[14] and OPBE.[15] There is a certain degree of fluctuation observed in the relative energies, spin state ordering and geometric details as commonly observed in nonheme iron complexes.[16] However, the results confirmed the assignment of the electron configuration of all complexes and reproduce experimental trends.

All optimizations and frequencies use a triple-ζ quality basis set (BS2) with LACV3P+ on iron and 6-311+G* on the rest of the atoms.[17] Previously, we used these methods extensively for the description of nonheme iron complexes and reproduced experimental free energies of activation within several kcal mol^{-1}.[18] To test the effect of the overall charge on the calculations we also performed a set of test calculations on charge neutral complexes, whereby the reactants and rate determining transition states were modified by counter-ions at a fixed distance of 15 Å from the axial nitrogen atom and with an angle of 120 degrees with respect to iron and the axial nitrogen atom. Point charges, Cl^- counter-ions and OH^- counter-ions were applied, but all results reproduced the solvent optimized results and did not give changes to the charge and spin distributions.

Kinetic isotope effects (KIEs) were calculated for the hydrogen atom abstraction reaction of ethylbenzene by **1** for the replacement of one or more hydrogen atoms of the substrate by deuterium atoms. We initially used the semi-classical Eyring equation (eqn (1)) to calculate KIE_E from the difference in free energies of activation ($\Delta G^{\ddagger}$) of the substrate and its deuterium substituted form following previously reported methods.[19] Eqn (1) uses the gas constant (R) and the actual temperature (273.15 K).

$$KIE_E = k_H/k_D = \exp\left\{\left(\Delta G^{\ddagger}_D - \Delta G^{\ddagger}_H\right)\Big/RT\right\} \qquad (1)$$

Further corrections due to tunnelling were applied using the Wigner model[20] that corrects KIE_E with the tunnelling ratio (Q_{tH}/Q_{tD}) as described in eqn (2) and (3).

 This journal is © the Owner Societies 2014

$$KIE_W = KIE_E \times Q_{tH}/Q_{tD} \quad (2)$$

$$Q_t = 1 + \frac{1}{24}\left(\frac{h\nu}{k_B T}\right)^2 \quad (3)$$

In eqn (3), k_B represents the Boltzmann's constant, h is Planck's constant and ν is the imaginary frequency in the transition state.

Results

Isolated reactants 1 and 2

Our study uses density functional theory (DFT) methods and is focused on the chemical systems of ref. 9 as described in Scheme 1, where we included an acetonitrile solvent molecule in the sixth ligand position of the metal: $[Fe(O)(BQEN)(NCCH_3)]^{2+}$ (**1**) and $[Fe(O)(BQEN)(NCCH_3)]^{3+}$ (**2**). These structures have the metal in formal oxidation state iron(IV) and iron(V), respectively. Before we will look into the reactivity patterns of structures **1** and **2** with substrates, we will describe the electronic properties of the optimized geometries of **1** and **2**, Fig. 1.

The lowest lying singlet, triplet and quintet spin states of **1** were calculated, but the singlet state was found to be high in energy. Similarly, **2** was investigated in the doublet and quartet spin states only. Fig. 1 displays the molecular valence orbitals of **1** and **2**, which are determined by the mixing of the metal 3d orbitals with its ligands. Thus, there are three π* molecular orbitals (π^*_{xy}, π^*_{yz}, π^*_{xz}) representing the anti-bonding interactions of the 3d iron orbitals with 2p orbitals on the oxo group. High in energy are two σ* orbitals for the anti-bonding interactions of the metal with the ligands in the *xy*-plane ($\sigma^*_{x^2-y^2}$) and with ligands along the *z*-axis ($\sigma^*_{z^2}$), whereby the *z*-axis is defined as parallel to the Fe–O bond. In the iron(IV)–oxo complex, *i.e.* ^{3,5}**1**, the set of orbitals shown in Fig. 1 is occupied by four electrons, which gives two low-lying solutions with either triplet or quintet spin: **1** has a triplet spin ground state with electronic configuration $\pi^*_{xy}{}^2\ \pi^*_{xz}{}^1\ \pi^*_{yz}{}^1$ (^{3}**1**) that is somewhat lower in energy than the quintet spin state with configuration $\pi^*_{xy}{}^1\ \pi^*_{xz}{}^1\ \pi^*_{yz}{}^1\ \sigma^*_{x^2-y^2}{}^1$ (^{5}**1**), *vide infra*. In both spin states **1** has the metal in formal oxidation state iron(IV). The spin state ordering matches previous studies on hexacoordinated non-heme iron biomimetic model complexes and also supports the experimentally reported absorption band at λ_{max} = 740 nm characteristic for triplet iron(IV)–oxo species and assigned by Nam *et al.* on $[Fe(O)(BQEN)(NCCH_3)]^{2+}$.[3,9,21]

Upon oxidation of ^{3,5}**1**, however, several possibilities arise for the electronic configuration of **2**. Firstly, ^{3}**1** can lose an electron from π^*_{yz} to give a doublet spin configuration with $\pi^*_{xy}{}^2\ \pi^*_{xz}{}^1$ orbital occupation or lose an electron from the

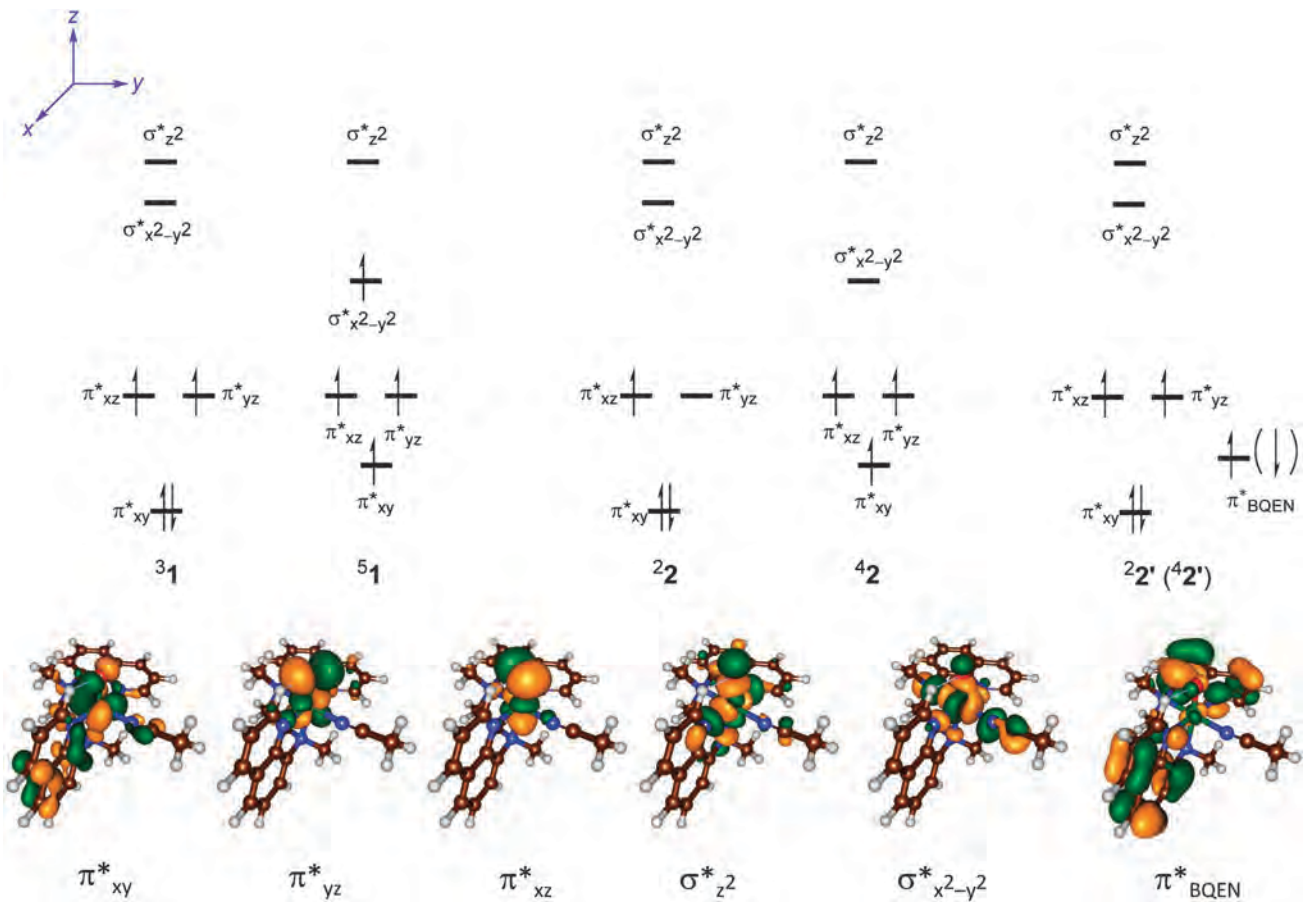

Fig. 1 High-lying occupied and low-lying virtual orbitals of **1** and **2**. The top panel shows the different electronic configurations of **1** and **2** considered and the bottom shows the orbital shapes of the valence orbitals.

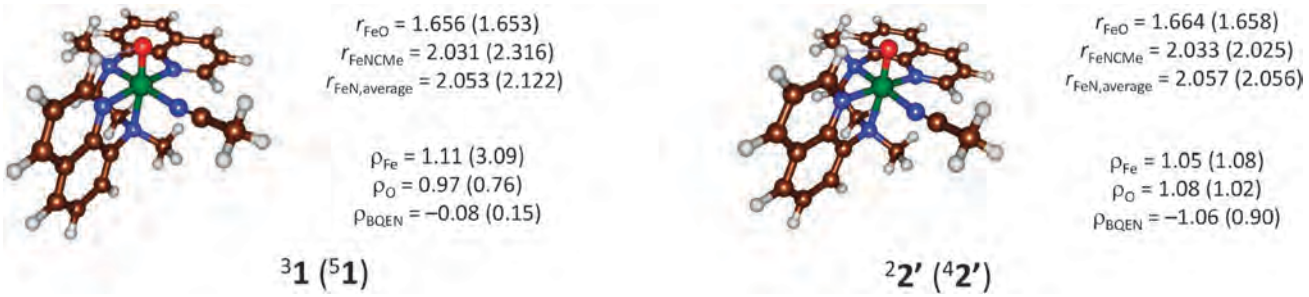

Fig. 2 Gas-phase optimized geometries (UB3LYP/BS1) of ^{3,5}**1** and ^{2,4}**2** with bond lengths in angstroms and group spin densities (ρ) in atomic units.

doubly occupied π^*_{xy} orbital to give a quartet spin complex with $\pi^*_{xy}{}^1\ \pi^*_{xz}{}^1\ \pi^*_{yz}{}^1$ configuration. These two states have the metal in formal oxidation state iron(v) and are labelled as ^{2,4}**2** in Fig. 1. In addition, the oxidation of ^{3}**1** can expel an electron from a ligand π-type orbital, such as π^*_{BQEN}, and lead to an electronic configuration $\pi^*_{xy}{}^2\ \pi^*_{xz}{}^1\ \pi^*_{yz}{}^1\ \pi^*_{BQEN}{}^1$, whereby the radical on the ligand can be either ferromagnetically or anti-ferromagnetically coupled to the metal-based unpaired electrons in an overall quartet or doublet spin state (^{4,2}**2**′). The latter, therefore, can be seen as an iron(IV)–oxo ligand cation radical species with configuration $[Fe^{IV}(O)(BQEN^{+\bullet})(NCCH_3)]^{3+}$ and is reminiscent of compound I of cytochrome P450 enzymes, which was characterized as an iron(IV)–oxo heme cation radical species, *i.e.* $[Fe^{IV}(O)(heme^{+\bullet})Cys]$.[22]

Details of the optimized geometries of ^{3,5}**1** and ^{2,4}**2**′ in the gas phase are reported in Fig. 2. In the gas-phase the triplet spin state is the ground state by ΔE + ZPE (ΔG) = 2.0 (0.2) kcal mol^{-1}. Optimized geometries are in line with previously reported structures on non-heme iron(IV)–oxo complexes with a short Fe–O bond of 1.66 Å, which implicates a double bond.[21,23] Group spin densities and charges confirm the orbital assignment of ^{3,5}**1** as described in Fig. 2 with electronic configuration of $\pi^*_{xy}{}^2\ \pi^*_{xz}{}^1\ \pi^*_{yz}{}^1$ for ^{3}**1** and $\pi^*_{xy}{}^1\ \pi^*_{xz}{}^1\ \pi^*_{yz}{}^1\ \sigma^*_{x^2-y^2}{}^1$ for ^{5}**1**.

Nam and co-workers[9] using absorption and infrared spectroscopy and extended X-ray absorption fine structure (EXAFS) studied the $[Fe(O)(BQEN)(NCCH_3)]^{2+}$ complex experimentally. They identified an iron–oxo bond of 1.67 Å and an average Fe–N distance of 1.97 Å. Our calculated Fe–O distances for ^{3,5}**1** in Fig. 2 match the experimental values excellently. The experimentally reported Fe–N distances are in good agreement with the triplet spin structures, but not with the quintet spin state structures due to single occupation of the $\sigma^*_{x^2-y^2}$ orbital that elongates the distances between the metal and its ligands. Therefore, the computational studies support the characterization of a triplet spin ground state of **1**.

Geometry optimizations of ^{2,4}**2**′, however, gives a low-lying solution with two singly occupied π* orbitals coupled to a radical on the BQEN unit with spin densities of ρ_{BQEN} = −1.06 (0.90) in the doublet and quartet spin states. The optimized geometries, therefore, correspond to an electronic state $[Fe^{IV}(O)(BQEN^{+\bullet})(NCCH_3)]^{3+}$, *i.e.* ^{2,4}**2**′ in Fig. 1, rather than the anticipated iron(v)–oxo species. Although we attempted to swap molecular orbitals to generate the iron(v) solution (^{2,4}**2**) these calculations converged back to ^{2,4}**2**′, which therefore is the molecular ground state.

As the complex has a large overall charge of +3, we decided to reoptimize these structures using the polarized continuum model mimicking an acetonitrile solution. However, the new model did not affect the spin state ordering and electronic configuration of the ground state and the same electronic state was found. It appears, therefore, that ^{2,4}**2**′ is the electronic ground state that can be described as $[Fe^{IV}(O)(BQEN^{+\bullet})(NCCH_3)]^{3+}$ with an iron(IV)–oxo group coupled to a ligand radical. As both doublet and quartet spin states represent the same orbital occupation, namely $\pi^*_{xy}{}^2\ \pi^*_{xz}{}^1\ \pi^*_{yz}{}^1\ \pi^*_{BQEN}{}^1$, we calculate them within 2 kcal mol^{-1}. This result is similar to the spin state energies of ferromagnetically *versus* antiferromagnetically coupled doublet and quartet spin states of compound I of P450, where these spin states were also found to be within a couple of kcal mol^{-1} from each other. Moreover, the energy gap was found to be sensitive to the local environment, including hydrogen bonding interactions to the oxidant as well as solvent effects.[24] Furthermore, these two spin states result in two-state-reactivity patterns with substrates on competing spin-state surfaces.[25] Analogously to P450 compound I, the iron(v)–oxo species is an excited state of the molecular ground state with configuration $[Fe^{IV}(O)(BQEN^{+\bullet})(NCCH_3)]^{3+}$. Geometrically ^{2,4}**2**′ has metal–ligand bond lengths close to those found for ^{3}**1**, which is also an iron(IV)–oxo species.

Reactant complexes

Subsequently, ethylbenzene (EB) was added to the model complexes to create a long-range reactant complex (**RC**) as this was one of the substrates used in the experimental study and we investigated the benzyl hydroxylation processes. The electronic features of ^{3,5}**RC**$_1$ or $^{3,5}[Fe(O)(BQEN)(NCCH_3)\cdots EB]^{2+}$ and ^{2,4}**RC**$_2$ or $^{2,4}[Fe(O)(BQEN)(NCCH_3)\cdots EB]^{3+}$ will be discussed prior to the investigation of the catalytic mechanism. Considering that computational modelling occasionally is sensitive to the choice of the density functional used as well as on environmental variables,[26] some thorough testing of the structures, spin-state energetics and electronic configurations of ^{3,5}**RC**$_1$ and ^{2,4}**RC**$_2$ using a selection of density functional methods and procedures was carried out. Thus, we performed geometry optimizations of all complexes in the gas-phase at UB3LYP/BS1, but also did a full geometry optimization in a dielectric constant mimicking acetonitrile at UB3LYP/BS2 and finally a full geometry optimization in a dielectric constant at the UB3LYP-D3/BS2. In addition, single point calculations on the UB3LYP/BS2 optimized geometries using B3LYP with 15% HF exchange (B3LYP*), UB3LYP-D3 and OPBE were

 This journal is © the Owner Societies 2014

Table 1 Spin state energies and optimized geometries of reactant complexes as calculated using various DFT methods

				ΔE + ZPE						
				UB3LYP	UB3LYP	UB3LYP-D3	UB3LYP-D3	UB3LYP	UB3LYP*	OPBE
Structure	r_{FeO} [a,b]	r_{FeO} [b,c]	r_{FeO} [b,e]	Gas[a,d]	Solv[c,d]	Solv[c,d]	Solv[d,e]	PC[c,f]	Solv[c,d]	Solv[c,d]
^{3}**RC**$_1$	1.656	1.633	1.657	0.0	0.0	0.0	0.0	0.0	0.0	0.0
^{5}**RC**$_1$	1.653	1.627	1.653	10.3	2.5	7.4	8.2	8.7	6.0	2.4
^{2}**RC**$_2$	1.664	1.638	1.656	0.0	0.0	0.0	0.0	0.0	0.0	0.0
^{4}**RC**$_2$	1.664	1.631	1.653	0.6	−3.6	10.0	8.4	10.0	6.9	3.8

[a] UB3LYP/BS1 geometry optimization in the gas-phase. [b] Values in Å. [c] UB3LYP/BS2 geometry optimization in solvent. [d] ΔE + ZPE value with energies at the BS2 level of theory in kcal mol^{-1}. [e] UB3LYP-D3/BS2 geometry optimization in solvent. [f] Structure with added point charges that neutralize the system at 15 Å.

performed. Finally, single point calculations in the gas-phase with additional counter-ions or point charges included in the model at a distance of 15 Å that neutralize the chemical systems were carried out.

Table 1 presents the optimized Fe–O distance and spin-state energies as obtained using these different DFT models and methods. As can be seen all methods, models and optimization techniques give the same spin state ordering, but a certain degree of variation in the relative energies is observed typical for DFT calculated iron complexes.[26] In all cases ^{3}**RC**$_1$ and ^{5}**RC**$_1$ are characterized as $[Fe^{IV}(O)(BQEN)(NCCH_3)\cdots EB]^{2+}$ with orbital occupation $\pi^*_{xy}{}^2\,\pi^*_{xz}{}^1\,\pi^*_{yz}{}^1$ and $\pi^*_{xy}{}^1\,\pi^*_{xz}{}^1\,\pi^*_{yz}{}^1\,\sigma^*_{x^2-y^2}{}^1$, respectively, in agreement with what was found for structure ^{3,5}**1** above. Regardless of the method and whether the optimization is done in the gas-phase or in solvent, a triplet spin ground state that is well separated from the quintet spin state by 2.4–10.3 kcal mol^{-1} is found. Although this appears to be a large variation in spin state energies, actually for transition metal complexes, and, in particular iron(IV)–oxo complexes a strong variation of the ordering and relative energies is normal in DFT upon changing the density functional method or environmental effects.[27] Nevertheless, all methods give a triplet spin ground state in support of experimental studies.[17]

The situation is dramatically changed when ^{2,4}**RC**$_2$ is investigated with these methods and models. Whereas ^{2,4}**2′** was found as the electronic ground state with configuration $[Fe^{IV}(O)(BQEN^{+\bullet})(NCCH_3)]^{3+}$ with two unpaired π* electrons coupled to a radical on the ligand, by contrast, in ^{2,4}**RC**$_2$ we find yet another electronic configuration with two unpaired π* electrons that are coupled to an ethylbenzene radical, *i.e.* orbital occupation $\pi^*_{xy}{}^2\,\pi^*_{xz}{}^1\,\pi^*_{yz}{}^1\,\pi^*_{BQEN}{}^2\,\pi_{EB}{}^1$, where the latter orbital is a singly occupied π-orbital on ethylbenzene. Therefore, addition of an ethylbenzene molecule to ^{2,4}**2′** results in an intermolecular electron transfer from the substrate into the π^*_{BQEN} orbital of the oxidant and the creation of a complex $[Fe^{IV}(O)(BQEN)(NCCH_3)]^{2+}\cdots EB^{+\bullet}$. This happens regardless of the method and whether gas-phase or solvent models are used. It implies that $[Fe^{IV}(O)(BQEN^{+\bullet})(NCCH_3)]^{3+}$ is a strong oxidant and can abstract electrons from substrates readily. Most probably this is caused by its extremely large electron affinity, *vide infra*.

Note that outer-sphere electron transfer upon approach of a substrate onto a metal–oxo species has been calculated before on metal–porphyrins,[28,29] including a potential intermediate of nitric oxide synthase, where the arginine substrate was found to donate an electron to an iron(IV)–oxo heme cation radical species quickly. Furthermore, approach of a Zn^{2+} ion onto a high-valent manganese(V)–oxo corrolazine also led to the formation of a manganese(IV)–oxo corrolazine cation radical through valence tautomerization.[29] Finally, studies on the comparative electronic features of the iron(IV)–oxo heme species of cytochrome *c* peroxidase (C*c*P) *versus* ascorbate peroxidase implicated differences in electronic configuration as a result of a bound cation at a distance of 15 Å from the heme. DFT modelling on compound **I** of C*c*P tested the effect of a point charge with magnitude $Q = -1/+1$ on the electronic configuration.[30] It was found that a charge of $Q = +1$ gave an electronic state $[Fe^{IV}(O)(heme^{+\bullet})\cdots Trp_{191}]$, whereas a value of $Q = -1$ resulted in an alternative state corresponding to $[Fe^{IV}(O)(heme)\cdots Trp_{191}{}^{+\bullet}]$. These studies have shown that seemingly small external (but long-range) perturbations can have a major impact on the electronic configuration of the oxidant and consequently on its ability to react with substrates. However, for nonheme metal–oxo species this would be the first example of outer-sphere electron transfer upon substrate approach and is likely caused by the large electron affinity of the ligand. In the following we will describe whether the change in electronic configuration is beneficial or disadvantageous to the catalysis.

Ethylbenzene hydroxylation by 1 and 2

Subsequently, the benzyl hydroxylation of ethylbenzene by ^{3,5}**RC**$_1$ and ^{2,4}**RC**$_2$ was calculated. Fig. 3 displays the calculated reaction mechanism with optimized geometries of the rate determining transition states of the reaction starting from ^{3,5}**RC**$_1$. We calculate a stepwise mechanism with an initial hydrogen atom abstraction from the benzyl position of ethylbenzene *via* a transition state (**TS**$_{HA}$) to form a radical intermediate (**I**) followed by hydroxyl rebound *via* a transition state (**TS**$_{reb}$) to form alcohol products (**P**). In all cases the hydrogen atom abstraction is rate determining and the rebound barriers are small or negligible, so that we will focus on the **TS**$_{HA}$ pathway only here. Full details of the rest of the mechanism are given in the ESI.† In the gas phase very little energy difference between hydrogen atom abstraction from the *pro-S versus pro-R* site of the benzyl position of ethylbenzene by iron(IV)–oxo complexes was found. Recent computational studies on *S*-mandalate synthase showed that the shape and size of the substrate binding pocket determines

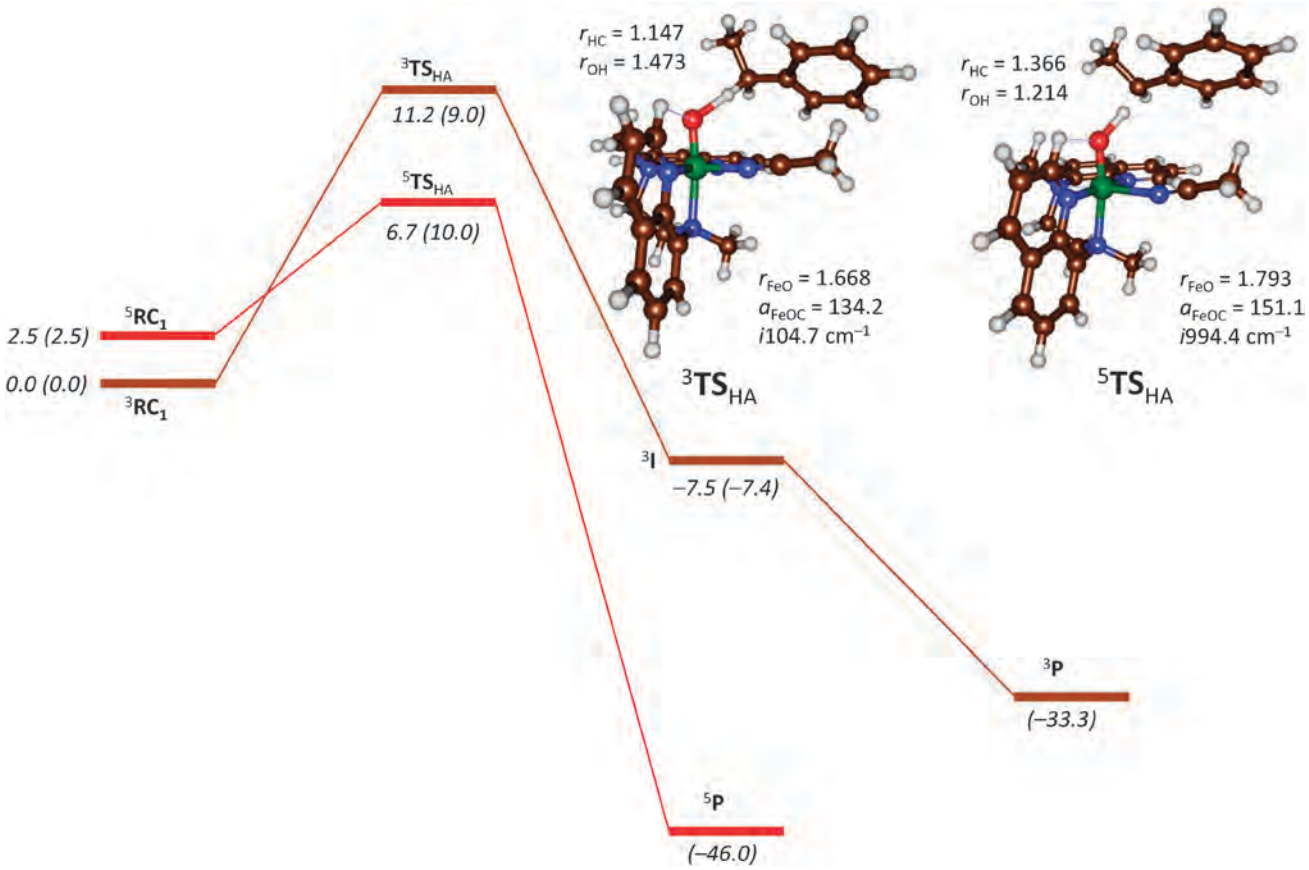

Fig. 3 DFT calculated potential energy profile for the hydrogen atom abstraction from EB by ^{3,5}**1** with energies given in kcal mol^{-1}. Also shown are optimized UB3LYP/BS2(solvent) geometries of ^{3,5}**TS**$_{HA}$ with bond lengths in angstroms, angles in degrees and the imaginary frequency in wave numbers. Relative energies represent ΔE + ZPE + E_{solv} values obtained after a full geometry optimization in solvent at the UB3LYP/BS2 (out of parenthesis) or at UB3LYP/BS2//UB3LYP/BS1 level of theory on a gas-phase optimized geometry.

whether the *pro-R* or *pro-S* hydrogen atom can be abstracted.[31] Indeed, site-selective mutations confirmed the computationally proposed hypothesis.

Geometrically, the ^{3,5}**TS**$_{HA}$ structures are quite distinct due to differences in electron transfer processes that happen in these transition states. In the triplet spin state the hydrogen atom transfer is accompanied with electron transfer from the substrate into the π^*_{xz} orbital and hence the substrate attacks under an angle (a_{FeOC} = 134.2°) to get ideal orbital overlap between donor and acceptor orbitals.[32] In the quintet spin state the hydrogen atom abstraction is accompanied with electron transfer from the substrate into the vacant $\sigma^*_{z^2}$ orbital and hence the substrate attacks from the top with considerably larger FeOC angles than found in the triplet spin state (a_{FeOC} = 151.1°), which gives an iron(III)–hydroxo complex with a fully exchange coupled metal 3d system with five singly occupied orbitals that is antiferromagnetically coupled to a benzyl radical: ^{5}**I** has electronic configuration $\pi^*_{xy}{}^1\,\pi^*_{xz}{}^1\,\pi^*_{yz}{}^1\,\sigma^*_{x^2-y^2}{}^1\,\sigma^*_{z^2}{}^1\,\pi_{EB}{}^1$. This exchange stabilization makes ^{5}**I** considerably lower in energy than the corresponding triplet spin complex. As a consequence, ^{5}**TS**$_{HA}$ is stabilized over ^{3}**TS**$_{HA}$, although dispersion corrections make them almost degenerate. Nevertheless, the barrier heights on both spin state surfaces are small and implicate an efficient hydrogen atom abstraction process in agreement with experiment.[9] When the enthalpy values from Fig. 3 are converted to a free energy of activation, a value of ΔG_{solv} = 10.8 kcal mol^{-1} on the triplet spin state surface is found, which is in reasonable agreement with the experimentally reported free energy of activation of Nam *et al.*[9]

The experimental studies on ethylbenzene hydroxylation by **RC**$_1$ were found to proceed with a kinetic isotope effect (KIE) of 10 for the replacement of hydrogen atoms by deuterium in the substrate. To estimate the isotope effects for replacement of the transferrable hydrogen atom by deuterium in the reaction passing ^{3}**TS**$_{HA}$ we used the Eyring and Wigner models (see Methods section) to estimate the KIE. Values of KIE$_E$ and KIE$_W$ of 4.9 and 5.4 were obtained, whereas these values increased up to 5.1 and 5.7, respectively, when the fully deuterated substrate was used. Our calculated isotope effect, therefore, predicts the same trends as experiment.

We then calculated a reaction complex of **2** with ethylbenzene (^{2,4}**RC**$_2$) in the gas phase as well as with solvent models included during the geometry optimizations. As mentioned above, the optimized geometry and group spin densities of ^{2}**RC**$_2$ characterize the reactant complex as ^{3}[Fe^{IV}(O)(BQEN)(NCCH$_3$)]$^{2+}\cdots{}^{2}$EB$^{+\bullet}$. The hydrogen atom abstraction from EB$^{+\bullet}$ by the iron(IV)–oxo complex then leads to electron transfer from the substrate into the π^*_{xz} orbital of the oxidant and spin density changes that are

 This journal is © the Owner Societies 2014

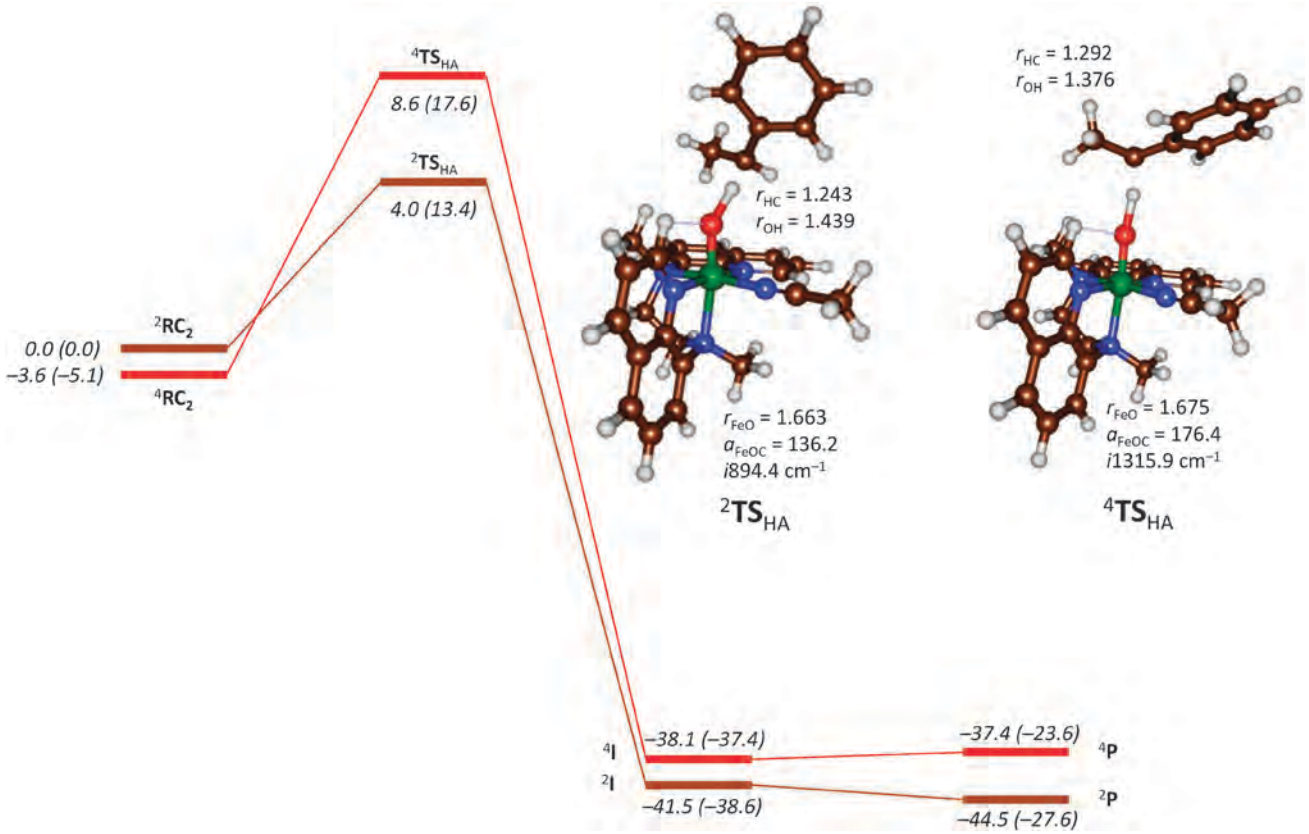

Fig. 4 DFT calculated potential energy profile for the hydrogen atom abstraction from EB by ^{2,4}**2** with energies given in kcal mol^{-1}. Also shown are optimized UB3LYP/BS2(solvent) geometries of ^{2,4}**TS**$_{HA}$ with bond lengths in angstroms, angles in degrees and the imaginary frequency in wave numbers. Relative energies represent ΔE + ZPE + E_{solv} values obtained after a full geometry optimization in solvent at the UB3LYP/BS2 (out of parenthesis) or at UB3LYP/BS2//UB3LYP/BS1 level of theory on a gas-phase optimized geometry.

very similar to those observed for ^{3}**TS**$_{HA}$. Technically, the differences in the hydrogen atom abstraction barrier between ^{3}**RC**$_1$ and ^{2}**RC**$_2$ should be very small as both are an iron(IV)–oxo oxidant. However, the outer-sphere electron transfer from the substrate to the oxidant has oxidized the approaching substrate, and hence the differences in barrier heights observed in Fig. 3 and 4 relate to hydrogen atom abstraction of the C–H bonds of EB and EB$^{+\bullet}$, respectively. Previously, it was shown that the hydrogen atom abstraction barrier correlates with the strength of the C–H bond of the substrate that is broken in the process.[33] Indeed, experimentally determined rate constants of hydrogen atom abstraction reactions by nonheme iron oxidants were shown to correspond to the bond dissociation energy (BDE$_{CH}$) for the breaking of the C–H bond of the substrate.[34] We, therefore, decided to calculate the BDE$_{CH}$ values of EB and EB$^{+\bullet}$ into $C_6H_5CHCH_3^{\bullet/+}$ and a hydrogen atom and find values of ΔE + ZPE = 82.3 and 41.2 kcal mol^{-1} in the gas phase, respectively. Thus, the oxidized ethylbenzene substrate has considerably weaker benzyl C–H bond strength as compared to the neutral system, and, therefore, the barrier heights for hydrogen atom abstraction obtained for **2′** are significantly lower than those for **1** in agreement with the differences in BDE$_{CH}$. Although, the higher reactivity of **2′** *versus* **1** is perceived as due to differences in the oxidation state of the two oxidants, it actually represents the same oxidant but a difference in the ionization state of the substrate with weakened BDE$_{CH}$. Also the reaction of **2′** with ethylbenzene incurs a significant KIE value, where we find a KIE$_E$ = 5.6 and a KIE$_W$ = 7.2. These values, therefore, are similar to those found for **1** above.

We also calculated the alternative quartet spin state of **2′** and the hydrogen atom abstraction *via* ^{4}**TS**$_{HA}$. Thus, ^{4}**RC**$_2$ has orbital occupation $\pi^*_{xy}{}^2\ \pi^*_{xz}{}^{\uparrow}\ \pi^*_{yz}{}^{\uparrow}\ \pi_{EB}{}^{\uparrow}$ and refers to ^{3}[Fe^{IV}(O)(BQEN)(NCCH$_3$)]$^{2+}\cdots{}^2$EB$^{+\bullet}$, but in contrast to ^{2}**RC**$_2$ the spin on EB is ferromagnetically coupled to the unpaired electrons on the metal. Energetically, ^{2}**RC**$_2$ and ^{4}**RC**$_2$ are close in energy. However, during the hydrogen atom abstraction in ^{2}**TS**$_{HA}$ the unpaired electron from EB$^{+\bullet}$ is transferred with down-spin to give a $\pi^*_{xy}{}^2\ \pi^*_{xz}{}^2\ \pi^*_{yz}{}^1$ configuration, but in ^{4}**TS**$_{HA}$ the unpaired electron has up-spin so a $\pi^*_{xy}{}^2\ \pi^*_{xz}{}^1\ \pi^*_{yz}{}^1\ \sigma^*_{z^2}{}^1$ configuration is formed. As this involves a higher lying orbital than in the corresponding doublet spin pathway, the barrier height for ^{4}**TS**$_{HA}$ is higher in energy than that for ^{2}**TS**$_{HA}$.

Discussion

Our DFT calculations on ^{3,5}**1** and ^{2,4}**2′** reported above show that both systems are in the iron(IV) oxidation state and the oxidation

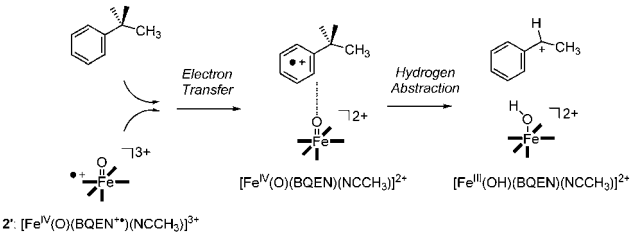

Scheme 2 Calculated reaction mechanism for **2** with oxidation states of critical intermediates identified.

of **2′** does not oxidize the metal to iron(VI) but rather keeps it at the lower oxidation state of iron(IV) due to electron release from the BQEN macrocycle rather than the metal. Therefore, although **2′** is perceived as an iron(V)–oxo species, it actually is an iron(IV)–oxo with BQEN cation radical. Moreover, the DFT calculations reported in this work show that approach of a substrate, *e.g.* ethylbenzene, onto ^{4,2}**2′**, leads to a long-range electron transfer upon formation of the reactant complex ^{4,2}**RC**$_2$: ^{3}[Fe^{IV}(O)(BQEN)(NCCH$_3$)]$^{2+}\cdots{}^2$EB$^{+\bullet}$, Scheme 2. The subsequent hydrogen atom abstraction then gives an iron(III)–hydroxo complex and a $C_6H_5CH^+CH_3$ cation.

In previous studies, we showed that the driving force of a hydrogen atom abstraction correlates linearly with the free energy of activation.[24d,27c,33] Therefore, to understand the thermodynamics and kinetics of the reaction mechanisms reported in Fig. 2 and 3 above, we did a detailed analysis of the individual thermodynamic reaction steps for electron and hydrogen atom transfer processes, which are summarized in Fig. 5. Panel (a) in Fig. 5 starts on the top left with ^{2}**2′** and the reaction to the right reflects a one-electron abstraction to form ^{3}**1** and the subsequent one-electron abstraction to form [Fe^{III}(O)(BQEN)(NCCH$_3$)]$^+$. The vertical arrows reflect the hydrogen atom abstraction processes from both ^{2}**2′** and ^{3}**1**. Thermodynamically, the energy for these reactions is associated with the bond dissociation energy of the O–H bond in the metal–hydroxo complex to revert back into the iron–oxo and an isolated H-atom, as defined as BDE$_{OH}$. The calculated BDE$_{OH}$ values for ^{2}**2′** and ^{3}**1** are virtually the same in the gas phase, which is not surprising as both complexes are iron(IV)–oxo intermediates. Therefore, geometrically very little differences in the hydrogen atom abstraction reactions will be obtained. The energy gap between the two BDE$_{OH}$ values widens to 10.2 kcal mol^{-1} in favour of ^{2}**2′** when solvent, thermal and entropical corrections to the energy are included.

In the case of BDE$_{OH}$, solvent corrections stabilize the value of **2′** over **1** by 7.3 kcal mol^{-1}, whereas thermal and entropic

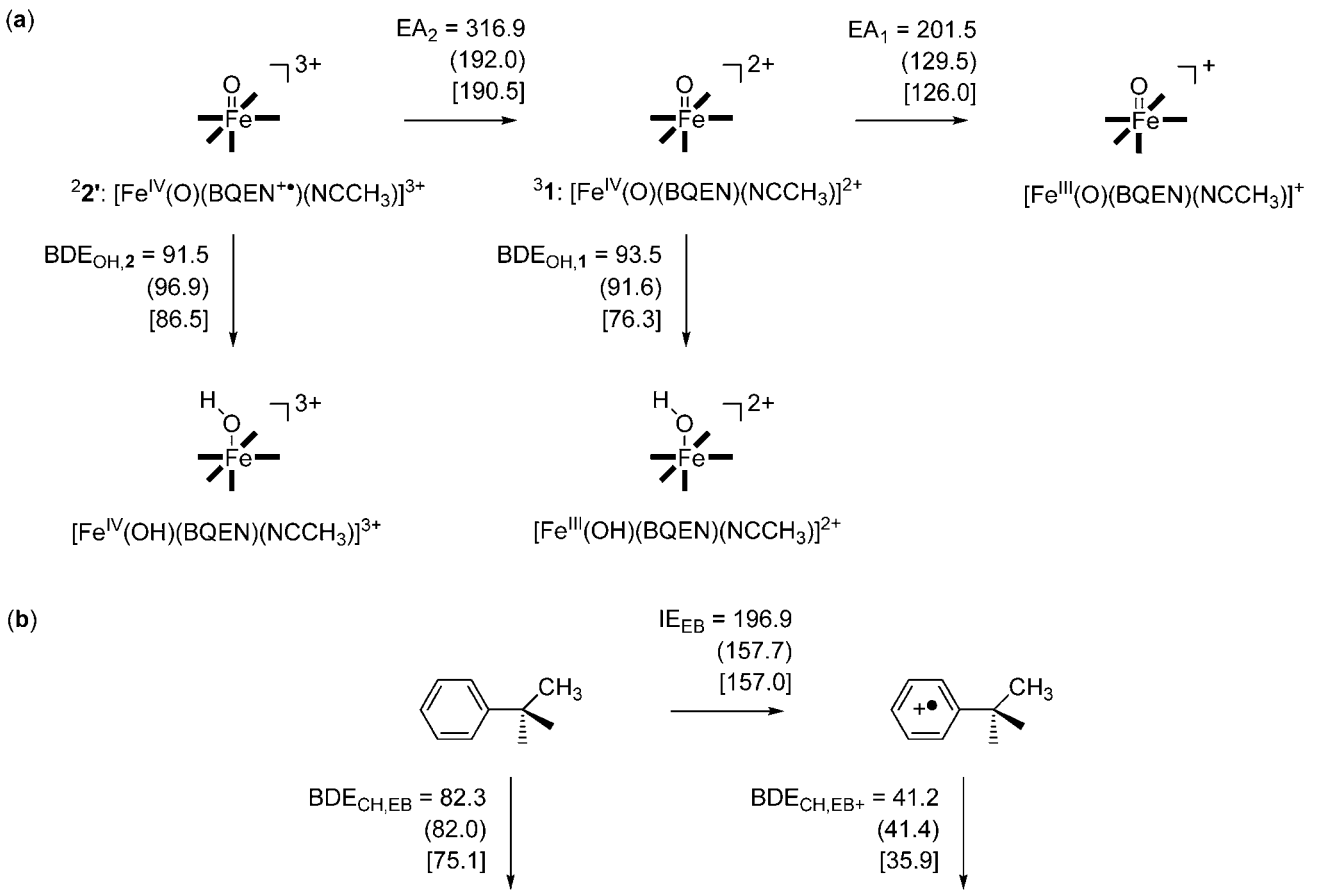

Fig. 5 (a) Thermodynamic reaction pathways for electron and hydrogen atom abstraction by **1** and **2**. (b) Thermodynamic reaction pathways for electron and hydrogen atom abstraction by EB. All data obtained from a geometry optimization at UB3LYP/BS2. Data (in kcal mol^{-1}) reported are ΔE + ZPE in the gas-phase (ΔE + ZPE in solvent) [ΔG in solvent].

 This journal is © the Owner Societies 2014

corrections add a further 4.9 kcal mol^{-1}. These BDE_{OH} values, therefore, would predict higher reactivity of $^2\mathbf{2}'$ over $^3\mathbf{1}$ in solvent for hydrogen atom abstraction reactions.

The major differences between **1** and **2′**, however, are related to their electron affinities or reduction potentials. Thus, $^2\mathbf{2}'$ has a large electron affinity (EA_2) of 316.9 kcal mol^{-1} in the gas-phase and ΔG_{solv} = 190.5 kcal mol^{-1}. It is worth noting that for all calculations we find almost equal values for ΔE + ZPE + E_{solv} and ΔG_{solv}, therefore, entropic and thermal corrections to the solvent corrected enthalpies have a negligible effect on the individual reactions studied. The electron affinity of $^2\mathbf{2}'$ is considerably larger than that found for $^3\mathbf{1}$, where values of EA_1 = 201.5 kcal mol^{-1} in the gas-phase and ΔG_{solv} = 126.0 kcal mol^{-1} are found. Consequently, $^2\mathbf{2}'$ has a ΔG_{solv} = 63.5 kcal mol^{-1} larger electron affinity than $^3\mathbf{1}$ and will be more susceptible to react by electron abstraction from substrates.

For completeness we also include in Fig. 6 the thermodynamics for the ethylbenzene substrate for removal of an electron and the C–H bond strengths of the benzyl group of ethylbenzene and the ethylbenzene cation radical. As already mentioned above the ethylbenzene cation radical has a considerably weakened C–H bond strength of ΔG_{solv} = 35.9 kcal mol^{-1} as compared to EB. Consequently, hydrogen atom abstraction from $EB^{+\bullet}$ will have a low barrier.

To find out whether a reaction of $^2\mathbf{2}'$ and $^3\mathbf{1}$ with EB would lead to a large thermodynamic driving force for electron transfer, the free energy in solvent for the reactions given in eqn (4) and (5) was calculated. Thus, the electron transfer from EB to $^2\mathbf{2}'$ is calculated to be exergonic by 33.5 kcal mol^{-1}, whereas the one originating from $^3\mathbf{1}$ is endergonic by 31.0 kcal mol^{-1} instead. These two reactions implicate that in a collision between $^2\mathbf{2}'$ and EB the driving force will trigger an electron abstraction from EB, whereas that will not be the case in a collision between $^3\mathbf{1}$ and EB. The large EA_2 value will, therefore, lead to a large driving force for electron transfer from suitable substrates including ethylbenzene to **2′**. Moreover, the thermodynamic reaction pathways given in Fig. 5 give further evidence of a likely electron transfer between EB and $^2\mathbf{2}'$.

$$^2\mathbf{2}' + EB \rightarrow {}^3\mathbf{1} + EB^{+\bullet} \quad [\Delta G_{solv} = -33.5 \text{ kcal mol}^{-1}] \quad (4)$$

$$^3\mathbf{1} + EB \rightarrow {}^4[Fe^{III}(O)(BQEN)(NCCH_3)]^+ + EB^{+\bullet} \quad [\Delta G_{solv} = +31.0 \text{ kcal mol}^{-1}] \quad (5)$$

Despite the fact that the BDE_{OH} values of **1** and **2′** are virtually the same, actually at the free energy level with solvent included they are separated by about 10 kcal mol^{-1}. However, much more dramatic differences in the electron affinity of both complexes are found. Thus, the bond dissociation energy to break the A–H bond (BDE_{AH}) – or hydrogen atom abstraction ability of compound A – can be split into an individual electron and proton transfer *via* eqn (6), whereby ΔG_{acid} represents the acidity of the weak acid AH, EA_A is the electron affinity of A, and IE_H the ionization energy of a H-atom. The experimentally reported value of IE_H is 13.598 eV.[35]

$$A\text{–}H \rightarrow A + H + BDE_{AH} \quad (6a)$$

$$BDE_{AH} = \Delta G_{acid,AH} - EA_A - IE_H \quad (6b)$$

Using the data from Fig. 5 and the known IE_H value we calculate a ΔG_{acid} of 590.5 kcal mol^{-1} for $[Fe^{IV}(OH)(BQEN)(NCCH_3)]^{3+}$, whereas proton transfer to **1** gives the complex $[Fe^{III}(OH)(BQEN)(NCCH_3)]^{2+}$ with ΔG_{acid} = 515.9 kcal mol^{-1}. The large difference between EA_2 and EA_1, therefore, has a direct impact on the acidity of the iron(III)–hydroxo group and makes it considerably more acidic. The origin of the difference in electron affinity of **1** and **2′** is due to difference in electron transfer processes. Upon reduction of $^2\mathbf{2}'$ an electron is transferred into the low-lying π^*_{BQEN} orbital to form a triplet spin $\pi^*_{xy}{}^2\,\pi^*_{xz}{}^1\,\pi^*_{yz}{}^1\,\pi^*_{BQEN}{}^2$ configuration.

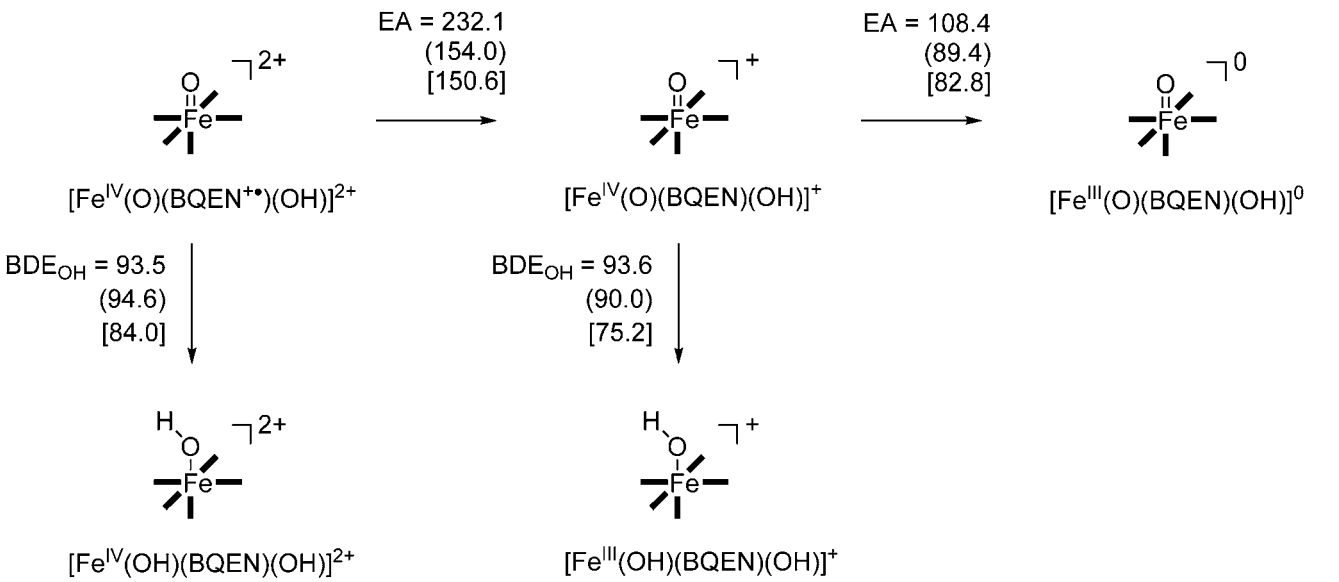

Fig. 6 Thermodynamic reaction pathways for electron and hydrogen atom abstraction by $[Fe(O)(BQEN)(OH)]^{2+}$ and $[Fe(O)(BQEN)(OH)]^{+}$. All data obtained from a geometry optimization at UB3LYP/BS2. Data (in kcal mol^{-1}) reported are ΔE + ZPE in the gas-phase (ΔE + ZPE in solvent) [ΔG in solvent].

On the other hand, reduction of ^{3}**1** leads to filling of the virtual $\sigma^*_{z^2}$ orbital with a single electron. As the $\sigma^*_{z^2}$ orbital is significantly higher in energy than the π^*_{BQEN} orbital this means the reduction of **1** will incur a much smaller electron affinity than adding an electron to π^*_{BQEN}, which is indeed what is found in Fig. 5.

To find out whether the *cis*-ligand of the metal–oxo group affects the EA and ΔG_{acid} values, we did a further set of calculations on the electron and hydrogen atom transfer reactions for complexes $[Fe^{IV}(O)(BQEN^{+\bullet})(OH)]^{2+}$ and $[Fe^{IV}(O)(BQEN)(OH)]^{+}$, *i.e.* complexes **2′** and **1** that have the acetonitrile ligand replaced by OH^-. We should note here that replacement of the acetonitrile equatorial ligand by hydroxide does not change the spin state ordering and electronic configuration and these complexes are characterized like **2′** and **1** above. Fig. 6 displays the thermodynamic reaction pathways for $[Fe^{IV}(O)(BQEN^{+\bullet})(OH)]^{2+}$ and $[Fe^{IV}(O)(BQEN)(OH)]^{+}$. Firstly, a very little effect of replacing the acetonitrile with hydroxide is found on the BDE_{OH} values of the complexes. For $[Fe^{IV}(OH)(BQEN)(OH)]^{2+}$ we find a BDE_{OH} value of ΔG_{solv} = 84.0 kcal mol^{-1}, whereas its one-electron reduced counterpart has a ΔG_{solv} = 75.2 kcal mol^{-1}. These values are within 2.5 kcal mol^{-1} from those obtained with an acetonitrile molecule in the *cis*-position. The situation, however, changes dramatically for the electron affinities and acidity values of the complexes when the acetonitrile ligand is replaced by hydroxide. Thus, $[Fe^{IV}(O)(BQEN^{+\bullet})(OH)]^{2+}$ has an electron affinity of ΔG_{solv} = 150.6 kcal mol^{-1}, whereas the much lower value of 82.8 kcal mol^{-1} is found for $[Fe^{IV}(O)(BQEN)(OH)]^{+}$. These lowered electron affinities with respect to complexes **2′** and **1** also mean reduced acidity of the protonated complexes, for which we find values of 548.2 and 471.6 kcal mol^{-1}, respectively.

In addition, a reaction of $[Fe^{IV}(O)(BQEN^{+\bullet})(OH)]^{2+}$ with ethylbenzene is calculated to give an endergonic electron transfer of 6.4 kcal mol^{-1} using the data given in Fig. 5 and 6. Therefore, replacing the acetonitrile equatorial ligand in complex **2′** with an anion such as a hydroxide will affect the stability and reactivity of the complex and will prevent a long-range electron transfer with substrates like ethylbenzene. The electron transfer from ethylbenzene to $[Fe^{IV}(O)(BQEN)(OH)]^{+}$ is calculated to be even more endergonic (ΔG_{solv} = 74.2 kcal mol^{-1}) and consequently is not likely to happen.

In summary, we establish reasons for the large thermodynamic driving force for electron transfer from ethylbenzene to **2′** as originating from a high electron affinity of the oxidant of ΔG_{solv} = 190.5 kcal mol^{-1}. This implies that the electron transfer to the approaching substrate could be spontaneous for substrates with an ionization potential below 190.5 kcal mol^{-1} or 8.26 eV. Although, we calculate an ionization energy of 8.54 eV in the gas phase actually in solution the value drops to ΔG_{solv} = 6.81 eV. Therefore, in solution the ionization potential of ethylbenzene is sufficiently low to incur a long-range electron transfer to the oxidant and create $^3[Fe^{IV}(O)(BQEN)(NCCH_3)]^{2+}\cdots{}^2EB^{+\bullet}$.

Finally, the thermodynamics values of Fig. 6 and 7 also enable us to predict the hydrogen atom transfer driving force in complexes $\mathbf{RC}_2$ and $\mathbf{RC}_1$. As described above, $\mathbf{RC}_2$ undergoes a long-range electron transfer and converts to $[Fe^{IV}(O)(BQEN)(NCCH_3)]^{2+}$ and $EB^{+\bullet}$. This complex reacts *via* hydrogen atom transfer *via*

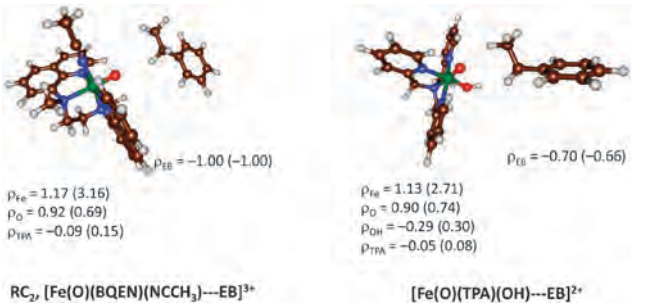

Fig. 7 Group spin densities of $^{4,2}\mathbf{RC}_2$ and $[Fe(O)(TPA)(OH)\cdots EB]^{2+}$ as calculated with UB3LYP/BS2 in solvent. High-spin data in parenthesis.

eqn (7) with a free energy change of −40.4 kcal mol^{-1}. The DFT calculations for this process, see ESI,† implicated a free energy change of ΔG_{solv} = −42.4 kcal mol^{-1} for the formation of the radical intermediate ^{2}**I**, and therefore its calculated value is in good agreement with the value estimated from our thermodynamic cycles.

$$[Fe^{IV}(O)(BQEN)(NCCH_3)]^{2+} + EB^{+\bullet} \rightarrow [Fe^{III}(OH)(BQEN)(NCCH_3)]^{2+} + C_6H_5CH^+CH_3\ [\Delta G_{solv} = -40.4\ \text{kcal mol}^{-1}] \quad (7)$$

By contrast, if we do the same for complex $\mathbf{RC}_1$ and take the difference in free energy between the BDE_{CH} and BDE_{OH} values of oxidant and substrate, we find an almost thermoneutral hydrogen atom abstraction reaction, eqn (8). Indeed, the DFT calculations above predict a radical intermediate with an exergonicity of 6.9 kcal mol^{-1} with respect to the reactant complex in good agreement with the thermodynamically estimated value.

$$[Fe^{IV}(O)(BQEN)(NCCH_3)]^{2+} + EB \rightarrow [Fe^{III}(OH)(BQEN)(NCCH_3)]^{2+} + C_6H_5CH^{\bullet}CH_3\quad [\Delta G_{solv} = -1.2\ \text{kcal mol}^{-1}] \quad (8)$$

To test whether the electron transfer observed here in our reactant complexes is a general feature that could be found in alternative iron(v)–oxo complexes as well, we also decided to investigate the well-studied $[Fe(O)(TPA)(OH)]^{2+}$, TPA = tris-(2-pyridylmethyl)amine, system of Costas and co-workers.[10b] Previously, $[Fe(O)(TPA)(X)]^{2+}$ with X = halide or OH^- has been used in studies of the *cis*-effect on substrate activation by metal–oxo species, but also as a model for non-heme iron halogenases. Technically the $[Fe(O)(TPA)(OH)]^{2+}$ is an iron(v)–oxo complex as indeed confirmed by DFT calculations.[36] The question, of course, arises whether the oxidation state of the complex stays in the iron(v) state upon approach of an ethylbenzene molecule. Thus, we optimized the reactant complex $[Fe(O)(TPA)(OH)\cdots EB]^{2+}$ in the doublet and quartet spin states at UB3LYP-D3/BS2 level of theory and show the structures and group spin densities of the complexes alongside those of $^{4,2}\mathbf{RC}_2$ in Fig. 7.

The results in Fig. 7 show that upon approach of an ethylbenzene molecule to an iron(v)–oxo center, a long-range electron transfer takes place from substrate to oxidant. Therefore, the group spin densities of $^{2,4}\mathbf{RC}_2$ and $[Fe(O)(TPA)(OH)\cdots EB]^{2+}$ both refer to an iron(iv)–oxo complex with a nearby $EB^{+\bullet}$ ion. Both complexes have a doublet spin state with $\pi^*_{xy}{}^2\ \pi^*_{xz}{}^1\ \pi^*_{yz}{}^1\ \pi_{EB}{}^1$ configuration,

 This journal is © the Owner Societies 2014

i.e. a triplet spin iron(IV)–oxo complex with a nearby doublet cation radical ethylbenzene. By contrast the quartet spin state configurations of these complexes have orbital occupation $\pi^{*}_{xy}{}^{2}$ $\pi^{*}_{xz}{}^{1}$ $\pi^{*}_{yz}{}^{1}$ $\sigma^{*}_{z^2}{}^{1}$ $\pi_{EB}{}^{1}$ configuration with the ethylbenzene radical anti-ferromagnetically coupled to three unpaired electrons on the iron(IV)–oxo complex. Note that without ethylbenzene the $[Fe(O)(TPA)(OH)]^{2+}$ complex converges to an iron(V)–oxo species and no ligand radical is found. The TPA ligand, therefore, has much lower lying molecular orbitals than a BQEN ligand system and as a result the π_{BQEN} orbitals become competitive with the $\pi^{*}_{xz}/\pi^{*}_{yz}$ orbitals on the FeO group. As a result of this $[Fe(O)(BQEN)(NCCH_3)]^{3+}$ has an electronic configuration representing an iron(IV)–oxo coupled to a ligand radical, whereas $[Fe(O)(TPA)(OH)]^{2+}$ is an iron(V)–oxo species.

Conclusions

In summary, we present here the first comparative study on the reactivity patterns of nonheme iron(IV)–oxo *versus* iron(V)–oxo intermediates. Upon approach of the substrate to the iron(IV)–oxo ligand cation radical it abstracts an electron from the substrate readily, and thereby creates an iron(IV)–oxo ligand cation radical species. The perceived reactivity of the iron(V)–oxo species, therefore, is due to the activity of the iron(IV)–oxo ligand cation radical instead. We also show that oxidation of ethylbenzene weakens the C–H bond strength of the substrate and thereby lowers the hydrogen atom abstraction barriers and leads to higher reactivity. This is an example of how outer-sphere (long-range) electron transfer can change the C–H bond strength of the substrate so that a more efficient H-transfer becomes possible. The outer-sphere electron transfer may be a common feature in transition metal catalysis, but further research will be needed to find more examples of this type of reactivity patterns.

Acknowledgements

SdV thanks the Royal Society for an International Exchanges with Korea grant. The National Service of Computational Chemistry Software (NSCCS) is acknowledged for cpu time. DK acknowledges Department of Science and Technology (New Delhi) for a Ramanujan Fellowship. The research at EWU was supported by NRF of Korea through CRI (NRF-2012R1A3A2048842) and GRL (NRF-2010-00353).

Notes and references

1 (*a*) E. I. Solomon, T. C. Brunold, M. I. Davis, J. N. Kemsley, S.-K. Lee, N. Lehnert, F. Neese, A. J. Skulan, Y.-S. Yang and J. Zhou, *Chem. Rev.*, 2000, **100**, 235; (*b*) T. D. H. Bugg and S. Ramaswamy, *Curr. Opin. Chem. Biol.*, 2008, **12**, 134; (*c*) M. J. Ryle and R. P. Hausinger, *Curr. Opin. Chem. Biol.*, 2002, **6**, 193; (*d*) Y. Mishina, E. M. Duguid and C. He, *Chem. Rev.*, 2006, **106**, 215; (*e*) *Iron-containing enzymes: Versatile catalysts of hydroxylation reactions in nature*, ed. S. P. de Visser and D. Kumar, RSC Publishing, Cambridge (UK), 2011; (*f*) P. He and G. R. Moran, *Curr. Opin. Chem. Biol.*, 2009, **13**, 443; (*g*) D. Buongiorno and G. D. Straganz, *Coord. Chem. Rev.*, 2013, **257**, 541.

2 (*a*) M. Costas, M. P. Mehn, M. P. Jensen and L. Que Jr, *Chem. Rev.*, 2004, **104**, 939; (*b*) S. V. Kryatov, E. V. Rybak-Akimova and S. Schindler, *Chem. Rev.*, 2005, **105**, 2175; (*c*) M. M. Abu-Omar, A. Loaiza and N. Hontzeas, *Chem. Rev.*, 2005, **105**, 2227; (*d*) R. van Eldik, *Coord. Chem. Rev.*, 2007, **251**, 1649; (*e*) P. C. A. Bruijnincx, G. van Koten and R. J. M. Klein Gebbink, *Chem. Soc. Rev.*, 2008, **37**, 2716; (*f*) S. P. de Visser, J.-U. Rohde, Y.-M. Lee, J. Cho and W. Nam, *Coord. Chem. Rev.*, 2013, **257**, 381; (*g*) W. Nam, Y.-M. Lee and S. Fukuzumi, *Acc. Chem. Res.*, 2014, **47**, 1146.

3 See, *e.g.*, (*a*) M. R. Bukowski, K. D. Koehntop, A. Stubna, E. L. Bominaar, J. A. Halfen, E. Münck, W. Nam and L. Que Jr, *Science*, 2005, **310**, 1000; (*b*) J.-U. Rohde, J.-H. In, M. H. Lim, W. W. Brennessel, M. R. Bukowski, A. Stubna, E. Münck, W. Nam and L. Que Jr, *Science*, 2003, **299**, 1037; (*c*) M. Martinho, F. Banse, J.-F. Bartoli, T. A. Mattioli, P. Battioni, P. Horner, S. Bourcier and J.-J. Girerd, *Inorg. Chem.*, 2005, **44**, 9592; (*d*) C. V. Sastri, M. S. Seo, M. J. Park, K. M. Kim and W. Nam, *Chem. Commun.*, 2005, 1405; (*e*) F. T. De Oliveira, A. Chanda, D. Banerjee, X. Shan, S. Mondal, L. Que Jr, E. L. Bominaar, E. Münck and T. J. Collins, *Science*, 2007, **315**, 835; (*f*) T. A. Jackson, J.-U. Rohde, M. S. Seo, C. V. Sastri, R. DeHont, A. Stubna, T. Ohta, T. Kitagawa, E. Münck, W. Nam and L. Que Jr, *J. Am. Chem. Soc.*, 2008, **130**, 12394.

4 (*a*) K. Chen, M. Costas, J. Kim, A. K. Tipton and L. Que Jr, *J. Am. Chem. Soc.*, 2002, **124**, 3026; (*b*) A. Company, L. Gómez, M. Güell, X. Ribas, J. M. Luis, L. Que Jr and M. Costas, *J. Am. Chem. Soc.*, 2007, **129**, 15766; (*c*) R. Mas-Ballesté, M. Fujita and L. Que Jr, *Dalton Trans.*, 2008, 1828; (*d*) P. Comba, M. Maurer and P. Vadivelu, *Inorg. Chem.*, 2009, **48**, 10348; (*e*) A. Company, Y. Feng, M. Güell, X. Ribas, J. M. Luis, L. Que Jr and M. Costas, *Chem. – Eur. J.*, 2009, **15**, 3359; (*f*) I. Prat, J. S. Mathieson, M. Güell, X. Ribas, J. M. Luis, L. Cronin and M. Costas, *Nat. Chem.*, 2011, **3**, 788.

5 (*a*) K. Chen and L. Que Jr, *J. Am. Chem. Soc.*, 2001, **123**, 6327; (*b*) A. D. Ryabov, *Adv. Inorg. Chem.*, 2013, **65**, 117.

6 (*a*) A. Nielsen, F. B. Larsen, A. D. Bond and C. J. McKenzie, *Angew. Chem., Int. Ed.*, 2006, **45**, 1602; (*b*) A. Lennartson and C. J. McKenzie, *Angew. Chem., Int. Ed.*, 2012, **51**, 6767.

7 S. H. Lee, J. H. Han, H. Kwak, S. J. Lee, E. Y. Lee, H. J. Kim, J. H. Lee, C. Bae, S. N. Lee, Y. Kim and C. Kim, *Chem. – Eur. J.*, 2007, **13**, 9393.

8 S. Kundu, J. Van Kirk Thompson, A. D. Ryabov and T. J. Collins, *J. Am. Chem. Soc.*, 2011, **133**, 18546.

9 J. Yoon, S. A. Wilson, Y. K. Jang, M. S. Seo, K. Nehru, B. Hedman, K. O. Hodgson, E. Bill, E. I. Solomon and W. Nam, *Angew. Chem., Int. Ed.*, 2009, **48**, 1257.

10 (*a*) *Jaguar, version 7.9*, Schrodinger, LLC, New York, NY, 2011; (*b*) *Gaussian-09, Revision C.01*, Gaussian Inc., Wallingford CT, 2010.

11 (*a*) A. D. Becke, *J. Chem. Phys.*, 1993, **98**, 5648; (*b*) C. Lee, W. Yang and R. G. Parr, *Phys. Rev. B: Condens. Matter Mater. Phys.*, 1988, **37**, 785.

12 (*a*) S. P. de Visser, *Angew. Chem., Int. Ed.*, 2006, **45**, 1790; (*b*) D. Kumar, W. Thiel and S. P. de Visser, *J. Am. Chem. Soc.*, 2011, **133**, 3869.
13 S. Grimme, *J. Chem. Phys.*, 2006, **124**, 034108.
14 M. Reiher, O. Salomon and B. A. Hess, *Theor. Chem. Acc.*, 2001, **107**, 48.
15 (*a*) N. C. Handy and A. J. Cohen, *Mol. Phys.*, 2001, **99**, 403; (*b*) J. P. Perdew, K. Burke and M. Ernzerhof, *Phys. Rev. Lett.*, 1996, **77**, 3865.
16 S. P. de Visser, M. G. Quesne, B. Martin, P. Comba and U. Ryde, *Chem. Commun.*, 2014, **50**, 262.
17 (*a*) P. J. Hay and W. R. Wadt, *J. Chem. Phys.*, 1985, **82**, 270; (*b*) W. J. Hehre, R. Ditchfield and J. A. Pople, *J. Chem. Phys.*, 1972, **56**, 2257.
18 (*a*) A. K. Vardhaman, C. V. Sastri, D. Kumar and S. P. de Visser, *Chem. Commun.*, 2011, **47**, 11044; (*b*) A. K. Vardhaman, P. Barman, S. Kumar, C. V. Sastri, D. Kumar and S. P. de Visser, *Angew. Chem., Int. Ed.*, 2013, **52**, 12288; (*c*) A. K. Vardhaman, P. Barman, S. Kumar, C. V. Sastri, D. Kumar and S. P. de Visser, *Chem. Commun.*, 2013, **49**, 10926.
19 (*a*) S. P. de Visser, *Chem. – Eur. J.*, 2006, **12**, 8168; (*b*) D. J. Heyes, M. Sakuma, S. P. de Visser and N. S. Scrutton, *J. Biol. Chem.*, 2009, **284**, 3762.
20 D. Kumar, S. P. de Visser, P. K. Sharma, S. Cohen and S. Shaik, *J. Am. Chem. Soc.*, 2004, **126**, 1907.
21 (*a*) D. Kumar, H. Hirao, L. Que Jr and S. Shaik, *J. Am. Chem. Soc.*, 2005, **127**, 8026; (*b*) S. P. de Visser, *J. Am. Chem. Soc.*, 2006, **128**, 15809; (*c*) S. Ye and F. Neese, *Proc. Natl. Acad. Sci. U. S. A.*, 2011, **108**, 1228.
22 (*a*) M. T. Green, *J. Am. Chem. Soc.*, 1999, **121**, 7939; (*b*) J. Rittle and M. T. Green, *Science*, 2010, **330**, 933; (*c*) K. Yoshizawa, Y. Shiota and T. Yamabe, *J. Am. Chem. Soc.*, 1999, **121**, 147.
23 (*a*) S. P. de Visser, *J. Am. Chem. Soc.*, 2006, **128**, 9813; (*b*) L. Bernasconi and E.-J. Baerends, *Eur. J. Inorg. Chem.*, 2008, 1672; (*c*) C. Y. Geng, S. Ye and F. Neese, *Angew. Chem., Int. Ed.*, 2010, **49**, 5717; (*d*) S. Shaik, H. Chen and D. Janardanan, *Nat. Chem.*, 2011, **3**, 19; (*e*) P. Comba, M. Maurer and P. Vadivelu, *Inorg. Chem.*, 2009, **48**, 10389.
24 (*a*) J. C. Schöneboom, H. Lin, N. Reuter, W. Thiel, S. Cohen, F. Ogliaro and S. Shaik, *J. Am. Chem. Soc.*, 2002, **124**, 8142; (*b*) S. P. de Visser, S. Shaik, P. K. Sharma, D. Kumar and W. Thiel, *J. Am. Chem. Soc.*, 2003, **125**, 15779; (*c*) S. P. de Visser, L. Tahsini and W. Nam, *Chem. – Eur. J.*, 2009, **15**, 5577; (*d*) D. Kumar, G. N. Sastry and S. P. de Visser, *Chem. – Eur. J.*, 2011, **17**, 6196.
25 S. Shaik, H. Hirao and D. Kumar, *Nat. Prod. Rep.*, 2007, **24**, 533.
26 M. G. Quesne, R. Latifi, L. E. Gonzalez-Ovalle, D. Kumar and S. P. de Visser, *Chem. – Eur. J.*, 2014, **20**, 435.
27 See, *e.g.*, (*a*) M. Güell, J. M. Luis, M. Solà and M. Swart, *J. Phys. Chem. A*, 2008, **112**, 6384; (*b*) R. Latifi, M. A. Sainna, E. V. Rybak-Akimova and S. P. de Visser, *Chem. – Eur. J.*, 2013, **19**, 4058; (*c*) D. Kumar, R. Latifi, S. Kumar, E. V. Rybak-Akimova, M. A. Sainna and S. P. de Visser, *Inorg. Chem.*, 2013, **52**, 7968.
28 S. P. de Visser and L. S. Tan, *J. Am. Chem. Soc.*, 2008, **130**, 12961.
29 P. Leeladee, R. A. Baglia, K. A. Prokop, R. Latifi, S. P. de Visser and D. P. Goldberg, *J. Am. Chem. Soc.*, 2012, **134**, 10397.
30 S. P. de Visser, *J. Phys. Chem. A*, 2005, **109**, 11050.
31 S. M. Pratter, C. Konstantinovics, C. L. M. DiGiuro, E. Leitner, D. Kumar, S. P. de Visser, G. Grogan and G. D. Straganz, *Angew. Chem., Int. Ed.*, 2013, **52**, 9677.
32 S. Sahu, L. R. Widger, M. G. Quesne, S. P. de Visser, H. Matsumura, P. Moënne-Loccoz, M. A. Siegler and D. P. Goldberg, *J. Am. Chem. Soc.*, 2013, **135**, 10590.
33 R. Latifi, M. Bagherzadeh and S. P. de Visser, *Chem. – Eur. J.*, 2009, **15**, 6651.
34 X. Wu, M. S. Seo, K. M. Davis, Y.-M. Lee, J. Chen, K.-B. Cho, Y. N. Pushkar and W. Nam, *J. Am. Chem. Soc.*, 2011, **133**, 20088.
35 S. G. Lias, in *Ionization Energy Evaluation in NIST Chemistry WebBook*, NIST Standard Reference Database Number 69: ed. P. J. Linstrom and W. G. Mallard, National Institute of Standards and Technology, Gaithersburg MD, 2005, p. 20899, http://webbook.nist.gov.
36 (*a*) Y. Ma and P. B. Balbuena, *J. Phys. Chem. B*, 2007, **111**, 2711; (*b*) P. Comba, G. Rajaraman and H. Rohwer, *Inorg. Chem.*, 2007, **46**, 3826; (*c*) A. Bassan, M. R. A. Blomberg, P. E. M. Siegbahn and L. Que Jr, *J. Am. Chem. Soc.*, 2002, **124**, 11056; (*d*) S. P. de Visser and W. Nam, *J. Phys. Chem. A*, 2008, **112**, 12887.

 This journal is © the Owner Societies 2014

ORGANOMETALLICS

Communication

pubs.acs.org/Organometallics

A "Hemilabile" Palladium–Carbon Bond: Characterization and Its Implication in Catalysis

Debajyoti Saha,[†] Ravi Verma,[‡] Devesh Kumar,[‡] Shubhrodeep Pathak,[§] Sourav Bhunya,[§] and Amitabha Sarkar*[,†]

[†]Department of Organic Chemistry, Indian Association for the Cultivation of Science, Raja S. C. Mullik Road, Kolkata 700032, India

[‡]Department of Applied Physics, School for Physical Sciences, Babasaheb Bhimrao Ambedkar University, Ramabai Ambedkar Raili Sthal Road, Lucknow 226 025, India

[§]Raman Centre for Atomic, Molecular and Optical Sciences, Indian Association for the Cultivation of Science, Raja S. C. Mullik Road, Kolkata 700032, India

Supporting Information

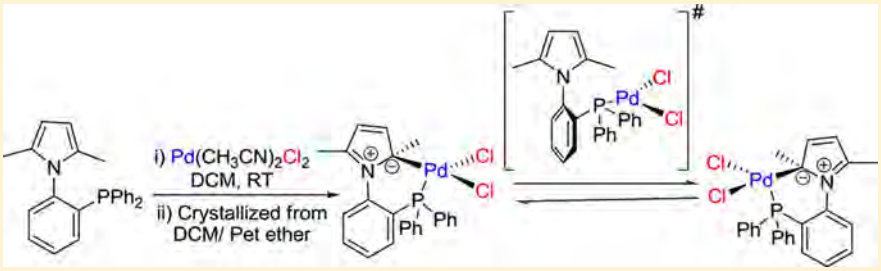

ABSTRACT: An unusual palladium–carbon bond was identified in the crystal structure of a Pd(II) complex (**VI**) derived from 1-(2-diphenylphosphinophenyl)-2,5-dimethyl-1*H*-pyrrole (**L4**). Theoretical calculations indicate that the Pd–C bond is covalent in nature. The complex exhibits fluxional behavior in solution at ambient temperature—the Pd binds alternately to C2 and C5 of pyrrole, generating equivalent, enantiomeric structures. Theory predicts that the transition state of this interconversion probably occurs through an unsaturated 14e complex, where the ligand binds the metal in a monodentate fashion. Comparison with related structures reported earlier has been made, and the possible implication of such unusual bonding in the context of catalysis of coupling reactions is discussed.

Palladium is known to have rather unusual bonding interactions with an ipso carbon of an aromatic ring in complexes with ligands featuring a β-aryl ring[1] or a biaryl motif,[2,3] as revealed in their crystal structures. Such structures are known for both Pd(0) and Pd(II) complexes, a selection of which, viz. **I**–**V**, are presented in Figure 1. A few of these have been scrutinized by theoretical calculations, and a covalent bond is inferred from the existence of a typical bond critical point between the metal and the carbon atoms.[4]

If we replace the ipso carbon with nitrogen as in 1-(2-diphenylphosphino)phenyl-2,5-dimethylpyrrole (**L4**), the biphenyl motif is technically retained and its similarity to the reported ligands **L1**–**L3** is evident (Figure 2).

We report herein the synthesis and structural characterization of a palladium(II) complex derived from ligand **L4**. The unusual η^1 bonding of palladium with the C2 of pyrrole in this molecule is indeed unique. The covalent nature of the bond is substantiated by theoretical calculations. We further established that the structure of the complex in solution is fluxional—the palladium can form a bond with either of the two equivalent carbons (C2 and C5) of pyrrole with equal facility—and metallotropy is fast on the NMR time scale at room temperature. Theory suggests that the interconversion most likely occurs via a monoligated 14e intermediate.

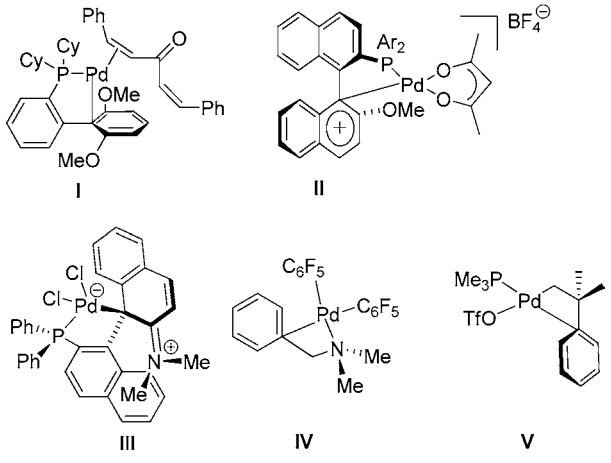

Figure 1. Palladium complexes with Pd–C_{arene} interactions.

Received: May 21, 2014
Published: July 2, 2014

 © 2014 American Chemical Society dx.doi.org/10.1021/om5005435 | *Organometallics* 2014, 33, 3243–3246

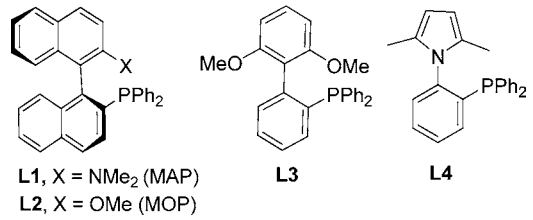

Figure 2. Structures of ligands.

Treatment of equimolar amounts of the ligand **L4** (for details of synthesis and characterization, see the Supporting Information) with $(CH_3CN)_2PdCl_2$ in dichloromethane (Figure 3a) afforded the red complex **VI**, a suitable crystal of which was grown from dichloromethane and light petroleum for crystal structure determination.

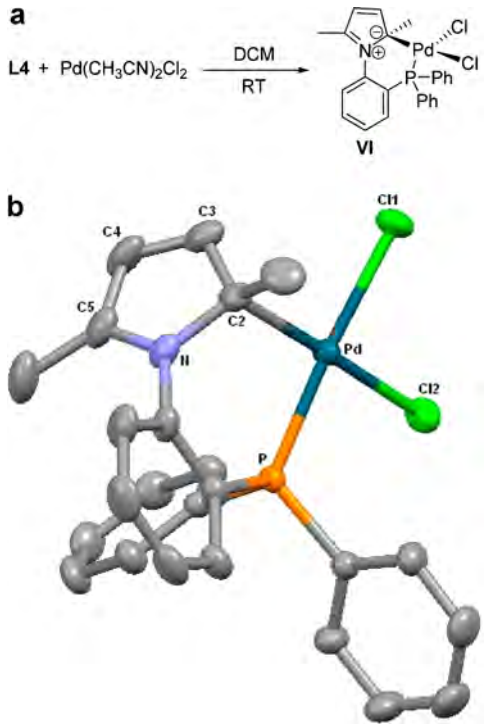

Figure 3. (a) Synthesis of complex **VI**. (b) ORTEP diagram for the molecular complex **VI** with ellipsoids at the 30% probability level. Selected bond lengths (Å): Pd–C2, 2.169(4); C2–C3, 1.434(6); C3–C4, 1.353(7); C4–C5, 1.386(6); C5–N, 1.344(5); N–C2, 1.437(5); Pd–P, 2.2373(9); Pd–Cl1, 2.3626(10); Pd–Cl2, 2.3125(10).

The ORTEP diagram (Figure 3b) reveals a near-planar ligand arrangement at the palladium center, where the metal is coordinated to the phosphorus and two chlorine atoms as anticipated. In addition, an unusual bond is formed between the C2 of pyrrole and palladium. There is no bonding interaction between the metal center and the nitrogen atom that substitutes for the ipso carbon in the heterocycle. Not only is the bonding site different in this unusual structure but also compound **VI** has by far one of the shortest metal–carbon bonds (2.169(4) Å) in such a complex.[5]

In some structures of palladium η^1-arene complexes, the planarity of the arene ring with sp^2-hybridized carbon atoms is said to be conserved despite the bonding interaction.[2] In the case of other complexes, however, pyramidality of the coordinated ipso carbon (as distinct from planarity of an aromatic system) has been mentioned.[3] Where the bonding interaction is strong, the Pd–C bond length is short (<2.22 Å) and deviation from planarity is significant. For structures with Pd–C bonds larger than 2.33 Å, the deviation from planarity is minimal. Complex **VI** presents another such unequivocal example where the C2 of pyrrole connected to Pd is clearly tetrahedral. The bond between N and C5 and the bond between C4 and C3 of pyrrole are shorter (1.344(5) and 1.353(7) Å) with pronounced double-bond character, while the bonds between C3 and C2 as well as between C2 and N are longer (1.434(6) and 1.437(5) Å) with greater single-bond character. These parameters prompted the formulation of the zwitterionic structure **VI** depicted in Figure 3a. The lone pair of nonbonded electrons of nitrogen is allowed to delocalize all the way to C2, where increased electron density would allow σ donation to palladium, which now attains the stable 16e configuration.[6]

The computed optimized geometry is shown in Figure 4a (see the Supporting Information for computational details).

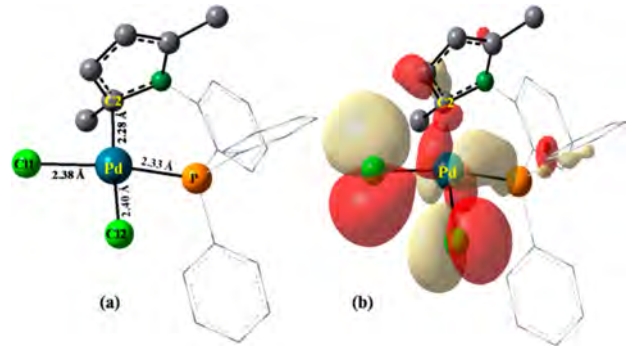

Figure 4. (a) Optimized geometry showing bond lengths and (b) highest occupied molecular orbitals showing overlap between Pd and C2.

The associated frontier molecular orbital picture clearly shows the presence of a significant bonding overlap between palladium and carbon of the pyrrole ring, as depicted in Figure 4b. The trend of bond length shrinkage or elongation observed in the crystal structure is reflected in the calculated bond lengths. Planarity around the palladium atom is also reproduced by the calculations. In many respects, therefore, the energy-minimized structure is similar to the crystal structure, as seen from a comparison of structural parameters (Table 1).

Table 1. Bond Lengths (r), Electron Density (ρ), and the Associated Laplacian ($\nabla^2\rho$) of Representative Bonds

	r (Å)	ρ	$\nabla^2\rho$	WBI[a]	NAO-BO[b]
Pd–P	2.33	0.09	−0.03	0.1486	0.5437
Pd–Cl1	2.38	0.07	−0.04	0.1603	0.4791
Pd–Cl2	2.40	0.07	−0.04	0.1522	0.4864
Pd–C2	2.28	0.07	−0.31	0.0745	0.3253

[a]Wiberg bond index. [b]Natural atomic orbital bond order.

Figure 5 indicates the presence of bond critical points (BCP) of the (3,−1) type. From Figure 5, it is clear that the BCP is centrally situated in the Pd–C2 bond and parameters ρ and $\nabla^2\rho$ (Table 1) suggest a covalent nature of the bond.[7]

The Mulliken population analysis places a net negative charge on the carbon bound to palladium and a net positive

dx.doi.org/10.1021/om5005435 | Organometallics 2014, 33, 3243–3246

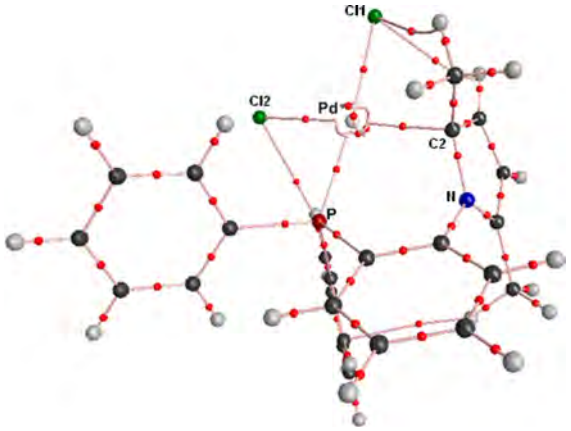

Figure 5. Calculated bond critical point of (3,−1) type.

charge on the nitrogen,[8] which is in agreement with our proposed zwitterionic structure **VI**.

The structure of complex **VI** implies that the symmetry of the pyrrole ring is destroyed; thus, the two methyl groups on pyrrole should have different chemical shift values in the proton NMR spectrum. However, the ^{1}H NMR spectrum of the complex recorded at ambient temperature exhibits one six-proton singlet at 1.46 ppm. Indeed, lowering the temperature led to decoalescence of the six-proton singlet. At −73 °C, two three-proton singlets are clearly seen to emerge at 1.71 and 1.04 ppm (Figure 6), which is to be expected from the nature of the

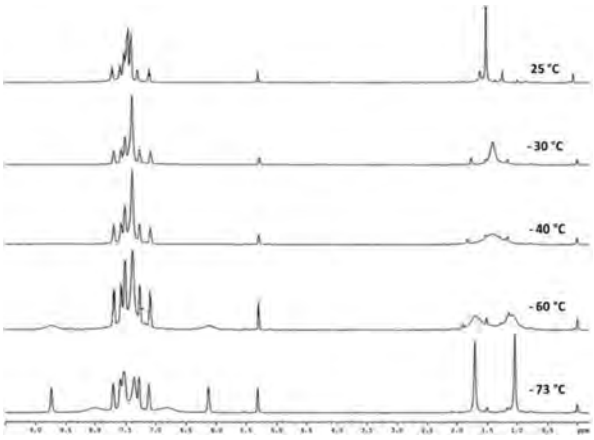

Figure 6. Low-temperature ^{1}H NMR spectra of complex **VI**.

two methyl groups depicted in the crystal structure. Similarly, two distinct and unsymmetrical pyrrole proton signals (H's at C3 and C4) also emerged at 8.74 and 6.13 ppm. A gradual shift of the ^{31}P signal of the phosphine coordinated to the metal was also observed (see the Supporting Information). Thus, the low-temperature NMR spectrum is consistent with the molecular structure of complex **VI**.

It is worthwhile to speculate on the mechanism of the fluxional process. The C−Pd bond is a relatively weak bond. It can be easily disrupted, allowing for a bond rotation along the arene−pyrrole axis leading to a similar bond formation on the other side of the pyrrole: the two structures are enantiomeric (Figure 7). The postulated metallotropy might involve an η^3-2-azaallyl group coordinated to palladium(II) as the transition state between two equal-energy ground-state conformations of η^1 complexes. Formation of an open-chain, coordinatively

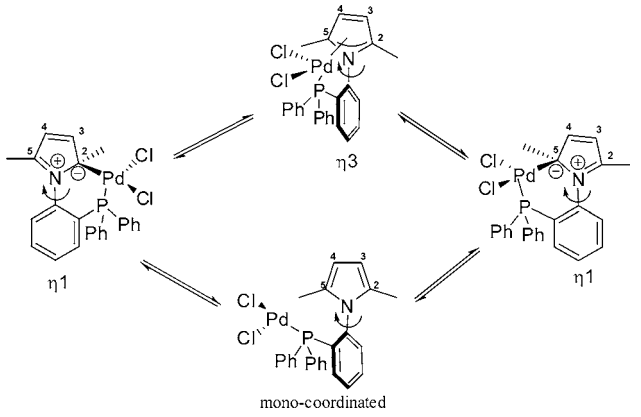

Figure 7. Possible modes of interconversion between two enantiomeric structures of **VI**.

unsaturated $-PPh_2PdCl_2$ intermediate that allows for rotation around the C−N bond is the other possibility.

A frontier molecular orbital analysis shows that the transition state goes through neither the η^3-2-azaallyl complex nor any Pd−N intermediate (see the Supporting Information for computational details). In the transition state there is no bonding overlap between the metal and the pyrrole ring (Figure 8), which suggests that the fluxional process involves

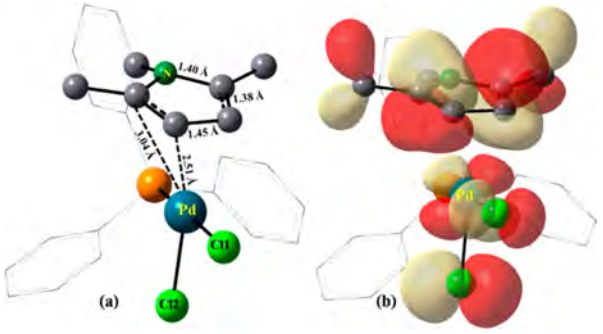

Figure 8. (a) Transition state geometry showing bond lengths and (b) highest occupied molecular orbitals of antibonding type.

Pd−C bond dissociation only. The free energy barrier for the fluxional process is calculated to be 11.5 kcal mol^{-1}. It is in good agreement with the value of 10.42 kcal mol^{-1} estimated[9] from DNMR data.

However curious the metal−pyrrole bond is, it appears to have a significant effect on the catalytic efficiency of the complex in coupling reactions of chloroarenes,[10] which are generally difficult substrates for such reactions. It is also a fact that several such complexes cited in the references do display significant catalytic activity.[11] It can perhaps be attributed to an unconventional, "hemilabile" participation on the part of the presumed monodentate phosphine that stabilizes reactive intermediates in the catalytic cycle.

Hemilabile ligands are potentially chelating ligands with one (or more) donor that has a strong affinity for the metal center and another which is "substitutionally labile".[12b] At the precatalyst stage or catalyst "resting" stage, the ligand acts as a bidentate ligand and stabilizes the metal species by a "chelating" effect. For hetero donor ligands of P, X type, where X = O, N, etc., the metal remains bound to phosphorus throughout the reaction; the weaker donor, O or N, dissociates

dx.doi.org/10.1021/om5005435 | *Organometallics* 2014, 33, 3243−3246

in the presence of the substrate molecules to trigger the catalytic cycle. It has also been stated that "hemilability of a chelate can be observed via fluxional processes that involve the dissociation and recoordination of weakly bonding moieties via intramolecular ligand exchange processes",[12a] which is exactly what we observed. It is possible that oxidative addition of ArCl takes place when the palladium is monocoordinated, as suggested earlier by Buchwald.[4a]

We cannot overlook the fact that several complexes that catalyze coupling reaction with ArCl feature a *triarylphosphine* as donor,[13] not an *aryldialkylphosphine*. Whether and how a weak Pd−C interaction can impart adequate electron richness of palladium to facilitate oxidative addition across a less reactive Ar−Cl bond remains an open question.

To sum up, we have isolated and structurally characterized an unusual palladium(II) complex which reveals an uncommon η^1 coordination of a pyrrole ring to metal that is characterized as a covalent bond by theoretical calculations. The bond is weak, however, as evidenced by a rapid interconversion between two enantiomeric structures at ambient temperature. However, such an interaction strengthens the possibility of "hemilabile" participation of the ligand to stabilize Pd(II) intermediates and facilitate coupling reaction of chloroarenes, notably with triarylphosphines. This merits a closer scrutiny, a theme that is currently being pursued in this laboratory.

■ ASSOCIATED CONTENT

Supporting Information

Text, figures, and a CIF file giving experimental details, characterization data, including ^{1}H, ^{13}C and ^{31}P NMR spectra for the compounds prepared in this paper, and crystallographic data for **VI**. This material is available free of charge via the Internet at http://pubs.acs.org.

■ AUTHOR INFORMATION

Corresponding Author

*E-mail for A.S.: ocas@iacs.res.in.

Notes

The authors declare no competing financial interest.

■ ACKNOWLEDGMENTS

We thank thr DST of India for financial support. D.K. is a Ramanujan Fellow of the Department of Science and Technology (DST), New Delhi, India. D.S. is grateful to the CSIR of India for a Senior Research Fellowship. Crystallographic studies were performed at the facility of the Department of Inorganic Chemistry, IACS. The authors thank Mr. Ranjan Dutta for his valuable assistance. We thank the reviewers for valuable suggestions and references. S.P. and S.B. thank their mentor, Dr. Ankan Paul for his support and encouragement.

■ REFERENCES

(1) (a) Falvello, L. R.; Fornies, J.; Navarro, R.; Sicilia, V.; Tomas, M. *Angew. Chem., Int. Ed.* **1990**, *29*, 891. (b) Falvello, L. R.; Fornies, J.; Navarro, R.; Sicilia, V.; Tomas, M. *J. Chem. Soc., Dalton Trans.* **1994**, 3143. (c) Cámpora, J.; López, J. A.; Palma, P.; Valerga, P.; Spillner, E.; Carmona, E. *Angew. Chem., Int. Ed.* **1999**, *38*, 147.

(2) (a) Murahashi, T.; Otani, T.; Okuno, T.; Kurosawa, H. *Angew. Chem., Int. Ed.* **2000**, *39*, 537. (b) Reid, S. M.; Boyle, R. C.; Mague, J. T.; Fink, M. J. *J. Am. Chem. Soc.* **2003**, *125*, 7816. (c) Wang, Y.; Li, X.; Sun, J.; Ding, K. *Organometallics* **2003**, *22*, 1856. (d) Walker, S. D.; Barder, T. E.; Martinelli, J. R.; Buchwald, S. L. *Angew. Chem., Int. Ed.* **2004**, *43*, 1871. (e) Chaouche, N.; Fornies, J.; Fortuno, C.; Kribii, A.; Martín, A. *J. Organomet. Chem.* **2007**, *692*, 1168.

(3) (a) Kočovsky, P.; Vyskočil, Š.; Cisařová, I.; Sejbal, J.; Tislerova, I.; Smrcina, M.; Lloyd-Jones, G. C.; Stephen, S. C.; Butts, C. P.; Murray, M.; Langer, V. *J. Am. Chem. Soc.* **1999**, *121*, 7714. (b) Dotta, P.; Kumar, P. G. A.; Pregosin, P. S. *Organometallics* **2003**, *22*, 5345.

(4) (a) Barder, T. E.; Walker, S. D.; Martinelli, J. R.; Buchwald, S. L. *J. Am. Chem. Soc.* **2005**, *127*, 4685. (b) Yamashita, M.; Takamiya, I.; Jin, K.; Nozaki, K. *J. Organomet. Chem.* **2006**, *691*, 3189. (c) Barder, T. E. *J. Am. Chem. Soc.* **2006**, *128*, 898.

(5) For comparable C_{ipso}−Pd bond distances, see 2.336(4) Å in ref 2a, 2.676(5) Å in ref 2b, 2.338(11) Å in ref 2c, 2.374(3) Å in ref 2d, 2.391(5) Å in ref 2e, 2.187 Å in ref 3a, and 2.226(8) and 2.129(2) Å in ref 3b.

(6) Kočovsky and Lloyd-Jones reported[3a] a structure that has a tetrahedral arene carbon bound to the Pd(II) center (see structure **III** in Figure 1). The lone pair of electrons on the nitrogen of the Me_2N− group is shown to delocalize (like an enamine) to increase electron density of the ipso carbon that coordinates with the palladium ion. The nitrogen now carries a positive charge; the palladium is shown as a "palladate" species in conformity with its +2 oxidation state. Similar polarizations have also been described by others.[3b]

(7) Zhang, L.; Ying, F.; Wu, W.; Hiberty, P. C.; Shaik, S. *Chem. Eur. J.* **2009**, *15*, 2979.

(8) Mulliken charges on different atoms of **VI**: Pd, 0.504499; P, 1.504727; N, 0.581628; C2, −0.346059.

(9) Eliel, E. L.; Wilen, S. H. In *Stereochemistry of Organic Compounds*; Wiley: New York, 1994; p 502.

(10) Selected reviews: (a) Littke, A. F.; Fu, G. C. *Angew. Chem., Int. Ed.* **2002**, *41*, 4176. (b) Zapf, A.; Beller, M. *Chem. Commun.* **2005**, 431. (c) Martin, R.; Buchwald, S. L. *Acc. Chem. Res.* **2008**, *41*, 1461. (d) Kambe, N.; Iwasaki, T.; Terao, J. *Chem. Soc. Rev.* **2011**, *40*, 4937. (e) Wong, S. M.; So, C. M.; Kwong, F. Y. *Synlett* **2012**, *23*, 1132. (f) Bruno, N. C.; Tudge, M. T.; Buchwald, S. L. *Chem. Sci.* **2013**, *4*, 916.

(11) (a) See refs 3a and 4a. See also: Iwasawa, T.; Komano, T.; Tajima, A.; Tokunaga, M.; Obora, Y.; Fujihara, T.; Tsuji, Y. *Organometallics* **2006**, *25*, 4665. (b) Preliminary experiments show that complex **VI** (2 mol %) catalyzes Suzuki−Miyaura coupling of 4-chloroanisole and 4-chlorotoluene with phenylboronic acid with 76% and 82% isolated yields of coupled products, respectively, in toluene at 100 °C for 6 h: Saha, D.; Sarkar, A. Unpublished results.

(12) (a) Slone, C. S.; Weinberger, D. A.; Mirkin, C. A. *Prog. Inorg. Chem.* **1999**, *48*, 233−350. (b) Braunstein, P.; Naud, F. *Angew. Chem., Int. Ed.* **2001**, *40*, 680.

(13) (a) Liu, S.-Y.; Choi, M. J.; Fu, G. C. *Chem. Commun.* **2001**, 2408. (b) Pramick, M. R.; Rosemeier, S. M.; Beranek, M. T.; Nickse, S. B.; Stone, J. J.; Stockland, R. A., Jr.; Baldwin, S. M.; Kastner, M. E. *Organometallics* **2003**, *22*, 523. (c) Kwong, F. Y.; Chan, K. S.; Yeung, C. H.; Chan, A. S. C. *Chem. Commun.* **2004**, 2336. (d) Mukherjee, A.; Sarkar, A. *Tetrahedron Lett.* **2004**, *45*, 9525. (e) So, C. M.; Chow, W. K.; Choy, P. Y.; Lau, C. P.; Kwong, F. Y. *Chem. Eur. J.* **2010**, *16*, 7996. (f) Chow, W. K.; Yuen, O. Y.; So, C. M.; Wong, W. T.; Kwong, F. Y. *J. Org. Chem.* **2012**, *77*, 3543. (g) See also ref 11a..

Published on 27 March 2014. Downloaded by INDIAN INSTITUTE OF TECHNOLOGY GUWAHATI on 30/09/2014 14:45:32.

Dalton Transactions

PAPER

View Article Online
View Journal | View Issue

Cite this: *Dalton Trans.*, 2014, **43**, 7522

Thioether-ligated iron(II) and iron(III)-hydroperoxo/alkylperoxo complexes with an H-bond donor in the second coordination sphere†

Leland R. Widger,[a] Yunbo Jiang,[a] Alison C. McQuilken,[a] Tzuhsiung Yang,[a] Maxime A. Siegler,[a] Hirotoshi Matsumura,[b] Pierre Moënne-Loccoz,*[b] Devesh Kumar,[c,d] Sam P. de Visser*[c] and David P. Goldberg*[a]

Received 25th January 2014,
Accepted 26th March 2014

DOI: 10.1039/c4dt00281d

www.rsc.org/dalton

The non-heme iron complexes, $[Fe^{II}(N3PySR)(CH_3CN)](BF_4)_2$ (**1**) and $[Fe^{II}(N3Py^{amide}SR)](BF_4)_2$ (**2**), afford rare examples of metastable Fe(III)-OOH and Fe(III)-OO*t*Bu complexes containing equatorial thioether ligands and a single H-bond donor in the second coordination sphere. These peroxo complexes were characterized by a range of spectroscopic methods and density functional theory studies. The influence of a thioether ligand and of one H-bond donor on the stability and spectroscopic properties of these complexes was investigated.

Introduction

Iron-(hydro)peroxo and (alkyl)peroxo species are postulated to be critical intermediates in a number of biologically relevant processes, from the utilization of dioxygen for substrate oxidation, to the processing and detoxification of reactive oxygen-derived species (ROS).[1–5] Some specific examples of non-heme Fe centers involved in this chemistry include isopenicillin N-synthase (IPNS),[6] superoxide reductase (SOR),[7] aromatic amino acid hydroxylase (AAH),[8] Bleomycin,[9] and cysteine dioxygenase (CDO) (Fig. 1).[10] In one case, the alkylperoxo intermediate of an extradiol ring-cleaving dioxygenase, homoprotocatechuate 2,3-dioxygenase (2,3-HPCD), was structurally characterized by X-ray crystallography.[2] The physical and spectroscopic properties of these species have been studied in a number of inorganic model complexes,[11–25] but most of these models utilize only polyamino/polypyridyl ligands. In contrast, some of the enzymes shown in Fig. 1 also include a sulfur donor in the first coordination sphere, but the incorporation of sulfur or other heteroatoms in model complexes is rare.[23,25–41] In addition, little work has been done to determine the effect of secondary sphere interactions, such as hydrogen-bonding networks, on the structures and spectroscopic properties of iron-peroxo complexes,[42,43] despite their roles in many of the corresponding enzyme intermediates. Recently our lab has focused on determining the first and second coordination sphere effects on non-heme iron model complexes, including the incorporation of S donors in the first coordination sphere, and oxidizable substrates or H-bond donors in the second coordination sphere.[44–47]

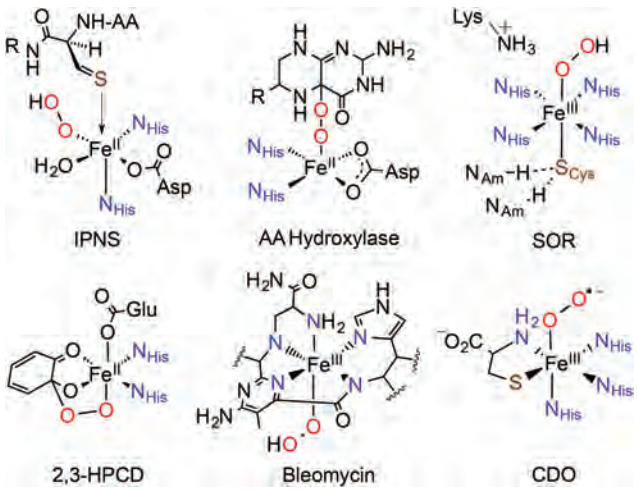

Fig. 1 Selected examples of iron-dioxygen complexes in biology.

The thiolate-ligated complex $[Fe^{II}(N3PyS)(CH_3CN)]BF_4$ was among the first examples of a biomimetic iron(II) complex to

[a]*Department of Chemistry, The Johns Hopkins University, 3400 North Charles Street, Baltimore, Maryland 21218, USA. E-mail: dpg@jhu.edu; Fax: +1-410-516-8420; Tel: +1-410-516-6658*
[b]*Oregon Health & Science University, Institute of Environmental Health, Mail code: HRC3, 3181 SW Sam Jackson Park Road, Portland, OR 97239, USA. E-mail: moennelo@ohsu.edu; Fax: +1-503-346-3427; Tel: +1-503-346-3429*
[c]*Manchester Institute of Biotechnology and School of Chemical Engineering and Analytical Science, The University of Manchester, 131 Princess Street, Manchester, M1 7DN, UK. E-mail: sam.devisser@manchester.ac.uk*
[d]*Department of Applied Physics, School of Physical Sciences, Babasaheb, Bhimrao Ambedkar University, Vidya Vihar, Rae Bareilly Road, Lucknow 226-025, India. E-mail: dkclcre@yahoo.com*

†Electronic supplementary information (ESI) available: Computational details. CCDC 976172–976174. For ESI and crystallographic data in CIF or other electronic format see DOI: 10.1039/c4dt00281d

This journal is © The Royal Society of Chemistry 2014

Published on 27 March 2014. Downloaded by INDIAN INSTITUTE OF TECHNOLOGY GUWAHATI on 30/09/2014 14:45:32.

undergo S-oxygenation with O_2 to yield a doubly-oxygenated sulfinate product.[44] This complex was also useful for studying the fundamental electronic structure and photolability of complexes while employing NO$^{\bullet}$ as a surrogate for O_2.[45] We have examined secondary coordination sphere effects by utilizing the aryl appended complexes, $[Fe^{II}(N4Py^{2Ph})(CH_3CN)](BF_4)_2$ and $[Fe^{II}(N4Py^{amide,2Ph})(CH_3CN)](BF_4)_2$. Without a stabilizing H-bond donor positioned near the open site on iron, the alkylperoxo complex $[Fe^{III}(N4Py^{2Ph})(OOtBu)]^{2+}$ likely undergoes rapid O–O bond cleavage to give a putative $Fe^{IV}(O)$ intermediate. The $Fe^{IV}(O)$ would then be situated for attack of the appended aryl group, giving the arene-hydroxylated product. However, in the presence of an amide H-bond donor, $[Fe^{III}(N4Py^{amide,2Ph})(OOtBu)]^{2+}$ is stabilized and only the alkylperoxoiron(III) complex is observed.[46] We also determined the influence of first and second coordination sphere modifications in a system in which an equatorial thioether donor was included in the first coordination sphere and an amide H-bond donor was included in the second coordination sphere. The $[Fe^{II}(N3Py^{amide}SR)](BF_4)_2$ starting material was shown to react with O-atom donors to give $[Fe^{IV}(O)(N3Py^{amide}SR)]^{2+}$ in CH_3CN at −40 °C. This complex is a rare example of a metastable $Fe^{IV}(O)$ complex with a pendant thioether donor, and it does not undergo *intramolecular* oxygen-atom transfer (OAT) to the thioether group. However, this complex does exhibit rapid *intermolecular* OAT to *exogenous* thioether substrates (PhSMe), and it was proposed that amide H-bond donation to the terminal oxo ligand was causing the significant rate accelerations seen for intermolecular OAT.[47]

Herein we report the synthesis and characterization of Fe(III)-OOH and -OO*t*Bu complexes derived from two biomimetic starting compounds, $[Fe^{II}(N3PySR)(CH_3CN)](BF_4)_2$ (**1**) and $[Fe^{II}(N3Py^{amide}SR)](BF_4)_2$ (**2**), shown in Scheme 1. These complexes were synthesized by metallation with $Fe(BF_4)_2$ of their respective purified ligand precursors. Both **1** and **2** possess a thioether ligand in the first coordination sphere, while complex **2** incorporates a single amide N–H group within H-bonding distance of the preferred binding site for anionic ligands. We demonstrate the generation of meta-stable Fe^{III}-OO(H/R) complexes in the presence of the thioether donor ligands starting from **1** and **2**. The influence of a first coordination sphere thioether donor and a second coordination sphere H-bond donor on the stability and spectroscopic properties of the (hydro/alkyl)peroxo iron(III) complexes is assessed.

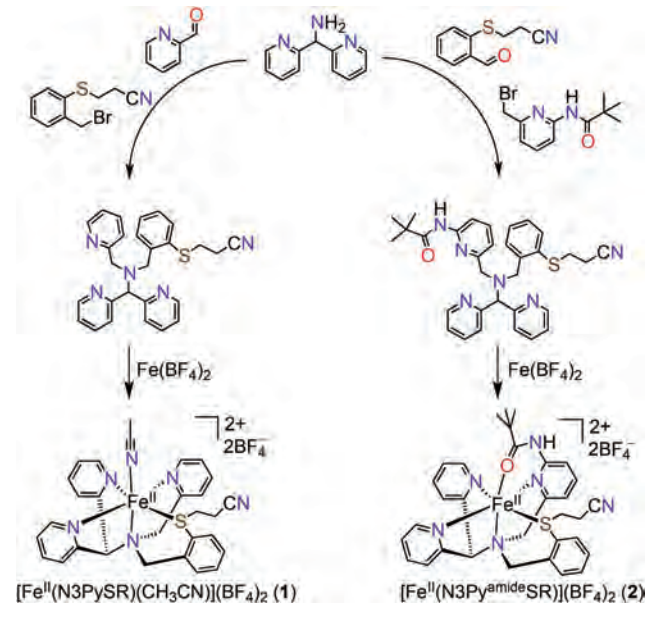

Scheme 1 Convergent syntheses of **1** and **2**.

Results and discussion

Synthesis and characterization

Compound **1** is prepared by metallation of the ligand N3PySR with $Fe(BF_4)_2$ in MeCN, followed by vapor diffusion of Et_2O into the resulting solution to give dark red blocks of **1** in 68% yield (Scheme 1). The structure of the cation of **1** is shown in Fig. 2 and structural data are summarized in Table 1. The ferrous ion is bound in a pseudo-octahedral geometry by three pyridyl and an aryl thioether donor in the equatorial plane, with a tertiary nitrogen donor and solvent nitrile molecule occupying the axial positions. The Fe–N bond distances (1.9260(14)–1.9969(13) Å, Table 2) are consistent with a low spin (ls) iron(II) center. The spin state was also confirmed by observation of a diamagnetic ^{1}H-NMR spectrum in $CDCl_3$.

Metallation of the ligand N3Py^{amide}SR with $Fe(BF_4)_2$, followed by vapor diffusion of Et_2O into the resulting dark orange solution yielded dark red crystals of **2** in 88% yield. The structure of the cation of **2** (Fig. 3) was reported previously and is repeated here for comparison with the other complexes.[47] As in **1**, the ferrous ion is low-spin and bound in a pseudo-octahedral geometry with three pyridyl and one aryl thioether donor in the equatorial plane, with the tertiary nitrogen donor occupying the axial position. In **2** however, the amide ligand has displaced the

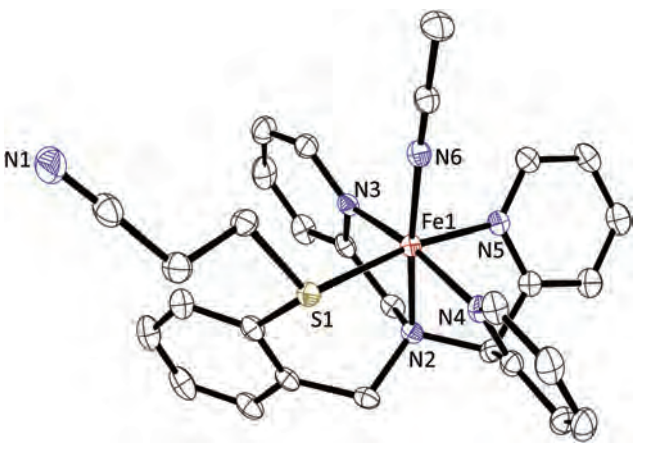

Fig. 2 Displacement ellipsoid plot of the cation of **1** shown at the 50% probability level. H-atoms are removed for clarity.

Published on 27 March 2014. Downloaded by INDIAN INSTITUTE OF TECHNOLOGY GUWAHATI on 30/09/2014 14:45:32.

Table 1 Summary of the crystallographic data for **1**, **3**·CH_3CN and **8**

Complex	**1**	**3**·CH_3CN	**8**
Formula	$C_{29}H_{28}B_2F_8FeN_6S$	$C_{34}H_{37}BF_{4.67}FeN_8OS$	$C_{44}H_{42}B_2F_8FeN_6OS$
Formula weight	722.10	761.13	932.37
T (K)	110	110	110
Color, morphology	Dark red, irregular shape	Yellow, lath	Yellow, block
Class	Triclinic	Orthorhombic	Triclinic
Space group	$P\bar{1}$	$Pbcn$	$P\bar{1}$
a (Å)	10.6689(2)	35.1087(4)	10.4419(3)
b (Å)	12.0355(2)	10.08753(9)	14.5834(3)
c (Å)	13.0403(3)	19.9277(2)	17.2950(4)
α (°)	80.5885(18)	90	90.6304(19)
β (°)	88.0024(18)	90	105.768(2)
γ (°)	68.543(2)	90	106.791(2)
V (Å^3)	1536.85(5)	7057.59(12)	2415.01(10)
ρ (g cm^{-3})	1.560	1.433	1.282
μ (mm^{-1})	0.640	4.546	0.425
$(\sin\theta/\lambda)_{max}$ (Å^{-1})	0.65	0.62	0.62
No. reflections collected	35 673	44 026	29 736
No. unique reflections	7051	6942	9709
R_{int}	0.0247	0.0273	0.0305
No. variable parameters	425	511	648
R_1 [$I > 2\sigma(I)$]	0.0325	0.0322	0.0401
wR_2 [$I > 2\sigma(I)$]	0.0877	0.0791	0.1117
R_1 [all data]	0.0373	0.0366	0.0475
R_2 [all data]	0.0905	0.0821	0.1155
Goodness-of-fit (GOF) on F^2	1.061	1.026	1.102
Largest difference in hold and peak (e A^{-3})	−0.50, 0.63	−0.33, 0.63	−0.46, 0.58

Table 2 Selected bond distances (Å) and angles (°) for **1**

Bond lengths		Bond angles	
Fe1 N6	1.9260(14)	N6 Fe1 N4	94.41(6)
Fe1 N4	1.9569(13)	N6 Fe1 N3	97.35(6)
Fe1 N3	1.9619(13)	N4 Fe1 N3	168.23(6)
Fe1 N5	1.9790(13)	N6 Fe1 N5	94.24(5)
Fe1 N2	1.9969(13)	N4 Fe1 N5	86.41(5)
Fe1 S1	2.2848(4)	N3 Fe1 N5	92.09(5)
		N6 Fe1 N2	175.10(5)
		N4 Fe1 N2	83.35(5)
		N3 Fe1 N2	84.88(5)
		N5 Fe1 N2	81.29(5)
		N6 Fe1 S1	93.13(4)
		N4 Fe1 S1	87.26(4)
		N3 Fe1 S1	92.70(4)
		N5 Fe1 S1	170.63(4)
		N2 Fe1 S1	91.12(4)

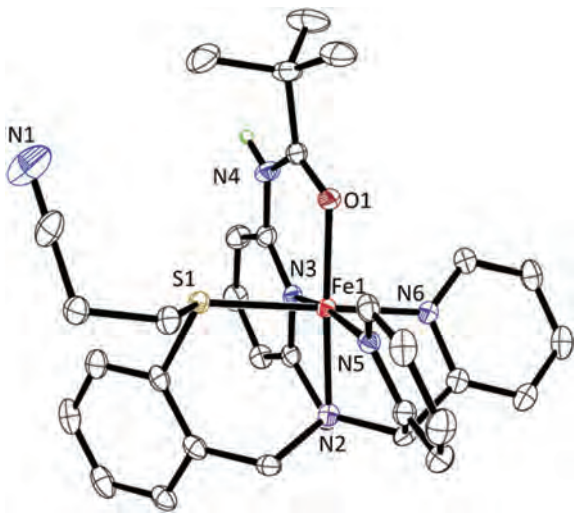

Fig. 3 Displacement ellipsoid plot for the cation of **2** shown at the 50% probability level. H-atoms, except the amide N–H, are removed for clarity. The existence of the H atom attached to N4 was confirmed by difference Fourier map.

bound solvent molecule and is coordinated through the amide oxygen.

When the propionitrile protecting group of the ligand for **1** is removed prior to metal binding, the corresponding Fe^{II}-thiolate complex is accessed, which has been shown to undergo sulfur oxidation in the presence of O_2.[44] However, in compounds **1** and **2** the thioether donor appears to make these complexes stable toward O_2, with no visible decomposition over several days stored under aerobic conditions.

Prior to attempting to make iron-peroxo complexes from **1** and **2**, we wanted to test the substitution chemistry of **2** toward anionic donors to show that the amide group could be displaced and reoriented into a favorable hydrogen-bonding position. We also wanted to confirm whether hydrogen bonding would be favored with the anionic ligands found in the axial position. Stirring of **2** with 1.0 equiv. NaN_3 in MeCN, followed by vapor diffusion of Et_2O into the solution produced a small amount of yellow crystals that were manually separated from the bulk precipitate for X-ray structure determination. This structure revealed the new compound, $[Fe^{II}(N3Py^{amide}SR)(F/N_3)]BF_4$ (**3**), which shows that the amide C=O donor has been displaced, and there is a mixture of F^- (67%) and N_3^- (33%) anions that are occupying the desired axial position.

 This journal is © The Royal Society of Chemistry 2014

Published on 27 March 2014. Downloaded by INDIAN INSTITUTE OF TECHNOLOGY GUWAHATI on 30/09/2014 14:45:32.

Table 3 Selected bond lengths (Å) and angles (°) for **3**

Bond lengths		Bond angles	
Fe1 F1	1.850(4)	F1 Fe1 N2	98.05(14)
Fe1 N7	2.063(14)	N7 Fe1 N2	105.6(5)
Fe1 N2	2.1703(16)	F1 Fe1 N1	108.09(14)
Fe1 N1	2.1892(14)	N7 Fe1 N1	102.8(4)
Fe1 N3	2.2012(14)	N2 Fe1 N1	82.68(6)
Fe1 N5	2.2448(13)	F1 Fe1 N3	173.68(12)
Fe1 S1	2.6007(5)	N7 Fe1 N3	176.6(4)
		N2 Fe1 N3	77.62(6)
		N1 Fe1 N3	76.14(5)
		F1 Fe1 N5	98.62(14)
		N7 Fe1 N5	103.3(4)
		N2 Fe1 N5	95.76(5)
		N1 Fe1 N5	153.22(5)
		N3 Fe1 N5	77.41(5)
		F1 Fe1 S1	94.88(14)
		N7 Fe1 S1	87.7(5)
		N2 Fe1 S1	166.53(5)
		N1 Fe1 S1	96.89(4)
		N3 Fe1 S1	89.18(4)
		N5 Fe1 S1	78.52(4)

The Fe–S bond is rather long (2.6007(5) Å), but the sulfur is oriented correctly for a weak bonding interaction with the Fe center (Table 3). The Fe^{II}–N(py) distances (2.1703(16)–2.2448(13) Å) for **3** are indicative of a high-spin (hs) ferrous center, and the difference in Fe–F and Fe–N_3 distances allows for reliable determination of the N_3^- ligand despite its low occupancy. The N_3^--containing component of **3** is shown in Fig. 4, as it more closely resembles the structure of an anionic peroxo ligand than does the F^- component. The source of fluoride for the F^--containing component of **3** can be assigned to BF_4^-. This structure shows that the axial amide carbonyl is labile, and can be displaced by anionic donors. The structure of **3** also shows that the pendant amide is positioned such that H-bonding interactions to anionic ligands are favored (N6···N7 = 2.914(16) Å, N6···F1 = 2.784(5) Å, N6–H–N7 = 174(2)°, N6–H–F1 = 170(2)°; amide N–H is located in the difference map). This complex provides good evidence that Fe-OO(H/R) complexes will likely exhibit the same H-bonding interaction.

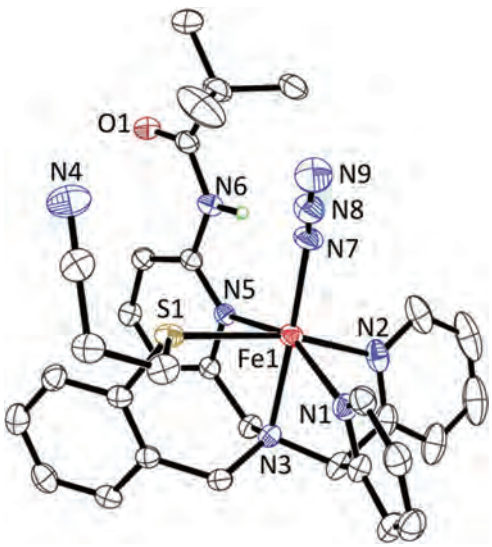

Fig. 4 Displacement ellipsoid plot of the N_3^--containing disordered component of the cation of **3** shown at the 50% probability level. H-atoms, except the amide N–H, are removed for clarity. The existence of the H atom attached to N6 was confirmed by difference Fourier map.

Fe^{III}-OOH complexes

Complex **1** reacts with excess H_2O_2 at 25 °C (Fig. 5) to generate a new transient red species, **4** ($t_{1/2} \approx 1$ min). Monitoring the reaction by UV-vis shows isosbestic conversion of the peaks corresponding to **1** (λ_{max} = 360, 430 nm) into a new spectrum for **4** (λ_{max} = 542 nm, ε = 1000 M^{-1} cm^{-1}). The peak at 542 nm is characteristic of a hydroperoxo-to-iron(III) LMCT band. Attempts to trap this species by generation at −40 °C were unsuccessful, leading only to decomposition, with no observable UV-vis peaks corresponding to **4**. Samples of **4** for analysis by EPR and resonance Raman were therefore prepared at 25 °C and flash-frozen immediately after mixing. From EPR and RR (*vide infra*) complex **4** is assigned as the Fe^{III}-OOH complex $[Fe^{III}(OOH)(N3PySR)]^{2+}$.

Complex **2** reacts with excess H_2O_2 at −40 °C (Fig. 6), and changes in color from orange to deep purple over the course of 30 min. The new purple species (**5**) persists for at least several hours at −40 °C, but immediately decays upon warming to 25 °C. Monitoring by low-temperature UV-vis spectroscopy shows isosbestic conversion from **2** (λ_{max} = 350, 450 nm) to a new peak (λ_{max} = 567 nm, ε = 900 M^{-1} cm^{-1}) that is characteristic of a hydroperoxo-to-iron(III) LMCT band. The EPR and RR spectra (*vide infra*), confirmed that the new species (**5**) is the Fe^{III}-OOH complex, $[Fe^{III}(OOH)(N3Py^{amide}SR)]^{2+}$.

The X-band EPR spectra of **4** and **5** are shown in Fig. 5 and 6, respectively. Both complexes show axial spectra corresponding to ls iron(III) centers with signals at g = 2.17, 2.11,

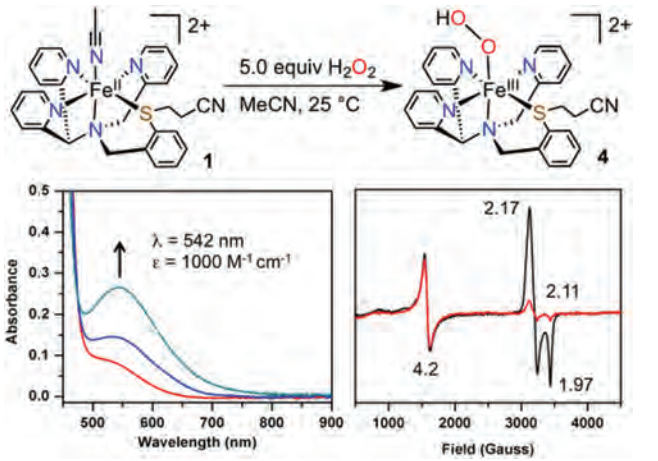

Fig. 5 Formation of $[Fe^{III}(OOH)(N3PySR)]^{2+}$ (**4**) (top). Changes in the electronic absorption spectrum for the reaction of **1** + H_2O_2 in CH_3CN (25 °C), red = **1**, blue = 30 s, green = 60 s (bottom left). X-band EPR spectra of the reaction mixture of **1** + H_2O_2, flash frozen after mixing at 25 °C for 1 min (black line) and 3 min (red line) (bottom right). EPR parameters: T = 15 K, frequency = 9.46 GHz, power = 2.01 mW.

Published on 27 March 2014. Downloaded by INDIAN INSTITUTE OF TECHNOLOGY GUWAHATI on 30/09/2014 14:45:32.

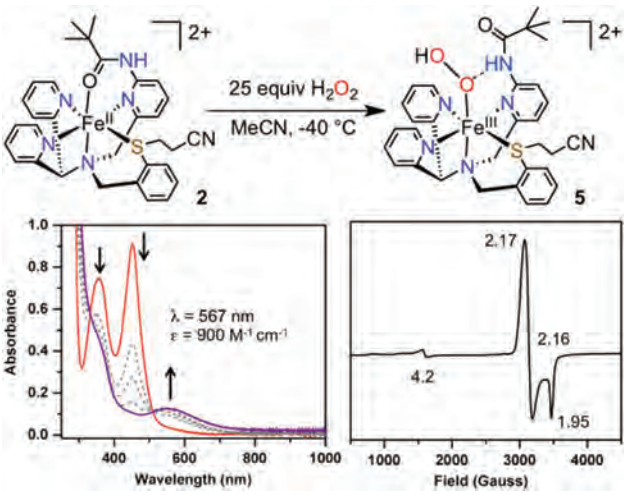

Fig. 6 Formation of $[Fe^{III}(OOH)(N3Py^{amide}SR)]^{2+}$ (**5**) (top). Changes in the electronic absorption spectrum for the reaction of **2** + H_2O_2 in CH_3CN, over 30 min at −40 °C (bottom left). X-band EPR spectrum of the reaction mixture of **2** + H_2O_2, flash frozen after mixing at −40 °C for 30 min. EPR parameters: T = 77 K, frequency = 9.46 GHz, power = 2.01 mW.

1.97, for **4** and g = 2.17, 2.16, 1.95, for **5**. These values are similar to other Fe^{III}-OOH complexes reported in the literature.[18] The mononuclear complex $[Fe^{III}(N4Py)(OOH)]^{2+}$ in methanol has a signal at g = 2.17, 2.12 and 1.97,[13] while the TPA analogue $[Fe^{III}(TPA)(OOH)]^{2+}$ affords a spectrum with g = 2.19, 2.15 and 1.96 in acetone/acetonitrile.[48] EPR spectra of reaction mixtures of **4**, taken at different timepoints (1–5 min) clearly show the rapid decomposition of the ls-Fe^{III} signal at room temperature. Samples frozen after 1 min show a relatively strong ls-Fe^{III} signal along with an additional signal at g = 4.2. After 3 minutes, the ls-Fe^{III} signal appears to be mostly decayed, and after 5 min no ls-Fe^{III} signal is observed. The peak at g = 4.2 does not increase with the decay of the Fe^{III}-OOH feature, indicating it is not a decomposition product and is likely a byproduct of Fe^{III}-OOH formation. The peak at g = 4.2 is much more prominent in **4** relative to that seen in the spectrum of **5**, which was prepared at −40 °C and frozen after 30 min, allowing for full formation of **5** with much less possibility for decay.

The identity of the Fe^{III}-OOH complex **4** was confirmed by RR spectroscopy. Frozen CD_3CN solutions were analyzed at 110 K with a 568 nm laser excitation to avoid overlap of RR bands with non-resonant vibrations from CH_3CN. The RR spectra of **4** show a cluster of bands in the ν(Fe–O) region with prominent bands at 615, 629, 647 and 664 cm^{-1}, and two bands at 787 and 809 cm^{-1} in the ν(O–O) region (Fig. 7A). Labeled samples prepared with $H_2{}^{18}O_2$ exhibit greatly simplified spectra with unique ν(Fe–O) and ν(O–O) modes at 590 and 763 cm^{-1}, respectively. RR spectra of samples prepared with D_2O_2 in the presence of excess D_2O also show a single set of ν(Fe–O) and ν(O–O) bands at 607 cm^{-1} and 809 cm^{-1}. These data clearly indicate that the complexity of the RR spectra of unlabeled complex **4** results from vibrational coupling of the

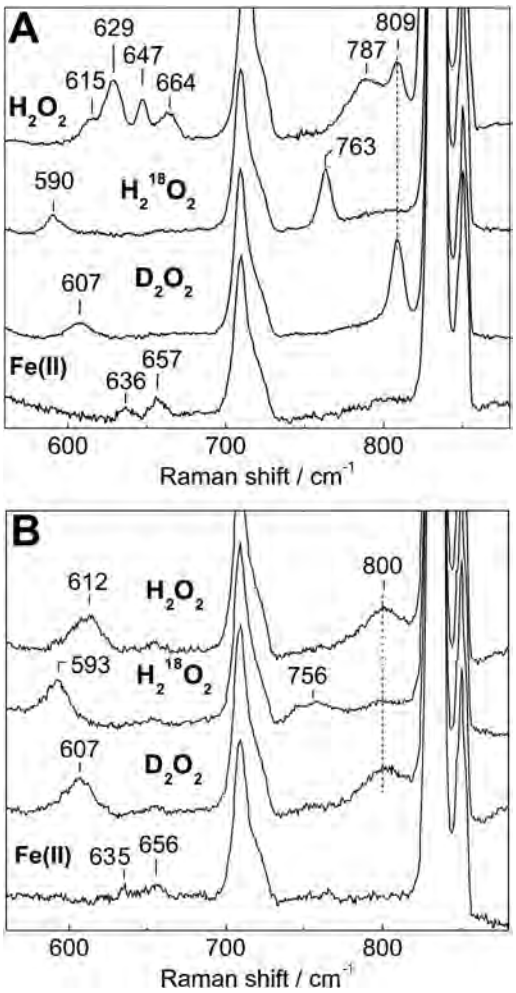

Fig. 7 Resonance Raman spectra of complexes **1** and **4** (A), and **2** and **5** (B) in CD_3CN.

Fe–O–O–H unit with internal vibrations of the (N3PyS) ligand. Using Hooke's law to calculate the $\nu(^{16}O–^{16}O)$ frequency based on an isolated diatomic oscillator with a $\nu(^{18}O–^{18}O)$ at 763 cm^{-1} leads to an 809 cm^{-1} value that matches the ν(O–O) mode seen in D_2O and the sharper component of the doublet observed with unlabeled complex **4**. Accordingly, the 809 cm^{-1} band is assigned to the ν(O–O) mode of **4**. Using the same approach to interpret the RR bands observed in the ν(Fe–O) region is less successful,[49] presumably because of admixture between Fe–O stretch and Fe–O–O bend vibrations, as seen previously with other Fe(III)-hydroperoxo complexes.[13,50]

The pendant amide complex $[Fe^{III}(N3Py^{amide}SR)(OOH)]^{2+}$ (**5**) was also studied by RR spectroscopy under the same conditions (Fig. 7b). In contrast with **4**, the RR spectra of **5** shows no evidence of vibrational coupling and assigning the ν(Fe–O) and ν(O–O) bands is straightforward. The unlabeled complex shows a single ν(O–O) mode at 800 cm^{-1} that downshifts to 756 cm^{-1} with samples prepared with $H_2{}^{18}O_2$ and that is unchanged in samples prepared with D_2O_2 in the presence of excess D_2O. A single band at 612 cm^{-1} in the ν(Fe–O) region shifts to 593 cm^{-1} with $H_2{}^{18}O_2$ and to 607 cm^{-1} with D_2O_2.

 This journal is © The Royal Society of Chemistry 2014

Published on 27 March 2014. Downloaded by INDIAN INSTITUTE OF TECHNOLOGY GUWAHATI on 30/09/2014 14:45:32.

Table 4 Comparison of RR data for ls non-heme Fe^{III}-OOH complexes

Complex	ν(Fe–O), [ν(O–O)]	$\Delta^{18}O_2$	ΔD_2O
$[Fe^{III}(N3PySR)(OOH)]^{2+}$	615, [809]	−25, [−46]	−8, [0]
$[Fe^{III}(N3Py^{amide}SR)(OOH)]^{2+}$	612, [800]	−19, [−44]	−5, [0]
$[Fe^{III}(N4Py)(OOH)]^{2+}$ [a]	632, [790]	−16, [−44]	−5, [0]
$[Fe^{III}(TPA)(OOH)]^{2+}$ [b]	624, [803]	−19, [44]	−3, [0]

[a] Ref. 13. [b] Ref. 51.

Comparing ν(Fe–O) and ν(O–O) frequencies for **4** and **5** with previously characterized Fe(III)-OOH complexes (Table 4), confirms their identity and suggests that the amide H-bond donor group exerts limited influence on the Fe–O–O unit.

Comparison of the RR data for complexes **4** and **5** with $[Fe^{III}(N4Py)(OOH)]^{2+}$ reveals a 19 ± 2 cm^{-1} downshift in ν(Fe–O), and a 10 to 19 cm^{-1} (for **5** and **4**, respectively) upshift of the $\Delta\nu$(O–O) upon incorporation of the thioether donor. This effect of the equatorial thioether donor on ν(O–O) differs from a previous study, where the replacement of an axial triflate (OTf^-) ligand with aryl-thiolate donors (ArS^-) in hs $[Fe^{III}(Me_4[15]aneN_4)(SAr)(OOR)]^+$ complexes was shown to have little influence on ν(O–O) ($\Delta\nu$(O–O) = 1 cm^{-1}).[23] In contrast, the effect of the equatorial thioether donor on ν(Fe–O) in **4** and **5** is similar to the effect previously seen for the aryl-thiolate complexes, in which inclusion of sulfur induced a lowering of this band.[23]

Fe^{III}-OO*t*Bu complexes

Complex **1** reacts with 10 equiv. of *t*BuOOH (Fig. 8) at −40 °C in MeCN to give a new deep blue species (**6**) that persists at low temperature for 15–20 min before slowly decaying. Monitoring the reaction by UV-vis spectroscopy shows the isosbestic conversion of the peaks corresponding to **1**, into a new spectrum (λ_{max} = 600 nm, ε = 1670 M^{-1} cm^{-1}) that is characteristic of an alkylperoxo-to-iron(III) LMCT band and is in good agreement with similar compounds reported in the literature.[14,29] The UV-vis spectra reveal that **1** reacts with *t*BuOOH to form **6** within 10 min, but is only stable for a short period and begins to decay after 15 min. The new species (**6**) is assigned as the alkylperoxo complex $[Fe^{III}(OOtBu)(N3PySR)]^{2+}$.

Complex **2** also reacts with *t*BuOOH at −40 °C to give a deep blue solution, similar to that seen for **1**. This new complex (**7**, Fig. 9) is formed *via* isosbestic conversion from **2**, to a new spectrum characteristic for Fe^{III}-OOR complexes (λ_{max} = 620 nm, ε = 2000 M^{-1} cm^{-1}) within 15 min. As seen for **6**, complex **7** is not stable at −40 °C, and slowly decays to a broad, featureless spectrum over 1 h. This species (**7**) is assigned as the ferric-alkylperoxo complex, $[Fe^{III}(OOtBu)(N3Py^{amide}SR)]^{2+}$.

It has been shown that a lowering in energy of peroxo-to-iron(III) charge transfer bands can be correlated with an increasing number of pyridine ligands bound to the iron center, as the π-accepting ability of py ligands lowers the energy of LMCT bands.[18,52] It is therefore interesting to compare the energy of the LMCT band for compounds **6** and **7**

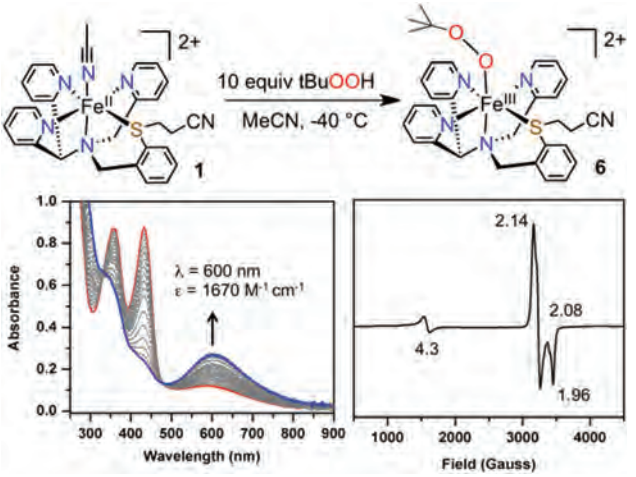

Fig. 8 Formation of $[Fe^{III}(OOtBu)(N3PySR)]^{2+}$ (**6**) (top). Changes in the electronic absorption spectrum for the reaction of **1** + *t*BuOOH in CH_3CN, over 10 min at −40 °C (bottom left). X-band EPR spectrum of the reaction mixture of **1** + *t*BuOOH, flash frozen after mixing at −40 °C for 15 min. EPR parameters: T = 15 K, frequency = 9.46 GHz, power = 2.01 mW.

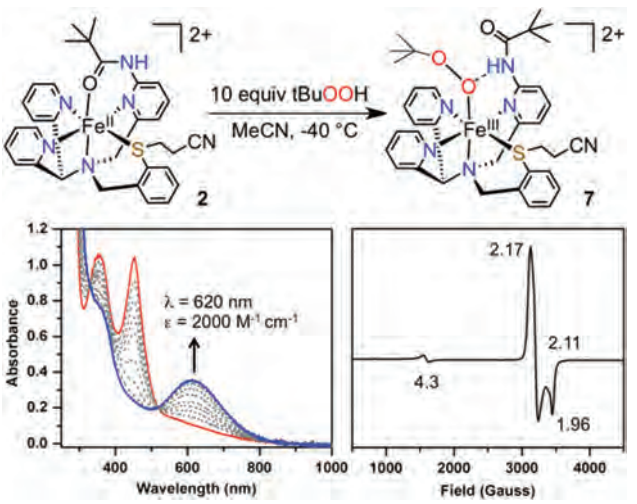

Fig. 9 Formation of $[Fe^{III}(OOtBu)(N3Py^{amide}SR)]^{2+}$ (**7**) (top). Changes in the electronic absorption spectrum for the reaction of **2** + *t*BuOOH in CH_3CN, over 10 min at −40 °C (bottom left). X-band EPR spectrum of the reaction mixture of **2** + *t*BuOOH, flash frozen after mixing at −40 °C for 15 min. EPR parameters: T = 77 K, frequency = 9.46 GHz, power = 2.01 mW.

to the parent $[Fe^{III}(N4Py)(OOtBu)]^{2+}$ compound (λ_{max} = 560 nm, ε = 2400 M^{-1} cm^{-1}).[15] Relative to N4Py, the thioether-ligated complexes exhibit bands that are shifted to lower energy by 40 nm for **6**, and 60 nm for **7**. These shifts indicate that replacement of a pyridine with a thioether donor causes a significant lowering of the energy of the LMCT band. This change is consistent with stabilization of the metal acceptor orbital caused by the weaker ligand field presented by the thioether donor. In addition, the LMCT bands for both the (hydro) and (alkyl) peroxo-iron(III) complexes are further lowered in energy by the

Published on 27 March 2014. Downloaded by INDIAN INSTITUTE OF TECHNOLOGY GUWAHATI on 30/09/2014 14:45:32.

addition of the H-bond donor, as evidenced by the ~20 nm red-shift in the absorption band for both **5** and **7**, relative to the non H-bonded **4** and **6**.

The X-band EPR spectra for **6** and **7** (Fig. 8 and 9) show that the alkylperoxo species are also low-spin iron(III) with *g* values of 2.14, 2.08, 1.96 (**6**), and 2.17, 2.11, 1.96 (**7**), that are in good agreement with similar compounds previously reported in the literature.[14,28,29] As seen with the hydroperoxo complexes, spectra of **6** and **7** do show a small peak at $g = 4.3$, consistent with a small amount of high-spin decomposition product.

Resonance Raman spectra of **6** and **7** were collected on frozen samples in CD_3CN at 110 K with a 647 nm laser excitation (Fig. 10). The spectrum of **6** shows two resonance-enhanced vibrations at 700 and 796 cm^{-1} that are in the expected range for ν(Fe–O) and ν(O–O), respectively. The RR spectrum of **7** shows similar vibrations at 691 and 796 cm^{-1}.

These ν(O–O) frequencies below 800 cm^{-1} are consistent with the ls configuration of **6** and **7** and both ν(O–O) and ν(Fe–O) closely match reported results for $[Fe^{III}(TPA)(OH_n)(OOtBu)]^{n+}$ (see Table 5). The presence of the intramolecular H-bond donor in **7** has no effect on the ν(O–O), but it results in a −9 cm^{-1} downshift of the ν(Fe–O) relative to **6**. RR spectra of complex **7** after H/D exchange of the amide N–H group showed that deuteration of the amide group has no effect on the ν(Fe–O) and ν(O–O) signals, which suggests that the H-bonding interaction might be weak. The 7 cm^{-1} downshift of the ν(Fe–O) in **7**, relative to $[Fe^{III}(TPA)(OOtBu)]^{2+}$, could be due to changes in Fe–O–O–R angle and level of admixture between Fe–O stretch and Fe–O–O bend rather than changes in Fe–O bond strength.

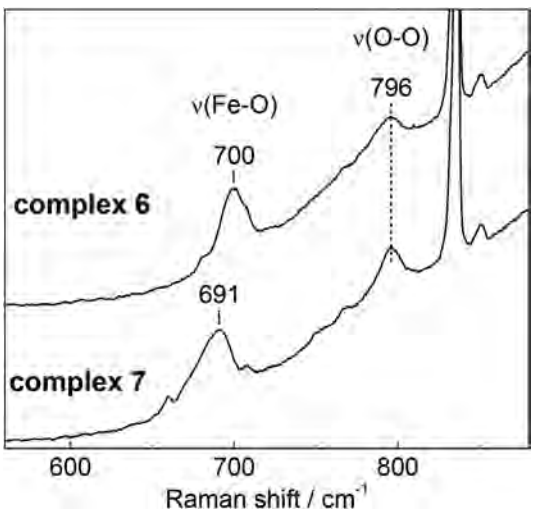

Fig. 10 Resonance Raman spectra of **6** and **7** in CD_3CN.

Table 5 Comparison of RR data for ls non-heme Fe^{III}-OO*t*Bu complexes

Complex	ν(Fe–O)	ν(O–O)	Reference
$[Fe^{III}(N3PySR)(OOtBu)]^{2+}$	700	796	This work
$[Fe^{III}(N3Py^{amide}SR)(OOtBu)]^{2+}$	691	796	This work
$[Fe^{III}(TPA)(OOtBu)]^{2+}$	696	796	22
$[Fe^{III}([15]aneN_4)(SPh)(OOtBu)]^{+}$	612	803	23

Density functional theory

Density functional computations at the UB3LYP-D level of theory were utilized to model complexes **4**–**7** (see ESI† for details). Our initial work explored the spin state ordering of complex **5**, for which we calculated the lowest lying doublet (^{2}**5**), quartet (^{4}**5**), and sextet (^{6}**5**) spin states. The doublet spin state was found to be the ground state by 1.5 and 8.5 kcal mol^{-1} over the sextet and quartet spin states, respectively. This spin state ordering reproduces the experimental EPR characterization of **5**, which indicates an $S = 1/2$ spin state. Optimized geometries of ^{2}**5** and ^{2}**7** are shown in Fig. 11 and are consistent with the proposed structures for complexes **5** and **7**, where the iron(III) center is bound in a pseudo-octahedral geometry by the equatorial pyridine and thioether donors, and the tertiary amine and (hydro/alkyl)peroxide ligands occupy the axial positions. The structures also show that the pendant amide H-bond donor has reoriented in both cases, and reveals an NH···O hydrogen bond, with calculated N···O distances of 2.774 Å (**5**) and 2.815 Å (**7**) and angles of 158.1° (**5**) and 153.3° (**7**).

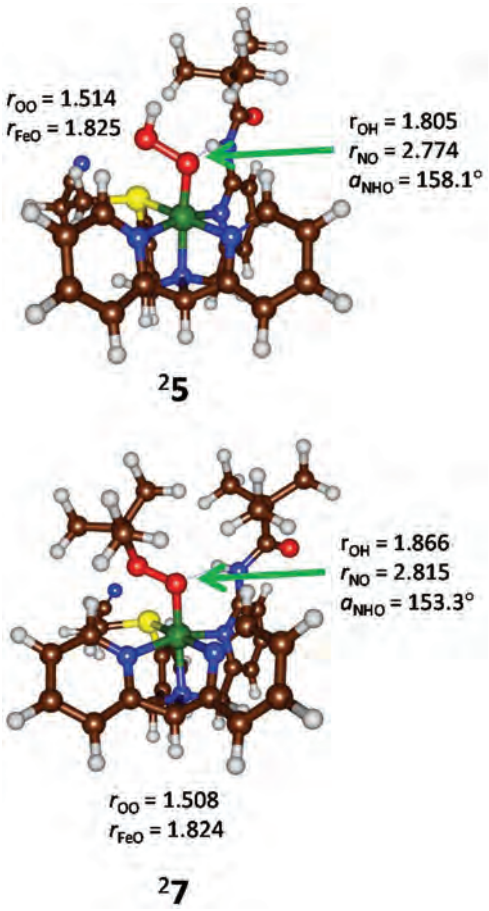

Fig. 11 DFT optimized structures of ^{2}**5** (top) and ^{2}**7** (bottom), calculated at the UB3LYP-D level of theory with bond lengths given in angstroms.

 This journal is © The Royal Society of Chemistry 2014

Published on 27 March 2014. Downloaded by INDIAN INSTITUTE OF TECHNOLOGY GUWAHATI on 30/09/2014 14:45:32.

Steric influences in the secondary coordination sphere

In further efforts to stabilize the Fe^{III}-OO(H/R) species, we synthesized the new ligand shown in Scheme 2. The resulting complex, $[Fe^{II}(N3Py^{amide,2Ph}SR)](BF_4)_2$ (**8**), incorporates two phenyl substituents in the second coordination sphere, providing additional steric protection around the putative peroxide binding site (Fig. 12). The synthesis of the $N3Py^{amide,2Ph}SR$ ligand is shown in Scheme 2. The key synthetic step, incorporation of the phenyl substituents onto the pyridine rings, was accomplished in high yield using Suzuki–Miyaura cross coupling reaction.[46] Metallation of the free ligand with $Fe(BF_4)_2$ was accomplished by stirring in MeCN, and single crystals of **8** were grown from vapor diffusion of Et_2O into the solution. The light yellow crystals reveal Fe–N bond distances (2.1842–2.2267 Å, Table 6) consistent with a high-spin (hs) iron(II) center. As in **2**, the iron(II) ion is bound in a pseudo-octahedral geometry with the 3 pyridine donors and aryl thioether occupying the equatorial positions, while the tertiary amine and the amide carbonyl are bound in the axial positions. The incorporated phenyl substituents are projected orthogonal to the pseudo-equatorial plane, and are oriented to provide significant steric protection around the axial binding site. In contrast to low-spin **1** and **2**, as well as some other hs Fe^{II} complexes,[28,46] **8** does not react with H_2O_2 or *t*BuOOH to afford the corresponding ferric-peroxo complexes, and appears to only undergo outer-sphere oxidation upon addition of a large excess of oxidant (150 equiv.). The lack of reactivity may be due to significant steric encumbrance around the metal center with incorporation of the new phenyl substituents. However, we should point out that the related diphenyl-substituted hs Fe^{II} complex, $[Fe^{II}(N4Py^{amide,2Ph})(CH_3CN)]^{2+}$, does react with *t*BuOOH to give an $Fe^{III}(OOtBu)$ complex at low temperature,[46] and therefore some additional factors may also be involved in inhibiting the reactivity of **8**.

Table 6 Selected bond distances (Å) and angles (°) for **8**

Bond lengths		Bond angles	
Fe1 O1	2.0085(13)	O1 Fe1 N4	83.37(6)
Fe1 N4	2.1842(16)	O1 Fe1 N3	159.27(6)
Fe1 N3	2.1954(15)	N4 Fe1 N3	76.66(6)
Fe1 N1	2.1959(15)	O1 Fe1 N1	111.24(6)
Fe1 N2	2.2267(16)	N4 Fe1 N1	98.60(6)
Fe1 S1	2.6097(5)	N3 Fe1 N1	77.62(6)
		O1 Fe1 N2	120.85(6)
		N4 Fe1 N2	154.51(6)
		N3 Fe1 N2	78.35(6)
		N1 Fe1 N2	80.75(6)
		O1 Fe1 S1	83.97(4)
		N4 Fe1 S1	84.45(4)
		N3 Fe1 S1	88.61(4)
		N1 Fe1 S1	164.70(4)
		N2 Fe1 S1	90.05(4)

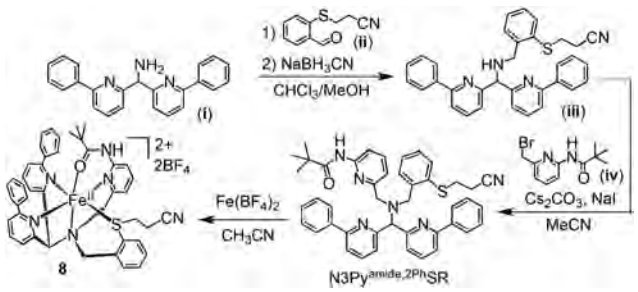

Scheme 2 Synthesis of the ligand precursor ($N3Py^{amide,2Ph}SR$) to **8**.

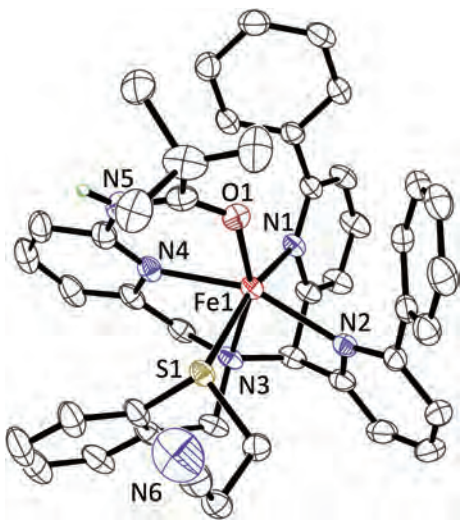

Fig. 12 Displacement ellipsoid plot of the cation of **8** shown at the 50% probability level. H-atoms, except the amide N–H, are removed for clarity.

Conclusions

We have synthesized a series of new biomimetic iron(II) model complexes that incorporate a pendant thioether ligand in the equatorial plane. Complexes **1** and **2** react to generate rare examples of Fe^{III}-hydroperoxo and -alkylperoxo complexes with a pendant thioether donor (**4**–**7**). These peroxo species were characterized by UV-vis, EPR and resonance Raman spectroscopy, and DFT calculations supported the proposed structures and spin states. All four peroxo complexes are low-spin species with rhombic EPR resonances centered around $g = 2$, and ν(O–O) at 800 ± 10 cm^{-1}. The hydroperoxo (**4** and **5**) and alkylperoxo (**6** and **7**) complexes show ν(Fe–O) at 618 ± 5 cm^{-1} and ν(Fe–O) at 695 ± 5 cm^{-1}, respectively, which are also in the expected range for ls peroxo species. While the addition of an equatorial thioether donor has minimal effects on the alkylperoxo Fe–O–O vibrations, substantial ν(Fe–O) and ν(O–O) upshifts are seen in the hydroperoxo complexes. The UV-vis data show a significant decrease in the energy of the alkylperoxo-to-iron(III) charge transfer bands, indicating that incorporation of a thioether donor in the first coordination sphere likely stabilizes the key metal acceptor orbital for the LMCT bands in **6** and **7**. Modification of the second coordination

Published on 27 March 2014. Downloaded by INDIAN INSTITUTE OF TECHNOLOGY GUWAHATI on 30/09/2014 14:45:32.

sphere by addition of a single H-bond donor was also shown to affect the properties of these non-heme Fe complexes. Structural characterization of the azide/fluoride-ligated complex **3** showed that the axial amide ligand was indeed labile toward displacement by anionic donors, and that formation of a single hydrogen bond between the amide N–H and anionic ligands in the open site is favored. The inclusion of an amide H-bond donor in the second coordination sphere also appears to shift the peroxo-to-iron LMCT band to lower energy by ~20 nm in both the hydro- and alkylperoxo cases. In contrast, the RR spectra of the peroxo complexes are minimally affected by the addition of the amide H-bond donor. The largest change corresponds to a 9 cm^{-1} downshift of the ν(Fe–O) in the Fe^{III}-OO*t*Bu complex **7**. It appears that the addition of the phenyl substituents in **8** inhibits formation of the Fe^{III}-OO(H/R) complexes, and further work is needed to tease out the factors that contribute to this second coordination sphere effect. The results presented here suggest that both first and second coordination sphere effects can be employed by non-heme iron complexes and proteins to subtly tune the reactivity and properties of Fe^{II} and Fe^{III}-OO(H/R) species.

Experimental section

General considerations

All reagents were purchased from commercial vendors and used without further purification unless noted otherwise. The N3PySR ligand[44] and **2**[47] were synthesized as previously reported. All reactions were carried out under an atmosphere of N_2 inside a glovebox or under Ar by standard Schlenk and vacuum line techniques. UV-visible spectra were recorded on a Varian Cary 50 spectrophotometer. Electron paramagnetic resonance (EPR) spectra were obtained on a Bruker EMX EPR spectrometer controlled with a Bruker ER 041 XG microwave bridge at 15 or 77 K. The EPR spectrometer was equipped with a continuous-flow liquid He or N_2 cryostat and an ITC503 temperature controller made by Oxford Instruments, Inc. NMR was performed on a Bruker Avance 400 MHz FT-NMR spectrometer at 25 °C. Elemental analysis was performed by Atlantic Microlab Inc., Norcross, GA. LDI-ToF mass spectra were obtained using a Bruker Autoflex III Maldi ToF/ToF instrument (Billerica, MA). Samples were dissolved in CH_2Cl_2 and deposited on the target plate in the absence of any added matrix. Samples were irradiated with a 355 nm UV laser and mass-analyzed by ToF mass spectrometry in the reflectron mode. Resonance Raman spectra were recorded at 110 K using a backscattering geometry with a McPherson 2061/207 spectrograph and a liquid-N_2-cooled CCD camera. The 568 and 647 nm excitations were obtained from a Kr and Ar ion laser, respectively (Innova 300, Coherent). Longpass filters (Razor-Edge, Semrock) were used to attenuate the Raleigh scattering. The samples were kept at 110 K inside a liquid-N_2 coldfinger and spun continuously to prevent photodamage. Frequencies were calibrated relative to an aspirin standard and are accurate to ±1 cm^{-1}. Density functional theory calculations were performed using previously calibrated and benchmarked methods[53] and are explained in detail in the ESI.†

Synthesis of reported compounds

$[Fe^{II}(N3PySR)(CH_3CN)](BF_4)_2$ (1). The free ligand N3PySR (399 mg, 0.89 mmol) was dissolved in CH_3CN (10 mL). A slurry of $Fe(BF_4)_2{\cdot}6H_2O$ (298 mg, 0.88 mmol) in CH_3CN (10 mL) was added dropwise to the ligand, affording a red suspension. The mixture was allowed to stir for 2 h, and filtered through celite. Diffusion of diethyl ether into a CH_3CN solution afforded dark red blocks after two days. Yield: 409 mg (68%). ^1H NMR ($CDCl_3$): δ 9.48 (2H), 9.34 (1H), 8.23 (1H), 8.14 (1H), 7.99 (2H), 7.76 (1H), 7.70 (1H), 7.56 (1H), 7.44 (3H), 7.21 (2H), 6.81 (1H), 6.71 (1H), 4.40 (1H), 4.26 (1H), 3.88 (1H), 3.66 (1H), 3.10 (1H), 2.73 (1H), 2.60 (1H). *Anal. Calc.* for $C_{29}H_{28}B_2F_8N_6SFe$: C, 48.24; H, 3.91; N, 11.64. Found: C, 48.22; H, 3.93; N, 11.70.

$[Fe^{II}(N3Py^{amide}SR)(F/N_3)](BF_4){\cdot}CH_3CN$ (F^- = 67%, N_3^- = 33%) (3·CH_3CN). A stock solution of NaN_3 (5.8 mg in 0.5 mL MeOH) was prepared, and 50 μL of this solution was added to complex **2** (6.5 mg, 9 μmol) dissolved in 0.5 mL MeCN. Vapor diffusion of Et_2O into the mixture resulted in a small amount of yellow crystals (**3**) suitable for X-ray structure determination, which were separated manually from the bulk material. UV-vis (CH_3CN): λ_{max} = 355, 430 nm, ε = 1620, 1680 M^{-1} cm^{-1}.

$[Fe^{III}(N3PySR)(OOH)]^{2+}$ (4). A solution of **1** (0.8 mM) was prepared in MeCN before H_2O_2 (30%, 5.0 equiv.) was added at 25 °C. The yellow solution immediately turned red, then brown. Monitoring by UV-vis (Fig. 5) showed the decay of peaks corresponding to **1** (λ_{max} = 350, 450 nm), with isosbestic conversion to a new spectrum (λ_{max} = 542 nm) that corresponds to **4**. Complex **4** was formed within 60 s and immediately began to decay to a brown species with no prominent UV-vis features. UV-vis: λ_{max} = 542 nm, ε = 1000 M^{-1} cm^{-1}; EPR: g = [2.17, 2.11, 1.97]; RR: ν(Fe–O) = 615, 629, 647 and 664 cm^{-1}, ν(O–O) = 809 cm^{-1}.

$[Fe^{III}(N3Py^{amide}SR)(OOH)]^{2+}$ (5). An amount of **2** (1.25 mg, 1.7 μmol) was dissolved in 4.0 mL of MeCN and cooled to −40 °C. A solution of H_2O_2 (0.88 M, 25 equiv., 0.05 mL) in MeCN was added and the color immediately began to change from orange to purple. Monitoring by UV-vis (Fig. 6) revealed full formation of **5** (λ_{max} = 567 nm) within 30 min. UV-vis: λ_{max} = 567 nm, ε = 900 M^{-1} cm^{-1}; EPR: g = [2.17, 2.16, 1.95]; RR: ν(Fe–O) = 612 cm^{-1}, ν(O–O) = 800 cm^{-1}.

$[Fe^{III}(N3PySR)(OO\mathit{t}Bu)]^{2+}$ (6). A solution of **1** (0.8 mM) was prepared in MeCN and cooled to −40 °C. A solution of *t*BuOOH (5.5 M, 10.0 equiv.) diluted in MeCN was added, and the yellow solution immediately turned green, then blue. Monitoring by UV-vis (Fig. 8) showed the peaks corresponding to **1** decay with isosbestic conversion to a new spectrum (λ_{max} = 600 nm) that corresponds to **6**. UV-vis: λ_{max} = 600 nm, ε = 1670 M^{-1} cm^{-1}; EPR: g = [2.14, 2.08, 1.96]; RR: ν(Fe–O) = 700 cm^{-1}, ν(O–O) = 796 cm^{-1}.

$[Fe^{III}(N3Py^{amide}SR)(OO\mathit{t}Bu)]^{2+}$ (7). A solution of **2** (1.1 mM) in MeCN was prepared and cooled to −40 °C. A solution of *t*BuOOH (5.5 M, 10 equiv.) in MeCN was then added and allowed to stir for 20 min. The orange solution of **2** turns

 This journal is © The Royal Society of Chemistry 2014

Published on 27 March 2014. Downloaded by INDIAN INSTITUTE OF TECHNOLOGY GUWAHATI on 30/09/2014 14:45:32.

green and finally deep blue, as monitoring by UV-vis (Fig. 9) shows the decay of the peaks corresponding to **2** with the isosbestic growth of a new peak (λ_{max} = 620 nm) corresponding to **7**. UV-vis: λ_{max} = 620 nm, ε = 2000 M^{-1} cm^{-1}; EPR: g = [2.17, 2.11, 1.96]; RR: ν(Fe–O) = 691 cm^{-1}, ν(O–O) = 796 cm^{-1}.

Secondary amine (iii). Primary amine (**i**)[46] (825 mg, 2.5 mmol) and aldehyde (**ii**)[47] (468 mg, 2.5 mmol) were dissolved in a 1 : 1 mixture of $CHCl_3$–MeOH (see Scheme 2). Molecular sieves (4 Å) were added and the mixture was stirred under Ar for 48 h. Excess $NaBH_3CN$ (315 mg, 5.0 mmol) was added and allowed to mix for 2 h before being quenched with 1 M HCl. The crude reaction mixture was concentrated, dissolved in $CHCl_3$, washed with H_2O, dried and re-concentrated, before being purified on neutral alumina (EtOAc–hexanes) to give 680 mg (53%) of secondary amine **iii** as a pale yellow solid. ^{1}H-NMR ($CDCl_3$): δ 8.09–8.07 (m, 4H), 7.72 (t, 2H), 7.63 (d, 2H), 7.54–7.49 (m, 6H), 7.46–7.42 (m, 6H), 5.30 (s, 1H), 4.06 (s, 2H), 3.06 (t, 2H), 2.47 (t, 2H).

N3Py^{amide,2Ph}SR. Secondary amine (**iii**) (200 mg, 0.4 mmol) and Cs_2CO_3 (196 mg, 0.6 mmol) were combined in 100 mL MeCN, followed by alkyl bromide (**iv**)[46] (109 mg, 0.4 mmol) and NaI (90 mg, 0.6 mmol) (see Scheme 2). After stirring for 72 h, the crude mixture was filtered through celite and concentrated. The crude solid was dissolved in $CHCl_3$, washed with H_2O, dried, and purified by column chromatography on neutral alumina (EtOAc–hexanes) to give 272 mg (97%) of the final ligand as a pale yellow solid. ^{1}H-NMR ($CDCl_3$): δ 8.07–8.03 (m, 5H), 7.92–9.90 (m, 2H), 7.73 (t, J = 8.1 Hz, 2H), 7.67 (dd, J = 8.8, 1.0 Hz, 2H), 7.60 (t, J = 7.8 Hz, 2H), 7.50–7.39 (m, 9H), 7.33 (dd, J = 7.6, 1.5 Hz, 1H), 7.25 (dd, J = 7.6, 1.3 Hz, 1H), 7.19 (td, 7.5, 1.8 Hz, 1H), 5.53 (s, 1H), 4.29 (s, 2H), 4.06 (s, 2H), 2.94 (t, J = 7.1 Hz, 2H), 2.37 (t, J = 7.1 Hz, 2H), 1.31 (s, 9H); ^{13}C NMR ($CDCl_3$): δ 177.2, 160.1, 159.1, 156.5, 150.8, 141.8, 139.8, 138.7, 137.1, 133.0, 131.4, 130.4, 129.1, 128.9, 127.9, 127.8, 127.3, 123.0, 119.1, 118.8, 118.3, 111.8, 72.0, 57.5, 54.6, 51.9, 40.0, 30.1, 27.8, 18.2, 8.6. FAB-MS (+): m/z = 703.32127 $[M + H]^+$ (calcd for $C_{44}H_{43}N_6OS$, 703.32191).

[Fe^{II}(N3Py^{amide,2Ph}SR)](BF$_4$)$_2$ (8). The free ligand N3Py^{amide,2Ph}SR (461 mg, 0.66 mmol) was dissolved in 5 mL MeCN before $Fe(BF_4)_2{\cdot}6H_2O$ (221 mg, 0.66 mmol) was added. After stirring for 2 h, the yellow solution was filtered through celite and vapor diffusion of Et_2O gave **8** as yellow crystals suitable for X-ray structure determination (510 mg, 83% yield). ^{1}H-NMR (CD_3CN): δ 80.67, 65.78, 64.29, 63.25, 53.03, 47.52, 32.37, 24.80, 20.33, 19.42, 13.40, 11.65, 9.19, 8.22, 7.38, 6.22, 4.08, 3.50, 2.33, 1.17, 0.45, −0.45, −2.33, −14.63, −32.73. LDI-MS: m/z = 757.6 $[M - H]^+$. UV-vis (CH_3CN): λ_{max} = 405 nm, ε = 2650 M^{-1} cm^{-1}. *Anal. Calc.* for [**8**] ($C_{44}H_{42}B_2F_8FeN_6OS$): predicted: C, 56.68, H, 4.54; N, 9.01; Found: C, 56.53; H 4.72; N, 9.44.

Acknowledgements

The NIH (D.P.G., GM62309 and GM101153, P.M.L. GM074785) is gratefully acknowledged for financial support. The National Service of Computational Chemistry Software (NSCCS) is thanked for providing cpu time to SdV. H.M. acknowledges support from the JSPS.

Notes and references

1 E. G. Kovaleva, M. B. Neibergall, S. Chakrabarty and J. D. Lipscomb, *Acc. Chem. Res.*, 2007, **40**, 475–483.
2 E. G. Kovaleva and J. D. Lipscomb, *Science*, 2007, **316**, 453–457.
3 E. I. Solomon, A. Decker and N. Lehnert, *Proc. Natl. Acad. Sci. U. S. A.*, 2003, **100**, 3589–3594.
4 M. Costas, M. P. Mehn, M. P. Jensen and L. Que, Jr., *Chem. Rev.*, 2004, **104**, 939–986.
5 E. I. Solomon, S. D. Wong, L. V. Liu, A. Decker and M. S. Chow, *Curr. Opin. Chem. Biol.*, 2009, **13**, 99–113.
6 P. L. Roach, I. J. Clifton, C. M. H. Hensgens, N. Shibata, C. J. Schofield, J. Hajdu and J. E. Baldwin, *Nature*, 1997, **387**, 827–830.
7 T. Santos-Silva, J. Trincão, A. L. Carvalho, C. Bonifácio, F. Auchère, P. Raleiras, I. Moura, J. J. G. Moura and M. J. Romão, *J. Biol. Inorg. Chem.*, 2006, **11**, 548–558.
8 P. C. A. Bruijnincx, G. van Koten and R. J. M. Klein Gebbink, *Chem. Soc. Rev.*, 2008, **37**, 2716–2744.
9 L. Que, Jr., *J. Biol. Inorg. Chem.*, 2004, **9**, 684–690.
10 S. Ye, X. Wu, L. Wei, D. M. Tang, P. Sun, M. Bartlam and Z. H. Rao, *J. Biol. Chem.*, 2007, **282**, 3391–3402.
11 M. J. Vasbinder and A. Bakac, *Inorg. Chem.*, 2007, **46**, 2921–2928.
12 G. Roelfes, M. Lubben, K. Chen, R. Y. N. Ho, A. Meetsma, S. Genseberger, R. M. Hermant, R. Hage, S. K. Mandal, V. G. Young, Y. Zang, H. Kooijman, A. L. Spek, L. Que, Jr. and B. L. Feringa, *Inorg. Chem.*, 1999, **38**, 1929–1936.
13 G. Roelfes, V. Vrajmasu, K. Chen, R. Y. N. Ho, J.-U. Rohde, C. Zondervan, R. M. la Crois, E. P. Schudde, M. Lutz, A. L. Spek, R. Hage, B. L. Feringa, E. Münck and L. Que, Jr., *Inorg. Chem.*, 2003, **42**, 2639–2653.
14 J. Kim, E. Larka, E. C. Wilkinson and L. Que, Jr., *Angew. Chem., Int. Ed.*, 1995, **34**, 2048–2051.
15 J.-U. Rohde, S. Torelli, X. P. Shan, M. H. Lim, E. J. Klinker, J. Kaizer, K. Chen, W. Nam and L. Que, Jr., *J. Am. Chem. Soc.*, 2004, **126**, 16750–16761.
16 A. Dey and E. I. Solomon, *Inorg. Chim. Acta*, 2010, **363**, 2762–2767.
17 A. J. Simaan, S. Döpner, F. Banse, S. Bourcier, G. Bouchoux, A. Boussac, P. Hildebrandt and J.-J. Girerd, *Eur. J. Inorg. Chem.*, 2000, 1627–1633.
18 M. Martinho, F. Banse, J. Sainton, C. Philouze, R. Guillot, G. Blain, P. Dorlet, S. Lecomte and J.-J. Girerd, *Inorg. Chem.*, 2007, **46**, 1709–1717.
19 A. E. Anastasi, A. Lienke, P. Comba, H. Rohwer and J. E. McGrady, *Eur. J. Inorg. Chem.*, 2007, 65–73.
20 M. R. Bukowski, P. Comba, C. Limberg, M. Merz, L. Que, Jr. and T. Wistuba, *Angew. Chem., Int. Ed.*, 2004, **43**, 1283–1287.

Published on 27 March 2014. Downloaded by INDIAN INSTITUTE OF TECHNOLOGY GUWAHATI on 30/09/2014 14:45:32.

21 N. Lehnert, R. Y. N. Ho, L. Que, Jr. and E. I. Solomon, *J. Am. Chem. Soc.*, 2001, **123**, 12802–12816.
22 N. Lehnert, R. Y. N. Ho, L. Que, Jr. and E. I. Solomon, *J. Am. Chem. Soc.*, 2001, **123**, 8271–8290.
23 F. Namuswe, T. Hayashi, Y. B. Jiang, G. D. Kasper, A. A. N. Sarjeant, P. Moënne-Loccoz and D. P. Goldberg, *J. Am. Chem. Soc.*, 2010, **132**, 157–167.
24 Y. B. Jiang, J. Telser and D. P. Goldberg, *Chem. Commun.*, 2009, 6828–6830.
25 J. Stasser, F. Namuswe, G. D. Kasper, Y. B. Jiang, C. M. Krest, M. T. Green, J. Penner-Hahn and D. P. Goldberg, *Inorg. Chem.*, 2010, **49**, 9178–9190.
26 J. Shearer, R. C. Scarrow and J. A. Kovacs, *J. Am. Chem. Soc.*, 2002, **124**, 11709–11717.
27 T. Kitagawa, A. Dey, P. Lugo-Mas, J. B. Benedict, W. Kaminsky, E. I. Solomon and J. A. Kovacs, *J. Am. Chem. Soc.*, 2006, **128**, 14448–14449.
28 D. Krishnamurthy, G. D. Kasper, F. Namuswe, W. D. Kerber, A. A. N. Sarjeant, P. Moënne-Loccoz and D. P. Goldberg, *J. Am. Chem. Soc.*, 2006, **128**, 14222–14223.
29 F. Namuswe, G. D. Kasper, A. A. N. Sarjeant, T. Hayashi, C. M. Krest, M. T. Green, P. Moënne-Loccoz and D. P. Goldberg, *J. Am. Chem. Soc.*, 2008, **130**, 14189–14200.
30 K. N. Green, S. M. Brothers, R. M. Jenkins, C. E. Carson, C. A. Grapperhaus and M. Y. Darensbourg, *Inorg. Chem.*, 2007, **46**, 7536–7544.
31 C. A. Grapperhaus and M. Y. Darensbourg, *Acc. Chem. Res.*, 1998, **31**, 451–459.
32 M. Sallmann, I. Siewert, L. Fohlmeister, C. Limberg and C. Knispel, *Angew. Chem., Int. Ed.*, 2012, **51**, 2234–2237.
33 C. S. Mullins, C. A. Grapperhaus, B. C. Frye, L. H. Wood, A. J. Hay, R. M. Buchanan and M. S. Mashuta, *Inorg. Chem.*, 2009, **48**, 9974–9976.
34 P. Lugo-Mas, W. Taylor, D. Schweitzer, R. M. Theisen, L. Xu, J. Shearer, R. D. Swartz, M. C. Gleaves, A. DiPasquale, W. Kaminsky and J. A. Kovacs, *Inorg. Chem.*, 2008, **47**, 11228–11236.
35 A. C. McQuilken and D. P. Goldberg, *Dalton Trans.*, 2012, **41**, 10883–10899.
36 G. Musie, C. H. Lai, J. H. Reibenspies, L. W. Sumner and M. Y. Darensbourg, *Inorg. Chem.*, 1998, **37**, 4086–4093.
37 E. Nam, P. E. Alokolaro, R. D. Swartz, M. C. Gleaves, J. Pikul and J. A. Kovacs, *Inorg. Chem.*, 2011, **50**, 1592–1602.
38 J. C. Noveron, M. M. Olmstead and P. K. Mascharak, *J. Am. Chem. Soc.*, 2001, **123**, 3247–3259.
39 M. G. O'Toole, M. Kreso, P. M. Kozlowski, M. S. Mashuta and C. A. Grapperhaus, *J. Biol. Inorg. Chem.*, 2008, **13**, 1219–1230.
40 M. J. Rose, N. M. Betterley, A. G. Oliver and P. K. Mascharak, *Inorg. Chem.*, 2010, **49**, 1854–1864.
41 L. A. Tyler, J. C. Noveron, M. M. Olmstead and P. K. Mascharak, *Inorg. Chem.*, 1999, **38**, 616–617.
42 D. C. Lacy, J. Mukherjee, R. L. Lucas, V. W. Day and A. S. Borovik, *Polyhedron*, 2013, **52**, 261–267.
43 R. L. Shook and A. S. Borovik, *Inorg. Chem.*, 2010, **49**, 3646–3660.
44 A. C. McQuilken, Y. B. Jiang, M. A. Siegler and D. P. Goldberg, *J. Am. Chem. Soc.*, 2012, **134**, 8758–8761.
45 A. C. McQuilken, Y. Ha, K. D. Sutherlin, M. A. Siegler, K. O. Hodgson, B. Hedman, E. I. Solomon, G. N. L. Jameson and D. P. Goldberg, *J. Am. Chem. Soc.*, 2013, **135**, 14024–14027.
46 S. Sahu, L. R. Widger, M. G. Quesne, S. P. de Visser, H. Matsumura, P. Moënne-Loccoz, M. A. Siegler and D. P. Goldberg, *J. Am. Chem. Soc.*, 2013, **135**, 10590–10593.
47 L. R. Widger, C. G. Davies, T. Yang, M. A. Siegler, O. Troeppner, G. N. L. Jameson, I. Ivanović-Burmazović and D. P. Goldberg, *J. Am. Chem. Soc.*, 2014, **136**, 2699–2702.
48 C. Kim, K. Chen, J. H. Kim and L. Que, Jr., *J. Am. Chem. Soc.*, 1997, **119**, 5964–5965.
49 Calculations based on an isolated diatomic oscillator with a ν(Fe–^{18}O) at 590 cm^{-1} predict a ν(Fe–^{16}O) at 617 cm^{-1} which does not match any of the most prominent bands seen in the ν(Fe–O) region of the RR spectra of unlabeled complex **4** nor the 607 cm^{-1} frequency observed in D_2O.
50 N. Lehnert, F. Neese, R. Y. N. Ho, L. Que, Jr. and E. I. Solomon, *J. Am. Chem. Soc.*, 2002, **124**, 10810–10822.
51 A. M. I. Payeras, R. Y. N. Ho, M. Fujita and L. Que, Jr., *Chem. – Eur. J.*, 2004, **10**, 4944–4953.
52 J.-J. Girerd, F. Banse and A. J. Simaan, *Struct. Bonding*, 2000, **97**, 145–177.
53 R. Latifi, M. A. Sainna, E. V. Rybak-Akimova and S. P. de Visser, *Chem. – Eur. J.*, 2013, **19**, 4058–4068.

 This journal is © The Royal Society of Chemistry 2014

ChemPubSoc Europe

DOI: 10.1002/chem.201303282

CHEMISTRY A European Journal Full Paper

DNA Damage

Quantum Mechanics/Molecular Mechanics Study on the Oxygen Binding and Substrate Hydroxylation Step in AlkB Repair Enzymes

Matthew G. Quesne,[a] Reza Latifi,[a, b] Luis E. Gonzalez-Ovalle,[a] Devesh Kumar,[c] and Sam P. de Visser*[a]

Abstract: AlkB repair enzymes are important nonheme iron enzymes that catalyse the demethylation of alkylated DNA bases in humans, which is a vital reaction in the body that heals externally damaged DNA bases. Its mechanism is currently controversial and in order to resolve the catalytic mechanism of these enzymes, a quantum mechanics/molecular mechanics (QM/MM) study was performed on the demethylation of the N^1-methyladenine fragment by AlkB repair enzymes. Firstly, the initial modelling identified the oxygen binding site of the enzyme. Secondly, the oxygen activation mechanism was investigated and a novel pathway was found, whereby the catalytically active iron(IV)–oxo intermediate in the catalytic cycle undergoes an initial isomerisation assisted by an Arg residue in the substrate binding pocket, which then brings the oxo group in close contact with the methyl group of the alkylated DNA base. This enables a subsequent rate-determining hydrogen-atom abstraction on competitive σ- and π-pathways on a quintet spin-state surface. These findings give evidence of different locations of the oxygen and substrate binding channels in the enzyme and the origin of the separation of the oxygen-bound intermediates in the catalytic cycle from substrate. Our studies are compared with small model complexes and the effect of protein and environment on the kinetics and mechanism is explained.

Introduction

Nonheme iron dioxygenases catalyse a range of important reactions in Nature including the biosynthesis of antibiotics in microbes and the metabolism of, for instance, cysteine in mammals.[1,2] In addition, nonheme iron dioxygenases have been linked to oxygen sensing and collagen cross-linking processes in the body, and as such they have vital functions for the biosystem,[3] but unfortunately there are many unanswered questions related to their activity and the catalytic transformation of substrates and detailed computational studies can shed light on this and predict a mechanism. The nonheme iron dioxygenases generally contain an iron active centre that is bound to the protein via a facial triad of amino acids that includes two histidine and one aspartate or glutamate residue in a 2-His/1-Asp feature.[4] They utilise a co-substrate (α-ketoglutarate, αKG) on an iron centre to convert molecular oxygen into a high-valent iron(IV)–oxo species, which has been proposed to be the active species of these enzymes.[5] For several nonheme iron dioxygenases, this active species has been characterised by spectroscopic methods, including resonance Raman and Mössbauer spectroscopies, and it was found that the iron(IV)–oxo intermediate reacts by hydrogen-atom abstraction from the substrate with a large kinetic isotope effect.[6] These experimental studies, however, mostly focused on the bacterial enzyme taurine/α-ketoglutarate dioxygenase.

A special class of enzymes within the nonheme iron dioxygenase family are the AlkB repair enzymes that repair methylated DNA (and RNA) bases that have been damaged by intra- or extracellular chemicals.[7] This has a dramatic effect on normal cellular function as, for instance, N^3-methylation of an adenine residue of a DNA strain blocks DNA replication through the prevention of formation of Watson–Crick base-pairs.[8] In addition, chemicals such as methylmethane sulfonate and methyl halides have been shown to generate N^1-methyladenine and N^3-methylcytosine. AlkB repair enzymes are the body's natural defence mechanism and react with damaged DNA and RNA chains by demethylation of these alkylated bases in a reaction that uses one molecule of αKG and molecular oxygen.[9] Biochemical studies were performed on the characterisation of the enzyme,[10] the protein structure,[11]

[a] M. G. Quesne, Dr. R. Latifi, L. E. Gonzalez-Ovalle, Dr. S. P. de Visser
Manchester Institute of Biotechnology and School of Chemical Engineering and Analytical Science
The University of Manchester, 131 Princess Street
Manchester M1 7DN (UK)
E-mail: sam.devisser@manchester.ac.uk

[b] Dr. R. Latifi
Department of Chemistry, Tufts University
Medford MA, 02155 (USA)

[c] Dr. D. Kumar
Department of Applied Physics, School of Physical Sciences
Babasaheb, Bhimrao Ambedkar University, Vidya Vihar
Rae Bareilly Road, Lucknow 226-025 (India)

Supporting information for this article is available on the WWW under http://dx.doi.org/10.1002/chem.201303282.

© 2013 The Authors. Published by Wiley-VCH Verlag GmbH & Co. KGaA. This is an open access article under the terms of the Creative Commons Attribution License, which permits use, distribution and reproduction in any medium, provided the original work is properly cited.

and the substrate selectivity and binding of inhibitors.[12] Moreover, crystal structure coordinates were measured for the reactant as well as the substrate and hydroxylated product bound complexes.[13] These studies highlight a tight bonding pocket for substrate and a catalytic mechanism that leads to hydroxylation of the methylated DNA base.

It has been hypothesised that the catalytic mechanism of AlkB repair enzymes is analogous to the nonheme iron dioxygenases and proceeds by aliphatic hydroxylation of the methyl group followed by release of formaldehyde.[7] Isotopic labelling and product distributions indeed confirmed that iron(II), αKG and molecular oxygen are needed in the process and that formaldehyde and CO_2 are formed.[7a,b] Crystallographic data provided further evidence that AlkB repair enzymes belong to the αKG-dependent dioxygenases and highlighted a nonheme iron active site, where the metal is bound to a 2-His/1-Asp ligand system (Figure 1).[14] However, a close inspection of the crystal structure coordinates reveals that the sixth binding site of the metal, that is, the O_2 binding site, is located perpendicular to the substrate orientation rather than in its vicinity. As such, an oxygen atom transfer within this conformation may be difficult and might proceed over a relatively large distance.

Furthermore, previous computational studies of the Gauld group on the catalytic cycle of the AlkB repair enzyme using active-site models found a rate-determining hydrogen-atom abstraction barrier of 20.9 kcal mol^{-1} for methylated adenine.[15] This is a relatively high barrier for a nonheme iron(IV)–oxo complex, since, for a series of hydrogen-atom abstraction reactions by analogous models much lower barriers were obtained for alternative substrates. As such, the value of 20.9 kcal mol^{-1} in the gas phase would compare to that found for a substrate like propane,[16] which as far as we know is not hydroxylated by nonheme iron enzymes. Consequently, a barrier with a magnitude over 20 kcal mol^{-1} may be a very slow process that is not efficient enough to happen in Nature. However, there may be effects of the protein and the local environment that were not taken into consideration in the models of Gauld et al. that have affected the barrier heights. The studies, therefore, warrant a further set of calculations and in particular one using quantum mechanics/molecular mechanics (QM/MM) that takes the full scale of the protein and solvent into effect.

Here we report this QM/MM study and focus on the catalytic mechanism of oxygen activation by AlkB enzymes and the hydroxylation of methylated DNA bases (Scheme 1). We investigate two possible oxygen binding positions on the iron(II) reactant complex with the superoxo either *trans* to His_{131} (structure **A**) or *trans* to His_{187} (structure **B**). In the following step in the catalytic cycle the superoxo group is expected to attack the α-keto-position of αKG to give an iron(IV)–oxo species, CO_2 and succinate.[17] Technically two isomeric iron(IV)–oxo struc-

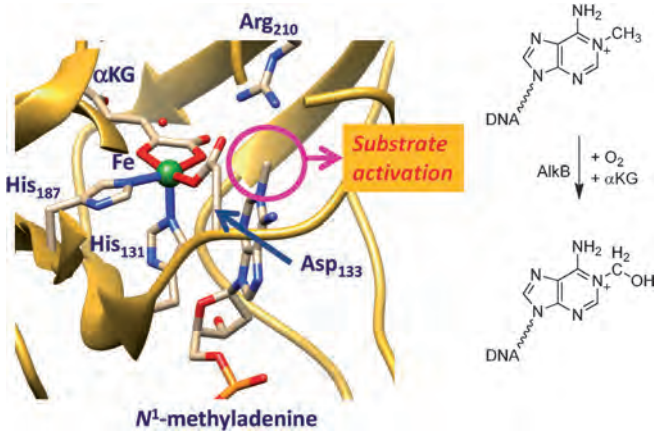

Figure 1. Extract of the active site of AlkB repair enzyme as taken from the 3I2O PDB file and the reaction catalysed by the enzyme. The proposed oxygen binding site *trans* to His_{131} is filled with a water molecule.

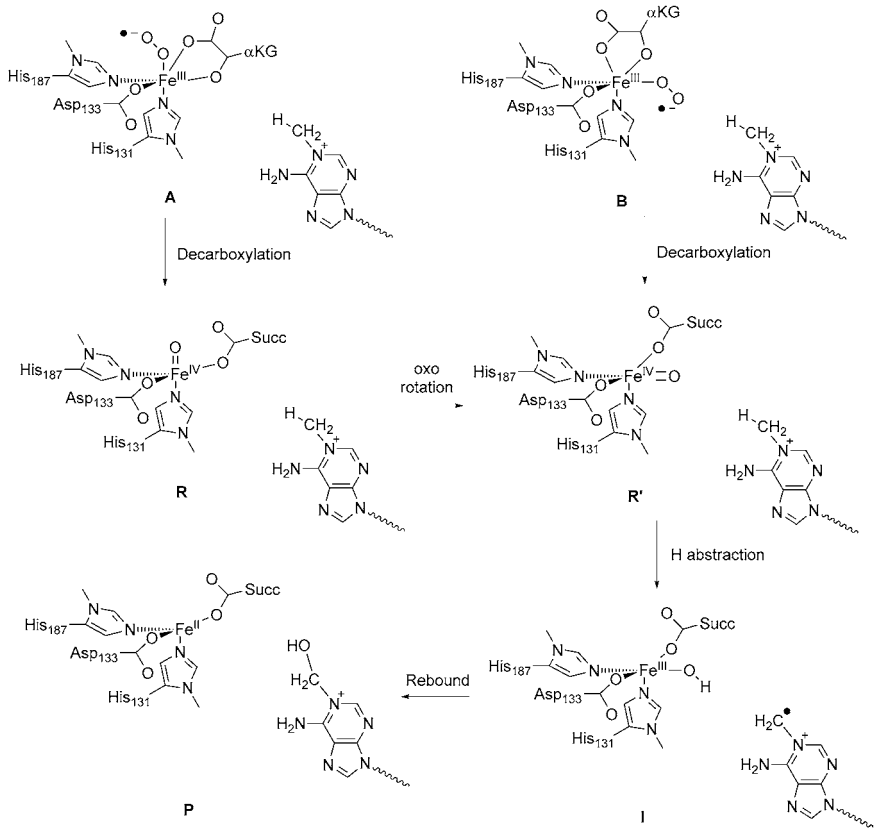

Scheme 1. Mechanism of substrate hydroxylation by an iron(IV)–oxo in AlkB repair enzymes.

 © 2014 The Authors. Published by Wiley-VCH Verlag GmbH & Co. KGaA, Weinheim

tures are possible (**R** and **R′**), which may interconvert into each other. In this work we identify **A** as the oxygen-binding position and propose a novel mechanism whereby the iron(IV)–oxo undergoes an isomerisation from **R** to **R′** prior to hydrogen-atom abstraction. We also highlight the electronic changes during the reaction and the effect the isomerisation has on the electron-transfer pathways and the barrier heights for the reaction.

Results and Discussion

Oxygen binding site on the metal

A recent QM/MM study investigated the hydrogen-atom abstraction step of N^1-methyladenine (CH_3Ade) by AlkB repair enzymes.[18] They used a molecular geometry, whereby the oxo group was aligned with the substrate, that is, *trans* to His_{187}, and an almost linear Fe-O-HCH_2-Ade angle, analogous to structure **R′** in Scheme 1. However, the iron(IV)–oxo species is formed in a catalytic cycle from an iron(III)–superoxo complex in a reaction with αKG (Scheme 1), and in the crystal structure displayed in Figure 1 there seems to be a dioxygen binding site *trans* to His_{131}. We decided, therefore, to first investigate the oxygen binding site of the enzyme, and thereby assign either **R** or **R′** as the reactant of the catalytic hydroxylation.

We started the work with locating the oxygen binding site of AlkB, whereby we attempted to model dioxygen into the protein structure at various metal binding sites, that is, create structures **A** and **B** (Figure 2). Firstly, molecular oxygen was inserted into the sixth binding site *trans* to His_{131} by replacing the water ligand. The binding pocket has sufficient space to accommodate molecular oxygen and no stereochemical clashes are noted that would prevent it from binding in this position. The binding pocket is lined up with apolar and aromatic residues, such as the side chains of Ile_{143}, Phe_{154} and Trp_{178}. Solvation of the protein still finds sufficient space in the binding pocket *trans* to His_{131} for two water molecules; this binding pocket, therefore, is large enough to accommodate molecular oxygen. Figure 2 gives the equilibrated MM structure of **A**.

Thereafter, we inserted molecular oxygen into the metal position *trans* to His_{187} with the distal oxygen atom on the line through the iron and the hydrogen atom from N^1-methyladenine that is abstracted by AlkB in order to generate structure **B**. However, this structure has considerable stereochemical constraints and we failed to optimise its geometry and converge it to a local minimum. In particular, the proximal oxygen atom of the iron(III)–superoxo with the oxygen *trans* to His_{187} gives close contacts (<1.7 Å) to the carboxylate group of Asp_{133} and the methyl group of N^1-methyladenine. Furthermore, the distal oxygen atom of the iron(III)–superoxo has close contact with the carboxylate group of αKG (1.75 Å), therefore, stereochemically it is not a stable structure. Consequently, these MM models show that molecular oxygen does not fit into the binding pocket in a position *trans* to His_{187} as it is too tight with too many closely packed residues. As structure **B** is not a stable entity it cannot be a catalytic cycle intermediate and as a result molecular oxygen can only bind in the position *trans* to His_{131}, that is, **A**. Our studies, therefore, have identified the molecular oxygen binding site as *trans* to His_{131} that in a reaction with αKG will give the iron(IV)–oxo species in the **R** conformation. This also implies that a subsequent isomerisation will be needed to form the rotated iron(IV)–oxo species (**R′**) with the oxo group *trans* to His_{187}, which is expected to precede the hydrogen-atom abstraction reaction.

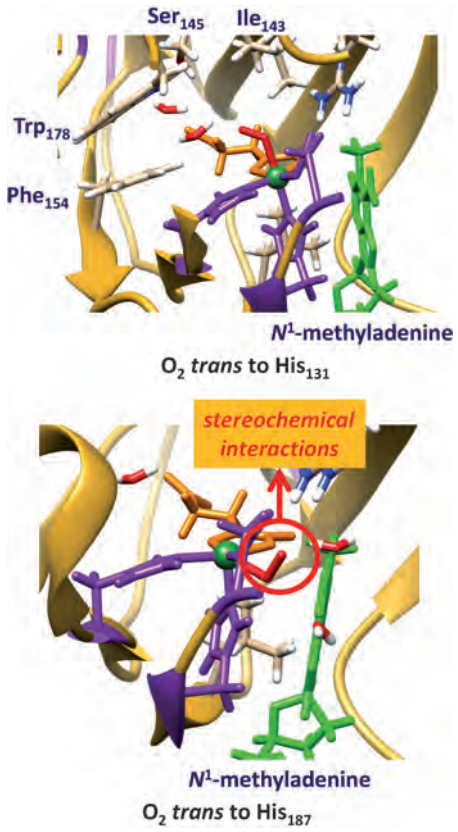

Figure 2. Isomeric structures for dioxygen binding to the iron(II) centre of AlkB enzymes with either the O_2 *trans* to His_{131} (top) or *trans* to His_{187} (bottom). The former structure is MM minimised, whereas the latter failed to converge due to stereochemical clashes. The 2-His/1-Asp structure is in purple, substrate in green and αKG in orange.

The reported QM/MM results in ref. [18] did not consider this isomerisation and as a result may not reflect the correct mechanism of the chemical reaction as they may have used a wrong starting structure of the chemical process. To gain further insight into the mechanism of substrate hydroxylation by DNA base repair enzymes, we decided to carry out a QM/MM study. We started the work from the iron(IV)–oxo species as displayed in Figure 1 and we followed the mechanism as described in Scheme 1 until hydroxylated products. The work started from the iron(IV)–oxo species with the oxo group *trans* to His_{131} (**R**), which is expected to isomerise to a position with the oxo group *trans* to His_{187} in **R′**. In the latter conformation the oxo group is in hydrogen bonding distance to the methyl group of N^1-methyladenine and takes up a hydrogen atom to form a radical intermediate (**I**) before hydroxyl rebound to form alcohol product complexes (**P**).

 © 2014 The Authors. Published by Wiley-VCH Verlag GmbH & Co. KGaA, Weinheim

QM/MM set up and validation

The work described in here uses the quantum mechanics/molecular mechanics (QM/MM) procedure, whereby the inner core of the enzyme is described by density functional theory methods and the rest of the protein and solvent with a molecular mechanics force field as explained in detail in the Experimental Section. Generally, the methodology follows previous QM/MM calculations of our group that were carefully benchmarked and calibrated.[19] The calculations start from the 3I2O PDB file,[14] which is a substrate bound iron(III)–water complexed with αKG as described in Figure 1. The water ligand was replaced by an oxo group and αKG by succinate to obtain our reactant structure (**R′**): an iron(IV)–oxo group in a 2-His/1-Asp ligand environment and succinate bound as a bidentate ligand. Subsequently, hydrogen atoms were added and the protonation state of residues checked as described below. Thereafter, the structure was subjected to an iterative solvation procedure to give a chemical model with a total amount of 10011 atoms.

After the set-up was completed we ran a molecular dynamics (MD) simulation for 800 ps at 298 K and 1 bar using the Charmm force field,[20] whereby the protein and solvent were allowed to relax. Figure 3 displays the total energy and the root mean square deviation (RMSD) of the protein structure of the MD trajectory of our reactant structure. As follows from Figure 3 after 20–30 ps of simulation the total energy reaches a plateau and the energy stabilises. At the same time the fluctuations in the protein structure and geometry stabilise and the RMSD values converges to a value of close to 1. These MD simulations match those found for the analogous nonheme iron enzymes proline hydroxylase that revealed conformational stability and rigidity after substrate binding.[21]

We selected three snapshots from the MD simulations as starting points for the QM/MM calculations after 300, 400 and 500 ps; designated Sn_{300}, Sn_{400} and Sn_{500}, respectively. An overlay of the three structures of these snapshots (Supporting Information, Figure S1) shows little differences in the protein orientation and the enzyme active site. The only differences obtained between these snapshots originate at distances far away from the reaction centre and generally are on the surface of the protein. We do not expect these motions and structural differences to be dramatic, but decided to carry out some test calculations for all three snapshots to determine the reproducibility and stability of the calculations. In all studies, we selected a large QM region containing the iron(IV)–oxo group, methylimidazole groups for His_{131} and His_{187}, acetate for succinate and Asp_{133}, methylguanidinium for Arg_{210}, and the N^1-methyladenine part of the substrate (Figure 4).

Subsequently, we optimised the geometry of the iron(IV)–oxo species using Sn_{300}, Sn_{400} and Sn_{500} in the lowest lying singlet, triplet, quintet and septet spin states. In all cases, the geometry optimisation converged to a structure corresponding to **R′**, in which the oxo-group bridges between the methyl group of methylated adenine and the iron atom. The quintet spin state is the ground state in each snapshot and the spin state ordering follows quintet–triplet–septet and singlet throughout, which implies that the quintet spin state will be

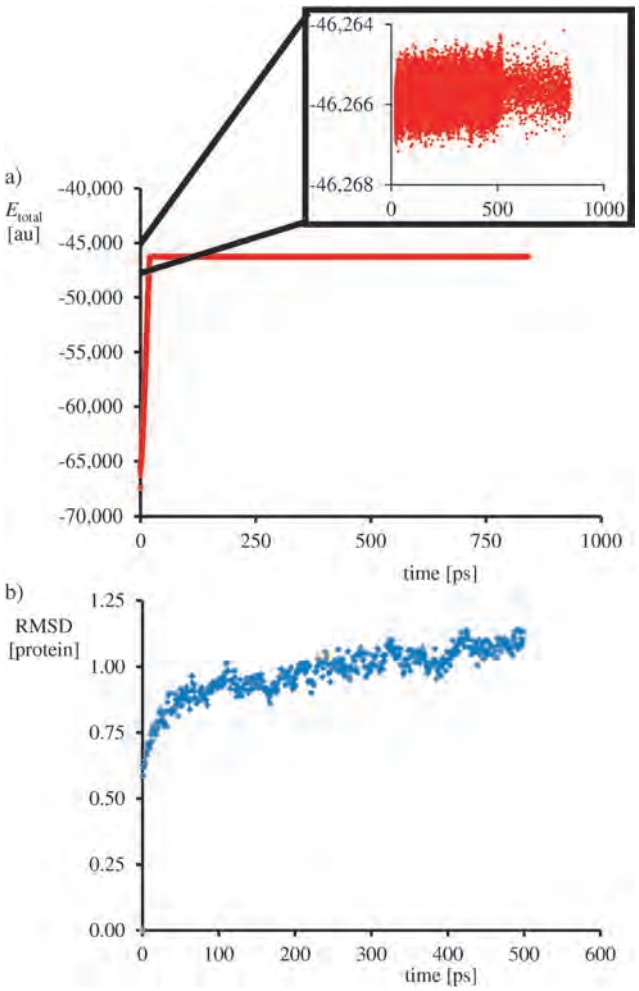

Figure 3. Molecular dynamics scan at 298 K of the protein. a) Plot of the total MM energy as a function of time. b) RMSD value of the protein structure as a function of time.

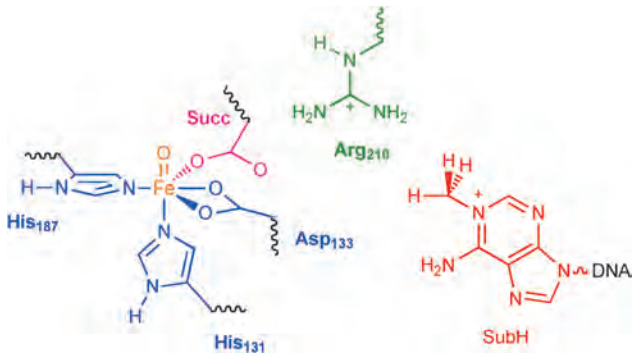

Figure 4. QM region selected for the QM/MM calculations. Waved lines represent QM/MM linkages that were described with the link atom method. Succ stands for succinate and SubH for substrate.

the reactive state. Previous studies of nonheme iron reactivities showed higher barriers on the triplet spin state than on the quintet spin state,[22] therefore, it is not expected that the triplet spin state will play a key role in this part of the catalytic cycle. Our calculations are in agreement with the experimental EPR characterisation of nonheme iron(IV)–oxo complexes in en-

 © 2014 The Authors. Published by Wiley-VCH Verlag GmbH & Co. KGaA, Weinheim

zymes that were found to be in a high-spin state.[23] Previous calculations on the iron(IV)–oxo species of DNA base repair enzymes[15,18] and analogous nonheme iron dioxygenases[24] also identified it as a high-spin ground state. This contrasts biomimetic nonheme iron(IV)–oxo complexes that generally are described with a triplet spin ground state.[25] Recent computations, however, showed that pentacoordinated iron(IV)–oxo complexes stabilise the quintet spin state, whereas hexacoordinated iron(IV)–oxo usually has a triplet spin ground state.[26]

All three snapshots give the same spin-state ordering and a well-separated quintet spin ground state from other states, therefore, we have focused in the following on the quintet spin mechanism of oxygen atom transfer only. Optimised geometries of ^{5}**R**′ as calculated in Sn_{300}, Sn_{400} and Sn_{500} are given in Figure 5. The iron(IV)–oxo bond is short, that is, 1.660–1.671 Å,

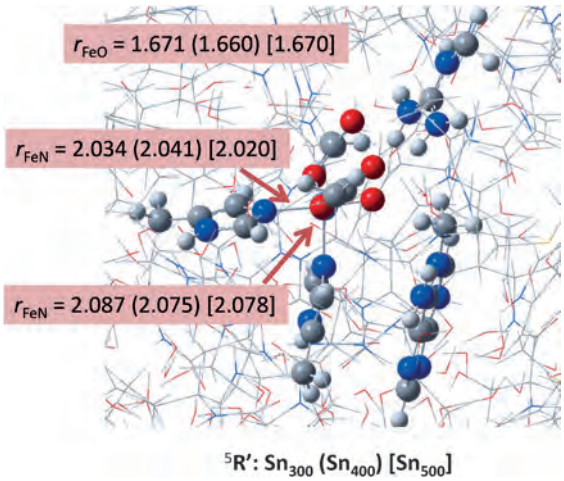

Figure 5. Optimised geometries of ^{5}**R**′ as obtained for Sn_{300}, Sn_{400} and Sn_{500} with bond lengths in Ångstroms.

which is indicative of a double bond and in agreement with previous calculations on related complexes.[24,27] The structures show little deviations between the three snapshots, and consequently the QM region is highly rigid and constraint. Furthermore, the optimised geometries of the three snapshots implicates that the reproducibility of the results is high and that little movement in the central components of the protein and in particular the catalytic centre has occurred during the MD simulation. Further test calculations using different density functional methods were carried out, namely B3LYP, B3LYP*, BP86 and M06.[28–31] In all cases a spin state ordering quintet < triplet < singlet was found with the quintet spin state as the ground state (see the Supporting Information). As the DFT methodology does not appear to give dramatic differences in spin-state ordering and relative energies, we decided to continue with UB3LYP only.

Iron(IV)–oxo group isomerisation

In the next set of calculations, we investigated ^{5}**R** as well as its barrier (^{5}**TS**$_I$) for the isomerisation into ^{5}**R**′. A comparison of the structure and electronic properties of ^{5}**R** and ^{5}**R**′ reveals some interesting features that may affect the reactivity of these complexes. Let us start with a description of the electronic changes upon rotation from ^{5}**R** to ^{5}**R**′. Thus, the rotation of the oxo group from a position *trans* to His_{131} in ^{5}**R** to a position *trans* to His_{187} in ^{5}**R**′ changes the shapes of the molecular orbitals. Figure 6 displays the valence orbitals of ^{5}**R** and ^{5}**R**′, in which we used the nomenclature of Shaik, Solomon and co-workers for nonheme iron oxidants.[22] The labelling uses a molecular *z* axis as taken along the Fe–O bond in ^{5}**R**. In the lowest quintet spin state of ^{5}**R** the metal 3d block of orbitals interact with ligands and split into a set of three π^* (π^*_{xz}, π^*_{yz}, π^*_{xy}) orbitals and a pair of two σ^* ($\sigma^*_{z^2}$, $\sigma^*_{x^2-y^2}$) orbitals. The π^* orbitals represent the antibonding combinations of the 3d atomic orbital on Fe with a $2p_{x/y}$ orbital on oxygen, whereas the $\sigma^*_{z^2}$ orbital reflects the antibonding combination of $3d_{z^2}$ on Fe with $2p_z$ on O. Finally, the $3d_{x^2-y^2}$ orbital on the metal forms antibonding combinations with ligands in the *xy* plane of symmetry. In pentacoordinated iron(IV)–oxo complexes the π^*_{xy} and $\sigma^*_{x^2-y^2}$ orbitals are close in energy and hence a high-spin situation is favourable.[32] Indeed, ^{5}**R**, as found for analogous complexes,[15,18,19,24] has orbital occupation $\pi^*_{xy}{}^1\pi^*_{xz}{}^1\pi^*_{yz}{}^1\sigma^*_{x^2-y^2}{}^1\sigma^*_{z^2}{}^0$. By contrast, the nearest triplet spin state is calculated to have $\pi^*_{xy}{}^2\pi^*_{xz}{}^1\pi^*_{yz}{}^1$ configuration.

Upon rotation of the oxo group, whereby ^{5}**R**′ is formed the molecular orbital interactions have altered. Thus, the Fe–O bond is now located along the molecular *y* axis and hence the labels of some of the orbitals have changed. In particular, the π^*_{xy} orbital in ^{5}**R**′ has a shape that matches the π^*_{xz} orbital in ^{5}**R** and the π^*_{xz} orbital in ^{5}**R**′ looks like the π^*_{xy} orbital in ^{5}**R**′. However, since both are singly occupied in ^{5}**R** and ^{5}**R**′, that will not affect the relative energies of these isomers dramatically. The major differences between ^{5}**R** and ^{5}**R**′ relate to the two σ^* orbitals, that is, the HOMO and LUMO orbitals, which, therefore, also affect the reactivities. In ^{5}**R** the $\sigma^*_{x^2-y^2}$ is singly occupied and the $\sigma^*_{z^2}$ orbital is virtual, whereas the ordering is reversed for ^{5}**R**′ and the $\sigma^*_{z^2}$ orbital is singly occupied instead. In this orientation the $\sigma^*_{z^2}$ orbital in ^{5}**R**′ has lesser antibonding interactions than the HOMO, that is, $\sigma^*_{x^2-y^2}$ in ^{5}**R** and consequently ^{5}**R**′ is more stable than ^{5}**R**. We calculated an isomerisation energy difference of $\Delta E + ZPE = -6.0$ kcal mol^{-1} for Sn_{500} at the UB3LYP level of theory. Changing the method to UB3LYP* gives negligible changes to the energy difference between ^{5}**R** and ^{5}**R**′ and a value of -7.0 kcal mol^{-1} is obtained.

Despite the fact that the orbital interactions have changed between ^{5}**R** and ^{5}**R**′, there are actually very little changes in the group spin densities and charges of these complexes (see the Supporting Information). The spin density on the metal is slightly increased from 2.96 in ^{5}**R** to 3.01 in ^{5}**R**′ and at the same time the oxygen atom loses spin density from 0.75 in ^{5}**R** to 0.69 in ^{5}**R**′. Generally, the more radical character obtained at the oxygen atom, the more reactive a metal–oxo group is, and it may be anticipated that this small change of spin polarisation from oxo to iron will make ^{5}**R**′ a slightly lesser oxidant than ^{5}**R**. Our group spin densities and electronic state assignment matches those reported in previous DFT and QM/MM studies on analogous systems.[15–20]

 © 2014 The Authors. Published by Wiley-VCH Verlag GmbH & Co. KGaA, Weinheim

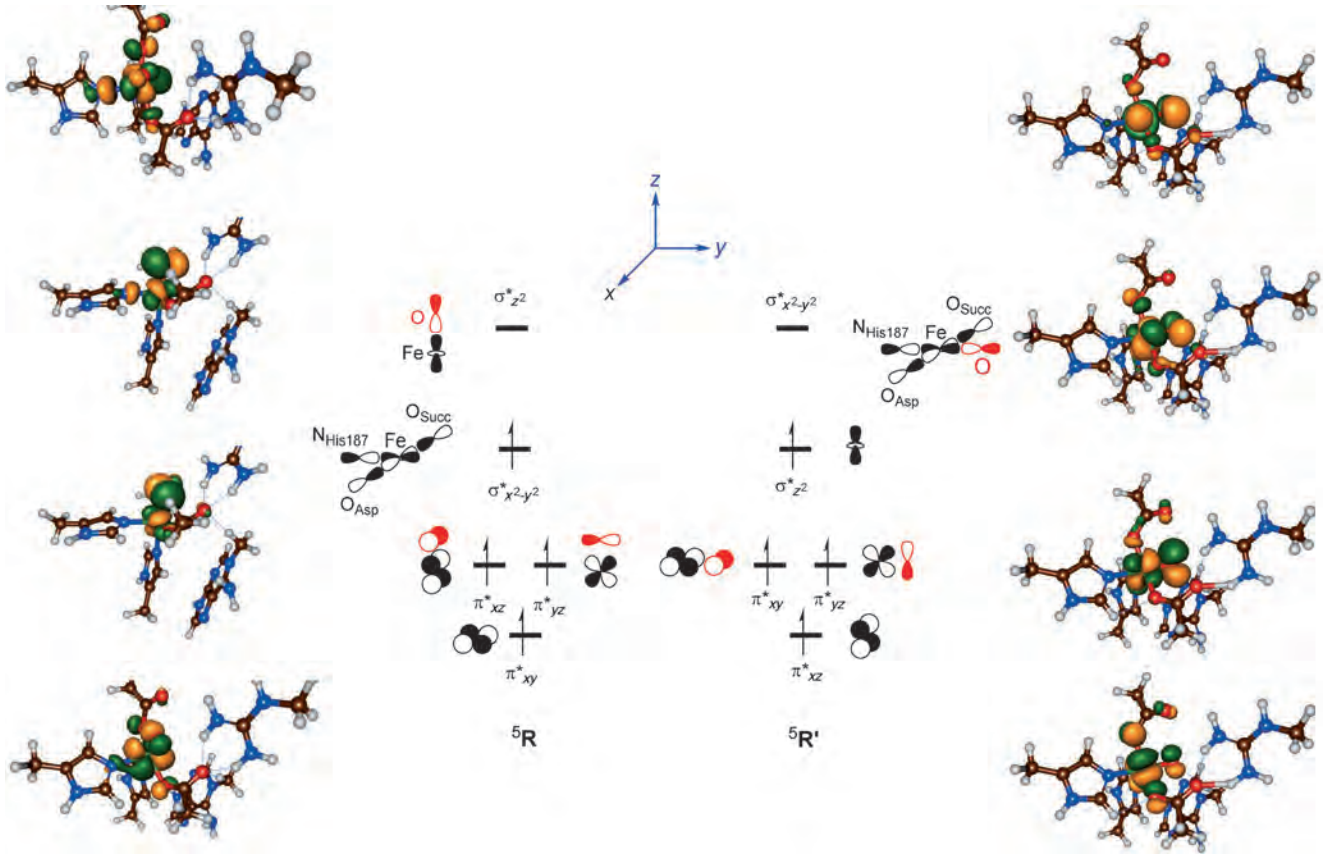

Figure 6. Orbital occupation of ^{5}**R** and ^{5}**R**′. Also given are the natural orbitals for ^{5}**R** and ^{5}**R**′.

In addition to differences in orbital interactions of the HOMO orbital in ^{5}**R** versus ^{5}**R**′ there are similar changes noted for the LUMO orbital. In ^{5}**R** the LUMO orbital is the antibonding interaction along the Fe–O bond, which shows little involvement of other ligands. By contrast, the $\sigma^*_{x^2-y^2}$ orbital displays interactions with four groups in the *xy* plane, namely the oxo, Asp_{133}, His_{187} and succinate groups, and, therefore, it will be considerably higher in energy than the LUMO in ^{5}**R**. Consequently, ^{5}**R**′ will have a much larger electron affinity than ^{5}**R** and it will cost ^{5}**R** more energy to abstract electrons from substrates. As hydrogen-atom abstraction is accompanied by a one-electron transfer from substrate to oxidant; this implies that ^{5}**R**′ will react with higher barriers than ^{5}**R**. There must, therefore, be a fundamental reason for the enzyme to initiate the reaction with an isomerisation from ^{5}**R** to ^{5}**R**′. A possible reason is that the enzyme has to separate the dioxygen and substrate binding processes to avoid side reactions and by-products. Thus, after dioxygen binding to the iron centre an iron(III)–superoxo complex is formed that reacts with αKG to form an iron(IV)–oxo and succinate.[24] In several nonheme iron enzymes, however, the iron(III)–superoxo complex is known to abstract hydrogen atoms from substrates directly. For instance, in the enzyme isopenicillin N synthase, the tripeptide δ-(L-α-amino adipoyl)-L-cysteinyl-D-valine, by four sequential hydrogen-atom abstraction reactions, is converted into isopenicillin N through two ring-closure processes.[33] The first step of this reaction proceeds via an iron(III)–superoxo intermediate. It may very well be that in AlkB repair enzymes the iron(III)–superoxo has to be separated from substrate to prevent multiple hydroxylation reactions to occur on the methylated group, which would prevent the subsequent demethylation reaction into formaldehyde.

To test the relative reactivity of an iron(III)–superoxo versus an iron(IV)–oxo complex with N^1-methyladenine, we set up a DFT model complex based on the QM region displayed in Figure 4 and calculated the hydrogen-atom abstraction of both complexes. We found a hydrogen-atom abstraction barrier of $\Delta E + \mathrm{ZPE} = 32.8\ \mathrm{kcal\,mol^{-1}}$ for the iron(III)–superoxo, whereas a value of $\Delta E + \mathrm{ZPE} = 23.4\ \mathrm{kcal\,mol^{-1}}$ for the iron(IV)–oxo was calculated. The latter matches the hydrogen-atom abstraction barrier reported by Gauld et al. well although slightly different methods were used.[15] Thus, the energy difference between the two hydrogen-atom abstraction barriers implicate faster reactivity of the iron(IV)–oxo than the iron(III)–superoxo complex. However, it is conceivable that the iron(III)–superoxo reacts with aliphatic groups by abstraction of hydrogen atoms although it probably will be slow.

Nevertheless, any reactivity of the iron(III)–superoxo species would lead to the disruption of the catalytic cycle and the failure to hydroxylate N^1-methyladenine to form N^1-hydroxymethyl adenine. It is, thus, very well possible that the enzyme has separated the oxygen binding and substrate binding positions in the active site of AlkB to prevent reactivity by the iron(III)–superoxo species. The substrate is shielded from the iron(III)–

 © 2014 The Authors. Published by Wiley-VCH Verlag GmbH & Co. KGaA, Weinheim

superoxo group by an arginine residue (Arg_{210}) in the binding pocket. The superoxo group is too bulky to slide underneath Arg_{210} and attack the substrate, but once the iron(III)–superoxo has reacted with αKG and formed an iron(IV)–oxo species an oxidant is formed that can migrate to a position *trans* to His_{187} and attack the substrate. This way the enzyme retains the regioselectivity of substrate hydroxylation and prevents the occurrence of by-products. Most probably the enzyme pays a small thermodynamic price for this isomerisation process, which now happens with elevated hydrogen-atom abstraction barriers.

Next we calculated the isomerisation barrier (^{5}**TS**$_I$) from ^{5}**R** to ^{5}**R**′ in Sn_{500} and the optimised geometry is given in Figure 7. Energetically, ^{5}**TS**$_I$ is higher in energy than ^{5}**R** by $\Delta E + ZPE = 9.0$ kcal mol^{-1}. QM/MM studies of the Borowski group[34] on the nonheme iron halogenase SyrB2 were also predicted to start

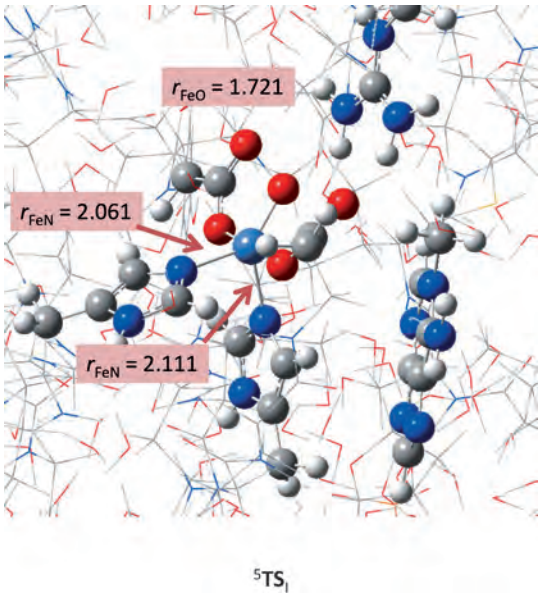

Figure 7. QM/MM optimised geometry of ^{5}**TS**$_I$ using snapshot Sn_{500} with bond lengths in Ångstroms.

with an isomerisation, whereby the positions of the oxo and halide ligands to the metal centre were interchanged. They calculated an isomerisation barrier of 13.4 kcal mol^{-1} for that process, which is not dramatically different from the value we found here. Our isomerisation is slightly lower in energy because in AlkB only the oxo group migrates whereas in SyrB2 both the oxo and halide groups interchange, which will raise the barrier heights.

The optimised geometry of ^{5}**TS**$_I$ shows some differences with respect to ^{5}**R** and ^{5}**R**′. Obviously the $NHis_{131}$-Fe-O angle changes along the rotation from 173.3° in ^{5}**R** to 135.7° in ^{5}**TS**$_I$ and to 97.2° in ^{5}**R**′. In addition in ^{5}**TS**$_I$ there is minor elongation of the two Fe–N distances with His_{131} and His_{187}, but more dramatically is the lengthening of the Fe–O bond to 1.721 Å. This is because of a tight interaction of the oxo group with one of the protons of Arg_{210}, which is shortened from 2.414 Å in ^{5}**R** to 1.888 Å in ^{5}**TS**$_I$ and then elongates again toward ^{5}**R**′ to a value of 2.470 Å. The Arg_{210} residue, therefore, acts as a switch and assists with the rotation of the oxo group from *trans* to His_{131} to a position *trans* of His_{187}.

Substrate hydroxylation by the iron(IV)–oxo complex

We subsequently continued with calculations of the rest of the potential energy profile for the hydrogen-atom abstraction and followed by radical rebound to form alcohol product complexes (**P**). The hydrogen-atom abstraction passes a transition state ($\mathbf{TS}_H$) to form a radical intermediate (**I**) that is separated from products by a rebound transition state ($\mathbf{TS}_{reb}$). We calculated the hydrogen-atom abstraction with QM/MM using snapshot Sn_{300}, Sn_{400} and Sn_{500}, whereas the rebound was only investigated for Sn_{500}. Despite the fact that we calculated the full potential energy profile of N^1-methyladenine hydroxylation on the singlet, triplet, quintet and septet spin state surfaces with QM/MM, actually only the quintet spin state is accessible for this part of the catalytic cycle and the other spin states are much higher in energy (see the Supporting Information). This is in agreement with previous studies of nonheme iron(IV)–oxo complexes in which single-state reactivity on a dominant quintet spin state surface was found.[24a] Hence, we will focus on the quintet spin state results only and the other spin state structures and energetics are given in the Supporting Information for completeness.

Figure 8 displays the complete potential energy profile from **R** to **P** as calculated with QM/MM in Sn_{500}. As mentioned above, the isomerisation barrier is about 9.0 kcal mol^{-1} and leads to the energetically more stable structure **R**′. Geometrically, the isomerisation step is assisted by Arg_{210} that hydrogen bonds with the oxo and succinate groups. Arg_{210} keeps the oxo group in a specific orientation and guides its rotation toward the substrate. To highlight the motion of the Arg residue upon rotation from **R** to **R**′ we have drawn a yellow box around its atoms. The isomerisation then brings the oxo group in close proximity to the substrate to enable a regioselective hydrogen-atom abstraction and prevent reactivity of its precursor the iron(III)–superoxo species. The tight substrate binding pocket and the Arg-assisted isomerisation mechanism enable regioselective hydroxylation of the methylated DNA base without activation of any of the other C–H bonds in the substrate.

We located two distinct pathways for hydrogen-atom abstraction by ^{5}**R**′. Hydrogen-atom abstraction from N^1-methyladenine by ^{5}**R**′ can either lead to electron transfer into the virtual $\sigma^*_{x^2-y^2}$ orbital, the so-called $^5\sigma$-pathway, or to double occupation of the π^*_{xz} orbital through the so-called $^5\pi$-pathway.[35] Usually, in nonheme iron(IV)–oxo complexes the $^5\sigma$-pathway is considerably lower in energy than the $^5\pi$-pathway, and, hence is the dominating quintet spin electron transfer mechanism.[22,24,26] Generally, in the $^5\sigma$-pathway the substrate attacks from the top and incurs little stereochemical interactions with the metal ligands, whereas in the $^5\pi$-pathway the substrate approaches under an Fe-O-H angle of about 120° that is stereochemically disfavoured.[36] Due to the rotation of the iron(IV)–oxo group and a change of orbital shapes (Figure 6), the $^5\sigma$-pathway is not the dominating pathway anymore. We located

 © 2014 The Authors. Published by Wiley-VCH Verlag GmbH & Co. KGaA, Weinheim

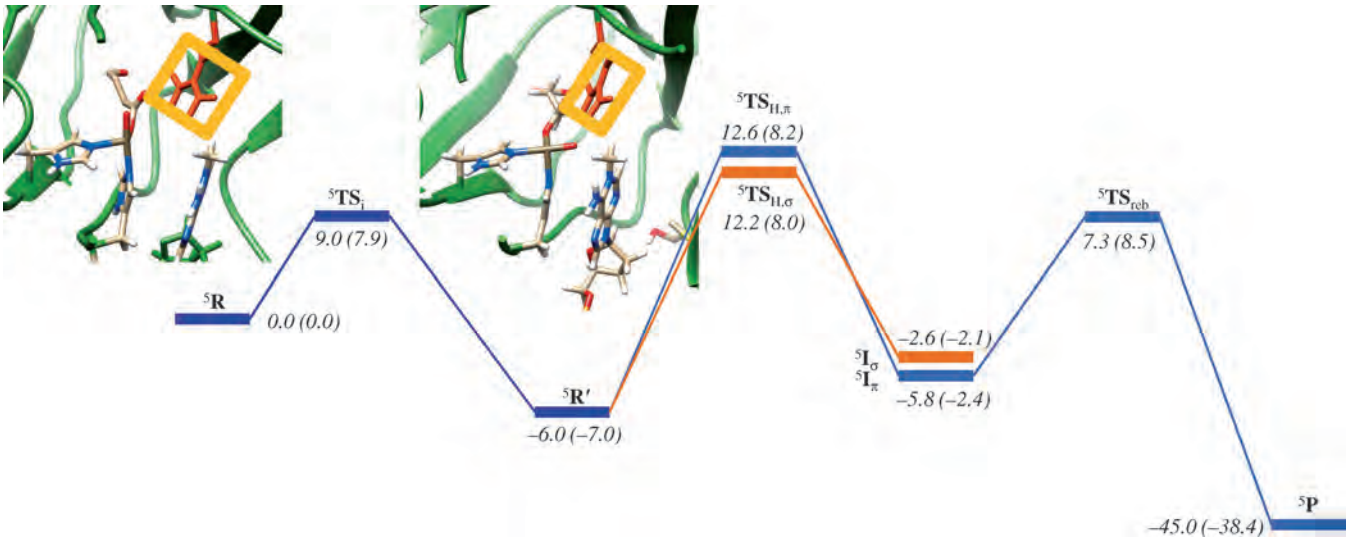

Figure 8. Potential energy landscape for the hydroxylation of N^1-methyladenine as calculated with QM/MM. Energies are obtained at UB3LYP/B2//UB3LYP/B1-Amber, whereas in parenthesis are given UB3LYP*/B2//UB3LYP/B1-Amber results. All energies contain zero-point corrections and are given in kcal mol^{-1}.

transition states for both pathways, designated ^{5}**TS**$_{H,\sigma}$ and ^{5}**TS**$_{H,\pi}$, as well as the two isomeric radical intermediates, ^{5}**I**$_\sigma$ and ^{5}**I**$_\pi$.

Based on the orbital diagram for ^{5}**R** and the unfavourable angle between the $\sigma^*_{z^2}$ and the substrate location, one might have expected high barriers for ^{5}**TS**$_{H,\sigma}$ but actually due to the change of the ordering of $\sigma^*_{z^2}$ and $\sigma^*_{x^2-y^2}$ upon rotation of the iron(IV)–oxo group from ^{5}**R** to ^{5}**R**′ the σ-pathway is still a viable reaction pathway. Moreover, the $^5\pi$-pathway is stabilised and becomes competitive with the $^5\sigma$-pathway. Nevertheless, the rate-determining step in the reaction mechanism in Figure 8 is the hydrogen-atom abstraction via barrier ^{5}**TS**$_H$, and both located transition states ^{5}**TS**$_{H,\sigma}$ and ^{5}**TS**$_{H,\pi}$ originate from the same reactant structure ^{5}**R**′. Thus, during the hydrogen-atom abstraction an electron is transferred into the $\sigma^*_{x^2-y^2}$ orbital in ^{5}**TS**$_{H,\sigma}$ to form an exchange coupled radical intermediate (^{5}**I**$_\sigma$) with $\pi^*_{xz}{}^{\uparrow}\pi^*_{yz}{}^{\uparrow}\pi^*_{xy}{}^{\uparrow}\sigma^*_{z^2}{}^{\uparrow}\sigma^*_{x^2-y^2}{}^{\uparrow}\phi_{Sub}{}^{\downarrow}$ configuration. By contrast in ^{5}**TS**$_{H,\pi}$ a low-lying π^* orbital is doubly occupied to give a radical intermediate (^{5}**I**$_\pi$) with configuration $\pi^*_{xz}{}^2\pi^*_{yz}{}^{\uparrow}\pi^*_{xy}{}^{\uparrow}\sigma^*_{z^2}{}^{\uparrow}\sigma^*_{x^2-y^2}{}^0\phi_{Sub}{}^{\uparrow}$. As the isomerisation has led to an inversion of the ordering of $\sigma^*_{z^2}$ and $\sigma^*_{x^2-y^2}$ the σ-pathway now involves electron transfer into the $\sigma^*_{x^2-y^2}$ orbital and an alignment of the substrate along the molecular *y* axis. Indeed, an Fe-O-C angle of 141.4° is found for ^{5}**TS**$_{H,\sigma}$, whereas ^{5}**TS**$_{H,\pi}$ gives a much smaller angle of 131.4°.

Because of the fact that the angle in ^{5}**TS**$_{H,\sigma}$ deviates significantly from the ideal angle of a linear Fe-O-C conformation due to constraints on the enzyme substrate and co-factor binding pocket, the σ-pathway is destabilised. By contrast, the π-pathway requires angles of typically 120° and indeed here we find an Fe-O-C angle of 131.4°. Because of the unfavourable angle in the σ-pathway, it is destabilised in energy and the π-pathway becomes competitive. This is fundamentally different from hydrogen-atom abstraction along the molecular *z* axis as is normally the case for nonheme iron enzymes that appear to mostly react through the σ-pathway. Note as well that the LUMO orbital in ^{5}**R**, that is, the $\sigma^*_{z^2}$ orbital is lower in energy than the LUMO orbital in ^{5}**R**′, that is, the $\sigma^*_{x^2-y^2}$ which has considerably more antibonding interactions between the metal and its ligands, and, therefore, it requires more energy to fill it.

Energetically in Sn_{500}, ^{5}**TS**$_{H,\sigma}$ and ^{5}**TS**$_{H,\pi}$ are of comparable energies: 18.2 versus 18.6 kcal mol^{-1} at UB3LYP level of theory, and 15.0 versus 15.2 kcal mol^{-1} at UB3LYP* level of theory with respect to ^{5}**R**′. We also calculated ^{5}**R**′ and ^{5}**TS**$_{H,\pi}$ in Sn_{300} and Sn_{400}, but similar group spin densities and charges are found and a minor stabilisation of the barrier heights is observed: 13.0 kcal mol^{-1} for Sn_{300} and 15.1 kcal mol^{-1} for Sn_{400}. As such there is a small effect of the protein on the barrier heights of the hydrogen-atom abstraction, although, geometrically they look very similar to the structure displayed in Figure 8 for Sn_{500} (see the Supporting Information). Our values are also close, but slightly lower in energy than those reported by Cisneros and co-workers.[18] Furthermore, DFT studies using an active-site complex found a rate-determining hydrogen-atom abstraction barrier of 20.9 kcal mol^{-1}.[15] It appears, therefore, that the protein has a minor but stabilising effect on the transition state of the reaction. These high energetic barriers are caused through the isomerisation of the iron(IV)–oxo species, which raises the electron affinities and the corresponding hydrogen-atom abstraction barriers.

Figure 9 gives QM/MM optimised geometries for hydrogen-atom abstraction transition states and intermediates on the competing σ- and π-pathways. In both cases the hydrogen-atom abstraction is late on the potential energy surface with short O–H distances of 1.141 and 1.160 Å for ^{5}**TS**$_{H,\sigma}$ and ^{5}**TS**$_{H,\pi}$, whereas their corresponding H–C distances are considerably longer: 1.367 and 1.500 Å, respectively. As previously shown,[37] late transition states generally correspond with high energetic barriers. Due to single occupation of the $\sigma^*_{x^2-y^2}$ orbital in ^{5}**TS**$_{H,\sigma}$ the Fe–O and Fe–$NHis_{187}$ distances are somewhat longer than those in ^{5}**TS**$_{H,\pi}$, in which this orbital is virtual. The Arg_{210} residue

 © 2014 The Authors. Published by Wiley-VCH Verlag GmbH & Co. KGaA, Weinheim

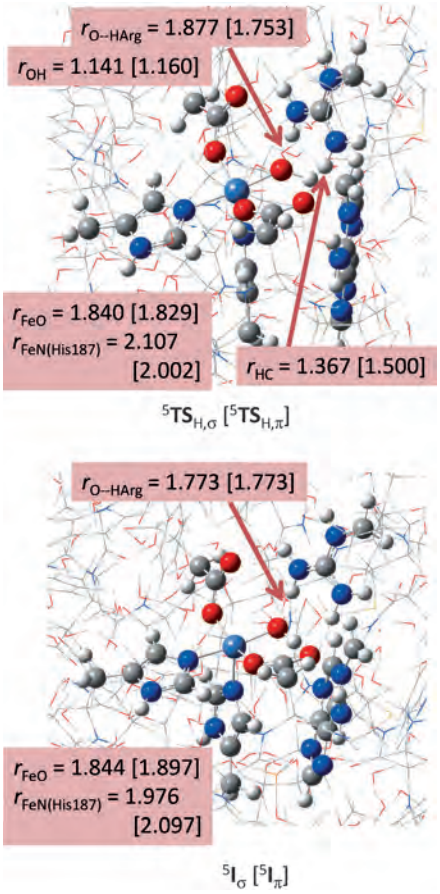

Figure 9. Optimised geometries of $^5TS_{H,\sigma}$, $^5TS_{H,\pi}$, $^5I_\sigma$ and $^5I_\pi$ as obtained from QM/MM calculations with bond lengths in Ångstroms.

forms hydrogen bonding interactions with the carboxylate groups of succinate and Asp_{133} as well as with the oxo group at a distance 1.877 (1.753) Å for $^5TS_{H,\sigma}$ ($^5TS_{H,\pi}$).

After the hydrogen-atom abstraction the system relaxes to a radical intermediate ($^5I_\sigma$ or $^5I_\pi$), whereby the former has orbital occupation $\pi^{*\uparrow}_{xz}\pi^{*\uparrow}_{yz}\pi^{*\uparrow}_{xy}\sigma^{*\uparrow}_{z^2}\sigma^{*\uparrow}_{x^2-y^2}\phi^{\downarrow}_{Sub}$ whereas it is $\pi^{*2}_{xz}\pi^{*\uparrow}_{yz}\pi^{*\uparrow}_{xy}\sigma^{*\uparrow}_{z^2}\sigma^{*0}_{x^2-y^2}\phi^{\uparrow}_{Sub}$ for the latter. The hydroxyl group in $^5I_\sigma$ and $^5I_\pi$ is locked in hydrogen-bonding interactions with the carboxylate group of Asp_{133} at a short distance of 1.701 (1.781) Å for $^5I_\sigma$ ($^5I_\pi$). As such it is not surprising that hydroxyl rebound to the substrate radical gives a significant barrier: on the π-pathway we located a $^5TS_{reb}$ barrier of 13.1 kcal mol^{-1} above $^5I_\pi$, although this is lower in energy than the hydrogen-atom abstraction barrier of 18.6 kcal mol^{-1} for the π-pathway. This substantial rebound barrier was previously shown to lead to rearrangement patterns and the formation of by-products due to the relatively long lifetime of the radical intermediate.[38] Despite the large rebound barriers, therefore, the hydrogen-atom abstraction step is still the rate-determining step in the reaction mechanism. The large rebound barrier obtained in this work contrasts the result of DFT model calculations,[15] in which a rebound barrier of just 0.6 kcal mol^{-1} was found. Clearly, the strong hydrogen-bonding interactions of the OH group to the carboxylate groups of succinate and Asp_{133} and the methylguanidinium group of Arg_{210} stabilise the radical intermediates and raise the barrier for OH transfer to the radical. This highlights the importance of inclusion of part of the protein and particularly the hydrogen bonding network in the model.

To find out whether the hydrogen abstraction barrier is dependent on the substrate, we also calculated it for N^1-methylguanine, N^1-methyladenine, N^3-methylcytosine and N^3-methylthymine using DFT model complexes and compared the results with the QM/MM studies described above (Figure 10). Our calculated hydrogen-abstraction barrier for N^1-methylade-

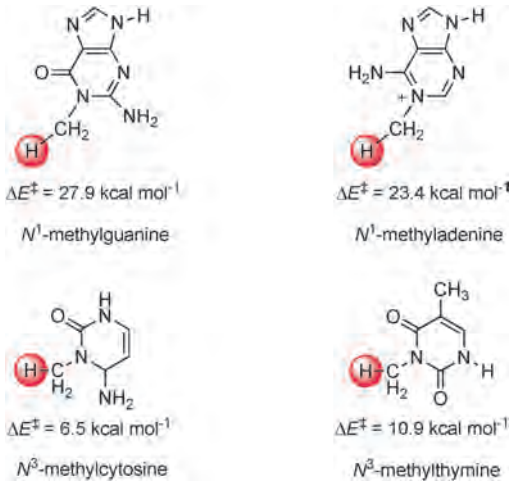

Figure 10. DFT calculated hydrogen-atom abstraction barriers from methylated DNA bases as calculated with DFT model complexes. All energies are in kcal mol^{-1} and contain ZPE and solvent corrections.

nine of 23.4 kcal mol^{-1} is close in energy to the one reported by Gauld and co-workers.[15] We located hydrogen-atom abstraction barrier heights from the *N*-methyl positions of N^3-methylcytosine, N^1-methylguanine and N^3-methylthymine of $\Delta E + ZPE = 6.5$, 27.9 and 10.9 kcal mol^{-1}, respectively. To find out whether this trend correlates with the strength of the C–H bond that is broken for these substrates, we calculated the bond dissociation energy (BDE_{CH}) for these bonds using procedures used before.[39] The BDE_{CH} value of substrates (SubH) was calculated from the energy difference of the isolated substrate with the sum of an isolated hydrogen atom and the substrate minus one hydrogen atom. As follows the BDE_{CH} values for these four substrates fall within a narrow window of about 5 kcal mol^{-1}, and should have resulted in very similar barrier heights for all substrates. Inspection of the optimised geometries (see the Supporting Information) shows that in the DFT model complexes the substrates have reoriented in several cases and formed multiple hydrogen-bonding interactions with the carboxylic acid groups of succinate and Asp_{133} as well as the oxo-group. As shown before,[26] hydrogen-bonding interactions reduce catalytic efficiency and raise hydrogen-abstraction barriers and therefore these model complexes are not a good representative of the catalysis in the actual enzyme. Thermodynamically, the AlkB repair enzyme should, therefore, also be able to hydroxylate, and, consequently, repair N^3-methylcytosine and N^3-methylthymine.

 © 2014 The Authors. Published by Wiley-VCH Verlag GmbH & Co. KGaA, Weinheim

Conclusion

In this work we report a series of QM/MM and DFT studies on the catalytic mechanism of substrate activation by AlkB repair enzymes. We analysed PDB structures and attempted to insert a dioxygen molecule in several positions and found only one feasible binding position to iron *trans* to His_{131}. The iron(III)–superoxo species is separated from the substrate by a considerable distance and its approach is blocked by an Arg residue. This Arg_{210} residue acts as a latch and only allows the isomerisation of iron(IV)–oxo and prevents the iron(III)–superoxo from reacting with substrate. It is proposed that the iron(III)–superoxo reacts with αKG to form iron(IV)–oxo, succinate and CO_2. The iron(IV)–oxo initially has the oxo *trans* to His_{131} and isomerises to a position *trans* to His_{187}. The isomeric iron(IV)–oxo species was found to react via hydrogen-atom abstraction on competing $^5\sigma$- and $^5\pi$-pathways to form a radical intermediate followed by rebound to give alcohol products. The hydrogen-atom abstraction is the rate-determining step in the reaction mechanism.

The studies presented in this work give important insight into the substrate and oxygen binding channels in the enzyme. We show that it is essential to separate the substrate and oxygen binding channels as otherwise the iron(III)–superoxo will react with substrate and prevent the repair reaction of the DNA. We also show that the isomerisation reorganises the high-lying occupied and low-lying virtual orbitals and, thereby, affects the electron transfer abilities of the oxidant. The isomeric iron(IV)–oxo reacts with substantially larger barriers as a result, which is a price the enzyme pays for separating the substrate and dioxygen binding channels.

Experimental Section

For the set-up of the QM/MM system we used well-tested and benchmarked methods as reported before.[19] Starting from the 3I2O PDB file,[14] hydrogen atoms were added to the structure using the PDB2PQR program package[40] and the active site was manually modified from the iron(II)—water αKG complex into an iron(IV)–oxo succinate (Succ) active site. Apart from the two histidine groups that are bound to the metal, all other histidine side chains were doubly protonated. Furthermore, we made sure that all arginine and lysine side chains were protonated and all glutamic acid and aspartic acid side chains were deprotonated. This resulted in a structure with overall neutral charge. Solvent (with sphere of radius of 35 Å) was added to this structure, and equilibrated, followed by a molecular dynamics minimisation and heating procedure to 298 K of the full structure using the CHARMM force field.[20] The total model has 10011 atoms and includes 2269 TIP3P water molecules. We selected several snapshots from this MD simulation as starting points for the QM/MM calculations at different time intervals. The iron(IV)–oxo reactant was geometry optimised in all low-lying and accessible spin states, that is, singlet, triplet, quintet and septet, and the spin state ordering and relative energies of these snapshots at 300, 400 and 500 ps (Sn_{300}, Sn_{400}, Sn_{500}) gave consistent and reproducible results. Subsequently, we investigated the full potential energy profile with Sn_{500} as well as the hydrogen-atom abstraction step by Sn_{300} and Sn_{400}. We chose to start the work from the iron(III)–superoxo complex and studied the mechanism until formation of alcohol product complexes as this procedure means the number of atoms in the model stays constant during the reaction.

QM/MM calculations employed the ONIOM program package as implemented in Gaussian 09.[41] The QM region was described by density functional theory and the unrestricted B3LYP functional,[28] while we used the Amber force field for the MM region.[42] The QM region contained the iron(IV)–oxo group, methylimidazole groups for His_{131} and His_{187}, acetate for succinate and Asp_{133}, methylguanidinium for Arg_{210}, and the N^1-methyladenine part of the substrate. All structures described here are the result of a full QM/MM geometry optimisation of all degrees of freedom. Stationary points were characterised by running an analytical frequency calculation on the QM region only at the same level of theory. Geometry optimisation and frequency were carried out with a double-ζ quality LACVP basis set on iron that contains a core potential and 6-31G on the rest of the atoms (basis set B1).[43] Single-point energy calculations with a Wachters all-electron basis set on iron and 6-31+G* on the rest of the atoms (basis set B2) was carried out on the optimised geometries at QM/MM to improve the energetics.[44] All energies reported in this work were obtained with basis set B2 and include ZPE corrections. Previous studies of our group on nonheme iron(IV)–oxo complexes showed these methods to be sufficiently accurate to match experimentally determined free energies of activation.[44] We used electronic embedding procedures whenever possible. To ascertain that the obtained results are reproducible we also calculated single-point energies using the UB3LYP* density functional in which the amount of HF exchange was reduced to 15%,[29] as well as single points using either the BP86 or M06 methods.[30,31]

To gain further insight into the reaction kinetics and energetics we supplemented our studies with DFT model calculations in which we took a model containing iron(IV)–oxo with two imidazole and two acetate groups as the active species of the enzyme in analogy to previous model calculations.[16,24a] We then treated this oxidant with methylated DNA bases: N^1-methyladenine, N^1-methylguanine, N^3-methylcytosine and N^3-methylthymine. The geometries were optimised with UB3LYP/B1 and characterised with a frequency calculation. Single-point calculations were carried out with UB3LYP/B2 and solvent corrections were included.

We also calculated a DFT model complex based on the above-mentioned QM region for an iron(III)–superoxo complex and calculated the hydrogen-atom abstraction from N^1-methyladenine at UB3LYP/B1. Geometries and frequencies were carried out in Gaussian using this level of theory and energies were corrected with single points at UB3LYP/B2 and solvent corrections.

Acknowledgements

The National Service of Computational Chemistry Software (NSCCS) is thanked for generous CPU time. M.G.Q. thanks the BBSRC for a studentship. D.K. is DST–Ramanujan Fellow (SR/S2/RJN-11/2008) and also acknowledges financial support from the Department of Biotechnology, New Delhi (BT/PR14510/BID/07/334/2010). Dr. Kakali Sen and Prof. Walter Thiel (Max Planck Institute in Mülheim an der Ruhr) are thanked for fruitful discussions and assistance with the QM/MM set-up.

Keywords: density functional calculations · DNA base repair · DNA damage · hydroxylation · nonheme iron enzymes

 © 2014 The Authors. Published by Wiley-VCH Verlag GmbH & Co. KGaA, Weinheim

[1] a) E. I. Solomon, T. C. Brunold, M. I. Davis, J. N. Kemsley, S.-K. Lee, N. Lehnert, F. Neese, A. J. Skulan, Y.-S. Yang, J. Zhou, *Chem. Rev.* **2000**, *100*, 235 – 349; b) T. D. H. Bugg, *Curr. Opin. Chem. Biol.* **2001**, *5*, 550 – 555; c) M. J. Ryle, R. P. Hausinger, *Curr. Opin. Chem. Biol.* **2002**, *6*, 193 – 201; d) M. Costas, M. P. Mehn, M. P. Jensen, L. Que Jr, *Chem. Rev.* **2004**, *104*, 939 – 986; e) M. M. Abu-Omar, A. Loaiza, N. Hontzeas, *Chem. Rev.* **2005**, *105*, 2227 – 2252; f) P. C. A. Bruijnincx, G. van Koten, R. J. M. Klein Gebbink, *Chem. Soc. Rev.* **2008**, *37*, 2716 – 2744; g) S. V. Kryatov, E. V. Rybak-Akimova, S. Schindler, *Chem. Rev.* **2005**, *105*, 2175 – 2226.

[2] a) M. H. Stipanuk, *Annu. Rev. Nutr.* **2004**, *24*, 539 – 577; b) G. D. Straganz, B. Nidetzky, *ChemBioChem* **2006**, *7*, 1536 – 1548; c) C. A. Joseph, M. J. Maroney, *Chem. Commun.* **2007**, 3338 – 3349.

[3] a) R. Chowdhury, A. Hardy, C. J. Schofield, *Chem. Soc. Rev.* **2008**, *37*, 1308 – 1319; b) J. M. Simmons, T. A. Müller, R. P. Hausinger, *Dalton Trans.* **2008**, 5132 – 5142; c) C. Loenarz, C. J. Schofield, *Nat. Chem. Biol.* **2008**, *4*, 152 – 156.

[4] a) L. Que Jr, *Nat. Struct. Biol.* **2000**, *7*, 182 – 184; b) E. G. Kovaleva, J. D. Lipscomb, *Nat. Chem. Biol.* **2008**, *4*, 186 – 193.

[5] a) W. Nam, *Acc. Chem. Res.* **2007**, *40*, 522 – 531; b) *Iron-Containing Enzymes: Versatile Catalysts of Hydroxylation Reaction in Nature* (Eds.: S. P. de Visser, D. Kumar), RSC, Cambridge, **2011**; c) A. R. McDonald, L. Que, Jr., *Coord. Chem. Rev.* **2012**, *257*, 414 – 428.

[6] a) D. A. Proshlyakov, T. F. Henshaw, G. R. Monterosso, M. J. Ryle, R. P. Hausinger, *J. Am. Chem. Soc.* **2004**, *126*, 1022 – 1023; b) P. J. Riggs-Gelasco, J. C. Price, R. B. Guyer, J. H. Brehm, E. W. Barr, J. M. Bollinger Jr, C. Krebs, *J. Am. Chem. Soc.* **2004**, *126*, 8108 – 8109.

[7] a) S. C. Trewick, T. F. Henshaw, R. P. Hausinger, T. Lindahl, B. Sedgwick, *Nature* **2002**, *419*, 174 – 178; b) P. Ø. Falnes, R. F. Johansen, E. Seeberg, *Nature* **2002**, *419*, 178 – 182; c) P. J. O'Brien, *Chem. Rev.* **2006**, *106*, 720 – 752; d) C. Yi, C. G. Yang, C. He, *Acc. Chem. Res.* **2009**, *42*, 519 – 529.

[8] a) Y. Mishina, E. M. Duguid, C. He, *Chem. Rev.* **2006**, *106*, 215 – 232; b) Y. Mishina, C. He, *J. Inorg. Biochem.* **2006**, *100*, 670 – 678; c) K. I. Ladwein, M. Jung, *Angew. Chem.* **2011**, *123*, 12347 – 12349; *Angew. Chem. Int. Ed.* **2011**, *50*, 12143 – 12145.

[9] a) B. Yu, J. F. Hunt, *Proc. Natl. Acad. Sci. USA* **2009**, *106*, 14315 – 14320; b) Y. Fu, Q. Dai, W. Zhang, J. Ren, T. Pan, C. He, *Angew. Chem.* **2010**, *122*, 9069 – 9072; *Angew. Chem. Int. Ed.* **2010**, *49*, 8885 – 8888; c) N. C. Giri, H. Sun, H. Chen, M. Costa, M. J. Maroney, *Biochemistry* **2011**, *50*, 5067 – 5076; d) D. Li, J. C. Delaney, C. M. Page, X. Yang, A. S. Chen, C. Wong, C. L. Drennan, J. M. Essigmann, *J. Am. Chem. Soc.* **2012**, *134*, 8896 – 8901.

[10] a) M. A. Kurowski, A. S. Bhagwat, G. Papaj, J. M. Bujnicki, *BMC Genomics* **2003**, *4*, 48 – 53; b) Y. Mishina, L. X. Shen, C. He, *J. Am. Chem. Soc.* **2004**, *126*, 16930 – 16936.

[11] B. Bleijlevens, T. Shivarattan, K. S. van den Boom, A. de Haan, G. van der Zwan, P. J. Simpson, S. J. Matthews, *Biochemistry* **2012**, *51*, 3334 – 3341.

[12] a) R. W. D. Welford, I. Schlemminger, L. A. McNeill, K. S. Hewitson, C. J. Schofield, *J. Biol. Chem.* **2003**, *278*, 10157 – 10161; b) S. C. Peck, H. A. Cooke, R. M. Cicchillo, P. Malova, F. Hammerschmidt, S. K. Nair, W. A. van der Donk, *Biochemistry* **2011**, *50*, 6598 – 6605; c) A. M. Maciejewska, J. Poznański, Z. Kaczmarska, B. Krowisz, J. Nieminuszczy, A. Polkowska-Nowakowska, E. Grzesiuk, J. T. Kuśmierek, *J. Biol. Chem.* **2013**, *288*, 432 – 441.

[13] C. Yi, G. Jia, G. Hou, Q. Dai, G. Zheng, X. Jian, C.-G. Yang, Q. Cui, C. He, *Nature* **2010**, *468*, 330 – 335.

[14] B. Yu, W. C. Edstrom, J. Benach, Y. Hamuro, P. C. Weber, B. R. Gibney, J. F. Hunt, *Nature* **2006**, *439*, 879 – 884.

[15] H. Liu, J. Llano, J. W. Gauld, *J. Phys. Chem. B* **2009**, *113*, 4887 – 4898.

[16] a) R. Latifi, M. Bagherzadeh, S. P. de Visser, *Chem. Eur. J.* **2009**, *15*, 6651 – 6662; b) S. P. de Visser, *J. Am. Chem. Soc.* **2010**, *132*, 1087 – 1097.

[17] a) A. Bassan, T. Borowski, P. E. M. Siegbahn, *Dalton Trans.* **2004**, 3153 – 3162; b) S. P. de Visser, *Chem. Commun.* **2007**, 171 – 173.

[18] D. Fang, R. L. Lord, G. A. Cisneros, *J. Phys. Chem. B* **2013**, *117*, 6410 – 6420.

[19] a) E. Godfrey, C. S. Porro, S. P. de Visser, *J. Phys. Chem. A* **2008**, *112*, 2464 – 2468; b) D. Kumar, W. Thiel, S. P. de Visser, *J. Am. Chem. Soc.* **2011**, *133*, 3869 – 3882.

[20] B. R. Brooks, R. E. Bruccoleri, B. D. Olafson, D. J. States, S. Swaminathan, M. Karplus, *J. Comput. Chem.* **1983**, *4*, 187 – 217.

[21] C. R. Wick, H. Lanig, C. M. Jäger, N. Burzlaff, T. Clark, *Eur. J. Inorg. Chem.* **2012**, 4973 – 4985.

[22] a) D. Kumar, H. Hirao, L. Que Jr, S. Shaik, *J. Am. Chem. Soc.* **2005**, *127*, 8026 – 8027; b) A. Decker, J.-U. Rohde, E. J. Klinker, S. D. Wong, L. Que Jr, E. I. Solomon, *J. Am. Chem. Soc.* **2007**, *129*, 15983 – 15996.

[23] a) J. C. Price, E. W. Barr, B. Tirupati, J. M. Bollinger, Jr., C. Krebs, *Biochemistry* **2003**, *42*, 7497 – 7508; b) D. Galonić Fujimori, E. W. Barr, M. L. Matthews, G. M. Koch, J. R. Yonce, C. T. Walsh, J. M. Bollinger Jr., C. Krebs, P. J. Riggs-Gelasco, *J. Am. Chem. Soc.* **2007**, *129*, 13408 – 13409; c) P. K. Grzyska, E. H. Appelman, R. P. Hausinger, D. A. Proshlyakov, *Proc. Natl. Acad. Sci. USA* **2010**, *107*, 3982 – 3987.

[24] a) S. P. de Visser, *J. Am. Chem. Soc.* **2006**, *128*, 9813 – 9824; b) T. Borowski, A. Bassan, P. E. M. Siegbahn, *Chem. Eur. J.* **2004**, *10*, 1031 – 1041; c) S. P. de Visser, *Angew. Chem.* **2006**, *118*, 1822 – 1825; *Angew. Chem. Int. Ed.* **2006**, *45*, 1790 – 1793; d) S. Ye, F. Neese, *Proc. Natl. Acad. Sci. USA* **2011**, *108*, 1228 – 1233; e) S. Aluri, S. P. de Visser, *J. Am. Chem. Soc.* **2007**, *129*, 14846 – 14847.

[25] a) S. Shaik, H. Chen, D. Janardanan, *Nat. Chem.* **2011**, *3*, 19 – 27; b) S. P. de Visser, J.-U. Rohde, Y.-M. Lee, J. Cho, W. Nam, *Coord. Chem. Rev.* **2013**, *257*, 381 – 393.

[26] R. Latifi, M. A. Sainna, E. V. Rybak-Akimova, S. P. de Visser, *Chem. Eur. J.* **2013**, *19*, 4058 – 4068.

[27] a) I. A. Topol, A. V. Nemukhin, K. Salnikow, R. E. Cachau, Y. G. Abashkin, K. S. Kasprzak, S. K. Burt, *J. Phys. Chem. A* **2006**, *110*, 4223 – 4228; b) C. Geng, S. Ye, F. Neese, *Angew. Chem.* **2010**, *122*, 5853 – 5856; *Angew. Chem. Int. Ed.* **2010**, *49*, 5717 – 5720.

[28] a) A. D. Becke, *J. Chem. Phys.* **1993**, *98*, 5648 – 5652; b) C. Lee, W. Yang, R. G. Parr, *Phys. Rev. B* **1988**, *37*, 785 – 789.

[29] M. Reiher, O. Salomon, B. A. Hess, *Theor. Chem. Acc.* **2001**, *107*, 48 – 55.

[30] J. P. Perdew, *Phys. Rev. B* **1986**, *33*, 8822 – 8824.

[31] Y. Zhao, D. G. Truhlar, *J. Chem. Phys.* **2006**, *125*, 1 – 18.

[32] H. Hirao, L. Que Jr, W. Nam, S. Shaik, *Chem. Eur. J.* **2008**, *14*, 1740 – 1756.

[33] a) J. E. Baldwin, M. Bradley, *Chem. Rev.* **1990**, *90*, 1079 – 1088; b) M. Lundberg, P. E. M. Siegbahn, K. Morokuma, *Biochemistry* **2008**, *47*, 1031 – 1042.

[34] T. Borowski, H. Noack, M. Radoń, K. Zych, P. E. M. Siegbahn, *J. Am. Chem. Soc.* **2010**, *132*, 12887 – 12898.

[35] a) L. Bernasconi, E.-J. Baerends, *Eur. J. Inorg. Chem.* **2008**, 1672 – 1681; b) S. D. Wong, C. B. Bell III, L. V. Liu, Y. Kwak, J. England, E. E. Alp, J. Zhao, L. Que Jr, E. I. Solomon, *Angew. Chem.* **2011**, *123*, 3273 – 3276; *Angew. Chem. Int. Ed.* **2011**, *50*, 3215 – 3218; c) S. Sahu, L. R. Widger, M. G. Quesne, S. P. de Visser, H. Matsumura, P. Moënne-Loccoz, M. A. Siegler, D. P. Goldberg, *J. Am. Chem. Soc.* **2013**, *135*, 10590 – 10593.

[36] S. P. de Visser, *J. Am. Chem. Soc.* **2006**, *128*, 15809 – 15818.

[37] a) S. P. de Visser, D. Kumar, S. Cohen, R. Shacham, S. Shaik, *J. Am. Chem. Soc.* **2004**, *126*, 8362 – 8363; b) S. Shaik, D. Kumar, S. P. de Visser, *J. Am. Chem. Soc.* **2008**, *130*, 10128 – 10140; c) D. Kumar, B. Karamzadeh, G. N. Sastry, S. P. de Visser, *J. Am. Chem. Soc.* **2010**, *132*, 7656 – 7667.

[38] a) S. P. de Visser, F. Ogliaro, S. Shaik, *Angew. Chem.* **2001**, *113*, 2955 – 2958; *Angew. Chem. Int. Ed.* **2001**, *40*, 2871 – 287; b) D. Kumar, S. P. de Visser, S. Shaik, *J. Am. Chem. Soc.* **2004**, *126*, 5072 – 5073; c) D. Kumar, S. P. de Visser, S. Shaik, *Chem. Eur. J.* **2005**, *11*, 2825 – 2835; d) S. M. Prather, C. Konstantinovics, C. L. M. DiGiuro, E. Leitner, D. Kumar, S. P. de Visser, G. Grogan, G. D. Straganz, *Angew. Chem.* **2013**, *125*, 9859 – 9863; *Angew. Chem. Int. Ed.* **2013**, *52*, 9677 – 9681.

[39] a) K. A. Prokop, S. P. de Visser, D. P. Goldberg, *Angew. Chem.* **2010**, *122*, 5217 – 5221; *Angew. Chem. Int. Ed.* **2010**, *49*, 5091 – 5095; b) K. A. Prokop, H. M. Neu, S. P. de Visser, D. P. Goldberg, *J. Am. Chem. Soc.* **2011**, *133*, 15874 – 15877; c) P. Leeladee, R. A. Baglia, K. A. Prokop, R. Latifi, S. P. de Visser, D. P. Goldberg, *J. Am. Chem. Soc.* **2012**, *134*, 10397 – 10400.

[40] T. J. Dolinsky, P. Czodrowski, H. Li, J. E. Nielsen, J. H. Jensen, G. Klebe, N. A. Baker, *Nucleic Acids Res.* **2007**, *35*, 522.

[41] Gaussian 09, Revision C.01, M. J. Frisch, G. W. Trucks, H. B. Schlegel, G. E. Scuseria, M. A. Robb, J. R. Cheeseman, G. Scalmani, V. Barone, B. Mennucci, G. A. Petersson, H. Nakatsuji, M. Caricato, X. Li, H. P. Hratchian, A. F. Izmaylov, J. Bloino, G. Zheng, J. L. Sonnenberg, M. Hada, M. Ehara, K. Toyota, R. Fukuda, J. Hasegawa, M. Ishida, T. Nakajima, Y. Honda, O. Kitao, H. Nakai, T. Vreven, J. A. Montgomery, Jr., J. E. Peralta, F. Ogliaro, M. Bearpark, J. J. Heyd, E. Brothers, K. N. Kudin, V. N. Staroverov, T. Keith, R. Kobayashi, J. Normand, K. Raghavachari, A. Rendell, J. C. Burant, S. S. Iyengar, J. Tomasi, M. Cossi, N. Rega, J. M. Millam, M. Klene, J. E. Knox,

 © 2014 The Authors. Published by Wiley-VCH Verlag GmbH & Co. KGaA, Weinheim

J. B. Cross, V. Bakken, C. Adamo, J. Jaramillo, R. Gomperts, R. E. Stratmann, O. Yazyev, A. J. Austin, R. Cammi, C. Pomelli, J. W. Ochterski, R. L. Martin, K. Morokuma, V. G. Zakrzewski, G. A. Voth, P. Salvador, J. J. Dannenberg, S. Dapprich, A. D. Daniels, O. Farkas, J. B. Foresman, J. V. Ortiz, J. Cioslowski, D. J. Fox, Gaussian, Inc., Wallingford CT, **2010**.

[42] W. D. Cornell, P. Cieplak, C. I. Bayly, I. R. Gould, K. M. Merz, Jr., D. M. Ferguson, D. C. Spellmeyer, T. Fox, J. W. Caldwell, P. A. Kollman, *J. Am. Chem. Soc.* **1995**, *117*, 5179 – 5197.

[43] P. J. Hay, W. R. Wadt, *J. Chem. Phys.* **1985**, *82*, 299 – 310.

[44] A. J. H. Wachters, *J. Chem. Phys.* **1970**, *52*, 1033 – 1036.

[45] a) A. K. Vardhaman, C. V. Sastri, D. Kumar, S. P. de Visser, *Chem. Commun.* **2011**, *47*, 11044 – 11046; b) A. K. Vardhaman, P. Barman, S. Kumar, C. V. Sastri, D. Kumar, S. P. de Visser, *Angew. Chem.* **2013**, *125*, 12514 – 12518; *Angew. Chem. Int. Ed.* **2013**, 52, 12288 – 12292.

Received: August 21, 2013
Published online on December 11, 2013

 © 2014 The Authors. Published by Wiley-VCH Verlag GmbH & Co. KGaA, Weinheim

ChemComm

RSC Publishing

COMMUNICATION

Mechanistic insight into halide oxidation by non-heme iron complexes. Haloperoxidase *versus* halogenase activity†

Cite this: *Chem. Commun.*, 2013, **49**, 10926

Received 5th September 2013, Accepted 8th October 2013

DOI: 10.1039/c3cc46792a

www.rsc.org/chemcomm

Anil Kumar Vardhaman,[a] Prasenjit Barman,[a] Suresh Kumar,[b] Chivukula V. Sastri,*[a] Devesh Kumar*[b] and Sam P. de Visser*[c]

This work presents the first detailed study on mechanistic aspects of halide oxidation by non-heme iron complexes. We show that while iron(III)–hydroperoxo complexes oxidise halides *via* oxygen atom transfer, the corresponding iron(IV)–oxo complex reacts *via* electron transfer.

A large variety of natural product biosynthesis reactions involve the halogenation of aromatic and aliphatic carbon centres.[1] Halogenating enzymes are divided into H_2O_2 required haloperoxidases (heme systems) and oxygen dependent halogenases (non-heme systems).[2,3] Over the years many heme containing haloperoxidases have been discovered that utilize chloride, bromide and iodide ions and in a reaction with hydrogen peroxide lead to hypohalide products.[4] The α-ketoglutarate dependent halogenases, by contrast, form a high-valent non-heme iron(IV)–oxo (halide) intermediate that abstracts a hydrogen atom from an aliphatic group and rebound the halide ligand to form a halogenated substrate in a stepwise radical process.[5] While haloperoxidases catalyse electrophilic halogenation (X^+) reactions, the non-heme iron halogenases, on the other hand, usually react *via* a radical process ($X^\bullet$).

Despite the fact that the enzymatic mechanism is well explored, surprisingly, few studies have been reported on analogous biomimetic models. As such, we report the first detailed mechanistic study on the reaction of halides with biomimetic iron(IV)–oxo complexes. The catalytic halogenation of organic substrates by these models was reported for a number of complexes that are likely to form a high-valent metal–oxo intermediate.[6] In addition, the reactivity of non-heme iron(III)–hydroperoxo intermediates as effective electrophilic oxidants in substrate halogenation has been reported, and it was found that under certain conditions they are catalytically more active than iron(IV)–oxo intermediates.[7] Further studies on the relative activity of non-heme iron(IV)–oxo *versus* iron(III)–hydroperoxo in aromatic hydroxylation and sulfoxidation of substrates have been reported.[8] To gain insight into the mechanistic pathways by non-heme iron(III)–hydroperoxo intermediates in electrophilic reactions, we decided to explore the direct reactivity of halides (X^- = F^-, Cl^-, Br^- and I^-) with $[Fe^{III}(OOH)(N4Py)]^{2+}$ (**1a**) and $[Fe^{III}(OOH)(Bn\text{-}tpen)]^{2+}$ (**2a**) and compare the kinetics with those of the corresponding iron(IV)–oxo complexes, *i.e.* $[Fe^{IV}(O)(N4Py)]^{2+}$ (**1b**) and $[Fe^{IV}(O)(Bn\text{-}tpen)]^{2+}$ (**2b**) (Fig. S1, ESI†).[9]

The iron(III)–hydroperoxo complexes, **1a** and **2a**, were generated *in situ* in a methanol solution at 253 K by addition of 10 equiv. of H_2O_2 following a reported procedure.[10] Subsequently, tetrabutyl ammonium halides (TBA–X; X = Cl^-, Br^-, I^-) were added to **1a** at the same temperature, which led to decay of the characteristic 548 nm peak in the UV-vis spectra. The second order rate constants extracted from these experiments (Fig. 1 and Table 1) showed a difference of as large as a factor of 6, and the reactivity decreased in the order $I^- > Br^- > Cl^-$. Surprisingly, the observed trend does not correlate with the electron affinities of these halides. Moreover, when TBA–F was added to **1a** no oxidation reaction of F^- was observed, which may be due to the fact that H_2O_2 lacks the thermodynamic potential to oxidize fluoride ions.[11]

In order to compare the reactivities of iron(III)–hydroperoxo with iron(IV)–oxo in halide oxidation, we generated **1b** and **2b** in CH_3CN using a procedure reported previously.[12] Addition of halides to **1b** under the same conditions as those for **1a** enabled us to evaluate the second order rate constants: **1b** reacted with halides (Cl^-, Br^-) with much lower rate constants than **1a**; *however, a reversal of the trend was observed in the presence of* I^-. In fact, for iodide oxidation, **1b** was found to react about six times faster than **1a**. This reversal in trend may be attributed to the steric factor influenced by the bulky I^- group upon approach of **1a**. Additionally, the reactivity of **1b** was found to be sensitive to the one electron oxidation potential of halides thus demonstrating that the reactivity of non-heme iron(IV)–oxo

[a] *Department of Chemistry, Indian Institute of Technology Guwahati, Assam 781039, India. E-mail: sastricv@iitg.ernet.in; Fax: +91-361-258-2349*

[b] *Department of Applied Physics, School for Physical Sciences, Babasaheb Bhimrao Ambedkar University, Vidya Vihar, Rai Bareilly Road, Lucknow 226 025, India. E-mail: dkclcre@yahoo.com*

[c] *Manchester Institute of Biotechnology and School of Chemical Engineering and Analytical Science, The University of Manchester, 131 Princess Street, Manchester M1 7DN, UK. E-mail: sam.devisser@manchester.ac.uk*

† Electronic supplementary information (ESI) available: Experimental and computational methods, and experimental and computational raw data in the form of tables and figures. See DOI: 10.1039/c3cc46792a

This journal is © The Royal Society of Chemistry 2013

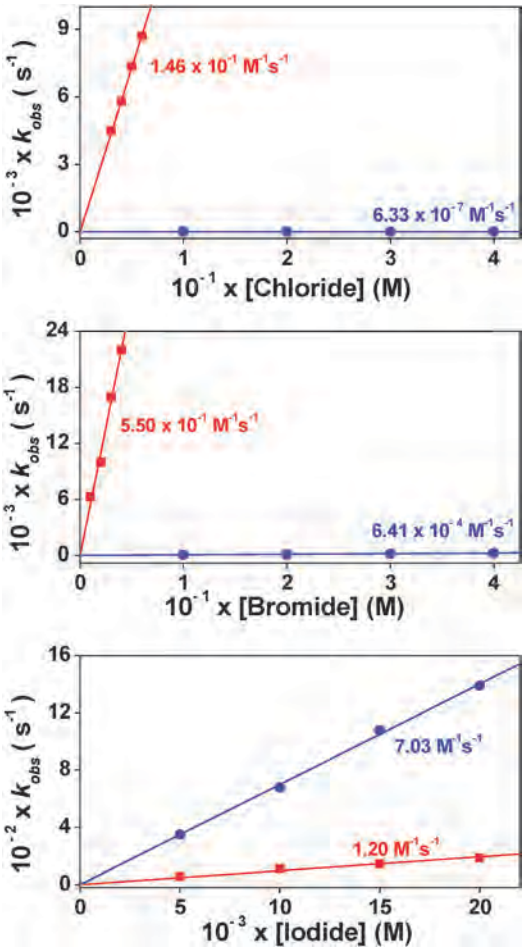

Fig. 1 Comparison of the second order rate constants for halide oxidation by **1a** (■) and **1b** (●) in the presence of (a) TBA-Cl, (b) TBA-Br and (c) TBA-I at 253 K.

Table 1 Second order rate constants for the oxidation of halides

	k_2 (M^{-1} s^{-1}) (253 K)			
X^-	**1a**	**1b**	**2a**	**2b**
Cl^-	1.46×10^{-1}	6.33×10^{-7}	4.00×10^{-2}	6.00×10^{-5}
Br^-	5.50×10^{-1}	6.41×10^{-4}	2.70×10^{-1}	1.00×10^{-2}
I^-	1.20	7.03	8.01×10^{-1}	19.01

complexes can be significantly affected by the identity of substrates. The difference in the reactivity between **1a** and **1b** was in the order of $\sim 10^3$ in the oxidation reaction of Br^- and increased to $\sim 10^5$ for Cl^-. A similar trend was observed when the halide oxidation reactions of **2a** and **2b** were compared.

To quantify the difference in the oxidation pathways for iron(III)–hydroperoxo and iron(IV)–oxo intermediates, we then made a plot of the second order rate constants log(k_2) against the one electron oxidation potential (E^0_{ox}) of these halides. A linear correlation was observed with a slope of –0.88 and –6.62 for **1a** and **1b** respectively (Fig. 2). Similar slopes were obtained for **2a** (–1.23) and **2b** (–5.16) (ESI†). Such large negative values of slopes from a plot of log(k_2) *versus* one electron oxidation potential implicates a rate determining electron transfer step in the reaction from halides to oxidants, *i.e.* **1b** and **2b**, rather than a group transfer.[13] The ease of a plausible electron transfer from I^- to

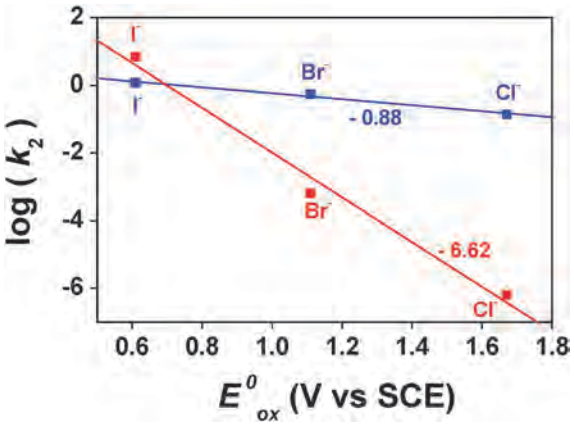

Fig. 2 Plot of log(k_2) against the one-electron oxidation potentials (E^0_{ox}) of halides of **1a** (■, blue) and **1b** (■, red) at 253 K.

iron(IV)–oxo can now account for the higher oxidation rates observed. The difference in the reaction mechanism for the oxidation of halides by iron(IV)–oxo as compared to iron(III)–hydroperoxo complexes can be attributed to the interactions of the negatively charged substrates with the electrophilic iron centre.

Further evidence of the mechanistic insights was obtained from the catalytic oxidation of anisole by **1a** and **1b** in the presence of TBA-Cl (see ESI† for details). These two chlorinating species yield different products with anisole. The oxidation of chloride involves either a one-electron oxidation ($Cl^- \rightarrow Cl^{\bullet} + e^-$) to form a chloride radical or an overall two electron oxidation ($Cl^- \rightarrow Cl^+ + 2e^-$) to give the chloronium ion. Chlorination by **1a** gave only monochlorinated products (*para* and *ortho* isomers). In stark contrast, the chlorination of anisole by **1b** gave a mixture of mono- and di-substituted chlorinated products, Scheme 1. The isomer distribution and product ratios indicate that the chlorinating agent in the presence of **1a** is Cl^+. The formation of di-substituted anisole and phenoxymethyl chloride is characteristic of free radical chlorination of anisole in the presence of **1b**.[14]

To gain further insight into the difference in reactivity of **1a** *versus* **1b** in a reaction with halides we performed a set of DFT studies on their reactivity with Br^-, as explained in detail in the ESI.†[15] Bromide oxidation by either **1a** or **1b** proceeds in a

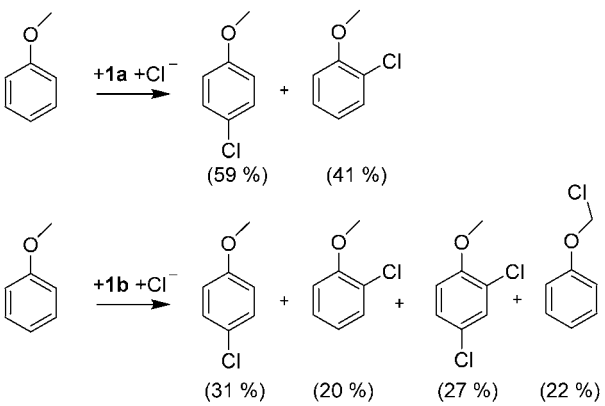

Scheme 1 Products obtained from the reaction of anisole with **1a** and **1b** in the presence of TBA-Cl at 298 K. The values in parentheses represent relative yields in mole%.

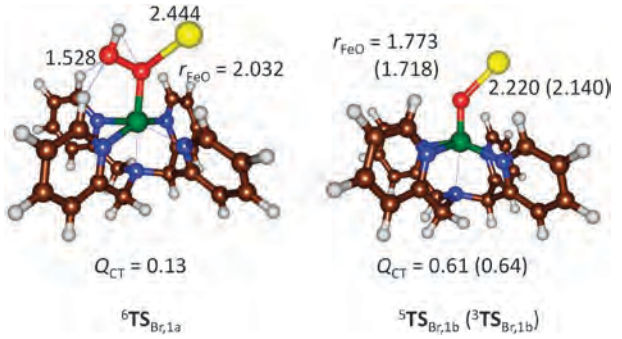

Fig. 3 Optimized geometries of bromide oxidation transition states by **1a** and **1b** with bond lengths (in Å) and spin densities and charges (in au).

concerted manner *via* a single transition state ($\mathbf{TS}_{Br}$) to form a product complex of hypobromide bound to iron(II)(N4Py). Fig. 3 displays the rate determining transition states for the reactions of **1a**/**1b** with Br^-. Geometrically, the reaction of **1a** with Br^- gives early transition states with longer O–Br distances as compared to the reaction of **1b** with Br^-. The large differences between the transition states, however, relate to the spin densities and charges. Thus, the iron(IV)–oxo complex reacts *via* an initial one-electron transfer to the substrate to produce a transition state with a large degree of radical character on the approaching halide: ρ_{Br} = −0.49 (−0.51) for $^5\mathbf{TS}_{Br}$ ($^3\mathbf{TS}_{Br}$), similar to what was observed before for electrophilic reaction mechanisms by non-heme iron(IV)–oxo complexes.[16] In addition, we calculated a large amount of charge transfer (Q_{CT}) from the oxidant to the substrate as obtained from the difference in charge of the halide in the reactant complex with respect to $\mathbf{TS}_{Br}$. This way, we obtained values of Q_{CT} to be 0.61 (0.64) for $^5\mathbf{TS}_{Br}$ ($^3\mathbf{TS}_{Br}$), respectively. On the other hand, the bromide oxidation transition state of **1a**, *i.e.* $^6\mathbf{TS}_{Br,1a}$, shows little changes in group spin densities with respect to the reactant complex and only a small degree of charge transfer (Q_{CT} = 0.13),[7] hence the iron(III)–hydroperoxo species reacts *via* group transfer rather than one-electron transfer.

These computational studies show that the electron transfer processes in electrophilic reaction mechanisms are dependent on the nature of the oxidant, whereby iron(IV)–oxo abstracts electrons early, whereas the electron transfer by iron(III)–hydroperoxo will happen after the transition state, on the way to product formation. The electron affinity difference of **1a** *versus* **1b** will, therefore, determine the electrophilic reaction rates with halides. We calculated electron affinities for **1a** and **1b** of ΔE + ZPE + E_{solv} = 102.6 and 108.7 kcal mol^{-1}, respectively. Thus, the larger electron affinity of the iron(IV)–oxo as compared to the iron(III)–hydroperoxo species will enable a much quicker and efficient electron transfer by the iron(IV)–oxo complexes. Indeed, the transition states show much earlier electron transfer from the iron(IV)–oxo as compared to the iron(III)–hydroperoxo species. These computational results are also in perfect agreement with the plot in Fig. 2 that shows a correlation of the reaction rate with the electron oxidation potential.

In summary, we reported a comparative study of the reactivity of non-heme iron(III)–hydroperoxo *versus* iron(IV)–oxo in halide oxidation reactions. We identified dramatic differences in the electron transfer processes for the two reactions, whereby iron(IV)–oxo reacts *via* a one-electron transfer and iron(III)–hydroperoxo by group transfer.

The authors acknowledge support from the Department of Science and Technology, India, for the Ramanujan Fellowship (SR/S2/RJN-11/2008) to DK and grants to CVS: SR/S1/IC-02/2009 and support from the Council for Scientific & Industrial Research (01(2527)/11/EMR-II). CPU time was provided by the National Service of Computational Chemistry Software (NSCCS) to SdV.

Notes and references

1 (*a*) G. W. Gribble, *J. Chem. Educ.*, 2004, **81**, 1441; (*b*) A. Butler and M. Sandy, *Nature*, 2009, **460**, 848.
2 (*a*) F. H. Vaillancourt, E. Yeh, D. A. Vosburg, S. Garneau-Tsodikova and C. T. Walsh, *Chem. Rev.*, 2006, **106**, 3364; (*b*) K. H. Van Peé, C. Dong, S. Flecks, J. Naismith, E. P. Patallo and T. Wage, *Adv. Appl. Microbiol.*, 2006, **59**, 127; (*c*) J. L. Anderson and S. K. Chapman, *Mol. Biosyst.*, 2006, **2**, 350; (*d*) D. G. Fujimori and C. T. Walsh, *Curr. Opin. Chem. Biol.*, 2007, **11**, 553.
3 L. P. Hager, D. R. Morris, F. S. Brown and H. Eberwein, *J. Biol. Chem.*, 1966, **241**, 1769.
4 (*a*) J. A. Manthey and L. P. Hager, *Biochemistry*, 1989, **28**, 3052; (*b*) J. A. Manthey and L. P. Hager, *J. Biol. Chem.*, 1985, **260**, 9654; (*c*) M. P. Roach, Y. P. Chen, S. A. Woodin, D. E. Lincoln, C. R. Lovell and J. H. Dawson, *Biochemistry*, 1997, **36**, 2197.
5 (*a*) C. Krebs, D. Galonić Fujimori, C. T. Walsh and J. M. Bollinger Jr, *Acc. Chem. Res.*, 2007, **40**, 484; (*b*) *Iron-containing enzymes: Versatile catalysts of hydroxylation reactions in nature*, ed. S. P. de Visser and D. Kumar, Royal Society of Chemistry Publishing, Cambridge, UK, 2011.
6 (*a*) T. Kojima, R. A. Leising, S. Yan and L. Que Jr., *J. Am. Chem. Soc.*, 1993, **115**, 11328; (*b*) A. Bakac, C. Shi and O. Pestovsky, *Inorg. Chem.*, 2004, **43**, 5416; (*c*) J. Y. Kravitz and V. L. Pecoraro, *Pure Appl. Chem.*, 2005, **77**, 1595; (*d*) P. Comba and S. Wunderlich, *Chem.–Eur. J.*, 2010, **16**, 7293; (*e*) W. Liu and J. T. Groves, *J. Am. Chem. Soc.*, 2010, **132**, 12847; (*f*) W. Liu, X. Huang, M.-J. Cheng, R. J. Nielsen, W. A. Goddard III and J. T. Groves, *Science*, 2012, **337**, 1322; (*g*) P. Galloni, M. Mancini, B. Floris and V. Conte, *Dalton Trans.*, 2013, **42**, 11963.
7 A. K. Vardhaman, C. V. Sastri, D. Kumar and S. P. de Visser, *Chem. Commun.*, 2011, **47**, 11044.
8 (*a*) A. Thibon, V. Jollet, C. Ribal, K. Sénéchal-David, L. Billon, A. B. Sorokin and F. Banse, *Chem.–Eur. J.*, 2012, **18**, 2715; (*b*) J. Cho, S. Jeon, S. A. Wilson, L. V. Liu, E. A. Kang, J. J. Braymer, M. H. Lim, B. Hedman, K. O. Hodgson, J. S. Valentine, E. I. Solomon and W. Nam, *Nature*, 2011, **478**, 502.
9 Abbreviations used: N4Py, *N*,*N*-bis(2-pyridylmethyl)-*N*-bis(2-pyridyl)-methylamine; Bn-tpen, *N*-benzyl-*N*,*N*′,*N*′-tris(2-pyridylmethyl)ethane-1,2-diamine.
10 (*a*) A. Hazell, C. J. McKenzie, L. P. Nielsen, S. Schindler and M. Weitzer, *J. Chem. Soc., Dalton Trans.*, 2002, 310; (*b*) K. D. Koehntop, J.-U. Rohde, M. Costas and L. Que Jr, *Dalton Trans.*, 2004, 3191.
11 (*a*) O. Nashiru, D. L. Zechel, D. Stoll, T. Mohammadzadeh, R. A. J. Warren and S. G. Withers, *Angew. Chem., Int. Ed.*, 2001, **40**, 417; (*b*) D. L. Zechel, S. P. Reid, O. Nashiru, C. Mayer, D. Stoll, D. L. Jakeman, R. A. J. Warren and S. G. Withers, *J. Am. Chem. Soc.*, 2001, **123**, 4350.
12 J. Kaizer, E. J. Klinker, N. Y. Oh, J.-U. Rohde, W. J. Song, A. Stubna, J. Kim, E. Münck, W. Nam and L. Que Jr., *J. Am. Chem. Soc.*, 2004, **126**, 472.
13 Y. Goto, T. Matsui, S.-I. Ozaki, Y. Watanabe and S. Fukuzumi, *J. Am. Chem. Soc.*, 1999, **121**, 9497.
14 F. S. Brown and L. P. Hager, *J. Am. Chem. Soc.*, 1967, **89**, 719.
15 (*a*) D. Kumar, W. Thiel and S. P. de Visser, *J. Am. Chem. Soc.*, 2011, **133**, 3869; (*b*) R. Latifi, M. A. Sainna, E. V. Rybak-Akimova and S. P. de Visser, *Chem.–Eur. J.*, 2013, **19**, 4058.
16 (*a*) D. Kumar, B. Karamzadeh, G. N. Sastry and S. P. de Visser, *J. Am. Chem. Soc.*, 2010, **132**, 7656; (*b*) D. Kumar, G. N. Sastry and S. P. de Visser, *Chem.–Eur. J.*, 2011, **17**, 6196.

 This journal is © The Royal Society of Chemistry 2013

Iron(IV)–Imido Complexes

DOI: 10.1002/anie.201305370

Comparison of the Reactivity of Nonheme Iron(IV)–Oxo versus Iron(IV)–Imido Complexes: Which is the Better Oxidant?**

Anil Kumar Vardhaman, Prasenjit Barman, Suresh Kumar, Chivukula V. Sastri, Devesh Kumar,* and Sam P. de Visser**

High-valent heme and nonheme iron(IV)–oxo complexes play key roles in biology as catalytic intermediates in enzymes, where they catalyze vital biotransformations for human health, including detoxification processes in the liver and also the biosynthesis of hormones.[1,2] Mono- and dioxygenases bind and utilize molecular oxygen on an iron center and form a catalytically active iron(IV)–oxo species that transfers the oxygen atom to substrate. Technically, using a nitrogen donor one should be able to synthesize the analogous iron(IV)–imido and/or iron(V)–nitrido complexes. Although these complexes are rare in nature, evidence exists of substrate aziridination by cytochrome P450 enzymes that presumably takes place by a high-valent iron(IV)–nitrido or –imido complex.[3] Several iron–porphyrin models with nitrene or imido ligands have been synthesized and their reactivity patterns implicated efficient aziridination of olefins.[4,5]

By contrast to iron(IV)–oxo complexes, which have been extensively studied over the years, only few studies have been reported on its closely related iron(V)–nitrido species ($Fe^{V}\equiv N$) or the iron(IV)–imido (Fe^{IV}=NR) species. In principle, these high-valent metal–nitrido/imido complexes should have strong oxidative power and capable to catalyze isolobal amination reactions. During the past decade, the chemistry of metal-catalyzed aziridination of alkenes and aminidation of aliphatic C–H bonds using iminoiodane reagents have been studied by several groups.[6,7] In recent years, the putative metal–nitrogen multiple-bonded species have been isolated and spectroscopically characterized, which led to significant progress on the understanding of its fundamental chemical properties.[6,8] However, details on its potential as nitrogen atom transfer agent are lacking and little knowledge exists in its relative reactivity with respect to the well-known iron(IV)–oxo species.[8h]

In nonheme iron chemistry, the aromatic amination of ligands by an iron–nitrido complex was reported by several groups,[6e,9] and recently, the spectroscopic characterization of the iron(IV)–tosylimido (tosylimido^{2-} = NTs) complex with pentadentate N4Py ligand (N4Py = *N*,*N*-bis(2-pyridylmethyl)-*N*-bis(2-pyridyl)methylamine), $[Fe^{IV}(NTs)(N4Py)]^{2+}$, was described (Figure 1).[10] As this species was shown to have a relatively long lifetime, it makes it highly suitable for reactivity studies, especially since the iron(IV)–oxo analogue can be studied in tandem. We therefore took the opportunity to pursue a comparative reactivity study of $[Fe^{IV}(NTs)(N4Py)]^{2+}$ (**1**) and $[Fe^{IV}(O)(N4Py)]^{2+}$ (**2**) with substrates.

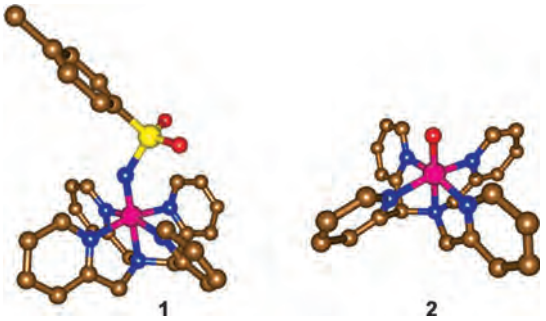

Figure 1. Structures of $[Fe^{IV}(NTs)(N4Py)]^{2+}$ (**1**) and $[Fe^{IV}(O)(N4Py)]^{2+}$ (**2**) derived from computational and crystallographic results. Hydrogen atoms are omitted for clarity. Fe magenta, C brown, O red, N blue, S yellow.

Complexes **1** and **2** were generated in an acetonitrile solution in situ using either PhINTs as tosylimido donor or PhIO as oxygen atom donor using procedures reported before.[10,11] The identity of complex **1** was confirmed on the basis of visible features with an intense LMCT band at 445 nm ($\varepsilon = 2700\ L\,mol^{-1}\,cm^{-1}$) and a low energy 660 nm band ($\varepsilon = 250\ L\,mol^{-1}\,cm^{-1}$) that arises from ligand field transitions characteristic for $S = 1$ iron(IV) complexes (Supporting Information, Figure S2). The electron spray ionization mass spectrum (Supporting Information, Figure S3) gave a major

[*] A. K. Vardhaman, P. Barman, Dr. C. V. Sastri
Department of Chemistry
Indian Institute of Technology Guwahati
Assam, 781039 (India)
E-mail: sastricv@iitg.ernet.in
S. Kumar, Dr. D. Kumar
Department of Applied Physics
Babasaheb Bhimrao Ambedkar University
School for Physical Sciences
Vidya Vihar, Rae Bareilly Road, Lucknow (UP), 226025 (India)
E-mail: dkclcre@yahoo.com
Dr. S. P. de Visser
Manchester Institute of Biotechnology and School of Chemical Engineering and Analytical Science, The University of Manchester
131 Princess Street, Manchester M1 7DN (United Kingdom)
E-mail: sam.devisser@manchester.ac.uk

[**] Research support was provided by the Department of Science and Technology, India (SR/S1/IC-02/2009) and Council for Scientific & Industrial Research (01(2527)/11/EMR-II) to C.V.S. The National Service of Computational Chemistry Software (NSCCS) is acknowledged for CPU time. D.K. acknowledges Department of Science and Technology (New Delhi) for a Ramanujan Fellowship.

Supporting information for this article is available on the WWW under http://dx.doi.org/10.1002/anie.201305370.

 © 2013 Wiley-VCH Verlag GmbH & Co. KGaA, Weinheim

peak at $m/z = 741.0751$ corresponding to {[Fe^{IV}(NTs)N4Py](OTf)}$^+$ with an isotope pattern that matches the theoretically expected distribution. Thioanisole was added to the solution of **1** at 273 K, which led to the decay of the characteristic peak at 660 nm in the UV/Vis spectrum concomitant with the appearance of its iron(II) precursor ($\lambda_{max} = 450$ nm) with an isosbestic point at 516 nm (Supporting Information, Figure S4). Aminidation of thioanisole to *N*-*p*-tosylmethylphenyl sulfilimine was obtained in about 85% yield,[12] and a second-order rate constant for this reaction was evaluated of 0.260 $L\,mol^{-1}\,s^{-1}$ (Supporting Information, Table S5). In contrast, the second-order rate constant for **2** determined under the same reaction conditions was found to be only 0.050 $L\,mol^{-1}\,s^{-1}$ (Figure 2a; Supporting Information, Table S6). It appears, therefore, that the [Fe^{IV}(NTs)(N4Py)]$^{2+}$ complex reacts with thioanisole with rate constants that are about five times higher than those found for the [Fe^{IV}(O)(N4Py)]$^{2+}$ complex.

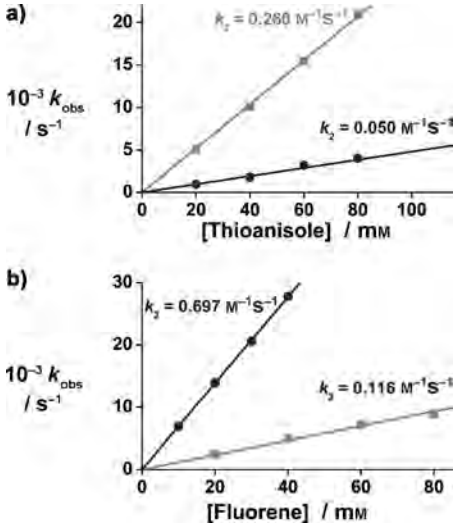

Figure 2. Second-order rate constants determined in the reactions of 1 mM [Fe^{IV}(NTs)(N4Py)]$^{2+}$ **1** (■) and [Fe^{IV}(O)(N4Py)]$^{2+}$ **2** (●) in CH_3CN solution against various concentrations of a) thioanisole at 273 K and b) fluorene at 298 K.

The pseudo first-order rate constants were then determined for the reaction of **1** and **2** with various *p*-substituted thioanisoles (Supporting Information, Table S7). From a direct comparison of the k_{obs} values for the reactions of **1** and **2** with different *para*-substituted thioanisoles, it is evident that the reactivity of **1** is more sensitive than that of **2** to substitution at the *para* position of the substrate. In fact, the difference in reactivity between **1** and **2** increased when electron-donating groups at the *para* position were employed; for instance, in the reaction with *p*-methoxythioanisole the difference in reactivity was found to be more than 50 times. We then created Hammett plots, for a quantitative examination of the substituent effect on the reaction rates. For **2**, a linear correlation with σ was found with a $\rho = -0.90$. In contrast, when a similar plot was made for **1**, non-linearity was observed with $\rho = -3.36$ (Supporting Information, Figure S8), which is likely as a result of additional stabilization of positive charge in the transition state by electron-donating groups in the *para* position of thioanisole and thus enhanced the overall rate of oxidation, as also will be discussed in the computational section. To accommodate the additional stabilization of the positive charge in the transition state, new Hammett plots were now made using σ^+ values leading to ρ values of -1.92 and -0.52, respectively, for **1** and **2** (Supporting Information, Figure S9). This difference is slopes quantitatively reflect that **1** is more sensitive to electronic effects of the *para* substituents than **2**. Further, the plot of $\log(k_X/k_H)$ values against the E^0_{ox} of sulfides gave a linear correlation with a slope of -7.1 and -1.92 for **1** and **2**, respectively (Supporting Information, Figure S10). Such a large negative slope obtained from these plots implicates a rate determining electron transfer from sulfides to **1** rather than a group transfer.[13]

Considering the high reactivity of **1** over **2** in the oxidation of thioanisole, we then evaluated the hydrogen atom transfer (HAT) capability of **1**. It has been shown that the rate constant of HAT reactions often correlates with the strength of the C–H bond that is broken, that is, BDE_{C-H} or bond dissociation energy,[14] we therefore studied the rates of HAT between **1** and substrates with a range of BDE_{C-H} values: xanthene, 9,10-dihydroanthracene (DHA), 1,4-cyclohexadiene (CHD), fluorene, and triphenylmethane. Indeed a plot of the logarithm of the rate constant of HAT by **1** versus the BDE_{C-H} value of the substrate gives a linear correlation, Figure 3, (Supporting Information, Table S11, Figure S12). However, when excess triphenylmethane ($BDE_{C-H} = 81$ kcal mol^{-1}) was added to a solution of **1** at 298 K, no change in 660 nm absorption band was observed, despite observable reactivity with fluorene, which has a comparable BDE_{C-H}.[11] Most probably the difference in reactivity between these two substrates with closely related BDE_{C-H} values is due to stereochemical clashes of **1** with the approaching substrate. This is particularly important for substrates with bulky groups adjacent to the hydrogen abstraction center, such as triphenylmethane.

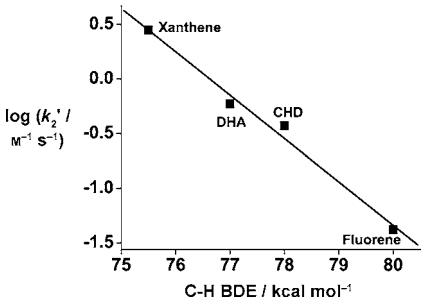

Figure 3. Correlation of the second-order rate constants (determined at 288 K) for HAT by **1** with BDE_{C-H} of substrates.

Subsequently, we compared the relative activity in HAT processes of **1** and **2** using fluorene as the substrate (Supporting Information, Table S13). The reaction of **1** and **2** follows pseudo first-order kinetics, and second-order rate constants were determined for each system (Figure 2b;

 © 2013 Wiley-VCH Verlag GmbH & Co. KGaA, Weinheim

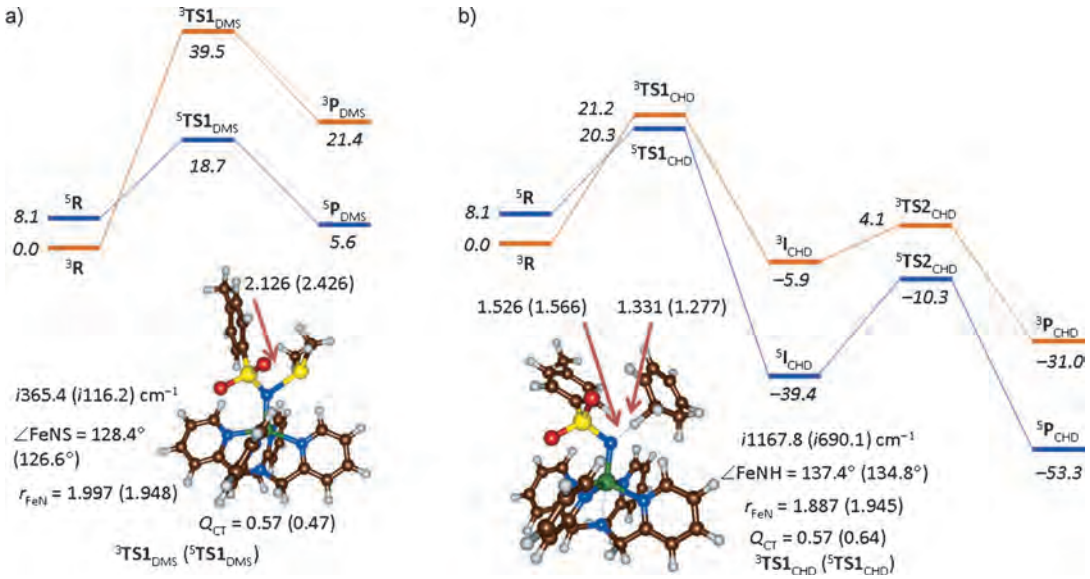

Figure 4. DFT calculated potential-energy landscapes for DMS sulfoxidation and hydrogen atom abstraction from CHD by $[Fe^{IV}(NTs)(N4Py)]^{2+}$. Energies are ΔG^{+} in kcal mol^{-1} relative to a reactant complex with solvent and dispersion energy corrections included. Also given are optimized geometries of the transition states with bond lengths [Å], the degree of charge transfer (Q_{CT}), and the imaginary frequency in the **TS** [cm^{-1}].

Supporting Information, Table S6). At 298 K, complex **1** decayed with a second order rate constant of 0.116 L mol^{-1} s^{-1} to form 9*H*,9′*H*-[9,9′]bifluorenyl (9,9′-bifluorene) products in about 32% yield. These results indicate that **1** effectively acts as a one-electron oxidizing agent in HAT reactions, whereby the 32% yield of 9,9′-bifluorene reflects the conversion of about 64% of iron(IV)–imido complex in two one-electron oxidation steps of fluorene. By comparison, complex **2** decays with a $k_2 =$ 0.697 L mol^{-1} s^{-1} to form fluorenone as the dominant product.[15] The observed slower rate (ca. 6 times) of **1** relative to **2** for C–H bond activation is opposite to that observed for thioanisole oxidation (see above). This observation indicates that iron(IV)–tosylimido complex is a less-effective oxidant than iron(IV)–oxo for hydrogen atom abstraction reactions. Indeed, recent computational studies on nonheme iron(IV)–oxo versus iron(IV)–nitrido complexes gave higher hydrogen atom abstraction barriers from methane for the latter system, in agreement with our results herein.[16]

Further evidence of a rate-determining HAT reaction comes from kinetic isotope effect (KIE) studies of **2** with fluorene (KIE = 30). Such large KIE values exceed the semi-classical limit and suggest strong tunneling behavior in the reaction mechanism. On the other hand, the reaction of deuterated fluorene with **1** gave a KIE of only 7, although it is still regarded as a HAT mechanism (Supporting Information, Figures S14, S15).

To gain insight into the details of the reaction mechanisms of substrate activation by iron(IV)–tosylimido complexes, we decided to do an additional density functional theory study and compare the work with the experimental work reported above and earlier computational studies on the reactivity of **2** with substrates.[17] We calculated the reaction mechanisms of **1** with dimethylsulfide (DMS) and CHD as model substrates for sulfoxidation and HAT reactions. Dehydrogenation of CHD is a stepwise process with two sequential hydrogen-atom abstraction barriers $\mathbf{TS1}_{CHD}$ and $\mathbf{TS2}_{CHD}$ by a radical intermediate $\mathbf{I}_{CHD}$ leading to benzene products $\mathbf{P}_{CHD}$. Figure 4 displays the calculated free energy landscapes and the rate-determining transition states (**TS1**) for the two reactions on the lowest lying triplet and quintet spin-state surfaces. Similar to previous studies, we find a concerted one-step,mechanism via a transition state $\mathbf{TS1}_{DMS}$ for substrate sulfoxidation by both **2** and **1**, leading to products $\mathbf{P}_{DMS}$.[18] Despite the fact that substrate sulfoxidation by either **1** or **2** appears to be concerted through a single rate-determining transition state, actually there are some critical differences between the two sulfoxidation processes that lead to changes in the Hammett plots for **1** versus **2**. In case of **1**, the analysis of the orbital occupation and group spin densities and charges of $^{3,5}\mathbf{TS1}_{DMS}$ shows that in the sulfoxidation transition states a large amount of charge transfer has taken place from substrate to oxidant; $Q_{CT} = 0.57$ (0.47) for $^3\mathbf{TS1}_{DMS}$ ($^5\mathbf{TS1}_{DMS}$), respectively. Furthermore, the orbital occupations and group spin densities (Supporting Information, Tables S18, S31) implicate a product-like electronic configuration. In contrast, the electron-transfer processes from substrate to iron(IV)–oxo happen at a much later timescale and give group spin densities much more in line with the reactant structure.[18] To find the origin of these differences in reactivity we calculated the electron affinities of **1** and **2**, which gave values of $\Delta E + \mathrm{ZPE} + E_{solv} =$ 120.5 and 94.6 kcal mol^{-1}, respectively. Therefore, **1** is more electrophilic than **2**.

The substrate sulfoxidation mechanism by $[Fe^{IV}(NTs)(N4Py)]^{2+}$ shows analogy to aromatic hydroxylation by **2**, where also a large energy difference between $^3\mathbf{TS1}$ and $^5\mathbf{TS1}$ was calculated.[17b] However, there are critical differences and one relates to the orientation of the substrate. Thus, on the quintet spin-state surface the substrate usually attacks from the top and aligns itself along the Fe–O/N bond owing to

© 2013 Wiley-VCH Verlag GmbH & Co. KGaA, Weinheim

electron transfer into the $\sigma^*_{z^2}$ orbital.[17,19] In $[Fe^{IV}(NTs)(N4Py)]^{2+}$ this alignment is not possible because of stereochemical constraints of the NTs group with the approaching substrate and thus a more sideways approach is essential. As a consequence, the quintet spin barriers have increased in energy and in the case of HAT from CHD ^{5}**TS1**$_{CHD}$ is competitive with ^{3}**TS1**$_{CHD}$. These studies support the experimental observation mentioned above that **2** will be better in catalyzing HAT reaction mechanisms owing to lesser stereochemical interactions between substrate and oxidant as compared to **1**. Furthermore, the stereochemical interactions between oxidant and the approaching substrate destabilize the transition states and increase the HAT process for **1**. This effect is larger for HAT processes by **1** than by **2** as the (almost) linearity of the Fe-O-H angle in the quintet spin state will ensure large distances between the rest of the substrate and the oxidant. Approach under an angle of 120° as in **1**, however, brings the substrate closer to the equatorial ligand of the oxidant and hence stereochemical repulsions are larger and barriers are raised. As a consequence, the HAT barriers for **1** are above those for **2** in support of the experimental rate constants in Figure 2.

The dehydrogenation reaction has low barriers **TS1**$_{CHD}$ on the triplet and quintet spin states, leading to a radical intermediate. However, the subsequent dehydrogenation of hydrogen atom abstraction via **TS2** encounters significantly larger barriers of well over $\Delta G + E_{solv} > 25$ kcal mol^{-1}, and consequently will be difficult. Instead theory predicts that the radical will dissipate from the reaction center rather than donating a second hydrogen atom to the oxidant. A subsequent collision of two of these radicals will then form a dimer at much lower energetic costs than dehydrogenation products, which is indeed what was observed experimentally. The fact that these dimers are not formed in the reaction of **1** with triphenylmethane may be due to stereochemical restrictions in dimer formation. The large **TS2** barrier obtained for the reaction of **1** with CHD contrasts that found for the reaction of **2** with CHD, where typically barriers of less than 5 kcal mol^{-1} are obtained.[20] This change in **TS2** barrier leads to fundamental differences in substrate activation and consequently product distributions.

So what is the origin of the differences in reactivity of **1** over **2** and why is sulfoxidation preferred for **1**, whereas hydrogen atom abstraction is favored by **2**? Hydrogen atom abstraction is accompanied by the breaking of the C–H bond of the substrate and the formation of an O/N–H bond with the oxidant. It has been shown that hydrogen atom abstraction barriers tend to correlate with the BDE_{C-H} bond of the substrate as well as the BDE_{O-H} bond of the oxidant.[14,21] We calculated values of $BDE_{N-H} = 94.4$ kcal mol^{-1} and $BDE_{O-H} = 96.7$ kcal mol^{-1} for **1** and **2**, respectively, which implies that **2** and **1** should be similarly good oxidants of HAT reactions. Instead, differences in HAT catalysis are most likely originated by stereochemical repulsions of the approaching substrate with the oxidant. Thus, as shown in Figure 4, during HAT the substrate attacks the NTs group under an angle Fe-N-H of 137.4° (134.8°) for ^{3}**TS**$_{CHD}$ (^{5}**TS**$_{CHD}$), respectively, whereas in $[Fe^{IV}(O)(N4Py)]^{2+}$ the approach will be along the Fe–O axis in the quintet spin state.[22] Consequently, the attack of substrate on **1** will be more stereochemically constraint than in **2** and thus generally higher barriers for HAT reactions.

In summary, we present herein the first comparative study on the reactivity patterns of nonheme iron(IV)–oxo versus iron(IV)–imido. We show that owing to the larger electron affinity of the oxidant iron(IV)–imido is a better oxidant of sulfoxidation reactions than iron(IV)–oxo. By contrast, these trends are reversed for stepwise one-electron transfer reactions, such as hydrogen atom abstraction reactions where stereochemical interactions upon substrate approach determine the relative rate constants.

Experimental Section

Detailed procedures and methods of the experiments and computations, which follow those of our previous studies in the field,[23] are given in detail in the Supporting Information.

Received: June 21, 2013
Revised: August 12, 2013
Published online: September 25, 2013

Keywords: C–H activation · enzyme models · imido ligands · iron · sulfoxidation

[1] a) M. Sono, M. P. Roach, E. D. Coulter, J. H. Dawson, *Chem. Rev.* **1996**, *96*, 2841 – 2888; b) J. T. Groves, *Proc. Natl. Acad. Sci. USA* **2003**, *100*, 3569 – 3574; c) *Cytochrome P450: Structure, Mechanism and Biochemistry*, 3rd ed. (Ed.: P. R. Ortiz de Montellano), Kluwer Academic/Plenum Publishers, New York, **2004**; d) *Handbook of Porphyrin Science* (Eds.: K. M. Kadish, K. M. Smith, R. Guilard), World Scientific Publishing Co., New Jersey, **2010**; e) *Iron-containing enzymes: Versatile catalysts of hydroxylation reactions in nature* (Eds.: S. P. de Visser, D. Kumar), RSC Publishing, Cambridge, **2011**.

[2] a) M. Costas, M. P. Mehn, M. P. Jensen, L. Que, Jr., *Chem. Rev.* **2004**, *104*, 939 – 986; b) S. V. Kryatov, E. V. Rybak-Akimova, S. Schindler, *Chem. Rev.* **2005**, *105*, 2175 – 2226; c) M. M. Abu-Omar, A. Loaiza, N. Hontzeas, *Chem. Rev.* **2005**, *105*, 2227 – 2252; d) R. van Eldik, *Coord. Chem. Rev.* **2007**, *251*, 1649 – 1662; e) P. C. A. Bruijnincx, G. van Koten, R. J. M. Klein Gebbink, *Chem. Soc. Rev.* **2008**, *37*, 2716 – 2744; f) A. R. McDonald, L. Que, Jr., *Coord. Chem. Rev.* **2013**, *257*, 414 – 428.

[3] a) R. E. White, M. B. McCarthy, *J. Am. Chem. Soc.* **1984**, *106*, 4922 – 4926; b) E. W. Svastits, J. H. Dawson, R. Breslow, S. H. Gellman, *J. Am. Chem. Soc.* **1985**, *107*, 6427 – 6428; c) J. Hohenberger, K. Ray, K. Meyer, *Nat. Commun.* **2012**, *3*, 1 – 13.

[4] a) D. Mansuy, P. Battioni, J.-P. Mahy, *J. Am. Chem. Soc.* **1982**, *104*, 4487 – 4489; b) J.-P. Mahy, P. Battioni, D. Mansuy, J. Fisher, R. Weiss, J. Mispelter, I. Morgenstern-Badarau, P. Gans, *J. Am. Chem. Soc.* **1984**, *106*, 1699 – 1706; c) J.-P. Mahy, P. Nattioni, D. Mansuy, *J. Am. Chem. Soc.* **1986**, *108*, 1079 – 1080.

[5] a) C.-M. Che, C.-Y. Zhou, E. L.-M. Wong, *Top. Organomet. Chem.* **2011**, *33*, 111 – 138; b) T. W.-S. Chow, G.-Q. Chen, Y. Liu, C.-Y. Zhou, C.-M. Che, *Pure Appl. Chem.* **2012**, *84*, 1685 – 1704.

[6] a) J. F. Berry, E. Bill, E. Bothe, S. DeBeer George, B. Mienert, F. Neese, K. Wieghardt, *Science* **2006**, *312*, 1937 – 1941; b) P. Comba, C. Lang, C. Lopez de Laorden, A. Muruganatham, G. Rajaraman, H. Wadepohl, M. Zajaczkowski, *Chem. Eur. J.* **2008**, *14*, 5313 – 5328; c) K. L. Klotz, L. M. Slominski, M. E. Riemer, J. A. Phillips, J. A. Halfen, *Inorg. Chem.* **2009**, *48*, 801 – 803; d) J. J. Scepaniak, J. A. Young, R. P. Bontchev, J. M. Smith,

 © 2013 Wiley-VCH Verlag GmbH & Co. KGaA, Weinheim

Angew. Chem. **2009**, *121*, 3204 – 3206; *Angew. Chem. Int. Ed.* **2009**, *48*, 3158 – 3160; e) P. Leeladee, G. N. L. Jameson, M. A. Siegler, D. Kumar, S. P. de Visser, D. P. Goldberg, *Inorg. Chem.* **2013**, *52*, 4668 – 4682.

[7] a) M. J. Zdilla, M. M. Abu-Omar, *J. Am. Chem. Soc.* **2006**, *128*, 16971 – 16979; b) S. Kundu, E. Miceli, E. Farquhar, F. F. Pfaff, U. Kuhlmann, P. Hildebrandt, B. Braun, C. Greco, K. Ray, *J. Am. Chem. Soc.* **2012**, *134*, 14710 – 14713; c) J. W. W. Chang, P. W. H. Chan, *Angew. Chem.* **2008**, *120*, 1154 – 1156; *Angew. Chem. Int. Ed.* **2008**, *47*, 1138 – 1140.

[8] a) T. Petrenko, S. DeBeer George, N. Aliaga-Alcalde, E. Bill, B. Mienert, Y. Xiao, Y. S. Guo, W. Sturhahn, S. P. Cramer, K. Wieghardt, F. Neese, *J. Am. Chem. Soc.* **2007**, *129*, 11053 – 11060; b) R. E. Cowley, N. A. Eckert, S. Vaddadi, T. M. Figg, T. R. Cundari, P. L. Holland, *J. Am. Chem. Soc.* **2011**, *133*, 9796 – 9811; c) M. P. Mehn, J. C. Peters, *J. Inorg. Biochem.* **2006**, *100*, 634 – 643; d) C. M. Thomas, N. P. Mankad, J. C. Peters, *J. Am. Chem. Soc.* **2006**, *128*, 4956 – 4957; e) I. Nieto, F. Ding, R. P. Bontchev, H. Wang, J. M. Smith, *J. Am. Chem. Soc.* **2008**, *130*, 2716 – 2717; f) E. R. King, E. T. Hennessy, T. A. Betley, *J. Am. Chem. Soc.* **2011**, *133*, 4917 – 4923; g) Y. Liu, X. Guan, E. L. M. Wong, P. Liu, J. S. Huang, C.-M. Che, *J. Am. Chem. Soc.* **2013**, *135*, 7194 – 7204; h) E. T. Hennessy, T. A. Betley, *Science* **2013**, *340*, 591 – 595.

[9] a) M. P. Jensen, M. P. Mehn, L. Que, Jr., *Angew. Chem.* **2003**, *115*, 4493 – 4496; *Angew. Chem. Int. Ed.* **2003**, *42*, 4357 – 4360; b) H. S. Soo, M. T. Sougrati, F. Grandjean, G. J. Long, C. J. Chang, *Inorg. Chim. Acta* **2011**, *369*, 82 – 91.

[10] E. J. Klinker, T. A. Jackson, M. P. Jensen, A. Stubna, G. Juhász, E. L. Bominaar, E. Münck, L. Que, Jr., *Angew. Chem.* **2006**, *118*, 7554 – 7557; *Angew. Chem. Int. Ed.* **2006**, *45*, 7394 – 7397.

[11] J. Kaizer, E. J. Klinker, N. Y. Oh, J.-U. Rohde, W. J. Song, A. Stubna, J. Kim, E. Münck, W. Nam, L. Que, Jr., *J. Am. Chem. Soc.* **2004**, *126*, 472 – 473.

[12] Small amounts (< 15 %) of methylphenylsulfoxide products were detected that are likely to be due to hydrolysis of sulfilimine.

[13] a) Y. Goto, T. Matsui, S.-I. Ozaki, Y. Watanabe, S. Fukuzumi, *J. Am. Chem. Soc.* **1999**, *121*, 9497 – 9502; b) J. Park, Y. Morimoto, Y.-M. Lee, W. Nam, S. Fukuzumi, *J. Am. Chem. Soc.* **2011**, *133*, 5236 – 5239.

[14] a) L. E. Friedrich, *J. Org. Chem.* **1983**, *48*, 3851 – 3852; b) F. G. Bordwell, J.-P. Cheng, *J. Am. Chem. Soc.* **1991**, *113*, 1736 – 1743; c) C. V. Sastri, J. Lee, K. Oh, Y. J. Lee, J. Lee, T. A. Jackson, K, Ray, H. Hirao, W. Shin, J. A. Halfen, J. Kim, L. Que, Jr., S. Shaik, W. Nam, *Proc. Natl. Acad. Sci. USA* **2007**, *104*, 19181 – 19186; d) J. J. Warren, T. A. Tronic, J. M. Mayer, *Chem. Rev.* **2010**, *110*, 6961 – 7001; e) K. A. Prokop, S. P. de Visser, D. P. Goldberg, *Angew. Chem.* **2010**, *122*, 5217 – 5221; *Angew. Chem. Int. Ed.* **2010**, *49*, 5091 – 5095.

[15] J. R. Bryant, J. M. Mayer, *J. Am. Chem. Soc.* **2003**, *125*, 10351 – 10361.

[16] H. Tang, J. Guan, H. Liu, X. Huang, *Inorg. Chem.* **2013**, *52*, 2684 – 2696.

[17] a) H. Hirao, D. Kumar, L. Que, Jr., S. Shaik, *J. Am. Chem. Soc.* **2006**, *128*, 8590 – 8606; b) S. P. de Visser, K. Oh, A.-R. Han, W. Nam, *Inorg. Chem.* **2007**, *46*, 4632 – 4641; c) S. P. de Visser, *J. Am. Chem. Soc.* **2010**, *132*, 1087 – 1097.

[18] a) S. Aluri, S. P. de Visser, *J. Am. Chem. Soc.* **2007**, *129*, 14846 – 14847; b) D. Kumar, S. P. de Visser, P. K. Sharma, H. Hirao, S. Shaik, *Biochemistry* **2005**, *44*, 8148 – 8158; c) D. Kumar, G. N. Sastry, S. P. de Visser, *Chem. Eur. J.* **2011**, *17*, 6196 – 6205.

[19] a) S. P. de Visser, *J. Am. Chem. Soc.* **2006**, *128*, 15809 – 15818; b) C. Y. Geng, S. F. Ye, F. Neese, *Angew. Chem.* **2010**, *122*, 5853 – 5856; *Angew. Chem. Int. Ed.* **2010**, *49*, 5717 – 5720; c) S. Sahu, L. R. Widger, M. G. Quesne, S. P. de Visser, H. Matsumura, P. Moënne-Loccoz, M. A. Siegler, D. P. Goldberg, *J. Am. Chem. Soc.* **2013**, *135*, 10590 – 10593.

[20] a) R. Latifi, M. A. Sainna, E. V. Rybak-Akimova, S. P. de Visser, *Chem. Eur. J.* **2013**, *19*, 4058 – 4068; b) S. M. Pratter, C. Konstantinovics, C. L. M. DiGiuro, E. Leitner, D. Kumar, S. P. de Visser, G. Grogan, G. D. Straganz, *Angew. Chem.* **2013**, *125*, 9859 – 9863; *Angew. Chem. Int. Ed.* **2013**, *52*, 9677 – 9681.

[21] a) J. M. Mayer, *Acc. Chem. Res.* **1998**, *31*, 441 – 450; b) J. Yoon, S. A. Wilson, Y. K. Jang, M. S. Seo, K. Nehru, B. Hedman, K. O. Hodgson, E. Bill, E. I. Solomon, W. Nam, *Angew. Chem.* **2009**, *121*, 1283 – 1286; *Angew. Chem. Int. Ed.* **2009**, *48*, 1257 – 1260; c) D. E. Lansky, D. P. Goldberg, *Inorg. Chem.* **2006**, *45*, 5119 – 5125.

[22] a) S. P. de Visser, *J. Am. Chem. Soc.* **2006**, *128*, 9813 – 9824; b) D. Kumar, W. Thiel, S. P. de Visser, *J. Am. Chem. Soc.* **2011**, *133*, 3869 – 3882.

[23] A. K. Vardhaman, C. V. Sastri, D. Kumar, S. P. de Visser, *Chem. Commun.* **2011**, *47*, 11044 – 11046.

 © 2013 Wiley-VCH Verlag GmbH & Co. KGaA, Weinheim

Inorganic Chemistry

Article

pubs.acs.org/IC

Synthesis and Ligand Non-Innocence of Thiolate-Ligated (N_4S) Iron(II) and Nickel(II) Bis(imino)pyridine Complexes

Leland R. Widger,[†] Yunbo Jiang,[†] Maxime A. Siegler,[†] Devesh Kumar,[⊥] Reza Latifi,[§] Sam P. de Visser,*[,§] Guy N. L. Jameson,*[,‡] and David P. Goldberg*[,†]

[†]Department of Chemistry, The Johns Hopkins University, 3400 North Charles Street, Baltimore, Maryland 21218, United States

[‡]Department of Chemistry, and MacDiarmid Institute for Advanced Materials and Nanotechnology, University of Otago, PO Box 56, Dunedin 9054, New Zealand

[§]Manchester Institute of Biotechnology and School of Chemical Engineering and Analytical Science, The University of Manchester, 131 Princess Street, Manchester M1 7DN, United Kingdom

[⊥]Department of Applied Physics, School for Physical Sciences, Babasaheb Bhimrao Ambedkar University, Vidya Vihar, Rae Bareilly Road, Lucknow (U. P.) 226 025, India

Supporting Information

ABSTRACT: The known iron(II) complex [$Fe^{II}(LN_3S)$-(OTf)] (**1**) was used as starting material to prepare the new biomimetic (N_4S(thiolate)) iron(II) complexes [$Fe^{II}(LN_3S)$-(py)](OTf) (**2**) and [$Fe^{II}(LN_3S)$(DMAP)](OTf) (**3**), where LN_3S is a tetradentate bis(imino)pyridine (BIP) derivative with a covalently tethered phenylthiolate donor. These complexes were characterized by X-ray crystallography, ultraviolet−visible (UV-vis) spectroscopic analysis, ^{1}H nuclear magnetic resonance (NMR), and Mössbauer spectroscopy, as well as electrochemistry. A nickel(II) analogue, [$Ni^{II}(LN_3S)$](BF_4) (**5**), was also synthesized and characterized by structural and spectroscopic methods. Cyclic voltammetric studies showed **1**−**3** and **5** undergo a single reduction process with $E_{1/2}$ between −0.9 V to −1.2 V versus Fc^+/Fc. Treatment of **3** with 0.5% Na/Hg amalgam gave the monoreduced complex [$Fe(LN_3S)$(DMAP)]^0 (**4**), which was characterized by X-ray crystallography, UV-vis spectroscopic analysis, electron paramagnetic resonance (EPR) spectroscopy (g = [2.155, 2.057, 2.038]), and Mössbauer (δ = 0.33 mm s^{-1}; ΔE_Q = 2.04 mm s^{-1}) spectroscopy. Computational methods (DFT) were employed to model complexes **3**−**5**. The combined experimental and computational studies show that **1**−**3** are 5-coordinate, high-spin (S = 2) Fe^{II} complexes, whereas **4** is best described as a 5-coordinate, intermediate-spin (S = 1) Fe^{II} complex antiferromagnetically coupled to a ligand radical. This unique electronic configuration leads to an overall doublet spin (S_{total} = 1/2) ground state. Complexes **2** and **3** are shown to react with O_2 to give S-oxygenated products, as previously reported for **1**. In contrast, the monoreduced **4** appears to react with O_2 to give a mixture of sulfur oxygenates and iron oxygenates. The nickel(II) complex **5** does not react with O_2, and even when the monoreduced nickel complex is produced, it appears to undergo only outer-sphere oxidation with O_2.

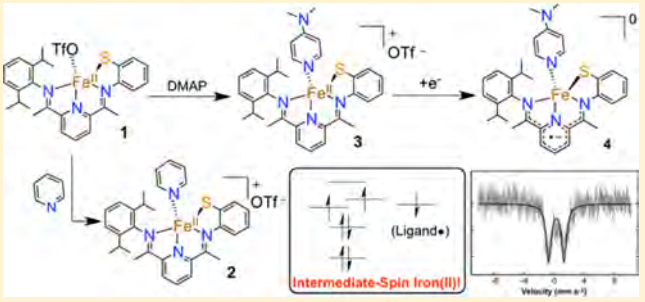

INTRODUCTION

Thiolate-ligated non-heme iron sites play key roles in biology, exhibiting diverse structural features as well as contributing to a wide range of reactivity.[1−7] The mononuclear, thiolate-ligated non-heme iron enzymes superoxide reductase,[8−12] nitrile hydratase,[13−15] and cysteine dioxygenase (CDO)[16−23] utilize single iron sites coordinated in mixed N/S ligand environments. Work by some of us has focused on the preparation of synthetic analogues of these sites, including some of the first structural and functional models of CDO.[1,24−33] A bis(imino)-pyridine (BIP) ligand scaffold was employed, leading to the synthesis of $Fe^{II}(LN_3S)$ complexes that mimicked certain structural and functional features of CDO.[24,25] The key thiolate donor was incorporated into these complexes by either covalent attachment to the BIP backbone, or by addition of an exogenous phenylthiolate (PhS^-) ligand to the iron(II) center, yielding $Fe^{II}(N_3S)$ complexes in both cases. These complexes were among the first mononuclear thiolato-iron(II) complexes to selectively react with O_2 to give S-oxygenated products, reproducing the gross reactivity of the enzymatic system. However, the Cys-bound iron(II) form of CDO contains an iron center held in an (N_4S) donor set, comprised of three His ligands and one Cys substrate chelated through both the amino and side-chain S groups. Thus, we are currently interested in the design and synthesis of $Fe^{II}(N_4S)$ complexes in which a fourth neutral N donor is included in the first coordination

Received: May 29, 2013
Published: August 30, 2013

 © 2013 American Chemical Society dx.doi.org/10.1021/ic4013558 | Inorg. Chem. 2013, 52, 10467−10480

sphere to more closely match the active site of CDO prior to S-oxygenation.

Herein, we describe the synthesis, spectroscopic characterization and O_2 reactivity of a new series of $Fe^{II}(N_4S)$ complexes (Figure 1) that contain a covalently linked, BIP-derived ligand

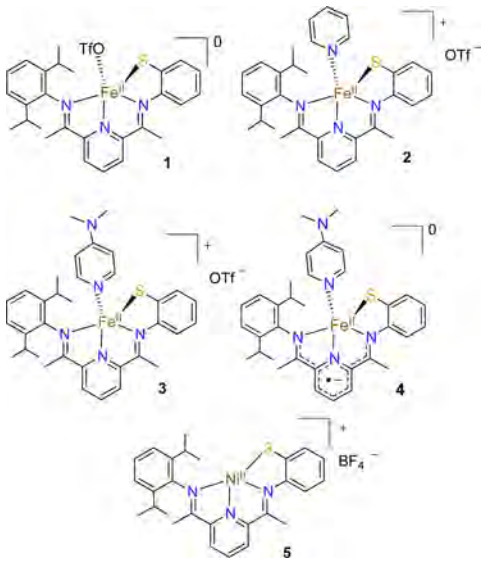

Figure 1. Complexes described in the present study.

providing an N_3S(thiolate) donor set (LN_3S^-), and a fourth N donor derived from exogenous pyridine derivatives. The general synthetic strategy was to incorporate a fourth N donor without the need for covalent modification of the BIP backbone. This strategy proved productive, and the new iron(II) complexes $[Fe^{II}(LN_3S)(py)](OTf)$ (**2**) and $[Fe^{II}(LN_3S)(DMAP)](OTf)$ (**3**) were synthesized and characterized by X-ray crystallography, NMR, electrochemistry, Mössbauer spectroscopy and density functional theory (DFT) calculations. A nickel(II) analogue, $[Ni^{II}(LN_3S)](BF_4)$ (**5**), was also prepared for comparative spectroscopic and reactivity studies.

The BIP platform is also well-known to behave as a non-innocent ligand, allowing for the storage of multiple reducing equivalents on the ligand backbone. The BIP framework has been shown to accept up to three electrons, which are stabilized by delocalization over the conjugated ligand scaffold.[34−45] However, the reduced analogues of these BIP complexes are generally restricted to derivatives in which only minor changes to the aryl substitution patterns on the imino positions have been made, with no major modification of the chelating abilities of the BIP framework. There is significant interest in the development of non-innocent, polydentate ligands for their use as redox-active partners in combination with metal ions to assist with various chemical transformations such as the reduction of small-molecules (e.g., CO_2, N_2) and other redox reactions. With the thiolate-modified LN_3S system in hand, we thus wanted to determine if it could also function as a non-innocent ligand, perhaps stabilizing one or more reducing equivalents across the ligand backbone. A question to be addressed concerns the influence of the additional, covalently linked phenylthiolate arm on the stability, spin delocalization, and spectroscopic and redox properties of possible (multi)reduced ligand−metal complexes. It is also of interest to determine if multiple reducing equivalents stored on both the ligand and the metal can be employed together for the activation of O_2, and how this combination will affect subsequent sulfur- or metal-based oxygenation steps.

The new complexes $[Fe^{II}(LN_3S)(py)]OTf$ (**2**), $[Fe^{II}(LN_3S)(DMAP)]OTf$ (**3**) and $[Ni^{II}(LN_3S)]BF_4$ (**5**) were shown to accept a single electron to give the respective monoreduced products. In one case, successful crystallization of the monoreduced species was achieved, and the structure of $[Fe(LN_3S)(DMAP)]^0$ (**4**) was obtained by X-ray crystallography. A detailed experimental and computational (DFT) investigation into the electronic and structural properties of **4**, as well as the other monoreduced analogues, was conducted, revealing several insights regarding the interplay between the structures and the electronic configurations of these complexes. The influence of the strong field thiolate donor, the extent of non-innocence in the BIP ligand, and the oxidation and spin state of the metal center are addressed. A major finding from these studies is that complex **4**, based on experimental and computational results, is a monoreduced bis(imino)pyridine complex with an intermediate-spin iron(II) center coupled with a stable ligand-based radical.

The O_2 reactivity of these complexes was also examined, and for the starting iron(II) complexes **2** and **3**, selective S-oxygenation to give sulfonato (RSO_3^-) products was observed, as seen previously for $[Fe^{II}(LN_3S)(OTf)]$ (**1**).[24] In contrast, the monoreduced complex **4** reacts with O_2, leading to a mixture of products that suggest both iron oxygenation and sulfur oxygenation readily occur for this monoreduced species. However, both the Ni^{II} complex **5**, and its monoreduced analog, do not exhibit any sulfur-based or metal-based oxygenation in the presence of O_2, even after prolonged reaction times. This lack of reactivity is in contrast to the iron analogues, as well as some nickel-thiolate complexes that do react with O_2 to give sulfur-oxygenated sulfinato and sulfonato products, although these reactions can be sluggish.[46−54]

EXPERIMENTAL SECTION

General Procedures. All reagents were purchased from commercial vendors and used without further purification, unless noted otherwise. All reactions were carried out under an atmosphere of N_2 inside a glovebox or under an argon atmosphere by standard Schlenk and vacuum line techniques. Ultraviolet−visible (UV-vis) spectra were recorded on an Agilent 8453 photodiode array spectrophotometer. Electron paramagnetic resonance (EPR) spectra were obtained on a Bruker EMX EPR spectrometer that was controlled using a Bruker ER 041 X G microwave bridge at 15 K. The EPR spectrometer was equipped with a continuous-flow liquid helium cryostat and an ITC503 temperature controller made by Oxford Instruments, Inc. Nuclear magnetic resonance (NMR) was performed on a Bruker Avance 400 MHz FT-NMR spectrometer at 25 °C. Elemental analysis was performed by Atlantic Microlab, Inc. (Norcross, GA). LDI-ToF mass spectra were obtained using a Bruker Autoflex III Maldi ToF/ToF instrument (Billerica, MA). Samples were dissolved in CH_2Cl_2 and deposited on the target plate in the absence of any added matrix. Samples were irradiated with a 355-nm UV laser and mass-analyzed by ToF mass spectrometry in reflectron mode. $Fe^{II}(LN_3S)(OTf)$ (**1**) was prepared according to a literature procedure.[24] ^{57}Fe Mössbauer spectra were recorded on a Mössbauer spectrometer from SEE Co. (Science Engineering & Education Co., Edina, MN) equipped with a closed-cycle refrigerator system from Janis Research Co. and Sumitomo Heavy Industries, Ltd. (SHI)). Approximately 10 mg of sample was placed in a custom sample holder made from Teflon and specifically designed for solid samples. Data were collected in constant acceleration mode in transmission geometry with an applied field of 47 mT parallel to the γ-rays. The zero velocity of the Mössbauer spectra refers to the centroid of the room

dx.doi.org/10.1021/ic4013558 | Inorg. Chem. 2013, 52, 10467−10480

temperature spectrum of a 25 μm metallic iron foil. Analysis of the spectra was conducted using the WMOSS program (SEE Co., formerly WEB Research Co., Edina, MN).

Computational Methods. Density functional theory calculations were performed on complexes **3**–**5**, using methods and procedures that we have tested and calibrated previously.[55,56] The complexes were calculated in several possible spin states. The spin state ordering of transition-metal complexes can be dependent on the density functional theory (DFT) functional chosen, and thus we tested several different methods for our calculations. In an initial set of calculations, the unrestricted hybrid density functional method B3LYP was used in combination with an LACVP basis set on the metal and 6-31G on the rest of the atoms (referenced as basis set B1) for geometry optimizations and frequencies.[57−59] Optimized structures were employed as the starting point for single-point calculations using (a) the LACV3P+ basis set on the metal and 6-311+G* on the rest of the atoms; (b) the M06/B1 method;[60] and (c) B3LYP/B1 with the polarized continuum model with a dielectric constant of ε = 5.7. In a second set of calculations, we used the unrestricted BP86 density functional method[61,62] in combination with an LACV3P+ basis set on the metal and 6-311+G* on the rest of the atoms (referenced as basis set B2). Full geometry optimizations were run with the Jaguar 7.6 program, followed by a frequency calculation using these methods.[63] Single-point calculations with dispersion-corrected DFT were performed as proposed by Schwabe and Grimme;[64] however, this had a negligible effect on the spin state ordering and relative energies.

Synthesis of [Fe^{II}(LN$_3$S)(py)]OTf (2). Crystalline [Fe^{II}(LN$_3$S)(OTf)] (**1**) (100 mg, 0.16 mmol) was dissolved in CH_2Cl_2 and pyridine (15 μL, 0.19 mmol) was added. After stirring for 2 h, the solution was filtered through Celite. Slow vapor diffusion of diethyl ether or layering with pentane gave the desired product as dark brown plates suitable for X-ray diffraction (XRD) analysis in 97% yield (110 mg). ^{1}H NMR (CD_2Cl_2): δ 107.0, 95.4, 91.6, 45.2, 13.1, 11.6, 3.1, 1.3, −4.1, −10.3, −16.2, −30.4. LDI-MS (+): m/z 484.2 ([**2**−py−OTf]$^+$). Anal. Calc. for Fe^{II}(LN$_3$S)(py)(OTf)·CH_2Cl_2 ($C_{34}H_{37}Cl_2F_3FeN_4O_3S_2$): C, 51.20; H, 4.68; N, 7.02. Found: C, 51.21; H, 4.88; N, 7.67.

Synthesis of [Fe^{II}(LN$_3$S)(DMAP)]OTf (3). Crystalline [Fe^{II}(LN$_3$S)(OTf)] (**1**) (110 mg, 0.17 mmol) was dissolved in CH_2Cl_2 and DMAP (25 mg, 0.21 mmol) was added. After stirring for 2 h, the solution was filtered through Celite. Slow vapor diffusion of diethyl ether or layering with pentane gave **3** as black plates suitable for XRD analysis in 95% yield (125 mg). ^{1}H NMR (CD_2Cl_2): δ 128.0, 102.4, 92.8, 37.6, 19.4, 10.4, 8.4, 3.1, 1.4, −4.9, −7.7, −10.4, −13.7, −22.8. LDI-MS (+): m/z 484.2 ([**3**−DMAP−OTf]). Anal. Calc. for Fe^{II}(LN$_3$S)(DMAP)(OTf) ($C_{35}H_{40}F_3FeN_5O_3S_2$): C, 55.63; H, 5.34; N, 9.27. Found: C, 55.37; H, 5.29; N, 9.07.

Synthesis of [Fe^{II}(LN$_3$S)(DMAP)]·2Et$_2$O (4·2Et$_2$O). Crystalline [Fe^{II}(LN$_3$S)(DMAP)](OTf) (**3**) (125 mg, 0.17 mmol) was combined with 1.5 equiv of 0.5% Na/Hg amalgam (6.0 mg Na^0, 1.15 g Hg) and suspended in 5 mL of Et_2O. Upon stirring, the insoluble starting material (**3**) slowly dissolves into solution as it reacts, giving a dark green/brown solution. After stirring for 2 h, the reaction mixture was filtered through Celite, layered with pentane, and placed in the freezer for several days, giving **4·2Et$_2$O** as dark brown crystals suitable for XRD in 37% yield (38 mg). UV-vis (THF) (nm): 566, 625, 785 (ε = 890 M^{-1} cm^{-1}). ^{1}H NMR (THF-d_8): δ 95.7, 33.8, 24.7, 5.8. EPR: g = 2.155, 2.057, 2.038. Mössbauer: $\Gamma_{L=R}$ = 0.8 mm s^{-1}, δ = 0.33 mm s^{-1}, ΔE_Q = 2.04 mm s^{-1}. Anal. Calc. for [**4** + Et_2O + 0.25 NaOTf] ($C_{38.25}H_{50}F_{0.75}FeN_5Na_{0.25}O_{1.75}S_{1.25}$): C, 63.48; H, 6.96; N, 9.68. Found: C, 62.85; H, 6.74; N, 9.73. Crystalline samples of **4·2Et$_2$O** coprecipitate with a small amount of white solid impurity that could not be separated from **4·2Et$_2$O**. The impurity was identified as NaOTf by ^{19}F NMR (see Figure S2). Inclusion of 0.25 equiv of NaOTf was necessary to obtain a good fit for elemental analysis.

Synthesis of [Ni^{II}(LN$_3$S)]BF$_4$ (5). An amount of 2-(O=CMe)-6-(2,6-(^{i}Pr$_2$−C_6H_3N=CMe)-C_5H_3N (50 mg, 0.155 mmol) and Ni^{II}(BF$_4$)$_2$·6H_2O (55 mg, 0.163 mmol) was suspended in EtOH (5 mL) and heated at 80 °C for 30 min. The solids slowly dissolved to give a deep green solution, and then a solution of 2-aminothiophenol (17 μL, 0.155 mmol) and triethylamine (22 μL, 0.155 mmol) in EtOH (1 mL) was added to the reaction mixture. The reaction was allowed to stir at 80 °C for 24 h before being cooled to room temperature and concentrated. The resulting solid residue was brought into a glovebox where it was redissolved in a minimum amount of CH_2Cl_2 and filtered through Celite. Slow vapor diffusion of diethyl ether into the filtrate yielded 96 mg (94% yield) of **5** as dark red crystals suitable for X-ray analysis, together with colorless crystals of $Et_3NH·BF_4$. Samples for elemental analysis were prepared by manual separation of crystals of **5** from the colorless $Et_3NH·BF_4$ crystals. ^{1}H NMR (CD_2Cl_2): δ 8.30 (br, 1H), 7.89 (br, 2H), 7.35 (t, 1H), 7.22 (d, 2H), 7.09 (d, 1H), 6.92 (t, 1H), 6.82−6.72 (m, 2H), 3.18 (br), 2.69 (s, 3H), 2.14 (s, 3H), 1.50 (d, 6H), 1.33 (br), (1.17 (d, 6H). LDI-MS (+): m/z 488.3 [**5**-BF$_4$]$^+$. Anal. Calc. for [Ni^{II}(LN$_3$S)](BF$_4$)·CH_2Cl_2 ($C_{28}H_{32}BCl_2F_4N_3NiS$): Predicted: C, 51.03; H, 4.89; N, 6.38. Found: C, 51.28; H 4.76; N, 6.66.

O_2 Reactivity. Reactions of **2**, **3**, and **5** with excess O_2 were conducted as previously reported for **1** in CH_2Cl_2.[24] The one-electron-reduced complexes were reacted with O_2 by freshly preparing solutions of **4** or reduced **5** via Na/Hg amalgam in Et_2O, followed by filtration through Celite, as described for the synthesis of **4**. Reaction mixtures following O_2 addition were then analyzed directly by LDI-MS.

RESULTS AND DISCUSSION

Synthesis of Iron(II) and Nickel(II) Complexes. The synthesis of the unsymmetrical, thiolate-ligated complex [Fe^{II}(LN$_3$S)(OTf)] (**1**) was accomplished by reacting the imino-ketone precursor[65] 2-(O=CMe)-6-(2,6-(^{i}Pr$_2$−C_6H_3N=CMe)-C_5H_3N with the commercially available 2-aminothiophenol and Fe(OTf)$_2$ in a metal-assisted template reaction as previously described.[24] We sought to determine if this complex could be used as a precursor to generate Fe^{II} complexes with biologically relevant [N_4S] donor sets via substitution at the OTf$^-$ position. Displacement of the OTf$^-$ ligand in **1** was an attractive route when compared to the more challenging strategy involving multistep organic synthesis to produce covalently linked N_4S-donating ligands.[26,66−68] The addition of 1 equiv of either pyridine or *N*,*N*′-dimethylaminopyridine (DMAP) to dark red-purple **1** in CH_2Cl_2 at room temperature does not result in any color change. However, vapor diffusion of diethyl ether into the reaction mixture after stirring for 2 h afforded single crystals as dark brown plates of the pyridine-ligated [Fe^{II}(LN$_3$S)(py)](OTf) (**2**), and black plates in the case of the DMAP-ligated [Fe^{II}(LN$_3$S)(DMAP)](OTf) (**3**). These crystals yielded the X-ray structures of **2** and **3** (Figures 2 and 3, vide infra), confirming that the OTf$^-$ anion was displaced by the pyridine derivatives. For large-scale preparations of **2** and **3**, layering of pentane was used in place of vapor diffusion of Et_2O to give both **2** and **3** in high yield.

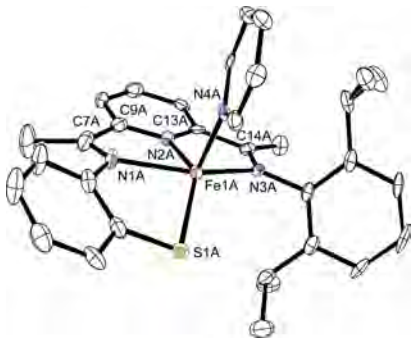

Figure 2. Displacement ellipsoid plot for the cation of complex **2** (50% probablility level). The H atoms are removed for clarity.

dx.doi.org/10.1021/ic4013558 | Inorg. Chem. 2013, 52, 10467−10480

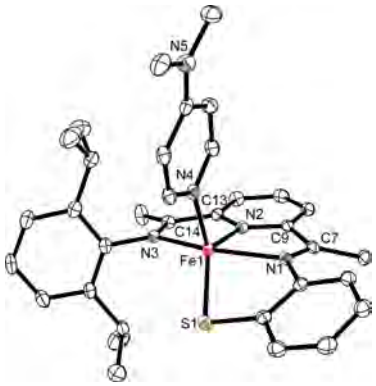

Figure 3. Displacement ellipsoid plot for the cation of complex **3** (50% probablility level). The H atoms are removed for clarity.

The synthesis of the Ni^{II} analogue of **1** was also targeted for comparison of spectroscopic features and its reactivity toward O_2. The use of $Ni^{II}(BF_4)_2$ in place of $Fe^{II}(OTf)_2$ in Scheme 1 results in a dark green solution. Vapor diffusion of Et_2O afforded dark red crystals, together with clusters of large colorless needles. The red crystals were separated by hand and analyzed by X-ray crystallography, revealing the Ni^{II} complex $[Ni^{II}(LN_3S)](BF_4)$ (**5**). The colorless crystals were presumed to be $Et_3NH^+BF_4^-$, the expected byproduct of the template reaction. Peaks corresponding to $Et_3NH^+BF_4^-$ were confirmed in the ^1H NMR of **5**. The coprecipitation of $Et_3NH^+BF_4^-$ could not be avoided even upon successive recrystallizations; therefore, it was necessary to isolate complex **5** by manual separation of crystalline material for elemental analysis and further reactivity studies.

X-ray Structures of the Iron(II) and Nickel(II) Complexes. The X-ray structures for the iron(II) complexes $[Fe^{II}(LN_3S)(py)](OTf)$ (**2**) and $[Fe^{II}(LN_3S)(DMAP)](OTf)$ (**3**) are shown in Figures 2 and 3. Selected bond distances and angles are given in Tables 1 and 2. The structures reveal that the triflate ligand has been displaced in each case by the heterocyclic N donor to afford the 5-coordinate $Fe^{II}(N_4S$-(thiolate)) products. There is a clear preference for forming the 5-coordinate complexes over the 6-coordinate species, in which the OTf^- would be retained in the first coordination sphere. The Fe−N distances of 2.073(5)−2.196(5) Å for **2** and 2.0667(14)−2.2179(15) Å for **3** are indicative of high-spin (S = 2) Fe^{II} complexes. The pyridine-derived Fe−N bonds are shorter than the imine N−Fe distances in both **2** and **3**, whereas the Fe−S bonds are nearly identical. There is minimal effect of substitution of the *para* position of the pyridine derivatives on the bond lengths in **2** and **3**. An analysis of the bond angles for **2** and **3** and their τ values (τ = 0.15 for **2**, and τ = 0.18 for **3**; where τ = 0 for square pyramidal and τ = 1 for trigonal bipyramidal)[69] show that, in both cases, the Fe^{II} ions are held in a distorted square pyramidal geometry, with the pyridine derivatives occupying the axial position. The molecular structure of **1** has been reported,[24] and selected bond distances are reproduced in Table 1. The Fe−N distances are very similar to those found in **2** and **3**, whereas the Fe−S distance appears slightly shorter. Complex **1** exhibits a more idealized square pyramidal geometry than **2** or **3**, with τ = 0.12, and a comparison of the τ values for **1**−**3** reveals that the geometry becomes more distorted from square pyramidal with increasing axial ligand donor strength ($\tau_{(OTf)}$ = 0.12 < $\tau_{(py)}$ = 0.15 < $\tau_{(DMAP)}$ = 0.18). In all three complexes **1**−**3**, the pyridine diimine backbone remains planar, while the ferrous ion sits 0.276 Å above the N_3 plane for **1**, but less out of plane for **2** (0.116 Å) and **3** (0.200 Å). In addition, the thiolate donor never sits in the ideal equatorial position, but rather lies well below the N_3 plane. For **1** and **2**, the N_{plane}−S distances are 0.824 and 1.18 Å, respectively, while for **3**, it is significantly more distorted with $d(N_{plane}-S)$ = 1.8 Å. The C_{imine}−N and $C_{imine}-C_{ipso}$ bond distances for the ligand are similar for complexes **1**−**3** (Table 1), and are consistent with a neutral-ligand bis(imino)pyridine backbone (LN_3S^-).[34,43]

The X-ray structure for the Ni^{II} complex $[Ni^{II}(LN_3S)](BF_4)$ (**5**) is shown in Figure 4. Selected bond distances and angles for **5** are given in Table 3. The molecular structure of **5** shows a square planar geometry for the Ni^{II} ion. The observed Ni−N distances are 1.8151(14)−1.9159(15) Å, and are somewhat shorter (∼0.1−0.4 Å) than other BIP-derived nickel(II) complexes.[45,70−73] The Ni−S distance of 2.1386(5) Å is significantly shorter than the Fe^{II}−S distances seen for **1**−**3**, as are the Ni−N distances. The bond angles about the Ni^{II} center deviate slightly from the idealized square-planar geometry (82.44°−102.37°), likely due to the constraints imposed by the three 5-membered chelate rings. The Ni^{II} ion and S atom sit directly in the plane of the bis(imino)pyridine ligand as seen by Ni−N_3(plane) and S−N_3(plane) distances of 0.030 Å and 0.082 Å, respectively. This structure contrasts those found for **1**−**3**, where both the metal ion and sulfur donor lie significantly

Scheme 1. Synthesis of Iron(II) Complexes (1−3), and Nickel(II) Complex (5)

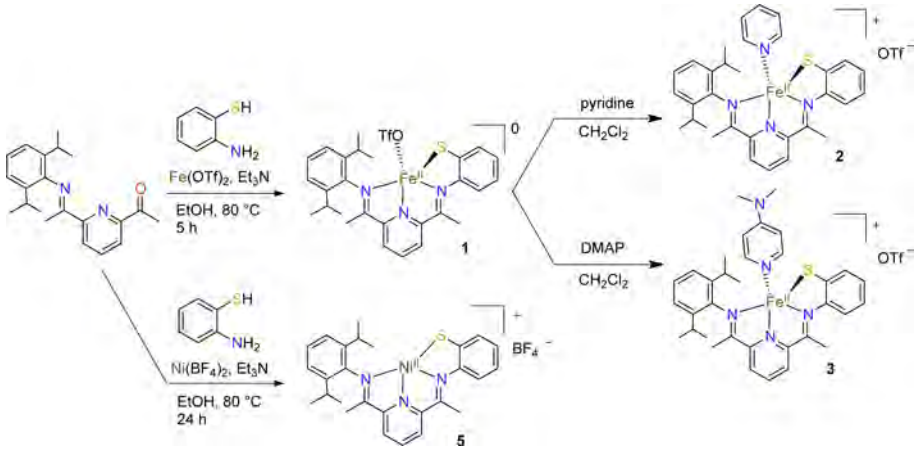

dx.doi.org/10.1021/ic4013558 | *Inorg. Chem.* 2013, 52, 10467−10480

Table 1. Selected Bond Distances for $[Fe(LN_3S)]^{n+}$ Complexes[a]

	Bond Distances (Å)			
	$[Fe^{II}(LN_3S)(OTf)]$[a]	$[Fe^{II}(LN_3S)(py)]OTf$	$[Fe^{II}(LN_3S)(DMAP)]OTf$	$[Fe^{II}(LN_3S)(DMAP)]^0$
Fe1−N1	2.188(2)	2.173(5)	2.1859(15)	1.9255(15)
Fe1−N2	2.072(2)	2.090(5)	2.0960(14)	1.8278(15)
Fe1−N3	2.184(2)	2.196(5)	2.2179(15)	1.9179(16)
Fe1−N4	N/A	2.073(5)	2.0667(14)	2.0508(16)
Fe1−S1	2.2942(8)	2.3246(18)	2.3295(5)	2.2179(5)
Fe−O1	2.0870(18)	N/A	N/A	N/A
N1−C7 (imine)	1.293(3)	1.298(8)	1.292(2)	1.347(2)
C7(imine)− C9(ipso)	1.480(4)	1.485(9)	1.486(2)	1.432(3)
C9(ipso)−N2(pyr)	1.343(3)	1.342(8)	1.341(2)	1.376(2)
N3−C14(imine)	1.284(3)	1.275(7)	1.290(2)	1.341(2)
C14(imine)−C13(ipso)	1.483(4)	1.494(8)	1.487(3)	1.426(3)
C13(ipso)−N2(pyr)	1.334(3)	1.334(8)	1.343(2)	1.381(2)

[a]Data taken from ref 24.

Table 2. Selected Bond Angles for $[Fe(LN_3S)]^{n+}$ Complexes

	Bond Angles (deg)		
	$[Fe^{II}(LN_3S)(py)]OTf$	$[Fe^{II}(LN_3S)(DMAP)]OTf$	$[Fe^{II}(LN_3S)(DMAP)]^0$
N4−Fe1−N2	109.79(19)	112.91(6)	99.92(6)
N4−Fe1−N1	95.3(2)	99.69(6)	95.84(6)
N2−Fe1−N1	74.0(2)	73.08(5)	81.26(7)
N4−Fe1−N3	99.29(19)	99.82(6)	99.88(6)
N2−Fe1−N3	73.4(2)	73.94(6)	80.65(7)
N1−Fe1−N3	147.24(19)	146.17(5)	157.78(7)
N4−Fe1−S1	106.05(15)	107.20(4)	105.25(5)
N2−Fe1−S1	138.08(14)	135.18(4)	153.58(5)
N1−Fe1−S1	81.79(15)	81.40(4)	88.27(5)
N3−Fe1−S1	121.28(13)	118.28(4)	102.49(5)

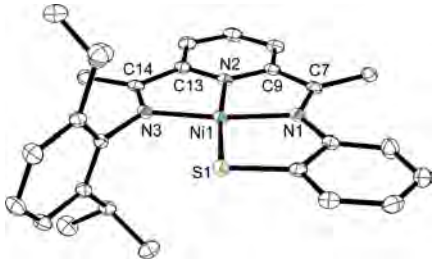

Figure 4. Displacement ellipsoid plot for the cation of complex **5** (50% probablility level). The H atoms are removed for clarity.

Table 3. Selected Bond Distances and Angles for Complex 5

Bond Distances (Å)	
Ni1−N1	1.8981(15)
Ni1−N2	1.8151(14)
Ni1−N3	1.9159(15)
Ni1−S1	2.1386(5)
N1−C7 (imine)	1.312(2)
C7(imine)−C9(ipso)	1.480(2)
C9(ipso)−N2(pyr)	1.341(2)
N3−C14(imine)	1.299(2)
C14(imine)−C13(ipso)	1.480(2)
C13(ipso)−N2(pyr)	1.338(2)
Bond Angles (deg)	
N2−Ni1−N1	83.56(6)
N2−Ni1−N3	82.44(6)
N1−Ni1−N3	165.91(6)
N2−Ni1−S1	175.17(5)
N1−Ni1−S1	91.64(5)
N3−Ni1−S1	102.37(5)

out of the bis(imino)pyridine plane for these 5-coordinate complexes.

NMR Spectroscopy. The paramagnetic ^{1}H NMR spectra for complexes **1**−**3** in CD_2Cl_2 are shown in Figure 5. Each complex exhibits sharp, paramagnetically shifted peaks over a broad range (from 130 ppm to −30 ppm), indicative of high-spin (S = 2) Fe^{II} complexes. Detailed ^{1}H NMR assignments have been made for bis(imino)pyridine iron(II) complexes that carry the same aryl imino substituents.[34,65,74,75] These data can be used as a guide for interpreting the spectra for **1**−**3**, although the unsymmetrical structures of **1**−**3** make their ^{1}H NMR patterns difficult to definitively assign. For all three complexes, the downfield region (130−80 ppm) contains three sharp peaks, with the exception of **3**, in which the most downfield resonance at 130 ppm is significantly broadened. In comparison to symmetrical (BIP)FeX_2 complexes, two of the three resonances in this region can be assigned to the *meta* and *para* pyridyl backbone protons, with the most intense resonance (82.8, 95.4, and 92.8 ppm for **1**−**3**, respectively) likely arising from the *meta* protons that are apparently not split in the local symmetry. We tentatively assign the third resonance to a proton on the phenylthiolate ring. No peaks appear in the spectrum for **1** between 80 ppm and 20 ppm, whereas complex **2** shows a broad peak at 45.2 ppm and complex **3** exhibits a sharp peak at 37.6 ppm and a broad feature at 43.5 ppm. The latter peaks for **2** and **3** can be assigned to the axial pyridine ligands, which are absent in **1**. This assignment was confirmed by the generation in situ of **2** with the addition of 1 equiv of pyridine-d_5 to **1**. As seen in Figure 5, the spectrum for deuterated **2**-d_5 is a good match for **2**, except for the disappearance of the resonance at 45.2 ppm. The broadness of the py peak and the absence of distinct signals for the *ortho*, *meta*, and *para* protons suggest that the py ligand in **2** is labile on the NMR time scale. In contrast, two peaks are observed for **3** in the region of the axial DMAP donor, and one is relatively sharp, suggesting that DMAP is significantly less labile than py; this observation is consistent with it being a more strongly donating py derivative. Further upfield, the diisopropyl methyl groups can easily be assigned to the intense singlets between 1.20 ppm and 1.36 ppm for **1**−**3**, and the peaks found from −14 ppm to −16 ppm are assigned to the *para* C−H on the

dx.doi.org/10.1021/ic4013558 | Inorg. Chem. 2013, 52, 10467−10480

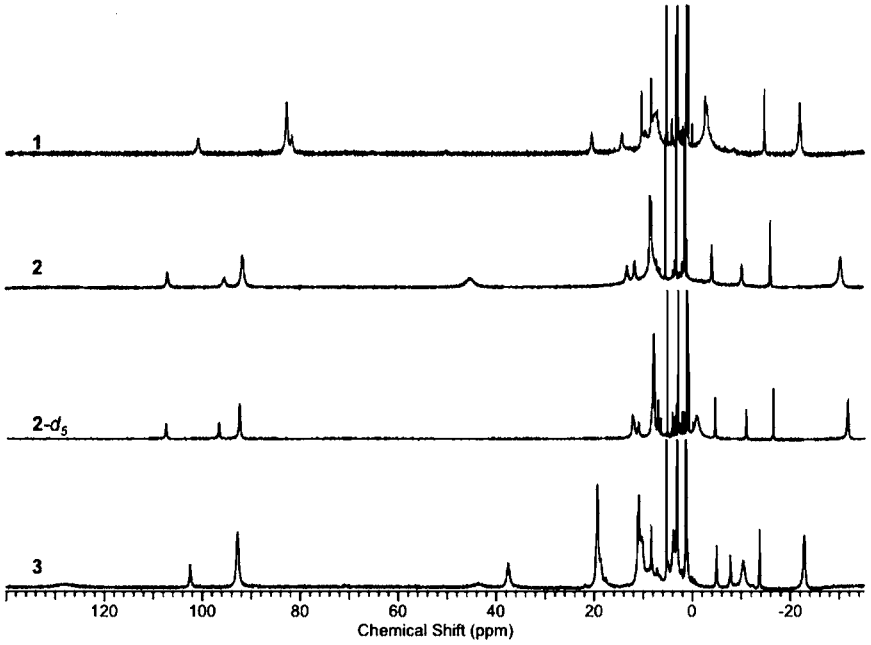

Figure 5. ^{1}H NMR spectra of complexes **1**−**3** in CD_2Cl_2 at 25 °C.

iPr$_2$Ph substituent based on earlier work.[34,65,74,75] The upfield resonances at −21.9, −30.3, and −22.8 ppm for **1**, **2**, and **3**, respectively, likely arise from the isopropyl methine protons.

The ^{1}H NMR spectrum of the diamagnetic Ni(II) complex **5** is shown in Figure 6. The peaks for the pyridyl protons are seen

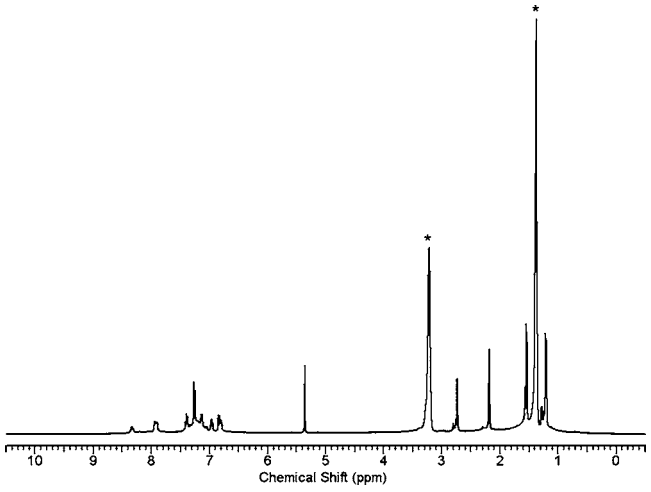

Figure 6. ^{1}H NMR spectrum of **5** in CD_2Cl_2 at 25 °C. The $Et_3NH^+BF_4^-$ impurity signal is denoted by an asterisk (*).

at δ 8.30 and 7.88, and the diisopropylphenyl peaks are assigned to δ 7.35 (t, 1H) and 7.22 (d, 2H). Other peaks in the aromatic region include δ 7.09 (d, 1H), 6.92 (t, 1H), and overlapping peaks at 6.79 (d, 1H) and 6.75 (t, 1H), which can be attributed to the phenylthiolate ring. The peaks found at 3.18 and 1.33 ppm come from a small amount of $Et_3NH^+BF_4^-$ impurity (vide supra), and the peak at 3.18 ppm likely masks the isopropyl methine C−H peaks for **5**. The ketimine CH_3 resonances are located at δ 2.70 (s, 3H) and 2.14 (s, 3H). There are two distinct isopropyl CH_3 peaks found at δ 1.50 (d, 6H) and 1.17 (d, 6H), indicating restricted rotation of the diisopropylphenyl substituent about the N_{imino}−C_{ipso} bond.

Electrochemistry. Cyclic voltammetry of the iron(II) and nickel(II) complexes was measured to gain insights regarding the influence of the exogenous py derivatives and covalently tethered phenylthiolato donor on the redox properties of these complexes. The cyclic voltammograms for compounds **1**, **2**, **3**, and **5** are shown in Figure 7. The triflate complex **1** and the

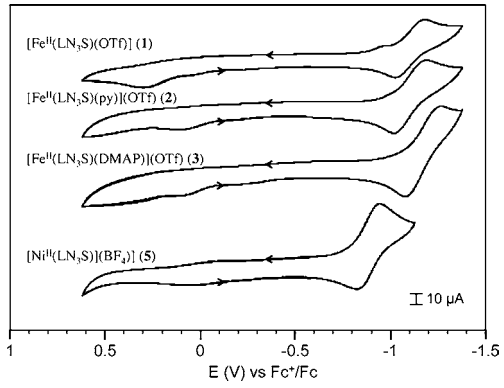

Figure 7. Cyclic voltammograms of compounds **1**−**3** and **5** in MeCN. $E_{1/2}$: **1** = −1.1 V, **2** = −1.1 V, **3** = −1.2 V, and **5** = −0.9 V; ΔE_p: **1** = 120 mV, **2** = 130 mV, **3** = 130 mV, and **5** = 66 mV. Working electrode, glassy carbon; counter electrode, platinum; and reference electrode, Ag/Ag^+. Electrolyte: $LiClO_4$, 100 mM. Scan rate = 100 mV/s.

pyridine complex **2** exhibit quasireversible waves at $E_{1/2}$ = −1.1 V, while the DMAP complex **3** reveals a more negative $E_{1/2}$ value (−1.2 V). No other obvious redox processes for these complexes are present within the solvent window for CH_3CN. The fact that the $E_{1/2}$ values for **1** and **2** are the same suggests that the axial pyridine donor in **2** does not exhibit any influence on the redox potential, but is also consistent with the pyridine ligand dissociating to some extent in solution, as indicated by the NMR data. Substitution of py for DMAP does have a clear impact, shifting the redox potential by ∼100 mV more negative in **3**, compared to **2**. This result is consistent with DMAP being a more strongly donating ligand than unsubstituted pyridine.

dx.doi.org/10.1021/ic4013558 | Inorg. Chem. 2013, 52, 10467−10480

Scheme 2. Reduction of Thiolate-Ligated M^{II} Bis(imino)pyridine Complexes

The nickel(II) complex is the easiest to reduce in the series, with $E_{1/2}$ = −0.9 V.

Non-innocent BIP ligands have been shown previously to undergo up to three sequential reductions in which the electrons are delocalized over the BIP backbone.[34−45] The negative $E_{1/2}$ values for **1**−**3** are consistent with ligand-based reduction, and covalent attachment of the phenylthiolate group exerts a strong influence on the redox properties, in comparison to other BIP complexes.[25] The non-thiolate-ligated BIP complexes typically show two reversible reduction waves, whereas **1**−**3** exhibit only one reduction process, suggesting that the next reduction for **1**−**3**, if it exists, lies outside the solvent window. Similarly, the nickel(II) analogue **5** exhibits only one redox process at −0.9 V, which is within the range of ligand-based reductions for the iron complexes, but is more positive by ≥200 mV. These data show that the BIP-derived ligand of the Ni^{II} complex **5** is significantly easier to reduce than **1**−**3**.

One-Electron Reduction of the Iron(II) and Nickel(II) Complexes. A summary of the possible redox transformations for the phenylthiolate-appended $[M(LN_3S)(L)]^+$ complexes are shown in Scheme 2. The CV data for **1**−**3** and **5** each show well-separated, quasi-reversible reduction waves, indicating that one-electron-reduced complexes should be synthetically accessible. The lack of a second reduction process suggests that the one-electron-reduced complexes can be isolated without the complication of forming two-electron-reduced species, in contrast to other BIP complexes.[39] Several methods have been employed to reduce M^{n+}(BIP) complexes, including treatment with aluminum/lithium alkyl reagents, $NaBEt_3H$, KC_8, and Na/Hg amalgam.[35,70,76,77] The latter method was a convenient choice for the controlled reduction of the thiolate-ligated complexes described here.

Reduction of the DMAP complex **3** was accomplished by stirring a suspension of **3** in Et_2O over a slight excess of 0.5% Na/Hg amalgam, affording the one-electron-reduced $[Fe(LN_3S)(DMAP)]^0$ (**4**), as shown in Scheme 3. The progress

Scheme 3. Synthesis of the Monoreduced Complex $[Fe(LN_3S)(DMAP)]^0$ (4)

of the reaction is easily followed by the colorless ethereal suspension of **3** converting to a deep green, homogeneous solution. The UV-vis spectrum following the Na/Hg reduction is shown in Figure 8, where the solvent is THF instead of Et_2O to maintain the solubility of **3**. Distinct features appear at 566, 625, and 785 nm that are indicative of **4**. It should be noted that solutions of **4** in either THF or Et_2O are extremely air-sensitive,

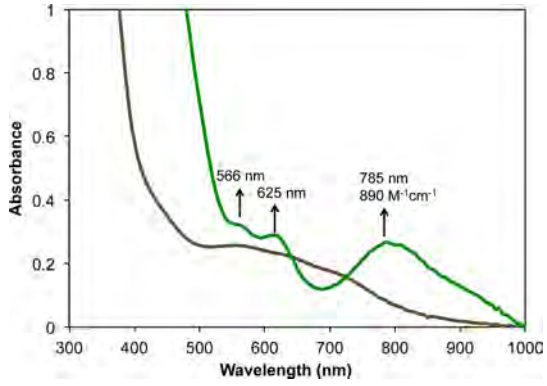

Figure 8. UV-vis spectral change for the conversion of **3** (brown trace) to **4** (green trace) with 0.5% Na/Hg amalgam in tetrahydrofuran (THF).

and will decompose upon prolonged standing, even at −35 °C in a drybox freezer, as seen by spontaneous conversion of dark green solutions of **4** to a brown precipitate. Crystals for XRD can be grown from layering of pentane into Et_2O at −35 °C, but the crystals must be obtained within 48 h or decomposition occurs and no crystalline product will form. Crystalline **4** is also difficult to isolate outside of the mother liquor without further decomposition. Attempts to scale up the reaction failed to give crystalline product: instead, it led to more-rapid decomposition.

Many reduced Fe(BIP) complexes have been reported, most involving doubly reduced species relative to the M^{II} complexes analogous to **1**−**3**. However, a few examples of monoreduced and triply reduced Fe(BIP) complexes have been described.[37−39] The monoreduced Fe(BIP) complexes were prepared by either reduction of iron(II) starting materials (e.g., $[(^{iPr}BIP)Fe^{II}Cl_2] + e^- \rightarrow [(^{iPr}BIP)FeCl]^0$), or oxidation of doubly reduced (formally Fe^0) Fe(BIP) complexes (e.g., $[(^{iPr}BIP)Fe(N_2)]^0 \rightarrow [(^{iPr}BIP)Fe(OEt_2)]^+ + e^-$) and, in both cases, yield 4-coordinate iron complexes.[37−39] The 5-coordinate complexes $[(^{iPr}BIP)Fe(Br)(THF)]$ and $[(^{iPr}BIP)Fe(CO)_2]^+$, were prepared via one-electron oxidation of their respective doubly reduced precursors, while $[(^{Et}BIP)Fe(Cl)(Et_2O)]$ was prepared by reduction of the starting material.[37,40,78] However, the doubly reduced species generally are more easily obtained than the monoreduced analogs, and careful stoichiometric control must be used to synthesize monoreduced complexes. In contrast, the putative doubly reduced analog of **3** is not accessible as seen by electrochemistry, and thus reduction of **3** leads to the selective isolation of a rare 5-coordinate, monoreduced complex.

Attempted reductions of the iron(II) complexes **1** and **2** suspended in Et_2O led to deep green solutions similar to those seen for **4**, but the products were highly soluble, even in mixtures with pentane, and crystals could not be isolated. The nickel(II) complex **5**, which is insoluble in Et_2O, reacts similarly with Na/Hg amalgam to give a homogeneous bright green solution which presumably contains the monoreduced nickel analogue. This product was also highly soluble and could not be

dx.doi.org/10.1021/ic4013558 | Inorg. Chem. 2013, 52, 10467−10480

crystallized, but provides a useful comparison to iron-containing **4**; therefore, it was prepared in situ from **5** and characterized by EPR spectroscopy (vide infra).

X-ray Structure of Monoreduced [Fe(LN$_3$S)(DMAP)]^0 (4). The crystal structure of **4** (Figure 9) shows an overall

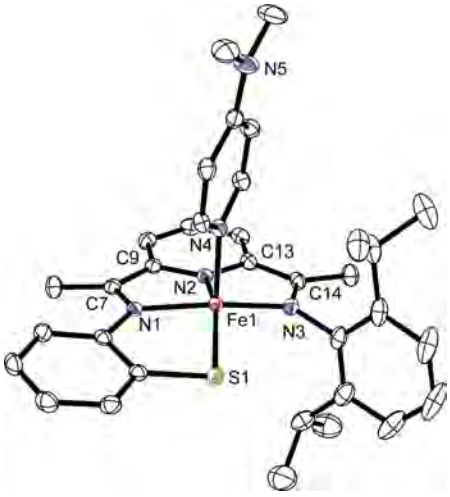

Figure 9. Displacement ellipsoid plot for **4** (50% probablility level). The H atoms are removed for the sake of clarity.

neutral iron complex with no additional counterions. Therefore, charge balance indicates that this complex is the one-electron-reduced analogue of the cation of **3**. The DMAP is retained in the axial position and, together with the LN$_3$S ligand, gives a 5-coordinate Fe center. Selected bond distances and angles are given in Tables 1 and 2. The Fe and S atoms in **4** have moved toward the equatorial plane of the bis(imino)pyridine backbone (Fe−N$_3$(plane) = 0.254 Å and S−N$_3$(plane) = 0.411 Å), compared to **3**. This flattening of the geometry around the Fe center is characterized by a change in τ value from τ = 0.18 for **3** to τ = 0.08 for **4**. There is a significant shortening of the Fe−N and Fe−S bonds for LN$_3$S, with the Fe−S bond decreasing by 0.1 Å and the Fe−N bonds decreasing by 0.3 Å. These changes are opposite to what would be expected for a metal-centered reduction to give a formal high-spin iron(I) complex, and they are more consistent with ligand-based reduction.

It has been shown that the C−C and C−N bond distances in BIP complexes are indicative of ligand reduction, and an analysis of ligand backbone distances is essential when assigning the locus of reduction in these complexes.[37−43] To gain insight into the electronic structure of **4**, it is useful to compare metrical parameters with other structurally characterized 5-coordinate monoreduced complexes reported in the literature. The complexes [Fe(^{iPr}BIP)(Br)(THF)][78] and [Fe(^{Et}BIP)(Cl)][40] exhibit similar C$_{imine}$−N$_{imine}$, C$_{imine}$−C$_{ipso}$, and C$_{ipso}$−C$_{pyridyl}$ bond distances in the BIP backbone that are consistent with one-electron ligand reduction. In contrast, [Fe(^{iPr}BIP)(CO)$_2$](BAr$^F_4$),[37] another monoreduced complex, has bond distances closer to a non-reduced BIP ligand and has been assigned as an iron(I) complex. The critical metrical parameters for **4** are highlighted in the structural fragments shown in Figure 10, in which **4** can be compared with its non-reduced precursor **3**. The C−N$_{imine}$ and C−N$_{pyridyl}$ bonds are elongated, while the C$_{imine}$−C$_{ipso}$ bonds are shortened in **4**, compared to **3**. These changes in the ligand backbone clearly point to the complex undergoing ligand-based reduction upon conversion of

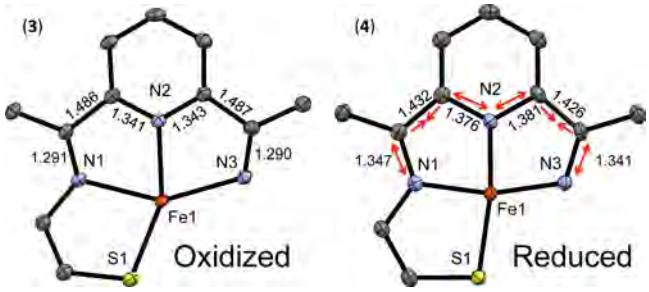

Figure 10. Comparison of selected ligand bond lengths for **3** (left) and **4** (right).

3 to **4**. A careful comparison of the bond distances in **4** to those reported in the literature suggests that the ligand in **4** is similar to a two-electron reduced BIP ligand. However, **4** would need to be formulated as an Fe^{III} complex with a doubly reduced (LN$_3$S)$^{3-}$ ligand, which is unlikely, given that iron(III) complexes are often not stable in the presence of monoanionic thiolate donors. Further evidence from Mössbauer spectroscopy and DFT calculations point to **4** as being an iron(II) complex with a one-electron-reduced ligand (vide infra). The phenylthiolate-appended LN$_3$S ligand appears capable of behaving as a non-innocent ligand by accommodating a reducing equivalent delocalized over the BIP backbone.

EPR Spectroscopy. Further information regarding the electronic structure of the monoreduced **4** was obtained by EPR spectroscopy. Crystalline **4** was dissolved in Et$_2$O and EPR data were recorded at 15 K. A nearly axial EPR spectrum was observed, and a good simulation was obtained for an S = 1/2 system with g values of 2.155, 2.057, and 2.038 (Figure 11).

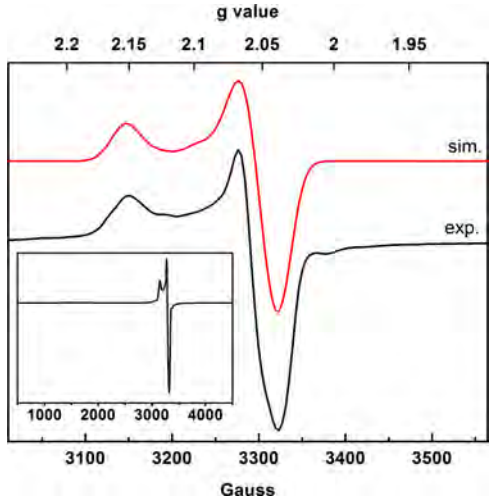

Figure 11. X-band EPR spectrum of **4** (2.4 mM) in Et$_2$O at 16 K (black line). Inset: full-range experimental spectrum. Parameters: frequency, 9.479 GHz; microwave power, 2 mW; modulation amplitude, 10 G; modulation frequency, 100 kHz. Parameters for simulation (red line): S = 1/2; g = [2.155, 2.057, 2.038]; Lorentzian linewidths, W = 33, 32, and 30 G.

The S = 1/2 ground state could arise from a low-spin (ls) iron(I) center resulting from metal-based reduction, a ls-iron(II) (S = 0) center with a ligand-based radical, or an intermediate-spin (is) iron(II) (S = 1) center antiferromagnetically coupled to a ligand-based radical. An additional possibility is a high-spin (hs) iron(II) (S = 2) antiferromagnetically

dx.doi.org/10.1021/ic4013558 | Inorg. Chem. 2013, 52, 10467−10480

coupled to a ligand-based radical, but this configuration would give rise to a total spin ground state of $S = 3/2$, which should exhibit g values spread over a much wider range than that observed in Figure 11.[38] To make a definitive assignment, it is useful to draw comparisons with other monoreduced BIP-Fe complexes. For the monoreduced complex $[(^{iPr}BIP)Fe(CO)_2](BAr^F{}_4)$, a rhombic EPR spectrum with $g = 2.111, 2.043, 1.994$ is observed and attributed to a low-spin Fe^I configuration with an $S = 1/2$ ground state.[37] In contrast, the monoreduced $[(^{iPr}BIP)Fe(OEt_2)](BAr^F{}_4)$ exhibits an EPR spectrum assigned to an $S = 3/2$ species derived from a high-spin Fe^{II} ion antiferromagnetically coupled to the BIP radical anion.[38] The spectrum in Figure 11 does not match the spectra for either of the former complexes. These results suggest that the LN_3S complex **4**, which contains a covalently tethered phenylthiolate group, exhibits a new electronic configuration, consisting of either ls-Fe^{II} and a ligand-based radical or an is-Fe^{II} center antiferromagnetically coupled to a ligand-based radical, not previously observed in other monoreduced complexes.

The in situ reduction of the nickel complex **5** helps clarify the EPR properties and electronic ground states of the LN_3S complexes described in this work. The monoreduced analogue of **5**, $[Ni(LN_3S)]^0$, was generated in situ and its EPR spectrum is shown in Figure 12. A sharp singlet at $g = 2.00$ ($\Delta pp = 20$ G)

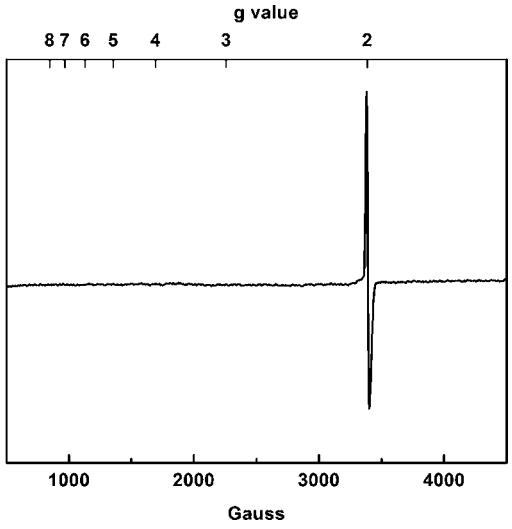

Figure 12. X-band EPR spectrum of **5** (3.0 mM) + Na/Hg (0.5%) amalgam in THF at 16 K. Parameters: frequency, 9.479 GHz; microwave power, 2 mW; modulation amplitude, 10 G; modulation frequency, 100 kHz.

is observed and can be assigned to a purely ligand-based radical.[70] Such a spectrum would be expected for **4** if this complex contained an ls-Fe^{II} ion and a single, unpaired e^- delocalized over the LN_3S ligand. Taken together, these data suggest that **4** may be best described as an intermediate-spin iron(II) ion antiferromagnetically coupled with a ligand radical, giving rise to the axial EPR spectrum in Figure 11.

Mössbauer Spectroscopy. Mössbauer spectra of microcrystalline samples of complexes **3** and **4** with natural abundance ^{57}Fe were collected at 5.3 K and with a weak applied field (47 mT) and are given in Figure 13. Mössbauer parameters for these complexes, together with complexes from the literature, are given in Tables 4 and 5. Both **3** and **4** produced spectra that consisted of broad quadrupole doublets. The broad spectra may be attributed to the fact that the

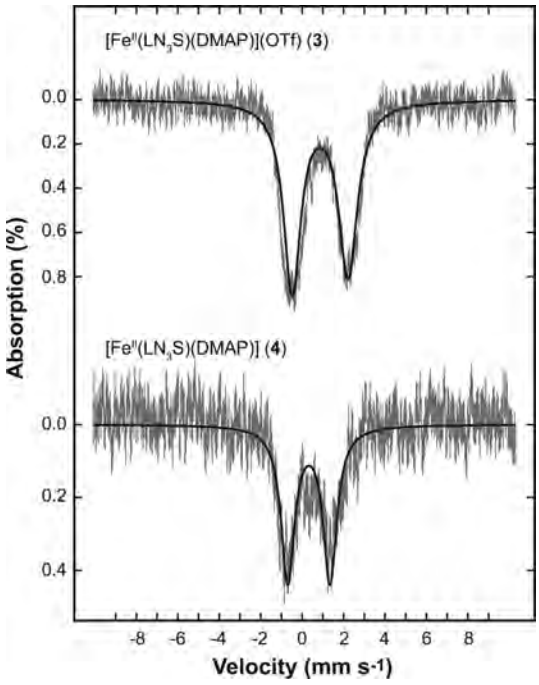

Figure 13. Mössbauer spectra at 5.3 K in a weak applied field (47 mT) of **3** (starting material) and **4** (monoreduced). Both spectra consist of broad quadrupole doublets ($\Gamma_{L=R} = 0.8$ mm s^{-1}). Complex **3** has parameters that can be assigned to a high-spin iron(II) species: ($\delta = 0.87$ mm s^{-1}; $\Delta E_Q = 2.70$ mm s^{-1}), while **4** is consistent with an intermediate-spin iron(II) species coupled to a S = 1/2 radical: ($\delta = 0.33$ mm s^{-1}; $\Delta E_Q = 2.04$ mm s^{-1}).

samples for **3** and **4** were mixtures of both crystalline and amorphous solids. The spectrum of **3** can be fitted to a quadrupole doublet with parameters that are highly distinctive[79] for a high-spin iron(II) ion ($\delta = 0.87$ mm s^{-1}; $\Delta E_Q = 2.70$ mm s^{-1}). However, the isomer shift is on the low end of the expected range, and this lowering is likely caused by both covalency of the thiolate iron bond and the five-coodinate nature of the complex. We previously reported an analogous ^{iPr}BIP complex, $[Fe^{II}(^{iPr}BIP)(SPh)Cl]$, which contains an exogenous thiolate donor in place of the tethered PhS^- group in **1**–**3** and Cl^- as the fifth ligand, and its Mössbauer spectrum was collected and is displayed in Figure S7 in the Supporting Information.[25] Complex **3** and $[Fe^{II}(^{iPr}BIP)(SPh)Cl]$ exhibit similar isomer shifts and quadrupole splittings, suggesting that substitution of the neutral DMAP ligand with the anionic Cl^- ligand has little effect on the Mössbauer spectra and, hence, electronic structure. These complexes can also be compared favorably with data for the thiolate-ligated non-heme iron enzymes CDO[20] and SOR.[81]

We next examined the one-electron-reduced complex **4** by Mössbauer spectroscopy. Analysis of crystalline **4** affords a Mössbauer spectrum distinct from **3**, with a significant decrease in both isomer shift and quadrupole splitting ($\delta = 0.33$ mm s^{-1}; $\Delta E_Q = 2.04$ mm s^{-1}). Comparison with the monoreduced and doubly reduced complexes in Table 5 shows that **4** exhibits Mössbauer parameters with values between those of monoreduced $[(BIP)Fe(CO)_2]^+$, which contains two strong-field CO donors and an ls-Fe^I center, and monoreduced $[(BIP)Fe(OEt_2)]^+$, which has a single, weak-field Et_2O donor and an hs-Fe^{II} ion. Surprisingly, the isomer shift and quadrupole splitting values for **4** are, in fact, closest to those seen for the *doubly*

dx.doi.org/10.1021/ic4013558 | Inorg. Chem. 2013, 52, 10467−10480

Table 4. ^{57}Fe Mössbauer Parameters for Selected High-Spin Iron(II) Complexes

	δ (mm s^{-1})	ΔE_Q (mm s^{-1})	ground state, S	source
[Fe^{II}(LN$_3$S)(DMAP)](OTf) (**3**)	0.87	2.70	2	this work
[(^{iPr}BIP)FeCl$_2$]	0.89	2.40	2	ref 39
[(^{iPr}BIP)FeCl$_2$]	0.92	2.40	2	this work
[(^{iPr}BIP)Fe(SPh)Cl]	0.78	2.62	2	this work
[(^{Mes}BIP)FeCl$_2$]	0.90	1.12	2	ref 80

Table 5. ^{57}Fe Mössbauer Parameters for Monoreduced and Doubly Reduced BIP-Iron Complexes

	δ (mm s^{-1})	ΔE_Q (mm s^{-1})	S_{total}	S_{Fe}	S_{ligand}	source
Monoreduced Complexes						
[Fe^{II}(LN$_3$S)(DMAP)] (**4**)	0.33	2.04	1/2	1	1/2	this work
[(^{iPr}BIP)Fe(CO)$_2$](BAr$^F_4$)	0.17	0.62	1/2	1/2	0	ref 37
[(^{iPr}BIP)Fe(OEt$_2$)](BAr$^F_4$)	1.13	2.51	3/2	2	1/2	ref 38
[(^{iPr}BIP)FeCl]	0.77	0.73	3/2	2	1/2	ref 39
Doubly Reduced Complexes						
[(^{iPr}BIP)Fe(DMAP)]	0.31	1.94	0	1	1	ref 39
[(^{iPr}BAP)Fe(DMAP)]^a	0.30	2.04	0	1	1	ref 82
[(^{iPr}BIP)Fe(CO)$_2$]	0.03	1.17	1	0	1	refs 39, 82

^{a}BAP = bis(aldimino)pyridine.

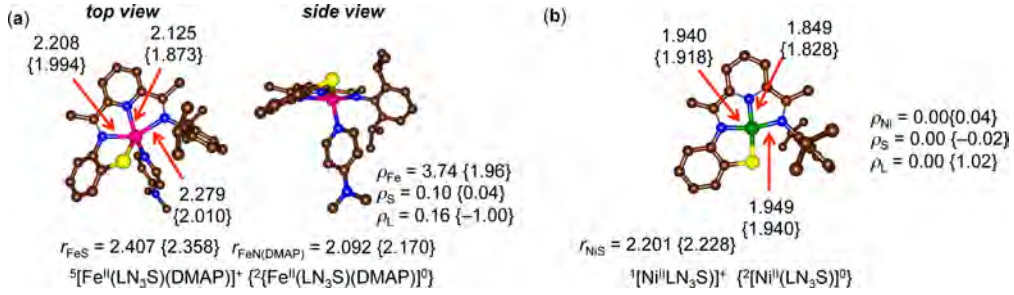

Figure 14. Optimized UB3LYP/B1 geometries of ^{5}[Fe^{II}(LN$_3$S)(DMAP)]$^+$ and ^{1}[Ni^{II}(LN$_3$S)]$^+$, and their reduced complexes (bond lengths given in angstroms). Also given are group spin densities.

reduced complexes, which have been assigned as intermediate-spin (is) iron(II) species with diradical ligands. The Mössbauer data for **4** thus point to an is-Fe^{II} center as the best assignment for this complex, and this conclusion is in good agreement with both the structural and EPR data. The strong-field thiolate ligand in **4**, coupled with the relatively weak-field DMAP donor, gives rise to this unique electronic configuration.

Computational Studies. The iron(II) and nickel(II) complexes, and their monoreduced analogues, were studied by DFT calculations to gain further insight into their structures and electronic configurations. The optimized geometries of [(LN$_3$S)Fe^{II}(DMAP)]$^+$ (**3**) and [Ni^{II}(LN$_3$S)]$^+$ (**5**) were calculated with the B3LYP functional on all low-lying spin states and are given in Figure 14. A quintet spin ground state (S = 2, hs-Fe^{II}) was found for **3**. At ΔE+ZPE level of theory, the quintet state (^{5}**3**) for the iron(II) complex is more stable than either the triplet state (S = 1, is-Fe^{II}, (^{3}**3**)) or the singlet state (^{1}**3**), by 13.8 and 17.0 kcal mol^{-1}, respectively. Inclusion of dispersion corrections further increases the energy gaps to 21.6 and 32.7 kcal mol^{-1}, respectively. These results indicate that the singlet and triplet spin states should be inaccessible at room temperature, and match nicely with the experimental observations (structural parameters, ^{1}H NMR) that show **3** has an hs-Fe^{II} ground state. The Fe−N bond lengths in the DFT-optimized structure of ^{5}**3** are within the range of 2.092−2.279 Å, and they are in good agreement with the X-ray structure (Fe−N for **3**: 2.073(5)−2.196(5)). The Fe−S distance of 2.407 Å for ^{5}**3** in Figure 14 is slightly elongated, compared to the X-ray structure (Fe−S = 2.3246(18) Å). Note that when geometry optimizations for **3** were run with a pure density functional such as BP86 instead of B3LYP, a different spin state ordering was found, in which a degenerate singlet/triplet ground state was obtained and the quintet spin state was calculated to be much higher in energy (see the Supporting Information). Consequently, pure density functional methods such as BP86 give results that are inconsistent with the experimental findings, and therefore we did not proceed further with these types of methods.

For the nickel(II) complex **5**, a closed-shell singlet spin state (S = 0) was found to be the ground state. We also calculated the triplet and quintet spin states for **5**, but we found these states to be higher in energy than ^{1}**5**, by 4.2 and 33.3 kcal mol^{-1}, respectively. No changes in spin state ordering were found for this complex when alternative density functional methods were employed. The optimized geometry for the ground state singlet is approximately square planar, consistent with the X-ray structure. The Ni−N distances for ^{1}**5** are in excellent agreement with those derived from the crystal structure (Table 3), although the Ni−S distance is slightly elongated (2.201 Å via the DFT method, 2.1386(5) Å according to the experimental data), similar to the trend seen for the Fe−S distance in ^{5}**3** versus the X-ray structure. The DFT calculations at the B3LYP level of theory often slightly overestimate metal−sulfur bond lengths.[83] The other main

dx.doi.org/10.1021/ic4013558 | Inorg. Chem. 2013, 52, 10467−10480

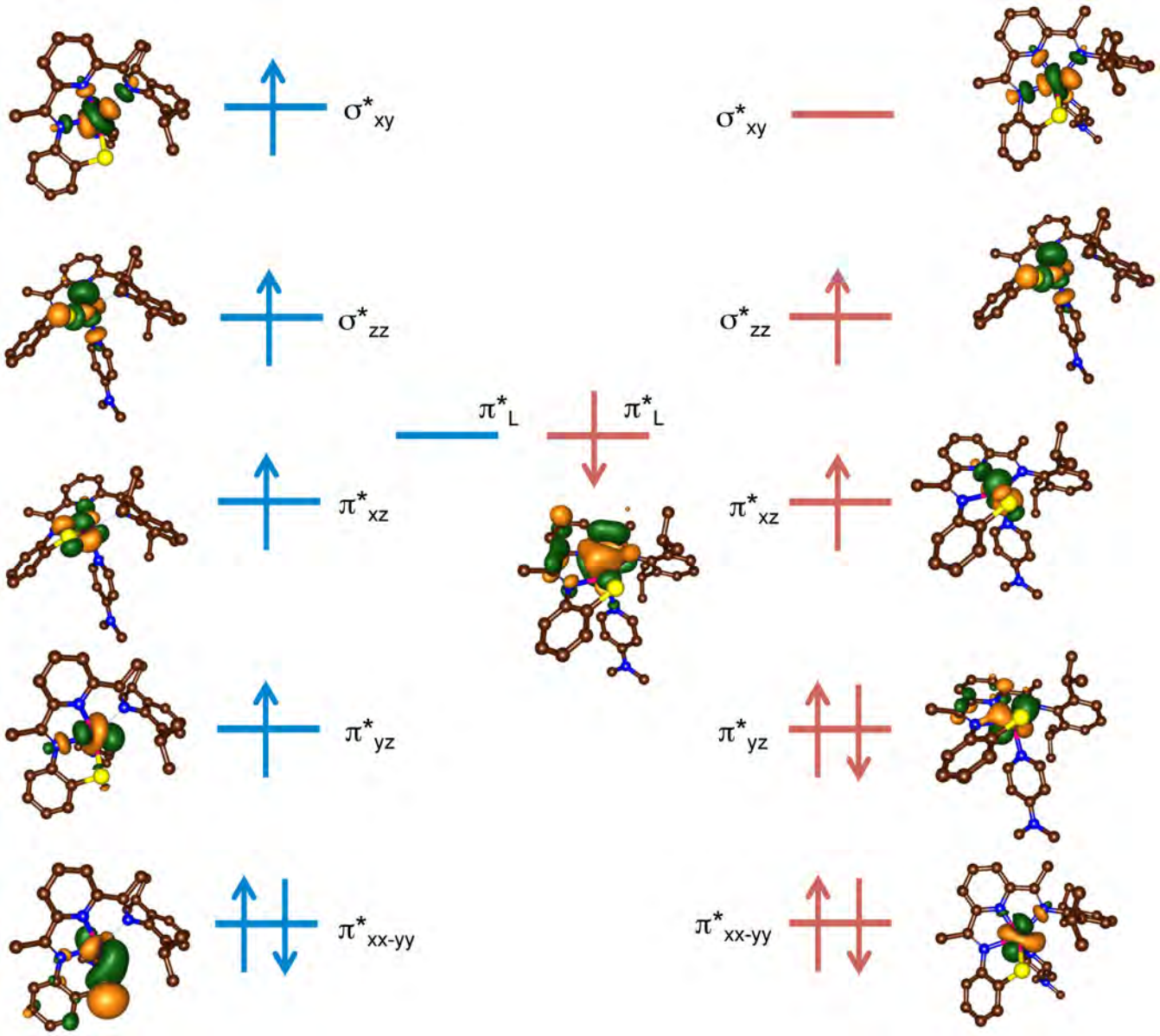

Figure 15. Orbital diagrams of $^{5}[Fe^{II}(LN_3S)(DMAP)]^{+}$ (left) and $^{2}[Fe^{II}(LN_3S)(DMAP)]^{0}$ (right).

structural features—and, importantly, the spin ground states—are well-reproduced by the calculations.

The monoreduced complex **4** was also studied at the B3LYP level of theory, taking into consideration the possible doublet (S = 1/2) and quartet (S = 3/2) spin states for this complex. Calculations were initiated by using the coordinates from the X-ray structure of **4** as a starting point, and the results led to an overall doublet spin ground state (S = 1/2) for the monoreduced complex. The doublet spin state is found to be stabilized by 6.3 kcal mol^{-1} over the quartet spin state, and solvent corrections raise this energy gap to 6.5 kcal mol^{-1}; however, dispersion corrections reduce it to 0.6 kcal mol^{-1}. The computationally derived S = 1/2 ground state thus matches that derived from the EPR spectrum observed in Figure 9 for complex **4**. The bond distances for the doublet spin ground state of **4** are shown in Figure 14, and both the Fe−N and Fe−S distances are significantly shortened compared to the starting complex **3**. The Fe−N bond lengths for the in-plane LN_3S ligand are in good agreement with the structural parameters for **4** (Table 1), but the Fe−S distance is somewhat longer, following the trend seen for **3** and **5**. In addition the Fe−N distance for the axial DMAP ligand is also slightly elongated (DFT, 2.170 Å; expt, 2.0508(16) Å).

The molecular orbital diagram for the doublet spin ground state of **4** is given in Figure 15, together with the MO diagram for the quintet spin ground state of starting complex **3**. For complex **4**, the computational results are consistent with an is-Fe^{II} (S_{Fe} = 1) center antiferromagnetically coupled with a ligand-based radical to give an overall doublet spin (S_{total} = 1/2) ground state. As seen in Figure 15, two α spin electrons reside in metal-based orbitals, while a predominantly ligand-based orbital (π^*_L) contains one β spin electron. The two unpaired electrons on the metal are reflected by a calculated spin density of ρ_{Fe} = 1.96, whereas the unpaired electron on the ligand leads to ρ_{LN3S} = −1.00 (Figure 14). In contrast, the MO diagram for **3** reveals four half-filled (α-spin) metal-based orbitals resulting in ρ_{Fe} = 3.74, as expected for a hs-Fe^{II} center. The calculations show that one-electron reduction of **3** occurs by the filling of a

dx.doi.org/10.1021/ic4013558 | Inorg. Chem. 2013, 52, 10467−10480

low-lying virtual ligand (π^*_L) orbital in preference to filling of an empty metal-based orbital, confirming the non-innocent nature of the LN_3S ligand. The spin state change that occurs at the Fe center upon reduction of **3** (hs-Fe^{II}) to **4** (is-Fe^{II}) appears to be a consequence of the destabilization of the σ^*_{xy} orbital. This destabilization is likely brought on by an increase in ligand field strength for the one-electron-reduced LN_3S ligand and a consequent shortening of the Fe−N and Fe−S bonds. Destabilization of σ^*_{xy} leads to depopulation of this orbital and occupation of the lower-lying π^*_{yz} orbital, resulting in an overall is-Fe^{II} center. Finally, the ligand-based β electron in **4** is mainly located on the bis(imino)pyridine backbone, which leads to the significant bond length perturbations shown in Figure 16, where the backbones for ^{5}**3** and ^{2}**4** are compared.

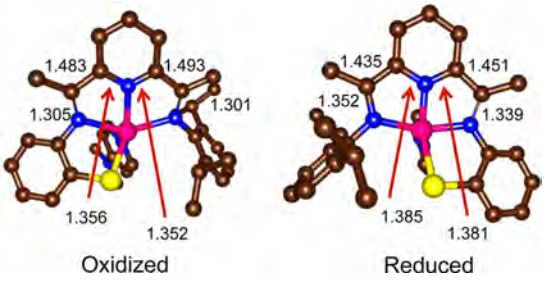

Figure 16. Optimized UB3LYP/B1 geometries of $^5[Fe^{II}(LN_3S)(DMAP)]^+$ and $^2[Fe^{II}(LN_3S)(DMAP)]^0$, highlighting BIP ligand backbone (bond lengths given in angstroms).

The trends in the perturbations provide a satisfying match to what is seen experimentally in Figure 10 and help to further validate the DFT results. The close agreement of the calculated ligand backbone bond distances (Figure 16) with the X-ray structure of **4** provides additional evidence for the assignment of **4** as a one-electron reduced ligand radical coupled to an is-Fe^{II} ion (ρ_{Fe} = 1.96, ρ_L = −1.00; see Figure 14a).

The monoreduced product of ^{1}**5** was also investigated by DFT, giving the optimized geometry for the doublet spin ground state of $^2[Ni^{II}(LN_3S)]^0$ shown in Figure 14. In this case, there are only very minor perturbations on the metal−ligand bond lengths, compared to the non-reduced starting material. Analysis of the spin density shows that the extra electron clearly lies on the LN_3S ligand and not the closed-shell nickel center, with an α electron occupying a π^*_L orbital (Figure S8 in the Supporting Information). The DFT calculations for the monoreduced nickel complex provide further confirmation that LN_3S functions easily as a non-innocent ligand, and the ligand-based radical predicted by DFT is in full agreement with the sharp organic radical seen in the EPR spectrum for monoreduced **5**.

O_2 Reactivity. We previously found that **1** reacts with excess O_2[24] in CH_2Cl_2 to give an S-oxygenated sulfonate complex, providing the first example of an Fe^{II}-thiolate complex that reacts with O_2 to give selective sulfur oxygenation. This reaction mimicked some of the general features of the reaction seen for CDO, but was lacking in the fact that the donor set at the metal center was N_3S(thiolate), not N_4S(thiolate), and the sulfur-oxygenated product was a triply oxygenated RSO_3^- complex, as opposed to the doubly oxygenated RSO_2^- product generated by the enzymatic system. In a subsequent report, we prepared an improved N_4S(thiolate) iron(II) model complex based on the tripodal N4Py ligand, $[Fe^{II}(N3PyS)(solvent)]^+$, and we found that it reacts with O_2 to give a biomimetic, doubly oxygenated sulfinato-iron(II) complex.[26] We thus sought to test the new N_4S(thiolate) iron(II) complexes **2** and **3** to determine their reactivity toward O_2.

Reactions of complexes **2** and **3** with excess O_2 in CH_2Cl_2 were analyzed directly by LDI-MS. The mass spectral data (Figures S3 and S4 in the Supporting Information) show dominant ions that correspond to the triply oxygenated sulfonato-iron(II) complex, $[Fe(LN_3SO_3)]^+$ (m/z = 532). This oxygenation pattern is the same as that seen for **1**.[24] Conversion of **1** to an N_4S(thiolate) coordination environment by addition of py or DMAP does not alter the O_2 reactivity such that sulfur oxygenation results in a doubly oxygenated sulfinato product, as seen for our other N_4S(thiolate) system.[25]

Some nickel(II) thiolate complexes can undergo sulfur oxygenation, most likely through a mechanism involving direct attack of O_2 on the coordinated sulfur atom, while other Ni^{II}-thiolates are inert toward O_2, and orbital compositions have been analyzed to explain these differences in O_2 reactivity.[46−54] We did not observe any reaction between complex **5** and excess O_2 in CH_2Cl_2, even after prolonged stirring for several days. Solutions of the monoreduced nickel(II) complex $[Ni(LN_3S)]^0$ generated from Na/Hg amalgam in THF were next tested for their reactivity toward O_2. In this case, a rapid reaction with O_2 was indeed observed by an immediate color change from bright to dark green, but LDI-MS analysis of the reaction mixture revealed only a peak (m/z = 488.3) for the starting material **5**, suggesting only outer-sphere oxidation had occurred. In contrast, a related Ni^{II}(BIP) complex undergoes outer-sphere reduction to give a one-electron-reduced product that then reacts with O_2 via an inner-sphere mechanism to afford ligand-oxidized products.[70]

The monoreduced compound **4** also exhibits rapid reactivity with O_2. Exposure of solutions of **4** in Et_2O to air, or bubbling O_2, leads to an immediate color change from dark green to brown with concurrent formation of a brown precipitate. Analysis by LDI-MS reveals a mixture that can be assigned to iron oxygenates and sulfur oxygenates, with multiple major peaks assigned to $[SOFe^{III}-O-Fe^{III}SO]^{2+}$ (m/z = 508.3), $[SO_2Fe^{III}-O-Fe^{III}SO_2]^{2+}$ (m/z = 524.4), and $[SO_3Fe^{III}-O-Fe^{III}-SO_3]^{2+}$ (m/z = 540.4). While complexes **1**−**3** exhibit S-centered oxidation, the monoreduced complex **4** appears to show significant oxidation at the Fe center. This represents a significant change in the observed reactivity of these complexes, as a result of the change in electronic structure.

■ CONCLUSIONS

The triflate-ligated ferrous complex $[Fe^{II}(LN_3S)(OTf)]$ (**1**) serves as a useful precursor for the facile synthesis of the biomimetic N_4S(thiolate) complexes $[Fe^{II}(LN_3S)(DMAP)]$-OTf (**2**) and $[Fe^{II}(LN_3S)(DMAP)]OTf$ (**3**). Template assembly with nickel(II) tetrafluoroborate leads to the Ni^{II} analogue $[Ni^{II}(LN_3S)]BF_4$ (**5**). Structural and spectroscopic methods show that the iron complexes are 5-coordinated, high-spin (S = 2) iron(II) species, while the nickel complex is a 4-coordinate square-planar nickel(II) species. Electrochemical measurements revealed that these complexes uniformly exhibit only one reversible reduction wave between −0.9 V and −1.2 V, vs Fc^+/Fc, within the CH_3CN solvent window. Bulk chemical reduction of **3** by Na/Hg amalgam gives the extremely air-sensitive, monoreduced complex $[Fe(LN_3S)(DMAP)]^0$ (**4**), which was isolated and crystallographically characterized. No evidence for a two-electron reduced product was observed, which was consistent with the electrochemical analysis. This

dx.doi.org/10.1021/ic4013558 | Inorg. Chem. 2013, 52, 10467−10480

behavior contrasts other bis(imino)pyridine complexes, which typically can house up to two or three reducing equivalents beginning at the $M^{2+}(BIP^0)$ redox level, and have been shown to form two-electron reduced products from Na/Hg reduction. It can be concluded that the anionic thiolate arm appended to the new LN_3S system likely causes multiple reductions to be thermodynamically unfavorable. The X-ray structure of **4** shows it is a 5-coordinated complex, with one DMAP ligand remaining coordinated in the axial position following reduction. The electronic structure of the monoreduced complex **4** was firmly established through a combination of structural analysis, EPR and Mössbauer spectroscopies as well as computational (DFT) methods. The ground state of **4** is clearly a doublet state that arises from an intermediate-spin ($S = 1$) iron(II) center antiferromagnetically coupled to a ligand-based radical. The spin state of the Fe center is reflected in the unusual Mössbauer parameters for this monoreduced BIP complex, with $\delta = 0.33$ mm s^{-1} and $\Delta E_Q = 2.04$ mm s^{-1}. These parameters differ significantly from other monoreduced Fe(BIP) complexes that exhibit either hs-Fe^{II} ($S = 2$) or ls-Fe^{II} ($S = 0$) configurations, and they, in fact, are consistent with the doubly reduced Fe(BIP) species, which have been previously assigned as is-Fe^{II} complexes carrying diradical ligands. The computational studies show that the doublet spin ground state is comprised of two α electrons occupying metal-based orbitals of d_{z2} and d_{xz} parentage and one β electron residing on a ligand-based π^* orbital with most of the spin density localized on the bis(imino)pyridine backbone and not on the phenylthiolate arm. The DFT results are nicely validated by their agreement with the findings from Mössbauer and EPR spectroscopies, as well as by their reproduction of the experimentally observed, yet subtle bond length distortions that occur in the BIP backbone upon one-electron reduction. This study shows that the tetradentate LN_3S ligand can serve as a non-innocent ligand in the same fashion as the parent BIP system; however, in this case, it only accepts one electron delocalized over the ligand backbone. Taken together, our experimental and computational data strongly suggest that monoreduction of the starting iron(II) complex provides the first example of an intermediate-spin iron(II) complex antiferromagnetically coupled with a ligand-based radical.

The O_2 reactivity of the new Fe^{II} complexes **2** and **3** seems to mirror that of **1**, to give sulfonato-iron complexes. Interestingly, the thiolate-ligated Ni^{II} complex **5** is completely unreactive toward O_2, as opposed to some thiolate-ligated Ni^{II} complexes that can become oxygenated at the sulfur positions. The monoreduced iron complex **4** is extremely air-sensitive and rapidly reacts with O_2, but instead of leading only to sulfur oxygenation, yields a mixture of products involving both Fe-centered and S-centered oxygenates. Now that the ability to store reducing equivalents on thiolate-appended BIP ligands has been established, future work may involve designing systems where reducing equivalents on both the non-innocent ligand and the metal can be harnessed in a more-controlled fashion for O_2 activation.

■ ASSOCIATED CONTENT

Supporting Information

Crystallographic details for $[Fe^{II}(LN_3S)(py)](OTf)$, $[Fe^{II}(LN_3S)(DMAP)](OTf)$, $[Fe(LN_3S)(DMAP)]^0$, and $[Ni^{II}(LN_3S)](BF_4)$ in CIF format. ^1H and ^{19}F NMR spectra of **4**, and LDI-MS data for O_2 reactions. Computational details, including energies and Cartesian coordinates for DFT calculated structures. This material is available free of charge via the Internet at http://pubs.acs.org.

■ AUTHOR INFORMATION

Corresponding Author

*E-mail: dpg@jhu.edu.

Notes

The authors declare no competing financial interest.

■ ACKNOWLEDGMENTS

The National Institute of Health (NIH) is gratefully acknowledged for financial support to D.P.G. (No. GM62309). The National Service of Computational Chemistry Software (NSCCS) is thanked for generous CPU time to S.P.d.V. D.K. is a DST-Ramanujan Fellow (SR/S2/RJN-11/2008). G.N.L.J. thanks the Marsden Fund and The International Mobility Fund administered by the Royal Society of New Zealand.

■ REFERENCES

(1) McQuilken, A. C.; Goldberg, D. P. *Dalton Trans.* **2012**, *41*, 10883.
(2) Fox, B. G. *Iron Cofactors: Non-heme Handbook of Proteins*; John Wiley & Sons, Ltd.: Chichester, U.K., 2007; pp 611−618.
(3) Kovacs, J. A.; Brines, L. M. *Acc. Chem. Res.* **2007**, *40*, 501.
(4) Mascharak, P. K. *Coord. Chem. Rev.* **2002**, *225*, 201.
(5) Solomon, E. I.; Decker, A.; Lehnert, N. *Proc. Natl. Acad. Sci. U.S.A.* **2003**, *100*, 3589.
(6) Ryle, M. J.; Hausinger, R. P. *Curr. Opin. Chem. Biol.* **2002**, *6*, 193.
(7) Bruijnincx, P. C. A.; van Koten, G.; Klein Gebbink, R. J. *Chem. Soc. Rev.* **2008**, *37*, 2716.
(8) Nivière, V.; Bonnot, F.; Bourgeois, D. *Handb. Metalloproteins* **2011**, 246.
(9) Yeh, A. P.; Hu, Y. L.; Jenney, F. E.; Adams, M. W. W.; Rees, D. C. *Biochemistry* **2000**, *39*, 2499.
(10) Matias, P. M.; Morais, J.; Coelho, A. V.; Meijers, R.; Gonzalez, A.; Thompson, A. W.; Sieker, L.; LeGall, J.; Carrondo, M. A. *J. Biol. Inorg. Chem.* **1997**, *2*, 507.
(11) Santos-Silva, T.; Trincão, J.; Carvalho, A. L.; Bonifâcio, C.; Auchère, F.; Raleiras, P.; Moura, I.; Moura, J. J. G.; Romão, M. J. *J. Biol. Inorg. Chem.* **2006**, *11*, 548.
(12) Adam, V.; Royant, A.; Niviere, V.; Molina-Heredia, F. P.; Bourgeois, D. *Structure* **2004**, *12*, 1729.
(13) Kobayashi, M.; Nagasawa, T.; Yamada, H. *Trends Biotechnol.* **1992**, *10*, 402.
(14) Endo, I.; Nojiri, M.; Tsujimura, M.; Nakasako, M.; Nagashima, S.; Yohda, M.; Odaka, M. *J. Inorg. Biochem.* **2001**, *83*, 247.
(15) Kobayashi, M.; Shimizu, S. *Nat. Biotechnol.* **1998**, *16*, 733.
(16) de Visser, S. P., Kumar, D., Eds. *Iron-Containing Enzymes: Versatile Catalysts of Hydroxylation Reactions in Nature*; Royal Society of Chemistry: Cambridge, U.K., 2011.
(17) Joseph, C. A.; Maroney, M. J. *Chem. Commun.* **2007**, 3338.
(18) Straganz, G. D.; Nidetzky, B. *ChemBioChem* **2006**, *7*, 1536.
(19) Siakkou, E.; Rutledge, M. T.; Wilbanks, S. M.; Jameson, G. N. L. *Biochim. Biophys. Acta, Proteins Proteomics* **2011**, *1814*, 2003.
(20) Tchesnokov, E. P.; Wilbanks, S. M.; Jameson, G. N. L. *Biochemistry* **2012**, *51*, 257.
(21) McCoy, J. G.; Bailey, L. J.; Bitto, E.; Bingman, C. A.; Aceti, D. J.; Fox, B. G.; Phillips, G. N. *Proc. Natl. Acad. Sci. U.S.A.* **2006**, *103*, 3084.
(22) Simmons, C. R.; Liu, Q.; Huang, Q. Q.; Hao, Q.; Begley, T. P.; Karplus, P. A.; Stipanuk, M. H. *J. Biol. Chem.* **2006**, *281*, 18723.
(23) Ye, S.; Wu, X.; Wei, L.; Tang, D. M.; Sun, P.; Bartlam, M.; Rao, Z. H. *J. Biol. Chem.* **2007**, *282*, 3391.
(24) Jiang, Y. B.; Widger, L. R.; Kasper, G. D.; Siegler, M. A.; Goldberg, D. P. *J. Am. Chem. Soc.* **2010**, *132*, 12214.
(25) Badiei, Y. M.; Siegler, M. A.; Goldberg, D. P. *J. Am. Chem. Soc.* **2011**, *133*, 1274.

(26) McQuilken, A. C.; Jiang, Y. B.; Siegler, M. A.; Goldberg, D. P. *J. Am. Chem. Soc.* **2012**, *134*, 8758.
(27) Kovacs, J. A. *Science* **2003**, *299*, 1024.
(28) Kovacs, J. A. *Chem. Rev.* **2004**, *104*, 825.
(29) Artaud, I.; Chatel, S.; Chauvin, A. S.; Bonnet, D.; Kopf, M. A.; Leduc, P. *Coord. Chem. Rev.* **1999**, *192*, 577.
(30) Cho, J.; Woo, J.; Nam, W. *J. Am. Chem. Soc.* **2012**, *134*, 11112.
(31) Sallmann, M.; Siewert, I.; Fohlmeister, L.; Limberg, C.; Knispel, C. *Angew. Chem., Int. Ed.* **2012**, *51*, 2234.
(32) Gonzalez-Ovalle, L. E.; Quesne, M. G.; Kumar, D.; Goldberg, D. P.; de Visser, S. P. *Org. Biomol. Chem.* **2012**, *10*, 5401.
(33) Kumar, D.; Sastry, G. N.; Goldberg, D. P.; de Visser, S. P. *J. Phys. Chem. A* **2012**, *116*, 582.
(34) Britovsek, G. J. P.; Bruce, M.; Gibson, V. C.; Kimberley, B. S.; Maddox, P. J.; Mastroianni, S.; McTavish, S. J.; Redshaw, C.; Solan, G. A.; Stromberg, S.; White, A. J. P.; Williams, D. J. *J. Am. Chem. Soc.* **1999**, *121*, 8728.
(35) Scott, J.; Gambarotta, S.; Korobkov, I.; Budzelaar, P. H. M. *Organometallics* **2005**, *24*, 6298.
(36) Scott, J.; Gambarotta, S.; Korobkov, I.; Knijnenburg, Q.; de Bruin, B.; Budzelaar, P. H. M. *J. Am. Chem. Soc.* **2005**, *127*, 17204.
(37) Tondreau, A. M.; Milsmann, C.; Lobkovsky, E.; Chirik, P. J. *Inorg. Chem.* **2011**, *50*, 9888.
(38) Tondreau, A. M.; Stieber, S. C. E.; Milsmann, C.; Lobkovsky, E.; Weyhermuller, T.; Semproni, S. P.; Chirik, P. J. *Inorg. Chem.* **2013**, *52*, 635.
(39) Bart, S. C.; Chlopek, K.; Bill, E.; Bouwkamp, M. W.; Lobkovsky, E.; Neese, F.; Wieghardt, K.; Chirik, P. J. *J. Am. Chem. Soc.* **2006**, *128*, 13901.
(40) Bouwkamp, M. W.; Bart, S. C.; Hawrelak, E. J.; Trovitch, R. J.; Lobkovsky, E.; Chirik, P. J. *Chem. Commun.* **2005**, 3406.
(41) Bart, S. C.; Lobkovsky, E.; Bill, E.; Wieghardt, K.; Chirik, P. J. *Inorg. Chem.* **2007**, *46*, 7055.
(42) Stieber, S. C. E.; Milsmann, C.; Hoyt, J. M.; Turner, Z. R.; Finkelstein, K. D.; Wieghardt, K.; DeBeer, S.; Chirik, P. J. *Inorg. Chem.* **2012**, *51*, 3770.
(43) Darmon, J. M.; Turner, Z. R.; Lobkovsky, E.; Chirik, P. J. *Organometallics* **2012**, *31*, 2275.
(44) Enright, D.; Gambarotta, S.; Yap, G. P. A.; Budzelaar, P. H. M. *Angew. Chem., Int. Ed.* **2002**, *41*, 3873.
(45) de Bruin, B.; Bill, E.; Bothe, E.; Weyhermuller, T.; Wieghardt, K. *Inorg. Chem.* **2000**, *39*, 2936.
(46) Farmer, P. J.; Solouki, T.; Mills, D. K.; Soma, T.; Russell, D. H.; Reibenspies, J. H.; Darensbourg, M. Y. *J. Am. Chem. Soc.* **1992**, *114*, 4601.
(47) Farmer, P. J.; Solouki, T.; Soma, T.; Russell, D. H.; Darensbourg, M. Y. *Inorg. Chem.* **1993**, *32*, 4171.
(48) Darensbourg, M. Y.; Tuntulani, T.; Reibenspies, J. H. *Inorg. Chem.* **1995**, *34*, 6287.
(49) Buonomo, R. M.; Font, I.; Maguire, M. J.; Reibenspies, J. H.; Tuntulani, T.; Darensbourg, M. Y. *J. Am. Chem. Soc.* **1995**, *117*, 5427.
(50) Grapperhaus, C. A.; Darensbourg, M. Y.; Sumner, L. W.; Russell, D. H. *J. Am. Chem. Soc.* **1996**, *118*, 1791.
(51) Grapperhaus, C. A.; Darensbourg, M. Y. *Acc. Chem. Res.* **1998**, *31*, 451.
(52) Mullins, C. S.; Grapperhaus, C. A.; Frye, B. C.; Wood, L. H.; Hay, A. J.; Buchanan, R. M.; Mashuta, M. S. *Inorg. Chem.* **2009**, *48*, 9974.
(53) Herdt, D. R.; Grapperhaus, C. A. *Dalton Trans.* **2012**, *41*, 364.
(54) Mullins, C. S.; Grapperhaus, C. A.; Kozlowski, P. M. *J. Biol. Inorg. Chem.* **2006**, *11*, 617.
(55) Kumar, D.; Karamzadeh, B.; Sastry, G. N.; de Visser, S. P. *J. Am. Chem. Soc.* **2010**, *132*, 7656.
(56) Vardhaman, A. K.; Sastri, C. V.; Kumar, D.; de Visser, S. P. *Chem. Commun.* **2011**, *47*, 11044.
(57) Becke, A. D. *J. Chem. Phys.* **1993**, *98*, 1372.
(58) Lee, C. T.; Yang, W. T.; Parr, R. G. *Phys. Rev. B* **1988**, *37*, 785.
(59) Hay, P. J.; Wadt, W. R. *J. Chem. Phys.* **1985**, *82*, 299.
(60) Grimme, S.; Antony, J.; Ehrlich, S.; Krieg, H. *J. Chem. Phys.* **2010**, *132*, 154104.
(61) Becke, A. D. *Phys. Rev. A* **1988**, *38*, 3098.
(62) Perdew, J. P. *Phys. Rev. B* **1986**, *33*, 8822.
(63) *Jaguar, version 7.9*; Schrödinger, LLC: New York, 2011.
(64) Schwabe, T.; Grimme, S. *Phys. Chem. Chem. Phys.* **2007**, *9*, 3397.
(65) Bianchini, C.; Mantovani, G.; Meli, A.; Migliacci, F.; Zanobini, F.; Laschi, F.; Sommazzi, A. *Eur. J. Inorg. Chem.* **2003**, 1620.
(66) Fiedler, A. T.; Halfen, H. L.; Halfen, J. A.; Brunold, T. C. *J. Am. Chem. Soc.* **2005**, *127*, 1675.
(67) Theisen, R. M.; Shearer, J.; Kaminsky, W.; Kovacs, J. A. *Inorg. Chem.* **2004**, *43*, 7682.
(68) Shearer, J.; Nehring, J.; Lovell, S.; Kaminsky, W.; Kovacs, J. A. *Inorg. Chem.* **2001**, *40*, 5483.
(69) Addison, A. W.; Rao, T. N.; Reedijk, J.; Vanrijn, J.; Verschoor, G. C. *J. Chem. Soc., Dalton Trans.* **1984**, 1349.
(70) Manuel, T. D.; Rohde, J. U. *J. Am. Chem. Soc.* **2009**, *131*, 15582.
(71) Fan, R. Q.; Fan, R. J.; Lv, Z. W.; Yang, Y. L.; An, F.; Gu, D. M. *J. Coord. Chem.* **2007**, *60*, 919.
(72) Dunn, T. J.; Ramogida, C. F.; Simmonds, C.; Paterson, A.; Wong, E. W. Y.; Chiang, L.; Shimazaki, Y.; Storr, T. *Inorg. Chem.* **2011**, *50*, 6746.
(73) Chen, Y. J.; Hao, P.; Zuo, W. W.; Gao, K.; Sun, W. H. *J. Organomet. Chem.* **2008**, *693*, 1829.
(74) Bryliakov, K. P.; Talsi, E. P.; Semikolenova, N. V.; Zakharov, V. A. *Organometallics* **2009**, *28*, 3225.
(75) Britovsek, G. J. P.; Gibson, V. C.; Spitzmesser, S. K.; Tellmann, K. P.; White, A. J. P.; Williams, D. J. *J. Chem. Soc., Dalton Trans.* **2002**, 1159.
(76) Bart, S. C.; Lobkovsky, E.; Chirik, P. J. *J. Am. Chem. Soc.* **2004**, *126*, 13794.
(77) Nakajima, Y.; Nakao, Y.; Sakaki, S.; Tamada, Y.; Ono, T.; Ozawa, F. *J. Am. Chem. Soc.* **2010**, *132*, 9934.
(78) Trovitch, R. J.; Lobkovsky, E.; Chirik, P. J. *J. Am. Chem. Soc.* **2008**, *130*, 11631.
(79) Gütlich, P.; Bill, E.; Trautwein, A. X. *Mössbauer Spectroscopy and Transition Metal Chemistry: Fundamentals and Applications*; Springer–Verlag: Berlin, Heidelberg, 2011.
(80) Britovsek, G. J. P.; Clentsmith, G. K. B.; Gibson, V. C.; Goodgame, D. M. L.; McTavish, S. J.; Pankhurst, Q. A. *Catal. Commun.* **2002**, *3*, 207.
(81) Moura, I.; Tavares, P.; Moura, J. J. G.; Ravi, N.; Huynh, B. H.; Liu, M. Y.; Legall, J. *J. Biol. Chem.* **1990**, *265*, 21596.
(82) Russell, S. K.; Milsmann, C.; Lobkovsky, E.; Weyhermuller, T.; Chirik, P. J. *Inorg. Chem.* **2011**, *50*, 3159.
(83) Kumar, D.; Thiel, W.; de Visser, S. P. *J. Am. Chem. Soc.* **2011**, *133*, 3869.

Biocatalysis

DOI: 10.1002/anie.201304633

Inversion of Enantioselectivity of a Mononuclear Non-Heme Iron(II)-dependent Hydroxylase by Tuning the Interplay of Metal-Center Geometry and Protein Structure**

*Sarah M. Pratter, Cornelia Konstantinovics, Cristiana M. L. Di Giuro, Erich Leitner, Devesh Kumar, Sam P. de Visser, Gideon Grogan, and Grit D. Straganz**

Natural stereoselective oxidations by molecular oxygen have long fascinated chemists and these chemically challenging, "green" reactions have great potential for industrial processes.[1] However, the natural enzymes have a finite synthetic repertoire. A major goal is therefore to control their stereoselectivity and to produce a desired stereo-center within a certain target molecule. There have been some major successes recently in the design of stereo-controlled reactions by cytochrome P450 enzymes (P450s),[2] which have great potential as a source for site-specific oxygenation reactions.[3] By contrast, O_2 and mononuclear non-heme (MNH) Fe^{II} dependent hydroxylases have not been the focus of enzyme design studies. This is surprising because the catalytic potential of MNH Fe^{II} dependent hydroxylases complements that of P450s, with their ability to oxidize aliphatic carbon atoms in a regio- and stereoselective manner.[4] One example is the (*S*)-selective *p*-hydroxymandelate synthase (HMS) from *Amycalotopsis orientalis* (*Ao*HMS), which has homologues in other organisms including *Streptomyces coelicolor* (*Sc*HMS).[5,6] Recently, it was found that the high enantioselectivity of *Sc*HMS, which naturally converts the substrate *p*-hydroxyphenylpyruvate, can be compromised by substituents on the aromatic ring of phenylpyruvate (PP).[7] However, no structural features have been identified that cause the generally observed (*S*)-enantioselectivity of HMS enzymes. Herein, we have used modeling, molecular dynamics (MD), and density functional theory (DFT) calculations to redesign the (*S*)-selective *Sc*HMS to give a biocatalyst of inverted enantioselectivity, yielding (*R*)-mandelate as the product.

The reaction mechanism of HMS enzymes follows that of α-ketoacid dependent MNH Fe^{II} enzymes: *p*-hydroxyphenylpyruvate binding primes the iron center for activation of O_2, which in turn decarboxylates the substrate. The resulting high-valent Fe^{IV}=O species abstracts a benzylic hydrogen atom. In a rebound reaction, the formed Fe^{III}–OH species transfers a hydroxyl radical to the benzylic position resulting in the *p*-hydroxymandelate product, which leaves the active site (Figure 1).[6,8] The crystal structure of the (*S*)-selective *Ao*HMS has been determined and shows the native reaction product coordinated to the metal center.[9]

Upon close inspection of in silico docked complexes of *Sc*HMS with mandelate (MA) analogues of the (*S*)-configuration, as well as in the *Ao*HMS crystal structure,[9] it was found that the ligands were oriented in a slightly distorted trigonal bipyramidal geometry at the metal center. The α-hydroxy group of MA and the metal-coordinating glutamate were in the axial positions and two nitrogen atoms from the coordinating histidines, together with the carboxylate oxygen of the ligand, formed the trigonal basis of the pyramid. In contrast, the analogous (*R*)-MA–enzyme complex showed more pronounced deviations from the ideal symmetry (Supporting Information, Figure S1).[7] DFT calculations of the reactive Fe^{IV}=O and Fe^{III}–OH species in the catalytic cycle of α-ketoacid dependent enzymes showed that a trigonal bipyramidal geometry was one of two probable organizations

[*] S. M. Pratter, C. Konstantinovics, Dr. C. M. L. Di Giuro, Dr. G. D. Straganz
Institute of Biotechnology and Biochemical Engineering
Graz University of Technology
Petersgasse 12, 8010 Graz (Austria)
E-mail: grit.straganz@tugraz.at
Prof. Dr. E. Leitner
Institute of Analytical Chemistry and Food Chemistry
Graz University of Technology
Stremayrgasse 9, 8010 Graz (Austria)
Dr. D. Kumar
Department of Applied Physics, School for Physical Sciences,
Babasaheb Bhimrao Ambedkar University
Vidya Vihar, Rae Bareilly Road, Lucknow 226-025 (India)
Dr. S. P. de Visser
Manchester Institute of Biotechnology and School of Chemical Engineering and Analytical Science
The University of Manchester
131 Princess Street, Manchester M1 7DN (UK)
Dr. G. Grogan
York Structural Biology Laboratory, Department of Chemistry,
University of York
Heslington, York, YO10 5DD (UK)

[**] The financial support by the Austrian Science Fund (FWF) grant W901-B05 DK Molecular Enzymology and FWF research grant P18828 is gratefully acknowledged. G.D.S. thanks the VVRC at the Graz University of Technology for computational resources and Kim Carstens for technical assistance. S.d.V. thanks the National Service of Computational Chemistry Software for CPU time. D.K. holds a Ramanujan Fellowship from the Department of Science and Technology (DST), New Delhi (India) and acknowledges its financial support (Research Grants SR/S2/RJN-11/2008 and SR/S1/PC-58/2009).

Supporting information for this article is available on the WWW under http://dx.doi.org/10.1002/anie.201304633.

© 2013 Wiley-VCH Verlag GmbH & Co. KGaA, Weinheim

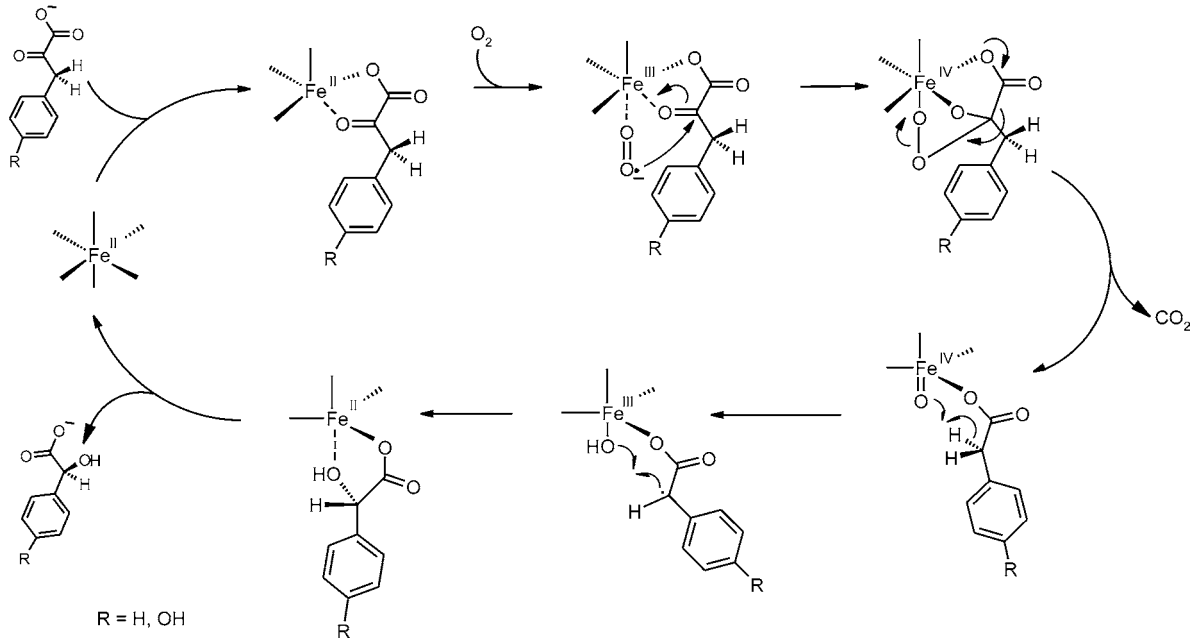

Figure 1. Generally accepted reaction mechanism of HMS enzymes.[8]

of these high-valent iron centers.[10] This posed the question of what impact the ligand field symmetry may have on enantioselectivity during catalysis. In models of (*R*)-MA and (*S*)-MA bound *Sc*HMS, in which the trigonal bipyramidal geometry was constrained, the (*R*)-MA ligand did not occupy the hydrophobic pocket that accommodates the aromatic substituent of (*S*)-MA. In contrast, the aromatic ring pointed toward the presumed substrate entrance channel and thereby collided with residue Tyr359 (Figure S1). *pro*-(*S*) and *pro*-(*R*) transition states of H-abstraction and rebound hydroxylation gave analogous principle spatial orientations when docked into the trigonal bipyramidal metal center of *Sc*HMS. Consequently, we investigated how the destabilization of the aromatic ring in the hydrophobic pocket and its stabilization in the alternative orientation influenced enantioselective catalysis. The steric clash with residue Tyr359 upon (*R*)-MA binding in our model could be removed by substituting it with alanine. To obstruct the hydrophobic pocket of *Sc*HMS, potentially effective point mutations were identified using in silico site-saturation mutagenesis with the following set of criteria: the variation 1) results in a low-energy apo-enzyme structure to prevent energetically driven reorganization of the active site; 2) has low-energy amino acid conformers that all interfere with the hydrophobic binding pocket; and 3) does not interact with the first coordination sphere of the metal ion and thus with its electronic or geometric structure. Using the algorithm described in the Supporting Information (Figure S2), six target single-point substitutions (Ser221Met, Val223Phe, Val223Met, Val223Trp, Ile236Phe and Tyr359Ala) were identified and introduced into the *Sc*HMS scaffold in vitro.

Spectra of PP conversion products by the wild-type (WT) and the resulting enzyme variants were subsequently analyzed using GC-MS and HPLC-MS (Table S1): all but one variation had a significant impact on the enantioselectivity of the WT enzyme, which gave an enantiomeric ratio (e.r.) of 0.4% (*R*)-MA:99.6% (*S*)-MA (Figure 2a). The most pronounced effect was an appoximately 1900-fold increase in (*R*)-selectivity with the mutation Ser221Met, which was predicted to obstruct the hydrophobic pocket, and resulted in the formation of 88.5% (*R*)-MA versus 11.5% (*S*)-MA. This efficacy was followed by the mutant Val223Phe, which gave an e.r. of 65.1% (*R*)-MA:34.9% (*S*)-MA. The opening of space for (*R*)-MA binding by the Tyr359Ala mutation resulted in only an approximately 47-fold increase of (*R*)-enantioselectivity compared to WT. Notably, Ser221, Val223, and Tyr359 are strongly conserved throughout all annotated putative *p*-hydroxyphenylpyruvate dioxygenases and HMSs. Combinations of the most successful substitutions further enhanced enantioselectivity: the best variant, triple mutant Ser221Met_Val223Phe_Tyr359Ala increased the e.r. to 97.4% in favor of (*R*)-selective hydroxylation, which corresponds to an approximately 9300-fold enhancement compared to WT. The latter translates to a difference in transition state energy $\Delta\Delta G^{\ddagger}$ of 22.6 kJ mol^{-1}. No reaction side products that are indicative of C2–C3 cleavage or uncoupled decarboxylation[11] were formed in detectable amounts and product recovery for MA was greater than 95% for all variants, except for variants Ile236Phe and Val223Trp, which showed substantial losses of approximately 60% and 20% that were not accounted for. This may indicate the formation of alternative oxygenation products in these variants that escaped our analysis. Notably, ring oxidation products have been reported from mutational studies of the active site of HMS.[12]

All *Sc*HMS variants had enzymatic activities towards PP that were roughly in the same range of the WT enzyme (Figure 2b, Table S1). The point mutations Val223Phe and Ser221Met increased catalytic efficiencies by an order of

 © 2013 Wiley-VCH Verlag GmbH & Co. KGaA, Weinheim

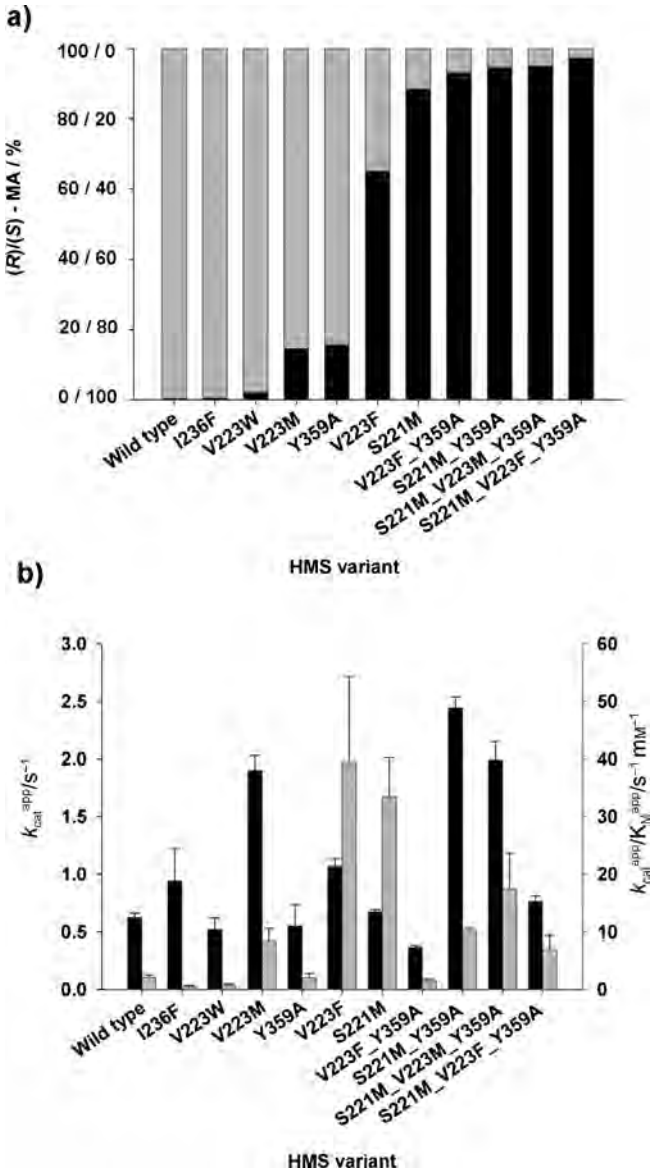

Figure 2. Enantioselectivities and activities of *Sc*HMS WT and variants. (a) The percentage of (*R*)-MA (black) and (*S*)-MA (gray) products and (b) steady-state kinetic constants k_{cat}^{app} (black) and k_{cat}^{app}/K_M^{app} (gray) are shown.

magnitude with k_{cat}^{app}/K_M^{app} values of 40 mM^{-1}s^{-1} and 34 mM^{-1}s^{-1} respectively, while the open active-site variant Tyr359Ala did not significantly alter WT efficiency ($k_{cat}^{app}/K_M^{app} = 2.1$ mM^{-1}s^{-1}). For the enzyme with the highest (*R*)-enantioselectivity, the triple mutant Ser221Met_Val223Phe_Tyr359Ala, the apparent turnover number was raised by 22% ($k_{cat}^{app} = 0.76$ s^{-1}) and the k_{cat}^{app}/K_M^{app} of 6.9 mM^{-1}s^{-1} was approximately three times higher compared to the WT enzyme.

The structure of the newly designed (*R*)-MA synthase, *Sc*HMS variant Ser221Met_Val223Phe_Tyr359Ala, in complex with (*R*)-MA and cobalt, which is a redox inactive Fe^{II} mimic,[9] was solved and refined to a resolution of 1.95 Å with an R_{cryst} value of 17.5% and an R_{free} value of 21.5% (Table S2). The aromatic substituent of the product filled the free space, which was created by the Tyr359Ala mutation, while Met221 and Phe223 occupied space in the hydrophobic binding pocket of the enzyme. Both protein molecules of the asymmetric unit showed (*R*)-MA ligation to the metal ions in a trigonal bipyramidal geometry and thus mirrored the product coordinated active site in the native structure of *Ao*HMS[11] (Figure 3a).

Computational MD studies of reaction intermediates in the scaffolds of WT *Sc*HMS and its Ser221Met_Val223Phe_Tyr359Ala variant shed light on the impact of particular catalytic steps for the overall enantioselectivity of the reaction. In each case, intermediates and transition states from phenylacetate (PA) ligated Fe^{IV}=O centers up to the final products were analyzed, whereby the ideal initial *pro*-(*S*) and *pro*-(*R*) geometries, which had been geometrically optimized by DFT calculations (Figure S3–S5), were the starting points of all simulations. The complexes generally showed two distinct localizations of the phenyl rings on the intermediates that were prototypical for either the *pro*-(*S*) or the *pro*-(*R*) pathway (Figure 3b and Figure S6–S13). Inspection of the ligand geometries and energies in the *Sc*HMS WT protein suggested that product chirality was determined by the final hydroxylation step. The pro-(*S*) mechanism, to which the ligand is predisposed by preceding catalytic steps,[7,10d] resulted in a PA radical that displayed considerable out-of-plane flexibility. It oscillated between a *pro*-(*S*) (43%) and a *pro*-(*R*) (57%) conformation, thus apparently making both hydroxylation pathways equally feasible (Figure S10 and Table S4). The *pro*-(*S*) rebound transition state was then kinetically favored compared to the (*R*)-selective pathway. By contrast, during MD simulations of the newly designed (*R*)-MA synthase the first, high-valent Fe^{IV}=O complex of both *pro*-(*R*) and *pro*-(*S*) starting geometries adopted the *pro*-(*R*) conformation. The subsequent PA radicals were entrapped in their respective *pro*-(*S*) (99%) and *pro*-(*R*) positions (97%) (Figure S10), while the *pro*-(*S*) pathway was kinetically favored during hydroxylation. This suggests that the primary Fe^{IV}=O complex geometry co-determines enantioselectivity in the variant and apparently compensates for the kinetically favored (*S*)-trajectory during hydroxylation (Table S4). Overall, our computational method rationalized the experimentally observed enantioselectivities of the two enantio-complementary enzymes.

In summary, we demonstrated for the first time how the interplay of metal-center geometry and protein structure control enantioselective hydroxylation in a metalloenzyme. The consideration of this principle has allowed for the design of a highly (*R*)-selective MA synthase from an enantio-complementary HMS through the in vitro construction of a total of only ten enzyme variants. The resulting approximately 9300-fold enantioselectivity switch, the most pronounced change ever reported for an oxygenation, is accompanied by a threefold improvement of enzyme efficiency. The designed hydroxylase, which has no natural precedent, may open up a new route for efficient, sustainable (*R*)-MA biosynthesis from readily available renewable feedstocks. This work and its underlying principles may, furthermore, be

 © 2013 Wiley-VCH Verlag GmbH & Co. KGaA, Weinheim

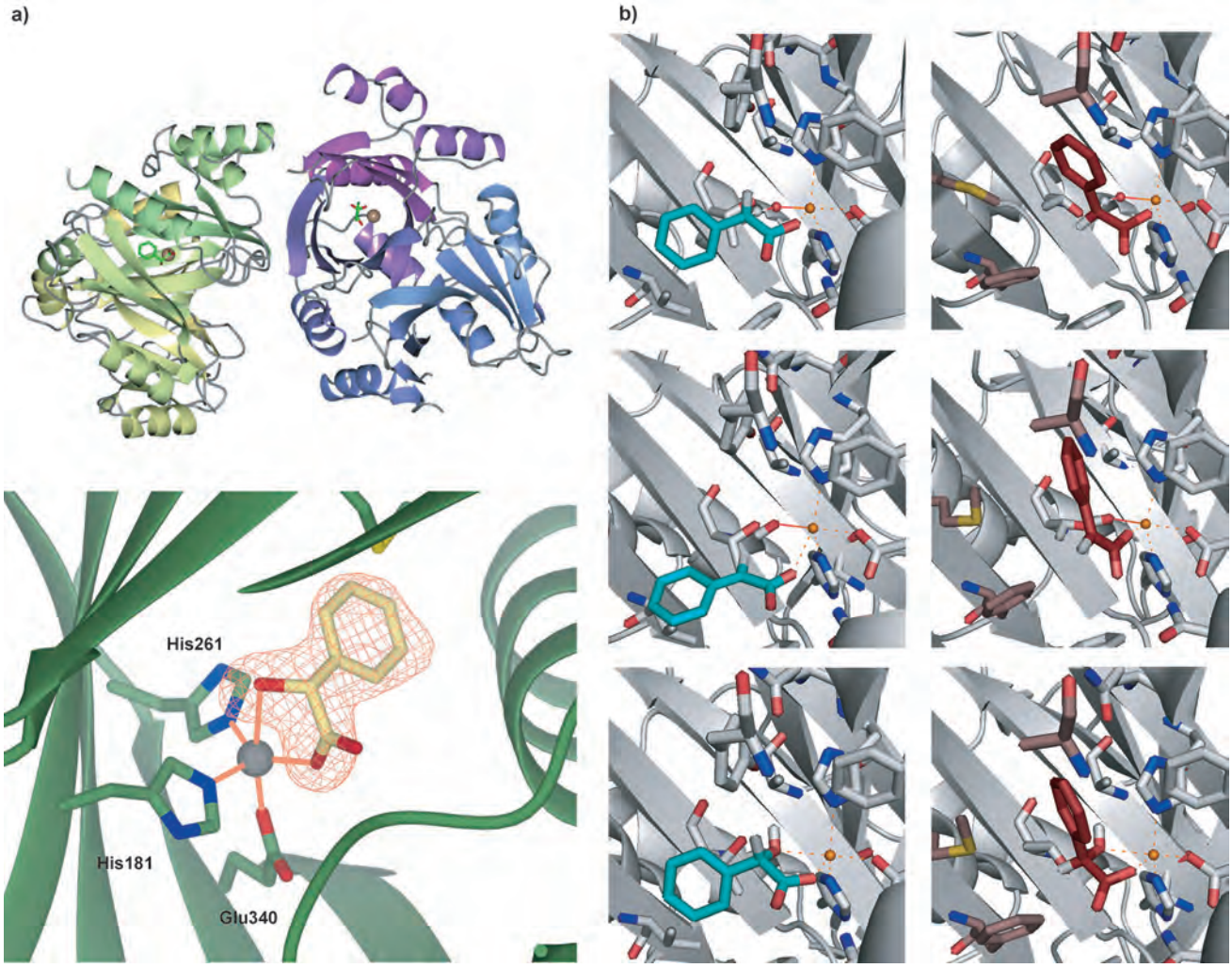

Figure 3. Interplay of protein structure and ligand orientation in the *Sc*HMS WT and the Ser221Met_Val223Phe_Tyr359Ala variant. a) Crystal structure of the (*R*)-selective *Sc*HMS triple variant. Top: overall structure of the observed dimer in complex with cobalt (brown) and the reaction product (*R*)-MA (green). Bottom: close-up of the active site. The coordinating oxygen atoms of (*R*)-MA (yellow) and the side chains of His261, His181, and Glu340 form a trigonal bipyramidal geometry around the cobalt atom (gray). The electron density of the ligand (coral) corresponds to the omit map (F_o-F_c map) contoured at a level of 3 σ obtained after the final rounds of refinement in the absence of the ligand. b) A structural representation of the catalytic steps that lead to chiral hydroxylation in WT *Sc*HMS (left) and in the (*R*)-selective triple mutant (right). The average structures of 10 ns MD simulations are shown, except in the lower right panel, which depicts the crystal structure of the mutant solved in this study. (Note that MD simulations gave similar active site geometries). The transition state of H-abstraction from PA by the Fe^{IV}=O center (upper row) results in an iron-bound hydroxy group and a substrate radical (middle row). The subsequent rebound step yields the chiral products (lower row). Residues within 5 Å of the metal (orange) are displayed—Ile335, Leu358, and Ile236 are omitted for clarity. Ligands of the (*S*)- and (*R*)-selective pathways are in teal and dark red, respectively. Mutations in the triple variant are shown in brown.

a first step in making enzymatic MNH Fe^{II} centers accessible as a resource for tailor-made biosynthetic oxygenations.

Received: May 29, 2013
Revised: July 1, 2013
Published online: July 23, 2013

Keywords: asymmetric catalysis · hydroxylation · metalloenzymes · non-heme iron · protein design

[1] K. Sanderson, *Nature* **2011**, *469*, 18–20.
[2] a) S. Kille, F. E. Zilly, J. P. Acevedo, M. T. Reetz, *Nat. Chem.* **2011**, *3*, 738–743; b) R. Agudo, G. D. Roiban, M. T. Reetz, *ChemBioChem* **2012**, *13*, 1465–1473; c) W. L. Tang, Z. Li, H. Zhao, *Chem. Commun.* **2010**, *46*, 5461–5463; d) S. Q. Pham, G. Pompidor, J. Liu, X. D. Li, Z. Li, *Chem. Commun.* **2012**, *48*, 4618–4620.
[3] V. B. Urlacher, M. Girhard, *Trends Biotechnol.* **2012**, *30*, 26–36.
[4] E. G. Kovaleva, J. D. Lipscomb, *Nat. Chem. Biol.* **2008**, *4*, 186–193.
[5] B. K. Hubbard, M. G. Thomas, C. T. Walsh, *Chem. Biol.* **2000**, *7*, 931–942.
[6] O. W. Choroba, D. H. Williams, J. B. Spencer, *J. Am. Chem. Soc.* **2000**, *122*, 5389–5390.
[7] C. M. L. Di Giuro, C. Konstantinovics, U. Rinner, C. Nowikow, E. Leitner, G. D. Straganz, *PLoS One* **2013**, DOI: 10.1371/journal.pone.0068932.
[8] D. D. Shah, J. A. Conrad, B. Heinz, J. M. Brownlee, G. R. Moran, *Biochemistry* **2011**, *50*, 7694–7704.

© 2013 Wiley-VCH Verlag GmbH & Co. KGaA, Weinheim

[9] J. Brownlee, P. He, G. R. Moran, D. H. Harrison, *Biochemistry* **2008**, *47*, 2002 – 2013.
[10] M. L. Neidig, A. Decker, O. W. Choroba, F. Huang, M. Kavana, G. R. Moran, J. B. Spencer, E. I. Solomon, *Proc. Natl. Acad. Sci. USA* **2006**, *103*, 12966 – 12973; b) S. P. de Visser, *Angew. Chem.*, **2006**, *118*, 1822 – 1825; *Angew. Chem. Int. Ed.*, **2006**, 45, 1790 – 1793; c) S. Sinnecker, N. Svensen, E. W. Barr, S. Ye, J. M. Bollinger, Jr., F. Neese, C. Krebs, *J. Am. Chem. Soc.* **2007**, 129, 6168 – 6179; d) A. Wojcik, E. Broclawik, P. E. Siegbahn, T. Borowski, *Biochemistry* **2012**, 51, 9570-9580.
[11] T. K. Paine, H. Zheng, L. Que Jr. , *Inorg. Chem.* **2005**, *44*, 474 – 476.
[12] a) M. Gunsior, J. Ravel, G. L. Challis, C. A. Townsend, *Biochemistry* **2004**, *43*, 663 – 674; b) J. M. Brownlee, B. Heinz, J. Bates, G. R. Moran, *Biochemistry* **2010**, *49*, 7218 – 7226.

 © 2013 Wiley-VCH Verlag GmbH & Co. KGaA, Weinheim

Inorganic Chemistry

Article

pubs.acs.org/IC

Rationalization of the Barrier Height for *p*-Z-styrene Epoxidation by Iron(IV)-Oxo Porphyrin Cation Radicals with Variable Axial Ligands

Devesh Kumar,*[,†] Reza Latifi,*[,‡,§] Suresh Kumar,[†] Elena V. Rybak-Akimova,[§] Mala A. Sainna,[‡] and Sam P. de Visser*[,‡]

[†]Department of Applied Physics, School of Physical Sciences, Babasaheb Bhimrao Ambedkar University, Vidya Vihar, Rae Bareilly Road, Lucknow 226-025, India

[‡]Manchester Institute of Biotechnology and School of Chemical Engineering and Analytical Science, University of Manchester, 131 Princess Street, Manchester M1 7DN, U.K.

[§]Department of Chemistry, Tufts University, Medford, Massachusetts 02155, United States

Supporting Information

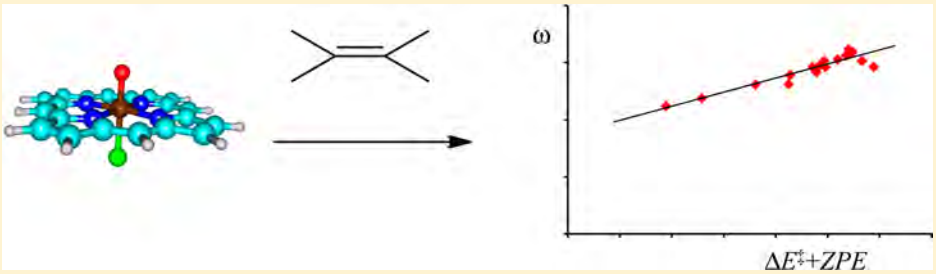

ABSTRACT: A versatile class of heme monoxygenases involved in many vital functions for human health are the cytochromes P450, which react via a high-valent iron(IV) oxo heme cation radical species called Compound I. One of the key reactions catalyzed by these enzymes is C=C epoxidation of substrates. We report here a systematic study into the intrinsic chemical properties of substrate and oxidant that affect reactivity patterns. To this end, we investigated the effect of styrene and para-substituted styrene epoxidation by Compound I models with either an anionic (chloride) or neutral (acetonitrile) axial ligand. We show, for the first time, that the activation enthalpy of the reaction is determined by the ionization potential of the substrate, the electron affinity of the oxidant, and the strength of the newly formed C−O bond (approximated by the bond dissociation energy, BDE_{OH}). We have set up a new valence bond model that enables us to generalize substrate epoxidation reactions by iron(IV)-oxo porphyrin cation-radical oxidants and make predictions of rate constants and reactivities. We show here that electron-withdrawing substituents lead to early transition states, whereas electron-donating groups on the olefin substrate give late transition states. This affects the barrier heights in such a way that electron-withdrawing substituents correlate the barrier height with BDE_{OH}, while the electron affinity of the oxidant is proportional to the barrier height for substrates with electron-donating substituents.

INTRODUCTION

An important class of enzymes in human physiology are the cytochromes P450, which are a large set of heme enzymes involved in the biodegradation and metabolism of toxic compounds in the liver.[1] These enzymes utilize molecular oxygen on a heme center in a catalytic cycle that uses two electrons and two protons to generate an iron(IV) oxo heme cation-radical active species called Compound I (CpdI).[2] This species is the active oxidant of the P450 enzymes and reacts with substrates via, for instance, aliphatic and aromatic hydroxylation, double-bond epoxidation, N-dealkylation, and sulfoxidation.[3] Because of its versatility in substrate activation, the group of enzymes has attracted interest from the biotechnological and pharmaceutical industries, although the intricate details of its catalytic mechanism and reactivity with substrates are still poorly understood. The epoxidation of olefins is a common reaction in P450 enzymes for a variety of important bioprocesses in the body including the activation of unsaturated fatty acids.[4] As a result, substrate epoxidation by P450 isozymes is well studied for a wide range of (non)natural substrates.[5] For instance, the reactions were shown to be highly enantioselective, whereby the *cis*-*β*-methylstyrene substrate gave an 89:11 epoxide product ratio of the 1*S*,2*R* form over the 1*R*,2*S* form.[6]

Because CpdI is a very versatile oxidant, many studies investigated synthetic analogues and models in substrate oxidation.[7] A number of these biomimetic studies focused on double-bond epoxidation mechanisms, and one of the most common substrates in these studies is styrene. Thus, a series of styrene epoxidation studies with a CpdI mimic and various axial ligands gave rate constants that were proportional to its

Received: February 27, 2013
Published: July 3, 2013

 © 2013 American Chemical Society dx.doi.org/10.1021/ic4005104 | *Inorg. Chem.* 2013, 52, 7968−7979

electron-donating ability.[8] Green and co-workers[9] characterized the axial-ligand effect as arising from changes in the pK_a values of the oxo group, which was confirmed with density functional theory (DFT) calculations on model complexes.[10]

Experimental studies reported rate constants for styrene epoxidation by synthetic iron(IV) oxo complexes: $[Fe^{IV}(O)(TPFPP^{\bullet+})X]^{0/+}$ with TPFPP = *meso*-tetrakis(pentafluorophenyl)porphyrinato and X = Cl^- or $NCCH_3$.[11] In an intriguing set of experiments, it was shown that the reaction of $[Fe^{IV}(O)(TPFPP^{\bullet+})NCCH_3]^+$ with ethylbenzene gave aromatic hydroxylation products, whereas the one using $[Fe^{IV}(O)(TPFPP^{\bullet+})Cl]$ as an oxidant led to benzylic hydroxylation instead; hence, the axial ligand in iron(IV)-oxo porphyrins seems to affect the product distributions in the reaction processes and the regioselectivity of aromatic over aliphatic hydroxylation.[11] The two oxidants with chloride versus acetonitrile as the axial ligand also gave differences in styrene epoxidation using para-substituted styrene derivatives. The work identified a correlation between the rate constant of styrene epoxidation with the ρ^+ Hammett factor, but the slopes were different for the CpdI models with anionic versus neutral axial ligands. The fundamental nature of this axial-ligand effect and how it affects the reaction mechanisms, rate constants and product distributions of iron(IV)-oxo porphyrins is unknown and, therefore, warrants a computational study. Thus, to gain insight into the effect of axial ligands on the reactivity of iron(IV)-oxo porphyrins with olefins, we have done a DFT study of the activation barriers using a selection of para-substituted styrenes as substrates and CpdI models with meso-substituted porphyrin.

Fujii and co-workers did a systematic investigation into the redox potentials of $[Fe^{IV}(O)(TMP^{+\bullet})X]^{n+}$ with TMP = 5,10,15,20-tetramesitylporphyrinate and X an axial ligand that is either anionic or neutral.[12] They found a positive $E_{1/2}$ shift upon binding of an anionic axial ligand that was virtually constant for a range of ligands. By contrast, binding of neutral ligands, such as imidazole, gave redox potentials in line with those found for peroxidases corresponding to a negative $E_{1/2}$ shift. They then replaced the TMP group with a meso-substituted porphyrin ligand with electron-withdrawing groups, which led to an increase of the $E_{1/2}$ values. Currently, it is not clear what factors determine the redox potentials of iron porphyrins and whether there is a relationship with catalysis. Therefore, to gain insight into the effect of meso substitution on the intrinsic chemical properties of the oxidant and the subsequent catalysis of substrates, we decided to include this study in the present work.

The model we chose for our studies presented here is given in Figure 1 and is based on the system used in ref 11. The basic features of the oxidant are an iron(IV) oxo group embedded in a protoporphyrin IX (Por) without side chains and with either chloride or acetonitrile as the axial ligand: $[Fe^{IV}(O)(Por^{\bullet+})X]^{0/+}$ with X = Cl^- or $NCCH_3$. In addition, we also investigated a more elaborate model that uses pentafluorophenyl substituents on the meso position of the porphyrin ring, i.e., TPFPP. Substrate epoxidation was studied using a range of *p*-Z-substituted styrenes with Z = H, F, Cl, CH_3, *t*-Bu, CN, NO_2, OCH_3, NH_2, and $N(CH_3)_2$. We show that para substitution affects the ionization potential of the substrate and its electron-donating ability, which leads to changes in the activation barrier of oxygen atom transfer. Although we reported a detailed analysis of substrate epoxidation by iron(IV)-oxo porphyrins before,[10] the systematic study described here goes beyond that of the previous work and highlights the differences in reactivity of substrates with electron-donating versus electron-withdrawing substituents. Moreover, a new model is presented that correlates with the obtained reactivity trends.

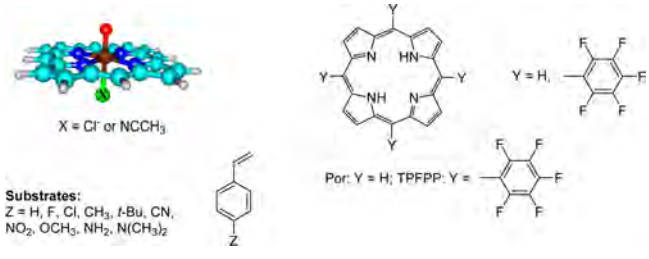

Figure 1. Oxidants and substrates used in this work.

METHODS

The study presented here uses DFT methods, as implemented in the *Jaguar*, *Gaussian03*, and *Gaussian09* program packages.[13] All geometries are the result of a full geometry optimization, whereby all degrees of freedom are minimized. A subsequent analytical frequency calculation characterized the structures as local minima (with real frequencies only) or first-order saddle points with one imaginary frequency for the correct mode. The hybrid B3LYP method[14] was employed throughout in combination with the Los Alamos-type LACVP basis set on iron and 6-31G on the rest of the atoms (BS1) for the geometry optimizations and frequencies.[15] Energies were then improved by single-point calculations with a triple-ζ-type basis set on iron (LACV3P+) and 6-311+G* on the rest of the atoms (BS2). Benchmark studies against experimental data reproduced free energies of activation using these methods to within 3 kcal mol^{-1}.[16] Previously, we calculated a full potential energy profile for substrate hydroxylation by an iron(IV)-oxo porphyrin cation-radical system at UB3LYP/BS2 and obtained relative energies within a few tenths of a kilocalorie per mole for local minima and first-order saddle points along a reaction mechanism compared to those obtained at UB3LYP/BS2//UB3LYP/BS1; hence, the latter method was used here.[17] Single-point calculations in a dielectric constant with ε = 37.5 mimicking acetonitrile with a probe radius of 2.1 Å were performed in *Jaguar* using basis set BS2. Free energies reported here were calculated at 298 K temperature and 1 bar pressure and are based on the UB3LYP/BS2//UB3LYP/BS1 energies and corrected with zero-point energy (ZPE), thermal and entropic corrections from the frequency file, and solvent corrections from the single-point solvent calculation. Further corrections to the energy were made by performing single-point calculations with dispersion-corrected B3LYP, B3LYP-D, as implemented in *Jaguar*.[18] For selected structures, we also did geometry optimizations and frequencies using UB3LYP-D/BS1 in *Jaguar*, although little changes in the optimized geometries were obtained.

We used two synthetic iron porphyrin models that are distinguished by the choice of the axial ligand, which was either chloride or acetonitrile. Note that $[Fe^{IV}(O)(Por^{\bullet+})Cl]^0$ is overall charge neutral, while $[Fe^{IV}(O)(Por^{\bullet+})NCCH_3]^+$ is positively charged. In our initial calculations, we used a bare porphyrin ring, whereby all side chains were replaced by hydrogen atoms. In a second set of calculations, we studied a TPFPP ligand system. We studied styrene epoxidation using a selection of para-substituted styrene substrates, as described in Figure 1.

To ascertain that the results are not influenced by the DFT method chosen here, we ran a selection of single-point calculations using dispersion-corrected DFT[18] and B3LYP with 15% HF exchange (designated as B3LYP*).[19] As before,[20] these test calculations reproduced the trends obtained with the B3LYP method, so that the results give a systematic error, which does not affect our discussion and analysis because we are dealing with trends only here. Nevertheless, for comparison, we give here the results obtained for ΔE + ZPE

dx.doi.org/10.1021/ic4005104 | *Inorg. Chem.* 2013, 52, 7968−7979

(UB3LYP), $\Delta G + E_{solv}$ (UB3LYP), and $\Delta G + E_{solv} + E_{disp}$ (UB3LYP-D).

RESULTS

We started the work with a detailed study into the electronic properties of iron(IV) oxo complexes, the effects of axial versus equatorial ligands, and finally the reactivity patterns with a selection of para-substituted styrenes. Our models include $[Fe^{IV}(O)(Por^{\bullet+})X]^{0/+}$, designated as $\mathbf{1}_X$, and $[Fe^{IV}(O)(TPFPP^{\bullet+})X]^{0/+}$, designated as $\mathbf{2}_X$, with X = Cl^- and $NCCH_3$ (Figure 1). Similar to previous studies on CpdI of P450 and biomimetic iron(IV)-oxo porphyrin complexes,[21] all complexes have the same electronic ground state with four electrons in metal 3d-type orbitals and a radical on the porphyrin macrocycle. High-lying occupied molecular orbitals include the $\delta_{x^2-y^2}$ orbital, which is nonbonding, doubly occupied, and located in the plane of the porphyrin. Slightly higher in energy are two π^*_{FeO} orbitals (π^*_{xz}, π^*_{yz}) for the antibonding interaction of the metal $3d_{xz/yz}$ with $2p_{x/y}$ atomic orbitals on oxygen. Higher-lying and virtual are the $\sigma^*_{z^2}$ and σ^*_{xy} orbitals for the antibonding interactions along the Fe−O axis and between the Fe−N groups in the plane of the porphyrin ring. In addition, there is a radical on a porphyrin-type orbital that in D_{4h} symmetry has the label a_{2u}. The orbital occupation gives close-lying doublet and quartet spin states with configuration $\delta_{x^2-y^2}{}^2\pi^*_{xz}{}^1\pi^*_{yz}{}^1a_{2u}{}^1$, whereby the two π^* electrons are either ferromagnetically or antiferromagnetically coupled to the a_{2u} electron in the quartet and doublet spin states. As a consequence, the two spin states are close in energy and the oxidant reacts via two-state-reactivity patterns on close-lying doublet and quartet spin state surfaces.[22]

Figure 2 gives optimized geometries of $^{4,2}\mathbf{1}_X$ and $^{4,2}\mathbf{2}_X$ with X = Cl^-/$NCCH_3$, as calculated with DFT. Optimized geometries of $^{4,2}\mathbf{1}_X$ (X = Cl^-/$NCCH_3$) are almost identical with those reported before.[23] The Fe−O distances are short and typical for an iron(IV) oxo species and shorten somewhat with an axially ligated acetonitrile molecule compared to chloride. This is due to mixing of the a_{2u} and π^* orbitals in $^{4,2}\mathbf{1}_{Cl}$ with 3p atomic orbitals on the chloride ligand,[23] which brings the metal more inside the plane through the porphyrin ring. This type of mixing has been identified before as the key reason for the intrinsic electronic differences of CpdI in monoxygenases and peroxidases.[24] We did additional geometry optimizations of $^2\mathbf{1}_X$ (X = Cl^-/$NCCH_3$) at the UB3LYP-D/BS1 level of theory, which reproduced the UB3LYP/BS1 structures within 0.010 Å.

As can be seen, meso substitution of the porphyrin ring with pentafluorophenyl groups has little effect on the optimized geometries, and the Fe−O, Fe−Cl, and Fe−N_{ax} distances for structures **1** and **2** are almost the same. Note also that very little saddling is found for the $[Fe^{IV}(O)(TPFPP^{\bullet+})X]$ structures. Not surprisingly, because the same molecular orbitals are singly occupied in the doublet and quartet spin-state structures, their geometries are virtually identical for each CpdI set of data. To establish whether the *meso*-pentafluorophenyl groups give electronic changes to the iron(IV) oxo species, we also show in Figure 2 the group spin densities (ρ), but only minor differences are observed between the data for structures **1** and **2**.

Subsequently, we calculated styrene epoxidation using a range of para-substituted styrene derivatives. Before we discuss the results on the substituted styrenes, let us focus on the general overall mechanism first. All epoxidation reactions described in this work proceed with the same stepwise

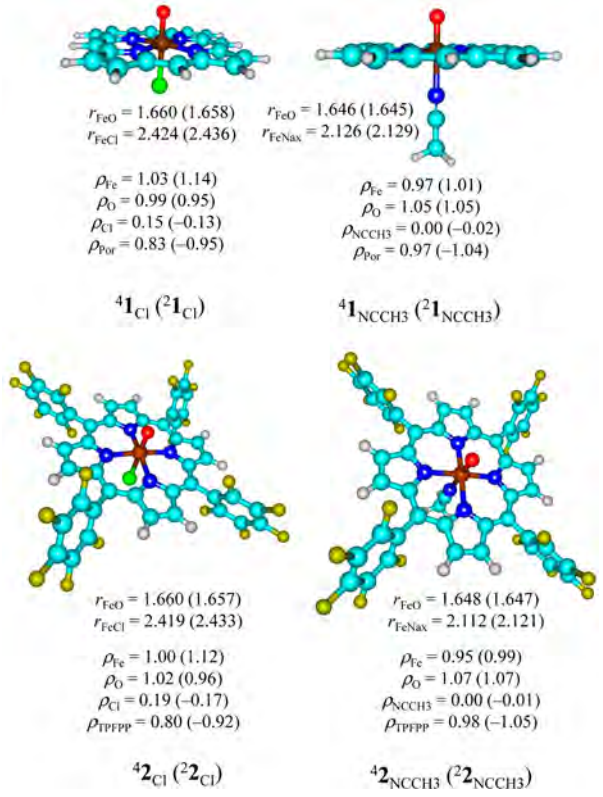

Figure 2. UB3LYP/BS1-optimized geometries of $^{4,2}\mathbf{1}_X$ and $^{4,2}\mathbf{2}_X$ in the gas phase with bond lengths in angstroms. Group spin densities are obtained at UB3LYP/BS2//UB3LYP/BS1 and are reported in atomic units.

mechanism that starts with the formation of a reactant complex between CpdI and substrate, **R**. As an example, we give the reaction profile for $[Fe^{IV}(O)(Por^{\bullet+})Cl]$ with *p*-H-styrene in Figure 3 on the lowest doublet and quartet spin states. The spin multiplicity is given as a superscript, and in the subscript, we give the axial ligand (X) and the *p*-Z substituent of styrene. The mechanism resembles that found in earlier studies of substrate epoxidation of olefins by metal(IV) oxo oxidants[23,25,26] and starts with an initial electrophilic addition of the oxo group to the double olefinic bond of styrene via a transition state $\mathbf{TS}_{X,Z}$ to form a radical intermediate ($\mathbf{I}_{X,Z}$), whereby the subscript X refers to the axial ligand, i.e., X = Cl^- or AN (acetonitrile), and the subscript Z to the para substituent of styrene. In a final reaction step, a ring-closure transition state ($\mathbf{TS}_{rc,Z}$) leads to epoxide product complexes ($\mathbf{P}_{X,Z}$). Optimized geometries obtained at UB3LYP-D/BS1 show little difference from those obtained at UB3LYP/BS1 (Figure 3).

Although the ring-closure barrier was calculated for a selection of chemical systems, in all cases its barrier was much smaller than the C−O bond-formation barrier via $\mathbf{TS}_{X,Z}$; therefore, we will focus here on the rate-determining barrier only. In particular, in the quartet spin state, ring-closure barriers were located and found to be small, whereas in the doublet spin state, the ring closure was virtually barrierless. The origin of this difference is due to differences in electron-transfer processes in the ring-closure step, whereby on the doublet spin-state surface, the π^*_{xz} orbital is filled with an extra electron, while on the quartet spin state, a higher-lying and virtual $\sigma^*_{z^2}$ orbital is filled with one electron.[26a] Energies obtained for the reaction of $[Fe^{IV}(O)(Por^{\bullet+})Cl]$ with *p*-H-styrene are very similar to those

dx.doi.org/10.1021/ic4005104 | Inorg. Chem. 2013, 52, 7968−7979

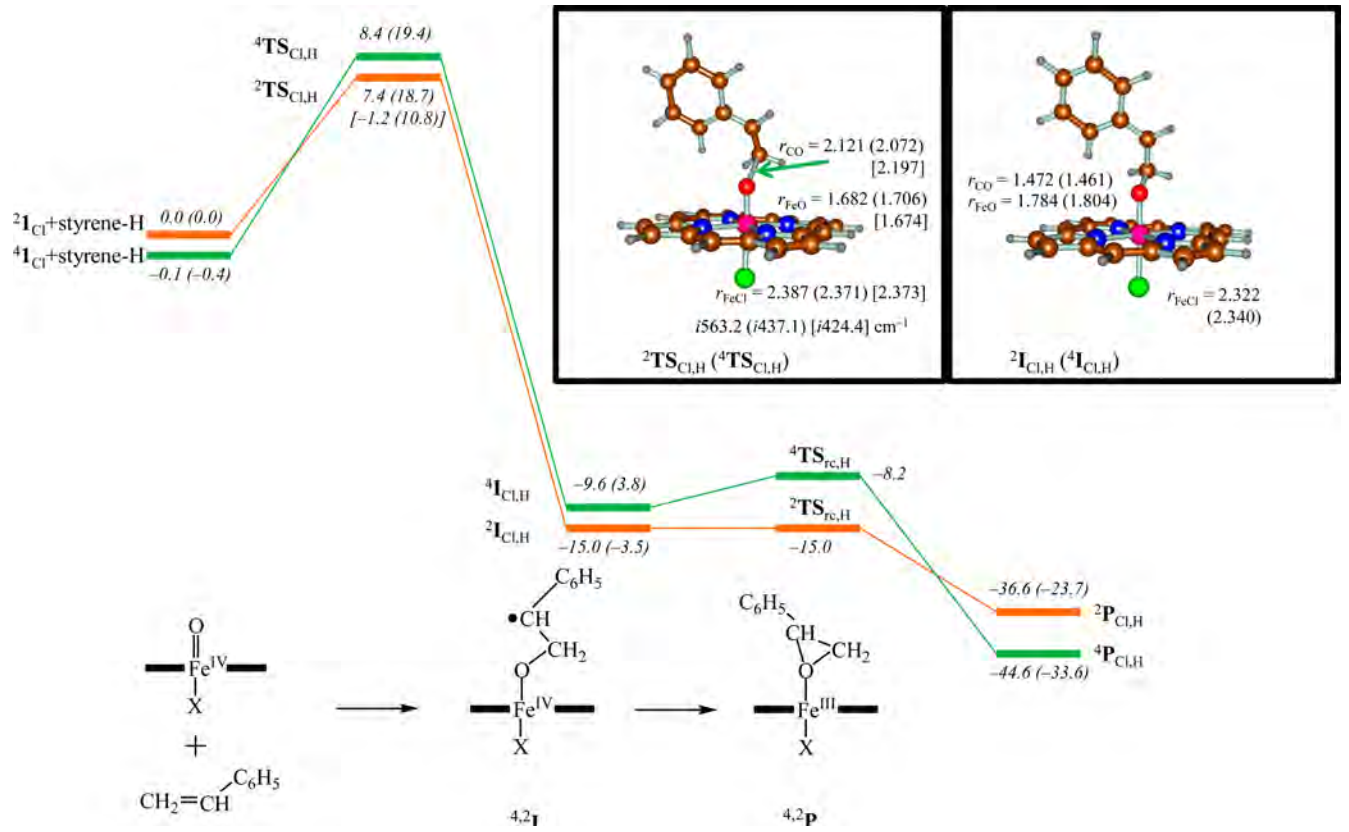

Figure 3. Potential energy profile of styrene epoxidation by $^{4,2}\mathbf{1}_{Cl}$ as calculated with UB3LYP/BS2//UB3LYP/BS1. All energies are in kilocalories per mole relative to isolated reactants in the doublet spin state and include ZPE corrections. Also shown are optimized geometries of critical points with bond lengths in angstroms and the imaginary frequencies in the transition state in wavenumbers. Free energies are given in parentheses and include UB3LYP/BS2 energies corrected with thermal and entropic corrections at 298 K. Data in square brackets were obtained from a UB3LYP-D/BS2//UB3LYP-D/BS1 calculation.

reported before using $[Fe^{IV}(O)(Por^{\bullet+})SH]$ as an oxidant.[23,26b] That is not surprising because the pK_a and electron affinity (EA) of $[Fe^{IV}(O)(Por^{\bullet+})X]$, X = Cl^-/SH^-, are virtually the same. Geometries are typical for epoxidation structures from previous calculations for P450-catalyzed reaction mechanisms.[25,26] In the transition state, the Fe−O bond elongates slightly with respect to reactants and further extends in the intermediate to 1.784 Å. At the same time, considerable shortening of the C−O distance occurs to a formally single bond in $^{4,2}\mathbf{I}_{Cl,H}$ of 1.472 Å.

Subsequently, we investigated the reaction mechanisms of $[Fe^{IV}(O)(Por^{\bullet+})X]^{0/+}$, X = Cl^- or $NCCH_3$, with para-substituted styrene, and the optimized geometries of the transition states are given in Figure 4. Interestingly, structural differences are found between the two axially ligated oxidants, whereby the Cl^--bound $\mathbf{TS}_{X,Z}$ structures are with styrene in an upright position, whereas the acetonitrile-bound ones are more sideways-bound. Test calculations using an upright starting structure and an acetonitrile axial ligand, however, converged back to the sideways-bound structure instead, which implies that the upright structures are higher in energy for the axially ligated acetonitrile transition states. The differences in the substrate orientation affect the bond distances of the respective transition states. For instance, the bond-forming C−O distances vary from 2.017 to 2.241 Å for the transition states with X = Cl^-, whereas for X = $NCCH_3$, distances between 2.083 and 2.439 Å are found. This implies that the barriers for the acetonitrile-ligated structures are somewhat earlier than the ones for the chloride-bound systems. Although variations in the Fe−O and Fe−X distances are considerably smaller than those for the C−O distance, variations between the oxidant with chloride and acetonitrile ligands are also found.

The epoxidation barriers ($\mathbf{TS}_{Cl,Z}$) range from 3.92 kcal mol^{-1} for *p*-N$(CH_3)_2$-styrene to 7.40 kcal mol^{-1} for *p*-H-styrene, i.e., vary by 3.48 kcal mol^{-1} upon para substitution. With acetonitrile as the axial ligand, the lowest barrier is 10.56 kcal mol^{-1} below isolated reactants for *p*-N$(CH_3)_2$-styrene, although it should be noted that the reactant complex is more stable than isolated reactants by 14.75 kcal mol^{-1}. Thus, the epoxidation barrier height varies by 20 kcal mol^{-1} between *p*-N$(CH_3)_2$-styrene and *p*-NO_2-styrene for $\mathbf{TS}_{AN,Z}$; hence, the substituent located at a distance of over 4 Å from the reaction center causes a rate constant change by a factor of ca. 10^{15} (estimated using transition state theory for an enthalpy-derived free energy change of 20 kcal mol^{-1}; the entropy of activation was not included in this estimate). The ordering of the barrier heights is virtually the same for the two oxidants studied, namely, Z = N$(CH_3)_2$ < NH_2 < OCH_3 < CH_3/*t*-Bu < F/Cl < CN < H. A plot of the barriers $^2\mathbf{TS}_{Cl,Z}$ versus those calculated for $^2\mathbf{TS}_{AN,Z}$ with the same methods gives a linear correlation; see Figure S27 in the Supporting Information (SI). Furthermore, calculations using a solvent model included give free energies of activation that follow the same trends as values found in the gas phase (Figure S28 in the SI). Inclusion of dispersion corrections on the solvent-corrected free energies of activation gives a further systematic change of the energetics, as shown in

dx.doi.org/10.1021/ic4005104 | Inorg. Chem. 2013, 52, 7968−7979

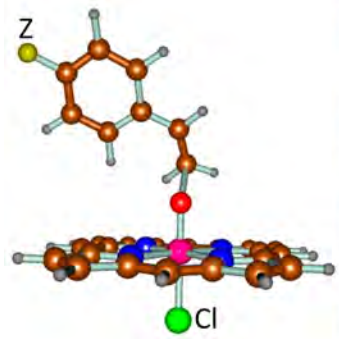

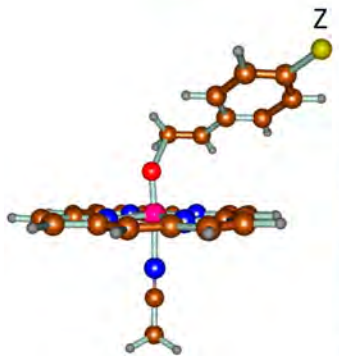

Z	H	F	Cl	CH_3	*t*-Bu	CN	NO_2	OCH_3	NH_2	$N(CH_3)_2$
X = Cl^-										
r_{C-O}	2.121	2.107	2.090	2.142	2.143	2.053	2.017	2.163	2.232	2.241
r_{O-Fe}	1.682	1.684	1.685	1.680	1.680	1.689	1.692	1.679	1.674	1.674
r_{Fe-Cl}	2.387	2.386	2.385	2.390	2.389	2.383	2.382	2.392	2.399	2.401
imag	*i*563.2	*i*600.4	*i*641.0	*i*500.3	*i*500.1	*i*693.3	*i*697.8	*i*421.5	*i*269.4	*i*245.7
ΔE+ZPE	7.40	7.01	7.06	6.79	6.85	7.30	7.28	5.97	4.80	3.92
$\Delta G+E_{solv}+E_{disp}$	13.8	11.2	11.9	9.4	11.3	12.7	11.8	10.1	6.5	−0.3
X = $NCCH_3$										
r_{C-O}	2.187	2.178	2.160	2.244	2.272	2.117	2.083	2.305	2.430	2.439
r_{O-Fe}	1.668	1.673	1.677	1.659	1.653	1.692	1.703	1.653	1.648	1.646
$r_{Fe-NCCH3}$	2.103	2.099	2.096	2.115	2.128	2.088	2.084	2.130	2.150	2.163
imag	*i*209.8	*i*220.3	*i*234.3	*i*181.1	*i*238.2	*i*274.4	*i*310.5	*i*147.8	*i*75.3	*i*66.0
ΔE+ZPE	3.55	4.15	4.66	1.39	1.25	8.30	9.44	-1.94	-7.11	-10.56
$\Delta G+E_{solv}+E_{disp}$	6.3	8.7	10.7	5.7	7.7	24.8	27.0		4.9	−1.0

Figure 4. Optimized geometries of rate-determining transition states $^2\mathbf{TS}_{X,Z}$ for the reaction of *p*-Z-styrene with $^2\mathbf{1}_X$ (X = Cl^-/$NCCH_3$). Geometries optimized at UB3LYP/BS1 with bond lengths given in angstroms and the imaginary frequencies in wavenumbers. Also given are barrier heights (ΔE + ZPE) for $^2\mathbf{TS}_{X,Z}$ with energies calculated at UB3LYP/BS2//UB3LYP/BS1+ZPE relative to isolated reactants in kilocalories per mole and free energies of activation in a solvent ($\Delta G + E_{solv} + E_{disp}$) relative to $^2\mathbf{RC}_{X,Z}$.

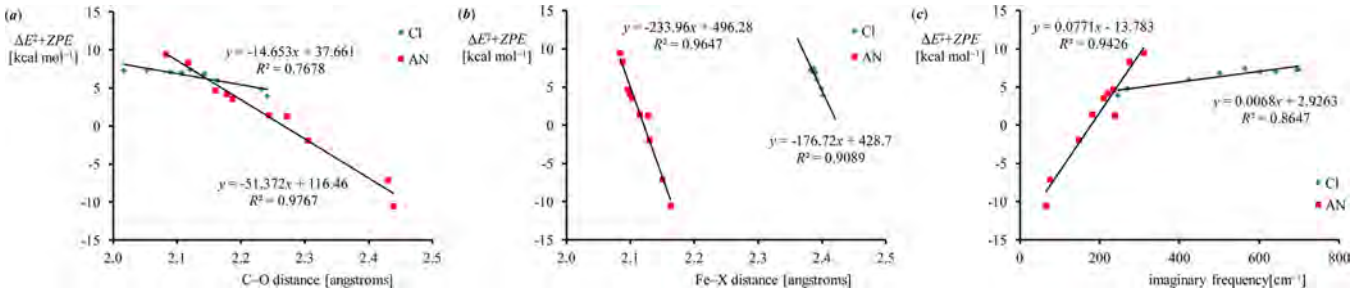

Figure 5. Analysis of the structural features of the transition states $\mathbf{TS}_{X,Z}$ calculated at UB3LYP/BS1 as a function of the height of the epoxidation barrier with respect to the (a) C−O distance, (b) Fe−X distance, and (c) imaginary frequency in the transition state. Data are given for X = Cl^- axial ligand (blue diamonds) and X = acetonitrile (red squares).

Figures S29 and S30 in the SI. This highlights the fact that for the assignment of reactivity trends it does not matter whether ΔE + ZPE, ΔG, $\Delta G + E_{solv}$, or $\Delta G + E_{solv} + E_{disp}$ energies are used. Because the enthalpies in a reaction mechanism are determined by the electronic changes of the reactants and we aim to establish the intrinsic chemical properties that determine the reactivity patterns, we will focus in the following on establishing trends through the ΔE + ZPE sets of data.

To understand the changes in the transition-state geometry between the para-substituted styrene substrates, we plot in Figure 5 a selection of bond distances versus the barrier height ($\Delta E^{\ddagger}$ + ZPE) for the two CpdI models with either a chloride or an acetonitrile axial ligand. Figure 5a shows the distance of the C−O bond that is formed in the process versus the barrier height. An almost perfect linear correlation (R^2 = 0.98) is obtained for the acetonitrile-ligated transition states, and a satisfactory linear correlation is found for the chloride-ligated system. Thus, a drop in the C−O bond length of 0.224 Å is found between the weakest epoxidating substrate (*p*-NO_2-styrene) and the strongest one [*p*-$N(CH_3)_2$-styrene] using a chloride axial ligand, whereas the difference between these substrates is 0.256 Å for an axially ligated acetonitrile molecule. This implies that the para substituent of styrene has a single possibly electrostatic effect on the C−O bond-formation step and, consequently, the barrier height of the reaction. To further ascertain that the optimized geometries and barrier heights are reproducible, we reoptimized a selection of **TS** structures with UB3LYP-D/BS1. Thus, $^2\mathbf{TS}_{AN,CN}$ and $^2\mathbf{TS}_{Cl,CN}$ give Fe−O distances of 1.683 and 1.680 Å and C−O distances of 2.131 and 2.107 Å, respectively. These values are close to those given in Figure 4 calculated at the UB3LYP/BS1 level of theory.

dx.doi.org/10.1021/ic4005104 | *Inorg. Chem.* 2013, 52, 7968−7979

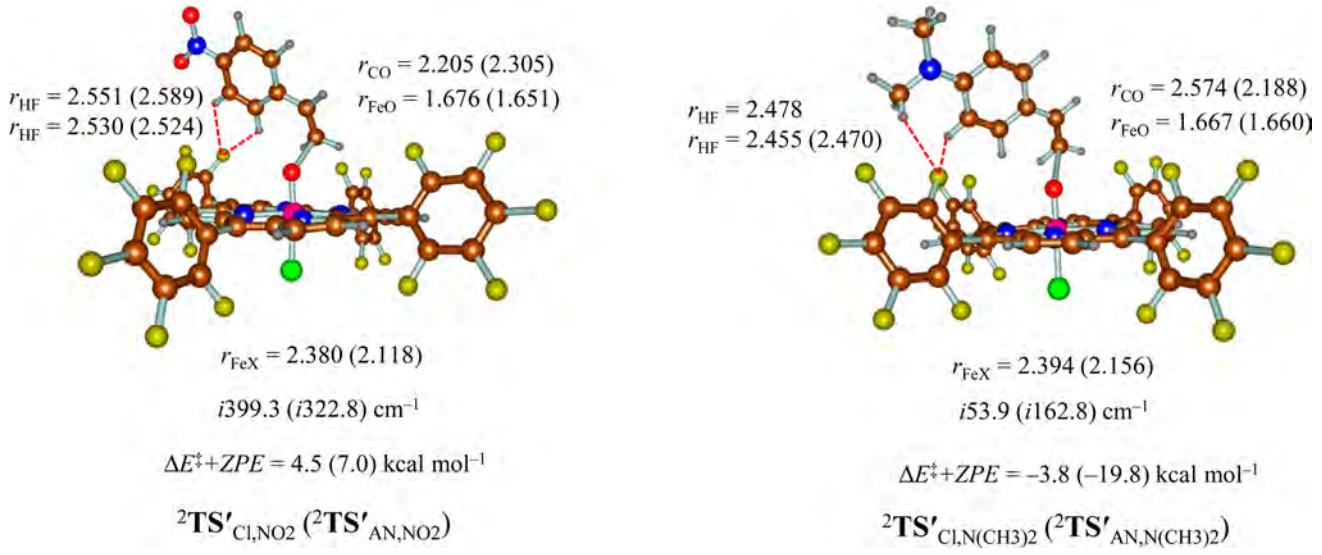

Figure 6. Optimized geometries of epoxidation transition states ^{2}**TS′**$_{X,Z}$ for the reaction of **2**$_{X}$ (X = Cl^{-}/NCCH$_3$) with *p*-Z-styrene. Bond lengths are in angstroms and the values of the imaginary frequencies in wavenumbers.

We also investigated the correlations of the epoxidation barrier height with the Fe−O and Fe−X distances in the transition states, and indeed these correlations are linear as well. With a chloride axial ligand, modest Fe−O and Fe−Cl changes are seen throughout the series of −0.018 and +0.019 Å, respectively, between the outer ranges for *p*-NO_2-styrene and *p*-$N(CH_3)_2$-styrene. Much larger differences are found for the weakly bound acetonitrile system, where the Fe−$NCCH_3$ distance is elongated from 2.084 to 2.163 Å (+0.079 Å shift) between *p*-NO_2-styrene and *p*-$N(CH_3)_2$-styrene. Thus, the para substituent of styrene affects bond distances well over 5 Å from the catalytic center and weakens the metal-to-axial ligand distances of the Fe−Cl and Fe−$NCCH_3$ bonds dramatically.

Interestingly, even the value of the imaginary frequency gives a linear correlation with the barrier height, i.e., are that the para substituent of styrene affects the height as well as the width of the potential energy curve around the transition state. Because both the height and width of the barrier change linearly for our series of substrates, this means that the area under the curve could stay the same for these substrates. However, changes to the width of the potential energy curve may have important effects on, for instance, the kinetic isotope effects (KIEs) for a reaction.[27] Thus, a small imaginary frequency correlates with a broad and wide potential energy surface, whereas a large imaginary frequency implies a narrow and high peak. Tunnelling through a narrow and high peak should be easier than through a broad peak; therefore, KIEs associated with this reaction may be affected as well. It is interesting to note that the imaginary frequencies are substantially larger for [Fe^{IV}(O)(Por$^{\bullet+}$)Cl] than for [Fe^{IV}(O)(Por$^{\bullet+}$)$NCCH_3$]$^{+}$; hence, the barriers for the latter oxidant will be much broader in shape. If this trend also applies to the hydrogen-atom-abstraction reaction, then this would imply that the calculations predict [Fe^{IV}(O)(Por$^{\bullet+}$)Cl] to react with considerably larger KIEs for the replacement of hydrogen by deuterium atoms than [Fe^{IV}(O)(Por$^{\bullet+}$)$NCCH_3$]$^{+}$ with substrates. Indeed, Nam and co-workers reported differences in the KIE values for the two oxidants in aliphatic hydrogen-atom-abstraction reactions.[11]

In a final set of calculations, we investigated the effect of meso substitution of the porphyrin ring on the electronic properties of CpdI and the epoxidation of para-substituted styrenes. We selected the TPFPP ligand system with pentafluorophenyl groups on the meso position of the porphyrin and calculated styrene epoxidation using the TPFPP oxidant: [Fe^{IV}(O)(TPFPP$^{\bullet+}$)X]$^{0/+}$ with X = Cl^{-} and $NCCH_3$ or **2**$_{X}$. We studied styrene epoxidation for *p*-$N(CH_3)_2$-styrene and *p*-NO_2-styrene and compared the mechanism and energy profiles with those observed above for **1**$_{X}$. Figure 6 displays optimized geometries of the epoxidation transition states **TS′**$_{X,Z}$ for the reaction of styrene with **2**$_{X,Z}$ with Z = NO_2 or $N(CH_3)_2$, as calculated with DFT methods.

Geometrically, there are striking differences between **TS**$_{X,Z}$, on the one hand, and **TS′**$_{X,Z}$, on the other hand. Thus, the epoxidation barriers with the TPFPP ligand system are characterized with long C−O and short Fe−O distances, which implies much earlier transition states along the potential energy surface. Furthermore, both acetonitrile- and chloride-ligated **TS′**$_{X,Z}$ structures are in the upright configuration, with a structure similar to the **TS**$_{Cl,Z}$ geometries reported in Figure 4. Probably, the stereochemical interactions with meso substituents prevent a substrate orientation analogous to **TS**$_{AN,Z}$ with a sideways attack on the oxo group. In addition, the structures are stabilized with hydrogen-bonding interactions of substrate C−H groups with the fluoride atoms from the TPFPP ligand and specifically those located in the ortho position of the meso substituent. As a consequence, both the reactant complexes and the transition states for epoxidation are considerably stabilized with respect to isolated reactants. Each transition state structure in Figure 6 is stabilized by at least two or three C−H---F hydrogen-bonding interactions with distances between 2.4 and 2.6 Å. F−H hydrogen-bonding interactions can be dramatic; for instance, trifluoromethanol as a solvent has been shown to lead to a considerable lowering of the epoxidation and halogenation barriers heights because of hydrogen-bonding and charge-transfer interactions.[28]

Recent computational studies of dehydrogenation of cyclohexadiene by [Fe^{IV}(O)(TPCPP$^{\bullet+}$)Cl] with TPCPP = *meso*-tetrakis(pentachlorophenyl)porphyrin also showed substrate stabilization due to weak hydrogen-bonding interactions of chloride atoms of the TPCPP ligand with C−H groups of the

dx.doi.org/10.1021/ic4005104 | *Inorg. Chem.* 2013, 52, 7968−7979

approaching substrate.[29] These interactions were shown to be particularly strong for epoxidation barrier heights because of a closer approach to the oxidant compared to hydrogen-atom-abstraction reactions and lowered epoxidation barriers significantly.[30] In line with this, it is not surprising that we find a considerable lowering of the epoxidation barriers from 7.3 to 4.5 kcal mol^{-1} for X = Cl/Z = NO_2, from 9.4 to 7.0 kcal mol^{-1} for X = AN/Z = NO_2, from 3.9 to −3.8 kcal mol^{-1} for X = Cl/Z = $N(CH_3)_2$, and from −10.6 to −19.8 kcal mol^{-1} for X = AN/Z = $N(CH_3)_2$ upon replacement of the equatorial ligand from Por to TPFPP. The big changes in geometry for $\mathbf{TS}_{X,Z}$ compared to $\mathbf{TS}'_{X,Z}$ also affect the shape of the potential energy surface and the values of the imaginary frequencies. Both $\mathbf{TS}'_{Cl,NO_2}$ and $\mathbf{TS}'_{Cl,N(CH_3)_2}$ structures have lower imaginary frequencies than $\mathbf{TS}_{Cl,NO_2}$ and $\mathbf{TS}_{Cl,N(CH_3)_2}$, whereas this is not the case for the axially ligated acetonitrile structures.

Thus, we report here the effect of meso substitution on the electronic and reactivity properties of iron(IV) oxo porphyrin cation-radical models. We find little changes in the electronic configuration of the various CpdI reactants. However, fluorine substituents on the meso position of TPFPP entice favorable electrostatic interactions with the approaching substrate and stabilize the epoxidation transition states. In the following, we will try to rationalize these observations.

DISCUSSION

In this work, we report a systematic set of epoxidations of substituted styrenes using four different oxidants, namely, $\mathbf{1}_{Cl}$, $\mathbf{1}_{NCCH_3}$, $\mathbf{2}_{Cl}$, and $\mathbf{2}_{NCCH_3}$. During the substrate epoxidation process, two electrons are transferred from the substrate to the oxidant, which is reduced from $[Fe^{IV}(O)(Por^{\bullet+})X]$ to $[Fe^{III}(Por)X]$. As a consequence, the EA of the oxidant and the ionization energy (IE) of the substrate should reflect the electron-transfer processes that take place. Indeed, several experimental studies found a correlation between the IE of substrates and the rate constant of substrate epoxidation and sulfoxidation.[7s,31] So far, no experimental studies have been reported on the activation parameters of substrate epoxidation by synthetic biomimetic iron(IV)-oxo porphyrin cation-radical models, but the rate constants are expected to correlate with the activation enthalpies. In earlier work, we reported a systematic study of olefin epoxidation by iron(IV) oxo complexes and set up a model that predicts barrier heights from known ionization potentials. Although that correlation still applies, we generalize it further in this work using the data described here.

To understand the individual contributions of the oxidant and substrate to the reaction process, i.e., transition states, we will investigate those separately. Let us start with a discussion of the differences and a comparison between $\mathbf{1}_{Cl}/\mathbf{2}_{Cl}$ and $\mathbf{1}_{NCCH_3}/\mathbf{2}_{NCCH_3}$ in styrene epoxidation reactions and their corresponding EAs. Thus, as shown in Figure 2, the reactant complexes give little differences in the geometric and electronic features upon a change in the equatorial ligand from Por to TPFPP.

We calculated EA values of 79.4 kcal mol^{-1} for $\mathbf{1}_{Cl}$, 101.4 kcal mol^{-1} for $\mathbf{2}_{Cl}$, 148.7 kcal mol^{-1} for $\mathbf{1}_{NCCH_3}$, and 163.8 kcal mol^{-1} for $\mathbf{2}_{NCCH_3}$ in the gas phase. Note here that, despite the fact that the valence orbital occupations and orbital shapes seem little influenced by the nature of the meso substituents of the porphyrin ring, actually the EA values increase by as much as 15.1−22.0 kcal mol^{-1}. This observation is in excellent agreement with the electrochemical studies of Fujii and coworkers, who found similar trends.[12]

Because the electrophilic reaction mechanism results in electron transfer from substrate to oxidant orbitals, these differences in the EAs of the four oxidants also affect the subsequent reaction mechanisms and reactivities with substrates. The transition state structures for these reactions, however, show dramatic differences in group spin densities, as displayed in Figure 7. Thus, generally the reaction proceeds

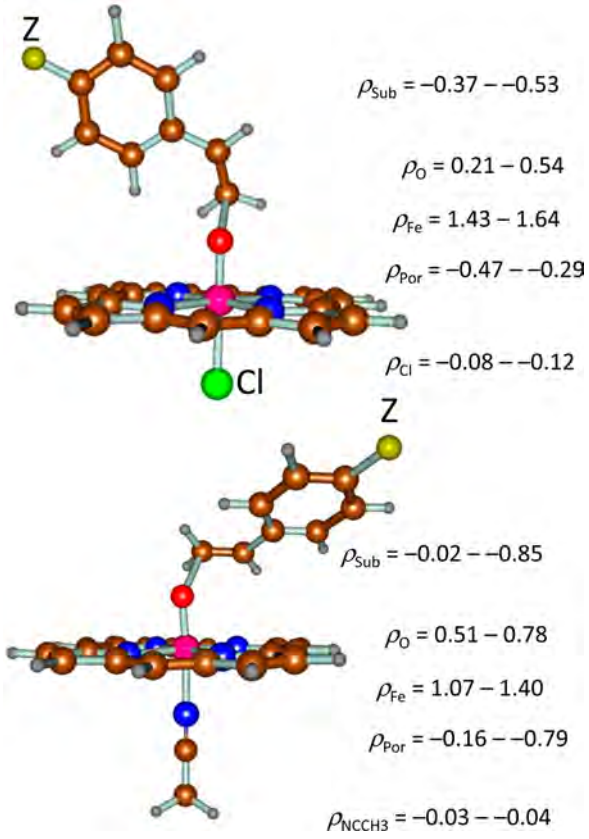

Figure 7. UB3LYP/BS2//UB3LYP/BS1-calculated group spin density ranges for *p*-Z-styrene epoxidation by $\mathbf{1}_{Cl}$ (top) and $\mathbf{1}_{AN}$ (bottom).

with electron transfer from the substrate to the half-filled a_{2u} porphyrin orbital, whereby a decrease in the spin density of the porphyrin group is found. The electronic configuration of the $\mathbf{TS}_{Cl,Z}$ structures is very much product-like with ρ_{Por} in the range from −0.29 to −0.47, whereas the $\mathbf{TS}_{AN,Z}$ values are reactant-like with considerably more spin density on the porphyrin ring.

Similarly, polarization of the FeO spin density from almost equal oxygen and iron spin densities in the reactants to a dominant iron radical in $\mathbf{TS}_{Cl,Z}$ occurs, whereby ρ_{Fe} ranges from 1.43 to 1.64 and ρ_O ranges from 0.21 to 0.54. By contrast, ρ_{Fe} varies from 1.07 to 1.40 and ρ_O ranges from 0.51 to 0.78 in the set of $\mathbf{TS}_{AN,Z}$ structures. The axial ligand, therefore, has an electronic effect on the charge and spin distributions in the rate-determining transition states, and, in particular, an anionic axial ligand, such as chloride, polarizes the FeO biradical toward the metal. Consequently, the anionic ligand will incur a "push" effect on the metal oxo group and formally change it from an $Fe^{V}O^{\bullet-}$ configuration in the reactant state to $Fe^{IV}O^{2-}$ in the transition state. By contrast, an iron(IV) oxo oxidant with a neutral axial ligand retains much larger radical character on the

dx.doi.org/10.1021/ic4005104 | Inorg. Chem. 2013, 52, 7968−7979

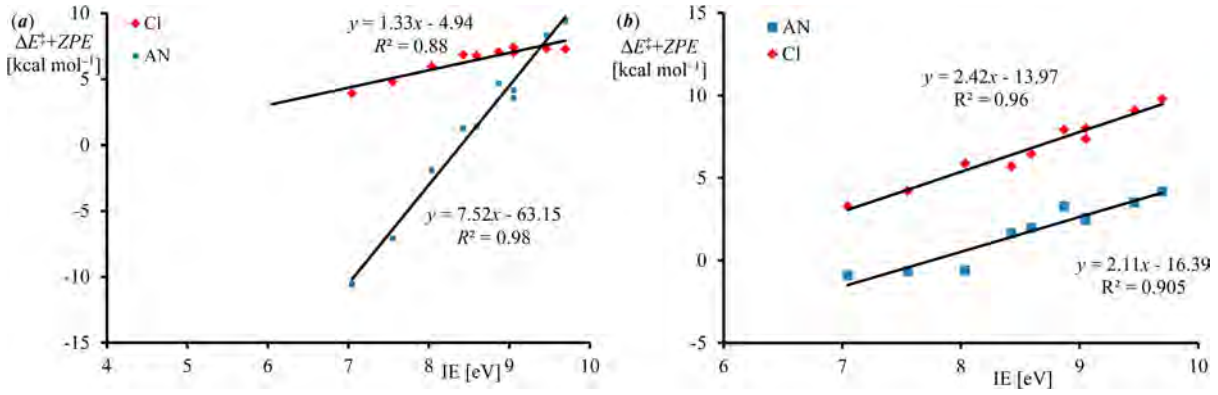

Figure 8. Styrene epoxidation barrier heights ($\Delta E^{\ddagger}$ + ZPE) of $^{2}\mathbf{TS}_{X,Z}$ plotted against the IE of the corresponding substrate. (a) Energies relative to isolated reactants. (b) Energies relative to a reactant complex (**RC**).

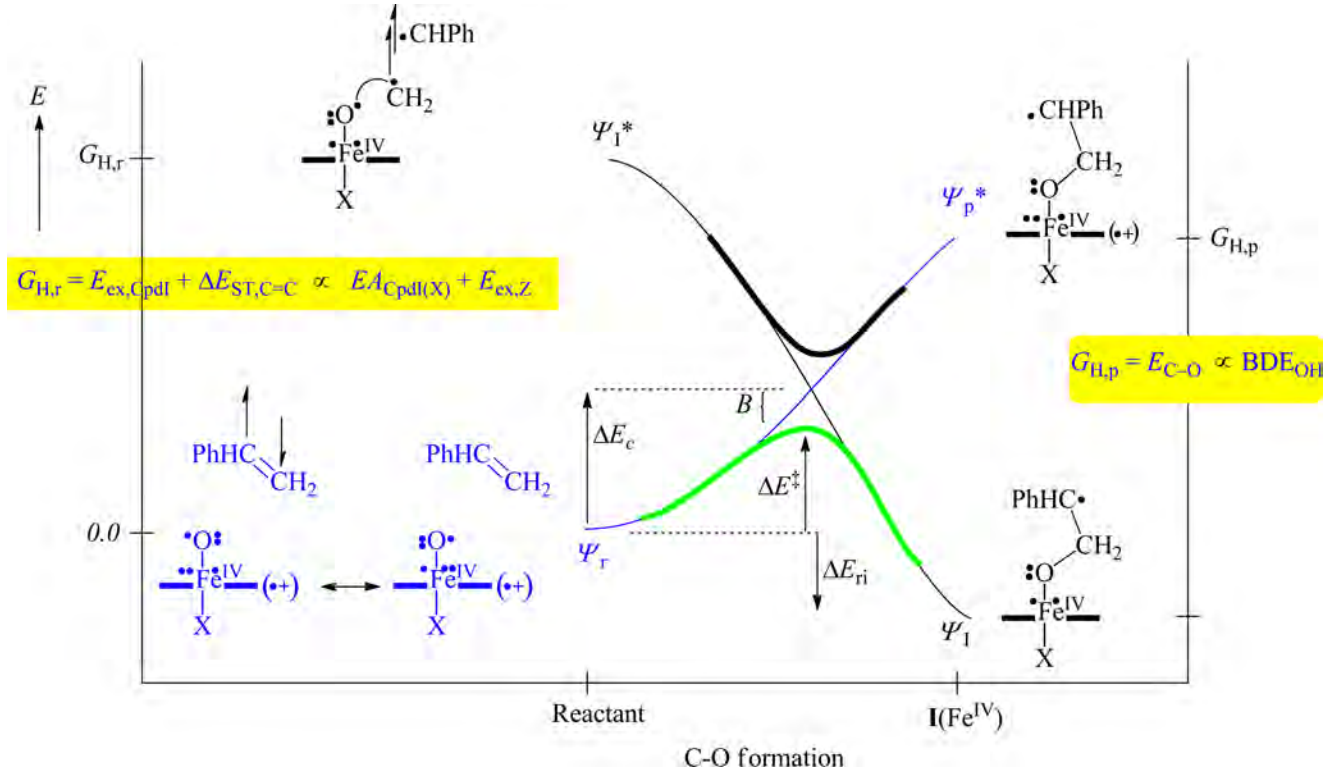

Figure 9. VB curve crossing diagram for *p*-Z-styrene epoxidation by iron(IV)-oxo porphyrin cation-radical oxidants. Lewis structures give relevant valence π orbitals with a dot.

oxygen atom in the electrophilic transition states and keeps the metal oxo group in a formal $Fe^{V}O^{\bullet-}$ configuration. This is important because it reduces the barrier heights of the electrophilic reaction mechanisms.

Let us in the following look into the barrier heights of styrene epoxidation and elucidate the enthalpic contributions to the relative values of the associated rate constants. Experimental studies on substrate sulfoxidation by P450 enzymes indicated a correlation between the rate constants and IEs of the selected substrates.[31] More recent mass spectrometric and computational studies showed that this correlation also applies to substrate epoxidation reactions.[7s,10] To test this relationship for the set of data studied here, we plot in Figure 8 the calculated barrier heights $^{2}\mathbf{TS}_{Cl,Z}$ and $^{2}\mathbf{TS}_{AN,Z}$ as a function of the IEs of the *p*-Z-styrene substrates. We calculated the trends using two sets of relative energies: In the first, we take the isolated reactants as a reference point, whereas in the second set, a reactant complex (**RC**) is used. DFT-calculated ionization potentials at the same level of theory as the transition states for the epoxidation reactions were used for consistency. Our calculated IE values are close to those reported in the literature;[32] however, because not all IE values are experimentally known, we will use the calculated data in our analysis here. As can be seen, both series of *p*-Z-styrene epoxidation reactions give barriers that correlate linearly with the ionization potential, whether energies relative to isolated reactants or a reactant complex are used. Interestingly, the two correlations that use energies relative to isolated reactants have different slopes and intercepts, and indeed the two curves cross at an IE of about 9.40 eV. Therefore, $[Fe^{IV}(O)(Por^{\bullet+})NCCH_3]^{+}$ in the gas phase is a better oxidant than $[Fe^{IV}(O)(Por^{\bullet+})Cl]$ in epoxidation reactions with substrates with IE below 9.40 eV,

dx.doi.org/10.1021/ic4005104 | Inorg. Chem. 2013, 52, 7968−7979

whereas it is reversed for substrates with higher ionization potentials, i.e., for *p*-CN-styrene and *p*-NO_2-styrene. This observation is in excellent agreement with the experimental studies of Nam et al.,[11] who also found improved reactivity of $[Fe^{IV}(O)(Por^{\bullet+})NCCH_3]^+$ over $[Fe^{IV}(O)(Por^{\bullet+})Cl]$ for the epoxidation of para-substituted styrenes with a large ρ^+_p Hammett value of the substituent. The study that uses a reactant complex as the reference point, by contrast does not find this change in reactivity but instead produces almost parallel trends (Figure 8b). It may very well be, therefore, that the reactant complexes are unrealistic models and do not compare well with the experiment. Thus, in a reactant complex, the structures of the oxidant and substrate are solvated by solvent molecules and the interactions between all particles. In our reactant complex, no solvent molecules were included, and as a consequence, full freedom of optimization was possible, which may have resulted in an experimentally unrealistic structure.

To further understand the reactivity trends and the effect of the substrate and oxidant on the obtained barrier heights and, by extension, the rate constants, we set up a valence bond (VB) curve crossing diagram for styrene epoxidation by iron(IV)-oxo porphyrin cation-radical systems (Figure 9). The VB curve crossing diagram displayed here is analogous to that presented before for hydrogen-atom-abstraction reactions by iron(IV) oxo oxidants[33] but is further generalized to accommodate substrate epoxidation reactions.

This diagram starts on the bottom-left with the reactant configurations, i.e., styrene and $[Fe^{IV}(O)(Por^{\bullet+})X]$. The latter appears in two VB configurations, where we highlight the valence π-orbital electrons with dots. Thus, the electronic ground state of $[Fe^{IV}(O)(Por^{\bullet+})X]$ is $\delta_{x^2-y^2}{}^2\pi_{xz}{}^2\pi_{yz}{}^2\pi^*_{xz}{}^1\pi^*_{yz}{}^1a_{2u}{}^1$ in both the quartet and doublet spin states, and its wave function is labeled as Ψ_r in Figure 9. The $\delta_{x^2-y^2}$ orbital is a nonbonding orbital in the plane of the porphyrin ring. The perpendicular set of orbitals, π_{xz}/π^*_{xz} and π_{yz}/π^*_{yz}, are the bonding and antibonding combinations of the metal $3d_{xz}/3d_{yz}$ with the oxygen $2p_x/2p_y$ atomic orbitals and contain three electrons in each pair.

In the C−O bond-formation step in the epoxidation mechanism, one electron is transferred from the substrate to the oxidant and it fills the a_{2u} orbital with a second electron to give the radical intermediate wave function Ψ_I. In VB theory,[33] the reactant (Ψ_r) and product (Ψ_I) wave functions cross each other and connect to excited states in the product and reactant conformations, respectively. Thus, Ψ_I* is an excited reactant state with an electronic configuration that represents a C−O bond pair, a radical on the styrene group, and a closed-shell a_{2u} orbital. The two VB curves give an avoided crossing and a barrier height for C−O bond formation, $\Delta E^{\ddagger}$. On the basis of a series of hydrogen-atom-abstraction reactions,[33,34] it was shown that $\Delta E^{\ddagger}$ is proportional to the curve crossing energy (ΔE_c) minus the resonance energy B via $\Delta E^{\ddagger} = \Delta E_c - B$. However, the curve crossing energy is proportional to the promotion gap ($G_{H,r}$) or excitation energy from the reactant to product configuration in the geometry of the reactants so that the barrier height can be written as

$$\Delta E^{\ddagger} = fG_{H,r} - B \quad (1)$$

In a recent study, we showed that the relationship in eq 1 is also valid for substrate epoxidation and sulfoxidation reactions and that the promotion gap $G_{H,r}$ reflects the excitation energy or ionization potential of the substrate.[10,35]

A comparison of the VB structures for the Ψ_r and Ψ_I* configurations shows that there is an electron transfer from the iron(IV) oxo group to the porphyrin a_{2u} orbital, reflecting an electron excitation in CpdI ($E_{ex,CpdI}$), which can be approximated with the EA of the oxidant. In addition, it can be seen that the electrons in the C=C bond are singlet-paired in the reactant ground state but triplet-coupled in the excited state in the reactant geometry, which implies a singlet−triplet energy gap in the C=C bond, ΔE_{ST}. Thus, a singlet−triplet energy gap in the C=C bond reflects the excitation energy of an electron in the π bond of the C=C moiety, namely, $E_{ex,Z}$, which, in turn, can be approximated with the IE of the substrate. Consequently, $G_{H,r}$ is proportional to $EA_{CpdI(X)} + E_{ex,Z}$ and so should the barrier height of the epoxidation reaction. Of course, electron excitation from the π orbital of the substrate, which is the highest occupied molecular orbital, is also proportional to the IE of the substrate. Indeed, the plot in Figure 8 confirms a relationship between the barrier height and ionization potential, as predicted by the VB diagram in Figure 9.

For the reverse reaction, that is, from radical intermediates to reactants, the epoxidation barrier height ($\Delta E^{\ddagger}_{rev}$) is equal to $\Delta E^{\ddagger}$ plus the exothermicity to form radical intermediates (ΔE_{ri}). In VB, the reverse barrier is proportional to the promotion gap in the radical intermediates, i.e., Ψ_I to Ψ_p* or $G_{H,p}$. The VB structures on the radical intermediate side of Figure 9 show that the excitation energy $G_{H,p}$ corresponds to the formation energy of the C−O bond plus the electron transfer from the substrate into the a_{2u} orbital. The VB structures in Figure 9 indicate that the electrons in the C−O bond are singlet-coupled in Ψ_I but triplet-coupled in Ψ_p*, which implies that a singlet−triplet excitation in the C−O bond has occurred. The singlet−triplet excitation in the C−O bond refers to the bond breaking of the C−O bond. In earlier work, we showed that the C−O bond-formation energy is proportional to a H−O bond-formation energy, so that it can be mimicked with BDE_{OH}, defined as the reaction enthalpy for eq 2.[10]

To test whether the VB curve crossing diagram can predict the barrier heights from empirical values, we calculated the gas-phase EAs of all four oxidants from Figure 1 and the π−π* excitation energies and IEs of all *p*-Z-styrene substrates, and the results are given in Table 1. We calculated the EA of the

Table 1. Substrate Chemical Properties and Charge-Transfer (Q_{CT}) Values in the Transition States

Z	IE_Z[a]	$E_{ex,Z}$[a]	$Q_{CT,Cl}$[b]	$Q_{CT,AN}$[c]
H	9.05	3.82	0.10	0.25
F	9.05	3.81	0.07	0.24
Cl	8.87	3.70	0.08	0.16
CH_3	8.59	3.75	0.12	0.32
t-Bu	8.43	3.76	0.12	0.42
CN	9.46	3.46	0.01	0.10
NO_2	9.70	2.88	−0.03	−0.01
OCH_3	8.03	3.73	0.16	0.42
NH_2	7.55	3.61	0.22	0.55
$N(CH_3)_2$	7.05	3.57	0.27	0.63

[a]In electronvolts. [b]Charge transfer in $^2TS_{Cl,Z}$. [c]Charge transfer in $^2TS_{AN,Z}$.

dx.doi.org/10.1021/ic4005104 | Inorg. Chem. 2013, 52, 7968−7979

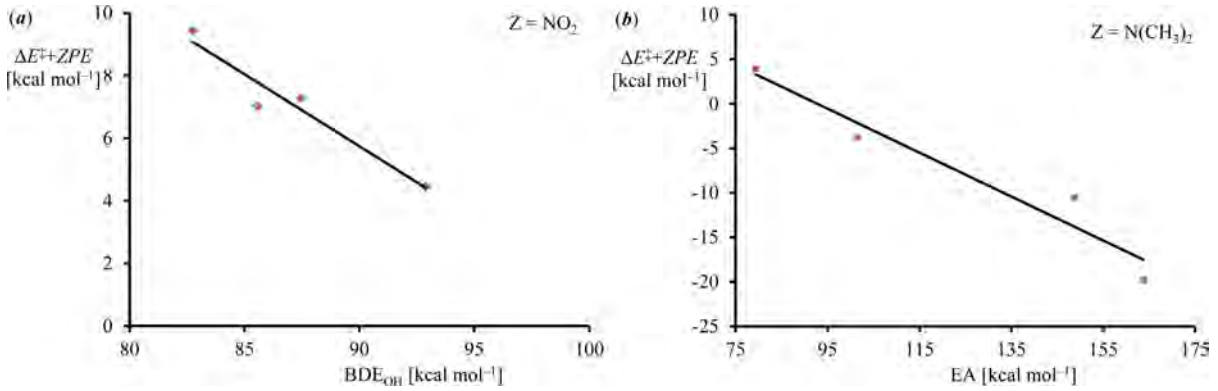

Figure 10. Correlations of (a) the epoxidation barrier height of *p*-NO_2-styrene with BDE_{OH} and (b) the epoxidation barrier height of *p*-$N(CH_3)_2$-styrene with $EA_{CpdI(X)}$.

oxidant, the $\pi-\pi^*$ excitation energy in the *p*-Z-styrene substrates, and the promotion gap via eq 2. Subsequently, we used these values to estimate $\Delta E^{\ddagger}_{VB}$ for all substrates. Although these VB-calculated barrier heights are, on average, within −0.05 kcal mol^{-1} of the DFT-calculated ones, actually the standard deviation is quite large (about 2 kcal mol^{-1}). This implies that the model has shortcomings, which we address with a slightly modified model as described below.

$$G_{H,r} = 2(EA_{CpdI(X)} + E_{ex,Z}) \quad (2)$$

$$[Fe^{IV}(O)(Por^{\bullet+})X] + H^{\bullet} \rightarrow [Fe^{IV}(OH)(Por)X] \quad (3)$$

Thus, the forward reaction barrier is dependent on the intrinsic chemical properties of the substrate, i.e., the IE, whereas the reverse reaction barrier depends on the variables of the oxidant, i.e., the BDE_{OH} value. We calculated gas-phase values of BDE_{OH} = 87.5 kcal mol^{-1} for $[Fe^{IV}(O)(Por^{\bullet+})Cl]$ and BDE_{OH} = 82.8 kcal mol^{-1} for $[Fe^{IV}(O)(Por^{\bullet+})NCCH_3]^+$, respectively.[23] This energy difference narrows to almost equal values in a dielectric constant of ε = 5.7: BDE_{OH} = 82.3 and 81.3 kcal mol^{-1} for $[Fe^{IV}(O)(Por^{\bullet+})X]$, X = Cl^- or $NCCH_3$, respectively.

The VB diagram of Figure 9 shows that the transition state described from reactants to intermediates, i.e., forward, is proportional to $EA_{CpdI(X)} + E_{ex,Z}$, whereas the transition state in the reverse reaction, i.e., backward, is proportional to the BDE_{OH} value of the oxidant. Thus, the location of the barrier on the potential energy surface will determine whether the barrier correlates with $EA_{CpdI(X)} + E_{ex,Z}$ or BDE_{OH}. So, for a substrate epoxidation reaction where the transition state has a very reactant-like electronic configuration, i.e., an early transition state, very little electron transfer from the substrate to the oxidant has taken place and consequently the reactant wave function dominates in the transition state. As a result, an early transition state should be proportional to BDE_{OH}. On the other hand, a late transition state has an electronic configuration closely resembling the radical intermediate state because of a significant amount of electron transfer that has taken place already. Therefore, late transition states, based on the VB diagram in Figure 8, should correlate with the EA of the oxidant. Indeed, the group spin density of the epoxidation transition state with *p*-NO_2-styrene as a substrate shows only a small amount of electron transfer from the substrate to the oxidant, and consequently the charge transfer from the substrate to the oxidant (Q_{CT}) is almost zero. This implies that the epoxidation barriers for *p*-NO_2-styrene will be early on the potential energy surface, and little electron transfer has taken place. As reasoned above, these barrier heights should, therefore, correlate with BDE_{OH} and not with $EA_{CpdI(X)} + E_{ex,Z}$. To test this, we display in Figure 10 the correlation of *p*-NO_2-styrene epoxidation with BDE_{OH} for $\mathbf{1}_X/\mathbf{2}_X$ (X = Cl^- and $NCCH_3$). As can be seen for this set of four data points, a linear correlation is found between the epoxidation barrier of *p*-NO_2-styrene and the corresponding BDE_{OH} value of the oxidant.

The group spin densities of $^2\mathbf{TS}_{X,N(CH_3)_2}$, in contrast to those found for $^2\mathbf{TS}_{X,NO_2}$, show considerably larger amounts of spin density on the substrate part of the structure. At the same time, the spin density on the porphyrin ring has dropped because of electron transfer from the substrate to the oxidant. Thus, the $^2\mathbf{TS}_{X,N(CH3)2}$ structures are electronically late and resemble product-type conformations. Because of that, in $^2\mathbf{TS}_{X,N(CH_3)_2}$, electron transfer has taken place already (or at least most of it) and, consequently, the barrier height will be driven by the differences in the EAs of the individual oxidants. To test this, we plot in Figure 10b the correlation between the epoxidation barrier height of *p*-$N(CH_3)_2$-styrene epoxidation by $\mathbf{1}_X/\mathbf{2}_X$ oxidants as a function of the EA of the oxidant. We find a linear correlation between the EA and barrier height, as predicted by the VB diagram in Figure 8.

As follows from the correlations depicted in Figure 10, the amount of electron transfer from the substrate to the oxidant determines whether a transition state correlates either with the sum of $EA_{CpdI(X)} + E_{ex,Z}$ or with BDE_{OH} instead. Thus, we extracted the degree of charge transfer from the substrate to the oxidant (Q_{CT}) from the UB3LYP/B2//UB3LYP/B1 calculations and summarize these values for the $^2\mathbf{TS}_{X,Z}$ transition states in Table 1. We now define the variable ω, which describes the position of the transition state on the potential energy profile through eq 4, and link ω to the degree of charge transfer (Q_{CT}), BDE_{OH}, and $EA_{CpdI(X)} + E_{ex,Z}$.

$$\omega = Q_{CT}BDE_{OH} + (1 - Q_{CT})(EA_{CpdI(X)} + E_{ex,Z}) \quad (4)$$

Essentially, ω is proportional to BDE_{OH} when the charge transfer is maximal, i.e.. an early transition state, but it is proportional to $EA_{CpdI(X)} + E_{ex,Z}$ for a late transition state with a small value of Q_{CT}. We calculated ω for all transition states $^2\mathbf{TS}_{X,Z}$, X = Cl^-/$NCCH_3$ and *p*-Z-styrene as substrates, and a plot of all data is given in Figure 11. Thus, the full set of transition states, irrespective of the axial ligand of the oxidant, fits a linear correlation. Consequently, we described the trend in epoxidation barriers for early as well as late transition states

dx.doi.org/10.1021/ic4005104 | Inorg. Chem. 2013, 52, 7968−7979

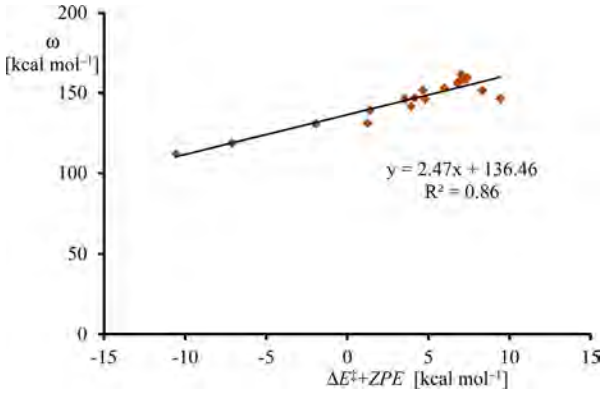

Figure 11. Correlation between the epoxidation barrier height of all data for $\mathbf{1}_X$ (X = Cl^-, $NCCH_3$) with parameter ω.

as a function of the intrinsic chemical properties of the oxidant and substrate and the amount of charge transfer in the TS during the reaction process.

In summary, we show here that the barrier height of an epoxidation reaction by a metal oxo oxidant is dependent on the electron-donating/withdrawing character of the substituents of the substrate. Thus, substrates with high electron-donating power such as *p*-$N(CH_3)_2$-styrene result in low barrier heights and rapid electron transfer from the substrate to the oxidant well before the epoxidation barrier height has been overcome. On the other hand, electron-withdrawing groups such as *p*-NO_2-styrene result in much later electron transfer from the substrate to the oxidant, and now the height of the barrier is determined by the strength of the C−O bond that is formed.

CONCLUSIONS

In this work, we report a systematic computational study into substrate epoxidation by four iron(IV)-oxo porphyrin cation-radical models. We investigated the effect of the axial ligand, chloride versus acetonitrile, as well as the equatorial ligand, Por versus TPFPP. It is shown that the substituents on the porphyrin ring can guide substrate binding through electrostatic interactions with halide atoms, which lowers the barrier heights. A neutral axial ligand leads to displacement of the metal from the plane through the porphyrin ring and results in different orbital interactions between the metal and porphyrin ring compared to systems with an anionic ligand. This has profound effects on the EA of the oxidant and the subsequent reactivity patterns. Finally, we investigated *p*-Z-styrene epoxidation by four iron(IV)-oxo porphyrin cation-radical models and highlight the differences in reactivity for olefins with electron-withdrawing versus electron-donating substituents. In particular, it is shown that electron-donating substituents give early transition states and lower reaction barriers than substrates with electron-withdrawing substituents.

ASSOCIATED CONTENT

Supporting Information

Tables with group spin densities, charges, and relative energies of all complexes described in this work as well as Cartesian coordinates of all optimized geometries. This material is available free of charge via the Internet at http://pubs.acs.org.

AUTHOR INFORMATION

Corresponding Author

*E-mail: sam.devisser@manchester.ac.uk (S.P.d.V.), dkclcre@yahoo.com (D.K.), rezalatifi@gmail.com (R.L.).

Notes

The authors declare no competing financial interest.

ACKNOWLEDGMENTS

The research was supported by the CPU time provided by the National Service of Computational Chemistry Software. D.K. is Ramanujan Fellow of the Department of Science and Technology, New Delhi, India (Research Grants SR/S2/RJN-11/2008), and also acknowledges financial support from the OSDD unit of the Council of Scientific & Industrial Research, New Delhi, India (Grant OSDD/HCP0001/12FYP/2012-13/Fin/2455). M.A.S. thanks the Petroleum Technology Development Fund of the Nigerian Government for a scholarship. E.V.R.-A. thanks the U.S. Department of Energy, Office of Basic Energy Science (Grant DE-FG02-06ER15799).

REFERENCES

(1) (a) Sono, M.; Roach, M. P.; Coulter, E. D.; Dawson, J. H. *Chem. Rev.* **1996**, *96*, 2841−2888. (b) Groves, J. T. *Proc. Natl. Acad. Sci. U.S.A.* **2003**, *100*, 3569−3574. (c) Ortiz de Montellano, P. R., Ed. *Cytochrome P450: Structure, Mechanism and Biochemistry*, 3rd ed.; Kluwer Academic/Plenum Publishers: New York, 2004. (d) Kadish, K. M., Smith, K. M., Guilard, R., Eds. *Handbook of Porphyrin Science*; World Scientific Publishing Co.: New York, 2010. (e) Ortiz de Montellano, P. R. *Chem. Rev.* **2010**, *110*, 932−948. (f) de Visser, S. P., Kumar, D., Eds. *Iron-containing enzymes: Versatile catalysts of hydroxylation reactions in nature*; RSC Publishing: Cambridge, U.K., 2011.

(2) (a) Denisov, I. G.; Makris, T. M.; Sligar, S. G.; Schlichting, I. *Chem. Rev.* **2005**, *105*, 2253−2277. (b) Rittle, J.; Green, M. T. *Science* **2010**, *330*, 933−937.

(3) (a) Groves, J. T.; Shalyaev, K.; Lee, J. In *The Porphyrin Handbook*; Kadish, K. M., Smith, K. M., Guilard, R., Eds.; Academic Press: New York; 2000; Vol. *4*, Chapter 27, pp 17−40. (b) Nam, W. *Acc. Chem. Res.* **2007**, *40*, 522−531.

(4) (a) Ruettinger, R. T.; Fulco, A. J. *J. Biol. Chem.* **1981**, *256*, 5728−5734. (b) Guengerich, F. P. *Arch. Biochem. Biophys.* **2003**, *409*, 59−71. (c) McLean, K. J.; Munro, A. W. *Drug Metabol. Rev.* **2008**, *40*, 427−446.

(5) (a) Groves, J. T.; Avaria-Neisser, G. E.; Fish, K. M.; Imachi, M.; Kuczkowski, R. L. *J. Am. Chem. Soc.* **1986**, *108*, 3837−3838. (b) Alcalde, M.; Farinas, E. T.; Arnold, F. H. *J. Biomol. Screen.* **2004**, *9*, 141−146. (c) Dansette, P. M.; Bertho, G.; Mansuy, D. *Biochem. Biophys. Res. Commun.* **2005**, *338*, 450−455. (d) Yuan, X.; Wang, Q.; Horner, J. H.; Sheng, X.; Newcomb, M. *Biochemistry* **2009**, *48*, 9140−9146. (e) Shinkyo, R.; Xu, L.; Tallman, K. A.; Cheng, Q.; Porter, N. A.; Guengerich, T. P. *J. Biol. Chem.* **2011**, *286*, 33021−33028.

(6) Ortiz de Montellano, P. R.; Fruetel, J. A.; Collins, J. R.; Campere, D. L.; Loew, G. H. *J. Am. Chem. Soc.* **1991**, *113*, 3195−3196.

(7) For example, see: (a) Groves, J. T.; Myers, R. S. *J. Am. Chem. Soc.* **1983**, *105*, 5791−5796. (b) Groves, J. T.; Watanabe, Y. *J. Am. Chem. Soc.* **1986**, *108*, 507−508. (c) Collman, J. P.; Kodadek, T.; Brauman, J. I. *J. Am. Chem. Soc.* **1986**, *108*, 2588−2594. (d) Ostović, D.; Bruice, T. C. *J. Am. Chem. Soc.* **1989**, *111*, 6511−6517. (e) Collman, J. P.; Brauman, J. I.; Hampton, P. D.; Tanaka, H.; Bohle, D. S.; Hembre, R. T. *J. Am. Chem. Soc.* **1990**, *112*, 7980−7984. (f) Groves, J. T.; Gross, Z.; Stern, M. K. *Inorg. Chem.* **1994**, *33*, 5065−5072. (g) Stephenson, N. A.; Bell, A. T. *Inorg. Chem.* **2006**, *45*, 2758−2766. (h) Collman, J. P.; Zeng, L.; Wang, H. J. H.; Lei, A.; Brauman, J. I. *Eur. J. Org. Chem.* **2006**, 2707−2714. (i) Hessenauer-Ilicheva, N.; Franke, A.; Meyer, D.; Woggon, W.-D.; van Eldik, R. *J. Am. Chem. Soc.* **2007**, *129*, 12473−12479. (j) Mas-Balleste, R.; Que, L., Jr. *J. Am. Chem. Soc.* **2007**, *129*,

15964−15972. (k) Comba, P.; Rajaraman, G. *Inorg. Chem.* **2008**, *47*, 78−93. (l) Bruijnincx, P. C. A.; Buurmans, I. L. C.; Gosiewska, S.; Moelands, M. A. H.; Lutz, M.; Spek, A. L.; van Koten, G.; Klein Gebbink, R. J. M. *Chem.—Eur. J.* **2008**, *14*, 1228−1237. (m) Hull, J. F.; Sauer, E. L. O.; Incarvito, C. D.; Faller, J. W.; Brudvig, G. W.; Crabtree, R. H. *Inorg. Chem.* **2009**, *48*, 488−495. (n) McGown, A. J.; Kerber, W. D.; Fujii, H.; Goldberg, D. P. *J. Am. Chem. Soc.* **2009**, *131*, 8040−8048. (o) Company, A.; Feng, Y.; Güell, M.; Ribas, X.; Luis, J. M.; Que, L., Jr.; Costas, M. *Chem.—Eur. J.* **2009**, *15*, 3359−3362. (p) Franke, A.; Wolak, M.; van Eldik, R. *Chem.—Eur. J.* **2009**, *15*, 10182−10198. (q) Hessenauer-Ilicheva, N.; Franke, A.; Wolak, M.; Higuchi, T.; van Eldik, R. *Chem.—Eur. J.* **2009**, *15*, 12447−12459. (r) Leeladee, P.; Goldberg, D. P. *Inorg. Chem.* **2010**, *49*, 3083−3085. (s) Lanucara, F.; Crestoni, M. E. *Chem.—Eur. J.* **2011**, *17*, 12092−12100.

(8) (a) Gross, Z.; Nimri, S. *Inorg. Chem.* **1994**, *33*, 1731−1732. (b) Gross, Z. *J. Biol. Inorg. Chem.* **1996**, *1*, 368−371. (c) Czarnecki, K.; Nimri, S.; Gross, Z.; Proniewicz, L. M.; Kincaid, J. R. *J. Am. Chem. Soc.* **1996**, *118*, 2929−2935.

(9) Green, M. T.; Dawson, J. H.; Gray, H. B. *Science* **2004**, *304*, 1653−1656.

(10) Kumar, D.; Karamzadeh, B.; Sastry, G. N.; de Visser, S. P. *J. Am. Chem. Soc.* **2010**, *132*, 7656−7667.

(11) Song, W. J.; Ryu, Y. O.; Song, R.; Nam, W. *J. Biol. Inorg. Chem.* **2005**, *10*, 294−304.

(12) (a) Takahashi, A.; Kurahashi, T.; Fujii, H. *Inorg. Chem.* **2011**, *50*, 6922−6928. (b) Cong, Z.; Kurahashi, T.; Fujii, H. *Angew. Chem., Int. Ed.* **2011**, *50*, 9935−9939.

(13) (a) *Jaguar*, version 7.9; Schrödinger, LLC: New York, 2011. (b) Frisch, M. J.; et al. *Gaussian03*, revision C.01; Gaussian, Inc.: Wallingford, CT, 2004. (c) Frisch, M. J.; et al. *Gaussian09*, revision A.1; Gaussian, Inc.: Wallingford, CT, 2009.

(14) (a) Becke, A. D. *J. Chem. Phys.* **1993**, *98*, 5648−5652. (b) Lee, C.; Yang, W.; Parr, R. G. *Phys. Rev. B* **1988**, *37*, 785−789.

(15) (a) Hay, P. J.; Wadt, W. R. *J. Chem. Phys.* **1985**, *82*, 270−283. (b) Hehre, W. J.; Ditchfield, R.; Pople, J. A. *J. Chem. Phys.* **1972**, *56*, 2257−2261.

(16) (a) de Visser, S. P.; Oh, K.; Han, A.-R.; Nam, W. *Inorg. Chem.* **2007**, *46*, 4632−4641. (b) Vardhaman, A. K.; Sastri, C. V.; Kumar, D.; de Visser, S. P. *Chem. Commun.* **2011**, *47*, 11044−11046.

(17) de Visser, S. P. *J. Am. Chem. Soc.* **2010**, *132*, 1087−1097.

(18) Schwabe, T.; Grimme, S. *Phys. Chem. Chem. Phys.* **2007**, *9*, 3397−3406.

(19) Reiher, M.; Salomon, O.; Hess, B. A. *Theor. Chem. Acc.* **2001**, *107*, 48−55.

(20) Kumar, D.; Thiel, W.; de Visser, S. P. *J. Am. Chem. Soc.* **2011**, *133*, 3869−3882.

(21) (a) Green, M. T. *J. Am. Chem. Soc.* **1999**, *121*, 7939−7940. (b) Ogliaro, F.; de Visser, S. P.; Cohen, S.; Kaneti, J.; Shaik, S. *ChemBioChem* **2001**, *11*, 848−851. (c) Kamachi, T.; Yoshizawa, K. *J. Am. Chem. Soc.* **2003**, *125*, 4652−4661. (d) Bathelt, C. M.; Zurek, J.; Mulholland, A. J.; Harvey, J. N. *J. Am. Chem. Soc.* **2005**, *127*, 12900−12908. (e) Lonsdale, R.; Oláh, J.; Mulholland, A. J.; Harvey, J. N. *J. Am. Chem. Soc.* **2011**, *133*, 15464−15474. (f) Isobe, H.; Yamanaka, S.; Okumura, M.; Yamaguchi, K.; Shimada, J. *J. Phys. Chem. B* **2011**, *115*, 10730−10738.

(22) Shaik, S.; Kumar, D.; de Visser, S. P.; Altun, A.; Thiel, W. *Chem. Rev.* **2005**, *105*, 2279−2328.

(23) de Visser, S. P.; Tahsini, L.; Nam, W. *Chem.—Eur. J.* **2009**, *15*, 5577−5587.

(24) de Visser, S. P.; Shaik, S.; Sharma, P. K.; Kumar, D.; Thiel, W. *J. Am. Chem. Soc.* **2003**, *125*, 15779−15788.

(25) (a) Linde, C.; Åkermark, B.; Norrby, P.-O.; Svensson, M. *J. Am. Chem. Soc.* **1999**, *121*, 5083−5084. (b) Kamachi, T.; Shiota, Y.; Ohta, T.; Yoshizawa, K. *Bull. Chem. Soc. Jpn.* **2003**, *76*, 721−732. (c) Quiñinero, D.; Musaev, D. G.; Morokuma, K. *Inorg. Chem.* **2003**, *42*, 8449−8455. (d) Sharma, P. K.; de Visser, S. P.; Ogliaro, F.; Shaik, S. *J. Am. Chem. Soc.* **2003**, *125*, 2291−2300. (e) Hirao, H.; Kumar, D.; Thiel, W.; Shaik, S. *J. Am. Chem. Soc.* **2005**, *127*, 13007−13018. (f) Kumar, D.; Derat, E.; Khenkin, A. M.; Neumann, R.; Shaik, S. *J. Am. Chem. Soc.* **2005**, *127*, 17712−17718. (g) Bassan, A.; Blomberg, M. R. A.; Siegbahn, P. E. M.; Que, L., Jr. *Angew. Chem., Int. Ed.* **2005**, *44*, 2939−2941.

(26) (a) de Visser, S. P.; Ogliaro, F.; Harris, N.; Shaik, S. *J. Am. Chem. Soc.* **2001**, *123*, 3037−3047. (b) de Visser, S. P.; Ogliaro, F.; Shaik, S. *Angew. Chem., Int. Ed.* **2001**, *40*, 2871−2874. (c) de Visser, S. P.; Ogliaro, F.; Sharma, P. K.; Shaik, S. *Angew. Chem., Int. Ed.* **2002**, *41*, 1947−1951. (d) de Visser, S. P.; Ogliaro, F.; Sharma, P. K.; Shaik, S. *J. Am. Chem. Soc.* **2002**, *124*, 11809−11826. (e) Kumar, D.; de Visser, S. P.; Shaik, S. *Chem.—Eur. J.* **2005**, *11*, 2825−2835.

(27) (a) Kumar, D.; de Visser, S. P.; Shaik, S. *J. Am. Chem. Soc.* **2003**, *125*, 13024−13025. (b) Kumar, D.; de Visser, S. P.; Sharma, P. K.; Cohen, S.; Shaik, S. *J. Am. Chem. Soc.* **2004**, *126*, 1907−1920. (c) Kumar, D.; de Visser, S. P.; Shaik, S. *J. Am. Chem. Soc.* **2004**, *126*, 5072−5073. (d) de Visser, S. P. *Chem.—Eur. J.* **2006**, *12*, 8168−8177.

(28) (a) Ben-Daniel, R.; de Visser, S. P.; Shaik, S.; Neumann, R. *J. Am. Chem. Soc.* **2003**, *125*, 12116−12117. (b) de Visser, S. P.; Kaneti, J.; Neumann, R.; Shaik, S. *J. Org. Chem.* **2003**, *68*, 2903−2912.

(29) Kumar, D.; Tahsini, L.; de Visser, S. P.; Kang, H. Y.; Kim, S. J.; Nam, W. *J. Phys. Chem. A* **2009**, *113*, 11713−11722.

(30) de Visser, S. P. *J. Am. Chem. Soc.* **2006**, *128*, 15809−15818.

(31) (a) Watanabe, Y.; Iyanagi, T.; Oae, S. *Tetrahedron Lett.* **1980**, *21*, 3685−3688. (b) Watanabe, Y.; Numata, T.; Iyanagi, T.; Oae, S. *Bull. Chem. Soc. Jpn.* **1981**, *54*, 1163−1170. (c) Watanabe, Y.; Iyanagi, T.; Oae, S. *Tetrahedron Lett.* **1982**, *23*, 533−536.

(32) Lide, D. R. *CRC Handbook of Chemistry and Physics*, 76th ed.; CRC Press: Boca Raton, FL, 1996.

(33) Shaik, S. S. *J. Am. Chem. Soc.* **1981**, *103*, 3692−3701.

(34) (a) Shaik, S.; Kumar, D.; de Visser, S. P. *J. Am. Chem. Soc.* **2008**, *130*, 10128−10140. (b) Latifi, R.; Bagherzadeh, L.; de Visser, S. P. *Chem.—Eur. J.* **2009**, *15*, 6651−6662.

(35) Kumar, D.; Sastry, G. N.; de Visser, S. P. *Chem.—Eur. J.* **2011**, *17*, 6196−6205.

Inorganic Chemistry

Article

pubs.acs.org/IC

Generation of a High-Valent Iron Imido Corrolazine Complex and NR Group Transfer Reactivity

Pannee Leeladee,[†] Guy N. L. Jameson,*[,‡] Maxime A. Siegler,[†] Devesh Kumar,[⊥] Sam P. de Visser,*[,∥] and David P. Goldberg*[,†]

[†]Department of Chemistry, The Johns Hopkins University, 3400 North Charles Street, Baltimore, Maryland 21218, United States

[‡]Department of Chemistry and MacDiarmid Institute for Advanced Materials and Nanotechnology, University of Otago, P.O. Box 56, Dunedin 9054, New Zealand

[⊥]Department of Applied Physics, Babasaheb Bhimrao Ambedkar University, Vidya Vihar, Rai Bareilly Road, Lucknow 226 025, India

[∥]Manchester Institute of Biotechnology and School of Chemical Engineering and Analytical Science, The University of Manchester, 131 Princess Street, Manchester M1 7DN, United Kingdom

Supporting Information

ABSTRACT: The generation of a new high-valent iron terminal imido complex prepared with a corrolazine macrocycle is reported. The reaction of $[Fe^{III}(TBP_8Cz)]$ (TBP_8Cz = octakis(4-*tert*-butylphenyl)corrolazinato) with the commercially available chloramine-T (Na^+TsNCl^-) leads to oxidative N-tosyl transfer to afford $[Fe^{IV}(TBP_8Cz^{+\bullet})(NTs)]$ in dichloromethane/acetonitrile at room temperature. This complex was characterized by UV−vis, Mössbauer (δ = −0.05 mm s^{-1}, ΔE_Q = 2.94 mm s^{-1}), and EPR (X-band (15 K), g = 2.10, 2.00) spectroscopies, and together with reactivity patterns and DFT calculations has been established as an iron(IV) species antiferromagnetically coupled with a Cz-π-cation-radical (S_{total} = $^1/_2$ ground state). Reactivity studies with triphenylphosphine as substrate show that $[Fe^{IV}(TBP_8Cz^{+\bullet})(NTs)]$ is an efficient NTs transfer agent, affording the phospharane product $Ph_3P{=}NTs$ under both stoichiometric and catalytic conditions. Kinetic analysis of this reaction supports a bimolecular NTs transfer mechanism with rate constant of 70(15) M^{-1} s^{-1}. These data indicate that $[Fe^{IV}(TBP_8Cz^{+\bullet})(NTs)]$ reacts about 100 times faster than analogous Mn terminal arylimido corrole analogues. It was found that two products crystallize from the same reaction mixture of $Fe^{III}(TBP_8Cz)$ + chloramine-T + PPh_3, $[Fe^{IV}(TBP_8Cz)(NPPh_3)]$ and $[Fe^{III}(TBP_8Cz)(OPPh_3)]$, which were definitively characterized by X-ray crystallography. The sequential production of $Ph_3P{=}NTs$, $Ph_3P{=}NH$, and $Ph_3P{=}O$ was observed by ^{31}P NMR spectroscopy and led to a proposed mechanism that accounts for all of the observed products. The latter Fe^{III} complex was then rationally synthesized and structurally characterized from $Fe^{III}(TBP_8Cz)$ and $OPPh_3$, providing an important benchmark compound for spectroscopic studies. A combination of Mössbauer and EPR spectroscopies led to the characterization of both intermediate spin (S = $^3/_2$) and low spin (S = $^1/_2$) Fe^{III} corrolazines, as well as a formally Fe^{IV} corrolazine which may also be described by its valence tautomer $Fe^{III}(Cz^{+\bullet})$.

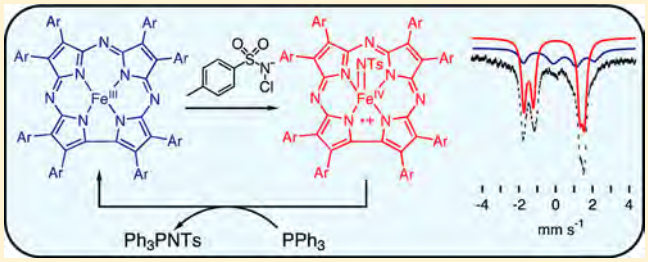

INTRODUCTION

Iron−nitrogen multiply bonded complexes have been implicated in biological systems and industrial processes. For instance, in the Haber−Bosch process, iron-bound surface nitrides have been postulated as the reactive intermediates responsible for ammonia production.[1,2] The iron-containing metalloenzyme nitrogenase likely relies upon one or more multiply bonded Fe−N intermediates during the dinitrogen reduction process.[3−5] An Fe=NR porphyrin species was suggested as the reactive intermediate for reactions involving NR insertion into C−H bonds by the heme enzyme Cytochrome P450-LM 3,4.[6] In analogy to this chemistry, much effort has gone into accessing transient Fe−N(R) multiply bonded species as potent catalysts for C−H activation and functionalization.[7−11] There is great interest in preparing metal-nitrido and metal-imido complexes, including iron-based systems, for similar potential applications in atom or group transfer processes.[12−17]

The synthesis of mid- to late-transition metal-imido complexes has been quite challenging. The stability of these compounds depends on their geometry, the oxidation state of the metal, and the nature of the ancillary ligands. In particular, 5- or 6-coordinate Fe-imido complexes are usually considered highly unstable, making it difficult to generate and/or characterize such species. It can be seen from qualitative d-orbital splitting diagrams that these high coordination number iron complexes would normally have filled, or partially filled,

Received: February 2, 2013
Published: March 25, 2013

 © 2013 American Chemical Society dx.doi.org/10.1021/ic400280x | Inorg. Chem. 2013, 52, 4668−4682

Chart 1. Representative Examples of Multiply-Bonded, Terminal-Imido/Nitrene Fe and Mn Complexes (Ad = adamantyl; Ts = tosyl; Mes = mesityl)

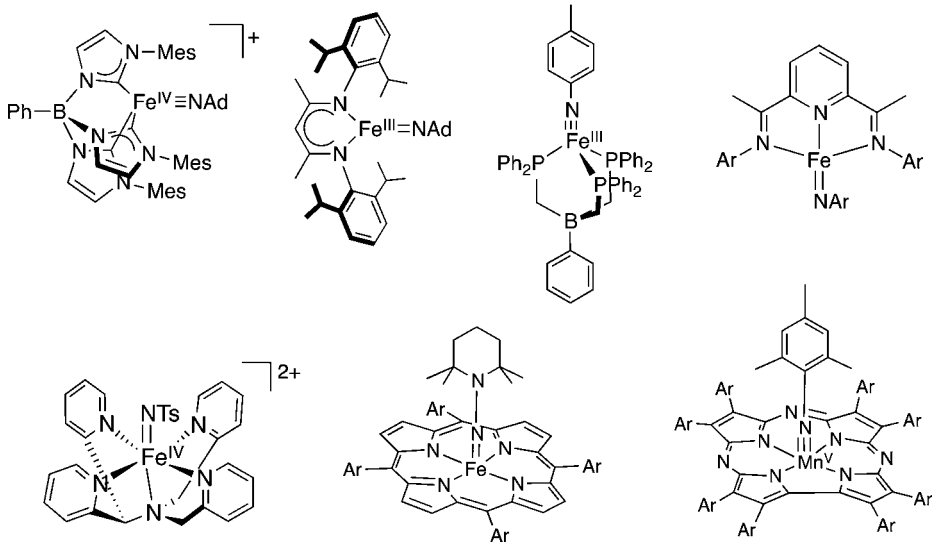

dπ-pπ antibonding orbitals with respect to the Fe−N interaction. The Fe ion needs to be in an unusually high oxidation state, e.g., Fe(6+), to avoid this destabilizing influence,[18] and iron compounds in relatively low oxidation states, e.g. Fe(2+), Fe(3+), are destabilized due to the population of the antibonding dπ(Fe)−pπ(N) orbitals.[9,10,17,19] To our knowledge, there is only one example of an Fe(NR) complex with a coordination number ≥5 that has been crystallographically characterized, and this complex is an iron porphyrin derivative.[20] Interestingly, this complex was formulated as a high-spin Fe^{II}-nitrene compound, as indicated by Mössbauer spectroscopy. In addition, a 6-coordinate, nonheme Fe^{IV}-imido complex supported by a tetrapyridylamine ligand was described, but this complex could not be characterized by X-ray crystallography (Chart 1).[21]

An alternative, elegant strategy to prepare stable Fe terminal imido complexes is to construct them from compounds with low coordination number (Chart 1). Peters and co-workers have shown that triply bonded Fe^{II}-, Fe^{III}-, and Fe^{IV}-imido complexes can be stabilized in pseudotetrahedral coordination environments by sterically encumbered tris(phosphino)borane, tris(phosphino)borate, and bis(phosphine)pyrazolyl ligands.[22−26] Similarly, Smith and co-workers introduced strong field, bulky tris(carbene)borate ligands to stabilize Fe^{III}- and Fe^{IV}-imido complexes with 3-fold symmetry.[27] Iron-imide complexes with redox-active bis(imino)pyridine (BIP) ligands have been constructed from distorted square planar geometries,[28,29] although the assignment of the iron oxidation states in these compounds is not straightforward.[28] Highly unsaturated, three-coordinate iron(III) terminal imido complexes have also been prepared with either bulky bidentate, β-diketiminate ligands,[30,31] or bidentate, dipyrromethene-based systems.[8] In all of these cases it seems that the steric encumbrance of the surrounding ligands is essential to engender the low-coordinate environments that stabilize iron-imido species.

Our group has focused on the stabilization and characterization of high-valent manganese and iron complexes with multiply bonded terminal ligands encapsulated in the heme-like corrolazine (Cz) platform. The strongly donating and oxidatively resistant Cz macrocycle has allowed for the isolation and X-ray crystallographic characterization of a high-valent Mn^{V}-imido complex, [Mn^{V}(TBP$_8$Cz)(NMes)] (Mes = 2,4,6-trimethylphenyl; TBP$_8$Cz = octakis(4-*tert*-butylphenyl)-corrolazinato) (Chart 1).[32] The related corrole (Cor) complex, [Mn^{V}(tpfc)(NMes)] (tpfc = *meso*-tris(pentafluorophenyl)-corrole), was also isolated and fully characterized, including an X-ray structure determination.[33] Isoelectronic Mn^{V} terminal oxo complexes have also been generated with Cz and Cor supporting ligands, and the first example of this class, Mn^{V}(O)(TBP$_8$Cz), was isolable and stable as a solid at room temperature.[34−38] In these cases the paradigm does not involve enforcing low-coordinate environments at the metal center; rather the Cz and Cor ligands are designed to provide strong, in-plane σ donation that helps stabilize metal ions in high-valent states, depopulating the key, dπ−pπ antibonding orbitals involved in terminal imido/oxo ligation.

The synthesis of these rare, manganese-imido/oxo complexes suggested to us that the Cz scaffold might support the preparation of analogous high-valent, iron-imido complexes. Indeed, we had already described the generation, low-temperature stabilization, and C−H activation chemistry of a high-valent, iron-oxo corrolazine π-cation-radical (Fe^{IV}(O)-(TBP$_8$Cz$^{+\bullet}$)), equivalent to the compound-I intermediate in heme enzymes.[39,40] It has been shown that Fe^{III} corroles can catalyze aziridinations using PhINTs as the nitrogen source, and a high-valent Fe-imido species was postulated as the reactive intermediate.[41] In the same study, an Fe^{IV} corrole was also found to be a potent catalyst for aziridinations when PhINTs was replaced with chloramine-T (Na^{+}TsNCl^{-}) as the nitrogen source. However, no direct spectroscopic evidence for the existence of high-valent Fe-imido corroles in this study, or any other, has thus far been obtained.

Herein, we report the generation of a high-valent iron-imido corrolazine, (TBP$_8$Cz$^{+\bullet}$)Fe^{IV}(NTs), and its characterization through a combination of UV−vis, EPR, and Mössbauer spectroscopies. Density functional theory (DFT) calculations were performed to support and analyze the electronic structure assignment, and simulate the Mössbauer parameters for the high-valent iron-imido complex. This complex is a rare example of a metastable Fe-imido porphyrinoid compound, and the first example of such a species housed in a corrole-type macrocycle.

dx.doi.org/10.1021/ic400280x | *Inorg. Chem.* 2013, 52, 4668−4682

It is shown that this compound is capable of NR group transfer to PPh_3 to give the $TsN{=}PPh_3$ product with concomitant two-electron reduction of the iron-imido complex. Kinetic studies show that the reactivity of the Fe=NTs complex is dramatically enhanced over Mn=NAr corroles. However, $(TBP_8Cz^{+\bullet})Fe^{IV}(NTs)$ is, in general, significantly more stable (and less reactive) than expected for a multiply bonded, iron-imido species. Crystal structures were determined for the PPh_3-derived products $[Fe^{IV}(TBP_8Cz)(NPPh_3)]$ and $[Fe^{III}(TBP_8Cz)(OPPh_3)]$, and these structures have aided in our understanding of the mechanism of NR transfer and subsequent product transformations. Combined EPR and Mössbauer studies on the series of iron complexes described here provide insights into the oxidation state assignments and ligand noninnocence for such compounds.

EXPERIMENTAL DETAILS

All reactions were performed using dry solvents and standard Schlenk or drybox techniques at room temperature unless otherwise noted. The complex $[Fe^{III}(TBP_8Cz)]$ (**1**)[42] and metal-free corrolazine TBP_8CzH_3[43] were synthesized as reported previously. The $^{57}FeCl_2$ was prepared according to a published procedure.[44] Dichloromethane and acetonitrile were purified via a Pure-Solv solvent purification system from Innovative Technologies, Inc. Deuterated solvents for NMR samples were purchased from Cambridge Isotope Laboratories, Inc. Chloramine-T trihydrate ($Na^+TsNCl^-{\cdot}3H_2O$) was purchased from Sigma-Aldrich and used as received. Triphenylphosphine (PPh_3) was received from Sigma-Aldrich and recrystallized from diethyl ether. Triphenylphosphine oxide (Ph_3PO) was purchased from Sigma-Aldrich and recrystallized from ethanol. Authentic samples of (*N*-tosylimino)triphenylphosphorane (Ph_3PNTs) and Ph_3PNH were synthesized according to published methods.[45,46]

Instrumentation. UV−vis spectroscopy was performed on a Varian Cary 50 Bio spectrophotometer. Kinetic experiments were run on a Hewlett-Packard 8542 diode-array spectrophotometer equipped with HPChemstation software. Electron paramagnetic resonance (EPR) spectra were obtained on a Bruker EMX EPR spectrometer controlled with a Bruker ER 041 X G microwave bridge at 15 K, and equipped with a continuous-flow liquid helium cryostat (ESR900) coupled to a TC503 temperature controller made by Oxford Instruments, Inc. ^1H NMR and ^{31}P NMR spectra were recorded on a Bruker Avance 400 MHz FT-NMR spectrometer. Chemical shifts were referenced to the residual solvent peaks for ^1H NMR and to the H_3PO_4 peak for ^{31}P NMR. Electrospray ionization mass spectra (ESI-MS) were collected on a Thermo Finnigan LCQ Duo ion-trap mass spectrometer fitted with an electrospray ionization source in positive ion mode. Samples were infused into the instrument at a rate of 25 μL/min using a syringe pump via a silica capillary line. The spray voltage was set at 5 kV, and the capillary temperature was held at 250 °C. ^{57}Fe Mössbauer spectra were recorded on a Mössbauer spectrometer from SEE Co. (Science Engineering & Education Co., MN) equipped with a closed cycle refrigerator system from Janis Research Co. and SHI (Sumitomo Heavy Industries Ltd.). Data were collected in constant acceleration mode in transmission geometry. The zero velocity of the Mössbauer spectra refers to the centroid of the room temperature spectrum of a 25 μm metallic iron foil. Analysis of the spectra was conducted using the WMOSS program (SEE Co, formerly WEB Research Co. Edina, MN). Magnetic spectra were fitted using the spin Hamiltonian:

$$H = D\left[\hat{S}_z^2 - \frac{1}{3}S(S+1)\right] + E(\hat{S}_x^2 - \hat{S}_y^2) + \beta\hat{S}\cdot g\cdot\hat{B} \qquad (1)$$

Computational Calculations and Spectroscopic Parameter Determination. All calculations were done using previously described methods[47] with density functional theory at the unrestricted hybrid density functional level UB3LYP[48,49] as implemented in the *Jaguar 7.9* and *Gaussian-03* program packages.[50,51] All geometries described here were the result of a full optimization without geometric constraints, and the local minima were ascertained with an analytical frequency calculation that established real frequencies only. These optimizations and frequencies were done with an LACVP basis set on Fe that includes a core potential and a 6-31G basis set on the rest of the atoms: basis set B1.[52] This basis set was shown to give adequate structures for the investigation of a potential energy profile of a chemical reaction by an iron(IV)-oxo species.[53] To improve the energetics we did single point calculations using a triple-ζ quality LACV3P+ basis set on Fe (with core potential) and 6-311+G* on the rest of the atoms: basis set B2. Energies reported in here are taken from the UB3LYP/B2 results and are corrected for zero-point energies at UB3LYP/B1. Free energies use UB3LYP/B2 energies and UB3LYP/B1 zero-point energies, thermal and entropic corrections. We also did single point calculations in Jaguar using the Polarized Continuum Model using a dielectric constant of $\varepsilon = 5.708$ and probe radius of 2.722 Å.

Spectroscopic parameters (Mössbauer and EPR parameters) were obtained from single point calculations on the optimized geometries using the ORCA program package.[54] These calculations used the B3LYP method in combination with the CP(PPP) basis set on Fe coupled to a TZVP basis set on the rest of the atoms.[55] The electric field gradients V_i ($i = x, y,$ or z) were used to calculate the quadrupole splitting (ΔE_Q) using eqs 2 and 3 with e the elementary charge of a proton/electron, Q the nuclear quadrupole moment, $Q(^{57}Fe) = 0.16$ barn, and η the asymmetry parameter of the nuclear quadrupole tensor.[56]

$$\Delta E_Q = \frac{1}{2}eQ\cdot V_z\cdot\sqrt{1+\frac{1}{3}\eta^2} \qquad (2)$$

$$\eta = (V_x - V_y)/V_z \qquad (3)$$

The isomer shift δ was calculated from the spin density at the iron nucleus $\rho_0(Fe)$ using previously determined fit-parameters in ORCA.[57] The magnetic hyperfine parameters, A_i ($i = x, y,$ or z), were obtained using the scalar relativistic zero-order regular approximation (ZORA) at the B3LYP level of theory. These methods were shown to reproduce well experimentally determined Mössbauer and EPR parameters of transition metal complexes.

Generation of $[Fe^{IV}(TBP_8Cz^{+\bullet})(NTs)]$ (2) in Situ. To a solution of $[Fe^{III}(TBP_8Cz)]$ (16 μM) in CH_2Cl_2 was added $Na^+TsNCl^-{\cdot}3H_2O$ (1 equiv dissolved in CH_3CN). A color change of the solution from green to brown was noted. The reaction was monitored by UV−vis spectroscopy, revealing isosbestic conversion from the spectrum for **1** to that of the new brown species $[Fe^{IV}(TBP_8Cz^{+\bullet})(NTs)]$ (**2**) (λ_{max} = 395, $\varepsilon = 4.3\times10^4\ M^{-1}\ cm^{-1}$). The spectrum for **2** is stable for at least 2 h at room temperature. An EPR sample was prepared as follows: to a solution of $[Fe^{III}(TBP_8Cz)]$ (2.0 mM) in toluene (300 μL) was added chloramine-T (1 equiv dissolved in CH_3CN) to give a final concentration of 1.5 mM of the iron complex. A color change from green to brown was observed. The reaction mixture was then transferred to a Wilmad quartz EPR tube (3 mm i.d.), and the sample was frozen and stored at 77 K.

Precipitation of Solid $[Fe^{IV}(TBP_8Cz^{+\bullet})(NTs)]$ (2). To an amount of $[Fe^{III}(TBP_8Cz)]$ (20.6 mg, 14.6 μmol) in CH_2Cl_2 (1.00 mL) was added $Na^+TsNCl^-{\cdot}3H_2O$ (6.2 mg, 22 μmol, 1.5 equiv) dissolved in CH_3CN (0.40 mL). The reaction mixture was stirred for 30 min, and the color change from green to brown was observed. An amount of CH_3CN was added until a solid precipitate had formed in the reaction mixture. The resulting solid was filtered, isolated on filter paper, and washed with CH_3CN to afford a dark brown-green solid (8.0 mg).

Kinetics of NR Group Transfer to Triphenyl Phosphine. In a custom-made 100-mL round-bottom flask adapted with a 1-cm path-length side arm UV−vis cell was prepared a solution of $[Fe^{IV}(TBP_8Cz^{+\bullet})(NTs)]$ (**2**) by addition of $Na^+TsNCl^-{\cdot}3H_2O$ (100 μL of an 0.8 mM stock solution in CH_3CN, 1 equiv) to a solution of **1** (16 μM) dissolved in CH_2Cl_2 (5 mL). The cell was placed in the spectrophotometer, and a 400 nm long-pass filter was placed between the spectrophotometer light source and the sample solution in order to

dx.doi.org/10.1021/ic400280x | Inorg. Chem. 2013, 52, 4668−4682

avoid any potential photodegradation of iron corrolazine. After complete conversion of **1** to **2** was noted by UV−vis, excess PPh_3 (30−75 equiv dissolved in CH_2Cl_2) was added to start the reaction, and an immediate color change from brown to green was noted, indicating the recovery of the starting material **1**. The time-course of the reaction was monitored by UV−vis and showed a smooth conversion of **2** to **1** over a 100−200 s period depending on the concentration of PPh_3. The pseudo-first-order rate constants, k_{obs}'s, for this reaction were obtained by nonlinear least-squares fitting of the plots of absorbance (Abs) at 440 nm versus time (t) to the following equation:

$$Abs_t = Abs_f - (Abs_f - Abs_0)e^{-k_{obs}t} \quad (4)$$

Here, Abs_f = final absorbance and Abs_0 = initial absorbance. The reaction was repeated over a range of substrate concentrations, and a plot of k_{obs} versus substrate concentration was found to be linear. The second-order rate constant (k) was obtained from the slope of the best-fit line to this plot.

Monitoring of NR Group Transfer by ^{31}P NMR Spectroscopy. To a solution of **1** (12−15 mM) in CD_2Cl_2 was added $Na^+TsNCl^-{\cdot}3H_2O$ (1−3 equiv dissolved in CD_3CN). A color change from green to brown was noted, consistent with formation of **2**. An aliquot of the reaction mixture was checked by UV−vis spectroscopy to ensure the complete formation of **2**. Excess PPh_3 (5−10 equiv dissolved in CD_2Cl_2) was added, causing an immediate color change from brown to green. An aliquot of the reaction mixture was removed and analyzed by UV−vis spectroscopy, revealing the return of **1**. The solution was then transferred to an NMR tube, and the reaction was monitored by ^{31}P NMR over 14 d.

Synthesis of [Fe(TBP$_8$Cz)(NPPh$_3$)] (3). A reaction of **2** with PPh_3 substrate was performed as described above for ^{31}P NMR experiments, and then the reaction mixture was allowed to stand in an NMR tube under ambient conditions. Good quality single crystals appeared after 2 weeks. A crystal was selected for X-ray structure determination and revealed the structure for [Fe(TBP$_8$Cz)(NPPh$_3$)] (**3**). ESI-MS, EPR, and Mössbauer data indicated that the bulk material of these crystals was contaminated with a small amount of [Fe(TBP$_8$Cz)(OPPh$_3$)], and a separate X-ray structure determination of a second crystal confirmed the presence of this complex, whose structure was solved as [Fe(TBP$_8$Cz)(OPPh$_3$)] (**4a**).

Synthesis of [Fe(TBP$_8$Cz)(OPPh$_3$)] (4b). To a solution of **1** (9.8 mg, 6.9 μmol) in CH_2Cl_2 (400 μL) was added Ph_3PO (5 equiv in 100 μL of CH_2Cl_2). An amount of CH_3CN (100 μL) was added, and good quality single crystals (black blocks) (8 mg, 68%) were obtained by slow evaporation of this mixture for one week. UV−vis (CH_2Cl_2): λ_{max} = 439, 607, 732 nm. ESI-MS (m/z): isotopic cluster centered at 1689.7 (M^+). ^{1}H NMR (CD_2Cl_2): δ (ppm) 13.05 (br), 11.26 (br), 9.95 (br), 7.47 (br), 2.00, 1.82, 1.66, 1.57, 1.26, 0.88. ^{31}P NMR (CD_2Cl_2): δ (ppm) 27.4. Anal. Calcd for $C_{114}H_{119}FeN_7OP$: C, 81.02: H, 7.10; N, 5.80. Found: C, 81.18; H, 7.03; N, 5.78.

X-ray Crystallography. All reflection intensities were measured at 110(2) K using a KM4/Xcalibur (detector: Sapphire3) with enhanced graphite-monochromated Mo Kα radiation (λ = 0.710 73 Å) under the program CrysAlisPro (Version 1.171.33.55 or 1.171.35.11, Agilent Technologies, 2010/2011). The temperature of the data collection was controlled using the system Cryojet (manufactured by Oxford Instruments). The program CrysAlisPro (Version 1.171.33.55 or 1.171.35.11, Agilent Technologies, 2010/2011) was used to refine the cell dimensions and data reduction. The structure was solved with the program SHELXS-97 and was refined on F^2 with SHELXL-97. Analytical numeric absorption corrections based on a multifaceted crystal model were applied using CrysAlisPro (Version 1.171.33.55 or 1.171.35.11, Agilent Technologies, 2010/2011). The H-atoms were placed at calculated positions using the instructions AFIX 23, AFIX 43, or AFIX 137 with isotropic displacement parameters having values 1.2 or 1.5 times U_{eq} of the attached C atoms.

The asymmetric unit of **3**, **4a**, and **4b** contains one Fe complex, and some lattice dichloromethane and acetonitrile solvent molecules. All structures are partly disordered. The t-butyl group C73→C76 of one aryl group is disordered over two orientations, and the occupancy factor for the major component refines to 0.876(5) for **3**, 0.870(5) for **4a**, and 0.895(4) for **4b**. In the structure of **3**, disorder was modeled for the four crystallographically independent dichloromethane molecules, and the occupancy factors for the major components are 0.831(4), 0.880(2), 0.695(5), and 0.529(8). In the structures of **4a** and **4b**, free variables for the major occupancy factors of one disordered CH_2Cl_2 and one ordered CH_3CN solvent molecules were used in the final refinement. Their refined values are 0.753(4), 0.131(3), and 0.902(8) for **4a**, and 0.792(4), 0.113(3), and 0.923(8) for **4b**. Other solvent molecules were found in the crystal lattice but were significantly more disordered, and therefore, their contributions were taken out by using the program SQUEEZE (Spek, 2003) for the final refinement.

Data for **3** follow: fw = 2068.75, black block, 0.34 × 0.31 × 0.26 mm^3, monoclinic, $P2_1/c$ (No. 14), a = 17.2124(2) Å, b = 33.4786(5) Å, c = 19.9855(2) Å, β = 102.6307(12)°, V = 11237.9(2) Å^3, Z = 4, D_x = 1.223 g cm^{-3}, μ = 0.390 mm^{-1}, abs corr range 0.894−0.923. There were 65 453 reflections measured up to a resolution of $(\sin\theta/\lambda)_{max}$ = 0.59 Å^{-1}. There were 19 786 unique reflections (R_{int} = 0.0377), of which 13 559 were observed [$I > 2\sigma(I)$]. There were 1354 parameters refined using 180 restraints. R1/wR2 [$I > 2\sigma(I)$]: 0.0666/0.1901. R1/wR2 [all reflns]: 0.0961/0.2026. S = 1.069. Residual electron density found between −0.93 and 0.78 e Å^{-3}.

Data for **4a** follow (asterisk indicates exclusion of the contribution of the unresolved residual electron density): *fw = 1802.09, *black block, 0.62 × 0.51 × 0.30 mm^3, monoclinic, $P2_1/c$ (No. 14), a = 17.2614(8) Å, b = 33.4143(11) Å, c = 19.9714(8) Å, β = 102.610(4)°, V = 11241.2(8) Å^3, Z = 4, D_x = 1.065 g cm^{-3}, *μ = 0.239 mm^{-1}, *abs corr range 0.899−0.941. *There were 59 539 reflections measured up to a resolution of $(\sin\theta/\lambda)_{max}$ = 0.59 Å^{-1}. There were 19 795 unique reflections (R_{int} = 0.0449), of which 15 006 were observed [$I > 2\sigma(I)$]. There were 1221 parameters refined using 63 restraints. R1/wR2 [$I > 2\sigma(I)$]: 0.0605/0.1733. R1/wR2 [all reflns]: 0.0759/0.1822. S = 1.069. Residual electron density found between −0.47 and 0.66 e Å^{-3}.

Data for **4b** follow: *fw = 1804.71, *black block, 0.35 × 0.24 × 0.20 mm^3, monoclinic, $P2_1/c$ (No. 14), a = 17.2502(2) Å, b = 33.4217(5) Å, c = 19.9821(2) Å, β = 102.7119(12)°, V = 11237.9(2) Å^3, Z = 4, D_x = 1.067 g cm^{-3}, *μ = 0.240 mm^{-1}, *abs corr range 0.900−0.937. There were *64 199 reflections measured up to a resolution of $(\sin\theta/\lambda)_{max}$ = 0.59 Å^{-1}. There were 19 786 unique reflections (R_{int} = 0.0375), of which 14 933 were observed [$I > 2\sigma(I)$]. There were 1221 parameters refined using 63 restraints. R1/wR2 [$I > 2\sigma(I)$]: 0.0611/0.1662. R1/wR2 [all reflns]: 0.0791/0.1750. S = 1.073. Residual electron density found between −0.40 and 0.66 e Å^{-3}.

Synthesis of [^{57}Fe^{III}(TBP$_8$Cz)]. The metal-free corrolazine TBP_8CzH_3 (62 mg, 0.046 mmol) was combined with $^{57}FeCl_2$ (29 mg, 0.23 mmol) in dimethylformamide (10 mL) and heated at reflux for 2 h. After removing the solvent *in vacuo*, the crude product was purified by flash column chromatography (CH_2Cl_2/MeOH 99:1 v/v; silica gel) to obtain [^{57}Fe^{III}(TBP$_8$Cz)] as a dark-green solid (51 mg, 79%). UV−vis (CH_2Cl_2): λ_{max} = 441, 610, 746 nm.

Samples for Mössbauer Studies. The ^{57}Fe-labeled complexes [^{57}Fe^{III}(TBP$_8$Cz)] and [^{57}Fe^{III}(TBP$_8$Cz)(NPPh$_3$)] were used for Mössbauer measurements. An isotopically labeled sample of **3** ([^{57}Fe^{III}(TBP$_8$Cz)(NPPh$_3$)]) was synthesized from [^{57}Fe^{III}(TBP$_8$Cz)] starting material. In the case of [Fe^{III}(TBP$_8$Cz)(OPPh$_3$)] (**4b**), Mössbauer data were collected on samples that were not enriched in ^{57}Fe. Samples were either measured as solid-state samples (~10 mg) or as frozen solutions (~400 μL) in toluene or pyridine in custom-made Teflon sample holders.

RESULTS AND DISCUSSION

Synthesis and Characterization of a High-Valent Iron Imido Corrolazine Complex. A variety of discrete metal-imido complexes have been synthesized by the reaction of the appropriate metal precursors and alkyl- or aryl-azides.[9,32,33,58−61] This strategy was used to synthesize the Mn^V-imido complex [Mn^V(TBP$_8$Cz)NMes], in which the Mn^{III}

dx.doi.org/10.1021/ic400280x | Inorg. Chem. 2013, 52, 4668−4682

precursor [$Mn^{III}(TBP_8Cz)$] was reacted with mesityl azide (2,4,6-$(CH_3)_3C_6H_2N_3$) at elevated temperature.[32] Corrole analogues [Mn(tpfc)NAr] (Ar = 2,4,6-$(CH_3)_3C_6H_2$, 2,4,6-$Cl_3C_6H_2$) have been similarly prepared.[33] Our initial efforts to gain access to a high-valent Fe-imido corrolazine followed the same methodology. Attempts were made to react the previously synthesized Fe^{III} complex [$Fe^{III}(TBP_8Cz)$] with both alkyl- and aryl-azides. For example, [$Fe^{III}(TBP_8Cz)$] was stirred with 50 equiv of mesityl azide in toluene for 24 h, but even at elevated temperature (90 °C) no evidence of reaction in the form of a color change, UV−vis spectroscopic conversion, or TLC change was noted. The azides AdN_3 (Ad = adamantyl), PhN_3, and Me_3SiN_3 were examined under similar conditions, but none led to any noticeable reaction with the Fe^{III} corrolazine. We speculated that the coordination of the azide reagents, or the triplet nitrene that potentially forms upon thermal activation of the azides,[61] was not occurring because even small changes in the UV−vis spectrum of [$Fe^{III}(TBP_8Cz)$] were not observed. The failure of the azide reagents to react with [$Fe^{III}(TBP_8Cz)$] prompted us to examine alternative NR group transfer reagents.

The inexpensive, commercially available reagent chloramine-T ($Na^+TsNCl^-\cdot 3H_2O$) was shown to be a good NTs-transfer agent in catalytic aziridinations involving Fe corrole [$(Fe^{IV}(tpfc)$],[41] and both chloramine-T and bromamine-T have been used as a nitrene source in metal-catalyzed C−H insertions.[41,62−65] Addition of a stock solution of chloramine-T in CH_3CN to [$Fe^{III}(TBP_8Cz)$] dissolved in CH_2Cl_2 at room temperature led to the conversion of green [$Fe^{III}(TBP_8Cz)$] (λ_{max} = 440, 611, 747 nm) to a new, brown species with λ_{max} = 395 nm (Figure 1). Isosbestic points are observed at 392, 490,

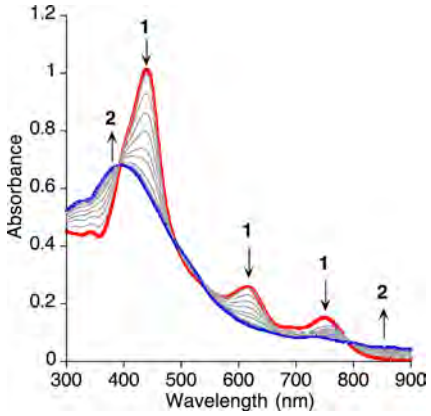

Figure 1. UV−vis spectral change upon addition of chloramine-T trihydrate (0−1.0 equiv) to [$Fe^{III}(TBP_8Cz)$] at 23 °C in CH_2Cl_2/CH_3CN.

538, and 792 nm. The new species with λ_{max} = 395 nm appears surprisingly stable for more than 2 h at room temperature as monitored by UV−vis. The changes in the UV−vis following addition of chloramine-T are similar to those observed for the reaction of [$Fe^{III}(TBP_8Cz)$] and pentafluoroiodosylbenzene to give the high-valent iron-oxo complex [$Fe^{IV}(TBP_8Cz^{+\bullet})(O)$], although in this case the iron-oxo product is thermally unstable and had to be observed at low temperature (−78 °C) (Figure 2). The UV−vis data are consistent with the formation of the expected product, [$Fe^{IV}(TBP_8Cz^{+\bullet})(NTs)$] (**2**), in which the tosylimido group replaces the terminal oxo ligand of [$Fe^{IV}(TBP_8Cz^{+\bullet})(O)$] and the Fe^{III} complex is oxidized by

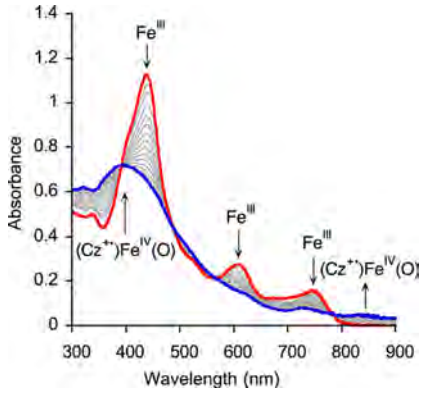

Figure 2. UV−vis spectral change upon addition of pentafluoroiodosylbenzene (PFIB) to [$Fe^{III}(TBP_8Cz)$] at −78 °C in CH_2Cl_2/CH_3OH.

two electrons, as shown in Scheme 1. The stoichiometry of the reaction was determined by titration of chloramine-T followed by monitoring by UV−vis spectroscopy, as shown in Figures 1 and S1. Addition of chloramine-T in 0.1 equiv increments results in isosbestic conversion of the Fe^{III} complex up to a total of 1 equiv, at which point a loss of isosbestic behavior is observed together with a decrease at 395 nm corresponding to the oxidized product. This spectral titration confirms that chloramine-T and [$Fe^{III}(TBP_8Cz)$] (**1**) react in a ratio of 1:1 to form [$Fe^{IV}(TBP_8Cz^{+\bullet})(NTs)$] (**2**). The imido complex **2** is thus remarkably stable in solution at room temperature, and this stability is likely a consequence of the previously established ability of the corrolazine platform to stabilize high-valent, multiply bonded terminal oxo and terminal imido complexes.

Several attempts were made to grow single crystals of the product from chloramine-T for X-ray structure determination, but thus far these efforts have remained unsuccessful. However, the complex can be isolated as a solid by solvent precipitation. Relatively concentrated solutions of [$Fe^{IV}(TBP_8Cz^{+\bullet})(NTs)$] (10 mM) can be generated in CH_2Cl_2 from [$Fe^{III}(TBP_8Cz)$] and chloramine-T, and the resulting Fe═NTs product is then precipitated from the reaction mixture by the addition of excess CH_3CN. Formation of a brown-green solid and a brown solution results, and the solid is then isolated by filtration. This solid exhibited similar UV−vis and other spectroscopic properties as seen for a sample of [$Fe^{IV}(TBP_8Cz^{+\bullet})(NTs)$] freshly generated in CH_2Cl_2, indicating that the precipitated material contains the [$Fe^{IV}(TBP_8Cz^{+\bullet})(NTs)$] complex prepared in situ. However, Mössbauer spectroscopic measurements show that this solid cannot be isolated in pure form, and contains up to ∼25% of the starting Fe^{III} complex (vide infra). Autoreduction of the iron-imido complex likely occurs upon precipitation, which is similar to what we have observed previously in attempts to isolate high-valent Mn-oxo corrolazines in the solid state.

NR Group Transfer. The brown complex **2**, generated from the reaction of chloramine-T and [$Fe^{III}(TBP_8Cz)$], was next examined for its ability to transfer the NTs group to phosphine substrates. The analogous reaction with corrole derivatives (e.g. [$Mn^V(tpfc)(NAr)$]) and phosphine substrates occurs smoothly, and has yielded kinetic and mechanistic information regarding NR group transfer.[66] Reaction of [$Fe^{IV}(TBP_8Cz^{+\bullet})(NTs)$] (freshly prepared in situ) with excess triphenylphosphine (Scheme 2) led to the isosbestic return of the spectrum for [$Fe^{III}(TBP_8Cz)$] as shown in Figure 3. Production of the two-

dx.doi.org/10.1021/ic400280x | Inorg. Chem. 2013, 52, 4668−4682

Scheme 1. Reaction of $Fe^{III}(TBP_8Cz)$ with Chloramine-T

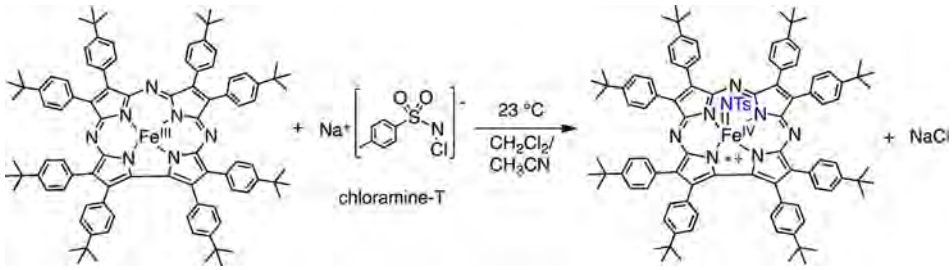

Scheme 2. Reaction of $[Fe^{IV}(TBP_8Cz^{+\bullet})(NTs)]$ with PPh_3

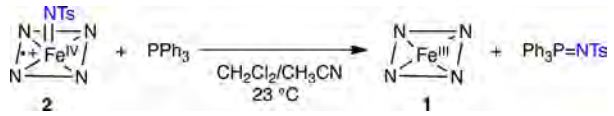

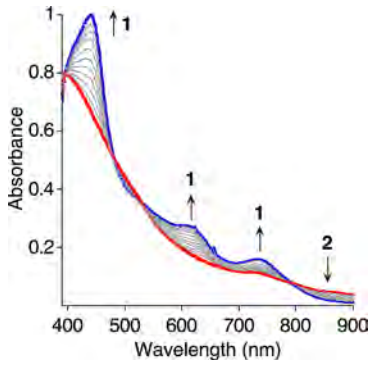

Figure 3. Time-resolved UV−vis spectra of $[Fe^{IV}(TBP_8Cz^{+\bullet})(NTs)]$ + PPh_3 (30 equiv) at 23 °C in CH_2Cl_2/CH_3CN (100:1 v:v).

electron-reduced Fe^{III} product is consistent with the formulation of $[Fe^{IV}(TBP_8Cz^{+\bullet})(NTs)]$, which is two oxidizing equivalents above that of the Fe^{III} starting material. Analysis of the reaction mixture by ^{31}P NMR following addition of PPh_3 reveals a single peak at 14.8 ppm (Figure S11). This peak matches that seen for the expected phosphorane product, $Ph_3P{=}NTs$, providing confirmation of NTs transfer to the phosphine substrate. No signal for unreacted PPh_3 was observed by ^{31}P NMR at the end of the NTs transfer reaction. This observation is consistent with the lack of a ^{31}P signal for independent solutions of $[Fe^{III}(TBP_8Cz)]$ + excess PPh_3, which is likely due to paramagnetic effects from the Fe^{III} complex on PPh_3. The PPh_3 also may coordinate to one or both axial positions at the Fe^{III} center, enhancing the paramagnetic influence.

The generation of $[Fe^{IV}(TBP_8Cz^{+\bullet})(NTs)]$ and subsequent reaction with PPh_3 was monitored by ^1H NMR spectroscopy (Figure S13). The initial spectrum for the Fe^{III} complex **1** reveals paramagnetically shifted peaks between −10 and +15 ppm. Addition of a slight excess of chloramine-T causes the clear disappearance of the paramagnetic signals for **1**, revealing a featureless paramagnetic spectrum for the iron-imido complex **2**. Subsequent addition of excess PPh_3 to the reaction mixture causes an immediate return of the peaks from −10 to 15 ppm associated with the starting complex **1**. These data are nicely consistent with the proposed mechanism of formation of the iron-imido complex and subsequent NTs transfer to PPh_3, which also causes the concomitant return of the Fe^{III} starting material.

Preliminary investigation of the reaction of the imido complex **2** with styrene was also performed to determine its potential reactivity toward aziridination of alkene substrates. As seen in Figure S14, a titration experiment with styrene leads to the reduction of **2** back to the starting Fe^{III} complex **1**, but a very large excess of substrate (48 000 equiv) is needed for this reaction to go to completion over a 25 min period. These data suggest that **2** is a very sluggish NR transfer agent for alkene substrates, and this finding is consistent with the general, inherent stability of **2** in solution at room temperature compared to other high-valent Fe-imido complexes. Given the low reactivity of **2** toward styrene, further studies regarding aziridination of styrene or other substrates were not pursued at this time.

Turnover. The UV−vis and NMR data suggested that the reactions involving the generation of the Fe=NTs complex and the subsequent NR transfer to PPh_3 were relatively fast, and therefore we attempted to determine if catalytic turnover could be achieved. The NR transfer reaction was run under catalytic conditions with a small excess of oxidant (3 equiv) and PPh_3 substrate (10 equiv). The initial formation of **2** from **1** + chloramine-T was first confirmed by UV−vis spectroscopy, and then the substrate was added immediately to initiate the NR transfer reaction. As seen in Figure 4, monitoring of this

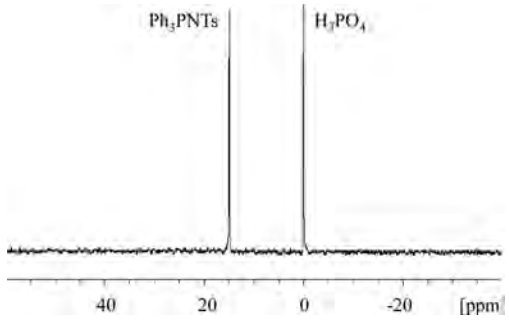

Figure 4. ^{31}P NMR spectrum showing the production of $Ph_3P{=}NTs$ from the reaction of $[Fe^{III}(TBP_8Cz)]$ + chloramine-T trihydrate (3 equiv) + PPh_3 (10 equiv) after 15 min in CD_2Cl_2/CD_3CN at 23 °C.

reaction by ^{31}P NMR showed the rapid production of $Ph_3P{=}NTs$ with no other phosphorane products. The catalytic cycle is summarized in Scheme 3. A background reaction does occur in the absence of **1** under these conditions; however, a significant amount of triphenylphosphine oxide is also produced in this case (Figure S12). The $OPPh_3$ is presumably obtained from oxidation of PPh_3 by hypochlorite anion (OCl^-), which is known to readily form from chloramine-T and exogenous H_2O. There is no $OPPh_3$ observed by ^{31}P NMR in Figure 4, indicating that the catalytic NR transfer must be highly efficient, preventing any background reaction from occurring. We can

dx.doi.org/10.1021/ic400280x | Inorg. Chem. 2013, 52, 4668−4682

Scheme 3. Catalytic Turnover

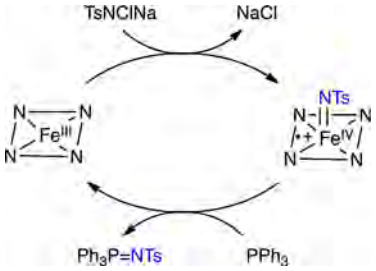

conclude that **1** is capable of catalytic turnover in the NR transfer to phosphines, and that the high-valent iron imido complex **2** is the likely active oxidant in the catalytic cycle.

Kinetics of NR Group Transfer. The kinetics of the reaction between $[Fe^{IV}(TBP_8Cz^{+\bullet})(NTs)]$ and PPh_3 were examined at 23 °C to gain further insight into the reaction mechanism for NR group transfer. The Fe═NTs complex was generated in situ, and excess PPh_3 (30−75 equiv) was added to yield pseudo-first-order conditions. An example of time-resolved UV−vis spectra used for kinetic measurements is shown in Figure 3. Monitoring this transformation at 440 nm over time gives the plot in Figure 5, which was satisfactorily fit

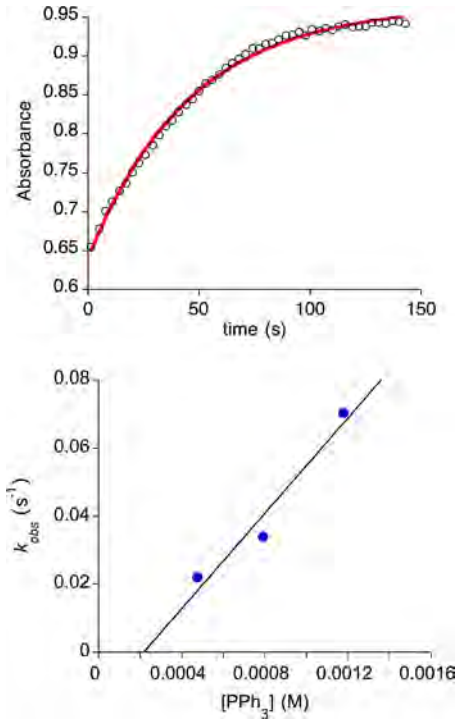

Figure 5. Representative change in absorbance at 440 nm vs time for **2** + PPh_3 corresponding to the return of $Fe^{III}(TBP_8Cz)$ (open circles), and best fit line (red) (top). Plot of the pseudo-first-order rate constants (k_{obs}) vs $[PPh_3]$ (bottom). A second-order rate constant of 70(15) M^{-1} s^{-1} was obtained from the best fit line (black).

with a first-order kinetics model and yielded a k_{obs} = 0.022 s^{-1}. The concentration of PPh_3 was varied and led to a linear correlation of k_{obs} versus $[PPh_3]$ as shown in Figure 5, consistent with an overall second-order rate law of rate = $k_2[Fe^{IV}(TBP_8Cz^{+\bullet})(NTs)][PPh_3]$. The slope of this plot gave a derived second-order rate constant of 70(15) M^{-1} s^{-1}. In comparison, the Mn^V-imido corrole $[Mn^V(tpfc)(NMes)]$ underwent NR group transfer to PPh_3 with a rate constant of 0.71(5) M^{-1} s^{-1}.[66] Thus, the Fe═NTs corrolazine exhibits a 100-fold rate enhancement over an Mn^V imido corrole analogue. These findings are in line with the enhanced reactivity of high-valent iron-oxo versus manganese-oxo corrolazines.[40] In addition, the electron-withdrawing nature of a tosyl group, as compared to a 2,4,6-trichlorophenyl substituent, can be expected to enhance the electrophilicity of **2** and make it more reactive for NR group transfer to nucleophiles such as PPh_3.

Structural Characterization of an NR Group Transfer Product. Efforts were made to obtain single crystals for structural characterization of the phosphine product following reaction of $[Fe^{IV}(TBP_8Cz^{+\bullet})(NTs)]$ with PPh_3. An NMR sample of this reaction mixture in CD_2Cl_2/CD_3CN was allowed to stand for two weeks, affording black crystalline blocks suitable for X-ray diffraction. The structure revealed an iron corrolazine complex with a phospharaniminato ligand coordinated in the axial position, corresponding to $[Fe^{IV}(TBP_8Cz)(NPPh_3)]$ (**3**). A displacement ellipsoid plot for complex **3** is shown in Figure 6, and selected bond distances and angles are

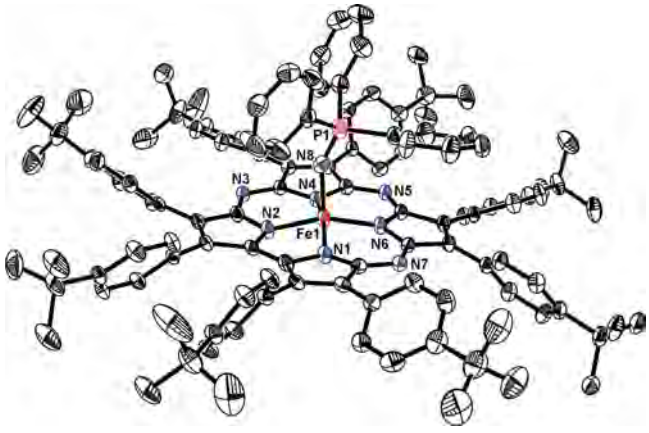

Figure 6. Displacement ellipsoid plot (50% probability level) of $[Fe(TBP_8Cz)(NPPh_3)]$ (**3**). H atoms and disorder are omitted for clarity.

given in Table 1. The tosyl substituent is absent, presumably having been hydrolytically cleaved from the initial Ph_3P═NTs product during crystallization. The remaining anionic Ph_3P═N^- axial ligand indicates that the iron is formally in the +4 oxidation state. We attempted to model the donor atom attached to Fe as an oxygen atom given the possibility of forming $OPPh_3$ in the reaction mixture. However, substitution of O for N in the axial position invariably leads to an unusually large thermal ellipsoid (Figure S3). In addition, substitution of O for N does not alter bond distances significantly, and the resulting P—O bond length would be unusually short (Table 2). These results rule out the presence of an $OPPh_3$ axial donor in **3**. The structural parameters for **3** are also not reasonable for a protonated Ph_3P═NH ligand, and no evidence for a hydrogen atom could be found in the final difference Fourier maps.

To our knowledge there are only two other crystallographically characterized mononuclear Fe—N═PPh_3 complexes reported to date, and relevant structural data for these complexes are given in Table 2. These iron complexes are four-coordinate iron(II) species derived from sterically encumbered tris(carbene)borate ancillary ligands. The Fe−N distance for

dx.doi.org/10.1021/ic400280x | Inorg. Chem. 2013, 52, 4668−4682

Table 1. Selected Bond Distances (Å) and Angles (deg) for 3, 4a, and 4b

	3	4a	4b
Fe(1)−N(1)	1.840(3)	1.843(2)	1.840(2)
Fe(1)−N(2)	1.844(3)	1.849(2)	1.848(2)
Fe(1)−N(4)	1.862(3)	1.867(2)	1.864(2)
Fe(1)−N(6)	1.866(3)	1.866(2)	1.865(2)
Fe(1)−$(N_{pyrrole})_{plane}$	0.292	0.291	0.291
Fe(1)−$(23\text{-atom})_{core}$	0.271	0.262	0.259
C_β−C_β (av)	1.393	1.388	1.390
C_α−C_β (av)	1.446	1.448	1.447
C_α−C_α (C4−C5)	1.425(5)	1.436(4)	1.430(4)
C_α−$N_{pyrrole}$(av)	1.373	1.367	1.369
C_α−N_{meso} (av)	1.338	1.338	1.339
Fe1−X (X = N8 or O1)	1.963(3)	2.002(2)	2.001(2)
P(1)−X	1.427(3)	1.494(2)	1.500(2)
N(1)−Fe(1)−N(2)	80.9(1)	81.12(9)	81.1(1)
N(2)−Fe(1)−N(4)	90.2(1)	90.45(9)	90.3(1)
N(4)−Fe(1)−N(6)	92.9(1)	92.62(9)	92.6(1)
N(6)−Fe(1)−N(1)	90.4(1)	90.17(9)	90.3(1)
N(1)−Fe(1)−X	97.9(1)	98.60(9)	98.50(9)
N(2)−Fe(1)−X	95.9(1)	96.13(8)	95.95(9)
N(4)−Fe(1)−X	100.1(1)	99.30(8)	99.47(9)
N(6)−Fe(1)−X	101.9(1)	101.72(8)	101.85(9)
Fe(1)−X−P(1)	154.5(2)	154.5(1)	154.4(1)

$[Fe^{IV}(TBP_8Cz)(NPPh_3)]$ of 1.963(3) Å is considerably longer than the Fe−N distances seen for the tris(carbene)borate complexes (Fe−N = 1.807(2)−1.894(2) Å). The shorter Fe−N bonds in the latter complexes may be assigned to the $NPPh_3$ ligand functioning as both a σ- and π-donor to the metal. In these approximate C_3-symmetric complexes, the d_{xz}/d_{yz} orbitals can serve as π-acceptors, whereas in the tetragonal Cz complex the orbitals of similar parentage are π^* in character with respect to the Fe−N bond and are partly filled, leading to the elongated Fe−N distance. In contrast, the N−P distance for **3** is significantly shorter than the N−P distances found in the other Fe—N═PPh_3 complexes in Table 2. The origin of this discrepancy is not known at this time, although the N−P distance for **3** is clearly shorter than that expected for either M−$OPPh_3$ or M−(H)$NPPh_3$ complexes, as seen in Table 2.

Efforts to characterize a bulk crystalline sample of $[Fe^{IV}(TBP_8Cz)(NPPh_3)]$ by ESIMS(+) revealed an isotopic cluster centered at m/z 1689.7, whose main peak was +2 above that expected for $[Fe(TBP_8Cz)(NPPh_3)]^{+\bullet}$, but a close match for $[Fe(TBP_8Cz)(OPPh_3)]^{+\bullet}$ (theoretical m/z 1689.8, see Supporting Information). However, the isotope pattern did not fit well for the $OPPh_3$ complex, and suggested that a possible mixture of Fe−$NPPh_3$ and Fe−$OPPh_3$ products crystallized in the same bulk material. This result prompted the analysis of a new batch of crystals from the PPh_3 reaction by X-ray diffraction. A unit cell check on an independently prepared crystal from the PPh_3 reaction mixture revealed a similar cell to that obtained for **3**. However, we speculated that an Fe^{III}−$OPPh_3$ complex might have nearly identical unit cell dimensions to those of **3**, and thus, another full set of data was collected. The structure solution for this second crystal revealed an $OPPh_3$ rather than $NPPh_3$ axial ligand. The crystal structure of this complex, $[Fe^{III}(TBP_8Cz)(OPPh_3)]$ (**4a**), is provided in the Supporting Information, and relevant bond distances and angles are given in Table 1. In this case, the presence of an O atom was confirmed, but the refinement of an N atom in the axial position was attempted. As expected, an N atom in this position led to a significantly smaller thermal ellipsoid, and three residual electron density peaks as large as 0.69 e^- $Å^{-3}$ were found at 0.43−0.48 Å from the N atom, which strongly suggests that not enough electron density has been assigned to this atomic site. The metrical parameters for the second crystal structure from the reaction of $[Fe(TBP_8Cz^{+\bullet})(NTs)]$ + PPh_3 are fully consistent with an Fe^{III}−$OPPh_3$ complex. These findings indicate that a mixture of Fe-$NPPh_3$ and Fe-$OPPh_3$ products ultimately form in the PPh_3 reaction and both crystallize under the same conditions.

Synthesis of $[Fe^{III}(TBP_8Cz)(OPPh_3)]$. The $Fe^{III}(OPPh_3)$ complex was independently prepared for comparison purposes. Addition of excess $OPPh_3$ to a solution of $[Fe^{III}(TBP_8Cz)]$ led to the crystalline complex $[Fe^{III}(TBP_8Cz)(OPPh_3)]$ (**4b**) in good yield (Scheme 4). A displacement ellipsoid plot is shown in Figure 7, and selected bond distances and angles are given in Table 1. The metrical parameters match well with those found for **4a**. The UV−vis and ESIMS spectra for **4b** are shown in Figure 8. The mass spectral data show a dominant cluster centered at m/z 1689.7, and its position and isotope pattern match nicely for $[Fe(TBP_8Cz)(OPPh_3)]^+$. This result can be contrasted with Figure S4, in which a different isotope pattern was obtained for the mixture of **3** + **4a** from the chloramine-T reaction. The UV−vis spectrum is similar to that of the Fe^{III} starting material, but a blue-shift of ∼15 nm is seen for the 732 nm band, resulting from coordination of $OPPh_3$ to Fe^{III}. Elemental analysis confirmed the high purity of **4b** as a bulk crystalline solid, and this material provided a key benchmark for further studies, including ^{31}P NMR and Mössbauer spectroscopies, while also confirming our assignment of the **3** + **4a** mixture from the PPh_3 oxidation reaction.

Scheme 4. Synthesis of $Fe^{III}(TBP_8Cz)(OPPh_3)$

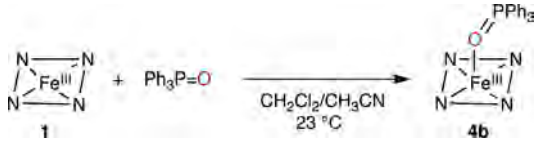

Monitoring Production of Hydrolyzed Products by ^{31}P NMR Spectroscopy. The reaction of $[Fe^{IV}(TBP_8Cz^{+\bullet})$-

Table 2. Comparison of Selected Bond Distances (Å) for Metal-$XPPh_3$ Compounds (X = N, O)

	M−X	P−X	ref
$[Fe^{IV}(TBP_8Cz)(NPPh_3)]$ (**3**)	1.963(3)	1.427(3)	this study
$[Fe^{III}(TBP_8Cz)(OPPh_3)]$ (**4b**)	2.001(2)	1.500(2)	this study
M-(H)$NPPh_3$ (M = Os, Cu, Zr, Ta)	1.931−2.367	1.511−1.843	67, 81−84
Fe^{III}−$OPPh_3$	1.912−2.056	1.483−1.507	85−89
$PhB(^tBuIm)_3Fe^{II}$−$NPPh_3$	1.894(2)	1.527(2)	59
$PhB(MesIm)_3Fe^{II}$−$NPPh_3$	1.807(2)−1.855(2)	1.524(2)−1.549(2)	90

dx.doi.org/10.1021/ic400280x | Inorg. Chem. 2013, 52, 4668−4682

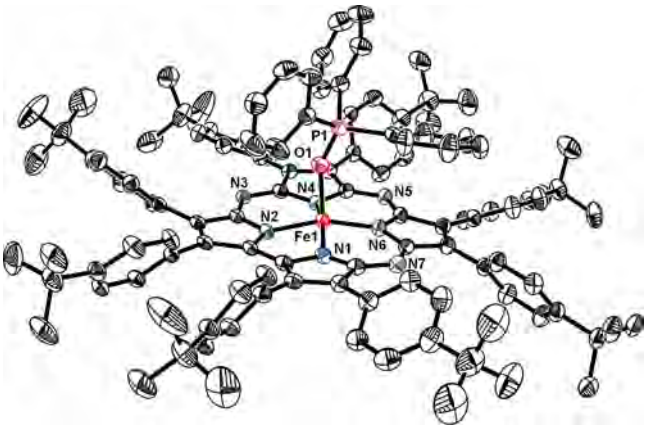

Figure 7. Displacement ellipsoid plot (50% probability level) of $[Fe^{III}(TBP_8Cz)(OPPh_3)]$ (**4b**). H atoms and disorder are omitted for clarity.

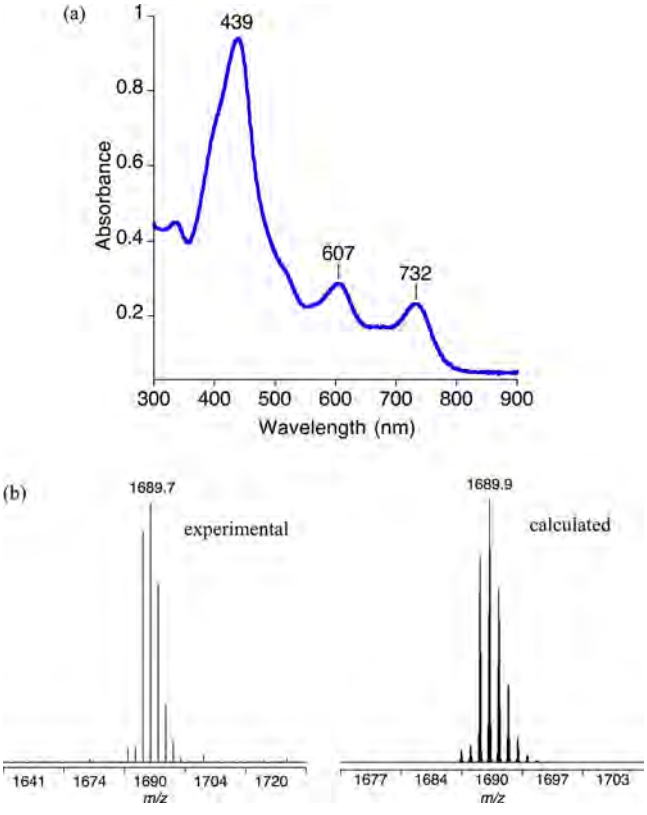

Figure 8. (a) UV–vis and (b) ESIMS spectra for $[Fe^{III}(TBP_8Cz)(OPPh_3)]$ (**4b**) as a crystalline solid dissolved in CH_2Cl_2.

(NTs)] (**2**) + PPh_3 was monitored by ^{31}P NMR spectroscopy over an extended time-course to gain insight into the mechanism of NR transfer and formation of the final phosphine-derived products $[Fe^{IV}(TBP_8Cz)(NPPh_3)]$ (**3**) and $[Fe^{III}(TBP_8Cz)(OPPh_3)]$ (**4**). Examination of the reaction mixture after day 1 shows only the Ph_3PNTs product, as expected (Figure 9). Following this initial spectrum, there is a slow build-up of the detosylated Ph_3PNH compound at 21.8 ppm (verified by comparison with an authentic sample). By day 7, a broad peak appears at 27.9 ppm, which then grows in intensity after a further week of reaction (day 14). An independent sample of pure $[Fe^{III}(TBP_8Cz)(OPPh_3)]$ (**4b**) exhibited the same broad peak in the ^{31}P NMR spectrum

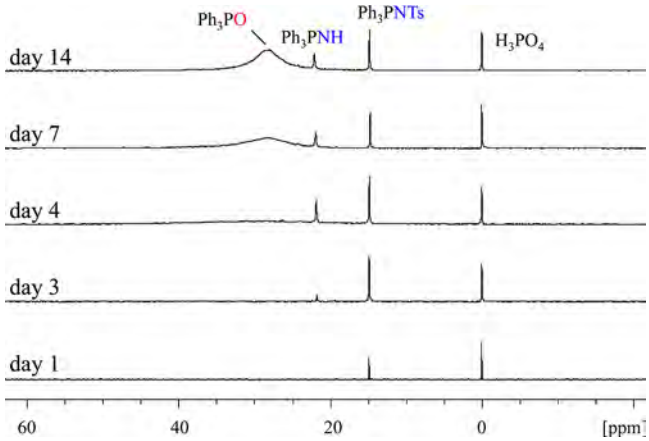

Figure 9. ^{31}P NMR spectra of the reaction of $[Fe^{III}(TBP_8Cz)]$ + chloramine-T trihydrate (3 equiv) + PPh_3 (10 equiv) in CD_2Cl_2/CD_3CN over 2 weeks.

(Figure S7). Thus, the ^{31}P NMR time-course shows the production of all three phosphorus products, Ph_3PNTs, $Ph_3PN(H)$, and Ph_3PO, over a two-week period.

Mechanism. A proposed mechanism for NR group transfer and generation of the different phosphine products is shown in Scheme 5. Initial formation of the Fe=NTs complex is followed by nucleophilic attack of PPh_3 to give Ph_3PNTs and an iron(III) corrolazine. The Ph_3PNTs may be activated by Fe^{III} toward hydrolytic cleavage of the tosyl group, resulting in production of Ph_3PNH. Coordination of this phosphinimine product can then lead to the formation of $Fe^{IV}(NPPh_3)$, following oxidation of an Fe^{III} precursor. Although the identity of the oxidant is not known, oxidation of Fe^{III} to Fe^{IV} is likely facilitated by a strong axial donor such as Ph_3PN^-. The generation of Ph_3PO occurs upon hydrolysis of Ph_3PNH, which is known to readily hydrolyze to Ph_3PO and NH_4OH in the presence of residual water.[67] The presence of Ph_3PO can then give rise to the final $Fe^{III}(OPPh_3)$ complex. This mechanism accounts for both the NMR time-course experiments and the observation of the different products from X-ray crystallography.

EPR and Mössbauer Spectroscopies. To obtain information about the oxidation states and spin states of the Fe corrolazine complexes described here, EPR and Mössbauer spectra were collected. Previous work on iron corrole complexes[68−71] has shown that it is often difficult to determine their electron configurations due to the noninnocent nature of the corrolate ligand. Similar complications arise with the related iron corrolazines presented in this study. Further complexity is to be expected when Mössbauer spectra of frozen solutions are collected because corrolazines, like other porphyrinoid compounds, are prone to aggregation, which can lead to intermolecular spin–spin relaxation.[72−74] For these reasons the Mössbauer and EPR data have to be treated as a whole. To support the Mössbauer and EPR assignments we ran a set of DFT calculations in tandem with the experiments.

A solid state, crystalline sample of **4b** formed from the reaction of $[Fe^{III}(TBP_8Cz)]$ with Ph_3PO provides a well-defined reference compound for spectroscopic measurements because the structure has been determined with high precision by single-crystal X-ray diffraction, and the oxidation state of the iron center can be definitively assigned as +3. A sample of **4** exhibits a Mössbauer spectrum at 5.3 K with a single, sharp

dx.doi.org/10.1021/ic400280x | Inorg. Chem. 2013, 52, 4668−4682

Scheme 5. Proposed Mechanism

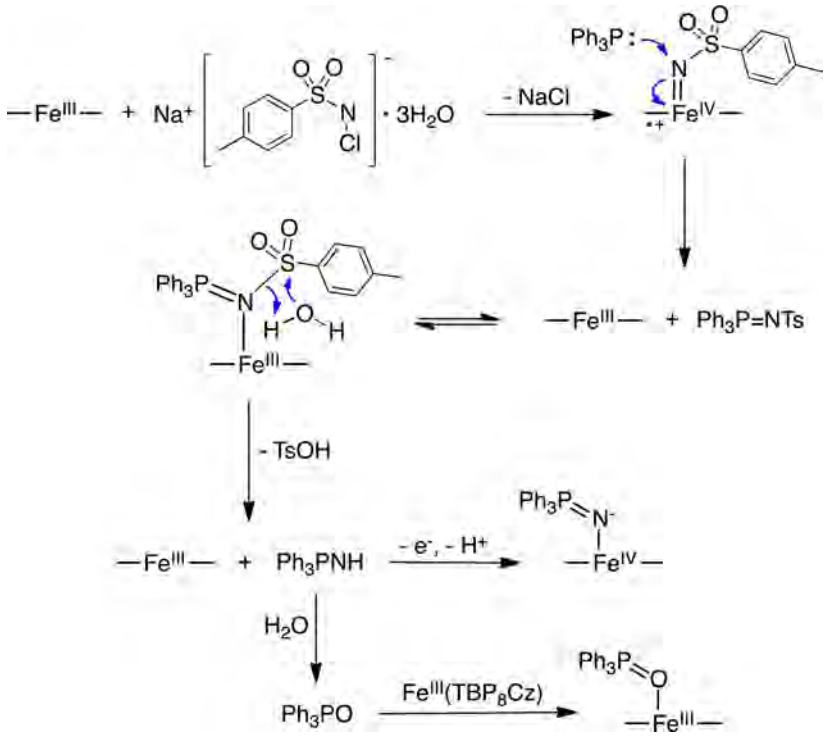

quadrupole doublet (δ = 0.13 mm s^{-1}; ΔE_Q = 4.40 mm s^{-1}, Figure 10). The isomer shift is consistent with an intermediate spin (S = $^3/_2$) Fe^{III} ion as seen by comparison with other intermediate spin iron(III) complexes (see Table 5 in ref 56), and the large quadrupole splitting is in part due to the square pyramidal geometry (see bond angles above). Indeed, the square pyramidal geometry of the iron center revealed by the crystal structure of [Fe^{III}(TBP$_8$Cz)(OPPh$_3$)] (Figure 7) and the presence of the strong-field equatorial corrolazine ligand should greatly destabilize the $d_{x^2-y^2}$ orbital relative to the other d orbitals and therefore stabilize the S = $^3/_2$ state relative to the high spin S = $^5/_2$ state. The intermediate spin state of this compound is further confirmed by EPR spectroscopy. The X-band EPR spectrum of a crystalline sample of **4** dissolved in toluene and measured at 15 K (Figure 11) shows an axial signal with $g_\perp$ = 4.43, $g_\parallel$ = 1.99, which is typical for an S = $^3/_2$ ion.

In comparison, the Mössbauer spectrum of solid [Fe^{III}(TBP$_8$Cz)], which lacks an OPPh$_3$ axial ligand, was measured at 293 K and consists of two quadrupole doublets (δ = 0.06 mm s^{-1}, ΔE_Q = 4.00 mm s^{-1} and δ = 0.30 mm s^{-1}, ΔE_Q = 1.00 mm s^{-1}, Figure 10) in a ratio of approximately 3:1.

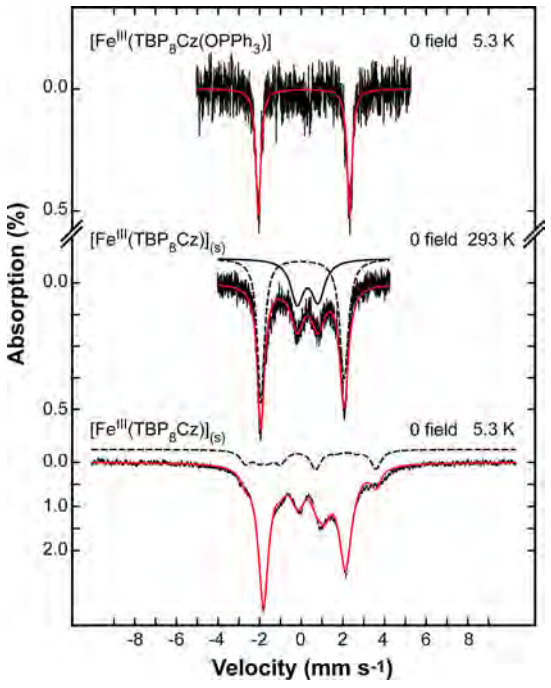

Figure 10. Mössbauer spectra of a crystalline sample of [Fe^{III}(TBP$_8$Cz)(O═PPh$_3$)] (**4b**) measured at 5.3 K and a solid sample of [Fe^{III}(TBP$_8$Cz)] (**1**) measured at 293 K (solid black line = high spin Fe^{III}; dashed black line = intermediate spin Fe^{III}) and 5.3 K with no applied magnetic field (dashed line = slow relaxing intermediate spin Fe^{III}). The red lines show the best fit to the data.

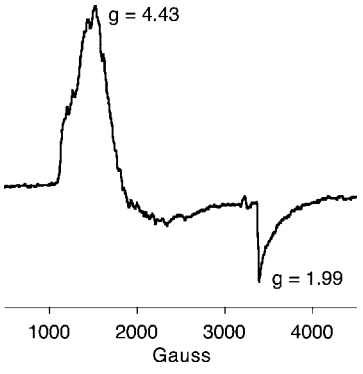

Figure 11. X-band EPR spectrum at 15 K of crystalline [Fe^{III}(TBP$_8$Cz)(OPPh$_3$)] (**4b**) dissolved in toluene. Experimental conditions: frequency = 9.49 GHz, microwave power = 0.201 mW, modulation amplitude 10.0 G, modulation frequency = 100 kHz.

dx.doi.org/10.1021/ic400280x | Inorg. Chem. 2013, 52, 4668−4682

These parameters and intensities are similar to those recently reported for [$Fe^{III}(TBP_8Cz)$] by Nakamura and co-workers,[75] who measured temperature-dependent Mössbauer spectra down to 77 K. In this study the quadrupole splitting was seen to be temperature-independent, but the isomer shift increased with a decrease in temperature, as one would expect, as a result of the second-order Doppler shift.[76] As seen in Figure 10, the spectrum at 5.3 K for **1** consists of two quadrupole doublets with a slight increase in the isomer shifts (δ = 0.15 mm s^{-1} and δ = 0.47 mm s^{-1}) as compared to the data at 293 K. These isomer shifts can be assigned to a mixture of intermediate spin Fe^{III} and high spin Fe^{III} ($S = {}^5/_2$) ions. Additionally, there is a broad component (~20%, dashed line Figure 10) caused by slow relaxation of the intermediate spin iron(III) centers relative to the Mössbauer time scale of ~10^7 s^{-1}, resulting in splitting of the nuclear magnetic spin states and giving rise to the broad spectrum observed. The parameters used to simulate this magnetic spectrum were those used to fit the frozen solution spectrum of [$Fe^{III}(TBP_8Cz)$] described below.

Dissolution of the [$Fe^{III}(TBP_8Cz)$] complex in toluene provides Mössbauer spectra that help to clarify the spectral assignments. A frozen toluene solution of the Fe^{III} complex produces a single quadrupole doublet at 100 K (δ = 0.11 mm s^{-1}, ΔE_Q = 3.96 mm s^{-1}, Figure 12), consistent with the

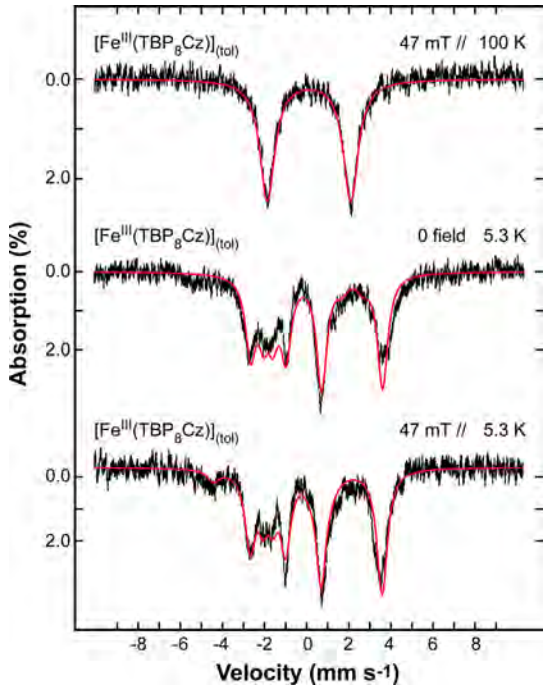

Figure 12. Mössbauer spectra of [$Fe^{III}(TBP_8Cz)$] dissolved in toluene and measured at 100 K with an applied magnetic field of 47 mT parallel to the γ-rays, 5.3 K with no magnetic field and 5.3 K with an applied magnetic field of 47 mT parallel to the γ-rays. The red line through the data shows the best fit using the parameters given in the text.

presence of a pure intermediate spin species. If the sample is then suitably diluted and carefully frozen,[72] the spectra collected at the lower temperature of 5.3 K are clearly in the slow relaxation regime (Figure 12), and can be fitted to a single $S = {}^3/_2$ species. This result is in good agreement with EPR spectra of the same complex in a frozen solution of toluene, which revealed an intermediate spin iron(III) spectrum at 15 K.[42] Careful comparison of the Mössbauer spectra in the presence and absence of a small magnetic field (47 mT) allows this species to be fitted with the values δ = 0.15 mm s^{-1}; ΔE_Q = +3.98 mm s^{-1}; $D = -4$ cm^{-1}; $E/D = 0$; $A_x = A_y = 19$ T, $A_z = 6$ T, which are comparable with intermediate spin Fe^{III} tetraamido complexes.[77] We can conclude that dissolution in toluene provides a uniform environment for complex **1** and leads to the observation of a single iron(III) intermediate spin ground state, in contrast to the solid state, in which stacking or other aggregation effects appear to give rise to a mixture of the two different spin states $S = {}^3/_2$ and $S = {}^5/_2$ for **1**.

The third possible spin state for an Fe^{III} species is a low-spin ($S = {}^1/_2$) configuration, and this state can be accessed for iron(III) corrolazine by addition of excess pyridine. Previous work has shown that addition of pyridine to [$Fe^{III}(TBP_8Cz)$] gives the axially ligated complex [$Fe^{III}(TBP_8Cz)(py)_2$], which reveals an intense rhombic EPR spectrum (g 2.39, 2.20, 1.90) that is characteristic of a low spin Fe^{III} porphyrinoid compound.[42] The Mössbauer spectrum of this species at 100 K consists of a symmetrical quadrupole doublet (δ = 0.01 mm s^{-1}, ΔE_Q = 3.99 mm s^{-1}, Figure 13). The isomer shift is consistent with low spin Fe^{III}, and indeed the value is lower than that of the intermediate spin species discussed above. At 5.3 K, the spectrum consists of both slow (dashed line, Figure 13) and fast relaxing low spin Fe^{III} signals (δ = 0.03 mm s^{-1}, ΔE_Q = 4.03 mm s^{-1}), as seen for the intermediate spin complex (Figure 10). These parameters are similar to, but slightly larger than, those recently described[75] for the analogous bis(cyano) complex [$Fe^{III}(TBP_8Cz)(CN)_2]^{2-}$ ($\delta = -0.09$ mm s^{-1}, ΔE_Q = 2.74 mm s^{-1} at 77 K).

The Mössbauer spectrum of bulk, crystalline **3** consists of a quadrupole doublet at 293 K (δ = 0.13 mm s^{-1}, ΔE_Q = 4.25 mm s^{-1}, Figure 13). However, a bulk sample of this material consists of both [$Fe^{IV}(TBP_8Cz)(NPPh_3)$] and [$Fe^{III}(TBP_8Cz)$-$(OPPh_3)$] as shown by independent X-ray analysis. An EPR spectrum of a bulk sample of **3** at 15 K revealed only a weak signal with broad features at g 5.39, 2.02 (Figure S10), consistent with the presence of [$Fe^{III}(TBP_8Cz)(OPPh_3)$] as a minor impurity. The Mössbauer spectrum of **3** at 5.3 K can be fitted to an Fe^{IV} (S = 1) species (δ = 0.13 mm s^{-1}; ΔE_Q = 4.25 mm s^{-1}; $D = +5$ cm^{-1}; $E/D = 0$; $A_x = A_y = 8$ T, $A_z = 10$ T; Figure 13) together with [$Fe^{III}(TBP_8Cz)(OPPh_3)$] as a minor component (~10%, fitted with the parameters found for the pure $Fe^{III}(OPPh_3)$ complex). Thus, Mössbauer and EPR spectroscopy are in agreement with the assignment of the bulk crystalline material for **3**. Interestingly, the isomer shift for the Fe^{IV} complex (δ = 0.13 mm s^{-1}) is comparable to the isomer shift found for the intermediate spin Fe^{III} corrolazines, which suggests that the Fe^{IV}–$NPPh_3$ complex may be better described as an intermediate spin Fe^{III} center coupled to a corrolazine π-cation radical. This dichotomy for iron(IV) corroles has been discussed at length by Walker and co-workers,[70] but these two options cannot be distinguished for the current complex from the available data. We note that the quadrupole splitting parameters are distinct for the Fe^{IV} complex **3** (4.25 mm s^{-1}) and the intermediate spin-Fe^{III} complex **4** (4.40 mm s^{-1}), although not by as much as might be expected. Future experimental/computational work may shed light on this issue.

Finally, Mössbauer spectroscopy was also employed to analyze a ^{57}Fe-labeled sample of [$Fe^{IV}(TBP_8Cz^{+\bullet})(NTs)$], which was isolated as a precipitated solid from the reaction

dx.doi.org/10.1021/ic400280x | Inorg. Chem. 2013, 52, 4668–4682

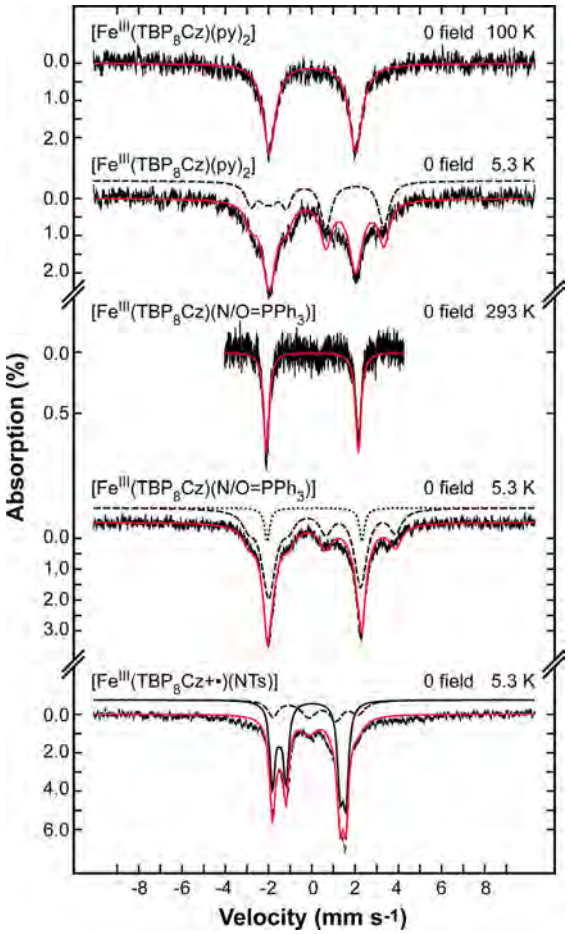

Figure 13. Mössbauer spectra of $[Fe^{III}(TBP_8Cz)]$ dissolved in pyridine at 100 and 5.3 K with no applied field (dashed line = slow relaxing low spin Fe^{III}). Mössbauer spectra of a solid sample of $[Fe^{III}(TBP_8Cz)(N/OPPh_3)]$ measured at 293 and 5.3 K (dotted line = $[Fe^{III}(TBP_8Cz)(OPPh_3)]$; dashed line = $[Fe^{IV}(TBP_8Cz)(NPPh_3)]$). Frozen solution spectrum of $[Fe^{IV}(TBP_8Cz^{+\bullet})(NTs)]$ measured at 5.3 K (dashed line = ~25% $[Fe^{III}(TBP_8Cz)]$). The red line through the data shows the best fit using the parameters given in the text.

mixture of $[Fe^{III}(TBP_8Cz)]$ and chloramine-T. The spectrum measured at 5.3 K in toluene (Figure 13) can be fitted to two species: ~25% of unreacted $[Fe^{III}(TBP_8Cz)]$ (dashed line, parameters given above), and an Fe^{IV} (S = 1) ion antiferromagnetically coupled to a Cz-π-cation-radical (δ = −0.05 mm s^{-1}; ΔE_Q = 2.94 mm s^{-1}; $A_x = A_y$ = 26 T, A_z = 3.5 T; J ~ 30 cm^{-1}). The sign of the quadrupole splitting cannot be unambiguously defined, but if positive, a rotation of the electric field gradient (EFG) relative to the principle axes is required. In fact there is no reason why the principal axes should be collinear and the EFG tensor can be rotated by a set of Euler angles α, β, and γ (0, 105, 0). The low isomer shift and smaller quadrupole splitting of this species as compared to those found for the Fe^{III} complexes strongly suggest that this complex contains an iron(IV) center as proposed.[68] In addition, EPR spectroscopy of this complex at 15 K gives a sharp axial signal with $g_\perp$ = 2.10, $g_\parallel$ = 2.00, consistent with an overall $S = {}^1/_2$ ground state as expected for an Fe^{IV}−Cz-π-cation-radical and in good agreement with the Mössbauer analysis.

Altogether, the Mössbauer data show consistent findings across all species as summarized in Table 3. The intermediate spin $S = {}^3/_2$ Fe^{III} species all have isomer shifts of ~+0.13 mm s^{-1}. The isomer shift for $[Fe^{IV}(TBP_8Cz)(NPPh_3)]$ also falls in this range, and this complex may be best described as an Fe^{III} coupled to a π-radical-cation. Conversion to a low spin Fe^{III} center by addition of pyridine to form $[Fe^{III}(TBP_8Cz)(py)_2]$ lowers the isomer shift to +0.03 mm s^{-1}. Further oxidation to form $[Fe^{IV}(TBP_8Cz^{+\bullet})(NTs)]$ leads to an isomer shift of −0.05 mm s^{-1}, consistent with a high-valent iron(IV) ion.

Computational Studies. To further confirm the spectroscopic data and gain structural insight into the iron-imido complex we have calculated the Mössbauer and EPR parameters of $[Fe^{IV}(H_8Cz^{+\bullet})(NTs)]$ in both the doublet and quartet spin states using DFT. To reduce calculation time a model where the eight peripheral ^{t}Bu-phenyl groups from the corrolazine ring were replaced by hydrogen atoms was implemented, H_8Cz. Initial geometric optimization led to a structure with reasonable bond lengths (Figure 15). The Fe−N

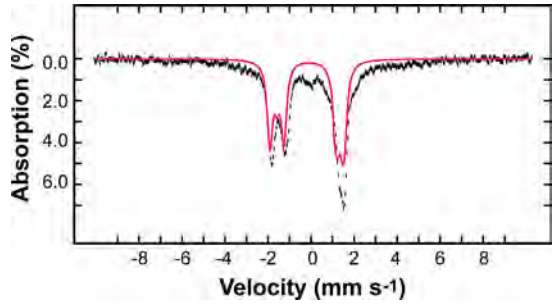

Figure 14. Mössbauer spectra of $[Fe^{IV}(TBP_8Cz^{+\bullet})(NTs)]$ measured at 5.3 K. Overlaid is a simulation (red line) using the parameters determined by DFT with the EFG and A rotated by the following Euler angles (19, 100, 51) and (70, 92, 3).

Table 3. Mössbauer Parameters for Iron Corrolazine Complexes

		spin state	δ (mm s^{-1})	ΔE_Q (mm s^{-1})	Γ (mm s^{-1})	D (cm^{-1})	E/D	$A_x/g_n\mu_n$ [a] (T)	$A_y/g_n\mu_n$ [a] (T)	$A_z/g_n\mu_n$ [a] (T)
$[Fe^{III}(TBP_8Cz)]$		$^3/_2$	0.15	+3.98	0.6	−4	0	19	19	6
$[Fe^{III}(TBP_8Cz)(py)_2]$		$^1/_2$	0.03	4.03	0.7					
$[Fe^{III}(TBP_8Cz)(OPPh_3)]$		$^3/_2$	0.13	4.40	0.3					
$[Fe^{IV}(TBP_8Cz)(NPPh_3)]$		1 [b]	0.13	4.25	0.7	+5	0	8	8	10
$[Fe^{IV}(TBP_8Cz^{\bullet+})(NTs)]$	expt	$^1/_2$ [c]	−0.05	2.95	0.3			26	26	3.5
	calcd	$^1/_2$ [d]	−0.12	+2.92				−4.8	24.0	30.9

[a] The sign of the hyperfine coupling constants cannot be determined. [b] The spin state is not fully determined and can be considered an intermediate spin Fe^{III} coupled to a radical cation, as the isomer shift suggests. [c] The S = 1 Fe^{IV} is antiferromagnetically coupled to a $S = {}^1/_2$ radical cation with an exchange coupling constant of ~30 cm^{-1}. The electric field gradient (EFG) is rotated using the following Euler angles (0, 105, 0). [d] η = 0.38. To fit experiment, both the EFG and A tensors have to be rotated by the following Euler angles (19, 100, 51) and (70, 92, 3), respectively, because the principal axes used are different.

dx.doi.org/10.1021/ic400280x | Inorg. Chem. 2013, 52, 4668−4682

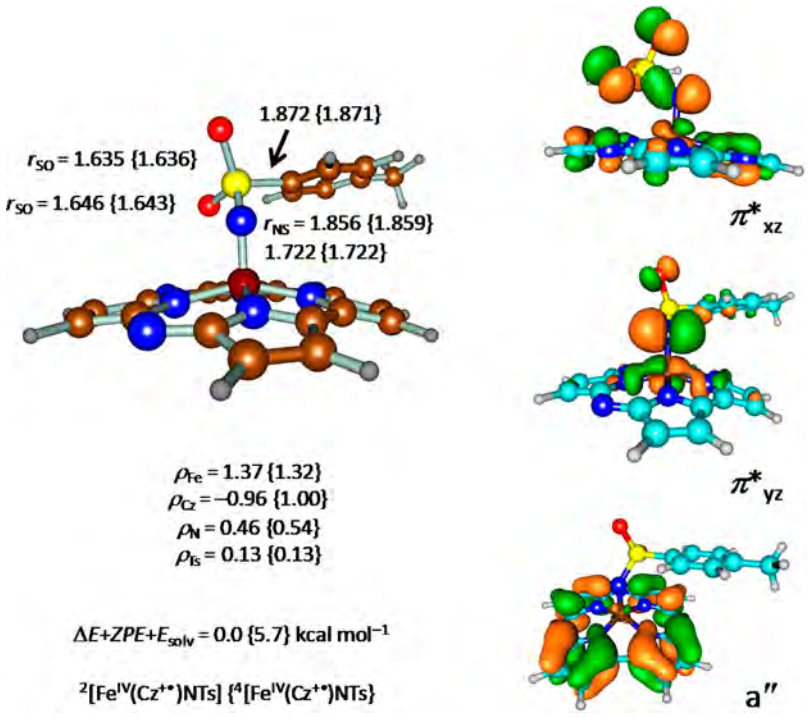

Figure 15. DFT calculated structures of ^{2,4}[Fe^{IV}(H$_8$Cz$^{+\bullet}$)(NTs)] with bond lengths in angstroms and group spin densities (ρ) in atomic units. Also given are the spin state energy differences in kcal mol^{-1} as calculated at UB3LYP/B2//UB3LYP/B1 including solvent and zero-point corrections. Orbital drawings of the singly occupied molecular orbitals are given on the right.

bond length of 1.722 Å is comparable to other iron-imido complexes both experimental and calculated.[8,78] The doublet spin state is the ground state and is found to lie 5.7 kcal mol^{-1} below the quartet spin state, consistent with the spectroscopic results given above. The spin densities were then calculated and molecular orbitals analyzed, which revealed two unpaired electrons in the $\pi^*_{xz/yz}$ orbitals antiferromagnetically coupled to a single electron in the a″-type Cz orbital. The orbital shapes and the electronic configuration show resemblance to that calculated for [Mn^V(H$_8$Cz$^{+\bullet}$)(O)], which also gave single occupation of the a″ orbital.[38] Due to mixing of the atomic $3d_{xz}/3d_{yz}$ orbitals on Fe with $2p_x/2p_y$ orbitals on nitrogen, the π^*_{xz} and π^*_{yz} orbitals are mixed iron/nitrogen antibonding orbitals, and consequently, considerable spin density is observed on the nitrogen and tosylate group. This mixing is similar to that observed on the oxo group in heme and nonheme iron(IV)-oxo species.[79,80]

Finally, the Mössbauer and EPR parameters were then calculated and are given in Table 3. The parameters compare favorably with the experimentally determined ones and provide further strong evidence that our understanding of the electronic state is correct. The calculated g values (2.00, 2.03, 2.07) are rhombic rather than axial, but the Mössbauer isomer shift and quadrupole splitting reproduce the experimental data within the error of the calculations. A simulation of the Mössbauer spectrum with these parameters is given in Figure 14 and shows graphically how close the match is. To obtain a reasonable fit both the electric field gradient (EFG) and hyperfine (A) tensors had to be rotated relative to each other. The following Euler angles were used: (19, 100, 51) for the EFG and (70, 92, 3) for A.

CONCLUSIONS

The reaction of [Fe^{III}(TBP$_8$Cz)] with the NR transfer agent chloramine-T results in the formation of the high-valent iron(IV) terminal imido complex [Fe^{IV}(TBP$_8$Cz$^{+\bullet}$)(NTs)] (**2**). Previously iron terminal imido complexes have been stabilized through a combination of steric encumbrance and the enforcement of relatively low-coordinate geometries about the iron center. The stability of **2** is likely a consequence of the oxidatively resistant, trianionic corrolazine supporting ligand favoring high-valent iron(IV) together with the strong σ and π donation of the terminal tosylimido donor. The stability of **2** is significant because high-valent, multiply bonded terminal imido complexes of the mid- to late-transition metals are normally considered to be highly reactive, but the data presented here indicates that **2** is much more stable (and consequently less reactive) than is expected for an iron-imido complex. Thus, catalytic mechanisms that rely on proposed intermediates of this type, especially in porphyrinoid chemistry, may need to be carefully scrutinized when identifying the actual oxidizing species.

Mössbauer and EPR spectroscopies show that [Fe^{IV}(TBP$_8$Cz$^{+\bullet}$)(NTs)] contains a high-valent Fe^{IV} ion with an extra oxidizing equivalent stored on the Cz ring as a π-cation-radical, analogous to the previously described compound-I-like terminal oxo complex [Fe^{IV}(TBP$_8$Cz$^{+\bullet}$)(O)].[39] This view has been further corroborated by DFT calculations. The spin state of both the imido and oxo complexes is proposed to be a doublet with iron(IV) antiferromagnetically coupled to the Cz π-cation-radical. It was demonstrated that **2** is capable of NR group transfer to triphenylphosphine to give Ph$_3$PNTs, leading to the two-electron reduction of **2** to give the Fe^{III} complex **1**. Catalytic NR transfer to PPh$_3$ by **1** was also successful, suggesting that further design of suitable metallocorrolazines (or corroles) may yield potent NR transfer

dx.doi.org/10.1021/ic400280x | Inorg. Chem. 2013, 52, 4668−4682

catalysts. The kinetic data For NR transfer from **2** to PPh_3 was in agreement with the proposed bimolecular mechanism, and a comparison of rate constants shows that **2** exhibits a dramatic rate enhancement (~100-fold) for NR transfer as compared to $Mn^V(NAr)$ corrole analogues. Structural analyses of complexes formed following initial NR transfer reveal that both $[Fe^{IV}(TBP_8Cz)(NPPh_3)]$ and $[Fe^{III}(TBP_8Cz)(OPPh_3)]$ crystallize from the same reaction mixture. A mechanism was described that can account for the NR transfer reactivity of **2** as well as the subsequent formation of the former complexes.

■ ASSOCIATED CONTENT

Ⓢ Supporting Information

Spectroscopic and crystallographic data (CIF), and details of the DFT calculations, including relative and absolute energies, group spin densities, charges, and Cartesian coordinates of all structures. This material is available free of charge via the Internet at http://pubs.acs.org.

■ AUTHOR INFORMATION

Corresponding Author

*E-mail: dpg@jhu.edu (D.P.G.); gjameson@chemistry.otago.ac.nz (G.N.L.J.); sam.devisser@manchester.ac.uk (S.P.d.V.).

Notes

The authors declare no competing financial interest.

■ ACKNOWLEDGMENTS

This work was supported by the NSF (CHE0909587 and CHE1213836 to D.P.G.). P.L. is grateful for the Queen Sirikit Scholarship (Thailand). We thank Dr. Yosra M. Badiei for the synthesis of $^{57}FeCl_2$ and Dr. Victoria J. A. Jameson for help with Mössbauer sample preparation. The computational work was supported by CPU time provided by the National Service of Computational Chemistry Software (NSCCS). D.K. holds a Ramanujan Fellowship from the Department of Science and Technology (DST), New Delhi (India), and acknowledges its financial support (Research Grants SR/S2/RJN-11/2008 and SR/S1/PC-58/2009).

■ REFERENCES

(1) Ertl, G. *Angew. Chem., Int. Ed.* **1990**, *29*, 1219−1227.
(2) Smil, V. *Enriching the Earth: Fritz Haber, Carl Bosch, and the Transformation of World Food Production*; MIT Press: Cambridge, 2004.
(3) Hoffman, B. M.; Dean, D. R.; Seefeldt, L. C. *Acc. Chem. Res.* **2009**, *42*, 609−619.
(4) Seefeldt, L. C.; Hoffman, B. M.; Dean, D. R. *Annu. Rev. Biochem.* **2009**, *78*, 701−722.
(5) Pickett, C. J. *J. Biol. Inorg. Chem.* **1996**, *1*, 601−606.
(6) Svastits, E. W.; Dawson, J. H.; Breslow, R.; Gellman, S. H. *J. Am. Chem. Soc.* **1985**, *107*, 6427−6428.
(7) King, E. R.; Betley, T. A. *Inorg. Chem.* **2009**, *48*, 2361−2363.
(8) King, E. R.; Hennessy, E. T.; Betley, T. A. *J. Am. Chem. Soc.* **2011**, *133*, 4917−4923.
(9) Berry, J. F. *Comments Inorg. Chem.* **2009**, *30*, 28−66.
(10) Mehn, M. P.; Peters, J. C. *J. Inorg. Biochem.* **2006**, *100*, 634−643.
(11) Saouma, C. T.; Peters, J. C. *Coord. Chem. Rev.* **2011**, *255*, 920−937.
(12) Zalatan, D. N.; Du Bois, J. *Top. Curr. Chem.* **2010**, *292*, 347−378.
(13) Müller, P.; Fruit, C. *Chem. Rev.* **2003**, *103*, 2905−2919.
(14) Chow, T. W. S.; Chen, G. Q.; Liu, Y. G.; Zhou, C. Y.; Che, C. M. *Pure Appl. Chem.* **2012**, *84*, 1685−1704.
(15) Eikey, R. A.; Abu-Omar, M. M. *Coord. Chem. Rev.* **2003**, *243*, 83−124.
(16) Abu-Omar, M. M. *Dalton Trans.* **2011**, *40*, 3435−3444.
(17) Smith, J. M.; Subedi, D. *Dalton Trans.* **2012**, *41*, 1423−1429.
(18) To our knowledge, there are only two reported Fe compounds with +6 oxidation state: Berry, J. F.; Bill, E.; Bothe, E.; DeBeer George, S.; Mienert, B.; Neese, F.; Wieghardt, K. *Science* **2006**, *312*, 1937−1941.
(19) Hohenberger, J.; Ray, K.; Meyer, K. *Nat. Commun.* **2012**, *3*, 720.
(20) Mahy, J. P.; Battioni, P.; Mansuy, D.; Fisher, J.; Weiss, R.; Mispelter, J.; Morgensternbadarau, I.; Gans, P. *J. Am. Chem. Soc.* **1984**, *106*, 1699−1706.
(21) Klinker, E. J.; Jackson, T. A.; Jensen, M. P.; Stubna, A.; Juhasz, G.; Bominaar, E. L.; Münck, E.; Que, L., Jr. *Angew. Chem., Int. Ed.* **2006**, *45*, 7394−7397.
(22) Brown, S. D.; Betley, T. A.; Peters, J. C. *J. Am. Chem. Soc.* **2003**, *125*, 322−323.
(23) Moret, M. E.; Peters, J. C. *Angew. Chem., Int. Ed.* **2011**, *50*, 2063−2067.
(24) Betley, T. A.; Peters, J. C. *J. Am. Chem. Soc.* **2003**, *125*, 10782−10783.
(25) Brown, S. D.; Peters, J. C. *J. Am. Chem. Soc.* **2005**, *127*, 1913−1923.
(26) Thomas, C. M.; Mankad, N. P.; Peters, J. C. *J. Am. Chem. Soc.* **2006**, *128*, 4956−4957.
(27) Nieto, I.; Ding, F.; Bontchev, R. P.; Wang, H. B.; Smith, J. M. *J. Am. Chem. Soc.* **2008**, *130*, 2716−2717.
(28) Bowman, A. C.; Milsmann, C.; Bill, E.; Turner, Z. R.; Lobkovsky, E.; DeBeer, S.; Wieghardt, K.; Chirik, P. J. *J. Am. Chem. Soc.* **2011**, *133*, 17353−17369.
(29) Bart, S. C.; Lobkovsky, E.; Bill, E.; Chirik, P. J. *J. Am. Chem. Soc.* **2006**, *128*, 5302−5303.
(30) Cowley, R. E.; Eckert, N. A.; Vaddadi, S.; Figg, T. M.; Cundari, T. R.; Holland, P. L. *J. Am. Chem. Soc.* **2011**, *133*, 9796−9811.
(31) Cowley, R. E.; Holland, P. L. *Inorg. Chem.* **2012**, *51*, 8352−8361.
(32) Lansky, D. E.; Kosack, J. R.; Sarjeant, A. A. N.; Goldberg, D. P. *Inorg. Chem.* **2006**, *45*, 8477−8479.
(33) Eikey, R. A.; Khan, S. I.; Abu-Omar, M. M. *Angew. Chem., Int. Ed.* **2002**, *41*, 3592−3595.
(34) Mandimutsira, B. S.; Ramdhanie, B.; Todd, R. C.; Wang, H. L.; Zareba, A. A.; Czernuszewicz, R. S.; Goldberg, D. P. *J. Am. Chem. Soc.* **2002**, *124*, 15170−15171.
(35) Lansky, D. E.; Mandimutsira, B.; Ramdhanie, B.; Clausén, M.; Penner-Hahn, J.; Zvyagin, S. A.; Telser, J.; Krzystek, J.; Zhan, R. Q.; Ou, Z. P.; Kadish, K. M.; Zakharov, L.; Rheingold, A. L.; Goldberg, D. P. *Inorg. Chem.* **2005**, *44*, 4485−4498.
(36) Prokop, K. A.; Goldberg, D. P. *J. Am. Chem. Soc.* **2012**, *134*, 8014−8017.
(37) Prokop, K. A.; de Visser, S. P.; Goldberg, D. P. *Angew. Chem., Int. Ed.* **2010**, *49*, 5091−5095.
(38) Prokop, K. A.; Neu, H. M.; de Visser, S. P.; Goldberg, D. P. *J. Am. Chem. Soc.* **2011**, *133*, 15874−15877.
(39) McGown, A. J.; Kerber, W. D.; Fujii, H.; Goldberg, D. P. *J. Am. Chem. Soc.* **2009**, *131*, 8040−8048.
(40) Cho, K.; Leeladee, P.; McGown, A. J.; DeBeer, S.; Goldberg, D. P. *J. Am. Chem. Soc.* **2012**, *134*, 7392−7399.
(41) Simkhovich, L.; Gross, Z. *Tetrahedron Lett.* **2001**, *42*, 8089−8092.
(42) Kerber, W. D.; Ramdhanie, B.; Goldberg, D. P. *Angew. Chem., Int. Ed.* **2007**, *46*, 3718−3721.
(43) Ramdhanie, B.; Stern, C. L.; Goldberg, D. P. *J. Am. Chem. Soc.* **2001**, *123*, 9447−9448.
(44) Aresta, M.; Nobile, C. F.; Petruzzelli, D. *Inorg. Chem.* **1977**, *16*, 1817−1818.
(45) Bittner, S.; Assaf, Y.; Krief, P.; Pomerantz, M.; Ziemnicka, B. T.; Smith, C. G. *J. Org. Chem.* **1985**, *50*, 1712−1718.
(46) Davidson, M. G.; Goeta, A. E.; Howard, J. A. K.; Lehmann, C. W.; McIntyre, G. M.; Price, R. D. *J. Organomet. Chem.* **1998**, *550*, 449−452.

(47) Kumar, D.; Karamzadeh, B.; Sastry, G. N.; de Visser, S. P. *J. Am. Chem. Soc.* **2010**, *132*, 7656−7667.
(48) Becke, A. D. *J. Chem. Phys.* **1993**, *98*, 5648−5652.
(49) Lee, C. T.; Yang, W. T.; Parr, R. G. *Phys. Rev. B* **1988**, *37*, 785−789.
(50) *Jaguar, version 7.9*; Schrodinger, LLC: New York, 2011.
(51) Frisch, M. J.; et al. *Gaussian 03, revision C.02*; Gaussian, Inc.: Wallingford, CT, 2004. See Supporting Information.
(52) Hay, P. J.; Wadt, W. R. *J. Chem. Phys.* **1985**, *82*, 270−283.
(53) de Visser, S. P. *J. Am. Chem. Soc.* **2010**, *132*, 1087−1097.
(54) Neese, F. *ORCA—An Ab Initio, DFT and Semiempirical SCF-MO Package, Version 2.9*; Bonn, Germany, 2009.
(55) Neese, F. *Inorg. Chim. Acta* **2002**, *337*, 181−192.
(56) Sinnecker, S.; Svensen, N.; Barr, E. W.; Ye, S.; Bollinger, J. M., Jr.; Neese, F.; Krebs, C. *J. Am. Chem. Soc.* **2007**, *129*, 6168−6179.
(57) Karamzadeh, B.; Kumar, D.; Sastry, G. N.; de Visser, S. P. *J. Phys. Chem. A* **2010**, *114*, 13234−13243.
(58) Betley, T. A.; Peters, J. C. *J. Am. Chem. Soc.* **2004**, *126*, 6252−6254.
(59) Scepaniak, J. J.; Fulton, M. D.; Bontchev, R. P.; Duesler, E. N.; Kirk, M. L.; Smith, J. M. *J. Am. Chem. Soc.* **2008**, *130*, 10515−15017.
(60) Mankad, N. P.; Muller, P.; Peters, J. C. *J. Am. Chem. Soc.* **2010**, *132*, 4083−4085.
(61) Abu-Omar, M. M.; Shields, C. E.; Edwards, N. Y.; Eikey, R. A. *Angew. Chem., Int. Ed.* **2005**, *44*, 6203−6207.
(62) Fructos, M. R.; Trofimenko, S.; Diaz-Requejo, M. M.; Perez, P. J. *J. Am. Chem. Soc.* **2006**, *128*, 11784−11791.
(63) Fantauzzi, S.; Caselli, A.; Gallo, E. *Dalton Trans.* **2009**, 5434−5443.
(64) Vyas, R.; Gao, G. Y.; Harden, J. D.; Zhang, X. P. *Org. Lett.* **2004**, *6*, 1907−1910.
(65) Harden, J. D.; Ruppel, J. V.; Gao, G. Y.; Zhang, X. P. *Chem. Commun.* **2007**, 4644−4646.
(66) Edwards, N. Y.; Eikey, R. A.; Loring, M. I.; Abu-Omar, M. M. *Inorg. Chem.* **2005**, *44*, 3700−3708.
(67) Bennett, B. K.; Saganic, E.; Lovell, S.; Kaminsky, W.; Samuel, A.; Mayer, J. M. *Inorg. Chem.* **2003**, *42*, 4127−4131.
(68) Cai, S.; Walker, F. A.; Licoccia, S. *Inorg. Chem.* **2000**, *39*, 3466−3474.
(69) Walker, F. A.; Licoccia, S.; Paolesse, R. *J. Inorg. Biochem.* **2006**, *100*, 810−837.
(70) Zakharieva, O.; Schünemann, V.; Gerdan, M.; Licoccia, S.; Cai, S.; Walker, F. A.; Trautwein, A. X. *J. Am. Chem. Soc.* **2002**, *124*, 6636−6648.
(71) Schwalbe, M.; Dogutan, D. K.; Stoian, S. A.; Teets, T. S.; Nocera, D. G. *Inorg. Chem.* **2011**, *50*, 1368−1377.
(72) Amusa, A.; Debrunner, P.; Frauenfe, H.; Münck, E.; DePasqua, G. *J. Phys. C* **1974**, *7*, 1881−1891.
(73) Teschner, T.; Yatsunyk, L.; Schunemann, V.; Paulsen, H.; Winkler, H.; Hu, C. J.; Scheidt, W. R.; Walker, F. A.; Trautwein, A. X. *J. Am. Chem. Soc.* **2006**, *128*, 1379−1389.
(74) Simonneaux, G.; Schunemann, V.; Morice, C.; Carel, L.; Toupet, L.; Winkler, H.; Trautwein, A. X.; Walker, F. A. *J. Am. Chem. Soc.* **2000**, *122*, 4366−4377.
(75) Kurahashi, S.; Ikeue, T.; Sugimori, T.; Takahashi, M.; Mikuriya, M.; Handa, M.; Ikezaki, A.; Nakamura, M. *J. Porphyrins Phthalocyanines* **2012**, *16*, 518−529.
(76) Gütlich, P.; Bill, E.; Trautwein, A. X. *Mössbauer Spectroscopy and Transition Metal Chemistry: Fundamentals and Applications*; Springer-Verlag: Berlin, 2011.
(77) Kostka, K. L.; Fox, B. G.; Hendrich, M. P.; Collins, T. J.; Rickard, C. E. F.; Wright, L. J.; Münck, E. *J. Am. Chem. Soc.* **1993**, *115*, 6746−6757.
(78) Jaccob, M.; Rajaraman, G. *Dalton Trans.* **2012**, *41*, 10430−10439.
(79) de Visser, S. P. *J. Am. Chem. Soc.* **2006**, *128*, 15809−15818.
(80) *Iron-Containing Enzymes: Versatile Catalysts of Hydroxylation Reactions in Nature*; de Visser, S. P., Kumar, D., Eds.; Royal Society of Chemistry Publishing: Cambridge, U.K., 2011.
(81) Stephens, J. C.; Khan, M. A.; Houser, R. P. *Inorg. Chem.* **2001**, *40*, 5064−5065.
(82) Chen, G.; Man, W. L.; Yiu, S. M.; Wong, T. W.; Szeto, L.; Wong, W. T.; Lau, T. C. *Dalton Trans.* **2011**, *40*, 1938−1944.
(83) Gröb, T.; Geiseler, G.; Harms, K.; Greiner, A.; Dehnicke, K. *Z. Anorg. Allg. Chem.* **2002**, *628*, 217−221.
(84) Schrumpf, F.; Roesky, H. W.; Noltemeyer, M. *Z. Naturforsch., B* **1990**, *45*, 1600−1602.
(85) Tomi, F.; Wah, H. L. K.; Postel, M. *New J. Chem.* **1988**, *12*, 289−292.
(86) Ding, Z. R.; Bhattacharya, S.; Mccusker, J. K.; Hagen, P. M.; Hendrickson, D. N.; Pierpont, C. G. *Inorg. Chem.* **1992**, *31*, 870−877.
(87) Chekhlov, A. N. *Russ. J. Inorg. Chem.* **2005**, *50*, 1207−1211.
(88) Atkinson, F. L.; Blackwell, H. E.; Brown, N. C.; Connelly, N. G.; Crossley, J. G.; Orpen, A. G.; Rieger, A. L.; Rieger, P. H. *J. Chem. Soc., Dalton. Trans.* **1996**, 3491−3502.
(89) Olejnik, Z.; Lis, T.; Ondrejkovicova, I. *Acta Crystallogr., Sect. C* **1995**, *51*, 2246−2249.
(90) Scepaniak, J. J.; Harris, T. D.; Vogel, C. S.; Sutter, J.; Meyer, K.; Smith, J. M. *J. Am. Chem. Soc.* **2011**, *133*, 3824−3827.